

WL-TR-96-2081

ADVANCED LASER DIAGNOSTICS DEVELOPMENT
AND APPLICATION



D. F. GROSJEAN

SYSTEMS RESEARCH LABORATORIES
AN OPERATION OF CALSPAN SRL CORPORATION
2800 INDIAN RIPPLE ROAD
DAYTON, OH 45440-3696

JUNE 1996

FINAL REPORT FOR 06/01/90 - 03/31/96

APPROVED FOR PUBLIC RELEASE; DISTRIBUTION UNLIMITED.

19961231 005

AERO PROPULSION AND POWER DIRECTORATE
WRIGHT LABORATORY
AIR FORCE MATERIEL COMMAND
WRIGHT-PATTERSON AIR FORCE BASE, OH 45433-7251

NOTICE

When Government drawings, specifications, or other data are used for any purpose other than in connection with a definitely Government-related procurement, the United States Government incurs no responsibility or any obligation whatsoever. The fact that the government may have formulated or in any way supplied the said drawings, specifications, or other data, is not to be regarded by implication, or otherwise in any manner construed, as licensing the holder, or any other person or corporation; or as conveying any rights or permission to manufacture, use, or sell any patented invention that may in any way be related thereto.

This report is releasable to the National Technical Information Service (NTIS). At NTIS, it will be available to the general public, including foreign nations.

This technical report has been reviewed and is approved for publication.

W. M. Roquemore

W. M. ROQUEMORE, Project Engineer
Combustion Branch
Fuels and Lubrication Division

Leo S. Harootyan, Jr.

LEO S. HAROOTYAN, JR., Chief
Fuels and Lubrication Division
Aero Propulsion and Power Directorate

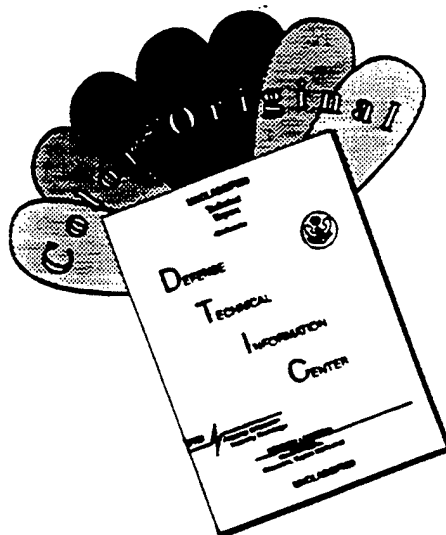
Royce P. Bradley

ROYCE P. BRADLEY, Chief
Combustion Branch
Fuels and Lubrication Division

If your address has changed, if you wish to be removed from our mailing list, or if the addressee is no longer employed by your organization please notify WL/POSC, WPAFB, OH 45433-7103 to help us maintain a current mailing list.

Copies of this report should not be returned unless return is required by security considerations, contractual obligations, or notice on a specific document.

DISCLAIMER NOTICE



THIS DOCUMENT IS BEST QUALITY AVAILABLE. THE COPY FURNISHED TO DTIC CONTAINED A SIGNIFICANT NUMBER OF COLOR PAGES WHICH DO NOT REPRODUCE LEGIBLY ON BLACK AND WHITE MICROFICHE.

REPORT DOCUMENTATION PAGE

FORM APPROVED
OMB NO. 0704-0188

Public reporting burden for this collection of information is estimated to average 1 hour per response, including the time for reviewing instructions, searching existing data sources, gathering and maintaining the data needed, and completing and reviewing the collection of information. Send comments regarding this burden estimate or any other aspect of this collection of information, including suggestions for reducing this burden, to Washington Headquarters Services, Directorate for Information Operations and Reports, 1215 Jefferson Davis Highway, Suite 1204, Arlington VA 22202-4302, and to the Office of Management and Budget, Paperwork Reduction Project(0704-0188), Washington DC 20503.

1. AGENCY USE ONLY (Leave Blank)		2. REPORT DATE June 1996	3. REPORT TYPE AND DATES COVERED FINAL 06/01/90 - 03/31/96	
4. TITLE AND SUBTITLE ADVANCED LASER DIAGNOSTICS DEVELOPMENT AND APPLICATION			5. FUNDING NUMBERS C F33615-90-C-2033 PE 62203 PR 3048 TA 05 WU AA	
6. AUTHOR(S) D. F. Grosjean			8. PERFORMING ORGANIZATION REPORT NUMBER 5579 Final	
7. PERFORMING ORGANIZATION NAME(S) AND ADDRESS(ES) Systems Research Laboratories An Operation of Calspan SRL Corporation 2800 Indian Ripple Road Dayton, OH 45440-3696			10. SPONSORING/MONITORING AGENCY REP NUMBER WL-TR-96-2081	
9. SPONSORING MONITORING AGENCY NAME(S) AND ADDRESS(ES) Wright Laboratory Aero Propulsion and Power Directorate Air Force Materiel Command Wright-Patterson Air Force Base, OH 45433-7251 POC: W. M. Roquemore, WL/POSC, 255-6813				
11. SUPPLEMENTARY NOTES				
12a. DISTRIBUTION/AVAILABILITY STATEMENT Approved for public release; distribution unlimited			12b. DISTRIBUTION CODE	
13. ABSTRACT Experimental and numerical investigations on gas-turbine combustion processes and jet-fuel thermal stability were undertaken. Advanced laser-based diagnostic techniques were developed and applied to the experimental study of combustion processes (jet diffusion flames and research combustors) and jet-fuel thermal-stability processes (autoxidation, global chemistry, and fuel-additive effects). In addition, numerical computational fluid dynamics with chemistry (CFDC) models detailing both the fluid dynamics and chemistry were developed to simulate realistic environments. The development, calibration, and evaluation of the numerical models employing fundamental combustion and fuel experiments was the ultimate goal of this research program.				
14. SUBJECT TERMS Advanced Laser Diagnostics, Fuel Thermal Stability, Computational Fluid Dynamics with Chemistry, Computational Fluid Dynamics, Vortex-Flame Interactions, Research Combustors, Combustion, Jet Diffusion Flames, Premixed Flames, Coherent Anti-Stokes Raman Spectroscopy, Laser Doppler Velocimetry, Particle Imaging Velocimetry, Laser-Induced Fluorescence, Fuel Additives, Fuel Deicers, Sprays, Droplets			15. NUMBER OF PAGES 889	
17. SECURITY CLASSIFICATION OF REPORT UNCLASSIFIED			16. PRICE CODE	
18. SECURITY CLASS OF THIS PAGE. UNCLASSIFIED		19. SECURITY CLASS OF ABSTRACT UNCLASSIFIED		20. LIMITATION ABSTRACT UL

TABLE OF CONTENTS

SECTION	PAGE
1. INTRODUCTION	1
2. DIAGNOSTIC DEVELOPMENT	2
2.1 Combustion and Aerodynamic Flow Diagnostics	2
2.1.1 General Overview	2
2.1.2 Coherent Anti-Stokes Raman Spectroscopy	2
2.1.3 Particle-Imaging Velocimetry	50
2.1.4 Thin-Filament Pyrometry and Velocimetry	127
2.1.5 Droplet and Spray Diagnostics	163
2.2 Thermally Stressed Jet-Fuel Diagnostics	200
2.2.1 General Overview	200
2.2.2 Conventional Diagnostic Techniques	200
2.2.3 Ultrafast Laser Diagnostics	237
3. DIAGNOSTIC APPLICATIONS	251
3.1 Combustion Studies	251
3.1.1 General Overview	251
3.1.2 Premixed Flames	251
3.1.3 Jet-Diffusion Flames	285
3.1.4 Research Combustors	399
3.2 Thermally Stressed Jet-Fuel Studies	482
3.2.1 General Overview	482
3.2.2 Autoxidation Experiments	482
3.2.3 Fuel-System Icing Experiments	595
4. COMPUTATIONAL FLUID DYNAMICS WITH CHEMISTRY CODE	607
4.1 Combustion Studies	607
4.1.1 General Overview	607
4.1.2 Numerical Simulations of Gaseous Combustion	607
4.1.3 Numerical Simulations of Droplet Combustion	714
4.2 Thermally Stressed Jet-Fuel Studies	806
4.2.1 General Overview	806
4.2.2 Numerical Simulations of Jet-Fuel Thermal Stability	806
5. REFERENCES	863
APPENDIX: Presentations, Publications, and Patents	865

LIST OF FIGURES

FIGURES		PAGE
1	Plots of Icing Temperatures as a Function of Aqueous-Solution Concentrations of Various FSII's as Measured with the NAWC Flowing Test Rig. Data provided by NAWC (Ref. 5)	597
2	Schematic Diagram of Low-Temperature Optical Test Apparatus	600
3	Plots of Water-Droplet Volume (a) and Bound-Water Content (b) as a Function of Fuel Temperature. Water-droplet volume was calculated from measured diameters; bound-water content was taken from Ref. 8	602
4	Concentration of Aqueous Solutions of Various FSII's as a Function of Measured Refractive Index. (a) DiEMGE, (b) DPG, (c) M-1, (d) M-2, (e) M-3	604
5	Plots of Particle Diameter as Function of Reactor Residence Time for POSF-2827 Fuel Without and With M-2 Icing Inhibitor After Stressing at 185°C	606
6	Plots of Surface-Deposit Rate as Function of Reactor Residence Time for POSF-2827 Fuel Without and With M-2 Icing Inhibitor After Stressing at 185°C	606
7	Development of Large-Scale Instabilities in an H ₂ -Air Jet Diffusion Flame When the Gravitational Force is 1/2g	609
8	Development of Large-Scale Instabilities in an H ₂ -Air Jet Diffusion Flame When the Gravitational Force is 1/6g	610
9	Magnitude of Flame-Surface Oscillation at Different Heights as a Function of Relative Gravitational Force	611

TABLES		PAGE
1	Measured Partition Ratios of Fuel-System Icing Inhibitors	603

PREFACE

This report was prepared by Dennis F. Grossjean and covers work performed during the period 1 June 1990 through 31 March 1996 under Air Force Contract F33615-90-C-2033. The contract was administered under the direction of Wright Laboratory, Aero Propulsion and Power Directorate, Wright-Patterson Air Force Base, Ohio, with W. M. Roquemore, Ph.D., as Government Project Monitor.

1. INTRODUCTION

This report describes the results of experimental and numerical investigations on gas-turbine combustion processes and jet-fuel thermal stability. Advanced laser-based diagnostic techniques were developed and applied to the experimental study of combustion processes (jet diffusion flames and research combustors) and jet-fuel thermal stability (autoxidation, global chemistry, and fuel-additive evaluation). In addition, numerical computational fluid dynamics with chemistry (CFDC) models detailing both the fluid dynamics and chemistry were developed to simulate realistic environments. The development, calibration, and evaluation of the numerical models employing fundamental combustion and fuel experiments was the ultimate goal of this research program.

The goals this research and development program were 1) to examine the state-of-the-art of advanced laser diagnostics, 2) determine which techniques would have the highest payoff for fundamental and applied combustion studies, 3) develop those techniques found to be most promising, and 4) apply the selected techniques to fundamental experimental studies that could be used for testing and evaluating CFDC models. Techniques that were determined to be useful for fuel-degradation studies were also developed and applied to fundamental experimental studies designed to achieve a cohesive model of jet-fuel thermal-degradation processes. In studies of both fuel and combustion, the combination of advanced laser diagnostics, well-designed fundamental experiments, and state-of-the-art CFDC models has led to a better understanding of the fundamental fluid-dynamic and chemical processes involved. Only through this combination of experimental and numerical approaches can a true picture of these underlying processes be obtained.

The research conducted during this program resulted in more than 200 publications and presentations as well as two patent applications; a list of these can be found in the Appendix. In this report the research efforts are summarized in the three following sections. Section 2 details the development of advanced laser techniques for combustion and fuel-degradation studies. Section 3 describes the application of these advanced techniques to the investigation of fundamental combustion and jet-fuel thermal stability. Section 4 documents the development, calibration, and evaluation of numerical CFDC codes for simulating combustion and jet-fuel thermal stability.

2. DIAGNOSTIC DEVELOPMENT

2.1 Combustion and Aerodynamic Flow Diagnostics

2.1.1 General Overview. The development of advanced diagnostic techniques continued to be a major driving force throughout this 5-year research and development program. Because of the extensive previous experience of the SRL staff with Coherent Anti-Stokes Raman Spectroscopy (CARS), this technique quickly became a research tool and was applied to the study of both laboratory and large-scale research combustors. Other techniques that were investigated and developed during the course of this program include Particle Imaging Velocimetry (PIV), Thin Filament Pyrometry - Velocimetry (TFP-TFV), and a variety of droplet and spray diagnostic techniques. Traditional laser diagnostic techniques such as Laser Doppler Velocimetry (LDV), Laser Induced Fluorescence (LIF and PLIF), and laser sheet-light visualization were developed into research tools and applied to the study of combustors and aerodynamic flowfields. Papers, presentations, and patents are included in this report to document the results of research efforts and instrumentation development in each area.

2.1.2 Coherent Anti-Stokes Raman Spectroscopy. In a review entitled, "CARS Instrumentation for Combustion Applications," the Principal Investigator on this program, Dr. Larry P. Goss, summarized the development of the CARS technique during this program. This invited book chapter (see pp. 3 - 39) details not only the application of the CARS technique to practical combustors but also the combination of the technique with an LDV system. A paper entitled, "Effect of Droplet-Induced Breakdown on CARS Temperature Measurements" (pp. 40 - 49) describes the problems (and solutions) involved with making CARS measurements in spray-combustion environments.

Chapter Four

CARS Instrumentation for Combustion Applications

LARRY P. GOSS

*Systems Research Laboratories, Inc. (A Division of Arvin/Calspan),
2800 Indian Ripple Road, Dayton, OH 45440-3696, USA*

I. Introduction	253
II. Background	254
III. Theoretical considerations and spectral synthesis	261
IV. Thermometry	270
V. Concentration measurements	273
VI. Instrument considerations	277
A. Optical arrangement	277
B. Data acquisition system	282
C. Data analysis	285
D. Calibration of instrument	288
E. Applications of CARS instrument	288
VII. Combined CARS-LDV instrument	292
A. LDV instrument	294
B. Description of combined instrument	294
C. Particle effects	297
D. Acquisition and analysis software	298
E. Seed effects	301
F. Flame measurements with combined instrument	305
VIII. Future considerations	313

NOTATION

B_{Fi}	density-weighted temperature probability
B_{ui}	unconditional temperature probability
c	speed of light

D	dispersion; relative temperature fitting error
$E(k, \omega)$	Fourier transform of applied electric field
$E(r, t)$	applied electric field in Cartesian coordinates
h	Planck's constant
I_{300}	CARS intensity at 300 K
I_i	intensity of i th laser beam
J	Jacobian matrix
J^\dagger	transpose of Jacobian matrix
k_i	i th photon wave vector
n_i	index of refraction of i th laser beam
N	number density of probed gas
N_T	number density at temperature T
N_{300}	number density at 300 K
NOBS	number of data points in spectrum
$P^{(n)}$	n th-order electric dipole polarization
R_T	band-shape ratio factor for concentration measurements
\bar{T}_F	Favre-averaged temperature
\bar{T}_i	density-weighted i th measured temperature
\bar{T}_U	unconditional averaged temperature
u_i^f	axial-velocity fluctuation
\bar{u}_T	axial velocity-temperature correlation coefficient
$\bar{u}\bar{v}$	axial-radial velocity correlation coefficient
$\bar{v}\bar{T}$	radial velocity-temperature correlation coefficient
δ	detuning frequency ($\omega_1 - \omega_2$)
Γ_j	Raman line width of j th transition
Δj	difference in rotational quantum number
ΔT	error correction for temperature fit
Δv	difference in vibrational quantum number
$\Delta \phi$	difference matrix between calculated and experimental spectra
$\Delta \omega_j$	frequency difference between Raman transitions involved in CARS process
ϵ	dielectric constant
σ	deviation of temperature fit
$\chi^{(n)}$	n th-order susceptibility
χ_{nr}	non-resonant part of third-order susceptibility
χ_r	resonant part of third-order susceptibility
χ'_i	real part of resonant third-order susceptibility
χ''_i	imaginary part of resonant third-order susceptibility
$\omega_i^{(0)}$	centre frequency of pump laser
ω_G	Gaussian slit function
ω_i	i th photon frequency
ω_L	Lorentzian slit function
ω_V	Voigt slit function
ω_1	pump laser frequency
ω_2	Stokes laser frequency
ω_3	CARS frequency
*	complex conjugate
$\langle \rangle$	convolution
$u\theta$	Reynolds-averaged correlations
m_i	Molecular weight of gases during i th measurement

1. Introduction

Coherent anti-Stokes Raman spectroscopy (CARS) has evolved over the past decade from a laboratory curiosity into a practical engineering tool for combustion research. The CARS technique has been applied to practical combustion systems, including small-scale burners, combustor cans, turbine engine afterburners, industrial furnaces, internal-combustion engines, magnetohydrodynamic (MHD) and coal-fired facilities, and burning propellants. This rapid growth in applications of the technique can be attributed to an enhanced understanding of the CARS process and the development of sophisticated spectral-synthesis codes which are necessary for quantitative interpretation of CARS data. While the CARS instrumentation and associated calculations are quite complex in many cases, the technique has survived to become a viable tool because of its unique ability to provide precise point-wise temperature and concentration measurements of major flame species in extremely hostile, particle-laden environments. This flexible technique combined with other diagnostic methods such as laser Doppler velocimetry (LDV) has allowed velocity-scalar measurements in turbulent reacting flow fields. From these combined data, correlation coefficients of velocity and temperature can be determined.

Although the CARS process had already been experimentally demonstrated by the mid-1960s (Maker and Terhune, 1965), its potential for the study of combustion was not realized until the mid-1970s through the pioneering efforts of J. P. Taran and coworkers (Regnier and Taran, 1973; Regnier *et al.*, 1973; Moya *et al.*, 1975, 1977; Pealat *et al.*, 1980). Today the technique is utilized by laboratories throughout the world for combustion studies, with practitioners including government laboratories, turbine engine manufacturers, automotive manufacturers and universities. The CARS technique, however, is not "user friendly"; that is, its practical implementation requires considerable knowledge and skill on the part of the user. As with most spectroscopic techniques, a working knowledge of both theory and instrumentation is required to ensure optimum results.

Quantitative measurements with the CARS technique require in-depth understanding of the instrumentation factors (slit function, laser statistics) as well as the spectroscopic factors (Raman line widths and spacing) which affect the CARS spectrum in a complex and non-linear manner. Parameters affecting the spectral shape and intensity include temperature, pressure, species concentration, non-resonant susceptibility, laser statistics, laser power, instrument slit function (resolution) and detector characteristics. These parameters must be taken into account to ensure accurate interpretation of CARS spectral data.

The major thrust of this chapter is the basic CARS instrumentation and its implementation relative to combustion studies. While a solid theoretical foundation is necessary for a full understanding of the principles of the CARS technique, a complete review of CARS theory is beyond the scope of this chapter. Such information can be found in a recently published book (Eckbreth, 1988) and several review articles (Greenhalgh, 1988; Hall and Eckbreth, 1984). Basic CARS theory will be reviewed briefly and various schemes for spectral synthesis discussed. As stated previously, the major emphasis will be on instrumentation, including optics, electronics and software, for operation of the CARS and combined CARS-LDV systems. Applications of the CARS technique to turbulent reacting flows will also be treated.

II. Background

When light interacts with matter, the response of the medium to the electromagnetic perturbation is fully described by the electric dipole polarization P . The response of the medium to an applied field is typically a complicated non-linear function of E , the applied electric field. In the linear case, however, P assumes the simple linear form

$$P(r, t) = \int_{-\infty}^{\infty} \chi^{(1)}(r - r', t - t') E(r', t') dr' dt' \quad (1)$$

where $\chi^{(1)}$ is the linear susceptibility and r and t represent the spatial and temporal variation, respectively, of the polarization. If E is a monochromatic plane wave, then the Fourier transform of equation (1) yields the well-known relation

$$P(r, t) = P(k, \omega) = \chi^{(1)}(k, \omega) E(k, \omega) \quad (2)$$

where k is the photon wave vector and ω the photon frequency.

The linear dielectric constant ϵ is related to the linear susceptibility as follows:

$$\epsilon(k, \omega) = 1 + 4\pi\chi^{(1)}(k, \omega) \quad (3)$$

In the non-linear case the polarization P is expanded into a power series of E , resulting in

$$P(r, t) = \int_{-\infty}^{\infty} \chi^{(1)}(r - r', t - t') E(r', t') dr' dt'$$

$$\begin{aligned}
& + \int_{-\infty}^{\infty} \chi^{(2)}(r-r_1, t-t_1; r-r_2, t-t_2) E(r_1, t_1) \\
& \times E(r_2, t_2) dr_1 dr_2 dt_2 \\
& + \int_{-\infty}^{\infty} \chi^{(3)}(r-r_1, t-t_1; r-r_2, t-t_2; r-r_3, t-t_3) \\
& \times E(r_1, t_1) E(r_2, t_2) E(r_3, t_3) dr_1 dr_2 dt_2 dr_3 dt_3 + \dots \quad (4)
\end{aligned}$$

where $\chi^{(n)}$ is the n th-order non-linear susceptibility. Fourier transformation of equation (4) in the case of monochromatic plane waves results in

$$P(k, \omega) = P^{(1)}(k, \omega) + P^{(2)}(k, \omega) + P^{(3)}(k, \omega) + \dots \quad (5)$$

with

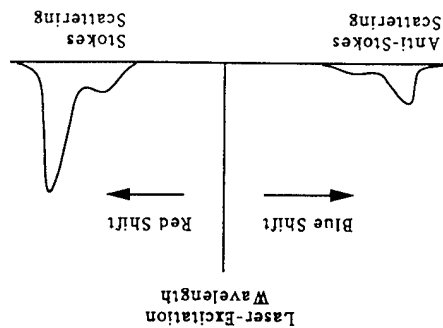
$$\begin{aligned}
P^{(1)}(k, \omega) &= \chi^{(1)}(k, \omega) E(k, \omega) \\
P^{(2)}(k, \omega) &= \chi^{(2)}(k = k_i + k_j, \omega = \omega_i + \omega_j) E(k_i, \omega_i) E(k_j, \omega_j) \\
P^{(3)}(k, \omega) &= \chi^{(3)}(k = k_i + k_j + k_l, \omega = \omega_i + \omega_j + \omega_l) E(k_i, \omega_i) E(k_j, \omega_j) \\
&\quad \times E(k_l, \omega_l) \quad (6)
\end{aligned}$$

The first term in equations (6) gives rise to linear scattering processes such as Mie and Raman scattering. The first non-linear term, $P^{(2)}$, is responsible for sum or difference three-wave-mixing processes observed in non-linear optical crystals—effects utilized extensively by the laser industry to shift the wavelength of laser sources. In media having an inversion symmetry (gases), the third-order non-linear susceptibility, $\chi^{(3)}$, is the lowest-order non-linearity allowed. CARS is among the many effects due to the $P^{(3)}$ non-linear term.

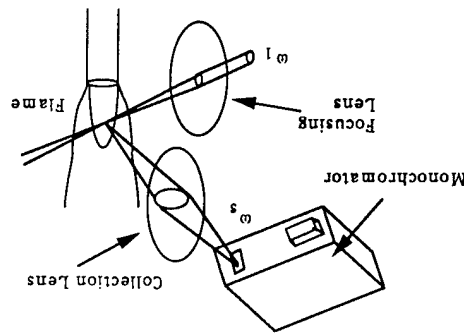
Since CARS is a *non-linear* Raman technique, a comparison with linear Raman spectroscopy is in order. The characteristics of the linear Raman technique are given in Figure 1. Photons at frequency ω_1 induce a linear polarization in a medium, causing energy to be exchanged. If the photon loses energy to the medium, the inelastically scattered photon is Stokes or red shifted with respect to its original frequency; if the photon gains energy, the photon is anti-Stokes or blue shifted. Through interaction of the photon with the energy levels of the medium, specific information concerning the medium can be obtained. This is in contrast to elastic scattering processes such as Mie scattering where no energy exchange occurs between the photon and the scattering medium and, thus, no specific information is obtained. Since specific information on the populations of the rotational and vibrational energy levels of the scattering medium are obtained with the Raman technique, temperature and species concentrations can be determined. Raman scattering from the medium occurs in all directions, and the

- Characteristics
- Weak scattering (1 photon in 10^7 scattered)
- Linear dependence upon density and laser power
- Weak dependence upon Raman linewidth
- Single laser source excites all allowed transitions
- 4 π -steradian scattering, low collection efficiency
- Relatively clean flames required, no soot or particles

• Spectrum



• Experimental Approach



• Energy Diagram

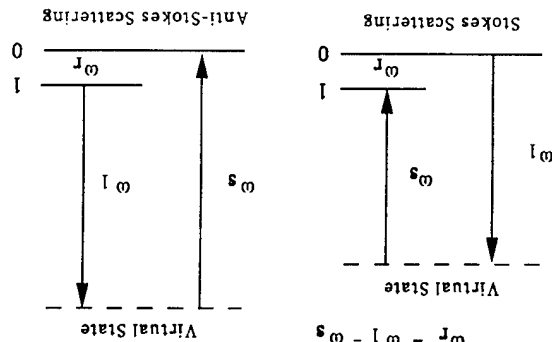
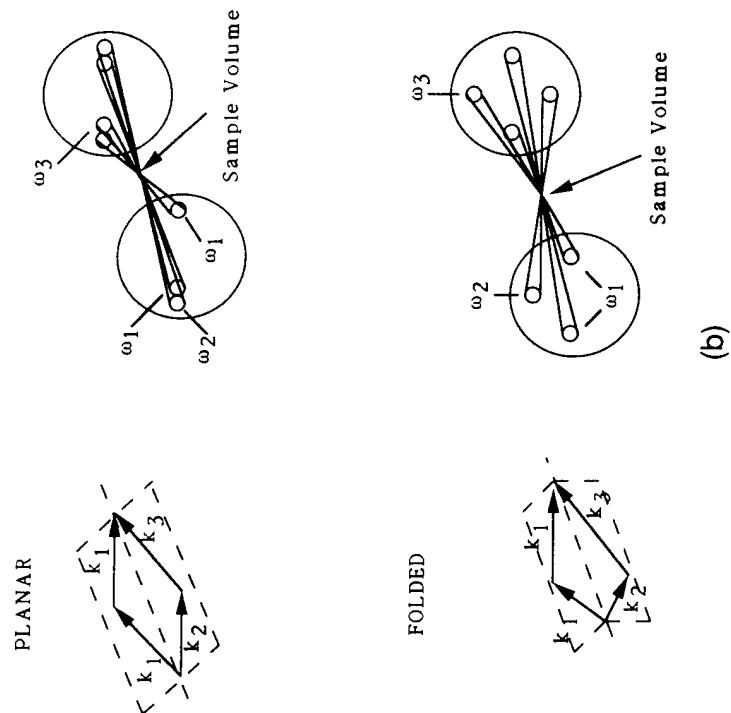
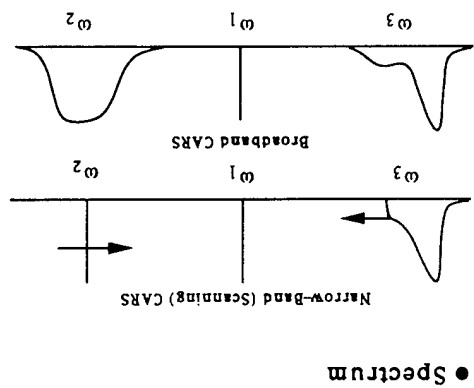
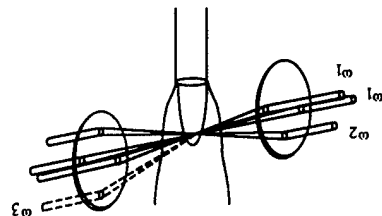


Figure 1 Properties of linear Raman scattering.

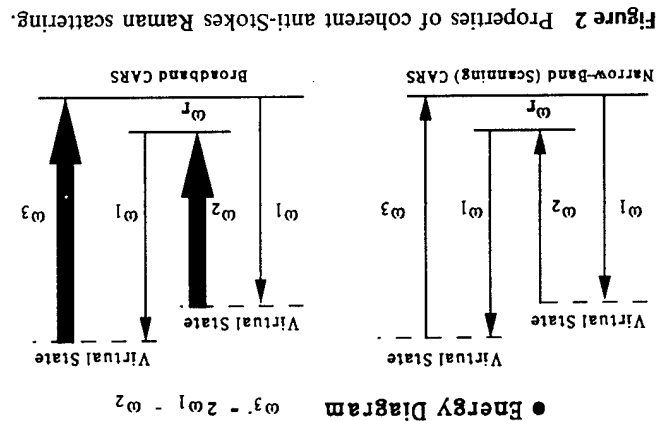


Experimental Approach



Characteristics

- Relatively strong scattering (1 photon in 10^6 scattered)
- Quadratic dependence upon density and laser power
- Strong nonlinear dependence upon Raman linewidth
- Multiple laser sources required for single species
- Highly directional CARS signal allows high collection efficiency
- Applicable to harsh, dirty flame environments



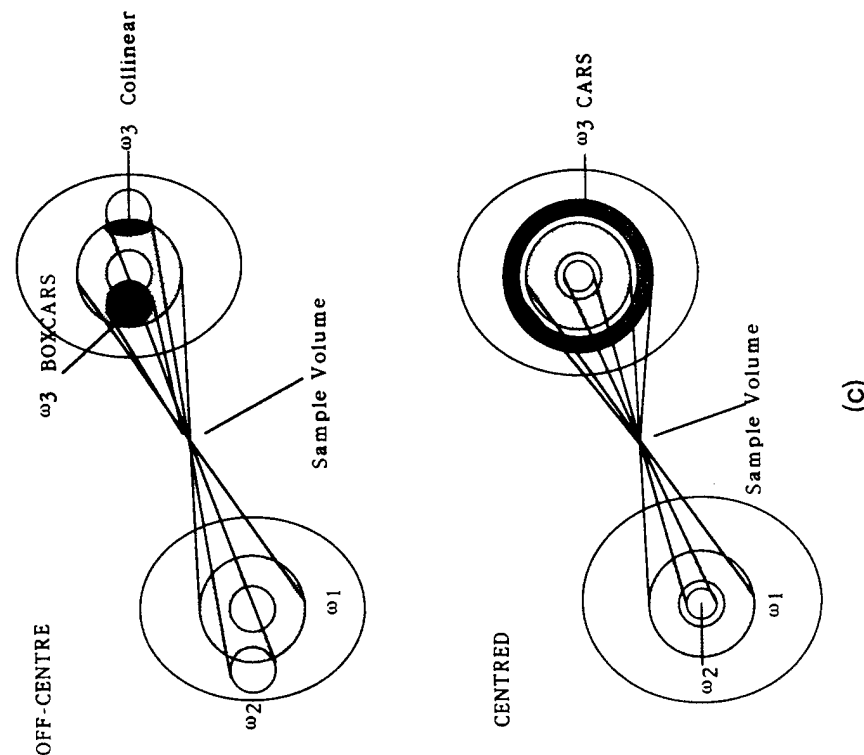


Figure 3 Possible phase-matching arrangements for the CARS technique, including (a) collinear CARS, (b) BOXCARS and (c) USED CARS. See text for explanation of acronyms.

inefficiency of the process (one in 10 million photons is inelastically scattered) necessitates the use of powerful laser sources for practical applications. Because of the low signal levels associated with the technique, applications to flame studies have been limited to relatively clean flame systems, i.e. hydrogen or lean methane.

The basic properties of the CARS process are listed in Figure 2. Laser beams of frequency ω_1 (pump) and ω_2 (Stokes) are combined via the third-order susceptibility of a molecule to induce a polarization which forms a third coherent beam at frequency $\omega_3 = (2\omega_1 - \omega_2)$. CARS is, thus, a non-

linear four-wave-mixing process. If the frequency difference ($\omega_1 - \omega_2$) is tuned to a Raman-allowed transition, the CARS signal is resonantly enhanced, and a "fingerprint" of the probed species results. Thus, as with the linear Raman technique, temperature and species concentration information can be obtained from the CARS spectrum of a species such as N_2 . Because the CARS beam at frequency ω_3 is laser-like, a high percentage of the signal can be detected (unlike Raman or fluorescence processes where signals are distributed over a 4π steradian). This high collection efficiency, along with conversion efficiencies (one photon in 10 000 is produced in the CARS process), translates into a much stronger CARS signal requiring less energetic lasers for implementation than those needed for linear Raman spectroscopy. However, with the CARS technique only one species can be probed at a time unless multiple Stokes laser sources are used (Eckbreth and Anderson, 1985; Eckbreth and Anderson, 1986; Lucht, 1987a), whereas with linear Raman techniques, all species can be probed using a single laser source (Lapp and Penney, 1974). In the CARS process the species of interest is probed by controlling the frequency difference between the pump and probe lasers. The pump laser is typically a pulsed narrow-bandwidth laser, and the Stokes laser can be either narrow-band (utilized for scanning CARS) or broad-band (utilized for single-shot CARS). With a broad-band Stokes laser, an entire Q-branch signature can be recorded in a single laser shot (Roh *et al.*, 1976). This permits single-shot thermometry to be performed, which is extremely important in turbulent reacting flows where the temperature can vary dramatically between laser pulses.

For maximum effectiveness of the CARS four-wave-mixing process, conservation of energy and momentum must be maintained. Momentum conservation of the CARS process requires phase matching of the photon wave vectors ($k_3 = 2k_1 - k_2$) to achieve constructive interference and optimum signal levels. Several of the beam-mixing geometries which satisfy the phase-matching condition are depicted in Figure 3. Because of the weak dependence of the refractive index of the gases upon wavelength, a collinear arrangement of the beams is possible. However, this configuration results in a large region of beam overlap which causes the CARS signal to be generated over a wide area. In making measurements in turbulent reactive flows, this overlap can constitute a problem because of the spatial distribution of the temperatures observed in such flows. If a temperature gradient exists over the CARS measurement volume, the low-temperature high-density regions will have a greater impact upon the observed spectrum, causing the measured temperatures to appear to be much lower than the flame temperatures (Boquillon *et al.*, 1988). Spatially resolved phase-matching schemes for circumventing this problem include BOXCARS (named from the apparent box-like shape of the vector matching)

(Eckbreth, 1978), folded BOXCARS (Prior, 1980; Shirley *et al.*, 1980) and USED-CARS (unstable-resonator spatially enhanced detection) (Marko and Rimai, 1979; Davis *et al.*, 1981; Klick *et al.*, 1981). The reduced sample volume of these spatial resolving techniques causes a large reduction in the CARS signal. Thus, practical implementation of the CARS technique requires a trade-off between signal intensity and desired spatial resolution. For most flame studies where optical access is *not* limited, folded BOXCARS is the phase-matching scheme of choice because of its ability to isolate the CARS signal from the stronger laser beams. If optical access is limited (internal combustors) or if refractive index gradients are large, then USED-CARS and collinear CARS schemes are normally favoured.

III. Theoretical considerations and spectral synthesis

Because the CARS signal intensity is dependent in a non-linear manner upon several parameters such as temperature, species concentration, Raman line width, and pressure, a computer model of the spectrum of the probed species must be employed to quantify the CARS signal intensity. CARS theory and spectral synthesis has been the subject of many publications over the past decade (Nibler and Knighten, 1979; Druet and Taran, 1981; Harvey, 1981; Hall and Eckbreth, 1984). The theory will be reviewed here only briefly, with emphasis on spectral calculation.

The intensity of the CARS signal for monochromatic waves is given in terms of the third-order susceptibility by

$$I(\omega_3) \sim I_1^2 I_2 |\chi^{(3)}|^2 \quad (7)$$

where I_1 , I_2 and I_3 represent the pump laser, Stokes laser and CARS intensities, respectively. The third-order susceptibility which governs the CARS process can be expressed in abbreviated form as

$$\chi^{(3)} = \chi_{nr}^{(3)} + \chi_r^{(3)} \quad (8)$$

where $\chi_{nr}^{(3)}$ is the non-resonant contribution and $\chi_r^{(3)}$ the Raman resonant contribution. The non-resonant susceptibility is real and proportional to the total number density of the gases in the sample volume. This part of the third-order susceptibility is made up of small contributions from off-resonant electronic transitions and is only a mild function of wavelength. The Raman resonant contribution is a complex quantity arising from Raman-allowed transitions of molecules in the probe volume. As in ordinary Raman spectroscopy, the isotropic part of the polarizability dominates the anisotropic part; thus, CARS spectra typically consist of Q-branch transitions ($\Delta v = 1$, $\Delta j = 0$; Herzberg, 1964). The lifetimes—and,

thus, line widths—of these Raman transitions are affected by pressure, temperature and rotational quantum number.

The resonant susceptibility will now be examined in greater detail to aid the understanding of the characteristics of a CARS spectrum and how it differs from a linear Raman spectrum. As stated earlier, the resonant susceptibility is a complex quantity which can be expressed as

$$\chi_r^{(3)} = \chi_r' + i\chi_r'' \quad (9)$$

where

$$\chi_r' = N \sum_j \frac{2 \Delta\omega_j K_j \Gamma_j}{4 \Delta\omega_j + \Gamma_j^2} \quad \text{and} \quad \chi_r'' = N \sum_j \frac{K_j \Gamma_j^2}{4 \Delta\omega_j + \Gamma_j^2}$$

with

$$K_j = \frac{(4\pi)^2 n_1 \epsilon_0 c^4 \Delta_j}{(n_2 h / 2\pi) \omega_j^4 \Gamma_j} \left(\frac{\partial \sigma}{\partial \Omega} \right)_j$$

Here $(\partial \sigma / \partial \Omega)_j$ is the Raman scattering cross-section of the j th transition, N the number density of the probed species, Δ_j the fractional population of the j th state (difference in the populations of the initial and final rotational levels involved in the Raman transition), $\Delta\omega_j$ the detuning frequency given by $\omega_j - \omega_1 + \omega_2$, where ω_j is the j th Raman transition frequency, Γ_j the Raman line width of the j th transition, c the speed of light, ϵ_0 the linear dielectric constant, n_1 and n_2 the indices of refraction for the pump and Stokes laser wavelengths, respectively, and h Planck's constant. Note that the CARS signal results from a summation made over all allowable Raman transitions. Thus, in addition to the Raman transition being probed, nearby Raman transitions contribute to the CARS signal.

The absolute square of the third order susceptibility, as denoted in equation (7), utilized to determine the CARS signal intensity is given by

$$|\chi_r^{(3)}|^2 = (\chi_{nr}^{(3)})^2 + 2N\chi_{nr}^{(3)}\chi_r' + N^2[(\chi_r')^2 + (\chi_r'')^2] \quad (10)$$

with the number density being written in front of the resonant susceptibility term to show its explicit dependence. Equation (10) shows that three terms make up the CARS signal. Figure 4 depicts the effect of each of the three terms upon a single Raman transition. The first term $(\chi_{nr}^{(3)})^2$ represents the square of the non-resonant susceptibility and manifests itself in a CARS spectrum as a constant background. The second contribution is a cross term between the resonant and non-resonant susceptibilities. This term is dispersive (due to the resonant contribution, see Figure 4), weighted by the inverse of the Raman line width of the transition, and linearly proportional to the concentration of the probed species. The third contribution to the CARS spectrum is the square of the real and imaginary parts of the resonant

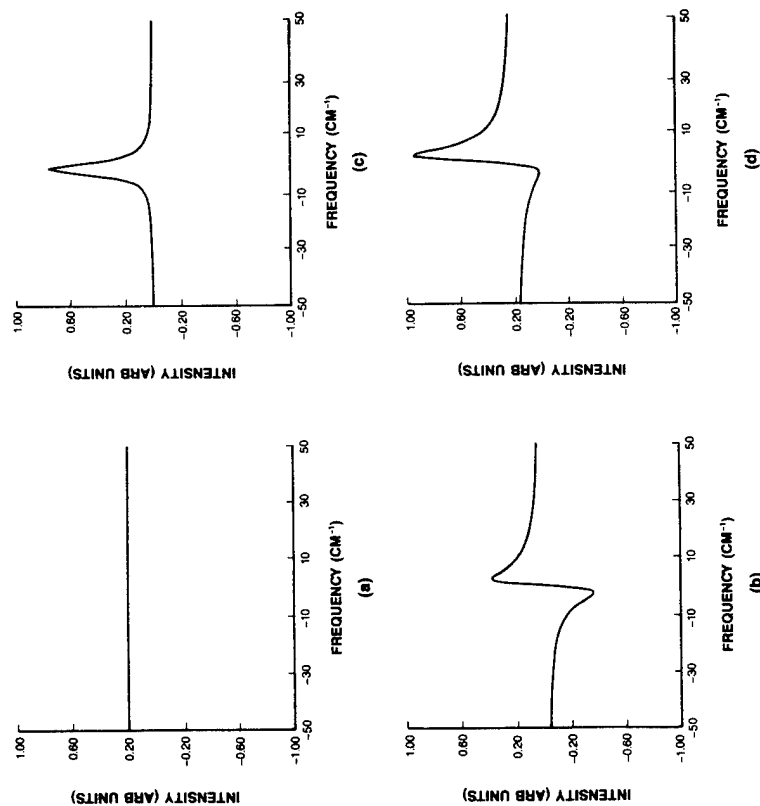


Figure 4 Influence of third-order-susceptibility terms upon the observed line shape of an isolated Raman transition at low species concentration. (a) Non-resonant background, (b) dispersive component, (c) Lorentzian component and (d) resulting CARS peak.

susceptibility and is characterized by a Lorentzian shape which is weighted by the inverse square of the Raman line width and the square of the concentration of the probed species.

For a given Raman line width, the concentration can have a considerable effect upon the intensity and spectral shape of the CARS spectrum (see Figure 4). At high concentration levels, the $(\chi_r')^2$ term dominates the CARS spectrum, producing a Lorentzian line shape peak whose intensity is proportional to the square of the concentration and the inverse square of the Raman line width. If the concentration is lowered significantly (below about 25% by volume), the cross term will begin to dominate the spectrum, resulting in a dispersive-shaped peak whose intensity is directly proportional to the concentration and inversely proportional to the Raman line width.

This effect has been used extensively in making concentration measurements, as will be discussed later in this chapter. If the concentration is lowered further, the non-resonant-background term will begin to dominate, with a constant background signal being observed. This signal limits the concentration at which a species can be detected (typically between 0.1 and 1% by volume). Detection below this level requires suppression of the background, which will be discussed in a later section.

Unlike a linear Raman spectrum, a CARS spectrum is highly sensitive to concentration, temperature, pressure and the Raman line width. In fact, only recently have the Raman line widths of N_2 been determined to the accuracy needed for precise calculations and measurements. Line width information for other species—especially polyatomic molecules—is urgently needed for combustion studies. Species for which CARS spectral synthesis codes have been developed include N_2 , O_2 , CO , H_2O , N_2O , SO_2 and (recently) CO_2 .

Real laser systems are not completely monochromatic and do not consist of plane waves; thus, the effect of the finite bandwidth of the laser sources upon the CARS spectrum must be taken into account. In the extensively used theory of Yuratich (Yuratich, 1979), the observed CARS intensities are obtained by a convolution of $|\chi^{(3)}|^2$ with the pump and Stokes spectral profiles. The CARS intensity distribution is given by

$$I(\omega_3) \sim I_1(\omega_1) \int I_2(\omega_1^{(0)} - \delta) I_1(\omega_1 - \delta) |\chi^{(3)}(\delta)|^2 d\delta \quad (11)$$

where I_1 and I_2 are the spectral densities of the pump and Stokes lasers, respectively, $\omega_1^{(0)}$ is the centre frequency of the pump laser and δ the detuning frequency ($\omega_1 - \omega_2$). In broad-band CARS, the Stokes bandwidth is sufficiently large that I_2 can be taken outside the integral; thus, the spectral resolution of the CARS signal is limited only by the bandwidth of the pump laser. This approach ignores the cross terms (Kataoka *et al.*, 1982; Teets, 1984) arising from the coherence between the polarization components when a single laser is used as the pump laser.

In the case where the pump line width is comparable to the Raman line width and the non-resonant part of the third-order susceptibility is of the same order as the resonant part, cross-coherence terms in the CARS spectrum must be taken into account. The Kataoka-Teets convolution which expresses the cross-coherence term is given by

$$I(\omega_3) = |\chi_{nr}^{(3)}|^2 + 2\chi_{nr}^{(3)} \langle R_c [\chi_r (\omega_3 - \omega_1)] \rangle + \frac{1}{2} \langle |\chi_r^{(3)}(\omega_3 - \omega_1)|^2 \rangle + \frac{1}{2} \langle \chi_r^{(3)}(\omega_3 - \omega_1) \chi_r^{(3)*}(\omega_3 - \omega_0) \rangle \quad (12)$$

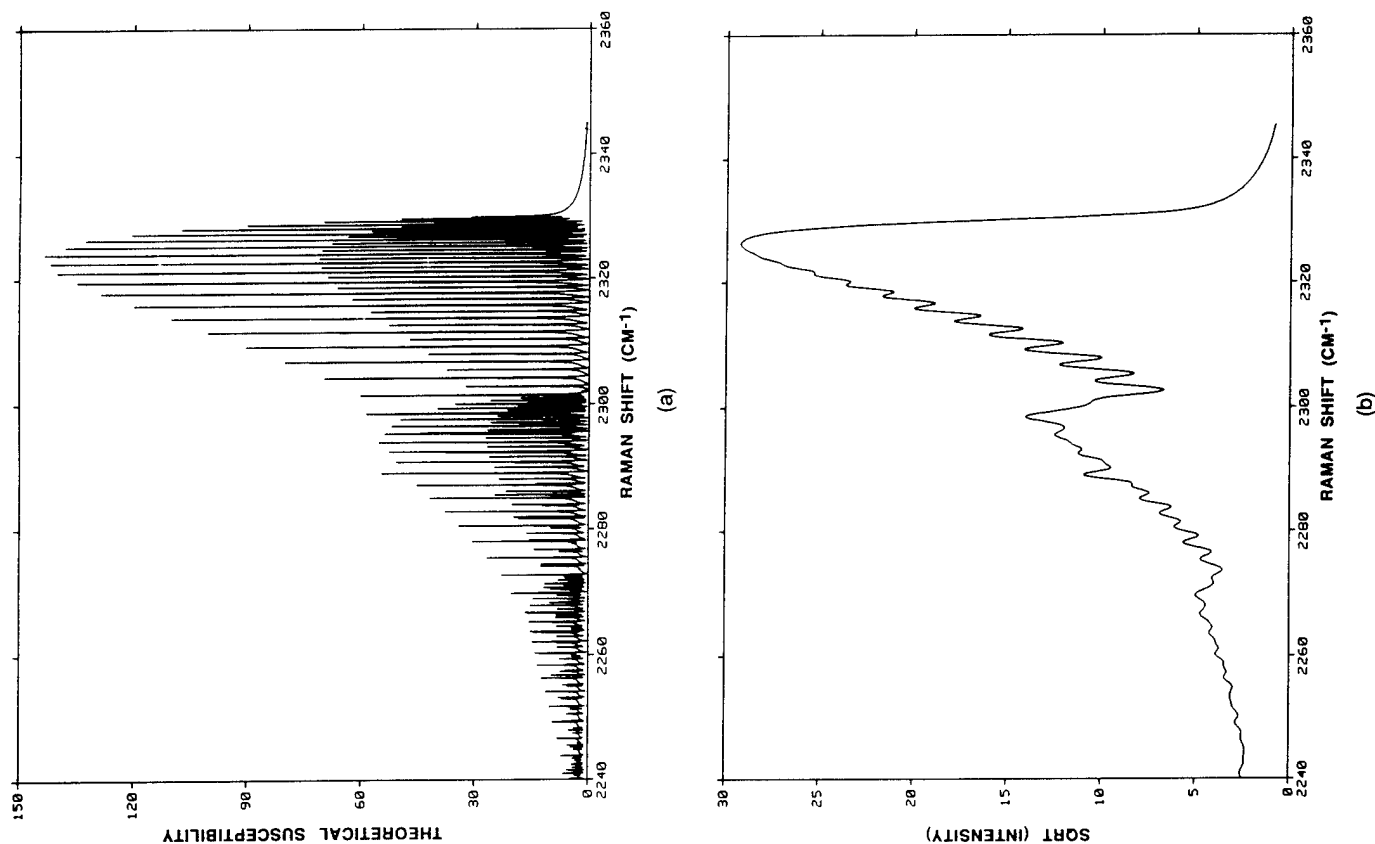
where ω_0 and ω_1 are the two pump photons, * represents a complex

conjugate, and $\langle \rangle$ indicates the convolution in equation (11). Note that the last term of equation (12) treats the two pump photons explicitly rather than assuming them to be equivalent. Because of the necessity to convolve the product $\chi_r^{(3)}(\omega_3 - \omega_1)\chi_r^{(3)*}(\omega_3 - \omega_0)$ over both ω_0 and ω_1 , this cross-coherence term requires a very time-consuming double integration. Analytical closed-form solutions of this term have been developed for the case of a Lorentzian pump laser (Teets, 1984) and a Gaussian pump laser (Greenhalgh and Hall, 1986) which allow realization of the fast calculation of the cross term.

Pressure broadens the Raman line widths and causes close-lying lines to overlap. When the pressure is sufficiently high (as in the case of internal-combustion engines), the adjacent lines interfere and collisional narrowing occurs (Bonamy *et al.*, 1977). Calculation of the effects of high pressure requires a detailed understanding of collisional dynamics and energy transfer. If these effects are to be taken into account in the generation of theoretical CARS spectra, the elements of the scattering matrix (G matrix) which describe the transition rate between the rotational states of the Raman Q branch must be known (Hall, 1983). The various scaling laws available for modelling the G matrix have been discussed in detail in the literature (Greenhalgh, 1988).

The spectral resolution of the CARS spectrum derived from equation (11) or (12) is limited by the bandwidth of the lasers employed in producing the CARS signal. In an ideal experiment the instrumentation used to detect the CARS signal would be capable of high spectral resolution and would not spectrally broaden the CARS signal during the detection process. In reality, the spectral resolving capability of the detection instrumentation is not sufficiently high to circumvent broadening; thus, a convolution over the instrument slit function must be performed to relate the detected CARS signal to the calculated CARS spectrum. In the narrow-band CARS case (both pump and Stokes lasers are spectrally narrow), a photomultiplier having a broad filter can be employed to detect the CARS signal without loss of resolution since spectral resolution is determined strictly by the laser sources. In the broad-band CARS case, however, the CARS signal is broad in nature, and the frequency-intensity information is obtained by dispersion with a grating (or prism). The CARS signal must then be detected by means of a multichannel detector system which captures the frequency-intensity information. This experimental approach is favoured for single-shot thermometry or line shape concentration measurements since the CARS information is obtained in a single laser shot.

The functional form most commonly employed for calculating the experimental slit function is a Voigt function combining the wings of a



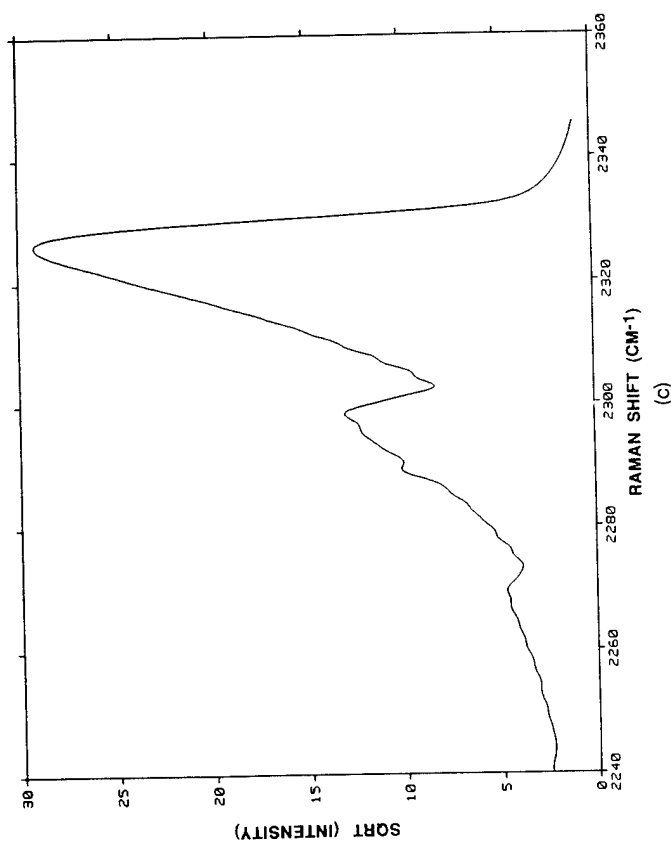


Figure 5 CARS spectrum of N_2 with (a) infinite instrument resolution, (b) broadening due to laser line widths and (c) broadening due to finite dispersion and detector resolution (Palmer, 1989).

Lorentzian (ω_L) function with the width of a Gaussian (ω_G) function. This function can be approximated by (Whiting, 1968)

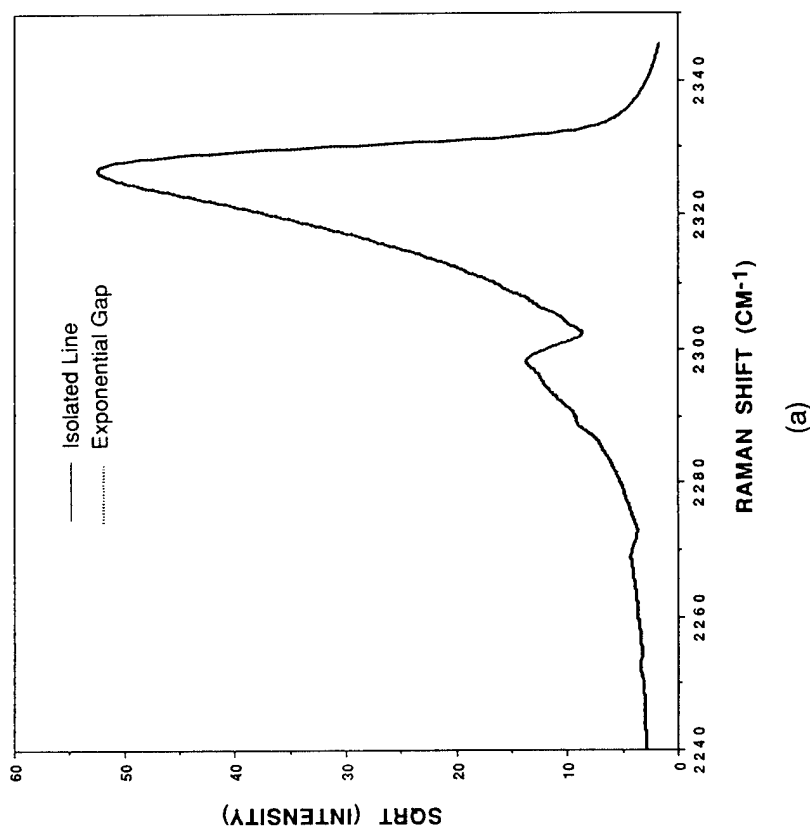
$$\omega_V = \omega_L + \left[\frac{\omega_L^2}{4} + \omega_G \right]^{1/2} \quad (13)$$

The slit function is normally determined from a direct comparison of data taken at room temperature and data taken at a known flame temperature; this allows both ω_L and ω_G to be determined at the temperature extremes of the experiment.

Figure 5(a) depicts the high resolution spectrum of N_2 at 2000 K which would be obtained if the laser and detector systems were infinitely resolvable. This resolution limit is only approached with high-resolution scanning CARS systems. For a typical moderate-resolution CARS system, the spectrum is broadened by the laser system, grating and detector used in the instrument. Figure 5(b) shows the effects of using an unseeded

neodymium:yttrium aluminium garnet (Nd:YAG) laser having a laser line width of 1.6 cm^{-1} (FWHM). With most broad-band CARS systems, the dye laser profile is sufficiently broad that a convolution over its band-shape is not required. However, if a narrow-band dye laser of finite bandwidth is employed, then a convolution over its bandwidth is necessary. In the broad-band CARS case, the CARS signal must be dispersed with a grating and recorded with a multichannel analyser having a finite detector element size. In a moderate-resolution system typically employed for single-shot thermometry, the combined grating-detector slit function is $\sim 2 \text{ cm}^{-1}$. Figure 5(c) depicts the convolution of the CARS spectrum with the instrument slit function. From Figure 5 it is obvious that instrument (lasers, grating, detector) effects upon the observed CARS signal are sizeable and, thus, must be taken into account for interpretation of the experimental CARS data.

It is vitally important that the correct calculation model be employed for



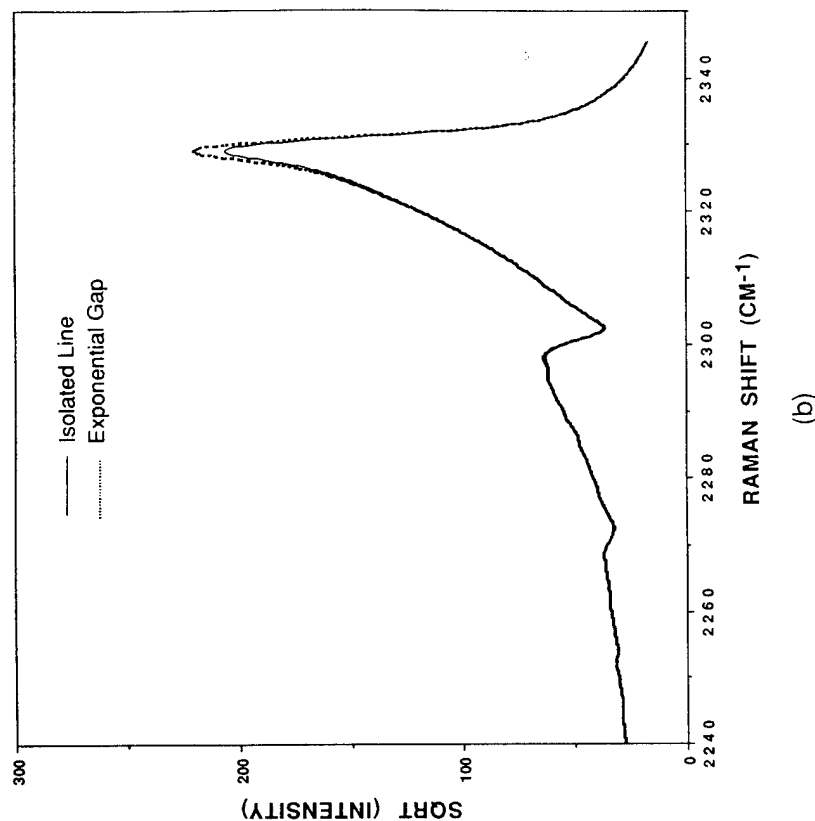


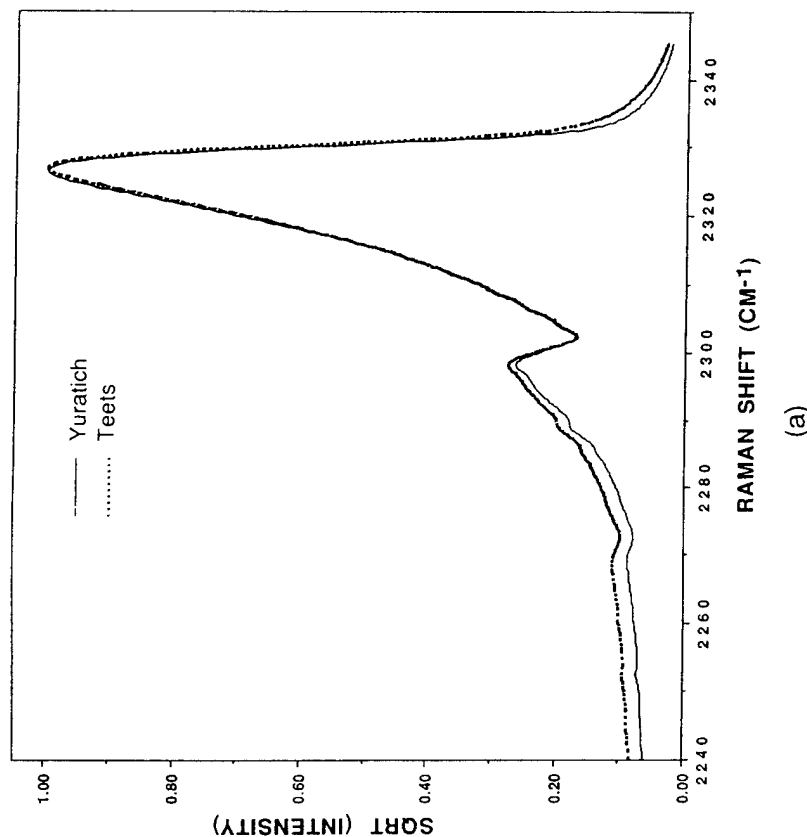
Figure 6 Comparison of isolated-line and collisional-narrowing models (experimental gap) for N_2 at (a) 1 atm pressure and (b) 10 atm pressure (Palmer, 1989).

the CARS experimental conditions. To illustrate this point, a comparison of the isolated-line, collisional-narrowing, Yuratich convolution and Kataoka-Teets convolution models was made (see Figures 6 and 7). The CARS N_2 spectral calculations depicted in these figures were made at a relatively high resolution to emphasize the differences in the models. Figure 6(a) shows that at 1 atm pressure, there is little difference between the isolated-line and collisional-narrowing spectra. However, as the pressure is increased to 10 atm, the difference (Figure 6(b)) between the models becomes quite obvious. At high concentrations of N_2 , only minor differences are observed in the calculated spectra of the Yuratich and Kataoka-Teets convolutions (Figure 7(a)). However, at relatively low N_2

concentrations, the differences between the two convolutions become obvious (Figure 7(b)). Thus, the experimental conditions under which CARS measurements are to be made must be closely examined to ensure that the correct synthesis model is being employed, bearing in mind that the more complex collisional narrowing and the Kataoka-Teets convolution exact a substantial penalty in computation time (increasing spectral-synthesis times from tens of minutes to hours on minicomputer systems).

IV. Thermometry

The temperature sensitivity of the CARS technique is the result of the variation in rotational-vibrational populations of the Raman transitions of the species being probed. Thus, a spectroscopic rather than a translational



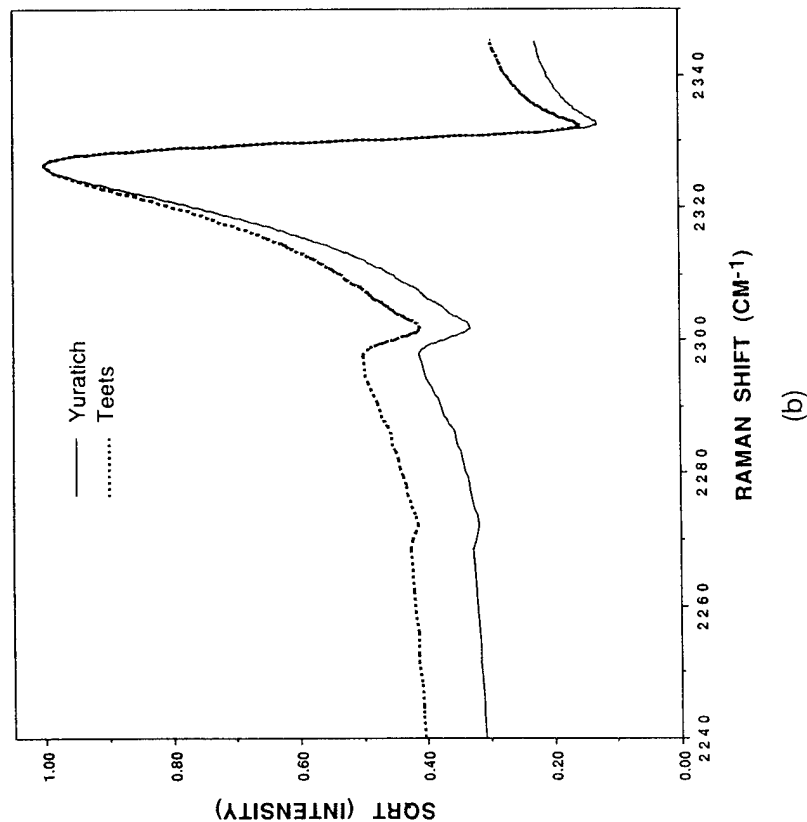


Figure 7 Comparison of Yuratich and Kataoka-Teets convolutions at (a) 78% by volume N_2 and (b) 10% by volume N_2 (Palmer, 1989).

temperature is actually determined by the technique. In most combustion situations, these two temperatures are equivalent; however, in plasmas this may not be the case (Nibler *et al.*, 1976; Shaub *et al.*, 1977; Pealat *et al.*, 1981; Taran, 1987; Yaney *et al.*, 1987). As a thermometric species, N_2 has received considerable attention because of its abundance in air-breathing combustion and the sensitivity of its Q-branch spectrum to temperature variations; this sensitivity is illustrated in Figure 8. Even when monitored under low spectral resolution, the Q branch displays a striking sensitivity to temperature. At low temperatures the N_2 spectrum is characterized by a strong band ($v = 0 \rightarrow v = 1$, where v denotes the vibrational level) whose width increases with temperature because of the increased population of high rotational levels. As the temperature approaches 1000 K, the hot-band

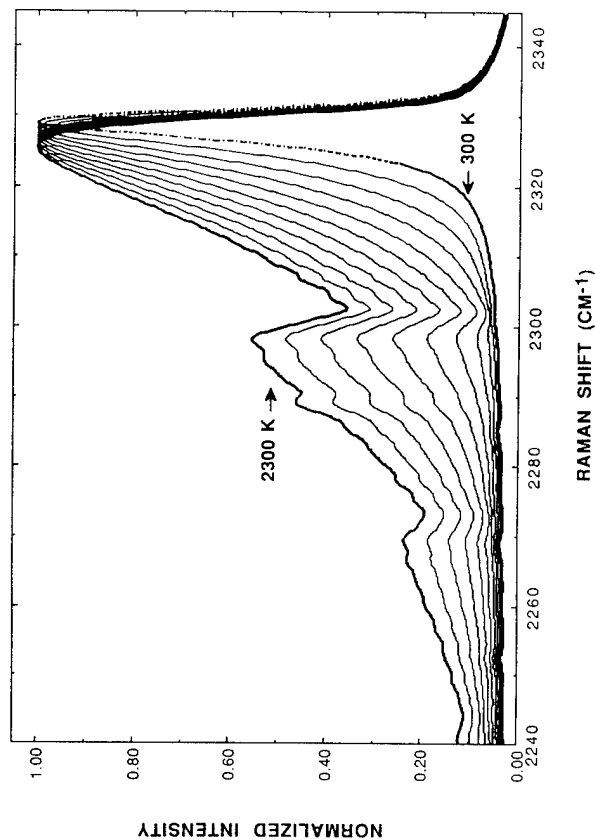


Figure 8 Variation of CARS N_2 spectrum as a function of temperature from 300 to 2300 K (Palmer, 1989).

transition ($v = 1 \rightarrow v = 2$) becomes populated. Thus, the band-shape of the N_2 Q-branch spectrum is clearly a good indicator of temperature, and most thermometric data reduction schemes employ a least-squares routine for fitting the calculated data and the observed experimental band-shape (Goss *et al.*, 1980). The single-shot precision of N_2 thermometry (uncertainty of the temperature measurement for a constant-temperature environment) is about ± 50 K, while the multiple-shot accuracy (CARS temperature versus real temperature measured by a standard technique) is $\sim 1\%$ of the average temperature.

The N_2 CARS spectra displayed in Figure 8 were calculated employing equations (9) and (10) and spectral constants (Gilson *et al.*, 1980; Rahn, 1985). The off-diagonal G -matrix elements and the Raman line widths were determined by means of the Sandia scaling law (Rahn and Palmer, 1986). Polarization derivatives were obtained from experimental Raman cross-sections and polarizability ratios (Farrow and Rahn, 1985). Non-resonant-susceptibility values (Rado, 1967) were scaled to recent measurements of N_2 (Farrow and Rahn, 1985; Rosasco and Hurst, 1985).

Other species which have been employed for thermometry include H_2 , H_2O and CO_2 . H_2 is a good candidate for thermometry because of its large

Raman scattering cross-section and the wide separation between rotational lines which aids in minimizing interference from the non-resonant susceptibility. H_2 has been used for thermometry in an H_2 -air diffusion flame (Shirley *et al.*, 1979). H_2O is a major product of air-fed combustion, and its concentration is a gauge of combustion efficiency; however, its CARS spectrum is quite complex, and the variation of the spectral line widths is not well known (Hall, 1979). Measurements of H_2O at elevated temperatures have been made in heated cells (Shirley *et al.*, 1980), in high-pressure steam (Greenhalgh *et al.*, 1983) and in a premixed methane-air flame (Hall and Shirley, 1983). CO_2 , like H_2O , is a major product of combustion and has been experimentally investigated in several propane-air and CO-air flames (Hall and Eckbreth, 1981; Hall and Stufflebeam, 1984) and in a high-temperature furnace (Papineau and Pealat, 1985).

V. Concentration measurements

While the major application of CARS in combusting flows is thermometry, the technique is also useful for concentration measurements of major flame species. Concentration measurements fall into two categories; in the first the species concentration is sufficiently high that interference due to the non-resonant background in the CARS spectrum is small, and in the second the concentration is sufficiently low that such interference can be observed.

In the high-concentration case ($> 30\%$ by volume), an absolute measurement of the CARS signal strength must be made in order to determine the concentration. The non-linear nature of the CARS process makes this a difficult—if not impossible—task. Therefore, a relative measurement of the flame conditions is usually made and the result compared with the CARS signal strength at a known (usually ambient) temperature. This procedure requires that variation of the signal with temperature be calculable and that the power fluctuations between the two measurements be taken into account. The former is accomplished through computer synthesis of the spectrum as a function of temperature. The latter requires incorporation of a power-referencing scheme (Goss *et al.*, 1983a, 1984c) which takes into account not only the temporal but also the spatial fluctuations of the laser sources for accurate normalization of the sample and reference signals.

The optical arrangement for concentration measurements in a small-scale burner is shown in Figure 9. This scheme employs a common lens to form both the sample and reference signal legs. A retroreflecting beam splitter splits off a small fraction of the main pump and Stokes beams just in front of the sample volume to form the reference volume (Figure 9(a)). This arrangement has been employed for N_2 and O_2 concentration

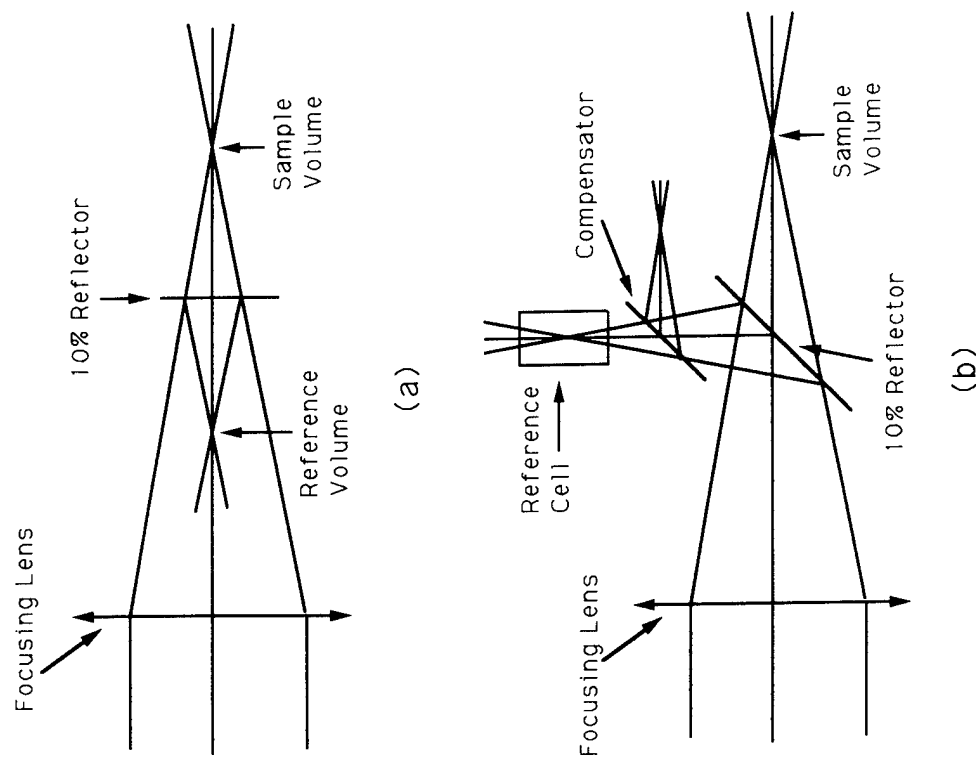


Figure 9 Optical schematic of reference paths used for concentration measurements for species above 20% by volume levels. (a) Single-lens retroreflection scheme for no reference cell case (N_2 and O_2) and (b) single-lens 45° scheme for inclusion of reference cell.

measurements (Switzer *et al.*, 1979, 1980; Goss *et al.*, 1983a, 1984c; Antcliff *et al.*, 1985; Antcliff, 1987; Antcliff and Jarret, 1987). For concentration measurements of a species whose natural abundance in the atmosphere is low (e.g. monitoring CO_2 in a CO_2 jet) or for monitoring the shot-to-shot fluctuation of the dye laser by the non-resonant CARS signal,

a reference cell must be employed. Use of this cell makes it necessary to rotate the beam splitter 45° to form the reference leg (Figure 9(b)). However, another optical element of the same thickness as the initial splitter must be placed in the reference leg at a point just before the beams cross to ensure that the sample and reference path lengths will be identical. The correlation between the sample and reference paths with this arrangement is nominally 90–95%, which translates into an uncertainty in the concentration measurement of $\sim 10\%$.

The power-referencing schemes shown in Figure 9 cannot be employed in large-scale combustors, which display a wide variation in refractive index because the deflection and defocusing of the sample path beams caused by variation of the refractive index are not taken into account by the reference leg. As a result, the sample and reference signals cannot track each other, and erroneously low concentration values result. Since a reference cell placed after the sample would tend to overcompensate for refractive effects, this scheme is unreliable. *In situ* referencing schemes in which the non-resonant signal produced in the sample volume is used as the reference have been proposed and tested successfully in a scanned CARS system (Farrow *et al.*, 1985). However, the photon-limited signals from a broad-band CARS system preclude utilization of this approach.

Interference between the resonant and non-resonant signals which occurs as the concentration of the species drops below 30% can be used to make concentration measurements in combusting flows (Eckbreth and Hall, 1979, 1981). In this approach the concentration is determined by the band-shape of the observed signal rather than from an absolute measurement of the signal strength. This scheme has two obvious advantages over power-referencing approaches. First, no external reference is required for the measurement since the non-resonant and resonant signals are recorded simultaneously, which simplifies the experimental arrangement. The second—and more important—advantage is that accurate measurements are possible because a band-shape is used to determine the concentration rather than an absolute intensity measurement. With this scheme a simple least-squares analysis approach can be taken in determining the species concentration.

Figure 10 demonstrates the sensitivity of the N_2 spectral band-shape to concentration at 1800 K. Although the band-shape is indeed a sensitive indicator of concentration, it is dependent upon the temperature, Raman line width (pressure) and non-resonant susceptibility as well as concentration. Therefore, an entire family of curves having different temperatures, pressures and non-resonant susceptibilities will yield the same spectral shape. Thus, the accuracy of the concentration determined in this manner is dependent upon the degree to which the temperature, pressure and non-

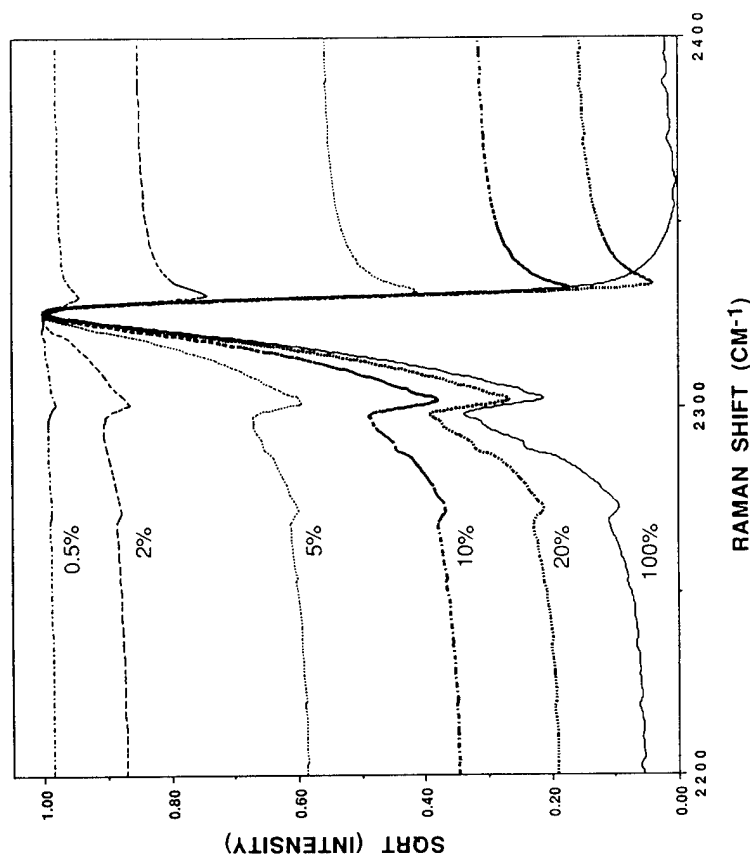


Figure 10 Sensitivity of the N_2 spectral band-shape to concentration variation at 1700 K (Palmer, 1989).

resonant susceptibility are known. Of these three parameters, the non-resonant background is likely to have the highest degree of uncertainty; in the case of turbulent combustion, an adiabatic calculation is required to determine the constituents of the flame. The non-resonant susceptibility of various constituents has been measured (Rado, 1967), but the addition of a scaling factor is required if the results are to be used in spectral synthesis (Eckbreth and Hall, 1981).

Sensitivity of the CARS technique to low species concentrations can be achieved in some cases by suppressing the non-resonant background. Such suppression is possible because the resonant and non-resonant parts of the third-order susceptibility have different tensor properties (Owyoung, 1971). Thus, with proper selection of pump and Stokes polarizations, the non-resonant polarization can be angularly separated from the resonant component and suppressed by a polarization analyser (Bunkin *et al.*, 1977;

Oudar *et al.*, 1979). Since resonant and non-resonant polarizations are not orthogonal, complete suppression of the non-resonant component cannot be realized without some loss of the resonant component (factor of 16 minimum). In the case of broad-band (single-shot) CARS, the signal levels are usually photon limited; thus, the loss in signal due to suppression cannot be tolerated. In the narrow-band CARS case, however, the signal level is usually limited by the background interference, and the loss in signal level with suppression can be tolerated, resulting in an extension of the lower concentration limit to $\sim 0.1\%$ (Eckbreth and Hall, 1981). Background suppression techniques have been applied to the measurement of CO (Attal *et al.*, 1979; Farrow *et al.*, 1980; Eckbreth and Hall, 1981), CO_2 (Attal *et al.*, 1980) and O_2 (Antcliff *et al.*, 1985; Antcliff, 1987; Antcliff and Jarret, 1987).

VI. Instrument considerations

A. Optical arrangement

Figure 11 shows the experimental arrangement for a broad-band CARS apparatus employed for flame studies at the Wright Laboratory/Aero Propulsion and Power Directorate at Wright-Patterson Air Force Base (WPAFB) (Goss *et al.*, 1983b). The pump source in this set-up is a frequency-doubled Nd:YAG laser capable of producing 200 mJ of 532 nm radiation at a repetition rate of 10 Hz. Commercial Nd:YAG lasers are presently capable of operation at frequencies up to 50 Hz, with energy levels in excess of 500 mJ/per pulse. The 532 nm output of the Nd:YAG laser serves as a pump for both the CARS process and the broad-band dye laser. A broad-band dye laser is used in this instrument to allow the entire Q branch of N_2 to be obtained in a single shot; the temperature is determined from the band-shape of the CARS signature. The dye laser consists of a simple Fabry-Perot oscillator cavity, ~ 30 cm long, followed by an amplifier stage. For excitation of the N_2 transition at 2331 cm^{-1} , the dye sulpharhodamine 640 is used and its frequency output is concentration tuned to 607.3 nm . The broad-band emission from this dye laser is $\sim 130\text{ cm}^{-1}$ wide, and the laser operates with a conversion efficiency of $\sim 25\%$ in the longitudinal pumping configuration. Other dye laser configurations have been discussed in the literature with regard to reduction of dye noise (Eckbreth and Stufflebeam, 1985; Greenhalgh and Whitley, 1985) and, thus, temperature uncertainty (Pealat *et al.*, 1985; Snelling *et al.*, 1985, 1987; Barton and Garneau, 1987; Kroll *et al.*, 1987).

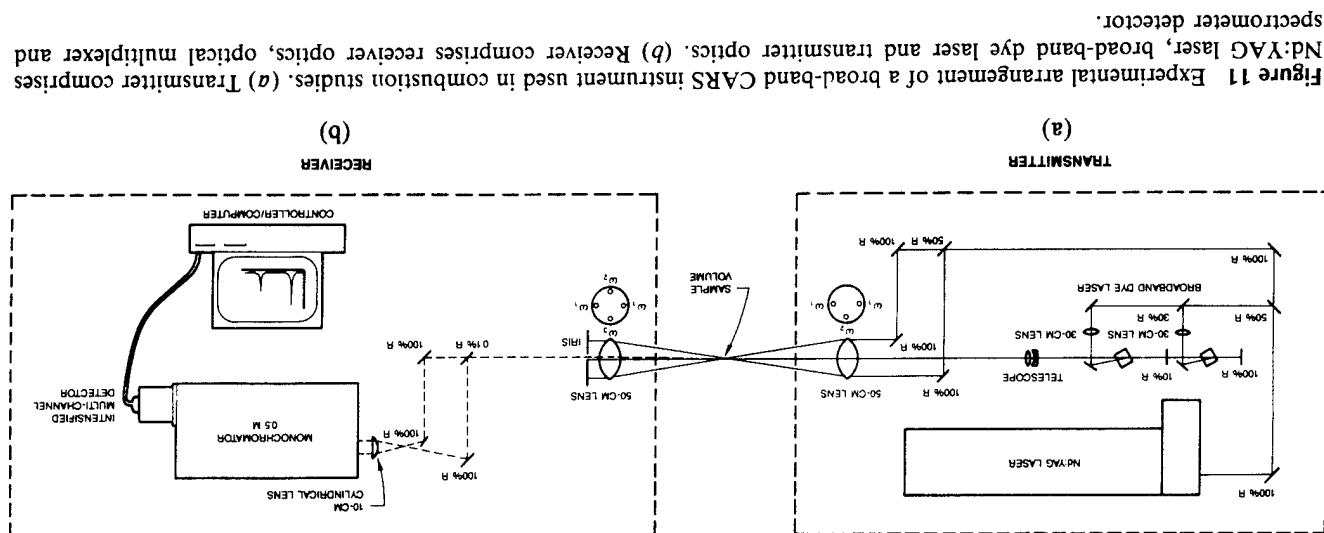


Figure 11 Experimental arrangement of a broad-band CARS instrument used in combustion studies. (a) Transmitter comprises Nd:YAG laser, broad-band dye laser and transmitter optics. (b) Receiver comprises receiver optics, optical multiplexer and spectrometer detector.

The 532 nm output of the Nd:YAG laser is split a second time to form two CARS pump beams. A path difference of a few centimetres is introduced into one of the beams to minimize pump coherence effects (Rahn *et al.*, 1984; Farrow and Rahn, 1985). To achieve spatial resolution with the 50 cm focal length primary lens, a folded BOXCARS arrangement is typically employed. The two pump laser beams are crossed with the dye laser beam at an angle of $\sim 2^\circ$ to maximize spatial resolution. Measurements of the spatial resolution with a 100 μm CO_2 jet indicated that the 90% region for CARS signal production in this arrangement is $< 1000 \times 250 \times 250 \mu\text{m}$. A telescope is used in the dye laser leg to ensure that the waist of the pump and dye beams will occur at a common focus.

Due to the non-linear dependence of the CARS signal upon laser power and mode fluctuations, a reference must be employed for measurements of major flame species. In the present set-up, a retroreflecting power reference was incorporated for this purpose. The reference is formed by a 20% beam splitter which is positioned in front of the focal point, perpendicular to the incident beams. That portion of the laser beams reflected by the splitter produces a second focus which generates a CARS signal from atmospheric N_2 ; this signal serves as the power reference for concentration measurements and, thus, allows the fluctuation of the laser powers to be normalized in the CARS intensity data. With this arrangement the correlation between sample and reference signals is typically 94–97%, which translates to a concentration uncertainty of $\sim 10\%$.

Both the reference and sample signals are collimated and steered by a right-angle prism towards a Spex 3/4-m monochromator. The monochromator contains a grating which spatially disperses the CARS signal as a function of wavelength. Thus, the band-shape information of the CARS spectrum is spatially separated and can be recorded by means of a multiplex element detector. An intensified detector is normally required for CARS measurements because of the relatively low CARS signals. These detectors are characterized by a dynamic range of only ~ 30 (upper count of 3000, lower count of 100) which is inadequate for turbulent-combustion studies where the temperature can vary dramatically from shot to shot, necessitating a dynamic range of ~ 900 (see Figure 12).

To overcome the dynamic-range problem, an optical-multiplexer arrangement (Goss *et al.*, 1983b) such as that shown in Figure 11 must be employed which simultaneously images two different sample beams on to the multichannel detector. Each beam represents a different fraction of the total CARS signal. Full coverage of temperature possible in turbulent flames can be achieved with a beam splitter combination of 30 to 1. As shown in Figure 12, the temperature range is divided into two regions, 300–1000 and 1000–2300 K. When the CARS signal is generated from a hot

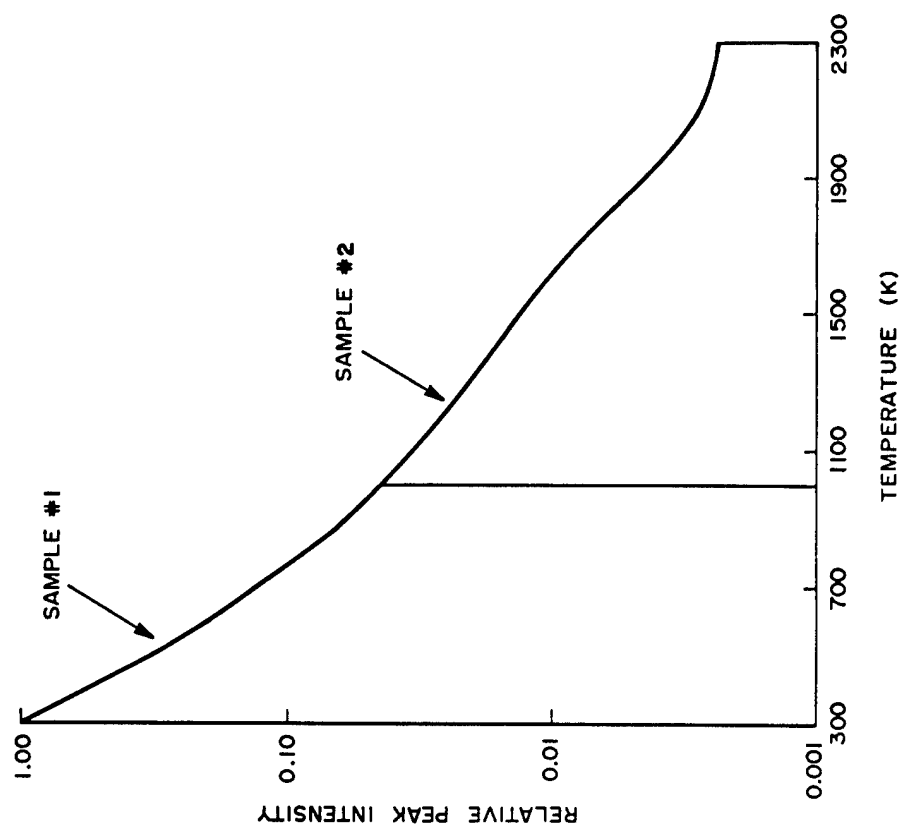


Figure 12 Relative peak intensity variation of the N_2 CARS signal as a function of temperature, with optical-multiplexer coverage indicated (Goss *et al.*, 1983b).

portion of the flame (Figure 13(a)), the more sensitive split of the optical multiplexer is in the proper count range on the multichannel detector and is used for data analysis. When the CARS signal originates from a cooler portion of the flame (Figure 13(b)), the detector is saturated in the most sensitive split of the multiplexer; however, the second split is in the correct intensity range and can be used for thermometry. An alternative arrangement for multiplexing the CARS signal has been utilized for N_2 thermometry (Eckbreth, 1983).

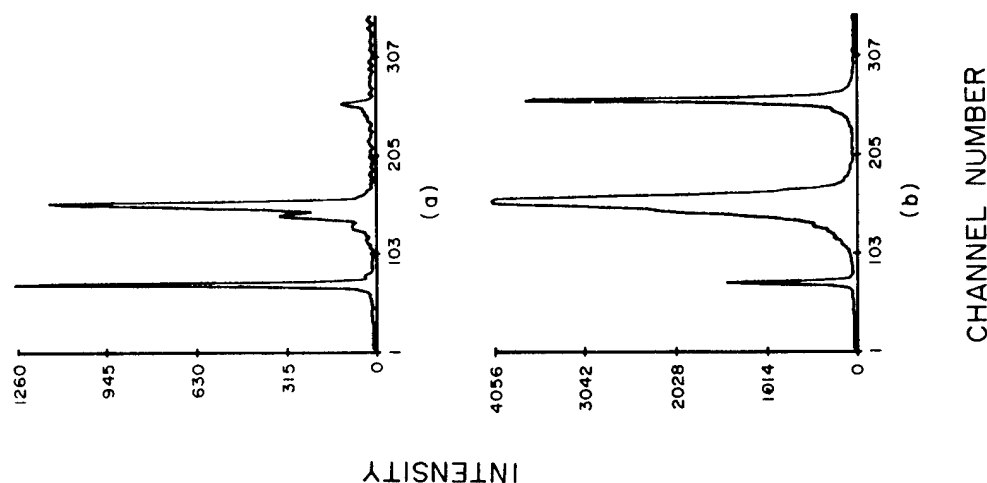


Figure 13 Experimental CARS N_2 spectra obtained from (a) a hot portion of the flame and (b) a cooler portion of the flame, depicting dynamic-range coverage of an optical multiplexer (Goss *et al.*, 1983b).

For simultaneous positioning of the two sample beams and the reference beam on to the multichannel detector, the slits of the monochromator are removed. The three beams (two samples and one reference) are then crossed 10 cm in front of a 10 cm cylindrical lens and enter the monochromator in parallel. A cylindrical lens is employed at the monochromator entrance to

ensure that a line rather than a point will be imaged on to the face of the multichannel detector, which helps to minimize saturation effects associated with the intensified detector (Antcliff *et al.*, 1984; Snelling *et al.*, 1984). The measured dispersion for this arrangement of the instrument was 1.25 cm^{-1} per channel element of the detector, with a measurement resolution of 2.3 cm^{-1} HWHM.

B. Data acquisition system

The basic components of the CARS data acquisition system are shown in Figure 14. The heart of the system is a Tracor-Northern 1710 multichannel analyser with a plug-in optical spectrometer and an intensified, gated diode array rapid-scanning spectrometer (IDARSS) detector. The detector incorporates a Reticon solid-state line scanner and a monolithic, self-scanning, 1024-element, linear photodiode array in a dual in-line package. The IDARSS provides thermoelectric cooling (for reduced dark counts) and is equipped with a gateable, continuously variable gain image intensifier. This detector displays little of the troublesome blooming encountered with vidicons (Liesgang and Smith, 1981). The dynamic-range data shown in Figure 15 were obtained from measurements with the IDARSS detector by averaging 100 shots of room temperature N_2 CARS signals. The input intensity was varied by insertion of calibrated neutral-density filters. The points on this plot indicate extension of the signal counts above the

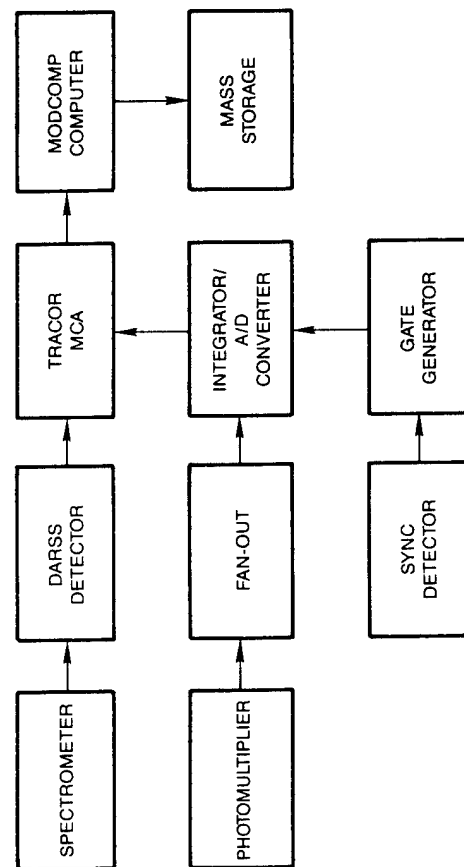


Figure 14 Basic components of a CARS data acquisition system (Goss *et al.*, 1983b).

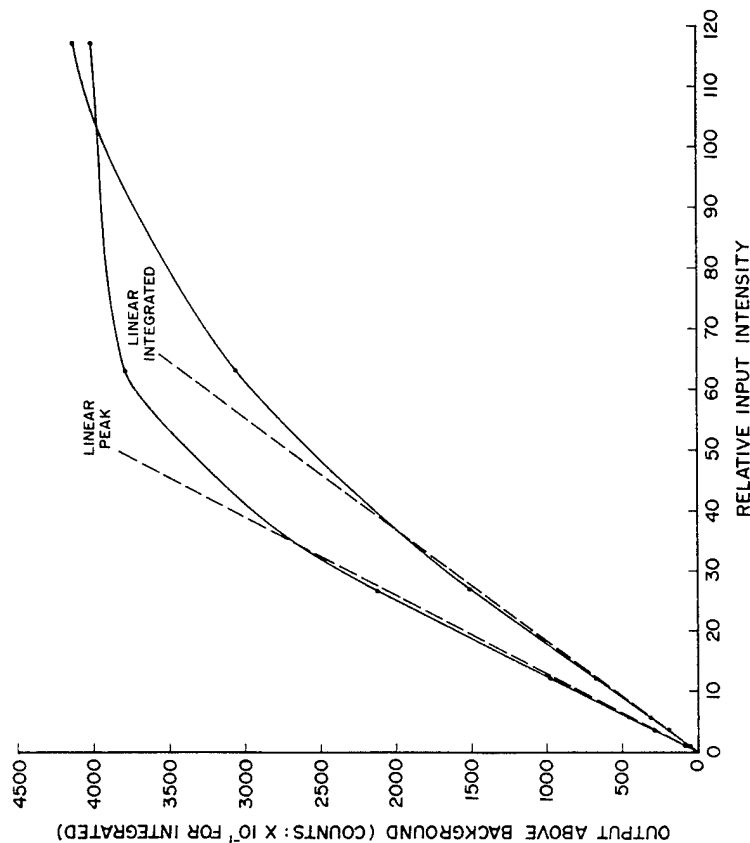


Figure 15 Integrated and linear peak responses of the intensified linear array to variation in the CARS signal intensity (Goss *et al.*, 1983b).

background levels for both peak (height of signal) and integrated (total area of signal) detector responses. These data suggest a maximum peak count constrained to ~ 3000 for linear operation. The lowest acceptable signal count with no interference from background noise sources is ~ 100 . Thus, for single-shot operation the useful dynamic range of the detector is ~ 30 .

An electronic interface has been constructed for synchronizing the firing of the Nd:YAG laser and the data acquisition cycle of the multichannel analyser. Upon receipt of an electronic trigger from the multichannel analyser, the laser synchronizer generates four signals—two (20 V pulses) which fire the laser flashlamps and Q switch and two (TTL) which trigger the multichannel analyser data acquisition electronics and gate the detector for background light reduction. Four variable delays are provided for adjusting the relative timing of the four signals. The laser may be fired in a single-shot mode or its firing can be controlled by the multichannel

analyser. The synchronizer allows the laser flashlamps to be pulsed continuously, regardless of laser firing mode, which maintains the laser cavity under constant thermal loading.

The video signals from the multichannel analyser detector are digitized and stored in the spectral data memory of the multichannel analyser. From this memory, data are transferred in 16-bit parallel format to a minicomputer. The transfer program (machine code) of the multichannel analyser controls the handshaking and data transfer on the sending side. On the receiving (minicomputer) side, a Fortran program in conjunction with a direct-memory processor channels the information to an 800 b.p.i. tape transport. When 1024-channel spectra are being taken at 10 Hz, a tape can be filled in ~ 15 minutes.

In addition to the spectral data from the multichannel analyser, the data acquisition system can acquire 10 Hz integrated-signal data from a photomultiplier tube (sample or reference). The desired CARS signals are time multiplexed via different lengths of fibre-optic cable to a single photomultiplier tube. The tube signals are fed to a LeCroy 428-F Fan-Out which splits the photomultiplier output into 12 parts, allowing up to 12 different CARS signals to be derived from a single photomultiplier. Each of the 12 signals drives one channel of a 12-channel integrator/analogue-to-digital (A/D) converter (LeCroy Camac model 2249SG). Each channel is gated to capture a single pulse from the pulse train of the photomultiplier tube. The custom-built gate generator provides 12 individually adjustable (start time and duration) gates triggered by a common synchronization signal from a p-i-n diode which monitors the laser event. Instructions in the data acquisition program cause the multichannel analyser to address and read out the requested number of A/D converter channels sequentially. This information is deposited into the spectral data memory (replacing the last 12 channels of the 1024-channel spectral data) and transferred along with the multichannel analyser data to the minicomputer.

A serious problem was encountered with earlier versions of the multichannel analyser detector during 10 Hz operation, namely that the detector possessed an image persistence which allowed information from one laser shot to be carried over to the next (Goss *et al.*, 1983b). Current detectors are much more efficient at reducing this image lag. The external exposure input of the optical-spectrometer plug-in was used to develop a special data acquisition cycle which reduced the image lag problem to $<0.1\%$ signal bleed-over. The acquisition cycle is depicted in Figure 16. After each laser shot, the detector integrates for a time period of 35 ms to acquire the full CARS signal. The detector is then scanned and its output digitized and deposited into the spectral data memory. If the minicomputer is ready, the spectrum is transferred via the input/output ports. Otherwise, the program

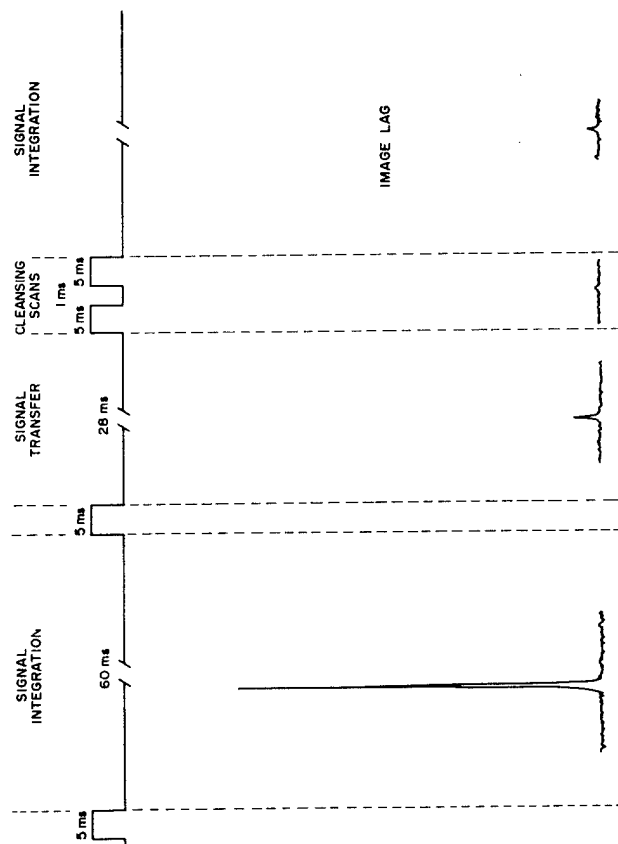


Figure 16 Data acquisition cycle for the intensified diode array, including cleaning scans to remove signal lag (Goss *et al.*, 1983b).

loops for a time equal to the transfer time, which maintains the laser firing rate at 10 Hz. The detector is then scanned to cleanse it of any leftover signal, and the cycle is repeated.

As mentioned previously, the raw CARS spectra are stored on tape for analysis at a later time. This analysis includes conversion of the raw single-shot spectra to temperature and species concentration values from which histograms, contour maps and correlation plots can be constructed.

C. Data analysis

Data reduction consists of fitting the observed spectral band-shape to obtain a temperature and integrating over the wavelength of the CARS signal to obtain species concentrations. However, since two sample CARS peaks are recorded during a single shot, the program must decide which peak is in the proper intensity range for temperature fitting. The basic program can be reduced to the following subprograms: (1) initial parameter set-up; (2) peak selection; (3) temperature fitting; (4) concentration determination and (5) data storage and display.

In the initial parameter set-up, the first step is to determine the sample reference intensity correlations of the CARS sample signal in ambient air, which involves ratioing the integrated sample signal by the integrated-power reference value for a total of 200 shots. This measurement is required for calibration of the flame concentration data and determination of the error in the concentration measurement. If concentration information is not requested by the operator, the correlation procedure is by-passed.

The program next searches through the file of spectra to be reduced and selects, for each of the two peaks, one spectrum in which the peak intensity falls between 100 and 3000 counts. Each spectrum is then frequency fitted (using a fitting procedure similar to the temperature fitting discussed below) to determine the starting channel, frequency and boundaries of the CARS peak. This procedure establishes the boundary conditions for each peak which will be used by the peak selection subprogram.

The peak selection subprogram determines which of the two sample peaks recorded during a single shot will be used for temperature fitting. Each peak is tested to determine whether it falls within the 100–3000 count range. Next, the initial parameters and boundary conditions which were determined in the set-up subprogram are applied to that peak which is found to be in the correct intensity range. Normalization for diode sensitivity variation, dye laser tuning, and detector non-linearity corrections is then performed, and the CARS spectrum is ready for temperature fitting.

The temperature-fitting subprogram employs a non-linear least-squares fit of the temperature which is based upon the matrix equation (Kim, 1970)

$$\Delta T = (J^T J)^{-1} J^T \Delta \phi \quad (14)$$

where J is the Jacobian matrix whose elements are defined by $J = dI/dT$ (I being the i th intensity and T the temperature), J^T the transpose of the J matrix, $\Delta \phi$ the matrix with elements $\Delta \phi = I_{i,obs} - I_{i,cal}$ (where $I_{i,obs}$ is the i th observed experimental intensity and $I_{i,cal}$ the i th calculated intensity), and ΔT the correction to be made to the temperature.

The fitting routine functions as follows. First, an initial guess of the temperature is made; next a spectrum is calculated and used to formulate the $\Delta \phi$ matrix. Then, the Jacobian is created by a numerical evaluation of the intensity-temperature derivative, and the transpose of the Jacobian and subsequent inverse of the product of the Jacobian and its transpose are formed. Next, the correction ΔT is calculated according to equation (14). The correction can then be made to the temperature and the resulting new temperature used as the initial guess for the next iterative cycle. The iterative process is continued until variation of the calculation spectrum yields no further improvement in the fitted temperature. The

dispersion—an indicator of the fitting error for each parameter—can be obtained from

$$D_i = (J^T J)^{-1} \sigma^2 / (\text{NOBS} - 1) \quad (15)$$

where $(J^T J)^{-1}$ is the i th diagonal element of the $(J^T J)^{-1}$ matrix, σ^2 the variance between the observed and calculated spectra, and NOBS the total number of data points in the observed spectrum. Three cycles of this iteration are usually required for fitting the temperature. To reduce the fitting time, a library of CARS spectra calculated in 10 K increments is stored for use by the fitting routine. The temperature-fitting subprogram retrieves the CARS spectrum from the library instead of calculating it for each fitting cycle. This reduces the data analysis time per experimental spectrum from 30 minutes to 1 second on a minicomputer. Figure 17 shows a fit which was made to single-shot data obtained from a premixed propane-air flame.

Once the temperature has been fitted, the concentration can be determined from the integrated CARS signal. The N_2 number density is given by

$$N_T = N_{300} \sqrt{\frac{R_T I_T}{I_{300}}} \quad (16)$$

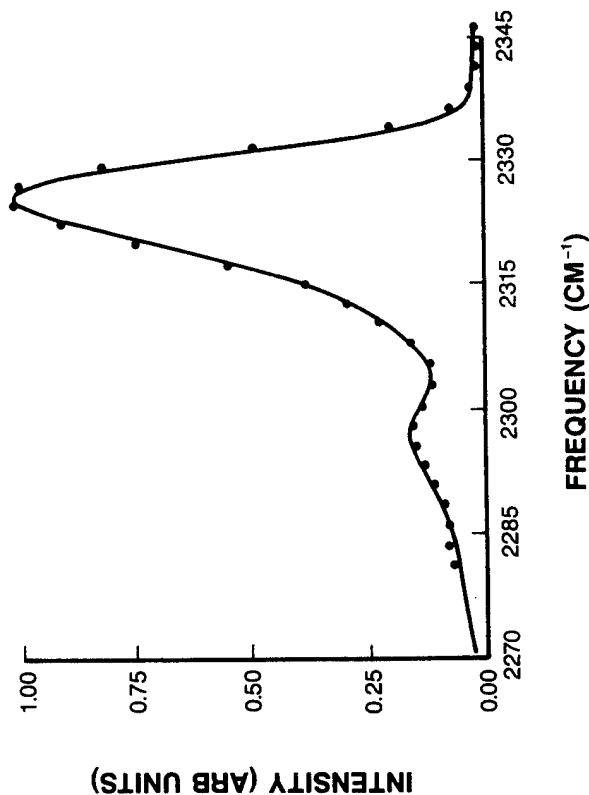


Figure 17 A numerical fit to an experimental CARS N_2 spectrum obtained with the non-linear least-squares Jacobian routine.

where N_T is the N_2 number density at temperature T , N_{300} the N_2 number density at 300 K, R_T the ratio of band-shapes of the CARS spectrum at 300 K to those of the CARS spectrum at temperature T (determined by the spectral synthesis program), and I_{300} the experimentally measured integrated CARS intensity at 300 K. The ratio R_T takes into account the change in Raman line width and population redistribution with temperature. Both I_T and I_{300} are normalized by the reference signal to remove intensity variations due to the pump and Stokes lasers. Once the raw spectral data file has been reduced to temperature and species concentration data, the results are stored by the data storage subprogram, and analysis of the next file of raw CARS spectra begins.

D. Calibration of instrument

Calibration of the CARS instrument is typically accomplished through the use of a platinum coiled furnace. The furnace is positioned in the sample area of the CARS instrument and measurements made over the range 573–1573 K. Two hundred single-shot measurements were made at each temperature, and the average and root mean square (r.m.s.) fluctuations are plotted in Figure 18. The oven temperature was monitored by a Pt–Rh thermocouple and compared with the CARS data. As indicated in Figure 18, the precision of the CARS single-shot temperature measurements is ~ 60 – 80° (fluctuation of the CARS temperature measurement is not due to actual temperature change). The accuracy of the CARS data (agreement of measured temperature with that determined by a standard thermocouple) was determined to be ~ 10 K. These results are consistent with the resolution and uncertainty predictions for the type of dye and pump lasers employed in this instrument.

E. Applications of CARS instrument

The CARS technique has been applied to the study of a wide variety of combustion processes, including laboratory-scale flames, large-scale combustion tunnels, jet engines, industrial furnaces, internal-combustion engines and burning propellants. A comprehensive review of the areas of application is not within the scope of this chapter and, thus, only a brief review is included here. The reader is referred to the references cited for complete details of this extensive body of work.

Probably the area which has been investigated most thoroughly by the CARS technique is small-scale laboratory flames. Temperature as well as species concentration studies have been performed on premixed flames (Hall, 1979; Goss *et al.*, 1980, 1988; Alden *et al.*, 1983; Antcliff and Jarret,

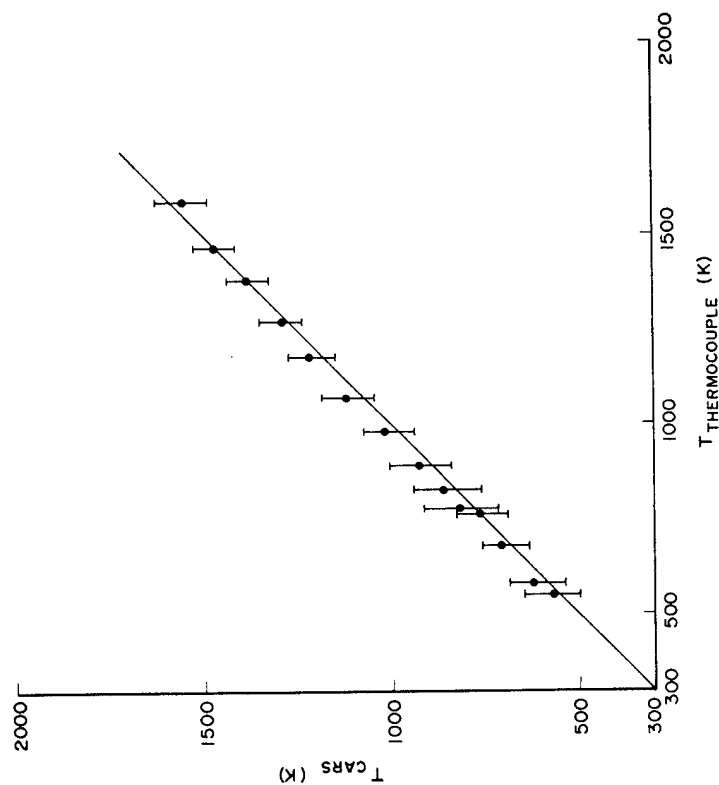


Figure 18 Calibration results for the CARS instrument obtained in a platinum coiled oven (Goss *et al.*, 1984a). Error bars indicate fluctuation of single-shot CARS temperatures, while the straight line indicates thermocouple readings.

1983; Aron *et al.*, 1983; Harris, 1983; Kreutner *et al.*, 1983; Chen *et al.*, 1988) and on jet diffusion flame systems (Fujii *et al.*, 1982; Goss *et al.*, 1984c; Roquemore *et al.*, 1989). The CARS technique was first demonstrated in the area of combustion research by Taran and coworkers (Moya *et al.*, 1975, 1977) on an H_2 -air flame. An example of nitrogen thermometry and concentration measurements on a turbulent premixed jet flame with the instrument located at WPAFB (Goss *et al.*, 1983a) is shown in Figure 19. Results of a radial scan by the CARS instrument across the turbulent reaction zone of this $Re \approx 6000$ flame are depicted. The temperature recorded along with a single species of the flame can be compared with adiabatic-flame calculation results which, in effect, shows how CARS data can be utilized for comparison with computational fluid dynamics (CFD) code results (Antcliff and Jarret, 1987).

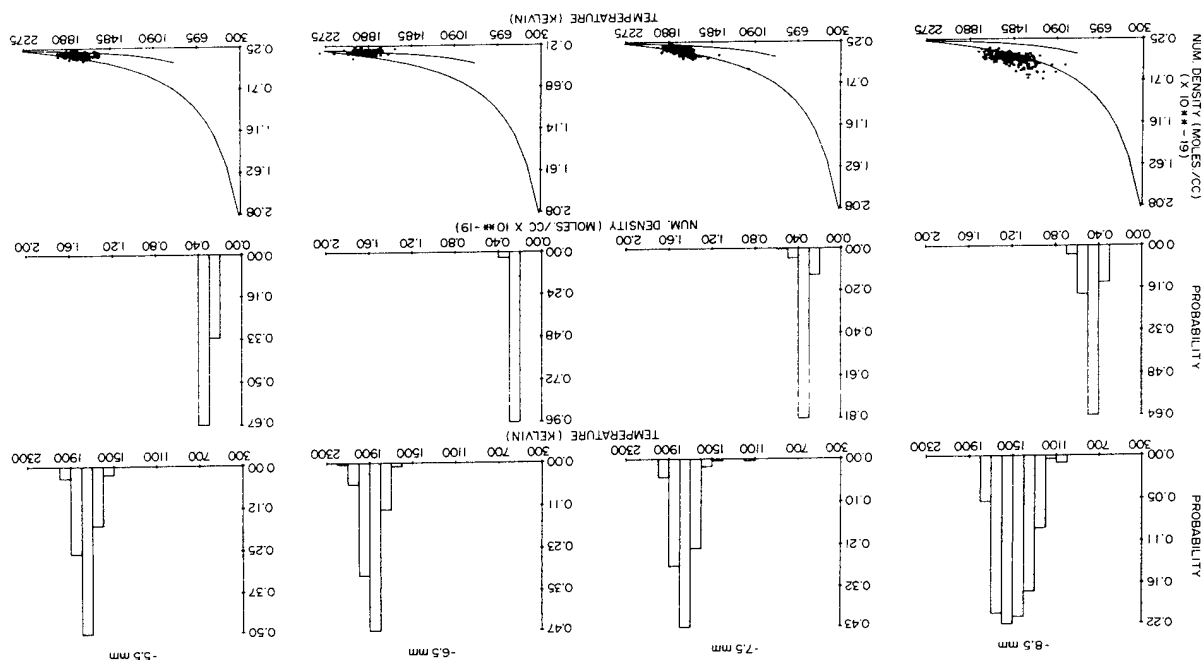


Figure 19 Temperature-concentration probability density functions (p.d.f.s) and correlation plots of temperature and concentration versus adiabatic equilibrium calculation results obtained in an $Re \approx 6000$ turbulent diffusion flame at four radial positions (about flame sheath) 30 cm above the burner surface (Goss *et al.*, 1983a).

A similar instrument developed at the NASA Langley Research Center is capable of measuring O₂ as well as N₂ concentration along with temperature. This capability is realized by incorporation of a second Stokes laser tuned for O₂. The experimental integrated O₂ CARS signal is converted to a concentration by ratioing to the calculated O₂ spectra at the temperature determined by the N₂ measurement. This system has been used for comparison with CFD computational results on subsonic jet diffusion flames (Antcliff *et al.*, 1984, 1985) and is presently being utilized for supersonic flames (Antcliff, 1987; Antcliff and Jarret, 1987; Chitsomboon *et al.*, 1988). Extensive investigations on laboratory burners have been conducted at the United Technologies Research Center (UTRC); these include concentration measurements (Eckbreth and Hall, 1979, 1981; Shirley *et al.*, 1979; Hall and Shirley, 1983; Hall and Stufflebeam, 1984) and the study of sooting flames (Eckbreth and Hall, 1979; Hall and Boedeker, 1984; Hall and Stufflebeam, 1984; Boedeker and Dobbs, 1985; Dobbs *et al.*, 1985). An extremely high-accuracy scanning CARS system developed at Sandia National Laboratories has been used for temperature and species concentration measurements (Rahn *et al.*, 1979; Farrow *et al.*, 1981, 1982, 1985).

In larger-scale combustion tunnel experiments, environmentally hardened CARS instruments have been used for measurements on a bluff-body at WPAFB (Switzer *et al.*, 1979, 1980, 1983, 1985; Switzer and Goss, 1982) and on combustor cans at UTRC (Eckbreth, 1979, 1980; Eckbreth *et al.*, 1983), at ONERA (Attal *et al.*, 1978, 1980; Taran and Pealat, 1982; Bedue *et al.*, 1984), at Harwell (Greenhalgh *et al.*, 1983) and at the National Aerospace Laboratory of Japan (Fujii *et al.*, 1983). The temperature field obtained on the bluff-body at WPAFB has been compared with that calculated by a TEACH code; the results are shown in Colour Plate I. While the comparison indicates qualitative agreement between theory and experiment, quantitative agreement has not yet been achieved. UTRC has extended the hardened-system development by producing a mobile CARS system which can function in harsh environments and is easily transportable (Anderson *et al.*, 1986).

An extensively engineered CARS system has also been constructed and used by UTRC for thermometry and concentration measurements on a fully augmented afterburner of a gas turbine engine (Eckbreth *et al.*, 1984). This system is operated remotely because of its proximity to the jet engine. Both scanned and single-shot measurements were made in a series of tests conducted at the Pratt and Whitney test site. This instrument has demonstrated that the CARS technique is indeed applicable in extremely harsh environments.

Studies of industrial furnaces have also been conducted with the CARS technique (Hartford *et al.*, 1983; Taylor, 1983; Alden *et al.*, 1984; Alden

and Wallin, 1985; Beiting, 1986; Gomi *et al.*, 1986; Greenhalgh and Porter, 1986). The ability of the technique in large-scale combusting flows in the presence of high levels of particulates has been clearly demonstrated in MHD facility investigations conducted at the Mississippi State University (Beiting, 1986). The scattering and optical breakdown associated with particle-laden flow fields introduce special problems in the case of CARS measurements. These problems are discussed in detail in Section VII.C.

The first practical demonstration of the CARS technique involved measurements in an internal-combustion engine (Klick *et al.*, 1981). Several subsequent investigations illustrated the capability of the technique in high-pressure combustion situations (Kaijiyama *et al.*, 1982; Rahn *et al.*, 1982; Green and Lucht, 1985; Greenhalgh *et al.*, 1985; Greenhalgh and Williams, 1986; Hassel *et al.*, 1986; Robertson, 1986; Lucht, 1987b).

Propellant combustion has also been investigated by the CARS technique (McIlwain and Harris, 1980; Harris and McIlwain, 1981, 1982; Aron *et al.*, 1983); these studies (along with the internal-combustor work) have spurred the development of spectral codes for high-pressure collisional narrowing.

VII. Combined CARS-LDV instrument

While the CARS technique has proven to be an invaluable tool in combustion studies, it is even more powerful when combined with a laser Doppler velocimeter. With the combined instrument, simultaneous temperature and velocity measurements can be made; these measurements allow determination of correlation coefficients which are extremely important in turbulent flame studies. The simultaneous non-intrusive measurement of velocity and temperature, however, is a difficult task and only a few such experiments have been reported in the literature. Non-intrusive techniques which have been combined with LDV include Rayleigh scattering (Dibble *et al.*, 1981), Raman scattering (Lederman and Posillico, 1981; Warshaw *et al.*, 1981; Dibble *et al.*, 1984) and CARS (Fujii and Eguchi, 1983; Fujii *et al.*, 1984; Goss *et al.*, 1984a, 1984b, 1988; Chen *et al.*, 1988). The advantages of the CARS technique for joint scalar measurements are: (1) measurement of temperature in diverse flame environments; (2) combination with the LDV system; and (3) examination of the effects of particles upon combined measurements. The last advantage is quite significant in demonstrating the density-weighted effect which occurs with LDV measurements.

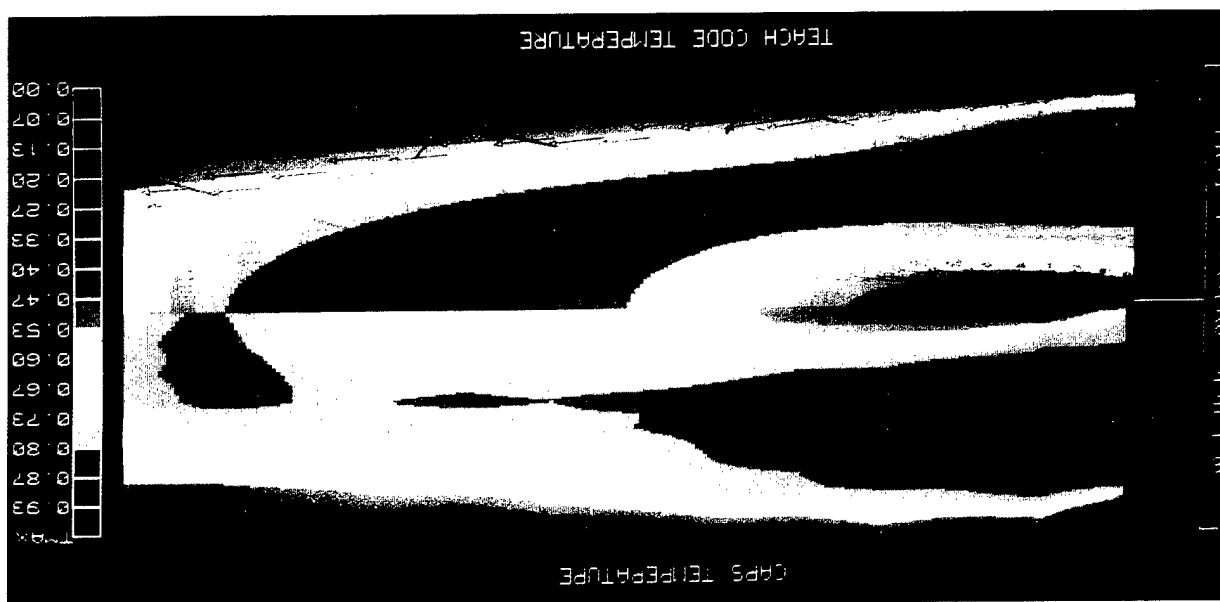


PLATE I Comparison of results from time-averaged CARS temperature measurements and TEACH-code predictions of temperature and velocity, with illustration of shed vortices (Switzer *et al.*, 1985).

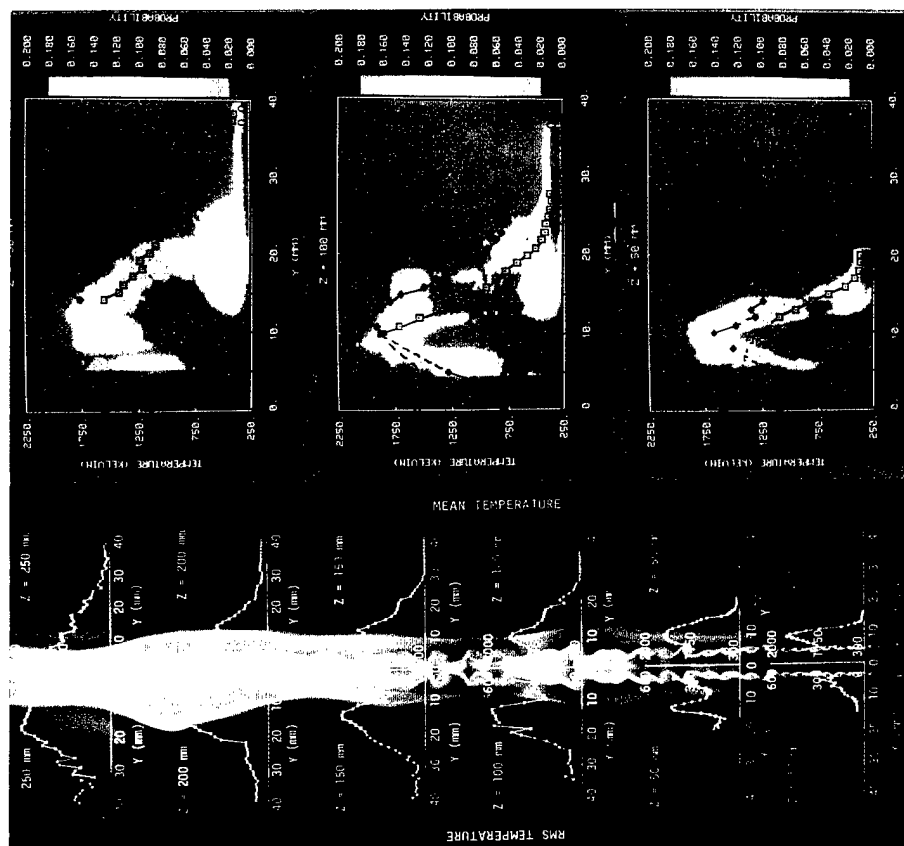


PLATE II Mean, r.m.s., and p.d.f. temperatures in a propane jet diffusion flame ($Re = 4000$) obtained by the CARS instrument (Goss *et al.*, 1989).

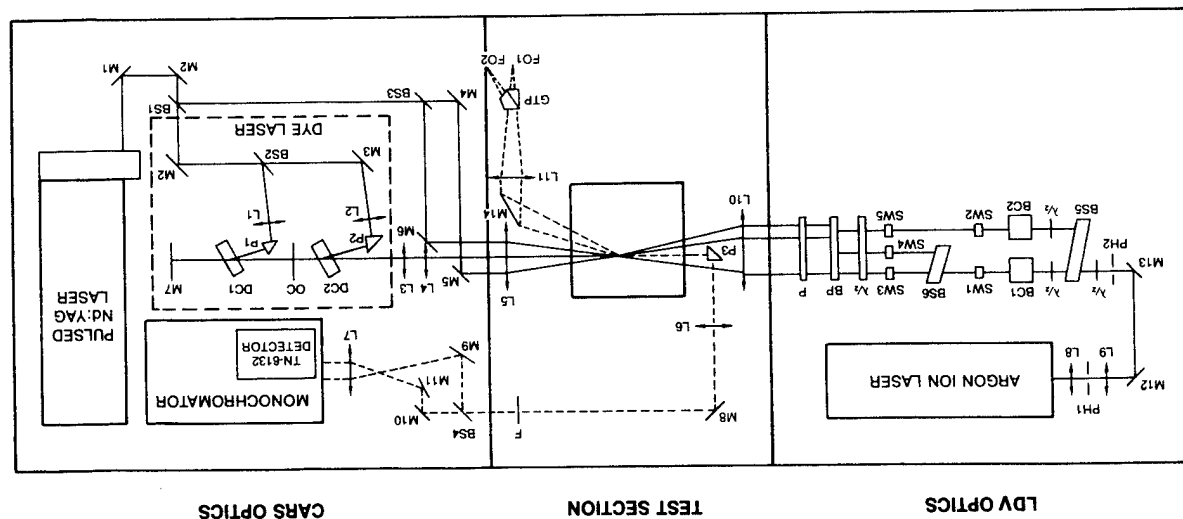


Figure 20 Optical arrangement of combined CARS-LDV instruments (Goss *et al.*, 1989). CARS optics: M1, M2, M3, M4, M5, M6, R_{max} 532 nm mirrors; BS1, BS3, 50% 532 nm beam splitters; BS2, 30% 532 nm beam splitter; M7, R_{max} 607 nm mirror; OC, output coupler 20% 607 nm mirror; L1, L2, 30 cm lens; L3, L4, 10 cm and 20 cm lenses (dye telescope); P1, P2, P3, right-angle prisms; L5, L6, 50 cm lenses; M8, M9, M10, M11, broad-band mirrors; F, 532 nm blocking filter; BS4, 3% beam splitter; L7, 10 cm cylindrical lens. LDV optics: L8, L9, 5 cm lenses; PH1, PH2, 100 μ m pinholes; M12, M13, R_{max} 514.5 nm mirrors; BS5, BS6, 50% beam splitters; $\lambda/2$, half-wave plates; BC1, BC2, 35 and 40 mHz Bragg cells; SW1, SW2, SW3, SW4, SW5, steering wedges; BP, beam positioning prisms; P, periscope; L10, 50 cm focusing lens; M14, collection mirror; L11, 20 cm collection lens; GTP, Glan-Thompson prism; FO1, FO2, fibre-optic cables.

A. LDV instrument

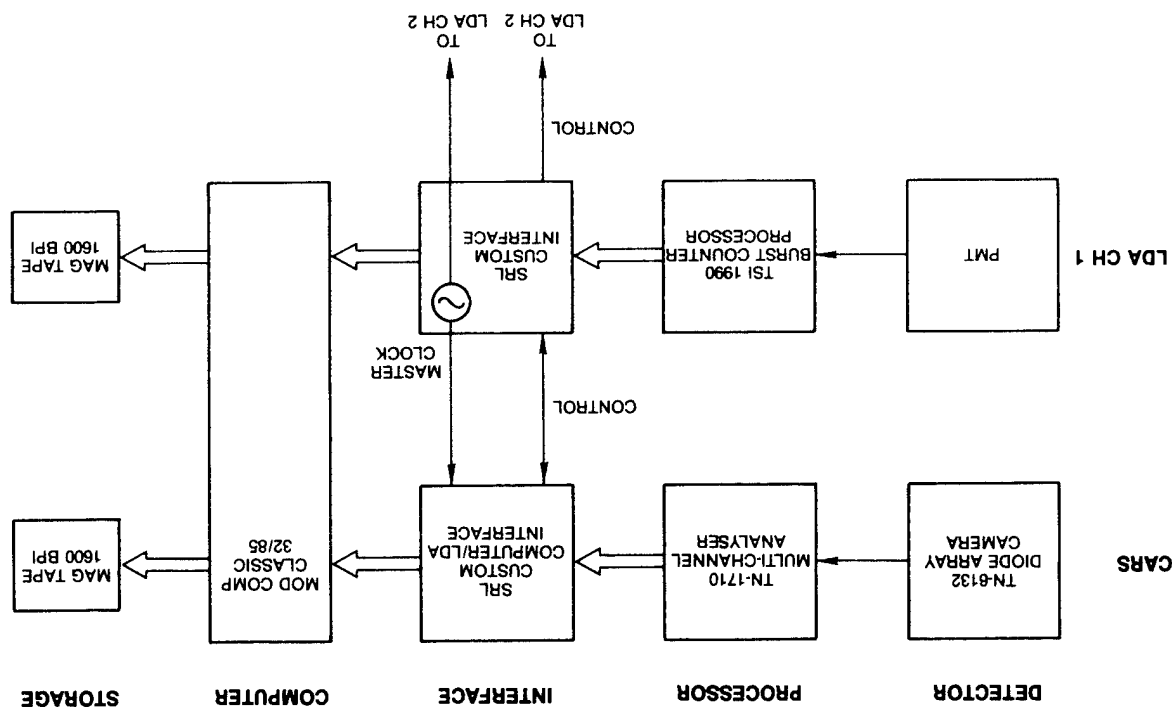
The LDV system (Lightman *et al.*, 1983) as combined with the CARS system at WPAFB is shown in Figures 20 and 21. This two-component real-firing system is based upon polarization separation of the velocity components. The 488 nm line from a Spectra-Physics argon ion laser is used as the light source, with $\sim 1 \mu$ m diameter alumina (Al_2O_3) particles serving as the scattering medium. The Doppler burst is collected in the forward direction slightly off-axis ($\sim 10^\circ$) to minimize interference with the CARS beams. The two velocity components are separated by a Glan-Thompson polarization beam splitter and sent to two 1990 TSI burst counter processors through fibre optics. Dual Bragg cells having a 5 MHz frequency difference are employed to remove directional ambiguities and maintain the Doppler burst frequencies in an optimum range for the velocities under study.

B. Description of combined instrument

The combined CARS-LDV instrument was arranged in such a way that changes to the optical systems were minimized. The two instruments are aligned head-on and have no common optics, allowing them to be operated separately or jointly without interference. Joint measurements must be not only temporally but also spatially coincident. To align the three beams from each system at a common focus, a 100 μ m circular aperture was used. The focus of each set of beams was determined first by examining the extinction of the beam by the edge of the aperture which acts as a knife edge. The power in the CARS laser was reduced from the level of normal operations by detuning the Q switch from the optimum delay; thus, the thermal loading and divergence of the Nd:YAG beams could be maintained while lowering the laser power. The main focusing lens of both the CARS and the LDV systems was adjusted to ensure that the foci would occur at a common point. The six beams were then crossed and aligned through the 100 μ m aperture. Once this alignment was complete, the system could not be adjusted because of the possibility of uncrossing the two sample volumes.

Basic operation of the CARS instrument involves repetitive firing of the Nd:YAG laser at a 10 Hz rate, while operation of the LDV instrument involves measuring the Doppler burst from a seed particle as it traverses the sample volume. This passage of the seed particle is a near-random event and is dependent upon the seeding as well as the flow conditions of the study. Since CARS measurements take place at 100 ms intervals, the problem lies in synchronizing a random and a repetitive event. To understand the magnitude of this problem, one must examine the firing sequence of the Nd:YAG

Figure 21 Schematic diagram of data acquisition components of CARS and LDV instruments (Goss *et al.*, 1989). CARS electronics include TN6132 camera, Tracor-Northern TN1710 multichannel analyser, custom-built computer/LDV interface, ModComp 32/85 Classic computer, LDV electronics include photomultiplier, TSI 1990 burst counter processors, custom-built LDV interface, ModComp computer.



laser, as shown in Figure 22. This sequence consists of discharging the flashlamps to obtain a population inversion and then pulsing the Q switch to depopulate the upper laser levels, which provides a giant laser pulse. The time separation between the flashlamp discharge and the Q-switch firing is 250 μ s. The Q-switch firing can be varied by ± 50 μ s about the 250 μ s value, with a loss of only $\sim 25\%$ power. However, because of thermal loading of the Nd:YAG laser rods by the flashlamp discharge, which affects the divergence of the laser beam, the Nd:YAG laser must be fired at a repetition rate of 8–14 Hz to prevent power loss; thus, the Nd:YAG laser is not a pulse-on-demand laser. Therefore, three different schemes were incorporated into the combined CARS-LDV instrument to allow simultaneous measurements.

The simplest of these approaches, mode 1, consists of permitting the two instruments to free-run. In order to establish time coincidence, a common clock is used for the instruments; when a measurement is made, the data are tagged with the time. Analysis software is then employed to sort the independent data according to time, based upon the tagword. This approach allows the two instruments to acquire data independently, each at its maximum rate. The disadvantage of this mode is that the LDV instrument acquires data at a much higher rate than the 10 Hz CARS system and, therefore, much of the LDV data is not sufficiently close in time to a CARS event to be considered coincident data. To circumvent this problem, a 10 ms gate was incorporated to window the LDV data acquisition about the CARS laser firing; this gate opens ~ 5 ms before the flashlamp discharge and remains open ~ 5 ms after laser firing. The Nd:YAG laser is fired even if no LDV realization has occurred in the gate.

In mode 2, LDV data acquisition is inhibited until the CARS flashlamp is ready to fire. As in mode 1, a 10 ms gate is opened about the flashlamp firing, and LDV realizations can be transferred only during this gate. If a velocity realization occurs, the flashlamps are discharged; 250 μ s later the Q switch fires. This guarantees at least one simultaneous measurement with

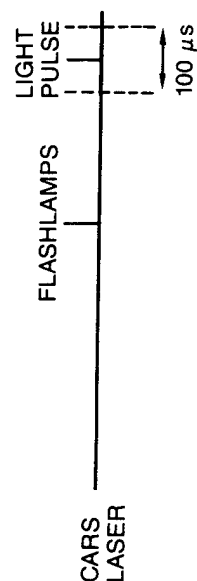


Figure 22 Firing sequence of the Nd:YAG laser used in the CARS system (Goss *et al.*, 1989).

a time coincidence of 250 μs . If no LDV realization occurs, the flashlamps are discharged at the end of the window, but—unlike in mode 1—the Q switch is not fired. Discharging the flashlamps guarantees that the thermal loading of the laser cavity (and, thus, the power level) will be maintained. All LDV realizations are collected during this 10 ms window to permit examination of all time coincidences. This method allows a moderate time coincidence with maximum data rates for both instruments and is best suited for low- to moderate-flow velocity studies.

Mode 3 is the most stringent in terms of both time coincidence and simultaneous data rates. In this approach the LDV system is gated as in mode 2, with the exception that the gate is only 100 μs wide and centred on the optimum 250 μs delay between the flashlamp and the Q switch firing. The flashlamps are discharged repeatedly and the narrow 100 μs gate opened 200 μs after each discharge. Any LDV realization occurring within this gate will fire the Q switch and allow a CARS measurement to be made. The coincidence time in this case is the time required by the TSI counters to process the Doppler burst and transmit a data-ready signal to the Tracor interface electronics which fires the Q switch. This entire process occurs in $\sim 4 \mu\text{s}$. Thus, mode 3 provides the optimum simultaneous measurement times and is well suited for moderate- to high-velocity flow studies. These advantages are not gained without sacrifice, however. The CARS laser fires at a 10 Hz rate, and during each pulse a 100 μs gate is opened for LDV realizations; thus, the LDV system is allowed to store data only over a period of 1 ms s^{-1} . Data acquisition rates are, thus, reduced by a factor of 100 as compared to those of modes 1 and 2. Mode 3 is, therefore, recommended only for those studies where flow rates preclude use of modes 1 and 2.

The flexibility of the CARS-LDV electronics and software allows the operator to choose one of these three modes at the CARS control console by loading an appropriate program from disk. In all three modes, the time tagword is stored along with the data during acquisition. After the raw LDV period data have been converted to velocities and the CARS spectral data to temperatures, the processed data are sorted according to the time tagword. The analysis software sorts the data about a time coincidence window which is selected by the operator and allows the velocity-temperature correlation to be studied as a function of this window. Correlation coefficients such as \overline{uT} , \overline{vT} , and \overline{uv} can then be determined for the flow field under study.

C. Particle effects

One of the major problems associated with combining the CARS and LDV instruments is the use of seed particles for the velocity measurement.

Because of the directionality of the CARS beams, Mie scattering from the particles which would preclude the use of ordinary Raman scattering is not a problem for the CARS technique. Seeds such as alumina, however, can adversely affect CARS data in numerous ways, including attenuation of the laser beams (and, thus, lowering of the CARS signal), production of a non-resonant signal whose contribution could increase the fitted temperature, and—in the worst case—catastrophic breakdown at the particle surface. Such breakdown occurs when a particle of sufficient size passes through the sample volume during Nd:YAG laser firing; the surface of the particle is heated to an extreme temperature, and a plasma is formed which acts to absorb the pump laser light, thus robbing the CARS process of needed power. The probability of breakdown occurring is dependent upon particle size and power in the laser beams; this effect can be minimized by employing the smallest possible seed particles and the lowest laser power. Breakdown is most notable inside a cold fuel jet where seed and gas densities are relatively large. When breakdown occurs, the CARS data are rejected and excluded from the analysis. This is accomplished by monitoring the amount of scattered laser light around the sample volume. If the scattered-light level reaches a preset threshold, then breakdown is assumed to have occurred and the data are rejected. Several studies have been conducted to determine whether the CARS signal can be utilized when breakdown occurs. In the case of coal ash, an increase in the non-resonant-background signal was observed upon breakdown (Beiting, 1985). In a more recent study involving liquid droplets, it was determined that breakdown contributed a direct-current level which could be accurately fitted and removed (Dunn-Rankin *et al.*, 1988).

D. Acquisition and analysis software

Approaches to mating the CARS and LDV instruments have involved combining the instruments both optically and electronically in such a way that a minimum of changes would be required. However, incorporation of the various acquisition modes outlined above has necessitated extensive changes in the interface electronics and acquisition software. The heart of the acquisition software is a machine language program which runs on the multichannel analyser control unit and controls (1) the transfer of CARS spectral data to a minicomputer system, (2) the firing sequence for the Nd:YAG laser, and (3) the necessary gating pulses to the LDV interfaces based upon the particular acquisition mode selected.

The timing schemes for the three acquisition modes are shown in Figure 23. When the program is initiated, the system is in the independent acquisition mode, which allows the operator to observe the CARS signal strength

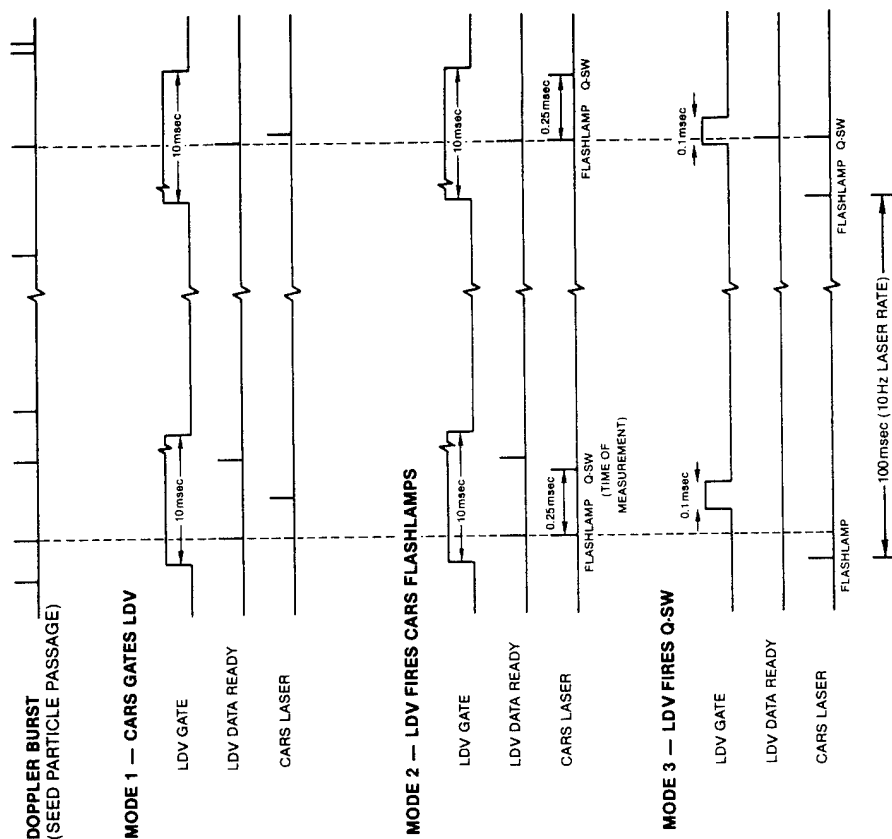


Figure 23 Timing diagram for three acquisition modes of the combined CARS-LDV Instrument (Goss *et al.*, 1989). Mode 1 LDV—data is windowed about a CARS event with a large 10 ms window. Both systems are essentially independent. Mode 2—LDV is windowed with a 10 ms window, and the CARS flashlamp fires if LDV realization occurs within the window. The maximum time coincidence is 250 μ s. Mode 3—the CARS flashlamp is fired independently of LDV. The 100 μ s window is open about the optimum delay for the Q switch. If LDV realization occurs, then the Q switch is fired. The maximum time coincidence is 4 μ s.

and determine whether optical adjustments must be made. By loading a different program, the operator can select the acquisition mode to be employed. The acquisition software is similar for the three modes. In mode 1, the program first opens a 10 ms gate to allow LDV data acquisition, waits 6 ms to discharge the flashlamps and another 250 μ s to fire the Q switch, and then interrogates the minicomputer interface to determine whether a data transfer request has been issued. The gate to the LDV system is open for ~ 10 ms, corresponding to the maximum window for variation of the 10 Hz Nd:YAG laser firing which results in no power loss. If the data transfer request from the minicomputer has been issued, the CARS spectral data are transferred in ~ 46 ms. The program must then wait another 55 ms before repeating the sequence. If no data transfer request has been sent, the multichannel analyser waits the full 100 ms by counting to itself. The last word in the CARS data is overwritten with the contents of the common clock (time tagword) before transfer.

In mode 2 the machine language program opens the 10 ms window and waits for a velocity data-ready signal from the LDV burst counter processors. If the signal is detected, the flashlamps are discharged and, 250 μ s later, the Q switch fires. The CARS spectral information is then transferred to the minicomputer. If a velocity data-ready signal has not been detected by the end of the 10 ms window, the flashlamps are discharged; however, the Q switch does not fire and no CARS data are transferred. In either case, the program waits another 90 ms, and the cycle is repeated.

In mode 3 the machine language program discharges the flashlamps, waits 200 μ s, and then opens a 100 μ s gate. If a velocity data-ready signal is detected during this gate, the Q switch is fired and the data subsequently transferred to the minicomputer. If no data-ready signal is detected, the program counts to itself for ~ 99 ms, and the process is repeated.

The acquisition software on the minicomputer for the CARS and LDV instruments is similar and controls the positioning of the burner system, the number of spatial locations at which data are to be taken, and the number of data points to be acquired at each location. Interface control is mainly the function of the multichannel analyser program, but analysis of the raw spectral and period data is conducted exclusively on the minicomputer.

The first steps in processing the raw data involve fitting the CARS spectra data to obtain temperatures and converting the period data from the TSI 1990 burst counters into velocities. The time tagword associated with each data point is then extracted and the data sorted according to time. Once these tasks have been accomplished, the mean, r.m.s., and correlation values between temperature and velocity components can be determined. By recording the time associated with each measurement, the simultaneous

CARS-LDV data can be examined as a function of the coincidence time. This allows investigation of the autocorrelations between the temperature and the velocity components. The reduced data can then be displayed as needed for study and presentation.

E. Seed effects

Individual CARS and LDV measurements can be used in conjunction with conditional-sampling techniques to determine whether seed effects are occurring in the combined CARS-LDV system. A CARS-LDV measurement is initiated by introducing a seed particle into the measurement volume during the time interval (window) over which the CARS laser is ready to fire. Since the distribution of seed particles in the flow determines the measurement sampling statistics, bias effects due to seeding may occur. When the LDV instrument alone is employed, the presence and magnitude of seed biasing effects cannot be easily assessed since accurate unbiased data are required for comparison. A CARS temperature measurement made simultaneously with an LDV measurement constitutes a conditional measurement since it is dependent upon the presence of seeds. However, unconditional CARS temperatures can be measured independently at a constant rate. These unconditional measurements will be unbiased as long as the measurement frequency (10 Hz) is not locked to an instability frequency in the flow. By comparing the mean and probability distribution functions (p.d.f.s) for conditional and unconditional temperature measurements, seed effects can be examined under different test conditions.

Three different seed biases are known to occur in LDV measurements in cold flows. First, if the seed particles are too large to track the flow field, then the velocity measurements will be biased towards low velocities. It is generally accepted that such errors do not exist in turbulent subsonic flows when the particles are $< 1 \mu\text{m}$ in diameter. The second type of bias is caused by a variation in seed density which results from non-uniform seeding. This error can occur even in the presence of only one flow stream; for example, a uniformly seeded jet ejected into still room air entrains unseeded air into the plume which can cause the velocities in the shear layer to be biased towards higher values since the higher velocities from the inner region of the jet are more likely to be measured. Biases due to non-uniform seeding have been reported in the literature (Durst, 1984; Yule *et al.*, 1980). The third type of bias occurs in a uniformly seeded flow (McLaughlin and Tiederman, 1973; Edwards and Baratuci, 1984; Chen and Lightman, 1985) and results from the higher probability that a seed particle will be present in faster-moving fluid elements than in slower-moving ones. This causes the velocity p.d.f.s and the average velocity to be biased towards the higher

values. These bias effects which are known to occur in cold flows can also occur in combustion flows.

Additional bias effects can occur as a result of combustion. High flame temperatures can cause a reduction in the effective scattering cross-sections of certain seed materials, which results in a higher probability of sampling low-temperature fluid elements. Such an effect was observed for TiO_2 (Ebrahimi and Kleine, 1977). Figure 24 demonstrates that the CARS-LDV system—through the use of conditional sampling—can detect this effect. The measurements depicted in Figure 24 were made on a Bunsen burner-type premixed propane-air flame. Each temperature p.d.f. contains ~ 1500 individual measured temperatures. The conditional p.d.f.s in column C, as compared to the unconditioned ones in column A, are strongly weighted towards lower temperatures. For example, the high-temperature peak shown in the unconditional measurements at $r = 0$ is extremely weak in the conditional p.d.f. Biasing of the conditional measurements towards low temperatures is also evident in the mean temperatures shown in Figure 24. However, the bias in the width (r.m.s. value) of the distribution is dependent upon the actual shape of the unconditional p.d.f.

Another bias effect which may occur in flames is caused by variation in gas density. Seed density is expected to be proportional to gas density; therefore, if samples cannot be collected at a constant rate, the probability of measuring low-temperature, high-density fluid elements is higher than that for measuring high-temperature, low-density ones. This bias effect may be somewhat offset by the McLaughlin-Tiederman high-velocity bias if the lower-density fluid elements are moving faster than the higher-density ones. However, these two bias effects need not cancel each other. A gas density bias effect has been suggested (Magill *et al.*, 1982) to explain a bias towards low-velocity, low-temperature fluid elements when high-velocity, high-temperature fluid elements were known to be present more than 60% of the time. Recently, a Favre-averaged p.d.f. (Heitor *et al.*, 1984) was computed from unconditional (constant sampling rate) thermocouple measurements and the results compared with a p.d.f. obtained from conditionally sampled simultaneous LDV and thermocouple measurements. Although the data samples in this study were not sufficiently large to rule out sampling errors, the Favre-averaged and conditional p.d.f.s were similar.

The low-temperature bias noted in Figure 24 may be due, in part, to gas density variations. To determine whether this is the case, the unconditional p.d.f.s were density weighted using

$$B_{Fi} = \frac{\bar{T}_F B_{ui}}{T_i}, \quad \bar{T}_i = \frac{1}{1/T_u} \quad (17)$$

where B_{Fi} is the density-weighted probability of measuring a temperature

Figure 24 CARS temperature p.d.f.s obtained at an axial location of 21.5 mm and radial locations of 0, 4 and 6 mm (Goss *et al.*, 1988). Column A represents the CARS temperatures measured independently of LDV velocities (unconditional). Column B represents the calculated Favre average of the temperature p.d.f.s in column A, and column C represents the CARS temperatures measured simultaneously with LDV velocities using TiO_2 seed particles (conditional).

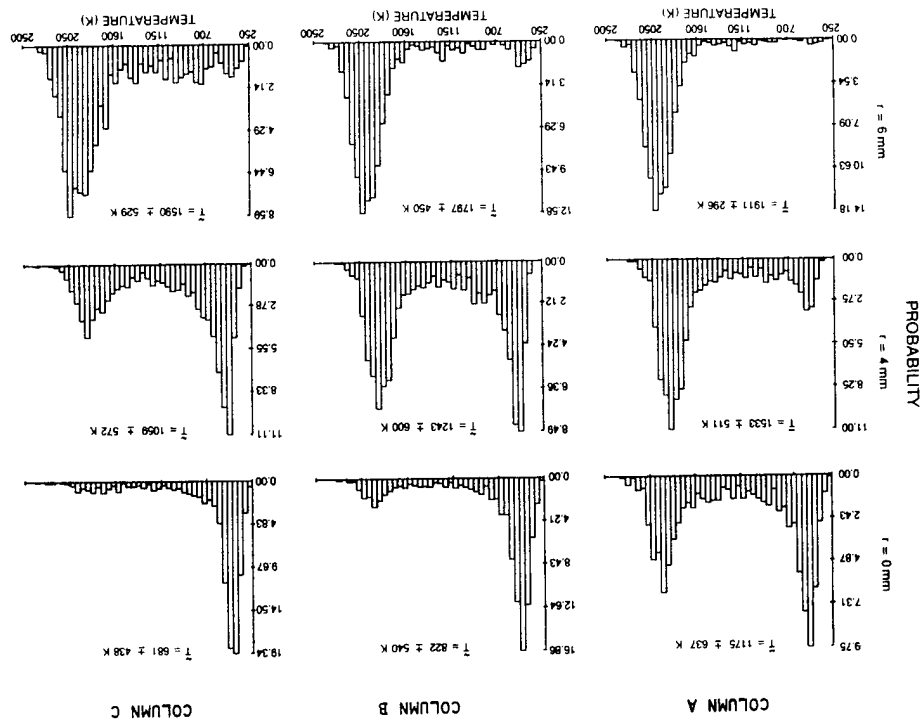
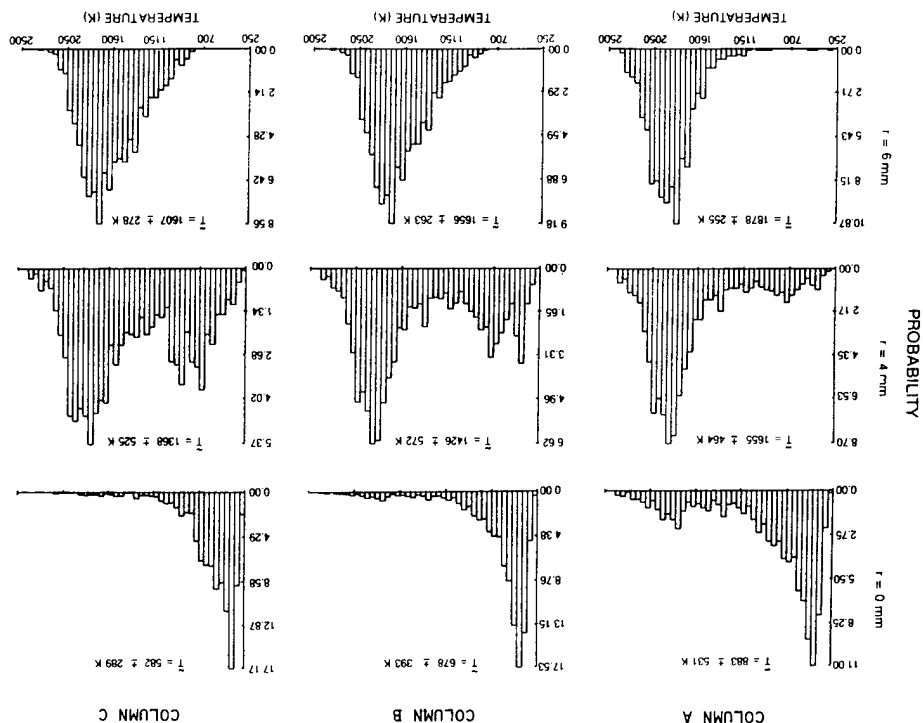


Figure 25 CARS temperature p.d.f.s obtained at an axial location of 15 mm and radial locations of 0, 4 and 6 mm (Goss *et al.*, 1988). Column A represents CARS temperature measurements made independently of LDV measurements (unconditional). Column B represents the calculated Favre average of temperature p.d.f.s in column A, and column C represents CARS temperature measurements made simultaneously with LDV measurements using Al_2O_3 seed particles (conditional).



4. CARS Instrumentation

T_i , T_F the Favre-averaged or density-weighted temperature, T_u the unconditional temperature, and B_{ui} the unconditional probability of measuring temperature T_i . A comparison of the p.d.f.s in columns B and C in Figure 24 reveals that the low temperatures are more pronounced than would be expected as a result of density weighting. Indeed, the drop-out rate of the LDV data taken with TiO_2 was almost a factor of three higher than that expected under the assumption that seed particle density varies with gas density. The data in Figure 24 indicate that TiO_2 is not a good seed particle for combusting flows.

Figure 25, which contains unconditional and conditional temperature p.d.f.s measured in a Bunsen burner flame, illustrates the density bias error which may result from the use of Al_2O_3 seed particles. The average conditional temperatures are more than 270 K lower than the unconditional ones, and the p.d.f.s are weighted towards low-temperature, high-density values. Comparison of the shapes of the density-weighted p.d.f.s (column B) and the conditional p.d.f.s (column C) lends strong support to the proposition that the measurements conditioned by the presence of seed particles are density weighted. Al_2O_3 is, thus, a better choice for seed particles than TiO_2 .

F. Flame measurements with combined instrument

1. Bunsen burner studies

One of the earliest studies with a combined CARS-LDV system was conducted on a turbulent Bunsen burner flame (Goss *et al.*, 1988). This flame was chosen for study because of previous work which demonstrated that large velocity-temperature correlations exist around the reaction zone. In two separate studies using an LDV-thermocouple instrument, both positive and negative correlations were observed in various regions of the flame (Yanagi and Mimura, 1981; Tanaka and Yanagi, 1983).

The average and r.m.s. temperatures and axial and radial velocities at two axial positions are plotted in Figures 26–28. These data were collected with the CARS and LDV systems operating independently. Superimposed on these plots is a time-averaged display of the premixed flame obtained from a long-exposure flame photograph. At an axial position of 15 mm, just inside the visible flame region, the temperature in Figure 26 decreases dramatically in the central region of the reaction zone and peaks in the surrounding plume, whereas the r.m.s. fluctuations peak at the centre and decrease sharply in the plume region. As can be seen in Figure 27, at this axial location the axial velocity and corresponding fluctuation are nearly constant throughout most of the flame. The radial-velocity profile at

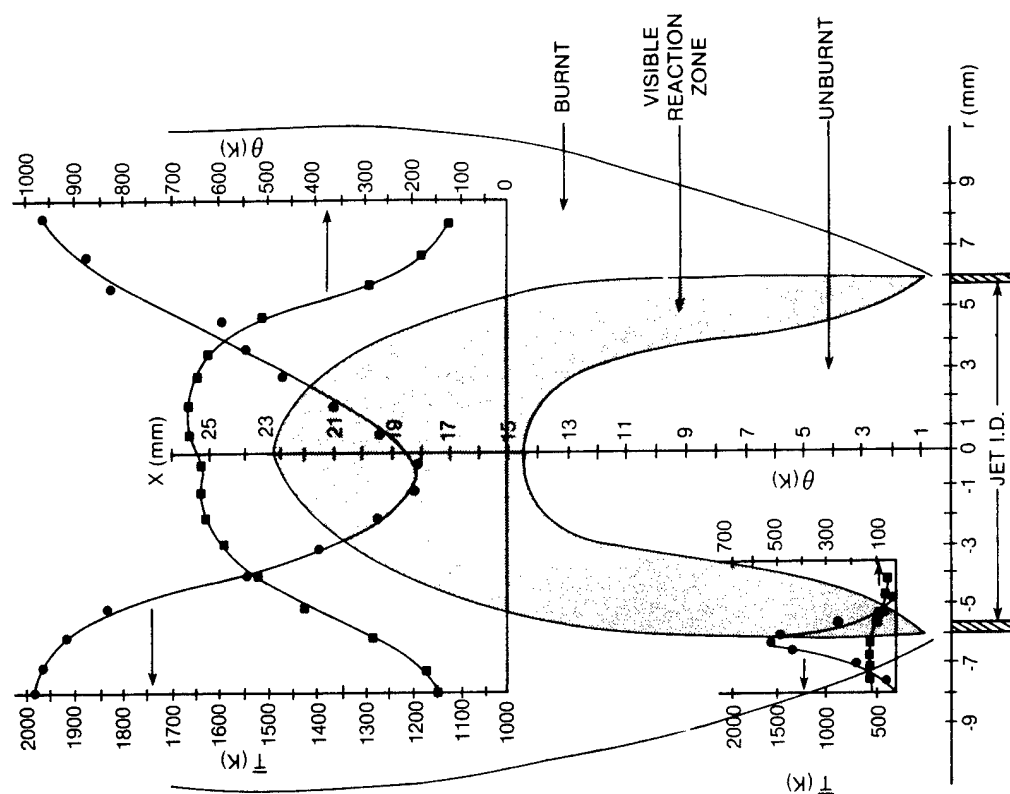


Figure 26 Time-averaged (\bar{T}) and r.m.s. (θ) temperature profiles at axial locations of 1.5 and 15 mm in a Bunsen burner flame (Goss *et al.*, 1988). CARS temperature measurements were made independently of LDV measurements at a rate of 10 Hz.

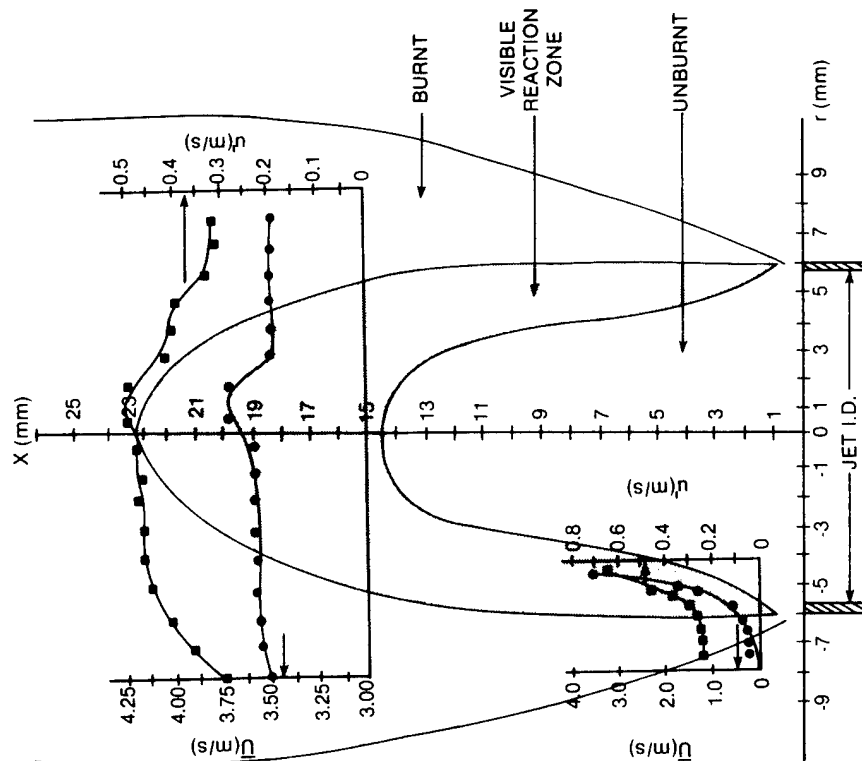


Figure 27 Time-averaged (\bar{U}) and r.m.s. (u') axial velocity profiles at axial locations of 1.5 and 15 mm in a Bunsen burner flame (Goss *et al.*, 1988). LDV measurements were made independently of CARS measurements at an average rate of 500 realizations s^{-1} .

15 mm, shown in Figure 28, is similar to the temperature profile, with a peak occurring just outside the flame zone very near the edge of the burner and the fluctuations being nearly flat.

The axial and radial velocity-temperature correlations which were determined from measurements by the CARS-LDV instrument at the base of the Bunsen burner (Figures 29 and 30) show trends which are the same as those observed by other investigators (Tanaka and Yanagi, 1983)—a negative correlation between axial velocity and temperature at the interface of the reaction zone and the burnt mixture and a positive correlation between

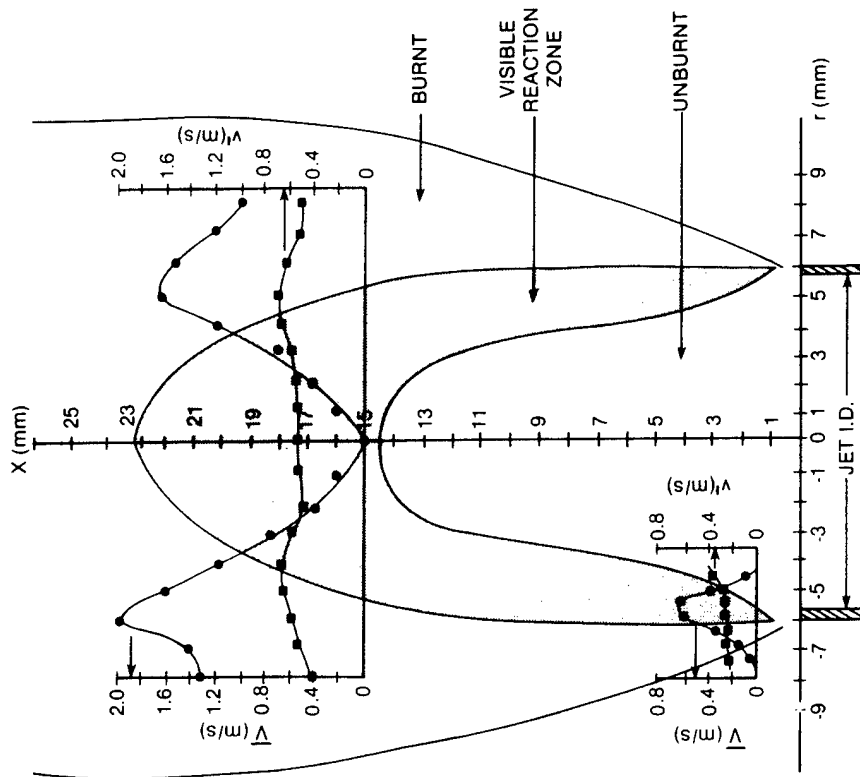


Figure 28 Time-averaged (\bar{V}) and r.m.s. (v') radial velocity profiles at axial locations of 1.5 and 15 mm in a Bunsen burner flame (Goss *et al.*, 1988). LDV measurements were made independently of CARS measurements at an average rate of 500 realizations s^{-1} .

radial velocity and temperature very near the same radial location. These trends are apparent in the 1.5 mm profiles shown in Figures 29 and 30.

Figures 29 and 30 also show velocity-temperature correlation profiles at the 15 mm position near the tip of the reaction zone. The axial velocity-temperature correlation displays a minimum at the centreline (where the average temperature is a minimum) and peaks near the plume-reaction zone interface. A maximum of 81 is observed, indicating strong positive correlation (high temperature, high velocity) in this region. Since the mean temperature gradient is also positive at this location, counter-gradient transport is occurring.

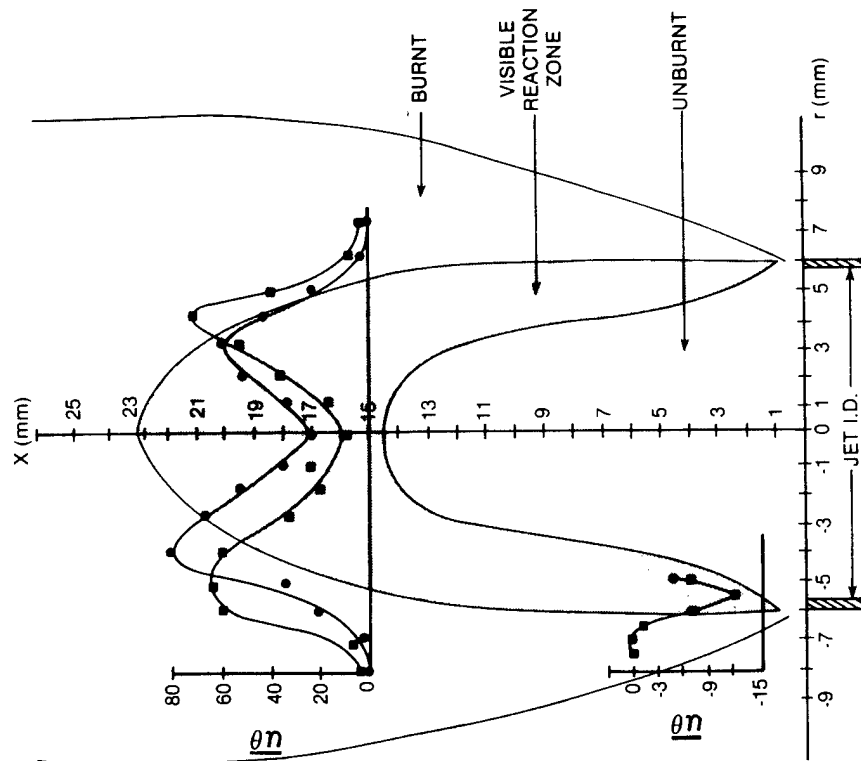


Figure 29 Favre (■) and Reynolds (●) averaged axial velocity-temperature correlations for a Bunsen burner flame about the mean at axial locations of 1.5 and 15 mm (Goss *et al.*, 1988). Al_2O_3 particles were used to seed the flow.

As discussed in Section VII.E, the velocity measurements appear to be density weighted when alumina seed particles are used and, thus, are Favre averaged. However, since temperature is determined simultaneously with velocity, the Reynolds-averaged correlations can be determined by correcting the individual measurements using

$$\overline{u\theta} = \frac{\sum_{i=1}^N (\bar{T}_i/M_i) u_i'' \bar{\theta}_i}{\sum_{i=1}^N \bar{T}_i/M_i} \quad (18)$$

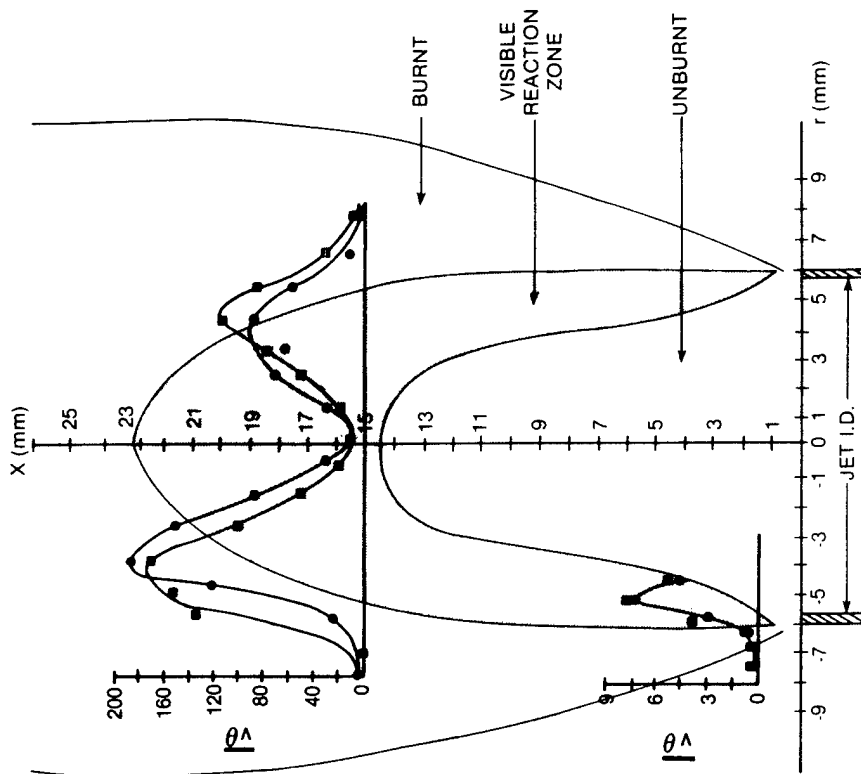


Figure 30 Favre (■) and Reynolds (●) averaged radial velocity-temperature correlations for a Bunsen burner flame about the mean at axial locations of 1.5 and 15 mm (Goss *et al.*, 1988). The LDV measurements were made using Al_2O_3 particles.

where u_i'' is the axial-velocity fluctuation about the Favre average of the i th measurement, \bar{T}_i the density-weighted i th measured temperature, $\bar{\theta}_i$ the i th measured temperature fluctuation about the Favre average, M_i the molecular weight of the gases during the i th measurement and N the total number of measurements. It was estimated that the molecular weights of the mixture and products for this premixed flame varied by only 1.5%. Thus, for the calculations using equation (18), the molecular weight is assumed to be constant, which causes no appreciable error. Equation (18) allows a direct comparison between the Reynolds- and Favre-averaged correlations.

The results of Figures 29 and 30 show the magnitude of the correlations to be lower in the density-weighted case, with the maxima being shifted from just inside the reaction zone-plume interface to the right of the interface. The difference in the magnitude of the correlations due to density weighting can vary by as much as a factor of 2. The observed shift in the maxima is of the order of 1 mm. The effect upon the radial and axial correlations is quite similar. Both an amplitude and a spatial difference are observed between the density-biased and corrected radial correlations. The amplitude difference in the radial-correlation case is somewhat smaller, ~ 1.4 ; but the spatial shift of the maxima is approximately the same, 1 mm. Thus, while the general features of the density-weighted correlations are the same as those of the corrected correlations, the amplitudes as well as the spatial locations of the maxima are different and must be taken into account for an accurate determination of the correlations.

2. Jet diffusion flame

To demonstrate the capabilities of the combined CARS-LDV instrument and to complement earlier CARS studies (Roquemore *et al.*, 1989), a propane jet diffusion flame was chosen for examination (Goss *et al.*, 1989). The burner set-up used for this flame consisted of a contoured 1 cm fuel jet surrounded by a 24 cm co-annular air jet. The fuel employed was propane at a flow rate of 8.5 standard litres min^{-1} . An air jet velocity of 15 cm s^{-1} was employed to reduce room air disturbances. Flow visualization studies on this flame have indicated the presence of large toroidal vortices which form outside the visible flame zone (Roquemore *et al.*, 1989). These vortices interact with the flame and are responsible for low-frequency oscillations or flame flicker. The vortices are believed to be the result of a Kelvin-Helmholtz-type instability which is formed by a buoyancy-driven shear layer. A sheet-lighting visualization photograph of the jet diffusion flame is shown in Colour Plate II. Superimposed on this photograph are the results of independent CARS measurements. The interaction between the outside vortices and the flame surface is evident. Colour Plate II displays bimodal temperature p.d.f.s in the areas associated with the flame bulge. The temperature p.d.f. can be interpreted as the fraction of time during which the flame zone is located in the sample volume. The bimodal behaviour is typical of a flame surface which is oscillating as a function of time. The oscillations are evident in the temperature r.m.s. data as well.

Simultaneous CARS and LDV measurements were made at the 200 mm axial location because of the presence of the flame bulge in this area. The uT , \overline{vT} and \overline{wT} correlation coefficients are depicted in Figure 31. The uT data indicate a strong correlation between axial velocity and

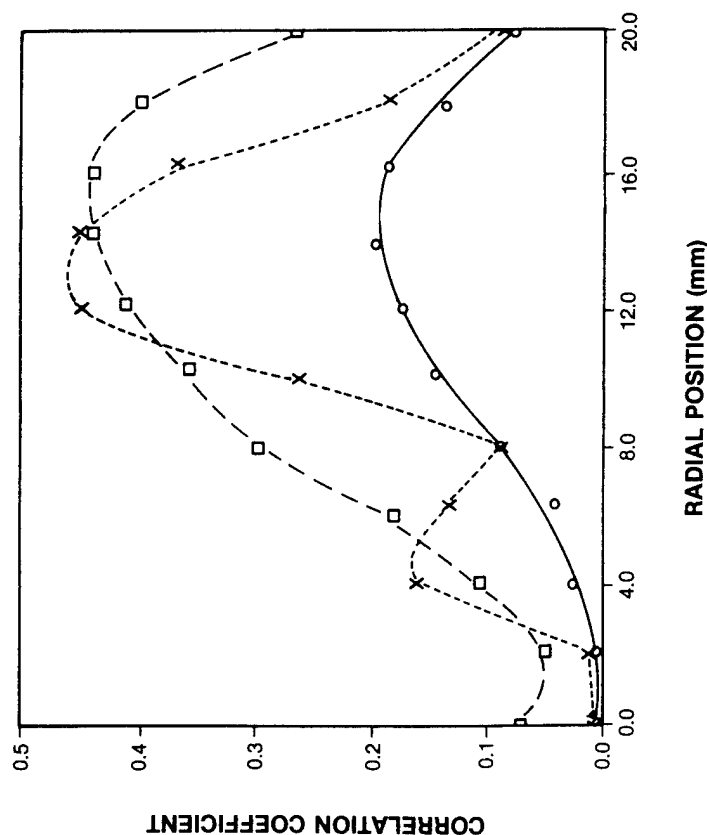


Figure 31 Correlation coefficients obtained at the 200 mm axial location in a propane jet diffusion flame (Goss *et al.*, 1989). ■, uT ; ●, vT ; ×, wT ; △, wv .

temperature in the flame bulge area associated with the acceleration of the flame front due to buoyancy. This large positive uT correlation is expected in a flow field dominated by buoyancy. The Reynolds shear stress \overline{uw} displays a similar behaviour, indicating the strong interaction between the outer vortices and the flame. The \overline{vT} correlation is lower in magnitude but peaks in the bulge vortex region. Thus, the dominance of the buoyancy effect in relatively low Reynolds number jet diffusion flames can be clearly seen from the visualization, independent temperature p.d.f., and simultaneous data.

3. Premixed "vee" gutter flame

Study of a "vee" gutter flame is important because of its strong association with real combustion devices (Beer and Chigier, 1972). This flame is relatively simple and yet can be used to simulate the fuel injection area in the primary zone of a combustor can or the flame holder of an afterburner.

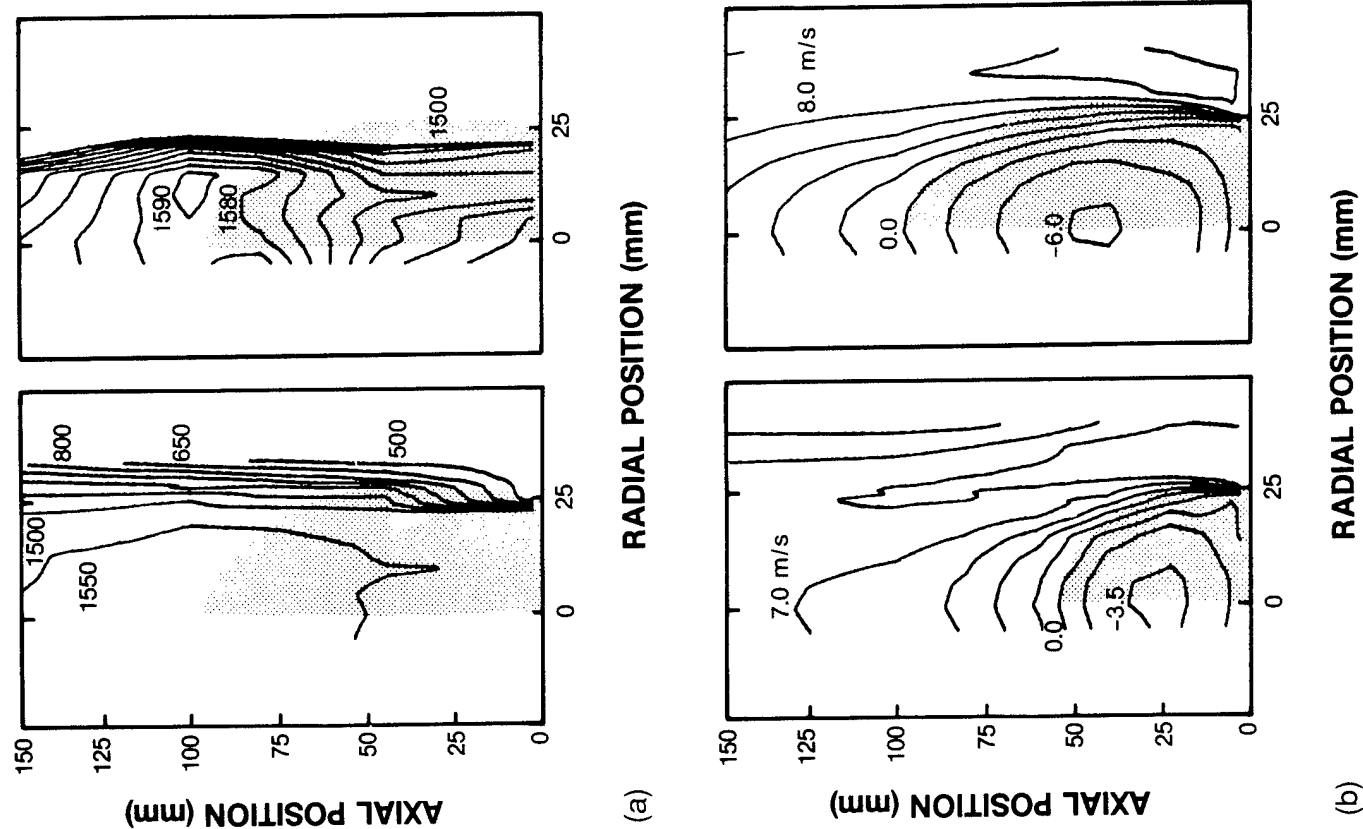
Interesting features of a "vee" gutter flame include a strong recirculating-zone structure, the surrounding shear layer which contains large-scale coherent structures, and the interaction of these coherent structures with the flame. Severe problems are associated with measuring the temperature in a recirculation zone by means of thermocouples because of the interaction of the recirculation flow field and the physical probe (Switzer *et al.*, 1985). Conventional velocity probes suffer not only from this interference but also from correlation factors due to the reacting flow. Thus, the integrated CARS-LDV system is an ideal tool for characterizing this reactive, recirculating flow field.

In this study both velocity and temperature fields were mapped in detail (Chen *et al.*, 1988). Their statistical values were compared in assessing the effects of heat release upon a recirculating flow field. It was found that heat release doubled the size and strength of the recirculation zone. Inside this zone, as shown in Figure 32, the temperature field was nearly constant, varying less than 100 K. The maximum entrainment velocity for the reactive flow was found to be smaller than that for a non-reactive flow having the same inlet velocity. This implies that the flame reduces the entrainment of air into the recirculation zone.

Turbulent thermal-exchange rates were determined through the joint temperature and velocity measurements shown in Figure 33. By means of a thermal-balance analysis, a global Damkoehler number of ~ 0.4 was deduced from the measurement. Since the flame under study was near the lean-blow-out limit, this global number represents the critical value for lean blow-out. The turbulent Prandtl number which is important in modeling this flow was also measured directly. Across the shear zone, this number was found to range from 0.55 to 0.8. The velocity-temperature correlation was found to have a maximum of 0.35, which is slightly higher than that of 0.27 for the case of swirling flow (Brum and Samuelsen, 1987). This maximum correlation occurs inside the flame brush. For comparison purposes, the maximum value for the cross-correlation of the axial-radial velocities was found to be ~ 0.6 and occurred in the shear zone. This was an indication that interaction was strong between the shear layer and flame brush and that these regions did not necessarily overlap at all times.

VIII. Future considerations

As discussed in Section VII, combination of the CARS and LDV techniques has greatly extended the capability to acquire data needed for combustor design codes. These studies will be continued, with emphasis upon spray combustion and future combination of a phase Doppler anemometer and



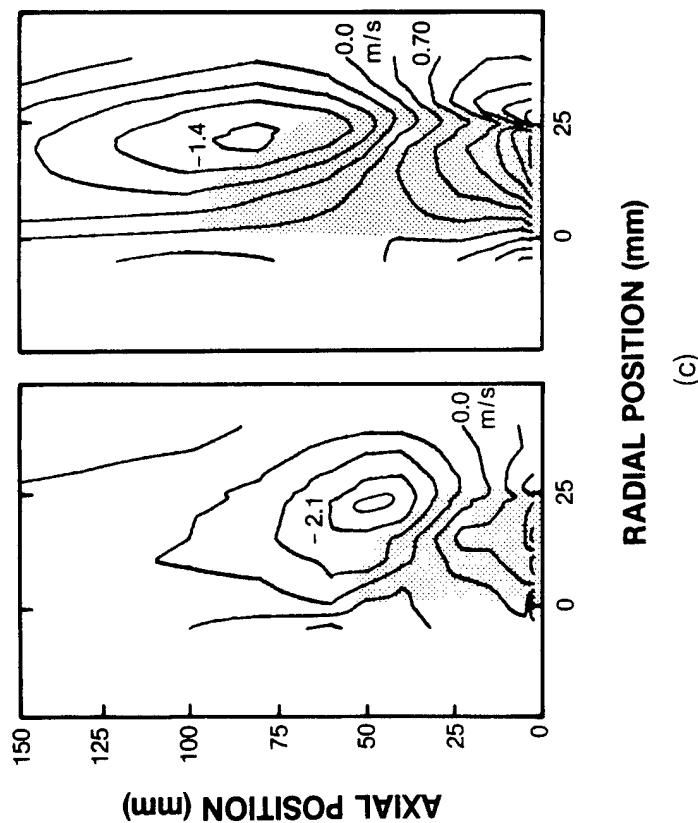


Figure 32 (a) Contour of mean temperature in the range 500–1550 K (left) and 1500–1590 K (right), (b) measured contours of axial velocity for cold flow (left) and reacting flow (right), and (c) measured contours of radial velocity for cold flow (left) and reacting flow (right) in a premixed "vee" gutter flame (Chen *et al.*, 1988). Shaded areas correspond to a bluff-body-stabilized recirculation zone.

a CARS instrument. The former instrument is capable of droplet size and velocity measurements and, thus, in combination with the latter will allow unique size-velocity-temperature correlations to be made in dense spray combustion environments. The phase Doppler instrument is being combined with the hardened CARS system at WPAFB for conducting tunnel tests. Major modifications to the optical layout will be required as well as to the electronics and software of the two systems. Combination of CARS and other techniques such as laser-induced fluorescence will allow temperature and major- and minor-species concentrations to be measured simultaneously.

The capabilities of the CARS technique would be extended by the development of more-powerful broad-band laser sources. Such an advance

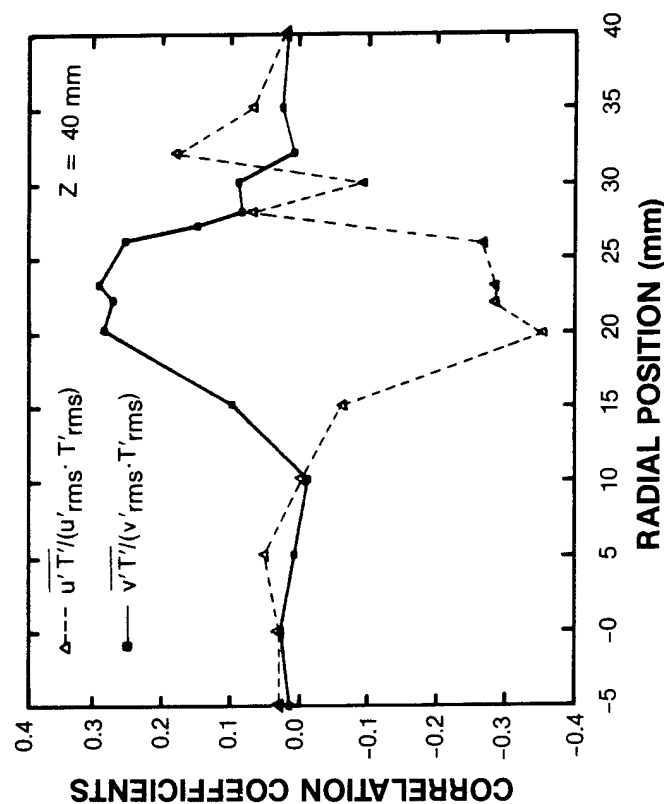


Figure 33 Measured correlation coefficients for temperature and velocity in a "vee" gutter flame; radial scans at $z = 40$ mm (Chen *et al.*, 1988).

in technology should aid the extension of the dual broad-band techniques for multiple species to atmospheric combustion processes (Eckbreth and Anderson, 1985, 1986). Presently these techniques are limited to high-pressure combustion situations because broad-band lasers are used as the pump in the CARS process. High-power broad-band lasers would allow these techniques to be applied to lower-pressure flame systems, which would result in a capability for monitoring several species during a single laser shot. Species which could be monitored in this manner include N_2 , N_2O , CO , HCN , NO , O_2 , CO_2 , hydrocarbons (CH stretching region) and H_2O .

In the CARS area another subject requiring investigation involves the fundamental spectroscopy of species of interest to combustion. As mentioned previously, because of the sensitivity of the CARS spectrum to spectral information (line widths and locations), it is imperative that fundamental spectroscopy studies be conducted. The spectroscopy of N_2 and the simple diatomic gases is relatively well known; however, the more-complex species such as H_2O and the hydrocarbon fuels require further

investigation. High-resolution CARS and inverse Raman studies should be conducted in this area.

Finally, higher repetition rate, high-power, pulsed-laser sources would allow the CARS technique to track the temperature variation in turbulent flames. Such laser sources would also aid in alleviating the low sampling rate problems associated with combined techniques. A recent article suggests a possible CARS system for this specific purpose (Deen and Thompson, 1989).

References

- Alden, M. and Wallin, S. (1985). *Appl. Optics* **24**, 3434.
- Alden, M., Edner, H. and Svanberg, S. (1983). *Physica Scripta* **27**, 29.
- Alden, M., Fredrickson, K. and Wallin, S. (1984). *9th Int. Conf. on Raman Spectroscopy, Tokyo*.
- Anderson, T. J., Dobbs, G. M. and Eckbreth, A. C. (1986). *Appl. Optics* **25**, 4076.
- Antcliff, R. R. (1987). NASA Contractor Report 178245, NASA Langley Research Center, Hampton, VA.
- Antcliff, R. R. and Jarret, O. (1983). AIAA Paper 83-1482, American Institute of Aeronautics and Astronautics, Washington, DC.
- Antcliff, R. R. and Jarret, O. (1987). *Rev. Sci. Instr.* **58**, 2075.
- Antcliff, R. R., Hillard, M. E. and Jarret, O. (1984). *Appl. Optics* **23**, 2369.
- Antcliff, R. R., Jarret, O. and Rogers, R. C. (1985). *J. Propul. Power* **1**, 205.
- Aron, K., Harris, L. E. and Fendell, J. (1983). *Appl. Optics* **22**, 3604.
- Attal, B., Schneep, O. O. and Taran, J. P. E. (1978). *Optics Commun.* **24**, 77.
- Attal, B., Pealat, M. and Taran, J. P. E. (1980). *Energy* **4**, 135.
- Barton, S. A. and Garneau, J. M. (1987). *Optics Lett.* **12**, 486.
- Bedue, R. P., Gastebois, R., Bailly, R., Pealat, M. and Taran, J. P. (1984). *Combust. Flame* **57**, 141.
- Beer, J. M. and Chigier, N. A. (1972). *Combustion Aerodynamics*. Wiley, New York.
- Beiting, E. J. (1985). *Appl. Optics* **24**, 3010.
- Beiting, E. J. (1986). *Appl. Optics* **25**, 1684.
- Boedeker, L. R. and Dobbs, G. M. (1985). *Combust. Sci. Technol.* **46**, 301.
- Bonamy, J., Bonamy, L. and Robert D. (1977). *J. Chem. Phys.* **67**, 4441.
- Boquillon, J. P., Pealat, M., Bourchard, P., Collin, G., Magre, P. and Taran, J. P. (1988). *Optics Lett.* **13**, 722.
- Brum, R. D. and Samuelsen, G. S. (1987). *Exp. Fluids* **5**, 95.
- Bunkin, A. F., Ivanov, S. G. and Koroteev, N. I. (1977). *Sov. Tech. Phys. Lett.* **3**, 182.
- Chen, T. H. and Lightman, A. J. (1985). *ASME Winter Annual Meeting* (Ed. A. Dybbs and P. A. Pfund), p. 231. ASME, New York.
- Chen, T. H., Goss, L. P., Trump, D. D. and Schmoll, W. J. (1988). AIAA Paper 88-3194, American Institute of Aeronautics and Astronautics, Washington, DC.
- Chitsomboon, T., Rogers, R. C., Northam, G. B., Jarret, O. and Antcliff, R. R. (1988). AIAA Paper 88-0095, American Institute of Aeronautics and Astronautics, Washington, DC.
- Davis, L. C., Marko, K. A. and Rimai, L. (1981). *Appl. Optics* **20**, 1685.
- Deen, M. J. and Thompson, E. D. (1989). *Appl. Optics* **28**, 1408.
- Dibble, R. M., Rambach, G. D., Hoilenback, R. E. and Ringland, J. T. (1981). *Fall Meeting of the Western States Section of the Combustion Institute, WSS/C 1*, pp. 81-84. The Combustion Institute, Pittsburgh.
- Dibble, R. M., Kollmann, W. and Schefer, R. W. (1984). *Combust. Flame* **55**, 307.
- Dobbs, G. M., Boedeker, L. R. and Eckbreth, A. C. (1985). *Technical Meeting of the Eastern States Section of the Combustion Institute, Philadelphia*.
- Druet, S. A. J. and Taran, J. P. E. (1981). *Prog. Quant. Electronics* **7**, 1.
- Dunn-Rankin, D., Switzer, G. L., Obringer, C. A. and Jackson, T. A. (1988). *Fall Meeting of the Western States Section of the Combustion Institute, Dana Point, CA*.
- Durst, F. (1984). *Workshop on Laser Velocimetry* (Ed. H. D. Thompson and W. H. Stevenson), Vol. 2, p. 471. Purdue University, West Lafayette.
- Ebrahimi, I. and Kleine, R. (1977). *16th (Int.) Symp. on Combustion*, p. 1711. The Combustion Institute, Pittsburgh.
- Eckbreth, A. C. (1978). *Appl. Phys. Lett.* **32**, 421.
- Eckbreth, A. C. (1979). *Appl. Optics* **18**, 3215.
- Eckbreth, A. C. (1980). *Combust. Flame* **39**, 133.
- Eckbreth, A. C. (1983). *Appl. Optics* **22**, 2118.
- Eckbreth, A. C. (1988). *Laser Diagnostics for Combustion Temperature and Species. Energy and Engineering Science Series*. Abacus Press, Cambridge, MA.
- Eckbreth, A. C. and Anderson, T. J. (1985). *Appl. Optics* **24**, 2731.
- Eckbreth, A. C. and Anderson, T. J. (1986). *Appl. Optics* **25**, 1534.
- Eckbreth, A. C. and Hall, R. J. (1979). *Combust. Flame* **36**, 87.
- Eckbreth, A. C. and Hall, R. J. (1981). *Combust. Sci. Technol.* **25**, 175.
- Eckbreth, A. C. and Stufflebeam, J. H. (1985). *Exp. Fluids* **3**, 301.
- Eckbreth, A. C., Dobbs, G. M., Stufflebeam, J. H. and Tellex, P. A. (1983). AIAA Paper 83-1294, American Institute of Aeronautics and Astronautics, Washington, DC.
- Eckbreth, A. C., Dobbs, G. M., Stufflebeam, J. H. and Tellex, P. A. (1984). *Appl. Optics* **23**, 1328.
- Edwards, R. V. and Baratuci, W. (1984). *9th Turbulence Symp., Rolla, MO*.
- Farrow, R. L. and Rahn, L. A. (1985). *J. Opt. Soc. Am.* **2**, 903.
- Farrow, R. L., Mattern, P. L. and Rahn, L. A. (1980). Sandia Technical Report SAND 80-8640, Sandia National Laboratories, Livermore, CA.
- Farrow, R. L., Mattern, P. L. and Rahn, L. A. (1981). AIAA Paper 81-0182, American Institute of Aeronautics and Astronautics, Washington, DC.
- Farrow, R. L., Mattern, P. L. and Rahn, L. A. (1982). *Appl. Optics* **21**, 3119.
- Farrow, R. L., Lucht, R. P., Clark, G. L. and Palmer, R. E. (1985). *Appl. Optics* **24**, 2241.
- Fujii, S. and Eguchi, K. (1983). *J. Fluids Eng.* **105**, 128.
- Fujii, S., Gomi, M. and Jin, Y. (1982). *Combust. Flame* **48**, 233.
- Fujii, S., Gomi, M. and Eguchi, K. (1983). *J. Fluids Eng.* **105**, 128.
- Fujii, S., Gomi, M., Eguchi, K., Yamayuchi, S. and Jin, L. (1984). *Combust. Sci. Technol.* **36**, 211.

- Gilson, T. R., Beattie, T. R., Black, I. R., Greenhalgh, D. A. and Jenny, S. N. (1980). *J. Raman Spectrosc.* **9**, 361.
- Gomi, K., Sohna, K. and Hishinuma, Y. (1986). *OSA/IEEE Conf. on Lasers and Electro Optics (CLEO '86)*, p. 114. Laser Institute of America, Toledo, OH.
- Goss, L. P., Switzer, G. L. and Schreiber, P. W. (1980). AIAA Paper 80-1543, American Institute of Aeronautics and Astronautics, Washington, DC.
- Goss, L. P., Switzer, G. L., Trump, D. D. and Schreiber, P. W. (1983a). *J. Energy* **7**, 403.
- Goss, L. P., Trump, D. D., MacDonald, B. G. and Switzer, G. L. (1983b). *Rev. Sci. Instr.* **54**, 563.
- Goss, L. P., Trump, D. D. and Roquemore, W. M. (1984a). AIAA Paper 84-1458, American Institute of Aeronautics and Astronautics, Washington, DC.
- Goss, L. P., Trump, D. D. and Roquemore, W. M. (1984b). *Experimental Measurements and Techniques in Turbulent Reactive and Non-Reactive Flows* (Ed. R. M. So, J. H. Whitelaw and M. Lapp), p. 215. American Society of Mechanical Engineers, New York.
- Goss, L. P., Trump, D. D., Switzer, G. L. and MacDonald, B. G. (1984c). *Combustion Diagnostics by Nonintrusive Methods* (Ed. J. A. Roux and T. D. McCay), Vol. 92, p. 24. American Institute of Aeronautics and Astronautics, Washington, DC.
- Goss, L. P., Trump, D. D. and Roquemore, W. M. (1988). *Exp. Fluids* **6**, 189.
- Goss, L. P., Trump, D. D., Lynn, W. F., Chen, T. H., Schmoll, W. J. and Roquemore, W. M. (1989). *Rev. Sci. Instr.* **60**, 638.
- Green, R. M. and Lucht, R. P. (1985). Sandia Technical Report SAND 85-8621, Sandia National Laboratories, Livermore, CA.
- Greenhalgh, D. A. (1988). *Advances in Non-linear Spectroscopy* (Ed. R. J. H. Clark and R. E. Hester). Wiley, London.
- Greenhalgh, D. A. and Hall, R. J. (1986). *Optics Commun.* **57**, 125.
- Greenhalgh, D. A. and Porter, F. M. (1986). AERE-Harwell Report AERE-R 12221, AERE-Harwell, Oxfordshire.
- Greenhalgh, D. A. and Whittley, G. (1985). *Appl. Optics* **24**, 907.
- Greenhalgh, D. A. and Williams, D. R. (1986). AERE-Harwell Report AERE-R 12222, AERE-Harwell, Oxfordshire.
- Greenhalgh, D. A., Hall, R. J., Porter, F. M. and England, W. A. (1983). *J. Raman Spectrosc.* **14**, 150.
- Greenhalgh, D. A., Porter, F. M. and England, W. A. (1983). *Combust. Flame* **49**, 171.
- Greenhalgh, D. A., Williams, D. R. and Baker, C. A. (1985). *Proc. of AutoTech. Conf.* Institution of Mechanical Engineers, London.
- Hall, R. J. (1979). *Combust. Flame* **35**, 47.
- Hall, R. J. (1983). *Opt. Eng.* **22**, 322.
- Hall, R. J. and Boedeker, L. R. (1984). *Appl. Optics* **23**, 1340.
- Hall, R. J. and Eckbreth, A. C. (1981). *Opt. Eng.* **20**, 494.
- Hall, R. J. and Eckbreth, A. C. (1984). *Laser Applications* (Ed. J. F. Ready and R. K. Erf), Vol. 5, p. 313. Academic Press, New York.
- Hall, R. J. and Shirley, J. A. (1983). *Appl. Spectrosc.* **37**, 196.
- Hall, R. J. and Stufflebeam, J. H. (1984). *Appl. Optics* **23**, 4319.
- Harris, L. E. (1983). *Combust. Flame* **53**, 103.
- Harris, L. E. and McIlwain, M. E. (1981). *Fast Reactions in Energetic Systems* (Ed. C. Capellos and F. Walker), p. 473. Reidel, Boston.

- Harris, L. E. and McIlwain, M. E. (1982). *Chem. Phys. Lett.* **93**, 335.
- Hartford, A., Cremers, D. A., Loiree, T. R., Quiglis, G. P., Radziemski, L. J. and Taylor, D. J. (1983). *Proc. SAE-International Society of Optical Engineering*, Vol. 411, p. 92. Society of Automotive Engineers, Warrendale, PA.
- Harvey, A. B. (1981). *Chemical Applications of Nonlinear Raman Spectroscopy*. Academic Press, New York.
- Hassel, E., Bruggeman, D., Daams, H. J., Dittie, G. and Schmidt, T. (1986). *21st Symp. (Int.) on Combustion*, p. 148. The Combustion Institute, Pittsburgh.
- Heitor, M. V., Taylor, A. M. K. P. and Whitelaw, J. H. (1984). *Experimental Measurements and Techniques in Turbulent Reactive and Non-Reactive Flows* (Ed. R. M. So, J. H. Whitelaw and M. Lapp). American Society of Mechanical Engineers New York.
- Herzberg, G. (1964). *Infrared and Raman Spectra of Polyatomic Molecules. Molecular Spectra and Molecular Structure*, Vol. 2, p. 239. Van Nostrand, New York.
- Kaijiyama, K., Sajiki, S., Katoaka, H., Maeda, S. and Hirose, C. (1982). SAE Technical Paper 821036, Society of Automotive Engineers, Warrendale, PA.
- Kataoka, H., Maeda, S. and Hirose, C. (1982). *Appl. Spectrosc.* **36**, 565.
- Kim, H. (1970). *J. Chem. Educ.* **47**, 120.
- Klick, D., Marko, K. A. and Ramai, L. (1981). *Appl. Optics* **20**, 1178.
- Kreutner, W., Stricker, W. and Just, T. (1983). *Phys. Chem.* **87**, 1045.
- Kroll, S., Alden, M., Berglind, T. and Hall, R. J. (1987). *Appl. Optics* **26**, 1068.
- Lapp, M. and Penney, C. M. (1974). *Laser Raman Gas Diagnostics*. Plenum Press, New York.
- Lederman, S. and Posillico, C. (1981). *AIChE J.* **19**, 824.
- Liesegang, G. W. and Smith, P. W. (1981). *Appl. Optics* **20**, 2604.
- Lightman, A., Magill, R. D. and Anderson, R. J. (1983). AFWAL-TR-83-044, Air Force Wright Aeronautical Laboratories, Wright-Patterson Air Force Base, OH.
- Lucht, R. P. (1987a). *Opt. Lett.* **12**, 78.
- Lucht, R. P. (1987b). *OSA/IEEE Conf. on Lasers and Electro Optics (CLEO '87)*, p. 232. Laser Institute of America, Toledo, OH.
- Magill, R. D., Lightman, A., Orr, C. E., Bradley, R. P. and Roquemore, W. M. (1982). AIAA Paper 82-0883, American Institute of Aeronautics and Astronautics, Washington, DC.
- Maker, P. D. and Terhune, R. W. (1965). *Phys. Rev.* **137**, A801.
- Marko, K. A. and Rimal, L. (1979). *Optics Lett.* **4**, 211.
- McIlwain, M. E. and Harris, L. E. (1980). *Proc. 17th JANNAF Conf. on Combustion*. CPIA Publ. 329, p. 693. Chemical Propulsion Information Agency, Laurel, MD.
- McLaughlin, D. K. and Tiederman, W. G. (1973). *Phys. Fluids* **16**, 2082.
- Moya, F. S., Druet, S. A. J. and Taran, J. P. E. (1975). *Optics Commun.* **13**, 169.
- Moya, F. S., Druet, S. A. J., Pealat, M. and Taran, J. P. E. (1977). *Progress in Astronautics and Aeronautics*, Vol. 53, p. 549. American Institute of Aeronautics and Astronautics, Washington, DC.
- Nibler, J. W., McDonald, J. R. and Harvey, A. B. (1976). *Optics Commun.* **18**, 371.
- Nibler, J. W. and Knighten, G. V. (1979). *Raman Spectroscopy of Gases and Liquids* (Ed. A. Weber), pp. 253-299. Springer-Verlag, Berlin.
- Oudar, J. L., Smith, R. W. and Shen, Y. R. (1979). *Appl. Phys. Lett.* **34**, 758.

- Owyoung, A. (1971). AFOSR Technical Report 71-3132, Air Force Office of Scientific Research, Washington, DC.
- Palmer, R. E. (1989). Sandia Technical Report SAND 89-8206 UC13, Sandia National Laboratories, Livermore, CA.
- Papineau, N. and Pealat, M. (1985). *Appl. Optics* **24**, 3002.
- Pealat, M., Taran, J. P. E. and Moya, F. (1980). *Optics Laser Technol.* **12**, 21.
- Pealat, M., Taran, J. P. E., Tallet, J., Bacal M. and Bruneteau, M. (1981). *J. Appl. Phys.* **52**, 2687.
- Pealat, M., Bouchardy, P., Lefebvre, M. and Taran, J. P. (1985). *Appl. Optics* **24**, 1012.
- Prior, Y. (1980). *Appl. Optics* **19**, 1741.
- Rado W. R. (1967). *Appl. Phys. Lett.* **2**, 123.
- Rahn, L. (1985). Unpublished results, Sandia National Laboratories, Livermore, CA.
- Rahn, L. A. and Palmer, R. E. (1986). *J. Opt. Soc. Am.* **3**, 1164.
- Rahn, L. A., Zych, L. J. and Mattern, P. L. (1979). *Optics Commun.* **39**, 249.
- Rahn, L. A., Johnston, S. C., Farrow, R. L. and Mattern, P. L. (1982). *Temperature, Its Measurement and Control in Science and Industry* (Ed. J. F. Schooley), Vol. 5. American Institute of Physics, New York.
- Rahn, L. A., Farrow, R. L. and Lucht, R. P. (1984). *Optics Lett.* **9**, 223.
- Regnier, P. R. and Taran, J. P. E. (1973). *Appl. Phys. Lett.* **23**, 240.
- Regnier, P. R., Moya, F. and Taran, J. P. E. (1973). AIAA Paper 73-702, American Institute of Aeronautics and Astronautics, Washington DC.
- Robertson, G. N. (1986). *Optical information processing II. SPIE Proc.* **674**, 562.
- Roh, W. B., Schreiber, P. W. and Taran, J. P. E. (1976). *Appl. Phys. Lett.* **29**, 174.
- Roquemore, W. M., Chen, L. D., Goss, L. P. and Lynn, W. F. (1989). *Turbulent Reactive Flows. Lecture Notes in Engineering* (Ed R. Borghi and S. N. B. Murthy), Vol. 40, pp. 49-63. Springer-Verlag, New York.
- Rosasco, G. J. and Hurst, W. S. (1985). *Phys. Rev. A: Gen. Phys.* **32**, 281.
- Shaub, W. M., Nibler, J. W. and Harvey, A. B. (1977). *J. Chem. Phys.* **67**, 1883.
- Shirley, J. A., Eckbreth, A. C. and Hall, R. J. (1979). *Proc. 16th JANNAF Combustion Meeting. CPIA* **309**, 487. Chemical Propulsion Information Agency, Laurel, MD.
- Shirley, J. A., Hall, R. J. and Eckbreth, A. C. (1980). *Optics Lett.* **5**, 380.
- Snelling, D. R., Sawchuk, R. A. and Smallwood, G. J. (1984). *Appl. Optics* **23**, 4083.
- Snelling, D. R., Sawchuk, R. A. and Mueller, R. E. (1985). *Appl. Optics* **24**, 2771.
- Snelling, D. R., Smallwood, G. J., Sawchuk, R. A. and Parameswaran, T. (1987). *Appl. Optics* **26**, 99.
- Switzer, G. L. and Goss, L. P. (1982). *Temperature: Its Measurement and Control in Science and Industry* (Ed. J. F. Schooley), Vol. 5, p. 583. American Institute of Physics, New York.
- Switzer, G. L., Roquemore, W. M., Bradley, R. B., Schreiber, P. W. and Roh, R. B. (1979). *Appl. Optics* **18**, 2343.
- Switzer, G. L., Goss, L. P., Roquemore, W. M., Bradley, R. P., Schreiber, P. W. and Roh, W. B. (1980). *J. Energy* **4**, 209.
- Switzer, G. L., Trump, D. D., Goss, L. P., Roquemore, W. M., Bradley, R. P., Stutrud, J. S. and Reeves, C. M. (1983). AIAA Paper 83-1481, American Institute of Aeronautics and Astronautics, Washington, DC.
- Switzer, G. L., Goss, L. P., Trump, D. D., Reeves, C. M., Stutrud, J. S., Bradley, R. P. and Roquemore, W. M. (1985). AIAA Paper 85-1106, American Institute of Aeronautics and Astronautics, Washington, DC.
- Tanaka, H. and Yanagi, T. (1983). *Combust. Flame* **51**, 183.
- Taran, J. P. E. (1987). *Pure Appl. Chem.* **59**, 1295.
- Taran, J. P. and Pealat, M. (1982). *Temperature: Its Measurement and Control in Science and Industry* (Ed. J. F. Schooley), Vol. 5, 575. American Institute of Physics, New York.
- Taylor, D. J. (1983). LASL Report LA-UR-1840, Los Alamos Scientific Laboratory, Los Alamos.
- Teets, R. E. (1984). *Optics Lett.* **9**, 226.
- Warshaw, S., Lapp, M., Penny, C. and Drake, M. C. (1981). *Laser Probes for Combustion Chemistry* (Ed. D. R. Crosley). The American Chemical Society, Washington, DC.
- Whiting, E. E. (1968). *J. Quant. Spectrosc. Rad. Trans.* **8**, 1379.
- Yanagi, T. and Mimura, Y. (1981). *18th Symp. (Int.) on Combustion. The Combustion Institute, Pittsburgh.*
- Yaney, P. P., Emmerich, C. J., Hodson, D. D. and Kizirnis, S. W. (1987). AIAA Paper 87-0615, American Institute of Aeronautics and Astronautics, Washington, DC.
- Yule, A. J., Chigier, N. A., Boulderston, R. and Ventura, J. (1980). AIAA J. **19**, 752.
- Yuratich, M. A. (1979). *Mol. Phys.* **38**, 625.

Effect of droplet-induced breakdown on CARS temperature measurements

Derek Dunn-Rankin, Gary L. Switzer, Cindy A. Obringer, and Tom A. Jackson

This research examines the potential for coherent anti-Stokes Raman scattering (CARS) to provide reliable gas temperature measurements in the presence of liquid droplets. The droplets cause dielectric breakdown by focusing the CARS laser beams. This breakdown produces a plasma that can disrupt or obscure the CARS signal. Specifically, we examine the influence of laser induced breakdown on the CARS signal, and we determine the importance of droplet position relative to the CARS focal volume and droplet concentration on the reliability of CARS temperature measurements in droplet-laden flows. In addition, we propose a reliable data reduction procedure to minimize the disruptive influence of laser induced breakdown on CARS temperatures.

I. Introduction

A. Background

Proper characterization of spray combustion flows requires spatially resolved maps of droplet size, droplet velocity, droplet composition, gas velocity, gas species concentration, and gas temperature. In addition, it is important to determine these properties without disturbing the flow field. Several nonintrusive optical diagnostic techniques have been designed and employed for this purpose (Roquemaire *et al.*,¹). For example, McDonnell *et al.*² and Mao *et al.*³ report Phase Doppler Particle Analyzer (PDPA) measurements of droplet size, droplet velocity, and gas velocity in a spray flame. Comparable nonintrusive temperature measurements in liquid spray flames have not been reported. Our eventual goal is to provide these temperature measurements, in addition to measurements of the flow field and the droplet field, by combining CARS thermometry with PDPA interferometry. Toward this goal, the present paper concentrates on resolving difficulties of CARS thermometry in droplet laden flows.

B. CARS in Particle Laden Environments

CARS is a nonlinear spectroscopic technique for measuring the energy spectrum from an ensemble of

molecules. Through quantum mechanics, the energy spectrum is a predictable function of temperature. CARS thermometry determines temperature by comparing the measured energy spectrum to calculated spectra using temperature as the fitting parameter. Because CARS thermometry relies on spectral fitting, disruption of the measured energy spectrum by scattered light has potentially serious consequences for the accuracy of the temperature measurements. Fortunately, in particle laden environments, CARS thermometry has significant advantages over other nonintrusive thermometric techniques such as Rayleigh scattering or spontaneous Raman scattering. The CARS signal is coherent so that spatial filtering prevents most of the light scattered by particles from entering the detector. In addition, CARS is an inelastic scattering process, and consequently the signal is spectrally separated from the pump and probe laser beams. Spectral filtering further eliminates particle-scattered background radiation. Eckbreth *et al.*⁴ present a review of CARS spectroscopy and further advantages of CARS thermometry in hostile measurement environments.

Utilizing the inherent background rejection capability of CARS, several researchers have reported nonintrusive temperature measurements in combustion flows with solid particles present. Eckbreth and Hall⁵ have demonstrated reliable temperature measurements in sooting flames. Goss and Trump⁶ have combined a laser Doppler anemometer (LDA) with a CARS system, and have successfully measured temperature with titanium dioxide LDA seed particles in the flow. These efforts have shown that small particles ($<1\ \mu\text{m}$) do not significantly affect the collection and analysis of CARS signals. However, Beiting,⁷

Derek Dunn-Rankin is with University of California, Irvine, Department of Mechanical Engineering, Irvine, California 92717; Gary L. Switzer is with Systems Research Laboratories, Dayton, Ohio 45440-3696; the other authors are with AFWAL Aero-Propulsion Laboratory, Wright-Patterson Air Force Base, Ohio 45433-6563.

Received 13 December 1988.

Lucht,⁸ Noda *et al.*,⁹ and Switzer *et al.*¹⁰ (1989) showed significant dielectric breakdown, and disruption of CARS signals with large particles (1–100 μm) present. Taylor,¹¹ using relatively low laser energy intensity, did not have breakdown problems during collinear CARS measurements in a coal gasifier. Both Beiting and Lucht demonstrated qualitatively that breakdown can be minimized by reducing laser power, but they did not present a systematic study of breakdown during CARS measurements.

C. Potential Effects of Particle Induced Breakdown on CARS Signals

Laser energy density of $\sim 10^{12}$ W/cm² at a wavelength of 532 nm causes laser induced breakdown of clean air at standard temperature and pressure. For a Gaussian spatial intensity profile, and a triangular temporal profile, this energy density corresponds to the peak intensity in a 200-mJ, 10-ns laser pulse focused to 0.1-mm diam beam waist. To maximize the CARS signal, most researchers operate near this threshold energy level. However, large particles in the sample volume reduce the breakdown threshold energy by 1–2 orders of magnitude. Consequently, any large particle in the CARS interaction volume will produce a breakdown.

The plasma generated by laser breakdown affects the CARS signal in several ways: (1) the bright plasma discharge produces a background signal that obscures the CARS signal; (2) the nonresonant CARS signal generated in the plasma competes with the resonant CARS signal, making analysis of the spectrum difficult; (3) the plasma prevents CARS generation by absorbing laser radiation. Switzer *et al.*¹⁰ and Lucht⁸ reported difficulties with (1) and (2), Beiting⁷ reported difficulties with (2). Although (3) has been reported in high density plasmas, it has not been significant for plasmas generated during CARS measurements in particle laden combustion systems.

The present work examines the effect of droplet induced laser breakdown on CARS temperature measurements. There are three objectives in the study: (1) determine the influence of droplet induced breakdown on the CARS spectrum, and how that influence affects the temperature fit of the experimental spectrum, (2) explore software tests to extract valid CARS temperature measurements from spectra affected by breakdown events, and (3) determine the droplet number density and spatial region where droplet breakdown has significant effects.

II. Experiments

A. Experimental Apparatus

Figure 1 is a schematic diagram of the experimental apparatus. The apparatus includes a CARS system, droplet generating hardware and electronics, an imaging system to visualize droplets, a PIN diode to record laser induced breakdown (LIB), and a propane burner and heat pipe to supply high temperature gas to the sample volume.

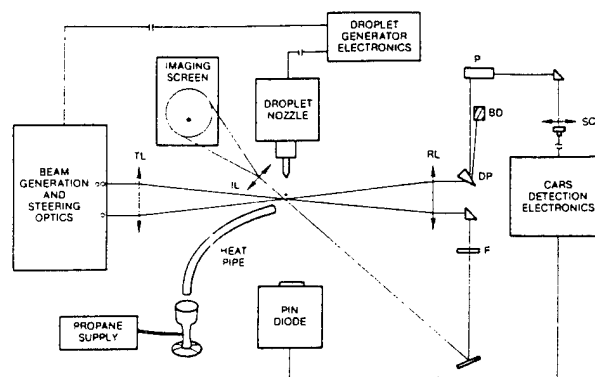


Fig. 1. Schematic diagram of the experimental apparatus: TL-transmitting lens, IL-imaging lens, RL-receiving lens, F-neutral density filter, DP-dispersing prism, BD-beam dump, P-periscope, SC-sample collection optics.

(1) CARS System

The CARS system uses the second harmonic (532 nm) of a pulsed Nd:YAG laser (Spectra-Physics DCR-2) as its primary photon source. Part of the 532-nm light pumps a Rhodamine 590 dye laser oscillator to generate a broadband (150-cm⁻¹) Stokes laser beam peaked at 607 nm. The peak of the dye laser output is concentration tuned to probe the N₂ Q-branch. The remaining 532-nm beam is split into a pair of pump beams. A 500-mm focal length lens combines the two pump beams and the one Stokes beam in an interaction volume ~ 2 mm long and 500 μm in diameter. The interaction volume was measured by scanning a small nitrogen gas jet near the beam crossing, and recording the variation in the CARS signal amplitude. Switzer and Goss¹² describe this nitrogen jet scanning technique. Each pump beam contains ~ 47 mJ of energy, and the Stokes beam contains ~ 30 mJ of energy. Assuming a 10-ns laser pulse, and uniform spatial and temporal intensity, these energies indicate an average intensity of 6×10^9 W/cm². Dispersing prisms separate the CARS signal beam from the pump beams, and focusing optics converge the CARS energy onto the face of an optical fiber. The fiber transmits the CARS signal to a spectrometer. A Tracor Northern TN-1710 DARSS linear array detector collects the spectrum and passes it to a ModComp computer for analysis. Additional details of the CARS system have been reported by Switzer and Goss.¹²

(2) Droplet Generators

We study the effect of laser induced breakdown on CARS measurements using three droplet sources: a drop-on-demand piezoelectric generator, a pressure atomizer, and a capillary breakup droplet stream generator. The droplet generators mount on a 3-D translation stage to place droplets or spray at different positions relative to the CARS focal volume. All of the measurements use water as the droplet fluid, and the droplets travel perpendicular to the laser beam direction.

The drop-on-demand droplet generator consists of a

glass nozzle encased in a cylindrical piezoelectric element. The generator produces droplets ($\sim 65\text{ }\mu\text{m}$ diameter) when the piezoelectric element squeezes fluid out of the glass nozzle. A high-voltage pulser, triggered by a function generator, drives the piezoelectric element with $\sim 75\text{-}\mu\text{s}$, 50-V pulses. The function generator is synchronized to the 10-Hz laser firing to ensure that a droplet is present during the 8-ns Nd:YAG laser pulse. A gravity-feed reservoir supplies the nozzle with liquid. The droplet generator can be a stable source of mono-sized droplets at frequencies from 10–500 Hz, but we had difficulty with its reliability. We used this droplet generator only for room temperature experiments because it did not perform adequately at high temperature.

The pressure atomizer is a Delavan, 45°, 0.5-gal/h nozzle. We operated this nozzle at three pressures (30 psi, 40 psi, and 50 psi) to produce different droplet size distributions and number densities. An Aerometrics phase Doppler particle analyzer measured the droplet size and number density. The Sauter mean diameter (D_{32}) for the droplet size distributions using 30-, 40-, and 50-psi pressures were 65, 56, and 45 μm , respectively. The pressure atomizer was used for room temperature CARS measurements only. We attempted to heat the surrounding air with a heat pipe from a propane/air burner, but unfortunately, the heat pipe did not provide sufficient quantities of high temperature air, and the spray cooled the air to nearly room temperature.

The capillary breakup droplet steam generator is similar to the commercially available Bergland-Liu droplet generator (TSI Incorporated). The generator forces a stream of fluid through a 50- μm pinhole while oscillating the stream with a piezoelectric element. At the proper frequencies the oscillation causes the fluid stream to break up into mono-sized droplets $\sim 80\text{ }\mu\text{m}$ in diameter. We used this droplet generator both at room temperature and in heated air. Unlike the spray, the single droplet stream did not affect the air temperature significantly. A propane/air burner provided the high temperature (800-K) gas via a heat pipe. We also translated the droplet stream along the laser beam axis to determine the effects of droplet position on laser induced breakdown.

B. Experiment Summary

Each experiment consists of 400 single shot CARS measurements. For each shot the reduced data contains the following: (1) *temperature*, the temperature fit to the experimental CARS spectrum; (2) *peak*, the peak amplitude of the CARS signal; (3) *baseline*, the average of 10 baseline pixels representative of the background intensity seen by the spectrometer; and (4) *breakdown*, the intensity of the laser breakdown recorded by a PIN diode with a very wide field of view. The PIN diode collects the breakdown signal 90° from the laser beam axis. The baseline pixels collect the breakdown noise from on-axis. In this work, the signal to noise ratio (SNR) is defined $\text{SNR} = (\text{peak} - \text{baseline})/\text{baseline}$.

The results include CARS temperature measurements in the following droplet environments:

(a) single drops from the drop-on-demand generator in room temperature air at different locations along the CARS laser beam axis,

(b) single drops from the capillary breakup drop generator in heated air at different locations along the CARS laser beam axis, and

(c) a spray of fluid drops from a pressure atomizer in room temperature air centered above the CARS focus; different atomizing pressure and different heights above the focus provide different droplet size and number density conditions.

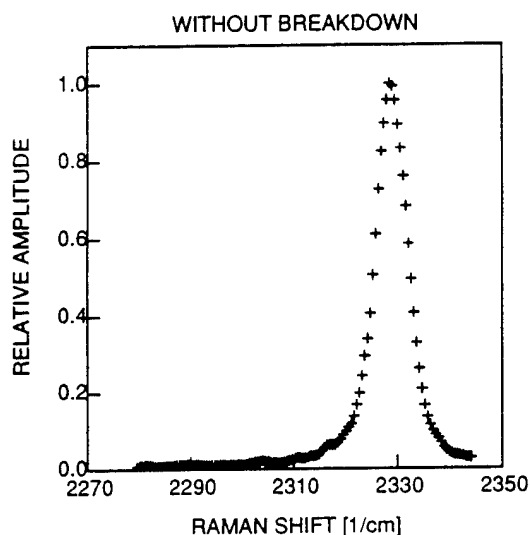
III. Results and Discussion

A. Effect of Droplet Breakdown on the CARS Signal

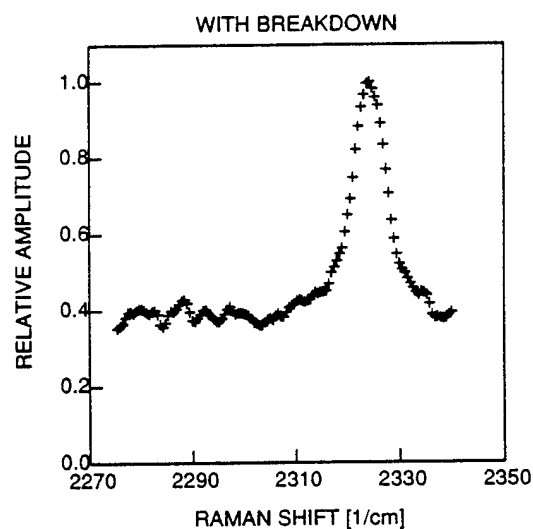
Several recent articles detail the physical processes of LIB of liquid droplets (Chang *et al.*,¹³ Zhang *et al.*,¹⁴ Hsieh *et al.*,¹⁵ Chýlek *et al.*,¹⁶ Zheng *et al.*,¹⁷). LIB in water droplets does not result from absorption, but rather the droplet acts as a lens, focusing the incident radiation just outside the shadow face of the droplet and inside the droplet, just within the shadow face. At high laser energy, breakdown first occurs in the gas outside the droplet, soon followed by breakdown within the droplet. The breakdown inside the droplet forms a highly absorbing plasma that absorbs incoming radiation. The absorption sustains a detonation wave that ejects plasma from the droplet at $\sim 10\text{ km/s}$. The plasma forms in the first few nanoseconds of the laser pulse.

Figure 2 demonstrates the effect of droplet breakdown on CARS measurements by comparing a room temperature CARS spectrum without droplet breakdown to a CARS spectrum with droplet breakdown. The breakdown reduces the peak amplitude of the CARS signal, and increases the baseline amplitude. This combination substantially degrades the SNR of the measurement, making temperature fitting difficult. Figure 3 shows the temperature fits for the two spectra of Fig. 2. Without breakdown, the CARS fit is accurate, and produces a temperature close to room temperature. With breakdown, however, the CARS fitting routine tries to accommodate the lifted baseline and reduced peak by adding a hot band to the calculated spectrum. Adding a hot band produces a very high, incorrect temperature.

Figure 4 shows the average CARS temperature as a function of signal to noise ratio. Three cases are shown in the figure: single drops in heated air, with the drops falling through the focus of the CARS interaction volume; single drops in room temperature air, with the drops falling through the focus of the CARS interaction volume; and a spray in room temperature air, with the spray centered above the CARS interaction volume. The drop-free temperature range is centered about the average CARS temperature with no droplets present. The range includes ± 1 standard deviation of the drop-free temperatures. All of the curves show an incorrectly high temperature for low

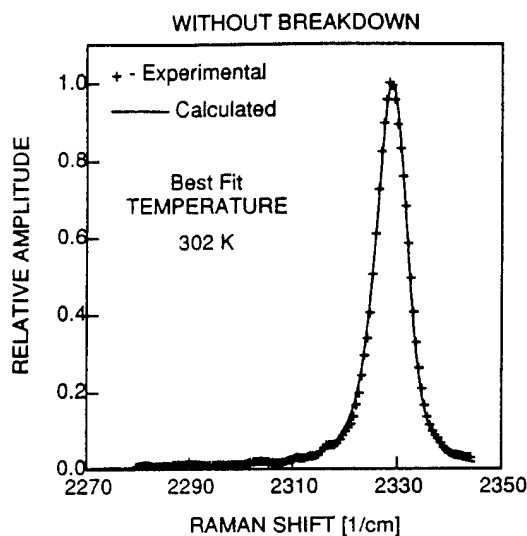


(a)

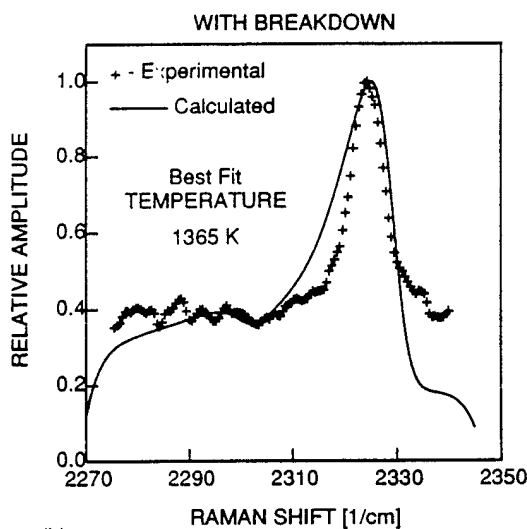


(b)

Fig. 2. Comparison between a CARS signal without droplet breakdown (a) and a CARS signal with droplet breakdown (b).



(a)



(b)

Fig. 3. Temperature fit to the experimental spectra of Fig. 2: (a) fit to CARS signal without droplet breakdown, (b) fit to CARS signal with droplet breakdown.

SNR, and an accurate temperature for high SNR. The cutoff between low and high SNR is ~ 20 .

Figure 5 shows the average baseline level and the average breakdown intensity as a function of SNR for the three cases shown in Fig. 4. The baseline level decreases rapidly with increasing SNR, while the breakdown intensity decreases more slowly. The difference between the baseline and breakdown variation with SNR results from droplet position variations. Droplets at the edge of the CARS sample volume may produce a relatively intense breakdown, but the collection optics spatially discriminate against plasma discharge from the fringe of the sample volume. This discrimination is particularly apparent in the spray case, where the spark intensity is nearly independent of SNR. In the spray, droplets far from the CARS collection volume cause dielectric breakdown, but be-

cause they are out of the collection optics view, the breakdown does not affect the CARS signal significantly. We discuss droplet position in a later section.

B. Effect of Droplet Breakdown on CARS Temperature Measurements

The results of the preceding section indicate that reliable average temperature measurements can be obtained by utilizing only CARS spectra with a high SNR. Unfortunately, however, even with a high (>30) SNR, the RMS temperature with droplets present is larger than the droplet-free RMS temperature. To improve our measurements of RMS temperature, we eliminate the influence of dielectric breakdown noise before we attempt a temperature fit. If the baseline lift is caused by plasma enhanced nonresonant back-

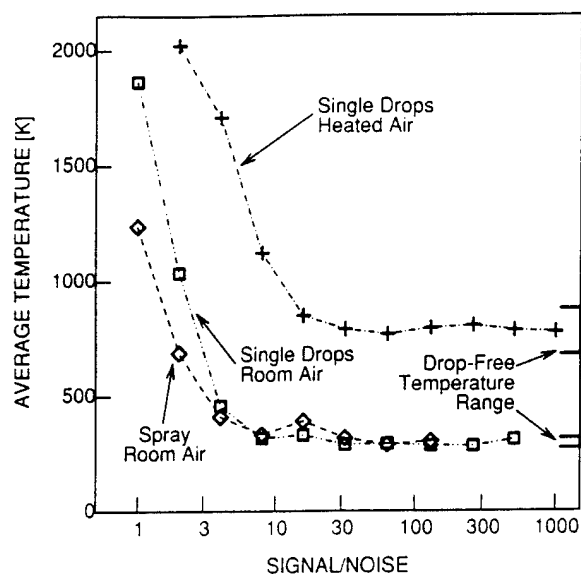
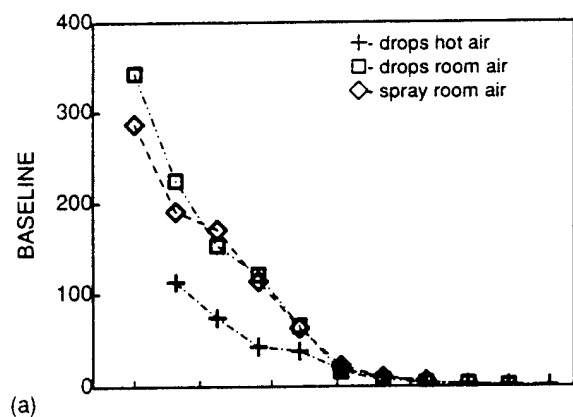
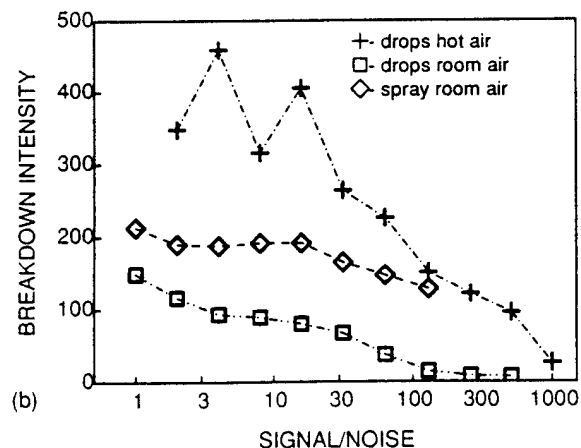


Fig. 4. Average CARS temperature as a function of SNR for single drops in heated air, single drops in room temperature air, and a spray in room temperature air.



(a)



(b)

Fig. 5. Average baseline intensity (a) and average breakdown intensity (b) as a function of SNR.

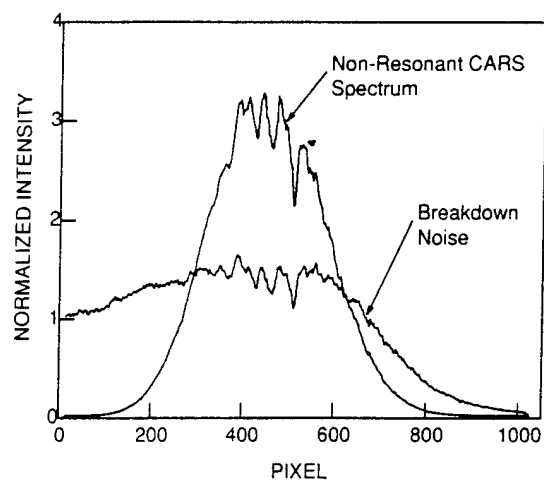


Fig. 6. Comparison between a normalized non-resonant reference spectrum and a normalized breakdown noise spectrum. The spectra are normalized to unit area.

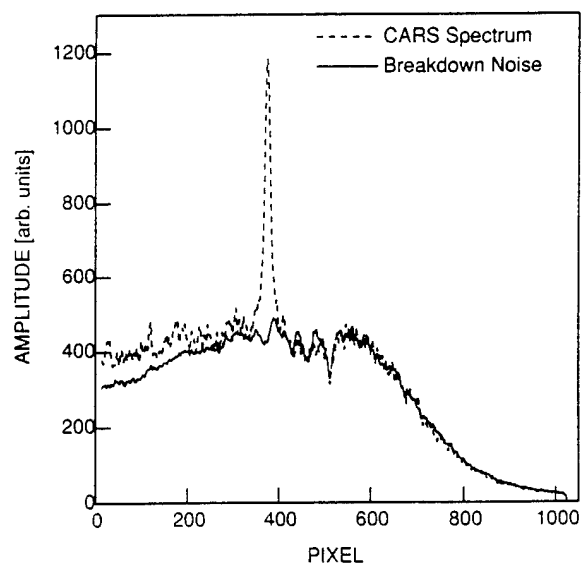
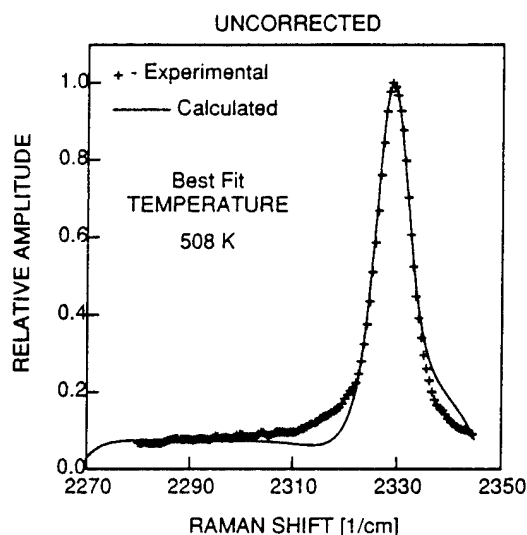


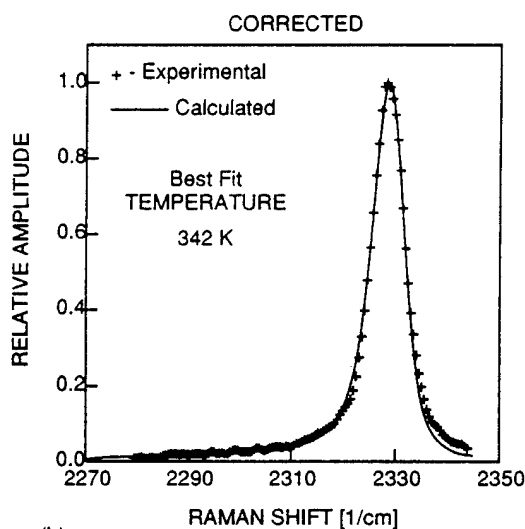
Fig. 7. Comparison between a CARS spectrum influenced by droplet breakdown and a breakdown noise spectrum with no CARS generation.

ground, as suggested by Beiting⁷ we must subtract a normalized nonresonant background. If the baseline lift is caused by stray light from plasma recombination, then we must subtract a normalized breakdown noise spectrum.

Figure 6 compares a normalized nonresonant reference spectrum to a normalized breakdown noise spectrum. The spectra are normalized to unit area. The noise spectrum is taken with the dye laser beam blocked to prevent CARS generation. The nonresonant spectrum is spectrally narrower than the noise spectrum. Figure 7 shows that the breakdown noise spectrum matches very closely the baseline structure of a CARS spectrum influenced by droplet breakdown. For our experiments, therefore, the dominant source of



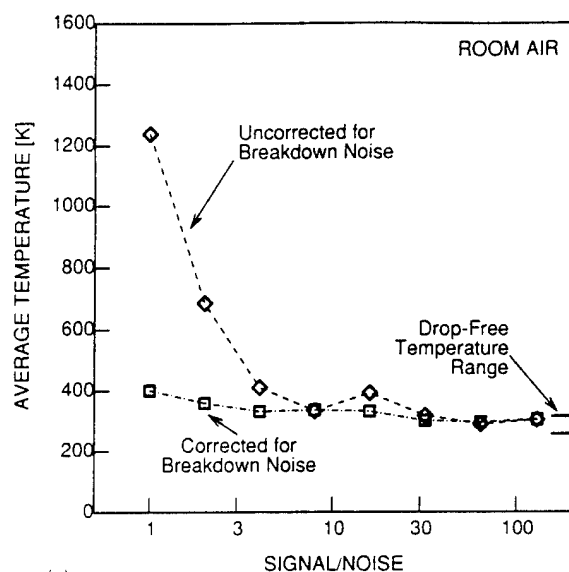
(a)



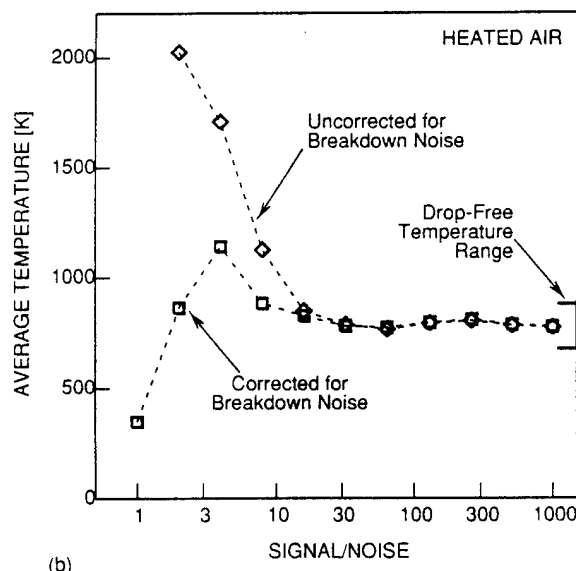
(b)

Fig. 8. Comparison between the CARS temperature fit to an uncorrected spectrum (a) and the CARS temperature fit to a corrected spectrum (b).

baseline lift comes from breakdown noise rather than from an enhanced nonresonant CARS contribution. This dominance may depend on droplet composition and on the gas environment. For example, hydrocarbons have large nonresonant susceptibilities (Farrow *et al.*,¹⁸) which may increase the nonresonant contribution, and as noted earlier, Beiting⁷ found a dominant nonresonant contribution when breakdown was caused by irradiation of solid flyash particles. It is also possible that our droplet breakdown occurs later in the laser pulse than does the breakdown in flyash (Beiting⁷) and coal (Lucht⁸). With a late breakdown, most of the CARS signal is generated before a nonresonant signal from the plasma occurs. Because our intensifier gate is quite wide (1 μ s), light from the plasma



(a)



(b)

Fig. 9. Average temperature as a function of SNR for spectra uncorrected and corrected for droplet breakdown noise: (a) measurements in a room temperature spray, (b) measurements with single drops in heated air.

recombination can be added to the signal after the laser pulse ends.

Based on the results shown in Fig. 7, we correct our experimental spectra for breakdown noise by subtracting a normalized breakdown spectrum from the raw data before we attempt a temperature fit. Beiting¹⁹ used a similar method to analyze CARS signals contaminated by coherent interference. The normalization factor is $(S_{p10} - S_b)/(B_{p10} - B_b)$. S is the measured CARS signal and B is an average breakdown spectrum. The subscript $p10$ refers to an average of 10 pixels and subscript b refers to the absolute baseline of the DARSS detector. Initially, we chose to average the first 10 pixels of the DARSS, however, these pixels did not accurately monitor the level of the breakdown

noise. In Fig. 7, for example, the largest deviation between the signal baseline and the average breakdown spectrum occurs in the first few pixels. Consequently, we determine S_{p10} from an average of 10 pixels located near the second hot band of the nitrogen CARS spectrum. At high temperatures, the second hot band contributes to the CARS signal, requiring a modified choice of pixels to average. Figure 8 compares the temperature fit between an uncorrected and a corrected room temperature CARS spectrum. While the corrected temperature is a little high, it is within the temperature uncertainty typical of low temperature CARS measurements.

Figure 9 compares the variation of temperature with SNR for corrected and uncorrected spectra. The figure shows results from measurements in a room temperature spray [Fig. 9(a)] and from measurements with single drops in heated air [Fig. 9(b)]. In Fig. 9(a), the correction procedure greatly improves the average temperature for spectra with SNR between 1 and 10. For SNR > 10, however, the signal is relatively good already, and the correction procedure adds little improvement. For the heated air case, Fig. 9(b), the correction procedure improves the average temperature for SNR between 3 and 10, but the improvement is

not as substantial as in the room temperature case. As in Fig. 9(a), there is little difference between the corrected and uncorrected results for SNR > 10.

The results of Fig. 9 indicate that spectral correction and conditional measurements based on SNR can produce reliable mean temperatures from CARS signals affected by droplet breakdown. However, the figure also indicates that droplet breakdown results in slightly higher mean temperatures than are measured in drop-free environments. For example, corrected spectra from room temperature spray measurements with SNR > 10 produce a mean temperature ~30 K (10%) higher than occurs in the drop-free temperature measurement. Similarly, corrected spectra from heated air with single drops with SNR > 10 produce a mean temperature ~25 K (3%) higher than occurs in the drop-free temperature measurement.

Figures 10 and 11 present temperature distributions for CARS measurements in a room temperature spray (Fig. 10) and with single drops in heated air (Fig. 11). The bottom distribution in each column is the temperature distribution without droplets present. The remaining histograms compare corrected and uncorrected temperature distributions for three SNR. For SNR > 5, the temperature distribution for uncorrected

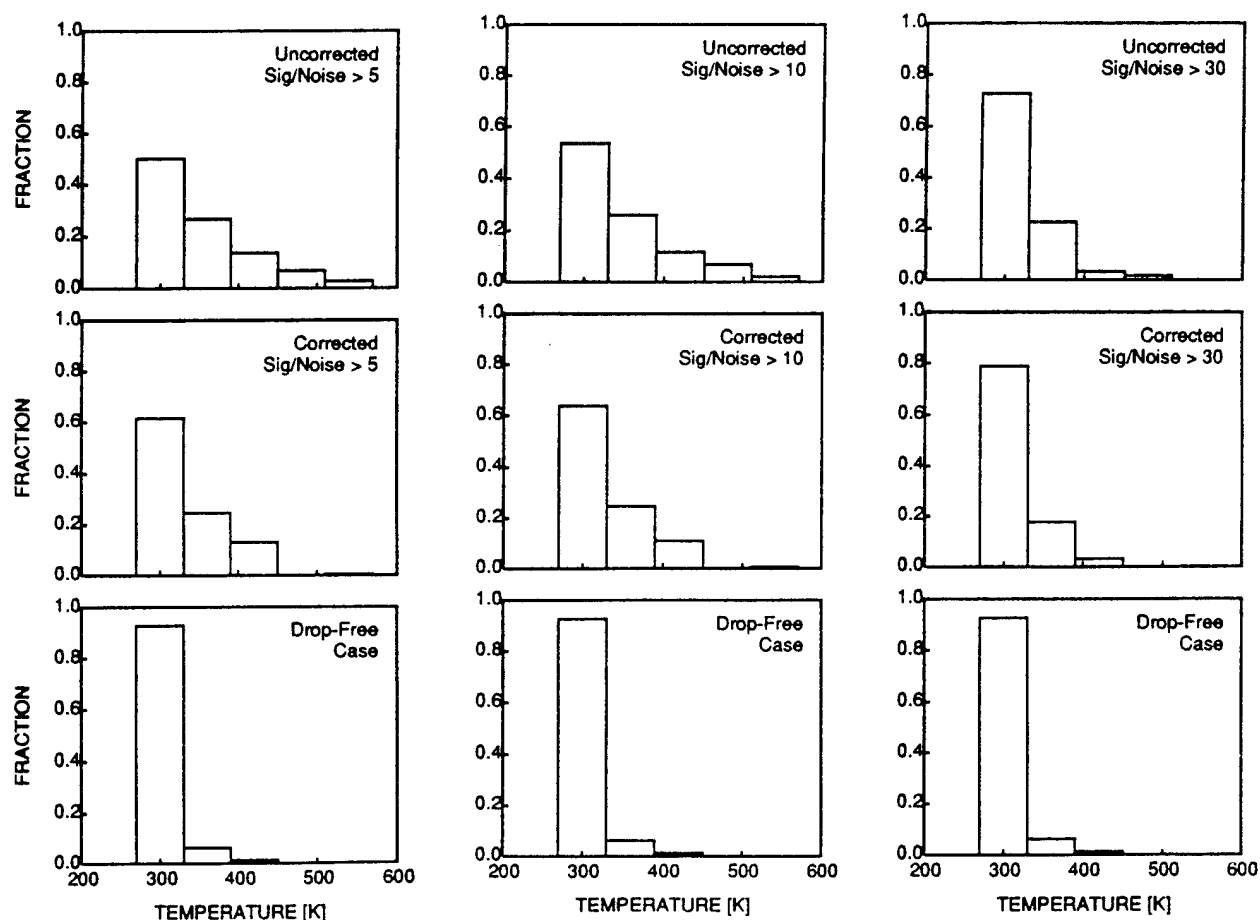


Fig. 10. Temperature distributions for CARS measurements in a room temperature spray. The bottom histogram in each column is the temperature distribution without droplets present. Distributions of uncorrected and corrected temperatures for three SNRs are shown.

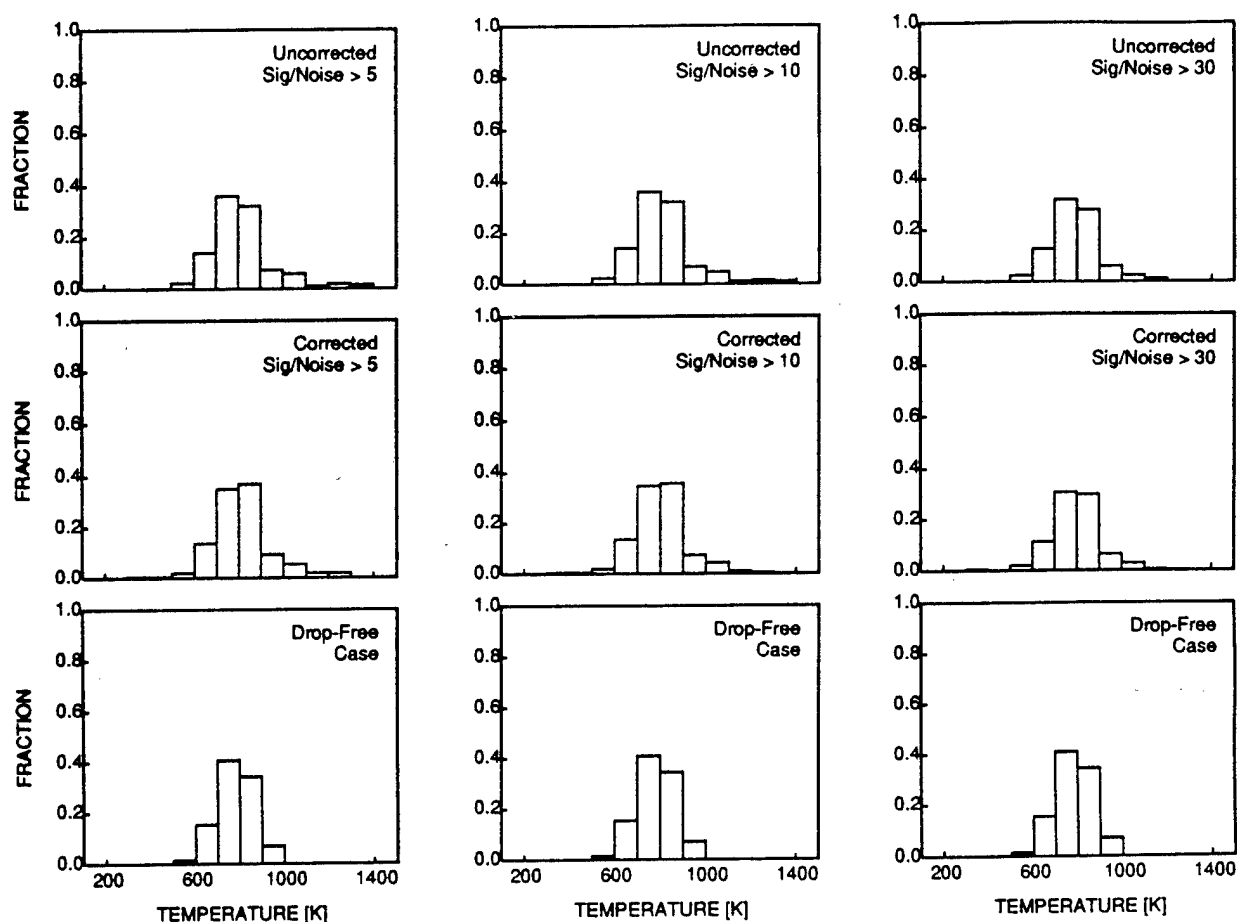


Fig. 11. Temperature distributions for CARS measurements with single drops in heated air. The bottom histogram in each column is the temperature distribution without droplets present. Distributions of uncorrected and corrected temperatures for three SNRs are shown.

spectra is much broader than the distribution for drop-free measurements. The temperature distribution from corrected spectra is narrower than the uncorrected distribution but still does not reproduce the drop-free distribution. Increasing the SNR condition improves the temperature distribution, however even for $\text{SNR} > 30$, the corrected temperature distribution does not reproduce the drop-free temperature distribution. The results from single drops in heated air (Fig. 11) demonstrate the same behavior as the distributions of Fig. 10. In heated air, however, there is little difference between distributions from corrected and uncorrected spectra.

Figures 10 and 11 show that CARS measurements in droplet laden flows produce a broader temperature distribution than measurements made in drop-free environments. The broadening is on the high temperature side of the distribution, and occurs because CARS spectra influenced by breakdown can be interpreted as high temperature spectra. The broadening is most severe at room temperature where the CARS spectra have few features to fit. Temperature measurements of corrected spectra in a room temperature spray with $\text{SNR} > 10$ have a standard deviation of 58 K compared to 29 K for measurements in drop-free room air. For

single drops in heated air, corrected spectra with $\text{SNR} > 10$ produce a temperature standard deviation of 128 K compared with 100 K for drop-free heated air.

C. Effect of Droplet Position on CARS measurements

Figure 12 shows the fraction of CARS measurements that result in a valid temperature as a function of axial droplet position relative to the CARS focus. For this figure, the fraction is the number of temperatures within ± 1 standard deviation of the drop-free temperature divided by the number of measurements containing a noticeable breakdown event. Both the room air experiments and the heated air experiments indicate that the valid fraction is relatively insensitive to axial droplet position when the droplet is near the CARS focus ($\approx \pm 2$ mm). With droplets in the near-focus region, we obtain valid temperatures in 30–40% of the measurements. The droplets travel across the narrow dimension of the CARS sample volume. Valid measurements occur when droplets break down above and below the sample volume because the collection optics spatially discriminate between the CARS signal and the plasma discharge. A similar discrimination does not occur with droplets at the axial edges of the sample volume because the collection optics are nearly

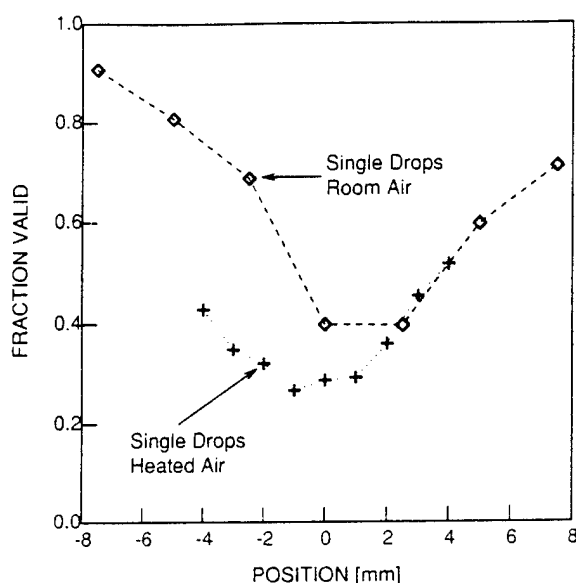


Fig. 12. Fraction of CARS measurements resulting in valid temperature measurements as a function of droplet position relative to the CARS focus. Valid measurements are within ± 1 standard deviation of drop-free temperature.

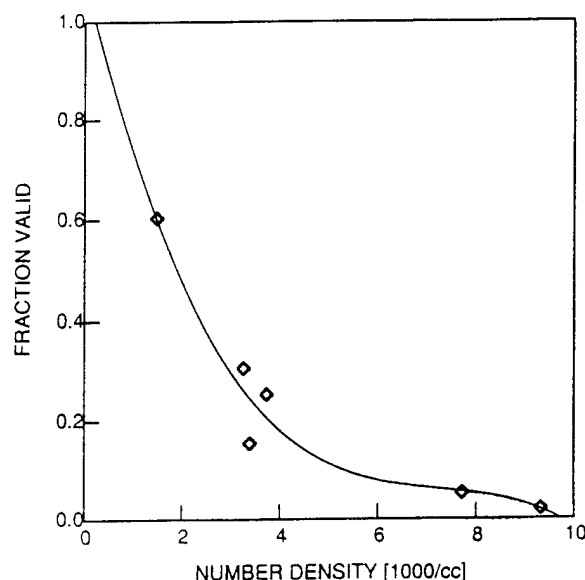


Fig. 13. Fraction of measurements in a room temperature spray that result in valid temperatures as a function of droplet number density. Valid temperatures are within ± 1 standard deviation of drop-free temperature measurements. The number density is measured with a phase-doppler particle analyzer.

on-axis and therefore insensitive to axial position variations. Our results suggest that a droplet breakdown will disrupt the CARS measurement if it is near the beam axis and in the primary CARS interaction volume.

From the above information and Poisson statistics we can estimate the upper bound on particle number density that will result in 40% valid temperature measurements. The number of particles in the CARS sample volume can be described with a Poisson distribution. The mean of the Poisson distribution is the product of the particle number density N and the probe volume V_p . Our CARS system has $V_p \approx 0.4 \text{ mm}^3$ based on the interaction volume dimensions measured with a nitrogen jet. For $N = 2500$ particles/cc, a particle will be present in the sample volume in 60% of the measurements. From this calculation, we expect that 2500 particles/cc is the number density limit for 40% valid temperature measurements. Figure 13 shows valid fraction as a function of particle number density from our CARS temperature measurements in a water spray. The solid line is a least squares cubic fit to the data. The experiments suggest 2500 particles/cc as the number density producing 40% valid measurements, in agreement with our estimate.

D. Minimizing the Effect of Droplet Breakdown on CARS Measurements

Our results suggest the following methods to minimize the effect of breakdown on CARS temperature measurements:

(1) Reduce laser power: reducing laser power decreases the size of the region with sufficient energy to generate breakdown. Unfortunately reducing laser

power also reduces the CARS signal. It is possible to compensate for the decrease in laser power with an increased interaction volume at the expense of degraded spatial resolution.

(2) Minimize optics field of view: restricting the optics field of view ensures that breakdown events outside the CARS interaction volume will not affect the CARS signal.

(3) Reduce detector gate time: the entire CARS signal is collected in less than 10 ns, while the plasma recombination occurs on the microsecond time scale. Gating the detector in a narrow time window around the CARS laser pulse will reduce the breakdown noise. Reducing the detector gate time will not reduce the nonresonant contribution to the noise. The detector gate time can be difficult to reduce in practice as it is often limited by detector hardware and shot-to-shot jitter.

(4) Software corrections and conditional sampling: CARS spectra that have been affected by breakdown noise can be improved by subtracting a normalized background characteristic of the breakdown. In addition, conditionally sampling the measurements to include only spectra with a high SNR allows accurate temperature measurements in droplet laden flows.

IV. Conclusions

Our experiments suggest the following conclusions:

Droplets that breakdown near the center of the CARS interaction volume influence the CARS signal by decreasing the peak signal intensity, and by raising the background intensity. There is little evidence of noise due to the plasma enhanced nonresonant CARS

signal that has been observed in similar experiments using solid particles rather than droplets to produce LIB.

LIB leads to inaccurate temperatures because the CARS fitting routine tries to fit the elevated background by enhancing the first nitrogen hot band. Subtracting a background spectrum characteristic of LIB improves the temperature fit. The improvement is more pronounced for low temperature spectra than for high temperature spectra.

Background subtracted CARS spectra with a high SNR provide reasonably accurate mean and RMS temperatures in droplet laden flows.

Droplets that generate breakdown plasma far from the CARS interaction volume do not influence the CARS measurement. Spatial filtering by the collection optics discriminates fairly well between the CARS signal and the plasma discharge.

Results from CARS measurements in sprays are very similar to results from CARS measurements with single droplets in the sample volume. It is likely, therefore, that the LIB process is a single droplet event. Our CARS sample volume ($\sim 1 \text{ mm}^3$) and 40% validation rate requires a particle number density less than 2500 particles/cc.

The authors appreciate the important insights provided by Larry Goss of Systems Research Laboratory. This research is sponsored by the Air Force Office of Scientific Research/AFSC, United States Air Force, under Contract F49620-87-R-0004.

References

1. W. M. Roquemore, *et al.*, "Development of Laser Diagnostics for Combustion Research," Invited paper of the Central States Section/The Combustion Institute Spring Meeting, NASA Lewis Research Center, May 5-6, 1986.
2. V. G. McDonell, C. P. Wood, and G. S. Samuelsen, "A Comparison of Spatially-Resolved Drop Size and Drop Velocity Measurements in an Isothermal Chamber and a Swirl-Stabilized Combustor," in *Proceedings Twenty-first Symposium (International) on Combustion* (The Combustion Institute, Pittsburgh, PA 1986), p. 685.
3. C. P. Mao, G. Wang, and N. A. Chigier, "An Experimental Study of Air-Assist Atomizer Spray Flames," in *Proceedings Twenty-first Symposium (International) on Combustion* (The Combustion Institute, Pittsburgh, PA 1987), p. 665.
4. A. C. Eckbreth, P. A. Bonczyk, and J. F. Verdick, "Review of Laser Raman and Fluorescence Techniques for Practical Combustion Diagnostics," Environmental Protection Agency Report EPA-600/7-77-006 (1977).
5. A. C. Eckbreth and R. J. Hall, "CARS Thermometry in a Sooting Flame," *Combust. and Flame* **36**, 87-98 (1979).
6. L. P. Goss and D. D. Trump, "Simultaneous CARS and LDA Measurements in a Turbulent Flame," AIAA Paper AIAA-84-1458, 20th Joint Propulsion Conference, Cincinnati, Ohio, June 11-13 (1984).
7. E. J. Beiting, "Coherent Interference in Multiplex CARS Measurements: Nonresonant Susceptibility Enhancement due to Laser Breakdown," *Appl. Opt.* **24**, 3010-3017 (1985).
8. R. P. Lucht, "Coherent Anti-Stokes Raman Scattering Measurements in Coal-Particle-Laden Flames," Sandia National Laboratories Technical Report SAND88-8721 (1988).
9. M. Noda, A. Gierulski, and G. Marowsky, (1987) "CARS-Studies of Coal and Coal-Water-Mixture Combustion," Paper 7C-109, Joint Meeting of the Western States and Japanese Sections/The Combustion Institute, Honolulu, Hawaii, November 22-25, 1987.
10. G. L. Switzer, T. A. Jackson, C. A. Obringer, and J. S. Stutrud, "An Integrated Spectroscopic-Interferometric Instrument for Spray Combustion Diagnostics," Western States Section/The Combustion Institute Fall Meeting, Sandia National Laboratories, Livermore, CA, October 23-24, 1989.
11. D. J. Taylor, "CARS Concentration and Temperature Measurements in Coal Gasifiers," Los Alamos National Laboratory Report LA-UR-83-1840 (1983).
12. G. L. Switzer and L. P. Goss, (1982) "A Hardened CARS System for Temperature and Species Concentration Measurements in Practical Combustion Environments," *Temperature: Its Measurement and Control in Science and Industry—Vol. 5*, J. F. Schooley, Ed. (Publ. City, 1982) p 583.
13. R. K. Chang, J. H. Eickmans, W.-F. Hsieh, C. F. Wood, J.-Z. Zhang, and J.-B. Zheng, "Laser Induced Breakdown in Large Transparent Water Droplets," *Appl. Opt.* **27**, 2377-2385 (1988).
14. J.-Z. Zhang, J. K. Lam, C. F. Wood, B.-T. Chu, and R. K. Chang, "Explosive Vaporization of a Large Transparent Droplet Irradiated by a High Intensity Laser," *Appl. Opt.* **26**, 4731-4737 (1987).
15. W.-F. Hsieh, J.-B. Zheng, C. F. Wood, B. T. Chu, and R. K. Chang, "Propagation Velocity of Laser-Induced Plasma Inside and Outside a Transparent Droplet," *Opt. Lett.* **12**, 576-578 (1987).
16. P. Chýlek, M. A. Jarzembki, V. Srivastava, R. G. Pinnick, J. D. Pendleton, and J. P. Cruncleton, "Effect of Spherical Particles on Laser Induced Breakdown of Gases," *Appl. Opt.* **26**, 760-762 (1987).
17. J.-B. Zheng, W.-F. Hsieh, S.-C. Chen, and R. K. Chang, "Temporally and Spatially Resolved Spectroscopy of Laser Induced Plasma from a Droplet," *Opt. Lett.* **13**, 559-561 (1988).
18. R. L. Farrow, R. P. Lucht, and L. A. Rahn, "Measurements of the Nonresonant Third-Order Susceptibilities of Gases using Coherent Anti-Stokes Raman Spectroscopy," *J. Opt. Soc. Am. B* **4**, 1241-1246 (1987).
19. E. J. Beiting, "Multiplex CARS Temperature Measurements in a Coal-Fired MHD Environment," *Appl. Opt.* **25**, 1684-1692 (1986).

2.1.3 Particle-Imaging Velocimetry (PIV). The two-color PIV technique was developed for quantifying previously used two-dimensional visualization methods and allows two-dimensional velocity measurements to be made free of directional ambiguities. The initial PIV analysis code was based on a combined correlator/particle tracker and was applied to the study of both aerodynamic flowfields ["Two-Color Particle Imaging Velocimetry in a Turbine Cascade" (pp. 51 - 60) and "Two-Color Particle-Imaging Velocimetry in Vortex Structures" (pp. 61 - 70)] and combustion flowfields ["Two-Color Particle-Imaging Velocimetry" (pp. 71 - 77)]. The technique was based on the use of two pulsed laser systems of different colors. For demonstrating that the technique could be effective with a single laser, multiple colors from an argon-ion laser were used to study a splitter-plate flowfield ["Two-Color Particle-Imaging Velocimetry Using a Single Argon-Ion Laser" (pp. 78 - 87)].

The technique was next extended to the development of new analysis software based upon a two-dimensional FFT correlator that allowed realization of high seed densities, resulting in valid velocity information throughout the PIV image. Other advantages of the new software included a simpler graphic user interface (GUI) and faster image processing. Thus, the two-color PIV technique evolved from a laboratory curiosity into a useful tool for fluid-dynamic measurements ["Investigation of a Jet in a Cross Flow Using PIV" (pp. 88 - 102) and "PIV Measurements of Periodically Forced Flat Plate Film Cooling Flows With High Free Stream Turbulence" (pp. 103 - 114)].

The latest step in the evolution of two-color PIV involved replacement of the film used for recording the color PIV images with an electronic recording device. Before high-resolution color-CCD cameras were available, experiments were attempted with a monochrome camera and dielectric mirror arrangement ["Two-Color Particle-Imaging Velocimetry Employing a Single CCD Camera" (pp. 115 - 120)]. This approach, however, was only marginally successful. Fortunately, a high-resolution color CCD camera soon became available, allowing convenient replacement of color film ["Two Color Particle-Image Velocimetry Employing a Color CCD Camera" (pp. 121 - 126)].



AIAA-91-0274

**TWO-COLOR PARTICLE-IMAGING
VELOCIMETRY IN A TURBINE CASCADE**

M. E. Post, L. P. Goss, and L. F. Brainard

Systems Research Laboratories, Inc.

A Division of Arvin/Calspan

2800 Indian Ripple Road

Dayton, OH 45440-3696

29th Aerospace Sciences Meeting

January 7-10, 1991/Reno, Nevada

TWO-COLOR PARTICLE-IMAGING VELOCIMETRY IN A TURBINE CASCADE

M. E. Post,* L. P. Goss,** and L. F. Brainard†

Systems Research Laboratories, Inc.

A Division of Arvin/Calspan

2800 Indian Ripple Road

Dayton, OH 45440-3696

Abstract

A novel method for determining two dimensional velocity flowfields has been developed and applied to a turbine test section. The technique, two-color particle-image velocimetry (PIV), is similar to existing PIV techniques except that two different-color laser sources are used to form the light sheets required for exposing the position of the particles. Analysis of the resulting color images consists of digitizing the exposed film with color filters and processing the digitized images with velocity-displacement software. The two-color PIV technique has the advantage that direction, as well as particle displacement, is uniquely determined. This technique is, thus, applicable to complex flowfields (i.e., recirculating), where the normal 180-deg. directional ambiguity of single-color techniques can be troublesome. Velocity measurements utilizing the two-color PIV technique on a turbine-cascade test section have been made and are discussed.

Introduction

In complex transient flowfields, it is important to obtain an instantaneous two-dimensional picture of the entire flowfield rather than a time-averaged pointwise map. Several techniques have been reported in the literature which have the capability to determine the two-dimensional flowfield. These techniques fall into three categories: particle-tracking schemes,¹⁻⁸ time-of-flight techniques,⁹⁻¹¹ and laser Doppler methods.¹²⁻¹⁵ For low-to-moderate velocity flowfields, particle-tracking techniques are effective, offering a wide velocity range and allowing a two-dimensional measurement of the velocity flowfield.

Particle tracking or particle-imaging velocimetry (PIV) is basically an extension of speckle

photography which has been employed extensively in solid mechanics. The PIV technique involves 1) double pulsing a particle-laden flowfield, 2) recording the scattered light either by conventional photography or holography, and 3) processing the photographs to obtain velocity information. While the first two steps are relatively simple to implement, the data analysis is typically complex and requires computerized image processing.

This paper describes the two-color PIV technique which allows measurements to be made in complex transient flow systems.¹⁶⁻¹⁷ This technique utilizes color to mark temporally the position of small seed particles in a flowfield. A laser sheet (green) formed by passing the output from a doubled Nd:YAG laser through a cylindrical lens is used to illuminate the seed particles in the flowfield. After a short time delay (ranging from a few microseconds for high-velocity flow systems to milliseconds for low-velocity flow systems), a second laser sheet (red) from a Nd:YAG-pumped dye laser is pulsed to illuminate the flowfield a second time. Any particles remaining in the plane of the laser sheets produce a "displacement-vector" pair which is made up of a green- and a red-particle image. The Mie scattering from the seeded particles is recorded on 100-ASA color film which is processed by direct digitization. The unique color coding helps to remove the directional ambiguities associated with single-color techniques because the red image appears after the green image by a known time delay.

In order to compare the experimental data with computational results, a multipoint, inverse-distance weighting algorithm was developed to estimate velocity values at specified coordinates. Computational models frequently make use of a regularly spaced set of node coordinates, while the experimental PIV data is determined at random locations (where seed particles are located during the laser pulses). The weighting algorithm employs an arbitrary number of nearest-neighbor experimental points to estimate the velocity at a selected point. Utilization of the interpolator allows the random

*Research Physicist, Member AIAA

**Chief Scientist, Optical Diagnos., Member AIAA

†Systems Analyst

experimental velocity distribution to be transformed onto a grid to facilitate comparisons with calculated data.

Theory of Particle-Tracking Velocimetry

Because the imaging aspects of two-color PIV are the same as those of single-color PIV techniques, the theoretical foundation developed by Adrian^{3-6,7} and coworkers for single-color PIV techniques can be used to predict the laser-power and recording-film requirements. For particle imaging, the exposure resulting from a particle in a laser light sheet of energy W and area $\Delta y \Delta z$ is given by⁴

$$\epsilon = \frac{4}{\pi k^2 d_e^2} \frac{W}{\Delta y \Delta z} \int_{\Omega} \sigma^2 d\Omega \quad (1)$$

where $k = 2\pi/\lambda$, Ω is the collection angle of the lens system, σ the Mie-scattering cross section of the particle, λ the wavelength of the laser light sheet, and d_e the nominal image diameter given by

$$d_e = (m^2 d_p^2 + d_s^2)^{1/2} \quad (2)$$

where

$$d_s = 2.44 (m + 1) f\# \lambda \quad (3)$$

with m being the magnification of the image, d_p the particle diameter, $f\#$ the ratio of the focal length to the lens diameter, and λ the wavelength of the laser source. The "diffraction limited" blur image due to the lens is given by d_s . For small seed particles the particle image recorded on film is actually the blur image and, thus, represents a lower limit to the image size.

Adrian,⁴ has calculated the Mie-scattering contribution to Eq. (1) and generated a family of curves for normalized exposure, $f\#$, and particle size. Normalizing the exposure to the light-sheet energy density allows comparison with experimental conditions other than those reported in Ref. 4. The minimum exposure level of the film is given by the inverse of the ASA speed rating in erg/cm^2 . For 100-ASA film, the minimum exposure corresponds to $1 \times 10^{-5} \text{ J/m}^2$. In order to compare this value with the family of curves generated by Adrian, the exposure must be normalized to the energy density of the laser light sheet. Because of the high speeds of the particles in the test chamber of these studies, a combination of a Nd:YAG laser (green sheet) and a Nd:YAG-pumped dye laser (red sheet) was employed. Assuming an energy level of 200

mJ/pulse from these lasers in a 10 cm x 1 mm sheet, the energy density available is $\sim 2000 \text{ J/m}^2$. With the minimum exposure or fog level for 100-ASA film, the normalized exposure, ϵ , is $\sim 5 \times 10^{-9}$. Since a density of one is considered to be an adequate exposure level, the optimum exposure (ϵ) level with these laser systems is $\sim 5 \times 10^{-8}$. Superimposing this level on the family of curves generated by Adrian indicates that sub-micron particles can be captured with an $f/8.4$ lens.

The precision of particle-tracking or PIV methods requires determination of the smallest displacement which can be accurately measured by the film (resolving power of the film). In order to understand the resolving capability of the film, one must examine the modulated transfer function (MTF) which is a measure of the ability of the film to resolve accurately line pairs separated by a given distance. The function is defined by

$$\text{MTF} = \frac{I_{\max} - I_{\min}}{I_{\max} + I_{\min}} \quad (4)$$

where I_{\max} is the intensity maximum of adjacent line pairs (or particle images) and I_{\min} the minimum intensity between the line pairs. As the line pairs per millimeter of the input image increases, a point is reached where the lines are no longer distinct and overlapping (cross-talk) occurs. For example, 100-ASA film exhibits an MTF value which corresponds to a resolution of 100 line pairs/mm. This color film is, thus, capable of resolving a 10- μm particle separation. However, the particle-image size given by Eq. (2) represents the ultimate limit to the velocity resolution since no two particles can be resolved closer than the distance between their centers (one particle diameter). The recorded particle diameter for an $f/8.4$ lens having a magnification of 0.4 is $\sim 30 \mu\text{m}$.

Assuming that the maximum velocity of the cascade test section is 340 m/sec and that a spatial resolution of 1 mm is required, the time separation between sequential pulses would be $\sim 3 \mu\text{sec}$. The minimum velocity would correspond to the minimum particle spacing, $\sim 30 \mu\text{m}$, divided by the pulse separation, 3 μsec , which would correspond to $\sim 10 \text{ m/sec}$ or $\sim 3\%$ of the full-scale velocity limit. Achievement of a lower minimum velocity with a double-pulsed system would require a longer time separation between pulses, which would result in a lower spatial resolution. The requirement for a 3- μsec separation between pulses cannot be achieved with a single double-pulsed Nd:YAG system. The double-pulsed Nd:YAG laser used in the present

study has a minimum separation between pulses of 26 μsec and a maximum of $\sim 250 \mu\text{sec}$. Thus, two separate Nd:YAG lasers were required for the cascade measurements.

TWO-COLOR IMAGE ANALYSIS

The two-color PIV technique utilizes color to remove directional ambiguities and reduce tracking errors. However, because the Young's-fringe analysis approach cannot distinguish between the different-color particle fields, an alternative correlation-tracker analysis approach was developed. The analysis procedure consists of 1) digitizing the color negative with a CCD array, 2) determining the spatial locations of the digitized particle images, 3) constructing a correlation map from which the most probable displacement vector can be determined, and 4) using this information in a tracker which identifies green/red particle-vector pairs from the digitized image. A detailed discussion of the analysis software can be found in Refs. 16 and 17; only the salient features will be discussed here.

Determination of Particle Coordinates

In order to take full advantage of the resolution available with the color film on which images are recorded, an enlarger was used to subdivide the image for analysis. The position of the enlarger was controlled by an automated x,y,z traversing mechanism that could set the position of the enlarger to within 20 μm in any direction. Each section of the enlarged image was digitized twice using a CCD camera system. The first digitized image was taken with a green filter to identify the green-particle images and the second with a red filter to identify the red-particle images. These digitized images were processed in an identical manner to permit determination of the coordinates of the green and red particles.

A typical digitized image displays peaks associated with the particles superimposed on a slowly varying background. In order to simplify procedures for finding the coordinates of each particle, components of the background, which are constant or slowly varying over the scale of the particle size, are removed by applying a two-dimensional Laplacian operator to the digitized image. This operator basically acts as a spatial-frequency filter, passing high-frequency (small-size) components of the image but suppressing low-frequency (background) components. The particle images can be further enhanced above the background and film noise if the step size of the Laplacian operator is approximately the

particle size. Next, the processed image is scanned in two dimensions for local maxima, and a series of tests is performed to identify those local maxima which correspond to particles. In brief, particles are identified by finding local maxima which 1) are above a threshold value, 2) do not constitute a peak shoulder, 3) have a local average intensity above a threshold value, and 4) have an estimated diameter within a specified range.

Determination of Most Probable Vector Displacement

The histogram approach to particle correlation is the method adopted for this study and, therefore, will be discussed in detail. The cross correlation between the green- and red-particle images is given by

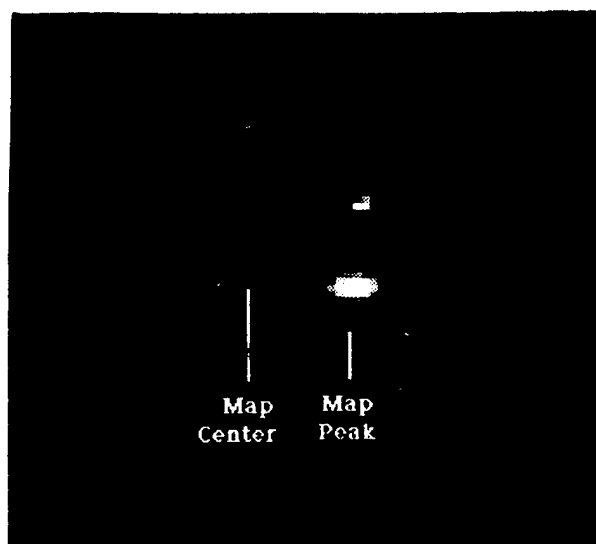
$$c(\xi, \psi) = \sum_x \sum_y g(x, y) r(x - \xi, y - \psi) \quad (5)$$

where $c(\xi, \psi)$ is the two-dimensional correlation map, $g(x, y)$ the digitized green image, $r(x, y)$ the digitized red image, and the limits of summation are over the pixel dimensions of the digitized image. The correlation in this form is computationally intensive since it represents a double summation of the entire digitized image. In the histogram approach a correlation histogram map is constructed from the green- and red-particle images; the maximum of these images contains the most probable displacement vector. The software for this analysis functions by first finding an initial particle image in the green digitized image. The exact location of the green particle is determined and used for mapping. A 64 x 64 pixel area of the red-particle image centered about the green-particle coordinates is then copied into a histogram map (correlation space). This procedure is then repeated for all the green-particle images and their associated surrounding fields in the red-particle images. This process is represented mathematically by

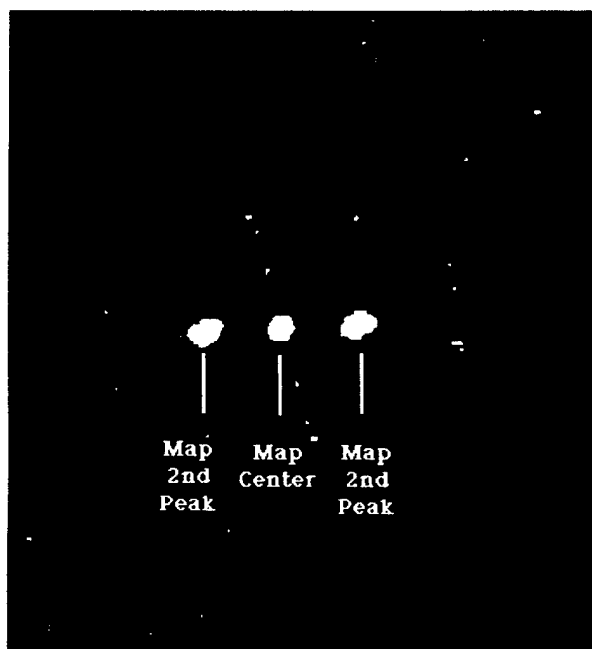
$$H(\xi, \psi) = \sum_n g(x_c, y_c) r(x_c - \xi, y_c - \psi) \quad (6)$$

where $H(\xi, \psi)$ is the correlation histogram, $g(x_c, y_c)$ the center coordinates of the green-particle images, $r(x_c - \xi, y_c - \psi)$ the red-particle images surrounding the green particle being mapped, and the summation is over all green-particle images. Because the double summation of Eq. (5) over all x and y pixels has been replaced with a single summation over the number of green particles, Eq. (6) is computationally more efficient and results in a cross-correlation histogram.

As green/red-particle pairs having the same velocity--and, thus, displacement--are mapped onto correlation space, peaks are built up on this map. The maximum of this map corresponds to the most probable displacement from the center coordinate, illustrated in Fig. 1(a). If only a single color image had been used instead of a two-color image, the resulting correlation map would have been symmetric and centered about a large self-correlation peak at the center of the map shown in Fig. 1(b). This would have resulted in a



(a)



(b)

Fig. 1. Correlation Maps Determined by Histogram Procedure for (a) Two-Color PIV and (b) Single-Color PIV Data.

180-deg. directional ambiguity which would have had to be resolved by phase shifting or by having an *a priori* knowledge of the flowfield. Because only the red-particle images were mapped into the histogram map with respect to the green, neither the self-correlation peak nor the symmetry and associated 180-deg. directional ambiguity is observed. Thus, both displacement and directional information are determined from the histogram map. The analysis software determines the direction and displacement by searching for the maximum. The displacement is then determined from the maximum to the center. This corresponds to the most likely velocity and direction averaged over the x,y array examined. To determine the individual velocity vectors, a tracker must be employed. The task of the tracker now, however, is simplified because the average velocity and direction have been determined, thus reducing the angles and displacements over which it must track.

Tracker for Matching Green/Red Pairs

Once the coordinates of the green- and red-particle images have been determined and the most probable displacement vector calculated from the correlation histogram, the individual velocity vectors of green/red-particle pairs can be identified in a relatively short time. A tracker routine was developed to permit use of the average velocity and directional information obtained from the correlation map to find green/red-particle pairs which fit this value within a preset uncertainty. The tracker functions by starting from each green-particle image, adding the most probable vector displacement, and searching for the corresponding red-particle pair. If a red particle is present at the projected coordinates, then a velocity match is made and a vector drawn. If no red particle is found at these coordinates, a small "box" is opened around the target coordinates. This "box" is expanded incrementally to a selected percentage of the vector length. The number and size of increments should be kept relatively small (usually three increments or less with a maximum size of 50% of the vector length at the last increment). If the number and size of increments becomes too large, the number of erroneous matches may become large. Generally, good results are obtained with three increments, with the maximum increment being about 20% of the vector length. The tracker portion of the analysis is very efficient, normally requiring approximately 30 sec on a full 384 x 576 digitized image for processing. The combination of a correlator and tracker was found to be the most efficient and effective approach to determining velocity

vectors in the two-color images recorded in this study.

Interpolator

By employing the techniques described above a two-dimensional velocity field is experimentally determined, with individual velocity vectors being located at random positions (location of the seed particles when the photographs were taken). It is desirable to determine the velocity vectors at specified coordinates in order to make comparisons with numerical models of the flowfield being studied. A multipoint, inverse-distance interpolation method was developed to estimate velocity data at a specific spatial location from nearest neighbor experimental data. This process is represented mathematically by

$$[V_x(x_s, y_s), V_y(x_s, y_s)] = \frac{\sum_{i=1}^N \frac{[V_x(x_i, y_i), V_y(x_i, y_i)]}{\sqrt{(x_i - x_s)^2 + (y_i - y_s)^2}}}{\sum_{i=1}^N \frac{1}{\sqrt{(x_i - x_s)^2 + (y_i - y_s)^2}}} \quad (7)$$

where (x_s, y_s) are the coordinates of the point where an interpolated velocity vector is desired, and $V_x(x_s, y_s)$ is the x component of velocity at the point (x_s, y_s) . In practice, the N velocity vectors "closest" to the selected point are used in the interpolation. This method was tested with several different exact vector patterns and was found to yield reasonable results for values of N = 3 or 4. Comparisons of length and direction were made with interpolated velocity vectors and vectors calculated from an exact pattern. It should be noted that coordinate sets which are not surrounded by experimental data result in extrapolations which may not accurately describe the experimental flow pattern. In other words, this is an interpolation method. It should not be used for extrapolation, and it should be used in close proximity to actual experimental data. If a set of coordinates is selected which matches exactly with the coordinates of an experimental point, the method correctly returns the experimental velocity vector for that point because the weighting factor goes to infinity.

Experimental

The experimental arrangement for two-color PIV measurements is shown in Fig. 2. Two Nd:YAG lasers are used in forming the different-color light sheets for exposing the position of the particles in the seeded flowfield. The green-laser-light sheet is formed from the doubled output of a Nd:YAG laser (Quanta-Ray DCR 1A) at

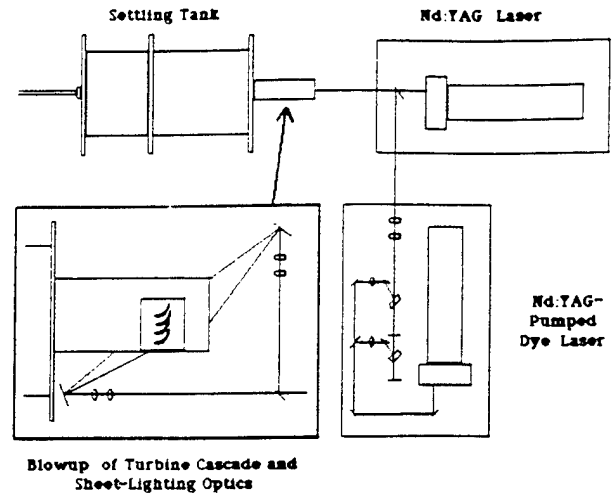


Fig. 2. Schematic Diagram of Experimental Arrangement Employed for Two-Color PIV Experiments on Turbine-Cascade Test Section. Both a Nd:YAG and a Nd:YAG-pumped dye laser employed for sheet lighting of test section. Forward and backward light sheets used to expose test section.

532 nm (this laser is capable of a single pulse in excess of 200 mJ). The second laser employed for the red-laser-light sheet is a broadband dye laser. The frequency-doubled output of a Nd:YAG laser (Quanta-Ray DCR 3A) is used to pump a dye laser consisting of an oscillator/amplifier combination which operates in a broadband mode for maximum conversion efficiency and output power. The dye laser is capable of a single pulse in excess of 100 mJ at 607 nm. The outputs from the dye and Nd:YAG lasers are combined by a dichroic mirror, split into two equal parts by a beamsplitter, and directed into sheet-forming optics. These optics consist of a cylindrical lens which spreads the laser beams two dimensionally and a plano-convex lens which controls the beam waist of the laser sheets. Two separate laser sheets of nearly equal intensity are required for lighting the turbine-cascade test section because of the limited optical access. The laser sheets are ~10 cm in height and 1 mm in thickness in the test section.

Synchronization of the two laser systems presented a special problem because of the difference in repetition rates between the two Nd:YAG laser systems (10 and 20 Hz). In the present setup the lamp output from the 20-Hz DCR 3 (dye) laser is frequency halved by a divided-by-two circuit and used to fire the flashlamps of the DCR 1 laser at 10 Hz. The internal Q-switch circuitry of the DCR 1 laser is used to control the

actual lasing of the 10-Hz laser. The Q-switch output from the DCR 1 is delayed by a pulse generator and fed into the Q-switch input of the DCR 3, thus firing the laser Q-switch at a fixed time delay after the DCR 1. This time delay is normally set to $5 \mu\text{sec} \pm 20 \text{ nsec}$. With this electronic arrangement, the DCR 3 laser discharges its flashlamps at a 20-Hz rate but fires its Q-switch at a 10-Hz rate.

A Nikon 35-mm-format camera was used to record the Mie scattering from the seeded flowfield. A macro zoom lens operating at an $f/8.4$ aperture and a shutter speed of 0.125 sec. was employed for the images reported in this study. This lens-aperture combination resulted in a magnification factor of 0.39. The shutter speed ensured that at least one double-pulse exposure would be obtained for every shutter opening, reducing the need for camera-synchronization electronics. If the flowfield emits a background light which will not allow the use of a low-speed shutter (i.e., a sooty flame or hot test section), then a high-speed shutter which can be synchronized to the laser firing must be employed. Color film of 100 ASA was used to record the two-color PIV images; the film was processed commercially.

The color film was digitized using the setup shown in Fig 3. A film projector was used to enlarge a section of the film onto a 384 x 576 Thompson CCD array camera (Photometrics, Ltd.) which digitized and stored the information for analysis. Each section of the film was digitized twice--once with a green-color filter and then with a red-color filter. The digitized film sections typically covered a 1.5 cm^2 area of the recorded image. This corresponded to a pixel resolution of $\sim 20 \mu\text{m}$ which was considered to be adequate for capturing the particle images. The 35-mm film was typically divided into 36 segments for digitization; these were stored on magnetic tape for analysis.

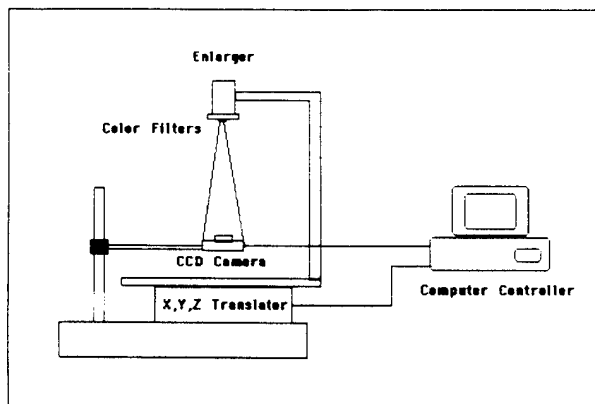


Fig. 3. Schematic Diagram of System for Digitization for Two-Color PIV Images.

The turbine-cascade test section (Fig. 4) consisted of four aluminum airfoils representative of the high-pressure-turbine, first-stage-nozzle guide-vane row of commercial transport engines. The vanes were one-half engine scale, having a chord of 3.66 cm and a span of 2.54 cm. Design turning was 72-deg., and the pitch spacing was 2.54 cm. Seeded, dry-air flow entered the cascade from a rectangular channel which was 28 cm in length and had a cross section of 23 cm^2 . The total throat area of the cascade was $\sim 5 \text{ cm}^2$. Each passage throat area was 1.61 cm^2 . The cascade was operated at an inlet total-to-exit static-pressure ratio of 2.15. Flow conditioning was provided upstream of the inlet channel by a large stagnation plenum containing screening and honeycomb flow straighteners. Access for the laser light sheets was provided by constructing one wall of the inlet channel and one of the exit tailboards of Plexiglas. Photographing the center passage of the cascade was done through a Plexiglas sidewall.

Results and Discussion

Analysis of the two-color PIV images was discussed in the theoretical section, and only a brief review will given here. The color negative is first divided into 36 sections which are digitized twice to distinguish color. Each green/red digitized section is then analyzed. The initial step of this analysis is to locate the center coordinates of the green- and red-particle images. Second, the digitized section (384×576) is subdivided into four or sixteen segments, depending upon the particle density and velocity variation from which correlation histograms are constructed for each segment. The final step in the analysis involves a particle tracker which employs the most probable displacement vectors determined from the correlation histogram of each segment to find green/red-particle velocity pairs. The reduced velocity vectors are then stored for statistical analysis and graphics display.

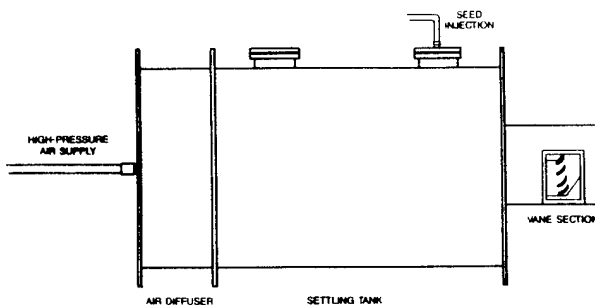


Fig. 4. Experimental Turbine-Cascade Test Section Employed for High-Speed-Flow Studies.

A two-color PIV image which was taken on the turbine-cascade test section is shown in Fig. 5. A 5- μ sec time separation between the green and red laser sheets was used for this photograph. The air flow is from left to right in the photograph. The seed employed in this study was plasma-produced alumina (Zyp Coatings, Inc.), consisting of 5- μ m hollow microballoons having an effective aerodynamic diameter of < 1 μ m. The hollow microballoons were chosen for this study to maximize particle visibility without sacrificing aerodynamic response. The seed is injected into the settling chamber just prior to the entrance of the test section. The flow speed of the air exiting the settling chamber is \sim 80 m/sec.

The processed two-color PIV vectors for the photograph shown in Fig. 5 are displayed in Fig. 6. The length of the vectors depicted in this plot indicates the speed of the air flow. Analysis of the two-color PIV image indicates that the air entering the turbine test section was flowing at a rate of \sim 80 m/sec. However, as the air entered

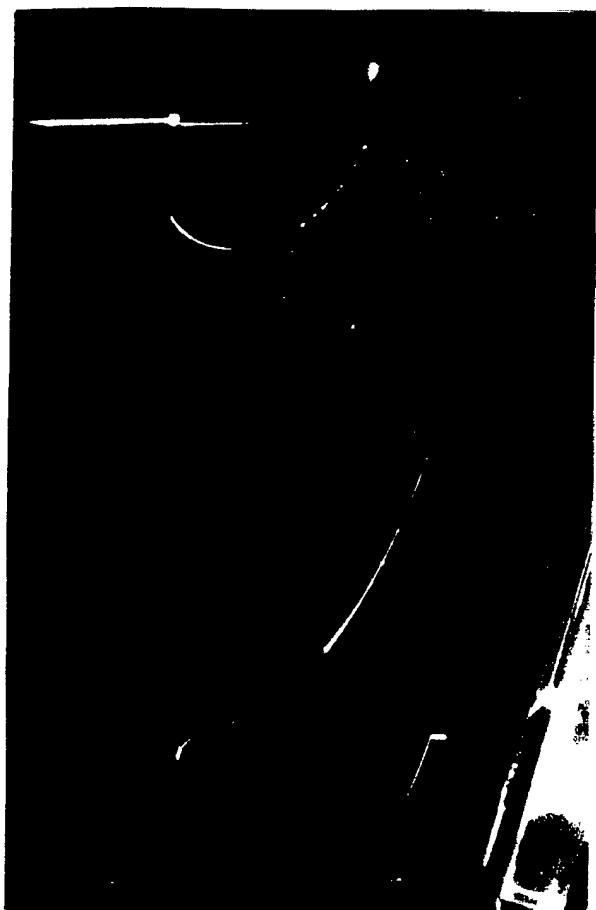


Fig. 5. Two-color PIV Image Obtained in Turbine-Cascade Test Section. Time delay between laser pulses of 5 μ sec employed for photograph.

the passages between the turbine blades, it initially slowed to \sim 60 m/sec and then continually accelerated to \sim 340 m/sec at the tip of the blades. The acceleration of the flow in the channel between the blades can be easily visualized in this plot.

In order to achieve consistent and reliable results, it was desirable to focus on a region sufficiently small that the velocity would be essentially constant but sufficiently large that a significant number of green/red-particle pairs would be present. This requirement resulted in digitization of regions of \sim 10 x 15 mm which were further divided into fourths or sixteenths, depending upon the particle density and the variation in velocity field. The subdivision of the sections into sixteenth regions was especially important in the areas near the blades where the velocity was accelerating rapidly. Although the two-color PIV technique allows determination of speed and direction with only one green/red-particle pair, statistically it is desirable to have a minimum of ten pairs.

Analysis of the experimental data results in a two-dimensional, instantaneous representation of the flowfield, with velocity vectors

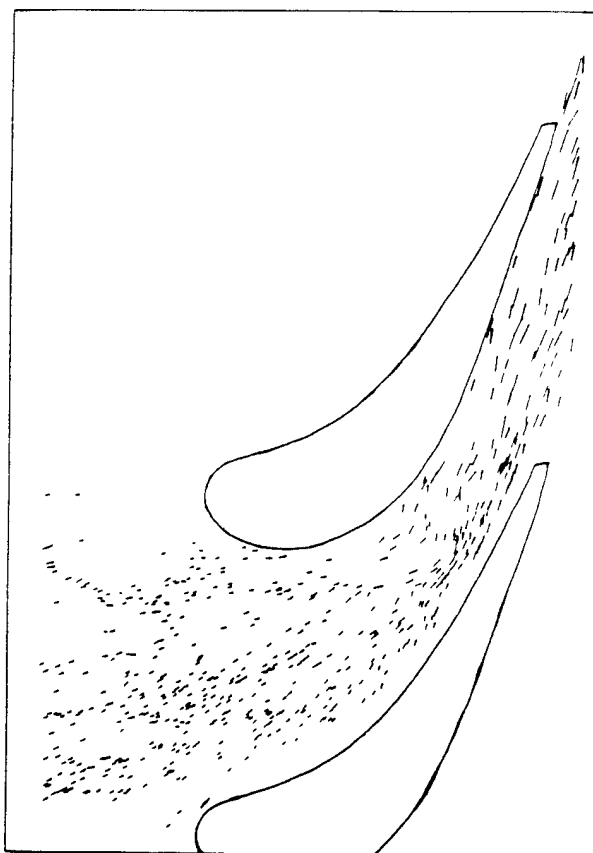


Fig. 6. Processed Velocity-Vector Map for Turbine Cascade.

located at random positions (location of the seed particles when the photographs were taken). The interpolator was used to estimate the velocity field for a selected set of coordinates corresponding to the node coordinates of a numerical model. Figure 6 shows a set of experimental data and Fig. 7, the corresponding interpolated data. The interpolator "smooths" the experimental data. Since the length scale over which the data were interpolated depends upon the distance to the specified number of nearest neighbors, the "smoothing" process may average out local spatial variations associated with structures in the flowfield. If regions exist where only a few experimental points are available, the interpolated data may be excessively weighted by the closest neighboring point. If the interpolator is to be reasonably accurate, the number of experimental velocity vectors should be sufficiently high that the distances to the nearest neighbors used in the interpolation are "short" compared to the length scales associated with the flow channels.

The interpolator results in Fig. 7 show the general flow features which were expected and

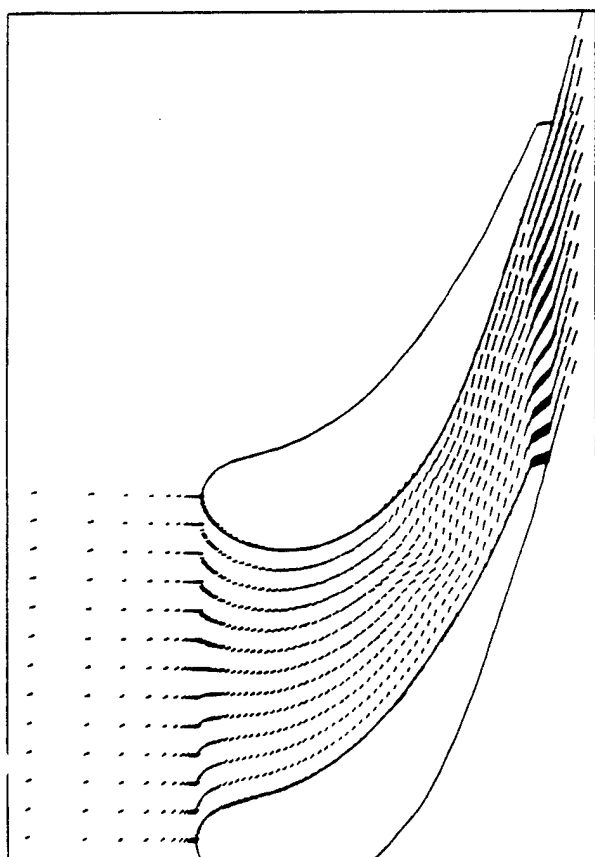


Fig 7. Interpolated Velocity Flowfield of Turbine Cascade.

measured experimentally. The inlet velocity field is uniform at ~ 80 m/sec, slows to a minimum of ~ 60 m/sec at the entrance to the channel between the blades, and accelerates through the channel to ~ 340 m/sec at the tip of the blades. A bubble is also evident in the middle of the flow channel. This bubble is thought to be an artifact for which at least two explanations can be given. It may be an artifact of the interpolation technique since only a few experimental velocity vectors were identified in this region (see Fig. 6). Another explanation may be that the seed particles cannot track the gas flow in the region behind the blades because of flow separation which would be a contributing factor to the low number of velocity realizations in this area.

Future work with the two-color PIV technique on the turbine cascade will involve evaluating the feasibility of imaging submicron particles for velocimetry and comparing the results with a computer model which was developed to simulate the flowfield of the cascade. Also, a high-resolution film digitizer will be utilized for digitizing the color film in a single step in under 15 min. which will help to reduce the analysis time and minimize problems with segment alignment.

Summary

In summary, the two-color PIV technique consists of 1) acquiring an image of green/red-particle positions, 2) separating the green from the red particles, 3) finding the coordinates of the particles, 4) determining the most probable vector displacement for green/red pairs, and 5) matching green/red pairs which are within a specified percentage of the most probable vector displacement. The two-color PIV technique has the advantage that direction as well as particle displacement is uniquely determined because the green-particle image occurs before the red one by a known time increment. The technique is, thus, applicable to complex flowfields (i.e., recirculating), where the normal 180-deg. directional ambiguity of single-color techniques can be troublesome. Velocity measurements using the two-color PIV technique in a turbine-vane cascade test facility indicated that the large changes in direction and flow speed associated with these flowfields can be tracked by this technique.

A multipoint, inverse-distance interpolation method was developed to estimate velocity data at specific spatial locations from nearest neighbor experimental data. Utilization of the interpolator allowed the random experimental velocity distribution to be transformed onto a

grid to facilitate comparison with calculated data. The interpolated data provide a "smoothed," two-dimensional visualization of the flowfield on a regular grid.

Acknowledgement

This work was supported by and performed at the Wright Laboratories/Aero Propulsion and Power Laboratory under Contract No. F33615-90-C-2033.

References

1. R. Meynart, *Appl. Opt.* 19, 1385 (1980).
2. R. Meynart, *Appl. Opt.* 22, 535 (1983).
3. C. S. Yao and R. J. Adrian, *Appl. Opt.* 23, 1687 (1984).
4. R. J. Adrian and C. S. Yao, *Appl. Opt.* 24, 44 (1985).
5. R. J. Adrian, *Appl. Opt.* 25, 3855 (1986).
6. C. C. Landreth, R. J. Adrian, and C. S. Yao, "Double-Pulsed Particle Image Velocimetry with Directional Resolution for Complex Flows," Tenth Biennial Symposium on Turbulence, Rolla, Missouri, 1986.
7. J. M. Coupland, C. J. D. Pickering, and N. A. Halliwell, *Appl. Opt.* 23, 11 (1987).
8. D. L. Ruess, R. J. Adrian, C. C. Landreth, D. T. French, and T. D. Fansler, "Instantaneous Planar Measurements of Velocity and Large-Scale Vorticity and Strain Rate in an Engine Using Particle-Image Velocimetry," SAE International Congress and Exposition, SAE Technical Paper 890616, 1989.
9. B. Hiller, R. A. Booman, C. Hassa, and R. K. Hanson, *Rev. Sci. Instrum.* 55, 1964 (1984).
10. R. B. Miles, J. Connors, E. Markovitz, P. Howard, and G. Roth, *Phys. Fluids A* 1, 389 (1989).
11. L. R. Boedeker, *Opt. Lett.* 14, 473 (1989).
12. B. J. Hiller, J. C. McDaniel, J. E. C. Read, and R. K. Hanson, *Opt. Lett.* 8, 474 (1983).
13. J. C. McDaniel, B. Hiller, and R. K. Hanson, *Opt. Lett.* 8, 51 (1983).
14. B. Hiller and R. J. Hanson, *Opt. Lett.* 10, 206 (1985).
15. B. Hiller and R. K. Hanson, *Appl. Opt.* 27, 33 (1988).
16. L. P. Goss, M. E. Post, D. D. Trump, B. Sarka, C. D. MacArthur, and G. E. Dunning, Jr., "A Novel Technique for Blade-to-Blade Velocity Measurements in a Turbine Cascade," AIAA Paper 89-2691 Presented at the AIAA/ASME/SAE/ASEE 25th Joint Propulsion Conference, Monterey, California, July 10-12, 1989.
17. L. P. Goss, M. E. Post, D. D. Trump, and B. Sarka, "Two-Color Particle-Imaging Velocimetry," Accepted for publication in the *Journal of Laser Applications*.



AIAA-93-0412

**TWO-COLOR PARTICLE-IMAGING
VELOCIMETRY IN VORTEX STRUCTURES**

M. E. Post and L. P. Goss

Systems Research Laboratories, Inc.

A Division of Arvin/Calspan

2800 Indian Ripple Road

Dayton, OH 45440-3696

**31st Aerospace Sciences
Meeting & Exhibit
January 11-14, 1993 / Reno, NV**

TWO-COLOR PARTICLE-IMAGING VELOCIMETRY IN VORTEX STRUCTURES

M. E. Post* and L. P. Goss**

Systems Research Laboratories, Inc.

A Division of Arvin/Calspan

2800 Indian Ripple Road

Dayton, OH 45440-3696

Abstract

The capability of two-color Particle-Imaging Velocimetry (PIV) for making velocity measurements in vortex structures has been demonstrated and the data used to calculate stream functions, shear, and vorticity. Two-color PIV photographs were obtained for two experimental systems which generate vortex structures, and these photographs were analyzed using a modified correlation technique. A driven shear-layer flow formed with a splitter plate was employed to produce a vortex train, and a toroidal vortex was obtained by impulsively forcing a gas mixture through a sharp-edged circular orifice. Two-color PIV was shown to be capable of measuring a near-instantaneous two-dimensional velocity field associated with vortex structures. In one case the flow pattern was complex and cyclical in time (shear-layer flow), and in the other case the flow was transient in nature (single-toroidal vortex traveling down a duct). The velocity data were used to calculate stream functions, shear, and vorticity for comparison with computational models.

Introduction

The principle of two-color Particle-Imaging Velocimetry (PIV) was suggested by Adrian¹ in 1986 as a means of removing the directional ambiguities associated with one-color PIV, and the technique was first implemented by Goss, *et al.*,² in 1989 in transient flow through a turbine-cascade system. This paper describes a new method for the digital analysis of a two-color PIV photograph and presents some recent experimental results. The new analysis method is a modified cross correlation technique referred to as point-array correlation which makes use of a reduced data set based on peak center locations (an array of point coordinates) of the seed particles photographed in two-color images. This technique makes it possible to reduce the input data set from digitized image arrays on the order of 50 Mbytes

to particle-center arrays on the order of 50 kbytes.

Applying the methods developed by Adrian¹ in one-color PIV, a number of researchers have employed the technique to obtain near instantaneous, two-dimensional velocity data in complex and transient flowfields. An instantaneous, two-dimensional picture of the entire flowfield yields information in transient experiments where time-averaged, pointwise measurements (LDV or hot wire) are not practical. Two dimensional measurements can also provide valuable insight into spatial correlations of flowfield data where time-averaged, pointwise data may be difficult to interpret. PIV methods should be viewed as complementary to time-averaged, pointwise data.

Overview of Two-Color PIV

The two-color PIV technique utilizes color to temporally mark the position of small seed particles in a flowfield. A laser sheet (green) formed by passing the output from a doubled Nd:YAG laser through a cylindrical lens is used to illuminate the seed particles in the flowfield. After a short time delay (ranging from a few microseconds for high-velocity flow systems to milliseconds for low-velocity flow systems), a second laser sheet (red) from a Nd:YAG-pumped dye laser is pulsed to illuminate the flowfield a second time. Any particles remaining in the plane of the laser sheets produce a "displacement vector" pair which is made up of a green- and a red-particle image. The result is a near-instantaneous, two-dimensional vector field. The unique color coding helps to remove the directional ambiguities associated with one-color techniques. The particle images are recorded on standard color film which is processed commercially. The color negative is digitized with a high-resolution color scanner to obtain separate color images associated with each laser pulse. The experimental arrangement for two-color PIV measurements in the pulsed-laser sheet-lighting mode is shown in Fig. 1 and is described in more detail elsewhere.³ A swept-beam mode of two-color PIV has also been demonstrated⁴ using an argon-ion laser.

*Research Physicist, Member AIAA

**Dir. of Research, Optical Diag., Member AIAA

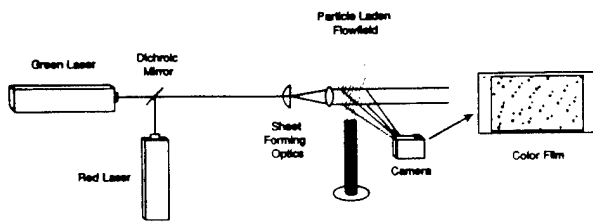


Fig. 1. Schematic Diagram of Two-Color PIV Arrangement Used in This Study.

The basic principle of PIV is straightforward. The average velocity of a two-color particle-image pair is the vector displacement divided by the time increment between pulses

$$(v_x, v_y) = (x_2 - x_1, y_2 - y_1) / \Delta t \quad (1)$$

where (x_1, y_1) and (x_2, y_2) are the positions of a particle when it is illuminated by Color-1 (first) and Color-2 (second) light sheets. This expression is obtained from a series expansion of position as a function of time and is strictly applicable only when Δt is sufficiently small that terms second order and higher in Δt are negligible. For complex flows and for high-seed density, the process of matching Color-1 and Color-2 images is accomplished with correlation methods. The analysis procedure consists of 1) determining the spatial locations of the digitized particle images, 2) constructing a set of local correlation maps from which the average displacement vectors can be determined, and 3) utilizing this information in a tracker which identifies particle vector pairs from the digitized image. These procedures have been described in more detail by Goss, *et al.*^{2,3}

A number of issues must be addressed in order to obtain PIV photographs. Optical access to the flowfield to be studied must be provided, and the flow must be seeded with particles or droplets that can serve as light scatterers. The ability of the particle to follow the flow must be considered. For two-color PIV, lasers must be selected to produce the two different-color light sheets, and a timing-control mechanism is required for controlling the time interval between successive light pulses. The output from the lasers is aligned and passed through sheet-forming optics to ensure that the light from the lasers will illuminate the same plane. The two colors must expose different layers of the color film. The image on the color film must be digitized and the color data separated into its two components. These issues have been addressed previously by Adrian,¹ Goss, *et al.*,² and Smallwood.⁵

Operational Modes

As with other PIV methods, two-color PIV can be implemented in three modes. When the number density of particles in the PIV photo is small, the process of matching particle image pairs is reduced to finding the closest red (Color-2) particle to a given green (Color-1) particle. The maximum expected displacement (d_{max}) is equal to the maximum expected velocity times the time interval between different-color light sheets. The condition for this mode is that the number of Color-2 particles per unit area of the image times the area of a circle with radius equal to d_{max} (maximum expected displacement) is less than 0.1. The value 0.1 is somewhat arbitrary and effectively indicates that about 90% of the close-neighbor matches will be correct. This first mode is very simple to implement, but it necessarily produces a very sparse data set.

The second mode is also a particle tracking mode that is guided by performing a local correlation analysis. The local correlation provides information concerning the direction and distance to a red (Color-2) particle from a given green (Color-1) particle. The correlation also gives an indication of the uncertainty in the expected vector displacement. This uncertainty is dependent on the spatial variation in the velocity field over the region where the local correlation is performed. The magnitude of the uncertainty in the vector displacement is labeled Δd . The condition for this second mode is that the number of particles per unit area of the image times the area of a circle with radius equal to Δd (the scale of the expected distribution of displacements) is less than 0.1.

In the third mode the number density of particles per unit area is higher than for the second mode, and particle tracking is no longer reliable. At this high number density, particle tracking would almost always find a match, but the probability of several particles being within the expected uncertainty (Δd) is high, and it is no longer clear which of the near particles is the correct match. In this mode of operation, a correlation analysis is performed on a subset of the data, and the average displacement is assigned to the center of the subset.

Overview of Correlation Methods

Correlation modes are required for the second and third operational modes of PIV described above. This section provides a brief review of some of the correlation techniques that have been utilized for PIV analysis.

The average particle displacement within a local region of the digitized image can be determined in several ways. Adrian,¹ developed an optical correlation technique for analyzing one-color PIV photographs. Here, the negative is interrogated with a laser beam to produce an optical Fourier transform of the particle-image pairs within the beam spot. An inverse transform of the Young's fringe pattern results in a correlation map that is analyzed to find the most probable particle displacement. The inverse-transform process can be performed digitally or optically. The resulting vector displacement is transformed into a velocity vector by dividing the displacement components by the time interval between laser pulses used to produce the PIV image. The velocity vector is assigned to a spatial location corresponding to the center of the beam spot. This method is generally used for the high-particle-density operational mode (Mode 3).

Some difficulties are associated with the analysis of the correlation map produced from one-color photographs. A 180-deg directional ambiguity is associated with one-color PIV because the order in which the two particle images is produced is not known, and there is a large central auto-correlation peak is present in the correlation map. Unless the flow is simple or there is *a priori* knowledge concerning the flow, the directional ambiguity causes uncertainty in the analysis of the data, and the large central correlation peak can interfere with low-speed measurements.

Because of these difficulties, Adrian¹ suggested several methods (including two-color methods) for eliminating the directional ambiguities in the one-color correlation map, and he has continued the analysis of one-color PIV methods utilizing an image-shifting technique. In this method a fixed displacement is added to all particle displacements. The directional ambiguity is eliminated because the correct peak is in the part of the correlation map on the side in the direction of the displacement shift. After analysis of the correlation map, the fixed displacement is subtracted from the average vector displacement.

The digital analog of the optical correlation can be performed by digitizing the PIV image and using the correlation function to find the average displacement between first and second particle images. To increase computational speed, FFT's are used to transform and inverse transform a section of the image corresponding to a beam spot. One problem with FFT methods is the requirement to use dimensions that are restricted to multiples of two or some other special set of values. Alternative methods for

performing digital correlations of PIV images will be presented for one-dimensional data sets and then extended to two-dimensional data sets.

One-Dimensional Auto-Correlation

In one dimension the correlation function for a discrete function is given by

$$C_0(s) = \sum_x f(x) f(x-s) \quad (2)$$

For one-dimensional functions this calculation can be performed in a straightforward manner. Note that the number of calculations required to calculate C_0 is proportional to the number of x values times the number of s values. The range of s values is limited by the Nyquist criteria to at most half the range of the x values. Figures 2-5 correspond to example calculations for this and the following one-dimensional auto-correlations and cross-correlations. The figures are discussed at the end of the section on cross-correlation.

An alternative method for correlating the function is to use a "histogram approach." The function is pre-processed to find the local maximum values, and the summation of Eq. (2) is only applied at the locations of the local maxima. This is represented by

$$C_1(s) = \sum_m f(x_m) f(x_m-s) \quad (3)$$

The number of operations to calculate C_1 is proportional to the number of local maxima (m) in $f(x)$ times the number of s values. The reduction in the number of operations to calculate C_1 is slightly offset by the requirement to pre-process the function to find the local maxima. However, the number of operations required to find the local maxima is only proportional to the number of x values, and the total number of operations to calculate C_1 is less than that required to calculate C_0 .

The logical extension of the histogram approach is a "point-array-correlation" technique. In this method only the local maximum values are compared. It is represented by

$$s' = x_{m_i} - x_{m_j}, \quad i, j = 1, \dots, m \quad (4)$$

$$C_2(s') = C_2(s') + f(x_{m_i}) f(x_{m_j})$$

The number of s' values is limited to at most the square of the number of local maxima. If s' for a given i, j pair exceeds the maximum expected displacement, it is not included in the

calculation of C_2 . The number of operations to calculate C_2 has been reduced to a number that is proportional to the product of the number of local maxima. The advantage of this method is that the original array of function values at all the discrete values of x can be reduced to an array of local maxima. As for the histogram calculation, the number of operations required to find the local maxima is proportional to the number of x values.

The histogram and point-array methods defined by (3) and (4) can be normalized to yield

$$C'_1(s) = \sum_m f'(x_m) f'(x_m - s) \quad (5)$$

$$s' = x_{m_i} - x_{m_j}, \quad i, j = 1, \dots, m \quad (6)$$

$$C_2(s') = C_2(s') + f'(x_{m_i}) f'(x_{m_j})$$

where the f' values are set equal to one. This corresponds to setting the point-array data to unity at each location where a local maximum is present.

Cross-Correlation

Analysis of two-color PIV data requires the cross-correlation of two functions. One corresponds to Color-1 data and the other to Color-2 data. The cross correlation of one-dimensional functions $f(x)$ and $g(x)$ is given by

$$CC_0(s) = \sum_x f(x) g(x - s) \quad (7)$$

where the cross-correlation has been identified as CC . The cross-correlation histogram and point-array expressions are obvious modifications of the auto-correlation functions described above. The normalized point-array cross-correlation is

$$s' = x_{m_i} - x_{m_j}, \quad i, j = 1, \dots, m \quad (8)$$

$$CC_2(s') = CC_2(s') + f'(x_{m_i}) g'(x_{m_j})$$

Example Calculations

Figures 2-5 show example calculations for the one-dimensional auto- and cross-correlations described above. Figure 2 shows the example data sets. The bottom row is a one-dimensional representation of three particle pairs in a one-color experiment. Each particle is shown as a Gaussian-shaped peak centered at one location and repeated with the center shifted by ten units. This corresponds to a double exposure of the three particles as they

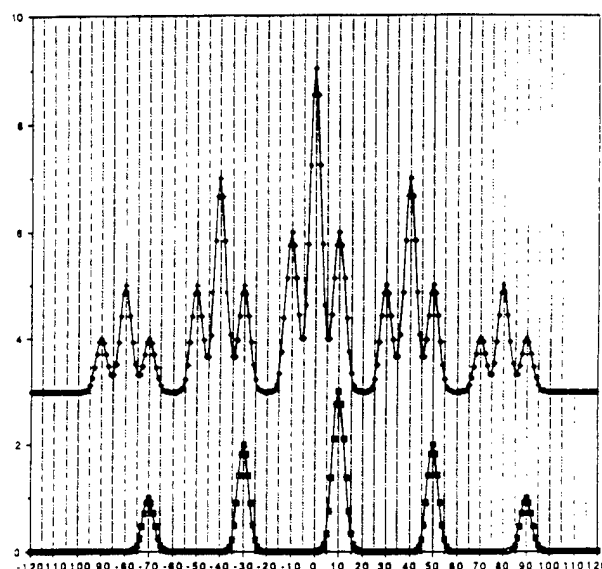


Fig. 2. Graph of Data Used in Example Calculations.

moved ten units to the right (or left). In this case the three particles are evenly spaced and identical in shape.

The top row corresponds to a picture of the three particles in one color and the middle row to a picture of the same three particles in a second color after moving ten units to the right (definitely right this time).

Figure 3 shows the auto-correlation of the one-color data (bottom row of Fig. 2) above the cross-correlation of the two-color data (top and middle rows of Fig. 2). Figures 4 and 5 show the corresponding histogram and point-array correlations, respectively.

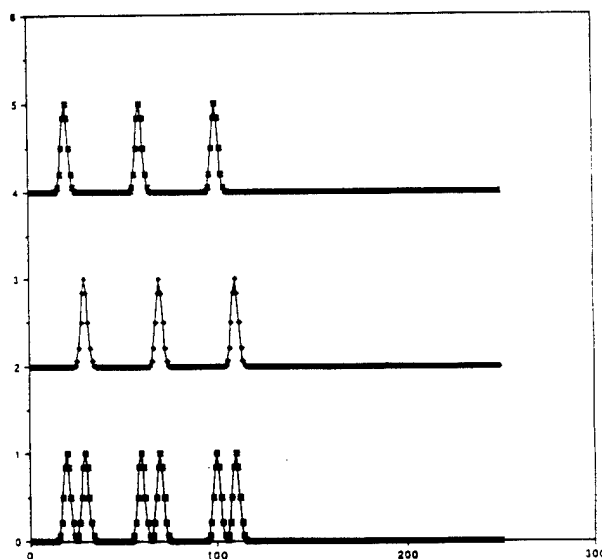


Fig. 3. Graph of Standard Auto- and Cross-Correlation Examples.

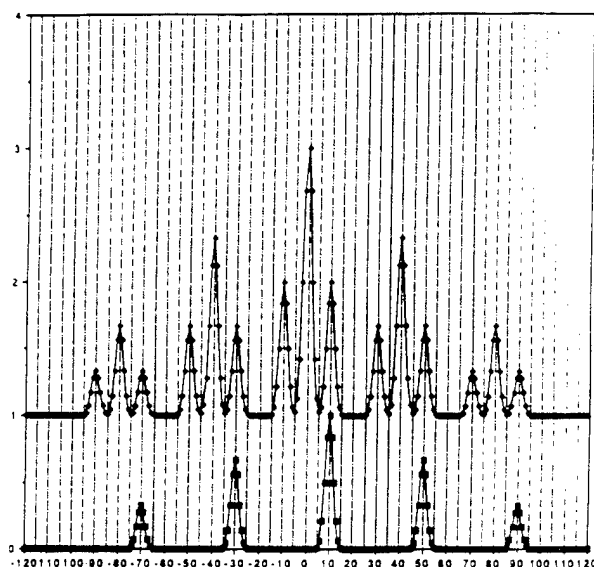


Fig. 4. Histogram Plot of Auto- and Cross-Correlation Examples

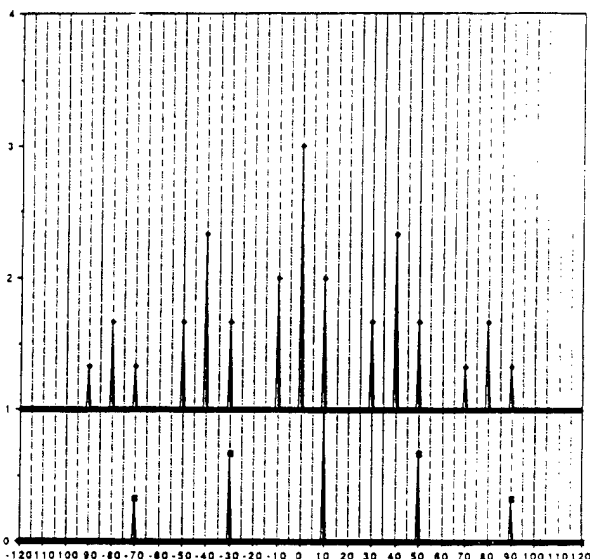


Fig. 5. Graph of Point-Array Auto- and Cross-Correlation Examples

The relatively broad peaks in a C_0 map are the result of the convolution of each peak shape with the peaks within the correlation dimension. The narrower peaks in the C_1 (histogram) map result from the peaks being scaled by peak intensities and added to the correlation map. The spikes in the C_2 (point-array correlation) are the products of peak intensities.

Note the differences between the graphs for auto-correlation and cross-correlation. The central peak in the auto-correlation map is not present in the cross-correlation map, and the peak in the cross-correlation map does not have

a symmetry peak as is present in the auto-correlation map.

Normalizing the data removes particle-intensity information from the analysis, and the peak-center correlation removes particle size and shape information from the analysis. Many PIV researchers who make use of intensity, shape, and size information when analyzing their data, but experience gained in this laboratory with processing many images from a variety of reacting and non-reacting flow experiments has shown that in many cases obvious particle image pairs have significantly different intensities or sizes. This occurs because of 1) nonuniformities in the laser sheets, 2) the distribution of laser energy across the laser sheets, and 3) particle-image variations associated with depth of focus. These variations would not introduce significant error into the analysis if all the particle image pairs were separated by exactly the same distance; however, the distribution of displacements observed in real data is distorted by the non-uniform weighting associated with variations in intensity, size, and shape.

It has been suggested that statistical variations in intensity, size, and shape will be averaged out for correlations that contain many particle image pairs and that the particle center correlations are somewhat overemphasized. This argument fails to recognize that spatial resolution is obtained by correlating small sections with necessarily smaller numbers of particle image pairs. A spatial resolution trade-off exists between reducing the dimension of the subsection to be correlated and increasing the dimension of the subsection to include sufficient particles to obtain an acceptable signal-to-noise ratio in the correlation map. This trade-off is especially important in regions where the velocity gradient is stronger.

Multi-Dimensional Correlations

The same approach can be applied to functions of more than one variable where the real savings in computational effort for point-array correlations becomes more apparent. For the two-dimensional case

$$CC_0(s,t) = \sum_x \sum_y f(x,y) g(x-s,y-t) \quad (9)$$

The number of operations required to calculate CC_0 is proportional to the product of the number of x , y , s , and t values. As noted for the one-dimensional functions described previously, the range of s and t values is limited by the Nyquist criteria. The expressions for the two

dimensional cross-correlation histograms and point-arrays are obvious. For comparison with CCO, look at the normalized point array correlation

$$s',t' = (xm_i - xm_j), (ym_i - ym_j), \quad i,j = 1,\dots,m \quad (10)$$

$$CC_2(s',t') = CC_2(s',t') + f'(xm_i,ym_i) g'(xm_j,ym_j)$$

The number of operations required to calculate C_2 is proportional to the square of the number of local maxima. The number of pre-processing operations required to find the local maxima is proportional to the size of the two-dimensional array for $f(x,y)$ and $g(x,y)$. For two-dimensional data, the relative number of operations for the point-array method is orders of magnitude less than that required for standard correlation techniques.

Geometry Restrictions

In optical-correlation methods, both first and second images of a particle must be within the beam spot. In analogous digital methods, a section of the PIV photograph corresponding to a beam spot is analyzed using auto-correlation techniques. This is a case where copying the optical technique has restricted the flexibility available with digital methods. An advantage of digital methods is the ability to cross-correlate sections of arbitrary shapes. The first-color particle images in a subsection of a photograph can be cross-correlated with the second-color particle images in a surrounding subsection. Since the particle displacement is not known in advance, the surrounding section is enlarged by an amount equal to the maximum expected displacement. This results in every first-color particle image retaining the possibility of being correlated with its second-color particle image, with the exception of particles near the edges of the PIV photograph. Cross-correlation edge effects are limited to the true edges of the PIV photograph. This approach was implemented in the first application of two-color PIV by Goss, *et al.*²

Analysis of Correlation Map

The advantages of the two-color cross-correlation map are the absence of paired correlation peaks with 180-deg ambiguity and the absence of the auto-correlation peak that can interfere with finding small particle displacements associated with low velocities. For the standard and histogram cross-correlations shown in Figs. 3 and 4, the average displacement

is determined by finding the maximum of the highest peak. For the point-array correlation, the average displacement is determined by finding the most dense cluster of points. Although this method is more complicated than usual peak-finding techniques, information on the distribution of displacements can be gained. Distribution information can also be determined from the peak in a standard or histogram correlation approach; however, it must be remembered that these peaks are a convolution of peak location, intensity, size, and shape. It is not a simple matter to deconvolute the information in the peaks without making assumptions about the peak shapes.

The most dense cluster in the point-array correlation map is found by integrating the data in the correlation map over a range of scales (essentially binning the data with a range of bin dimensions). This procedure is initiated by integrating the data over a small dimension with an overlapping grid and finding the local maxima in the grid. Next, the integration dimension is incremented, and the process is repeated. The cycle is interrupted when the ratio of the highest peak to the second highest peak begins to decrease or when the highest peak is equal in value to the number of first-color particles used to construct the correlation map (any additional increase can only add background counts to the signal). The integration dimension is a measure of the scale of the distribution of displacements for the data being correlated.

Applications to Two-Color PIV

Toroidal Vortex

A toroidal vortex was generated with an experimental apparatus used by Roberts, *et al.*,⁶ to study flame-vortex interactions. The system was an 11.4 x 11.4 x 61.0 cm duct in a vertical orientation. A Plexiglas window on the front allowed observation, and slit windows on the sides allowed transmission of the laser sheets. A loudspeaker mounted on top of the duct was pulsed to drive gas through a sharp-edged circular orifice (3.81-cm diameter). As the pulse passed through the orifice, a single downward-traveling toroidal vortex was generated. When visualized with fine TiO₂ smoke, the vortex has the appearance of a well-defined doughnut-shaped smoke ring traveling down the duct.

A 35-mm Nikon camera was used to collect the PIV photographs. Customized electronics were used to synchronize the laser pulses and time separation with the arrival of the vortex in the camera field of view. The film (Kodak Gold ASA 100) was processed commercially.

The laser pulses were generated with a frequency doubled Nd:YAG laser (green light, 532 nm) and a Nd:YAG pumped dye laser (red light, 640 nm). For the PIV photographs the gas in the duct was seeded with alumina microballoons having a nominal diameter of 6 μm .

Figure 6 shows the measured velocity field in the cross section of a toroidal vortex. The only initial information on the velocity field was the maximum expected particle displacement in the 1.0-msec interval between laser pulses. A calibration photograph was used to find the equivalent length of a digitized pixel. The counter-rotating structures are clearly visible as are the compressed and expanding flows along the translational axis. The lack of data in the vortex centers was due to difficulties associated with seeding the gas in the vicinity of the speaker and with the ability of the seed particles to follow the flow in regions where they are effectively being centrifuged out of the vortex. Additional studies of the interaction of the toroidal vortex with a flame surface are underway.

Vortex Structures in Two-Dimensional Shear Layer

Shear-layer experiments have been performed in an experimental apparatus used by Hancock, *et al.*,⁷ to study droplet-vapor interactions. A splitter plate divides a 12.7-cm square duct equally. Dry air was used on both sides of the splitter plate, with the high velocity set at 0.7 m/sec and the low velocity at 0.35 m/sec. Both sides were seeded with alumina microballoons having a nominal diameter of 6 μm . The same lasers described above were used to illuminate the particles, and the same 35 mm camera was utilized. The flow was driven at 20 Hz with a loudspeaker that perturbed the low-speed flow. This produced a set of well-defined,

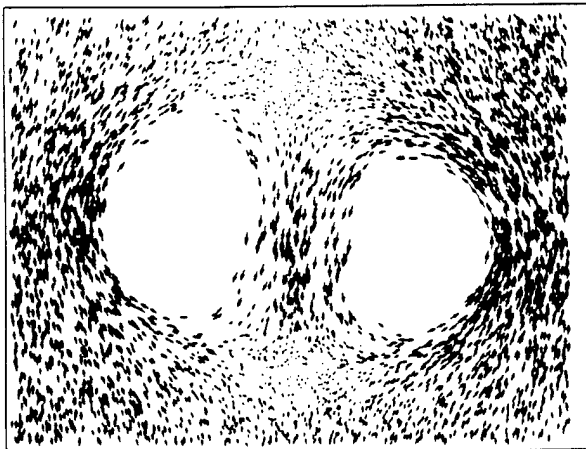


Fig. 6. PIV Vector Field for Toroidal Vortex.

periodic vortex structures that were visualized with TiO_2 particles.

Figure 7(a) shows the measured the velocity field in a shear layer produced with a splitter plate. This flow was somewhat simpler since all particles move in the upward direction. Subtracting the average flow velocity from the data transforms to a reference frame that is moving at the translational speed of the vortex structures commonly observed in shear-layer flow [Fig. 7(b)]. The rotational motion of three vortex structures is evident. All three structures are rotating in a clockwise direction, as seen in this view.

Initially the only information concerning the velocity field was the maximum expected particle displacement in the 1.5-msec interval between laser pulses. A calibration photograph was used to find the equivalent length of a digitized pixel (17.1 $\mu\text{m}/\text{pixel}$). The maximum expected displacement was about 1.1 mm which corresponds to about 64 pixels in the digitized image. A single-pixel displacement is equivalent to a velocity of 1.14 cm/sec. The digitized field of view was $\sim 6.5 \text{ cm} \times 9.8 \text{ cm}$.

A multi-point, inverse-distance, weighted interpolation function has been used to estimate the velocity at positions on grids for calculations of shear, vorticity, and stream function and for comparisons with numerical models. Stream lines and vorticity contours for the shear-layer flow were prepared with a commercial software package (Surfer) and are shown in Figs. 8 and 9. Note that Fig. 8(a) shows the stream function for the velocity vectors of Fig. 7(a) and that Fig. 8(b) shows the stream lines for Fig. 7(b). The stream lines in the laboratory frame [Fig. 8(a)] are not especially remarkable and show the upward motion

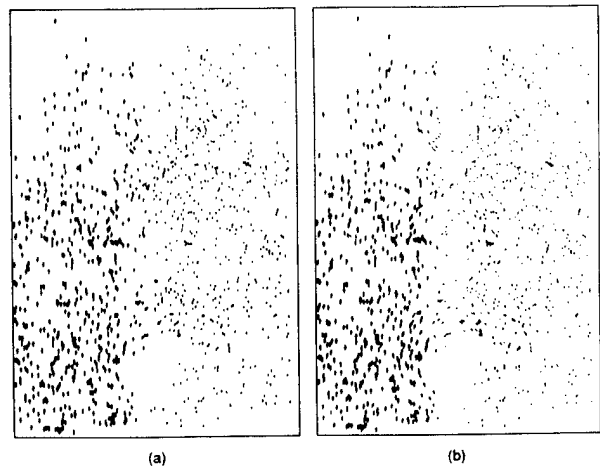


Fig. 7. PIV Vector Field for Shear Layer in (a) Laboratory Frame and (b) Moving Reference Frame.

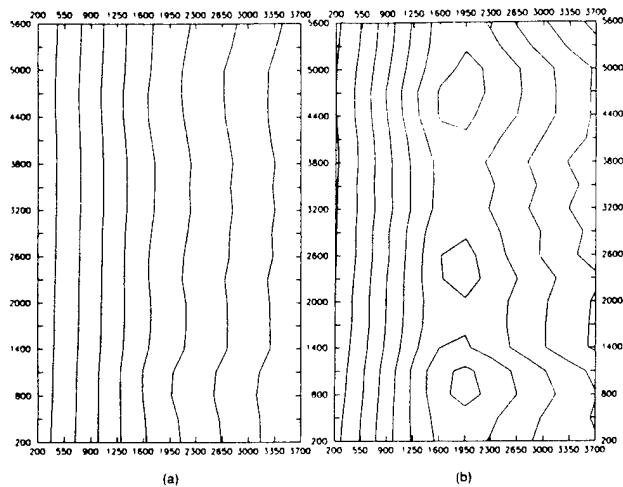


Fig. 8. Stream Lines for Shear Layer in (a) Laboratory Frame and (b) Moving Reference Frame.

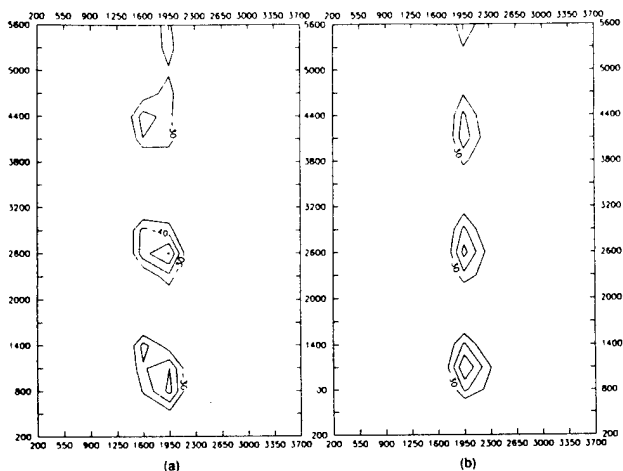


Fig. 9. Vorticity Contours (a) for Shear Layer and (b) From Numerical Model

expected. By subtracting a vector equal to the average velocity of the shear layers makes the frame of reference stationary with respect to the vortex structures, and three circular stream lines corresponding to the vortex structures are observed.

The vorticity contours shown in Fig. 9 are the same in both reference frames. They show the three vortex structures and have the same sign since they are rotating in the same direction. Figure 9(b) shows a set of vorticity contours prepared with the same grid and software used for the experimental data, but the underlying velocity field was calculated with a CFD code developed by Katta, *et al.*⁸

Summary

Two-color PIV has been utilized to measure a two-dimensional cross section of the velocity field in a toroidal vortex propagating down a square duct and in a two-dimensional shear layer. Both data sets were characterized as intermediate seed density (Operational Mode 2) and were analyzed with particle tracking methods.

A number of techniques are available for performing the correlation analysis used to find local average velocities, and the normalized, point-array correlation described here requires the fewest number of calculations of any of the techniques discussed in this paper. The correlation need not be restricted to correlations of data subsets of the same size for either auto- or cross-correlations. By correlating a first-color subsection with an expanded second-color subsection, edge effects are limited to the true edges of the photograph.

Future work will involve high-particle-density measurements as well as comparisons of point-array and FFT correlation methods. Since the number of calculations for point-array correlations is proportional to the number of particles, it may be possible to extend the technique to three dimensions with a relatively small increase in complexity. The current limitation appears to be the lack of an experimental technique for finding the simultaneous positions of particles in three dimensions.

Acknowledgement

This work was supported by the Aero Propulsion and Power Directorate of Wright Laboratory, Wright-Patterson Air Force Base, Ohio, under Contract No. F33615-90-C-2033.

References

1. Adrian, R. J., "Image Shifting Technique to Resolve Directional Ambiguity in Double-Pulsed Velocimetry," *Appl. Opt.* 25, 3855 (1986).
2. Goss, L. P., Post, M. E., Trump, D. D., Sarka, B., MacArthur, C. D., and Dunning, G. E., Jr., "A Novel Technique for Blade-to-Blade Velocity Measurements in a Turbine Cascade," AIAA Paper 89-2691 presented at the AIAA/ASME/SAE/ASEE 25th Joint Propulsion Conference, Monterey, California, July 1989.

3. Goss, L. P., Post, M. E., Trump, D. D., and Sarka, B., "Two-Color Particle Velocimetry," *J. Laser Appl.* 3(1), 36 (1991).
4. Post, M. E., Trump, D. D., Goss, L. P., and Hancock, R. D., "Two-Color PIV Using a Single Argon-Ion Laser," submitted for publication in *Experiments in Fluids* in October 1992.
5. Smallwood, G. J., *A Technique for Two-Color PIV*, Masters Thesis (University of Ottawa, Canada, 1992).
6. Roberts, W. L., Driscoll, J. F., Drake, M. C., and Ratcliffe, J. W., "Hydroxyl Fluorescence Images of the Quenching of a Premixed Flame During an Interaction with a Vortex," *24th Symposium (International) on Combustion* (The Combustion Institute, Pittsburgh, 1992), In Press.
7. Hancock, R. D., Jackson, T. A., and Nejad, A. S., "Technique for Visualizing Vapor Lines Emanating from Water Droplets," *Appl. Opt.* 31(9), 1163 (1992).
8. Katta, V. R., Goss, L. P., and Roquemore, W. M., "Numerical Investigations on the Dynamic Behavior of a H_2-N_2 Diffusion Flame under the Influence of Gravitational Force," AIAA Paper 92-0335 presented at the AIAA 30th Aerospace Sciences Meeting, Reno, Nevada, January 1992.

Two-Color Particle-Imaging Velocimetry*

Larry P. Goss, Michael E. Post, Darryl D. Trump, and Benjamin Sarka
Systems Research Laboratories, Inc.

A Division of Arvin/Calspan
2800 Indian Ripple Road, Dayton, OH 45440-3696 USA

Key Words: correlation analysis, flow visualization, fluid-flow measurements, particle-imaging velocimetry, two-dimensional velocimetry, velocity measurements

ABSTRACT

A novel experimental method for determining two-dimensional velocity flowfields has been developed. The technique, two-color particle-imaging velocimetry (PIV), is similar to existing PIV techniques except that two different-color laser sources are used to form the light sheets required for exposing the position of particles in a seeded flowfield. A green-colored laser sheet (formed by a doubled Nd:YAG laser) and a red-colored laser sheet (formed by an Nd:YAG-pumped dye laser) are employed sequentially to expose the particle positions, which are recorded on 35 mm color film. Analysis of the resulting images involves digitizing the exposed film with color filters to separate the green- and red-particle image fields and processing the digitized images with velocity-displacement software. The two-color PIV technique has the advantage that direction, as well as particle displacement, is uniquely determined because the green-particle image occurs before the red one by a known time increment. Velocity measurements utilizing the two-color PIV technique on a propane jet diffusion flame have been made and are discussed.

INTRODUCTION

IN COMPLEX FLOWFIELDS (i.e., recirculating flows), it is important to obtain an instantaneous two-dimensional picture of the entire flowfield rather than a time-averaged pointwise map. Several techniques have been reported in the literature that have the capability to determine the two-dimensional velocity of a flowfield. These techniques can be divided into three categories: particle-tracking schemes[1-8], time-of-flight techniques[9-11], and planar-laser-induced-fluorescence (PLIF) methods[12-15]. For low-to-moderate velocity flowfields, particle-tracking techniques are efficient, offering a wide velocity range and allowing a two-dimensional measurement of the velocity flowfield. Particle tracking or particle-imaging velocimetry (PIV) is basically an extension of speckle photography, which has been employed extensively in solid mechanics. The PIV technique consists of 1) double-pulsing a particle-laden flowfield, 2) recording the scattered light either by conventional photography or holography, and 3) processing the photographs to obtain

velocity information. While the first two steps are relatively simple to implement, the data analysis is typically complex and requires computerized image processing.

This paper introduces the two-color PIV technique, which was designed to remove directional ambiguities, allowing measurements to be made in complex flow systems. The technique consists of employing small particles to seed a gas stream exiting a nozzle or passing through a test section. A laser sheet (green), formed by passing the output from a doubled Nd:YAG laser through a cylindrical lens, is used to illuminate the seed particles in the flowfield. After a short selected time interval (ranging from a few microseconds for high-velocity flow systems to milliseconds for low-velocity flow systems), a second laser sheet (red) from an Nd:YAG-pumped dye laser is pulsed to illuminate the flowfield a second time. Any particles remaining in the plane of the laser sheets produce a "displacement-vector" pair composed of a green- and a red-particle image. The Mie scattering from the seeded particles is recorded on 100-400 ASA color film and processed by direct digitization. The unique color coding helps to remove directional ambiguities associated with single-color techniques because the red image occurs after the green one.

Particle-Tracking Velocimetry

Particle-tracking velocimetry methods involve 1) making multiple exposures of a particle-laden flowfield with a sheet of laser light, 2) recording the Mie-scattered light either by conventional photography or holography, and 3) processing the photographs to obtain velocity information. Each step in this process requires careful consideration if the technique is to measure two-dimensional flowfields accurately.

For particle imaging, the exposure resulting from a particle in a laser light sheet of energy W and area $\Delta y \Delta z$ is given by [4]

$$e = \frac{4}{\pi k^2 d_e^2} \frac{\Omega}{\Delta y \Delta z} \int_n \sigma^2 d\Omega \quad (1)$$

where $k = 2\pi/\lambda$, Ω is the collection angle of the lens system, σ the Mie-scattering cross section of the particle, λ the wavelength of the laser light sheet, and d_e the nominal image diameter given by

$$d_e = (m^2 d_p^2 + d_s^2)^{1/2} \quad (2)$$

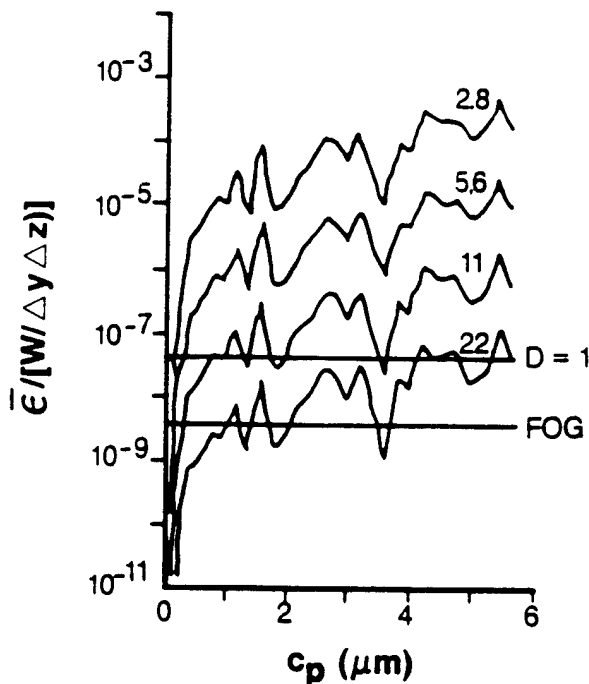
where

$$d_s = 2.44 (m+1) f \# \lambda \quad (3)$$

with m being the magnification of the image, d_p the particle

*This work was supported by the Wright Research and Development Center/Aero Propulsion and Power Laboratory under Contract No. F33615-85-C-2562.

FIGURE 1. Nondimensional exposure (ϵ) as function of particle size (c_p) for various f# collection optics.



diameter, and f# the ratio of the focal length to the lens diameter. The "diffraction-limited" blur image of the lens is given by d_s . For small seed particles the particle image recorded on film is actually the blur image and, thus, represents a lower limit to the image size.

Adrian[4] has calculated the Mie-scattering contribution to Eq. (1) and generated the family of curves for normalized exposure, f#, and particle size shown in Figure 1. Normalizing the exposure to the light-sheet energy density allows comparison with experimental conditions other than those reported in Reference 4. The minimal exposure level of a film used for particle imaging is given by the inverse of the ASA speed rating in erg/cm^2 . For the 400 ASA color film employed in these experiments (Kodacolor Gold 400), the minimum film exposure (fog level) corresponds to $1 \times 10^{-5} \text{ J}/\text{m}^2$. In order to compare this value with the family of curves in Figure 1, the exposure must be normalized to the energy density of the laser light sheet. Assuming that an energy of 20 mJ/pulse is employed for both the red (dye) and green (frequency-doubled Nd:YAG) lasers in a 10 cm x 1 mm sheet, the energy density available is $\sim 200 \text{ J}/\text{m}^2$. With the minimum exposure or fog level for 400 ASA film, the normalized exposure, ϵ , is $\sim 5 \times 10^{-8}$. Since a density of one above the fog level is required for acceptable particle-image quality, the optimum exposure (ϵ) level is $\sim 5 \times 10^{-7}$. Superimposition of this level on the family of curves generated by Adrian (see Figure 1) confirms that micron particles can be captured with the f/8.4 lens system employed in this study.

The precision of particle-tracking methods requires determination of the smallest displacement that can be accurately measured by the resolving capability of the

film. In order to understand this capability, one must examine the modulated transfer function (MTF), which is a measure of the ability of the film to resolve accurately line pairs separated by a given distance. An MTF value of ~ 300 line pairs/mm is exhibited by 400 ASA color film. This implies that color film is capable of resolving a $6 \mu\text{m}$ particle separation (with one-to-one imaging). If the particle position can be determined to the resolution of the film, then the velocity resolution is given by

$$V_r = \frac{R_p(\mu\text{m})}{\Delta t(\mu\text{s})} \quad (4)$$

where V_r represents the velocity resolution, R_r the resolving power of the film, and Δt the time interval between double exposures. In the experiments discussed here, V_r was determined to be $\sim 1.2 \text{ mm}/\text{s}$. The particle blur image size given by Eq. (2) represents the actual lower velocity limit since no two particles can be resolved closer than their diameters. The recorded particle diameters (diffraction-limited image) for the f/8.4 lens utilized in this experiment (having a magnification factor of 0.4) was $\sim 30 \mu\text{m}$. If a 5-ms time separation is used between the exposures, a lower velocity limit of $\sim 6 \text{ mm}/\text{s}$ is possible. The upper velocity limit is determined by the maximum allowable spatial separation of the particle images over the time interval between double exposures. If 1-mm spatial resolution is required, then the maximum velocity measurable in the 5-ms interval is $\sim 5 \text{ m}/\text{s}$.

IMAGE ANALYSIS

The two-color PIV technique utilizes color to remove directional ambiguities and reduce tracking errors. However, because the standard Young's-fringe analysis approach cannot distinguish between the different-color particle fields, an alternative correlation-tracker analysis approach was developed[1]. The analysis procedure consists of 1) digitizing the color negative with a CCD array, 2) determining the spatial locations of the digitized particle images, 3) constructing a correlation map from which the most probable displacement vector can be determined, and 4) utilizing this information in a tracker that identifies green/red-particle vector pairs from the digitized image.

Determination of Particle Coordinates

In order to take full advantage of the resolution available with the color film on which images were recorded (~ 300 line pairs/mm), an enlarger was employed to subdivide the image for analysis. An automated x,y,z traversing mechanism was used to set the position of the enlarger to within 20 mm in any direction. Each section of the enlarged image was digitized twice using a CCD camera system. The first digitized image was taken with a green filter for identifying the green-particle images and the second with a red filter for identifying the red-particle images. These digitized images were processed in an identical manner to determine the coordinates of the green and red particles.

(Continued next page)

A typical digitized image displays peaks associated with the particles superimposed on a slowly varying background. In order to simplify the procedures for determining the coordinates of each particle, components of the background that are constant or slowly varying over the scale of the particle size are removed by applying a two-dimensional Laplacian operator to the digitized image. This Laplacian operator basically acts as a spatial-frequency filter, passing high-frequency (small-size) components of the image but suppressing low-frequency (background) components. The particle images can be further enhanced above the background and film noise if the step size of the Laplacian operator is approximately the particle size. Next, the processed image is scanned in two dimensions for local maxima, and a series of tests is performed to identify those local maxima that correspond to particles. In brief, particles are identified by finding local maxima that 1) are above a threshold value, 2) do not constitute a shoulder, 3) have a local average intensity above a threshold value, and 4) have an estimated diameter within a specified range. Once the local maxima are determined to be a particle, the geometric center of the particle image is determined to subpixel accuracy.

Determination of Most Probable Vector Displacement

Several methods have been used to determine the most probable displacement (correlation) for vector pairs in a section of the image. Beginning with the simplest and moving to the most mathematically complex, these include 1) vector comparison, 2) histograms, and 3) Fourier transforms. The histogram (correlation-map) approach to particle correlation was found to be computationally efficient; therefore, this method was chosen for the present study and will be discussed in detail here. The cross correlation between the green- and red-particle images is given by

$$c(\xi, \Psi) = \sum_x \sum_y g(x, y) r(x - \xi, y - \Psi) \quad (5)$$

where $c(x, y)$ represents the two-dimensional correlation map, $g(x, y)$ the digitized green image, $r(x - x, y - y)$ the digitized red image, and the limits of summation are over the pixel dimensions of the digitized image. The correlation in this form is computationally intensive since it represents a double summation of the entire digitized image. In the histogram approach, a correlation-histogram map is constructed from the green- and red-particle images; the maximum of this map contains the most probable displacement vector. The method is displayed schematically in Figure 2. The software for this analysis functions by first finding an initial particle image in the green digitized image. The exact location of the green particle is determined and used for mapping. A 64×64 pixel area of the red-particle image centered about the green-particle coordinates is then summed into a histogram map (correlation space). This procedure is repeated for all the green-particle images and their associated surrounding fields in the red-particle images. This process is represented mathematically by

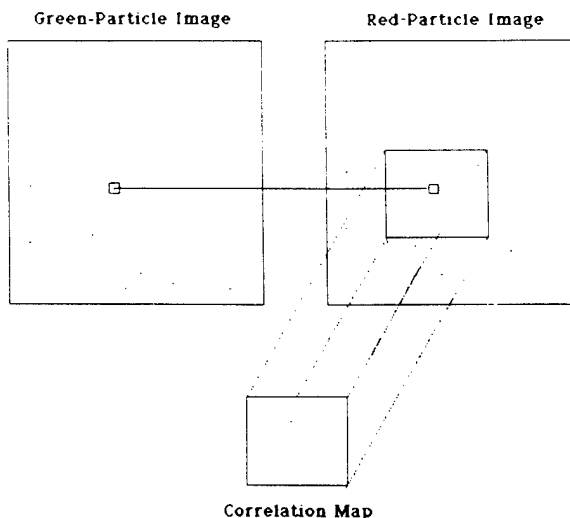
$$H(\xi, \Psi) = \sum_n g(x_c, y_c) r(x_c - \xi, y_c - \Psi) \quad (6)$$

where $H(x, y)$ represents the correlation histogram, $g(x_c, y_c)$ the center coordinates of the green-particle images, $r(x_c - x, y_c - y)$ the red-particle images surrounding the green particle being mapped, and the summation is over all green-particle images. Because the double summation of Eq. (5) over all x and y pixels has been replaced with a single summation over the number of green particles, Eq. (6) is computationally more efficient and results in a cross-correlation map.

As green/red-particle pairs having the same velocity—and thus displacement—are mapped into correlation space, peaks are built up on the map surface. The maximum of this map corresponds to the most probable displacement from the center coordinate, illustrated in Figure 3. If a single-color image had been used instead of a two-color image, the resulting correlation map would have been symmetric and centered about a large self-correlation peak at the center of the map. This would have resulted in a 180-degree directional ambiguity, which would have had to be resolved by phase shifting or by having an *a priori* knowledge of the flowfield. Because only the red-particle images were mapped into the histogram with respect to the green, neither the self-correlation peak nor the symmetry and associated 180-degree directional ambiguity is observed. Thus, both displacement and directional information are determined from the histogram map. Note that since self-correlation between the green- and red-particle images is avoided with the two-color technique, a significant reduction in erroneous peaks is possible (see Figure 3) and, thus, an improvement in signal-to-noise ratio over that possible in conventional single-color techniques.

The analysis software determines the direction and displacement by searching for the maximum of the

FIGURE 2. Schematic diagram of mapping from image to correlation space for two-color PIV technique. For each green particle, 64×64 area of red-particle image centered on green-particle coordinates is summed into correlation map.



correlation map. The displacement is then determined from the maximum to the center. This corresponds to the most likely velocity and direction averaged over the x,y array that was examined. To determine the individual velocity vectors, a tracker must be employed. The task of the tracker is simplified because the average velocity and direction have been determined, thus reducing the angles and displacements over which it must search.

Determination of Vector Pairs (Tracker)

Once the coordinates of the green- and red-particle images have been determined and the most probable displacement vector calculated from the correlation histogram, the individual velocity vectors of green/red-particle pairs can be identified in a relatively short time. A tracker routine was developed to permit one to use the average velocity and directional information obtained from the correlation map to find green/red-particle pairs. The tracker functions by first starting from each green-particle image, adding the most probable vector displacement, and searching for the corresponding red particle. If there is a red particle at the projected coordinates, then a velocity match is made and a vector drawn. If no red particle is found at these coordinates, a small *window* is opened around the target coordinates. This window is expanded incrementally to a predetermined percentage of the vector length. Figure 4 is a graphic representation of this process. If the number and size of the window increments become too large, the number of erroneous matches may become large. Generally, good results are obtained with three window increments, the maximum increment being 20% of the vector length. The tracker portion of the analysis is very efficient, normally requiring <30 sec to process a full 384

x 576 digitized image. The combination of a correlator and tracker was found to be the most efficient and effective approach to determining velocity vectors in the two-color images recorded in this study.

EXPERIMENTAL

The experimental arrangement for two-color PIV measurements is shown in Figure 5. Two separate Nd:YAG lasers are used in forming the different-color light sheets for exposing the position of the particles in the seeded flowfield. The green-laser-light sheet is formed from the doubled output of an Nd:YAG laser (Quanta-Ray DCR 1A) at 532 nm. This laser is capable of a single pulse in excess of 200 mJ. The second laser employed for the red-laser-light sheet is a broadband dye laser. The frequency-doubled output of an Nd:YAG laser (Quanta-Ray DCR 3A) is used to pump a dye laser consisting of an oscillator-amplifier combination that operates in a broadband mode for maximum conversion efficiency and output power. The dye laser is capable of over 100 mJ/pulse at 607 nm. The outputs from both the dye and Nd:YAG lasers are combined by a dichroic mirror and directed into sheet-forming optics. These optics consist of a cylindrical lens that spreads the laser beams two dimensionally and a planoconvex lens, which controls the beam waist of the laser sheets. The laser sheet in the test area was ~ 10 cm high and 1 mm thick.

Synchronization of the two laser systems presented a special problem because of the different repetition rates of the two Nd:YAG laser systems (10 and 20 Hz). In the

(Continued next page)

FIGURE 3. Correlation map of two-color PIV double-pulsed image. Notice absence of self-correlation center peak.

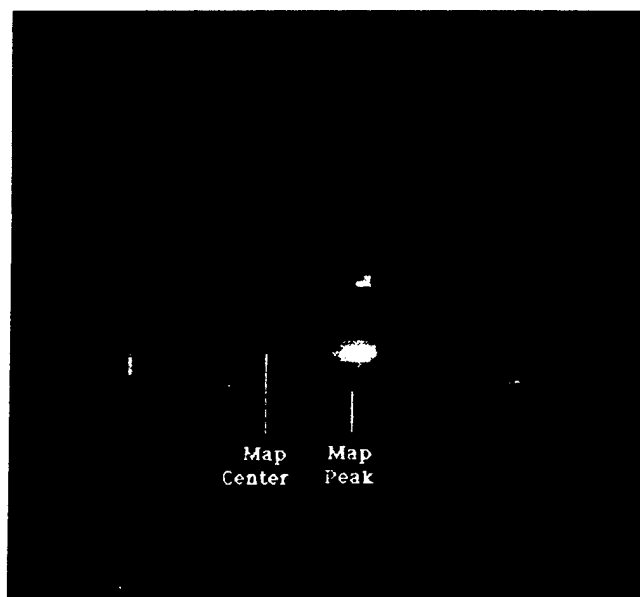
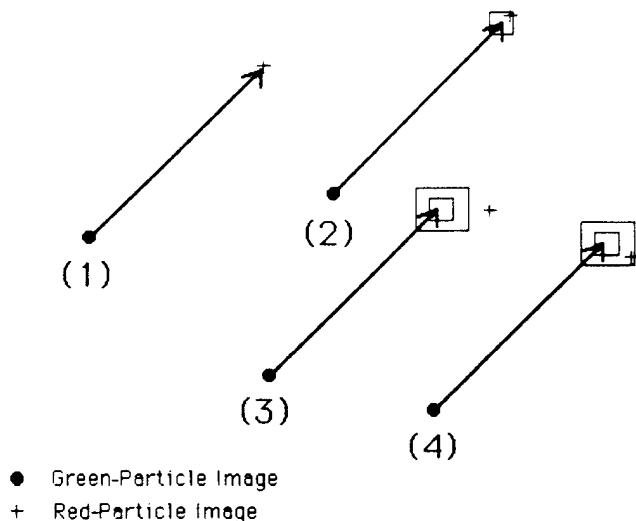


FIGURE 4. Schematic illustration of two-color PIV tracker. Most probable velocity vector is drawn from each green-particle image (●) to locate corresponding red-particle image (+). Case (1) depicts exact match; Case (2), match obtained with first uncertainty box; Case (3), no match; Case (4), match obtained with second uncertainty box.

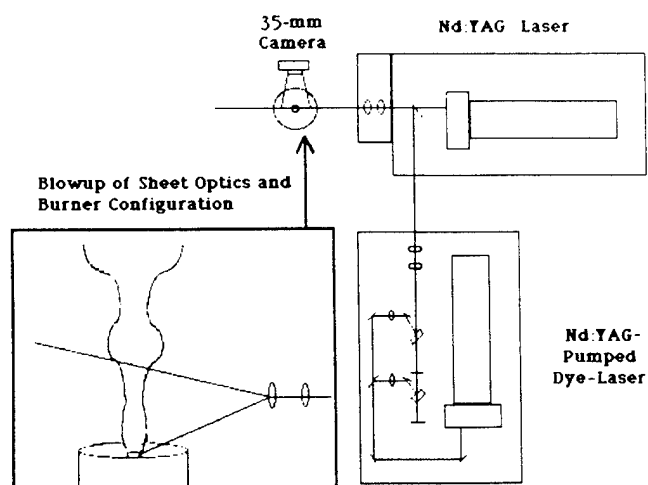


present setup the lamp output from the 20-Hz DCR 3 (dye) laser is frequency-halved by a divided-by-two circuit and used to fire the flashlamps of the DCR 1 laser at 10 Hz. The internal Q-switch circuitry of the DCR 1 laser is used to control the actual lasing of the 10-Hz laser. The Q-switch output from the DCR 1 is delayed by a pulse generator and feed into the Q-switch input of the DCR 3, thus firing the laser Q-switch at a fixed time delay after the DCR 1. This time delay is normally set to 500 msec \pm 20 nsec. With this electronic arrangement, the DCR 3 laser discharges its flashlamps at a 20-Hz rate but fires its Q-switch at a 10-Hz rate.

A Nikon 35 mm-format camera was used to record the Mie scattering from the seeded flowfield. A macro zoom lens operating at an f/8.4 aperture was employed for the images reported in this study. This lens-aperture combination resulted in a magnification factor of 0.52. To reduce the contribution of the soot emission of the flame, a Uniblitz high-speed camera shutter operating at a 1/500-sec. exposure was employed. Synchronization of the camera shutter with the laser firing was controlled by custom-built timing electronics. Color film of 100-400 ASA was used to record the two-color PIV images; the film was processed commercially.

The color film was digitized by a 384 x 576 Thompson CCD array camera (Photometrics, Ltd.), and a film projector was used to enlarge a section of the film onto the camera. Each section of the film was digitized twice—first with a green-color filter and then with a red-color filter. The digitized film sections typically covered a 1.5 cm² area of the recorded image (which was \sim 54 cm²). This corresponded to a pixel resolution of \sim 20 mm, which was considered to be adequate for capturing the particle images. The 35 mm film was generally divided into 36 segments for digitization; these were stored on magnetic tape for analysis.

FIGURE 5. Schematic diagram of experimental arrangement for two-color PIV technique on propane jet diffusion flame. Both an Nd:YAG and an Nd:YAG-pumped dye laser are employed for sheet lighting the flame.



The experimental arrangement for the jet diffusion flame consisted of a 22.5 mm-diam. round central jet surrounded by a 254 mm-diam. annular coflowing air jet. The velocity of the central fuel jet and annular air was \sim 30 cm/sec. The fuel used in this study was propane diluted with 50%-by-mass nitrogen. This flame has been studied experimentally by means of the reactive Mie scattering (RMS) and thin-filament pyrometry (TFP) techniques in which visualization and temperature profiles, respectively, were obtained; these profiles were compared with numerical predictions of Davis, *et al.*[16-17]. Experimental as well as numerical evidence indicates that the low-velocity propane jet is unusual in that a stagnation (weak-recirculation) zone is established approximately two diameters downstream of the nozzle. This stagnation zone is caused by the high density of propane, which tends to overcome the weak momentum of the fuel jet, eventually stopping the upward fuel flow. The flame develops downstream from the stagnation zone due to the acceleration effects of buoyancy. The flowfield is, thus, relatively complex and provides a good test for two-dimensional velocity methods, which can distinguish direction.

A 500-msec time separation was used between the green- and red-laser sheets for this study. If a maximum velocity in the flowfield of 3 m/sec is assumed, the minimum spatial resolution at this velocity is \sim 1.5 mm. The lowest observable velocity is determined by the minimum detected particle separation divided by the time separation between laser pulses. For the collection optics and film used in this study, the smallest detectable particle separation was \sim 15 mm; thus, the smallest detectable velocity was \sim 0.03 m/sec. The seed, alumina of \sim 1 mm nominal size, was injected into both the fuel jet and coannular air jet just prior to exiting the tubes.

RESULTS AND DISCUSSION

Analysis of the two-color PIV images was discussed in the theoretical section and will be reviewed here only briefly. The color negative is first divided into 36 sections, which are digitized twice to distinguish color. Each green/red digitized section is then analyzed separately. The initial step of this analysis involves locating the center coordinates of the green- and red-particle images. Next, the digitized section (384 x 576) is subdivided into four or 16 segments (depending upon the particle density and velocity variation), from which correlation histograms are constructed. The final step in the analysis involves a particle tracker, which uses the most probable displacement vectors determined from the correlation histogram of each segment to find green/red-particle velocity pairs. The reduced velocity vectors are then stored for statistical analysis and graphic display. At present \sim 16 hr is required to complete the entire digitization, analysis, and graphics procedure on each two-color image. More rapid digitization and analysis procedures are under development, which should greatly reduce the data-reduction time.

In order to achieve consistent and reliable results, it was desirable to focus on a region sufficiently small that the velocity would be essentially constant, but sufficiently

large that a significant number of green/red-particle pairs would be present. A typical image had a field of view of $\sim 60 \times 90$ mm. This view was digitized into $\sim 10 \times 15$ mm regions which were further divided into fourths or sixteenths, depending upon the particle density and variation in velocity field. The subdivision of the sections into 16 regions was especially important in areas where the velocity was changing rapidly. Although the two-color PIV technique allows determination of speed and direction with only one green/red-particle pair, statistically a minimum of ten pairs is desirable.

The processed two-color PIV image for the 22.5-mm propane jet is shown in Figure 6. The initial velocity of the fuel jet was ~ 30 cm/sec at the nozzle exit. As the fuel jet progressed downstream, its velocity decayed, approaching zero at ~ 1.5 diameters downstream. The development of the stagnation zone was due to the high density of the propane fuel, which overcame the initial momentum of the fuel jet. Just above this stagnation zone, the fuel jet accelerated due to the proximity of the fast, hot-burning gases. Notice that these hot regions displayed a velocity that was much higher than that of the cold central fuel jet. This high velocity was thought

to be due to the buoyancy effect, which accelerates the hot (low-density) combusting gases. The gases in the combusting areas reach a velocity of ~ 3 m/sec. Notice that the cooler outer air was entrained into the flame at downstream locations. This process acted to mix burning fuel with air and, thus, sustain combustion at downstream locations.

The existence of the stagnation zone and flowfield acceleration due to buoyancy have been qualitatively demonstrated using the RMS flow-visualization technique on this jet diffusion flame[16]. Numerical results of Davis, *et al.* have confirmed the importance of the role of buoyancy in giving this flame its unique character[16-17]. Future work on this flame will be directed toward obtaining velocity vorticity in this flowfield. Also, spatial interpolation techniques are under development that would allow the randomly oriented velocity vectors to be transposed to a spatial grid, which would facilitate comparison with computational-fluid-dynamic code results.

SUMMARY

In summary, the two-color PIV technique consists of 1) acquiring an image of green/red-particle positions, 2) separating the green particles from the red ones, 3) finding the coordinates of the particles, 4) determining the most probable vector displacement for green/red pairs, and 5) matching green/red pairs that are within a specified percentage of the most probable vector displacement. This technique has the advantage that direction as well as particle displacement is uniquely determined because the green-particle image occurs before the red one by a known time increment. The technique is, thus, applicable to complex flowfields (i.e., recirculating), where the normal 180-degree directional ambiguity of single-color techniques can be troublesome. Velocity measurements using the two-color PIV technique on a propane jet diffusion flame indicate that the sizable change in flow speed and direction associated with this flowfield can be studied by this technique.

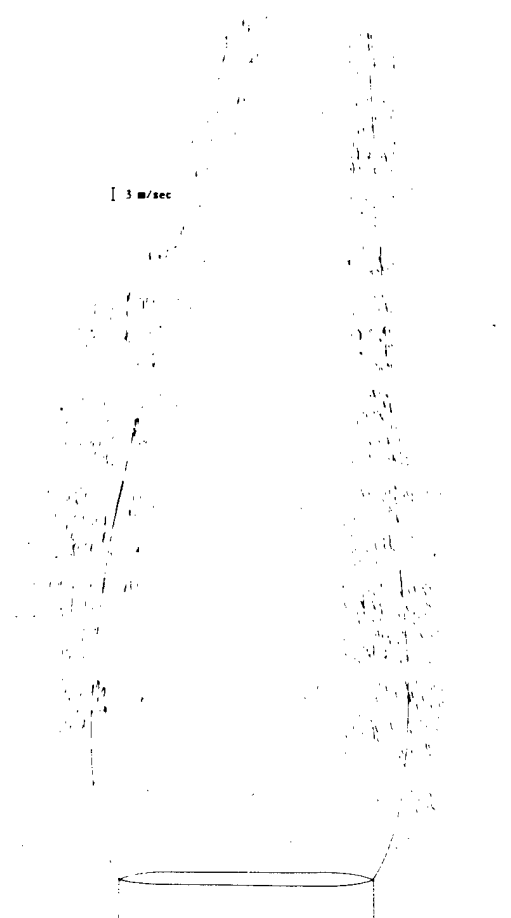
ACKNOWLEDGMENTS

The authors are indebted to Drs. W. M. Roquemore and C. D. MacArthur for support and discussions concerning this work and to M. Whitaker for editorial assistance and preparation of the manuscript.

REFERENCES

1. Meynart, R.: "Equal Velocity Fringes in a Rayleigh-Benard Flow by a Speckle Method," *Applied Optics* 19:1385-1386, 1980.
2. Meynart, R.: "Instantaneous Velocity Field Measurements in Unsteady Gas Flow by Speckle Velocimetry," *Applied Optics* 22:535-540, 1983.
3. Yao, C. S. and Adrian, R. J.: "Orthogonal Compression and 1-D Analysis Technique for Measurement of 2-D Particle Displacements in Pulsed Laser Velocimetry," *Applied Optics* 23:1687-1689, 1984.

FIGURE 6. Processed velocity-vector map of propane jet diffusion flame. Solid line in flow represents visible flame surface.



(Continued next page)

4. Adrian, R. J. and Yao, C. S.: "Pulsed Laser Technique Application to Liquid and Gaseous Flows and the Scattering Power of Seed Materials," *Applied Optics* 24:44-52, 1985.
5. Adrian, R. J.: "Image Shifting Technique to Resolve Directional Ambiguity in Double-Pulsed Velocimetry," *Applied Optics* 25:3855-3858, 1986.
6. Landreth, C. C., Adrian, R. J. and Yao, C. S.: "Double-Pulsed Particle Image Velocimetry with Directional Resolution for Complex Flows," Tenth Biennial Symposium on Turbulence, Rolla, Missouri, 1986.
7. Coupland, J. M., Pickering, C. J. D. and Halliwell, N. A.: "Particle Image Velocimetry: Theory of Directional Ambiguity Removal Using Holographic Image Separation," *Applied Optics* 26:1576-1578, 1987.
8. Ruess, D. L., Adrian, R. J., Landreth, C. C., French, D. T. and Fansler, T. D.: "Instantaneous Planar Measurements of Velocity and Large-Scale Vorticity and Strain Rate in an Engine Using Particle-Image Velocimetry," SAE Technical Paper 890616.
9. Hiller, B., Booman, R. A., Hassa C. and Hanson, R. K.: "Velocity Visualization in Gas Flows Using Laser-Induced Phosphorescence of Biacetyl," *Review of Scientific Instruments* 55:1964-1967, 1984.
10. Miles, R. B., Connors, J. Markovitz, E., Howard, P. and Roth, G.: "Instantaneous Supersonic Velocity Profiles in an Underexpanded Sonic Air Jet by Oxygen Flow Tagging," *Physics of Fluids A* 1:389-393, 1989.
11. Boedeker, L. R.: "Velocity Measurement by H₂O Photolysis and Laser-Induced Fluorescence of OH," *Optics Letters* 14:473-475, 1989.
12. Hiller, B. J., McDaniel, J. C., Rea, E. C., Jr. and Hanson, R. K.: "Laser-Induced Fluorescence Technique for Velocity Field Measurements in Subsonic Gas Flows," *Optics Letters* 8:474-476, 1983.
13. McDaniel, J. C., Hiller, B. and Hanson, R. K.: "Simultaneous Multiple-Point Velocity Measurements Using Laser-Induced Iodine Fluorescence," *Optics Letters* 8:51-53, 1983.
14. Hiller, B. and Hanson, R. K.: "Two-Frequency Laser-Induced Fluorescence Technique for Rapid Velocity-Field Measurements in Gas Flows," *Optics Letters* 10:206-208, 1985.
15. Hiller, B. and Hanson, R. K.: "Simultaneous Planar Measurements of Velocity and Pressure Fields in Gas Flows Using Laser-Induced Fluorescence," *Applied Optics* 27:33-48, 1988.
16. Davis, R. W., Moore, E. F., Chen, L.-D., Vilimpoc, V., Goss, L. P. and Roquemore, W. M.: "Numerical/Experimental Study of the Dynamic Structure of a Buoyant Jet Diffusion Flame," 1989 Spring Technical Meeting of the Central States Section of The Combustion Institute, Dearborn, Michigan, April 30 - May 3, 1989.
17. Davis, R. W., Moore, E. F., Chen, L.-D., Vilimpoc, V., Goss, L. P. and Roquemore, W. M.: "Preliminary Results of Numerical/Experimental Study of a Buoyant Jet Diffusion Flame," Submitted to *Combustion and Flame*, May 1989.

AUTHORS

LARRY P. GOSS

Ph.D. degree in Physical Chemistry, University of Georgia, 1978; was an NRC Post-Doctoral Fellow at the Naval Research Laboratory in 1979; has been associated with Systems Research Laboratories, Inc., for the past 12 years in the development of advanced diagnostic techniques for combustion research; AT present Chief Scientist of the Optical Diagnostics Group at SRL and has been involved in the development of several diagnostic techniques including Coherent Anti-Stokes Raman Spectroscopy (CARS) for thermometry and major-flame-species measurements, Reactive Mie Scattering (RMS) for visualization of flowfields, Thin-Filament Pyrometry (TFP) for line and two-dimensional temperature measurements, and—more recently—Two-Color Particle-Imaging Velocimetry for two-dimensional velocity measurements; member of the Laser Institute of America, the Optical Society of America, the Combustion Institute, and the American Institute of Aeronautics and Astronautics.

MICHAEL E. POST

M.S., Chemical Engineering, University of Dayton, 1989; has been involved in the development of advanced diagnostics for the study of complex turbulent flowfields, including the development of software for the Two-Color Particle-Imaging Velocimetry Technique; efforts have also involved use of a two-component Laser Doppler Velocimetry system for pointwise velocity measurements in turbulent flowfields; member of the Combustion Institute and AIAA.

DARRYL D. TRUMP

B.S. Electrical Engineering, Ohio Northern University, 1979; professional engineering license for the State of Ohio in 1983; research efforts over the past 10 years have involved the development of advanced laser-based diagnostic techniques for combustion environments; member of the Institute of Electrical and Electronics Engineers and the Combustion Institute.

BENJAMIN SARKA

Involved in electronics and mechanics for the past 30 years, specializing in support of the development of advanced diagnostics for the past 10 years; recently engaged in research and development on closed-cycle, rare-gas-halide lasers. During the course of this effort, developed considerable expertise in pulsed gas discharges, high-speed-switch (thyatron) technology, optics, electronics, laser technology, and vacuum and materials technology. He is a member of the Combustion Institute.

Editor's Note:

Accepted for publication December 14, 1990

Two-color particle-imaging velocimetry using a single argon-ion laser*

M. E. Post¹, D. D. Trump¹, L. P. Goss¹, R. D. Hancock²

¹ Systems Research Laboratories, Inc., A Division of Arvin/Calspan, 2800 Indian Ripple Road, Dayton, OH 45440-3696, USA

² Aero Propulsion and Power Directorate, Wright Laboratory, Wright-Patterson Air Force Base, OH 45433-7103, USA

Received: 22 October 1992 / Accepted: 22 June 1993

Abstract. A swept-beam, two-color particle-imaging velocimetry (PIV) technique has been developed which utilizes a single argon-ion laser for illuminating the seed particles in a flowfield. In previous two-color PIV techniques two pulsed lasers were employed as the different-color light sources. In the present experiment the particles in a two-dimensional shear-layer flow were illuminated using a rotating mirror to sweep the 488.0-nm (blue) and 514.5-nm (green) lines of the argon-ion laser through a test section. The blue- and green-particle positions were recorded on color film with a 35-mm camera. The unique color coding eliminates the directional ambiguities associated with single-color techniques because the order in which the particle images are produced is known. Analysis of these two-color PIV images involved digitizing the exposed film to obtain the blue and green-particle image fields and processing the digitized images with velocity-displacement software. Argon-ion lasers are available in many laboratories; with the addition of a rotating mirror and a few optical components, it is possible to conduct flow-visualization experiments and make quantitative velocity measurements in many flow facilities.

List of symbols

d	length of displacement vector
d_m	distance between rotating mirror and concave mirror
n_f	number of facets on rotating mirror
R	seed-particle radius
v	velocity in x, y plane
v_s	sweep velocity of laser beams, assumed to be in y direction from top to bottom of field of view
v_x, v_y, v_z	x, y , and z components of velocity
x_1, y_1	color-1 particle coordinates
x_2, y_2	color-2 particle coordinates
y_{max}	y dimension of field of view, assumed to be the long dimension
Δs	spatial separation of beams as they approach rotating mirror
Δt	time separation of laser sheets or of swept beams passing fixed point
Δt_b	time between successive sweeps through test section by same beam
Δt_s	time required for both beams to sweep through test section

$\Delta\theta$	angular separation of beams reflecting from rotating mirror
μ	fluid viscosity
ν	angular velocity of rotating mirror in cycles per second
ρ	seed-particle density
τ	seed-particle response time
$\sigma_v, \sigma_d, \sigma_t$	standard deviation of velocity, displacement, and time
ω	vorticity

1 Introduction

In the characterization of complex flows (e.g., recirculating), it is advantageous to obtain an instantaneous picture of the entire flowfield rather than a time-averaged pointwise map. The global view resulting from instantaneous two-dimensional measurements can provide insight into spatial correlations of systems such as unsteady or cyclical flows where interpretation of time-averaged pointwise data may be difficult.

Several techniques which can be used to determine the two-dimensional velocity of a flowfield have been reported in the literature; these include: PIV methods based on the correlation of particle displacements (Meynart 1980, 1983, Yao and Adrian 1984, Adrian and Yao 1985, Adrian 1986, Landreth et al. 1986, Coupland et al. 1987, and Ruess et al. 1989), time-of-flight techniques (Hiller et al. 1984, Miles et al. 1989, and Boedeker 1989) and planar-laser-induced-fluorescence (PLIF) methods (Hiller et al. 1983, McDaniel et al. 1983, Hiller and Hanson 1985, 1988). For low-to-moderate velocity flowfields, particle-displacement techniques such as particle-imaging velocimetry (PIV) are effective and offer a wide velocity-measurement range. The PIV technique involves 1) double pulsing a particle-laden flowfield, 2) photographing the light scattered by the particles and 3) processing the photographs to obtain velocity information.

The principle of two-color PIV was suggested by Adrian (1986) and first implemented by Goss et al. (1989). This technique provides a means of removing the directional ambiguities associated with double-pulsed,

* This work was supported, in part, by the Aero Propulsion and Power Directorate of Wright Laboratory under Contract No. F33615-90-C-2033.

Correspondence to: M. E. Post

one-color PIV methods because the order in which the particle images are produced is known. In the pulsed-laser sheet-lighting mode of two-color PIV, seed particles are illuminated with a light sheet (Color-1) produced by passing the output from a pulsed laser through a cylindrical lens. After a selected time interval (ranging from a few microseconds to milliseconds for high- and low-velocity flow systems, respectively), a co-planar light sheet (Color-2) from a second pulsed laser is used to illuminate the particles. Particles which remain in the plane of the laser sheets produce a "displacement-vector" pair comprised of a Color-1 and a Color-2 particle image. The Mie scattering from the seed particles is recorded on color film and processed by direct digitization. This mode of PIV has been utilized to measure two-dimensional flowfields in a turbine-cascade test section with velocities ranging from 50 to 340 m/s (Goss et al. 1989) and in a propane diffusion flame with velocities ranging from 0 to 3 m/s (Goss et al. 1991).

In most PIV applications, correlation analysis is used to find the average displacement of particle pairs within the correlation region. High seed densities provide many pairs in a small region. This results in high spatial resolution and a statistically accurate average of the particle displacement. If the seed density is in a lower range, it is possible to match individual particle pairs (particle tracking) using correlation analysis to guide the particle-tracking algorithm. The modified correlation technique employed in this study utilizes particle-coordinate information rather than intensity information and requires fewer operations than standard correlation methods; the dimensions of the correlation region are limited neither by optical constraints nor by size constraints associated with digital FFT algorithms.

The pulsed-laser sheet-lighting mode of operation has been used for most one- and two-color PIV measurements. The exceptions are Kawahashi and Hosoi (1989, 1991) and Gray et al. (1991) who used the continuous output of an argon-ion laser to perform one-color PIV in a swept-beam mode. For the experiments described in the present paper, the swept-beam concept was extended to two-color PIV by making use of the fact that the argonion laser has several distinct lines which can be separated and swept through the sample volume in a selected order.

2 Theory

2.1 Velocity calculation

The basic principle of PIV is straightforward – the average velocity of a two-color particle-image pair is determined by dividing the vector displacement by the time increment between pulses

$$(v_x, v_y) = (x_2 - x_1, y_2 - y_1) / \Delta t \quad (1)$$

where (x_1, y_1) and (x_2, y_2) are the positions of the particles when illuminated by Color-1 (first) and Color-2 (second) light sources, respectively. An overview of the methods used to find average displacement and track individual particle pairs is presented in Sect. 2.4 (image analysis).

In previous two-color PIV experiments in this laboratory, the seed particles were illuminated by successive light sheets, and all particles in the test region were imaged simultaneously for each color. In swept-beam experiments a correction is required to account for the fact that all particles are not illuminated simultaneously. When the beams sweep through the test section in an orientation perpendicular to the vertical dimension, the separation between the Color-1 and Color-2 images of a seed particle is given by

$$x_2 - x_1 = v_x(\Delta t) \frac{v_s}{v_y + v_s} \quad (2)$$

$$y_2 - y_1 = v_y(\Delta t) \frac{v_s}{v_y + v_s} \quad (3)$$

where Δt is the time interval between the Color-1 and Color-2 beams entering the test section, v_s is the "sweep" velocity of the beams as they pass through the test section, and the sweep direction is assumed to be the y direction (thus, the denominator of each term contains v_y). As the sweep velocity increases, the velocity ratio in Eqs. (2) and (3) approaches unity, and these expressions for particle displacement approach those which would be obtained using Eq. (1).

2.2 Light scattering

The amount of light scattered by a particle is a function of the particle size and shape, the wavelength of the laser beam, and the intensity of the light incident on the particle. The detection of the scattered light is dependent upon the collection optics and the scattering angles. As particle size decreases, the energy density of the light beam must be increased to produce sufficient scattered light for imaging the particle. These issues are treated by Adrian and Yao (1985), Goss et al. (1989), and Smallwood (1992). With the swept-beam PIV technique, the laser beam retains its high-energy density because it is not formed into a sheet. This makes possible the imaging of small particles with a source that might have insufficient energy density if it were spread into a light sheet.

2.3 Particle flow response

The ability of the seed particles to follow the flowfield is dependent upon the size, density, and shape of the particle and the viscosity, density, and speed of the fluid. For

low-velocity flows the response time of a spherical particle is given by

$$\tau = \frac{2R^2\rho}{9\mu} \quad (4)$$

where R is the particle radius, ρ is the particle density, and μ is the fluid viscosity. Hollow microballoons (phenolic resin) were used to seed the flow in this study; their low density decreases their response time, enabling them to follow the fluid flow more closely than solid particles of the same size. The large surface area of the microballoon also makes it more effective as a light scatterer. As the ratio of the particle response time to the characteristic time of changes in the flow decreases, particles can follow the flow more closely.

2.4 Image analysis

The analysis procedure consists of 1) determining the spatial locations of the particle images, 2) constructing a correlation map from which the average displacement vector can be determined, and 3) utilizing this information in a tracker which locates vectors between particle-image pairs.

The color negatives were digitized with a high-resolution (4096×6144 pixels) color scanner. This produces a separate digital image for each emulsion layer of the film. In this experiment the blue and green emulsion layers were utilized. An important factor in the success of this analysis is that the "cross-talk" between emulsion layers must be minimized. This minimization is dependent on the spectral sensitivity of the film, the intensity of the scattered light, and the transmission characteristics of the scanner. These issues have been reviewed by Smallwood (1992).

The digitized images are processed to find the particle locations. In this study particle-location information is used to perform a modified correlation analysis and to match particle-image pairs. Particle-location information makes it possible to reduce substantially the number of operations in the correlation analysis, to identify regions where no particles are present (no correlation is possible), and to eliminate intensity weighting. The disadvantages associated with finding particle locations are that the process is somewhat subjective in nature and may be relatively slow.

The parameters used to identify particles are minimum radius, maximum radius, and intensity threshold. The values of these parameters are somewhat subjective, and it is possible to select values that identify only those particles that are clearly evident from a visual inspection of the photograph or values that identify nearly every local intensity maximum as a particle. Minimum and maximum radius parameters can be estimated with

reasonable accuracy by examining the photograph. A useful intensity criterion is to identify particles having an intensity that is one standard deviation above the average intensity of all local intensity maxima that satisfy the size criteria. In practice this procedure tends to identify some local noise peaks as particles, but, in general, the correlation methods are effective, even in cases where some random noise is present. If the number of particles identified by this process is found to be too large or too small, the intensity criterion can be altered using some multiple of the standard deviation to modify the threshold intensity.

Since light-scattering properties are dependent on particle diameter, a range of particle diameters has the potential to introduce complexity into the particle-finding process. When the imaging system is optimized for a given particle size, smaller particles may not scatter sufficient light to expose the film, while larger particles may saturate the film (with the possibility of exposing both the blue and the green layers of film emulsion at the same time). If all particles were overexposed and imaged in both the blue and the green emulsion layers, the data obtained would be equivalent to that obtained in a one-color, double-pulsed experiment. The experimental approach in the present study was to vary the laser intensity, magnification, $f\#$, and film speed to determine operating values which would minimize the amount of "cross-talk" between the layers of film emulsion.

After the particles have been identified, the images are divided into sub-sections and a modified cross-correlation method used to obtain an estimate of the average particle displacement within each subsection. The average displacement is identified as the location of the maximum in the correlation map. The base of each displacement vector is assigned to the center of the subsection used to construct the correlation map.

The particle-tracking algorithm is based on the interpolation of the average displacements. The location of a Color-1 (blue) particle is identified, and the average displacements for the image subsection are interpolated to obtain a local estimate of the displacement of the blue particle. The estimated displacement is added to the position of the blue particle to obtain a "target" location for a Color-2 (green) particle. A search of the green particle locations is made to find a green particle within a specified uncertainty of the "target" position. If a green particle can be found which satisfies this criterion, it is accepted as the match. The overall number density of green particles should be such that the probability of making a random match is low. The criterion used in this study was that the number of particles per unit area times the area of the uncertainty in the "target" position must be less than 0.1. This criterion is arbitrary and corresponds roughly to a requirement that no more than 10% of the matches can be due to random effects. These procedures have been

discussed in more detail by Goss et al. (1989) and Post (1994).

3 Experimental

3.1 System components

The experimental arrangement for swept-beam, two-color PIV measurements is shown in Fig. 1. The output of a multiple-line argon-ion laser was separated into its individual components using a dispersion prism, and the 488.0-nm (blue) and 514.5-nm (green) laser lines were employed to sweep the test section. The laser was operated at ~ 1.5 W (all lines). The power of the blue beam was ~ 0.5 W and that of the green beam was ~ 0.6 W; the remaining power was distributed among the other beams produced by the laser. The beams were directed to a rotating mirror (10 facets, axis rotating at 25 Hz), swept across a concave mirror (15-cm diameter, 75-cm focal length), and reflected through the test section one after the other. The concave mirror was used to orient the scanning beams perpendicular to the major flow axis of the test section. A PIN diode was employed to detect the beams as they passed through the test section, and a time delay of 2.0 ms between beams was measured by viewing the output of the diode on an oscilloscope. In the present study the sweep velocity was 220 m/s, and the maximum v_y value was about 1 m/s. For this case the error introduced by neglecting the velocity ratio in Eqs. (2) and (3) is $< 0.5\%$.

For the shear-layer flow, the experimental arrangement (Fig. 2) consisted of a square duct (12.7 cm on a side), with a splitter plate dividing the inlet into two equal sections. The air velocity was 0.94 m/s on the high-speed side and 0.47 m/s on the low-speed side (based on volume flow rates and cross-sectional areas). This setup is being used as part of a study of the interaction of droplets with the large coherent structures produced by the shear-layer flow. The swept-beam two-color PIV technique was employed to measure the two-dimensional velocity profile of the shear-layer flow prior to introduction of droplets into the system. The flow was driven at 30 Hz with a loud speaker placed in the air-supply line for the low-velocity side of the flow. The seed – phenolic microballoons (UCAR Phenolic Resin, Union Carbide) of 100- μ m nominal diameter (range 5–200 μ m) – was injected into both flow channels upstream of the splitter plate. The microballoons have an average wall thickness of about 1 μ m and an average density of 0.104 gm/cm³. The response time of the microballoons in room-temperature air was calculated to be 2.91 ms [Eq. (4)]. The characteristic time based on the average shear-layer thickness (6.3 mm) divided by the velocity difference across the shear layer (0.47 m/s) is 13.4 ms.

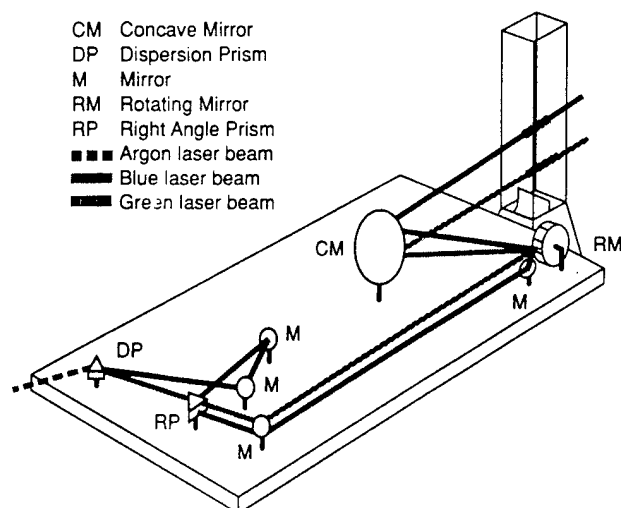


Fig. 1. Experimental arrangement for swept-beam two-color PIV technique

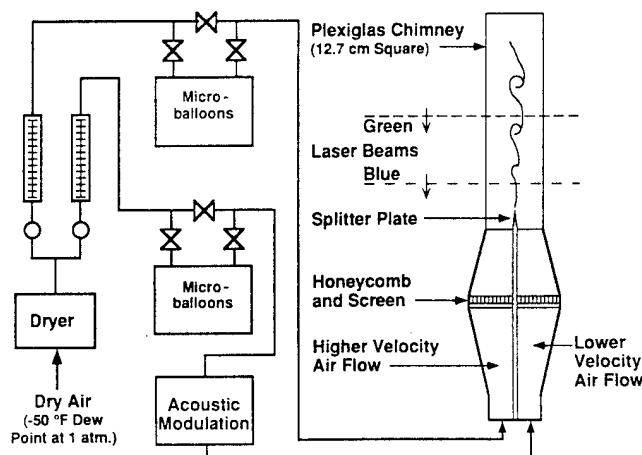


Fig. 2. Schematic diagram of splitter-plate test facility

A 35-mm Nikon camera with an exposure time of 1/250 s was employed to record the Mie scattering of the particles in the seeded flowfield. Photographs were taken using a focal-plane shuttered camera with a 50-mm lens, and the camera aperture was set at $f/2.6$. The magnification factor was 0.15. Kodak Gold-400 color film was used to record the two-color PIV images, and the film was processed commercially.

The success of any PIV experiment depends upon the care with which the optical components of the system are aligned. The beams must be co-planar as they sweep through the test section; otherwise, the two color images obtained will be of particles in different planes. The windows of the test section should be oriented perpendicular to the laser beams in such a way that reflections within the

test section will be in the same plane as the swept beams. Otherwise, a set of ghost images of particles will be produced in a different plane. These images introduce noise into the PIV photograph and interfere with analysis of the data. Finally, the camera should be oriented perpendicular to the plane of the swept beams.

The relationship between distance in the plane of the swept beams and digitized pixels in the actual PIV picture was determined by photographing a scale. The plane of the scale was placed at an angle to the plane of the swept beams that facilitated visualization of the edge of the sweep plane. The length-per-pixel factor ($39.2 \mu\text{m}/\text{pixel}$) was calculated by dividing the length of the scale by the number of pixels used to digitize that length. The scale photograph was also used to verify that the sweep plane of the laser beams was in the center of the depth of field and to estimate the beam width (less than 1 mm) in the sweep plane.

3.2 Timing

Application of swept-beam two-color PIV techniques to other experiments requires adjustment of several time intervals and synchronization of a number of events. The time intervals involved are 1) the time separation of the swept beams, 2) the time required for one sweep of the entire test section by both beams, 3) the time separation of successive sweeps by the same beam, and 4) the time required for illumination of a single particle. The most important synchronization event involves opening the camera shutter while the beams are sweeping through the test section; it may also be necessary to synchronize the camera shutter and swept beams with a transient or cyclical event.

The relevant time intervals are dependent upon the speed (v_s) at which the beams are swept across the concave mirror surface and through the test section

$$v_s = 4\pi d_m v \quad (5)$$

where d_m is the distance between the rotating and the concave mirrors and v is the angular velocity of the rotating mirror in cycles per second (4π is the usual 2π factor for axial rotation multiplied by 2 for the reflection from the plane mirror surfaces of the rotating mirror). The sweep speed should be set at a value which is high compared to the maximum expected velocity in the experimental system in order that the velocity ratio in Eqs. (2) and (3) will approach unity.

The first time interval (Δt) of interest is that between the swept beams. This interval can be adjusted by two methods. First, for parallel beams the spatial separation (Δs) results in a temporal separation (Δt) since the rotating-mirror face causes the Color-1 (blue) beam to reach the edge of the concave mirror before the Color-2 (green) beam. As Δs is increased, Δt increases; however, Δs is

limited, in practice, by the size of the faces of the rotating mirror. For the case where the beams are parallel, Δt is calculated using

$$\Delta t = \frac{\Delta s}{v_s} = \frac{\Delta s}{4\pi d_m v} \quad (6)$$

The range of Δt values can also be adjusted by changing the angle ($\Delta\theta$) between the swept beams as they are reflected from the rotating-mirror surface. For this case, Δt is calculated using

$$\Delta t = \frac{\Delta\theta}{4\pi v} \quad (7)$$

In either case, the time delay is measured from the output of a PIN diode on an oscilloscope.

The product of Δt and the expected velocity is the expected particle displacement. The maximum expected displacement is of the same order as the minimum spatial resolution; thus, it is desirable to decrease this displacement by decreasing Δt . As the displacement decreases, the relative error in measuring the displacement increases. The trade-off between these two factors must be considered when selecting the value of Δt .

The second time interval (Δt_s) of interest is that required for both beams to sweep the test section. The camera shutter must be open for at least this amount of time to permit illumination of the full test section with both beams. This interval is calculated using

$$\Delta t_s = \frac{y_{\max}}{v_s} + \Delta t \quad (8)$$

where y_{\max} is the dimension of the field of view perpendicular to the sweep direction. Note that as v_s increases, Δt_s approaches Δt .

The third time interval (Δt_b) of interest is that between successive sweeps of the same beam. The camera shutter must be open for a time period which is shorter than this interval; otherwise, a portion of the test section will be illuminated twice by successive scans of the same beam. This interval is inversely proportional to the product of the angular velocity of the rotating mirror, v , and the number of facets on the mirror, n_f . For a multi-faceted mirror of the type used in this experiment, this product can be adjusted by altering the angular velocity of the mirror or by changing the number of facets on the mirror, e.g., by blackening facets with paint or tape. This time interval is calculated using

$$\Delta t_b = \frac{1}{vn_f} \quad (9)$$

The fourth time interval of interest is that required for illumination of a single particle. This interval should not be confused with the time period during which the camera shutter is open. The shutter may be open for a relatively

long time, but the particles are illuminated for a very short time. In the pulsed-laser sheet-light mode of two-color PIV, all particles in the field of view are illuminated for a time equal to the pulse length (about 10 ns). In the swept-beam mode, individual particles are imaged in a time which is equal to the beam diameter divided by v_s (assuming the particle diameter to be much smaller than the beam diameter and the sweep velocity to be much higher than the particle velocity). For the sweep speed of 220 m/s and the beam diameter of 1.0 mm in this experiment, the illumination time was 4.55 μ s. The maximum expected velocity was 1.0 m/s; thus, the particles moved a maximum distance of 4.55 μ m while being illuminated. This distance represents only a fraction of a pixel in the digitized image and was negligible in comparison to the maximum expected displacement of 51 pixels.

The most important synchronization event involves opening the camera shutter while the beams are sweeping through the test section; this can be accomplished by placing a color filter in front of a photodiode to detect the approach of one of the beams. Adjustment of a time delay triggers the camera shutter to open as the first beam enters the test section. It is also possible to operate in an asynchronous mode where the camera shutter is opened at random for a time longer than required for both beams to sweep the test section but shorter than that between successive sweeps by the same beam; however, in this mode some of the PIV photographs will not be useful. If synchronization with transient or cyclical events is necessary, customized electronics and detectors are required.

In the present study the sweep velocity and the required time intervals discussed above were calculated as follows. Equation (5) was used to calculate a sweep velocity of 220 m/s (for a 10-facet rotating mirror operating at an angular velocity of 25 Hz with a distance of 70 cm between the rotating and the concave mirrors). This value met the criterion that the sweep velocity must be much higher than the maximum expected flow velocity which was 1.0 m/s. A maximum displacement of 2.0 mm was chosen for a blue/green-particle pair. This distance was small compared to characteristic dimensions of changes in the flowfield but sufficiently large to have an equivalent length of 51 pixels in the digitized image. A 1-pixel error in this length would result in a relative error of 2.0%. The required time separation of the swept beams (2.0 ms) was calculated by dividing the maximum particle displacement by the maximum expected velocity. Equation (7) was used to calculate the 36-deg. angular separation of the beams as they were reflected from the rotating mirror. Equations (8) and (9), respectively, were used to calculate the minimum (3.4 ms) and maximum (4.0 ms) times during which the camera shutter would be open.

3.3 Accuracy and resolution

The accuracy of an individual velocity measurement is dependent upon the accuracy with which the time interval between the two swept beams is measured and the position of the two particle centers is determined. Wernet and Edwards (1990) used the following expression to estimate the error in a velocity measurement

$$\frac{\sigma_v}{v} = \sqrt{\left(\frac{\sigma_d}{\Delta d}\right)^2 + \left(\frac{\sigma_t}{\Delta t}\right)^2} \quad (10)$$

where v , d , and t are the velocity, displacement, and time, respectively. In the present study the positions of the first- and second-color images were determined to within 0.5 pixels; thus, the displacement is accurate to within 0.7 pixels, and the relative error is on the order of 0.7 pixels divided by the displacement in pixels. The relative error increases as the particle displacement decreases. The time interval between pulses is measured with an oscilloscope to within 2%. This uncertainty could be reduced through the use of a digital electronic counter and a fast-response diode.

The incremental velocity change (0.0196 m/s) associated with a displacement of 1 pixel was determined by dividing the equivalent length of a single pixel (39.2 μ m) by the time separation between laser pulses (2.0 ms). The 0.7-pixel uncertainty in particle displacement corresponds to an absolute error on the order of 0.0139 m/s.

The uncertainty of the displacement for a matched pair is 0.7 pixels. For interpolated values of displacement, the uncertainty is a function of the weighting factors used in the interpolation and the uncertainties of the values being interpolated. Since the sum of the weighting factors is unity and the uncertainty in the individual displacements is 0.7 pixels, the uncertainty in the interpolated displacements is also on the order of 0.7 pixels.

In one-color PIV the diffraction-limited particle image size represents the lowest resolvable distance between images of a particle since no two images of a particle can be resolved closer than their diameters. This problem can be eliminated by shifting the second-pulse images relative to the first-pulse images. Adrian (1986) discussed methods (including color) for accomplishing this and has successfully implemented a shifting-mirror technique and a polarization technique. In two-color PIV the particles are imaged in different layers of the color-film emulsion. In image-shifted PIV methods, the uncertainty in measuring average displacements is the sum of the uncertainty in finding the center of the peak in the correlation map and the uncertainty in the shift. For two-color methods the shift is zero.

The maximum resolvable displacement is one-half the dimension of the correlation region. In practice, it is difficult to measure displacements that have a peak on the

edge of the correlation map, and a practical limit of 0.4 times the dimension of the correlation region was used in this study.

The average particle displacements were obtained by performing a correlation analysis of subsections of the data. The size of the correlation regions is the spatial distance over which the data are averaged, and the average displacements cannot resolve changes over shorter distances. The lower limits of the correlation scale are set, in practice, by the seed-particle density since a sufficient number of particles must be included within the subsection to render the correlation meaningful.

3.4 Alternative experimental configuration

An alternative experimental configuration would involve separation of the two different-color beams from the argon-ion laser, use of Bragg cells to pulse the beams, and direction of the pulsed outputs through sheet-forming optics. This configuration is similar to the pulsed-laser sheet-light mode of operation. At the low power levels available for the present study (argon-ion laser operating at 1.5 W), the energy density in the light sheets would have been insufficient for production of adequate PIV photographs. It may be possible to achieve success in this configuration with a laser operating at higher power levels, but the average power for CW lasers is generally lower than the instantaneous pulse power available from pulsed lasers. It may also be possible to maintain a high energy density by restricting the light sheets to a smaller area and focusing on a smaller field of view. In the present study the laser lines were selected because of their relatively high power.

4 Results and discussion

Swept-beam two-color PIV was demonstrated in this study by measuring the two-dimensional velocity field above the trailing edge of a splitter plate. An image of the flow is visualized using the Reactive Mie Scattering (RMS) technique (Chen and Roquemore 1986) is shown in Fig. 3. This image, collected under the same flow conditions as the PIV photograph, shows the interface between the two fluids and is included to give the reader a view of the vortex structures. Two-color PIV photographs have been omitted because they do not reproduce well in black and white. The PIV photograph was digitized and particle-finding software used to locate the positions of the blue- and green-particle centers (Fig. 4a). In this case 2543 blue particles and 2381 green particles were located. Not every blue-particle image has a matching green-particle image in this data set since out-of-plane components of the velocity transport particles out of the field of view. If the beams are perfectly aligned, $1 - (v_z \Delta t / w)$ represents the

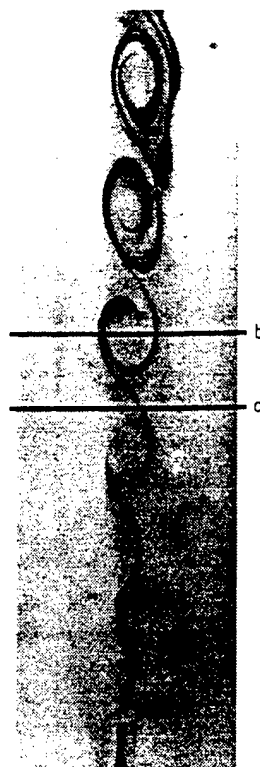


Fig. 3. Visualization of shear layer by reactive Mie scattering. Flow conditions and driving frequency are same as for PIV experiment. Line *a* marks position between vortex structures; line *b* marks position through vortex center

fraction of blue particles which have a matching green particle (v_z is the out-of-plane velocity component, and w is the light-sheet thickness). Differences in beam diameters and sweep-plane locations as well as the efficiency of the particle-finding algorithm must also be considered. The maximum number of matches possible is the number of blue or green particles, whichever is lower.

The particle-center coordinates were grouped into sections and analyzed with correlation techniques. The number of matches totaled 896, which represents 38% of the number of matches possible if all 2381 green particles had been matched. The displacement-vector pairs are shown in Fig. 4b. The origin of the velocity vectors is the position of the blue particles. The length and direction of the vectors are directly proportional to the particle velocities. The velocity vectors (obtained by dividing the displacement by the time interval between laser pulses) are tangent to the streamlines of the flow at the instant when the photograph was taken. In Fig. 4 the direction of the flow is upward, with high speed on the left and low speed on the right. For the digitized image resolution of $39.2 \mu\text{m}/\text{pixel}$ and a time separation of 2.0 ms between beams, a single pixel in a displacement vector represents 0.0196 m/s . The tip of the splitter plate is at pixel coordinates $x=950$, $y=50$, and the field of view is $6.7 \times 15.7 \text{ cm}$.

A three-point, inverse-distance algorithm was used to calculate an interpolated velocity field on a two-dimensional grid for graphical representations of the data

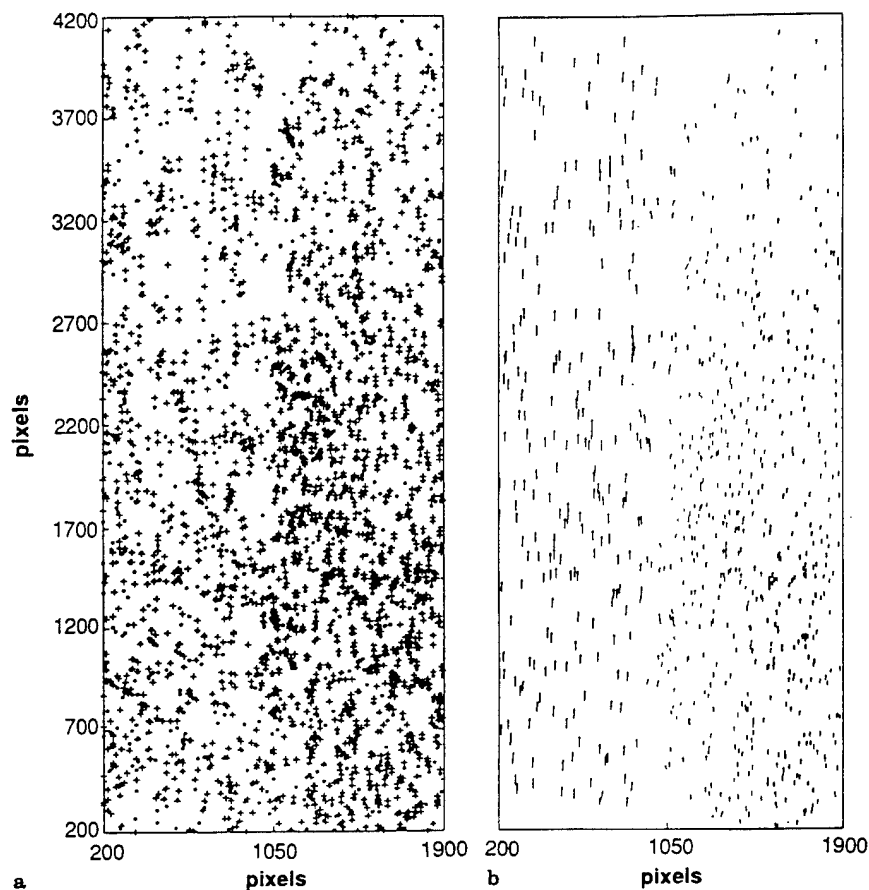


Fig. 4. **a** Blue- and green-particle coordinates obtained from PIV image; **b** displacement vectors between matched blue/green pairs obtained from PIV image

with contour plotting software. The interpolated velocity field was employed to calculate the magnitude of the velocity using

$$v = \sqrt{v_x^2 + v_y^2} \quad (11)$$

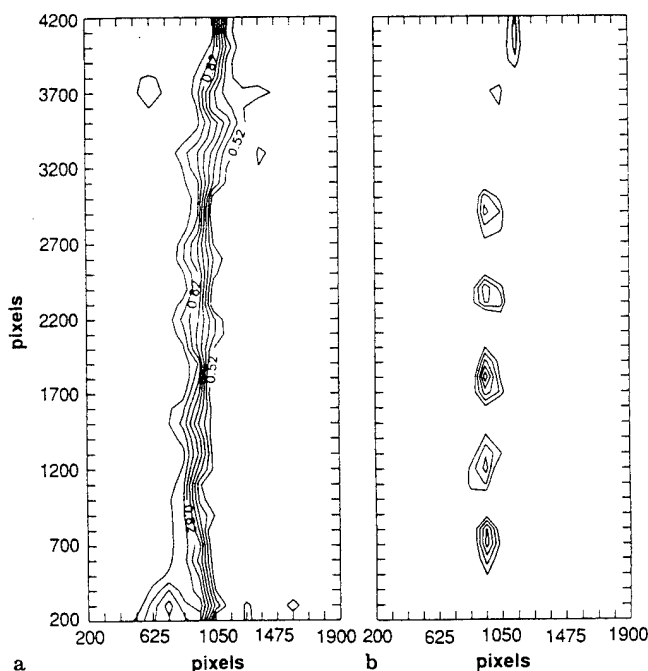
The velocity contours in Fig. 5a show the expected gradient between the high- and low-velocity sides of the shear layer.

Figure 6 is a plot of velocity as a function of x for two values of y – one through the vortex center at $y=1800$ (6.9 cm above the splitter plate) and one between the vortex structures at $y=1500$ (5.7 cm above the splitter plate). Outside the shear layer the average velocity was 1.01 m/s on the high-speed side and 0.47 m/s on the low-speed side. These values compare favourably with those of 0.94 m/s and 0.47 m/s calculated from volume flow rates and cross-sectional areas. The measured velocity difference across the shear layer was 0.54 m/s.

The vorticity is calculated from the interpolated velocity field using

$$\omega = \frac{\Delta v_x}{\Delta y} - \frac{\Delta v_y}{\Delta x} \quad (12)$$

The vorticity contours in Fig. 5b show the location of the vortex structures. The magnitude of the vorticity at the



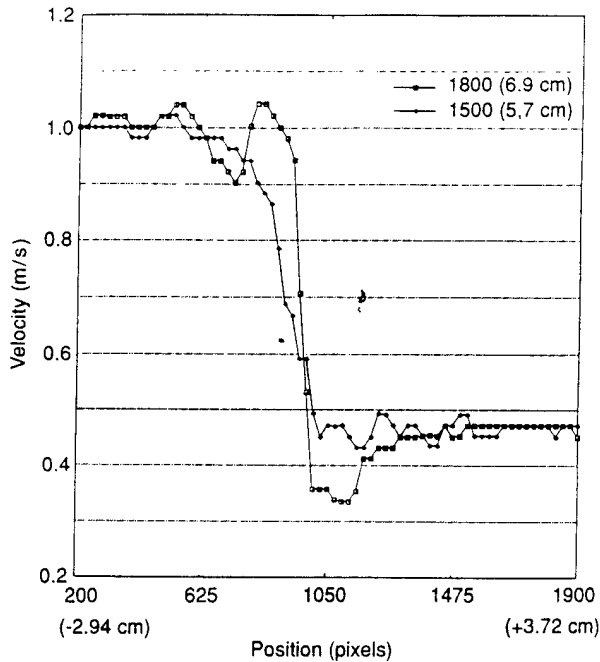


Fig. 6. Velocity profiles at $y=1500$ pixels and $y=1800$ pixels from interpolated PIV data. $y=1500$ pixels was between vortex structures, 5.7 cm above splitter plate. $y=1800$ pixels profile was through vortex center, 6.9 cm above splitter plate

vortex centers was on the order of 250 s^{-1} . The spacing between the vortex centers was estimated to be about 550 pixels (21.6 mm).

A comparison of Figs. 4 and 5 indicates that fewer particles are present in the vortex centers than in the region surrounding the vortices. Fewer vector matches are identified in areas where the particle number density is low. One reason for this is that the particles are too large to follow the flow near the vortex center. It may be possible to improve this situation through the use of smaller seed particles.

A comparison of Figs. 5a and 5b reveals that the locations of the vortex structures correspond to the steepest velocity gradients. This may seem contrary to intuition, based upon the flow visualization in Fig. 3. A steep velocity gradient would usually be inferred along Line *a* where a distinct boundary is present between the high- and low-speed fluids; a more gradual velocity gradient would be inferred along Line *b* where the boundary between fluids is stretched and wrapped into its characteristic spiral shape. The PIV data (Fig. 5) indicate that this is not the case and show that the steeper velocity gradient does, in fact, pass through the vortex. Katta (1992) has used CFD methods to model shear-layer flow under conditions very similar to those in this study. The CFD and PIV data exhibit similar behavior (i.e., steeper velocity gradients through vortex centers and more gradual gradients between vortex structures).

The relative steepness of the velocity gradients through a vortex center and between vortex structures was measured by determining the positions where the velocity reached values of 10% and 90% of the difference across the shear layer for the profiles in Fig. 6. The corresponding speeds were 0.524 and 0.956 m/s, respectively. The width of this layer through the vortex center ($y=1800$ pixels, 6.9 cm above splitter plate) was 2.4 mm and between the vortex structures ($y=1500$ pixels, 5.7 cm above splitter plate) was 10.2 mm. As noted above, the spacing between vortex centers (vortex diameter) is about 22 mm (550 pixels). The width of the velocity layer through the vortex center is significantly less than might be inferred based upon the size of structures visualized in Fig. 3. The average shear rate at the location $y=1800$ pixels was 180 s^{-1} and that at $y=1500$ pixels was 42 s^{-1} .

The apparent differences between the velocity field inferred from the visualization data (Fig. 3) and the velocity contours (Fig. 5) calculated from PIV data are attributed to the fact that the visualization data reveal the location of particles produced by reaction of trace components in the high and low-speed fluids. The concentration and location of these particles are influenced by the underlying velocity field, but the particle positions do not directly reveal the velocity magnitudes or gradients.

5 Summary

A new swept-beam two-color PIV technique has been developed which utilizes a single argon-ion laser to illuminate the particles in a seeded flowfield. Two-color PIV has the advantage that direction as well as particle displacement is uniquely determined because the first-color particle image occurs before the second-color one by a known time increment. The technique is applicable to complex flows (e.g., recirculating), where the normal 180° directional ambiguity of single-color techniques can be troublesome. An advantage of swept-beam PIV is that a single laser is used to produce the different-color laser beams, rather than two pulsed lasers. Argon-ion lasers are available in many laboratories; with the addition of a rotating mirror and a few optical components, it is possible to conduct flow-visualization experiments and make quantitative velocity measurements in many flow facilities.

Acknowledgements

The authors are indebted to Dr. W. M. Roquemore for support and discussions concerning this work and to M. Whitaker for editorial assistance and preparation of the manuscript.

References

- Adrian, R. J. 1986: Image shifting technique to resolve directional ambiguity in double-pulsed velocimetry. *Appl. Opt.* 25, 3855-3858
- Adrian, R. J.; Yao, C. S. 1985: Pulsed laser technique application to liquid and gaseous flows and the scattering power of seed materials. *Appl. Opt.* 24, 44-52
- Boedeker, L. R. 1989: Velocity measurement by H_2O photolysis and laser-induced fluorescence of OH. *Opt. Lett.* 14, 473-475
- Chen, L. D.; Roquemore, W. M. 1986: Visualization of Jet Flames. *Combust. Flame* 66, 81-86
- Coupland, J. M.; Pickering, C. J. D.; Halliwell, N. A. 1987: Particle image velocimetry: theory of directional ambiguity removal using holographic image separation. *Appl. Opt.* 26, 1576-1578
- Goss, L. P.; Post, M. E.; Trump, D. D.; Sarka, B.; MacArthur, C. D.; Dunning, G. E. Jr. 1989: A novel technique for blade-to-blade measurements in a turbine cascade. *AIAA-89-2691*
- Goss, L. P.; Post, M. E.; Trump, D. D.; Sarka, B. 1991: Two-color particle-imaging velocimetry. *J. Laser Appl.* 3, 36-42
- Gray, C.; Greated, C. A.; McCluskey, D. R.; Easson, W. J. 1991: An analysis of the scanning beam PIV illumination system. *Meas. Sci. Technol.* 2, 717-724
- Hiller, B.; Booman, R. A.; Hassa, C.; Hanson, R. K. 1984: Velocity visualization in gas flows using laser-induced phosphorescence of biacetyl. *Rev. Sci. Instrum.* 55, 1964-1967
- Hiller, B.; Hanson, R. K. 1985: Two-frequency laser-induced fluorescence technique for rapid velocity-field measurements in gas flows. *Opt. Lett.* 10, 206-208
- Hiller, B.; Hanson, R. K. 1988: Simultaneous planar measurements of velocity and pressure fields in gas flows using laser-induced fluorescence. *Appl. Opt.* 27, 33-48
- Hiller, B. J.; McDaniel, J. C.; Rea, E. C.; Jr Hanson, R. K. 1983: Laser-induced fluorescence technique for velocity field measurements in subsonic gas flows. *Opt. Lett.* 8, 474-476
- Katta, V. R. 1992: Systems Research Laboratories, Inc., Dayton, Ohio, Private communication
- Kawahashi, M.; Hosoi, K. 1989: Beam-sweep laser speckle velocimetry. *Exp. Fluids* 8, 109-111
- Kawahashi, M.; Hosoi, K. 1991: Dual-beam-sweep laser speckle velocimetry. *Exp. Fluids* 11, 278-280
- Landreth, C. C.; Adrian, R. J.; Yao, C. S. 1986: Double-pulsed particle image velocimetry with directional resolution for complex flows. Tenth Biennial Symposium on Turbulence, Rolla, Missouri, 1986
- McDaniel, J. C.; Hiller, B.; Hanson, R. K. 1983: Simultaneous multiple-point velocity measurements using laser-induced iodine fluorescence. *Opt. Lett.* 8, 51-53
- Meynart, R. 1980: Equal velocity fringes in a Rayleigh-Bernard flow by a speckle method. *Appl. Opt.* 19, 1385-1386
- Meynart, R. 1983: Instantaneous velocity field measurements in unsteady gas flow by speckle velocimetry. *Appl. Opt.* 22, 535-540
- Miles, R. B.; Connors J.; Markovitz E.; Howard P.; Roth G. 1989: Instantaneous supersonic velocity profiles in an underexpanded sonic air jet by oxygen flow tagging. *Phys. Fluids A* 1, 389-393
- Post, M. E. 1994: Two-dimensional velocity fields of vortex structures measured with two-color particle-imaging velocimetry. Ph.D. Dissertation. Cincinnati: University of Cincinnati
- Ruess, D. L.; Adrian R. J.; Landreth C. C.; French D. T.; Fansler T. D. 1989: Instantaneous planar measurements of velocity and large-scale vorticity and strain rate in an engine using particle-image velocimetry. *SAE Technical Paper* 890616
- Smallwood, G. J. 1992: A technique for two-color particle image velocimetry. Masters Thesis, Ottawa, Ontario, Canada: University of Ottawa
- Warnet, M. P.; Edwards, R. V. 1990: New space domain processing technique for pulsed laser velocimetry. *Appl. Opt.* 29, 3399-3417
- Yao, C. S.; Adrian, R. J. 1984: Orthogonal compression and 1-D analysis technique for measurement of 2-D particle displacements in pulsed laser velocimetry. *Appl. Opt.* 23, 1687-1689



AIAA-95-0790

**INVESTIGATION OF A JET IN A CROSS FLOW
USING PIV**

S. GOGINENI and D. SUTKUS
Wright Laboratory
Wright-Patterson AFB, OH

L. GOSS
Systems Research Laboratories, Inc.
Dayton, OH

A. GLEZER
Georgia Institute of Technology
Atlanta, GA

**33rd Aerospace Sciences
Meeting and Exhibit**
January 9-12, 1995 / Reno, NV

INVESTIGATION OF A JET IN A CROSS FLOW USING PIV

S. Gogineni* and D. Sutkus†

Wright Laboratory

Aero Propulsion and Power Directorate

Wright-Patterson AFB, OH 45433-7103

L. Goss‡

Systems Research Laboratories

A Division of Space Industries International, Inc.

2800 Indian Ripple Road

Dayton, OH 45440-3696

and

A. Glezer§

School of Mechanical Engineering

SSTC Building, 225 First Street

Georgia Institute of Technology

Atlanta, GA 30332-0405

ABSTRACT

The effect of streamwise excitation on the mixing and velocity field of a jet in a cross flow is investigated for jet-to-cross flow velocity ratios of 0.33, 0.6, and 1.0 using the two-color PIV technique. The jet emanates from a square conduit and is manipulated by four piezoelectric actuators, one mounted along each side of the jet conduit near the jet exit plane. Time- and phase-averaged cross stream and spanwise distributions of velocity and rms velocity fluctuations are also obtained. A novel approach is employed for processing of PIV images which makes it possible to distinguish between the jet fluid and the cross flow based on the size of the seeding particle. In addition, reactive Mie scattering images are used to assess the effect of excitation on molecular mixing. The present results show that manipulation of the upstream and downstream segments of the jet shear layer leads to diminution of the low-velocity domain in the wake of the jet, an increase in its penetration into the cross flow (up to 30%) and substantial mixing enhancement.

1. INTRODUCTION

The study of jet in a cross flow is of importance in a number of engineering applications, including blade and combustor cooling in gas turbines

and thrust vectoring and reversal. It is well known that a jet discharging into cross flow creates a complex flow field with distinguishable features such as a curvature of the jet trajectory and the formation of a pair of counter-rotating vortices along the jet centerline that result in a kidney-shaped cross section. Experimental and numerical investigations of this flow are reviewed in a recent article by Margason.¹

While most of the previous experimental investigations of a jet in a cross flow have been focused on the fundamental mechanisms and global features of the base flow, the present work is concerned with manipulation of the jet for mixing enhancement. Furthermore, unlike previous work in this area which utilized pointwise velocity measurements, the present work employs a global velocimetry technique, namely, particle image velocimetry (PIV). The jet in the present investigation emanates from a square conduit and is manipulated by four piezoelectric actuators one mounted along each side of the jet conduit near the jet exit plane. Although piezoelectric actuators were successfully employed for flow modification as early as the mid-sixties^{2,3} their use apparently has been limited because of the diminution in their response when operated outside of a narrow frequency band centered around their resonance frequency. Wiltse and Glezer⁴ developed a new technique which overcomes this difficulty and allows effective manipulation of turbulent shear flows over a broad frequency range and they demonstrated its utility in a square-air-jet experiment. The effectiveness of these actuators for mixing modification was later demonstrated in the combustion laboratory at Wright-Patterson AFB in a square jet issuing into a cross-channel flow using chemical reaction⁵ and surface

* NRC Post-Doctoral Research Associate, AIAA Member

† Aerospace Engineer, AIAA Member

‡ Chief Scientist, Optical Diagnostics, AIAA Member

§ Associate Professor, AIAA Member

cooling.⁶ More recently, this work has been focused on the flow mechanisms that bring about mixing modifications. The present paper is concerned with implementation of a two-color PIV system in this complex flow field and a novel approach for processing PIV images which makes it possible to distinguish between the jet fluid and the cross flow based on particle size.

2. EXPERIMENTAL APPARATUS AND PROCEDURE

The experimental apparatus is shown schematically in Figure 1(a). The test section is a 61-cm long vertical channel having a square cross section measuring 8.9 cm on a side. The flow in the channel is driven from an air supply system.⁵ A flat (6.5-mm-thick) plate having a sharp leading edge is mounted across the span of the channel parallel to and 6.35 cm from one of the side walls such that the leading edge is located 7.62 cm downstream from the channel inlet. A provision is made to bleed off the channel flow between the underside of the plate and the duct wall to ensure that the flow upstream of the plate will be uniform across the channel cross section. An air jet is emanating normal to the channel flow from a 34 cm long square conduit measuring 1.52 cm on a side (hydraulic jet diameter of 1.72 cm) that is flush-mounted on the center span of the plate such that its upstream side is parallel to and located 23 cm downstream of the plate's leading edge. The cross flow in the channel is conditioned by a honeycomb flow straightener and screens of progressively finer mesh size mounted in the upstream ducts to maintain the free stream turbulence level at less than 2%. The nominal jet to cross flow velocity ratios ($R = U_{jet}/U_{channel}$) in the present experiment are 0.33, 0.6, and 1.0. The corresponding jet Reynolds numbers based on equivalent jet diameter (Re_d) are 427, 776, and 700.

A piezoelectric actuator is mounted on each of the four interior walls of the jet. Each actuator consists of a thin stainless-steel blade which is 1.25-cm wide and 3.0-cm long. The upstream section of the blade is sandwiched between two slabs of piezoceramic material, each 1.9 cm long. The actuator is clamped along its upstream edge and is cantilevered across a shallow cavity that extends through the jet exit plane. When the actuator is driven at its resonance frequency (nominally 500 Hz), the free end of the blade vibrates normal to the jet flow. Low-frequency instabilities (up to 25 Hz) of the jet column are introduced by amplitude modulation of the resonance waveform. The resonance waveform is common to all four actuators but can be independently modulated for each actuator; thus the modulation frequencies and the relative phase between the modulating waveforms can be independently varied. In the work reported here, the pair of opposite actuators having tip displacements in the streamwise direction is

simultaneously activated with excitation waveforms of equal amplitude and identical modulation frequency (referred to below as streamwise excitation).

Flow-visualization studies are conducted using reactive Mie scattering. The jet is seeded with titanium-tetrachloride ($TiCl_4$) vapor which reacts with water vapor in the cross-flowing air stream to form titanium-dioxide (TiO_2) particles (nominally 1- μm in diameter) at the interface between the two streams. Cross sections of the flow are illuminated by a light sheet from a frequency-doubled Nd:YAG laser and are visualized by light (Mie) scattered from the particles.

3. TWO-COLOR PARTICLE IMAGE VELOCIMETRY

PIV techniques have been used for a number of years to measure velocity distributions in planar cross sections of a given flow field, as described in detail in earlier work.^{7,8} One of the difficulties involved in implementing this otherwise attractive velocimetry technique is the directional ambiguity, namely, the inability to determine the temporal sequence of particle pairs and thus the direction of the measured velocity. Several techniques that have been developed to resolve this ambiguity use single-color lasers and image shifting by means of either scanning, or rotating mirrors, pulse tagging, calcite crystals, and polarizing beam splitters. The mechanical motion associated with the mirrors imposes some limitations on velocity measurements. Pulse tagging uses pulses of different duration,⁹ but is limited to low-velocity flows, since the time resolution is not adequate to prevent image blurring in high-speed flows. Calcite crystals exploit the polarization of the light scattered from the seed particles, but the magnitude and orientation of the shift can change in the film plane because the light is collected from a finite solid angle.¹⁰ In addition, for a given camera magnification, the velocity bias cannot be altered unless the crystal thickness is changed or several crystals are used in series. A polarizing beam splitter and two quarter wave plates arrangement also utilizes the polarization principle and provides constant velocity bias throughout the flow field, making synchronization with other hardware unnecessary.¹¹

A two-color PIV system that was developed by Goss et al.¹² (Figure 1b) has the following advantages: (i) the directional ambiguity is resolved using the color coding of the particle images, (ii) higher data yields are attainable, and (iii) the system is particularly suitable for combustion diagnostics. The system uses color to temporally mark the location of the seed particles in the flow field. The green (532-nm) laser output from a frequency-doubled Nd:YAG laser and the red (610 nm) laser output from a Nd:YAG-pumped dye laser are combined by a dichroic beam splitter and directed through sheet-forming optics. The laser sheet energy is typically 20 mJ/pulse, and the sheet thickness is less

than 1 mm at the test section. The temporal delay between the two lasers is controlled by a pulse generator and is set as a function of the gas velocity, optical magnification, and interrogation spot size. In the present experiments, the time delay is varied from 300 to 800 μ sec and is monitored by a photo-diode.

The channel and jet fluids are seeded with 1- μ m size aluminum-oxide particles and sub-micron (nominally 0.5 μ m) smoke particles, respectively. Mie scattering from the seed particles is recorded on commercial 35 mm color film that is digitized into individual red, green, and blue components at a resolution of 2700 pixels per inch. Several techniques such as Young's fringe analysis and auto-correlation are available for image analysis for monochromatic double-pulse images. However, these methods do not take into account the color information in the present PIV images. The cross-correlation technique implemented in the present work exploits the spectral separation of the red and green images and eliminates approximately one half of the possible particle images from each interrogation region.

Figure 2 shows a typical double-exposed image of the unforced jet issuing into the cross flow ($R = 1$) in the x - y plane $z = 0$. As discussed above, the flow is illuminated by two successive pulses from a YAG laser and because the cross flow and jet fluids are seeded with particles of different diameters, it is possible to distinguish between the jet and cross flow fluids by the intensity levels of the scattered light. It is noteworthy that unlike images of reactive Mie scattering (e.g., Figure 4 below), images similar to Figure 2 enable not only PIV processing but also, in principle, determination of the composition of the mixed fluid within any finite domain of the image. The contrast in the present image is set such that the smoke particles are barely visible; thus the channel fluid appears almost clear. The particles that are present immediately downstream of the jet (within the "wake" region) result from the entrainment of the cross flow fluid.

The present cross-correlation technique is based on intensity maps of the red and green images of the scattered light. Consider the intensity distributions of the red and green images $r(x,y)$ and $g(x,y)$ and their corresponding Fourier transforms $R(a,b)$ and $G(a,b)$. The two-dimensional cross-correlation function

$$\begin{aligned} h(x,y) &= \int_R \int_R r(\alpha,\beta) g(x+\alpha, y+\beta) d\alpha d\beta \\ &= F^{-1}[F(r(x,y)) F^*(g(x,y))] \\ &= F^{-1}[R(\alpha,\beta) G^*(\alpha,\beta)] \end{aligned} \quad (1)$$

is employed to determine the magnitude and direction of the average velocity over the interrogation area. (Note

that unlike in processing methodologies that are based on autocorrelation, the direction of the velocity vectors is uniquely determined.)

The correlation function (1) is calculated over small segments (interrogation domains) of the PIV image. In order to process the digitized PIV image, it is dissected into small subregions. The dimensions of each interrogation domain depend on the particle density, estimated local velocity gradients, particle image size, and the desired spatial resolution. The maximum displacement of each particle must be less than one-half the interrogation spot. In the present experiments, the interrogation domain measured 64 x 64 pixels corresponding to 0.5 x 0.5 mm in the measured flow. In order to enhance the overall resolution, the interrogation domains are overlapped by one-half the domain size. The peak of the correlation map calculated by Eq. (1) corresponds to the average velocity displacement within the interrogation spot. An intensity-weighted peak-searching routine is used to determine the exact location of the peak to a sub-pixel accuracy. The number of particle pairs that are normally necessary to ensure a desirable signal-to-noise ratio is reduced to four or five pairs when the cross-correlation analysis is employed.

A typical instantaneous velocity field obtained by the application of the correlation scheme described above is shown in Figure 3a. While each PIV image typically contains a grid of 100 x 70 (or 7000) vectors, only 35 x 21 grid points are actually plotted for clarity. This distribution demonstrates that a few of the vectors are erroneous, resulting from out-of-plane motions or low concentrations of seeding particles. Thus, the next steps in the processing procedure include filtering and interpolation techniques for the removal of the erroneous vectors. Once all the velocity vectors are determined for a given image, the vectors are post-processed. The post-processing procedure consists of a series of operator-selectable filter and interpolation routines. The "nearest neighbor" filter compares the average variation between a given vector and its nearest neighbors. If the variation exceeds a desired level, the vector in question is disregarded. The resulting image is shown in Figure 3b. Once all the vectors are removed, an interpolation procedure is used to estimate the magnitude of the missing vectors based upon their nearest neighbors (Figure 3c). Since the grid size is large and each measured vector includes an error which is statistically independent from point to point (caused by pseudo-white noise up to the spatial frequencies corresponding to the grid spacing), derived quantities such as vorticity and strain rate can be adversely affected.¹³ Hence, the interpolated velocity data is resampled using a bi-linear interpolation method to provide a new grid size of 500 x 200 which yields 100,000 vectors (Figure 3d). This process does not change the velocity field because the measured vector is already a spatially filtered version of the flow field but

dramatically improves the quality of the quantities derived from the field.

4. RESULTS AND DISCUSSION

Reactive Mie Scattering is used to visualize the interaction of the jet with the channel cross flow. As noted in section 2 above, a chemical reaction between titaniumtetrachloride ($TiCl_4$) vapor seeded in the jet fluid and water vapor in the channel cross flow leads to the formation of sub-micron titaniumdioxide (TiO_2) particles. These particles are formed as a result of mixing at the molecular level when the jet and channel fluids come into contact. Because the two species are advected by coflowing streams, the rate of formation of the TiO_2 particles is dependent on, and is clearly an indication of, the degree of mixedness. The presence of these particles (and, thus, of reaction product) in planar cross sections of the flow can be easily detected by light scattered from a laser light sheet (YAG laser in the present study). Because molecular mixing in free-shear flows typically increases by an order of magnitude following the appearance of small-scale three-dimensional motions within the shear layer between the streams,¹⁴ it is expected that manipulation of the jet shear layer will lead to substantial enhancement of mixing and to an increase in concentrations of TiO_2 particles. An important attribute of this flow visualization is that at any instant in time, only the present and past reaction product is visualized while nonreacting parts of the flow remain invisible.

Figure 4(a,b,c) shows pairs of images of the light scattered by TiO_2 particles in the x-y plane $z = 0$ of the unforced (on the left) and streamwise-forced jet for $R = 0.33$, 0.6, and 1.0, respectively. The field of view measures 12.2 cm x 6.8 cm in the x and y directions respectively. As observed by a number of previous investigators, the penetration distance of an unforced jet into the cross flow increases with R . However, a remarkable feature of the unforced jet is that aside from the relatively thin shear layers upstream and downstream of the jet column, the jet fluid in the plane $z = 0$ remains virtually unmixed over a substantial downstream distance; this unmixed region decreases with increasing R . The mixed fluid in the wake of the jet is apparently mixed and transported by the counter-rotating streamwise vortex pair that is formed along the spanwise edges of the jet column. It appears that mixing is substantially increased following the formation of "secondary" vortices around the circumference of the jet, presumably through interaction with the "primary" streamwise vortex pair. The formation of such vortices is evident along the upstream interface between the jet fluid and the cross flow which exhibits an instability having a characteristic streamwise wavelength that decreases with increasing R ; thus, suggesting that this is primarily a wake-like effect

(a train of three secondary vortices is visible in Figure 4c).

The most prominent effect of streamwise forcing (on the right in Figure 4) is the substantial increase in mixing between the jet and the cross flow. Mixing apparently begins near the jet orifice, as evidenced by the disappearance of the core of unmixed fluid in the unforced jet. As in the experiments of Wiltse and Glezer,⁴ forcing the jet shear layer at the resonance frequency of the actuators leads to the formation of a train of secondary spanwise vortices having a characteristic length scale that is approximately two orders of magnitude smaller than the wavelength of the predominant jet core instability; thus, their appearance promotes molecular mixing far more effectively than the formation of the secondary vortices in the unforced flow. Figure 4c demonstrates that the low-frequency modulation of the actuators' resonance waveform leads to substantial modifications of the primary streamwise vortices. Even though the streamwise wavelength that is associated with the modulation frequency is longer than the extent of the streamwise domain shown here, Figure 4c suggests that the primary vortices undergo streamwise rollup at the modulation frequency as indicated by the engulfment of unmixed fluid from the cross flow and its transport toward the flat plate. Figure 4c further suggests that the cross-stream penetration of the forced jet also increases compared to that of the unforced flow.

Pairs of instantaneous two-dimensional velocity distributions of the unforced and forced flow in the x-y plane $z = 0$ are shown in Figure 5 for $R = 0.33$ (a), 0.6 (b), and 1.0 (c). The field of view measures 4.71 cm x 3.34 cm ($3.1w \times 2.2w$, where w is the width of the jet orifice) in the x and y directions, respectively. The velocity distributions for the unforced flow reveal a region in the "wake" of the jet where the magnitude of the velocity is very low compared to the cross-flow velocity, indicating that the fluid contained in this low-velocity region is almost stagnant. As the velocity of the jet is increased, the fluid in the low-velocity region appears to be moved away from the wall by the flow induced by the streamwise counter-rotating vortex pair. In Figure 5c, the low-velocity region is lifted away from the surface and is surrounded by upward moving flow. Figures 5a-c show that when the jet is forced, the instantaneous flow field changes dramatically. Of particular note is the absence of the low-velocity region in the "wake" of the jet. The disappearance of the low-velocity region near the surface of the plate and the entrainment of cross-flow fluid suggests that heat transfer from the plate is enhanced when the jet is forced, in accord with the observations of Sutkus et al.⁶

As discussed above, the jet and the cross flow are separately seeded with particles of different nominal diameter and, thus, it is possible to distinguish, in post processing, between particles that originated from each

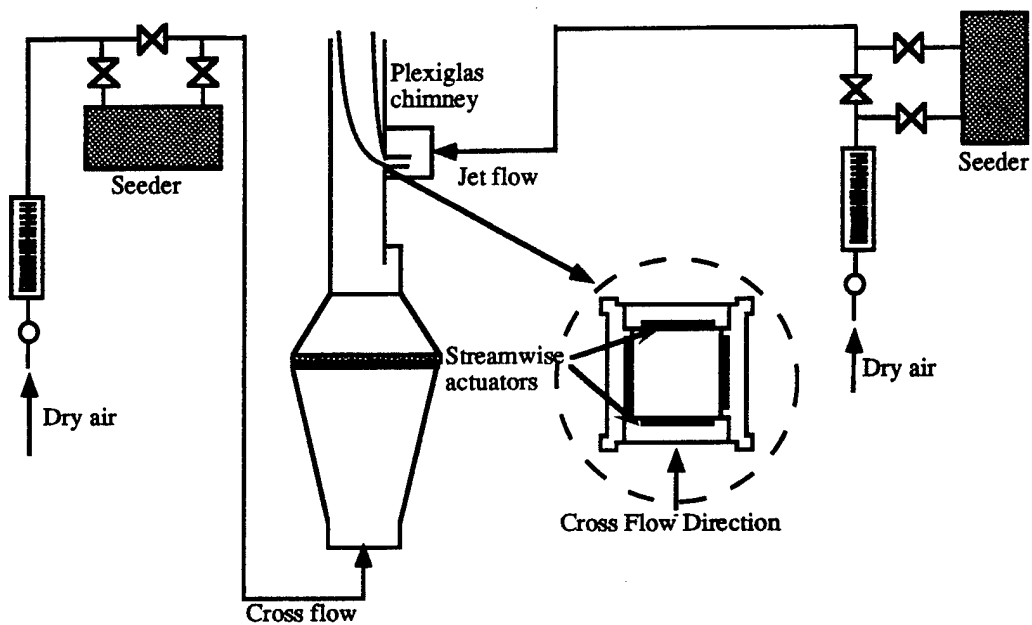


Figure 1a. Schematic of the experimental setup

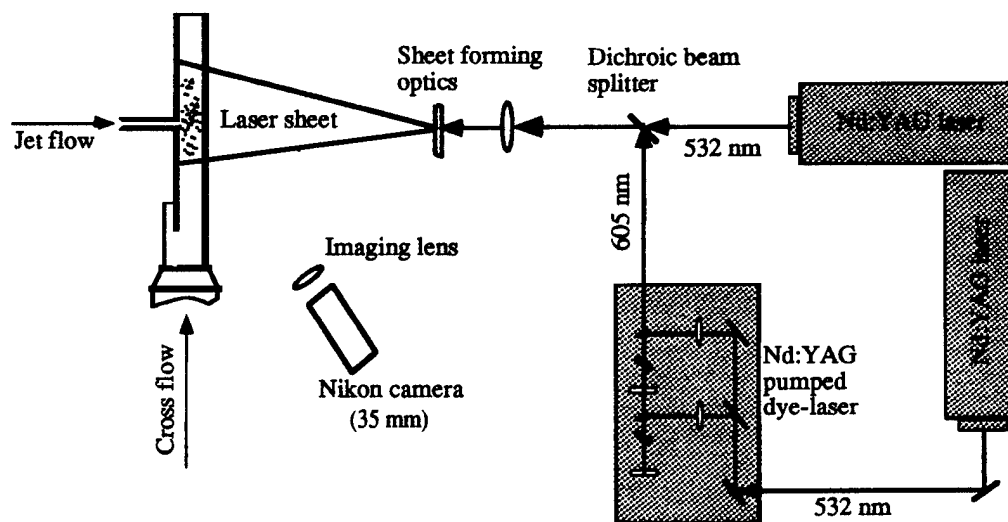


Figure 1b. Optical system for two-color PIV

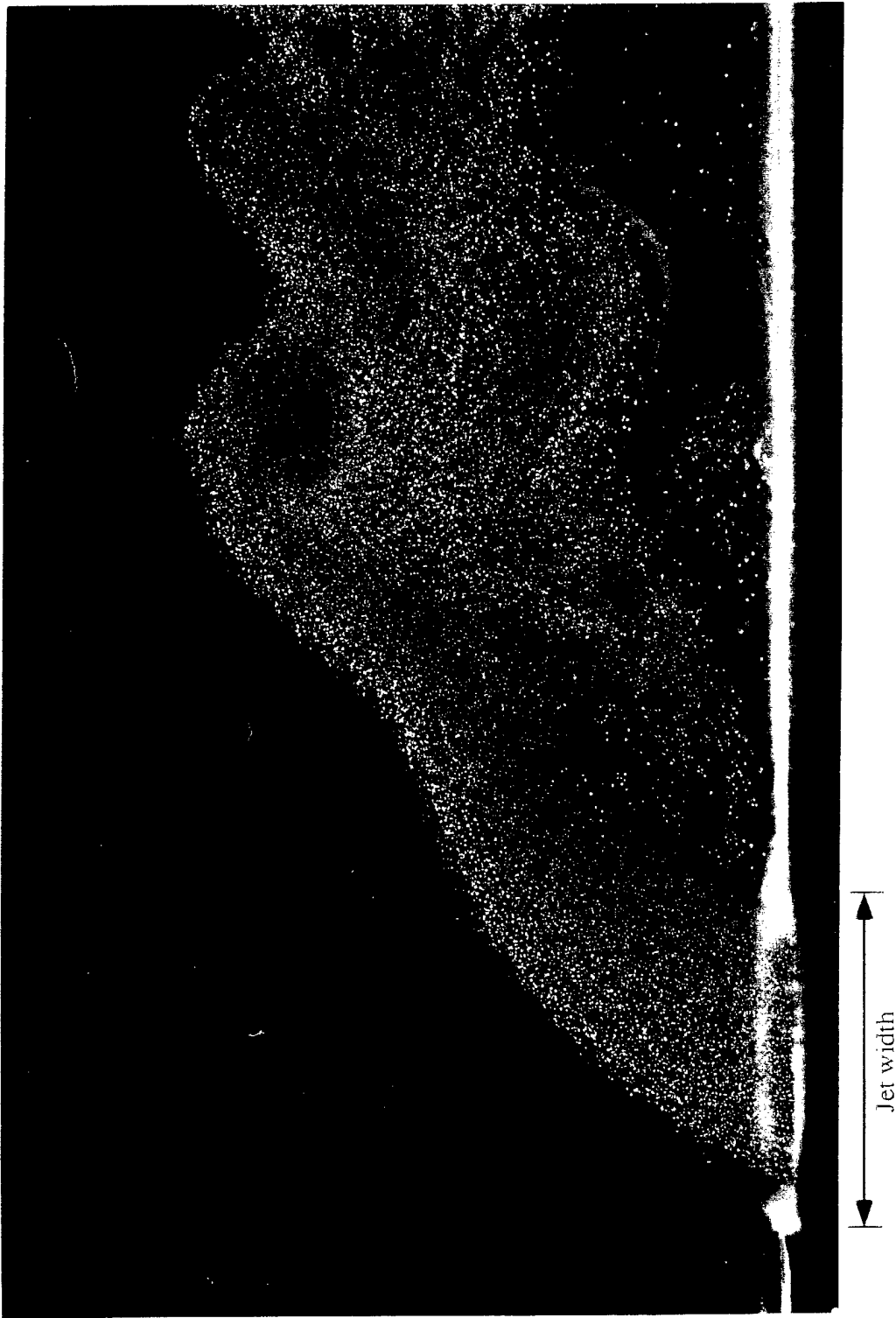


Figure 2. A typical double exposed PIV image (unforced jet, $R = 1.0$)

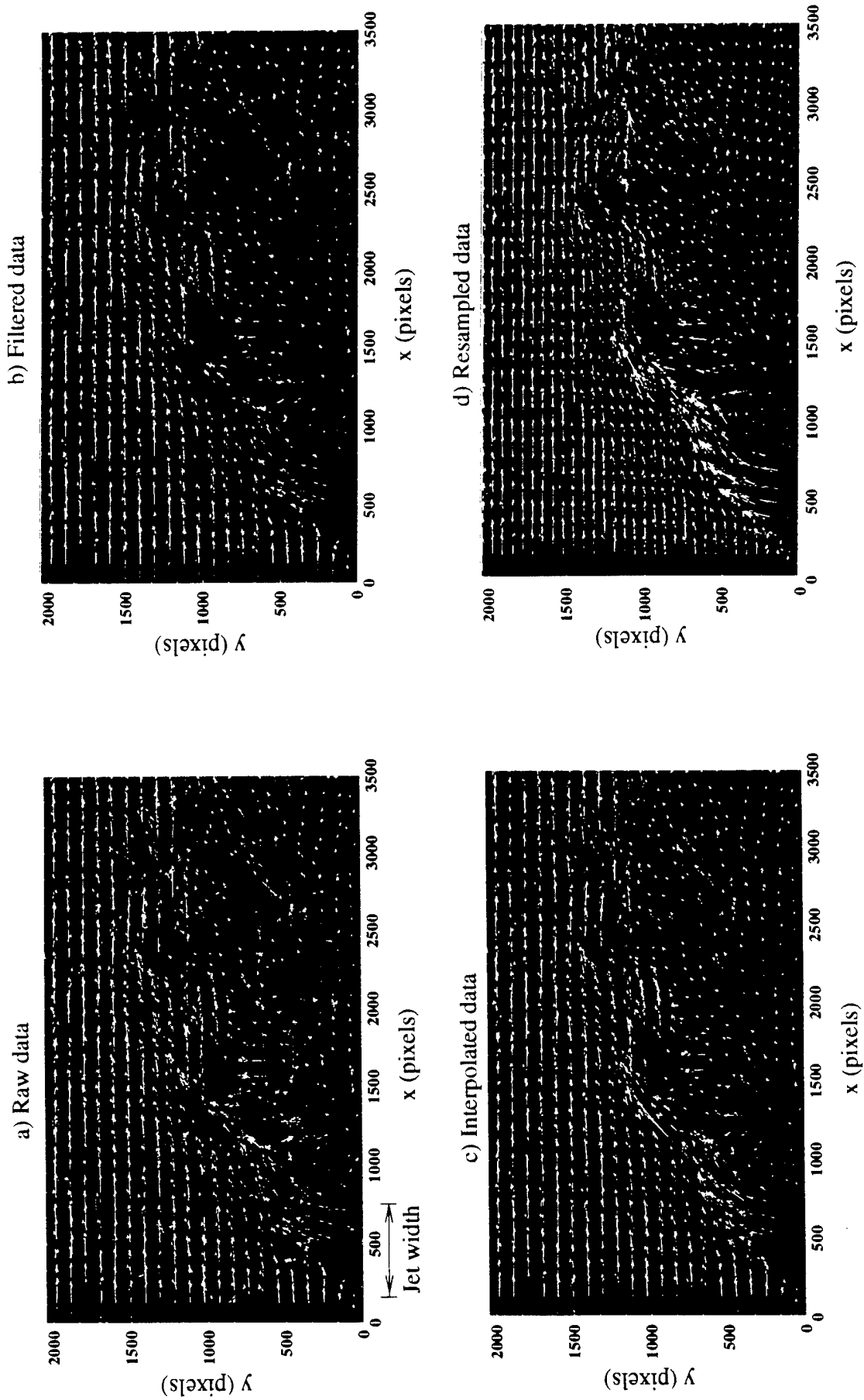


Figure 3. Post processing of PIV data

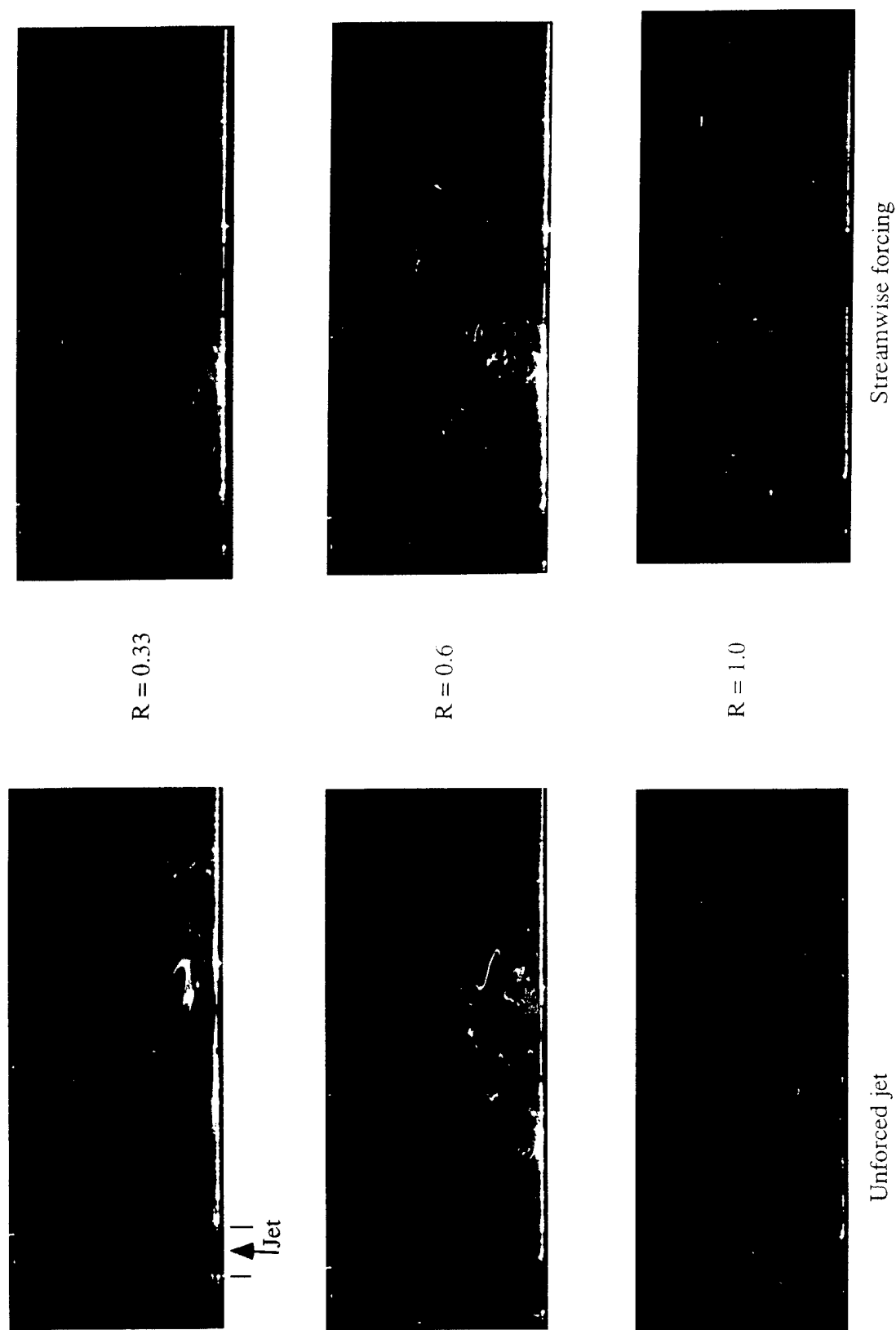


Figure 4. Reactive Mie Scattering Images (x-y plane)

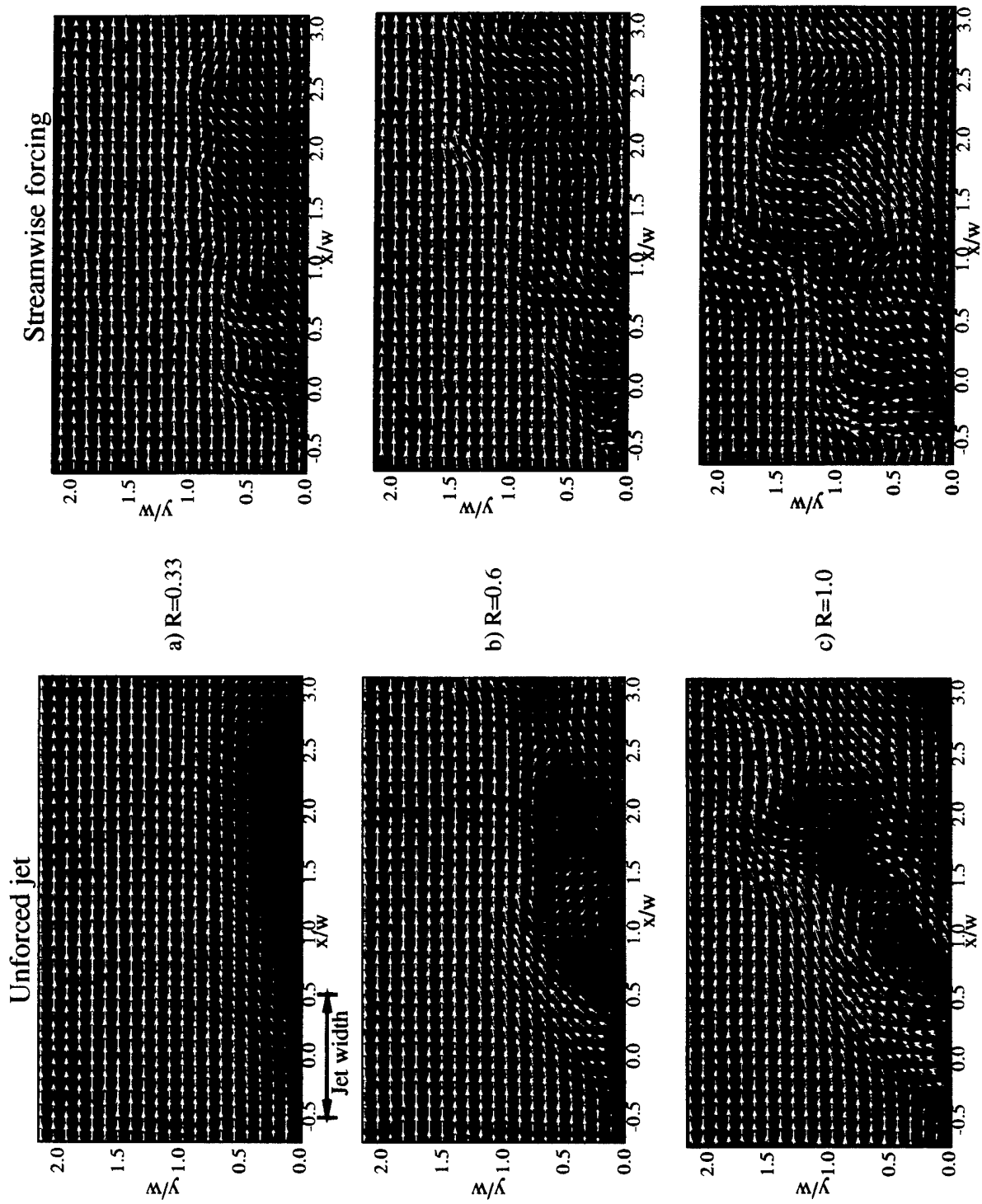


Figure 5. Instantaneous velocity distribution (x - y plane)

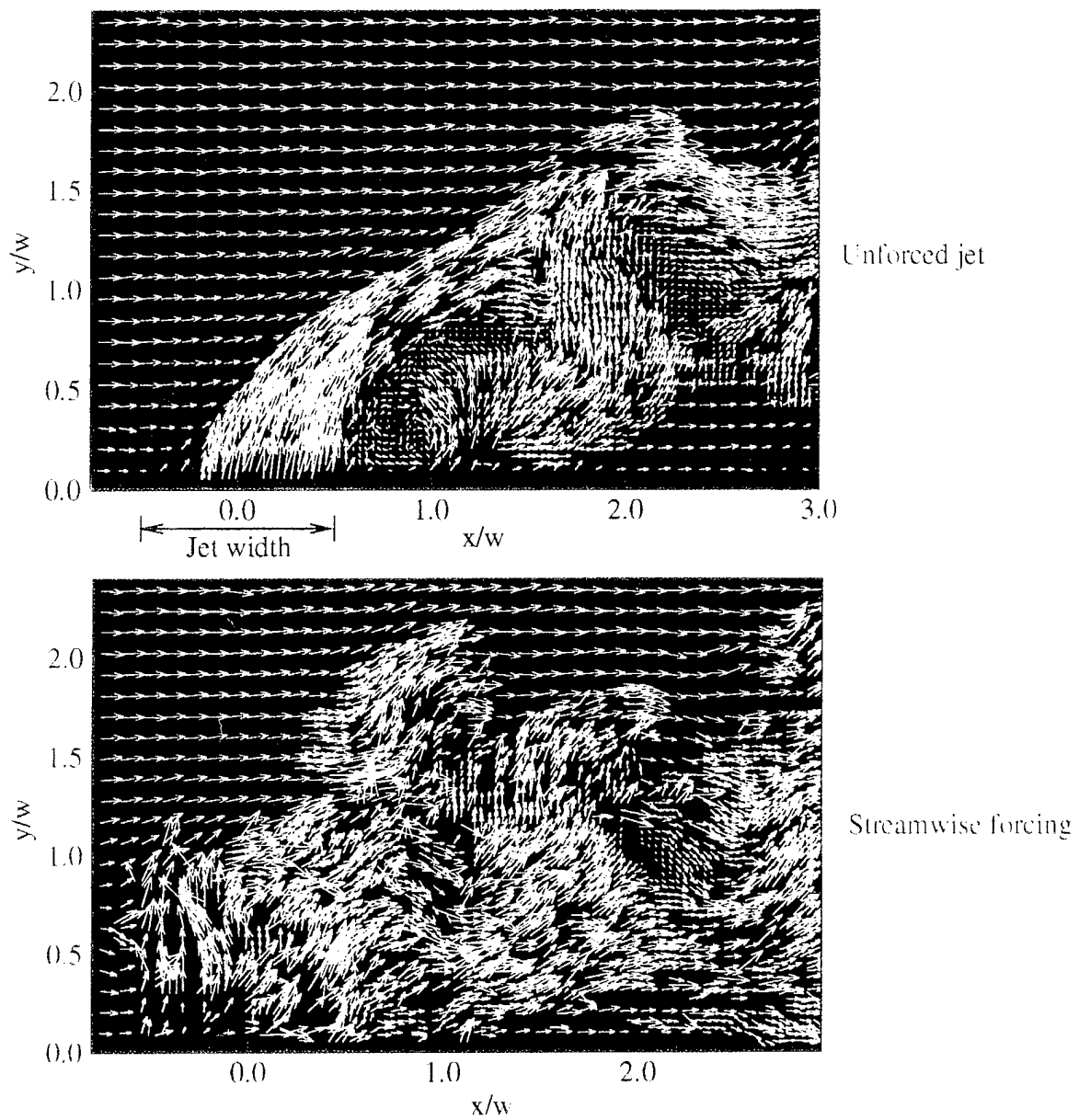
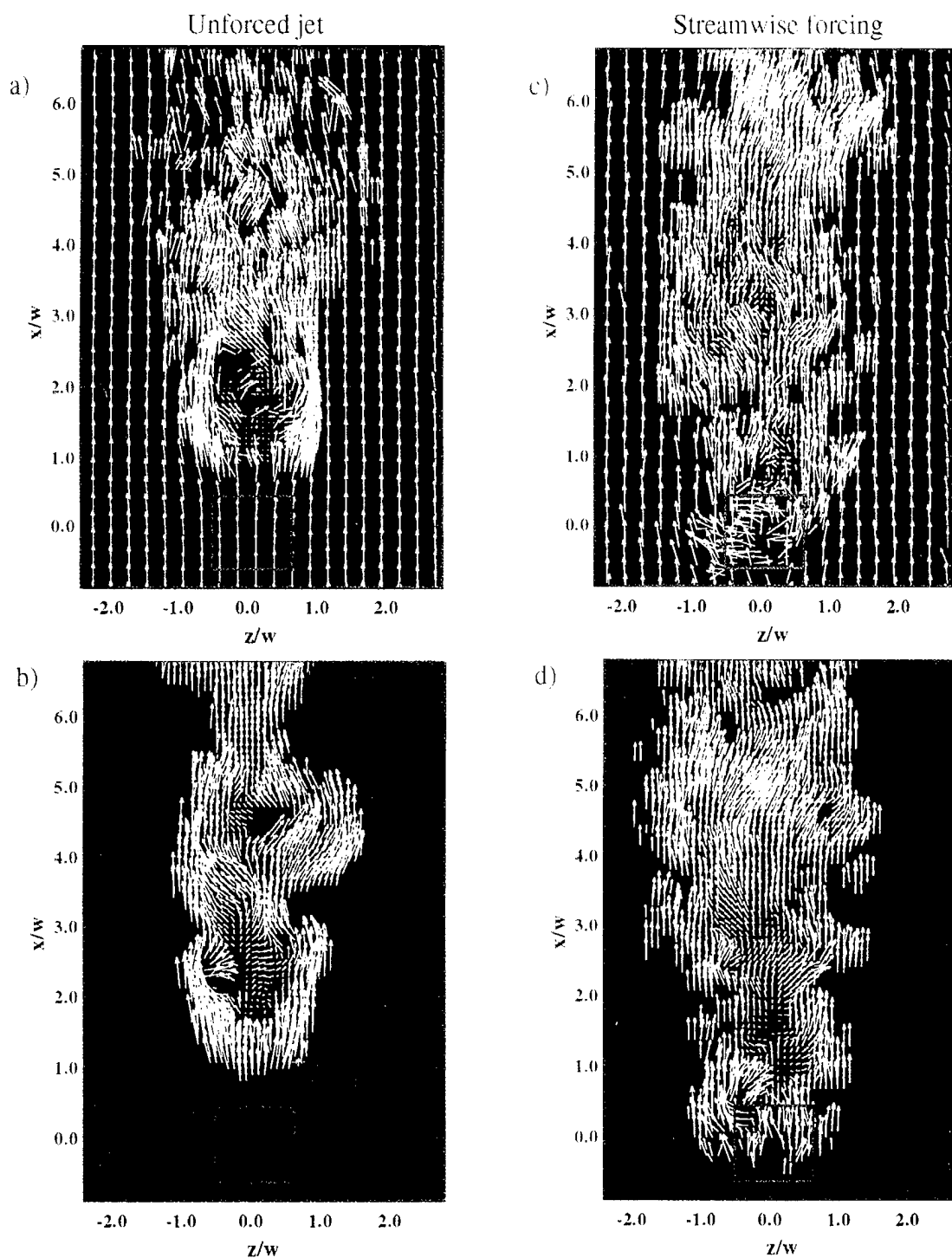


Figure 6. Image analysis based on particle size (x-y plane)



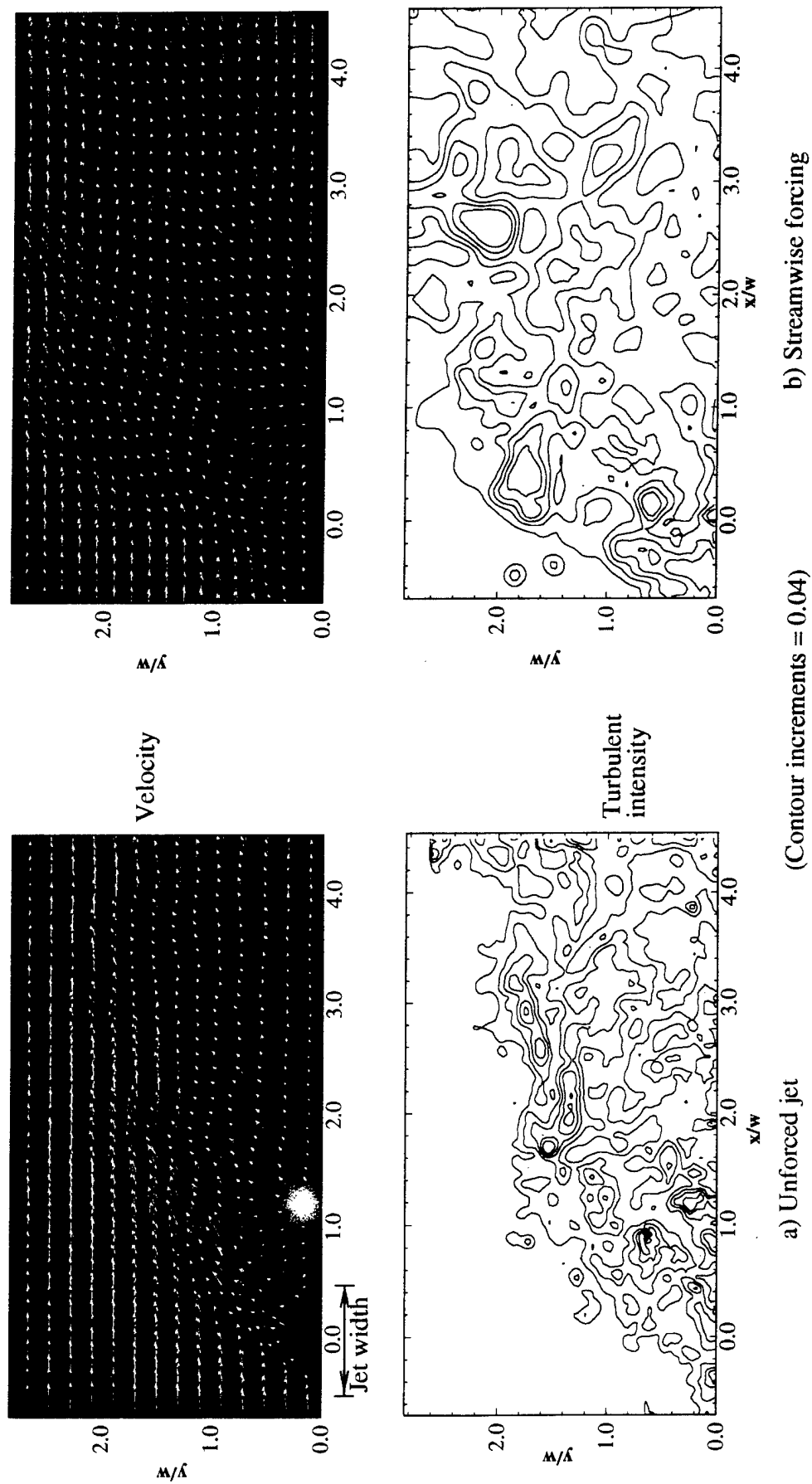


Figure 8. Velocity and normalized turbulent intensity (u_{rms}/U_{mean}) distributions ($R = 1.0$)



AIAA 96-0617

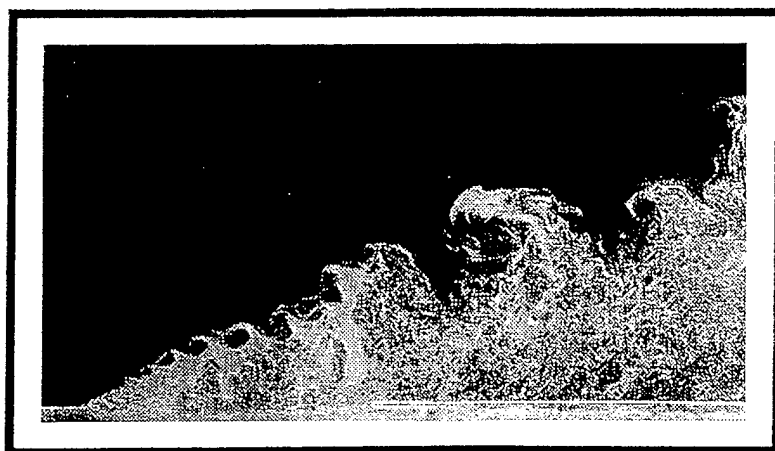
**PIV MEASUREMENTS OF FLAT PLATE FILM
COOLING FLOWS WITH HIGH FREE STREAM
TURBULENCE**

Sivaram P. Gogineni
Systems Research Labs
Dayton, OH

Richard B. Rivir
Aero Propulsion and Power Directorate
Wright Patterson AFB, OH

David J. Pestian
Univ. of Dayton Research Institute
Dayton, OH

Larry P. Goss
Innovative Scientific Solutions Inc.
Dayton, OH



**34th Aerospace Sciences
Meeting & Exhibit**
January 15-18, 1996 / Reno, NV

PIV MEASUREMENTS OF FLAT PLATE FILM COOLING FLOWS WITH HIGH FREE STREAM TURBULENCE

Sivaram P. Gogineni
Systems Research Labs
Dayton, OH

David J. Pestian
University of Dayton Research Institute
Dayton, OH

Richard B. Rivir *
Aero Propulsion and Power Directorate
Wright Patterson AFB, OH

Larry P. Goss
Innovative Scientific Solutions Inc.
Dayton, OH

Abstract

Two color double pulsed Particle Image Velocimetry measurements of simulated turbine film cooling flows have been made for blowing ratios of 0.5, 0.7, 1.0, and 1.5 in the near field of the film cooling hole, $x/d \leq 2.5$ for free stream turbulence levels of 1%, 6%, 12%, and 17%. Increases in the jet spread with free stream turbulence are up to 2 times the 1% free stream turbulence case for blowing ratios up to 1.0.

Nomenclature

- d film cooling hole diameter (1.905 cm)
- M coolant blowing (mass flux) ratio ($\rho_c U_c / \rho_{fs} U_{fs}$)
- Re Reynolds Number based on film cooling hole diameter ($\rho_c U_c d / \mu$)
- Tu x turbulence intensity (u' / U)
- U time mean local streamwise velocity (m/s)
- x streamwise distance measured from the downstream lip of the injection hole (cm)
- y vertical distance from the injection surface (cm)
- Λ integral turbulence scale (cm)

Introduction

The character of the flow into the axial turbine rotor blade row of a gas turbine engine is largely determined by the upstream nozzle guide vanes. The close spacing of vanes and blades subject the blades to unsteady flows with scales which may range from half of the passage width, due to the passage vortex, to the order of the blade boundary layer thickness.

Many modern turbine stages employ film cooling to permit near stoichiometric combustor operating temperatures. Film cooling air is injected through rows of small (0.5mm diameter typical) holes in the blade surface. The coolant air is supplied from the compressor exit flow and is maintained at essentially constant pressure.

The objective of the present study is to provide a more detailed characterization of the coolant injection phenomenon and its interaction with the free stream disturbances. The Reynolds number based on the coolant hole diameter of 1.9 cm is approximately 20,000, which is typical for a turbine. The facility can be supplied with freestream turbulence levels ranging from less than 1% to over 17%. Freestream turbulence is an important feature of gas turbines which must be present to properly simulate the turbine aerodynamics and heat transfer. The velocity ratio (coolant velocity / freestream velocity) varies depending on where the film cooling is located on the blade, so this parameter will also be investigated. Because the effectiveness of film cooling is governed by the rate at which the coolant jets mix with the hotter surrounding flow, both freestream turbulence and the velocity ratio influence the rate of mixing and therefore the performance of any specific film cooling design. PIV measurements provide a simultaneous realization of a plane of the flow with a spatial resolution of 1.4mm for 3 diameters downstream of the film injection hole. These measurements allow computation of vorticity and dissipation.

Experimental Facility

The measurements of this study were made in an open loop film cooling wind tunnel described in detail

* AIAA Associate Fellow
Copyright © 1996 by the American Institute of Aeronautics and Astronautics, Inc. All rights reserved.

by Bons, et al. 1994, and 1995. Figure 1 shows an overall view of the facility and a top view of the cooling hole arrangement and the heat transfer surface. The main flow passes through a conditioning plenum containing perforated plates, honeycomb, screens, and a circular-to-rectangular transition nozzle. Downstream of the transition nozzle, at the film cooling station location, free stream turbulence levels of 0.7 to 17% can be achieved with velocity and temperature profiles uniform to within 1% at the film cooling station.

A single row of 1.905 cm film cooling holes at an injection angle of 35 degrees to the primary flow is investigated. The length to diameter ratio of the film cooling holes evaluated is 2.4. The integral turbulence scale to film hole diameter is 2.88 to 4.23, depending on the turbulence level and turbulence generation mechanism (Bons et al., 1994). The momentum thickness to hole diameter ratio typically is 0.05, and a typical film cooling hole Reynolds number is 20,000.

Two-Color Particle Image Velocimetry

PIV techniques have been used for a number of years to measure velocity distributions in planar cross sections of a given flow field as described in detail in earlier work (Lourenco et al., 1989 and Adrian, 1991). One of the difficulties involved in implementing this otherwise attractive velocimetry technique however, is the directional ambiguity, namely, the inability to determine the temporal sequence of particle pairs and thus the direction of the measured velocity. Several techniques that have been developed to resolve this ambiguity use a single color lasers and image shifting by means of either scanning, or rotating mirrors, pulse tagging, calcite crystals, and polarizing beam splitters. The mechanical motion associated with the mirrors imposes some limitations on velocity measurements. Pulse tagging uses pulses of different duration (Grant et al., 1990), but limits the technique to low velocity flows, since the time resolution is not adequate to prevent image blurring in high speed flows. Calcite crystals exploit the polarization of the light scattered from the seed particles but the magnitude and orientation of the shift can change in the film plane because the light is collected from a finite solid angle (Landreth et al., 1988). In addition, for a given camera magnification, the velocity bias can not be altered unless the crystal thickness is changed or several crystals are used in series. A polarizing beam splitter and two quarter wave plates also utilize polarization principle and provide constant velocity bias throughout the flow field so that synchronization with other hardware is not necessary (Lourenco, 1993).

A two-color PIV system that was developed by Goss et al., 1991, (Figure 1) has the following advantages: (i) the directional ambiguity is resolved using the color coding of the particle images, (ii) higher data yields are attainable, and (iii) the system is particularly suitable for combustion diagnostics. The system uses color to temporally mark the location of the seed particles in the flow field. The green (532 nm) laser output from a frequency-doubled Nd:YAG laser and the red (610 nm) laser output from a Nd:YAG pumped dye laser are combined by a dichroic beam splitter and directed through sheet forming optics. The laser sheet energy is typically 20 mJ/pulse and the sheet thickness is less than 1 mm in the test section. The Laser sheet orientation is illustrated in Figure 1. The temporal delay between the two lasers is controlled by a pulse generator and is set as a function of the gas velocity, optical magnification and interrogation spot size. In the present experiments, the time delay is 12 μ sec and is monitored by a photodiode.

The jet fluid is seeded with sub-micron (nominally 0.5 μ m) smoke particles. Mie scattering from the seed particles is recorded on commercial 35 mm color film that is digitized into individual red, green, and blue components at a resolution of 2700 pixels per inch. Several techniques such as Young's fringe analysis, auto-correlation, etc. are available for image analysis for monochromatic double pulse images. However, these methods do not take into account the color information in the present PIV images. The cross correlation technique implemented in the present work exploits the spectral separation of the red and green images and eliminates approximately one half of the possible particle images from each interrogation region.

The present cross-correlation technique is based on intensity maps of the red and green images of scattered light. Consider the intensity distributions of the red and green images $r(x,y)$ and $g(x,y)$ and their corresponding Fourier transforms $R(a,b)$ and $G(a,b)$. The two-dimensional cross-correlation function

$$\begin{aligned} h(x,y) &= \int_R \int_R r(\alpha,\beta) g(x+\alpha, y+\beta) d\alpha d\beta \\ &= F^{-1} [F(r(x,y)) F(g^*(x,y))] \\ &= F^{-1} [R(\alpha,\beta) G^*(\alpha,\beta)] \end{aligned} \quad (1)$$

is employed to determine the magnitude and direction of the average velocity over the interrogation area. (Note that unlike processing methodologies that are based on autocorrelation, the direction of the velocity vectors is uniquely determined.)

The correlation function (1) is calculated over small segments (interrogation domains) of the PIV image. In order to process the digitized PIV image, it is dissected into small sub regions. The dimensions of each interrogation domain depend on the particle density, estimated local velocity gradients, particle image size, and the desired spatial resolution. The maximum displacement of each particle must be less than half of the interrogation spot. In the present experiments, the interrogation domain measuring 64×64 pixels corresponding to 1.4×1.4 mm in the measured flow. In order to enhance the overall resolution, the interrogation domains are overlapped by one-half the domain size. The peak of the correlation map calculated by Eq. (1) corresponds to the average velocity displacement within the interrogation spot. An intensity weighted peak searching routine is used to determine the exact location of the peak to a sub-pixel accuracy. The number of particle pairs that are normally necessary to ensure a desirable signal to noise ratio is reduced to four or five pairs when the cross-correlation analysis is employed.

Uncertainty Analysis

The experimental uncertainties are calculated based on knowledge of the instrumentation used and a simple root-mean-squared error analysis (Kline and McClintock 1953). This method assumes contributions to uncertainties arise mainly from unbiased and random sources. The large out of plane velocities and large fluctuating components required dense seeding and very short interpulse times which began to challenge the capability of the film for temporal resolution. Uncertainty in the velocity measurement arises from the time required to keep the large out of plane velocities and fluctuating components within the laser sheet during both pulses. The resulting number of pixels, typically 12, of displacement and the sub pixel resolution of 0.25 pixels then dictate the uncertainty of $\pm 2\%$. The spatial resolution used in the data presented is 2.8mm. The data was acquired at a resolution of 1.4mm using 45 pixels per mm for a spatial resolution accuracy of 1.5%.

Results and Discussion

The film flow has been seeded with a 50% mixture of water and Propylene Glycol with a nominal diameter of 1 micron or less. This technique allows measurements of the film flow only. Blowing ratios of 0.5, 0.7, 1.0, and 1.5 were investigated for 1%, 6%, 12%, and 17% turbulence intensities. 10 to 30 images were taken for each flow case. The double pulsed PIV images and the reduced velocity plots will be presented. There is a very large mean velocity distribution in the vicinity of the film hole as shown in previous publications, Schauer and Bons, 1994, resulting in a vulcano like structure for this flow condition with a velocity ratio of up to +120% to 80% of free stream over the film hole. This range of velocities is also observed in the PIV measurements.

Shown in Figures 2 and 3 are typical double pulsed two color measurements for blowing ratios of 0.7, and 1.0 at the four turbulence levels. At the same blowing ratio the free stream turbulence levels of 1 % and 17% in the Figure 2 comparison clearly shows near doubling of the jet spread for the 17% turbulence case. This is consistent with previous averaged hot wire and thermocouple measurements. The film jet spread angle has two slopes, one nominally over the film hole, and a second slope after the film hole opening. Also illustrated in Figures 2 and 3 is the roll up of the film cooling jet boundary layer in the opposite direction of what would be the anticipated free stream shear layer roll up. The free stream has not been seeded in this case which is why the free shear layer does not appear in these realizations of the flow. The corresponding instantaneous velocity vector fields are shown in Figures 4 and 5. The range of film jet velocities at the exit are comparable to those observed in Schauer and Bons, 1994. Extensive regions of low velocity flow are indicated following the exit with very high activity in the shear layer. Again the jet spread with turbulence intensity is quite clear.

The indicated jet spread, growth of the shear layer, and growth of the scales was obtained from these realizations of the flow by digitizing their envelopes. The angle of the flow over the film cooling hole and the angle after the film cooling hole for 2.5 diameters is illustrated in Figure 6 for all blowing ratios and turbulence levels investigated. A least squares fit has been plotted for both angles in Figure 6. In Figure 7 we have digitized the thickness of the shear layer as a function of turbulence and blowing ratio. Figure 7 shows a regular growth in shear layer thickness with turbulence intensity and blowing ratio until we reach a blowing ratio of 1.5. At 1.5 the jet

momentum dominates the turbulence and the two curves remain coincident for 1.5 diameters. Although we have attempted to choose representative realizations, these are individual realizations of the flow. In reality there should be an envelope around each of these sets of data. The film injection angle is 35° as previously indicated. The initial blowing angle is less than the injection angle for blowing ratios less than 1, and approximately equal to the injection angle at a blowing ratio of 1.0 and 1% turbulence intensity. Both angles are observed to decrease with turbulence intensity for the 1.5 blowing ratio case. Both angles increase up to a blowing ratio of 1.0 with increasing turbulence intensity. At a blowing ratio of 1.5 the film momentum dominates that of the free stream with both angles decreasing with increasing turbulence. The shear layer over the film hole, is clearly driven primarily by the blowing ratio and the free stream then dominating the eddy size after the film hole. The shedding frequency of the shear layer increases, the scale size decreases, over the film hole with blowing ratio. The roll up frequency for the shear layer after the film hole decreases, the scale size increases, with both blowing ratio and turbulence level.

In Figure 8 the vorticity distribution has been calculated from $\omega = 1/2(\partial U/\partial y - \partial V/\partial x)$ and the contours plotted for the blowing ratio of 1.0 case. The vorticity plots for all cases investigated show an increase in vorticity activity with both blowing ratio and turbulence intensity. The peaks in vorticity are well correlated with the shear layer velocities as is indicated in Figures 3, 5, and 8. These representations need to have the seeding optimized by further reducing the amount of seed introduced.

Concluding Remarks

PIV measurements of film cooling flows have indicated augmentation of jet spread for increased turbulence for $M \leq 1$. A systematic increase in jet and shear layer spread with turbulence intensity and blowing ratio has been documented near the film cooling hole for a Reynolds number of 20K. The blowing ratios of 0.5, 0.7, and 1.0 showed a doubling for the spread angles in going from turbulence levels of 1% to 17% with nearly a linear relationship with blowing ratio and turbulence level, while the 1.5 blowing ratio showed a decrease in spread angles. Increased jet spread implies a lower effectiveness and a proportionately higher mixed out temperature or lower cooling effectiveness.

Acknowledgments

This work was performed under partial sponsorship of the Air Force Office of Scientific Research project 2307S. Dr. James McMichael was the program manager.

References

- Adrian, R. J., 1991, "Particle Imaging Techniques for experimental fluid mechanics," *Ann Rev Fluid Mech*, 23, pp. 261-304.
- Bons, MacArthur, and Rivir, 1994, "The Effect of High Freestream Turbulence on Film Cooling Effectiveness," ASME 94-GT-51, International Gas Turbine and Aeroengine Congress and Exposition, The Hague, Netherlands.
- Bons, Rivir, MacArthur and Pestian, 1995, "The Effect of Unsteadiness on Film Cooling Effectiveness," AIAA 95-0306, 33rd Aerospace Sciences Meeting and Exhibit, Reno NV.
- Grant, I. And Liu, A., 1991, "Directional Ambiguity Resolution in Particle Image Velocimetry by Pulse Tagging," *Experiments in Fluids*, 10, 71-76, 1990. 3, pp. 36-42.
- Goss, L. P., Post, M. E., Trump, D. D., and Sarka, B., 1991, "Two Color Particle Imaging Velocimetry," *J. Laser Applications*, 3, pp. 36-42.
- Kline, S. J. and McClintock, F. S., Jan 1953, "Describing Uncertainties in Single-Sample Experiments," *Mechanical Engineering*, pp. 3-8.
- Landreth, C. C. and Adrian, R. J., 1988, "Electro-Optical Image Shifting for Particle Image Velocimetry," *Appl. Optics*, 27 pp. 4216-4220.
- Lourenco, L. M., 1993, "Velocity Bias Technique for Particle Image Velocimetry Measurements of High Speed Flows," *Appl. Optics*, 32, pp. 2159-2162.
- Lourenco, L. M., Krothapalli, A., and Smith, C. A., 1989, "Particle Image Velocimetry," *Advances in Fluid Mechanics Measurements* (M. Gad-el-Hak, ed.), Springer-Verlag, Berlin, pp. 127-199.
- Schauer, J. J., and Bons, J. P., 1994, "Film Cooling Jet Mixing with Free Stream Turbulence," 1994 ICHMT International Symposium on Turbulence, Heat and Mass Transfer, Lisbon, Portugal.

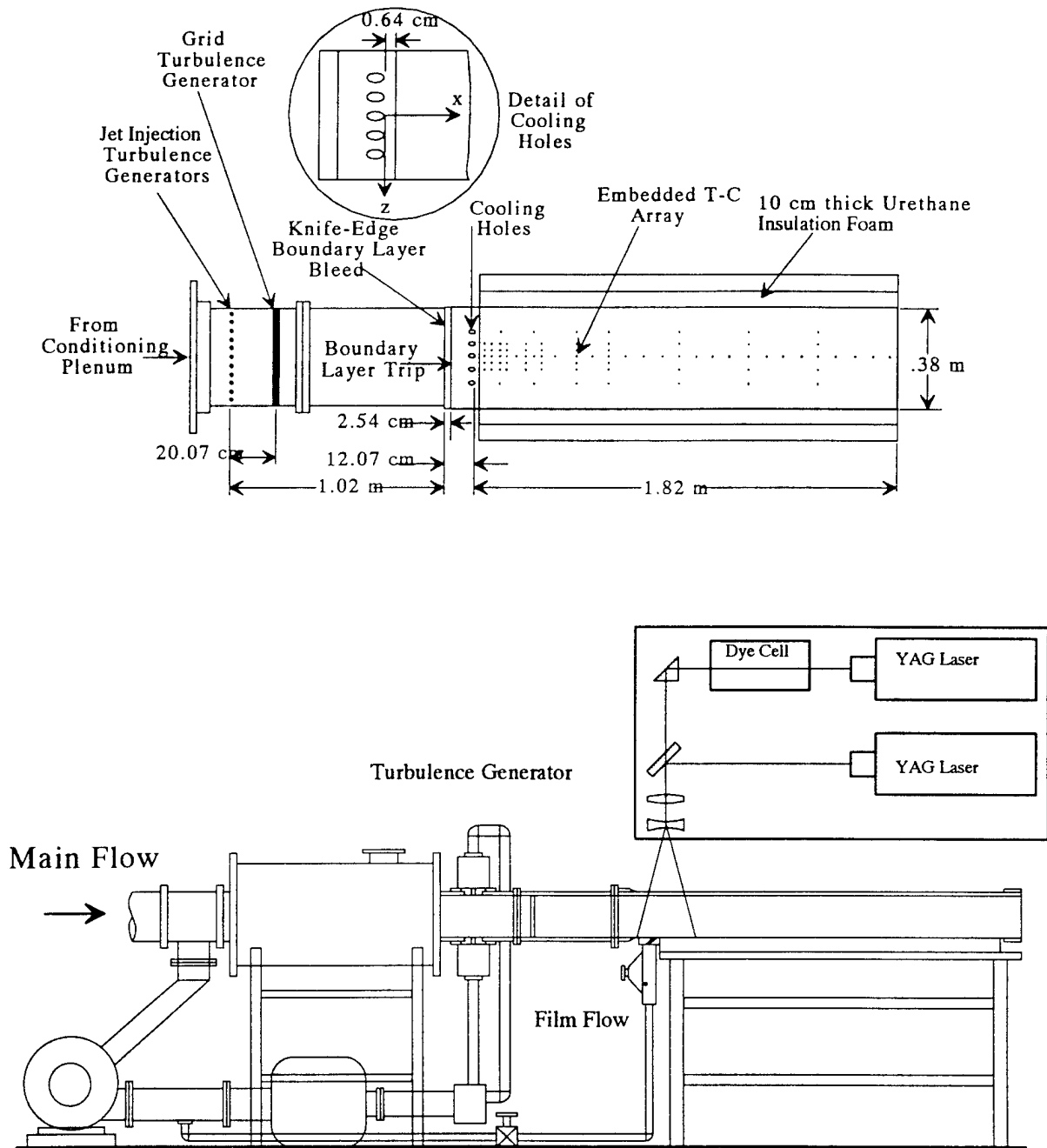


Figure 1. Top View of Facility and PIV Installation Schematic

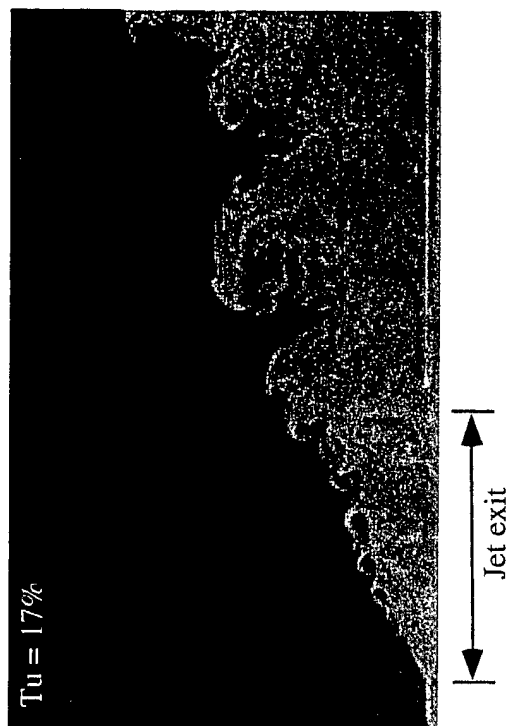
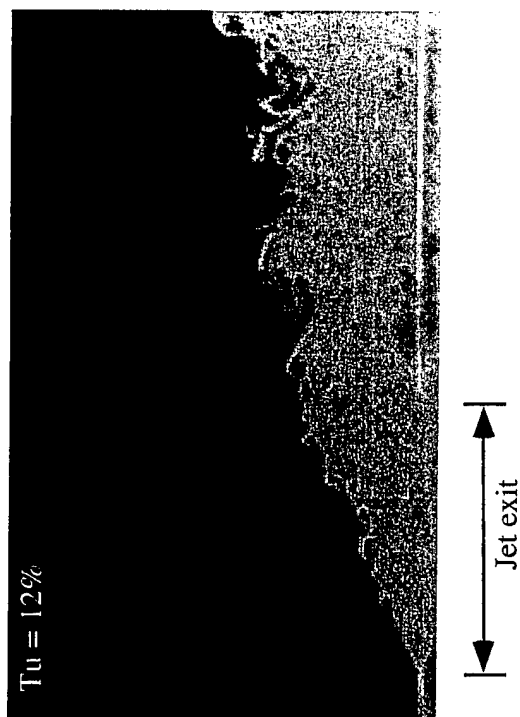
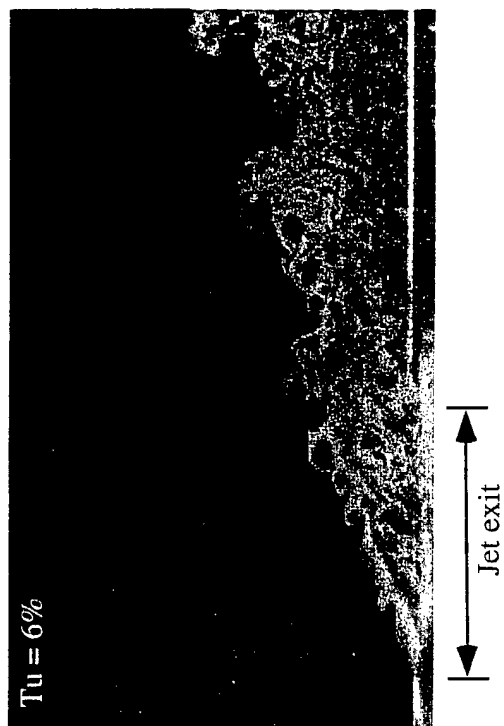
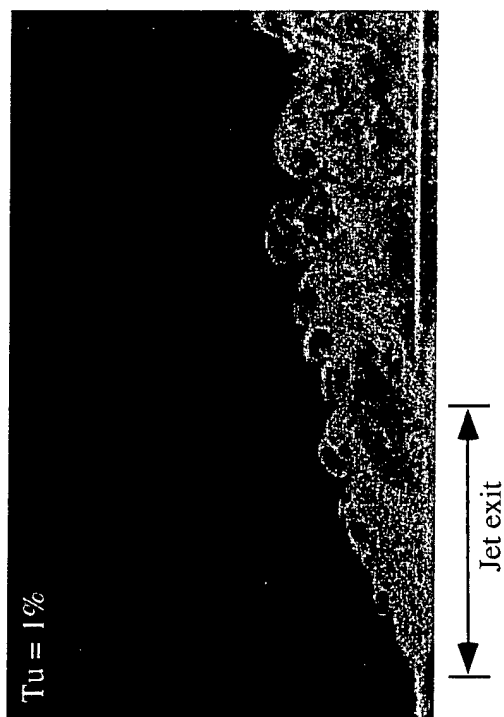


Figure 2. Double Pulsed PIV Images ($M = 0.7$, $Re = 20K$)

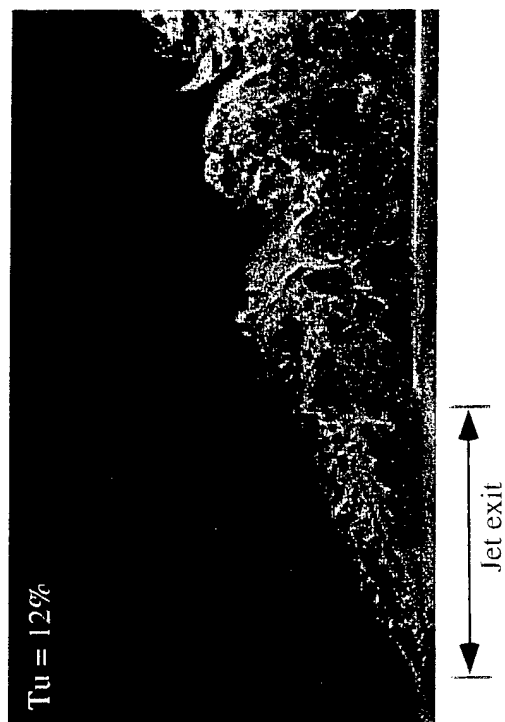
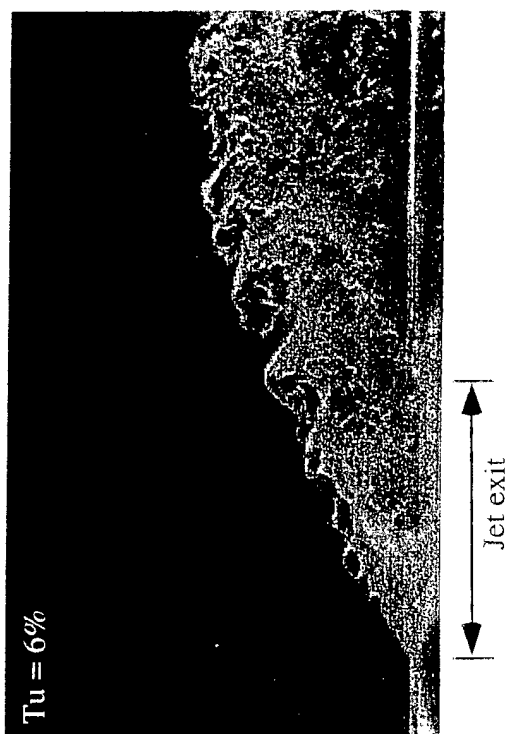
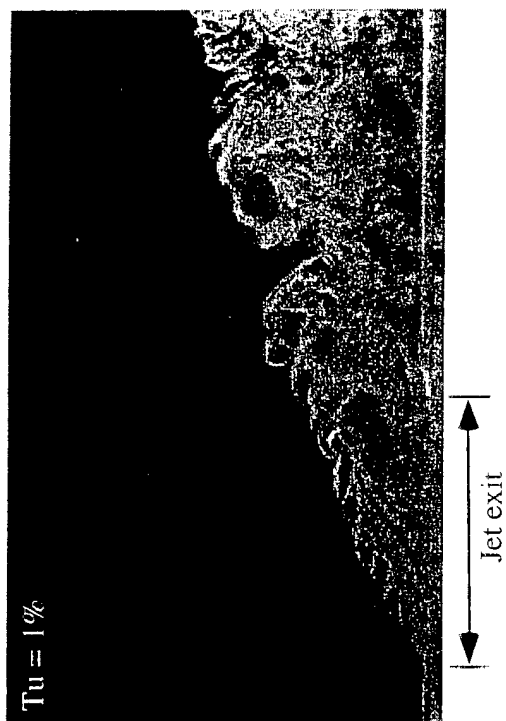


Figure 3. Double Pulsed PIV Images ($M = 1.0$, $Re = 20K$)

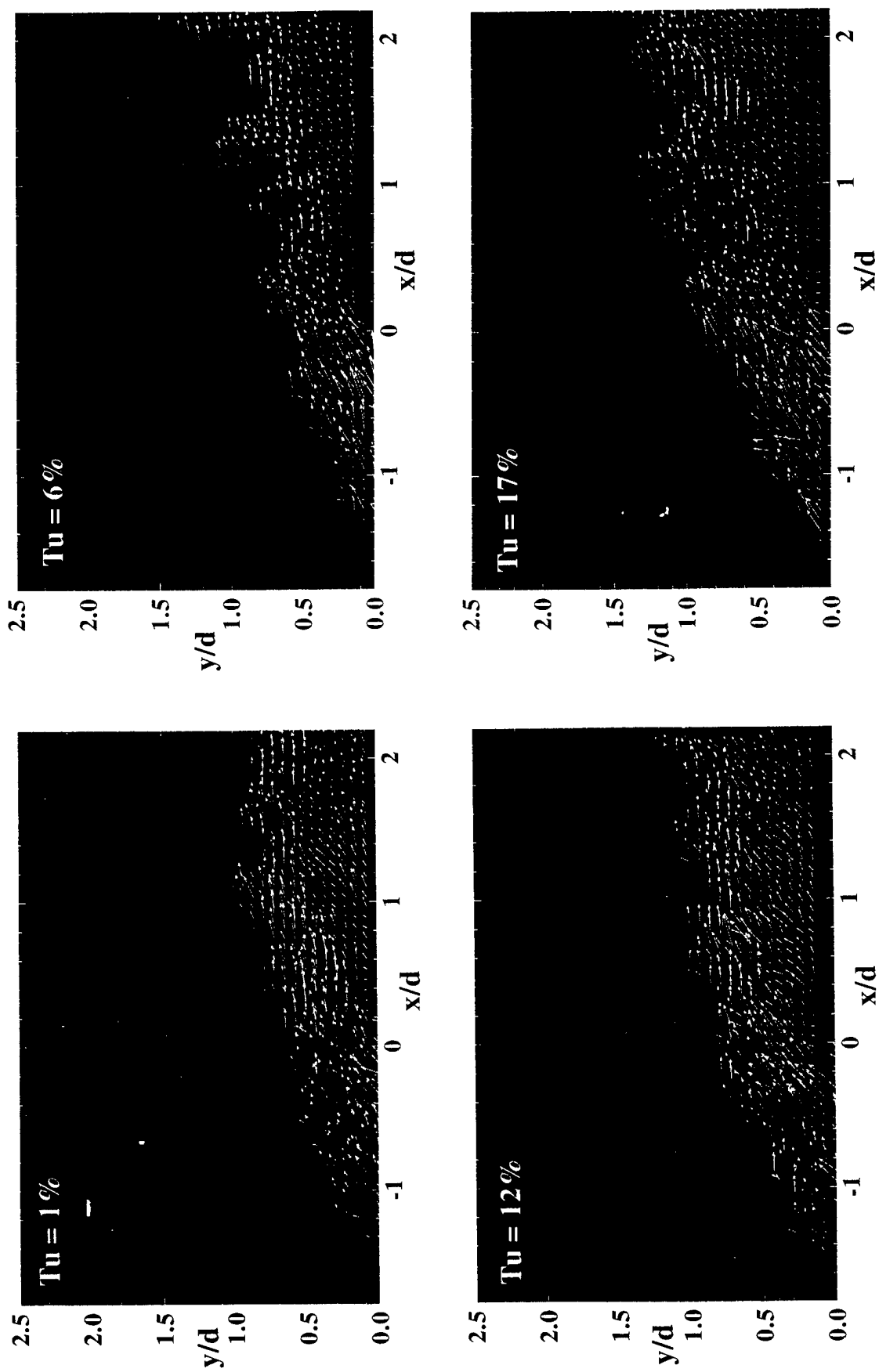


Figure 4. Instantaneous Velocity Distributions ($M=0.7$, $Re=20,000$)

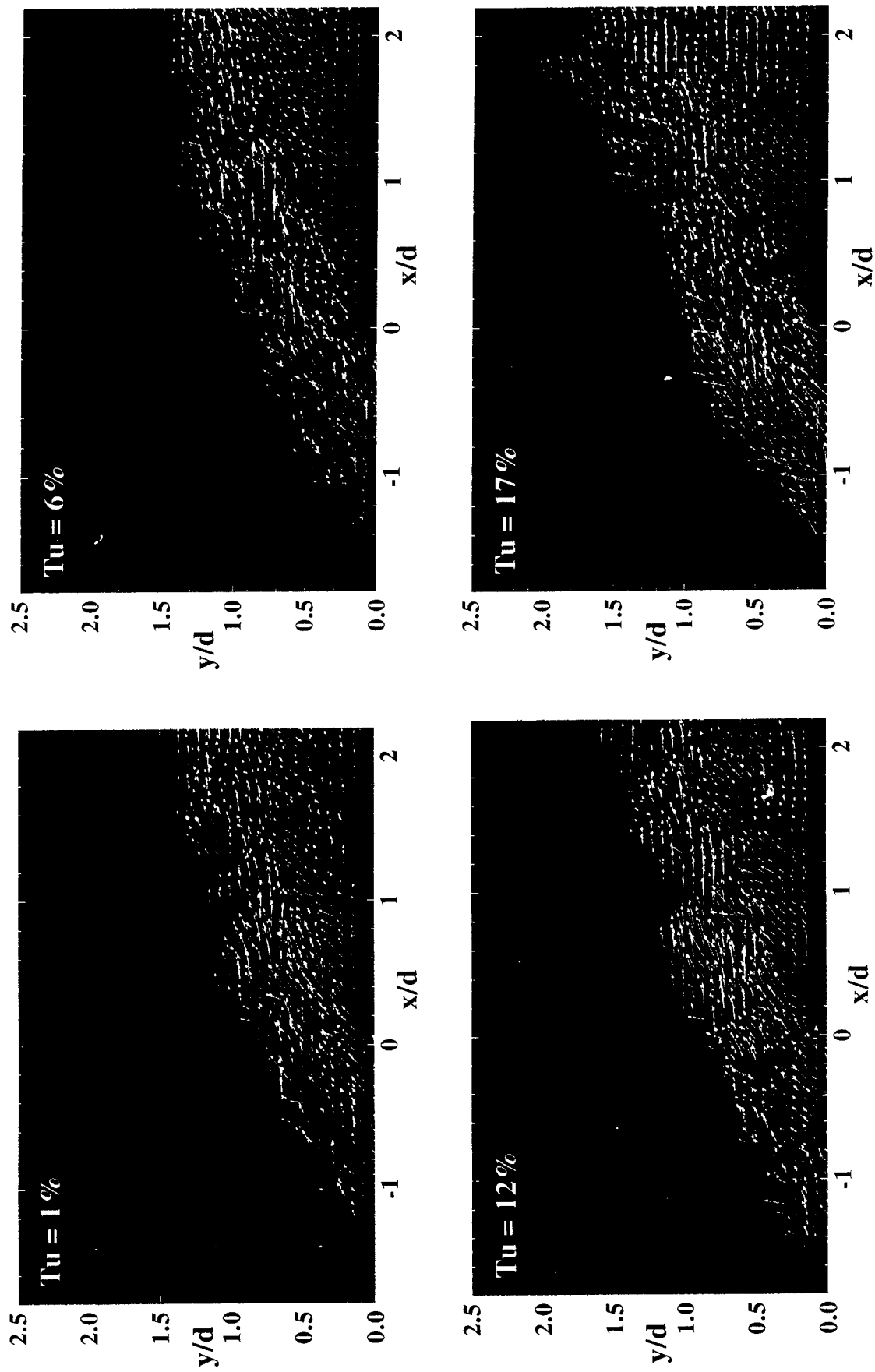


Figure 5. Instantaneous Velocity Distributions ($M=1.0$, $Re=20,000$)

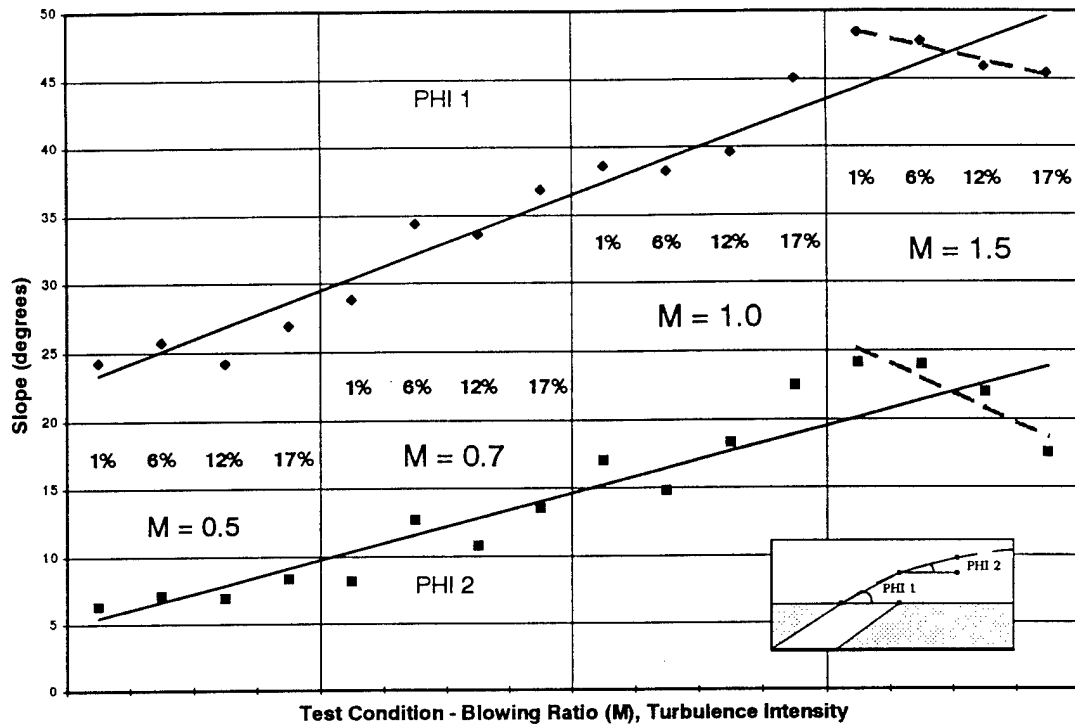


Figure 6. Angles of the Exiting Film Cooling Flow for the First 2.5 Diameters

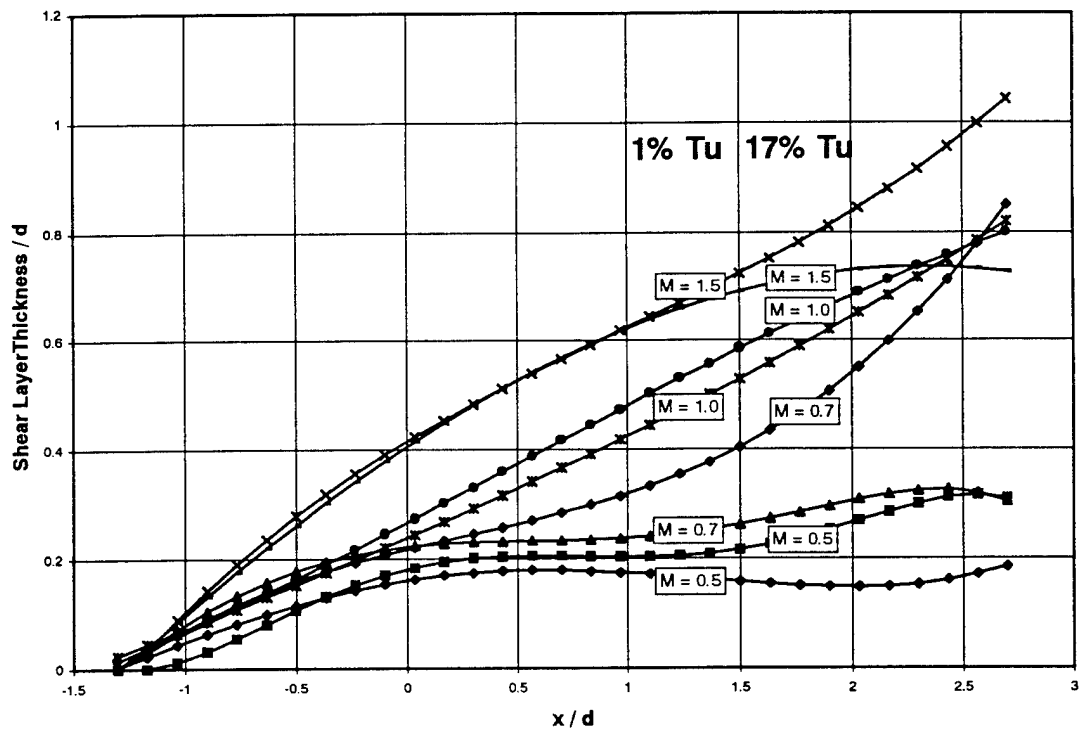


Figure 7. Growth of the Shear Layer Thickness Near the Film Cooling Jet Exit

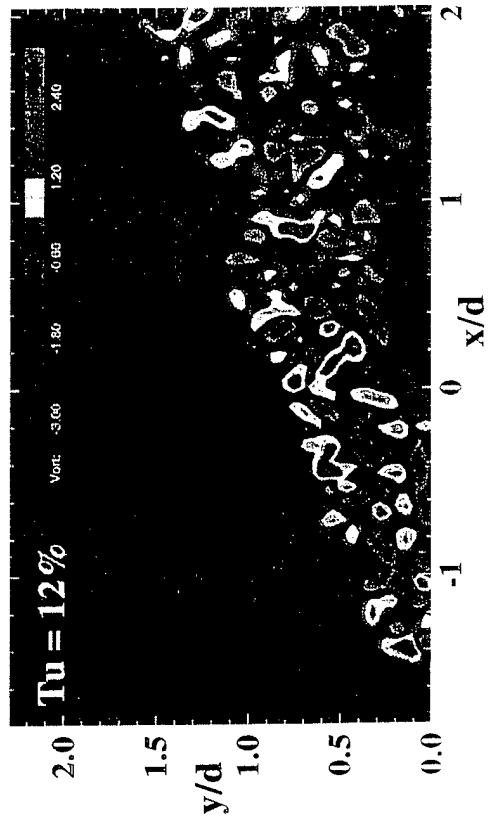
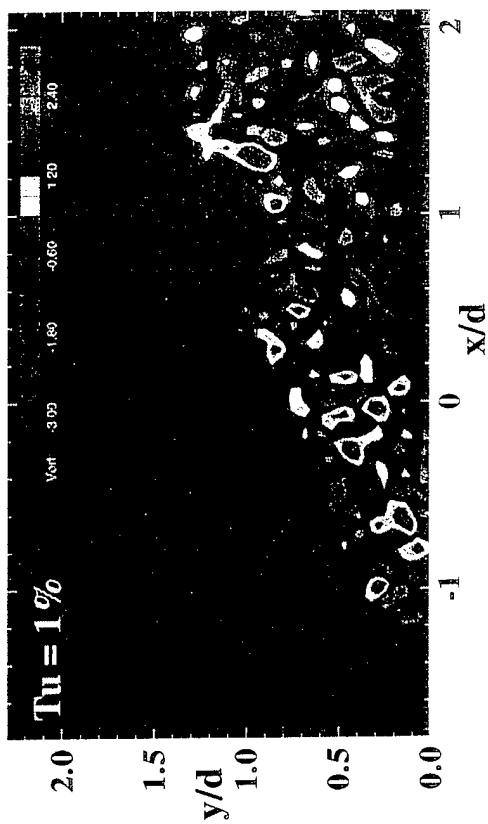
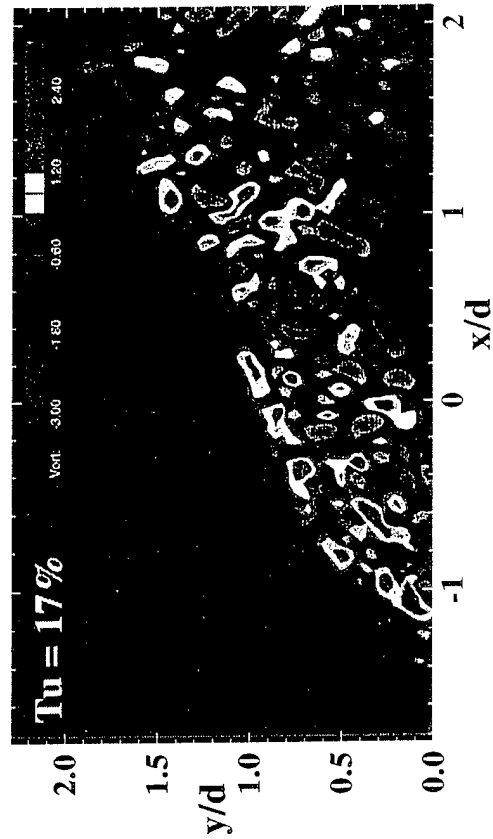
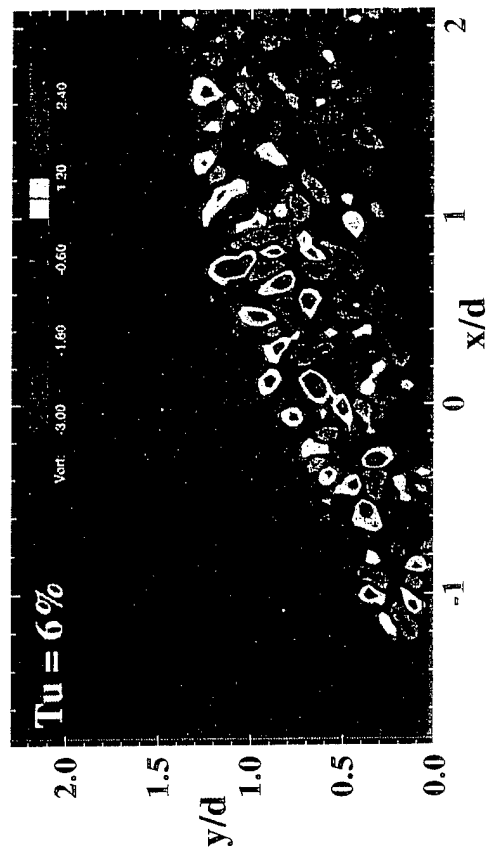


Figure 8. Instantaneous Vorticity Distributions ($M=1.0$, $Re=20,000$)

TWO-COLOR PARTICLE-IMAGING VELOCIMETRY EMPLOYING A SINGLE CCD CAMERA

Larry P. Goss and Darryl D. Trump
Systems Research Laboratories, Inc.
A Division of Calspan Corporation
2800 Indian Ripple Road
Dayton, OH 45440-3696

Jonathan H. Frank
Department of Mechanical Engineering
and Center for Laser Diagnostics
Yale University
New Haven, CT 06520

Introduction

Particle-Imaging Velocimetry (PIV) is a proven technique for the measurement of two-dimensional velocity in a flowfield.¹⁻³ Seed particles, which follow the flow, are illuminated by two pulses of laser light having a known time delay between them. Mie scattering from the particles is imaged onto a two-dimensional detector. Each particle is imaged twice--once from each laser pulse. The particle images provide a measurement of the distance that a particle travels between laser pulses, and a velocity can be calculated since the interpulse time is known. An advantage of PIV over point-measurement velocimetry is the ability to measure velocity gradients and vorticity at an instant in time. Of particular interest is the ability to compare instantaneous and time-averaged velocity fields to gain an understanding of the importance of transient-flow phenomena.

One of the difficulties with implementing PIV in complex flows is the directional ambiguity. Unless some means exists for distinguishing the temporal sequence of particle images, it is not known whether the measured velocity is $+v$ or $-v$. Directional ambiguity can be resolved through a variety of methods including those which employ pulse tagging,⁴ fluorescent particles,⁵ two colors,⁶ and image shifting.⁷⁻⁹ The present work demonstrates a new approach to image shifting--the use of two colors and a dichroic mirror in the collection optics to impose an image shift. Previously, image-shifting techniques have employed a single color and a variety of shifting mechanisms including a rotating mirror, detector translation, and electro-optics. The first two incorporate mechanical motion which imposes some limitations on velocity measurements. The use of either electro-optics or two-color PIV removes these limitations. For two-color PIV systems, seed particles are illuminated by pulsed lasers of two different colors. Particle images are recorded on color film which is subsequently digitized with a CCD array.⁶ The two colors of recorded particle images are digitized separately, enabling the determination of the temporal sequence of the images. However, the use of film has a variety of disadvantages, some of which can be overcome by imaging directly onto a two-dimensional CCD array. Two-color PIV could be performed by imaging each color onto either a separate CCD or different areas of a single CCD, although this would be an inefficient use of the limited resolution (relative to that of film) of these detectors. In the present work both color

images are superimposed on the same region of a single CCD detector, but one color image is shifted slightly to ensure that even the largest negative velocity has a positive displacement of particle images.

Experimental

The experimental arrangement for two-color PIV with image shifting is shown in Fig. 1. Two pulsed lasers are used to illuminate the flowfield. Green light ($\lambda = 532$ nm) is produced by a Q-switched Nd:YAG laser with a doubling crystal. A second Nd:YAG laser is used to pump a broadband dye laser (maximum energy output at $\lambda \sim 605$ nm). The red and green beams are overlapped via a dichroic beamsplitter, formed into sheets by lenses, and directed through the flowfield. In the imaged region of the flow, the beam height is ~ 8 cm with a waist of ~ 1 mm. The delay time between the red and green lasers is adjusted by varying the phase of the 10-Hz electronic oscillator that drives each Nd:YAG laser. A photodiode is used to measure the time between laser pulses.

Mie scattering from the seed particles is collected by a camera lens and imaged onto a 1024×1024 pixel Thompson CCD array. Red-particle images are displaced relative to green-particle images by a dichroic mirror placed between the flowfield and the imaging lens. Particles having zero velocity thus produce red and green images having a known separation that is determined by the magnification of the collection optics and the thickness of the dichroic mirror. In the present work a magnification of 0.24 was used and a dichroic mirror thickness of 1 cm which produces a horizontal shift of 100 pixels. Each red-particle image is shifted to the right of its corresponding green image and, thus, each measured displacement vector must have a component to the right (a positive x-component.) The particle-image separation actually measured in a flow depends on the imposed image displacement, the flow velocity, the image magnification, and the time delay between laser pulses. In order to ensure the resolution of directional ambiguity, one must have prior knowledge of the maximum velocities in the flowfield. The interpulse time is adjusted such that the largest negative x-component of the velocity field still generates red-particle images to the right of their corresponding green images.

Analysis

The procedure for deriving a velocity-field measurement from a single CCD image containing superimposed red- and green-particle images is as follows. Each vector is determined from the average separation between red-particle images and their associated green-particle images within a 128×128 pixel subregion of the digitized image. To obtain actual particle displacements, the image shift imposed by the dichroic mirror must be subtracted from the measured separations. The velocity components are given by the following expressions:

$$v_x = \frac{\Delta x_{\text{tot}} - \Delta x_{\text{shift}}}{\Delta t \times M} \times (\text{Pixel Size}), \quad v_y = \frac{\Delta y_{\text{tot}} - \Delta y_{\text{shift}}}{\Delta t \times M} \times (\text{Pixel Size}) \quad (1)$$

where Δx_{tot} and Δy_{tot} represent the displacement of the green- and red-particle images in pixels, Δx_{shift} and Δy_{shift} represent the imposed shift in pixels, Δt is the delay time between laser pulses, and M is the magnification of the collection optics. This calculation is repeated throughout the 1024×1024 pixel image with overlapping subregions to produce a vector field of 15×15 vectors.

Computation of the average separation of particle images within a subregion is automated by an image-correlation technique performed on a computer. One of two modes of processing is used, depending on the size of the imposed image shift. In one mode an auto-correlation is performed on each subregion. The resulting auto-correlation of the particle images has a central peak and two secondary peaks [Fig. 2(a)]. The displacement vector is determined by drawing a vector from the central to a secondary peak. However, the auto-correlation is symmetric about the central peak; therefore, the secondary peaks are 180 degrees apart, which is a manifestation of the directional ambiguity. The direction of the imposed shift determines the correct peak. In the present configuration the displacement having a positive x-component is selected.

The auto-correlation technique is valid when the particle-image separation is less than one-half the subregion dimension. For experimental configurations that produce larger particle separations, the subregion size must be increased, thus reducing the number of resolvable vectors. However, a cross-correlation technique allows the use of smaller subregions. For example, in the present experimental arrangement, constraints on magnification and the thickness of the available dichroic mirror produce a particle-image shift of 100 pixels. As an alternative to the use of a 256 x 256 pixel auto-correlation, a cross-correlation is performed with two separate 128 x 128 pixel subregions that are displaced from each other by 60 pixels [Fig. 2(b)]. In this particular case the cross-correlation has two peaks—one from the self-correlation resulting from the overlap of the two subregions and the other from the particle-image pairs. The relative displacement vector is drawn from the center of the cross-correlation to the latter of these peaks.

Results and Discussion

The PIV technique described above has been demonstrated with a stagnation-point flow. An air jet, seeded with ~ 5-mm-diameter alumina microballoons, issues from a circular 8-cm-diameter nozzle into ambient air. The average exit velocity is ~ 1 m/s. One nozzle diameter downstream of the exit, the jet impinges on a flat plate, producing a stagnation flow. The time delay between laser pulses is 1.5 ms. The imposed shift is determined throughout the field of view by imaging a piece of sandpaper illuminated with both red and green laser light. The processed sandpaper images yield a zero-velocity vector field which is then subtracted from the raw vectors [Eq. (1)] to yield the actual flow velocities in Fig. 3. The flow is from the top, and the splitting of the flow direction near the plate can be seen. Cross-talk between the red and green images due to an imperfect color separation by the dichroic mirror was not a significant problem.

An estimate of the precision of the velocity measurements was determined as follows. To simulate particle images from a uniform flowfield, a sandpaper target was attached to a translation stage having a digital position readout. First, the sandpaper was illuminated with green light and a green image acquired. Then, the sandpaper was translated a known distance and a red image acquired. After superimposing the red and green images, the displacement was measured using the PIV processing described above. Ideally, the displacement vectors throughout the image should be identical. However, the actual distribution of vector magnitudes has a standard deviation of 0.4 pixels. For this measurement of precision, systematic variations across the image field resulting from distortion by the collection optics are not completely eliminated. Although the precision is a fraction of a pixel, the accuracy of an actual velocity measurement depends on a variety of factors including seeding density, particle-size distribution, background signal, the ability of particles to follow

the flow, and the amount of particle motion normal to the laser sheets. Significant velocity gradients within a subregion add noise to the velocity measurement.

Conclusions

In conclusion, a new implementation of two-color PIV has been demonstrated in a stagnation-point flow. The resolution of directional ambiguity has been achieved by shifting red and green images with a dichroic mirror. In this method of PIV, film is not required. However, the resolution of a CCD is limited by the number of pixels on the detector. The ongoing development of larger format CCD arrays will expand the usefulness of the digital PIV technique.

Acknowledgement

This research was sponsored in part and conducted at the Wright Laboratory, Aero Propulsion and Power Directorate, Wright-Patterson Air Force Base, Ohio, under Contract No. F33615-90-C-2033.

References

1. L. M. Lourenco, A. Krothapalli, and C. A. Smith, *Advances in Fluid Mechanics Measurements* (Springer-Verlag, Berlin, 1989).
2. R. J. Adrian, *Appl. Opt.* **23**, 1690 (1984).
3. R. J. Adrian, *Int. J. Heat Fluid Flow* **7**, 127 (1986).
4. I. Grant and A. Liu, *Exp. Fluids* **10**, 71 (1990).
5. M. Gharib, M. A. Hernan, A. H. Yarrouian, and V. Sarcoma, AIAA-85-0172.
6. L. P. Goss, M. E. Post, D. D. Trump, and B. Sarka, *J. Laser Appl.* **3**, 36 (1991).
7. R. J. Adrian, *Appl. Opt.* **25**, 3855 (1986).
8. M. Grobel and W. Merzkirch, *Proceedings, International Conference on Optical Methods in Flow and Particle Diagnostics*, San Diego, CA, Laser Inst. Am. Proc. **63**, 97 (1988).
9. C. C. Landreth and R. J. Adrian, *Appl. Opt.* **27**, 4216 (1988).

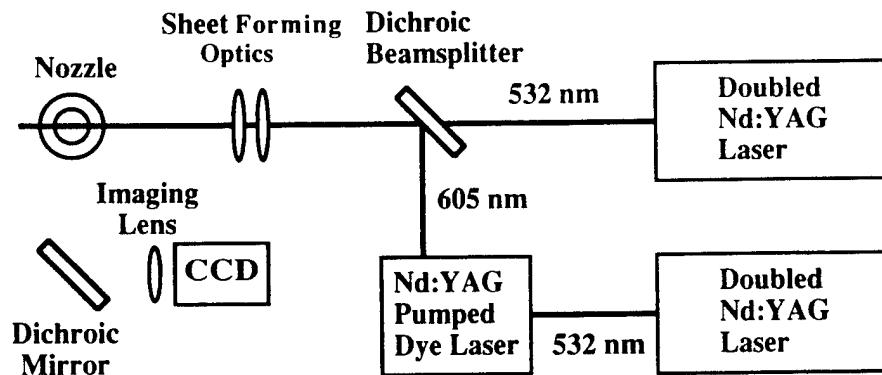


Fig. 1. Experimental Arrangement for Two-Color PIV with Image Shifting.

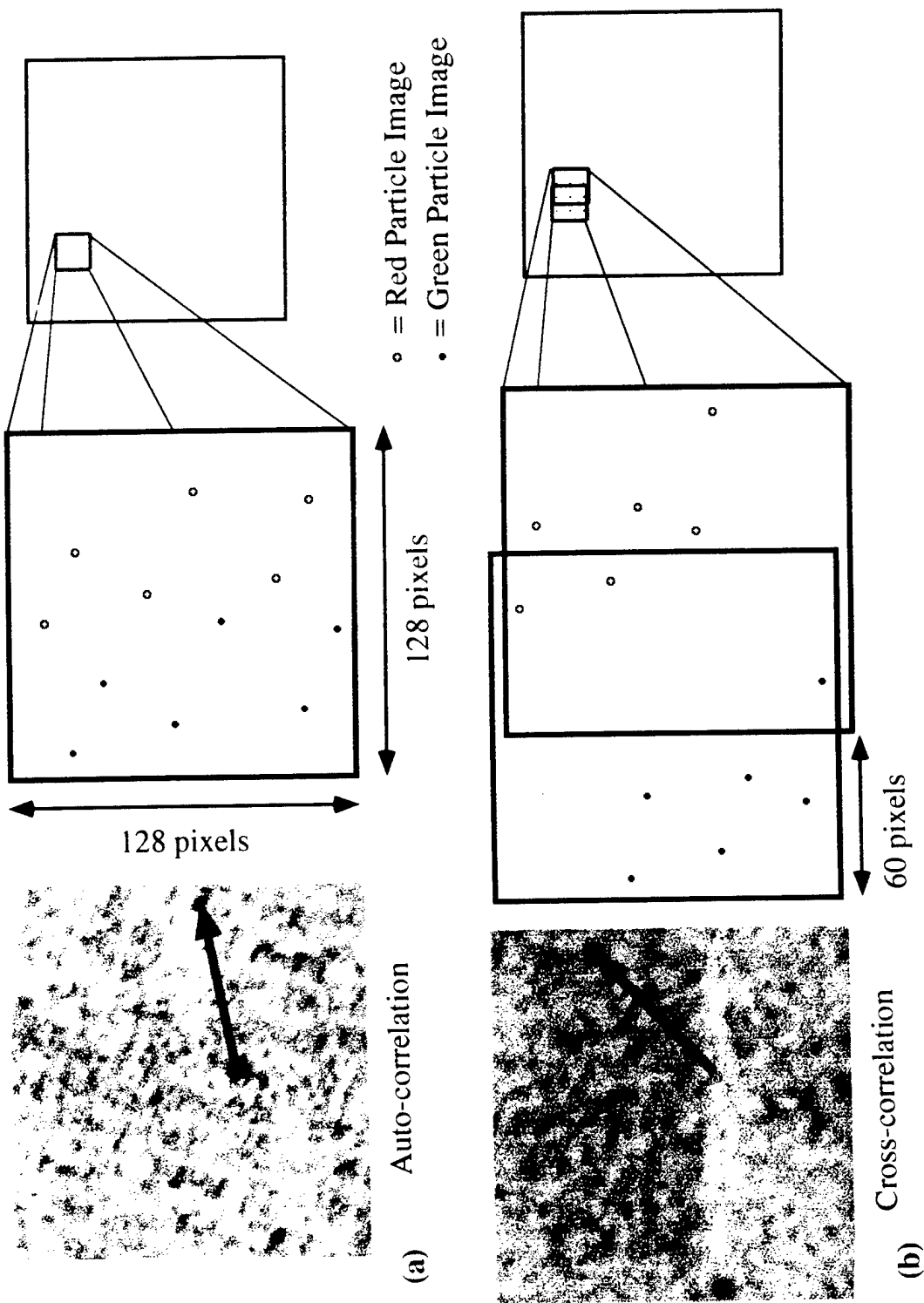


Fig. 2. (a) Illustration of the Use of Auto-correlation to Evaluate the Average Spacing of Red- and Green-Particle Images; (b) Representation of the Cross-correlation Method for Calculating the Average Spacing of Red- and Green-Particle Image Pairs.

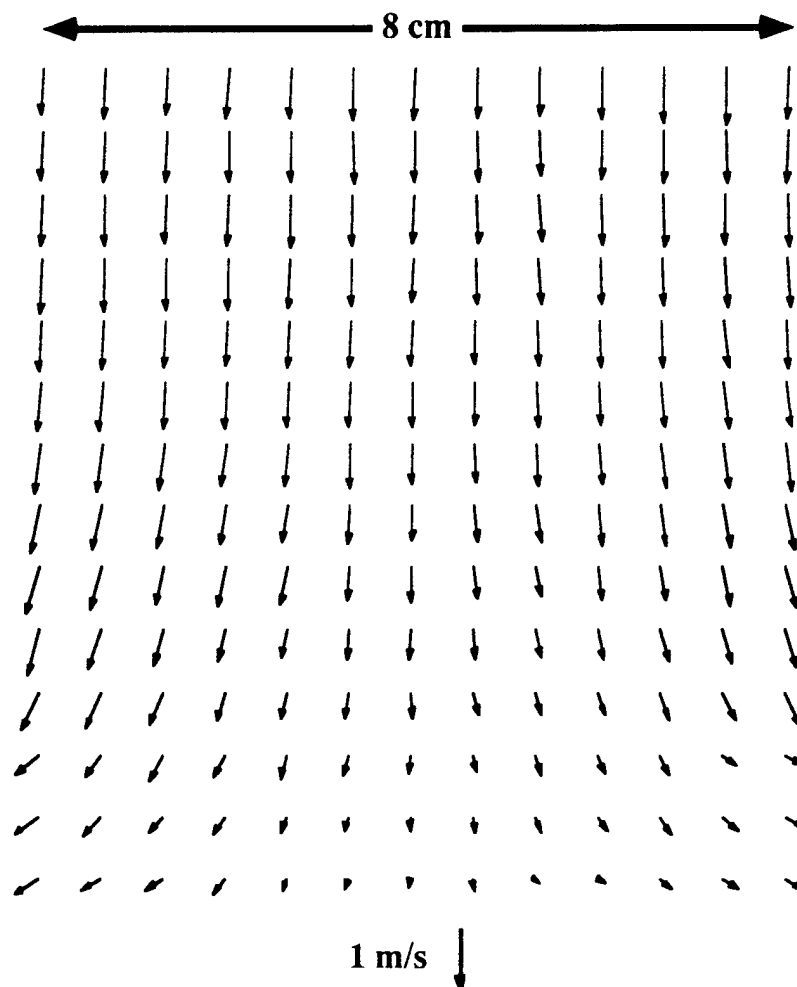


Fig. 3. Corrected Vector Field of a Stagnation-Point Flow Measured by the Two-Color PIV Technique.

Presented 7th Int. Symp. on Flow Visualization, 11-13 Sept 1995, Seattle, WA.
In *Flow Visualization VII* (J. P. Crowder, Ed.) (Bagell House, Inc., New York,
1995), pp. 622-627.

TWO-COLOR PARTICLE-IMAGE VELOCIMETRY EMPLOYING A COLOR CCD CAMERA

Darryl D. Trump, Sivaram P. Gogineni, and Larry P. Goss
Systems Research Laboratories, Inc.
2800 Indian Ripple Road, Dayton, OH 45440-3696

Introduction

Particle-Image Velocimetry (PIV) has been used for a number of years to measure velocity distributions in planar cross sections of aerodynamic flowfields (see, for example, Lourenco [1] and Adrian [2]). One of the difficulties involved in implementing this velocimetry technique is the 180-deg directional ambiguity which results from the inability to determine the temporal sequence of the particle pairs. Several techniques have been developed to resolve this ambiguity problem; most involve imposing a shift between consecutive image exposures by means of scanning or rotating mirrors, pulse tagging, calcite crystals, or polarizing beam splitters [3-5]. To overcome the difficulties inherent in these techniques, a two-color PIV system was developed [6]. The advantages of this system are: (i) the directional ambiguity is resolved using the color coding of the particle images, which is inherent in the system. (ii) higher data yields and signal-to-noise levels are attainable, and (iii) the technique is suitable for both combustng and non-combustng flowfields.

In early experimental approaches involving the PIV technique, the particle images were recorded on photographic film. However, this type of recording is time consuming because of the need to wet-process the film before digitization and computer processing. This disadvantage can be overcome by recording the particle images directly onto a two-dimensional charge-coupled device (CCD) array. Several investigators [7-10] have implemented this approach; but because of the low-resolution of their cameras, the results were limited to low velocities and small spatial resolutions. Lourenco et al. [11] recently introduced a fully digital and operator-interactive PIV system which utilizes a high-resolution CCD area sensor and is a significant improvement over earlier CCD-based PIV systems.

The extension of the two-color PIV technique to include CCD cameras has been hampered in the past by the lack of commercially available high-resolution color CCD camera systems. Goss et al. [12] attempted to utilize a single CCD camera and dichroic mirror to record the two-color PIV images of a stagnation-point flow. However, several problems were encountered, including a non-uniform shift across the image and degraded signal-to-noise ratios. Recent developments in high-resolution color cameras have significantly reduced the difficulty in utilizing color CCD cameras for two-color PIV.

The present paper describes the extension of two-color PIV to the recording of color images onto a single high-resolution color CCD camera, thus eliminating the processing time associated with color film and the complexities associated with conventional image-shifting techniques. To demonstrate the direction-resolving capabilities of this technique, a calibration test was performed using a rotating wheel. A jet in a cross flow was also utilized to permit comparison of results with data from previous PIV studies [13] and because of the wide range of practical applications and the involvement of complex flow features.

Experimental Setup and Procedures

The experimental apparatus is shown schematically in Figure 1(a). The test section is a 61-cm-long vertical channel having a square cross section measuring 8.9 cm on a side. The flow in the channel is driven from an air-supply system [14]. An air jet emanates from a hole having an elliptical cross section with a major axis of 27 mm and a minor axis of 15 mm. The cross flow in the channel is conditioned by a honeycomb flow straightener and screens of progressively finer mesh mounted in the upstream ducts to maintain the free-stream turbulence level at < 2%. The nominal jet-to-cross flow velocity ratio ($R = U_{jet}/U_{channel}$) in the present experiment was 1.0. The corresponding jet Reynolds number based on the minor axis was 600.

The two-color PIV system shown in Figure 1(b) uses color for temporal marking of the location of the seed particles in the flow field. The green (532-nm) laser output from a frequency-doubled Nd:YAG laser and the red (650-nm) laser output from a Nd:YAG-pumped dye laser (DCM dye) are combined by a dichroic beam splitter and directed through sheet-forming optics. The laser-sheet energy is typically 20 mJ/pulse, with a thickness of < 1 mm at the test section. The temporal delay between the two lasers is controlled by a pulse generator and is determined to be a function of the gas velocity, optical magnification, and interrogation spot size. In the present experiments, the time delay between the two color lasers is set at 250 μ sec. A photo-diode is utilized to ensure that the desired time delay is being employed.

Experimentally the channel and jet fluids are seeded with alumina and smoke particles, respectively, and the Mie scattering from the seed particles is recorded on a Kodak NC 2000 CCD array. This CCD sensor has a resolution of 1024 x 1280 pixels, each pixel being 16 square microns. The spatial resolving power of this sensor array is equivalent to ~ 67 line pairs/mm which is comparable to that of many films currently used in PIV recordings. The CCD camera has a built-in 12-bit analog-to-digital converter for increased dynamic range and a frame rate of 2 frames/sec in bursts of 6 frames. It also features a removable and re-usable credit-card-size PC-MCIA storage drive which delivers about 60 exposures, with each PIV image occupying ~ 4 Mbytes. A 105-mm micro lens with an f-number of 5.6 is used to record the images.

The color response of the NC2000 CCD array is accomplished by overlaying the individual pixels of the camera with a series of red, green, and blue color filters. The green and red laser outputs were situated near the peak of the transmission of the green and red camera filters, respectively. Because the camera was built to respond to color, in part, in the same way as a human eye, the majority of the pixels are green sensitive. The relative percentage of green, blue, and red pixels is 75, 12.5, and 12.5%, respectively. The distribution of the red and blue pixels is random to minimize straight-edge effects. The output from the camera controller to the computer is a 24-bit RGB tiff image; thus, the 12-bit ADC camera output must be mapped into three 8-bit colors, each with a spatial resolution equivalent to the chip size (1024 x 1280). This is accomplished through proprietary software developed by Kodak which involves some form of interpolation to increase the spatial resolution of the camera. Because of the unknown nature of this interpolation software, it was uncertain that the resulting resolution of the color camera would be sufficient for accurate PIV measurements. This study was directed toward evaluation and demonstration of the use of the Kodak color CCD camera for PIV studies.

Once the PIV image has been captured and digitized, the velocity field is obtained using a cross-correlation technique [6]. The correlation function is calculated over small segments (interrogation domains) of the PIV image. The dimensions of each interrogation domain are dependent on the particle density, estimated local velocity gradients, particle-image size, and desired spatial resolution. The maximum displacement of each particle must be less than one-half the size of the interrogation spot. In the present experiments the interrogation domain measured 32 x 32 pixels, corresponding to 1 x 1 mm in the measured flow. For enhancement of the overall resolution, the interrogation domains are overlapped by one-half the domain size. The peak of the correlation map corresponds to the average velocity displacement within the interrogation spot. An intensity-weighted peak-searching routine is used to determine the exact location of the peak to sub-pixel accuracy. The number of particle pairs normally necessary to ensure a desirable signal-to-noise ratio is reduced to four or five when the cross-correlation analysis is employed.

Results and Discussion

To test the ability of the color CCD camera to capture images of sufficient quality for PIV analysis, a series of rotating-wheel images was obtained. In this experiment, a small square of foam material was secured to a rotating wheel. The foam acted as a random scattering surface and served as a convenient means of calibrating the PIV system. The output from the green and red laser was directed unexpanded onto a scattering plate which diffusely scattered the light onto the surface of the rotating foam material. The CCD camera then captured a double-pulse red-green image for analysis. A typical vector field from the rotating wheel is shown in Fig. 2. The

relationship between velocity and radius from the center of the rotating wheel is evident as well as the ability of the approach in uniquely determining velocity direction.

The next step in evaluation of the CCD camera was to apply it to the study of a realistic particle-seeded flowfield. For this purpose a jet in a cross flow was chosen, the main features of this jet being the mutual deformation due to the interaction of the jet and the cross flow, formation of the wake region behind the jet injection location, change in shape of the jet from a circular cross section to a kidney shape, domination of the counter-rotating vortex pair, entrainment, and the effects of mixing on the expansion of the jet. Although these features are dependent on the blowing ratios, the shear layer exists above the wake region where the streamwise velocity changes and a very complex three-dimensional, turbulent flow occurs downstream of the jet exit.

First attempts at obtaining PIV quality images with small seed particles meet with little success. With the use of solid seed particles, a wide variation in particle size resulting from particle agglomeration is typically observed. While this was not an issue when film was employed for image recording, it was a significant problem with the color CCD camera. Film typically displays a logarithmic response to light, while CCD cameras and amplifiers are especially designed to respond in a linear fashion. Because the size of the seed particle has a dramatic effect on the amount of scattered light, large particles or clumps appear to be especially bright to linear detectors. This is a problem in the cross-correlation analysis because two-dimensional FFTs are utilized for this purpose. These FFTs are known to be intensity and size weighted, i.e., a large bright particle would dominate a multitude of small dim particles, making it difficult--if not impossible--to determine the real correlation peak accurately. This problem is especially troublesome when different-size seed particles are intentionally used for PIV studies (see discussion below). For minimizing this effect the output of the linear camera was convolved with a logarithm-like function to equalize the intensity of large- and small-size particles. This greatly improved the analysis of the seeded flowfields and was utilized in the remainder of this study. Because the computer time required for calculating logarithms is prohibitive, a power-series expression consisting of five terms was used to approximate the behavior of a logarithm.

Figure 3(a) shows the PIV image for a blowing ratio of $R = 1.0$ in the jet and cross-flow experiment. In this case the jet fluid has significantly penetrated the cross flow. This PIV image was analyzed using a 32×32 pixel interrogation size to obtain about 4000 vectors, and the resulting instantaneous two-dimensional velocity distribution can be seen in Figure 3(b). This figure shows a uniform cross flow and the deflection of the jet flow when it interacts with the cross flow. A low-velocity region just behind the jet exit is also noticeable and corresponds to the "wake" region. These results are in close agreement with those obtained using a film-based PIV system.

As discussed above, the jet and the cross flow are separately seeded with particles of different nominal diameter; thus, it is possible to distinguish, in post processing, those particles that originated from each flow. Because the intensity of the scattered light is proportional to the particle surface area, image separation can be accomplished using a threshold level such that pixels having light intensities that are below a set value (nominally 65% of the full scale) are reset to the background level. Figure 3(c) shows the resulting velocity field. In order to emphasize the jet fluid, the velocity vectors of particles that are seeded in the jet are plotted at twice the density of the velocity vectors of fluid particles in the cross flow. This type of analysis would be useful for understanding the interaction between the jet and the cross-flow fluids, for identifying the penetration of the jet flow toward the wall, and also for recognizing the entrainment of the cross flow into the wake region. Other methods which take into account the particle size were also considered but discarded because of a substantial increase in the complexity level of the processing.

Conclusions

A new implementation of the two-color PIV technique replaces the conventional photographic recording and processing steps with a color CCD sensor. The proprietary interpolation software developed by Kodak appears to be effective in maintaining equal red, green, and blue pixel spatial resolution even though the pixels are not distributed equally. It was

determined that optimum results in seeded flowfields were obtained by applying a logarithm-like function to the camera image before cross-correlation analysis. Tests on a rotating wheel showed the directional-velocity capabilities of the two-color approach, and the system was successfully applied to a jet in a cross flow involving complex flow features and multiple-size seed particles. Seeding the jet flow and the cross flow simultaneously with particles of different nominal diameter allowed the interaction between the jet and the cross-flow fluids to be studied. Ongoing development of larger-format color-CCD arrays will expand the usefulness of this color-based digital PIV technique.

Acknowledgments

The authors gratefully acknowledge the help of W. C. Gray of Envision Associates and T. E. Bahan of Eastman Kodak Company for providing the Kodak CCD camera and the associated hardware. The authors also acknowledge a number of valuable discussions with Dr. W. M. Roquemore and the assistance of B. Sarka of Systems Research Laboratories with the instrumentation. The editorial assistance of M. Whitaker (SRL) is greatly acknowledged. This work was supported by AFOSR and USAF Contract F33615-90-C-2033.

References

1. Lourenco, L. M., Krothapalli, A., and Smith, C. A. 1989 "Particle Image Velocimetry," in *Advances in Fluid Mechanics Measurements* (M. Gad-el-Hak, ed.) (Springer-Verlag, Berlin), pp 127-199.
2. Adrian, R. J. 1991 "Particle Imaging Techniques for Experimental Fluid Mechanics," *Ann Rev Fluid Mech*, **23**, 261-304.
3. Grant, I. and Liu, A. 1990 "Directional Ambiguity Resolution in Particle Image Velocimetry by Pulse Tagging," *Exp Fluids*, **10**, 71-76.
4. Landreth, C. C. and Adrian, R. J. 1988 "Electro-optical Image Shifting for Particle Image Velocimetry," *Appl Opt*, **27**, 4216-4220.
5. Lourenco, L. M. 1993 "Velocity Bias Technique for Particle Image Velocimetry Measurements of High Speed Flows," *Appl Opt*, **32**, 2159-2162.
6. Goss, L. P., Post, M. E., Trump, D. D., and Sarka, B. 1991 "Two Color Particle Image Velocimetry," *J Laser Appl*, **3**, 36-42.
7. Cho, Y.C. 1989 "Digital Image Velocimetry," *Appl Opt*, **28**, 740-748.
8. Okada, E., Enomoto, H., Fukuoka, Y., and Minamitani, H. 1990 "Instantaneous Particle Image Velocimetry with Electronic Specklegram," in *Proceedings of Applications of Laser Techniques to Fluid Mechanics* (Springer-Verlag, New York, 1990), pp 464-475.
9. Westerwell, J., Nieuwstadt, F. T., and Flor, J. B., 1990 "Measurement of Dynamics of Coherent Flow Structures Using Particle Image Velocimetry," in *Proceedings of Applications of Laser Techniques to Fluid Mechanics* (Springer-Verlag, New York, 1990), pp 476-479.
10. Willert, C. E. and Gharib, M., 1991 "Digital Particle Image Velocimetry," *Exp Fluids*, **10**, 181-193.
11. Lourenco, L. M., Gogineni, S. P., and LaSalle, R. T., 1994 "On-line Particle Image Velocimeter: an Integrated Approach," *Appl Opt*, **33**(13), 2465-2470.
12. Goss, L. P., Trump, D. D., and Frank, J. H., 1994 "Two Color Particle Imaging Velocimetry Employing a Single CCD Camera," in *Combustion Fundamentals and Applications* (Proceedings of the 1994 Technical Meeting, Central States Section, The Combustion Institute) (The Combustion Institute, Pittsburgh, PA), pp 237-242.
13. Gogineni, S., Sutkus, D., Goss, L., and Glezer, A. 1995 "Investigation of a Jet in a Cross Flow Using PIV," AIAA Paper No. 95-0790, Presented at the 33rd Aerospace Sciences Meeting and Exhibit, Reno, Nevada, 9-12 January.
14. Hancock, R. D., Glezer, A., and Roquemore, W. M. 1992 "Manipulation of the Mixedness of a Jet in Cross Flow," Presented at the Annual Meeting of the American Physical Society, Division of Fluid Dynamics, Tallahassee, FL, 22-24 November.

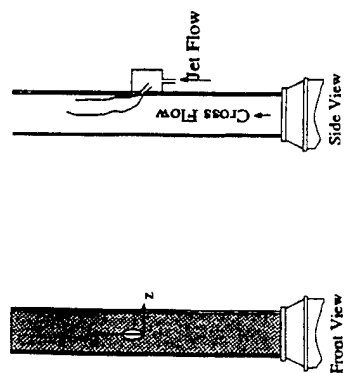


Figure 1(a). Schematic of a Jet in a Cross flow

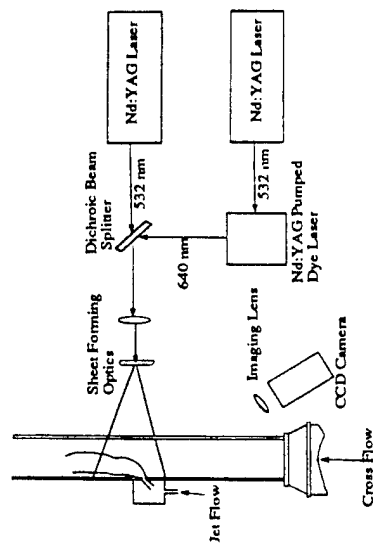


Figure 1(b). Experimental setup for two-color PIV

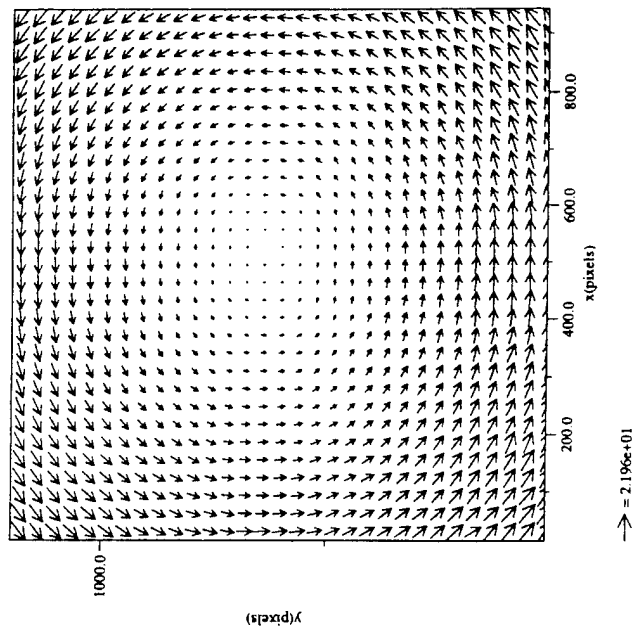


Figure 2. Vectors of solid body rotation

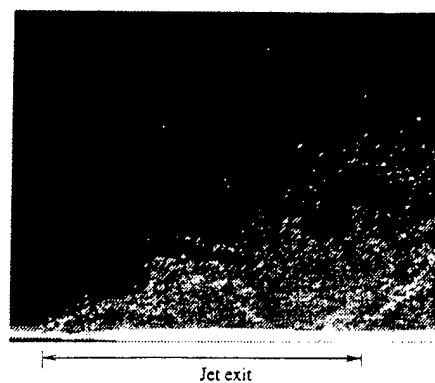


Figure 3(a). Double exposed PIV image

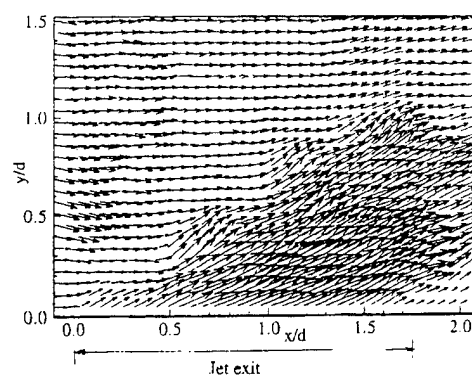


Figure 3(b). Instantaneous velocity distribution

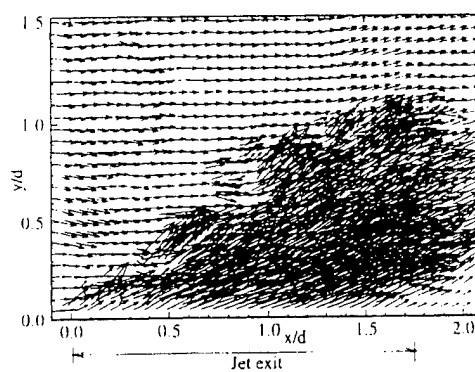


Figure 3(c). Image analysis based on particle size

2.1.4 Thin Filament Pyrometry (TFP). The TFP technique was extended from the measurement of line-temperature profiles to the thermometric measurement of multiple lines in sooting flames ["Multiple-Line Thermometry in Sooting Flames Using Thin-Filament Pyrometry" (pp. 128 - 133)] to the conditional sampling of LDV velocity measurements in combusting flows ["Conditional Velocity Measurements at the Base of Turbulent, Lifted Jet Flames" (pp. 134 - 140)] and finally to the simultaneous measurement of temperature and velocity ["Thin-Filament Velocimetry" (pp. 141 - 150) and "Simultaneous Thin-Filament Velocimetry and Pyrometry" (pp. 151 - 162)].

MULTIPLE-LINE THERMOMETRY IN SOOTING FLAMES USING THIN-FILAMENT PYROMETRY

L. P. Goss, V. Villimpoc, and M. E. Post

Systems Research Laboratories, Inc.

A Division of Arvin/Calspan

2800 Indian Ripple Road

Dayton, OH 45440-3696

Introduction

The Thin-Filament-Pyrometry (TFP) technique was developed to study the high-frequency thermometric characteristics of non-sooting flame systems. With this technique the graybody emission from a small ceramic filament (SiC) is focused onto a rotating mirror which collects the image along the length of the filament and focuses it onto a single-element detector. The filament emission is recorded as a function of time (and, therefore, position along the filament) and converted to temperature through the use of calibration curves. Examples of the development and utilization of the technique can be found in several recent articles.¹⁻⁵ The disadvantages of the technique as originally implemented were the limited spatial information from a single filament and the restriction to relatively clean non-sooting flame systems. To overcome these limitations the single-element detector used in the original technique was replaced with a two-dimensional CCD detector which allows incorporation of multiple filaments.

Experimental

The experimental arrangement used in this study is shown in Fig. 1. A multiple-filament holder was designed to contain ten filaments ~ 10 cm in length and spaced ~ 2 cm apart. The filaments were oriented perpendicular to the jet flow to allow the large-scale motion of the flame to be captured. A small amount of tension was maintained on each filament to prevent sagging. The emission from the ten filaments was recorded by a Photometrics Model 200 CCD Camera System. The imaging chip employed in this system was a Thompson CSF THX31156 having a 1024 x 1024 pixel format, each pixel being ~ 25 μm in diam. The shutter was a Uniblitz Model 225L2A2T5 employing a Model SD-10 Controller having a custom interface to allow direct computer control. To minimize motion blurring of the captured image, the camera was operated at the fastest possible shutter speed (~ 3 ms) with an f/22 aperture. The imaging system had a spatial resolution of 274 $\mu\text{m}/\text{pixel}$, which is comparable to the thermal-spread function of the filament.²

The jet diffusion flame employed consisted of a tapered (7-deg.) 23-mm-diam. nozzle surrounded by a 25-cm annular-air jet. The fuel was a mixture of propane and nitrogen in equal mass fractions, flowing at an exit velocity of 10 cm/sec. The coflowing annular-air jet had an exit velocity of 15 cm/sec and stabilized and reduced outside disturbances to the flame. This flame system was characterized by large-scale buoyancy-driven structures which are presently under experimental and numerical investigation.⁶ These flames exhibit 10-17 Hz oscillations in association with the large-scale structures which can be easily tracked by means of the TFP technique.

Image Analysis

The image-acquisition procedure consisted of 1) triggering the camera system to open the shutter, which exposed the CCD to the flame and filament emission, 2) closing the shutter, and 3) transferring the data to a Macintosh IIfx Computer for storage and analysis. Each image consisted of an $\sim 10 \times 25$ cm region in which the lowest filament was suspended 5 cm above the nozzle and each of the other nine filaments was located 2 cm from its nearest neighbor. The emission from each filament was located and separated from its surroundings by the analysis software.

The first step in the analysis software involves locating the individual filaments. This multi-step process takes advantage of the small size of the filament whose spatial frequency is much higher than that of the slowly varying background from the flame. Thus, spatial filters can be employed to separate the high- (filament) and low- (flame) frequency components. The filtering process consisted of convoluting the emission image with the matrix elements given in Fig. 2(a). The differential operator represented by this matrix allows filtering only in the direction perpendicular to the filament. This minimizes effects due to soot boundaries and greatly intensifies the filament intensity over the background [see Fig. 2(a)]. The exact location of the filament is determined by filling a box (~ 20 pixels in depth and the length of the image) with the filtered image of each filament and its surroundings. A threshold is then applied to the box which corresponds to 10% of the maximum intensity for the filtered filament. The pixel locations above the threshold are fed into an array and a third-degree polynomial fit made to determine the filament locations. This process is repeated for all filaments and the coefficients saved for background subtraction.

Once the filament locations have been determined, background subtraction is carried out. An intensity plot perpendicular to a filament is shown in Fig. 2(b). Note the almost uniform soot emission on either side of the filament which indicates the additive nature of the filament and flame emissions. Background subtraction involves taking the centerline location of the filament and fitting the adjacent background intensity perpendicular to the filament on either side. This is accomplished by filling an array with the intensity information from the unfiltered image, 5 to 10 pixels on either side perpendicular to the center of the filament, and fitting the background intensity (array) with a fourth-order polynomial [see Fig. 2(b)]. The fitted background is then subtracted from the filament image. This procedure is repeated along the entire length of the filament, resulting in a background-free image of the filament emission.

Once the background-free emission of the filament has been determined, the intensity can be converted to a temperature. For relating the emission of the SiC filament to the temperature of the gas, the Planck blackbody equation must be employed. Experimentally, the filament emission is detected over a limited spectral bandwidth with a detector having a varying response to the wavelength of the emission. The Planck blackbody must then be multiplied by the detector response and integrated over the detector-response bandwidth to form a calibration curve which accurately predicts the filament emission as a function of temperature. The normalized filament intensity is converted to a temperature by the calibration curve calculated in this manner from the CCD detector response. The experimentally determined filament-temperature profiles must then be corrected for heat loss due to radiation.

Results and Discussion

Temperature profiles obtained on the propane-nitrogen sooting jet diffusion flame were superimposed on the filament-flame image and are displayed in Fig. 3. Note the incipient formation of the large-scale buoyancy-driven structure and the expansion and contraction of high-temperature zones following the passage of this structure. At most locations in the flame, excellent data were obtained which reveal the essential features of the temperature fields under study. However, where the soot intensity approached that of the filament, a low signal-to-noise ratio resulted in some loss of accuracy. The accuracy of the TFP technique in non-sooting flames was compared with temperature measurements made by the CARS technique and reported in Ref. 2. An interesting problem which manifested itself in the sooting-flame experiments was the coating of the filament with soot. The coating appeared experimentally as an increase in the local emission and, thus, temperature of the flame. The increase in emission was determined to be due to the increased diameter (and, thus, surface area) of the filament as it became coated with soot. Since a filament-coating time of ~ 10 min. was required before noticeable results could be observed, the filaments were kept out of the flame until measurements were to be made. The filament could be easily cleaned of the soot deposit by burning it with a propane-air torch; thus, for these experiments soot deposition on the filament represented only a minor problem.

Conclusions

In conclusion, this study demonstrated that through the extension of the TFP technique by means of multiple filaments and a CCD detector, instantaneous multiple-line temperature profiles can be obtained in a sooting flame. It was also shown that it is possible to minimize the interference of the soot and filament emissions by application of a suitable data-analysis algorithm.

Acknowledgement

This research was supported by USAF Contract No. F33615-90-C-2033. The authors wish to thank Dr. W. M. Roquemore for stimulating discussions.

References

1. Nicalon, Silicon Carbide Fiber, Dow Corning Corp., Midland, MI 48686-0995.
2. L. P. Goss, V. Vilimpoc, B. Sarka, and W. F. Lynn, *Trans. ASME, J. Eng. Gas Turb. Power* **111**, 46 (1989).
3. V. Vilimpoc, B. Sarka, S. Kizirnis, M. Fernandez, and W. Roh, 1988 Spring Technical Meeting of the Central States Section of the Combustion Institute, Indianapolis, IN, May 2 - 3, 1988.
4. V. Vilimpoc, L. P. Goss, and B. Sarka, *Opt. Lett.* **13**, 93 (1988).
5. R. W. Davis, E. F. Moore, L.-D. Chen, W. M. Roquemore, V. Vilimpoc, and L. P. Goss, *AICHE Conference on Combustion and Reaction Engineering I: Numerical Methods*, San Francisco, CA, November 5 - 10, 1989.
6. R. W. Davis, E. F. Moore, W. M. Roquemore, L.-D. Chen, V. Vilimpoc, and L. P. Goss, 1989 Spring Technical Meeting of the Central States Section of the Combustion Institute, Dearborn, MI, April 30 - May 3, 1989.

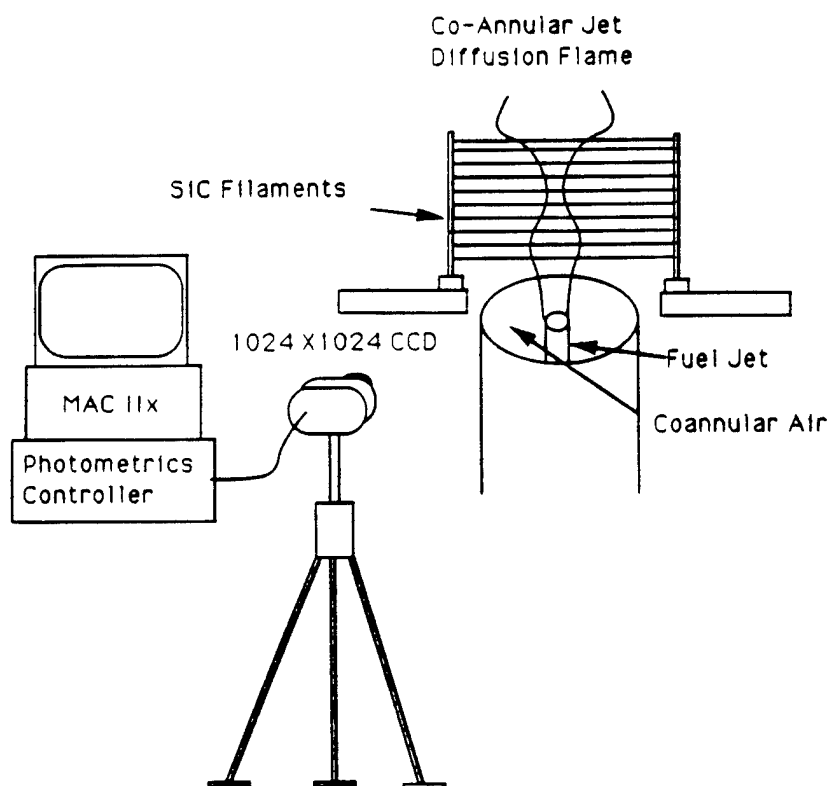


Fig. 1. Experimental arrangement for multiple-filament TFP technique.

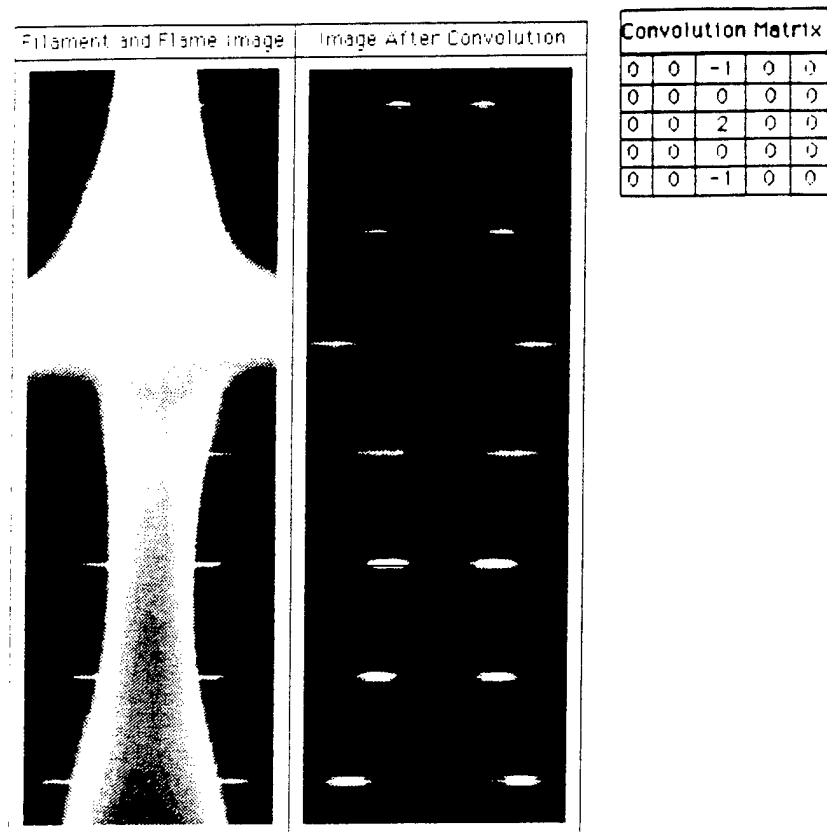


Fig. 2(a). Filament-flame image before and after convolution with high-bandpass filter.

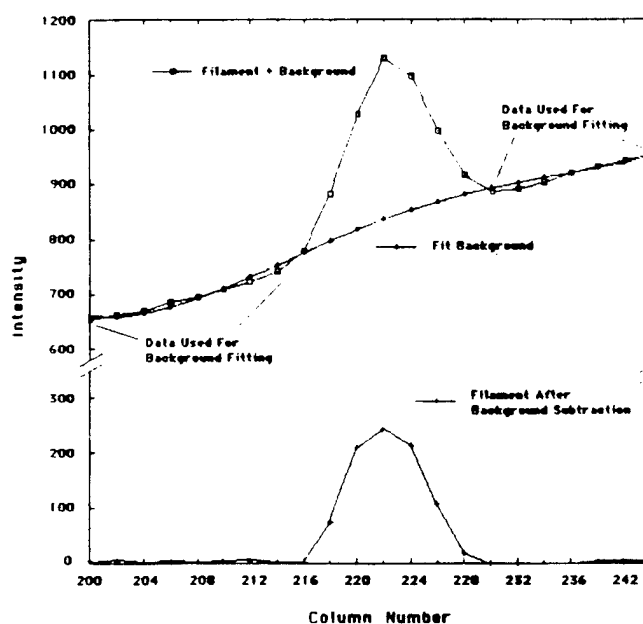


Fig. 2(b). Cross section of filament-flame image depicting filament and background, fitted background, and filament after background subtraction.

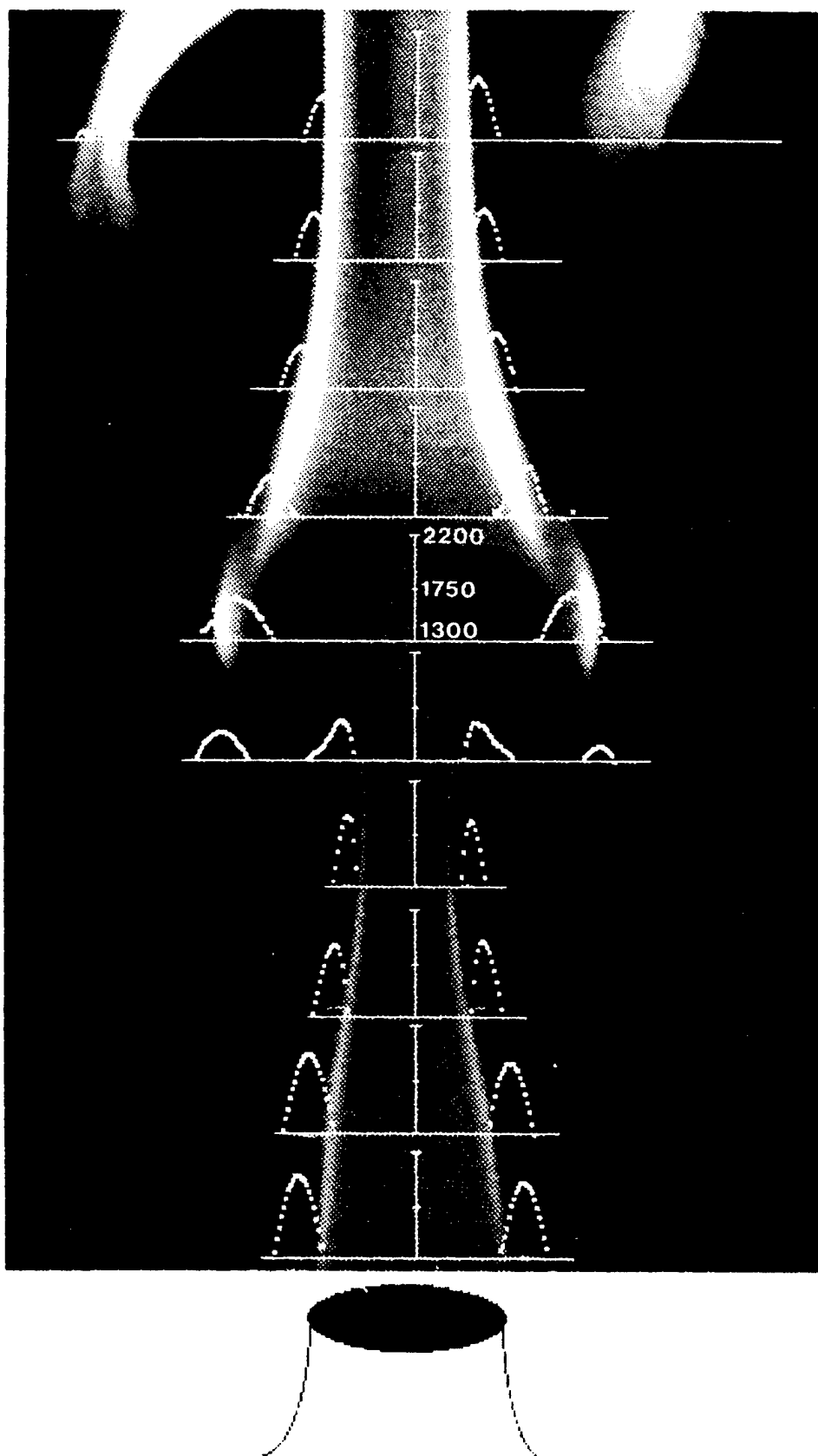


Fig. 3. Overlay of experimentally determined multiple-filament temperatures and filament-flame image. Vertical scale bars: length corresponds to temperature range from 1300 to 2200 K.



AIAA-90-2725

**Conditional Velocity Measurements at
the Base of Turbulent, Lifted Jet Flames**

Tzong H. Chen, Darryl D. Trump, and Larry P. Goss

Systems Research Laboratories, Inc.
A Division of Arvin/Calspan
2800 Indian Ripple Road
Dayton, OH 45440-3696

**AIAA/SAE/ASME/ASEE
26th Joint Propulsion Conference
July 16-18, 1990/Orlando, Florida**

CONDITIONAL VELOCITY MEASUREMENTS AT THE BASE OF TURBULENT, LIFTED JET FLAMES

Tzong H. Chen,* Darryl D. Trump,** and Larry P. Goss†

Systems Research Laboratories, Inc.

A Division of Arvin/Calspan

2800 Indian Ripple Road

Dayton, Ohio 45440-3696

Abstract

A novel technique has been developed for use in flame studies to condition LDV velocity measurements to the presence (or absence) of combustion. This technique utilizes Thin-Filament-Pyrometry (TFP) to determine whether combustion gases are present during a velocity measurement by an LDV system. TFP was selected for this purpose because of its effective flame-detection capability, ease of implementation with Laser Doppler Velocimetry (LDV), and low cost. The conditioning measurement technique was applied to the study of lifted methane and propane jet flames. Flame regions which exhibited the most pronounced difference between conditional and unconditional measurements were primarily areas having a high correlation between temperature and velocity. The velocity profiles obtained highlight the differences between methane and propane jet flames.

Nomenclature

U_j	Mean axial jet exit velocity
U_c	Mean axial velocity at jet axis at downstream location of liftoff height
U_{fb}	Mean axial velocity at flame base
u'	Root-mean-square (rms) axial-velocity fluctuation
z	Axial ordinate

Introduction

Flame-lifting and blowout mechanisms remain an important subject for study in the combustion-research community. Recent experimental efforts have been directed toward the measurement of scalar dissipation rates in order to gain insight into the phenomena of local flame quenching which can cause flame lifting and blowout. Approaches based upon premixed-flame and vortex-mixing concepts have been successfully applied in attempts to understand blowout in swirler-stabilized flames. Here velocity information is critical in assessing the effects of turbulent mixing upon flame stabilization.

Traditional velocity-measurement techniques (e.g., LDV) require introduction of seed particles into the

flowfield under study. Particle-based techniques have been shown to be biased in several ways including density weighting.¹ For accurate measurement of the velocity field of intermittent combusting gas mixtures, a technique capable of detecting the presence of the flame in the LDV probe volume during the velocity measurement would allow assessment of the extent of biasing. Thermocouple probes are intrusive and cannot precisely resolve thin flame sheets. Laser diagnostic techniques which have been employed for conditional measurements, i.e., combined Coherent Anti-Stokes Raman Spectroscopy (CARS) and LDV,¹⁻³ are complex, costly, and difficult to implement. The recently developed Thin-Filament-Pyrometry (TFP)⁴ technique which displays high spatial and temporal resolution is an ideal choice for a conditional experiment. In the TFP technique, the blackbody emission from a SiC filament which is $\sim 14 \mu\text{m}$ in diam. is employed to determine the local flame temperature with negligible intrusion of the flame. The application of TFP for conditioning LDV measurements is simpler and more cost effective than the use of other laser diagnostic methods.

In this study both conditional and unconditional velocity measurements were made at the base of turbulent, lifted jet flames. In the conditional-velocity-measurement case, a two-component LDV system was used in conjunction with the TFP technique to condition the velocity measurement to the presence (or absence) of the flame. Velocity data were taken only when the flame was present (as detected by the TFP technique). In the unconditional-measurement case, the LDV system was allowed to collect velocity data without regard to the conditions of the flame. Both propane and methane fuel were used with a 5-mm short tapered nozzle. Previous combustion studies with the 5-mm nozzle have shown that the interaction of the flame sheet and the fuel-jet shear layer is stronger for the methane flame than for the propane flame under the critical liftoff conditions. This result indicates that for this nozzle, different lifting mechanisms are dominant in the methane and propane flames. To elucidate these differences, conditional and unconditional velocities were measured near the flame base for jet-flame conditions ranging from liftoff to near blowout.

*Senior Research Scientist, Senior Member AIAA

**Senior Engineer

†Chief Scientist, Optical Diagnostics, Member AIAA

Experimental

Flow Conditions

The fuel jet employed in this study consisted of a short tapered 5-mm-id nozzle surrounded by a 25-cm annular air duct. The contraction ratio of the contoured nozzle was 20 to 1 and was designed to yield a flat exit-velocity profile. The exit velocity of the annular air flow was fixed at 15 cm/sec. The fuels employed for this study were methane and propane. For the unconditional velocity measurement, the axial profile along the centerline and the radial profile at the liftoff height (LOH) were made. For the conditional measurement, the focus was on the flame base. Three measurement points were chosen—inner edge, center, and outer edge of the flame base.

LDV and TFP Conditioning

A schematic diagram of the experimental setup employed for the conditional velocity measurements is shown in Fig. 1. The LDV system was a two-component,

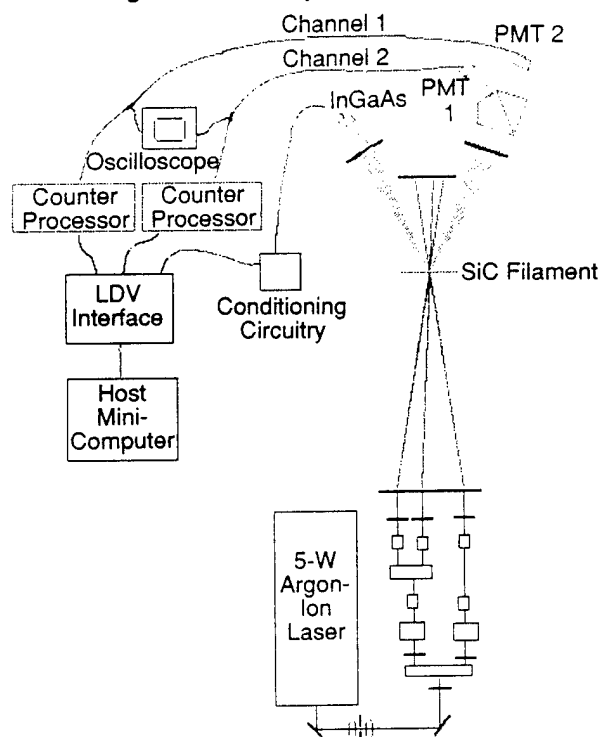


Fig. 1. Schematic diagram of combined LDV and TFP experimental setup.

forward-scattering single-color system utilizing polarization for component separation.⁵ A 5-W argon-ion laser was used as the light source at a wavelength of 488 nm. The seed particle employed for this study was Al_2O_3 having an average diameter of 0.5 μm . For the fuel jet a TSI fluidized-bed seeder was employed; for the coflowing jet, a custom-made cyclone-type seeder was used. A low seeding density in both the coflowing air and the fuel was

maintained to allow steady, long-duration operation; and the density was balanced to avoid biasing. Doppler bursts from the sample volume were converted to periods by two 1990 TSI burst counters. The output from each counter was fed into a mini-computer for analysis.

For flame detection a TFP setup was utilized. The TFP technique has been applied in numerous turbulent jet flame studies.⁶ Its unique features include high temporal and spatial resolution, capability of measuring temperature distribution along a line, and ease of implementation. The filament employed was $\sim 14\text{-}\mu\text{m}$ -diam. SiC and was held by a "U"-shaped steel strip under proper tension. The span of the holder was $\sim 12\text{ cm}$, which covered the flame diameter. When placed in the flame, the filament becomes visibly "red hot" due to blackbody radiation. In this experiment the radiation from the filament was imaged onto a InGaAs photodiode detector and used to indicate the presence (or absence) of the flame. Previous studies have shown that such an arrangement displays a low-temperature detection limit to $\sim 1000\text{ K}$.

For the conditional velocity measurements, the thin filament was placed $\sim 0.5\text{ mm}$ upstream of the LDV probe, as indicated in Fig. 2. Care was exercised to

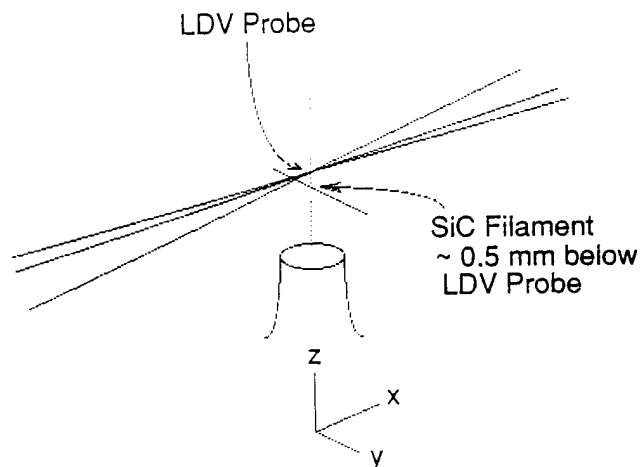


Fig. 2. Alignment of thin filament with respect to LDV probe.

ensure that the proper tension would be placed on the filament; otherwise, a filament that was too loose could vibrate into the LDV probe or one that was too tight might break after limited flame exposure.

The signal from the InGaAs detector was sent to a custom-built electronic interface which amplified the signal and generated a gate pulse when the signal was above a preset threshold (see Fig. 3). The width of the gate pulse was determined by the duration of the TFP signal above the preset threshold. The threshold in these experiments was chosen to correspond to an approximate flame temperature of 1800 K. This approach was taken to ensure that actual combustion would be sampled rather than hot-combustion products. The gate pulse was fed

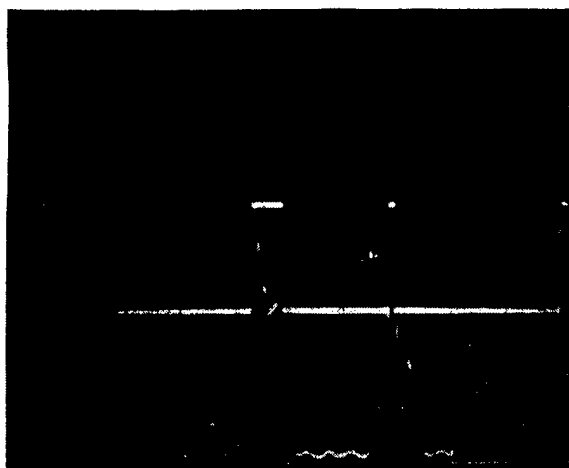


Fig. 3. TFP signals and generated gate pulses for LDV data sampling.

into the LDV-computer-interface inhibit circuit to allow the LDV system to acquire data when the gate was open and inhibit acquisition when closed. This was referred to as the flame-gating mode of operation. The TFP interface could also be operated in a nonflame-gating mode in which the LDV was allowed to acquire data only in the absence of flame. For the unconditional measurements the LDV system was allowed to collect velocity data without regard to the status of the flame (free-run mode).

Results and Discussion

General Observations

The general flame characteristics observed in this study are summarized in Table I. For each flame condition, attention was focused at the LOH where the mean-radial-flame-base location, R_f , was measured by means of the SiC filament. The flame fluctuates around this mean location and covers the range radially from $R_f - \Delta R$ (inner edge) to $R_f + \Delta R$ (outer edge). At the LOH the velocities at both the centerline (U_c) and the flame base (U_{fb}) were measured and are given in Table I.

To achieve a LOH of 90 mm, the methane flame required a much higher exit velocity ($U_j = 45$ m/s) than the propane flame ($U_j = 38.5$ m/s). At the LOH the central jet velocity for methane was 12.5 m/s and for propane, 21.4 m/s. However, the velocities measured at the flame base, U_{fb} , for methane and propane flames were

very similar in magnitude, resulting in a high normalized velocity, U_{fb}/U_c , for the methane flame. The rms velocity fluctuations at the propane-flame base were higher than those at the methane-flame base. Since the propane flame had a higher centerline velocity at the LOH, the normalized values, u'/U_c , are very similar for the two flames under these conditions.

For the five conditions given in Table I, both flames display interesting trends. First, the velocity at the jet center at the LOH, U_c , was ~ 12 m/s for all three methane-flame conditions listed. For propane flames this velocity was ~ 22 m/s for the two conditions listed. Second, the mean axial velocity at the flame base, U_{fb} , was ~ 2 m/s for all flame conditions. As a result the normalized flame-stabilization velocity, U_{fb}/U_c , was $\sim 9\%$ and 15% for the propane and methane flames, respectively.

The similarity in flame-base velocity can be attributed to the fact that the thermal time scale--the ratio of laminar flame thickness to laminar flame speed--for the methane and propane flames is approximately the same (1/430 and 1/400 sec, respectively). Whereas, the differences in velocity development along the centerline can be attributed to the variation in density, reaction rate, stoichiometric fuel-air ratio, and other effects.

Conditional and Unconditional Velocity PDF's

Figure 4 displays the probability distribution functions (pdfs) for the conditional and unconditional axial velocities taken at the inner edge, $R_f - \Delta R$, of the flame base for a lifted methane jet flame. The pdf of the conditional velocity shown in Fig. 4(a) indicates that the local axial flow velocity where the flame exists is ~ 1.5 m/s. It also shows that the diffusion flamelets cease to exist when the local jet velocity exceeds ~ 4.0 m/s. With unconditional velocity measurements, both hot and cold gases are measured which, in this case, significantly alters the observed pdf [see Fig. 4(b)]. Since the velocity data were taken at the inner edge of the flame, which is near the jet shear layer, velocities higher than 4 m/s were also measured. The difference in the conditional and unconditional velocity pdfs at the inner edge of the flame is the result of high shear, incomplete mixing, and associated high intermittent velocity and scalar fluctuations. At this location where the jet shear is high, the probability of stabilizing the flame is rather low.

Table I. Flame Characteristics Observed

Fuel	U_j (m/s)	LOH (mm)	U_c (m/s)	R_f (mm)	ΔR (mm)	U_{fb} (m/s)	U_{fb}/U_c (%)	u' (m/s)	u'/U_c (%)
CH ₄	32.0	60.	13.0	14.5	± 3.0	1.86	14.3	1.0	7.7
CH ₄	45.0	90.	12.5	21.0	± 4.0	1.89	15.1	0.86	6.8
CH ₄	52.0	120.	11.8	27.0	± 5.5	2.27	19.2	1.05	8.9
C ₃ H ₈	26.0	50.	23.0	9.0	± 2.5	2.04	8.87	1.50	6.5
C ₃ H ₈	38.5	90.	21.4	16.0	± 4.0	1.86	8.69	1.39	6.5

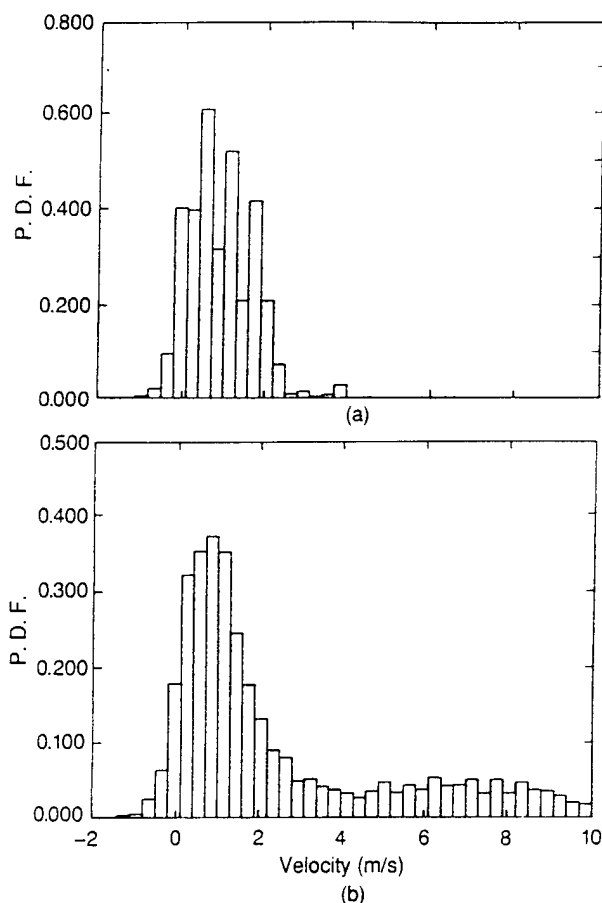


Fig. 4. PDFs of (a) conditional and (b) unconditional axial velocities taken at inner edge of methane-flame base.

The conditional and unconditional velocity pdfs under several flame conditions at the mean radial flame location, R_f , were made. Although distinct differences between the conditional and unconditional velocity pdfs were found in the inner edge of the flame, minor differences were observed at location, R_f . Figure 5 displays an example of the near-Gaussian-shaped conditional and unconditional velocity pdfs obtained in this region. These pdfs indicate that the mean axial velocity is ~ 2 m/s; whereas, the rms velocity fluctuation is ~ 1 m/s (also see Table I). The near-Gaussian-shape distribution may be the result of the flat profiles for both axial and radial velocities which indicates a low-velocity gradient in the flame zone.

At the outer edge of the flame, $R_f + \Delta R$, the measured conditional and unconditional velocities display similar pdfs since the velocity profiles in this area are relatively flat. These results indicate that at the base of a lifted flame, most of the flame area displays only minor differences between conditional and unconditional velocity pdfs. This implies that the velocity pdfs for the hot and cold gas pockets do not differ significantly. Thus, the LDV sampling bias which favors cold gas pockets¹

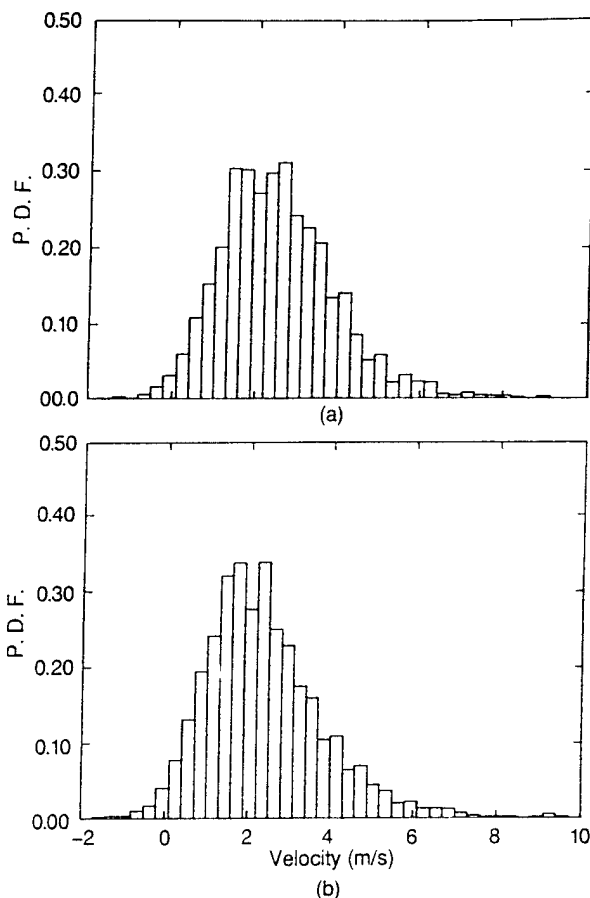


Fig. 5. PDFs of (a) conditional and (b) unconditional axial velocities taken at mean position of methane-flame base.

should not result in a biased pdf or velocity statistics for the flame. This is consistent with previous studies which have indicated that the temperature or scalar fields, in general, display bi-modal distributions in intermittent flow regions where velocity fields seldom show a distinct bi-modal distribution.¹⁻³

Velocity Profiles

Both similarities and differences observed in general comparisons of the methane and propane flames are given in Table I. To obtain a more detailed comparison of the jet flames, the velocity profiles along the centerline and radially at the LOH were made.

The mean velocity and rms velocity fluctuation of the axial component along the centerline are depicted in Figs. 6-7. Figure 6 shows results for the methane jet flame with a LOH of 60 mm. The maximum turbulent fluctuation was observed to occur at ~ 30 mm ($z/D = 6$); the flame LOH was ~ 60 mm ($z/D = 12$). Figure 7 shows results for the propane flame with a LOH of 50 mm. In this case the maximum rms fluctuation occurs at ~ 50 mm ($z/D = 10$),

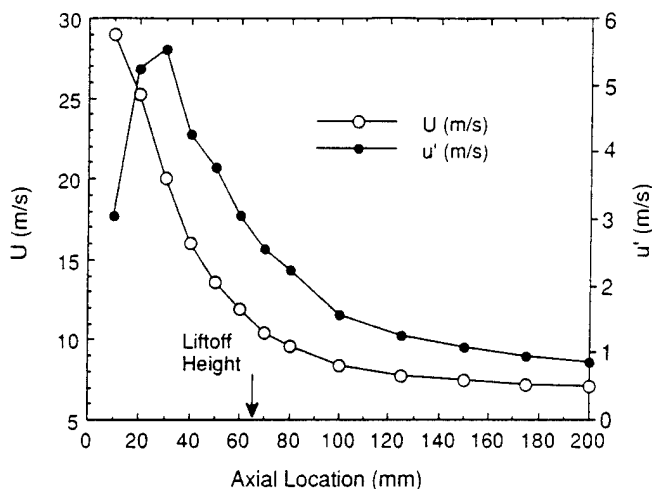


Fig. 6. Centerline mean and RMS axial velocity profiles for methane flame with LOH of 60 mm.

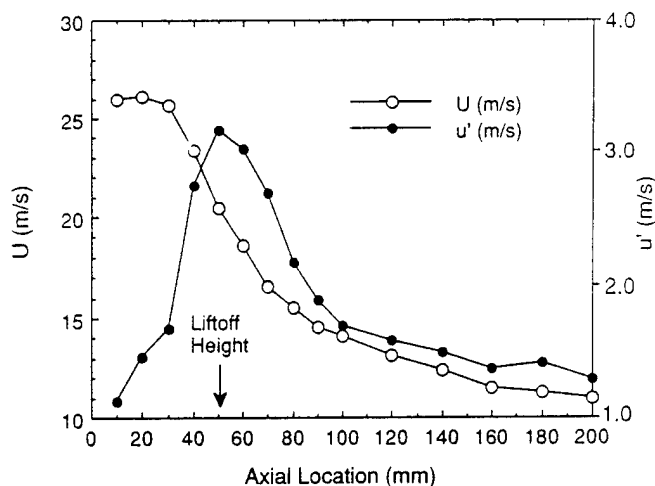


Fig. 7. Centerline mean and RMS axial velocity profiles for propane flame with LOH of 50 mm.

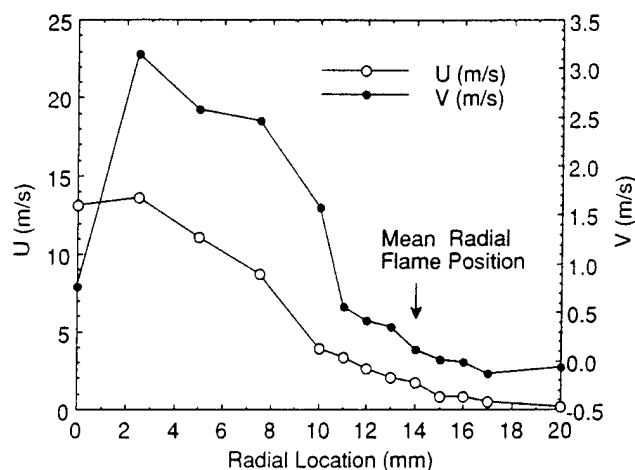


Fig. 8. Radial scan of velocity profiles at base of lifted methane flame with LOH of 60 mm.

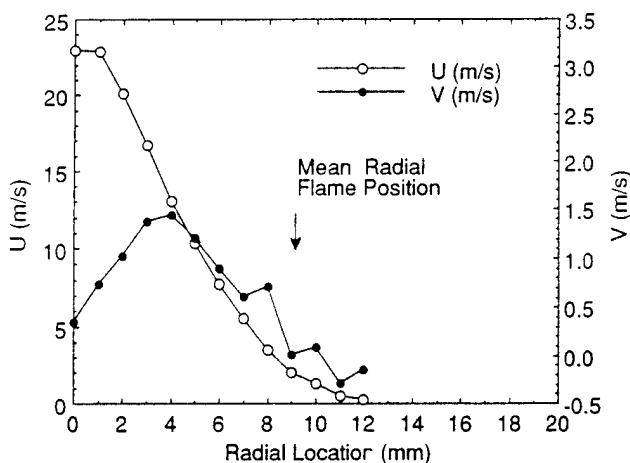


Fig. 9. Radial scan of velocity profiles at base of lifted propane flame with LOH of 50 mm.

which was the LOH. A comparison of these two figures indicates that the velocity field of the methane jet decays much faster than that of the propane jet due to the lower density of methane. As a result the methane jet is less stable, with the onset of turbulent fluctuations occurring nearer the jet exit. In addition, the rms fluctuation is of higher magnitude for the methane jet than for the propane jet.

The effects of density upon the development of the velocity field can also be observed in the velocity profiles taken radially at the LOH (see Figs. 8-9). Figures 8 and 9 show results for the methane flame with a LOH of 60 mm and for the propane flame with a LOH of 50 mm, respectively. The methane jet in this case displays a lower axial velocity in the LOH region than the propane jet; yet, the radial velocity of the methane jet is higher than that of the propane jet. This is consistent with results from a previous study⁶ in which both OH imaging and TFP measurements of the flame-surface fluctuation indicated that the methane flame displays stronger

flame/flow interactions than the propane flame under the critical lift-off condition. The shear-layer vortices of the methane jet have a higher probability of spinning out at a high radial velocity and can strongly interact with the flame under these conditions. As a result the methane flame displays a higher probability for hole formation than the propane flame at the critical lift-off jet velocity.

Conclusion

A novel technique for conditioning LDV velocity measurements to the presence of the flame has been developed. Measurements in flame regions which display a high correlation between temperature and velocity require some means of distinguishing the presence (or absence) of the flame. For detecting the flame, the TFP technique was found to be easy to implement and cost effective. The combined LDV/TFP technique was successfully utilized to measure conditional and unconditional velocities at the base of lifted hydrocarbon jet

flames. The present study indicates that the combined LDV/TFP technique is a reliable tool for conditional studies of jet flames. Future efforts will be directed toward obtaining correlation measurements with the combined instrument.

Acknowledgement

This work was supported by and performed at the Wright Research and Development Center, Aero Propulsion and Power Laboratory under Contract Nos. F33615-85-C-2562 and F33615-90-C-2033. The authors are indebted to Dr. W. M. Roquemore for support and discussions concerning this work. The authors also wish to thank Ms. M. Whitaker for editorial assistance.

References

1. L. P. Goss, D. D. Trump, and W. M. Roquemore, "Combined CARS/LDA Instrument for Simultaneous Temperature and Velocity Measurements," *Exp. Fluids* 6, 189 (March 1988).
2. L. P. Goss, D. D. Trump, W. F. Lynn, T. H. Chen, W. J. Schmoll, and W. M. Roquemore, "Second-Generation Combined CARS-LDV Instrument for Simultaneous Temperature and Velocity Measurements in Combusting Flows," *Rev. Sci. Instrum.* 60, 638 (April 1989).
3. T. H. Chen, L. P. Goss, D. D. Trump, and W. J. Schmoll, "Studies of a Turbulent Premixed Flame Using CARS-LDV Diagnostics," *J. Prop. Power* 6, 106 (March-April 1990).
4. L. P. Goss, V. Vilimpoc, B. Sarka, and W. F. Lynn, "Thin-Filament Pyrometry: A Novel Thermometric Technique for Combusting Flows," *J. Engrg. Gas Turb. Pow., Trans. ASME* 111, 46 (1989).
5. A. Lightman, P. D. Magill, and R. J. Andrews, "Two-Dimensional Laser Doppler Anemometer Studies of Isothermal Flowfield in A Ducted Center-body Combustor," AFWAL-TR-83-2044, Air Force Wright Aeronautical Laboratories, Wright-Patterson Air Force Base, OH, June 1983.
6. T. H. Chen, and L. P. Goss, "Propagation and Fractals of Turbulent Jet Flames," AIAA-89-2524 (to appear in *J. Prop. Power*); T. H. Chen and L. P. Goss, "Flame Lifting and Flame/Flow Interactions of Jet Diffusion Flames," AIAA-89-0156; T. H. Chen, L. P. Goss, D. Talley, and D. Mikolaitis "Stabilization Zone Structure in Jet Diffusion Flames from Liftoff to Blowout," AIAA-89-0153.



AIAA-93-0518

THIN-FILAMENT VELOCIMETRY

L. P. Goss, J. R. Gord, D. D. Trump, and M. E. Post

Systems Research Laboratories, Inc.

A Division of Arvin/Calspan

2800 Indian Ripple Road

Dayton, OH 45440-3696

**31st Aerospace Sciences
Meeting & Exhibit
January 11-14, 1993 / Reno, NV**

THIN-FILAMENT VELOCIMETRY

L. P. Goss,* J. R. Gord,** D. D. Trump,† and M. E. Post††

Systems Research Laboratories, Inc.

A Division of Arvin/Calspan

2800 Indian Ripple Road

Dayton, OH 45440-3696

Abstract

The Thin-Filament-Velocimetry (TFV) technique that has been developed for velocity measurements in cold or hot combusting flows is the optical analog of hot-wire anemometry. The energy flux from a laser is used to heat a section of a 14- μm β -SiC filament, and the temperature relaxation of the filament is determined by its graybody emission. Heat-transfer coefficients are directly measured allowing gas properties to be determined. A modified King's-Law Nusselt-number correlation was found to yield the best agreement with experimental results. A full explicit time-dependent model was developed and the predictions of the model compared with the experimental results. Three different operational modes for velocity determination are reported, and the results calibrated by a conventional Laser-Doppler-Velocimetry (LDV) system.

Introduction

Previous studies by the authors have utilized the graybody emission from a small β -SiC filament to investigate the temperature profiles of premixed and diffusion flames.¹⁻⁶ The filament emission can be recorded spatially along the length of the filament, allowing the radial temperature distribution to be evaluated. The β -SiC filament is commercially available, has a diameter of 14 μm , and displays a low thermal conductivity along the filament axis, making it ideal for the spatial determination of temperature profiles. The small size of the filament allows it to respond quickly to temperature (and velocity) changes in its surroundings; its high emissivity (0.88), which is constant over a wide temperature range, allows for the quantitative conversion of filament emission intensity to gas

temperature. The technique called Thin Filament Pyrometry has been applied to several flame studies involving non-sooting laminar,¹ turbulent,²⁻⁶ and sooting flames.⁷ The thermal properties of the filament were modeled (steady state) in two earlier studies⁸⁻⁹ and a full non-steady time-dependent heat-transfer model has also been developed.⁷ Because of the strong dependence of the filament response upon Reynolds number and the thermal properties of the flowfield, velocity as well as temperature information can be obtained from the filament emission.

Post and co-workers¹⁰ demonstrated that the temporal phase lag of the emission from a filament when heated with a sinusoidal energy flux from a laser can be related to the velocity of the surrounding flowfield. From this earlier work it was concluded that Thin-Filament Velocimetry (TFV) was a viable technique for the determination of velocities in the range of 0 - 10 m/s. The advantage of this technique over conventional hot-wire probes is that temperature and velocity can be determined simultaneously and that the technique can be applied to combusting flowfields. The study reported in this paper extends the earlier velocity work by investigating three separate approaches to obtaining velocities by laser heating of the filament including 1) steady state, 2) impulse (square wave), and 3) sinusoidal heating of the filament with a laser source. The response of the filament to heating by a laser is modeled with an explicit time-dependent model which will be discussed in detail in the next section.

Experimentally, the energy flux of a laser is used to heat a small section of the filament, the emission from which is observed by an InGaAs detector and converted to filament temperature and velocity. In the constant-laser-flux (steady-state) heating case, a drop in temperature (emission intensity) with an increase in velocity is observed, allowing the surrounding gas velocity to be determined. In the impulse-flux-heating case (square wave), the relaxation of the filament temperature to that of the ambient surroundings is followed to determine the

*Dir. of Research, Optical Diag., Member AIAA

**Senior Research Chemist, Member AIAA

†Senior Engineer

††Research Physicist, Member AIAA

gas velocity. In the sinusoidal heating case, the phase lag of the filament emission is utilized for velocity determination. A comparison of the velocities obtained by the TFD technique with those obtained by a conventional Laser Doppler Velocimetry (LDV) instrument is discussed.

Theory and Model

Detected Filament Emission

Since the filament is known to be a gray-body,¹¹ its emission is related to its temperature by the Planck blackbody equation multiplied by the emissivity of the filament

$$I(\lambda, T) = \frac{\epsilon(\lambda, T) C_{1p}}{\lambda^5 [\exp(\frac{C_{2p}}{\lambda T}) - 1]} \quad (1)$$

where $\epsilon(\lambda, T)$ is the emissivity; C_{1p} is Planck's first radiation constant; C_{2p} is Planck's second radiation constant; and λ is the emission wavelength. Studies by several groups have shown that the filament emissivity is relatively constant with temperature and wavelength, having a value of 0.88.^{9,11} Experimentally, the emission from the filament is observed with a detector having a limited wavelength response which requires that the calculated filament emission be convoluted over the spectral response of the detector. Assuming that the transmission characteristics of the optical components are constant over the wavelength range of the detector, the experimentally detected signal is given by

$$D_{exp} = k_{exp} \int_{\lambda_1}^{\lambda_2} I(\lambda, T) R(\lambda) d\lambda \quad (2)$$

where k_{exp} is the experimental constant which takes into account the light-collection efficiency and the gain of the detector electronics; $R(\lambda)$ is the wavelength response of the detector; and the integral extends over the lower, λ_1 , and upper wavelength, λ_2 , range of the detector response. Notice that the detected signal is a function of filament temperature only. Figure 1 shows the relationship between filament temperature and emission obtained for the InGaAs detector utilized in this study. The efficiency constant can be removed by normalizing the observed signal at a known temperature. The complications which arise with techniques that rely upon the filament emission do not involve determining the filament temperature but relating the filament temperature to the properties of the surrounding gases.

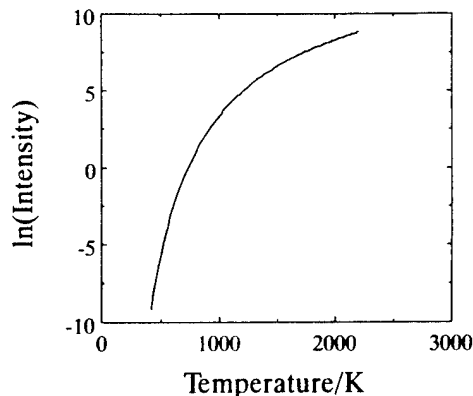


Fig. 1. Natural logarithm of filament-emission intensity vs. filament temperature as calculated for InGaAs photodiode detector.

Filament Temperature

The filament temperature is dependent upon the physical properties of the filament (heat capacity, thermal conductivity, emissivity, density, and diameter) and upon its heat-transfer processes with the surrounding gases (convection, conduction, radiation, and external energy flux). A numerical model for calculating the temperature of the filament was developed by considering a differential section of a long cylinder. The rate of energy transfer (units of energy per time) along the filament axis by conduction is modeled as

$$q_{conduction} = -kA_{cross} \frac{dT}{dx} \quad (3)$$

where k is the thermal conductivity of the filament; A_{cross} ($\pi d^2/4$) is the cross-sectional area of the filament; T is the filament temperature; and lower-case x refers to distance along the filament axis.

The rate of convective heat transfer is modeled as

$$q_{convection} = hA_{surface}(T - T_{gas}) \quad (4)$$

The convective heat transfer coefficient (h) is dependent on the velocity and the physical properties of the gases surrounding the filament. $A_{surface}$ is $\pi d \Delta x$, where Δx is the length of the differential section of the filament and T_{gas} is the bulk temperature of the gases surrounding the filament.

The rate of radiation heat transfer is modeled as

$$q_{radiation} = \sigma \epsilon A_{surface}(T^4 - T_{ref}^4) \quad (5)$$

It is assumed that the filament exchanges energy with a distant surrounding enclosure at temperature T_{ref} , and the view factor is unity. σ is the Stefan-Boltzmann constant, and ϵ is the filament emissivity.

The rate of energy transfer to the filament from an external energy flux (laser focused on the filament) is modeled as

$$q_{external} = A_{normal} \Gamma \quad (6)$$

where A_{normal} is $d\Delta x$; and Γ is the laser energy flux. The value of Γ is an effective flux that includes the efficiency factors for the varying incidence angles of the laser on the curved surface of the cylinder.

The time-dependent energy accumulation in a differential section of the filament is modeled as

$$E_{accum} = \rho CV \frac{dT}{dt} \quad (7)$$

where ρ is the filament density; C is the heat capacity of the filament; V is the volume ($\pi d^2 \Delta x / 4$) of the differential section of filament; and lower-case t refers to time.

These terms can be combined in an energy balance and rearranged to yield a time dependent expression for the filament temperature

$$\begin{aligned} \frac{\partial T}{\partial t} = & \frac{k}{\rho C \partial x^2} - \frac{4h}{\rho C d} (T - T_{gas}) \\ & - \frac{4\sigma\epsilon}{\rho C d} (T^4 - T_{ref}^4) + \frac{4\Gamma}{\pi \rho C d} \end{aligned} \quad (8)$$

A more exact analysis would require simultaneous solutions of momentum and energy equations for the fluid surrounding the filament and the internal temperature profile of the filament. Such an analysis is beyond the scope of this study. The energy balance presented in Eq. (8) assumes that the filament energy balance is coupled with the exact transport solutions for the surrounding fluid through only the heat-transfer coefficient. All fluid properties are included in the calculation of h and do not appear explicitly in the filament energy balance. Radiation, absorption, and emission from surrounding gases or soot have been neglected because of the additional requirements to model the surrounding fluid and combustion processes. In addition, it is assumed that no temperature gradient is present within the differential section of the filament.

Equation (8) was used as the basis for an explicit, finite-difference numerical calculation of filament temperature as a function of time. The heat-transfer coefficient was calculated with a Nusselt-number correlation and could be varied as a function of position and time to correspond to spatial and time-dependent velocity profiles. The gas temperature and external-energy-flux term could also be varied as a function of position and time.

The numerical model has sufficient flexibility to provide a computational comparison for every experimental variation attempted in this study. For example, it is possible to drive the filament in response to gas-temperature or laser-flux terms that are dependent on time and position, or it is possible to consider steady-state operations under conditions where conduction and radiation heat transfer are negligible.

Equation (8) can be rearranged for calculating the heat-transfer coefficient, h , from the filament and surrounding-gas temperatures taken as a function of time and position.

$$\begin{aligned} h = & \frac{\rho C d}{4(T - T_{gas})} \left[-\frac{\partial T}{\partial t} + \frac{k}{\rho C} \frac{\partial^2 T}{\partial x^2} \right. \\ & \left. - \frac{4\sigma\epsilon}{\rho C d} (T^4 - T_{ref}^4) + \frac{4\Gamma}{\pi \rho C d} \right] \end{aligned} \quad (9)$$

Using a correlation for the relationship between Nusselt number and Reynolds number, it is possible to calculate the velocity of a fluid flowing perpendicularly to the filament.

Dependence of Heat-Transfer on Gas Properties

Equation (9) explicitly demonstrates that the filament temperature is dependent on the heat transfer coefficient of the the surrounding gases. The heat-transfer coefficient is determined through the Nusselt number. According to King's Law, the Nusselt number for convective flow across a cylinder when the Reynolds number is between 1 and 1000 is given by

$$Nu = \frac{hd}{k_{gas}} = 0.4 + 0.518\sqrt{Re} \quad (10)$$

where k_{gas} is the thermal conductivity of the gas; Re is the Reynolds number; and all properties are evaluated at the mean film temperature. Experimentally it was observed that the King's-Law correlation over-predicted the heat transfer coefficient. This is not surprising since the

Reynolds number for the experiments reported in this study ranged from 0 to 3, which is well below the nominal values for the King's-Law correlation. The following modification to the Nusselt-number correlation was required

$$Nu = \frac{hd}{k_{\text{gas}}} = 0.4 + 0.185\sqrt{Re} \quad (11)$$

This correlation was utilized for all calculations in this study.

To understand the sensitivity of the filament emission to the temperature and velocity field of the surrounding gases, the convective time constant should be examined. To simplify the derivation for the convective time constant, the radiation, conduction and laser-flux terms of the energy balance of Eq. (8) are assumed to be negligible ($T < 1000\text{K}$ and laser off). In this case, the energy balance for the filament is given by

$$\frac{\partial T}{\partial t} = -\frac{4h}{\rho Cd}(T - T_{\text{gas}}) \quad (12)$$

Rearranging Eq. (12) and solving for temperature yields

$$T = T_{\text{gas}} + (T - T_{\text{gas}})_0 \exp\left(-\frac{t}{\tau}\right) \quad (13)$$

where

$$\tau = \frac{\rho Cd}{4h} \quad (14)$$

is the convective time constant of the filament for a given gas temperature and velocity. From Eq. (14) it can be seen that the convective time constant is a function of filament properties, i.e., density, heat capacity and diameter (all of which are assumed to be constant in this study), and gas properties through h . A plot of the variation of the convective time constant with temperature and velocity is shown in Fig. 2. The convective time constant is a maximum for low temperature and velocity and a minimum for high temperature and velocity. To maximize the sensitivity to velocity for the thin filament technique requires that the experiment be conducted at the lowest possible temperature. The low-temperature limit of the experiment is determined by the choice of detector (wavelength response of detector) and the background noise of the detector electronics. For the experimental setup utilized in this study, the lower-temperature limit was $\sim 800\text{ K}$. The majority of the experiments were conducted with the filament temperature in the range $800 - 1200\text{ K}$.

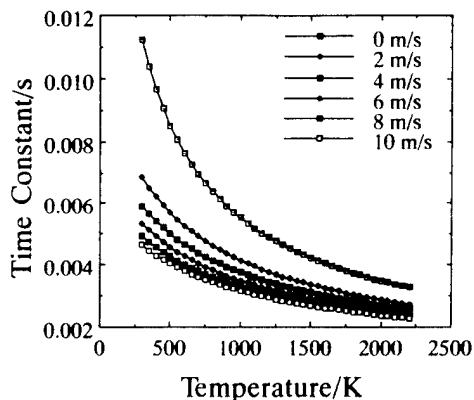


Fig. 2. Convective time constant (τ) vs. gas temperature and velocity as calculated with modified King's-Law Nusselt-number correlation.

Experimental

The experimental apparatus employed to perform TFV measurements is depicted in Fig. 3. A thin ceramic filament heated by a focused laser beam is suspended above a 30-mm diameter tube configured to direct room-temperature air across the filament. Convective cooling of the heated filament is monitored through collection of its graybody emission. The filament used in this study is composed of ultrafine β -SiC crystals with excess carbon¹² and is distributed by Dow Corning under the trade name NICALON. Nominal filament diameter is $14\text{ }\mu\text{m}$; density is 2550 kg/m^3 ; and thermal conductivity along the fiber axis at room temperature is 11.6 W/m-K . The reported heat capacity of SiC is 711 J/kg-K .¹³ Previous experiments in this laboratory⁸

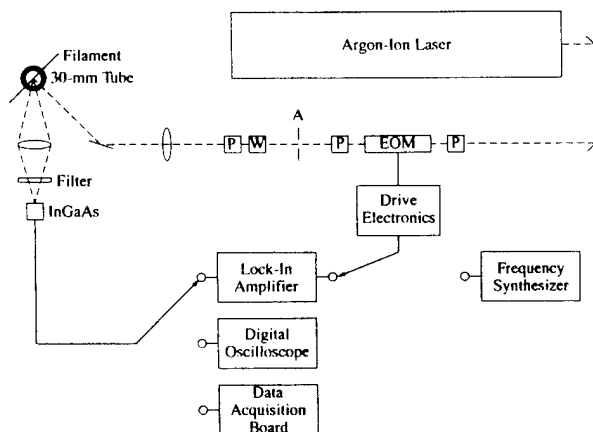


Fig. 3. Schematic diagram of experimental apparatus employed to perform Thin-Filament Velocimetry measurements. A: aperture, EOM: electro-optic modulator, P: Glan-laser polarizer, W: $1/2$ waveplate.

indicated that the filament emissivity is 0.88 \pm within 1% over the temperature range 300 - 2200 K.

An air-handling system designed around Tylan Model FC 262 mass-flow controllers delivered air flows between 0 and 300 slpm to the heated filament. These flows produced axial velocities at the filament (located in the central core of the 30-mm-diameter tube) ranging from 0 to 12 m/s as calibrated with a two-component Laser Doppler Velocimeter (LDV).

Three distinct operational modes were developed for collecting data with the thin-filament velocimeter. In the first, the 488.0-nm output of a Spectra-Physics Model 2020 argon-ion laser was focused at the filament using a 0.4-m focal-length lens. The resulting filament emission was imaged onto an InGaAs photodiode employing a 0.125-m focal-length lens, and the photodiode signal was processed with a Preston Model 8300 XWB amplifier. A Schott optical glass filter was positioned in front of the photodiode to eliminate scattered laser light at the detector. The laser power was maintained at a constant value of 300 mW for these experiments. The gas flow was adjusted under these constant-laser-flux conditions, and the average emission intensity, which is related to the filament temperature, was recorded at 30-slp (1 m/s) gas-flow intervals between 0 and 300 slpm. The amplified InGaAs photodiode output was digitized for 0.8 s at each gas flow using a National Instruments LAB-NB board installed in a Macintosh IIx computer. Averaging these data produced an intensity-vs.-velocity calibration.

In the second operational mode, gas velocity is determined by measuring the filament response to a square-wave-modulated laser flux. The argon-ion laser output was electro-optically modulated using a ConOptics Model 370 ADP modulator situated between two Glan-laser polarizers. A Wavetek Model 144 frequency synthesizer provided a 5-Hz bipolar square wave to a ConOptics Model 25 drive electronics assembly, which powered the electro-optic modulator. The modulator was configured to ensure extinction of the laser beam during the low portions of the square wave (i.e., 100% depth of modulation). An aperture placed after the second polarizer served to eliminate stray beams produced through optical vignetting in the modulator. A waveplate-polarizer pair permitted variable attenuation of the modulated laser flux, and the power at the filament was adjusted as described below over the range 75 - 395 mW. In these experiments, the amplified photodiode signal was captured with a LeCroy Model 9314L digital storage oscilloscope. The decay of the filament

emission upon transition from the laser-on to laser-off state was digitized and averaged for 100 to 1000 cycles. The temporal response of the filament when heated with an average laser power of 270 mW and bathed in a 150-slp (5.3 m/s) gas flow is depicted in Fig. 4. Averaged decay profiles were collected at 30-slp (1 m/s) gas-flow intervals between 0 and 300 slpm. During the course of a velocity study, the laser flux and alignment were adjusted to obtain the same maximum emission signal and, therefore, filament temperature at each mass flow. Complete sets of decay vs. velocity data were collected at several different filament temperatures for evaluation of the effects of temperature on the convective heat-transfer coefficient and the resulting filament-emission decay.

The third operational mode of the TFV involves measurement of the filament response to sinusoidal modulation of the laser flux. The experimental arrangement was much the same as that described above; however, a Stanford Research Systems Model SR850 DSP lock-in amplifier was employed to drive the electro-optic modulator with a bipolar 50-Hz sine wave and to monitor the phase difference between the filament emission and the driving laser flux. A typical trace of the modulator-driving waveform and the phase-shifted filament emission at a gas flow of 150 slpm (5.3 m/s) and average laser power of 340 mW is depicted in Fig. 5. The phase shift of the filament emission with respect to the driving sinusoid was determined through measurement of the in-phase and quadrature components of the emission signal. The lock-in amplifier was configured with a 100-ms output time constant, and the phase difference was sampled and averaged over a 50-s period at each mass flow. The laser power was adjusted between 125 and 375 mW, and complete phase

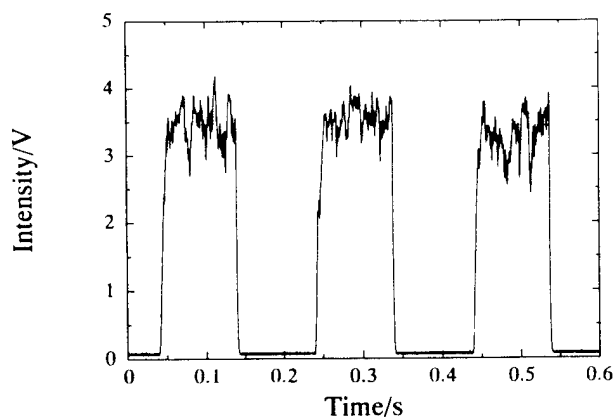


Fig. 4. Emission from filament when heated by 270-mW square-wave-modulated laser beam and bathed in 150-slp (5.3 m/s) gas flow.

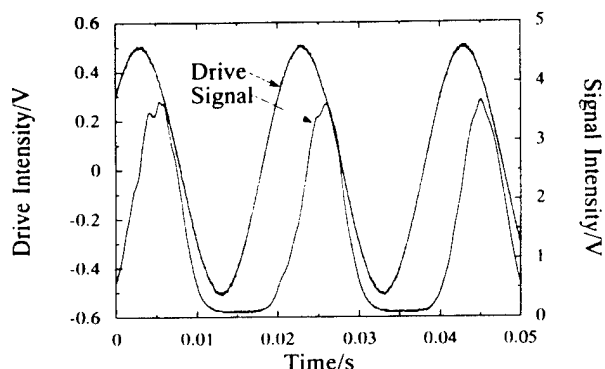


Fig. 5. Sinusoidal modulation waveform and emission from filament when heated by 340-mW sine-wave-modulated laser beam and bathed in 150-slpn (~ 5.3 m/s) gas flow.

difference-vs.-velocity data were collected at each of several constant filament temperatures as in the decay-vs.-velocity experiments.

Several experiments were performed to verify that the observed phase shift was produced at the filament. A reflection from the focusing lens was positioned onto a photodiode, and the phase shift introduced at 50 Hz by the lock-in amplifier and laser-modulation apparatus was determined to be negligible. Similarly, a fast-rise-time, infrared light-emitting diode (LED) was modulated sinusoidally and imaged onto the detector to demonstrate that the phase shift at 50 Hz in the InGaAs photodiode and associated electronics is negligible as well.

To estimate the filament temperature at which data were collected, a single-point intensity-vs.-temperature calibration was performed by measuring the photodiode signal produced when the filament was heated with a propane torch ($T = 2200$ K). The focused laser beam irradiates only a small section of the filament, while the propane torch heats a much larger section; therefore, limiting apertures were positioned between the filament and the detector during the torch experiments to achieve a reliable temperature calibration.

Results and Discussion

Steady-State Laser Heating

In this approach to velocity measurements, the filament is heated with a constant energy flux from the argon-ion laser. The emission from the filament is observed by an InGaAs detector and recorded as a function of the surrounding air flow. As the surrounding air velocity is increased, the filament cools and the emission intensity drops accordingly. The rate

of cooling in this case is determined by the heat transfer from the filament to the surrounding cold gases and the energy losses due to radiation effects. This case is the simplest to model and implement experimentally. In the low temperature region (< 1000 K) where the radiative heat loss and thermal conductivity along the filament are small, the energy balance to the filament can be written as

$$\frac{\partial T}{\partial t} = -\frac{4h}{\rho C d}(T - T_{\text{gas}}) + \frac{4\Gamma}{\pi \rho C d} \quad (15)$$

Since the filament is allowed to achieve a steady-state temperature before the measurement is made, Eq. (15) reduces to

$$T = T_{\text{gas}} + \frac{4\Gamma}{\pi \rho C d} \tau \quad (16)$$

indicating that the steady-state constant-flux temperature achieved by the filament is directly proportional to the convective time constant. To compare the predictions of Eq. (16) with the experimental results, the filament temperature must be converted to an experimental intensity. This is accomplished through the relationship between filament temperature and emission intensity depicted in Fig. 1. The results of a constant-flux experiment on the 30-mm air jet are shown in Fig. 6. A marked decrease in the emission intensity is observed as the velocity of the air jet is increased. The experimental results agree well with both the simple [Eq. (16)] and the explicit model results for a filament temperature of 1000 K and a laser flux of 3.8 W/mm^2 . Notice the deviation of the experimental results from both the simple and explicit

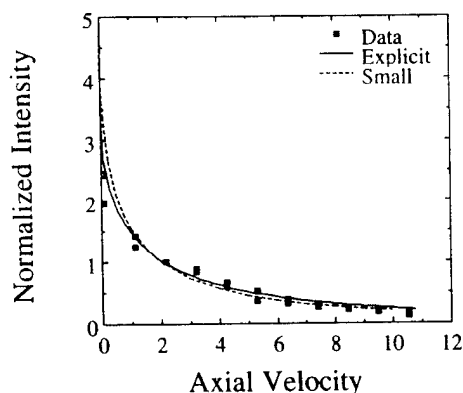


Fig. 6. Filament emission intensity vs. gas velocity when filament is heated at constant laser power of 300 mW. Also plotted are results obtained from simple and explicit energy-balance models.

model results at the zero velocity point. This deviation is not surprising since the Nusselt-number correlation is not accurate for such a low velocity, and it is experimentally difficult to maintain a zero-velocity condition with an unconfined experimental setup.

In the steady-state laser-flux case, the time step for the explicit model was 10 μ s, and the calculation was allowed to run for 40 ms (10 time constants) to ensure a steady-state filament temperature. Notice the over-prediction of the filament intensity at the zero velocity point for the simple model [Eq. (16)] as compared to the explicit model. This is due to the neglect of the radiation term by the simple model which would tend to cool the filament. For determining k_{exp} the emission intensity for the experiment and the calculations were normalized at the 2.16-m/s velocity point before comparison.

The steady-state laser-flux approach is the most simple to implement; however, the requirement that the filament be at a steady-state temperature necessitates a minimum wait period of 5 - 10 convective time constants (10 - 30 ms). While this may not be a problem for steady flowfields, unsteady flowfields require a higher temporal response. Both impulse heating and sinusoidal methods can accomplish this task. One important application of the steady-state heating approach, however, is the accurate determination of heat-transfer coefficients.

Impulse Laser Heating

In the impulse-heating approach, the laser output is modulated electro-optically to yield a square-wave-shaped laser flux. The filament emission resulting from a driving waveform for this experiment is depicted in Fig. 4. The length of the square pulse was chosen to ensure that the filament would obtain a steady temperature, eliminating the need to determine a separate temperature for each velocity. In practice, this is not necessary as long as the temperature and velocity measurements are made simultaneously. The temporal decay of the filament emission, which occurs after the laser flux is interrupted, is indicative of the heat-transfer processes of the filament with the surrounding gases. The low-temperature energy-balance equation [Eq. (12)] can be used to model the decay after the heat pulse. Rearranging Eq. (12) allows the following expression for filament temperature

$$T = T_{gas} + (T - T_{gas})_0 \exp(-\frac{t}{\tau}) \quad (17)$$

The filament temperature can then be converted to intensity, as discussed in the steady-state case.

To simulate the square-wave effect in the explicit model, either a square gas-temperature pulse or square external-flux pulse can be employed. These two approaches were found to be equivalent. The square gas-temperature pulse is easier to implement for the case in which the temperature of the filament is kept constant as the velocity is varied (the conditions of the experiment); thus, this approach was employed for the impulse-heating calculations. The experimental decay curves obtained on the 30-mm air jet are shown in Fig. 7. The difference in the filament emission decay with time can be enhanced by taking the natural logarithm as shown in Fig. 8. Good agreement is obtained between the explicit model and the experimental data while only moderate agreement is obtained with the simple model as shown in Fig. 9. Of the three approaches described in this study, the impulse approach is the most sensitive to the accuracy of the model. This approach, however, offers the most promise for dynamic velocity measurements in time-variant flowfields.

Sinusoidal Laser Heating

If the energy flux from the laser is modulated in a sinusoidal manner, the filament temperature can be shown to vary sinusoidally at the same frequency as the laser-flux modulation, with a phase delay that depends on the heat-transfer coefficient. An analytical expression for this relationship can be derived if the filament temperature is maintained in a range

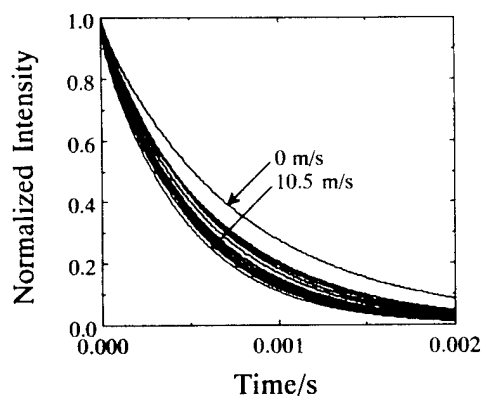


Fig. 7. Time-resolved decay of filament emission after heating with square-wave-modulated laser beam for gas velocities ranging from 0 to 10.5 m/s.

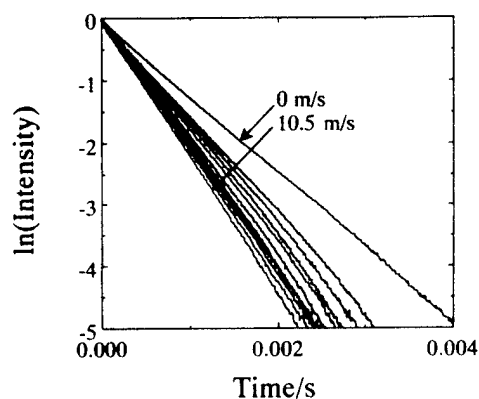


Fig. 8. Natural logarithm of filament-emission decay after heating with square-wave-modulated laser beam for gas velocities ranging from 0 to 10.5 m/s.

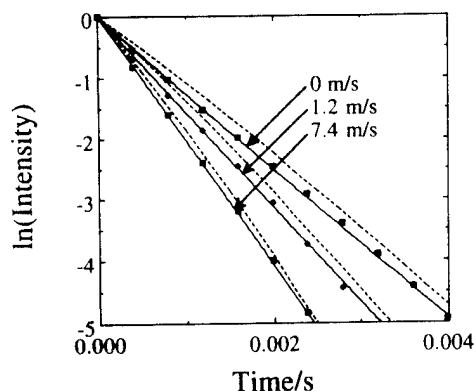


Fig. 9. Comparison of natural logarithm of filament emission decay results with simple (dashed) and explicit (solid) energy balance models for gas velocities of 0, 1.2, and 7.4 m/s.

where radiation heat transfer is small relative to convective heat transfer. If radiation and conduction effects are negligible compared to convection and laser-heating effects, the energy balance is described in Eq. (15). If the laser energy flux is modulated sinusoidally, it can be represented as

$$\Gamma = a_0 + a_1 \sin \omega t \quad (18)$$

Assuming that all parameters are constant, it can be shown that

$$T - T_{\text{gas}} = b_0 + b_1 \sin(\omega t - \phi) \quad (19)$$

where

$$b_0 = \frac{a_0}{\pi h}$$

$$b_1 = \frac{a_1}{\pi h \sqrt{1 + \omega^2 \tau^2}} \quad (20)$$

$$\tan \phi = \omega \tau = \omega \left(\frac{\rho C d}{4h} \right)$$

This last expression shows the relationship among the tangent of the phase angle, the modulation frequency of the laser, and the heat-transfer coefficient. By measuring the phase delay for a given modulation frequency, it is possible to calculate h . Then h can be used to calculate velocity with an expression for Nusselt number as a function of Reynolds number.

Note that for low or high frequencies the phase delay approaches limiting values of zero or 90 deg, respectively. The application of phase-delay methods for measuring h (and v) requires the ability to measure small changes in phase delay. This limits the dynamic range of the experimental measurements. For a larger dynamic range, the modulation frequency can be adjusted until the phase delay is ~ 45 deg when the velocity (and h) is in the mid-range of expected values. During the course of experimental measurements, it was observed that best results were obtained when the modulation frequency was adjusted in such a way that high velocity (high h) produced a phase delay of 45 deg. The non-linear dependence of h on v and of the tangent function resulted in an effectively linear curve for phase delay versus velocity.

An analytical solution for the explicit model has not been found, but the signal from the filament is a modified sinusoid with an observed phase delay. While the radiation term is most significant at higher temperatures, the value of the heat-transfer coefficient changes throughout the heat cycle because of the temperature dependence of the gas properties. The detector has a low-temperature limit of ~ 800 K, which results in a truncation of the filament-emission signal.

Figure 10 displays the experimentally determined phase delays as a function of air jet velocity for three different filament temperatures. Notice that as predicted by the model, with increasing temperature, the sensitivity to velocity is reduced, i.e., the phase shift decreases as the temperature increases. The results of both the simple [Eq. (20)] and the

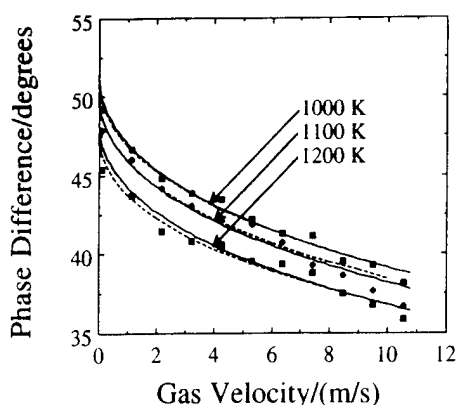


Fig. 10. Phase difference between sine-wave-modulated laser beam and filament emission vs. gas velocity at filament temperatures of 1000, 1100, and 1200 K. Also plotted are results obtained from simple (dashed) and explicit (solid) energy-balance models.

explicit model support the phase-delay data, with the usual exception at the zero-velocity point.

Because of the requirement to wait at least one full excitation cycle, the dynamic capabilities of the sinusoidal-heating approach are limited. Increasing the excitation frequency would help, but this also compresses the dynamic range, requiring the measurement of small phase shifts. This technique, like the steady-state approach, is best suited for slowly varying flowfields or for direct measurement of heat-transfer coefficients.

Summary

The Thin-Filament Velocimetry technique is essentially the optical analog of hot-wire anemometry. A numerical model has been developed to predict the temperature of a filament when heated by a laser energy flux. Combining this model with correlations between the Nusselt number and Reynolds number allows the prediction of fluid velocity. A modified King's Law correlation was found to yield the best agreement with experimental data. Experiments have been performed in several operational modes to demonstrate the technique in the velocity range 0.0 - 10.0 m/sec. Several follow-on opportunities exist for both experimental and numerical studies in areas including simultaneous velocity measurements along the filament, simultaneous temperature and velocity measurements, and velocity measurements as a function of time.

References

1. Vilimpoc, V., Goss, L. P., and Sarka, B.: *Optics Letters* 13, 93 (1988).
2. Chen, T. H., and Goss, L. P.: *J. Propul. Power* 8(1), 16 (1992).
3. Chen, T. H., and Goss, L. P.: "Flame Lifting and Flame/Flow Interactions of Jet Diffusion Flames," AIAA-89-0156.
4. Davis, R. W., Moore, E. F., Roquemore, W. M., Chen, L.-D., Vilimpoc, V., and Goss, L. P.: *Comb Flame* 83, 263 (1991).
5. Takahashi, F., and Goss, L. P.: "Near-Field Turbulent Structure and the Local Extinction of Jet Diffusion Flames," Presented at the Twenty-Fourth (International) Symposium on Combustion, Sydney, Australia, July 1992.
6. Hsu, K., Chen, L., Katta, V., and Goss, L.: "Experimental and Numerical Investigations on the Flame-Vortex Interactions in a Driven Jet Diffusion Flame," AIAA-93-0455.
7. Goss, L. P., Chen, T. H., Vilimpoc, V., Post, M. E., Trump, D. D., and Sarka, B.: "Optical Diagnostics for Reacting and Non-Reacting Flows: Recent Developments and Results," AIAA-90-0156.
8. Vilimpoc, V., and Goss, L. P.: *Twenty-Second Symposium (International) on Combustion* (The Combustion Institute, Pittsburgh, PA, 1988), p. 1907.
9. Goss, L. P., Vilimpoc, V., Sarka, B., and Lynn, W. F.: *ASME Trans., J. Eng. Gas Turbines Power* 111, 46 (January 1989).
10. Post, M. E., Gord, J. R., Goss, L. P., Trump, D. D., Sarka, B., Brainard, L. F., and Govind, R.: "Thin Filament Velocimetry," Presented at the 1992 Technical Meeting of the Central States Section of the Combustion Institute, Columbus, OH, April 1992.
11. Touloukian, Y. S., *Thermal Properties of High Temperature Solid Materials, Vol. 5 Nonoxides and Their Solutions and Mixture Including Miscellaneous Ceramic Material Properties* (MacMillan, London, 1967), pp. 118-140.
12. New Product Information (Dow Corning Corporation, Midland, MI 48686-0995, 1986).
13. Kern, E. L., Hamill, D. W., Deem, H. W., and Sheets, H. D., "Thermal Properties of β -SiC from 20 to 2000 C," Special Issue, *Mater. Res. Bull.* 4, S25-S32 (1969).



AIAA-94-0495

**SIMULTANEOUS THIN-FILAMENT
VELOCIMETRY AND PYROMETRY**

L. P. Goss, W. L. Weaver, and D. D. Trump

**Systems Research Laboratories, Inc.
A Division of Calspan Corporation
2800 Indian Ripple Road
Dayton, OH 45440-3696**

J. R. Gord

**Wright Laboratory
Aero Propulsion and Power Directorate
Wright-Patterson AFB, OH 45433-7103**

**32nd Aerospace Sciences
Meeting & Exhibit
January 10-13, 1994 / Reno, NV**

SIMULTANEOUS THIN-FILAMENT VELOCIMETRY AND PYROMETRY

L. P. Goss,* W. L. Weaver,** and D. D. Trump,†
Systems Research Laboratories, Inc.
A Division of Calspan Corporation
2800 Indian Ripple Road
Dayton, OH 45440-3696

J. R. Gord††
Wright Laboratory
Aero Propulsion and Power Directorate
Wright-Patterson Air Force Base, OH 45433-7103

Abstract

A novel technique which employs a thin ceramic filament has been developed for the simultaneous measurement of temperature and velocity in combustng flowfields. The technique utilizes the optical analog of hot-wire anemometry for velocimetry and blackbody emission for thermometry. The energy flux from a laser is used to heat a section of 14- μm -diameter β -SiC filament, and the temperature relaxation of the filament is tracked by its graybody emission. Heat-transfer coefficients are measured directly, allowing determination of gas properties. A modified King's-Law Nusselt-number correlation was found to provide the best agreement with experimental results. A fully explicit time-dependent model was employed for numerical fitting of the experimental velocity results. Profiles of a premixed propane-air flame were obtained and compared to the results of LDV measurements. The effects of gas composition on the observed velocity-measurement results are discussed.

Introduction

In previous studies by the authors, the graybody emission from a small β -SiC filament has been utilized to investigate the temperature profiles of premixed and diffusion flames.¹⁻⁶ The filament emission can be recorded spatially along the length of the filament, allowing evaluation of the radial-temperature distribution. The β -SiC filament is commercially available, has a diameter of 14 μm , and displays a low thermal conductivity along the filament

axis, making it ideal for spatial determination of temperature profiles. Because of the small size of the filament, it is able to respond quickly to temperature (and velocity) changes in its surroundings; its high emissivity (0.88), which is constant over a wide temperature range, allows quantitative conversion of filament emission intensity into gas temperature. The technique known as Thin-Filament Pyrometry has been applied in several studies involving non-sooting laminar,¹ turbulent,²⁻⁶ and sooting flames.⁷ The thermal properties of the filament have been modeled (steady state) in two earlier studies,⁸⁻⁹ and a full nonsteady time-dependent heat-transfer model has also been developed.⁷ Because of the strong dependence of the filament response on Reynolds number and the thermal properties of the flowfield, velocity as well as temperature information can be obtained from the filament emission.

The advantages of this technique over the use of conventional hot-wire-anemometer probes is that both temperature and velocity can be determined simultaneously and that the technique can be applied to combustng flowfields. The authors previously investigated the velocimetry capabilities of the thin filament in the case of a laminar air jet.¹⁰ Three separate approaches to obtaining velocities by heating the filament with a laser source were examined: 1) steady state, 2) impulse (square wave), and 3) sinusoidal. The response of the laser-heated filament was modeled using an explicit time-dependent model; this model was modified for numerical fitting of experimental decays in the present study. The present study represents the first application of the joint thin-filament velocimetry and pyrometry techniques in a combustng environment.

Experimentally, the energy flux of a laser is used to heat a small section of the filament, the emission from which is observed by an

*Dir. of Research, Optical Diag., Member AIAA

**Research Chemist, Member AIAA

†Senior Engineer

††Research Chemist, Member AIAA

InGaAs detector and converted to filament temperature and velocity. In the impulse-flux-heating case (square wave) utilized in this study, the relaxation of the temperature to the temperature of the ambient surroundings after being heated by the laser is tracked to determine the gas velocity. The velocities obtained by the Thin-Filament Velocimetry (TFV) technique in a premixed propane-air flame and those obtained by a conventional Laser Doppler Velocimetry (LDV) instrument are compared.

Theory and Model

Detected Filament Emission

Since the filament is known to be a gray-body,¹¹ its emission is related to its temperature by the Planck blackbody equation multiplied by the emissivity of the filament

$$I(\lambda, T) = \frac{\epsilon(\lambda, T) C_{1p}}{\lambda^5 [\exp(\frac{C_{2p}}{\lambda T}) - 1]} \quad (1)$$

where $\epsilon(\lambda, T)$ is the emissivity, C_{1p} is Planck's first radiation constant, C_{2p} is Planck's second radiation constant, and λ is the emission wavelength. Studies by several groups have shown that the filament emissivity is relatively constant with temperature and wavelength, having a value of 0.88.¹² Experimentally, the emission from the filament is observed by means of a detector having a limited wavelength response; this requires the calculated filament emission to be convoluted over the spectral response of the detector. If the transmission characteristics of the optical components are assumed to be constant over the wavelength range of the detector, the experimentally detected signal is given by

$$D_{\text{exp}} = k_{\text{exp}} \int_{\lambda_1}^{\lambda_2} I(\lambda, T) R(\lambda) d\lambda \quad (2)$$

where k_{exp} is the experimental constant that takes into account the light-collection efficiency and the gain of the detector electronics, $R(\lambda)$ is the wavelength response of the detector, and the integral extends from the lower, λ_1 , to the upper, λ_2 , wavelength range of the detector response. Notice that the detected signal is a function of filament temperature only. Figure 1 shows the relationship between filament temperature and emission obtained for the InGaAs detector utilized in this study. The experimental constant can be removed by normalizing the observed signal at a known temperature.

Filament Temperature

The filament temperature is dependent upon the physical properties of the filament (heat capacity, thermal conductivity, emissivity, density, and diameter) and upon heat-transfer processes (convection, conduction, radiation, and external energy flux). A numerical model for calculating the temperature of the filament was developed by considering a differential section of a long cylinder. The conduction, convection, radiation, and laser-heat-flux terms can be combined in an energy balance and rearranged to yield a time-dependent expression for the filament temperature

$$\begin{aligned} \frac{\partial T}{\partial t} = & \frac{k}{\rho C} \frac{\partial^2 T}{\partial x^2} - \frac{4h}{\rho C d} (T - T_{\text{gas}}) \\ & - \frac{4\sigma\epsilon}{\rho C d} (T^4 - T_{\text{ref}}^4) + \frac{4\Gamma}{\pi \rho C d} \end{aligned} \quad (3)$$

where k is the thermal conductivity of the filament, T is the filament temperature, T_{gas} is the temperature of the surrounding gases, T_{ref} is a reference temperature, x refers to the distance along the axis of the filament, ρ is the density of the filament, h is the convective heat-transfer coefficient, d is the diameter of the filament, σ is the Stefan-Boltzmann constant, ϵ is the emissivity of the filament, Γ is the laser flux used to heat the filament, and C is the heat capacity of the filament.

A more exact analysis would require simultaneous solutions of momentum and energy equations for the fluid surrounding the filament and the internal temperature profile of the filament. Such an analysis is beyond the scope of this study. The energy balance presented in Eq. (3) assumes that the energy balance of the filament is coupled with the exact transport solutions for the surrounding fluid only through the heat-transfer coefficient. All fluid properties are included in the calculation of h and do not appear explicitly in the filament energy balance. Radiation, absorption, and emission from surrounding gases or soot have been neglected because of the additional requirements to model the surrounding fluid and combustion processes. In addition, it is assumed that no temperature gradient exists within the differential section of the filament.

Equation (3) was used as the basis for an explicit, finite-difference, numerical calculation of filament temperature as a function of time. The heat-transfer coefficient was calculated using a Nusselt-number correlation and could be varied as a function of position and time to correspond to spatial and time

dependent velocity profiles. Gas-temperature and external-energy-flux terms could also be varied as a function of position and time.

Equation (3) can be rearranged for calculating the heat-transfer coefficient, h , from the temperature of the filament and that of the surrounding gas as a function of time and position

$$h = \frac{\rho C d}{4(T - T_{\text{gas}})} \left[-\frac{\partial T}{\partial t} + \frac{k}{\rho C} \frac{\partial^2 T}{\partial x^2} - \frac{4\sigma\epsilon(T^4 - T_{\text{ref}}^4)}{\rho C d} + \frac{4\Gamma}{\pi \rho C d} \right] \quad (4)$$

If a correlation is employed for the relationship between Nusselt number and Reynolds number, it is possible to calculate the velocity of a fluid flowing in the direction perpendicular to the filament.

Dependence of Heat Transfer on Gas Properties

Equation (4) explicitly demonstrates that filament temperature is dependent on the heat-transfer coefficient of the surrounding gases. The heat-transfer coefficient is determined through the Nusselt number. The experimentally obtained modified King's-Law correlation of the Nusselt number for convective flow across a cylinder when the Reynolds number is between 0 and 44 is given by

$$Nu = \frac{hd}{k_{\text{gas}}} = 0.425 + .45 \sqrt{Re} \quad (5)$$

where k_{gas} is the thermal conductivity of the gas, Re is the Reynolds number, and all properties are evaluated at the mean film temperature.

The sensitivity of the filament emission to the temperature and velocity field of the surrounding gases can be understood by examining the convective time constant. The derivation for the convective time constant can be simplified by assuming the radiation, conduction, and laser-flux terms of the energy balance of Eq. (3) to be negligible ($T < 1000$ K and laser off). In this case, the energy balance for the filament is given by

$$\frac{\partial T}{\partial t} = -\frac{4h}{\rho C d} (T - T_{\text{gas}}) \quad (6)$$

Rearranging Eq. (6) and solving for temperature yields

$$T = T_{\text{gas}} + (T - T_{\text{gas}})_0 \exp\left(-\frac{t}{\tau}\right) \quad (7)$$

where

$$\tau = \frac{\rho C d}{4h} \quad (8)$$

is the convective time constant of the filament for a given gas temperature and velocity. Equation (8) shows that the convective time constant is a function of filament properties (i.e., density, heat capacity, and diameter--all of which are assumed to be constant in this study), and gas properties through the heat-transfer coefficient, h . A plot of the variation of the convective time constant with temperature and velocity is shown in Fig. 2. The convective time constant is a maximum for low temperature/low velocity and a minimum for high temperature/high velocity.

Experimental

The experimental apparatus employed to perform thin-filament pyrometry and velocimetry is depicted in Fig. 3. A thin ceramic filament heated by a focused laser beam is suspended above the flowfield to be studied. Convective cooling of the heated filament is monitored through collection of its graybody emission. The filament used in this study is composed of ultrafine β -SiC crystals with excess carbon¹¹ and is distributed by Dow Corning under the trade name NICALON. Nominal filament diameter is 14 μm ; density is 2550 kg/m^3 ; and thermal conductivity along the fiber axis at room temperature is 11.6 W/m-K . The reported heat capacity of SiC is 711 J/kg-K .¹³ Previous experiments in this laboratory⁸ indicated that the filament emissivity is 0.88 to within 1% over the temperature range 300 - 2200 K.

Experimentally, the gas velocity is determined by measuring the response of the filament to a square-wave-modulated laser flux. The output from a Spectra-Physics Model 2020 Argon-Ion Laser was electro-optically modulated using a ConOptics Model 370 ADP Modulator situated between two Glan-laser polarizers. An HP Model 3314A Function Generator provided a 10-Hz bipolar square wave to a ConOptics Model 25 Drive Electronics Assembly which powered the electro-optic modulator. The modulator was configured to ensure extinction of the laser beam during the low portions of the square wave (i.e., 100% depth of modulation). An aperture placed after the second polarizer served to eliminate stray beams produced through optical vignetting in the modulator. A waveplate-polarizer pair permitted variable attenuation of the modulated laser flux, and the power at the filament was adjusted as described below over the range 75 - 395 mW. In these experiments, the amplified photodiode signal was captured with a LeCroy Model 9314L Digital Storage Oscilloscope. The

decay of the filament emission upon transition from the laser-on to laser-off state was digitized and averaged for 100 cycles. Averaged decay profiles were collected on a 2-mm radial grid and a 6-mm axial grid in a premixed propane-air flame. The flow rates for the flame were 0.3 slpm of propane and 5.2 slpm of air. The flame was slightly fuel-rich and displayed the usual inner-reaction-zone cone of ~ 20 mm in length.

As the temperature of the filament increased as a result of the hot gases from the flame, the laser flux used to heat the filament was reduced to minimize breakage of the filament. A temperature rise of ~ 10 K was more than adequate to achieve reliable velocity measurements in the hot portions of the flame; however, in the cold regions the filament required heating to at least the lower detectivity limit of the InGaAs detector (~ 800 K). Thus, in the cold regions, a temperature rise of 500 K was required. This high-heat-flux requirement can be reduced by employing a detector that is more sensitive in the infrared region of the spectrum; however, no adverse effects were observed when the filament was heated as described above. Extensive profiling of the flame was undertaken to demonstrate the wide range of velocity and temperature conditions under which the technique was applicable.

For determination of the filament temperature, a single-point intensity vs. temperature calibration was performed by measuring the InGaAs photodiode signal produced when the filament was heated with a propane torch ($T = 2200$ K). The focused laser beam irradiates only a small section of the filament, while a laser torch heats a much larger section; therefore, limiting apertures were positioned between the filament and the detector during all flame experiments to achieve reliable temperature measurements.

Analysis of Data

Analysis of the temperature data involves 1) normalizing the filament-emission intensity to that at a known temperature, 2) taking the natural log of the normalized emission intensity, and 3) converting the emission intensity to temperature by convoluting the blackbody equation over the wavelength-response region of the detector. Figure 1 displays the filament intensity-temperature response for the InGaAs detector utilized in this study. A least-squares fit of this curve allows the experimentally measured normalized emission intensity to be converted directly to a filament temperature. The filament temperature must then be corrected for radiation losses.

The velocity analysis is slightly more complicated because the temporal response of the filament emission must be calculated as a function of time in order to take into account the temperature and heat transfer of surrounding gases. The first step in the velocity analysis is to convert the emission intensity to a filament temperature. The next step involves a numerical fit of the experimental decay curve to obtain a velocity. A non-linear least-squares approach was adopted in which the laser flux, surrounding-gas temperature, and gas velocity were varied to match the experimentally measured decay curve. A time-dependent explicit model based upon Eq. (3) was utilized to calculate the filament-emission intensity which was then used in the fitting procedure. A Jacobian-matrix routine was employed for the least-square fitting iteration to permit the fitted parameters to be varied either together or independently.¹³ The independent fitting approach was found to be preferable because of the strong coupling between the fitted parameters. The procedure for fitting the experimental decay curve to obtain a velocity involved fitting 1) the laser flux, 2) the surrounding-gas temperature, and 3) the gas velocity. The goodness of fit (square root of the sum of the deviation of the calculated decay curve from the experimental) was utilized as the indicator of fitted error. Several iterations of the fitting process were often necessary to obtain the best fit to the experimental data.

An example of the types of fits obtained with this approach is shown in Fig. 4. Figure 4(a) displays the fit obtained under ambient conditions for an ~ 0.2-m/s nitrogen jet. The displayed data are digitized at the dropping edge of the argon-ion-laser impulse, and only the temperature decay is shown in this figure. Because the detector cannot "see" a filament emission below 670 K, the experimental temperature curve bottoms out before the calculated one. In the moderate- and high-temperature flame cases, shown in Figs. 4(b) and 4(c), the detector can accurately follow the complete decay of the filament temperature. The temperature at the end of the full decay is taken to be the actual flame temperature.

Results and Discussion

To test the TFCV technique in cold flow, a series of measurements was made on a 6-mm-diameter nitrogen laminar jet. The velocity measurements were made 2 mm above the jet exit and covered a wide range of flow conditions (0.5 - 25 slpm). Velocities obtained using the TFCV technique were compared with those obtained using an LDV instrument. The results are

shown in Fig. 5. In this figure, the velocity obtained with the TFM technique is plotted as a function of that obtained with the LDV instrument under each flow condition. Ideally the slope of the resulting line should be 1. The experimentally observed slope was 1.012, indicating close agreement between the results from the two velocimetry techniques.

To test the TFM technique under flame conditions, a premixed propane-air flame was chosen for study because of the small change in gas properties which occurs between products and reactants. This point is important when velocity measurements are to be made since both the kinematic viscosity and the thermal conductivity of the gas affect the observed rate of cooling (or heating) of the filament. In the propane-air case, a small correction was made to the calculations for kinematic viscosity and thermal conductivity to account for the compositional change. If one is studying a flame system (i.e., methane or hydrogen) in which the gas properties of the products and reactants differ significantly, then a knowledge of the variation in composition is required.

A 7 x 12 point two-dimensional grid was adopted for studying the premixed flame. Starting from 1 mm above the exit of the 10-mm-diameter burner tube, a 2-mm radial and 6-mm axial grid were used to profile the flame. Because of the symmetry of the flame, only one-half of the flame was profiled. A comparison of results obtained with the LDV and TFM instruments for the centerline profile of the flame is shown in Fig. 6. The agreement between the results achieved with the two techniques is quite good. The flame has a fuel flow rate of 0.3 slpm and an air flow rate of 5.2 slpm, resulting in an initial jet exit velocity of 0.8 m/s. The centerline velocity remains constant until the flame zone is encountered. Because of the rapid heating that occurs in the reaction zone, the gases are accelerated to ~ 2 m/s. In the post-reaction-zone regions, the hot flame gases are slowly accelerated by buoyancy to ~ 2.3 m/s. Both the LDV and the TFM techniques were able to "observe" this phenomenon.

The individual profiles obtained by the TFM technique are shown in Figs. 7 and 8. Figure 9 displays the same information but in image and contour form. Unlike the LDV technique which is restricted to the measurement of velocity, the TFM technique allows both the velocity and temperature of the flowfield to be determined. Notice that the velocity profile 1 mm above the burner [Fig. 7(a)] is a parabolic profile typical of pipe flow. Notice also that the flame is attached to the burner surface but is relatively narrow in width. At the 7-mm axial location

[Fig. 7(b)], the flame temperature has increased dramatically, and the parabolic profile has become broader due to the acceleration of hot gases. At the 13-mm position [Fig. 7(c)], the hot gases are flowing at 2 m/s, as compared to 0.8 m/s in the cold flow. The velocity profile is now dominated by the acceleration resulting from these hot gases. At the 19-mm position [Fig. 7(d)], the previously cold central core of the flame has been heated by its proximity to the hot surrounding gases, and the resulting velocity profile is flat-top in nature.

At the 31-mm position [Fig. 7(f)], the once-cold central jet has disappeared and the temperature is more uniform, resulting in a uniform flat profile. From this location to the last one at 67 mm [Fig. 8(f)], the temperature and velocity profiles narrow as the flame narrows. The temperature data indicate that the temperature profile peaks at the 43-mm location and gradually drops off, becoming more parabolic in nature downstream of this location. The velocity profiles generally follow the shapes of the temperature profiles at these downstream locations, but the overall central axial velocity of the flow gradually increases as a result of buoyancy. Notice that all aspects of the initial velocity and temperature profiles are lost at the downstream locations. The dominant effect in the velocity profile at the downstream locations is the initial rapid acceleration in the reaction zone. The near-field velocity profile, however, is very important in stabilizing the flame.

Figure 9(a) displays an overlay of the velocity contour and temperature image of the flame. For this figure the acceleration of the velocity field resulting from the high-temperature zones can be clearly seen. The slower velocity acceleration resulting from buoyancy can also be seen in the downstream portions of the flame. Figure 9(b) displays an overlay of the temperature contour and velocity image of the flame. The height of the cold inner cone is evident, along with the flame velocity acceleration with temperature.

Summary

A novel technique has been developed which allows the simultaneous measurement of temperature and velocity in combustive environments. The technique is based upon the black-body emission of a 14- μm β -SiC ceramic filament. When immersed in a combustive flowfield, the filament reacts to the hot surrounding gases and emits blackbody radiation which can be used to determine the filament temperature. Velocity measurements can be made with the

technique by heating the filament above the temperature of its surroundings and then monitoring the cooling of the filament. The velocity-measurement technique, Thin-Filament Velocimetry, is essentially the optical analog of hot-wire anemometry. A numerical fitting algorithm has been developed to predict the velocity of a filament when heated by a laser energy flux. A comparison of the results obtained with the Thin-Filament-Velocimetry method with those from a Laser-Doppler-Velocimetry technique on a cold laminar nitrogen jet indicated good agreement. Simultaneous velocity and temperature profiles were obtained on a premixed propane-air flame.

Acknowledgement

This work was supported, in part, by USAF Contract F33615-90-C-2033. The authors wish to acknowledge the technical contributions of Dr. K. Hsu and Mr. M. Post and the editorial assistance of Mrs. M. Whitaker.

References

1. V. Vilimpoc, L. P. Goss, and B. Sarka, *Opt. Lett.* **13**, 93 (1988).
2. T. H. Chen, *J. Propul. Power* **8**(1), 46 (1992).
3. T. H. Chen and L. P. Goss, AIAA-89-0156.
4. R. W. Davis, E. F. Moore, W. M. Roquemore, L. D. Chen, V. Vilimpoc, and L. P. Goss, *Combust. Flame* **83**, 263 (1991).
5. F. Takahashi and L. P. Goss, in *Twenty-Fourth Symposium (International) on Combustion* (The Combustion Institute, Pittsburgh, PA, 1992), pp. 351-359.
6. K. Hsu, L. Chen, V. Katta, and L. Goss, AIAA-93-0455.
7. L. P. Goss, T. H. Chen, V. Vilimpoc, M. E. Post, D. D. Trump, and B. Sarka, AIAA-90-0156.
8. V. Vilimpoc and L. P. Goss, in *Twenty-Second Symposium (International) on Combustion* (The Combustion Institute, Pittsburgh, PA, 1988), p. 1907.
9. L. P. Goss, V. Vilimpoc, B. Sarka, and W. F. Lynn, *Trans. ASME, J. Eng. Gas Turbines Power* **111**, 46 (1989).
10. L. P. Goss, J. R. Gord, D. D. Trump, and M. E. Post, AIAA-93-0518.
11. New Product Information (Dow Corning Corporation, Midland, MI 48686-0995, 1986).
12. Y. S. Touloukian, *Thermophysical Properties of High Temperature Solid Materials, Vol. 5, Non-oxides and Their Solutions and Mixture Including Miscellaneous Ceramic Material Properties* (MacMillan, New York, 1967), pp. 118-140.
13. E. L. Kern, D. W. Hamill, H. W. Deem, and H. D. Sheets, Special Issue, *Mater. Res. Bull.* **4**, S25-S32 (1969).

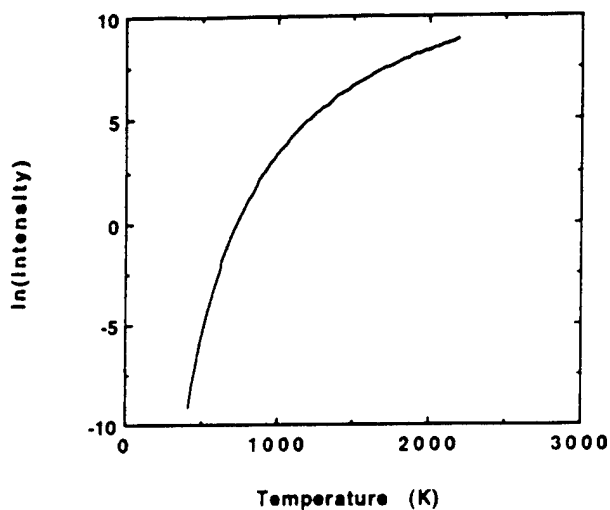


Fig. 1. Natural logarithm of filament-emission intensity as function of filament temperature, as calculated for InGaAs photodiode detector.

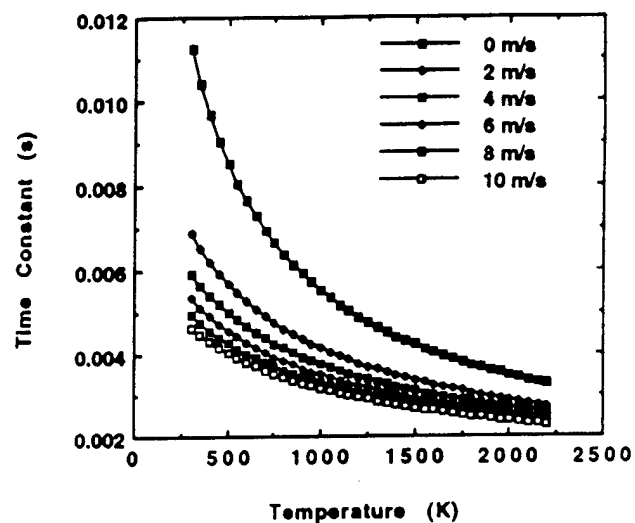


Fig. 2. Plot of convective time constant (τ) as function of gas temperature and velocity, as calculated using a modified King's-Law Nusselt-number correlation.

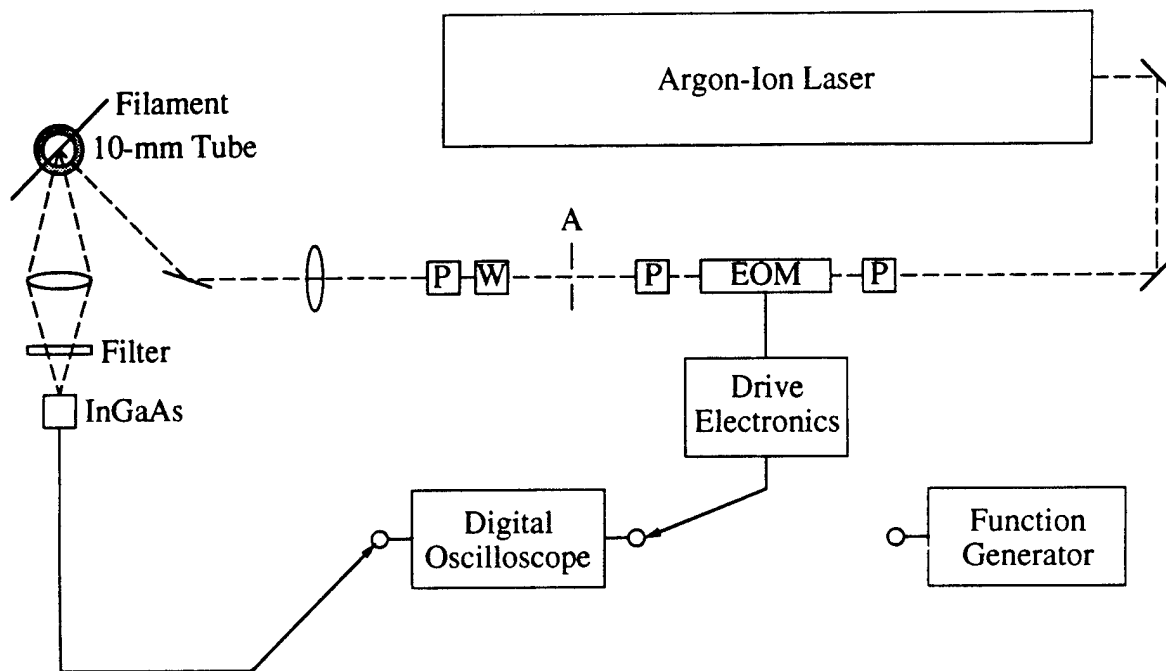
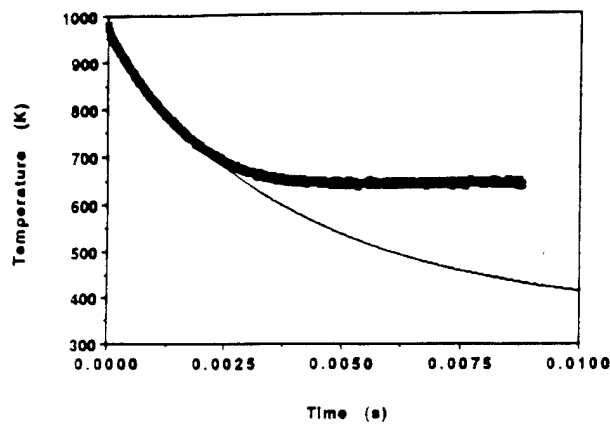
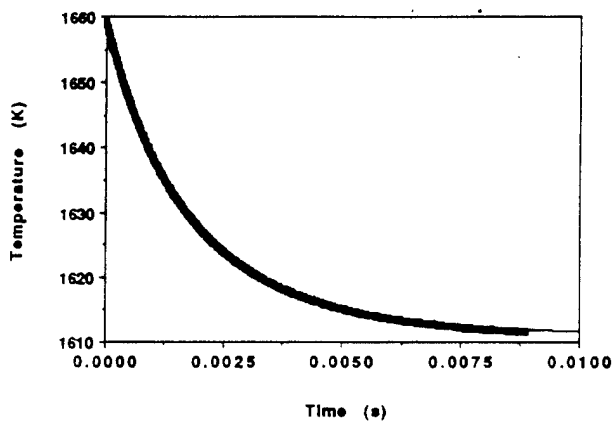


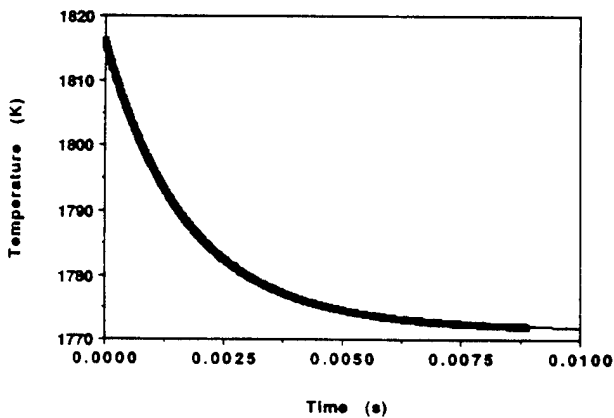
Fig. 3. Schematic diagram of experimental apparatus employed to perform Thin-Filament Velocimetry. A: aperture, EOM: electro-optic modulator, P: Glan-laser polarizer, W: $\lambda/2$ waveplate.



(a)



(b)



(c)

Fig. 4. Experimental (■) and fitted (—) temperature decays obtained in (a) cold - 0.2-m/s nitrogen jet, (b) moderate temperature - 1.8-m/s propane-air flame, and (c) high temperature - 2.3-m/s propane-air flame.

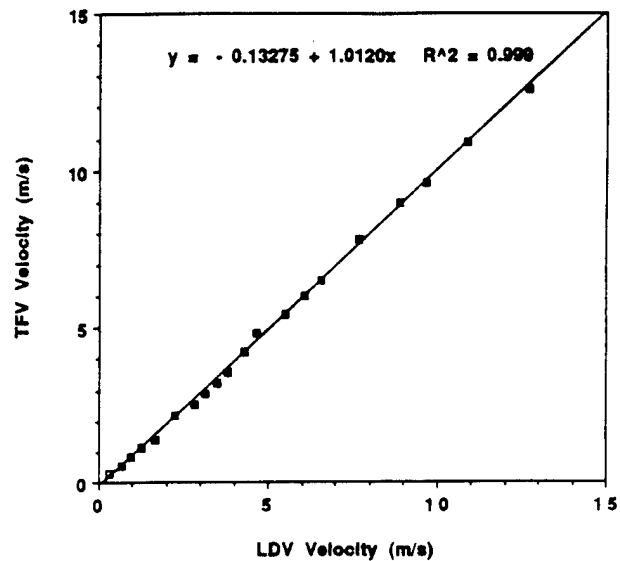


Fig. 5. Comparison of LDV and TFV velocity-measurement results obtained 2 mm above centerline of 6-mm nitrogen jet. Flow rate was varied from 0.5 to 25 slpm. Slope of linear fit to data is 1.012.

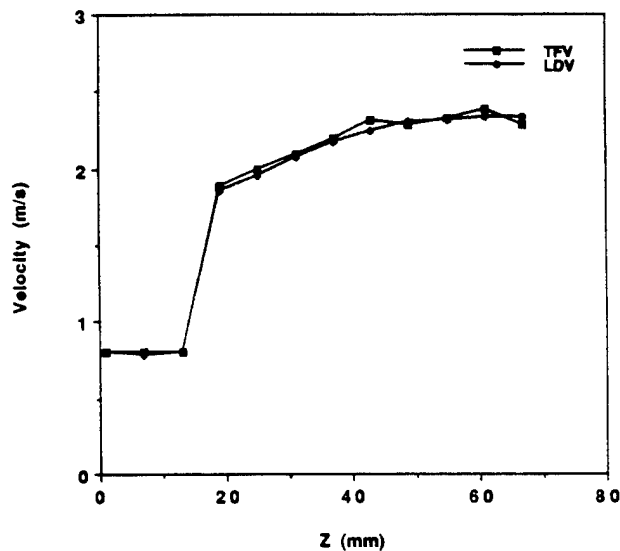


Fig. 6. Comparison of LDV and TFV velocity-measurement results obtained on centerline of premixed propane-air flame. Flow rates for flame were 0.3 slpm of propane and 5.2 slpm of air.

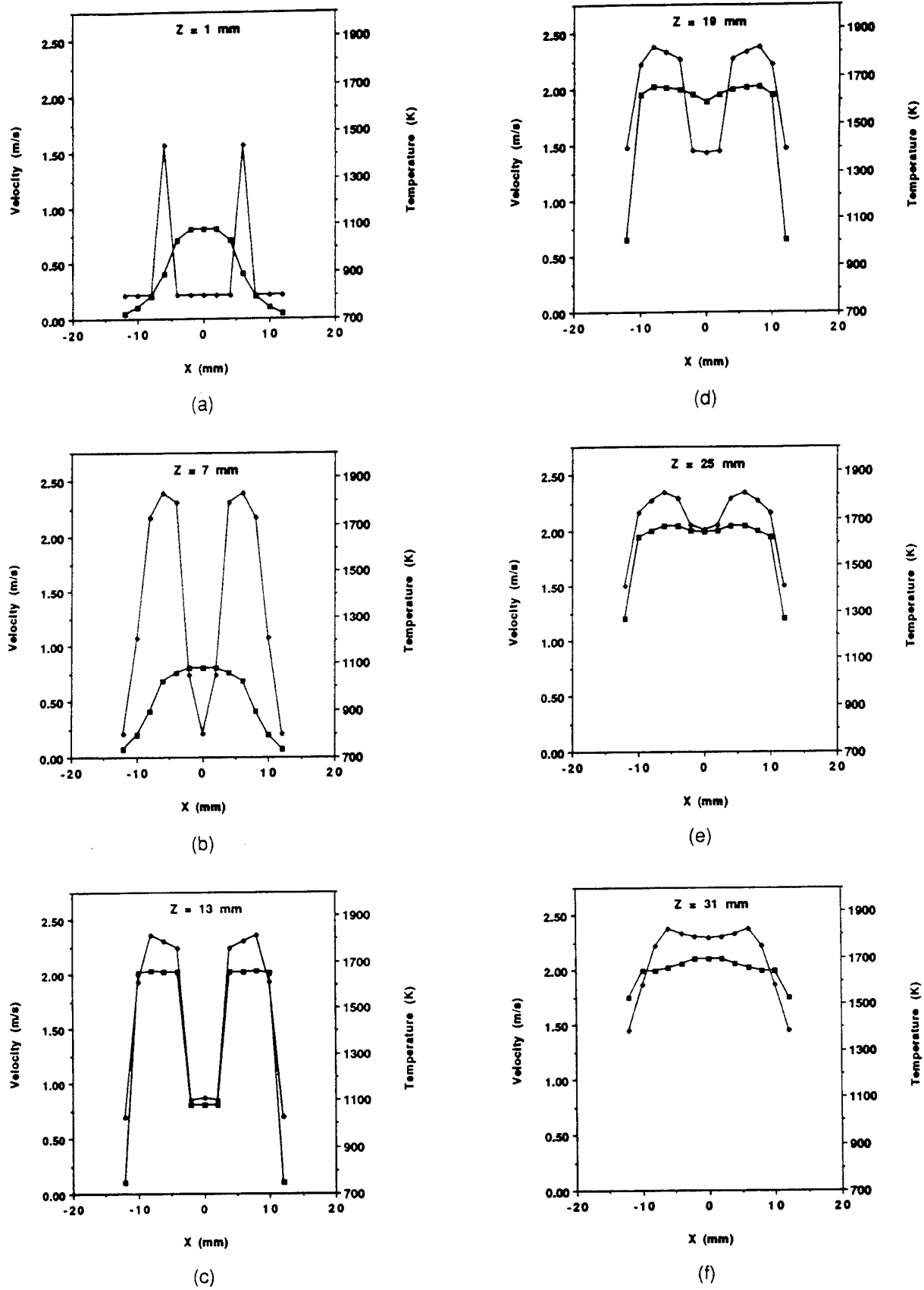


Fig. 7. Radial temperature (♦) and velocity (□) profiles at different axial locations (1 - 31 mm) in premixed propane-air flame. Flow conditions same as in Fig. 6.

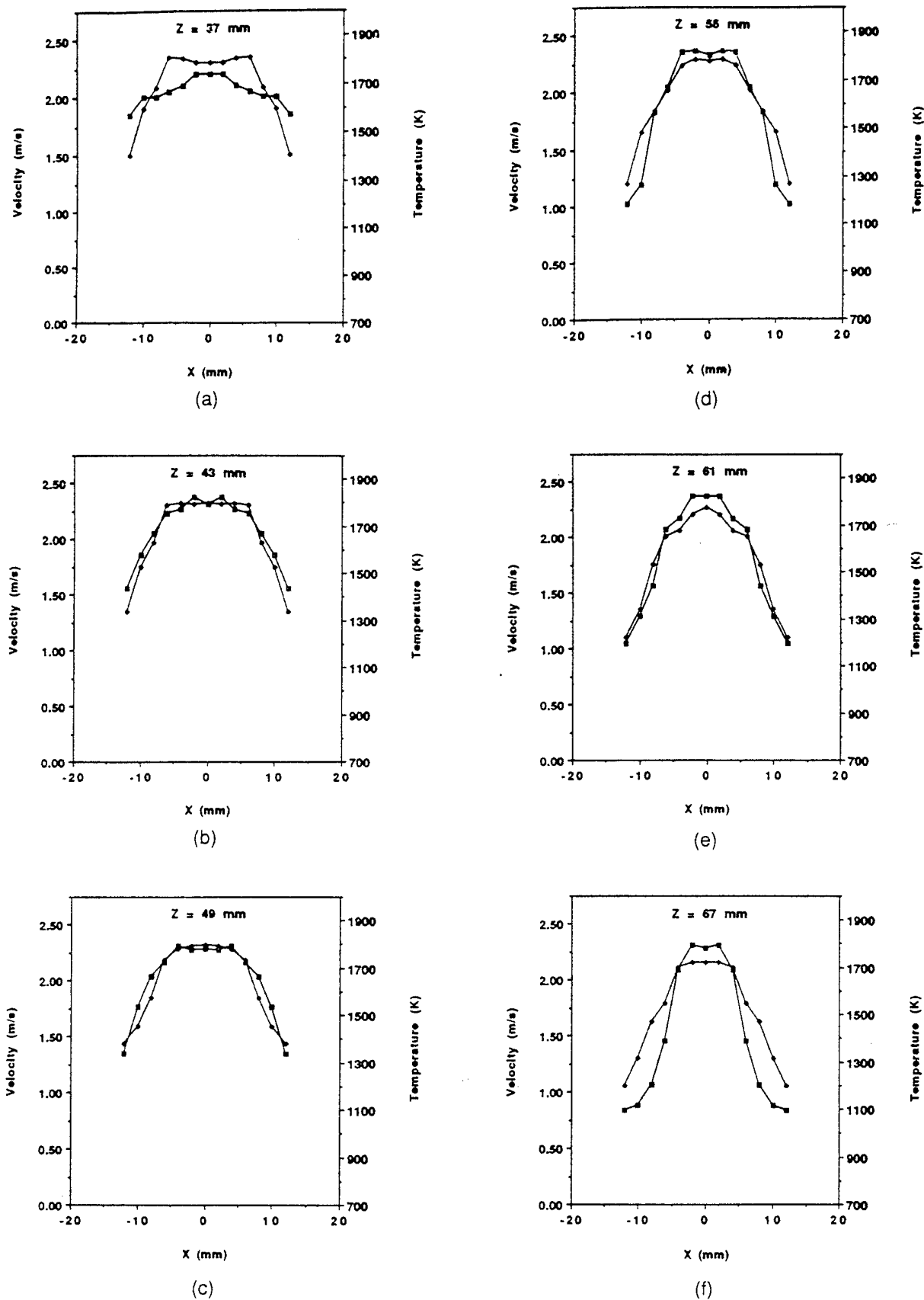


Fig. 8. Radial temperature (\diamond) and velocity (\square) profiles at different axial locations (37 - 67 mm) in premixed propane-air flame. Flow conditions same as in Fig. 6.

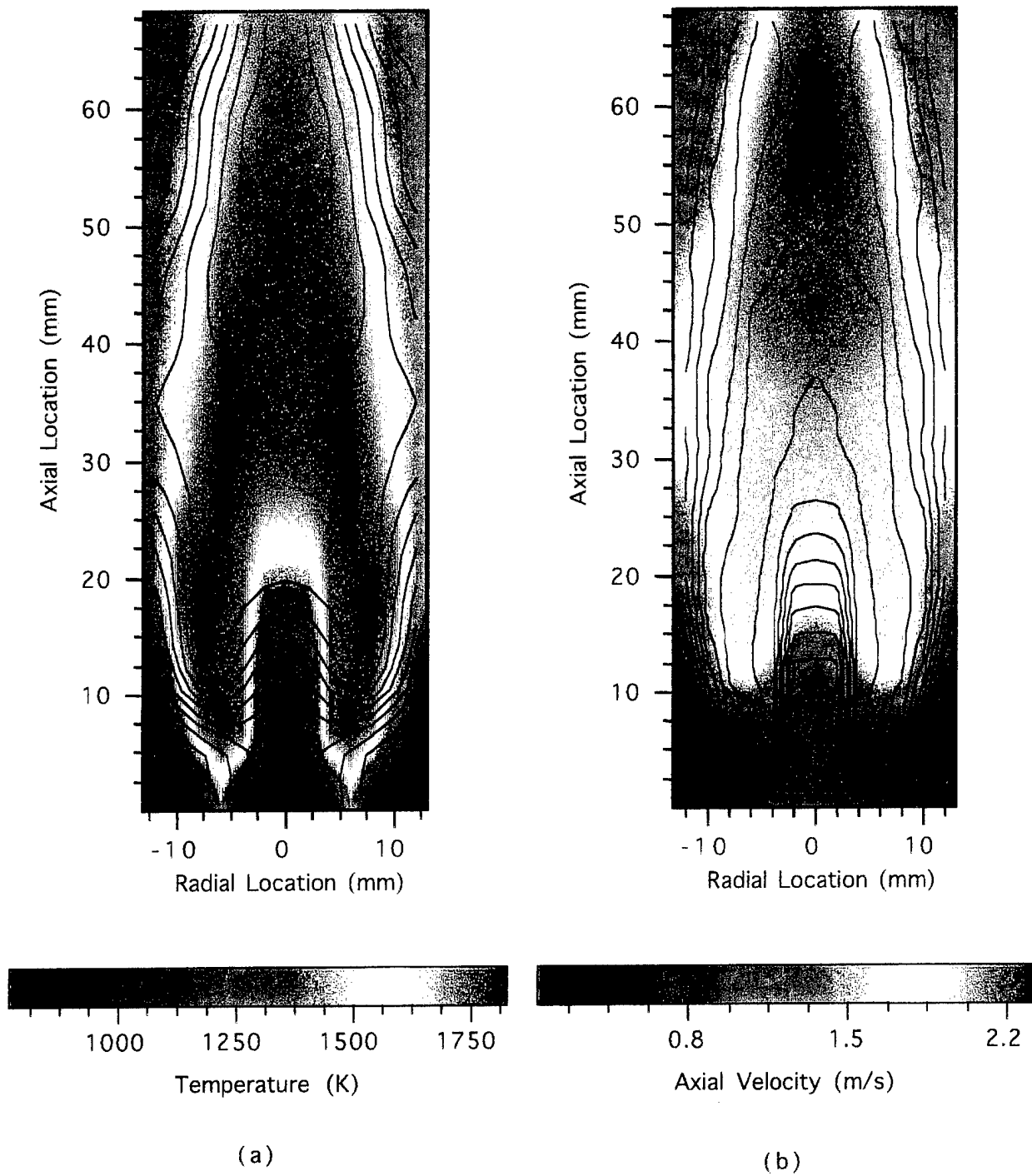


Figure 9 : Overlays of (a) velocity contours over temperature image and (b) temperature contours over velocity image of premixed propane-air flame obtained with TFM technique.

2.1.5 Droplet and Spray Diagnostics. Development and evaluation of droplet and spray diagnostic techniques requires the use of a well-characterized droplet generator. Such a generator was developed and a patent application submitted during the course of this program ["Uniform Droplet Generator: A Versatile System for Stable Generation of Uniform Droplets" (pp. 164 - 170)]. With this generator droplet evaporation rates were studied using the Phase Doppler Particle-Sizing Instrument ["Vaporization Behavior of Fuel Droplets in a Hot Air Stream" (pp. 171 - 175) and "Droplet Distributions from the Breakup of a Cylindrical Liquid Jet" (pp. 176 - 185)]. The Reactive Mie Scattering (RMS) technique was used to study droplet-vortex interactions in splitter-plate flowfields ["Two-Dimensional Shear-Layer Entrainment and Interface-Length Measurements" (pp. 186 - 199)].

A versatile system for stable generation of uniform droplets

Gary L. Switzer

Systems Research Laboratories, Inc., A Division of Arvin/Calspan, 2800 Indian Ripple Road, Dayton, Ohio 45440-3696

(Received 1 May 1991; accepted for publication 12 July 1991)

A system for the production of liquid droplets of uniform size and velocity is described. The precise control of the operating fluid provided by this system allows the generator to function in a droplet-on-demand, burst, or continuous mode of operation. The basic component of the uniform droplet generator is a radially contracting piezoelectric cylinder which forces liquid through a glass-capillary nozzle. Droplet diameters ranging from 5 to 500 μm have been produced by appropriate selection of nozzle aperture and operating mode. Further control of size, velocity, and interdroplet spacing is exercised through the voltage- and fluid-control elements of the system. In addition to its ability to operate in any orientation, the droplet generator is designed with a small cross section and a water cooling feature for operation in coflowing, elevated-temperature environments. The uniform-droplet-generation system has exhibited long-term stability in operations ranging from a single isolated droplet to a stream of calibration-standard droplets separated by center-to-center spacings of less than two diameters. Its capabilities in controlling droplet development and dynamics make it an attractive candidate for use in a wide range of liquid-droplet applications.

I. INTRODUCTION

Within the research and industrial communities involved in spray technology, the need exists for the controlled generation of liquid droplets having uniform characteristics. From the considerable amount of literature on droplet generation, two major areas of interest can be identified. In the first, the droplet produced is employed as the primary subject under scrutiny.¹⁻⁶ To reduce the potential complexity of spray or droplet systems during examination, simple interaction environments can be created with proper control over droplet production. Thus, observations of liquid-droplet dynamics can be made either in the simplest environment of an individual isolated droplet or in the progressively more complex environment of interacting or colliding droplets. In the second area of application, controlled droplet generation is employed as a source for droplets of precisely known size which serve as calibration standards for various particle diagnostic techniques.⁷⁻⁹ Although the requirements placed upon droplet-generation systems are as many and varied as the applications, these systems share certain performance considerations such as the type of liquid used, droplet size, velocity, frequency, and stability and reproducibility of operation. The most versatile system would be one exhibiting a high degree of control over each of these parameters.

Described herein is a system which has been developed to satisfy the requirements of both of these areas of application for droplet generation. The system consists of a uniform droplet generator (UDG) and associated fluid- and electrical-control components. The versatility of this system is evidenced by its ability to operate not only in any orientation and under a variety of environmental constraints but also in any one of three distinct modes. When

operating as a droplet-on-demand generator, the system can generate droplets at rates from a single droplet up to ~ 4 kHz with diameters ranging from 5 to 250 μm , depending upon the nozzle aperture selected, and velocities from 0.4 to 12 m/s. In the burst mode of operation, the droplet-on-demand action of the generator is controlled to produce bursts or packets containing a selected number of closely spaced droplets at selected intervals. For the third or continuous mode of operation, the generator operates by inducing the controlled breakup of a liquid jet as described by Rayleigh¹⁰ into droplets of desired size. Droplets ranging in diameter from 10 to 500 μm can be generated by variation of nozzle aperture, liquid pressure, and generation frequency. This mode provides a source of droplets not only for size-calibration standards but also for very closely spaced, high-volumetric flow.

II. SYSTEM DESCRIPTION

A block diagram of the complete UDG system is shown in Fig. 1. As indicated, the system consists of three separate components: a nozzle assembly (the UDG), a fluid-control component, and an electrical-control component. A detailed description of each of these elements will be given along with the operational considerations required for their optimum performance.

A. Nozzle assembly

The heart of the UDG is a lead-zirconate-titanate piezoelectric cylinder (PZT) which is 25 mm in length, having an i.d. of 0.76 mm and an o.d. of 1.27 mm. The inner and outer surfaces of the cylinder are nickel-coated elec-

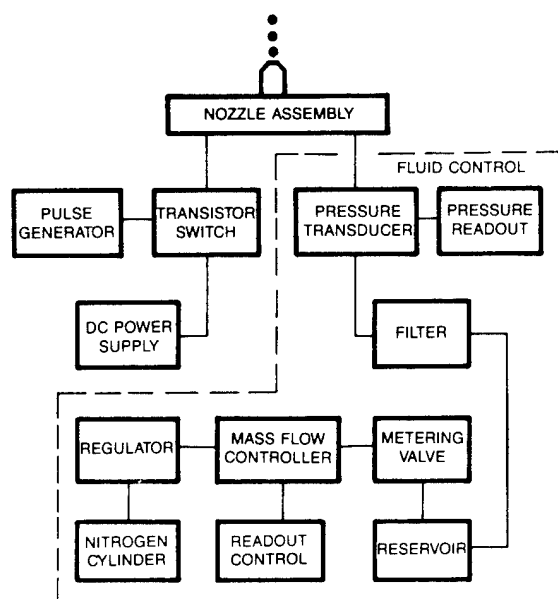


FIG. 1. Block diagram of droplet-generation system.

trodes. In operation, the cylinder is filled with a fluid, and a positive-polarity electrical pulse is applied to the inner electrode. This pulse excites the PZT to contract radially, creating a pressure wave within the fluid. The pressure wave radiates along the axis of the cylinder and is focused into a circular orifice by a tapered glass nozzle. With a proper balance among fluid viscosity, static pressure, orifice quality, and dynamic pressure (PZT drive-voltage amplitude), a single drop will be formed from the liquid which is forced through the orifice.

The most versatile configuration of the droplet generator is shown schematically in Fig. 2. The PZT is held by a mild press-fit in a threaded stainless-steel holder and sealed in place by two "O" rings. The tight fit of these two pieces provides electrical contact with the outer (ground) electrode of the PZT. Approximately 2 mm of the outer electrode is removed from each end of the PZT to ensure that electrical isolation will be maintained between the inner and outer electrodes in the presence of the working fluid. The output end of the PZT is capped by a glass nozzle which is epoxied into a nylon nozzle holder. This nonconducting holder is sealed by the upper O ring in the area where the electrode has been removed to prevent leakage of either the flowing liquid or the electrical charge carried by the inner electrode. The nozzle holder is pressed into position by threading a tapered nylon tip onto the PZT holder. This combination of tip and nozzle holder provides a very convenient and reliable method for removing a nozzle for cleaning, changing aperture size, or incorporating a different type of aperture. The opposite end of the PZT receives the fluid and electrical inputs. Contact with the inner electrode is accomplished through a connector fabricated from 0.58 mm i.d. \times 0.81 mm o.d. \times 5 mm long stainless-steel tubing. A 0.1-mm-wide slot is made along the length of the tube to produce a split ring which can be compressed, inserted into the end of the PZT, and

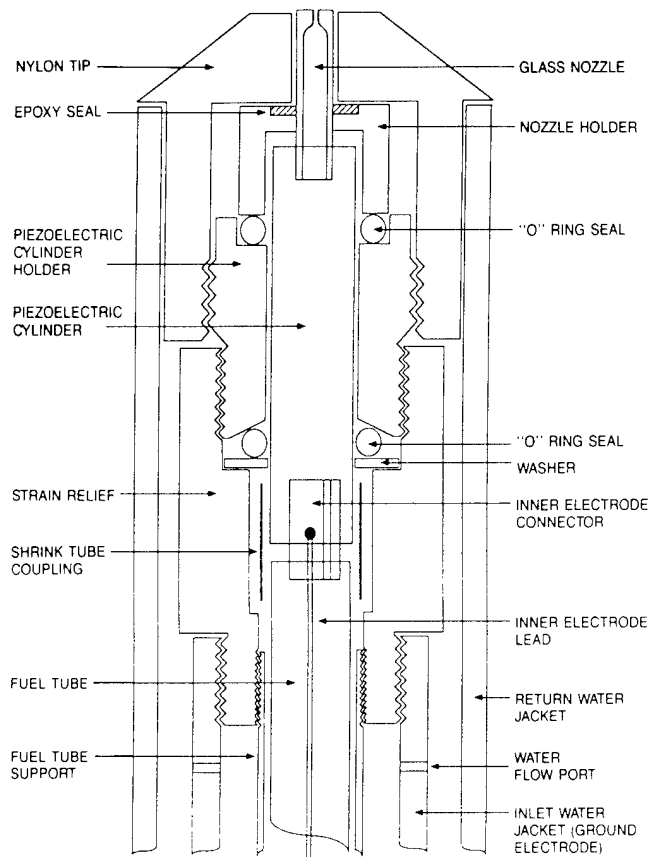


FIG. 2. Schematic diagram of temperature-controlled uniform droplet generator.

allowed to expand to contact the inner surface. A single fold in the end of a stripped 30 AWG wire is sufficient to make a firm contact with the inside of the split ring and completes the connection for the inner electrode lead. The remaining input to the PZT, the liquid path, is accomplished by the coupling of a 0.56 mm i.d. \times 0.86 mm o.d. piece of Teflon fuel tubing to the PZT. This coupling is made with shrinkable Teflon tubing applied between the fuel tube and the outer (electrode-free) end of the PZT.

One of the major assets of the UDG design is the small diameter of the piezoelectric cylinder. Its small size allows it to be placed very near the nozzle to optimize dynamic control over fluid pressure at the orifice. Since the total diameter of the configuration in Fig. 2 is 5.18 mm, the resulting small cross section of the PZT and its mounting allows convenient insertion into flowing external media with a minimum of perturbation. It should be pointed out that this small size of the PZT also constitutes a weakness. That is, the 0.51-mm-thick shell of the PZT is somewhat fragile and, therefore, susceptible to breakage by compressional or torsional forces. The mounting of the piezoelectric cylinder consisting of the PZT holder and strain relief was designed to protect the PZT as much as possible from mechanical stress by providing an external anchor for the necessary attachments. If the limitations associated with larger size were not a consideration, the UDG could, of

course, be designed to employ a larger diameter, more rugged PZT cylinder.

The remaining components shown in Fig. 2 (the fuel-tube support and inlet and return water jackets) are employed to extend the utility of this generator to operation in elevated-temperature environments. For studies such as those to determine droplet-evaporation rates,⁴ it is advantageous to inject droplets into coflowing, heated air. To accomplish this, two additions are made to the basic UDG. First the fuel and electric feed paths are lengthened to permit insertion of the UDG coaxially into the flow a sufficient distance to facilitate development of a laminar environment; this can result in feed lines being as long as 1 m. The second addition involves insulation of the fuel tube from the potentially high-temperature surrounding environment by means of a water jacket. With low-boiling-point liquids such as hexane and decane, the heat from the surrounding flow field can cause vaporization of the fuel within the fuel tube before it reaches the generator tip, prohibiting droplet formation.

The addition of two concentric tubes [inner (2.36 mm i.d. \times 3.07 mm o.d.) and outer (4.29 mm i.d. \times 5.18 mm o.d.)] creates a water jacket in which temperature-controlled water is forced through the inner water tubing and flows along the fuel tube through holes near the generator tip and returns inside the outer tubing. This cooling configuration has been demonstrated to be effective at temperatures up to 600 K. These two tubes also provide a very stable support structure for the droplet generator. Water cooling of the UDG probe required one other design consideration. The disturbance of the cooling water flowing around the Teflon fuel tube creates pressure fluctuation in the fuel flow which is sufficient to prevent stable droplet formation. To eliminate this problem, a fuel-tube support fabricated from 1.07 mm i.d. \times 1.47 mm o.d. stainless-steel tubing is used to protect and hold the flexible fuel tube.

Without the considerations for cooling of the droplet liquid or aerodynamic compatibility, the complexity of this generator can be reduced considerably. The schematic diagram in Fig. 3 shows the basic configuration and its complete feed connections as contained in a 7.5 cm \times 10.0 cm \times 2.5 cm package. Designed for bench-top applications, this compact configuration operates very reliably in environments not requiring streamlined delivery or cooling capability.

B. Nozzle fabrication

Three types of apertures have been adapted for use with the UDG. Two of these are commercially available. The first is a 3 mm disk made from 40- μ m-thick nickel containing a laser-drilled pinhole. A wide range of these aperture sizes is readily available from several suppliers. The second is a 0.90-mm-diam \times 0.24-mm-thick synthetic ruby substrate containing an 80- μ m-diam drilled hole. While droplet-on-demand operation was possible with these two types of apertures, performance was unstable and a greatly increased PZT pump-voltage threshold (150–200 V) was required. The third type of aperture, which is a custom-made glass nozzle as shown in Fig. 4, has proved to

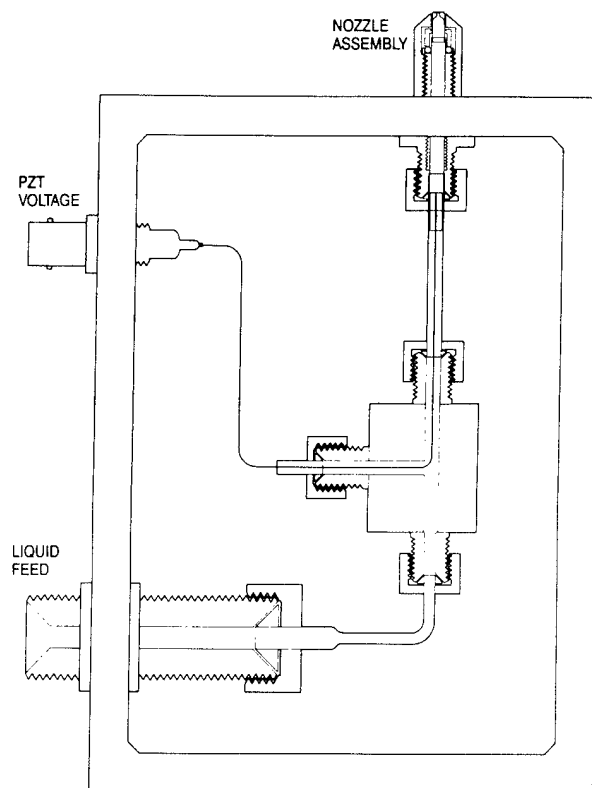


FIG. 3. Schematic diagram of basic generator configuration.

be the most desirable. The glass nozzle used in this configuration is fabricated from round-capillary Pyrex tubing (0.5 mm i.d. \times 0.7 mm o.d.). The tubing is cleaved into 19 mm blanks; one end of the blank is polished using a water

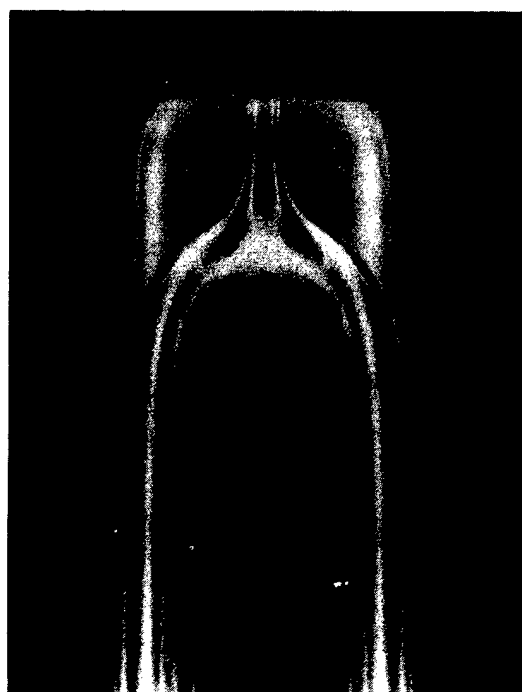


FIG. 4. Photograph of glass nozzle.

slurry of 17 μm aluminum-oxide powder to yield a uniform, normal surface. The blank is cleaned and then rotated with its axis held vertically over a small propane flame which gently and uniformly heats the polished end. As the end of the capillary is heated, it slowly contracts in length and inside diameter while its outside diameter remains nearly constant. As observed through a microscope, this contraction can be halted at any desired diameter by removing the flame. At this point the tip end of the blank contains a smooth, uniformly tapered transition between the original inside diameter of the capillary and a circular passage of the desired reduction. The rounded tip surface produced by the fire "polishing" is then removed by polishing with successively finer grades of aluminum-oxide polishes until a flat, scratch-free surface is obtained; a 1 μm micropolish is usually sufficient. The nozzle is completed by cleaving ~ 6.0 mm off the tip end of the blank. This nozzle can then be mounted in the nozzle holder.

In nozzle fabrication, several parameters greatly influence the efficiency and quality of droplet generation. The inside bore of both the capillary and its reduced passage should be smooth, coaxial, and symmetric. A short, uniform-taper transition section leading into a short, round passage is most desirable. Perhaps the characteristic most critical to successful performance is that defined during the final-polishing phase in nozzle construction. The main objective of the fine polish is to obtain a sharp, clean edge on the glass orifice since any crack or chip in this edge can facilitate the formation of multiple droplets or undesirable satellites.

C. Fluid control

Stable control over the fluid pressure is essential to the long-term production of uniform droplets. Additionally, since the volume flow of fluid required for generation of micron-sized droplets on demand is quite small, extremely high resolution in control is needed. The fluid-control elements employed to meet these requirements in the UDG system are outlined in Fig. 1. Bottled nitrogen is used as a pressurizing source gas. Its output is pressure regulated, and the gas volume flow is regulated by use of a mass-flow controller. A steady flow of ~ 100 ml/min enters the fluid reservoir. The pressure within the reservoir is set by venting excess gas through a fine bellows metering valve. The fluid is forced from the reservoir and filtered of particles, and its pressure is monitored as it is fed into the UDG. This configuration provides pressure resolution which is better than 7 Pa and stability on the order of ± 20 Pa/h.

While the fluid-control system described provides optimum control for long-term stable operation in all modes, shorter periods of operation can be attained with less sophisticated pressure delivery. Compressed or "shop" air regulated to a sufficiently low pressure and restricted by a series flow valve has been used to replace the nitrogen bottle and mass-flow controller. A syringe pump can be used to provide the total fluid-control element for those applications where the generator is operating in the continuous mode and a measured volumetric flow is of greater

importance. For the droplet-on-demand and burst modes of operation, the stability and resolution of syringe pumps are presently inadequate. The simplest fluid-control system, a gravity-fed reservoir, exhibits quite adequate performance, primarily in applications where the position of the droplet source can remain stationary.

D. Electrical control

Electrical control over the operation of the piezoelectric cylinder is exercised by three elements, as shown in Fig. 1. The amplitude of the potential impressed upon the PZT is developed and controlled by a 0–300 V dc power supply. An *n-p-n* switching transistor or an *N*-channel metal-oxide-semiconductor field effect transistor (MOSFET) is used in series with a high-wattage ballast resistor across the power-supply output to form the transistor switch. The transistor-switching action is controlled by a pulse generator. The positive-voltage pulse developed across the transistor in this manner is impressed upon the PZT.

For optimum system operation, the dc power supply must fulfill several requirements. The maximum voltage is chosen such that it will not exceed the voltage limitations of between 500 and 1000 V/mm for depolarization or dielectric breakdown of the piezoelectric material. A wide range of adjustment in the supply is required. To initiate droplet generation, a 250–300 V pulse amplitude is occasionally required; however, once the fluid path becomes purged of gas pockets, a voltage threshold of 20–30 V is commonly required to maintain operation. Additionally, a stable output with highly resolved adjustment is essential. Output-amplitude variations as small as 10 mV have been observed to affect droplet characteristics. A ten-turn potentiometer has proved to provide adequate resolution of the 0–300 V dc supply.

Pulse characteristics such as width, rise and fall times, and repetition rates are controlled through the pulse generator. Typically, a square-edged pulse of 30 to 60 μs duration is required. Investigations into the effects of edge-transition times have shown that there is little or no improvement in operation to be gained by varying pulse shape. Repetition-rate requirements can range from a single pulse up to ~ 20 kHz for continuous operation. Burst-mode operation requires a second pulse generator which can be used to regulate or gate the operation of the first.

III. SYSTEM PERFORMANCE

A. Droplet-on-demand operation

Operation of the UDG in the droplet-on-demand mode is shown in Fig. 5. This composite of five photographs depicts the evolution of a 50 μm droplet having a velocity of 1 m/s (vertically upward) from the initial PZT compression of the water column (bottom) to a fully formed, stable liquid sphere (top). This transition from puddle to droplet is influenced (for a given liquid) by the PZT voltage amplitude and pulse width, liquid pressure, and aperture size. The diameter of the droplet produced is generally

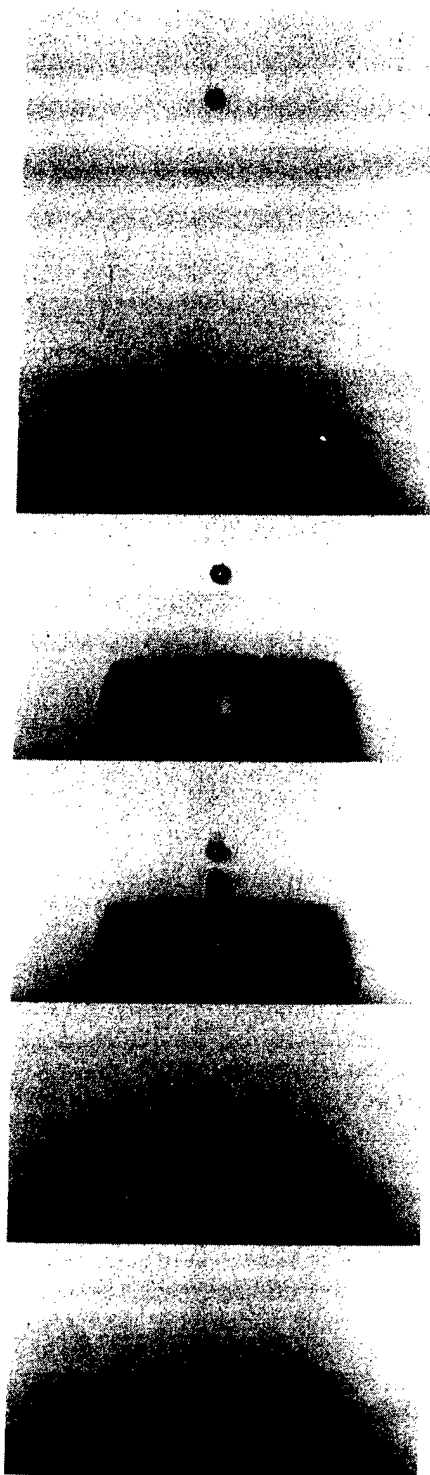


FIG. 5. Photographs showing droplet-on-demand evolution.

the same as that of the nozzle orifice, although much smaller or much larger droplets can be "locked in" during operation. Fine adjustments to droplet diameter (in the range of $\pm 10\%$) can be accomplished by exploiting the direct relationship which exists between the diameter and the PZT voltage and liquid pressure. The sensitivity of the droplet velocity to the PZT voltage can be exploited for independent adjustment of the velocity of a droplet of

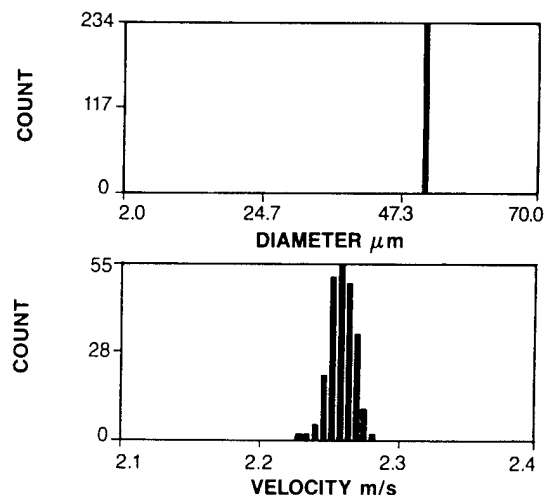


FIG. 6. Histogram of size and velocity for 1 Hz droplet generation. Rate: 224 droplets/228.2 s; Diameter mean: 52.0 μm ; Velocity: mean=2.260 m/s, rms=0.009 m/s.

given diameter. Velocity adjustments by a factor of 2 or more are possible within the limits of stable droplet formation.

The uniformity and stability of the droplets generated in this mode are indicated for generation rates of 1 Hz, 100 Hz, and 2 kHz from an $\sim 55\text{-}\mu\text{m}$ -diam orifice in Figs. 6, 7, and 8, respectively. These plots obtained with the phase Doppler particle analyzer⁹ indicate uniform size droplets at each repetition rate to within the 1.4 μm resolution of the diameter range plotted. The small fluctuation in the mean velocity indicated in each of the velocity distributions is believed to be due primarily to slight turbulence in the coflowing air into which these drops are generated. Although the longest period of operation for the data accumulation indicated in these plots is ~ 5 min (Fig. 7), similar "snapshots" of uniformity have demonstrated long-term stability over periods of time as long as 4 h.

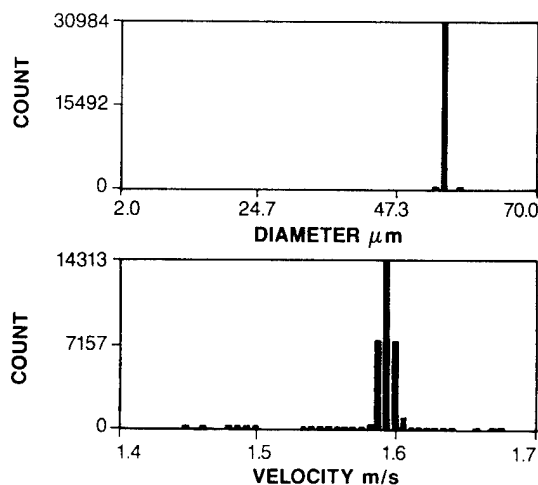


FIG. 7. Histogram of size and velocity for 100 Hz droplet generation. Rate: 30001 droplets/304.6 s; Diameter mean: 56.1 μm ; Velocity: mean=1.781 m/s, rms=0.005 m/s.

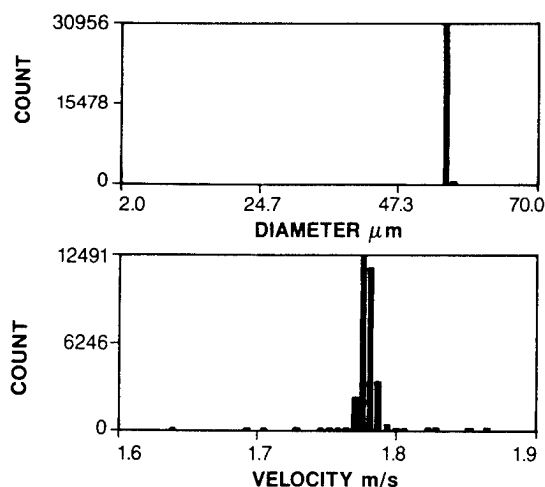


FIG. 8. Histogram of size and velocity for 2 kHz droplet generation. Rate: 30004 droplets/15.2 s; Diameter mean: 56.1 μm ; Velocity: mean=1.596 m/s, rms=0.005 m/s.

Since droplet-on-demand velocities are controlled primarily by the PZT-drive-voltage amplitude and pulse width, caution against the application of excessive voltage is warranted. Two adverse conditions can be created if the amplitude of the driving voltage becomes excessively high for a given liquid. The first and more obvious of these is the production of multiple droplets of varying size with a single pulse. The second condition is related to the pumping action of the PZT and the vapor pressure of the liquid. Excessive expansion of the PZT can cause cavitation within the liquid, resulting in the creation of vapor bubbles. These bubbles can become trapped within the UDG nozzle and destroy the uniformity and stability of droplet production. Under most circumstances the difference which exists between the voltage amplitude required for stable performance and that which produces cavitation is sufficient to prevent overlap. For example, water droplets having velocities of several meters per second can be produced stably with 30 V, while vapor bubbles begin to form at ~ 140 V. It is primarily in situations where the PZT voltage must be increased in order to overcome a grossly inefficient nozzle or to produce droplets having very large velocities that problems due to cavitation effects arise.

B. Burst-mode operation

Generator operation in the burst mode is basically the same as that described for droplet-on-demand operation. However, the addition of a second pulse generator in the electrical-control element allows modification of the PZT-drive-voltage pulse train for production of a burst or packet of individual droplets. An example of burst-mode operation is shown photographically in Fig. 9, with droplets being generated vertically upward. In this example, the primary pulse generator is set to drive the PZT with ~ 40 μs pulses at a rate of 1 kHz (1 ms between droplets). The second pulse generator is employed to gate the 1 kHz oscillator into operation for a period of 3.5 ms at a rate of 100 Hz. These conditions result in bursts containing three

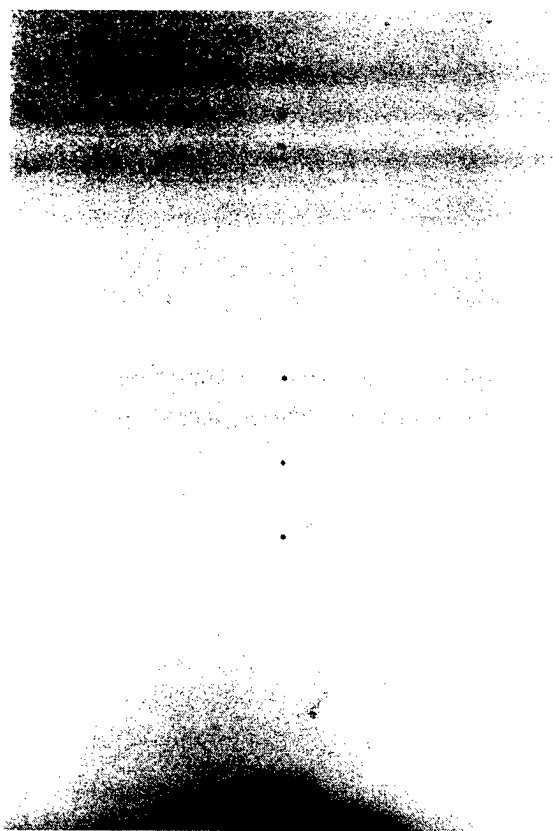


FIG. 9. Photograph showing burst-mode operation.

droplets having interdroplet temporal spacings of 1 ms and packet separations of 10 ms. Any combination of burst dimensions can be achieved by simple adjustment of these three parameters.

The utility of burst-mode UDG operation makes it advantageous for studies such as interaction of droplets in controlled proximity as well as flow-field dynamics. Some effect of flow dynamics upon droplet behavior are evident in Fig. 9. Here the local turbulence and nonlinear slip velocities experienced by the upper packet in the surrounding air flow have noticeably modified the upper burst structure.

C. Continuous-mode operation

To achieve continuous-mode UDG operation such as that shown in Fig. 10, the liquid pressure is increased until a continuous jet is formed through the orifice. The PZT excitation is then adjusted to a suitable resonance frequency which forces the jet to break up into uniform droplets. In the figure, 116 μm droplets are being produced at a rate of 8.2 kHz from an ~ 55 μm orifice. Since the volumetric flow of the liquid is defined by the liquid pressure and the orifice size, the frequency driving the droplet breakup is the major size-controlling factor. The stability of the droplets generated is also primarily a function of pressure and frequency. An inverse relationship between frequency and droplet size exists which allows a wide range of regularly sized and spaced droplets to be generated.

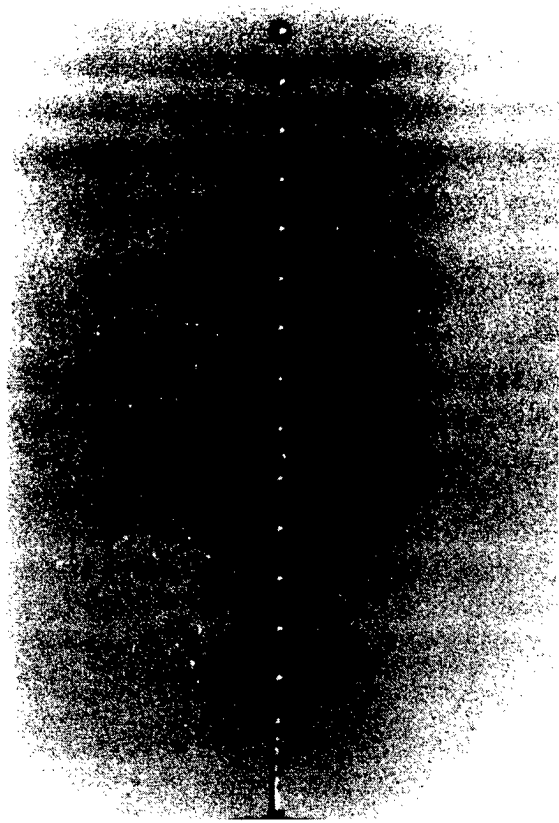


FIG. 10. Photograph showing continuous-mode operation.

In contrast to the other two operating modes, the droplet diameter generated in the continuous mode is generally twice that of the orifice employed. This relationship can be exploited to allow selection of the orifice diameter required to produce a desired droplet size or, conversely, to estimate

the orifice size based upon an observed droplet diameter. The amplitude and waveshape of the driving voltage are also much less critical in the case of continuous operation. Voltages of less than 5 V are sufficient to cause jet breakup, with higher amplitudes forcing breakup only slightly sooner. The waveshape driving the PZT can vary among sinusoidal, square, triangular, and pulsed, with little or no detrimental effect upon droplet formation.

ACKNOWLEDGMENTS

The pioneering efforts of Benjamin Sarka, Jr. in the initial development of a droplet-on-demand capability are gratefully acknowledged. This work was supported by and performed at the Aero Propulsion and Power Directorate, Wright Laboratory, Wright-Patterson Air Force Base, Ohio, under contract F33615-90-C-2033.

¹W. A. Sirignano and C. K. Law, in *Advances in Chemistry Series, No. 166-Evaporation-Combustion of Fuels*, edited by J. T. Zung (American Chemical Society, Washington, DC, 1978), pp. 3-26.

²I. K. Puri and P. A. Libby, "Droplet Behavior in a Counterflowing Flame," AIAA-88-42, American Institute of Aeronautics and Astronautics, Washington, DC, 1988.

³R. W. Park and E. J. Crosby, *Chem. Eng. Sci.* **20**, 39 (1965).

⁴S. K. Aggarwal, C. Chen, T. A. Jackson, and G. L. Switzer, *Int. J. Heat Mass Trans.* (to be published).

⁵Z. T. Deng and S. M. Jeng, "Numerical Simulation of Droplet Deformation in Convective Flows," AIAA-90-2309, American Institute of Aeronautics and Astronautics, Washington, DC, 1990.

⁶D. Dunn-Rankin, G. L. Switzer, C. A. Obringer, and T. A. Jackson, *Appl. Opt.* **29**, 3150 (1990).

⁷R. N. Berglund and B. Y. H. Liu, *Environ. Sci. Technol.* **7**, 147 (1973).

⁸B. Y. H. Liu, R. N. Berglund, and J. K. Agarwal, *Atmos. Environ.* **8**, 717 (1974).

⁹W. D. Bachalo and M. J. Houser, "Development of the Phase/Doppler Spray Analyzer for Liquid Drop Size and Velocity Characterizations," AIAA-84-1199.

¹⁰L. Rayleigh, *Proc. London Math. Soc.* **10**, 4 (1879).

Vaporization behavior of fuel droplets in a hot air stream

S. K. AGGARWAL and G. CHEN

Department of Mechanical Engineering, University of Illinois at Chicago,
 P.O. Box 4348, Chicago, IL 60680, U.S.A.

and

T. A. JACKSON and G. L. SWITZER

Wright Patterson AFB, OH 45433, U.S.A.

(Received 24 January 1990 and in final form 14 November 1990)

1. INTRODUCTION

THE GASIFICATION behavior of a liquid droplet provides a fundamental input for the modeling of many spray systems, and has been studied extensively [1–4]. Theoretical analysis for the multicomponent fuel droplet presents several complexities absent in a similar analysis for the single component droplet. First, the phase-change process at the droplet surface and the transport of a fuel vapor mixture in the gas phase need to be properly described. Second, the evaporation process is inherently time varying due to the continuous change in the composition and temperature of the droplet as vaporization proceeds. Another difference between the two cases is due to the phenomenon of microexplosion [2].

The earlier viewpoint [2] of multicomponent droplet vaporization assumes that the composition and temperature within the droplet are spatially uniform but time varying. Such theories predict that the gasification process is similar to batch distillation in that the sequence of gasification is controlled by the volatility differentials among the different components. However, Sirignano [4] showed that even in the limit of high vortex strength, the internal liquid circulation can only reduce the characteristic length scale for diffusion by a factor of three. Landis and Mills [5] investigated the vaporization of a bi-component fuel droplet in a stagnant atmosphere. A quasi-steady gas-phase model was used and the equations governing the unsteady mass and heat diffusion within the droplet were solved numerically. Results when compared with rapid mixing behavior showed significant differences. A unique feature of the diffusion-dominated droplet gasification mechanism is the possible attainment of approximately steady-state temperature and concentration profiles within the droplet, which then leads to a steady-state gasification rate. Based on this concept, Law and Law [6] formulated a d^2 -law model for multicomponent droplet vaporization and combustion.

As indicated above, the literature on the gasification behavior of an isolated droplet is extensive. However, most of these studies deal with droplet combustion or evaporation under high-temperature conditions. Not much information is available on the behavior of evaporating droplets in relatively low-temperature air streams. Under such conditions, the possibility of an envelope flame is precluded and the droplet gasification rate is low. The droplet heat-up time may not be negligibly small compared to its lifetime, although the latter is relatively large and the liquid-phase transient processes may still be important.

In this paper, the vaporization behavior of pure and multicomponent fuel droplets flowing in a well-characterized laminar flow is studied. The predictions of three vaporization models are compared with the experimental data.

2. THEORETICAL MODEL

The theoretical model involves the calculation of velocity, size, and surface properties of an evaporating droplet along

its trajectory in a laminar hot air flow. The time-dependent Lagrangian equations for the droplet position, velocity, and size are solved numerically.

In most circumstances, the gas-phase transient time is much smaller than the characteristic time for the liquid-phase processes. Consequently, the gas-phase processes can be considered as quasi-steady and the equations can be solved analytically [3] for the non-dimensional mass evaporation rate \dot{m} , the fractional mass evaporation rate ε , and the effective latent heat \hat{H} as

$$\dot{m} = \ln \left(1 + \frac{Y_{fs} - Y_{fx}}{1 - Y_{fs}} \right) \quad (1)$$

$$\varepsilon = \frac{\dot{m}_i}{\dot{m}} = Y_{fs} + (1 - Y_{fs}) \frac{Y_{fs} - Y_{fx}}{Y_{fs} - Y_{fx}} \quad (2)$$

$$\hat{H} = \frac{(1 - Y_{fs})(\hat{T}_x - \hat{T}_s)}{Y_{fs} - Y_{fx}} \quad (3)$$

At any given time instant, the gas-phase species mole fraction at the droplet surface can be obtained by means of Raoult's law

$$X_{is} = X_i X_{oi} \quad (4)$$

where X_{oi} is the equilibrium vapor mole fraction for the pure liquid i given by the Clausius–Clapeyron relation

$$X_{oi} = (1/P) \exp \{ L_i W_i / R[(T_{ib})^{-1} - (T_i)^{-1}] \}. \quad (5)$$

Finally, X_{is} is related to the gas-phase species mass fraction, Y_{is} , through

$$Y_{is} = X_{is} W_i \left\{ \left(1 - \sum_{i=1}^n X_{is} \right) + \sum_{i=1}^n X_{is} W_i \right\} \quad (6)$$

where W_i is the ratio of the molecular weight of the i th vaporizing species to an average molecular weight of all the non-condensable inert species at the droplet surface. As indicated above, the liquid-phase transient processes appear through the variables X_{is} and T_s . To examine their influence, three liquid-phase models considered are the infinite-diffusion, diffusion-limit and thin-skin models. The first two models have been described elsewhere [7, 8]. The implicit assumption in the infinite-diffusion model is that the internal circulation is so fast that the droplet temperature and composition are maintained spatially uniform, though still temporally varying. The volatile components are continuously brought to the droplet surface where they are preferentially vaporized. The temporal variations of droplet composition and temperature are determined from the overall mass and energy conservation equations [8]. In the diffusion-limit model, the transient heat and mass transport in the liquid are assumed to be governed by the unsteady heat and mass diffusion equations [7].

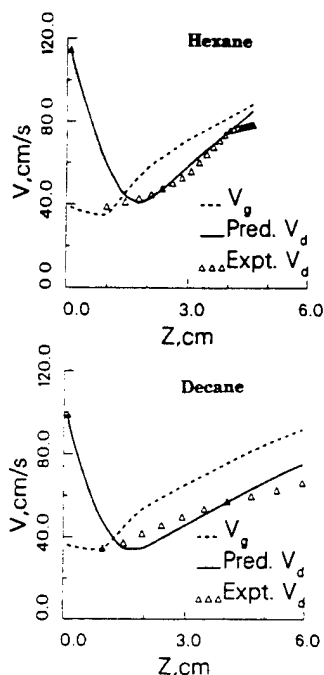


FIG. 1. Comparison of predicted and experimental droplet velocity along the trajectory.

Figure 2 shows the variation of the droplet diameter squared obtained experimentally and predicted by the thin-skin, diffusion-limit and infinite-diffusion models. Note that several data sets were obtained to assess the repeatability of data, although only one is shown. The overall agreement between predictions and experiments is quite good. For hexane, the calculated values are not very sensitive to the models. However, for decane, some sensitivity to the models is indicated, where the diffusion limit and infinite diffusion models show better agreement with the experimental data compared to the thin-skin model. These results can be explained by following the droplet surface temperature history. For hexane, the boiling temperature is relatively low, and the evaporation proceeds at a relatively fast rate. However, the latent heat needed for phase change is more than the heat transferred to the droplet surface. Consequently, the surface temperature would decrease until the heat needed for evaporation is provided by the ambience. Therefore, the wet-bulb temperature is below the initial droplet temperature. The liquid-phase transient time is very short, and all three models predict almost the same surface temperature and, therefore, the droplet size variation is not sensitive to the models. For decane, however, the wet-bulb temperature is relatively high and the droplet transient heating becomes important. As a result, the vaporization behavior is sensitive to the models. Initially, the evaporation rate is very low and the amount of heat needed for evaporation is smaller than the heat transferred to the droplet surface. Consequently, the droplet temperature keeps increasing until it reaches an equilibrium temperature. Because the thin-skin model neglects the transient droplet heating, it predicts a faster vaporization rate than the other two models. Thus, the important observation is that the difference between the models is more significant for heavier fuels which have higher boiling temperatures and, thus, a longer transient heating period. It is also important to note that for the conditions considered the rate of heat transport to the surface is not much faster than the rate of heat transport within the droplet for the diffusion-limit model. Conse-

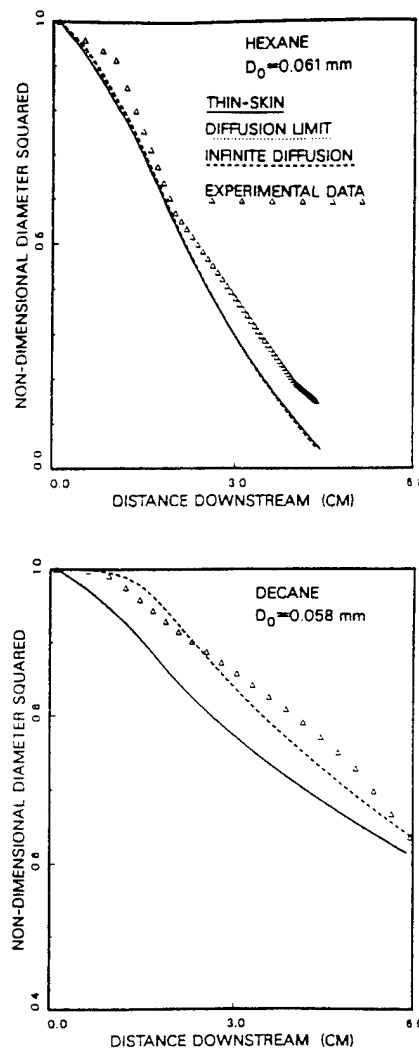


FIG. 2. Diameter squared along the trajectory of a fuel droplet.

quently, this model predicts almost the same vaporization rate as the infinite-diffusion model. However, for higher ambient temperatures, the rate of heat transfer to the droplet surface would be higher, and the difference between these two models will become apparent [8].

Figure 3 shows the variation of the diameter squared along the trajectory of a hexane/decane droplet with the initial mass fraction of each being 0.5. It is interesting to note that the experimental data indicates a batch-distillation type of behavior, which is better simulated by the infinite-diffusion model. It means that the assumption of a spatially uniform liquid temperature and composition may be a good approximation for the present case. This is due to the slow rate of vaporization at relatively low environment temperature which makes the droplet evaporation time comparable to the thermal/mass diffusion times. The thin-skin model does not show as good an agreement as the other two models. This is due to the excessively slow rate of evaporation and long liquid transient time causing the assumption of constant temperature and composition profiles to deviate from the real situation.

Figure 4 shows the variation of the surface mass fraction of liquid hexane and the surface temperature along the droplet

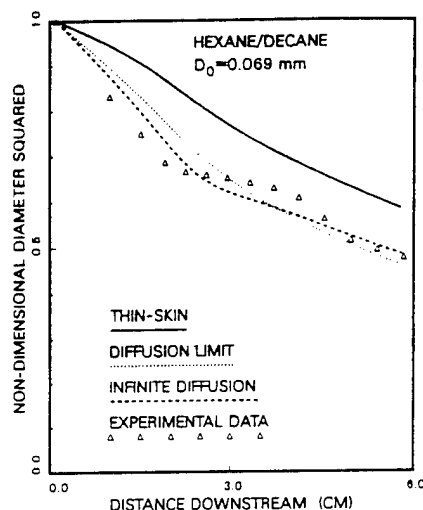


FIG. 3. Diameter squared along the trajectory for a multicomponent fuel droplet.

trajectory. Significant disagreements exist among the three models. For the thin-skin model, the surface concentration as well as temperature, by definition, have constant values. For the diffusion-limit model, the surface concentration initially decreases much faster than that for the infinite-diffusion model and then attains an almost constant value. For the latter model, the mass fraction of hexane decreases steadily due to the preferential vaporization of more volatile species, whereas the surface temperature initially has a constant value given by the wet-bulb temperature of the hexane component. It then continues to increase slowly as the wet-bulb temperature increases following the change in the liquid surface composition. Finally it approaches the wet-bulb temperature of decane. There is a transition region in between the two inflexion points of the curve which corresponds to the depletion of the hexane component.

The differences in the surface temperature and liquid concentrations cause differences in the predictions of surface vapor concentrations. It is observed, though not shown here, that the liquid concentration has a more dominant effect on the surface vapor concentration. As a result, the diffusion-limit model underpredicts the vaporization rate compared to the infinite-diffusion model. Note that this behavior is observed for low ambient temperatures. At relatively high ambient temperatures, the behavior is significantly different [3].

Figure 5 shows the sensitivity of predictions to the methods of calculating reference properties. For methods 1 and 2, the commonly-used one-third rule is employed. For method 3, the scheme of Law and Williams [11] is used to obtain the reference properties. An important observation is that method 1 which only considers the variable temperature effect shows significant differences with the experimental results. The difference between methods 2 and 3, which consider the temperature as well as fuel vapor effects, is negligible.

4. CONCLUSIONS

The vaporization behavior of pure and multicomponent fuel droplets in a laminar hot air flow has been studied. Predictions of three vaporization models have been compared with experimental data. Important conclusions are:

(1) The predicted droplet velocity shows excellent agreement with the measured data, indicating that the solid-sphere drag law is quite adequate for the conditions considered. However, an accurate calculation of the gas-film properties

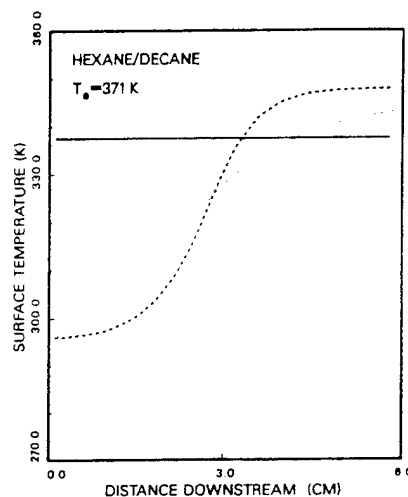
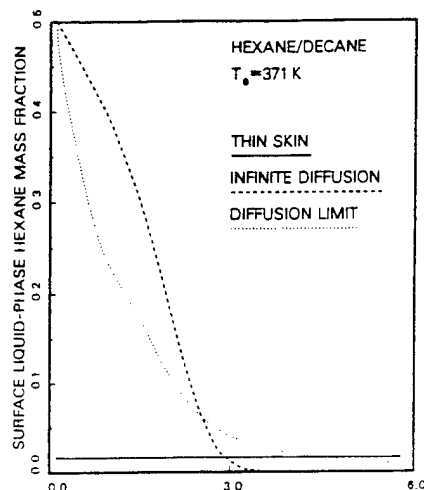


FIG. 4. Liquid hexane mass fraction and temperature at the droplet surface along the trajectory.

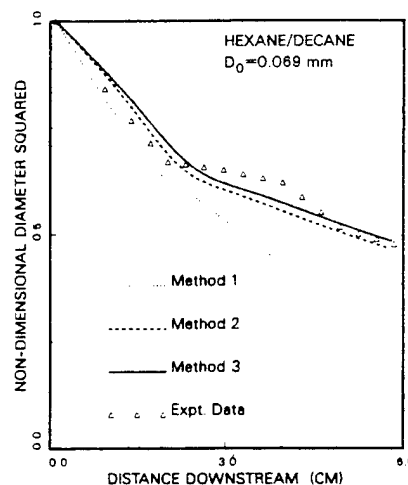


FIG. 5. Comparison of droplet size squared along the trajectory with different methods of calculating thermo-physical properties.

has a strong effect on the predictions. The vaporization behavior of a hexane fuel droplet is not sensitive to the vaporization models. However, for less volatile fuels such as decane, the vaporization behavior shows some sensitivity to the models. The thin-skin model is not as accurate as the other two models which show excellent agreement with experimental data.

(2) The vaporization behavior of a multicomponent fuel droplet is better simulated by the infinite-diffusion model. However, the difference between the infinite-diffusion and diffusion-limit models is not very significant. The thin-skin model shows significant deviation from the experimental values.

(3) The variable property effects are important for an accurate prediction of droplet velocity and size. Not only the effect of temperature but also that of fuel vapor should be considered for calculating the thermophysical properties of the gas film surrounding the droplet. For low ambient temperatures, the accurate evaluation of the latent heat of fuel also has a noticeable effect on predictions.

To conclude, the present study illustrates that for relatively low ambient temperatures, both the infinite-diffusion and diffusion-limit methods can accurately predict the vaporization of pure as well as multicomponent fuel droplets. However, it is important to include the effects of variable thermophysical properties of the gas film outside the droplet as well as of the liquid-phase properties in a comprehensive manner. The present study also indicates the need for measuring the surface properties of a vaporizing multicomponent fuel droplet.

Acknowledgement—The financial support from the Air Force Office of Scientific Research is gratefully acknowledged.

REFERENCES

1. G. A. E. Godsave, Studies of the combustion of drops in a fuel spray—the burning of single drops of fuel, *Fourth Symposium (International) on Combustion*, p. 818. Williams and Wilkins, Baltimore (1953).
2. C. K. Law, Recent advances in droplet vaporization and combustion, *Prog. Energy Combust. Sci.* **8**, 169–199 (1982).
3. S. K. Aggarwal, A. Tong and W. A. Sirignano, A comparison of vaporization models in spray calculations, *AIAA J.* **22**, 1448–1457 (1984).
4. W. A. Sirignano, Theory of multicomponent fuel droplet vaporization, *Arch. Thermodyn. Combust.* **9**, 231–247 (1978).
5. R. B. Landis and A. F. Mills, Effect of internal diffusional resistance on the evaporation of binary droplets, Fifth Int. Heat Transfer Conf., Tokyo, Japan, Paper B7-9 (1974).
6. C. K. Law and H. K. Law, A d^2 -law for multicomponent droplet vaporization and combustion, *AIAA J.* **20**, 522–527 (1982).
7. A. Y. Tong and W. A. Sirignano, Multicomponent droplet vaporization in a high temperature gas, *Combust. Flame* **66**, 221–235 (1986).
8. G. Chen, Vaporization behavior of pure and multicomponent fuel droplets in a hot air stream, M.S. Thesis, The University of Illinois at Chicago (1989).
9. G. A. Agoston, H. Wise and W. A. Rosser, Dynamic facts affecting the combustion of liquid spheres, *Sixth Symposium (International) on Combustion*, pp. 708–717. Reinhold, New York (1957).
10. R. A. Ingebo, Drag coefficients for droplets and solid spheres in clouds accelerating in air streams, NACA Technical Note 3762 (1956).
11. C. K. Law and F. A. Williams, Kinetics and convection in the combustion of alkane droplets, *Combust. Flame* **29**, 393–405 (1972).
12. T. A. Jackson, G. L. Switzer and S. K. Aggarwal, Measurements of droplet size and velocities in a laminar flow (under preparation).

Droplet distributions from the breakup of a cylindrical liquid jet

L. P. Chin, P. G. LaRose, and R. S. Tankin
Northwestern University, Evanston, Illinois 60208

T. Jackson and J. Stutrud
Wright Patterson Air Force Base, Dayton, Ohio 45433

G. Switzer
Systems Research Laboratories, Inc., Dayton, Ohio 45440

(Received 11 January 1991; accepted 24 April 1991)

A phase/Doppler particle analyzer is used to measure the size and velocity distributions of the droplets generated by the disintegration of a cylindrical liquid jet. This type of liquid jet breakup is commonly called Rayleigh breakup. Metered liquid flow rates agree with the rates computed from the droplet measurements made with the phase/Doppler particle analyzer. The maximum entropy principle is used to predict the droplet size and velocity distributions. The constraints imposed in this model involve conservation of mass, momentum, surface energy, and kinetic energy. Agreement between measurements and predictions is very good.

I. INTRODUCTION

The process of producing droplets by the breakup of a cylindrical liquid jet is commonly called Rayleigh breakup.^{1,2} The use of a stimulated mechanism (forcing function) has been widely employed by many researchers to obtain uniform droplets. Such droplets are essential in calibrating spray sizing instruments and in studying the fundamental aspects of droplet combustion. For a stream of droplets with uniform size and velocity, the only mathematical representation of droplet distribution is a coupled delta function $\delta(D - D_0)\delta(U - U_0)$. Here, D_0 denotes the uniform droplet size and U_0 denotes the uniform droplet velocity. Generally, this result is difficult to achieve—even when experiments are carefully conducted in a vibration-isolated environment. Unforced disturbances and complicated nonlinear breakup mechanisms normally produce a stream of droplets deviating slightly from the ideal distribution. At times such a jet, as a result of nonlinear instability, also has a propensity to produce relatively small "satellite"³ droplets interspersed among the main droplets. The existence and behavior of these satellite droplets depends on the initial flow conditions and the physical properties of the liquid jet. The stream of droplets with satellites must be described by a bimodal distribution function. In this study, we will not consider flows where satellite droplets exist. To control the production of satellite droplets, which is important for the jet printer operation, several studies have been made to understand the formation mechanism at various stimulating disturbances.⁴⁻⁷ For example, Pimbley and Lee⁵ obtained a map showing the behavior of satellite droplets under different stimulating conditions. There is a region in this map where the satellite droplet can be totally eliminated. In this study, the measurements recorded by a phase/Doppler particle analyzer (PDPA) of an unforced cylindrical jet (as well as photographs) show that there are no satellite droplets produced over the range of operation under consideration.

With a PDPA, it is possible to measure both the droplet velocity and size. The PDPA is a single-point scattering

technique, making a measurement of each droplet as it passes through a small probe volume. In these measurements, the attempts and validations are recorded. It is important that the acceptance ratio (validations/attempts) be close to one; otherwise, the cause of the rejections should be determined. In many complicated sprays (hollow cone, swirl atomizers), an acceptance rate of 60% or less, over portions of the spray, is often obtained. The advantages of using a small-diameter cylindrical jet, from an experimentalist's point of view, are twofold: (1) the acceptance rate in the PDPA measurements is very high—approximately 100%, and (2) the probe area is not a variable in the problem.

The concept of information entropy was developed by Shannon,⁸ and Jaynes⁹ later extended this concept into the now well-known method of maximum entropy formalism. This formalism can be applied to problems that involve probability, i.e., where insufficient information is available to obtain exact solutions. Tribus¹⁰ used the principle of this formalism in thermodynamics and showed that the concepts of heat and temperature in thermodynamics could be defined through the formalism of maximum entropy. Haken's book on synergetics¹¹ established links between dynamical systems theory and statistical theory with information theory as its basis. This maximum entropy formalism allows one to determine the probability distribution functions for complex systems in physics, chemistry, and biology, as well as in many other disciplines by measuring relatively few average (macroscopic) quantities. In the present study, we will confine our attention to its application to liquid sprays in order to predict the droplet size and velocity distributions in sprays. Since the application to these kinds of problems has been adequately discussed by several researchers—Kelly,¹² Sellens and Brzustowski,^{13,14} and Li and Tankin,¹⁵⁻¹⁷ it will not be necessary to develop the background materials once again.

The maximum entropy principle has been applied by the authors to the spray from a pressure nozzle under isothermal flow condition.¹⁸ In order to compare the theory with experiment data obtained at the position 2.5 mm downstream of

the liquid sheet breakup region, aerodynamic drag is employed. One disadvantage of this old formulation is the physical constraint for the total energy to be conserved. This, in turn, provides insufficient information regarding the individual effects of surface energy and kinetic energy. This shortcoming will be overcome in this study by balancing these two energy terms separately since the two energy terms have different contributions on the droplet distributions. In addition, the control volume chosen is extended to the region where the measurement was made; so that the complicated computation of drag effect on the droplets can be avoided.

The primary purpose of this study is to compare the theoretical predictions based on a modified maximum entropy principle concerning droplet size and velocity distributions with the experimental results. In the process of making these comparisons, estimates will be made of the source terms that appear in the conservation equations. From a computational point of view, there is an advantage in using the cylindrical liquid jet instead of a hollow or solid cone spray—reasonably accurate estimates can be made of the source terms associated with these constraints (conservations of mass, momentum, surface energy, and kinetic energy). The pattern of droplets formed after breakup in the Rayleigh problem is different from the regular hollow cone or solid cone spray system. Therefore the problem is formulated differently than in previous analyses.

II. EXPERIMENT

A critical component in this experiment is the hole that forms the orifice plate. In these experiments, the hole is formed by an electroforming process that is commonly used to make bimetal masks for photolithography. With this process, precise openings of various shapes (in this case, circular) and sizes (in this case, $50\text{ }\mu\text{m}$) can be made in a thin metal plate such as nickel. The nickel metal is bonded to a layer of another metal for strength. This technique is used to construct contact exposure masks in the production of printed circuit boards (see Dressler and Kraemer¹⁹).

The liquid used in this study is distilled water with the following additives to prevent corrosion at the orifice: ethylene glycol 1%, sodium nitrite 0.1%, borax 0.1%, and traces of bacterial inhibitors. The liquid is forced through the orifice by applying a constant air pressure to a liquid reservoir (see Fig. 1). By changing the air pressure, the flow rate is changed. The water exiting the orifice forms a cylindrical jet that is approximately $50\text{ }\mu\text{m}$ in diameter. This cylindrical jet breaks up into droplets. It is desirable to measure the droplets as close as possible to the breakup region, thus reducing aerodynamic effects (drag); but beyond the point where the droplets are oscillating (nonspherical). Figure 2 is a typical photograph that was taken through a microscope using a strobe as a light source ($100\text{ }\mu\text{sec}$ flash). In this photograph, the droplets, as well as a fringe pattern, is seen. The fringe pattern, where measurements were made, is due to the laser beams used to determine simultaneously the droplet velocity and size. It can be seen from this photograph that the droplets are spherical at the point where the measurements were taken.

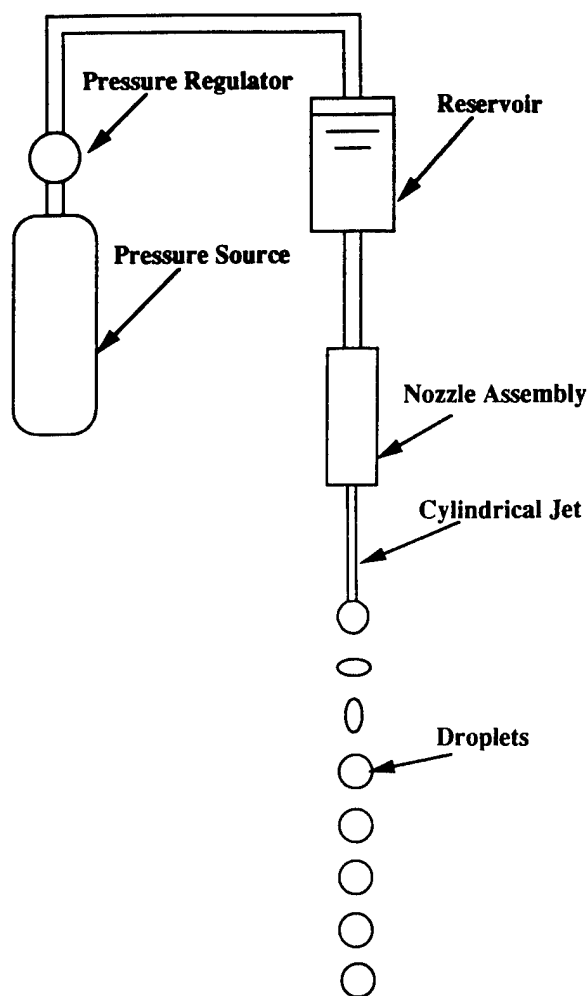


FIG. 1. Schematic drawing of the droplet generator setup.

Droplets are sized with an Aerometrics Inc., two-color, four-beam PDPA; although only one color (green— $5154\text{ }\text{\AA}$) was used in these experiments. This instrument has a probe volume of 0.002 mm^3 . It sizes a droplet by measuring its radius of curvature. The instrument is configured like a standard laser Doppler anemometer; the beam pair yields a measurement of the axial component of the droplet velocity. In each test run, 5000 droplets are measured. Collection times for this many samples are of the order of 4 sec. Sample sizes as large as 10 000 droplets were taken before determining that 5000 samples are more than sufficient to yield stable mean and rms statistics.

One could have used microscopic photography as shown in Fig. 2 and with double exposures and multiple pictures obtained the size and velocity distributions. There are two reasons for using the PDPA unit. First, in an earlier study, we examined a complex spray from a pressure atomizer and found the metered flow rate was an order of magnitude greater than the flow rate obtained from the PDPA measurements. Thus we decided to use a simple spray system—a jet that breaks up into a single column of drops—to test the accuracy of our system. The PDPA measurements

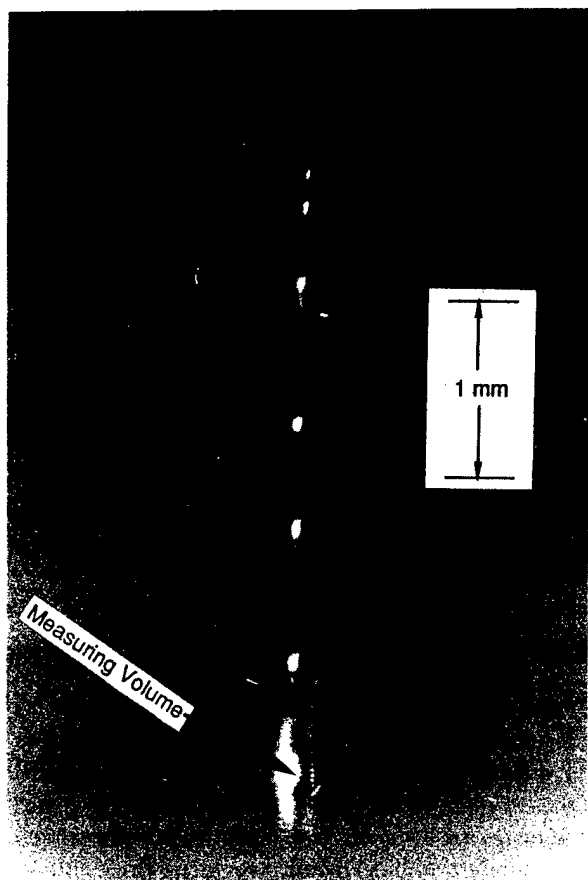


FIG. 2. Photograph showing the stream of droplets produced by the droplet generator.

agreed with the metered flow rate as well as with the sizes estimated from photographs. This will be discussed later. Second, when the distributions are relatively broad (as they were in some cases), analyses of many such photographs (in the hundreds or thousands) would be required to obtain accurate velocity and size distributions. This would have been tedious and time consuming.

Several constraints inherent in the PDPA must be addressed. First, the measured droplets must be spherical. This requires that the measurement station be sufficiently far from the breakup region so that droplets are not oscillating (nonspherical). Second, the PDPA has a dead time of 16 μsec associated with each measured droplet. Another droplet entering the probe volume during this dead time will not be measured and may prevent the measurement of the first droplet by invalidating the signal. In these experiments, the stream of droplets is not dense; thus, there is little probability of having a droplet entering the probe volume during this dead time. These two considerations influence the percentage of valid signals versus the total attempts. That is, the PDPA attempts to process all Doppler signals. It performs checks on the quality of each signal and rejects those that exceed certain limits. In these experiments, there were seven different flow rates analyzed; the valid signals are almost 100% of the signals collected. For example, in one test, there are 5022 attempts and 5022 validations—yielding an accep-

tance ratio of 100%; in the experiment having the worst acceptance ratio, there were 5492 attempts and 5004 validations—yielding an acceptance ratio of 91%.

The experimental data for size distribution is normalized by the mass mean diameter D_{30} . This value is determined from PDPA measurements. The droplet velocity is normalized by the axial velocity at the orifice U_{jet} . This value is determined by dividing the measured liquid flow rate by the cross-sectional area of the cylindrical jet issuing from the nozzle (50 μm diam). The diameter of the cylindrical jet was verified by magnifying the jet with a microscope and projecting an image onto a screen—from which measurements could be made. Also, direct examination of the cylindrical jet with a microscope with a built in measuring reticle yielded the same result. The cylindrical jet diameter is 50 μm .

III. THEORY

As stated, detailed formulation and derivation of the maximum entropy principle have been published,¹⁷ and will not be reiterated here. However, there are two significant modifications: (1) Instead of combining the kinetic energy and the surface energy into one energy constraint, these two energy constraints were separated. The need for this will be described later; (2) the control volume chosen here is the region of liquid jet between the orifice plate (nozzle) and the location downstream where the droplets were measured by the PDPA. That means the distribution obtained from this formulation will be the droplet distribution at the same location as the measurements, not the breakup region of liquid jet normally used by Li and Tankin.¹⁷ The reason we chose the measuring position as the downstream boundary is that, later, we will make use of some measured mean values to estimate the source terms. In addition, the aerodynamic effects on the droplet velocities are negligible.

A schematic drawing for the breakup of a liquid jet and its control volume is shown in Fig. 3. The control volume begins at the outlet of the orifice (nozzle) and extends far enough downstream so that all of the droplet oscillations have damped out. The downstream boundary is the location where the measurements were made. The liquid jet that enters the control volume through surface 1 has a diameter

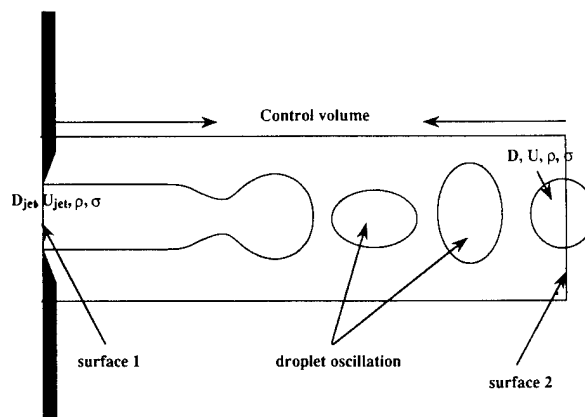


FIG. 3. Control volume used in this study for the liquid jet and droplets.

D_{jet} , velocity U_{jet} , density ρ , and surface tension σ . The droplets that emerge from the control volume through surface 2 have diameter D , velocity U , and arrive at a frequency \dot{n} (number/time). The surface tension and density are assumed to be unchanged because of the breakup.

By applying maximum entropy formulation, the most probable droplet distribution due to the breakup of cylindrical liquid jet is obtained based on the well-known conservation laws involving a few physical quantities. In this study, these physical quantities include mass flux, axial momentum flux, kinetic energy flux, and surface energy flux, which are conserved in the control volume. Because of the existence of individual droplets crossing surface 2, the mass, momentum, and energy leaving the control volume are not constant but occur in a temporal oscillating manner whose frequency depends on \dot{n} . Thus there are changes of these quantities (mass, momentum, kinetic energy, and surface energy) within the control volume with time. To maintain a steady-state formulation, the conservation equations employed here will be derived using a time-averaged base.

A. Conservation of mass flux, momentum flux, and energy fluxes

If the droplets are produced in a saturated air environment, there is no mass flux loss nor gain during the breakup process and the mass flow rate at surface 1 and surface 2 should be equal on a time-averaged base. That is

$$\frac{\pi}{6} \rho \sum_i \sum_j P_{i,j} D_i^3 \dot{n} = \dot{m}_i = \frac{\pi}{4} \rho D_{\text{jet}}^2 U_{\text{jet}} \quad (1)$$

Similarly, a balance in the momentum and energy fluxes of liquid jet and droplets yield

momentum:

$$\begin{aligned} \frac{\pi}{6} \rho \sum_i \sum_j P_{i,j} D_i^3 U_j \dot{n} &= \dot{m}_i U_{\text{jet}} + S_{\text{mv}} \\ &= \frac{\pi}{4} \rho D_{\text{jet}}^2 U_{\text{jet}}^2 + S_{\text{mv}}, \end{aligned} \quad (2)$$

kinetic energy:

$$\begin{aligned} \frac{1}{2} \frac{\pi}{6} \rho \sum_i \sum_j P_{i,j} D_i^3 U_j^2 \dot{n} &= \frac{1}{2} \dot{m}_i U_{\text{jet}}^2 + S_{\text{ke}} \\ &= \frac{1}{2} \frac{\pi}{4} \rho D_{\text{jet}}^2 U_{\text{jet}}^3 + S_{\text{ke}}, \end{aligned} \quad (3)$$

surface energy:

$$\pi \sigma \sum_i \sum_j P_{i,j} D_i^2 \dot{n} = \pi \sigma D_{\text{jet}} U_{\text{jet}} + S_{\text{se}}, \quad (4)$$

where $P_{i,j}$ is the joint probability of finding a droplet with diameter D_i and velocity U_j ; S_{mv} , S_{ke} , and S_{se} are the momentum, kinetic energy, and surface energy source terms, respectively. They include the effects of transport between two phases (liquid and air) within the control volume and the effects of external surface force and body force exerted on the liquid. These three source terms could be positive, zero, or negative. In addition, there is the requirement that the sum of the joint probabilities be equal to unity. That is

normalization:

$$\sum_i \sum_j P_{i,j} = 1. \quad (5)$$

The droplet size and the droplet velocity are nondimensionalized by D_{30} (mass mean diameter) and U_{jet} (initial jet velocity), respectively. Thus the five constraints expressed in integral form are as follows:

normalization:

$$\int \int f d\bar{D} d\bar{U} = 1, \quad (6)$$

mass conservation:

$$\int \int \bar{D}^3 d\bar{D} d\bar{U} = 1, \quad (7)$$

momentum conservation:

$$\int \int \bar{D}^3 \bar{U} d\bar{D} d\bar{U} = 1 + \bar{S}_{\text{mv}}, \quad (8)$$

kinetic energy conservation:

$$\int \int \bar{D}^3 \bar{U}^2 d\bar{D} d\bar{U} = 1 + \bar{S}_{\text{ke}}, \quad (9)$$

surface energy conservation:

$$B \int \int \bar{D}^2 d\bar{D} d\bar{U} = \frac{2B}{3\bar{D}_{\text{jet}}} + \bar{S}_{\text{se}}, \quad (10)$$

where

$$B = 12/\text{We}, \quad \text{We} = \rho U_{\text{jet}}^2 D_{30}/\sigma,$$

and f , the continuous joint probability density function (pdf) of $P_{i,j}$, can be obtained by maximizing Shannon's entropy^{8,11} subject to the above five constraints. Thus f will have the following form:

$$\begin{aligned} f = 3\bar{D}^2 \exp(-\alpha_0 - \alpha_1 \bar{D}^3 - \alpha_2 \bar{D}^3 \bar{U} - \alpha_3 \bar{D}^3 \bar{U}^2 \\ - \alpha_4 B \bar{D}^2), \end{aligned} \quad (11)$$

where the Lagrange multipliers, α_0 , α_1 , α_2 , α_3 , and α_4 , are the undetermined parameters of the distribution function depending on the flow conditions. The formulation in the present study is slightly different from that of Li and Tankin.¹⁷ The previous formulation conserves the combined energy flux—kinetic energy flux and surface energy flux—as one single constraint instead of two separate constraints. The shortcoming of the previous formulation is that no information is provided as to how the total energy source is distributed between the kinetic energy and the surface energy. Any combination of constant total energy source will result in the same probability density function. However, the kinetic energy source term primarily affects the droplet velocity distribution and the surface energy source term primarily affects the droplet size distribution. The difference between the distributions, based on these two formulations, will be clearer when the calculated results are presented later.

B. Estimates of source terms

Because of the complexity of the breakup mechanism for a spray system, normally the source terms (\bar{S}_{mv} , \bar{S}_{ke} , \bar{S}_{se}) can be roughly estimated according to some simple physical phenomena (see, e.g., Li *et al.*¹⁸). In the present study, the

disintegration of the liquid cylinder results in a spray of droplets of nearly uniform size and uniform velocity. This implies that the distributions are very steep and narrow. Under such circumstances, the results obtained from this formulation are extremely sensitive to the source terms assigned. A minor variation of a source term (less than 1%) could change the droplet distributions dramatically. This

situation requires an accurate estimate of source terms for this problem to yield reliable results.

Estimating these source terms accurately will require the use of some average quantities that are obtained from experimental measurements—such as mass mean diameter, mean velocity, etc. The relationships between source terms and experimental data are derived as follows:

$$\bar{S}_{mv} = \int \int \bar{D}^3 \bar{U} d\bar{D} d\bar{U} - 1 = \bar{D}_{30}^3 \int \int \bar{U} d\bar{D} d\bar{U} - 1 = \bar{U}_m \bar{D}_{30}^3 - 1 = \bar{U}_m - 1, \quad (12)$$

$$\begin{aligned} \bar{S}_{ke} &= \int \int \bar{D}^3 \bar{U}^2 d\bar{D} d\bar{U} - 1 = \bar{D}_{30}^3 \int \int \bar{U}^2 d\bar{D} d\bar{U} - 1 \\ &= \bar{D}_{30}^3 \int \int f(\bar{U} - \bar{U}_m)^2 d\bar{D} d\bar{U} + 2\bar{D}_{30}^3 \bar{U}_m \int \int \bar{U} d\bar{D} d\bar{U} - \bar{D}_{30}^3 \bar{U}_m^2 - 1 \\ &= \bar{D}_{30}^3 \int \int f(\bar{U} - \bar{U}_m)^2 d\bar{D} d\bar{U} + \bar{D}_{30}^3 \bar{U}_m^2 - 1 \\ &= \bar{D}_{30}^3 (\bar{U}_m^2 + \bar{U}_{rms}^2) - 1 = (\bar{U}_m^2 + \bar{U}_{rms}^2) - 1, \end{aligned} \quad (13)$$

$$\bar{S}_{sc} = B \int \int \bar{D}^2 d\bar{D} d\bar{U} - \frac{2B}{3\bar{D}_{jet}} = \frac{B}{\bar{D}_{32}} - \frac{2B}{3\bar{D}_{jet}}, \quad (14)$$

where \bar{D}_{30} is the mass mean diameter (equal to 1) from experiments, \bar{U}_m is the mean droplet velocity from experiments, \bar{U}_{rms} is the root mean square of droplet velocity fluctuations from experiments, \bar{D}_{32} is the Sauter mean diameter from experiments, \bar{D}_{jet} is the diameter of cylindrical jet at the orifice, and $2B/3\bar{D}_{jet}$ is the surface energy flux of the cylindrical jet at the orifice.

In making these estimates of \bar{S}_{mv} and \bar{S}_{ke} , it was assumed that all the droplets have the same velocity so that \bar{D}_{30} can be extracted from the integrals. That is, the velocity and size are uncoupled. This will be seen to be a reasonable assumption for the sprays under consideration.

IV. RESULTS AND DISCUSSION

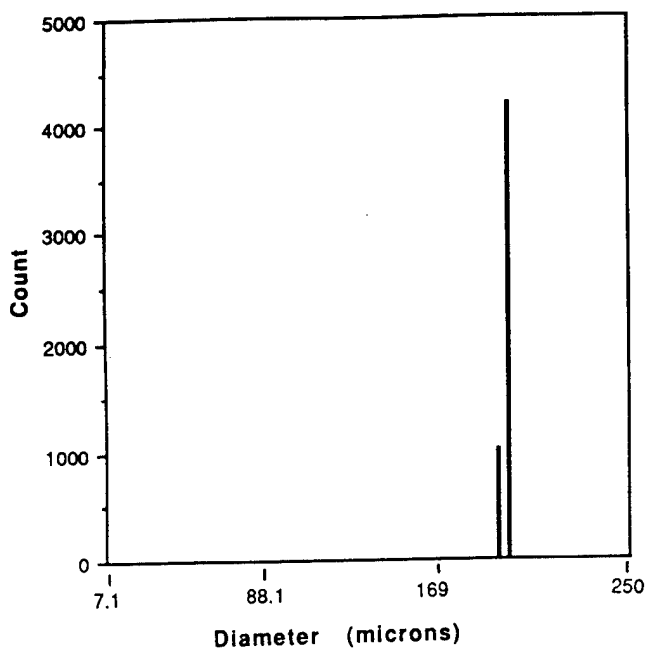
In this section, two sets of experimental data will be chosen to illustrate their corresponding distribution functions for droplet size and droplet velocity. In one set of data, the distributions are very narrow—almost delta functions; in the other set of data, the distributions are broad. We have selected these two sets of data because they represent the two extremes from the seven sets of data collected. Figures 4 and 5 show these two sets of experimental data; one set has an acceptance ratio of 1.0 (highest) and the other an acceptance ratio of 0.91 (lowest). The narrow distributions, as in Fig. 4, occur over a very restricted range of nozzle exit velocities, U_{jet} . It was only with great care (remember these were not externally stimulated jets) that these data were obtained. The nozzle exit velocity (U_{jet})—based on a jet diameter of 50 μm —equals 2.76 m/sec in Fig. 4. Changing U_{jet} (either increasing or decreasing) results in broader distributions. For example, the distributions at $U_{jet} = 2.32$ m/sec is shown in Fig. 5. Similar results (but not quite as broad as those in Fig. 5) occurred when $U_{jet} = 3.64$ m/sec. Intermediate

widths of the distributions occur when 3.64 m/sec $> U_{jet} > 2.76$ m/sec and 2.32 m/sec $< U_{jet} < 2.76$ m/sec.

For each set of experiments, there are two distribution curves—one is the number of droplets versus droplet diameter [Figs. 4(a) and 5(a)] and the other curve is the number of droplets versus droplet velocity [Figs. 4(b) and 5(b)]. Accompanying these two plots are the experimental parameters and measured mean values of droplets. The terms \bar{D}_{30} , \bar{D}_{32} , \bar{U}_m , and \bar{U}_{rms} are used in estimating the source terms. It was assumed in these initial estimates [Eqs. (12)–(14)] that the droplet size is independent of droplet velocity. This assumption needs justification.

The assumption for estimating \bar{S}_{mv} and \bar{S}_{ke} can be verified from the experimental data recorded by the PDPA. If one examines the raw data—for example, for the test shown in Fig. 5(b)—one can plot the mean diameter (\bar{D}_{30}) and its rms value for each velocity bin. This is shown in Fig. 6(a) for velocity bins having more than 10 drops/bin. The mean diameter is nearly independent of velocity and the rms of the drop diameter in each velocity bin is small compared to the mean diameter (1). The largest deviation of \bar{D}_{30} from 1 occurs at velocity bins (U/U_{jet}) greater than 0.35; but even in these bins the D/D_{30} is greater than 0.97 and the rms is less than 0.15. In addition, the number of drops in the velocity bins greater than 0.35 only amounts to 10% of the total drops measured. Thus the assumption that the droplet diameter is independent of velocity is valid. Therefore one would expect the estimated source terms to be reasonably accurate.

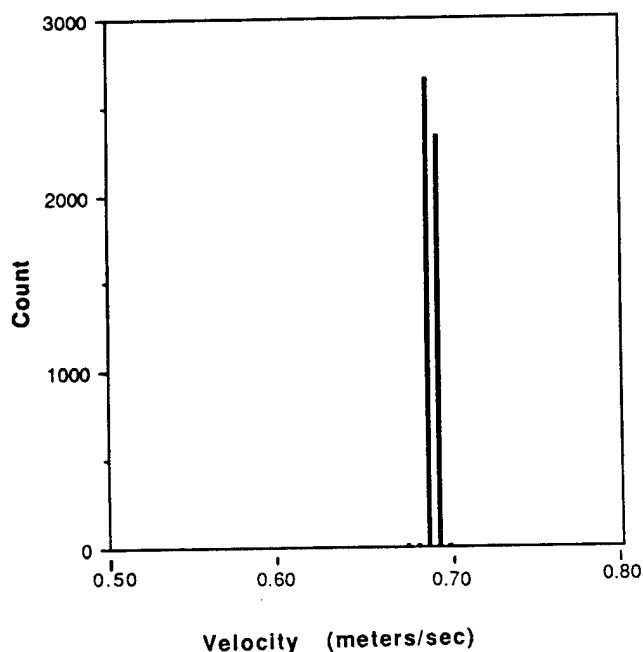
As an alternate approach, one could assume a uniform velocity (\bar{U}_m) instead of a uniform droplet size when making estimates for \bar{S}_{mv} and \bar{S}_{ke} in Eqs. (12) and (13). By employing this assumption, the only difference from the previous approach is that $\bar{S}_{ke} = \bar{U}_m^2 - 1$. The term \bar{U}_{rms}^2 disap-



(a)

Arithmetic Mean (D_{10}) = 194.5 μm
 Area Mean (D_{20}) = 194.5 μm
 Volume Mean (D_{30}) = 194.5 μm
 Sauter Mean (D_{32}) = 194.6 μm

Probe Area = 9.92 E-004 cm^2
 Number Density = 2.07 E+004 /cc
 Vol. Flow Rate = 5.43 E-003 cc/s
 Volume Flux = 5.47 cc/s/ cm^2



(b)

Attempts = 5022
 Validations = 5022
 Corrected Count = 5210
 Run Time = 3.57 sec

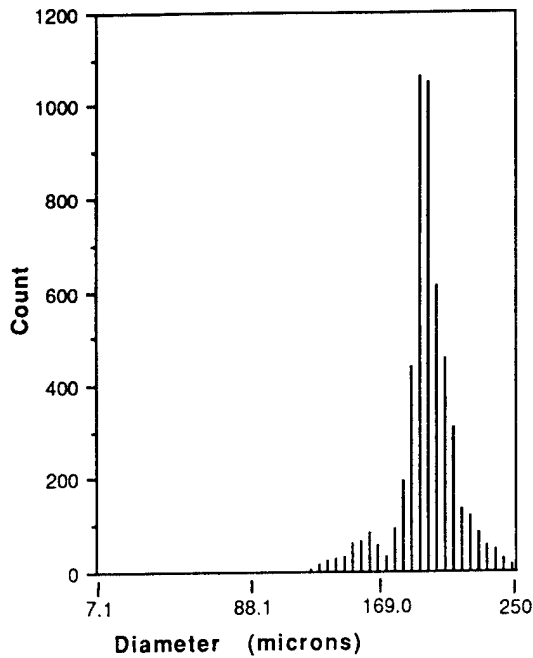
Mean Velocity = 0.687 m/s
 RMS Velocity = 0.003 m/s

FIG. 4. Printout of the measurements obtained from PDPA for data set No. 1. (a) The number of droplets versus droplet diameter and (b) the number of droplets versus droplet velocity.

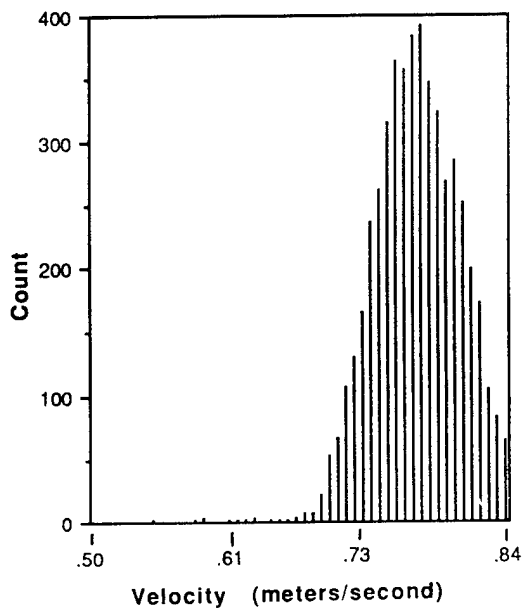
pears because of the assumption that the velocity is constant. It is interesting to note that the influence of the droplet size distribution on the estimates of the source terms is the same in these two approaches. The assumption of uniform velocity is verified experimentally by plotting the mean and rms values of the droplet velocity in each size bin as shown in Fig.

6(b). The rms values for the velocity in each bin is less than 0.02 (6%).

A third approach can be used without making any assumption about the droplet size or droplet velocity distributions. This approach is based on two additional mean variables that are not directly measured by PDPA. If one defines



(a)



(b)

Arithmetic Mean (D_{10}) = 199.7 μm
 Area Mean (D_{20}) = 200.4 μm
 Volume Mean (D_{30}) = 201.1 μm
 Sauter Mean (D_{32}) = 202.4 μm

Probe Area = 1.62 E-003 cm^2
 Number Density = 8.66 E+003 /cc
 Vol. Flow Rate = 4.56 cc/s/ cm^2

Attempts = 5492
 Validations = 5004
 Corrected Count = 5148
 Run Time = 4.00 sec

Mean Velocity = 0.766 m/s
 RMS Velocity = 0.035 m/s

FIG. 5. Printout of the measurements obtained from PDPA for data set No. 2. (a) The number of droplets versus droplet diameter and (b) the number of droplets versus droplet velocity.

the mean velocity and rms values of the velocity in terms of droplet volume instead of droplet number, then the source terms \bar{S}_{mv} and \bar{S}_{ke} can be derived by simply replacing the number-based mean velocity and the rms of the velocity in Eqs. (12) and (13) with volume-based variables. Although these two mean variables are not directly available from the

standard PDPA output, they could be obtained from the raw data.

The droplet distributions obtained from these estimated source terms only provide an initial result, which will probably require modification of the source terms in order to yield distributions that agree with the experimental data.

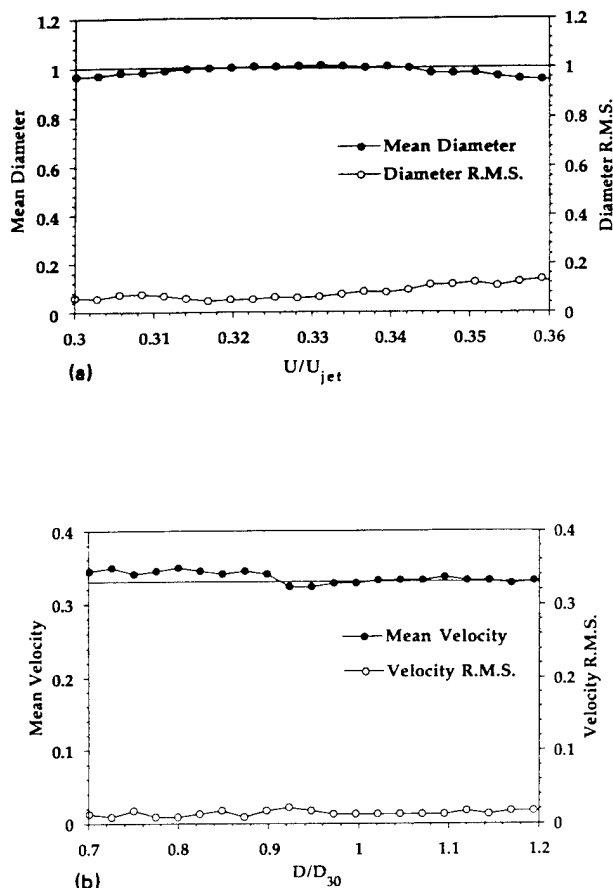


FIG. 6. Plots showing the dependence of the droplet velocity on droplet diameter. (a) Plot of the mean diameter and its rms values versus droplet velocity. (b) Plot of the mean velocity and its rms values versus droplet diameter.

Therefore we will not concern ourselves with the different possible results obtained from these three approaches for estimating the source terms, but choose the first approach—constant droplet diameter. It is believed that any one of these three approaches will provide sufficiently accurate estimates of the source terms needed to make the initial calculations. Once the source terms are estimated, the corresponding distribution functions of droplet size and droplet velocity are obtained by integrating Eq. (11) along \bar{D} and \bar{U} , respectively. They are

$$\frac{dN}{d\bar{D}} = \frac{3}{2} \left(\frac{\pi \bar{D}}{\alpha_3} \right)^{1/2} [\text{erf}(X_{\max}) - \text{erf}(X_{\min})] \times \exp \left[-\alpha_0 - \left(\alpha_1 - \frac{\alpha_2^2}{4\alpha_3} \right) \bar{D}^3 - \alpha_4 B \bar{D}^2 \right], \quad (15)$$

$$\frac{dN}{d\bar{U}} = \int f d\bar{D}, \quad (16)$$

where $\text{erf}(X)$ is the error function of X :

$$X_{\max} = (\bar{U}_{\max} + \alpha_2/2\alpha_3)(\alpha_3 \bar{D}^3)^{1/2},$$

$$X_{\min} = (\bar{U}_{\min} + \alpha_2/2\alpha_3)(\alpha_3 \bar{D}^3)^{1/2}.$$

Since there is no closed-form solution for the droplet velocity distribution, Eq. (16) is calculated by numerical

integration. Here, N is the normalized droplet number. “Estimated” distributions (based on estimated source terms) for these two set of data are also shown in Figs. 7 and 8. The estimated source terms and the corresponding parameters ($\alpha_0, \alpha_1, \alpha_2, \alpha_3, \alpha_4$) for these predicted distributions are listed in Tables I and II. Agreement between measurements and estimated correlations is reasonably good. However, there is a discrepancy between the peaks of estimated distributions and the experimental data.

The “estimated” distribution function was further modified by adjusting the source terms—resulting in “fitted” distribution functions. The fitting technique applied, in this case, relies on the fact that the We number and the surface energy source term \bar{S}_{se} have a major effect on the droplet size distribution and a minor effect on the velocity distribution. On the other hand, the other two source terms \bar{S}_{mv} and \bar{S}_{ke} have a major effect on the velocity distribution, but minor effect on the size distribution. The procedure used for fitting is described briefly as follows.

(1) To fit the droplet size distribution, the We number was fixed and the surface energy source \bar{S}_{se} was adjusted until the maximum amplitude of $dN/d\bar{D}$ of the experimental data and the fitted data matched. In this manner, the size distribution is fitted while the velocity distribution remains essentially unchanged.

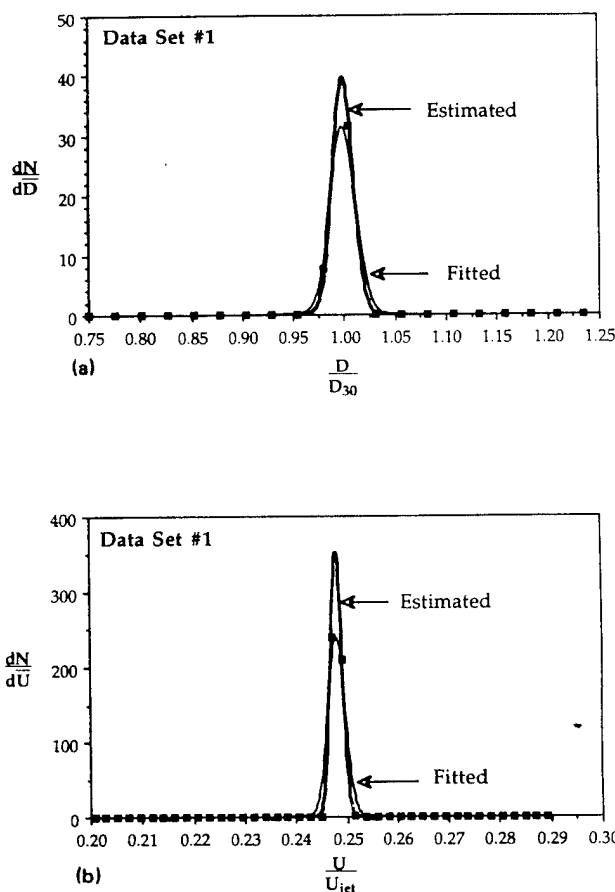


FIG. 7. Comparison between experimental data, “estimated” and “fitted” results for data set No. 1. (a) The droplet size distributions and (b) the droplet velocity distributions.

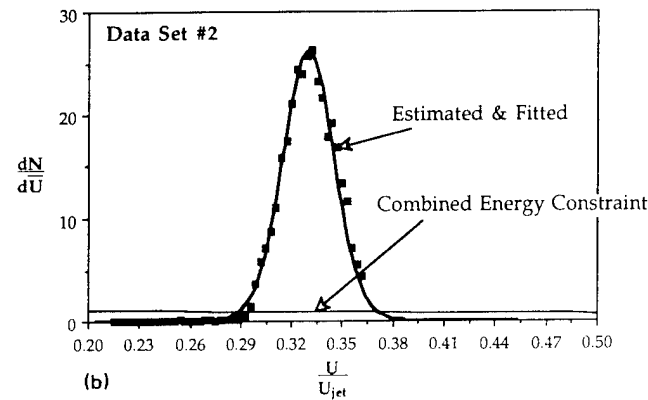
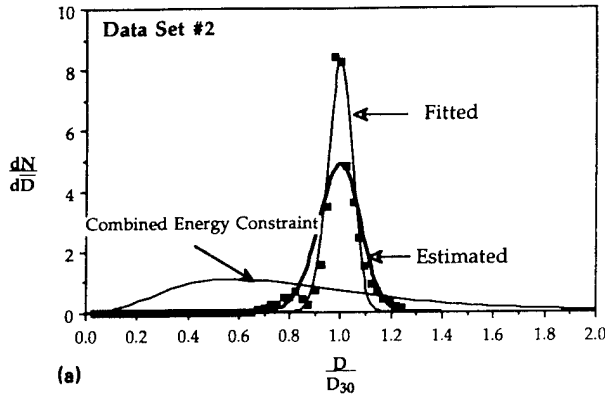


FIG. 8. Comparison between experimental data, "estimated" and "fitted" results for data set No. 2. (a) The droplet size distributions and (b) the droplet velocity distributions.

(2) To fit the droplet velocity distribution, the source term \bar{S}_{mv} was fixed and the kinetic energy source term \bar{S}_{ke} was adjusted. Thus the velocity distribution is fitted while the size distribution remains essentially unchanged.

The results for the combined changes in \bar{S}_{sc} and \bar{S}_{ke} are shown in Figs. 7 and 8. The corresponding parameters and source terms are listed in Tables I and II. The difference in the source terms used in the "estimated" and "fitted" curves varied by only a fraction of a percent! For example, in Fig. 7, the difference in \bar{S}_{sc} is only 0.0038%; the difference in \bar{S}_{ke} is only 0.00016%. In Fig. 8, these differences are only

TABLE I. Source terms and distribution parameters for data set No. 1.

	Estimated	Fitted
We	20.400 02	20.400 02
\bar{S}_{mv}	- 0.751 750 3	- 0.751 750 3
\bar{S}_{ke}	- 0.938 370 8	- 0.938 369 3
\bar{S}_{sc}	- 0.937 611 9	- 0.937 648 0
α_0	1639.5249	1017.7057
α_1	27 249.1459	13 110.0542
α_2	- 192 972.6902	- 89 091.7504
α_3	388 666.5124	179 439.7947
α_4	- 8405.5046	- 5231.043 00

TABLE II. Source terms and distribution parameters for data set No. 2.

	Estimated	Fitted
We	14.870 16	14.870 16
\bar{S}_{mv}	- 0.669 871 6	- 0.669 871 6
\bar{S}_{ke}	- 0.890 784 4	- 0.890 785 4
\bar{S}_{sc}	- 1.361 976 0	- 1.358 450 0
α_0	20.9063	66.3845
α_1	285.8760	378.9142
α_2	- 1430.1208	- 1436.3431
α_3	2166.0070	2175.4309
α_4	- 92.2844	- 263.3113

0.0001% and 0.259%. Similar results were obtained for the other five sets of data collected and examined. Thus one can see the importance of "accurately" estimating the source terms.

The distributions using the previous formulation¹⁷ of a single energy flux constraint was examined. Attempts were made to determine the corresponding droplet distributions for the two sets of data based on the formulation that there is only one constraint for the energy flux. The combined energy source term is the sum of two separate energy source terms (\bar{S}_{sc} and \bar{S}_{ke}) estimated earlier (see Tables I and II). For the data set in Fig. 7, the numerical calculations did not converge. The results for the data set in Fig. 8 reveal that the velocity and size distributions disagree with the experimental data. Thus the conservation of the combined energy source term does not provide enough information for this spray system.

Finally, the computed flow rate using the PDPA measurements is compared with the measured flow rate obtained by weighing a sample of the droplets collected over a period of time. The following equation was used to compute the flow rate:

$$\dot{Q} = \pi \sum_i n_i \frac{D_i^3}{6}, \quad (17)$$

where D_i is the diameter of the droplet in the i th bin and n_i is the number of droplets per unit time in the i th bin.

A comparison of the difference between the calculated flow rate using the PDPA and the measured flow rate is 8%. However, since the diameter is raised to the third power, the measured diameter of the droplets is within 3% of the actual diameter. This implies a consistency between the measured data and the PDPA data. In making the calculation represented by Eq. (17), the droplet diameter D_i is the lower limit of the droplet diameter in the i th bin. If one used an average droplet diameter in the i th bin, the difference between the metered flow rate and the calculated flow rate would be about 3%; thus resulting in a discrepancy of only 1% in droplet diameter.

V. CONCLUSIONS

The agreement between theory and experiments is reasonably good for the Rayleigh problem under investigation. In order to obtain these results, it was necessary to modify the previous theory of Li and Tankin,¹⁵⁻¹⁷ by separating the

energy source term into a kinetic energy source term and a surface energy source term. It was possible to evaluate the source terms for the breakup of a cylindrical jet within a fraction of a percent. In the experiments conducted in this study, it was not necessary to involve the probe area of the PDPA (a possible source of error) since all the droplets passed through the measuring volume. Also, the acceptance ratio exceeded 0.91 in these experiments. The measured liquid flow rate agrees to within 8% of that obtained from the PDPA measurements.

ACKNOWLEDGMENTS

The authors wish to thank the assistance provided by Fluid Jet Associates and, in particular, Dr. J. L. Dressler, president. He supplied the nozzle and supervised the operation of the droplet generator.

¹L. Rayleigh, Proc. London Math. Soc. **4**, 10 (1878).

²L. Rayleigh, Proc. R. Soc. London **34**, 130 (1882).

³D. B. Bogey, Annu. Rev. Fluid Mech. **11**, 207 (1979).

⁴E. F. Goedde and M. C. Yuen, J. Fluid Mech. **40**, 495 (1970).

⁵W. T. Pimbley and H. C. Lee, IBM J. Res. Dev. **21**, 21 (1977).

⁶K. C. Chaudhary and T. Maxworthy, J. Fluid Mech. **96**, 287 (1980).

⁷D. W. Bousfield, I. H. Stockel, and C. K. Nanivadekar, J. Fluid Mech. **218**, 601 (1990).

⁸C. E. Shannon, Bell Syst. Tech. J. **27**, 379 (1948); *Key Papers in the Development of Information Theory*, edited by D. Slepian (IEEE, New York, 1974).

⁹E. T. Jaynes, Phys. Rev. **106**, 620; **108**, 171 (1957).

¹⁰M. Tribus, *Thermostatistics and Thermodynamics* (Van Nostrand, New York, 1961).

¹¹H. Haken, *An Introduction to Synergetics* (Springer-Verlag, Berlin, 1978).

¹²A. J. Kelly, J. Appl. Phys. **47**, 5264 (1976).

¹³R. W. Sellens and T. A. Brzustowski, Atom. Spray Tech. **1**, 89 (1985).

¹⁴R. W. Sellens and T. A. Brzustowski, Combust. Flame **65**, 273 (1986).

¹⁵X. Li and R. S. Tankin, Combust. Sci. Tech. **56**, 65 (1987).

¹⁶X. Li and R. S. Tankin, Combust. Sci. Tech. **60**, 345 (1988).

¹⁷X. Li, Ph.D. thesis, Northwestern University, Evanston, Illinois, 1989.

¹⁸X. Li, L. P. Chin, R. S. Tankin, T. Jackson, J. Stutrud, and G. Switzer, to appear in Combust. Flame.

¹⁹J. L. Dressler and G. O. Kraemer, in *Liquid Particle Size Measurement Techniques-Vol. II*, edited by E. D. Hirleman, W. D. Bachalo, and P. G. Felton (American Society for Testing and Materials, Baltimore, MD, 1990), p. 30.



AIAA 92-0382

**Two-Dimensional Shear-Layer
Entrainment and Interface-Length
Measurements**

Tzong H. Chen
Systems Research Laboratories, Inc.
A Division of Arvin/Calspan
Dayton, OH 45440-3696

Robert D. Hancock
Wright Laboratory
Wright-Patterson AFB, OH 45433-6563

**30th Aerospace Sciences
Meeting & Exhibit**
January 6-9, 1992 / Reno, NV

TWO-DIMENSIONAL SHEAR-LAYER ENTRAINMENT AND INTERFACE-LENGTH MEASUREMENTS

Tzong H. Chen*
Systems Research Laboratories, Inc.
2800 Indian Ripple Road
Dayton, OH 45440-3696

Robert D. Hancock**
Aero Propulsion and Power Directorate
Wright Laboratory
Wright-Patterson AFB, OH 45433-6563

Abstract

A novel approach to measuring the effect of vortex roll-up on interface length, entrainment, and mixing enhancement has been developed and demonstrated for two-dimensional shear-layer flows. The shear layer is marked by TiO_2 seed particles that chemically form at the interface of the two fluids and is illuminated by a light sheet from a pulsed laser. This measurement technique involves tracing the interface between the two free streams directly from CCD images collected under phase-locked conditions. Interface-length elongation factors for the vortices under several driving frequencies were compared. The entrainment of the free-stream fluid and the area of the product were also measured and compared at several driving frequencies. The technique allows direct measurement of the ratio of the product area and the interface length. It was found that driving the flow at its resonant frequency results in the optimum interface-elongation factor and mixing enhancement.

1.0 Introduction

Large-scale vortices has been studied extensively for many years.¹⁻⁴ The development of these vortices are viewed as a key mechanism in the promotion of macro-scale mixing which creates the environment in which chemical reactions can take place due to micro-scale mixing. Numerous approaches have been taken to defining and determining vortex velocities and entrainment ratios.⁵⁻⁹ Much of this effort has been conducted under turbulent conditions and in liquid mixing layers. However, efforts on gaseous shear layers have been limited.^{10,11}

Konrad measured the molecular mixing layer in several turbulent two-dimensional shear flows using a concentration probe.¹² When fast-reacting chemicals were introduced into the stream, the amount of chemical product formed was proportional to the molecular-scale mixing at the reaction's equivalence ratio. Hernan and Jimenez¹⁰ extracted quantitative information on a turbulent mixing layer by digitizing 16-mm shadowgraph ciné film. Using this approach, they were able to develop statistics to describe the life history of

the eddy currents, the structure of the amalgamation process, and the amount of entrainment. Their results clearly show vortex coalescence and the general shape and size of the vortices as they move downstream. Koochesfahani and Dimotakis⁶ investigated a non-reacting, uniform-density, liquid mixing layer to determine the composition of the vortical structures. A fluorescent dye was mixed into the low-speed free-stream fluid, and then the fluorescence intensity was measured along an argon laser beam extending across the width of the shear layer using a linear photodiode array. They found that the vortical structures in the mixing-layer rolled up with a large excess of high-speed fluid in the cores. Masutani and Bowman examined a chemically reacting, gas-phase, two-stream plane mixing layer using planar laser-induced fluorescence.¹¹ Roberts completed a comprehensive study of a reacting liquid shear layer. He characterized the shear layer behavior under a variety of frequency regimes¹³ and refers to a particular region of the flow called the "pre-mixing-transition" region. It is in this region that entrainment of the high- and low-speed fluid is dominated by the two-dimensional vortices, and the mixing is primarily due to molecular diffusion along the material interface separating the high- and low-speed fluids. It is in this region that the data for this paper was acquired.

In this present study, a novel approach was utilized to investigate the effect of vortex roll-up on entrainment and interface length and mixing. The unique interface-tracing technique developed and demonstrated in this investigation allows direct study of the mixing and reaction along the interface. Unlike the direct scalar measurement used in other imaging techniques, the entrainment of the fluids from both sides of the mixing layer was measured after locating the interfacial boundary. Thus, the mixing and reaction enhancement can be directly compared to the measured interface elongation. This allows direct access of the mixing-enhancement efficiency by increasing the interface length through vortex roll-up. The results will shed light on the detailed mechanism involved in vortex mixing. This exploratory investigation is performed in preparation for future experimental and theoretical

*Senior Member AIAA, ** Member AIAA

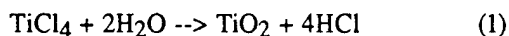
Copyright © 1992 by the American Institute of Aeronautics and Astronautics, Inc. All rights reserved.

studies that will involve direct numerical simulation of these flow.

2.0 Experimental

Two-dimensional vortices are generated from a splitter plate which separates two parallel flowing-air streams contained within a 12.7-cm-square Plexiglas duct. A schematic diagram of the facility is shown in Fig. 1. The 12.7-cm-wide splitter plate divides the duct into two equal areas of dimensions 6.35 x 12.7 cm. Dry air is used in both the high- and low-speed flows. An established technique known as Reactive Mie Scattering is used to visualize the vortical flow. Air on the high-speed side of the splitter plate is passed over a liquid TiCl_4 bath, collecting TiCl_4 vapor. Air on the low-speed side of the splitter plate is passed over a water bath, collecting water vapor. The TiCl_4 in the higher velocity air flow reacts with the moist air on the low-velocity side of the flow, forming micron-sized TiO_2 particles that follow the gas flow and distinctly mark the molecular interface of the two air streams. Vortex formation and shedding are driven by acoustic stimulation of the low-speed flow, which can be controlled with excellent stability over a range of frequencies from 15 to 25 Hz.

The TiO_2 particles are formed at the stoichiometric surface between the TiCl_4 - and H_2O -seeded sides of the flow. These seed particles form only where the two seeded air streams come in contact on the micro-scale level. Thus, the TiO_2 particles essentially mark the molecular interface between the two air streams. Equation (1) describes this chemical reaction



The amount of product, or TiO_2 particles, and the location of the stoichiometric surface where the product forms are dependent on the concentration of the reactants. The data for this experiment were obtained with unknown, but consistent, molecular concentrations of TiCl_4 and H_2O on the higher (left) and lower (right) velocity sides of the splitter plate, respectively.

The flow field is recorded as a digital image on a portion of a 1024 x 1024 diode array. Typically, the image size was 250 x 1024 pixels, with the 1024 pixels oriented parallel to the flow direction. The scale was 192 $\mu\text{m}/\text{pixel}$ for all the images collected. Therefore, the images show a 4.8 x 19.7 cm region of the flow. The light source is the frequency-doubled output (532 nm) of a Nd:YAG laser. The 10-ns pulse-length light sheet essentially freezes the flow, enabling the digitized images to be collected. The resulting images possess an intensity value for each x-y pixel combination of the array. A major advantage of this technique is that the digitized images do not require scanning as would a shadowgraph of some other

photograph. The image is collected with the CCD camera and analyzed directly in its original form. The TiO_2 seed creates fairly distinct high-intensity lines that mark the interface between the two streams.

3.0 Results and Discussion

Vast amounts of data can be collected with this technique in a very short period of time. The process of collecting a CCD image of the two-dimensional shear layer flow and measuring the interface length is straightforward. However, the analysis is a new approach to measure entrainment interface length of individual vortices moving in a Lagrangian frame of reference. Obviously, the boundaries within which measurements are made can dramatically alter entrainment and interface-length results. Furthermore, the concentrations of the reactants play a major role in determining the entrainment and interface length and measured product. Although these concentrations were not measured, the data presented were collected in a single continuous run under a constant flow condition in order to provide consistent measurements. Despite the unknowns related to the reactant concentrations and the analysis method, some insight can be gained and trends observed by comparing individual vortices as well as total mixing-layer results in natural and driven laminar flows.

Data are presented for a two-dimensional shear-layer flow at a Reynolds number based on the velocity difference and vortex width yielding, $\Delta u \delta / \nu \sim 10^3$. The velocity of the air on the high-velocity (left) side of the flow was 0.94 m/s and that on the low velocity (right) side was 0.47 m/s. Some data were obtained in undriven shear layers with additional measurements being made in identical flows driven at 15, 20, and 25 Hz. Examples of these images are shown in Fig. 2 as inverted images (black on white) to improve print clarity. It was observed that for the undriven flow, the shear-layer vortices were subject to some degree of randomness. However, the vortices shed at dominant frequencies corresponding to the most unstable modes of the flow near 25 Hz. When the flow was driven at 25 Hz, the interface is thicker than in the undriven case. When the drive frequency was 15 Hz, the vortex width grew rapidly, but the vortex spacing was quite large.

By performing a "flip" experiment (flipping the sides in which the H_2O and TiCl_4 are introduced into the flow) similar to those described in the literature^{11,14,15} it was determined that less TiO_2 product was formed. Figure 3 shows images collected before and after the TiCl_4 and H_2O were flipped. Based on Equation (1) and the fact that the shear layer entrains more fluid from the high-speed side of the flow, it is apparent that the concentration of the TiCl_4 was low and became the limiting reactant in the process of forming the TiO_2 seed particles. The two images in Fig. 3 demonstrate the impact of the reactant

concentrations upon the appearance of the shear layer and amount of product. While it would be informative to analyze and compare sets of images from a flip experiment, the images analyzed in this study were only of the type shown on the left in Fig. 3 (TiCl₄ on high speed side of flow).

Figure 4 shows, at six different phase angles, a two-dimensional shear layer being driven at 20 Hz. These images were obtained by increasing the delay time between the generation of the vortex and the exposing CCD camera. Once again, the images were inverted in order to improve print clarity. The excellent repeatability of the driven flow makes phase-locked measurements possible.

A computer algorithm was developed for tracing two lines of constant intensity on the shear layer in the digitized images. These constant-intensity contour lines are illustrated in Fig. 5. These two lines mark interface surfaces for the fluid on the left and right sides of the flow with the TiO₂ product. The area between the two lines then represents the mixed region, or the region where the TiO₂ product resides.

Most techniques employ a stationary laser beam through which vortical flows doped with some visualizing agent pass. With such a technique a maximum shear-layer width can be used to set boundaries within which to measure the composition of the shear layer. The technique presented in this paper differs from these techniques in that it allows vortices to be followed in a Lagrangian frame of reference because the flow is laminar and phase locked with the CCD camera. Since individual vortices were singled out in the flow, a method was needed for establishing a bounded region within which to measure areas and interface lengths. The method selected was to draw a box around the vortex with the top and bottom edges of the box being located halfway between adjacent vortex centers near the stagnation points. The sides of the box were drawn tangent to the extreme edges of the vortex. The area interface lengths were then calculated with the computer algorithm developed for that purpose. This method of placing the vortex in a box is a new technique and will result in different values of entrainment from those traditionally reported in the literature. For the data presented in this paper it was a consistent way in which the individual vortices could be measured and compared. From these measurements, the entrainment and resultant interface length were derived and studied parametrically as a function of drive frequency. This technique becomes more difficult to use as the vortices begin to merge since it becomes more difficult to single out individual vortices. Therefore, all the data analyzed in this study were collected from the region which exists prior to merging. In the future, more effort will be devoted to comparing this method, or some derivative method, with traditional entrainment-measurement techniques.

Insight was gained into several questions upon inspection of the data images. 1) The effect of drive frequency on the length of the interface between the two air streams--For example, does the large vortex width of the 15-Hz driven case result in the largest increase in the interface length where molecular mixing occurs. 2) The effect of drive frequency upon the entrainment and composition of the vortices 3) Whether an increase of the interface length yields a proportional increase in mixing area.

These questions will be addressed by first examining in detail data from a flow driven at 20 Hz to find a general trend with regard to variation of length scales and areas for a vortex traveling downstream. Finally, comparisons between the length scale and area results for selected flow conditions will be made.

3.1 Convective Velocity

The convective velocity of the vortices is an important parameter in the study of shear layers. Under incompressible flow conditions, the convective velocity of the vortex structure can be described by Equation (2) as proposed by Dimotakis.⁷

$$\frac{U_c}{u_1} = \frac{1 + rs^{1/2}}{1 + s^{1/2}} \quad (2)$$

where U_c is the large structure convective velocity; $r = u_2/u_1$; $s = \rho_2/\rho_1$; u_2 and u_1 are the free-stream velocities; and ρ_2 and ρ_1 are the free-stream densities. For this experiment, $r = 0.47/0.94$ and $s = 1$. According to Eq. (2), the large-structure convective velocity should be 0.705 m/s, which is simply the average velocity of u_2 and u_1 . The actual convective velocity of the large vortical structures in the shear layer for different forcing frequencies was derived from linear curve fits to the data in Fig. 6. The location of each vortex center was found as a function of time. As expected, the vortices traveled a distance which is linearly proportional to the delay time for all three drive frequencies. The slope of the lines in Fig. 6 represents the vortex convective velocity. This slope was 0.78 m/s for all three drive frequencies which is ~12% higher than the predicted value. This discrepancy can be attributed to the fact that the flow conditions in this experiment were in a lower velocity region ($Re = 10^3$) than that in which this equation is typically applied. Additionally, up to a $\pm 5\%$ error is associated with the velocities for u_1 and u_2 used in the vortex convective-velocity calculation.

3.2 Individual-Vortex Measurements

The data presented in this portion of the paper give information about individual vortices analyzed by drawing a box around each vortex (refer to Fig. 5) and calculating the corresponding interface lengths and areas

of the high-speed, low-speed, and product regions for each vortex.

3.2.1 Vortex Width, Vortex Spacing, Interface Length, and Elongation Factor

The formation of vortical structures is important for increasing the interface length of two fluids. It is at this interface that molecular diffusion and chemical reaction take place. The large-scale vortices, similar to the ones investigated for this study, serve to stir the two fluids together on a macroscopic level in order to increase the interface length and provide the environment for enhanced mixing on a molecular level. Without the formation of vortices, the interface between the two fluids would be a straight line and the molecular-mixing surface would be limited.

To account for the effect of individual vortex roll-up on interface length, the following convention was followed. The width of the vortex was measured as the spanwise distance between lines drawn tangential to the edges of the vortex. Typically, the vortex length is defined as the distance between the leading stagnation point and the trailing stagnation point of a given vortex. In this study, the central point between two adjacent vortices was used rather than the actual stagnation point. Therefore, the vortex spacing figures described in this paper were obtained by measuring the distance between the leading central point and the trailing central point of a vortex. This vortex spacing was taken as the reference length scale for the computation of the interface elongation factor for each vortex.

Figure 7 shows the measured vortex interface length, width, and spacing as a function of the downstream location of the associated vortex. The driving frequency was 20 Hz. As expected for a driven shear layer, the vortex width and spacing increased only slightly as the vortices moved downstream. The vortex spacing was typically twice as large as the vortex thickness. These data indicate that the interface of Fluid 1 with the product region grew at a faster rate than the interface of Fluid 2 with the product region. This would support the idea of asymmetric entrainment into a shear layer.

Over a region from 7-14 cm downstream of the splitter plate, the vortex width increased by ~22% and the vortex spacing increased by ~17%. Typically, the growth of the shear layer should follow the Abramowich-Sabin expression

$$\delta = C_{\delta} \left(\frac{u_1 - u_2}{u_1 + u_2} \right) x \quad (3)$$

For a well-developed turbulent shear layer, the proportional constant C_{δ} is in the range²

$$0.25 < C_{\delta} < 0.45. \quad (4)$$

The constant C_{δ} corresponding to the vortex width shown in Fig. 7 ranged from 0.46 at $x = 7$ cm to 0.33 at $x = 14$ cm. This indicates that for the selected flow regime, the shear-layer vortex grew at a rate initially at the high end of the range for the flow in the turbulent region. However, the high growth rate was not maintained; rather, it decayed to the value at the lower end of the normal shear-layer growth range. The Strouhal number defined by the driving frequency, f_0 , vortex thickness, δ , and convective velocity, U_c , was held constant at ~0.5.

$$St = \frac{f_0 \delta}{U_c} \quad (5)$$

In Eq. (5), if vortex spacing is used rather than vortex thickness, then the Strouhal number is 1.0. The Strouhal number defined in this way for all other flow conditions with different driving frequencies selected in this study remains ~1.0.¹³ Also, recall that the convective velocity, U_c , remains the same regardless of driving frequency. Thus, lower driving frequencies are expected to yield larger vortex widths and spacings.

Examination of the interface length for the 20-Hz driven flow indicated that the high-velocity side of the flow contributed more fluid to the vortex. Furthermore, the interface between fluid 1 and the product was longer and grew faster than the interface between Fluid 2 and the product. In the remainder of this section, the interface lengths between Fluid 1 and the mixed product are compared at 15-, 20-, and 25-Hz drive frequencies.

Figure 8 shows the interface length of Fluid 1 with the product area for individual vortices normalized by the associated vortex spacing. These normalized values (elongation factor) indicate the degree of increased interface length over a case in which no roll-up was present. The data indicate that the interface length increase the greatest when the flow is driven at 25 Hz. The elongation factor decreased with lower drive frequencies. Within the measurement region, the elongation factor of Fluid 1 followed a linear relation with respect to the downstream location of the vortex center. Linear curve fits through the data give similar slopes of ~0.46 for the three frequencies shown. Not illustrated is the normalized interface lengths of Fluid 2 with the product for which a slope of 0.24 was found.

The undriven case, whose natural frequency is much closer to 25 Hz, had normalized interface lengths closer to those of 15 Hz. Clearly, the driving has a significant effect on the onset and degree of roll-up as well as the shape of the vortices. This can be seen by referring to Fig. 2. Notice that the same number of vortices are present at similar positions in the flow for both the undriven and 25-Hz driven flow, but the shapes and degree of roll-up are much different.

3.2.2 Entrainment, Entrainment Ratio, and Entrainment Area

The areas of Fluid 1, Fluid 2, and the product as functions of downstream location are shown in Fig. 9 for a 20-Hz driven flow. It was found that the product inside the vortex located at $x = 7$ cm was 0.5 cm^2 and increased to 2.0 cm^2 when the vortex was at $x = 14$ cm. A calculation can be done for the area-growth rate of the product. It proceeds as follows:

$$\frac{dA}{A_i dx} = 0.34 \text{ cm}^{-1} \text{ from the data,} \quad (6)$$

$$\text{since } \frac{dA}{A_i dx} = \frac{dA}{A_i U_c dt}, \quad (7)$$

$$\text{then } \frac{dA}{A_i dt} = 27 \text{ sec}^{-1} \quad (8)$$

where the reference value, A_i , is the area of the product at the location $x = 7$ cm. The characteristic time corresponding to the driving frequency of 20 Hz is 0.05 sec. Therefore during one complete cycle, the product area inside a vortex will increase by a factor of 1.35.

Figures 10, 11, and 12 show the areas of Fluid 1, Fluid 2, and product normalized by the individual vortex areas. With the exception of four points at the 25-Hz drive frequency, the data are grouped around 60% for Fluid 1, 20-30% for Fluid 2, and 10-20% for the product. While the number of data points is limited, it appears that driving the flow near its natural frequency of about 25 Hz has increased the amount of product, or mixed area, in the individual vortices. Additional data collected under more controlled reactant-concentration conditions will be required to substantiate conclusions about this observation. It is important to remember that if the entrainment is measured by some other technique, or under other reactant concentration levels, the results may be different.

Based on the data, the entrainment ratio of Fluid 1 to Fluid 2 yields a value of 2.0. As expected, this value does not compare well with the predicted value of 1.23 obtained from an entrainment measurement equation proposed by Dimotakis.⁷ It is expected that if the composition of the vortices were measured at a fixed downstream position in the flow the entrainment ratio may decrease and approach the predicted value.

3.3 Comparison of Total Mixing Layer

In Sections 3.1 and 3.2, individual vortices were compared relative to their vortex-center location downstream of the splitter plate. In this section, comparisons will be based on the entire shear layer and not individual vortices. Therefore, when a point is plotted on a graph, it is important to remember that the point represents not just one vortex but the entire shear layer from the tip of the splitter plate to the particular downstream location marked by the point. The total interface length is measured from the tip of the splitter

plate to the specified downstream location. This location corresponds to either the leading or the trailing midpoint between the vortices. The total product area is simply the area between the two interface lines.

3.3.1 Interface Length

Figure 13 shows the total interface length of Fluid 1 with the product as a function of downstream distance for the four flow conditions analyzed. The total interface length of the 15-Hz case is similar to the natural shear-layer flow. Although the images of the 15-Hz case show that very wide vortices were generated in the shear layer, the formation of the initial vortex was delayed and the vortex spacing was larger than in the other higher frequency cases. As a result, driving the flow at 15 Hz did not elongate the interface and increase product area. The total interface length in the 20-Hz case shows appreciable improvement over the natural and 15-Hz case. The limited 25-Hz data indicate a slightly longer interface length than that of the other frequencies. The ratio of the interface length and the downstream distance can be viewed as the elongation factor of the vortex roll-up. This elongation factor for the 20-Hz case ranges from 2.1 at $x = 12.5$ cm to 2.6 at 17.8 cm.

3.3.2 Area

Roberts showed that the total amount of chemical product in the shear layer can be altered upon shear layer forcing.¹³ Additionally, Koochesfahani and MacKinnon state that it is impossible to obtain unambiguous information on molecular mixing for a chemically reacting experiment at a single stoichiometric ratio.¹⁶ Some correlations between the product area and the elongated interface are presented in this section. Clearly, these correlations and the relating conclusions may not be general, but the results are interesting and worth attention. More data collected under a variety of stoichiometries and carefully controlled conditions may help in obtaining generalized information of about the molecular mixing in a two-dimensional gaseous shear layer.

The total product area as measured from the splitter plate to selected downstream locations is plotted in Fig. 14. The flow driven at 25 Hz continues to yield the best results, followed by that driven at 20 Hz and then at 15 Hz. The undriven flow yields results similar to those of the 20-Hz case.

One way of examining the correlation between the product area and the elongated interface is to obtain the ratio of these two quantities. The units of this ratio is one of length and is equivalent to the definition of the overall transverse diffusion thickness. This diffusion length is plotted in Fig. 15. The diffusion thickness for the 20 Hz case is fairly constant at ~ 0.08 cm. This indicates that the area of mixing or reaction is linearly proportional to the interface length.^{17,18} Again, the 25-Hz case yields the largest transverse

diffusion length, whereas, the 15-Hz case yields the smallest. According to the theory,¹⁹ the transverse diffusion length can be reduced by stretching. Therefore, the fact that the 15 Hz case has the smallest transverse diffusion length may indicate the largest amount of stretching along the interface. Although it can be expected that high stretching should yield a high elongation factor, the artificial driving of the shear-layer vortex formation follows a fundamental rule. For example, the Strouhal number must remain constant.¹³ Driving the flow at 15 Hz certainly did not yield the highest elongation factor. It is, therefore, speculated that driving the flow at the non-resonant frequency may result in more stretching and in less elongation.

4.0 Conclusions

The interface of the reactive mixing layer has been traced to allow detailed examination of mixing enhancement due to the roll-up process of the vortex. The mixing layer employed in this study has fixed free-stream velocities and density ratios. Artificial driving of the flow at several frequencies including the resonant frequency was performed to study the effect of such perturbations on vortex entrainment. The unique interface-tracing technique developed and demonstrated in this investigation allows direct study of the mixing and reaction along the interface. The entrainment of the fluids from both sides of the mixing layer was also measured after locating the interfacial boundary. Therefore, the mixing and reaction enhancement can be directly compared to the measured interface elongation. This technique loses its simplicity when merging and coalescence of vortices occur. Under these circumstances, the direct measurement of entrained fluid using a scalar imaging technique would be more appropriate.

For the flow conditions selected and the flow region analyzed in this study, the following conclusions can be made.

1. The convective velocity of the vortex and ratio of the entrained fluid from the fast side to the total vortex area remain fairly constant, regardless of driving frequency.
2. The entrainment ratio of the fast to slow fluid was found to be ~ 2.0 , which is higher than the theoretical prediction. The shear-layer growth rate follows the trend observed in well-developed shear flows.
3. The interface length, entrainment, and product were enhanced by driving the flow. The resonant driving frequency of 25 Hz enhances the interface length, entrainment, and product more than the lower frequencies. The 15-Hz case provided the widest vortex (shear-layer width). However, the vortex spacing also increased, resulting in the least effective mixing and reaction enhancement among all the cases. This observation implies that

judging mixing enhancement by shear-layer width may not be a valid approach, especially in very low Reynolds number flows such as those investigated in this study.

4. The interface-length elongation factor for each vortex can be significant. However, the total interface length for the entire shear layer, which includes a large portion of laminar transition area, increase by a much smaller amount.
5. The ratio of the product area and interface length, which is equivalent to the transverse diffusion length, for the mixing layer has been directly measured by the technique developed in this study. For the flow condition studied, this length is on the order of 1 mm.

5.0 Acknowledgements

This work was supported by the Aero Propulsion and Power Directorate of the Wright Laboratory under Contract No. F33615-90-C-2033. The authors are indebted to W. M. Roquemore and L. P. Goss for helpful discussions, G. L. Switzer and D. D. Trump for technical assistance, and M. Whitaker for editorial assistance.

References

1. Oster, D. and I. Wygnanski, *The Forced Mixing Layer between Parallel Streams*. J. Fluid Mech., 1982. 123: p. 91-130.
2. Dimotakis, P.E., *Turbulent Free Shear Layer Mixing and Combustion*. 1991, California Institute of Technology: GALCIT Report FM91-2.
3. Ho, C.-M. and P. Huerre, *Perturbed Free Shear Layers*. Ann. Rev. Fluid Mech., 1984. 16: p. 365-424.
4. Hussain, A.K.M.F., *Coherent Structures - Reality and Myth*. Phy. Fluids, 1986. 26: p. 2816-2850.
5. Brown, G.L. and A. Roshko, *On Density Effects and Large Structure in Turbulent Mixing Layers*. J. Fluid Mech., 1974. 64: p. 775-816.
6. Koochesfahani, M.M. and P.E. Dimotakis, *Laser Induced Fluorescence Measurements of Concentration in a Plane Mixing Layer*. AIAA-84-0198, 1984.
7. Dimotakis, P.E., *Two-Dimensional Shear-Layer Entrainment*. AIAA Journal, 1986. 24(11): p. 1791-1796.
8. Koochesfahani, M.M. and P.E. Dimotakis, *A Cancellation Experiment in a Forced Turbulent Shear Layer*. 88-3713-CP, 1988.
9. Coles, D., *Dryden Lecture: The Uses of Coherent Structure*. AIAA-85-0506, 1985.
10. Hernan, M.A. and J. Jimenez, *Computer Analysis of a High-Speed Film of the Plane Turbulent Mixing Layer*. J. Fluid Mech., 1982. 119: p. 323-345.

11. Masutani, S.M. and C.T. Bowman, *The Structure of a Chemically Reacting Plane Mixing Layer*. J. Fluid Mech., 1986. 172: p. 93-126.
12. Konrad, J.H., *An Experimental Investigation of Mixing in Two-dimensional Turbulent Shear flows with Application to Diffusion-Limited Chemical Reactions*. 1976, California Institute of Technology: Dissertation
13. Roberts, F.A., *Effects of a Periodic Disturbance on Structure and Mixing in Turbulent Shear Layers and Wakes*. 1985, California Institute of Technology: Dissertation
14. Koochesfahani, M.M. and P.E. Dimotakis, A "Flip" Experiment in a Chemically Reacting Turbulent Mixing Layer. AIAA J., 1985. 23(8): p. 1191-1194.
15. Mungal, M.G. and P.E. Dimotakis, *Mixing and Combustion with Low Heat Release in a Turbulent Shear Layer*. J. Fluid Mech., 1984. 148: p. 349-382.
16. Koochesfahani, M.M. and G.G. MacKinnon, *Influence of Forcing on the Composition of Mixed Fluid in a Two-Stream Shear Layer*. Phys. Fluids A, 1991. 3(5): p. 1135-1142.
17. Broadwell, J.E. and M.G. Mungal, *Large-Scale Structures and Molecular Mixing*. Phys. Fluids A, 1991. 3(5): p. 1193-1206.
18. Aref, H. and S.W. Jones, *Enhanced Separation of Diffusing Particles by Chaotic Advection*. Phys. Fluids A, 1989. 1(3): p. 470-474.
19. Marble, F.E. and J.E. Broadwell, *The Coherent Flame Model for Turbulent Chemical Reactions*. 1977: Project SQUID TRW-9-PU.

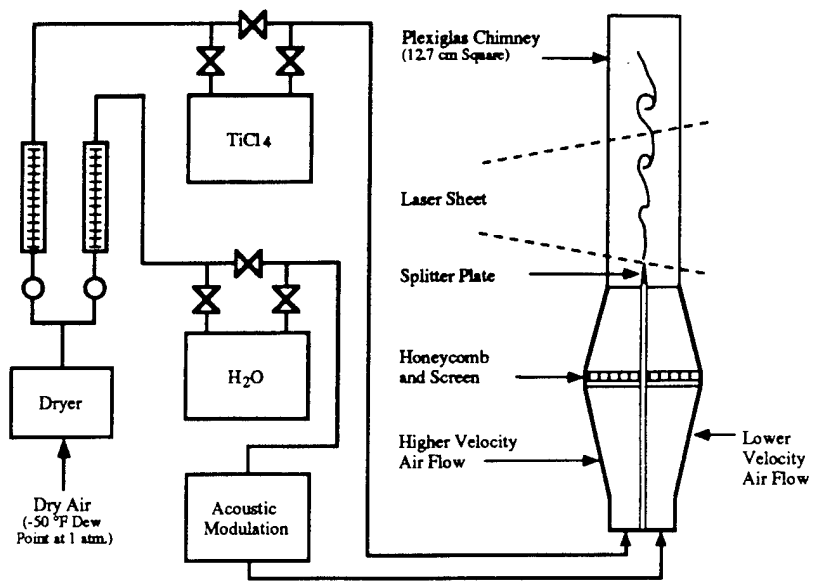


Fig. 1. Two-dimensional shear layer facility schematic.

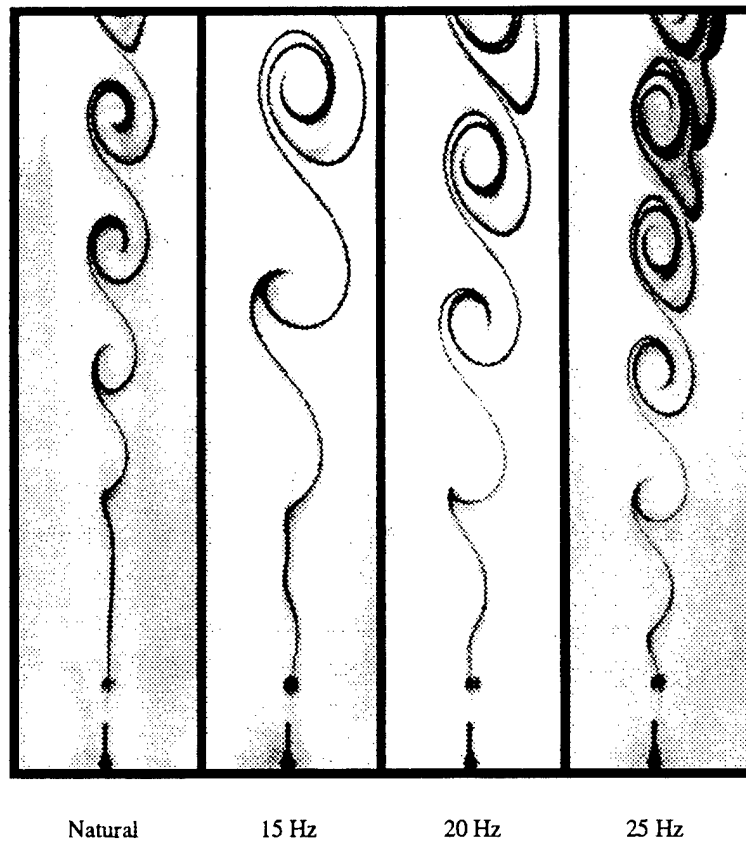
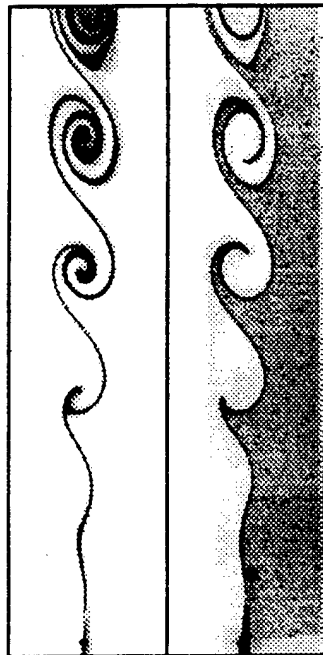


Fig. 2. Phase-locked Mie-scattering images of a 2-d shear layer.



TiCl₄ H₂O H₂O TiCl₄

Fig. 3. Flip experiment images

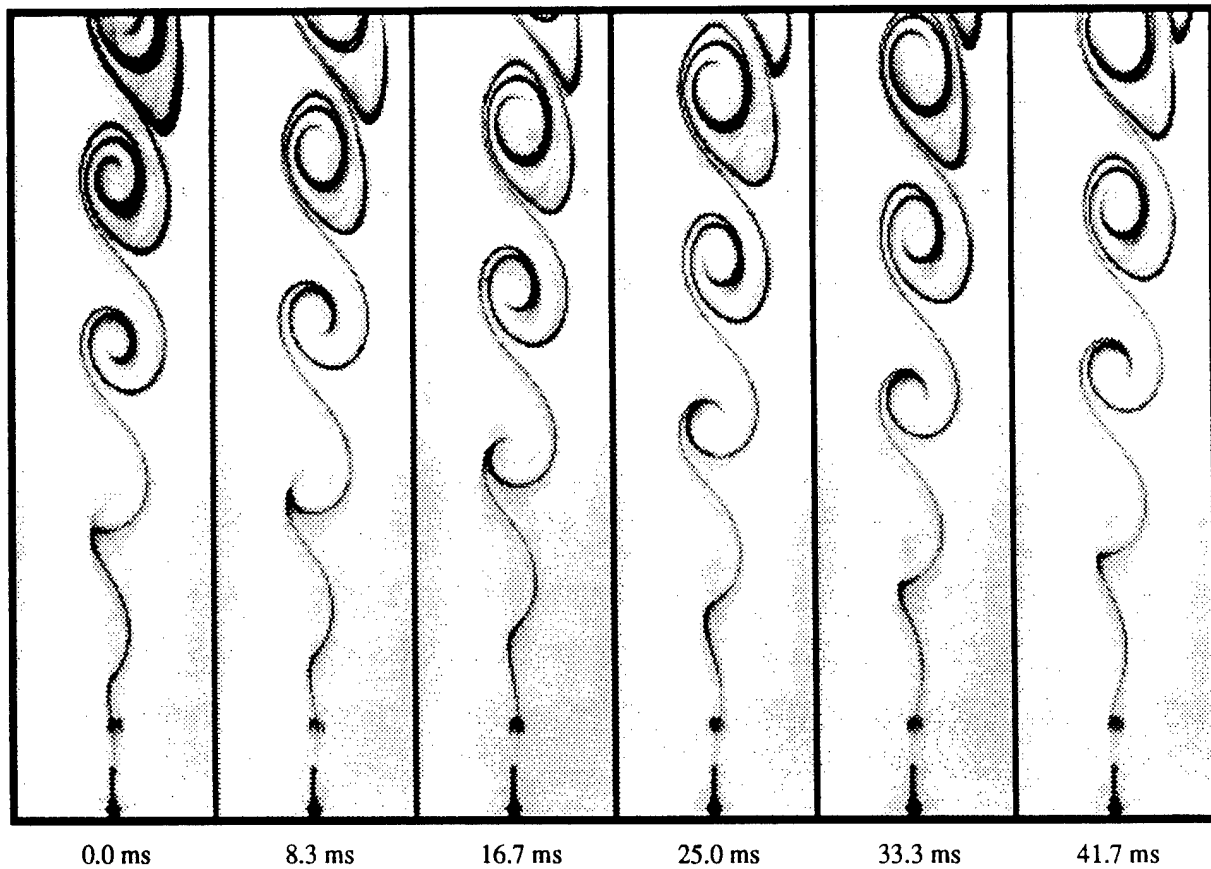


Fig. 4. Phase-locked images of a 2-d shear layer driven at 20 Hz

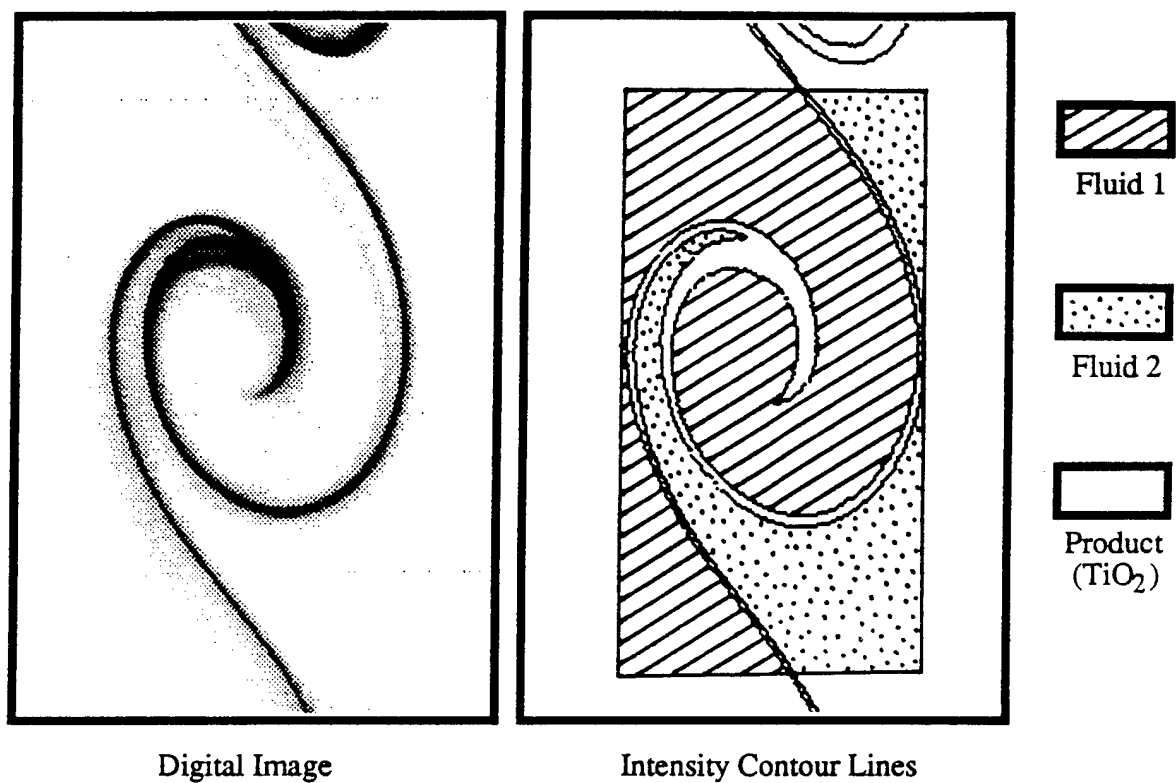


Fig. 5. Image Analysis Technique

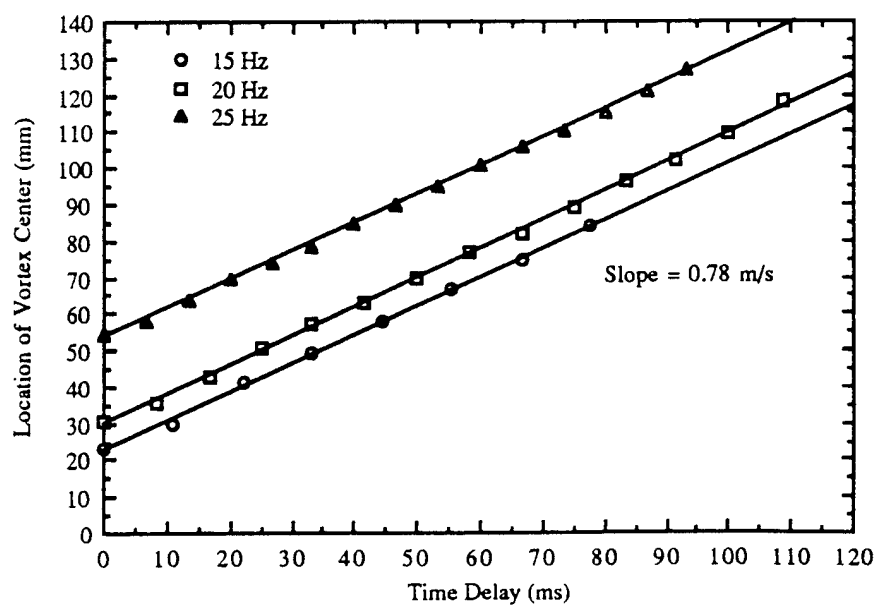


Fig. 6. Vortex center location vs time delay.

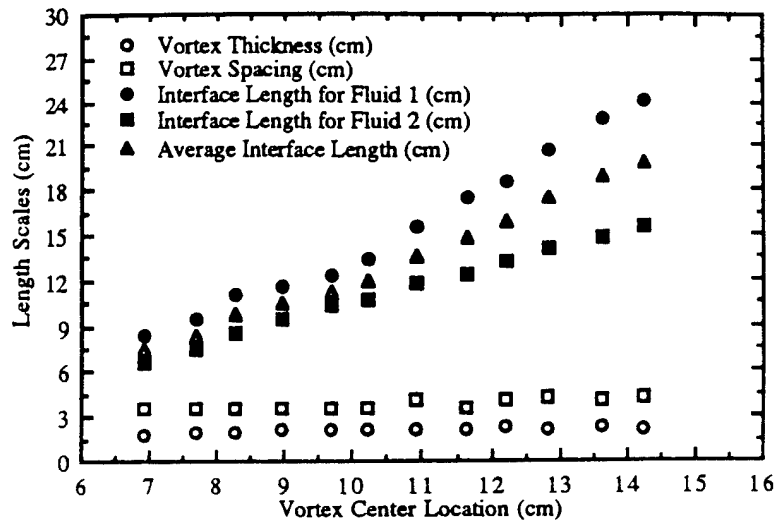


Fig. 7. Measured vortex and interface values at 20 Hz.

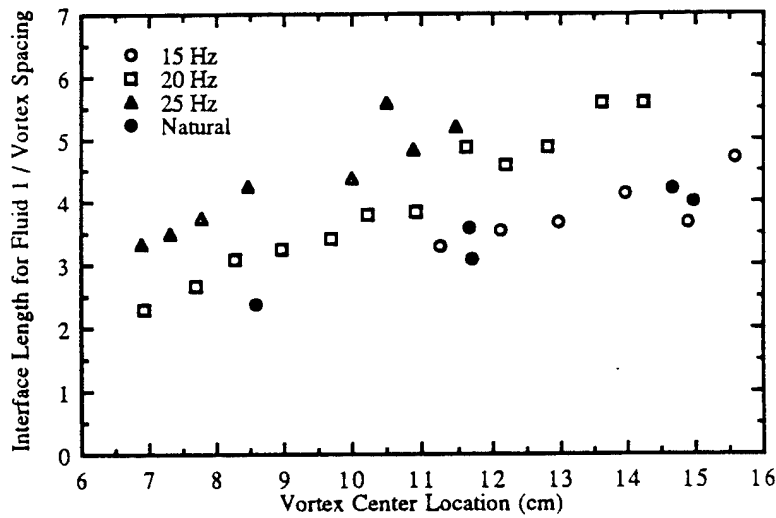


Fig. 8. Normalized interface length for fluid 1.

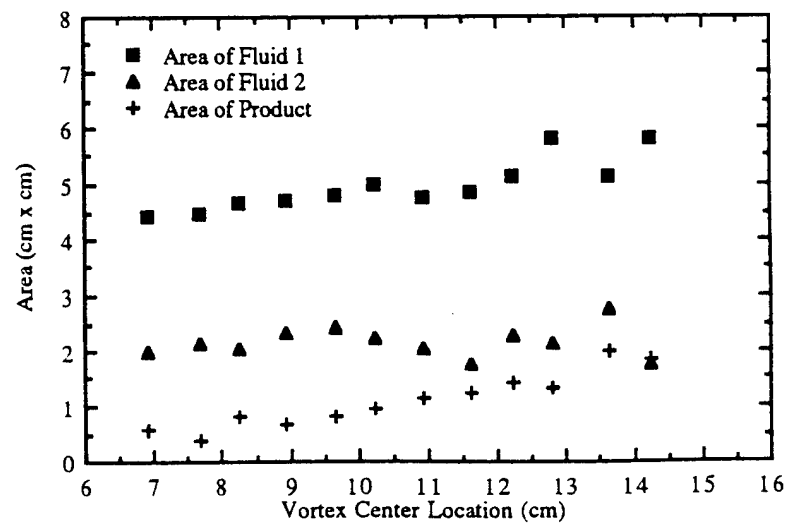


Fig. 9. Measured areas of fluid 1, fluid 2, and product at 20 Hz.

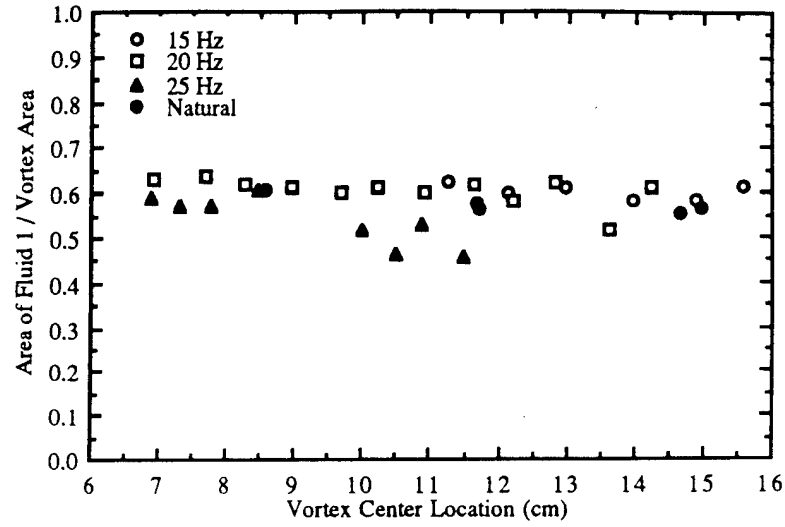


Fig. 10. Normalized Area of fluid 1.

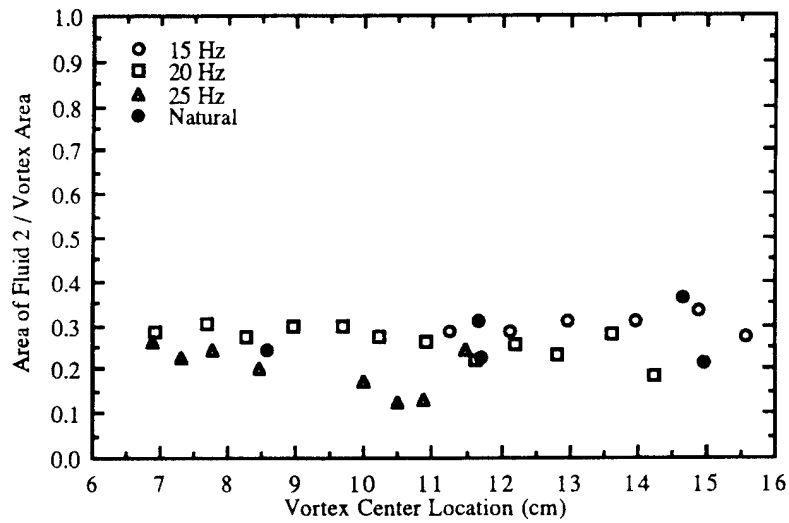


Fig. 11. Normalized area of fluid 2.

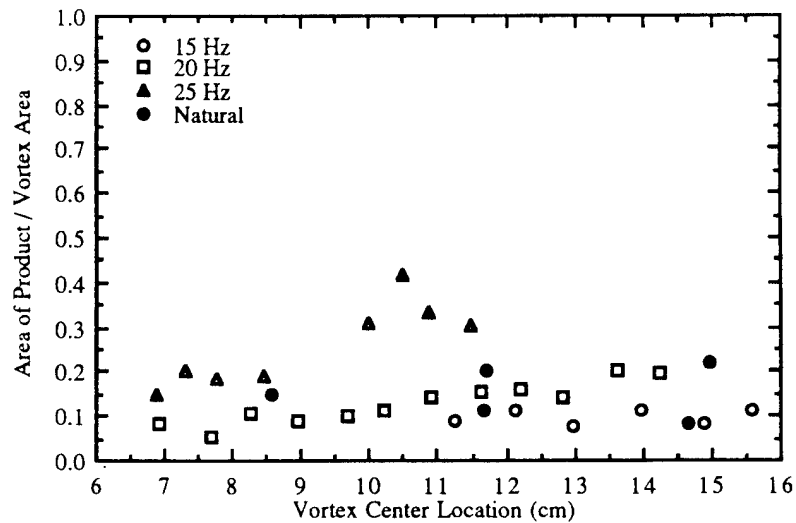


Fig. 12. Normalized area of product.

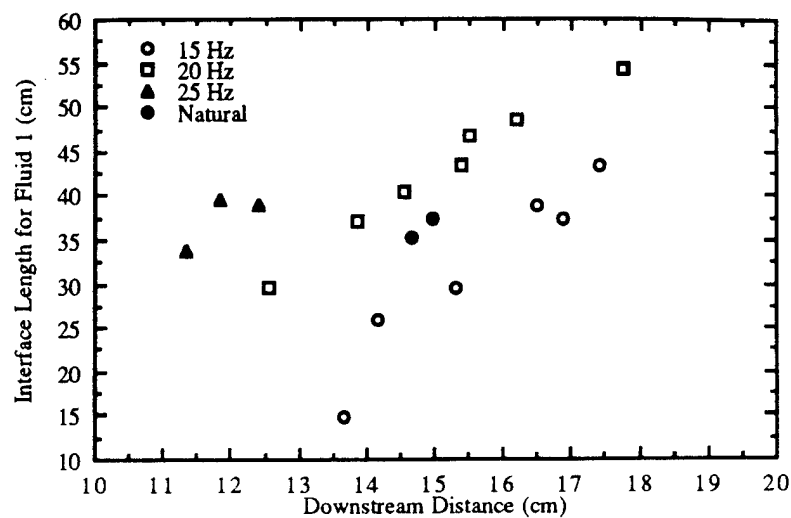


Fig. 13. Total interface length.

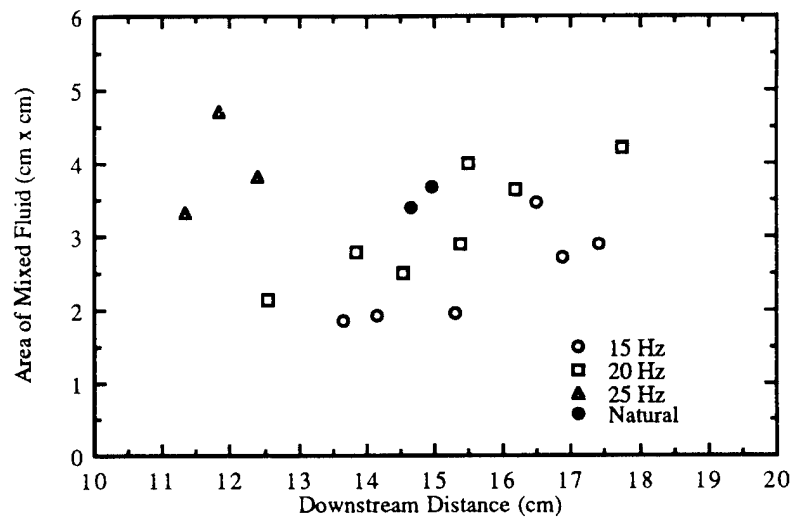


Fig. 14. Total product area.

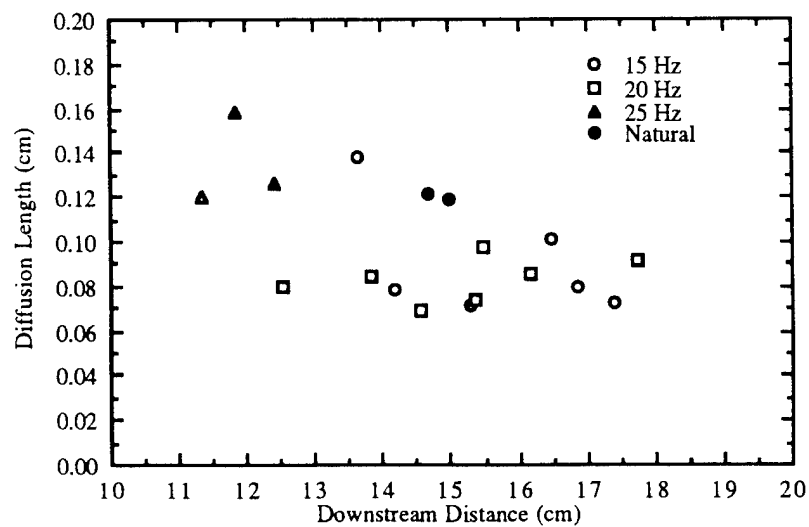


Fig. 15. Measured transverse diffusion thickness.

2.2 Thermally Stressed Jet-Fuel Diagnostics

2.2.1 General Overview. The ultimate goal of this portion of the program was to investigate and develop diagnostic techniques that would be used to aid the study of jet-fuel thermal stressing. The scope was later broadened to include de-icing studies. Two approaches were taken to achieve the program goals. Conventional diagnostic techniques such as Dynamic Light Scattering and the Quartz Crystal Microbalance were chosen and extended to meet *in situ* measurement needs. The second approach involved the development of ultrafast laser diagnostic techniques. These routes resulted in the development of research tools for jet-fuel stressing and de-icing studies.

2.2.2 Conventional Diagnostic Techniques. Fuel degradation is a complex problem. Measurement of the quantity of surface deposits as a function of time and temperature provides some insight into the basic processes involved. Measurement of the growth of particles with time and temperature provides additional information, as does the measurement of oxygen consumption. These parameters, when measured separately, are very useful but their correlation is difficult. However, simultaneous measurements of particle size, mass-deposition rate, and oxygen consumption have the potential to provide a greater understanding of the kinetics involved in thermal decomposition.

The conventional diagnostic techniques focused on particle sizing (Dynamic Light Scattering) and deposition measurements (Quartz Crystal Microbalance). These techniques were developed for their off-line (after stressing) and *in situ* (during stressing) capabilities. Results of studies conducted with the combined techniques on thermally stressed jet fuel are given in papers entitled, "Application of Photon-Correlation Spectroscopy and Quartz-Crystal Microbalance to the Study of Thermally Stressed Jet Fuel" (pp. 201 - 225), "Simultaneous Application of Photon Correlation Spectroscopy and Quartz Crystal Microbalance to the Study of Thermally Stressed Jet Fuel" (pp. 226 - 228), and "Simultaneous Measurement of Particle Size, Mass Rate of Deposition, and Oxygen Concentration in Thermally Stressed Jet Fuel" (pp. 229 - 236).

Application of Photon-Correlation Spectroscopy and Quartz-Crystal Microbalance to the study of Thermally Stressed Jet Fuel

V. Vilimpoc* and B. Sarka

Systems Research Laboratories, Inc., A Division of Space Industries International, Inc., 2800 Indian Ripple Road, Dayton, OH 45440-3696

The thermal degradation of jet fuel is characterized by the formation of particulates and gum deposits. The lack of sensitivity of previous methods of testing thermally stressed jet fuel required acceleration of the test conditions. Recently, two techniques have been integrated into a single instrumented platform to permit simultaneous in-situ real-time measurements of particle-size growth rate and surface mass-deposition rate in these fuels. With this arrangement, the particle growth rate is determined using Photon Correlation Spectroscopy (PCS), and the surface mass-deposition rate is measured with a Quartz Crystal Microbalance (QCM). The resolution and sensitivity of these techniques permit the study of particle-size growth rate and mass-deposition rate at temperatures and times representative of those found in aviation fuel systems.

Introduction

Fuel is used as the coolant for avionics and hydraulic systems in modern aircraft. Exposure of fuel to high temperature results in the formation of particulates and deposits that clog valves and filters and degrade injection-nozzle performance. Several studies have shown that auto-oxidation of hydrocarbons is the main reaction leading to formation of insoluble products and deposits (Katta and Roquemoire, 1992; Krazinski et al., 1990; Anderson et al., 1994; Jones et al., 1995; Jones and Balster, 1995; Chin and Katta, 1995). Efforts to develop highly stable jet fuels would benefit from an understanding of the relationship between particle-size growth rate and the rate of particle deposition on a surface resulting from thermally induced degradation of jet fuel. No single analytical technique exists that can provide all the required information. Therefore,

integration of existing applicable techniques into a single instrumented platform where the required parameters can be measured simultaneously and in-situ would be highly desirable. This paper reports progress on such an effort.

Experimental Techniques

PCS is a dynamic light-scattering technique capable of measuring particle size in the range 10^{-8} to 10^{-6} m. Laser light incident on a sample of particles undergoing Brownian motion will be scattered by particles having different phases, depending on the position of each particle in the laser beam and on the distance between the particle and the detector. Thus, the composite light scattered from the group of particles in the scattering volume will form an interference pattern at the detector. As the particles randomly diffuse through the solution, the pattern produced will be modulated by the particle motion. The intensity fluctuations associated with the interference pattern at the detector, although random, will be more rapid for small, rapidly diffusing particles than for larger, more slowly diffusing ones. The random-noise signal produced by the detector as a result of the scattered light can be characterized by its autocorrelation function, $g(t)$, defined by

$$g(t) = \langle I[T] I[T+t] \rangle \quad (1)$$

where $I[T]$ is the intensity at the detector at time T and the angular brackets denote a time average over T . The autocorrelation function is a measure of the similarity, or correlation, between the configuration of particles T and that at a later time $T+t$. At short t the configuration of the particles within the scattering volume will remain essentially unchanged, and the correlation with the configuration at T will be high. At longer t the particles will have diffused such that their new positions will be statistically uncorrelated with their former ones. For a system of particles of uniform size and shape undergoing Brownian motion, the autocorrelation function will be a decaying exponential:

$$g(\tau) = A \exp[-2\Gamma\tau] + B \quad (2)$$

where Γ is a decay constant characteristic of particles of that size and A and B are experimental constants dependent on the geometry, optical collection efficiency, and counting efficiency of the electronics. $1/\Gamma$ is the decay time of the Brownian motion, i.e., the time required for any particular configuration of particle positions within the scattering volume to become uncorrelated with its former positions. The decay constant is related to the diffusion constant of the particles and to the geometry of the experiment through

$$\Gamma = q^2 D; \quad q = 4\pi n \sin(\theta/2)/\lambda \quad (3)$$

where q is the magnitude of the scattering vector, D the diffusion constant of the particles, n the refractive index of the fluid, θ the scattering angle, and λ the laser wavelength. For spherical particles, the diffusion constant is related to the particle diameter through the Stokes-Einstein equation

$$D = kT/3\pi\eta d \quad (4)$$

where k is the Boltzmann constant, T absolute temperature, η the fluid viscosity, and d the particle diameter.

When the sample contains particles of different sizes, the autocorrelation function will be the sum of decaying exponentials weighted by the intensity of light scattered from particles of each characteristic size, and the autocorrelation function can be described by

$$g(\tau) = \int_a^b X(s) \exp[-\Gamma(s)\tau] ds \quad (5)$$

where the index s denotes the size of the particles and $X(s)$ is the particle-size distribution which yields the relative proportion of scattering from particles of size s . The constants a and b are the

lower and upper limits of particle size, respectively. This integral equation must be numerically inverted to extract $X(s)$ from the measured autocorrelation function (Bott, 1987). CONTIN (Provencher, 1979, 1982), a widely used FORTRAN program for this type of data analysis, was employed.

QCM is a technique for measuring extremely small mass accumulation on a quartz-crystal surface. It is designed around a piezoelectric wafer, sliced from a single crystal of quartz. The quartz wafer is sandwiched between two gold electrodes bonded to the wafer surface. As a piezoelectric material, the quartz deforms slightly in the electric field applied between the two electrodes. The oscillating electric field perpendicular to the wafer surface induces mechanical oscillation, in the form of a standing wave, in the bulk of the quartz wafer. In the QCM an AT-cut quartz wafer efficiently produces mechanical shear oscillation with displacement parallel to the wafer surface. A resonant oscillation is usually achieved by including the wafer in an appropriately designed oscillator circuit. Sandia National Laboratories (Martin et al., 1991) developed the oscillator circuit used in this study. In such a circuit, the frequency of the electrical and mechanical oscillation centers at a characteristic fundamental frequency. Mechanical oscillation of the crystal is at a maximum where the electrodes overlap and diminishes rapidly in areas where they do not. Thus, the QCM is most useful when probing processes that occur uniformly across the QCM surface--processes that can be represented as a change in mass per unit area. The oscillation frequency is dependent upon several factors: 1) factors that are normally constant include the physical properties of the quartz wafer (thickness, density, and shear modulus) and 2) factors that normally are held constant include the density and viscosity of the phases in contact with the QCM wafer and the pressure and temperature differences across the wafer. The theory relating the measured frequency changes to the surface mass deposition has been presented previously (O'Hern, 1993) and is given by

$$\Delta f \approx - 2f^2/N(\mu_q \rho_q)^{1/2} [\rho_s + (\rho\eta/4\pi f)^{1/2}] \quad (6)$$

where Δf is the change in oscillation frequency, f the unperturbed resonant frequency, N the overtone mode number, μ_q the quartz shear modulus ($2.947 \times 10^{11} \text{ g cm}^{-1} \text{ s}^{-2}$), ρ_q the density of quartz (2.648 g cm^{-3}), ρ_s the surface mass density, and ρ and η the liquid density and viscosity, respectively. The first term in Eq. (6) relates the surface mass density to the change in frequency, and the second relates the change in fluid properties to that in oscillation frequency. When all other factors are held constant, the variation in mass of an adsorbate or thin film attached to the electrode can be determined from the change in frequency. Under such conditions the surface mass deposition can be related to the change in the fundamental resonant frequency by

$$\rho_s = - 2.21 \times 10^5 \text{ g cm}^{-2} \text{ s}^{-1} \Delta f/f^2 \quad (7)$$

Although QCM has been applied by Zabarnick and Grinstead (1994) and by Martin et al. (1991) to the study of thermally stressed jet fuel, the system employed has shortcomings. First, the reactor used was a stirred-tank type with a large fluid volume, requiring a long heat-up time. At high temperature the reaction rates are accelerated; therefore, mass deposition would be completed well before their reactors achieved thermal equilibrium. Second, the reactor has an air space which introduces an additional step of mass transfer from the gas phase to the liquid phase during the course of the reaction. This complication can be avoided by the proper design of the QCM cell and holder.

Experimental Setup and Procedures

The experimental setup is shown in Fig. 1. Light from a 35-mW HeNe laser is focused into a quartz optical cell from above, while the time-varying light scattered from particles is collected at a fixed angle in the horizontal plane by a photomultiplier. The time-varying signal from the photomultiplier is converted into pulse trains by an amplifier/discriminator whose output is processed by a digital correlator (Langley Ford Instrument Correlator Model 1096). The outputs

from the correlator (exponential decay curve for each run) are stored and later processed off-line on a workstation to yield size data.

The experimental test cell is a cylindrical block (56 mm in diam and 64 mm long) made of 304 stainless steel, into which four 3.2-mm-diam holes are drilled symmetrically. Two sections of these blocks are connected and surrounded by cylindrical heating jackets. The entire apparatus is wrapped with fiberglass insulation to minimize temperature fluctuation. The fuel is pumped through the test cell by an HPLC syringe pump (ISCO 500D). Typical flow rates required to obtain 1 - 20 min of residence time are in the range 4.212 - 0.211 cc/min. Either an optical quartz cell or a QCM cell (or both) can be attached to the end of the reactor to obtain *in-situ* size and mass-rate data. At high temperature the PCS signal-to-noise ratio was observed to be low; therefore, some experiments were conducted by pumping fuel through the reactor into the QCM cell (maintained at the test-cell temperature) and then through a 0.15-mm-od stainless-steel tube immersed in a water bath into a 4-mm-square optical-quartz cell at room temperature.

The QCM cell consists of an outer stainless-steel shell with an SMA-type RF feedthrough (Del Weld Model VAC 925 1000) welded to the end. The support for the electrical contacts is machined from a ceramic block (Corning Glass MACOR ceramic). The electrical contacts are beryllium copper posts on springs sliding against beryllium copper fingers. O-ring seals are used to protect the contacts from deposition. Fuel flows around the QCM crystal and deposits on both sides of the crystal; therefore, no differential pressure develops across the crystal. Both the test cell and the QCM cell are completely filled and pressurized to ~ 250 - 300 psig to prevent boiling and to avoid overhead space. In operation, both the test cell and QCM cell are oriented in the horizontal direction to avoid convective current and sedimentation.

Results and Discussion

With PCS particle size is measured indirectly by inference from the rate of signal decorrelation due to Brownian motion of a group of particles at successive instances in time. A question arises as to the effect on the measurement accuracy of a directed flow velocity superposed

on the Brownian motion. For calibrating the PCS system, calibration runs with three different sizes of polystyrene spheres (Nanosphere, Duke Scientific Corp.) were made. Solutions of the spheres in distilled water were made and pumped through the optical test cell at different flow rates, covering more than five times the range of the flow rates to be used in the actual thermal-stressing experiments. Results from the PCS calibration runs are shown in Fig. 2. As can be seen, the smaller the particles, the larger the superimposed velocity must be to affect the accuracy of the measured diameter. This is to be expected since smaller particles diffuse with faster Brownian motion; thus, as long as the superimposed velocity is much smaller than the Brownian velocity, the effect of the superimposed velocity will be negligible. The PCS system is expected to yield accurate size data at all flow rates used in the actual thermal-stressing experiments because at high flow rates the residence time in the reactor is short and, thus, the particle size is expected to be small; therefore, the effect of the flow velocity on the measured size will be negligible. At low flow rates and longer residence times, the particle size is expected to be large; however, because the flow velocity is low, the effect of the superimposed velocity is also expected to be negligible.

A number of experiments were conducted in which a typical jet fuel (POSF2827) was thermally stressed for different durations and the resultant particulates measured with the PCS system. Two sets of measurements were made. Initially fuel was pumped through the optical cell at the rate used to obtain the desired residence time while PCS measurements were made. Then measurements of the same fluid were repeated with zero fluid velocity in the optical cell. The results are shown in Fig. 3. If spherical particles form, one would expect that at the flow rates used in these experiments, the resultant particle size would converge to within the span of the experimental errors for both static and dynamic experiments. However, as can be seen from Fig. 3, the particle-size profiles obtained when fuel is flowing through the optical cell are consistently smaller than those obtained when fuel is not flowing. As stated previously the superimposed flow velocity is expected to have a negligible effect on the measured particle size in this velocity range if the particles are spherical. The reason for the difference in values may be that the particles have a tubular shape (Baker et al., 1982) and when a velocity is superimposed, the long axis of the

particles becomes aligned with the flow direction; when no velocity is superimposed, the particles are free to rotate, resulting in a larger particle size being measured in the static fluid. Note also that the dynamic and static diameter approach the same value as the flow velocity decreases toward zero, as expected.

The mechanism of particulate formation during thermal degradation of jet fuel remains a mystery. Do particles form as a result of physical processes which occur with a change in the physical or chemical properties of the fuel, for example, by condensation resulting from differences in solubility between the solvent and solute phases (Oswald ripening) or by agglomeration resulting from collisions and sticking together of small particles? Or do particles form and grow as a result of chemical reaction? In-situ measurements during particle formation would answer this question unambiguously. A typical result from a number of attempts to make in-situ particle-size measurements is shown in Fig. 4. At short residence times, the few small-size particles generated do not scatter sufficient light (scattered-light intensity is proportional to particle number density and particle size) to allow meaningful correlation by the PCS system. The poor signal-to-noise ratio is reflected in the large uncertainty in particle size at short residence times. In fact, at a residence time of < 1.5 min, no particle was detected. It is probable that the large standard deviation in particle size at short residence time masked any observable trend in the particle growth rate.

A complication in conducting in-situ PCS experiments is that at high temperature, small particles move in and out of the probe volume very rapidly because of the large Brownian velocity resulting from its high kinetic energy. The short transit times of small particles through the probe volume result in a low signal-to-noise ratio caused by the low scatter intensity. As particles grow in size, move more slowly, and are produced in larger quantities at longer residence times, they become detectable by the PCS system. Unfortunately, beyond the detection threshold, these particles are no longer growing in size with increasing residence time, although they are produced and deposited in ever-increasing quantities. To obviate these difficulties, the decision was made to quench post-stressed fuel to room temperature prior to measurements by PCS. However, first it

was necessary to ascertain whether the act of quenching the post-stressed fuel sample to room temperature would interfere with any of the kinetic processes responsible for the formation and growth of particles.

For ascertaining the effect of temperature changes on particle size, fuel was heated at a long residence time to generate particles sufficiently large for detection; then fuel flow to the test cell and power to the heater were shut off. PCS was used for continuous in situ monitoring of particle size as the fuel cooled to obtain data on particle size as a function of temperature. As can be seen from Fig. 5, the particle size increases continuously and slowly, while the scattered-light intensity increases to a maximum and then slowly decreases. A plausible explanation for the observed profiles is that as temperature decreases, the average-particle Brownian velocity also decreases, resulting in longer transit times for particles in the probe volume and, thus, more scattered light per unit time during the first 10 min of elapsed time. Although the particles become larger, the scattered-light intensity decreases after 10 min. The increase in particle size is probably caused by agglomeration which would account for the reduction of scattered-light intensity. This result indicates that post-stressed PCS measurements should yield accurate size data since the time scale is so short during quenching and measurement that particles have no time to grow by agglomeration except at very low flow rates.

For obtaining particle-size growth rate as a function of exposure time to high temperature, fuel thermally stressed for different lengths of time was quenched to room temperature and studied with PCS, while mass-deposition rates were monitored in-situ with QCM. All tests in this study were conducted with a JET-A fuel (POSF2827). At the start of an experiment, a computer commands the syringe pump to begin pumping fuel through the test cell at a predetermined flow rate to achieve a given exposure time. The computer then monitors the volume of fuel flow and the fuel temperature in the QCM cell. The quartz-crystal oscillation frequency is a function of both the temperature and the amount of mass deposit on the crystal surface; therefore, the QCM temperature must remain relatively constant when mass-deposition-rate data are being collected. When at least two reactor volumes (30 cc) of fuel have been purged through the reactor-QCM cell and the fuel

temperature in the QCM cell has remained constant to within 0.1°C for 16 min, the computer begins taking PCS and QCM data for subsequent processing. At each flow rate 20 PCS and QCM data points are taken at 2-min intervals. Therefore, the rates of mass deposition are measured over a period of 40 min. The benefit of this procedure is that some statistical confidence can be gained on the size of particles and the scattered intensity measured. When sufficient data are collected, the pump is commanded to pump at a new flow rate, and the entire process is repeated. Because of the large thermal mass of the reactor-QCM cell, ~ 2 hr is required to achieve a steady-state temperature from initial room temperature; however, once steady state is reached, the temperature remains very stable.

Typical results for a fuel thermally stressed for different exposure times at 165°C and 195°C are shown in Figs. 6 and 7, respectively. In these figures, the scattered-light intensities are normalized to the minimum and maximum particle size to ensure that they will be on the same scale for demonstrating the relationships among the variables. At 165°C , particle size and scattered-light intensity increase with increasing residence time but at decreasing rates. Particle size and scattered-light intensity begin to level off at a 20-min residence time, while the rate of mass deposition peaks at 14 min. In comparison, at 195°C the mass-deposition rates and scattered-light intensity reach their maxima at about 3.5 min, while the particle-size growth profile does not level off until about 10 min. Note the similarity between the scattered-light intensity, which represents the total number density of particles, and the rate of mass deposition. Both profiles show progressively longer residence times required to reach a maximum, from 3.5 min at 195°C to 20 min at 165°C . From a comparison of the profiles at 195 and 165°C , it is obvious that the 165°C profiles from 2 to 20 min residence time mimic those at 195°C from 1 to 5 min residence time--but at a much lower particle number density and mass deposition rate and at a much slower pace. This result clearly suggests that particulates are formed and deposited as a result of chemical reactions--hence, the longer residence time required to reach maxima at lower temperatures.

Comparison of the scattered-light-intensity profiles and mass-deposition rates in Figs. 4 and 7 shows a striking similarity in behavior of these profiles whether the experiments are

conducted in-situ or under post-test quenching. It is interesting that the profiles track each other--regardless of the experimental method used to obtain the data--which suggests that scattered intensity profiles indeed provide a good approximation to the total number of particles produced. This result seems to suggest that settling in the quenched line between the reactor and the PCS optical cell does not cause the observed decrease in the scattered-intensity and mass-deposition rates. Profiles of particle diameter in the range 165 - 195°C as a function of residence time are shown for comparison in Fig. 8. Note the progressively slower particle-size growth rate at 165°C in comparison to the growth rate at 195°C.

Figures 9 and 10 show scattered-light-intensity and mass-deposition-rate profiles, respectively. Note the difference in magnitude of the scattered-light intensity at different temperatures. The scattered-light-intensity profiles seem to suggest that the higher the temperature, the larger the quantity of particles formed as a function of fuel-exposure time at high temperature. One interpretation of the two profiles would be that at any given temperature, a maximum in the rate of particle production and surface deposition corresponds to the maximum amount of dissolved oxygen that can be consumed by the reactants at the prevailing reaction rates. The maxima in the two profiles are reached when the dissolved oxygen is consumed up to the limit dictated by the thermodynamic equilibrium of the system. Logically, particles are produced in the bulk phase and then deposited onto the surface in contact with the bulk phase, as evidenced by the fact that the mass-deposition rates track the scattered-light-intensity profiles very closely. When less particles are produced at a longer residence time, the rate of mass deposition also declines. The thermodynamic equilibrium of the fuel-dissolved-oxygen system dictates the extent of oxygen consumption, while the kinetic rate of reactions dictates the rate of particle growth and the number of particles produced; hence, at lower temperature the rate of particle growth and the quantity of particles produced are much lower.

From observation of the larger scattered-light intensities in Fig. 9, it can be deduced that more particles may be produced at 195 and 185°C than at 175°C. However, the mass-deposition rates in Fig. 10 show a reversal in magnitudes at longer residence times. It is interesting to note

that the rate of mass deposition dropped off rapidly at 195 and 185°C after reaching a maximum, and at long residence times the mass-deposition rates at 195 and 185°C are lower than at 175°C. If the scattered-light intensity is considered to represent the total number of particles in the bulk fuel and the total quantity of particles produced in the fuel is fixed for a given rate of oxygen consumption, then when more particles are deposited on the QCM surface, the total number of particles remaining in the bulk solution must decrease according to the law of conservation of mass. This explanation seems to be consistent with the behavior of the two profiles.

Conclusion

The combination of QCM and PCS has provided insight into the relationship between particle-size growth rate and mass-deposition rate. Scattered-light-intensity and mass-deposition rates exhibit similar behavior in in-situ and post-test-quenched experiments, suggesting that qualitative particle number density can be approximated by the scattered-light intensity. Particle-growth, scattered-light-intensity, and mass-deposition rates appear to be dictated by chemical kinetics and thermodynamic equilibrium between dissolved oxygen and fuel. It has been shown that the simultaneous use of these techniques can provide powerful insight into the interplay among the various mechanisms.

Acknowledgment

This study was performed at and supported by Wright Laboratory, Aero Propulsion and Power Directorate, Wright-Patterson Air Force Base, OH, under USAF Contract No. F33615-90-C-2033.

Literature Cited

- Anderson, S. D.; Jones, E. G.; Goss, L. P.; Balster, W. J. Effect of Additives on the Formation of Insolubles in a Jet A Fuel. In *Proceedings of the 5th International Conference on Stability and Handling of Liquid Fuels, Rotterdam, The Netherlands, 3-7 October 1994; Vol. 1*, Giles, H. N., Ed.; U. S. Department of Energy: Washington, D. C., 1994, pp 291-301.
- Baker, R. T. K.; Yates, D. J. C.; Dumesic, J. A. Filamentous Carbon Formation over Iron Surfaces. In *Coke Formation on Metal Surfaces, ACS Symposium Series 202*, Albright, L. F., and Baker, R. T. K., Eds.; American Chemical Society: Washington, D. C., 1982, pp 1-21.
- Bott, S. E. Submicrometer Particle Sizing by Photon Correlation Spectroscopy: Use of Multiple-Angle Detection. In *Particle Size Distribution - Assessment and Characterization, ACS Symposium Series 332*, Provder, T., Ed.; American Chemical Society: Washington, D. C., 1987, pp 74-88.
- Chin, L. P.; Katta, V. R. Numerical Modeling of Deposition in Fuel-Injection Nozzles. AIAA Paper No. 95-0497, Presented at the AIAA 33rd Aerospace Sciences Meeting and Exhibit, Reno, NV, Jan 1995.
- Jones, E. G.; Balster, W. J. Surface Fouling in Aviation Fuel: Short- vs Long-Term Isothermal Tests. *Energy and Fuels*. **1995**, In Press.
- Jones, E. G.; Balster, W. J.; Post, M. E. Degradation of a Jet-A Fuel in a Single-Pass Heat Exchanger. *J. Energy Gas Turbines Power* **1995**, *117*, 125.
- Katta, V. R.; Roquemore, W. M. A Numerical Method for Simulating the Fluid-Dynamic and Heat-Transfer Changes in a Jet Engine Injector Feed-Arm due to Fouling. AIAA Paper No. 92-0768, Presented at the AIAA 30th Aerospace Sciences Meeting and Exhibit, Reno, NV, Jan 1992.

- Krazinski, J. L.; Vanka, S. P.; Pearce, J. A.; Roquemore, W. M. A Computational Fluid Dynamics and Chemistry Model for Jet Fuel Thermal Stability. Presented at the 35th ASME International Gas Turbine and Aeroengine Congress and Exposition, Brussels, Belgium, June 1990.
- Martin, S. J.; Granstaff, V. E.; Frye, G. C. Characterization of a Quartz Crystal Microbalance with Simultaneous Mass and Liquid Loading. *Anal. Chem.* **1991**, *63*, 2272.
- O'Hern, T. J.; Trott, W. M.; Martin, S. J.; Klavetter, E. A. Advanced Diagnostics for In Situ Measurement of Particle Formation and Deposition in Thermally Stressed Jet Fuels. AIAA Paper No. 93-0363, Presented at the AIAA 31st Aerospace Sciences Meeting and Exhibit, Reno, NV, Jan 1993.
- Provencher, S. W. Inverse Problems in Polymer Characterization: Direct Analysis of Polydispersity with Photon Correlation Spectroscopy. *Makromolec. Chem.* **1979**, *180*, 201.
- Provencher, S. W. CONTIN: A General Purpose Constrained Regularization Program for Inverting Noisy Linear Algebraic and Integral Equations. *Comp. Phys. Commun.* **1982**, *27*, 229.
- Zabarnick, S.; Grinstead, R. R. Studies of Jet Fuel Additives Using the Quartz Crystal Microbalance and Pressure Monitoring at 140°C. *I&EC Res.* **1994**, *33*, 2771.

Figure Captions

- Figure 1. Schematic diagram of experimental setup.
- Figure 2. Plot of apparent diameter as function of flow rate of polystyrene calibration spheres.
- Figure 3. Plot showing effect of fluid velocity on apparent particle size.
- Figure 4. Results of in-situ experiment to measure particle size and mass-deposition rate.
- Figure 5. Results of cool-down experiment to measure effect of temperature on particle size.
- Figure 6. Typical results for quenched-product PCS/QCM measurements at 165°C.
- Figure 7. Typical results for quenched-product PCS/QCM measurements at 195°C.
- Figure 8. Particle-growth rates at different temperatures.
- Figure 9. Profiles of scattered-light intensity at different temperatures.
- Figure 10. Mass-deposition rates at different temperatures.

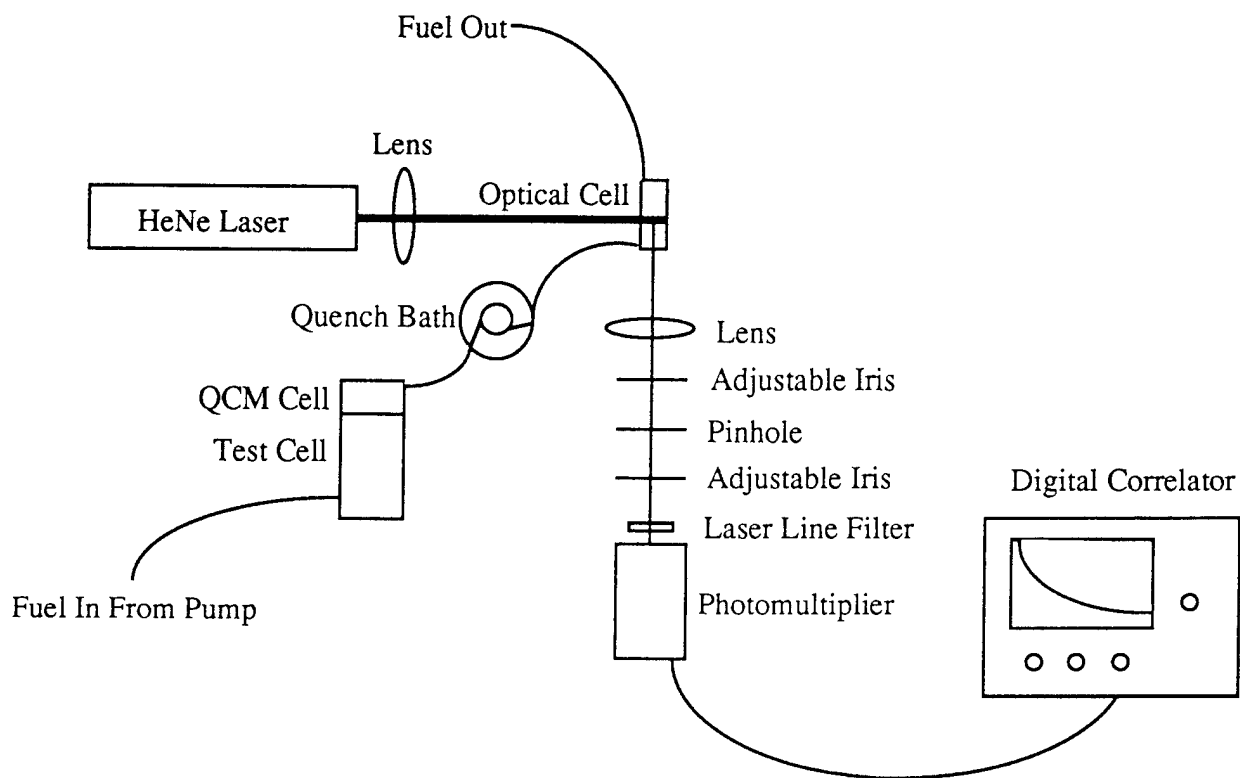


Figure 1. Schematic diagram of experimental setup.

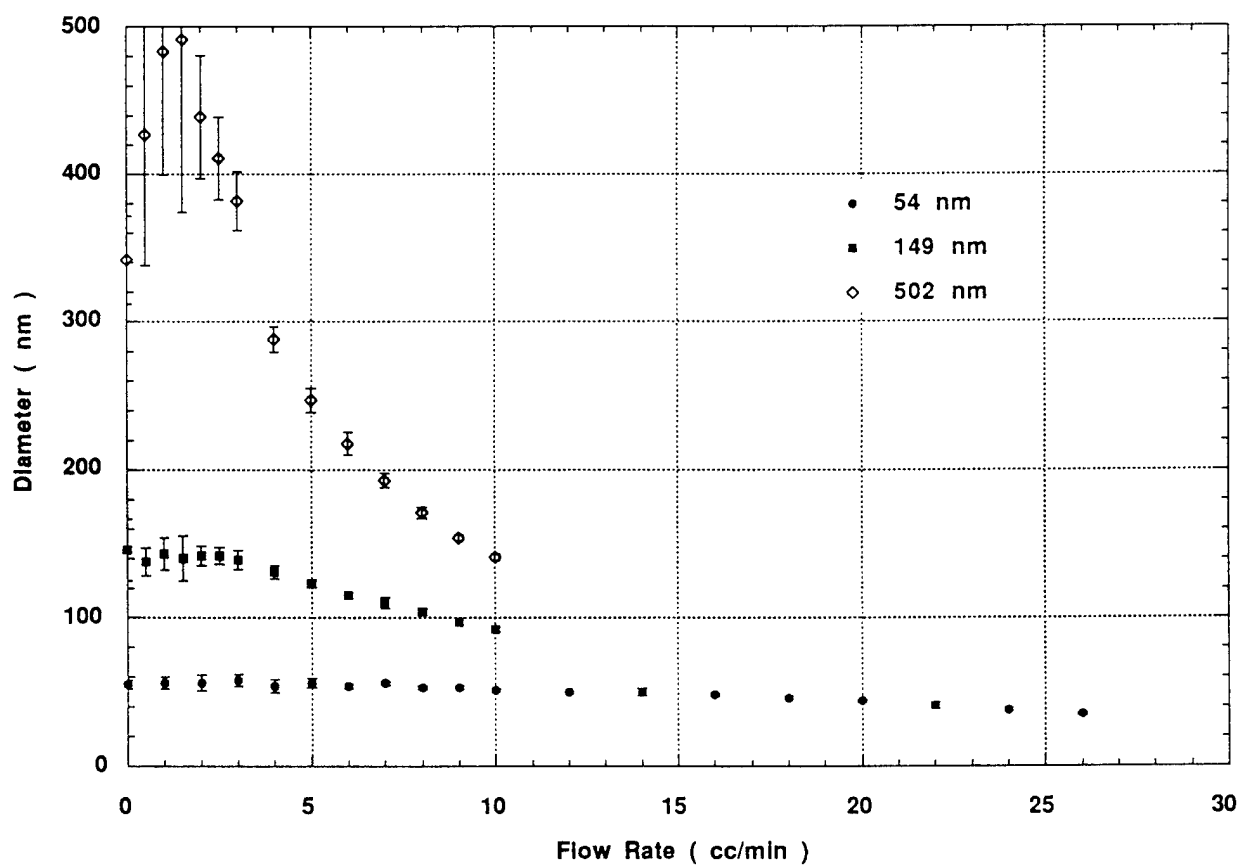


Figure 2. Plot of apparent diameter as function of flow rate of polystyrene calibration spheres.

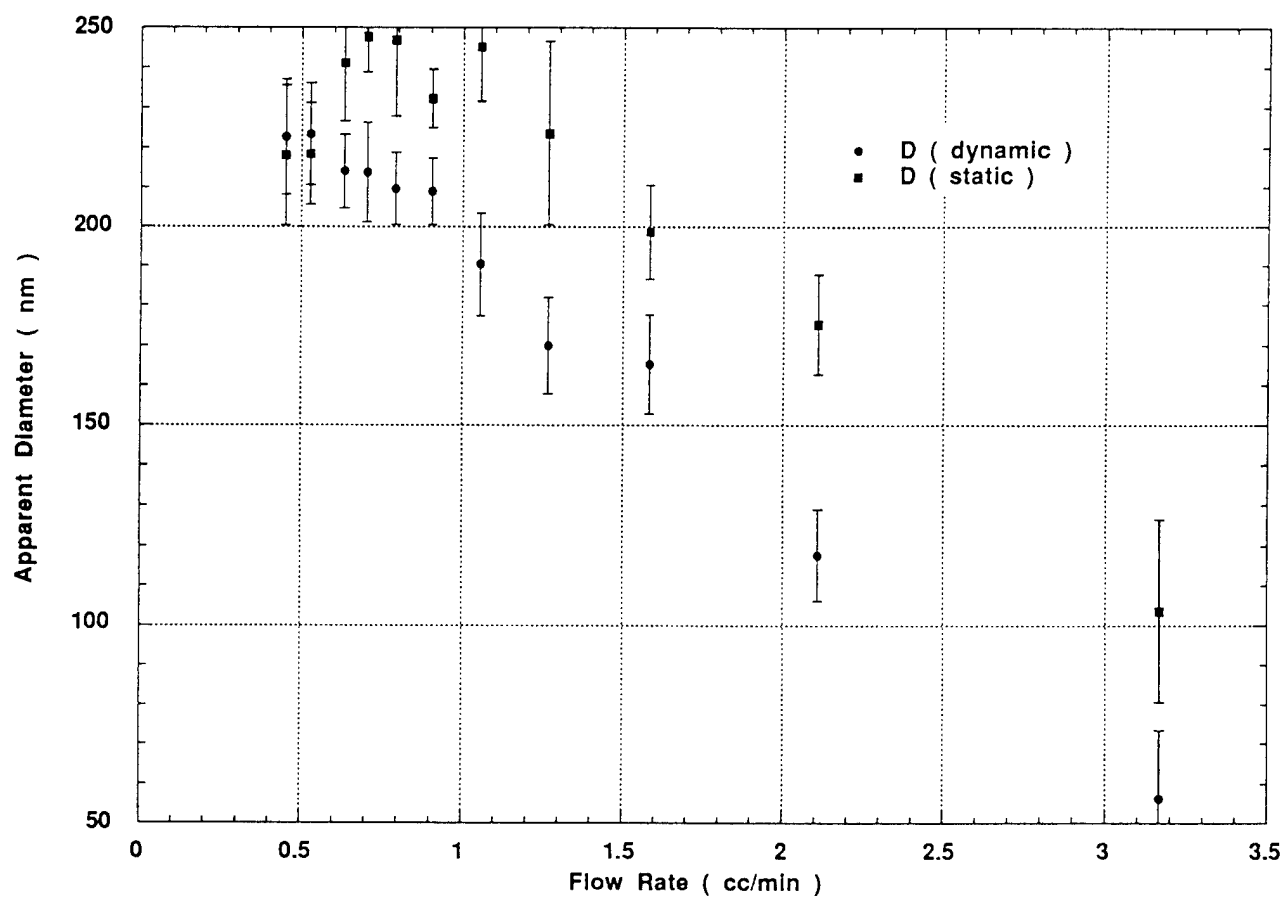


Figure 3. Plot showing effect of fluid velocity on apparent particle size.

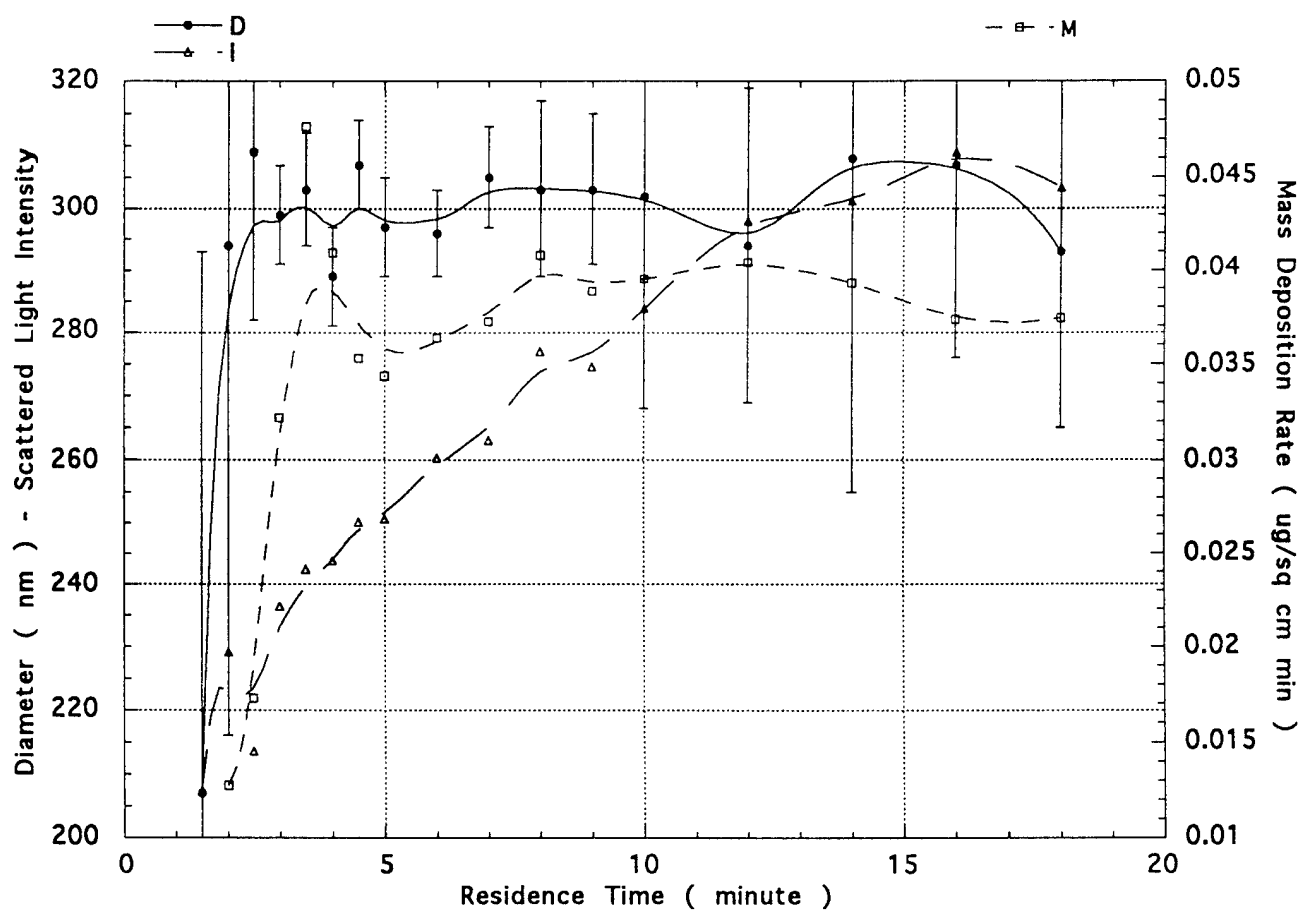


Figure 4. Results of in-situ experiment to measure particle size and mass-deposition rate.

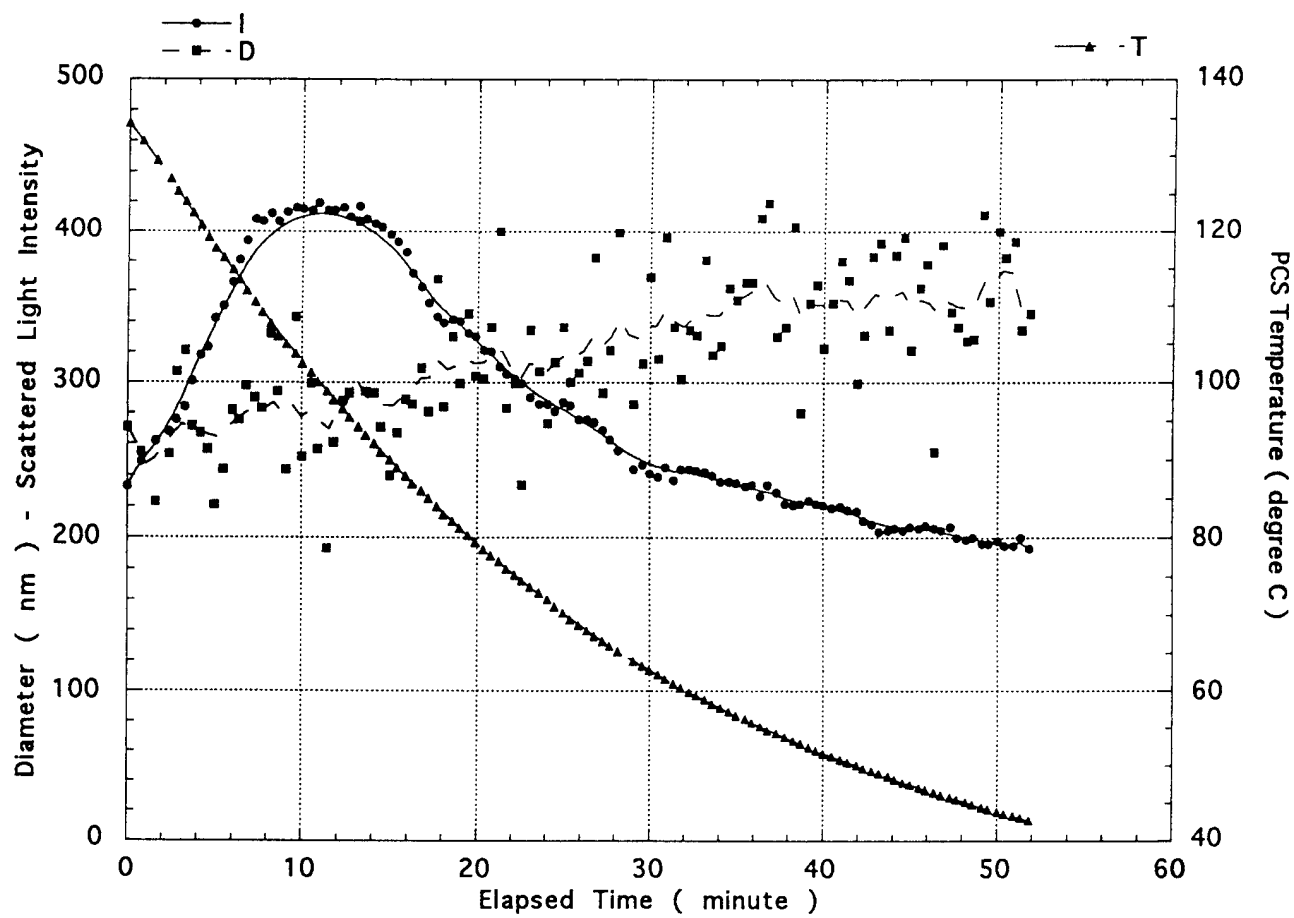


Figure 5. Results of cool-down experiment to measure effect of temperature on particle size.

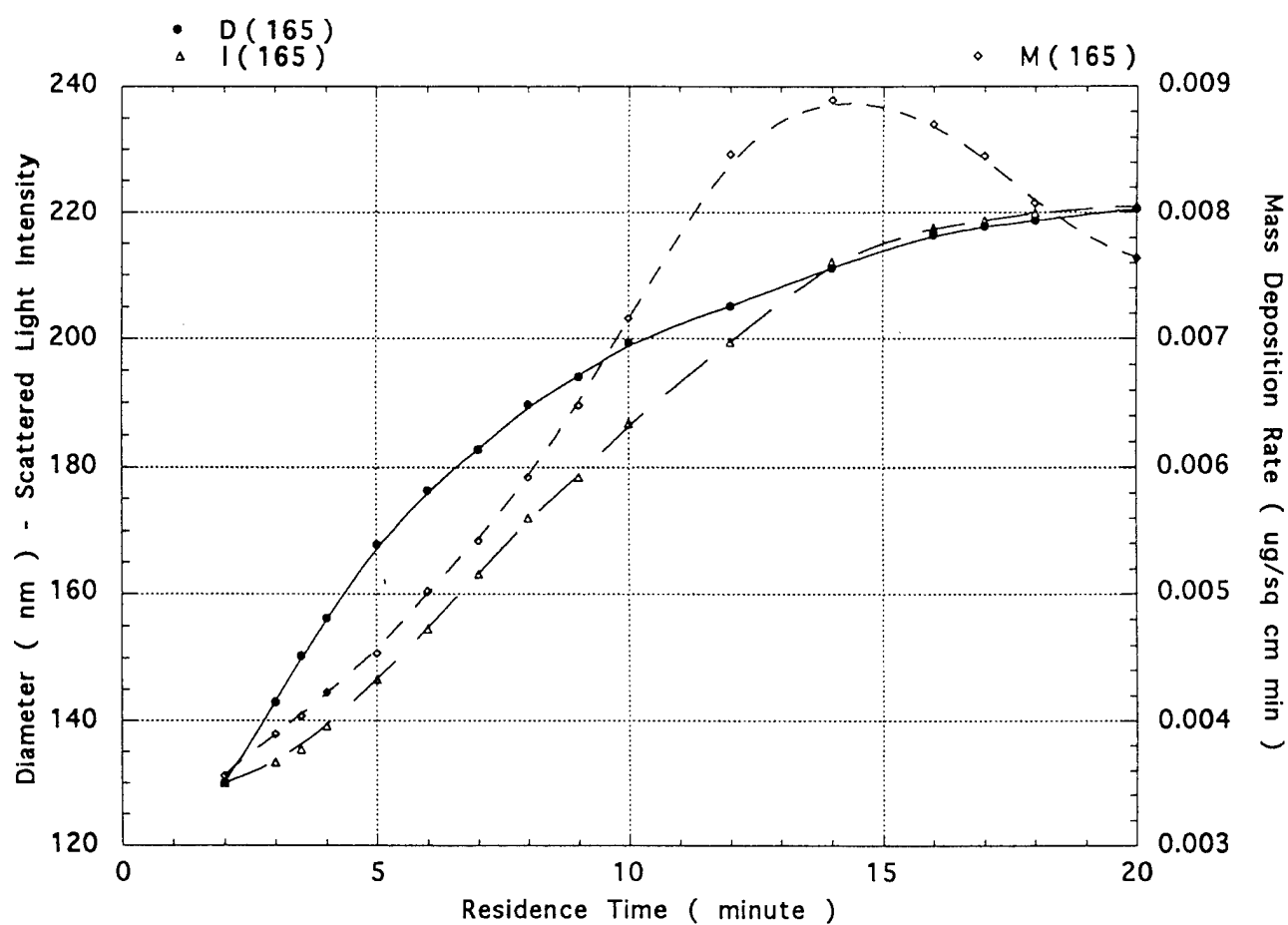


Figure 6. Typical results for quenched-product PCS/QCM measurements at 165°C.

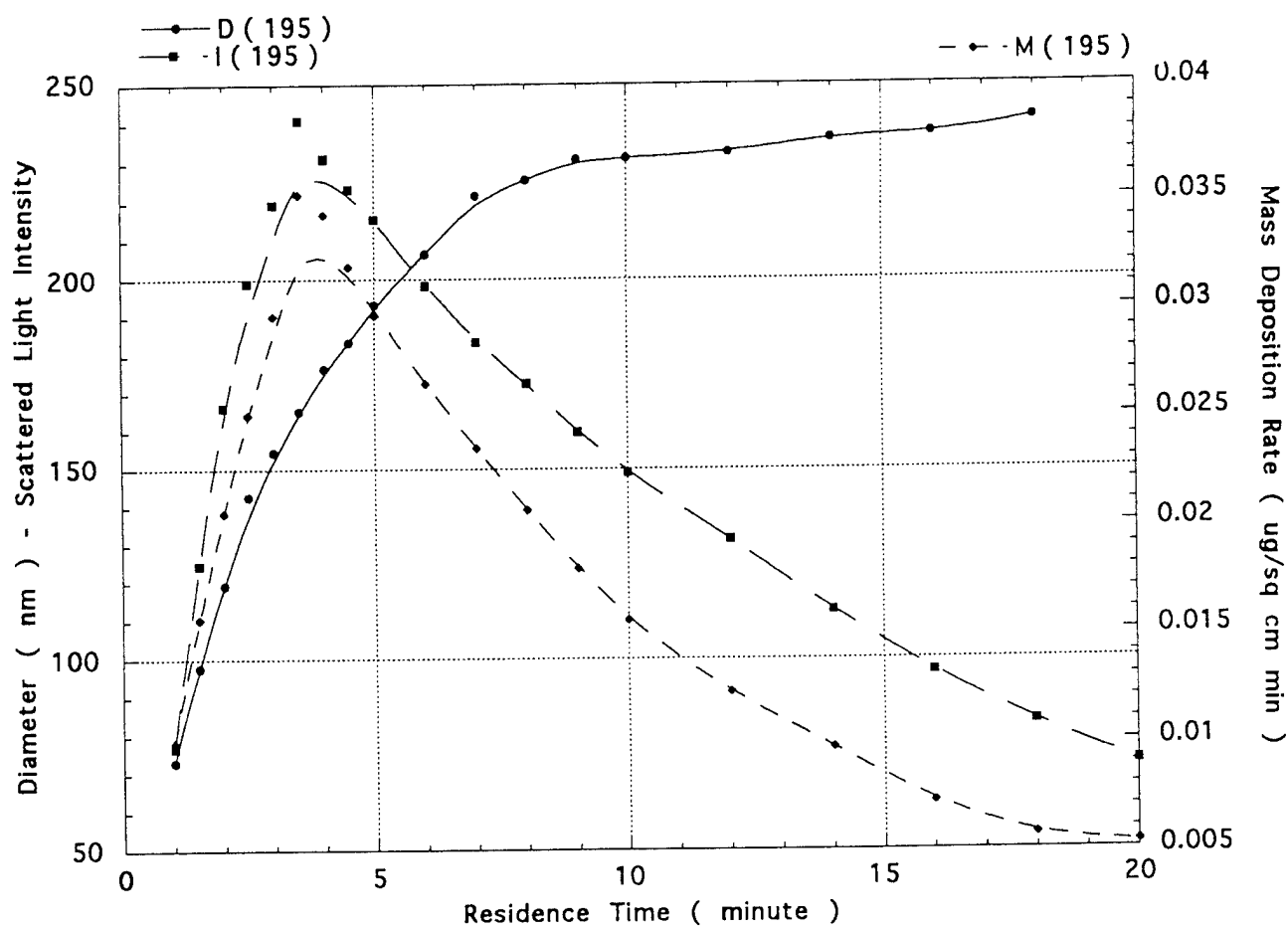


Figure 7. Typical results for quenched-product PCS/QCM measurements at 195°C.

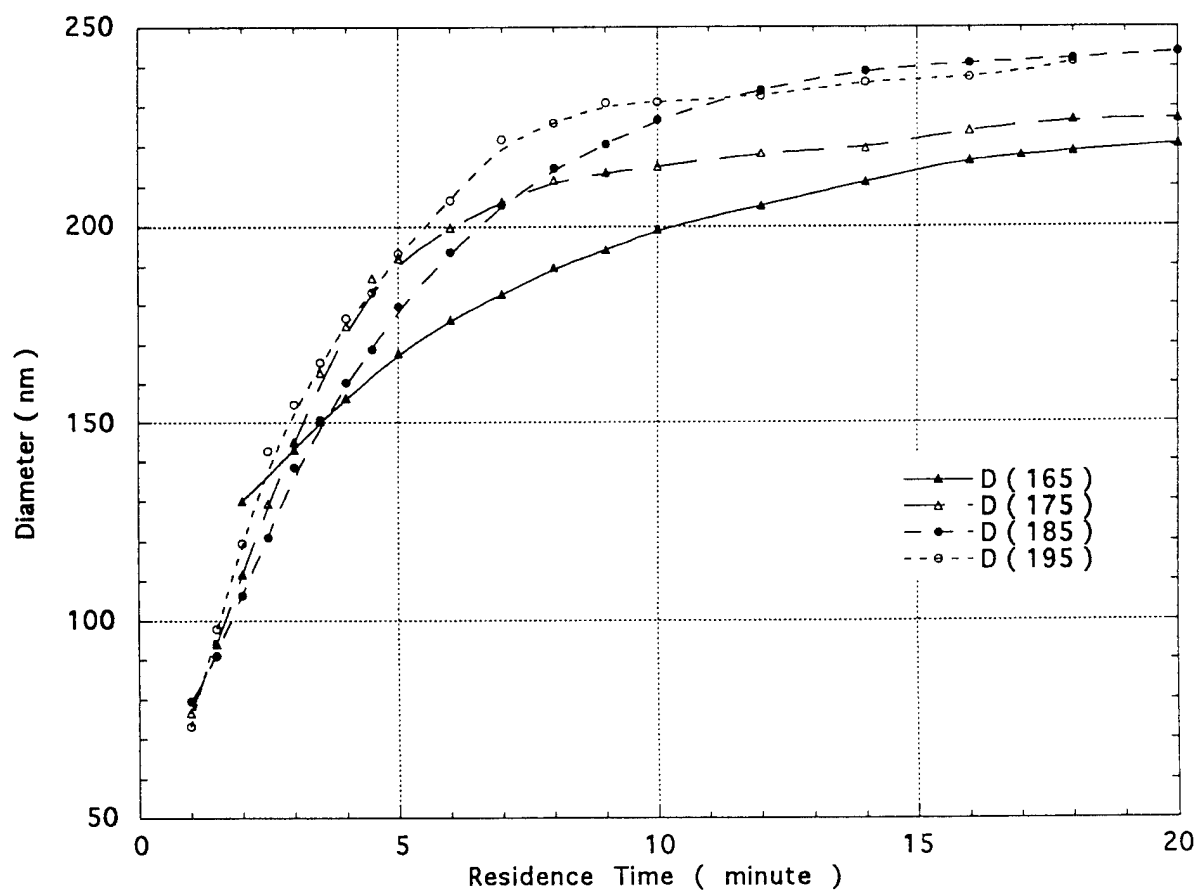


Figure 8. Particle-growth rates at different temperatures.

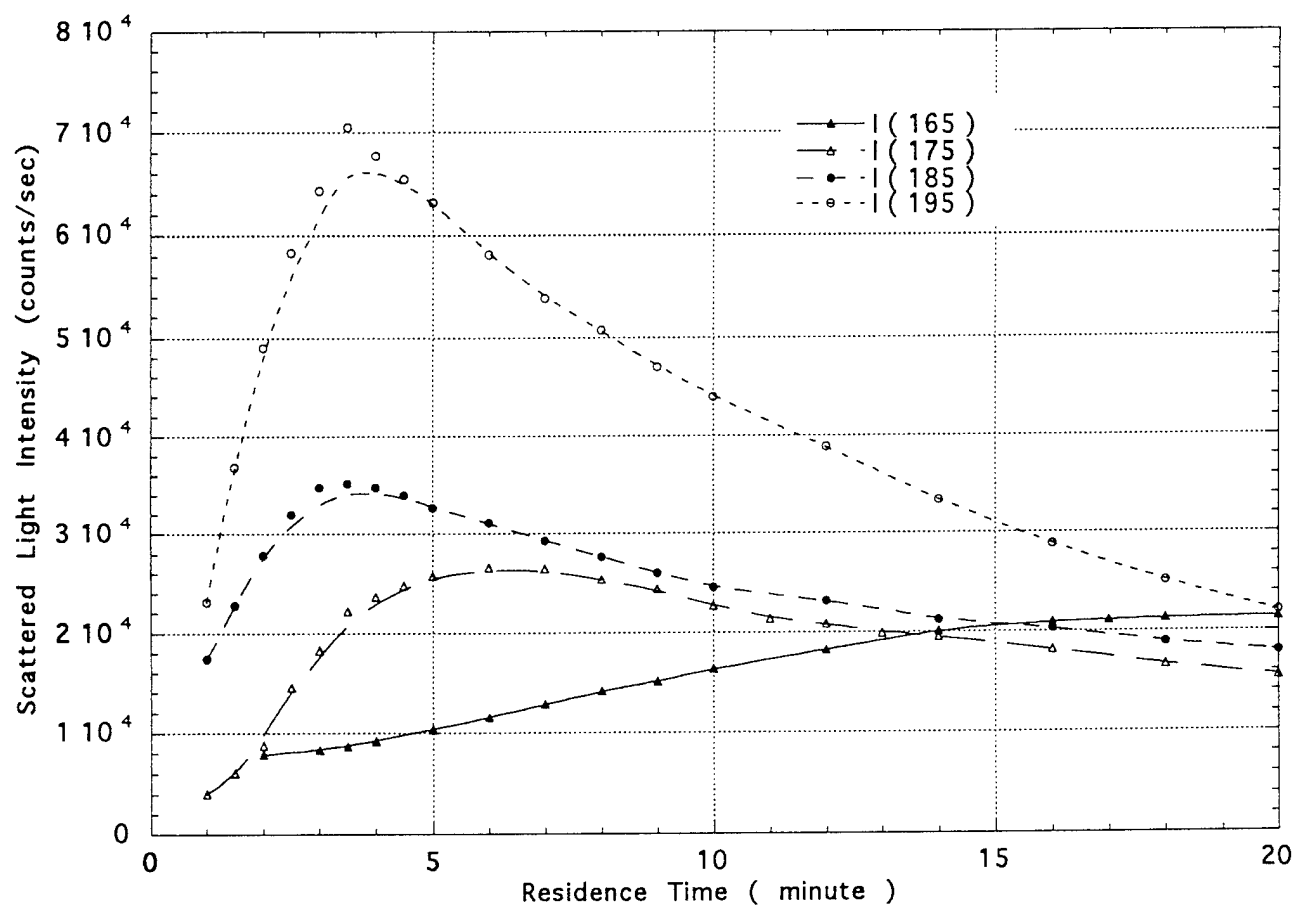


Figure 9. Profiles of scattered-light intensity at different temperatures.

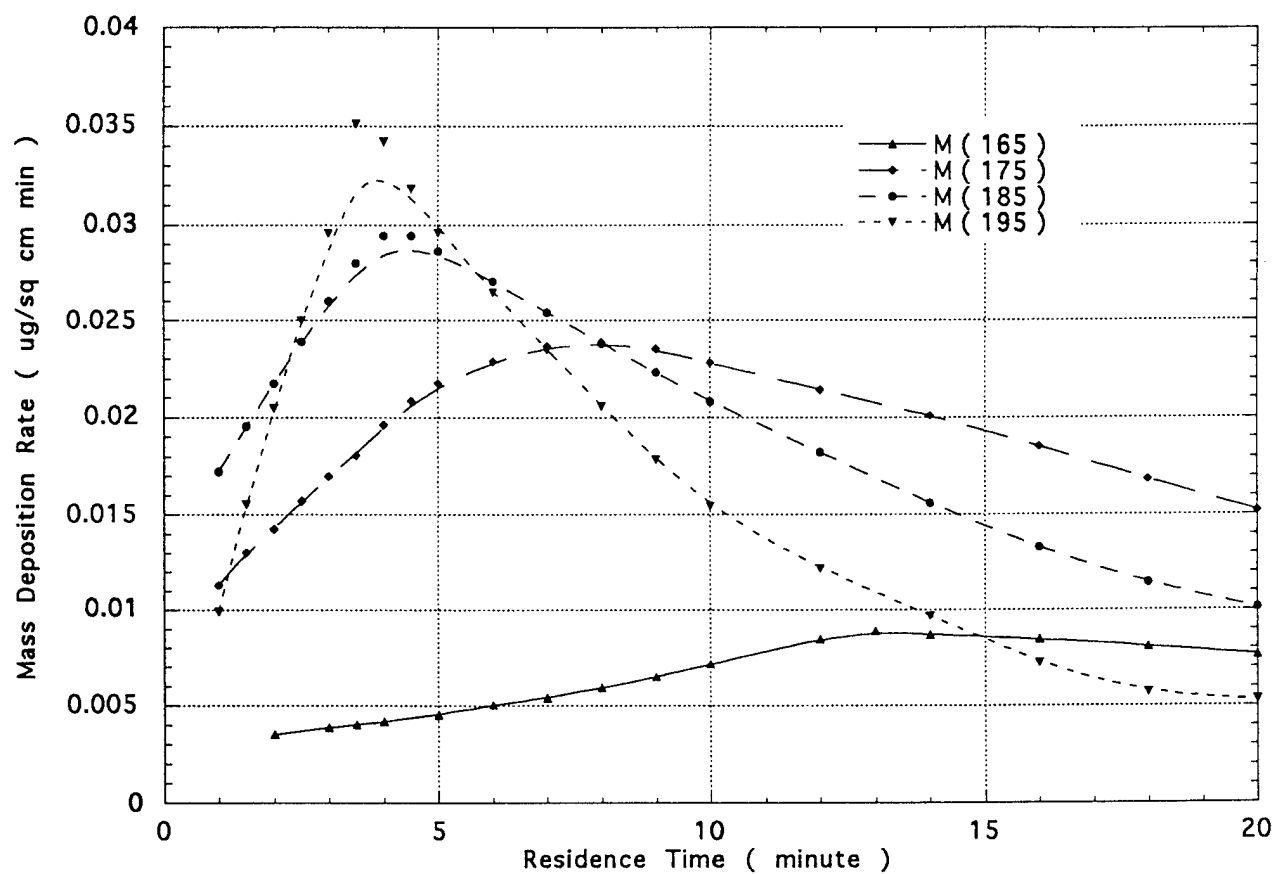


Figure 10. Mass-deposition rates at different temperatures.

Symposium on Coke Formation and Mitigation
Presented before the Division of Petroleum Chemistry, Inc.
210th National Meeting, American Chemical Society
Chicago, IL, August 20-25, 1995

Simultaneous Application of Photon Correlation Spectroscopy and Quartz Crystal Microbalance to the Study of Thermally Stressed Jet Fuel

V. Vilimpoc and B. Sarka
Systems Research Laboratories, Inc.
A Division of Space Industries International, Inc.
2800 Indian Ripple Road
Dayton, OH 45440-3696

INTRODUCTION

Fuels are used as the coolant in avionics and hydraulic systems in modern aircraft. Exposure of fuels to high temperature results in the formation of particulates and deposits which clog valves and filters and degrade injection-nozzle performance. Several studies have shown that the auto-oxidation of hydrocarbons is the main reaction leading to formation of insoluble products and deposits (1-6). Efforts to develop highly stable jet fuels would benefit from a model relating the size and growth rate of particles and the rate of particle deposition on a surface in thermally induced degradation of jet fuel. The application of two techniques for measuring these parameters will be discussed in this paper. The first technique, Photon Correlation Spectroscopy (PCS), is a dynamic light-scattering technique for measuring hydrodynamic particle diameter in the 10^{-6} to 10^{-9} m. The second technique is Quartz Crystal Microbalance (QCM) where the rate of mass deposition over the surface area of a quartz crystal is deduced from the shift in the resonant oscillation frequency of the crystal.

EXPERIMENTAL

Techniques and Procedures

Excellent discussions on the fundamentals of both techniques have been given elsewhere (7-11). The test cell and data collection will be discussed in some detail here.

To assure uniform heating and repeatability, the experimental test cell was made of 304 stainless-steel cylindrical block, 56 mm in diameter and 64 mm long, into which four 3.2

mm diameter holes were drilled symmetrically. Two sections of these blocks are connected and surrounded by cylindrical heating jackets. The entire apparatus is wrapped with Fiberglas insulation to minimize temperature fluctuation. An HPLC syringe pump is used to pump fuel through the test cell. Typical flow rates to obtain 1 - 20 min of residence time are in the range 4.212 - 0.211 cc/min. Either an optical quartz cell or a QCM cell (or both) can be attached to the end of the reactor to obtain in-situ size and mass rate data.

At high temperature the PCS signal-to-noise ratio was observed to be low; therefore, all experiments were conducted by pumping fuel through the reactor into the QCM cell, which was maintained at the test-cell temperature, and then through a 0.15 mm-od stainless-steel tube immersed in a water bath into a rectangular optical quartz cell at room temperature.

A 35-mW HeNe laser beam is focused into a quartz optical cell from above, while the time-varying light scattered from particles is collected at a fixed angle in the horizontal plane by a photomultiplier. The time-varying signal from the photomultiplier is converted into pulse trains by an amplifier/discriminator whose output is processed by a digital correlator. The outputs from the correlator (an exponential decay curve for each run) stored and later processed off-line on a workstation to yield the size data.

At the beginning of an experiment, a computer commands the syringe pump fuel through the test cell at a predetermined flow rate to achieve a given exposure time. The computer then monitors the volume of fuel flow and the fuel temperature in the QCM cell. When at least two reactor volumes (30 cc) of fuel have been purged through the reactor-QCM cell and the fuel temperature in the QCM cell has remained constant to within 0.1°C for 16 min, then the computer begins taking PCS and QCM data and logs to storage files for subsequent processing. At each flow rate 20 PCS and QCM data points are taken at 2-min intervals; therefore, the rates of mass deposition are measured over a period of 40 min. When sufficient data are collected, the pump is commanded to pump at a

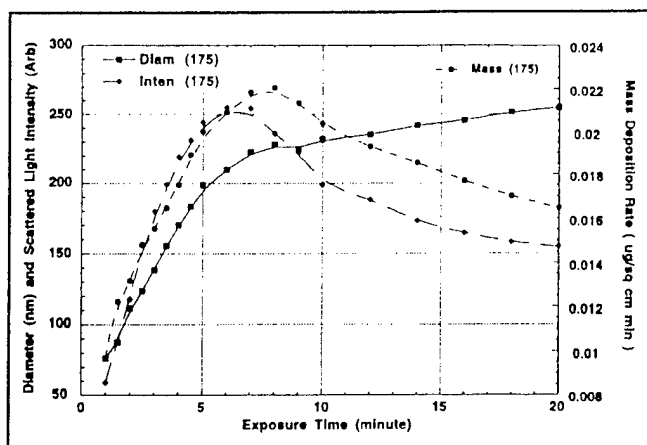


Figure 1. Plot of particle diameter, scattered light intensity, and mass deposition rate as a function of exposure time for POSF2827 fuel at 175°C.

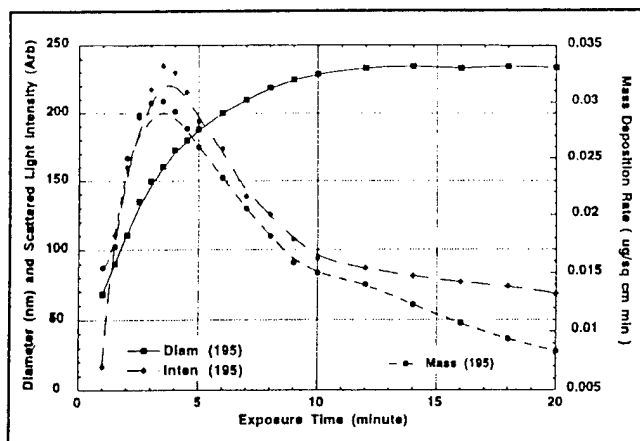


Figure 2. Plot of particle diameter, scattered light intensity, and mass deposition rate as function of exposure time for POSF2827 fuel at 195°C

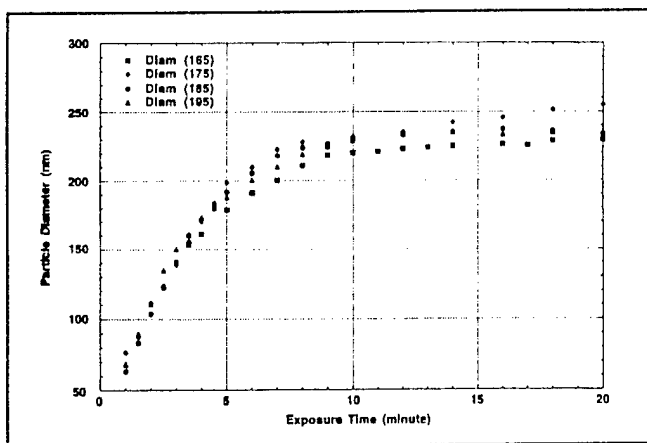


Figure 3. Plot of diameter as function of temperature for POSF2827 fuel.

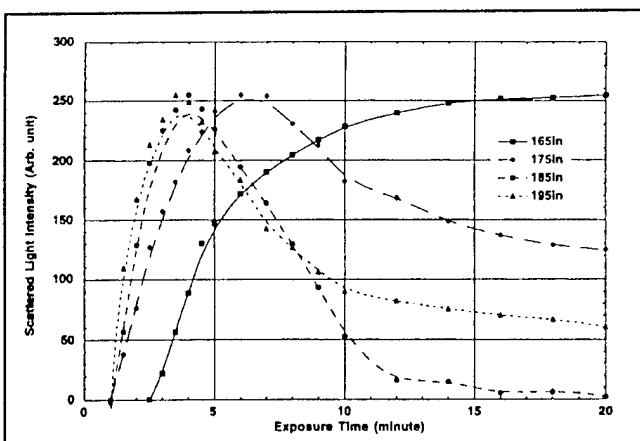


Figure 4. Plot of scattered light intensity as function of temperature for POSF2827 fuel.

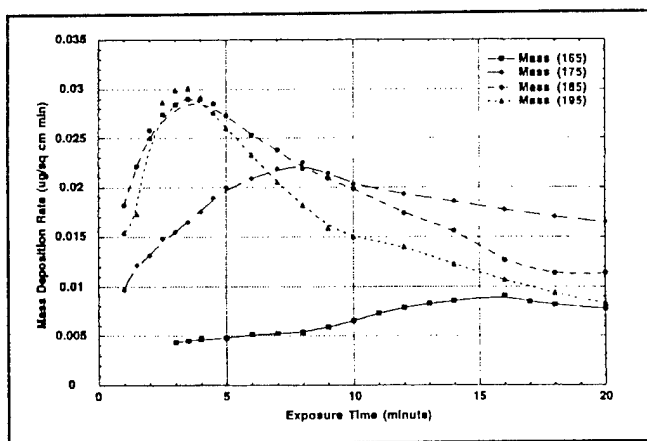


Figure 5. Plot of mass deposition rate as function of temperature for POSF2827 fuel.

new flow rate, and the entire process is repeated. Because of the large thermal mass of the reactor-QCM cell, ~2 hr is required to achieve a steady-state temperature from initial room temperature; however, once steady-

change in the rates of particle growth and mass deposition at these two temperatures can probably be attributed to the rate of oxygen consumption and the amount of residual oxygen available to form additional

state is reached, the temperature remains very stable.

RESULTS AND DISCUSSION

Typical results for a fuel (POSF2827) thermally stressed at different exposure times at 175 and 195°C are shown in Figures 1 and 2, respectively. The

particles and to cause existing particles to grow. Obviously, at lower temperature particle-growth, mass-deposition, and oxygen consumption rates will be slower than at higher temperature; therefore, some dissolved oxygen will remain in solution and, as a result, particles already formed will continue to grow.

Figure 3 shows the rate of particle growth as a function of temperature. Note that at higher temperatures (195 and 185°C), the particle size increases to some asymptotic value and remains constant with increasing time, while at lower temperatures (175 and 165°C), the particle size continues to increase, albeit at a much slower rate than the initial growth rate. It is conceivable that at high temperature, most of the dissolved oxygen is depleted in the initial formation of the

particles which means that no oxygen remains to fuel particle growth in the second stage. It is conjectured that the second growth process may well be due to particle agglomeration which requires only a small amount of dissolved oxygen.

Figures 4 and 5 are scattered-light-intensity and rate-of-mass-deposition profiles, respectively, as a function of both exposure time and temperature. Note the longer exposure time required for each profile to reach its lower temperature. These profiles are very similar, which suggests that the scattered light intensity has a much stronger functional dependence on the total number density of the scattered particles than on their size.

CONCLUSIONS

The combination of two techniques has provided insight into the relationship of particle size, growth rate, and mass deposition rate. This information will be beneficial in the quest to understand the mechanisms involved in the thermal degradation of jet fuel. Although the scattered-light-intensity data could be construed as partially representing the contribution from the total number density of the particles, Mie theory must be used to subtract the contribution from size dependence to obtain a true picture of the total number density of the particles. Fortunately, the rate of mass deposition obtained by QCM seems to indicate that the qualitative interpretation of scattered-light-intensity data representing number density is correct.

ACKNOWLEDGMENTS

This study was conducted at and supported by Wright Laboratory,

Aero Propulsion and Power Directorate, Wright-Patterson Air Force Base, OH, USAF Contract No. F33615-90-C-2033.

LITERATURE CITED

- (1) Katta, V. R. and Roquemore, W. M., "A Numerical Method for Simulating the Fluid-Dynamic and Heat-Transfer Changes in a Jet Engine Injector Feed-Arm due to Fouling," AIAA Paper No. 92-0768, Presented at the 30th Aerospace Sciences Meeting and Exhibit, Reno, NV, January 6-9, 1992.
- (2) Krazinski, J. L., Vanka, S. P., Pearce, J. A. and Roquemore, W. M., "A Computational Fluid Dynamics and Chemistry Model for Jet Fuel Thermal Stability," Presented at the 35th ASME International Gas Turbine and Aeroengine Congress and Exposition, Brussels, Belgium, 11-14 June 1990.
- (3) Anderson, S. D., Jones, E. G., Goss, L. P. and Balster, W. J., "The Effect of Additives on the Formation of Insolubles in a Jet A Fuel," Presented at the 5th International Conference on Stability and Handling of Liquid Fuels, Rotterdam, The Netherlands, 3-7 October 1994.
- (4) Jones, E. G., Balster, W. J. and Post, M. E., *J. Energy Gas Turb. Power*, **117**, 12 (January-March 1995).
- (5) Jones, E. G. and Balster, W. J., "Surface Fouling in Aviation Fuel: Short- vs. Long-Term Isothermal Tests", accepted for publication in *Energy and Fuels*.
- (6) Chin, L. P. and Katta, V. R., "Numerical Modeling of Deposition in Fuel-Injection Nozzles," AIAA Paper No. 95-0497, Presented at the 33rd AIAA Aerospace Sciences Meeting and Exhibit, Reno, NV, 9-12 January 1995.
- (7) Bott, S. E., "Submicrometer Particle Sizing by Photon Correlation Spectroscopy: Use of Multiple-Angle Detection," in *Particle Size Distribution - Assessment and Characterization*, ACS Symposium Series 332, (T. Provder, ed.), Chapter 5, American Chemical Society, Washington, D. C., p. 74-88 (1987).
- (8) Zabarnick, S., *I&EC Research* **33**(5), 1348 (1994).
- (9) Martin, S. J., Granstaff, V. E. and Frye, G. C., *Anal. Chem.*, **63**, 2272 (1991).
- (10) Zabarnick, S. and Grinstead, R. R., *I&EC Research*, **33**, 2771 (1994).
- (11) O'Hern, T. J., Trott, W. M., Martin, S. J. and Klavetter, E. A., "Advanced Diagnostics for In Situ Measurement of Particle Formation and Deposition in Thermally Stressed Jet Fuels," AIAA Paper No. 93-0363, Presented at the 31 Aerospace Sciences Meeting and Exhibit, Reno, NV, 11-14 January 1993.

Presented at the ASME Forum on Measurement Techniques in Multiphase Flows, ASME Winter Annual Meeting, November 1995, San Francisco

SIMULTANEOUS MEASUREMENT OF PARTICLE SIZE, MASS RATE OF DEPOSITION, AND OXYGEN CONCENTRATION IN THERMALLY STRESSED JET FUEL

V. Villimpoc, B. Sarka, and W. L. Weaver
Systems Research Laboratories, Inc.
A Division of Space Industries International, Inc.
Dayton, OH 45440-3696

J. R. Gord
Wright Laboratory, Aero Propulsion and Power Directorate
Wright-Patterson Air Force Base, OH 45433-7103

ABSTRACT

Three techniques integrated into a single instrumented platform allow simultaneous measurement in real time of particle size and growth rate, surface mass-deposition rate, and concentration of dissolved oxygen in thermally stressed jet fuel. Particle growth rate is studied using Photon Correlation Spectroscopy (PCS); surface mass-deposition rate is measured with a Quartz Crystal Microbalance (QCM); and dissolved oxygen concentration is monitored by Pyrene Fluorescence Quenching (PFQ).

INTRODUCTION

Fuels are used as the coolant for avionics and hydraulic systems in modern aircraft. Exposure of fuels to high temperature results in formation of particulates and deposits that clog valves and filters and degrade injection-nozzle performance. Several studies have shown that the auto-oxidation of hydrocarbons is the main reaction leading to formation of insoluble products and deposits (Katta and Roquemore, 1992; Krazinski et al., 1990; Anderson et al., 1994; Jones et al., 1995; Jones and Balster, 1995; Chin and Katta, 1995). Efforts to develop highly stable jet fuels would benefit from an understanding of the relationship among particle size and growth rate, rate of particle deposition on a surface, and dissolved-oxygen concentration resulting from thermally induced degradation of jet fuel. No single analytical technique exists that can provide all the required information. Therefore, integration of existing applicable techniques into a single instrumented platform where all the required parameters can be measured simultaneously and in-situ would be highly desirable. In this paper progress on such an effort is reported.

EXPERIMENTAL TECHNIQUES

PCS is a dynamic light-scattering technique capable of measuring particle size in the range 10^{-8} to 10^{-6} m. Laser light incident on a sample of particles undergoing Brownian motion will be scattered with different phases, depending on the position of each particle in the laser beam and on the distance between the particle and the detector. Thus, the composite light scattered from the group of particles in the scattering volume will form an interference pattern at the detector. As the particles randomly diffuse through the solution, the pattern produced will be modulated by the particle motion. The intensity fluctuations associated with the interference pattern at the detector, although random, will be more rapid for small, rapidly diffusing particles than for larger, more slowly diffusing ones. The random-noise signal produced by the detector as a result of the scattered light can be characterized by its autocorrelation function, $g(t)$, defined by

$$g(t) = \langle I[T] I[T+t] \rangle \quad (1)$$

where $I[T]$ is the intensity at the detector at time T and the angular brackets denote a time average over T . The autocorrelation function is a measure of the similarity, or correlation, between the configuration of particles contributing to an intensity I at T and that at a later time $T+t$. At short t the configuration of the particles within the scattering volume will remain essentially unchanged, and the correlation with the configuration at T will be high. At longer t the particles will have diffused such that their new positions will be statistically uncorrelated with their former ones. For a system of particles of uniform size and

shape undergoing Brownian motion, the autocorrelation function will be a decaying exponential:

$$g(\tau) = A e^{-2\Gamma\tau} + B \quad (2)$$

where Γ is a decay constant characteristic of particles of that size and A and B are experimental constants dependent on the geometry, optical collection efficiency, and counting efficiency of the electronics. $1/\Gamma$ is the decay time of the Brownian motion, i.e., the time required for any particular configuration of particles within the scattering volume to become uncorrelated with its former configuration. The decay constant is related to the diffusion constant of the particles and to the geometry of the experiment through

$$\Gamma = q^2 D; \quad q = 4\pi n \sin(\theta/2)/\lambda \quad (3)$$

where q is the magnitude of the scattering vector, D the diffusion constant of the particles, n the refractive index of the fluid, θ the scattering angle, and λ the laser wavelength. For spherical particles, the diffusion constant is related to the particle diameter through the Stokes-Einstein equation

$$D = kT/3\pi\eta d \quad (4)$$

where k is the Boltzman constant, T the absolute temperature, η the fluid viscosity, and d the particle diameter.

When the sample contains particles of different sizes, the autocorrelation function will be the sum of decaying exponentials weighted by the intensity of light scattered from particles of each characteristic size, and the autocorrelation function can be described by

$$g(\tau) = \int_a^b X(s) e^{-\Gamma(s)\tau} ds \quad (5)$$

where the index, s , denotes the size of the particles and $X(s)$ is the particle-size distribution, which yields the relative proportion of scattering from particles of size s . The constants a and b are the lower and upper limits of particle size. This integral equation must be numerically inverted to extract the size distribution, $X(s)$, from the measured autocorrelation function (Bott, 1987). CONTIN (Provencher, 1979, 1982), a widely used FORTRAN program for this type of data analysis, was employed.

QCM is a technique for measuring extremely small mass accumulation on a quartz-crystal surface. It is designed around a piezoelectric wafer, sliced from a single crystal of quartz. The quartz wafer is sandwiched between two gold electrodes bonded to the wafer surface. As a piezoelectric material, the quartz deforms slightly in the electric field applied between the two electrodes. The oscillating electric field perpendicular to the wafer surface induces mechanical oscillation, in the form of a standing wave, in the bulk of the quartz wafer. In the QCM, an AT-cut quartz wafer

efficiently produces mechanical shear oscillation with displacement parallel to the wafer surface. A resonant oscillation is usually achieved by including the wafer in an appropriately designed oscillator circuit. Sandia National Laboratories (Martin et al., 1991) developed the oscillator circuit used in this study. In such a circuit, the electrical and mechanical oscillation centers at a characteristic fundamental frequency. Mechanical oscillation of the crystal is at a maximum where the electrodes overlap and diminishes rapidly in areas where they do not. Thus, the QCM is most useful when probing processes that occur uniformly across the QCM surface--processes that can be represented as a change in mass per unit area. The oscillation frequency depends on several factors: 1) factors that are normally constant include the physical properties of the quartz wafer (thickness, density, and shear modulus); 2) factors that normally are held constant include the density and viscosity of the phases in contact with the QCM wafer and the pressure and temperature differences across the wafer. The theory relating the measured frequency changes to the surface mass deposition has been presented previously (O'Hern, 1993) and is given by

$$\Delta f = -2f^2/N(\mu_q \rho_q)^{1/2} [\Delta\rho_s + (\rho\eta/4\pi f)^{1/2}] \quad (6)$$

where Δf is the change in oscillation frequency, f the unperturbed resonant frequency, N the overtone mode number, μ_q the quartz shear modulus ($2.947 \times 10^{11} \text{ g cm}^{-1} \text{ s}^{-2}$), ρ_q the density of quartz (2.648 g cm^{-3}), ρ_s the surface mass density, and ρ and η the liquid density and viscosity, respectively. The first term in Eq. (6) relates the change in surface mass density to the change in frequency, and the second relates the change in fluid properties to that in oscillation frequency. When all other factors are held constant, the variation in mass of an adsorbate or thin film attached to the electrode can be determined from the change in frequency. Under such conditions the change in surface mass deposition can be related to the change in the fundamental resonant frequency by

$$\Delta\rho_s = -[2.21 \times 10^5 (\text{g/cm}^2 \text{ s})] \Delta f/f^2 \quad (7)$$

PFQ is based on determination of the fluorescence lifetime of pyrene doped in the fuel at the parts-per-million level. Spectroscopically, molecular oxygen is difficult to study in solution (Herzberg, 1945). It does not absorb in the infrared, and its electronic transitions lie far in the ultraviolet where fuel components absorb strongly. Oxygen has a Raman-allowed transition, but Raman spectroscopy is not the technique of choice for trace analysis. Oxygen also has a unique ESR (electron-spin-resonance) signature, but the expense and limited sensitivity of this technique prohibit its use for this application. An alternative optical approach involves quantitating dissolved oxygen indirectly through its influence on the fluorescence of a probe molecule (Cox, 1985) such as pyrene. Oxygen

efficiently and reproducibly quenches the fluorescence of pyrene as a result of the energy match between the singlet-triplet gap in oxygen and the energy of the first excited singlet state of pyrene (Lakowicz, 1983). This process provides the basis for a spectroscopic technique for quantitating dissolved molecular oxygen. The technique is based on the propensity of dissolved molecular oxygen to quench probe-molecule fluorescence excited with a pulsed nitrogen laser. Linear calibration curves based on Stern-Volmer kinetics are generated through measurement of the time-resolved fluorescence signal produced by pyrene.

Collisions between photoexcited pyrene and oxygen molecules result in the non-radiative transfer of energy from pyrene to oxygen because of the energy match between the singlet-triplet gap in oxygen and the energy of the first excited singlet state of pyrene. At a given temperature, a decrease in the dissolved-oxygen concentration reduces the oxygen-pyrene collision frequency, resulting in an increase in both the total fluorescence quantum yield and the lifetime of the excited state of pyrene. Instrumentally, it is a simpler task to measure the total fluorescence intensity, which may be converted to a quantum yield. However, previous work has shown this approach to be intractable for quantitating dissolved oxygen during fuel-thermal-stability studies since the amount of pyrene doped into the fuel must be precisely controlled. If pyrene is consumed (or produced) during oxidation of the fuel, the total fluorescence intensity will vary, independent of the presence of oxygen. However, the lifetime of the excited state of pyrene is independent of pyrene concentration (within certain limits). Thus, the pyrene fluorescence lifetime is a reliable and reproducible indicator of the dissolved-oxygen concentration at a given fuel temperature. After photoexcitation of an ensemble of pyrene molecules, the excited species return to their ground states, producing an observed fluorescence signal that can be described by the single exponential decay in

$$\Phi_f(t) = \Phi_f^0 \exp(-k_f t) \quad (8)$$

where Φ_f^0 is the fluorescence radiant power immediately following excitation. The fluorescence power decays with an overall rate constant, k_f , that contains contributions from the first-order (natural or radiative) decay rate constant, k_r , and a second-order rate constant for dynamic quenching with oxygen, k_q , as shown in

$$k_f = k_r + k_q[\text{O}_2] \quad (9)$$

Using the relationship between the rate constant (k) and the lifetime (τ) of a single exponential decay ($k=1/\tau$), Eq. (9) can be written in terms of the fluorescence lifetime, as in the Stern-Volmer Equation,

$$\tau_0/\tau_f = 1 + \tau_0 k_q [\text{O}_2] \quad (10)$$

where τ_f is the measured lifetime of the observed fluo-

rescence (Dynamically Quenched Fluorescence Lifetime, DQFL) and τ_0 is the measured lifetime of the observed fluorescence in the absence of quenching. By measuring τ_0 at $[\text{O}_2] = 0$ and the DQFL at known values of $[\text{O}_2]$, a linear calibration curve can be constructed that relates the lifetime of the observed pyrene fluorescence to the concentration of dissolved oxygen (as measured by existing gas-chromatographic and electrochemical methods).

EXPERIMENTAL SETUP AND PROCEDURES

The experimental setup is as shown in Fig. 1. Light from a 35-mW HeNe laser beam is focused into a quartz optical cell from above, while the time-varying light scattered from particles is collected at a fixed angle in the horizontal plane by a photomultiplier. The time-varying signal from the photomultiplier is converted into pulse trains by an amplifier/discriminator whose output is processed by a digital correlator (Langley Ford Instrument Correlator Model 1096). The outputs from the correlator (exponential decay curve for each run) are stored and later processed off-line on a workstation to yield size data. A N_2 laser beam is directed into the test cell from below to occupy the same probe volume as the PCS HeNe laser beam. A small portion of the N_2 laser beam is split off with a flat glass into a photodiode. The output of the photodiode initiates data acquisition by a LeCroy 9354 digital storage oscilloscope. Fluorescence from the pyrene is collected by an RCA 931A photomultiplier tube. For each data set, 100 fluorescence decay curves were averaged. Typical fluorescence decays have time constants of 20 - 300 nsec.

The experimental test cell is a cylindrical block, 56 mm in diam and 64 mm long, made of 304 stainless-steel; into this block four 3.2-mm-diam holes are drilled symmetrically. Two sections of these blocks are connected and surrounded by cylindrical heating jackets. The entire apparatus is wrapped with fiberglass insulation to minimize temperature fluctuation. The fuel is pumped through the test cell by an HPLC syringe pump (ISCO 500D). All tests in this study were conducted with a JET-A fuel (POSF2827). Typical flow rates to obtain 1 - 20 min of residence time are in the range 4.212 - 0.211 cc/min. Either an optical quartz cell or a QCM cell (or both) can be attached to the end of the reactor to obtain *in-situ* size and mass rate data. At high temperature the PCS signal-to-noise ratio was observed to be low; therefore, some experiments were conducted by pumping fuel through the reactor into the QCM cell (maintained at the test-cell temperature) and then through a 0.15-mm-od stainless-steel tube immersed in a water bath into a 4-mm-square optical quartz cell at room temperature.

RESULTS AND DISCUSSION

The mechanism of particulate formation during thermal degradation of jet fuel remains a mystery. Do particles

form as a result of physical processes when there is a change in the physical or chemical properties of the fuel, for example, by condensation due to differences in solubility between the solvent and solute phases (Oswald ripening) or by agglomeration resulting from collisions and sticking together of small particles? Or do particles form and grow as a result of chemical reaction?

In-situ measurement while particles are being formed would answer this question unambiguously. A typical result from a number of attempts to make an in-situ particle-size measurement at 185°C is shown in Fig. 2. A complication in conducting an in-situ PCS experiment is that at high temperature, particles move in and out of the probe volume very rapidly because of its large Brownian motion. These fast movements that result in low signal-to-noise ratio necessitate the use of small time bins to capture the rapid exponential decays that are typical of small particles. The consequence is obvious from examination of Fig. 2; at short residence times, the small size and the small number of particles generated do not scatter sufficient light (scattered-light intensity is proportional to particle number density and particle size) to permit meaningful correlation by the PCS system. As particles grow in size, move more slowly, and are produced in larger quantities at longer residence times, they become detectable by the PCS system. Unfortunately, beyond the detection threshold, these particles are no longer growing in size with increasing residence time, although they are produced and deposited in ever-increasing quantities. The poor signal-to-noise ratio is reflected in the large uncertainty in particle size at short residence times. No attempt was made to measure in-situ oxygen concentration with PFQ at high temperature because small changes in very short fluorescence decay times cannot be measured accurately.

For ascertaining the effect of temperature changes on particle size, fuel was heated at a long residence time to generate particles sufficiently large for detection; then fuel flow to the test cell and power to the heater were shut off. PCS was used for continuous monitoring of particle size as the fuel cooled down to obtain data on particle size as a function of temperature. The result is shown in Fig. 3. As can be seen from the figure, the particle size increases continuously, while the scattered-light intensity increases to a maximum and then slowly decreases. The scattered-light intensity is a function of particle residence time in the probe volume, particle number density, and particle size. A plausible explanation for the observed profiles is that as temperature decreases, the average-particle Brownian motion also decreases, resulting in longer residence times for particles in the probe volume and, thus, more scattered light per unit time during the first 10 min of elapsed time. Although the particles are becoming larger, beyond 10 min the scattered-light intensity is decreasing. The increase in particle size is probably due to agglomeration which would account for the reduction of scattered-light intensity. This result indicates that growth in particle size by a physical process is slow compared to that by chemical kinetics.

For obtaining the particle-size growth rate as a function of exposure time to high temperature, fuel thermally stressed for different lengths of time was quenched to room temperature and studied with PCS and PFQ, while mass-deposition rates were monitored in-situ with QCM. At the start of an experiment, a computer commands the syringe pump (ISCO 500D) to begin pumping fuel through the test cell at a predetermined flow rate to achieve a given exposure time. The computer then monitors the volume of fuel flow and the fuel temperature in the QCM cell. The quartz-crystal oscillation frequency is a function of both the temperature and the amount of mass deposit on the crystal surface; therefore, the QCM temperature must remain relatively constant when mass-deposition-rate data are being obtained. When at least two reactor volumes (30 cc) of fuel have been purged through the reactor-QCM cell and the fuel temperature in the QCM cell has remained constant to within 0.1°C for 16 min, then the computer begins taking PCS and QCM data for subsequent processing. At each flow rate 20 PCS and QCM data points and five PFQ fluorescence decay times are taken at 2-min intervals. Therefore, the rates of mass deposition are measured over a period of 40 min. When sufficient data are collected, the pump is commanded to pump at a new flow rate, and the entire process is repeated. Because of the large thermal mass of the reactor-QCM cell, ~ 2 hr is required to achieve a steady-state temperature from initial room temperature; however, once steady state is reached, the temperature remains very stable.

Typical results for a fuel thermally stressed for different exposure times at 165 and 195°C are shown in Figures 4 and 5, respectively. In these figures, scattered-light intensity and oxygen concentration are normalized to minimum and maximum particle size to ensure that they will be on the same scale for demonstrating the relationships among the variables. At 165°C, particle size and scattered-light intensity increase with increasing residence time but at decreasing rates, while oxygen concentration decreases in a reciprocal manner. Particle size and scattered-light intensity begin to level off at a 20-min residence time, while the rate of mass deposition peaks at 14 min. In comparison, at 195°C the mass-deposition rates and scattered-light intensity reach their maxima at about 3.5 min, while the particle-size growth profile does not level off for about 10 min. Note the similarity between the scattered-light intensity, which represents the total number density of particles, and the rate of mass deposition. Both profiles show progressively longer residence times required to reach a maximum, from 3 - 4 min at 195°C to 15 - 20 min at 165 °C. This result clearly suggests that particulates are formed and deposited as a result of chemical reactions. The higher the temperature, the larger the quantity of particles formed and the faster they are formed as a function of fuel-exposure time to temperature. Particle-diameter profiles in the range 165 - 195°C as a function of residence time are shown for comparison in Fig. 6. Figures 7 and 8 show scattered-light-intensity and mass-deposition-rate profiles, respec-

tively. Comparison of the scattered-light-intensity profiles in Figs. 2 and 7 shows a striking difference between in-situ and post-test quenched experiments. In Fig. 2, the scattered-light-intensity profiles increase slowly toward a plateau for long residence times, while in Fig. 7 the profiles reach a peak at about a 3-min residence time and then decrease.

One plausible explanation for the scattered-light-intensity profiles decreasing after peaking in the post-test experiments is competition between different mechanisms. A larger quantity of particles and larger particles are produced as the residence time increases; therefore, the scattered-light intensity increases. However, flow velocity is lower for longer residence times, thus permitting particle-removal processes such as settling or agglomeration to take place in the quench line between the test cell and the optical cell; this results in decreasing scattered-light intensity for longer residence times. The quantity of particles removed by settling and agglomeration will be proportional to the length of time available for the processes and, therefore, inversely proportional to the flow velocity of the fuel. PCS and QCM measurements were made by pumping fuel at different flow rates through the test cell to obtain different residence times; therefore, if the scattered-light intensity and mass-deposition rates are normalized by the flow rates, the results will be somewhat independent of the influence of flow velocity. The results of such normalization are shown in Figs. 9 and 10, respectively. The normalized scattered-light intensity can now be thought of, to a first approximation, as concentration of particles per cubic centimeter of fuel and the rate of mass deposition in units of micrograms of deposit per square centimeter of quartz crystal surface per cubic centimeter of fuel flow over the surface. From a comparison of the profiles at 195 and 165°C, it is obvious that the 165°C profiles from 2 to 20 min residence time mimic those at 195°C from 1 to 5 min residence time—but at a much lower particle number density and mass deposition rate and at a much slower pace. The normalized profiles suggest the existence of two mechanisms in the particle formation and deposition rates. The initial rates are fast and exhibit an S-shaped curve characteristic of autocatalytic reaction, while the rates for longer residence times are slow and linear. Both regimes exhibit decreasing rates with decreasing temperature, suggesting a dependence on reaction mechanisms as the primary cause.

Figure 11 contains oxygen-concentration profiles at different temperatures. Dissolved oxygen is almost depleted at 195°C after about a 5-min residence time in the reactor, while ~50% of the oxygen remains after 20 min at 165°C. Many particles are generated during the first 5 min of reaction time at 195°C; therefore, little oxygen remains to fuel further particle production at longer residence times. The result is a large rate decrease. At 165°C the rate of particle production is much slower; therefore, some oxygen remains at long residence times and the rate decrease is small. Obviously at lower temperature the rate of particle growth, mass deposition, and oxygen consumption will be slow;

therefore, more dissolved oxygen will remain in the fuel and, as a result, reaction can proceed for a longer time at a lower temperature. The rates of particle growth and mass deposition as a function of temperature seem to be closely tied to the concentration of dissolved oxygen.

CONCLUSION

The combination of three techniques has provided insight into the relationship among particle size, growth rate, mass-deposition rate, and oxygen concentration. Scattered-light-intensity profiles for in-situ and post-test quenched experiments do not exhibit the same shape, suggesting that settling or agglomeration, in addition to reaction kinetics, may play a role in determining the size and quantity of particles formed. Further experiments are required to delineate the differences in the observed scattered-light-intensity profiles.

ACKNOWLEDGMENT

This study was performed at and supported by Wright Laboratory, Aero Propulsion and Power Directorate, Wright-Patterson Air Force Base, OH, in part, under USAF Contract No. F33615-90-C-2033.

REFERENCES

- Anderson, S. D., Jones, E. G., Goss, L. P., and Balster, W. J., 1994, "The Effect of Additives on the Formation of Insolubles in a Jet A Fuel," Presented at the 5th International Conference on Stability and Handling of Liquid Fuels, 3-7 October, Rotterdam, The Netherlands.
- Bott, S. E., 1987, "Submicrometer Particle Sizing by Photon Correlation Spectroscopy: Use of Multiple-Angle Detection," *Particle Size Distribution - Assessment and Characterization*, ACS Symposium Series 332, T. Provder, ed., American Chemical Society, Washington, D. C., pp. 74-88.
- Chin, L. P., and Katta, V. R., 1995, "Numerical Modeling of Deposition in Fuel-Injection Nozzles," AIAA Paper No. 95-0497.
- Cox, M. E., and Dunn, B., 1985, *Applied Optics*, Vol. 24, p. 2114.
- Herzberg, G., 1945, *Infrared and Raman Spectra of Polyatomic Molecules*, Van Nostrand, New York.
- Jones, E. G., and Balster, W. J., 1995, "Surface Fouling in Aviation Fuel: Short- vs Long-Term Isothermal Tests," Accepted for publication in *Energy and Fuels*.
- Jones, E. G., Balster, W. J., and Post, M. E., 1995, *Journal of Energy for Gas Turbines and Power*, Vol. 117, p. 125.
- Katta, V. R., and Roquemore, W. M., 1992, "A Numerical Method for Simulating the Fluid-Dynamic and Heat-Transfer Changes in a Jet Engine Injector Feed-Arm due to Fouling," AIAA Paper No. 92-0768.

Krazinski, J. L., Vanka, S. P., Pearce, J. A., and Roquemore, W. M., 1990, "A Computational Fluid Dynamics and Chemistry Model for Jet Fuel Thermal Stability," Presented at the 35th ASME International Gas Turbine and Aeroengine Congress and Exposition, 11-14 June, Brussels, Belgium.

Lakowicz, J. R., 1983, *Principles of Fluorescence Spectroscopy*, Plenum Press, New York.

Martin, S. J., Granstaff, V. E., and Frye, G. C., 1991, *Analytical Chemistry*, Vol. 63, p. 2272.

O'Hern, T. J., Trott, W. M., Martin, S. J., and Klavetter, E. A., 1993, "Advanced Diagnostics for In Situ Measurement of Particle Formation and Deposition in Thermally Stressed Jet Fuels," AIAA Paper No. 93-0363.

Provencher, S. W., 1979, *Makromolecular Chemistry*, Vol. 180, p. 201.

Provencher, S. W., 1982, *Computer Physics Communications*, Vol. 27, p. 229.

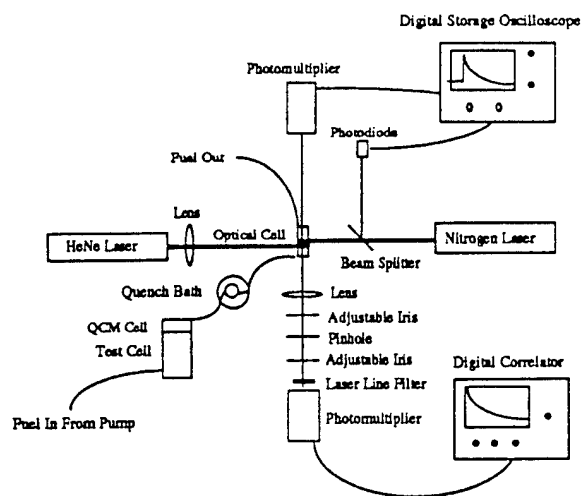


Fig. 1. Diagram of Experimental Setup.

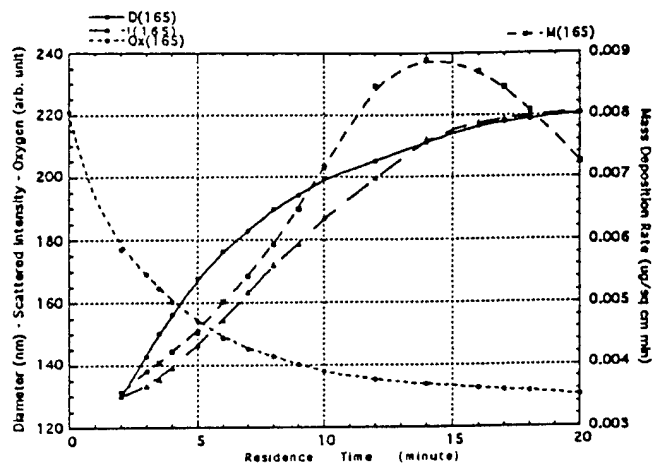


Fig. 4. Post-Test Quenched Results at 165°C.

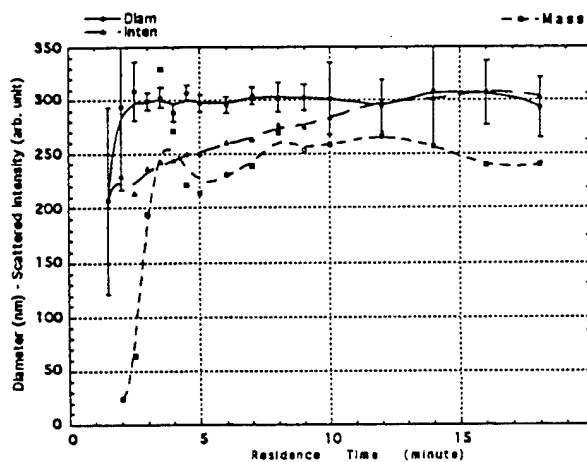


Fig. 2. In-situ Experimental Results.

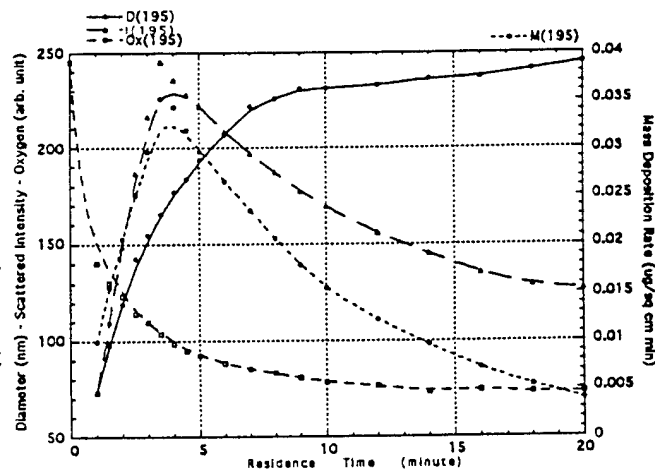


Fig. 5. Post-Test Quenched Results at 195°C.

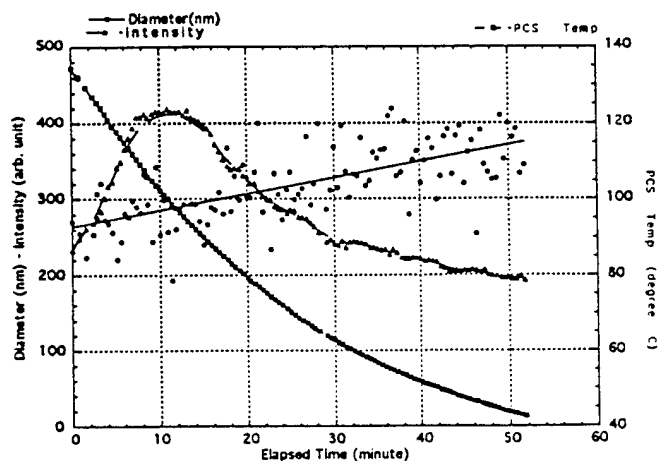


Fig. 3. In-situ Cooling Results.

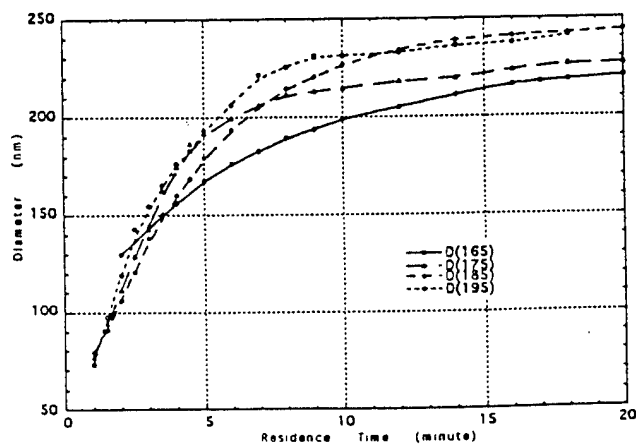


Fig. 6. Post-Test Quenched Diameter Profiles.

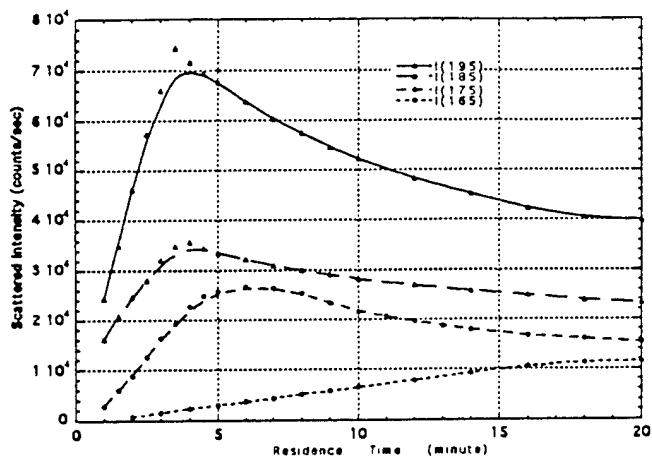


Fig. 7. Post-Test Quenched Scattered-Light Intensity.

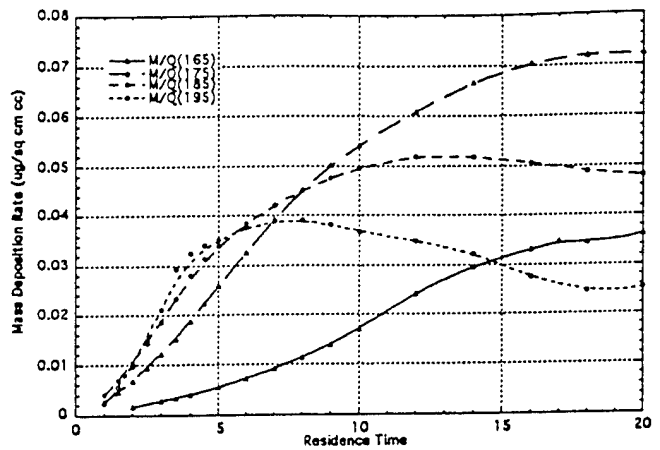


Fig. 10. Normalized Mass-Deposition Rates.

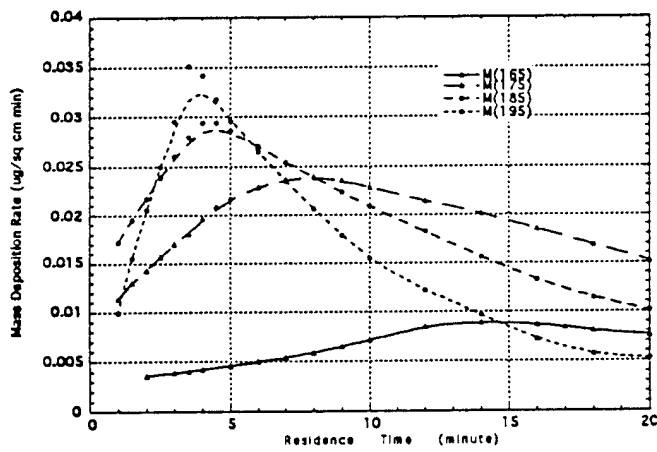


Fig. 8. Post-Test Quenched Mass-Deposition Rates.

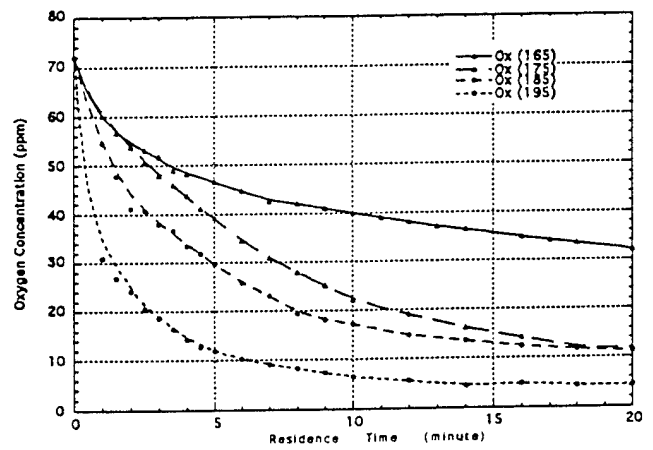


Fig. 11. Post-Test Quenched Oxygen Concentration.

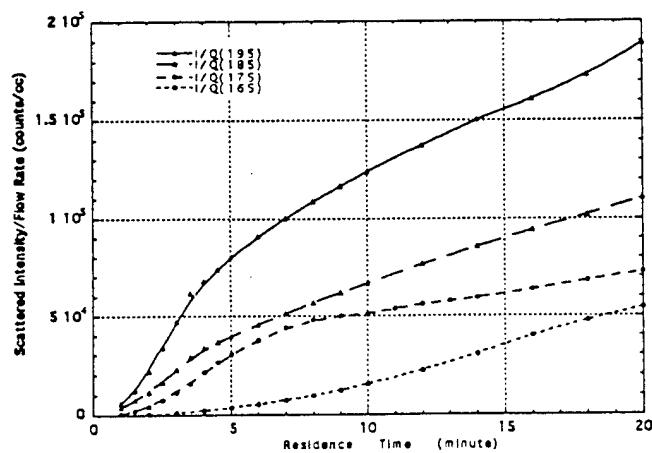


Fig. 9. Normalized Scattered-Light Intensity.

2.2.3 Ultrafast Laser Diagnostics. In response to the needs of this research program, SRL established an on-site laboratory in the scientific field of ultrafast laser spectroscopy for the development of ultrafast laser diagnostics to characterize ultrafast chemistry and kinetics in the combustion and decomposition of sub- and supercritical hydrocarbon jet fuels.

The ultrafast laboratory group collaborated with other scientists including representatives from Purdue University, The Colorado School of Mines, The Ohio State University, State University of New York at Buffalo, Columbus College (Georgia), Yale University, Princeton University, Sandia National Laboratory, and Oak Ridge National Laboratory. These collaborations yielded several scientific presentations and journal publications. By the conclusion of this contract, four areas of study had been identified; namely, combustion, supercritical jet fuel, subcritical jet fuel, and dissolved-oxygen-concentration monitoring in liquid jet fuel. The combustion and supercritical fuel studies utilized nearly identical time-resolved ultrafast laser techniques. The subcritical jet fuel studies included the use of non-ultrafast spectroscopic techniques to provide support for the more advanced ultrafast experiments, while the oxygen-concentration monitoring in liquid jet fuel represented the first time-resolved ultrafast diagnostic produced by the laboratory.

The ultrafast group devised the following approach to the development and validation of new ultrafast diagnostics for combustion and supercritical fuels. In Phase I ultrafast sample lifetime data would be acquired using the commercially available technique of Time-Correlated Single-Photon Counting (TC-SPC). In Phase II an ultrafast instrument based on the technique of Synchronous Pump-Probe Spectroscopy (SPPS) would be developed and the Phase I data used to validate these measurements. In Phase III the SPPS instrument would be extended to an ultrafast one, based on the technique of Asynchronous Optical Sampling (ASOPS). In Phase IV the relative performance of the SPPS and ASOPS methods would be evaluated. In Phase V combustion and supercritical fuel diagnostics would be developed based on the superior method.

The ultrafast laboratory was one of the first to utilize now widely available commercial Ti:sapphire-based lasers. Early Phase I efforts involved the exploration and documentation of the characteristics specific to this new class of lasers. In one of the studies performed, a collaborative effort with Prof. Mark A. Linne of the Colorado School of Mines, the noise and tuning properties of the Ti:sapphire laser were measured and a journal publication describing the results prepared. At the completion of Phase I, the TC-SPC system constructed was used to make time-resolved fluorescence measurements in wavelength regions inaccessible to other commonly used laser systems. This capability led to a collaboration with The Ohio State University, and several presentations and publications were generated in the area of time-resolved fluorescence spectroscopy. The development of the SPPS instrument in Phase II involved the characterization of system performance using previously studied potassium-doped premixed flames. In collaboration with Dr. Linne, along with Dr. Gregory J. Fiechtner of Sandia National Laboratory, the results of published

studies were duplicated with this instrument to explore its operation; presentations at several local and national meetings resulted. In Phase II the SPPS instrument was extended to permit the study of sub- and supercritical jet fuel.

A collaboration with Mr. Keith D. Grinstead of Purdue University initiated the development of an ultrafast-laser-pumped Two-Photon-Excited Fluorescence Spectroscopy (TPEFS) based diagnostic for the study of additive performance in jet fuels. Several publications and presentations at local and national scientific meetings described the initial success of the technique [see, for example, "Fuel-Thermal-Stability Studies with Photon Fluorescence Spectroscopy" (pp. 239 - 244)].

To aid the study of thermal stability of jet fuels, the ultrafast group investigated, developed, and demonstrated the utility of a noninvasive, *in situ* optical method for the quantification of dissolved molecular oxygen in jet fuel. In collaboration with Prof. Steven W. Buckner of Columbus College (Georgia), this time-resolved, laser-based diagnostic enhanced efforts in other laboratories to study the thermal decomposition of jet fuel and to screen fuel-additive candidates for inclusion in a recently defined Air Force fuel-additive package. The success of this diagnostic in the rapid quantification of dissolved oxygen at part-per-million levels was discussed in presentations at several regional and international meetings ["Dissolved Oxygen Quantification in Fuel Through Measurements of Dynamically Quenched Fluorescence Lifetimes" (pp. 245 - 250)].

Fuel-Thermal-Stability Studies with Two-Photon Fluorescence Spectroscopy

James R. Gord
Wright Laboratory
Aero Propulsion and Power Directorate
Wright-Patterson Air Force Base, OH 45433-7103

William L. Weaver
Systems Research Laboratories, Inc.
A Division of Calspan Corporation
2800 Indian Ripple Road
Dayton, OH 45440-3696

Keith D. Grinstead and Fred E. Lytle
Department of Chemistry
Purdue University
West Lafayette, IN 47907

Introduction

In the development of advanced military aircraft, thermal management is an increasingly important driver. Aviation fuel, which is the primary aircraft coolant and serves lubrication and hydraulic functions as well, must possess sufficient stability to perform without thermal decomposition that leads to fuel-system fouling and unacceptable downtime. Since thermal loads in future aircraft will be significantly increased, the Air Force has initiated a far-reaching program to enhance the thermal stability of fuels.¹ Non-intrusive, laser-based diagnostic techniques are playing a key role in characterization of fundamental decomposition mechanisms and in evaluation of fuel-additive performance.

Laser-induced fluorescence (LIF) is a well-established technique for selective quantitation in condensed- and gas-phase environments. Unfortunately, interfering chromophores or optically dense sample matrices often limit the potential of analytical fluorimetry in "real-world" samples such as aviation fuel. In addition, interfering fluorophores can complicate quantitation of a particular analyte. Recently, Parker and coworkers have developed laser-based diagnostics for fuel-fouling studies.² Their work demonstrates the challenges associated with LIF measurements in the complex mixture of chemicals which is typical of aviation fuel. This mixture includes many fluorescent components and produces broad, unstructured fluorescence spectra under laser excitation.

The present study explored the use of two-photon excitation to produce fluorescence signals of increased analytical utility in the characterization of aviation fuel. Two-photon fluorescence studies performed to date indicate that only a limited number of chemical compounds possess sufficiently strong transitions to produce measurable signals. This significantly reduces the number of compounds in the fuel mixture that will fluoresce and should simplify the resulting emission spectrum. In addition, near-infrared lasers can be employed to excite two-photon fluorescence in the fuel, reducing problems associated with the optical density of the sample.

Past applications have exploited a number of potential advantages associated with this technique. In addition to its analytical capabilities in optically dense media,³⁻⁶ this approach provides information that is complementary to one-photon techniques, because different selection rules govern the two processes.⁷ Since two-photon excitation has a power-squared dependence, focusing the source yields increased absorption. Applications that exploit this three-dimensional excitation control include confocal microscopy,⁸ photolithography for microelectronics construction,⁹ and optical data storage.¹⁰

The principal disadvantage of two-photon fluorescence spectroscopy is its inherently weak signals. Excitation requires that the analyte simultaneously absorb two photons, and the cross section for this event is typically four to eight orders of magnitude smaller than that of the corresponding one-photon process, depending on the peak power and focusing characteristics of the excitation source.⁶ The governing equation for two-photon fluorescence illustrates the effects of source parameters on the signal produced

$$P_f = KP_{av}[\delta l(P_{peak}/A)]C(\Phi/2) \quad (1)$$

where P_f is the two-photon fluorescence, K is a group of experimental parameters describing the collection efficiency of the instrument, P_{av} is the average power of the excitation source, δ is the two-photon cross section in $\text{cm}^4 \text{ s photon}^{-1} \text{ molecule}^{-1}$, l is the path length, P_{peak} is the peak power of the excitation source, A is the cross-sectional area of the laser beam, C is the analyte concentration, and Φ is the fluorescence quantum yield.¹¹ Inspection of this equation indicates that modelocked laser sources are ideal for two-photon fluorescence studies because of their high $P_{av}P_{peak}$ product. However, even with these sources, measurements of the weak two-photon fluorescence have been plagued by laser scatter.

Recent successful approaches to measuring two-photon fluorescence have separated the linear and nonlinear components of the signal to isolate the two-photon fluorescence from scattering interferences. Freeman, *et al.*, describe a *temporal* approach to separation.¹² They model the total fluorescence intensity, I_f , in terms of linear interactions, A_1 , and nonlinear (i.e., two-photon) interactions, A_2 , with the instantaneous laser intensity, I_{laser} ,

$$I_f = A_1 I_{laser} + A_2 I_{laser}^2 \quad (2)$$

Sinusoidal intensity modulation at ω with a dc offset of a and a modulation amplitude of b yields

$$I_{laser} = a + b \cos \omega t. \quad (3)$$

If Eqs. (2) and (3) are combined and the appropriate trigonometric identity employed, the result is

$$I_f = (aA_1 + a^2A_2 + \frac{1}{2}b^2A_2) + (bA_1 + 2abA_2) \cos \omega t + \frac{1}{2}b^2A_2 \cos 2\omega t. \quad (4)$$

Thus, modulating the laser at ω places a fraction of the two-photon signal at 2ω where it is isolated from linear interferences. A lock-in amplifier referenced to the modulation source and configured for second-harmonic operation will capture this "background-free" two-photon signal.

Focusing the excitation source *spatially* separates the nonlinear signal from the linear signal.¹³ Imaging only the fluorescence that occurs in the tightly focused region of the beam significantly increases the ratio of the desired signal to the scatter background. The temporal and spatial approaches, when used in concert, provide improved detection limits for two-photon fluorescence spectroscopy.¹¹

Experimental

Figure 1 depicts the instrumentation for two-photon fluorescence spectroscopy. A Spectra-Physics Model 2080-25 Argon-Ion Laser pumps a Spectra-Physics Model 3960 Tsunami Titanium:Sapphire Laser to produce an ~82-MHz train of modelocked pulses that can be tuned spectrally from 690 to 1080 nm. This system yields pulsewidths that can be adjusted from ~40 fs to ~30 ps by controlling the intracavity

group velocity dispersion. The system typically delivers 1-2.5 W of power; however, up to 4 W is available under high-pump-power conditions. Experiments were performed over a wide range of wavelengths, pulsewidths, and powers as described below.

The vertically polarized Tsunami pulsetrain passes through a Hinds photoelastic modulator operated at ~50 kHz and then through a Fresnel rhomb and a broadband polarizing beamsplitter cube. This collection of polarization elements trapezoidally modulates the amplitude of the incoming pulsetrain at 50 kHz with essentially no second-harmonic content. The rejected, horizontally polarized component strikes a fast-wired FND-100Q photodiode,¹⁴ providing pulsetrain and modulation diagnostics. For some experiments, neutral-density filters are placed after the cube to attenuate the beam. A beamsplitter picks off a small fraction of the vertically polarized component passed by the beamsplitter cube. This fraction provides continuous, real-time temporal and spectral diagnostics through an InRad Model 5-14BX Autocorrelator and a Princeton Instruments Model RY-1024 Photodiode Array coupled to an Acton SpectraPro-275 Spectrograph. The majority of the modulated pulsetrain is focused to a spot in the sample cuvette by a 10x microscope objective and then passes into a beam terminator. A second 10x microscope objective collects the resulting two-photon fluorescence and images it through a Schott Glass BG-39 Colored-Glass Filter onto a fast-wired RCA Model 931A Photomultiplier Tube (PMT)¹⁵ biased at -1000 V. The equipment employed in this experiment has been selected and configured to minimize the second-harmonic "blank" observed at ~100 kHz in the absence of two-photon fluorescence.

As described above, detection at the second harmonic of the modulation frequency isolates the two-photon signal from one-photon interferences. A TTL output from the photoelastic modulator driver provides a 50-kHz signal to a Stanford Research Systems Model SR850 Digital-Signal-Processing Lock-In Amplifier. With the anode current of the 931A PMT coupled to the lock-in via a 1-k Ω shunt resistor, the lock-in measures a background-free, two-photon fluorescence signal when configured to detect at 100 kHz. Operating with a 1-s time constant, the SR850 samples the signal at 0.5-Hz for 60 s to provide an average two-photon signal with good statistics. Through IEEE-488 connections, a 486 DX computer captures the two-photon signal as well as the pulse autocorrelation trace and spectral characteristics for post processing. A Coherent Labmaster power meter configured with an LM-3 head provides average-power information for the modulated pulsetrain.

The Heisenberg uncertainty principle dictates that femtosecond pulses have very large spectral bandwidths. For example, a transform-limited, 80-fs, sech^2 pulse centered at 800 nm has a spectral bandwidth of 8.4 nm FWHM. The wavelength dependence of the refractive index disperses or "chirps" these pulses, stretching them out in time as they pass through optical elements. The modulation elements in the beam path represent a significant amount of glass through which the pulses must pass. To ensure that accurate pulsewidths are employed in post processing of the two-photon signals, the autocorrelator pick-off is placed just upstream of the microscope objective. This scheme does not take into account any group velocity dispersion that occurs in the objective optics and the sample itself.

The chemicals employed in these studies include Coumarin-480 laser dye purchased from Exciton and methanol purchased from Burdick and Jackson. Each fuel sample was assigned an alphanumeric code such as POSF-2827.

Results and Discussion

Figure 2 depicts the calibration curve obtained for Coumarin-480 dissolved in methanol when excited with a 2-W pulsetrain of 130-fs pulses. Past two-photon studies revealed no spectroscopic blank when synchronously pumped dye lasers were used to excite two-photon fluorescence; however, the high average and peak powers achieved with the modelocked Ti:sapphire laser produce a small but measurable signal ($S/N \sim 2$) when the laser is focused into a neat methanol sample. A weighted least-squares fit to the data in Fig. 2 coupled with correction for the small methanol blank yields a Coumarin-480 detection limit of ~0.1 nM ($S/N=3$). A detection limit of 7.55 nM was achieved in previous picosecond experiments

with Coumarin-480.¹¹ A future publication will describe the features associated with this instrument that are responsible for this significant improvement.

A two-photon excitation spectrum for Coumarin-480 in methanol is obtained by tuning the modelocked Ti:sapphire laser across its gain curve while monitoring the second-harmonic signal at the lock-in amplifier. Figure 3 depicts the uncorrected two-photon signal obtained for Coumarin-480 as a function of excitation wavelength. Inspection of Eq. (1) reveals that the two-photon fluorescence signal is dependent directly on the square of the laser power through $P_{av}P_{peak}$ and inversely on the pulsewidth through P_{peak} . Experience has shown that straightforward correction of the two-photon signal for laser power and pulsewidth is difficult with a multimode source such as a pulsed laser;¹⁶ this careful study reveals the importance of the second-order coherence properties of the source. Utilizing a single-mode dye laser for two-photon excitation, the authors obtained corrected spectra. In continuing studies, a single-mode ring Ti:sapphire laser will be employed for evaluating the effects of second-order coherence.

Future two-photon studies in aviation fuel will be focused on two distinct experiments. First, fuel-additive candidates that have been chemically tagged with strong two-photon fluorophores will be synthesized. Monitoring the two-photon signal from fuels doped with these tagged additives will provide detailed information on the lifetimes and thermal stabilities of the additives. Second, two-photon-active species that are native to the fuel will be studied. Measurements reveal that many of the fuels produce significant two-photon fluorescence under modelocked Ti:sapphire excitation. The list of two-photon-active fluorophores identified to date is relatively limited; however, the complicated mixture that constitutes aviation fuel contains one or more two-photon-active components. This fortunate situation permits the direct study of these components and their associated chemistry.

Figure 4 contains results that address both of these experimental goals. This calibration curve for Coumarin-480 in POSF-2827 aviation fuel was obtained with a 150-mW pulsetrain of 130-fs pulses. The fuel itself produces a significant two-photon fluorescence signal. In addition, submicromolar quantities of Coumarin-480 produce a measurable signal in the presence of the fuel background.

The bars in Fig. 5 represent the two-photon signal measured for each fuel in a group of six representative samples. Averaging over several laser powers and pulsewidths produced the data depicted in this figure. In each laser configuration, the fuel signals were normalized to that of POSF-2818. POSF-2980, -2922, and -2827 are commercial Jet-A fuels; POSF-2934 is a military JP-8 fuel; POSF-2976 is a fuel formulated for high thermal stability (JPTS); and POSF-2818 is a highly refined JP-7 fuel. Thermal-stability experiments conducted by Systems Research Laboratories, the University of Dayton Research Institute, and USAF in-house researchers indicate that POSF-2980, -2922, -2934, and -2827 produce substantial fuel-fouling deposits when thermally stressed. POSF-2976 and -2818 are more thermally stable than the other four fuels. Interestingly, the low-thermal-stability fuels produce relatively large two-photon fluorescence signals, while the high-thermal-stability fuels produce relatively small signals. The signals from these two classes of fuels differ in another way: The former produce a blue-green two-photon-excited emission, while the latter produce a violet-blue emission.

Conclusion

Modelocked Ti:sapphire laser excitation coupled with spatial filtering and second-harmonic detection yields outstanding performance for two-photon fluorescence spectroscopy. This approach yields a detection limit of ~0.1 nM Coumarin-480 in methanol and a linear dynamic range covering over four orders of magnitude. In addition, this scheme provides a rapid and reproducible means for obtaining two-photon fluorescence excitation spectra. Future studies will verify the effects of second-order coherence on these spectra. Preliminary experiments in aviation fuel indicate that strong two-photon fluorophores doped in the fuel and two-photon-active species native to the fuel produce abundant fluorescence signals. Future studies will focus on exploiting these signals to characterize the chemistry and physics responsible for fuel fouling and the potential for thermal-stability enhancement.

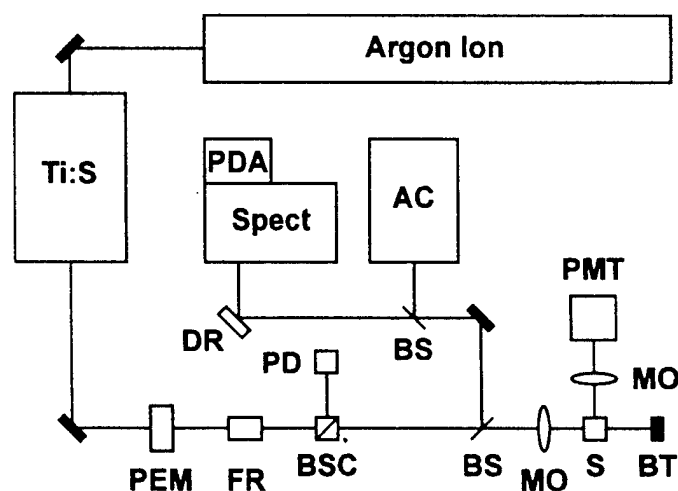
Acknowledgements

This work was supported, in part, by the Air Force Office of Scientific Research, Air Force Contract F33615-90-C-2033, and National Science Foundation Grant CHE-8822878. The authors would like to thank Marian Whitaker for her invaluable assistance in preparing the manuscript.

References

1. T. Edwards, W. M. Roquemore, W. E. Harrison, and S. D. Anderson, "Research and Development of High Thermal Stability Fuels," AGARD Conference Proceedings 536 (AGARD, Neilluy-Sur-Seine, France, 1993), p. 18-1.
2. T. E. Parker, R. R. Foutter, and W. T. Rawlins, *Ind. Eng. Chem. Res.* **31**, 2243 (1992).
3. D. M. Dinkel and F. E. Lytle, *Anal. Chim. Acta* **263**, 131 (1992).
4. R. L. Steffen and F. E. Lytle, *Anal. Chim. Acta* **215**, 203 (1988).
5. R. L. Steffen and F. E. Lytle, *Anal. Chim. Acta* **200**, 491 (1987).
6. M. J. Wirth and F. E. Lytle, *Anal. Chem.* **49**, 2054 (1977).
7. W. Kaiser and C. G. Garrett, *Phys. Rev. Lett.* **7**, 229 (1961).
8. W. Denk, J. H. Strickler, and W. W. Webb, *Science* **248**, 73 (1991).
9. E. S. Wu, J. H. Strickler, W. R. Harrell, and W. W. Webb, *SPIE Proc.* **1674**, 776 (1992).
10. J. H. Strickler and W. W. Webb, *Opt. Lett.* **16**, 1780 (1991).
11. W. G. Fisher and F. E. Lytle, *Anal. Chem.* **65**, 631 (1993).
12. R. G. Freeman, D. L. Gilliland, and F. E. Lytle, *Anal. Chem.* **62**, 2216 (1990).
13. M. J. Wirth and H. O. Fatunmbi, *Anal. Chem.* **62**, 973 (1990).
14. J. M. Harris, W. R. Barnes, Jr., T. L. Gustafson, T. H. Bushaw, and F. E. Lytle, *Rev. Sci. Instrum.* **51**, 988 (1980).
15. J. M. Harris, F. E. Lytle, and T. C. McClain, *Anal. Chem.* **48**, 2095 (1976).
16. M. C. Johnson and F. E. Lytle, *J. Appl. Phys.* **51**, 2445 (1980).

Figure 1. Two-photon fluorescence spectrometer. Abbreviations: Ti:S-Ti:sapphire laser, PEM-photoelastic modulator, FR-Fresnel rhomb, BSC-beamsplitter cube, PD-photodiode, BS-beamsplitter, AC-autocorrelator, DR-diffuse reflector, Spect-spectrograph, PDA-photodiode array, MO-microscope objective, S-sample, PMT-photomultiplier tube, BT-beam terminator.



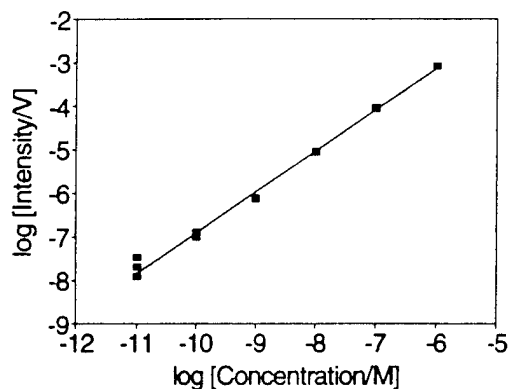


Figure 2. Calibration curve for Coumarin-480 in methanol obtained using a 2-W pulsetrain of 130-fs pulses.

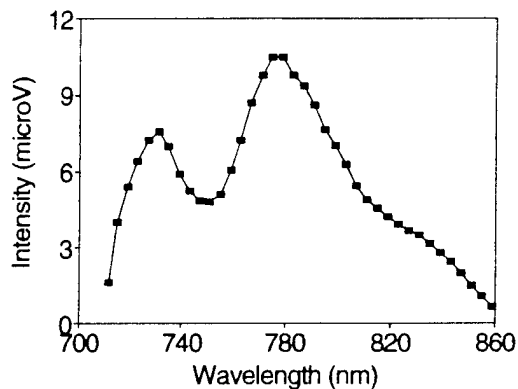


Figure 3. Uncorrected two-photon fluorescence excitation spectrum for Coumarin-480 in methanol.

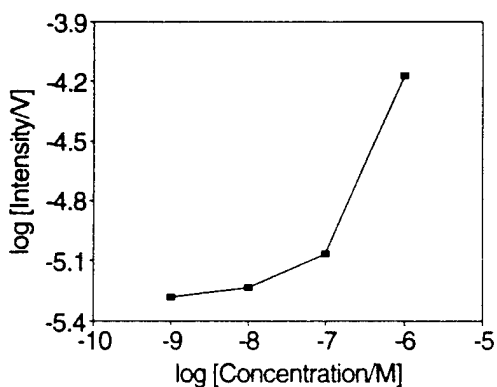


Figure 4. Calibration curve for Coumarin-480 in POSF-2827 aviation fuel obtained using a 150-mW pulsetrain of 130-fs pulses.

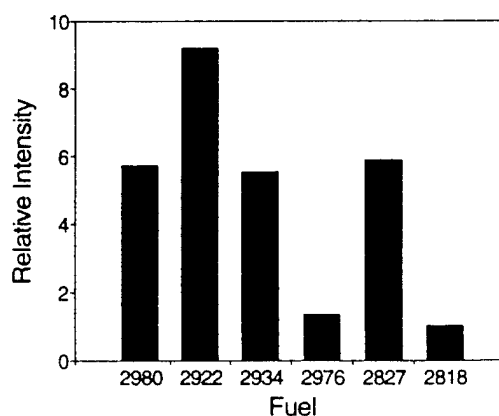


Figure 5. Relative two-photon fluorescence signals for POSF aviation fuels.

Dissolved Oxygen Quantitation in Fuel Through Measurements of Dynamically Quenched Fluorescence Lifetimes

James R. Gord

Wright Laboratory, Aero Propulsion and Power Directorate
Wright-Patterson AFB, OH 45433-7103

Steven W. Buckner

Columbus College, Department of Chemistry and Geology
Columbus, GA 31907

and

William L. Weaver

Systems Research Laboratories, Inc.,
A Division of Space Industries International, Inc.
2800 Indian Ripple Rd, Dayton, OH 45440-3696

Abstract — An optical method for the quantitation of dissolved molecular oxygen in aviation fuels has been developed to aid the study of thermally induced fuel oxidation. The technique is based on the propensity of dissolved molecular oxygen to quench probe molecule fluorescence excited with a pulsed nitrogen laser. Linear calibration curves based on Stern-Volmer kinetics are generated through measurement of the time-resolved fluorescence signal produced by pyrene doped into aviation fuel at parts per million (ppm) levels. The advantages of nondestructive *in-situ* monitoring, reduced measurement time, and enhanced capabilities (including spatially resolved and rapidly time-varying measurements) make this optical technique a very attractive complement to current chromatographic and electrochemical methods. Application to flowing-fuel simulators demonstrates the technique.

INTRODUCTION

In advanced aircraft, fuel is used as the primary coolant for on-board heat sources. Thermally induced reactions between the fuel and dissolved oxygen generate insoluble products and deposits within the aircraft fuel system. In order to develop rational solutions to the problem of deposit formation, an understanding of the oxidation of these fuels under conditions of high temperature and low oxygen concentration is essential [1-3]. One of the difficulties in this area is the determination of oxygen concentration in the fuel. The oxygen-saturated concentration is on the order of 70 ppm [4,5]; thus, limit of detection is an issue.

The techniques currently employed to quantitate dissolved oxygen include gas chromatography/mass spectrometry (GC/MS), gas chromatography with thermal-conductivity detection (GC/TCD) [4-6], and electrochemical methods. The GC/MS and GC/TCD techniques suffer from the fact that they are off-line and destructive. In addition the GC column must be purged of excess

liquid fuel between samples, resulting in an average acquisition time of 20 min per measurement. Electrodes provide a much faster response time (30 s), but they consume oxygen and are affected by sample flow rate, stirring, and high pressure [7]. Material incompatibilities between electrodes and the high-temperature aviation fuel are also a concern. It would be advantageous to supplement the GC and electrochemical techniques with a non-destructive, *in-situ* optical spectroscopic probe for molecular oxygen [1].

Spectroscopically, molecular oxygen is difficult to study in solution [8]. It does not absorb in the infrared, and its electronic transitions lie far in the ultraviolet where fuel components absorb strongly. Oxygen has a Raman-allowed transition, but Raman spectroscopy is not the technique of choice for trace analysis. Oxygen also has a unique ESR (electron spin resonance) signature, but the expense and limited sensitivity of this technique prohibit its use for this application. An alternative optical approach involves quantitating dissolved oxygen indirectly through its influence on the fluorescence of a probe molecule [9] such as pyrene. Oxygen efficiently and reproducibly quenches the fluorescence of pyrene due to the energy match between the singlet-triplet gap in O₂ and the energy of the first excited singlet state of pyrene [10]. This process provides the basis for a spectroscopic technique for quantitating dissolved molecular oxygen.

EXPERIMENTAL

Materials

Isooctane (Fischer Scientific, CAS#0540-84-1), cyclohexane (Mallinckrodt, CAS#110-82-7), and pyrene (Kodak, CAS#129-00-0) were purchased from their respective suppliers and used without further purification. Aviation fuels provided by the Fuels

and Lubrication Division of Wright Laboratory at Wright-Patterson Air Force Base included three Jet-A fuels (POSF-2827, POSF-2980, POSF-2926) and a JP-7 fuel (POSF-2818).

Instruments

The concentrations of dissolved molecular oxygen in the samples used during development of the technique were varied by sparging the samples with controlled mixtures of air and nitrogen [Tylan General mass flow controllers, Model RO-28 system with FC-280S controllers]. The oxygen concentration in each of the standard samples was determined using a GC/MS [Hewlett-Packard, Model 5980 (GC)/Model 5988 (MS)] system, with selected ion monitoring of the $m/z=32$ ion. The determination of $[O_2]$ in fuel by GC/MS has been described in detail elsewhere [6]. Additional experiments were conducted to determine the reproducibility and uncertainty of the optical technique employing an amperometric Pt/Ag electrode oxygen sensor [Ingold, Model 4300] to calibrate the oxygen standards.

The on-line studies were performed with the Wright Laboratory near-isothermal flowing test rig (NIFTR) [11] in which air-saturated fuel is pumped through a fuel line maintained at or near typical gas-turbine-engine operating temperatures and pressures. Thermally induced chemical reactions consume dissolved oxygen in the NIFTR. The fuel lines used in this study included both coated and uncoated stainless steel. Following the heated section, the fuel flows through 1 m of unheated stainless-steel tubing in which it rapidly returns to room temperature. No oxygen is consumed in this region. The fuel stream then passes through a quartz flow cell with flat faces, providing optical access for the laser-based technique. The oxygen concentration is obtained optically and verified by diverting some of the post test stream to a GC/TCD (Hewlett Packard, Model 5980) [6].

Time-Resolved Fluorimeter

All fluorescence measurements were made on a fluorimeter whose construction is described below. A block diagram of the instrument is shown in Fig. 1. Excitation of samples is accomplished using a nitrogen laser (Laser Sciences, Inc., Model VSL-337ND) with a 337-nm output power of 300 μ J/pulse, a pulsewidth of 3 ns, and a maximum pulse repetition rate of 20 Hz. A small portion ($\sim 4\%$) of the laser beam is split off with a glass slide into a photodiode [Texas Instruments TIED-56] which is fast-wired to yield a 200-ps risetime [12]. The photodiode output is used as the trigger source for a LeCroy Model 9354 digital storage oscilloscope (DSO). Following the glass slide, the laser beam is focused into the sample. The fluorescence emission from the sample passes through a neutral density filter [Melles Griot, OD=3] and a pair of glass filters [Schott Glass Technologies, GG375 and BG37] to reject scatter from the 337-nm beam and ambient room light. The filtered fluorescence is detected by an RCA 931A photomultiplier tube (PMT) that has been fast-wired to yield a risetime of ~ 1.3 ns [13]. The signal from the PMT is connected to the input of the DSO which is configured to average

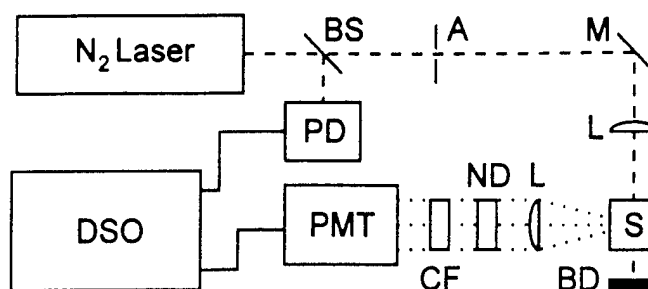


Figure 1. Block diagram of time-resolved fluorimeter. BS - Beam Splitter; A - Aperture; M - Mirror; L - Lens; S - Sample; BD - Beam Dump; ND - Neutral Density Filter; CF - Color Filter; PMT - Photomultiplier Tube; PD - Photodiode; DSO - Digital Storage Oscilloscope.

100 traces over a 1- μ s time window with a 2-GHz sampling rate at a bandwidth of 500 MHz. The resulting fluorescence decays are transferred via an IEEE-488 connection to a host computer for post processing.

KINETIC MODEL

Collisions between photoexcited pyrene and oxygen molecules result in the non-radiative transfer of energy from pyrene to oxygen because of the energy match between the singlet-triplet gap in oxygen and the energy of the first excited singlet state of pyrene. At a given temperature, a decrease in the dissolved-oxygen concentration reduces the oxygen-pyrene collision frequency, resulting in an increase in both the total fluorescence quantum yield and the lifetime of the excited state of pyrene. Instrumentally, it is a simpler task to measure the total fluorescence intensity, which may be converted to a quantum yield. However, previous work has shown this approach to be intractable for quantitating dissolved oxygen during fuel-thermal-stability studies since the amount of pyrene doped into the fuel must be precisely controlled. If pyrene is consumed (or produced) during oxidation of the fuel, the total fluorescence intensity will vary, independent of the presence of oxygen. However, the lifetime of the excited state of pyrene is independent of pyrene concentration (within certain limits). Thus, the pyrene fluorescence lifetime is a reliable and reproducible indicator of the dissolved-oxygen concentration at a given fuel temperature.

After photoexcitation of an ensemble of pyrene molecules, the excited species return to their ground states, producing an observed fluorescence signal that can be described by the single exponential decay in Eq. (1),

$$\Phi_f(t) = \Phi_f^0 \exp(-k_f t), \quad (1)$$

where Φ_f^0 is the fluorescence radiant power immediately following excitation. The fluorescence power decays with an overall rate constant, k_f , that contains contributions from the first-order (natural or radiative) decay rate constant, k_r , and a second-

order rate constant for dynamic quenching with oxygen, k_q , as shown in Eq. (2),

$$k_t = k_r + k_q[O_2]. \quad (2)$$

Using the relationship between the rate constant (k) and the lifetime (τ) of a single exponential decay ($k=1/\tau$), Eq. (2) can be written in terms of the fluorescence lifetime, as in the Stern-Volmer Equation,

$$\tau_0/\tau_f = 1 + \tau_0 k_q [O_2], \quad (3)$$

where τ_f is the measured lifetime of the observed fluorescence (dynamically quenched fluorescence lifetime, DQFL) and τ_0 is the measured lifetime of the observed fluorescence in the absence of quenching. By measuring τ_0 at $[O_2] = 0$ and the DQFL at known values of $[O_2]$, a linear calibration curve can be constructed that relates the lifetime of the observed pyrene fluorescence to the concentration of dissolved oxygen (as measured by existing gas-chromatographic and electrochemical methods).

RESULTS

Model Systems

Cyclohexane and isooctane were studied first as model systems. Neither of these neat solvents produces a detectable fluorescence signal when excited at the wavelength used in these studies. Figure 2 shows the decay of the detected fluorescence signal as a function of time for a 10-ppm solution of pyrene in cyclohexane after sparging with nitrogen (a) and air (b). The decrease in both integrated fluorescence intensity and lifetime is evident when the deoxygenated sample is sparged with air (oxygen).

The lifetime of the decays can be obtained by fitting the traces to an exponential function using nonlinear fitting techniques. However, since the traces are composed of single exponential decays, the data were linearized by taking the natural logarithm of the intensity, and decay constants were extracted by fitting the resultant data to a straight line with a least-squares algorithm, as demonstrated in Fig. 3.

The concentration of dissolved oxygen in the pyrene/cyclohexane sample was varied and then measured with the time-resolved fluorimeter and the electrochemical probe. A Stern-Volmer plot for this sample is shown in Fig. 4. Linear behavior, as predicted by the model, is observed. This plot serves as a calibration curve for the determination of $[O_2]$ in cyclohexane. This procedure was used to construct Stern-Volmer calibration curves for all of the samples used in this study.

Analysis of Uncertainty: The vertical error bars in Fig. 4 and all subsequent Stern-Volmer calibration curves represent two standard deviations on averages of fitted DQFL values (τ_0/τ_f) calculated using 16 replicate experiments averaged over 100 decay traces at each oxygen concentration. Since the fluorescence lifetime is inversely proportional to the

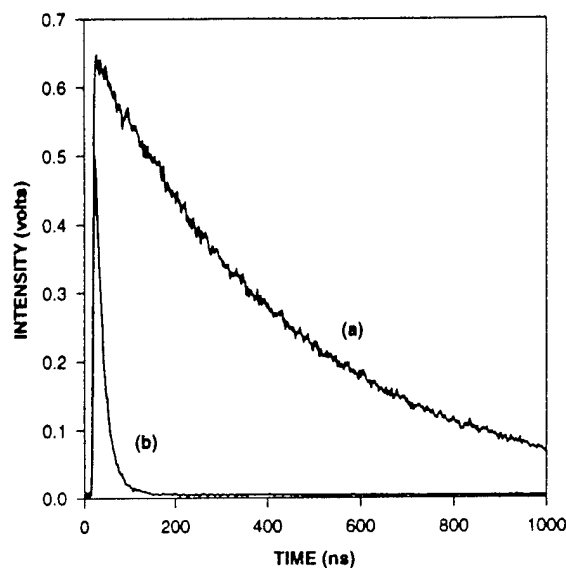


Figure 2. Plots of time-resolved fluorescence intensity for a solution of 10-ppm pyrene in cyclohexane after sparging with nitrogen (a) and air (b).

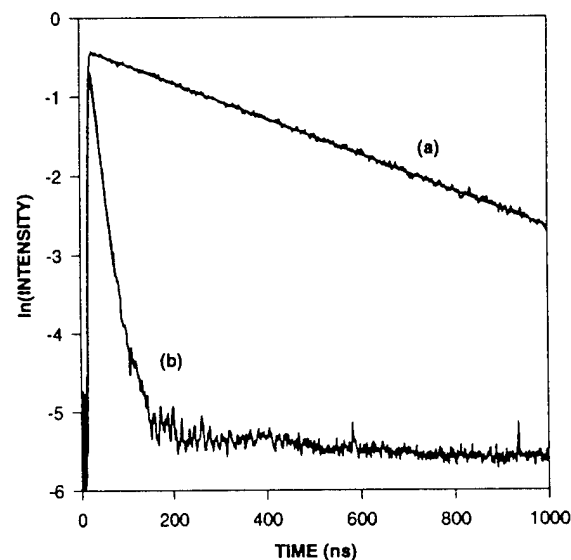


Figure 3. Linearized data for 10-ppm pyrene in cyclohexane sparged with nitrogen (a) and air (b). Linear region is fit with a least squares algorithm over the range of 90% to 10% maximum intensity.

concentration of dissolved molecular oxygen, samples that contain very little dissolved oxygen produce decays with much longer lifetimes than samples containing dissolved oxygen at concentrations close to that of the saturation value (as in Fig. 2). The uncertainty in the fit to the linearized decay of the average of 100 traces (as in Fig. 3) increases from ~0.2% to ~1.6% relative error as the concentration of dissolved oxygen increases from 0%

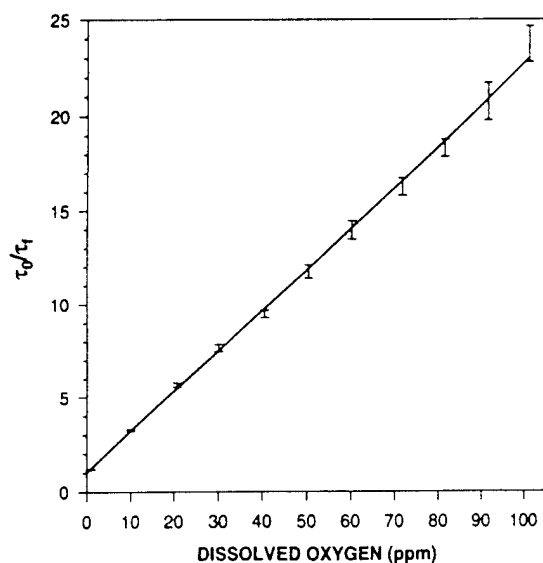


Figure 4. Stern-Volmer calibration plot for 10-ppm pyrene in cyclohexane.

to 100% saturation. The uncertainty in 16 replicate averages of 100 decays increases from 3.2% to 7.8% relative error over the same range. It is the precision of these replicate measurements that is offered as the uncertainty in the technique rather than the error in the fit.

The inverse relationship between signal and oxygen concentration is clearly nonlinear. As a result the technique not only yields improved precision but also enjoys greater sensitivity as the concentration of dissolved oxygen decreases, providing an optical technique that is very complementary to both the chromatographic and electrochemical techniques whose signals decrease into their noise levels as the concentration of dissolved oxygen decreases to zero.

Undoped Aviation Fuel

The neat aviation fuels used in this study produce an intrinsic fluorescence signal when excited at 337 nm. Use of this native fuel fluorescence would obviate the need to dope the fuel with pyrene for oxygen analysis. Unfortunately, analysis of the time-resolved signal from neat fuel reveals that there are many fluorescent components there in. The fluorescence from each of these components is quenched by dissolved oxygen with different efficiency, resulting in a multi-exponential fluorescence-decay signal that is under-determined by the Stern-Volmer analysis used in this study.

Pyrene-Doped Fuels

To achieve quantitation of dissolved oxygen, the aviation fuels under study were doped with pyrene at levels ranging from 10 to 50 ppm. The fluorescence quantum yield of pyrene is larger than that of the neat fuel. This condition, coupled with the longer

fluorescence lifetime of pyrene as compared to that of fuel (~300 ns and ~100 ns, respectively, at 0 ppm O_2), produces a signal from the doped fuel samples that is dominated by the single-exponential pyrene fluorescence decay. Stern-Volmer calibration plots for these doped fuels display excellent linearity as a result. A typical plot for 10-ppm pyrene in POSF-2827 (Jet-A) is shown in Fig. 5.

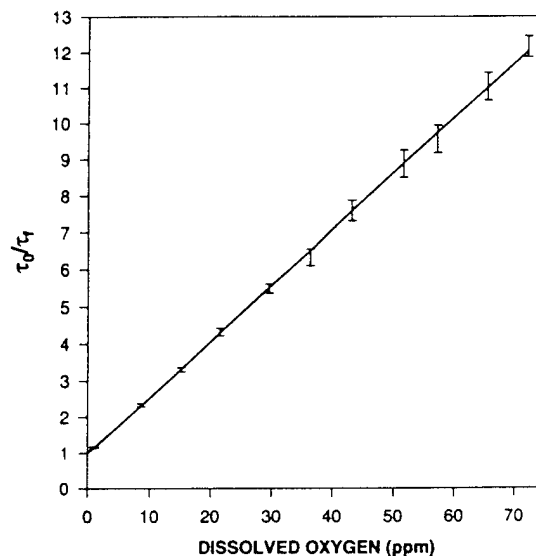


Figure 5. Stern-Volmer calibration plot for 10-ppm pyrene in POSF-2827 (Jet-A).

To confirm the independence of the time-resolved fluorescence lifetime technique from the effects of high-temperature conditions that may consume pyrene, a sample of 20-ppm pyrene in Jet-A was thermally stressed in the NIFTR at 185°C for sufficient time to consume all of the dissolved oxygen. When the sample was reoxygenated, it produced DQFL values that were identical to those from a 20-ppm pyrene in Jet-A sample that had not been thermally stressed. Additionally, doped and undoped fuel samples display identical oxygen-consumption behavior (within the uncertainty of the GC/TCD technique), providing evidence that the levels of pyrene used for this study do not affect the oxygen-consumption chemistry.

Flowing Simulators

The NIFTR is used to simulate the flow of aviation fuel through a heated jet fuel line. Thermally induced oxidation reactions are limited to consumption of oxygen initially dissolved in the fuel since there are no headspaces in the simulator. By varying the flowrate of the fuel through the heated tube, it is possible to control the residence time of the fuel in the heated section and, hence, the reaction (stress) time. The concentration of oxygen as a function of stress time and reactor temperature is measured to

yield an oxygen-consumption curve for the fuel/additive sample under study.

To test the utility of the DQFL technique, the NIFTR was configured with a quartz cell to permit concurrent measurement of oxygen with the DQFL optical technique and the GC/TCD. The stressed fuel returns to room temperature before the oxygen-concentration measurements are performed with either instruments, thereby ensuring a constant temperature for the optical technique. Several studies of different fuel/additive samples and coated/uncoated reaction tubes were performed with the DQFL and GC/TCD diagnostics. The two techniques for oxygen determination were in agreement within their respective experimental uncertainties ($\pm 5\%$ for the GC/TCD). A typical oxygen-consumption curve is shown in Fig. 6 for a sample of POSF-2980 (Jet-A) with a jet fuel additive (metal deactivator, MDA) in a coated tube. It is important to mention that each of the points on the curve produced by the GC/TCD technique represents 20 min of analysis time, while each point acquired with the DQFL technique required only 10 s.

The operational protocol for the NIFTR is currently designed around the analysis time required by the GC/TCD technique. The temperature of the test section is held constant, while the sample flow rate (stress time) is varied. After adjustment to a different flow rate, the NIFTR is permitted to achieve steady state (30 min to 1 hr) before the oxygen analysis is made (additional 20 min). This protocol produces an oxygen-consumption curve after as much as a week of analysis time. Utilizing the fast time response of the DQFL technique (10 s), we are currently investigating a protocol based on modulated fuel flow that is designed to produce a complete oxygen-consumption curve in a few hours.

SUMMARY

Time-resolved measurement of the oxygen-quenched fluorescence of pyrene has been demonstrated to be a viable technique for determining dissolved-oxygen concentration in aviation fuel. Although the intrinsic fluorescence of the fuel is quenched by oxygen, the time-resolved behavior of this native fuel fluorescence is multiexponential and inconvenient for use as a diagnostic tool. The addition of trace amounts of pyrene overcomes this problem, and a Stern-Volmer kinetic model yields good results in both static and flowing simulator studies. The advantages of lower cost, non-destructive *in-situ* monitoring, shorter measurement time, and capabilities for spatially resolved and rapidly time-varying measurements make this technique a very attractive alternative to current chromatographic and electrochemical approaches.

ACKNOWLEDGEMENTS

This work was funded, in part, by USAF Contract F33615-90-C-2003. Dr. Buckner wishes to thank the Air Force Office of Scientific Research and Wright Laboratory for support through the Summer Faculty Research Program. The authors wish to thank Lt. Col. Gary C. Hale (USAF Rsrvs.) for his assistance in

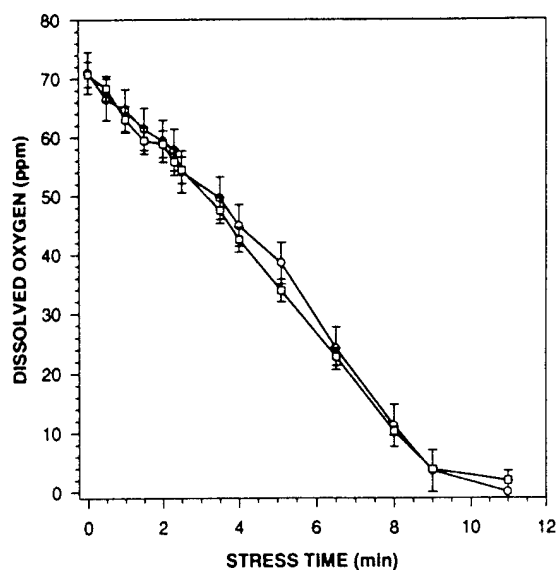


Figure 6. Dissolved oxygen concentration measured by the DQFL (\square) and GC/TCD (\circ) techniques as a function of stress time at 185°C. Sample is 20-ppm pyrene in POSF-2980 (Jet-A). acquiring data for the reproducibility studies. The authors are also indebted to Mrs. Marian Whitaker for her editorial assistance in preparation of this manuscript.

REFERENCES

- [1] W. M. Roquemore, J. A. Pearce, W. E. Harrison, J. L. Krazinski, and S. P. Vanka, *Prepr.-Am. Chem. Soc., Div. Pet. Chem.* vol. 34, p. 841, 1989.
- [2] T. E. Parker, R. R. Foutter, and W. T. Rawlins, *Ind. Eng. Chem. Res.* vol. 31, no. 9, pp. 2243-2251, 1992.
- [3] S. Zabarnick, *Ind. Eng. Chem. Res.* vol. 33, no. 5, pp. 1348-1354, 1994.
- [4] R. Battino, T. R. Rettich, and T. Tominaga, *J. Phys. Chem. Ref. Data*, vol. 12, p. 163, 1983.
- [5] R. Battino, *Oxygen and Ozone*, ed. R. Battino. Oxford: Pergamon, 1981.
- [6] R. C. Striebig and W. A. Rubey, *Prepr.-Am. Chem. Soc., Div. Pet. Chem.* pp. 47-50, 1994.
- [7] M. C. Hitchman, *Measurement of Dissolved Oxygen*, New York: John Wiley & Sons, 1978.
- [8] G. Herzberg, *Infrared and Raman Spectra of Polyatomic Molecules*, New York: Van Nostrand, 1945.
- [9] M. E. Cox and B. Dunn, *Appl. Opt.* vol. 24, pp. 2114-2120, 1985.
- [10] J. R. Lakowicz, *Principles of Fluorescence Spectroscopy*, New York: Plenum, 1983.
- [11] E. G. Jones and W. J. Balster, *Energy and Fuels* vol. 7, no. 6, pp. 968-977, 1993.
- [12] J. M. Harris, F. E. Lytle, and T. C. McCain, *Anal. Chem.* vol. 48, p. 2095, 1976.
- [13] J. M. Harris, W. T. J. Barnes, T. L. Gustafson, T. H.

Bushaw, and F. E. Lytle, *Rev. Sci. Instrum.* vol. 51, p. 988, 1980.

3. DIAGNOSTIC APPLICATIONS

3.1 Combustion Studies

3.1.1 General Overview. The application of advanced laser diagnostics to combustion studies was one of the most productive areas of this program. The combustion studies ranged from small-scale laboratory burners to large-scale engine components. Diagnostics as simple as visualization to as complex as CARS were employed to obtain state-of-the-art information concerning combustion processes. The resulting information was utilized for CFDC development, calibration, and evaluation.

3.1.2 Premixed Flames. Because of the nature of the goals of this research, namely, to study processes that aid the understanding of jet turbine combustors, only two premixed flame studies were performed. The first was in collaboration with Professor Jim Driscoll of the University of Michigan in which the interaction of a speaker-generated ring vortex and a premixed propane-air flame were studied using LIF of the OH radical and TFP ["Images of the Quenching of a Flame by a Vortex - To Quantify Regimes of Turbulent Combustion" (pp. 252 - 265)] and PIV ["The Strain Exerted by a Vortex on a Flame - Determined from Velocity Field Images" (pp. 266 - 278)].

In the second study the effects of a DC electric field on a premixed flame were evaluated. Although the body of work on the effects of DC electric fields on flames is large, the exact mechanism responsible for the rather dramatic alterations in the size, shape, and stability of hydrocarbon flames is not well understood. The PIV and TFP optical diagnostic techniques can lend additional insight into physical effects by providing medium-resolution two-dimensional velocity profiles and time-dependent temperature measurements. The application of these techniques to a premixed propane-air flame in a laboratory burner was described in a presentation entitled, "The Effect of a DC Electric Field on the Velocity and Temperature of a Premixed Flame" (pp. 279 - 284).

Images of the Quenching of a Flame by a Vortex—To Quantify Regimes of Turbulent Combustion

WILLIAM L. ROBERTS and JAMES F. DRISCOLL

Department of Aerospace Engineering, University of Michigan, Ann Arbor, MI 48109

MICHAEL C. DRAKE

General Motors Research Laboratories, Warren, MI 48090

LARRY P. GOSS

Systems Research Laboratories, Dayton, OH 45440

A laminar toroidal vortex is interacted with a laminar premixed flame in order to isolate and to visualize some of the fundamental physics of turbulent combustion. Localized quenching of the flame was observed using planar laser-induced fluorescence imaging of superequilibrium OH molecules in the counterflow flamefront region near the vortex leading edge. A quenching limit curve was measured as a function of vortex size and strength. In the second part of the study, the measurements are combined with concepts proposed by Poinot, Veynante, and Candel in order to infer the thin flame limit, namely, the onset of distributed reactions, on a classical premixed turbulent combustion regime diagram. The measured thin flame limit indicates when laminar flamelet theories become invalid, since quenching allows hot products and reactants to coexist. Results are compared with the Klimov–Williams criterion. Vortex core diameters were as small as the flame thickness in some cases. The main conclusion is that small vortices are less effective at quenching a flame than was previously believed; therefore the inferred regime within which thin flame theories are valid extends to a turbulence intensity that is more than an order of magnitude larger than that which was previously predicted. Results also indicate that micromixing models, which assume that the smallest eddies exert the largest strain on a flame, are not realistic. Measured trends are in agreement with direct numerical simulations of Poinot et al., but absolute values differ. The measured vortex Karlovitz number that is required to quench a flame is not constant but decreases by a factor of four as vortex size increases from one to five flame thicknesses. Thin-film pyrometry was used to quantify the radiative heat losses; quenching occurs when the products cool to approximately 1300 K, which is in agreement with stretched laminar flame calculations that include detailed chemistry. The quenching Karlovitz number for propane–air flames differs from that of methane–air flames, indicating the importance of detailed chemistry and transport properties. Flame curvature was observed to cause enhancement (or reduction) of the local reaction rate, depending on the Lewis number, in a manner that is consistent with stretched flame theory.

INTRODUCTION

The present work is an investigation of the vortex strength that is required for a single eddy in a turbulent flow to locally quench a premixed flame, and thereby alter the flame structure. This quenching condition is denoted the thin flame limit. When a flame is locally quenched, the reactants can coexist with hot products prior to chemical reaction, which can result in a distributed reaction. This coexistence of reactants and products violates the assumptions made in thin flame theories.

Therefore it is useful to quantify the thin flame limit in order to determine the range over which thin, strained flamelet models are valid.

The classical regime diagram for turbulent premixed flames appears in Ref. 1 and is discussed below. The predicted thin flame limit is reached when the turbulence intensity is sufficient to cause the nondimensional stretch rate (Karlovitz number) that is based on the Taylor microscale $(u'_{rms}/\Lambda)/(S_L/\delta)$ to equal unity. This prediction has been denoted the Klimov–Williams criterion [2]; the Taylor microscale (Λ) is assumed to be the appropriate

scale because it is the characteristic scale of the strain rate in a nonreacting turbulent flow [3]. The rms velocity fluctuation is u'_{rms} , S_L is the laminar burning velocity, and δ is the laminar flame thickness. Previously there have been no measurements available to assess how vortices quench flames or to determine if quenching occurs at a constant Karlovitz number. Numerical results have been reported by Poinso et al. [4, 5], which predict when a single vortex can quench a flame; Poinso et al. also show how to relate single vortex simulations to the regime diagram for turbulent combustion. However, none of the simulations to date can yield quantitative values because the simulations include unrealistic heat loss terms and unrealistic one-step chemistry. Flame quenching is especially sensitive to both assumptions, so quantitative results must come from experiment.

A second research issue is whether or not small vortices play a dominant role in the process of flame wrinkling and flame quenching. Micromixing models [6] assume that small vortices having a core diameter (d_c) near the Kolmogorov or the Taylor scales play a dominant role because in a nonreacting flow the strain rate U_θ/d_c that is associated with eddies of diameter d_c scales as $d_c^{-2/3}$ and thus is largest for small eddies. That is, eddy rotational velocity U_θ is assumed to be unaffected by the flame and to scale as $d_c^{1/3}$, according to turbulent energy cascade concepts [3]. In contrast, simulations by Poinso et al. [4, 5] and the present measurements show that small eddies do not strain out the flame because they are destroyed by viscous forces. The importance of this finding is that it means that direct numerical simulations of turbulent flames need not attempt to resolve all of the small scales of turbulence. However, measurements such as those herein are needed to determine the range of small scales that can be ignored.

The approach taken has been to interact a single laminar, toroidal vortex with a laminar flame. The smallest vortex used had a toroid diameter of 1.27 cm and a vortex core diameter (d_c) of 0.25 cm. It was decided to operate near the lean flammability limit in order to achieve a large value of the thermal thickness of the flame (δ) of 0.26 cm so that values of

d_c/δ as small as unity could be achieved. Our previous studies [7, 8] provided the first conclusive experimental evidence that a premixed flame can be quenched by a vortex. Only one vortex size was considered in that work, so the present work utilizes a range of vortex diameters, vortex strengths, and several different values of Lewis number. A toroidal vortex was chosen because two-dimensional linear vortices tend to be unstable, especially at the large rotational velocities desired. Another requirement was that naturally-occurring radiative heat losses must be sufficient to prevent the hot products from immediately reigniting the flame; in addition, the vortex must have sufficient residence time in the flame to cause quenching.

Figure 1 illustrates that the physics of the present flame quenching process is similar to that of a counterflow flame that is produced between a stream of cold reactants and an opposing stream of hot products. The counterflow flame problem has been solved by several researchers, including Darabiha et al. [9, 10]. Near the vortex leading edge in Fig. 1 there exists a stagnation point; cold reactants approach the stagnation point from above, and due to the vortex downward motion, hot products approach the stagnation point from below. It is relatively difficult to quench a counterflow flame without sufficient heat loss because hot products always remain in contact with reactants. However, Darabiha et al. [9] show that sufficient strain forces the flame to move across the stagnation point. For such conditions, incomplete reaction occurs, since most of the reactants remain on the reactant side of the

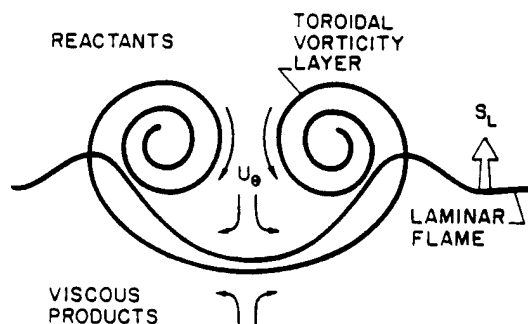


Fig. 1. Schematic showing how the flame near the vortex leading edge is similar to a counterflow flame.

stagnation point. Only those reactants that can diffuse across the opposing convection field can be consumed at the flame. The maximum temperature and the rate of reactants consumed per unit volume of the reaction zone do not decrease due to strain in Darabiha's solution. Instead the increasing strain reduces the reaction zone thickness to zero, the reactants bypass the flame, and the flame is quenched.

Heat losses are important in nearly all flame quenching experiments and substantial heat losses had to be added to the numerical simulations of Poinso et al. [4, 5] in order to observe quenching. Therefore, the present strategy was not to attempt to eliminate heat losses but to quantify the naturally occurring radiation losses in the experiment. Measurements were made of the rate at which gas temperature decreases with distance behind the flame due to radiation; the measured temperature profiles could be used to insure that numerical simulations properly match the realistic radiative losses typical of the present experiment.

The counterrotating vortex pair chosen for this study, as shown in Fig. 1, is not the only possible arrangement of vortices upstream of a turbulent flame. However, this arrangement, which exerts extensive strain on the flame, was chosen because it is the most probable quenching mechanism, as demonstrated by direct simulations [11, 12]. If one considers any vortex in the reactants ahead of the flame and one proceeds along the flame until an adjacent vortex is encountered, the two vortices can be (a) corotating, (b) counterrotating with the reactants between the vortices directed away from the flame, thereby exerting compressive strain on the flame, and (c) counterrotating with the reactants between the vortices directed towards the flame, thereby inducing extensive strain on the flame. The compressive strain case (b) is least probable because the flame will propagate most rapidly over this vortex pair since reactants between the vortices are moving in the direction of flame propagation. The extensive strain case (c) is most probable because the flame spends a significantly longer residence time attempting to propagate over a flowfield that is directed against the propaga-

tion direction. Wu and Driscoll [13] have quantified the different residence times associated with the above three cases.

EXPERIMENTAL ARRANGEMENT

The experiment is shown schematically in Fig. 2 and is discussed in detail in Refs. 7 and 8. It consists of a rectangular flame tube having dimensions of 11.4 cm by 11.4 cm by 61 cm. A single toroidal laminar vortex is formed by using a loudspeaker to impulsively force fluid downward through a sharp edged orifice. The orifice diameter is denoted D and was varied between 1.27 and 5.1 cm. Laser velocimetry [8] was used to measure the vortex velocity profiles. It was found that the diameter of the toroidal vortex ring is equal to the orifice diameter D , as is shown in Fig. 1, to within 10% accuracy. The diameter of the vortex core is denoted d_c ; the core is defined as the region of solid body rotation. The core diameter d_c was found to equal $0.2D$ at the measurement loca-

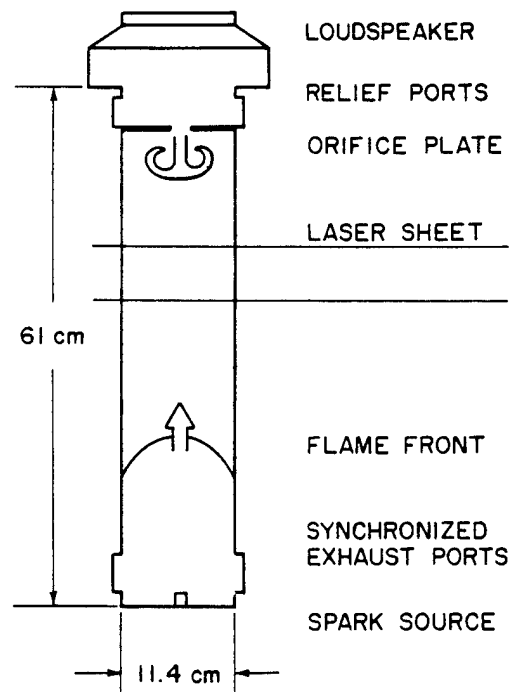


Fig. 2. Schematic of the flame-vortex interaction apparatus.

tion for the vortices considered. At other locations downstream, the vortex diameter will increase due to entrainment of fluid into the vortex. The quantity U_θ is the maximum rotational velocity within the vortex, which occurs at a distance of $d_c/2$ from the center of the core, which is expected for a Rankine vortex.

A homogeneous fuel-air mixture flows through the chamber before the chamber is sealed and the charge is ignited, causing a laminar flame to propagate upward. The equivalence ratio was varied between 0.50 and 0.70 and three fuels (methane, propane and ethane) were used. Tables 1 and 2 list the laminar burning velocities (S_L) and thermal thicknesses of the flames studied. S_L was determined by subtracting the gas velocity ahead of the flame (which was measured using laser velocimetry to be 34 cm/s for methane, $\phi = 0.6$), from the flame speed in lab coordinates, which was determined to be 42 cm/s for methane, $\phi = 0.6$, using motion picture images of Mie scattering. The resulting values of S_L are in agreement with those reported in Refs. 18-20.

The thermal thickness of the flame (δ) is defined as the temperature difference across the flame divided by the maximum temperature gradient. Four previous studies [14-17] report temperature profiles that indicate that δ equals $7.4 \alpha/S_L$ for lean hydrocarbon flames to within an accuracy of 10%; α is the thermal diffusivity of the cold reactants. Therefore δ was determined from this relation. It is noted

TABLE 2

Properties of the Flames Studied

Fuel	ϕ	S_L (cm/s)	δ^a (cm)	$T_{\max, \text{meas}}^b$ (K)	T_{ad}^c (K)
Methane	0.55	6.5	0.26	1525	1573
Methane	0.60	8.0	0.20	1605	1664
Methane	0.70	12.0	0.14	1810	1838
Propane	0.50	8.0	0.20	1479	1507
Propane	0.60	14.0	0.12	1688	1700

^a The thermal thickness of the flame δ is $7.4 \alpha/S_L$ as discussed in the text.

^b $T_{\max, \text{meas}}$ is maximum temperature measured with thin filament pyrometry.

^c T_{ad} is adiabatic flame temperature calculated by the NASA CEC-72 equilibrium code.

that others [4, 5] use a somewhat different definition of δ . Two conflicting requirements that had to be met were that the vortex Karlovitz number $(U_\theta/S_L)/(d_c/\delta)$ must be of order unity for quenching to occur, while the Reynolds number $U_\theta D/\nu$ must be less than 1200 to maintain a laminar vortex [8]. It follows that $S_L D$ must be less than 255ν , so it is advantageous to operate near the lean flammability limit to minimize the burning velocity S_L .

The maximum rotational velocity within the vortex was defined as U_θ and was found to increase linearly with $\Delta V^2/(t_r D^5)$, [8], where ΔV is the volume displaced by the loudspeaker and t_r is the time duration of loudspeaker motion. This relation is derived by equating the circulation of the vortex, which is propor-

TABLE 1

Parameters Associated with the Images Shown in Figs. 3-8

Fig.	Fuel	ϕ	d_c/δ	Ka_v	d_c (cm)	U_θ (cm/s)	U_θ/S_L	K (s ⁻¹)	T_Q (K)
3a	methane	0.55	1.0	14.0	0.25	91	14.0	365	1300
3b	methane	0.55	2.0	6.2	0.51	80	12.3	157	1300
3c	methane	0.55	3.1	4.5	0.76	90	13.8	119	1300
7a	methane	0.55	2.0	6.3	0.51	82	12.5	160	1300
7b	propane	0.60	4.6	2.0	0.51	130	9.3	255	no quen.
7c	propane	0.50	5.3	3.8	1.02	160	20.0	157	no quen.
7d	ethane	0.56	5.1	3.9	1.02	160	20.0	157	no quen.
8a	propane	0.50	2.0	6.0	0.38	96	12.0	252	no quen.
8b	propane	0.50	4.0	2.8	0.76	90	11.3	118	no quen.
8c	ethane	0.55	3.8	3.0	0.76	90	11.3	118	no quen.
8d	methane	0.56	2.0	6.2	0.51	80	12.3	157	no quen.

Strain rate $K = U_\theta/d_c$; Core diameter $d_c = 0.2 D$; D = orifice diameter; Vortex Karlovitz number $Ka_v = (U_\theta/S_L)/(d_c/\delta)$; δ = flame thickness = $7.4 \alpha/S_L$; T_Q = temperature of products when quenching occurs.

tional to $U_\theta D$, to the circulation within the segment of the boundary layer that exits the orifice during time t_r . The boundary layer circulation is proportional to the product of the boundary layer vorticity (which scales with U/δ , where U is the orifice velocity and δ is the boundary layer height) and the boundary layer area, which scales with $\delta U t_r$. U is eliminated by equating it to $(\Delta V/t_r)/(\pi D^2/4)$ in order to satisfy conservation of mass.

Flame quenching was detected using a planar laser induced OH fluorescence system. A Nd:YAG pumped dye laser with a frequency doubled output of 2 mJ at 282.7 nm was tuned to the $Q_1(5)$ line of the (1,0) band of the $X^2\Pi-A^2\Sigma^+$ transition of the OH molecule as described by Drake and Pitz [21]. The laser light sheet is 5.1 cm in height and less than 200 μm thick at the chamber centerline. The laser frequency was tuned after every ten runs by optimizing the OH laser induced fluorescence signal from a Bunsen burner. Fluorescence was collected in the wavelength range from 300 to 390 nm using a WG-305 cutoff filter and a UG-11 glass filter and was collected by an f 2.8 UV Nikkor lens which has a 100-mm focal length. Images were recorded by a Princeton Instruments ICCD-576 intensified, cooled CCD array camera that has a 576×384 pixel array. Each pixel was sampled with 14-bit resolution and stored on an IBM compatible 386/33-MHz computer having a 687-Mbyte hard disk. Each image was corrected for laser sheet intensity variations by normalizing by an image of the Rayleigh scattering from room temperature air.

A Thin Filament Pyrometer (TFP) was employed to measure the time history of temperature on the centerline in order to quantify heat losses from the product gases. The arrangement was similar to that reported by Goss et al. [22]. The concept is that the infrared greybody emission from a very thin filament is proportional to the fourth power of the filament temperature and thus provides a sensitive measure of the gas temperature in the range 700–2400 K. A time response of 0.3 ms was calculated by using the standard relation for the time response of a thermocouple. A 15- μm -diameter, 15-cm-long SiC filament extended horizontally across the chamber and was attached to the sidewalls. A 1-mm section

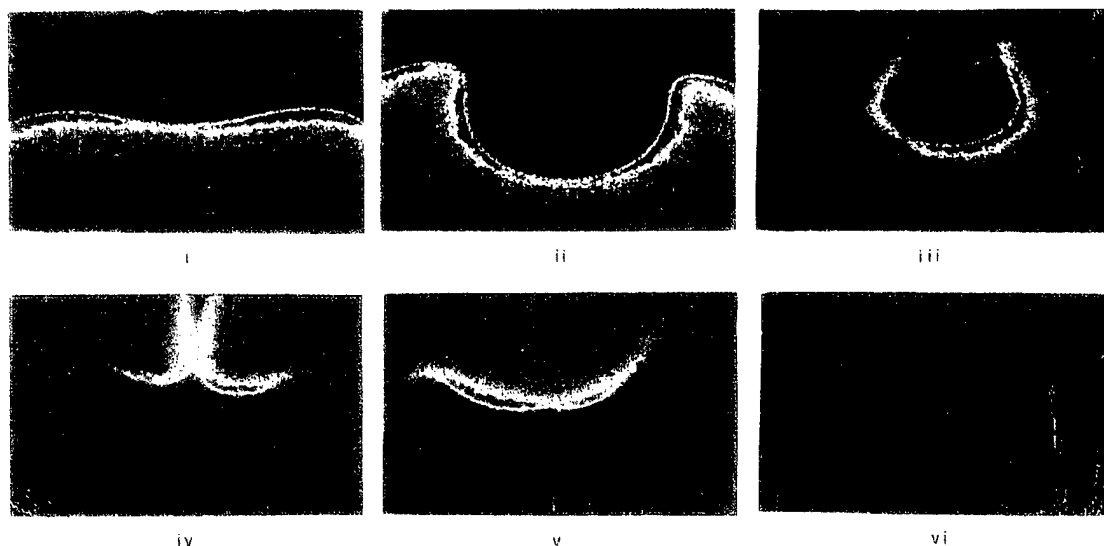
of the filament was focused onto a InGaAs infrared detector using a 10-cm focal length lens and optical filters with a bandpass of 0.8–1.8 μm . Gas temperature differs from the filament temperature by only 1%–5%; this difference was determined by using the standard relation that is used to correct thermocouples for radiation and conduction losses [22]. The TFP output signal was calibrated by placing a stoichiometric propane–air grid-stabilized flame directly under the filament.

RESULTS

OH Images of the Quenching Process

Figure 3 illustrates some images of the quenching of a methane–air flame by small, medium and large vortices. The properties of the vortices and flames are listed in Tables 1 and 2. The flame in Fig 3a appears as a red line, where the red color indicates locations where the OH fluorescence intensity is in the range 50%–100% of the maximum intensity. Note that the product gases, which are below the flame in Figure 3a, appear black, indicating that the fluorescence from the equilibrium OH in the products is less than 10% of the fluorescence from the superequilibrium OH in the flamefront. Drake and Blint [23] have shown that the ratio of superequilibrium OH to equilibrium OH concentrations typically exceeds ten for very lean (or rich) flame conditions but will be less than two for adiabatic stoichiometric flames. Therefore, since the present flames are near the lean limit, the OH fluorescence intensity serves as a marker of the leading edge and the trailing edge of the flame.

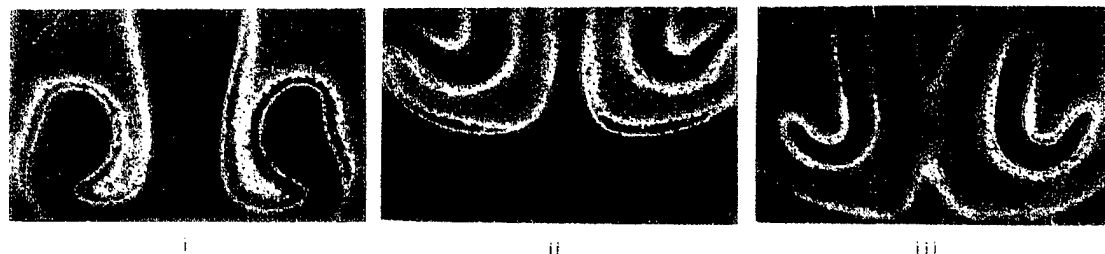
It is observed that the pocket of reactants formed by the small vortex does not roll up but retains an oval shape in Fig. 3a, image iii. The following image (iv) shows that the pocket of reactants quenches near the vortex leading edge, where the image appears black and the superequilibrium OH intensity is measured to be less than 2% of the maximum intensity in an undisturbed flame. Numerical simulations by Poinso et al. [4, 5] for d_c/δ of approximately unity also show that the pocket fails to roll up and it quenches at the leading edge. The quenching of flames about pockets of re-



(a) SMALL VORTEX, $d_0/\delta=1.0$, $Ka_v=14.0$, METHANE



(b) MEDIUM VORTEX, $d_0/\delta=2.0$, $Ka_v=6.2$, METHANE



(c) LARGE VORTEX, $d_0/\delta=3.1$, $Ka_v=4.5$, METHANE

Fig. 3. Quenching of a methane-air flame ($\phi = 0.55$) during an interaction with a vortex. Additional parameters appear in Tables 1 and 2. Each image represents 5 cm by 3 cm. Colors represent the percentage of maximum superequilibrium OH fluorescence intensity: red = 50%–100%; yellow = 30%–50%; green = 20%–30%; blue = 10%–20%; and black = 0%–10%.

actants, as seen in Fig. 3, may be responsible for some of the unburned hydrocarbons and CO emitted by practical combustors. For the medium sized vortex, shown in Fig. 3b, there also is no roll-up of the flame into the vortex.

For the larger vortices, Figs. 3b and 3c show that the flame rolls up about one revolution, which causes the pocket of reactants to be distorted into a thin, highly curved strip. Therefore, flame curvature effects can be just as pronounced, or even more pronounced for interactions involving large vortices than for interactions involving small vortices. That is, flame stretch in real interactions may not scale linearly with U_θ/d_c and thus the vortex Karlovitz number at quenching cannot be expected to have a single universal value. Flame burn-through in the large vortex creates three separate pockets, which does not occur in the smaller vortex.

Determination of the Thin Flame Limit on a Combustion Regime Diagram

Two curves were determined from the OH images. The first is denoted the single vortex quenching curve and is shown in Fig. 4. This curve is then used to infer a second curve that is denoted the thin flame limit. To obtain the single vortex quenching curve shown in Fig. 4, vortices having six different core diameters

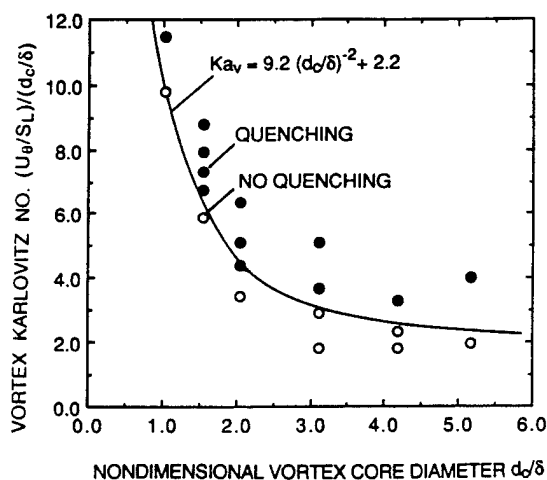


Fig. 4. Single vortex quenching curve. Methane-air flame, $\phi = 0.55$. Quenching is determined from OH images such as Fig. 3. Solid curve represents best fit to the data.

were chosen and U_θ was increased until local quenching was detected; i.e., the peak OH intensity of a segment is less than 1% of that of the undisturbed flame. The vortex Karlovitz numbers (Ka_v) that result in the quenching of the methane air flame ($\phi = 0.55$) are shown in Fig. 4, where Ka_v is defined as $(U_\theta/S_L)/(d_c/\delta)$. It is seen that small vortices are much less effective at quenching a flame (i.e., require larger Karlovitz numbers) than larger vortices, which has been predicted previously [4, 5]. Smaller vortices have smaller values of Reynolds number ($U_\theta D/\nu$) and thus decay more rapidly as they enter the flame, where the kinematic viscosity is more than ten times larger than that of the unreacted gas. The single vortex quenching curve is represented by a Karlovitz number of:

$$(U_\theta/S_L)/(d_c/\delta) = 9.2(d_c/\delta)^{-2} + 2.2 \quad (1)$$

for the methane-air flame at equivalence ratio of 0.55. Other flames have different chemistry and radiative heat losses and may not be represented by Eq. 1.

The single vortex quenching curve has been replotted in Fig. 5 in order to compare measurements to the numerical results of Poinso et al. [4, 5]. It is concluded that both curves display similar parabolic shapes. Absolute values differ because the simulation assumes single step chemistry as well as a radiative loss that differs from the experiment. In addition, the flame in the experiment experiences three-dimensional stretch and curvature whereas the simulations are two dimensional.

The thin flame limit is inferred from the present data using concepts discussed by Mennevau and Poinso [24]. A turbulent flame is defined to exist in the thin flame regime if none of the eddies in its spectrum lie in the single vortex quenching region. A typical spectrum of the vortices within a hypothetical turbulent flowfield is shown in Fig. 5. The right-most point of the spectrum is defined by the rms velocity fluctuations (u'_{rms}) and the integral scale (L). The slope of the spectrum is one-third since U_θ scales as $u'_{rms}(d_c/L)^{1/3}$ in the turbulent cascade process [3]. To determine the thin flame limit, we seek values of u'_{rms} and integral scale L such that the spectrum in Fig.

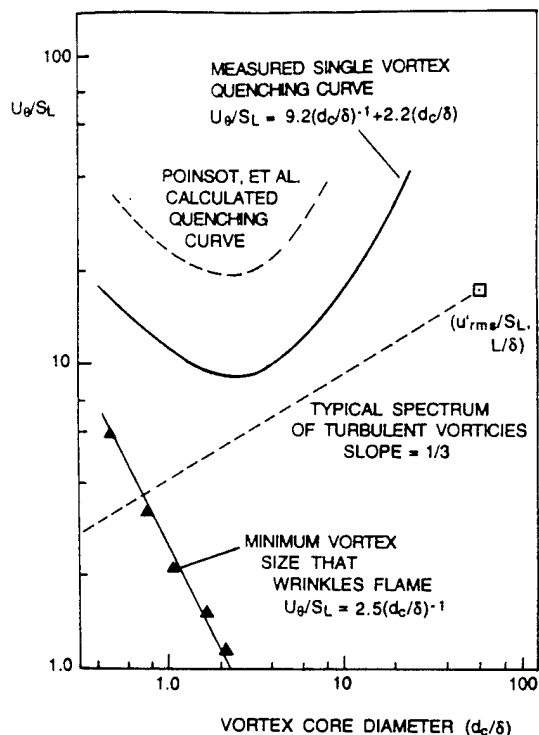


Fig. 5. The measured single-vortex quenching curve of Fig. 4 compared to the numerical results of Ref. 4. Methane-air, $\phi = 0.55$. The measured minimum vortex size that wrinkles the flame was reported previously in Ref. 8.

5 lies below the measured single vortex quenching curve. Therefore a value of L/δ is chosen and a value of u'_{rms}/S_L is chosen and a spectrum of vortices is plotted in Fig. 5 similar to that shown by the dashed line. The rectangular symbol in Fig. 5 represents chosen conditions of u'_{rms}/S_L and L/δ equal to 16 and 61, respectively. Holding L/δ constant, u'_{rms}/S_L is then increased, causing the rectangular symbol to move upwards, until the dashed line that represents the spectrum first intersects the measured single vortex quenching curve. For this condition the values of u'_{rms}/S_L and L/δ are plotted as one point on the thin flame limit of Fig. 6. The procedure is repeated for all other values of L/δ , yielding the entire thin flame limit curve in Fig. 6, which is given by

$$u'_{rms}/S_L = 5.7(L/\delta)^{-1} + 5.8(L/\delta)^{1/3} \quad (2)$$

for the methane-air flame ($\phi = 0.55$). This thin flame limit is expected to depend on the fuel type and ϕ which control the chemical

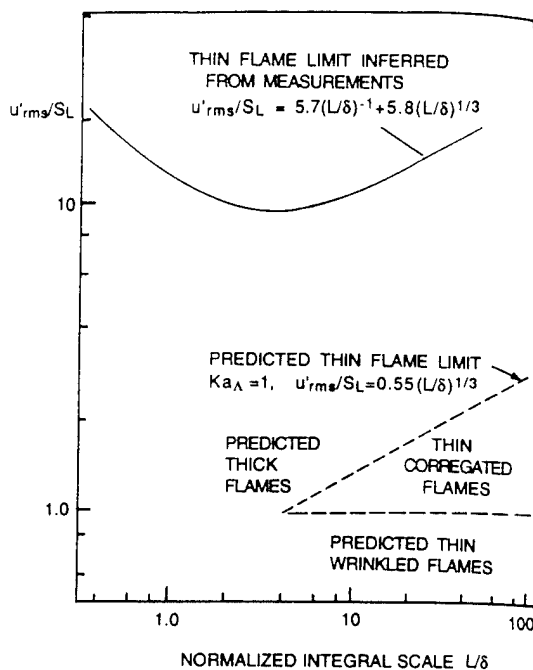


Fig. 6. The thin flame limit on a combustion regime diagram. Upper curve is inferred from the data shown in Fig. 4.

kinetic, molecular transport, and radiative losses.

Figure 6 represents the regime diagram for turbulent premixed flames. The inferred thin flame limit that is given by Eq. 2 is plotted in Fig. 6 and is compared to the Klimov-Williams criterion ($Ka_A = 1$). The Taylor microscale [3] is defined to exactly equal $L(u'_{rms}L/\nu)^{-1/2}$; Prandtl number is 0.72, and flame thermal thickness δ is $7.4 \alpha/S_L$ as discussed above. It is seen that the present measurements yield a thin flame limit in Fig. 6 that is an order of magnitude larger than the $Ka_A = 1$ criterion. The implication is that turbulent flames are expected to remain thin for significantly larger values of turbulence intensity than previously believed. A physical explanation is that the eddies at the Taylor microscale may characterize the maximum strain in nonreacting flows, but they are too small to survive the viscous forces within a flame.

The physical reasons why the thin flame limit in Fig. 6 has regions of negative and positive slopes are as follows. For large integral scale, the curve has positive slope, in agreement with the lower curve denoted the

predicted thin flame limit because larger vortices exert less strain on a flame than smaller vortices, since strain scales as U_θ/d_c . Thus as the integral scale is increased, an increased turbulence intensity is required for the vortices to strain out and thicken the flame. However, as the integral scale is decreased sufficiently, the upper curve in Fig. 6 has a negative slope. The smaller vortices are attenuated by viscous effects due to their small Reynolds number and significantly larger turbulence are required to change the flame structure.

Turbulence Scales That Can Be Neglected in Simulations

Measurements were made to determine the smallest vortex core diameter that wrinkles the flame, that is, causes a 5% variation in the flame perimeter. Results are indicated by the lowermost curve in Fig. 5, which is given by

$$U_\theta/S_L = 2.5(d_c/\delta)^{-1}. \quad (3)$$

Poinsot et al. [4, 5] define a cutoff scale as the value of d_c/δ for which the lowermost curve in Fig. 5 intersects the turbulence spectrum. A general relation for the cutoff scale for methane-air flames ($\phi = 0.55$) is deduced by combining Eq. 3 and the equation for the spectrum ($U_\theta = u'_{rms}(d_c/L)^{1/3}$), which yields

$$(d_c/\delta)_{\text{cutoff}} = 2.0(u'_{rms}/S_L)^{-3/4}(L/\delta)^{1/4}. \quad (4)$$

Vortex core diameters smaller than this cutoff scale have no effect on the flame in the present experiment. Therefore it is believed that such scales could be neglected from direct numerical simulations, discrete vortex simulations, or stochastic simulations of turbulent flames [25, 26]. For typically turbulent flows the cutoff scale determined from Eq. 4 is substantially larger than the Kolmogorov or Taylor microscales. It is noted that lean methane-air flames are diffusionally unstable; we showed previously [8] that other fuels display significantly more diffusional stability and thus will have larger cutoff scales than a lean methane-air flame, so Eq. 4 is a conservative estimate of scales that can be neglected.

Lewis Number Effects on Flame Curvature and Quenching

The present images provide some of the first verification that flame curvature has a direct effect on the local reaction rate for conditions that simulate turbulent flames. Figure 7a illustrate the effects of flame curvature for a flame having Lewis number less than unity. At location 1, where there is strong positive flame curvature, the reaction rate is enhanced and the region appears red. These results are in agreement with the analysis of Law [2], who shows how the reaction rate should increase where the local burned gas temperature is enhanced by the thermodiffusive effects. The local burned gas temperature T_b is affected by flame stretch according to

$$T_b/T_{ad} = 1 + (Le^{-1} - 1)Ka, \quad (5)$$

where T_{ad} is the adiabatic unstretched flame temperature [2]. At location 1 in Fig. 7a, the Karlovitz number is positive due to the positive flame curvature and $(Le^{-1} - 1)$ is positive. Therefore, Eq. 5 predicts that T_b should be relatively large at location 1, which is in accordance with the red region observed in Fig. 7a. Conversely, at location 2 the flame curvature is negative and the reaction rate (and the superequilibrium OH concentration, as indicated by the lower fluorescence intensity) are reduced, as denoted by the blue color. The opposite trends are observed in Fig. 7b for a flame having Lewis number greater than unity. Positive flame curvature at location 3 causes a reduction in the reaction rate and the flame appears to be blue. Physically the heat flux vectors that are directed towards the reactants at location 3 are diverging. Negative flame curvature at location 4 enhances the reaction rate, as denoted by the red color. At location 4 the heat flux vectors are directed towards the reactants and they are focused, which enhances the reactant temperature. Thus all of the trends shown in Fig. 7 are in agreement with Eq. 5.

The present images also visualize the mechanism of flame sheet area reduction that has been predicted to occur in turbulent flames by Cant et al. [28] and Carrier et al. [29]. Figures

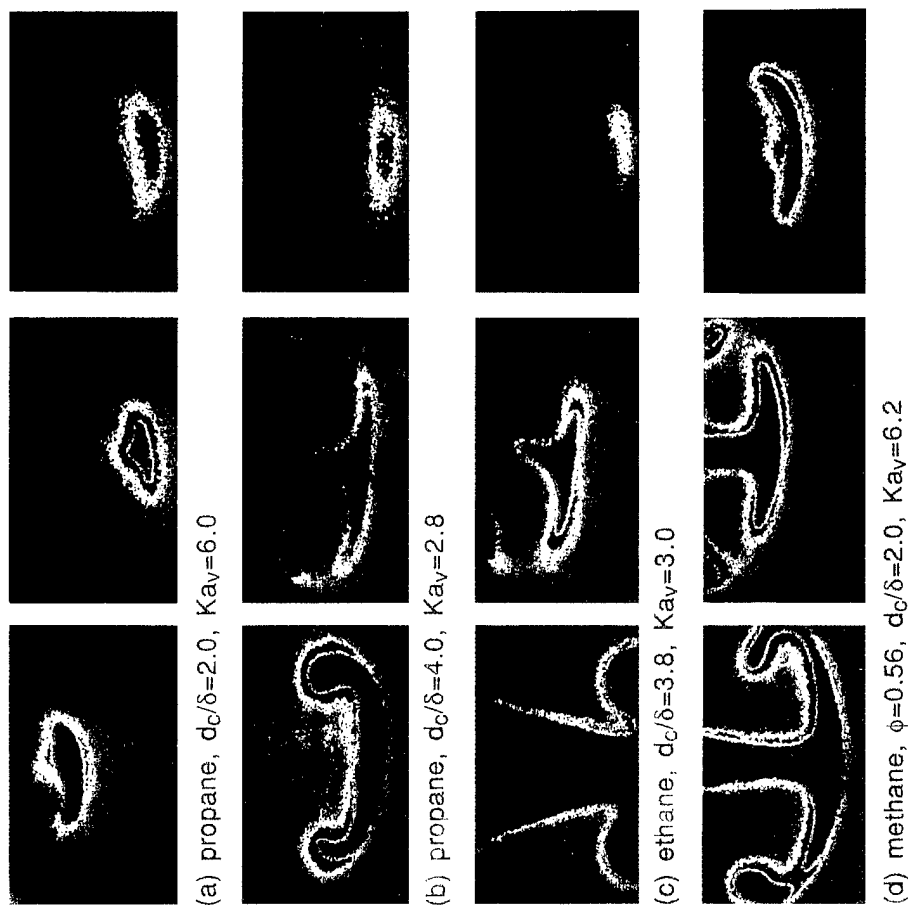


Fig. 8. Flame-vortex interactions for which quenching does not occur—pockets of reactants are consumed. Additional parameters are listed in Tables 1 and 2. Red indicates maximum super-equilibrium OH fluorescence intensity. Image size is 5 cm by 3 cm.

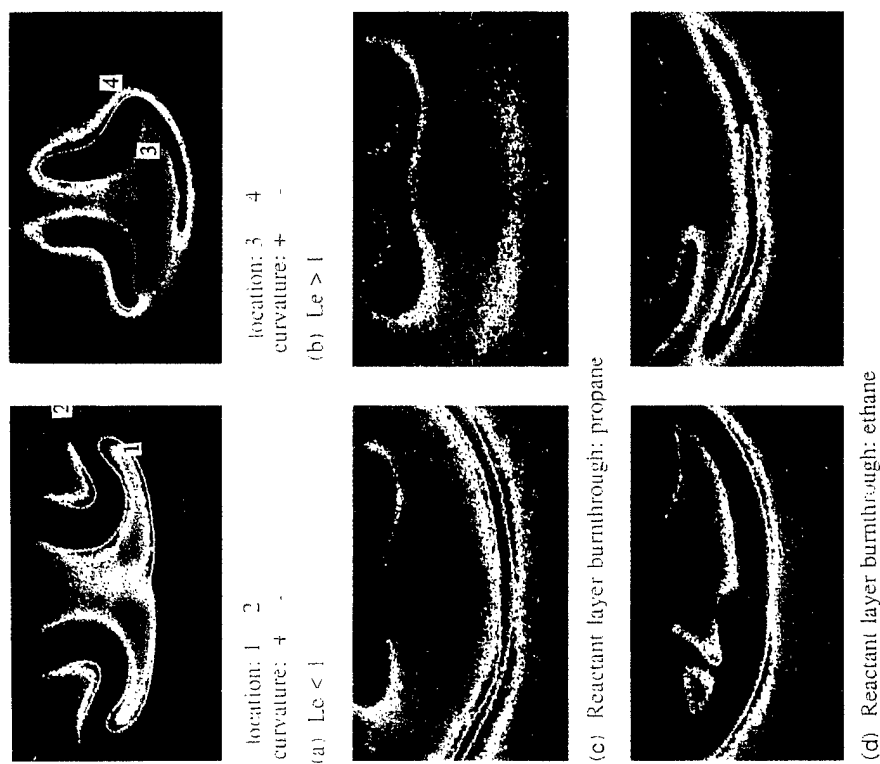


Fig. 7. (a,b) Effects of flame curvature on reaction rate. Enhanced reaction rate (red) occurs where flame curvature is positive for $Le < 1$ (a) and negative for $Le > 1$ (b). (c,d) Images of flames burning towards each other, which causes destruction of flame area (i.e., negative stretch) as modeled by Cant et al. Flame parameters are listed in Tables 1 and 2.

7c and 7d show that a thin strip of reactants can exist between two flames that burn towards each other. The thin strip of reactants in Fig. 7 is a pocket that has been greatly elongated by positive stretch. As the two flames merge the total flame area rapidly decreases to zero in this region and the flame stretch ($A^{-1} dA/dt$) must be negative. This mechanism of flame sheet destruction is believed to be present in turbulent flames and it prevents a flame from becoming infinitely wrinkled after long residence times in the turbulence field.

A similar set of experiments was run using both lean propane-air flames and lean ethane-air flames in order to study the effects of Lewis number on flame quenching. Figure 8a shows that a propane-air flame ($\phi = 0.52$, $Le = 1.8$) does not quench for a Karlovitz number of 6.0. This Karlovitz number of 6.0 is larger than the value of 3.9 that is required to quench a methane-air flame for the same vortex size (Fig. 4); therefore it can be concluded that lean propane-air flames are more difficult to quench than lean methane-air flames. The theory of strained flames [2] predicts a trend that is opposite to that observed, namely that it should be easier to quench a lean propane-air flame ($Le > 1$) with positive strain than a lean methane-air flame. The contradictory observations are believed to be due to complex chemistry at extinction that is not included in most theories.

Attempts were made to measure the quenching limit curves for lean propane-air

and lean ethane-air flames, but quenching of such flames could not be achieved using the present experiment. Vortices became turbulent before quenching was observed if either U_θ or d_c was increased. When d_c was decreased in order to increase the Karlovitz number, quenching also was not observed because of the rapid decay of the curve in Fig. 4. Figures 8a-8d show how it was deduced that quenching did not occur for various interactions. Pockets of reactants are observed to be entirely consumed for these cases.

Measurements to Quantify Radiative Heat Losses

The heat losses from the product gases were quantified by measuring the gas temperature on the combustor centerline as the flame passes over the TFP probe that was described earlier. Results are shown in Fig. 9. The maximum temperatures measured are 1%-3% less than the calculated adiabatic flame temperature for the five cases shown. The deviation is believed to be due to radiation losses from the product gases. Figure 9 shows that the temperature of the products decays in time by approximately 185 K during the first 200 ms after flame passage. To determine if radiative heat loss could be responsible for the entire observed temperature decay, the following calculation was performed. Gas at the same conditions as the products behind the methane-air flame ($\phi = 0.60$, $T = 1665$ K, 6% CO_2 , 12% H_2O)

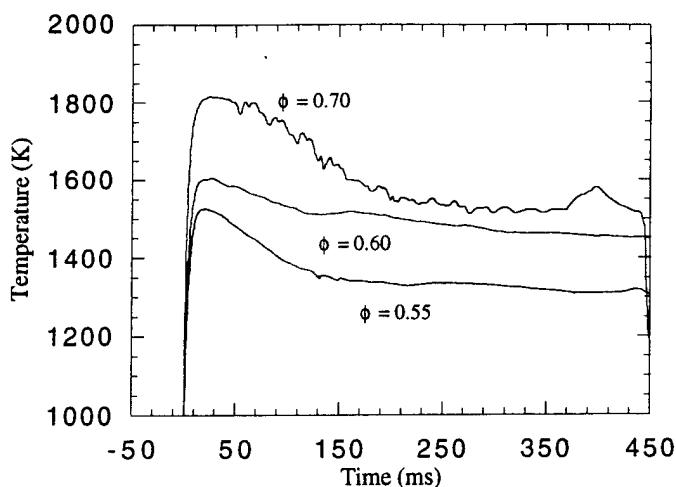


Fig. 9. Temperature time histories on centerline as the flame passes over the TFP filament for methane-air flames at various equivalence ratios. No vortex.

was considered. The rate of temperature decay of the products due to radiative losses is predicted using

$$\rho V c_p dT/dt = -\epsilon_g \sigma T^4 A, \quad (6)$$

where the surface-to-volume ratio A/V of the chamber is 0.25 cm^{-1} . The gas emissivity ϵ_g for the above partial pressures of CO_2 and H_2O and the chamber dimensions is 0.04 [30]. Integration of Eq. 6 yields product temperatures equal to $T_{\text{ad}}^{-3} + 3\sigma\epsilon_g((A/V)/(\rho c_p))t)^{-1/3}$. The calculated temperature decrease at 200 ms is somewhat larger than the measured temperature decrease of 185 K. Therefore it is concluded that radiative heat losses are sufficient to cause the measured temperature decay.

Figure 10 is a comparison of the measured temperature decay to that assumed for the numerical simulation of Poinso et al. [4, 5]. The distance x was computed for a given time after flame passage by using the measured velocity of the products in the laboratory coordinates. The distance that is required for the gas temperature to decay to $0.85 T_{\text{ad}}$ is found to be 30δ , which is the three times larger than that calculated in the numerical simulations. Since Eq. 6 shows that heat loss is proportional to dT/dt , it is concluded that the heat loss assumed in the simulation is approximately three times larger than the realistic heat loss rate of the present experiment. It is not surprising that the propane-air flame of the numerical simulations was quenched by relatively weak vortices whereas the experimental pro-

pane-air flames could not be quenched. Table 1 shows that the product gases must be cooled by radiation to approximately 1300 K before quenching could be observed, for the strain rates achieved in the present experiment. These results are in agreement with calculations of Darabiha et al. [10] who showed that quenching of methane-air premixed flames required that products be cooled to less than 1400 K.

CONCLUSIONS

The physics of the quenching of a premixed flame by a vortex was studied using laser induced OH fluorescence imaging and thin filament pyrometry. By using a relatively thick laminar flame and small vortices, a ratio of the vortex core diameter to the thermal thickness of the flame was as small as unity.

1. Nondimensional vortex stretch rates (Ka_v) that characterize the size and strength of a vortex that quenches a premixed flame were found to increase as the vortex size decreases. Therefore, small vortices are significantly less efficient at quenching a flame than larger vortices.
2. The measured vortex quenching limit curve was:

$$U_\theta/S_L = 9.2(d_c/\delta)^{-1} + 2.2(d_c/\delta).$$

The measured curve displayed the same trends as predicted by direct numerical simulations, but absolute values differ because

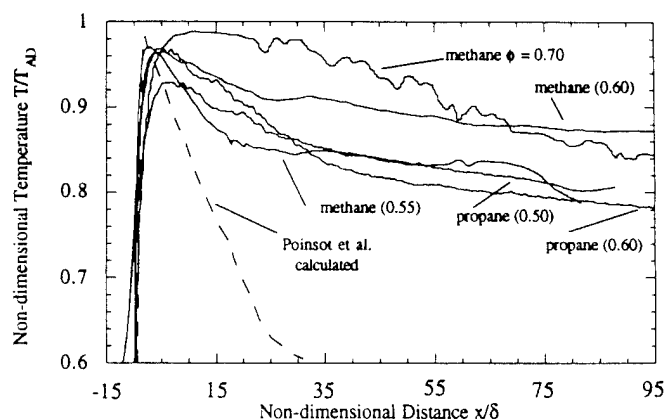


Fig. 10. Heat losses from the products, as characterized by TFP measurements of center-line temperature, compared with heat loss assumed in numerical simulations of Ref. 4 and 5. No vortex. Values of adiabatic flame temperature T_{ad} and flame thickness δ are given in Table 2.

the simulation was two-dimensional, assumed unrealistically large heat losses, and used single-step chemical kinetics. The temperature of the products at which quenching was first detected was 1300 K, which is in agreement with counterflow flame calculations with full chemistry.

3. The thin flame limit on the classical combustion regime diagram (Fig. 6) was inferred from the present data and the concepts proposed by Poinso et al. to be

$$u'/S_L = 5.7(d_c/\delta)^{-1} + 5.8(d_c/\delta)^{1/3}.$$

Results indicate that thin flames extend over a larger range of turbulence intensities than previously assumed.

4. It is inferred from the above experimental conclusion, combined with the theoretical work of Poinso et al. that a significant fraction of the small scale turbulence can be neglected from direct simulations of flame-turbulence interactions. It also follows that micromixing models that assume that small vortices play a dominant role are unrealistic.
5. Positive flame curvature can be observed to enhance the local reaction rate for Lewis number less than one, which is in agreement with the asymptotic analyses of Law and others.
6. Lean propane-air and ethane-air flames (having $Le > 1$) require significantly larger Karlovitz numbers in order to achieve quenching than lean methane-air flames ($Le < 1$); and $Le > 1$ flames could not be quenched in the present apparatus. This observation disagrees with current stretched flame theory and may be attributed to complex chemistry effects.

The authors acknowledge useful discussions with Dr. Thierry Poinso and Professor S. Candel during the stay of one of the authors (J. Driscoll) at Ecole Central de Paris. The effort of J.F.D. was partially supported by National Science Foundation Grant CTS 9123834. The cooperation of Dr. C. M. Roquemore made possible the TFP measurements; D. Trump and J. Ratcliffe assisted in the TFP and OH measurements.

REFERENCES

1. Williams, F. A., *Combustion Theory*, Addison Wesley, Palo Alto, CA, 1989.
2. Williams, F. A., *Combust. Flame* 26:269-270 (1976).
3. Tennekes, H., and Lumley, J. L., *A First Course in Turbulence*, MIT Press, Cambridge, 1972.
4. Poinso, T., Veynante, D., and Candel, S., *Twenty-Third Symposium (International) on Combustion*, The Combustion Institute, Pittsburgh, 1990, pp. 613-619.
5. Poinso, T., Veynante, D., and Candel, S., *J. Fluid Mech.* 228:561-606 (1991).
6. Magnussen, B. F., and Hjertager, B. H., *Sixteenth Symposium (International) on Combustion*, The Combustion Institute, Pittsburgh, 1977, p. 719.
7. Roberts, W. L., Driscoll, J. F., Drake, M. C., and Ratcliffe, J. W., *Twenty-Fourth Symposium (International) on Combustion*, The Combustion Institute, Pittsburgh, 1993, p. 169.
8. Roberts, W. L., and Driscoll, J. F., *Combust. Flame* 87:245-256 (1991).
9. Darabiha, N., Candel, S., and Marble, F. E., *Combust. Flame* 64:203-217 (1986).
10. Darabiha, N., Candel, S., Giovangigli, V., and Smooke, M. D., *Combust. Sci. Technol.* 60:267-272 (1988).
11. Ashurst, W. T., Sivashinsky, G. I., and Yakhot, V., *Combust. Sci. Technol.* 62:273-284 (1988).
12. Haworth, D. C., and Poinso, T. J., *J. Fluid Mech.* 244:405-436 (1992).
13. Wu, M.-S., and Driscoll, J. F., *Combust. Flame* 91:310-322 (1992).
14. Warnatz, J., *Eighteenth Symposium (International) on Combustion*, The Combustion Institute, Pittsburgh, 1980, pp. 369-383.
15. Bechtel, J. H., Blint, R. J., Dasch, C. J., and Weinberger, D. A., *Combust. Flame* 42:197-213 (1981).
16. Friedman, R., *Fourth Symposium (International) on Combustion*, The Combustion Institute, Pittsburgh, 1952, p. 259.
17. Dixon-Lewis, G., and Williams, A., *Eleventh Symposium (International) on Combustion*, The Combustion Institute, Pittsburgh, 1966, p. 951.
18. Yamaoka, I., and Tsuji, H., *Twentieth Symposium (International) on Combustion*, The Combustion Institute, Pittsburgh, 1984, pp. 1883-1892.
19. Yu, G. Law, C. K., and Wu, C. K., *Combust. Flame* 63:339-347 (1986).
20. Lewis, B., and von Elbe, G., *Combustion, Flames, and Explosions of Gases*, Academic, New York, 1961.
21. Drake, M. C., and Pitz, R. W., *Exp. Fluids* 3:283 (1985).
22. Goss, L. P., Vilimpoc, V., Sarka, B., and Lynn, W. F., *Trans. ASME* 111:46-52, (1989).
23. Drake, M. C., and Blint, R. J., *Combust. Sci. Technol.* 75:261 (1991).
24. Meneveau, C., and Poinso, T., *Combust. Flame* 86:311-332 (1991).
25. Wu, M. S., Kwon, S., Driscoll, J. F., and Faeth, G. M., *Combust. Sci. Technol.* 83:187-202 (1992).

26. Kwon, S., Wu, M. S., Driscoll, J. F., and Faeth, G. M., *Combust. Flame* 88:221-238 (1992).
27. Law, C. K., *Twenty-Second Symposium (International) on Combustion*, The Combustion Institute, Pittsburgh, 1988, pp. 1381-1402.
28. Cant, R. S., Pope, S. B., and Bray, K. N. C., *Twenty-Third Symposium (International) on Combustion*, The Combustion Institute, Pittsburgh, 1990, pp. 809-815.
29. Carrier, G. F., Fendell, F. E., and Marble, F. E., *SIAM J. Appl. Math* 28:2,463 (1975).
30. Siegel, R., and Howell, J. R., *Thermal Radiation Heat Transfer*, 2nd ed., Hemisphere, New York, 1981, pp. 597-671.

Received 27 November 1992; revised 12 February 1993



AIAA 93-0362

**The Strain Exerted by a Vortex on a Flame -
Determined from Velocity Field Images**

James F. Driscoll¹, D.J. Sutkus², Wm. L. Roberts³,
M.E. Post⁴, and L. P. Goss⁴

¹Dept. of Aerospace Engineering, University of Michigan,

²Aero Propulsion and Power Lab, Wright-Patterson AFB,

³Lockheed Engr. and Sciences Corp., Hampton VA,

⁴Systems Research Laboratories, Dayton OH

**31st Aerospace Sciences
Meeting & Exhibit
January 11-14, 1993 / Reno, NV**

The Strain Exerted by a Vortex on a Flame - Determined from Velocity Field Images

James F. Driscoll¹, D.J. Sutkus², Wm. L. Roberts³,
M.E. Post⁴, and L. P. Goss⁴

¹Dept. of Aerospace Engr., Univ. of Michigan, ²Aero Propulsion and Power Lab., Wright-Patterson AFB, ³Lockheed Engr. and Sciences Corp., Hampton VA, ⁴Systems Research Lab., Dayton OH

Abstract

Velocity field imaging techniques were used to observe how a single toroidal vortex, which represents one eddy in a turbulent flow, exerted aerodynamic strain on a premixed flame. By achieving dense seeding of the flow, the spatial derivatives of velocity were determined accurately, which allowed the following to be measured as a function of space and time: the aerodynamic strain rate tangential to the flame, the rate of flame stretch, the vorticity field, the shear strain rate field and the flow pattern near the forward stagnation point. The vortex strength was sufficient to cause quenching of the flame.

An unexpected result was that the maximum strain on the flame did not occur on the centerline near the forward stagnation point. Instead the strain rate distribution was significantly different from numerical simulations of Poinso, Veynante and Candel, for which strain is maximum on centerline. The difference is due to the different vortex sizes considered, which indicates that small vortices exert a different strain rate distribution on a flame than larger vortices, and that the process cannot be modelled as being self-similar. During flame quenching, the maximum local strain rate was measured to be 35 sec^{-1} , which is similar to the value of 42 sec^{-1} that is required to quench a steady, planar counterflow flame of the same equivalence ratio.

The velocity field images also show how the flame created vorticity in the products. This flame-generated turbulence resulted from gas expansion and the baroclinic torque term in the vorticity transport equation. The velocity field ahead of the flame also was affected by the flame, but no vorticity was generated in the reactants; this validates the assumption made in many models that the turbulence in the reactants is undisturbed by the flame.

Introduction

The motivation for the present work is the need to better understand the phenomenon known as aerodynamic strain and to develop consistent ways to add aerodynamic strain to models of turbulent flames [1-8]. The effects of strain can be large; for example, as the turbulence level ahead of a premixed flame is increased, the turbulent burning velocity eventually no longer increases; instead the burning velocity eventually decreases to zero and the entire flame is strained out [9]. Strain also steepens the scalar gradients within flames, which enhances preferential diffusion effects and which in turn can cause a two-fold change in the turbulent burning velocity, as reported by Wu, Kwon, Driscoll and Faeth [10].

One promising way to add strain to models of high Reynolds number turbulent flames is to use a thin-interface simulation. With this approach the reaction zone is represented as a thin, wrinkled interface that propagates normal to itself at a local burning velocity that depends on the local aerodynamic strain rate and flame curvature [3-8]. The relation between burning velocity and strain is determined from measurements or calculations performed for a counterflow flame having a known strain rate. The velocity field and resulting strain rate are simulated by either a discrete vortex method or by a stochastic method. The thin-interface simulations to date [3-8] produce instantaneous images of very wrinkled flames that are encouragingly similar to experiment.

In order to develop such turbulent flame models, it is important that the vortices in the numerical simulation behave in a manner that is similar to the way actual vortices behave in the presence of a flame. The present work uses an advanced velocity field imaging technique to measure the strain rate that is exerted on a flame during a flame-vortex interaction. Previous papers describe how the apparatus used in the

present work was used to visualize flame wrinkling [11] and flame quenching [12,13] by a vortex. The measurements herein relate the local strain rate on the flame to the global strain rate, as defined below, during the quenching process. The results also will allow for future comparisons of certain scalar profiles, such as profiles of OH concentration and temperature, in this unsteady, wrinkled, strained flame to the profiles calculated for steady, planar, counterflow flames at the same local strain rate, in order to determine if the flame can be modelled as a strained laminar flame as turbulent flow conditions are approached.

The geometry of the flame-vortex interaction that is studied is shown in Fig. 1. A laminar premixed flame propagates upward and the toroidal vortex has a downward convective velocity (U_c). The convective velocity is partially self-induced and partially due to the momentum imparted during vortex creation. Therefore, in the vortex frame of reference the hot products below the vortex in Fig. 1 have a relative velocity of magnitude U_c that is upward, which creates a forward stagnation point below the flame. The velocity components in the x and y directions defined in Fig. 1 are u and v , respectively, while u_T is the velocity component that is tangential to the flame surface. The coordinate that is tangential to the flame surface is denoted s . The quantities of interest include the stretch rate K , which is defined as $(1/A)dA/dt$, where A is the flame sheet area; analysis has shown [14,15] that the contribution to the stretch rate from the velocity components in the two-dimensional plane shown in Fig. 1 is:

$$K_{2D} = \partial u_T / \partial s - S_L / R \quad (1)$$

where S_L is the laminar burning velocity and R is the local radius of curvature of the flame. The first term in Eq. 1 represents the aerodynamic tangential strain rate on the flame which is denoted S_{tt} . The second term is the rate of area increase due to flame curvature. Also of interest is the normal strain rate S_{xx} , the shear strain rate S_{xy} , and the vorticity component in the z direction ω_z which are:

$$\begin{aligned} S_{xx} &= \partial u / \partial x & S_{xy} &= (1/2) (\partial u / \partial y + \partial v / \partial x) \\ \omega_z &= \partial v / \partial x - \partial u / \partial y \end{aligned} \quad (2)$$

Simple formulas for the quantities S_{tt} , S_{xx} , S_{xy} , and ω_z can be obtained for the theoretical example of two potential vortices, of circulation $+\Gamma$ and $-\Gamma$ respectively, that are separated by a distance $2a$, as shown in Figure 1. Far ahead of the vortex the freestream velocity is U_c . This theoretical example does not include several physical processes of importance, however because of the simplicity of the

formulas, it provides a useful comparison to the measurements discussed below. For this theoretical example the velocity and strain fields are:

$$u = -(\Gamma/(2\pi)) [(y+a)(x^2+(y+a)^2)^{-1} - (y-a)(x^2+(y-a)^2)^{-1}] + U_c \quad (3a)$$

$$v = -(\Gamma/(2\pi)) [-x(x^2+(y+a)^2)^{-1} + x(x^2+(y-a)^2)^{-1}] \quad (3b)$$

$$S_{xy} = (\Gamma/(2\pi)) [(y-a)^2 x^2 (x^2+(y-a)^2)^{-2} - ((y+a)^2 x^2 (x^2+(y+a)^2)^{-2})] \quad (4)$$

$$S_{xx} = -S_{yy} = (\Gamma/\pi) [-(y-a)x(x^2+(y-a)^2)^{-2} + (y+a)x(x^2+(y+a)^2)^{-2}]$$

During the earliest phase of the interaction, the flame surface, in general, can be represented as a horizontal plane located a distance L below the vortex shown in Fig. 1. The tangential strain rate S_{tt} equals $\partial v / \partial y$ and differentiation of Eq. 3b, for x equal to $-L$, yields:

$$S_{tt}(\text{planar flame}) = (\Gamma L / \pi) [(y+a)[L^2+(y+a)^2]^{-2} - (y-a)[L^2+(y-a)^2]^{-2}] \quad (5)$$

Therefore, the tangential strain rate S_{tt} is distributed along a planar flame as shown in Figure 1b, which was calculated using Eq. 5. The strain is seen to reach a maximum on centerline for the planar flame. The planar flame case represents the initial phase of a flame-vortex interaction; this strain distribution also represents an interaction involving a weak vortex, since a vortex with a relatively small rotational velocity will not distort the flame significantly from its initially planar geometry.

For the case of a strong vortex, the flame surface is best represented by the circle of radius R that is shown in Figure 1a. The calculation of the strain rate is straightforward because the tangential velocity u_T is simply the azimuthal velocity $((xv/R)-(yu/R))$. S_{tt} is the derivative of u_T with respect to y , multiplied by dy/ds , where the derivative of the tangential coordinate along the interface (ds) is $Rd\theta$. Since y equals $R\sin\theta$, differentiation shows that ds is $R(R^2-y^2)^{-1/2}dy$. It follows that along a circular flame interface the tangential velocity and strain rates are:

$$\begin{aligned} u_T &= (\Gamma/(2\pi R)) [(R^2-ay)(R^2+a^2-2ay)^{-1} - (R^2+ay)(R^2+a^2+2ay)^{-1}] + U_c y / R \end{aligned} \quad (6)$$

$S_{tt}(\text{circular flame}) =$

$$\Gamma / (2\pi) [(a/R^2)(R^2 - a^2)] (R^2 - y^2)^{1/2} [(R^2 + a^2 - 2ay)^{-2} + (R^2 + a^2 + 2ay)^{-2}] + (U_c/R^2)(R^2 - y^2)^{1/2} \quad (7)$$

The tangential velocity u_T and the tangential strain rate S_{tt} given by Eq. 7 are plotted in Figure 1b for values of Γ , a , R and U_c equal to 524 cm²/s, 1 cm, 2 cm and zero respectively.

The observation that immediately follows from Figure 1b is that the tangential strain exerted on the flame is highly dependent on how the flame is distorted; the portion of the flame that happens to be located closest to a vortex center will experience the largest strain rate. Therefore the strain is especially sensitive to the flame structure, the vortex structure, and the relative distances between the flame and the vortex. It is believed that models of turbulent flames that correctly simulate the instantaneous flame surface have the potential to incorporate the correct strain effects, which is a major advantage over time-averaged models.

Experimental Arrangement

Two-color particle imaging velocimetry (PIV) diagnostics that were developed by Goss, Post, Trump and Sarka [16] were applied to the flame-vortex experiment developed by Roberts and Driscoll [11]. The experimental apparatus consists of an 11.4 cm x 11.4 cm x 61 cm rectangular chamber with a loudspeaker and orifice plate on the top surface and a spark plug on the lower surface. The chamber is filled with a methane-air mixture at an equivalence ratio of 0.55; the loudspeaker is pulsed to create a toroidal vortex which moves downward and the spark ignites a flame which propagates upward. While many vortex sizes, vortex strengths and flame speeds have been studied in our previous work [13], all of the velocity field imaging reported herein was conducted with a single vortex having a toroid diameter (D) of 3.81 cm and a vortex core diameter (d_c) of 0.76 cm. The maximum rotational velocity of the vortex (U_θ) was measured to be 107 cm/s using a laser velocimeter [11]. This velocity occurs at the edge of the vortex core which is defined as the region where the rotational velocity increases linearly with radial distance from the vortex center. Therefore the global strain rate associated with this vortex (U_θ/D) is 28 sec⁻¹. The laminar burning velocity of the flame was measured to be 7.5 cm/sec; this is the difference between the velocity of the flame in the laboratory coordinates (36.5 cm/sec) and the velocity of gas in front of the flame (29 cm/s) on centerline. The former was determined from the flame transit time between two thin filament pyrometers and

the latter was determined from the PIV images. A similar laminar burning velocity was measured for these conditions using a video camera and a laser velocimeter [13]. All times that are reported are referenced to the time when the vortex core is a distance $2D$ from the flame, which defines the beginning of the interaction.

The two-color PIV system developed by Goss and Post [16] uses a frequency doubled Nd:YAG laser to create a green laser light sheet at 532 nm and a second Nd:YAG laser, which pumps a dye laser, to form a red laser light sheet at 640 nm. Laser energy is 20 mJ/pulse; each laser sheet has a height of 25 cm and a thickness of 0.1 cm. The experiment is seeded with alumina microballoon particles having a mean diameter of six microns. The green laser sheet is pulsed one millisecond before the red laser sheet and the positions of the particles within a typical 8 cm by 6 cm field of view are recorded on 35 mm color film. Therefore a typical maximum particle velocity of 100 cm/s results in a particle displacement of 1 mm. Directional ambiguity is eliminated with the two-color system because each particle that appears green (which is denoted a "green particle") is imaged at an earlier time than the corresponding red particle. Both light sheets were forced to overlap in space by using a dichroic mirror and the same cylindrical optics. Customized electronics were required to pulse each laser on demand, since the lasers normally operate at fixed repetition rates. Kodak Gold 400 film was used because it has a resolution of 300 line pairs/mm, thus it is able to resolve a 6 micron particle separation with one-to-one imaging. Each color photograph was digitized using an Imapro QCS-35 digital scanner which was hooked to an Apple Macintosh IIx computer.

The present PIV system uses an efficient three-step algorithm to determine the velocity vector field from a digitized PIV image. The first step is to determine the locations of red and green particles on the digitized image. This is accomplished by use of an algorithm which applies red and green filters to the digitized image and finds particles based on relative pixel intensity counts. The second step is to determine the most probable vector displacement in each 5 mm by 5 mm section of the image by use of the spatial cross-correlation function, which is defined as:

$$c(\xi, \eta) = \sum_x \sum_y g(x, y) r(x - \xi, y - \eta) \quad (8)$$

where g and r represent the coordinates of each green particle and red particle respectively. The correlation function c will have a maximum value in the ξ, η plane and the vector drawn from the origin to this maximum represents the most probable vector displacement in that 5 mm by 5 mm section. The third step is to use a tracking algorithm to pair up the individual red and green particles. For each green particle considered, the

tail of a probable displacement vector is placed at the green particle position. This probable displacement vector is determined by a spatially weighted average of the most probable displacement vectors associated with the three sections closest to the green particle. Near the head of the vector a search is conducted for the nearest red particle. A small search window is opened and the window size is increased, typically to be no more than 10% of the vector length, until a red particle is identified. If no red particle is identified in the window, no velocity vector is associated with that particular green particle. The tracker algorithm is efficient, requiring less than 30 seconds to process the digitized image. A typical image of the velocity field is shown in Figure 2a. The density of valid particle pairs is typically 100 per square cm of the image.

One problem that was encountered was that particles were not observed in the vortex core region, as is seen in Figure 2a. The vortex core is made up of fluid that originated in the wall boundary layer near the orifice plate and was forced out through the orifice. The chamber above the orifice plate was heavily seeded by passing the incoming fuel-air mixture through two separate seeders; one seeded flow entered the chamber below the orifice and one entered above the orifice. However, centrifugal forces or perhaps electrostatic attraction of particles to the orifice wall resulted in insufficient seeding of the vortex cores. Fortunately, for the strong vortex considered, the flame is quenched before it enters the vortex core so the seeding of the vortex cores is not a significant problem. Another problem was that particles acquired a static charge and adhered to the windows, which obscured the view of the camera. A commercial anti-static fabric softener was applied to the windows to solve the problem.

Results

For the case of the vortex alone, with no flame present, the velocity field is shown in Figure 2a. The velocity vectors are in the vortex frame of reference in this figure. To represent the vectors in the lab frame of reference, a downward-pointing vector of magnitude 33.5 cm/s must be added to each vector. Solid lines have been added to identify the forward and rear stagnation points; the flowfield about the vortex with its convective downward velocity is observed to be similar to the laminar flow about a sphere.

Figure 2b shows the flame alone, with velocity vectors represented in the laboratory frame of reference. The flame acts like a piston and forces the fluid ahead of it to move upward at a velocity of 29 cm/s on centerline, as seen in Figure 2b, while the flame itself moves upward at 36.5 cm/s. It is seen that the flame does not disturb the gas that is more than 2 cm ahead of

the flame. In the 2 cm region ahead of the flame, the flame does create velocity gradients; but it is shown below that these induced velocity gradients are such that no vorticity is created in the reactants. Figure 2b also shows that there is a rotational motion set up in the product gases below the flame; it is shown below that this motion is associated with vorticity produced by the flame.

Figure 3 shows the flame-vortex interaction at a time of 26 milliseconds where time zero is defined above; this point in the interaction is denoted the intermediate phase. The flame position is defined as the boundary in the PIV photograph where an abrupt change in the particle number density occurs due to gas expansion. This boundary is more distinct in the photograph than in the final velocity images because the photograph contains many small particles that are too small to yield valid velocity vectors; the photograph is similar to an image of Mie scattering from oil drops, which is a common method used to accurately identify the flame surface. The other lines drawn in Figure 3 represent the stagnation point streamlines.

Figure 3 indicates that the flame exists on the reactant-flow side of the stagnation point, as expected. Counterflow flame calculations [17] indicate that the flame can be forced to cross to the opposite side of the stagnation point, but only for extremely large, unrealistic strain rates. It also is observed that the flame curvature is such that the curvature reduces the strain on the flame. It can be observed in Figure 3 that the velocity vectors are all nearly normal to the flame in the region near the centerline. Below the flame, near the forward stagnation point, the velocity vectors are rapidly turned away from the centerline. The velocity field at the late stage of the interaction ($t = 34$ milliseconds) is shown in Fig. 4.

The velocity tangential to the flame surface (u_T) was determined by use of a computer algorithm. A flame contour approximation was defined in the algorithm by a polynomial fit of flame contour points that were chosen by eye from the original PIV photograph. Velocities at various points on the flame contour were determined by spatially averaging PIV velocity vectors. These spatially averaged velocities were then transformed to a coordinate system having one axis tangential to the approximate flame contour at the point of interest. The velocity component along this axis was defined as u_T . Tangential velocities u_T are shown in Figure 5 for the two different interaction times. The consistent trends observed in Figure 5 indicate that there is sufficient spatial resolution in the measuring technique to resolve u_T from the raw data.

The tangential strain rate S_{θ} , which is $\partial u_T / \partial s$, was determined from the slope of Figure 5 and was added to the curvature term in Eq. 1 to yield the total stretch rate K which is plotted in Figure 6. The curvature term is approximately -2 sec^{-1} over most of the flame, which represents a 6% contribution where the strain rate is maximum. The measured stretch rates display the same trend as the theoretical strain rates shown in Figure 1 that were calculated using Eq. 7 for the theoretical example discussed previously. Near the centerline the strain rates are small because the flame must remain relatively far from the vortex cores, due to the large counterflow velocity directed toward the flame on centerline. At other locations the flame can propagate closer to the vortex cores and the strain rate reaches a local maximum. Poinso, et al. [18] calculated the strain exerted by a vortex of smaller diameter, normalized by the flame thickness, than used herein. Their maximum strain occurred on the centerline, because the smaller vortex did not distort the flame as severely as in the present experiment; for smaller flame distortions, the strain rate profile should correspond more closely to the profile in Figure 1 that is maximum on centerline.

The conditions at which the flame is quenched is a sensitive measure of the chemistry-strain interaction. The maximum stretch rate on the flame just prior to quenching is seen in Figure 6 to be 35 sec^{-1} (quenching occurs at a time of 39 msec, as deduced from previous OH images [13]). This value of stretch is similar to the measured value of 42 sec^{-1} that is required to quench a steady, planar counterflow flame having the same methane-air stoichiometry [13]. This agreement is encouraging evidence that there are similarities between a planar, steady strained flame and a time-varying, wrinkled flame for the same local stretch rate. It is still not conclusively known if the properties of a turbulent flame can be modelled by using the profiles that are calculated for a counterflow flame, since unsteady effects may be important and local flame properties may depend on more than one parameter (ie., stretch). However, using the known counterflow stretch rate at extinction (of 42 sec^{-1}) would correctly predict the observed quenching process in the present study.

The vorticity field was deduced by evaluating $\partial v / \partial x - \partial u / \partial y$ and several contours are shown in Figures 7 and 8. The largest measured vorticity of 30 sec^{-1} occurs at a distance of 0.9 cm from the vortex center. Larger values of vorticity will occur near the vortex core boundary, which is 0.4 cm from the vortex center, however it was not possible to measure vorticity near the vortex cores because of insufficient seeding. The maximum vorticity is estimated to be $2 U_0 / r_c$, which is 450 sec^{-1} , since the core has a solid body rotation.

Laser velocimetry previously was used to show that U_0 and r_c are 107 cm/s and 0.4 cm respectively; the sub-micron oil drops that were used were small enough to uniformly seed the vortex cores. The large difference between measured vorticity at $r = 0.9 \text{ cm}$ and the expected vorticity at $r = 0.4 \text{ cm}$ is not surprising; for a Rankine vortex (having solid body core rotation surrounded by a potential vortex) the vorticity suddenly decreases from a constant value to zero at the core boundary.

Another observation that was made is that vorticity is generated by the flame, as shown by Figure 7. The flame-generated vorticity results from the flame curvature and is seen to be positive in the products on the left side of the flame and is negative on the right side. Flame curvature arises because of two factors: buoyancy forces [20] and the reduction in burning velocity near the non-adiabatic walls. The only possible sources of vorticity in the flowfield, away from the walls, are given by the four terms in vorticity transport equation:

$$D\omega/Dt = \omega \cdot \nabla \mathbf{v} - \omega \nabla \cdot \mathbf{v} + \mathbf{v} \nabla^2 \omega + (\nabla \rho \times \nabla p) / \rho^2 \quad (7)$$

The $\omega \cdot \nabla \mathbf{v}$ term is due to vortex stretching and is zero for the axisymmetric conditions considered herein. The diffusion term $\mathbf{v} \nabla^2 \omega$ redistributes the vorticity but cannot cause any net change in the vorticity. The $\omega \nabla \cdot \mathbf{v}$ term represents vorticity that is created as the gas expands due to heat release. The baroclinic torque term $((\nabla \rho \times \nabla p) / \rho^2)$ does create vorticity that is of the same sign as the flame generated vorticity observed in Figure 7. The ∇p vector points toward the reactants and the pressure gradient vector ∇p results from gravitational forces and points downward. Thus the cross product results in negative vorticity behind the right hand side of the flame, which causes the clockwise rotation of the velocity vectors observed in Figure 2. From a physical standpoint, a square fluid element can be placed on the flame surface to the right of centerline; the pressure force due to buoyancy acts vertically upward on the center of pressure, which is located at the center of the square element. The center of mass is in the reactant half of the element, so the net torque about the center of mass is clockwise.

The vorticity field at two different times during the flame-vortex interaction is shown in Figure 8. The vortex remains sufficiently strong so that it prevents the flame from propagating over the vortex core where most of the vorticity is located during the time interval considered. Therefore no appreciable decrease in the net circulation can be deduced. Ashurst and McMurtry [21] have used a discrete vortex simulation to evaluate each of the terms in the vorticity transport equation for a

flame-vortex interaction. They found that a flame will generate vorticity that is of the same sign as the incident vorticity at some locations and will generate vorticity of opposite sign at other locations; they concluded that their simulated flame-generated vorticity is a reasonable explanation for the flame-generated vorticity measured by Driscoll and Gulati [22].

To complete the description of the strain field, the shear strain rate S_{xy} , which is $(\partial u/\partial y + \partial v/\partial x)/2$, was determined. Contours appear in Figure 9. The measured contours for the vortex only (Figure 9b) and for the flame and vortex (Figure 9c) are similar to those of a theoretical Rankine vortex. The shear strain contours have eight lobed-shaped regions, four of which have positive shear. Measurements of shear strain in a turbulent flowfield can be of benefit because they allow the determination of the principle axes of the strain field [23], which are rotated from the x, y axes by the angle $0.5 \arctan(2S_{xy}/(S_{xx}-S_{yy}))$. There is evidence that a turbulent flame aligns itself with the principle axes of strain [24].

Conclusions

1. The distributions of the tangential strain rate $\partial \Gamma / \partial s$ and the stretch rate K have been directly measured along a distorted premixed flame contour, as the flame interacts with a vortex, using velocity field imaging techniques
2. The tangential strain rate is not a maximum on centerline because the velocity field prevents the flame from propagating to a location that is close to the vortex core. Instead, the maximum strain occurs at a location where the distorted flame is able to propagate to a location close to the vortex core, where the velocity gradients are largest.
3. The strain rate distribution on the flame for a smaller vortex, as calculated by direct numerical simulations, is maximum on centerline and differs significantly from the present measurements. It follows that the strain rate distribution on a flame cannot be modelled as a self-similar process but is dependent on the vortex size.
4. The maximum local strain rate also increases with residence time because portions of the flame continue to propagate closer to the high-strain vortex core region.
5. The flame quenches when the maximum local stretch rate is measured to be 35 sec^{-1} , which is similar to the measured stretch rate of 42 sec^{-1} that quenches a steady, planar counterflow flame of similar stoichiometry. It is concluded that unsteady

strain effects do not have a major effect on quenching, at least for the conditions of the present experiment.

6. Velocity field images show that the flame generates vorticity due to the action of a baroclinic torque.

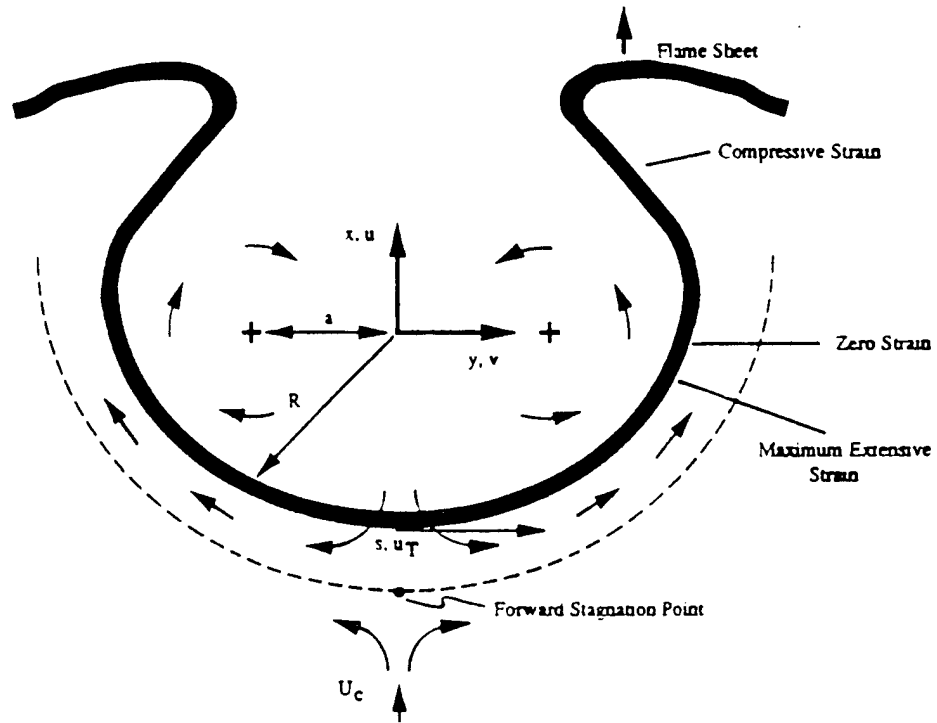
Acknowledgements

The measurements were performed at Wright-Patterson AFB in the laboratory that is under the direction of Dr. C.M. Roquemore, whose support and encouragement is appreciated. D. Trump and B. Sarka were instrumental in the development of the PIV diagnostics.

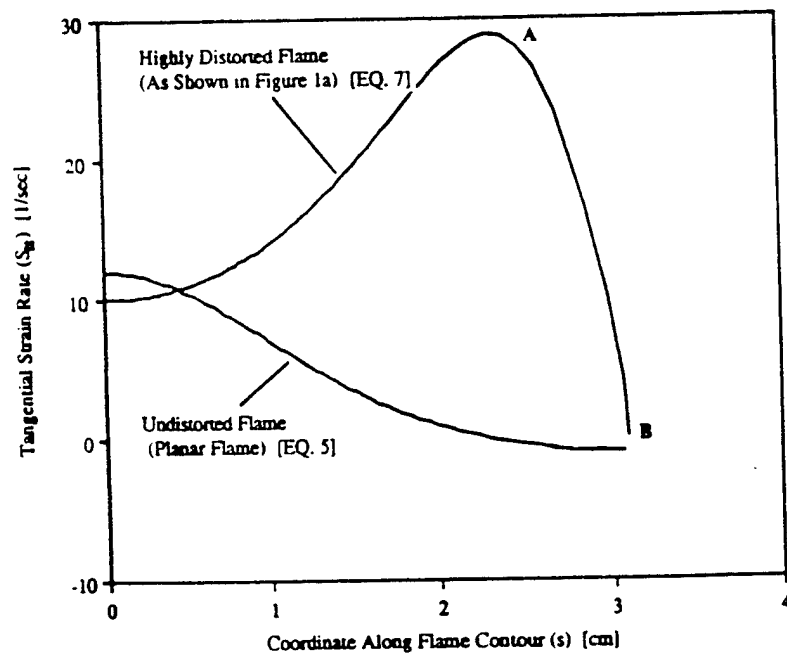
REFERENCES

1. Meneveau, C., and Poinot, T. (1991). *Combust. Flame* 86: 311-332.
2. Cant, R.,S., Pope, S.B., and Bray, K.N.C. (1990). Twenty-Third Symposium (International) on Combustion, The Combustion Institute, Pittsburgh, pp.809-815.
3. Ashurst, W.T.(1987). "Vortex Simulation of Unsteady Wrinkled Laminar Flames", *Combust. Sci. Technol.* 52:325.
4. Wu, M.S., Kwon, S., Driscoll, J.F., and Faeth, G.M.(1992). *Comb. Sci.and Technol.* 83: 187-202 .
5. Kwon, S., Wu, M.S., Driscoll, J.F., and Faeth, G.M. (1992). *Combust. Flame* 88: 221-238 .
6. Wu, M.-S., and Driscoll, J.F. (1993) *Combust. Flame*, to appear.
7. Kerstein, A.R. Ashurst, W.T., and Williams, F.A.(1988) *Phys. Rev. A*: 37:2728-2731.
8. Lee, T.W. and Santavicca, D.A.(1993) "Flame Front Geometry and Stretch During Interactions of Premixed Flames With Vorticies", to appear, *Combust. Sci. Technol.*
9. Abdel-Gayed, R.G., Bradley, D., Hamid, N.M., and Lawes, M. (1984). "Lewis Number Effect on Turbulent Burning Velocity", Twentieth Symposium (International) on Combustion, The Combustion Institute, Pittsburgh, p. 505.

10. Wu, M.S., Kwon, S., Driscoll, J.F., and Faeth, G.M. (1991). "Preferential Diffusion Effects on the Surface Structure of Turbulent Premixed Hydrogen-Air Flames" *Comb. Sci. Technol.* 83: 187-202.
11. Roberts, W.L. and Driscoll, J.F., *Combust. Flame*, 87: 245-256 (1991).
12. Roberts, W.L., Driscoll, J.F., Drake, M.C., and Ratcliffe, J.W. (1992). Twenty-Fourth Symposium (International) on Combustion, The Combustion Institute, Pittsburgh, to appear.
13. Roberts, W.L., Driscoll, J.F., Drake, M.C. and Goss, L.P. (1993) "Images of the Quenching of a Flame by a Vortex-To Quantify Regimes of Turbulent Combustion", submitted to *Comb. and Flame*.
14. Law, C.K., Twenty-Second Symposium (International) on Combustion, The Combustion Institute, Pittsburgh, 1988, pp. 1381-1402.
15. Candel, S.M. and Poinso, T.J. (1990) "Flame Stretch and the Balance Equation for the Flame Area", *Combust. Sci. Technol.* 70:1-15.
16. Goss, L.P., Post, M.E., Trump, D.D. and Sanka, B. (1991). "Two Color Particle Imaging Velocimetry", *J. Laser Applic.*, Winter 1991, pp. 36-42.
17. Darabiha, N., Candel, S.M., and Marble, F.E. (1986). "The Effect of Strain Rate on a Premixed Laminar Flame", *Combust. Flame* 64: 203-217.
18. Poinso, T., Veynante, D., and Candel, S. (1990). Twenty-Third Symposium (International) on Combustion, The Combustion Institute, Pittsburgh, pp. 613-619.
19. Poinso, T., Veynante, D., and Candel, S., *J. Fluid Mech.* 228: 561-606 (1991).
20. Pelce-Savorin, C., Quinard, J. and Searby, G. (1988). "The Flow Field of a Curved Flame Propagating Freely Upwards", *Combust. Sci. Technol.* 58: 337-346.
21. Ashurst, W.T. and McMurtry, P.A. (1989). "Flame Generation of Vorticity: Vortex Dipoles from Monopoles", *Combust. Sci. Technol.* 66: 17-37.
22. Driscoll, J.F. and Gulati, A. (1986). "Measurement of Various Terms in the Turbulent Kinetic Energy Balance Within a Flame and Comparison with Theory", *Combust. Flame* 72:131-152.
23. Beer, F.P., and Johnston, E.R., Mechanics of Materials, McGraw Hill, NY, 1981.
24. Haworth, D.C. and Poinso, T.J. (1992). "Numerical Simulations of Lewis Number Effects in Turbulent Premixed Flames", *J. Fluid Mech.* 244:405-436.

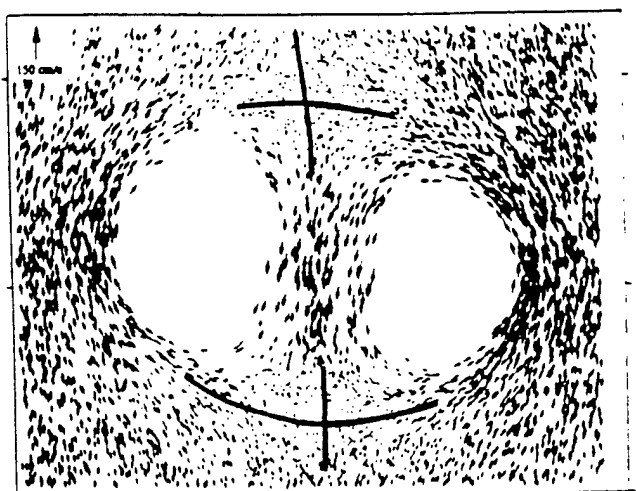


(a)

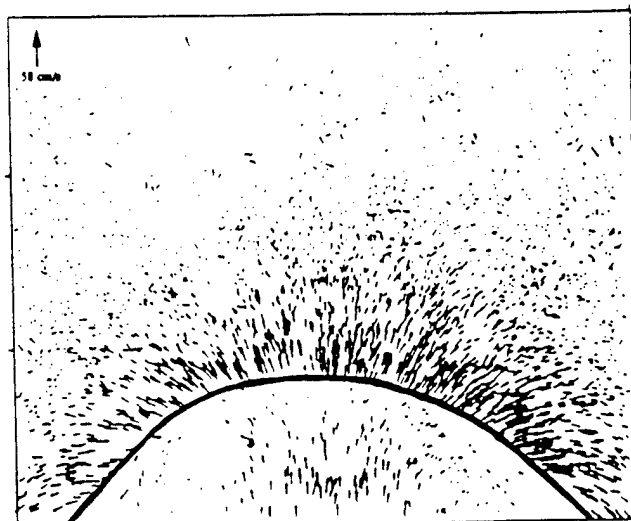


(b)

Figure 1. (a) Schematic of the Velocity Field for a Flame-Vortex Interaction., (b) Theoretical Tangential Strain Rate Profiles for a Flame-Vortex Interaction

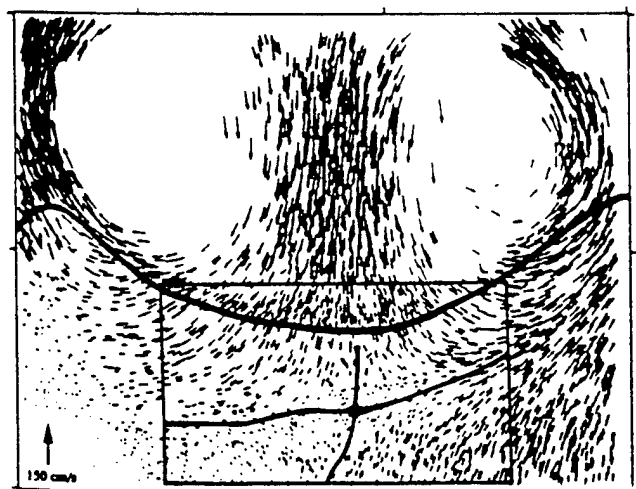


(a)

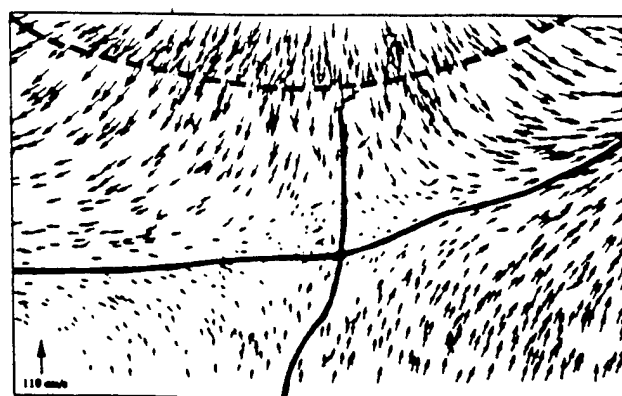


(b)

Figure 2. Velocity Field Images for (a) Vortex Only (In Vortex Frame of Reference), maximum rotational velocity $U_\theta=107$ cm/s, distance between vortex centers $D=3.8$ cm, (b) Flame Only (In Lab Frame), burning velocity $S_L=7.5$ cm/s. Field of view for each image is approximately 8 cm wide by 6 cm high.



(a)



(b)

Figure 3. (a) Velocity Field Image of Intermediate Phase of Flame-Vortex Interaction (In Vortex Frame of Reference, $t=26$ ms), (b) Magnified View of the Intermediate Phase Forward Stagnation Point.

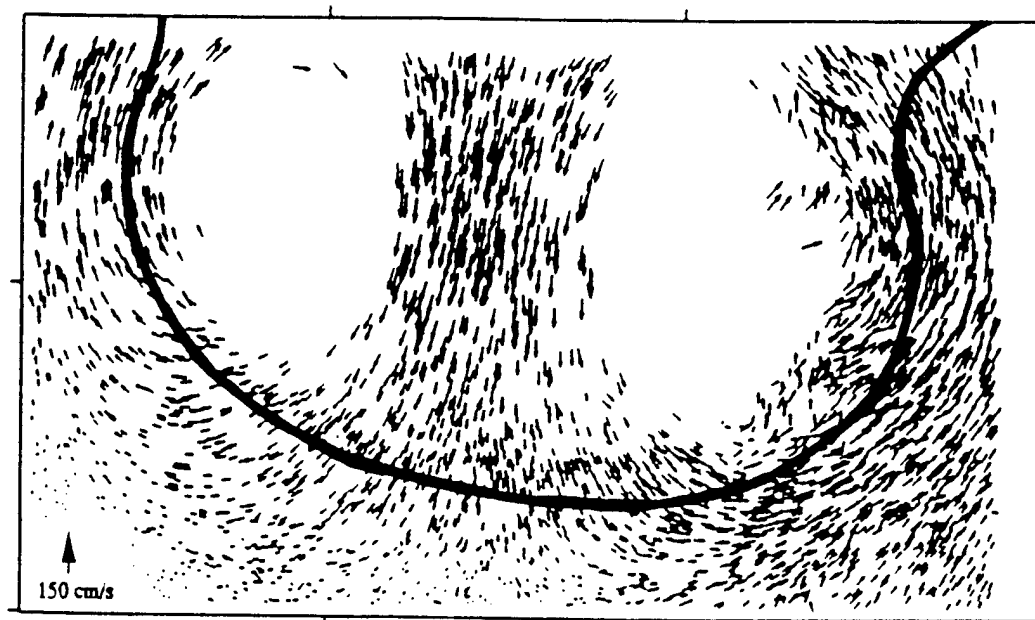


Figure 4. Velocity Field Image of the Late Phase of the Flame-Vortex Interaction (In Vortex Frame of Reference, $t = 34$ ms).

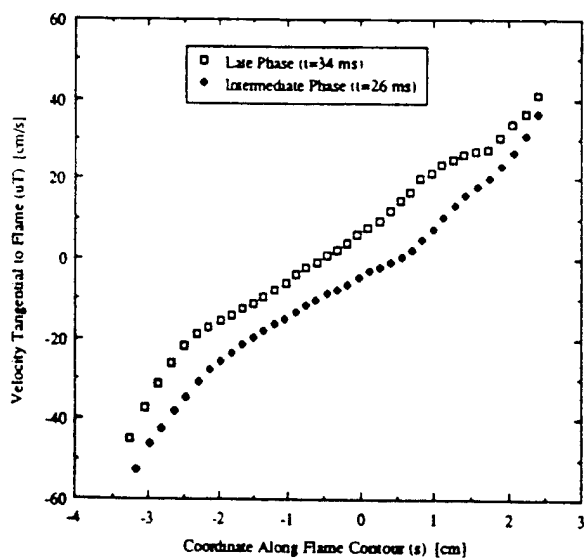


Figure 5. Velocity Tangential to Flame Contour for Intermediate Phase and Late Phase of Flame-Vortex Interaction.

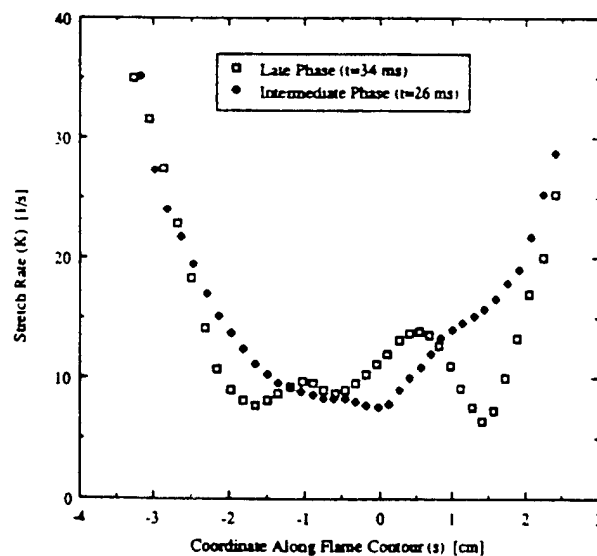


Figure 6. Measured Stretch Rate (K) Obtained by Applying Equation 1 to PIV Velocity Data.

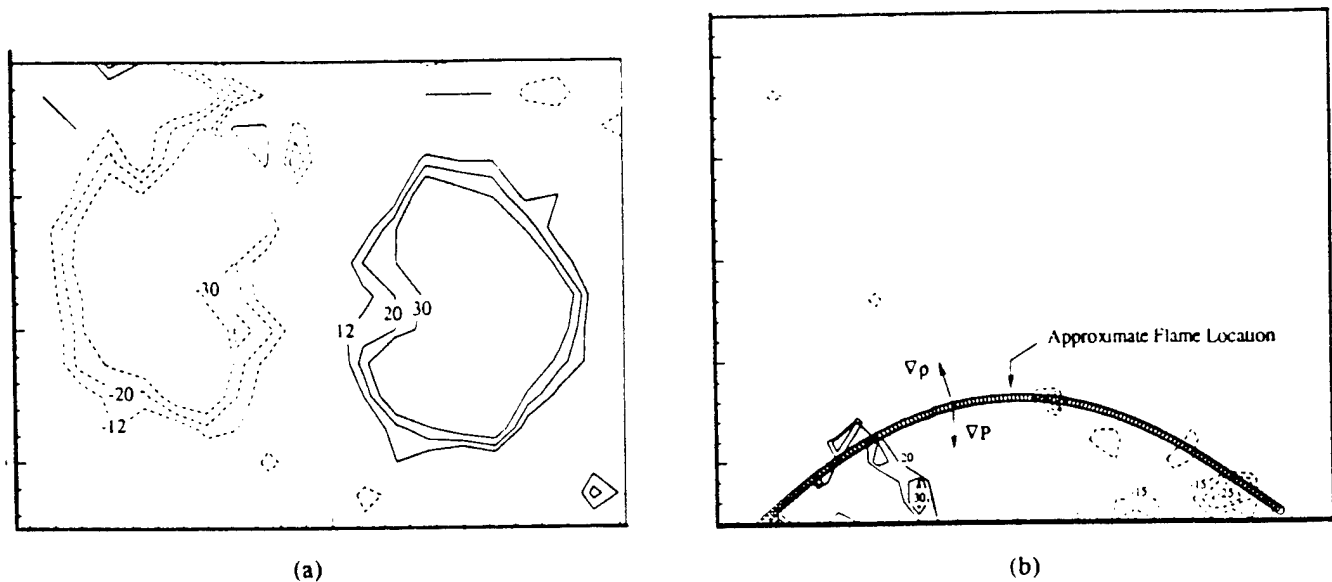


Figure 7. Contours of Vorticity (ω_z) Measured for (a) Vortex Only Case, (b) Flame Only Case. Units are sec^{-1}

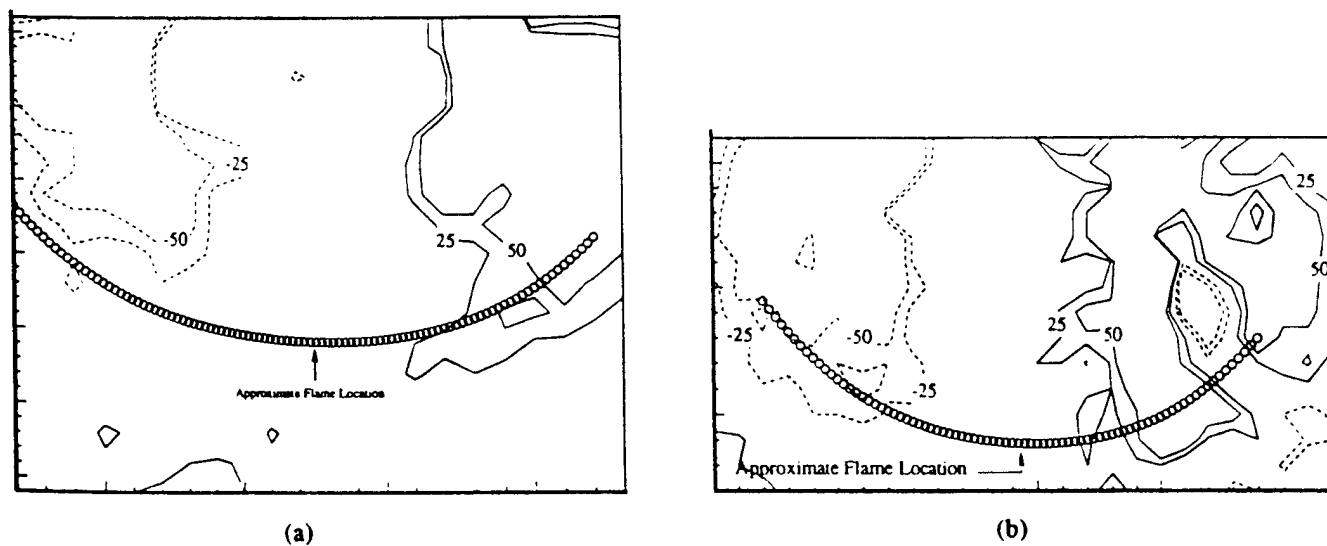
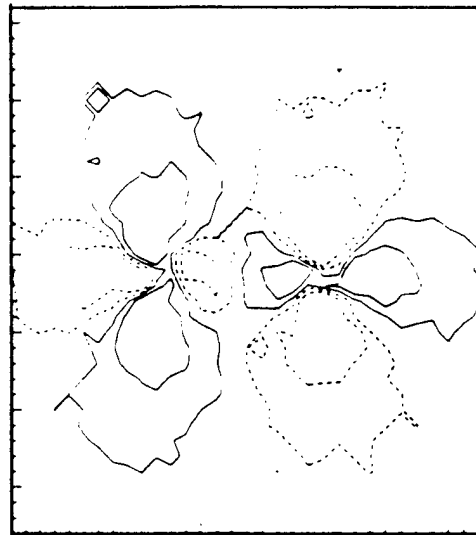
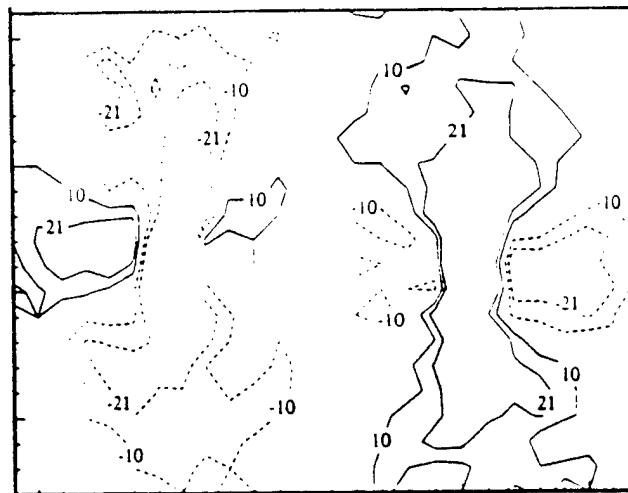


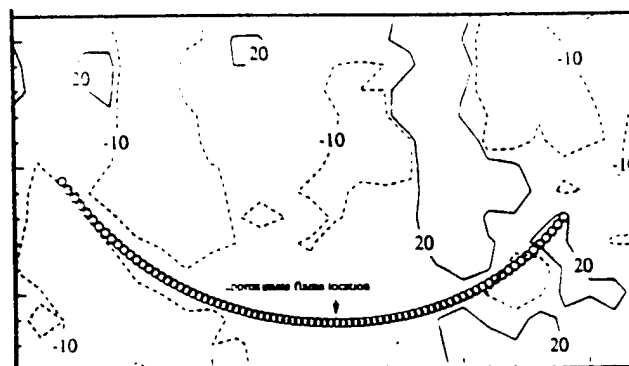
Figure 8. Vorticity Contours for (a) Intermediate Phase, $t = 26 \text{ ms}$ and (b) Late Phase, $t = 34 \text{ ms}$ of Flame-Vortex Interaction. Units are sec^{-1} .



(a)



(b)



(c)

Figure 9. Shear Strain Rate (S_{xy}), (a) Theoretical Example, (b) Vortex Only, (c) Late Phase of Flame-Vortex Interaction, $t = 34$ ms.

The Effect of a DC Electric Field on the Velocity and Temperature of a Premixed Propane-Air Flame

Dennis F. Grosjean
Systems Research Laboratories, Inc.
A Division of Calspan Corporation
2800 Indian Ripple Road
Dayton, OH 45440-3696

INTRODUCTION

A large body of work has been reported on the various effects of electric fields on flames. However, the exact mechanisms responsible for the rather dramatic field-induced effects on the size, shape, and stability of hydrocarbon flames are still not well understood. Excellent coverage of the subject is given by Lawton and Weinberg,¹ and an updated review is provided by Bradley.² Electric-field-induced effects can alter the flame geometry as well as the flame-blowout limit, increase the flame stability, improve the heat transfer to solid surfaces, increase the burning velocity, and elevate the electron temperatures in the flame.

Emphasis in the present study was on the dramatic change in shape of a cylindrical premixed propane-air flame induced by an axial electric field. Particle-Imaging Velocimetry (PIV) was employed to obtain a two-dimensional image of the gas velocity; Thin-Filament Pyrometry (TFP) permitted a one-dimensional time-dependent measurement of temperature distributions; and high-resolution point measurements of gas velocity were attempted using Thin-Filament Velocimetry (TFV).

EXPERIMENTAL ARRANGEMENT AND RESULTS

Figure 1 is a diagram of the burner system employed for the measurements reported here. The burner head is a 42-mesh wire cloth made from 0.010-in.-diam. stainless-steel wire welded to a 0.75-in.-diam. thin-wall (0.020-in.) stainless-steel tube. Premixing was accomplished within the 48-in. supply tube by naturally occurring diffusion and turbulence. A 0.75-in.-long honeycomb plug, consisting of hexagonal 1/16-in. cells, was located 1 in. below the wire cloth as an aid in straightening the flow. This technique did not remove all the nonuniformities in the flow but did result in a highly reproducible flame that could be readily seeded. In fact, definite flow gradients--attributed to the edge nonuniformities of the surface screen--were observed, but stable temperature profiles indicated adequate premixing.

The electric field was applied between the burner surface and a wire mesh located 4.4 cm above (downstream of) the burner surface. Although the wire mesh is not necessary for the production of the observed effect, the mesh enhances the coupling of the field to the flame. When a 1.25-in.-ID brass cylinder without the mesh was used, changes in flame shape were apparent upon application of an electric field (cylinder positive with respect to burner), but the flame often fluctuated erratically. Presumably, this was a result of the position-dependent conductivity of the downstream portion of the flame and the changing position of contact between the flame and the electrode caused by buoyancy-driven turbulence.

Photographs of the flame produced by the burner system are shown in Fig. 2. These photos were taken at approximately the location where the PIV recordings were made, with the camera focus being set at the center of the flame. The effect of the electric field is dramatic. Although the shape of the flames is quite similar when the voltage applied is in the range 0 - 200 V, some jitter can be observed for voltages as low as 100 V. Dramatic changes in shape are apparent when the voltage applied is 400 V and greater. For potentials above 600 V, turbulence becomes significant, as demonstrated in the 800-V photograph.

Although the effect of an electric field is dramatic when the downstream electrode is positive with respect to the burner surface, it is nonexistent when the DC polarity is reversed. That is, when a negative potential is applied to the downstream electrode, the flame shape remains completely unchanged [same as Fig. 2 (0 volts)] until the field is sufficiently large to produce corona. For the present study, interest was limited to field amplitudes below the corona-inception point.

Thin-Filament Pyrometry (TFP)

The basic technique of TFP, as described by Vilimpoc, *et al.*,³ was applied to the burner system under study. A single 13- μ m-diam. SiC fiber was suspended within the flame, and the resulting gray-body radiation was scanned at 200 - 2000 Hz via a rotating mirror having 10 facets. In this manner, the time-dependent temperature was recorded. The temporal response of the SiC fiber limited the frequency of temperature fluctuations to < 750 Hz,³ and the optical setup limited the spatial resolution to ~ 1 mm along the 13- μ m fiber.

Representative temperature profiles are shown in Fig. 3. The high temperatures indicate the location of the reaction zone and the post-burn gases. The lower temperatures indicate the region outside the flame as well as the region of unburned gas, upstream of the reaction zone. A frequency analysis revealed only frequencies of < 30 Hz. These buoyancy-driven oscillations are typically < 20 Hz at both the inside and outside edges of the hot zones and 20 - 30 Hz near the center of the hot gases downstream of the reaction zone. Although the frequency may vary upon application of an electric field, the changes in frequency induced by the field were minor and were attributed to changes in flame shape rather than local momentum effects.

Particle-Imaging Velocimetry (PIV)

Two-dimensional velocity profiles of the flame were obtained by a two-color PIV technique described by Post and co-workers.⁴ The plane of observation was illuminated by a red light source (broadband emission of Nd:YAG-pumped dye laser utilizing SR640 dye) and by the green emission of a frequency-doubled Nd:YAG laser. The two short-pulse sources were separated by 50 - 100 μ sec. After digitization of the color images which were captured on 35-mm film, the spatial shift of the red and green Mie scattering from 6- μ m-diam. (nominal) seed particles was determined by a cross-correlation technique. Velocity vectors were then calculated.

Results from a propane-air flame with equivalence ratio of 1.47 are shown in Fig. 4. The position of the flame front, where the velocity vectors change in size and direction,

is clearly visible. Although the flame-front position changes when an electric field is applied, no obvious change is detected in the magnitude of the velocity. The PIV technique is useful for pictorial demonstrations of large changes in velocity vectors; however, the resolution is insufficient to provide insight into the phenomenon responsible for the changes in flame shape effected by an electric field.

Thin-Filament Velocimetry (TFV)

An attempt was made to apply the technique of TFV, as developed by Goss and co-workers,⁵ in order to obtain a high-resolution measurement of velocity in close proximity to the reaction zone. Unfortunately, reliable data have not yet been obtained within the desired area. Measurement results within the hot, post-burn region agreed well with results of PIV measurements, but data obtained near the reaction zone were erratic. More work is needed for resolution of difficulties caused by low-frequency fluctuations.

DISCUSSION

Over the last 25 years, most of the studies on the effect of sub-breakdown DC electric fields on premixed flames have suggested that a heavy-particle mechanism provides the coupling between the field and the flame.^{1,2} The exact mechanism, however, has not been identified. Although it appears that the majority of energy transfer from the electric field is via momentum transfer by heavy charged particles, it is not clear whether this kinetic-energy gain of the gas merely induces a directed motion or contributes to increased reaction rates by effecting a change in the transport properties of the gas in the vicinity of the reaction zone.

For the premixed propane-air system studied here, the dependence of the field effect on polarity constitutes the strongest evidence that momentum transfer is the dominant energy-coupling mechanism. That is, when the downstream electrode was negative with respect to the burner surface, no measurable effect on gas velocity or temperature was observed. Only after the electric field exceeded the corona-inception point was any visible or measurable effect noted. However, when the electrode was positive with respect to the burner, both visual and measurable effects were observed for potentials as low as 100 V across a 4.4-cm gap.

Qualitatively, the polarity dependence has been explained by the difference in the masses of the negative charge carriers when the field is reversed.² That is, for a positive potential downstream of the reaction zone, the major charge carriers are high-mobility, low-mass electrons at a relatively high density. Negative-ion destruction processes can be significant in this high-temperature region.⁶ However, when the field is reversed, the electrons generated within the reaction zone become rapidly attached, resulting in the negative charge carriers being low-mobility negative ions. It appears, then, that a net directed energy will be imparted toward the burner when the downstream electrode is positive with respect to the burner, while the net directed energy for the case of a negative electrode will be zero since the positive and negative charge carriers have similar masses.

In addition, the mobilities of ions differ considerably, depending upon their position. That is, mobilities are both temperature and gas-density dependent. Mobilities for a given ionic species would be much higher in the hot downstream area of the flame than in the much cooler upstream zone. The resulting difference in diffusion rates as well as the significant difference in mobilities resulting from the significant difference between electron and ion masses can lead to self-generated electric fields which can be readily modified by an external electric field.

An often-neglected parameter is the effect of the local electric field. The current carriers within the hot zone (downstream of the reaction zone) are expected to be electrons and positive ions. A balance of electrons, positive ions, and--to a lesser extent--negative ions consistent with space-charge effects and charged-particle diffusion will exist. The charge carriers within the relatively cold region below (upstream of) the reaction zone will be positive and negative ions. Here, a balance of positive and negative ions consistent with space-charge effects and diffusion will exist. Because current continuity must be maintained, the charge density and local electric field are strongly coupled. In other words, a quantitative analysis requires the inclusion of charged-particle drift and diffusion parameters along with flame chemistry.

Sheath effects at the electrodes, necessary for current continuity, can be extremely important in the determination of local electric fields.^{7,8} This is particularly critical at the burner when the burner surface is the negative electrode. Since the burner is relatively cool, electron emission is insignificant and current is carried by positive ions only, requiring a high electric field.

It seems reasonable to assume that the relatively small amount of directed kinetic energy is highly leveraged in the vicinity of the reaction zone to produce the dramatic effects shown in Fig. 2. However, it is not yet clear what pathways are followed. The measurements discussed above indicate that the momentum coupling must occur on a small scale since the only measurable effect was a change in the position of the reaction zone. Spatial resolution was generally limited to dimensions of > 1 mm.

CONCLUSIONS

Some of the effects of a DC electric field on a premixed hydrocarbon flame were demonstrated. The discussion indicates that more work is needed in order to delineate the pathways through which energy is coupled from the electric field to the flame constituents. Future measurements should concentrate on high-resolution, fast-response techniques for detecting short-range turbulence. Modeling of the combustion process in the presence of an electric field must include a reasonable value of local electric field and cannot ignore the significance of differing charged-particle mobilities.

ACKNOWLEDGMENTS

This research was supported by and conducted at the Wright Laboratory, Aero Propulsion and Power Directorate, Wright-Patterson Air Force Base, Ohio, under Contract Nos. F33615-88-C-2832 and F33615-90-C-2033.

REFERENCES

1. J. Lawton and F. J. Weinberg, *Electrical Aspects of Combustion* (Clarendon Press, Oxford, 1969).
2. D. Bradley, "The Effects of Electric Fields on Combustion Processes," in *Advanced Combustion Methods* (F. J. Weinberg, Ed.) (Academic Press, New York, 1986), pp. 331-394.
3. V. Vilimpoc, L. P. Goss, and B. Sarka, "Spatial Temperature-Profile Measurements by the Thin-Filament-Pyrometry Technique," *Opt. Lett.* 13, 93 (February 1988).
4. M. E. Post and L. P. Goss, "Two-Color Particle-Imaging Velocimetry in Vortex Structures," AIAA Paper No. 93-0412, Presented at the 31st Aerospace Sciences Meeting and Exhibit, Reno, NV, 11-14 January 1993.
5. L. P. Goss, J. R. Gord, D. D. Trump, and M. E. Post, "Thin Filament Velocimetry," AIAA Paper No. 93-0518, Presented at the 31st Aerospace Sciences Meeting and Exhibit, Reno, NV, 11-14 January 1993.
6. J. M. Goodings, D. K. Bohme, and Chun-Waing, "Detailed Ion Chemistry in Methane-Oxygen Flames. II. Negative Ions," *Combust. Flame* 36, 45 (1979).
7. S. D. Marcum and B. N. Ganguly, "The Effect of DC Electric Fields on Pre-Mixed Hydrocarbon Flames," AIAA Paper No. 93-0803, Presented at the 31st Aerospace Sciences Meeting and Exhibit, Reno, NV, 11-14 January 1993.
8. M. J. Wolf and B. N. Ganguly, "Rydberg State Stark Spectroscopic Measurements of Electric Field Profile in a Propane-Air Flame," *Combust. Flame* 90, 284 (1992).

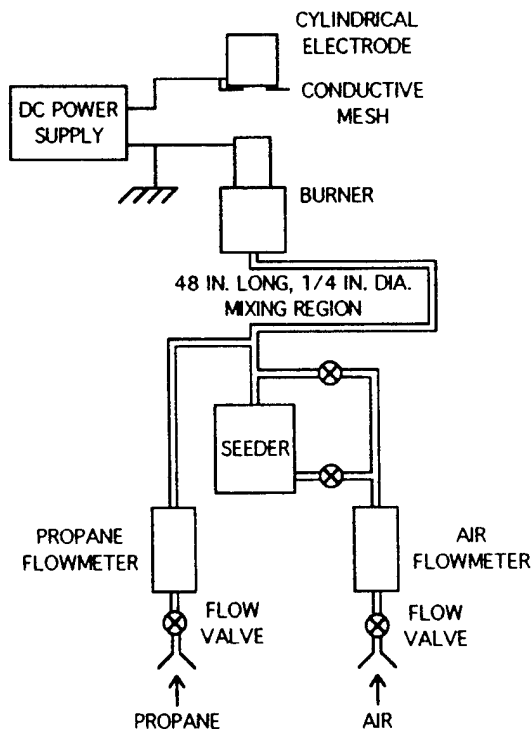


Fig. 1. Schematic Diagram of Laboratory Burner System. Electrode located 4.4 cm above burner surface.

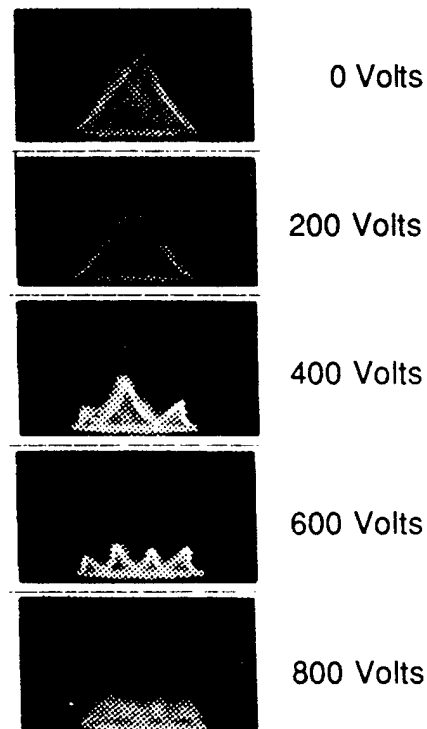


Fig. 2. Visual Effect of Electric Field on Laboratory Flame Burner. Downstream electrode is positive with respect to burner.

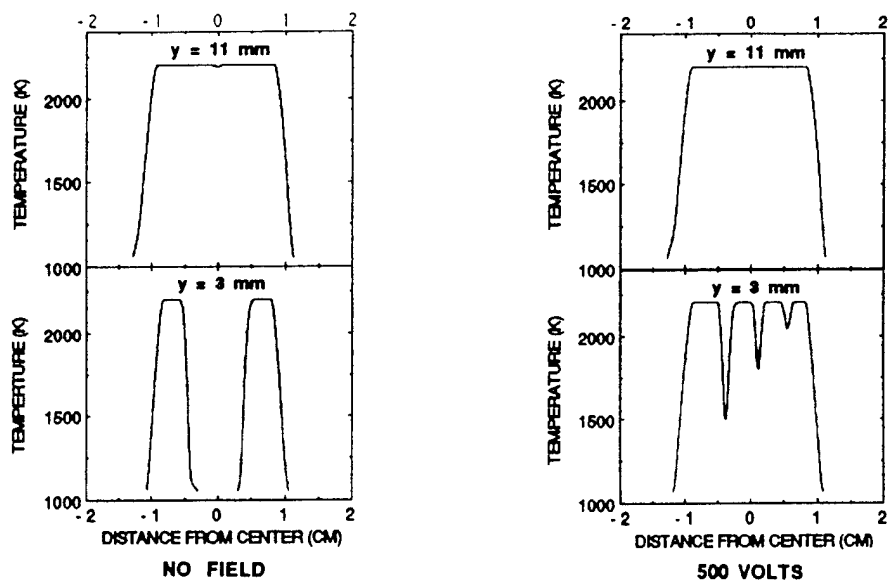


Fig. 3. Representative Temperature Profiles of Laboratory Flame for Field Potentials of 0 V and 500 V.

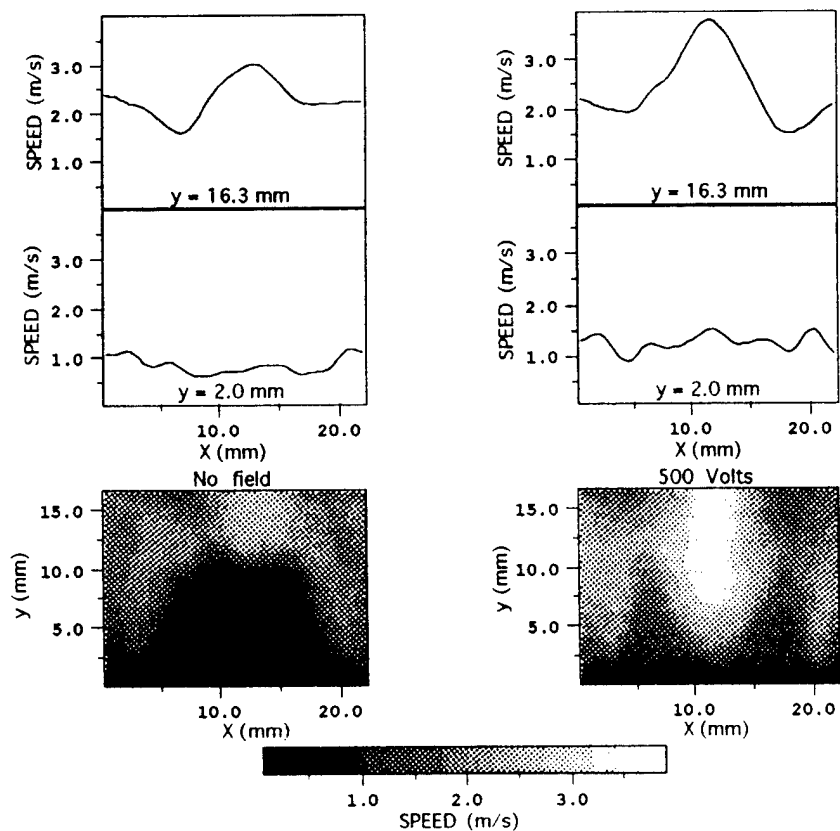


Fig. 4. Representative Measurements of Velocity Magnitude within Laboratory Flame for Field Potentials of 0 V and 500 V.

3.1.3 Jet Diffusion Flames. Jet diffusion flames have frequently been studied as an analogue of more complex combusting flows because, although geometrically simple, they exhibit many of the features found in complex practical systems. In particular, the dynamic interactions of the flame surface and the surrounding flow structures are of great importance in many applications such as furnaces and combustors. The dynamic interactions occurring in jet diffusion flames have been the subject of numerous experimental investigations during the course of this program. Studies on the dynamic structure of jet diffusion flames were reported in papers entitled, "Preliminary Results of a Numerical/Experimental Study of a Buoyant Jet Diffusion Flame" (pp. 286 - 295), "A Numerical/Experimental Study of the Dynamic Structure of a Buoyant Jet Diffusion Flame" (pp. 296 - 306), "Time Evolution of a Buoyant Jet Diffusion Flame" (pp. 307 - 314), and "Vorticity Generation in Jet Diffusion Flames" (pp. 315 - 331). Studies of the stabilization of a jet diffusion flame under near-lift-off conditions were reported in papers entitled, "Statistical OH-Zone Structures of Turbulent Jet Flames from Liftoff to Blowout" (pp. 332 - 345), "Dynamic Stabilization Zone Structure of Jet Diffusion Flames from Liftoff to Blowout" (pp. 346 - 350), and "Near-Field Turbulent Structures and the Local Extinction of Jet Diffusion Flames" (pp. 351 - 359).

In modeling the turbulent jet diffusion flame, the complex interaction between chemistry and fluid turbulence is the major difficulty. The CFD codes used for gas-turbine-combustor design rely heavily on the accuracy of turbulence models. Therefore, it is important to understand the interaction between vortex and flame. Moderate interactions can aid the combustion process by increasing the flame surface, while strong interactions may lead to local extinction, lift off, and blow-out of the flame and, as a result, reduce combustion efficiency and increase emissions. Vortex-flame interactions were studied with advanced laser diagnostics and the results reported in papers entitled, "Vortex-Flame Interactions and the Local Extinction of Turbulent Jet Diffusion Flames" (pp. 360 - 370), "Experimental and Numerical Investigations of the Vortex-Flame Interactions in a Driven Jet Diffusion Flame" (pp. 371 - 386), "Finite-Rate Chemistry Effects During Vortex-Flame Interactions in a Driven-Jet Diffusion Flame" (pp. 387 - 392), and "The Structure of a Dynamic Nonpremixed H₂-Air Flame" (pp. 393 - 398).

Preliminary Results of a Numerical-Experimental Study of the Dynamic Structure of a Buoyant Jet Diffusion Flame

R. W. DAVIS and E. F. MOORE

Center for Chemical Technology, National Institute of Standards and Technology, Gaithersburg, MD 20899

W. M. ROQUEMORE

WRDC/Aero Propulsion Lab, Wright-Patterson AFB, OH 45433-6563

L.-D. CHEN

Department of Mechanical Engineering, The University of Iowa, Iowa City, IA 52242

V. VILIMPOC and L. P. GOSS

Systems Research Laboratories, Inc., Dayton, OH 45440-3696

Preliminary results of a joint numerical-experimental investigation of the dynamic structure of a buoyant jet diffusion flame are presented. The purpose of this effort is to determine the nature of the unsteady interactions between flames and their associated vortex motions. A direct numerical simulation of an unsteady low-speed propane-air jet diffusion flame is carried out utilizing the flame sheet and conserved variable approximations. Counterrotating vortex structures internal and external to the flame surface appear and move upward along with flame sheet bulges. Tip-cutting (flickering) occurs with a frequency of 11-15 Hz. These dynamic features bear close resemblance to those observed experimentally by means of the reactive Mie scattering (RMS) technique. Comparisons between computational and experimental (determined using thin filament pyrometry) near-instantaneous radial temperature profiles at four heights in the flame also show good agreement. The assumption of zero gravity in the computation results in the complete cessation of dynamical activity, thus demonstrating the important role that buoyancy plays in the behavior of this flame.

INTRODUCTION

The study of combustion processes is difficult because of the complex interactions between the fluid dynamics and the chemistry. In any complicated situation such as this, it is desirable to isolate certain critical aspects of the physics by investigating simplified systems. Even after simplification, however, the coupling among the remaining processes can be very difficult to sort out. Jet diffusion flames are often used to study

the interactions among the physical and chemical processes occurring in combusting flows. Indeed, much of the current understanding of non-premixed combustion processes has resulted from the study of these flames, beginning with the development of laminar diffusion flame theory by Burke and Schumann [1].

The idea of a laminar jet diffusion flame has been extended to the turbulent case by conceptualizing the flame surface as wrinkled and stretched. In this school of thought, the turbulent

flame is represented by an ensemble of stretched laminar flamelets. This appears to be a reasonable method of accounting for the transition from laminar to turbulent flame structure, although the concept has recently been challenged by Bilger [2]. Investigation of the basic processes underlying the transition from laminar to turbulent structure in these flames is very difficult from an experimental viewpoint because of the various types of fluid dynamic and chemical data that are required simultaneously over a large spatial region. This difficulty can be reduced by combining an experimental combustion study with a powerful simulation technique that can provide the required amount of instantaneous spatially resolved data. The resulting experimental-computational data set can then be employed to gain insights into the underlying physical processes, with the added power that the impact of changing parameters in the computation can readily be evaluated. Experiments with jet diffusion flames [3-6] have clearly shown that any computational method must correctly describe large-scale, time-dependent processes involving buoyancy and large density variations. A direct numerical simulation based on the governing unsteady equations of motion appears to be a reasonable way of proceeding and is the approach that is followed here.

The configuration that has been selected to initiate a joint experimental-numerical investigation is a low-speed buoyant jet diffusion flame. This configuration has been chosen for several reasons. First, the lower regions of this flame are laminar, thus eliminating the extreme scale disparities caused by turbulence, as well as allowing use of a simple flame sheet approximation in the model. Second, this buoyant flame has many distinctive structural features that can be employed to aid in evaluating the fluid dynamic and thermodynamic aspects of the model. Third, buoyancy is clearly a dominant factor in low-speed jet diffusion flames. In particular, the role of buoyancy in establishing the large vortical structures outside of the flame sheet and their relationship to flame flicker is not fully understood. The impact of these structures on the mean flow field properties measured in many previous combustion studies has not been fully appreciated. This

has become dramatically apparent throughout the recent use of the reactive Mie scattering (RMS) technique to visualize the structure of these flames [5, 7]. Finally, an experimentally validated model in which the time-dependent conservation equations are coupled with a laminar flame sheet approximation will provide an excellent basis on which these flame sheet models can be systematically studied at higher jet Reynolds numbers.

NUMERICAL MODEL

The nondimensional continuity, momentum, and state equations for the unsteady axisymmetric flow of a multicomponent fuel jet surrounded by a coflowing oxidizer stream are

$$\frac{\partial \rho}{\partial t} + \nabla \cdot (\rho \mathbf{q}) = 0, \quad (1)$$

$$\begin{aligned} \rho \frac{\partial \mathbf{q}}{\partial t} + \rho (\mathbf{q} \cdot \nabla) \mathbf{q} \\ = -\nabla \tilde{p} - \rho Ri \hat{e}_z \\ + \frac{1}{Re} \{ -\nabla \times (\nabla \times \mu \mathbf{q}) \\ + 4/3 \nabla (\mu \nabla \cdot \mathbf{q}) \\ + \nabla (\mathbf{q} \cdot \nabla \mu) - \mathbf{q} \nabla^2 \mu \\ + \nabla \mu \times (\nabla \times \mathbf{q}) - (\nabla \cdot \mathbf{q}) \nabla \mu \}, \end{aligned} \quad (2)$$

$$\rho T \sum_i R_i Y_i = p_0, \quad (3)$$

respectively, where ρ is density, μ is viscosity, T is temperature, $\mathbf{q} = (v, u)$, where v and u are velocity components in an axisymmetric reference frame (r, z) , Y_i is the mass fraction of species i with gas constant R_i , and \hat{e}_z is the unit normal in the axial direction. The pressure consists of a constant background pressure, p_0 , plus a perturbation pressure, $\tilde{p}(r, z, t)$, where $p_0 \gg \tilde{p}$. As discussed by Rehm and Baum [8], the omission of \tilde{p} from Eq. 3 is entirely appropriate here, resulting in the suppression of acoustic waves while admitting the low-frequency motions due to buoyancy effects. All quantities in Eqs. (1-3) have been nondimensionalized with respect to conditions in the coaxial oxidizer stream at the

burner inlet. Thus Re = Reynolds number = $U_0 L / \nu_0$ and Ri = Richardson number = gL / U_0^2 , where U_0 and ν_0 are the entering oxidizer stream velocity and kinematic viscosity, L is the fuel jet radius, and g is gravitational acceleration.

In order to reduce the complexity of the problem while still providing a good approximation to the physical situation, a flame-sheet model (infinite rate kinetics) will be employed here. In addition, the Lewis number (ratio of thermal to species diffusivities) is assumed to be unity. Therefore, conserved variables, β_i , for species mass fractions and enthalpy can be utilized. These obey the simple nondimensional convection-diffusion equation

$$\frac{\partial(\rho\beta_i)}{\partial t} + \nabla \cdot (\rho\mathbf{q}\beta_i) = \frac{1}{Pe} \nabla \cdot (\rho D \nabla \beta_i), \quad (4)$$

where D is binary diffusion coefficient and Pe = Peclet number = $U_0 L / D_f$, with D_f taken as the diffusion coefficient of fuel into nitrogen at the burner inlet. The conserved variables are defined as

$$\beta_1 = \frac{\alpha Y_{ox} + Y_f^I - Y_f}{\alpha Y_{ox}^I + Y_f^I},$$

$$\beta_2 = \frac{h - h_{ox}^I + Y_f Q / \alpha}{(Y_f^I / \alpha) Q + h_f^I - h_{ox}^I},$$

where h is enthalpy, Q is heat release per unit mass of oxygen consumed, $\alpha = \nu_f M_f / \nu_{ox} M_{ox}$, where ν is stoichiometric coefficient and M is the molecular weight, the subscripts f and ox refer to fuel and oxidizer (with diluent accounted for in the enthalpy), the superscript I refers to burner inlet conditions. A flame sheet exists at the locations where $\beta_1 = Y_f^I / (\alpha Y_{ox}^I + Y_f^I)$. The analytical model for the jet diffusion flame under discussion here consists of Eqs. 1-4 along with appropriate boundary conditions.

This analytical model is solved numerically by means of a modified version of the finite difference scheme employed previously by Davis and

Moore [9] to simulate cold mixing layer dynamics. This scheme utilizes a variably-spaced staggered mesh in which pressures are defined at cell centers and normal velocities at cell faces. Quadratic upwind differencing is used for convection, and an explicit Leith-type of temporal differencing is employed. At each time step ($\Delta t = 2.5 \times 10^{-3}$), a Poisson equation for perturbation pressure is solved by a direct method. Variable thermophysical properties are calculated as described by Mitchell [10], and no turbulence or radiation models are employed. Species binary diffusion is taken as fuel into nitrogen inside the flame and oxygen into nitrogen outside. All relevant variables are specified at the burner inlet ($z = 0$), axisymmetry is enforced along the burner centerline, and zero or constant gradients are employed at very large axial and radial distances (i.e., no shroud). Mesh dimensions are 5000 fuel jet radii axially (145 mesh cells) and 50 radially (84 cells), both attained by employing rapidly expanding mesh cell sizes away from the flame. The smallest axial grid spacings (0.2) are employed in the initial mixing region at the base of the flame, while the smallest radial grid spacings (0.05) are employed for $r \leq 1.5$. In some cases, dynamic mesh rezonings have been utilized in order to maximize the number of grid cells inside the flame at any given time. Run times on the NIST CYBER 205 are typically several hours, with initial solution fields obtained by means of a steady-state flame simulation [11]. After awhile, flame flickering commences in the unsteady computation without the triggering required in the cold jet case [9].

EXPERIMENTAL

The experimental setup [5, 7] consists of a round central jet with a 22.5 mm diameter surrounded by an annular coflow with a 254 mm diameter. The velocities of the central and annular jets are 10 and 15 cm/s, respectively. This low-velocity flame is very susceptible to room air disturbances. Screens placed around the burner do a reasonably good job of shielding the flame from outside disturbances; however, some asymmetry

in the flame is noted. The fuel for the central jet is propane diluted with 50% by mass of nitrogen.

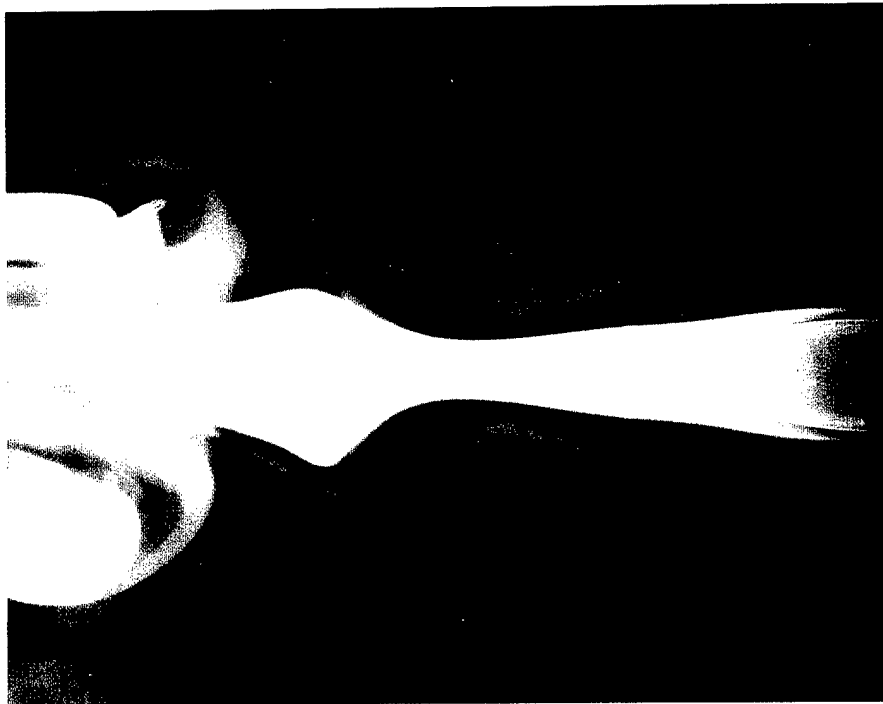
The RMS technique [7] is used to visualize the mixing of the fuel and products inside the flame surface and the air and products outside the flame surface. This technique involves seeding the dry fuel and air with TiCl_4 vapor. Regions where the water product mix with the TiCl_4 in the fuel and air are marked by the formation of micron-sized TiO_2 particles. These particles are visualized by Mie scattering observed at right angles to a sheet of laser light.

Simultaneous radial temperature profiles are measured using blackbody radiation from five 15- μm -diameter silicon carbide filaments (thin filament pyrometry). A digitized image of the intensity of the graybody radiation (spectral emissivity at a nearly constant value greater than 0.9 over the temperature range 1400–2300 K) from the five filaments and soot in the flame is recorded using a charge couple device (CCD). An approximately 10-cm by 15-cm area of the flame is recorded in a 384×576 pixel format, with each pixel being approximately 25 μm in diameter. The imaging system has a spatial resolution of about 274 μm per pixel, and the filaments are located axially about every 30 mm. Soot emissions obtained from background intensity measurements near a filament are subtracted from the graybody radiation of that filament. The filaments were calibrated in place using a hydrogen flame where the peak intensity along a filament was assumed to correspond to the stoichiometric flame temperature minus the temperature associated with the radiation loss from the flame. The intensity data for the propane flame after soot background subtraction are scaled by the known hydrogen flame temperature and converted to temperature data by using Planck's equation and the convolution of the detector response as a function of wavelength. It is feasible to subtract the soot background from the total intensity of a filament because the filament is a more effective radiator than soot particles for an optically thin flame. Also, since soot formation is a relatively low-temperature process, the intense sooting zone and the high-temperature zone where the filament intensity is highest do not coincide. Errors associ-

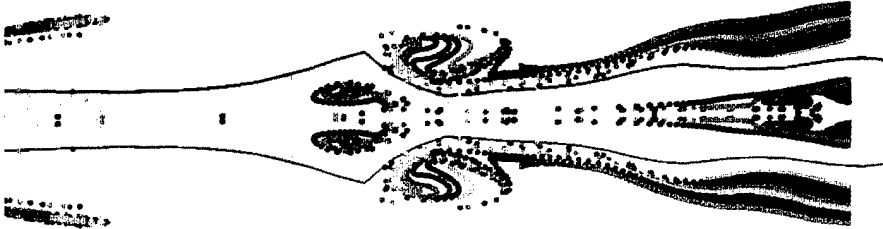
ated with the temperature measurements are expected to be less at the peak temperature and will increase as the temperature decreases. Precisions (8% at 1000 K and 0.3% at 2370 K) comparable to those obtained for hydrogen-air diffusion flames in Ref. 12 are expected for the present measurements because the high temperature zone is usually located outside the luminous sooting area. Good estimates of the errors associated with the temperature measurements inside the luminous sooting surface have not been obtained. Only temperatures greater than about 1400 K are measured in these experiments. The details of the thin filament pyrometry technique are described elsewhere [12].

RESULTS AND DISCUSSION

Computations of the aforementioned jet diffusion flame have been carried out with $\text{Re} = 112$, $\text{Ri} = 4.9$, and $\text{Pe} = 156$. In the absence of experimental data, slug flow velocity profiles have been assumed at the burner inlet. Computations assuming the opposite extreme (a fully developed parabolic fuel jet profile) yield virtually identical results. This is due to the buoyancy-dominated nature of this low-speed flame, where the initial velocity profiles are rapidly distorted by the large buoyant acceleration. Figure 1 shows both a visualization of the computed flame and an experimental view as obtained by the RMS technique. Both the theoretical and experimental visualization techniques provide a streak-line representation (snapshot) of the flow field at one instant of time. The flame is not intentionally forced either experimentally or computationally. The computational flow field is illuminated via multicolored passive marker particles, with the solid red line representing the flame sheet. Experimentally, the shape of the sooting surface is believed to be a reasonable representation of the shape of the flame surface [13] and, as can be seen, the shape of the computed laminar flame is very similar to that of the observed sooting surface. The shapes of the large outer-vortex structures are also very well reproduced computationally. Even the counter rotating vortices located in the flame bulge are predicted. Another interesting feature of the ex-



EXPERIMENTAL FLOW VISUALIZATION



COMPUTATIONAL STREAKLINE PLOT

Fig. 1. Experimental and computational visualizations of jet diffusion flame.

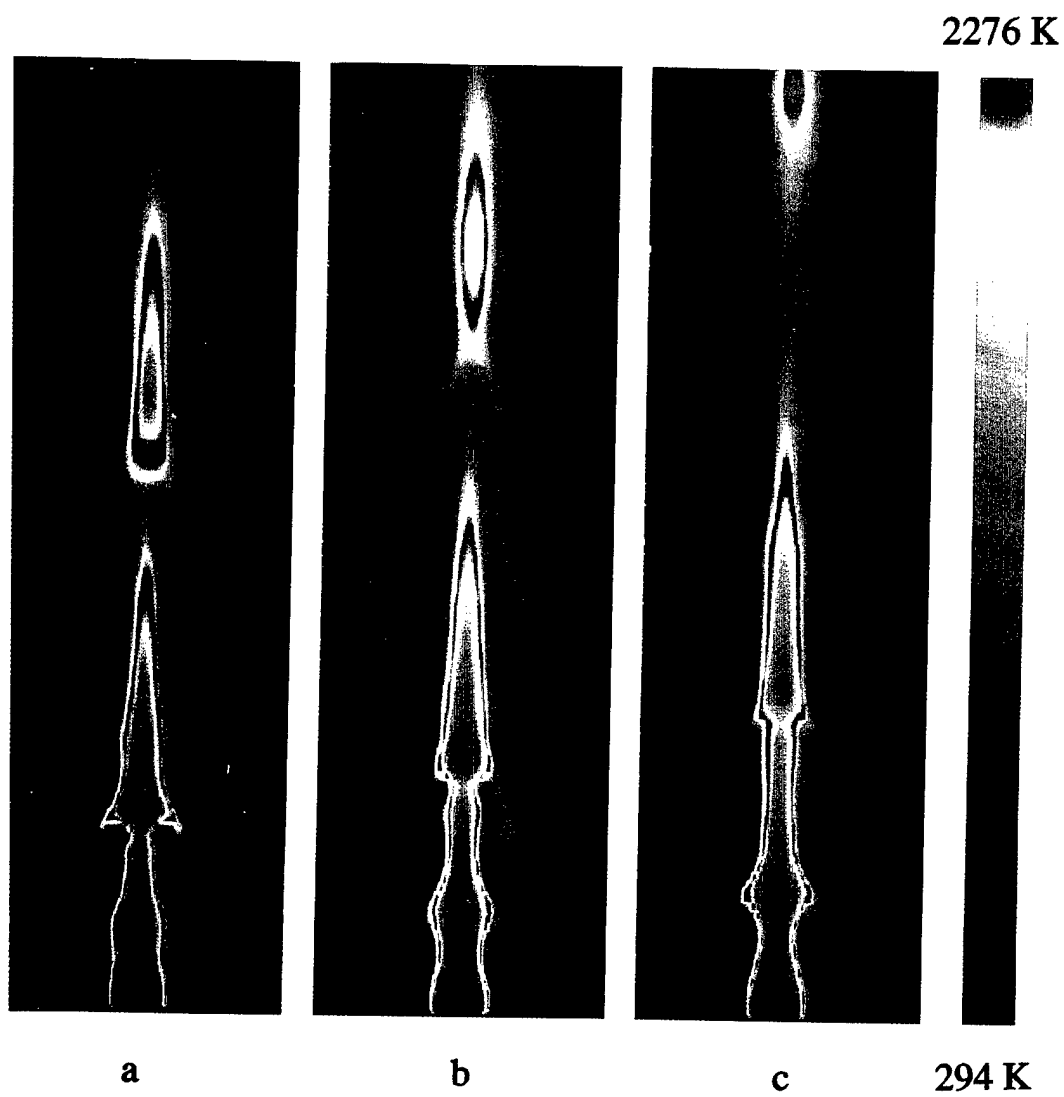


Fig. 2. Computed isotherms for three times (a-c) 18.8 ms apart. The red contour represents the flame surface.

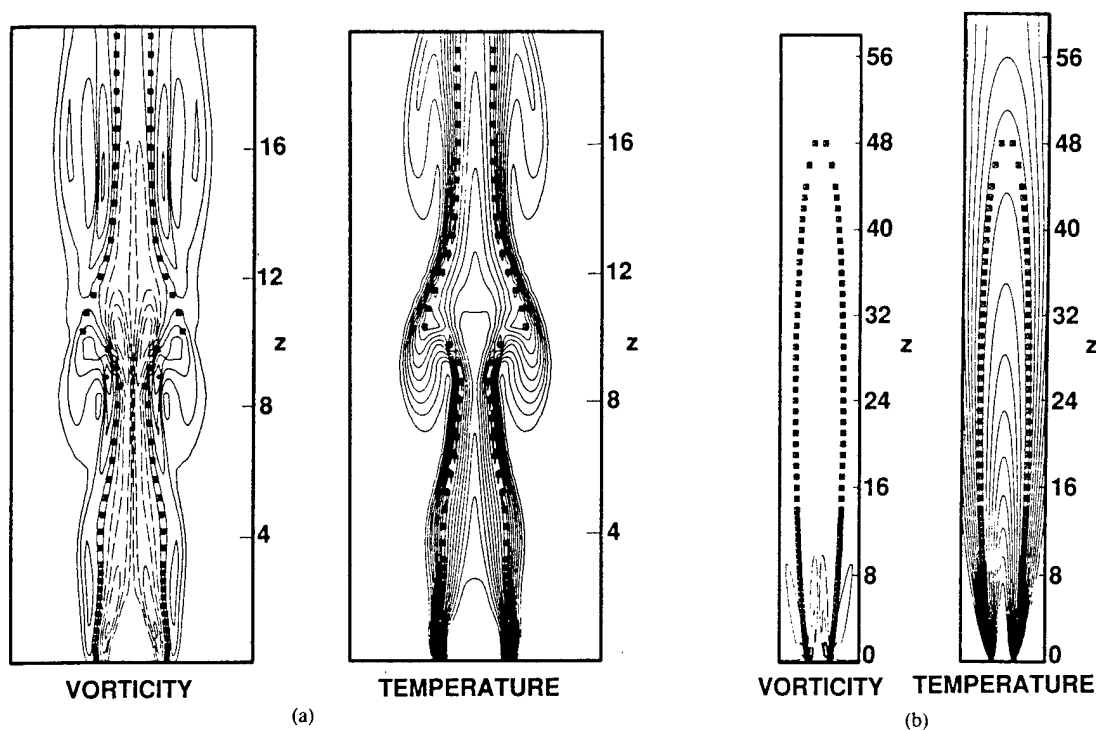


Fig. 3. Computed vorticity and temperature contours in jet diffusion flame, with squares denoting the flame sheet. (a) Normal gravity. (b) Zero gravity.

perimental flame is the location of a stationary recirculation zone in the potential core of the jet flame [7]. This recirculation exists because of negative buoyancy effects, i.e., propane is denser than air. The computation also predicts this stationary recirculation zone. Thus, it is evident from Fig. 1 that the model is able to qualitatively predict the important dynamic features of this rather complex flame.

The large vortex structures outside the flame surface have been known for many years [14], but their impact on the dynamic characteristics of the flame has only recently been recognized [5, 15, 16]. These structures' dynamic importance is apparent from Fig. 2, which presents computed isotherms (with a red flame surface) for three different times. The large outer structures (in blue) are clearly identified, as is the separation of the tip (flickering) from the main body of the flame, an effect that is apparently associated with the motion of these large vortices. The predicted dominant frequency range of 11–15 Hz (as com-

puted over numerous flickering cycles) compares well with the experimentally determined range of 12 to 14 Hz for this jet flame. Buckmaster and Peters [15] postulated that flame flicker is the result of a buoyancy induced Kelvin-Helmholtz type of instability. Their analysis of an idealized infinite candle flame resulted in a flicker frequency of 17 Hz. The impact of buoyancy on the flame is shown in Fig. 3, where in one case gravity is included in the calculation and in the other case the gravitational constant is set equal to zero. The zero-gravity case results in a long steady flame with no moving vortex structures, thus implying that buoyancy is the dominant force in jet diffusion flame dynamics. The delineation of the large outer vortices by both the isovorticity lines and the isotherms can be seen in Fig. 3a.

Figure 4 presents near-instantaneous radial temperature profiles and snapshots to about the same scale of the computed and measured flame visualizations. Figure 4a shows the digitized image of the sooting flame surface with background

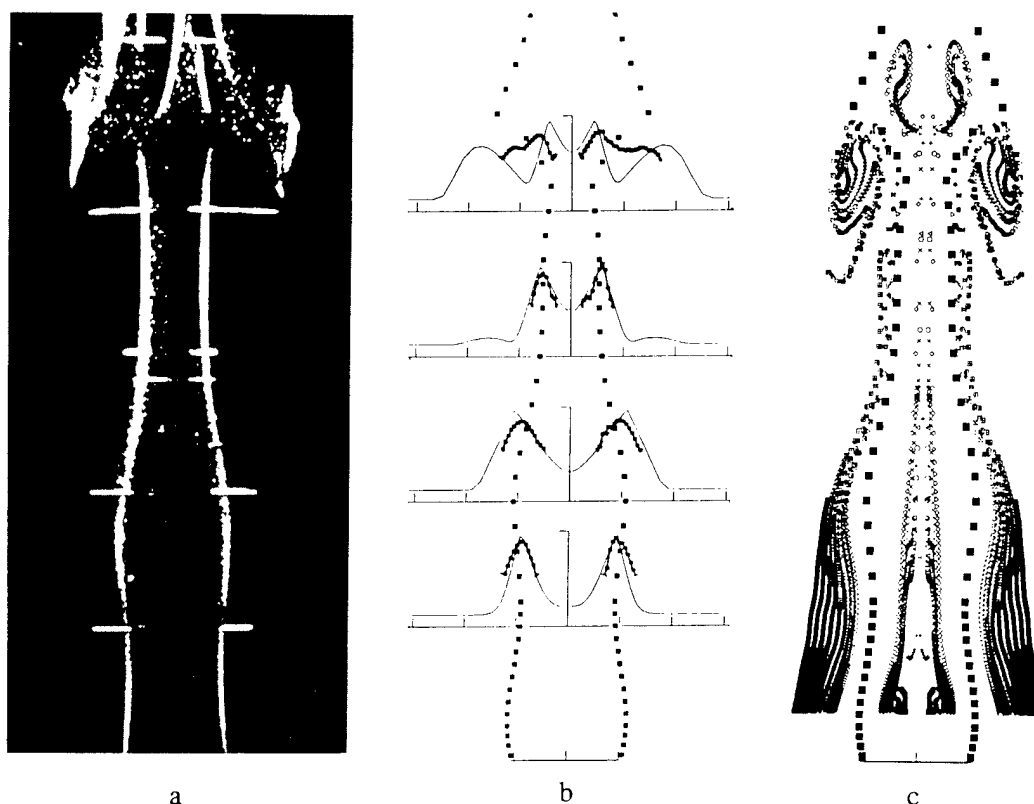


Fig. 4. Experimental/computational temperature comparison. (a) Digitized image of sooting flame. (b) Near-instantaneous experimental (dotted curves) and computational (solid curves) radial temperature profiles. (c) Computational streakline plot at same phase as digitized image.

subtraction along with the SiC filaments at four different axial locations. In Fig. 4b, the near-instantaneous temperature profiles measured by the SiC filaments and those calculated by the model at about the same phase are overlaid on the calculated flame surface plot, with this surface being represented by solid squares. The filament-measured temperature profiles have a lower cutoff temperature of about 1400 K, and the temperature scale is from 0 to 2350 K. The axial locations of the calculated and measured temperatures agree to within a few millimeters. Figure 4c is a computational streakline snapshot of the flame from which the calculated radial temperature profiles in Fig. 4b were obtained. Note that the sooting surface in Fig. 4a has about

the same shape as the flame surface represented by the solid squares in Fig. 4c.

As just noted, the phase of the experimental flame was chosen so that the shapes of the experimental and theoretical flame surfaces were about the same, thus matching peak temperature locations radially. This method of comparison could give misleading results because it has not been determined how well the experimental and theoretical flame shapes actually correlate throughout their respective flickering cycles. As can be seen, the agreement between the measured and calculated temperature profiles in Fig. 4b is quite good. This is illustrated by comparing the width of the temperature profiles at different axial locations. Both the predicted and measured widths of

the profiles nearest the jet exit are narrow. At the next higher axial location, the profiles become broader as the flame starts to bulge outward. In the contraction region at the next higher filament location (third filament up) they are narrow again. Double peaks are noted just below the large flame bulge at the highest filament location, with the predicted peaks more pronounced than the measured ones. The predictions and the measurements agree, however, that the outer peak is much broader than the inner one. This is believed to be due to the entrainment of hot gases into the large outer vortex shown in Fig. 4c. Examination of the RMS visualizations (not shown) indicates that three-dimensional effects are beginning to set in at this location. These effects may be at least partially responsible for the differences in the predicted and measured widths of the double temperature peaks. The transition to a fully three-dimensional flow at greater heights is currently under study experimentally.

The compressed temperature scale in Fig. 4b does not give a highly accurate comparison between the calculated and measured temperatures. In general the peak measured temperatures are 5%–15% lower than the calculated adiabatic flame-sheet temperature. A radiative temperature loss of about 10%, which is unaccounted for in the model, is not unreasonable for this sooting flame.

The higher predicted flame temperatures, and thus buoyant accelerations, may account for another observed difference between the model and the experimental results. A comparison of numerous snapshots of predicted and RMS-measured flame shapes shows that the calculated flow develops faster than the observed flow. The axial location of the calculated recirculation zone just above the fuel jet exit is usually closer to the nozzle than is observed experimentally. Likewise, the outer vortex structures, and consequently the flame bulge with its inner counter-rotating vortices, are predicted to form closer to the nozzle than indicated by experiment. Consistent with this reasoning, computational experiments in which the flame temperature is lowered by about 10% show a slight retardation in flow field development.

CONCLUSIONS

A direct numerical simulation of an axisymmetric, low-speed propane–air jet diffusion flame has been performed. The computational results have been compared with the results of an experimental investigation of the same flame. The computations have been shown to predict the correct qualitative features of the dynamic vortex structures observed both inside and outside the flame surface as well as the stationary recirculation zone seen in the potential core of the fuel jet. The model and experiment also closely agree regarding the dominant flame flicker frequency range. Comparisons of computational and experimental near-instantaneous radial temperature profiles at four heights in the flame have shown good agreement. The predictions show that both flame flicker and double-peaked temperature profiles are closely associated with buoyancy-induced vortices outside the flame surface. The model, however, predicts a faster development of the inner and outer vortex structures than is observed experimentally. This is believed to be due, at least in part, to the fact that the predicted flame sheet temperature is higher than that in the actual flame where radiative heat losses occur. Finally, important three-dimensional effects have been observed to eventually appear as the flame bulges and vortex structures move upward, thus rendering the axisymmetric model inadequate at large heights in the flame. It is clear that additional experimental–numerical comparisons of instantaneous results are needed over entire flickering cycles before the model's region of validity can be firmly established for this buoyant propane–air jet diffusion flame.

REFERENCES

1. Burke, S. P., and Schumann, T. E. W., *Ind. Eng. Chem.* 29:998 (1928).
2. Bilger, R. W., in *Annual Review of Fluid Mechanics* (J. L. Lumley, M. van Dyke, and H. L. Reed, Eds.), Annual Reviews, Palo Alto, CA, 1989, Vol. 21, p. 101.
3. Yule, A. J., Chigier, N. A., Ralph, S., Boulderstone, R., and Ventura, J., *AIAA J.* 19:752 (1981).
4. Eickhoff, H., and Winandy, A., *Combust. Flame* 60:99 (1985).
5. Roquemore, W. M., Chen, L.-D., Goss, L. P., and

- Lynn, W. F., in *Turbulent Reactive Flows, Lecture Notes in Engineering* (R. Borghi and S. N. B. Murthy, Eds.), Springer-Verlag, Berlin, 1989, Vol. 40, p. 49.
6. Takahashi, F., Mizomoto, M., and Ikai, S., *J. Heat Transf.* 110:182 (1988).
 7. Chen, L.-D., and Roquemore, W. M., *Combust. Flame* 66:81 (1986).
 8. Rehm, R. G., and Baum, H. R., *J. Res. Natl. Bur. Std.* 83:297 (1978).
 9. Davis, R. W., and Moore, E. F., *Phys. Fluids* 28:1626 (1985).
 10. Mitchell, R. E., Sandia National Laboratories Report SAND 79-8236, 1980.
 11. Davis, R. W., and Moore, E. F., Paper 15, Eastern Section of the Combustion Institute, Fall Meeting, 1987.
 12. Vilimpoc, V., and Goss, L. P., *Twenty-Second Symposium (International) on Combustion*, The Combustion Institute, Pittsburgh, 1988, p. 1907.
 13. Miake-lye, R. C., and Toner, S. J., *Combust. Flame* 67:9 (1987).
 14. Wohl, K., Kapp, N. M., and Gazley, C., *Third Symposium (International) on Combustion*, The Combustion Institute, Pittsburgh, 1949, p. 3.
 15. Buckmaster, J., and Peters, N., *Twenty-First Symposium (International) on Combustion*, The Combustion Institute, Pittsburgh, 1986, p. 1829.
 16. Chen, L.-D., Seaba, J. P., Roquemore, W. M., and Goss, L. P., *Twenty-Second Symposium (International) on Combustion*, The Combustion Institute, Pittsburgh, 1988, p. 677.

Received 12 May 1989; revised 7 February 1990

A Numerical/Experimental Study of the Dynamic Structure of a Buoyant Jet Diffusion Flame

R.W. Davis and E.F. Moore

Chemical Science and Technology Laboratory,
National Institute of Standards and Technology,
Gaithersburg, MD 20899, U.S.A.

L.-D. Chen

Department of Mechanical Engineering, The University of Iowa,
Iowa City, IA 52242, U.S.A.

W.M. Roquemore

Wright Research and Development Center, Aero Propulsion and Power Laboratory,
Wright-Patterson Air Force Base, OH 45433-6563, U.S.A.

V. Vilimpoc and L.P. Goss

Systems Research Laboratories, Inc., Division of Arvin/Calspan,
Dayton, OH 45440-3696, U.S.A.

Communicated by Ashwani Kapila

Received 24 January 1993 and accepted 5 September 1993

Abstract. An overview of a joint numerical/experimental investigation of the dynamic structure of a low-speed buoyant jet diffusion flame is presented. The dynamic interactions between the flame surface and the surrounding fluid mechanical structures are studied by means of a direct numerical simulation closely coordinated with experiments. The numerical simulation employs the full compressible axisymmetric Navier–Stokes equations coupled with a flame sheet model. Counterrotating vortex structures both internal and external to the flame surface are seen to move upward along with flame sheet bulges. These buoyancy-driven dynamic features compare well with those observed experimentally by means of phase-locked flow visualizations over entire flame-flickering cycles. The flicker frequencies measured both computationally and experimentally also compare well. Other aspects of this investigation which are discussed include sudden jumps in flicker frequency with increasing coflow velocity and the utilization of background pressure changes to simulate gravitational force variations experimentally.

1. Introduction

Jet diffusion flames have been frequently studied as an analog for more complex combustions flows ever since the original development of the basic theory by Burke and Schumann (1928). This is because, although geometrically simple, these flames exhibit many of the features found in more complex physical systems. In particular, the dynamic interactions of the flame surface with the

surrounding flow structures are of great importance in many practical applications such as furnaces and combustors. The dynamic interactions occurring in jet diffusion flames have been the subject of numerous experimental investigations (e.g., Yule *et al.*, 1981; Eickhoff and Winandy, 1985; Strawa and Cantwell, 1985; Vandsburger *et al.*, 1988; Chen *et al.*, 1988; Lovett and Turns, 1990). Additionally, recent advances in both computer power and numerical techniques have now made possible the direct numerical simulation of many of these same interactions (Hosangadi *et al.*, 1990; Mahalingam *et al.*, 1990; Davis *et al.*, 1991; Ellzey *et al.*, 1991; Chen *et al.*, 1992). Note that these dynamic flame simulations are distinctly different from numerical models for steady jet diffusion flames (Mitchell *et al.*, 1980; Smooke *et al.*, 1989). The steady flame models are able to simulate more sophisticated chemical reaction mechanisms but are only applicable over a narrow range of operating conditions where transient phenomena, such as flame flicker, do not occur.

Despite the recent addition of numerical modeling to the arsenal of tools available for investigating the dynamic features of jet diffusion flames, the real advance in research productivity has yet to be achieved. This advance, which is the subject of this paper, is to join both direct numerical simulation and experimentation into a single unified effort to understand at least some aspects of these complex unsteady reacting flows. The first step toward this goal is a closely knit numerical/experimental investigation to assess computational predictions both qualitatively and, as much as possible, quantitatively. It is the purpose of this paper to provide an overview of such a joint numerical/experimental investigation involving a low-speed buoyant jet diffusion flame.

The configuration under investigation here is a low-speed coflowing propane/air jet diffusion flame in an unconfined environment. The operational parameters were chosen so as to produce a highly repeatable flame-flickering cycle amenable to phase-locked experimental measurements. Because of the low speeds involved, turbulence is not a factor here, and there are many distinctive large-scale features available for numerical/experimental comparisons. As will be seen, these comparisons are made over entire flickering cycles in order to provide as comprehensive an assessment as possible of the computational results.

2. Numerical Model

The nondimensional continuity, momentum, and state equations for the unsteady axisymmetric flow of a multicomponent fuel jet surrounded by a coflowing airstream are

$$\frac{\partial \rho}{\partial t} + \nabla \cdot (\rho \mathbf{q}) = 0, \quad (1)$$

$$\rho \frac{\partial \mathbf{q}}{\partial t} + \rho (\mathbf{q} \cdot \nabla) \mathbf{q} = -\nabla \bar{p} - \rho Ri \hat{\mathbf{e}}_z + \frac{1}{Re} \left\{ -\nabla x (\nabla x \mu \mathbf{q}) + \frac{4}{3} \nabla (\mu \nabla \cdot \mathbf{q}) + \nabla (\mathbf{q} \cdot \nabla \mu) - \mathbf{q} \nabla^2 \mu \right. \\ \left. + \nabla \mu x (\nabla x \mathbf{q}) - (\nabla \cdot \mathbf{q}) \nabla \mu \right\}, \quad (2)$$

$$\rho T \sum_i R_i Y_i = p_0. \quad (3)$$

Here ρ is the density, μ is the viscosity, T is the temperature, $\mathbf{q} = (v, u)$, where v and u are velocity components in an axisymmetric reference frame (r, z) , Y_i is the mass fraction of species i with gas constant R_i , and $\hat{\mathbf{e}}_z$ is the unit normal in the axial direction. The pressure consists of a constant background pressure, p_0 , plus a perturbation pressure, $\bar{p}(r, z, t)$, where $p_0 \gg \bar{p}$. As discussed by Rehm and Baum (1978), the omission of \bar{p} from (3) is entirely appropriate here, resulting in the suppression of acoustic waves while admitting the low-frequency motions due to buoyant effects. This type of filtering is applicable because the time scale associated with these buoyant motions is much larger than the time scale required for acoustic signals to equilibrate the flowfield pressure. This would not be the case, for instance, at Mach numbers approaching unity. All quantities in (1)–(3) have been nondimensionalized with respect to conditions in the coaxial airstream at the burner inlet. Thus $Re = \text{Reynolds number} = U_0 L / \nu_0$ and $Ri = \text{Richardson number} = g L / U_0^2$, where U_0 and ν_0 are the

entering airstream velocity and kinematic viscosity, L is the fuel jet radius, and g is the gravitational acceleration.

In order to reduce the complexity of the problem while still providing a good approximation to the physical situation, a flame sheet model (infinite rate kinetics) is employed here. In addition, the Lewis number (ratio of thermal to species diffusivities) is assumed to be unity. Therefore, conserved variables, β_i , for species mass fractions and enthalpy can be utilized. These obey the simple nondimensional convection-diffusion equation

$$\frac{\partial(\rho\beta_i)}{\partial t} + \nabla \cdot (\rho\mathbf{q}\beta_i) = \frac{1}{Pe} \nabla \cdot (\rho D \nabla \beta_i), \quad (4)$$

where D is the binary diffusion coefficient and $Pe = \text{Peclet number} = U_0 L / D_f$, with D_f taken as the diffusion coefficient of fuel into nitrogen at the burner inlet. The conserved variables are defined as

$$\beta_1 = \frac{\alpha(Y_{0x}^I - Y_{0x}) + Y_f}{\alpha Y_{0x}^I + Y_f^I},$$

$$\beta_2 = \frac{h - h_{0x}^I + (Y_f Q / \alpha)}{(Y_f^I / \alpha) Q + h_f^I - h_{0x}^I}.$$

Here h is the enthalpy, Q is the heat release per unit mass of oxygen consumed, $\alpha = v_f M_f / v_{0x} M_{0x}$, where v is the stoichiometric coefficient and M is the molecular weight, the subscripts f and $0x$ refer to fuel and oxidizer (with nitrogen accounted for in the enthalpy), and the superscript I refers to the burner inlet conditions. The analytical model for the jet diffusion flame under discussion here consists of (1)–(4) along with appropriate boundary conditions. A flame sheet exists at locations where $\beta_1 = \alpha Y_{0x}^I / (\alpha Y_{0x}^I + Y_f^I)$. The mass fraction of the nitrogen diluent is simply $Y_{N_2} = \beta_1 (Y_{N_2}^{FI} - Y_{N_2}^{OXI}) + Y_{N_2}^{OXI}$, where the superscripts FI and OXI refer to burner inlet values in the fuel and oxidizer streams, respectively. Finally, the product mass fractions are $Y_w = \gamma Y_c$ and $Y_c = (1 - Y_f - Y_{0x} - Y_{N_2}) / (1 + \gamma)$, where $\gamma = v_w M_w / v_c M_c$ and the subscripts w and c refer to water and CO_2 , respectively.

The analytical model described above is solved by means of the QUICKEST finite-difference scheme (Leonard, 1979; Davis and Moore, 1982, 1985; Davis, 1984). This scheme employs a variably spaced staggered mesh in which all variables except velocities are defined at cell centers and normal velocities are specified at cell faces. Quadratic upwind differencing is used for convection, and an explicit Leith-type of temporal differencing is employed. At each time step, a Poisson equation for the perturbation pressure is solved by a direct method utilizing the FISHPAK package of FORTRAN subprograms for the solution of separable elliptic partial differential equations (Swarztrauber and Sweet, 1975). Variable thermophysical properties (viscosities, binary diffusion coefficients, and specific heats) are calculated as described by Mitchell (1980), and no turbulence or radiation models are employed. Species binary diffusion is taken as fuel into nitrogen inside the flame and oxygen into nitrogen outside.

The computational procedure at each time step begins with the explicit solution of (4) utilizing a linear extrapolation in time of the density from the previous time step. One solution pass provides values of both β_1 and β_2 since both have identical boundary conditions (as will be discussed) and thus $\beta_1 = \beta_2 = \beta$. The relationship between β_2 and temperature is calculated prior to the initiation of time stepping, thus enabling temperatures at each time step to be obtained from simple interpolations. This allows computation of densities from (3) following determination of species mass fractions from values of β_1 . Equations (2) are solved next, with the solution of the Poisson equation for perturbation pressure ensuring that (1) is satisfied. This is accomplished by first solving the momentum equations in conservation form without pressure gradient terms for an intermediate value $(\rho\mathbf{q})^*$. The final velocity field at time step $(N + 1)$ is then obtained from

$$\frac{(\rho\mathbf{q})^{N+1} - (\rho\mathbf{q})^*}{\Delta t} = -\delta \tilde{p}^{N+1}, \quad (5)$$

$$\delta^2 \tilde{p}^{N+1} = \frac{-\delta \cdot (\rho\mathbf{q})^{N+1} + \delta \cdot (\rho\mathbf{q})^*}{\Delta t} = \frac{((\rho^{N+1} - \rho^N) / \Delta t) + \delta \cdot (\rho\mathbf{q})^*}{\Delta t}, \quad (6)$$

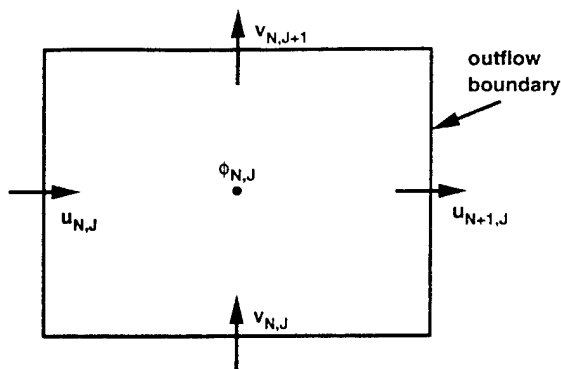


Figure 1. Detail of mesh cell adjacent to outflow boundary.

where δ and δ^2 are central difference approximations to ∇ and ∇^2 , and it is assumed that

$$\delta \cdot (\rho q)^{N+1} = - \left(\frac{\rho^{N+2} - \rho^{N+1}}{\Delta t} \right) = - \left(\frac{\rho^{N+1} - \rho^N}{\Delta t} \right) \quad (7)$$

from (1). The calculation of \bar{p}^{N+1} from (6) followed by the determination of q^{N+1} from (5) completes the solution at time step $(N + 1)$. The boundary conditions employed here are now discussed.

All relevant variables are specified at the burner inlet ($z = 0$); axisymmetry is enforced along the burner centerline; and constant normal gradients (thus allowing inflow) are specified at a large radial distance from the centerline. In order to provide sufficient oxidizer flow for entrainment into the flame, the inlet coflow velocity is doubled for $r > 6$. Note that this is a negligible increase compared with the order of magnitude buoyancy-induced increases in axial velocity occurring near the flame surface. The value of β at the burner inlet is unity inside the fuel stream and zero outside. The boundary conditions employed downstream of the flame are more complex and are described next.

In early versions of the simulation, greatly expanding axial mesh spacings were employed far downstream of the flame. All temperatures were set to 293 K (the inlet value) at axial distances greater than about ten flame heights. This effectively eliminated buoyancy effects and allowed the imposition of zero axial gradients at the mesh exit. However, this procedure was computationally inefficient. Thus, later versions of the model employ a set of continuative outflow conditions which enable the mesh exit to be placed virtually anywhere, even through the flame itself. These outflow conditions are now discussed.

Figure 1 shows a typical grid cell in the final downstream column of the mesh. The outflow boundary is coincident with the right face of this cell, where the computation requires an estimate of $\varphi = (\rho, \beta, \text{etc.})$. This is determined by specifying φ at this face to equal $\varphi_{N,J}$ at the previous time step. The axial velocity at this face, $u_{N+1,J}$, is determined from applying continuity (equation (1)) within the cell, whereas velocities at all other cell faces are computed similarly to $\varphi_{N,J}$. The values of φ at all other cell faces are calculated using simple first-order upwinding as opposed to the quadratic upwinding used elsewhere in the mesh. Although other computational outflow schemes could obviously be applied here, the one just described reliably allows the flow to exit the mesh with no noticeable disturbance.

The mesh employed in the early versions of this simulation noted above contained 145 cells axially and 84 cells radially. Rapid cell expansion with axial distance allowed the outflow boundary to be placed at $z = 5000$; similarly the outer radial boundary was at $r = 50$. In the later versions of the model, a computation usually only covered the lower portion of the flame, typically $z < 10$ or 20. An example of the mesh for this latter case is shown in Figure 2 for $r < 10$, with alternate radial grid lines removed for clarity. This mesh is approximately twice as fine in the region shown as the earlier (145×84) mesh described above. However, there are no significant differences in the large-scale flame features, such as flicker frequency, as calculated on the two meshes. Over the course of this investigation, computations have been carried out on the NIST CYBER 205 and then on its replacement, a CRAY Y-MP. The FORTRAN code is highly vectorized and runs at an average speed of 150 MFLOPS on the latter machine. Typically, 50–60 flickering cycles (at 10–15 Hz) can be computed

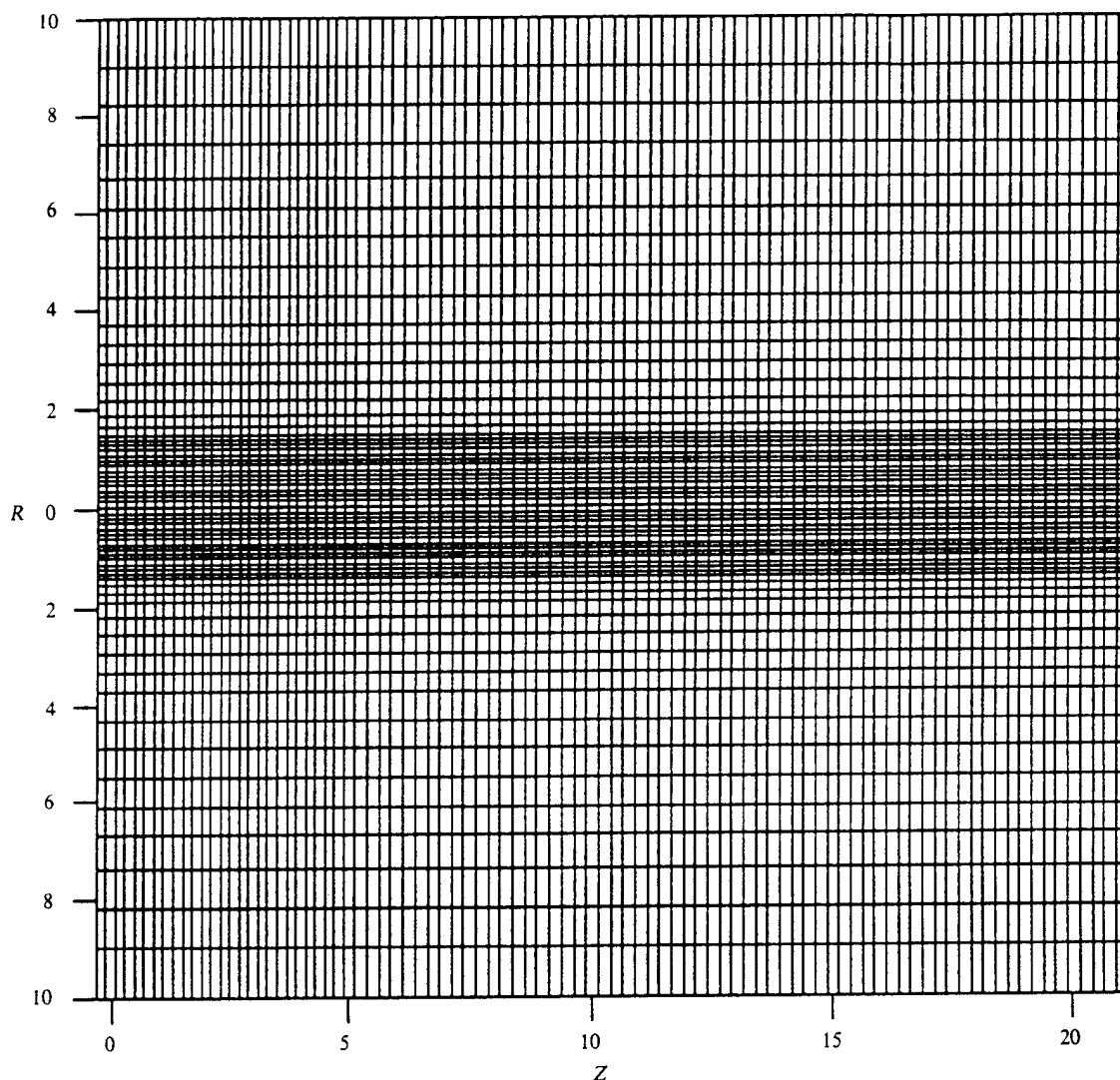


Figure 2. 92 axial \times 83 radial mesh for computation of lower flame region; alternate radial grid lines removed.

per cpu hour on the CRAY Y-MP, with no artificial triggering necessary to initiate this flickering behavior.

3. Experimental Technique

The experimental technique is discussed in Davis *et al.* (1991) and Chen *et al.* (1992) and, thus, is only briefly described here. A vertically mounted 23-mm diameter fuel tube is surrounded by a 254-mm diameter annular air stream. The fuel is propane with 50% by mass nitrogen diluent. The fuel and air burner inlet velocities are 6.4 and 18 cm/s, respectively, since these conditions produce a reasonably axisymmetric flame with a highly repeatable flickering cycle. The Reynolds number, Richardson number, and Peclet number for this case are $Re = 137$, $Ri = 3.48$, and $Pe = 191$.

The Reactive Mie Scattering (RMS) technique is used for visualization of the flame structure. This technique involves seeding the fuel and dry air with $TiCl_4$ vapor which reacts with the water vapor combustion products to form micron-sized TiO_2 particles. These particles are visualized by the Mie scattering from a laser sheet formed via a pulsed Nd:YAG laser. Phase-locked images of the flame are then recorded by a CCD camera. The camera is triggered by the motion of the flame determined from

the deflection of an He-Ne laser beam at a height (74 mm) where oscillations are first evident. These images are obtained at seven 10-ms intervals corresponding to phase angles of 0° , 50° , 101° , 151° , 202° , 252° , and 302° based on the measured flicker period of 71 ms (14 Hz frequency).

4. Results and Discussion

Over the course of this investigation, computations have been carried out for the experimental conditions described in the previous section (Chen *et al.*, 1992) and for a case utilizing the same reactants and burner but with fuel and air velocities of 10 and 15 cm/s, respectively (Davis *et al.*, 1991). This latter flame exhibits very similar features to the former but its flickering cycle is not as repeatable. Figure 3 presents the vorticity field for the 10/15 cm/s flame, with the bluish regions

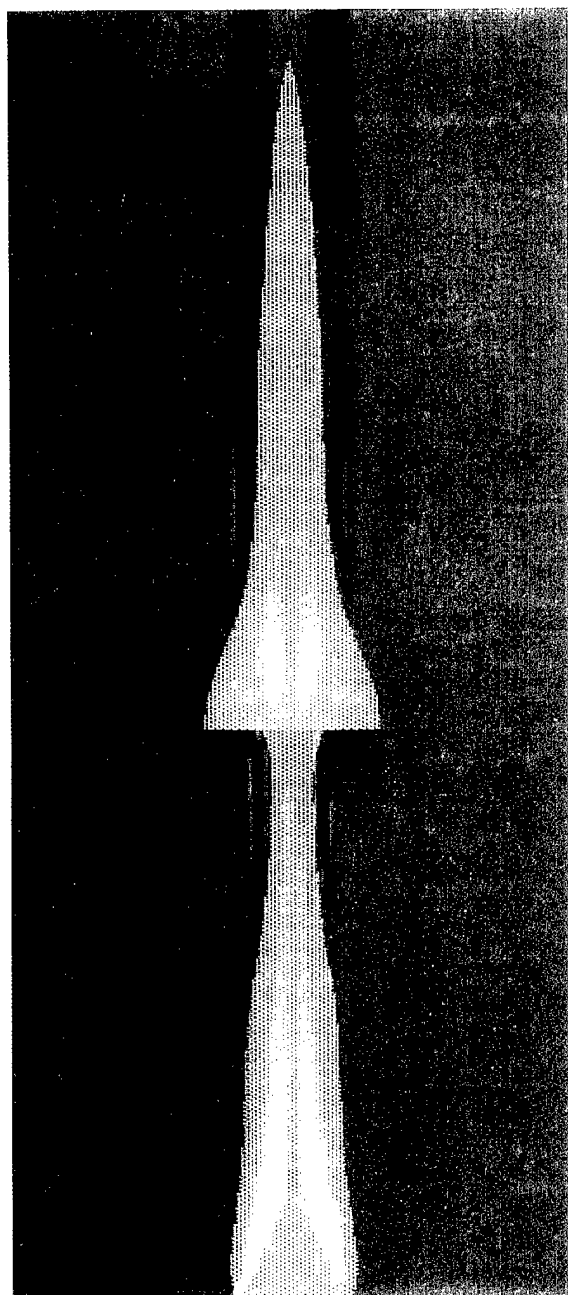


Figure 3. Vorticity field with translucent flame surface for the 10/15 cm/s diluted propane/air flame.

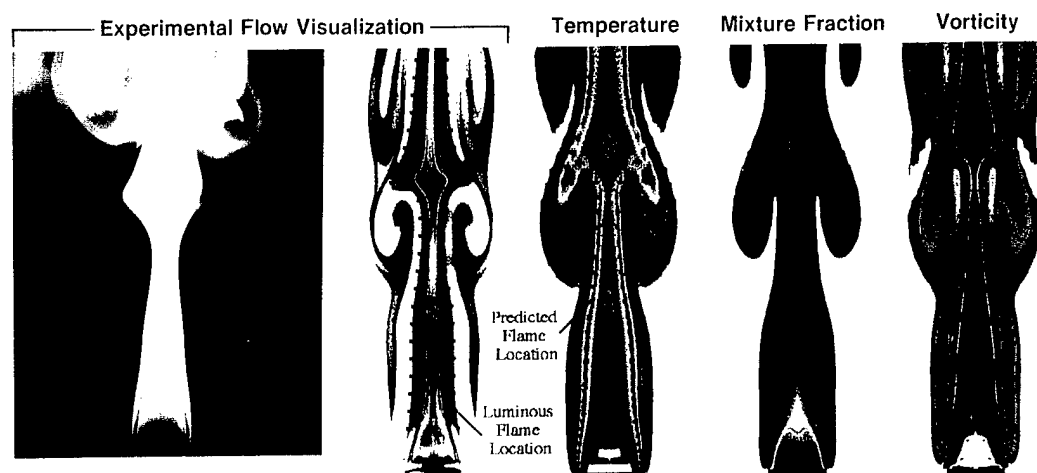


Figure 4. Various experimental and computational visualizations for the 6.4/18 cm/s diluted propane/air flame at a phase angle of 101° .

indicating the outer vortex structures and the bright yellow regions denoting the counterrotating vortices inside the translucent hatched flame surface. The prominent bulge in this surface moves rapidly upward due to buoyant acceleration and eventually detaches from the lower flame. This tip-cutting, which occurs at 11–15 Hz, is visually observed as flame flickering.

Various means of visualizing the flame structure both experimentally and computationally are presented in Figure 4 for (arbitrary) phase angle $\theta = 101^\circ$. The two experimental visualizations shown are for the two cases described above. The leftmost RMS image is for the 10/15 cm/s case, while the computer-enhanced RMS image (with false colors) to its right is for the 6.4/18 cm/s case. Despite the difference in flow conditions, each image shows a prominent flame bulge with both inner and outer vortex structures. Note also the presence of a stationary recirculation zone in the base region of both flames due to negative buoyancy effects, i.e., fuel denser than air. The three images on the right in Figure 4 are generated from numerical results for the 6.4/18 cm/s flame. The isotherm visualization (with red indicating the adiabatic flame temperature of approximately 2250 K) also contains streaklines of passive marker particles injected with the fuel stream in order to image the vortex structures inside the flame bulge. This visualization, along with the mixture fraction (conserved variable) and vorticity visualizations, all show the same features seen experimentally. These include the large outer vortex structures, the counterrotating inner vortices, the flat-based flame bulge, and the stationary recirculation zone in the base region. It becomes clear that all these features have their origin in buoyancy effects when gravity is set to zero in the computations. The result is a steady,

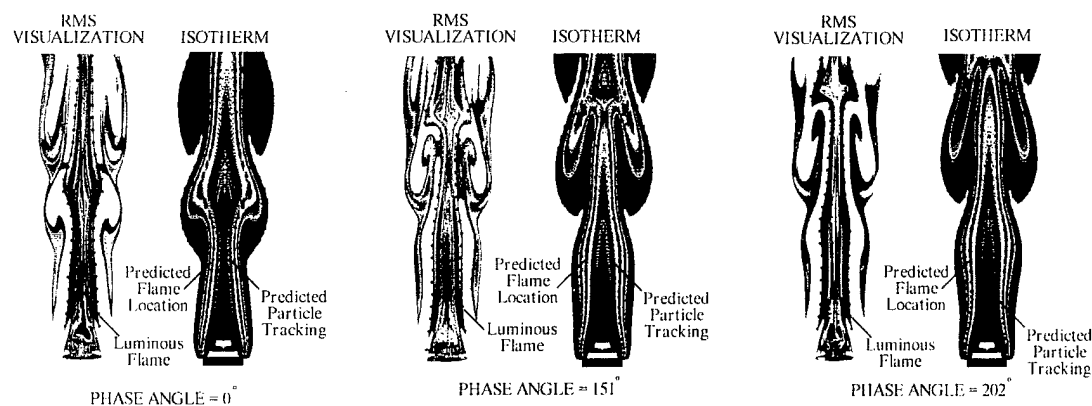


Figure 5. Experimental phase-locked RMS and computational isotherm visualizations of the 6.4/18 cm/s diluted propane/air flame at phase angles of 0° , 151° , and 202° .

almost featureless flame with no moving vortex structures (Davis *et al.*, 1991). This is in conformity with results from experimental drop tower investigations of microgravity jet diffusion flames (Bahadori *et al.*, 1990).

Figure 5 presents a comparison of phase-locked experimental (RMS) and computational (isotherm) visualizations of the time evolution of the 6.4/18 cm/s flame for three of the seven phase angles studied. The angles shown here are $\theta = 0^\circ$, 151° , and 202° , with $\theta = 101^\circ$ having been presented in Figure 4. Note that the experimental and computational flickering cycles are both highly repeatable, with frequencies of 14 Hz and 12 Hz, respectively. These cycles have been referenced to one another at $\theta = 101^\circ$, as can be seen from Figure 4. The formation and upward movement of the flame bulge can be readily traced in Figures 4 and 5, with both types of visualizations exhibiting reasonable agreement. Note from $\theta = 202^\circ$, however, that the upward velocity of the bulge is greater computationally than experimentally near the top of the flame. This is attributed to the greater buoyant acceleration in the numerical model due to the higher temperatures caused primarily by lack of radiation. It is noted that the outflow boundary conditions are not a factor in this phenomenon since the location of this boundary (either far above the flame or through its upper levels) appeared irrelevant. Also seen in Figure 5 is the axial stretching of the outer vortices due to this buoyant acceleration both experimentally and computationally. Another feature seen in this figure is that the computational flame usually appears wider than the experimental one. This is at least partially attributable to the fact that the luminous flame surface marked experimentally is slightly inside the high-temperature contour or stoichiometric surface marked computationally (Davis *et al.*, 1991). Finally, it is noted that quantitative numerical/experimental comparisons of instantaneous radial temperature profiles at ten heights in the flame have been made and show reasonable agreement (Chen *et al.*, 1992).

Another interesting aspect of this investigation has been a study of the effects on dominant flicker frequency of varying the annulus air velocity in the 6.4/18 cm/s flame. The results from both experiments and predictions are shown in Figure 6. The numerical predictions are presented for both full chemical heat release ($100\%Q$) and reduced heat release ($80\%Q$). The objective of the 20% reduction in heat release is to decrease the adiabatic flame temperature (to approximately 1900 K) as a crude means of accounting for radiative losses. The striking features seen in Figure 6 are the very

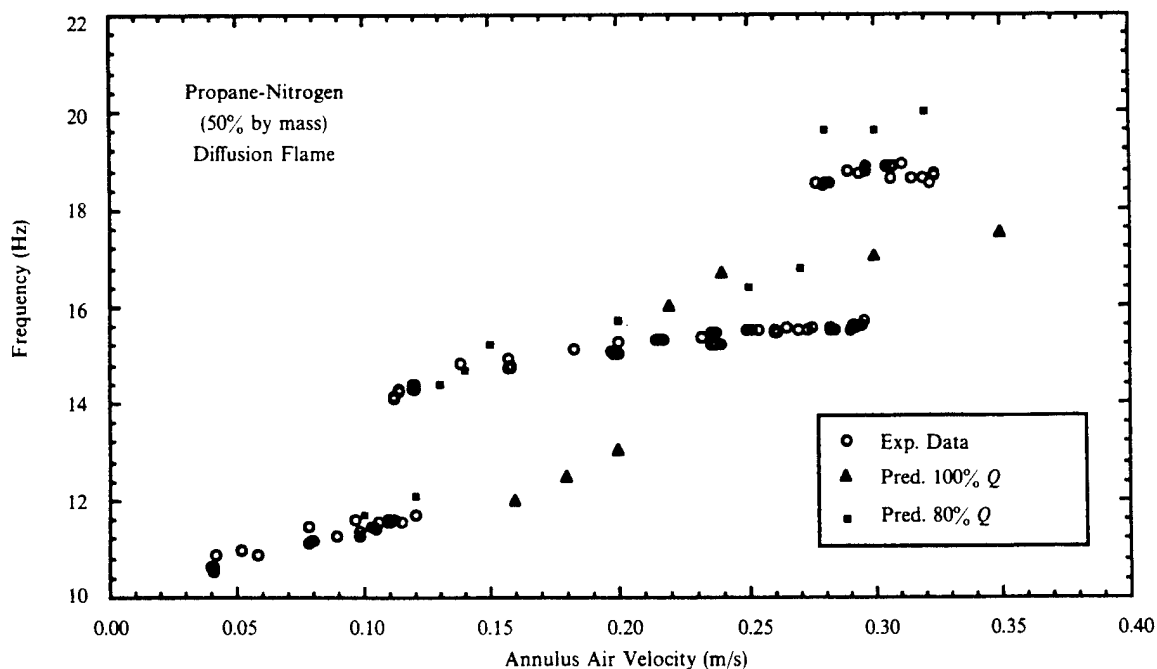


Figure 6. Dominant flicker frequency versus annulus air velocity for the diluted propane/air jet diffusion flame (from Sui *et al.*, 1991).

sudden transitions in dominant frequency both experimentally and numerically with increasing annulus air velocity. In fact, the numerical/experimental comparison is very good at 80% Q (transitions at approximately 12 cm/s and 27 cm/s), while the 100% Q predictions show only one transition at about 21 cm/s. Experimental spectra near these transitions are complex, while away from them there is only a single important frequency component (Sui *et al.*, 1991). The physical mechanism responsible for the sudden transitions is not presently understood.

Buoyancy has been seen to play a dominant role in the behavior of the low-speed jet diffusion flames under investigation here. Isolation of buoyancy effects in these flames is simple computationally (just vary the gravitational acceleration, g) but obviously difficult experimentally. However, as discussed in Davis *et al.* (1990), if the background pressure, p_0 , is varied while maintaining constant mass flows of fuel and oxidizer into the burner, the numerical model behaves as if g itself were changing. In fact, the effective gravitational acceleration acting on the simulated flame varies as p_0^2 . Experiments have indicated that this may also be true in laboratory flames, at least over some limited range of background pressure variations (Davis *et al.*, 1990). Thus, the means may now be available for isolating buoyancy effects in experimental jet diffusion flames utilizing a fairly simple procedure.

In addition to the low-speed flames that have been discussed here, the numerical model is also capable of simulating higher-speed transitional (i.e., approaching turbulent) jet diffusion flames. These flames typically exhibit both large outer vortex structures and trains of roll-up vortices in the shear layer between the incoming fuel jet and the annulus air stream (Chen *et al.*, 1988). Since these transitional flames are usually longer than the low-speed ones, it becomes essential to restrict the computational domain to the base region in order to resolve the small inner shear layer vortices adequately. This is illustrated in Figure 7, which is the vorticity field in the base region of a methane/air flame with fuel and air inlet velocities of 3.2 m/s and 15 cm/s, respectively. The axial velocity in the wall region of the fuel jet is forced with white noise in order to trigger the inner vortex roll-ups, which exhibit a dominant frequency of 278 Hz. There are 92 axial grid points employed here with the mesh exit at $z = 10.6$. The grid is, in fact, that shown in Figure 2 but with the axial

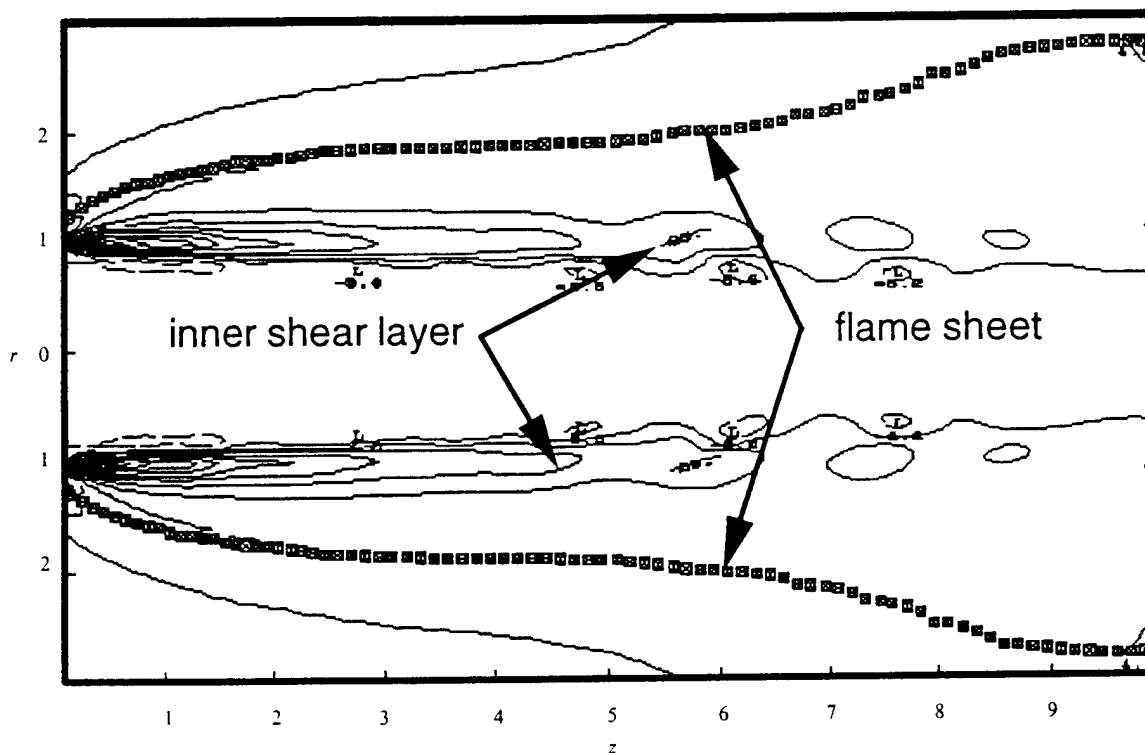


Figure 7. Vorticity field in the base region of a 3.2/0.15 m/s methane/air jet diffusion flame with white-noise forcing.

mesh spacing reduced by half. Comparisons with experimental results for this case have yet to be undertaken.

5. Concluding Remarks

An overview of a joint numerical/experimental investigation of the dynamic structure of a low-speed buoyant jet diffusion flame has been presented. It has been shown that an axisymmetric direct numerical simulation embodying a simple flame sheet model adequately reproduces the dynamic large-scale structures observed experimentally. These include upward moving flame bulges and both inner and outer vortex structures. The flame-flicker frequency is also reasonably predicted. The successful simulation of the large-scale features utilizing such a simple combustion model implies that the accurate modeling of buoyant convection is the overriding concern in this type of flow. Since the simulation exhibits too large a buoyancy force due to a peak temperature about 15% higher than measured experimentally, the addition of a radiation model would represent an important improvement. Another significant enhancement to the model would be the addition of full three-dimensionality in order to simulate the nonaxisymmetric behavior observed in the upper regions of experimental flames. Finally, the addition of some simple chemical kinetics to the combustion model would allow the simulation of such effects as flame stretch and local quenching. Thus, the investigation described in this paper should be looked upon as only one step toward the goal of developing a comprehensive model for the dynamic behavior of jet diffusion flames.

References

- Bahadori, M.Y., Edelman, R.B., Stocker, D.P., and Olson, S.L. (1990). Ignition and behavior of laminar gas-jet diffusion flames in microgravity. *AIAA J.*, **28**, 236–244.
- Burke, S.P., and Schumann, T.E.W. (1928). Diffusion flames. *Indust. Engrg. Chem.*, **29**, 998–1006.
- Chen, L.-D., Seaba, J.P., Roquemore, W.M., and Goss, L.P. (1988). Buoyant diffusion flames. *Proceedings of the Twenty-Second Symposium (International) on Combustion*, pp. 677–684. The Combustion Institute, Pittsburgh, PA.
- Chen, L.-D., Vilimpoc, V., Goss, L.P., Davis, R.W., Moore, E.F., and Roquemore, W.M. (1992). Time evolution of a buoyant jet diffusion flame. *Proceedings of the Twenty-Fourth Symposium (International) on Combustion*, pp. 303–310. The Combustion Institute, Pittsburgh, PA.
- Davis, R.W. (1984). Finite difference methods for fluid flow. In *Computational Techniques and Applications: CTAC-83* (J. Noye and C. Fletcher, eds.), pp. 51–69. North-Holland, Amsterdam.
- Davis, R.W., and Moore, E.F. (1982). A numerical study of vortex shedding from rectangles. *J. Fluid Mech.*, **116**, 475–506.
- Davis, R.W., and Moore, E.F. (1985). A numerical study of vortex merging in mixing layers. *Phys. Fluids*, **28**, 1626–1635.
- Davis, R.W., Moore, E.F., Santoro, R.J., and Ness, J.R. (1990). Isolation of buoyancy effects in jet diffusion flame experiments. *Combust. Sci. Technol.*, **73**, 625–635.
- Davis, R.W., Moore, E.F., Roquemore, W.M., Chen, L.-D., Vilimpoc, V., and Goss, L.P. (1991). Preliminary results of a numerical-experimental study of the dynamic structure of a buoyant jet diffusion flame. *Combust. Flame*, **83**, 263–270.
- Eickhoff, H., and Winandy, A. (1985). Visualization of vortex formation in jet diffusion flames. *Combust. Flame*, **60**, 99–101.
- Ellzey, J.L., Laskey, K.J., and Oran, E.S. (1991). A study of confined diffusion flames. *Combust. Flame*, **84**, 249–264.
- Hosangadi, A., Merkle, C.L., and Turns, S.R. (1990). Analysis of forced combustions jets. *AIAA J.*, **28**, 1473–1480.
- Leonard, B.P. (1979). A stable and accurate convective modelling procedure based on quadratic upstream interpolation. *Comput. Methods Appl. Mech. Engrg.*, **19**, 59–98.
- Lovett, J.A., and Turns, S.R. (1990). Experiments on axisymmetrically pulsed turbulent jet flames. *AIAA J.*, **28**, 38–46.
- Mahalingam, S., Cantwell, B.J., and Ferziger, J.H. (1990). Full numerical simulation of coflowing, axisymmetric jet diffusion flames. *Phys. Fluids A*, **2**, 720–728.
- Mitchell, R.E. (1980). A Theoretical Model of Chemically Reacting Recirculating Flows. Report SAND 79-8236, Sandia National Laboratories, Livermore, CA.
- Mitchell, R.E., Sarofim, A.F., and Clomburg, L.A. (1980). Experimental and numerical investigation of confined laminar diffusion flames. *Combust. Flame*, **37**, 227–244.
- Rehm, R.G., and Baum, H.R. (1978). The equations of motion for thermally driven, buoyant flows. *J. Res. Nat. Bur. Standards*, **83**, 297–308.
- Smooke, M.D., Mitchell, R.E., and Keyes, D.E. (1989). Numerical solution of two-dimensional axisymmetric laminar diffusion flames. *Combust. Sci. Technol.*, **67**, 85–122.
- Strawa, A.W., and Cantwell, B.J. (1985). Visualization of the structure of a pulsed methane-air diffusion flame. *Phys. Fluids*, **28**, 2317–2320.

- Sui, P.C., Chen, L.-D., Davis, R.W., Moore, E.F., and Roquemore, W.M. (1991). Low-frequency flame oscillation of a nitrogen-diluted propane diffusion flame: an experimental and numerical study. *Proceedings of the 1991 Fall Technical Meeting: Eastern Section of the Combustion Institute*, pp. (3-1)–(3-4).
- Swartztrauber, P.N., and Sweet, R. (1975). Efficient FORTRAN Subprograms for the Solution of Elliptic Equations. Technical Note IA-109, National Center for Atmospheric Research, Boulder, CO.
- Vandsburger, V., Seitzman, J.M., and Hanson, R.K. (1988). Visualization methods for the study of unsteady non-premixed jet flame structure. *Combust. Sci. Technol.*, **59**, 455–461.
- Yule, A.J., Chigier, N.A., Ralph, S., Boulderstone, R., and Ventura, J. (1981). Combustion–transition interaction in a jet flame. *AIAA J.*, **19**, 752–760.

TIME EVOLUTION OF A BUOYANT JET DIFFUSION FLAME

L.-D. CHEN

*Department of Mechanical Engineering
The University of Iowa
Iowa City, Iowa 52242 USA*

V. VILIMPOC AND L. P. GOSS

*Systems Research Laboratories, Inc.
Division of Arvin/Calspan
Dayton, OH 45440-3696 USA*

R. W. DAVIS AND E. F. MOORE

*Chemical Science and Technology Laboratory
National Institute of Standards and Technology
Gaithersburg, MD 20899 USA*

AND

W. M. ROQUEMORE

*Wright Research and Development Center
Aero Propulsion and Power Laboratory
Wright-Patterson AFB, Ohio 45433-6563 USA*

Predictions of the time and spatial evolutions of a buoyant jet diffusion flame by a direct numerical simulation are experimentally evaluated. The simulation involves the solution of the full time-dependent Navier-Stokes equations in conjunction with a flame sheet model. The experiments involve a vertical, buoyant diffusion flame in a coflowing air environment. The fuel is a propane and nitrogen mixture (50% by mass) and the burner is a long tube (22.94 mm inside diameter) with a sharp lip at the exit. Planar visualizations and thin-filament-pyrometry temperature measurements are phase-locked to the naturally periodic oscillation of the flame. A comparison of experimental and theoretical results for seven phase angles shows that the model gives an adequate representation of the time evolution of the flame. Temperature profiles obtained at ten axial locations show reasonable agreement when a 20% reduction in heat release is used to approximate the radiative heat loss from the flame. Time-averaged velocity measurements in the near-nozzle region also compare favorably with the prediction.

Introduction

Numerical modeling is an effective tool for studying chemically reacting flows representative of combustion systems. In recent years, time-dependent simulations have been applied to the modeling of these flows by, for example, McMurtry, et al.,¹ Riley, et al.,² and Ghoniem and Ng³ on reacting shear layers; Ellzey and Oran,⁴ Mahalingam, et al.,⁵ Yamashita et al.,⁶ and Davis, et al.,⁷ on unconfined diffusion flames; and Ellzey, et al.⁸ on confined diffusion flames. Although different numerical schemes

have been employed for the flow calculations and different models for the chemical reactions, these studies have clearly shown that large-scale vortical structures are a dominant feature of the time evolution of reacting flows. Verification of these complex simulations, however, has proven difficult. Past practice has involved the comparison of the predicted flow structure with experimental visualization. Quantitative assessments of these simulations have generally not been attempted. Recently, numerical simulations have successfully reproduced the flicker frequency of buoyant jet diffusion flames.^{4,7}

It has also been shown that when gravity is set to zero computationally, flickering ceases,^{1,7} and that when gravity is reduced to one-half of its normal value, or its direction is reversed, the low-frequency oscillations virtually disappear.⁴ To quantitatively verify the numerical simulation beyond the comparison of frequencies (e.g., velocity and temperature) has been difficult. One difficulty involves matching the experimental and computational times. Also, the temporal requirements of data acquisition preclude the simultaneous, multiple-point measurements necessary to quantitatively describe the evolution of the entire flowfield.

The objective of this paper is to evaluate the ability of a time-dependent model to predict the time and spatial evolution of a buoyancy dominated jet diffusion flame. This is an extension of the study reported in Ref. 7, in which the structure of a jet diffusion flame, at one instant in time, is compared to that predicted by the model. In this paper, the "natural" oscillation (or flicker)^{9,10} of buoyant jet flame is used to obtain phase-locked visualizations and temperatures of the flame as it evolves in time and space. The experimental results are compared to predictions from a time-dependent numerical model.

Numerical Model

The numerical model is described by Davis, et al.⁷ In short, non-dimensional continuity, momentum and state equations for the unsteady axisymmetric flow of a two-component fuel jet surrounded by a coflowing air stream are numerically solved, along with a conserved scalar equation for species and temperature (i.e., a flame-sheet model) which requires a unity Lewis number assumption. The numerical scheme employs a variably spaced, staggered mesh and quadratic upwind differencing for convection. At each time step ($\Delta t = 0.16$ ms), a Poisson equation for perturbation pressure is solved by a direct method. Variable thermophysical properties are calculated following Mitchell,¹¹ and no turbulence or radiation models are employed. Binary diffusion of species is taken as fuel into nitrogen inside the flame and oxygen into nitrogen outside. All relevant variables are specified at the burner exit; axisymmetry is enforced along the burner centerline; and zero or constant gradients are employed at very large axial and radial distances (i.e., no shroud). The dimensions of the highly non-uniform mesh are 2500 burner diameters in the axial direction with 145 mesh cells and 25 burner diameters in the radial direction with 84 mesh cells. The smallest axial grid spacings (one-fifth of the burner radius) are employed in the initial mixing region at the base of the flame. The smallest radial grid spacings (one-twentieth of the burner radius)

are employed for $r/r_o \leq 1.5$ (r is the radius and r_o is the burner radius). A run time of one hour on the NIST CYBER 205 was sufficient to compute approximately five flame flickering cycles, with no artificial triggering necessary to initiate this flickering behavior.

Experimental Methods

The experimental setup and procedure are similar to those described in Refs. 7, 12. Thus, only a brief description will be given here. A vertically mounted fuel tube (22.94 mm in diameter) was surrounded by a low-speed, 254 mm diameter annulus air jet which helps to shield the unconfined flame from outside disturbances. A 50% by mass mixture of propane and nitrogen, which satisfies the unity Lewis number assumption of the model, was used as fuel.

Considerable effort was devoted to finding a condition which has repeatable, periodic flame oscillations as required for phase-locked measurements. Although flame flicker was first observed some time ago (e.g., see Chamberlin and Rose¹³), it has only been recently shown that the flicker frequency spectrum is often quite complex.¹⁴ However, a flame has been observed that has a single predominate frequency, as required for phase-locked measurements, when the fuel and air velocities are maintained at 0.06 and 0.18 m/s, respectively. This condition was chosen for comparison with model prediction.

The Reactive Mie Scattering (RMS) technique¹² was used for visualization of the flame structure. This technique involves seeding the fuel and dry air with TiCl_4 vapor which reacts with the water-vapor combustion products to form micron sized TiO_2 particles. These particles are then visualized by the Mie scattering from a laser-sheet formed by a pulsed Nd:YAG laser.

Temporally- and spatially-resolved temperature measurements were obtained by Thin Filament Pyrometry (TFP).^{15,16} This technique records the graybody emission from SiC filaments with a diameter of 13 μm . A calibration relating the radiance (intensity) to temperatures can be readily established since the filament emissivity is independent of temperature. Only temperatures above 1300 K were measured because of sensitivity limitations of the detector. A CCD camera (Photometrics Model 200 Camera System; 1000 \times 1000 format) was used for simultaneous intensity measurements from ten filaments stretched radially across the flame. These filaments were located at $z = 24, 40, 54, 74, 84, 103, 118, 133, 148, \text{ and } 162$ mm, where z is the height above the burner. The filament locations are also superimposed on the RMS images in the discussion which follows (cf., Fig. 3). The imaging sys-

tem displays a spatial resolution of 270 $\mu\text{m}/\text{pixel}$. The heat transfer characteristics and filament time response allow nearly instantaneous radial temperature profiles to be obtained.

The analysis of the filament data requires a multiple-step process. The filaments were located and their intensity extracted from the surrounding soot emission. A Laplacian operator, which acts as a high spatial bandpass filter, was used. The axial and radial pixel locations of each filament were obtained and fitted with a fourth order polynomial. Once the filament location was determined, the background soot emission was subtracted from the image. The resulting soot-free emission intensity was converted to temperature following a blackbody curve, using the filament emission measurements from a H_2 flame with a known temperature. Correction for heat loss was included in the data reduction following Refs. 16, 17, with a measurement precision anticipated similar to that reported in Ref. 17, i.e., better than 80 K. Forty repeated tests were performed at each phase angle for phase-averaging purposes. Twenty repeated tests were performed for the RMS visualization at each phase angle, with only one image being randomly selected for comparison with prediction.

Phase-locked images of the flame and filaments were obtained by a CCD camera. The camera was triggered by the motion of the flame that was recorded by monitoring the deflection of a He-Ne laser beam. The laser beam was positioned tangent to the luminous flame at a height just above the fourth filament ($z = 74$ mm) where the luminous flame starts to oscillate. Different phases of flame oscillation were captured by setting the time delays with respect to the signal of the deflected laser beam. The results were obtained at seven 10 ms intervals which correspond to phase angles of 0, 50, 101, 151, 202, 252, and 302 degrees based on the measured period of 71 ms (14 Hz frequency). The time delay could be repeated to within ± 0.2 ms.

Simultaneous axial and radial velocity measurements were made with a frequency-shifted (dual Bragg cell operated at 5 MHz frequency shift) two-component laser Doppler anemometer (LDA) system. This system has an effective measurement size of 200 μm by 500 μm . Both the fuel and annular-air jets were seeded by alumina particles (1 μm in diameter). The LDA measuring volume was scanned in increments of 500 μm or 1000 μm in the 200 μm measurement-volume direction for radial profiles. An ensemble average of 3000 velocity realizations was performed for each data point presented. With this sample size and assuming a Gaussian error distribution, both the mean and rms have a confidence level better than 95%.

Results and Discussion

The purpose of this paper is to experimentally evaluate the ability of the numerical model to cor-

rectly describe the time and spatial evolution of a near-laminar jet diffusion flame. A nondimensional parameter, phase angle, is used to follow the time evolution of the jet flame oscillations. This proved necessary since there is a slight difference between the measured (14 Hz) and the computed (12 or 13 Hz) flame oscillation frequencies. The experimental phase angle is referenced to the numerical simulation by matching the shape of the luminous flame with the predicted stoichiometry surface at a phase angle of 151 degrees, i.e., $\theta = 151^\circ$.

The nearfield visualization of the experimental flame at $\theta = 101^\circ$ is shown in Fig. 1. False color is used to highlight the Mie scattering from TiO_2 particles and the luminous flame. The edge of the luminous flame is shown just inside the predicted stoichiometric surface, which is denoted by the large dots. The luminous flame is attached to the burner a few mm below the burner lip, which is not shown in the figure. The TiO_2 particles outside the luminous flame mark the mixing of the combustion products and annulus air while those inside mark the mixing of the combustion products and fuel. A stationary recirculation zone is observed inside the luminous flame, located 8 to 18 mm above the burner.

The radial profiles of mean axial velocities at $z = 0.85, 24, 40, 54$ mm and temperatures at $z = 24, 40, 54$ mm, are superimposed on the flame image in Fig. 1. The LDA velocity is ensemble-averaged, while the TFP data and the velocity and temperature predictions are arithmetic means of seven phase angles. The velocity and temperature scales are also shown in the figure, with the baseline of the temperature scale being 294 K. The velocity scale at $z = 0.85$ mm is magnified five times compared to other locations. Although it is not evident in Fig. 1, the measured instantaneous peak temperatures are approximately 200 K lower than the predicted stoichiometric temperature as will be discussed directly. This discrepancy is believed to be due to the radiative heat loss from the flame. The measured maximum temperature appears 1 to 2 mm outside the luminous flame, in agreement with Mitchell, et al.¹⁷ The radial locations of the measured peak temperatures are displaced about 1 mm outside the location of the predicted temperatures, but, in general, the agreement between predictions and measurements is reasonably good.

The predicted and measured averaged velocities in Fig. 1 are also in reasonable agreement. Near the jet exit, $z = 0.85$ mm, a uniform axial velocity of 0.20 m/s is measured in the annular air jet outside the luminous flame. This is slightly higher than the 0.18 m/s axial velocity of the air jet used as an initial condition in the model. The axial velocity increases at the stoichiometric flame location and then decreases to near zero at the jet centerline. The increase in velocity at the location of the peak flame

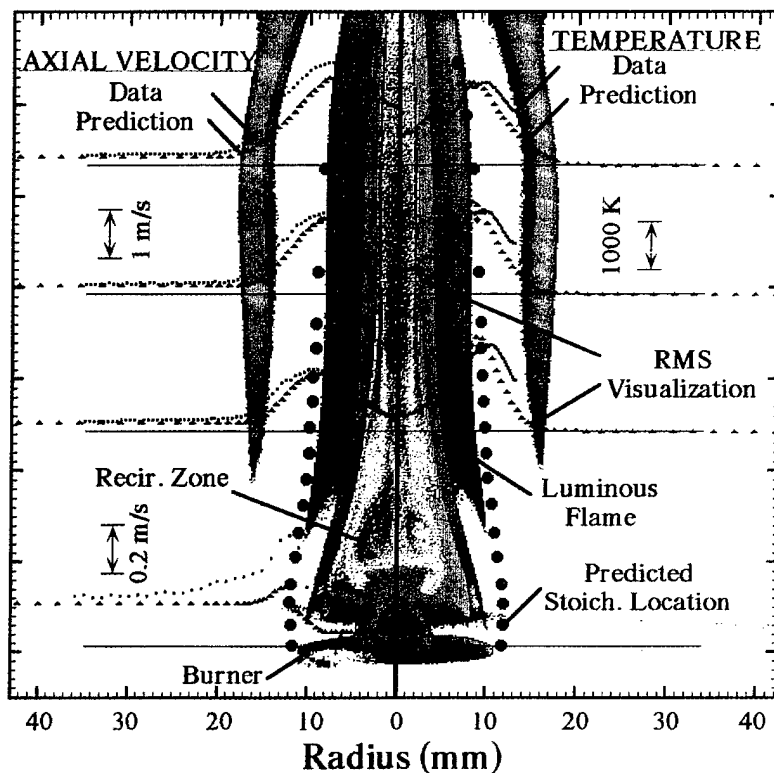


FIG. 1. Nearfield Axial Mean Velocity, Mean Temperature and Planar RMS Imaging of the C_3H_8/N_2 Diffusion Flame (with Same Length Scales for Horizontal and Vertical Coordinates).

temperature is due to buoyancy; whereas, the decrease in velocity at the jet centerline is due to the fuel and nitrogen mixture being heavier than air, i.e., negative buoyancy. The buoyant acceleration becomes increasingly evident in the axial velocity profiles at the higher locations of the flame. For example, the maximum measured axial velocity increases from 0.45 m/s at $z = 0.85$ mm to 1.24 m/s at $z = 24$ mm. The model slightly underestimates the peak velocities and the width of the velocity profile. In general, the data in Fig. 1 demonstrates that the predicted results are in reasonable agreement with the measurements in the nearfield where the flame oscillations are small.

Figure 2 illustrates that the model captures the detailed structure of the flame when visualized in the appropriate way. The experimental RMS image of the flame and the computed isotherm with a superposition of streaklines and vorticity contours are shown for $\theta = 101^\circ$. The squares in the RMS image denote the locations of the luminous flame surface. In the isotherm and vorticity images, they represent the location of the stoichiometric flame surface. The large vortices outside the luminous

flame are well represented by the isotherm and the vorticity images. However, the smaller vortex at the bulge of the flame is most clearly marked by the vorticity contours and the streaklines from tracking passive, massless particles. The massless particles are released inside the flame near the base; their instantaneous positions are superimposed on the isotherms of Fig. 2. This isotherm/streakline plot reproduces the essential flow features and will henceforth be used for numerical/experimental visualization comparisons. The color code is blue for low temperatures (down to 294 K), and red for high temperatures (up to 2250 K). A short potential core is shown in Fig. 2 by the temperature contours and the very low vorticity region (white colored) above the burner. The prediction generally yields positive vorticity outside the zero contour and negative vorticity inside. Concentrated, positive vorticity (yellow-orange color) is predicted near the necking location just below the flame bulge.

Figure 3 shows a comparison of phase-locked experimental and theoretical visualizations of the time evolution of the flame for four of the seven phase angles. The results at $\theta = 101^\circ$ have been pre-

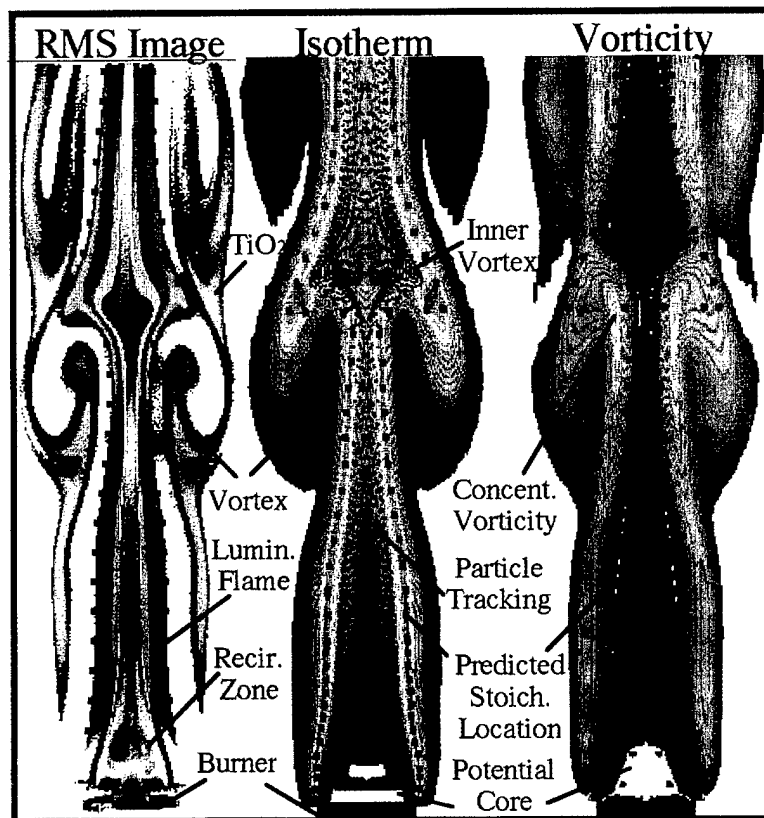


FIG. 2. Comparison of Theoretical and Experimental Visualizations of the Phase-Locked Results of the C_3H_8/N_2 Diffusion Flames at $\theta = 101^\circ$.

sented in Fig. 2, and the visualizations at $\theta = 50^\circ$ and 302° are quite similar to that shown at $\theta = 0^\circ$. As can be seen, the general flame shape is clearly reproduced by the simulation. The flame bulge and its movement as a function of time (phase angle) are also reasonably predicted. The flame bulge is seen to move with the outer vortex, with a sudden acceleration to pass the vortex "saddle point" seen at $\theta = 202^\circ$. At $\theta = 252^\circ$, the flame bulge moves out of the field of view and the outer vortex is seen to be stretching in the axial direction. This stretching of the outer vortex is attributed to the buoyant acceleration which results in a higher velocity at the upper "saddle point," an observation which is consistent with Ref. 9. A new flame bulge with its trailing vortex is subsequently seen forming at $\theta = 252^\circ$. Thus, Figure 3 illustrates that the simulation not only reproduces the global flow structure at one instant of time,⁷ but also provides a reasonable representation of the time evolution of this flame. The major discrepancy between simulation and experiment is that the predicted bulge moves upward faster than the experimental one, as can be seen at

$\theta = 202^\circ$. This is attributed to the increased buoyancy due to the higher temperatures present in the simulation, which does not account for radiative heat losses.

Quantitative comparisons of instantaneous radial temperature profiles were obtained for the seven phase angles, with the results at $\theta = 101^\circ$ presented in Fig. 4. The predicted adiabatic stoichiometric temperature (2250 K) is higher than the measured maximum temperature (approximately 2000 K). A 20% reduction of enthalpy of combustion was employed in the simulation in a highly simplified attempt to account for radiative heat loss¹⁸ by lowering the flame temperature. The lower stoichiometric temperature is approximately 1900 K and clearly improves the quantitative comparison, cf. Fig. 4. The frequency prediction is also improved: a 13 Hz frequency is now predicted, compared to a 12 Hz frequency with the adiabatic flame and a 14 Hz measured frequency. The prediction based on 20% heat loss is also in general agreement with the measured temperature profiles including locations of peaks. Note that the prediction underestimates the

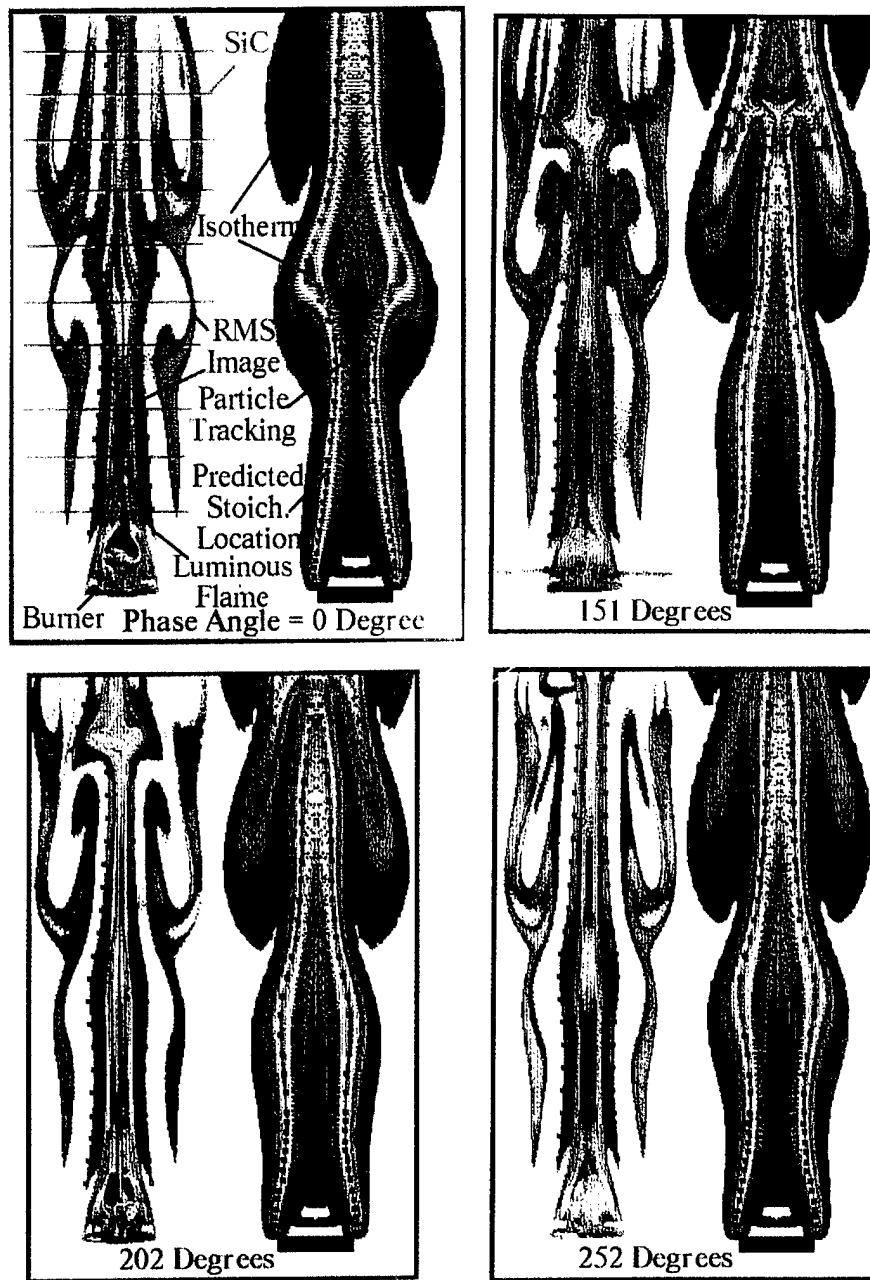


FIG. 3. Phase-Locked Visualizations of the C_3H_8/N_2 Diffusion Flame at $\theta = 0^\circ$, 151° , 202° , and 252° .

flame spread by about 2 mm for the phase angle examined. The computation is seen to reproduce the double peak in the temperature measurements at $z = 103$ mm, which is just below the flame bulge, i.e., the sixth filament above the burner in Fig. 3.

A double peak in temperature is also predicted at $z = 84$, 148 , and 162 mm. At these locations, the second peak is below the 1300 K cut-off temperature of the filaments and, therefore, could not be detected by them. The formation of these double

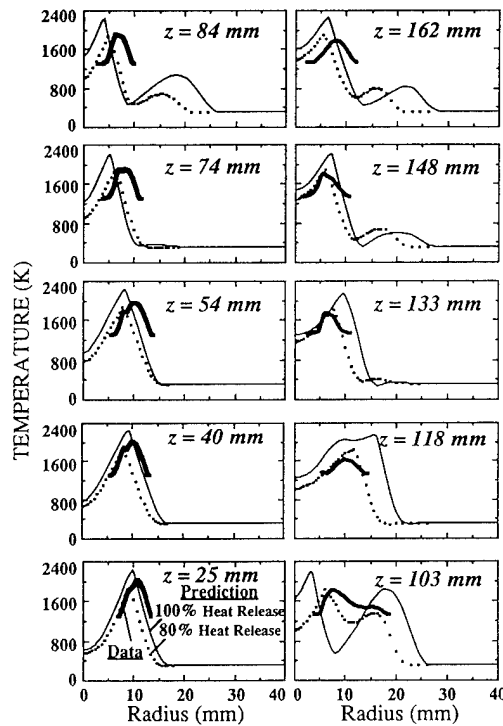


FIG. 4. Comparison of Predicted and Measured Temperatures at $\theta = 101^\circ$; Thick Solid Line—TFP (Thin Filament Pyrometry) Data; Thin Solid Line—Prediction with 0% Reduction in Enthalpy of Combustion; Dotted Line—Prediction with 20% Reduction in Enthalpy of Combustion.

peaks in temperature is attributed to the outer vortex motion which entrains high temperature gas along the flame and convects it outward.

Summary and Conclusions

A combined experimental and numerical investigation of a near-laminar, buoyant jet diffusion flame has been conducted. The flame exhibits a naturally occurring low frequency oscillation of 14 Hz. This frequency was used to obtain phase-locked RMS (Reactive Mie Scattering) visualizations and TFP (Thin Filament Pyrometry) temperature measurements. The phase-locked data were used to evaluate the time and spatial evolution of jet flame as predicted by a time-dependent numerical simulation based on the Navier-Stokes equations and a conserved scalar formulation. The major findings and conclusions derived from this study are:

1. The numerical simulation adequately reproduces the temperature and velocity fields in the base region of the flame studied here.
2. The numerical simulation reproduces the time and spatial evolution of the global structures of the flame studied, e.g., the large vortex structures, the flame bulge with its counterrotating inner vortices, and the stationary recirculation zone above the burner. The numerical simulation is also in general agreement with measured phase-averaged temperatures and is close to the experimental flicker frequency. A 20% reduction in enthalpy of combustion improves the quantitative numerical/experimental comparisons. However, this is only a crude approximation to simulate the effects of radiative heat loss from the flame.
3. The simple flame-sheet model employed in the present study is found to be adequate for describing the time evolution of the flame studied. This observation suggests that the accurate modeling of buoyant convection is the most important element required for predicting the interactions between this flame and its surrounding flow structures.

Acknowledgment

This work was supported in part by the Aerospace Sciences Division of AFOSR and NSF. Technical assistance from J.-G. Lee, S.-H. Wu, and D. D. Trump is acknowledged.

REFERENCES

1. MCMURTRY, P. A., JOU, W.-H., RILEY, J. J. AND METCALFE, R. W.: AIAA J. 24, 962 (1986).
2. RILEY, J. J., METCALFE, R. W. AND ORSZAG, S. A.: Phys. Fluids 25, 406 (1986).
3. GHONEIM, A. F. AND NG, K. N.: Phys. Fluids 30, 706 (1986).
4. ELLZEY, J. L. AND ORAN, E. S.: Twenty-Third Symposium (International) on Combustion, p. 1635, The Combustion Institute, 1991.
5. MAHALINGAM, S., CANTWELL, B. J. AND FERGIGER, J. H.: Phys. Fluids A, 2, 720 (1990).
6. YAMASHITA, H., KUSHIDA, G. AND TAKENO, T.: Proc. R. Soc. Lond. A, 431, 301 (1991).
7. DAVIS, R. W., MOORE, E. F., ROQUEMORE, W. M., CHEN, L.-D., VILIMPOC, V. AND GOSS, L. P.: Comb. Flame 83, 263 (1991).
8. ELLZEY, J. L., LASKEY, K. J. AND ORAN, E. S.: Combust. Flame, 84, 249 (1991).
9. CHEN, L.-D., SEABA, J. P., ROQUEMORE, W. M. AND GOSS, L. P.: Twenty-Second Symposium (International) on Combustion, p. 677, The Combustion Institute, 1989.

10. BUCKMASTER, J. AND PETERS, N.: Twenty-First Symposium (International) on Combustion, p. 1829, The Combustion Institute, 1988.
11. MITCHELL, R. E.: Sandia National Laboratories Report SAND 79-8236 (1980).
12. CHEN, L.-D. AND ROQUEMORE, W. M.: *Combust. Flame* 66, 81 (1986).
13. CHAMBERLAIN, D. S. AND ROSE, A.: First Symposium on Combustion (*Ind. Eng. Chem.* 20), p. 1013, The Combustion Institute, 1928.
14. SUI, P. C., CHEN, L.-D., ROQUEMORE, W. M. AND DAVIS, R. W.: in *Proceedings of 1991 Spring Technical Meeting of the Central States Section of The Combustion Institute*, p. 113, The Combustion Institute, 1991.
15. VILIMPOC, V., GOSS, L. P. AND SARKA, B.: *Optics Letters* 13, 93 (1988).
16. VILIMPOC, V. AND GOSS, L. P.: Twenty-Second Symposium (International) on Combustion, p. 1907, The Combustion Institute, 1989.
17. MITCHELL, R. E., SAROFIM, A. F. AND CLOUMBURG, L. A.: *Combust. Flame* 37, 227 (1980).
18. JENG, S.-M., CHEN, L.-D. AND FAETH, G. M.: Nineteenth Symposium (International) on Combustion, p. 349, The Combustion Institute, 1983.

COMMENTS

Dr. John De Ris, Factory Mutual Research Corp., USA. Please explain the mechanism controlling the pulsation frequency of the flame. In particular, does the vorticity supplied from the fuel source have any role in the mechanism, or is all the controlling vorticity generated by buoyancy?

Author's Reply. The buoyancy acceleration is responsible for the flame flicker or pulsation frequency of the flame. The flame flicker is a result of the interaction of toroidal vortices outside the stoichiometric surface and the stoichiometric surface. We have done the numerical experiment of setting gravity to zero, and the simulation resulted in a non-oscillating flame. Thus, it appears that the controlling vorticity is generated by buoyancy in the diffusion flames we studied.

Shankar Mahalingam, University of Colorado, Boulder, USA. Your computed flicker frequency decreased from 14 Hz to 13 Hz when you reduced the heat release. Although this reduces ΔU , it is not clear from your presentation what is the physical mechanism for the decrease in computed frequency. Secondly, do you observe the same behaviour by diluting the fuel and oxidizer streams and thereby reducing the flame temperature?

Author's Reply. When the heat release was reduced in the simulation by 20%, the flicker frequency *increased* from 12 Hz to 13 Hz. This change in flicker frequency agrees with the effect of the annular air, which shows that the flicker frequency increases as the annular air velocity is increased (i.e., ΔU is decreased). We do not understand the mechanism that is responsible for the increase in frequency. When the fuel is diluted by inert gas (e.g., N_2), a similar increase in frequency is observed. The dilution, however, can result in a non-oscillating flame when the flame length (defined by the stoichiometric surface) is reduced below the onset of the unsteady flow.

M. A. Delichatsios, Factory Mutual Research Corp., USA. Is it true that the oscillation frequency is independent of the nozzle diameter? If so, why?

Author's Reply. We have examined one nozzle diameter in this Symposium paper, and only three diameters in our past work. The nozzle diameter dependence is not evident from our work. A better reference is the paper of Hamins, Yang and Kashiwagi at this Symposium, which has shown that the frequency is inversely proportional to the square root of diameter.

Vorticity Generation in Jet Diffusion Flames

L.-D. CHEN *Department of Mechanical Engineering, The University of Iowa,
Iowa City, Iowa 52242*

W. M. ROQUEMORE *WRDC/Aero Propulsion and Power Laboratory,
Wright-Patterson AFB, Ohio 45433*

L. P. GOSS and V. VILIMPOC *Systems Research Laboratories, Division of
Arvin/Calspan, Dayton, OH 45440*

(Received June 23, 1989; in final form November 26, 1990)

Abstract—A novel method to analyze the vorticity generation or destruction in jet diffusion flames is presented. The analysis employs a generic flame structure and a single conserved scalar to examine the vorticity generation or destruction in jet diffusion flames. The analysis shows that the volumetric expansion and baroclinicity can result in vorticity destruction or generation depending on the flame structure, or the stoichiometry. Three regimes concerning vorticity generation or destruction are identified for jet diffusion flames. The analysis also defines a non-dimensional parameter, describing the relative importance of baroclinicity to volumetric expansion. The parameter is the ratio of Reynolds number to Froude number and multiplied by the square root of the Schmidt number.

Key words: Vorticity, turbulent jet diffusion flames, non-premixed jet flames.

NOMENCLATURE

d	burner diameter
D	binary diffusion coefficient
f	mixture fraction
Fr	Froude number based on ρ , u' , ρ_∞ , g and l ; Eq. (17)
Fr	Froude number based on ρ , u , ρ_∞ , g and l_f ; Eq. (15)
g	gravitational acceleration vector
i, j, k	unit vectors in x, y, z directions
l	velocity (vorticity) length scale
l_f	scalar transport length scale
l^*	dimensionless length scale, Figure 3
p	pressure
Re	Reynolds number based on u' , l and ν ; Eq. (17)
Re	Reynolds number based on u , l_f and ν ; Eq. (15)
Ro	dimensionless number, Eq. (15)
Sc	Schmidt number, Eq. (15)
S_v	baroclinicity term in the vorticity equation, Eq. (1)
S_v	volumetric expansion term in the vorticity equation, Eq. (1)
t	time
T	temperature
u	characteristic velocity, Eq. (15)
u'	characteristic velocity, Eq. (17)
u^*	dimensionless velocity, Figure 3
v	specific volume
V	velocity vector

V_G	vorticity generation parameter, Eq. (13)
x, y, z	coordinates defined in Figure 2
\mathbf{x}	positive vector
Y_i	mass fraction of i th species

Greek Letters

ρ	density
ν	kinematic viscosity
ω	vorticity vector

Subscripts

o	burner exit condition
s	stoichiometric condition
∞	ambient quantity

INTRODUCTION

There have been many studies of turbulent jet diffusion flames due to their practical importance and fundamental significance. Turbulent jet diffusion flames are typical of many industrial processes, ranging from domestic heating to aero-propulsion applications. They represent the simplest geometry of chemically reactive flows that retain many generic features important to the flows of practical combustion systems. For these and other reasons, jet diffusion flames have become one of the "standard" flame configuration for conducting combustion research.

Rapid development of computational and diagnostic capabilities in recent years allows one to conduct detailed and sophisticated studies (measurements and numerical simulation) of jet diffusion flames. Some examples are the utilization of laser diagnostics to study the physics of turbulent and laminar jet diffusion flames, *e.g.* Masri, *et al.* (1988) and Roquemore, *et al.* (1987a), and direct numerical simulation of reacting flows, *e.g.* Gohniem, *et al.* (1988) and Davis, *et al.* (1990). These studies have qualitatively as well as quantitatively illustrated the effects of combustion on flow fields and have advanced our understanding of the underlying physics concerning the dynamics of jet diffusion flames. This paper presents a theoretical analysis that addresses the vorticity generation and destruction in jet diffusion flames. Specifically, the effects on vorticity generation and destruction due to volumetric expansion and baroclinicity resulting from the combustion of turbulent jet diffusion flames are examined.

The exothermic reaction of combustion yields high temperature combustion products typically around 2300 K for hydrocarbon fuels burning in air. Density variation of order of ten can exist in flames. Three effects can arrive from density variation, *e.g.*, thermal or volumetric expansion, buoyancy effects and vorticity generation. The first two effects are evident as one examines the continuity and momentum equations. The linear deformation of fluids ($\nabla \cdot \mathbf{V} \neq 0$) complicates the analysis since the incompressible fluid assumption can no longer be applied. The buoyancy forces appear in the momentum equation as a source term which accelerates the flow resulting in dynamic changes in the flame structure of vertical jet diffusion flames. This dynamic change can be noted in the mean velocity profiles when the radial locations of the peak axial

velocity and maximum temperature are about the same and by a reduced rate of velocity decay along the jet centerline as compared to constant density jets. The dynamic change can also be seen from a Kelvin-Helmholtz type instability which is attributed to buoyancy induced shear layer around the flame (Buckmaster and Peters, 1988) and regularly occurring vortices outside the luminous flame (Roquemore *et al.*, 1987a). These vortices are buoyancy driven as shown from the numerical simulation in which outer vortices are suppressed as the gravitational acceleration is artificially set to zero (Davis *et al.*, 1990). The suppression of the outer vortices yields a steady flame without the low frequency flame oscillation (or flame flicker) typically observed in buoyant jet diffusion flames.

The effect of combustion on vorticity transport is not as straight forward as the general perception that states the volumetric expansion tends to suppress the vorticity generation and that the buoyancy forces act as a vorticity generation term (baroclinicity) in a vertically upward jet flame. This paper employs a generic flame structure to study the vorticity generation in jet diffusion flames. A non-dimensional parameter, V_G that is related to the ratio of Reynolds number to Froude number, is derived from the analysis to characterize the relative importance of baroclinicity and volumetric expansion.

ANALYSIS

The governing equation for vorticity transport in variable density flows is as follows (Kuo, 1986):

$$\frac{\partial \omega}{\partial t} + (\mathbf{V} \cdot \nabla) \omega = (\omega \cdot \nabla) \mathbf{V} + \nu \nabla^2 \omega - \omega (\nabla \cdot \mathbf{V}) - \nabla \frac{1}{\rho} \times \nabla p, \quad (1)$$

where the vorticity (ω) is defined as $\nabla \times \mathbf{V}$ and \mathbf{V} is the velocity vector. Two terms are retained in the above equation to account for density variation. One is associated with the thermal or volumetric expansion, *i.e.*, $S_v = -\omega (\nabla \cdot \mathbf{V})$. The other is coupled with

the pressure variation, known as the baroclinicity, *i.e.*, $S_B = \nabla p \times \nabla \frac{1}{\rho}$, or

$S_B = \nabla p \times \nabla v$, where v is the specific volume ($v = 1/\rho$).

The volumetric expansion acts as a sink term when the divergence of the velocity is positive. The divergence of the velocity can be evaluated from the continuity equation, *i.e.*,

$$\nabla \cdot \mathbf{V} = -\frac{1}{\rho} \left(\frac{\partial \rho}{\partial t} + \mathbf{V} \cdot \nabla \rho \right). \quad (2)$$

The volumetric expansion can be evaluated for jet diffusion flames by expressing the thermochemical properties as functions of a single conserved scalar, *e.g.*, mixture fraction (Bilger, 1976). For example, thermochemical properties can be considered as a passive scalar, *i.e.*,

$$\phi = \phi(\mathbf{x}, t) = \phi(f), \quad (3)$$

where $\phi = \rho, T$, or Y_i (density, temperature, or *i*th-component species mass fraction), f is the mixture and \mathbf{x} is the position vector. The mixture fraction is defined as the

effective mass fraction originating from the injected fluid (*e.g.*, see Jeng and Faeth, 1984). Employing the conserved scalar approach, one can evaluate the property variation as follows:

$$\frac{\partial \phi}{\partial t} = \frac{d\phi}{df} \frac{\partial f}{\partial t} \quad \text{and} \quad \nabla \phi = \frac{d\phi}{df} \nabla f. \quad (4)$$

Substituting Eq. (4) into Eq. (2), one obtains

$$\nabla \cdot \mathbf{V} = -\frac{1}{\rho} \frac{d\rho}{df} \left(\frac{\partial f}{\partial t} + \mathbf{V} \cdot \nabla f \right). \quad (5)$$

The transport equation for mixture fraction (Williams, 1985) is:

$$\rho \left(\frac{\partial f}{\partial t} + \mathbf{V} \cdot \nabla f \right) = \nabla \cdot (\rho D \nabla f), \quad (6)$$

where D is the binary diffusion coefficient. The volumetric expansion term (S_v) then becomes

$$S_v = -\omega (\nabla \cdot \mathbf{V}) = \omega \left(\frac{1}{\rho^2} \frac{d\rho}{df} \nabla \cdot (\rho D \nabla f) \right) \text{ or,} \quad (7)$$

$$S_v = -\frac{dv}{df} \nabla \cdot (\rho D \nabla f) \omega. \quad (8)$$

The baroclinic effect can be evaluated following a similar approach. Assuming that the pressure gradient is due to hydrostatic pressure alone, the baroclinicity can be expressed as

$$\mathbf{S}_B = -\nabla \frac{1}{\rho} \times \nabla p = -\nabla v \times \nabla p = -\nabla v \times \rho_x \mathbf{g}, \quad (9)$$

where ρ_x is the ambient fluid density and \mathbf{g} is the gravitational acceleration (a vector quantity). Employing the conserved scalar approach, one obtains the following expression for baroclinicity:

$$\mathbf{S}_B = -\rho_x \frac{dv}{df} \nabla f \times \mathbf{g}. \quad (10)$$

DISCUSSION

The significance of Eqs. (8) and (10) is that the vorticity generation/destruction due to volumetric expansion and baroclinicity is now related to the variation of a physical property, *i.e.* specific volume in the mixture fraction space and to the transport of a conserved scalar, *i.e.* mixture fraction. In other words, the flame structure in the mixture fraction space is an important parameter to determine whether generation or destruction of vorticity in jet diffusion flames is likely to occur. To illustrate this, a planar two-dimensional jet is considered. Invoking the boundary layer approximations, the volumetric expansion term becomes

$$S_v = -\frac{dv}{df} \frac{\partial}{\partial y} \left(\rho D \frac{\partial f}{\partial y} \right) \omega \mathbf{k}, \quad (11)$$

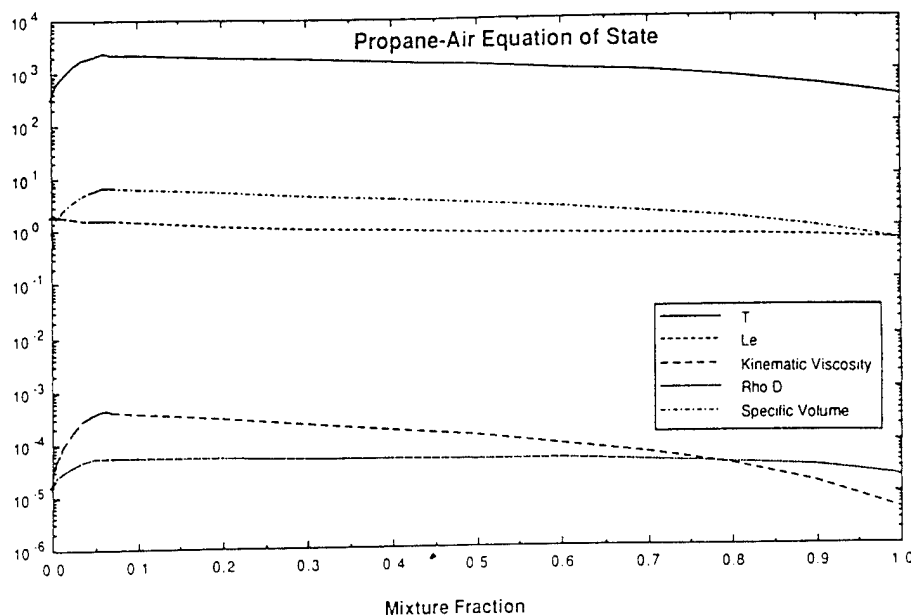


FIGURE 1 State Relationship for Propane-Air Diffusion Flames.

where k is the unit vector in the z direction. The term $\frac{dv}{df}$ is typically negative (density increases as the mixture fraction is increased) in the fuel rich regime inside the flame envelope ($f_s < f < 1$) and positive in the fuel lean regime outside the flame envelope ($0 < f < f_s$) where f_s is the stoichiometric mixture fraction. As an example, the state relationship for propane-air diffusion flame is shown in Figure 1. The state relationship was constructed assuming partial equilibrium in jet diffusion flames similar to past practice, *e.g.* see Jeng, *et al.* (1982) and Jeng and Faeth (1984). The equilibrium computation employed the NASA equilibrium code (Gordon and McBride, 1976) and the equilibrium limit at the fuel rich side was set at equivalence ratio of 1.2. Adiabatic mixing was assumed for the fuel rich regime beyond this equivalence ratio.

Equation (11) states that volumetric expansion can result in vorticity generation when it has the same sign as the vorticity. In the discussion herein, the sign convention shown in Figure 2 is adopted. In other words, the vorticity originated from the jet is positive for the domain bounded by positive x and positive y , and negative for the regime bounded by negative x and positive y . To examine the effects due to volumetric expansion on vorticity transport, let's consider the positive x and positive y domain,

and approximate $\frac{\partial}{\partial y} \left(\rho D \frac{\partial f}{\partial y} \right)$ with $\rho D \frac{\partial^2 f}{\partial y^2}$ *i.e.*, $\rho D = \text{constant}$ or $\frac{\partial(\rho D)}{\partial y} \frac{\partial f}{\partial y} = 0$. The

constant ρD assumption was introduced to illustrate the diffusional transport; however, it is not a pre-requisite for the analysis. An inflection point in mixture fraction

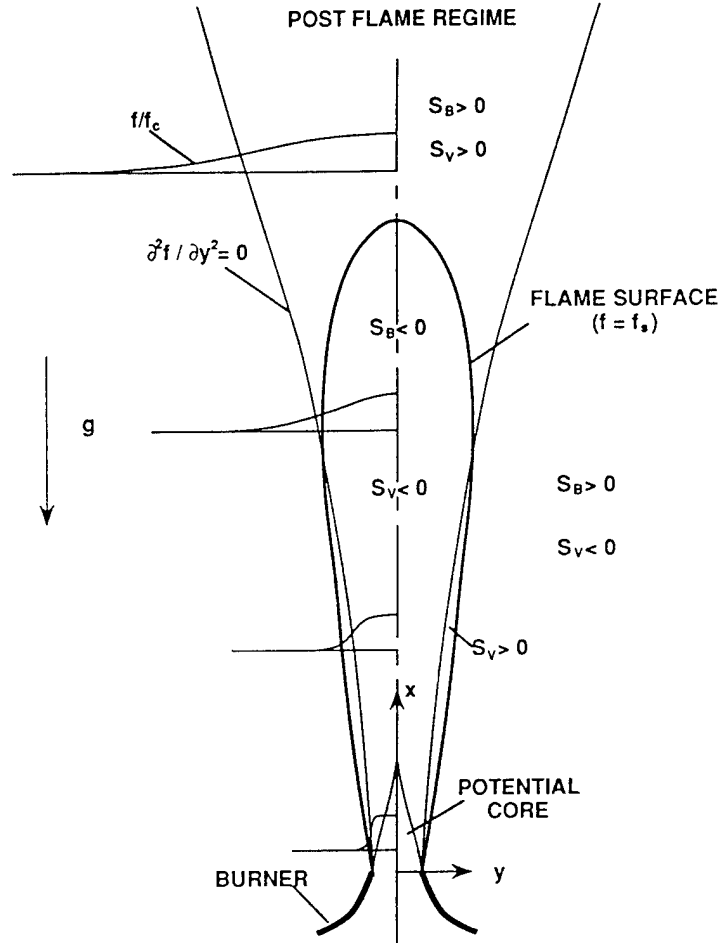


FIGURE 2 Illustration of Vorticity Generation/Destruction in Jet Diffusion Flames.

$\left(\frac{\partial^2 f}{\partial y^2} = 0\right)$ exists in the y -direction for jet diffusion flames; the sign of $\frac{\partial^2 f}{\partial y^2}$ changes

from negative to positive as one moves from the center of the jet toward the flame. As a result, vorticity generation as well as destruction can result from volumetric expansion; in specific, $S_v < 0$ (or $S_v/\omega < 0$) in the fuel lean regime, $S_v > 0$ in the regime bounded by the stoichiometric contour and inflection-point contour of the fuel rich regime, and $S_v < 0$ in the core regime—see the illustration in Figure 2. It should be noted that volumetric expansion can result in vorticity generation in the post-flame regime which will be discussed later.

The baroclinicity for a two-dimensional planar flow is

$$S_B = -\rho_x \frac{dv}{df} \left(\frac{\partial f}{\partial y} \mathbf{j} \times (-g) \mathbf{i} \right) = -\rho_x g \frac{\partial f}{\partial y} \frac{dv}{df} \mathbf{k}, \quad (12)$$

where g is the gravitational acceleration constant, and i and j are unit vectors in x and y directions, respectively. As discussed earlier, the state relationship for hydrocarbon-air diffusion flames yields $\frac{dv}{df} < 0$ in the fuel rich regime and $\frac{dv}{df} > 0$ in the fuel lean

regime. Since $\frac{\partial f}{\partial y}$ is less than zero for jet flows, the baroclinicity is negative ($S_b < 0$) in the fuel rich regime but positive ($S_b > 0$) in the fuel lean regime. The analysis showed that the baroclinicity suppresses vorticity in the fuel rich regime (or inside the luminous flame) of a jet diffusion flame, yielding laminarization effects to the flow. The baroclinicity, however, can generate vorticity in the fuel lean regime (or outside the luminous flame). Although the discussion above for S_b is based on the sign convection for the positive x and positive y regime, the same conclusion will be obtained for the positive x and negative y regime as ω assumes a minus sign in that regime.

In the post-flame regime, the vorticity generation becomes qualitatively similar to that of buoyant jets. The post-flame regime is defined as the regime downstream of the flame height at which the mixture fraction at the jet center reached the stoichiometric value, *e.g.* See Figure 2. In the post-flame regime, the mixture fraction is less than the stoichiometric value ($f < f_s$) which results in $\frac{\partial v}{\partial f} > 0$. Since $\frac{\partial f}{\partial y} < 0$, the baroclinicity is a source term for vorticity generation. The volumetric expansion term, S_v however, depends on the sign of $\frac{\partial^2 f}{\partial y^2}$; it becomes a source term when $\frac{\partial^2 f}{\partial y^2} < 0$ but a sink term when $\frac{\partial^2 f}{\partial y^2} > 0$. As a result, vorticity generation due to volumetric expansion is expected in the core regime, *i.e.* from the center of the jet to the inflection point location ($\frac{\partial^2 f}{\partial y^2} = 0$), but vorticity destruction is expected in the outer regime, *i.e.*, from the inflection point to the edge of the jet.

A non-dimensional parameter V_G can be defined to assist the discussion of vorticity generation in jet diffusion flames. The parameter is the ratio of the magnitude of baroclinicity to that of volumetric expansion in jet diffusion flames:

$$V_G = \frac{|S_b|}{|S_v|} = \frac{\left| \rho_x g \frac{\partial f}{\partial y} \frac{dv}{df} \right|}{\left| \frac{dv}{df} \frac{\partial}{\partial y} \left(\rho D \frac{\partial f}{\partial y} \right) \omega \right|} \approx \frac{\left| \rho_x g \frac{\partial f}{\partial y} \right|}{\left| \rho D \left(\frac{\partial}{\partial y} \frac{\partial f}{\partial y} \right) \omega \right|} \approx \frac{\rho_\infty g l_f}{\rho D |\omega|}, \quad (13)$$

where l_f is a characteristic length of the diffusional transport of mixture fraction. Substituting the Froude number (Fr), Reynolds number (Re) and Schmidt number (Sc) into Eq. (13), one obtains

$$V_G = \frac{Sc Re}{Fr} Ro, \text{ where} \quad (14)$$

$$Fr = \frac{\rho u^2}{\rho_\infty g l_f}, \quad Re = \frac{u l_f}{\nu}, \quad Sc = \frac{\nu}{D}, \quad \text{and} \quad Ro = \frac{u l_f}{\omega}. \quad (15)$$

In the above equations, u is the characteristic velocity of the convective flow, ν is the kinematic viscosity, and Ro is the ratio of the characteristic time of the vortex motion to that of the translational flow. One can estimate the vorticity by defining a characteristic velocity u' for vortex motion and associated length scale l , *i.e.* $\omega \approx \frac{u'}{l}$.

Equation (13) then becomes

$$V_G = \frac{R_1}{F_1} Sc^{1/2}, \quad (16)$$

where F_1 and R_1 are respectively the Froude and Reynolds numbers based on u' and l , *i.e.*

$$F_1 = \frac{\rho u'^2}{\rho_\infty g l} \quad \text{and} \quad R_1 = \frac{u' l}{\nu}. \quad (17)$$

Equation (16) also assumed that the ratio of the length scales l and l_f is proportional to the square root of the Schmidt number, *i.e.*

$$\frac{l}{l_f} = Sc^{1/2}. \quad (18)$$

The above equations were derived considering a planar two-dimensional jet; it can also be applied to axisymmetric jets. To illustrate this, one can substitute the diffusional transport term of axisymmetric jet flow to Eq. (11), yielding a volumetric expansion term:

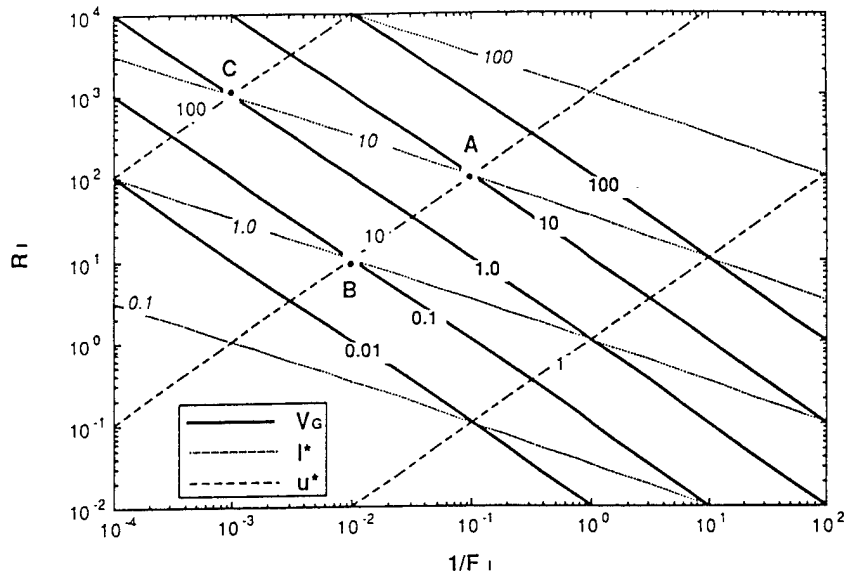
$$S_v = - \frac{dv}{df} \frac{1}{y} \frac{\partial}{\partial y} \left(y \rho D \frac{\partial f}{\partial y} \right) \omega \mathbf{k}. \quad (19)$$

In the above equation, the boundary layer assumptions are invoked. The non-dimensional parameter V_G retains the same form as Eqs. (13) and (14):

$$V_G = \frac{|S_B|}{|S_I|} = \frac{\left| \rho_\infty g \frac{\partial f}{\partial y} \frac{dv}{df} \right|}{\left| \frac{dv}{df} \frac{\partial}{\partial y} \left(y \rho D \frac{\partial f}{\partial y} \right) \omega \right|} \approx \frac{\left| \rho_\infty g \frac{\partial f}{\partial y} \right|}{\left| \rho D \left(\frac{1}{y} \frac{\partial}{\partial y} y \frac{\partial f}{\partial y} \right) \omega \right|} \approx \frac{\rho_\infty g l_f}{\rho D |\omega|},$$

$$V_G = \frac{Sc \, Ro \, Re}{Fr}, \quad \text{or} \quad V_G = \frac{R_1}{F_1} Sc^{1/2}. \quad (20)$$

The relative importance of baroclinicity to volumetric expansion can be estimated following Eq. (20). This was done by plotting V_G (*e.g.* $V_G = 0.01, 0.1, 1, 10$ and 100) versus R_1 and F_1 as shown in Figure 3. The calculated V_G assumed a unity Schmidt number, *cf.* solid lines in the diagram. However, the results can be interpreted as $\frac{V_G}{Sc^{1/2}}$

FIGURE 3 Vorticity Generation Parameter, V_G , as Functions of R_1 and F_1 .

when a non-unity Schmidt number is desired. Also plotted are the dimensionless length l^* ($l^* = \frac{l}{(\mu\nu/\rho_x g)^{1/3}}$) and dimensionless velocity u^* ($u^* = \frac{u'}{(\rho_x g \nu/\rho)^{1/3}}$) respectively shown as the dotted and dashed lines. The scaling parameters for l^* and u^* are chosen, recognizing the importance of gravitational acceleration and molecular transport on the vorticity. The dimensionless length is essentially the cubic root of the

Grashof number, $Gr = \frac{l^3 \rho_x g}{\mu\nu}$, and the dimensionless velocity can be expressed in

terms of R_1 (Reynolds number) and $Gr \frac{R_1}{Gr^{1/3}}$. It is apparent that the upper right corner

(say $V_G \geq 10$) of the figure denotes a regime where the baroclinicity or buoyancy effects are important, typically with a large length scale (say $l^* > 10$). A small length scale ($l^* < 1$), however, is also possible for baroclinicity being dominant as long as the Froude number is sufficiently small ($F_1 < 10^{-2}$). The volumetric expansion, on the other hand, becomes dominant ($V_G \leq 0.1$) in the lower left corner of the diagram, typically with a small length scale ($l^* < 1$) or a large length scale with high Froude number ($F_1 > 10^4$). It is clear from the diagram that Reynolds number alone cannot fully characterize jet diffusion flames.

It is of interest to identify known experimental conditions in the V_G diagram. As a starting point, the buoyancy driven vortices in jet diffusion flames were considered. These vortices appeared outside the luminous flame with a characteristic length of the order of 10 mm ($l = 0.01$ m) and buoyancy induced velocity of the order of 1 m/s ($u' = 1$ m/s), e.g. see Chen, *et al.* (1988). Employing $Sc = 1$, $\rho D = 10^{-4}$ kg/m-s, $\rho = 1$ kg/m³, $\rho_x g = 10$ kg/m²s², and $l = 0.01$, one obtains $F_1 = 10$, $R_1 = 100$ and $V_G = 10$ (Point A in Figure 3). The same V_G can be calculated if one

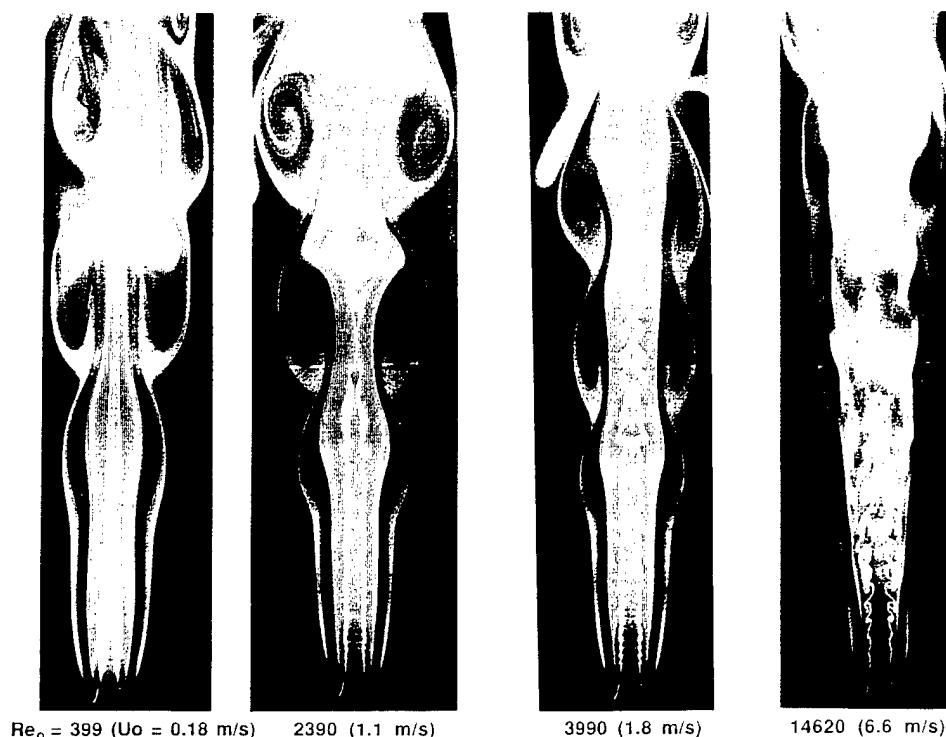


FIGURE 4 Reactive Mie Scattering Visualization of Propane Jet Diffusion Flames (10 mm Contoured Nozzle) (see color plates at end of issue).

follows Eq. (13), setting $l_f = l = 10$ mm ($Sc = 1$), $\frac{\rho_z g l_f}{\rho D} = 10^3 \text{ s}^{-1}$ and $\omega = 10^2 \text{ s}^{-1}$.

This analysis in which $V_G = 10$, suggests that at this condition, baroclinicity is the dominant vorticity generation/destruction mechanism. A net vorticity generation is expected in the fuel lean regime which is consistent with the experimental observation of large vortical structures outside the luminous flame surface. To illustrate the vortical structures, the Reactive Mie Scattering visualization of propane jet diffusion flames at four burner Reynolds number conditions ($Re_0 = 399, 2390, 3990$ and 14620) was shown in Figure 4. The experiments were conducted in a small vertical combustion tunnel in which the fuel nozzle (10 mm contoured nozzle) was surrounded by a low velocity coflowing annular air (0.15 m/s at the burner exit), the apparatus is identical to that described by Chen and Roquemore (1986). The orange color of the photographs marked the two-dimensional projection of the three-dimensional luminous flame surface. The green colour marks the TiO_2 particles illuminated by a thin laser sheet (Nd: YAG pulsed laser) which passed through the center of the jet. The photographs were taken by a still camera positioned at a right angle to the laser sheet. The photographs clearly illustrated the existence of large vortices outside the luminous flame, even at relatively high burner Reynolds number conditions (e.g., $Re_0 = 14620$) for propane jet diffusion flame. In the near injector region, the inner vortices (vortices appeared inside the luminous flame) of propane jet diffusion flames at $Re_0 = 3990$ has a characteristic length of the order 1 mm and velocity of 1 m/s, the

corresponding location in the diagram is Point B. At this location, V_G is 0.1 which suggests that the volumetric expansion overwhelms the baroclinicity. One interesting observation of the Reactive Mie Scattering visualization of the flame ($Re_0 = 3990$) is that the vortices changed the rotational direction in the downstream regime ($x > 15d_0$). This effect has also been observed by Eickhoff and Winandy (1985). A kinematic explanation of the phenomenon is that the buoyancy forces accelerated the fluid near the flame, developing a local peak axial velocity (in radial profile) near the flame which resulted in a change of the rotational direction of vortices. This is consistent with the vorticity analysis. Recall that both volumetric expansion and baroclinicity behave as a sink term in the core regime of the flow, *e.g.* see Figure 2; consequently, when the initial vorticity can not overcome the sink term, a change of the sign of vorticity will occur. As a result, inward rotation as opposed to the outward rotation of inner vortices was observed (also see the Reactive Mie Scattering visualization of propane diffusion flames at $Re_0 = 2390$).

To elaborate the effects of combustion to the core region of the flow, the visualization of cold and combusting jets at an identical burner exit condition (*i.e.*, the same d_0 and u_0) was shown in Figure 5. The flow condition is the same as one of the conditions shown in Figure 4, *i.e.* $Re_0 = 3990$. Figure 5, however, emphasized the near-injector regime and the comparison between the cold and combusting jets. It is evident that the flow structures of cold and combusting jets are quite different at this condition. In the cold jet, the transition of roll-up vortices to more turbulent-like eddies was seen to occur at three to four jet diameters downstream of the nozzle, marking a relatively short potential core at $x/d_0 = 3-4$. Unlike the cold jet, the roll-up vortices inside the luminous flame (termed inner vortices) retained its identities for a substantially longer distance. The jet diffusion flame also showed a much longer potential core. Merging or pairing of inner vortices observed in jet diffusion flames often leads to a turbulent-like 3d structure. The "ordered" inner structure of the flow is common to transitional jet diffusion flames, *e.g.* see Yule *et al.* (1981) and Roque-more, *et al.* (1987b). The laminarization effect on the flow due to combustion is a well known fact, see Yule *et al.* (1981) and, from time to time, it was attributed to the high viscosity associated with the flame (or lower local Reynolds number). The present analysis identified an additional mechanism responsible for laminarization of jet diffusion flames, namely, the vorticity destruction in the flow. It was found that both baroclinicity and volumetric expansion suppressed the vorticity of the flow inside the fuel rich regime (or inside the luminous flame). Conversely, the combustion of jet diffusion flames tends to return the flow inside the fuel rich regime to an irrotational state, yielding a laminarization effect. The suppression of vorticity also suggested that it retards the growth of vortices in the jet shear layer (forced convection shear layer). As a result, the rate of entrainment into the jet shear layer is reduced (entrainment is dominated by large structures), yielding a longer potential core and a reduced jet spread.

The suppression of vorticity in the core regime of jet diffusion flame has been discussed; however, a question yet to answer is how does this differ from the vorticity generation/destruction of buoyant (*e.g.*, methane in air) and negatively buoyant jets (*e.g.*, propane in air). As discussed on vorticity generation in the post-flame regime, in a buoyant jet the baroclinicity acts as a source term but the volumetric expansion can be a source or a sink term depending on the net diffusional transport. As for negatively buoyant jets, the baroclinicity will be a sink term while the volumetric expansion can be a sink (in the core regime) or source term (in the outer regime). The vorticity generation/destruction in buoyant and negatively buoyant jets is illustrated in the scheme shown in Figure 6. The negatively buoyant jets are qualitatively similar

PROPANE JETS

10 mm NOZZLE

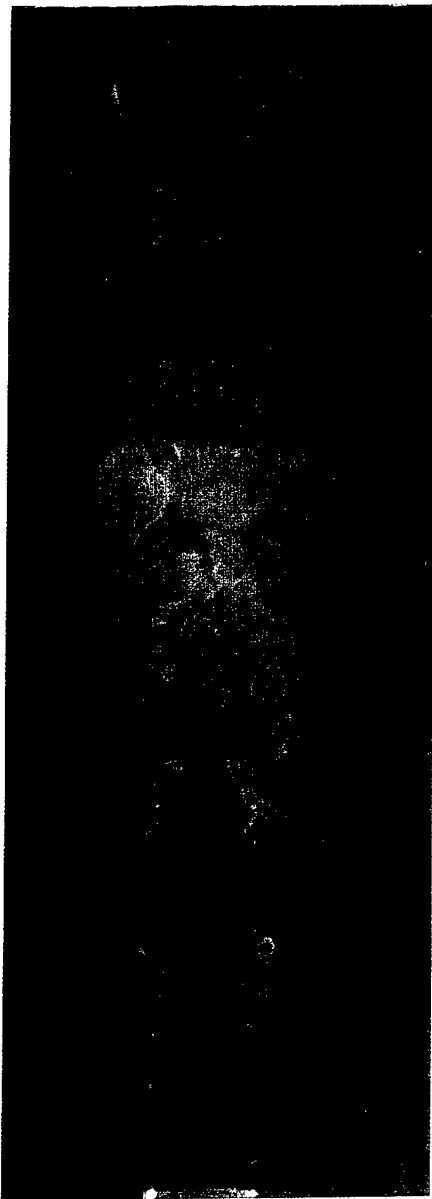
 $Re = 3988$  $Re = 3988$ 

FIGURE 5 Comparison of Propane Cold and Combusting Jets (10mm Contoured Nozzle and $Re_0 = 3990$) (see color plates at end of issue).

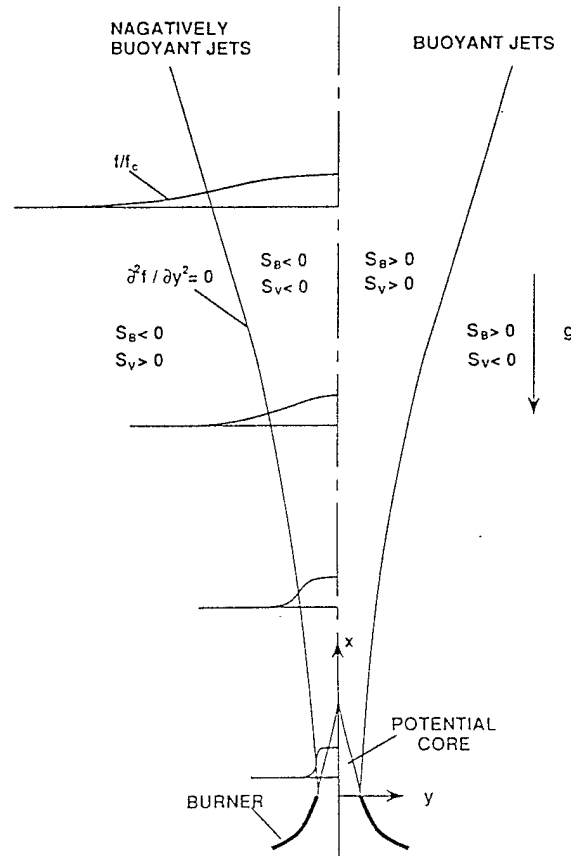


FIGURE 6 Illustration of Vorticity Generation/Destruction in Buoyant and Negatively Buoyant Jets.

in vorticity generation/destruction in the core region as jet diffusion flames; unlike propane jet diffusion flames, the propane cold jets did not reveal the laminarization in the jets, *cf.* Figure 5. This will become clear as one examines the state relationships of jet mixing and jet diffusion flames. Recall that, in the core regime, the volumetric expansion overwhelms the baroclinicity (V_G is of the order of 0.1). The volumetric expansion, in term, is proportional to the gradient of specific volume in the mixture fraction space, *cf.* Eq. (19). For buoyant and negatively buoyant jets, the mixing results in a specific volume of

$$v = fv_0 + (1 - f)v_\infty, \quad (21)$$

where v_0 and v_∞ are densities of the jet fluid and ambient fluid, respectively. The corresponding $\frac{dv}{df}$ is $-0.2923 \text{ m}^3/\text{kg}$ for the cold propane jet and $-6.427 \text{ m}^3/\text{kg}$ for

propane jet diffusion flame. The diffusion flame calculation was performed with a specific volume of $6.601 \text{ m}^3/\text{kg}$ at the flame (from the equilibrium calculation) and a linear approximation for specific volume in the fuel rich regime ($0.06 \leq f \leq 1$). The

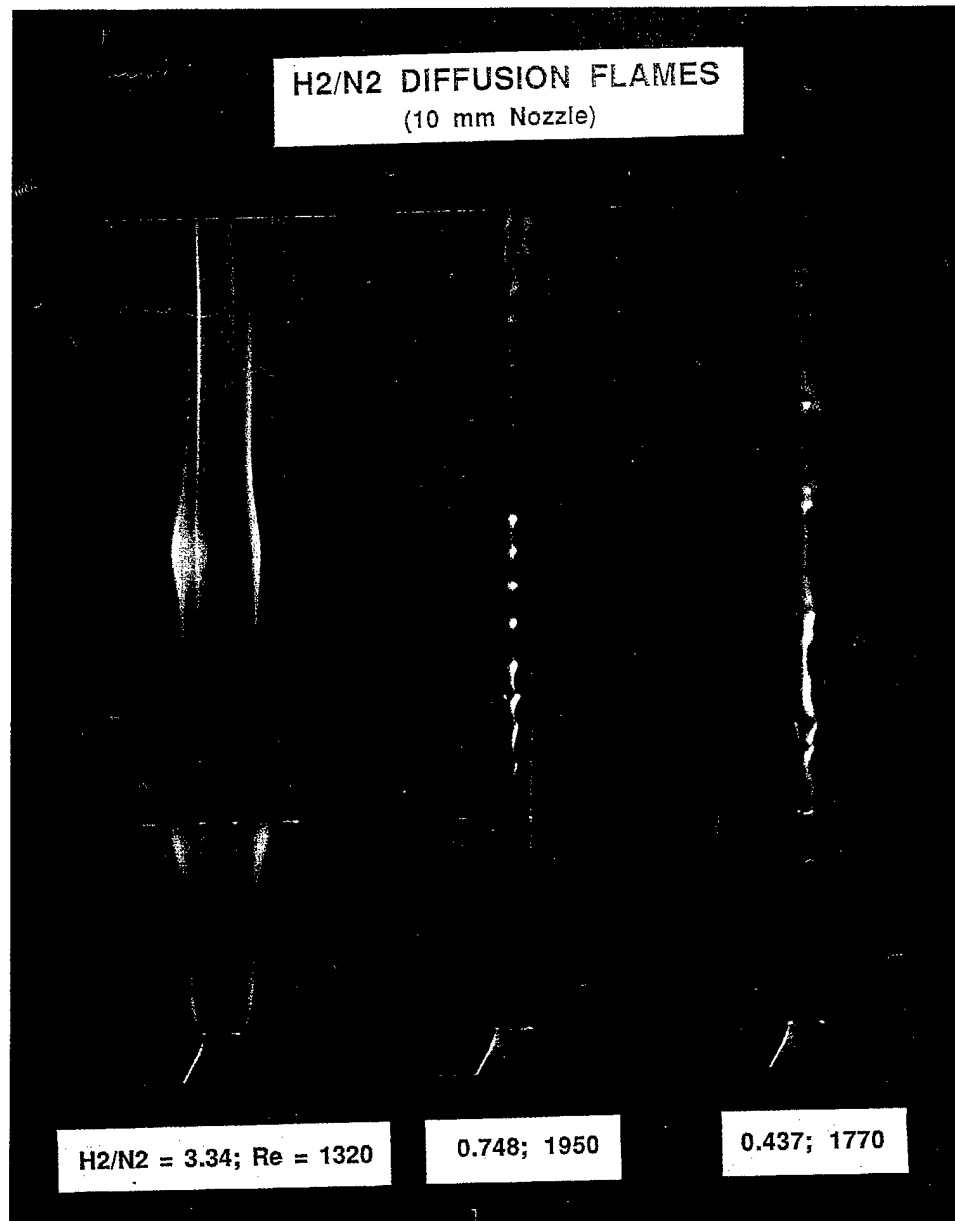


FIGURE 7 Reactive Mie Scattering Visualization of Hydrogen/Nitrogen Jet Diffusion Flames (10 mm Contoured Nozzle) (See colorplates at end of issue).

vorticity suppression due to volumetric expansion is an order of magnitude higher in jet diffusion flames than that in negatively buoyant jets.

The length scale of the flow appears to have a more dominant role in determining the vorticity source/sink term than the velocity scale. For example, as one moves along a constant I^* line in Figure 3, the V_G is reduced by a factor ten when the velocity is increased by ten times (*e.g.*, Point A to Point C). The same ten-fold reduction in

length scale (*e.g.*, Point A to Point B in Figure 3), however, results in a hundred times reduction in V_G . Since the baroclinicity and volumetric expansion have opposite signs in the regime outside the luminous flame, the maximum V_G for net zero vorticity production is $V_G = 1$. This can be accomplished by increasing the velocity scale or decreasing the length scale. The velocity increase can be accomplished by increasing the co-flowing air velocity or the jet exit velocity. It, however, requires a local velocity of the order 10 m/s to suppress the vorticity generation—a difficult condition to accomplish from increasing the jet velocity alone. This can be seen from that the stoichiometric mixture fraction is quite low (*e.g.*, 0.06) for hydrocarbon–air diffusion flames, resulting in a flame location at the outer edge of jet boundary, *i.e.* a low velocity at the flame location. The 10 m/s velocity, however, can be accomplished by increasing the coflowing air velocity—an interesting experimental condition to consider. The length scale consideration requires a length scale of 3 mm to reach $V_G = 1$ condition while the velocity scale is kept unchanged. This suggests that the outer vortices have a minimum length scale of the order 3 mm. Indeed, this seems to be the case for buoyancy driven structures at high jet exit velocities. It should be noted that the length scale discussed here is associated with the velocity scale employed in the analysis; conversely, the length scale is that in the cross-stream direction or y -direction (*e.g.* see Figure 2).

In an effort to study the interaction of the flame and the flow, the flame location in jet shear layer was varied. This was accomplished by diluting the fuel gas with an inert gas (nitrogen, for example) to move the stoichiometric location from the buoyancy induced shear layer (or free convection shear layer) to jet shear layer (or forced convection shear layer). Quite different flow and flame structures were observed when substantial dilution of the fuel was made, *e.g.*, see the Reactive Mie Scattering visualization of hydrogen (diluted with nitrogen) jet diffusion flames shown in Figure 5. The test facility and annular air flow condition were the same as that employed in Figure 4. Three different H_2 – N_2 mixture ratios were examined, they are H_2/N_2 (mole ratio) = 3.34, 0.784 and 0.437 with corresponding $f_s = 0.131$, 0.3648 and 0.4907. Similar jet exit velocities were maintained for the three mixture conditions, *e.g.*, 4.39, 3.95 and 3.25 m/s (in descending mixture ratios). Hydrogen–air flames are non-luminous; the orange color shown in the photographs was due to thermal radiation from reactively formed TiO_2 particles in the flow. At $H_2/N_2 = 3.34$, the Reactive Mie Scattering visualization is similar to buoyant jet diffusion flames fueled with pure hydrogen and hydrocarbons. As the H_2/N_2 ratio was decreased (*e.g.*, $H_2/N_2 = 0.748$), the “luminous” portion of the flame was located closer to the centerline than the higher H_2/N_2 ratio condition, and it did not reveal a spatial periodicity as seen in the $H_2/N_2 = 3.34$ flame. At $H_2/N_2 = 0.748$, the vortical structure was formed at downstream locations and was less identifiable. Further decrease the H_2/N_2 ratio, the vortical structure was completely suppressed. The suppression of buoyancy driven structures can be explained consulting the vorticity generation diagram, Figure 3, or Eq. (20). Two effects may arrive as the flame moved into the jet shear layer, namely, a higher velocity at the flame location and a decrease in length scales. The net effect is a decrease in V_G . When the V_G is reduced to one or smaller, buoyancy effects in vorticity generation is suppressed by the volumetric expansion in the fuel rich regime—a sufficient condition to suppress the buoyancy driven vortices in jet diffusion flames.

Dilution of the hydrogen jet diffusion flame with nitrogen decreases the stoichiometric temperature, for example, the predicted adiabatic flame temperatures, employing the CEC code (Gordon and McBride, 1976) are 1942 K at $H_2/N_2 = 0.8$ and 1735 K at $H_2/N_2 = 0.5$. The decrease in temperature is accompanied by an

increase in stoichiometric density; the decrease in the Grashof number, however, is within 1% for the conditions examined. The decrease in stoichiometric temperature also results in a lower viscosity at the flame. Conversely, the local Grashof number should increase if other parameters (length scale and density difference) remain unchanged. The thermal effects (on the properties) alone, therefore, cannot explain the suppression of vortical structures due to the dilution of the fuel jets. The vorticity analysis presented in this paper offers a useful insight into the observed phenomenon.

SUMMARY AND CONCLUSIONS

A new method to analyze the vorticity generation/destruction in jet diffusion flames due to combustion was presented. The analysis employs a generic flame structure of jet diffusion flames in the context of single conserved scalar to obtain a non-dimensional vorticity generation parameter which describes the relative importance of baroclinicity to volumetric expansion. The non-dimensional parameter, V_G , was found to be the ratio of the Reynolds number to Froude number, and multiplied by the square root of the Schmidt number.

The analysis showed that the jet flame can be divided into three regimes concerning the vorticity generation, as opposed to the usual perception of vorticity destruction due to volumetric expansion and vorticity generation due to buoyancy effects. In the fuel lean regime or outside the luminous flame, the baroclinicity yields vorticity generation but the volumetric expansion results in vorticity destruction. Inside the luminous flame, both the volumetric expansion and baroclinicity suppressed the vorticity production, except in a sub-regime close to the flame sheet where the volumetric expansion acts as a source term. In the post flame regime, the baroclinicity is a vorticity generation term but the volumetric expansion can be a source term in the core regime or sink term in the outer regime, divided by the inflection point in the mixture fraction. The vorticity production in the post flame regime is qualitative similar to a buoyant jet; and conversely, opposite effects are expected for a negatively buoyant jet (heavier fluid injected in to a lighter ambient fluid).

The major assumptions of the present analysis are the single-conserved scalar, boundary layer approximation for the diffusional transport of vorticity, two-dimensionality, and constant ρD . As a result, the conclusions can only be applied to the two-dimensional thin shear layer flows with fast chemistry (or at the infinitely large Damkohler number limit). The approach cannot be applied to high Reynolds number flows in which a convoluted flamelet structure, or folding of the flamelet, is present.

ACKNOWLEDGEMENT

This work was supported in part by the Aerospace Sciences Division of AFOSR and a subcontract GC-1416-87-014 of AFWAL F33615-84-2412. LDC also acknowledged the sponsorship of AFSC/AFOSR University Resident Research Program. The authors acknowledged technical assistance from J. P. Seaba, P. Tschen, R. Britton and D. Trump at various stages of the experiments.

REFERENCES

- Bilger, R. W. (1976) Turbulent Jet Diffusion Flames, *Prog. Energy Comb. Sci.*, **1**, 87-109.
- Chen, L.-D. and Roquemore, W. M. (1986) Visualization of Jet Flames, *Combust. Flame*, **66**, 81-86.
- Chen, L.-D., Seaba, J.P., Roquemore, W.M., and Goss, L. P. (1988) Buoyant Diffusion Flame, *22nd International Symposium on Combustion* The Combustion Institute, 677-684.

- Davis, R. W., Moore, E. F., Chen, L.-D., Roquemore, W. M., Vilimpoc, V., and Goss, L. P. (1990) Numerical/Experimental Study of the Dynamic Structure of a Buoyant Jet Diffusion Flame. *Combustion and Flame* (in press).
- Eickhoff, H. and Winandy, A. (1985) Visualization of Vortex Formation in Jet Diffusion Flames. *Combust. Flame.*, **60**, 99-101.
- Gordon, S. and McBride, B. J. (1976) *Computer Program for Calculation of Complex Chemical Equilibrium*. NASA SP-273, NASA, 1976.
- Gohniem, A. F., Heidarinejad, G., and Krishnan, A. (1988) On Mixing, Baroclinicity and the Effect of Strain in a Chemically Reacting Shear Layer, AIAA 26th Aerospace Sciences Meeting, AIAA-88-0729.
- Jeng, S.-M., Chen, L.-D., and Faeth, G. M. (1982) The Structure of Methane and Propane Diffusion Flames. *19th Symp. (Int.) Combust.*, The Combustion Institute, 349-358.
- Jeng, S.-M. and Faeth, G. M. (1984) Predictions of Mean and Turbulence Properties in Buoyant Methane Diffusion Flames. *ASME J. Heat Transfer*, **106**, 891-893.
- Kuo, K. K. (1986) *Principles of Combustion*, John Wiley & Sons, p. 429.
- Masri, A. R., Bilger, R. W., and Dibble, R. W. (1988) Conditional Probability Density Functions Measured in Turbulent Nonpremixed Flames of Methane Near Extinction. *Combustion and Flame*, **74**, 267-284.
- Roquemore, W. M., Chen, L.-D., Goss, L. P., and Lynn, W. F. (1987a) Structure of Jet Diffusion Flames. Proceedings of The United States - France Joint Workshop on Turbulent Reactive Flows; Also in *Turbulent Reactive Flows* (Lecture Notes in Engineering, Vol 40) R. Borghi and S. N. B. Murthy, Eds, Springer-Verlag, 1989, pp. 49-63.
- Roquemore, W. M., Chen, L.-D., Seaba, J. P., Tschen, P. S., Goss, L. P., and Trump, D. D. (1987b) Jet Diffusion Flame Transition to Turbulence. *APS The Physics of Fluids*, **30**, 2600.
- Yule, A. J., N. A. Chigier, S. Ralph, R. Boulderstone and Ventura, J. (1981) Combustion-Transition Interaction in a Jet Flame. *AIAA J.*, **19**, 752-760.
- Williams, F. A. (1985) *Combustion Theory*, Benjamin/Cummings, p. 73.

Statistical OH-Zone Structures of Turbulent Jet Flames from Liftoff to Near-Blowout

TZONG H. CHEN and LARRY P. GOSS *Systems Research Laboratories, Inc.,
A Division of Arvin/Calspan, 2800 Indian Ripple Road, Dayton,
OH 45440-3696, (513) 252-2706*

(Received July 12, 1990; in final form May 6, 1991)

Abstract—Joint Reactive-Mie-Scattering (RMS) and Planar-Laser-Induced-Fluorescence (PLIF) techniques have been employed to study the impact of jet-shear-layer development upon flame behavior. Images of the complete penetration of the shear-layer vortex through the flame surface have been successfully captured utilizing these planar imaging techniques. Studies of these images have indicated that the degree of flame/flow interaction varies with respect to a wide range of flame conditions and results in the observation of several different types of flame zones—flamelets, multiple flamelets, thick flame zones, and local extinction. The probability of observing the different types of flame behavior was measured, and the results are presented. Analysis of the probability data indicates that the root-mean-square (rms) flame-surface fluctuation, L , provides a proper length for correlating the statistical behavior of the flame. Significant changes in the flame behavior were observed to occur at two critical values of L —the minimal thermal thickness (~ 1 mm) and the nozzle diameter (5 mm).

Key words: Flame, stabilization, measurement, OH, PLIF, probability.

INTRODUCTION

Information on the detailed flame/flow interaction is an important key to understanding flame-stabilization mechanisms for jet flames under attached or lifted flow conditions. Three different theories (Pitts, 1988) have been applied in attempts to explain flame lifting: (1) the laminar flamelet model (Peters and Williams, 1983), (2) the premixed combustion model (Vanquickenborne and van Tiggelen, 1966), and (3) the large-scale structural-mixing model (Broadwell and Bredenthal, 1982; Dahm and Dibble, 1988; Miake-Lye and Hammer, 1988). Although these models were established through sound experimental and theoretical efforts, under many circumstances they are contradictory. Disagreement between the various theories may be due, in part, to the vast differences in the turbulence states of mixing and combustion processes in the jet flowfield which result from the development of large-scale vortices. As an example, earlier work of Shekarchi *et al.* (1988) indicated that the flame lifting begins at the nozzle mouth, regardless of the fuel, for a tapered nozzle jet exhibiting a flat velocity profile. However, it has been experimentally observed that this is *not* the case for a methane flame (Chen and Goss, 1989); the observed difference in lifting characteristics between the methane and propane flames in this study was attributed to the difference in the degree of interaction of the flame surface and the vortices initiated from the fuel jet. Thus, a thorough statistical characterization of this interaction can aid the understanding of flame-lifting mechanisms.

Two important aspects of large-scale vortices have opposite effects upon flame stabilization: (1) promotion of fuel-air mixing which stabilizes the flame, and (2) stretching and penetration of the flame zone which destabilizes the flame. The weight of these counter-effects may be determined by means of associated scales such as the thickness of the combustible mixing zone, the size of the large-scale structure, and the thickness of the OH-zone which provides a potential source of reignition.

Studies of the stabilization effect have received more attention; however, due to the availability of laser diagnostics, considerable interest has now been shown in the destabilization effect. This study is concerned with the destabilization effects of large-scale vortices as imaged by planar-laser-imaging techniques.

The Planar-Laser-Induced-Fluorescence (PLIF) (Hanson, 1986) and Reactive-Mie-Scattering (RMS) (Roquemore *et al.*, 1989) techniques were employed in the present study to characterize the flame/flow interactions of turbulent jet flames. For the PLIF technique, the OH-radical fluorescence was utilized. The existence of the OH-radical is an indicator of ongoing combustion processes and can mark the area of the thermal zone. For the RMS technique, TiO_2 seed particle formed by the reaction of TiCl_4 with water were used for Mie scattering. When properly introduced into the fuel jet, TiCl_4 forms TiO_2 in the fuel-mixing layer. By tracking the vortex motion with Mie scattering and marking the flame zone by OH-fluorescence, the impact of large-scale structures upon flame behavior can be observed. By statistical analysis of the experimentally observed OH-profiles, the thickness of the thermal zone, the magnitude of the flame fluctuation, and the probability of observing flamelets, thick flame zones, and holes can be determined. This analysis allows evaluation of the dependence of the statistical flame properties upon the degree of flame/flow interaction. A proper representation of the degree of flame/flow interaction will be described.

EXPERIMENTAL

Flow conditions

The fuel jet employed in this study consisted of a short, tapered 5 mm-id nozzle surrounded by a 25 cm annular air duct. The contraction ratio of the contoured nozzle, 20 to 1, was designed to yield a flat exit-velocity profile (Seaba, 1990). The exit velocity of the annular air flow was fixed at 15 cm/sec. The fuels employed included propane and methane, with jet velocities ranging from flame liftoff to near blowout. The critical velocity for the propane flame was measured to be 19.5 m/s and that for the methane flame, to be 29.0 m/s. Under the critical liftoff condition, the flame can be either attached or lifted. The measurement locations were chosen in the near-field region from the flame base (liftoff height) up to 60 jet diameters downstream, $x/d = 60$. In this region the fuel-jet shear layer and flame surface interact strongly, allowing the deformation of the flame surface to be studied.

Diagnostic Techniques

The optical setup utilized in this study for joint RMS/OH-PLIF measurements is shown in Figure 1. A Quanta-Ray DCR-3:PDL:WEX laser system was employed to produce the UV radiation required to excite the $(v = 0 \rightarrow v = 1)Q_1(6)$ transition of the OH-radical. The UV beam of 283 nm wavelength was passed through the sheet-forming optics (cylindrical lens combination) and directed through the flame zone. The thickness of the laser sheet was ~ 1 mm. Laser-induced fluorescence from the OH-radical was observed at right angles to the laser sheet by an intensified two-dimensional CCD camera (Photometrics CC200). The intensifier was coupled with the CCD by optical fibers. The gate width of the intensifier was 2 μsec . The 384×576 pixel density of the CCD camera combined with the optical arrangement resulted in a 98 $\mu\text{m}/\text{pixel}$ spatial resolution which allowed observation of a 37.5 mm \times 55 mm area of the flame.

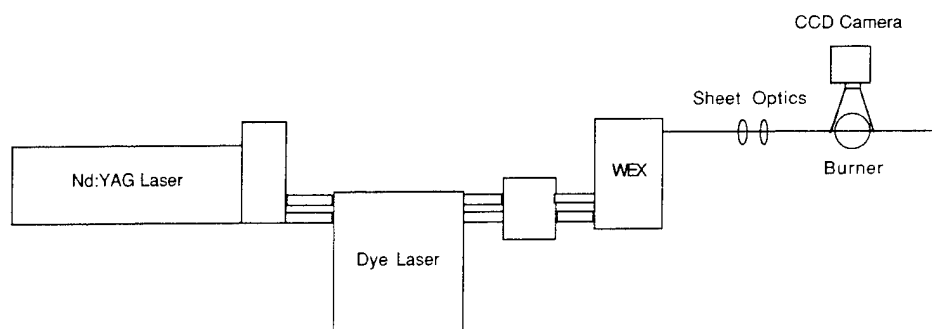


FIGURE 1 Optical arrangement of joint RMS/OH-PLIF systems.

Joint RMS/OH-PLIF measurements were made by introducing a small amount of TiCl_4 into the gaseous fuel. TiCl_4 reacts with water formed as a combustion byproduct to produce small seed particles which can scatter laser light. Care was taken to ensure that the seed concentration would be maintained at a low level such that the OH-fluorescence signal would not be overwhelmed by the Mie-scattering signal. In this arrangement the Mie-scattering and OH-PLIF signals are observed simultaneously by a single camera system. For independent OH-PLIF measurements, a spike filter with 30% efficiency centered at 314 nm, half-width of 10 nm, was used to filter out the Mie scattering from the dust particles and soot. For most flame conditions tested, the flame base was blue in color and soot emission was not observed to be a problem.

Probability Analysis and Signal Detectability

For constructing a statistical description of the flame properties, hundreds of scalar measurements are required. In the case of two-dimensional imaging techniques, this can constitute a problem due to the massive amount of data required (443 KBytes of information per image). To solve this problem, a line-image system was employed. In this case the laser-excitation beam is mildly focused into a cylinder or line, the fluorescence from which is captured by a 1024-element intensified-diode-array system. For each flame condition, several axial locations were chosen for measurement. At each location 750 line images were acquired and stored for analysis.

Because the laser beam intercepts the jet-flame axis perpendicularly, it crosses the flame cone twice. For the flame region and flow conditions measured, the magnitude of the flame-surface fluctuation is $< 5\%$ of the diameter of the flame cone (Chen *et al.*, 1989). Therefore, it can be assumed that the laser beam intercepts the flame surface perpendicularly. In addition, the relatively small radial flame fluctuation cannot cause the flame to drift out of the laser beam. Thus, absence of the OH-signal in an area where the flame surface should be located can be due to flame extinction, *i.e.*, hole formation. With the exception of hole formation, the experimentally observed thermal zones were of three types: thin flamelets (~ 1 mm in thickness), thick flame zones (> 3 mm), and multiple flame zones (combination of multiple thin or thick zones). The multiple flame zone may be the result of the flame wrapping around the vortices. For data-presentation purposes, multiple flamelets were considered to be a thick flame.

The small ratio of flame fluctuation to flame-cone diameter also ensures that the flame surface will not cross the jet axis. Thus, the measured OH-signal was divided

into two regions, separated by the jet axis, for examination. At each side of the axis, the thin flamelets, thick flames, and local extinctions were counted. By recording the number of times each of these zones was observed, one could determine the probability of their occurrence. For example,

$$\text{Probability of flamelet occurrence} = \text{Number of times flamelets were counted}/N_i$$

where N_i is the number of line images collected (N_i is the number of images collected (N_i is 750 for every flame condition and location measured in this study).

Although quantitative temperature information is not required for this type of analysis, the signal-detectability limit must be considered. To ensure that the OH-signal would not disappear due to insufficient laser power or inefficient detectability, several measures were taken. First, the Nd: YAG laser was operated at full power. Measurements of the OH-signal intensity as a function of laser power indicated that the OH-fluorescence was in the saturated regime for the line-measurement conditions studied. For the optical setup utilized in this study, the linear OH-fluorescence exists only under very low power conditions—less than 50% of full power. Second, results from the line-OH measurements, when compared with temperatures measured by thin-filament pyrometry (TFP) (Chen and Goss, 1989; Chen *et al.*, 1989), indicated that the OH-signal was detected only in a region where the temperature was above ~ 1000 K. Therefore, when the local flame temperature was higher than the ignition temperature and the fuel-air mixture was combustible, the OH-radical existed and could be detected by the optical setup employed.

RESULTS AND DISCUSSION

Local Extinction and Non-Flamelet Behavior

Evidence of discontinuities (or holes) in the flame sheet of jet diffusion flames has been reported by several groups (Roquemore *et al.*, 1985; Schefer *et al.*, 1988; Takahashi *et al.*, 1982). The existence of holes in the flame surface is thought to result from the penetration of the flame by vortices by the fuel jet. Since flame-stabilization behavior is linked to the evolution of these vortices (Pitts, 1988; Miake-Lye and Hammer, 1988), an experimental investigation was initiated to study these flame/vortex interactions.

Figure 2 is a joint RMS/OH-PLIF image taken in the near field of an attached CH_4 diffusion flame at the critical liftoff velocity. The vortex penetration through the flame surface can be seen clearly in this figure. The flame surface, indicated by the outer OH fluorescence, displays an area of local extinction corresponding to the size of the penetrating vortex which is marked by the Mie scattering associated with the fuel jet. In this particular case the propagation of the flame surface is passive and dominated by the vortex motion which is driven by the fuel jet. For most jet diffusion flames, the separation of the flame surface from the shear layer (Roquemore *et al.*, 1989; Masri *et al.*, 1984) is well defined. However, this separation is not so well defined in the methane as in the propane flame, resulting in a stronger flame/flow interaction for the former. In addition, the density of the methane jet is lower than that of the co-flowing air, thus, the shear-layer vortex has a higher probability of spinning out and interacting with the flame. As a result, the methane flame displays a higher probability of hole formation than the propane flame at the critical liftoff jet velocity. The high probability of hole formation at a location ~ 60 mm downstream causes the methane flame to

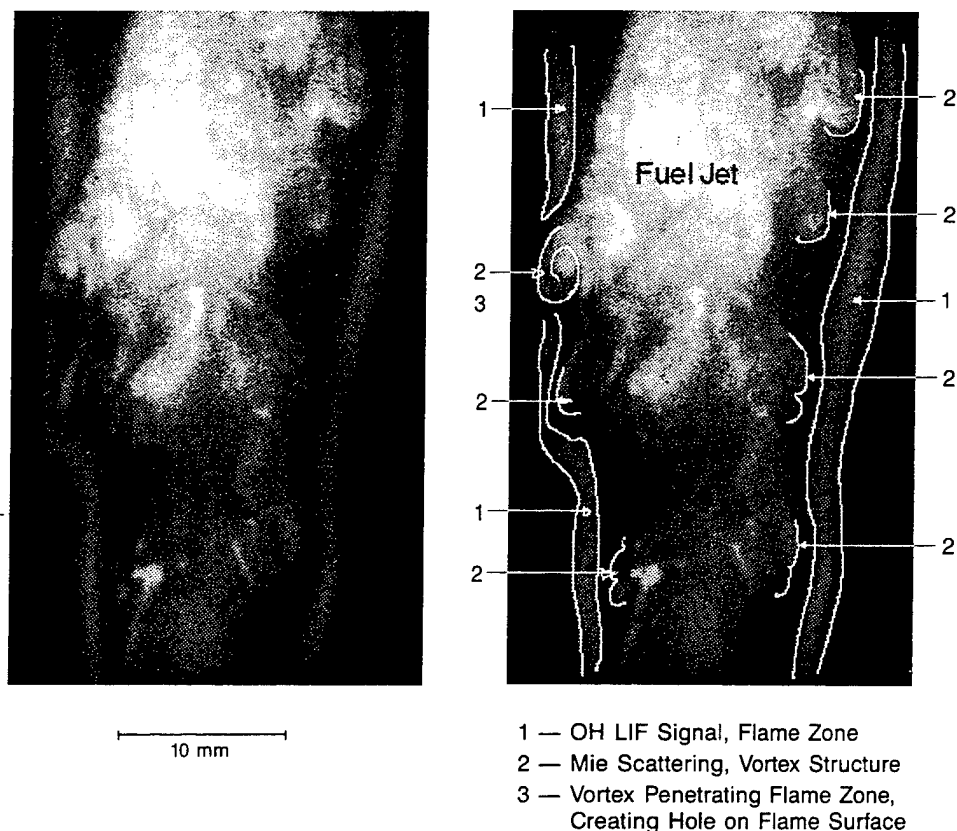


FIGURE 2 Image of penetration of vortex through surface of CH_4 diffusion flame under critical liftoff condition: flame surface is marked by OH-fluorescence and jet by Mie scattering.

split before complete lifting occurs. The observation was confirmed by the probability data which will be presented in the next section.

Seven large vortices can be identified in the RMS/OH-PLIF image displayed in Figure 2. The flame surface is distorted by only three of these. The other four have little effect because of their greater separation from the surface which reduces the strength of the interaction. As a result the flame surface fluctuates at a frequency which is lower than that of vortex passage. This result is consistent with those of previous studies in which the flame surface was found to fluctuate in the frequency range ~ 50 to 125 Hz. Based upon the liftoff height, jet exit velocity, and flame-crossing frequency, the values of the Strouhal number for this flame were determined to be ~ 0.10 – 0.15 (Chen *et al.*, 1989).

As can be seen from Figure 2, the OH-zone thickness remains fairly constant, ~ 1 mm, at the flame base for both the propane and methane flames operating under the critical liftoff condition. This slow growth of the thermal zone was also observed by Schefer *et al.* (1988) and Stepowski *et al.* (1988). For comparison, the OH zone thickness for the laminar propane and methane flames was also experimentally measured, and the smallest value was found to be 1 mm. As the jet velocity increased beyond flame liftoff, the interaction between the flame and the vortex layer becomes



FIGURE 3 First type of flame base of CH_4 diffusion flame under near-blowout condition.

stronger, resulting in an increase in the probability that local extinction (holes) will occur at the flame surface. In this case the flame attempts to stabilize at a downstream location where the interaction is weaker. Under the near-blowout condition, the flame base is stabilized far downstream where fuel-air mixing is nearly complete. This results in a premixed combustion zone which is thick in nature and tends to wrap around the vortices. In this region tribrachial flames (Buckmaster and Matalon, 1988) may exist, which can also contribute to a thick thermal zone. The measured thickness of the OH-zone near the flame base under this condition varies from ~ 10 to 30 mm, which compares favorably with previous temperature results (Chen and Goss, 1989).

Figures 3–5 depict planar OH-images taken around the base of a lifted methane flame operated under near-blowout conditions. Under these conditions 1-mm-thick flamelets can still be observed, but the probability of observing them is lower. The observed flame-base structures fall into three categories. The first, shown in Figure 3, is a simple flame tip. The second is a thick vortical structure, as shown in Figure 4. Inside the thick thermal zone, two small non-burning zones can be observed, corresponding to pockets which are extremely fuel-rich (Barlow, 1989). The third type of flame base, shown in Figure 5, is characterized by two distinct islands of combustion located outside the main flame base. These images indicate that flame shape and size vary dramatically as a function of time and space.



10 mm

FIGURE 4 Second type of flame base of CH_4 diffusion flame under near-blowout condition: local extinction found inside thick thermal zone.

Probability of Observing Flamelets, Holes, and Thick Zones

The flames shown in Figures 4 and 5 would display multiple OH-signal peaks if observed by a line CCD detector. The presence of such peaks was reported in an earlier study (Chen *et al.*, 1989). The multiple flame zones in this case were classified as thick flames, as was mentioned previously. In addition to the thick zone, flamelets and holes can also be observed at different downstream locations. The probability of observing these events is shown in Figure 6–9 for methane and propane flames under the critical liftoff condition. Figures 6–9 display data for the attached methane flame, the lifted methane flame, the attached propane flame, and the lifted propane flame, respectively. The probability of observing thin flamelets is highest at the flame base. Farther downstream, the probability of observing hole and thick OH-zones increases. The methane flame displays a higher probability of developing holes than the propane flame, as explained previously. The coexistence of thin flamelets, holes, and thick flame zones is indeed challenging to the modelling community (Haworth *et al.*, 1989; Chen and Kollmann, 1989; Corea and Gulati, 1989).

Comparison of Figures 6 and 7 leads to the conclusion that under the critical liftoff condition, flamelets, thick flame zones, and holes have the same probability of occurring in attached and lifted flames. This is primarily due to the fact that the exit

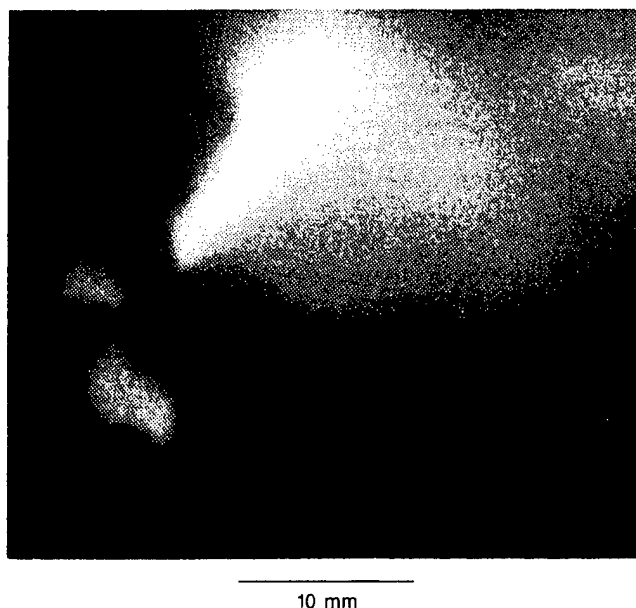


FIGURE 5 Third type of flame base of CH_4 diffusion flame under near-blowout condition; island of combusting zone located away from main thermal zone.

velocities are the same. This conclusion can also be drawn from the propane-flame results displayed in Figure 8-9. At the 300 mm downstream location, the probability of observing holes approaches that of observing flamelets for the flow conditions presented in Figures 6-9. Data for the methane flame, having an exit velocity of 40 m/s, are plotted in Figure 10. As the jet velocity is increased, the flame/flow interaction is observed to become stronger. The probability of observing holes is higher than that of observing flamelets at the 225 mm downstream location. For a methane flame having an exit velocity of 60 m/s, the corresponding location is ~ 175 mm.

The effect of the changing scales upon flame stabilization can be appreciated by examining Figure 6 which shows that at $\cong 60$ mm, there is a local high probability that holes will be observed and, thus, a low probability that the flame will be observed. Eventually, with a small increase in velocity from the critical liftoff value, flame necking will occur at this location. The probability of holes being displayed at this location may be at the local maximum; however, the highest probability of holes being observed occurs farther downstream, as shown in Figure 6-10. The reason for local splitting of the methane flame at ~ 60 mm but not at other locations having higher probabilities of displaying holes (local quenching) may be related to the variety of scales, each of which is changing with respect to space and time. Near the nozzle exit mixing is incomplete, and the mixing layer and the flammable zone are thin. As a result the measured flame zone is thin, ~ 1 mm. The vortex at this location can be as large as 5 mm, which is greater than the flame thickness and can completely penetrate the flame, as shown in Figure 2. Under these conditions the flame can be quenched and cannot be reignited easily. Farther downstream, however, more efficient mixing is achieved which results in a thick mixing layer and flammable zone. Thus, in this

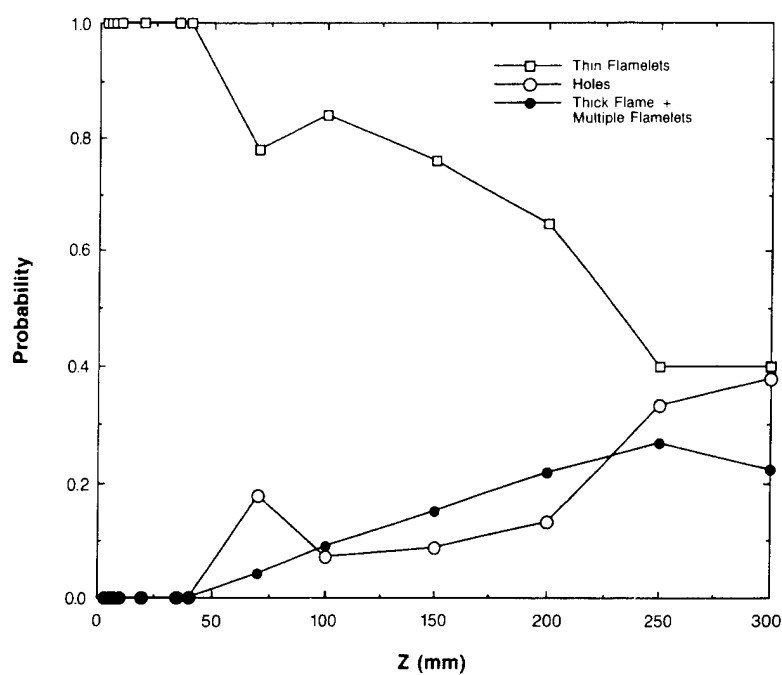


FIGURE 6 Plot of probability of observing flamelets, thick flame, and holes for attached CH₄ flame under critical liftoff condition.

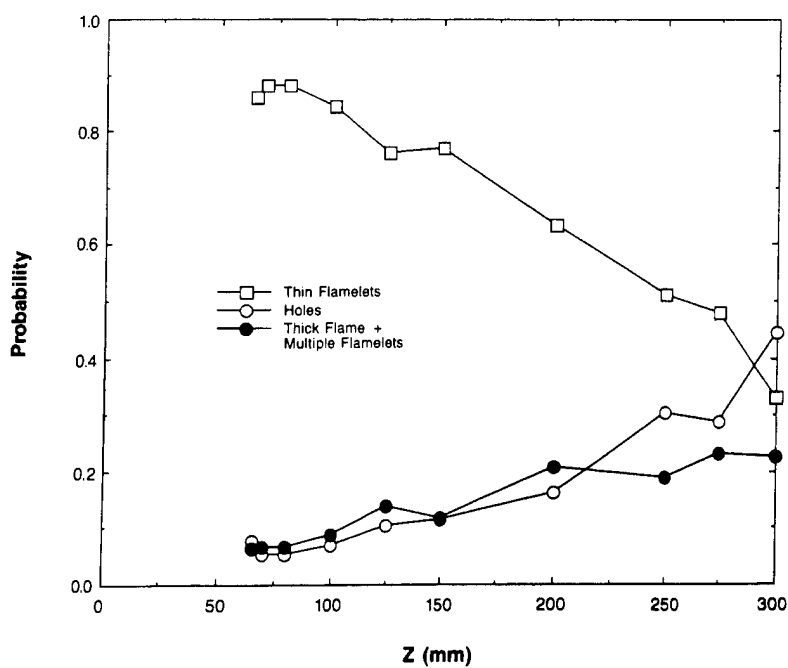


FIGURE 7 Plot of probability of observing flamelets, thick flame, and holes for lifted CH₄ flame under critical liftoff condition.

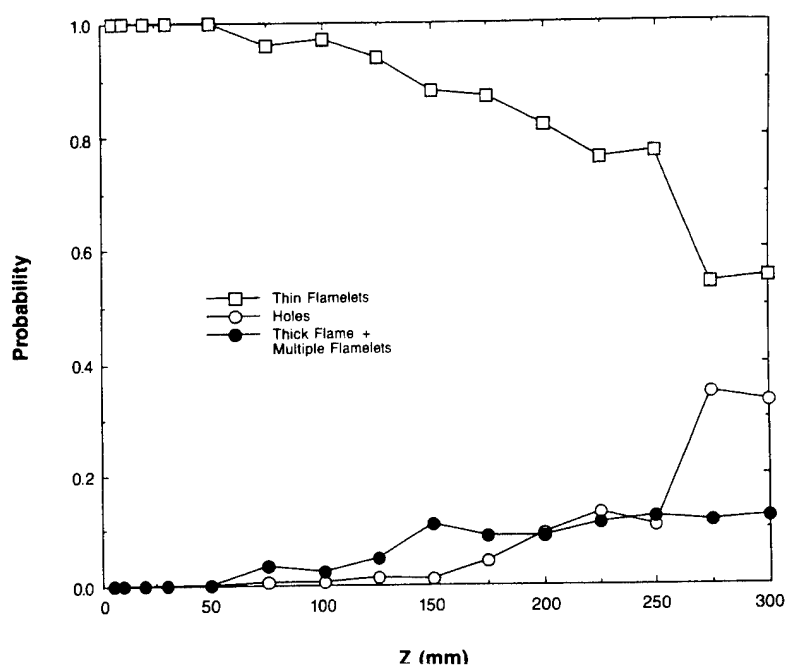


FIGURE 8 Plot of probability of observing flamelets, and holes for attached C_3H_8 flame under critical liftoff condition.

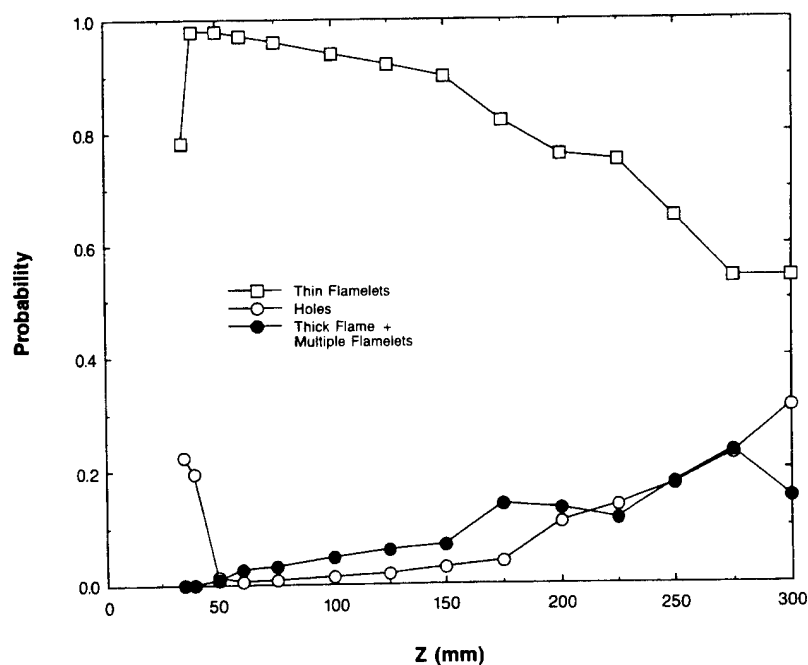


FIGURE 9 Plot of probability of observing flamelets, thick flame, and holes for lifted C_3H_8 flame under critical liftoff condition.

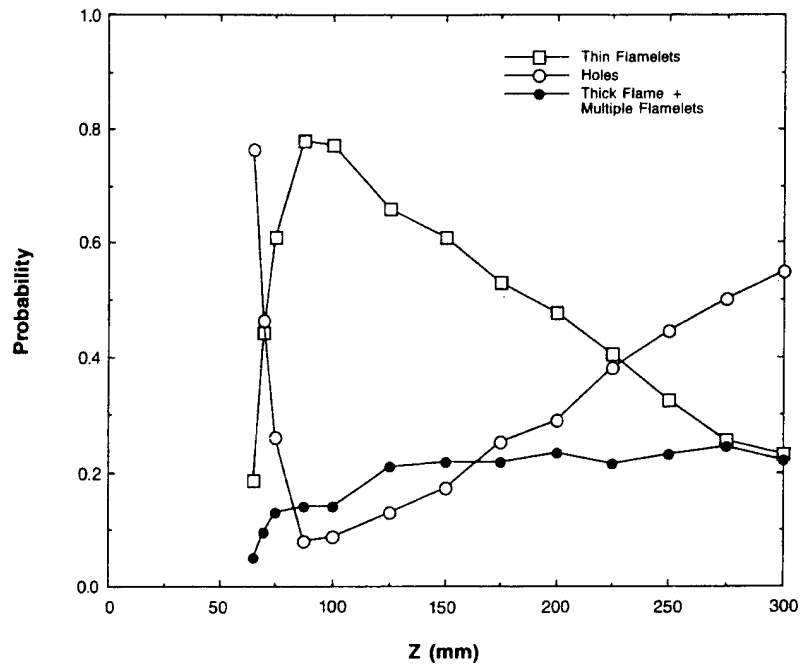


FIGURE 10 Plot of probability of observing flamelets, thick flame, and holes for lifted CH_4 flame with exit velocity of 40 m/s.

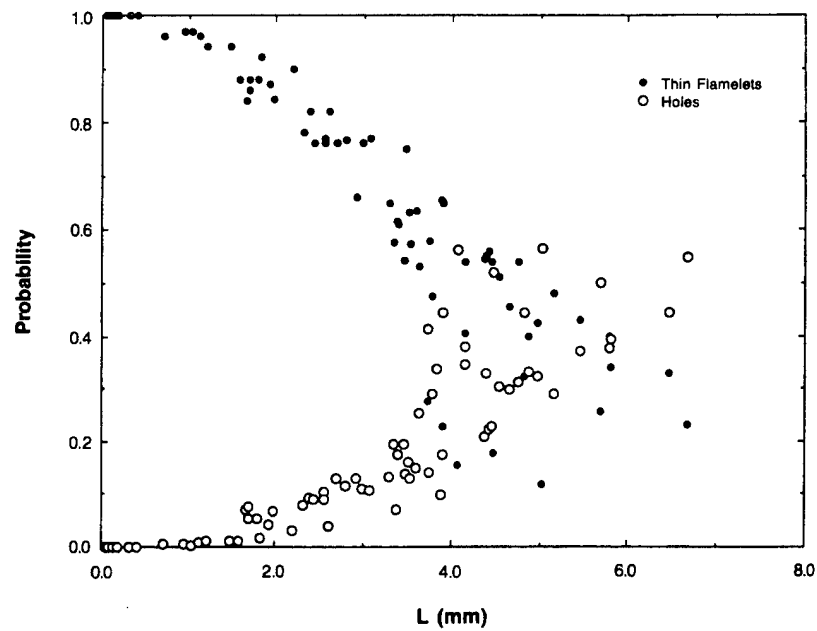


FIGURE 11 Correlation between rms flame fluctuation, L , and probability of observing flamelets and holes for wide range of flame conditions.

region the probability of holes being displayed increases (which may be due to the increasing importance of large buoyancy instability structures); however, since the probability of reignition is also greater, the flame will not split at these locations.

Correlation of Statistical Properties and the Degree of Flame/Flow Interactions

As the flow is perturbed by large structures in the jet shear layer, the flame surface fluctuates about its stationary (reference) position. At the measurement location, the mean flame location can be derived by statistically analyzing the 750 line images acquired. The root-mean square (rms) value of the flame fluctuation, which also results from statistical analysis, is a good measure of the flame/flow interaction. This rms flame fluctuation is denoted by L which is a length scale corresponding to the degree of interaction. The value of L can be related to the local strain rate, provided the local velocity scale is known. A similar approach was employed in earlier studies to determine the degree of flame/flow interaction using the thin-filament-pyrometry (TFP) technique (Chen and Goss, 1989; Chen *et al.*, 1989).

The probability data, as discussed in the previous section, indicated that at the critical liftoff velocity, the methane flame has a higher probability of displaying holes than the propane flame. This is due to the stronger flame/flow interaction in the methane-flame case. However, the thermal time scale—the ratio of laminar flame thickness to laminar flame speed—for the methane and propane flames is approximately the same (1/430 and 1/400 sec, respectively). Therefore, if the degree of flame/flow interaction is the same, the probability of displaying holes or local extinction should be the same. To test this hypothesis, the probability of observing thin flamelets and holes for both methane and propane flames was plotted as a function of the rms flame fluctuation, L ; the results are displayed in Figure 11.

Data for the propane and methane flames under critical liftoff conditions, both attached and lifted, are summarized in Figure 11. In addition, data for methane flames in operation beyond the flame-lifting condition and having jet exit velocities of 40, 50, and 60 m/s are included. For the wide range of flame conditions studied, the maximum rms flame fluctuation was observed to be < 7 mm for the flame in the 300 mm downstream range ($x/d < 60$). Under the same flame condition, the flame/flow interaction becomes stronger (L becomes larger) at locations farther downstream. At a given downstream location, the flame/flow interaction becomes stronger with increasing jet exit velocity. Therefore, use of L as the independent variable inherently includes the fuel-type, fuel-velocity, and downstream-distance dependence of the flame/flow interaction. Figure 11 indicates that the probability of observing flamelets decreases with increasing L , while the probability of observing holes increases with increasing L . Indeed, the probability data which represent a wide range of flame conditions fall within a relatively narrow band, indicating strong correlation between the flame characteristics and the value of L .

A detailed examination of Figure 11 indicates that for two important values of L , the statistical properties of the flame behavior change dramatically. The first is the minimum thermal thickness, measured to be ~ 1 mm, while the second is the nozzle diameter of the jet (5 mm). When L is smaller than 1 mm, the probability of observing flamelets and holes is constant, 1 and 0, respectively. This implies that when interaction is small such that L remains less than the minimal thermal thickness, the flame displays thin-flamelet behavior and no local extinction occurs. When L is larger than 1 mm, the probability of observing flamelets decreases linearly, while that of observing holes increases linearly. When the value of L reaches ~ 5 mm, the probability of observing holes becomes greater than that of observing flamelets.

CONCLUSIONS

Hydrocarbon jet diffusion flames under liftoff to near-blowout conditions have been characterized using joint RMS/OH-PLIF techniques. The shear-layer zone observed by the RMS technique and the flame zone revealed by line and planar OH-imaging display many degrees of interaction. As a result three types of OH zones—thin flames, multiple flamelets, and thick flames—are observed. In addition, local flame extinction through the flame surface has been observed and may be governed by a strong convection, dissipation, strain, and heat-loss mechanisms.

The statistical description of various types of OH-zones under a wide range of flow conditions has been given. From a statistical viewpoint, the following conclusions have been drawn:

- For both the methane and propane flames, the thinnest flamelets observed are ~ 1.0 mm. Near the flame blowout condition, the thermal thickness of the flame base may be as large as 30 mm.
- Local extinction inside a thick thermal zone and small pockets of combustion located outside the main flame zone are observed near the flame base when the flame is operated under near-blowout conditions.
- The flame/flow interaction is stronger for the methane than for the propane flame under the critical liftoff condition. Consequently, the methane flame has a higher probability of displaying holes.
- Good correlation is observed between the rms flame fluctuation, L , and the probability of displaying holes and flamelets for the methane and propane flames. The statistical analysis indicates that when the value of L approaches the nozzle diameter, the probability of observing holes in the flame surface is higher than that of observing flamelets. If the interaction is small, such that L remains less than 1 mm (the minimal thermal thickness), the flame displays thin-flamelet behavior and no local extinction occurs.

ACKNOWLEDGEMENT

This work was supported by and performed at the Wright Laboratory /Aero Propulsion and Power Directorate under Contract No. F33615-85-C-2562. The authors are indebted to Dr. W. M. Roquemore for support and discussions concerning this work. The authors wish to thank Drs. R. Dibble, J. Driscoll, D. Mikolaitis, W. Shyy, F. Takahashi, and D. Talley for the discussion regarding the structure of the lifted flame base. Technical assistance from D. D. Trump and M. Whitaker is appreciated. A version of this paper was presented at the AIAA 28th Aerospace Sciences Meeting as AIAA Paper No. 90-0159.

REFERENCES

- Barlow, R. (1989). Sandia National Laboratories, private communication.
- Broadwell, J. E. and Breidenthal, R. E. (1982). A simple model of mixing and chemical reaction in a turbulent shear layer. *J. Fluid Mech.*, **125**, 397.
- Buckmaster, J. and Matalon, M. (1988). Anomalous Lewis number effects in tribrachial flames. In *Twenty-Second Symposium (International) on Combustion*, The Combustion Institute, Pittsburgh, Pennsylvania, pp. 1527–1535.
- Chen, J-Y. and Kollmann, W. (1989). PDF modelling of chemical nonequilibrium effects in turbulent nonpremixed hydrocarbon flames. In *Twenty-Second Symposium (International) on Combustion*, The Combustion Institute, Pittsburgh, Pennsylvania, pp. 645–653.
- Chen, T. H. and Goss, L. P. (1989). Flame lifting and flame/flow interactions of jet diffusion flames, AIAA Paper No. 89-0156.

- Chen, T. H., Goss, L. P., Talley, D. and Mikolaitis, D. (1989). Stabilization zone structure in jet diffusion flames from liftoff to blowout, AIAA Paper No. 89-0153.
- Correa, S. M. and Gulati, A. (1989). Non-premixed turbulent CO/H₂ flames at local extinction conditions. In *Twenty-Second Symposium (International) on Combustion*, The Combustion Institute, Pittsburgh, Pennsylvania, pp. 599-606.
- Dahm, W. J. A. and Dibble, R. W. (1988). Combustion stability limits of coflowing turbulent jet diffusion flames. AIAA Paper No. 88-0538.
- Eickhoff, H., Lenze, B. and Leuckel, W. (1985). Experimental investigation on the stabilization mechanism of jet diffusion flames. In *Twentieth Symposium (International) on Combustion*, The Combustion Institute, Pittsburgh, Pennsylvania, pp. 311-318.
- Hanson, R. K. (1986). Combustion diagnostics: planar imaging techniques. In *Twenty-First Symposium (International) on Combustion*, The Combustion Institute, Pittsburgh, Pennsylvania, pp. 1677-1691.
- Haworth, D. C., Drake, M. C., Pope, S. B. and Blint, R. J. (1989). The importance of time-dependent flame structures in stretched laminar flamelet models for turbulent jet diffusion flames. In *Twenty-Second Symposium (International) on Combustion*, The Combustion Institute, Pittsburgh, Pennsylvania, pp. 589-597.
- Long, M. B. and Yip, B. (1988). Measurement of three-dimensional concentrations in turbulent jets and flames. In *Twenty-Second Symposium (International) on Combustion*, The Combustion Institute, Pittsburgh, Pennsylvania, pp. 701-709.
- Masri, A. R., Starnes, S. H. and Bilger, R. W. (1984). Transition and transport in the initial region of a turbulent diffusion flame. In Bowen, J. E. (Ed.), *Dynamics of Flames and Reactive Systems*, American Institute of Aeronautics, Washington, D.C., Vol. 95 of *Progress in Astronautics and Aeronautics*, pp. 293-304.
- Miake-Lye, R. C. and Hammer, J. A. (1988). Lifted turbulent jet flames: a stability criterion based on the jet large-scale structure. In *Twenty-Second Symposium (International) on Combustion*, The Combustion Institute, Pittsburgh, Pennsylvania, pp. 817-824.
- Namazian, M., Schefer, R. W. and Kelly, J. (1988). Scalar dissipation measurements in the developing region of a jet. *Comb. Flame*, **74**, 147.
- Peters, N. and Williams, F. A. (1983). Liftoff characteristics of turbulent jet diffusion flames. *AIAA J.*, **21**, 423.
- Pitts, W. M. (1988). Assessment of theories for the behavior and blow out of lifted turbulent jet diffusion flames. In *Twenty-Second Symposium (International) on Combustion*, The Combustion Institute, Pittsburgh, Pennsylvania, pp. 809-816.
- Roquemore, W. M., Chen, L.-D. and Lynn, W. F. (1989). Structure of jet diffusion flames. In Borghi, R. and Murthy, N. B. (Eds.), *Turbulent Reactive Flows (Lecture Notes in Engineering)*, Springer-Verlag, New York, Vol. 40, pp. 49-63.
- Schefer, R. W., Namazian, M. and Kelly, J. (1988). Structural characteristics of lifted turbulent-jet flames. In *Twenty-Second Symposium (International) on Combustion*, The Combustion Institute, Pittsburgh, Pennsylvania, pp. 833-842.
- Seaba, J. P. (1990). *Burner Statistics of Jet Diffusion Flames*, Ph.D. Dissertation, University of Iowa, Iowa City, Iowa.
- Shekarchi, S., Savas, O. and Gollahalli, S. R. (1988). Structure of a split gas flame. *Comb. Flame*, **73**, 221.
- Stepowski, D., Labbaci, K. and Borghi, R. (1989). Instantaneous radial profiles of OH fluorescence and Rayleigh scattering through a turbulent H₂-air diffusion flame. In Borghi, R. and Murthy, S. N. B. (Eds.), *Turbulent Reacting Flows (Lecture Notes in Engineering)*, Springer-Verlag, New York, Vol. 40, pp. 64-80.
- Takahashi, F., Mizomoto, M. and Ikai, S. (1982). Transition from laminar to turbulent free jet diffusion flames. *Comb. Flame*, **48**, 85.
- Vanquickenborne, L. V. and van Tiggelen, A. (1966). The stabilization mechanism of lifted diffusion flames. *Comb. Flame*, **10**, 59.

Dynamic Stabilization Zone Structure of Jet Diffusion Flames from Liftoff to Blowout

Tzong H. Chen* and Larry P. Goss†

Systems Research Laboratories, Inc., A Division of Arvin/Calspan, Dayton, Ohio 45440

Douglas G. Talley‡

University of Michigan, Ann Arbor, Michigan 48109
and

David W. Mikolaitis§

University of Florida, Gainesville, Florida 32611

Structures of methane and propane jet diffusion flames under liftoff to blowout conditions are studied. The focus of this investigation is on the dynamic, time-varying features of flame propagation and stabilization near the flame base. The turbulent velocity and length scales of the flame motion were *directly* measured using the thin-filament pyrometry (TFP) technique at high sampling rates. A significant change in the turbulent velocity and length scales of the measured flame was observed as the jet velocity increased, approaching the blowout condition. The deduced turbulent diffusivity displayed over one order of magnitude increase from liftoff to blowout. The strain rate, however, never exceeded ~ 600 1/s. Near blowout, the flame base became very broad.

Nomenclature

- D_t = measured turbulent diffusivity associated with flame-surface fluctuation
 f = flame crossing frequency
 h = flame liftoff height, mm
 Δh = magnitude of liftoff-height fluctuation, mm
 L = length scale of flame-surface motion; root-mean-square value of radial flame location, mm
 S_r = measured strain rate deduced from turbulent-flame-surface motion
 S_r = Strouhal number
 S_u = maximum value of laminar burning velocity
 U_e = jet exit velocity, m/s
 v' = velocity scale of flame-surface motion; root-mean-square value of radial velocity, m/s
 ν = kinematic viscosity
 $\bar{\rho}$ = density ratio of fuel to ambient air

I. Introduction

TOPICS related to propagation and stabilization of turbulent, lifted jet diffusion flames have been widely investigated.¹⁻¹¹ The investigative tools used in these studies included flame visualization and point and two-dimensional measurements. Point measurements typically included determination of velocity, temperature, and species concentration as well as joint measurement of the above properties using laser Doppler velocimetry (LDV), Raman spectroscopy, coherent anti-Stokes Raman spectroscopy (CARS), LDV/Raman, and LDV/CARS. Two-dimensional measurements of the above properties were achieved through the use of techniques such as Rayleigh imaging, Raman scattering, and laser-induced fluorescence (LIF). Despite these efforts, only limited

information has been obtained on the progress of the flame motion near the flame base.

Information on the time-varying properties of the lifted flame is required for an understanding of dynamic flame-stabilization processes. Such information can be obtained through the use of the thin-filament pyrometry (TFP) technique recently developed by Goss et al.¹² With this technique the line temperature of the hydrocarbon turbulent jet diffusion flame can be profiled—an extremely difficult, if not impossible, task using other experimental methods. The spatially and temporally resolved temperature profile obtained by TFP at a high sampling rate yields the time-dependent flame characteristics, e.g., the location of the flame and the thickness of the flame zone. From this time-dependent information, statistical flame characteristics can be derived. In an earlier study, Chen and Goss¹³ utilized the TFP technique to profile the temperature of turbulent jet flames at high sampling rates. In that study, the velocity and length scales associated with flame motion were derived for methane and propane flames under critical liftoff conditions. The thermal-zone thickness and the velocity and length scales were found to increase significantly after flame liftoff. However, the time scale associated with large-scale flame movement remained within a narrow range. As a result, the derived turbulent diffusivity increased with increasing jet velocity and downstream location, while the strain rate remained essentially constant. For methane and propane flames at the critical liftoff velocity, the strain rate sustained by the flame surface was measured to be ~ 450 1/s. This result was consistent with that of other researchers.⁵

In the present paper lifted flames having an exit velocity greater than the critical liftoff velocity were examined. Questions of particular interest included: 1) how the thermal zone varies along the flame under various liftoff conditions; 2) whether the strain rate remains limited and the range of strain rate that the flame sustains when approaching blowout; and 3) whether the time scale of the dominant flame motion remains constant and, if so, why. In addition, attempts have been made to quantify intermittent flame-base motion.

II. Experimental

In these studies the fuel jet was issued from a short, tapered, 5-mm-i.d. contour nozzle having a contraction ratio of 20:1.

Presented as Paper 89-0153 at the AIAA 27th Aerospace Sciences Meeting, Reno, NV, Jan. 9-12, 1989; received April 11, 1990; revision received Aug. 1, 1991; accepted for publication Aug. 8, 1991. Copyright © 1989 by the American Institute of Aeronautics and Astronautics, Inc. All rights reserved.

*Senior Research Scientist. Senior Member AIAA.

†Chief Scientist, Optical Diagnostics. Member AIAA.

‡Currently, Research Physical Scientist, Phillips Laboratory, Edwards Air Force Base, CA 93523.

§Associate Professor.

To isolate the flame from room-air disturbances, a 25-cm duct was used that confined the co-annular air jet having a constant exit velocity of 0.15 m/s. The experimental setup using the TFP technique to study flame lifting and flame/flow interactions of turbulent jet diffusion flames is described in detail in Refs. 12 and 13. Therefore, only a brief description is given here.

Time-dependent temperature profiles for the propane and methane jet flames were made at a rate of $>3000/s$ from the blackbody emission of a $\sim 10\text{-}\mu\text{m}$ -diam SiC thin filament having a frequency response of $\sim 1000\text{ Hz}$. The spatial resolution of the current configuration was varied from 60 to $150\text{ }\mu\text{m}$. The total length of the filament, $\sim 12\text{ cm}$, was sufficient to allow radial examination of the entire jet-flame zone. The curve-fitting process was applied to each temperature profile to permit accurate determination of the radial position of the flame surface and the thickness of the thermal zone. Because the data were taken at a high sampling rate, the time-varying information could be captured and recorded. From the time-series trace of the flame surface, the radial velocity and length scales of the flame propagation could be deduced. The radial velocity is the time derivative of the flame trace; this trace is obtained by aligning the filament in the radial direction. The root-mean-square (rms) value of the radial velocity v' is defined as the velocity scale; whereas, the rms value of the radial flame location y' is defined as the length scale L .

The experimental conditions are summarized in Table 1. For the propane flame the heat released was very intense. As a result a high-velocity propane flame could not be operated for long periods of time in the exhaust facility. Thus, the propane flame was not tested for jet velocities $>40\text{ m/s}$. For the methane flame this problem was less severe. However, for a methane flame having an exit velocity $>60\text{ m/s}$, the liftoff height was $>140\text{ mm}$ and fluctuated at an amplitude $>35\text{ mm}$. In addition, the flame was no longer flamelet-like in character. Use of the fitting process for locating the flame peaks¹³ could not be justified in this case. Therefore, temperature profiles for the methane flames having a velocity of 70 m/s were made, but the data were not analyzed by means of the fitting process. The flame conditions shown in Table 1 (labeled Case Nos. 1–5) were examined, and the results are presented herein. The measurement locations were chosen in the near-field region from the flame base (liftoff height) up to 40 jet diameters downstream, $x/d = 40$. In this region the fuel-jet shear layer and flame surface interact strongly, allowing deformation of the flame surface to be studied.

III. Results and Discussion

It has been shown¹³ that under critical liftoff conditions, the methane diffusion flame experiences stronger flame/flow interaction than the propane flame. This was later confirmed using laser-induced OH fluorescence¹⁴ to study the statistical flame-zone characteristics. In the present study it was found that when the flame condition approaches blowout, the flame/flow interaction becomes stronger for both flames. For examining the progress of the flame behavior, data are presented in the following order: 1) general flame-liftoff characteristics;

2) thermal-zone thickness and velocity and length scales; 3) deduced diffusivity and strain rate; and 4) crossing frequency that behaves in a manner similar to the strain rate.

A. Liftoff Height and Fluctuations

In the study of the stabilization of lifted flames, the classical approach involves an initial examination of the liftoff height.^{15,16} Measurement of liftoff height has most often been accomplished by direct observation, but it can be achieved more effectively through the use of a thin filament to indicate the presence of the flame. The observed flame height fluctuates, indicating the dynamic interaction of the shear zone and the flame zone. This interaction becomes even stronger after the flame lifts and can be influenced by 1) chemical kinetics of the mixture in the fuel jet; 2) fluid properties of the fuel jet and coflowing jet; 3) initial flow conditions; and 4) geometry effects that may be inherent in the flow conditions. This non-steady interaction can cause intermittent flame behavior. In the present study the range of intermittent flame-base motion is characterized by recording both the lower and upper bounds of the liftoff height along with the average height.

The average liftoff height h and the difference in liftoff height between the lower and upper bounds Δh are plotted in Figs. 1 and 2, respectively, as a function of exit velocity. The exit velocity was calculated from the volume flow rate and the nozzle diameter of 5 mm . The exit velocity profiles are described in detail in Ref. 17. The initial liftoff condition for the methane and propane flames is indicated in Fig. 1. After the flame lifts, it jumps to an initial liftoff height. A reduction in jet velocity will decrease the liftoff height and eventually cause the flame to re-attach. This re-attaching regime in the figure is the region where the velocity is lower than the initial liftoff velocity. After initial liftoff an increase in the jet velocity will increase the liftoff height and eventually cause the flame to blow out. The blowout velocity for the methane flame is $\sim 80\text{ m/s}$ and that for the propane flame is $>90\text{ m/s}$.

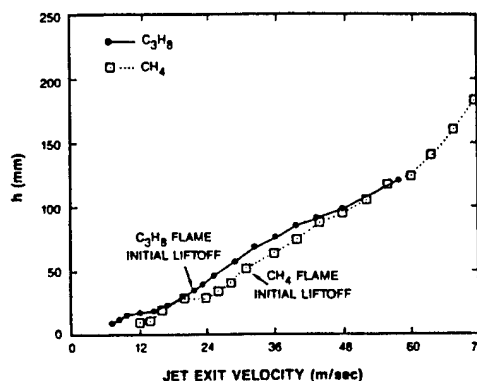


Fig. 1 Plot of average liftoff height as function of jet exit velocity.

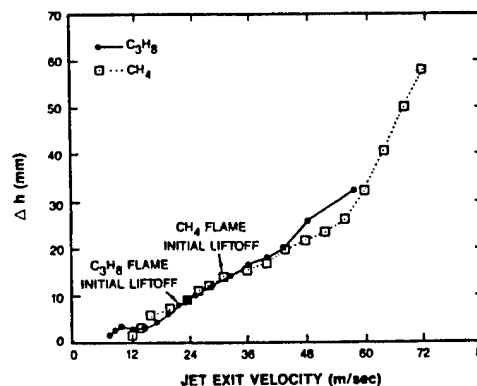


Fig. 2 Plot of amplitude of liftoff-height fluctuation as function of jet exit velocity.

Table 1 Experimental conditions

Fuel	Exit velocity, m/s	Flame status	Origin of data	Case no.
Propane	19.5	Attached	Ref. 13	
Propane	19.5	Lifted	Ref. 13	
Propane	29.0	Lifted	Present study	1
Propane	38.5	Lifted	Present study	2
Methane	31.0	Attached	Ref. 13	
Methane	31.0	Lifted	Ref. 13	
Methane	40.0	Lifted	Present study	3
Methane	50.0	Lifted	Present study	4
Methane	60.0	Lifted	Present study	5
Methane	70.0	Lifted	Present study	6

For the methane and propane flames, a linear relationship is observed between liftoff height h and jet velocity U_e , which confirms the results of a previous study of Kalghatgi.¹⁵ This relation for the propane flame is given by

$$h = -21.74 + 2.50 U_e \quad (1)$$

and for the methane flame by

$$h = -28.45 + 2.61 U_e \quad (2)$$

with h being in millimeters and U_e in meters per second. Figure 1 shows that the initial liftoff height for the propane flame is ~ 30 mm, which is much lower than that of the methane flame, ~ 52 mm.

A linear relationship also exists between U_e and Δh for the methane and propane flames. Over the jet-velocity range 16–45 m/s, Δh for the two flames is nearly equal. The relation is

$$\Delta h = -5.66 + 0.626 U_e \quad (3)$$

Considering the differences in the reaction kinetics and fluid properties of methane and propane flames, the equal Δh shown in Fig. 2 requires further investigation. Comparing Δh to h for the flames studied, Δh was $\sim 20\%$ of h and $\sim 50\%$ of the flame diameter, or 100% of the flame radius. The fluctuation of the flame height is mainly large scale in nature. As the blowout condition was approached, h was ~ 200 mm and $\Delta h \sim 60$ mm, as shown in Figs. 1 and 2, respectively.

Because coflowing air was employed, the results cannot be directly compared with those obtained by other investigators. However, for modeling-comparison purposes, one can apply the nondimensional analysis of Kalghatgi.¹⁵ For hydrocarbon gases the relationship between h and U_e was given by Kalghatgi¹⁵ as

$$h = C_1 (U_e \nu / S_u^2) (\bar{\rho})^{1.5} \quad (4)$$

where ν is the kinematic viscosity, S_u the maximum value of the laminar burning velocity, and $\bar{\rho}$ the density ratio of fuel to ambient air. C_1 in this equation is an empirical constant that is independent of the gas employed. If the fluid properties of the gases employed are known, C_1 can be obtained by comparing Eqs. (1), (2), and (4). For the case of methane and propane flames, C_1 was determined to be 59 and 61, respectively. These two numbers are essentially equal within the experimental uncertainty of this measurement. Thus, these measurements support the universal law described in Eq. (4), with $C_1 \approx 60$. The value of C_1 cited by Kalghatgi is 50; the flow conditions relative to the coflowing air and the nozzle geometry employed in the present study could account for this difference.

B. Velocity Scale, Length Scale, and Thermal-Zone Thickness

Because the turbulent flame has been viewed as an ensemble of flamelets, the radial velocity and length scales associated with turbulent flame motion and the thermal-zone thickness were measured in order to characterize the progress of the propagation and stabilization of lifted jet flames. The results are shown in Figs. 3, 4, and 5, respectively.

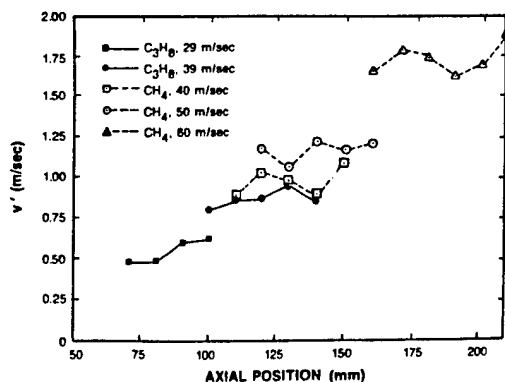


Fig. 3 Plot of measured rms value of radial velocity fluctuation as function of axial location.

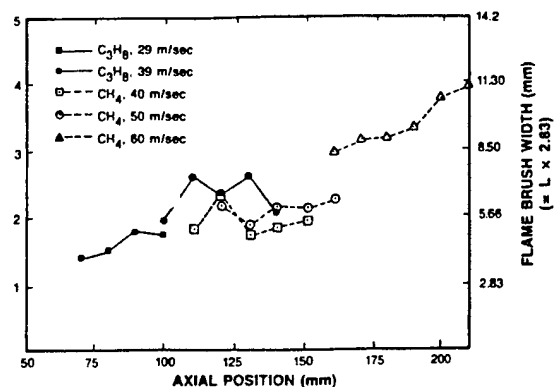


Fig. 4 Plot of measured rms value of flame fluctuation as function of axial location.

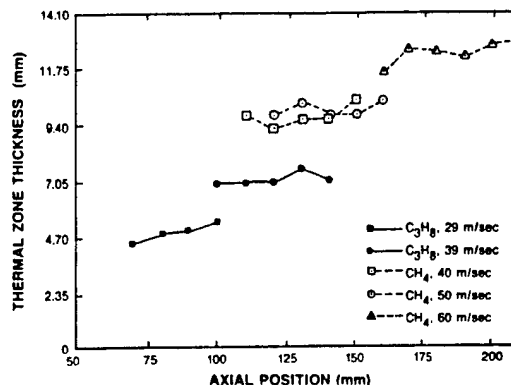


Fig. 5 Plot of thermal-zone thickness as function of axial location.

In Fig. 3 the radial velocity fluctuation v' for the motion of the flame surface is plotted as a function of axial location for the five flame conditions selected for study. With increasing jet velocity and downstream location, v' for both propane and methane flames consistently increased. The methane flame displayed a higher fluctuation than the propane flame.¹³ The maximum radial velocity observed was ~ 1.8 m/s for the lifted methane flame having a jet exit velocity of 60 m/s. The local maximum axial velocity at the measurement location was estimated to be ~ 12 m/s. Under these circumstances the normalized velocity fluctuation was $\sim 15\%$, which is comparable to the jet turbulent intensity. For this flame condition, the flame surface motion may be passive and dominated by the flowfield. The measured maximum turbulent velocity is approximately four to five times the maximum laminar flame velocity.

The rms value of the flame fluctuation L is shown in Fig. 4. Because L is an rms value, the actual range of the inner and outer bounds of the flame position should be $\sim 2.83 L$. This range is the flame-brush width and is shown on the right-hand vertical axis in Fig. 4. The dependence of L upon the flame conditions and axial location was similar to that of v' . When the flame-brush width was normalized by the radius of the flame cone, the normalized value was found to be $\sim 20\%$ for most of the flame conditions tested. For Test Condition No. 5 in Table 1 (the methane flame having an exit velocity of 60 m/s), the above normalized value approached 58%.

Figure 5 is a plot of the thermal-zone thickness, which is defined as the width of the flame zone for temperatures above ~ 1300 K. For measurements of the reaction-zone thickness, a spectroscopic technique¹⁰ is required; such measurements were not attempted in the present study. The thermal zone should be thicker than the reaction zone because the thickness of the former is equal to the thickness of the latter plus the thermal-boundary-layer thickness. However, measurement of the thermal-zone thickness yields the size of the area confining the hot combustion products that have a temperature higher than the ignition temperature. The results in Fig. 5 clearly indicate that the methane flame has a thicker thermal zone

than the propane flame, presumably due to the higher thermal diffusivity of methane.¹³

For Test Condition No. 5 (see Table 1), the observed thickness was ~ 13 mm. For the methane flame having a slightly higher exit velocity of 70 m/s (very near blowout), the thermal zone became extremely thick; in this case, the entire flame cone may assume the characteristics of distributed combustion. This is demonstrated in Fig. 6 by the evolution of the temperature profile near the flame base, at a location ~ 175 mm downstream. Here it is clear that the entire flame cone is filled with hot combusting gases. The intermittent flame motion can be observed in this figure. When the flame is stabilized at a location above the filament, no signal appears; when the flame moves down toward the filament, the high-temperature zone can be observed. This transition clearly shows that under the near-blowout condition, the thermal zone is thick, even at the stabilized flame base.

C. Turbulent Diffusivity and Strain Rate

In the near field of the jet, the flame is perturbed by the flow turbulence, and the flame becomes contorted; the surface area increases accordingly, raising the consumption rate of the reactant mixture. However, the contorted flame surface is also accompanied by an increase in strain rate. If the strain rate reaches a certain value, the flame will be quenched locally.¹⁸ The strain rate sustained by the flame surface can be estimated from the length and velocity scales associated with the flame-surface motion. In this experiment, the flame motion was directly tracked by the TFP technique. The measured velocity scale v' and the length scale L associated with the flame fluctuation can be used to determine the important parameters turbulent diffusivity and strain rate using the following relations:

$$D_t = v' L \quad (5)$$

$$S_r = v'/L \quad (6)$$

The units for D_t and S_r are the same as those for turbulent diffusivity and strain rate, respectively. In a typical flame study when information on the direct flame-surface motion is not available, the velocity and length scales are derived from the velocity measurement of the flowfield. The velocity measured in this way, however, does not necessarily characterize the flame motion because the flame may not completely respond to the flow motion and, as a result, the turbulent Prandtl number will not be unity. Because these two quantities were measured for the first time in the present study, no comparison with previous literature was possible. Therefore, for reference purposes, the value of D_t was referred to as turbulent diffusivity with an assumed proportional constant of unity. The same convention was applied to the value of S_r , which was referred to as strain rate.

Figures 7 and 8 show turbulent-diffusivity and strain-rate results, respectively. Under high jet-velocity conditions, the flame base could not be characterized as an ideal flamelet for either the methane or the propane flame. The probability of observing multiple flamelets and thick flame zones increased with increasing jet velocity, an observation which was con-

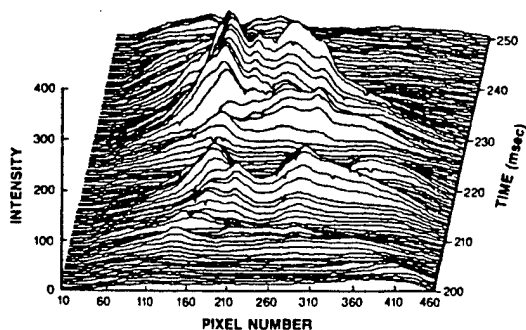


Fig. 6 Three-dimensional plot of TFP results for methane flame base at 70 m/s.

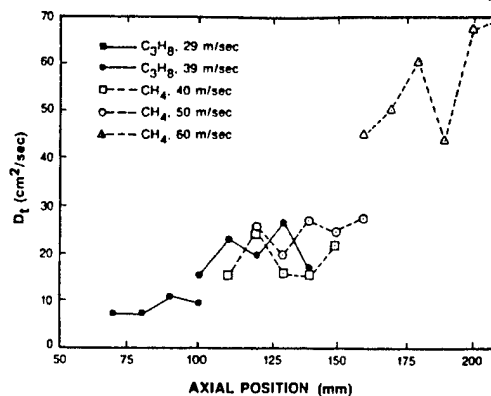


Fig. 7 Plot of turbulent diffusivity associated with turbulent-flame-surface motion as function of axial location.

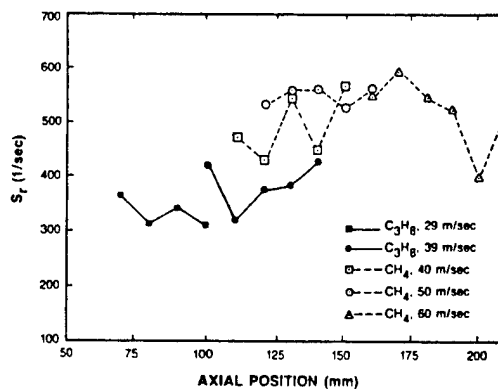


Fig. 8 Measured strain rate deduced from turbulent-flame-surface motion.

firmed in a later experimental study.¹⁴ This nonflamelet behavior reduced the success rate of curve fitting and, thus, the quality of the data. For the methane flame the quality of the data was lower than for the propane flame. Furthermore, the total number of profiles sampled at each location was only 720. Under-sampling constitutes a special problem for diffusivity and strain-rate calculations that are composed of two measured quantities; therefore, the data presented should not be considered benchmark results. Instead, attention should be focused on the trend and range of the results.

At the critical liftoff velocity, the turbulent diffusivity at the liftoff height for the propane flame is ~ 2 cm²/s and for the methane flame is ~ 10 cm²/s. Figure 7 shows that turbulent diffusivity increased with an increase in jet velocity and downstream location. However, the strain rate sustained by the flame surface remained relatively constant, as shown in Fig. 8. For the propane flame, the strain rate for the lifted flame remained at ~ 350 1/s, which is lower than that for the attached flame at the critical liftoff velocity. For the methane flame the strain rate for the lifted flame remained at ~ 540 1/s, which is higher than that for the attached flame at the critical liftoff velocity. It seems that the flame sustains a certain strain rate over a wide range of flame conditions. Note that the strain rate was deduced from the statistical quantities, as shown in Eq. (6). The instantaneous strain rate sustained by the flame may be different. However, a later study by Seaba¹⁷ indicated that this deduced strain rate is very similar to the result obtained by mean-flow-velocity measurements made around the flame base.

D. Crossing Frequency of Flame Surface

As reported in a companion study,¹³ the flame can influence the flowfield and be influenced by it. This is evident from data on the crossing frequency, which is defined as the frequency at which the flamefront crosses its mean position. Before reaching the end of the potential core, the jet-shear-layer structure becomes larger after the flame lifts and, consequently, the flame-crossing frequency decreases after the

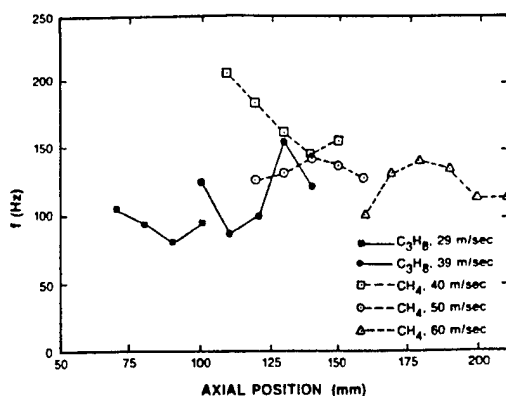


Fig. 9 Measured crossing frequency of flame surface at different downstream locations.

flame has lifted. For the methane flame the interaction is strong and the structure less coherent; as a result the frequency decreases irregularly. However, the frequency of the lifted methane flame falls between 100 and 150 Hz. For the propane flame in which the interaction of the shear zone and the flame zone is weaker, the frequency decreases by one-half from 200 to 100 Hz.¹³ Under the flame conditions selected for this study, which range from liftoff to blowout, this trend was observed and the measured frequency remained in the 100–150 Hz range, as shown in Fig. 9.

The exact reason for the crossing frequency of the methane and propane flames falling into the range ~100–150 Hz over a wide exit-velocity region is not clear. Nevertheless, this indicates the dominant time scale over which the lifted flame responds to flow modulation. Because the region between the lifted flame base and the nozzle mouth is a preferred location for entrainment of air,¹³ it is physically sound to assume that the liftoff height is an important length scale that affects flame behavior. Variation of liftoff height may, in turn, affect air entrainment, local fuel-air mixing, and, thus, flame stabilization. To quantify the consequence of this unsteady flame/flow coupling, a nondimensional ratio equivalent to the Strouhal number S_f can be defined as

$$S_f = fh/U_e \quad (7)$$

where f is the dominant frequency. In the above definition, global parameters such as h and U_e are used. From the data in Figs. 1 and 9, the Strouhal number is found to range from ~0.10 to 0.15. Note that over a wide range of flame conditions, the ratio h/U_e remains constant, as shown in Fig. 1. Thus, if the Strouhal number defined in Eq. (7) for characterizing the unsteady flame/flow coupling is to be constant, then the frequency f must be constant, as shown in Fig. 9.

IV. Conclusions

A novel approach was taken to the characterization of the stabilization-zone structure of jet flames. Methane and propane flames having an exit velocity ranging from liftoff to near blowout were examined and the results compared. Emphasis in this study was placed on the measurement of time-varying properties in order to characterize the dynamic behavior related to flame propagation and stabilization. The results are summarized below.

- 1) In the near-field region of the lifted flame, the thermal-zone thickness and the velocity and length scales associated with the flame motion increased with respect to an increase in the jet velocity and downstream distance. Under the same jet-velocity conditions, the methane flame fluctuated at higher velocity and amplitude than the propane flame.

- 2) The strain rate sustained by the flame remained relatively constant for the wide range of flame conditions tested.

- 3) The intermittent behavior of the flame-stabilization zone was characterized. The fluctuation of the liftoff height was measured to be ~20% of the average value.

- 4) Unsteady flame/flow coupling resulted in a Strouhal number ranging from ~0.10 to 0.15. The liftoff height is considered to be an important physical length scale.

- 5) Approaching the near-blowout condition, the flame base fluctuated violently and the flame may take on distributed-combustion characteristics.

Acknowledgments

This work was supported in part by the Aero Propulsion and Power Directorate, Wright Laboratory, Wright-Patterson Air Force Base, under Contract F33615-85-C-2562. The authors are indebted to W. M. Roquemore for helpful discussions and support of this work and to M. Whitaker, D. D. Trump, V. Vilimpoc, and B. Sarka for technical assistance.

References

- ¹Vanquickenborne, L., and van Tiggelen, A., "The Stabilization Mechanism of Lifted Diffusion Flames," *Combustion and Flame*, Vol. 10, No. 3, 1966, pp. 59–69.
- ²Eickhoff, H., Lenze, B., and Leuckel, W., "Experimental Investigation on the Stabilization Mechanism of Jet Diffusion Flames," *Twentieth Symposium (International) on Combustion*, The Combustion Institute, Pittsburgh, PA, 1985, pp. 311–318.
- ³Roquemore, W. M., Chen, L. D., Goss, L. P., and Lynn, W. F., "Structure of Jet Diffusion Flames," *Turbulent Reactive Flows (Lecture Notes in Engineering)*, edited by R. Borghi and N. B. Murthy, Vol. 40, Springer-Verlag, New York, 1989, pp. 49–63.
- ⁴Peters, N., and Williams, F. A., "Liftoff Characteristics of Turbulent Jet Diffusion Flames," *AIAA Journal*, Vol. 21, No. 3, 1983, pp. 423–429.
- ⁵Bilger, R. W., "Turbulent Diffusion Flames," *Annual Review of Fluid Mechanics*, Annual Reviews Inc., Palo Alto, CA, 1989, Vol. 21, pp. 101–135.
- ⁶Broadwell, J. E., and Breidenthal, R. E., "A Simple Model of Mixing and Chemical Reaction in a Turbulent Shear Layer," *Journal of Fluid Mechanics*, Vol. 125, No. 12, 1982, pp. 397–410.
- ⁷Dahm, W. J. A., and Dibble, R. W., "Combustion Stability Limits of Coflowing Turbulent Jet Diffusion Flames," *AIAA Paper 88-0538*, Reno, NV, 1988.
- ⁸Haworth, D. C., Drake, M. C., Pope, S. B., and Blint, R. J., "The Importance of Time-Dependent Flame Structures in Stretched Laminar Flamelet Models for Turbulent Jet Diffusion Flames," *Twenty-Second Symposium (International) on Combustion*, The Combustion Institute, Pittsburgh, PA, 1989, pp. 589–597.
- ⁹Masri, A. R., Starnes, S. H., and Bilger, R. W., "Transition and Transport in the Initial Region of a Turbulent Diffusion Flame," *Dynamics of Flames and Reactive Systems*, edited by J. R. Bowen, N. Manson, A. K. Oppenheim, and R. I. Soloukhin, Vol. 95, Progress in Astronautics and Aeronautics, AIAA, Washington, DC, 1984, pp. 293–304.
- ¹⁰Schefer, R. W., Namazian, M., and Kelly, J., "Structural Characteristics of Lifted Turbulent-Jet Flames," *Twenty-Second Symposium (International) on Combustion*, The Combustion Institute, Pittsburgh, PA, 1988, pp. 833–842.
- ¹¹Takahashi, F., Mizomoto, M., and Ikai, S., "Structure of the Stabilizing Region of a Laminar Jet Diffusion Flame," *Journal of Heat Transfer*, Vol. 110, No. 2, 1988, pp. 182–189.
- ¹²Goss, L. P., Vilimpoc, V., Sarka, B., and Lynn, W. F., "Thin-Filament Pyrometry: A Novel Thermometric Technique for Combusting Flows," *Journal of Engineering for Gas Turbines and Power*, Vol. 111, 1989, pp. 46–52.
- ¹³Chen, T. H., and Goss, L. P., "Flame Lifting and Flame/Flow Interactions of Jet Diffusion Flames," *AIAA Paper 89-0156*, Reno, NV, Jan. 1989.
- ¹⁴Chen, T. H., and Goss, L. P., "Statistical OH-Zone Structures of Turbulent Jet Flames from Liftoff to Near-Blowout," *Combustion Science and Technology*, Vol. 79, 1991, pp. 311–324.
- ¹⁵Kalghatgi, G. T., "Lift-off Heights and Visible Lengths of Vertical Turbulent Jet Diffusion Flames in Still Air," *Combustion Science and Technology*, Vol. 41, 1984, pp. 17–29.
- ¹⁶Pitts, W. M., "Assessment of Theories for the Behavior and Blowout of Lifted Turbulent Jet Diffusion Flames," *Twenty-Second Symposium (International) on Combustion*, The Combustion Institute, Pittsburgh, PA, 1988, pp. 809–816.
- ¹⁷Seaba, J. P., "Burner Statistics of Jet Diffusion Flames," Ph.D. Dissertation, Univ. of Iowa, Iowa City, IA, 1990.
- ¹⁸Lewis, B., and von Elbe, B., *Combustion, Flames and Explosions of Gases*, 3rd ed., Academic Press, New York, 1987.

NEAR-FIELD TURBULENT STRUCTURES AND THE LOCAL EXTINCTION OF JET DIFFUSION FLAMES

FUMIAKI TAKAHASHI

*University of Dayton
Research Institute
300 College Park
Dayton, Ohio 45469-0140 USA*

AND

LARRY P. GOSS

*Systems Research Laboratories
2800 Indian Ripple Rd.
Dayton, Ohio 45440-3696 USA*

The aerodynamic structure of turbulent jet diffusion flames of methane stabilized on a thick-walled fuel tube in coflowing air has been studied by using laser-Doppler velocimetry and Mie scattering techniques to elucidate the local flame extinction and subsequent lifting phenomena. Instantaneous planar flow visualization and real-time line measurements revealed large-scale vortical structures, constituting the intermittent mixing layer, and sporadic radial mass ejection from the jet-fluid core. By seeding the jet and coflow separately in the LDV measurement, conditioned joint probability-density functions (pdf's) of the axial and radial velocity components and their statistical moments, i.e., the conditioned (zone) averages, root-mean-square fluctuations, skewnesses, kurtoses, and Reynolds shear stress, were determined. The unconditioned pdf and, in turn, the statistical moments were obtained from the conditioned pdf's and intermittency of the jet fluid. The jet-fluid parcels had a higher mean axial velocity than that of the external-fluid parcels and a positive mean radial velocity in contrast to a negative value for the external-fluid parcels. These differences are responsible, to a great extent, for creating highly-distorted turbulent structures in the intermittent layer adjacent to the flame zone. Since diffusion processes require significantly longer time than convective processes associated with the large-scale vortices and the radial mass ejection, the radial location of the flame zone is insensitive, at least in the near-jet field, to the high-frequency jet-fluid concentration fluctuation in the core. As a result, the ejected jet fluid, or the large-scale vortex itself, can reach the flame-zone location without disturbing the concentration field, thereby locally quenching the already strained diffusion flame.

Introduction

Although various phenomena in jet diffusion flames have been studied since early days in combustion research, there remain certain aspects of the subject that need further investigation. The flame stabilization phenomena, e.g., liftoff and blowout, are of both fundamental and practical interest. It has recently¹ been clarified that there exist several distinct lifting mechanisms for jet diffusion flames, depending on the burner and flow configurations and the fuel type. In many cases, the flame stabilization and the detachment from the burner rim are controlled by local conditions near the flame base^{2,3} (Type I in Ref. 1). The Type I case is likely to happen particularly if the lip thickness of the fuel

tube or nozzle is small. However, if the flame base is stabilized securely on the burner rim by using, for example, a thick-lip fuel tube, the flame zone will be quenched locally at typically a few jet diameters downstream where the laminar flame zone becomes turbulent (i.e., breakpoint). For hydrogen⁴⁻⁷ or propane⁸ flames, the local extinction leads to formation of a stable split flame, i.e., a combination of a small laminar flame in the vicinity of the burner rim and a turbulent lifted-like flame downstream (Types II(b) and II(c) in Ref. 1). However, for methane flames,^{1,3,9-11} the local extinction causes lifting of the flame almost immediately (Type II(a) in Ref. 1). Takeno and Kotani⁵ postulated that, for hydrogen flames, the local extinction is a result of the excess transport rate as compared to the reac-

tion rate at the transition point of turbulent flames. More recently, the event when inner vortices interfere with the flame front was captured in methane flames by using instantaneous schlieren⁹ or laser-sheet flow visualization^{12,10} techniques. Eickhoff et al.⁹ speculated that the diffusion flame was quenched because too much heat was diffused by the small scale turbulence superimposed in these vortices. Unfortunately, detailed flame structure data related to the local flame extinction phenomena are only slowly becoming available.

Turbulent diffusion flames are described in most cases as being composed of wrinkled, moving, laminar sheets of reaction, i.e., flamelets.^{13, 15} The concept of local flamelet extinctions due to high strain rate has been applied to the base of turbulent lifted flames to determine the liftoff height and blowout conditions.¹⁶ Extinction processes have initially been considered to occur within small-scale turbulent structures.^{16,17} More recent work¹⁸⁻²² has suggested that large-scale structures are responsible for extinction. Since the flame zone is located generally outside of the large-scale vortex structure in burner-rim-attached turbulent jet diffusion flames, the large-scale vortex structure must play a major role also in the local extinction phenomena near the breakpoint. Unlike the lifted turbulent flame base, the transition region of attached flames is more stationary and continuous, and there is no complication due to the fuel-air premixing prior to combustion. Therefore, the near-jet field of rim-attached turbulent jet diffusion flames provide a unique, well-defined diffusion flame structure suitable to the study of dynamic turbulence-flame interactions. The major objective of this study is to gain a better understanding of the mechanisms of local extinction and subsequent lifting phenomena (Type II(a) in Ref 1).

Experimental Techniques

The experimental apparatus and the LDV system have been described in detail elsewhere.¹¹ The burner consists of a thick-walled, flat-end fuel tube (9.45 mm i.d., 2.4 mm lip thickness) and a concentric air tube (26.92 mm i.d.) through which annulus coflow air flows, centered in a low-speed (~ 0.5 m/s) general air stream in a vertical combustion chimney. Methane ($>98\%$) was used as the fuel. Submicron ZrO_2 particles were used for the LDV measurement.

The details of the instantaneous (10 ns) planar flow visualization and the real-time line measurements have been reported elsewhere.^{10,12,23,24} For planar visualization, Mie scattering from TiO_2 particles, formed from the reaction of seeded $TiCl_4$ vapor and water vapor in the combustion products, are visualized at right angles to a sheet of laser light (~ 0.25

mm thickness) from a pulsed Nd:YAG laser (Quanta-Ray DCR-3; frequency doubled, 532 nm, ~ 250 mJ). For the real-time line measurements, the output from an Argon ion laser (Spectra Physics 2000; multiline, 1-3W) is focused to a line above the burner. TiO_2 particles are preformed and introduced into the fuel tube. The scattered light is collimated by a $f/2.5$ lens and directed toward a multi-faceted rotating mirror wheel which sweeps the collimated light from the flame through a $f/2$ focusing lens onto a 50 μm aperture. The scattered light exiting the aperture is then detected by a photomultiplier, the output of which is amplified and digitized at a high rate. The digitization of the scattered light is synchronized with the rotation of the mirror by monitoring the reflection of a HeNe laser beam with a silicon diode detector, thereby triggering a 512 clock burst which is sent to the digitizer. A delay circuit is used to temporally adjust the clock burst to the sweep of the scattered light to ensure the correct signal is digitized. A transient recorder (Lecroy TR8818) with ECL memory is used to digitize the data with 8 bit resolution. For the experiments reported in this paper, the rotational speed of the multi-faceted mirror was 500 rpm which with 10 facets translates into 5000 sweeps per second. Each individual sweep was digitized at a rate of 8 MHz. The effective spatial resolution of the experiment was measured to be 75 μm /pixel, where a pixel is defined as one digitized channel or 1/512th of a single sweep.

Results and Discussion

Mie Scattering Measurements:

Figure 1 shows instantaneous planar flow visualization photographs. At a low mean jet velocity (Fig. 1a), the boundary between the $TiCl_4$ -laden jet fluid and the combustion products is clearly marked by TiO_2 particles as smooth green streaks up to the height from the jet exit, $z \sim 30$ mm. It should be noted, however, that the flow inside the fuel tube is turbulent, as the Reynolds number ($Re_j = U_j d / \nu_j = 3380$; d , the jet diameter; ν_j , the kinematic viscosity of the fuel) exceeds a critical value (~ 2300), and that the pipe flow turbulence is confined inside the visualized boundary. Notice that the blue visible flame zone is well separated (2-3 mm) from the visualized boundary. The instability of the boundary and the subsequent roll-up process, forming large-scale vortices, are seen downstream ($z > 30$ mm) until yellow luminous flame cover the inside structure. Although the behavior of this breakpoint to turbulence has been studied^{5,25} extensively by using schlieren photography, the detailed flow structure such as visualized here has never been revealed.

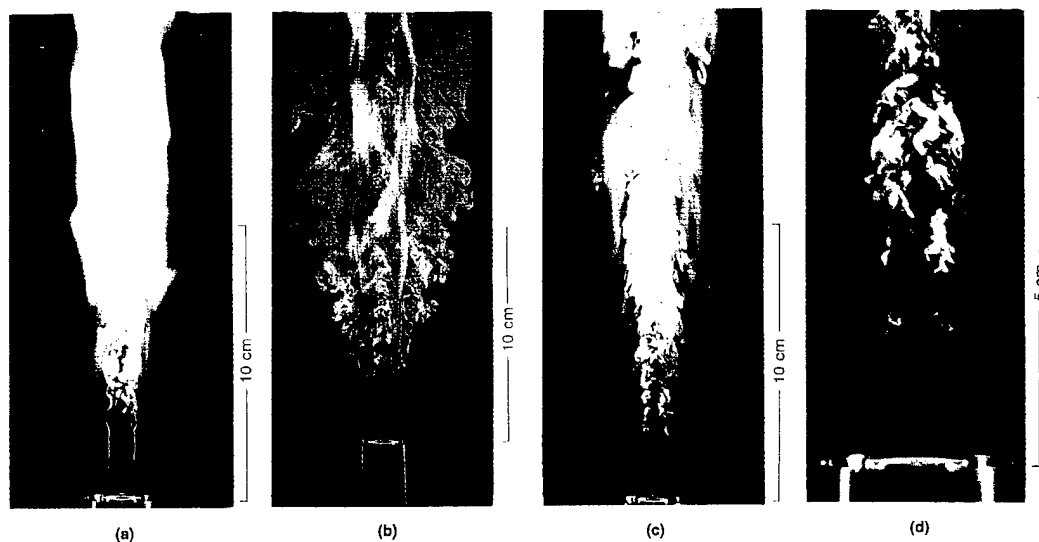


FIG. 1. Instantaneous (10 ns) laser-sheet reactive Mie scattering images superimposed with time-exposure direct photographs of methane/air coflow jet diffusion flames. Scattering particles (TiO_2) were formed from seeded TiCl_4 and water vapor in the combustion products $U_a = 3$ m/s. (a) Jet seed, exposure 1/60 s, $U_j = 6$ m/s ($Re_j = 3380$). (b) Jet and annulus air seed, exposure 1/250 s, $U_j = 10$ m/s ($Re_j = 5630$). (c) Jet seed, exposure 1/60 s, $U_j = 15$ m/s ($Re_j = 8460$). (d) Jet seed, exposure 1/125 s, $U_j = 15$ m/s.

Figure 1b is a moderate velocity case, where TiCl_4 vapor is introduced into both the jet and annulus air to show the entrainment pattern. Due to the continuous radiation from the particles entrained into the flame zone, the color of the flame is no longer natural. It is notable that mixing on the air-side of the flame zone takes place also intermittently by large-scale vortices created in the shear layer of the annulus air jet. Many fine streaks engulfed into the inner large-scale vortices are seen. The observations augment further the recent view of entrainment based on the large-scale structures,^{19,26,27} which differs significantly from a classic view based on the time-averaged flow pattern.

At a high mean jet velocity (Figs. 1c and 1d) near the critical mean jet velocity at lifting ($U_{jc} = 16.5 \sim 17$ m/s at $U_a = 3$ m/s),^{1,11} more turbulent activities are observed. The large-scale vortices grow in the intermittent mixing layer. Although the large structures are not as orderly, or coherent, as observed in low-speed nozzle jet flames,^{12,24} symmetric evolution of the vortices is evident as shown in Figs. 1c and 1d. At other times, it appears as though the large structures are more helical, as observed also in the far field,²⁶ or less orderly. The blue flame zone is locally quenched momentarily in the range $10 < z < 60$ mm. It is noticed in the closed-up view (Fig. 1d), that the blue flame zone is essentially stationary despite the violent movement of the jet-fluid in the core region. The large-

scale vortices are very close to the flame zone ($0 \sim 1.5$ mm), and smaller-scale radial mass ejection from the jet-fluid core extruding beyond the flame zone can be seen in the figure.

Figure 2 shows real-time traces of Mie scattering intensities along a line for the high velocity case. The radial movement of the boundary of the jet and external fluids increases toward downstream as a result of the growth of the large-scale structure. At the highest position (Fig. 2c), lower frequency movement associated with the slowed large-scale structures is more noticeable, and the external fluid reaches the centerline region occasionally. The images such as shown in Fig. 2 were then processed such that each pixel had a binary value determined by comparing to a threshold value (typically set at $\sim 50\%$ of the maximum value of the average scattering intensity along a line). The processed binary image directly relates to an intermittency function^{13,28,29} defined as a stochastic function having a value $I(z, r, t) = 1$ in the jet fluid and $I(z, r, t) = 0$ in the external fluid. The intermittency ($\bar{I}(z, r)$), i.e., the mean value of the intermittency function, represents the fraction of time that the jet fluid is present at the position in question. The crossing frequency (f_c), i.e., the number of crossings from the jet to external fluid per unit time then can be determined. Figure 3 shows the intermittency and crossing frequency obtained from the binary images. The radial locations of the visible flame

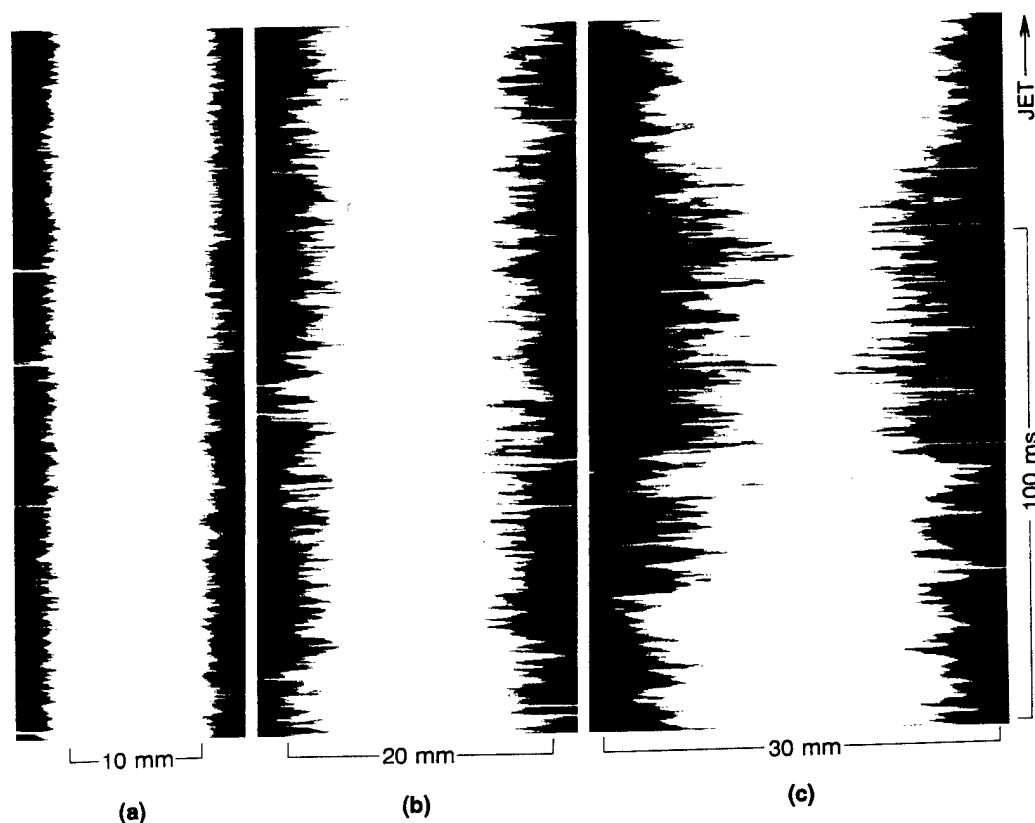


FIG. 2. Real-time traces of Mie scattering intensities along a line in methane/air coflow jet diffusion flames. Scattering particles (TiO_2) were preformed from TiCl_4 and water vapor prior to the fuel tube inlet. $U_j = 15$ m/s, $U_a = 3$ m/s. (a) $z = 15$ mm, (b) $z = 50$ mm, (c) $z = 100$ mm.

zone, measured by using a stationary telescope and by moving the burner with the translational stage ($5 \mu\text{m}$ precision), and the burner rim location are also included. In all cases, f_c peaked at $\bar{I} = 0.5$, as expected. As U_j was increased (Figs. 3a and 3b), the intermittent mixing layer spread outwards due to transition to turbulent jet-external fluid mixing as observed in Fig. 1, approaching to a closer proximity of the thickened visible flame zone. At $U_j \approx U_{jc}$ (Figs. 3c and 3d), the radial location where f_c peaked remained the same at different heights ($5 < z < 50$ mm), and the mixing layer spread on both sides. Although the line Mie scattering measurement was made up to $z = 125$ mm, only the results in the potential core zone, where $\bar{I} = 1$ at the centerline, were presented here. The crossing frequency for $\bar{I} = 0.5$ ($f_{c1/2}$) provides a crude estimate for the scale of the large-scale turbulent structure which accompany intermittency.²⁹ The length between crossings is given by $U_{1/2}/f_{c1/2}$, where $U_{1/2}$ is the local mean axial velocity at $r = r_{1/2}$ where $\bar{I} = 0.5$. A typical scale of the large eddies (l) can be calculated by taking half that length

as $l = 0.5U_{1/2}/f_{c1/2}$. Table I summarizes characteristics of the large-scale vortical structure.

LDV Measurements:

Since a LDV instrument measures the velocities of individual seed particles to obtain the probability distribution of velocity components, there exist various statistical bias problems. To clarify limits of velocity bias due to non-uniform seeding, particles were added only to the fuel jet or annulus coflow air at a time, following previous investigators.³⁰ This technique is found to be useful not only to provide information related to bias problems but also details concerning the turbulent structure. Figure 4 shows the radial profiles of the conditioned means and root-mean-square (rms) fluctuations of the axial and radial velocity components and Reynolds shear stress. The unconditioned profiles in the figure will be discussed later. The innermost annulus-seed data point and the outermost jet-seed data point, where the particle arrival rate becomes extremely low, are consistent with the distribution of \bar{I} (Fig. 3a).

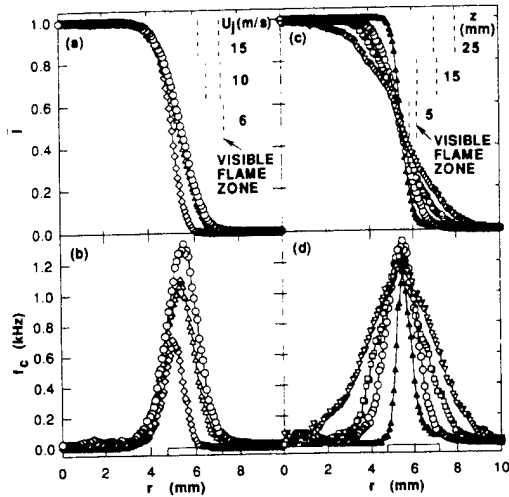


FIG. 3. Radial profiles of the intermittency and crossing frequency of the jet fluid in a methane/air coflow jet diffusion flame. $U_a = 3$ m/s. (a)(b) $z = 15$ mm. \diamond , $U_j = 6$ m/s; \triangle , $U_j = 10$ m/s; \circ , $U_j = 15$ m/s. (c)(d) $U_j = 15$ m/s. \blacktriangle , $z = 5$ mm; \circ , $z = 15$ mm; \square , $z = 25$ mm; ∇ , $z = 50$ mm.

In the mixing layer, the jet fluid parcels had a higher mean axial velocity than that of the external fluid parcels (Fig. 4a). The radial profiles of the mean radial velocity component (Fig. 4b) revealed a rather striking feature, namely, that the jet fluid parcels were moving outwardly on the average, whereas the external fluid parcels were moving inwardly. These results were uniquely captured by conditional sampling and demonstrate the intermittent mixing process due to large-scale vortices, the occasional radial jet fluid ejection, and the engulfment of the external fluid into the large-scale structure.

The rms fluctuations of the axial and radial velocity components of the jet fluid (Figs. 4c and 4d)

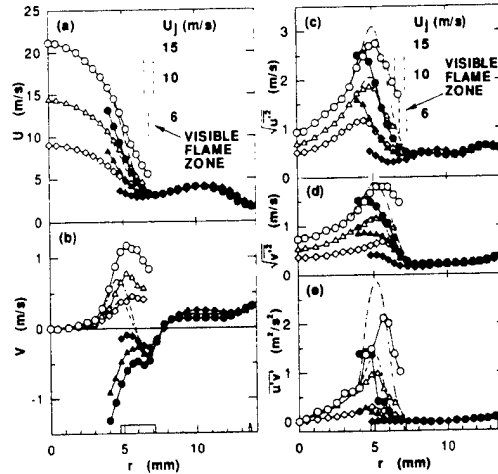


FIG. 4. Radial profiles of (a) the mean axial and (b) radial velocity components, (c) the root-mean-square fluctuation velocity of axial and (d) radial components, and (e) Reynolds shear stress in methane/air coflow jet diffusion flames. $U_a = 3$ m/s. $z = 15$ mm. \diamond , $U_j = 6$ m/s; \triangle , $U_j = 10$ m/s; \circ , $U_j = 15$ m/s. Open: conditioned on jet seed; filled: conditioned on annulus-air seed. \cdots , $---$, Unconditioned.

were generally larger than those of the external fluid, as expected because the jet fluid issuing from the fuel tube was a high-velocity turbulent flow and the external fluid in the mixing layer consisted of high-temperature combustion products with a high viscosity and a lower velocity. Further, the rms axial fluctuation was everywhere larger than that of the radial component, i.e., anisotropic. The Reynolds shear stress (Fig. 4e) of the external fluid was nearly zero on the air-side of the flame, displaying no active contribution to the turbulent transport.

Figure 5 shows the radial profiles of the radial gradients of the mean axial and radial velocity components and the skewness and kurtosis of the axial velocity component. The peaks of the Reynolds shear stress and the rms's (and therefore, turbulent kinetic energy) of the jet fluid coincided approximately with the points where the magnitude of the gradient of the mean axial velocity was maximum. This result is indicative of the gradient-type momentum diffusion in turbulent transport processes of small-scale eddies superimposed with the large structure and of the production of the turbulent kinetic energy through the product of the Reynolds shear stress and strain.

The unconditioned joint probability-density function (pdf) of the axial and radial velocity components $P(u, v; z, r)$ is determined from the pdf's conditioned on the jet fluid $P_j(u, v; z, r)$ and the

TABLE I
Characteristics of Large Structures

U_j (m/s)	z (mm)	$r_{1/2}$ (mm)	$U_{1/2}$ (m/s)	$f_{1/2}$ (Hz)	l (mm)
6	15	5.0	5.1	704	3.6
10	15	5.3	7.0	1100	3.2
15	5	5.5	3.6 ^{a,b}	1130	1.6
15	15	5.5	9.1	1330	3.4
15	25	5.3	12.1 ^a	1230	4.9
15	50	5.4	—	1190	—

^aRef. [1]

^bExtrapolated

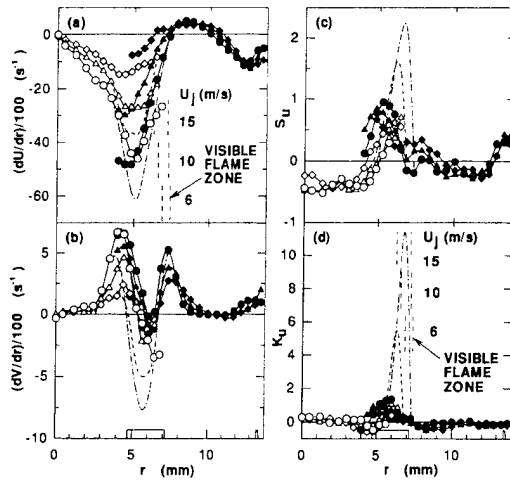


FIG. 5. Radial profiles of (a) the gradients of the mean axial and (b) radial velocity components and (c) skewness and (d) kurtosis of the axial velocity component in methane/air coflow jet diffusion flames. $U_a = 3$ m/s, $z = 15$ mm. \diamond, \blacklozenge , $U_j = 6$ m/s; $\triangle, \blacktriangle$, $U_j = 10$ m/s. \circ, \bullet , $U_j = 15$ m/s. Open: conditioned on jet seed; filled: conditioned on annulus-air seed. \cdots , $---$, $----$, Unconditioned.

external fluid originated from annulus-air $P_a(u, v; z, r)$ and the intermittency $(\bar{I}(z, r))$ as^{13,28}

$$P(u, v; z, r) = [1 - \bar{I}(z, r)]P_a(u, v; z, r) + \bar{I}(z, r)P_j(u, v; z, r).$$

The unconditioned statistical moments then can be retrieved from the unconditioned pdf as shown in Figs. 4 and 5. It is noteworthy that because the conditioned (zone) averages are used to determine conditioned moments and the zone averages are different for the jet and external fluids, the unconditioned values, except for the time-averaged means, cannot be obtained simply by taking a weighted average of the conditioned values and the intermittency. This conventional method²⁸ is valid only if the time average is used for determining conditioned moments, and it is feasible for time-series measurements for which the time average is readily available. Figure 6 shows an example of the conditioned and unconditioned pdf's with contour plots. The pdf's conditioned on the jet fluid (Fig. 6a) and the external fluid (Fig. 6b) are broadly spread due to high rms values and shows a positive correlation ($\overline{u'v'} \sim 1.5$ m²/s²; Fig. 4e), typical of the shear layer, and the external fluid's pdf is more skewed ($S_u \sim 1$; Fig. 5c). More importantly, due to the differences in the zone averages between the jet and external fluids, the unconditioned pdf (Fig. 6c) be-

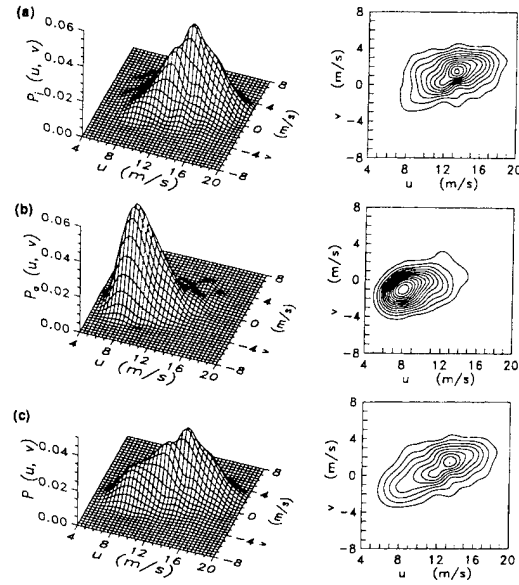


FIG. 6. Joint pdf's of the axial and radial velocity components in a methane/air coflow jet diffusion flame and their contour plots. $U_j = 15$ m/s, $U_a = 3$ m/s, $z = 15$ mm, $r = 4.8$ mm. $\bar{I} = 0.77$. Contour interval: every 0.004 from 0.004. (a) Conditioned on jet seed, (b) conditioned on annulus-air seed, (c) unconditioned.

comes more elongated shape, thus creating a large correlation $\overline{u'v'}$ (~ 2.7 m²/s²; Fig. 4e). This effect is even more apparent in the vicinity of the flame zone, where the unconditioned higher moments show highly-distorted turbulent structure (Figs. 5c and 5d).

Local Flame Extinction:

In general, the extinction of laminar diffusion flames occurs due to nonequilibrium effects as a result of decreased Damköhler number, i.e., the ratio of the local diffusion time to chemical reaction time. The critical strain rate (velocity gradient) beyond which the flame cannot be stabilized has been reported^{31,32} for methane as 350–500 s⁻¹. It is remarkable that, in Fig. 5b, the radial velocity gradient of the mean radial velocity component of the approach flow (external fluid) into the flame zone increases with increasing U_j and reaches approximately 500 s⁻¹ at the near extinction condition ($U_j = 15$ m/s). Although the actual value may fluctuate since the mean velocity was used here, the high velocity gradient means a thin diffusion layer and low Damköhler number, and thus the flame zone is highly strained.

An important observation made by the planer flow

visualization is that the blue flame zone in the near-jet region is essentially stationary despite the violent movement of the inner large-scale vortices. This indicates that the concentration field near the flame zone is insensitive to the high frequency variations in the core region. The characteristic fluctuation time associated with the axial convection of the large-scale structure can be estimated as $\tau_l = 1/f_{c1/2} \sim 0.8$ ms ($U_j = 15$ m/s and $z = 15$ mm; Table I). The radial jet-fluid mass ejection must need even shorter time compared to τ_l , to reach the flame zone from the core. If the mass ejection velocity (v_m) is assumed to be the maximum mean radial velocity component of the jet fluid (1.2 m/s; Fig. 4b) plus three times maximum rms value (1.8 m/s; Fig. 4d), the characteristic time for the radial mass ejection would be, $\tau_m = \delta_d/v_m \sim 0.2$ ms. Here, the diffusion layer thickness (δ_d) is ~ 1.5 mm, since $r_{1/2} \sim 5.5$ mm (Table I), and the outer edge of the visible flame zone is $r \sim 7$ mm. The fuel molecules must diffuse from the jet-fluid core to the flame zone. By using the diffusion coefficient of methane at 1500 K ($D \sim 0.7$ cm²/s) the characteristic diffusion time would be, $\tau_d = \delta_d^2/D \sim 30$ ms. The diffusion process requires an order of magnitude longer time than the jet-fluid core fluctuations. Thus, there is not enough time to re-establish the concentration field in response to variations in the core and the flame zone location remains stationary. Therefore, the radial mass ejection or the large-scale vortex itself can reach the flame zone location without causing significant disturbances in the concentration field, and thus, the diffusion flame is locally quenched by simply displacing the stoichiometric fuel-air mass flux field with nearly-pure fuel. This condition is eased downstream as the convective velocities decrease and the flame zone shifts radially away from the jet-fluid core. As a result, τ_l would increase faster than the increase in τ_d . Therefore, the local extinction occurs only in the mid-range of the near-jet region ($10 < z < 60$ mm).

Conclusions

The Mie scattering and LDV measurements in the near-field region of methane/air coflow turbulent jet diffusion flames provided a physical insight into the local extinction and subsequent lifting phenomena. The diffusion process needs at least an order of magnitude longer time compared to the concentration fluctuation time associated with the large-scale vortices in the core region and the radial jet-fluid mass ejection. As a result, the flame zone location is insensitive to the high-frequency inner fluctuation, and the fuel packets can reach the already strained flame zone and locally extinguish it. Due to the differences in the zone average velocities between the jet and external fluids, highly-dis-

torted turbulent structures are created in the vicinity of the flame zone. Further, unconditioned quantities must be retrieved from the unconditioned pdf, rather than taking weighted averages from conditioned quantities and the intermittency.

Acknowledgement

This work was supported by the U.S. Air Force, Wright Laboratory, Aero Propulsion and Power Directorate, Ohio, under Contract No. F33615-87-C-2767. Special appreciation is given to Drs. W. M. Roquemore (AF Technical Monitor) and D. R. Ballal for their support and helpful comments, Prof. T. Takeno for stimulating discussions, Messrs. W. J. Schmoll, G. L. Switzer, D. D. Trump, and B. Sarka for their assistance in conducting experiments.

REFERENCES

1. TAKAHASHI, F. AND SCHMOLL, W. J.: Twenty-Third Symposium (International) on Combustion, p. 677, The Combustion Institute, 1991.
2. TAKAHASHI, F., MIZOMOTO, M., IKAI, S. AND FUTAKI, N.: Twentieth Symposium (International) on Combustion, p. 295, The Combustion Institute, 1985.
3. COATS, C. M. AND ZHAO, H.: Twenty-Second Symposium (International) on Combustion, p. 685, The Combustion Institute, 1989.
4. VRANOS, A., TABACK, E. D. AND SHIPMAN, C. W.: Combust. Flame 12, 253 (1968).
5. TAKENO, T. AND KOTANI, Y.: Acta Astronaut. 2, 999 (1975).
6. HALL, L., HORCH, K. AND GUNTHER, R.: Brennst. Wärme Kraft 32, 26 (1980).
7. TAKAHASHI, F., MIZOMOTO, M., IKAI, S. AND TSURUYAMA, K.: Stability Limits of Hydrogen/Air Coflow Jet Diffusion Flames. AIAA Paper No. 90-0034, 1990.
8. SHEKARCHI, S., SAVAS, Ö. AND GOLLAHALLI, S. R.: Combust. Flame 73, 221 (1988).
9. EICKHOFF, H., LENZE, B. AND LEUCKEL, W.: Twentieth Symposium (International) on Combustion, p. 311, The Combustion Institute, 1985.
10. CHEN, T. H. AND GOSS, L. P.: Combust. Sci. Tech. 79, 311 (1991).
11. TAKAHASHI, F., SCHMOLL, W. J. AND VANGSNES, M. D.: 1990: Effects of swirl on the stability and turbulent structure of jet diffusion flames. AIAA Paper No. 90-0036.
12. ROQUEMORE, W. M., CHEN, L.-D., GOSS, L. P. AND LYNN, W. F.: Turbulent Reactive Flows (R. Borghi and S. N. B. Murthy, Ed.), p. 49, Springer-Verlag, 1989.
13. WILLIAMS, F. A.: Combustion Theory, 2nd ed., Benjamin/Cummings, 1985.

14. PETERS, N.: Twenty-First Symposium (International) on Combustion, p. 1231, The Combustion Institute, 1988.
15. BILGER, R. W.: Twenty-Second Symposium (International) on Combustion, p. 475, The Combustion Institute, 1989.
16. PETERS, N. AND WILLIAMS, F. A.: AIAA J. 21, 423 (1983).
17. BYGGSTØYL, S. AND MAGNUSSEN, B. F.: Turbulent Shear Flow 4 (L. J. S. Bradbury et al. Eds.), p. 381, Springer, 1985.
18. BROADWELL, J. E., DAHM, W. J. A. AND MUNGAL, M. G.: Twentieth Symposium (International) on Combustion, p. 303, The Combustion Institute, 1985.
19. DAHM, W. J. A. AND DIBBLE, R. W.: Twenty-Second Symposium (International) on Combustion, p. 801, The Combustion Institute, 1989.
20. MIAKE-LYE, R. C. AND HAMMER, J. A.: Twenty-Second Symposium (International) on Combustion, p. 817, The Combustion Institute, 1989.
21. PITTS, W. M.: Twenty-Second Symposium (International) on Combustion, p. 809, The Combustion Institute, 1989.
22. PITTS, W. M.: Twenty-Third Symposium (International) on Combustion, p. 661, The Combustion Institute, 1991.
23. VILIMPOC, V. AND GOSS, L. P.: Twenty-Second Symposium (International) on Combustion, p. 1907, The Combustion Institute, 1989.
24. ROQUEMORE, W. M., GOSS, L. P., LYNN, W. F. AND CHEN, L.-D.: Structure of Jet Diffusion Flames. Paper presented at the Central States/The Combustion Institute Meeting, May 1987.
25. TAKAHASHI, F., MIZOMOTO, M. AND IKAI, S.: Combust. Flame 48, 85 (1982).
26. MUNGAL, M. G. AND O'NEIL, J. M.: Combust. Flame 78, 377 (1989).
27. BROADWELL, J. E. AND MUNGAL, M. G.: Phys. Fluids A 3, 1193 (1991).
28. LIBBY, P. A. AND WILLIAMS, F. A.: Turbulent Reacting Flows, p. 21, Springer-Verlag, 1980.
29. LIBBY, P. A., CHIGIER, N. AND LaRUE, J. C.: Prog. Energy Combust. Sci. 8, 203 (1982).
30. DIBBLE, R. W., HARTMAN, V., SCHEFER, R. W. AND KOLLMAN, W.: Exp. Fluids 5, 103 (1987).
31. TSUJI, H.: Prog. Energy Combust. Sci. 8, 93 (1982).
32. CHELLIAH, H. K., LAW, C. K., UEDA, T., SMOOKE, M. D. AND WILLIAMS, F. A.: Twenty-Third Symposium (International) on Combustion, p. 503, The Combustion Institute, 1991.

COMMENTS

Dr. S. H. Stårner, University of Sydney, Australia. You determine the crossing frequency f , as I understand it, from your Mie scattering measurements. The dual effects of zero particulate diffusivity and thermophoresis are likely to affect f : it is well known that a Mie image in a diffusion flame has a more contorted edge, with sharper gradients, than the 'superlayer' of your flame zone. Hence, f is likely to have been substantially above the true value. Have you been able to verify your measurements of f by doing CARS, Rayleigh or other measurements? I think this is an important issue, since your conclusions seem to be based on f in part.

Author's Reply. First, it is necessary to make it clear that our definitions of intermittency and crossing frequency are based on the conditioning that a jet-fluid (continuum) parcel be present. We have used Mie scattering from jet-seeded particles to mark the convective motion of the jet-fluid parcel and, in turn, the boundary between the jet and external fluids. We did not intend to measure the concentration fluctuation for the conserved scalar based on an assumption conventionally employed for highly turbulent flames that particles follow fuel atoms by turbulent transport processes. Second, Mie-scattering results were used quantitatively only in the near

field, particularly the potential core region ($z < 6d$) where the intermittency on the centerline is known to be unity (thus, $f_c = 0$) and the jet-external fluid boundary is relatively clear due to unmixedness. Further, the intermittency was used to determine the unconditioned $P(u,v)$ with the conditioned $P(u,v)$ and $P_a(u,v)$ measured by LDV. It is consistent that both intermittency and LDV measurements utilize Mie scattering and the same conditioning criterion.

Since we have tried to trace jet-fluid parcels rather than fuel atoms, zero particulate diffusivity is rather a necessary condition. The effect of thermophoresis must be small since the jet-seeded particles are not subjected to high-temperature gradients in the near field, except for the jet-external fluid interface; and it would even play a favorable role, if any, to keep cold-jetseeded particles from mingling into the external fluid of hot combustion products. Similarly, the sharp gradient of the edges of the Mie-scattering intensities is desirable to obtain the crossing frequency which indicates the idealized bimodal switching frequency from the jet to external fluid. We have used nitrogen CARS spectra uniquely to determine the intermittency of the jet fluid (methane) by taking a ratio of the number of CARS realizations which are subjected to broadband in-

terference by methane to the total number of measurements at a fixed location.¹ Although this is an indirect method of determining the intermittency defined, the results are found to be in qualitatively good agreement with the Mie-scattering measurement.

REFERENCE

1. TAKAHASHI, F., VANGSNESS, M. D. AND GOSS, L. P.: Dynamic Vortex-Flame Interactions in Turbulent Jet Diffusion Flames near Local Extinction. Paper presented at the Central States Section/The Combustion Institute Meeting, April 1992.

•

A. R. Masri, *The University of Sydney, Australia*.
In your presentation you have indicated that the

study of turbulence-chemistry interactions is one of the objectives of the study. The highest jet Reynolds number is of the order 8000, and turbulence levels in the flame are relatively low. I think it is important to indicate that the local extinction you refer to is not due to turbulence-chemistry interaction but rather to physical effects.

Author's Reply. Our focus is on dynamic vortex-flame interactions leading to local flame extinction in the laminar-to-turbulent flame breakpoint region. It has long been postulated that the local extinction near the breakpoint is also a result of turbulence-chemistry interactions, i.e., the excess turbulent transport rate as compared to the finite reaction rate (Refs. 5 and 9 in the paper). Our new findings, however, have revealed that the primary cause of the local extinction in question is due to the physical process associated with the large-scale vortex structure and the radial mass ejection from the jet-fluid core.



AIAA 95-0139

**Vortex-Flame Interactions and the Local
Extinction of Turbulent Jet Diffusion
Flames**

F. Takahashi and W. J. Schmoll
University of Dayton
Dayton, Ohio

D. D. Trump and L. P. Goss
Systems Research Laboratories
Dayton, Ohio

**33rd Aerospace Sciences
Meeting and Exhibit
January 9-12, 1995 / Reno, NV**

VORTEX-FLAME INTERACTIONS AND THE LOCAL EXTINCTION OF TURBULENT JET DIFFUSION FLAMES

Fumiaki Takahashi* and W. John Schmoll**
University of Dayton, Dayton, Ohio

Darryl D. Trump† and Larry P. Goss‡
Systems Research Laboratories, Dayton, Ohio

Abstract

Dynamic vortex-flame interactions and subsequent local extinction have been investigated in turbulent methane jet diffusion flames stabilized on a thick-walled fuel tube using joint real-time Mie scattering/thin-filament pyrometry and particle image velocimetry. Local extinction occurred as a result of both (1) inner shear-generated large-scale fuel vortices extending outward to the flame zone and (2) radial influx velocity perturbations created by the outer shear-buoyancy-induced vortical structure. Consequently, cold annulus air passed through the quenched holes in the flame zone into the inner large vortices in the intermittent mixing layer. The total entrainment velocity at the flame-zone location increased substantially after local extinction. The local flame extinction can be attributed to (1) an order-of-magnitude longer characteristic diffusion time of the fuel compared to a convection time associated with the rapid growth of the inner large structure and (2) stretch-induced extinction as a result of excess annulus-fluid influx into the strained flame zone.

INTRODUCTION

In turbulent jet diffusion flames, dynamic interactions between the large-scale vortices and flame

zone may lead to local extinction near the laminar-to-turbulent flame transition point before the flame lifts off if the flame base is stabilized securely by a bluff body or pilot flame [1]. Local extinction leads to the formation of a stable split flame (i.e., a combination of a small laminar flame in the vicinity of the burner rim and a "lifted" turbulent flame downstream) in the case of hydrogen [2-6] or propane [7], or causes lifting of the flame almost immediately in the case of methane [1, 8-10]. The vortex-flame interaction is a common feature in turbulent flames, although the turbulence scales and intensities vary widely, and the flame extinction and stability are of both fundamental and practical importance. If the mechanisms of vortex-flame interactions and local extinction are revealed in relatively simple laboratory flames, their essential features must be applicable to various turbulent flames in more complex practical combustion systems, such as gas-turbine combustors and industrial furnaces.

The vortex-flame interactions in turbulent methane jet diffusion flames have been studied [11-13] by means of various laser diagnostic techniques (including planar flow visualization, real-time Mie scattering, laser-Doppler velocimetry [LDV], and coherent anti-Stokes Raman spectroscopy [CARS]) and by numerical experiments [14]. One physical aspect of the vortex-flame interactions has been identified as the dominant process in a series of events leading to local extinction, at which finite-rate chemistry takes over the process. More specifically, the fuel diffusion process requires an order-of-magnitude longer time compared to the convective motion associated with the large-scale vortex structure growth, including the radial mass ejection (side jets) from the jet-fluid core. A Pecret number (Pe), defined as the ratio of the characteristic diffusion time to convection time, determines the response of the flame zone to the vortical motion [14].

* Research Engineer, Research Institute, Senior Member AIAA

** Associate Research Physicist, Research Institute

† Senior Engineer, Optical Diagnostics

‡ Director of Research, Optical Diagnostics, Member AIAA

If Pe is large, fuel packets can reach the flame zone location without causing significant disturbances in the adjacent concentration field. Consequently, they replace the gases on the passage through the flame zone, thereby quenching the flame locally.

This paper reports new results obtained using the joint real-time Mie scattering and thin filament thermometry, and particle image velocimetry (PIV). Particularly, the effect of the outer vortical structure is investigated as well as the internal shear-layer vortices. The primary purpose of this study is to gain a better understanding of the dynamic vortex-flame interactions which lead to the local extinction and subsequent lifting of jet diffusion flames.

EXPERIMENTAL TECHNIQUES

The burner system, described elsewhere in detail [1, 11, 12], consists of a thick-walled fuel tube (9.45-mm inner diameter, 806-mm length, 2.4-mm lip thickness, flat-end stainless-steel tube) and a concentric air tube (26.92-mm inner diameter) – through which annulus coflow air is supplied – centered in a low-speed (~ 0.5 m/s) external airstream in a vertical combustion chimney (150- × 150-mm rounded-square cross section; 483-mm length; quartz windows on three sides). Methane (>98%) was used as the fuel.

The unique capabilities of the real-time line measurements techniques, including line Mie scattering and thin-filament pyrometry (TFP) [15, 16], were combined to study the real-time interactions of flames and their flow fields. The combination of the two line-measurement techniques is depicted in Fig. 1. As in the previous experiments [11], a rotating mirror is employed to sweep the scattered or emitted light from a jet diffusion flame past a point detector. In the case of line-Mie scattering, seed particles (ZrO_2 ; $< 1 \mu m$, 97%) are introduced into the fuel jet and allowed to pass through a line formed from the focused output of an Argon ion laser (Spectra Physics 2000; multi-line, 1-3W). The scattered light from the sample region is collimated and focused by a lens system toward the multifaceted rotating mirror wheel which sweeps the converging light onto an optical fiber. The optical fiber collects the scattered light and directs it into a photomultiplier for detection. The TFP technique is simultaneously implemented by placing a small SiC filament ($\sim 15 \mu m$ diameter) near the laser beam location. As the flame heats the small filament,

blackbody emission is collected by the same lens system and reflected to a second optical fiber. This fiber directs the blackbody light to a InGaAs detector whose peak response is at $1.7 \mu m$. This experimental arrangement allows both the line-Mie scattering and the TFP signals to be simultaneously recorded as a function of space and time. For the experiments reported in this paper, the rotational speed of the multifaceted mirror was 500 rps which with 10 facets translates into 5000 sweeps per second.

The experimental scheme utilized for two-dimensional velocity measurements was similar to that reported by Goss et al. [17] and is shown in Figure 2. In this scheme, a seeded flow field is illuminated by two different colored (green and red) pulsed laser sheets. Because color is used to mark the particle positions as a function of time, the direction and displacement of the particles (velocity) can be uniquely determined. The green (532 nm) laser output from a frequency-doubled pulsed (~ 8 ns) Nd:YAG laser and the red (640 nm) laser output from a Nd:YAG-pumped dye laser are combined and routed through sheet forming optics. The laser sheet energy is typically 20 mJ/pulse with a thickness ~ 0.5 mm at the test section. The temporal delay between the two lasers is controlled by a pulse generator and is a function of the gas velocity, optical magnification, and interrogation spot size. In the present experiments, the time delay between the two color lasers was varied from 9 to 18 msec. A photodiode was used to ensure that the desired time delay was being employed. Mie scattering from the seed particles was recorded on commercial 35-mm color film (ASA 400) with a Nikon camera with a 105-mm lens (typical f-number: 4). The color film was digitized by a Nikon CoolRay Electronic Imaging scanner. The scanner digitized the image into individual red, green, and blue components at a resolution of 2702 pixels per inch. The digitized image was then processed by customized PIV analysis software.

Because two distinct image fields (red and green) are recorded by the color film, a cross-correlation technique is used for the PIV analysis. The two-dimensional cross-correlation can be written as

$$h(x, y) = F^{-1} [R(\alpha, \beta) G^*(\alpha, \beta)] \quad (1)$$

where $R(a, b)$ is the Fourier transform of the red-color image and $G(a, b)$ the Fourier transform of the green-color image. While the cross-correlation analysis

requires more time than an autocorrelation analysis, the self-correlation peak and the 180 deg. directional ambiguity associated with an autocorrelation approach are overcome, and the velocity is uniquely determined by the peak in the cross-correlation map. The processing of the digitized image requires that it be dissected into small subregions over which the cross-correlation is applied. The small subregions are referred to as interrogation spots and their size is dependent on the particle density, local velocity gradients, particle image size, and the desired spatial resolution. The maximum recorded displacement of the particle must be less than half the interrogation spot. In the experiments reported in this paper, the interrogation spot size was either 64 or 128 square pixels which translates to the spatial resolution of 0.6×0.6 mm with the 1.0 magnification employed. To enhance the overall resolution, the interrogation spots are overlapped by one-half the spot size.

The peak of the correlation map calculated by Eq. (1) corresponds to the average velocity displacement within the interrogation spot. The size, shape, and intensity of this peak are determined by the corresponding information in the particle images. An intensity-weighted peak-searching routine was used to determine the exact location of the peaks center to a subpixel accuracy. The number of particle pairs needed to ensure a good signal-to-noise ratio is reduced in the cross-correlation analysis. However, a minimum of four to five red-green particles pairs is preferred.

Once the velocity vectors are determined for a given image, the vectors are post-processed. The post-processing procedure consisted of a series of operator-selectable filter and interpolation routines. The "nearest neighbor" filter consists of comparing the average variation between a given vector and its nearest neighbors. If the variation exceeds a desired level, the vector in question is discarded. Further "manual" filtering is sometimes necessary to correct for inconsistent vectors not removed or created by the data validation techniques. Once all the bad vectors are removed, an interpolation procedure is used to estimate the magnitude of the missing vectors based upon their nearest neighbors. From the post-processed vectors, contour maps and gradient quantities (i.e. shear and vorticity) can be determined.

RESULTS AND DISCUSSION

Real-Time Mie/TFP Visualization

Figure 3 shows real-time line intensities of Mie scattering (ZrO_2) and thin filament radiation for two different mean jet velocities ($U_j = 6$ and 15 m/s) and three different heights from the jet exit ($x = 15, 25$, and 50 mm). The left edge of each image coincides with the jet axis, and the elapsed time is longer in the upper portion. The Mie scattering is on the left and the thin-filament radiation is on the right in each photograph. At a low mean jet velocity (Fig. 3a), the high-temperature zone marked by the filament is thin and continuous, and the particle-laden jet fluid rarely reaches the hot zone. The visible (blue) flame zone for the same flow condition is located at the radial distance from the axis of $y = 6.8$ to 7.3 mm [11, 12]. By contrast, at a high mean jet velocity under the condition of local extinction (Fig. 3b), the jet fluid sometimes pokes through the flame zone, and the high temperature zone discontinues sporadically. This result is consistent with the previous observation [17] of local extinction using joint planar Mie scattering and laser-induced fluorescence of OH radicals. However, in other instances, local extinction occurred even if the jet fluid stayed in the jet core region. The visible flame location is pushed inwardly to $y = 6.2$ to 7.2 mm at this condition due to a higher radial velocity component in the flame zone [11]. The crossing frequency of the jet and external fluids increased from 702 Hz to 1330 Hz [11], and the mean flame temperature dropped from ~ 2050 K to ~ 1820 K [12] for these two conditions. At a downstream location (Figs. 3c and 3d), the high-temperature zone shifted outward, thickened, and lumped to form large packets. The radial movement of the interface of the jet fluid and external fluid increased downstream as a result of the growth of the large-scale structure.

Planar Flow Visualization

Planar particle scattering images taken for PIV are also useful to extract qualitative information on the vortical structures and local extinction. Figure 4 shows examples of the visualization photographs, showing a relatively wide field of view. The green and red lasers were fired with a relatively long separation (20 to 40 μs). The jet and annulus fluids can be identifiable in the images mainly because of the differences in the number density of the seed particles. The local laser intensity and flow velocity (which determines the particle displacement during the time separation) also contribute to the properties of images. Furthermore, as

a result of thermal expansion of the gases in a hot region and associated reduction in the particle number density, the hot regions near the flame zone can also be identified as dark regions particularly in the near field. This nature is of great advantage in that it allows instantaneous recognition of local flame extinction, whereas the visible flame zone is a time-exposure (typically 1/15 s) record. These features could not be obtained by one-color (green) laser-sheet visualization using either preformed particles [12] or reactive-Mie scattering [11].

At a low mean jet velocity (Fig. 4a), the evolution and growth of large-scale vortices in both the central fuel jet and annulus air jet are clearly seen. The internal vortical structure is purely shear-induced. Although the external structure evolves in the shear layer between the annulus air jet and the external airstream, buoyancy apparently contributes to the scale of the vortices. The effect of the flame becomes evident by contrasting images of a stable flame (Fig. 4a) and a lifted flame (Fig. 4c). Since the liftoff height is large (~ 10 cm), the region below the flame base is essentially identical to a cold jet. The scale of vortices of the outer structure is much larger for a stable flame because of presence of the flame. The visible (blue) flame zone is barely recorded in the photograph in the near field, and it turns to yellow because of soot formation downstream ($x > 5$ cm). The dark hot zone is recognizable in the vicinity (inside and outside) of the visible (blue) flame zone and near the yellow flame downstream. The inner vortex occasionally extends toward the visible flame zone (see $x \approx 33$ mm on the left side), but the dark hot zone is still thick, indicating the continuous flame zone. The large outer structure engulfs the external air close to the visible flame zone, thus squeezing the hot zone. The hot zone bulges out as the outer vortex rolls outwardly (see $x \approx 36$ mm on the left side). The yellow flame bulges out due to both inner and outer vortices.

At a high mean jet velocity under the local extinction condition (Figs. 4b and 4c), the inner vortices become smaller with more random shapes. The local extinction can be identified because the dark hot zone discontinues. As was investigated in detail [11, 12], the inner vortex extrudes to reach the flame zone and extinguish the flame (see Fig. 4b: $x \approx 38$ mm on the left side and $x > 19$ mm on the right side). Figure 4c shows an image with only annulus-seeded particles; thus, the jet fluid appears black. It should be noted that the engulfment of the external air into the outer vortex (see Fig. 4c: $x \approx 28$ mm on the both sides)

pushes the annulus air layer inward, and the dark hot zone discontinues (i.e., local extinction). Consequently, cold annulus air passes through the quenched hole and contacts the fuel directly. This mechanism of local flame extinction has not been revealed previously. This result explains the large temperature fluctuations (the room temperature to flame temperature) near the flame zone observed under a similar jetting condition [12]. Moreover, the annulus air reaches deep into the mixing region and nearly reaches the jet axis (see Fig. 4c: $x > 6$ cm). This observation is consistent with the real-time line-Mie scattering measurement reported earlier [11].

Figure 5 shows a schematic illustrating several features of vortex-flame interactions. As the fuel jet velocity is increased, the velocity of annulus air entrained into the flame zone increases in the near field, thus pushing the flame zone toward the jet-annulus fluid boundary. As a result, the thickness of the transport layer becomes thin and the flame zone becomes strained; thus, the flame loses its mobility. Consequently, the flame zone is locally extinguished if the internal fuel jet vortices approach to the flame zone in a short period or the entrainment velocity is forced to increase due the outer vortical structure, as described in the next section. However, in the downstream region where the visible flame turns to yellow due to soot formation, the transport processes slow down and the scales of the vortices become larger. Thus, the flame can bulge due to vortical motion in both internal and external structures.

PIV Measurements

Figure 6 shows planar particle images for the PIV measurement in the near-jet field, and Figure 7 shows the vector field with some characteristic boundaries determined from the images. Figures 6a and 7a demonstrate local extinction due to internal vortices. The image (Fig. 6a) clearly shows a wake region (of the tube wall) where almost no particle is present. The visible (blue) flame zone anchors at the upper part of the wake region. The large-scale vortices grow downstream and extend outward to the location where the flame zone was formed. Consequently, the dark hot zone became thin and discontinued at $x \approx 13$ mm on the left and $x \approx 22$ mm on the right. The instantaneous velocity vector field (Fig. 7a) shows some interesting features that could not be revealed by point-measurement techniques such as LDV. In general, the jet fluid elements almost always have much high velocities (typically 5 to 22 m/s) compared to the

annulus fluid (mostly < 5 m/s except for the fluid elements engulfed deeply in the vortex), even in the extended vortices or fragmented packets (5 to 10 m/s). This observation is consistent with the conditionally sampled LDV measurement [11]. The instantaneous velocity vectors along $y = -6$ mm reveals typical features in the vortex-flame interactions and local extinction. In the region where the flame zone exists ($x < 10$ mm), the annulus fluid elements pass through the flame zone with a narrow angle at low velocities (< 1 m/s). In the region where the visible flame zone fades out but the dark hot zone remains ($10 < x < 16$ mm), the total velocities increase (2 to 3 m/s). Once the flame zone is locally extinguished ($25 < x < 27$ mm), the cold annulus air is engulfed into the inner large-scale vortices with larger angles (typically $\sim 45^\circ$) and higher velocities (4 to 5 m/s). The kinematic viscosity is a function of $T^{1.7}$; thus, it decreases ~ 15 times as the gas temperature decreases from 1500 K to 300 K. Therefore, the cold annulus air would be easily engulfed into the vortex and accelerate more quickly than the highly viscous hot combustion products. The zigzag changes in the directions of the velocity vectors along the jet-annulus-fluid boundary are typical of large-scale vortices. Consequently, if the average axial transit velocity of the vortex train is subtracted from the velocity vectors, rotation of the vortices can be visualized more clearly.

The vortex transit time between two consecutive vortices, estimated by dividing a typical inter-vortex distance (~ 8 mm) by a typical axial velocity component of the vortex (~ 10 m/s), is ~ 0.8 ms, a consistent measurement of the characteristic convection time of the large-scale vortex structure estimated by the crossing frequency of the jet fluid (~ 1330 Hz) [11, 12]. Thus, the instantaneous fuel concentration changes in a short period compared to the characteristic diffusion time (~ 30 ms [11, 12]) estimated by dividing the square of the characteristic transport layer thickness (~ 1.5 mm) by the diffusion coefficient of methane at 1500 K ($0.7 \text{ cm}^2/\text{s}$). Consequently, the Pecret number (the ratio of the characteristic times of diffusion and convection) is large (> 30). Therefore, if the inner large-scale vortex grows and reach the flame zone location, there is not sufficient time to establish the fuel concentration field. Consequently, when the fuel vortex reaches the flame zone, the flame is subjected to a steep fuel concentration gradient (i.e., large diffusion flux) around the jet-fluid vortex, while the oxygen influx remains

unchanged. The stoichiometric balance between the fuel and oxygen fluxes can no longer be achieved; thus, the flame zone extinguished locally.

Figures 6b and 7b show local extinction due to the influence of the external large-scale vortical structure. The image was captured above the jet exit ($17 < x < 37$ mm). Because the visible (blue) flame zone was recorded within a film exposure period (1/15 s), it does not match the instantaneous particle image. The outer vortices create a necking of the annulus fluid's outer boundary, thereby pushing the annulus fluid toward the flame zone. The velocity of the stream passing the flame zone may increase; thus, the convective contribution of the oxygen transport into the flame may increase. To compensate for the change, the flame needs to be formed at a radial position closer to the fuel jet to obtain a larger diffusive flux of the fuel. However, at the high mean jet velocity close to the extinction limit, the flame zone must be formed already at the innermost position where the fuel and oxygen transport is maximum to be consumed by chemical reactions. Thus, the flame zone (and transport layer) must be thin, and the flame is strained and loses mobility. Therefore, any increase in the entrainment velocity would decrease the chemical reaction rate (in turn, the Damkhöler number), the flame temperature decreases, and stretch-induced local extinction occurs.

CONCLUSIONS

The laser diagnostic measurements have shed light on the dynamic interaction processes between the diffusion flame zone and the internal and external vortical structures and mechanisms of local extinction. Both the internal shear-generated large-scale vortices and external shear-buoyancy-induced vortices are responsible for local flame extinction. The flame zone is locally extinguished if the internal fuel jet vortices approach the flame zone in a short period of time or the entrainment velocity is forced to increase due to the outer vortical structure. The former can be attributed to an order-of-magnitude longer characteristic diffusion time of the fuel compared to a convection time associated with the rapid growth of the inner large structure (large Pe effect). The latter is caused by stretch-induced extinction as a result of excess annulus-fluid influx into the strained flame zone.

ACKNOWLEDGMENTS

This work was supported by the U.S. Air Force, Wright Laboratory, Aero Propulsion and Power Directorate, Fuels and Lubrication Division, Wright-Patterson Air Force Base, Ohio, under Contract No. F33615-92-C-2207 (Technical Monitor: C. W. Frayne).

REFERENCES

1. Takahashi, F., and Schmoll, W. J., "Lifting Criteria of Jet Diffusion Flames," *Twenty-Third Symposium (International) on Combustion*, The Combustion Institute, Pittsburgh, 1991, pp. 677-683.
2. Hattori, H., "Stability of Diffusion Flame," *Transactions of the JSME*, Vol. 30, 1964, pp. 320-332.
3. Vranos, A., Taback, E. D., and Shipman, C. W., "An Experimental Study of the Stability of Hydrogen-Air Diffusion Flames," *Combustion and Flame*, Vol. 12, 1968, pp. 253-260.
4. Takeno, T., and Kotani, Y., "An Experimental Study on the Stability of Jet Diffusion Flames," *Acta Astronautica* 2, 999-1008 (1975).
5. Hall, L., Horch, K., and Günther, R., "Die Stabilität von Freistrah-Diffusionsflammen," *Brennst. Wärme Kraft* 32, 26-31 (1980).
6. Takahashi, F., Mizomoto, M., Ikai, S., and Tsuruyama, K., "Stability Limits of Hydrogen/Air Coflow Jet Diffusion Flames," AIAA Paper 90-0034, 1990.
7. Shekarchi, S., Savas, Ö., and Gollahalli, S. R., "Structure of a Split Flame," *Combustion and Flame*, 73, 221-232 (1988).
8. Eickhoff, H., Lenze, B., and Leuckel, W., "Experimental Investigation on the Stabilization Mechanism of Jet Diffusion Flames," *Twentieth Symposium (International) on Combustion*, The Combustion Institute, Pittsburgh, 1985, p. 311.
9. Chen, T. H., and Goss, L. P., "Flame Lifting and Flame/Flow Interactions of Jet Diffusion Flames," AIAA Paper 89-0156, 1989.
10. Coats, C. M., and Zhao, H., "Transition and Stability of Turbulent Jet Diffusion Flames," *Twenty-Second Symposium (International) on Combustion*, The Combustion Institute, Pittsburgh, 1989, pp. 685-692.
11. Takahashi, F., and Goss, L. P., "Near-Field Turbulent Structures and the Local Extinction of Jet Diffusion Flames," *Twenty-Fourth Symposium (International) on Combustion*, The Combustion Institute, Pittsburgh, 1992, pp. 351-359.
12. Takahashi, F., and Vangsness, M. D., "Near-Field CARS Measurements and the Local Extinction of Turbulent Jet Diffusion Flames," *Dynamics of Heterogeneous Combustion and Reacting Systems*, A. L. Kuhl, J.-C. Leyer, A. A. Borisov, and W. A. Sirignano (eds.), *Progress in Astronautics and Aeronautics*, Vol. 152, AIAA, Washington, D. C., 1993, pp. 37-55.
13. Hsu, K. Y., Chen, L. D., Katta, V. R., Goss, L. P., and Roquemore, W. M., "Experimental and Numerical Investigation of the Vortex-Flame Interactions in a Driven Jet Diffusion Flames," AIAA Paper No. 93-0455, 1993.
14. Takahashi, F., and Katta, V. R., "Numerical Experiments on the Vortex-Flame Interactions in a Jet Diffusion Flames," *Journal of Propulsion and Power*, to appear (1995).
15. Vilimpoc, V., and Goss, L.P., *Twenty-Second Symposium (International) on Combustion*, The Combustion Institute, 1989, p. 1907.
16. Roquemore, W. M., Chen, L. -D., Goss, L. P., and Lynn, W. F., "The Structure of Jet Diffusion Flames," *Turbulent Reactive Flows*, R. Borghi and S. N. B. Murthy (eds.), Springer-Verlag, New York, 1989, pp. 49-63.
17. Goss, L. P., Post, M. E., Trump, D. D., and Sarka, B., "Two-Color Particle Imaging Velocimetry," *Journal of Laser Applications* 3, 36-42 (1991).
18. Chen, T. H., and Goss, L.P., *Combustion Science and Technology* 79, 311 (1991).

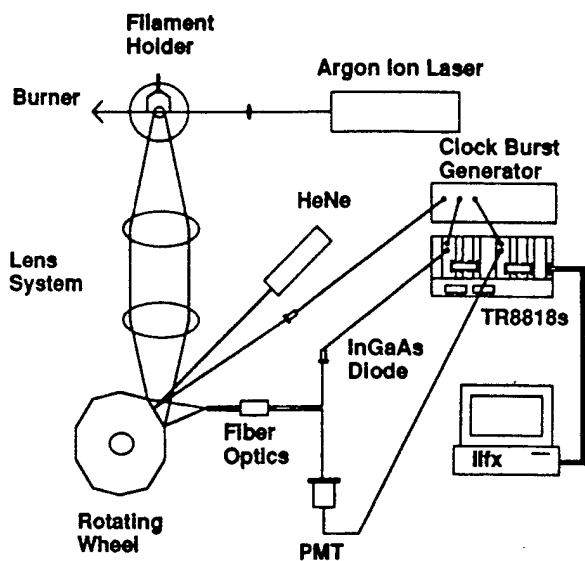


Fig. 1 Schematic of the joint real-time Mie/TFP instrument.

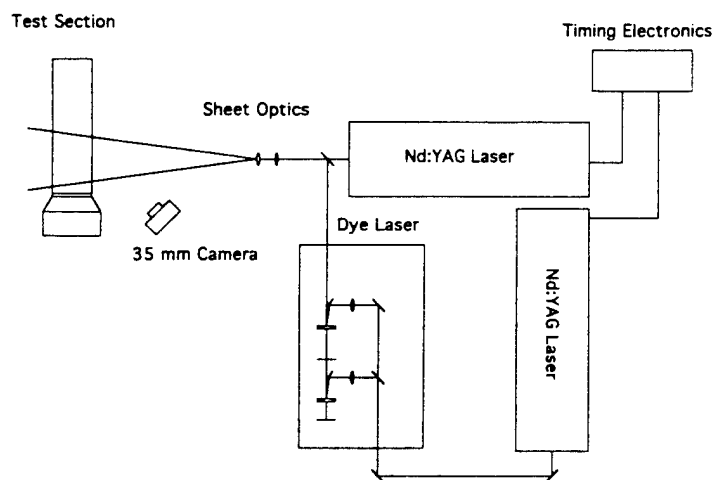


Fig. 2 Schematic of the PIV setup.

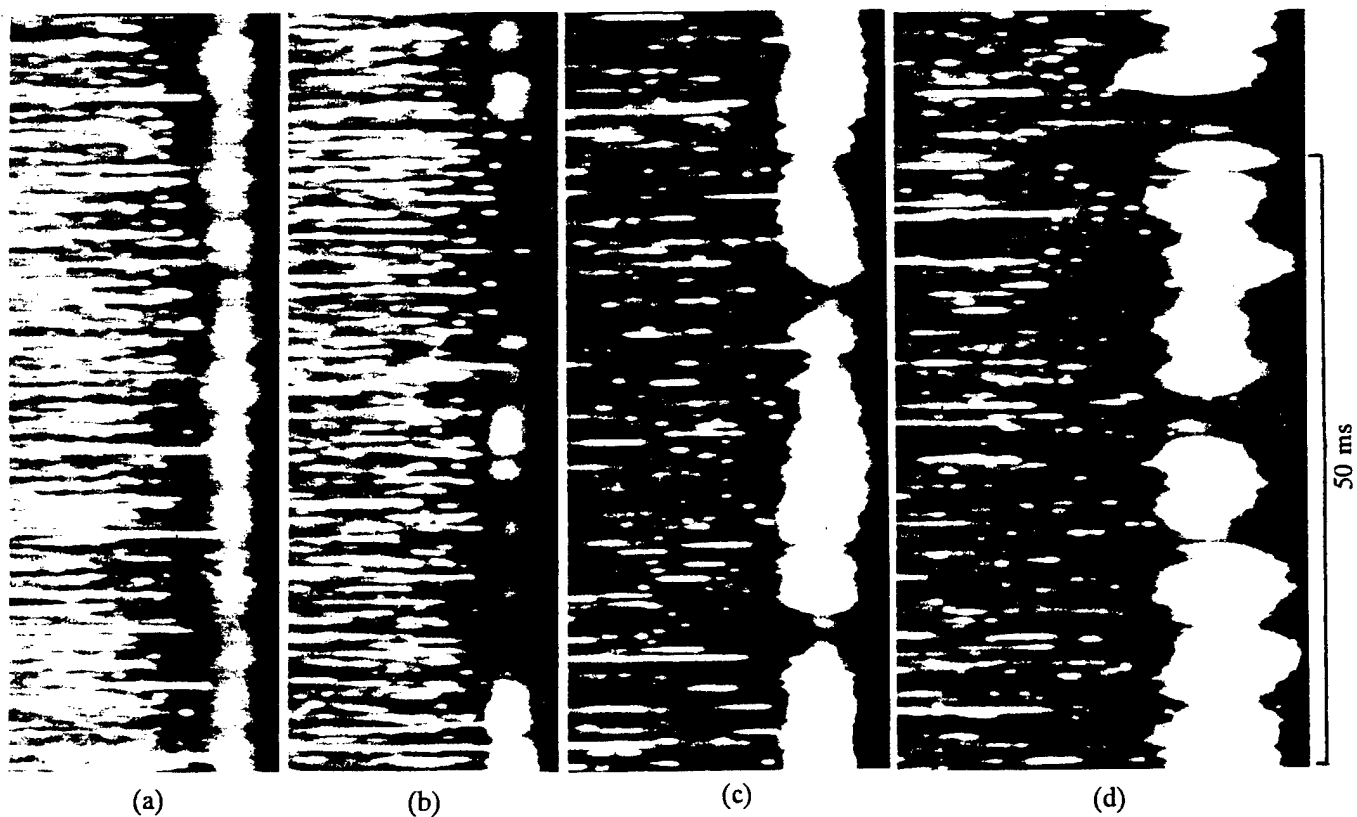


Fig. 3 Real-time Mie scattering (ZrO_2) and TFP intensities along a line. $U_a = 3$ m/s. (a) $U_j = 6$ m/s, $x = 15$ mm; (b) $U_j = 15$ m/s, $x = 15$ mm; (c) $U_j = 15$ m/s, $x = 25$ mm; and (d) $U_j = 15$ m/s, $x = 50$ mm.

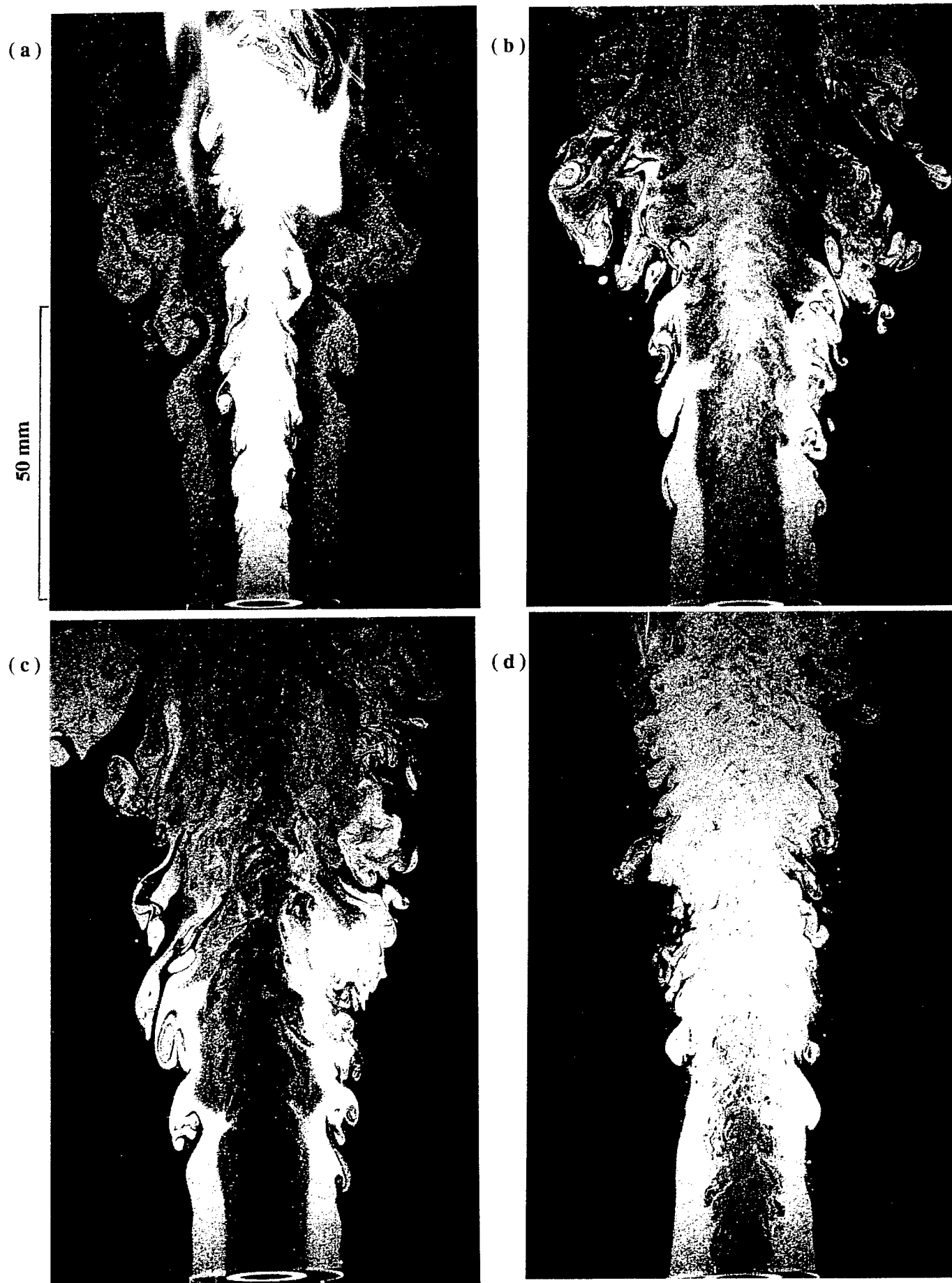


Fig. 4 Planar flow visualization photographs of methane jet diffusion flames. $U_a = 3$ m/s. (a) $U_j = 6$ m/s, $\Delta t = 40 \mu\text{s}$; (b)(c) $U_j = 15$ m/s, $\Delta t = 20 \mu\text{s}$; and (d) $U_j = 16$ m/s, $\Delta t = 20 \mu\text{s}$.

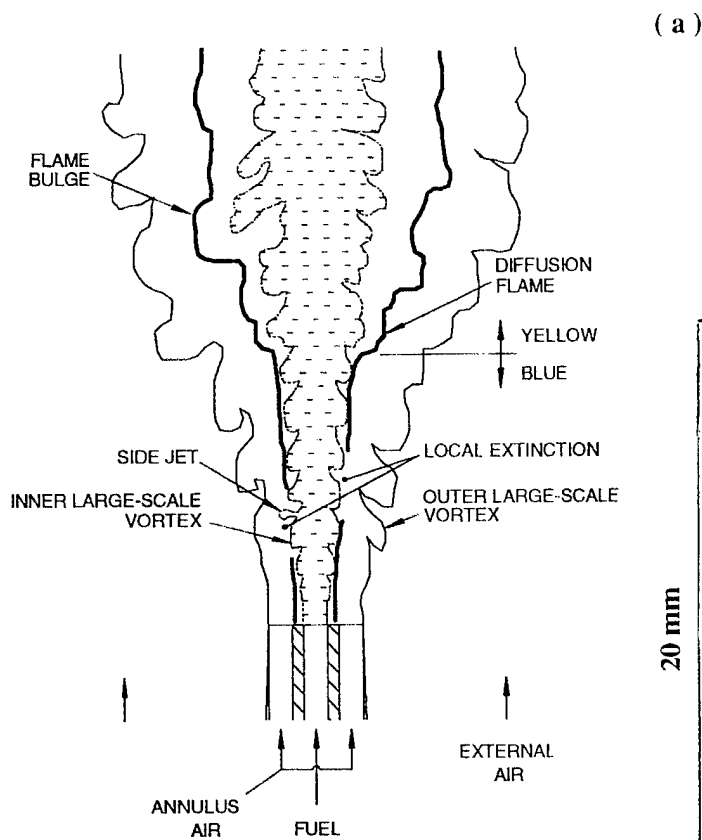


Fig. 5 Schematic of vortex-flame interactions in a double-concentric jet diffusion flame.

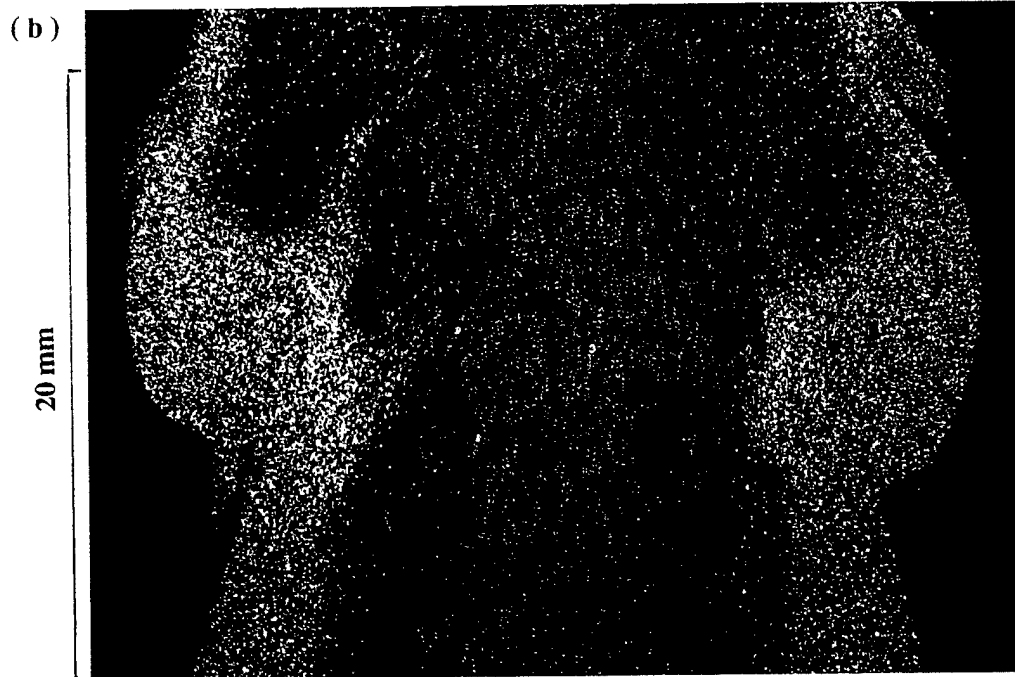


Fig. 6 Particle image photographs of methane jet diffusion flames under local extinction. $U_a = 3$ m/s, $U_j = 15$ m/s, $\Delta t = 9$ μ s. (a) Internal vortex interference and (b) external vortex interference.

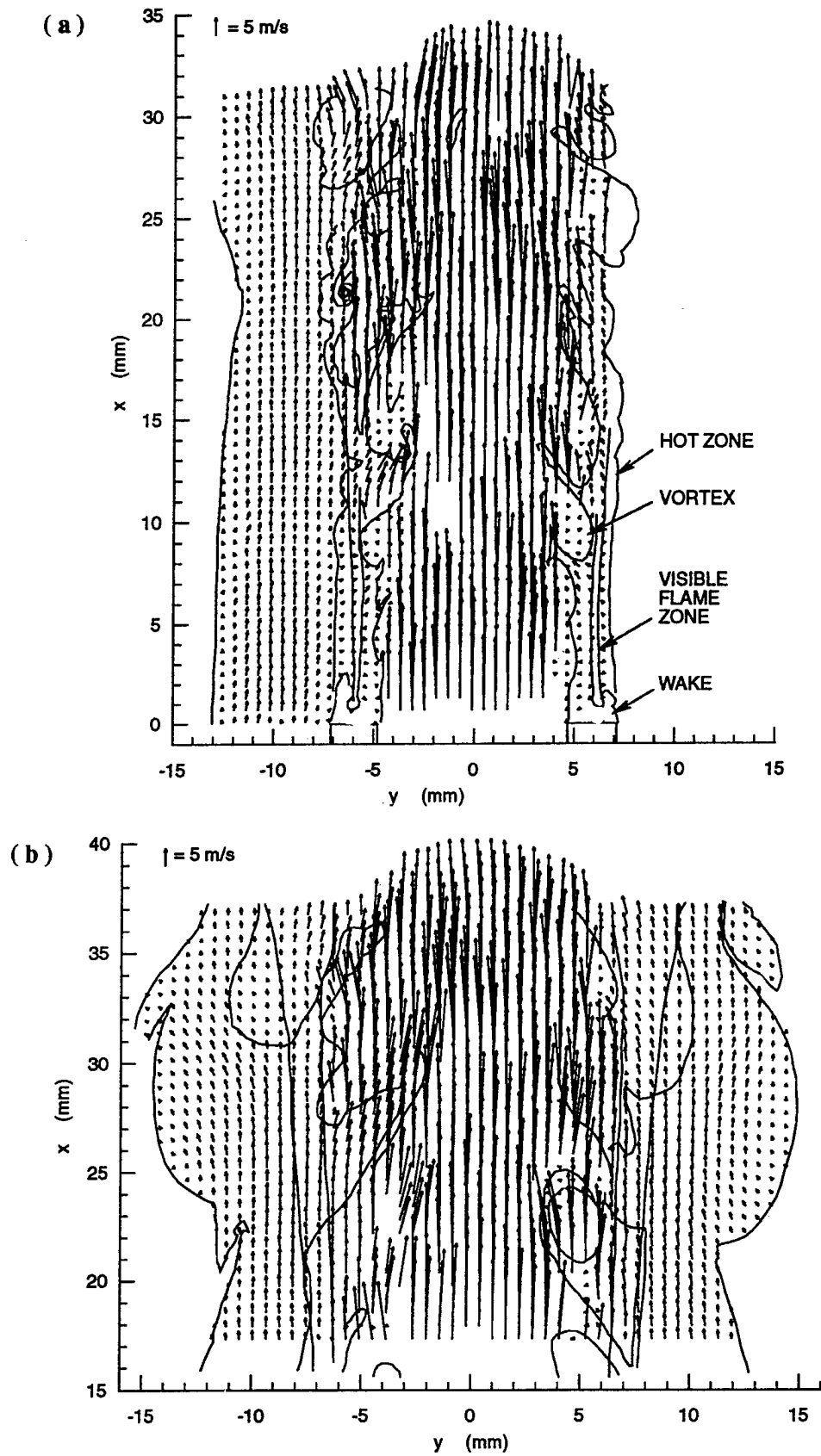


Fig. 7 Velocity vectors in methane jet diffusion flames under local extinction. $U_a = 3 \text{ m/s}$, $U_j = 15 \text{ m/s}$, $\Delta t = 9 \mu\text{s}$. (a) Internal vortex interference. (b) External vortex interference.



AIAA 93-0455

**Experimental and Numerical Investigations of
the Vortex-Flame Interactions in a Driven Jet
Diffusion Flame**

K. Y. Hsu and L. D. Chen
Department of Mechanical Engineering
The University of Iowa
Iowa City, IA

V. R. Katta and L. P. Goss
System Research Laboratories, Inc.
Dayton, OH

W. M. Roquemore
Wright Laboratory
Wright-Patterson Air Force Base, OH

**31st Aerospace Sciences
Meeting & Exhibit
January 11-14, 1993 / Reno, NV**

EXPERIMENTAL AND NUMERICAL INVESTIGATIONS OF THE VORTEX-FLAME INTERACTIONS IN A DRIVEN JET DIFFUSION FLAME

K. Y. Hsu and L. D. Chen*
Department of Mechanical Engineering
The University of Iowa
Iowa City, IA 52242

V. R. Katta** and L. P. Goss**
System Research Laboratories, Inc.
Dayton, OH 45440-3696

W. M. Roquemore†
Wright Laboratory
Wright-Patterson Air Force Base, OH 45433

Abstract

This paper presents the initial results of a vortex-flame interaction that is periodically reproduced. The interaction has features that are similar to those observed in a turbulent jet diffusion flame. An acoustic speaker is used to form axisymmetric, counter rotating ring vortices inside the flame surface. Phase-locked Reactive-Mie-Scattering (RMS) and Planar-Laser-Induced-Fluorescence (PLIF) are used to visualize the vortex structure and OH zone, respectively. The evolution of the vortex-flame interaction is presented. The forcing vortex, convected in the radial direction, causes the flame to bulge outward. When the flame surface is further stretched, a local quenching around the flame is observed. Thin-Filament-Pyrometry (TFP) is used to record the temperature variation during the interaction process. A sudden decrease in flame temperature indicates the occurrence of local quenching. The thinning and disappearance of the OH zone during the quenching process is also illustrated by OH-PLIF imaging. A time-dependent numerical simulation reproduces the vortex structure and the dynamic vortex-flame interaction observed in the experiment. Although the fast chemistry model fail to predict the quenching, the calculation demonstrates the importance of transport phenomena during the vortex-flame interaction.

Introduction

Lean blowout, high altitude relight, emissions, and combustion efficiency are of practical importance

* Professor, Member

** Research and Application Division, Member

† Fuel and Lubrication Division, Member

This paper is declared a work of the U.S. Government and is not subject to copy right protection in the United States

in the design of gas turbine combustors. They all involve turbulent combustion processes that need to be better understood if accurate combustor design models are to be developed. Turbulent jet diffusion flames are used to gain insight into turbulent combustion processes and to develop numerical models for use in combustor design. Because of their practical importance, they have been studied for over 40 years. Although considerable progress has been made in understanding turbulent jet diffusion flames, there still remain many important questions about the turbulent combustion processes and the simplifying assumptions required to effectively model them. The conceptual view of turbulent reaction zones and the interplay between turbulence and chemistry are germane to the modeling approaches. Recent research has focused on whether turbulent flames can be viewed as an ensemble of strained laminar flamelets or distributed reaction zones (Bilger, 1989; Correa, 1992). In this paper the statistical fabric of a turbulent reaction zone is viewed as an ensemble of vortex-flame interactions. The statistics of the problem are eliminated by isolating and studying a single vortex-flame interaction event that has similar characteristics to those occurring in turbulent jet diffusion flames.

Many of the basic characteristics of turbulent jet diffusion flames were described by Hottel and Hawthorne (1949), Scholefield and Garside (1949), and Wohl et al, (1949). According to their description, a vertically-mounted jet diffusion flame is considered fully turbulent when its entire surface area becomes a flame brush, which means that the flame has a highly wrinkled, bumpy, or rough appearance.

Improved visualization techniques have provided additional insights into the structure of a turbulent flame and the events that happen as the flame becomes turbulent (Roquemore, et al., 1988). Although the turbulent transition processes can be

observed in flames established with fuel tubes (Takeno and Kotani, 1977; Takahashi, et al. 1982), they are more clearly observed when the jet flame is established by a contoured nozzle with a flat velocity exit profile (Yule et al. 1981; Eickhoff, 1982; Savas and Gollahalli, 1986; Coats and Zhao 1988; and Roquemore et al. 1988). At transitional jet velocities, well organized, axisymmetric vortex structures are observed to exist inside the laminar flame surface for many jet diameters downstream. As the jet velocity increases, the inner vortices begin to coalesce at a downstream location in the flame. The coalescence process is highly unstable and results in the break-down of the organized vortices into smaller but identifiable three dimensional fluid elements. The flame becomes turbulent when these small three-dimensional structures interact with the flame creating the turbulent flame brush. The height at which this takes place is called the break-point. As the jet velocity increases, the break-point moves toward the nozzle exit. When the break-point is occurred near the lip of the nozzle, the flame is considered to be fully turbulent. Thus, the wrinkles or bumps in the flame are localized protrusions of the flame surface that result when three-dimensional fluid elements of different size, shape, velocity, and rotational strength interact with reaction zones of different thicknesses.

There is a question about whether or not the small three-dimensional fluid elements formed in the coalescence process are vortices. In a vortex, the fluid mass moves around a common axis (Lugt, 1979). Some of the small structures in turbulent jet flames are easily recognized in a two-dimensional visualizations as vortex pairs that are associated with mushroom-shaped vortices. Other fluid elements are not so easily recognized as vortices in the laboratory reference frame. However, three-dimensional calculations show that the small fluid elements resulted from the coalescence of two-dimensional vortices are vortex structures (Knio and Ghoniem, 1989). Since this process is similar to that occurring in jet flames, it will be assumed that the three-dimensional fluid elements that interact with the flame are vortices. The interaction processes will be referred to as vortex-flame interactions.

Individual vortex-flame interactions are important to understand for several reasons. First, they can increase or decrease the turbulent reaction rate. When the vortex-flame interactions is moderate, they increase the surface area of the flame which leads to an overall increase in the global reaction rate and a reduction in the length of the flame. However, if a vortex has a sufficiently high radial velocity, it can pass through the flame creating a localized hole in

which no chemical reactions take place (Takahashi and Schmoll, 1990; Chen and Goss, 1991; Takahashi and Goss, 1992). The holes can cause the flame to split or lift when they form near the jet exit. If the holes covers two much of the flame surface the global reaction rate can decrease. This can lead to reduction in combustion efficiency and blow-out. Second, flame vortex interactions may be building blocks for statistical theories of turbulent flames. It is conceivable that an ensemble of only a relatively few basic types of vortex-flame interactions need to be considered to accurately represent the statistical result of what, on first sight, might appear to be an endless number of interactions. If this idea is supported by experimental results, it might be feasible to construct a statistical turbulent combustion model.

Vortex-flame interactions have been studied experimentally as well as computationally. However, most of the studies are for premixed systems (Roberts et al., 1992; Rutland and Ferziger, 1989; Poinot et al., 1991). The studies of diffusion flames appear to involve vortex-flame interactions that apply to the flame interacting with the large buoyancy induced vortex structures formed outside transitional jet flames (Karagozian and Marble 1986; Laverdant and Candel 1989). In turbulent jet diffusion flames surrounded by nearly still air, the vortices must be transported from the fuel side of the flame towards the diffusion flame surface. To our knowledge, only one individual vortex-flame interaction study has been performed under these conditions and it was complicated by the coupling of a large, buoyancy induced, vortex that was outside of the flame surface with the vortex inside the flame surface (Lewis, 1988).

This paper presents the initial results of a vortex-flame interaction that has some features like those observed in turbulent jet diffusion flames. A counter rotating pair of ring vortices are formed by driving the flow. Planar visualization and line-temperature measurement techniques are phase-locked to the driving pulse so that the interaction can be strobe at different time steps. A direct numerical simulation with infinitely fast chemistry, unity Lewis number, and temperature and concentration dependent transport coefficients (Katta et al., 1992) is used to investigate the dynamic characteristics of the vortex-flame interaction.

Experimental Descriptions

The vortex-flame interactions are produced in an externally driven methane jet diffusion flame shown schematically in Fig. 1. This is a very flexible

system that allows the frequency, intensity, and shape of the driving pulse to be varied. A speaker connected to a 25 mm diameter fuel tube is used to periodically generate the vortices. The speaker is placed inside a chamber with the speaker diaphragm oriented vertically upward along the flow direction. The chamber is sealed from the surrounding air. The fuel enters the speaker chamber through side inlet ports. Another fuel inlet, at a location just above the chamber, is used for seeding in visualization. A power amplifier in conjunction with a pulse generator are used to drive the speaker, which forces the fuel through the fuel tube. Vortices are formed inside the flame near the tip of a 10 mm diameter long-tapered nozzle. The strength and the frequency of the generated vortices can be adjusted by the pulse generator. The flame is shielded from room air disturbances by a slowly co-flowing annulus air. The air duct (152 mm diameter) consist of diffusion and contraction sections and layers of screens and honeycombs for flow straightening so the surrounding air flow is relative quite. The vortex-flame interaction is studied using visualization, velocity and temperature measurement techniques that are phased-locked to the driving pulse.

Reactive-Mie-Scattering Imaging

The detailed structures of the driven vortices and the flame are visualized using a Reactive-Mie-Scattering (RMS) technique (Chen and Roquemore, 1986). The output beam (532 nm) of a pulsed Nd:YAG laser is used to form a laser sheet (1 mm thickness) vertically along the center-line of the jet flame as shown in Fig. 1. The vortical structures are visualized by the scattering of micron-size TiO_2 particles formed from the chemical reaction between the TiCl_4 vapor seeded in the fuel and the combustion product, H_2O . A 35 mm camera placed at a right angle to the laser sheet is used to photograph the vortical structure and the flame. A gated mechanical shutter mounted on the camera is triggered externally. In order to visualize the detailed dynamics of the flame-vortex interaction, a synchronization circuit is used to trigger the Nd:YAG laser, speaker, and camera shutter. A master pulse generator in combination with a delay circuit is used to create an adjustable time delay between the speaker and the Nd:YAG laser for phase-locked visualization.

Joint RMS-PLIF Imaging

The vortex structure and the OH zone are visualized simultaneously using Reactive-Mie-

Scattering (RMS) and Planar-Laser-Induced-Fluorescence (PLIF). The experimental setup of the RMS-PLIF system is shown in Fig. 2. The frequency-doubled laser beam (532 nm) of a pulsed Nd:YAG laser is used to pump a dye laser. The output UV beam (282.7 nm) from the wavelength extender is tuned to excite the OH-radical (Hanson, 1986). A quartz focusing lens and a cylindrical lens are combined to expand the UV laser sheet vertically along the center-line of the flame. A gated intensified-CCD camera is used to record the fluorescent image of the OH-radical at a right angle to the laser sheet. The phase-locked measurement is accomplished by precise synchronization between the laser, speaker pulse, and CCD camera. The intensifier, gated by a pulse generator with 1.5 ms gate width, is used to eliminate the flame background emission. The Mie scattering of the TiO_2 particle marks the region where the fuel and products, H_2O , are mixed.

Laser-Doppler-Anemometry

A frequency-shifted Laser-Doppler-Anemometry (LDA) system is used for velocity measurement. The fuel is seeded with Al_2O_3 particles (5 μm mean diameter). The time history of the velocity is measured by employing a phase-locked, conditional sampling method. A 5 ms time window is used to register 1000 samples at each phase angle.

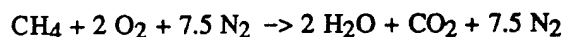
Thin-Filament Pyrometry

The line temperature is measured by Thin-Filament Pyrometry (TFP) technique (Vilimpoc and Goss, 1988) as shown schematically in Fig. 3. A fine SiC fiber with approximately 15 μm diameter is supported and placed horizontally across the center of the flame. The thermal radiation from the heated filament is focused onto a ten-facets spinning mirror. An InGaAs detector with spectral range of 900 to 1500 nm is used to measure the radiative signal from the filament. The emission intensity along the filament is scanned continuously onto the detector by the spinning mirror. A 12-bit waveform recorder is used to digitize and store filament intensity. A He-Ne laser and a photodiode are used as the triggering signal for initiating data acquisition. The line intensity of the filament is scanned on to the InGaAs detector at a 2 kHz frequency. The InGaAs detector signal is digitized by the waveform recorder at 5 MHz frequency. A program is used to interface the waveform recorder and a Macintosh IIfx for data

acquisition and transfer. The digitized TFP data consist of 1024 points in spatial direction and 512 segments in temporal direction. The recorded TFP data has spatial and temporal resolutions of 35 μm and 500 μs , respectively. The time trace of the driving pulses is digitized by a multi-channel 16-bit A/D converter. The TFP data is collected at 20 different axial locations above the nozzle exit. The flame background emission is also recorded at those same locations. Background subtraction with precise phase-matching is performed on the TFP data to eliminate the flame emission. The recorded time trace of the driving pulses ensure precise phase-matching in data reduction. Temperature is calculated from the processed TFP data. The detailed calibration and correction of the TFP measurement has been discussed by Vilimpoc and Goss (1988). Phase-averaging on temperature is performed over 7 cycles at each axial location. The phase-averaged temperature profiles calculated at each location are used to reconstruct the two-dimensional temperature field at different phase angles.

Numerical Scheme

The diffusion flame considered in this work is formed between a central methane jet and a low speed co-annular air flow. Time dependent governing equations, expressed in cylindrical coordinates, consist of mass continuity, axial and radial momentum conservation, and two scalar conservation equations (Katta et al. 1992). Shvab-Zel'dovich formulation in conjunction with the flame-sheet model is assumed. This formulation is primarily used in understanding the mechanism leading to large vortices that are observed in the experiments and their effects on the flame surface. Body-force term, due to the gravitational field, is included in the axial momentum equation. The following global chemical kinetics between methane and oxygen is considered :



Nitrogen in this system is assumed to be an inert gas. The system of governing equations is completed by using the state equation. Transport properties (viscosity and diffusion coefficient) are considered to vary with temperature and species concentrations. The enthalpy of each species is calculated from polynomial curve-fits, while the viscosity of the individual species is estimated from Chapman-Enskog collision theory. The binary diffusion coefficient between any two species on the fuel side of the flame is assumed to be identically

equal to that of the fuel and nitrogen. Similarly, on the oxidizer side of the flame it is made identical to that of the oxygen and nitrogen. Chapman-Enskog theory and the Lennard-Jones potentials have been used to estimate these two binary diffusion coefficients.

The finite-difference form of the governing equations are constructed on a staggered grid system based on an implicit QUICKEST numerical scheme. It is third-order accurate in both space and time and has a very low numerical diffusion error. At every time-step, the pressure field is accurately calculated by solving the system of algebraic pressure Poisson equations simultaneously, at all grid points by using LU decomposition technique. An orthogonal grid system with rapidly expanding cell sizes in both z and r directions is utilized. The outer boundaries of the computational domain are shifted sufficiently far enough to minimize the propagation of disturbances into the region of interest. Outflow boundary in these flows is the most difficult one to treat because the flow leaving this boundary continuously evolves in time as the large vortices convect through this boundary. A simple extrapolation procedure with weighted zero- and first-order terms is used to estimate the flow variables on the boundary in the present calculations. The main criterion used in selecting the weighting functions is that the vortices crossing the outflow boundary should leave smoothly without being distorted.

Calculations, using a mesh size of 151 x 61 have been made for the unsteady flow in a 250 mm x 150 mm computational domain. Flat initial velocity profiles, with the measured mass-averaged values of 1.5 and 0.4 m/s, have been used at the exit planes of a 10 mm-center-nozzle and a 150 mm annulus-duct, respectively. Because of the gravity term in the axial-momentum equation the computed flame developed a low-frequency oscillation of about 20 Hz. However, no roll-up of the buoyancy-induced vortex occurred within an axial distance of 250 mm.

The large driven-vortices in the experiment are then simulated by periodically perturbing the fuel mass-flow-rate at the exit of the fuel-nozzle at a frequency of 30 Hz. The modified velocity at this section, for a period of one perturbation cycle, is shown in Fig. 4 along with that of the measured one. Note that there is a suction pulse of -1.5 m/s for a period of about 6 ms making the modified velocity zero. This stagnant condition at the nozzle exit pulls the flame surface and thereby, the viscous fluid closer to the axis. The following sudden injection of additional fuel at a velocity of 6 m/s (modified velocity is 7.5 m/s) makes a collision with the highly

viscous combustion products. This process results in sending an axisymmetric, counter rotating pair of ring vortices radially toward the flame surface. The growth and the interaction of this vortex with the flame is further discussed in the results and discussion sections

Results

The purpose of this study is to investigate vortex-flame interactions that result in flame stretch and extinction processes that are similar to those observed in turbulent jet diffusion flames. With this purpose in mind, but realizing that actual vortex-flame interactions in turbulent combustion processes are three-dimensional and that this seriously complicates both the modeling and experimental efforts, the following characteristics of the vortex-flame interaction were sought. 1) The outward radial velocity of the vortex should be controllable so that vortex-flame interactions results in either the production of a flame bulge, which does not extinguish the flame, or a flame bulge that is stretched to the point that the flame is extinguished, a hole is produced. Similar effects are known to occur in turbulent jet diffusion flames. 2) The interaction should be axisymmetric, since this would facilitate the use of direct numerical simulation and also simplify the experiment. 3) The vortex should interact with a thin, laminar flame so that a flame-sheet model can be used in the simulation. 4) The shape of the vortex was not a major consideration since visualizations have shown that many different shape fluid elements interact with the flame. However, a counter rotating vortex pair are often seen in two-dimensional visualizations of turbulent jets and turbulent jet flames so it would be desirable to produce this type of vortex structure. 5) The vortex-flame interaction should be periodically produced so that phased-locked measurements could be made. This allows the vortex-flame interaction to be studied at discrete time-delays during the interaction process.

A significant investigation was required to determine the driving conditions and the fuel flow rate that would generate a vortex-flame interaction that had the characteristics described above. RMS visualizations were used to systematically investigate the influences of frequency, intensity, and pulse shape on the vortex formation, growth, and flame interaction processes for different air and fuel flow rates. Several problems were encountered. First, it was difficult to find conditions at which a vortex would grow radially to the extent needed to interact with the flame surface. Second, when such conditions were found, the flame would usually lift,

hence the interaction process would not be periodic. Third, the flame would go three-dimensional. Fourth, large buoyancy induced vortices, formed outside the flame, would couple with the inner vortices formed by the driving pulse, so the system would become very complicated. It was found that large internal vortex structures were most evident for flow rates below about 2 m/s and at driving frequencies of 30, 45, 60, and 90 Hz. The calculated resonance frequency of the fuel tube (or the organ pipe effect) was 240 Hz. The frequencies of rapid vortex growth were subharmonics of this frequency, or linear combinations of the subharmonics. However, increasing the amplitude of a sinusoidal wave at a favorable frequency did not produce a desirable vortex-flame interaction for the reasons stated above. The key parameter that lead to the desired vortex-flame interaction was the shape of the driving pulse.

A suitable vortex-flame interaction is produced when the fuel flow rate is maintained at a mean mass velocity of 1.59 m/s and an annulus air velocity of 0.39 m/s. Without driving, the flame is laminar up to a height of 50 mm above the nozzle tip. When a fast rising pulse, with a 12 ms exponential decay, is applied to the speaker at a rate of 30 Hz, a counter-rotating vortex ring is observed to produce a bulge in the blue flame surface. Increasing the intensity of the driving pulse causes a visible hole to form in the stretched flame at a height of 20 mm above the nozzle. The vortex-flame interaction is axisymmetric, periodic, and very repeatable. The dynamics of vortex-flame interaction can be observed with 0.5 ms resolution of the time delay.

The sharp rise, 12 ms decay driving pulse to the speaker results in the axial velocity pulse shown in Fig. 4. The Phase-locked velocity measurements were made on the nozzle centerline, at $z = 4$ mm. A thousand velocity realizations were averaged at each 1 ms time delay. Data were collected at 33 time-delays which corresponds to one period of the 30 Hz driving frequency. The time-delay was measured from the leading edge of the driving pulse to the middle of the LDA data sampling window. The sampling window had to be opened to 5 ms to obtain a reasonable sampling rate. This means that the measurements at each time-delay were actually averaged over two and a half time-delays on each side of the recorded time-delay. This resulted in the large uncertainties noted by the error bars on the velocity data.

It is seen from Fig. 4 that the mean axial velocity increased from 1.5 m/s and reached a peak of 7 m/s in about 8 ms. This was followed by a gradual decay to 1.5 m/s over a period of 22 ms. There appears to be three inflection points in the decay part

of the velocity pulse. They are located at $t = 16, 22$ and 28 ms. These inflection points are probably due to the mechanical damping of the speaker.

Phase-Locked RMS visualizations at $8, 10, 12$ and 14 ms time-delays are shown from left to right in Fig. 5(a). The vortex structures captured by the RMS visualizations can be recognized by their dark green-yellow appearance. These images are frozen by the 10 ns flash of the laser sheet passing through the center of the flame and thus, accurately represent the time and spatial evolution of the vortices. This is not necessarily the case for the images of the flame.

The apparent flame locations in Fig. 5(a) are marked by the yellow and blue colors in the photograph. The yellow color is from the blackbody radiation of the soot particles and the blue is the emissions from the CH radicals in reaction zone of the flame. Both the yellow and blue flames are three-dimensional structures that are superimposed on to a two-dimensional photograph. However, at the outer radial location of the flame, they can be a reasonable two-dimensional representations of the flame surface. Unfortunately the camera shutter had to be opened for 5 ms to capture enough light to see the blue flame. This means that the flame images are not truly reflecting the flame "location" at the reported time-delay. This is evident from the image of the blue flame in the 8 ms time-delay case. For example, there is an apparent hole in the blue flame that is located above the vortex. This is a false image and only reflects the fact that, during the 5 ms shutter opening, centered about the 8 ms time-delay, the blue flame spent most of the time at the location where the hole was formed. However, at the higher time-delays, the location of the blue flame doesn't appear to change much, which indicates that the actual changes in the location of the blue flame during the shutter opening are reasonably correct.

The vortex-flame interaction are evident in Fig. 5(a). At the 8 ms time-delay, a large vortex that rotates downward is observed. There is also a counter rotating "secondary" vortex on top of the large "primary" vortex but it is too small to be clearly observed. Two milliseconds later, however, the "secondary" vortex is as large as the "primary" vortex. It is clear that they form a pair of counter rotating vortex rings. Almost all of the outward radial motion of the vortices occurs between 0 and 10 ms. This corresponds to the time that the axial velocity reaches its peak, as noted in Fig. 4. The vortex interaction with the flame produces a hole that occurs between 8 and 10 ms. This is confirmed by the OH images in Fig. 9. It is also confirmed in Fig. 9 that the vortex never extends radially beyond the flame surface. This

indicates that flame stretch is involved in the flame quenching process. Once the hole is formed and vortex has reached its maximum radial location. The vortex pair then appear to rotate inward as can be observed for time-delays of 12 and 14 ms. The hole, which is clearly a ring, as noted by the dark band across the flame, remains open for a long time.

The relative axial velocities of the fuel at different radial locations are reflected by the line connecting the vortices on the right and left sides of the flame in Fig. 5(a). The center of the connecting line probably represents a stagnation point as observed by Lewis et al. (1988). At the 8 ms time-delay, the vortex connecting line is curved upward, indicating that the vortices, at their outer radial location, have a higher axial velocity than the fluid at the center of the jet. At 10 ms, the axial velocities, at the height of the vortices, are nearly independent of radial location. For the 12 and 14 ms time-delays, the central region of the flow is moving much faster than the outer radial region where the vortices are located. Indeed, the stagnation point moves upward about 10 mm between 10 and 12 ms time delays. This gives a velocity of 5 m/s, which is in agreement with the data in Fig. 4 for the 11 ms time-delay. There is very little vertical motion of the vortices at time-delays between 10 and 14 ms; however, there is a very large acceleration of the central jet fluid above the vortices. This is caused by inward radial motion of the vortices which produces a jetting action of the central fluid. It is anticipated that this will suck air in towards the fuel stream to replace the volume of fluid being accelerated upwards. The accelerating fluid cannot be replaced by the fluid below the vortex pair because its axial velocity is decreasing (See Fig. 4 for time-delays greater than 10 ms) by the inward contraction of the vortices.

The numerical simulation at approximately the same time-delays as those of the experiments of Fig. 5(a) are shown in Fig. 5(b). Composite figures of isotherms (left) and color-coded particle trackings (right) are presented for each time-delay. Also shown in the figure are the predicted instantaneous stoichiometric mixture fraction locations, marked by the white dots outside the particle trackings. The numerical simulation reproduces the evolution of the primary vortex of the experiments using the particle tracking technique. The counter-rotating vortex ring is also evident in the simulation. The isotherm representation did not identify the vortex pair that is shown by particle trackings. In fact, the temperature field prediction seems to suggest the existence of a single vortex region. The numerical simulation appears to produce nearly the same time and spatial

evolution of the ring vortex as observed in with the experimental visualizations.

The simulation shows a thinning of the reaction zone and a decrease in the flame temperature as the flame is being stretched by the vortex-flame interaction. This is noted by the temperature contours in Fig. 5(b). The thinning of the flame seems reasonable but, the actual reduction in the stoichiometric flame temperature is not physically correct for a flame sheet model with fast chemistry. This happens because the reaction zone becomes much thinner than the grid spacing. The grids containing the stoichiometric reaction zone also contains an excess of fuel, so the inadequate grid resolution results in a lower flame temperature.

Phase-locked TFP measurements at 10 and 14 ms are shown in Fig. 6. The TFP temperature data are superimposed on their respective RMS images. The results show that the local peak temperatures (at fixed axial heights) are usually situated along the luminous flame, as one would expect for a laminar or near-laminar jet diffusion flame, except for the region where the vortex is located. The phase-averaged temperature profiles show double peaks in the measurements of the second and third filaments above the burner tube at 10 ms time-delay, and in the upper filaments at 14 ms time delay. At 14 ms time-delay, the outer peak temperature at $z = 18$ mm (fifth filament above the burner) is 850 K at a radial location $r = 12$ mm. This radial location is where the local quenching of the "blue" flame is visually observed.

The time trace of the filament temperature in Fig. 7, illustrates that the outward movement of the flame, as noted by the location of the peak temperature, is accompanied by a decrease in the hot zone thickness and a reduction in the peak temperature. The peak temperature location is superimposed on the TFP time trace. When an flame bulge is observed, the "flame" temperature decreases to below the detection limit of 800 K. This decrease in "flame" temperature is accompanied by the appearance of a second temperature peak at a radial location closer to the jet center line. This second peak corresponds to the inner peak shown by the TFP data in Fig. 7. The radial locations of the flame (the outer peak) and the inner peak are also shown in Fig. 7 as a function of time delay. As the flame moves outward, the inner peak in Fig. 7 starts to appear. When the flame is quenched by the vortex-flame interaction, the inner peak temperature becomes higher than the outer peak temperature. The time-evolution of the outer and inner peak temperatures are shown in Fig. 8. The duplicate sets of triangles

illustrate the symmetry of the TFP measurements. The outer peak temperature is seen to decrease from 1800 K to 800 K within the first 3 ms during the rapid growth of the flame radius. The local peak temperature gradually recovers the unperturbed flame temperature.

The time response of the filaments is significant in comparison with the temperature time traces of the flame. The time response of the filament, as the temperature is instantaneously dropped from 1750 K to 300 K, is shown in Fig. 8. The flow remains at 300 K for cooling times of 1, 3, and 5 ms. The response to the filament for these cooling times and a gas flow velocity of 1 m/s are also shown in Fig. 8. The calculated filament temperatures decrease from 1800 K to 1360 K, 850 K, and 650 K for 1ms, 3 ms, and 5 ms cooling pulse widths, respectively. A 3.5 ms cooling period is required, to reach the detector cut-off temperature of 800 K. This suggest that the filament is exposed to a low temperature environment as shown by the time trace in Fig. 7. The time response of the filament is currently being investigated for different convective flow conditions (Post and Gord, 1993).

Four OH-PLIF images at $t = 9, 11, 13$, and 15 ms are shown in Fig. 9. These LIF images were taken with the intensifier gate width set at 1.5 ms. Also shown on the LIF images are the RMS visualization taken simultaneously. The vortex interaction with the OH zone (or hot zone) is clearly illustrated in Fig. 9. As the "primary" ring vortex evolves and grows in size, the OH becomes contoured. A local thinning of the OH zone is evident in the visualization taken at the 9 ms time-delay. The radial movement (or growth) of the vortex is sufficient to form a flame bulge. Further outward radial movement of the ring vortex results in a decrease in the local OH fluorescence signal below the detection limit. At this point a hole is formed in the flame, as noted in the 11 ms time-delay image. This local "quenching" persists for a few millisecond, as illustrated by the images at $t = 13$ and 15 ms. A protruding of the ring vortex is also evident at these two time delays.

Discussion

The vortex-flame interaction of Figs. 4-9 shows local extinction due to the flame stretch as opposed to other types of the vortex-flame interaction, for example, that resulting from penetration of the fast moving vortices through the flame (reaction) zone as in the formation of the flamelets in jet diffusion flames (e.g., see Roquemore

et al., 1988). The length scale of the ring-vortex pair of the present experiments is much larger than that of the flame zone, and the time scale much longer. These characteristics, however, need not always to be the case for turbulent flames in propulsion systems.

The stretching of the flame due to the vortex action appears to lead to local extinction of the hot (or OH) zone. To obtain a better understanding of the transport process that may be critical to the vortex-flame interaction studied, the numerical simulation at a phase angle similar to the 10 ms time delay of the experiment is studied. The results are shown in Fig. 10(a), using a similar composite image format of Fig. 5(b). The radial profiles of temperature and mole fractions at three axial locations, $z = 18, 28$ and 40 mm, are shown in Fig. 10 (b), by the side of the composite image. The phase angle of 10 ms time delay is chosen because it is in the initial stage of the local extinction and the counter-rotating ring vortex is just being formed. Thus, a better understanding can be obtained for the transport processes critical to these phenomena.

On the formation of the counter-rotating ring vortex, the simulation shows a high radial velocity component in the primary ring vortex. The particle trackings clearly show an outward motion of the jet fluid. This outward motion was deflected at the flame location, due to its inability to penetrate the flame zone, perhaps, due to the barrier of the high viscosity at the flame and/or the large density ratio between the entrained fluid and the flame. While the downward deflected fluid is being entrained into the primary ring vortex, the upward moving fluid forms a counter-rotating ring vortex on top of the primary vortex. The particle tracking of the radial motion mimics a "stagnation-like" layer shown by RMS visualization.

On the transport of species and thermal energy, the radial profiles of temperature and species concentration at $z = 28$ mm, i.e., location inside the vortex, show sharp gradients of these quantities by both sides of the stoichiometric location. These sharp gradients suggest an enhanced transport of reactants (as can be measured by local scalar dissipation rates) into the reaction zone, and enhanced conductive heat loss from the flame zone. When the fast chemistry assumption is employed, the prediction states that all the reactants transported to the reaction zone will be consumed by the chemical reaction, and at the unity Lewis number limit, the increased heat release rate due to enhanced chemical reaction rates will be balanced by the enhanced conductive heat loss as reflected by the sharp temperature gradients. Thus, an adiabatic flame is always present at the predicted stoichiometric location. In reality, however, the

reaction rate can not keep up, without limit, with enhanced transport of the reactants. As a result, local extinction will occur. In fact, the phase-locked data taken at 10 ms time delay (through 15 ms time delay) suggests that local extinction indeed is present. An interesting observation of the predicted temperature profiles is that at $z = 28$ mm of Fig. 10(b), the species concentration gradient is so sharp that the present numerical grid resolution is not sufficient to capture the instantaneous stoichiometric location.

On the instantaneous temperature profiles, double peaks in temperature are predicted at the axial location where the primary vortex is present, e.g., $z = 28$ mm. The prediction shows that the outer peak at this location ($z = 28$ mm) corresponds to the stoichiometric location; thus, it has a higher temperature than the inner peak. The TFP data of Figs. 6(a), however, show that the maximum temperature appears at the inner peak location rather than the outer peak. The predicted inner peak temperature at $z = 28$ mm is a result of the convective transport of hot combustion products into the primary vortex. At the fast chemistry limit, the predicted inner peak temperature is 500 K. The TFP data show an inner peak temperature of 1300 K and the outer peak temperature below 800 K. The convective transport of combustion products from an upstream flame location can not explain the much higher inner peak temperature determined by the TFP measurements. Due to local quenching, it is likely that oxygen can be entrained into the vortex core or it can leak through the reaction zone. As a result, partially premixed flames can exist inside the ring vortex, as well as the convoluted stoichiometric surfaces. To verify the aforementioned hypotheses for the temperature double peaks, the experiments call for concentration measurements inside the ring vortex, and to advance our understanding on the type of the vortex-flame interaction studied, the numerical simulation requires to incorporate the finite rate chemistry for study of the reaction zone structures inside the vortex and the extinction phenomenon.

Summary and Conclusion

This paper reports the initial results of a joint experimental and numerical study of the vortex-flame interaction in diffusion flame.

The experimental system periodically reproduces an isolated vortex-flame interaction event that provides a unique opportunity for study of a specific type of the vortex-flame interaction, that leads to local quenching of the flame. The time evolution and the dynamics of the vortex-flame

interaction are quantified by phase-locked measurements of the fuel-jet exit velocity and the flow field temperature, along with phase-locked RMS visualization and PLIF OH imaging.

A ring vortex is periodically reproduced by the driving of the fuel jet using a acoustic speaker, starting near the fuel-jet exit location. This vortex grows in size as time evolves and pushes the location of the luminous flame radially outward. A flame bulge is subsequently formed. During the growth of the primary vortex, e.g., vortex entrainment of the fuel jet fluid, and the time-varying mass addition of the driving, a counter-rotating vortex ring (secondary vortex) is formed. This secondary vortex was initially situated on top of the primary vortex. A "solid-body" type of rotation is subsequently observed from RMS visualizations, showing the rotation of the secondary vortex ring around the primary vortex, or vice versa. This "solid-body" rotation is a result of the faster moving primary vortex.

When the flame bulge is formed, the PLIF images shows a local thinning of the OH zone at the maximum radius location. The thinning of the OH zone suggests the flame being stretched due to the interaction of the vortex and the flame. The continued growth of the vortex size, or the flame bulge radius, eventually results in a local disappearance of the OH fluorescence, coincident with where the filament emissive power falls below the detection limit (i.e., 800K). At this condition the TFP data showed double peaks in radial profiles, unlike without artificial driving, the TFP data show a single peak located outside the luminous flame. The double peak temperature profile shows a higher temperature at the inner peak location.

The numerical model assumes an infinitely fast chemical reaction rate, within the context of the flame sheet model. A finite difference scheme (QUICKEST) is used to obtain solutions to the 2-D, time dependent Navier-Stokes equations, coupled with the continuity and mixture fraction equations. The simulation is seen to reproduce the formation of the primary and secondary vortex pair, and the formation of the flame bulge due to the vortex-flame interaction. The axial height of the flame bulge is also adequately reproduced. Due to the infinitely fast chemistry assumption, the local quenching of the flame is not predicted. The simulation nevertheless shows a double peak temperature profile at the axial location where local quenching was experimentally observed. At this location, the gradients of temperature and concentration are much sharper than the single peak profiles. Due to this sharp gradient, the present numerical grid resolution is not sufficient to precisely

locate the stoichiometry. The maximum temperature, on contrary to the TFP data, is located at the outer peak. The predicted inner peak temperature, however, is much lower than that observed in the experiment.

While the simulation shows the enhanced mass transport to the reaction zone and the transport process being important during the vortex and flame interaction, it fails to predict the flame stretch that leads to local extinction. The much higher inner peak temperature of the TFP data suggest that the finite rate chemistry might be important within the vortex, a result of the premixing of fuel-product mixture with the oxygen that leaks through the quenching location or highly stretched the flame. Thus, it is possible to observe distributed reaction zones or convoluted stoichiometric surfaces inside the ring vortex pair.

This joint experimental and numerical investigation presents an experimental system for study the vortex-flame interaction that undergoes a thin flame regime, through a stretched flame regime, to local extinction. The experimental results suggest the possibility of partial premixing inside the ring vortex pair which is yet to be confirmed.

Several improvements of the current capabilities are obvious. The finite rate chemistry must be incorporated in the numerical model to investigate the reaction zone structure inside the vortex ring. Similarly, the experiment call for species concentration measurements of the ring-vortex pair and quantification of the TFP time response to advance our understanding of the type of vortex-flame interaction studied in this paper.

Acknowledgement

This work was sponsored by AFOSR Grant No. F49620-92-J-0462. The authors are indebted to Dr. F. Takahashi for his helpful discussion, D.D. Trump, B. Sarka and M. Post for their assistance.

References

- Bilger, R. W., "The Structure of Turbulent Nonpremixed Flames," *Twenty-Second (International) Symposium on Combustion*, The Combustion Institute, Pittsburgh, PA, pp. 475-488, 1989.
- Chen, L.-D. and Roquemore, W. M., "Visualization of Jet Flames," *Comb. and Flame*, Vol. 66, pp. 81-86, 1986.
- Chen, T. H. and Goss, L. P., "Statistical OH-zone Structures of Turbulent Jet Flames from Liftoff to Near-Blowout," *Combust. Sci. and Tech.*, Vol. 79, pp. 311-324, 1991.
- Coats, C. M., and Zhao, H., "Transition and Stability of Turbulent Jet Diffusion Flames," *Twenty-Second Symposium (International) on Combustion*, The

Combustion Institute, Pittsburgh, PA, pp. 685-692, 1988.

Correa, S. M., "Relevance of Non-premixed Laminar Flames to Turbulent Combustion," Major Research Topics in Combustion, Hussaini, M. Y., Kumar, A., and Voight, R. G., Eds., Springer-Verlag, pp. 45-69, 1992.

Eichkoff, H., "Instability and Coherent Structures in Jet Flames," Recent Contributions to Fluid Mechanics, Hasse, Ed., Springer-Verlag, Berlin, 1982.

Hanson, R. K., "Combustion Diagnostics: Planar Imaging Techniques," Twenty-first Symposium (International) on Combustion, The Combustion Institute, Pittsburgh, Pennsylvania, pp. 1677-1691, 1986.

Hottel, H. C. and W. R. Hawthorne, "Diffusion in Laminar Flame Jets," Third Symposium (International) on Combustion, Flame and Explosive Phenomena, pp. 254-266, 1949.

Karagozian, A. R., and Marble, R. E., "Study of a Diffusion Flame in a Stretched Vortex," Combust. Sci. and Tech., Vol. 45, pp. 65-84, 1986.

Katta, V. R., Goss, L. P., and Roquemore, W. M., "Numerical Investigations on the Dynamic Behavior of a H₂-N₂ Diffusion Flame under the Influence of Gravitational Force," AIAA Paper 92-0335, 1992.

Knio, O. M. and Ghoniem, A. F., "Three Dimensional Vortex Simulation of Entrainment Augmentations Due to Streamwise Structures," AIAA Paper 89-0574, 1989.

Lavdant, A. and Candel, S., "Combustion of Diffusion and Premixed Flames Rolled-up in Vortex Structures," AIAA J. Propulsion and Power, Vol. 5, p. 134, 1989.

Lewis, G. S., et al., "An Investigation of the Structure of a Laminar Non-Premixed Flame in an Unsteady Vortical Flow," Twenty-Second Symposium (International) on Combustion, The Combustion Institute, Pittsburgh, Pennsylvania, pp. 515-521, 1988.

Lugt, J., "The Dilemma of Defining a Vortex," Theoretical and Experimental Fluid Mechanics, Muller, U., Rosner, F. G., and Schmidt, B., Eds., Springer-Verlag, 1979.

Masri, A. R., R. W. Bilger, and R. W. Dibble, "Turbulent Nonpremixed Flames of Methane Near Extinction: Probability Density Functions," Comb. and Flame, 73, pp. 261-285, 1988.

Poinsot, T., Veynante, D. and Candel, S., "Quenching Processes and Premixed Turbulent Combustion Diagrams," J. Fluid Mech., Vol. 22, pp. 561-606, 1991.

Post, M., Gord, J. and Goss, L. P., "Thin-Filament Pyrometry," To be presented in 31st Aerospace Sciences Meeting and Exhibit, AIAA, Reno Nevada, 1993.

Roberts, W. L., Driscoll, J. F., Drake, M. C. Ratcliffe, J. W., Twenty-Fourth Symposium (International) on Combustion, The Combustion Institute, Pittsburgh, Pennsylvania, 1992, to appear.

Roquemore, W. M., L.-D. Chen, L. P. Goss and W. F. Lynn, "Structure of Jet Diffusion Flames," Turbulent Reactive Flows, Lecture Notes in Engineering, Vol. 40, pp. 49-63, 1988.

Rutland C., and Ferziger, J., "Interaction of a Vortex and a Premixed Flame," AIAA Paper 89-0127, 1989.

Savas, O. and Gollahalli, S. R., "Flow Structure in the Near-Nozzle Region of Gas Jet Flames," AIAA Journal, Vol. 24, No. 7, pp. 1137-1140, 1986.

Scholefield D. A., and J. E. Garside, "The Structure and Stability of Diffusion Flames," Third Symposium (International) on Combustion, Flame and Explosive Phenomena, pp. 102-110, 1949.

Takahashi, F., M. Mizomoto and S. Ikai., "Transition from Laminar to Turbulent Free Jet Diffusion Flames," Comb. and Flame, Vol. 48, pp. 85-95, 1982.

Takahashi, F., Schmoll, W. J., "Lifting Criteria of Jet Diffusion Flames," Twenty-Third Symposium (International) on Combustion, The Combustion Institute, Pittsburgh, Pennsylvania, pp. ????, 1991.

Takahashi, F. and Goss L., "Near-Field Turbulent Structures and the Local Extinction of Jet Diffusion Flames," Twenty-fourth Symposium (International) on Combustion, The Combustion Institute, Pittsburgh, Pennsylvania, pp. 351-359, 1992.

Takeno, T. and Kotani, Y., "Transition and Structure of Turbulent Jet Diffusion Flames," AIAA Paper 77-97, 1977.

Vilimpoc, V. and Goss, L. P., "SiC-Based Thin Filament Pyrometry: Theory and Thermal Properties," Twenty-Second Symposium (International) on Combustion, The Combustion Institute, Pittsburgh, Pennsylvania, pp. 1907-1914, 1988.

Wohl, K., Kapp, N. M., and C. Gazley, "Flame Stabilization and Quenching," Third Symposium (International) on Combustion, Flame and Explosive Phenomena, PP 3-21, 1949.

Yule, A. J., Chigier, S. R., Boulderstone, R., and Ventura, J., "Combustion-Transition Interaction in a Jet Flame," AIAA Journal, pp. 725-760, 1981.

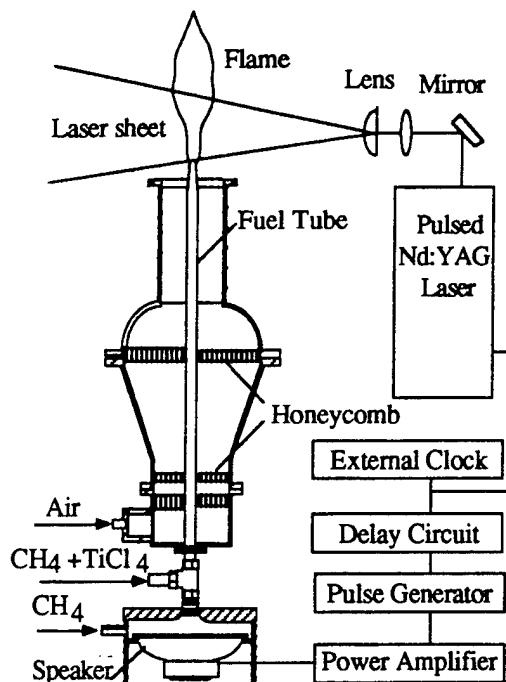


Figure 1. Schematics of Driven Diffusion Flame

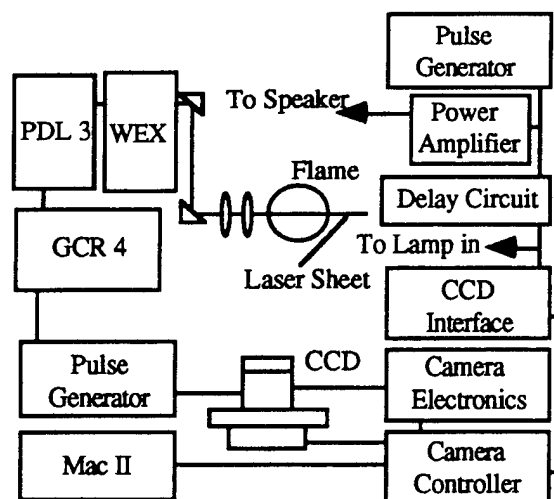


Figure 2. Experimental Setup of Phase-Locked Joint RMS and OH-PLIF Imaging

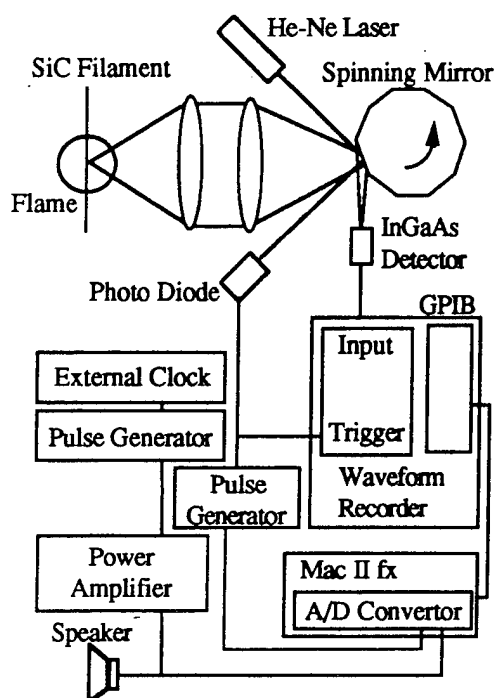


Figure 3. Experimental Setup of Thin-Filament Pyrometry Measurement

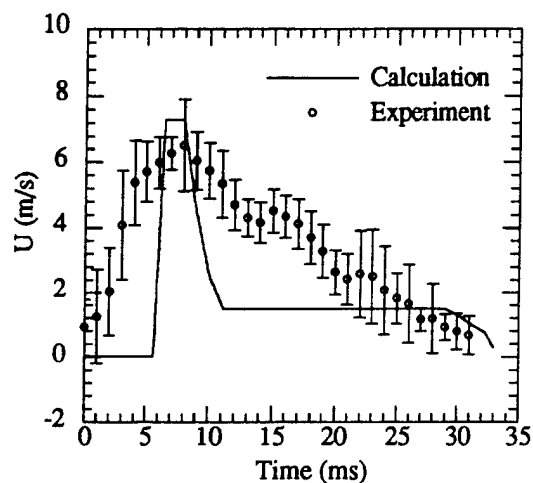
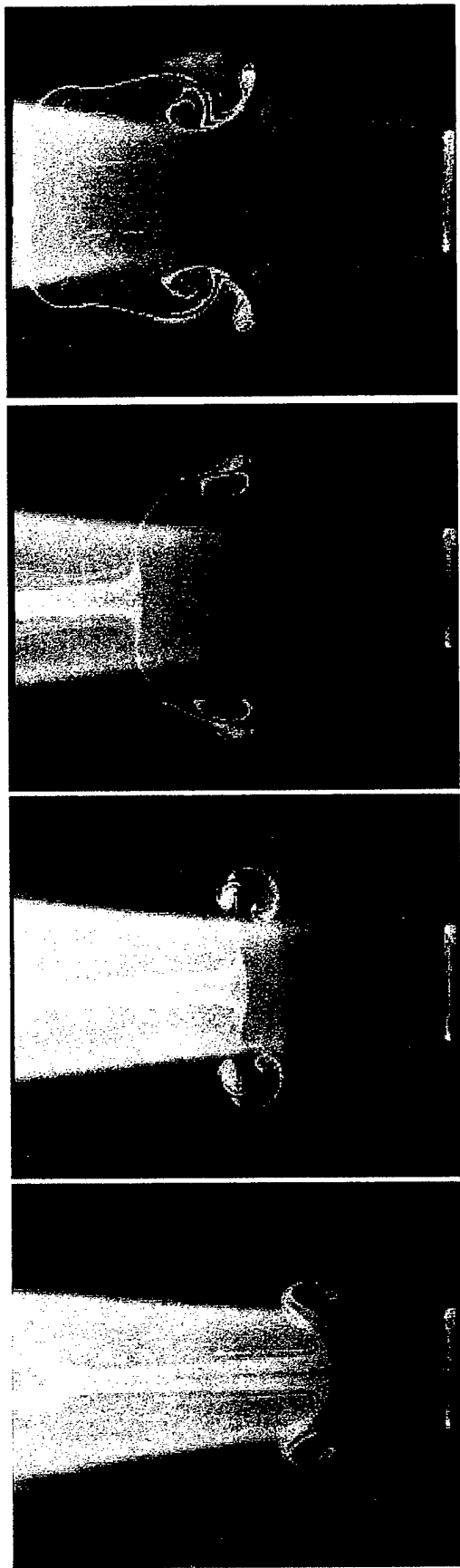
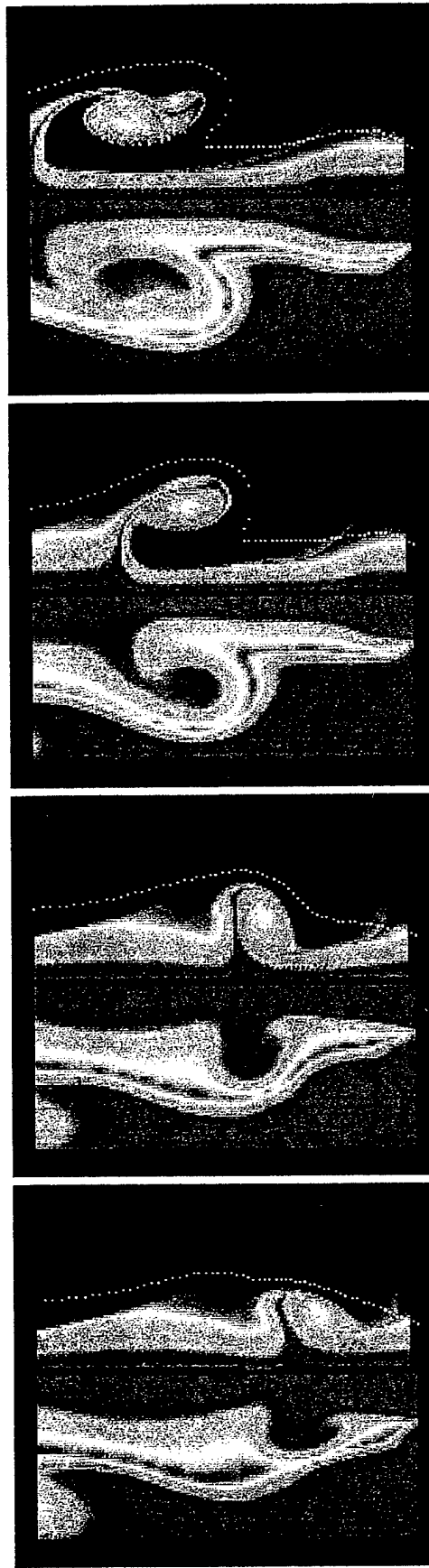


Figure 4. Time History of Axial Velocity Near the Centerline of the Nozzle Exit

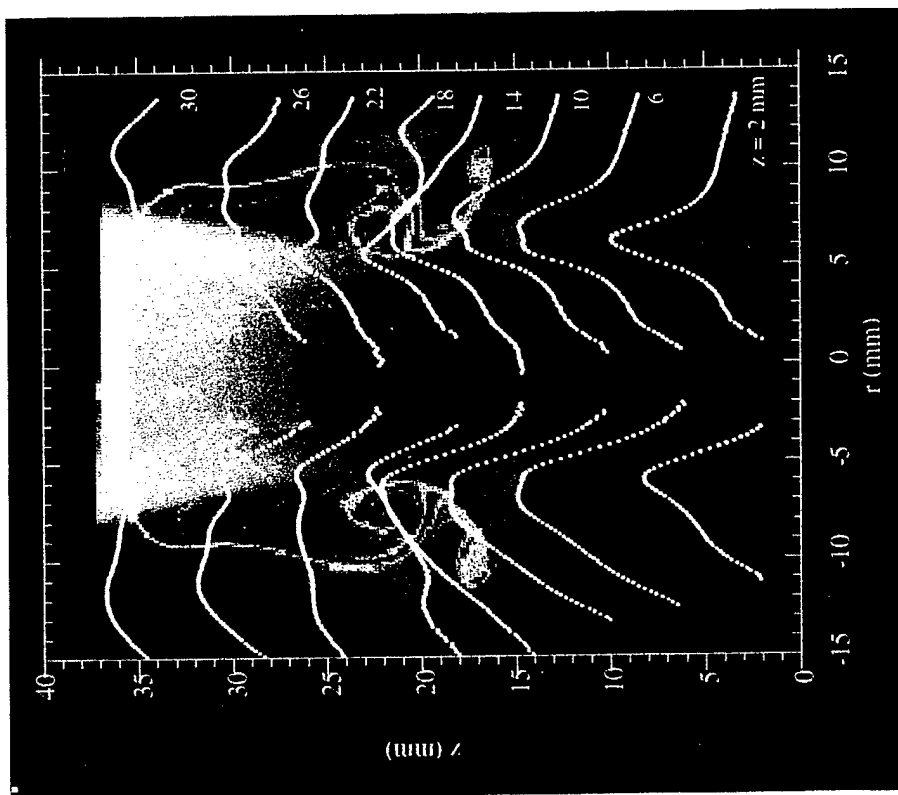


(a)

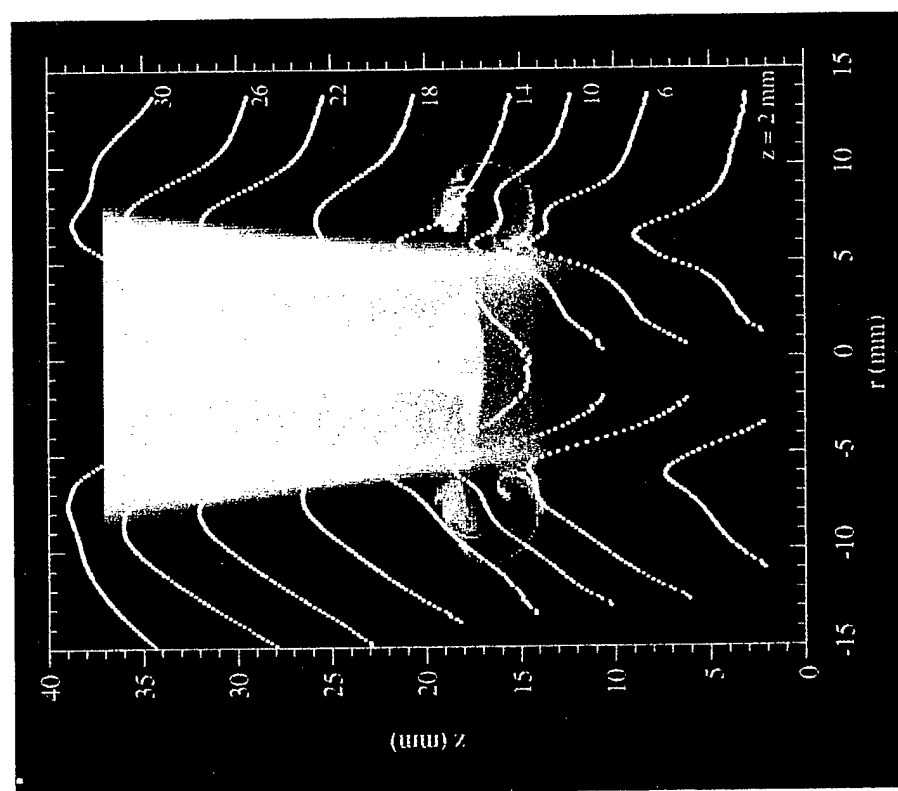


(b)

Figure 5. The Evolution of Flame-Vortex Interaction by (a) reactive-Mie-scattering Flame Imaging, and (b) Time-dependent Numerical Simulation



(a)



(b)

Figure 6. Composite Images of Flame and Phase-Averaged Temperature at (a) $t = 10$ ms, and (b) $t = 14$ ms

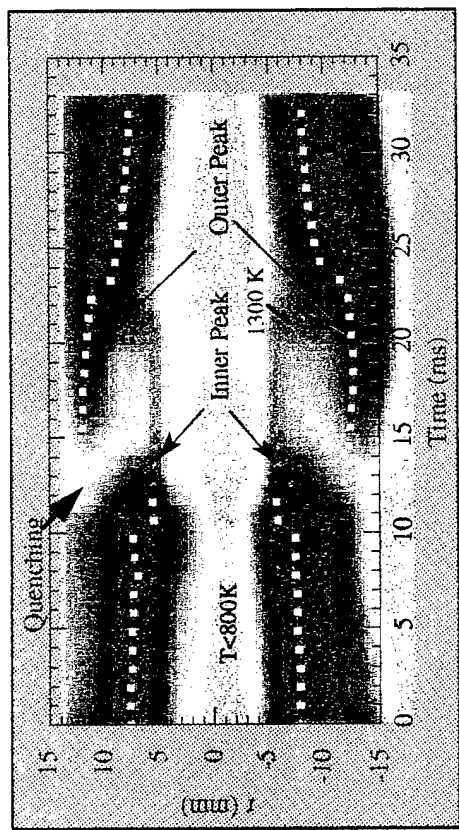


Figure 7. TFP Temperature Image and Locations of Peak Temperature
($z = 18$ mm)

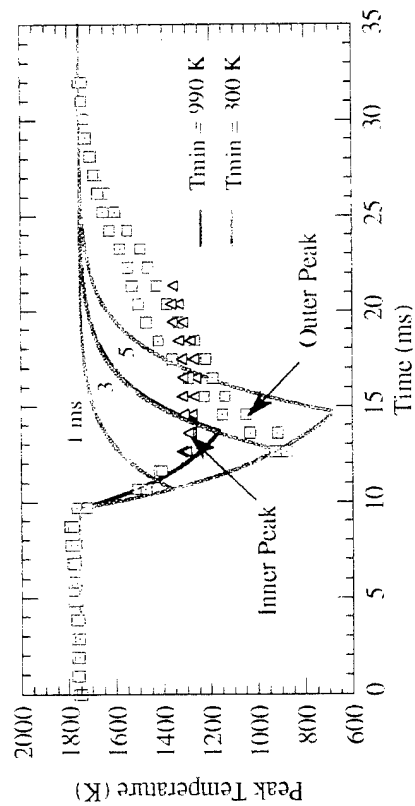


Figure 8. Peak Temperatures versus Time, and Filament Response
($z = 18$ mm)

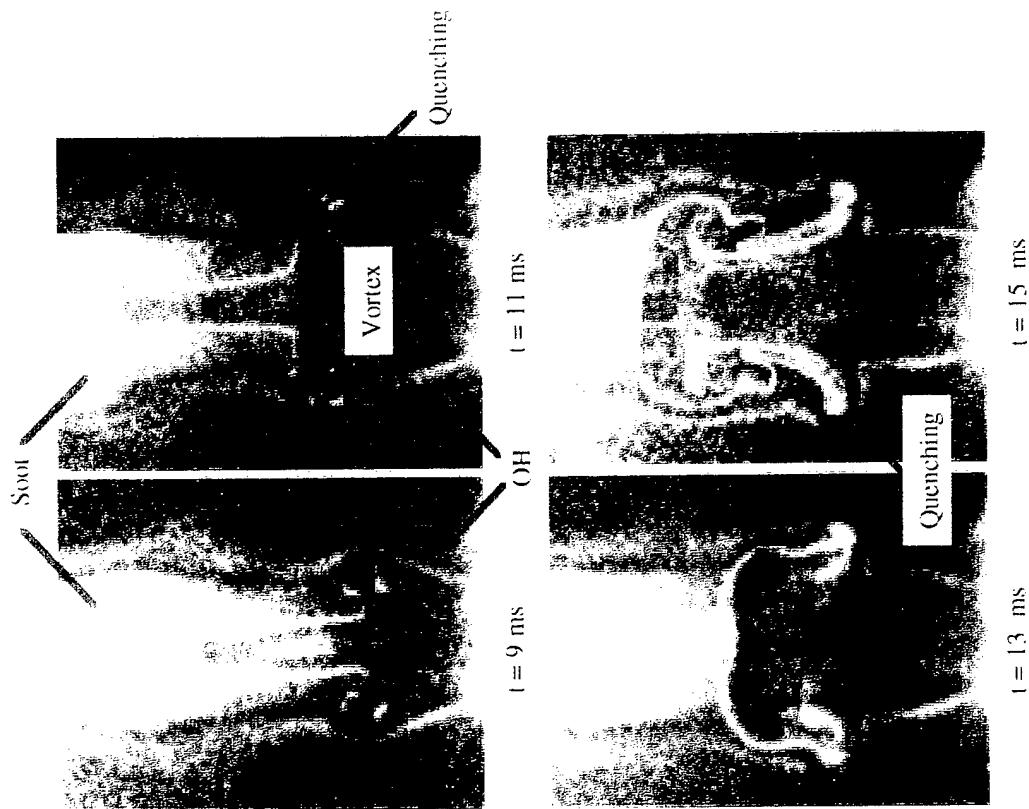


Figure 9. Joint RMS and OH-PLIF Images at Various Phase Angles

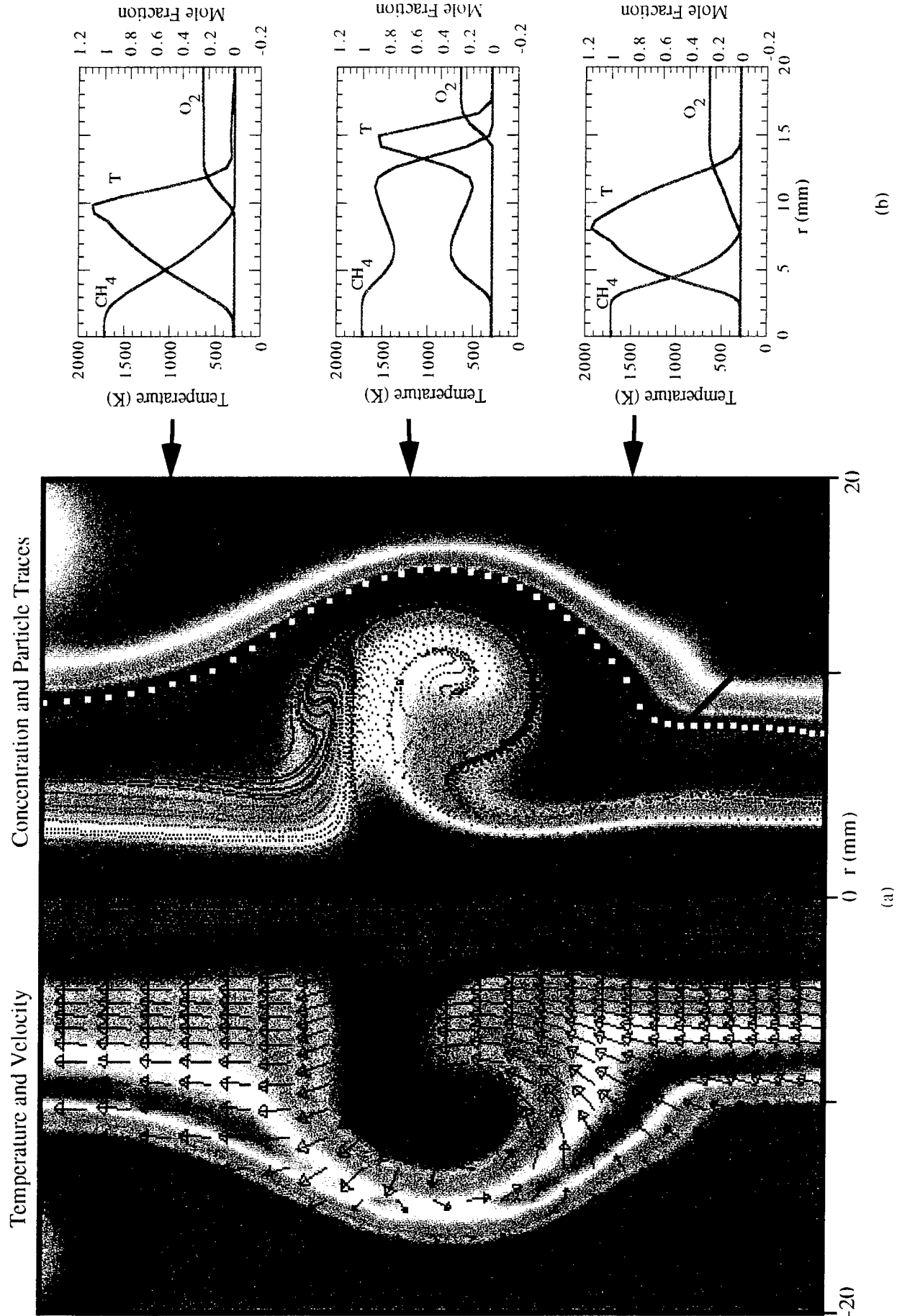


Figure 10. (a) Instantaneous Temperature and Concentration Fields with Superimposed Velocity Vectors and Particle Traces, (b) Radial Profiles of Temperature, Mole Fractions of Fuel and Oxygen

Finite-Rate Chemistry Effects During Vortex-Flame Interactions in a Driven-Jet Diffusion Flame

R. D. HANCOCK* and R. P. LUCHT

University of Illinois, Mechanical & Industrial Engineering, 1206 West Green Street, Urbana, IL 61820

** Also with Wright Laboratory, Aero Propulsion and Power Directorate, Wright-Patterson AFB, OH 45433*

V. R. KATTA and K. Y. HSU

Systems Research Laboratories, Inc., A Division of Arvin/Calspan, 2800 Indian Ripple Road, Dayton, OH 45440

An experimental and numerical investigation of vortex-flame interactions in a driven-jet diffusion flame is described. In the experimental investigation, the fuel jet is driven with a loud speaker to produce repetitive, toroidal-shaped vortices that push radially outward on the diffusion flame surface, creating regions of positive and negative stretch. The interaction of this induced vortex with the flame serves as a model for similar interactions in turbulent flames. The induced vortex structure has been visualized using reactive Mie scattering and the spatial reproducibility is better than 100 μm from laser shot to laser shot. Since the interaction is repeatable, the temperature and species concentration fields can be examined, both experimentally and theoretically, in great detail.

The jet is a mixture of hydrogen, nitrogen, and helium that has a local Lewis number less than unity on the fuel side of the diffusion flame. Flame temperature is determined from coherent anti-Stokes Raman scattering (CARS) spectra of nitrogen. These measurements, along with numerical results, indicate that the flame temperature decreases near the outer bulge of the vortex and the flame zone thins appreciably at this bulge. For the undriven flame, the CARS temperature profiles are in good agreement with numerical modeling results obtained with a third-order-accurate computational fluid dynamics code with elementary chemical kinetics included. For the driven flames, the CARS experimental and computed temperature profiles exhibit qualitative agreement. Future work includes three-laser CARS [1] temperature and oxygen concentration measurements in a variety of driven hydrogen flames as well as laser-induced fluorescence measurements of NO.

INTRODUCTION

Turbulent flames are typically composed of a multitude of random vortex-flame interactions. The gas temperature at a fixed spatial location within a flame will vary significantly with time. Thermocouples can be used to obtain temperature measurements in turbulent flames, but they are intrusive and their response is often much slower than the turbulent events in the flow. Laser diagnostic techniques such as coherent anti-Stokes Raman scattering (CARS) can be used to obtain average or single-shot temperature measurements in these flames. Probability density functions of temperature can then be obtained from the single-shot data for each location in the flame. While this has proven to be a useful way to characterize the behavior of turbulent flames, it has not provided the ability to precisely investigate the actual vortex-flame interaction events. Much of the dynamic behavior of the vortex-flame interaction is lost with the probability density function approach. The experiment described in this paper was designed to produce a single, repetitive, vortex-flame interaction that is similar to a typical turbulent event [2]. Since this vortex-flame interaction is highly repeatable, gas temperatures can be measured quite accurately using CARS at a variety of locations and phase angles of the flame.

The particular jet diffusion flame studied was a mixture of H_2 , N_2 , and He. Driving of the jet repeatedly with a loud speaker forces vortices to collide with the flame surface, producing curved flame surfaces with regions of positive and negative stretch. Within these regions, significant deviations in the local peak flame

temperature from the adiabatic flame temperature are predicted. In addition to flame stretch, the local Lewis number, Le , has an impact on the flame temperature. Le is defined as the ratio of the conductive-heat transport of the mixture to the mass transport of the species. In many flames, Le is assumed to be unity. This assumption is generally not appropriate for hydrogen flames. It has been shown theoretically by Katta, et al. [3] that for jet diffusion flames with $Le \neq 1$ the local flame temperature can deviate significantly from the adiabatic flame temperature obtained using a $Le=1$ assumption. The transient flame curvature and local Lewis number combine to determine whether a particular location in the flame will have an increase or decrease in temperature from the adiabatic flame temperature. In regions of the flame where the temperature is higher than the diffusion flame temperature, increased production of the pollutant species nitric oxide (NO) often results. It is anticipated that the combination of experimental and computational results for these driven flames will give additional insight into the effect of local Lewis number and flame stretch on flame temperatures and NO production.

This paper describes a combined experimental and numerical investigation of the influence of vortex-flame interactions on a non-unity Lewis number flame. CARS temperature measurements were obtained in the $\text{H}_2/\text{N}_2/\text{He}$ diffusion flame for undriven and driven conditions. The time-averaged flowrate was the same for both the undriven and driven flame, and three phase angles, or time delays after pulsing a loud speaker in the fuel line were investigated for the driven flame. Temperature profiles were obtained at the $z=25.4$ mm axial location downstream

of the nozzle exit. The diffusion flame was driven to produce strong vortices on the fuel side of the flame surface which can produce both positive (stretch) and negative (compression) flame stretch factors [4] when interacting with the flame surface. The flame was modeled using a third-order-accurate computational fluid dynamics code that provides direct numerical solutions to the time-dependent conservation equations and incorporates buoyancy, finite-rate chemistry, and transport coefficients that depend on temperature and species concentration. This code is discussed in detail elsewhere [5].

EXPERIMENTAL

Burner and Flow System

Figure 1 is a schematic drawing of the experimental setup. A master controller produces a signal at 20 Hz. This signal is the input to a pulse generator that produces the waveform required to drive the speaker (and ultimately the jet) effectively. The master controller signal is also used to trigger the frequency-doubled Nd:YAG laser. The combustible mixture is passed over the pulsating speaker and through the fuel tube. The master controller has a built-in variable delay that is used to adjust the time between the pulsing of the jet and the firing of the laser. This allows the vortex-flame interaction to be investigated at various time delays relative to the driving signal. The vortex and flame structures have been found to be reproducible to within $\sim 100\ \mu\text{m}$ from cycle to cycle.

Tylan mass flow controllers (0°C reference) are used to provide flowrates of 3.00 SLPM of H_2 , 9.78 SLPM of He, and 3.65 SLPM of N_2 , giving a calculated top-hat velocity profile of $\sim 3.8\ \text{m/s}$ at room temperature. An annular flow of dry air with a calculated average velocity of $0.33\ \text{m/s}$ surrounds the fuel tube. The annulus air protects the flame from room air disturbances and can also be used to move the location of the flame zone radially with changes in axial velocity.

Imaging of the Flame

The vortex flame interaction is visualized using phase-locked Reactive Mie Scattering (RMS) [6]. The fuel flow is passed over a chamber holding liquid TiCl_4 where it picks up TiCl_4 vapor. The fuel and annulus air flows are initially very dry and so the only water in the experiment is that formed during the combustion process. The TiCl_4 reacts with the water vapor to form submicron TiO_2 particles at the fuel/ H_2O product interface, marking a surface that corresponds roughly to the shear layer.

The images collected for this paper were obtained with a Photometrics 512 x 512 unintensified CCD camera. The camera shutter speed was 5 ms. The laser pulse was $\sim 10\ \text{ns}$ long resulting in a Mie scattering image that was frozen in time. The flame luminosity was very low compared to the Mie scattering. However, the flame luminosity present is smeared slightly due to the 5 ms exposure time. In the future, an intensified camera that is phase-locked to the flow will be used to observe flame

luminosity and OH fluorescence in order to more precisely visualize the location of the flame zone.

CARS Experimental Setup

A schematic drawing of the CARS system is shown in Fig. 2. A Continuum injection-seeded frequency-doubled Nd:YAG laser was used to produce 532 nm laser light for the pump beams and input to the modeless dye laser [7]. The full width at half maximum (FWHM) of the output of the YAG laser was $0.0045\ \text{cm}^{-1}$. The dye laser was centered spectrally near 607 nm and had a FWHM of $\sim 100\ \text{cm}^{-1}$. The CARS signal was spectrally dispersed using a 1-m spectrometer and detected using the 512 x 512 unintensified CCD camera.

The CARS spectra were fit using the CARSFIT code developed at Sandia National Laboratories [8]. Each spectrum was fit individually using the isolated line model. An example of a typical CARS spectrum and associated least-squares fit is shown in Fig. 3. Each data spectrum is the average of 100 laser shots. Averaging is acceptable in this flow because the flame structures are repetitive to within $100\ \mu\text{m}$ from laser shot to laser shot. A conservative estimate of the accuracy of the CARS temperature measurements is $\pm 50\ \text{K}$ at 1500 K.

RESULTS

CARS temperature profiles were obtained in the undriven flame and at three different phase angles in the driven flame. Flame A corresponds to an undriven diffusion flame. Flames B, C, and D are all at the same flow rates as flame A, but they are driven with the loud speaker placed below the fuel tube. The difference between flames B, C, and D is that the data was collected at successive time delays, or phase angles, relative to the signal used to drive the loud speaker. All of the CARS temperature profiles were collected at the $z=25.4\ \text{mm}$ location downstream of the nozzle tip. Figures 4-7 each show an image of the particular flame, the experimental and computational temperature profiles, and the computed mole fraction profiles. The $z=25.4\ \text{mm}$ location on each flame is marked with a horizontal black line and 1 mm increments in the radial direction are indicated with tick marks. At the left side of Figs. 4a-7a is the computed image and the right side is the experimental image. The computed images show the temperature distribution in gray scales, with the range going from dark to light to dark again with increasing temperature. As discussed above, the experimental images are a combination of Mie scattering from TiO_2 particles and flame luminosity. Computed particle traces are also shown for flames B, C, and D. The computed images were selected out of a complete time-dependent simulation and displayed with the corresponding experimental images. The mole fraction information was used to calculate the buffer background susceptibility that is used in the CARS calculations. The mole fraction information, particularly the OH

concentration profile, indicates the location and width of the calculated flame.

DISCUSSION

In order to effectively model vortex-flame interactions in driven flames it is essential that the basic undriven flame is first correctly modeled. Figure 4b illustrates that excellent temperature agreement is obtained between the experiment and the computations for the undriven flame. It was found, however, that the location and width of the flame zone depend strongly on the diffusion coefficients and the velocity flow field. For this experiment, the jet and annulus air flow velocities were calculated based on volume flow rates and assumed top-hat velocity profiles. As detailed velocity measurements of the inlet flow conditions are completed, even better temperature agreement may result.

For the driven flame, the shapes of the experimental and computed temperature profiles are in qualitative agreement and several interesting trends were observed. The calculated peak flame temperatures for flames B, C, and D are 1627 K, 1592 K, and 1521 K, respectively. The measured peak flame temperatures for flames B, C, and D are 1395 K, 1373 K, and 1323 K. Obviously, the peak temperatures and magnitude of the temperature drops are not in agreement. However, the decrease in temperature at the bulge is as expected due to intense stretching of the flame at that location. It is possible that the flame becomes slightly lifted and/or locally extinguished during the driving cycle which would lead to lower measured flame temperatures. The driven flame has local regions where the Damkohler number decreases because the residence time decreases as compared to the undriven flame. If the jet is not driven as intensely, a weak bulge in the flame surface appears and preferential diffusion can become a major contributor to the flame behavior. This could produce temperatures in the flame zone at the bulge that are above the flame temperatures elsewhere [3]. Both the computation and the experiment show that the width of the flame zone narrows near the bulge due to stretching. It is also apparent from Flame D that hot products are entrained into the core of the jet due to the roll-up of the vortex.

The difference between the experimental and computational temperature profiles probably results from a lack of knowledge about the time-dependent jet velocity profile. The three driven experimental images were obtained at increments of 1 ms. The matching images from the computations were 1.5 ms apart in time, indicating that a higher axial velocity input may be required. A higher axial velocity input to the computations would also result in a higher radial velocity because the faster moving fluid collides with the slower moving fluid in front of it and is forced radially outward. The data seem to support this idea since the location of the flame front moves radially outward faster for the experiment than for the computations. Quantitative

agreement should improve when detailed time-dependent velocity profiles at the exit of the nozzle are obtained. Future hot wire measurements of velocity for a cold jet should provide this essential information about the velocity profile at the exit.

The radial location of the flame zone is very dependent on the velocity profile during the driving sequence. The annular air velocity, though small (~ 0.33 m/s), was also found to alter the flame temperature. As the time-dependent velocity profiles are measured and used as input to the CFD code, better quantitative agreement should result.

SUMMARY AND FUTURE WORK

A driven non-unity Lewis number jet diffusion flame ($H_2/N_2/He$) was investigated using CARS and a third-order accurate, finite-rate chemistry, fluid dynamics code. The agreement between the experimental and computational temperature profiles for the undriven flame was excellent. The qualitative behavior of the experimental and computed temperature profiles in the driven flame was similar. More simultaneous CARS measurements of nitrogen temperature and oxygen concentration are planned for the near future. Computational results obtained using measured inlet conditions will be compared to the experimental results. Additionally, laser-induced fluorescence measurements of NO concentration will be conducted for flames in which the NO concentrations are significant. This will be done to determine the increase in NO production in the hottest regions of the flames due to coupled stretching and non-unity Lewis number effects.

The University of Illinois would like to acknowledge the support of the Air Force Aero Propulsion and Power Directorate of Wright Laboratory and Systems Research Laboratories, Inc. (Contract D5358).

REFERENCES

1. Lucht, R. P., *Optics Letters* 12:78-80 (1987).
2. Hsu, K. Y., Chen, L. D., Katta, V. R., Goss, L. P., and Roquemore, W. M., AIAA Paper 93-0455, 31st Aerospace Sciences meeting and Exhibit, Reno, 1993.
3. Katta, V. R., Roquemore, W. M., *Combust. Flame* 100:61-70 (1995).
4. Law, C. K., *Twenty-second Symposium (International) on Combustion*, The Combustion Institute, Pittsburgh, 1988, p.1381.
5. Katta, V. R., Goss, L. P., and Roquemore, W. M., *Combust. Flame* 96:60-74 (1994).
6. Chen, L.-D., Roquemore, W. M., *Combust. Flame* 66:81-86 (1986).
7. Ewart, P., Mode - X Laser Systems, 55 Benmead Road, Kidlington, Oxon. OX5 2DB, U.K.
8. Palmer, R. E, Sandia Report, SAND89-8206, February 1989.

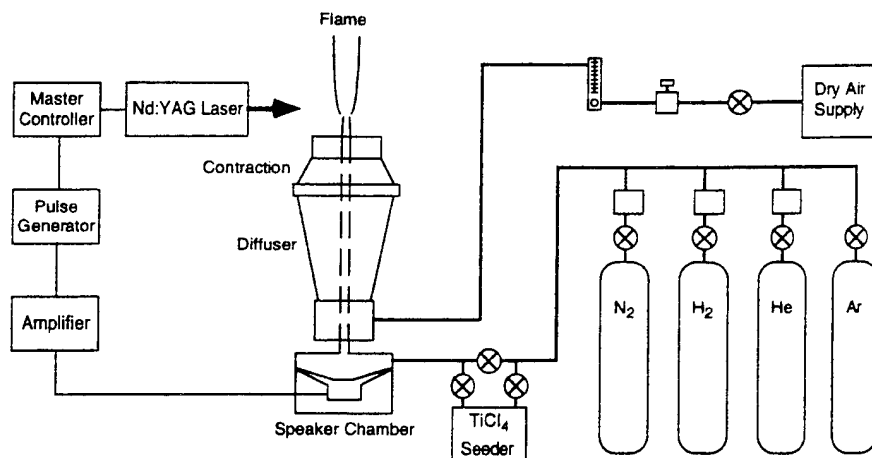


Figure 1. Experimental Setup

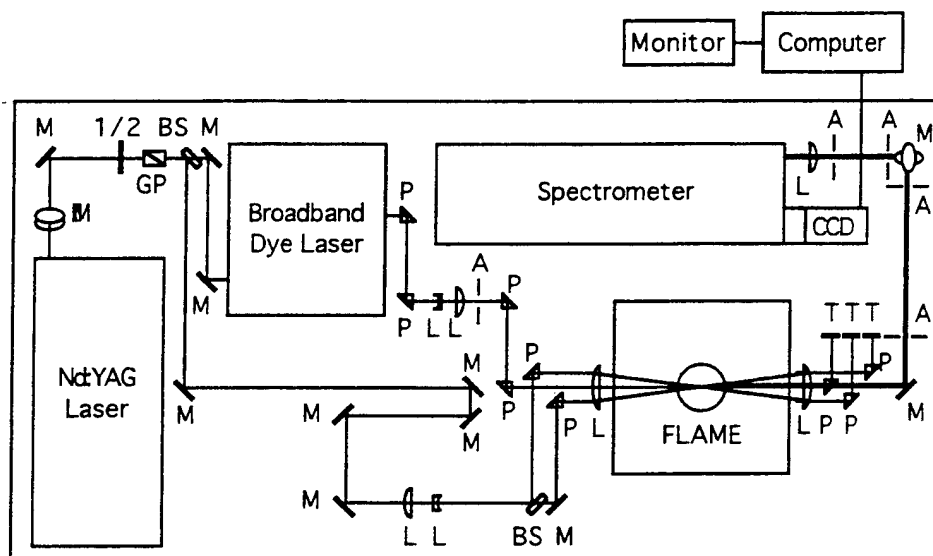


Figure 2. CARS System Schematic

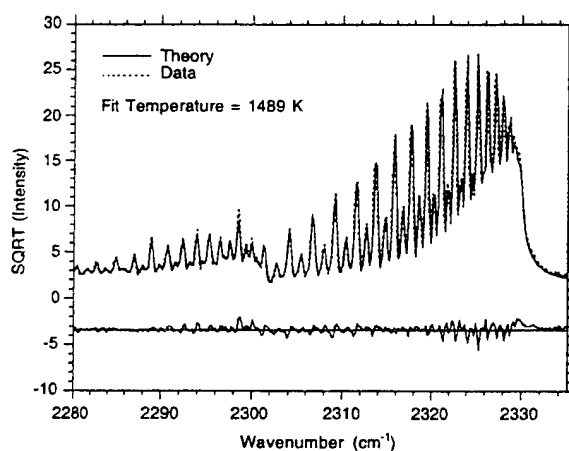


Figure 3. CARS Spectrum Example

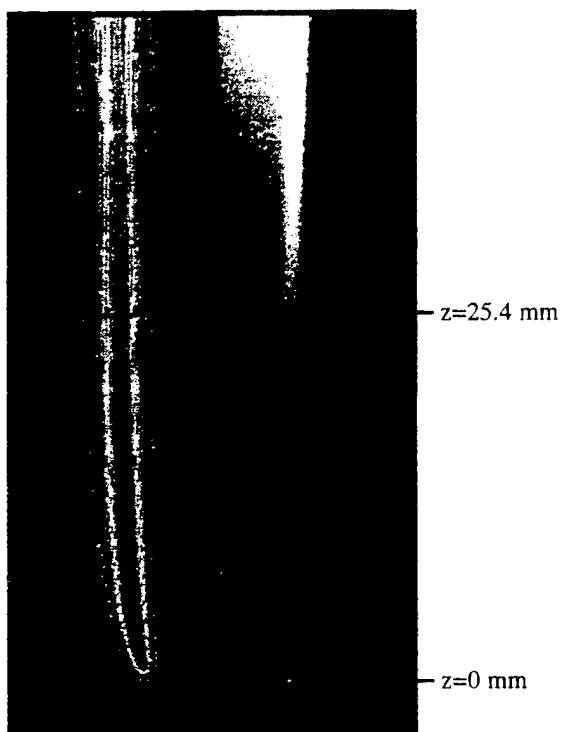


Figure 4a. Flame A (Undriven)



Figure 5a. Flame B (5 ms Delay)

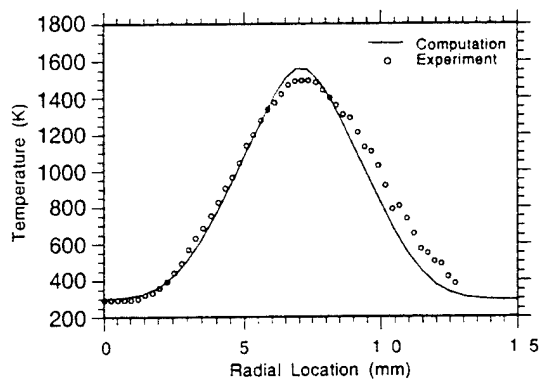


Figure 4b. Temperature Profile (Flame A)

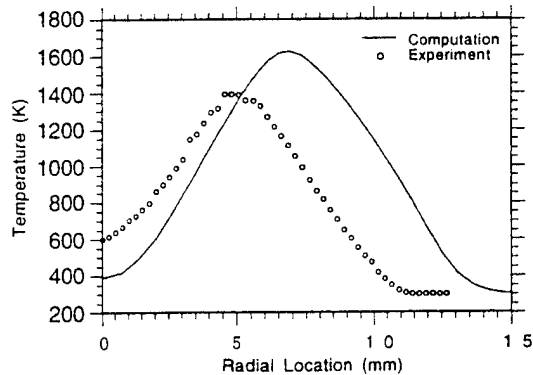


Figure 5b. Temperature Profile (Flame B)

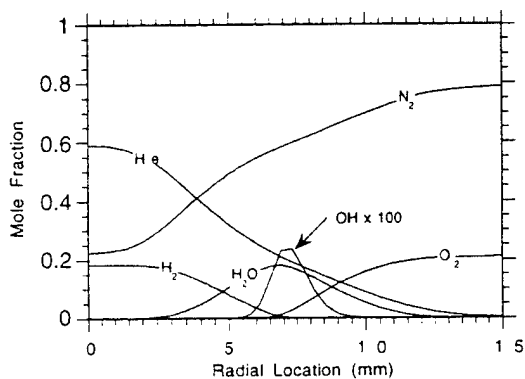


Figure 4c. Calculated Mole Fraction (Flame A)

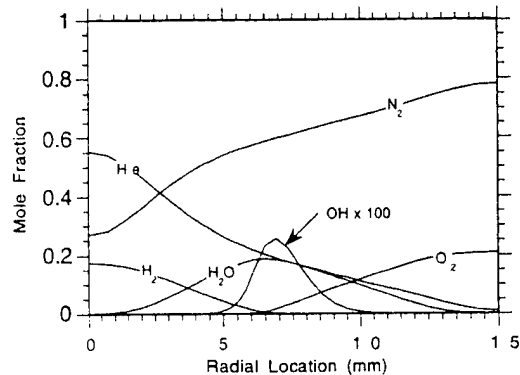
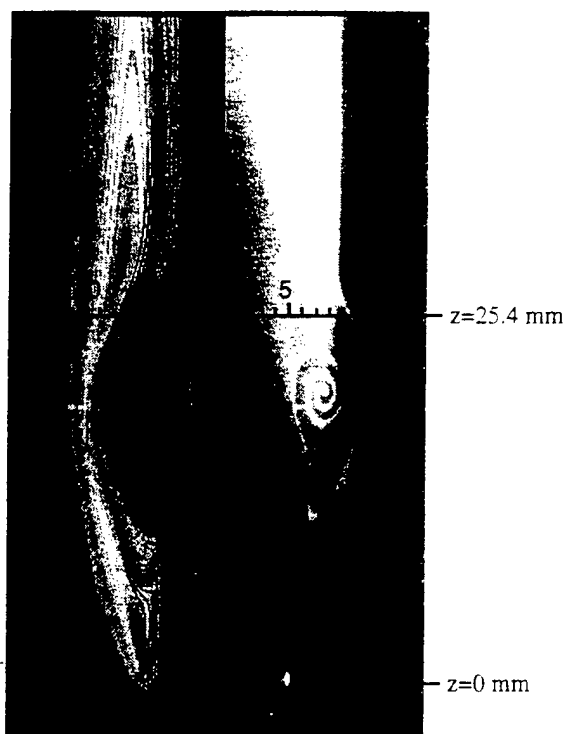


Figure 5c. Calculated Mole Fraction (Flame B)



Computation Experiment
Figure 6a. Flame C (6 ms Delay)



Computation Experiment
Figure 7a. Flame D (7 ms Delay)

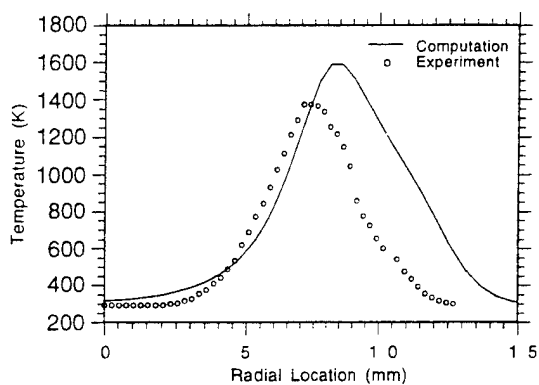


Figure 6b. Temperature Profile (Flame C)

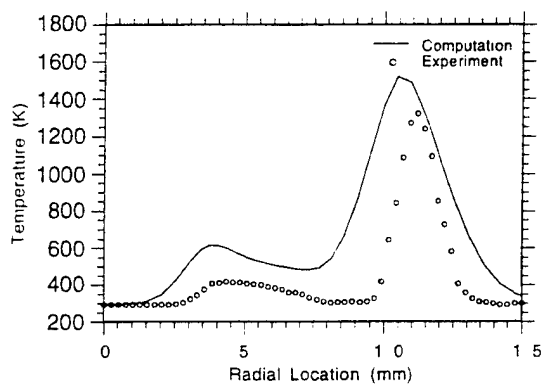


Figure 7b. Temperature Profile (Flame D)

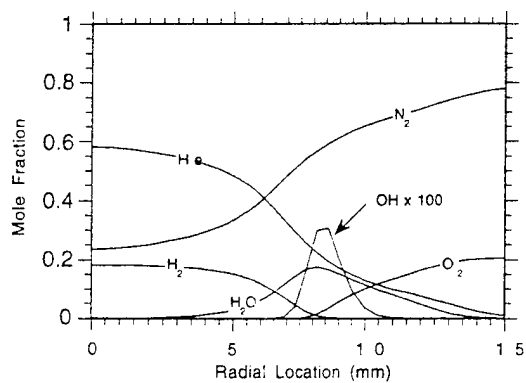


Figure 6c. Calculated Mole Fraction (Flame C)

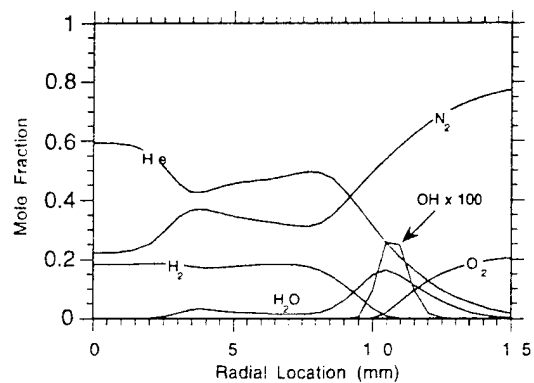


Figure 7c. Calculated Mole Fraction (Flame D)

The Structure of a Dynamic Nonpremixed H₂-Air Flame

C. D. Carter, L. P. Goss, K. Y. Hsu, V. R. Katta, and D. D. Trump

Systems Research Laboratories, Inc.
A Division of Space Industries International, Inc.
2800 Indian Ripple Rd.
Dayton, OH 45440-3696

INTRODUCTION

Studies of simple vertically oriented nonpremixed jet flames have shown that when the co-flow velocity is sufficiently low, buoyancy-induced, periodic toroidal vortices form outside the flame surface. These vortices wrinkle the flame surface and produce stretched and compressed flamelets, thereby providing a relatively simple means of studying flame-vortex interactions. Recent calculations by Katta et al. [1,2] suggest that preferential diffusion due to nonunity Lewis number in these H₂-air flames influences the gas temperature along the flame surface. In particular, Katta et al. [1,2] find that the flame temperature increases in the compressed regions of the flame and decreases in the stretched regions. That the flame temperature varies in this manner has been confirmed in part by previous experimental studies [3,4].

To characterize the structure of a dynamic nonpremixed H₂-air flame, we have made sequential point measurements of temperature using thin-filament-pyrometry (TFP) and concentrations of hydroxyl (OH) and nitric oxide (NO) using laser-induced fluorescence (LIF). We have chosen three downstream locations of 135 mm, 85 mm, and 50 mm from the jet exit; for each of these positions, we have recorded the radial and temporal variation of these scalars. For this paper, we will focus on measurements recorded at 135 mm.

EXPERIMENTAL METHODS

Facilities and Techniques

Shown in Fig. 1 is a schematic of the experimental facility. The burner consists of a tapered fuel tube (1-cm ID) surrounded by a co-annular air section (15-cm ID); both the burner and the co-annular section are mounted to an *x-y-z* translation system employing stepper motors. Assuming a uniform velocity profile, the

flow velocities for the fuel and air were 4.62 m/s and 0.40 m/s, respectively. These flow rates resulted in a buoyant frequency of 15.2 Hz. Although a range of frequencies (10 to 20 Hz) can be obtained by varying the gas flow rates, the 15-Hz frequency is optimum for the available laser system (a 30-Hz Nd:YAG pump laser), insofar as the laser is triggered at twice the frequency of the buoyant fluctuations. The laser and detection electronics were phase locked to the 15.2-Hz buoyant frequency using the passage of these structures through a cw laser beam; the beam steering induced by the passage of the flame bulge moved the laser beam on and off a photodiode at the frequency of 15.2 Hz; with the flame isolated from disturbances, the variation in the trigger frequency was only ± 0.2 Hz. To maintain the trigger signal, we mounted both the cw laser and the photodiode detector to the burner/co-flow housing. Thus, the detection electronics were triggered from the same flame structure, regardless of the burner position. Finally, to reduce the maximum temperatures and, thereby, extend the lifetimes of the filaments, we

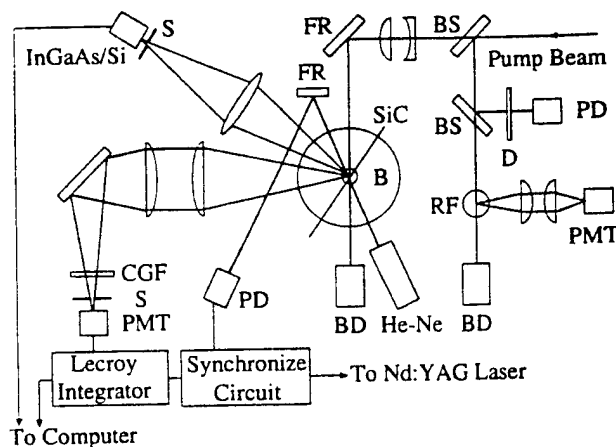


Fig. 1. Schematic of experimental setup

employed a diluted fuel mixture in the ratio of 2.22 parts H_2 to 1 part N_2 .

Originally the filament emission and NO fluorescence were recorded simultaneously. However, the flame proved to be reproducible, and subsequent to our initial simultaneous measurements, each (NO fluorescence, OH fluorescence, and temperature) was recorded sequentially. The β -SiC filaments, due to their small diameter (14 μm) and low thermal conductivity (10 kcal/m-hr-K or about 40 times lower than that of a type S or R thermocouple) exhibit excellent temporal response and spatial resolution. The filament acts as a graybody with an emissivity of 0.88. The detection limit for the filament corresponds to ~ 900 K; the high-temperature limit, ~ 2300 K in practice, is determined by the sublimation point of the β -SiC material.

We overlapped the filament and LIF probe volumes using a 500- μm pinhole--which was mounted on a kinematic magnetic base assembly--in combination with a He-Ne alignment laser; the pinhole defined the spatial resolution of both the LIF and the TFP measurements. The light from the He-Ne laser was split into two beams, which were made to pass through the alignment pinhole. The intersection of the two beams was then used as a marker for the probe volume, and the filament was properly aligned when scattering from both He-Ne beams was observable. With all three measurements, we translated the burner to the axial and radial position of interest. The signals were then recorded as a function of delay relative to the trigger signal; the 2-D maps (signal vs. time and radius) were then constructed from the individual signal vs. time traces. With temperature we recorded the signals in real time; that is, we sampled the filament emission at a frequency of ~ 1 kHz. Typically, we averaged the filament emission over 45 cycles for each spatial location. Strong emission from H_2O was also present in the hottest regions of the flame; consequently, recording the background flame emission was necessary. Thus, subsequent to recording the filament emission map (i.e., in time and space), the filament was broken and the background was recorded for the same phases and radial positions. With the LIF measurements, we were limited by the 30-Hz pulse repetition frequency of the laser; thus, we obtained measurements on successive cycles of the buoyant structures. Typically, we averaged the fluorescence from 45 laser pulses--corresponding to 45 successive buoyant cycles--for each temporal and spatial location.

The filament emission was collected with a conventional camera lens and focused onto a dual photodiode detector. This dual photodiode is composed of sandwiched InGaAs and Si diodes having respective spectral ranges of about 0.9 to 1.8 μm and 0.45 to 1.0 μm . Because the temperature is derived from a ratio of the photodiode signals, the measurement is less sensitive to possible variation in the filament emissivity (due to long exposure at high temperatures, for example) and to small variations in the optical alignment. The frequency response of the filament is better than 1 kHz for flame conditions. Therefore, we expect that the filament will accurately reflect the temporal variations in gas temperature.

The laser-beam diameters for OH and NO excitation were adjusted to allow $\sim 90\%$ of the beam energy through the alignment pinhole. The probe-volume beam energies for OH and NO were kept below the 10- μJ level to ensure that the fluorescence would remain within the linear regime. We collected the fluorescence with two 100-mm-diameter fused-silica lenses--a 250-mm focal length collection lens and a 500-mm focal length focusing lens--which resulted in a system magnification of ~ 2 . A slit-and-photomultiplier-tube housing was positioned at the focus of the fluorescence beam. For both NO and OH fluorescence collection, the slit width was set to ~ 1.0 mm, resulting in a resolution of ~ 0.5 mm along the axis of the LIF laser beams.

For NO and OH fluorescence excitation, we employed a Nd:YAG-pumped dye laser system with a 30-Hz pulse repetition frequency. To generate the wavelength for NO excitation, the frequency-doubled output of the dye laser was mixed with the residual IR radiation from the Nd:YAG. We tuned this system to the $Q_1(28)$ transition of the $A^2\Sigma^+-X^2\Pi(0,0)$ band ($\lambda = 225.20$ nm). A Schott UG-5 colored-glass filter, a KrF excimer-laser turning mirror, and the spectral response of a solar-blind PMT photocathode were used to isolate the NO fluorescence from the ($v'=0$, $v''=1-5$) bands and reject background radiation. Although interfering fluorescence from vibrationally hot O_2 is present, the level of interference in this flame is small relative to the NO fluorescence [5]. For OH excitation, we tuned the same laser system (using the frequency-doubled dye laser beam) to the $S_{21}(8)$ line of the $A^2\Sigma^+-X^2\Pi(1,0)$ band ($\lambda = 278.91$ nm). By pumping a satellite transition, we greatly reduced absorption of the laser beam propagating through the flame [6]. Schott colored-glass filters, WG-295 and UG-11, blocked

scattered radiation and transmitted fluorescence from the dominant (1,1) and (0,0) bands, where the (0,0) band fluorescence is preceded by vibrational energy transfer from $v'=1$ to $v'=0$ [7]. Some of the fluorescence, principally the (0,0)-band component, is strongly absorbed as it propagates through the flame. For this reason, we collected fluorescence from the *near* half of the flame. For both LIF measurements, we recorded the laser energy in addition to the OH or NO fluorescence from a laminar, near-adiabatic reference flame (Fig. 1). The reference flame served two purposes: first, the LIF signal allowed easy tuning of the laser wavelength to the desired transition; second, the recorded fluorescence allowed correction of the LIF signal in the H_2 -air flame for minor wavelength drift of the dye laser.

Calibrations and Corrections

The filament was calibrated using a near-stoichiometric H_2 -air flame produced by a Hencken burner [8]. This 25-mm-square burner consists of an array of small fuel tubes surrounded by a Hastelloy honeycomb matrix which provides for the flow of air. The uncooled burner thus produces an array of nonpremixed flames; with sufficiently high flow rates of H_2 and air (total cold-gas flow rates of ~ 50 slpm for this 25-mm-square burner), the heat loss to the burner is negligible and the temperature is near the adiabatic value [8]. The hot-gas velocity—which is necessary for calculation of the radiation correction—can easily be calculated due to the 1-D nature of the flow field; additionally, the gas properties can be obtained from equilibrium calculations. Because of the nonpremixed nature of the burner, one can obtain a wide range of temperatures (from below 1000 K to greater than 2300 K) simply through variation of the H_2 flow rate [8]. A comparison of the derived filament temperature (calibrating the filament at one Hencken flame condition) and the adiabatic equilibrium temperature showed excellent agreement between the calculated temperatures and those obtained from the filament.

To convert the emission measurement into gas temperature, the measured filament temperature must be corrected for radiative losses [4]. A numerical simulation of the flame (described below) shows that the velocity field is relatively uniform—i.e., a factor of two variation—in the region of interest; thus, we have simply used a constant velocity of 3.6 m/s for all the radiation corrections. However, to assess the sensitivity of the derived temperature to the time-

varying velocity and temperature fields, we have used the calculated fields and gas properties as inputs into the radiation correction algorithm. The difference in temperatures derived by means of the two approaches, one using uniform velocity and gas properties and the other using the time-varying calculated values, is small due to the relatively high velocity of the gas.

To calibrate the OH fluorescence, we used the same burner. At heights greater than ~ 2 cm above the burner, the OH fluorescence is constant, indicating that the OH has equilibrated. We used the measured [OH] reported by Barlow and Carter [8] for a lean ($\phi = 0.94$) H_2 -air flame. This concentration, $[OH] = 2.16 \times 10^{16} \text{ cm}^{-3}$, compares well with the adiabatic equilibrium value of $2.31 \times 10^{16} \text{ cm}^{-3}$. Unlike the concentrations of OH, those of NO are too small for reliable absorption measurements and are typically far below equilibrium at reasonable distances above the burner. Consequently, the approach taken was to dope a lean laminar flame with a small, known concentration of NO (from a bottle with ~ 200 ppm of NO in N_2). The calibration procedure consists of measuring NO fluorescence signals in a doped flame and in an undoped flame, where a portion of the pure N_2 is substituted for the NO-doped N_2 . Thus, except for the NO levels, the flames are identical; by subtracting the signal from the undoped flame from that of the doped flame, we obtain the signal corresponding to the doped NO.

Using quantities obtained from the calibration flame (those quantities denoted with the subscript *cal*), we have converted the linear fluorescence signals S_f to mole fraction with the following equation:

$$X_i = \frac{S_f}{N_T} \left[\frac{N_i}{S_f} \right]_{cal} \left(\frac{[F_B]_{cal}}{F_B} \right) \left(\frac{[E_L/Q]_{cal}}{E_L/Q} \right).$$

Here, N_T is the total number density; $[N_i/S_f]_{cal}$ is the fluorescence calibration factor (species number density divided by fluorescence signal); F_B is the Boltzmann fraction; E_L is the laser energy; and Q is the net quenching rate. For the NO fluorescence, we also took into account the effect of line broadening; however, its affect on the derived concentrations is small for the range of temperatures recorded with the filament. Of course, for both OH and NO LIF the transitions were chosen to minimize the temperature sensitivity of the respective ground-state populations over the temperature range appropriate for the filament (i.e., 900 to 2300 K).

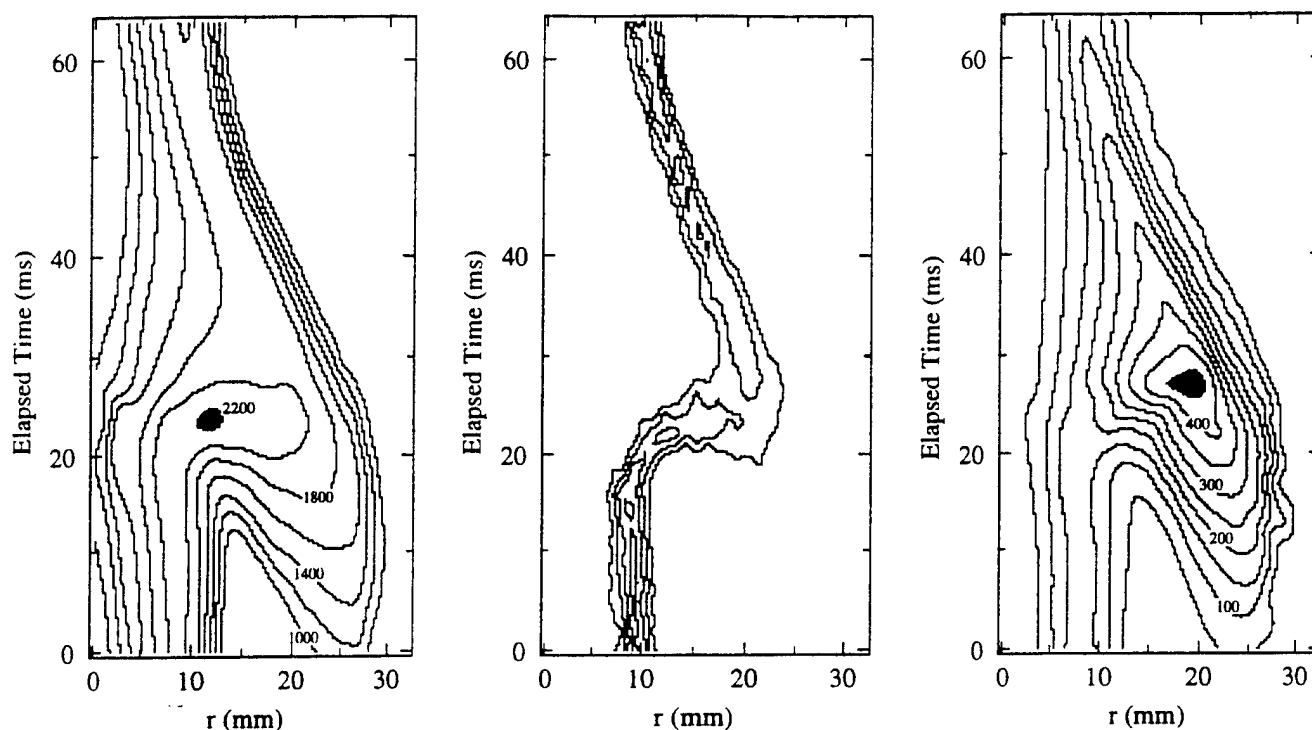


Fig. 2. Contour plots of measured temperature (left), OH concentration (middle), and NO concentration (right) in space (radius) and time. For temperatures and NO concentrations, contour levels are shown (temperature increments of 200 K with a maximum level of 2200 K; NO mole fraction increments of 50 ppm with a maximum level of 450 ppm). For OH mole fraction, contours are in increments of 0.2 percent with a maximum contour of 0.8 percent (fourth-level contour).

Currently we can only approximate the quenching variation using the recorded temperatures. Because one can distinguish fuel-rich from fuel-lean regions, the mix of species necessary to produce the measured temperatures can be estimated from equilibrium calculations. Because OH exists over only a limited range of conditions, its fluorescence is minimally affected by this estimate; for NO fluorescence, however, the quenching rate can vary by a factor of two over the range 1000 K to 2200 K. Consequently, to correct the fluorescence for the quenching variation across the flame, we constructed a *look-up* table of the quenching rate vs. temperature, which was based on an adiabatic temperature and the corresponding equilibrium mixture of species. The corrections differ for rich and lean conditions; thus, the correction algorithm distinguishes between the fuel-rich (inner) and fuel-lean (outer) regions of the flame. The models for OH and NO quenching include the quenching cross sections recently described by Paul et al. [Refs. 9 and 10 for NO; Refs. 11 and 12 for OH quenching].

RESULTS AND DISCUSSION

Shown in Fig. 2 are the measurements of temperature and mole fraction of OH and NO (again, at the

downstream location of 135 mm) versus radial position and time, relative to the photodiode trigger signal. The temperature and mole fractions are represented with contour plots. Smooth curves have been drawn through the NO and temperature data for ease of interpretation; the same was not done for the OH plot, due to the course mapping resulting from 1-mm radial steps. The maximum observed temperature, ~ 2250 K, occurs at the location of the flame bulge, i.e., the compressed region of the flame. In the stretched regions of the flame, the maximum temperatures across the flame drop to ~ 1900 to 2000 K. Currently, we are investigating this drop in temperature below the adiabatic value of ~ 2200 K.

As expected, OH exists only over a relatively narrow region of space. This region matches well that bracketed by the $T > 1800$ K contour; consequently, the OH marks the high-temperature regions where we expect NO to be produced. For OH we find that the maximum concentrations of 0.8 to 0.9 percent by volume are in the thin stretched regions; at the bulge, the peak concentrations are lower. Katta et al. [4] attribute this behavior to flame curvature effects. Unfortunately, the flame stability was somewhat worse on the day when the OH was recorded (0.4 Hz vs. 0.2

Hz); as a consequence, the sharpest features of the OH map have probably been lost and the contour plot appears *noisy*. For NO the higher temperatures within the bulge result in concentrations in excess of 400 ppm. As expected, away from the bulge, even along the flame surface, the NO concentration is lower. Of course, once the NO is produced, it is transported as a relatively stable product; thus, we observe considerable concentrations of NO even in fuel-rich regions.

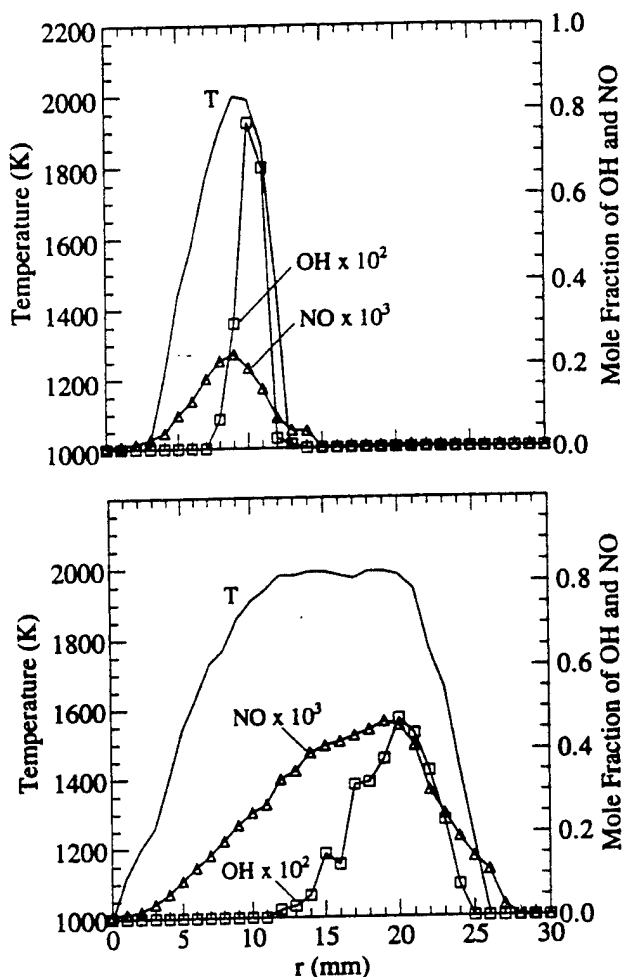


Fig. 3. Line plots of temperature, X_{OH} , and X_{NO} vs. radius at two times (top plot, 59 ms; bottom plot, 28 ms) relative to the trigger signal.

In Fig. 3 we show radial profiles at two times (i.e., phases), 28 and 59 ms, corresponding respectively to profiles across the compressed and stretched portions of the flame. The profiles from the stretched regions show narrow distributions of temperature, of X_{NO} , and especially of X_{OH} . The OH peaks slightly to the lean side—based on the temperature profile—of stoichiometric at ~0.8 mole fraction; the peak X_{NO} (~220 ppm) corre-

lates well with the peak temperature (~2000 K). In the compressed region, the profiles of temperature, X_{NO} , and X_{OH} are broad. The NO peaks at about the same radial location (20 mm) as the OH. As mentioned above, the NO concentration is at its maximum value at this location; on the other hand, the peak OH concentrations are somewhat less than in the stretched regions.

Finally, in Fig. 4 we show results from the aforementioned numerical simulation, which has been described in detail by Katta et al. [1,2]. Briefly, the time-dependent Navier-Stokes equations, along with the species- and energy-conservation equations, are integrated on a nonuniform staggered-grid system. The detailed chemistry model includes 13 species and 52 elementary reactions. The effective binary-diffusion coefficient of the individual species in the local mixture is calculated using molecular dynamics and Lennard-Jones potentials. Across the compressed region, we find the maximum concentrations in the range of 420 to 480 ppm, in good agreement with the measured values. The maximum OH concentrations, occurring along the stretched regions, are between 0.8 and 1.0 percent mole fraction. Again, this matches well the experimental maximum of about 0.8 to 0.9 percent mole fraction. However, across the bulge, the calculated X_{OH} are somewhat larger than the measured values. Perhaps a more significant area of disagreement, however, is in the temperature field: while the measured temperatures drop 200 to 300 K in the stretched regions of the flame, the drop in the calculated values is less than 100 K.

CONCLUSIONS

We have investigated the structure of a dynamic nonpremixed H_2 -air flame. In particular, we have mapped in space and time through sequential point measurements the temperature through thin filament pyrometry and the concentrations of OH and NO through laser-induced fluorescence. The measurements show that OH is confined to relatively narrow regions, especially in the stretched portion of the flame. The peak values across the stretched regions of the flame are $X_{OH} \approx 0.8$ to 0.9 percent mole fraction. The OH distribution across the compressed region is significantly broader (10 mm vs. 4 mm) and the peak concentrations are reduced.

NO is distributed over a wide region of the flame (from lean to rich, whereas the OH is found primarily in fuel-lean mixtures), with peak concentrations of ~450 ppm in the compressed (bulge) region; in contrast, peak X_{NO} across the stretched region are as

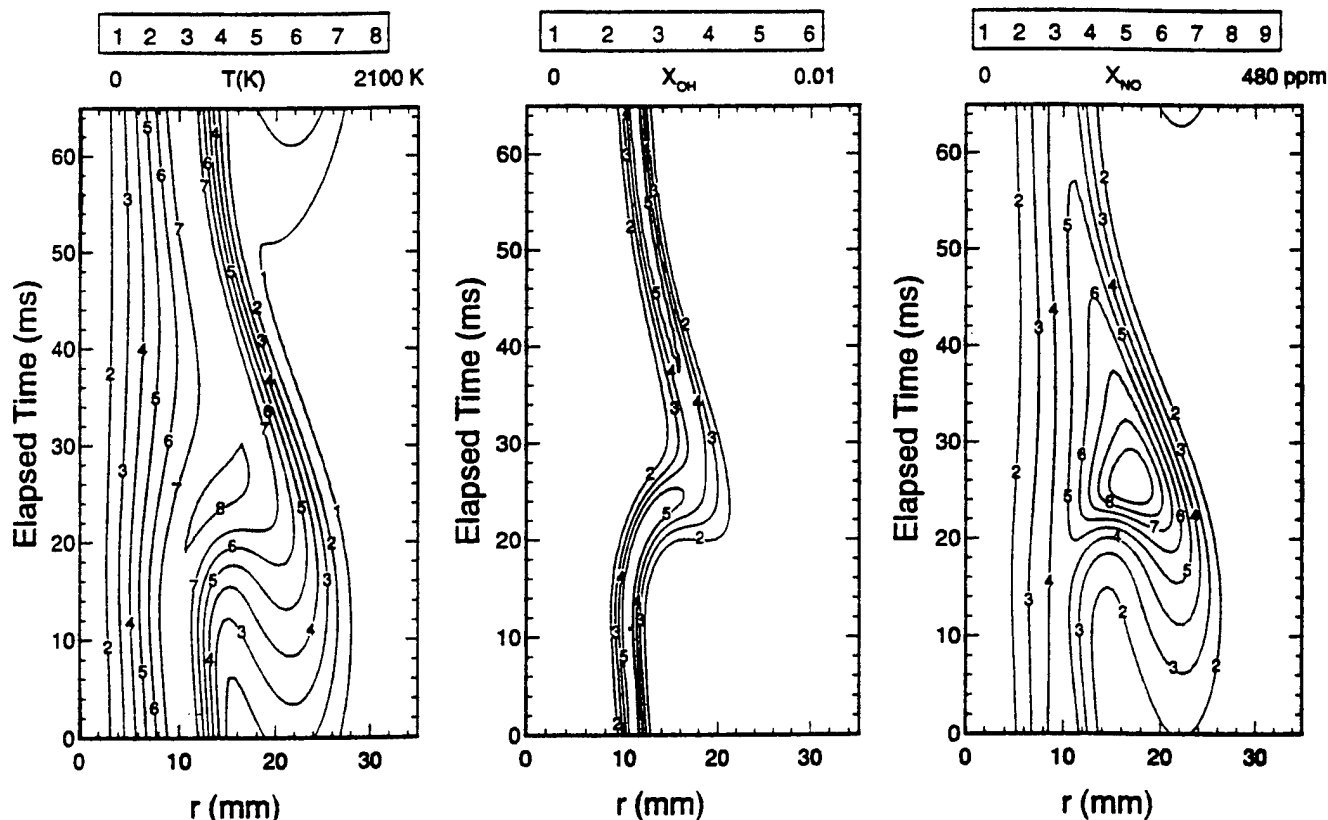


Fig. 4. Contour plots of calculated temperature (left), OH concentration (middle), and NO concentration (right) in space (radius) and time. Contour levels are indicated above each plot.

low as ~180 ppm. A numerical simulation of the flame produced good agreement with the measured NO concentrations. Both calculations and measurements show peak NO concentrations of 450 to 480 ppm in the bulge and significantly reduced concentrations in the stretched regions. Currently, the most significant area of disagreement between simulation and experiment is the temperature field. We expect that future measurements and calculations will resolve this discrepancy.

ACKNOWLEDGMENTS

This work was supported by Wright Laboratory, Wright-Patterson Air Force Base, OH, under Contract No. F 33615-90-C-2033.

REFERENCES

- Katta, V. R., Goss, L. P., and Roquemore, W. M., *Combust. Flame* **96**: 60-74 (1994).
- Katta, V. R. and Roquemore, W. M., *Combust. Flame* **100**: 61-70 (1995).
- Vilimpoc, V. and Goss, L. P., *Twenty-Second Symposium (International) on Combustion*. The Combustion Institute, Pittsburgh, 1988, pp. 1907-1914.
- Goss, L. P., Vilimpoc, V., Sarka, B., and Lynn, W. F., *ASME Trans.* **111**: 46-52 (1989).
- Carter, C. D. and Barlow, R. S., *Opt. Lett.* **19**: 299-301 (1994).
- Chidsey, I. L. and Crosley, D. R., *J. Quant. Spectrosc. Radiat. Transfer* **23**: 187-199 (1980).
- Smith, G. P. and Crosley, D. R., *Appl. Opt.* **22**: 1428-1430 (1983).
- Barlow, R. S. and Carter, C. D., *Combust. Flame* **97**: 261-280 (1994).
- Paul, P. H., Carter, C. D., Gray, J. A., Durant Jr., J. L., and Furlanetto, M. R., *Correlations for the NO A²Σ⁺ (v'=0) Electronic Quenching Cross-section*, Sandia Report SAND94-8237, Sandia National Laboratories, Livermore, CA 94551 (1995).
- Paul, P. H., Gray, J. A., Durant Jr., J. L., and Thoman Jr., J. W., *AIAA J.* **32**: 1670 (1994).
- Paul, P. H., Carter, C. D., Gray, J. A., Durant Jr., J. L., Thoman, J. W., and Furlanetto, M. R., *Correlations for the OH A²Σ⁺ (v'=0) Electronic Quenching Cross-section*, Sandia Report SAND94-8244, Sandia National Laboratories, Livermore, CA 94551 (1994).
- Paul, P. H., *J. Quant. Spectrosc. Radiat. Transfer* **51**: 511 (1994).

3.1.4 Research Combustors. Several research combustors were studied using advanced laser diagnostic techniques. The unique features of these combustors bridged the gap between laboratory flames and turbine engine combustors. One of the first combustors studied was gas fueled and consisted of confined coaxial jets with a sudden expansion. The results of studies conducted on this combustor are contained in a paper entitled, "Experimental and Theoretical Studies in a Gas-Fueled Research Combustor" (pp. 400 - 416) .

The next step in the evolution of the research combustor was the incorporation of a commercial fuel injector. This combustor consisted of a single swirl cup housed in a vertical tunnel with quartz windows for optical access. CARS, LDV, LIF, and visualization measurements were made and the results reported in papers entitled, "Observations of Flame Behavior From a Practical Fuel Injector Using Gaseous Fuel in a Technology Combustor" (pp. 417 - 428) and "Structure of a Spray Flame Stabilized on a Production Engine Combustor Cup" (pp. 429 - 437). The effects on the swirl combustor of the addition of wall jets were reported in a paper entitled, "The Role of Traverse Air Jets in the Formation of Gas Turbine Emissions" (pp. 438 - 449).

One of the design issues of a gas turbine combustor is flame stabilization which determines the lower operating condition and the turn-down ratio of the gas turbine engines. A lower operating condition results in lower specific fuel-consumption rate which reduces both the cost and the problem of relight. In typical gas turbine engines, swirl and bluffbodies are used for flame stabilization. During the course of this program, a new concept for flame stabilization was developed--the trapped-vortex combustor (TVC) which employs a properly sized cavity for flame stabilization ["Performance of a Trapped-Vortex Combustor" (pp. 450 - 464)]. The lean blow-out of the TVC was found to be an order of magnitude lower than that of conventional gas turbine combustors over a wide range of flow conditions. The excellent stability of the TVC prompted the Air Force to apply for a patent on this advanced method of flame stabilization. The configuration of the combustor was also modified to make it more suitable for implementation in real combustors. The performance of the combustor was tested extensively over a wide range of flow conditions and configurations at atmospheric pressure. A series of experiments on lean blow-out and pollution emission was conducted and the results analyzed. The experience gained from these tests was very useful in identifying key design factors for future development.

The largest-scale combustor studied during this program was a four-injector representation for a practical annular combustor which was made into a planar configuration. CARS temperature measurements and isothermal flow CFD calculations provided field information that led to a consistent picture of the blowout behavior of the combustor. The results of this study were reported in the paper entitled, "Relation of CARS Temperature Fields to Lean Blowout Performance in an Aircraft Gas Turbine Generic Combustor" (pp. 465 - 481).



AIAA 91-0639

Experimental and Theoretical Studies in a Gas-Fueled Research Combustor

W. M. Roquemore and V. K. Reddy

WL, Wright-Patterson Air Force Base, OH

P. O. Hedman

Brigham Young University

M. E. Post, T. H. Chen, L. P. Goss, D. Trump, V. Vilimpoc
Systems Research Laboratories, Inc.

G. J. Sturgess

Pratt and Whitney, East Hartford, CT.

29th Aerospace Sciences Meeting

January 7-10, 1991/Reno, Nevada

Experimental and Theoretical Studies in a Gas-Fueled Research Combustor

W. M. Roquemore and V. K. Reddy
Wright Laboratory
Aero Propulsion and Power Directorate
Wright Patterson AFB, OH 45433-6563

P. O. Hedman
Chemical Engineering Department
Brigham Young University
Provo, UT 84602

M. E. Post, T. H. Chen, V. Vilimpoc, L. P. Goss, B. Sarka, D. Trump
Systems Research Laboratories, Inc.
A Division of Arvin/Calspan
Dayton, OH 45440-3696

G. J. Sturgess
Pratt and Whitney
East Hartford, CT 06108

ABSTRACT

This paper reports the results of an investigation to determine the flow and flame characteristics of a burner which has been carefully designed to "specifically reproduce recirculation patterns and lean-blow-out (LBO) processes that occur in a real gas turbine combustor" [1]. When operated in a fuel rich mode, the flame is very stable and is anchored in the jet shear layer by a pilot flame attached to the step, near the outer edge of the air supply tube. As the equivalence ratio is reduced, the flame becomes less stable, and eventually reaches a point where the pilot flame becomes detached (lifts) from the base region, and the entire flame structure becomes stabilized downstream. Thus, there are two distinct operating modes for the combustor: a fully attached flame and a lifted flame. As the fuel equivalence ratio is further reduced, the flame becomes progressively less stable in its lifted condition, and eventually blows out. Photographs of the flame clearly illustrate the attached and lifted flame operational regimes of the combustor. However, visual observation and conventional photographic techniques are unable to quantify the precise details of the flame transition from an attached to a lifted condition. A Computational Fluid Dynamics (CFD) model with one step chemistry was used to investigate the time-averaged features of the reacting and non-reacting flow fields. The difficulties of predicting the characteristics of the attached flame with a time averaged CFD type model are discussed. Measurements, using OH emissions and graybody radiation from 14 μm diameter filaments located near the base of the flame, clearly indicate the dynamic or intermittent nature of both the attached and lifted flames.

It is theorized that unburned hydrocarbon combustion products are transported into the recirculation zone by the intermittent process; and it is these products that provide the fuel needed for the flame to attach to the outer edge of the step.

INTRODUCTION

Advancements in gas turbine engine technology are reducing design tolerances and increasing the need to have precise design methods. Of all the design requirements for combustion chambers, several may be categorized as being critical to safety and reliability. One of these is combustion stability, an aspect of which is lean-blow-out (LBO). LBO is of special concern since recent design trends appear to result in an erosion of stability margins. This concern is exacerbated by the weakness in current methods of calculating LBO limits, and by the limited design criteria for obtaining good stability. A research program that results in improved calculation procedures for LBO enhances design capability and will provide a most valuable contribution.

There are several difficulties that make modeling LBO a serious challenge. LBO is usually encountered during engine transients and it may, therefore, be difficult to separate overall system behavior from the combustor characteristics. The phenomenon itself is a transient process, and it may involve non-stationary flow behavior. Hence, LBO is rather difficult to study in detail. The physics involved can be extremely complex since it concerns interactions between several processes. This means that the mechanisms of blow-out in one combustor

design might be different from that of another design so that the impact of changing operational parameters, such as pressure or air flow, could have opposite effects. Also, the blow-out process may be very sensitive to small design changes even to the point that manufacturing and assembly tolerances in a system component, such as the fuel nozzle, may be a significant factor. An equal challenge is presented by the state-of-the-art in computational fluid dynamic (CFD) based codes for engineering use. In general, these provide stationary-state solutions, and the near-term prospects for realistic time-dependent calculations for engineering applications are not good.

This paper presents the results of an investigation to determine the flow and flame characteristics of a burner designed for the study of the fundamental LBO process. The burner has confined, coannular jets that discharge into a sudden expansion. This simple geometry provides a recirculation zone that is similar to those in modern gas turbine combustors. The present work is part of a larger study to investigate the flow and flame structure within the combustor over a wide range of fuel equivalence ratios and loading conditions. The results presented in this paper are considered preliminary in that the Reynolds numbers associated with flow conditions are lower than those found in gas turbine combustors. The transitional Reynolds number limitation was required to prevent overheating of the facility exhaust hood. The facility is currently being modified to accommodate the higher heat loads associated with fully turbulent flows. Future studies performed in this facility will be conducted at engine representative Reynolds number flow conditions. The general descriptions of the flame attachment and lifting processes reported in this paper were also observed in the facility at fully turbulent Reynolds number conditions. However, these conditions were only maintained for only short periods of time. Earlier studies conducted with this combustor were performed in a high Reynolds number flow facility that did not have the heat load problem [1,5,6].

The objectives of this paper are to: 1) characterize the flame structure for a wide range of equivalence ratios; 2) identify phenomena that contribute to the transition from an attached to a lifted flame since this clearly represents the beginning of lean blowout; and 3) gain insight into the characteristics that a model must have to correctly predict the LBO process.

The experimental approach used in this study involves: 1) visual observations, 2) 2-D flow visualization of the combustion flows using Reactive Mie Scattering, 3) spontaneous OH emission measurements in the ultraviolet (uv) to characterize the fuel equivalence ratio where the flame transitions from an attached flame to a lifted flame, 4) uv laser sheet lighting to stimulate OH laser induced fluorescence (LIF) emission, and 5) thin

filament graybody radiation studies of the flame frequency oscillations. A CFD model is also used to investigate the time averaged flow field characteristics of the burner. Experimental and model results are discussed in the following sections.

EXPERIMENTAL DESCRIPTION

Combustor. The combustor is shown schematically in Figure 1. The combustor has been carefully designed to "specifically reproduce recirculation patterns and LBO processes that occur in a real gas turbine combustor"[1]. The research combustor consists of coaxial jets with a 29.7 mm inside diameter central fuel jet surrounded by a 40 mm diameter annular air jet. The fuel is gaseous propane. The jets are located centrally in a 150 mm diameter duct. A backward facing step at the jet discharge plane completes the sudden expansion, giving a step height of 55 mm. The step provides a recirculation region that can stabilize the flame. The combustor test section incorporates flat quartz windows to accommodate laser and other optical access to the flame. Curved metal fillets, located in the corners of the test section, reduce and distribute the vorticity, generated by secondary wall flows, and thereby minimizes its impact on the bulk flow field in the combustor. This hybrid cross-section of the combustor allows reasonable optical access for laser diagnostics, while providing a good two-dimensional, axisymmetric flow approximation.

Test Conditions. Tests reported herein were all conducted at an air flow rate of 1000 lpm (referenced to 1 atm and 21°C) with a mean velocity of 31.6 m/s. Nominal propane flow rates were 30, 41, 52, and 63 lpm propane (referenced to 1 atm, and 0°C) with velocities of 0.8, 1.01, 1.35, and 1.64 m/s, respectively. These flow rates correspond to fuel equivalence ratios of 0.78, 1.05, 1.31, and 1.56, respectively. The Reynolds number for the annular air jet based on the width of the air jet is 18,360. Fuel jet Reynolds numbers are 5,223, 7,138, 9,053, and 10,968, respectively. Thus both the air and fuel jets are in the transitional flow region.

Reactive Mie Scattering (RMS). Mie scattering of a laser sheet from TiO_2 particles was used to obtain instantaneous (10 ns) images of the flame and flow patterns. The TiO_2 seed was obtained from the near instantaneous reaction of TiCl_4 vapor and moisture to form the TiO_2 particles. Either dry air or dry propane were seeded with TiCl_4 vapor. Moisture was added to the opposite flowing stream to provide ample H_2O for the chemical reaction. Moisture generated in the combustion process also participated in the chemical reaction. A sheet of light from a frequency doubled Nd-Yag laser was used to illuminate a cross section of the flow through the centerline of the burner. Images were collected with a 1024x1024 array intensified CCD camera that was located normal to the laser sheet.

OH Emissions. An instrument was set up to observe the spontaneous emission from the OH radical through a very narrow region of the flame near the flame attachment point. A simple lens and aperture were used to focus a narrow, cylindrical region of the combustor into a spectrometer. The waist of the focal volume was located about 15 mm above the base of the burner and in the region where the characteristic blue flame sheet was observed when the flame was attached. The focal volume integrated the OH emission along the entire path across the burner, but the most intense region, at least from visual observations was in the circular ring just outside of the air jet, where the flame appeared to attach.

The spectrometer was tuned to an OH emission line near 308 nm that gave a strong signal. The signal was captured with a photomultiplier tube, amplified, converted to a digital signal, and recorded on a mini computer. The 20,000 separate digital points collected over a 20 second time period were used to obtain a mean and standard deviation of the measured signal. Even though the spectrometer and photomultiplier tube were shielded from the radiation of the combustor, there was sufficient thermal loading to cause considerable background instrument noise that changed during a test. Consequently, an average background was obtained for each set of OH emission measurements. An average background was obtained from 20,000 data points collected after each test with the entrance to the spectrometer blocked. The average background signal was subtracted from each of the uv signal data points to obtain as representative a set of uv emission data as possible.

Laser-Induced Fluorescence (LIF). A thin sheet of laser light was also used to capture instantaneous (10 ns) two dimensional images of the flame and flow structure from the laser induced fluorescence (LIF) emission of OH. A frequency doubled Nd-Yag laser was used to generate a uv laser beam at about 283 nm. This frequency was used to pump a fluorescence transition of OH which resulted in a LIF signal at about 308 nm. As in the TiCl_4 seeded experiments, the plane of the laser light bisected the centerline of the test section. A 384x576 element intensified CCD camera, located normal to the laser sheet, was used to capture the rather faint images from the laser induced OH fluorescence. The intensified CCD camera was able to capture the full width of the optical window, but was limited in vertical height to about a 77 mm section of the combustor. To get a more complete record of the OH images, data were collected at four axial locations: 0 mm, 75 mm, 150 mm, and 225 mm.

Thin-Filament Pyrometer (TFP). A thin-filament pyrometer was used to study the time variations in temperature of the flame near the inlet of the combustor. The 14 μm SiC₄ filament is capable of

measuring temperatures at high sampling rates and is described in detail in [7]. The filament was not calibrated for these studies and was used only to indicate relative temperatures. The emissivity of the SiC₄ filament is independent of temperature which means that the intensity of the radiation from the filament is exponentially proportional to the temperature as determined by Planck's blackbody radiation law. The response time of the filament is of the order of 700 Hz, which causes the intensity signal from the filament to rise and fall as the temperature varies inside the combustor. The lower detectable temperature limit of the filament was about 1300 K, based on past experiences [7]. The radiation from a chosen filament was imaged onto a single InGaAs photodiode detector through the use of a cylindrical lens and a rotating mirror. The filament was located about 1 cm above the exit of the fuel-air jet. The filament radiation scanned and imaged with 256 pixels, digitized, and stored during each gated scan. For a fixed optical layout, the physical length scanned can be adjusted by changing the mirror scan rate and the digitization rate. This scanned length divided by 256 yields the pixel resolution. In this study the pixel resolution was $\sim 75 \mu\text{m}$.

To achieve the high sampling rates used in this experiment, a transient recorder was used. The output signal from the InGaAs detector was amplified and fed into the memory unit of the transient recorder. During the gated time period, 256 bytes of data were digitized at a selected rate in the range 1 - 4 Mbyte/s. The digitized data, which can be used to derive the line temperature profile, were then fed into a micro computer for data processing and storage. For this study, the line TFP signal was scanned at 250 and 500 lines per second. It was found that inside the recirculation zone near the step surface, the flame oscillation occurs at very low frequencies, i.e., less than 20 Hz. Therefore, only the results of scans at 250 lines per second are shown.

From the stored line signal taken at known scan rate, spectral information related to the flame oscillation can be obtained by spectral analysis using fast Fourier transform (FFT). For example, once a spatial location was chosen for the spectral analysis, the intensity data corresponding to that location was graphed as a function of time. Then, that array of data was fed into an FFT routine to yield spectral density. The FFT results are used to identify significant frequency patterns in the temperature signal produced by the filament.

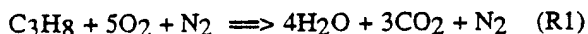
CFD MODEL DESCRIPTION

Both the nonreacting and the reacting flows in the research combustor are numerically simulated using a not-yet-published CFD code that is capable of predicting nonequilibrium and weakly compressible flows. It uses a non-staggered grid system and solves time-dependent

governing equations that are written in cylindrical polar coordinate system. An isotropic k- ϵ turbulence model has been used. When N_S number of species are considered in the given problem then, this two-dimensional code solves (N_S+5) governing equations namely; two momentum, continuity, turbulent energy, turbulent energy dissipation, enthalpy and (N_S-1) species conservation equations. Density is obtained from the state equation while pressure is directly obtained by solving the Poisson pressure equation instead of the continuity equation. One species mass fraction is always determined from the global species continuity equation. The specific enthalpy of each species is calculated from a polynomial curve-fit. In the present version of the code, all the species transport properties such as viscosity, thermal conductivity and diffusivity are assumed to be constant and identical to those of nitrogen.

The finite-difference form of the nondimensional governing equations are obtained by using a hybrid numerical scheme [8]. In general, it uses central differencing for the convective terms everywhere in the flow domain except at the locations where the local Peclet number falls below 2. In these regions the scheme automatically switches over to an upwind or backwind differencing to improve the convergence. Even though all the governing equations are solved in an uncoupled manner, the turbulence equations and the species conservation equations are coupled through the source terms in the solution process. Solution for the system of algebraic equations deduced from each governing equation at all grid points is obtained by adopting an Alternate Direct Implicit (ADI) technique. When the grid aspect ratio (Dx/Dr) is large, this ADI technique fails to converge. To circumvent this problem, the u-momentum equation is solved using a point-relaxation scheme. Finally, the usual no slip, adiabatic and chemically inert wall boundary conditions are made. Also the wall functions approach [9] is employed to avoid grid clustering near the walls.

In the present analysis for the combusting flows, a simple global reaction scheme involving propane, oxygen, water, carbon dioxide and inert nitrogen species is used and is expressed as follows:



The specific reaction rate is written in Arrhenius form and the pre-exponential is adjusted to match the peak temperatures for the experimentally measured propane diffusion flames.

Parabolic velocity profiles have been specified at the inlets of the fuel and air tubes. During cold flow simulations, the air jet is replaced with a pure oxygen jet and the thermophysical properties of both propane and oxygen are set equal. This enables identification of fuel mixing patterns when there is no flame. All the cold flow

simulations are made on a 89×46 uniformly spaced grid system, whereas the reacting flow solutions are obtained on a relatively coarse mesh having 40×40 nodes. Due to the small recirculation bubble in the fuel jet, calculations are made with a Courant-Friedrichs-Lewy (CFL) number close to 0.9 and the converged solution is obtained after several thousand time steps.

RESULTS

Visual Observations. When operated in a very fuel rich mode with gaseous propane fuel, the flame is very stable and is attached to the bluff body near the outer edge of the air tube. Figure 2a shows a photograph of such an attached flame at a fuel equivalence ratio (ϕ) of 1.56. As ϕ is reduced, the flame becomes less stable, and eventually reaches a point where it detaches (lifts) from the base region, and is stabilized about 150 mm downstream on the outer recirculation zone as shown in Fig. 2b. The end of the outer recirculation zone is located at a height very near the base of the very bright flame zone shown in Fig. 2b. As the fuel equivalence ratio is further reduced, the flame becomes very unstable, and eventually blows out. The lean blowout limit was found [1] to closely correspond to a fuel equivalence ratio ($\phi = 0.5$) very close to the lean flammability limit ($\phi = 0.51$) of the propane fuel and air [2]. Other studies suggest the combustor may behave like a well stirred reactor [3, 4] when the flame is in the lifted condition [1,5,6]. The instability that results just before blowout appears visually to correspond to a longitudinal oscillation of the lifted flame in the interfacial shear layers of the jets. The flame lifting process is required before lean blow out can occur. It is believed that an understanding of how the flame attaches and detaches from the combustor at rich and lean equivalence ratios will provide insight into the blowout process.

OH Emissions. The time-average view of the flame, as obtained from visual observations and photographs of the flame, clearly illustrates the qualitative effect of fuel equivalence ratio on the attached and lifted flame regimes of the burner. However, visual observation and conventional photographic techniques were unable to quantify the precise fuel equivalence ratio where the flame transitioned from an attached flame to a lifted flame. This was made difficult by the stochastic nature of the flame, and the integrating nature of observations by the human eye. At a given fuel equivalence ratio, the flame would appear to alternately attach then lift similar to what happens near lean blowout but not as vigorously. The visual appearance was such that the flame appeared to be attached most of the time, when the burner was operated very fuel rich; and lifted most of the time, when the burner was operated near or below a stoichiometric fuel equivalence ratio. Consequently, a measurement technique was sought that would give a more quantitative

measurement of the fuel equivalence ratio where the flame transitioned from an attached flame to a fully lifted flame.

It was reasoned that the signal obtained from the uv emission detection device described in the Experimental Section would be sensitive to the spontaneous OH uv emission, and would show a strong signal when the flame was attached, and a rather weak signal when the flame was lifted. The device could also give some insight into the periodicity of the flame attachment phenomena. Visual observations suggested that the flame would be attached for some period of time, and be lifted for some period of time. The fraction of time for attachment and fraction of time for lifted flames appear to be a function of fuel equivalence ratio. It was also thought that the intensity of the flame (i.e., the concentration of OH in the flame) would be somewhat proportional to the fuel equivalence ratio - a higher fuel equivalence ratio should lead to higher OH concentration, and consequently, a higher signal as measured by the device.

Measurements of OH emission from the flame in the region of the attachment point are presented in Fig. 3. Both the mean signal intensity and the standard deviation of the signal intensity show the same trends. Reproduced data points show that the data were very repeatable. In the fuel rich region, a general decrease in signal intensity with decreasing fuel equivalence ratio (decreased fuel flow at an air flow fixed at 1000 lpm) was readily apparent down to a fuel equivalence ratio of about 1.05. It was at about this fuel equivalence ratio that visual observations had suggested that the flame was fully lifted. Further reductions in fuel equivalence ratio cause little further change in the signal until the fuel equivalence ratio falls below about 0.8. After this point, the signal intensity continued to drop as the flame became more unstable, and as the fuel equivalence ratio approached the lean blow out limit of about 0.5.

These measurements identify the two operational regions of the flame, and have quantified a point of demarcation between the regimes of attached and lifted flames at a fuel equivalence ratio of about 1.05. Measurements at higher air flow rates showed different levels of signal intensity, but the curve had the same characteristic shape shown in Fig. 3, and the point of demarcation was always at a fuel equivalence ratio of about 1.05 even at the highest air flow rate tested, which was 3000 lpm. Consequently, further measurements were performed for two lifted conditions (the point of demarcation, $\phi = 1.05$ and a fuel lean case $\phi = 0.78$), and at two fuel rich cases where the flame was expected to be well attached ($\phi = 1.31$, and $\phi = 1.56$ respectively).

RMS Results. Figure 4a shows an example of results obtained by seeding the air stream with TiCl_4 vapor and adding moisture to the fuel tube. The flow conditions were 30 lpm of propane and 1000 lpm of air,

which gave a lifted flame. The flame is stabilized near the end of the recirculation zone and is not visible in Fig. 4a. The flow structure associated with the flow through the fuel tube, the eddies in the shear layer between the fuel jet and the annular air jet, and the turbulent structure downstream are clearly evident. It appears that the turbulent eddies that exist between the fuel and air jets are of about the same scale as the gap between the edge of the fuel tube and the outer diameter of the annular air jet.

A recirculation zone, where there is a high concentration of TiO_2 particles, is also observed near the fuel tube exit in Fig. 4a. The recirculation zone is similar to that formed behind bluff bodies and originates in much the same way. The high velocity annular air jet expands and entrains surrounding fluid as it enters the combustion chamber. The entrainment requirements of the air jet cannot be satisfied by the relatively small mass of fuel exiting the fuel jet and the air fuel mixture turns back on itself and is entrained back into the air jet much like the flow behind a bluff body. The recirculation zone appears to be somewhat egg-shaped and is very unstable. At relatively low fuel flow rates, it would momentarily attach at one location on the edge of the fuel tube and then move to another location. It seemed to dance back and forth around the fuel tube, always being attached to one edge or another; however, there appeared to be one location where it preferentially attached. This egg-shaped recirculation can be seen in Fig. 4a, and appears to be attached to the right side of the fuel tube. This appears to be a low Reynolds number effect since an increase in fuel flow caused the recirculation zone to lift out of the fuel tube, reduce in size, and became more or less stable in a location on the centerline of the burner above the jet exit.

CFD Model Results. The steady state CFD streamline calculation in Fig. 4b also shows the recirculation zone at the base of the fuel jet. The calculation is for a nonreacting flow of air in both the annular and central jets but for the same volumetric flow conditions as the reacting flow shown in Fig. 4a. The nonreacting flow calculation seems appropriate, since in the combusting flow case, the lifted flame sits near the end of the outer recirculation zone and no reaction is taking place in the near field shown in Fig. 4b. The spatial scales for Figs. 4a and 4b are about the same so only the flow observed in the width of the combustion chamber window is shown. The calculated recirculation zone has about the same size and shape as that determined experimentally and shown in Fig. 4a. Also, the streamlines converge towards the centerline just above the recirculation zone much like the experimentally observed shear layer. However, the calculated streamlines do not diverge further downstream as is observed experimentally.

The outer or step recirculation zone plays a major role in characterizing the performance of the research combustor. The recirculation zone is critical to the

understanding of the attached flame because it is responsible for the transport of unburned fuel and hot products that maintain this flame. In the case of a lifted flame as shown in Fig. 4a, it is particularly important to understand how much fuel and air are transported into the recirculation zone. This may determine whether a flammable fuel to air mixture might exist in the recirculation zone. If so, the flame, stabilized at the end of the recirculation zone, could ignite and flash back towards the face of the combustor. Such a process can be envisioned as being responsible for the low frequency oscillation of the lifted flame that will be reported later. It seems appropriate to use the model in a nonreacting flow simulation to examine the characteristics of the recirculation zone for the lifted flame.

The calculated steady-state or time-averaged streamlines and fuel mixture fraction contours for a nonreacting flow in the combustor are shown in Fig. 5a. The calculation is for the same nonreacting flow condition as shown in Fig. 4b. The zero axial velocity surface and the vortex center are important to the understanding of the fuel and air transport around the recirculation zone and are also shown in Fig. 5a. As noted by the radial component of the fuel mass flux vector on the zero axial velocity surface, the fuel is being transported out of the recirculation zone at axial locations up-stream of the vortex center and is transported into the recirculation zone at axial locations downstream of the vortex center. The magnitude of the radial component of the fuel flux vectors suggests that the largest transport of fuel into the outer recirculation zone occurs near the attachment point and the largest transport out of the recirculation zone occurs near the face of the combustor. The fraction of fuel at different axial locations can be obtained by integrating the mass flux between the outer wall and the zero axial velocity surface. A plot of the integrated mass fraction, shown in Fig. 5b, peaks at an axial location very near that of the vortex center. Although not shown, the integrated air mass fraction in the recirculation also peaks at an axial location corresponding to the vortex center. The integrated fuel to air ratio in the recirculation zone as a function of axial location is also shown in Fig. 5b. The fuel to air ratio is larger near the end of the recirculation zone and decreases as the flow is transported back towards the combustor base. The fuel to air ratio is essentially constant once the reverse flow passes the vortex center. This constant fuel to air ratio in the near field of the recirculation zone is about the same as the inlet fuel to air ratio. The stoichiometric fuel to air ratio by mass is 0.0638 and the largest fuel to air ratio in the recirculation zone is 0.023 which is below the flammability limit of 0.0319. Thus, a flammable mixture does not exist for this condition in the recirculation zone, according to the calculation.

Additional nonreacting flow calculations show that the trends noted in Fig. 5 also apply for other fuel and

air flow rate conditions. The fuel to air ratio in the recirculation zone is of prime importance because it determines whether a flammable mixture exists that might flash back into the recirculation zone if ignited. Plots for the fuel to air ratio at the end of the recirculation zone and at the face of the combustor are shown in Fig. 6. Inlet air flow rates of 1000 and 3000 lpm were used in these calculations. The fuel to air normalization appears to be good choice and there was no impact of air flow rate on the plotted results. The model predicts that there will be a linear relationship between the fuel to air ratio in the recirculation zone and inlet fuel to air ratio. Indeed, the calculations suggest that the recirculation zone behaves something like a well stirred reactor with the fuel to air ratio in the near region of the recirculation zone being approximately the same as the inlet fuel to air ratio even though the sources of fuel and air into the combustor are different.

The isotherms and streamlines calculations for an attached flame are shown in Fig. 7. Comparisons of Figs. 5a and 7 illustrate that the recirculation zone for the combustor flow is much smaller than for the nonreacting case. The attachment point of the zero axial velocity surface at the face of the combustor is located much closer to the wall than that for the nonreacting case. This is not understood but may be associated with the large volumetric expansion of the heated gases. The shape of the experimental flame surface, as taken from photographs like that shown in Fig. 2, and the computed flame surface are also shown in Fig. 7. The calculated and measured flame surfaces nearly coincide for axial locations above 50 mm. However, the calculated and measured locations of the attachment point at the combustor face are different. Experimentally, the flame attaches at the outer edge of the step; whereas, in the calculation, the flame attaches near the edge of the fuel jet. The calculations are obviously reflecting the incomplete physics and chemistry that have been put into the model. Indeed, the calculation does not require any high temperature sources or flammable fuel and air mixture ratios in order to burn. Also, there is no provision for incomplete combustion in a computational cell except when fuel remains unburned because the local equivalence ratio is larger than one. However, attempts have been made to put these features, as well as wall quenching effects, into a CFD model. The result is that the flame always appears to attach near the edge of the fuel tube. Even when the rate of chemical reaction is slowed down, it was not possible to get the flame to attach in a way similar to that observed experimentally. Indeed, it is difficult to understand the physics and chemistry that lead to an attached flame on the step side of the air jet. This difficulty will be considered in the Discussion Section. However, for present purposes it is suggested that the source of the difficulty may be associated with an intermittent property of the flame. This line of thinking led to using diagnostic techniques that provide the

temporally and spatially resolved measurements reported below.

LIF Results. A series of images were obtained at four axial locations (0, 75, 150, and 225 mm) and at four propane flow rates (30, 41, 52, and 63 lpm). These fuel flow rates corresponded to equivalence ratios of $\phi = 0.78$, 1.05, 1.31, and 1.56, respectively. Two of the flow rates corresponded to a lifted flame ($\phi = 0.78$ and 1.05), and the other two corresponded to an attached flame ($\phi = 1.31$, and 1.56). These images have been used to examine the location and shape of the flame zones in the burner. An example of an image for the attached flame when $\phi = 1.56$ is shown in Fig. 8. The image shows regions of high OH concentration, and consequently illustrates the actual flame structure that existed during the 10 ns exposure. Note that the OH appears to be concentrated in vortex structures that are apparently shed from the rearward facing step. There is evidence that the vortices merge and the burning becomes more intense as they move downstream. This is suggested by the vortex train on the left side of the step. The flame surface, as marked by the OH fluorescence, is not continuous but has holes that appear to be located in the braid region of the vortex train. The flame is not symmetric in an instantaneous view. Rayleigh scattering from the fuel is also apparent and some scattered light from the edge of the windows can also be observed. Nevertheless, the instantaneous image of the flame at axial locations between 0 and 70 mm clearly indicates the complex structure of the flame and the importance of thinking about the combustion processes in a dynamic way instead of on a time-averaged basis.

A sequence of images at different equivalence ratios and at different axial locations is presented in Fig. 9. The four images at the extreme left of Fig. 9 correspond to a fuel flow rate of 30 lpm. They show no OH image in the two regions from 0 to 152 mm. Significant OH emission (flame) is apparent in the region from 150 mm to 227 mm and evidence of a rather thick flame zone exists in the shear layers shown in the region from 225 mm to 302 mm. It is clear from this set of images that the flame is lifted, and is being stabilized by the outer recirculation zone. Examination of the images at the four different axial positions that correspond to a fuel flow rate of 41 lpm show a similar trend, i.e., no OH flame structure in the region from 0 to 152 mm, but significant flame stabilized by the outer recirculation zone in the regions above 150 mm. There is a faint image in the primary fuel jet that shows some evidence of the jet mixing structure between the fuel and air jets. Flame has never been seen visually in this region. Consequently, this image has been caused by a mechanism other than LIF. This image is thought to have been caused by Rayleigh scattering of the dye laser beam by the propane in the fuel tube.

The two sets of images on the right-hand side of Fig. 9 correspond to conditions for an attached flame ($\phi = 1.31$ and 1.56). Not only has the intensity of the OH emission in the two downstream zones increased, but there is OH emission evident for both ϕ 's in the regions between 0 and 152 mm. In the bottom region (0 to 77 mm), the OH emission shown in the moderately attached case ($\phi = 1.31$) is not continuous, but shows some evidence of being fragmented and only partially attached. This is consistent with visual observations where the flame seemed to be attached part of the time, and lifted part of the time. The OH emission shown in the $\phi = 1.56$ case between 0 and 77 mm clearly shows the sheet like nature of the flame zone, and also shows that the flame is wrapped up into one of the vortices associated with the eddy mixing between the fuel and air jets.

The thin flame structure near the entrance to the combustor in the well attached flame, $\phi = 1.56$, is clearly evident in Fig. 9 (also see Fig. 8). However, the flame zone appears to thicken in the downstream locations. The discontinuous and unsymmetrical nature of the flame is also apparent in all of the images. The packets of flame appear to be increasing in size as the flame progresses downstream. One might speculate that these flame packets represent vortices that have merged.

These observations suggest that the flame will be attached or lifted depending on the fuel equivalence ratio and attachment between the lifted point of demarcation and the well attached flame is periodic with the degree of attachment increasing as the fuel equivalence ratio is increased above $\phi = 1.05$. These results also suggest that the major heat release in the reactor occurs in the region above about 150 mm whether the flame is attached or lifted.

Thin-Filament Pyrometer Results. A time sequence of nearly instantaneous radial profiles of relative temperature 1 cm above the face of the combustor is shown in Fig. 10 at an equivalence ratio of 1.56 and an air flow of 1000 lpm. Each profile was obtained in 266 μ s and are separated by 8 ms. Approximately one period of the time evolving profile is shown. The graybody radiation intensity profiles along a SiC₄ filament were obtained using a rotating mirror arrangement, as described in the Experimental Section. The intensities are proportional to the instantaneous temperatures along the filament with a resolution in the radial direction of better than 75 μ m. Visual observations of the glow of the filament indicated that a temperature region of 1300 K or more extended from near the edge of the step to about 20 mm from the wall of the combustor. However, the combustion chamber window limited the radial observation of the filament, when the rotating mirror was used. The zero radial position in Fig. 10 is the approximate location of the edge of the step that is 20

mm from the combustor centerline. The sharp drop in intensity at 15.5 mm denotes the edge of the window.

Figure 10 shows that the flow behind the step is hot (e.g., higher than the cut-off-temperature of 1300 K) all the time, and that the temperature peaks at different radial location in time. The temperature peak is about 5 mm wide and is believed to be associated with the visible flame shown in Fig. 2a and the LIF image in Figs 8 and 9. Indeed, the radial motion of the temperature peak may be the result of vortices, like those shown in Figs. 8 and 9, convecting pass the measurement station. If this is the case, the radial displacement of the temperature peak can be taken as the width of the vortices at about 10 mm above the combustor face. This scale is about 4 mm and is comparable to the size of the vortices shown in Figs 8 and 9. The average radial location of the mean temperature peak is approximately 4 mm from the edge of the step.

The intermittent nature of the flame was investigated by observing the graybody radiation at one location on the filament. Time traces and frequency data are shown for both attached and lifted flames in Fig. 11a and 11b, respectively. In both flames, there appears to be an intermittent process that brings hot products down near the face of the combustor at a low frequency rate of less than 10 Hz, which is similar to the period for the time traces shown in Fig. 10. There was a continuum of frequencies above 25 Hz that continued for several hundred Hz but, no distinguishing high frequency peaks were observed in the TFP spectra.

DISCUSSIONS

Results of this study show that the operation of the combustor is very complex. The combustor operates in two distinct modes. In one mode, the flame is attached to the face of the combustor near the edge of the step, Figs. 2a. and 7. In the second mode, the flame is stabilized downstream near the end of the recirculation zone established by the step, Fig. 2b. The sheet lit LIF visualizations of OH in Figs. 8 and 9 and the TFP measurements in Figs 10 and 11 show that even when the flame is fully "attached", there is a degree of lifting, i.e., the flame fluctuates between an attached mode and the lifted mode with some degree of periodicity. The spontaneous OH emissions measurement in Fig. 3 suggests that when the inlet flow equivalence ratio is greater than 1.05, the flame is attached most of the time, whereas it is lifted most of the time when the equivalence ratio is less than this. As the equivalence ratio nears 0.5, the flame becomes very unsteady to the eye and goes out. This lean blow out limit is about the same as the lower flammability limit of propane and air mixtures.

The modeling results shown in Figs. 5-7, provide some insights into the time averaged flow field, but considerable difficulties have been encountered in

correctly predicting the attached flame condition. The problem is that the model does not predict sufficient entrainment of fuel into the step recirculation zone to stabilize a flame on the face of the combustor, near the edge of the step. Attached flames are observed at fuel rich conditions and the model predicts that almost all of the excess fuel exits the combustor unburned. The challenge is to understand the physics and chemistry responsible for the entrainment, mixing, transport, and combustion of fuel and hot products into the step recirculation zone so that a physically sound model can be developed. Unfortunately, the presented results are not sufficient to establish a confident explanation of the observed characteristics of this research combustor. However, there is sufficient information to allow some speculation about the possible causes of the observed effects.

Figure 12 illustrates the authors' postulate of the key characteristics of the reacting flow field of the research combustor. Several zones of distinct thermal/fluid action are identified. In the reported experiments, the air flow rate (1000 lpm) is much higher than the fuel flow rates (23, 30, 45, and 63 lpm). As a result, a fuel jet recirculation zone is formed at the fuel jet exit. This is also indicated in the CFD model results. The Rayleigh images in Figs. 8 and 9 show that only a small percentage of air is entrained into the fuel recirculation zone so it is probably above the rich flammability limit and unable to support combustion. Also, the computed isotherms in Fig. 7 show that the temperature in the fuel recirculation zone is about 400 K, which is not sufficient to ignite and sustain a flame even if a flammable mixture were present.

In the case of an attached flame, intense combustion and mixing is taking place in the region where the shear layers of the step and fuel jet intersect. This interaction occurs about two air jet diameters downstream and involves the merging of vortices shed from the step (air jet) and the fuel jet. The vortex merging is believed to be responsible for the thickening of the flame observed in Fig. 2a. This is illustrated between stations 2 and 3 in Fig. 12. The intersection of the shear layers and the merging of flame vortices from the step are clearly shown in Fig. 8 at a distance of 35 to 40 mm downstream. This is illustrated by location 2 in Fig. 12. It was observed that this also occurs at an axial location where the time averaged attached flame shown in Fig. 2a, extends radially toward the centerline before being pulled toward the wall by the outer, or step, recirculation zone. The time averaged result of the merging of the vortices may give the appearance that the flame moves toward the centerline. Since this maximum inward motion of the flame occurs near the end of the fuel recirculation zone established behind the fuel jet the two events may be related.

The flame established in the merged shear layer between locations 2 and 3 in Fig. 12 is being fed directly

by fuel coming from the fuel jet, as noted in Fig. 7. However, this region of intense combustion is actually piloted by the weaker flame that is attached to the face of the combustor near the edge of the step as illustrated by location 1 in Fig. 12. The fuel and the high temperature combustion products that sustain the attached flame appear to come from the step recirculation zone. A major concern is how the unburned fuel crosses the intense flame zone in the shear layer of the step and enters the step recirculation zone without being consumed.

Entrainment of a rich fuel and product mixture into the step recirculation zone for the attached flame is believed to involve an intermittent process. The entrainment into the step recirculation zone occurs in the merged shear layer between locations 2 and 3. This is a region of intense combustion. However, the combustion process is discontinuous in that it involves regions of intense burning and regions where there appears to be holes in the flame as shown by the OH images in Figs 8 and 9. The holes appear to be formed in the braid regions of the vortex train. Stretching and fast mixing normally occur in the braid regions which might lead to quenching of the flame (i.e. formation of holes) by finite rate chemistry. It is proposed that entrainment into the step recirculation zone is by an intermittent process involving discrete packets of fuel and products. Rich fuel packets may be transported through the holes into the recirculation zone essentially unburned. The probability of hole formation increases the probability that unburned fuel is transported into the recirculation zone. This probability is extremely high in the shear region between stations 2 and 3. TFP data shown in Figs. 10 and 11 indicate that the gases in the recirculation zone are sufficiently hot to ignite the fuel if oxygen is present. Thus, it is believed that most of the oxygen is consumed in the shear layer and only a small quantity enters into the recirculation zone. The predominance of fuel over oxygen in the recirculation zone is favored for fuel rich inlet conditions. This is believed to be the reason why the attached flame only occurs at equivalence ratios greater than one. The unburned fuel is mixed with the hot products and transported by the recirculation zone to location 1 in Fig. 12. The hot fuel mixes with the air in the step shear layer and burns as a relatively thin flame between the face and location 2 shown in Fig. 12. This flame may be fuel starved at discrete times due to the intermittent way it was initially entrained into the step recirculation zone. Thus, the flame might attach and lift periodically, which is consistent with observation.

As the inlet fuel equivalence ratio is reduced, a condition will develop in which the amount of fuel entrained into the step recirculation zone cannot sustain the flame stabilized at location 1 in Fig. 12. Since this pilots the flame at location 2, the flame will lift and reestablish near location 3. This is most likely to occur at fuel lean conditions, since very little fuel will be

entrained into the recirculation zone. Once lifting has occurred, the intense mixing of fuel, air, and hot combustion products from the step recirculation zone sustains the flame which becomes more like a premixed flame than a diffusion flame. The model calculation in Fig. 5 indicates that the fuel and air mixture in the recirculation zone under noncombusting conditions will be about the same as that entering the combustor. It seems possible that intermittent entrainment of hot products could ignite the fuel and air mixture in the step recirculation zone. This would result in a premixed flame propagating to the face of the combustor. This would account for the measured low frequency oscillations (3 to 10 Hz) noted in the TFP data in Fig. 11.

At increasing lean inlet conditions, the probability of having insufficient fuel inside the step recirculation zone increases. In this case, the flame will be lifted most of the time. Decreasing the fuel flow rate further results in a fuel-air mixture in the recirculation zone that is too lean to support combustion. Although intense mixing of the fuel, air, and combustion products is taking place in the primary fuel-air mixing zone, combustion does not take place because there is not sufficient heat and unburned combustion products coming from the recirculation zone to sustain a flame. Lean blow out results.

CONCLUDING REMARKS

The operational characteristics of a step stabilized research combustor designed to study lean blow out processes have been established at low Reynolds number conditions. A variety of measurement techniques and CFD modeling are used to examine both the time averaged and dynamic nature of the flame for a wide range of equivalence ratios. The flame appears to be attached near the combustor face at the edge of the step most of the time for equivalence ratios greater than 1.05. It is stabilized at the end of the recirculation zone for lower equivalence ratios. The presented measurements are not sufficient to establish the fundamental processes responsible for this behavior. However, they do show that the flame established near the mixing layers is not continuous in space and time. This suggests that unburned fuel is transported into the recirculation zone in discrete packets in an intermittent process that involves holes in the flame. Packets of hot fuel and products in the recirculation zone are mixed and transported to the face of the combustor where they are mixed with the air in the shear layer of the step. The fuel and air is sufficiently hot that an attached flame results. This process is most likely to occur at fuel rich conditions. At lean conditions, insufficient fuel is entrained into the recirculation zone to sustain the flame; lifting then occurs.

The potential importance of the intermittent nature of the burning process in this combustor offers significant challenges to conventional combustion

models. The biggest difficulty is to correctly model the processes responsible for entraining and transporting fuel, products, and heat into and out of the recirculation zone. The models must account for mixing of fuel, air, and hot products by relatively large vortices in the shear layers of the fuel jet and air jets. Also, they must account for burning in the vortex structures, holes in the flame, and intermittent transport and mixing of fuel and hot products into the recirculation zone. These requirements are believed to be beyond the capabilities of the current models.

ACKNOWLEDGEMENTS

This research was supported by the Air Force Office of Scientific Research (AFOSR) through a Summer Faculty Research Program (SFRP) and direct funding to the Aero Propulsion and Power Laboratory. Special appreciation is given to Mr. Royce Bradley, Dr. Tom Jackson, Dr. Tim Edwards, and Dr. David Sloan for their helpful comments and suggestions during this study and to Ms Gayle Byrd and Ms Carol Lucas for editorial corrections and aid in printing.

REFERENCES

1. Sturgess, G.J., D.G. Sloan, A.L. Lesmerises, S.P. Henneghan and D.R. Ballal. "Design and Development of a Research Combustor for Lean Blowout Studies", 35th International Gas Turbine and Aeroengine Congress and Exposition. Brussels, Belgium (June 1990).
2. Lewis, B., and G. von Elbe, Combustion, Flames and Explosions of Gases, 3rd Edition, Academic Press, Inc. (1987).
3. Longwell, J.P., E.E. Frost, and M.A. Weiss, "Flame Stability in Bluff Body Recirculation Zones", Industrial and Engineering Chemistry, 45 (8), pp 1629-1633 (August 1953).
4. Longwell, J.P., and M.A. Weiss, "High Temperature Reaction Rates in Hydrocarbon Combustion", Industrial and Engineering Chemistry, 47 (8), pp 1634-1643 (August 1955).
5. Sturgess, G. J., et al., "Lean Blowouts in a Research Combustor at Simulated Low Pressures." To Be Presented at the 36th ASME International Gas Turbine and Aeroengine Congress and Exposition, Orlando, FL, June 1991.
6. Henneghan, S.P., et al. "Acoustic Characteristics of a Research Step Combustor." AIAA Paper 90-1851, AIAA/SAE/ASME/ASEE 26th Joint Propulsion Conference, Orlando, FL, July 1990.
7. L. P. Goss, V. Vilimpoc, B. Sarka, and W. F. Lynn, "Thin-Filament Pyrometry: A Novel Thermometric Technique for Combusting Flows," J. Engrg. Gas Turbines & Power, Transactions ASME, vol. 111, pp. 46-52, January 1989.
8. Spalding, D. B., A Novel Finite Difference Formulation for Difference Expressions involving both First and Second Derivatives, International Journal for Numerical Methods in Engineering, Vol. 4, 1972, pp. 551-559.
9. Launder, B. E. and Spalding D. B., The Numerical Computation of Turbulent Flows, Computer Methods in Applied Mechanics and Engineering, Vol. 3, 1974, pp. 269-289.

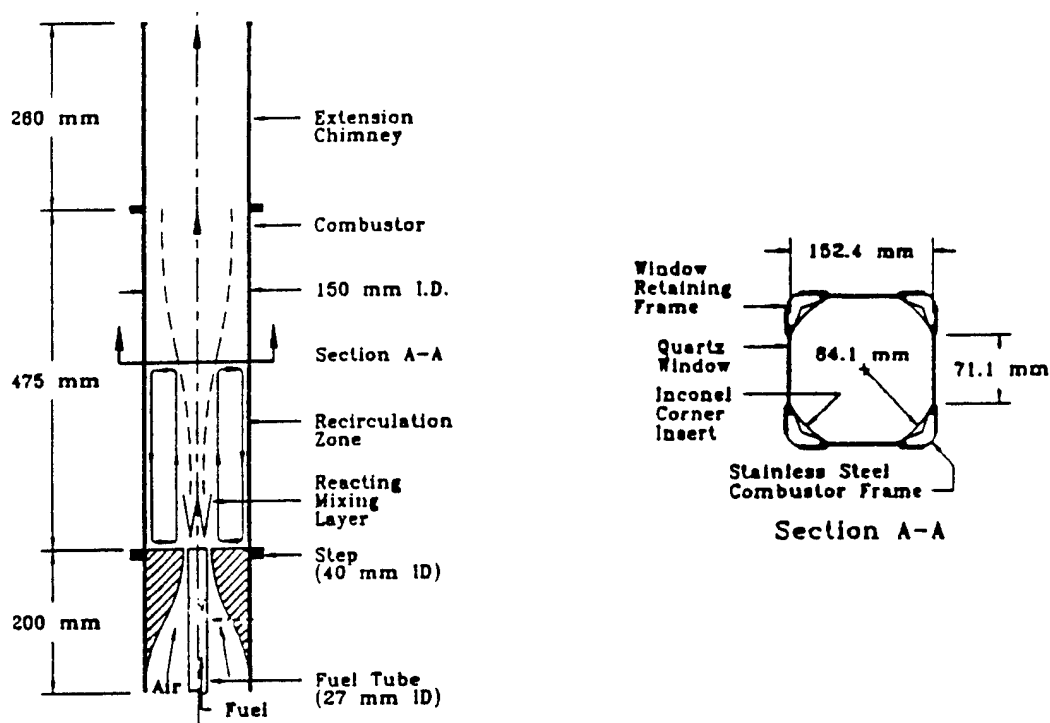


Figure 1. Schematic of the Confined Coaxial Jet Combustor with a Sudden Expansion [1].

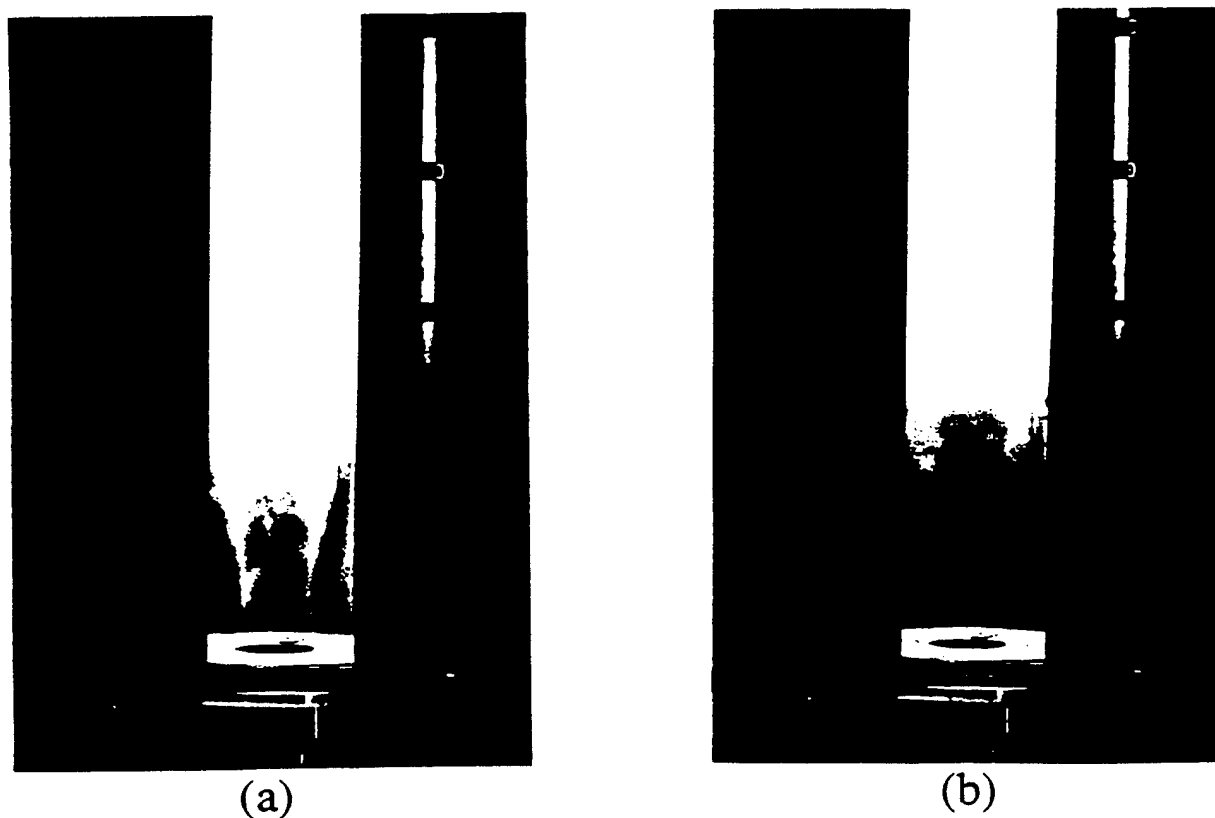


Figure 2. Photographs of Combustor with (a) Attached Flame 63 lpm Propane, $\phi = 1.56$, and (b) Lifted Flame 30 lpm Propane, $\phi = 0.78$, Air = 1000 lpm.

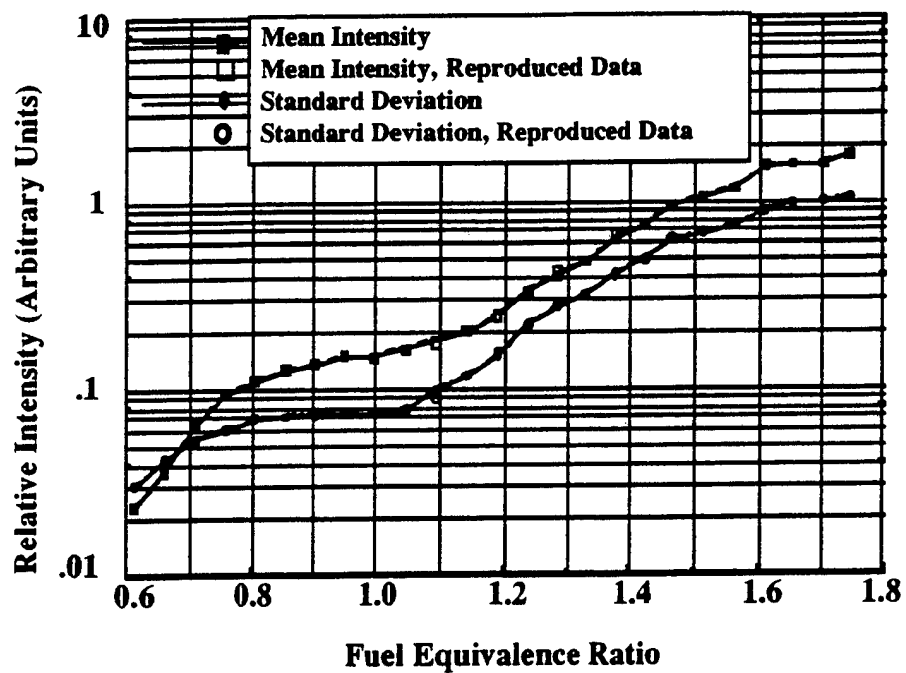
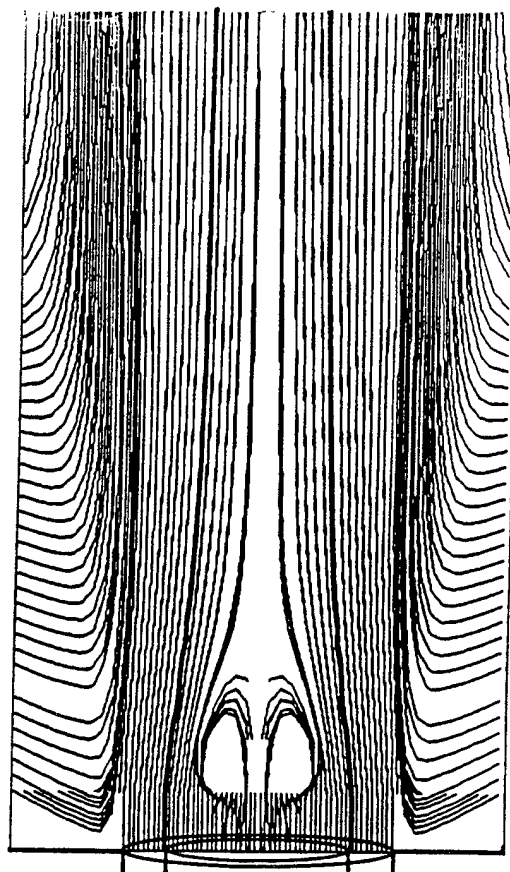


Figure 3. Relative Intensities of OH Emission for Different Equivalence Ratios with Air Flow Rate of 1000 lpm.



(a)



(b)

Figure 4. a) Laser Sheet Lighted Image of TiCl_4 Seeded Flame 1000 lpm Air, 30 lpm Propane, TiCl_4 Seed in Air, H_2O in Fuel, $\phi = 0.78$. b) CFD Model Streamline Calculations for Nonreacting Flow Conditions 1000 lpm Air and 30 lpm Air in the Fuel Jet.

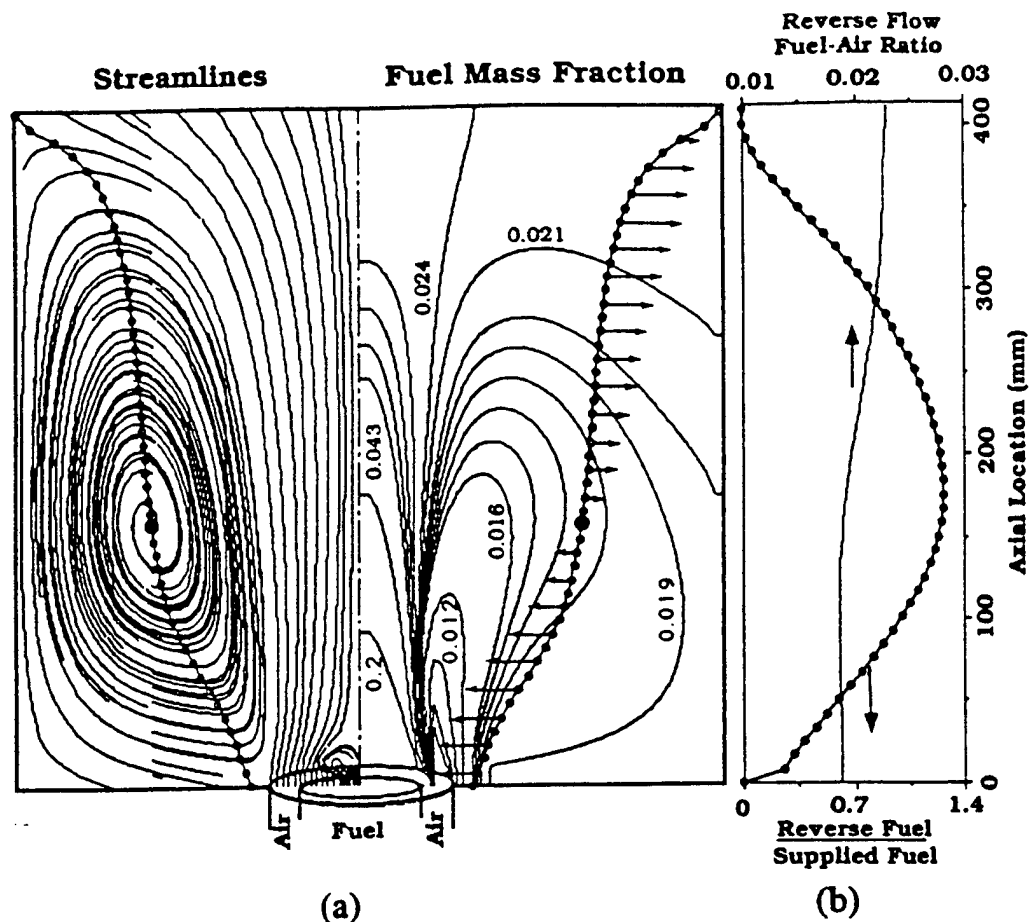


Figure 5. a) CFD Calculations of Streamlines, Fuel Mass Fraction and Zero Axial Velocity Surface and b) Integrated Fuel Mass Fraction and Fuel to Air Ratio in the Recirculation Zone for Air in Both Fuel and Annular Jets with $\phi = 0.78$.

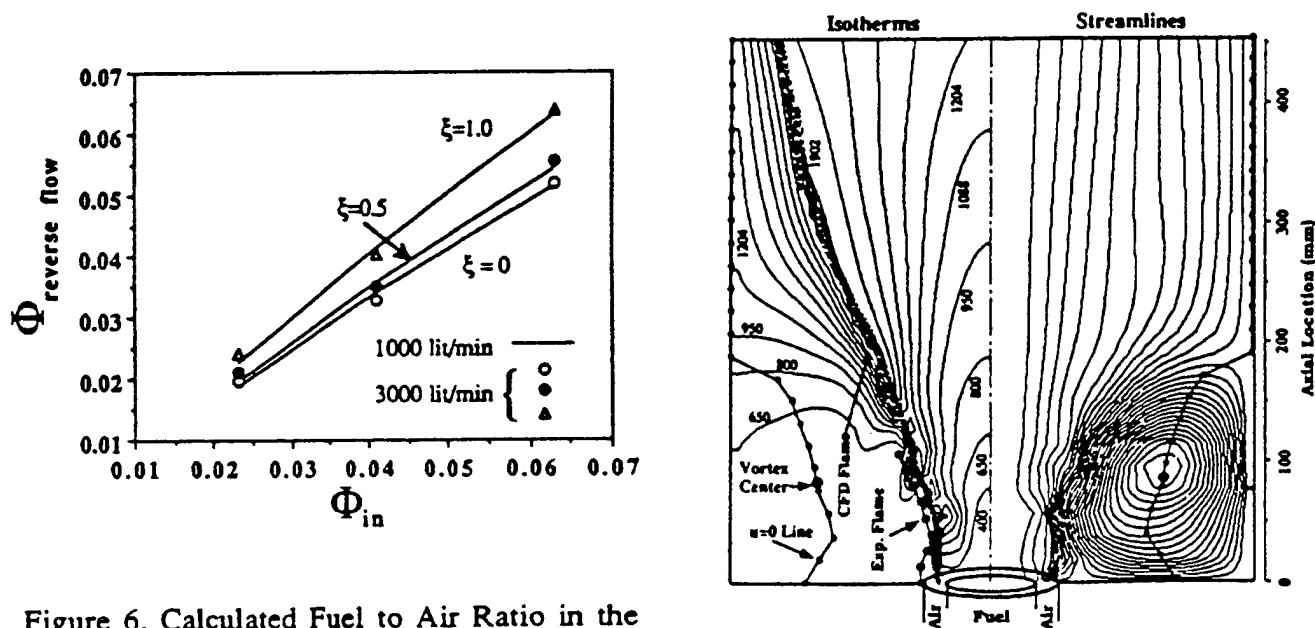


Figure 6. Calculated Fuel to Air Ratio in the Recirculation Zone for Nonreacting Flow with $\phi = 0.78$ and at Axial Locations Measured by the Fraction of the Recirculation Zone Length ξ .

Figure 7. Calculated Isotherms, Streamlines and Flame Surface for Propane Flame with $\phi = 1.56$.

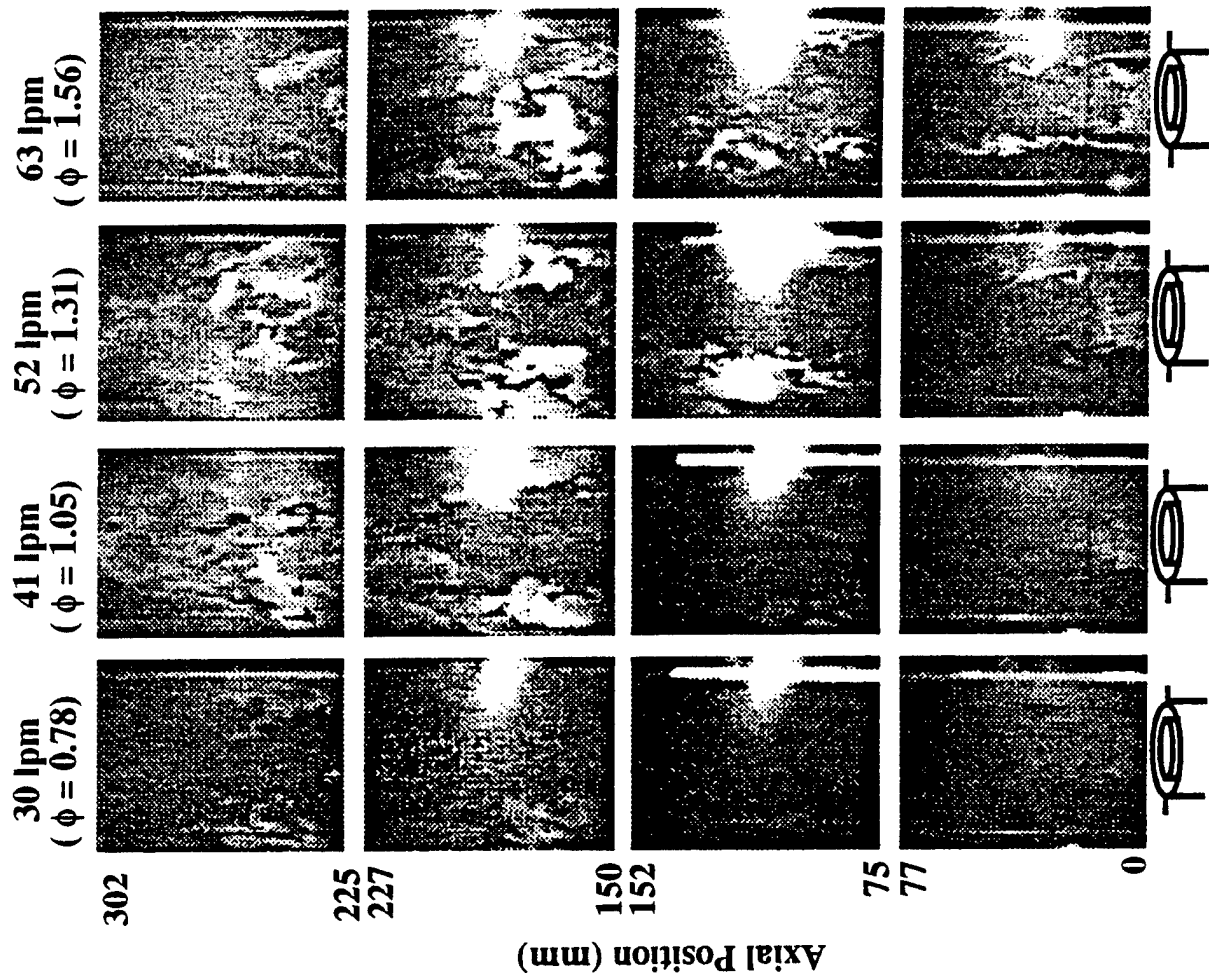


Figure 9. Images of Laser Induced OH Fluorescence at Various Axial Positions, and at Various Fuel Equivalence Ratios (1000 lpm Air)

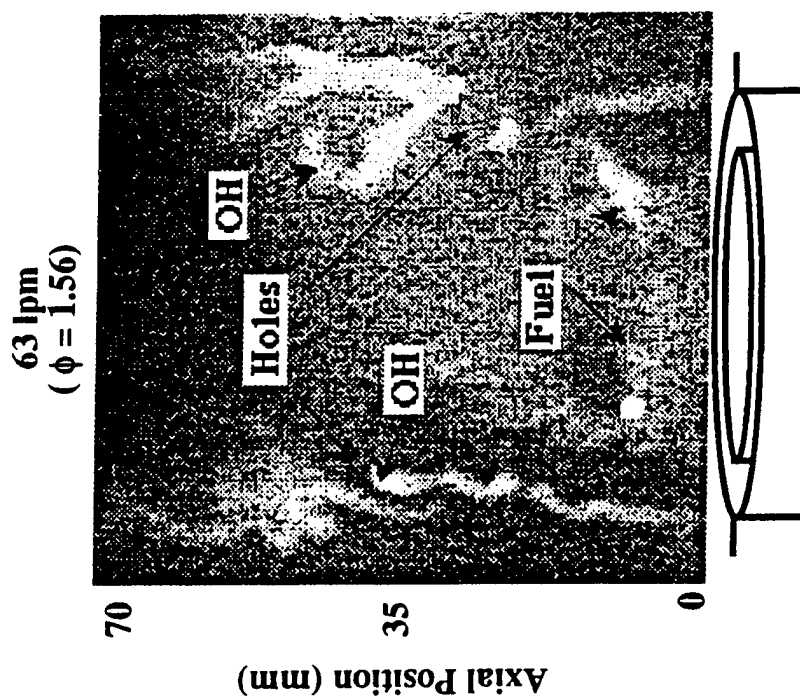


Figure 8. Image of Laser Induced OH Fluorescence for the Attached Flame with 63 lpm Propane, 1000 lpm Air, $\phi = 1.56$.

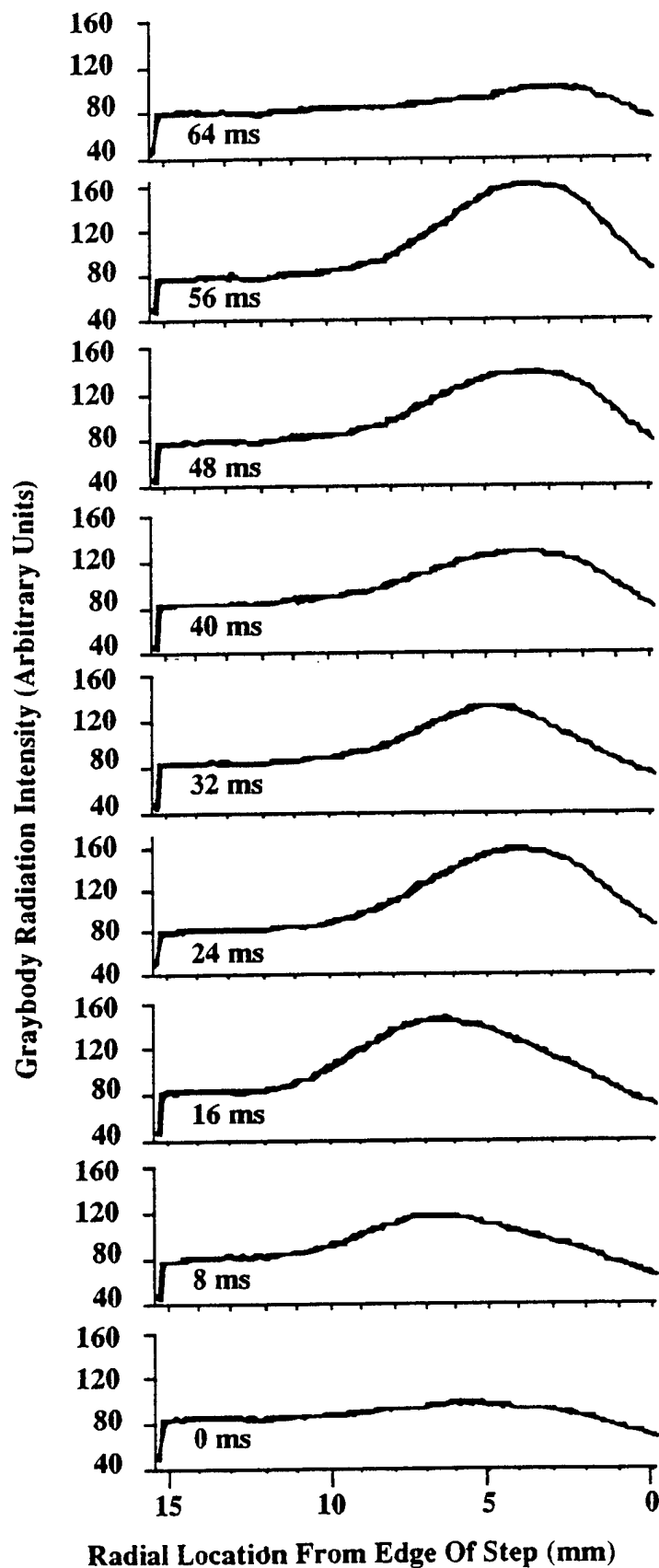


Figure 10. TFP Radial Traces at Indicated Times for Filament 10 mm Above Face of Combustor with $\phi = 1.56$.

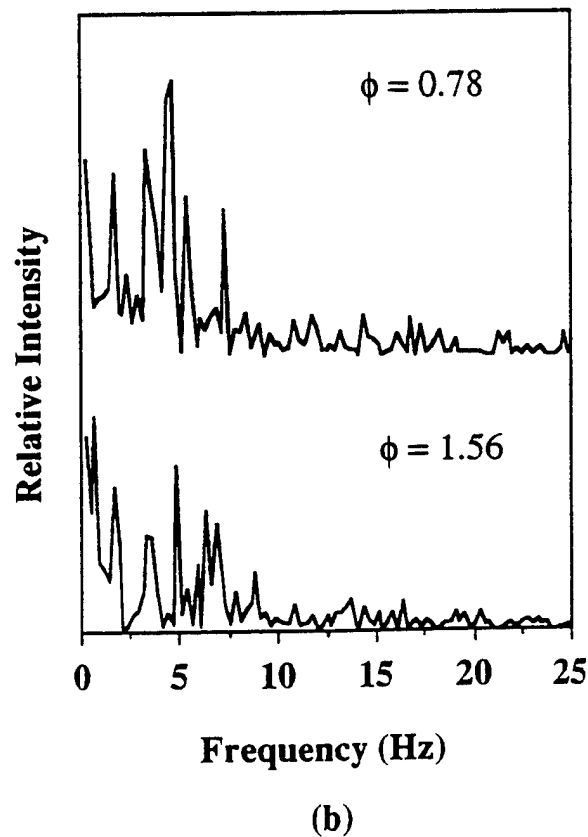
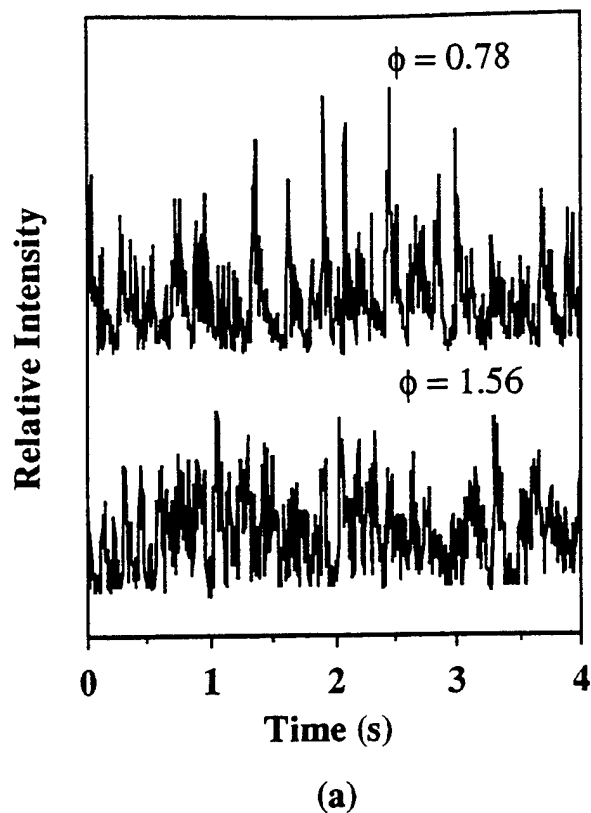


Figure 11. Time Trace and Spectrum of Filament, 10 mm Above Combustor Face, $r \sim 4$ mm from Step, $\phi = 1.56$.

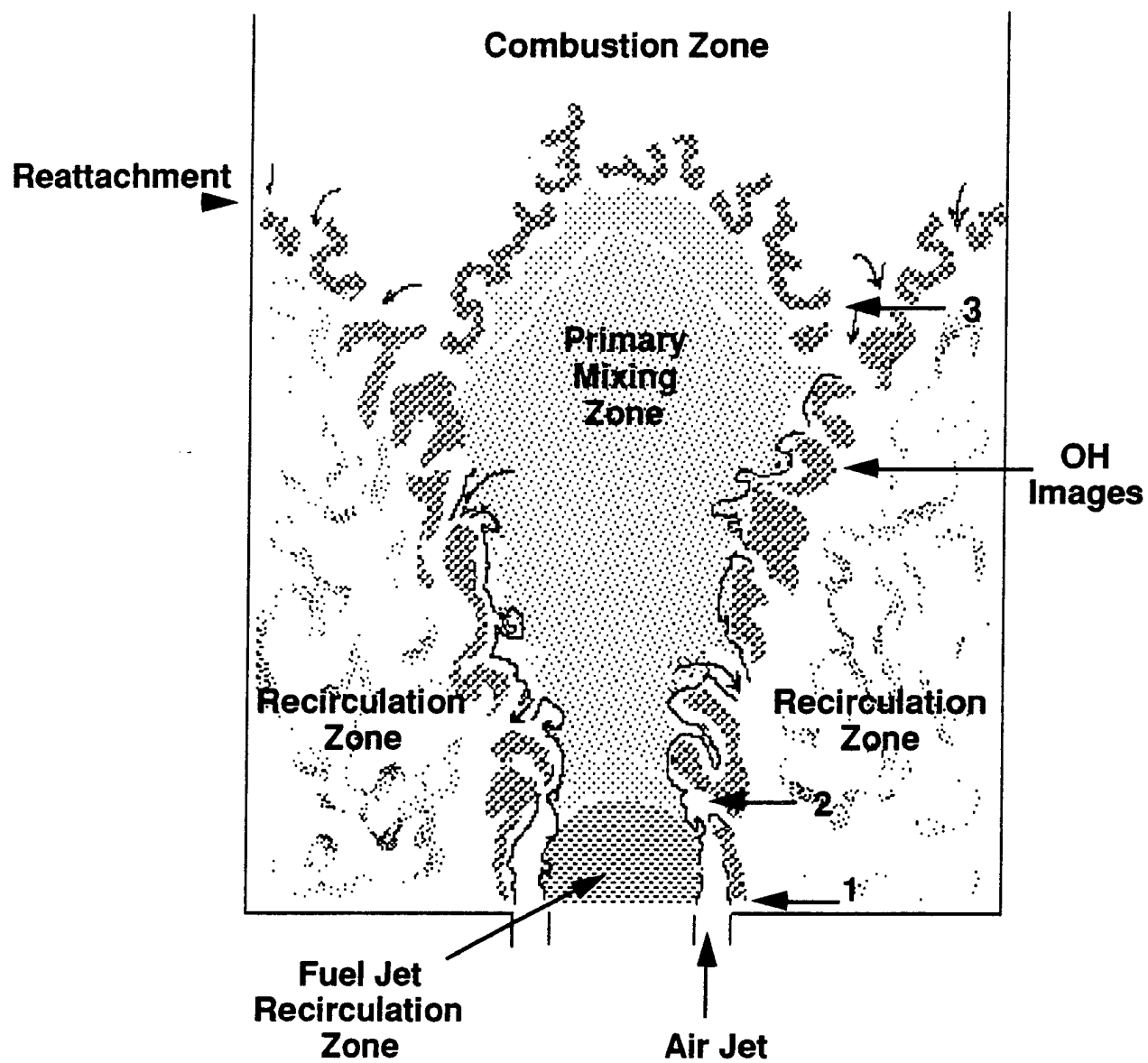


Figure 12. General flame/flow characteristics of near-field research combustor.

P. O. Hedman

Department of Chemical Engineering,
Advanced Combustion,
Engineering Research Center,
Brigham Young University,
Provo, UT 84602

G. J. Sturgess

Pratt & Whitney,
East Hartford, CT 06108

D. L. Warren

Department of Mechanical Engineering,
Advanced Combustion,
Engineering Research Center,
Brigham Young University,
Provo, UT 84602

L. P. Goss

Systems Research Laboratories, Inc.,
A Division of Arvin/Calspan,
Dayton, OH 45440

D. T. Shouse

Wright Laboratory,
Wright-Patterson AFB, OH 45433

Observations of Flame Behavior From a Practical Fuel Injector Using Gaseous Fuel in a Technology Combustor

This paper presents results from an Air Force program being conducted by researchers at Brigham Young University (BYU) Wright-Patterson Air Force Base (WPAFB), and Pratt and Whitney (P&W). This study is part of a comprehensive effort being supported by the Aero Propulsion and Power Laboratory at Wright-Patterson Air Force Base, and Pratt and Whitney in which simple and complex diffusion flames are being studied to understand better the fundamentals of gas turbine combustion near lean blowout. The program's long-term goal is to improve the design methodology of gas turbine combustors. This paper focuses on four areas of investigation: (1) digitized images from still film photographs to document the observed flame structures as fuel equivalence ratio was varied, (2) sets of LDA data to quantify the velocity flow fields existing in the burner (3) CARS measurements of gas temperature to determine the temperature field in the combustion zone, and to evaluate the magnitude of peak temperature, and (4) two-dimensional images of OH radical concentrations using PLIF to document the instantaneous location of the flame reaction zones.

Introduction

As part of a comprehensive Air Force program, three different combustors have been utilized to investigate lean blowout in aircraft gas turbine engines. These vehicles consist of a simplified research combustor (Task 100), a technology combustor (Task 150), and a simplified, generic gas turbine combustor (Task 200). The technology combustor (Task 150) incorporates the practical fuel injectors used in the generic gas turbine combustor (Task 200) into the simpler research combustor (Task 100), to permit study of injector characteristics in isolation. The work presented concerns work with the Task 150 technology combustor. While many detailed studies exist in the literature concerning jet flames, both free and enclosed, almost nothing is available on the flame characteristics produced by practical ways of introducing the reactants into an engine combustor. This work goes some way toward remedying this situation.

The Task 150 technology combustor uses a practical liquid fuel injector with a classic gas turbine engine air blast atomizing configuration, involving coswirling airsheets on either side of a coswirling annular (normally liquid) fuel sheet, with the outer air passage and the fuel passage both converging on the central air passage. For this study, the burner was fueled by gaseous propane. Two injectors of this same configuration have been used, high-swirl (HS) and low-swirl (LS) injectors. Only data from the high-swirl configuration are reported in this paper. The technology combustor has been configured so that the geometry around the injector is nearly axisymmetric with a diameter of about 150 mm. However, the combustor incorporates flat quartz windows about 60 mm in width on each of four sides so that

laser-based optical diagnostic instruments can be used. This unique configuration allows complex diagnostic measurements to be made in a simpler geometry than the Task 200 generic gas turbine combustor, but which embodies most of the features of an actual jet engine combustor in a near axisymmetric configuration that is easier to model mathematically. Four methods of measurement have been used to characterize the flame. These include still film photographs, LDA measurements of velocity, CARS measurements of gas temperature, and images from PLIF measurements of the OH radical.

Experimental tests have been conducted on the research combustor at both BYU and WPAFB locations. These tests included operational characteristics, flow partitioning in various injector passages, visual flame structure, planar laser induced fluorescence (PLIF) imaging of OH radicals in the flame boundary, laser-Doppler anemometry (LDA) velocity information, and coherent anti-Stokes Raman spectroscopy (CARS) temperature data. The effects of various parameters on the fuel equivalence ratio at lean blowout (LBO), an important operational characteristic, have also been investigated but are not reported in this paper.

Intriguing flame structures have been visually observed, and captured in video images, digitized still photographs, and PLIF images of the OH radical with the Task 150 configuration. The digitized images from still photographs have characterized the flame shapes observed visually. The instantaneous two-dimensional PLIF images have frozen flame structures missed with the visual observations. The partitioning of air flows through the dome and insert jets, and the primary and the secondary air swirlers was also determined. Preliminary analysis of PLIF images of the OH radical, combined with air flow split information, have helped describe the basic mixing patterns observed as the fuel equivalence ratio is changed. The flame attaches to the burner or lifts from the burner as the fuel equivalence ratio is changed.

LDA measurements have quantified the axial, radial, and tangential velocity components in the combustor for two op-

Contributed by the International Gas Turbine Institute and presented at the 39th International Gas Turbine and Aeroengine Congress and Exposition, The Hague, The Netherlands, June 13-16, 1994. Manuscript received by the International Gas Turbine Institute March 4, 1994. Paper No. 94-GT-389. Associate Technical Editor: E. M. Greitzer.

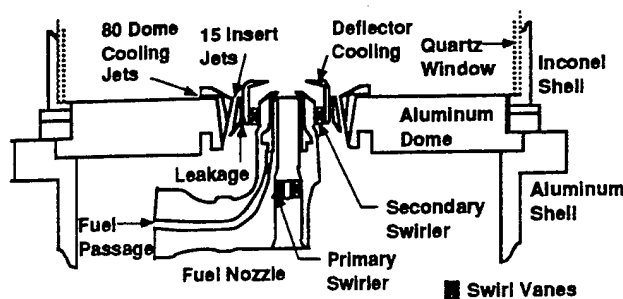


Fig. 1 Schematic of the T150 high-swirl injector

erating conditions ($\phi = 0.72$ and $\phi = 1.49$) at an air flow rate of 500 slpm. This information has yielded local velocity and turbulence data and preliminary analysis of zero axial velocity contours has been used to identify the major recirculation zones. Data from both isothermal flows and combustor hot flows have been collected. Mean axial, tangential, and radial velocity LDA data for combustor hot flow data are presented in the paper. These data are also useful for model validation.

CARS gas temperature data have also been collected for the Task 150 technology combustor with the high swirl injector at an air flow rate of 500 slpm and at fuel equivalence ratios (ϕ) of 0.75, 1.00, 1.25, and 1.50. This unique set of data shows the corresponding geometric changes in the structure of the mean gas temperature distribution as fuel equivalence ratio is changed, and quantifies the change in the magnitude of the peak temperature as the fuel equivalence ratio changes from lean, to stoichiometric, to fuel rich. Mean gas temperature data for $\phi = 0.75, 1.00$, and 1.50 are presented in the paper.

Combustor Test Facility

Three burners are being utilized as part of a comprehensive Air Force program to investigate lean blowout in the combustors of aircraft gas turbine engines (Sturgess et al., 1991b). These vehicles consist of the simplified Task 100 research combustor, the Task 150 technology combustor, and the Task 200 simplified, generic gas turbine combustor. This work provides a bridge between the combustion characteristics of confined, co-annular fuel and air jets discharged into a sudden expansion (Task 100 research combustor) and the characteristics of a linear array of four swirling fuel injectors installed in a rectangular combustion chamber that simulates a segment of a real jet engine combustor (Task 200 simplified, generic gas turbine combustor). The Task 150 technology combustor incorporates one of the practical fuel injectors used in the Task 200 generic gas turbine combustor into the simpler Task 100 research combustor, to permit study of its characteristics in isolation. The use of the Task 150 technology combustor allows the combustion characteristics of a real injector to be investigated in a simple geometry where various diagnostic measurements (primarily laser-based optical measurements) can be more easily made.

In an actual engine combustor, additional combustion and cooling air is added to the combustor downstream of the actual fuel injector. This adds an additional complexity to the flow and combustion characteristics, which is being investigated in a subsequent study. Only the characteristics in the zone near the injector are presented in this paper.

The work reported herein was accomplished in identical burners available in the Combustion Laboratories at BYU and WPAFB, respectively. The burners were designed by researchers at P&W (Sturgess et al., 1992) and fabricated at WPAFB. The features of the dome and injector can be seen in Fig. 1. The type injector used in this study is a classic gas turbine engine air blast atomizing configuration, involving coswirling airsheets on either side of a coswirling annular (normally liquid)

fuel sheet, with the outer air passage and the fuel passage both converging on the central air passage.

Two injectors of this same configuration were used. The high-swirl (HS) injector has a nominal swirl number (based on vane angle) of 1.41, and the low-swirl (LS) injector has a nominal swirl number of 1.05. The total air passage effective areas were 0.176 in^2 for the HS injector and 0.266 in^2 for the LS injector, with outer to inner flow splits of 2.8 and 2.2, respectively. The outer swirler vane angle was 55° for both injectors, while the inner swirler vane angle was 70° for the HS injector and 45° for the LS injector. The injectors were mounted in a plain bulkhead dome containing insert jets angled at 12.5° into the flame, and radially outward flowing film cooling jets. This arrangement closely simulates that of an engine combustor. The total effective air flow area of the dome, excluding the fuel injector, was 0.160 in^2 .

The combustor chamber, shown in Fig. 2, has been designed to be nearly axisymmetric and incorporate quartz windows to allow optical diagnostics (primarily laser-based optical measurements) to be made. The combustor cross section is square with generously filleted corners to minimize secondary flow development. The hydraulic diameter is 150 mm. This box-section combustor with corner fillets allows reasonable optical access while providing a cross section that approximates a two-dimensional axisymmetric cross section. The bluff body provides a recirculation region that can stabilize the flame. Optical windows of fused quartz are provided on the four flat sides for a downstream length of 490 mm. The combustor overall length to hydraulic diameter ratio is 4.9, and the exit blockage is 45 percent by means of an orifice plate. The only air addition in this configuration is through the dome.

The combustor is mounted on a 240 mm long spool piece containing a mounting pad for the fuel injector flange. The combustor and spool piece are situated on an inlet air conditioning section, also shown in Fig. 2. Reactants are supplied at ambient temperature and pressure. Ignition is by means of a removable torch ignitor. This combustion chamber allows the combustion characteristics of a practical injector to be investi-

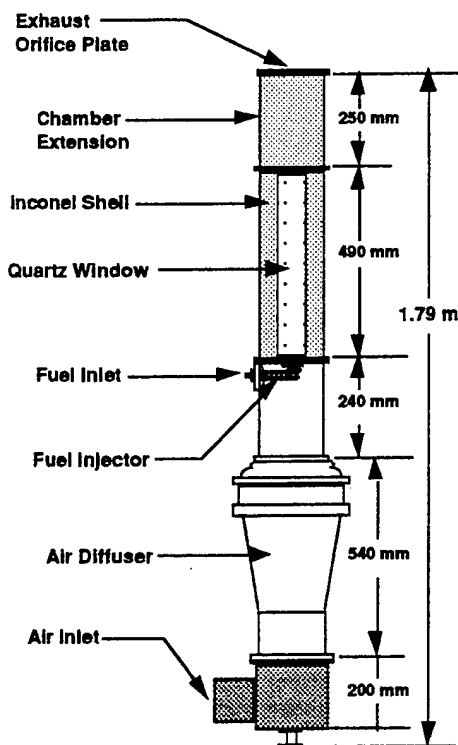


Fig. 2 Laboratory-scale gas turbine combustor

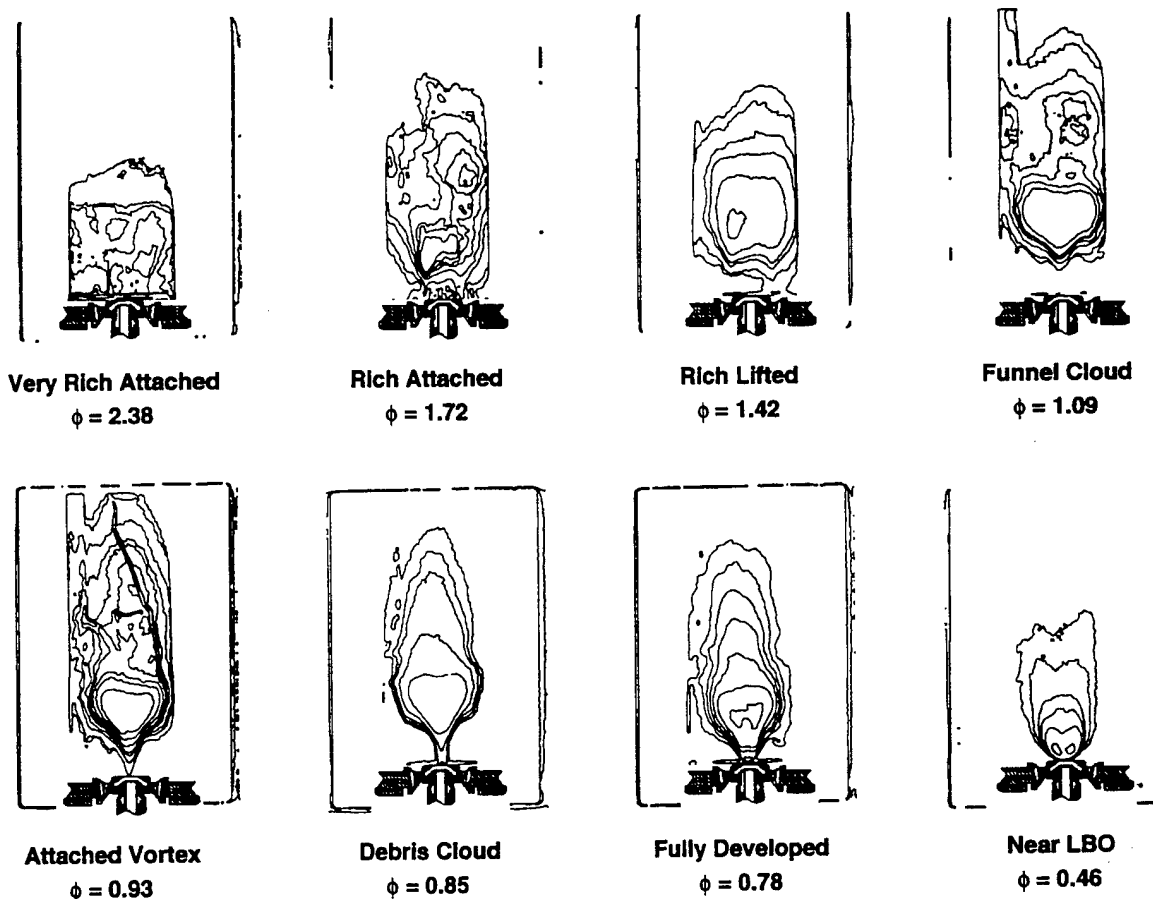


Fig. 3 Characteristic flame shapes from digitized still photographs (T150-HS nozzle, 310 slpm air)

gated in a simple geometry where various diagnostic measurements can be made.

In order to separate the effects of liquid fuel atomization and spray droplet evaporation from the effects associated with fuel/air mixing and aerodynamic flow pattern, these first evaluations involved the use of a gaseous propane fuel. Planned subsequent evaluations will use liquid ethanol. Liquid ethanol is expected to simulate closely the combustion characteristics of the liquid jet fuels, but without significant soot formation. Extensive sooting could cloud the quartz windows precluding easy optical access. The present paper deals exclusively with propane results with the HS injector.

The results presented concern work with the Task 150 technology combustor using the high-swirl injector and gaseous propane fuel. While many detailed studies exist in the literature concerning jet flames, both free and enclosed, almost nothing is available on the flame characteristics produced by practical ways of introducing the reactants into an engine combustor. This work goes some way toward remedying this situation.

Photographic Flame Characterization

A complex series of intricate flame structures have been observed in the Task 150 technology combustor according to the operating conditions and fuel injector used. Some of the flame behavior could be related to that seen in the Task 100 research combustor (Sturgess et al., 1991a, 1993), and some of the structures to those seen in the Task 200 generic combustor (Sturgess and Shouse, 1993). These flame structures were studied directly with use of visual observations, video recordings, and still photography. The still film photographs have been digitized and filtered using computer techniques to produce isochromatic contour plots, Fig. 3, for quantitative purposes.

One of the traits of the Task 150 technology combustor is the wide variety of flame structures observed. Each flame shape indicates a different mode of operation, which differs from the others in the location of the flame fronts, or by some structure such as thickness or intensity. The different structures observed arise from changes in the flow fields, mixing patterns, or fuel equivalence ratio as operating conditions are varied. The differences and similarities of the flame structures for the swirling injectors together with the results from the co-axial jet diffusion flame (Task 100 combustor) provide significant insights to the combustion processes. The shape of the flame, at the minimum, provides qualitative information on the mixing process and location of flame fronts. Such information can yield insights into the processes present. Flames fronts exist because fuel and oxidizer have been transported to a point where combustion can be supported. The location of these fronts relative to the outlet orifices of fuel and air are of obvious interest.

The fuel equivalence ratios where the transitions from one flame structure to another were determined are a function of fuel flow rate. The flames for both Task 150 injectors were attached to the outside of the insert air jets when the burner was operated very fuel rich. The flame would then lift, reattach, and lift again as the fuel equivalence ratio was progressively reduced depending on the injector (high swirl versus low swirl) and the air flow rate. During the reattachment phase, the flame would take on many of the characteristics of a strong vortex, and shared many features associated with a tornado. Consequently, the terminology of funnel cloud, tornado, and debris cloud were adopted to differentiate some of the observed flame structure from the general description of a vortex flow. The characterization of the flame structure was carried out by visual observations. Still film photographs were taken of the different

Table 1 Summary of experimental conditions for LDA measurements

Injector	Flow	Air slpm (70 F)	C ₃ H ₈ slpm (0 C)	N ₂ slpm (0 C)	ϕ
T150HS	Cold	500		14	0.72
T150HS	Hot	500	14		0.72
T150HS	Cold	500		29	1.49
T150HS	Hot	500	29		1.49
T100	Cold	1000		23	0.59

structures. These images were digitized and manipulated using various computer programs into the isochromatic contour plots found in Fig. 3 for the high swirl injector. The major factor affecting flame structure was the overall fuel equivalence ratio in the burner determined from total air and fuel flow rates, and to a much lesser extent the air flow rate. At a given air flow rate, the fuel would be reduced until a transition in flame structure was judged to have been reached. These observations were not easily made. With the high swirl nozzle, the flame structures flowed smoothly from one mode to another. These smooth transitions left no sharp break point in flame behavior. Consequently, the images presented in Fig. 3 are only representative of the types of flame structures observed.

At very fuel-rich conditions ($\phi = 2.38$ and $\phi = 1.72$), the flame was attached to the insert jets, in a manner similar to that observed with the Task 100 technology combustor at rich conditions. Unlike the Task 100, however, these flames were very short, presumably because of the much faster mixing due to the swirling motion of the gases. As the amount of fuel was further reduced (decreasing fuel equivalence ratio at a constant air flow rate), the still rich flame lifted and stabilized on a downstream recirculation zone that appeared to be associated with the injector ($\phi = 1.42$). The primary combustion zone continued to lengthen as relatively less fuel entered the combustion chamber ($\phi = 1.42$ to $\phi = 1.09$).

After the rich lifted condition, further reductions in fuel equivalence ratio caused the flame to stabilize in the rapidly swirling vortex at the center of the combustor, with flame structures that resembled the development of a tornado. As seen in Fig. 3, a structure that resembled a funnel cloud formed within the rich lifted flame ($\phi = 1.09$) and gradually descended as the fuel flow was continually decreased ($\phi = 1.09$ to $\phi = 0.93$) forming a tornado-like flame structure. Further reductions in ϕ caused the tornadolike flame to enter the primary swirler passage in the injector ($\phi = 0.93$). Continued reduction in fuel equivalence ratio caused a flame in the shape of a bowl, which looked much like the debris cloud of a tornado, to attach to the nozzle on the outside of the tornadolike structure ($\phi = 0.85$). The minute detail of the debris cloud was lost in the process of converting from the still photograph to the image presented in Fig. 3. Continued reduction of the fuel flow resulted in the growth in size and intensity of the debris cloud-like flame structure while the funnel cloud-like structure was simultaneously decreasing. The total disappearance of the funnel cloud structure marked a transition to a fully developed flame that was strongly attached to the center of the injector ($\phi = 0.78$). At lower air flow rates (less than ca 500 slpm), this strongly attached flame would weaken until the lean blowout limit ($\phi = 0.46$) was reached (blowout occurred from an attached flame). At high air flow rates (greater than ca 500 slpm), the flame would once again lift, attach to a downstream recirculation zone, and eventually blowout from the separated flame structure ($\phi = 0.42$), much like that observed in the Task 100 research combustor.

Gas Velocity Measurements

A laser-Doppler anemometer (LDA) was used to make extensive measurements of gas velocity in the burner at five separate

experimental conditions. The experimental conditions used are summarized in Table 1.

The LDA measurements reported in this paper are for the Task 150 burner with the high-swirl injector installed. Measurements were made for lean conditions ($\phi = 0.72$) where the flame was well attached to the central part of the injector, and also at fuel-rich conditions ($\phi = 1.49$) where the flame was attached to the dome and insert jets. LDA measurements were also obtained in isothermal, nonreactive flows where nitrogen was substituted for the propane fuel. This has allowed the effect of the flame temperature on the flow field and gas velocities to be determined for at least two of the test conditions used. However, only the data from the combustor flow experiments are reported in this paper.

A schematic of the LDA experimental setup is presented in Fig. 4. The beam from the argon-ion laser was split into two beams, frequency shifted (40 and 34 MHz), polarized, and focused into a diagnostic volume in the test section. The forward-scattered LDA signals for the radial (or tangential) and axial velocity components were focused into fiber optic cables and passed to a photomultiplier tube to be amplified and converted to electrical signals. These electrical signals were collected with TSI, Inc., counters and analyzed with a Macintosh IIfx computer. A Le Croy 9314L Quad 300 MHz oscilloscope was used to monitor the Doppler bursts to help in the alignment of the LDA system and to insure quality data were being collected. Even with careful alignment, there was still some noise, which was filtered using a data analysis program.

A brief investigation was made to evaluate the effect of the number of points taken at a given test location on the accuracy of the gas velocity measurement. Three different sets of data were collected, a set with 5000 points, a set with 2000 points, and a set with 1000 points. In general, there was little difference observed in the mean axial and tangential velocities determined from the different number of points in the data sets. However, the fluctuating velocity components (i.e., rms velocities) were better described by the data sets containing the largest number of points. Nevertheless, for this study, 1000 data points were collected at each test location. This allowed a greater number of experimental conditions and geometries to be evaluated, albeit at slightly reduced data accuracy.

The two component velocity data (either axial and radial, or axial and tangential) were obtained for each of the test conditions described above (Table 1). The burner was translated with respect to the laser diagnostic volume in an X, Y, and Z coordinate system. Translation in the Z coordinate direction allowed different axial locations to be sampled. Translation in the X or Y axis allowed different radial locations to be sampled. For these tests, the X or Y translations were done along a coordinate centerline. Translation in the X coordinate direction along the Y coordinate centerline allowed axial and radial velocity data to be obtained. The edge of the windows limited transla-

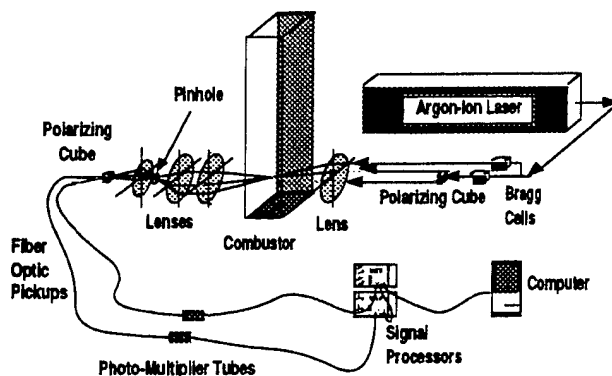


Fig. 4 Setup for LDA velocity measurements

tion in this coordinate direction to about ± 30 mm. Translation in the Y coordinate direction along the X coordinate centerline allowed axial and tangential velocity data to be obtained. As the diagnostic volume was brought near the quartz windows, significant optical noise was added to the Doppler signals. The quartz windows were approximately ± 75 mm from the center of the reactor. The optical noise from the windows generally limited data collection to ± 65 mm, although with especially clean windows, it was sometimes possible to get good data at ± 70 mm.

Typically, data were collected at 0.5 or 1.0 mm radial increments where the velocity gradients were large. Data were collected at up to 10 mm increments where velocity profiles were relatively flat. A typical set of data was taken at axial locations of 10, 15, 20, 25, 50, 75, 100, 125, 150, 200, and 240 mm above the dome of the reactor. Occasionally, other intermediate locations were examined where large velocity gradients or other interesting behavior were found.

The basic flow field in the combustor was derived by interpolation of the velocity data obtained. The field is dominated by multiple regions of flow recirculation. The axial velocity from both the X and Y coordinate traverses has been combined for one of the Task 150-HS cold flow cases (14 slpm N_2 , 500 slpm air), interpolated, and the zero axial velocity contours plotted in Fig. 5. Each zero axial velocity contour bisects a recirculation zone. While the data have not been analyzed in the detail needed to quantify the recirculation patterns totally, estimates of the recirculation zones are indicated. Eventually, flow streamlines will be plotted to identify the various flow fields better. However, for this paper, only axial, tangential, or radial data have been used.

Figure 5 identifies several important recirculation zones. Although the near field is similar to that in a real gas turbine combustor, the downstream region is not due to the absence of air addition by means of transverse jets, as is usual practice. Since current interest is concentrated on the near field, this deviation is not of great significance. It is interesting to note that there is a zone of flow reversal on the centerline of the burner very near the discharge of the injector. This flow reversal is undoubtedly caused by the highly swirling flow, and is consistent with the strong vortex structures observed earlier (Fig. 3). A recirculation zone is also apparent in the lower corners of the combustion chamber. This zone appears to be driven by the dome cooling jets, and is consistent with the observed horizontal flow in the radial direction that emanates from these cooling jets.

Another major recirculation zone is centered on the zero axial contour that angles from the face of the injector outward till it reaches the wall of the combustor at a downstream location at about 140 mm. This large recirculation zone seems to have a major impact in stabilizing the flame under certain operating conditions. The last observed recirculation zone surrounds the zero isovelocity contours that exist between the 100 mm and 240 mm axial locations. This recirculation pattern was very weak as judged by the magnitude of the velocities measured, and was only observed in the isothermal case. It was not seen in the combustor cases. The influence of the combustion was sufficient to eliminate this pattern from the flow field. Combustion also altered the shape and location of the other recirculation zones, but each of the other zones remained in the combustion cases.

Figures 6(A), 6(B), and 6(C) present the isocontour plots for the mean axial, mean tangential, and mean radial velocity measurements respectively for the fuel lean case ($\phi = 0.72$). In each figure, the velocity contour plot from the centerline to the maximum measurement radius was created using commercial computer software, duplicated, and reversed. The reversed image was combined with the original image and superimposed on a schematic of the burner to provide an indication of the flow characteristics with respect to the burner. The data presented in

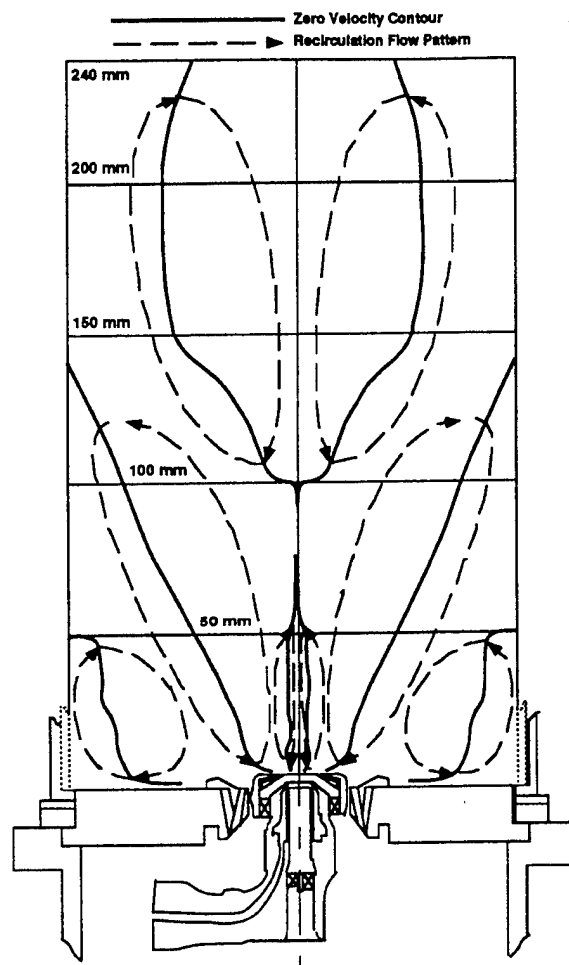


Fig. 5 Recirculation patterns with the high-swirl fuel injector

Figs. 6(A) and 6(B) were collected along the Y coordinate direction out to about 60 mm. The data in Fig. 6(C) are limited to a radial location of about 30 mm because of the width constraints of the windows. The flow fields and recirculation patterns presented here are generally consistent with those observed in Fig. 5.

The flame at the operating condition was well attached to the center of the injector, and was considered to be fully developed, as was shown earlier in the discussion of Fig. 3. Mass balance calculations based on isothermal axial velocity measurements have been used to determine the overall accuracy of the LDA measurements. It was found that the mass flow rate was strongly influenced by the gradient assumed near the wall, but reasonable velocity interpolations gave reasonable mass balance closure.

The sharp peak in axial velocity component shown in Fig. 6(A) near the injector is clearly evident. The rapid decay of the high-velocity region near the injector as one moves downstream is also apparent. The recirculation zone directly over the injector is dramatic, and clearly shows a significant region of flow reversal. The tangential velocity in this zone is very high as seen in Fig. 6(B). The other major recirculation pattern in the combustor is of a somewhat different shape and in a somewhat different location than observed in the isothermal case (Fig. 5). The recirculation patterns caused by the dome jets are notably absent. Visual observations confirmed that the corner recirculation still existed in the combustor flow cases, but it was not possible to collect LDA data close to the window near the bottom of the reactor because of excess optical noise.

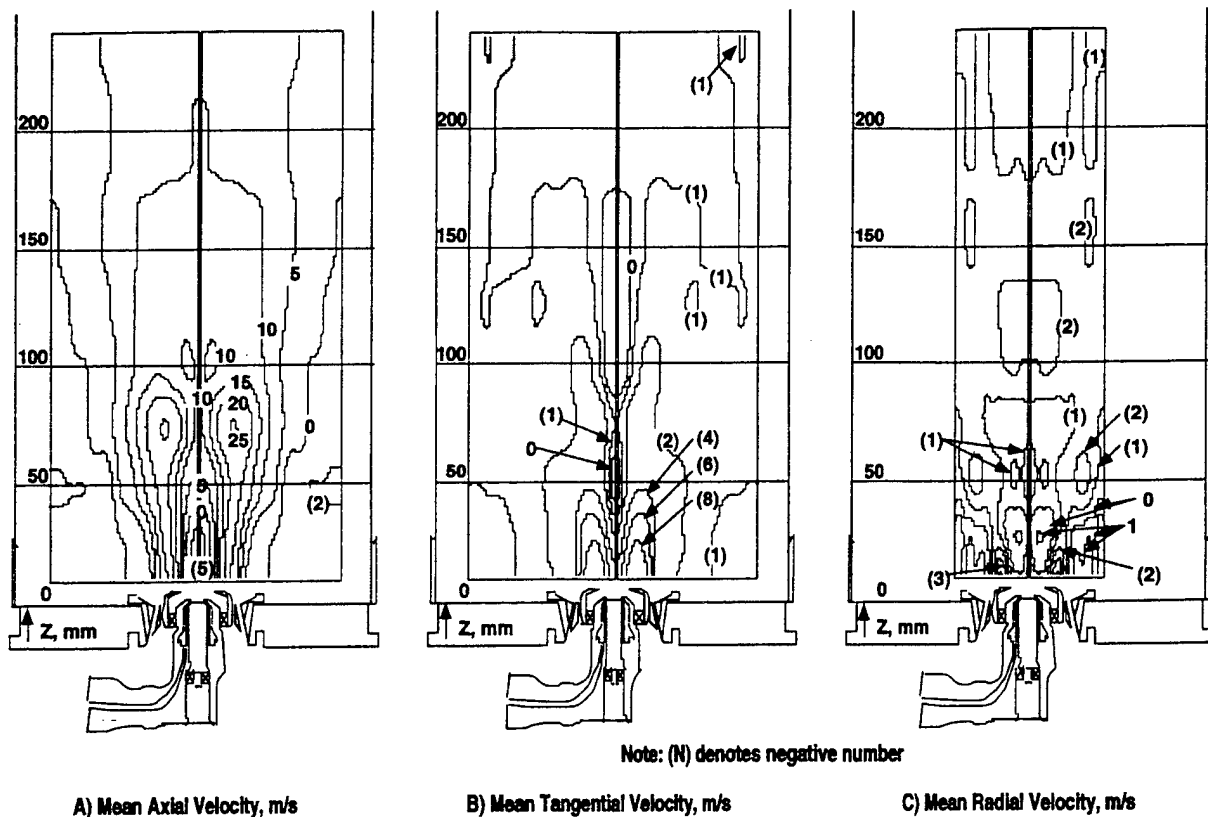


Fig. 6 Isovelocity contours for the T150-HS burner at $\phi = 0.72$ and 500 slpm air flow rate

The radial velocity data are presented in Fig. 6(C). These data are limited to a radial location of about 30 mm. The radial flow velocities are all very low in magnitude, but do show some interesting structures. The low magnitudes of these velocities are close to the resolution of the LDA instrument. A similar set of gas velocity data for the Task 150-HS combustor operating at a fuel equivalence ratio of 1.49 is presented in Figs. 7(A), 7(B), and 7(C) for the mean axial, mean tangential, and mean radial velocity measurements, respectively. The flame at this operating condition was attached to the insert and dome jets as was shown earlier in the discussion of Fig. 3. As above, the radial data in Fig. 7(C) are limited to a radial location of about 30 mm, but the axial and tangential data in Figs. 7(A) and 7(B) were collected out to about 60 mm. The flow fields and recirculation patterns presented here are also generally consistent with those observed in Figs. 5 and 6.

As for the $\phi = 0.72$ case, the sharp peaks in mean axial velocity component associated with the injector are still clearly evident, but seem to decay more rapidly than in the $\phi = 0.72$ case. The recirculation zone directly over the injector is still dramatic, and shows little difference in the magnitude of the reversed velocity or in the size and shape of the recirculation pattern when compared to the $\phi = 0.72$ case. The other major recirculation pattern in the combustor is of a similar shape to that observed with the $\phi = 0.72$ case, but seems to be much stronger (i.e., has much larger reversed flow velocity components). The recirculation patterns caused by the dome jets are still absent. As in the $\phi = 0.72$ case, visual observations confirmed that the corner recirculation still existed in this combustion flow case, but it was not possible to collect LDA close to the window near the bottom of the reactor because of optical noise near the quartz windows.

The radial velocity data are presented in Fig. 7(C). Again, the radial flow velocities are all very low in magnitude, but do show some interesting structures, that are quite different than

seen with the lean flame. The low magnitudes of these velocities are also close to the resolution of the LDA instrument.

The differences in velocities between the lean flame and the rich flame show that there is a strong influence of the location of the flame zone on the flow fields as characterized by the measured velocity fields.

Gas Temperature Measurements

Coherent anti-Stokes Raman spectroscopy (CARS) was used to obtain a set of gas temperature measurements in the Task 150-HS combustor at fuel equivalence ratios of 0.75, 1.00, 1.25, and 1.50; and at an air flow rate of 500 slpm. The details of the CARS facility have been well documented in previous publications (Boyack and Hedman, 1990; Hancock et al., 1991, 1992). The CARS setup used for this study, as shown in Fig. 8, is very similar to the folded box-CARS phase matching scheme employed by Boyack (Boyack and Hedman, 1990). Boyack located his combustor directly on the CARS optical table, and was able to focus the laser beams easily directly into his combustor. In this experimental setup, the combustor was remotely located. Consequently, the laser beams were directed off the optics table over a distance of about 10 m onto a set of optical bread boards located on either side of the Task 150-HS combustor. The optical components needed to create the box-CARS phase matching were located on these remote optical breadboards. As with Boyack's work, the CARS signal was focused into the end of the fiber optic used to transfer the signal back to the spectrometer. The CARS lasers and spectrometer were kept in an optics room distant from the combustion facilities in an effort to keep the optical components relatively clean.

Like the gas velocity measurements, the CARS temperature measurements were taken at closely spaced radial increments where large gradients in temperature were found and in a coarser grid where the temperature gradients were found to be relatively

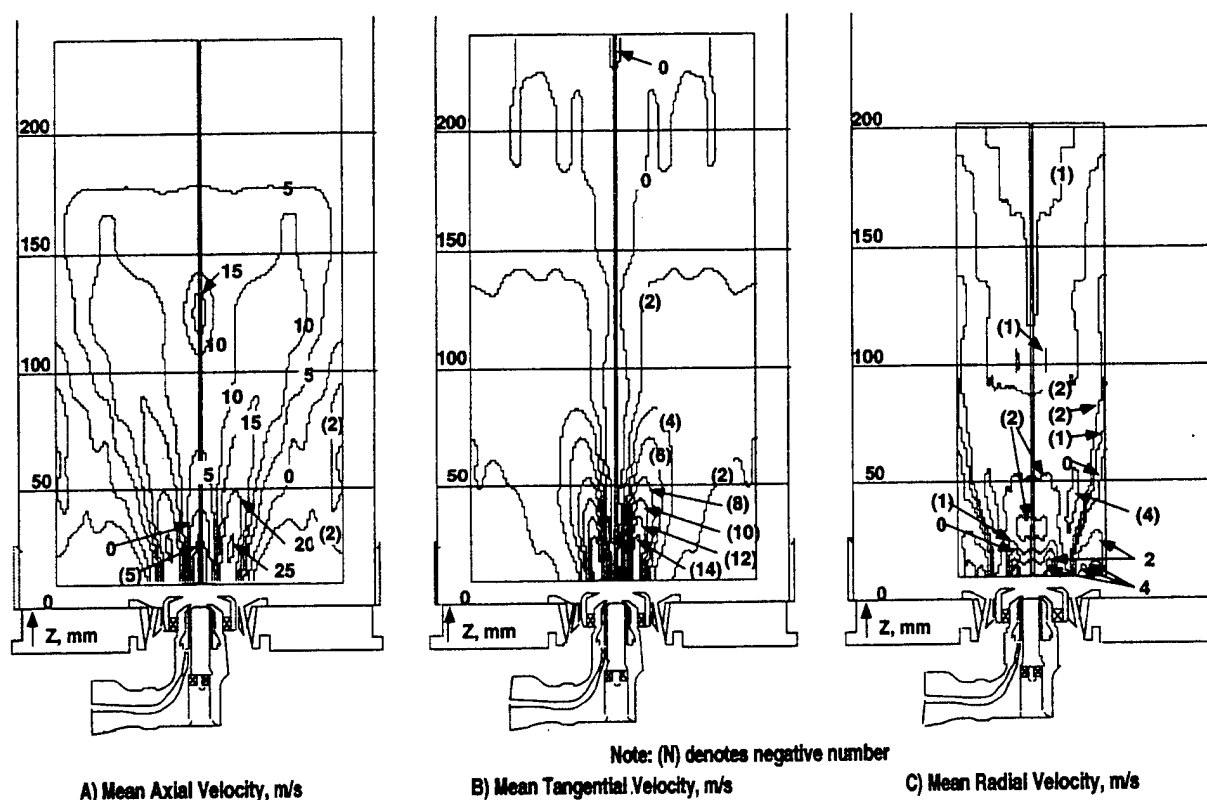


Fig. 7 Isovelocity contours for the T150-HS burner at $\phi = 1.49$ and 500 slpm air flow rate

shallow. Temperature data were taken at similar axial locations as well. The temperature data were taken along the X coordinate, and consequently are available only out to a radius of about 30 mm, but were taken to an axial location of about 300 mm. Attempts at obtaining data along the Y axis to radial locations near the quartz window resulted in laser damage to the quartz window. Nevertheless, the CARS temperature data obtained have provided adequate temperature measurements to well quantify the temperatures in the region of most interest near the injector.

Figure 9 presents isocontour plots of temperature data for the Task 150-HS combustor operating with an air flow rate of 500 slpm and at fuel equivalence ratios of 0.75, 1.00, and 1.50. The data at $\phi = 1.25$ have been excluded from the paper because of space considerations. Two hundred discrete temperature data points were taken at each of 92 separate diagnostic locations from the centerline to a 30 mm radial location, and from 10 mm to 300 mm axial location. These sets of data were used to determine the mean temperatures used to create the isothermal contour plots shown. In order to show the symmetry of the flame, the contour plot was duplicated, and computer software was used to flip the image and add it to the opposite side of the combustor. The flow fields are very symmetric about the centerline in this highly swirled flame. The doubled image gives a better representation of the temperature field in the vicinity of the injector.

The relatively cold region (600 K to 1000 K) directly above the injector in all three cases generally corresponds to the central recirculation zone seen in the gas velocity plots (Figs. 6 and 7). Surrounding the cold central zone is an intermediate temperature region that seems to be associated with the penetration of the very high axial velocity into the combustor. Higher temperatures exist on either side of this penetration zone. It is unfortunate that temperature data could not be obtained in the lower corners of the combustor where the recirculation zones near the dome are located. The data do suggest that this region is rela-

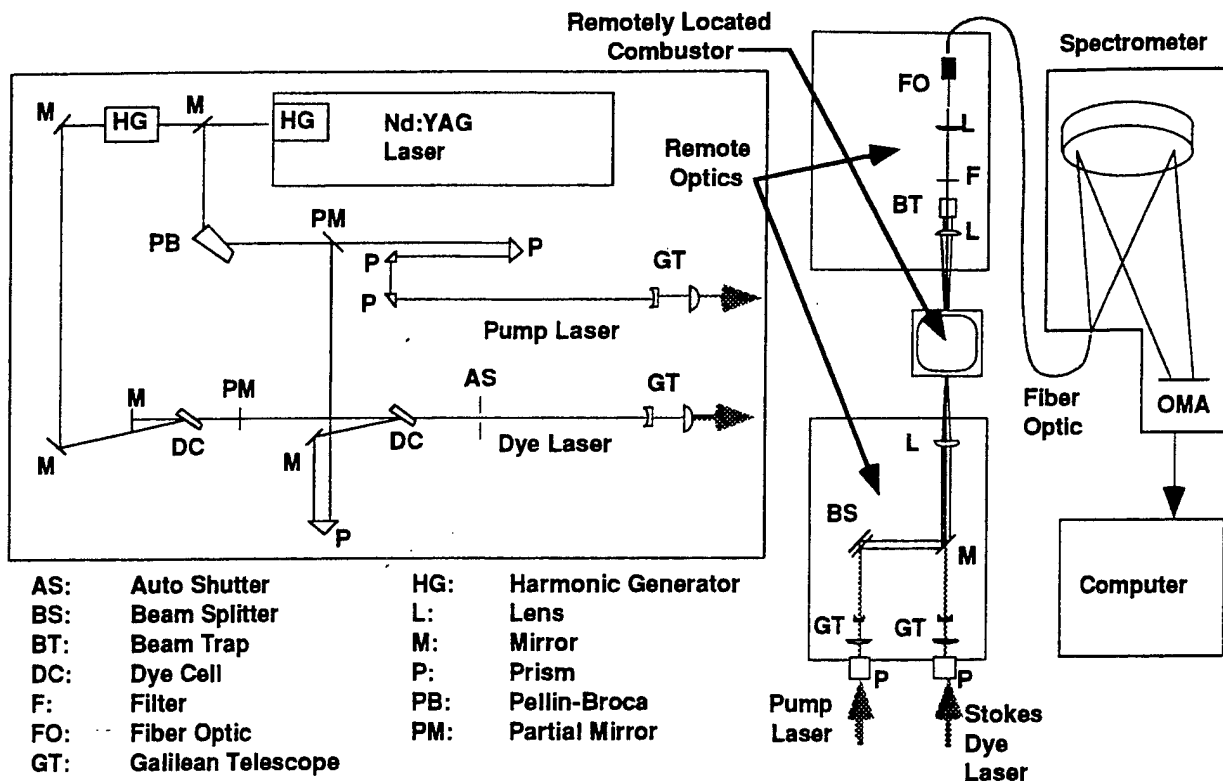
tively cool for the $\phi = 0.75$ case, but seem to indicate a relatively hot region in this corner recirculation zone for the $\phi = 1.5$ case. This observation seems to be consistent with the observed relocation of the flame zone from the central core of the vortex when operating fuel lean to the outer recirculation zone when operating fuel rich, as noted in the digitized film images and in the PLIF images of OH radical discussed in the last section of this paper.

Temperatures in excess of the $\phi = 0.75$ adiabatic flame temperature (1963 K) are seen in a zone near the centerline at an axial location of about 100 mm for the fuel lean case. Since this is a non-premixed flame, this suggests that this diffusion zone may be operating with near-stoichiometric ($\phi = 1.00$) mixtures of fuel and air. The peak temperature that was measured was 2085 K which is about 178 K below the theoretical stoichiometric adiabatic flame temperature of 2263 K.

In the stoichiometric case ($\phi = 1.00$), the peak measured temperature is 67 K below the theoretical stoichiometric adiabatic flame temperature of 2263 K. The zone of near-peak temperature extends from an axial location of about 100 mm to about 170 mm and forms a toroidal shaped ring around the centerline. Beyond the high-temperature region, the temperatures decrease, dropping to about 1800 K at the combustor exit (not shown).

Isocontour plots of gas temperature measurements for the $\phi = 1.50$ case are shown in Fig. 9(C). It is interesting to note that the peak temperature (1875 K) in the fuel-rich case, like the stoichiometric case, is just below the predicted ($\phi = 1.50$) adiabatic flame temperature of 1974 K. It seems reasonable that the peak measured temperature in this case would be close to the adiabatic flame temperature, since all of the oxygen would be consumed early in the flame, preventing a zone near stoichiometric from ever existing.

The variation in temperature field as the fuel equivalence ratio changes from fuel lean to fuel rich seems to be consistent with the observations made from the still photographs. At $\phi =$



0.75, the flame is well attached to the burner, with a narrow vortex penetrating into the injector and a fully developed flame structure attached to the injector. The temperature distributions at $\phi = 1.0$ and $\phi = 1.25$ (not shown) were very similar, and seemed to agree with the flame structures described in Fig. 3 as a rich lifted flame and a funnel shaped flame. At $\phi = 1.50$ (Fig. 9C), the center cold zone has been reduced in size, and there are higher temperatures at the outer edge of the measurement region that support the visual observation that the flame is attached to the insert jets. These results also suggest that a fairly high temperature exists in the corner recirculation zone when the combustor is operating in a fuel rich mode. In general, the temperature measurements are consistent with the visual flame conditions, the PLIF images of the OH radical, and the velocity measurements for this particular test condition.

PLIF Imaging of OH Radical

In PLIF (planar laser induced fluorescence) imaging, a dye laser is tuned to a resonant frequency, which causes the particular combustion radical or molecule to fluoresce at a different resonant frequency. This fluorescence is then recorded and the two-dimensional image preserved with an electronic camera. In these experiments, OH radicals were excited with an ultraviolet (ca 283 nm) light sheet produced by a tunable dye laser pumped with a 10 ns pulse from a Nd:Yag laser. This sheet of laser light was passed through centerline of the reactor. An intensified CCD camera, located normal to the laser sheet, captured the 75 mm high two-dimensional UV (ca 308 nm) image (Fig. 10). This nearly instantaneous map of OH radical concentration in the flame zone was then stored by a Macintosh computer. The images have been analyzed and enhanced using conventional computer software.

OH radicals are commonly chosen for PLIF because they are important markers in hydrocarbon flames. These radicals are produced in large quantities during the combustion process, and are a good indicator of flame fronts. However, in some

circumstances, these radicals may persist for long distances downstream of the actual flame front, limiting their usefulness. Also, as in any laser diagnostic technique, there is a concentration level below which the OH radical will not be detected. With these limitations in mind, conclusions based solely on PLIF images of the OH radical must be carefully drawn.

Many PLIF images of the OH radicals were obtained in the Task 150-HS combustor at 500 slpm air flow and at fuel equivalence ratios that ranged from 0.62 to 1.75. Images were taken at values of fuel equivalence ratio that roughly correspond to the changes in flame structure that had been observed visually and documented with still photographs (Fig. 3). Comparison of the two types of flame image, and the relation of these images to the time-mean flow field and bulk equivalence ratios, explains much about the flame structures. However, comparison of a sequence of instantaneous OH images at fixed operating conditions, e.g., Fig. 11, also reveals the highly nonstationary character of the flame zone. This behavior is similar to that observed previously in the Task 100 research combustor (Roquemore et al., 1991).

The experimental behavior of the Task 100 research combustor is quite different from the predictions by computational fluid dynamics (CFD) programs. These computer codes predict the flame to be anchored in the jet shear layer for all fuel equivalence ratios. However, the flame has been experimentally observed (Roquemore et al., 1991) to attach to the backward-facing step just outside the air tube at fuel equivalence ratios (ϕ) in excess of 1.08. In these operating conditions, a small "coke bottle" shaped flame pilots a thicker flame sheet, which is much lower in the combustor than the CFD programs predict. A waisting in the flow field is predicted by the CFD code, but the mixture is predicted to be too lean to burn. Roquemore postulates that a discrete and intermittent process is responsible for the entrainment of the fuel into the step recirculation zone. This type of transport would require passageways in the flame in order to deliver the unburned fuel from the fuel tube to the

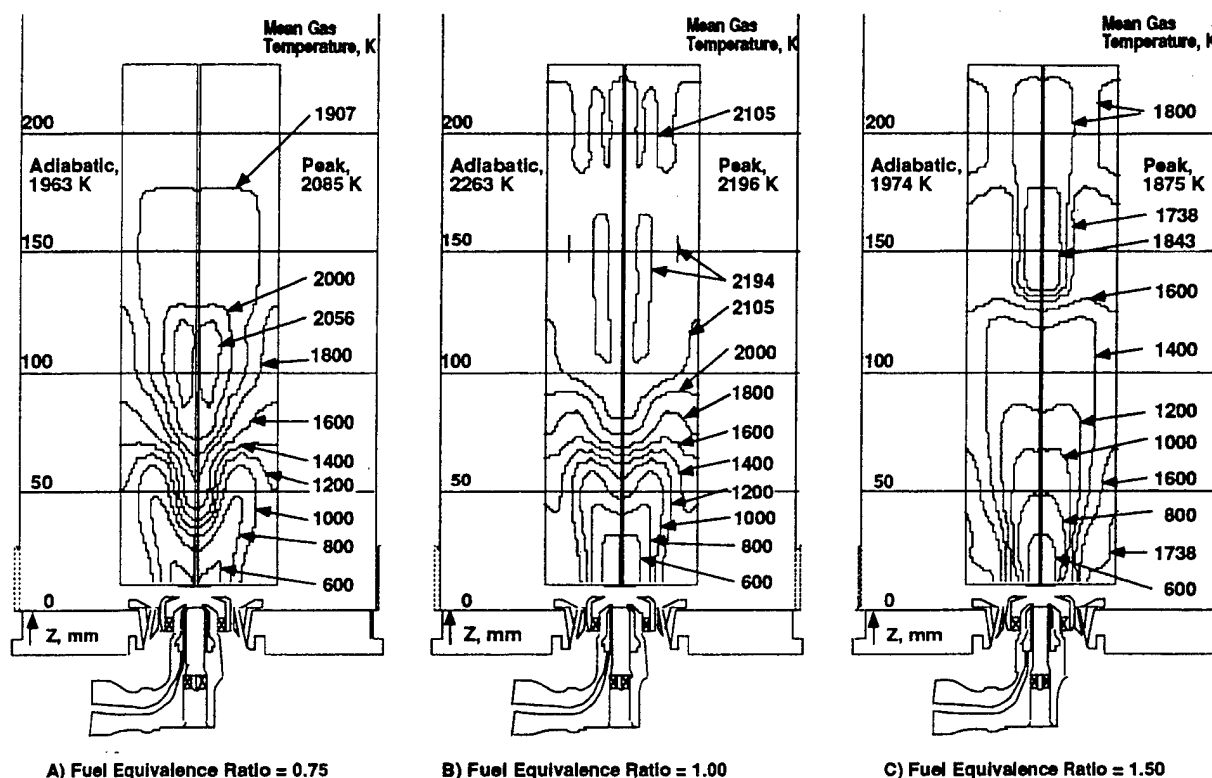


Fig. 9 Mean gas temperature isocontours for the T150-HS burner at 500 slpm air flow rate

step recirculation zone. These passageways would appear as a region with little to no OH radical present.

Much of what Roquemore postulated has been found in PLIF images of the OH radical collected in the Task 100 research combustor. In the well-attached flame ($\phi = 1.56$), the OH radicals appear in vortex structures being shed off the backward step. These structures were very clear in the images collected. In the lean condition, OH radicals were not observed below 150 mm in the reactor, with relatively small amounts between 150–200 mm and very large amounts beyond. Similar observations have been made in the PLIF (images of the OH radical for the Task 150 technology combustor (e.g., Fig. 11 and Fig. 12A, 12B, and 12C). Figure 11 shows four separate instantaneous images at two different axial locations at $\phi = 1.29$. Figure 12 shows composites of several single PLIF images of OH radical grouped as a collage in the appropriate locations within the combustor at a fuel lean condition ($\phi = 0.62$), near-stoichiometric ($\phi = 1.08$), and at a fuel-rich condition ($\phi = 1.49$). These images dramatically illustrate the characteristics of swirling flames and the highly variable nature of the instantaneous flame shape. Therefore, it seems likely that the conclusion reached for the co-axial jet system of the Task 100 research combustor (Roquemore et al., 1991; Sturgess et al., 1992, 1991b), that mass transport by axisymmetric, turbulent, recirculating flames is dominated by nonstationary flow phenomena, and not by gradient transport is confirmed, even in a practical injection system. The implication of this finding for accurate mathematical modeling of practical turbulent combustion systems is very important.

It is informative to correlate these OH images with the information known about the partitioning of the air flow rates through the various air passageways through the nozzle. The local fuel equivalence ratios shown in Table 2 were calculated from the air flow through each of the different passageways and the total fuel flow. Implicit in these calculations are two assumptions. First, the fuel is assumed to mix uniformly within each combination of partitions before mixing with remaining air. Second, any fuel blockage

effects (which would change the partitioning as a function of fuel flow) are assumed to be negligible. At this air flow rate (500 slpm), LBO occurs at a fuel equivalence ratio of about 0.42.

With these assumptions in mind, and knowing the flammability limits (ϕ) of propane are roughly 0.5 to 2.5, some conclusions can be cautiously applied to these images. In every case, the air in the primary swirler alone does not provide sufficient oxidizer to permit combustion. Thus, the fuel must mix with at least the secondary swirled air before combustion is possible. As shown in Fig. 12 (A), with a fuel equivalence ratio of 0.62, the funnel structure expected in a swirl stabilized flame is clearly evident. The local fuel equivalence ratio with the air from the two swirled jets is 1.11, indicating little air from the insert jets is needed to complete the combustion. Although Fig. 12(A) shows high concentrations of OH radical extending above the funnel-like structure, visual observations reveal the visible flame region is apparently only a thin sheet, much like a horn, or funnel, with a rounded cusp.

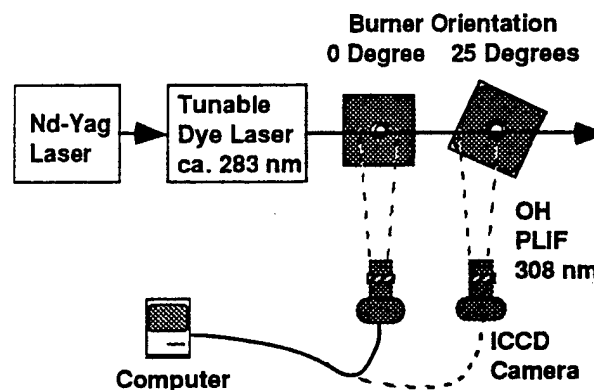


Fig. 10 Instrumentation for PLIF imaging of OH radical

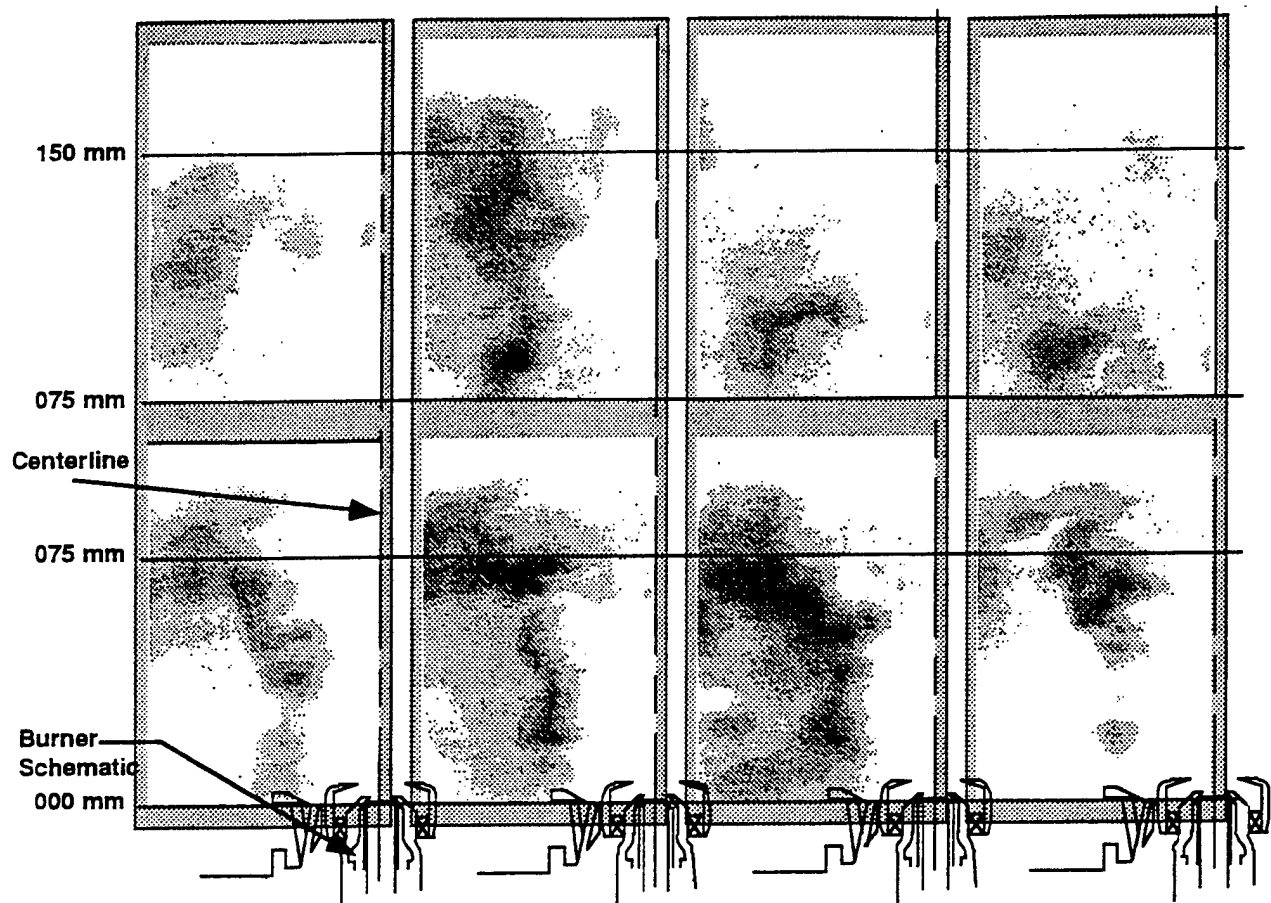


Fig. 11 Instantaneous flame images by PLIF of the OH radical (T150-HS nozzle, 500 slpm air, $\phi = 1.29$)

As the overall fuel equivalence ratio is increased to 1.08 (Fig. 12B), the swirled air/fuel mixture was still within flammability limits. What changed was the extra fuel left to mix with the insert jets. This additional fuel, as shown in Fig. 12(B), apparently burned on the shoulders of the funnel like structure. Finally, as the overall fuel equivalence ratio is increased to 1.49 (Fig. 12C), the very fuel-rich swirled air directly over the injector can no longer support combustion. The estimated fuel equivalence ratio in this central zone is estimated to be about 2.67, which exceeds the rich flammability limits for propane and air. The characteristic funnel of a swirl stabilized flame is no longer visible in Fig. 12(C). The combustion is only taking place where air from the insert and dome jets has reduced the local fuel equivalence ratio to within the flammability limits of propane and air. This can be illustrated by comparing Fig. 12(A) with Fig. 12(C). These two images appear to be negatives of each other—where one is black the other is white. This tends to support an assumption of the fuel mixing with each air passageway in turn from the inside out.

Observations and Conclusions

There have been considerable insights into the operational characteristics of a practical injector gained from this study. However, there is much to be done before a full understanding of the combustion characteristics of a practical gas turbine combustor is achieved.

A complex series of intricate flame shapes have been observed in the Task 150 technology combustor. Each flame shape indicates a different mode of operation, which differ from one another in the location of the flame fronts, or by some structure such as thickness or intensity. The different structures observed arise from changes in the flow fields, mixing patterns, or fuel

equivalence ratio as operating conditions are varied. The fuel equivalence ratio where the flame transitions from one structure to another is the major operating variable affecting flame structure. The flames were attached to the insert air jets when the burner was operated very fuel rich. The flame would then lift, reattach, and lift again as the fuel equivalence ratio was progressively reduced. During the reattachment phase, the flame would take on many of the characteristics of a strong vortex and showed characteristics much like a tornado. Consequently, the terminology of funnel cloud, tornado, and debris cloud were adopted to describe some of the observed flame structure.

Gas velocity measurements were made where the flame is well attached to the injector ($\phi = 0.72$), at fuel-rich conditions ($\phi = 1.49$) where the flame is attached to the dome and insert jets, and in isothermal, nonreactive flows where nitrogen was substituted for the propane fuel. These velocity data have allowed the effect of the flame temperature on the flow field and gas velocities to be determined.

Gas velocity data near the injector have shown sharp peaks in mean axial velocity near the outlet of the injector, and a corresponding strong tangential component in this same location. The insert jets had a marked influence on the axial and radial components, but seemed to have little effect on the tangential velocity components. The sharp gradients in axial velocity component were observed to decay quite rapidly with increasing downstream position. The strong tangential velocities associated with the injector decayed rapidly and diffused to the outer edges of the reactor becoming nearly uniform (ca -1 m/s across the duct by the 150 mm axial location. Mass balance calculations based on isothermal axial velocity measurements have been used to determine the accuracy of the LDA measurements, and to assist in the extrapolation of the velocity to the

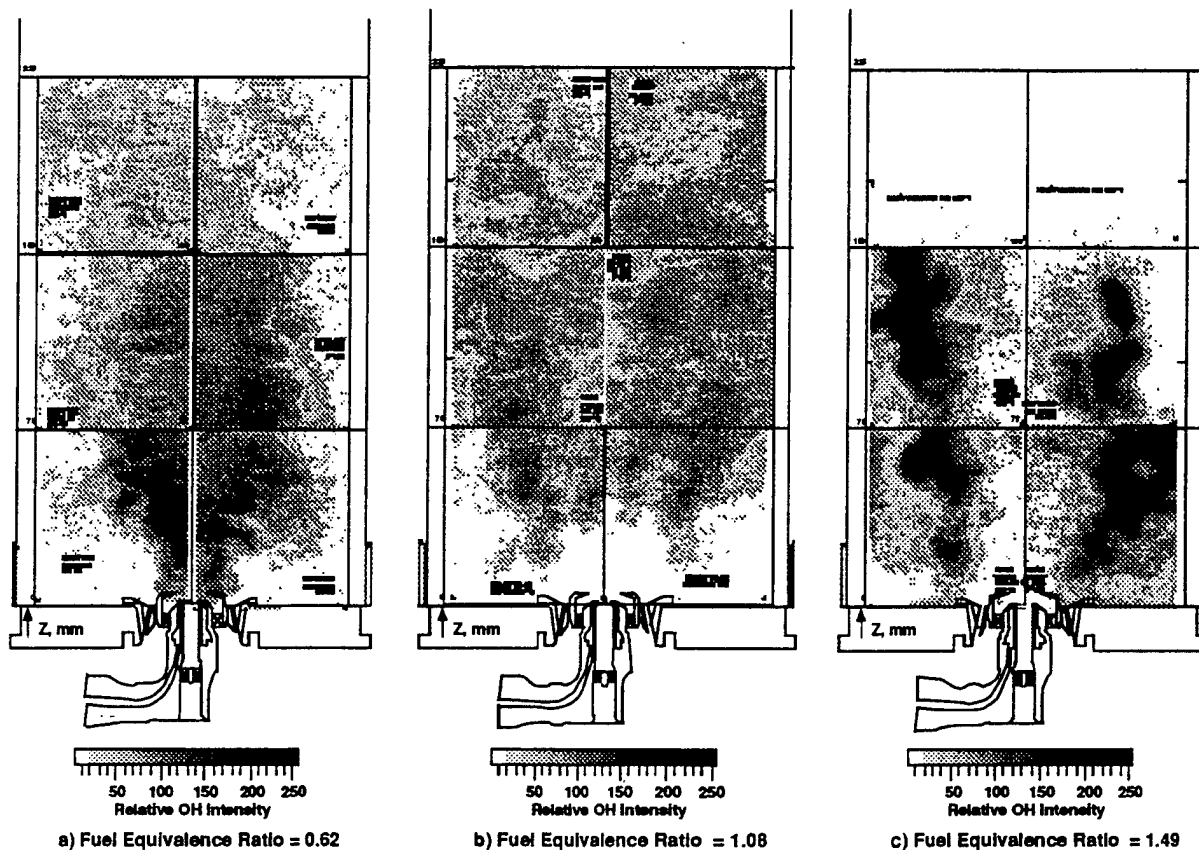


Fig. 12 Instantaneous PLIF contours of OH radical (T150-HS burner, 500 slpm air)

wall. The mass flow rate is strongly influenced by the gradient assumed near the wall, but reasonable velocity interpolations gave reasonable mass balance closure.

Images from still photographs and angular velocity data deduced from the tangential velocity measurements have shown that the flow in the region behaves much like that observed in a strong vortex, with the rotational speed in rpm increasing toward infinity as the zero radius position is approached. The high rotational speeds are consistent with visual observations of the flames. The steep gradients in angular velocity suggest the shear stresses in the swirling eddies are very high.

An analysis of the zero axial velocity contours for one of the isothermal flow cases (14 slpm N_2 , and 500 slpm air) has been used to show the complex flow structure that includes four recirculation zones: one at the bottom edge of the reactor driven by the dome jets, a second small but intense recirculation zone associated with the injector swirlers directly over the injector, a third major recirculation zone that begins at the edge of the injector and angles upward to the wall of the reactor, and a weak fourth recirculation zone high up in the combustor. The

weak fourth zone was not seen in the combustor flows. The recirculation zones are consistent with the visual observations and video images taken of the reactor.

CARS gas temperature measurements have been successfully made in the Task 150 technology combustor. The measured peak temperatures were slightly below the predicted adiabatic flame temperature for the stoichiometric and fuel rich cases. The peak temperature was slightly higher than the adiabatic flame temperature for the lean case, which suggests a local diffusion zone within the flame that is close to a stoichiometric fuel equivalence ratio.

The variation in temperature field as the fuel equivalence ratio changes from fuel lean to fuel rich seemed to be consistent with the observations made from the still photographs. In general, the temperature measurements are consistent with the visual flame conditions, the PLIF images of the OH radical, and the velocity measurements for this particular test condition.

The PLIF images of the OH radical taken with the Task 150-HS technology burner dramatically illustrate the characteristics of swirling flames and the highly variable nature of the flame shape. The air from the insert jets significantly affects the flame structure, and the different modes of operation observed. Correlation of these OH images with the partitioning of the air flow rates through the various air passageways of the injector showed a consistent correlation between the local fuel equivalence ratio and the location of the flame structure. The images at low overall fuel equivalence ratio where the flame is well attached to the burner, and the images at high overall fuel equivalence ratio where the flame is attached to the insert jets are negatives of each other—where one is black the other is white. This supports the assumption of the fuel mixing with each passageway in turn from the inside out.

Table 2 Local ϕ from total fuel flow and air for each flow passage combination

Overall ϕ	ϕ with air from primary swirler	ϕ with air from primary + secondary swirlers	ϕ with air from primary + secondary swirlers + insert jets
0.62	4.17	1.11	0.80
1.08	7.26	1.94	1.39
1.49	10.02	2.67	1.92

Acknowledgments

This paper presents results from an Air Force Office of Scientific Research (AFOSR) program being conducted at Brigham Young University (BYU), Provo, Utah, and at Wright-Patterson Air Force Base (WPAFB). This study is part of an extensive research effort being carried out by the Fuels Combustion Group of the Aero Propulsion and Power Laboratory at Wright-Patterson Air Force Base (APPL, WPAFB), Dayton, Ohio, in which simple and complex diffusion flames are being studied to understand better the fundamentals of gas turbine combustion. The program's long-term goal is to improve the design methodology of gas turbine combustors.

References

- Boyack, K. W., and Hedman, P. O., 1990, "Dual-Stokes CARS System for Simultaneous Measurement of Temperature and Multiple Species in Turbulent Flames," *Twenty-Third Symposium (International) on Combustion*, The Combustion Institute, Pittsburgh, PA.
- Hancock, R. D., Hedman, P. O., and Kramer, S. K., 1991, "Coherent Anti-Stokes Raman Spectroscopy (CARS) Temperature and Species Concentration Measurements in Coal-Seeded Flames," *Combustion and Flame*, Vol. 71, pp. 593-604.
- Hancock, R. D., Boyack, K. W., and Hedman, P. O., 1992, "Coherent Anti-Stokes Raman Spectroscopy (CARS) in Pulverized Coal Flames," *Advances in Coal Spectroscopy*, Henk L. C. Meuzelaar, ed., Plenum Publishing Company, pp. 373-407.
- Roquemore, W. M., Reddy, V. K., Hedman, P. O., Post, M. E., Chen, T. H., Goss, L. P., Trump, D., Vilimpoc, V., and Sturgess, G. J., 1991, "Experimental and Theoretical Studies in a Gas-Fueled Research Combustor," Paper No. AIAA 91-0639.
- Sturgess, G. J., Heneghan, S. P., Vangsness, M. D., Ballal, D. R., and Lesmerises, A. L., 1991a, "Lean Blowout in a Research Combustor at Simulated Low Pressures," ASME Paper No. 91-GT-359.
- Sturgess, G. J., Sloan, D. G., Roquemore, W. M., Reddy, V. K., A. L. Shouse, D., Lesmerises, A. L., Ballal, D. R., Heneghan, S. P., Vangsness, M. D., and Hedman, P. O., 1991b, "Flame Stability and Lean Blowout—A Research Program Progress Report," *Proceedings of the 10th ISABE Conference*, Nottingham, United Kingdom, pp. 372-384.
- Sturgess, G. J., Sloan, D. G., Lesmerises, A. L., Heneghan, S. P., and Ballal, D. R., 1992, "Design and Development of a Research Combustor for Lean Blowout Studies," ASME JOURNAL OF ENGINEERING FOR GAS TURBINES AND POWER, Vol. 114, pp. 13-19.
- Sturgess, G. J., Heneghan, S. P., Vangsness, M. D., Ballal, D. R., Lesmerises, A. L., and Shouse, D., 1993, "Effects of Back-Pressure in a Lean Blowout Research Combustor," ASME JOURNAL OF ENGINEERING FOR GAS TURBINES AND POWER, Vol. 115, pp. 486-498.
- Sturgess, G. J., and Shouse, D., 1993, "Lean Blowout Research in a Generic Gas Turbine Combustor With High Optical Access," ASME Paper No. 93-GT-332.

STRUCTURE OF A SPRAY FLAME STABILIZED ON A PRODUCTION ENGINE COMBUSTOR SWIRL CUP

FUMIAKI TAKAHASHI AND W. JOHN SCHMOLL

*University of Dayton Research Institute
Dayton, OH 45469, USA*

GARY L. SWITZER

*Systems Research Laboratories, Inc., A Division of Arvin/Calspan
Dayton, OH 45440, USA*

AND

DALE T. SHOUSE

*Wright Laboratory, Aero Propulsion and Power Directorate
Wright-Patterson Air Force Base, OH 45433, USA*

The near-field structure of a turbulent flame stabilized on a production gas-turbine engine combustor fuel injector/air swirler system (i.e., swirl cup) has been studied using phase-Doppler anemometry and coherent anti-Stokes Raman spectroscopy (CARS) at atmospheric pressure. A Jet-A fuel spray from a simplex atomizer impinges onto a coaxially located liquid filming surface between countervailing air streams for secondary atomization using high shear forces. An inverted conical flame with a cone angle of $\sim 90^\circ$ was formed in the inner shear layer of the low-temperature droplet-laden hollow-cone air jet, which divides high-temperature internal and external recirculation zones. Small droplets disappeared in the inner and downstream spray regions by evaporation along the droplet trajectories at higher temperatures and longer residence times, thereby increasing arithmetic and Sauter mean diameters. No fuel droplets were found in the internal recirculation zone. Despite frequent laser-induced breakdown in the dense spray region, CARS thermometry successfully determined the gas temperature. The temperature histograms show a wide distribution inside the flame zone, indicating enhanced stirring of cold air, vaporized fuel, and hot combustion products. On the other hand, the fate of fuel droplets, which did not participate in the combustion process directly in the near field, must play an important role in determining the combustion efficiency and pollutant emission levels.

Introduction

In advanced combustion systems for aircraft gas-turbine engines, a large portion of combustion air is admitted into the primary zone through air swirlers in the dome in order to provide uniform fuel-air mixing and to reduce pollutant (NO_x) emissions [1]. Consequently, the development of a high-performance fuel injector/air swirler system plays a key role in achieving good fuel-lean stability at a low power operating condition, and thorough fuel-air mixing, efficient combustion, and low pollutant emissions at a high power condition. Despite the necessity of a fundamental understanding of spray-flame aerodynamics in the flow field generated by the swirler, quantitative measurements using nonintrusive laser diagnostic techniques have only begun in recent years. Thus, physical and chemical processes taking place simultaneously in such spray flames (i.e., the

dynamic interactions between the swirling turbulent flow, fuel droplet vaporization, fuel vapor transport/mixing, and combustion) have not been fully understood.

Swirling flows have long been used in many practical combustion devices to control the stability and intensity of combustion and the size and shape of the flame region [2]. Early studies [3-8] on the characteristics of swirl combustion were mostly based on gaseous fuels. Characterization of swirl combustion has progressed with the development of various laser diagnostic techniques. Laser-Doppler velocimetry has long been a major tool in revealing the turbulent flow field in a combustor [5,7,8]. Recent studies [9-15] using phase-Doppler anemometry (PDA) have contributed greatly to the characterization of both swirling and nonswirling, combustive and noncombustive sprays. PDA provides spatially resolved information on the size and velocity of individual drop-

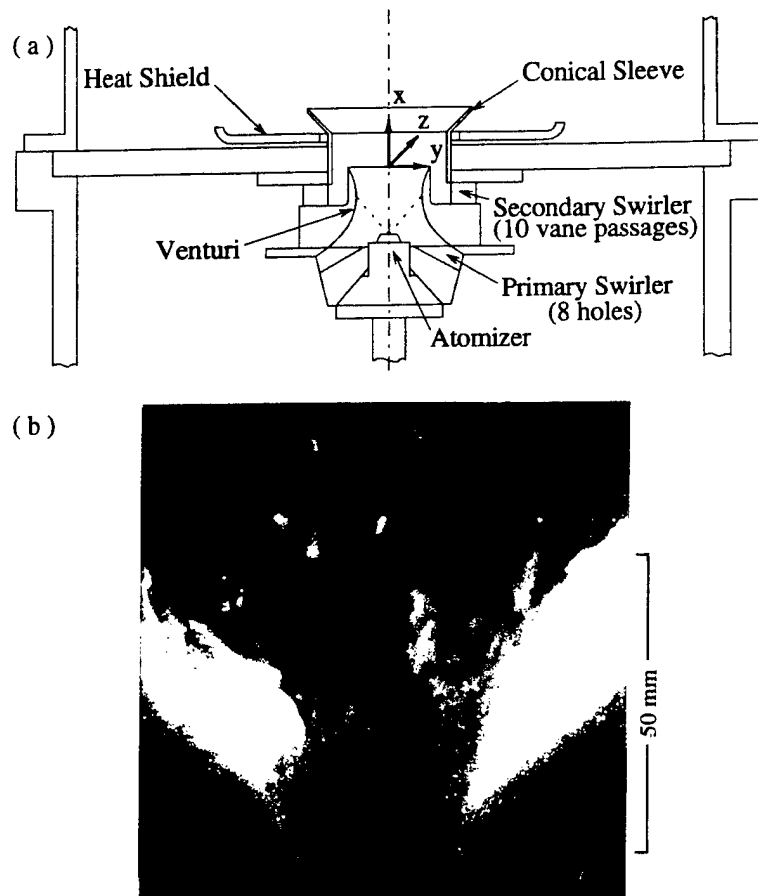


FIG. 1. (a) Schematic of the research combustor with a production gas-turbine engine combustor swirl cup. (b) A time-exposure (1/125 s) direct photograph of the Jet-A spray flame with instantaneous (10 ns) planar visualization of fuel droplets.

lets and gas velocity within the spray. More recently, attempts to measure scalars in the gas phase in spray flames have been made using various nonintrusive diagnostic techniques. A common difficulty in these measurements is the interference of liquid droplets. Species concentration has been measured with some success using exciplex fluorescence [16], laser-induced fluorescence [17], and absorption [15,18–20]. Comparable nonintrusive temperature measurements in spray flames have not been reported. Coherent anti-Stokes Raman spectroscopy (CARS) has been known to have significant advantages over other nonintrusive techniques [21]. The feasibility for CARS thermometry to provide reliable gas temperature measurements in practical combustion environments including the presence of liquid droplets has been examined [22–26].

In this study, droplet size, velocity components, and gas-phase scalar (temperature) have been measured using three-component PDA and CARS in a spray flame stabilized on a practical engine combus-

tor swirl cup at atmospheric pressure. Although, in practical combustors, typical inlet air temperatures and pressures are substantially higher and multiple swirl cups are frequently used, the current single-cup research combustor must preserve some fundamental features of the spray combustion phenomena in real hardware. On the other hand, because slight changes in the hardware would result in significant differences in the combustion characteristics, it is meaningful to use actual combustor parts to avoid oversimplification. The purposes of this study are (1) to gain a better understanding of the coupled physical processes in a spray flame in a swirling flow generated by the swirl cup, and (2) to provide basic information useful for developmental and modeling efforts of the fuel atomizer/air swirler unit.

Experimental Techniques

In the research combustor used (Fig. 1a), a production engine (General Electric CFM56) combus-

tor dome swirl cup is attached on a mounting plate with small cooling holes placed in the inlet of a combustion chimney (150×150 -mm rounded square cross section; 483-mm length) with quartz windows on three sides for laser diagnostics. The dome swirl-cup assembly consists of several separate parts: a 90° -spray-angle simplex atomizer, a primary swirler with eight holes (clockwise rotation if viewed from downstream), a venturi, a secondary swirler with 10 vane passages (counterclockwise rotation if viewed from downstream), and a 90° -cone-angle flare/sleeve. Jet-A fuel injects from the central simplex atomizer at a mass flow rate of 1.30 g/s (liquid pressure drop: 169 kPa), partially convecting downstream and partially impinging on the venturi inner surface to form a thin film for the secondary atomization by the counterrotating swirling air at room temperature. The total air mass flow rate through the swirl cup and the mounting plate cooling holes is 29.7 g/s (pressure drop: 508 mm H_2O , $\sim 5\%$ atmospheric pressure). Approximately 78% of the total air flows through the swirler. The calculated equivalence ratios based on the total and swirler air are approximately 0.67 and 0.86, respectively.

The three-component PDA (Dantec Measurement Technology) consists of an optic system and a covariance-type signal processor. An argon-ion laser (Coherent Innova 200) is used as a light source. The optic system includes a color separator/fiber-optic coupler unit with a Bragg cell, a two-dimensional (2D) fiber-optic transceiver probe with a velocity component separation based on color (514.5 nm: axial component; 488 nm: radial component), a one-dimensional (1D) transmitter probe (476.5 nm: tangential component), and a receiver. The Bragg cell is used to split the light from the laser (typical operating output: 5 W) into two beams with one beam frequency-shifted at 40 MHz to avoid directional ambiguity. The focal lengths of the 2D and 1D probe focusing lenses are 310 and 400 mm, respectively. The calculated fringe spacings of the 514.5-, 488-, and 476.5-nm beams are 4.1, 4.0, and 5.0 μm , respectively. The scattering light of 514 and 488 nm is detected by the receiver at a 70° -off-axis forward scattering mode, and that of 476.5 nm is detected by the 2D probe at a 90° -off-axis mode. The measuring volume is approximately $210\text{-}\mu\text{m}$ diameter \times $100\text{-}\mu\text{m}$ length.

The construction and capabilities of the CARS system employed have been described in detail elsewhere [23]. The CARS system is based upon a frequency-doubled Nd:YAG laser (Quanta-Ray DCR-2) that provides 10-ns pulses of 532-nm radiation at a repetition rate of 10 Hz and a broadband (150 cm^{-1}) dye laser that is tuned to the Stokes vibrational frequency of the nitrogen molecule (607 nm). The system is configured with a folded-BOXCARS [21] optical geometry to produce a sampled spatial volume of $\sim 1\text{ mm}^3$, with the CARS information being gen-

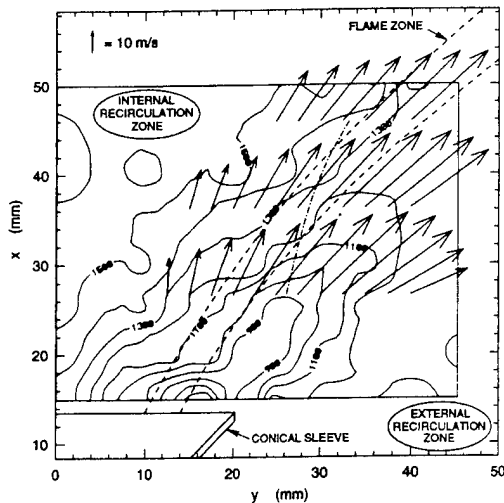


FIG. 2. Mean droplet velocity vector field and isotherms. ---, maximum PDA data rate locus. Temperature in K.

erated within a path length of 2 mm. The accuracy of the CARS temperature determinations is estimated to range between 10% near room temperature and 5% near stoichiometric flame temperature, with the largest contribution to uncertainty resulting from shot-to-shot variation in the Stokes-laser spectral distribution.

Results and Discussion

Optical Observations:

Figure 1b shows a time-exposure direct photograph of the spray flame investigated with illumination by a sheet (~ 0.5 -mm thickness) of Nd:YAG pulsed (10 ns) laser. The inverted conical sleeve (cone angle: $\sim 90^\circ$) was stabilized inside the flared sleeve adjacent to its exit plane. The visible flame zone was blue near the swirl cup and deflected upward near the chimney windows. Yellow streaks caused by soot formation were seen downstream. The laser sheet illuminated the fuel droplets in the vertical plane containing the axis. A large number of droplets were seen along the flame zone, spreading out downstream. A densely populated droplet stream was observed, even outside the flame zone in the extension of the conical sleeve. A high-speed (5000 fps) color cinematography (not shown) revealed intense flame movement downstream, which made the flame zone in the time-exposure photographs appear thick.

PDA Measurements:

Figure 2 shows the mean droplet velocity vector field in the near-exit region. The PDA measurements

were made at three different heights from the exit plane of the venturi ($x = 26.7, 36.4, 46.1$ mm). The approximate location of the visible flame zone in the figure was measured by processing a scanned image of a time-exposure photograph. The isotherms from the CARS measurements and the locus of the maximum PDA data rate, also included in the figure, will be described in more detail later. The general direction of the droplet velocity vectors is in the extension of the 90° -cone-angle sleeve. The flame zone is located in the middle of the spray region nearly parallel to the droplet velocity vectors. This result represents a unique feature of the swirl-cup-stabilized spray flames, whereas simple pressure-atomizing spray flames are typically formed outside the entire spray (similar to gaseous diffusion flames) [13] or in the inner edge region of the spray (in case of swirl-stabilized flames [12]), where enough oxygen is available. Thus, the current result of the swirl-cup-stabilized flame shows enhanced oxygen penetration into the spray region as a result of turbulent stirring associated with the geometric configuration of the fuel atomizer and air swirler. Particularly, functional merits of the means for secondary atomization must be significant.

Figure 3 shows the total and size-classed data (droplet arrival) rates in the PDA measurements and the probability density functions (pdf's), or histograms, of the droplet diameter [$P(d)$] at selected locations. The total data rate was determined by dividing the number of attempted samples by the elapsed time, and the data rates for various droplet size classes were determined from the total data rate and the probability (the pdf times the bin width). The total data rate at $x = 26.7$ mm (Fig. 3a) reached a peak of 6000 Hz at $y = 26$ mm and decreased rapidly on both sides to ~ 10 Hz at $y = 12.5$ mm and 40 mm. No droplets were detected in the core region ($y < 12$ mm). This is consistent with the laser-sheet visualization results (Fig. 1b). The histograms show a shift in the size distribution in the radial direction. In the outer region ($y > 30$ mm), a relatively sharp peak in a small diameter range ($5\text{--}10\text{ }\mu\text{m}$) is seen, whereas in the inner region ($y < 25$ mm), the probability of small droplets decreased and the distribution became wider. Consequently, the size-classed data rates show high number fluxes of small droplets in the outer region. As will be discussed in more detail later, the droplets in the outer region pass through a relatively low-temperature region, compared to those in the inner region. Apparently, disappearance of the droplets by evaporation started from smaller particles whose trajectories passed through a high-temperature region. The peak value of the total data rate decreased rapidly downstream [2400 Hz at $z = 36.4$ mm (Fig. 3b), 750 Hz at $z = 46.1$ mm (Fig. 3c)]. Because the droplet trajectories are inclined at $\sim 45^\circ$ with respect to the axis and expand downstream, dispersion of droplets is certainly a factor

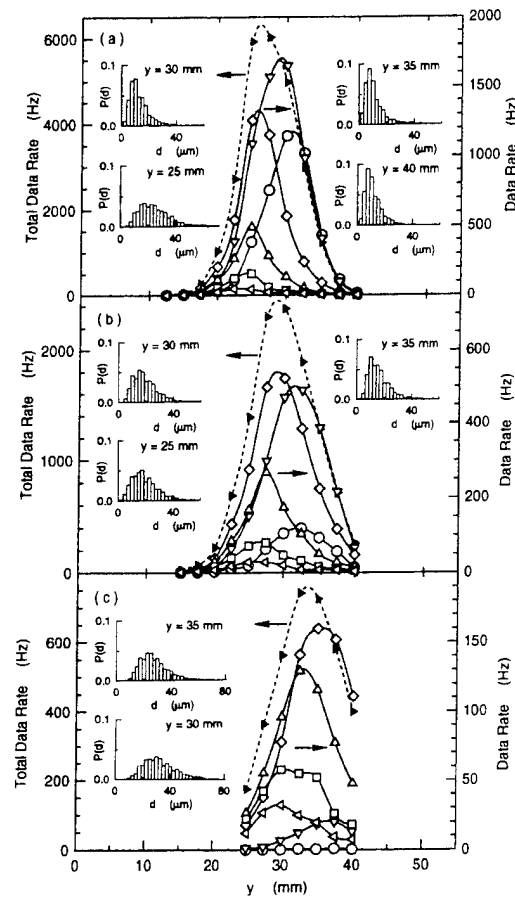


FIG. 3. PDA data rates and histograms of the droplet diameter. (a) $x = 26.7$ mm, (b) $x = 36.4$ mm, and (c) $x = 46.1$ mm. --- \blacktriangleright ---, total; \circ , $5\text{ }\mu\text{m}$; ∇ , $10\text{ }\mu\text{m}$; \diamond , $20\text{ }\mu\text{m}$; Δ , $30\text{ }\mu\text{m}$; \square , $40\text{ }\mu\text{m}$; \triangleleft , $50\text{ }\mu\text{m}$.

contributing to the lowered data rate. Furthermore, disappearance of small droplets by evaporation occurred at longer residence times downstream.

In contrast to the present results on the reacting case, PDA measurements in an isothermal (water) spray from a similar swirl cup reported by Wang et al. [14] showed substantially high data rates of small droplets in the central region. The current results indicate that the engulfment of the droplets into the internal recirculation zone in the flame is prevented in two ways: (1) the droplets injected toward the recirculation zone are evaporated—the flux of droplets directly from the atomizer is low compared to that from secondary atomization, and (2) perhaps no droplets exist in the downstream stagnation region to come back into the recirculation zone.

Figure 4 shows the radial variations in the arithmetic (D_{10}) and Sauter (D_{32}) mean diameters at three different heights. The radial locations of the visible flame zone are also included in the figure. At

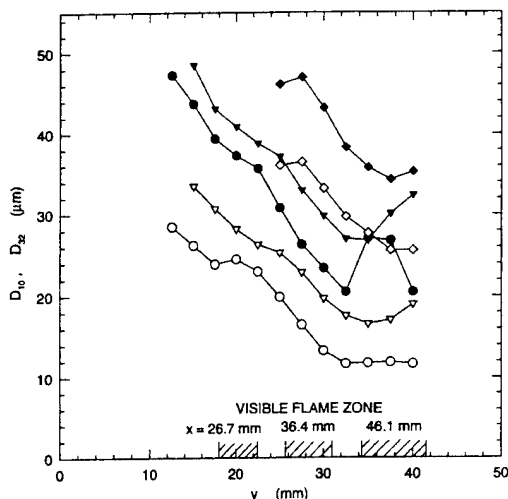


FIG. 4. Mean droplet diameters. \circ , \bullet , $x = 26.7$ mm; ∇ , \blacktriangledown , $x = 36.4$ mm; \diamond , \blacklozenge , $x = 46.1$ mm. Open: arithmetic mean (D_{10}); filled: Sauter mean (D_{32}).

$x = 26.7$ mm. D_{10} was small ($\sim 12 \mu\text{m}$) in the outer spray region ($y > 30$ mm) and increased inwardly. As small droplets disappeared in the inner region, as described before, the mean diameter increased. In the downstream positions, the same trend was observed, and D_{10} increased because of evaporation at longer residence times. Here D_{32} was larger than D_{10} , as expected, because D_{32} reflects the volume of the droplets. Because D_{32} is influenced by the occasional arrival of droplets having large diameters (volumes), it exhibited more scatter than D_{10} in the outer spray region where the progress of evaporation was less than in the inner region.

Figure 5 shows the mean and root-mean-square (rms) fluctuations of the axial, radial, and tangential droplet velocity components for different size classes at $z = 26.7$ mm. The bin width used is $5 \mu\text{m}$, and the diameter shown is the center value of each bin. For both axial and radial components, the mean velocity for a smaller size class showed a sharper peak than that of a larger size class. The mean tangential velocity component of a small size class was higher than that of a larger size class in the inner region and vice versa in the outer region. The rms's of a small size class for all three components were higher than those of a large size class. Small droplets follow the gas flow more closely because they possess lower inertia and drag forces. The mean axial and radial velocity components for the smallest size class ($5 \mu\text{m}$), which must be closest to the gas flow, peaked at $y = 31$ mm, indicating that the main airflow injected along the extension of the conical sleeve at 45° , creating the low-temperature zone outside the flame zone. Thus, the flame zone was formed in the inner shear layer of the air jet. As the flow diverged down-

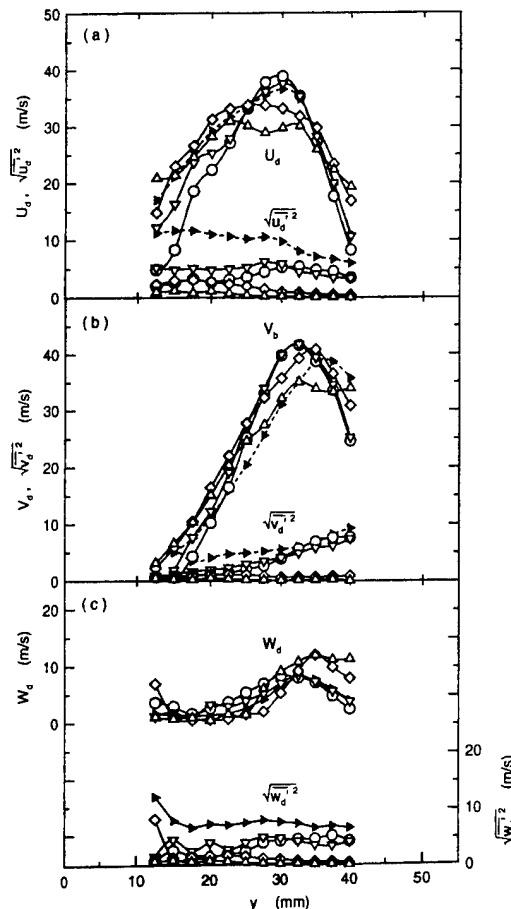


FIG. 5. Mean and root-mean-square fluctuation of (a) axial, (b) radial, and (c) tangential droplet velocity components. $-\triangle---$, total; \circ , $5 \mu\text{m}$; ∇ , $10 \mu\text{m}$; \diamond , $30 \mu\text{m}$; \square , $50 \mu\text{m}$.

stream, the maximum values of the velocity components decreased (not shown), but the trends were similar to those at $x = 26.7$ mm.

CARS Measurements:

The liquid fuel spray of this combustor presented a challenging environment for the CARS measurement technique. A high density of liquid droplets exhibited near the nozzle exit and at the edge of the visible flame contributed to several effects that complicated temperature measurements. Among these were beam steering, nonresonant CARS generation, and droplet-induced breakdown. Index of refraction gradients created by the high concentrations of droplets affected steering of the CARS pump and Stokes beams, thus prohibiting the necessary beam overlap and resulting in a loss of some temperature samples

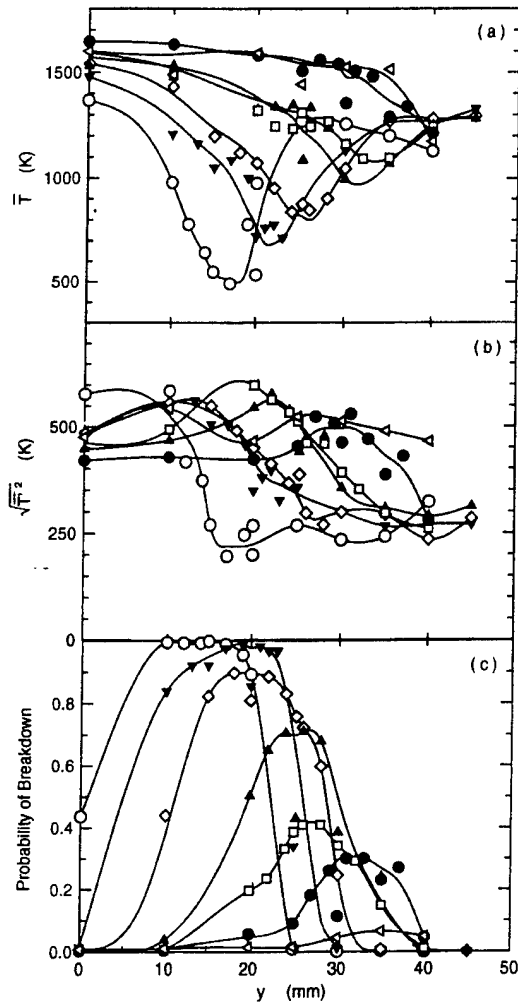


FIG. 6. (a) Mean and (b) root-mean-square fluctuation gas temperatures and (c) CARS droplet-induced breakdown rate. \circ , $x = 15$ mm; \blacktriangledown , $x = 20$ mm; \diamond , $x = 25$ mm; \blacktriangle , $x = 30$ mm; \square , $x = 35$ mm; \bullet , $x = 40$ mm; \triangleleft , $x = 50$ mm.

at certain locations. The background contributions arising from nonresonant CARS and droplet-induced breakdown have been described [25] and were minimized for these measurements. Corrections for the nonresonant contribution were accommodated in the spectral fitting routines while background subtraction was employed to compensate for the background produced by droplet-induced breakdown.

Figure 6 shows the radial distributions of the mean and rms fluctuation temperatures and the probability of droplet-induced breakdown at various heights. The frequency of breakdown occurrence will be discussed later. The isotherms shown in Fig. 2 were derived from the results in Fig. 6a. The mean tem-

peratures on the centerline in the internal recirculation zone were in the range of 1400–1650 K, and those in the outermost data points ($y = 45$ mm) in the edge of the external recirculation zone were ~ 1300 K. The low-temperature (500–1100 K) zone was formed along the direction of the cold droplet-laden air jet (see Fig. 2). The visible flame zone was formed just inside and along the low-temperature zone in the shear layer of the air jet. The low-temperature zone became less evident downstream ($x > 40$ mm). The rms fluctuation temperature (Fig. 6b) was higher (400–600 K) in the internal recirculation zone with the maximum just inside the flame zone, compared to that outside (~ 300 K), indicating enhanced stirring of hot and cold fluid packets in the shear layer where the flame zone resided.

Figure 7 shows the temperature pdf's (histograms) with a bin width of 100 K at three different heights ($x = 20, 30$, and 40 mm). Four radial locations are selected: the centerline, a few millimeters inside the flame zone, the low-temperature zone, and $y = 40$ mm. In general, wide temperature distributions were observed in the central region inside the visible flame zone (Figs. 7a, 7b, 7e, 7f, 7i, and 7j), compared to the outer region including the low-temperature zone (Figs. 7c, 7g, and 7k) and the external recirculation zone (Figs. 7d, 7h, and 7l). The results show enhanced turbulent stirring between the high-temperature combustion products and the cold air near the flame zone. The minimum value in the temperature distribution decreased toward the nozzle along the centerline down to 300 K (Fig. 7a), indicating stirring between the cold air directly from the swirl cup and the combustion products recirculated. In the lower part of the low-temperature zone (Fig. 7c), a slight tendency of bimodal distribution was observed as a result of the occasional arrival of the hot gases (> 2000 K) into the cold air. The narrower peaks of the temperature distribution in the external recirculation zone (Figs. 7d, 7h, and 7l) indicate that the hot combustion products and cold air are mixed well.

The probability of droplet-induced breakdown (Fig. 6c) was determined as the number of breakdown occurrences in the total attempted CARS samples at each location. The background subtraction scheme implemented into the spectral fitting routines made it possible to retrieve temperature information if the background shift was relatively small. Thus, the number of samples with breakdown includes both successful temperature measurements and discarded samples due to the disrupted signal. The breakdown probability reached ~ 0.99 in the near-exit dense spray region ($x < 20$ mm). The peak value greatly decreased downstream (~ 0.07 at $x = 50$ mm). Comparisons between the breakdown probability and the PDA data rate (Fig. 3) show both similarities and differences. Basically, both the breakdown probability and the PDA data rate depend on how dense the spray is at the point where the probe

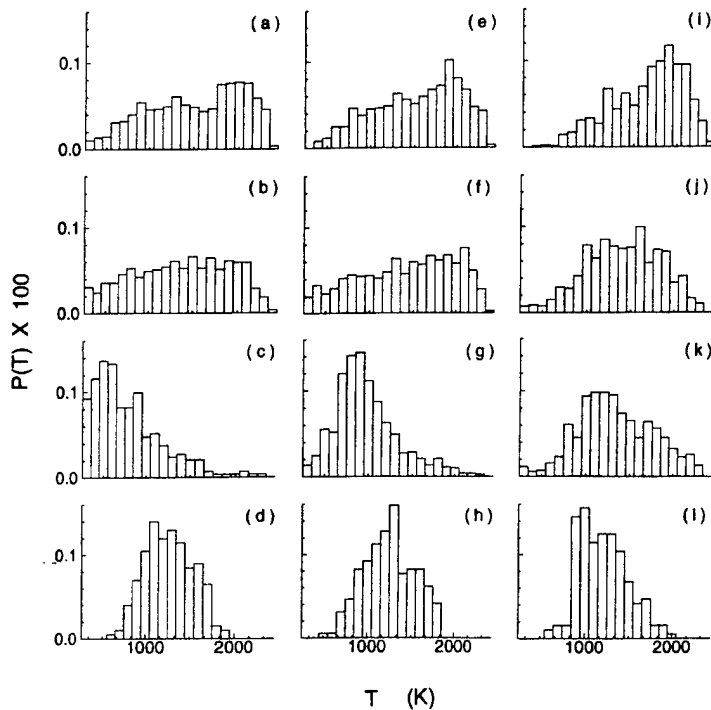


FIG. 7. Histograms of the gas temperature. $x = 20$ mm: (a) $y = 0$ mm, (b) $y = 10$ mm, (c) $y = 22$ mm, and (d) $y = 40$ mm. $x = 30$ mm: (e) $y = 0$ mm, (f) $y = 20$ mm, (g) $y = 30$ mm, and (h) $y = 40$ mm. $x = 40$ mm: (i) $y = 0$ mm, (j) $y = 30$ mm, (k) $y = 37$ mm, and (l) $y = 40$ mm.

volume is located; thus, in general, both peak in a dense region and decrease downstream. However, the breakdown curves show substantially broader distribution with tailing inwardly, and their peak locations, if interpolated for the heights for the PDA measurements, are closer to the centerline compared with the total PDA data rates. Major reasons for the differences must stem from the breakdown occurrence along the CARS laser beams. The energy flux of the focused beams of the CARS system is approximately 10^{11} W/cm², which is close to the breakdown threshold (order of 10^{12} W/cm²) in a "clean" environment. Because the introduction of liquid droplets into these beams reduces the threshold by several orders of magnitude, breakdown occurs well before the beams attain their normal focus. The quality of measured variables and the size of each probe volume may contribute, to some extent, to the differences in the PDA data rate and the CARS breakdown probability measurements. The PDA data rate represents the number flux of the droplets times the cross-sectional area measured over the elapsed time, whereas the CARS breakdown is an instantaneous spatial quantity directly related to the number density of the droplets. The probe volume of CARS is three orders of magnitude larger than that of PDA, and the horizontal cross-sectional area is two orders of magnitude larger. Because of the large probe volume, the CARS breakdown data must have a significantly higher possibility of multiple droplets inside the probe volume in the dense spray region.

Near-Swirl-Cup Structure:

The combustion process in a combustor becomes evaporation-rate-controlled if the evaporation of droplets does not complete within a residence time in the system. A crude estimate for the critical mean droplet size above which evaporation starts to limit combustion efficiency can be made by considering a simple droplet evaporation process [2]. The residence time of the droplets from the swirl-cup exit to the height where the droplets would impinge on the chimney window, for example, determined by dividing the trajectory distance (~ 0.1 m) by the maximum velocity for large droplets (~ 30 m/s), is ~ 3 ms. The critical mean drop size at the residence time of 3 ms is estimated for kerosene (Jet-A) as ~ 60 μ m [2]. Measured D_{32} is less than 60 μ m in the whole measurement range (Fig. 2); thus, the evaporation rate must not be rate-controlling, in a global sense, if all droplets pass through the high-temperature region. However, a close examination of the structure of the spray flame revealed that a considerable portion of the fuel droplets outside the flame zone does not participate in the combustion process in the near-swirl-cup region. Some of these droplets must burn downstream, and others must enter into the external recirculation zone, evaporate, pyrolyze, and mix with the cooling air. In a practical combustor, the external recirculation may be small or does not exist, depending on the shape of the dome. Furthermore, in a multiple-cup combustor, interaction between the ad-

jacent flames may occur. In any case, the fate of the droplets escaping from the flame in the near-exit region must be important in achieving a high combustion efficiency and reducing emissions of various pollutants.

Conclusions

The PDA and CARS measurements have provided useful information on the structure of a spray flame in a research combustor using actual engine combustor hardware. In spite of a high probability of laser-induced breakdown, CARS thermometry successfully determined the temperature field in the dense spray region of a simulated practical combustion system. An inverted conical flame zone is formed in the inner shear layer of the low-temperature droplet-laden hollow-cone jet, which divides the high-temperature internal and external recirculation zones. A large temperature fluctuation occurs inside the flame zone, as a result of intense stirring of packets of cold air, vaporized fuel, and hot combustion products. The droplet size distribution and, in turn, mean diameters are affected strongly by the level of evaporation, which depends on the temperature history and the residence time along the droplet trajectories. The mean and rms fluctuation velocity components depend on droplet size because of the difference in the traceability of a droplet to the turbulent flow. Although a crude estimate for the critical mean drop size shows that, in a global sense, the evaporation rate is not a rate-controlling factor, a significant portion of the droplets does not participate in the combustion process in the near field. The fate of these droplets is an important issue in terms of combustion efficiency and emission characteristics.

Acknowledgments

This work was supported by the U.S. Air Force, Wright Laboratory, Aero Propulsion and Power Directorate, Fuels and Lubrication Division, Wright-Patterson Air Force Base, OH, under Contract No. F33615-92-C-2207 (Technical Monitor: C. W. Frayne). Special thanks to GE Aircraft Engines for providing the swirl-cup hardware, Dantec Measurement Technology for loaning a PDA system, and Messrs. M.D. Vangsness, F. Timko, D. Sutkus, M. Burns, and M. Russell for assisting in the preparation of the experiments.

REFERENCES

1. Dodds, W. J., *Gas Turbine Industry Needs*, Gas Turbine Combustion Challenges and Laser Diagnostics Workshop, Ohio Aerospace Institute, April 1993.
2. Lefebvre, A. H., *Gas Turbine Combustion*, Hemisphere, New York, 1983, p. 127.
3. Beer, J. M., and Chigier, N. A., *Combustion Aerodynamics*, Applied Science, London, 1972.
4. Syred, N., and Beer, J. M., *Combust. Flame* 23:143-201 (1974).
5. Chigier, N. A., and Dvorak, K., *Fifteenth Symposium (International) on Combustion*, The Combustion Institute, Pittsburgh, 1975, pp. 573-585.
6. Lilley, D. G., *AIAA J.* 15:1063 (1977).
7. Gupta, A. K., Beer, J. M., and Swithenbank, J., *Sixteenth Symposium (International) on Combustion*, The Combustion Institute, Pittsburgh, 1977, pp. 79-91.
8. Gouldin, F. C., Depsky, J. S., and Lee, S. E., *AIAA J.* 23:95-102 (1985).
9. Mao, C.-P., Wang, G., and Chigier, N., *Twenty-First Symposium (International) on Combustion*, The Combustion Institute, Pittsburgh, 1988, pp. 665-673.
10. McDonell, V. G., Wood, C. P., and Samuelsen, G. S., *Twenty-First Symposium (International) on Combustion*, The Combustion Institute, Pittsburgh, 1988, pp. 685-694.
11. Cameron, C. D., Brouwer, J., and Samuelsen, G. S., *Fourth International Conference on Liquid Atomization and Spray Systems*, Sendai, Japan, August 1988, pp. 145-152.
12. Edwards, C. F., and Rudoff, R. C., *Twenty-Third Symposium (International) on Combustion*, The Combustion Institute, Pittsburgh, 1991, pp. 1353-1359.
13. Presser, C., Gupta, A. K., Avedisian, C. T., and Semerjian, H. G., *Twenty-Third Symposium (International) on Combustion*, The Combustion Institute, Pittsburgh, 1991, pp. 1361-1367.
14. Wang, H. Y., McDonell, V. G., and Samuelsen, G. S., *Twenty-Fourth Symposium (International) on Combustion*, The Combustion Institute, Pittsburgh, 1992, pp. 1457-1463.
15. McDonell, V. G., and Samuelsen, G. S., *Twenty-Fourth Symposium (International) on Combustion*, The Combustion Institute, Pittsburgh, 1992, pp. 1557-1564.
16. Melton, L. A., and Verdick, J. F., *Twentieth Symposium (International) on Combustion*, The Combustion Institute, Pittsburgh, 1985, pp. 1283-1290.
17. Allen, M. G., and Hanson, R. K., *Twenty-First Symposium (International) on Combustion*, The Combustion Institute, 1988, pp. 1755-1762.
18. Chraplyvy, A. R., *Appl. Optics* 20:2620 (1981).
19. Adachi, M., McDonell, V. G., and Samuelsen, G. S., *Combust. Sci. Technol.* 75:179 (1991).
20. Drallmeier, J. A., and Peters, J. E., *Atomiz. Sprays* 1:63 (1991).
21. Eckbreath, A. C., *Laser Diagnostics for Combustion Temperature and Species*, Abacus Press, Cambridge, MA, 1988.
22. Switzer, G. L., Goss, L. P., Roquemore, W. M., Bradley, R. P., Schreiber, P. W., and Roh, W. B., *J. Energy* 4:209-215 (1980).
23. Switzer, G. L., and Goss, L. P., in *Temperature: Its Measurement and Control in Science and Industry* (J.

- F. Schooley, Ed.), American Institute of Physics, New York, 1982. pp. 583-387.
24. Bedue, R., Gastebois, P., Bailly, P., Pealat, M., and Taran, J. P. E., *Combust. Flame* 57:141-153 (1984).
 25. Dunn-Rankin, D., Switzer, G. L., Obringer, C. A., and Jackson, T. A., *Appl. Opt.* 29:3150-3159 (1990).
 26. Zhu, J. Y., Tsuruda, T., Sowa, W. A., and Samuelson, G. S., *J. Eng. Gas Turbine Power* 115:515-521 (1993).

COMMENTS

Ruey-Hung Chen, *University of Central Florida, USA*. The amount of fuel droplets not participating in the near-field combustion may depend on, and increases with, the ratio of the vaporization time scale (which is not a concern in gas phase combustion) to the near-field internal recirculation zone time scale (or velocity and length scales). In a previous study on gas-fueled swirl flames, the recirculation zone scales and flame length were shown to depend on the degree of recirculation and the ratio of fuel jet momentum to the recirculating flow momentum [1,2]. Would you please comment on how one should try to characterize the ratio of the two time scales, since it has implications for the completeness of combustion and pollutant emissions.

2. Chen, R.-H. et al., *Combust. Sci. and Tech.* Pittsburgh, 71:197 (1990).

Author's Reply. The amount of fuel droplets not participating in the near-field combustion is independent of the *internal* recirculation zone time scale. Unlike many other initially unmixed flames, whether spray- or gas-fueled, in which the flame zone envelops the fuel jet, the structure of the present swirl-cup-stabilized spray flame is peculiar: The flame is formed radially inside the main fuel (spray) zone. This structure is due in part to, besides swirl, the unique air flow configuration and means of secondary atomization that define the boundary conditions at the swirl-cup exit. As a result, a substantial flux of fuel droplets is ejected outside the flame zone in the near field and partially engulfed in the *external* recirculation zone. The residence time and vaporization time scales can be determined using the regional characteristic velocity and temperature. However, since the characteristics of the external recirculation zone (and the subsequent downstream region) are highly system configuration dependent, the fate of the unburned fuel droplets should be assessed under more realistic conditions.

REFERENCES

1. Chen, R.-H., and Driscoll, J. F. *Twenty-Second Symposium (International) on Combustion*, The Combustion Institute, Pittsburgh, 1989.



AIAA 96-0705
The Role of Transverse Air Jets
in the Formation of
Gas Turbine Emissions

D.T. Shouse, C. Frayne, J. Stutrud
Aero Propulsion and Power Directorate
Wright-Patterson AFB, Ohio

S. Gogineni
Systems Research Laboratories
Dayton, Ohio

G.J. Sturgess
Innovative Scientific Solutions Inc.
Beavercreek, Ohio

34th Aerospace Sciences
Meeting & Exhibit
January 15-18, 1996 / Reno, NV

THE ROLE OF TRANSVERSE AIR JETS IN THE FORMATION OF GAS TURBINE EMISSIONS

D. Shouse, C. Frayne, J. Stutrud
Aero Propulsion and Power Directorate
Wright-Patterson AFB, Ohio

S. Gogineni
Systems Research Laboratories
2800 Indian Ripple Road
Dayton, Ohio

G.J. Sturgess
Innovative Scientific Solutions Inc.
3845, Woodhurst Court,
Beavercreek, Ohio

Abstract

Results are presented of emissions and lean blowout measurements in a generic combustor primary zone for the effects of opposed, circular combustion air jets of a range of sizes, positioned half a dome height downstream from the dome. The primary zone was operated at simulated engine high power conditions, and representative dome and liner pressure drops. It is shown that most of the NO_x is generated in the jets. Although an optimum jet size is identified, the lowest overall emissions resulted from a no combustion air jet configuration; air jets are necessary however, to confer lean blowout stability and short flame length.

Introduction

In 1987 the U.S. Air Force Wright Laboratory, Aero Propulsion and Power Directorate (WL/PO), Wright-Patterson Air Force Base, Ohio, established the *Combustor Design Model Evaluation (CDME) Program*. This effort is a comprehensive joint Government, Industry and University research program aimed at improving the design and analysis capabilities for the combustors of aircraft gas turbine engines. The CDME program is addressing many important aspects of combustor design.

One study that is currently in progress is an investigation into the minimization of engine exhaust emissions, and the relationships between generation of these emissions and combustor operability characteristics. As part of this study a broad-ranging

investigation of combustor primary zone behavior is being conducted.

Program Objectives

The overall intent of this part of the CDME program is to understand the detailed behavior of the major flame holding of a modern generic combustor for aircraft gas turbine engines, and to establish an appropriate database suitable for design purposes.

Test Vehicle

A relatively simple combustor developed under an earlier program¹ has been adapted for the experimental study of the influence of simulated engine primary zone flow structures on the emissions generation and lean stability characteristics.

The combustor consists of a single representative fuel injector and its associated dome interface, mounted in a plain bulkhead. The injector is a high-swirl airblast atomizer², and the dome interface consists of a small, discrete-jet swirler co-annular with the injector, together with a dome heat shield fed with cooling air that is discharged radially across the bulkhead face. The cross-section of the combustor is square for optical access by laser diagnostics, but generous fillets are provided in the corners to suppress vorticity generation that might result in spurious flameholding. The hydraulic diameter is 153 mm and the length is 490 mm. The combustor outlet is restricted by a 45 percent geometric blockage orifice plate to provide representative back pressure of the unsimulated portion of a real combustor.

The combustor is mounted horizontally, and the top and bottom walls are removable, uncooled metal plates that accommodate appropriate arrays of combustion air jets. One combustor side-plate (at 90 degrees to the liner plates containing the air jets) contains a fitting for application of a torch ignitor; the other side contains a full-length quartz window for visual access.

Figure 1 shows the combustor with its air entrance conditioning unit. Air supplies to the dome and the combustion air jets are separately metered, and may be electrically preheated to a maximum temperature of about 500F (533K).

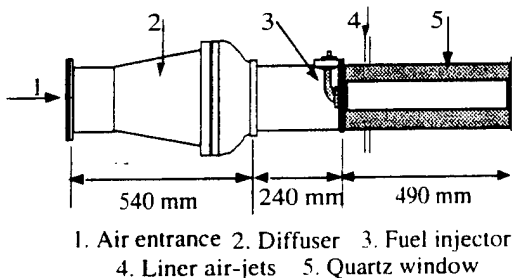


Figure 1a): Laboratory-Scale Gas Turbine Combustor

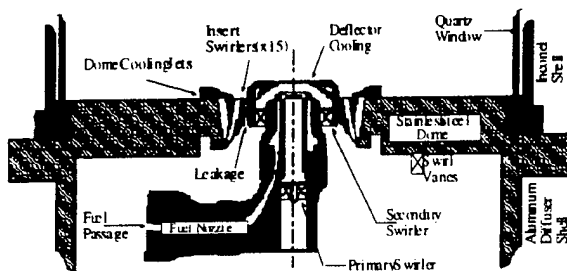


Figure 1b): Combustor Fuel Injector and Dome

Engine Power Simulation

The efficacy of the combustor for its intended purpose is discussed in detail in Reference 2. The combustor represents a "single-cup" planar segment of an annular combustor, and simulates the primary zone only.

It is operated at atmospheric pressure for convenience and cost reasons. Engine high power conditions are simulated by closely matching Spalding's partial modeling flow criterion K_f ,

reasonably approximating the temperature rise term $\Delta T/T_{in}$, and by substituting gaseous propane for liquid JP/Jet fuel. Together, these ensure that engine flow patterns are closely approximated and that liquid evaporation is not a problem. It was concluded that the combustor can reproduce reasonably well and to an acceptable degree the flow patterns of an engine combustor.

Description of the Rig

The test combustor is installed horizontally in a test cell at Wright Patterson Air Force Base, Ohio. Reference 2 gives a detailed description of the rig and facility in which the combustor is installed. Of relevance here is the fact that inlet air was dried to very low dew points prior to entering the compressors.

Experimental Variables

The array of combustion air ports presently to be described is confined to an opposed pair of circular flush holes (in upper and lower liners) placed inline with the fuel injector centerline. Diameters of 0.25 in. (6.35 mm), 0.375 in. (9.53 mm), 0.50 in. (12.70 mm) and 0.75 in. (19.05 mm) are reported. Although these pairs of jets could be situated 1.0, 0.75 and 0.5 dome heights (H_d) downstream from the dome, only the latter position is used in the results to be presented.

The inlet air temperature was held constant at a nominal 500F (533K). This value was selected in order to first, satisfy the simulation criteria, and second, to ensure the generation of sufficient NOx without a large burnup of CO; thus, trends and effects in these two pollutants could be detected easily and measured accurately.

Pressure drop across a combustor is in practice, not a free variable but is set by engine performance considerations. Generally, the allowable pressure drop across a dome is a little higher than that across liners due to the recovery of some dynamic head from the compressor. For the majority of the work to be presented the dome pressure drop was held fixed at a nominal value of 4.3 percent of the upstream pressure, and the liner pressure drop was 3.0 percent. These values are representative of typical engine conditions. Under these conditions all of the transverse jets with different initial diameters penetrated to the combustor centerline.

To extend the generality of the results the normal range of liner air pressure drops for each hole size was 1-5 percent of the upstream pressure. To explore the effects of jet turbulence this range was extended to as high as 12 percent for the 0.5 in. (12.70 mm) hole.

Emissions Measurements

The emissions sampling probe is a water-cooled, quick-quench, single-point type, and is made of stainless steel with an Inconel tip. The sample enters a converging nozzle of orifice diameter 0.059 in. (1.5 mm), which then diverges to the 0.180 in. (4.6 mm) I.D. of the stainless tube. This arrangement results in a supersonic expansion which reduces the gas stream temperature. Together with the water cooling of the probe, this achieves quenching of chemical reactions.

The sample is transferred from the probe by heated lines that avoid condensation, to the emissions measuring equipment, which is fairly standard. Again, detailed descriptions are given in Reference 2.

The axial measurement plane for gaseous emissions was 14 in. (356 mm) downstream from the face of the dome. Kinetics calculations indicated that at this position the bulk NOx was not changing too rapidly, and CO consumption rates were reasonably slow. Furthermore, at this axial station the profiles of measured emissions were flat enough over the entire range of equivalence ratios (for all jet sizes at the $H_d/2$ position) for centerpoint and area-weighted mean values to be in exceptionally close agreement, thus permitting centerpoint values to be used for economy, (errors less than ± 10 percent). Since the emissions probe was introduced into the combustor from the rear through the exit orifice plate, the extent of the radial traverses was determined by the size of this orifice plate. The extent of the radial profile traverses was ± 1.75 in. (± 44 mm) from the combustor centerline. Traverses were made both horizontally and vertically.

Comparisons were made of the metered fuel/air ratios to the measured exhaust fuel/air ratios based on the carbon balance. The agreements were better than 10 percent for metered equivalence ratios of 1.0 and less.

As the inlet air was dried in the facility prior to entering the rig the NOx levels to be quoted are all dry values.

Test Procedure

For each air-port size, axial position and pressure drop, the fuel flow rate was varied to cover a range of overall equivalence ratios such that the anticipated minimum in the CO-curve and the maximum in the NOx-curve could be fully established.

It is usual to present emissions measurements as a function of an appropriate equivalence ratio. The presumption is that the flow patterns in the combustor are established by the geometry and remain unchanged with this method (varying fuel flow rate) of operating, thus making equivalence ratio a good single descriptor of the emissions. Since the combustion air jets established by the different liner hole sizes all penetrated to the combustor centerline, this is a reasonable supposition. However, the high engine power simulation assumed that flow patterns were not affected to first order by the fuel flow. With a gaseous fuel having flow rate as a prime operational variable, this assumption must be verified due to fuel momentum considerations.

It is difficult to establish a true uniqueness test of the data due to the large number of variables involved. However, at fixed dome and liner pressure drops turbulence generated will be fixed, and variations in NOx with overall equivalence ratio for fixed jet size can be compared against variations in NOx with overall equivalence ratio for fixed fuel flow rate but with a range of combustion air jet initial diameters, i.e. variable airflow.

Such a comparison is complicated by the postulated mechanism for jet NOx formation² (see below also), which is proportional to jet size. However, provided that jet NOx is not a large proportion of the total NOx (small jets and/or low equivalence ratios), and, provided that the comparison is restricted to jet sizes equal to or less than the fixed jet size of the comparison, and that the range of constant fuel flows examined is selected to be within the range of flows for the fixed jet data, such comparisons may be made.

Figure 2 compares NOx emission indices (EI's in gm NOx as NO_2/kg fuel burned) data for the 0.5 in. (12.7 mm) jet case over a range of equivalence ratios obtained by varying fuel flow, with NOx data for 0.5 in. (12.7 mm), 0.375 in. (9.5 mm) and 0.25 in. (6.35 mm) at fixed fuel flow rates of 0.075, 0.100, 0.125 and 0.150 lbm/min. (0.034, 0.045, 0.057 and 0.068 kg/min. respectively). Rich and lean points are included.

The plotted data in Figure 2 on both lean and rich sides correlate within the measurement accuracy and repeatability of the single-test data scatter².

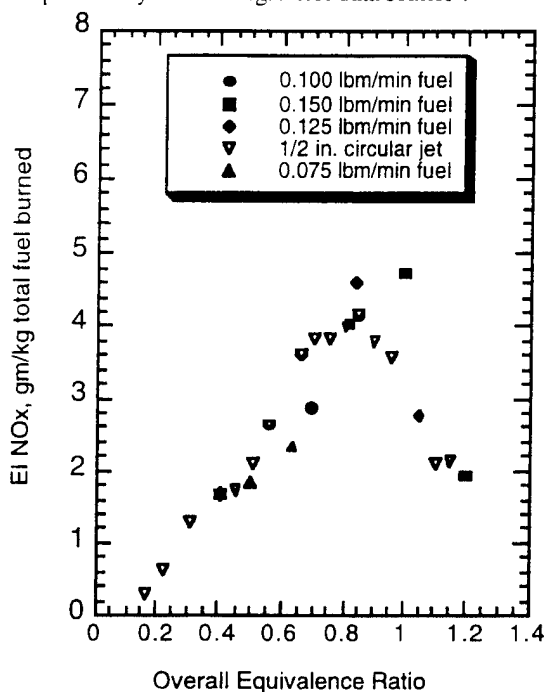


Figure 2: Uniqueness Plot Based on NOx, to Evaluate Fuel Momentum Effects

The conclusion can therefore be drawn that fuel momentum does not affect the flow field, and as a consequence, that for fixed pressure drop, equivalence ratio is a unique parameter describing NOx.

Dome Characteristics

The combustor can be operated with zero combustion air jets to obtain the characteristics of the dome alone.

Figure 3 is a plot of the emission index (EI) of NOx for the dome alone, as a function of dome equivalence ratio (metered). As expected, the measured NOx reaches a peak of about 3.6 at a dome equivalence ratio of 0.82. As the dome equivalence

ratio exceeds unity NOx falls due to decreasing bulk flame temperatures, but unburned fuel leaves the combustor.

Also shown on Figure 3 are calculated NOx curves using two approaches. First, assuming "experimentally-perfect premixing" of fuel and air, and second, representing the dome flow field as a reactor network having a degree of partial stirring.. For the "experimentally-perfect premixing" case the empirical correlation of Roffe & Venkataramani³ for lean propane and air systems was used. In this correlation the residence times were estimated for volumes based on observed flame dimensions. The reactor network was based on computational fluid dynamic calculations for this injector and hole pattern¹, with reactor dimensions based on observed flame dimensions and having fuel heating value reduced to account for estimated heat losses from the combustor. The network consisted of a well-stirred reactor with a parallel plug-flow reactor that processed 13 percent of the total flow that was recirculated back into the dome.

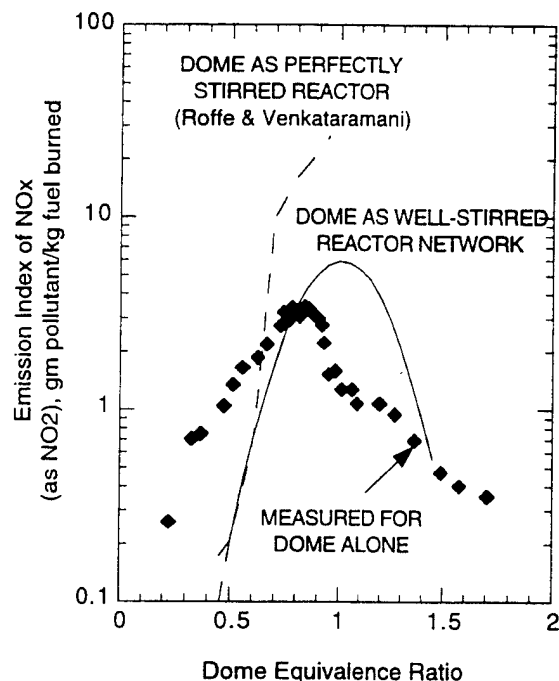


Figure 3: Assessment of Dome NOx Characteristics

The effect of improved mixing as represented in the two calculations, is to increase the peak NOx and to narrow the NOx curve across equivalence ratio; furthermore, the peak NOx occurs at dome equivalence ratios around unity.

Comparing the measured dome NOx against the two calculations demonstrates that despite the use of a gaseous fuel and the intimate association of fuel and air in the fuel injector, the fuel is burned in the dome in far from premixed form, and consequently, exhibits some degree of diffusion flame burning.

Overall Burning Characteristics

In Reference 2 the NOx data were analyzed in terms of a rich/lean burning system, where excess fuel from a fuel-rich dome was assumed to burn fuel-lean in the combustion air jet system, as was described in Reference 4. If this is so, the question concerning the nature of the flame in these two burning zones arises. It was assumed in Reference 2 that it was the same in both zones, i.e. based on the previous section, flames exhibiting some degree of diffusion burning.

Figure 4 is a plot of overall NOx EI's for several jet systems at $H_d/2$ from the dome, including the dome alone, plotted against dome equivalence ratio, at fixed pressure drops.

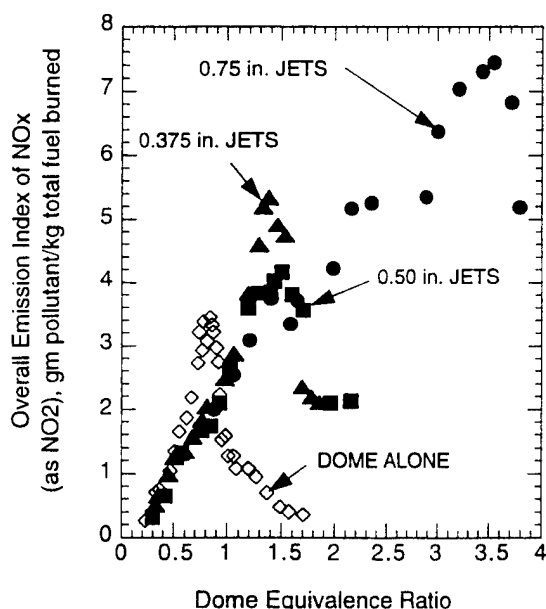


Figure 4: Overall Burning Characteristics for NOx

The characteristic of the dome-alone NOx is that from Figure 3. The characteristics for the individual combustion air jet cases collapse onto a common curve for dome equivalence ratios up to about 1.15. For dome equivalence ratios of 0.55 and less, this collapsed data is co-incident with the dome

alone data. This behavior indicates that basic flame characteristics in the dome are unaffected by the presence of the jets.

The NOx peak for jets being present is shifted to higher dome equivalence ratios, in the range 1.3 - 1.55, from the nominal 0.82 equivalence ratio for the dome alone. The levels of NOx at the peak, and the subsequent behavior on the dome rich-side of the peak, are dependent on the individual jet size.

The shifted NOx peak from 0.82 with no jets to 1.3 - 1.55 dome equivalence ratio with jets, indicates that in addition to peak temperatures being reached at lower equivalence ratios (0.82 rather than about 0.92-1.0) due to unmixedness effects, some of the combustion jet air is actually active in the dome. The co-occurrence of the data for individual jets at equivalence ratios less than 1.15 suggests that the dome aerodynamics are not strongly influenced, or least modified, by the details of the air jets, i.e. that any additional air introduced into the dome takes part in chemical reactions in a region somewhat separate from the jets themselves, and, that this region is not far upstream in the dome itself. Flame photographs identify a small luminous region on the injector centerline, just upstream of the confluence of the transverse combustion air jets. CFD analysis of this type of combustion system¹, identifies a well-mixed recirculation bubble in this position. This bubble could be where the small quantity of jet air is utilized in the dome. The centerline penetration of all jets at 3 percent liner pressure drop ensures that this bubble is present whenever the jets are present.

It will be noted that for the 0.75 in. (19.05 mm) jets, where, as was shown in Reference 2, most of the total NOx produced originates in the jets, high levels of NOx are eventually produced after the initial NOx-peak that denotes a stoichiometric dome. This is mainly due to jet NOx as the equivalence ratio increases. These high levels of NOx fall onto the same general curve as for the other jets, and for the dome alone at dome equivalence ratios less than 0.55. The existence of this "common curve" indicates that that there is no substantial difference in the flame characteristics of dome and jets, and, that the NOx produced in both regions is produced by the same kinetic mechanism.

Jet System Behavior

In Reference 2 the adopted analysis strategy for emissions data reduction was one of

treating the generic primary zone as being a quasi-staging[†], rich/lean burning combustor. The dome region was generally fuel-rich, and the importance of NO_x generation in the "lean burning" combustion air jet system itself was highlighted.

This aspect is illustrated here in Figure 5 where the percentage of total NO_x that is generated in the jets for each initial jet size is plotted in terms of overall equivalence ratio. The jet NO_x was obtained from the total NO_x at given overall equivalence ratio by subtracting from it the dome-alone NO_x at an appropriate dome equivalence ratio. Such a procedure is only valid if the predominant mechanism for NO_x generation is the same in both regions of the combustor. As was demonstrated above, this appears to be the case. The percent NO_x was obtained by multiplying the calculated emission indices for the jets by the mass flow rate of fuel burned in the jets, and dividing by the measured overall emission index for the primary zone at the same equivalence ratio, multiplied by the total fuel flow rate.

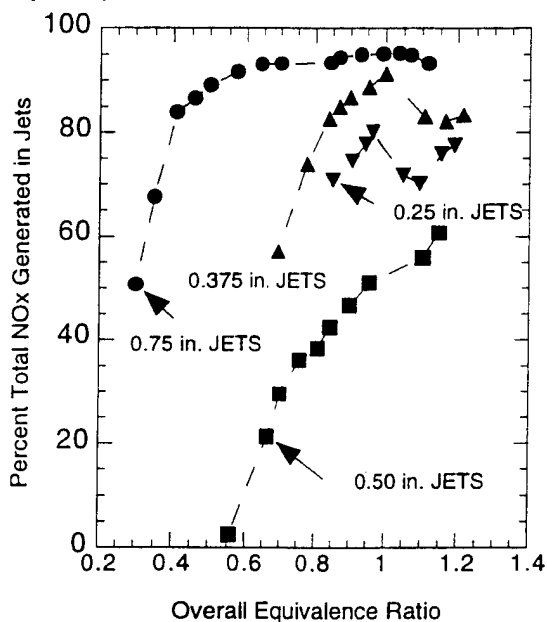


Figure 5: Contribution of Jet-Generated NO_x

Figure 5 shows that for the 0.75 in. (19.05 mm) initial jet size more than half of the NO_x originates in the jets for all operating equivalence ratios; for the 0.50 in. (12.7 mm) jet the jet NO_x only reaches 50 percent of the total for a stoichiometric primary zone. The general behavior is for the percent jet NO_x to increase with overall equivalence ratio, and to do so rather steeply initially until a plateau level is reached. This behavior is

repeated for each jet system, and the plateau level is lower for smaller jets than for the larger jets. For the 0.75 in. (19.05 mm) jets the plateau is for about 95 percent jet NO_x; for the 0.375 in. (9.53 mm) jets it is about 85 percent, and for the 0.25 in. (6.35 mm) jets it is about 75 percent. The 0.5 in. (12.70 mm) jet system has not yet reached its plateau level in the range of overall equivalence ratios covered. This jet system is the exception to the general behavior. If overall equivalence ratio is increased above unity, percent combustion air jet NO_x contribution to overall NO_x would eventually start to fall as the jet system became over-rich. This is clearly evident for the two smaller jets.

The 50 percent jet NO_x condition is reached at overall equivalence ratios that increase with decreasing jet size, and that corresponds to the condition where the dome equivalence ratio exceeds unity in each case. For the 0.50 in. (12.70 mm) jet system the 50 percent jet NO_x condition is reached at an overall equivalence ratio of 0.96. From stoichiometry plots this corresponds to a dome equivalence ratio of 1.7. This jet system generates lower jet NO_x levels at all overall equivalence ratios than either larger or smaller jets. Clearly, the 0.5 in. (12.70 mm) jet system behaves differently to all of the others.

Figure 6 is a plot from Reference 2 with additional information added for the smaller jets. The plot shows the EI's of jet NO_x for each jet as a function of jet equivalence ratio.

For jet equivalence ratios less than 0.8-0.9 (where a NO_x peak is expected) the NO_x for the 0.375 (9.53 mm), 0.50 in. (12.7 mm) and 0.75 in. (19.05 mm) jets is essentially independent of jet equivalence ratio. This suggests that the fuel burned in the jets at these lower equivalence ratios is reacted in stoichiometric interfaces associated with the fresh air entering through the jets. The jet NO_x EI's consistently begin to decrease at higher jet equivalence ratios. This is because unburned fuel is now exiting the combustor. The jet NO_x EI plateau levels for the lower jet equivalence ratios decrease with increasing jet initial diameter, with the exception of the 0.50 in. (12.7 mm) jet system, which again has the lowest values. For the 0.25 in. (6.35 mm) jets the jet NO_x EI's continuously decrease with increasing jet equivalence ratio over the entire range covered. This suggests that there is something different about this jet system.

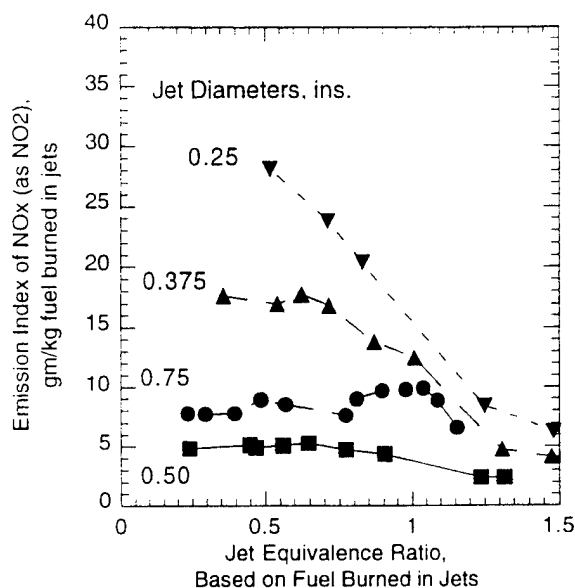


Figure 6: Demonstration of Stoichiometric Burning in Jet Systems

When the absolute jet NOx, in gm/min., is plotted against jet equivalence ratio, Figure 7, the behavior exhibits the characteristic equivalence ratio dependency, with NOx peaks occurring in the jet equivalence ratio range of 0.8-1.0. The absolute NOx levels decrease with decreasing jet size, which is the opposite behavior to that of the EI's. This is accounted for by the different amounts of the total fuel actually burned in the jets, where the 0.75 in. (19.05 mm) jet burns the most fuel and the 0.25 in. (6.36 mm) the least, and where, for a given jet size, the amount of jet fuel decreases with decreasing overall equivalence ratio. Once again, the 0.50 in. (12.7 mm) jet system shows as the optimum, having the lowest absolute jet NOx.

The optimum behavior of the 0.50 in. (12.7 mm) jet system is demonstrated in Figure 8 where the EI's of jet NOx are plotted against jet diameter for three primary zone (overall) equivalence ratios in the range of peak bulk-flame temperatures. Note that for all jet sizes, the jet NOx EI's decrease with increasing primary zone equivalence ratio, and the sensitivity to jet size decreases also.

Behavior in Relation to Primary Zones

From individual plots of overall NOx emissions against overall equivalence ratio for each jet size, values of NOx EI's at specific primary zone equivalence ratios can be extracted. From such values

plots of overall NOx emissions as a function of jet size can be produced.

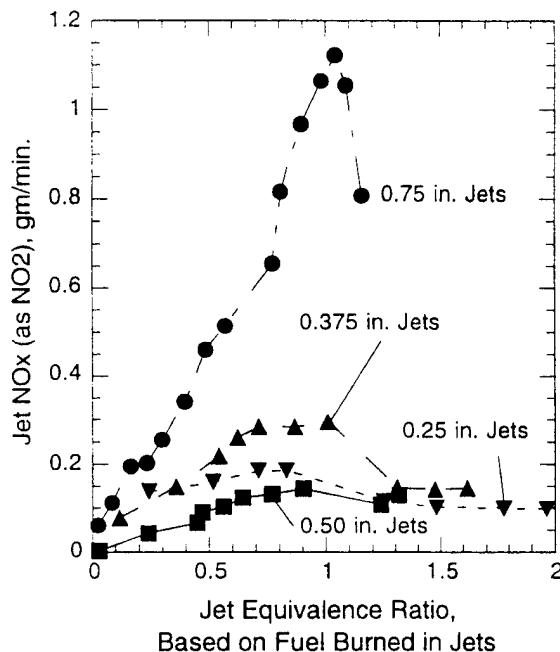


Figure 7: Absolute Values of Jet NOx

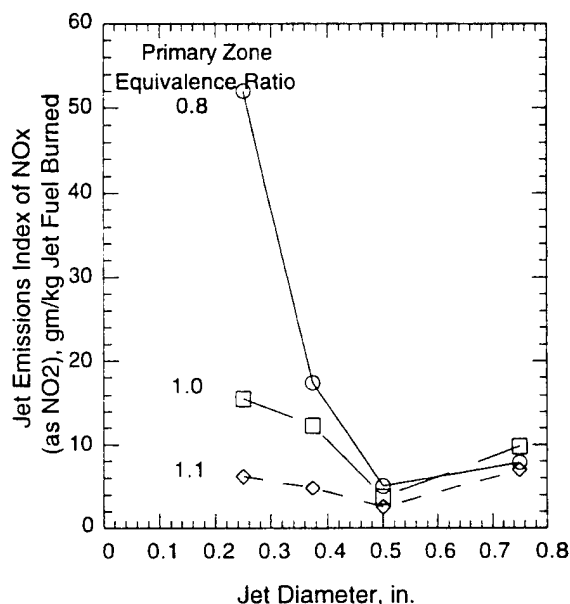


Figure 8: Indication of Optimum Jet Diameter

Figure 9 shows such a plot for primary zone equivalence ratios of 0.5, 0.8, 1.0 and 1.1. Since a particular primary zone equivalence ratio represents a specific bulk temperature, thermal NOx should be independent of jet size. That it is not, implies that the different jet sizes do result in some changes to flame

structure in the jets, (since most of the NO_x is generally generated in the jets) as was suggested, and that these changes are responsible for the observed increase in NO_x.

Remembering that the overall NO_x consists of NO_x produced in the dome and NO_x produced in the jets, the NO_x EI for total fuel burned characteristics with jet diameter are similar at each primary zone equivalence ratio. NO_x EI increases from the dome-alone value with the addition of combustion air jets. This is due to participation of some jet air in dome burning, as discussed above, and this increases with jet size for the 0.25 in. (6.35 mm) and 0.375 in. (9.53 mm) jets, together with a growing, and eventually dominating, contribution of jet NO_x. At unity primary zone equivalence ratio and above, there appears to be an optimum jet size at 0.50 in. (12.7 mm) diameter. There is a sharp increase in overall NO_x EI at all primary zone equivalence ratios, that is associated with the use of 0.75 in. (19.05 mm) diameter jets. The lowest NO_x at each of the primary zone equivalence ratios is achieved by the dome alone configuration.

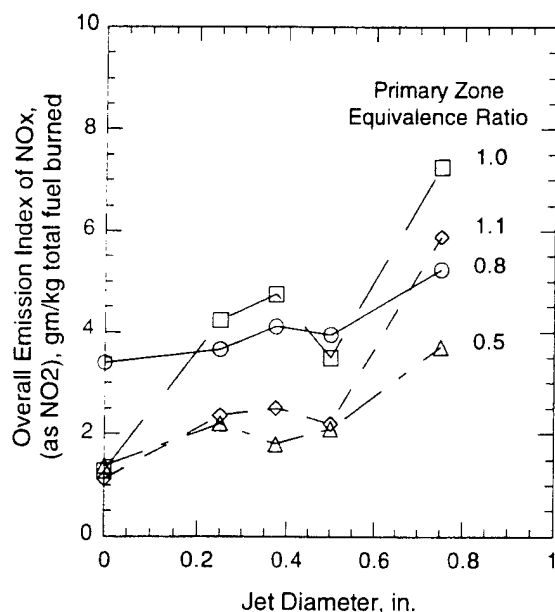


Figure 9: Optimum Jet Size for Overall Primary Zone

Figure 10 is a similar plot, but where the overall NO_x is expressed as an absolute value, in gm/min., and is plotted against the mass flow rate ratio of jet air to dome air. In this plot at given primary zone equivalence ratio, the mass flow ratio

varies as the jets are changed, and fuel flow rate increases with air mass flow ratio. Thus, as air mass flow rate ratio increases the dome gets progressively richer since its air flow is fixed.

The stoichiometry breakdowns for the combustor² show that for all but the highest air mass flow ratio shown on Figure 10, the dome is fuel-lean at 0.5 primary zone equivalence ratio, and is around stoichiometric or less at 0.8 primary zone equivalence ratio; the jet systems are always fuel-lean. Thus, primary zone equivalence ratios less than 0.8 generally represent overall lean burning in this combustor. For higher primary zone equivalence ratios, the dome is always very fuel-rich, and jet equivalence ratio becomes stoichiometric at unity primary zone equivalence ratio. Thus, primary zone equivalence ratios of unity or greater generally represent overall rich burning.

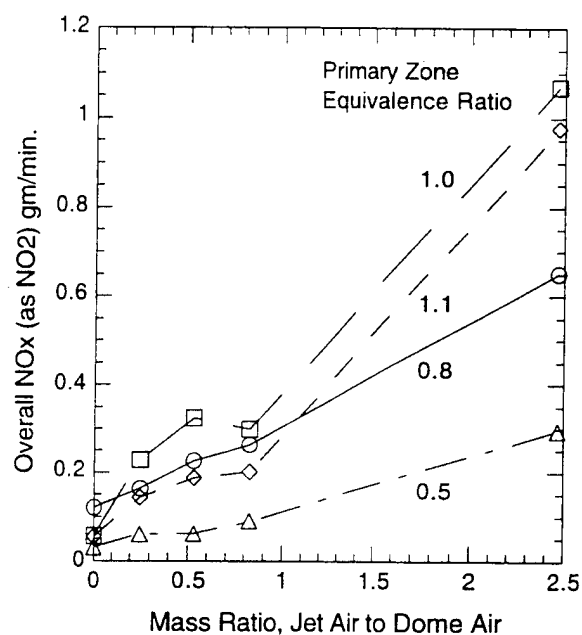


Figure 10: Dependence of Absolute NO_x Emissions on Jet to Dome Mass Flow Ratio

Figure 10 shows a clear difference in NO_x characteristics between these two primary zone equivalence ratio regimes. For 0.5 and 0.8 primary zone equivalence ratios the absolute NO_x level increases essentially linearly with increasing air mass flow rate ratio. As the primary zone equivalence ratio is increased the NO_x levels increase due to the increased bulk temperature, and the sensitivity to air mass flow rate ratio is increased. At any primary zone equivalence ratio the increase in overall NO_x with

increase in air mass flow rate ratio is due to the growing contribution of jet NO_x.

It is not sufficient to confine consideration to NO_x alone as the indicator of low emissions; the inefficiency emissions must also taken into account.

Figure 11 is a plot of overall NO_x emissions indices against overall CO emissions indices for each of the jet sizes, including the dome alone; the data for each jet size is limited on the left-hand-side by 0.5 primary zone equivalence ratio and on the right-hand-side by 1.1 primary zone equivalence ratio. Such a plot represents the emissions trades between NO_x and CO that might be made. If a box is placed around the data for any particular jet size in the plot, bounded on one side by the maximum CO, on the top by maximum NO_x, and, on the remaining side and the bottom by the respective axes, then that box is a qualitative measure of the total emissions production of the particular configuration. Data for any other configuration over the **same equivalence ratio range** that falls wholly *inside* the box, represents a **truly lower emissions configuration**.

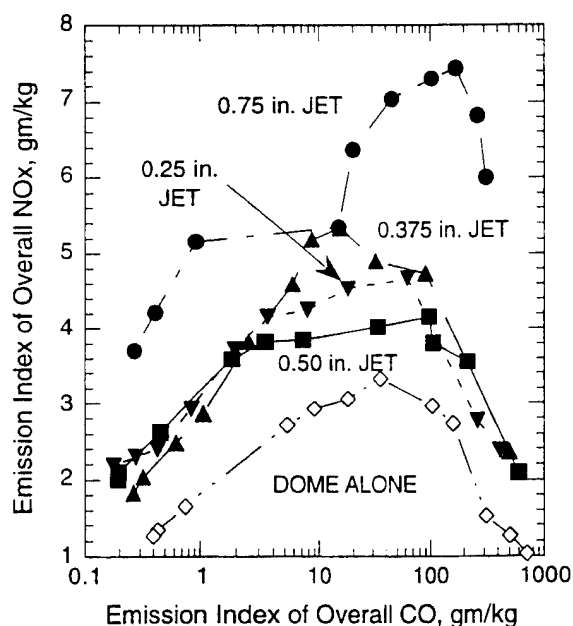


Figure 11: Overall Emissions Assessment for Range of Jet Sizes

Review of the figure reveals several interesting facts. First, the dome-alone configuration does truly represent the lowest emissions configuration, since it has the smallest box. Second,

the 0.50 in. (12.70 mm) jet does indeed represent some kind of optimum jet configuration for this primary zone since its box is smaller than the boxes for the other jets, i.e. it does not achieve its low NO_x by producing large amounts of CO. Third, the 0.75 in. (19.05 mm) jet is the worst emissions producer, and this is through its jet NO_x generation.

The levels of CO over the equivalence ratio range in Figure 11 are all at or very close to, the appropriate equilibrium levels for the test conditions. For lower equivalence levels outside the range there is an upwards departure from equilibrium CO as a lean blowout condition is approached; similarly, at higher equivalence ratios there is also an upwards departure from equilibrium CO due to a lack of oxygen. Combustion efficiencies for the dome alone and for the 0.5 in. (12.70 mm) jet, for example, are essentially 100 percent to an overall equivalence ratio of about 0.8, and then fall off more or less together.

The finding that the dome alone configuration, i.e. no traverse air jets whatsoever, gives the lowest emissions, raises the valid question as to the need for the separate combustion air jets.

The combustion air jets are needed to reduce flame length and to enhance lean stability. Figure 12 shows some limited stability data for the dome alone and for the dome with the 0.50 in. (12.70 mm) jets, in the form of blowout overall equivalence ratio against the air loading parameter, ALP. The ALP is as defined in Reference 5. The blowouts were conducted at atmospheric pressure, with variation of dome pressure drop for the dome alone, and liner pressure drop at fixed dome pressure drop for the with-jet case. In addition for the dome alone case, two inlet air temperatures were used - ambient and 500F (533K). The plot shows that for given ALP the with-jets case blows out at lower equivalence ratio than does the dome alone. For the dome alone situation there were several flame modes observed¹. Blowouts for the range of ALP's in Figure 12 were governed by lifted and attached flame conditions⁶; the presence of the combustion air jets exerts a back-pressure on the flame that modifies the flame behavior.

Figure 13 presents the dependency of overall equivalence ratio at blowout on jet size at fixed dome and liner pressure drops. It can be seen that the 0.50 in. jet size again represents an optimum for this dome.

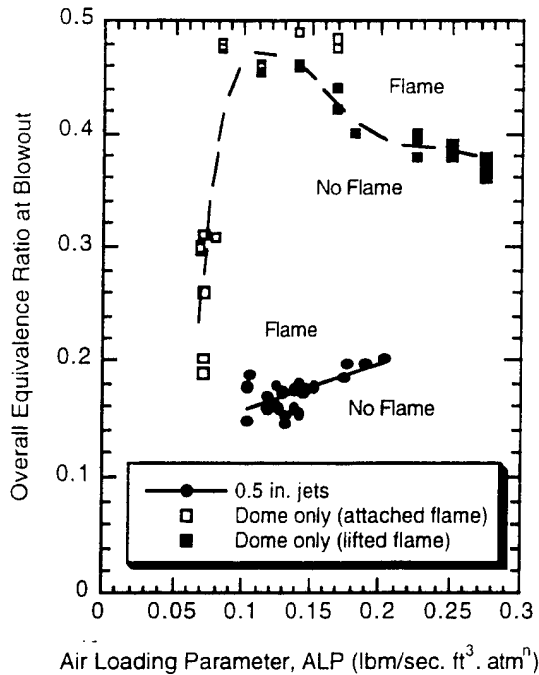


Figure 12: Stability Plot for Dome Alone and Dome with 0.5 in. Jets

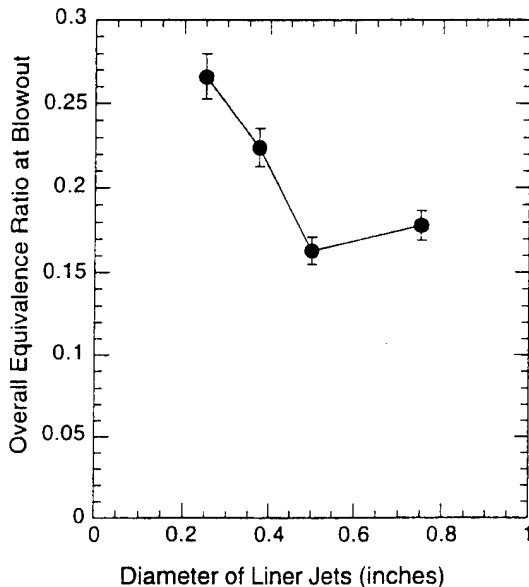


Figure 13: Blowout Equivalence Ratio as a Function of Jet Size

Discussion

Initial results, consisting of emissions measurements and lean blowout data, have been presented for a number of circular, single hole,

opposed, combustion air jet sizes at a fixed liner position close to the dome, and at fixed dome and combustor liner pressure drops that are representative of engine design values. The absolute levels of emissions are dependent on the way that the simulations were conducted, and therefore the present results ideally should not be used for predictive purposes by scaling. However, the trends that are produced are valid, and will eventually (when complete) be useful for design purposes.

The series of emissions measurements gathered over wide ranges of test conditions for the different geometric configurations investigated, could form a useful data-set for evaluating the response of CFD modeling to realistic combustor geometries.

It was established that equivalence ratio was a suitable and unique parameter with which to consider the emissions measurements in this combustor and with the manner in which it was operated. The data have been analyzed in terms of a rich dome/lean jet burning behavior. This approach appeared to account nicely for the effects observed.

The combustor dome behaves as a partially stirred reactor, and shows significant unmixedness effects in its NO_x characteristic. The partial set of results demonstrates that the jets play a significant role in generating the total NO_x measured over equivalence ratio ranges that are typical of many primary zones. The jet contribution appears to arise from stoichiometric burning in the jets system. This stoichiometric jet burning is clearly identifiable for all but the smallest of the jets (0.125 in. dia.). As a consequence of the jet contributions to total NO_x, the dome alone configuration emerges as the lowest producer of NO_x and CO emissions. The jets are needed to shorten flame length, and to enhance lean blowout stability of the primary zone. Of the jet systems examined, that for the 0.5 in. (12.70 mm) diameter jet shows distinct optimum behavior in terms of minimum NO_x emissions and maximum lean blowout stability.

The results to date indicate the need to use advanced optical diagnostic techniques to determine the exact flame structures existing in the jet systems, and how these are affected by the flow interactions between the dome and the jets. Detailed flow visualization is clearly most desirable. In particular, quantitative information on recirculation zone mass flow rates is essential. The parametric variations in liner pressure drop and combustion air jet axial

position will also be of assistance in this respect. An explanation for the optimum behavior of the 0.50 in. (12.70 mm) jet must be obtained.

Although there was no attempt in this combustor to achieve a true rich burn/quick quench/lean burn low emissions design, the present primary zone does function somewhat in this fashion. The findings here indicate how difficult it will be in such low emissions designs to achieve the quick quench portion and hence, to get a true lean burn.

The limited stability characteristics presented demonstrate that low emissions characteristics in a combustor cannot be pursued without regard to the other design criteria that must be satisfied for successful practical combustor designs.

Conclusions

1. Most of the NO_x generated in the generic primary zone appears to originate from stoichiometric burning in the combustion air jet system.
2. Minimum total emissions are produced when all of the reactants are introduced through the combustor dome.
3. Combustion air jets are necessary to reduce flame length and confer lean blowout stability.
4. For at present undefined reasons, the 0.50 in. (12.70 mm) dia. opposed circular jets exhibit a clear optimum for the dome when the jets are positioned half a dome height downstream. This optimum is for minimum No_x and lean blowout stability.

Acknowledgments

The enthusiasm, motivation, support and contributions of Dr. W.M. Roquemore are greatly appreciated. The authors wish to thank Ron Britton, Mike Burns and Melvin Russell for their help in operating the test facility and in making the emissions measurements. This on-going research was sponsored by the U.S. Air Force, Wright Laboratory, Aero Propulsion and Power Directorate.

References

1. Sturgess, G.J., *Combustor LBO Design Model Evaluation, Final Report*, (Draft) Pratt & Whitney Doc. No. FR-23400, 1 May, 1995

2. Gogeneni, S., Shouse, D., Frayne, C., Stutrud, J., and Sturgess, G., "Influence of Combustion Air Jets on Primary Zone Characteristics for Gas Turbine Combustors," *proc. ISABE 12th. Intl. Symp. on Air Breathing Engines*, editor F. Billig, Vol. 1, Melbourne, Australia, Sept. 10-15, 1995, pp. 475-487.

3. Roffe, G. and Venkataramani, K.S., "Emissions Measurements for Lean Premixed Propane/Air Systems at Pressures up to 30 Atmospheres," NASA Rept CR-159421, 1978.

4. Sturgess, G.J., McKinney, R.G. and Morford, S.A., "Modifications of Combustor Stoichiometry for Reduced No_x Emissions from Aircraft Engines," *Trans. ASME, J. Engrg. Gas Turbines and Power*, Vol. 115, No. 3, 1993, pp. 570-580.

5. Sturgess, G.J. and Shouse, D., "Lean Blowout in a Generic Gas Turbine Combustor with High Optical Access," ASME Paper No. 93-GT-332, May 1993, to appear in ASME *Trans. J. Engrg. for Gas Turbines and Power*.

6. Hedman, P.O., Sturgess, G.J., Warren, D.L., Goss, L.P. and Shouse, D.T., "Observations of Flame Behavior From a Practical Fuel Injector Using Gaseous Fuel in a Technology Combustor," *Trans. ASME, J. Engrg. for Gas Turbines and Power*, Vol. 117, No. 3, July 1995, pp. 441-452.



AIAA 95-0810

Performance of a Trapped-Vortex Combustor

K.-Y. Hsu, L. P. Goss, D. D. Trump
Systems Research Labs, Inc.
Dayton, OH

W. M. Roquemore
Wright Laboratory
Wright-Patterson AFB, OH

**33rd Aerospace Sciences
Meeting and Exhibit
January 9-12, 1995 / Reno, NV**

For permission to copy or republish, contact the American Institute of Aeronautics and Astronautics
370 L'Enfant Promenade, S.W., Washington, D.C. 20024

PERFORMANCE OF A TRAPPED-VORTEX COMBUSTOR

K.-Y. Hsu*, L. P. Goss* and D. D. Trump
System Research laboratories, Inc.
Dayton, OH

W. M. Roquemore**
Wright Laboratory
Wright-Patterson Air Force Base, OH

ABSTRACT

This paper describes the performance characteristics of a unique combustor that utilizes a trapped vortex (TV) in a cavity to provide flame stability. In this study, the cavity is formed between two axisymmetric disks mounted in tandem. The upstream disk is referred to as the forebody and the downstream disk is called the afterbody. Co-flowing annular air forms a vortex that is trapped in the cavity. The strength of the vortex is increased by injecting the primary air and gaseous propane directly into the cavity through multiple jets located on the upstream face of the afterbody. Particle Imaging Velocimetry (PIV) measurements show that when the length of the cavity is 0.59 of the forebody diameter, a vortex is trapped in the cavity. This cavity length also gives a minimum pressure drop across the combustor. Very low overall lean-blow-out (LBO) equivalence ratios are obtained for the TV combustor over a wide range of annular and primary air flow rates. Temperature profiles measured with a Coherent Anti-Stokes Raman Spectroscopy (CARS) system show that as the primary air flow increases, the temperature in the vortex increases. Increasing the primary air flow rate also results in a decrease in flame length and peak combustion efficiencies. Peak combustion efficiency varied between about 96.7 and 99%. Peak combustion efficiencies increased to 98.8 and 99.8% when a second trapped vortex is added to the combustor. This is accomplished by adding a 2nd afterbody just downstream of the first afterbody.

INTRODUCTION

In practical combustors and burners, swirl is used to create the recirculation zones that aerodynamically stabilizes the flame. Recirculation zones provide regions of low velocity fluid where mixing, ignition and burning can take place. Considerable efforts go

into designing the domes and fuel nozzles that establish the recirculation zones. To meet the performance constraints being placed on advanced gas turbine combustors, the dome and fuel nozzles are becoming very complex. This paper investigates a new concept for stabilizing flames that is simple and compact and has the potential of providing improved performance over a wide operating envelope. This concept is referred to as the Trapped Vortex (TV) concept.

The concept of a TV combustor is very simple, use a vortex trapped in a cavity to provide flame stability. The cavity has to be properly sized to trap a vortex which remains stable over a wide range of flow conditions. It turns out that the design rules for doing this were established many years ago by several investigators^{1,2,3} who were interested in reducing the drag behind disk. They demonstrated that the drag that normally results from the unsteady vortex motion behind disks could be reduced by trapping a vortex in a cavity formed between two disks mounted in tandem. To our knowledge, no one has investigated this idea for stabilizing a flame. The initial results of an investigation of the TV combustor concept are presented in this paper.

EXPERIMENTAL DESCRIPTIONS

The combustor used in this study consists of a forebody and an afterbody as shown in Fig. 1 (a). The afterbody is connected to two concentric tubes along the centerline of the forebody. The parts used in this study were made from 304 stainless steel. Fuel and primary air are delivered through concentric tubes into separate chambers in the afterbody which is 50.8 mm in diameter. The forebody, with diameter (d_f) of 70 mm, is located at the exit plane of the vertically-mounted co-annular air duct which has a diameter of 80 mm. The cavity length, H , is defined as the axial distance between the forebody and afterbody as noted in Fig. 1 (a). An axisymmetric cavity created in the void region between the forebody and the afterbody. The cavity length is adjustable and is used as one important parameter in this study. The blockage ratio defined as the area ratio between the forebody and the annular air duct is 76%. An annular air with maximum velocity of 42 m/s can

* Research and Application Division, Member AIAA

** Wright Laboratory, Member AIAA

This paper is declared a work of the U.S. Government and is not subject to copy right protection in the United

be achieved in the facility. The annular and primary air, originated from two air supplies, are controlled and metered separately.

A schematic diagram of the fuel and primary air injection plane is shown in Fig. 1 (b). Gaseous propane fuel is injected through eight orifices (1.75 mm in diameter), and the primary air is supplied through 24 orifices (2.29 mm diameter) surrounding the fuel jets. The locations of fuel and primary air jets are arranged so as to reinforce the vortex created in the cavity. Direct injection of primary air serves the following purposes : 1) provides direct control of the local equivalence ratio inside the recirculation zone, 2) enhances mixing by increasing the mixing region through distributed fuel and surrounding air jets, and 3) provides cooling for the injector assembly. A water manometer is used to measure the static pressure drop across the combustor for a range of cavity length. The LBO limits of the combustor are also established for a range of primary and annular air flow conditions.

A 35 mm camera and video recorder were used to record the flame images at various flow conditions. The instantaneous velocity field was obtained by employing the two-color Particle-Imaging Velocimetry (PIV)^{4,5} technique. A pulsed Nd:YAG laser and a Nd:YAG-pumped dye laser were used for generating two different wavelengths to eliminate the ambiguity in determining flow direction. Cylindrical lenses were used to form a laser sheet vertically across the centerline of the burner. The mono-spherical particles Al_2O_3 (5 μm in diameter) were seeded through primary air jets. A 35 mm camera mounted at a right angle to the laser sheet was used to take images of particles scattered from laser illumination. A synchronization circuit was used to control the time separation between the two laser pulses. Typical time separation between two lasers was about 30 μs for the flow conditions studied. A color scanner was then used to digitize the images and the data were stored in a computer for further analysis. The theory and experimental setup of the PIV technique are treated in detail in Refs. 4 and 5.

Radial temperature profiles, at different axial locations, inside the recirculation zone were measured using Coherent Anti-Stokes Raman Spectroscopy (CARS). The CARS system employed in this study was based on a Nd:YAG-broad band dye laser combination which was tuned for N_2 excitation. An intensified CCD camera interfaced with the computer was used for single-shot broad-band spectrum detection. At each location, one thousand samples were collected at a rate of 10 Hz, and the spectra were stored for data analysis. The temperature information was obtained by using a nonlinear least-square routine to fit the measured spectra.

The emission measurements were conducted for

various flow conditions to further characterize the performance of the combustor. A portable emission sampling/analyzer unit was used to measure the concentrations of CO, NO, NO_2 , O_2 and unburned hydrocarbon based on electrochemical sensors. The CO_2 concentration was calculated from measured O_2 concentration assuming equilibrium. A routine was then used to calculate the equivalence ratio and combustion efficiency based on the sample collected. The flow was confined by a Pyrex tube (80 mm I.D.) of 910 mm in length to eliminate the uncertainty in the measurement as result of entrained ambient air. The gas samples were collected at 860 mm downstream measured from the face of the forebody. The preliminary measurements was made by using a stainless steel tubing (3 mm I.D.) as sampling probe. A K-type thermocouple was used in conjunction with the sampling probe to obtained the temperatures at locations where the gas samples were taken. The radial profiles of emission species were mostly uniform except for some flow conditions. In order to obtain global emission characteristics of the combustor, a probe with multiple-holes was used to measure the "averaged" emission data over a range of flow conditions. The probe was place inside the glass chimney and was intersected with the centerline of the flow. There were five holes (0.4 mm in diameter) located on different radial locations to collect area-weighted samples. The differences between the measured equivalence ratios and the metered overall equivalence ratios were found to be within 10 % over the flow conditions studied. During the emission measurements, the flame lengths were also measured visually at various flow conditions. The averaged data are presented to illustrate the influence of primary air on the emission behavior of this combustor.

RESULTS

Preliminary experiments were performed to determine the impact of afterbody diameter and cavity length on flame structure. The diameter of the forebody was fixed at 70 mm for this study. Afterbodies with three different diameters were investigate and the cavity length for each afterbody was systematically varied under combustng conditions. Although this was not an extensive investigation, it did show that the flame structure was strongly dependent on afterbody diameter and cavity length. The most stable flame was observed with an afterbody diameter of $0.73 d_f$ where d_f is the diameter of the forebody. An afterbody with this diameter was used in the studies presented in this paper. Detailed results of these studies will be presented in the following sequence. The optimal cavity length is chosen based on the criteria of low pressure drop and

low LBO limits. The impact of primary air on LBO, flame structure, velocity and temperature fields, flame length is investigate for the TV combustor. The impact of adding a second afterbody on combustion efficiency is also examined followed by discussions of the fundamental processes believed to be important in understanding the results.

Choosing Cavity Length

Figure 2 shows the impact of cavity length on pressure drop across the combustor. The flow was confined by an 80 mm diameter, 150 mm long Pyrex tube. The measured pressure drop does not include that across the fuel and primary air jets. The pressured drop for the cold flow is plotted at three annular air velocities of 14, 28 and 42 m/s, respectively. The pressure drop increases with the annular air flow rate. As the cavity length was varied, the pressure drop for the cold flow conditions was observed to pass through a minimum. The minimum, which is more noticeable at the high annular air flow condition, occurred at a cavity length of about $0.6 d_f$ for the three curves shown in Fig. 2. It is noted that the pressure drop across the TV combustor is relatively small. At velocities that are somewhat higher than those in gas turbine combustors, the pressure drop was only 0.65%. The pressure drop for all conditions studied was less than 1.2 %.

Mair¹ and Little and Whipkey² conducted systematic studies of drag reduction for disks mounted in tandem. Their results showed that minimum drag was achieved with an afterbody diameter of $0.75 d_f$ and a cavity length of $0.6 d_f$. The cold flow data plotted in Fig. 2 are in very good agreement with their findings.

Although the combusting flow showed very little change in pressure drop with cavity length (Fig. 2), there was a noticeable change in the stability of the flame. A stable flame, with a well defined vortex, was visually observed when the cavity length range between $0.45 d_f$ and $0.65 d_f$. Multiple vortices and vortex shedding were observed at cavity lengths longer than $0.65 d_f$. For cavity lengths less than about $0.45 d_f$, a quasi-steady flame existed, but there was no clear evidence of a vortex in the cavity. These results are consistent with the cold flow results of Little and Whipkey² who observed that a stable vortex existed in the cavity when the cavity length corresponded to that of minimum drag.

A stable vortex is very desirable for good combustion stability. Since vortex stability changes with cavity length, one might expect that the LBO limits would also vary with cavity length. This was investigated for three annular air flow conditions with zero primary air. The results are shown in Fig. 3. The overall LBO equivalence ratio is less than 0.05 for all

conditions studied. However, the overall equivalence ratio at the LBO limits increases dramatically for cavity lengths greater than $0.65 d_f$. Visualization observation of the flame indicated that this increase in LBO limit is probably the result of vortices being shed from the cavity. Visually, the most stable flame occurred at a cavity length of $0.59 d_f$. This cavity length was chosen in the experiments described in the following sections.

Flame and Flow Field Characteristics

Flame photographs and PIV were used to determine if a stable vortex is formed in the TV combustor. The Pyrex tube was removed for these experiments, so the flame was unconfined. There were several differences between the unconfined and confined flames. The unconfined flames were shorter and had a larger diameter near the vortex center, but they had the same general features as the confined flames.

A typical image of a lean flame is shown in Fig. 4(a). The flame is stabilized inside the cavity. This region will be referred to as the primary zone of the combustor. The overall equivalence ratio is about 0.06 which is considerably below the LBO limit of typical swirl or bluff-body stabilized flames. The annular air velocity is 28 m/s. The equivalence ratio in the primary zone (Φ_p) as calculated from the fuel and primary air only, is about 1.2. The actual equivalence ratio in the primary zone may be less than this due to entrainment of annular air. However, the amount of entrainment changes with primary air and fuel flows and has not been accurately measured. The flame is blue and is attached in the shear layer around the circumference of the forebody. This is typical characteristic of TV combustor with primary air injection. The visible appearance of the flame indicates that a stable vortex is formed in the cavity at these conditions.

PIV was used to obtain the instantaneous velocity field in Fig. as shown 4(b). The flow domain is outlined in Fig. 4(a). Repeated measurements showed that velocity field does not change significantly from shot to shot. The velocity field shows a strong recirculating flow that is expected for a toroidal vortex. The center of the vortex is located at a radius just shorter than that of the afterbody. The radial location of the vortex center did not appear to change significantly for different primary air, annular air, and fuel flow conditions. However, the axial location of the vortex did change. For this condition it is about $0.25 d_f$ from the face of the forebody. At the primary and fuel flow rates increased, it moved back towards the afterbody.

The primary air and fuel jets control the local equivalence ratio, mixing, residence time, and stability in the primary zone. For good combustor performance,

these jets should be injected in a way that they reinforce the vortex so that it remains stable for a wide range of flow conditions. This appears to be the case for the multiple jet arrangement as shown in Fig. 1 (b). The velocity field in Fig. 4(b) includes flow from the fuel and primary air jets as noted by the large velocity vectors near the afterbody face. The jets appear to dissipate before they reach the face of the forebody. They also seem to be mixed into the recirculation zone and convected around the vortex center in a way that the vortex becomes stronger. The flow around the vortex center has a large axial velocity component well inside of the forebody radius. Most of this fluid seems to mix with the annular air and be convected past the afterbody. However, the flow just outside of the vortex center appears to be recirculated back into the primary zone. This fluid contains hot products and radicals that will ignite the incoming fuel and air mixtures. This process of reingested the hot products is the key to the excellent stability of a TV combustor.

The general structure of the vortex, as visualized by the flame, appeared to be the same as those shown in Figs. 4(a) and 4(b) for a wide range of fuel and air flow conditions. This is illustrated by the flame images in Figs. 5(a), (b), and (c). The Φ_p 's for the three images were obtained by changing the primary air flow rate. The primary air flow rates were 56, 140, and 280 slpm with corresponding velocities of 10, 24 and 48 m/s, respectively. The annular air flow rate was fixed at 3000 slpm and had a velocity of 42 m/s. The fuel flow rate was also fixed at 25 slpm with a velocity of 22 m/s. The overall equivalence ratio was 0.2, which did not change significantly for each of the primary air flow rates, since they are small in comparison with the annular air flow rate. Although the color of the flame varied with Φ_p , the shape of the flame in the cavity is about the same for all flow conditions. This is additional evidence that the primary zone has been stabilized by correctly sizing the cavity to trap a vortex. Furthermore, injecting the primary air and fuel from jets in the afterbody face seems to reinforce the trapped vortex as noted by the change in color around the vortex center.

Although the flow field in the primary zone does not change dramatically for different flow conditions, the temperature field does. This is noted in the temperature profiles in Figs. 5(a), (b), and (c) obtained with a CARS system. Radial profiles of temperature are shown for axial locations of $z = 5$, and 39 mm, as measured from the forebody face. The third axial measurement was made at the vortex center which changed from $z = 23$ mm to 28 mm as the primary air was increased. The closed symbols denote the rms temperature.

The locations of the air and fuel jets are very

evident in the temperature profiles in Fig. 5. The primary air jets are located at $r = 11$ and 19 mm, and the fuel jets are located at $r = 15$ mm, as shown in Fig. 1 (b). For the weaker primary air flow, $\Phi_p = 11.1$, the air jet trajectories are affected by the annular air. This is evident by the cold temperature zone shifted from $r = 11$ mm to $r = 8$ mm. At higher primary air flow rates (lower Φ_p), the air jets are not disturbed by the entrained air. However, the colder jet temperatures are not noted near the forebody, which suggest that the jet flows are mixed and dissipated before they reach the face of the forebody. These profiles provide additional support to the idea that the fuel and primary air injection technique does not disrupt the trapped vortex but enhances it.

The flame length and soot concentration decrease as the primary air flow rate increases. The increase in temperature as Φ_p decreases is evident in the flat temperature region ($20 \text{ mm} < r < 30 \text{ mm}$) in Fig. 5 at $z = 40$ mm. The temperature increases by about 700 K as the primary air is increased. A maximum temperature of 2150 K (equivalent to the stoichiometric flame temperature) was measured at the highest primary flow condition; however, the fluctuation in temperature is only about 200 K, as compared to 400 K for the lower primary air flow condition. The higher temperature occurs near the face of the afterbody for the higher primary air flow rate and at the vortex center at the lower flow rates. This is believed to be the result of different residence times, local equivalence ratio, and reingestion of hot products into the recirculation zone as the primary air velocity is increased. At the highest primary air flow rate, the flame bulges out radially toward the annular air. At this condition, the primary zone may not be affected by entrainment of cold annular air, which, if entrained, would lower the flame temperature and increase the temperature fluctuations. The higher temperatures at this condition should result in lower soot concentrations, shorter flames, good combustion efficiency, but higher NOx. However, the higher air jet velocities may make the flame more susceptible to LBO. These points are examined in the next sections.

Lean-Blow-Out

LBO is an important parameter for aircraft gas turbine engines because it determines the lower operating limits of the engine. In gas turbine combustors, LBO is often preceded by an unstable flame. This is believed to occur because of non-uniform mixing process in the swirl stabilized recirculation zone. This results in intermittent, flame-vortex interactions that locally quench the flame. This intermittence in combustion directly impact the ignition

source, therefore, the unsteadiness tends to grow until the flame blows out. In the TV combustor, the flame is shielded from high annular air flow rate by the cavity. The vortex trapped in the cavity provides a stable ignition source through reingestion of hot products and radicals back into the recirculation zone, as indicated by the velocity field in Fig. 4 (b). Since the vortex is stable over a wide range of flow conditions, a TV combustor should have excellent LBO characteristics. The data in Fig. 3 indicates that this is case, when the primary air flow rate is zero. The question is what is the influence of the primary air flow rate on the LBO limits?

The fuel and primary air flow rates at LBO conditions are shown in Fig. 6 to illustrate the influence of primary air. The LBO experiments were conducted by fixing the primary air flow rates and varying the fuel flow rate until LBO occurred. Then, a different primary air flow rate was selected and the procedure repeated. This process was repeated for two annular air flow rates. The data in Fig. 6 show that the largest differences between the LBO at the low and high annular air flow rates occurs at low primary air flow rates. To examine this point in more detail, it is useful to consider the annular air entrainment into the vortex when the primary air is zero.

The only air involved in the LBO process has to be entrained into the vortex from the annular flow, when there is no primary air. The amount of entrainment can be estimated using some assumptions and the data in Fig. 3 for a cavity length of 0.59 d_f . Assuming that the flow in the vortex is well mixed (which is only correct for a first order approximation), then, with zero primary air, the Φ_p at LBO would correspond to the lower flammability limit of premixed propane air flames. This is about 0.55. Using $\Phi_p = 0.55$ and the LBO data for high annular air flow rates in Fig. 3, it is estimated that only about 3% of the annular air is entrained into the cavity. For low annular air flow rates (less than about 1500 slpm), the first approximation of entrainment is poor because the mixing in the trapped vortex is poor. However, at higher annular air flow rates, the estimations of entrainment are more reasonable. Values for air entrainment between 2.5 and 3.5% were obtained for different annular flow rates. This implies that the percentage of air entrained into the trapped vortex is relatively constant at the higher annular air flow rates. This means that the fuel flow rate at LBO should be directly proportional to the annular air flow rate. Inspection of Fig. 3, at $H/d_f = 0.59$, shows that Φ_p at LBO is indeed relatively constant at the two higher annular air flow rates.

The percentage of air entrained into the trapped vortex is expected to decrease as the primary air flow

increases. This is indicated by an analysis of the fuel and primary air flow LBO data in Fig. 6. Figure 6 shows that the fuel flow rate at LBO does not change significantly until the primary air flow rate is above 60 slpm. A linear relationship between the fuel and primary air flow rate starts to develop at the primary air flow rate is about 75 and 150 slpm for annular air flow rates of 500 and 3000, respectively. At a primary air flow rate of 175 slpm, the two curves in Fig. 6 will merge as noted by the dashed line. Beyond this point, the LBO depends only on the primary air flow rate and thus, is independent of the annular air flow rate. A primary air flow rate of 150 slpm represents a 5% entrainment of the 3000 slpm annular air flow, and the 75 slpm conditions corresponds to a 15% entrainment of the 500 slpm annular flow. It seems reasonable that the entrainment of annular air into the vortex is reduced as the primary air flow rate is increased. When the primary air flow rate is sufficiently large, there is probably no annular air entrained into the vortex. Under these conditions, LBO is determined solely by the characteristics of the fuel and primary air jets.

The slope of the linear section in Fig. 6 corresponds to a primary zone equivalence ratio of 1.3. This is calculated assuming that there is no entrainment of the annular flow. Since a LBO equivalence ratio of 1.3 at LBO is much larger than the flammability limit, it appears that the mixing is not approaching that of a well stirred reactor. The mixing is a function of the size, number, and locations of the air and fuel jets. By optimizing the jet injector design, the LBO limits at high primary air flows should improve.

The overall LBO limits (determined by using the total air flow rate) for the TV combustor are considerable better than those of swirl and bluff-body stabilized flames. A gas turbine combustor dome operating with gaseous propane and room-temperature air has LBO Φ 's that vary between about 0.15 to 0.4, depending on the air flow rates and dome design. The LBO Φ 's, for the TV combustor, range from 0.005 to 0.02 with low primary air flow rates and up to 0.12 at the highest primary air flow rate tested. In general, the TV combustor has LBO limits that are about an order of magnitude better than those in conventional swirl-stabilized combustors. The excellent stability limits of the TV combustor occur because the trapped-vortex is very stable over a wide range of flow conditions and hot products and radicals that are reingested into the vortex provides a stable source of ignition. Only a small fraction of the main air actually participates in the combustion process at LBO conditions. However, this is not of practical concern. LBO occurs under transit conditions when an aircraft is maneuver at high altitude. When the pilot pulls back on the throttle, the key factor is to maintain the flame until a stable operating

condition is reestablished. The very low LBO limits of a TV combustor would have significant advantages over conventional swirl stabilized flames under these conditions.

Flame Length

Flame lengths are important in practical combustors. Aircraft gas turbine combustors are typically short and compact. This is very desirable because the combustor weight is proportional to the size. A light-weight combustor results in a good thrust-to-weight ratio. Modern combustors are 15 to 25 cm long. This means that the flame must be confined to this length, otherwise, combustion will take place around the nozzle guide vanes and in the turbine. This leads to poor turbine performance and short operating life. Advanced gas turbine combustors operate at pressures of about 40 atms with combustor inlet temperatures around 1000 K. These high pressure and high temperature conditions result in fast reaction rates and thus give rise to short flames. Diffusion flames, operated at room temperature and atmospheric pressure, are much longer than the length of a combustor. Studies of flame lengths as well as emissions at these conditions is not realistic as far as trying to estimate what the flame length and emissions would be at practical operating conditions. However, fundamental studies are often conducted at ambient conditions to understand how the flame changes as different flow parameters are changed. The intention of this section is to investigate the impact of fuel, annular air, and primary air on the flame length for the TV combustor.

Figure 7(a) shows how the flame length changes with fuel and annular air flow rate. Experiments were conducted by fixing the primary air flow rate at 140 slpm. The annular air flow rate was then fixed at 1000, 2000, or 3000 slpm. The fuel flow rate was then increased and the visible length of the flame measured. In Fig. 7 (a), the data at the higher annular air flow conditions collapsed on a single curve, when the flame length was plotted as the ratio of fuel to annular air. The linear plot for the lower annular air flow rate condition has the same slope as that for the higher flow rate condition, but, it has a different y-intercept. These results are typical of diffusion flames. An increase in fuel flow with a fixed annular air flow rate results in a longer flame. This is easily understood in that it takes a longer time to consume a large amount of fuel. An increase in air flow rate with the fuel flow fixed, results in a shorter flame. We believe the reason for this is that local vortex-flame interactions due to turbulence tend to increase as the air flow rate increases. The vortex-flame interactions can result in local quenching of the flame. This implies that the combustion

efficiency (% of fuel consumed) decreases with increasing annular air flow rate. This issue will be examined in more detail in the Discussion section. In summary, the flame length in a TV combustor behaves like a typical diffusion flame when the fuel and annular air flow rates are changed.

Figure 7(b) shows how the flame length varies with Φ_p . These experiments were conducted at a fixed fuel flow rate of 20 slpm and a fixed annular air flow rate to either 1000, 2000, and 3000 slpm. The primary air flow rate was varied and the flame length recorded. We have not found a way of plotting the data so that it all collapses on one curve. Thus, it is more difficult to understand. This range of Φ_p corresponds to primary air flow rates of about 240 and 311 slpm, respectively. Remembering that an increase in primary air flow results in a decrease in Φ_p , it is noted that the flame length becomes shorter as the primary air flow rate is increased. The cause of this rapid decrease in flame length will be examined in the Discussions section.

A flame length of 17 cm is where all the curves tend to merge ($\Phi_p = 2$) in Fig. 7(b). This can be understood by examining the wake region behind the afterbody. The 17 cm length corresponds to the end of the recirculation zone established downstream of the afterbody. The end of the recirculation zone fluctuates in time, but on an average it occurs about at 2.2 afterbody diameters downstream of the afterbody (about 17 cm from the face of the forebody). At this location the time average velocity is zero and the residence time is long. Thus, there is a tendency for the fuel to be consumed near this location. This is probably the reason that the flame lengths tend to merge at a height of 17 cm.

A Two-Cavity TV Combustor

The wake region behind the afterbody provides a low speed region to consume the excess fuel, however, the vortex shedding can also cause local quenching. This can lead to reduced combustion efficiency. The initial combustion efficiency measurements made on the TV combustor indicated that this was the case. Little and Whipkey² had shown that adding a second afterbody resulted in a significant reduction in drag. Basically, a second properly sized cavity results in another trapped-vortex between the first and second afterbody. The location of the second trapped-vortex would normally be the unsteady wake region of the afterbody, when only one afterbody is used. The second trapped-vortex reduces the drag because it reduces the unsteady wake motion. In a combustor flow, the second vortex should also reduce local quenching of the flame by reducing the flame-vortex quenching interactions. This was the idea leading to the two-cavity TV combustor

shown in Fig. 8.

The diameter of the second afterbody was determined by using the same forebody scaling used in designing the one cavity combustor. The cavity length of the second vortex, however, was not scaled. Some preliminary experiments indicated that a length of 41.3 mm resulted in a reasonably stable vortex. So this cavity length was used for the second cavity length. The different combustion regions are identified in Fig. 8 for the purpose of later discussions.

Combustion Efficiency and Emissions

Figure 9 presents data on combustion efficiency, unburned hydrocarbons (UHC), carbon monoxide (CO), and oxides of nitrogen (NO_x) for the one cavity (open symbols) and two cavity (closed symbols) combustors. The experiments were conducted in the same way as described for the flame length data in Fig. 7(b). The fuel flow rate was fixed at 20 slpm (corresponding to a velocity of 17 m/s) and the annular air flow rate was fixed at either 1000, 2000, or 3000 slpm (corresponding to velocities of 14, 28, and 42 m/s). Emissions data were then collected for different primary air flow rates. The results are plotted as a function of Φ_p .

The shapes and trends of the curves for the one and two cavity combustors are the same for all of the data in Fig. 9. In Fig. 9(a), the efficiency for the lowest annular air flow rate is flat over a wide range of Φ_p . At the highest annular air flow rate, the efficiency peaks at Φ_p 's between 1.8 and 2.6. There is a very rapid decay of efficiency at low values of Φ_p (high primary air flow rates) and a more gradual decay at higher Φ_p 's. It is also very evident that the addition of a second cavity substantially improves the efficiency but does not change the locations of the peaks nor the decay regions of the curves. Figures 9(b) and (c) show that the inefficiency in the combustion process is the result of both UHC and CO. But most interestingly the improvements in efficiency obtained by adding the second cavity is completely due to the reduction of UHC emissions. It is also evident in comparing Figs. 9(a) and (d) that the NO_x and combustion efficiency curves are very similar. That is, the NO_x and combustion efficiency peaks and decays at the same values of Φ_p . The lowest NO_x and combustion efficiency occur at the highest annular air flow rate. The addition of the second cavity results in only a small difference in NO_x as compared to that in the one cavity combustor. The combustion processes responsible for these features will now be discussed.

DISCUSSION

Insights into the data in Fig. 9 can be gained by

examining what happens to the fuel during its consumption history. Figure 8 has been annotated to aid in this process. Frequent inspection of this figure may be helpful in following the discussion. The fuel injected from the 1st afterbody is: (i) mixed with the primary air, hot products and heat that are recirculated back into the primary zone, and (ii) entrained products from the shear layer denoted by (b) in Fig. 8. The mixture is ignited by the hot products and radicals that are returned back into the recirculation zone. The fuel that is not consumed in the primary vortex is transported into the shear layer at the rim of the forebody at location (1) in Fig. 8. As the reacting fuel mixture travels downstream in the shear layer identified as (b), part of it is entrained into the primary vortex at location (2) and rest is convected on downstream. At location (3) some fraction of the reacting mixture is mixed with the hot products that are transported out of the secondary vortex (c). The resulting mixture continues downstream in the shear layer. Part of it is entrained into the secondary vortex at location 4. At location 5, some fraction of the convected unburned fuel will mix with the hot products being transported out of the wake region d. The remaining mixture will continue to be convected downstream and entrained into the wake region at region 6 or carried on downstream past location 7. The reactions will continue until all of the fuel is consumed or the flame is quenched. The processes that occur at different locations in the combustor depend on the fuel, and the primary and annular air flow rates. The details of the processes occurring during the fuel history are responsible for the different features in the data presented in Figs. 7(b) and 9. Some of these details will be examined.

The first feature to be discussed is the rapid decay that occurs in combustion efficiency, NO_x and flame length in Figs. 9 and 7(b) for Φ_p 's less than 2. Starting at $\Phi_p = 2$, Φ_p approaches 1 as the primary air flow rate is increased. For this range of Φ_p , the primary air flow rates are very large (240 to 311 slpm). The jet injection velocities are also large (40 to 52 m/s) so the residence times of the reacting mixture are small (1 to 0.8 ms). These low residence times result in low consumption of the fuel in the primary zone even though a higher heat release might be expected as Φ_p approaches 1. The low consumption of fuel means that the heat release rate and thus the temperature in the primary zone decreases as the high primary air flow rates increase. Both the low temperature and reduced residence time of the reacting fuel in the primary zone are responsible for the rapid decay in NO_x when $\Phi_p < 2$. Most of the NO_x is believed to be formed in the primary zone. This is supported by the temperature data in Fig. 5(c). Note that near stoichiometric temperatures occur near the face of the first afterbody at

$\Phi_p = 2.2$. This of course results in very high NO_x production rates. If most of the NO_x is formed in the primary zone, then adding the second cavity should not impact the NO_x emissions. Inspection of Fig. 9 (d) shows that this is the case.

The way the fuel mixture is transported into the annular air region (location 1 in Fig. 8) is the key to understanding the decay in efficiency and flame length data in Figs. 7 (b) and 9. There is an involved chain of events that are believed to be taking place. The reacting fuel mixture, being transported out of the primary zone at location 1 in Fig. 8, results in a bulge in the flame near the center of the primary vortex. The bulge in the flame is very evident in Fig. 5 (c) at high primary air flow. It is less evident in confined flows but is still present. The way the bulge is formed is evident from the velocity field data in Fig. 4 (b). The bulge extends out into the annular air stream causing a turbulent wake to be formed downstream of it. This process is analogous to what happens for a jet in cross-flow. The increase in turbulence in the wake region of the shear layer results in the formation of a large number of vortex structures. Vortices are also created in the annular air adjacent to the flame. The air expands as it passes through the narrow passage between the bulge and the wall. This increases the turbulence and thus the vortex formation on the air side of the shear layer. Whether the reacting products turn into the air stream or visa versa depends on their relative velocities. For $\Phi_p < 2$, the primary air velocity is about 1.2 to 2 times larger than the annular air velocity. This means that cold air is entrained into the hot products as they are convected downstream in the shear layer. This is not favorable from a stoichiometric view, since it takes 25 volume units of air to consume one volume unit of propane.

As the reacting fuel mixture is transported downstream, the vortices created in the wake behind the bulge interact with the vortices created in the adjacent air stream. This results in local vortex-flame interactions. Some of these interactions cause local quenching of the flame. The quenched packets of fuel that are not reignited result in reduced combustion efficiency and shorter flames. Vortices are also formed in the wake behind the 1st afterbody in the one cavity combustor and in the wake behind the 2nd afterbody in the two cavity combustor. These vortices also interact with the flame. Some of the interactions result in local quenching of the flame and contribute to combustion inefficiencies. The flame quenching events in the wake regions of the afterbodies are not believed to be important for the very high primary air flow rates but will be shown to be important for low primary air flows. The reason that they are not important for high primary air flows is that the unburned fuel in the wake

of the flame bulge is radially displaced sufficiently far out in the shear layer that very little of it interacts with the vortices formed in the wakes of the afterbody. Also, the flame lengths are sufficiently short that very little unburned fuel reaches the wake region behind the afterbody [See Fig. 7 (b)]. In summary, increasing the primary air flow rate to very large values, extends the flame bulge into the annular air stream. This creates a wake that increases the turbulence in the shear layer downstream of the bulge. The number of vortex-flame interactions are increased in this shear layer region. This results in an increase in the number of local vortex-flame quenching interactions, which increases the number of quenching events that do not get reignited. This chain of events causes a rapid reduction in flame length and combustion efficiency, thus increasing UHC and CO. This somewhat speculative explanation of the rapid decrease in combustion efficiency for $\Phi_p < 2$ seems consistent with all of our results. These ideas will be built upon as the discussion develops.

In Fig. 9 (a), it is noted that the peak values in efficiency decrease as the annular air flow rate increases. The explanation of this involves understanding which shear layers and wakes are responsible for the combustion inefficiencies. Vortex structures are formed as the annular air expands after passing through the gap between the wall and the forebody. These shear layer vortices interact with the flame sometimes causing local quenching that leads to combustion inefficiencies. The combustion inefficiency is defined as $1 - \text{combustion efficiency}$ and can be interpreted physically as the fraction of unburned fuel. The wake regions behind the afterbodies and the shear layers generated at locations 3 and 5 in Fig. 8 also form vortices that can interact with the flame in ways that cause local quenching and combustion inefficiencies. For these wake and shear layer generated vortices, the frequency and number of local quenching events increase as the annular air flow rate increases. Thus, the combustion efficiency and the flame length are expected to decrease as the annular air flow rate increases. The inefficiencies that result at the peak values of combustion efficiency in Fig. 9 (a) are believed to be the result of the vortex-flame interactions occurring in the shear layer and wake regions of the flow outside of the primary vortex. There will also be vortex-flame interactions causing local quenching in the primary vortex. But, the temperatures in the trapped vortex are sufficiently high that quenched fuel packets have a higher probability of being reignited.

When the 2nd cavity was added to the combustor, the peaks in combustion efficiency increased at all flow rates [See Fig. 9 (a)]. The reason for this is that many of the vortices that contribute to vortex-flame quenching interactions are not present so the combustion efficiency is improved. The improvement in combustion

efficiency that results when the second cavity is added is an approximate measure of combustion inefficiency resulting from the vortex-flame quenching interactions in the wake of the 1st afterbody in the one cavity combustor. It is noted in Fig. 9 (a) that the improvements in combustion efficiency resulting from the addition of the 2nd cavity were greater for the higher annular air flow rates. This is consistent with the idea that the improvements in combustion efficiency is a measure of the inefficiency occurring in the wake of the 1st afterbody. The number of vortex-flame quenching interactions occurring in the wake and shear layer behind the 1st afterbody increase as the annular air velocity increases. So, a larger improvement can be realized in combustion efficiency when the local quenching events are eliminated. This happens when the secondary vortex is added.

It was previously noted that the improvements in combustion efficiency resulting from the 2nd cavity are solely due to reductions of UHC's. In fact, the CO concentration increased [See Figs. 9 (b) and (c)]. The secondary cavity provides an additional recirculation zone for the fuel to be consumed. It is believed that the mixture is locally fuel-rich in the 2nd cavity. Combustion of UHC's in the fuel rich secondary vortex results in the formation of CO instead of CO₂ as noted in Fig. 9 (c).

The decay in combustion efficiency at large Φ_p is evident in Fig. 9 (a). This decay for annular air flow rates of 2000 and 3000 slpm is believed to be related to the amount of fuel consumed in the primary zone. This is important because: (1) the amount of fuel consumed controls the temperature in the primary zone and (2) the fuel that escapes the primary zone experiences vortex-flame quenching interactions that lead to combustion inefficiencies. High reaction temperatures normally result in high efficiencies. This trend is noted by comparing the temperatures in Figs. 5 (a) and (b) with the combustion efficiencies in Fig. 9 (a) for Φ_p 's of 4.4 and 2.2. The peak temperatures of 1800 K and 2150 K correspond to efficiencies of 92 and 97%, respectively. We believe that the decay in combustion efficiency for $\Phi_p > 2.6$ is due to decreasing primary zone temperatures as Φ_p increases. In these experiments, the fuel flow rate is fixed and Φ_p increases because the primary air flow rate decreases. The decrease in primary air velocity results in poor mixing in the primary zone and this leads to an increase in unburned fuel being transported out of the primary zone. The mixing inside the cavity decreases because the velocity of the primary air jets approach the fuel velocity. Mixing is a complicated process involving entrainment of one fluid into another. Entrainment often controls the mixing process. In shear layers, the lower velocity fluid is always entrained into the higher velocity fluid with the

velocity gradient being the driver. From stoichiometric considerations, the air velocity should be larger than the fuel velocity so that the fuel, being the lower stoichiometric component, is entrained into the air. The entrainment of fuel into the air jets increase as the air velocity becomes much larger than the fuel velocity. Thus, the mixing is enhanced under this condition. Alternately, the entrainment, hence mixing, decreases as the primary air velocity approaches the velocity of the fuel. This happens for Φ_p 's larger than 2.6. For example, the velocity ratios of primary air to fuel at $\Phi_p = 2.6$ and 4.4 are 1.8 and 1.2, respectively. This means that the amount of fuel escaping from the primary zone increases as Φ_p increases, the temperature in the primary zone decreases, and the combustion efficiency decreases. This the case for the data in Fig. 9 (a).

Note, that the combustion efficiency for the 2000 slpm annular flow rate is higher over a wider range of Φ_p than that for the 3000 slpm annular flow rate. The reason for this is that the fuel escaping at the higher annular flow rate is subject to more vortex-flame quenching interactions than the fuel that escapes at the lower annular flow rate. Thus, the combustion efficiency for the lower annular flow rate will remain higher over a wider range of Φ_p 's. This is evident from the flatness in the low annular air flow rate combustion efficiency curve in Fig. 9 (a). It is noted that the combustion efficiency for the one cavity combustor is about 99% for Φ_p between 4.4 and 1.8 and is 99.8% for the two cavity combustor. This means that only 1% to 0.2% of the fuel is not consumed in this range of Φ_p .

SUMMARY AND CONCLUSIONS

A new trapped vortex (TV) concept has been investigated as a means of stabilizing a flame. In a TV combustor, a cavity is sized to trap a vortex when air flows past it. Fuel and primary air are injected directly into the vortex from multiple jets in the downstream wall of the cavity. This injection location was found to be satisfactory in that it did not disrupt the trapped vortex and may have even reinforced it. It was found that combustion did not make much difference in properly sizing the cavity. The guidelines established by Mair¹ and Little and Whipkey² for trapping a vortex in a cavity for the purpose of drag reduction appear to work in this study.

The idea behind the TV combustor is that a flame established in the trapped vortex should remain stable over a wide range of air and fuel operating conditions. This idea was evaluated in this paper and combustion parameters such as LBO, pressure drop, flame length, combustion efficiency, and NO_x emissions were examined for a wide range of conditions. A somewhat

speculative theory is presented that gives some insights into how different flow conditions influence these combustion parameters.

The most impressive performance characteristic of the TV combustor is its extremely low LBO limit. The low LBO limit is due to the stability of the trapped vortex over a wide operating range. The overall LBO limit equivalence ratio (Φ) was 0.018 for the highest annular velocity tested (42 m/s). At flow velocities typical of those in gas turbine combustors, the LBO limit was less than 0.005. This is considerably below what is typically obtained with bluff-body and swirl stabilized flames. The lowest LBO limits were achieved at low primary air flow rates. At higher primary air flows, the fuel flow rate at the LBO limit was found to increase linearly with the primary air flow rate. The LBO limit in the primary vortex at high primary air flow rates was about $\Phi_p = 1.3$. This high value indicates that the mixing by the multiple jets needs to be improved.

Another feature of the TV combustor was the very low pressure drop across the cavity. It was about 0.5% when the air velocity in the combustor was about the same as that in typical gas turbine combustors. This suggests that significant reductions in specific fuel consumption might be realized in a properly designed TV combustor.

Combustion efficiencies of about 99% were recorded at an velocity typical of gas turbine combustors. At 3 times this velocity, the peak efficiency was about 97%. This efficiency was increased to almost 99% when a second cavity was added to the combustor. This high velocity flow condition resulted in a minimum EINO_x of 3.4. Almost all of the NO_x is formed in the fuel rich primary zone where near stoichiometric temperatures were measured.

In conclusion, the TV concept offers the promise of being a simple, compact, and low pressure drop combustor which has good stability limits and reasonable combustion efficiencies at high flow conditions. However, considerable work is required before the practical aspects of a TV combustor can be demonstrated. Future investigations will focus on methods of maintaining good performance characteristics while substantially reducing the NO_x. Approaches that involve operating the primary zone in a lean or prexed condition will be investigated.

ACKNOWLEDGMENT

This work was supported by Air Force Contract

F-33615-90-C-2033 and AFOSR Aerospace Science Division. The authors would like to thank Dr. G. J. Sturgess and Mr. D. Burrus for their helpful discussion, and Mr. B. Sarka for his assistance in experimental work and Mrs. M. M. Whitaker in preparing the manuscript.

REFERENCES

1. Mair, W. A., "The Effect of a Rear-Mounted Disc on the Drag of a Blunt-Based Body of Revolution," *The Aeronautical Quarterly*, pp. 350-360, Nov. 1965.
2. Little, Jr., B. H., and Whipkey, R. R., "Locked Vortex Afterbodies," *J. of Aircraft*, Vol., 16, No. 5, pp. 296-302, 1979.
3. Gharib, M., and Roshko, A., "The Effect of Flow Oscillations on Cavity Drag," *J. Fluid Mech.*, Vol. 177, pp. 501-530, 1987.
4. Goss, L. P., Post M. E., Trump, D. D., and Sarka, B., "Two-Color Particle Imaging Velocimetry", *J. Laser Appl.*, pp. 36-42, 1991.
5. Post, M. E. and Goss, L. P., "Two-Color Particle-Imaging Velocimetry in Vortex Structures," 31st Aerospace Sciences Meeting and Exhibit, AIAA-93-0412, 1993.

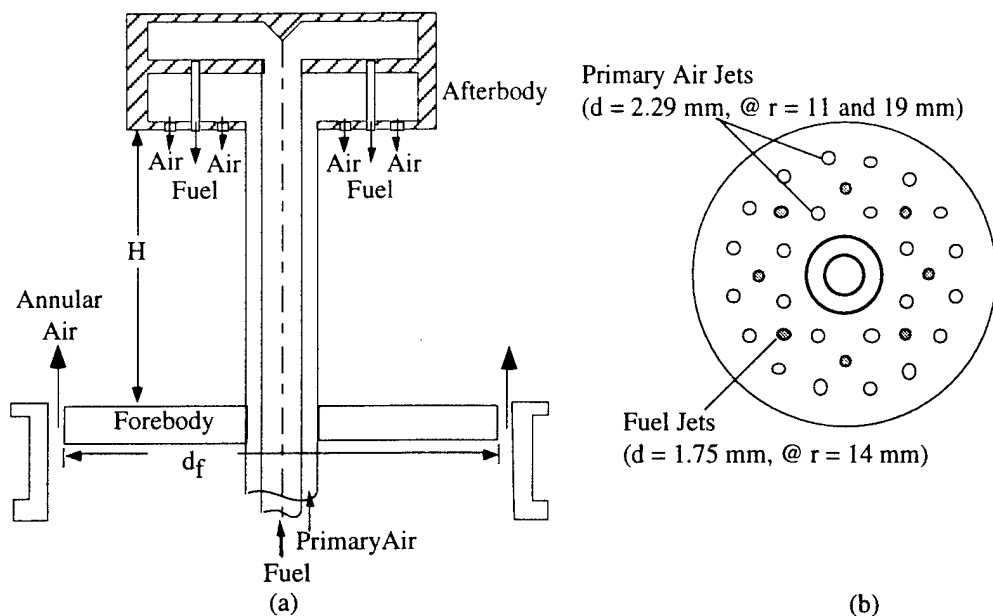


Figure 1. Schematic Diagrams of (a) Trapped-Vortex Combustor and (b) Injection Plane of Afterbody

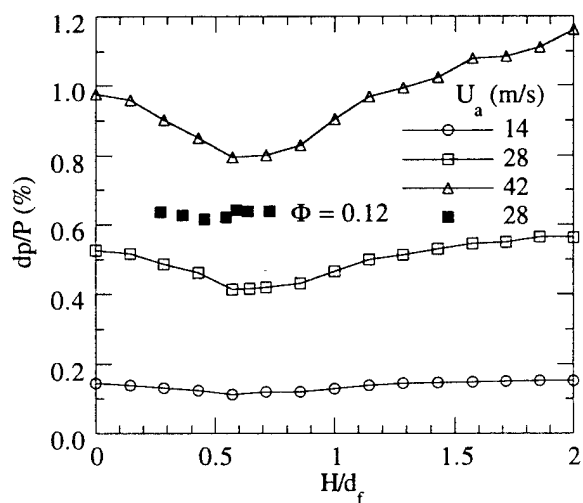


Figure 2. Comparison of Pressure Drops between Cold and Combusting Flows

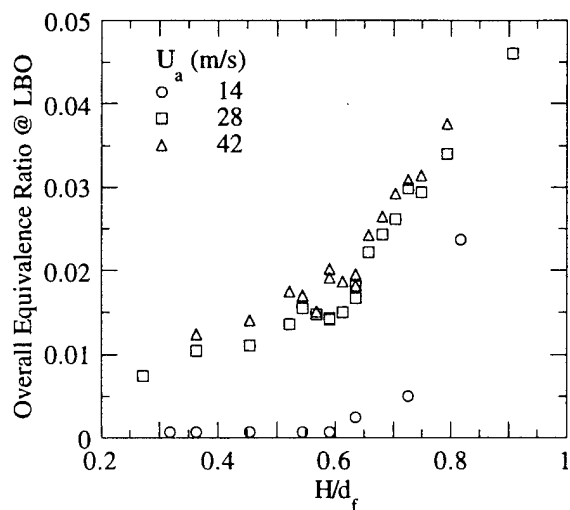


Figure 3. Effect of H/d_f on Lean Blow-out under Various Annular Air Flow Conditions

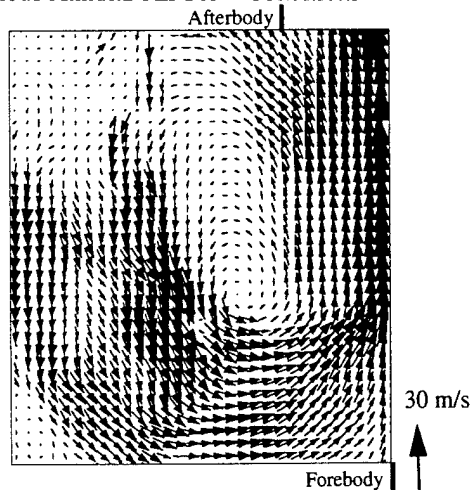
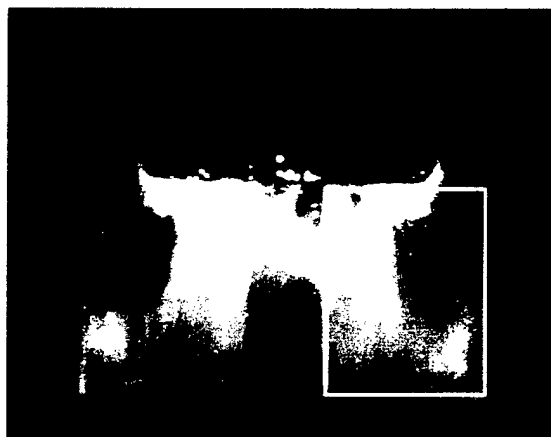


Figure 4. Stable Flame Image and Corresponding Instantaneous Velocity Field Obtained by PIV at $U_{air} = 28$ m/s

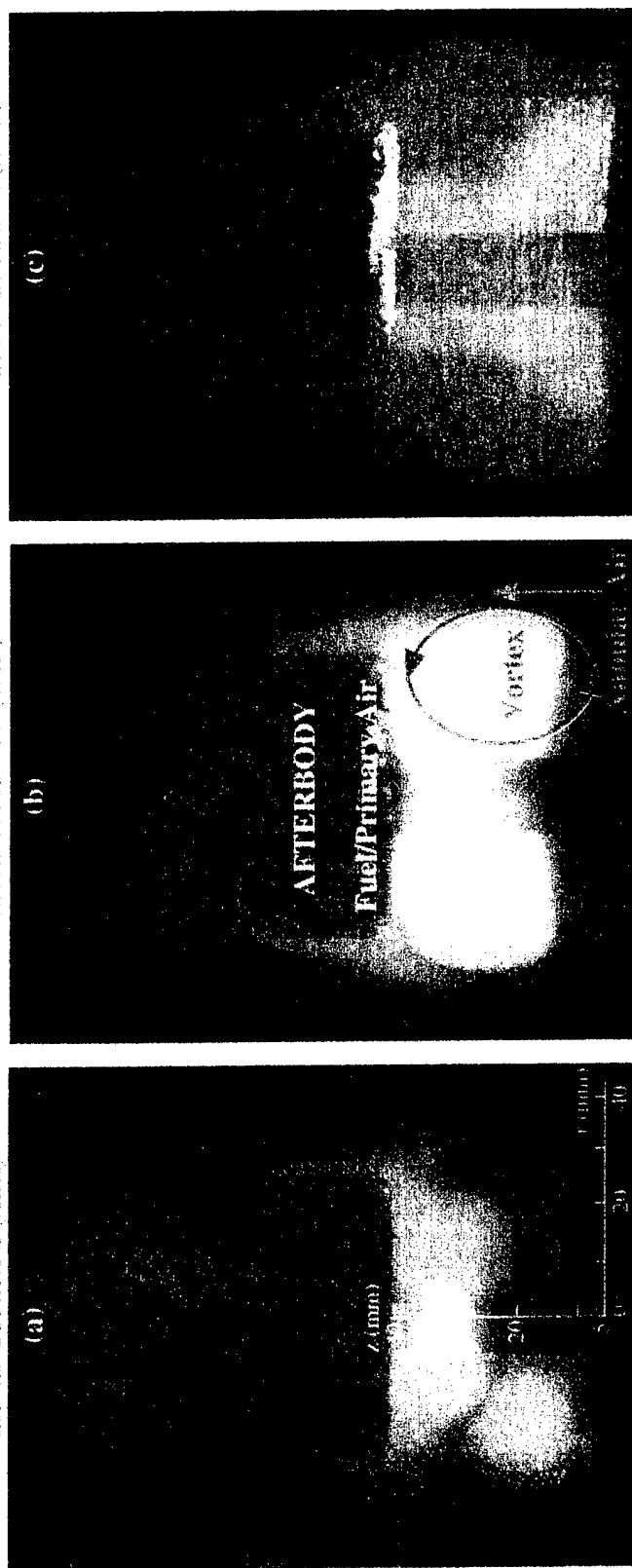
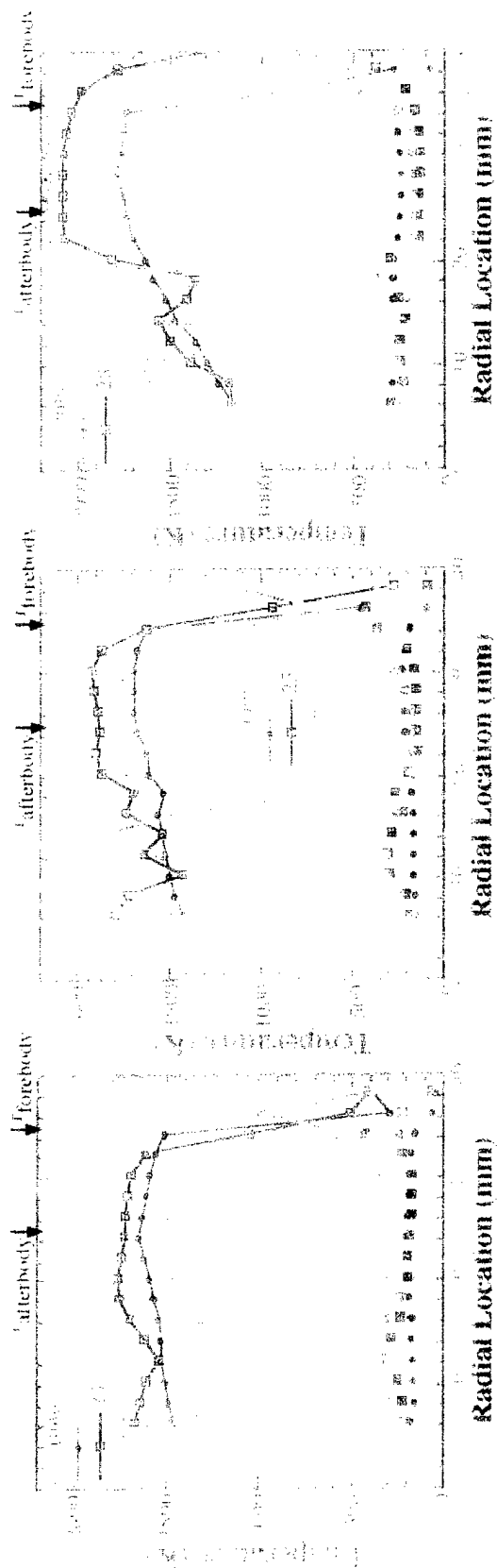


Figure 5. Effect of Primary Air on Flame Structures and Temperature Profiles at $U_{\text{air}} = 42 \text{ m/s}$ and $\Phi_{\text{Overall}} = 0.24$
 (a) $\Phi_{\text{Primary}} = 1.1$, (b) $\Phi_{\text{Primary}} = 4.4$ and (c) $\Phi_{\text{Primary}} = 2.2$

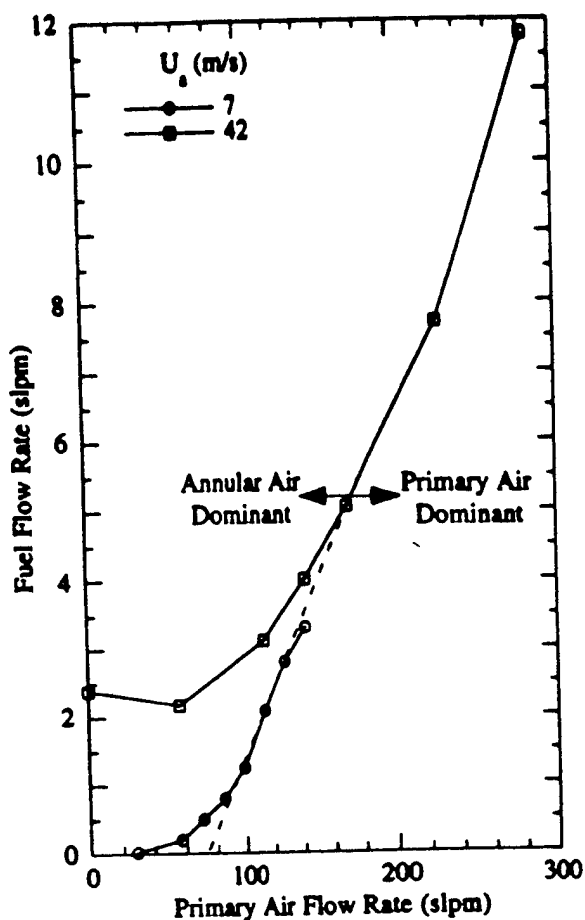


Figure 6. Effect of Primary Air Flow on Lean Blow-Out at $H/d_f = 0.59$

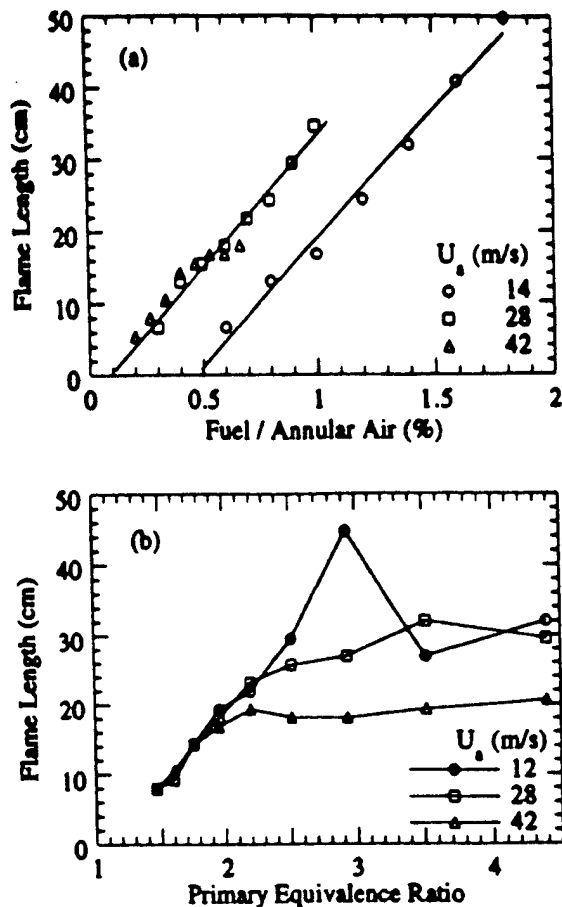


Figure 7. Impact of Flame Length due to (a) Fuel Flow and (b) Primary Equivalence Ratio

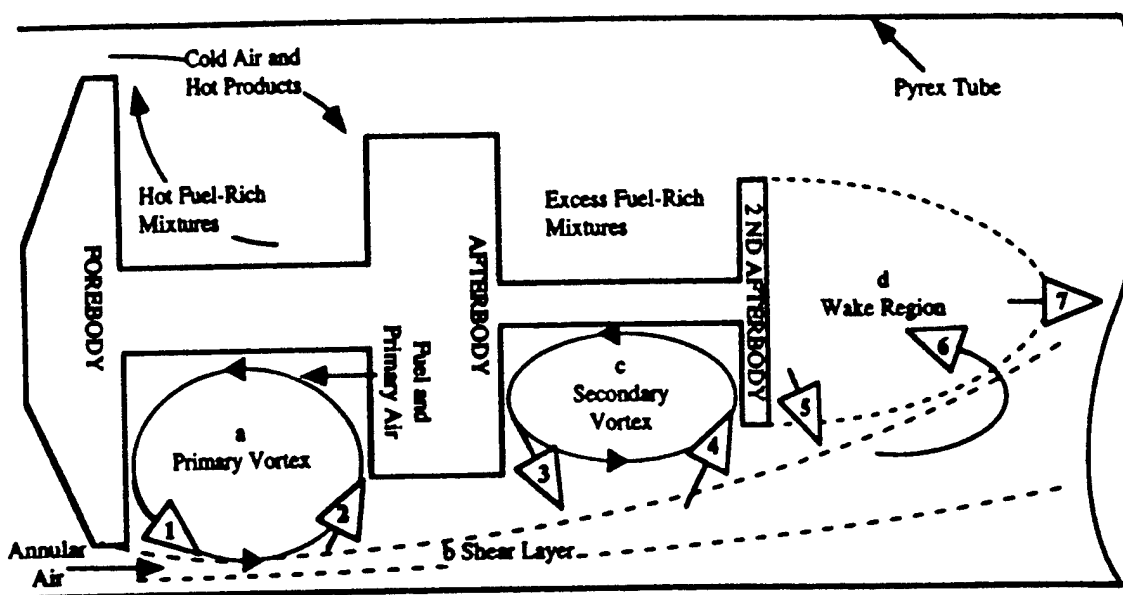


Figure 8. Illustration of Flow Field and Combustion Zones : a. Primary Vortex, b. Shear Layer, c. Secondary Vortex, and d. Wake Region.

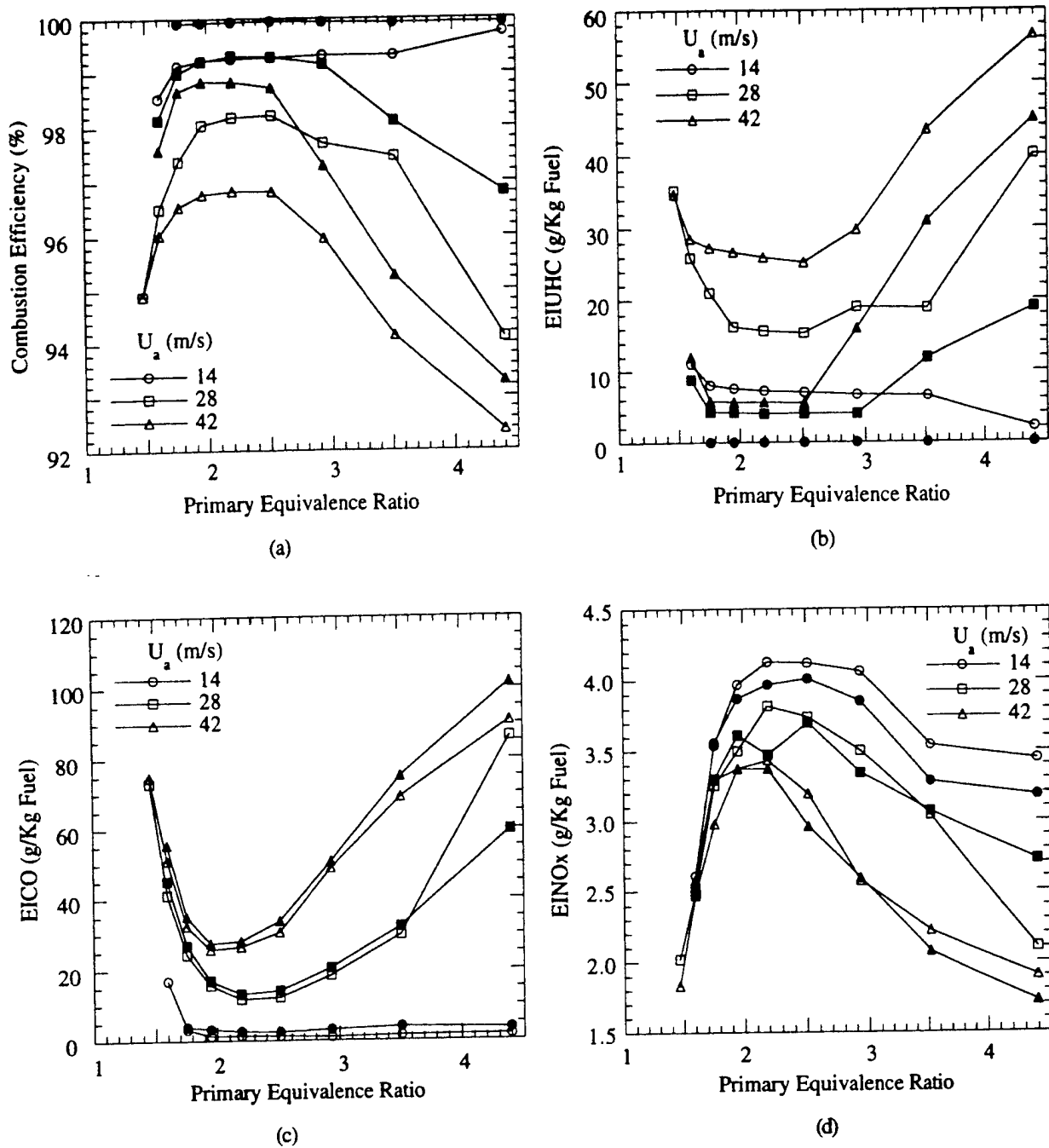


Figure 9. Impact of Primary Air and Annular Air on (a) Combustion Efficiency, and Emission Indices of (b) Unburned Hydrocarbon, (c) Carbon Monoxide and (d) Oxides of Nitrogen at a Fixed Fuel Flow. The Open and Closed Symbols Denote Configurations with One Cavity and Two Cavities, respectively.



AIAA 94-3271

**Relation of CARS Temperature Fields to
Lean Blowout Performance in an
Aircraft Gas Turbine Generic Combustor**

G. Switzer, Systems Research Labs., Inc., Dayton, OH
G. Sturgess, D. Sloan, Pratt & Whitney, East Hartford, CT
and D. Shouse, Wright Laboratory, Dayton, OH

**30th AIAA/ASME/SAE/ASEE Joint
Propulsion Conference**

June 27-29, 1994 / Indianapolis, IN

RELATION OF CARS TEMPERATURE FIELDS TO LEAN BLOWOUT PERFORMANCE IN AN AIRCRAFT GAS TURBINE GENERIC COMBUSTOR

G.L. Switzer, Systems Research Laboratories, Inc., Dayton, Ohio,
G.J. Sturgess* Pratt & Whitney, East Hartford, Connecticut,
D.G. Sloan, Pratt & Whitney, East Hartford, Connecticut, +
D. Shouse, Wright Laboratory, Wright-Patterson Air Force Base, Ohio.

Abstract

A four-injector representation of a practical annular combustor has been made in planar configuration and tested. Although the desirable test matrix for full understanding and description of the lean blowout behavior of this combustor is large, sufficient has been accomplished to present a reasonably complete picture of this behavior. Phenomenological modeling has been used to order the data, and provided correlation of blowout equivalence ratios. Field information for the combustor has been provided through isothermal flow computational fluid dynamic calculations, and CARS temperature measurements in reacting flow. The pictures of the combustor behavior at blowout provided by these three approaches are complimentary, and are remarkably consistent.

Introduction

Combustion stability is extremely important in gas turbine engines for aircraft use. However, it is becoming increasingly more difficult to ensure that adequate stability margins are maintained in the future because of current design trends. These trends include enhanced fuel/air mixing, via better atomization of the liquid fuel in airblast-type injectors for improved temperature traverse quality, high temperature rise (increased fuel turndown ratio), and, low emissions combustors and their associated technologies. At the higher pressure, higher temperature operating conditions of current and projected engines, considerations of combustor durability demand minimum surface area designs, with consequent tendencies to reduce combustor volume. The potential stability difficulties due to these trends are exacerbated by the lack of a satisfactory and reliable *a priori* prediction procedure for lean blowouts.

The majority of the relevant published material on flame stability is for bluff-body flameholders of various types or, is for well-stirred reactors, as reviewed by Lefebvre¹. The quantity of experimental data published in the open literature for practical gas turbine combustors is much less extensive, and systematic investigations are largely lacking, although some such work of limited scope for can-type combustors is reported by Jeffs² and Stewart³. Almost all of the information on the annular-type of combustor currently used for aircraft applications is confined to relatively inaccessible private company reports. The information that is available for practical combustors is expressed in global terms, and there are no detailed interior flowfield descriptions at near-blowout conditions. The large number of geometric and flow variables encountered makes rational comparison of data difficult.

In 1987 the U.S. Air Force Wright Laboratory, Aero Propulsion and Power Directorate (WL/PO), established the Combustor Design Model Evaluation (CDME) program, with the goal of improving physical modeling to facilitate design work. To address the developing stability concerns, the Air Force under the CDME effort, initiated a comprehensive joint Government, Industry and University research program aimed at improving the design and analysis capabilities for flame stability and lean blowout (LBO) in the combustors of aircraft gas turbine engines⁴.

The intent of the stability research program is to investigate, understand, and model lean blowout in the context of combustors of aircraft gas turbine engines. The approach adopted in this program is a step-by-step one that moves from gaining an understanding of the basic flow behavior in, initially, a simplified environment, and then through progressively more realistic situations, leading to a simplified version

* Member, AIAA.

+ Current address: Asea Brown Boveri, Windsor, Connecticut.

of a real gas turbine combustor. In order to separate the effects of liquid fuel atomization and spray evaporation from the aerothermochemical effects, it was decided to approach the LBO problem in two distinct stages - initially, with gaseous fuels (propane and methane) and then, with liquid fuels (ethanol and JP8).

The experimental portion of the program utilizes three combustors as test vehicles to achieve the desired progression in flow complexity. These combustors consist of a research combustor⁵, a technology-development combustor⁶ and a generic gas turbine combustor⁷.

The research combustor is simple in configuration, but nevertheless, contains the essential primary zone flow features of a practical gas turbine combustor. The technology combustor incorporates the practical fuel injectors of the generic combustor into the simplicity of the research combustor to permit study of their characteristics in isolation. The generic combustor is a geometrically-flexible, highly-controllable, yet simplified, four injector, planar version of an annular gas turbine combustor. Its purpose is to provide an experimental database against which lean blowout modeling of various types might be evaluated and calibrated.

All three combustors feature high optical access to permit direct flame observation and extensive use of laser diagnostic techniques. They operate at atmospheric pressure, and utilize an excess-nitrogen dilution technique⁸ to simulate the effects of low combustion pressure on LBO, by slowing down chemical reaction rates.

Modeling of the LBO process follows several approaches⁴. Conventional phenomenological modeling was applied to the research combustor to derive a stability criterion, as was a computational fluid dynamics (CFD) approach using a finite rate chemistry model⁹ and one¹⁰ using the Eddy Dissipation Concept combustion model of Magnussen¹¹. A hybrid method was applied to the generic combustor using conventional CFD with the Eddy Break-Up combustion model, to establish a well-stirred reactor network to represent the combustor flowfield, and upon which the detailed chemistry is solved⁴. In addition, CFD calculations of the generic combustor are being made using finite rate chemistry with a reduced mechanism for propane.

Some of the results from the research combustor are presented in References 8, 9, 10, 12, 13,

14, 15; limited results from the technology combustor are given in Reference 6, and limited results from the generic combustor are contained in Reference 7.

The more sophisticated the modeling that is used in a calculation procedure to describe a phenomenon, the more complex is the validation process necessary for that modeling. If the overall procedure utilizes a number of physical models, as does any CFD-based approach for example, it is not sufficient just to validate these models individually. The interactions of these models when working together must also be validated. Furthermore, given current computer and calculation grid limitations, it is essential that a comprehensive validation be made in a geometry similar to that of the intended application. Unfortunately, the number of suitable validation test cases for modern gas turbine combustor applications extant in the open literature is extremely limited; Reference 16 is a recent exception. Cases with operating parameters representative of lean blowout do not exist.

Contribution

The intended purpose of the generic gas turbine combustor is to provide an experimental database against which LBO modeling might be evaluated. In this context, a set of temperature measurements obtained in reacting flow with suitable operating conditions is presented, together with a description of the basic flow field in the combustor as obtained by CFD calculation. Together, these data are used to explain the measured LBO behavior of the generic combustor.

Generic Combustor Rig and Test Facility

The generic combustor rig design was selected to satisfy the following criteria: 1.) The combustor should represent current design practice. 2.) The combustor geometric boundary conditions should be simple so as to avoid introducing any grid restraints on calculation accuracy. 3.) The rig configuration should permit high optical access for flame visualization and application of laser diagnostics. 4.) The rig design should maximize geometric flexibility and operating condition controllability to permit extensive parametric studies of the major combustor design parameters.

The aerothermodynamic design of the base annular combustor was selected to follow present Pratt & Whitney design practice, and it utilized airblast-atomizing fuel injectors with integral air swirlers, together with "inside-out" recirculation^{4, 5, 15}. The

basic design is embodied in an engine that is currently in regular airline service throughout the world. The configuration adopted for the rig was a four-injector, planar-section, simplified geometry version of this annular combustor design.

The fundamental rig design to accommodate the combustor configuration was carried out by United Technologies Research Center, with subsequent modifications made by Wright Laboratory at Wright-Patterson Air Force Base, Dayton, Ohio. These Air Force modifications were made to improve rig handling, optical access and window durability. The fuel injectors used were actual engine hardware, with sets modified, calibrated and individually balanced with Lee-Jets to flow gaseous or liquid fuels. Sets with two swirl strengths air swirlers were available. The replaceable sets of combustion liners contain patterns of flush, circular air ports to admit additional air into the combustor. The port patterns were based on engine experience. On the shroud-side of the liners were welded several longitudinal I-beams for structural stiffness at high metal temperatures.

The rig delivers separately-metered air supplies to the combustor dome and, the upper and lower shrouds that feed the liners. These supplies were isolated from each other by means of an upstream array of sonic venturis. The exits from the combustor and shrouds are throttled by independent water-cooled valves that control bypass flows. The shroud bypass flows are set to realistic values to result in correct air jet trajectories into the combustor; bypass flows also provide backside convective cooling of the liners. Excess nitrogen, when used for low pressure simulation, is introduced and mixed with the main air supply upstream of the sonic venturis.

Major optical access to the combustor volume is provided by sidewall windows of fused quartz. In addition, direct vertical access can be provided via a set of fused quartz liners containing the appropriate pattern of air ports.

Fig. 1 gives a cross-sectioned elevation of the rig, that shows the major features described. Complete details of the combustor and rig, including leading dimensions, are given in Ref. 7.

The rig was mounted horizontally in a test cell (Room 20) of Wright Laboratory. The cell provides metering and control of air, fuel (gaseous propane), excess (gaseous) nitrogen, and cooling water to the combustor rig; gaseous hydrogen and separate air for

the combustor torch ignitor are also provided. The discharge from the rig enters an atmospheric pressure exhaust duct, and exits the facility to ambient conditions. Mounted under and on either side of the rig test section is a hardened CARS system. The facility is also described in more detail in Ref. 7.

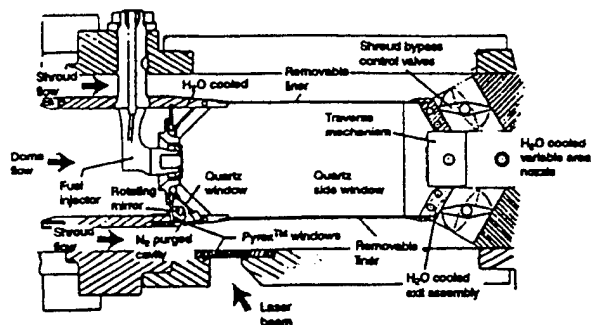


Fig. 1: Cross-section of the Generic Combustor

The planar configuration adopted for the combustor represents a compromise between realism and, optical access and simplicity. Jet flows into the rig combustor from the upper and lower shrouds via the liners will be into respective cross-sectional areas that are different from those of a real annular combustor due to the absence of wall circumferential curvatures. However, the rig upper and lower (planar) liners have identical hole sizes and patterns, just as they would have in the real outer and inner circular cross-section liners. Therefore, air jet penetration and jet lateral spreading will be slightly different in the rig from what they would be in the equivalent annular combustor. The resulting net blockage, and its radial distribution across the combustor height, for the gases exiting primary zones will also be different. This will exert some second order influence on flame stability, but, based on experience, this is not as serious for LBO as it is for some other aspects of combustor performance.

Lean Blowout Characteristics

The lean blowout characteristics of the generic combustor when operating on gaseous propane as fuel are described in Ref. 7. They are complex, and would have been difficult to understand with direct observations of flame behavior over the range of combustor loadings at which blowouts were obtained.

Combustor loading was set by air mass flow rate, (determining residence time) and the quantity of excess nitrogen that was introduced (determining the

simulated low pressure); air inlet temperature and combustor actual pressure were constant at ambient values. Blowouts were obtained by incrementally reducing fuel mass flow rate at fixed loading, with thermal stability being re-established after each successive fuel decrement. This was continued until flame extinction took place.

The equivalence ratios at LBO were correlated by a generalized form of the Kretschmer & Odgers¹⁷ combustor loading parameter LP, defined in Ref. 7 as,

$$LP = \frac{\dot{m}_{Tot}}{VP^n F}$$

where,

$$\dot{m}_{Tot} = \dot{m}_f + \dot{m}_a + \dot{m}_{N_2} \quad \text{lbm/sec.}$$

$$\dot{m}_f = \text{fuel mass flow rate}$$

$$\dot{m}_a = \text{air mass flow rate}$$

$$\dot{m}_{N_2} = \text{excess nitrogen mass flow rate}$$

$$V = \text{reactor volume, ft}^3$$

$$P = \text{combustion pressure, atmos.}$$

$$n = 2\phi_{LBO} / (1 + \dot{m}_{N_2} / \dot{m}_a)$$

apparent global reaction order

$$F = \frac{10^{0.00143T}}{3.72} \quad (\text{to correct to } 400K)$$

$$T = \text{inlet temperature, K}$$

This definition of loading parameter derives from phenomenological modeling that considers the flame-holding region of the combustor as a well-stirred reactor⁷. It may be applied on a global basis to the whole combustor (including the redundancy of the dilution zone), or, to a local burning zone within the combustor.

Figure 2 illustrates the lean stability characteristic for a configuration where 10 percent of the total combustor airflow is introduced through the combustor dome. The dome airflow consists of the sum of fuel injector, insert swirler (a smoke-control device¹⁸ surrounding each fuel injector and consisting of a ring of small circular ports each with a compound angle to the injector centerline), and dome cooling airflows⁷. The appropriate volume is here based on the total for the combustor, and the equivalence ratio at blowout is an overall one involving the total fuel flow and all of the combustor airflow. This is the usual definition for this quantity as used in combustor/engine development.

The LBO behavior shown in Fig. 2 exhibits an initial region of continuous but slow loss of stability at low and moderate values of combustor loading, followed at higher loadings (where values greater than 10 lbm/sec.(ft³atmos.) are reached) by a region of discontinuous behavior, where there are sudden losses in stability followed by recoveries and subsequent losses. This saw-tooth pattern of behavior has a net loss of stability that becomes increasingly severe as loading increases. A condition of peak heat release rate is not reached in these results.

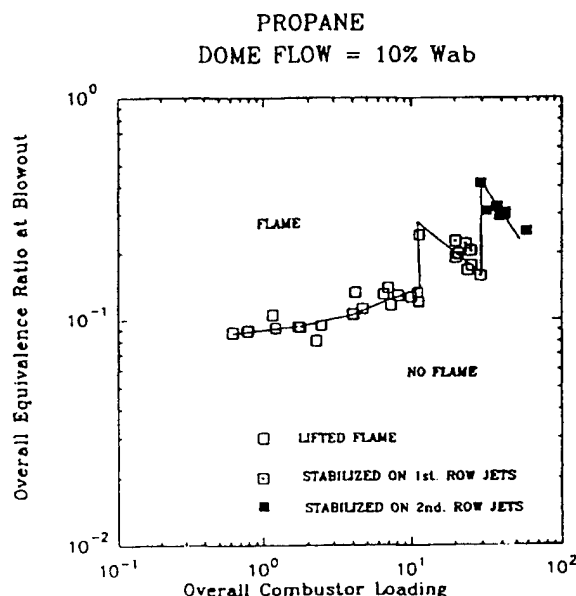


Fig. 2: Correlated LBO Data for 10% Dome Flow Combustor, Showing Different Flame Stabilization Modes

Flame observations confirmed conclusions based on estimates of local equivalence ratios, that up to a loading of 10 lbm/sec.(ft³atmos.), flame was stabilized in the volume between the fuel injector discharges and the plane of the first row of combustion air jets, (commonly known as the "primary zone") and involved shear layer burning of fuel in the individual insert air jets surrounding each fuel injector. For the higher loadings (achieved by increasing excess nitrogen while essentially maintaining residence time through constant airflow), there can be insufficient oxygen to allow complete burning in this upstream position, so flame expands downstream to become anchored on the first transverse row of combustion air jets. Eventually, at yet higher loadings achieved with additional excess nitrogen, the flame expands even further downstream to

become anchored on the second row of combustion air jets.

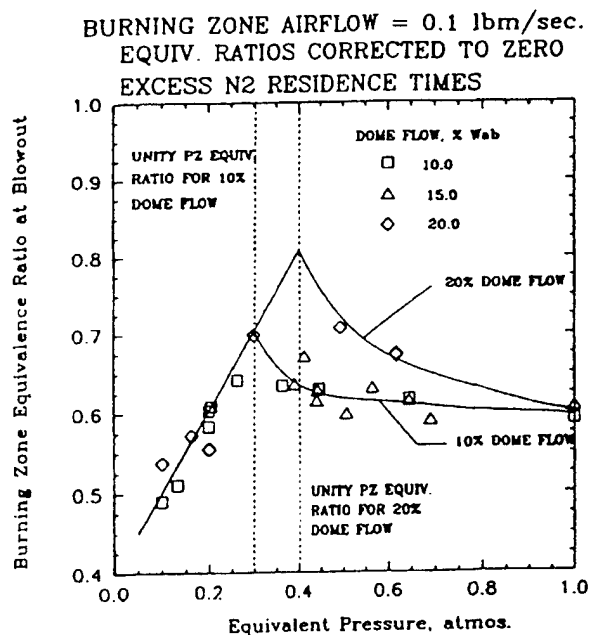
It is this progressive growth of the flame with increasing combustor loading, resulting in different methods and positions of flame holding, that gives the saw-tooth stability characteristic since the flame behavior as blowout is approached is different for each burning mode. LBO curves of this general character have been observed in other practical combustors, e.g. Ref. 4, where the reason for the behavior could only be speculated.

When the percentage of total combustor airflow introduced through the dome is increased, the saw-tooth stability behavior of overall LBO equivalence ratio is not encountered until much higher combustor loadings. This is because the local equivalence ratios in the primary zone do not approach unity until the higher loadings, by virtue of the additional dome air.

Figure 3 illustrates this behavior for 10 and 20 percent dome airflow combustor configurations. The term "burning zone" is now used to account for the expanding flame as equivalent pressure is reduced. Thus, "burning zone equivalence ratio" is based on the total fuel flow and the airflow associated with the axial extent of the visible flame in the combustor; the volume term in the loading parameter is determined similarly. The vertical dashed lines mark the appropriate equivalent pressures for each dome flow at which the primary zone reaches unity equivalence ratio. Values to the left of these lines represent equivalent pressures where the primary zone is over-rich, and the flame consequently extends beyond the primary zone.

The lines shown on the figure for 10 and 20 percent dome flows are curve fits to the data that are forced to intersect the combined (linear) data fit line at the respective values of equivalent pressure for which the primary zone equivalence ratio reaches unity. When the flame is anchored by the jets, the stability becomes independent of dome flow, as the correlated data show.

While the flame is stabilized in the primary zone, the effect of reducing pressure is to increase the burning zone blowout equivalence ratio. When the flame becomes stabilized on the transverse air jets, more air is involved even through fuel flow at blowout is increasing as pressure falls; therefore, the (extended) burning zone equivalence ratio at blowout falls.



The main flame structure in the primary zone for the 10 percent dome air configuration is characterized as being "lifted" for loadings less than 10 lbm/sec. (ft³atmos.). A "lifted flame" was the normal operating mode, and was one where visual flame was distributed rather widely over the primary zone. It is associated with the flame being anchored in the shear layers associated with the individual insert swirler air jets surrounding each fuel injector.

At higher primary zone absolute airflows, and for lower primary zone equivalence ratios, the visual flame becomes distinctly attached in tight conical form to the fuel injectors. This is referred to as an "attached flame." Figure 4 illustrates the occurrence of this for the 15 percent dome flow combustor. In this condition there is sufficient air available for combustion to be associated with the shear layers formed between the swirling annulus of fuel introduced by the injector and the swirling air from the integral outer air swirler. As will be shown, the additional air comes from the first row of combustion air jets as well as the increased injector air. An attached flame condition is acoustically quieter than a lifted flame condition.

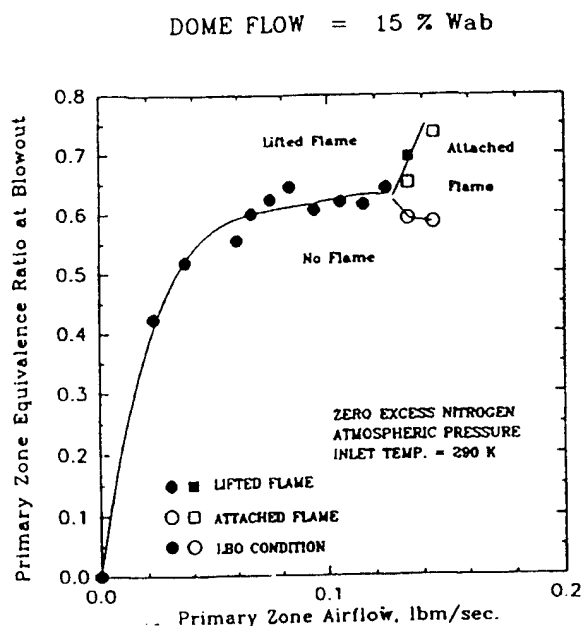


Fig. 4: Delineation of Lifted and Attached Flames at Atmospheric Pressure

A given combustor loading in this rig can be obtained in two ways: 1.) low or zero excess nitrogen together with high airflow, or, 2.) low airflow together with high excess nitrogen. Therefore, at given combustor loading, the flame structure may be either lifted or attached, depending on how the loading is achieved. Therefore, since the flame holding can be different according to the flame structure, two stability curves at a given percentage dome flow are possible for primary zone-anchored flames. Fig. 5 demonstrates this for the 10 percent dome flow combustor, where it can be seen that the attached flame, in addition to being quieter, also has better stability than the lifted flame.

CFD Calculations of Flowfield

Direct observations of the flame structure and the LBO behavior described above and in Ref. 7, indicated that interactions of the swirling fuel/air jets issuing axially into the combustor from the fuel injectors with the transverse jets of combustion air introduced through the liners, are extremely important in this design of combustor. To better understand these interactions, computational fluid dynamics (CFD) calculations of the flow field were made.

The CFD calculations were made using the NASTAR¹⁹ stationary-state solution computer code. The combustor configuration was represented as a

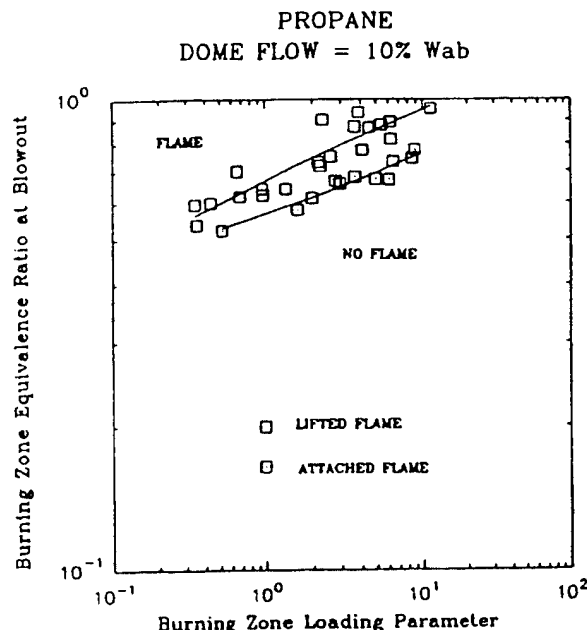


Fig. 5: Correlated LBO Data with Primary Zone Burning, Showing Improved Stability for Attached Flames

(repeating) single fuel injector segment, to which periodic boundary conditions were applied on the lateral sides. The calculation domain was filled by a 109 x 53 x 49 (283,073 nodes) body-fitted grid; grid independent solutions are not claimed however, even with this nodal density. The operating conditions for the calculation were an air temperature of 304K and the combustor pressure was 14.31 psia. The combustor total airflow was 0.1716 lbm/sec., with flow splits of 15 percent dome flow, upper liner 42.41 percent and lower liner 42.56 percent. Liner flows were introduced as individual jets, according to the hole patterns and effective areas given in Ref. 7.

The calculation was made for isothermal flow to avoid questions concerning the suitability of various combustion models for these operating conditions. Air was the sole fluid used. This is considered as acceptable since the major flow features in the combustor will not be significantly modified by the heat release associated with combustion at near-blowout conditions.

Fig. 6 shows calculated iso-surfaces of mean axial velocity at fixed velocity of, for reference purposes, magnitude 1. This figure conveys a good three-dimensional impression of the flow field existing in the combustor. Immediately identifiable, from the front of the combustor, are the axial swirling jet from the

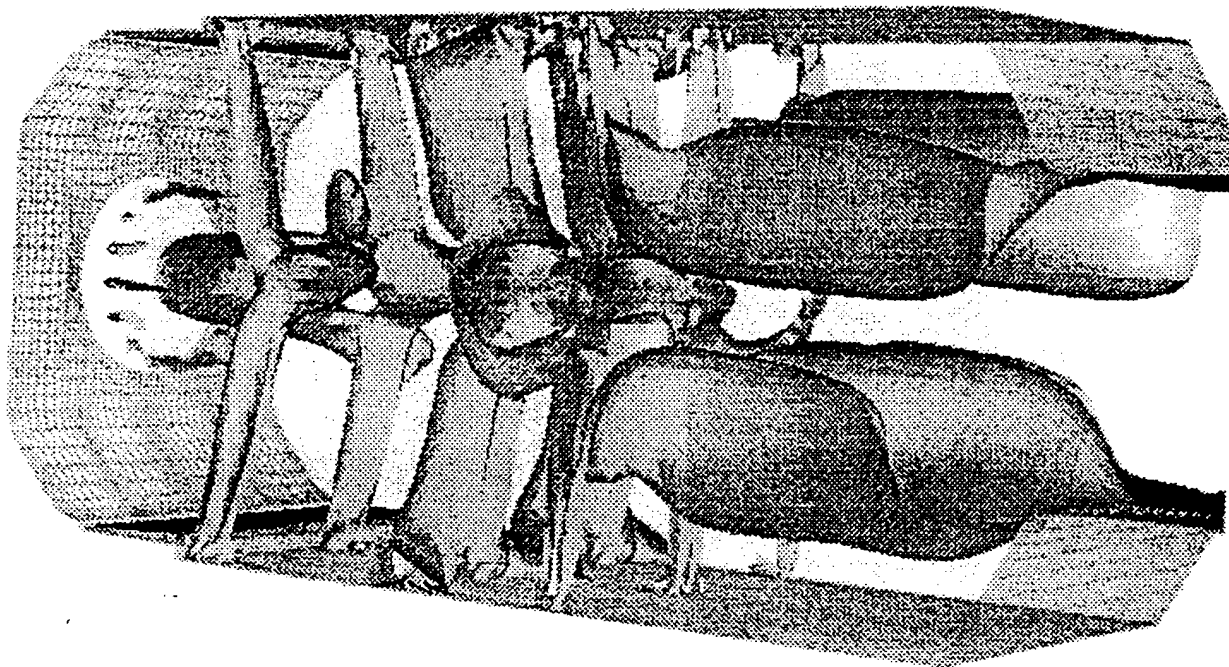


Fig. 6: Isothermal CFD Calculation with Iso-Surfaces of Mean Axial Velocity at Level 1 Magnitude, Showing Swirling Jet from Fuel Injector with Lobate Formation at First Row Combustion Air Jets

airblast fuel injector, the individual insert swirler jets (surrounding the fuel injector and with zero relative swirl in this instance, and zero angle relative to the injector discharge centerline), the first row of combustion air jets as opposed pairs on either side of, and inline with, the fuel injector jet, the second row of liner air jets as larger diameter, opposed pairs that are laterally disposed between the first row jets, and so on, along the combustor. Note that the effects of shroud bypass flows on liner jet initial angles are accounted for in the calculation (as a boundary condition, calculated separately from phenomenological modeling). The spent dome impingement cooling air is discharged axially as a liner cooling film at the upper and lower liner/dome interfaces.

The insert swirler jets act to prevent the weakly-swirling jet leaving the fuel injector from spreading much radially. It can be seen that the first row air jets penetrate to the combustor horizontal centerline before completing their turn to flow axially downstream.

The lateral spreading of the combustion air jets resulting from their high penetration and resulting collision can be seen in Fig. 7, where Level 2 velocity is less than Level 1 velocity in Fig. 6. The view in

Fig. 7 is from the top of the combustor, with the upper liner removed for clarity. As in Fig. 6, the bounds of the calculation domain that are physical wall are shown by means of the calculation grid projected onto these surfaces.

The consequential blockage to primary zone flow represented by the colliding combustion air jets causes the coherent swirling jet from the airblast fuel injector to divide into two, diagonally-opposed lobes in order to escape from the combustor primary zone. The asymmetric splitting of the fuel injector jet into two lobes is due to the swirl velocity component that this jet contains.

Figs. 8 and 9 respectively show contour plots of mean axial velocities on vertical planes inline with, and between, the fuel injectors; the plots reveal the regions of flow reversal (shown as hatched areas).

Note that the blockage of the pair of combustion air jets inline with the injector produces reverse flow in the center of the fuel injector jet as it begins to split into lobes, and that this causes diagonally-opposed lateral flows of combined combustion jet air and injector fluid into the regions between fuel injectors. Thus, the major recirculation zones are between injectors, with smaller recirculation zones in the injector plane that are placed

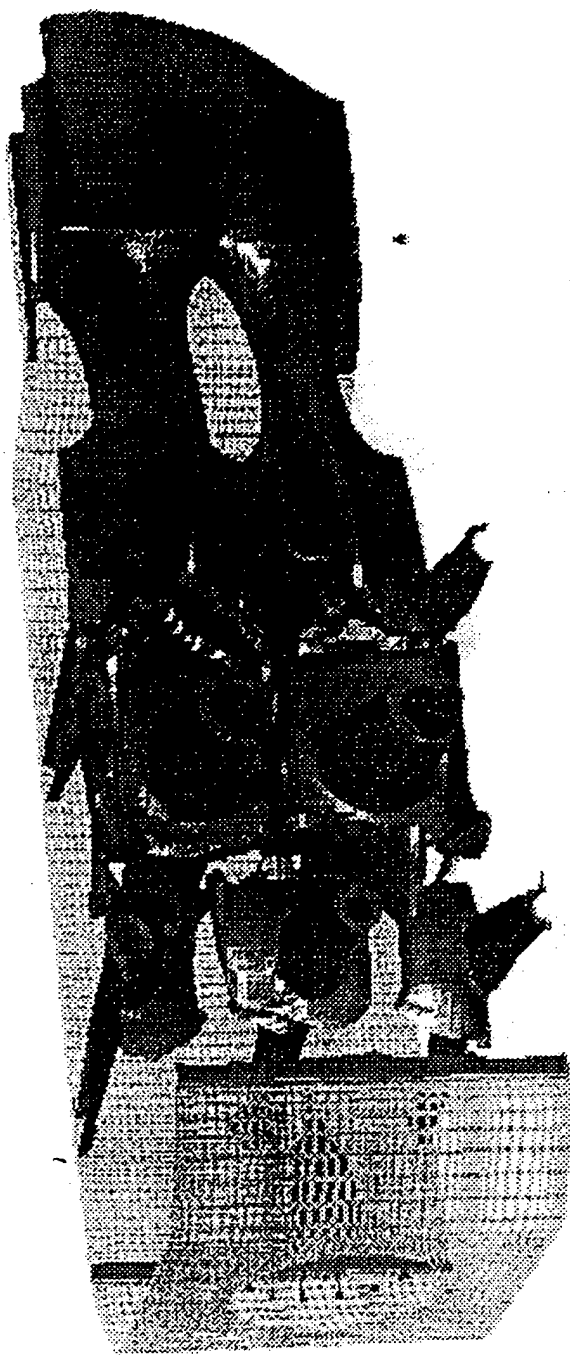


Fig. 7: Vertical View of Isothermal CFD Calculation with Iso-Surfaces of Mean Axial Velocity at Level 2 Magnitude, Showing Lateral Spreading of Colliding Transverse Combustion Air Jets

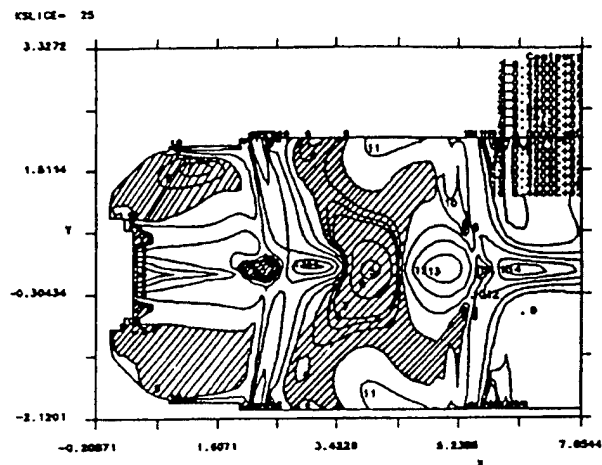


Fig. 8: Section Through Fuel Injector with Calculated Iso-Vels of Mean Axial Velocities Showing Reverse Flow Regions

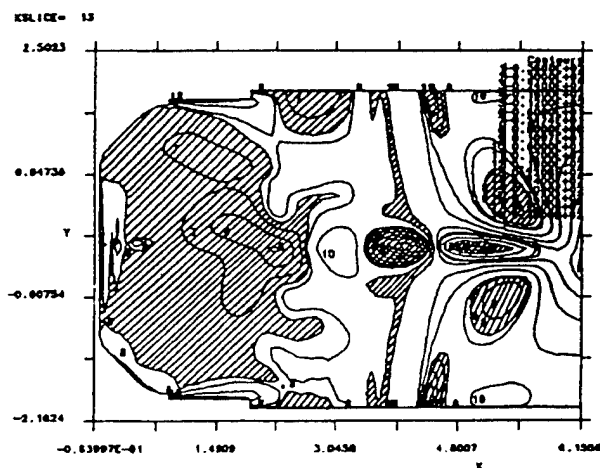


Fig. 9: Section Out of Fuel Injector Plane with Iso-Vels of Calculated Mean Axial Velocities, Showing Reverse Flow Regions

radially about the injector jets, outboard of the insert swirler jets. Further regions of reverse flow exist in the wake structures downstream of the first row combustion air jets and, upstream and downstream of the second row of combustion air jets.

The isothermal flow CFD calculations confirm that the swirling jet of fluid from the fuel injector is closely coupled with the first row of opposed combustion air jets. The swirling jets from the fuel injectors are sufficiently confined by their surrounding insert swirler air jets that fuel does not have much opportunity for spreading radially prior to reaching the combustion air jets. The combustion air jet system establishes ample

regions of reverse flow to provide jet flameholding if supplied with suitable fuel/air mixture.

Test Conditions for Temperature Measurements

As indicated above, the normal operating mode of the combustor was a lifted flame. However, the attached flame was interesting because of its quiet operation and improved stability (Fig. 5). It was therefore decided to make the temperature measurements to also include this condition.

The more typical engine combustor dome flow was the 15 percent case, so this was selected for the temperature measurements. Fig. 4 was used to determine the attached flame operating point. The total combustor airflow (all four injectors) was 0.7383 lbm/sec., with a primary zone airflow of 0.1422 lbm/sec. (see Ref. 7 for detailed calculation information); there was no excess nitrogen used, and the fuel was gaseous propane. The normal lifted flame became an attached flame at 0.69 primary zone equivalence ratio, and the combustor blew out for this airflow at just less than 0.60 equivalence ratio. Measurements were taken for a propane flow rate of 0.35 lbm/min. The combustor loading for these conditions was a low one so that the attached flame holding is confined to the primary zone.

CARS System

Temperature measurements in the combustor were performed using Coherent Anti-Stokes Raman Spectroscopy (CARS); the CARS system is described in detail by Switzer & Goss²⁰. It is based on a frequency-doubled Nd:YAG laser that provides 8 nano-second pulses at 532 nano-meters wavelength with a repetition rate of 10 hertz, and, a broadband dye laser that is tuned to the Stokes vibrational frequency of the nitrogen molecule. The system is configured to employ a folded BOXCAR optical geometry²¹ with a 50 cm focal length focussing lens. This combination yields a sampled spatial probe volume of about 1 mm^3 , with the CARS information being generated within a path-length of 2 mm. The anti-Stokes signal produced within the probe volume is collected and directed into a spectrometer where its spectral content is dispersed; signal detection is then accomplished with a gate-diode array detector which allows single-shot temperature determination from the Q-branch spectrum of nitrogen.

The accuracy of the CARS temperature determination made in this manner is estimated to range

between 10 percent at near-room temperatures and 5 percent at near-stoichiometric flame temperatures, with the largest contribution to uncertainty resulting from shot-to-shot variation in the Stokes-laser spectral distribution.

Four important combustion-diagnostic parameters are determined from the CARS data. Temperature means, fluctuations about the mean, probability distribution functions (pdf's), and the ratio of standard deviation of the distribution of temperature to the mean temperature, were obtained from instantaneous temperatures obtained in populations ranging from 1250 to 2000 at each measurement location.

Data repeatability is a difficult issue to resolve satisfactorily. It takes considerable elapsed time to acquire adequate data for extensive mapping. In this situation, repeatability is not determined by the CARS system, but by the constancy of the combustor air and fuel flows, and the precision with which a selected operating condition can be set and held. Both the fuel and air flows are continuously monitored and are electronically controlled to within 5 percent.

Measurement Considerations

The most desirable region to take detailed field measurements in this planar combustor is about the rig centerline, i.e. with two injectors on either side. This would result in minimum effect on the data due to the unwanted presence of the rig side-walls. However, use of this central region would necessitate that the laser beams traverse the maximum width of the combustor. Initial measurements made along this path, as feared, gave unreliable results because of insufficient CARS signal strength. The lack of signal was found to be the result of turbulent beam-steering as the laser beams passed through the flows associated with the near-pair of fuel injectors. The beam-steering was sufficient to prevent the essential overlap of the CARS pump and Stokes beams, (Fig. 10).

This problem was avoided in subsequent measurements by defining a measurement grid that extended through the first and second near-pair of injectors, and terminated at the line of local symmetry between the second and third injectors. This assumes that the flow field is identical on either side of this line of symmetry. It also supposes that data from the first injector, nearest to the side-wall, might have to be rejected due to side-wall effects. This indeed was found to be the case.

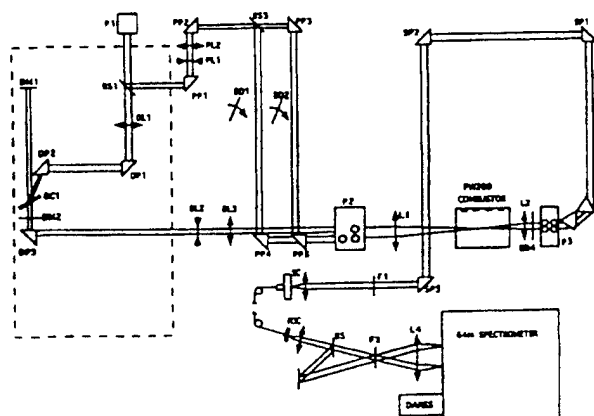


Fig. 10: Layout of CARS Optical Path in BOXCARS Configuration

A further consideration that influenced the determination of the measurement grid locations was the potential for damage to the optical windows by the laser beams. Initially, holes were burned in the combustor windows by the beams. To ensure that the high intensity laser beam focus would be a safe distance from the admitting windows, the sample region was restricted to a maximum distance of 11 cm from the combustor symmetry line, towards the sidewall.

With these two constraints to the possible measurement grid, a horizontal plane through the centerline of all four injectors ($y = 0$ cm) was selected. This plane extended transversely across the combustor from the axis of symmetry ($x = 0$ cm) to 11 cm towards the near-side combustor wall. It extended axially (z axis) from 1 - 15 cm downstream from the combustor dome. This area was covered with a 1 cm square measurement grid. An additional, smaller, transverse grid was applied normal to the horizontal grid at $z = 5$ cm, approximating the position of the first row of combustion air jets. The width of this vertical plane extended from $x = 0$ cm to $x = 7$ cm; thus, the second fuel injector centerline was located near its center. Again, a 1 cm square grid covered the region of this plane for 3 cm above and below the horizontal plane.

A caution is appropriate. As was unfortunately learned, the focussed laser beams contained sufficient energy to serve as an ignition source for flammable mixture in the combustor. Attention is necessary therefore, in sequencing purging system on shut-down,

laser beam aligning, and start-up procedures, when attempting such measurements!

Temperature Fields

It was found that the major effect of the rig side-walls on the flow and temperature fields in the combustor was through their effects on the shroud flows. The combination of the structural-support I-beams on the shroud-sides of the liners, and the presence of the rig side-walls, reduced the local velocities in the shroud flows near the walls significantly from the mean values. This in turn increased the initial trajectory angles of all the combustion and dilution air jets nearest to the walls. For example, on the combustor horizontal center-plane, the center of the first row air jet is only displaced downstream by one port diameter, compared to three to four port diameters for the jets away from the side-walls.

In the primary zone, the steeper angles of the first row air jets near the side-walls resulted in the reverse flow region at the impact plane of these jets (Fig. 8) exerting more influence on the axial jets of fuel/air mixture from the fuel injectors (Nos. 1 and 4) nearest the side-walls. The lobe formation (Fig. 6) takes place earlier, and is more effective in recirculating combustion jet air forward into the fuel injector jet. Consequently, the combustion region of highest temperatures (1500K) is pushed upstream, well inside the swirling fuel/air jet. In turn, this increases the temperature of the hot gases recirculated back to the combustor dome between injectors number 1 and 2, and, 4 and 3. The temperatures at the dome are about 1250K versus 1150-1200K between injectors 2 and 3.

With the spurious, side-wall affected, data removed from consideration, only the field between the centers of injectors 2 and 3 can be considered as being reasonably representative of the real combustor. Discussion of the temperature field is therefore confined to this region of measurements only.

Fig. 11 shows the measured mean isotherms on the horizontal (on the left of the figure) and vertical (on the right of the figure) cross-sectional planes, placed with

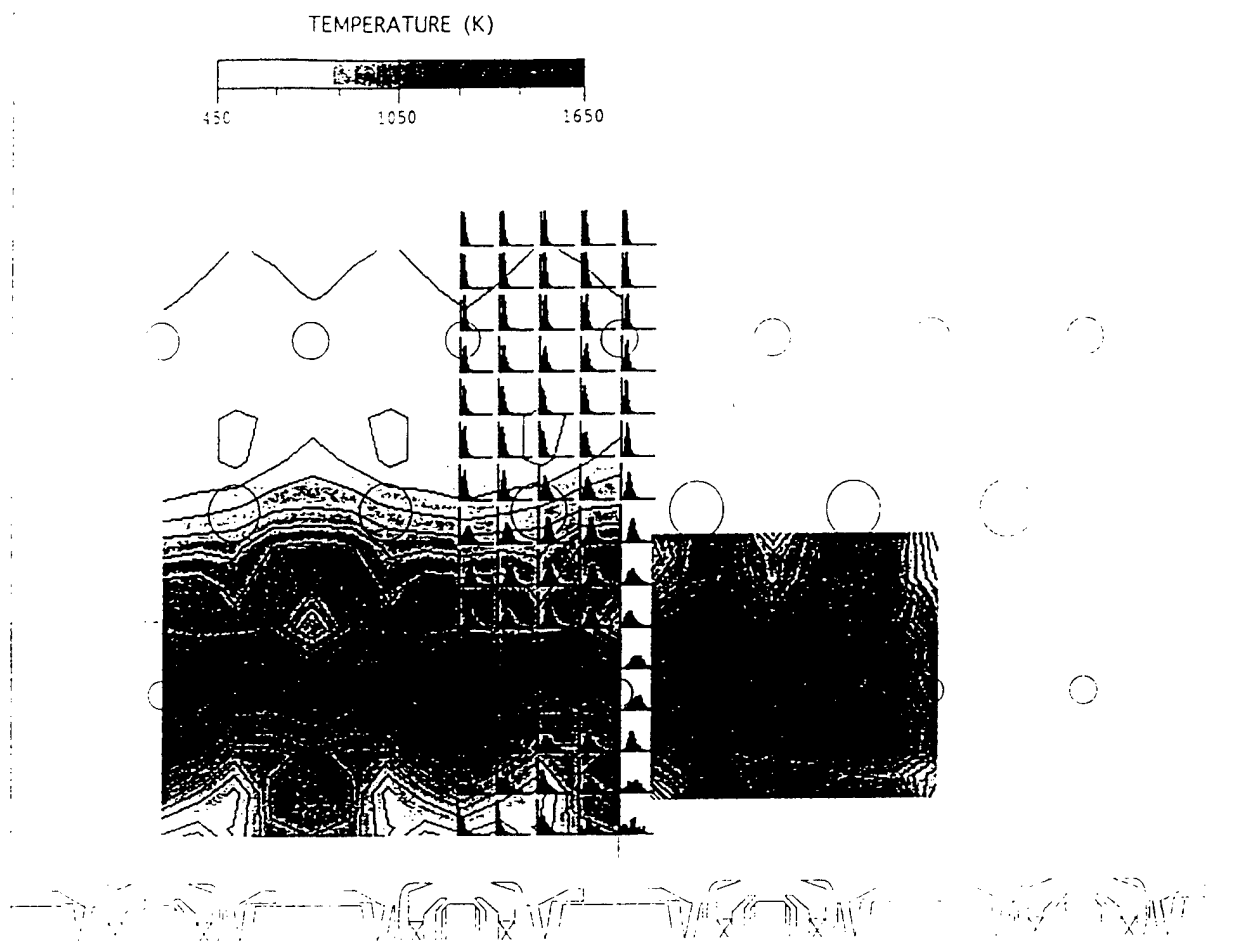


Fig. 11: Isotherms Representing Measured Mean Temperatures on Central Horizontal Plane and a Vertical Plane 5 cm Downstream, Together with PDF's for the Horizontal Plane Temperatures

the horizontal center of the vertical plane at its correct downstream position (just downstream of the first row of air jets) and the vertical center correctly aligned with an injector centerline. The vertical plane is viewed from the rear of the combustor. Super-imposed on the horizontal plane are the temperature pdf's at each measurement point in the plane. Note that the measured data in the horizontal plane for the right-hand side of injector No. 2 have been flipped to the left-hand side also. The symmetrical image so-formed makes it easier to understand the temperature field for a single, representative injector. While this is convenient, it should be remembered that the effects of swirl introduce some asymmetries in reality. For this particular set of

fuel injectors the effective swirl strength is low, so that any asymmetries would not be especially large. The data in the vertical plane are not flipped.

On the horizontal plane the peak gas temperatures of around 1500K are reached inline with the fuel injectors at 5 - 6 cm downstream, and are clearly associated with the region of recirculating flow (Fig. 8) in the center of the combustor just upstream of the colliding opposed jets of the first row combustion air.

In the vertical plane one of the diagonally-opposed lobes (Fig. 6) formed by the splitting fuel injector jet can be identified as being a region of high temperature (about 1350 - 1400K). Regions of high temperature (about 1300K) move laterally at mid-

combustor height following the spreading due to jet impact (Fig. 7). It should be noted that, inline with the injectors, the penetration of the lower combustion air jet is not so evident as that for the upper air jet in this ($z = 5$ cm) plane. This indicates different jet penetrations, top to bottom of the combustor. It can also be observed that between injectors both combustion air jets can be seen at this plane, but again, the lower jet appears to have lesser penetration than the upper one.

Note the downstream displacement of temperature events on the central horizontal plane at the position of the first row of air ports due to the initial jet trajectory angles not being normal to the liner surfaces. The hot gases moved laterally from inline with the injectors enter the reverse flow region between injectors, (Figs. 11, 6 and 9), and, are mixed with jet air and recirculated back upstream to the combustor dome at temperatures about 1150 - 1200K.

Temperatures downstream of the first row of combustion air jets are fairly uniform on the central horizontal plane at 1000 - 1200K, until the second row of combustion air jets is encountered. Combustion is essentially over on the center plane when the second row of combustion air jets is added, with temperatures falling to less than 800K. This is the dilution zone of the combustor, and was referred to earlier in connection with the definition of loading parameter, as "redundant" at LBO conditions. The reason for this description is now apparent. At higher values of combustor loading, when the flame region expands beyond the primary zone, some of this redundancy is lost.

The flow from the injectors is initially cold at inlet temperatures. Temperature increases radially outwards from the injector centerlines as the insert swirler jets entrain the hot gases recirculated to the dome from downstream. By 2 cm downstream the local temperatures in these jets is about 750 - 800K. By 2 - 3 cm downstream, temperature rise is evident on the centerline of the jets issuing from the fuel injectors. This is clearly induced by the lobe-splitting of this jet due to the central reverse flow from the first row combustion air jets, and does not propagate from the peripheral shear layers associated with the insert swirler jets.

At the conditions for this test the equivalence ratio of the flow emerging from the fuel injector is 1.488, and with account of all the insert swirler air it would fall to 1.159. All of the insert air could not be involved in any case, so the additional air for

combustion has to be provided by the reverse flow of combustion jet air. If this is so, then the reverse flow of combustion air penetrates forwards of the order of 2 - 3 cm on the centerline of the injector jet. It is most probably this penetration that gives the attached flame its conical shape, by introducing a radial velocity component into the injector jet. The CFD velocity vector results (not shown) confirm this.

The average of the mean temperature levels in the downstream regions of the measured horizontal field indicate that if they are typical of the complete exit plane from the combustor, then the upstream combustion efficiency is far from 100 percent. This is not too surprising at these operating conditions.

Consideration of the temperature pdf's reveals behavior that is not unexpected. In the injector fuel/air jet region the probabilities are skewed towards the lower inlet temperature, with evidence of intermittency towards the jet edges. In the downstream region where the bulk of the heat release takes place, they are more symmetrical about the mean values. For the dome recirculation zones they show broadened peaks, indicating equal probabilities of a wide range of temperatures as poorly-mixed combustion products and unreacted combustion air and fuel are returned together towards the dome region by the reverse-flow velocities present. The isotherms confirm that chemical reaction does take place in this recirculating flow.

Note that the region where pdf's are shown represents the only side-to-side extent of this plane where the measured data are considered to be acceptable.

Fig. 12 shows the fluctuating temperatures, expressed as a local intensity. As might be expected, the highest temperature intensities, 40 - 50 percent, are encountered on the centerline of the fuel/air jet issuing from the injector, and in the flow recirculated back to the dome. Intensities in the insert jets are about 30 percent, rising to 36 - 38 percent in the lobes of the dividing fuel/air injector jet. In the reverse flow region immediately upstream of the first row of combustion air jets (where the highest mean temperatures are attained) the intensities are 30 percent or less. Downstream of the second row of combustion air jets the temperature fluctuations increase to give intensities of 32 - 36 percent, reflecting the mixing activity that might be anticipated from Figs. 8 and 9.

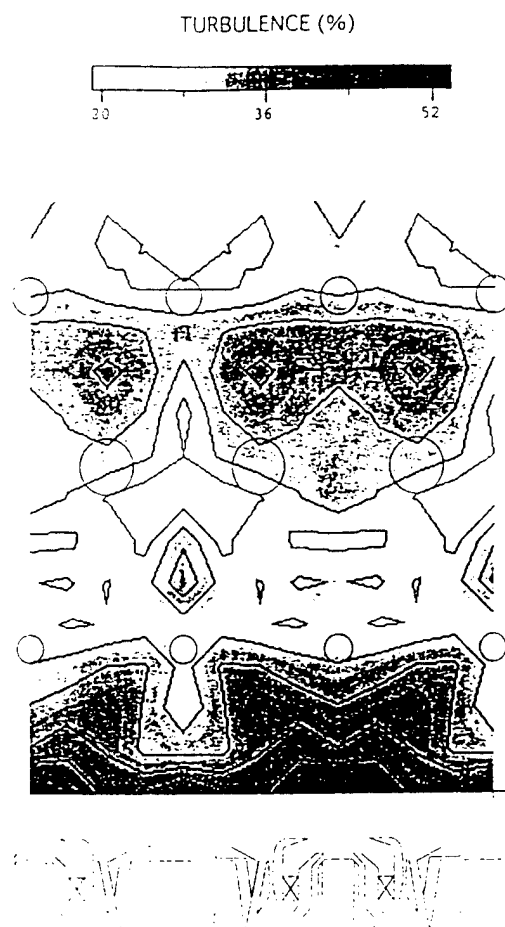


Fig. 12: Dimensionless Turbulent Fluctuations (RMS Values) of Temperature on the Central Horizontal Plane

Discussion

The conflicting difficulties of achieving a satisfactory benchmark test case in reacting flows for practical annular combustor geometries that have any pretence of reality, are well-demonstrated in the present work. A planar configuration is necessary to provide adequate optical access for the essential non-intrusive laser diagnostic probing. There are certain compromises that are inherent in making this configurational change to the combustor. In addition, the artificial side-walls so-introduced then perturb the flows near to them, and do so for significant distances normal to the walls, out into the reacting flowfield, causing non-typical behavior. To minimize this effect, a large number of fuel injectors pitches are necessary, four as a minimum with five being better. However, advantage of the increased combustor lateral dimension so obtained cannot be taken due to optical disturbances resulting

from the extensive turbulent, reacting near-field through which the laser beams must then pass in order to reach the central, unperturbed flow region.

With due care, it is possible to obtain flow field measurements that are reasonably representative of real combustor flow (to the degree that a planar combustor can be considered to adequately represent an annular combustor). Such results can certainly be of value as a diagnostic in explaining aspects of combustor behavior. Their value as a database for evaluating combustion modeling in CFD codes remains to be established.

For the present combustor, three separate approaches have been used to describe one feature of its behavior: 1.) Phenomenological modeling to correlate LBO data, 2.) isothermal CFD analysis of an unperturbed segment of the flowfield at near-LBO conditions, and, 3.) CARS measurements of a narrow, but representative section of the temperatures in the reacting flow at near-LBO conditions. Each of the three approaches separately yields information that is remarkably consistent with that of the other two approaches. No single approach on its own provides an adequate picture of blowout. Taken together, the lean blowout behavior of the inside-out recirculation primary zone is extremely well described.

Many questions have been answered, but several more have been raised. For an example of the answers, the saw-tooth behavior (Fig. 2) of the lean stability loop as peak heat release rate is approached (seen in many combustors) is explained as a change in the flame holding mechanism as combustor loading increases above critical values. For just two examples of the new questions, how much air is recirculated back to the dome, and, what is the exact role of the insert swirler air jets in confining the fuel injector jet, and, in determining the coupling with the first row of combustion air jets?

It is apparent from the information presented for this combustor, that a simple, or even relative complex, phenomenological approach to modeling LBO in practical combustors is doomed to failure. The flow behavior even in the few geometric variations presented here and in Ref. 7, is far too complex to permit a useful generalized description to be obtained. Phenomenological modeling will only be useful with practical combustors for correlation of fairly wide-ranging experimental data sets for a particular combustor, or for a family of similar designs with only limited geometric variation. In this capacity

phenomenological modeling can make a useful contribution in combustor development of a particular design, and for small, incremental design or scale changes to an existing combustor configuration.

For an *a priori* design tool it is abundantly clear that a CFD-based approach is necessary for LBO. Unfortunately, the combustion model required to make this realistic is a major stumbling block at this time; for example, see Ref. 10. Significant research is necessary in this area.

The aerodynamic and combustion close-coupling of the fuel/air jet from the fuel injectors with the first row of combustion air jets in this combustor illustrates why airblast-atomizing fuel injectors have to be designed in close co-operation with the engine companies, and developed in conjunction with the combustor. "Off-the-shelf" and "plug-in" fuel injectors of this type are now virtually items of the past.

The general primary zone characteristics revealed in this simplified gas turbine generic combustor can be related to the basic flow field established and studied in the research combustor⁷, and the fuel injector behavior studied separately in the technology combustor⁶, using more comprehensive diagnostics in both instances. The information gathered in the additional combustors greatly assisted in interpreting the present results.

The CARS temperature measurements confirm that the recirculated partially-mixed flow of hot combustion products and reactants back to the dome is important in providing flame stability. However, they reveal the major role played by the reverse flow of a small but important quantity of first row combustion jet air directly into the centers of the otherwise fuel-rich, swirling axial jets from the airblast fuel injectors. The blockage to the injector jets established by the colliding and laterally-spreading first row combustion air jets, then produces the necessary low velocity regions that allow flame-holding. It is the heat release associated with these flames that contributes enthalpy and chemically-active species to the between-injector dome recirculation, which results in further combustion in this dome region.

The action of the insert swirler individual jets in confining the mixture from the injector, increases the coupling of the injector flow to that of the first row combustion air jets.

Conclusions

1. Correlated experimental LBO data for a generic gas turbine combustor have been presented which show that the prime flame holding mechanism can change as the combustor loading increases, to give a lean stability characteristic that becomes saw-tooth in shape as the condition of peak heat release rate is approached.
2. The primary zone flow behavior of the generic combustor, due to its basic design, is such that the discharges from the airblast fuel injectors are closely-coupled with the first row of combustion air jets, and this coupling dominates LBO for lower values of combustor loading.
3. The CFD results and CARS temperatures show that the close-coupling in the primary zone is due to excessive confinement of the discharge from the airblast fuel injectors by the surrounding insert-swirler air jets, and by the severe blockage produced by the penetration and lateral spreading of the first row of combustion air jets.
4. The difficulties of making laser-based measurements for benchmarking in a practical combustor configuration are severe, and limit the extent of the field for which reliable data can be obtained. The reliability itself is generally determined by the constancy of flows within the rig over the lengthy measurement times involved, rather than the behavior of the optical and electronic processing systems.
5. The best approach to generalized modeling or calculation of LBO lies in the CFD approach, although this will require combustion models that are beyond the current state-of-the-art.

Acknowledgements

The authors wish to acknowledge the contributions to this work from their colleagues at Wright-Patterson Air Force Base and Pratt & Whitney. Special thanks are due to J.S. Stutrud and M. Russell at Wright Laboratory for support with the experimental work, and to A. Cheung at Pratt & Whitney for assistance in producing the manuscript. The enthusiasm, encouragement and support of Dr. W.M. Røquemoire of Wright Laboratory has been particularly appreciated. The work was supported by the U.S. Air Force Wright Laboratory under Contract No. F33615-87-C-2822 to Pratt & Whitney, East Hartford, Connecticut, and Contract No. F33615-90-C-2033 to Systems Research Laboratories, Inc., (Division of Calspan), Dayton,

Ohio. The authors thank Pratt & Whitney for permission to publish these results.

References

1. Lefebvre, A.H., Gas Turbine Combustion, Hemisphere Publishing Co., McGraw-Hill Book Co., 1983.
2. Jeffs, R.A., "The Flame Stability and Heat Release Rates of Some Can-Type Combustion Chambers," Eighth Symposium (International) on Combustion, Williams and Wilkins, Baltimore, 1962, pp. 1014-1027.
3. Stewart, D.G., Selected Combustion Problems II, AGARD/NATO, Butterworths, London, 1956, pp. 384-413.
4. Sturgess, G.J., Sloan, D.G., Roquemore, W.M., Reddy, V.K., Shouse, D., Lesmerises, A.L., Ballal, D.R., Heneghan, S.P., Vangsness, M.D., and Hedman, P.O., "Flame Stability and Lean Blowout - A Research Program Progress Report," Proc. Tenth International Society on Air-Breathing Engines, Nottingham, England, 1991, pp. 372-384.
5. Sturgess, G.J., Sloan, D.G., Lesmerises, A.L., Heneghan, S.P., and Ballal, D.R., "Design and Development of a Research Combustor for Lean Blowout Studies," Trans. ASME, J. Engineering for Gas Turbines and Power, Vol. 114, 1992, pp. 13-19.
6. Hedman, P.O., Sturgess, G.J., Warren, D.L., Shouse, D., and Goss, L.P., "Observations of Flame Behavior from a Practical Fuel Injector Using Gaseous Fuel in a Technology Combustor," to be presented at ASME Intl. Turbo Expo '94, The Hague, The Netherlands, June, 1994.
7. Sturgess, G.J. and Shouse, D., "Lean Blowout Research in a Generic Gas Turbine Combustor with High Optical Access," ASME Paper No. 93-GT-332, presented at the ASME Intl. Turbo Expo '93, Cincinnati, Ohio, May 1993, (to appear in ASME Transactions).
8. Sturgess, G.J., Heneghan, S.P., Vangsness, M.D., Ballal, D.R. and Lesmerises, A.L., "Lean Blowout in a Research Combustor at Simulated Low Pressures," ASME Paper No. 91-GT-359, presented at the Gas Turbine and Aeroengine Congress and Exposition, Orlando, Florida, 1991.
9. Roquemore, W.M., Reddy, V.K., Hedman, P.O., Post, M.E., Chen, T.H., Goss, L.P., Trump, D., Vilimpoc, V. and Sturgess, G.J., "Experimental and Theoretical Studies in a Gas-Fueled Research Combustor," AIAA Paper No. AIAA-91-0639, 29th. Aerospace Sciences Meeting, Reno, Nevada, January 1991.
10. Sloan, D.G. and Sturgess, G.J., "Modeling of Local Extinction in Turbulent Flames," to be presented at ASME Intl. Turbo Expo '94, The Hague, The Netherlands, June 1994.
11. Magnussen, B.F., "Heat Transfer in Gas Turbine Combustors - A Discussion of Mathematical Modeling of Combustion, Heat and Mass Transfer with Emphasis on Heat Transfer in Gas Turbine Combustors," AGARD Conference Preprint No. 390, Heat Transfer and Cooling in Gas Turbines, Paper No. 23, 1985.
12. Heneghan, S.P., Vangsness, M.D., Ballal, D.R., Lesmerises, A.L. and Sturgess, G.J., "Acoustic Characteristics of a Research Step Combustor," AIAA Paper No. AIAA-90-1851, AIAA/SAE/ASME/ASME 26th. Joint Propulsion Conference, Orlando, Florida, July 1990.
13. Sturgess, G.J., Heneghan, S.P., Vangsness, M.D., Ballal, D.R., and Lesmerises, A.L., "Isothermal Flow fields in a Research Combustor for Lean Blowout Studies," Trans. ASME, J. Engineering for Gas Turbines and Power, Vol. 114, 1992, pp. 435-444.
14. Sturgess, G.J., Heneghan, S.P., Vangsness, M.D., Ballal, D.R., Lesmerises, A.L. and Shouse, D., "Effects of Back-Pressure in a Lean Blowout Research Combustor," Trans. ASME, J. Engineering for Gas Turbines and Power, Vol. 115, No.3, 1993, pp. 486-498.
15. Ballal, D.R., Vangsness, M.D., Heneghan, S.P. and Sturgess, G.J., "Studies of Lean Blowout in a Research Combustor," AGARD Conference Proceedings No. 536, Fuels and Combustion Technology for Advanced Aircraft Engines, Section 23, September 1993.
16. Nikooj, M., Mongia, H.C., Sullivan, J.P. and Murthy, S.N.B., "Flow Interaction Experiment - Aerothermal Modeling II," Final Report, Vols. I and II, NASA Rept. CR-189192, November 1993.

17. Kretschmer, D. and J. Odgers, "Modeling of Gas Turbine Combustors - A Convenient Reaction Rate Expression," Trans. ASME, J. Energy Power, 1972, pp. 173-180.

18. Sturgess, G.J., McKinney, R. and Morford, S., "Modification of Combustor Stoichiometry Distribution for Reduced NO_x Emissions from Aircraft Engines," Trans. ASME, J. Engineering for Gas Turbines and Power, Vol. 115, July 1993, pp. 570-580.

19. Rhie, C.M. and Stowers, S.T., "Numerical Analysis of Reacting Flows Using Finite Rate Chemistry Models," AIAA Paper No. AIAA-89-0459, 1989.

20. Switzer, G.L. and Goss, L.P., "A Hardened CARS System for Temperature and Species Concentration Measurements in a Practical Combustion Environment," Temperature: Its Measurement and Control in Science and Industry, Ed. J.F. Schooley, American Institute of Physics, New York, 1982, pp. 583-587.

21. Eckbreth, A.C., "BOXCARS: Crossed-Beam-Phase-Matched CARS Generation in Gases," Appl. Phys. Lett., Vol. 32, 1978, p. 421.

3.2 Thermally Stressed Jet-Fuel Studies

3.2.1 General Overview. During the course of this program, methodology was developed to address the complicated surface and bulk fuel-fouling problems associated with the use of fuel as the primary heat sink available for cooling aircraft components. The approach used was consistent in quantifying both bulk and surface insolubles primarily under isothermal conditions. Experimental approaches used in the study of thermally stressed jet fuel varied from simple flask experiments to complicated multiple-day isothermal experiments. Oxygen uptake was a key indicator of fouling processes and was monitored off-line by a gas chromatograph (GC). Fuel deposition on tube walls was measured using a carbon analyzer. Variables which could be controlled in thermal-stressing experiments included temperature, fuel stress time (flow rate), initial oxygen content, and addition of fuel additives.

3.2.2 Autoxidation Experiments. Flask experiments were initiated to study the role of oxygen in the formation of bulk filterables and in deposition on stainless-steel discs suspended in actual fuels ["Formation of Insolubles in Jet Fuels: Effects of Oxygen" (pp. 484 - 493)] and in sulfur-doped hexadecane ["Application of a Sulphur-Doped Alkane System to the Study of Thermal Oxidation of Jet Fuels" (pp. 494 - 499)]. As it became clear that flask tests provided a continuous supply of oxygen and resulted in extensive conversion--particularly for fast-oxidizing fuels--it was decided to limit the available oxygen by the use of dynamic isothermal experiments. These experiments utilized existing technology, namely, single-pass heat exchangers under conditions of very slow fuel flow rate, to provide isothermal reaction conditions for extended stressing. This apparatus used under constant-wall-temperature conditions was designated NIFTR (Near-Isothermal Flowing Test Rig). Under these conditions fuels containing a fixed amount of oxygen (saturated with respect to air at room temperature) were stressed at a fixed temperature for a sufficient time to consume all of the oxygen and complete the deposition processes. Results of experiments with this apparatus--coupled with GC detection of dissolved oxygen--have been the basis of the current understanding of fuel thermal stability. Measurements of oxidation and surface quantification of surface carbon have provided a complementary test methodology for assessing fuel stability and the effect of additives developed under the JP-8+100 program. One Jet-A fuel (POSF-2827) was considered using this approach and the conclusion reached that surface deposits originate as particles formed in the bulk fuel which subsequently diffuse and adhere to the heated walls ["Phenomenological Study of the Formation of Insolubles in a Jet-A Fuel" (pp. 500 - 509)]. Studies on the autoxidation kinetics ["Kinetics and Modeling for Jet-Fuel Autoxidation" (pp. 510 - 513)] and the effects of temperature ["Formation of Insolubles in a Jet-A Fuel: Temperature Effects" (pp. 514 - 517)] were also conducted for this fuel. Mass spectral analyses of some of the bulk-formed gums were performed ["Composition of Aviation-Fuel Gums" (p. 518)].

The role of stainless-steel surfaces in catalyzing autoxidation and the passivating effects of surface deposits were treated in two papers ["Surface Fouling: Short- vs Long-Term Tests" (pp. 519 - 524) and "Surface Fouling in Aviation Fuels: Short- vs Long-Term Isothermal Tests" (pp. 525 - 530)]. The effects of four additives on the autoxidation and deposition of POSF-2827 fuel were studied ["Effect of Additives on the Formation of Insolubles in a Jet Fuel" (pp. 531 - 541)]. Further refinements of the dynamic isothermal techniques with application to turbines were reported in two ASME publications ["Degradation of a Jet-A Fuel in a Single-Pass Heat Exchanger" (pp. 542 - 548) and "Surface Fouling in Aviation Fuels: An Isothermal Chemical Study" (pp. 549 - 556)]. Improvements offered by the Silcosteel process in mitigating surface fouling were first reported in a paper entitled, "Fouling of Stainless Steel and Silcosteel Surfaces during Aviation Fuel Autoxidation" (pp. 557 - 561). The availability of passivated tubing has simplified the understanding of fuel autoxidation under conditions of reduced surface catalysis ["Application of Isothermal Calorimetry to Jet Fuel Autoxidation Kinetics" (pp. 562 - 567)]. Some additives such as JFA-5 and 8Q405 have been shown to reduce surface interaction and, thereby, reduce surface catalysis ["Application of JFA-5 as an Anti-Fouling Additive in a Jet-A Fuel" (pp. 568 - 574) and "Quantitative Evaluation of Jet-Fuel Fouling and the Effect of Additives" (pp. 575 - 581)]. The latter paper is the most complete treatment of the current status of the techniques in addressing a matrix of three fuels and four additives at 185°C.

The impact of fuel blending on thermal stability and the quantitative assessment of surface catalysis have been addressed in two papers ["Thermal Stability of Jet-A Fuel Blends" (pp. 582 - 588) and "Autoxidation of Aviation Fuels in Heated Tubes: Surface Effects" (pp. 589 - 594)].

Symposium on Structure of Jet Fuels III
Presented before The Division of Petroleum Chemistry, Inc.
American Chemical Society
San Francisco Meeting, April 5-10, 1992

Formation of Insolubles in Jet Fuels:
Effects of Oxygen

E. G. Jones and W. J. Balster
Systems Research Laboratories, Inc.
A Division of Arvin/Calspan
2800 Indian Ripple Road
Dayton, OH 45440-3696

S. D. Anderson
Wright Laboratory
Aero Propulsion and Power Directorate
Wright-Patterson Air Force Base, OH 45433

Introduction

Jet fuels provide a significant heat sink as the primary coolant in military aircraft. Heat, coupled with the presence of dissolved oxygen, causes thermo-oxidative degradation of the fuels leading to the formation of bulk and surface insolubles. From ambient to $\sim 300^{\circ}\text{C}$, the predominant degradation mechanism of hydrocarbons in fuel is autoxidation involving hydroperoxides formed in Reaction 1.



Fodor, et al. (1) have shown that in jet fuels, peroxide decomposition is the main free-radical initiation step. Such free radicals are early precursors of the production of insolubles by means of very complex reaction chemistry.

In the current studies, the emphasis is not placed upon the initial precursors of deposits but rather upon the actual deposits found in the bulk fuel and on

surfaces. To assure measurable quantities in 6-hr tests, jet fuels were subjected to accelerated stress conditions. Pyrolytic degradation processes involving direct bond scission are very important above 300°C but are considered to be relatively unimportant under the current experimental conditions. Thus, products collected in the current study are considered to be the result of autoxidation of the fuel. A global or phenomenological approach was taken whereby fuel degradation was quantified based upon the amount of solids generated during the course of accelerated stressing. First, the growth of filterable solid material formed directly in the bulk fuel was measured; second, the growth of insolubles on stainless-steel discs suspended within the fuel was measured. The filterable solids are broken down into three solubility categories; namely, insoluble solids, insoluble gums, and soluble gums as defined in Table 1. The quantity of solids was determined by the method of carbon burnoff following solvent rinse. For example, the fraction of

sample remaining after heptane/acetone rinse is IS, and the fraction remaining after heptane rinse is IS + IG; finally, the unrinsed or total filterable residue is IS + IG + SG. Insoluble residue collecting on stainless steel was similarly quantified by carbon burnoff following heptane/acetone rinse (IS) or heptane rinse (IS + IG). Only minor (<20%) differences between the last two values were observed.

water-cooled condenser. Six stainless-steel (302) discs of area 1.7 cm² were suspended on stainless-steel wire in the fuel.

At 1-hr intervals, one disc was removed and three liquid aliquots, typically 3-10 cm³, were drawn from the flask. The aliquots were dispersed onto glass-fiber filters and were vacuum filtered after 10 min of cooling. The filters and discs were treated as described earlier and

Table 1. NOMENCLATURE

Filterable Solids:	Solids removed by glass-fiber filters (Gelman A/E, 1 μ nominal).
SG (Soluble Gums):	Filterable products which are soluble in heptane.
IG (Insoluble Gums):	Filterable products which are insoluble in heptane but which are soluble in acetone.
IS (Insoluble Solids):	Filterable products which are insoluble in both heptane and acetone.

Experimental

Experiments were conducted at ambient pressure in a five-necked 500-ml glass reaction flask equipped with an inline mechanical glass stirrer driven by an electric motor. Oxygen or air was supplied through a porous glass frit (ASTM 40-60) at fixed flows ranging from 0.03 to 0.8 cm³ min⁻¹ per cm³ of solution. In order to reduce reaction during initial heat up, helium was bubbled through 250-350 cm³ of solution until experiment onset, at which time oxygen or air flow was initiated. The flow was set with a flowmeter (Matheson 601) and was reduced throughout the experiment to maintain a fixed flow per unit volume. Temperatures in the flask (~185°C) were determined with a glass-enclosed thermocouple and a mercury thermometer; temperatures were 5-10°C lower than that of the oil bath (Fisher, $\pm 2^\circ\text{C}$) due to heat of vaporization and the return of condensibles from the

were placed in a vacuum oven (115°C) overnight. Carbon was measured using a surface carbon analyzer (LECO RC-412); bulk data are given as micrograms of carbon per cubic centimeter of filtered solution, and surface data are presented as micrograms of carbon per square centimeter of surface areas. It is assumed that over the course of the reaction, the percentage of carbon in the bulk and surface deposits remains constant (~80%). Also, no attempt was made to relate the sampled liquid volume to standard temperature conditions. The combined corrections to yield grams of deposit per cubic centimeter (20°C) are anticipated to increase the reported rate values by about 40% in the bulk. Similarly, the surface rates in grams of deposit per square centimeter would be ~20% higher than those reported.

The glassware was cleaned with Li-quinox using ultrasound and scrubbing.

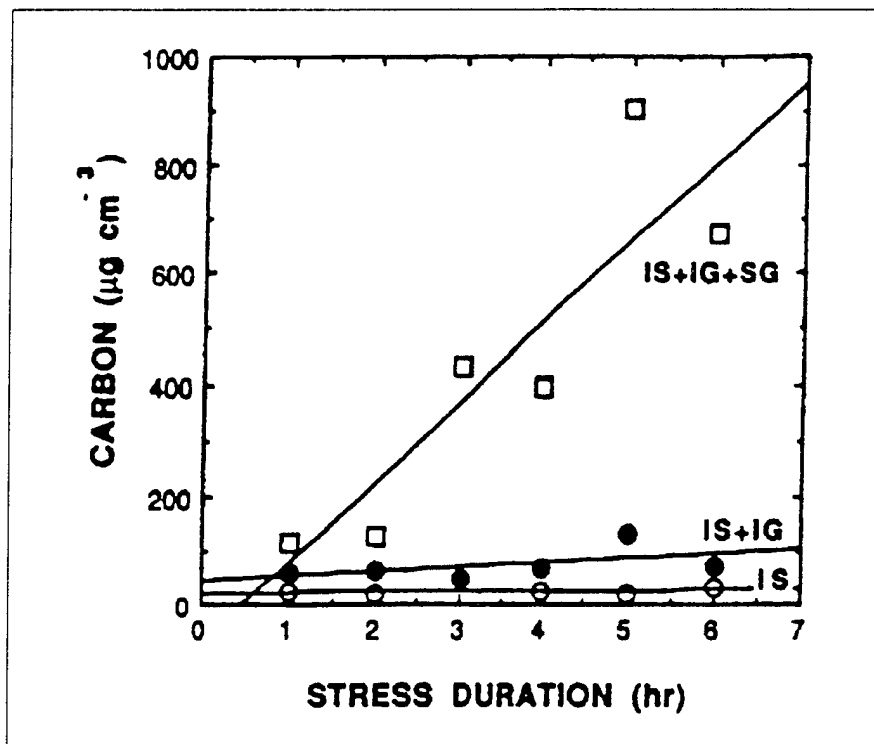


Figure 1. Hexadecane, 185°C, oxygen flow 0.25 cm³ min⁻¹ per cm³ of solution: Weight of carbon in samples removed by bulk filtration of liquid samples as function of stress duration.

Following a water and methanol rinse, the glassware was placed in a muffle furnace programmed to heat slowly to 550°C, following by slow cooling. This temperature was chosen based upon the surface-carbon-burnoff profile and the LECO furnace program (initial temperature 150°C, final temperature 650°C, heating rate 40°C min⁻¹) used to quantify deposits adhering to both the filters and the discs. The stainless-steel discs were cleaned with a 10% Blue Gold (2) solution using ultrasound followed by water and methanol rinses. Background carbon levels on discs are < 1 μg cm⁻²; the lower detection limit for the rate of surface carbon deposition is estimated to be 0.5 μg cm⁻² hr⁻¹. The amount of carbon on a blank filter paper is typically 200 μg. Depending upon the aliquot size, the lower limit for rates of

forming bulk insolubles is estimated to be 2-5 μg cm⁻³ hr⁻¹. Reproducibility of measured rates is estimated to be ± 20% for total bulk measurements and ± 30% for surface measurements.

Results and Discussion

Rate Measurements

Prior to investigating complicated jet fuels, it was of interest to study the behavior of a model hydrocarbon system such as hexadecane which is known to readily undergo autoxidation but which does not tend to form insolubles (3). It should be noted that under the test conditions, alkanes are rapidly converted to a complex mixture of products and, therefore, hexadecane does not represent a

simple system. Jensen, et al., (4) have reported detailed analysis of the primary autoxidation products of hexadecane.

Formation of bulk filterables from hexadecane is shown in Figure 1. The data are best represented by a linear fit, implying a pseudo-zeroth order reaction over the 6-hr stress duration. Using the rates of forming (IS), (IS + IG), and (IS + IG + SG), the rates of forming IS, IG, and SG were calculated to be < 1 , 7, and $137 \mu\text{g cm}^{-3} \text{ hr}^{-1}$, respectively. The rate of forming insolubles is clearly at or below the detection limit. The SG category includes the polar oxygenated products which have exceeded the soluble limits of the stressed system. Due to their significant aliphatic character, they are soluble in fresh fuel or, in this case, heptane and would not pose a fouling problem in a flowing system. The measured rate of forming IS on the surface, $< 0.4 \mu\text{g cm}^{-2} \text{ hr}^{-1}$, is below the lower detection limit for this technique and is consistent with the low rate of forming IS and IG in the bulk fluid.

Table 2 shows the nomenclature and classification of jet fuels studied. The results for the bulk filtered deposits from Jet A (SUN), Jet A (SHELL), and JPTS are given in Figures 2, 3 and 4, respectively. The results for the surface deposits from Jet A (SUN) and Jet A (SHELL) are shown in Figures 5 and 6, respectively. The level of surface carbon from JPTS was below detectable limits. As found to be the case with hexadecane, the data are best fit with straight lines, indicating pseudo-zeroth-order reactions. The successive contributions of IS, IG, and SG were directly calculated from the slopes in Figures 2-4 and are summarized in Table 3. In comparing the three fuels, note that the rate of producing SG is large in both Jet A (SUN) and JPTS but is near the detection limit in Jet A (SHELL).

Oxygen Dependence

At 185°C , oxygen dissolved in hexadecane is consumed rapidly by free radical scavenging. Korcek, et al., (6) have reported significant changes in the distribution of autoxidation products from hexadecane over the temperature range 160 - 190°C , depending upon the oxygen overpressure. Blaine and Savage (5) have noted increases in the quantity of autoxidation products such as ketones and carboxylic acids over the oxygen flow range 0.3 - $1.3 \text{ cm}^3 \text{ min}^{-1}$ per cm^3 of solution. These results indicate that at 185°C , dissolved oxygen in solution is being consumed faster than it can be replenished by an increase in flow rate. An oxygen non-limited regime, if achievable, would require a large overpressure of pure oxygen. Thus, for hexadecane, it is doubtful that a steady state could be achieved.

The dependence of rates upon oxygen flow has been measured for the two Jet A fuels and is shown in Figures 7 and 8. The hydrotreated fuel, Jet A (SUN), shows no signs of achieving a steady state, and the rates of forming IS and IG appear to have a pseudo-first-order dependence upon oxygen. This is analogous to the increase in autoxidation products in hexadecane reported by Blaine and Savage. The Jet A (SHELL), however, behaves quite differently. First, measured rates are much lower and do not display a monotonic increase with oxygen. The data points at zero oxygen flow were obtained using a continuous flow of inert gas (He) and represent estimated rates of $< 1 \mu\text{g cm}^{-3} \text{ hr}^{-1}$. The rate of IG formation appears to increase when oxygen is available and then remain approximately constant. The rate for IS displays an increase followed by a steady slowing at higher oxygen flow. These data show the need for oxygen in the initial production of IS and IG but also indicate an inhibition at higher oxygen flow, leading to a pseudo-steady state for the

Table 2.
Jet Fuels

	<u>Jet A (SUN)</u>	<u>Jet A (SHELL)</u>	<u>JPTS</u>
Source	Sun Oil	Shell Oil	Exxon
Designation	POSF-2747	POSF-2827	POSF-2799
Description	Hydrotreated	Straight Run Distillate	Specialty Fuel Composed of Three Blended Stocks
Aromatics (vol. %)	19	19	9
JFTOT BP(K)	605	539	672
Sulphur (mass %)	0.0	0.1	0.0

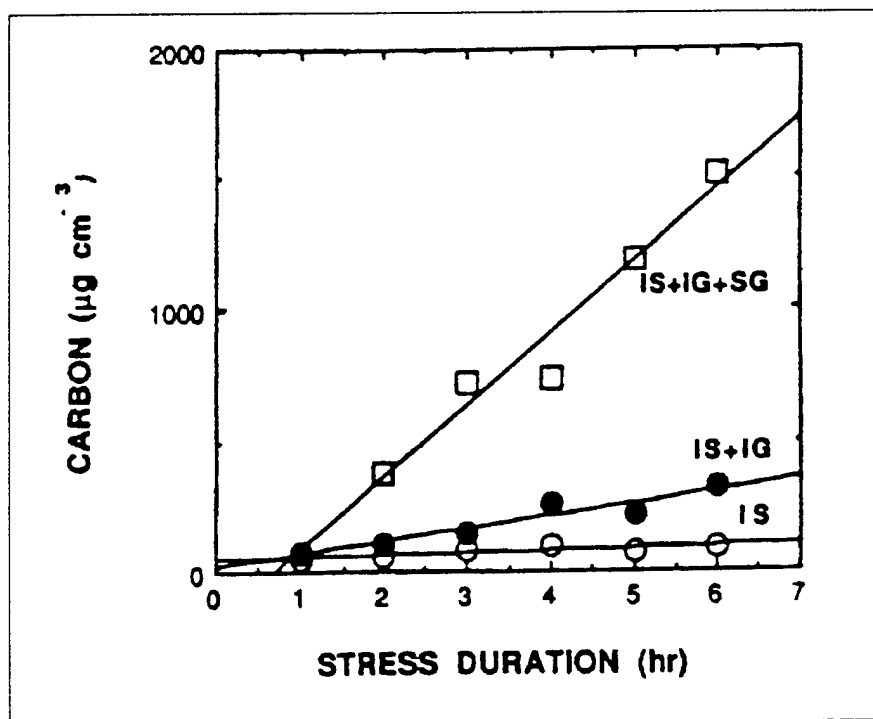


Figure 2. Jet A (SUN), 185°C, oxygen flow 0.20 cm³ min⁻¹ per cm³ of solution: Weight of carbon in samples removed by bulk filtration of liquid samples as a function of stress duration.

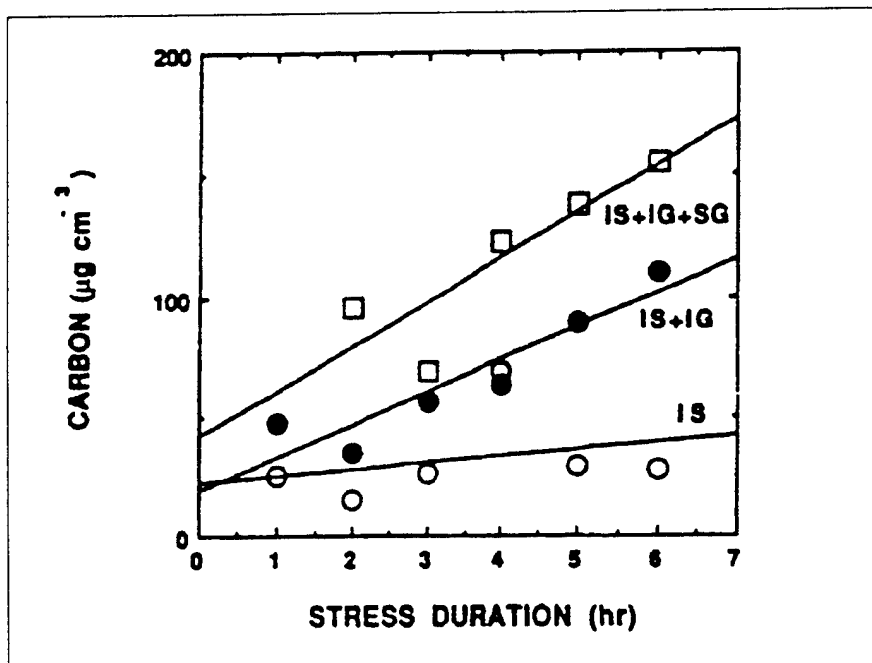


Figure 3. Jet A (SHELL), 185°C, oxygen flow 0.20 cm³ min⁻¹ per cm³ of solution: Weight of carbon in samples removed by bulk filtration of liquid samples as function of stress duration.

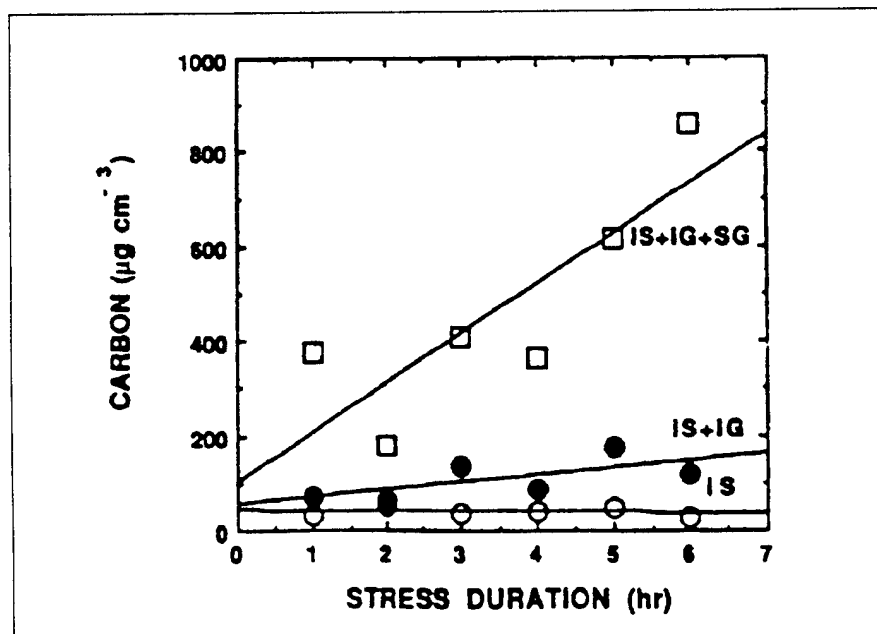


Figure 4. JPTS, 185°C, oxygen flow 0.20 cm³ min⁻¹ per cm³ of solution: Weight of carbon in samples removed by bulk filtration of liquid samples as function of stress duration.

Table 3.
Rate of Solid Formation: Bulk, Surface

	<u>Jet A (SHELL)</u>	<u>Jet A (SUN)</u>	<u>JPTS</u>
Surface ($\mu\text{g cm}^{-2} \text{ hr}^{-1}$)			
IS	3.5	7.8	< 1
Bulk ($\mu\text{g cm}^{-3} \text{ hr}^{-1}$)			
IS	2.9	7.9	< 1
IG	11.	40.	15
SG	4.8	226.	85

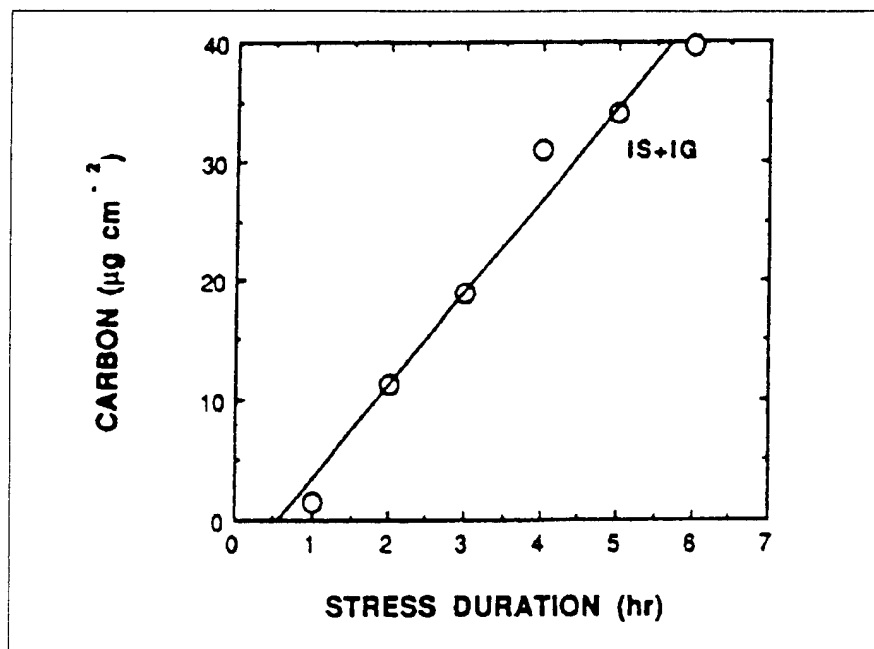


Figure 5. Jet A (SUN), 185°, oxygen flow $0.20 \text{ cm}^3 \text{ min}^{-1} \text{ cm}^2$ of solution: Weight of carbon in samples deposited as IS + IG on stainless-steel surface as function of stress duration.

largest fraction (IG). In the case of SG, the rates in Figure 8 were determined from the difference in two numbers of similar magnitude (cf, Figure 3). Thus, the structure displayed by the interpolated fit may not be reproducible. Suffice it to say that any SG formed in Jet A (SHELL) is near the detection limit of this technique.

The difference in the absolute rates of forming insolubles and their oxygen dependence appears to be related to the fact that one of the fuels is hydrotreated and the other contains a significant amount of sulphur. Kendall and Mills (7) have looked at similar hydrotreated and sulphur-containing jet fuels with respect to their oxidation rate. Their conclusions (7) were that

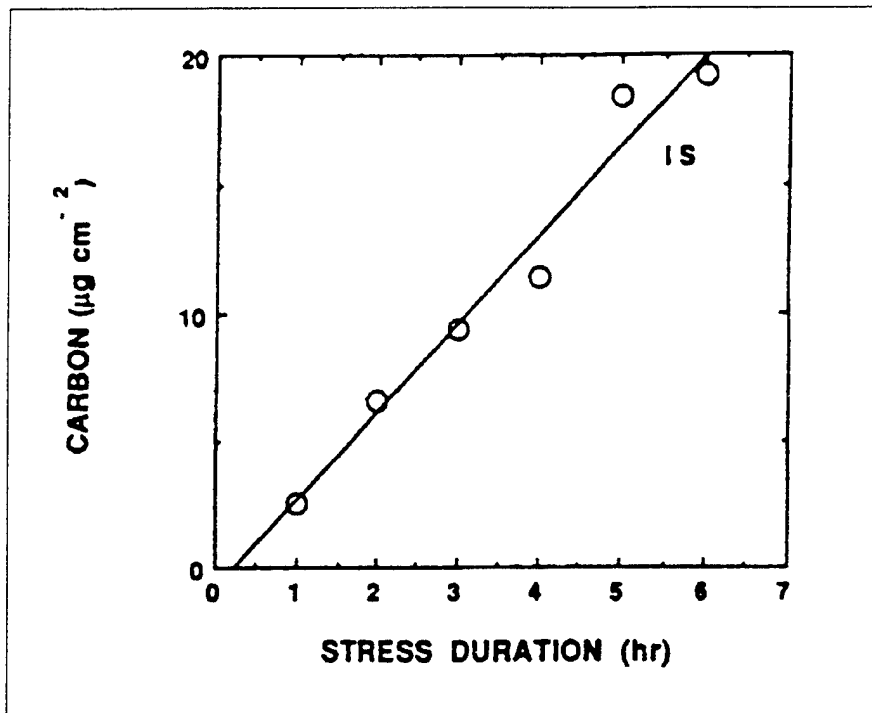


Figure 6. Jet A (SHELL), 185°C, oxygen flow 0.20 cm³ min⁻¹ per cm³ of solution: Weight of carbon in samples deposited as IS on stainless-steel surface as function of stress duration.

in the latter fuel, oxidation is autoinhibiting with a near-steady-state oxidation rate. This was attributed to the presence of sulphides and their oxidized product, sulphenic acids which can destroy hydroperoxides and scavenge peroxy radicals (8). Precisely this autoinhibiting action would account for the observation that rates of forming insolubles in Jet A (SHELL) do not increase with oxygen. These effects reduce solid formation under oxygen-rich conditions but do not eliminate it under oxygen-lean conditions, as evidenced by the measurable rates for forming IS and IG. Presumably the scavenging reactions form polar insolubles. The absence of natural sulphur inhibitors in the hydrotreated fuel Jet A (SUN) permits rapid autooxidation with oxygen-dependent rates. The current findings for insoluble formation are con-

sistent with the conclusions drawn by Kendall and Mills for oxidation rates.

A linear dependence of rates upon oxygen flow may reflect oxygen solubility effects or autocatalysis (9). The manifestation of autooxidation in the present experiments is the high rates of forming SG contrasted with those of forming IS and IG. The existence of near-zero rates of forming SG in the sulphur-containing fuel, Jet A (SHELL), indicates the absence of significant fuel autooxidation.

The surface deposition rate of the Jet A (SHELL) reflects similar oxygen behavior, as noted in the bulk rate of IG and IS formation.

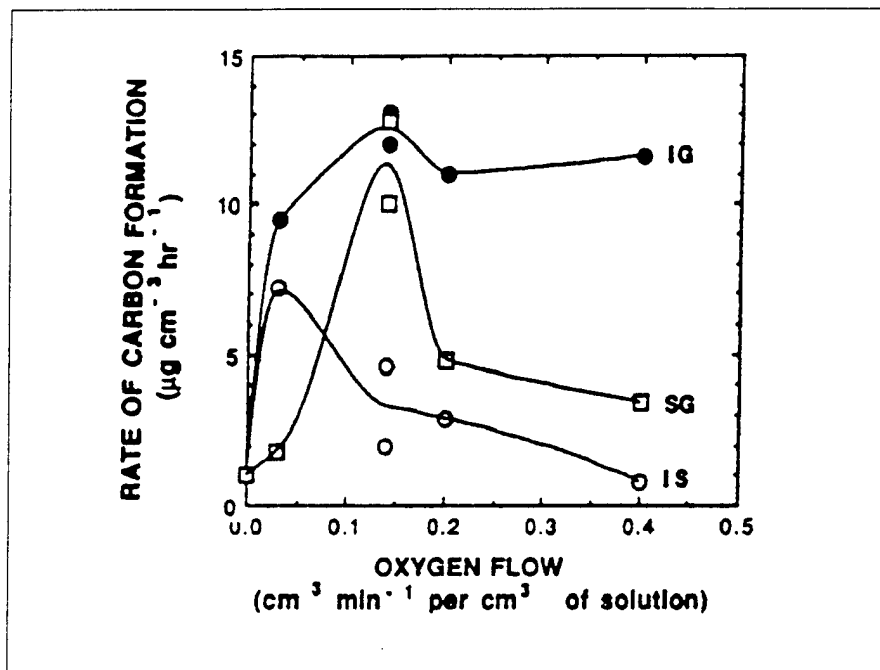


Figure 7. Jet A (SHELL) 185°C: Dependence of rate of forming IS, IG and SG upon oxygen flow.

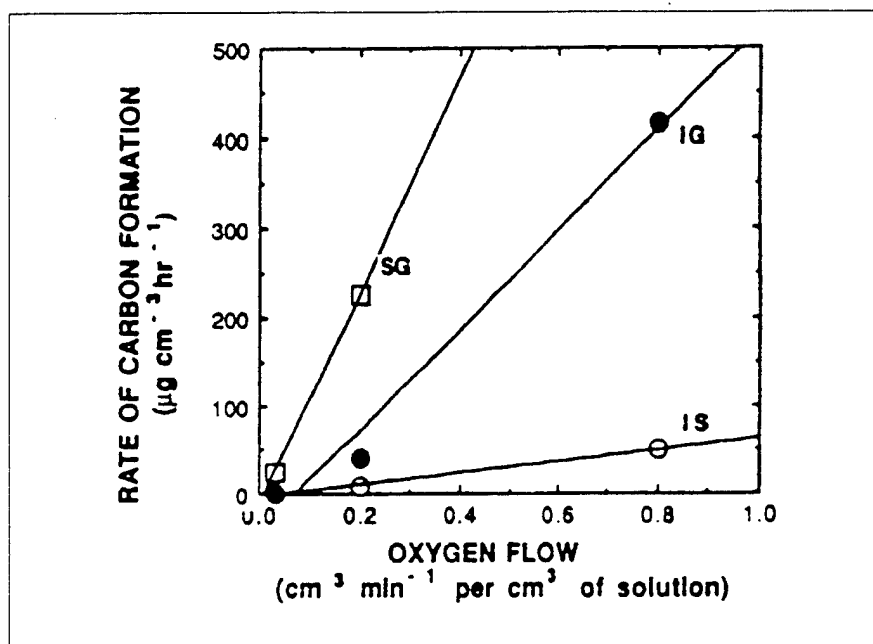


Figure 8. Jet A (SUN), 185°C: Dependence of rate of forming IS, IG and SG upon oxygen flow.

Summary and Conclusions

Global rates for forming three groups of filterable solids and also for surface deposits have been measured for three fuels. In each case the data reflect pseudo-zeroth order reactions to form IS, IG, and SG. The linearity of the bulk carbon versus time data up to 6 hr of accelerated stressing suggests that these are independent channels with no inter-conversion between SG, IG, and IS. Linearity was even maintained for Jet A (SHELL) in an extended 18-hr. test A similar independence of IS, IG, and SG channels has been noted in the model system diphenyldisulphide/hexadecane (10).

Experiments with oxygen variation have indicated achievement of a pseudo-steady-state condition in a sulphur-containing fuel and a pseudo-first-order dependence upon oxygen for a hydrotreated fuel. Results for solid formation are consistent with conclusions initially invoked to explain oxidation rates (7).

A comparison of the hydrotreated fuel and the sulphur-containing fuel reveals that the former exhibits lower rates of bulk and surface insoluble deposit formation under oxygen-lean conditions but higher rates under oxygen-rich conditions (see Figures 7 and 8). Finally, the presence of high rates of forming SG may be a criterion for assessing the significance of hydrocarbon autoxidation.

Acknowledgments

This work was supported in part by and performed at the Wright Laboratory, Aero Propulsion and Power Directorate, Wright-Patterson Air Force Base, Ohio, under USAF Contract No. F33615-90-C-2033. One of the authors (EGJ) would like to acknowledge the analytical advice of

W. H. Edwards (Pratt and Whitney) and kinetic discussions with M. L. Post (SRL).

Literature Cited

- (1) Fodor, G. E., Naegeli, D. W. and Kohl, K. B., *Energy Fuels*, **2**, 729 (1988).
- (2) Blue Gold Company, Ashland, OH.
- (3) Bol'shakov, G. F., FTM-MT-24-416-74 (Foreign Technology Division, Air Force Systems Command, Wright-Patterson Air Force Base, OH, 9 April, 1974), Chapter I.
- (4) Jensen, R. K., Korcek, S., Mahoney, L. R. and Zinbo, M., *J. Am. Chem. Soc.*, **101**, 7574 (1979); **103**, 1742 (1981).
- (5) Blaine, S. and Savage, P. E., in *Symposium on the Chemistry of Lubricants and Lubrication* (ACS Meeting, Boston, MA, April 22-27, 1990) (American Chemical Society, Washington, DC, 1990), pp. 239-244.
- (6) Korcek, S., Jensen, R. K., Zinbo, M. and Mahoney, L. R., in *Symposium on Hydrocarbon Oxidation* (ACS Meeting, New Orleans, LA, August 30-September 4, 1987) (American Chemical Society, Washington, DC, 1987), pp. 833-840.
- (7) Kendall, D. R. and Mills, J. S., *I&EC Prod. R&D*, **25**, 360 (1986).
- (8) Bridgewater, A. J. and Sexton, M. D., *J. Chem. Soc. London, Perkin Trans. II*, 530 (1978).
- (9) Walling, C., in *Free Radicals in Solution* (Wiley, New York, 1957), Chapter 9.
- (10) Jones, E. G. and Balster, W. J., "Application of a Sulphur-Doped Alkane System to the Study of Thermal Oxidation of Jet Fuel," To be presented at the International Gas Turbine Institute 1992 ASME Turbo Expo - Land, Sea, and Air, Cologne, Germany, June 1-4, 1992.



The Society shall not be responsible for statements or opinions advanced in papers or in discussion at meetings of the Society or of its Divisions or Sections, or printed in its publications. Discussion is printed only if the paper is published in an ASME Journal. Papers are available from ASME for fifteen months after the meeting.
Printed in USA.

Application of a Sulphur-Doped Alkane System to the Study of Thermal Oxidation of Jet Fuels

E. G. JONES and W. J. BALSTER

Systems Research Laboratories, Inc.
A Division of Arvin/Calspan
Dayton, OH 45440-3696

ABSTRACT

A system of diphenyldisulphide in hexadecane was selected for modeling the formation of insolubles in jet fuels. The system was stressed in a series of flask tests at 185°C under fixed oxygen flow. The quantity of filterable insoluble solids and insoluble gums was measured as a function of time and found to increase linearly following an initial induction period. Rates associated with the linear growth were evaluated for a series of oxygen flows to obtain the oxygen dependence of insoluble-solid and insoluble-gum formation. Results indicate that insoluble gums and insoluble solids are formed by independent processes. Bulk and surface rates show a linear correlation, indicating that the precursors to insolubles formed in the bulk and those formed on the surface are similar.

NOMENCLATURE

DPDS : Diphenyldisulphide
IS : Insoluble Solids (insoluble in heptane and acetone)
IG : Insoluble Gums (insoluble in heptane, soluble in acetone)
SG : Soluble Gums (soluble in heptane)

INTRODUCTION

Jet fuels are increasingly providing a significant heat sink as the primary coolant in military aircraft, thereby imposing more severe thermal stress which causes thermo-oxidative degradation. While the extent of this degradation is small, the accompanying formation of bulk insolubles and surface deposits can, over time, seriously degrade engine performance and may indeed cause failure. Degradation below about 350°C involves an autoxidation mechanism which utilizes dissolved oxygen in a series of free-radical reactions, producing a mixture of soluble gums, insoluble gums, and insoluble solids (Taylor and Frankenfeld, 1986). Because of the complex composition and variability in jet fuels, it is advantageous to study a simplified, or model,

system which mimics the behavior of jet fuel under thermal stress.

Long-chain alkanes which constitute a large fraction of jet fuels undergo autoxidation reactions but do not tend to form insolubles. However, the addition of small amounts (< 0.1% w/w) of a sulphur-containing compound such as diphenyldisulphide (DPDS) to a C₁₆ alkane (hexadecane) yields a system which rapidly produces both bulk and surface insolubles under thermo-oxidative stress. Although the deposits contain sulphur, their formation involves alkane autoxidation; as a result these deposits contain many functional groups which are observed in fuel deposits (FTIR spectra) and display morphology similar to that reported from augmentor rigs and other fouled regions (Schirmer, 1970).

The goal of the current study was to gain insight into the more complex fuel systems through a series of flask tests designed to investigate the global behavior of the simpler DPDS/hexadecane system, particularly in the area of formation of insoluble gums and insoluble solids.

EXPERIMENTAL

Experiments were conducted at ambient pressure in a five-necked, 500-ml glass reaction flask equipped with a porous glass frit (ASTM 40-60) for oxygen or air sparge and a water-cooled condenser to return most volatiles to the flask. An in-line mechanical glass stirrer driven by an electric motor (600 rpm) was used for mixing. The other two necks were used for sampling and a thermometer. Temperatures in the flask were determined using a glass-enclosed thermocouple and a mercury thermometer; temperatures were 5-10°C lower than that of the regulated oil bath (Fisher, ± 2°C) due to the return of condensibles.

In order to reduce reaction during initial heat up, helium was bubbled through 200 ml of solution until experiment onset, at which time oxygen was provided at a fixed flow rate. After specific time intervals, two sets of 3-ml aliquots were removed, cooled for 10 min, and vacuum filtered through glass-fiber filters (Gelman A/E, 1 μ nominal). One aliquot, rinsed with heptane, contained insoluble gums (IG) and insoluble solids (IS); the second, rinsed with both

heptane and acetone, contained only IS. In more recent experiments a third aliquot was collected and vacuum filtered without rinsing. This fraction was viewed as containing IS, IG, and fuel-soluble components designated soluble gums (SG). Samples were dried overnight in a vacuum oven at 115°C.

Carbon in the filter was quantified using a surface carbon analyzer (LECO RC-412). Deposits on suspended stainless-steel (302, finished with 240-grit paper) discs were similarly rinsed with both heptane and acetone and vacuum dried; the carbon was then evaluated as above. In some experiments several discs were suspended in the heated sample and removed sequentially along with the liquid aliquots.

Most experiments in the current study were conducted with saturated DPDS solutions estimated at 467 ppm (molar). Undissolved solute was removed by filtration; oxygen flows of 0 to 1 cm³ min⁻¹ per cm³ of solution were used to investigate the effects of oxygen. Reaction temperatures varied from 160 to 200°C, but most experiments were conducted at 185°C. Hexadecane (99%), DPDS, and thiophenol were obtained from Aldrich Chemical. Hexadecane was filtered with a 0.2-μ silver filter (Selas) and used without further purification.

The combined technique of thermogravimetry and mass spectrometry (TGMS) was used to investigate volatile products released from IS and IG during linear programmed heating.

RESULTS AND DISCUSSION

Measurement of Bulk and Surface Insolubles

Several experimental factors affect the rate of bulk and surface deposit formation. First, temperature changes have a pronounced effect upon autoxidation rates of forming hydroperoxide and subsequent oxygenated products such as alcohols, ketones, aldehydes, and carboxylic acids. Second, the amount of oxygen available in solution to react with free radicals is provided by an oxygen sparge at a fixed flow rate. Increasing the oxygen flow rate replaces the rapidly depleting dissolved oxygen. The combination of small bubble size and rapid stirring tends to assist the dissolving of oxygen. Blaine and Savage (1990) have shown that in pure hexadecane at 180°C, the distribution of autoxidation products changes for oxygen flow increases from 200 to 800 cm³ min⁻¹ for 600 cm³ of solution. Finally, Taylor and Wallace (1968) have reported that an increase in the level of sulphur compounds increases the amount of deposits in flowing experiments.

Data are expressed in terms of weight of carbon per cubic centimeter of filtered solution. The filtered solids are not carbon; rather they are oxygenated products, with levels of sulphur enhanced over that in bulk liquid. It is assumed that the percentage of carbon (typically 80%) in the bulk and surface deposits remains constant throughout the stress duration. The rate of formation of total filtered deposits will be greater than that resulting from the carbon measurements. Also no corrections have been applied to relate the sampled liquid volume to standard temperature conditions. The combined corrections outlined above to yield grams of deposit per cubic centimeter (20°C) are anticipated to increase the reported rate values by about 40% in the bulk. Similarly, the surface deposition rates in grams of deposit per square centimeter would be 20% higher than those reported.

Figures 1 and 2 show the results of carbon measurements in the bulk solution and on stainless-steel surfaces, respectively, for a saturated solution stressed at 163°C (the lowest temperature studied) and an oxygen flow of 0.14 cm³ min⁻¹ per cm³ of solution. It was found that the data were best

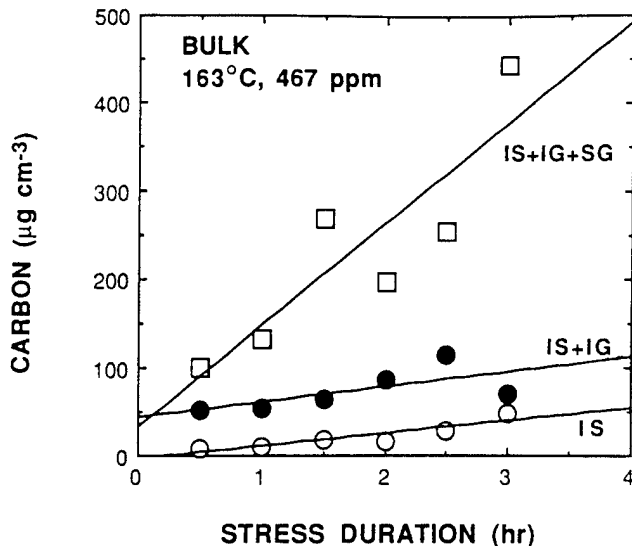


Figure 1. DPDS in Hexadecane, 467 ppm (molar), 163°C, Oxygen Flow 0.25 cm³ min⁻¹ per cm³ of Solution: Weight of Carbon in Samples Removed by Bulk Filtration of Liquid Samples as Function of Stress Duration.

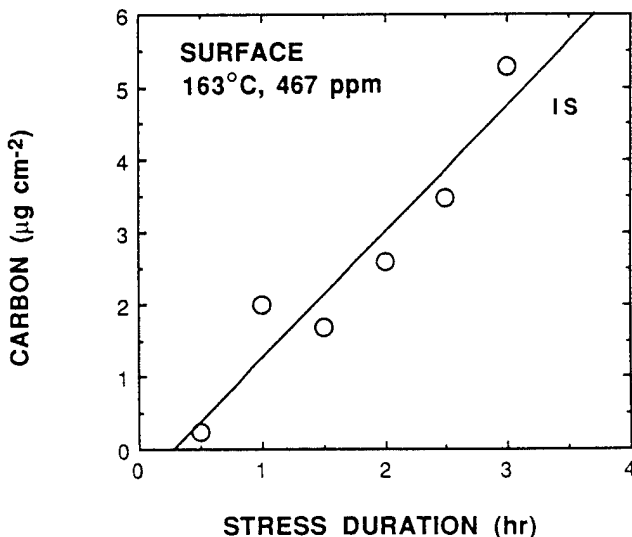


Figure 2. DPDS in Hexadecane, 467 ppm (molar), 163°C, Oxygen Flow 0.25 cm³ min⁻¹ per cm³ of Solution: Weight of Carbon in Samples Deposited as IS on Stainless-Steel Discs as Function of Stress Duration.

represented by linear fits. Frequently induction periods of 1-2 hr are observed. Based upon the observed linearity, the reaction under these experimental conditions follow pseudo-zeroth-order kinetics with respect to deposit formation. Rates corresponding to the best linear fit of data following an induction period were calculated. The pronounced effect of dopant concentration upon IS formation is shown in Fig. 3. Note the longer induction period and slower rate at low concentration. No attempt was made to remove trace inhibitors from the hexadecane. As a result induction periods should be expected in experiments where non-specific products such as IS, IG, or SG are monitored, analogous to the observation

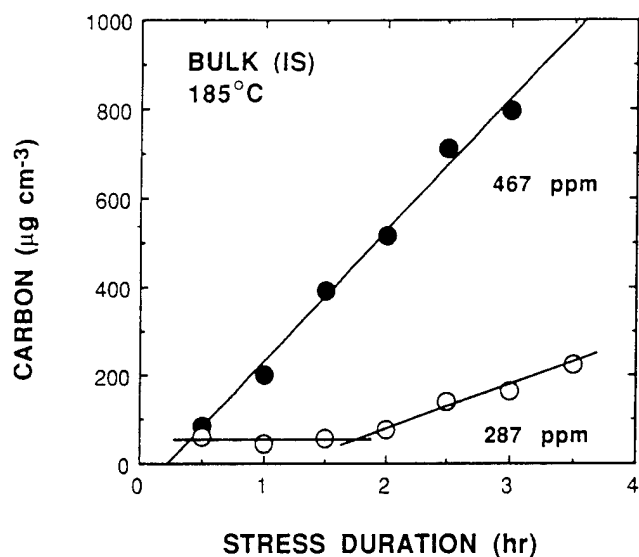


Figure 3. DPDS in Hexadecane, 185°C, Oxygen Flow 0.125 cm³ min⁻¹ per cm³ of Solution: Comparison of Weight of Carbon in IS Removed by Bulk Filtration of Liquid Samples [467 ppm and 287 ppm (molar)] as Function of Stress Duration.

of induction periods in hydroperoxide formation at lower temperature, as reported by Fodor, *et al.* (1988). Another possible contribution to an induction period arises from the inherent sampling and definition of filterable solids. First, measured solids must be trapped by glass-fiber filters (1 µ nominal); second, they must survive solvent rinse(s). Clearly, submicron particles will be collected very inefficiently, if at all. Particles with diameters near the filter pore size may be dissolved by solvent rinses, the result being that the quantity of detected material will display an induction period until particles become sufficiently large to be filtered and survive solvent rinses. A final, and possibly most important, factor is the need for sufficient product material to exceed the solubility of the reaction mixture. Polar and/or aromatic products will be less soluble in the hexadecane solvent system.

Dependence of IS and IG Formation Rates upon Oxygen Flow

The results of a complete series of rate measurements at 185°C as a function of oxygen flow are plotted in Fig. 4. These data were obtained prior to routine collection of SG; hence, the data include only IS and IG. Some very interesting facts are apparent. First, from onset, the rate of IS formation increases linearly with oxygen flow, suggesting rates which are pseudo-first order in oxygen. Clearly, observation of the pseudo-zeroth-order reaction kinetics described above results from maintaining a constant oxygen supply over the course of the reaction. Above a flow of 0.2 cm³ min⁻¹ per cm³ of solution, the rate levels off and decreases at higher oxygen flow. The region from 0.2 to 0.5 cm³ min⁻¹ per cm³ of solution appears to be an oxygen non-limited regime and may indicate saturation of the solution with respect to oxygen or the achievement of a steady state in some of the free-radical precursors to solid formation. Second, the rate of forming IG shows a much less pronounced oxygen dependence and is lower than the rate of forming IS, with the possible exception of the very lowest oxygen flow. Third, the rate dependence of IS and IG upon oxygen is quite different, suggesting that the

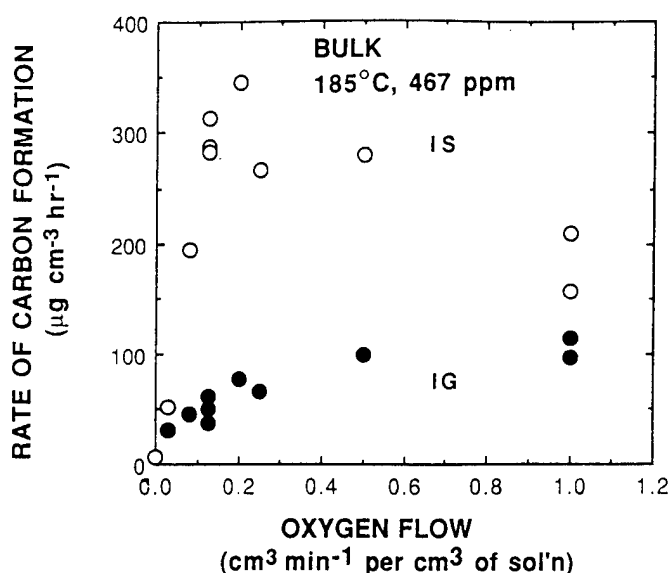


Figure 4. DPDS in Hexadecane, 467 ppm (molar): Rate of Forming IS and IG at 185°C as Function of Oxygen Flow.

experimentally designated IS and IG categories are independent.

The choice of solvents which defines designated categories is quite arbitrary. If a more aggressive solvent such as methanol or a solvent mixture such as Trisolve had been used, the region differentiating IS from IG would have been shifted slightly and the relative amount of IG would have increased at the expense of IS. However, the overall oxygen dependence would not have been altered. Thus, the concept of independent channels leading to IS and IG may be a general one in this system. The linear fits to the rate data indicate time-independent or pseudo-zeroth-order rates under conditions of constant oxygen flow, which reinforces the concept of independent reaction channels leading to IS and IG. Also, the large abundance of insolubles present in the bulk near the end of the 3-hr experiments (*viz.*, ~ 0.3 mg cm⁻³ IG and ~ 1 mg cm⁻³ IS) would promote numerous collisions and subsequent aggregation of the two categories of insolubles. The fact that under the test conditions, no growth of IS at the expense of diminution of IG was observed over a 3-hr stress duration indicates that conversion of IG to IS is not occurring. Recent experiments in our laboratory (Jones, *et al.*, 1992) on the more complex situation of thermo-oxidative degradation of turbine fuels indicate no interconversion between SG, IG, and IS, in agreement with the above findings for the model system.

Bulk/Surface Correlation

The current paper treats the phenomenological aspects of bulk and surface fouling in flask tests in the absence of fluid-dynamic complications which would be present in cases where fuel is flowing through heated tubes. A common question arises as to the origin of surface insolubles, *i.e.*, are they formed directly on the surface or are they formed as insoluble solids in the bulk which are subsequently transported and stick to the surface. Data from the present study can address this question for a model fuel. If aggregation and transport of IS and IG to the surface are assumed, increases in the surface rates will correlate with increases in the bulk rate. Figure 5 is a plot of bulk vs. surface rates,

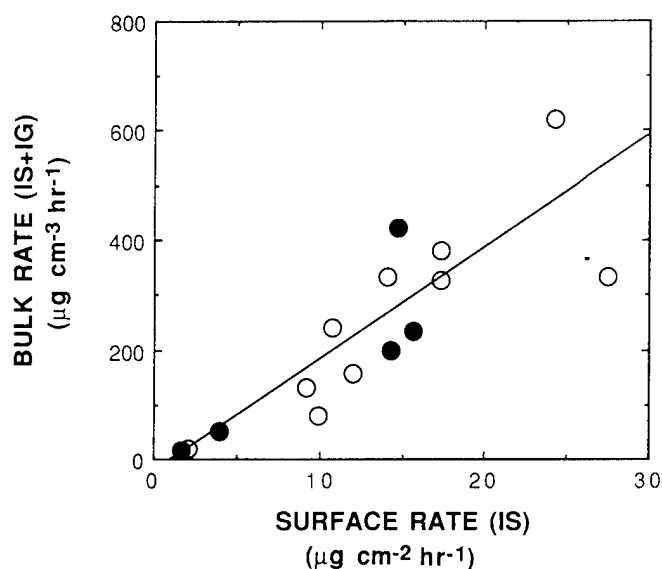


Figure 5. DPDS in Hexadecane: Rate of Forming Carbon in IS and IG Removed by Bulk Filtration of Liquid Samples as Function of Corresponding Rate of Forming Carbon in IS on Stainless-Steel Surfaces. Open Circles: Data from Single Disc; Closed Circles: Data from Six Discs.

including data collected in this study under varying conditions of oxygen flow, dopant concentration, and system temperature. The solid circles represent surface rates obtained from fitting six data points, while the open circles represent surface rates evaluated from deposition on a single stainless-steel disc which was suspended in the fuel for the entire stress duration. In these experiments, a linear correlation exists between the rates of forming bulk particles and surface deposits. This indicates either that the bulk particles are transported to the surface and stick or that within the stressed fuel the chemistry associated with both surface and bulk phenomena are directly linked, i.e., they have similar precursors. If the current findings obtained for a model system also prevail in jet fuels, then deposition within fuel tubes in the absence of fluid-dynamic effects will be determined by the rate of bulk particle production and the exposure time.

Further support for this point of view is obtained in a comparison of the fraction of total insolubles present as IS both in the bulk and on the surface. This fraction is given directly by the ratio of the quantity of residue following heptane/acetone rinse to that following heptane rinse. For six experiments, duplicate sets of stainless-steel discs were used to make this evaluation. The average ratios of 0.86 and 0.80, respectively, for surface deposits and bulk deposits indicate similar partitioning of IS and IG in the bulk and surface deposits.

Impact of Neat Hexadecane Contributions

The significant role played by DPDS can be appreciated by considering the results from a blank run employing neat hexadecane at 185°C and an oxygen flow of 0.25 cm³ min⁻¹ per cm³ of solution. The estimated bulk rates for forming IS, IG, and SG are 1, 7, and 137 μg cm⁻³ hr⁻¹, respectively. The estimated surface-deposition rate on stainless steel is ~ 0.2 μg cm⁻² hr⁻¹. Thus, any corrections to the rates for IS formation plotted in Fig. 4 for contributions from hexadecane autooxidation in the absence of DPDS are < 1% and are

negligible. Corrections for IG formation are 10-20% and are considered to be within the experimental uncertainty. The corresponding corrections to the rate of surface deposition in Fig. 5 are negligible.

Role of Sulphur Dopant

The Arrhenius plot in Fig. 6 was obtained using the rates of forming IS over the temperature range 163-193°C. Rate corrections discussed earlier are approximately constant over this temperature range and will not affect the slope. In each case the oxygen level was maintained in the range 0.1-1.0 cm³ min⁻¹ per cm³ of solution to ensure reaction on the plateau region. The measured activation energy of 50 kcal mole⁻¹ compares favorably with that calculated for Reaction (1) from tables by Lias, *et al.* (1988)



This is an obvious first step based upon the Taylor and Wallace (1968) conclusion that the thermal stability of the sulphur additive determines its propensity to influence deposit formation. The less-stable dopants tend to cause more deposits. The chemistry of thiophenol is closely related to that of DPDS; in fact, the former is readily oxidized to the latter under these experimental conditions. Recently, some detailed studies of thiophenol and its role in producing insolubles have been conducted by Hazlett, *et al.* (1991), and Mushrush, *et al.* (1988). The postulated mechanism involves the formation of sulphonic acids which can catalyze or directly participate in insoluble formation. Oxidation is known to progress from thiol to sulphenic acid to sulphinic acid and finally to sulphonic acid (Goldwhite, 1965). Prior to selection of DPDS for the current investigation, the thiophenol/hexadecane system exposed to ambient air at 170 and 190°C was studied in 16-hr flask tests. The results are shown in Fig. 7. Interpretation of the unusual concentration dependence is as follows. At very high concentrations, thiophenol is converted to DPDS according to Reaction (2)

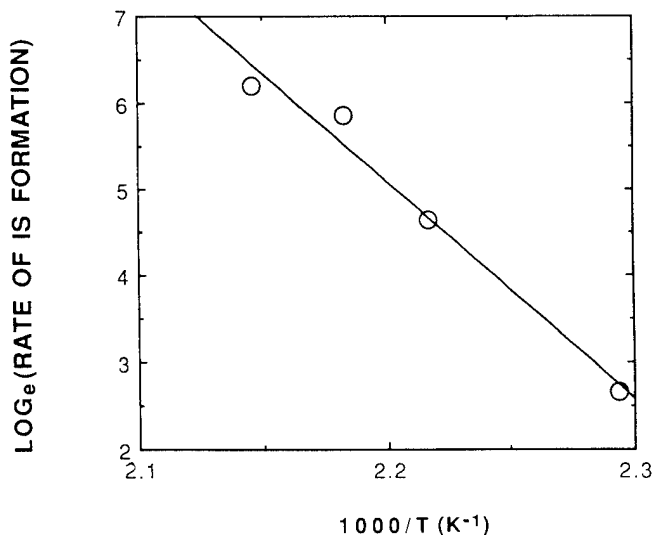
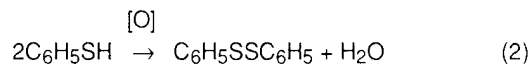


Figure 6. DPDS in Hexadecane, 467 ppm (molar): Arrhenius Plot of IS Formation in Bulk Fluid.

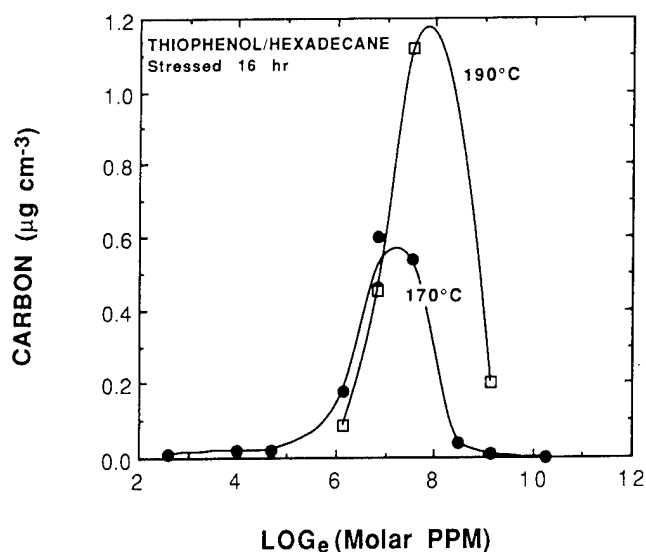


Figure 7. Thiophenol in Hexadecane: Weight of Particles Removed by Bulk Filtration of Liquid Samples After 16-hr Stress Duration as Function of Thiophenol Concentration. Solid Circles: LECO RC-412 Carbon Evaluation; Open Squares: Gravimetric Determination.

with the oxidant being the hydroperoxide, ROOH, or hydroperoxyl radical, ROO[•]. However, not all of the thiophenol is consumed during the 16-hr test. If some thiophenol is present, it can act as an inhibitor to autoxidation and the resultant formation of insolubles. At intermediate concentration (near the maximum), thiophenol is completely oxidized to DPDS. Once consumed, the resultant system is heavily doped in DPDS and produces deposits prolifically, as shown above. At low concentrations, thiophenol becomes entirely converted to DPDS, but at a doped level which is relatively low. It is clear from Fig. 3 that at lower doped levels, the rate of IS formation is greatly reduced and, as a result, fewer particles are formed. Thus, thiophenol can act both as an inhibitor and as an agent for IS formation, with the intermediate agent being DPDS. Watkins, *et al.* (1989), recently reported the role of thiophenol in reducing and/or controlling hydroperoxides which are early precursors to the formation of solids in jet fuels.

Nature of Insolubles

The IS were typically brown spheroidal particles, with diameters < 5 µ. Under high oxygen flow, the morphology of the particles changed markedly, resulting in large black spheroids with diameters exceeding 20 µ. Both types of particles are similar to those reported by Schirmer (1970) in aircraft and engine fuel systems. Visually IS and IG were indistinguishable. Both were analyzed using TGMS. Although most of the volatiles are released concurrently and cannot be distinguished, some of the identified volatile products include hexadecanol, SO₂, and a series of C₆H₅S-containing products such as C₆H₅SH, C₆H₅SC₆H₅, and DPDS. The temperature dependence of these products from the IS is shown in Fig. 8. Hexadecanol, one of the major autoxidation products, is not present in an adsorbed form; rather it is the product of thermal degradation. The energy required to release hexadecanol was estimated from fitting the temperature dependence to be 20 kcal mole⁻¹. It should be noted that unbound hexadecanol would be pumped away

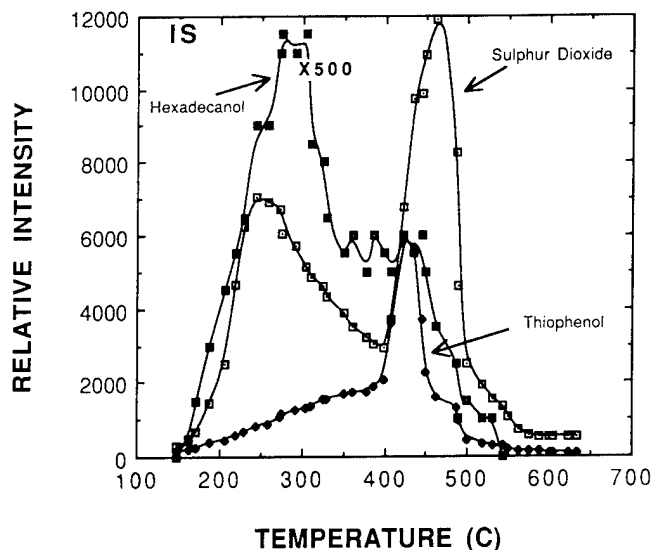
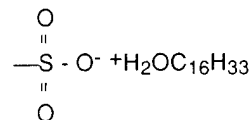


Figure 8. DPDS/Hexadecane IS: Temperature Dependence of Hexadecanol, Sulphur Dioxide, and Thiophenol Released During Linear Programmed Heating (4°C min⁻¹).

in the vacuum and heat pre-treatment. In previous TGMS investigations of polymers having salt groups such as -SO₃⁻ + R, low-temperature (400°C) release of SO₂, H₂O, and RH has been observed by Jones (1992). The current observation of SO₂ and hexadecanol around 250°C in both IS and IG may indicate the presence of salt in the form



The role of salts has frequently been invoked in discussions of fuel insolubles; and Hazlett, *et al.* (1991), recently reported sulphonic acids participating directly in the formation of insolubles in distillate fuels by salt formation with organic bases. The FTIR spectra indicate the presence of benzene-sulphonic acid in the IS and IG fractions. One distinct difference in the TGMS data from the two fractions is the observation of a pronounced doublet in SO₂ production from the IS fraction (see Fig. 8). The higher temperature release of SO₂ in the vicinity of C₆H₅S-containing products (see thiophenol in Fig. 8) indicates that other forms of sulphur are characteristic of the IS fraction. Little emphasis has been placed upon formation of the SG, primarily because inherent fuel solubility reduces their importance in fuel-fouling problems. The SG fraction may be the soluble hexadecane autoxidation products.

CONCLUSIONS

A series of flask tests on a model fuel system, DPDS/hexadecane, has shown that the quantity of IS, IG, and SG formed in the bulk increases linearly with stress duration after an induction period of 1-2 hr. Similarly, IS formed on stainless-steel surfaces has been found to increase linearly with stress duration. Rates of forming IS in the bulk can exceed 300 µg cm⁻³ hr⁻¹. Bulk and surface rates show a linear correlation, indicating either similar precursors or transport of bulk particles to the surface in the doped system.

The pseudo-zeroth-order dependence of the insolubles under fixed oxygen flow and the different oxygen dependences suggest that IS and IG are formed by independent processes and that IG is not a precursor of IS. The diagram in Fig. 9 is consistent with the observed macroscopic behavior.

The current fundamental study addresses solely the static situation within a model system. Under these conditions, surface deposition occurs and is influenced by the bulk-fuel reaction chemistry. Surface deposition rates measured in static tests are lower than those observed in dynamic tests due to the additional contribution from bulk particles being driven to the surface.

In summary, the sulphur-doped alkane system DPDS/hexadecane under thermo-oxidative stress has been shown to produce IS, IG, and SG which are analogous to those formed in more complicated jet fuels. Some of the conclusions, specifically, those which pertain to independence of global reaction channels, must be validated in more complicated systems.

ACKNOWLEDGEMENTS

This work was supported by and performed at the Wright Laboratory, Aero Propulsion and Power Directorate, Wright-Patterson Air Force Base, Ohio, under USAF Contract No. F33615-90-C-2033. One of the authors (EGJ) would like to acknowledge valuable discussions with W. H. Edwards (Pratt and Whitney) and with S. D. Anderson and W. M. Roquemore (Wright Laboratory).

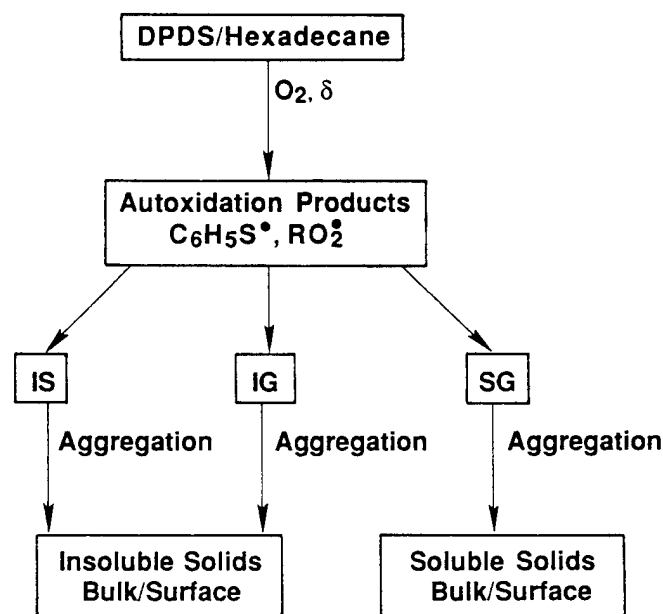


Figure 9. Global Reaction Diagram.

REFERENCES

- Blaine, S., and Savage, P. E., 1990, "Hexadecane Autoxidation: Product Analysis and Reaction Pathways," *Symposium on the Chemistry of Lubricants and Lubrication* (ACS Meeting, Boston, MA, April 22-27, 1990), American Chemical Society, Washington, D. C., pp. 239-244.
- Fodor, G. E., Naegeli, D. W., and Kohl, K. B., 1988, "Peroxide Formation in Jet Fuels," *Energy and Fuels*, Vol. 2, pp. 729-734.
- Goldwhite, H. J., 1965, "Sulphur Analogues of the Alcohols and Their Derivatives," in *Aliphatic Compounds*, Vol. 1, Part B of *Rodd's Chemistry of Carbon Compounds*, S. Coffey, ed., Elsevier, New York, pp. 73-92.
- Hazlett, R. N., Schreifels, J. A., Stalick, W. M., Morris, R. E., and Mushrush, G. W., 1991, "Distillate Fuel Insolubles: Formation Conditions and Characterization," *Energy and Fuels*, Vol. 5, pp. 269-273.
- Jones, E. G., 1992, Unpublished results.
- Jones, E. G., Balster, W. J., and Anderson, S. D., 1992, "Formation of Insolubles in Jet Fuels: Effects of Oxygen," *Symposium on the Structure of Jet Fuels III*, American Chemical Society National Meeting, San Francisco, CA.
- Lias, S. G., Bartmess, J. E., Liebman, J. F., Holmes, J. L., Levin, R. D., and Mallard, W. G., 1988, *Gas-Phase Ion and Neutral Thermochemistry*, Vol. 17 in *Journal of Physical Chemistry Reference Data, Supplement 1* (American Institute of Physics, Inc., New York).
- Mushrush, G. W., Hazlett, R. N., Hardy, D. R., and Watkins, J. M., Jr., 1988, "Jet Fuel Instability: Organo-Sulfur Hydroperoxide Interactions," *Proceedings of the Third International Conference on Long Term Storage Stabilities of Liquid Fuels* (London, September 13, 1988), pp. 294-306.
- Schirmer, R. M., 1970, "Morphology of Deposits in Aircraft and Engine Fuel Systems," SAE Paper No. 700258.
- Taylor, W. F., and Frankenfeld, J. W., 1986, "Chemistry and Mechanism of Distillate Fuel Stability," *Proceedings of the Second International Conference on Long-Term Storage Stabilities of Liquid Fuels* (San Antonio, Texas, July 29 - August 1, 1986), Southwest Research Institute, San Antonio, TX, pp. 496-511.
- Taylor, W. F., and Wallace, T. J., 1968, "Kinetics of Deposit Formation from Hydrocarbons: Effect of Trace Sulphur Compounds," *I&EC Product Research and Development*, Vol. 7, pp. 198-202.
- Watkins, J. M., Jr., Mushrush, G. W., Hazlett, R. N., and Beal, E. J., 1989, *Energy and Fuels*, Vol. 3, pp. 231-236.

Phenomenological Study of the Formation of Insolubles in a Jet-A Fuel

E. Grant Jones* and Walter J. Balster

Systems Research Laboratories, Inc., A Division of Arvin/Calspan, 2800 Indian Ripple Road,
Dayton, Ohio 45440-3696

Received May 11, 1993. Revised Manuscript Received August 2, 1993*

An aviation fuel in the Jet-A class has been stressed during flow through stainless-steel tubes under near-isothermal conditions at 185 °C. The quantity of insolubles in the bulk and on the stainless-steel surface has been measured as a function of stress duration. Surface deposits are shown to arise primarily from an adhering or reacting precursor formed initially in the bulk fuel. Other bulk insolubles do not contribute to surface fouling at this temperature. The formation of bulk and surface insolubles is shown to be tightly coupled to the measured depletion of dissolved oxygen. A mechanism is proposed to represent the inhibited oxidation based on the presence of sulfur-containing components in the fuel.

Introduction

Fuels serve as the primary coolant in aircraft. With enhanced aircraft performance, a greater thermal load must be dissipated into the aviation fuel by heat exchangers. Elevated temperatures cause oxidative degradation of the fuel, producing both bulk insolubles and surface deposits.¹ The former can lead to nozzle and filter blockage, and the latter can reduce heat-transfer efficiency. Such problems can be alleviated somewhat by operation at lower temperatures, selection of more stable aviation fuels, and the judicious use of additive packages comprising antioxidants, detergents, dispersants, and metal deactivators. A primary goal in this laboratory is to develop global computational-fluid-dynamics (CFD) models for predicting the time dependence of surface fouling under severe temperature and flow conditions that cannot be readily achieved or studied in the laboratory.² However, the development of global CFD models requires, as a basis, an understanding of some of the simple reaction chemical kinetics associated with fuel fouling: namely, the rates of formation of both bulk and surface insolubles.

The very detailed studies by Jensen et al.^{3,4} of model compounds such as *n*-hexadecane at elevated temperatures attest to the extreme diversity of product distribution and reaction pathways that are developed in relatively short reaction times. The complexity of detailed chemical analysis of reaction channels for an aviation fuel containing a broad mixture of hydrocarbons is formidable. Furthermore, it is difficult—if not impossible—to ascribe particular reaction channels to the production of insolubles. Because of these inherent difficulties, the approach to this problem taken in the present study and our previous studies is a phenomenological one, whereby the focus is on the quantity of bulk and surface insolubles without

initial regard for the detailed chemistry. In such a treatment the global formation of insolubles is monitored as a function of reaction time or fuel-stress duration at a fixed temperature. Insolubles are quantified by standard surface-carbon burnoff of filters and stainless-steel surfaces. This approach has been pursued in this laboratory in both static^{5,6} and dynamic⁷ studies at elevated temperatures (~185 °C) where degradation is dominated by autoxidation reaction chemistry and the effects of pyrolysis can be neglected.

Results reported herein relate to dynamic tests in which fuel is passed slowly through stainless-steel tubes that are maintained at a fixed temperature by surface contact within a heated copper block. The important features of the current heat-exchanger tests are the very slow flow rates and long path lengths which ensure that the bulk fuel and wall temperatures are equivalent and that reaction takes place under near-isothermal conditions. The residence time of the fuel within the tube is the chemical reaction time or the stress duration. Numerous studies^{8–11} have been reported which employed high wall temperatures, fast fuel flow, and concomitant large variations in temperature both along and across the tubes for approximation of certain engineering aspects of the fouling processes. The current experiments were initiated to minimize complications arising from both fluid dynamics and temperature nonuniformity and to study the chemical degradation of the fuel as a function of time at a fixed

* Abstract published in *Advance ACS Abstracts*, October 1, 1993.

(1) Hazlett, R. N. *Thermal Oxidation Stability of Aviation Turbine Fuels*; ASTM Monograph 1; American Society for Testing and Materials: Philadelphia, PA, 1991.

(2) Reddy, K. V.; Roquemore, W. M. *Prepr. Pap.—Am. Chem. Soc., Div. Fuel Chem.* 1990, 35 (4), 1346–1357.

(3) Jensen, R. K.; Korcek, S.; Mahoney, L. R.; Zinbo, M. *J. Am. Chem. Soc.* 1979, 101, 7574–7584.

(4) Jensen, R. K.; Korcek, S.; Mahoney, L. R.; Zinbo, M. *J. Am. Chem. Soc.* 1981, 103, 1742–1749.

(5) Jones, E. G.; Balster, W. J. ASME Paper 92-GT-122; American Society of Mechanical Engineers: New York, 1992.

(6) Jones, E. G.; Balster, W. J.; Anderson, S. D. *Prepr.—Am. Chem. Soc., Div. Pet. Chem.* 1992, 37 (2), 393–402.

(7) Jones, E. G.; Balster, W. J.; Post, M. E. Degradation of a Jet-A Fuel in a Single-Pass Heat Exchanger. ASME paper 93-GT-334, presented at the 38th International Gas Turbine and Aeroengine Congress and Exposition, Cincinnati, OH, May 24–27, 1993, accepted for publication in *Trans. ASME*.

(8) Heneghan, S. P.; Martel, C. R.; Williams, T. F.; Ballal, D. R. ASME Paper 92-GT-106; American Society of Mechanical Engineers: New York, 1992. To be published in *Trans. ASME*.

(9) Marteney, P. J.; Spadaccini, L. L. *J. Eng. Gas Turbines Power* 1986, 108, 648–653.

(10) Giovanetti, A. J.; Szelata, E. J. AIAA Paper 86-0525; American Institute of Aeronautics and Astronautics: Washington, DC, 1986.

(11) Chin, J. S.; Lefebvre, A. H.; Sun, F. T.-Y. ASME Paper 91-GT-114; American Society of Mechanical Engineers: New York, 1992.

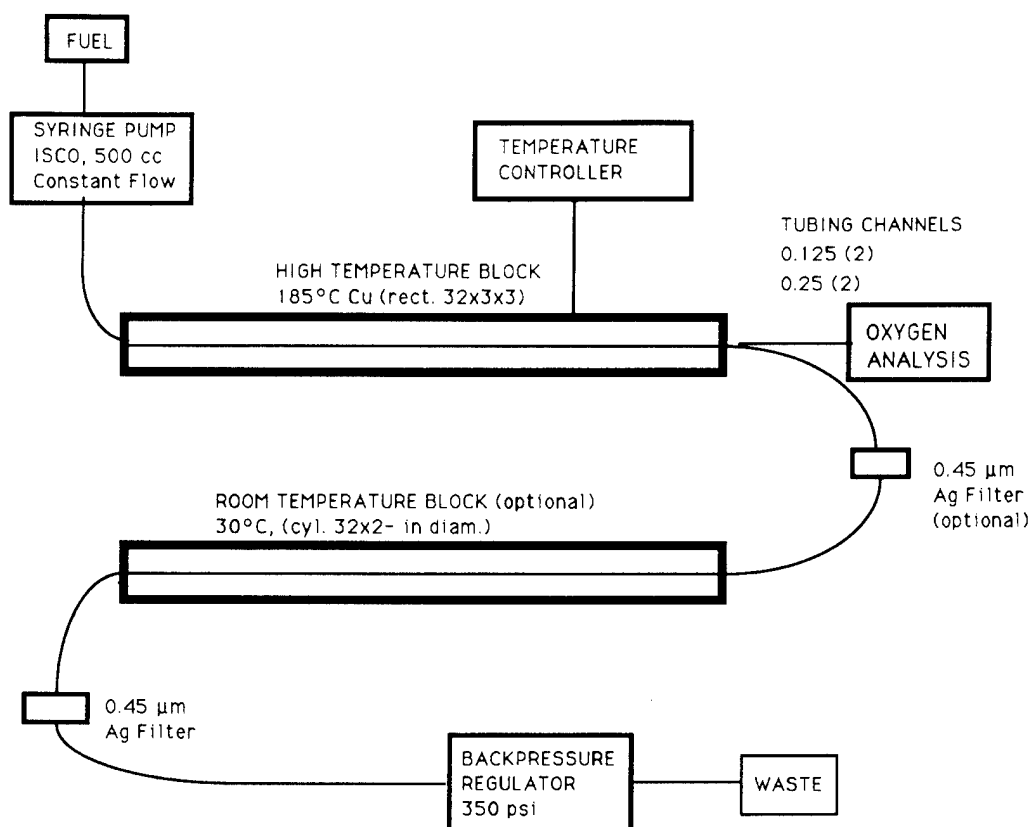


Figure 1. Schematic diagram of the near-isothermal flowing test rig (NIFTR) in single-pass configuration.

temperature. Fuel entering the heat exchanger contains a fixed amount of oxygen determined by the level of oxygen in air-saturated fuel at room temperature. Since this is the only source of oxygen for subsequent reactions, the conversion of fuel to oxygenated products is limited, and product buildup is minimal. An aviation fuel in the Jet-A class, designated POSF-2827, was chosen for study. This has served as a laboratory baseline fuel that meets USAF specifications and has been reported⁸ to form deposits in single-pass heat-exchanger tests at 300 °C.

The paper is structured as follows. After a description of the experimental apparatus and techniques, the Results and Discussion section treats, in turn, data format, surface deposition, filtered insolubles (qualitative), total insolubles (quantitative), oxygen consumption, and reaction mechanism. Data will be presented showing the existence of a unique, stress-time-dependent deposition profile which correlates closely with the consumption of oxygen. Results will be shown that demonstrate the bulk origin of surface deposits via the existence of a deposition precursor initially formed in the bulk fuel. This precursor will be shown to differ from other classes of bulk insolubles that do not contribute to surface fouling. Finally, the role of oxygen and its relation to the observed deposition is addressed in terms of the presence of autocatalysis and the global Arrhenius parameters describing oxygen consumption. The implication of these data to the problems of fuel fouling are summarized in the Conclusions.

Experimental Section

The Jet-A fuel in this study was used as received, without filtration. It contains 0.079% (wt) of sulfur and has a jet fuel thermal oxidation test (JFTOT) breakpoint of 539 K. The fuel was pumped through stainless-steel (304) tubing clamped tightly in a heated copper block. Two sizes of tubing were used: namely,

0.125-in. o.d., 0.085-in. i.d. and 0.25-in. o.d., 0.18-in. i.d. Tubing was ultrasonically cleaned using 10% Blue Gold solution¹² and was rinsed with distilled water and methanol. The criterion for clean tubing was minimal surface carbon as measured using a LECO RC-412 surface-carbon analyzer. The background level of carbon on 2-in. sections (0.125-in. o.d.) was typically about 10 µg, exhibited variation along the tubes and also with tubing batch, and was not subtracted from the observed signals.

Figure 1 is a schematic diagram of the near-isothermal flowing test rig (NIFTR). The system consists of a syringe pump which forces fuel through a 32-in.-long heated tube section, through a filter housing containing a 47-mm (0.45-µm) silver membrane filter, and finally through a backpressure regulator which maintains a minimum pressure of 350 psi. In selected experiments a 32-in.-long cooled section was inserted, and filtration was shifted downstream as shown in Figure 1. The major effect of this section is to provide additional cooling time prior to filtration. When additional fuel stress time was required, a third configuration was used in which the tubing was looped back through a second channel in the same heated block, and the membrane filter was accordingly moved downstream. For a flow rate of 1.8 cm³/min—which, in the current study, represents a worst-case situation for achieving isothermal conditions—at least 75% of the heated section has equivalent wall and bulk-fuel temperatures.⁷ The NIFTR was operated in the horizontal configuration; under the current test conditions, deposition differences in horizontal and vertical configurations could not be detected.⁷ Some discrimination against the collection of bulk particles is expected due to gravitational effects, particularly at the slowest flows.

Following a 6-h test the tube was allowed to drain overnight, and the heated region was cut into 16 2-in. sections. These sections were subsequently rinsed with heptane, placed in a vacuum oven (115 °C) for a minimum of 12 h, and subjected to surface-carbon analysis. The in-line filters were sectioned into two equal pieces; one was rinsed with heptane and the other with heptane followed by acetone. On occasion, one of the halves was

(12) Blue Gold Company, Ashland, OH.

Table I. Nomenclature

IS	insoluble solids (insoluble in both heptane and acetone)
IG	insoluble gums (insoluble in heptane, soluble in acetone)
SG	soluble gums (soluble in heptane, the implication being that filterables are insoluble with respect to stressed fuel but may be soluble in unstressed fuel, i.e., heptane)

left unrinsed for comparison purposes. The filters were then subjected to the same vacuum-oven and surface-carbon-analysis treatment as the tube sections. Based upon the residual following rinsing, the filtered insolubles were subdivided into three categories—IS, IG, and SG—as defined in Table I. The quantity of bulk insolubles present on the filters as IS was obtained directly from the heptane/acetone-rinsed filter. The quantity present as IG was determined from the heptane-rinsed filter and the quantity of IS. The quantity present as SG was estimated from unrinsed filters and the quantity of IS and IG. It should be noted that filterables in these experiments are defined with respect to 0.45- μm filters. It is expected that both quantity and distribution of insolubles are functions of pore size.

Surface deposits were not specified as IS or IG but rather as the total IS + IG. Previous static flask experiments employing stainless-steel discs suspended in the fuel at 185 °C yielded surface deposits composed primarily of IS (>80%).⁶

Two types of experiments were performed. In the first, surface deposits and bulk insolubles were quantified over a series of fuel flow rates using a heated block at 185 °C. A 6-h experimental test time was sufficient to produce measurable insolubles. In separate experiments the residual amount of dissolved oxygen was measured for a series of flow rates which provided different stress intervals in the heated section. Residence-time calculations were based on tube dimensions and plug flow, assuming a 15% volume expansion at 185 °C. An in-line Hewlett-Packard gas chromatograph modified by Rubey et al.¹³ was used for dissolved-oxygen measurements. Data are presented as percent residual oxygen as a function of residence time or stress duration, with 100% corresponding to fuel saturated with respect to air at room temperature. Based on recent measurements by Striebig,¹⁴ the saturated value for POSF-2827 fuel is 64.9 ppm (w/w). All signals were corrected for naturally occurring argon which is not chromatographically distinguishable from oxygen.

Results and Discussion

Data Format. As discussed above, deposition data are acquired as micrograms of carbon on each of 16 2-in. heated tube sections. The basic assumption made in such studies is that the deposits have a uniform elemental composition along the tube, i.e., the amount of deposit is proportional to the measured surface carbon. Based upon previous analyses, carbon constitutes ~80% of the total mass. Throughout this paper reference is made to deposited carbon and filtered carbon; the term carbon refers to the 80% carbon content of the carbonaceous insolubles. Resolution of the surface data is limited by the length of the tube sections, which should be reflected by presentation of the deposition data in histogram format; however, for ease of comparison these data are presented as points centered at the middle of each tube. One presentation of typical deposition data (flow rate 0.50 cm^3/min) where the weight of carbon (μg) is plotted as a function of the tube number is given in Figure 2a. Under isothermal conditions and a fixed flow rate, distance along the tube can be related to residence time or stress duration, assuming plug flow and a 15% volume expansion. Thus,

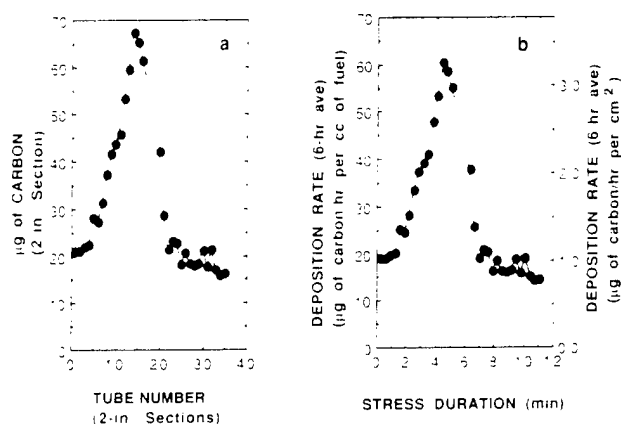


Figure 2. Data format: 185 °C, flow rate of 0.50 cm^3/min . (a) Carbon vs tube number and (b) time-averaged deposition rates vs fuel stress duration.

Figure 2a could be plotted equally well as micrograms of carbon as a function of fuel-stress duration.

It is important to distinguish two time frames. First is the experiment test time (6 h), representing an integration period to collect measurable deposits; this time along with flow determines the total quantity of fuel passed through the tube. Second is the fuel-stress duration, reaction time, or residence time in the heated block (1–30 min for the current data); this time controls the reaction conversion.

Deposition data can also be expressed as an experiment-time-averaged carbon-deposition rate. First, a rate in units of micrograms per unit stress time per cubic centimeter of fuel passed is calculated by dividing the micrograms of carbon on a tube section by the fuel residence time in that section and then by the total amount of fuel passed through the system. This is equivalent to micrograms per unit experiment time per unit volume of tube section. Data plotted in this manner are shown in Figure 2b with respect to the ordinate scale on the left. When viewed as a histogram, the area under the curve represents the total micrograms of surface carbon per cubic centimeter of fuel passed. Deposition results can then be readily compared with filter data which are experimentally integrated to yield micrograms of filtered carbon per cubic centimeter of fuel passed. A second way of expressing the experiment-time-averaged deposition rate is to divide the micrograms of carbon on a tube section by the internal surface area of the tube section and then by the total experiment test time. This format has been employed conventionally in the literature; however, its use with data covering broad temperature ranges is questionable. The units in this case are micrograms per hour per square centimeter. Data plotted in this manner are shown in Figure 2b with respect to the ordinate scale on the right. The two rate expressions differ only by the surface-to-volume ratio ($4/d$). With isothermal data the convention employed here is to plot as in Figure 2b with respect to the ordinate scale on the left, except when comparing tubes of different diameter and then as in Figure 2b with respect to the ordinate scale on the right.

Surface Deposition. Figure 3 shows the residual dissolved oxygen at 185 °C and the 6-h-averaged surface deposition for seven different fuel flow rates—0.10, 0.125, 0.25, 0.50, 0.75, 1.0, and 1.88 cm^3/min . In each case, fuel saturated with respect to air at room temperature was passed through 0.125-in. tubes. In contrast, the blank shown in Figure 4 was obtained at a flow of 0.25 cm^3/min using He-sparged fuel under conditions where the dissolved

(13) Rubey, W. A.; Tissandier, M. D.; Striebig, R. C.; Tirey, D. A.; Anderson, S. D. *Prepr.—Am. Chem. Soc., Div. Pet. Chem.* 1992, 37 (2), 371–376.

(14) Striebig, R. C. Private communication.

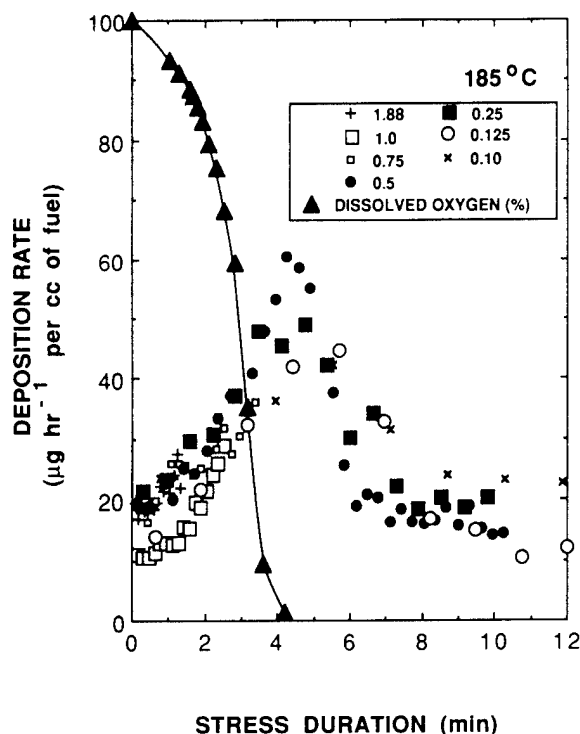


Figure 3. POSF-2827 fuel initially saturated with respect to air at room temperature. Deposition rate on 0.125-in.-o.d. tubing at a series of flow rates (cm^3/min) vs stress duration at 185°C . Superimposed is dissolved oxygen vs stress duration.

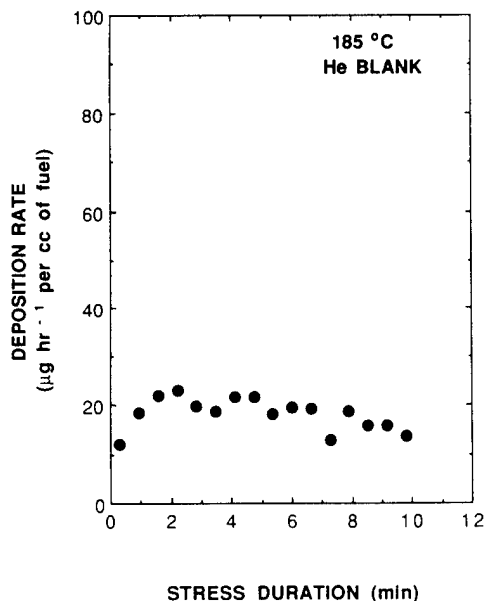


Figure 4. POSF-2827 fuel initially sparged with He. Deposition rate on 0.125-in.-o.d. tubing at a flow rate of $0.25 \text{ cm}^3/\text{min}$ vs stress duration at 185°C .

oxygen is estimated at less than 5% of the air-saturated value. The blank includes all non-oxygen-related surface contributions. Clearly, the observed deposition in Figure 3 arises primarily from the presence of dissolved oxygen. This is additionally confirmed by the oxygen consumption and the existence of a deposition rate that increases, passes through a maximum, and returns to baseline. Deposition is complete after 10 min of stressing.

Note in Figure 3 that at the three fastest flow rates, only the initial portions of the deposition profile are collected. Such conditions do not provide sufficient stress time for completion of either the oxygen consumption or the

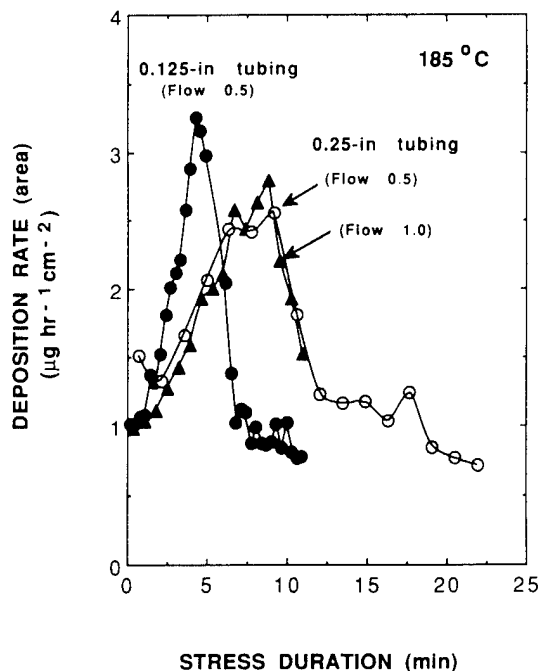


Figure 5. POSF-2827 fuel initially saturated with respect to air at room temperature. Comparison of deposition on 0.125-in.-o.d. and 0.25-in.-o.d. tubing.

deposition process within the 32-in. heated tube. At the other extreme, data obtained at the slowest flow rate ($0.10 \text{ cm}^3/\text{min}$) extend past 25 min; hence, about one-half of the data points exceed the plot range. The data set for a flow rate of $0.50 \text{ cm}^3/\text{min}$ was obtained from two passes through the heated block in order to provide 10 min of stressing. The observed deposition processes are consistent with the autoxidative basis of fuel fouling.

Maxima have been reported in most tube deposition studies; however, the existence of a large temperature drop along the tube has made it difficult to ascertain whether the maximum arises from oxygen consumption or from temperature-related chemical-kinetic changes. Isothermal conditions simplify the interpretation. The fuel becomes totally depleted of oxygen, and deposition processes can no longer be maintained. The fact that the deposition profile is approximately independent of fuel flow rate implies that the deposition maps a bulk-fuel reaction-time-dependent process. This indicates that surface deposits originate in the bulk fuel.

The existence of a deposition-rate maximum that occurs after complete oxygen consumption indicates a delay in the deposition process. This may arise, in part, from the time required to complete chemical reactions, e.g., to convert peroxy radicals, ROO^\bullet , into surface deposits. If surface deposits originate primarily from chemical reactions occurring in the bulk, then the time necessary for diffusion to the wall may be significant. That is, the walls may serve as a collector, with an inherent delay due to diffusion.

The possibility of bulk origin of the surface deposits can also be checked by comparing the deposition observed in Figure 3 on 0.125-in. tubes with that from similar experiments on 0.25-in. tubes. Presumably, the mean time to diffuse to the wall will be greater in the larger-diameter tubes and will be manifested by a broadened deposition profile. Figure 5 shows this comparison for a flow rate of $0.50 \text{ cm}^3/\text{min}$. The shift and broadening seen in Figure 5, when considered with the oxygen-loss data in Figure 3,

imply that almost all of the observed oxygen-related deposition originates from the bulk fuel. Shown in Figure 3 are additional data obtained at a $0.25\text{-cm}^3/\text{min}$ flow rate which confirm that the deposition process for the larger-diameter tubes is also independent of flow rate.

In summary, data at 185°C support the premise that surface deposition arises mainly from oxygen-dependent formation of a product within the bulk fuel which diffuses to the tube walls and either adheres or reacts to leave a residue. This product is defined here as a deposition precursor, P. The total surface carbon per cubic centimeter of fuel passed through the heat exchanger is approximately constant and independent of flow. The area under the profile in Figure 3 for 0.125-in. tubes is about $3\text{ }\mu\text{g}/\text{cm}^3$. Significantly, the total deposition on the 0.25-in. tube is the same within experimental uncertainty. This indicates that P is not appreciably consumed by competitive processes during the additional diffusion time to the wall and implies that it can be quantitatively evaluated.

Contributions to deposition related to nonoxidative processes are difficult to evaluate because of the large background. As mentioned earlier, no background corrections have been made. Such effects would be included along with some contribution from the residual oxygen in the blank run in Figure 4. Approximately one-half of the total carbon in Figure 4 arises from a clean-tube background. The remainder comprises two contributions, one being the presence of some residual oxygen not eliminated during sparging and the other being related to fuel exposure. The magnitude of the second contribution is proportional to the internal surface area and does not appear to be related to exposure or stress time.

Filtered Insolubles (Qualitative). For each of the above flow rates, the corresponding bulk filtered insolubles have been quantified. Two distinct situations become evident. First, in all cases where surface deposition has been completed within the heated tube (i.e., slow flow rates or long stress duration), the total filtered carbon is $\sim 2\text{ }\mu\text{g}/\text{cm}^3$, with equal amounts of IS and IG being present on the filter. Figure 6 shows the surface-carbon-burnoff dependence which is the detected carbon-dioxide signal formed during the linear programmed heating of the filtered sample in pure oxygen. The fuel flow rate was $0.10\text{ cm}^3/\text{min}$ for obtaining this filtered sample. Note that the burnoff dependences are nondescript, having equal abundance (area under curve) of IS and IG. In the second situation which arises when the surface-deposition process has not been completed within the heated tube (for example, a flow rate of $1.0\text{ cm}^3/\text{min}$), the IG portion of the filterables is dominant and has a unique bimodal carbon-burnoff dependence as shown in Figure 7. Similar profiles are obtained for IG in cases where the preceding surface deposition fails to return to baseline. The filtered material in these cases is almost entirely the deposition precursor, P, which has passed through the hot tube before diffusion to the walls. Thus, the filter data further support the bulk origin of oxygen-related surface deposits in this fuel and, in addition, place P in the category of an IG that is capable of being collected on $0.45\text{-}\mu\text{m}$ filters. In recent experiments a second filter having a pore size of $0.20\text{ }\mu\text{m}$ has been placed in series. Under the current experimental conditions, less than 10% of P is collected on the second filter. Thus, the mean precursor diameter must be on the order of $0.5\text{ }\mu\text{m}$ or larger at the point of filtration. Since some cooling of the fuel has occurred, no information

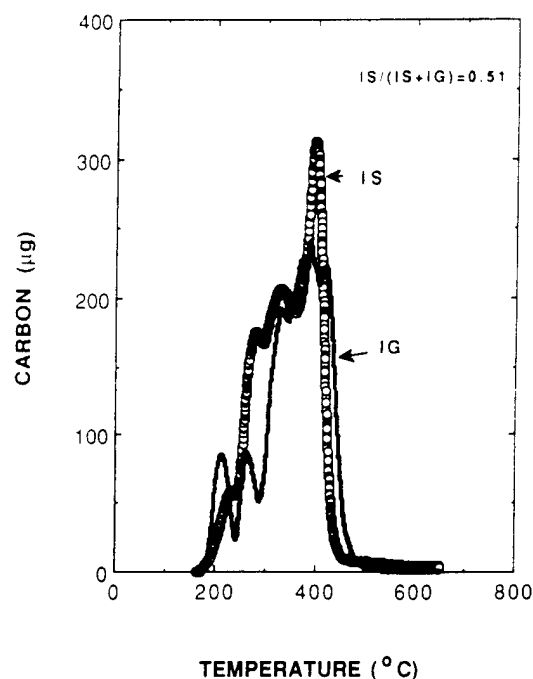


Figure 6. Output from RC-412 surface-carbon burnoff of a filtered sample. Sample collected using air-saturated POSF-2827 fuel and a flow rate of $0.10\text{ cm}^3/\text{min}$ at 185°C .

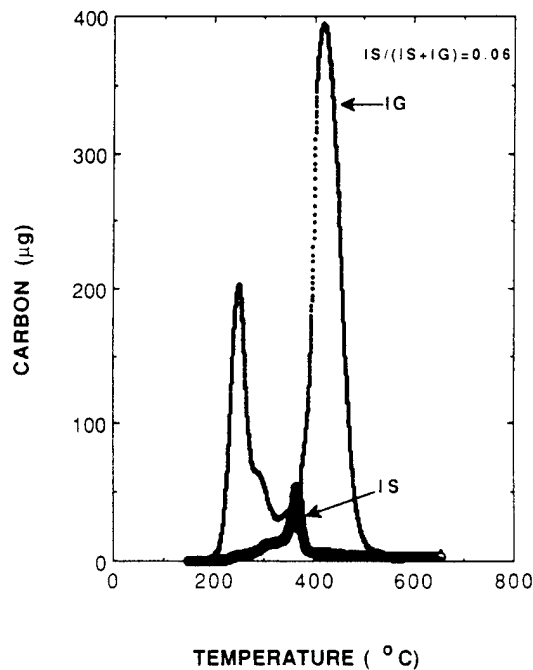


Figure 7. Output from RC-412 surface-carbon burnoff of a filtered sample. Sample collected using air-saturated POSF-2827 fuel and a flow rate of $1.0\text{ cm}^3/\text{min}$ at 185°C .

concerning the *in-situ* precursor size at 185°C can be obtained from these data.

A question arises concerning whether the precursor to deposition at 185°C may also cause surface deposits at other temperatures. This question has been addressed for deposition on 30°C stainless-steel surfaces by passing the fuel first through the hot tube at 185°C under conditions where P will be present in the effluent and then immediately through a 32-in. tube maintained in a room-temperature copper block. The recorded temperature was $\sim 30^\circ\text{C}$. The results of two such experiments are given in Figure 8. Both data sets show a sharp discontinuity between the two blocks. Evidently, no

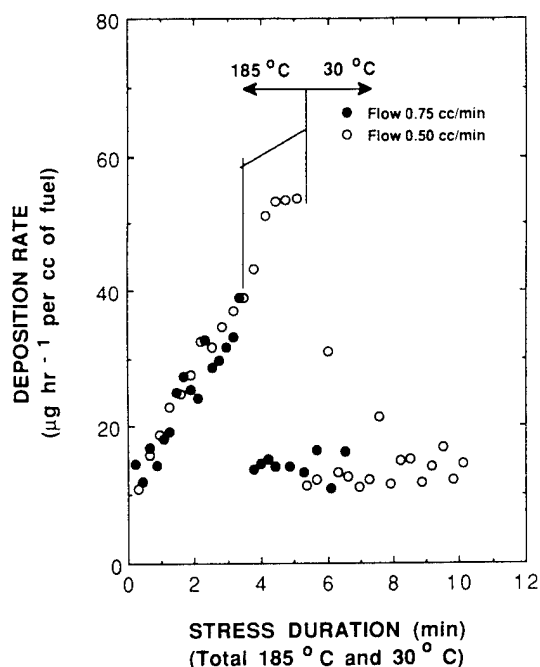


Figure 8. Deposition rate in successive tubes at 185 and 30 °C vs total tube residence time. Flow rates are 0.75 and 0.50 cm³/min. Vertical lines mark the transition from the hot to the cold block, i.e., 3.4 min (flow 0.75 cm³/min) and 5.2 min (flow 0.50 cm³/min).

significant deposition occurs on the cold tube because P either does not diffuse to the wall or, upon arrival, does not adhere or react; this dilemma cannot be resolved from the currently available data. The fact that P is still present in the effluent from the cold tube is confirmed by the filter data. In both experiments IG are dominant and the surface-carbon dependences appear as in Figure 7. It should be noted that the baseline deposition in the cold tube includes the same non-oxygen-related contributions observed in the heated sections.

Total Insolubles (Quantitative). Arguments made previously can be clarified by considering the *total* quantity of carbon, i.e., surface carbon plus filtered carbon produced

under different oxidative-stress conditions. The total filtered carbon is obtained directly from the filter burnoff, and the total surface carbon is obtained by taking the sum of the total carbon above baseline on each tube section or integrating the area under the profiles in Figure 3. Integration excludes the baseline or nonoxygen-related contribution. Since different quantities of fuel are passed through the tube at each flow rate, the data are normalized per cubic centimeter of fuel. Figure 9a shows the dependence of the total carbon and also that fraction of carbon contained on the filter as a function of fuel residence time in the tube or total stress duration. Note that for short stress times, most of the carbonaceous material is swept through to the filter with minimal loss to the walls. For stress times longer than 10 min, P is lost to the walls, and only nonadhering bulk particles are filtered. About 40% of the total filterables fall into the nonadhering category, and 60% are characterized as P.

In Figure 9a the total carbon increases with stress time up to 5 min, at which time the oxygen has been totally consumed (see Figure 3); the total carbon remains approximately constant over the next 20 min of additional stressing. Earlier it was concluded that a direct correlation exists between the surface deposits and the consumption of dissolved oxygen. The data in Figure 9a show a correlation between the total carbon (bulk + surface) and the presence of dissolved oxygen. The near-linear rise in total carbon as a function of total stress duration reflects the fact that an increasingly larger fraction of the oxygen is consumed over the first 5 min of reaction. The time behavior of total carbon is not surprising if one considers that the degradation is via autoxidation at this temperature. However, it is surprising that both surface-deposition precursors, P, and bulk particles have achieved a size that exceeds 0.45 µm in such short reaction times. Clearly, the observed insolubles are early products in the autoxidation chemistry.

If the oxygen is totally consumed in fuel saturated initially at room temperature with respect to air, then the maximum amount of insolubles formed from 1 cm³ of POSF-2827 aviation fuel is 5 µg. The partitioning shown

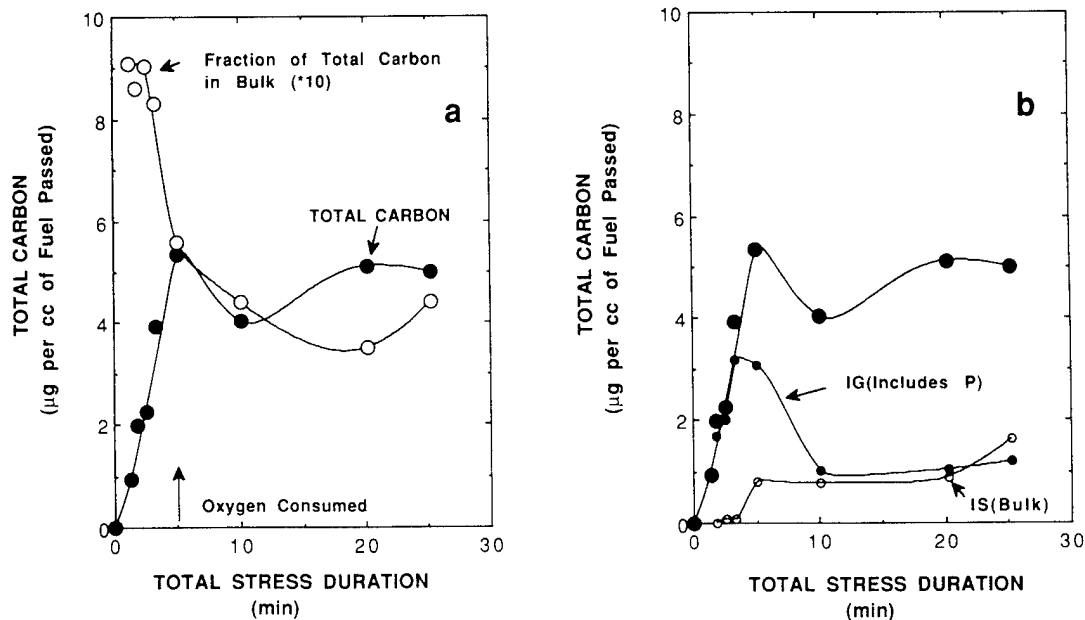


Figure 9. (a) Total carbon and fraction in bulk vs total stress duration at 185 °C. (b) Total carbon, IS (bulk), and IG (bulk + precursor) vs total stress duration at 185 °C.

in Figure 9a indicates that 60%, or $\sim 3 \mu\text{g}$, is P and 40%, or $2 \mu\text{g}$, is nonadhering bulk insolubles. In Figure 9b the distribution of IS and IG collected on the filter is superimposed on the total-carbon dependence. The IS which do not adhere to the tube surface are detected after an induction period of a few minutes and rapidly increase to $1 \mu\text{g}$. After consumption of oxygen is complete, the quantity of IS does not increase over an additional 20-min period of stressing. This is in contrast to the behavior of the IG. For the first few minutes, IG constitute almost 100% of the total collected carbon, exhibiting a maximum at around 4–5 min where the oxygen is totally consumed and finally dropping to a constant level of $\sim 1 \mu\text{g}$. The maximum arises from that fraction of IG that leads to surface fouling, i.e., P. For short residence times these precursors are swept through to the filter. At longer residence times within the heated tube, they are lost to the walls; as a result the filtered amount drops to a constant level of $\sim 1 \mu\text{g}$ which constitutes the nonadhering portion of the IG. Again, the quantity of this material does not increase with an additional 20 min of stressing, i.e., after complete oxygen consumption. Note that for long residence times, the ratio of IS to IG is about unity.

In summary, 1 cm^3 of air-saturated fuel has the potential (provided the oxygen is totally consumed) to produce a total of $5 \mu\text{g}$ of insolubles: $3 \mu\text{g}$ of a surface-fouling precursor, P, in the form of an IG, $1 \mu\text{g}$ of a nonsurface-fouling IG, and $1 \mu\text{g}$ of a non-surface-fouling IS. The contribution from inherent insolubles present in the initial fuel is $<0.08 \mu\text{g}/\text{cm}^3$.

Oxygen Consumption. Using the previous quantitative data, one can estimate that fraction of total reacted oxygen which can be ascribed to the observed insolubles. If the insolubles are estimated to be 20% oxygen,¹⁵ then $5 \mu\text{g}$ of total insolubles from 1 cm^3 of fuel corresponds to $1 \mu\text{g}$ of oxygen per cubic centimeter. If the dissolved-oxygen level at room temperature is assumed to be 64.9 ppm (w/w)¹⁴ and the fuel density to be $0.80 \text{ g}/\text{cm}^3$, $\sim 52 \mu\text{g}$ of oxygen is dissolved in 1 cm^3 of unstressed fuel. Thus, the total measured insolubles can account for only 2% of the total reacted oxygen. Presumably, the other 98% reacts to produce soluble products. The absence of an increase in the total insolubles formed during 20 min of stressing at 185°C following oxygen consumption implies that such soluble oxygen-containing products do not contribute to further near-term insoluble formation. At this point it should be mentioned that estimates of filtered SG have been made for several flow rates, based upon data from unrinsed filters. In all cases filtered SG are below detectable limits.

Despite the fact that only a small fraction of the total dissolved oxygen participates in the formation of insolubles, its presence is the basis of insoluble formation. Some experiments have been conducted in this laboratory using fuel sparged initially with pure oxygen. The equilibrium quantity of dissolved oxygen is proportional to the partial pressure of oxygen above the fuel. Hence, sparging with pure oxygen, as opposed to air, yields fuel having about five times more dissolved oxygen. Once this oxygen-rich fuel is loaded in the syringe pump at a system pressure of 350 psi, it can be depleted only by reaction. For a flow rate of $0.25 \text{ cm}^3/\text{min}$ and a second pass through the heated block, a total of $25.1 \mu\text{g}$ of insolubles was collected from

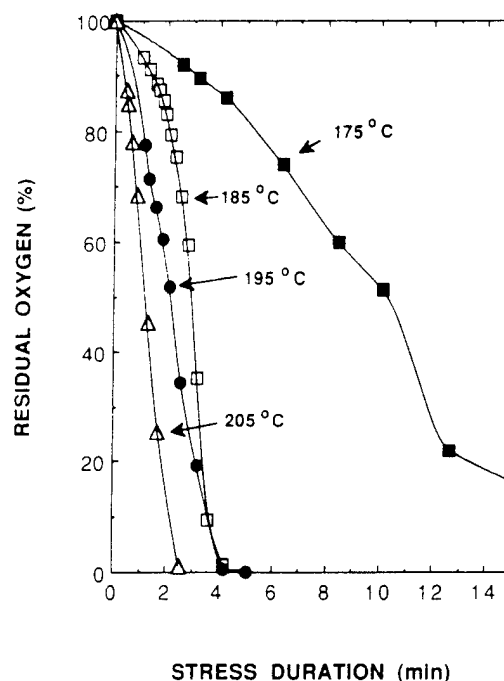


Figure 10. Residual dissolved oxygen vs stress duration (100% corresponds to initial saturation with respect to air at room temperature).

each cubic centimeter of fuel passed through the system. This factor-of-five increase in the total insolubles reflects the five-fold oxygen enrichment and the proportionality between total insolubles and dissolved oxygen.

Clearly the amount of oxygen consumed and the time dependence or rate of oxygen consumption are of extreme importance in assessing the extent of fouling in the fuel. Although a specific reactant, namely, oxygen, is being monitored as a function of stress time at elevated temperature, it should be noted that its reaction partners are a diverse family of free radicals, R^\bullet ; hence, consumption of oxygen is viewed as a global reaction, in the same vein as the phenomenological quantification of reaction insolubles.

Oxygen loss has been measured as a function of stress duration at 10-deg increments from 155 to 205°C . Experimental limitations preclude extending this range significantly. At higher temperatures the system departs significantly from isothermal conditions, and at lower temperatures the long times necessary to achieve significant oxygen loss result in excessive instrument drift. The data for the four highest temperatures are shown in Figure 10. At 205 and 195°C the oxygen decays approximately linearly up to 70% conversion and then tails off. Results from a study in this laboratory have shown⁷ that the global oxygen consumption is best described by zeroth-order kinetics or oxygen-non-limited rates down to 20–30% residual oxygen. Subsequently, insufficient oxygen remains to satisfy the R^\bullet radicals, and the reaction becomes oxygen limited, following first-order kinetics. This observation is important because it indicates that fuel saturated with respect to air at room temperature reacts predominantly in an oxygen-rich or oxygen-non-limited regime. At the lower temperatures of 185 and 175°C , the oxygen loss has a sigmoid shape that is characteristic of autocatalysis. This is well-known in the autoxidation of pure hydrocarbons, particularly in the absence of an initiator.¹⁶ In such cases the rate of oxygen consumption increases with reaction conversion. In the current study

(15) This value is confirmed by XPS analysis of surface deposits formed on stainless-steel discs in static tests.

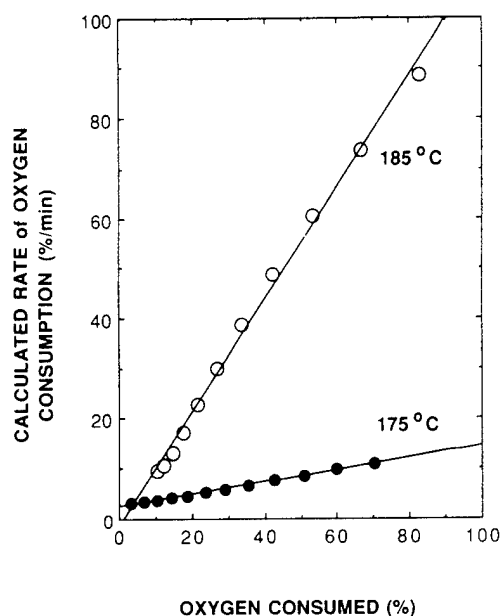


Figure 11. Rate of oxygen consumption (calculated from numerical fit to data in Figure 11) vs total oxygen consumed.

the rate increase is directly proportional to the amount of oxygen consumed, as shown in Figure 11. This plot was obtained by taking the data from Figure 10, fitting it with a third-order polynomial, and numerically calculating the first derivative, $d[O_2]/dt$.

Two possible explanations for a linear dependence such as that in Figure 11 are briefly outlined below. These explanations are based on the autoxidation of hydrocarbons to form the hydroperoxide, ROOH, which is known to play an important role in fuel degradation. The outline is based, to a great extent, on the treatments outlined in Walling¹⁷ and in Scott.¹⁸ The overall oxygen consumption and ROOH formation in an oxygen-rich case where the primary termination reaction is the bimolecular recombination of ROO^* are given by

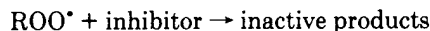
$$\frac{-d[O_2]}{dt} = k_p[RH] \left\{ \frac{R_i}{2k_t} \right\}^{1/2} = \frac{d[ROOH]}{dt}$$

where k_p and k_t are the rate coefficients for propagation and termination, respectively; R_i is the initiation rate; and $[RH]$ is the hydrocarbon concentration. The first explanation applies to long-term oxidation of pure hydrocarbons where $[ROOH]$ can become sufficiently high that R_i is enhanced due to ROOH formation and the subsequent bimolecular contribution to the free-radical pool from

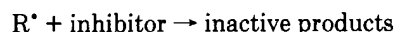


The occurrence of reaction 1 leads to $R_i \propto [ROOH]^2$, i.e., the rate of oxygen consumption is proportional to the amount of hydroperoxide formed or the total amount of oxygen consumed, as observed in Figure 11. Although this is an appealing explanation, it requires very high values for $[ROOH]$. These values are not substantiated by recent measurements in this laboratory which place 0.1 milliequivalents/L as an upper limit for $[ROOH]$ under the test conditions employed.¹⁹

Kendall and Mills²⁰ have reported that sulfur-containing fuels react more slowly with oxygen under inhibited-oxidation kinetics. Flask tests in this laboratory have shown⁶ that the current sulfur-containing fuel falls into this category, reacting under inhibited oxidation to achieve a pseudo-steady state with low rates of forming insolubles. Under inhibited oxidation the dominant termination step, according to Walling,¹⁷ is



or



in which case the rate of oxygen consumption is given by

$$-d[O_2]/dt = R_i k_p [RH] / n k_{inh} [inh]$$

where n represents the number of chains stopped by each inhibitor molecule and $[inh]$ is the inhibitor concentration. In this case the rate of oxygen consumption varies as R_i or $[ROOH]$ if the initiation is primarily the unimolecular dissociation of ROOH. The concentration, $[ROOH]$, will be proportional to the oxygen consumed, and hence the behavior shown in Figure 11 is expected. Fodor et al.,^{21,22} for a series of fuels, have experimentally demonstrated that dissociation of hydroperoxide is the primary free-radical initiation step. The inhibited-oxidation explanation for Figure 11 would appear to be the more appropriate under the experimental test conditions due not only to the large amount of sulfur present in this fuel but also to the oxygen-consumption rates that are relatively lower than those for hydrotreated fuels which are low in sulfur. The latter point will be explained below. It is not clear at this time whether the absence of obvious autocatalytic effects at the higher temperatures is due to the absence of ROOH or the fact that the global rate is so fast that autocatalytic enhancement is negligible.

If it is assumed that the global oxygen loss obeys Arrhenius kinetics, i.e., $k = A \exp(-E/RT)$ where A is the preexponential factor, E is the Arrhenius activation energy, and T is the temperature in K, then a plot of $\ln k$ vs $1000/T$ will have a slope $-E/R$ and an intercept A . Rates were determined from the initial oxygen consumption where autocatalytic effects are minimal. The plot is shown in Figure 12. For comparison purposes similar data are shown for the hydrotreated fuel POSF-2747 which contains much less heteroatom impurities. Note that over the entire temperature range, the POSF-2827 fuel reacts more slowly with oxygen than the hydrotreated fuel.

The Arrhenius parameters for oxygen loss in POSF-2827 fuel are $E = 35.8 \text{ kcal mol}^{-1}$ and $A = 3 \times 10^{11} \text{ mol L}^{-1} \text{ s}^{-1}$. Heneghan et al.⁸ have reported Arrhenius parameters for this fuel based on deconvoluting oxygen loss in a single dynamic experiment over a broad temperature range, assuming first-order loss of oxygen. The activation energies are in good agreement (compare $35.5 \text{ kcal mol}^{-1}$). More recently Heneghan et al.²³ have revised their calculations assuming zeroth-order oxygen loss; the revised values are 10^{15} ppm/s (i.e., $1.6 \times 10^{12} \text{ mol L}^{-1} \text{ s}^{-1}$ for A and $30.5 \text{ kcal mol}^{-1}$ for the activation energy). Oxygen loss in

(19) Jones, E. G.; Balster, W. J.; Kauffman, R. E. Unpublished results.

(20) Kendall, D. R.; Mills, J. S. *Ind. Eng. Chem. Prod. Res. Dev.* **1986**, 25, 360-366.

(21) Fodor, G. E.; Naegeli, D. W.; Kohl, K. B. *Energy Fuels* **1988**, 2, 729-734.

(22) Fodor, G. E.; Naegeli, D. W. *Prepr. Pap.—Am. Chem. Soc., Div. Fuel Chem.* **1990**, 35 (4), 1267-1276.

(16) Bateman, L.; Hughes, H.; Morris, A. L. *Discuss. Faraday Soc.* **1953**, 14, 190-199.

(17) Walling, C. *Free Radicals in Solution*; John Wiley and Sons, Inc.: New York, 1957.

(18) Scott, G. *Atmospheric Oxidation and Antioxidants*; Elsevier: New York, 1965.

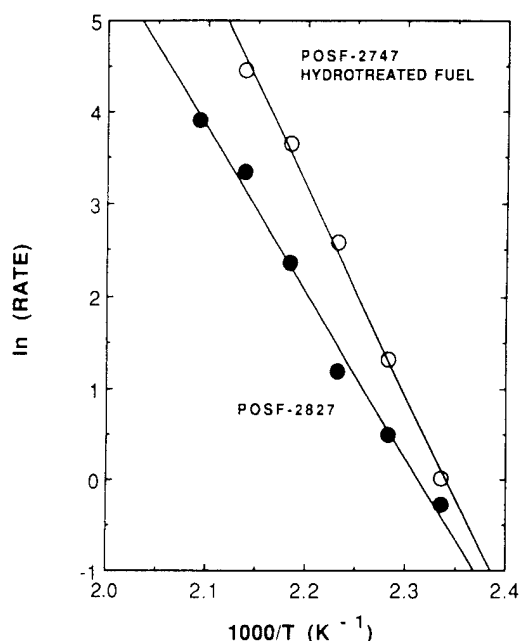


Figure 12. Arrhenius plot for oxygen consumption in aviation fuels POSF-2827 and POSF-2747 (hydrotreated). Rate in units of %/min.

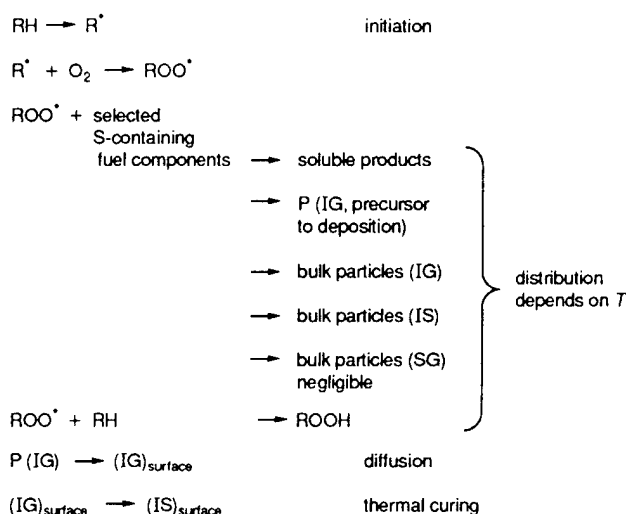
the comparison hydrotreated fuel, POSF-2747, is much faster over the temperature range studied and is given by $A = 2 \times 10^{16} \text{ mol L}^{-1} \text{ sec}^{-1}$ and $E = 45.2 \text{ kcal mol}^{-1}$ based upon the data in Figure 11.

In summary, the global oxygen loss is described by Arrhenius kinetics over the temperature range 155–205 °C. Fodor and co-workers^{21,22} have found that the global rate constant for ROOH formation which is pseudo-half-order in ROOH fits Arrhenius kinetics over the temperature range 43–120 °C in a series of fuels. Under conditions of oxygen-nonlimited kinetics, it is conceivable that the same autoxidation chemistry is dominant both in the storage stability regime and under the higher temperature conditions of the current study. Since the data are predicated on initial oxygen-consumption rates, the Arrhenius parameters are most appropriate for application under conditions of low oxygen conversion. In practice, particularly at the lower temperatures, autocatalytic effects at higher conversion can lead to much faster oxygen consumption. In fact, under autocatalytic conditions the POSF-2827 fuel can react with a rate that is comparable to that of the hydrotreated fuel POSF-2747. The profile for oxygen consumption, particularly at 185 °C, is very important in establishing the time distribution of ROO• which, in turn, determines the time distribution of insoluble formation. The stress-time-dependent deposition profile in Figure 3 is the manifestation of oxygen loss, subsequent chemistry to form P, and finally the diffusion of P to the walls. The initial product is assumed to be the family of peroxy radicals, ROO•. When only 2% of these lead to insolubles, it is important to focus on the deleterious reactions and to exclude, in some way, those reactions associated with the production of the less-troublesome soluble products.

Reaction Mechanism. In static tests with the same POSF-2827 fuel in this laboratory⁶ under fixed oxygen

concentration, it was found that bulk insolubles and surface deposits are formed with pseudo-zeroth-order kinetics, i.e., the rates are time independent. The primary conclusions from these observations were that IS, IG, and SG in the bulk²⁴ and also surface deposits follow along independent channels with no interconversions such as $\text{SG} \rightarrow \text{IG} \rightarrow \text{IS}$ and that measured bulk insolubles which increase linearly with time in the reaction flask do not contribute to the surface deposition, presumably because they do not adhere to surfaces. From static tests the existence of a specific surface-deposition precursor did not emerge; however, the introduction from the current dynamic tests of distinct adhering and nonadhering insolubles lends credence to the concept of independent reaction channels.

The inhibited nature of the oxidation is attributed to the presence of sulfur-containing compounds which deplete the peroxy-radical, ROO•, concentration and lead directly to insolubles. The following global mechanism is proposed to account for the current observations at 185 °C:



Conclusions

A sulfur-containing Jet-A fuel has been stressed isothermally at 185 °C in a single-pass heat exchanger. Quantification of the bulk and surface insolubles leads to the following conclusions:

Insoluble formation occurs during oxygen consumption.

At 185 °C deposition as a function of stress time yields a characteristic profile in 0.125-in. tubes. A similar time-delayed profile is observed in 0.25-in. tubes. Profiles are independent of flow rate.

Insolubles are no longer formed when dissolved oxygen is depleted.

Insolubles formed in the bulk fuel are IS and IG (SG are negligible).

IS do not adhere to tube walls and can be filtered (0.45 μm).

IG comprise a nonadhering fraction that can be filtered (0.45 μm) and also a surface-reacting or adhering fraction designated P, which can be filtered (0.45 μm).

When dissolved oxygen is totally consumed, 1 cm³ of fuel forms 1 μg IS, 1 μg IG, and 3 μg P, accounting for ~2% of the total oxygen dispersal.

(23) Heneghan, S. P.; Martel, C. R.; Williams, T. F.; Ballal, D. R. Effects of Oxygen and Additives on the Thermal Stability of Jet Fuels. ASME paper 93-GT-130, presented at the 38th International Gas Turbine and Aeroengine Congress and Exposition, Cincinnati, OH, May 24–27, 1993, accepted for publication in *Trans. ASME*.

(24) The definition of insolubility in static tests was based on Gelman A/E glass-fiber filters having a nominal pore size of 1 μm. The efficiency with which precursors identified in the current study would have been collected in static tests is expected to be low.

Surface deposits arise predominantly from a precursor, P, which is formed in the bulk fuel and which diffuses to the tube walls. At 185 °C, P either adheres to or reacts with the surface.

P does not cause deposition on stainless-steel surfaces at 30 °C.

Exposure of metal surfaces to POSF-2827 fuel produces surface insolubles that appear to be time and temperature independent. Their contribution is less than that of the oxygen-related deposits; however, it is not negligible.

Surface deposits originate as P, an IG, but ultimately are detected as IS. It is postulated that IG on the surface cure to IS during the 6-h experiment.

The initial rates of oxygen loss obey Arrhenius kinetics.

Significant autocatalysis occurs at 185 and 175 °C.

The inhibition (compared to a hydrotreated fuel) of oxygen loss is attributed to sulfur-containing fuel components which consume peroxy radicals.

A mechanism has been proposed to account for the oxygen-dependent processes. Current areas of investigation with POSF-2827 aviation fuel include the effect of stress temperature and additives on insoluble formation.

Acknowledgment. This work was supported by Wright Laboratory, Aero Propulsion and Power Directorate, Wright-Patterson Air Force Base, OH, under USAF Contract No. F33615-90-C-2033. The authors would like to thank Mr. Tim Gootee for performing the surface-carbon analyses and Mrs. M. Whitaker and Mr. M. L. Post for helpful comments. The authors acknowledge valuable discussions with University of Dayton personnel T. F. Williams and C. R. Martel concerning the heat-exchanger construction and with W. A. Rubey and R. C. Striebig concerning oxygen analysis.

Symposium on Distillate Fuel Auto-Oxidation Chemistry
Presented before the Division of Petroleum Chemistry, Inc.
207th National Meeting, American Chemical Society
San Diego, CA, March 13-18, 1994

Kinetics and Modeling for Jet-Fuel Autoxidation

E. Grant Jones, Walter J. Balster, Monica R. Vonada and James M. Pickard
Systems Research Laboratories, Inc.
A Division of Calspan Corporation
2800 Indian Ripple Road
Dayton, OH 45440-3696

INTRODUCTION

Engine fouling arising from fuel autoxidation is a primary factor in decreased aircraft-engine performance. Knowledge of jet-fuel oxidation and stability is essential in the design of antioxidant and/or inhibitor systems which minimize surface deposition within engine components. Typical jet fuels are known to contain large concentrations of saturated and aromatic hydrocarbons and—to a lesser extent—heteroaromatic, sulphur, and phenolic compounds (1). The phenolic and sulphur compounds, in some instances, can act as natural antioxidants and/or inhibitors (2). Unfortunately, these compounds may also play a fundamental role in deposit formation which leads to fouling and decreased engine performance (3).

In the last decade, single-pass heat exchangers have been used to study deposit formation and the phenomenological kinetics of oxygen depletion of various fuels (3). The advantage of these types of experiments is that real-life conditions may be simulated in a laboratory setting. Recently a study was undertaken to measure the initiation kinetics for a commercial jet fuel using added initiators and the single-pass heat-exchanger technique. The fuel studied, PSOF-2827, was chosen because previous research (3) has shown it to be an excellent candidate for surface deposition. Rate parameters derived from these efforts were used in numerical kinetic modeling for the overall depletion of dissolved oxygen in the fuel.

EXPERIMENTAL

The fuel employed had a breakpoint of 539°K from the Jet-Fuel Thermal-Oxidation Test (JFTOT) and a total sulphur content of 0.079%. Azobis(2,2'-cyanopropionitrile, AIBN, from Fisher Scientific was used without additional purification as an external initiator. Rate data were obtained using the single-pass heat-exchanger technique modified for oxygen measurements by employing an in-line Hewlett-Packard gas chromatograph according to procedures previously described (3, 4). Rate data were collected in the range 383-403°K, and the [AIBN] was varied from 5×10^{-5} to 5×10^{-4} M. Blank experiments conducted for neat fuel without added initiator indicated that the self-initiation rate was negli-

gible in the temperature range 383-403°K.

Rates of reaction for oxygen (percent min⁻¹) were calculated from the oxygen loss and stress time from data obtained in the initial stages of reaction (< 20% O₂ depletion). Rates were converted to absolute concentration units of moles per liter based on 65-ppm oxygen for air-saturation (3) and a fuel-specific gravity of 0.8072.

RESULTS

Representative curves for oxygen depletion in the range 383-403°K initiated with [AIBN] = 1×10^{-4} M are illustrated in Figure 1. The fact that PSOF-2827 contains natural antioxidants and/or inhibitors suggests that the global-oxygen depletion may be described by a retardation/inhibition mechanism. For retardation the steady-state assumption for chain carriers may be expressed as $R_i = \xi k_x[XH][RO_2] + 2k_t[RO_2]^2$, where R_i is the initiation rate, k_x and $2k_t$ are rate constants for inhibition and termination, [XH] is the inhibitor concentration, ξ is the number of radicals removed by one inhibitor molecule, and [RO₂] is the concentration of peroxy radicals (5). This expression may be combined with $-d[O_2]/dt = k_p[RH][RO_2]$, where k_p is the rate constant for propagation and [RH] is hydrocarbon concentration, to obtain

$$- \frac{d[O_2]}{dt} = \frac{2k_p R_i [RH]}{\xi k_x [RH] + (\xi^2 k_x^2 [XH]^2 + 8k_t R_i)^{1/2}} \quad (1)$$

From the assumption that $\xi k_x [XH] \ll 8k_t R_i$, Equation 1 simplifies to

$$- \frac{d[O_2]}{dt} = k_p \left(\frac{R_i}{2k_t} \right)^{1/2} [RH] \quad (2)$$

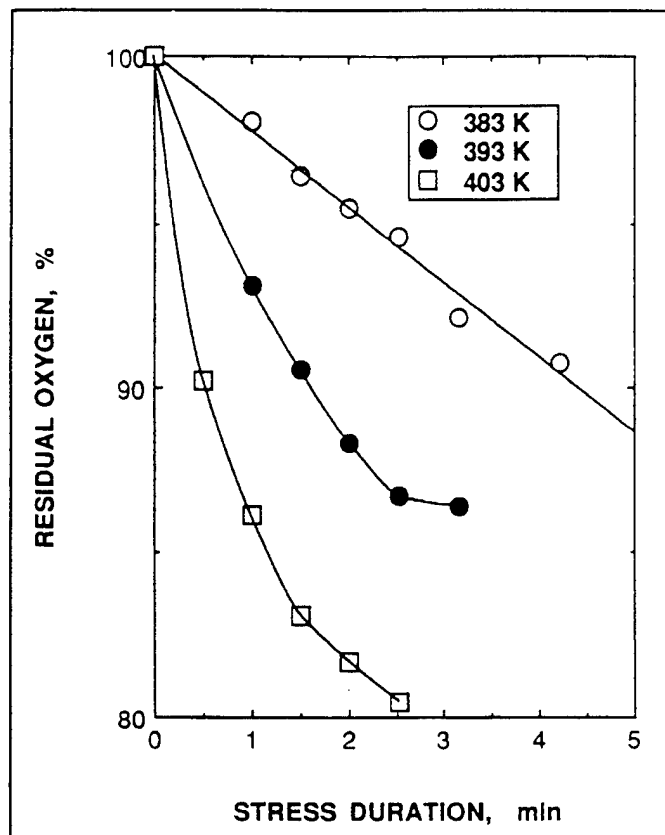


Figure 1. Variation of residual oxygen with stress time for $[I] = 1 \times 10^{-4} M$ (each data point is the average of four observations).

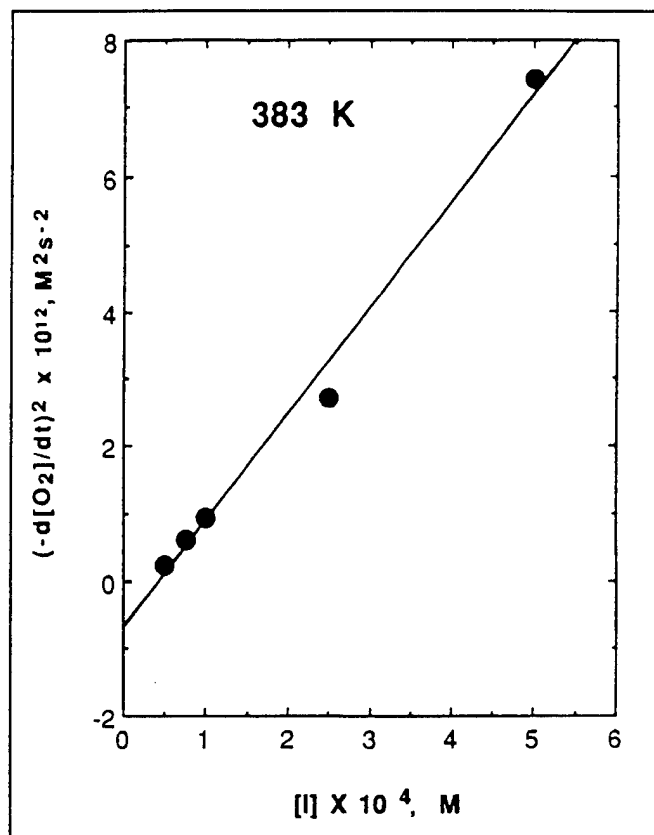


Figure 2. Rate plot of oxygen depletion.

Equation 2 is equivalent to the usual steady-state expression for a chain oxidation mechanism involving second-order termination (6). The steady-state assumption for chain carriers, $R_i = \xi k_x [XH][RO_2] + 2k_t [RO_2]^2$, may also be combined with $-d[O_2]/dt = k_p [RH][RO_2]$ and $R_i = 2ek_d [I]$ to obtain

$$\left(\frac{d[O_2]}{dt} \right)^2 = \frac{2ek_d k_p^2 [I]}{(2k_t)} - \xi k_x (k_p^2 / 2k_t) [XH][RO_2] \quad (3)$$

where k_d is the rate constant for initiator dissociation, $[I]$ is the initiator concentration, and e is the efficiency. Equation 3 should be a linear function of $[I]$, with a slope of $2ek_d k_p^2 / (2k_t)$ and an intercept of $-\xi k_x (k_p^2 / 2k_t) [XH][RO_2]$. A plot of Equation 3 illustrated in Figure 2 for a ten-fold variation in AIBN with $\log(k_d / s^{-1}) = 15.2 - 30.8/\theta$ (7), where $\theta = 2.303RT$ kcal mol^{-1} (R is the ideal gas constant and T is absolute temperature), indicates that the reaction is first-order with respect to AIBN (8). The ratio $k_p / (2k_t)^{1/2}$ was evaluated from

Table 1.
Reactions and Rate Parameters^a for Jet-Fuel Oxidation

No.	Reaction	Log(A)	E	Reference
1	$I = 2R$	11.9	34.3	This work
2	$RO_2H = RO + OH$	14.0	43.0	10
3	$R + O_2 = RO_2$	9.5	0.0	10
4	$A + O_2 = AO_2$	8.3	9.5	Est
5	$RO_2 + RH = RO_2H + R$	8.5	14.0	10
6	$RO_2 + XH = RO_2H + X$	10.6	10.8	This work
7	$XO_2 + RH = XO_2H + R$	8.5	14.0	Est
8	$XO_2 + XH = XO_2H + X$	8.5	14.0	Est
9	$RO + RH = ROH + R$	9.5	10.0	11
10	$RO = R' + H_2CO$	16.0	15.0	11
11	$OH + RH = H_2O + R$	9.5	10.0	11
12	$R' + RH = R'H + R$	9.5	10.0	11
13	$RO_2 = R + O_2$	14.0	28.0	10
14	$2RO_2 = R_2O_4$	8.7	0.0	12
15	$2XO_2 = X_2O_4$	9.5	9.7	Est
16	$R_2O_4 = R_2O_{4c}$	16.5	17.0	12
17	$R_2O_{4c} = 2RO + O_2$	11.5	0.0	Est
18	$R_2O_{4c} = RO_2R + O_2$	11.5	0.0	Est
19	$2R = R_2$	9.5	0.0	11
20	$2X = X_2$	8.3	9.5	Est
21	$2RO = RO_2R$	9.5	0.0	11

^aUnits of E are kcal mol^{-1} ; units of A are $M^{-1}s^{-1}$ for second-order reactions.

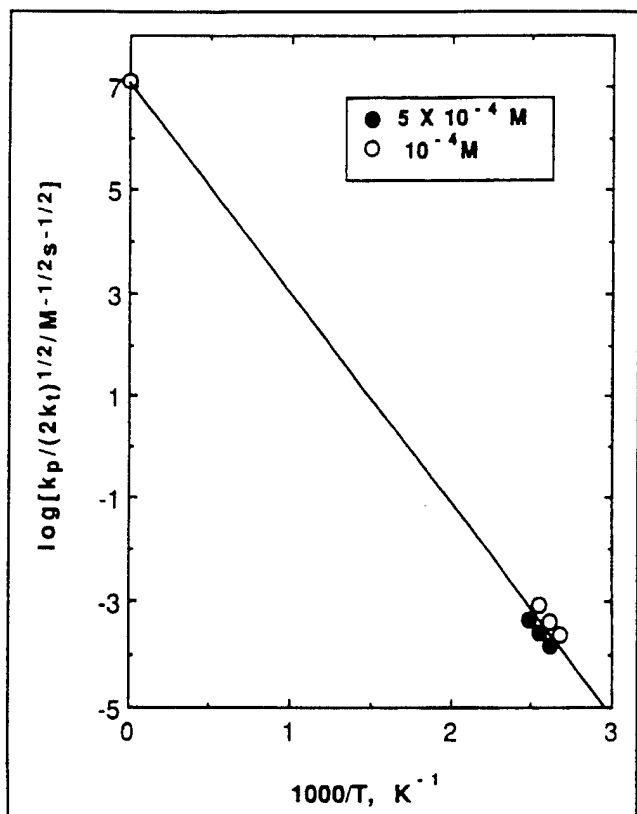


Figure 3. Arrhenius plot for $k_p/(2k_t)^{1/2}$ from 383 to 403 K (intercept is bracketed by experimental values).

Equation 2 for data such as that given in Figure 1, assuming $e = 0.6$ and $\xi = 1$. The concentration of [RH] was estimated to be 4.38 from the fuel-specific gravity and an average hydrocarbon chain length of 13. An Arrhenius plot of $k_p/(2k_t)^{1/2}$ is illustrated in Figure 3 (the intercept is bracketed by the experimental values obtained for each AIBN concentration). Statistical analysis of the data resulted in

$$\log \left[\frac{k_p}{(2k_t)^{1/2}} / M^{-1/2} s^{-1/2} \right] = 7.08 \pm 0.27 - \frac{(18.6 \pm 0.5)}{\theta} \quad (4)$$

where the error estimates for $A_p/(2A_t)^{1/2}$ and $(E_p - E_t/2)$ correspond to one standard deviation. Jones and Balster (3) have determined that the self-initiated reaction of PSOF-2827 over the temperature range 428–478°K may be expressed as $\log(-d[O_2]/dt/Ms^{-1}) = 11.33 - 35.8/\theta$. The data reported by Jones and Balster (3) were used with Equations 2 and 4 and [RH] = 4.38 M in order to calculate the rate for initiation. Such an approach led to

A stiff differential equation solver coded by Ebert, Ederer, and Isenhour (9) was used to solve the initial value problem for oxygen depletion from air-saturated fuel over the temperature range 428–478°K (3). Oxygen depletion was based on the series of reactions and rate parameters summarized in Table 1. In Table 1, RO_2H and XO_2H are hydroperox-

ides, RO_2R and XO_2R are peroxides, R_2O_4 is a tetroxide, and R, RO, and X are radicals. The subscript c in reactions 16–18 represents a solvent cage.

Rate constants for initiation and inhibition (reactions 1 and 6) were evaluated from the experimental data reported in the Results section of this paper and the reasonable assumptions that $[I] = 1 \times 10^{-5}$ M and $[XH] = 2.5 \times 10^{-4}$ M. Rate constants for reactions 2, 3, and 13 were assigned values selected by Benson (10). Rate

$$\log(R_i/Ms^{-1}) = (7.22 \pm 0.27) - \frac{(34.3 \pm 0.5)}{\theta} \quad (5)$$

for the spontaneous initiation rate of PSOF-2827. From Figure 2 $(-d[O_2]/dt)^2$ is zero for $[AIBN] = 5 \times 10^{-5}$, and Equation 3 may be simplified to $(2k_t R_i)^{1/2} = \xi k_x [XH]$ for $[RO_2] \cong (R_i/(2k_t)^{1/2})$. This approximation resulted in

$$\log(k_x [XH]/s^{-1}) = (7.02 \pm 0.5) - \frac{(10.8 \pm 1)}{\theta} \quad (6)$$

where the error estimates represent one standard deviation.

KINETIC MODELING

parameters for reaction 20 were equated to those for reaction 4; parameters for reactions 7 and 8 were equated to those for reaction 5. Reaction 4 would be expected to be equivalent to a radical recombination; however, it was necessary either to adjust $\log(k_4/M^{-1} s^{-1})$ well below the diffusion limit of 9.5 (10) or to assign a finite activation energy in order to achieve reasonable results for oxygen depletion. Reactions 9–12, 19, and 21 were based on the assign-

ments of Zabarnick (11); reactions 14 and 16–18 for cage termination were taken from and/or estimated from kinetic and thermochemical data of Ingold et al. (12).

An initial sensitivity analysis revealed that the calculated oxygen depletion was not strongly dependent upon rate parameters for reactions 8, 10, 12, 13, and 15–21; all subsequent integrations were based solely on ten parameters describing reactions 1–7, 9, 11, and 14. Figures 4(a) and 4(b) illustrate the agreement between the observed and calculated oxygen depletion over the range of 428–478°K for the data reported by Jones and Balster (3).

DISCUSSION

Figures 4(a) and 4(b) reveal that the calculated oxygen depletion is in reasonable agreement with the experimental results. The largest deviations between the calculated and observed data occur at 468 and 478°K; errors in this temperature regime may be the result of non-isothermal conditions associated with the experimental measurements (3). Calculated oxygen depletion was based on two fundamental assumptions. First, chain termination was assumed to be dominated by a second-order reaction. For this case, the inhibitor acts as

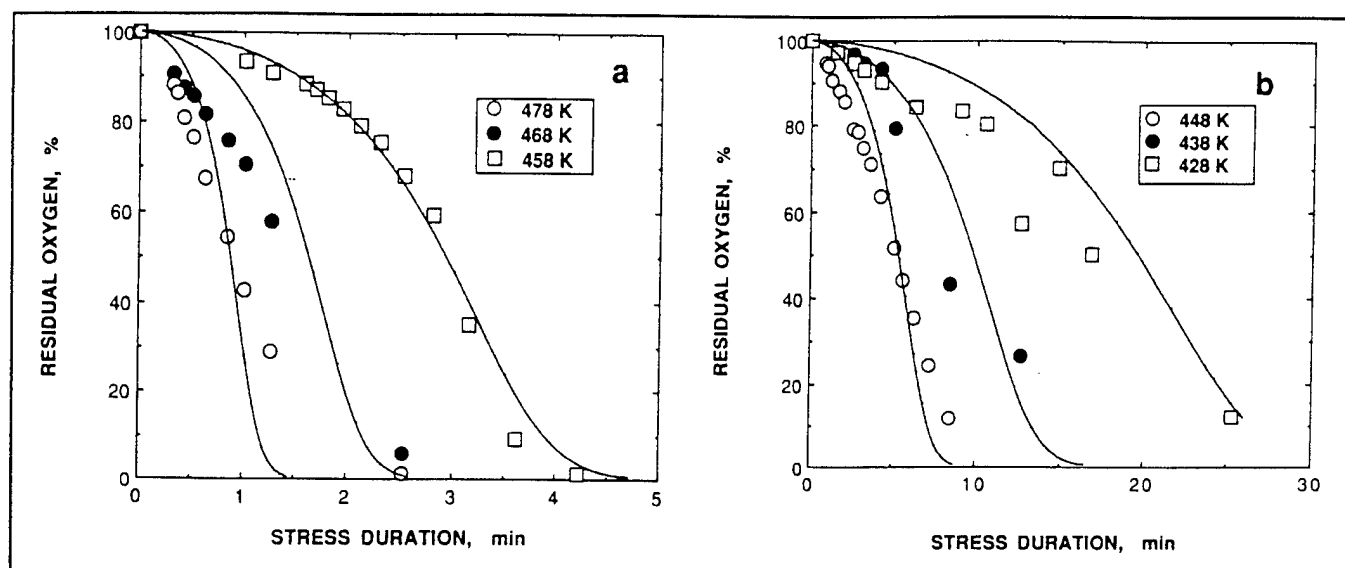


Figure 4. Comparison of calculated and observed residual oxygen versus stress duration. Solid line is calculated data.

a retarder. The data could also be analyzed as an inhibition mechanism according to Equation 1 for $k_x[XH] \gg 8k_tR_i$. Both models provided reasonable fits to the observed data; however, the inhibition mechanism suffers from large errors in the ratio $k_p/(k_x[XH])$ which overestimates R_i . In contrast, the retardation model implies a negative temperature dependence for the overall second-order termination rate constant, $2k_t$. A negative activation energy for second-order termination is consistent with thermochemical calculations but contrary to experimental observation (13), at least for the case of pure hydrocarbons. Secondly, $\log(A_i/s^{-1}) = 11.9$ was calculated on the basis of a homogeneous unimolecular reaction from the data of Jones and Balster (3) for $[I] = 1 \times 10^{-5}$ M. Although the assigned A factor is low in view of expectations from gas-phase kinetics (a low A factor may be indicative of surface initiation), reported kinetics for several hydroperoxide decompositions in solution exhibit $\log(A/s^{-1})$ in the range 10 to 13 (14).

ACKNOWLEDGMENTS

This work was sponsored by Wright Laboratory, Aero Propulsion and Power Directorate, Wright-Patterson Air Force Base, OH, under USAF Contract No. F33615-90-C-2033.

LITERATURE CITED

- (1) Kendall, D. R. and Mills, J. S., *Ind. Eng. Chem. Prod. Res. Dev.*, **25**, 360 (1986).
- (2) Jones, E. G., Balster, W. J. and Anderson, S. D., *PREPRINTS, Div. of Petrol. Chem., ACS*, **37**(2), 393 (1992).
- (3) Jones, E. G. and Balster, W. J., *Phenomenological Study of the Formation of Insolubles in a Jet-A Fuel*, *Energy Fuels*, To appear in November/December 1993 issue.
- (4) Rubey, W. A., Tissandier, M. D., Striebich, R. C. and Tirey, D. A., *PREPRINTS, Div. of Petrol. Chem., ACS*, **37**(2), 371 (1992).
- (5) Koelewijn, P. and Berger, H., *Recl. Trav. Chim. Pays-Bas*, **91**, 1275 (1972).
- (6) Howard, J. A., *Free Radicals Volume II* (Kochi, J. K., Ed.), John Wiley and Sons, New York, p. 4 (1973).
- (7) Strausz, O. P., Lown, J. W. and Gunning, H. E., *Comprehensive Chemical Kinetics Volume 5* (Bamford, C. H. and Tipper, C. H. F., Eds.) Elsevier, Amsterdam, p. 580 (1972).
- (8) A conventional order plot of $\log(-d[O_2]/dt)$ versus $\log[I]$ implies a reaction order of 0.7, consistent with implications of Equation 1 that retardation involves both first- and second-order termination.
- (9) Ebert, K., Ederer, H. and Isenhour, H. M., *Computer Applications in Chemistry*, VCH, New York, pp. 510-522 (1989).
- (10) Benson, S. W., *J. Am. Chem. Soc.*, **87**(5), 972 (1965).
- (11) Zabarnick, S., *Ind. Eng. Chem. Res.*, In press.
- (12) Adamic, K., Howard, J. A. and Ingold, K. U., *Can. J. Chem.*, **47**, 3804 (1969).
- (13) Bowman, D. F., Gillan, T. and Ingold, K. U., *J. Am. Chem. Soc.*, **93**, 6555 (1971).
- (14) Richardson, W. H. and O'Neal, H. E., *Comprehensive Chemical Kinetics Volume 5* (Bamford, C. H. and Tipper, C. H. F., Eds.), Elsevier, Amsterdam, p. 545 (1972).

Symposium on Distillate Fuel Auto-Oxidation Chemistry
Presented before the Division of Petroleum Chemistry, Inc.
207th National Meeting, American Chemical Society
San Diego, CA, March 13-18, 1994

Formation of Insolubles in a Jet-A Fuel: Temperature Effects

*E. Grant Jones and Walter J. Balster
Systems Research Laboratories, Inc.
A Division of Calspan Corporation
2800 Indian Ripple Road
Dayton, OH 45440-3696*

INTRODUCTION

High-performance aircraft rely heavily upon cooling provided by the aviation fuel. Projected improvements in aircraft performance will necessitate fuels that can withstand severe thermo-oxidative stress (1). Such conditions cause the formation of insolubles which can result in severe surface fouling, leading to inefficient heat transfer, and subsequent failure in heat exchangers as well as plugging of nozzles. The problem is caused mainly by dissolved oxygen in autoxidation reactions, aggravated by the presence of heteroatoms such as sulfur and nitrogen (2).

One criterion used to assess the thermo-oxidative stability of aviation fuels is the amount of surface and bulk insolubles formed during extended stress at elevated temperatures. As part of a broad program to study the behavior of aviation fuels, these insolubles have been quantified under near-isothermal conditions over a stress interval sufficient for complete dissipation of dissolved oxygen. Reported recently (3, 4) were the results of a detailed study conducted in this laboratory at 185°C using a single-pass heat exchanger for one fuel, designated POSF-2827, which meets USAF specifications and has served as a baseline. This fuel is amenable to study because of its propensity for fouling heated surfaces (5, 6). Surface deposition at 185°C has been found (3, 4) to be tightly coupled to oxygen consumption and to originate as the bulk insoluble designated a surface-deposition precursor, P.

Other bulk insolubles do not lead to surface fouling. One milliliter of fuel stressed to complete oxygen conversion at 185°C produces 5 µg of insolubles, partitioned as 3 µg of surface deposits and 2 µg of bulk particles.

In attempts to gain detailed knowledge of fuel behavior under diverse temperature conditions, very similar tests were conducted in which the reaction temperature ranged from 155 to 225°C; the results are reported herein. The goal of this study was twofold: 1) to determine systematic temperature trends in surface and bulk fuel fouling within the autoxidation-chemistry regime, and 2) to provide a quantitative baseline for a representative Jet-A fuel with which to evaluate the effectiveness of additives. For normalization purposes the fuel was initially saturated with respect to air at room temperature and then stressed at elevated temperature

to 100% oxygen conversion and also completion of surface-deposition processes.

EXPERIMENTAL

The instrument and experimental techniques have been described previously (4) and will be reviewed here only briefly. The aviation fuel POSF-2827 was used as received, with measured inherent insolubles being 0.08 µg/mL and sulfur being 0.079% (w). Fuel was passed from a syringe pump through 0.125-in.-od., 0.085-in.-id. commercial stainless-steel (304) tubing that was tightly clamped within the heated copper block of the Near-Isothermal Flowing Test Rig (NIFTR) shown in Figure 1. Pressure was maintained near 350 psi to ensure a single liquid-fuel phase. Surface insolubles were collected over a 6-hr experiment test time on the 32-in. heated tube, and bulk insolubles were collected on in-line 0.45-µm Ag-membrane filters. For each temperature a flow rate was chosen that would stress the fuel for a sufficient time to allow completion of surface-deposition processes within the heated tube. Dissolved oxygen was totally consumed, based upon either direct measurement in separate experiments or calculation from Arrhenius parameters (4). Oxygen was measured at the end of the tube for a series of residence times; data are expressed as residual oxygen, with 100% corresponding to saturation with respect to air at room temperature. Recently improved detector stability has allowed the determination of more accurate oxygen-loss profiles at the lower temperatures, particularly at higher oxygen conversion.

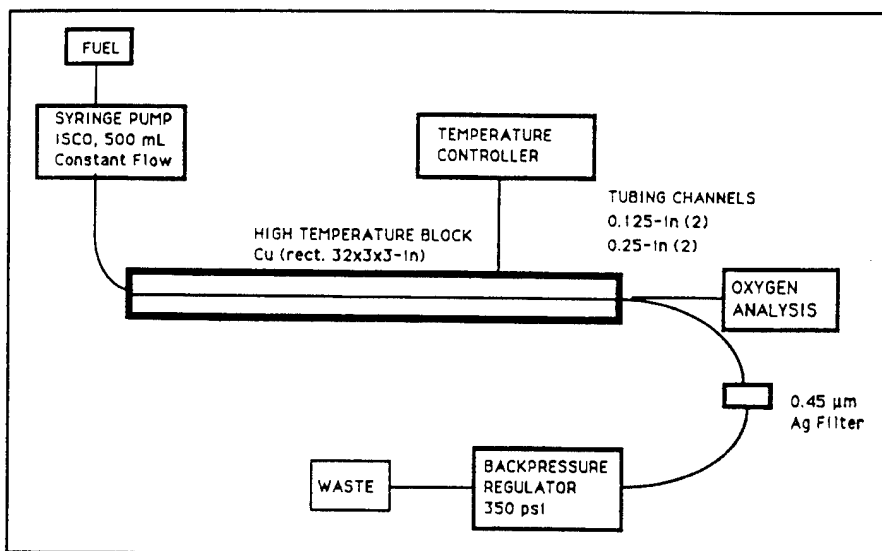


Figure 1. Diagram of Near-Isothermal Flowing Test Rig (NIFTR).

In the deposition experiments, segments of the tube walls are exposed to fuel which has been stressed for varying periods of time. For any distance along the tube, fuel stress time can be calculated from the flow rate and tube dimensions. The surface carbon deposition rate obtained under near-isothermal conditions has been shown to be independent of the flow rate when expressed as a function of fuel stress time rather than distance (3, 4). Surface deposits were quantified for sixteen 2-in. sections cut from the heated tube. Each section was rinsed with heptane, dried for 12 hr in a vacuum oven (115°C), and analyzed using a LECO RC-412 surface-carbon analyzer. Results are expressed as carbon-deposition rates (6-hr time averaged) versus fuel stress duration.

Bulk insolubles on the filters were quantified after heptane rinse and vacuum drying in the same manner as surface deposits on the tube sections.

RESULTS AND DISCUSSION

Measured deposition rates and dissolved oxygen are plotted in Figure 2. At 215 and 225°C the oxygen reaction was too rapid to be directly measured accurately and was calculated from Arrhenius parameters that

were determined from initial reaction rates (4). The fuel flow rate ranged from 1.5 mL/min (225°C) down to 0.07 mL/min (155°C) for the deposition experiments. Results over the entire temperature range indicate a tight coupling between oxygen consumption and deposition. The rate of deposition increases, passes through a maximum, and returns to baseline centered near complete oxygen loss. Background carbon not associated with autoxidation reactions was not subtracted, and this accounts for the baseline rate of 10 - 20 μg/hr per milliliter of fuel. The corrected maxima

in deposition rate range from 15 to 50 μg/hr per milliliter of fuel. This is a small dynamic range considering the temperature variation.

Autocatalysis, reported initially at 185°C (3), is most apparent at the lower temperatures, as evidenced by sigmoid profiles for the oxygen loss. The effect is an increased rate of oxygen consumption at higher conversion. It has been shown at 185 and 175°C that this increase in rate is proportional to the total oxygen consumed (4).

It is assumed that the concept of a bulk-formed surface-deposition precursor prevails over the temperature range studied, and the extended stress time permits differentiation between P and the non-adhering bulk particles by allowing all oxygen to be consumed and all P to diffuse to the walls. Thus, the distribution of insolubles into surface and filtered fractions represents the partitioning between the adhering component, P, and other non-adhering bulk particles. At each temperature bulk insolubles were quantified from the filters and P, or surface carbon, was determined from the integrated total carbon on the tube less the baseline contribution; the results are given in

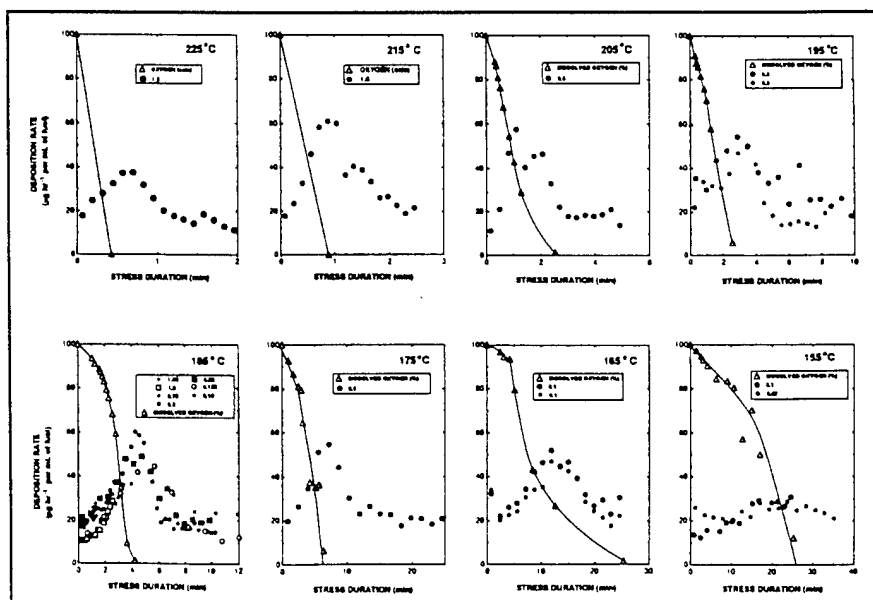


Figure 2. Plots of deposition rates and dissolved oxygen as a function of stress duration. Legend shows fuel flow rate. Data at 185°C previously published in Reference 4.

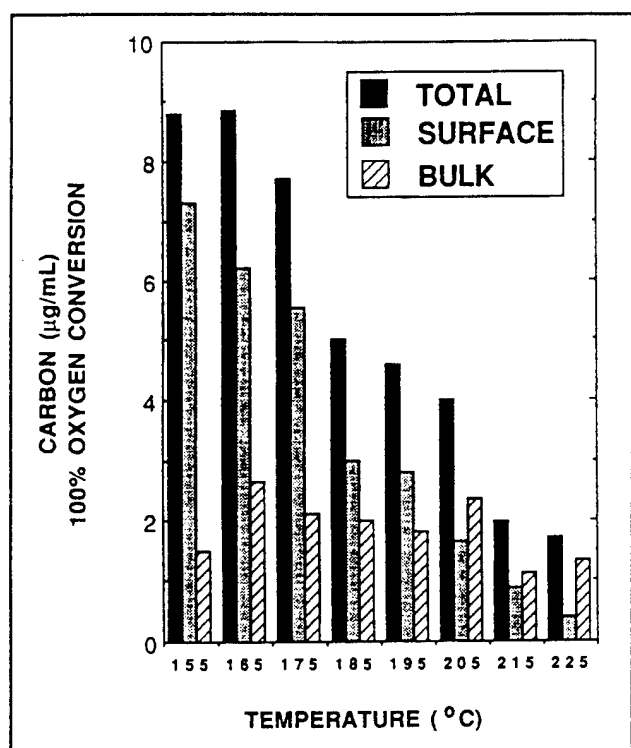


Figure 3. Histogram showing efficiency of converting dissolved oxygen into insolubles.

Figure 3. Since the quantity of oxygen consumed is the same for all temperatures, Figure 3 can be viewed as the temperature-dependent efficiency of converting oxygen into insolubles for POSF-2827 aviation fuel. As the reaction temperature is lowered, a steady increase in total carbon is displayed, clearly as a result of the surface component. The filtered amount, on the other hand, is relatively constant with temperature.

Through quantification of insolubles as a function of temperature, as shown in Figure 3, the primary goals of this study are achieved. The obvious question arises as to why the efficiency of converting oxygen into surface insolubles increases at low temperature. One possible explanation is that reaction channels leading to soluble products may, for thermodynamic reasons, become less important at lower temperature. Since insolubles account only for about 2% of the reacted oxygen at 185°C (4), any reduction in the soluble-reaction channels that causes an equivalent increase in the insolubles may have a significant impact. For example, a

10% reduction may lead to a five-fold increase in insolubles. Other possible explanations would involve temperature-related dissociation or solvation of P.

From Figure 2 it is apparent that the full-width-half-maximum time, t_{FWHM} , of the deposition profiles decreases with increasing temperature. The reciprocal of t_{FWHM} is a measure of the rate of oxygen consumption, reflecting an average over complete oxygen conversion. For example, the Arrhenius activation energies determined

using rates obtained from the reciprocal of t_{FWHM} or from a linear fit through the oxygen-loss profile are the same (7). The extent of oxygen conversion determines whether the Arrhenius parameters that describe the initial rates or those that describe global average rates are more appropriate.

The surface data in Figure 3 provide the efficiency of converting oxygen into surface deposits at each temperature. If this efficiency is defined as Ω , then at each temperature, $\Omega = (dS/dt)_{max} \times t_{FWHM}$, where $(dS/dt)_{max}$ is the observed maximum in the deposition rate. Replacing $1/t_{FWHM}$ by the average rate of oxygen loss, $-(dO_2/dt)_{ave}$, the deposition rate can be given by the relation

$$\left(\frac{dS}{dt}\right)_{max} = -\Omega \left(\frac{dO_2}{dt}\right)_{ave} \quad 1)$$

where the units of $(dS/dt)_{max}$, Ω , and $(dO_2/dt)_{ave}$ are $\mu\text{g/mL}$ per unit time, $\mu\text{g/mL}$, and fraction per unit time, respectively. All three are functions

of temperature. In this simple representation, the deposition rate is equal to the rate of oxygen loss multiplied by the efficiency of converting oxygen into surface deposits.

It is clear from Equation 1 why the dynamic range in the deposition rate is small, despite the large temperature variation. At lower temperature the observed deposition rates are enhanced by 1) autocatalysis which tends preferentially to increase the rate of oxygen loss at low temperature, and 2) Ω which increases as the temperature decreases. Both factors apply under conditions of 100% oxygen conversion prevailing in the current study.

CONCLUSIONS

The Jet-A aviation fuel POSF-2827 is found to produce insolubles over the temperature interval 155 - 225°C. Good correlation is found between surface deposits and the consumption of dissolved oxygen. The current experiments were designed to separate P from the non-adhering bulk insolubles. The former is found to vary inversely with temperature, and the latter is approximately constant. A baseline for the neat fuel has been established for evaluation of the effectiveness of additives over the temperature range 155 - 225°C.

In aviation applications POSF-2827 fuel may be less desirable under conditions of extended stress at lower temperatures. Further research is needed to determine whether the findings in this study are specific to POSF-2827 or are representative of the behavior of a general class of aviation fuels.

ACKNOWLEDGMENTS

This work was supported by Wright Laboratory, Aero Propulsion and Power Directorate, Wright-Patterson Air Force Base, OH, under USAF Contract No. F33615-90-C-2033. The authors would like to thank Mr. Tim Gootee for completing the

surface-carbon analyses, Mrs. Marian Whitaker for editorial assistance, and Dr. James M. Pickard for valuable discussions.

LITERATURE CITED

- (1) Edwards, T., Anderson, S. D., Pearce, J. A. and Harrison, W. E., High Temperature Thermally Stable JP Fuels--An Overview, AIAA Paper No. 92-0683, Presented at the 30th Aerospace Sciences Meeting and Exhibit, January 6-9, 1992, Reno, NV.
- (2) Hazlett, R. N., Thermal Oxidation Stability of Aviation Turbine Fuels, ASTM Monograph 1, American Society for Testing and Materials, Philadelphia, PA (1991).
- (3) Jones, E. G., Balster, W. J. and Post, M. E., Degradation of a Jet-A Fuel in a Single-Pass Heat Exchanger, ASME Paper No. 93-GT-334, Presented at the 38th International Gas Turbine and Aeroengine Congress and Exposition, May 24-27, 1993, Cincinnati, OH. To be published in Trans. ASME.
- (4) Jones, E. G. and Balster, W. J., Phenomenological Study of the Formation of Insolubles in a Jet-A Fuel, Energy Fuels, To appear in November/December 1993 issue.
- (5) Heneghan, S. P., Martel, C. R., Williams, T. F. and Ballal, D. R., ASME Paper No. 92-GT-106, Presented at the 37th ASME International Gas Turbine and Aeroengine Congress and Exposition, June 1-4, 1992, Cologne, Germany. To be published in Trans. ASME.
- (6) Jones, E. G., Balster, W. J. and Anderson, S. D., PREPRINTS, Div. Petrol. Chem., ACS, 37(2), 393 (1992).
- (7) Jones, E. G. and Balster, W. J., In preparation.

COMPOSITION OF AVIATION-FUEL GUMS

E. G. Jones, J. M. Lavoie, Systems Research Labs, 2800 Indian Ripple Rd., Dayton, OH 5440-3696
S. H. Hoke, II, Department of Chemistry, Purdue University, W. Lafayette, IN 47907-1393

Aviation fuel serves as the primary heat sink in modern aircraft. During heat exchange, fuel containing dissolved oxygen can undergo a series of free-radical reactions classified as autoxidation. Fuels consist of a diverse mixture of hydrocarbons, a small fraction of which contain hetero-atoms such as S and N. These trace fuel components disrupt the free-radical chain reactions by 1) slowing the rate of oxygen consumption and 2) forming S- and N-rich insoluble gums and solids.¹ Some of these insolubles leave deposits on heated surfaces, leading to reduced aircraft performance, costly repairs, and possible system failure. Unfortunately, all projected future high-performance aircraft will require even greater heat dissipation. Recent studies with a S-containing Jet-A fuel designated POSF-2827 show deposition to originate as a surface-deposition precursor, P, which is an insoluble gum (insoluble in heptane, soluble in acetone) that forms during autoxidation in the bulk fuel, diffuses to the metal surface, and reads or cures, leaving an intractable solid on the surface.² This paper reports some results of the mass-spectral analysis of these gums.

Uncured gums formed at 185°C have been collected on Ag-membrane in-line filters in a heat-exchanger experiment [Near-Isothermal Flowing Test Rig (NIFTR)]. These gums have been analyzed using X-Ray Photoelectron Spectroscopy (XPS) and mass spectrometry. The latter includes vacuum TGMS, Desorption Electron Impact (DEI), and Desorption Chemical Ionization (DCI) tandem mass spectrometry (MS/MS). A Finnigan TSQ 700 was employed for the collision activation experiments. The goal was to identify the primary classes of products comprising the uncured gums.

XPS data show values of N (3.7%) and S (3.5%) that are typical of fuel insolubles. S is primarily present as SO₂ and is enhanced approximately 50-fold in the insolubles. TGMS experiments indicate a bimodal SO₂ release at 150 and 230°C, a complex mixture of products, and a residual char of ~ 50%. The dominant ion series (m/z 146, 160, 174, 188, ...) has the same temperature dependence as SO₂. Desorption EI (15-eV) and CI (NH₃) spectra are shown in Figs. 1 and 2, respectively. The ions m/z 162, 176, 190, 204, 218, and 232 in the CI spectrum are viewed as protonated molecular ions (M+1)⁺ of a composite homologous series of products. With this as a basis, the dominant series of EI ions, m/z 147, 161, 175, 189, 203, 217 and 231, is interpreted as M⁺ analogues of the same series, defined as Series A. The DEI spectrum reveals two lesser M⁺ series—namely, 157, 171, 185, 199, ... (Series B) and 121, 135, 149, ... (Series C)—which can also be seen as (M+1)⁺ analogues in the DCI spectrum.

The DEI spectrum using 70-eV ionization has very few abundant ions with m/z < 121. This coupled with the odd-mass M⁺ ions and the presence of N from XPS data indicates that the homologues are alkyl-substituted aromatic N compounds. The collisional spectrum from m/z 121 is very similar to that from the molecular ion of the model compound 2,4,6-trimethylpyridine, suggesting that Series C is composed of alkyl-substituted pyridines. Similarly, the collisional spectrum from m/z 157 (Series B) is very similar to that from the model compound 2,4-dimethylquinoline, indicating that Series B consists of alkyl-substituted quinolines. The collisional spectrum from m/z 147 (Series A) is similar to that from the model compound 5,6,7,8-tetrahydroquinoline, but other isomers such as 1,2,3,4-tetrahydroquinoline or isoquinoline analogues may be better candidates. The collisional spectra of (M+1)⁺ ions from Series A show primarily losses from the alkyl chains. All three of these identified classes of volatile products are known components in petroleum crude oils³ and coal liquids.⁴

In summary, the surface-deposition precursor in the form of an uncured gum degrades in vacuum to form char (curing) and the volatiles SO₂ and three homologous series of alkyl-substituted aromatic N species. Since all the identified aromatic volatiles are bases, it is conceivable that the surface-deposition precursor is a series of salts generated from intrinsic bases, as observed in the volatiles and S-containing acids (sulphenic, sulphonic, or sulphonic) that are formed during oxidative stressing of the fuel. Upon heating, such salts⁵ would release SO₂, free the volatile bases, and leave an intractable char consisting of cured less-volatile aromatics.

The authors would like to acknowledge the advice and cooperation of Professor R. G. Cooks. This work was supported, in part, by Wright Laboratory, Aero Propulsion and Power Directorate, Wright-Patterson Air Force Base, OH, under USAF Contract No. F33615-90-C-2033.

1. Hazlett, R. N., *Thermal Oxidation Stability of Aviation Turbine Fuels*, ASTM Monograph 1; American Society for Testing and Materials: Philadelphia, PA, 1991.
2. Jones, E. G. and Balster, W. J., *Energy Fuels*, 1993, 7, 968-977.
3. Lochte, H. L. and Littmann, E. R., *Petroleum Acids and Bases*, Chemical Publishing Co.: New York, 1956.
4. Wood, K. V., Schmidt, C. E., Cooks, R. G., and Batts, B. D., *Anal. Chem.*, 1984, 56, 1335-1337.
5. Jones, E. G. and Balster, W. J., "Application of a Sulphur-Doped Alkane System to the Study of Thermal Oxidation of Jet Fuel," ASME Paper 92-GT-122.

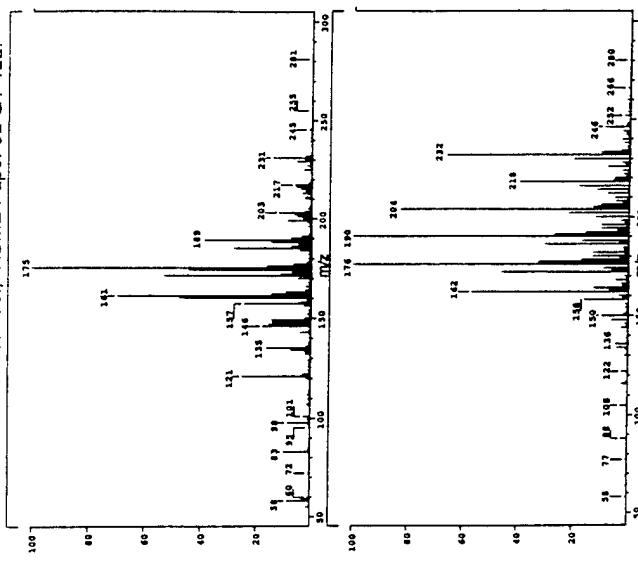


Fig. 1. Desorption EI Spectrum (15 eV)

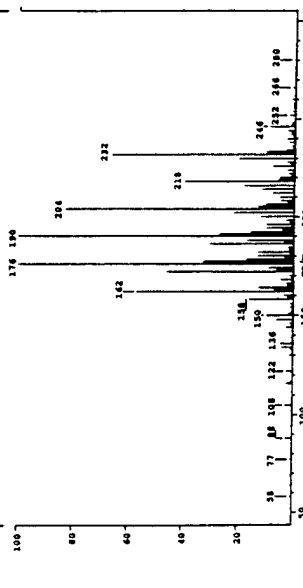


Fig. 2. Desorption CI Spectrum (NH₃)

SURFACE FOULING: SHORT- VS. LONG -TERM TESTS

E. Grant Jones and Walter J. Balster
Systems Research Laboratories, Inc.
A Division of Calspan Corporation
2800 Indian Ripple Road
Dayton, OH 45440-3696

Keywords: Autoxidation, Autocatalysis, Surface Fouling

INTRODUCTION

Problems associated with surface fouling of fuel lines, nozzles, and heat exchangers caused by thermo-oxidative stressing of aviation fuel have been documented.¹ With enhanced aircraft performance, heat loads from both the airframe and the engine that must be dissipated via the fuel become greater. The resultant additional fuel degradation exacerbates aircraft system failures. Since the extent of surface fouling depends strongly upon the particular aviation fuel, it is important to be able to assess each fuel in a simple accelerated laboratory test for simulating the thermo-oxidative stress experienced in aircraft fuel lines.

In the present study a simple dynamic test is employed, whereby the fuel is stressed under well-defined chemical-oxidation conditions that are near-isothermal. Quantification of surface and filtered insolubles provides an objective evaluation of fuel behavior at each temperature. In addition, the dependence of deposition rate upon stress duration provides a temporal profile of the reaction. The general laboratory goal is to evaluate fuel at several temperatures in an attempt to simulate thermo-oxidative stress but not the fluid-dynamic conditions in aircraft. These results can then be used to calibrate Computational-Fluid-Dynamics (CFD) models² for calculating fouling under the diverse temperature and fuel-flow conditions that are found within aircraft but are difficult to achieve experimentally with small-scale rigs.

The present investigation has involved fouling of heated stainless-steel surfaces caused by a particular Jet-A aviation fuel designated POSF-2827. Although this is a representative fuel that meets USAF specifications, it has a propensity for fouling heated surfaces at low temperatures, making it an ideal candidate for experimental study.³ Recent results were reported from this laboratory on surface deposition on stainless-steel surfaces as a function of stress duration for fuel flowing through a heat exchanger at 185°C under near-isothermal conditions.^{4,5} These results indicated that deposition arises from a bulk-formed species designated a surface-deposition precursor, P, and that deposition is complete within 10 min of stressing inside 0.125-in-o.d. stainless-steel tubing. Deposition over the temperature range 155-225°C was found to occur during a time interval that correlates with the measured time for oxygen consumption.^{6,7} The experimental test time in these prior experiments was set at 6 hr to ensure measurable deposits yet maintain surface fouling predominantly on the steel rather than on previously deposited surfaces.

The goal of the current study was to compare deposition in short-term (6-hr) tests with that in long-term tests where most of the deposition occurs on previously deposited surfaces. Results reported here show that the average surface fouling rates measured during extended test times differ from those measured during a 6-hr test. Since the bulk-fuel/wall temperature is held constant during the course of these experiments as a result of the low flow rate, deposits serve only to change the surface layer without influencing the bulk temperature of the fuel.

As the test time is extended, the deposition-rate-versus-stress-duration profile broadens, the maximum is reduced, and its location shifts to longer stress duration. These observations made at 155 and 185°C are shown to arise from a transition in the rate of oxygen loss as a result of surface fouling and a reduction in adherence to a fouled surface. The implications of these findings with respect to inherent surface fouling within aviation fuel systems are discussed.

EXPERIMENTAL

POSF-2827 fuel has a JFTOT breakpoint of 266°C and a sulfur level of 0.079% (w/w). This fuel falls into a category described by Kendall and Mills⁸ where the presence of sulfur compounds tends to inhibit oxidation but at the expense of increased insoluble formation.³

Data were collected using the Near-Isothermal Flowing Test Rig (NIFTR) which has been described previously.^{4,5} The advantage of the NIFTR experiment is the ability to measure deposition rates and dissolved oxygen as a function of reaction time at a fixed temperature. For each selected fuel-flow rate, the reaction time or stress duration is determined by tube dimensions and location along the tube axis. In the present experiment deposits were collected on 0.125-in.-o.d., 0.085-in.-i.d. commercial stainless-steel (304) tubing. The standard heated section was 32 in.; however, for test times longer than 6 hr, the spatial distribution of the deposition broadened and the complete profile could not be collected on a single pass through the heat exchanger. Three approaches were taken: 1) only the limited profile was collected on a single pass, 2) the fuel was passed back through a second tube within the NIFTR to double the path length, and 3) the fuel-flow rate was reduced to extend the stress duration accordingly within a single pass. It is important to distinguish stress duration from experimental test time in dynamic isothermal experiments. Stress duration is the reaction time at temperature, and the experimental test time (along with the fuel-flow rate) determines the total quantity of fuel passed through the system. The total fuel ranged from 25 to 1035 mL. Dissolved oxygen was measured in separate experiments using the entire tube as a reaction region, with stress time being varied by changing the fuel-flow rate.

Deposition rates at 185 and 155°C are based on the quantity of carbon in the deposits determined from surface-carbon burnoff (LECO RC-412) of 2-in. sections cut from the 32-in. heated tube. Rate is expressed in units of micrograms of carbon per unit volume of tube section per unit test time which is equivalent to micrograms of carbon per unit stress time within a tube section per unit volume of fuel passed through the system.⁵ In each case the fuel is saturated with respect to air, with oxygen being measured as 64 ppm (w/w).⁹

RESULTS AND DISCUSSION

Deposition. The measured deposition rate averaged for 6, 24, 30, 32, 48, and 69 hr is shown in Figure 1 as a function of stress duration at 185°C for a fixed fuel-flow rate of 0.25 mL/min. The following observations describe the changes in surface deposition with extension of integration time: 1) the profile broadens with significant tailing; 2) the maximum in the deposition rate is reduced; and 3) the center of the deposition peak shifts to slightly longer stress times. Also, the profiles appear to approach a common shape at the longest experimental times. Extended reaction time in the 30- and 69-hr experiments was afforded by a second pass through the heat exchanger. Results of similar experiments at 155°C are presented in Figure 2. The same trends are observed; however, the reaction time frame is extended to permit completion of the deposition processes at lower temperature.

Note that when comparing rates averaged over different experimental times, the baseline drops as the experimental time is increased. Background carbon which is independent of experimental test time has not been subtracted, and its impact is reduced in the longer-term averages.

The major difference between 6-hr tests and those of much longer duration is the nature of the surface. Initially the deposition occurs on cleaned stainless-steel tube surfaces. As the experimental time is extended, the surface gradually makes a transition to a completely carbonaceous-coated one. Deposition should be constant after complete coverage of the stainless-steel surfaces; for example, after the 48-hr test at 185°C, the surface density at the maximum is 90 $\mu\text{g cm}^{-2}$. The maximum deposition rate per unit area is 1.1 $\mu\text{g cm}^{-2}$ per hour of experiment. The observed variation in deposition is related to surface changes, and the major factor will be shown to be the rate of oxygen consumption.

Oxygen Loss. The residual dissolved oxygen for this fuel has been reported as a function of reaction time in stainless-steel tubes.⁵ Accelerated oxygen consumption observed at higher conversion was attributed to autocatalysis. Figure 3 shows the oxygen loss at 185°C measured using 1) a 32-in. cleaned stainless-steel tube,⁵ 2) a tube that previously had been coated with carbonaceous deposits containing 0.27 mg of carbon, and 3) a tube coated with the same deposits containing 1.5 mg of carbon. The initial rates are similar. Autocatalysis causes the rapid increase in rate at higher conversion in the cleaned tube; however, this appears to be a surface-related phenomenon that is no longer observed when the surface becomes coated with deposits. Rates measured with the coated tubes remain constant, indicating a predominantly zeroth-order or oxygen-non-limited reaction.⁴ After 8-9 min all of the oxygen is converted, and the source of the deposits (namely, P) can no longer be maintained. This

time corresponds to the location of the maximum in the shifted deposition profile at 185°C. Similarly, oxygen loss measured at 155°C (Figure 4) shows the same trend.

If the stainless-steel tubing is viewed as the norm, then deposits perturb the oxygen consumption by eliminating autocatalysis. If the coated (passivated) tubing is viewed as the norm--an alternative and preferable view--then the stainless steel perturbs the oxygen consumption by providing active catalytic sites which, at higher conversion, lead to an increased oxygen reaction rate. Deposition in short-term (6-hr) tests over the temperature range 155-225°C correlates with oxygen loss measured in cleaned stainless-steel tubes;⁶ similarly, deposition in long-term tests is expected to correlate with oxygen loss measured using tubes that have been passivated by deposits. The higher deposition rate observed in 6-hr experiments results from the oxygen loss that occurs during surface-induced autocatalysis. The reduction in surface deposition rate, the broadening of the deposition profile, and the shift in the maximum in the long-term experiments are manifestations of the slower, constant rate of oxygen loss.

The deposition profiles in long-term tests have tails that extend well beyond the region of 100% oxygen conversion. For example, at 185°C, despite complete oxygen depletion at 9 min, the deposition continues beyond 17 min. This is interpreted as reduced surface adherence of P.

Implications. Autocatalysis has been attributed to thermal dissociation of an oxidation product such as hydroperoxide.⁵ The present results indicate that autocatalytic effects in POSF-2827 fuel are caused by a surface-induced reaction of an oxidation product involving active sites on stainless steel. Carbonaceous deposits remove active sites, thereby eliminating autocatalysis.

Carbon-burnoff techniques generally require the use of cleaned surfaces for minimizing background. Based upon the current findings, when surface-induced autocatalysis occurs, the maximum deposition and the oxygen reaction rates will be faster in short-term experiments that are carried to high conversion. Fuel evaluation in this laboratory is predicated on accelerated short-term tests that stress the fuel to complete oxygen conversion. In rating fuels, a deposition-rate criterion has not been applied; instead a total integrated quantity of deposit, i.e. the area under the deposition profile in units of micrograms/milliliter, has been used.

Catalytic effects of metals dissolved in fuels, in particular, copper from copper tubing as in Naval applications, can reduce fuel thermal stability, even at low concentrations.¹ Kendall and Mills⁸ observed this effect in flask tests, and Morris and Turner¹⁰ observed it in expanded JFTOT experiments. Conceivably, the role of dissolved copper in catalyzing oxygen loss is analogous to the role of stainless-steel walls in what has been termed surface-induced autocatalysis.

Fuel-evaluation techniques such as the JFTOT and Hot Liquid Process Simulator (HLPS) which make use of clean aluminum and stainless-steel surfaces, respectively, would be expected to be sensitive to the nature of the surface and also the manner in which oxygen is consumed. For example, Clark et al.¹¹ have reported that a metal deactivator (MDA) functions optimally on clean metal surfaces; however, once a lacquer layer has formed, MDA does not reduce deposition. The vulnerability of JFTOT results in short-term tests has been discussed by Clark and Bishop.¹² The initial surface-passivation effects of MDA may mask problems detectable only during extended time periods. In view of the current results, the short-term benefit of MDA may be surface passivation which prevents autocatalysis. The reduced deposition would then be explained in terms of MDA slowing oxygen consumption rather than hindering adherence to the surface. In recent studies the DuPont fuel additive JFA-5 which contains the MDA, N,N'-disalicylidene-1,2-propanediamine, has been found to eliminate autocatalytic oxygen loss in POSF-2827 fuel.¹³

CONCLUSIONS

The dependence of the surface deposition rate of POSF-2827 fuel on isothermal stress duration at 155 and 185°C has been found to be a function of the experimental test time. In short-term (6-hr) tests, initial deposition is governed by the autocatalytic consumption of oxygen. For long-term (~ 70-hr) tests during which the initial stainless-steel surface becomes covered with deposits, the deposition profile changes to one governed by a slower loss of oxygen.

Oxygen loss in cleaned stainless-steel tubes is enhanced at high conversion as a result of surface-induced autocatalysis. After deposits have completely covered the stainless-steel surfaces, active sites necessary for autocatalysis are removed.

ACKNOWLEDGMENTS

This work was supported by Wright Laboratory, Aero Propulsion and Power Directorate, Wright-Patterson Air Force Base, Ohio, under USAF Contract No. F33615-90-C-2033. The authors would like to thank Mr. Tim Gootee for conducting the surface-carbon analyses, Mrs. Marian Whitaker for editorial assistance, and Dr. James M. Pickard for valuable discussions.

REFERENCES

1. Hazlett, R. N. *Thermal Oxidation Stability of Aviation Turbine Fuels*, ASTM Monograph 1; American Society for Testing and Materials: Philadelphia, 1991.
2. Katta, V. R., Jones, E. G. and Roquemore, W. M. "Development of Global-Chemistry Model for Jet-Fuel Thermal Stability Based on Observations from Static and Flowing Experiments," Paper No. PEP-19, Presented at the 81st AGARD Symposium on Fuels and Combustion Technology for Advanced Aircraft Engines, May 10-14, 1993, Colliferro, Italy.
3. Jones, E. G., Balster, W. J. and Anderson, S. D. *Prepr. - Am. Chem. Soc., Div. Petroleum Chem.* **1992**, 37(2), 393-402.
4. Jones, E. G., Balster, W. J. and Post, M. E. "Degradation of a Jet-A Fuel in a Single-Pass Heat Exchanger," ASME Paper No. 93-GT-334, Presented at the 38th International Gas Turbine and Aeroengine Congress and Exposition, May 24-27, 1993, Cincinnati, OH. To be published in *Trans. ASME*.
5. Jones, E. G. and Balster, W. J. *Energy Fuels* **1993**, 7, 968-977.
6. Jones, E. G. and Balster, W. J. *Prepr.-Am Chem. Soc., Div. Petroleum Chem.* **1994**, 39(1), 78-81.
7. Jones, E. G., Balster, W. J. and Pickard, J. M. "Effect of Temperature in the Formation of Jet-Fuel Insolubles," Submitted to *Energy Fuels*.
8. Kendall, D. R. and Mills, J. S. *I&EC Prod R&D* **1986**, 25, 360-366.
9. Striebich, R. C. and Rubey, W. A. *Prepr.-Am Chem. Soc., Div. Petroleum Chem.* **1994**, 39(1), 47-50.
10. Morris, R. E. and Turner, N. H. *Fuel Sci. Tech. Int.* **1990**, 8, 327.
11. Clark, R. H., Delargy, K. M. and Heins, R. J. *Prepr.-Am. Chem. Soc., Div. Fuel Chem.* **1990**, 35(4), 1223-1232.
12. Clark, R. H. and Bishop, G. H. "Measure of Fuel Thermal Stability - Which Answer is Correct?" *Aviation Fuel: Thermal Stability Requirements*. ASTM STP 1138, P. W. Kirklin and P. David, Eds.; American Society for Testing and Materials: Philadelphia, 1992.
13. Jones, E. G., Balster, W. J. and Goss, L. P. "Application of JFA-5 as an Anti-Fouling Additive in a Jet-A Aviation Fuel," In preparation.

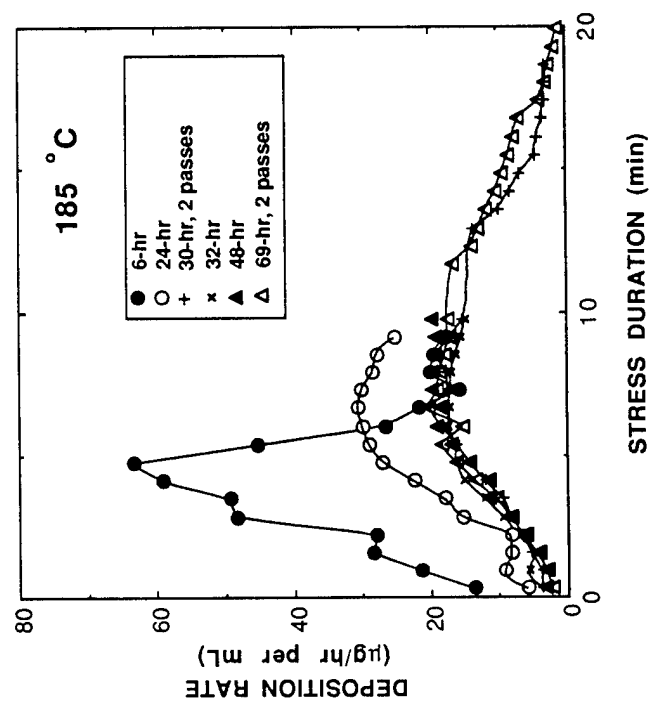


Fig 1. Deposition Rate vs. Stress Duration for POSF-2827 Fuel at 185°C for a Series of Experimental Test Times Measured with a Fuel-Flow Rate of 0.25 mL/min.

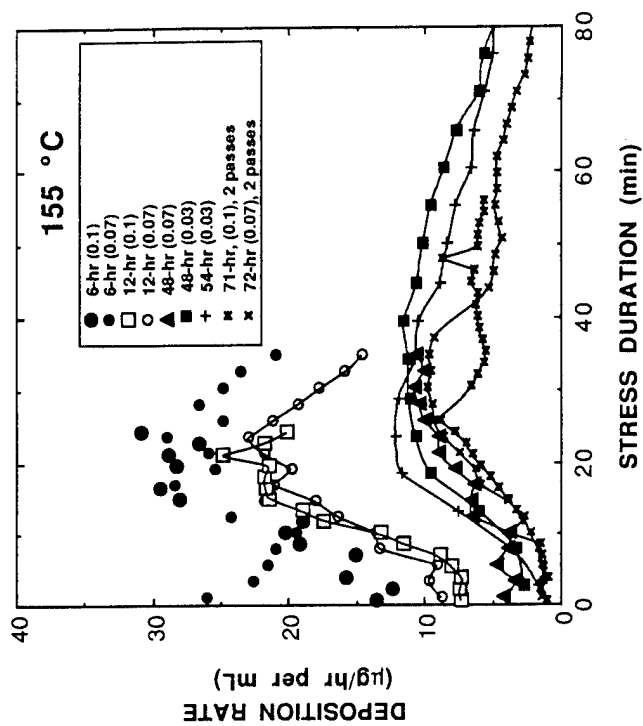


Fig 2. Deposition Rate vs. Stress Duration for POSF-2827 Fuel at 155°C for a Series of Experimental Test Times.

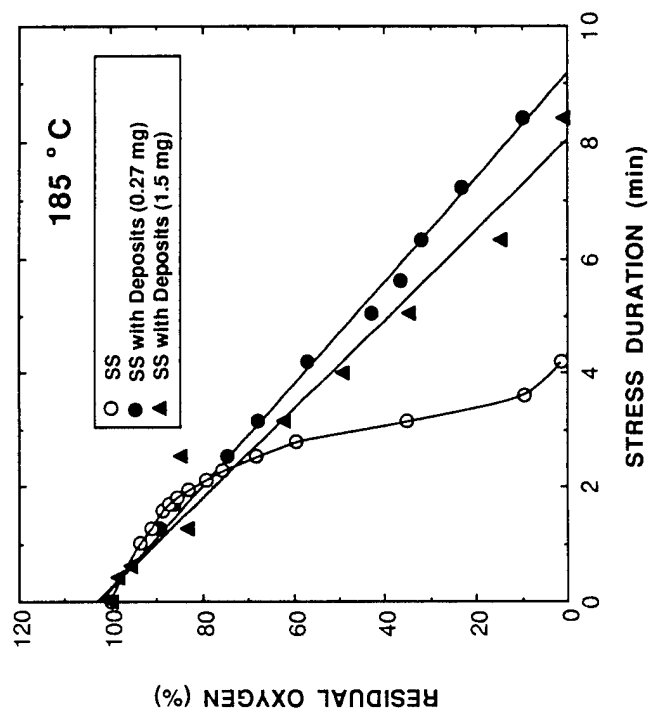


Fig 3. Residual Dissolved Oxygen vs. Stress Duration for POSF-2827 Fuel at 185°C. Measurements Made in 1) Cleaned Stainless-Steel Tubing, 2) Tubing Pre-deposited with 0.27 mg of Insolubles, and 3) Tubing Pre-deposited with 1.5 mg of Insolubles.

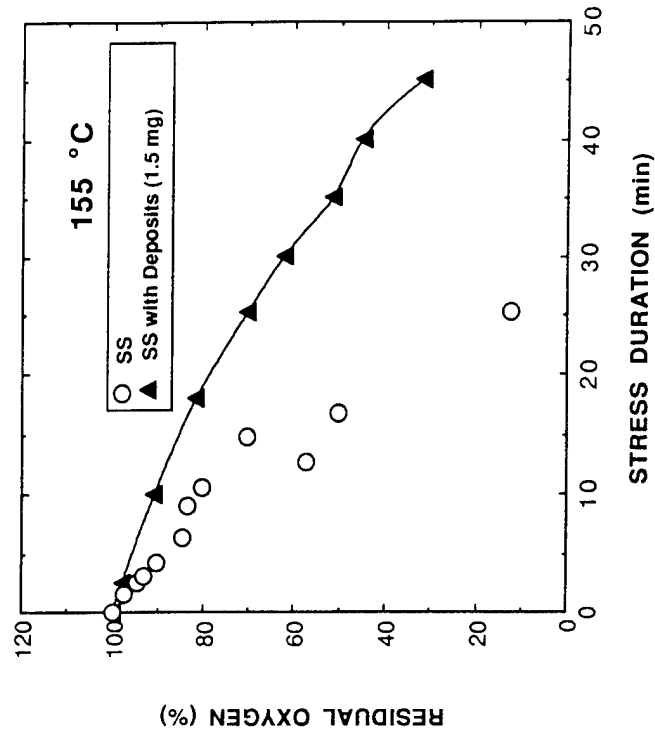


Fig 4. Residual Dissolved Oxygen vs. Stress Duration for POSF-2827 Fuel at 155°C. Measurements Made in 1) Cleaned Stainless-Steel Tubing and 2) Tubing Pre-deposited with 1.5 mg of Insolubles.

Surface Fouling in Aviation Fuel: Short- vs Long-Term Isothermal Tests

E. Grant Jones* and Walter J. Balster

*Systems Research Laboratories, Inc., A Division of Space Industries International, Inc.,
2800 Indian Ripple Road, Dayton, Ohio 45440-3696*

*Received January 16, 1995. Revised Manuscript Received March 20, 1995**

The rate of surface fouling has been studied using the aviation fuel POSF-2827 under near-isothermal reaction conditions during flow through heated stainless-steel (304) tubing. We previously reported rates of fouling stainless-steel walls as determined from measurements of surface carbon collected over a 6-h integration period. The goal of the current study was to complete similar experiments but with the integration time being extended to include contributions from deposition on previously fouled surfaces. In this paper, results of short-term (6 h) and long-term (>70 h) tests are compared. Differences in both deposition rate and its stress-time dependence are explained in terms of the changes in the rate of consumption of dissolved oxygen that result from surface interactions. The nature of the surface is shown to be important in controlling both oxygen reaction and deposition.

Introduction

Problems associated with surface fouling of fuel lines, nozzles, and heat exchangers caused by thermooxidative stressing of aviation fuel have been documented.¹ Heat loads from both the airframe and the engine that must be dissipated via the fuel are increasing with improvements in aircraft performance. Since the extent of surface fouling depends strongly upon the particular aviation fuel, it is important to be able to assess each fuel in a simple accelerated laboratory test that simulates the thermooxidative stress experienced in aircraft fuel lines. Although the Jet-Fuel Thermal-Oxidation Test (JFTOT) has traditionally been used, subjectivity in assessing lacquer color is considerable,² and surface temperatures up to 260 °C result in reactions taking place over a broad temperature range.

Over the past 3 years, we have been studying fuels using a simpler dynamic test in which fuel is stressed in a single-pass heat exchanger (stainless-steel tube) under well-defined *near-isothermal* chemical-oxidation conditions. The combination of very slow fuel flow rates (<0.5 mL/min), small tubing diameter, and large heater block (>40 kg) creates long residence times and reaction conditions which are predominantly free from radial and axial temperature gradients. During initial heating as fuel enters the block, temperature gradients occur and are the basis for describing the experiments as *near-isothermal*. With this approach, the chemistry of fuel fouling can be studied at a single temperature, thus avoiding complexities such as nonuniform temperature distributions existing in actual aircraft fuel lines due to the fluid dynamics. If autoxidation of fuel controls

the deposition processes, then this should be apparent in constant-temperature simulations. Also, in actual fuel lines the fraction of oxygen consumed is usually small and difficult to assess because of high flow rates and short residence times. In the current isothermal experiments fuel entering the heat exchanger is saturated with respect to air, and all of the oxygen is consumed during the reaction time at temperature; hence, the quantity of both bulk and surface insolubles is normalized based on the total quantity of oxygen consumed. Experiments at a series of temperatures can provide the rate of oxygen consumption, the deposition rate and its dependence on stress duration, and quantification of both bulk and surface insolubles; the result is a global-chemical description of a fuel. Conceivably, at some later stage, the chemical description can then be used to calibrate computational fluid dynamics (CFD) models³ for calculating fouling under the complicated temperature and fuel-flow conditions within aircraft fuel lines which cannot be simulated with small-scale rigs.

The goal of the current study was to exploit the near-isothermal tests for the purpose of readdressing a fundamental question; namely, does the deposition rate change as the surface of the stainless-steel tube becomes fouled? This question has been addressed primarily by workers from UTRC⁴⁻⁶ and SHELL Thornton,^{7,8} and their results have been summarized by Hazlett.¹ All of

* Abstract published in *Advance ACS Abstracts*, May 15, 1995.

(1) Hazlett, R. N. *Thermal Oxidation Stability of Aviation Turbine Fuels*, ASTM Monograph 1; American Society for Testing and Materials: Philadelphia, 1991.

(2) Clark, R. H.; Bishop, G. H. Measure of Fuel Thermal Stability—Which Answer is Correct? In *Aviation Fuel: Thermal Stability Requirements*; ASTM STP 1138; Kirklin, P. W., David, P., Eds.; American Society for Testing and Materials: Philadelphia, 1992; pp 117–137.

(3) Katta, V. R.; Jones, E. G.; Roquemore, W. M. Development of Global-Chemistry Model for Jet-Fuel Thermal Stability Based on Observations from Static and Flowing Experiments. Paper No. PEP-19, presented at the 81st AGARD Symposium on Fuels and Combustion Technology for Advanced Aircraft Engines, Colliferro, Italy, 10–14 May 1993.

(4) Marteney, P. J.; Spadaccini, L. J. Thermal Degradation of Aircraft Fuels. Report NAPC-PE-143C, United Technologies Research Center on contract with Naval Air Propulsion Center, Trenton, NJ, December 1984.

(5) Giovanetti, P. J.; Szetela, E. J. Long Term Deposit Formation in Aviation Turbine Fuel at Elevated Temperature. NASA Report CR-179579, United Technologies Research Center on contract with National Aeronautics and Space Administration, Cleveland, OH, April 1985.

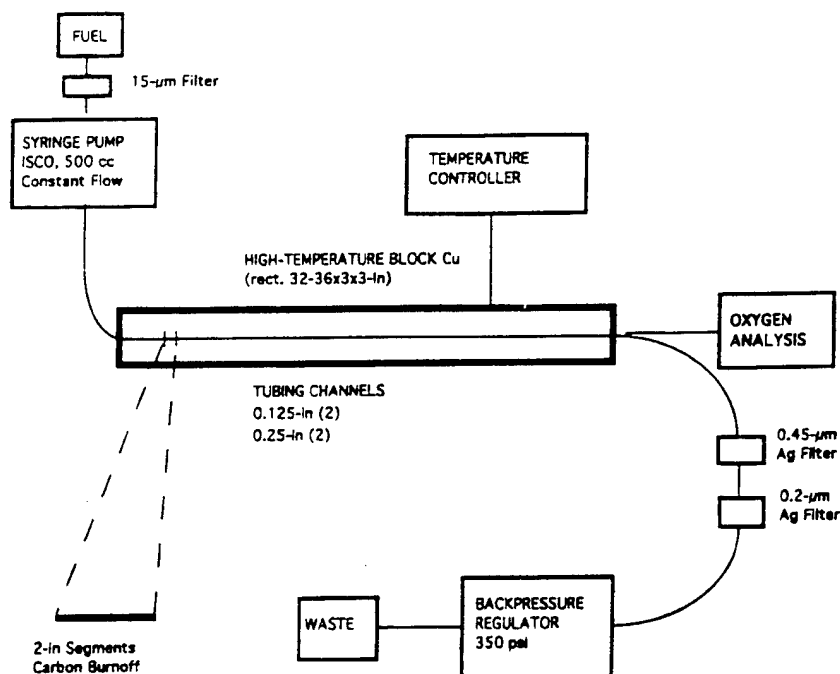


Figure 1. Schematic diagram of apparatus (NIFTR).

these test methods, including modified JFTOTs,⁹ have some intrinsic advantages for studying surface fouling. The large rigs more closely simulate actual aircraft systems. In particular, the SHELL systems use "real-time" measurements of deposits, but these measurements are predicated on wall-temperature increases as deposits build up. Our current tests using a small rig with slow flow are the most simple dynamic simulation. However, from a chemical standpoint there may be distinct advantages for such tests in which the bulk-fuel and fuel/wall-interface temperatures are equal and constant during fouling and in which deposits do not influence the bulk temperature of the fuel.

The experimental test time in prior near-isothermal experiments was set at 6 h to ensure that surface fouling would occur predominantly on cleaned stainless-steel surfaces. For longer test times more fuel is passed, more deposits are formed along the tube walls, and the measured deposition rate being averaged over longer times reflects differences associated with reaction and deposition on fouled tubes.

This paper reports the results of tests designed to measure surface fouling on both cleaned stainless-steel surfaces (short-term tests of 6-h duration) and fouled surfaces (long-term tests of > 70-h duration) at a series of temperatures within the autoxidation regime. The

Jet-A aviation fuel chosen for study, POSF-2827, is a representative fuel that passes the JFTOT criterion, meets all USAF specifications, and, unlike hydrotreated fuels which cause minimal surface fouling, creates measurable deposits during 6-h tests, making it an ideal candidate for experimental study. Surface and bulk fouling in this fuel has already been reported in detail at 185 °C^{10,11} and in general over the temperature range 155–225 °C.¹² Furthermore, deposition in this fuel has been shown to have a direct correlation with oxygen consumption; this offers distinct advantages for data interpretation.

Experimental Section

POSF-2827 fuel has a JFTOT breakpoint of 266 °C and a sulfur level of 0.079% (w/w). This fuel falls into a category described by Kendall and Mills¹³ where the presence of sulfur compounds tends to inhibit oxidation but at the expense of increased insoluble formation.¹⁴

Data were collected using the Near-Isothermal Flowing Test Rig (NIFTR) which has been described previously^{10,11} and will be briefly outlined here. The schematic diagram in Figure 1 shows a single-pass heat exchanger with 0.125-in.-o.d., 0.085-in.-i.d. commercial stainless-steel (304) tubing clamped tightly in a heated copper block. Fuel is passed through the system at a slow flow rate and a pressure of 2.3 MPa. Currently, two channels in the copper block permit a second pass for doubling the reaction time. Tubes were initially cleaned ultrasonically with a 10% Blue Gold solution.¹⁵ Dissolved oxygen was measured using a 32-in. tube as a reaction cell; stress duration was changed by varying the flow rate. Deposition rates were measured in a separate set of uninterrupted experiments at a

(6) Marteney, P. J. Thermal Decomposition of JP-5 in Long Duration Tests. Report NAFPC-PE-201C, United Technologies Research Center on contract with Naval Air Propulsion Center, Trenton, NJ, June 1989.

(7) Kendall, D. R.; Houlbrook, G.; Clark, R. H.; Bullock, S. P.; Lewis, C. The Thermal Degradation of Aviation Fuels in Jet Engine Injector Feed Arms. Part 1—Results from a Full Scale Rig. Paper 87-IGTC-49, presented at the International Gas Turbine Congress, Tokyo, October 1987.

(8) Clark, R. H.; Stevenson, P. A. The Thermal Degradation of Aviation Fuels in Jet Engine Injector Feed-Arms: Results from a Half-Scale Rig. *Prepr. Pap.—Am. Chem. Soc., Div. Fuel Chem.* **1990**, 35 (4), 1302–1314.

(9) Kamin, R. A.; Nowack, C. J.; Darrah, S. Thermal Stability Measurements Using the Fiber Optic Modified Jet Fuel Thermal Oxidation Tester. In *Proceedings of the 3rd International Conference on Stability and Handling of Liquid Fuels*; Institute of Petroleum: London, November 1988; p 240.

(10) Jones, E. G.; Balster, W. J.; Post, M. E. *J. Eng. Gas Turb. Power* **1995**, 117, 125–131.

(11) Jones, E. G.; Balster, W. J. *Energy Fuels* **1993**, 7, 968–977.

(12) Jones, E. G.; Balster, W. J. *Prepr.—Am. Chem. Soc., Div. Pet. Chem.* **1994**, 39 (1), 78–81.

(13) Kendall, D. R.; Mills, J. S. *Ind. Eng. Chem. Prod. Res. Dev.* **1986**, 25, 360–366.

(14) Jones, E. G.; Balster, W. J.; Anderson, S. D. *Prepr.—Am. Chem. Soc., Div. Pet. Chem.* **1992**, 37 (2), 393–402.

(15) Blue Gold. Modern Chemical, Jacksonville, AR.

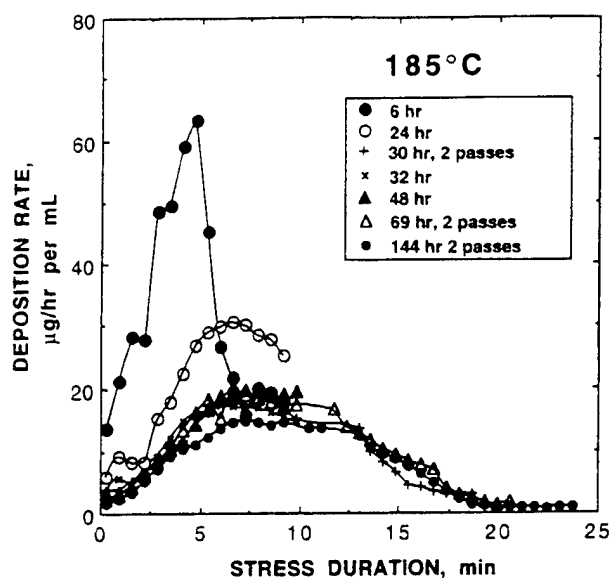


Figure 2. Deposition rate vs stress duration for POSF-2827 fuel at 185 °C for a series of experimental test times and a fuel-flow rate of 0.25 mL/min.

fixed fuel-flow rate; reaction time or stress duration was determined from the flow rate, tube dimensions, and location along the tube axis. The calculated times were reduced by 15% to compensate for fuel expansion. At the end of each test the heated tube was cut into 2-in. sections, and the quantity of carbon in the deposits was determined from surface-carbon burnoff (LECO RC-412). Deposition rates were based upon the amount of carbon in each 2-in. segment, the stress time within that segment, and the total amount of fuel passed. Each segment provides one data point, representing the rate averaged over the entire test time (i.e., minimum of 6 h and maximum of 144 h). The rate is expressed in units of micrograms of carbon per unit stress time (h) within a tube section per unit volume (mL) of fuel passed through the system.¹¹ The rate has not been corrected for fuel expansion.

The heater blocks used were 32, 34, and 36 in. in length. For longer test times the spatial distribution of the deposition broadened, frequently making it impossible to collect the complete profile at that flow rate during a single pass through the heat exchanger. Two attempts were made to collect a complete profile; in the first the fuel was passed back through a second tube within the NIFTR to double the path length and reaction time, and in the second the fuel-flow rate was reduced to extend the stress duration accordingly within a single pass. In dynamic isothermal experiments it is important to distinguish stress duration from experimental test time. Stress duration is the reaction time at temperature, and the experimental test time (along with the fuel-flow rate) determines the total quantity of fuel passed through the system. In the present study the total quantity of fuel ranged from 25 to 2160 mL. Obviously, "long-term" has a different connotation for isothermal tests and for tests in larger rigs where 2000 to 50 000 L of fuel may be used per test.^{7,8} Two in-line Ag-membrane filters (0.45 and 0.2 µm) collected the nonadhering bulk insolubles.

Experiments were conducted at 155, 165, 175, and 185 °C. In each case the initial fuel was saturated with respect to air, with oxygen being measured as 64 ppm (w/w).¹⁶

Results and Discussion

Deposition Profiles. The deposition rates averaged for 6, 24, 30, 32, 48, 69, and 144 h are shown in Figure

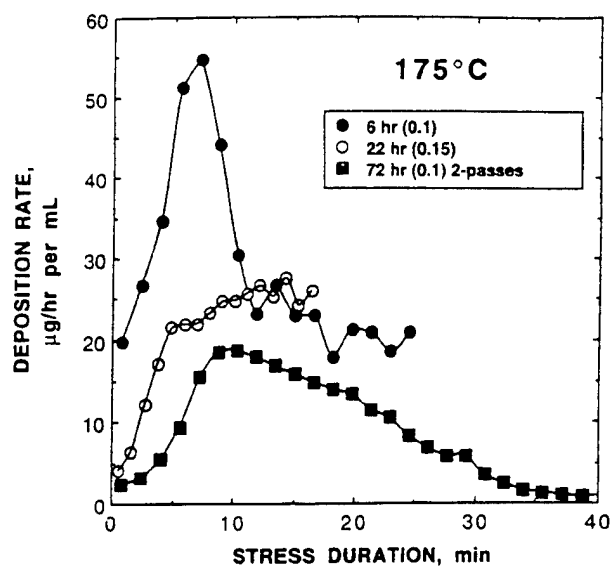


Figure 3. Deposition rate vs stress duration for POSF-2827 fuel at 175 °C for a series of experimental test times and fuel-flow rates (in parentheses).

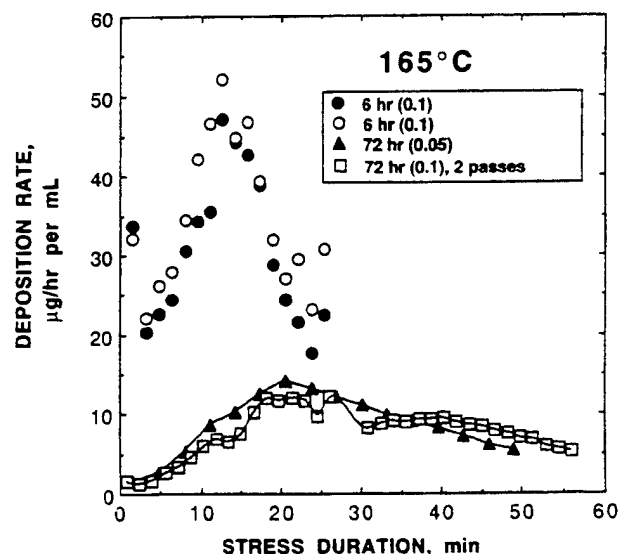


Figure 4. Deposition rate vs stress duration for POSF-2827 fuel at 165 °C for a series of experimental test times and fuel-flow rates (in parentheses).

2 as a function of stress duration at 185 °C for a fixed fuel-flow rate of 0.25 mL/min. The following changes in surface deposition are observed with extension of integration time: (1) the profile broadens with significant tailing, (2) the maximum in the deposition rate is reduced, and (3) the center of the deposition peak shifts to slightly longer stress times. Also, the profiles appear to approach a common shape at the longest experimental times. Extended reaction time in the 30- and 69-h experiments was achieved by a second pass of the fuel through the heat exchanger; note the discontinuity from the external loop. Results of similar experiments at 175, 165, and 155 °C are presented in Figures 3, 4, and 5, respectively. Flow rates (in parentheses) and experimental test times are shown on the figures. Similar trends are observed; however, the reaction times have been extended to permit completion of the deposition processes at lower temperatures.

In making a comparison of rates which are averaged over different experimental times, one must take into

(16) Striebig, R. C.; Rubey, W. A. *Prepr.-Am. Chem. Soc., Div. Pet. Chem.* 1994, 39 (1), 47-50.

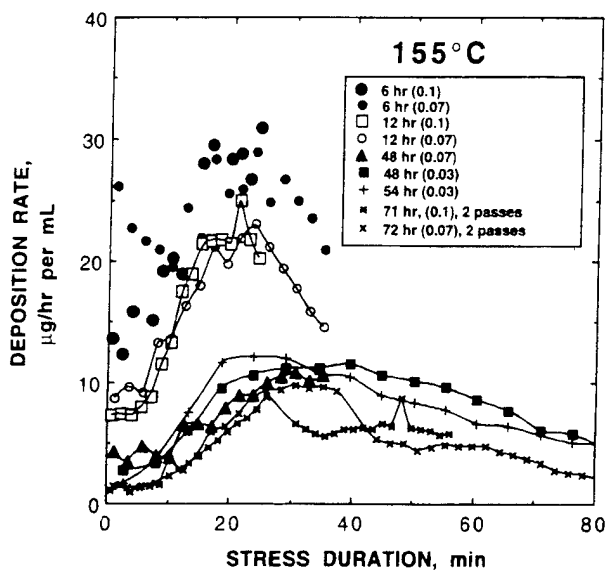


Figure 5. Deposition rate vs stress duration for POSF-2827 fuel at 155 °C for a series of experimental test times and fuel-flow rates (in parentheses).

account that the baseline arising from background carbon on the tube drops as the experimental time is extended. The major difference between 6-h tests and those of much longer duration concerns the nature of the tube surface. Initially, deposition occurs on cleaned stainless-steel tube surfaces. As the experiment time is extended, this surface gradually becomes completely carbonaceous coated. For example, at the end of the 69-h test at 185 °C, the surface density at the maximum is $75 \mu\text{g cm}^{-2}$. If it is assumed that the deposit has a density of unity and is distributed uniformly, the thickness is $0.75 \mu\text{m}$. Deposition should be constant after complete coverage of the initially cleaned stainless-steel surfaces; based on Figure 2 the deposition rate becomes constant after 30 h or at $\sim 30 \mu\text{g cm}^{-2}$ coverage. The observed variation in deposition rate is related to surface changes, the dominant factor being the rate of oxygen consumption, as shown below.

Oxygen Loss. The residual dissolved oxygen for this fuel has been reported¹¹ as a function of reaction time in stainless-steel tubes. The decrease in dissolved oxygen for reaction at 185 °C is shown in Figure 6; the accelerated reaction rate at higher conversion is attributed to autocatalysis. The 6-h deposition profile displays a maximum when the dissolved oxygen drops to zero. Also shown in Figure 6 is the oxygen loss measured using a tube that had been fouled in a previous fuel-stressing experiment and was estimated to have a uniform deposit containing $37 \mu\text{g cm}^{-2}$ of carbon. The initial rates of oxygen loss measured in the two tubes are similar. The acceleration in oxygen reaction is either no longer present or greatly diminished in importance once the surface becomes coated with deposits. These results indicate that autocatalysis in POSF-2827 fuel is a surface-related phenomenon.

The rate measured with the fouled tube remains constant over a wide conversion range, indicating a predominantly oxygen-non-limited reaction.¹⁰ After 8 min the rate slows as oxygen is further depleted and the source of the deposits is reduced. This time corresponds to the location of the maximum in the shifted deposition profile obtained in long-term tests at 185 °C. Similar behavior is observed at 155 °C (cf. Figure 7).

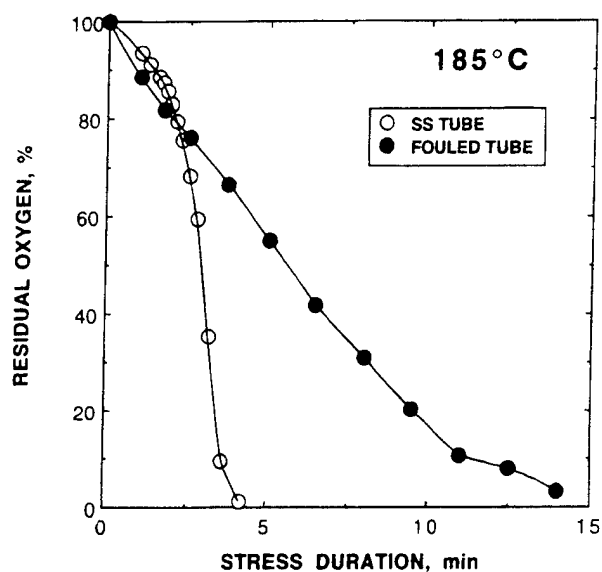


Figure 6. Residual dissolved oxygen vs stress duration for POSF-2827 fuel at 185 °C. Measurements made in (1) cleaned stainless-steel tubing and (2) stainless-steel tubing fouled with $37 \mu\text{g/cm}^2$ of carbonaceous deposit.

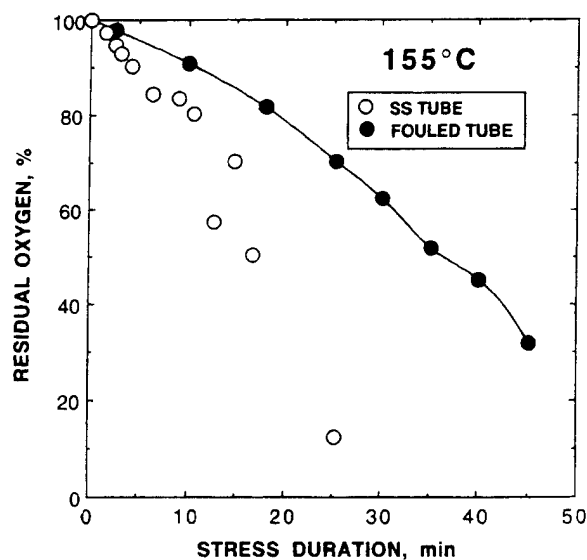


Figure 7. Residual dissolved oxygen vs stress duration for POSF-2827 fuel at 155 °C. Measurements made in (1) cleaned stainless-steel tubing and (2) stainless steel tubing fouled with $37 \mu\text{g/cm}^2$ of carbonaceous deposit.

Short- and long-term data sets differ as a result of the presence of deposits. If the cleaned stainless-steel tubing is viewed as the norm, then oxygen consumption is perturbed (i.e., slowed) by deposits. If the coated tube which has been somewhat passivated is viewed as the norm—an alternative and preferable view—then faster autoxidation observed in the stainless steel arises from active sites associated with the stainless-steel surface. Deposition in short-term (6-h) tests over the temperature range 155–225 °C correlates with oxygen loss measured in cleaned stainless-steel tubes;¹² similarly, deposition in long-term tests is expected to correlate with oxygen loss measured in tubes that have been passivated by deposits. The higher deposition rate observed in 6-h experiments results from the faster oxygen loss. The reduction in surface deposition rate, the broadening of the deposition profile, and the shift

Table 1. Insolubles (Average from Long-Term Tests, $\mu\text{g/mL}$)

temp ($^{\circ}\text{C}$)	insolubles		
	bulk	surface	total
185	2.7 ± 1.0	2.6 ± 0.6	5.3 ± 1.2
	2 ^a	3 ^a	5 ^a
	1.8 ^b	3.2 ^b	5.0 ^b
175	2.4 ± 0.5	5.9 ± 0.4	8.3 ± 0.1
	2.1 ^a	5.6 ^a	7.7 ^a
165	2.4 ± 0.3	7.3 ± 0.2	9.7 ± 0.6
	2.7 ^a	6.2 ^a	8.9 ^a
155	2.2 ± 0.6	6.8 ± 2.6	9.0 ± 2.1
	1.5 ^a	7.3 ^a	8.8 ^a

^a 6-h tests from ref 12. ^b 144-h test.

in the maximum in the long-term experiments are manifestations of slower autoxidation.

Quantification of Insolubles. Table 1 summarizes the bulk and surface insolubles averaged at each temperature for the extended-duration tests up to 72 h. Shown for comparison are the reported¹² 6-h averages and values for the longest test (144 h). It should be noted that in earlier 6-h tests, contributions from a single 0.45- μm filter were used, while the more recent long-term tests include additional bulk contributions from a second filter (0.20 μm). The surface contributions were evaluated by summing the total surface carbon or integrating the area under the complete deposition profiles. In each case an estimated baseline contribution was subtracted. Within the reproducibility of the data, the short- and long-term results are in agreement, the latter displaying the same inverse temperature dependence as reported in the 6-h tests.¹²

Implications. The findings from these simple tests have important implications for POSF-2827 fuel and possible significance with regard to the general thermal oxidative stability of fuels.

Autocatalysis. This process has been attributed to thermal dissociation of an oxidation product such as hydroperoxide.¹¹ The present results indicate that the accelerated autoxidation observed in POSF-2827 fuel is heterogeneous. Carbonaceous deposits passivate the surface by blocking active sites, thereby reducing or eliminating autocatalysis.

Quantity of Surface Insolubles. The quantity of surface insolubles can be used to rank fuels based on thermal oxidative stability. Our evaluations are predicated on accelerated short-term tests in which deposition processes have progressed to completion. When the entire profile of deposit is captured on the heated tube, the total deposit is independent of deposition rate, i.e., autocatalysis which may increase the deposition rate does not alter the total amount of surface carbon. If the basis for estimating surface deposits were the quantity formed within a fixed stress time t , then fuel evaluation would be based on the area under the deposition profile up to t and would be rate dependent. Clearly, fuels such as POSF-2827, which react slowly with oxygen at low conversion, would be ranked differently if a low-conversion (i.e., fixed reaction time) criterion rather than a complete-conversion criterion were used.

The current results indicate that quantification based on longer-term tests has distinct advantages, the primary one being the increased signal-to-noise ratio in the data. Also, initial surface catalytic effects occurring at

the shortest test times are mitigated by averaging over longer test times.

Fuel-Evaluation Techniques. Techniques such as the JFTOT and Hot Liquid Process Simulator (HLPS) which make use of clean aluminum and stainless-steel surfaces, respectively, should be sensitive to the nature of the surface and also the manner in which oxygen is consumed. For example, Clark et al.¹⁷ reported that a metal deactivator (MDA) functions optimally on clean metal surfaces but does not reduce deposition once a lacquer layer forms. The vulnerability of JFTOT results in short-term tests has been discussed by Clark and Bishop.² The initial surface-passivation effects of MDA were reported to mask problems detectable only during extended test times.

We conjectured in a preliminary report on some of these data¹⁸ that the short-term benefit of MDA might be surface passivation which delays oxygen consumption by reducing surface catalysis. Reduced deposition or an improved JFTOT result might then be explained in terms of MDA slowing oxygen consumption rather than hindering adherence to the surface. Since that report we have measured the oxygen consumption in POSF-2827 fuel containing the DuPont metal deactivator *N,N'*-disalicylidene-1,2-propanediamine present at 2 mg/L and have found that MDA slows the rate of oxygen consumption by preventing autocatalysis.¹⁹

Comparison with Results from Large Rigs. Investigators at Shell,⁸ using large rigs, have found common behavior among several fuels and additives. Weight vs time profiles indicate a three-stage process, consisting of induction (barely measurable deposition), take-off (constant deposition rate), and tail-off (reduced deposition rate) regions. They attributed induction to the time required to cover virgin metal with a complete lacquer layer that can provide different chemical reactivity and more rapid subsequent deposition. It is questionable whether any attempt should be made to compare results from the current isothermal experiments with those from the larger rigs. Different fuels and very different test conditions make detailed comparisons difficult; however, some general comments can be made. It is clear that we do not observe increased deposition rates at longer test times for POSF-2827 fuel. We attribute the apparent higher rates in the short-term (6 h) tests solely to catalyzed oxygen consumption. That is, if the oxygen reaction rate were constant, the deposition-rate profile would be independent of test time.

If the concept of induction period is applicable to POSF-2827 fuel, then our experiments characterized by a constant deposition rate must relate to either the induction or the postinduction period. After a 30-h test, the region of the tubes where deposition rates maximize should be totally covered with carbonaceous deposits, and subsequent deposition should occur at a constant rate. This is based on calculated deposit thickness, the constancy of observed deposition-rate profiles, and visual inspection. If we were to relate these results to the Shell-group three-stage process, then our rates (6–144 h average) would pertain to the second or constant-rate stage and any induction period would be <6 h.

(17) Clark, R. H.; Delargy, K. M.; Heins, R. J. *Prepr. Pap.-Am. Chem. Soc., Div. Fuel Chem.* **1990**, 35 (4), 1223–1232.

(18) Jones, E. G.; Balster, W. J. *Prepr. Pap.-Am. Chem. Soc., Div. Fuel Chem.* **1994**, 39 (3), 952–957.

(19) Jones, E. G.; Balster, W. J. manuscript in preparation.

According to Clark and Wolveridge,²⁰ it is preferable to collect data in this region rather than in the first stage. JFTOT standard operation relates to the first stage. We would not expect a third stage in the current isothermal experiments.

Nature of the Surface. The existence of virgin stainless-steel surfaces either in aircraft fuel lines or in the current experiments is highly unlikely. The term "cleaned" in the present context is used to describe not only the initial state of the tube prior to fuel and heat exposure but also, in a nebulous way, surfaces early in the experiments. It is anticipated that adsorption or chemisorption of fuel components will always occur. For example, with POSF-2827 fuel it has been observed, using both XPS and Auger spectroscopy, that a thin sulfur-rich coating forms within the first 15 min of stressing at 185 °C.²¹ It is not clear at present whether this layer results from an inherent fuel component or an oxidized product. In either event, surface activity ascribed to cleaned stainless steel may be associated with this layer. Carbonaceous deposits eventually mask details of the initial surface.

(20) Clark, R. H.; Wolveridge, P. E. Induction Periods: Are You Measuring the Right Rate? Presented at the Coordinating Research Council Meeting, Alexandria, VA, 21–22 April 1993.

(21) Jones, E. G.; Balster, W. J.; Kauffman, R. E. Surface Deposits—Sulfur Aspects. Presented at the Symposium on Sulfur Chemistry of Jet Fuels, Wright Laboratory, Aero Propulsion and Power Directorate, Wright-Patterson Air Force Base, OH, 6 April 1994.

Conclusions

The dependence of the surface deposition rate of POSF-2827 fuel on isothermal stress duration over the temperature range 155–185 °C has been found to be a function of experimental test time. In short-term (6 h) tests, initial deposition is governed by the autocatalytic consumption of oxygen. For long-term (>70 h) tests during which the initial stainless-steel surface becomes covered with deposits, the deposition profile is governed by a slower loss of oxygen.

Oxygen loss in cleaned stainless-steel tubes is accelerated as a result of surface interactions. After deposits build up, active sites necessary for autocatalysis are removed.

In dynamic experiments with POSF-2827 aviation fuel, the effect of surface interactions on both dissolved-oxygen consumption and subsequent surface deposition rates has been shown to be very significant. These evaluations must be extended to other fuels in order to assess the generality of the current findings.

Acknowledgment. This work was supported by Wright Laboratory, Aero Propulsion and Power Directorate, Wright-Patterson Air Force Base, Ohio, under USAF Contract No. F33615-90-C-2033. The authors thank Mr. Tim Gootee for conducting the surface-carbon analyses, Mrs. Marian Whitaker for editorial assistance, and Dr. James M. Pickard for valuable discussions.

EF9500090

In *Proceedings 5th International Conference on Stability and Handling of Liquid Fuels, Rotterdam, The Netherlands, 3-7 October 1994*, Vol. 1 (H. N. Giles, Ed.) (U. S. Department of Energy, Washington, D. C., 1995), pp. 291-301.

EFFECT OF ADDITIVES ON THE FORMATION OF INSOLUBLES IN A JET FUEL

Steven D. Anderson¹, E. Grant Jones*², Larry P. Goss², and Walter J. Balster²

¹Fuels Branch, WL/POSF, Aero Propulsion and Power Directorate, Wright Laboratory, Wright-Patterson AFB, OH 45433-7103, USA;

²Systems Research Laboratories, Inc., A Division of Space Industries International, Inc., 2800 Indian Ripple Road, Dayton, OH 45440-3696, USA.

ABSTRACT

Dynamic near-isothermal techniques have proven to be valuable in assessing the tendency of aviation fuels to form surface and bulk insolubles under thermal stress. These methods are applied in this study to the investigation of the neat Jet-A fuel POSF-2827 and changes introduced by a series of four candidate additives. In each case fuel is stressed while flowing through a heat exchanger under near-isothermal conditions at 185°C. The average surface deposition rate as a function of stress duration and the quantity of both surface and bulk insolubles have been determined after complete consumption of the dissolved oxygen. The additives, introduced individually, include a common antioxidant, a metal deactivator, a dispersant, and a combination detergent/dispersant. Of the four additives, only the dispersant-types are found to improve fuel thermal stability.

INTRODUCTION

Aviation fuels, when subjected to heat in the presence of oxygen, undergo degradation from autoxidation reactions.¹ Insoluble products formed in these reactions tend to foul heated surfaces, causing reduced efficiency and possible blockage in heat exchangers, hysteresis in servocontrols, and changes in nozzle geometry. Being the primary heat sink in modern aircraft, fuel will experience increased thermal stress as aircraft performance is enhanced.² Minor fuel constituents containing sulfur and nitrogen have been implicated as the primary cause of insoluble formation.

Methods of improving the stability of poorer quality fuels that are based on hetero-atom removal, such as clay- or hydro-treatment, do not always represent practical solutions because of the cost involved. The introduction of low-cost additives which may improve the thermal-oxidative stability is appealing. Additives such as antioxidants for slowing oxygen consumption, metal deactivators for chelating dissolved metals or passivating tubing walls, and dispersants for increasing solubility would appear to be the most promising from a thermal-stability standpoint.

Martel³ has summarized jet-fuel additives including, in addition to the above, corrosion inhibitors, lubricity improvers, icing inhibitors, static dissipators, and pipeline drag reducers.

Since each fuel has a different chemical composition, the behavior of an additive for reducing insolubles will be dependent upon the reaction kinetics within the fuel. No additive is expected to be universally effective. For example, the DuPont additive JFA-5 is specified for use in JPTS (thermally stable jet fuel) because it contains a mixture of a high-temperature antioxidant, a dispersant, and a metal deactivator.³ Similarly, to promote storage stability, hydrotreated fuels require the addition of low-temperature antioxidants to replace the natural antioxidants removed during processing.⁴

The approach in the current study was to 1) select a typical Jet-A fuel exceeding US Air Force requirements, 2) investigate its tendency to form insolubles at 185°C, and 3) individually add several candidate additives and investigate changes in the formation and quantity of insolubles. Deposition experiments were conducted over long test times to emphasize deposition on previously fouled surfaces.⁵ Several criteria were applied in assessing beneficial or possibly deleterious effects introduced by the additives. The additive producing the most improvement was then subjected to further testing at several other temperatures. The goal was to address some fundamentals of additive behavior in altering the thermal-oxidation stability. In future studies beneficial synergism among these additives will be investigated by studying combinations. The advantage of the isothermal approach employed in this study is the ability to focus on chemical effects without the additional complexities associated with fluid dynamics at higher flows and without the surface-temperature changes that can occur as deposits accumulate.

EXPERIMENTAL

The baseline fuel, POSF-2827, has a JFTOT breakpoint of 266°C and a sulfur level of 0.079% (w/w). The presence of sulfur probably accounts for interest in this fuel and makes it a good candidate for the study of insoluble formation. In seeking improvement in thermal stability through the introduction of additives, it is important to select a representative, average fuel that produces measurable insolubles rather than an excellent fuel in which improvements would be difficult to detect. POSF-2827 is a typical Jet-A fuel. Kendall and Mills⁶ addressed fuels of this type in which oxidation is inhibited by the presence of sulfur--but at the expense of increased insoluble formation.

The experiments were conducted using the Near-Isothermal Flowing Test Rig (NIFTR) which has been described previously.⁷ Figure 1 shows the heat exchanger which was operated in the double-pass mode to extend reaction time. Fuel, which is saturated initially with respect to air and which contains 64 ppm (w/w) of oxygen, is pumped at a pressure of 350 psi through 0.125-

in.-o.d., 0.085-in.-i.d. commercial stainless-steel (304) tubing clamped tightly in a 36-in. heated copper block. Two in-line Ag-membrane filters (0.45 and 0.2 μm) collect the non-adhering bulk insolubles.

Deposition rates were measured in 72-hr experiments that were run continuously at a fixed fuel-flow rate; reaction time or stress duration was determined from the flow rate, tube dimensions, and location along the tube axis. At the end of each test, the heated tube was cut into 2-in. sections, and the quantity of carbon in the deposits was determined from surface-carbon burnoff (LECO RC-412). Deposition rates were determined from the amount of carbon in each 2-in. segment and the stress time calculated to its midpoint. Each section provides one data point representing the rate averaged over the entire test time (i.e., ~ 72 hr). Rate is expressed in units of micrograms of carbon per unit stress time per unit volume of fuel passed through the system.⁷ Dissolved oxygen was measured in separate experiments using a 32-in. tube as a reaction cell and GC detection;⁸ stress duration was changed by varying the flow rate. In long-term (72-hr) tests, most deposition occurs on previously fouled surfaces; for this reason a passivated tube (Silcosteel⁹) was used to minimize catalytic wall effects during oxygen measurements. In dynamic isothermal experiments, stress duration differs from experimental test time. Stress duration is the reaction time at temperature, and the experimental test time (along with the fuel-flow rate) determines the total quantity of fuel passed through the system.

Photon-correlation spectroscopy was selected for sizing of sub-micron particles, based on the techniques outlined by O'Hern et al.¹⁰ Fuel was stressed within the NIFTR for selected times at 185°C, and particles in the effluent were sized after cooling to room temperature. The size measurements are viewed as an upper limit to the *in-situ* sizes.

The four selected additives are listed in Table 1. These include an antioxidant, a metal deactivator, a dispersant, and a combination detergent/dispersant. Concentrations of dispersants were based on manufacturers' suggestions, cost constraints, and previous tests in this laboratory.¹¹ Since the neat fuel does not contain measurable dissolved metals, MDA concentration was set at 2 mg/L for possible wall passivation.

RESULTS AND DISCUSSION

Oxygen Loss. The behavior of the dissolved oxygen as a function of stress duration at 185°C is shown in Fig. 2. Oxygen in the neat fuel is totally converted in about 20 min. The rate is constant down to 30% residual oxygen, indicating oxygen non-limited kinetics. Below 30% the rate becomes oxygen limited, as evidenced by tailing. Walling¹² has summarized the rate expressions for the disappearance of oxygen at high and low oxygen concentrations. Neither BHT nor MDA alters the oxygen consumption. The presence of certain types of sulfur compounds

causes hydroperoxide concentration to remain low and the kinetic chain length to approach unity. Chain-breaking antioxidants such as BHT (hindered phenol) are ineffective since a molecule of antioxidant is destroyed for every molecule of oxygen consumed.¹³ In the absence of dissolved metals and with inactive wall surfaces, a metal deactivator is similarly not expected to have a pronounced effect. Only one of the additives, MCP-147B, seems to perturb the oxygen consumption by increasing the reaction rate. At a concentration of 300 mg/L, this additive is directly participating in the reaction as a pro-oxidant or as an initiator.

Ideally, an additive should retard or certainly not increase the rate of autoxidation. In aircraft fuel lines, the fuel spends very little time at elevated temperature; therefore, oxygen conversion, in practice, is minimal. However, the very large fuel throughput offsets the conversion and leads to the observed fouling. In isothermal simulations only small amounts of fuel are used (~ 1.1 L); however, with 100% oxygen conversion, the extent of fouling per unit volume of fuel used is significant. In either case an additive such as MCP-147B that increases the autoxidation rate is of concern and its use should be decided based on further testing.

Dependence of Deposition Rate on Stress Duration. Figure 3 shows the deposition profiles at 185°C obtained at a flow rate of 0.25 mL/min. The 72-hr-average rate profiles for the additives BHT and MDA as well as the neat fuel appear to be the same within experimental reproducibility, displaying maxima around 9 min and completed deposition around 20 min which is consistent with the observed consumption of oxygen. The additives MCP-147B and 8Q405 cause significant changes in the deposition profiles. For stress times of less than 3 min, the former exhibits a reduced deposition rate but at longer times leads to a higher rate, maximizing around 6 min with no tailing. This additive appears to be promoting the deposition rate, as might be expected from the oxygen-loss data. The latter additive reduces the deposition rate for over 15 min of stressing and delays the maximum to around 12 min. The 8Q405 appears to behave as might be expected for an effective additive based upon a deposition-rate criterion, namely, reduced rate and delayed deposition. The MCP-147B displays undesirable behavior, based on a deposition-rate criterion.

Quantification of Insolubles. Other criteria for evaluating the additives on the basis of data from the same experiments are quantity of surface insolubles (integral under the rate profiles), bulk insolubles (carbon burnoff of the in-line filters), and finally the total insolubles (sum). In each case these quantities are expressed in terms of micrograms of insolubles per milliliter of fuel that is initially saturated with respect to air at room temperature. Insolubles are plotted in Fig. 4 for the neat fuel and each additive. Clearly, neither BHT nor MDA has a beneficial effect for POSF-2827 fuel under the test conditions; however, these additives do not reduce thermal stability. In contrast, both dispersants cause significant reduction in surface and

bulk insolubles. Using quantity of insolubles produced from POSF-2827 as a criterion, both MCP-147B and 8Q405 result in a 50% reduction and would be rated as effective additives.

Bulk insolubles are quantified only at the end of 24-min of stressing or complete oxygen conversion. Surface insolubles, on the other hand, can be evaluated after any selected stress time, t , at 185°C by integrating under the curves in Fig. 3 up to time t . Thus, the performance of each additive in reducing surface deposits can also be evaluated as a function of stress duration.

Selection of Most Effective Additive. Based on the above evaluation criteria, neither BHT nor MDA improves the thermal behavior of the fuel as tested. The detergent/dispersant MCP-147B, while reducing insolubles, showed less than desirable signs both in the oxygen experiments and in the deposition rate by initiating or promoting thermal degradation. The dispersant 8Q405 does not alter the oxygen reaction rate but reduces both the deposition rate and total quantity of insolubles. For these reasons 8Q405 was selected for further testing.

It should be noted that the current study is limited to a single fuel and four additives. Development of any additive package requires the consideration of a broad family of fuels and additive combinations. Both MCP-147B and 8Q405 have quite different proprietary structures and chemistry. We expect their behavior to be different in every fuel.

Other Tests with 8Q405 Additive. Figure 5 shows a comparison between the deposition using neat and additized fuel at 165, 185, 205, and 225°C. Significant reduction in deposition rates is observed at each temperature. Similar improvements in the quantity of insolubles would be expected (see Fig. 6). Note that the inverse temperature dependence of the total insolubles that has been reported in 6-hr tests¹⁴ is also reflected in the 72-hr experiments for both the neat and the additized fuel.

The fact that a dispersant-type additive shows the most promise in POSF-2827 fuel suggests that its role is to keep potential insolubles in solution, possibly by delaying agglomeration processes. The 8Q405 does not slow the autoxidation rate, but the subsequent chemical and physical steps leading to insolubles are delayed and the quantities are reduced. Insolubles that do come out of solution may be dispersed and kept small. Particles formed during the stressing of POSF-2827 fuel have been sized using photon-correlation spectroscopy. The measured diameter for the neat and 8Q405-doped fuel is shown in Fig. 7 as a function of stress duration at 185°C. The dispersant causes significant reduction in both particle size and number density (not shown), consistent with the earlier discussion.

CONCLUSIONS

The effect of four additives in improving the thermal stability of a particular Jet-A fuel has been evaluated in long-term (~ 70-hr) tests in which most of the deposition occurs on previously fouled surfaces. Neither the antioxidant (BHT) nor the metal deactivator exhibit beneficial effects. Some limited improvement was observed for a detergent/dispersant; however, indications of increased rates of oxygen consumption and deposition raise concerns as to its overall benefit. A dispersant additive 8Q405 exhibited significant reduction in deposition rates and quantity of insolubles over the temperature range 165 - 225°C. Improvement is explained in terms of particle-size reduction and decreased total insolubles caused by efficient dispersant activity.

Dynamic near-isothermal studies have provided details of oxidation and deposition kinetics for the Jet-A fuel, POSF-2827. These methods are currently being applied to evaluate the use of additives in other Jet-A and JP-8 aviation fuels.

ACKNOWLEDGMENTS

This work was supported, in part, by Wright Laboratory, Aero Propulsion and Power Directorate, Wright-Patterson Air Force Base, OH, under USAF Contract No. F33615-90-C-2033. The authors would like to thank Mr. Tim Gootee for performing the surface-carbon analyses, Ms. Lori M. Balster for making the oxygen measurements, and Mrs. M. Whitaker for lending editorial assistance. The authors acknowledge valuable discussions with W. A. Rubey, University of Dayton Research Institute.

LITERATURE CITED

- (1) Hazlett, R. N. *Thermal Oxidation Stability of Aviation Turbine Fuels*, ASTM Monograph 1; American Society for Testing and Materials: Philadelphia, 1991.
- (2) Edwards, T.; Anderson, S. D.; Pearce, J. A.; Harrison, W. E. "High Temperature Thermally Stable JP Fuels--An Overview," AIAA Paper No. 92-0683, Presented at the 30th Aerospace Sciences Meeting and Exhibit, January 6-9, 1992, Reno, NV.
- (3) Martel, C. R. "Military Jet Fuels, 1944-1987," Air Force Wright Aeronautical Laboratory Technical Report AFWAL-TR-87-2062; Air Force Wright Aeronautical Laboratory: Wright-Patterson Air Force Base, OH, November 1987.

- (4) Turner, L. M.; Kamin, R. A.; Nowack, C. J.; Speck, G. E. "Effect of Peroxide Content on the Thermal Stability of Hydrocracked Aviation Fuel," in *Proceedings, 3rd International Conference on Stability and Handling of Liquid Fuels*; Institute of Petroleum: London, England, November 1988; p 338.
- (5) Jones, E. G.; Balster, W. J. *Prepr.-Am. Chem. Soc., Div. Fuel. Chem.* **1994**, 39 (3), 952-957.
- (6) Kendall, D. R.; Mills, J. S. *I&EC Prod R&D* **1986**, 25, 360-366.
- (7) Jones, E. G.; Balster, W. J. *Energy Fuels* **1993**, 7, 968-977.
- (8) Rubey, W. A.; Tissandier, M. D.; Striebich, R. C.; Tirey, D. A.; Anderson, S. D. *Prepr.-Am. Chem. Soc., Div. Petrol. Chem.* **1992**, 37(2), 371-376.
- (9) SILCOSTEEL tubing, Restek Corporation, Bellefonte, PA.
- (10) O'Hern, T. J.; Trott, W. M.; Martin, S. J.; and Klavetter, E. A. *31st Aerospace Sciences Meeting and Exhibit*, Paper No. AIAA 93-0363, **1993**, Reno, NV, January 11-14.
- (11) Pratt and Whitney R&D Status Report No. FR 22635-18 under Contract No. F33615-93-C-15 with the United States Air Force, Wright Laboratory, Aero Propulsion and Power Directorate, Wright-Patterson Air Force Base, OH; Pratt and Whitney: West Palm Beach, FL, September 1994.
- (12) Walling, C. *Free Radicals in Solution*; John Wiley and Sons, Inc.: New York, 1957.
- (13) Scott, G., *Atmospheric Oxidation and Antioxidants*; Elsevier: New York, 1965; p 115.
- (14) Jones, E. G.; Balster, W. J. *Prepr.-Am. Chem. Soc., Div. Petrol. Chem.* **1994**, 39 (1), 78-81.

TABLE 1

ADDITIVES TESTED WITH POSF-2827 FUEL

CLASS	NAME	CHEMICAL NAME	MANUFACTURER	CONCENTRATION (mg/L)
Antioxidant	BHT	2,6-di-tert-butyl-p-cresol	DuPont	25
Metal Deactivator	MDA	N,N'-disalicylidene-1,2-propanediamine	DuPont	2
Dispersant	8Q405	Proprietary	Betz	100
Detergent/Dispersant	MCP-147B	Proprietary	Mobil	300

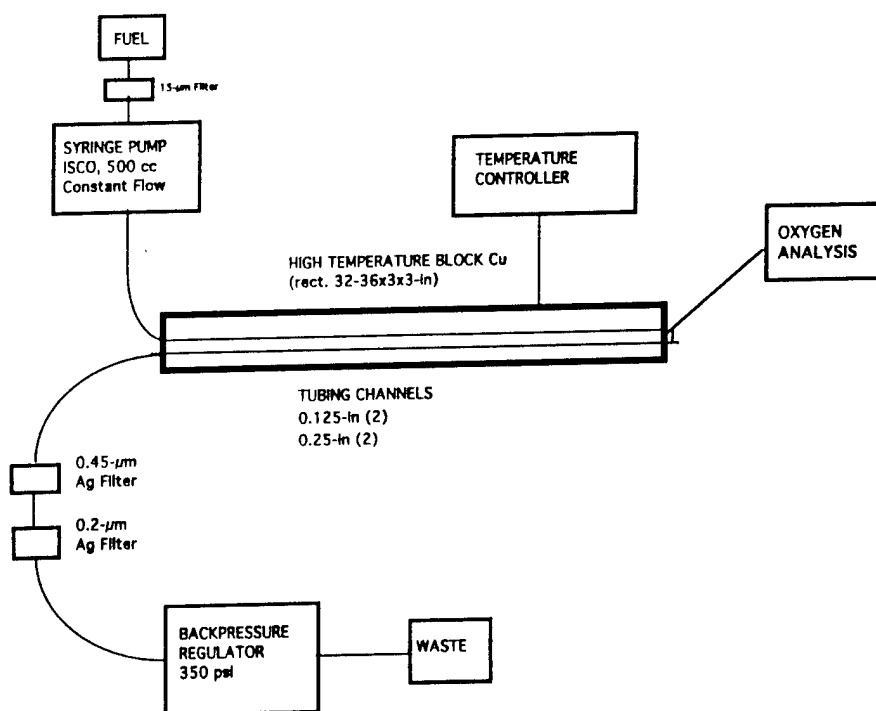


Figure 1. Schematic Diagram of Apparatus (NIFTR)

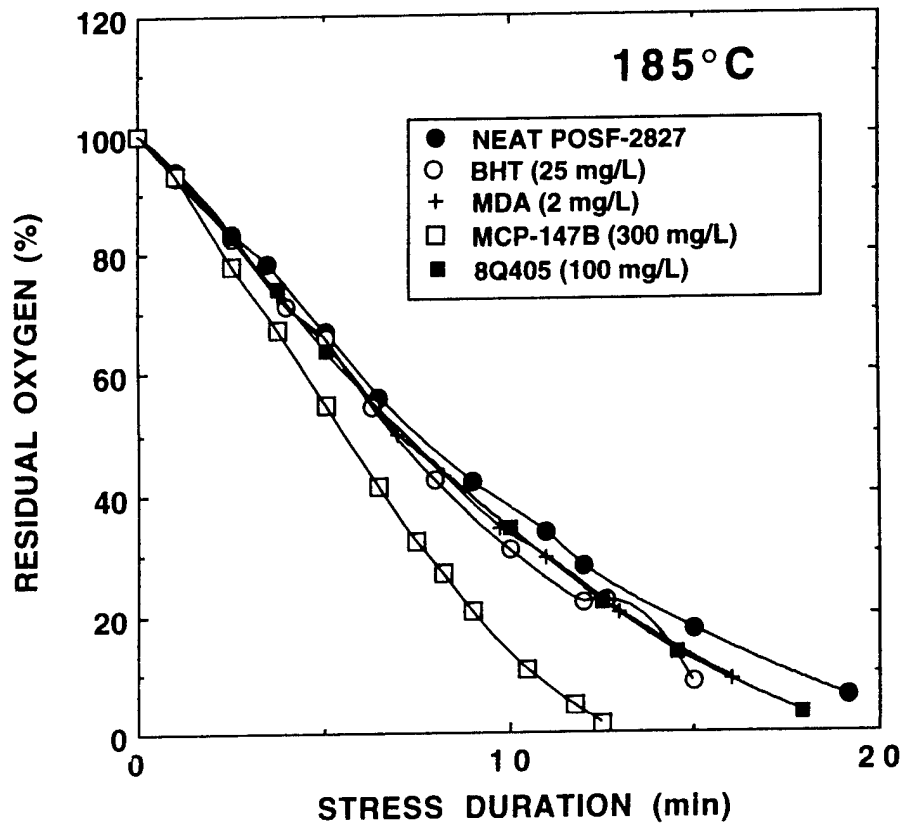


Figure 2. Consumption of Dissolved Oxygen at 185°C in Neat and Additized Fuel.

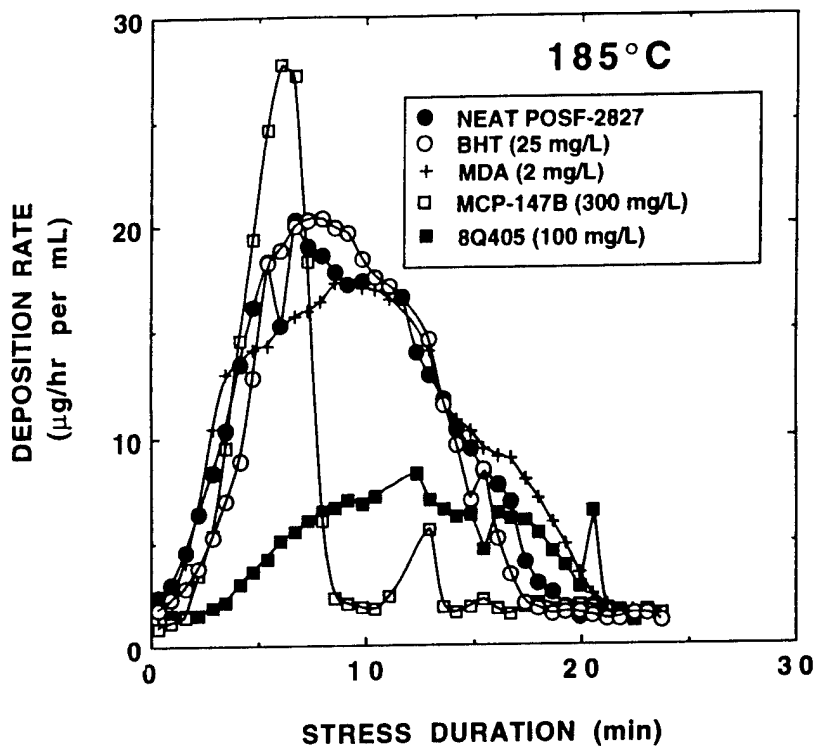


Figure 3. Surface Deposition Rates for Neat and Additized Fuel as a Function of Stress Duration at 185°C.

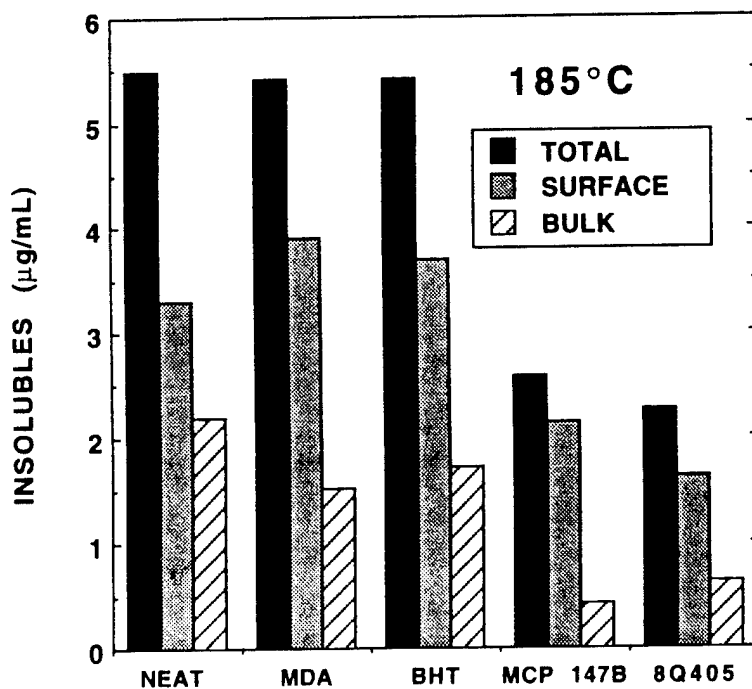


Figure 4. Bulk, Surface, and Total Insolubles Formed at 185°C.

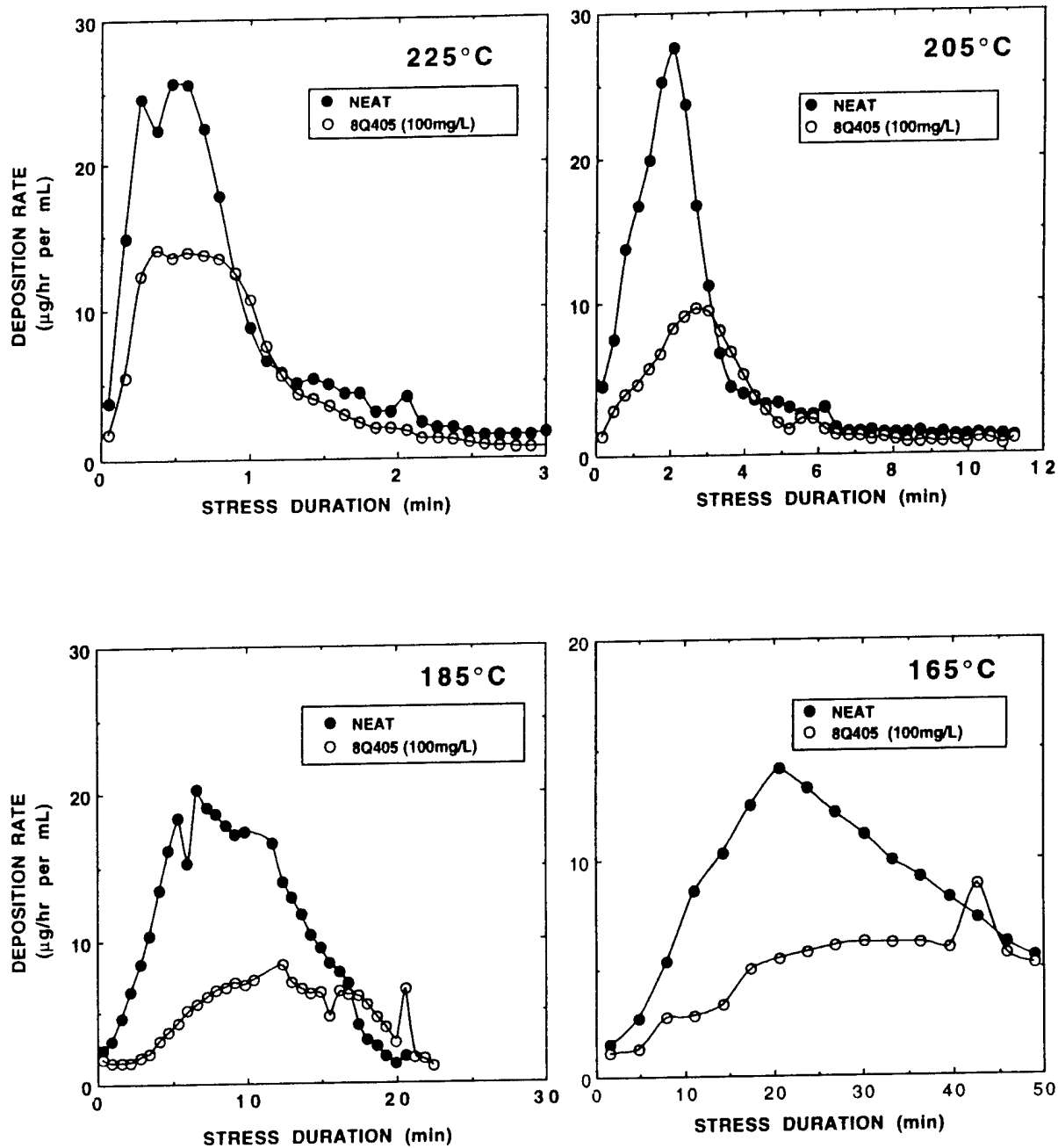


Figure 5. Deposition Rate. Stress Time Dependence at Series of Temperatures

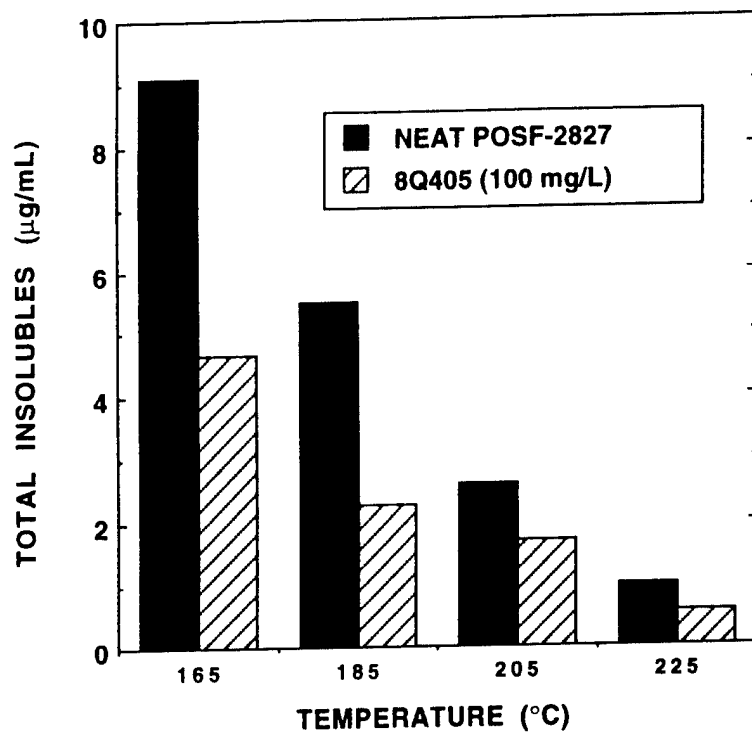


Figure 6. Total Insolubles as a Function of Temperature.

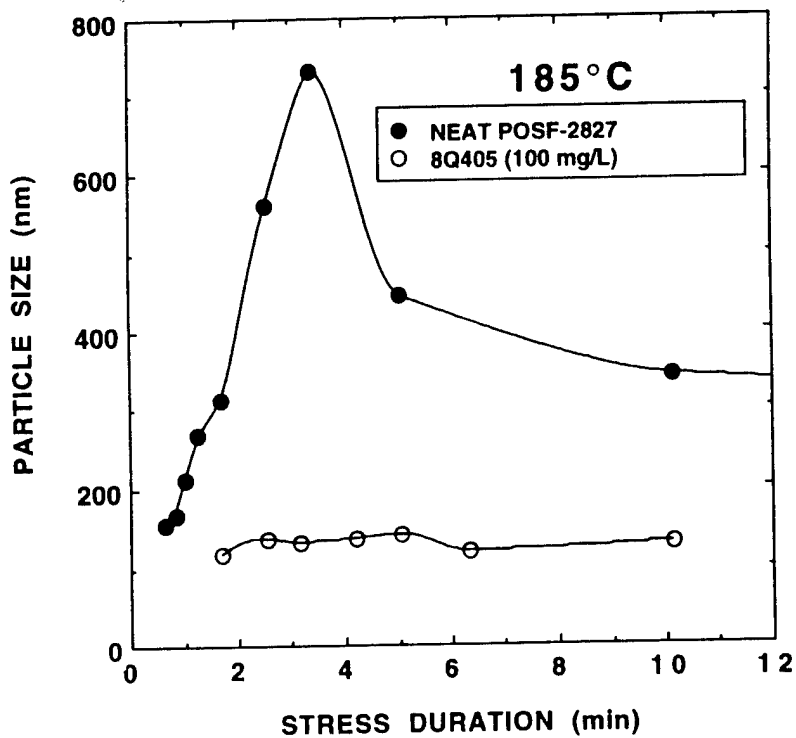


Figure 7. Particle Size of Insolubles as a Function of Stress Duration at 185°C.

E. G. Jones

W. J. Balster

M. E. Post

Systems Research Laboratories, Inc.,
Dayton, OH 45440

Degradation of a Jet A Fuel in a Single-Pass Heat Exchanger

The formation of bulk and surface insolubles in a Jet A fuel during a single pass through heated stainless-steel tubes has been studied. Low temperature and low flow rates were utilized to produce near-isothermal conditions. In a second series of experiments, depletion of oxygen in the fuel saturated with respect to room-temperature air was measured under identical isothermal conditions. At a wall/bulk-fuel temperature of 185°C, rates of surface deposition and oxygen depletion were correlated; the maximum in the surface-deposition rate was found to occur after the Jet A fuel was stressed sufficiently that the dissolved oxygen was totally consumed. Results are discussed in terms of the autoxidation of the Jet A fuel and the concurrent production of deleterious bulk and surface insolubles.

Introduction

The thermal oxidative stability of jet fuels is of major importance because of the use of fuel as the primary heat sink in military aircraft. Increased aircraft performance creates a greater heat load to be dissipated through heat exchangers into the aviation fuel. At elevated temperatures oxidative degradation of the fuel takes place with the concurrent formation of bulk insolubles and surface deposits, both of which can greatly reduce engine performance and lead to downtime or engine failure.

Knowledge of the mechanism and kinetics of fuel degradation can be used to improve aircraft performance through fuel selection, blending, or the introduction of additives. In addition, acquisition of kinetic parameters describing the degradation processes can be used in conjunction with global-modeling programs to predict surface fouling under conditions that may not be readily achieved in the laboratory. Recent modeling by Katta and Roquemore (1992) has been successful in predicting accumulated wall deposition in injector feed-arm rigs.

The goal of the current study was to select a typical aviation fuel, subject it to isothermal stress within stainless-steel tubing using a single-pass heat exchanger, study the rates of both oxygen consumption and surface deposition, and evaluate bulk-particle formation. Typically fuel deposition studies in flowing rigs have involved high temperature, high flow, and large variation in bulk-fuel and wall temperatures in attempts to approximate actual engine conditions (Marteny and Spadaccini, 1986; Giovanetti and Szetela, 1986; Kendall et al., 1987; Chin et al., 1992; Chin and Lefebvre, 1993). Achievement of isothermal conditions in the current study required the use of relatively low flow rates

($< 2 \text{ cm}^3 \text{ min}^{-1}$) and wall temperatures ($< 205^\circ\text{C}$); however, the constancy of wall and bulk-fuel temperatures greatly simplified the kinetic analysis.

The particular aviation fuel chosen for this study was a straight-run distillate fuel, meeting all USAF specifications, obtained from Shell Oil and designated Jet A (SHELL) or POSF-2827. Previous USAF-funded studies (Jones et al., 1992; Heneghan et al., 1993) have shown this fuel to have a propensity for surface deposition; it was considered an ideal candidate for thermal-oxidative degradation studies.

Experimental

The Jet A (SHELL) had a breakpoint of 539 K from the Jet-Fuel Thermal-Oxidation Test (JFTOT) and a sulfur level of 0.079 percent (w/w). Kendall and Mills (1986) have shown that the presence of certain sulfur-containing compounds tends to inhibit oxidation, but at the expense of increased insoluble formation. A similar finding has been reported in static flask tests for the currently studied fuel (Jones et al., 1992). The Jet A (SHELL) fuel was used as received, without filtration.

All experiments were conducted inside stainless-steel (304) tubes using the isothermal heat exchanger shown in Fig. 1. The tubing (0.125-in. OD, 0.020-in. wall) was cleaned with 10 percent Blue Gold solution using ultrasound, followed by water and methanol rinses. Background surface carbon in 2-in. tube sections was typically 10–20 μg and varied slightly from batch to batch. A syringe pump (ISCO Model 500D) was employed to transfer the fuel in a single pass through a 32-in.-long heated section. As will be discussed later, a long heat exchanger is necessary for capturing a large fraction of the surface-depositing material. In fact, in some experiments it was necessary to pass the fuel through two lengths of heated section. This was accomplished by an external loop and a second pass through another groove in the heater block.

Contributed by the International Gas Turbine Institute and presented at the 38th International Gas Turbine and Aeroengine Congress and Exposition, Cincinnati, Ohio, May 24–27, 1993. Manuscript received at ASME Headquarters March 17, 1993. Paper No. 93-GT-534. Associate Technical Editor: H. Lukas.

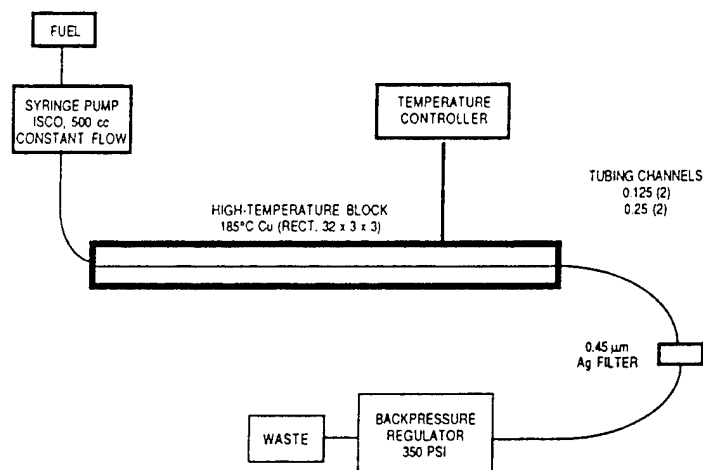


Fig. 1 Schematic diagram of isothermal heat exchanger

System pressure was maintained at 350 psi throughout the experiments to ensure a single phase. The fuel was stressed and then passed through an in-line 0.45- μm Osmonics silver-metal membrane filter. Deposition experiments were typically conducted over a 6-h time period, after which the tube was allowed to drain overnight and was then cut into sixteen 2-in. sections, which were rinsed with heptane and placed in a vacuum oven (115°C) for a minimum of 12 h. The filter was rinsed with heptane to remove residual fuel and was subjected to the same vacuum-oven conditions. Quantification of the total carbon in the filter and in the tube section was completed using a LECO RC-412 surface carbon analyzer. Deposits of this type generally contain ~ 80 percent carbon. Based on the nomenclature and heptane insolubility, the increased surface carbon was in the form of insoluble solids (*IS*) or insoluble gums (*IG*). Additional analyses of the filter deposits indicated that soluble gums (*SG*) were negligible and that the bulk particles were ~ 50 percent *IS* and ~ 50 percent *IG*.

Two basic experiments were conducted. In the first the fuel was passed through the tube at a fixed flow rate for 6 h, and the surface and bulk insolubles were quantified as described above. Initially the fuel was passed at room temperature until all the trapped air pockets were removed; then the desired fuel flow rate was set, and the copper-block heaters were turned on. Figure 2 shows the time required for the block to reach a setpoint of 185°C; the 10 min required to achieve equilibrium is considered negligible compared to the 360-min test duration. In the second type of experiment, the relative amount of dissolved oxygen present in the stressed fuel was measured using an in-line Hewlett-Packard gas chromatograph modified at the University of Dayton Research Institute (Rubey et al., 1992). In these experiments dissolved oxygen was evaluated for a series of flow rates, providing different stress intervals in the heated section. The data were represented as percent residual oxygen versus stress duration, with 100 percent corresponding to the amount

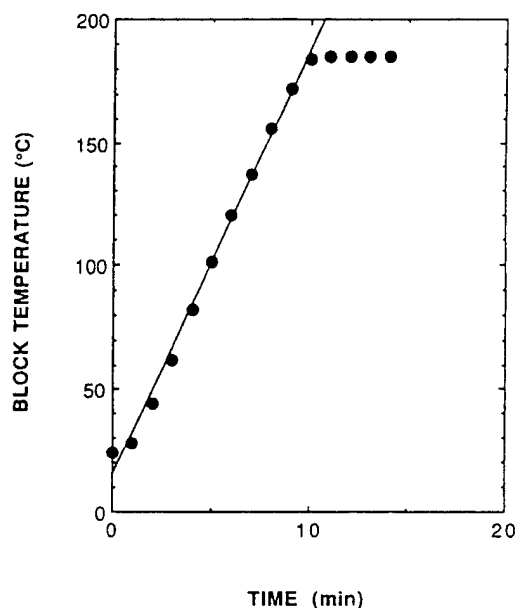


Fig. 2 Time required to achieve preset block temperature (185°C). Flow 1.0 $\text{cm}^3 \text{min}^{-1}$.

of oxygen in Jet A (SHELL) fuel saturated with respect to air at room temperature. Fuel was initially sparged with air under ambient conditions for 15 min to establish equilibrium air saturation. For some experiments where more dissolved oxygen was required, the fuel was initially sparged for 30 min with pure oxygen to achieve equilibrium levels of dissolved oxygen before the pump was filled. Similarly, for blank experiments where minimal oxygen was required, the fuel was sparged with helium for 30 min prior to the experiment. Although some residual dissolved oxygen remains after he-

Nomenclature

IS = Insoluble Solids (insoluble in heptane and acetone)
IG = Insoluble Gums (insoluble in heptane, soluble in acetone)
SG = Soluble Gums (soluble in heptane)

A = Arrhenius pre-exponential factor
E = Arrhenius activation energy
T = temperature (K)
R = gas constant
 JFTOT = Jet-Fuel Thermal-Oxidation Test

t = fuel stress duration
t' = experimental test duration
s = distance along heated tube
v = fuel velocity
k = rate coefficient
 USAF = United States Air Force

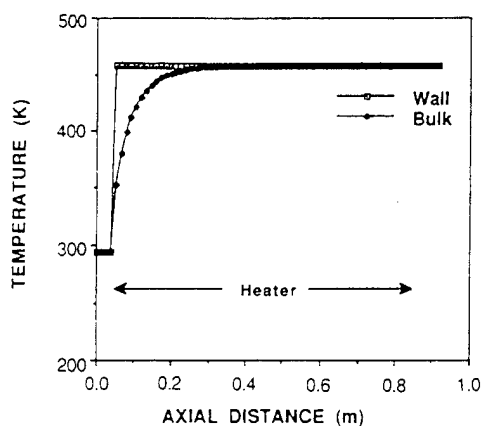


Fig. 3 Approach of bulk temperature to wall temperature. Flow $1.8 \text{ cm}^3 \text{ min}^{-1}$, block temperature 185°C .

lium sparge, it is estimated to be < 5 percent of the air-saturated value and effectively serves as a comparison blank. The air-saturated dissolved oxygen is typically taken to be 50 ppm (w/w), although absolute measurements were not made. All signals were corrected for naturally occurring argon that is not chromatographically separated.

Results and Discussion

In this section the following subjects will be addressed:

- Approach to isothermal test conditions
- Reaction time frame and experimental time frame
- Deposition
- Mass balance
- Effects of buoyancy/gravity
- Oxygen consumption and Arrhenius parameters

The thermo-oxidative reactions of Jet A fuel over the temperature range studied are described generally as auto-oxidation. The pertinent reaction steps have been well addressed in many texts. Some of the major aspects are summarized in the appendix, based on the treatment of Walling (1957).

Approach to Isothermal Test Conditions. Isothermal conditions are achieved when the cold fuel reaches the same temperature as the tube walls or the copper block. Figure 3 shows the calculated (Katta, 1992) approach to isothermal conditions for the bulk fuel at room temperature passing through a tube maintained at 185°C at a flow rate of $1.8 \text{ cm}^3 \text{ min}^{-1}$. It should be noted that for deposition studies discussed herein, $1.8 \text{ cm}^3 \text{ min}^{-1}$ represents a fast flow or a worst-case situation with respect to the achievement of isothermal test conditions. Clearly at least 75 percent of the tube experiences isothermal conditions at this flow rate.

Reaction Stress Duration and Experimental Test Time. In dynamic tests conducted isothermally, two distinct time frames are important. The first, or stress duration, is the time during which the fuel experiences the isothermal heated-block temperature. From a chemical standpoint, this represents the average time allotted for thermal-oxidative fuel degradation. At a fixed flow any position(s) along the tube is directly related to the reaction time or stress duration by the relation $t = s/v$. The average velocity, v , in turn, is directly proportional to the flow; and if an estimate is made for fuel expansion at 185°C (15 percent), the stress duration can be directly calculated from the flow and tube dimensions. In the current experiments this time frame is typically in the range 1–30 min.

The second time frame, t' , is the test duration. For exam-

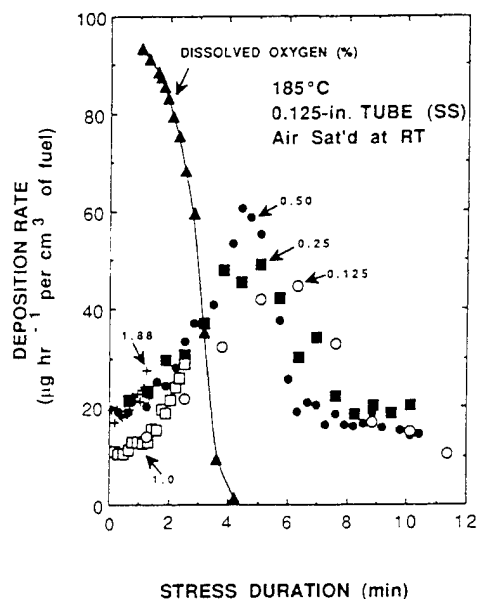


Fig. 4 Deposition from room-temperature air-saturated Jet A (SHELL) fuel at 185°C , 350 psi in 0.125-in. stainless-steel tubing as function of stress duration. Superimposed is dissolved oxygen (percent of air-saturated level at room temperature) as function of stress duration.

ple, $t' = 6 \text{ h}$ represents a reasonable time for achieving deposits above the background levels. For other fuel types such as hydrotreated fuels having reduced amounts of heteroatoms and containing antioxidant additives, much longer experimental test times are necessary for achieving consistently measurable deposition.

Deposition. Surface carbon burnoff provides information on the quantity of carbon in the deposit collected in a 2-in. section of tube over a 6-h test period. A deposition rate (μg carbon per time in the tube section per cm^3 of fuel) is calculated by dividing the amount of carbon in the tube section by the residence time in the tube section and the total amount of fuel passed through the tube. The deposition rate is equivalent to micrograms of carbon per time per volume of tube section and can be converted to micrograms of carbon per time per unit area of the tube section by dividing by the surface-to-volume ratio. For example, Fig. 4 is a plot of deposition rate ($\mu\text{g h}^{-1} \text{ per cm}^3$ of fuel passed) as a function of time, where the time is the stress duration t , for five different flows ranging from 0.125 to $1.88 \text{ cm}^3 \text{ min}^{-1}$.

Several important points should be made. First, at the highest flows, namely 1.88 and 1.0, the 32-in.-long tube encompasses only a small portion of the total profile since the fuel is passing through the tube so quickly that complete deposition is not possible. Presumably, a much longer tube, which would permit longer stress duration ($\sim 10 \text{ min}$), would encompass the entire deposition profile. This, in fact, is shown in the data at a flow of $0.5 \text{ cm}^3 \text{ min}^{-1}$, where a second pass was required for collecting all the data points. Second, for the slower flows, deposition rates increase with time, pass through a maximum, and finally decrease to the baseline. This observation indicates completion of a reaction within 10 min. Since background carbon levels have not been subtracted from the raw data, the baseline in Fig. 4 is ~ 10 – $20 \mu\text{g h}^{-1} \text{ per cm}^3$ of fuel. Third, within the noise of the data, the deposition rates peak in the vicinity of 4–6 min.

The equilibrium level of dissolved oxygen is dependent upon the partial pressure of oxygen during sparging; hence, sparging the fuel with pure oxygen as opposed to air will produce about five times more dissolved oxygen. The deposi-

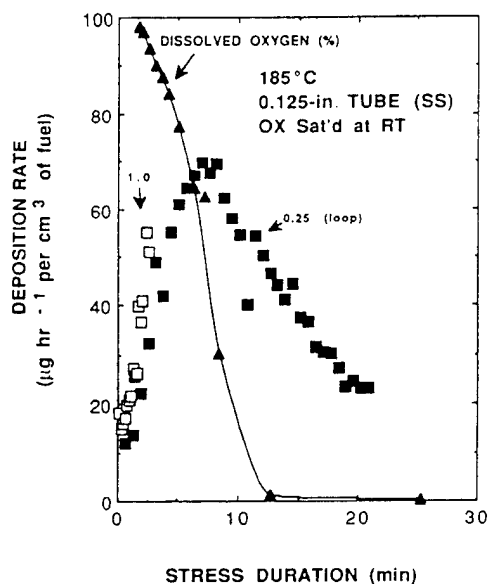


Fig. 5 Deposition from room-temperature oxygen-saturated Jet A (SHELL) fuel at 185°C, 350 psi in 0.125-in. stainless-steel tubing as function of stress duration. Superimposed is dissolved oxygen (percent of oxygen-saturated level at room temperature) as function of stress duration.

tion shown in Fig. 5 was obtained under the same conditions as those in Fig. 4; however, the plots in Fig. 5 were made with fuel saturated with respect to oxygen at room temperature. As noted above, the deposition rate increases from baseline, passes through a maximum, and slowly drops, approaching baseline. The data collected at a flow rate of 0.25 $\text{cm}^3 \text{ min}^{-1}$ were obtained in two complete heat-exchanger passes, i.e., 64 in. of stainless-steel tubing. The effects of additional oxygen are not manifested in significantly higher deposition rates but in a broadened deposition profile. The maximum shifts to ~7–8 min, and the total deposition remains incomplete after 21 min. Clearly, the total amount of deposit has increased. The quantification of the total surface deposit and the filter deposit will be discussed in the following section.

Mass Balance. Figure 4 shows that plotting the deposition rate as a function of stress duration brings the deposition peaks into near coincidence. It is not clear whether the small apparent differences in peak location are significant or whether the profiles are the same within experimental uncertainty. However, it should be obvious that when the flow rate is such that the stress duration is < 8 min, not all of the precursors to deposition will have a chance to deposit by diffusion to the walls. In other words, many deposition precursors will pass through the tube and be trapped on the filter, provided they can be stopped either by adsorption or filtration. In Fig. 6, the total amount of deposit evaluated by integrating all the surface-deposited carbon and adding the filtered carbon is plotted as a function of stress duration.

Note that the total carbon produced from 1 cm^3 of fuel increases with stress duration for ~5 min and remains nearly constant for the next 20 min. These data clearly show that there is a maximum amount of carbonaceous material that can be made in one cubic centimeter of fuel at 185°C. This value is ~5 $\mu\text{g cm}^{-3}$ for air-saturated fuel. If the data from Fig. 5 are used, with fuel saturated with respect to pure oxygen, the total is 25.1 $\mu\text{g cm}^{-3}$ or five times more than that for the air-saturated fuel. This factor represents the difference in the total amount of oxygen available for reaction and points to the crux of the observed deposition, namely, the quantity of dissolved oxygen.

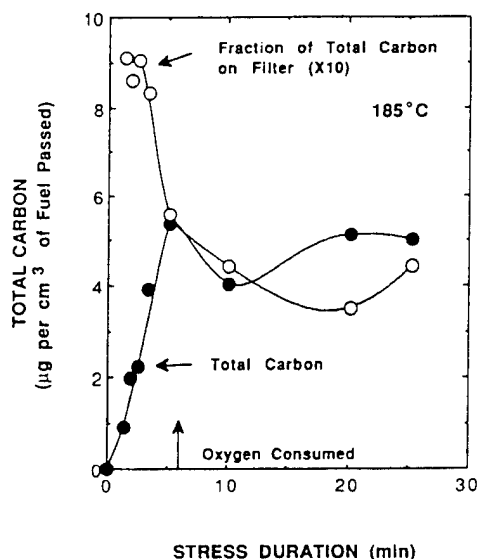


Fig. 6 Total carbon in surface deposits and bulk insolubles formed as function of stress duration. Superimposed is that fraction of total carbon measured on filter.

Also plotted in Fig. 6 is the fraction of the total material present in the filter. As discussed above, for slow flows where the total deposition can be completed within the heat exchanger, the filtered bulk fraction is minimal (~40 percent of the total). At high flows where the deposition cannot be completed within the heat exchanger owing to its limited length, the deposition precursors are captured preferentially by the filter, and the fraction approaches 100 percent for the shortest stress duration or fastest flow. In summary, the total amount of carbonaceous material is being partitioned between the tube surface and the in-line filter.

It is important to note that some fraction of the bulk particles will not adhere to the tube walls. These are *IS* and *IG* formed in the bulk stressed fuel that are distinct from the deposition precursors. From Fig. 6 one can estimate that of the total 5 μg of carbon collected from each cubic centimeter of fuel, 40 percent, i.e., 2 μg , is obtained even when the maximum amount of deposition has occurred. These nondeposition bulk particles, as mentioned earlier, are present ~50 percent as *IS* and ~50 percent as *IG*. The remaining 3 μg of carbon is associated with deposition precursors and, after 10 min of stressing, will be deposited on the inner tube walls or, with shorter stress time, in part on the filter. Such precursors, when present on the filter, are acetone soluble, i.e., *IG*. In summary, at 185°C, given sufficient stressing (~5 min), one cubic centimeter of the Jet A (SHELL) fuel will produce 1 μg of nondeposition *IG*, 3 μg of deposition precursor in the form of *IG*, and 1 μg of a nondeposition *IS*. Stressing up to 25 min fails to produce additional insolubles because the insoluble-forming reactions are complete.

Despite the fact that the deposition precursor collected in the bulk is an *IG*, the deposit is subjected to up to 6 h of further heating after deposition occurs. As a result, surface deposits cure to become primarily *IS*.

Buoyancy/Gravity. The single-pass heat exchanger used to obtain the data in Figs. 4 and 5 was operated in a horizontal configuration. Concerns arise about the possible role of buoyancy or, more seriously, gravity in the observed deposition. The low flow rates and the near-equilibrium conditions would tend to reduce the significance of buoyancy; however, gravitational effects must be addressed. In some of the previous studies in this laboratory with flasks operated in

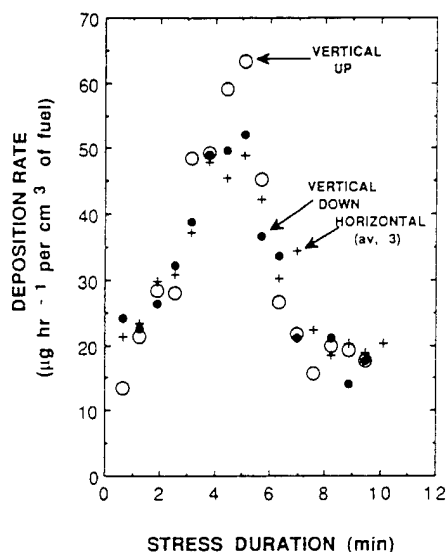


Fig. 7 Deposition measured using horizontal or vertical configuration of heat exchanger: buoyancy/gravity check. Flow $0.25 \text{ cm}^3 \text{ min}^{-1}$.

a static mode, it was concluded that surface deposition follows pseudo-zeroth-order kinetics and that bulk insolubles (which are most influenced by gravity) do not contribute to surface deposition (Jones et al., 1992). In order to compare deposition on tubes with and without gravitational effects along the tube, the deposition was studied both horizontally and vertically. Also, deposition was studied for fuel passing upward and downward through the heat exchanger in the vertical configuration. The results, shown in Fig. 7, clearly demonstrate that under the current test conditions (namely, 185°C , slow flow, and 0.125-in. tubes), buoyancy/gravitational effects are negligible.

Oxygen Depletion and Arrhenius Parameters. The oxygen depletion measured in a separate experiment but under the same deposition conditions is also plotted in Figs. 4 and 5. The very close coupling between oxygen loss and surface deposition is obvious. In contrast, in a hydrotreated fuel where the dissolved oxygen is removed at faster rates, concomitant deposition at 185°C is not observed. Based upon the stress duration required for deposition and that required for oxygen depletion, the precursor to deposition must be an early and primary autoxidation product. This further explains the existence of a maximum in the deposition rate. Once the oxygen has been totally consumed, the deposition precursor soon forms and subsequently diffuses to the wall.

The importance of oxygen in determining the total amount of bulk or surface deposits is readily apparent in Fig. 6 where the total amount of bulk and surface deposits increases until the oxygen is totally consumed (~ 4 min) and then remains constant for up to 20 min of additional heat stressing. The close coupling of both surface deposits and bulk particles to the availability of oxygen is pronounced.

It is apparent from the oxygen loss depicted in Figs. 4 and 5 that the rate of oxygen consumption increases as the oxygen is consumed. This sigmoid behavior is well known in the autoxidation of hydrocarbons, particularly in the absence of an initiator, and it arises from autocatalysis (cf. appendix). It is beyond the scope of the current paper to address this area; however, hydroperoxides, ROOH, are a primary autoxidation product and when they are formed in abundance, the biomolecular reaction R(1) can occur

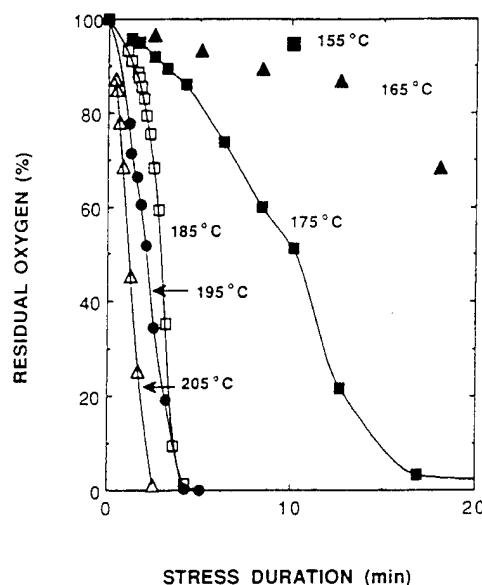


Fig. 8 Residual dissolved oxygen in Jet A (SHELL) fuel as function of fuel stress duration (100 percent corresponds to air saturation at room temperature)

This provides a lower energy free-radical initiation route, thereby increasing the overall oxygen consumption with ROOH production. Walling (1957) has discussed this area in detail.

The depletion of oxygen has also been monitored at 205, 195, 175, 165, and 155°C . A representation of most of the data is shown in Fig. 8. Because of the strong dependence of rate upon temperature, not all of the data can be visualized in a single plot. Significantly at temperatures such as 205 and 195°C where autocatalysis is less pronounced, it is clear from the linear oxygen loss that the reaction kinetics are zeroth order down to at least 20 percent residual oxygen and possibly lower. Recent data obtained using the Jet A (SHELL) fuel with an additive package have indicated that zeroth order describes the reaction down to < 10 percent residual oxygen (Jones and Balster, 1993). Under the experimental test conditions, results indicate reaction in an oxygen nonlimited regime. Clearly, at lower oxygen concentration the reactions must convert to oxygen-limited behavior when insufficient oxygen molecules are present to react with all the hydrocarbon free radicals. Reactions in flowing rigs with fuel saturated with respect to air are best described by oxygen nonlimited kinetics (i.e., zeroth order in oxygen). This explains the anomaly in Figs. 4 and 5 where five times more oxygen does not produce a significant increase in the deposition rate. It does produce five times more insolubles but much more time is required.

Assuming that the oxygen loss obeys Arrhenius kinetics, i.e., $k = A \exp(-E/RT)$, a plot of $\ln k$ versus $10^3/T$ has a slope E/R and an intercept A . The Arrhenius plot for the rate data is given in Fig. 9 over a 50-deg temperature range. It should be noted that experimental difficulties preclude extending this range significantly. At higher temperatures, oxygen consumption is so rapid that faster flows are needed, and these introduce large errors due to the time required to reach isothermal conditions. At low temperatures, relatively long times are required to establish equilibrium, and signal drift in the oxygen analyzer becomes significant.

The Arrhenius parameters best fitting the data are $E = 35.8 \text{ kcal mole}^{-1}$ and $A = 2.2 \times 10^{11} \text{ mole liter}^{-1} \text{ s}^{-1}$. The units of A are consistent with zeroth-order oxygen loss. Heneghan et al. (1993) have reported Arrhenius parameters

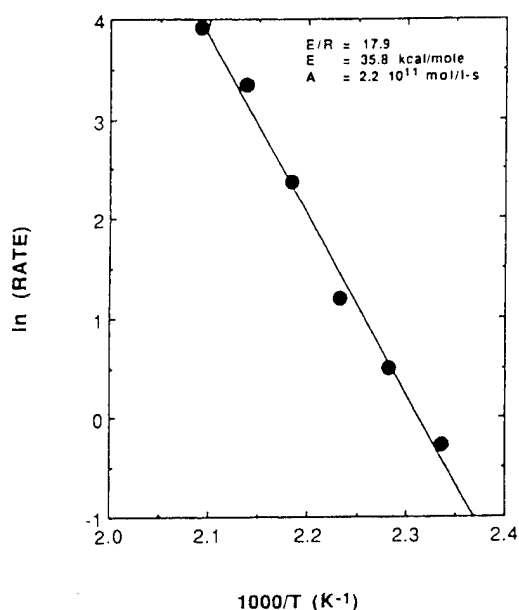


Fig. 9 Arrhenius plot for Jet A (SHELL) fuel over temperature range 155–205°C (units of rate are percent air saturation at room temperature per min)

for this fuel, which are calculated from deconvoluting oxygen loss over a broad temperature range, assuming first-order loss of oxygen. Despite the order difference, the activation energies are remarkably similar (compare 35.5 kcal mole⁻¹). The pre-exponential factors cannot be compared due to the order difference.

Conclusions

The thermo-oxidative behavior of a commercial Jet A fuel has been studied isothermally as a function of stress time at 185°C by monitoring the dissolved oxygen, the time-dependent surface deposition, and the total amount of bulk insolubles. All conclusions are based upon isothermal low-flow conditions that, by experimental design, are not representative of engine conditions. Turbulence under high-flow conditions tends to sweep deposition precursors and other insolubles downstream; these effects can be addressed only by global modeling. Modeling studies with the methods of Katta and Roquemore (1992) are currently under way using the fundamental chemical results reported herein. The following conclusions are drawn:

- All oxygen is consumed in 4 and 12 min, for room-temperature air- and oxygen-saturated fuel, respectively.
- Oxygen loss is characterized by zeroth-order kinetics, with autocatalysis occurring as oxygen is consumed. From 155 to 205°C the initial rate of oxygen loss is accurately described by the Arrhenius rate expression, with $A = 2.2 \times 10^{11}$ mole liter⁻¹ s⁻¹ and $E = 35.8$ kcal mole⁻¹.
- Air-saturated fuel reacts in an oxygen nonlimited regime.
- As oxygen is depleted, deposition on the inner wall of the fuel lines increases, passes through a maximum, and then decreases to baseline, indicating the formation and consumption of a deposition precursor. In general, the occurrence of a maximum in deposition rate along a heated tube is ascribed to oxygen depletion.
- Deposition profiles are brought into near coincidence by plotting deposition rate as a function of stress duration.
- When one cubic centimeter of air-saturated fuel is stressed more than 5 min, insoluble products contain ~5 µg of carbon; 1 µg is ascribed to both IS and IG, which do not

adhere to the tube, and 3 µg is assigned to a deposition precursor existing as an IG.

- The total quantity of insolubles is proportional to the dissolved oxygen.
- Low flow rates tend to focus the fouling problem near the heat source; high flow rates tend to sweep the deposition precursors and other bulk particles downstream and effectively change the location of the fouling problem.
- The close coupling between oxygen consumption and the observation of deposits is ascribed to the presence of deleterious sulfur compounds. For example, although a hydrotreated Jet A-1 fuel with diminished sulfur content reacts about three times faster than the Jet A (SHELL), it does not display significant deposition concurrent with oxygen consumption.

Acknowledgments

This work was supported by and performed at Wright Laboratory, Aero Propulsion and Power Directorate, Wright-Patterson Air Force Base, OH, under USAF Contract No. F33615-90-C-2033. The authors would like to thank Mr. Tim Gootee for performing the surface carbon analyses. The authors acknowledge valuable discussions with T. F. Williams and C. R. Martel concerning the heat-exchanger construction and with W. A. Rubey concerning oxygen analysis.

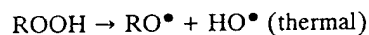
References

- Chin, J. S., Lefebvre, A. H., and Sun, F. T.-Y., 1992, "Temperature Effects of Fuel Thermal Stability," *ASME JOURNAL OF ENGINEERING FOR GAS TURBINES AND POWER*, Vol. 114, pp. 353–358.
- Chin, J. S., and Lefebvre, A. H., 1993, "Influence of Flow Conditions on Deposits From Heated Hydrocarbon Fuels," *ASME JOURNAL OF ENGINEERING FOR GAS TURBINES AND POWER*, Vol. 115, pp. 433–438.
- Giovanetti, A. J., and Szelata, E. J., 1986, "Long Term Deposit Formation in Aviation Turbine Fuel at Elevated Temperature," *AIAA Paper No. 86-0525*.
- Heneghan, S. P., Martel, C. R., Williams, T. F., and Ballal, D. R., 1993, "Studies of Jet Fuel Thermal Stability in a Flowing System," *ASME JOURNAL OF ENGINEERING FOR GAS TURBINES AND POWER*, Vol. 115, pp. 480–485.
- Jones, E. G., Balster, W. J., and Anderson, S. D., 1992, "Formation of Insolubles in Jet Fuels: Effects of Oxygen," *Preprints Symposia—Structure of Jet Fuels III*, Division of Petroleum Chemistry, Inc., American Chemical Society, Washington, DC, Vol. 37, No. 2, pp. 393–402.
- Jones, E. G., and Balster, W. J., 1993, to be published.
- Katta, V. R., and Roquemore, W. M., 1992, "A Numerical Method for Simulating the Fluid-Dynamic and Heat-Transfer Changes in a Jet-Engine Feed Arm Due to Fouling," *AIAA Paper No. 92-0768*.
- Katta, V. R., 1992, private communication.
- Kendall, D. R., and Mills, J. S., 1986, "Thermal Stability of Aviation Kerosines: Techniques to Characterize Their Oxidation Properties," *I & EC Product Research and Development*, Vol. 25, pp. 360–366.
- Kendall, D. R., Houlbrook, G., Clark, R. H., Bullock, S. P., and Lewis, C., 1987, "The Thermal Degradation of Aviation Fuels in Jet Engine Feed-Arms: Part I—Results From a Full-Scale Rig," 30th International Gas Turbine Congress, Tokyo, Japan, Oct. 26–31.
- Marteney, P. J., and Spadaccini, L. L., 1986, "Thermal Decomposition of Aircraft Fuels," *ASME JOURNAL OF ENGINEERING FOR GAS TURBINES AND POWER*, Vol. 108, pp. 648–653.
- Rubey, W. A., Tissandier, M. D., Striebig, R. C., and Tirey, D. A., 1992, "In Line Gas Chromatographic Measure of Trace Oxygen and Other Dissolved Gases in Flowing, High-Pressure, Thermally Stressed Fuel," *Preprints Symposia—Structure of Jet Fuels III*, Division of Petroleum Chemistry, Inc., American Chemical Society, Washington, DC, Vol. 37, No. 2, pp. 371–376.
- Walling, C., 1957, *Free Radicals in Solution*, Wiley, New York.

APPENDIX

Autoxidation

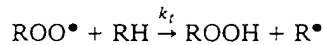
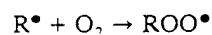
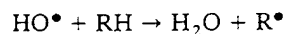
Initiated with trace amount of hydroperoxide (ROOH)



Initiated with large amounts of hydroperoxide



Propagation $\text{RO}^\bullet + \text{RH} \rightarrow \text{ROH} + \text{R}^\bullet$



Termination $2\text{ROO}^\bullet \xrightarrow{k_t} \text{nonradicals}$

Assuming steady state in R^\bullet and ROO^\bullet , it can be shown that given sufficient dissolved oxygen,

$$-\frac{d[\text{O}_2]}{dt} = \frac{d[\text{ROOH}]}{dt} = k_p[\text{RH}] \left(\frac{R_i}{2k_t} \right)^{1/2}$$

where R_i is the rate of initiation.

Sulfur-containing fuel components react with ROO^\bullet , deplete the peroxy-radical concentration, and reduce the rate of oxygen consumption.



The Society shall not be responsible for statements or opinions advanced in papers or discussion at meetings of the Society or of its Divisions or Sections, or printed in its publications. Discussion is printed only if the paper is published in an ASME Journal. Authorization to photocopy material for internal or personal use under circumstance not falling within the fair use provisions of the Copyright Act is granted by ASME to libraries and other users registered with the Copyright Clearance Center (CCC) Transactional Reporting Service provided that the base fee of \$0.30 per page is paid directly to the CCC, 27 Congress Street, Salem MA 01970. Requests for special permission or bulk reproduction should be addressed to the ASME Technical Publishing Department.

95-GT-45

Copyright © 1995 by ASME

All Rights Reserved

Printed in U.S.A.

SURFACE FOULING IN AVIATION FUELS: AN ISOTHERMAL CHEMICAL STUDY

E. Grant Jones, Walter J. Balster, and James M. Pickard
Systems Research Laboratories, Inc.
A Division of Space Industries International, Inc.
Dayton, Ohio

ABSTRACT

Surface fouling in aircraft fuel lines that results from autoxidation of aviation fuel remains a serious and very complicated problem. This area has been studied using two Jet-A fuels, POSF-2827 and POSF-2980. The results of a series of dynamic experiments conducted in a single-pass, tubular heat exchanger operated at very slow flow rates under near-isothermal conditions are reported herein. Such studies, by minimizing complications resulting from fluid dynamics and heat flow, constitute a simpler global approach to the chemistry of fouling. The basis for the selection of experimental test conditions is discussed, and data from measurements of dissolved oxygen and surface deposition as a function of fuel stress duration are presented. The effects of parameters such as reaction temperature, tube diameter, experimental test time, and fuel dopants are considered.

NOMENCLATURE

BHT	:	2,6-di-tert-butyl-p-cresol, Antioxidant
CFD	:	Computational Fluid Dynamics
GC	:	Gas Chromatograph
JFTOT	:	Jet-Fuel Thermal-Oxidation Test
NIFTR	:	Near-Isothermal Flowing Test Rig
POSF-2827	:	Jet-A Fuel, Straight Run
POSF-2980	:	Jet-A Fuel, MEROX-Treated
USAF	:	United States Air Force

INTRODUCTION

Aviation fuels, when subjected to heat in the presence of oxygen, undergo degradation from autoxidation reactions, as summarized by Hazlett (1991). Insoluble products

formed in these reactions tend to foul heated surfaces, causing reduced efficiency and possible blockage in heat exchangers, hysteresis in servocontrols, and changes in nozzle geometry. As the primary heat sink in modern aircraft, fuel will experience increased thermal stress as aircraft performance is enhanced (Edwards, *et al.*, 1992). Each fuel has a unique composition; thus, the chemical reactions describing the autoxidation of one fuel will be different from those of all other fuels. Similarly, the reaction steps from formation of the initial free radical to the final production of insoluble carbonaceous surface deposits or bulk insolubles are too complex to have been outlined for aviation fuels. Minor fuel constituents containing hetero-atoms such as sulfur and nitrogen have been identified either as the primary cause of insoluble formation or as the source of catalysis which can accelerate autoxidation. Also, the conditions of high fuel velocity and nonuniform wall and bulk-fuel temperatures present in fuel lines create complicated fluid-dynamic conditions which are difficult to simulate and which change during each segment of a flight cycle.

Simulating the fuel-stress conditions experienced in fuel lines during flight requires expensive full-scale rigs and large fuel batches. An alternative approach taken in this laboratory has been the use of a simpler Near-Isothermal Flowing Test Rig (NIFTR) to simulate only the chemical conditions (i.e., the temperature and reaction time) by conducting experiments under near-isothermal conditions. The advantage of this approach is three-fold: 1) many complications from fluid dynamics are removed, 2) wall and bulk-fuel temperatures are the same, and 3) the global aspects of deposition can be described in terms of rate of deposition as a function of reaction time or fuel-stress duration. Since

reactions are studied over 100% oxygen conversion, an inherent normalization occurs through the use of a fixed amount of reactant, namely, the total amount of oxygen present in air-saturated fuel. It is assumed in this approach that 1 L of fuel stressed to 100% conversion will form the same quantity of insolubles as 1,000 L of fuel stressed to 0.1% conversion. The latter condition more nearly approximates that experienced in an actual aircraft; however, if chemistry is a controlling factor, then the reaction chemistry in controlled isothermal experiments will be the same as that which occurs in the field. This forms the basis for the near-isothermal approach to the study of fuel fouling. Clearly, when isothermal conditions are used, the thermal behavior of fuel must be studied over a range of different temperatures to obtain a broad view of fuel thermal stability.

The goals of the isothermal approach are to 1) isolate the global-chemical processes, 2) collect experimental data that describe the fouling chemistry as a function of reaction time, and 3) compare the thermal behavior of different fuels and establish a baseline for evaluating the efficiency of additives in reducing or delaying surface fouling. Additives such as antioxidants for slowing oxygen consumption, metal deactivators for chelating dissolved metals or passivating tubing walls, and dispersants or detergents for increasing solubility would appear to hold the most promise from a thermal-stability standpoint. Martel (1987) has summarized jet-fuel additives including (in addition to the above) corrosion inhibitors, lubricity improvers, icing inhibitors, static dissipators, and pipeline-drag reducers. Changes introduced by the hindered-phenol antioxidant additive BHT in both Jet-A fuels are presented, and several possible criteria for rating fuels and additives based upon near-isothermal test results are reviewed.

Longer-term goals, not addressed in the current study but a simple extension of the current approach, are to collect data at several temperatures, to derive kinetic parameters which may ultimately describe surface-fouling processes over a broad temperature range, and to use these values in CFD models for predicting fouling under actual aircraft conditions that are difficult to achieve in the laboratory. Models such as those developed by Katta (1993) have been successful in describing surface fouling for several rigs.

This paper describes progress toward obtaining baseline data at 185°C to reflect the surface fouling that occurs in two Jet-A fuels, POSF-2827 and POSF-2980. Included is the establishment of the optimum experimental conditions for studying fouling and for differentiating the fuels in a series. Experimental parameters such as tubing size, reaction-temperature range, surface conditions, and test duration must be considered. For example, a 6-hr test has been found to be adequate for quantifying insolubles and identifying reaction trends in POSF-2827 fuel (Jones and Balster, 1993); however, arguments presented herein indicate that, in general, longer tests of ~ 70-hr duration may be preferable.

EXPERIMENTAL ARRANGEMENT

Some general properties of the two fuels are given in Table 1. Although both fuels contain a significant amount of total sulfur, they meet all USAF specifications. POSF-2980 fuel has been treated using the MEROX technique to reduce the mercaptan odor through oxidation to the corresponding disulfide. Both are Jet-A fuels representative of those in commercial service. The antioxidant BHT was obtained from DuPont. Fuels were used as received, with minimal filtration (15 µm) for protection of the syringe pump.

The experiments were conducted using the NIFTR which has been described previously (Jones, *et al.*, 1993a,b). Figure 1 shows the heat exchanger as operated in the extended-pass mode to double the total reaction time. Fuel, which is saturated initially with respect to air and which contains 64 ppm (w/w) of oxygen, is pumped at a pressure of 350 psi through commercial stainless-steel (304) tubing clamped tightly in a 36-in. heated copper block. Most of the experiments were conducted using tubing with dimensions of 0.125-in.-o.d. and 0.085-in.-i.d.; in a few experiments larger tubing with dimensions of 0.25-in.-o.d. and 0.18-in.-i.d. was used. A pair of in-line Ag-membrane filters (0.45 and 0.2 µm) collected the non-adhering bulk insolubles.

Deposition rates were measured in 6-hr and ~ 70-hr experiments that were run continuously at a fixed fuel-flow rate; reaction time or stress duration was determined from the flow rate, tube dimensions, and location along the tube axis. The calculated times were reduced by 15% to compensate for fuel expansion. When the total test time was increased tenfold, the total volume of fuel increased tenfold. At the end of each test, the heated tube was cut into 2-in. sections, and the quantity of carbon in the deposits was determined from surface-carbon burnoff (LECO RC-412). Deposition rates were determined from the amount of carbon in each 2-in. segment, the increment of stress time within that segment, and the total quantity of fuel used. Each section provides one data point, representing the rate averaged over the entire test time (i.e., 6 - 70 hr). Deposition rate is expressed in units of micrograms of carbon per unit stress time per unit volume of fuel passed through the

Table 1
FUEL PROPERTIES

	POSF-2827	POSF-2980
Treatment	Straight Run	MEROX-treated
JFTOT Breakpoint	266	288
Total Sulfur (%)	0.079	0.061
Freezing Point (°C)	- 43	- 44
Aromatics (% vol)	19	17
Total Acid No. (mg KOH/g)	0.001	0.001

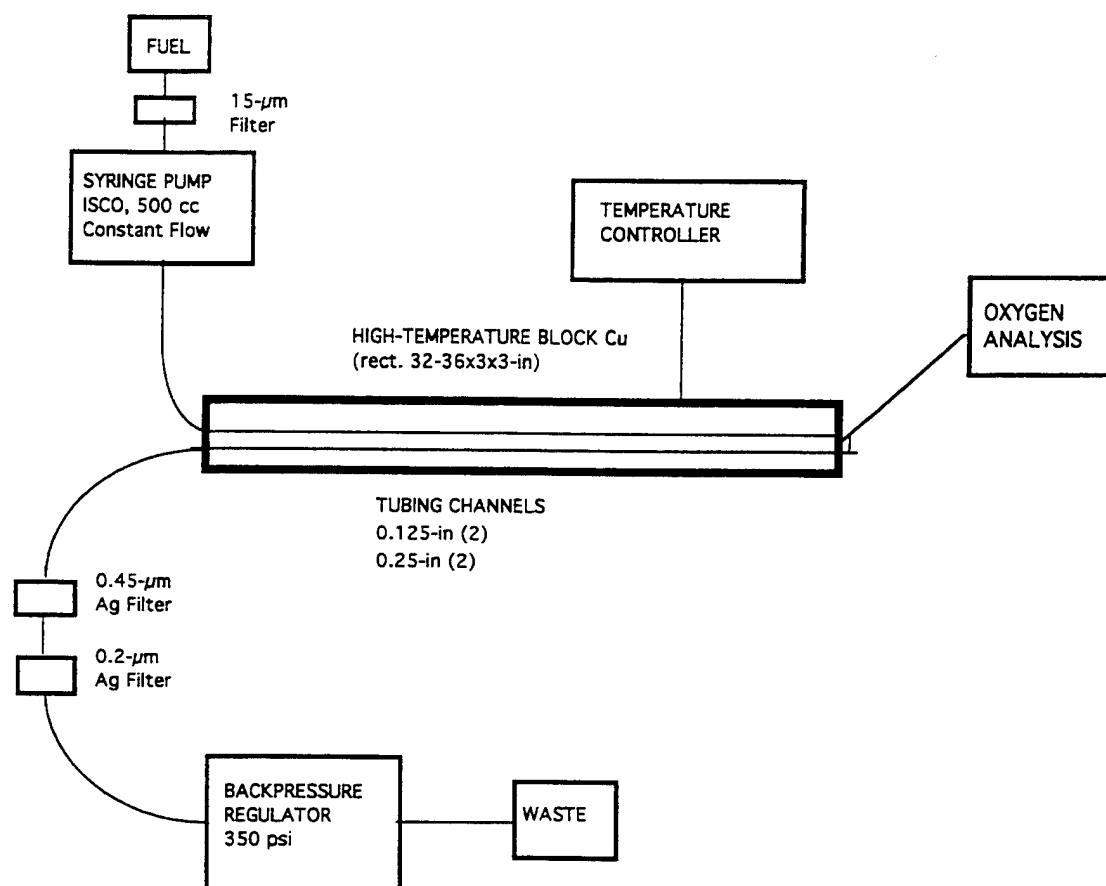


Figure 1. Schematic Diagram of Apparatus (NIFTR).

system. Nonadhering bulk insolubles were quantified by surface carbon burnoff of the in-line filters. Dissolved oxygen was measured in separate experiments using a 32-in. heated tube as a reaction cell and GC detection (Rubey, *et al.*, 1992); stress duration was changed by varying the flow rate. Cleaned stainless-steel tubes were used for measurements related to 6-hr deposition experiments where deposition occurs primarily on cleaned surfaces. In long-term tests, most deposition occurs on previously fouled surfaces; for comparison with deposition in this case, passivated tubes (Silcosteel, Restek Corporation) were used to minimize catalytic wall effects that occur during oxygen measurements.

RESULTS AND DISCUSSION

Selection of Optimum Test Conditions

Temperature Range. In many fuels a close correlation exists between oxygen consumption and deposition; thus, the temperature ranges of interest for oxygen depletion and surface deposition overlap. Experimentally, oxygen depletion can only be measured over a limited

temperature range of ~ 50 - 60°C for the following reason. At the high-temperature end, the reaction is very rapid, and higher fuel-flow rates are necessary for maintaining short residence times within the heated block. As a result the fuel does not achieve block temperature rapidly, i.e., the experiments depart significantly from isothermal. At the low-temperature end, the reaction is very slow, and residence times on the order of hours are necessary for complete consumption of the dissolved oxygen. Maintenance of GC-detector stability over extended periods of time can introduce significant errors into the measurements. Oxygen depletion in about 15 fuels has been studied in this laboratory, and dissolved oxygen has been found to be completely converted after 1 - 20 min of stressing at 185°C. The practical temperature range for oxygen measurements using the current techniques is 155 - 215°C.

Surface-fouling measurements are subject to similar temperature constraints. At the highest temperatures, reaction and subsequent deposition occur over a very narrow time interval; depending upon the fuel-flow rate, deposition occurs only in a limited region of the heated tube. Spatial deposition can be extended through higher flow rates, but at the expense of departure from isothermal conditions. At the lowest temperatures, very slow flow rates must be used

for total reaction of the dissolved oxygen. The difficulty arises from the fact that in a 6-hr test at 155°C, only about 25 mL of fuel are passed and a limited, minimal amount of deposit is collected. The practical temperature range for near-isothermal surface-fouling experiments is 145 - 225°C. A temperature of 185°C, the mid-point of the experimental range, was selected as the standard temperature for stressing neat jet fuels to obtain baseline surface deposition and dissolved-oxygen information.

Stress Duration. This parameter is controlled by rates of oxygen consumption and the deposition profile. The primary requirement is to provide sufficient residence time for completion of the oxygen reaction and subsequent deposition within the heated tube. Passing fuel through the heated block once or twice at a flowrate of 0.25 mL/min provides, respectively, 12 and 24 min of stressing at temperature. For the fuels studied, this time is sufficient for complete deposition to occur at 185°C within the heated block.

Test Time. This parameter was established for deposition experiments and determines the total amount of fuel passed through the system. The longer the test time, the greater the quantity of insolubles formed and the greater the signal/noise ratio. The measured deposition rates represent averages over the total test time. It has been reported (Jones and Balster, 1994a) that the dependence of deposition rate upon stress duration for POSF-2827 aviation fuel changes as the test time is extended from 6 to 70 hr. This observation was explained in terms of surface-dependent changes in the rate of oxygen consumption. The initial deposition on clean stainless-steel tubing is governed by a more rapid oxygen loss that is catalyzed by active sites on the cleaned surface. As deposits collect along the walls, active sites become covered, oxygen depletion is no longer surface catalyzed, and its rate and the rate of surface deposition decrease. This is manifested by a reduced deposition rate and a shift in the deposition profile to slightly longer stress times, i.e., residence times. Once the surface is completely covered by deposits, the deposition profile becomes independent of test time.

Figures 2 and 3 show the deposition rate for POSF-2827 and -2980, respectively, as measured in 6-hr (initial catalyzed rate) and in ~70-hr tests (constant deposition). The rate plotted has been corrected by subtracting the effects of background surface carbon not related to autoxidation. Also shown is the corresponding decay in dissolved oxygen as measured in a cleaned stainless-steel tube and in an inert tube. In general, POSF-2980 has a slower deposition rate and a faster oxidation rate. The profiles pertain to different conditions. The first (6-hr) describes deposition on cleaned stainless-steel tubing, and the second, the deposition mainly on previously fouled surfaces. Evidently POSF-2980 fuel displays deposition changes very similar to those reported for POSF-2827, namely, reduced rate and shift in the deposition profile as the test time is extended. The

amount of deposition with POSF-2980 fuel is less and, hence, the surface coverage and passivation will be less than for POSF-2827. Also, regions exist near the entrance and exit of the tubes where deposition is minimal, and these surfaces may continue to catalyze autoxidation.

Table 2 outlines some of the distinct advantages associated with both short- and long-term tests. One of the major considerations is the signal-to-noise ratio. For the current treatment, long-term tests which better reflect

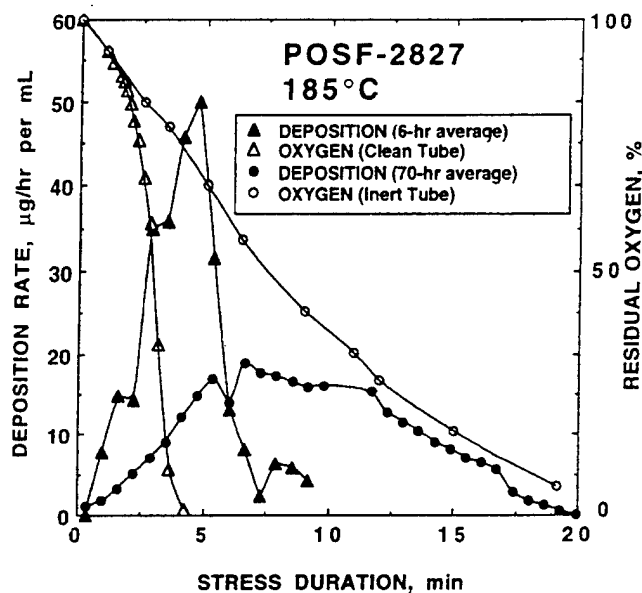


Figure 2. Deposition Rate and Residual Oxygen vs. Stress Duration for POSF-2827 Fuel Measured in 0.125-in.-o.d. Tubes.

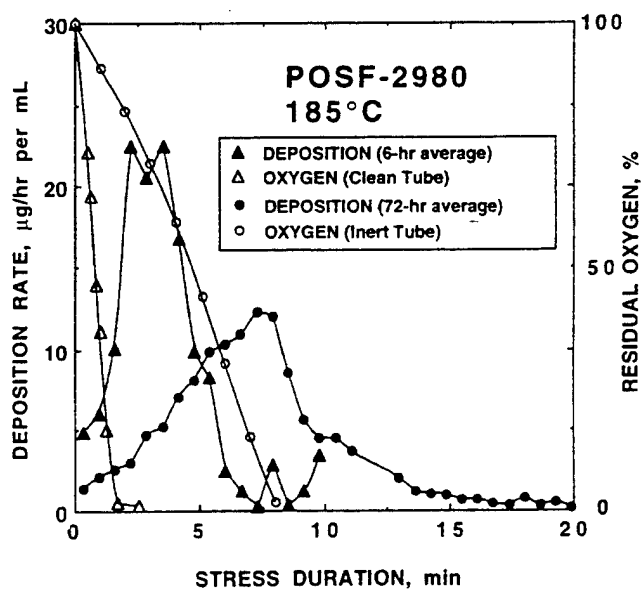


Figure 3. Deposition Rate and Oxygen Consumption vs. Stress Duration for POSF-2980 Fuel Measured in 0.125-in.-o.d. Tubes.

Table 2

ADVANTAGES: SHORT- VS. LONG-TERM TESTING

<u>Short Term (6 hr)</u>	<u>Long Term (~ 70 hr)</u>
One-day experiment	Weekend experiment
Deposition on cleaned surfaces	Better signal-to-noise ratio
Faster oxygen reaction (catalyzed)	Deposition on fouled surfaces
—	Slower oxygen reaction (surface passivated)
—	Reduced baseline correction to rate
Total insolubles per mL constant	Total insolubles per mL constant

deposition on fouled surfaces were selected to simulate conditions encountered in actual aircraft fuel lines. However, fuels which make few deposits may never lead to complete coverage of the original surfaces, even in 70-hr experiments. It is doubtful that virgin clean surfaces would be common in fuel lines, except for servocontrols where very clean surfaces are required for minimization of hysteresis. In the latter case there may be cause for concern since auto-oxidation in both of the fuels under study is catalyzed by cleaned surfaces.

Tubing Size. Since deposition in isothermal tests is expressed as a function of stress duration rather than axial tube distance, the rate profiles should be similar in tubing with different internal diameters. The deposition measured for POSF-2827 fuel using larger diameter tubes is shown in Fig. 4. As the test time is extended, the trends observed are the same as those in Fig. 2. Rates are reduced by about a factor of two because of the reduced surface-to-volume ratio. For most studies 0.125-in. tubes were selected to

minimize fuel volume within the heated block and also to minimize the time needed to achieve isothermal conditions. For example, to achieve the same stress time within the heated section using tubing with twice the internal diameter would require a four-fold increase in flow rate. The higher the flow rate, the longer the time required to bring fuel to temperature and the greater the departure from isothermal reaction conditions.

Tubing Surface. The nature of the initial surface is a controlling factor in deposition in 6-hr tests; however, once deposits have covered the metal surface, the deposition profile becomes constant. Thus, for long-term tests which produce deposits, the initial tubing surface is not a significant factor. It is for this reason that oxygen measurements were made using inert tubes.

Changes in Deposition Using Antioxidant BHT

POSF-2827 Fuel. The results of oxygen measurements at 185°C using the neat and additized fuel are shown in Fig. 5. Changes introduced by BHT at 25 mg/L fall within the reproducibility of the measurements. The rates are constant down to 30% residual oxygen, indicating oxygen unlimited kinetics. Below 30% the rate becomes oxygen limited, as evidenced by tailing. Walling (1957) has summarized the rate expressions for the reaction of oxygen at high (oxygen-unlimited) and low (oxygen-dependent) concentrations. The presence of certain types of sulfur compounds causes hydroperoxide concentration to remain low. Chain-breaking antioxidants such as BHT (hindered phenol) are ineffective in fuels containing large quantities of naturally occurring autoxidants. POSF-2827 fuel does produce hydroperoxides, but the measured steady-state concentration is very low (< 70 μ equivalents/L).

The corresponding deposition in the neat and additized fuel is given in Fig. 6. The two profiles are very similar. At this time it is not known whether the slight differences are real or whether they fall within experimental reproducibility. Based upon the similarity of the oxygen curves, it is concluded that BHT does not slow oxygen consumption nor does it significantly change the surface deposition rate in POSF-2827 fuel.

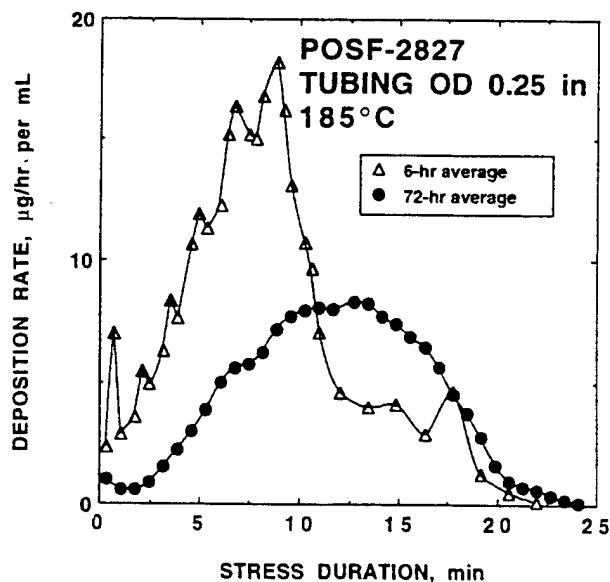


Figure 4. Deposition Rate vs. Stress Duration for POSF-2827 Fuel Measured in 0.25-in.-o.d. Tubes.

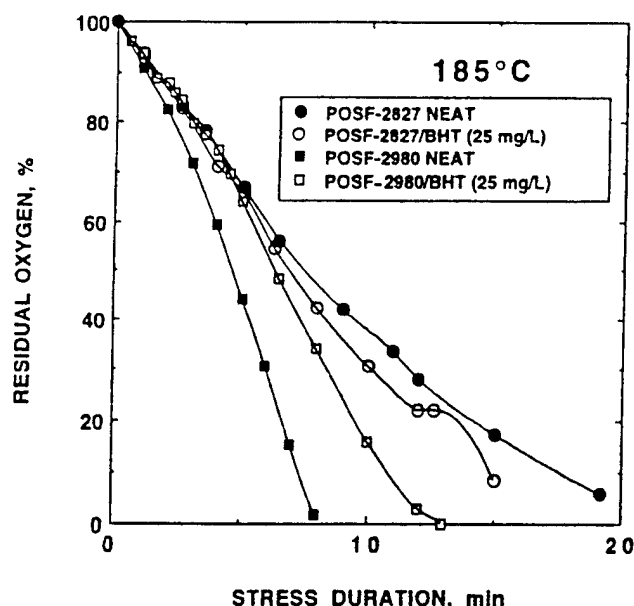


Figure 5. Oxygen Consumption in Neat and Additized POSF-2827 and -2980 Fuels.

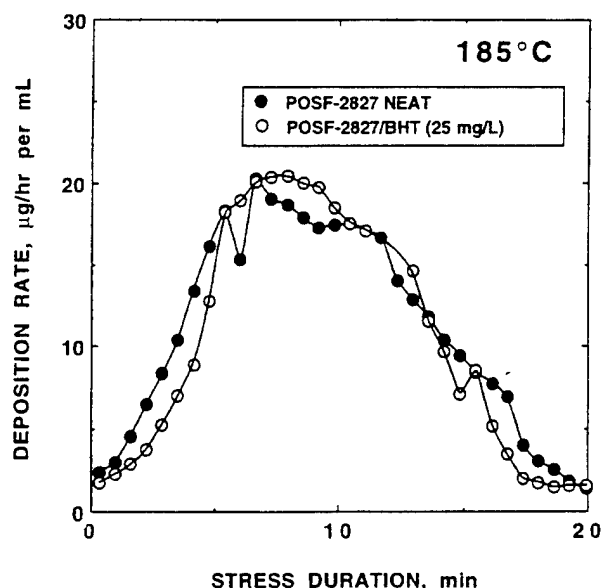


Figure 6. Deposition Rate in Neat and Additized POSF-2827 Fuel.

POSF-2980 Fuel. In contrast to the above results, BHT significantly slows the rate of oxygen consumption (see Fig. 5). The overall effect is a delay of ~ 2 min at 50% conversion and ~ 4 - 5 min at complete conversion. Clearly, fundamental differences exist in the autoxidation of these two Jet-A fuels. The hindered-phenol antioxidant at a concentration of 25 mg/L has a negligible effect on POSF-2827 and yet is very efficient in retarding oxygen reaction in POSF-2980.

The effect of BHT on the deposition profile is shown in Fig. 7. BHT causes a dramatic delay in surface deposition, as might be expected from the oxygen behavior and previous reports of correlation between oxygen reaction and deposition in Jet-A fuels (Jones and Balster, 1994b). The delay in the maximum of the deposition profile is 3 - 4 min, in reasonable agreement with the oxygen-loss data. However, as with POSF-2827 fuel, the total quantity of deposit (integral under curves) is unaffected by BHT.

Criteria for Comparing Fuels and the Effect of Additives

Based on the previous considerations, two obvious criteria for comparing fuels are the rate of oxygen consumption and the shape of the deposition-rate profile. Other quantitative criteria are the amount of bulk insolubles obtained directly from the in-line filters and the amount of surface insolubles obtained by integrating the area under the deposition profile. These quantities in units of micrograms per milliliter are summarized in the histogram in Fig. 8.

First, consider the impact of BHT. It does not reduce the amount of surface insolubles in POSF-2827 and causes a minor (10%) reduction in POSF-2980. BHT delays reaction in POSF-2980; but, given sufficient time to complete deposition, the total surface insolubles remain about the same. In actual service it is doubtful that all oxygen will be converted. This suggests that a more equitable way to assess the impact of BHT may be to compare surface insolubles formed after a limited stress duration, which is equivalent to considering the integral of the surface carbon as a function of stress duration; this is given in Fig. 9 for POSF-2980. Also plotted in this figure is the fractional

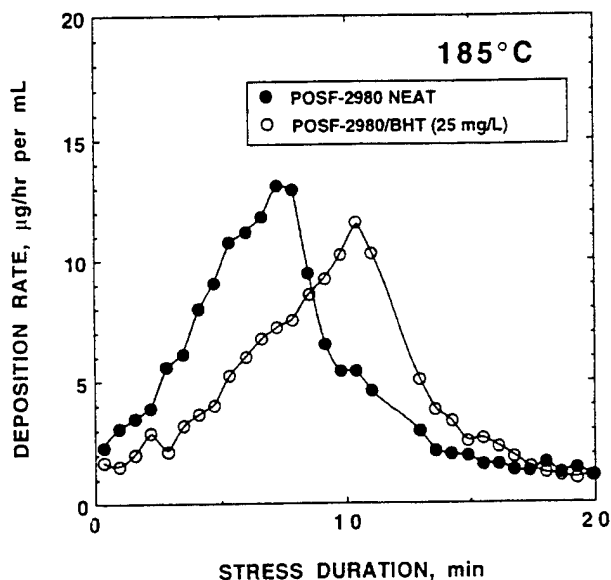


Figure 7. Deposition Rate in Neat and Additized POSF-2980 Fuel.

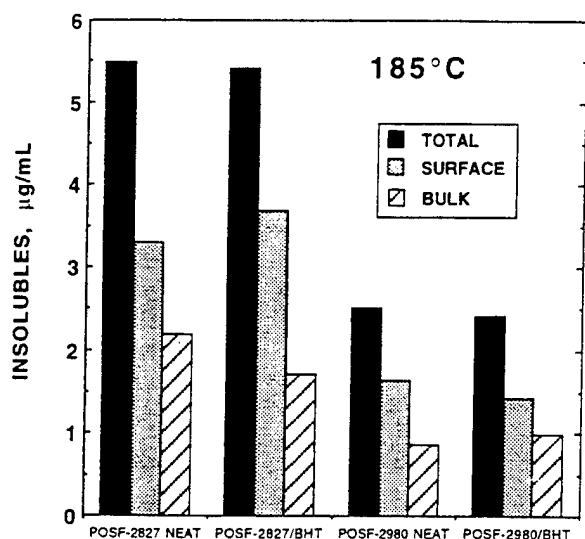


Figure 8. Quantification of Surface, Bulk, and Total Insolubles.

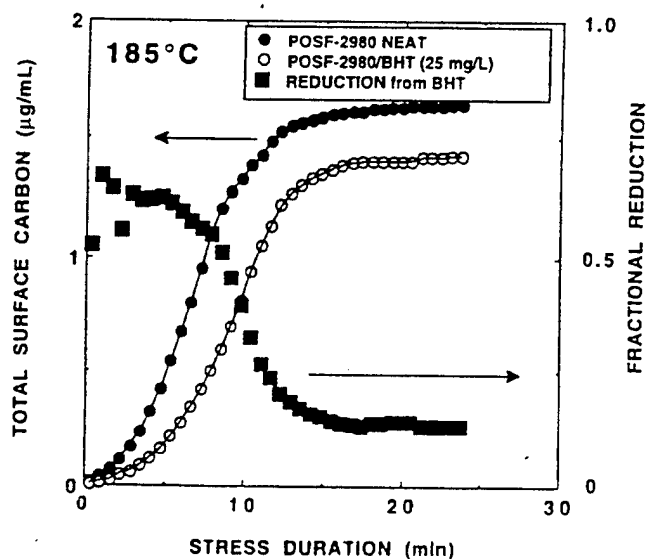


Figure 9. Plot of Total Surface Carbon (POSF-2980; neat, additized) and Fractional Reduction vs. Stress Duration.

reduction in surface deposits as a function of stress duration. After 10 min of stressing, BHT has reduced the total surface deposits by 35%; after only 5 min of stressing, the reduction is 60%. Clearly, comparison after shorter stress times best reflects the potential benefits of an antioxidant that serves primarily to delay reaction.

Second, compare the two Jet-A fuels. Figure 8 shows that POSF-2980 fuel produces less surface, bulk, and total insolubles at 185°C than POSF-2827 when these fuels are stressed to complete oxygen conversion and deposition. The difference is approximately a factor of two. However, if the comparison is based on the use of total surface

carbon formed over limited stressing as shown in Fig. 10, then the difference between the two fuels is much less for a shorter stress duration. Isothermal test results provide information for comparing fuels using many criteria. It should be noted that all current comparisons relate only to reaction at 185°C. Data collected at other temperatures may rank fuels differently. For example, POSF-2827 fuel has an inverse temperature dependence for total surface insolubles (Jones and Balster, 1994b). It is not known whether POSF-2980 behaves similarly or has a very different temperature dependence. Clearly, refinement of a ranking scheme for fuels and additives is a complicated process.

Finally, Table 2 indicates that short- and long-term tests produce the same amount of insolubles when expressed per unit volume of fuel. For example, the bulk, surface, and total insolubles from 6-hr tests with POSF-2827 fuel are 2, 3, and 5 μg/mL, respectively. The corresponding values for POSF-2980 are 0.83, 1.5, and 2.3. These sets of numbers are the same as the long-term values plotted in Fig. 8, within the experimental uncertainty of 10%.

CONCLUSIONS

Surface fouling that occurs at 185°C in two Jet-A fuels has been studied. Test conditions have been optimized to reflect fuel-dependent differences, and possible criteria have been outlined for ranking fuels and additives based on near-isothermal tests. Unique differences are observed both in the behavior of the neat fuels and in the impact of the antioxidant BHT. Autoxidation of both fuels is catalyzed by cleaned stainless-steel surfaces; the effect is greatly reduced or eliminated by surface passivation that occurs

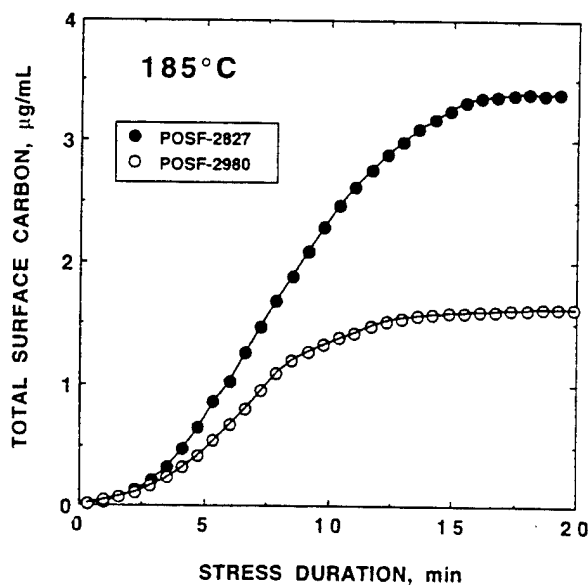


Figure 10. Plot of Total Surface Carbon vs. Stress Duration at 185°C for POSF-2827 and -2980 Fuels.

with the accumulation of surface deposits. Fuels which undergo surface catalysis may be of some concern under conditions where clean surfaces are encountered, as in ser-vocontrols.

ACKNOWLEDGEMENTS

This work was supported, in part, by Wright Laboratory, Aero Propulsion and Power Directorate, Wright-Patterson Air Force Base, Ohio, under USAF Contract No. F33615-90-C-2033. The authors would like to thank Mr. Tim Gootee for performing the surface-carbon analyses, Ms. Lori Balster for making the oxygen measurements, and Mrs. Marian Whitaker for lending editorial assistance. The authors acknowledge valuable discussions with Dr. Larry Goss of SRL, Mr. Steve Anderson of the USAF, and Mr. Wayne Rubey of the University of Dayton Research Institute.

REFERENCES

- Edwards, T., Anderson, S. D., Pearce, J. A., and Harrison, W. E., 1992, "High Temperature Thermally Stable JP Fuels--An Overview," AIAA Paper 92-0683 (30th Aerospace Sciences Meeting and Exhibit, January 6-9, 1992, Reno, NV).
- Hazlett, R. N., 1991, *Thermal Oxidation Stability of Aviation Turbine Fuels*, ASTM Monograph 1, American Society for Testing and Materials, Philadelphia.
- Jones, E. G., Balster, W. J., and Post, M. E., 1993a, "Degradation of a Jet-A Fuel in a Single-Pass Heat Exchanger," ASME Paper 93-GT-334.
- Jones, E. G., and Balster, W. J., 1993b, "Phenomenological Study of Formation of Insolubles in a Jet-A Fuel," *Energy and Fuels*, Vol. 7, pp. 968-977.
- Jones, E. G., and Balster, W. J., 1994a, "Surface Fouling: Short- vs. Long-Term Tests," *Preprints-American Chemical Society, Division of Fuel Chemistry*, Vol. 39(3), pp. 952-957.
- Jones, E. G., and Balster, W. J., 1994b, "Formation of Insolubles in a Jet-A Fuel: Temperature Effects," *Preprints-American Chemical Society, Division of Petroleum Chemistry*, Vol. 39(1), pp. 78-81.
- Katta, V. R., Jones, E. G., and Roquemore, W. M., 1993, "Development of Global-Chemistry Model for Jet-Fuel Thermal Stability Based on Observations from Static and Flowing Experiments," Paper No. PEP-19, 81st AGARD Symposium on Fuels and Combustion Technology for Advanced Aircraft Engines, May 10-14, 1993, Colliferro, Italy.
- Martel, C. R., 1987, "Military Jet Fuels, 1944-1987," 1987, Air Force Wright Aeronautical Laboratory Technical Report AFWAL-TR-87-2062, Wright-Patterson Air Force Base, Ohio.
- Rubey, W. A., Tissandier, M. D., Striebich, R. C., Tirey, D. A., and Anderson, S. D., 1992, "In-Line Gas Chromatographic Measure of Trace Oxygen and Other Dissolved Gases in Flowing High-Pressure, Thermally Stressed Jet Fuel," *Preprints-American Chemical Society, Division of Petroleum Chemistry*, Vol. 37(2), pp. 371-376.
- Walling, C., 1957, *Free Radicals in Solution*, John Wiley and Sons, Inc., New York.

Symposium on Coke Formation and Mitigation
Presented before the Division of Petroleum Chemistry, Inc.
210th National Meeting, American Chemical Society
Chicago, IL, August 20-25, 1995

Fouling of Stainless Steel and Silcosteel Surfaces During Aviation-Fuel Autoxidation

E. Grant Jones and Walter J. Balster
Systems Research Laboratories, Inc.
A Division of Space Industries International, Inc.
2800 Indian Ripple Road
Dayton, OH 45440-3696

Wayne A. Rubey
University of Dayton Research Institute
Environmental Sciences Group
KL102, 300 College Park
Dayton, OH 45469-0132

INTRODUCTION

The fouling of surfaces from carbonaceous deposition in aircraft fuel lines is a serious problem which results in costly downtime for the cleaning or replacement of critical components. Most of the deposition occurs in hot sections such as heat exchangers; however, all regions experience some deposition. This problem is predicted to be more serious for future aircraft where greater heat loads will require dissipation by the fuel (1). Fouling arises mainly from insolubles which are formed in temperature-dependent autoxidation reactions involving minor fuel components and oxygen dissolved in the fuel. Some fuels containing heteroatoms such as sulfur or nitrogen have a propensity for fouling surfaces at elevated temperatures (2). Possible solutions to this problem that have been pursued include use of: 1) better quality fuels; 2) refining methods such as hydrotreatment to reduce heteroatom content; 3) engineering designs to reduce the temperature loads from hot components; 4) individual additives or fuel additive packages, consisting of antioxidants, dispersants, detergents, and metal deactivators, and, 5) surface-treated tubing that may delay the initial deposition processes or reduce the quantity of deposits. The goal of the current study was to investigate possible mitigation of initial surface fouling through the use of surface treatment. When deposits cover all of the fuel-exposed surfaces, any initial advantage of passivated tubing will be negated; however, depending on the temperature and total exposure time, initial reductions may significantly reduce maintenance.

Based on dynamic isothermal experiments, we have reported that the rate of autoxidation in the Jet-A fuel

POSF-2827 depends on the nature of nearby surfaces (3). Cleaned stainless-steel (304) surfaces were found to

accelerate autoxidation; whereas when the same surfaces were heavily fouled by deposits, the result was slower autoxidation. It was argued that active surface sites on the stainless steel were blocked as the surface became fouled. These findings suggested that the use of tubing with surfaces passivated, not by deposits but by prior surface treatment with inert coatings, might offer significant benefits by slowing autoxidation reactions and, thereby, reducing surface fouling.

Recent studies which were performed using inverse chromatographic procedures (4, 5) have shown interesting results with respect to adsorptive behavior. With the use of a variety of sulfur- and nitrogen-containing organic substances (chemical probes), it has been demonstrated (5) that coated and inerted tubing provides much higher transport efficiency than conventional stainless-steel tubing. This same inerting technology has been applied to passivation of gaseous sample-collection devices (6) where non-interacting surfaces are required.

Glass-lined tubing, for example, which has been used for many years by chromatographers to achieve improved transport of trace chemicals was a potential candidate for consideration; however, Silcosteel which is a more robust tubing with passivated inner walls has recently been marketed by Restek Corporation for use in chromatography to reduce surface adsorption. This tubing, made to the same dimensions as commercial stainless-steel tubing, has an inert silica-treated inner surface covered with a monolayer of a specific stain-

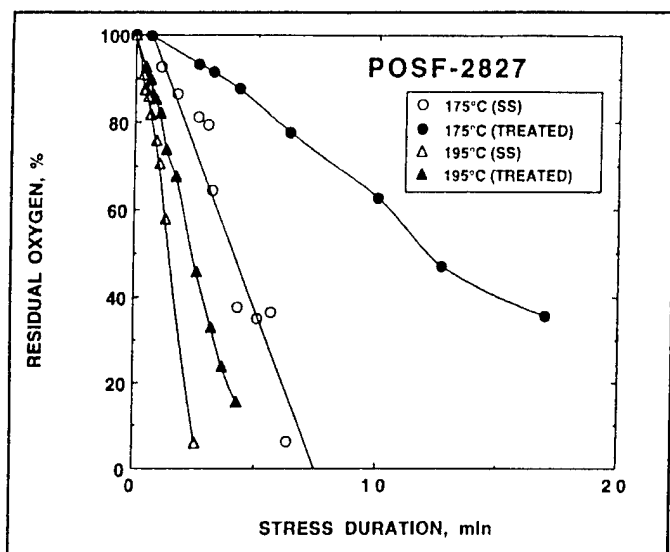


Figure 1. Plots of oxygen loss at 175°C and 185°C measured in stainless-steel and treated tubes.

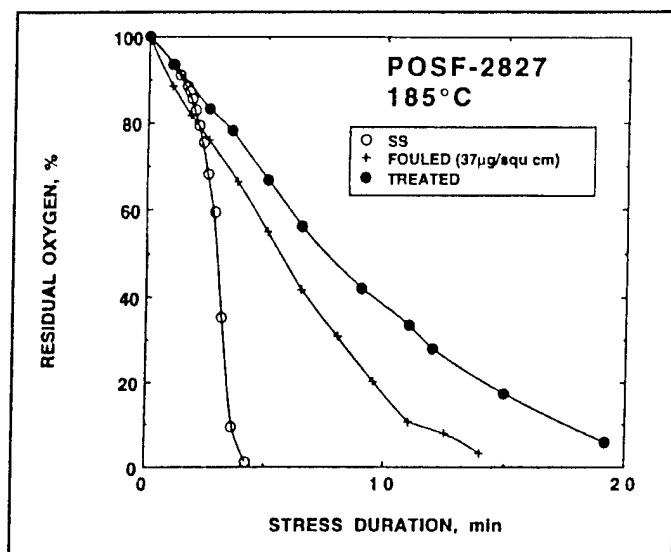


Figure 2. Plots of oxygen loss at 185°C measured in stainless-steel, fouled and treated tubes.

less-steel tubing with respect to surface fouling. Measurements of the rate of autoxidation, the rate of surface deposition, and the quantity of insolubles formed have been made during passage of POSF-2827 aviation fuel through each type of tubing clamped inside a single-pass heat exchanger. Results are reported for block temperatures of 155, 185, 255 and 300°C. Additives—in particular, dispersants—have been shown to reduce surface deposits in this fuel (7, 8). In order to investigate potential synergism from a combination of surface and fuel treatment, we have also compared deposition occurring at 185°C in each type of tubing for POSF-2827 fuel treated with the detergent 8Q405.

EXPERIMENTAL

A straight-run Jet-A fuel POSF-2827 which meets all aviation specifications was used for these tests. Experiments were conducted using Near-Isothermal Flowing Test Rig (NIFTR) single-pass heat exchanger. This rig has been described in detail elsewhere (9) and is reviewed here only briefly. Fuel (saturated with respect to air at room temperature) was pumped at a pressure of 2 MPa through 0.125-in O.D., 0.085-in I. D. tubing tightly clamped in a 42-kg copper block maintained at reaction

temperature. In-line filters (0.45- and 0.20-µm) capture bulk insolubles at the end of the heated section, and subsequent reaction occurred under isothermal conditions. Two separate experiments were conducted to monitor autoxidation using GC oxygen analysis (10) and surface deposition using carbon burnoff. In the first, oxygen dissolved in the fuel was monitored for fuel passage through a fixed-length (32-in) tube. Residence time or reaction time was varied by changing the flow rate to provide profiles of residual dissolved oxygen (%) as a function of time. In the second, a fixed flow rate was used for test times ranging from 6 to 72 hr, after which the tubing was cut into 2-in. sections and the carbon measured using a LECO RC-412 surface-carbon analyzer. For isothermal reaction conditions, the distance along the heated tube could be converted to reaction time, and profiles of deposition rate as a function of stress duration could be obtained. Since the carbon measurements were made after completion of each test, the calculated deposition rate represents an average over the entire test time.

The two types of experiments (autoxidation and deposition) were conducted under identical conditions using stainless-steel (304) tubing and

Silcosteel tubing, and results obtained for reaction occurring in each type of tubing were directly compared. In most cases reaction was taken to 100% conversion of dissolved oxygen, leading to an inherent normalization for quantification of insolubles. Finally, reaction in each type of tubing was studied using POSF-2827 fuel treated with the dispersant fuel additive 8Q405 (Betz Corp., 100 mg/L).

RESULTS AND DISCUSSION

Autoxidation

Figure 1 shows the dissolved oxygen measured in POSF-2827 fuel as a function of stress time at 175 and 195°C. The rate of autoxidation is significantly reduced (by a factor of two or three) when reaction occurs in the treated rather than the stainless-steel tubing. The explanation for this effect is as follows. The steel surface offers active sites to promote autoxidation. These sites are eliminated by the passivating effects afforded by the Silcosteel process. This observation is consistent with our earlier reports of reduced autoxidation rates measured in tubing that had previously been passivated by deposits (see, for example, Figure 2 which shows results at the intermediate temperature, 185°C, using 1) stainless-steel tubing, 2) Sil-

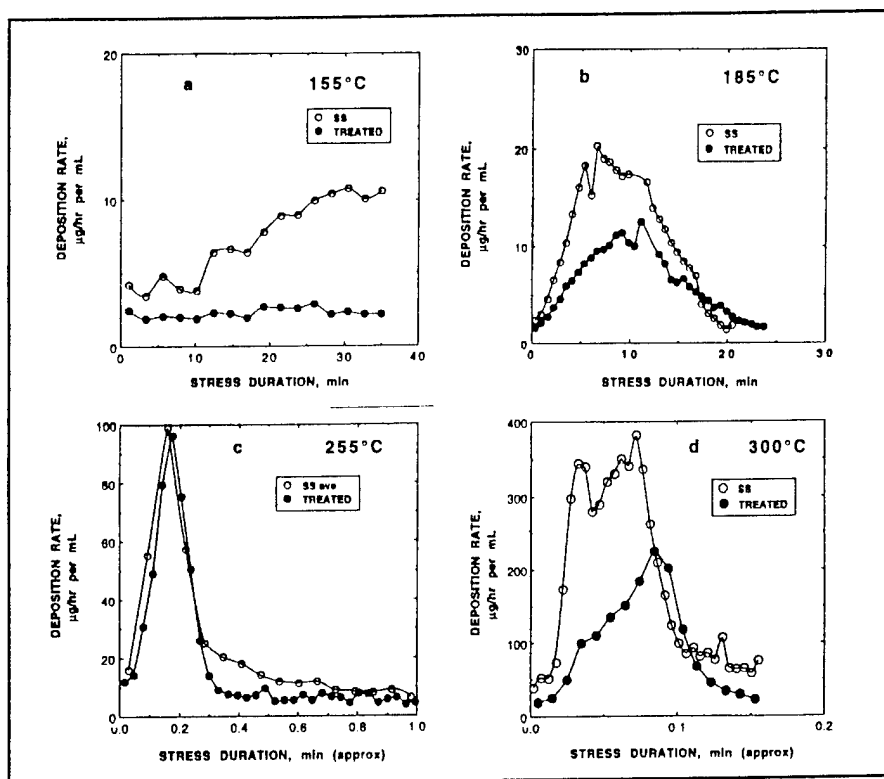


Figure 3. Deposition rate profiles; a) 155°C (48 hr, 0.07 mL/min), b) 185°C (72 hr, 0.25 mL/min), c) 225°C (18 hr, 2.5 mL/min), and d) 300°C (6 hr, 16 mL/min) for stainless-steel and treated tubes.

costeel-treated tubing, and 3) stainless-steel tubing fouled approximately uniformly by carbonaceous deposits ($37 \mu\text{g}/\text{cm}^2$) from the current fuel). The order of surface activity for autoxidation is SS > Deposit-Fouled > Silcosteel. Reduced autoxidation is achieved through the use of passivated tubes. The magnitude of this effect will be both temperature- and conversion-dependent. Based on autoxidation changes alone, we would expect reduced deposition rates and delays (stress duration) in overall deposition on the treated tubes.

Deposition

The results of a series of deposition experiments are given in Figure 3. The reaction conditions for the two types of tubing were identical. The reaction at 155°C and 185°C was isothermal as a result of the slow flow rate and low block temperatures. However, the high-temperature runs required faster flow rates, resulting in

a significant departure from isothermal conditions. Thus, much of the deposition occurs at temperatures below the block setting, and stress times are approximate (upper limit). With the exception of the reaction occurring at 255°C, the deposition rates are significantly lower on the treated tubes. The location of the maximum occurs at longer stress times. The measured rates are averages over the entire test time which varies from 6 to 72 hrs. As the test time is extended and more deposits accrue, eventually the deposition-rate profiles for the different types of tubing should become equal, representing the profile for deposition on a heavily fouled tube. This test time may be short at higher temperatures because of more total fuel being passed through the system and reaction rates being faster, but evidently at 155°C the amount of deposition on the treated tube is barely detectable; thus, very long test-time averages will be necessary to achieve sufficient surface cov-

erage to mask completely the original treated surface.

Quantification

The quantity of bulk insolubles (filter) and surface insolubles (integral under deposition profiles) and their sum are shown in histogram form (Figure 4). The quantity of surface deposits is significantly reduced on the treated tubes. One would not expect the quantity of bulk insolubles to be reduced by surface treatment unless the oxygen conversion were less in the treated tube. This may be the case at 155°C. The quantity of bulk insolubles measured at the two highest temperatures is unaffected by treated tubing. We have no explanation for the reduction at 185°C, except that slower autoxidation may produce smaller particles which are able to pass through the in-line filters.

Dispersant Additive

Figure 5 shows changes in reaction at 185°C introduced by the dispersant additive. In this 18-hr test, significant reductions in surface deposition rates and total surface carbon are observed. For reaction in steel tubes, compare the reduction in total surface carbon from 3.3 to 2.6 $\mu\text{g}/\text{mL}$ using the additive. For reaction in treated tubes, compare the reduction in total surface carbon from 2.5 to 1.2 $\mu\text{g}/\text{mL}$ using the additive. Reductions in surface and bulk insolubles have been reported with the use of 8Q405 in POSF-2827 fuel (7, 8), but synergism appears to be present in the combination of dispersant-treated fuel and treated tubes. The origin of this effect does not appear to be related to autoxidation; we have studied autoxidation in treated fuel and found no significant differences in the rates measured in steel and those measured in treated tubes. Rather, this effect may be related to solubility, particle size, and adherence of insolubles to different types of surfaces. For example, 8Q405 has

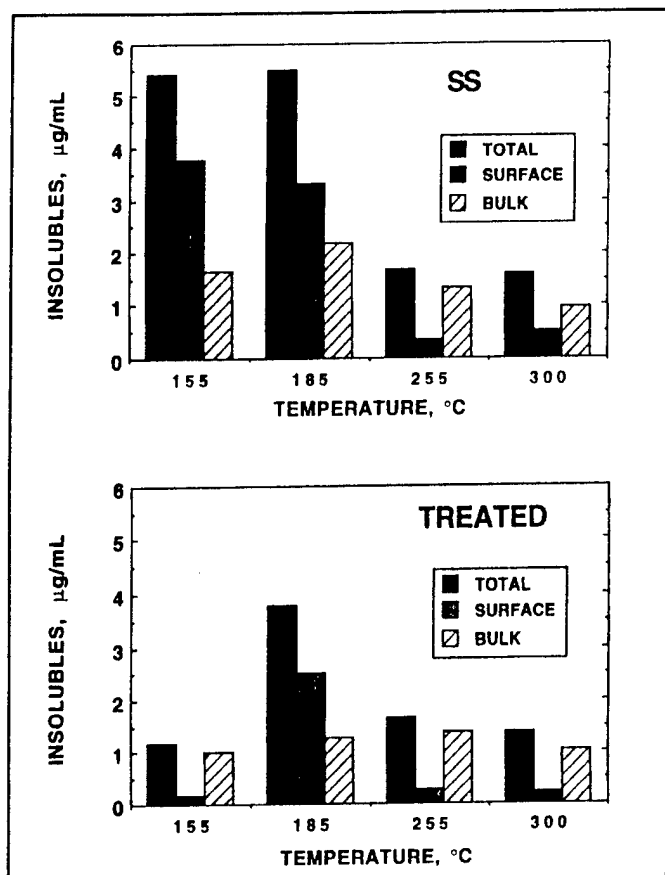


Figure 4. Insolubles formed in reaction in stainless-steel and treated tubes.

been found to reduce the diameter of bulk insolubles formed at 185°C (8).

The strength of adherence of insolubles to Silcosteel and stainless-steel surfaces is not clear from the current laminar flow tests. However, the improvement observed with the dispersant additive suggests that: 1) a combination detergent/dispersant fuel additive possessing better surface cleaning properties, and 2) periodic abrasive cleaning may offer additional improvement if the initial surface bonding to Silcosteel surfaces is weak. These areas are currently being studied.

CONCLUSIONS

The rates of autoxidation and deposition occurring during passage of aviation fuel through heated tubes are found to depend strongly on the

Silcosteel process is characterized by a reduced rate of autoxidation which, in turn, causes a reduced deposition rate. Once a significant amount of surface deposit has accrued, the inner walls cannot be distinguished and rates will be comparable. Thus, advantages in the use of treated tubing will be most significant during the initial deposition processes. Depending on the surface temperature and region of the aviation fuel lines, periodic replacement with treated tubes may be cost effective. Servocontrols and nozzles which have tight tolerances and which are particularly sensitive to minimal surface fouling would be ideal candidates for surface treatment. The introduction of a fuel additive (dispersant) coupled with surface treatment has been shown to offer additional mitigation of surface fouling.

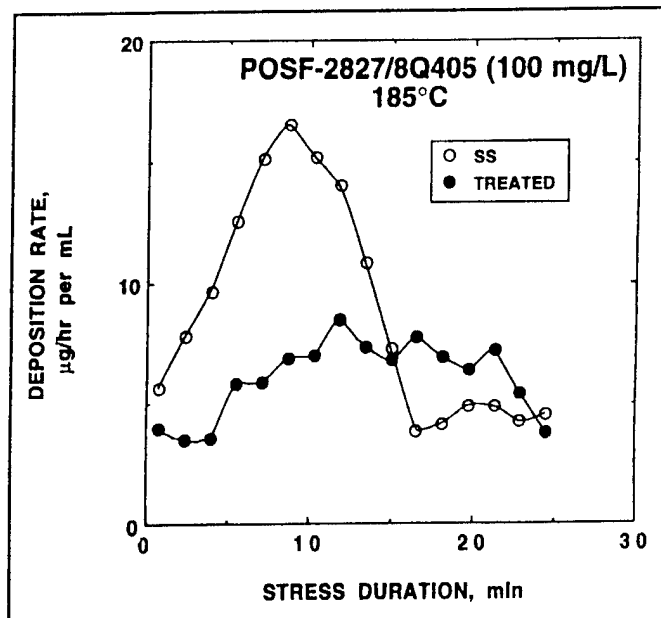


Figure 5. Deposition-rate profiles (185°C, additized fuel, 18 hr, 0.25 mL/min) for reaction in stainless-steel and treated tubes.

nature of the surface layer. As compared to reaction in stainless-steel tubes, reaction in tubes treated with the

ACKNOWLEDGMENTS

This work was supported by Wright Laboratory, Aero Propulsion and Power Directorate, Wright-Patterson Air Force Base, OH, under USAF Contract Nos. F33615-90-C-2033 and F33615-92-C-2207. The authors would like to thank Mr. Tim Gootee for performing the surface-carbon analyses and Mrs. M. Whittaker for lending editorial assistance.

LITERATURE CITED

- (1) Edwards, T., Anderson, S. D., Pearce, J. A. and Harrison, E. E., "High Temperature Thermally Stable JP Fuels—An Overview", AIAA Paper No. 92-0683, Presented at the 30th Aerospace Sciences Meeting and Exhibit, Reno, NV, January 6-9, 1992.
- (2) Bol'shakov, G. F., FTM-MT-24-416-74 (Foreign Technology Division, Air Force Systems Command, Wright-Patterson Air Force Base, OH, Chapter 1, April 9, 1974.

- (3) Jones, E. G. and Balster, W. J., "Surface Fouling in Aviation Fuel: Short- vs. Long-Term Isothermal Tests", Submitted to Energy and Fuels.
- (4) Anthony, L. J. and Holland, R. A., J. Noncryst. Solids, 120, 82 (1990).
- (5) Striebich, R. C., Rubey, W. A. and Anderson, S. D., PRE-PRINTS, Div. of Petrol. Chem., ACS, 39(1), 64 (1994).
- (6) Shelow, D. M. and Schuyler, A., "Fused Silica-Lined Canisters as a Viable Alternate to SUMMA Polished Canisters for the Collection and GC Analysis of Volatile Organic Compounds in Air", Presented at the Pittsburgh Conference, New Orleans, LA, March 1995.
- (7) Zabarnick, S. and Grinstead, R. R., Ind. Eng. Chem. Res., 33, 2771 (1994).
- (8) Anderson, S. D., Jones, E. G., Goss, L. P. and Balster, W. J., "Effect of Additives on the Formation of Insolubles in a Jet-A Fuel", Proceedings of the 5th International Conference on Stability and Handling of Liquid Fuels, Rotterdam, the Netherlands, October 3-7, 1994.
- (9) Jones, E. G. and Balster, W. J., Energy Fuels, 7, 968 (1993).
- (10) Rubey, W. A., Striebich, R. C., Tissandier, M. D., Tirey, D. A. and Anderson, S. D., "Gas Chromatographic Measurement of Trace Oxygen and Other Dissolved Gases in Thermally Stressed Jet Fuel", accepted for publication in the Journal of Chromatographic Science.

In Proceedings of the 24th North American Thermal Analysis Society Conference, 10-13 September 1995, San Francisco, CA (S. A. Mikhail, Ed.) (CANMET, Ottawa, Ontario, Canada, 1995), pp. 216-221.

APPLICATION OF ISOTHERMAL CALORIMETRY TO

JET FUEL AUTOXIDATION KINETICS

J. M. Pickard[†], E. G. Jones[‡], and W. J. Balster^{##}

[†]Kinetica, Inc., P. O. Box 182, Miamisburg, OH 45343-0182, [‡]ISSI, Dayton, OH 45440-3696, and ^{##}Systems Research Laboratories, Inc., 2800 Indian Ripple, Dayton, OH 45440

ABSTRACT

A preliminary examination of the autoxidation for air-saturated (65 ppm O₂) POSF-2827 jet fuel was conducted with isothermal calorimetry. The conversion versus time plot derived from the calorimetry data was found to correlate with the kinetics of O₂ depletion obtained with a Near-Isothermal Flowing Test Rig (NIFTR). It is proposed that kinetics for O₂ depletion may be described by a simple exponential function of the form, $100 \cdot \exp(-k^n t^n)$ where k^n is the rate constant and n is the order of the time-dependence.

INTRODUCTION

Engine fowling associated with insoluble gum and varnish formation arising from fuel autoxidation is a primary factor in decreased aircraft engine performance. In the last decade, the use of a Near-Isothermal Flowing Test Rig (NIFTR) to study the phenomenological kinetics for fuel autoxidation and deposit formation of various fuels has been reported(1). A major advantage of the NIFTR experiments is that real conditions may be simulated in a laboratory setting; a major disadvantage is that several days may be required to characterize fuel at a single temperature. In this presentation, we report preliminary results for an isothermal constant volume calorimetric analysis for air-saturated POSF-2827 jet fuel to demonstrate the feasibility of a calorimetric approach. The significance of the global kinetic parameters that may be inferred from this approach are compared to the NIFTR data and discussed in reference to

the conventional mechanism proposed for fuel autoxidation.

EXPERIMENTAL

The isothermal calorimetric data were obtained with a Setaram DSC-111 using stainless steel crucibles. Prior to data collection, a fuel sample was sparged for 30 min to insure air-saturation. For analysis at a particular temperature, a volume of fuel was chosen so that upon expansion from ambient conditions head space within the DSC crucible was minimized. This was necessary to insure that flashing of the dissolved O_2 did not occur when the crucible was injected into the calorimeter. Conversion was determined by integration of the DSC curve. The NIFTR technique has been described in detail elsewhere; briefly, this involves passing air-saturated fuel through as single-pass heat exchanger coupled to a gas chromatograph to monitor O_2 depletion(1,2). At the end of a NIFTR measurement, surface deposits on the heat-exchanger were quantified by combustion analysis and reported as total surface carbon(TSC).

RESULTS

Representative oxygen loss and TSC deposition obtained at 185 °C with the NIFTR technique are illustrated in Figure 1; the corresponding isothermal heat flow versus stress time curve obtained with DSC is given in Figure 2. The TSC deposition rate and the DSC heat flow curves both exhibit shapes characteristic of an autocatalytic reaction. These observations suggest that the integral O_2 loss data of Figure 1 may be represented by Equation (1).

$$[O_2] = [O_2]_0 \exp(-k^n t^n) \quad (1)$$

In Equation (1) $[O_2]_0$ and $[O_2]$ are the initial and intermediate percent O_2 at time greater than zero, k^n is the rate constant and n is the reaction order.

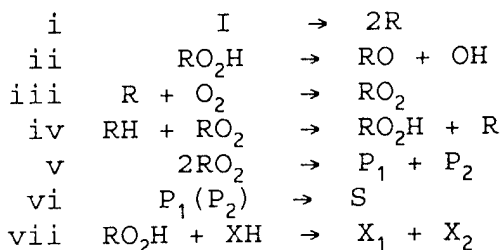
Differentiation of Equation (1) leads to Equation (2) for the rate of O_2 depletion.

$$\frac{d[O_2]}{dt} = [O_2]_0 n k^n t^{n-1} \exp(-k^n t^n) \quad (2)$$

The parameters, k^n and n , were evaluated from nonlinear least squares fitting using the O_2 loss data at each temperature. This approach indicated that the best value of n was 2; all subsequent regressions to determine the values of the rate coefficients were derived by setting n to the constant value of 2. A rate plot for the O_2 loss and the derived rate parameters are given in Figure 3. Figure 4 compares plots for conversion versus time for the DSC and NIFTR O_2 analysis at 185 °C as well as the predicted O_2 conversion based on Equation (1) using average rate parameters summarized in Figure 3.

DISCUSSION

Fuel oxidation may be approximated by the following simplified reaction mechanism:



where I is the initiator, RO_2 is a peroxy radical, RO_2H is hydroperoxide, RH is fuel, R is any radical, P_1 and P_2 are molecular species formed by termination (P_1 and or P_2 are assumed to be precursors to deposition), S is the surface deposit, XH is a natural inhibitor or retarder, and X_1 and X_2 are molecular products from reaction of hydroperoxide with inhibitor (1,3).

Application of the steady state principle with the assumption of second-order termination yields the rate for oxidation (4) given by Equation (3). In Equation (3), R_i is the rate of initiation, k_p is the rate constant for propagation, and $2k_t$ is the rate constant for termination. With the assumptions, $R_i = k_1[I] + k_2[\text{RO}_2\text{H}]$

$$-\frac{d[O_2]}{dt} = k_p \left[\frac{R_i}{2k_t} \right]^{1/2} [RH] \quad (3)$$

$\approx k_2[RO_2H]$, $[O_2] = [O_2]_o(1-\alpha)$, $[RO_2H] = \alpha[O_2]_o$, $[RH] = [RH]_o(1-\alpha)$, and $\alpha_o = k_1[I]/k_2[O_2]_o$ (where α is the extent of reaction), Equation (3) may be rearranged to obtain,

$$\begin{aligned} \frac{d\alpha}{dt} &= k_p \left(\frac{k_2}{2k_t} \right)^{1/2} \frac{[RH]_o}{[O_2]_o^{1/2}} (\alpha + \alpha_o)^{1/2} (1 - \alpha) \\ &= k(\alpha + \alpha_o)^{1/2} (1 - \alpha) \end{aligned} \quad (4)$$

Equation (4) is equivalent to the simple law of autocatalysis; it is also the appropriate differential of Equation (1) (5).

The feasibility of the calorimetric approach to monitor the fuel autoxidation may be assessed from the conversion versus time plots illustrated in Figure 4. Although the actual NIFTR O_2 conversion at 185 °C is slower than expected from the DSC analysis, the predicted O_2 conversion (based on the average rate parameters for the NIFTR data over the whole temperature range) compares favorably with the DSC analysis. This indicates that constant volume calorimetry should be a reliable method to assess fuel autoxidation stability.

ACKNOWLEDGEMENT

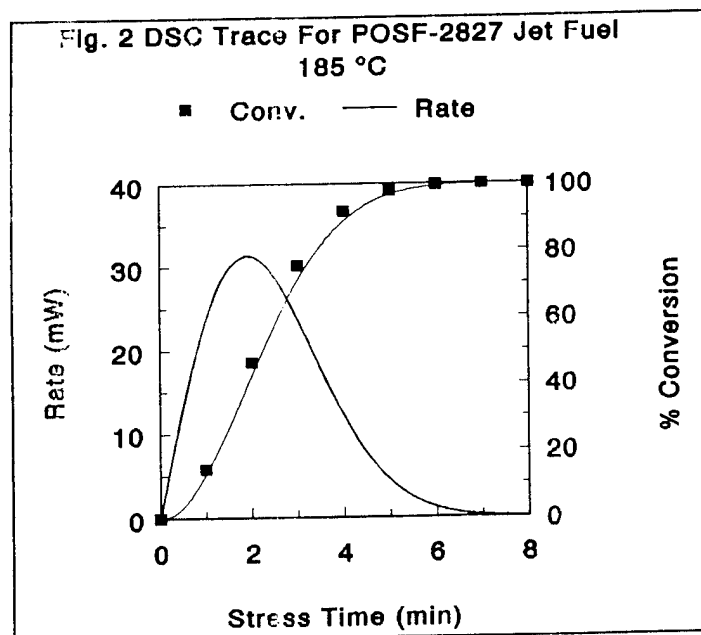
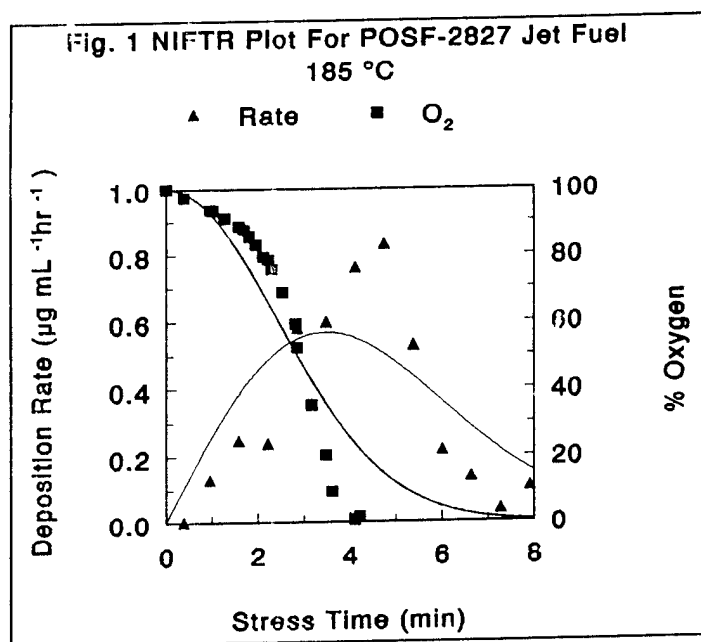
This work was sponsored by Wright Laboratory, Aero Propulsion and Power Directorate, Wright-Patterson Air Force Base, OH under USAF Contract No. F33615-90-C-2033.

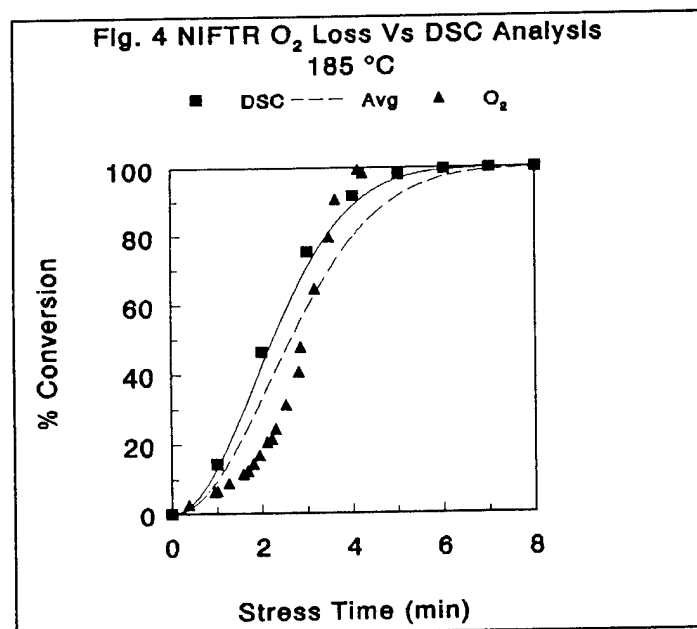
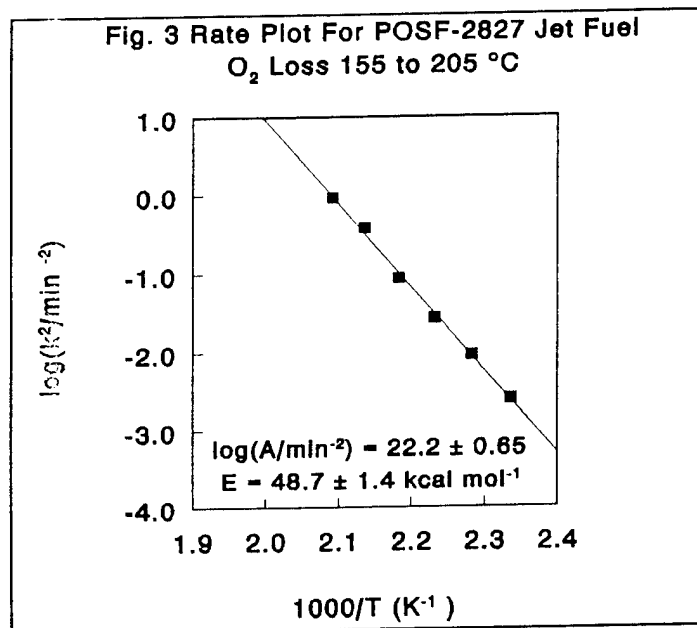
REFERENCES

- (1) Jones, E. G.; Balster, W. J.; Post, M. E. ASME JOURNAL OF ENGINEERING FOR GAS TURBINES AND POWER **1995**, 117, 125.
- (2) Rubey, W. A.; Tissandier, M. D.; Striebich, R. C.; Tirey, D. A.; Anderson, S. D. Preprints, Div. of Petrol. Chem., ACS, **1992** 37(2), 371.

Res. Dev., 1986 25, 360.

- (4) Howard, J. A. Free Radicals Volume II, Wiley: New York, 1973, Ch. 1.
- (5) Sestak, J.; Berggren, G. Thermochim. Acta, 1971 3, 1.





Application of JFA-5 as an Antifouling Additive in a Jet-A Fuel

E. Grant Jones,^{*,†} Walter J. Balster, and Larry P. Goss[†]

Systems Research Laboratories, An Operation of Calspan SRL Corporation, 2800 Indian Ripple Road, Dayton, Ohio 45440-3696

A commercial Jet-A aviation fuel, POSF-2827, was treated with an antifouling additive package, DuPont Jet Fuel Additive No. 5 (JFA-5), at a concentration of 12 mg/L. Fouling of heated stainless-steel (304) tubes from the neat and treated fuels was studied over the temperature range 155–300 °C using a single-pass heat exchanger and at 185 °C in flask tests. The rate of autoxidation in the treated fuel was slowed over the temperature range 155–225 °C, but total surface fouling evaluated after 100% conversion of dissolved oxygen was not reduced. Significant reduction (factor of 2–3) in surface fouling was observed at the higher temperatures, 255 and 300 °C. This improvement was traced to one component of the package, namely, a metal deactivator present at 2 mg/L. Additive packages such as JFA-5 which contain antioxidant, dispersant, and—in particular—metal-deactivator components may reduce Jet-A fuel fouling in certain temperature regimes.

Introduction

The proprietary DuPont Jet Fuel Additive No. 5, known as JFA-5, is used in military aviation fuels to improve thermal oxidation stability. In particular, since 1970 (according to MIL T-25524), it has been required for use in a U.S. Air Force specialty fuel, Thermally Stable Jet Fuel (JPTS), at concentrations of 9–12 mg/L (Martel, 1987). The antifouling additive package JFA-5 is an ashless mixture of polymers, organic amines, and amides in kerosene (Martel, 1987); the package contains dispersant, antioxidant, and metal-deactivator components. A recent Materials Safety Data Sheet lists nonproprietary components and their percentages (DuPont, 1991). Treatment with JFA-5 has been reported to reduce Coker-tube deposit ratings and filter pressure differentials (DuPont, 1960). Recently, reductions in surface deposition on 316-stainless-steel surfaces have been reported (Heneghan et al., 1993) through the use of 12 and also 50 mg/L JFA-5 in a Jet-A aviation fuel (POSF-2827) during studies conducted at 300 °C in a single-pass heat exchanger. The Jet-Fuel Thermal-Oxidation Tester (JFTOT) breakpoint of a shale-derived JP-4 fuel has been reported to be improved by use of JFA-5 (Boos and Dues, 1986).

As part of a broad-range investigation into thermal oxidation stability of aviation fuels, POSF-2827 has served as a reference since it meets all USAF specifications and is amenable to study because it has a propensity to foul heated surfaces (Heneghan et al., 1993; Jones et al., 1993; Jones and Balster, 1993). Quantification of surface and bulk insolubles formed in POSF-2827 fuel during thermal stressing under near-isothermal conditions has provided a very detailed picture of this fuel at 185 °C (Jones et al., 1993; Jones and Balster, 1994) and an outline of its behavior over the temperature range 155–225 °C (Jones and Balster, 1994). Deposition profiles as a function of stress duration have been found to correlate closely with autoxidation. Knowledge of autoxidation and the temperature dependence for the formation of insolubles has established POSF-2827 fuel as a baseline for ranking the performance of individual additives and additive pack-

ages in reducing surface and bulk fouling (Anderson et al., 1994). From a fundamental standpoint, documented changes resulting from the use of additives may aid in understanding the complex routes leading to insolubles and also in developing new additive combinations to minimize fouling. We now report the behavior of JFA-5 in mitigating surface and bulk insolubles in the Jet-A aviation fuel POSF-2827 over a broad temperature range.

The goal of the current study was to make a simple one-to-one empirical comparison between POSF-2827 fuel, neat and treated with 12 mg/L JFA-5. Comparison is predicated on the quantity of surface and filtered insolubles measured after conversion of 100% of the dissolved oxygen, primarily in dynamic tests. Results include those from (1) near-isothermal (low-flow-rate) dynamic deposition experiments at 155–225 °C (10-deg increments), (2) direct measurements of dissolved oxygen as a function of stress time over the temperature range 155–205 °C, (3) non-isothermal (higher-flow-rate) dynamic deposition experiments at 255 and 300 °C, (4) particle-size measurements at 185 °C, and (5) static flask experiments conducted isothermally at 185 °C. Experiments at 255 and 300 °C were conducted to determine whether earlier findings (Heneghan et al., 1993) that JFA-5 reduces deposition on 316-stainless-steel surfaces also hold for 304 stainless steel and to ascertain which of the three major constituents of JFA-5—namely, antioxidant, dispersant, or metal deactivator—makes the most significant contribution.

In order to aid in visualizing the effects of JFA-5, most data are presented as graphs that directly compare the results from both neat and treated fuel. Cases where the neat-fuel results have been reported elsewhere are referenced and briefly reviewed along with the impact of fuel treatment. It should be noted that additive performance is specific to each fuel and the current results relate to JFA-5 performance in a single fuel.

Experimental Section

The baseline is a commercial straight-run distillate Jet-A fuel designated POSF-2827. It meets all USAF specifications and has a breakpoint of 539 K from the JFTOT. Formation of insolubles has been attributed to autoxidation reactions of inherent sulfur compounds (0.079 wt %) which may also tend to inhibit autoxidation

[†] Present address: Innovative Scientific Solutions, Inc., 3845 Woodhurst Court, Beavercreek, OH 45430. FAX: (513) 429-9734.

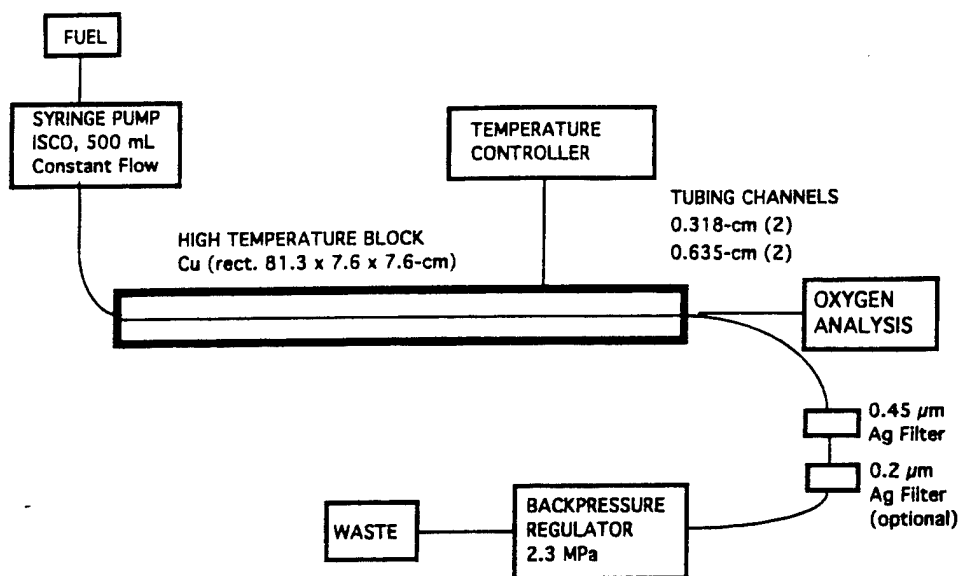


Figure 1. Schematic diagram of near-isothermal flowing test rig (NIFTR).

(Jones and Balster, 1993; Jones et al., 1992). Fuel was used without prior filtration.

The proprietary additive JFA-5, obtained from DuPont, was used at a concentration of 12 mg/L. The individual components comprising JFA-5—namely, antioxidant (PL-1694), dispersant, and metal deactivator (MDA; *N,N'*-disalicylidene-1,2-propanediamine)—were received in a carrier solvent and used in selected experiments at concentrations of 3, 4.9, and 2 mg/L, respectively. The concentration selected for each component was based upon its inherent level in JFA-5 (DuPont, 1994).

The instrument and techniques used for the dynamic experiments have been described previously (Jones et al., 1993; Jones and Balster, 1993) and will be reviewed here only briefly. All dynamic experiments were conducted using air-saturated fuel flowing through 304-stainless-steel tubing clamped in the copper block of the Near-Isothermal Flowing Test Rig (NIFTR) shown in Figure 1. The instrument is a single-pass heat exchanger with a 81.3-cm heated section; when used under conditions of slow fuel-flow rates and low block temperatures, this instrument provides near-isothermal conditions for reaction along the tube. System pressure was maintained above 2.3 MPa in order to ensure a single liquid phase. Fuel was passed through 0.318-cm (0.125-in.) o.d., 0.216-cm (0.085-in.) i.d. commercial tubing and an in-line 0.45- μ m filter. In non-isothermal experiments at higher temperature, a second in-line filter (0.2 μ m) was used. Surface deposits on 5.1-cm (2-in.) segments of tubing and insolubles on the filter were quantified by carbon burnoff using a LECO RC-412 surface-carbon analyzer.

Reaction time or stress duration in isothermal tests was determined from the flow rate, tube dimensions, and location along the tube axis. The calculated times were reduced by 15% to compensate for fuel expansion. Deposition rates were determined from the amount of carbon in each segment, the increment of stress time within that segment, and the total quantity of fuel passed. Each segment provides one data point, representing the deposition rate averaged over the entire test time (i.e., usually 6 h). Deposition rate is expressed in units of micrograms of carbon per unit stress time per unit volume of fuel passed through the system. In the

non-isothermal tests at 300 °C, deposition rate is expressed in units of micrograms per square centimeter per hour of testing, and the abscissa is shown as distance along the tube rather than stress duration.

Dissolved oxygen was measured in separate experiments using the entire 81.3-cm tube as a reaction cell; stress duration was changed by varying the flow rate. An in-line gas chromatographic detector, designed and built by Rubey and co-workers (1995), was employed for oxygen measurements.

Photon correlation spectroscopy (PCS) was used for submicron particle sizing after the isothermally stressed fuel had cooled to room temperature. The instrument and techniques were based on those outlined by O'Hern et al. (1993).

Static tests were conducted isothermally under ambient pressure at 185 °C using a Pyrex flask with continuous stirring and oxygen sparging. Bulk insolubles were collected by aliquot filtration every 30 min, and surface deposits were collected on a series of 302B-stainless-steel disks; each disk was suspended in the fuel for a different period of time. Both surface and bulk insolubles measured in flask tests exhibited a zero-order growth with time; thus, pseudo-zero-order rates could be determined. These techniques have been described previously (Jones et al., 1992).

Results and Discussion

Near-Isothermal Dynamic Studies. A comparison of the 6-h-averaged surface-deposition rates at 185 °C (flow 0.25 mL/min) and at 205 °C (0.5 mL/min) is shown in Figure 2. These results are typical of experimental data obtained over the temperature range 155–225 °C. Differences between surface deposition from neat and from treated fuel are evidently minor at 205 °C but are more pronounced at 185 °C. Generally, deposition profiles from the treated fuel extend to longer times at lower temperatures. The integrated area under these profiles is the total surface deposit arising from complete reaction of the dissolved oxygen present in 1 mL of fuel saturated initially with respect to air at room temperature. In other experiments the quantity of deposits was reduced to a negligible level (<10% of that from air-saturated fuel) when both neat and treated fuel were

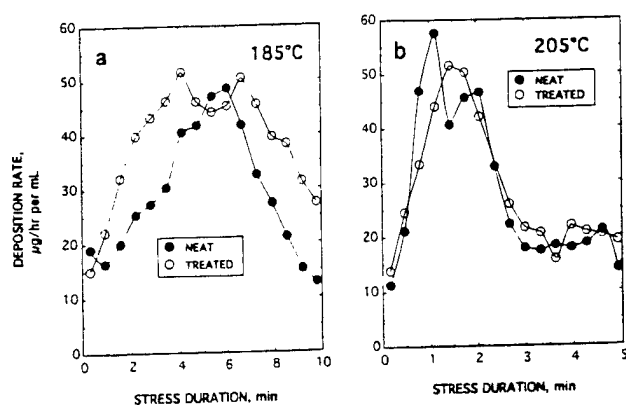


Figure 2. Deposition rate vs stress duration for neat and treated POSF-2827 fuel for stressing at 185 °C at flow rate of 0.25 mL/min (a) and 205 °C at flow rate of 0.5 mL/min (b).

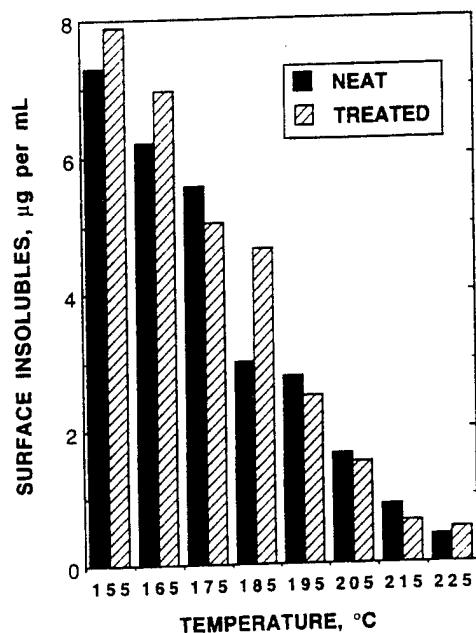


Figure 3. Total surface insolubles from neat and treated fuel as function of stress temperature.

sparged with He to remove most of the dissolved oxygen; this indicates that deposits arise from autoxidation.

Our previous studies with POSF-2827 fuel at 185 °C showed that insolubles originate within the bulk fuel and that one fraction of these (designated a surface-deposition precursor) leads to deposits on heated surfaces, while a second fraction does not and can be collected on in-line filters (Jones et al., 1993; Jones and Balster, 1993). Since filters are at room temperature, bulk insolubles include an additional contribution from fuel cooling. Extended stressing under isothermal conditions allows the completion of all surface-deposition processes within the heated tube. Thus, the insolubles can be separated into surface and filtered fractions that approximately represent the partitioning between adhering and nonadhering components.

Figures 3 and 4 are summary histograms of the total surface insolubles and the filtered insolubles, respectively, evaluated from the near-isothermal experiments over the temperature range 155–225 °C. These histograms represent the efficiency of making surface insolubles and filtered insolubles from 1 mL of air-saturated fuel. The greatest difference in the amount of surface deposits collected using neat and treated fuels is the increase at 185 °C for the treated fuel. However,

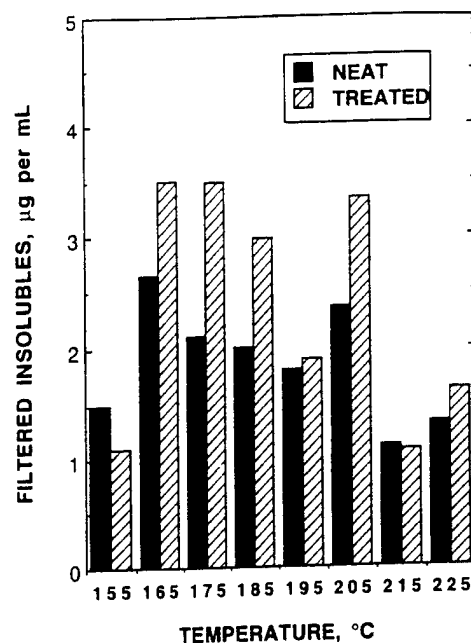


Figure 4. Filtered insolubles from neat and treated fuel as function of stress temperature.

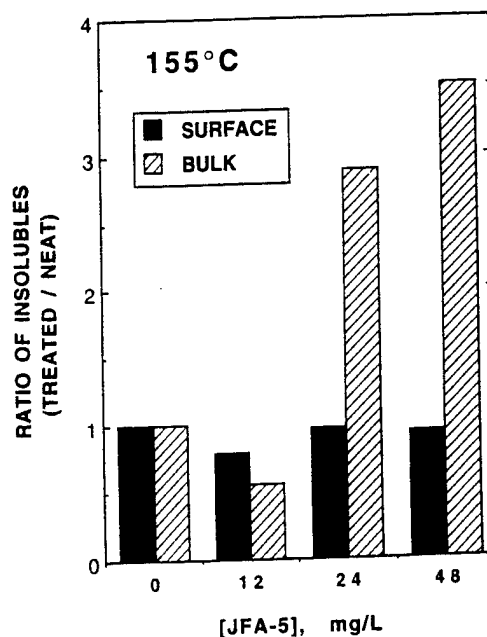


Figure 5. Ratio of insolubles formed at 155 °C vs concentration of JFA-5. Fuel flow rate is 0.1 mL/min, and test duration is 48 h.

on the average, JFA-5 appears to have no net effect on the amount of *total* surface deposits over the entire temperature interval. The origin of the rather unusual temperature dependence of surface deposits is not well understood and is the subject of current study. The presence of JFA-5 does appear to have a slight detrimental effect on filtered insolubles, as evidenced by the totals in Figure 4.

A cursory investigation was completed using higher concentrations of JFA-5 (24 and 48 mg/L). In order to enhance the detection of insolubles, test time was extended to 48 h and reaction was studied at 155 °C, a temperature at which the efficiency of producing insolubles is high. The results shown in Figure 5 indicate that higher concentrations of JFA-5 have no effect on the quantity of surface deposits but do increase the quantity of bulk insolubles. In summary, for isothermal

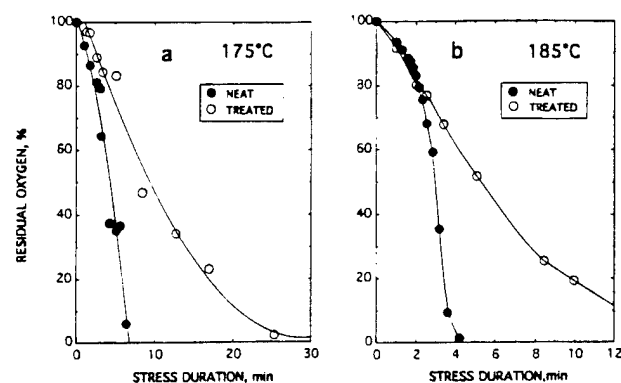


Figure 6. Residual oxygen in neat and treated fuel vs stress duration at 175 °C (a) and 185 °C (b).

tests JFA-5 does not alter surface deposits but increases bulk insolubles, particularly at higher concentrations. These observations support the selection of 12 mg/L as the optimum concentration of additive. Zabarnick and Grinstead (1994) have also studied the effects on surface deposition of using different concentrations of JFA-5 in POSF-2827 fuel. On the basis of quartz crystal microbalance (QCM) methods used in 15-h static tests at 140 °C, they found JFA-5 to increase fuel thermal stability early in the run but ultimately to decrease thermal stability under extended stressing, as evidenced by an increase in the total surface deposits using 6, 12, and 24 mg/L JFA-5. It is unclear why these tests differ in the assessment of surface deposits. This may be related to differences in temperature, surface-to-volume ratio, test methodology (static vs dynamic), or, possibly, the buildup of bulk particles in the QCM tests. Zabarnick and Grinstead (1994) reported complications due to the formation of a viscous film on the crystal; this film may cause anomalous increases in deposition with the use of additives such as JFA-5.

It should be emphasized that the quantification of insolubles discussed above relates to 100% reaction of oxygen and conditions under which the deposition processes are complete at temperature. This may have important implications in assessing improvements introduced by an additive. For example, if the rate of reaction of dissolved oxygen in the neat fuel differs from that in the treated fuel, the rate of forming insolubles will be significantly affected; however, rate differences may not be reflected in the *total quantity of insolubles* based on complete oxygen conversion. For this reason it is important to consider the rates of autoxidation in both neat and treated fuel.

Autoxidation Studies. Figure 6 shows the residual dissolved oxygen as a function of stress duration at 175 and 185 °C. The sigmoid shape observed in the case of the neat fuel is attributed to autocatalysis (Jones and Balster, 1993). The addition of JFA-5 effectively extends the time needed for complete oxygen consumption. Initial rates of autoxidation appear to be similar; however, the increase in rate at higher oxygen conversion observed in the neat fuel is eliminated in the treated fuel. The overall result of slower autoxidation is that the deposition processes are extended to longer stress times (see Figure 2a). Slower autoxidation may be the result of antioxidant behavior from JFA-5 or a bulk/surface activity. For example, recent studies (Jones and Balster, 1995) in this laboratory have shown that the presence of surface deposits reduces the bulk/wall interaction and slows oxygen consumption, as observed in Figure 2a. Thus, in addition to JFA-5 slowing

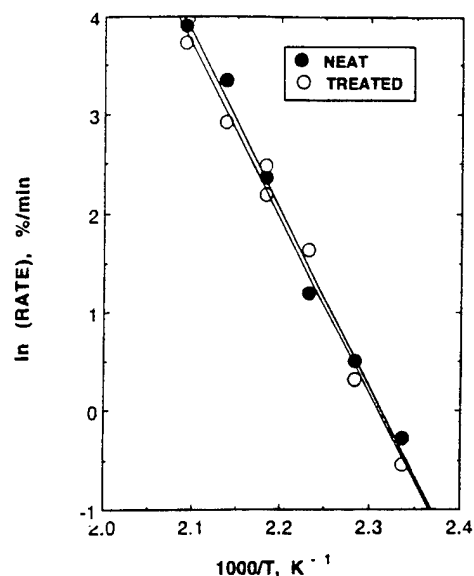


Figure 7. Arrhenius plot of oxygen reaction in neat and treated fuel. Reaction rate is in units of percentage of oxygen (air-saturated fuel) per minute.

autoxidation by a traditional antioxidant route, similar results may be effected by passivation of the stainless-steel surfaces by the dispersant or MDA components.

For temperatures of 175 and 185 °C, all oxygen in the neat fuel has reacted in about 7 and 4 min, respectively. Over the same time interval, less than 50% of the oxygen in the treated fuel has reacted. When POSF-2827 is stressed at 175 or 185 °C, JFA-5 will have a negligible effect on the oxygen reaction rate for up to 20% conversion, but it will have a pronounced effect in slowing autoxidation for any additional stressing. Thus, comparisons of the effects of additives such as JFA-5 should be made at several stress times corresponding to low, intermediate, and high oxygen conversion. Results predicated on complete reaction, as in Figures 3 and 4, do not take into account beneficial delays in autoxidation introduced by JFA-5.

Arrhenius parameters describing the *initial* autoxidation of the neat fuel have been reported (Jones and Balster, 1993); Figure 7 shows Arrhenius plots for both neat and treated fuel over the temperature range 155–205 °C. The former is determined from the initial reaction rate (i.e., slower rate) for the neat fuel, and the latter is based on a linear fit over the complete range of oxygen loss for the treated fuel. Note that the latter rate, as shown in Figure 6, is approximately constant over 80% conversion. The Arrhenius parameters describing oxygen consumption for the neat and treated fuels are the same within experimental uncertainty. The Arrhenius activation energy for the two data sets is 35 ± 1 kcal/mol. Thus, the rate coefficients for initiation, propagation, and termination must be very similar at low oxygen conversion (20%) for both neat and treated fuels.

Particle Sizing. Figure 8 shows the mean particle diameter (measured after cooling) for the neat and treated fuels as a function of stress time at 185 °C. Note the presence of a maximum diameter in the neat fuel around 3.5 min of stressing; this time correlated with the maximum rate of autoxidation (see Figure 6). Note also that the treated fuel shows no maximum, again consistent with Figure 6b. The mean particle size in the treated fuel is reduced by (1) the slower rate of autoxidation and (2) the presence of the dispersant

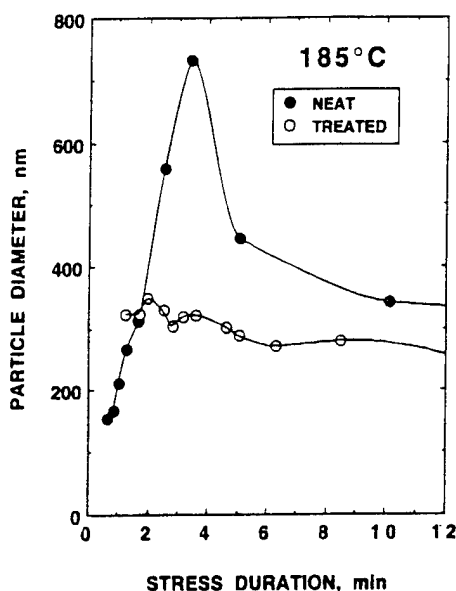


Figure 8. Particle diameter in neat and treated fuel vs stress time at 185 °C. Measurements made after cooling to room temperature.

Table 1. Ratio of Rates of Insoluble Formation (Treated/Neat)

oxygen flow (mL/min per mL of fuel)	surface	filterables ^a
0.03	0.7	1.7
0.2	2.0	3.7
0.4	0.8	1.2
	av 1.2 ± 0.7	av 2.2 ± 1.3

^a Filterables in static tests are defined with respect to Gelman A/E glass membrane filters with nominal pore size of 1 μm .

component in JFA-5 which acts to prevent agglomeration of insolubles. The Betz dispersant additive 8Q405 has been reported to introduce similar particle-diameter reductions for POSF-2827 fuel (Anderson et al., 1994). Although particle sizing provides direct information concerning the initial production of insolubles, photon correlation spectroscopy yields no information related to their quantity. If the surface adherence of bulk-formed insolubles is size dependent, then particle sizing may play a significant role in the understanding of surface fouling. Clearly, sizing data collected *in situ* at stress temperature would be more valuable. Experiments in this area are currently underway in our laboratory (Vilimpoc, 1994).

Static Isothermal Tests. Rates of forming filterable insoluble solids and gums and the rate of surface deposition on stainless-steel disks have been measured in flask tests at 185 °C. Similar experiments have been conducted with the treated fuel. The ratio of the pseudo-zero-order rates (treated/neat) shows the relative change in both surface and filtered insolubles with the introduction of JFA-5. These values are given in Table 1 for three different oxygen-spargate rates. The averaged results from the static tests at 185 °C are in fair agreement with findings from the dynamic tests. That is, JFA-5 tends to have only a minor impact on surface insolubles but leads to more bulk insolubles.

Non-Isothermal Dynamic Studies. The absence of significant benefit from the use of JFA-5 over the temperature interval 155–225 °C raises questions concerning the application of this additive in a Jet-A fuel. The possibility of benefits that are manifested only at higher temperatures and higher flow rates was

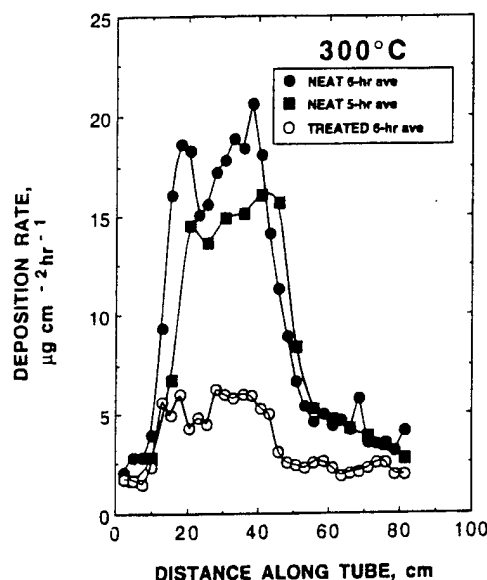


Figure 9. Deposition rate at 300 °C per unit area for neat fuel and treated fuel as function of distance along heated tube. Flow rate is 16 mL/min, and test duration is 6 h.

investigated. The single-pass heat-exchanger experiments of Heneghan et al. (1993) using a 300 °C block and a fuel-flow rate of 16 mL/min were repeated under virtually the same test conditions, except that 304 rather than 316 stainless steel was used in order to confirm reduction in surface deposits using JFA-5. The results plotted in Figure 9 show JFA-5 to introduce a 3-fold reduction in surface deposits on 304 stainless steel as compared to a 2-fold reduction on 316 steel (Heneghan et al., 1993). Total deposits (micrograms per milliliter of fuel) were reduced from 0.46 (average) to 0.15. The corresponding filterables (micrograms per milliliter of fuel) collected after cooling were unchanged [cf. 0.76 (average) and 0.78 (sum of insolubles from 0.45- and 0.2- μm filters)]. Evidently, JFA-5 is beneficial in reducing surface fouling in POSF-2827 fuel under conditions of fast fuel flow and high wall temperatures. Note in Figure 9 that some of the fine structure is reproduced in all three data sets. The fuel temperature increases along the axis of the tube, and the second broad maximum is attributed to the transition from laminar to turbulent flow which assists in mixing at the higher temperatures where reaction is becoming diffusion-limited.

Surface deposition in the neat and treated fuel was also studied at an intermediate temperature, namely 255 °C, at a flow rate of 2.5 mL/min—conditions which are also non-isothermal. The test time of the experiment was extended to 18 h to enhance signal levels. The results, plotted in Figure 10a, show a pronounced reduction in surface fouling with the treated fuel, as seen at 300 °C. The introduction of JFA-5 caused a reduction in surface deposits from 0.36 to 0.14 $\mu\text{g/mL}$, comparable to the reduction observed at 300 °C. Bulk insolubles are $\sim 0.5 \mu\text{g/mL}$ in both cases.

The results of the non-isothermal tests at 255 and 300 °C show that JFA-5 has very distinct benefits in reducing surface fouling while not changing the total quantity of bulk insolubles. This seems to contradict the previously discussed isothermal test results (155–225 °C) which indicated no benefit in reducing surface insolubles; however, there may be a rather simple explanation for this discrepancy. We know from Figure 6 that the time required for total conversion of all

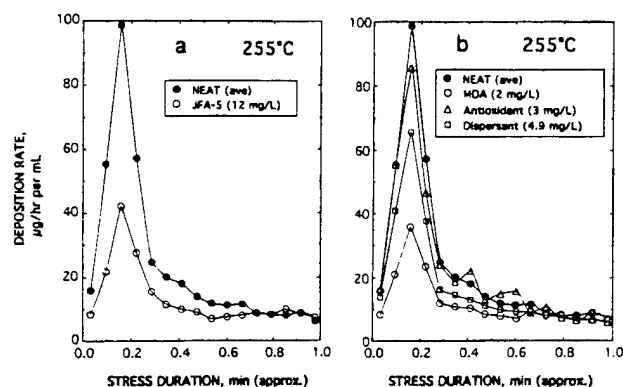


Figure 10. Deposition rate vs stress duration. Neat and fuel treated with (a) JFA-5 and (b) MDA, dispersant, and antioxidant components of JFA-5. Flow rate is 2.5 mL/min, and test duration is 18 h.

oxygen is extended when the fuel is treated with JFA-5. Hence, total reaction in treated fuel is delayed beyond that for neat fuel. This is not a factor in isothermal tests; however, in non-isothermal tests, fuel temperature increases with time in the heat exchanger. Thus, treated fuel will react on the average at a higher temperature. The efficiency of making surface insolubles, according to Figure 3, has an inverse temperature dependence, and as a result, less surface insolubles would be expected in the treated fuel. The bulk insolubles, according to Figure 4, show no pronounced temperature dependence, and no change in bulk insolubles would be expected. This essentially is the effect observed for non-isothermal tests.

The individual effects of introducing the metal deactivator (MDA), the dispersant, and the antioxidant at concentrations present in the composite JFA-5 are shown in Figure 10b. Clearly, the benefits realized from the use of JFA-5 (cf. 0.14 $\mu\text{g/mL}$) can be attributed primarily to the metal deactivator (cf. 0.12 $\mu\text{g/mL}$), with only a slight effect being the result of the dispersant (cf. 0.23 $\mu\text{g/mL}$) and the effect from the antioxidant (cf. 0.32 $\mu\text{g/mL}$) being negligible. Metal deactivators have been shown to be of value with fuels known to contain dissolved metals because of their ability to chelate metal and metal ions in solution (Downing et al., 1939; Pedersen, 1949); this area has been reviewed by Hazlett (1991). However, dissolved metals are not significant in this fuel; for example, Cu is <5 ppb and Fe is \approx 8 ppb. Clark (1988) has suggested that a metal deactivator, when added to a metal-free fuel, can also improve fuel performance in short-term tests such as the JFTOT but may present serious problems in long-term tests. The current tests of 6-h duration which show the beneficial effects of the MDA component of JFA-5 probably fall into the small-rig or short-term test category; conceivably, the measured reduction in our tests is a quantification of the qualitative JFTOT result. Further testing of MDA treatment of POSF-2827 using long-term experiments at high flow rates and high surface temperatures are planned.

Conclusions

The JFA-5 package has been added to POSF-2827 jet fuel at a concentration of 12 mg/L, and the neat and treated fuels have been compared in a series of tests to simulate fuel stressing at elevated temperature. In isothermal tests at low temperature (155–225 °C), quantification of surface and bulk insolubles after 100%

conversion of oxygen showed no net reduction. When added at 24 and 48 mg/L, JFA-5 was found to increase bulk insolubles significantly; however, it delayed the onset of rapid autooxidation (autocatalysis) which may lead to benefits in reducing insolubles for conditions where more than 20% of the oxygen in the neat fuel is converted to products. The size of the bulk particles was reduced by JFA-5, consistent with the presence of the dispersant component and the slower rate of autooxidation.

Under non-isothermal stress conditions which match more closely conditions experienced in the field, JFA-5 offers significant reduction in total surface deposits (factor of 2–3), while leaving the quantity of bulk filterables unchanged. The MDA component has been identified as the primary source of this effect. The observed changes introduced by JFA-5 under non-isothermal test conditions have been explained in terms of changes in autooxidation arising from JFA-5 and the observed temperature dependence of insolubles in POSF-2827 fuel.

Additive packages such as JFA-5 which contain antioxidant, dispersant, and—in particular—metal-deactivator components may reduce Jet-A fuel fouling in certain temperature regimes.

Acknowledgment

The authors would like to acknowledge Mr. Steve Anderson (USAF) for his coordination of the USAF additive program and Dr. Cyrus P. Henry of E. I. DuPont de Nemours and Co., Inc. (presently at Octel America, Inc., New Jersey), for providing the proprietary JFA-5 components and their equivalent concentration levels in JFA-5. The authors would like to thank Mr. Tim Gootee (USAF) for performing the surface-carbon analyses and Mrs. Marian Whitaker for editorial comments. This work was supported by and performed at the Wright Laboratory, Aero Propulsion and Power Directorate, Wright-Patterson Air Force Base, Ohio, under USAF Contract No. F33615-90-C-2033.

Literature Cited

- Anderson, S. D.; Jones, E. G.; Goss, L. P.; Balster, W. J. Effect of additives on the formation of insolubles in a jet fuel. In *Proceedings of the fifth international conference on stability and handling of liquid fuels*, Rotterdam, The Netherlands, Oct 3–7, 1994; Giles, H. N., Ed.; U.S. Department of Energy: Washington, DC, 1994, Vol. 1, pp 291–301.
- Boos, T. A.; Dues, T. L. Shale JP-4 additive evaluation. Technical Report AFWAL-TR-85-2118; Air Force Wright Aeronautical Laboratories: Wright-Patterson Air Force Base, OH, Oct 1986.
- Clark, R. H. The role of a metal deactivator in improving the stability of aviation kerosines. In *Proceedings of the third international conference on stability and handling of liquid fuels*; Institute of Petroleum: London, UK, 1988; p 283.
- Downing, F. B.; Clarkson, R. G.; Pedersen, C. J. Suppression of metal catalysts in gasoline gum formation. *Oil Gas J.* **1939**, *38* (11), 97–101.
- DuPont de Nemours Co. Product bulletin A-13611, January 1960.
- DuPont de Nemours Co., Materials Safety Data Sheet, MSDS 1682PC, September 1991.
- DuPont de Nemours Co. Private communication for component use, 1994.
- Hazlett, R. N. *Thermal oxidation stability of aviation turbine fuels*; ASTM Monograph 1; American Society for Testing and Materials: Philadelphia, PA, 1991.
- Heneghan, S. P.; Martel, C. R.; Williams, T. F.; Ballal, D. R. Studies of jet fuel thermal stability in a flowing system. *J. Eng. Gas Turbines Power* **1993**, *115*, 480–484.

- Jones, E. G.; Balster, W. J. Phenomenological study of the formation of insolubles in a Jet-A fuel. *Energy Fuels* **1993**, 7, 968-977.
- Jones, E. G.; Balster, W. J. Formation of insolubles in a Jet-A fuel: temperature effects. *Prepr.-Am. Chem. Soc., Div. Pet. Chem.* **1994**, 39 (1), 78-81.
- Jones, E. G.; Balster, W. J. Surface fouling: short- vs. long-term isothermal tests. *Energy Fuels* **1995**, 9, 610-615.
- Jones, E. G.; Balster, W. J.; Anderson, S. D. Formation of insolubles in jet fuels: effects of oxygen. *Prepr.-Am. Chem. Soc., Div. Pet. Chem.* **1992**, 37 (2), 393-402.
- Jones, E. G.; Balster, W. J.; Post, M. E. Degradation of a Jet-A fuel in a single-pass heat exchanger. *J. Eng. Gas Turbines Power* **1995**, 117, 125-131.
- Martel, C. R. Military jet fuels, 1944-1987. Technical Report AFWAL-TR-87-2062; Air Force Wright Aeronautical Laboratories: Wright-Patterson Air Force Base, OH, November 1987.
- O'Hern, T. J.; Trott, W. M.; Martin, S. J.; Klavetter, E. A. Advanced diagnostics for in situ measurement of particle formation and deposition in thermally stressed jet fuels. AIAA Paper No. 93-0363, Presented at the AIAA 31st Aerospace Sciences Meeting and Exhibit, Reno, NV, January 1993.
- Pedersen, C. J. Inhibition of deterioration of cracked gasoline during storage. *Ind. Eng. Chem.* **1949**, 41, 924.
- Rubey, W. A.; Striebich, R. C.; Tissandier, M. D.; Tirey, D. A.; Anderson, S. D. Gas chromatographic measurement of trace oxygen and other dissolved gases in thermally stressed jet fuel. *J. Chromatogr. Sci.* **1995**, 33, 433-437.
- Vilimpoc, V. Private communication, 1994.
- Zabarnick, S.; Grinstead, R. R. Studies of jet fuel additives using the quartz crystal microbalance and pressure monitoring at 140 °C. *Ind. Eng. Chem. Res.* **1994**, 33, 2771-2777.

Received for review May 25, 1995

Revised manuscript received October 23, 1995

Accepted November 10, 1995*

IE9503151

* Abstract published in *Advance ACS Abstracts*, January 15, 1996.

Quantitative Evaluation of Jet-Fuel Fouling and the Effect of Additives

E. Grant Jones,* Lori M. Balster, and Walter J. Balster

*Systems Research Laboratories, Inc., A Division of Space Industries International, Inc.,
2800 Indian Ripple Road, Dayton, Ohio 45440-3696*

*Received February 13, 1995. Revised Manuscript Received May 31, 1995**

Dynamic near-isothermal techniques have proven to be valuable in assessing the tendency of aviation fuels to form surface and bulk insolubles under conditions of thermal-oxidative stress. These methods are applied to the investigation of three representative jet fuels, POSF-2827, POSF-2980, and POSF-2934, and changes in these fuels caused by the introduction of four candidate additives. Neat and additized fuels are evaluated during flow through a tubular heat exchanger at 185 °C. The average surface-deposition rate as a function of stress duration and the quantity of both surface and bulk insolubles are determined during complete conversion of the dissolved oxygen. The additives, introduced individually, include a common antioxidant, a metal deactivator, a dispersant, and a combination detergent/dispersant. The impact of each additive is discussed. Dispersants are found to cause the greatest reduction in total quantity of bulk and surface deposits. Several criteria are considered for evaluating fuels and fuel/additive combinations.

Introduction

Consideration of the thermal-oxidative stability of aviation fuels is becoming more important as fuels are subjected to increased stress at elevated temperatures. Enhanced aircraft performance creates additional heat and, in turn, stressing of the aviation fuel. Being the primary heat sink, fuels must be capable of withstanding severe oxidative stress without bringing about system failures.¹ Unfortunately, the reaction products of autoxidation include insolubles which tend to foul heated surfaces, causing reduced efficiency and blockage in heat exchangers and other undesirable changes in nozzles and servo-controls. Such problems are exacerbated by the presence of small quantities of fuel components containing heteroatoms such as nitrogen and sulfur. In general, fuels having fewer polar components are preferable because they produce fewer insolubles.^{2a}

One approach to improving the stability of fuels is based on heteroatom removal. Clay or hydro treatment may accomplish the removal of some polar components but does not always represent a practical solution because of the cost involved. Another approach involves the introduction of low-cost additives—an approach that is particularly appealing when lesser quality or borderline fuels can be upgraded. Additives such as antioxidants for slowing oxygen consumption, metal deactivators for chelating dissolved metals or passivating tube walls, and dispersants for increasing solubility would appear to hold the most promise from the standpoint of

surface fouling. Additives for achieving other specific objectives include corrosion inhibitors, lubricity improvers, icing inhibitors, static dissipators, and pipeline-drag reducers. Their application to jet fuels has been summarized by Martel.³ As an aid in the selection of appropriate additives or additive packages, we need data from simple laboratory tests on each neat fuel and its additized analogue and, in addition, straightforward criteria for their interpretation.

One of the challenges facing those studying aviation fuels is to gain a basic understanding of insoluble formation that will assist in the ranking of fuels and the prediction of their behavior at elevated temperatures. This is a formidable task, considering the diversity of fuel chemistry. Nevertheless, dynamic near-isothermal techniques, developed within our laboratory, have provided new insight into the formation of bulk and surface insolubles in the Jet-A fuel POSF-2827 under controlled chemical conditions.⁴⁻⁷ These methods have proven to be valuable in assessing the tendency of fuels to form surface and bulk insolubles at selected elevated temperatures. The objective of the current study was to apply these techniques to a limited matrix of three jet fuels and four additives. The neat and additized fuels were studied to determine (1) differences in the neat fuels, (2) beneficial or deleterious changes from additives within a single fuel, and (3) criteria for evaluating and comparing different combinations of fuels and additives.

(3) Martel, C. R. Military Jet Fuels, 1944–1987, Technical Report AFWAL-TR-87-2062; Air Force Wright Aeronautical Laboratory: Wright-Patterson Air Force Base, OH, 1987.

(4) Jones, E. G.; Balster, W. J. *Energy Fuels* **1993**, *7*, 968–977.

(5) Jones, E. G.; Balster, W. J. *Prepr.-Am. Chem. Soc., Div. Pet. Chem.* **1994**, *39* (1), 78–81.

(6) Jones, E. G.; Balster, W. J. *Prepr. Pap.-Am. Chem. Soc., Div. Fuel. Chem.* **1994**, *39* (3), 952–957.

(7) Anderson, S. D.; Jones, E. G.; Goss, L. P.; Balster, W. J. Effect of Additives on the Formation of Insolubles in a Jet Fuel. *Proceedings of the 5th International Conference on Stability and Handling of Liquid Fuels, Rotterdam, 3–7 Oct 1994*, Giles, H. N., Ed.; U. S. Department of Energy: Washington, DC, 1994; Vol. 1, pp 291–301.

* Author to whom correspondence should be addressed. Tel: (513) 252-4264.

† Abstract published in *Advance ACS Abstracts*, July 15, 1995.

(1) Edwards, T.; Anderson, S. D.; Pearce, J. A.; Harrison, W. E. High Temperature Thermally Stable JP Fuels—An Overview. AIAA Paper 92-0683, Presented at the 30th Aerospace Sciences Meeting and Exhibit, Reno, NV, 6–9 January 1992.

(2) Hazlett, R. N. *Thermal Oxidation Stability of Aviation Turbine Fuels*, ASTM Monograph 1; American Society for Testing and Materials: Philadelphia, 1991; (a) pp 150–151; (b) Chapter IX.

Table 1. Fuel Properties

	POSF-2827	POSF-2980	POSF-2934
type	Jet-A	Jet-A	JP-8
treatment	straight run	MEROX-treated	JP-8 additives
JFTOT breakpoint (°C)	266	288	266
total sulfur (%)	0.079	0.061	0.076
mercaptan sulfur (%)	0.001	0.000	0.000
freezing point (°C)	-43	-44	-52
aromatics (vol%)	19	17	21
total acid no. (mg of KOH/g)	0.001	0.001	0.043
iron content (ppb)	8	<5	10
copper content (ppb)	<5	<5	53
inherent insolubles (μg/mL)	0.08	0.04	0.08

Table 2. Additives Tested

class	name	chemical name	manufacturer	concentration (mg/L)
antioxidant	BHT	2,6-di- <i>tert</i> -butyl- <i>p</i> -cresol	DuPont	25
metal deactivator	MDA	<i>N,N'</i> -disalicylidene-1,2-propanediamine	DuPont	2
dispersant	8Q405	proprietary	Betz	100
detergent/dispersant	MCP-147B	proprietary	Mobil	300

Each of the three selected fuels produces measurable quantities of deposits during stressing and, thus, is amenable to study using near-isothermal techniques. Hydro-treated and other very stable fuels were avoided because they produce minimal amounts of insolubles and, therefore, are of less interest and are more difficult to study. The additives selected are the commercial antioxidant BHT, a common metal deactivator, a proprietary dispersant, and a proprietary detergent/dispersant. Additives were used individually at fixed concentrations. All of these additives are potential candidates for use in future additive packages as part of the USAF JP-8 + 100 program⁸ which is designed to extend the operating temperature range of JP-8 fuels by 100 °F. The synergism arising from combinations of additives is an important consideration in additive packages; this is a logical extension but beyond the scope of the current study.

Fouling experiments were conducted over extended test times at 185 °C to emphasize deposition on previously fouled surfaces and to reduce complications arising from heterogeneous catalysis and its effect on oxygen consumption.⁶ We consider several simple criteria in ranking fuels and additives. For near-isothermal experiments at 185 °C, the most obvious criteria are the rate of consumption of dissolved oxygen, the dependence of deposition rate on stress duration, the total quantity of surface insolubles, the quantity of bulk insolubles, and finally the sum of surface and bulk insolubles. One additional criterion for evaluating fuel behavior under limited stress is presented and applied to the current data.

Experimental Section

Two of the selected fuels fall into the Jet-A category (POSF-2827 and -2980) and contain no additives. The third is a JP-8 fuel (POSF-2934) and, by definition, contains the standard JP-8 additive package consisting of icing inhibitor (DIEGME), corrosion inhibitor/lubricity improver (DCI-4A), and static dissipator (Stadis 450).⁹ These three fuels pass the JFTOT test and meet all Jet-A specifications; they also meet all USAF specifications (except for POSF-2934 which has an elevated total acid level). Table 1 contains some pertinent data on the three fuels. The sulfur concentrations are within specification (<0.1%) but are sufficiently high to account for the selection of these fuels as good candidates for the study of insoluble formation. One of the fuels, POSF-2980, was MEROX-treated

to convert mercaptans to disulfides for odor reduction. One fuel, POSF-2934, because of its high acid level, acquired some dissolved metals, in particular, Cu. Clearly, in seeking to measure improvement in thermal stability through the introduction of additives, it is important to select representative, average fuels rather than ideal fuels. In the three fuels selected for study, oxidation is inhibited by the presence of sulfur compounds, but at the expense of increased insoluble formation.¹⁰

The four selected additives, an antioxidant (BHT), a metal deactivator (MDA), a dispersant (8Q405), and a combination detergent/dispersant (MCP-147B), are described in Table 2. Concentration levels of BHT and the proprietary additives were provided by the USAF (JP-8 + 100 program) and were based on optimization tests,¹¹ original manufacturer's suggestions, and cost restraints. MDA was used at a concentration of 2 mg/L to chelate low levels of dissolved metals and possibly to passivate initial metal surfaces.

The experiments were conducted using the Near-Isothermal Flowing Test Rig (NIFTR) which has been described previously.^{4,6} Figure 1 shows the heat exchanger which was operated for deposition experiments in the extended-pass mode to double the reaction time. Fuel, which is saturated initially with respect to air and which contains ~64 ppm (w/w) oxygen, is pumped at a pressure of 2.3 MPa through 0.318-cm-o.d., 0.216-cm-i.d. commercial stainless-steel (304) tubing clamped tightly in a 91.4-cm heated copper block. Two in-line Ag-membrane filters (0.45 and 0.2 μm) at ambient temperature collect the nonadhering bulk insolubles formed at 185 °C as well as an additional contribution from fuel cooling. The stress temperature is maintained at 185 °C for all experiments.

All deposition measurements were made using stainless-steel tubing in 69–72 h experiments that were run continuously at a fixed fuel-flow rate of 0.25 mL/min; reaction time or stress duration was determined from the flow rate, tube dimensions, and location along the tube axis. Times were reduced by 15% to correct for fuel expansion at temperature.

(8) The JP-8 + 100 program is designed to extend the operating range of JP-8 fuels by 100 °F. See review by: Edwards, T.; Roquemore, W. M.; W. E. Harrison; Anderson, S. D. Research and Development in High Thermal Stability Fuels. Paper No. PEP-18, Presented at the 81st AGARD Symposium on Fuels and Combustion Technology for Advanced Aircraft Engines, Collifero, Italy, 10–14 May 1993.

(9) Martel, C. R. Properties of JP-8 Jet Fuel, Technical Report AFWAL-TR-88-2040; Air Force Wright Aeronautical Laboratory: Wright-Patterson Air Force Base, OH, 1988.

(10) Kendall, D. R.; Mills, J. S. *Ind. Eng. Chem. Prod. Res. Dev.* **1986**, 25, 360–366.

(11) R&D Status Report No. FR 22635-18 (under Contract No. F33615-93-C-2301 with the United States Air Force, Wright Laboratory, Aero Propulsion and Power Directorate, Wright-Patterson Air Force Base, OH); Pratt and Whitney: West Palm Beach, FL, September 1994.

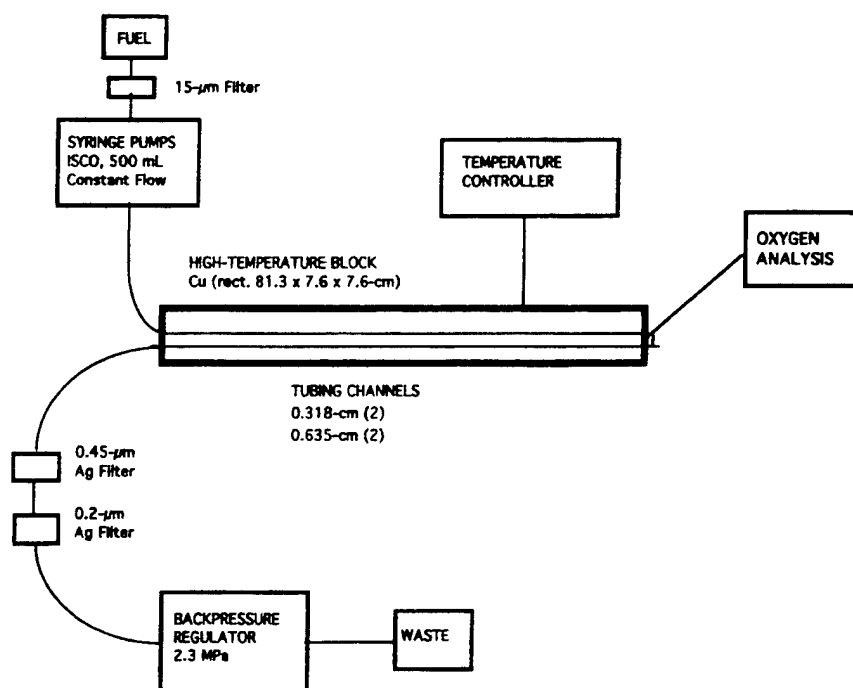


Figure 1. Schematic diagram of apparatus (NIFTR).

At the end of each test, the heated tube was cut into 5.1-cm segments, and the quantity of carbon in the deposits was assessed from surface-carbon burnoff (LECO RC-412). Deposition rates were determined from the amount of carbon in each segment, the stress time within that segment, and the total amount of fuel passed. Rates were not corrected for fuel expansion. Each carbon evaluation provides one data point, representing the rate averaged over the entire test time (i.e., ~72 h). The rate is expressed in units of micrograms of carbon per unit stress time per unit volume of fuel passed through the system. In dynamic near-isothermal experiments, stress duration refers to the reaction time at temperature; the experimental test time (along with the fuel-flow rate) determines the total quantity of fuel passed through the system. Bulk insolubles (insoluble in heptane) were quantified using surface carbon burnoff of the in-line filters. The term "dynamic" indicates that these tests are flowing as opposed to static. The term "near" reflects the fact that immediately after the fuel enters the block, some reaction occurs below the block temperature. Use of the slow flow rate limits this effect to the first data point.

Dissolved oxygen was measured in separate experiments using a fixed-length heated tube (81.3 cm) as a reaction cell and GC detection according to the methods of Rubey et al.¹² Stress duration was changed by varying the flow rate. It has been shown that autoxidation in POSF-2827 fuel is catalyzed by stainless-steel tubing and that the accumulation of surface deposits tends to passivate the metal surfaces.¹³ The current deposition experiments were conducted over extended time periods which allowed surface passivation from deposit accumulation to occur within the first few hours and all subsequent deposition to be governed by a slower rate of autoxidation. It is desirable to make oxygen measurements for the reaction which best approximates the test conditions present during deposition experiments, i.e., minimal catalytic wall effects. The decision was made not to use tubing which was passivated by deposits, but to use Silcosteel¹⁴ tubing. This

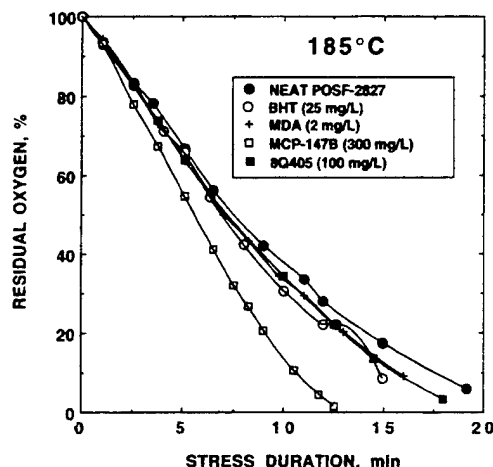


Figure 2. Oxygen consumption at 185 °C in neat and additized POSF-2827 fuel.

tubing, made to the same dimensions as commercial stainless-steel tubing, has an inert silica-treated inner surface covered with a monolayer of a specific siloxane polymer to further reduce surface activity. Background surface carbon is below levels for stainless-steel tubing.

Results and Discussion

In the following sections, the results obtained for each fuel are treated separately with respect to three evaluation criteria: oxygen loss, dependence of deposition rate on stress duration, and quantification of insolubles. Another criterion for fuel ranking is introduced, and finally we consider the impact of each additive.

POSF-2827. Oxygen Loss. Reaction of the dissolved oxygen as a function of stress duration at 185 °C is shown in Figure 2. All oxygen in the neat fuel reacts in about 20 min, and the rate is constant down to 30–40% residual oxygen. Neither BHT nor MDA signifi-

(12) Rubey, W. A.; Tissandier, M. D.; Striebig, R. C.; Tirey, D. A.; Anderson, S. D. *Prepr.-Am. Chem. Soc., Div. Pet. Chem.* **1992**, 37 (2), 371–376.

(13) Jones, E. G.; Balster, W. J. Surface Fouling in Aviation Fuel: Short- vs Long-Term Isothermal Tests. *Energy Fuels* **1995**, 9, 610–615.

(14) SILCOSTEEL tubing, Restek Corp., Bellefonte, PA.

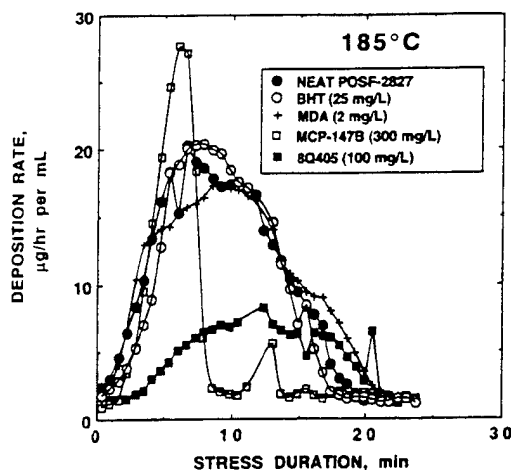


Figure 3. Deposition rate at 185 °C in neat and additized POSF-2827 fuel.

cantly alters the oxygen consumption. The presence of certain types of sulfur compounds causes hydroperoxide concentration to remain low.¹⁰ Hydroperoxide concentrations do not increase in this fuel; measurements in this laboratory using the RULER technique of Kauffman¹⁵ indicate maximum concentrations less than 0.1 mmol/L over 15 min of stressing.¹⁶ Chain-breaking antioxidants such as BHT (hindered phenol) are ineffective in this fuel since it contains such an abundance of natural antioxidants. Similarly, MDA is not expected to have a pronounced effect because of the low level of dissolved metals and the use of tubing with passivated walls. Only one of the additives, MCP-147B, perturbs the oxygen consumption by increasing the reaction rate. At a concentration of 300 mg/L, this additive directly participates in the reaction either as a pro-oxidant or as an initiator.

Dependence of Deposition Rate on Stress Duration. Figure 3 shows deposition profiles at 185 °C. The 72-h-average rate profiles for the additives BHT and MDA as well as the neat fuel are not distinguishable within experimental reproducibility, displaying maxima around 9 min and complete deposition around 20 min, which is consistent with the observed consumption of oxygen. The additives MCP-147B and 8Q405 cause significant changes in the deposition profiles. For stress times of 4–7 min, the former increases the deposition rate, maximizing around 6 min; however, for longer times it decreases the rate with minimal tailing. The increase in deposition rate using MCP-147B might be expected from the increased oxygen reaction rate (see Figure 2). 8Q405 decreases the deposition rate up to 15 min of stressing and delays the maximum to around 12 min. Based upon a deposition-rate criterion, 8Q405 is an effective additive because it delays deposition and reduces its rate.

Quantification of Insolubles. Other criteria for evaluation of the additives using data from the same experiments are total quantity of surface insolubles (integral under the rate profiles), bulk insolubles (carbon burnoff of the in-line filters), and finally the sum of these insolubles. These quantities are expressed in terms of

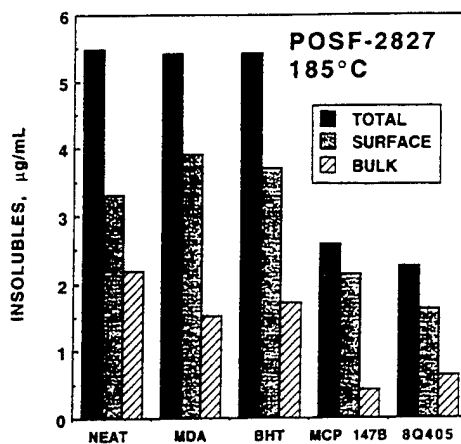


Figure 4. Quantification of surface, bulk, and total insolubles formed at 185 °C in neat and additized POSF-2827 fuel.

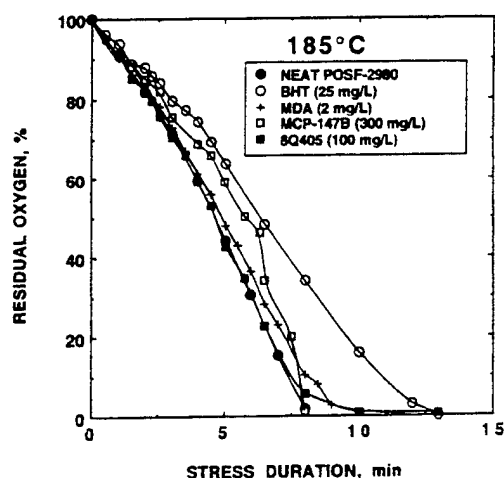


Figure 5. Oxygen consumption at 185 °C in neat and additized POSF-2980 fuel.

micrograms of insolubles per milliliter of fuel initially saturated with respect to air at room temperature. An inherent normalization results from the fixed amount of oxygen consumed in each experiment. The histogram in Figure 4 shows insolubles formed in the neat and additized fuel. BHT and MDA have minimal impact on the quantity of surface and bulk insolubles. In contrast, the other two additives, which are both dispersants, cause significant reduction. In the neat fuel, inherent bulk insolubles (0.08 µg/mL, see Table 1) make a negligible contribution to the measured bulk insolubles, except in cases where the dispersants have severely depressed the insoluble reaction products.

POSF-2980. Oxygen Loss. Figure 5 shows the reaction of dissolved oxygen as a function of stress duration. In the neat fuel all of the oxygen has reacted within 8 min. In contrast to POSF-2827, the oxygen reaction rate increases with conversion which is indicative of self-initiation or autocatalysis. This effect is common in both neat and additized fuel. Introduction of the additives MDA and 8Q405 does not cause the oxygen-loss profile to differ from that of the neat fuel. However, changes are apparent with the use of MCP-147B and BHT. The most significant change occurs with the introduction of BHT which requires an additional 2 min to achieve 50% conversion and ~4–5 min to achieve complete conversion. The detergent/dispersant MCP-147B slightly retards the initial reaction, but the time

(15) Kauffman, R. E. *Prepr.-Am. Chem. Soc., Div. Pet. Chem.* **1994**, 39 (1), 42–46.

(16) Jones, E. G.; Balster, L. M.; Balster, W. J. Manuscript in preparation.

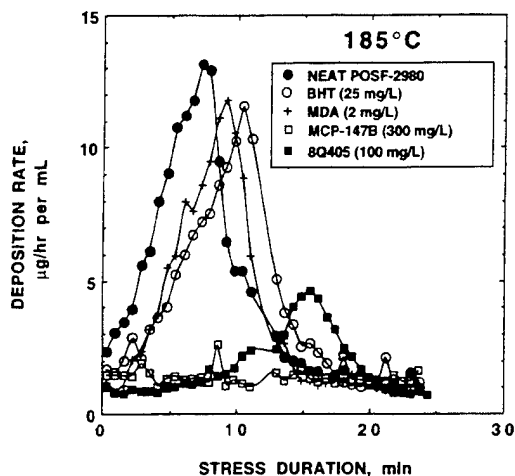


Figure 6. Deposition rate at 185 °C in neat and additized POSF-2980 fuel.

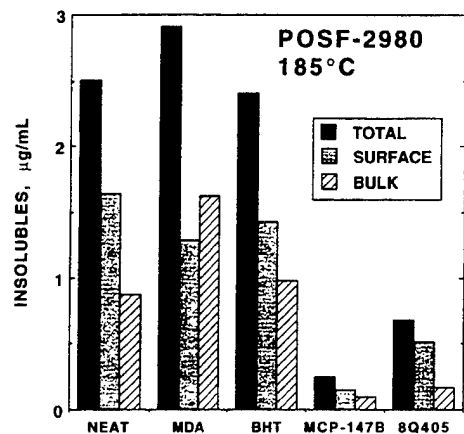


Figure 7. Quantification of surface, bulk, and total insolubles formed at 185 °C in neat and additized POSF-2980 fuel.

required for complete conversion is the same as that with the neat fuel.

Dependence of Deposition Rate on Stress Duration. The deposition profiles in Figure 6 indicate the impact of each additive on the deposition process. The hindered-phenol antioxidant BHT introduces a delay of 3–4 min in the location of the maximum, consistent with the observed delays in oxygen loss. Once deposition begins, however, the rate has a similar time dependence. This observation is consistent with antioxidants acting to retard autoxidation but not interfering with its ultimate course.

MDA causes a similar but smaller shift, indicating possible antioxidant capability in its phenol end groups. As with POSF-2827, the additives 8Q405 and MCP-147B have a significant impact. The former delays deposition and reduces the rate, while the latter reduces the deposition rate to levels near the baseline noise over the entire stress time.

Quantification of Insolubles. The results for the neat and additized fuel are given in Figure 7. The amount of total surface insolubles (area under profiles in Figure 6), as noted above, is unaffected by BHT and MDA but is reduced by a factor of three using 8Q405 and by a factor of 10 using MCP-147B. Bulk insolubles suffer large reductions when the dispersant and detergent/dispersant additives are used; bulk quantities approach the limiting value 0.04 µg/mL which would be expected

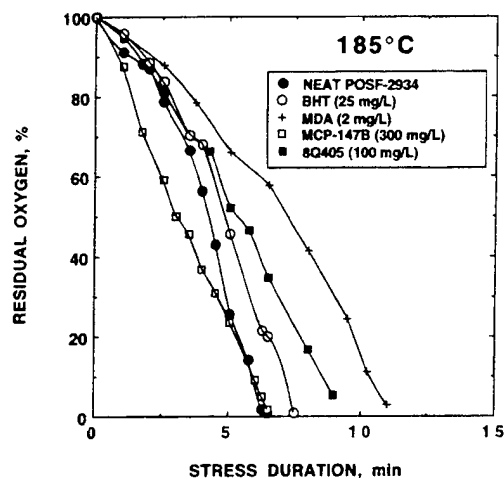


Figure 8. Oxygen consumption at 185 °C in neat and additized POSF-2934 fuel.

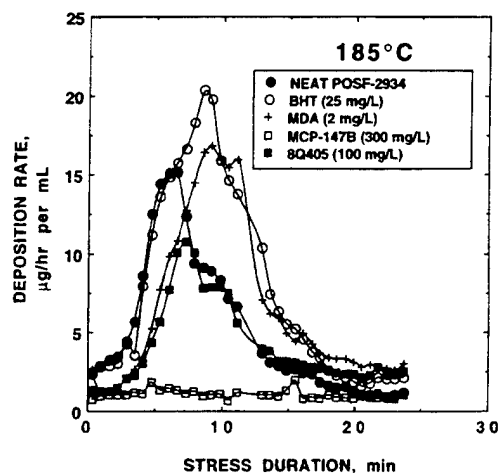


Figure 9. Deposition rate at 185 °C in neat and additized POSF-2934 fuel.

from inherent insolubles (see Table 1). Total insolubles, a combination of bulk and surface contributions, are minimally affected by BHT and MDA and significantly reduced by 8Q405 and MCP-147B.

POSF-2934. Oxygen Loss. The reaction of dissolved oxygen as a function of stress duration at 185 °C is shown in Figure 8. Oxygen reaction in this neat fuel is complete after about 6 min. All four additives cause changes in oxygen reaction. Three of the additives, BHT, 8Q405, and MDA, delay reaction, while MCP-147B accelerates reaction. MDA introduces the major delay due to chelation of dissolved metals.

Dependence of Deposition Rate on Stress Duration. As with POSF-2980, the introduction of each additive creates a new deposition profile which differs from that of the neat fuel (see Figure 9). Both BHT and MDA cause delays in achieving the maximum deposition rate that correspond to the delays observed in autoxidation. The former delay arises from antioxidant action and the latter, from dissolved metal chelation. The dispersant 8Q405 introduces a slight delay but overall causes the least change. MCP-147B effectively reduces the deposition rate to baseline levels after 24 min of stressing. The absence of deposition in this instance is very interesting, particularly considering the faster autoxidation apparent in Figure 8. Intuitively, additives which delay autoxidation are desirable, and those which accelerate

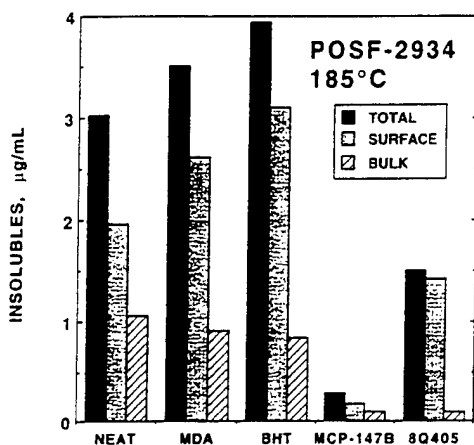


Figure 10. Quantification of surface, bulk, and total insolubles formed at 185 °C in neat and additized POSF-2934 fuel.

the reaction are not; however, this becomes a moot point in the absence of surface fouling. An additive that accelerates oxygen loss but prevents deposition may be partitioning oxidation reactions into soluble channels and, thus, may be an ideal candidate. MCP-147B is proprietary, and its molecular weight is not available; however, since its concentration is comparable to that of dissolved oxygen, it is conceivable that this additive is diverting the course of the autoxidation reactions.

Quantification of Insolubles. The histogram in Figure 10 displays a familiar trend; namely, significant reduction in bulk and surface insolubles with the use of 8Q405 and MCP-147B and no benefit from BHT and MDA. BHT and MDA do not alter the bulk filterables significantly but tend to increase the total amount of surface insolubles.

In very recent studies¹⁷ using the gravimetric JFTOT,¹⁸ Pande and Hardy have observed that for fuels of typical thermal stability, which would include POSF-2934, some of the deleterious aspects of Cu can be offset only if MDA is added soon after fuels leave the refinery; this permits aging to occur in the presence of MDA. In the current study MDA was added to POSF-2934 only after extended storage at ambient temperature. This may explain why the beneficial chelating effects of MDA in delaying autoxidation and deposition are observed, but overall benefits in reducing the quantity of insolubles are not. Many questions remain concerning the role of MDA.

Another Criterion for Ranking Fuels and Additives

The quantification discussed above refers to complete oxygen conversion. Distinct advantages result from comparing different fuel/additive combinations because the total amount of dissolved oxygen is approximately fuel independent. However, it can be argued that an additive which delays the deposition process may have a very beneficial impact in experiments conducted over limited conversion, the most obvious examples in the current data being the role of BHT and MDA in delaying

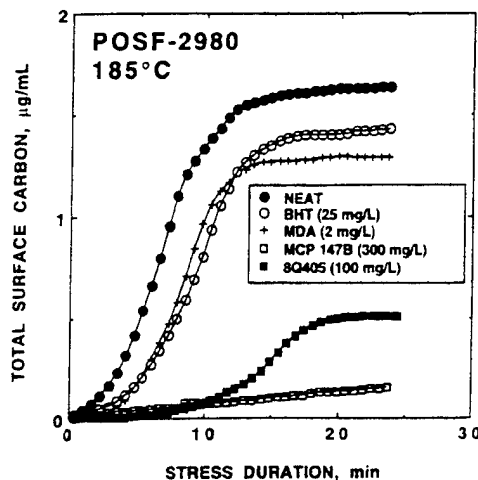


Figure 11. Total surface carbon formed at 185 °C in neat and additized POSF-2980 fuel.

deposition in POSF-2980. For example, after 7 min of stressing (location of maximum in neat fuel), much less total deposit (area under the curve in Figure 6) is present in both additized fuels. Another way of viewing the differential rate data in Figure 6 is to present it in integral form, as a total surface carbon (TSC) plot (see Figure 11). When evaluating this quantity, it is necessary to correct for a common background carbon level from each tube segment within each test. Since background levels are dependent on both tubing and fuel, some subjectivity is involved. Baseline corrections are relatively smaller in long-term tests. The use of integral plots has two advantages: (1) a smoothing of noise in differential data and (2) the immediate comparison of total surface fouling arising from any fuel/additive combination as a function of stress duration at temperature. For example, based on Figure 11 all four additives reduce surface fouling for POSF-2980 under conditions of limited stress time. TSC plots for the other two fuels are not shown. Analogous to Figure 11, the behavior of POSF-2934 shows significant delays in TSC from the additives MDA and 8Q405, as well as extended baseline from MCP-147B. The plot for POSF-2927 shows a significant delay from 8Q405. The extent of the reduction in surface fouling can be determined for any desired time from the TSC plot, and this may provide a better criterion for comparing fuels and the effect of additives.

As part of the current approach, we are monitoring two aspects of the fouling processes in jet fuels; namely, oxygen loss and growth of deposits. Peroxide formation is very closely related to oxygen loss. Fodor and co-workers¹⁹⁻²¹ have measured peroxide formation in many jet fuels at lower temperatures (40–120 °C) using a stirred reactor and have observed induction periods on the order of hours and a stress-time dependent increase in peroxide concentrations. Hindered-phenol antioxidants were found to extend the induction periods.²¹ The current experiments using BHT in both POSF-2980 and -2934 which show extended delays on the order of minutes in both oxygen loss and deposition

(17) Pande, S. G.; Hardy, D. R. *Energy Fuels* **1995**, *9*, 177–182.

(18) Beal, E. J.; Hardy, D. R.; Burnett, J. C. *Proceedings of the 4th International Conference on Stability and Handling of Liquid Fuels*, Orlando, FL, Nov 1991; American Society for Testing and Materials: Philadelphia, 1991; pp 245–259.

(19) Fodor, G. E.; Naegeli, D. W.; Kohl, K. B. *Energy Fuels* **1988**, *2*, 729–734.

(20) Fodor, G. E.; Naegeli, D. W. *Prepr. Pap.-Am. Chem. Soc., Div. Fuel Chem.* **1990**, *35* (4), 1267–1276.

(21) Fodor, G. E.; Naegeli, D. W.; Turner, L. M. *Prepr.-Am. Chem. Soc., Div. Pet. Chem.* **1992**, *37* (2), 403.

are a complementary observation of the same induction-period phenomenon observed by Fodor and indicate that autoxidation processes occurring at 185 °C are similar to those controlling fuel-storage stability at lower temperature. It is not clear, however, that the same deposition processes prevail over the entire temperature range.

Summary by Additive

Note, in considering the following summary, that each additive was evaluated at a single concentration. Assessment of the impact of each dispersant at equivalent molar concentration is precluded by not knowing the fraction of active ingredient in the proprietary samples.

BHT. The quantity of bulk insolubles formed in the three fuels studied is not reduced by use of BHT at a concentration of 25 mg/L. Also, BHT does not reduce the total quantity of surface insolubles in either POSF-2827 or POSF-2980 and increases it in POSF-2934. Significant improvement in POSF-2980 occurs during limited conversion from the delay in autoxidation; this potential for improvement at low conversion may be justification for the general inclusion of BHT in additive packages.

MDA. The rate of oxygen consumption is unchanged by introduction of MDA into POSF-2827 and -2980, consistent with the low level of dissolved metals. The significant delay in autoxidation and the corresponding delay in deposition from its use in POSF-2934 indicates the presence of dissolved metals, in particular, Cu at 53 ppb; however, we cannot exclude surface passivation. Again, the potential for benefits, particularly in the presence of dissolved metals, may be sufficient justification for its inclusion in additive packages.

MCP-147B. The behavior of the proprietary detergent/dispersant MCP-147B in these fuels is intriguing in that total insolubles are significantly reduced in all three fuels. This indicates that dispersant action is preventing particle growth. Undoubtedly, this is the primary effect; however, the autoxidation rate in two of the fuels increases, which is indicative of the direct chemical involvement of MCP-147B either as an initiator or as a pro-oxidant. In POSF-2827 increased oxygen consumption is manifested in an increased deposition rate. In contrast, surface deposition rates in POSF-2980 and POSF-2934 are so low that the amount of surface carbon is near the minimum detectable level.

8Q405. Insolubles are reduced in all three fuels, and no deleterious changes in autoxidation chemistry are evident with the use of the proprietary dispersant 8Q405. While this additive seems ideal, the reduction of insolubles is somewhat less than with MCP-147B. Zabarnick and co-workers, also working on the JP-8 + 100 program, have recently shown pronounced reduction in total surface deposits at 140 °C using the additive 8Q405 in POSF-2827 and -2980 fuels based on 15-h quartz crystal microbalance (QCM) experiments.²²

Conclusions

The thermal-oxidative behavior of a limited matrix of three jet fuels and four additives used in fixed concentrations has been studied for reaction at 185 °C. When deposition could be measured, it closely tracked

the reaction of dissolved oxygen, as expected for autoxidation reactions. Six criteria have been applied for assessment of thermal-oxidative stability: (1) reaction of dissolved oxygen, (2) shape of the deposition rate vs stress duration profile, (3) quantity of bulk insolubles (100% conversion), (4) quantity of surface insolubles (100% conversion), (5) sum of bulk and surface insolubles (100% conversion), and finally (6) total surface carbon formed after limited stressing. The last criterion may be the most significant since it relates to conditions of limited oxygen conversion which exist in typical aircraft.

Of the four additives considered, the dispersant and detergent/dispersant types were found to be the most effective in reducing insolubles. Their primary role appears to be reduction of potential insolubles by preventing particle growth. Each fuel and additive combination displays a unique deposition profile, indicative of specific reaction chemistry. The potential benefits of MDA may be better reflected under different test conditions. Under certain circumstances MDA and BHT offer benefits in delaying reaction, particularly at low conversion.

Current work has been limited to fuel behavior at 185 °C. Since aviation fuels experience a broad range of stress conditions, it is necessary to determine the dependence of fouling on temperature. The temperature dependence of POSF-2827 fuel has been studied. The surface fouling was found to have an inverse temperature dependence.⁵ Similar studies for the other two fuels are in progress. Because of the abundance of additive studies^{2b} involving a diverse range of fuels, it is difficult to make specific comparisons. It would be advantageous to compare the *same* fuel/additive combination in rigs which emphasize different temperature and flow regimes. For example, comparison of quantitative data collected using NIFTR and gravimetric JFTOT¹⁸ (both small-scale rigs) with those from full-²³ and half-scale²⁴ rigs would be valuable.

Further work is required to determine whether selected combinations of the above additives offer improvements beyond those discussed above. The current work indicates that such additive packages should include dispersant/detergent components; based on low-conversion results, arguments could be made for the inclusion of both antioxidant and metal-deactivator components.

Acknowledgment. This work was supported, in part, by Wright Laboratory, Aero Propulsion and Power Directorate, Wright-Patterson Air Force Base, OH, under USAF Contract No. F33615-90-C-2033. E.G.J. acknowledges Mr. Steven Anderson for many valuable discussions in his capacity as coordinator of the USAF additive program. The authors thank Mr. Tim Gootee (USAF) for performing the surface-carbon analyses, Mr. Wayne Rubey (University of Dayton Research Institute) for advice concerning oxygen measurements and the use of Silcosteel tubing, and Mrs. Marian Whitaker (SRL) for lending editorial assistance.

EF950033D

(23) Kendall, D. R.; Houlbrook, G.; Clark, R. H.; Bullock, S. P.; Lewis, C. Paper 87-IGTC-49, Presented at the International Gas Turbine Congress, Tokyo, October 1987.

(24) Clark, R. H.; Stevenson, P. A. *Prepr. Pap.-Am. Chem. Soc., Div. Fuel Chem.* **1990**, 35 (4), 1302-1314.

(22) Zabarnick, S.; Grinstead, R. R. *Ind. Eng. Chem. Res.* **1994**, 33, 2771-2777.

Thermal Stability of Jet-A Fuel Blends

E. Grant Jones*,†

Innovative Scientific Solutions, Inc., 3845 Woodhurst Ct., Beavercreek, Ohio 45430

Lori M. Balster and Walter J. Balster

*Systems Research Laboratories, An Operation of Calspan SRL Corporation,
2800 Indian Ripple Road, Dayton, Ohio 45440-3696*

*Received September 28, 1995. Revised Manuscript Received December 22, 1995**

The thermal stability of a high-quality hydrotreated Jet-A fuel, an average-quality straight-run Jet-A fuel, and several blends of each fuel has been studied during flow through a single-pass tubular heat exchanger at 185 °C. The goal was to obtain fundamental information concerning the thermal stability of fuel blends using dynamic isothermal methods. Autoxidation was tracked as a function of stress duration by measurements of dissolved oxygen and hydroperoxides; insoluble formation was determined by measurements of the average surface deposition rate and the total quantity of bulk insolubles collected on in-line filters. On the basis of several thermooxidative stability criteria, some of the blends were found to be less stable than either neat fuel. Furthermore, benefits of blending were not realized until the lesser-quality fuel had been diluted more than 8-fold. The implications of blending high- and lesser-quality fuels are discussed in the context of autoxidation and insoluble formation.

Introduction

Thermooxidative stability is a very important factor in the selection of aviation fuels. Storage at low temperature can cause discoloration, buildup of hydroperoxides, and the formation of insoluble gums and solids. Stressing at higher temperature that occurs during passage over hot surfaces of heat exchangers, nozzles, and flow-divider valves of aircraft fuel lines can cause fouling, which has serious consequences in terms of engine downtime and long-term aircraft operation. Since advanced aircraft will generate increased heat loads, the search for methods of mitigating the effects of surface fouling has taken on increased importance. Two such approaches based on enhancing fuel thermal stability are special refining techniques and the incorporation of additives.

Fuels with certain S- and N-containing components tend to have reduced stability or increased tendency toward surface fouling as compared to similar fuels which have been subjected to hydrotreatment at the refinery and, therefore, contain reduced levels of polar components.¹ Previous studies^{2,3} of fuel stability within our laboratory were conducted on the former (the lesser-quality fuels), with the primary goal of creating measurable quantities of insolubles and addressing potential methods for their reduction. Such straight-run fuels are subject to slower autoxidation because they contain natural inhibitors.⁴ However, frequently the basis of the inhibition (namely, reactions of S- and N-containing

components with peroxy radicals and hydroperoxides) is also the source of the insolubles.⁵ Fuels in the latter category are frequently costly prime fuels that are of less interest for study because they produce negligible surface fouling in laboratory simulations. Hydrotreated fuels, like pure hydrocarbons, contain few natural inhibitors and, thus, at elevated temperatures undergo more rapid autoxidation, hydroperoxide buildup, and autocatalysis, forming gums but few surface insolubles. Chain-breaking antioxidants such as butylated hydroxytoluene (BHT) are usually added to these fuels to reduce gum formation and improve long-term storage stability.⁶

Our laboratory has been interested in fundamental methods for quantitatively assessing fuel thermal stability, with the goal of identifying lesser-quality fuels and improving them by introducing additives; such an approach may be more practical and less costly than refining techniques. An obvious extension of this approach is to consider the potential impact on thermal stability of adding or blending a second fuel. For example, if straight-run and hydrotreated fuels represent the two extremes with respect to surface fouling, it would be of interest to determine the fouling tendency of different blends of each fuel. Blending may be viewed alternatively as (1) the contamination of a high-quality fuel with its lesser-quality counterpart or (2) the dilution of a lesser-quality fuel with a prime fuel.

Fuel blending has frequently led to thermal-stability problems.^{7–11} For example, the process of introducing

† Tel.: (513) 252-4264.

* Abstract published in *Advance ACS Abstracts*, February 1, 1996.

(1) Hazlett, R. N. *Thermal Oxidation Stability of Aviation Turbine Fuels*, ASTM Monograph 1; American Society for Testing and Materials: Philadelphia, 1991.

(2) Jones, E. G.; Balster, W. J. *Energy Fuels* 1993, 7, 968–977.

(3) Jones, E. G.; Balster, L. M.; Balster, W. J. *Energy Fuels* 1995, 9, 906–912.

(4) Bolshakov, G. F. *Sulfur Rep.* 1987, 7, Part 5, 379–392.

(5) Kendall, D. R.; Mills, J. S. *Ind. Eng. Chem. Prod. Res. Dev.* 1986, 25, 360–366.

(6) Turner, L. M.; Kamin, R. A.; Nowack, C. J.; Speck, G. E. Effect of Peroxide Content on the Thermal Stability of Hydrocracked Aviation Fuel *Proceedings of 3rd International Conference on Stability and Handling of Liquid Fuels*; Institute of Petroleum: London, Nov 1988.

(7) Gomes, H. O.; Pereira, R. C. L. *Prepr. Pap.-Am. Chem. Soc., Div. Fuel Chem.* 1994, 39 (3), 917–922.

light cycle oil (LCO) into diesel formulations which has been used at the refinery to meet the increasing need for diesel fuels has been reported to reduce thermal stability.⁷ Datschefschi⁹ and Speck¹⁰ have also observed decreased stability with the introduction of heavier components at a level of 1–10%. Upon storage, certain blends fail to pass thermal-stability tests such as the Jet Fuel Thermal Oxidation Test, JFTOT; this problem has been traced to fuel incompatibility.¹¹ In contrast, thermal stability has been reported to improve following dilution of a Jet-A fuel with a paraffinic solvent blend, Exxsol D-80.¹² Although blending can be accomplished by design at the refinery, it occurs routinely during storage-tank and aircraft refilling operations. Such blending is rarely documented, and its consequences remain unknown.

The goal of the current study was to investigate the impact on thermal stability of blending two distinct types of fuels; namely, a hydrotreated Jet-A-1 (POSF-2747) and a straight-run Jet-A (POSF-2827). Both fuels were obtained from a local airport and meet all commercial and USAF specifications; recent results indicate that the hydrotreated fuel is of excellent quality and that the straight-run fuel is a very typical Jet-A aviation fuel having average thermal stability. These fuels have served as references in our laboratory and have been the subject of USAF-sponsored research.¹³ The neat fuels and selected blends of each were studied in order to sample the continuum between the two fuels and to determine whether the stability of blends could be predicted based simply upon the thermal behavior of the neat fuels. If the addition of small quantities of a prime fuel to an average fuel were found to improve thermal stability, the result would be an inexpensive method of upgrading fuel.

The approach was to conduct a simulation of the complicated stressing that occurs in aircraft fuel lines using simplified laboratory tests under well-defined chemical-reaction conditions. The neat fuels and several blends were stressed under high-pressure, isothermal conditions at 185 °C during flow through the heated tubes of a single-pass heat exchanger, and the results of each experiment were compared with respect to established thermal-stability criteria.³ The stress conditions were selected to allow the complete conversion of initial oxygen (air-saturated at room temperature) and the completion of the major deposition processes. For each blend the following measurements were made as a function of stress duration: (1) the concentration of the primary reactant, oxygen, (2) the concentration of one of the first autoxidation products, hydroperoxide, (3) the surface-deposition rate, and (4) the quantity of surface insolubles. In addition, the total quantity of

Table 1. Fuel Properties

	POSF-2747	POSF-2827
type	Jet-A-1	Jet-A
treatment	hydrotreated	straight run
JFTOT breakpoint (°C)	332	266
total sulfur (%)	0.004	0.079
mercaptan sulfur (%)	0.000	0.001
freezing point (°C)	-60	-43
viscosity at -20 °C (cSt)	4	5
aromatics (vol%)	19	19
total acid no. (mg of KOH/g)	0.0	0.001
Cu (ppb)	<5	<5
Fe (ppb)		8
Zn (ppb)	18	<5

insolubles (surface and bulk) was evaluated after complete oxygen conversion. The potential benefits and problems associated with blending fuels of disparate thermal stabilities are discussed.

Experimental Section

The physical properties of the neat fuels are summarized in Table 1; these fuels have been available for study for several years and have been stored underground for extended periods. Mixing was done with measured volumes, with no account being taken of volume changes upon mixing. Fuels and fuel blends were initially saturated with respect to air at room temperature. The dissolved-oxygen concentration in POSF-2827 and POSF-2747 has been measured by Striebig and Rubey¹⁴ to be 64.7 and 72.5 ppm (w/w), respectively; however, for all current experiments this initial value was assumed to be constant and was set at 100%. Before use, each neat and blended fuel was passed through a 15- μ m filter.

Fuel was stressed at 185 °C during passage through 0.318 cm o.d., 0.216 cm i.d. tubing, clamped tightly within a Cu-block heat exchanger. System pressure was maintained at 2.3 MPa to ensure a single reaction phase. Two experimental arrangements were utilized, differing only in the length of the heat exchanger.

The concentration of O₂ and the steady-state concentration of hydroperoxides, [ROOH]_{ss}, were measured using the first or standard setup with the Near-Isothermal Flowing Test Rig (NIFTR) which has been described in detail elsewhere.² Dissolved O₂ was measured in-line at system pressure using a GC technique developed by Rubey and co-workers.¹⁵ Based on the difference between O₂ readings for the unstressed and stressed fuel, the percentage of residual O₂ was determined as a function of the calculated reaction time. Hydroperoxide concentration in millimoles was determined by cyclovoltammetry (RULER method of Kauffman¹⁶) using 10-mL samples of stressed fuel collected as effluent from the heat exchanger. The tubing selected for both O₂ and ROOH experiments was passivated by the Silcosteel¹⁷ process in order to minimize possible surface catalytic effects from stainless-steel tubing walls.¹⁸

Deposition experiments were conducted using the second experimental arrangement with an extended-length NIFTR-2 (see Figure 1). Under a fixed flow rate of 0.25 mL/min, this unit has a continuous, isothermal 183-cm heated pathlength that provides 23 min of stressing to accommodate the complete deposition profile of all fuels and blends used in this study. Deposits were collected over a relatively long test duration (72

(8) Hazlett, R. N., *Fuel Sci. Technol. Int.* **1988**, 6, 185–208.

(9) Datschefschi, G. *Fuel Sci. Technol. Int.* **1988**, 6, 609–631.

(10) Speck, G. E. Feasibility of Marine Diesel Fuel as an Emergency Aircraft Fuel, Report NAPC-PE 44; Naval Air Propulsion Center: Trenton, NJ, Feb 1981.

(11) Goetzinger, J. W.; Ripley, D. L.; French, C. *Prepr.-Am. Chem. Soc., Div. Pet. Chem.* **1989**, 39 (1), 804–808.

(12) Zabarnick, S.; Zelesnik, P.; Grinstead, R. R. Jet Fuel Deposition and Oxidation: Dilution, Materials, Oxygen, and Temperature Effects. ASME Paper No. 95-GT-050, Presented at the International Gas Turbine and Aeroengine Congress and Exposition, Houston, TX, 5–8 June, 1995.

(13) Edwards, T.; Anderson, S. D.; Pearce, J. A.; Harrison, W. E. High Temperature Thermally Stable JP Fuels—An Overview. AIAA Paper No. 92-0683, Presented at the 30th Aerospace Sciences Meeting and Exhibit, Reno, NV, 6–9 January 1992.

(14) Striebig, R. C.; Rubey, W. A. *Prepr.-Am. Chem. Soc., Div. Pet. Chem.* **1994**, 39 (4), 47–50.

(15) Rubey, W. A.; Striebig, R. C.; Tissandier, M. D.; Tirey, D. A.; Anderson, S. D. *J. Chromatogr. Sci.* **1995**, 33, 433–437.

(16) Kauffman, R. E. *Prepr.-Am. Chem. Soc., Div. Pet. Chem.* **1994**, 39 (1), 42–46.

(17) Silcosteel tubing, Restek Corp., Bellefonte, PA.

(18) Jones, E. G.; Balster, W. J. *Energy Fuels* **1995**, 9, 610–615.

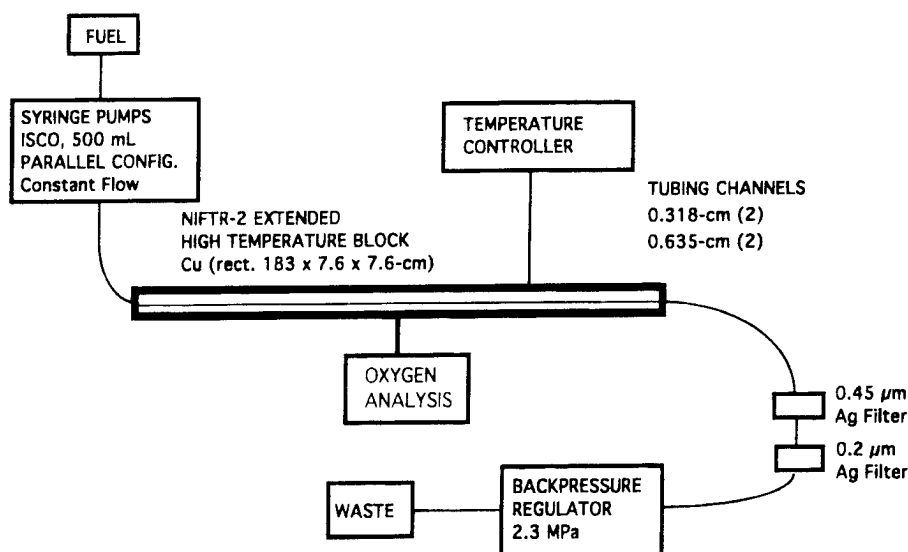


Figure 1. Schematic diagram of NIFTR-2 apparatus.

h), resulting in the passage of 1080 mL of air-saturated fuel during the course of each experiment. Commercial stainless-steel tubing was used for all deposition experiments; during the first few hours of each test, the original stainless-steel surfaces (except for reaction with neat POSF-2747 fuel) became covered with deposits and were considered passivated with respect to autoxidation.¹⁸ Thus, deposition and autoxidation experiments were conducted under very similar test conditions where the tubing walls were passivated.

Because of the slow fixed flow rate used in deposition experiments, isothermal conditions prevail after fuel has passed ~5 cm into the block; thus, reaction time is proportional to the distance along the heated tube. Reaction time is calculated from tubing dimensions and flow rate, making corrections for fuel expansion. At completion of the test, the tube was cut into a total of 36 segments, each 5.1 cm long. Following heptane rinse and vacuum drying (130 °C for 12 h), the carbon associated with the surface deposit was quantified by conventional surface-carbon burnoff techniques. The surface deposition rate on each tubing segment was calculated from the amount of carbon measured in burnoff, the fuel residence time within that tubing segment, and the total amount of fuel passed (1080 mL). Rate is expressed in units of micrograms of carbon/hour per milliliter of fuel, representing an average over the entire 72-h test period, and is plotted as a function of stress duration. The total surface carbon ($\mu\text{g/mL}$) was obtained as a function of stress duration by integrating the differential rate data.

Bulk insolubles were collected over the entire 72-h test period on two sets of in-line Ag-membrane filters (0.45 and 0.2 μm). Filter housings located ~10 cm from the heat exchanger remained near room temperature; thus, measurable filterables include additional contributions resulting from fuel cooling. Filterables were quantified as insoluble gums, IG (insoluble in heptane and soluble in acetone), and insoluble solids, IS (insoluble in both heptane and acetone), by cutting each filter into two equal sections and rinsing with heptane or heptane/acetone. Following rinse, filters were vacuum dried and subjected to carbon burnoff as described above. The quantity of bulk insolubles from the two filter sets was summed and expressed in units of micrograms per milliliter, representing an average over complete oxygen conversion.

Results and Discussion

Autoxidation and Deposition in Neat-Fuel Blend-stocks. Figure 2 shows the behavior of dissolved O_2 and deposition rate as a function of stress duration at 185 °C for the two neat fuels. POSF-2747, like all

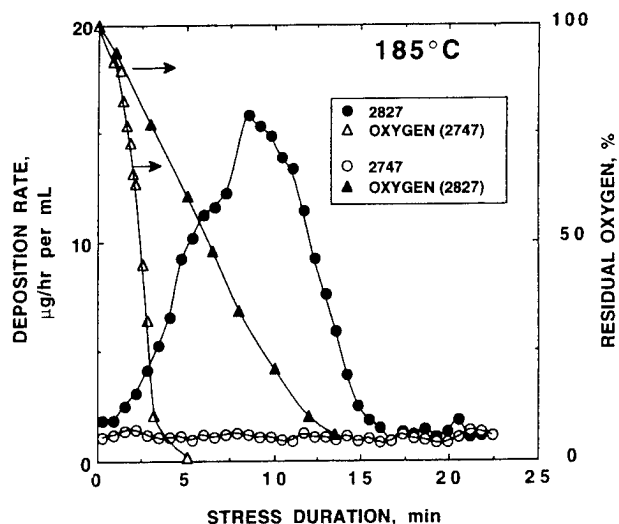


Figure 2. Oxygen consumption and deposition rate in neat POSF-2747 and POSF-2827 fuels.

hydrotreated fuels, has few natural inhibitors and undergoes rapid autoxidation (<3 min) with negligible deposition. The calculated deposition rate is at the threshold of detection and reflects the known benefits of hydrotreatment in minimizing surface fouling. The bulk and total surface insolubles (integral) were determined to be, respectively, 0.48 and 0.12 $\mu\text{g/mL}$; these values are in the same range as those of fuels having the highest stability such as JPTS. As a blend component, POSF-2747 is essentially a nondepositing fuel under the stress conditions selected.

Autoxidation in the straight-run fuel, POSF-2827, is slowed and ~13 min is required for complete oxygen conversion. The deposition rate passes through a maximum and tracks autoxidation; deposition is complete within ~17 min. Bulk insolubles and total surface carbon are found to be 2.0 and 2.6 $\mu\text{g/mL}$, respectively, values typical of average-quality aviation fuels. These compare favorably with our previously published values for this fuel obtained from short-term tests of 6-h duration (2.0 and 3.0 $\mu\text{g/mL}$)² and long-term tests of 72-h duration (2.7 ± 1.0 and 2.6 ± 0.6)¹⁸ using the original NIFTR. Mixing POSF-2747 and -2827 creates

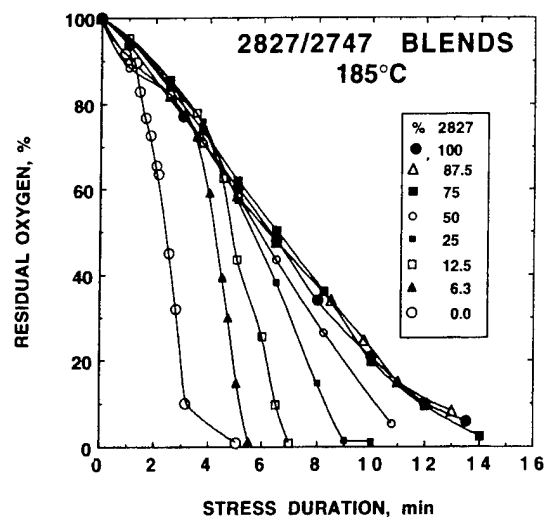
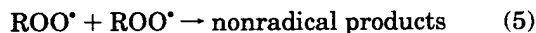
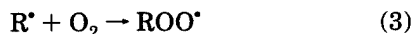


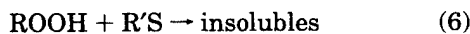
Figure 3. Oxygen consumption in POSF-2827 and POSF-2747 blends.

a blend of one nondepositing and one average-depositing fuel.

Dissolved O₂ in Fuel Blends. Reaction of O₂ and formation of ROOH involve a series of free-radical chain processes termed autoxidation. A simple mechanism includes initiation (reactions 1 and 2), propagation (reactions 3 and 4), and termination (reaction 5)



Based on the observed inhibited autoxidation of the straight-run fuel and the noted correlation between deposition and autoxidation, it is posited that an excess of S-containing natural inhibitors, R'S, is available for rapid destruction of ROOH, as in reaction 6. This is



the primary mechanism for slowing autoxidation by reducing self-initiation and one of the first steps in the formation of insolubles. Oxidation becomes autocatalytic when the inhibitors cannot slow the reaction sufficiently and the concentration of ROOH increases; reaction 2 initiates further reaction and accelerates the loss of oxygen. Results will be discussed in the context of this mechanism and the impact of inhibitor concentration on rates of autoxidation and insoluble formation.

In this and all subsequent sections, blends will be designated based on percentage of the POSF-2827 component, and the discussion of results will consider blending from two opposite points of view, namely, contamination of the hydrotreated fuel and dilution of the straight-run fuel. The depletion of dissolved O₂ in two neat and six blended fuels is plotted in Figure 3 as a function of stress duration. First, as progressively more POSF-2827 is added to the hydrotreated fuel, the concentration of natural inhibitors increases and autoxidation slows. As a result, the initial induction time

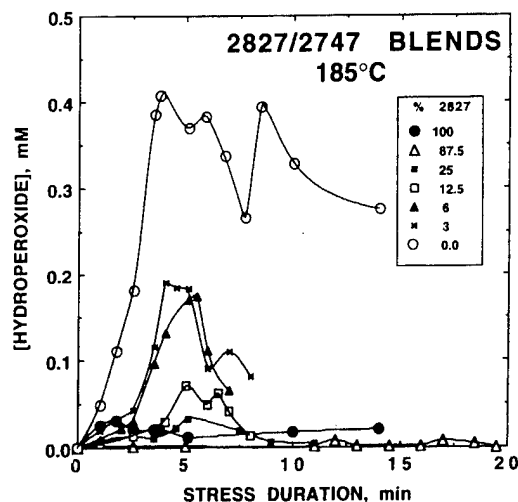


Figure 4. Hydroperoxides formed in POSF-2827 and POSF-2747 blends.

of ~1 min is extended in each successive blend until, at ~75% POSF-2827, no induction time is evident and the rate of autoxidation becomes approximately constant, changing little with further addition. Also, the autocatalytic rate following induction slows with addition of the straight-run fuel. The observed behavior is consistent with the addition of an antioxidant, R'S, to a hydrotreated fuel. Taking the alternative point of view, dilution of the straight-run fuel reduces the concentration of natural inhibitors and slows reaction 6; once the inhibitor concentration has been reduced by a factor of 4, slow autoxidation can no longer be maintained to the completion of O₂ conversion, and the reaction eventually becomes autocatalytic, as evidenced by the pronounced sigmoid shape for the leaner blends. Further dilution and reduced concentration of antioxidants lead to an earlier onset of autocatalysis from self-initiation.

ROOH in Fuel Blends. The measured steady-state concentration of hydroperoxides, [ROOH]_{ss}, in the two neat fuels and five blends is plotted in Figure 4. In neat POSF-2747, [ROOH]_{ss} increases rapidly and maximizes near 3 min, as expected from the complementary O₂-loss data in Figure 3. Over the next 10 min, the concentration decays slowly. The low concentration of S-containing components in the hydrotreated fuel allows [ROOH]_{ss} to build to a maximum, with only negligible decay. Stepwise contamination with POSF-2827 causes increasingly longer induction times and a slower increase in [ROOH]_{ss} to a reduced maximum, followed by a more rapid decay. Once the blend contains 25% POSF-2827, [ROOH]_{ss} is negligible at all stress times. Note that the times in Figure 3 at which the rate of autoxidation accelerates (autocatalysis becomes dominant) show good correlation with the times at which [ROOH]_{ss} in Figure 4 exceeds an estimated baseline value of ~0.03 mM. These data, by virtue of the reduction and the decay in [ROOH]_{ss}, illustrate the importance of reaction 6 in regulating autoxidation.

In the alternative view, dilution with the hydrotreated fuel reduces the concentration of the natural antioxidants that were able to maintain slow autoxidation for ~13 min or complete oxygen conversion in the neat fuel. Now, slow autoxidation can only be provided for shorter intervals (induction times), after which the rates of O₂

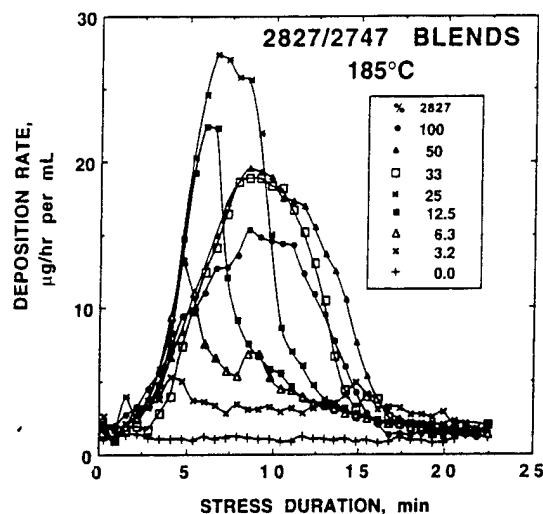


Figure 5. Surface deposition rate in POSF-2827 and POSF-2747 blends.

depletion and ROOH formation increase due to autocatalysis. $[\text{ROOH}]_{ss}$ increases briefly during the 3–7 min reaction-time interval. For example, in a 6.3% blend, autoxidation (Figure 3) is inhibited for 3.5 min and then accelerates until all O_2 has been converted (5.5 min). In the complementary hydroperoxide data in Figure 4 (6% blend), $[\text{ROOH}]_{ss}$ remains low for 2.5 min, followed by an increase to a maximum at 5.5 min and finally a decay. Once all oxygen has been converted, the source of ROOH is depleted and $[\text{ROOH}]_{ss}$ decays due to reaction 6. The complementary measurements of dissolved O_2 and ROOH show that autoxidation in the blends is controlled by reaction 6 and the concentration of natural antioxidants that originate in the straight-run fuel.

It should be pointed out that inhibition caused by slowed propagation cannot be distinguished from that resulting from ROOH destruction. Phenols and amines can act as antioxidants through a chain-breaking mechanism to reduce the propagation rate;¹⁹ however, this inhibition mechanism is considered to be less important than reaction 6 due to the abundance of S in the straight-run fuel.

Surface Deposition in Fuel Blends. Figure 5 shows the deposition rate for the two neat fuels and six blends. All deposition is complete within ~17 min of stressing. With addition of the straight-run fuel, the rate begins to deviate from the baseline established by POSF-2747. Even the 3.2% blend exhibits an increase in rate over all stress times. The deposition rate for each blend passes through a maximum and decreases at longer times. As more POSF-2827 is added, the maximum in the deposition rate increases and its location shifts to longer stress times; blends richer than 33% display a maximum in the vicinity of 9 min. On the basis of the autoxidation data presented earlier, the observed lag in deposition is a manifestation of delays in autoxidation with increasing antioxidant concentration. Contamination of POSF-2747 with the straight-run fuel leads to progressively reduced thermal stability, as evidenced by increased surface deposition rate and total deposits (area under rate curves).

When blending is viewed in terms of dilution of POSF-2827, the location of the maximum in deposition rate shifts to earlier stress intervals, particularly for the leaner blends, changing from ~9 min (neat fuel) to 7 min (25%), 6 min (12.5%), and <5 min (6.3 and 3.2%). These times correspond very closely to the maximum rates in autoxidation in Figure 3, viz., 7 min (25%), 5.5 min (12.5%), and 4.5 min (6.3%), and reflect the reduction in available antioxidants in the lean blends. The maximum deposition rates for 50, 33, 25, and 12.5% blends all exceed the maximum rate observed in neat POSF-2827 fuel. Even the 6.3% blend results in a maximum deposition rate which exceeds that of the neat fuel at early stress times. Also, the time over which deposition occurs (represented by the full width at half maximum, fwhm, of the profiles in Figure 5) is significantly compressed for the lean blends. Faster deposition rates occurring after shorter induction times result from autocatalysis in the lean blends (see Figure 3). According to the above reaction scheme, increases in the rates of autocatalysis and deposition occur with increases in $[\text{ROOH}]_{ss}$.

A tight correlation between autoxidation and deposition has been reported for the neat POSF-2827 fuel over a broad temperature range.^{18,20} Clearly, blends made with POSF-2827 and -2747 fuels display a similar strong dependence, indicating that autoxidation is the rate-limiting step leading to surface fouling. The link between surface fouling and autoxidation appears to be the inhibition reaction 6. Any reduction in surface fouling anticipated from diluting the lesser-quality fuel is offset by resultant shorter induction times and faster autocatalytic rates. Together, these lead to faster rates of deposition that occur after shorter stress times, both of which exacerbate the fouling problem.

Quantification of Insolubles after Complete Conversion. Figure 6a shows, in histogram form, the quantities of surface and bulk insolubles evaluated after 23 min of stressing. Note that surface insolubles initially increase with addition of the straight-run fuel (3.2, 6.3, 12.5, and 25% blends) and then remain unchanged for all richer blends. Even though the deposition rates were shown above to be faster in several blends, the total amount of deposit remains approximately constant. If blending is viewed as dilution of the straight-run fuel, no significant reduction occurs in either surface or bulk insolubles until 15-fold dilution (6.3% blend) is reached.

The quantity of bulk insolubles and their IS and IG components in Figure 6b generally tracks that of the surface insolubles. In most cases the quantity of IS and IG from the blends exceeds that from either neat fuel, and both are a maximum for the 12.5 and 25% blends. The magnitude of this effect cannot be explained by uncertainty in the data; it may be related to decreased solubility for certain blending ratios.

Deposition rates are controlled by reaction kinetics, but the total quantity of insolubles is determined not by reaction kinetics but by (1) the initial amount of dissolved O_2 that is available for reaction and (2) the concentration of natural inhibitors. The partitioning of O_2 into insolubles is determined only by temperature, provided an excess of natural inhibitors is present to

(19) Scott, G. *Atmospheric Oxidation and Antioxidants*; Elsevier: New York, 1965; p 115.

(20) Jones, E. G.; Balster, W. J. *Prepr.-Am. Chem. Soc., Div. Pet. Chem.* **1994**, 39 (1), 78–81.

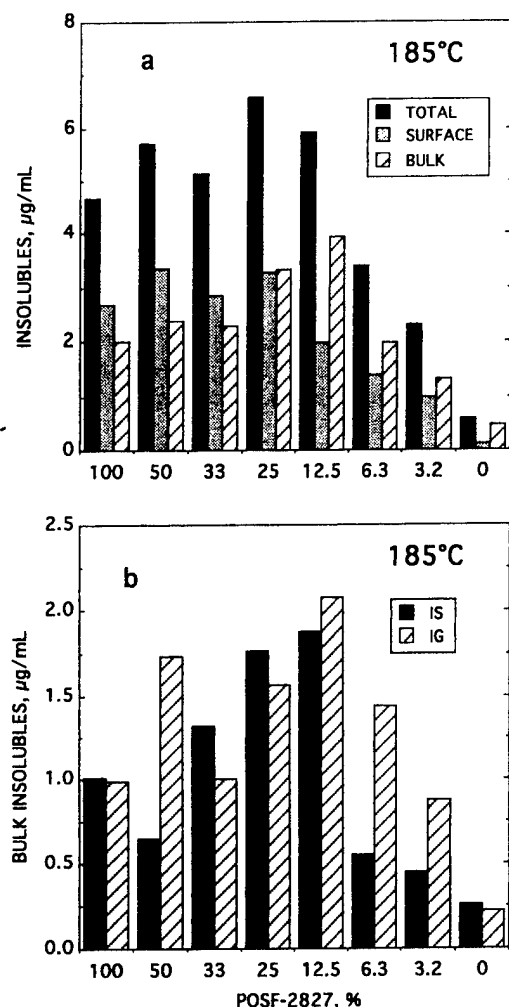


Figure 6. Histogram of quantity of insolubles formed in POSF-2827 and POSF-2747 blends: (a) total, surface, and bulk, (b) IS and IG.

react with ROOH. In the lean blends the amount of natural inhibitors is reduced sufficiently that the total quantity of insolubles becomes limited by the diluted concentration of inhibitors.

Surface Fouling under Conditions of Limited Conversion. In the current tests, fuels were stressed isothermally from onset to completion of the deposition process. In actual aircraft fuel lines, fuel flows rapidly and is subjected to stress for limited times under nonisothermal conditions; the resulting O_2 conversion may be minimal. The extent of surface fouling for limited conversion or shorter stress times can be determined by integrating the differential rate data from Figure 5. Use of the resultant stress-time dependence of total surface carbon (TSC) plots was introduced³ to put into perspective, particularly for isothermal tests, the potential benefits of additives such as antioxidants which may have significantly reduced initial surface fouling by delaying autoxidation but ultimately, after long stress times, may not have reduced the total deposits.

It is important to determine changes to TSC relative to each blendstock. Changes can be evaluated for each stress time by subtracting the TSC in the neat fuel from that in the blend. The resultant quantity (total surface fouling with respect to each fuel) is shown in Figure 7, a and b, respectively, for POSF-2747 and POSF-2827.

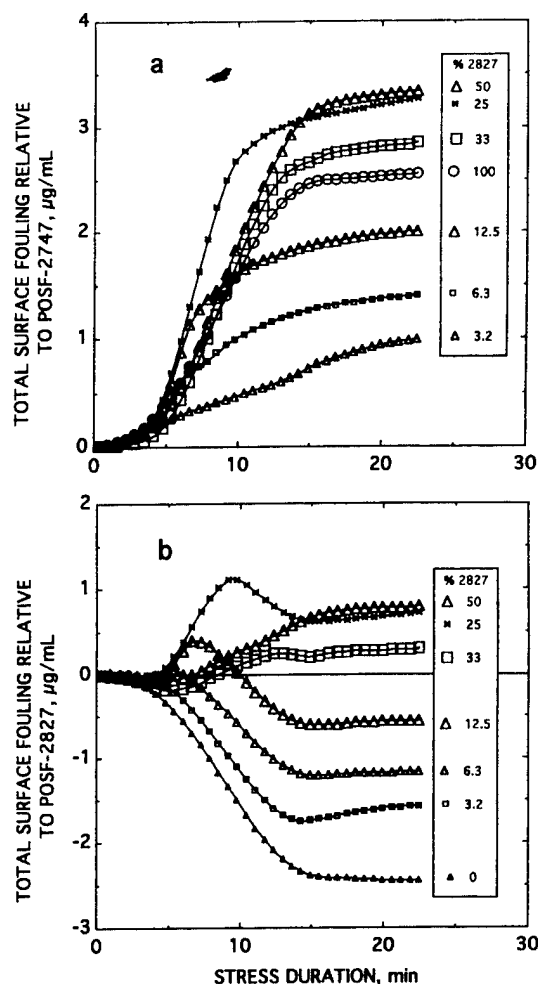


Figure 7. Total surface carbon with respect to (a) POSF-2747 and (b) POSF-2827.

Blending is considered to be contamination of POSF-2747 with the straight-run fuel in Figure 7a and dilution of POSF-2827 with a hydrotreated fuel in Figure 7b. Figure 7a is coincident with a TSC plot in this system because the POSF-2747 reference fuel does not make a contribution. The hydrotreated fuel produces less total surface insolubles than any blend for any stress time; i.e., the hydrotreated fuel is always the most stable. Fouling increases progressively with the addition of POSF-2827; 12.5 and 25% blends are less stable over short stress times. Once the blends have been stressed for 10 min, the relative assessment of their thermal stability does not change. In Figure 7b the neat POSF-2827 fuel is represented by the line through zero. The fact that some data are above and some below zero indicates that certain blends decrease thermal stability, while others increase it. The lower-stability blends at 12.5 and 25% display maxima, indicating a 0.5- to 1- $\mu\text{g/mL}$ reduction in thermal stability. Benefits are achieved only after considerable dilution which results in pure hydrotreated fuel at the limit and an overall improvement in thermal stability of $\sim 2.5 \mu\text{g/mL}$ after 15 min of stressing.

Summary. On the basis of any thermal-stability criteria that may be applied to the current data for assessing the two blendstocks [including rate of autoxidation, maximum surface deposition rate, total surface carbon after short- or long-term stressing, and total bulk insolubles (IG or IS)], few benefits are achieved from

blending. Contamination of the hydrotreated fuel with the straight-run fuel only serves to reduce thermal stability. Dilution of the straight-run fuel with the hydrotreated fuel results in benefits only when the lesser-quality stock is diluted more than 8-fold. If an average-quality fuel such as POSF-2827 requires significant dilution with an expensive hydrotreated fuel before improvement is achieved, then blending can never be cost effective. Furthermore, the stability of some blends may be less than that of either stock. To obtain a blend with stability only slightly better than that of the lesser-quality fuel would only reduce the original cost of hydrotreatment by about 10%.

The antioxidants present in excess in the straight-run fuel are the key species in all blends. Reaction 6 slows autoxidation during complete oxygen conversion in the neat fuel. Antioxidant concentration in the blends decreases with dilution but still influences the oxidation rate, induction time, $[ROOH]_{ss}$, and, to some extent, the autocatalytic rate and the rate of forming insolubles. Diluting lesser-quality fuels with readily oxidized hydrotreated fuels may be self-defeating since the same amount of insolubles can be made in 100% and in 12.5% POSF-2827 blends and since surface insolubles track autoxidation. The primary problem appears to be the abundance of inhibitors in POSF-2827. The rate of reaction 6 is proportional to $[ROOH]_{ss} \times [R'S]$; thus, dilution serves to (1) slow reaction 6, (2) shorten induction times for rapid autoxidation, and (3) increase the rate of autocatalysis with increasing $[ROOH]_{ss}$. If antioxidants were originally present in large excess and 2 mM of residual antioxidants remained after dilution, reaction 6 could proceed to completion, albeit at a slower rate. The previous observation² that the amount of total insolubles made from oxygen- and air-saturated POSF-2827 fuel is proportional to the initial dissolved oxygen (differing by a factor of 5) suggests an inherent capacity of this fuel to generate at least 5 times more total reaction products than observed with air-saturated fuel. Similarly, from the current experiments it may be inferred that antioxidants capable of destroying ROOH must be present in large excess if at least 8-fold dilution is necessary to reduce fouling. Dilution can improve thermal stability only when it reduces the concentration of residual antioxidants to such a level that the quantity of insolubles becomes limited by the antioxidant concentration. Such reduction occurs somewhere between 8- and 15-fold dilution of the current straight-run fuel; as a result, blending would not be feasible for the selected blendstocks. This finding is independent of the nature

of the high-quality fuel. Replacing the straight-run fuel with one containing a reduced level of natural antioxidants would probably result in more stable blends; however, the replacement fuel having better stability would not be a likely candidate for dilution. Thus, blending may be neither cost effective nor worthwhile.

The current findings with Jet-A fuels may be applicable, in general, to the blending of fuels with disparate thermal stabilities. This may be the origin of the thermal-stability problems associated with dilution of cracking products.⁷ Fuels such as POSF-2827 which oxidize very slowly possess an excess of natural antioxidants. Knowledge of the surface-fouling behavior of the neat blendstocks would not be sufficient to predict behavior in the blends.

Conclusions

The thermooxidative stability of a hydrotreated Jet-A fuel, a straight-run Jet-A fuel, and a series of blends of each fuel has been studied at 185°C. On the basis of measurements of dissolved oxygen, hydroperoxides, and insolubles, some blends have been found to be less stable than either blendstock; benefits from blending are only achieved when the lesser-quality fuel has been diluted more than 8-fold. It is concluded, therefore, that blending in the case of the selected fuels cannot be justified based on reasons of either resultant thermal stability or cost considerations.

An excess of natural inhibitors present in the straight-run fuel appears to be the source of reduced thermal stability upon blending. The current results have been explained in terms of hydroperoxide destruction by these natural inhibitors as the primary control of autoxidation rates. Furthermore, attributing insoluble formation to hydroperoxide destruction can explain the observed interdependence of surface fouling and autoxidation in all blends. The explanations offered for reduced thermal stability in blends of the two Jet-A fuels may account for reported problems in the analogous dilution of cracking products at the refinery.

Acknowledgment. This work was supported by Wright Laboratory, Aero Propulsion and Power Directorate, Wright-Patterson Air Force Base, Ohio, under USAF Contract No. F33615-90-C-2033 to SRL. The authors thank Mr. Tim Gootee for conducting the surface-carbon analyses and Mrs. Marian Whitaker for editorial assistance.

EF950190C

Autoxidation of Aviation Fuels in Heated Tubes: Surface Effects

E. Grant Jones*

Innovative Scientific Solutions, Inc., 3845 Woodhurst Court, Beavercreek, Ohio 45430

Lori M. Balster and Walter J. Balster

*Systems Research Laboratories, An Operation of Calspan SRL Corporation,
2800 Indian Ripple Road, Dayton, Ohio 45440-3696*

*Received October 6, 1995. Revised Manuscript Received February 8, 1996**

Recently it has been reported that autoxidation of a Jet-A fuel which occurs during passage through heated stainless-steel tubing is accelerated by the tubing walls and that this effect is mitigated as the surface becomes fouled. To investigate the generality of this finding, we have studied the depletion of dissolved oxygen in 16 aviation fuels in a single-pass tubular heat exchanger. Experimental conditions of temperature and tube dimension were held constant, but the chemical composition of the inner wall surfaces was varied. Reaction was compared in commercial stainless-steel (304) tubes and in passivated or surface-treated (Silcosteel) tubes which are noted for their inert inner walls. The aviation fuels selected for study ranged from the highly thermally stable JP TS to an unstable Cu-doped Jet-A. The fuels contained a fixed amount of oxygen (air-saturated at room temperature) and were stressed under identical conditions at 185 °C during passage through 0.216-cm-i.d. tubing. Results reported herein show that autoxidation occurring as fuel flows through stainless-steel tubes is accelerated as compared to that occurring in treated tubes. The magnitude of this effect is fuel dependent, ranging from a low of 10–20% (barely detectable) to ~75%. The role of surfaces in catalyzing aviation-fuel autoxidation in narrow-bore tubing and possible ramifications with regard to surface fouling in aircraft fuel lines are discussed.

Introduction

Aviation fuels containing dissolved oxygen undergo autoxidation involving a complex series of free-radical chain reactions; this process can ultimately lead to formation of insolubles including solids and gums that collect on fuel lines—a phenomenon known as fuel coking. Such surface fouling can reduce fuel flow, lower the efficiency of heat exchangers, alter nozzle dimensions, and cause hysteresis in servocontrols and flow-divider valves. Although all fuels undergo these deleterious reactions, the distribution of components in each fuel is unique, causing a different response to thermal stressing. Fuels containing trace quantities of heteroatoms such as S, N, and O show a propensity for surface fouling.^{1a} Fouling problems are projected to become more severe with advanced aircraft since the airframe and engine will generate higher heat loads which must be dissipated by the fuel.² Future concerns encompass both autoxidative and pyrolytic fuel degradation; the present study addresses only autoxidation.

An understanding of the complex processes involved in the formation of surface and bulk insolubles in

aviation fuels can be gained through determination of the rate of reaction of dissolved oxygen and the kinetic parameters that describe this rate. Factors which may alter the rate of autoxidation are also important from a fundamental standpoint. The introduction of additives such as antioxidants potentially delays and slows autoxidation and enhances the performance of certain fuels. On the other hand, presence in the fuel of dissolved metals such as Cu can initiate autoxidation.^{1b} Any mechanism whereby autoxidation is accelerated will be detrimental because of the potential for increasing the rate of surface fouling. For example, it was recently reported that the rate at which dissolved oxygen reacts at elevated temperatures (155–185 °C) in a particular Jet-A fuel, POSF-2827, is controlled in certain cases by the proximity and nature of nearby surfaces.^{3,4} The fact that surface fouling in this fuel correlates directly with autoxidation^{5,6} implies that the nature of the surface can impact both autoxidation and subsequent surface fouling. The onset of accelerated autoxidation or autocatalysis observed in this fuel was attributed to heterogeneous reactions occurring at the tubing walls; furthermore, this effect was reported to be greatly reduced or eliminated once the reaction tube surfaces became coated with deposits. Stainless-steel walls, it was argued, have active sites which accelerate

* Author to whom correspondence should be addressed. Tel: (513) 252-4264.

* Abstract published in *Advance ACS Abstracts*, April 1, 1996.

(1) Hazlett, R. N. *Thermal Oxidation Stability of Aviation Turbine Fuels*; ASTM Monograph 1; American Society for Testing and Materials: Philadelphia, 1991; (a) pp 79–84, (b) p 111, (c) p 73.

(2) Edwards, T.; Anderson, S. D.; Pearce, J. A.; Harrison, W. E. High Temperature Thermally Stable JP Fuels—An Overview. AIAA Paper 92-0683, presented at the 30th Aerospace Sciences Meeting and Exhibit, Reno, NV, 6–9 January 1992.

(3) Jones, E. G.; Balster, W. J. *Prepr. Pap.-Am. Chem. Soc., Div. Fuel Chem.* **1994**, 39 (3), 952–957.

(4) Jones, E. G.; Balster, W. J. *Energy Fuels* **1995**, 9, 610–615.

(5) Jones, E. G.; Balster, W. J. *Energy Fuels* **1993**, 7, 968–977.

(6) Jones, E. G.; Balster, W. J. *Prepr.-Am. Chem. Soc., Div. Pet. Chem.* **1994**, 39 (1), 78–81.

oxidation, and these sites can become blocked by the passivating effects of deposits. Since this effect was observed for only one fuel, it was important to ascertain whether such findings apply for other fuels. If most fuels do, in fact, exhibit similar behavior, then fouling reactions would be exacerbated by conditions of high surface-to-volume ratio and the presence of clean metal surfaces—precisely those conditions that are desirable for certain components in aircraft fuel lines, namely, servocontrols, flow-divider valves, and nozzles.

The goal of the current study was to investigate the generality of this previous finding by studying autoxidation of an array of fuels using experiments designed to emphasize surface effects; the premise here is that if wall interactions are significant in autoxidation, then the rate of autoxidation measured as fuel flows through clean stainless-steel tubes will differ from that measured as fuel flows through passivated tubes. For the latter case, we selected Silcosteel⁷ tubes reported to have high thermal stability and an inert interior. The extent to which Silcosteel tubing is inert for autoxidation reactions is unknown; however, for purposes of comparison, results for reaction in this tubing are considered to be representative of autoxidation occurring primarily in the bulk fuel (minimal surface activity), whereas results for reaction in stainless-steel tubing are considered to be representative of bulk autoxidation coupled with additional effects from possible surface interactions.

A series of 16 aviation fuels was selected for study—a choice based primarily on their interest to the USAF and current availability. Both thermally stable and thermally unstable fuel candidates were used, all having been the subject of other USAF-funded research. The dissolved oxygen in each fuel was measured directly during autoxidation as the fuel passed through heated stainless-steel tubing and also through passivated tubing of the same dimensions. It is important to note that the current data were obtained from dissolved-oxygen measurements in fuel reacting in a single phase at high pressure rather than from oxygen-takeup measurements in the headspace above fuel. The empirical approach in the current study addresses differences in autoxidation which may be attributed directly to surface activity.

Experimental Techniques

All experiments were conducted using the Near-Isothermal Flowing Test Rig (NIFTR) which has been described in detail elsewhere.⁵ Reaction occurred as the fuel was pumped through 0.318 cm (0.125 in.) o.d., 0.216 cm (0.085 in.) i.d. tubing clamped tightly within a 81.3 cm (32 in.) heated Cu block (~40 kg) heat exchanger maintained at 185 °C. The temperature range accessible by the techniques employed in this study is limited to 145–225 °C. The block temperature selected was midrange and provided test conditions under which the total dissolved oxygen in most fuels reacts within 20 min. System pressure was maintained at 2.3 MPa to ensure a single reaction phase. Stress duration, the residence time within the heated tube, was varied by changing the fuel flow rate and was calculated based on plug flow. A 15% correction to the stress duration has been applied to accommodate fuel expansion at 185 °C. At slow flow rates the fuel achieves block temperature in times that are short compared to the total residence time, and isothermal conditions apply. However,

under conditions of rapid flow rate, the system may depart significantly from isothermal. When the measured stress time is less than ~1.5 min, the actual time that the fuel spends at temperature becomes significantly less than the calculated time. The resulting error is an overestimation of the dissolved oxygen, i.e., an underestimation of the extent of reaction. This error can be significant on an absolute basis but is of less concern for relative comparisons. Fuel entered the heated section saturated with respect to air at STP. The initial dissolved O₂ concentration was equated to 100%, and the residual dissolved O₂ following reaction was measured at the end of the tube. The absolute quantity of O₂ dissolved in jet fuels at room temperature has been reported to be in the range 47–93 ppm (w/w), as measured using a GC-MS technique.⁸ In the current study the methodology employed for measuring dissolved O₂ at elevated pressures utilizes GC detection as developed by Rubey and co-workers.⁹

Each fuel was studied during reaction in (1) 304 stainless-steel (ss) tubing which was replaced after each test (i.e., daily), and (2) Silcosteel tubing (henceforth referred to as treated) of identical dimensions. The latter has an inert silica-treated inner surface covered with a monolayer of a specific siloxane polymer to further reduce surface activity. It has been demonstrated using a variety of S- and N-containing substances (chemical probes) and inverse chromatographic procedures that treated tubing provides much higher transport efficiency than conventional ss tubing.¹⁰ In the present study the treated tubing was used for only two experiments and then replaced to minimize surface changes arising from deposit buildup. Three of the 16 fuels selected for study were also evaluated for reaction in tubing that had previously been fouled by deposits. Fouling of the ss tube was achieved during earlier stressing of POSF-2827 fuel; based on the surface-carbon burnoff of tubes exposed similarly, it was estimated that the fouled ss tube contained an approximately uniform deposit layer of 37 µg/cm². Fouling of the treated tube was achieved by long-term exposure to heated fuel. Fuels were passed through a coarse (15 µm) filter for pump protection but were otherwise used as received. The treated tubing was cleaned using a methanol rinse in accordance with the manufacturer's instructions; ss tubing was cleaned with Blue-Gold and ultrasound to remove oils and to ensure consistency with deposition experiments which require minimum background surface carbon. Results obtained from O₂ measurements made in tubing (ss) cleaned by methanol rinse could not be distinguished from those made in tubing (ss) cleaned with BlueGold.

Fuels of categories Jet-A, Jet-A-1, JP-5, JP-8, and JPTS as well as one Cu-doped fuel were studied and are summarized in Table 1; Columns 2–5 contain some general background information including breakpoint temperatures from the Jet Fuel Thermal Oxidation Test (JFTOT) and data on dissolved Cu and Fe for most fuels.

Results and Discussion

Reaction in Treated Tubes. Figure 1 contains plots (closed circles) of residual dissolved O₂ as a function of residence time for 16 fuels. The time required for complete conversion ranges from 1.5 to 13 min. With few exceptions, the curves show delay times or induction periods followed by reaction acceleration at higher conversion. This sigmoid behavior is characteristic of autocatalysis, i.e., self-initiation caused by dissociation of reaction products such as hydroperoxides.

(8) Striebig, R. C.; Rubey, W. A. *Prepr.-Am. Chem. Soc., Div. Pet. Chem.* 1994, 39 (1), 47–50.

(9) Rubey, W. A.; Striebig, R. C.; Tissandier, M. D.; Tirey, D. A.; Anderson, S. D. *J. Chromatogr. Sci.* 1995, 33, 433–437.

(10) Anthony, L. J.; Holland, R. A. *J. Noncryst. Solids* 1990, 120,

(7) Silcosteel tubing, Restek Corp., Bellefonte, PA.

Table 1. Fuel Properties and Autoxidation Summary

fuel no.	class	JFTOT temp, K	total S, ppm	dissolved metals, ppb ^a	time difference 50% conv, min	reduction (ss), %	Figure 1 ref
2959	Jet-A, Merox-treated	566	1652	Cu, <5; Fe, <5	0.4	9	a
3084	Jet-A	541	527	Cu, 35; Fe, <5	0.7	14	b
3056	JP-8				0.6	16	c
3119	Jet-A	(fails)	1000	Cu, 7; Fe, 26	0.9	16	d
2857	Jet-A, hydrotreated				0.3	17	e
2922	Jet-A, hydrotreated	550	210	Cu, 7; Fe, <5	0.3	18	f
2799	JPTS, thermally stable		0	Cu, 7; Fe, 17	0.5	26	g
2985	JP-5, hydrotreated	535 (fails)	233	Cu, 14; Fe, 18	0.7	30	h
2962	JP-5		438		1.9	39	i
2963	JP-5, Cu-doped	505 (fails)	438	Cu, 98; Fe, 60	0.3	41	j
2747	Jet-A-1, hydrotreated	605	37	Cu, <5	1.1	48	k
2827	Jet-A, straight run	539	790	Cu, <5; Fe, 8	3.5	55	l
2976	JPTS, thermally stable	700	0		1.6	57	m
2934	JP-8	539	755	Cu, 34; Fe, <5	2.7	65	n
2980	Jet-A, Merox-treated	561	614	Cu, <5; Fe, <5	3.4	71	o
2926	Jet-A	561	524	Cu, <5; Fe, 10	2.1	76	p

^a Measurements made for USAF using graphite furnace Zeeman/5000 System atomic absorption spectrometer by United Technologies, Pratt and Whitney.

The delays observed are analogous to induction periods for the formation of hydroperoxides, as reported by Fodor and co-workers¹¹⁻¹³ at much lower temperatures. Fodor's data show a distinct transition following induction in plots of $[\text{ROOH}]^{1/2}$ vs stress duration. The transition to faster rates in the current oxygen data is gradual, and no sharp onsets are observed; this behavior may arise from the higher-temperature reaction conditions. Not all of the fuels in the current study produce a measurable steady-state concentration of hydroperoxides. The presence of certain types of S-containing compounds tends to destroy the hydroperoxides either directly by reaction or indirectly by intercepting their precursor. We have measured the concentration of hydroperoxides as a function of stress time for more than half of the current fuels and have observed the region of accelerated autoxidation to occur at stress times when the concentration of hydroperoxides begins to exceed ~ 0.03 mM.

Two of the fuels studied do not exhibit noticeable autocatalysis in treated tubes. These are the fuels in Figure 1, j and l, which require the minimum and maximum reaction time, respectively, for complete conversion of the dissolved oxygen. The first, POSF-2963 (Figure 1j), is the fastest reacting fuel in this series because of the presence of 98 ppb of Cu. In this case, since data were collected at the extreme upper limit of rates that can be measured using this methodology, large errors are present and, thus, it is difficult to observe rate increases with conversion. In the second, POSF-2827 (Figure 1l), autoxidation appears to be slowed over the entire reaction range. The steady-state concentration of hydroperoxides formed by this fuel in treated tubes remains at or below detectable limits; thus, self-initiation by the bulk dissociation of hydroperoxides is not expected to be significant.

All the rapidly oxidized fuels are specialty fuels such as hydrotreated or JPTS having low S levels and minimal natural antioxidants; these contain added antioxidant protection such as amines or hindered phenols in hydrotreated fuel and as JFA-5 in JPTS.

Reaction in ss Tubes. Data for reaction in ss tubes are represented in Figure 1 by open circles. For some fuels achieving reproducible O_2 readings over extended time periods was difficult. Data collected using the treated tubes were stable and readily reproducible; however, with ss tubes, frequently the observed reaction slowed somewhat during data collection. We attribute such changes to surface modification during the course of the testing; this includes changes resulting from deposits which collect on the inner walls of the tubing during the sequence of oxygen measurements. Also we could not distinguish surface activity caused by the initial ss from that due to changes occurring on a time scale that is short compared to the time scale of the measurements. For these reasons ss tubes were replaced daily and used for one fuel only. The profiles in Figure 1 contain data collected before surface fouling became significant.

The most obvious feature in Figure 1 is that the time required for complete O_2 conversion is shorter for reaction in ss tubes. This time difference is fuel dependent; in some cases differences are sufficiently small to be within the experimental uncertainty, and in other cases the times differ by a factor of 3-4. A simple estimate of the difference can be obtained by comparing the stress times required to achieve the same extent of O_2 conversion. For example, Table 1 (columns 6-7) summarizes the estimated difference in time required to reach 50% conversion of O_2 for reaction in each type of tubing, along with the percentage change in time (reduction) introduced by the use of ss tubing. Fuels in both Table 1 and Figure 1 are arranged in order of increasing magnitude of the values in column 7. The first six fuels differ by less than 20% and may be considered borderline; all others differ by more than 25%. In cases where induction periods and autocatalysis are observed for reaction in treated tubes, they are also observed for reaction in ss tubes. The induction periods are always shorter and the autocatalyzed rates are either the same or faster for reaction in ss tubes. For example, the fuels POSF-2747 (Figure 1k), POSF-2985 (Figure 1h), and POSF-2976 (Figure 1m) have significantly shorter (1-2 min) induction periods but similar catalyzed rates. The fuels POSF-2827 (Figure 1l), POSF-2926 (Figure 1p), POSF-2934 (Figure 1n), POSF-2962 (Figure 1i), and POSF-2980 (Figure 1o) have

(11) Fodor, G. E.; Naegeli, D. W.; Kohl, K. B. *Energy Fuels* 1988, 2, 729-734.

(12) Fodor, G. E.; Naegeli, D. W. *Prepr. Pap.-Am. Chem. Soc., Div. Fuel Chem.* 1990, 35 (4), 1267-1276.

(13) Fodor, G. E.; Naegeli, D. W.; Turner, L. M. *Prepr.-Am. Chem. Soc., Div. Pet. Chem.* 1992, 37 (2), 403.

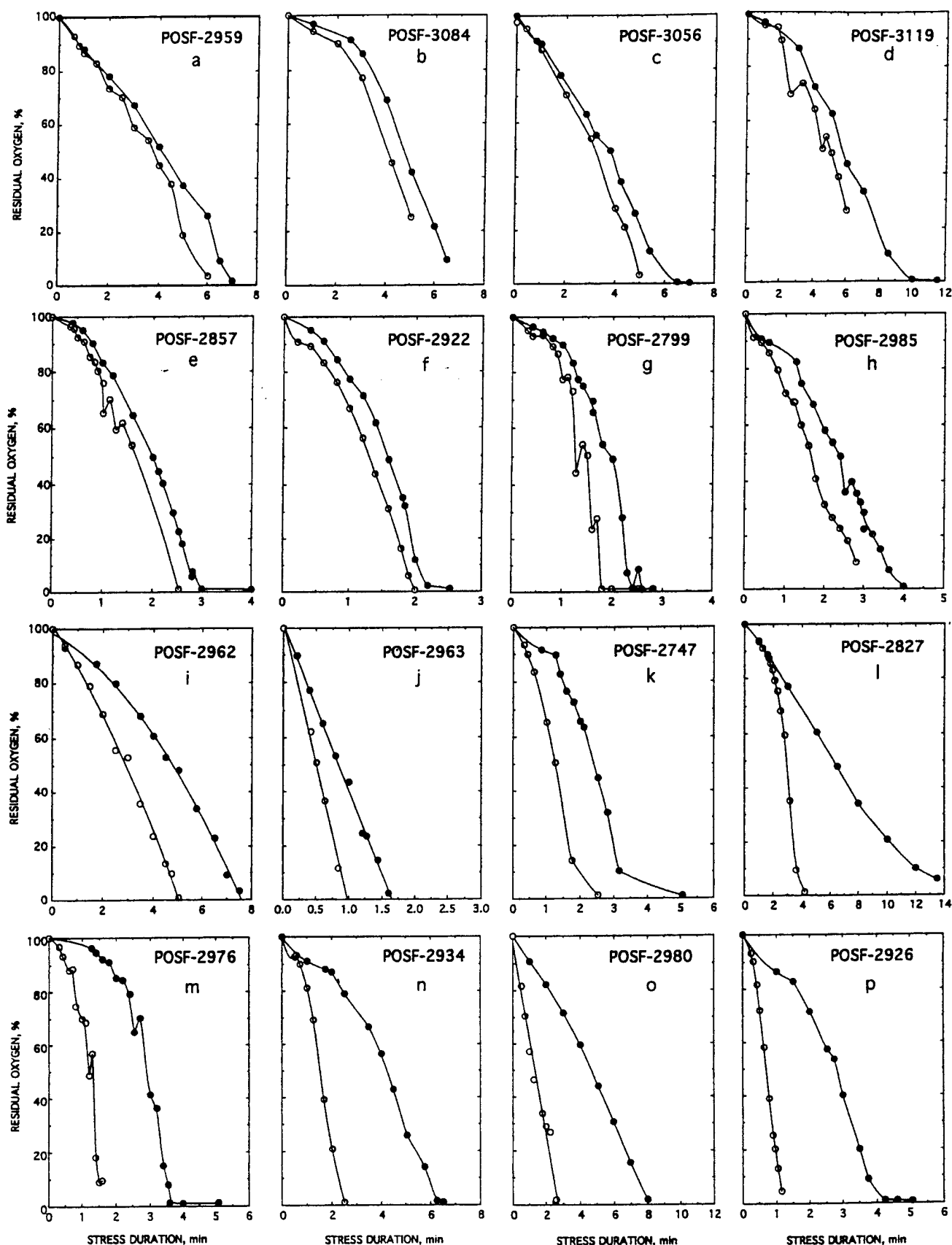


Figure 1. Reaction of dissolved oxygen in series of 16 fuels as function of stress duration at 185 °C as measured in ss (open circles) and treated (closed circles) tubes.

shorter induction periods but also exhibit significantly faster autocatalyzed rates in ss tubes.

Reaction in Fouled Tubes. From Figure 1 it is obvious that treated tubes are passivated compared to

ss for most of the 16 fuels. The question then is whether a deposit-fouled surface exhibits more or less activity for autoxidation than the treated surface. Figure 2 shows autoxidation in POSF-2827 as measured using

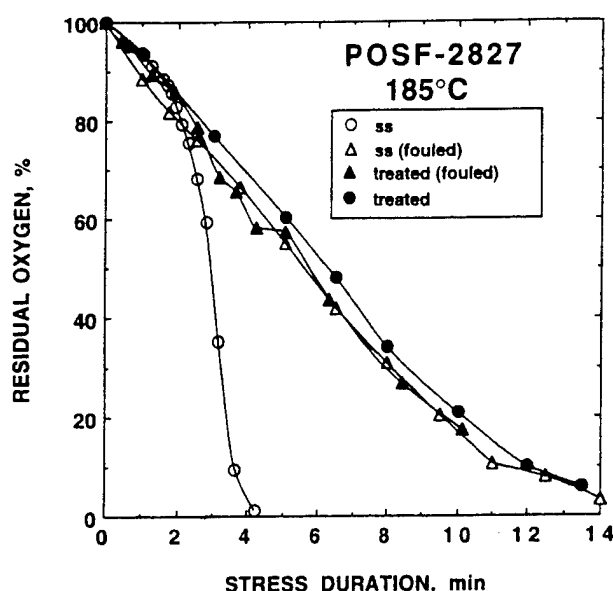


Figure 2. Reaction of dissolved oxygen in POSF-2827 fuel at 185 °C as measured in (1) ss tube, (2) ss tube fouled with deposits (37 $\mu\text{g}/\text{cm}^2$), (3) treated tube fouled with deposits, and (4) treated tube.

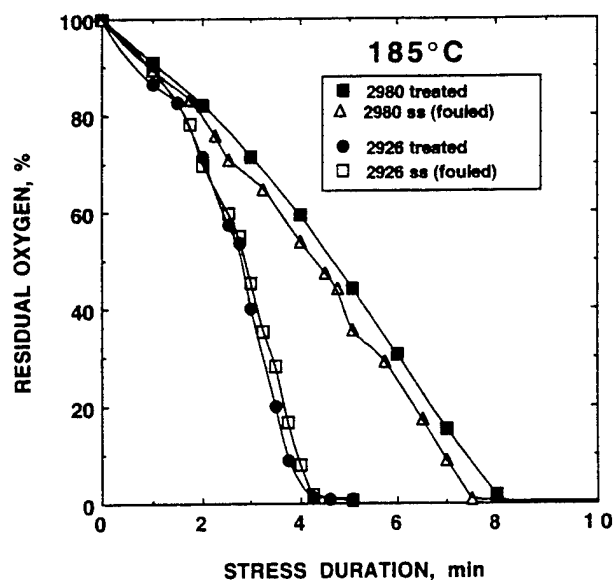


Figure 3. Reaction of dissolved oxygen in POSF-2980 and -2926 fuels at 185 °C as measured in treated and fouled ss (37 $\mu\text{g}/\text{cm}^2$) tubes.

tubing with inner walls that are (1) ss, (2) ss fouled by deposits (estimated at 37 $\mu\text{g}/\text{cm}^2$), (3) treated but fouled by deposits (unknown surface density), and (4) treated. The fouled surface exhibits minimal activity that is very similar to that of the treated tube. Also, Figure 2 shows that once the surface (ss or treated) is fouled by deposits, the nature of the underlying original surface becomes immaterial, as expected. Autoxidation in fouled tubes remains inhibited over the complete range of oxygen conversion. Surface activity related to the fouled tube is relatively minor.

Autoxidation in two other fuels (POSF-2980 and POSF-2926) that display a large difference in time required for 50% oxygen conversion in ss and treated tubes was investigated for reaction in the heavily fouled ss tube described above. Results in Figure 3 indicate that autoxidation in fouled and treated tubes is similar,

offering additional confirmation of the passivating effects of surface deposits.

Possible Explanations. Clearly, the nature of the inner surface of the heated walls is an important factor in autoxidation. If we assume that reaction in treated tubes involves primarily bulk chemistry with minimal wall interaction, then ss surfaces are viewed as catalyzing autoxidation. The three main processes in autoxidation are initiation, propagation, and termination. Propagation and termination are bulk reactions, but initiation at lower temperatures is frequently assisted or dominated by heterogeneous reactions.¹⁶ The following general explanation for the current observations is offered, bearing in mind that no single reaction scheme is expected to prevail over this broad range of fuels.

First, we expect active sites on the ss surface to be a source of free-radical initiation; this may be a heterogeneous catalytic reaction such as surface-assisted thermal dissociation of hydroperoxide



or any other trace fuel component having a weak bond. Metal-catalyzed autoxidation involving salts of heavy metals has been summarized by Walling¹⁴ and usually involves redox reactions between metal cations and hydroperoxides as a homogeneous source of free-radical initiation. Among the current fuels POSF-2963 (Figure 1j) doped with Cu may be typical of this mechanism. Contrast this behavior with the much slower reaction in the same fuel without Cu, POSF-2962 (see Figure 1i, closed circles). Compare also the acceleration resulting from the surface (POSF-2962 (Figure 1i; ss to treated)) with that resulting from the dissolved Cu. The presence of a homogeneous catalyst in the form of dissolved Cu at 98 ppb is more deleterious than heterogeneous reactions at the ss walls.

Any process such as reaction 1 or a redox reaction which lowers the activation energy for initiation also lowers the overall activation energy for autoxidation. The same active surface sites may not be available on heavily fouled tubes; thus, autoxidation would be expected to become slower as the ss walls become covered with deposits. Presumably, treated surfaces would have considerably fewer active sites for reaction 1.

It was pointed out earlier that the rate of autoxidation in POSF-2827 fuel, as measured in a treated tube, remains slow until oxygen conversion is complete. The presence of S-containing natural inhibitors, designated R'S, protects the fuel from rapid autoxidation by removing hydroperoxides as in reaction 2 and, thereby,



reducing self-initiation. We have placed this fuel into a common category previously described by Kendall and Mills¹⁵ in which reaction is slowed by S-containing components¹⁶ but at the expense of forming insolubles. Other antioxidants such as hindered phenols act by a chain-breaking mechanism to slow propagation.¹⁷ At

(14) Walling, C. *Free Radicals in Solution*; John Wiley and Sons, Inc.: New York, 1957; p 427.

(15) Kendall, D. R.; Mills, J. S. *Ind. Eng. Chem. Prod. Res. Dev.* **1986**, 25, 360-366.

(16) Bol'shakov, G. F. *Sulfur Rep.* **1987**, 7, Part 5, 379-392.

(17) Scott, G. *Atmospheric Oxidation and Antioxidants*; Elsevier: New York, 1965; p 115.

a concentration of 25 mg/L, the hindered-phenol antioxidant BHT does not further delay autoxidation, as measured in treated tubes, indicating that the natural inhibitors in POSF-2827 fuel are more efficient antioxidants than BHT.¹⁸ Although autoxidation is inhibited for reaction in treated tubes, the reaction does become autocatalytic during flow through ss tubes,⁵ as evidenced by the sigmoid behavior in Figure 2. In treated tubes reaction 2 maintains a low steady-state hydroperoxide concentration, $[ROOH]_{ss}$, minimizing self-initiation. In ss tubes, however, the additional initiation afforded by reaction 1 increases the free-radical pool so rapidly that slow autoxidation cannot be maintained and the reaction becomes autocatalytic.

Pure hydrocarbons and hydrotreated fuels which have few natural inhibitors and require the addition of chain-breaking antioxidants for storage stability¹⁹ form hydroperoxides readily, and autoxidation becomes autocatalytic even in treated tubes. At 185 °C the rate of thermal dissociation of ROOH is slow; however, any dissociation will significantly increase the free-radical pool. The additional contribution from the heterogeneous reaction 1 will cause autocatalysis at earlier stress times. For example, thermally stable POSF-2976 used in the U-2 aircraft contains the antioxidant package JFA-5 which provides an induction time of ~2 min in treated tubes before the onset of rapid autoxidation. The additional contribution from reaction 1 in ss tubes reduces the induction time by ~1.5 min, and this is reflected in the 1.6-min time difference at 50% conversion given in Table 1.

Implication of Results. Current results show that autoxidation in most of the fuels studied is accelerated by interaction with ss walls. At elevated temperature, regions of aircraft fuel lines having a high surface-to-volume ratio and exposed ss surfaces are vulnerable to surface interaction manifested by higher oxygen conversion and more insoluble formation. Servocontrols and flow-divider valves (which adjust fuel flow by movement of closely mating surfaces) as well as nozzles have tight tolerances and are very susceptible to additional surface fouling from fuel/ss interaction. High temperatures and extended residence times exacerbate the problem. Even minimal surface fouling of flow-divider valves causes serious hysteresis problems which disrupt fuel distribution. These specific regions of the fuel line may benefit most from surface treatment to reduce or eliminate fuel/metal interaction. Natural passivation resulting from accumulation of deposits may be beneficial in slowing autoxidation and subsequent deposition in many regions of the fuel lines, but this is clearly not an acceptable solution for critical regions.

Surface deposition in short-term tests such as JFTOT or 6-h NIFTR experiments will be governed by faster autoxidation caused by the initial metal surface. In

contrast, surface deposition in long-term tests where a passivating deposit layer may develop will be mainly controlled by a slower rate of autoxidation. In isothermal experiments this results in reduced deposition rates for fuels such as POSF-2827⁴ and POSF-2980.²⁰

If active sites on ss are responsible for accelerated autoxidation, then the possibility of using fuel additives to block such sites should be considered. We have reported that additives such as JFA-5 and MDA eliminate some of the autocatalytic effects in POSF-2827 for reaction in ss tubes.^{4,5} On the basis of the current results, one role of additives may be to reduce fuel/metal interactions and, thereby, slow autoxidation—an area of current interest in this laboratory.

Conclusions

The goal of the current investigation was to study autoxidation in 16 fuels using experiments designed to emphasize surface effects. Autoxidation is found to be faster for reaction in ss than in treated tubes. Frequently, reactions in ss tubes were found to have shorter induction periods before autocatalysis and faster autocatalytic rates. The magnitude of this difference was found to be fuel dependent.

Results indicate that the previous finding⁴ for a specific Jet-A fuel, namely, that autoxidation slows as the initial ss tubing becomes fouled by deposits, may be common to many fuels. Autoxidation for three fuels (POSF-2827, -2926, and -2980) during reaction in tubing fouled by deposits is considerably slower and closely approaches that achieved in treated tubing. These effects are explained by heterogeneous reactions at active catalytic sites on ss which can initiate autoxidation and/or destroy natural inhibitors. These sites can become blocked by deposits and are either much fewer in number or absent on the treated tubes.

Current findings support the use of passivated surfaces to reduce the extent of autoxidation and, presumably, the amount of surface insolubles, particularly in regions of aircraft fuel lines which are sensitive to surface fouling, including flow-divider valves and nozzles.

Acknowledgment. This work was supported by Wright Laboratory, Aero Propulsion and Power Directorate, Wright-Patterson Air Force Base, Ohio, under USAF Contract No. F33615-90-C-2033 with Systems Research Laboratories, Inc. The authors acknowledge Mr. Wayne Rubey of the University of Dayton Research Institute (UDRI) for developing and installing the dissolved-oxygen detector and suggesting the use of Silcosteel tubing. Also discussions with Dr. Jim Pickard (SRL) and Mr. Steve Anderson (USAF) and the editorial assistance of Mrs. Marian Whitaker (SRL) are acknowledged.

EF9502012

(18) Jones, E. G.; Balster, L. M.; Balster, W. J. *Energy Fuels*, **1995**, *9*, 906–912.

(19) Turner, L. M.; Kamin, R. A.; Nowack, C. J.; Speck, G. E. Effect of Peroxide Content on the Thermal Stability of Hydrocracked Aviation Fuel. *Proceedings of 3rd International Conference on Stability and Handling of Liquid Fuels*; Institute of Petroleum: London, November 1988; pp 338–349.

(20) Jones, E. G.; Balster, W. J.; Pickard, J. M. Surface Fouling in Aviation Fuels: An Isothermal Chemical Study. Paper No. 95-GT-45. Presented at International Gas Turbine and Aeroengine Congress and Exposition, Houston, TX, 5–8 June 1995; accepted for publication in *J. Eng. Gas Turb. Power*.

3.2.3 Fuel-System Icing

Historical Background. Ice accumulation within aircraft fuel filters was observed as early as 1947 (see Ref. 1 for an excellent review of early work). The solution at that time was the addition of alcohol. Fuel-system icing was not considered to be a serious problem, however, until 1958 when a report of a B-52 crash positively identified ice in the fuel-system filters and controls as the cause of the accident. As a result, the late 1950's and early 1960's saw sponsored work in fuel drying and fuel additives aimed at preventing ice formation.

Technical reports regarding icing-inhibitor development are sketchy and limited in number. The two most comprehensive were published in 1960 during the flurry of activity to solve the problem demonstrated by the B-52 crash. Langer¹ conducted tests in JP-4 fuel to identify the factors influencing ice formation in fuel systems. These tests showed that it was relatively common to observe the lack of ice formation at temperatures as low as -40°C. That is, water droplets may be highly supercooled. However, the temperature at which ice formation was observed was much higher when the solution was agitated. Also, the presence of a small amount of emulsifier appeared to promote ice formation, while a large quantity (1 vol%) prevented ice formation at the lowest temperatures tested (-46°C). This work demonstrated an obvious connection between droplet size and the temperature at which ice formation was observed.

Netzel, et al.² attempted to determine the optimum additive for ice prevention. These investigators tested numerous compounds by measuring the temperature at which the flow of fuel (containing an additive and excess water) through a mesh filter became blocked. Their conclusion was that the optimum performance was achieved through the use of organic compounds having a large number of functional groups per molar volume and having a ratio of carbon atoms to number of functional groups of two or less. Functional groups considered were primary, secondary, and tertiary amines; hydroxyl group; coordinating covalent phosphorus-oxygen bond; covalent nitrogen-phosphorus bond; and, in the presence of other groups, ether linkage.

As a result of these and other studies, in 1961 ethylene glycol monomethyl ether (EGME) was added to the specification for military jet fuels. At that time, a small amount of glycerol was included for protection of seals in the presence of EGME but was removed from the specification in 1970 when studies showed that it was of no benefit in the presence of an antioxidant if the EGME was well dissolved. In 1984, the Navy began to use diethylene glycol monomethyl ether (DiEGME) in an attempt to raise the flashpoint.³ In 1994, the Air Force also began to use DiEGME because its toxicity is much lower than that of EGME.

Because of its success in preventing icing in aircraft fuel systems and in preventing micro-organism growth within fuel storage tanks, DiEGME appears to be an ideal fuel-system icing inhibitor (FSII) compound. Its low toxicity makes it compatible with current disposal regulations, including disposal into municipal treatment facilities. Future disposal, however, may be much

more difficult as regulations become more demanding. In addition, the relatively high biological oxygen demand (BOD--sometimes referred to as biochemical oxygen demand) requires that the rate of disposal be limited. That is, fuel-tank water-bottoms contaminated with DiEGME must be held in storage tanks or settling ponds for a period of time before their release to the environment or treatment facilities. Premature release could kill aquatic life as well as lower treatment-plant efficiency.

An effort is presently underway to develop an alternative to DiEGME that is nontoxic and can be disposed of easily. Dr. George Mushrush of George Mason University has synthesized several compounds from simple sugars.⁴ His goal is to find a compound that is sufficiently soluble in JP-5 and JP-8 fuels (minimum of 0.2 vol% of FSII in fuel at - 50°C) but partitions to free water in such a way that its concentration in the free water is sufficient to prevent ice formation.

FSII Effectiveness. Currently FSII effectiveness is tested in a rig operated by the Naval Air Warfare Center (NAWC) in Trenton, NJ, using a technique similar to that employed by Langer.¹ That is, the efficacy of an FSII is determined by the ability of the additive to prevent ice blockage of a fuel flow containing ~ 250 ppm total water flowing at 40 ml/sec through a 30- μ m (absolute) wire mesh filter.⁵ Thus far, one candidate (designated M-2) has been shown to be effective, although not so effective as DiEGME. Figure 1 shows a comparison of data obtained from the test rig for DiEGME and three alternatives--dipropylene glycol methyl ether (DPG), acetone adduct of glycerol (M-1), and formaldehyde adduct of glycerol (M-2, commercially known as glycerol formal). Although DPG performs best, the glycerol-based compounds are of more interest as non-toxic FSII's. Alternative compounds are being synthesized at George Mason University.⁶

As shown in Fig. 1, a large amount of scatter is present in the measured value of icing-point temperatures for the rig-test results. Potential alternative tests for FSII effectiveness were evaluated in an attempt to reduce the variability of these results. The techniques evaluated employ 1) ultrasonics to monitor the accumulation of ice, 2) dielectric-constant measurements to detect the phase change of water to ice, 3) a quartz crystal microbalance to detect the formation of ice on a metal surface, 4) a commercial particle-sizing instrument to measure water-droplet and ice-crystal growth, 5) photon correlation spectroscopy (PCS) to measure the size of water droplets, and 6) depolarized light scattering to detect the formation of ice crystals.

The usefulness of ultrasonics in measuring the thickness of an ice layer on container surfaces is determined by the impedance mismatch of the liquid/ice and ice/surface interfaces. Some relevant published values⁷ of impedance are:

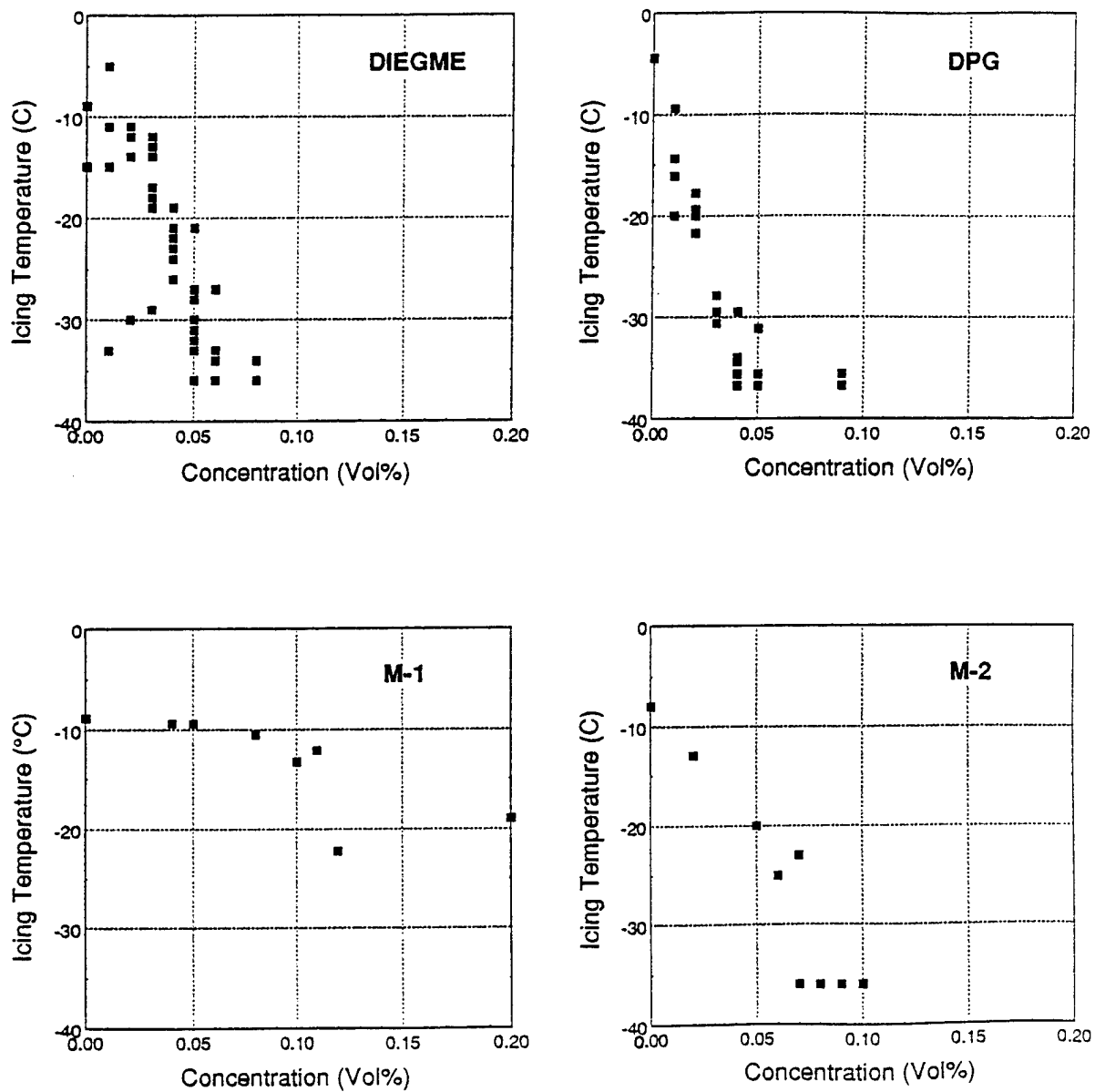


Figure 1. Plots of Icing Temperatures as a Function of Aqueous-Solution Concentrations of Various FSIs as Measured with the NAWC Flowing Test Rig. Data provided by NAWC (Ref. 5).

Material	Impedance ($\times 10^6 \text{ kg-cm}^{-2}\text{-sec}^{-1}$)
Diesel Oil	1.0
Water	1.5
Ice	3.6
Quartz	14.5
Steel	45

With these values, 5% of the energy of a reflected ultrasonic wave from a water/ice/steel path will result from the water/ice interface. If a layer of ice is uniform, measurement of its thickness is feasible. Initial ice deposition in a fuel/water solution, however, generally results from suspended droplets or droplets on the container surface. Ultrasonics is not feasible for discrimination of small ice crystals in the vicinity of water droplets. It may, however, be useful for detection of partial filter blockage.

The feasibility of utilizing the large difference in relative dielectric constant (ϵ_r) between water ($\epsilon_r = 78$) and ice ($\epsilon_r = 4.2$) for the detection of ice formation was investigated. The limitation of capacitance measurements arises from the small percentage (0.005 - 0.025 vol%) of water typically present in fuel.⁸ For a water content of 0.025%, the contribution of the water to the total capacitance of the dielectric fluid (fuel + water) is $\sim 1\%$. For detection of water freezing, a capacitance-measurement resolution of 0.05 - 0.1% is required. Also, a testing device having a large surface area and/or small plate separation is required to ensure that the total capacitance will be in the range of commercially available capacitance meters. For example, two 1-in.-diam. plates separated by 1 mm produce only 4 pF of capacitance with a fuel dielectric. An increase in the plate area or decrease in the gap by a factor of 100 would allow accurate capacitance measurements, but uniform cooling would then become difficult and nonuniformities in ice formation might occur.

In addition, a decrease in the temperature of a fuel solution causes an increase in the free-water concentration,⁸ affecting the total-solution capacitance. Other physical changes such as phase changes of other fuel components may also affect the solution capacitance. Netzel, et al.,² reported a linear change in capacitance as a function of fuel-solution temperatures above and below the expected icing point and a slight change in slope near the expected icing point. Their measurements produced only five data points and were limited to a single fuel solution; additional study is needed before the conclusion can be drawn that the effect was due exclusively to ice formation. Considering the variability in fuel chemistry, a significant amount of effort is required to prove that the capacitance technique is useful for the measurement of ice-inhibitor effectiveness. It was not prudent to perform such studies for the present effort.

The use of a quartz crystal microbalance⁹ (QCM) to detect ice formation on a metal surface (gold) appeared feasible. However, in laboratory tests no ice was detected while the QCM element remained in a water-saturated fuel solution. As the temperature of the solution was lowered, the resonant frequency of the crystal decreased and the damping factor increased monotonically. At $\sim -15^{\circ}\text{C}$, the crystal oscillation circuit ceased to function after the element had been removed from the fuel, exposed to air for ~ 10 sec, and then reinserted into the solution. The cessation of oscillation can indicate ice attachment to the gold crystal surface; however, no ice was observed to attach while the crystal was in the solution. It appears that the ice simply does not stick to the gold surface of the plated quartz electrode in a fuel solution.

The use of a commercial instrument (Horiba Model LA-900 Laser Scattering Particle Size Distribution Analyzer) to measure the size of suspended particles was severely limited by condensation on the outside sample-cell walls. A coating of antifreeze on the walls seemed to delay the effect of condensation, but the coating was difficult to maintain. Since the instrument configuration was not conducive to a nitrogen purge, it was concluded that use of this instrument in low-temperature applications is not feasible.

The feasibility of utilizing zero-angle depolarized dynamic light scattering,¹⁰ was determined initially using a 0.5-in.-diam. copper tube configured with an outer sleeve in a heat-exchanger arrangement. Windows attached at each end of the tube created a 16-in.-long optical path. Polarizing optics located at each end created a highly polarized optical source at one end and a polarization analyzer at the other to permit monitoring of the loss of polarization due to ice-crystal formation within the tube. Unfortunately, the 16-in. path length proved to be excessive, and refractive-index gradients caused beam deflection. Beam polarization could not be monitored because the beam moved to the tube walls and became severely distorted.

A heat-exchanger and optical-cell arrangement was constructed for making optical measurements on fuel solutions at temperatures down to -40°C . An assembly drawing is shown in Fig. 2. A copper block is cooled with chilled fluid supplied by a circulating bath/chiller. A cold finger, soldered to the block, protrudes into a double-walled Pyrex tubular arrangement. The solution to be observed is contained within the inner 0.75-in.-diam. Pyrex tube, and a vacuum is drawn and sealed between the inner and outer tubes. The 0.5-in.-diam. copper tube serves as a heat conductor from the fuel to the block. Although a thick-walled copper tube would be more desirable, a thin-walled tube was used because the thicker material was not available at the time of construction.

The low-temperature cell assembly was first employed for droplet-size measurements utilizing PCS.¹¹ PCS is a dynamic light-scattering technique for measuring the diameters of light scatterers suspended in a medium and undergoing Brownian motion. This technique is well suited for measuring the size of water droplets in fuel, provided the fuel viscosity is known and the droplet

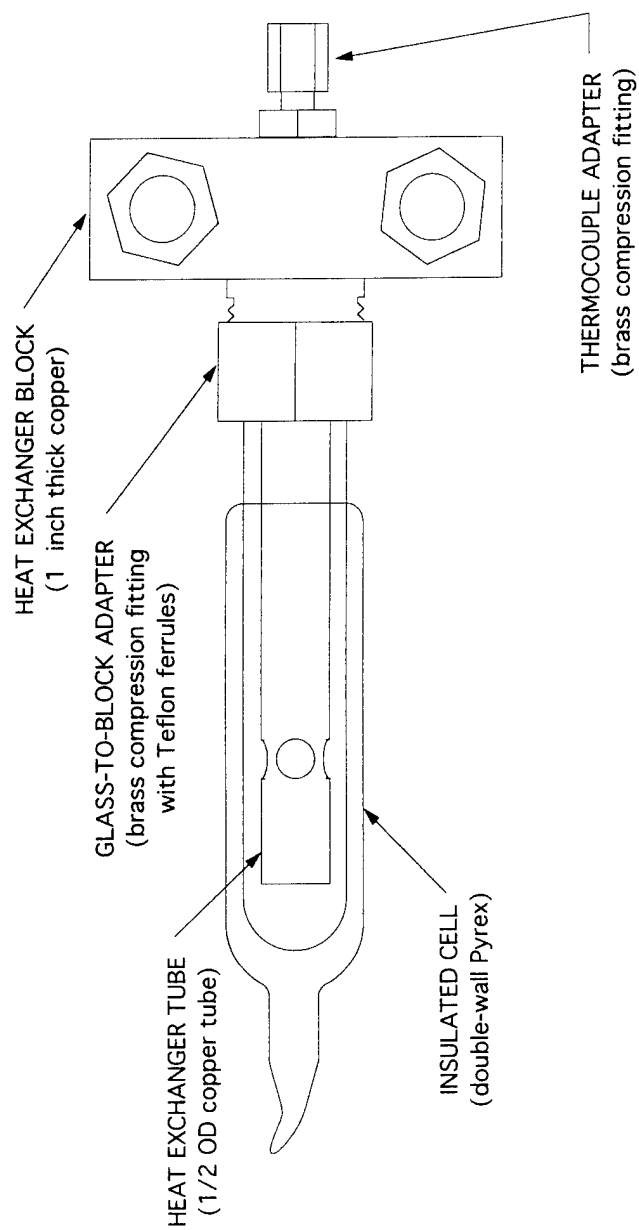


Figure 2. Schematic Diagram of Low-Temperature Optical Test Apparatus.

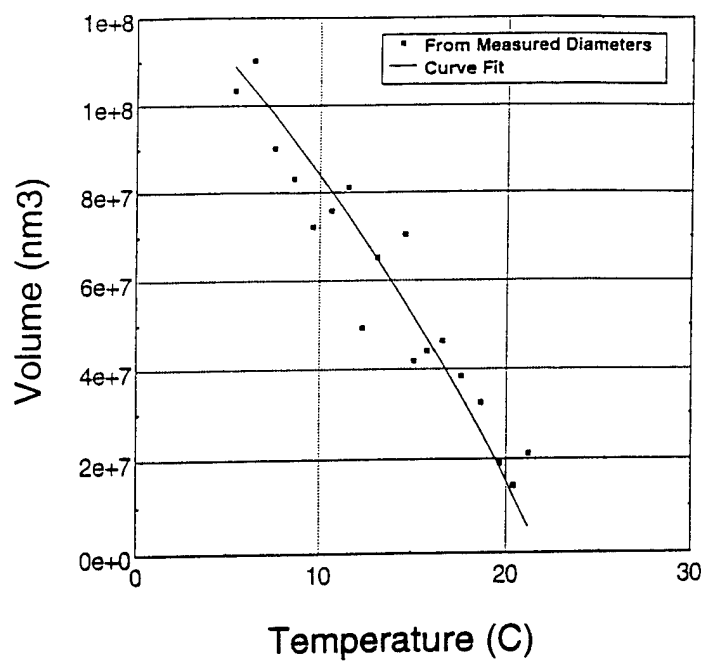
diameters are in the range 50 - 1000 nm (for a 633-nm light source). Preliminary measurements indicated a monotonic increase in water-droplet diameter from 400 to 650 nm as the temperature of the water-saturated Jet-A fuel decreased from 22 to 10°C. Below 10°C, the change in droplet diameter with temperature was negligible. This saturation in size may be a result of surface tension at the droplet/fuel interface or may be caused by agglomeration of droplets or condensation on the external cell wall in the initial setup.

The monotonic increase in droplet size with decrease in temperature indicates that PCS can be used for measurements of solubility as a function of temperature. Assuming that the density of droplets within the solution volume (e.g., droplets/cm³) does not change after some initial nucleation density, the increase in volume of droplets is proportional to the amount of water released from the fuel. This is a reasonable assumption for a limited range of droplet sizes since slow growth of a droplet can be energetically more favorable than nucleation of new droplets. Figure 3(a) shows a curve fit to droplet volume (calculated from measured diameters in a water-saturated Jet-A fuel) as a function of temperature. This fit is then compared to published values of water solubility in a typical Jet-A fuel in Fig. 3(b). The functional dependence shows good agreement, although an independent technique must be used to determine the absolute offset.

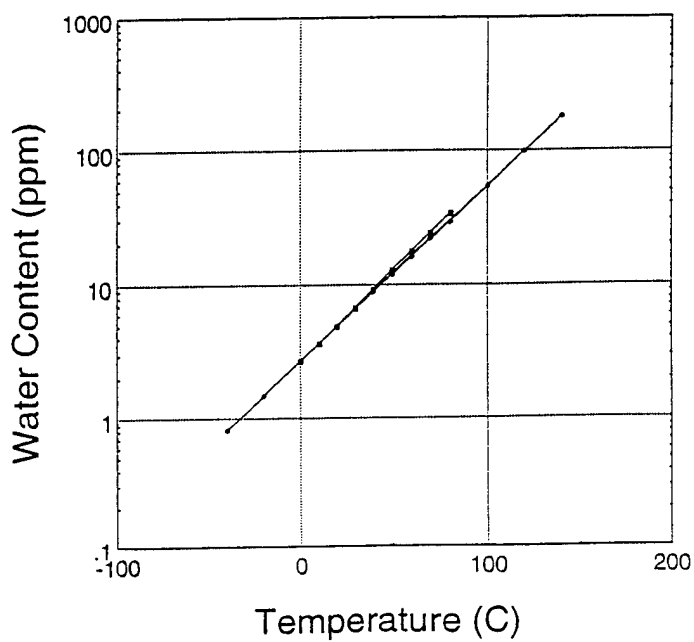
The optical cell was also configured for detection of zero-angle depolarized light scattering in order to monitor ice-crystal formation. In numerous attempts to detect a depolarization of a highly polarized (minimum 10,000:1) probe beam at temperatures as low as - 30°C, two difficulties were encountered--multiple scattering and convective currents. The intensity of the depolarized scattering detected in the forward direction became high for large droplet density, even when ice-crystal formation was unlikely, as in the presence of an ice inhibitor. This increased intensity was probably the result of multiple scattering. In addition, a periodic oscillation appeared to be superimposed on the intensity autocorrelation function--an indication of the presence of convective currents.¹¹

Of major importance in determining the effectiveness of a compound as a FSII is the partitioning of the compound from the fuel to the free water present in the fuel--often referred to as the "partition function;"¹² this term is confusing, however, since it may also refer to energy partitioning. Here, "partition ratio" will be used to refer to the ratio of FSII concentration in the aqueous solution to the concentration of FSII in the fuel, under equilibrium conditions, i.e., the partition ratio is a measure of the amount of FSII that will migrate to the free water and act as an antifreeze to prevent ice formation.

The first step in the procedure for measurement of the partition ratio of FSII candidate compounds is the thorough mixing of a known quantity of FSII in a fuel. Then, a carefully measured quantity of deionized water is added and thoroughly mixed by agitating numerous times over a 24-hr period. The water-bottom of the solution is removed, after settling, from a separatory



(a)



(b)

Figure 3. Plots of Water-Droplet Volume (a) and Bound-Water Content (b) as a Function of Fuel Temperature. Water-droplet volume was calculated from measured diameters; bound-water content was taken from Ref. 8.

funnel and analyzed with a refractometer for FSII concentration; this is the final concentration of FSII in the aqueous phase. The final concentration of FSII in the fuel is the initial amount added to the fuel less the quantity partitioned to the water.

The relationship between concentration and refractive index is determined with carefully measured aqueous solutions that have been mixed in the laboratory. Figures 4(a) - 4(e) show the measured values along with third-order fits. No published values exist for M-1, M-2, and M-3. For DPG, the aqueous concentrations determined from the measured refractive index agree with the manufacturer's literature¹³ within 2% for values of 20 - 50 vol%. Measured values for DiEGME differ from published values¹⁴ by as much as 20%, but it appears that the catalog values contain an offset; measured values were used in the concentration measurements since several batches yielded the same results, and the measured values represent the actual material used.

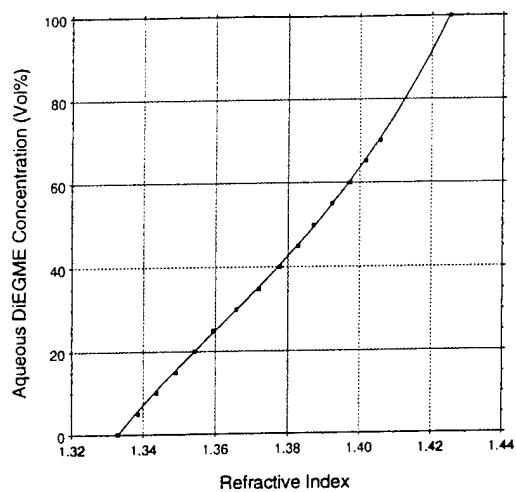
Measured partition ratios for DiEGME and several potential FSII compounds are given in Table 1. The principal merit of this table is the comparison of the relative values of partitioning. That is, the values of both M-2 and DPG are larger than that of DiEGME. These compounds, therefore, have potential as replacements for DiEGME. M-1 and M-3, however, have lower partition ratios and are, therefore, not suitable since the initial additive concentration in fuel required to provide adequate icing protection would be excessive (> 0.2 vol%).

Table 1
Measured Partition Ratios of Fuel-System Icing Inhibitors

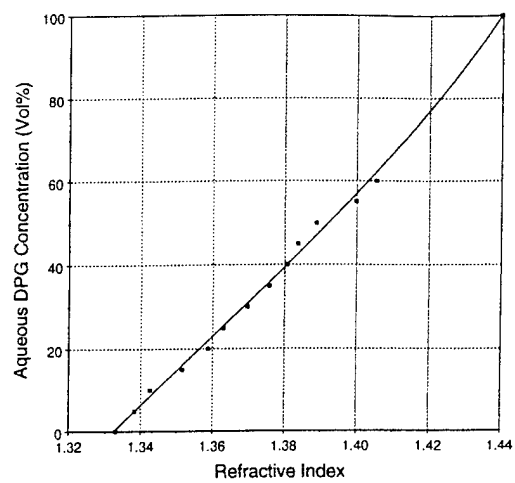
<u>Compound</u>	<u>Short Name</u>	<u>Partition Ratio</u> ($\pm 15\%$)
Diethylene Glycol Monomethyl Ether	DiEGME	480
Acetone Adduct of Glycerol	M-1	155
Formaldehyde Adduct of Glycerol	M-2	570
Acetylaldehyde Adduct of Glycerol	M-3	210
Dipropylene Glycol		> 600

A large uncertainty was encountered in the measured partitioning values of DPG because of the concentrations chosen and the limited number of measurements. Since DPG is a glycol, it is not currently being considered as a replacement compound for DiEGME; therefore, no effort was made to obtain more accurate values.

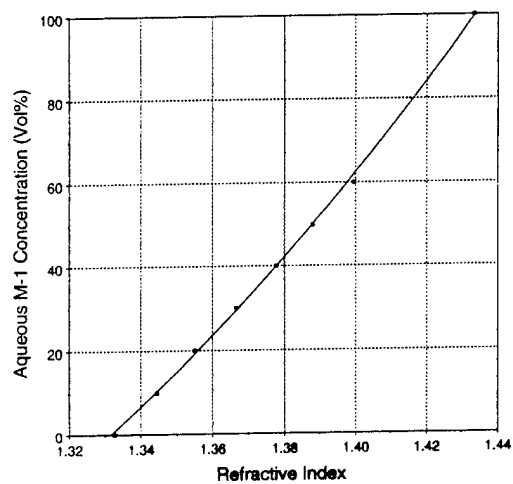
The use of differential scanning calorimetry (DSC) for measurement of the freezing point of icing inhibitors was investigated. Measurements of aqueous solutions of 15, 30, and 45 vol% of



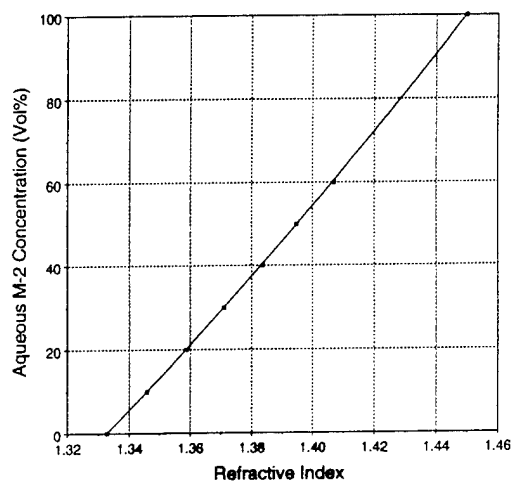
(a)



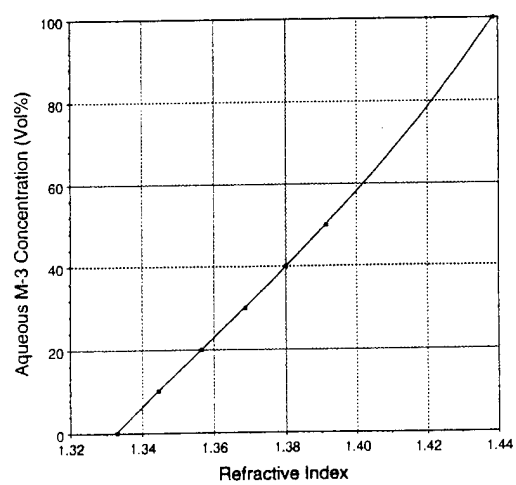
(b)



(c)



(d)



(e)

Figure 4. Concentration of Aqueous Solutions of Various FSIIIs as a Function of Measured Refractive Index. (a) DiEMGE, (b) DPG, (c) M-1, (d) M-2, (e) M-3.

DiEGME were made by Kinetic, Inc.,¹⁵ and the results were in fair agreement with the manufacturer's data when the DSC temperature change was limited to 1°C/min. A temperature rate of change of 5°C/min produced large errors for small concentrations of DiEGME. The advantage of the DSC technique over the generally accepted ASTM test for antifreeze freezing point¹⁶ is the ability of the DSC to test very small sample sizes. Most of the new icing inhibitors are difficult to synthesize and are not available in sufficiently large quantities to satisfy the ASTM testing requirements. The DSC technique is useful where sample availability is limited.

FSII Effect on Fuel Degradation. The moderate success of the M-2 icing-inhibitor additive prompted a screening test which would indicate the propensity of the additive to affect the high-temperature characteristics of the fuel. Consequently, the presence and growth of particles and the rate of surface-deposit formation were monitored at elevated temperature using the PCS/QCM apparatus described in Section 2.2.2.

A typical Jet-A fuel (POSF-2827) was prepared in two batches--one containing 0% and the other 0.15% (by volume) of glycerol formal, the commercial equivalent of M-2. Measurements were made of the change in amount of surface deposit on a gold-coated quartz crystal⁹ (via a frequency change) at an elevated temperature and in the diameter of particles existing within the liquid fuel after heating and thermal quenching to room temperature. For size measurements PCS was utilized; this technique is valid for diameters in the range ~ 50 - 1000 nm.

Figure 5 is a plot of measured particle diameter as a function of residence time at 185°C. Particles formed in the neat fuel are not a strong function of residence time for times greater than ~ 3 min and reach a maximum size at ~ 6 - 8 min. Size variation is slight for residence times > 8 min. In the presence of M-2, however, particle size appears to be a strong function of residence time up to ~ 12 - 14 min after which only slight changes are observed, the size increase apparently having reached saturation. The maximum particle size for the neat fuel is ~ 300 nm but reaches nearly 1000 nm in the presence of M-2. Although the measurements indicate that M-2 (at least the commercial equivalent) contributes to increased particle size when the fuel is thermally stressed, more study is required before definite conclusions can be drawn. It is possible that agitation during mixing of the additive/fuel combination causes introduction of air into the solution, and the increased particle size is a direct result of an increased concentration of oxygen--not the presence of M-2.

Of primary concern, however, is the surface deposition resulting from thermal stressing. As shown in Fig. 6, the deposit rate is not appreciably affected by the addition of M-2. The measurements should be repeated with greater care if the data are to be correlated quantitatively with fuel surface deposits observed in operational environments. The data from the current measurements, however, indicate that M-2 does not appreciably contribute to fuel-line fouling that results from thermal stress at temperatures up to 185°C.

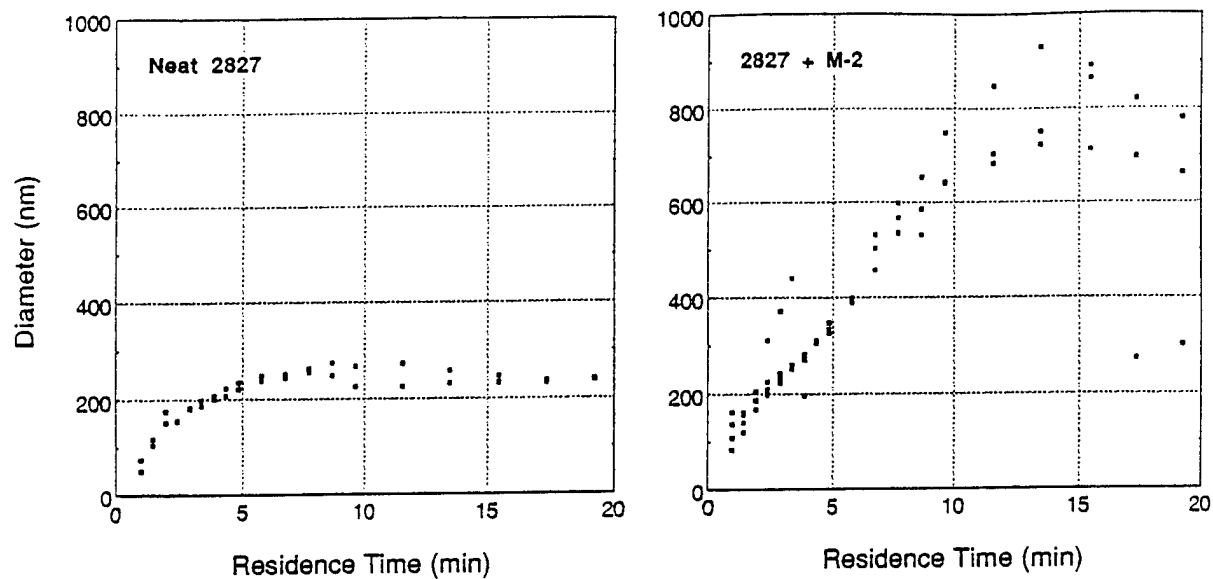


Figure 5. Plots of Particle Diameter as Function of Reactor Residence Time for POSF-2827 Fuel Without and With M-2 Icing Inhibitor After Stressing at 185°C.

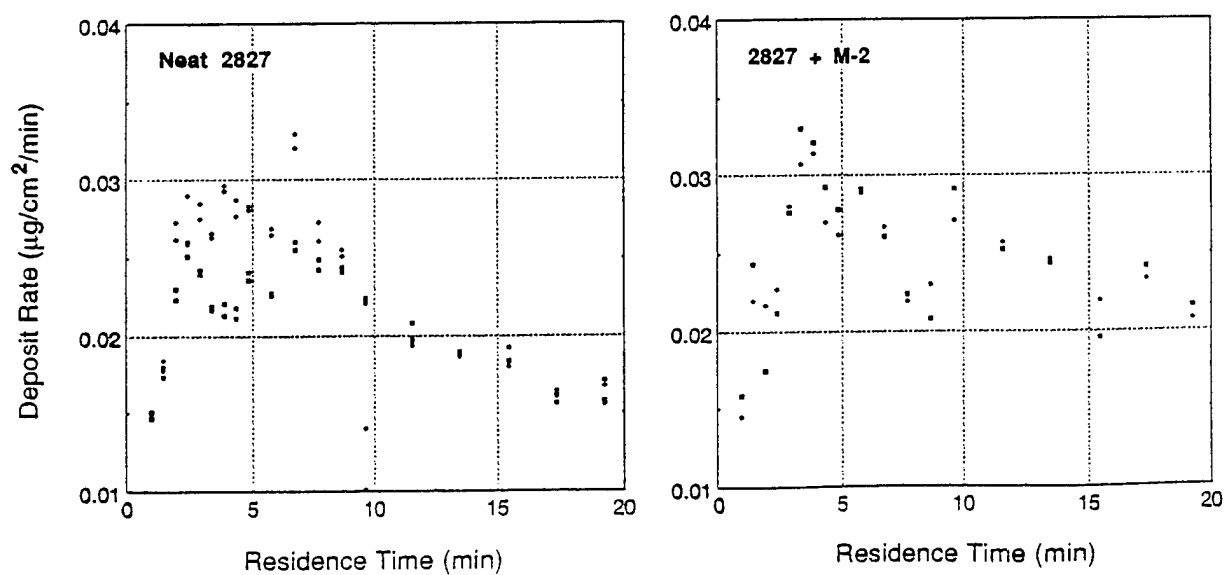


Figure 6. Plots of Surface-Deposit Rate as Function of Reactor Residence Time for POSF-2827 Fuel Without and With M-2 Icing Inhibitor After Stressing at 185°C.

4. COMPUTATIONAL FLUID DYNAMICS WITH CHEMISTRY CODE DEVELOPMENT AND APPLICATIONS

4.1 Combustion Studies

4.1.1 General Overview. Combustion research has benefited from the development of new methods in advanced-diagnostics and computational-fluid-dynamics technologies. By incorporating chemical kinetics in CFDC codes either through a set of global reactions or using detailed kinetics models, researchers are addressing complicated flow problems in combustion. In efforts to understand the physical and chemical processes taking place in the various experimental rigs at Wright Laboratory, several time-dependent CFDC codes were developed and validated. Numerical experiments were also performed using these CFDC codes for the design of more efficient test rigs. Details of the investigations performed using these codes are given in the following subsections.

4.1.2 Numerical Simulations of Gaseous Combustion.

Double-Vortex Structure of Jet Diffusion Flames. Vortex structures in flames are very different from those in cold jets under the same flow conditions. The small-scale structures in a combusting flow grow very slowly and maintain their identities or coherence over a long distance as compared to their rapid formation and decay in cold flows. In addition to these high-frequency vortices, significantly lower-frequency vortices are also observed in flames. These vortices are located outside the flame surface and, hence, are referred to as outer vortices. It is generally believed that the large-scale vortices which are located outside the flame surface are small perturbations amplified by a modified Kelvin-Helmholtz-type instability. On the other hand, the small-scale vortices that are enclosed by the flame are generated by the flow perturbations at the nozzle exit and are amplified by the Kelvin-Helmholtz-type instability of the fuel-jet shear layer. Computational experiments were performed to investigate the importance of buoyancy and shear-layer forcing in the development of the outer and inner vortices. The relative importance of these vortices in hydrogen ["Numerical Investigations of Transitional H_2/N_2 Jet Diffusion Flames" (pp. 614 - 624)] and propane ["Role of Inner and Outer Structures in a Jet Diffusion Flame" (pp. 625 - 635)] jet diffusion flames was investigated. The rotational characteristics of these vortices in a transitional-velocity propane flame were studied by injection of particles. The strong interaction between the first visible outer structure and the flame was identified from the pdf plots. The details of these studies were reported in a paper entitled, "Simulation of Vortical Structures in a Jet Diffusion Flame" (pp. 636 - 647).

Instabilities of a Jet Diffusion Flame. The transient behavior of an H_2 -air diffusion flame was studied. For the first time, the numerical simulations indicated that the mechanism generally thought to be responsible for the development of the large-scale outer vortices in a flame

should be re-examined. The outer vortices are now thought to result from the convective unstable flowfield. Recent simulations in this laboratory suggested that these vortices arise as a result of the absolute instability of the flow near the flame surface.

A steady, nonoscillating flame was initially obtained using steady-state governing equations. Starting with this solution, calculations for the transient flame-behavior were performed using a time-dependent formulation. However, during the initial 200 ms of computation, the unsteady terms in the governing equations were forced to zero. This constraint was suddenly relaxed at $t = 200$ ms, and unsteady calculations were made from that point onward. The radial location of the flame (stoichiometric location) was recorded at several heights and the data plotted as a function of time in Figs. 7 and 8. Gravitational forces equal to $1/2$ and $1/6$ that of the earth were used in the simulations of Figs. 7 and 8, respectively. No artificial perturbations were used in these calculations. It is believed that the noise in the numerical simulations is responsible for the flame oscillations. The following observations can be made from these plots: 1) After a certain time flames began to oscillate periodically at frequencies equal to 8.5 and 4.8 Hz for the $1/2g$ and $1/6g$ cases, respectively; 2) The growth rate of the noise was very small initially; however, the fluctuations grew rapidly just before approaching stable conditions (limit cycle); 3) The time required to establish a stable oscillating flame increased with a decrease in gravitational force. These are typical characteristics of an absolutely unstable flow. To confirm this, a test was made. If the flames are absolutely unstable, then a critical value for g should exist, below which oscillations at all locations should vanish. The maximum flame-surface movement of a periodically oscillating flame at different axial locations is plotted in Fig. 9 for different values of gravitational force. This figure clearly shows that the oscillations at all heights tend to converge to zero at $g \sim 0.05$, which is a critical value in this case for flame oscillation. This study was performed in collaboration with Professor Peter Monkewitz of the University of California.

Effects of Finite-Rate Chemistry and Nonunity Lewis Number on Jet Flame Structure. The temporal and spatial evolution of the outer and inner vortices change the stretch along the flame surface, which results in a wrinkled laminar flame. The local Lewis number on the fuel side of an H_2 /air diffusion flame is known to be lower than unity. When a high-Damkohler-number hydrogen flame is stretched, the flame temperature changes--not because of incomplete chemical reactions, but because of the preferential diffusion resulting from the non-unity Lewis number. The effects of Lewis number and finite-rate chemistry on the steady-state and dynamic flame structures were examined using a time-dependent, axisymmetric mathematical model having a detailed-chemical-kinetics mechanism for H_2 -air combustion. Results obtained with different mathematical models ["Effect of Nonunity Lewis Number and Finite-Rate Chemistry on the Dynamics of a Hydrogen-Air Jet Diffusion Flame" (pp. 648 - 660)] indicate that the size and shape of the outer structures are unaffected by the unity-Lewis-number and fast-chemistry assumptions

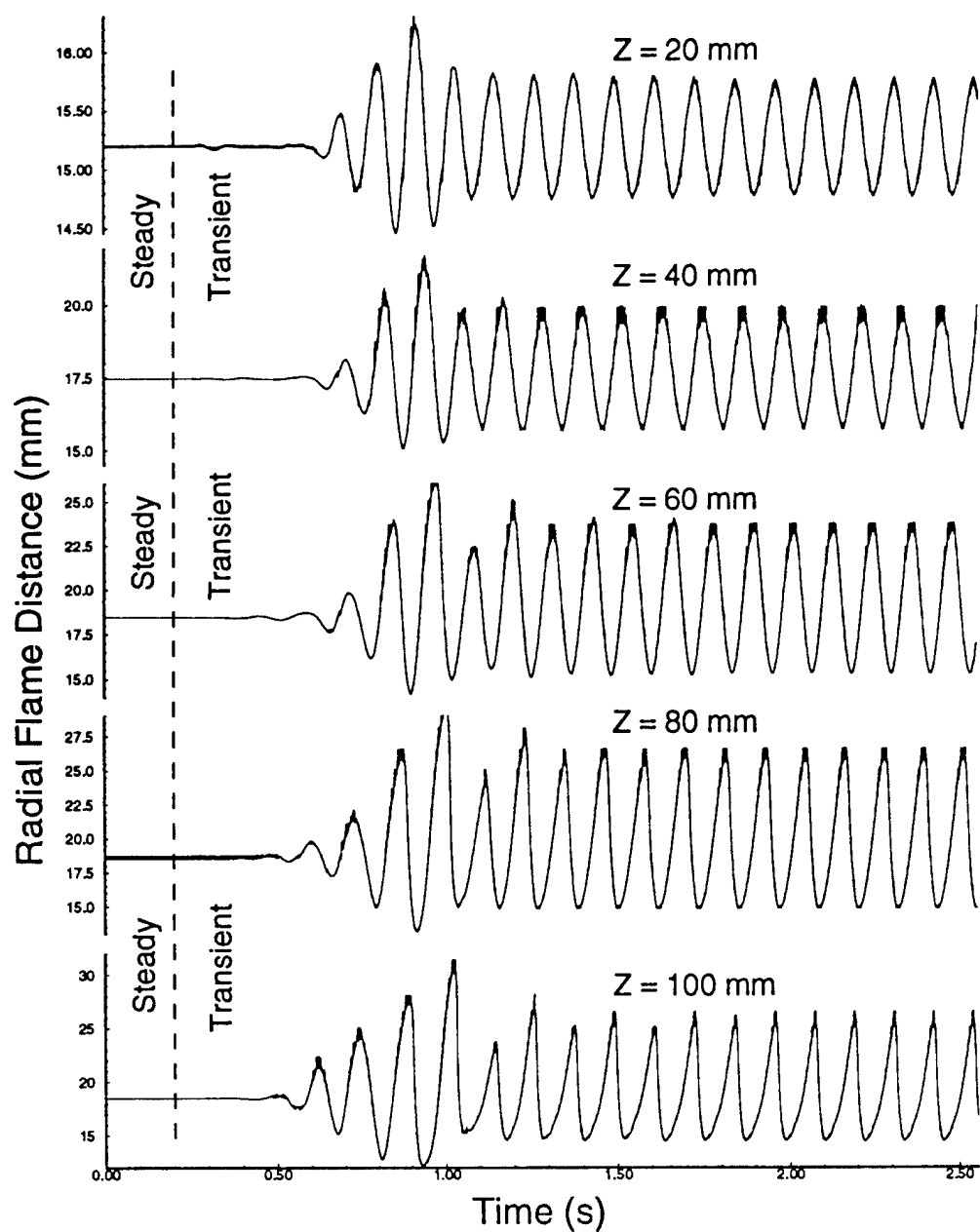


Figure 7. Development of Large-Scale Instabilities in an H_2 -Air Jet Diffusion Flame When the Gravitational Force is $1/2g$.

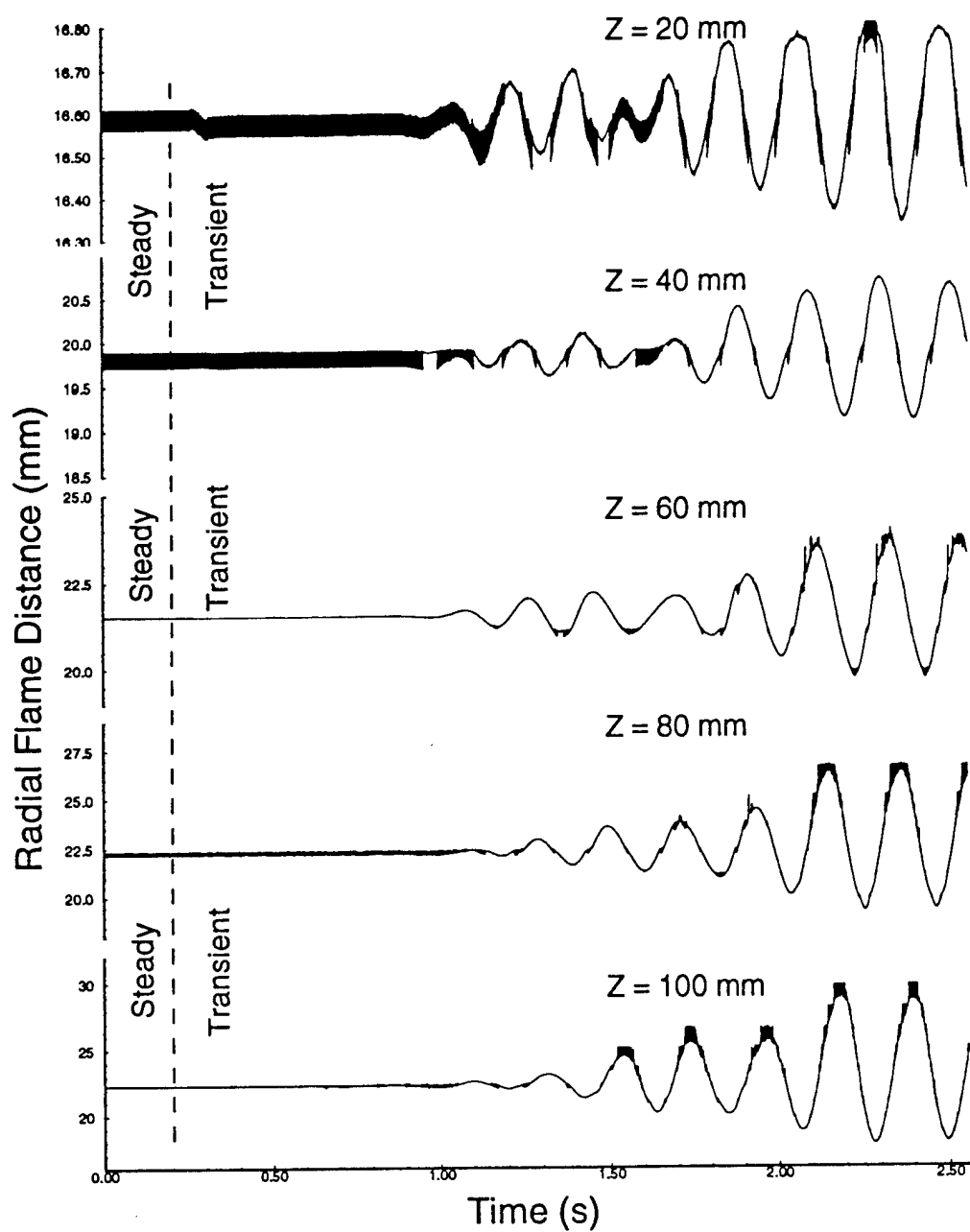


Figure 8. Development of Large-Scale Instabilities in an H_2 -Air Jet Diffusion Flame When the Gravitational Force is $1/6g$.

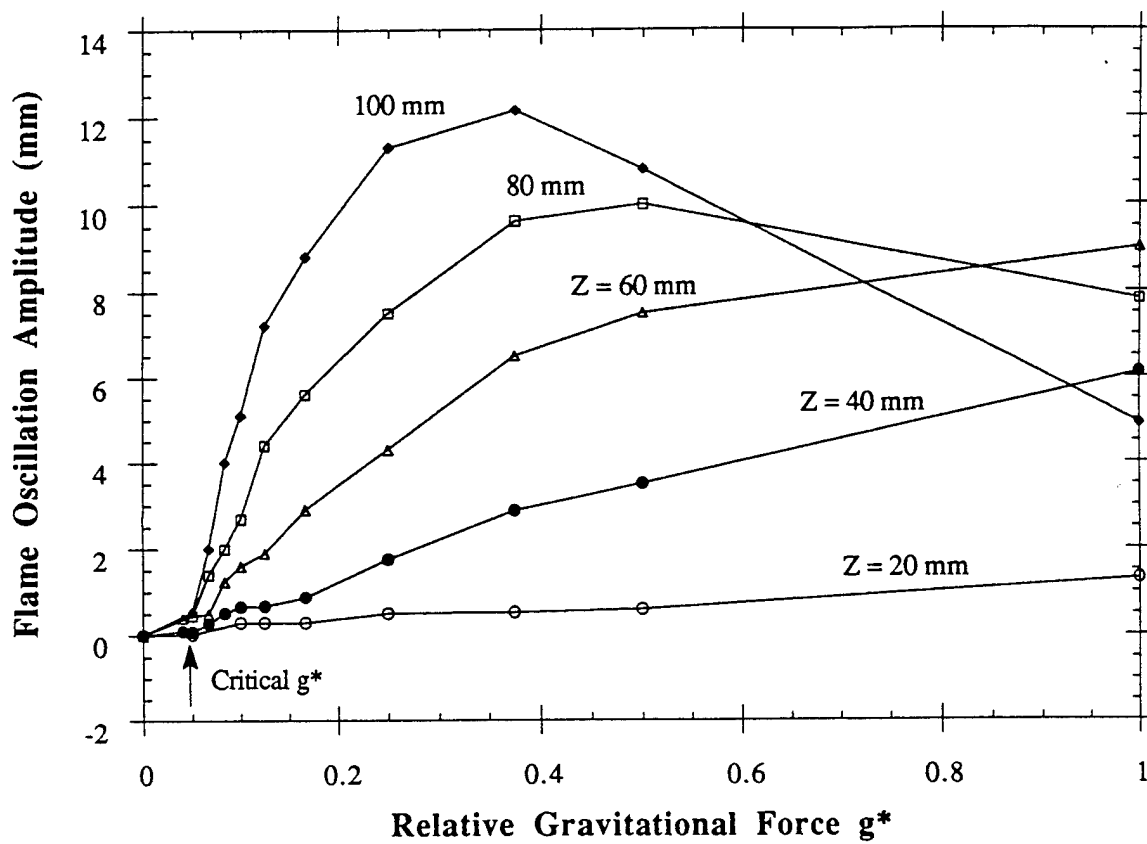


Figure 9. Magnitude of Flame-Surface Oscillation at Different Heights as a Function of Relative Gravitational Force.

Experiments revealed that the flame temperature tends to increase when the flame is bulging and to decrease when it is squeezing. The lower Lewis number inside the flame--not the increased Damkohler number--was found to be responsible for the observed fluctuations in the flame temperature. Preferential mass diffusion of different species causes an increase in water in the bulging regions of the flame and an increase in radicals in the squeezing regions.

The effects of nonunity Lewis number were further studied by subjecting a low-speed hydrogen flame to stretch using two vortices--one located on the fuel side of the flame and the other on the air side ["On the Structure of Stretched/Compressed Laminar Flamelet--Influence of Preferential Diffusion" (pp. 661 - 670)]. Both vortices create positive (stretch) and negative (compression) flame-stretch factors when interacting with the flame. The temperature of the positively stretched flamelet was found to decrease when the vortex is located on the air side and to increase when it is on the fuel side. Similarly, compression of the flamelet resulting from the air-side vortex increases the flame temperature, whereas that resulting from the fuel-side vortex decreases the flame temperature. Among the 11 species considered in this model, production of NO in the flame zone appeared to be the most sensitive to flame stretching or compression. Concentration of NO was found to be maximum in the compressed flamelet formed during the outside vortex-flame interaction. Finally, a comparison of the mean NO-concentration profiles obtained by averaging over several cycles of outside vortex-flame interactions and the time-averaged measurements yielded favorable agreement.

The burning characteristics of a premixed, H₂/air Bunsen-type flame depend on the local Lewis numbers. The computed temperature, species concentration, and velocity fields were investigated under fuel-lean, stoichiometric, and fuel-rich conditions ["Numerical Studies on the Structure of Two-Dimensional H₂/Air Premixed Jet Flame" (pp. 671 - 691)]. The calculations showed that under fuel-lean conditions, the flame exhibits the "tip-opening" phenomenon, while under fuel-rich conditions, the tip of the flame burns intensely. To further investigate the impact of local Lewis number on the premixed-flame structure, numerical experiments were performed by modifying the local Lewis numbers of the individual species. Results for the fuel-lean condition confirmed that the local Lewis number is responsible for the tip-opening phenomenon. Indeed, when the local Lewis number is set equal to 2, the burning pattern of the fuel-lean premixed flame resembles that of a fuel-rich flame with a closed tip. The spatial distributions of NO in the fuel-lean, stoichiometric, and fuel-rich flames were also examined. Under fuel-lean and stoichiometric conditions, the NO was formed along the high-temperature cone of the flame, as expected. In the fuel-rich case, a dual flame structure was observed. The NO production occurred primarily in the secondary "diffusion" flame which was established at the interface of the excess fuel and ambient oxygen. Buoyancy-induced toroidal vortices were found to form in the vertically mounted

premixed flames. However, the dynamic characteristics of a premixed flame, in contrast to those of a jet diffusion flame, were observed to be dependent on the inlet velocity profile of the fuel jet.

Vortex-Flame Interactions. A new theoretical study was initiated to understand the interaction between a vortex and a diffusion flame zone. Interactions between large vortices and the flame zone were studied using a unique numerical approach. A highly stretched methane diffusion flame that was stabilized with the help of a thick-lipped nozzle was numerically generated using a time-dependent, third-order-accurate mathematical model. Pockets of fuel were ejected from different locations inside the flame surface toward the flame zone at different velocities. A pair of counter-rotating toroidal vortex rings associated with the ejected fuel mass penetrated into the high-temperature, highly viscous layer of the flame zone and created a flow configuration similar to that of a strained counterflow diffusion flame. The flame bulge was studied with reference to convection times of the vortex pair and fuel diffusion times. The methodology and results are discussed in a paper entitled, "Numerical Experiments on the Vortex-Flame Interactions in a Jet Diffusion Flame" (pp. 692 - 699).

The interaction process which led to local quenching was studied experimentally using phase-locked measurements and numerically using a time-dependent mathematical model. The preliminary results were presented in a paper entitled, "Vortex Dynamics in a Driven Jet Diffusion Flame" (pp. 700 - 705).

Numerical Studies on Swirl Combustor. The CFDC model developed for simulating reactive flow in practical combustors was used to understand the stability mechanism for flames in a model combustor. This code solves time-dependent Navier-Stokes equations along with swirl, turbulent energy, species conservation, and enthalpy equations that are written in the z-r cylindrical coordinate system. A one-step global-chemistry model was used to represent the combustion processes of hydrocarbon fuels. Predictions were compared with experimental results in a paper entitled, "Study of Flame Stability in a Step Swirl Combustor" (pp. 706 - 713).

Numerical Investigations of Transitional H_2/N_2 Jet Diffusion Flames

V. R. Katta* and L. P. Goss†

Systems Research Laboratories, Inc., Dayton, Ohio 45440

and

W. M. Roquemore‡

Wright Laboratory, Wright-Patterson Air Force Base, Ohio 45433

A numerical method for accurate simulation of the time and spatial characteristics of the inner and outer vortex structures in transitional H_2/N_2 jet diffusion flames is presented. The direct numerical simulation, incorporating buoyancy, a simple one-step chemistry model, and transport coefficients that depend on temperature and species concentration, is described in detail. The species and energy equations are simplified by introducing two conserved scalars β_1 and β_2 and by assuming that the Lewis number of the flow is equal to unity. An implicit, third-order-accurate, upwind numerical scheme having very low numerical diffusion is used to simulate the inner small-scale structures and the outer large-scale structures simultaneously. Although the outer structures develop without introducing perturbations, the inner structures are manifested from artificially introduced computer-generated random noise. The buoyancy-driven outer instabilities and the shear-driven inner ones are found to roll up into vortices at frequencies of ~ 14 and 350 Hz, respectively. Unlike the structures in cold jets, the shear-driven vortices in flames propagate over a long distance without losing their identity or spreading radially. These vortices undergo an unusual axial-growth and merging process that is shown to result from their interactions with the outer vortices. The complex spectral characteristics of the flame are interpreted in terms of the dynamics of this interaction process. The inner vortices appear to have very little impact on the flame since the flame surface is located well outside the jet shear layer.

Introduction

THE structural changes that occur in jet diffusion flames during the laminar-to-turbulent transition have been the subject of several studies.¹⁻⁷ A typical axisymmetric, transitional jet diffusion flame is illustrated in Fig. 1. The fuel jet emerges from a contoured nozzle having a flat velocity profile at the exit and is surrounded by a low-speed coflowing airstream. Large coherent vortices are observed outside the flame surface, and smaller coherent ones appear inside the flame. The inner vortices develop from a Kelvin-Helmholtz type instability that is amplified by the jet shear layer, similar to the development of the vortex structures in cold jets. However, in cold jets the structures remain coherent for a few jet diameters downstream and then coalesce, which results in the radial growth of the shear layer and the transition to a three-dimensional turbulent flow. This transition sequence is also observed in jet diffusion flames, but the vortices can remain coherent for more than 20 jet diameters downstream before coalescing.⁵ During the time that the vortices are coherent, the shear layer does not grow radially. As the vortices coalesce, the shear layer begins to spread radially, the coherence of the inner structures is lost, and a three-dimensional turbulent flow is established. However, the turbulent flame cannot develop until the turbulent fluid interacts with the flame surface. The height in the flame where this occurs is called the break point. At all heights above the break point, the flame surface appears to be highly wrinkled, and the flame is said to be turbulent. The break-point distance decreases with increasing fuel

flow rate until either the flame lifts from the nozzle or the entire flame, with the exception of a short region near the nozzle, becomes turbulent. The transition from laminar to turbulent flow occurs at higher velocities in jet flames than in cold jets. A similar transition of the inner structures occurs in jet flames established with fuel tubes; however, the transition process is dependent on the pipe-flow Reynolds number, and the coherent structures are evident only over short distances, as is the case in cold jets.^{4,7}

The outer vortex structures shown in Fig. 1 are the dominant characteristic of laminar and transitional jet diffusion flames. Only in the last few years^{5,12} has it been realized that these structures are responsible for the much-studied phenomenon referred to by Chamberlin and Rose as "flame flicker."⁸ At transitional fuel-jet

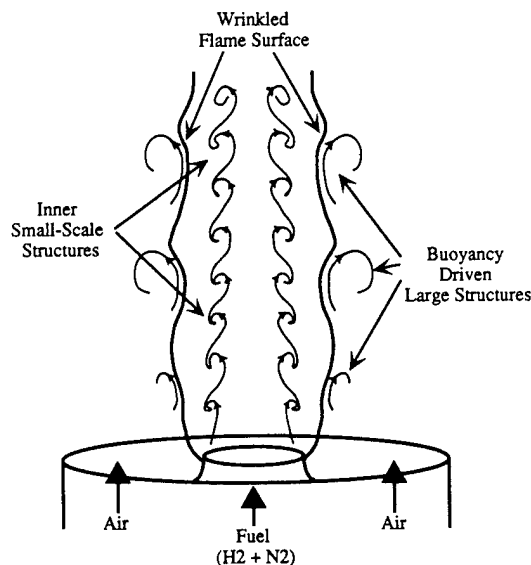


Fig. 1 Structure of hydrogen jet diffusion flame near transitional fuel-jet velocity and with low coannulus airflow.

Presented as Paper 92-0335 at the AIAA 30th Aerospace Sciences Meeting, Reno, NV, Jan. 6-9, 1992; received April 11, 1992; revision received May 11, 1993; accepted for publication June 9, 1993. Copyright © 1992 by the American Institute of Aeronautics and Astronautics, Inc. All rights reserved.

*Senior Engineer, Research and Engineering Center, 2800 Indiana Ripple Road, Member AIAA.

†Director of Research, Optical Diagnostics, Research and Engineering Center, 2800 Indiana Ripple Road.

‡Senior Scientist, Fuels and Lubrication Division, Aero Propulsion and Power Directorate, Member AIAA.

velocities, the slowly moving outer toroidal-vortex structures interact strongly with the flame, creating an outward bulge in the flame surface. The flickering appearance of the flame is the result of the upward convective motion of the flame bulge. In the early 1960s, Kimura⁹ used linear instability theory to estimate the flame-flicker frequency. Although he obtained a reasonable result, his theory did not explain that this frequency is nearly independent of fuel type, nozzle size, and Reynolds number.^{10,11}

Buckmaster and Peters¹² were the first to recognize that buoyancy is responsible for the flow-frequency instability associated with flame flicker. They argued that the natural convection of the flame and the forced convection of the jet are decoupled because the stoichiometric flame surface is located outside the shear layer of the jet, and thus the buoyancy-induced instability is nearly independent of jet characteristics such as fuel exit velocity, nozzle diameter, and fuel type. They performed a linear instability analysis on a two-dimensional infinite candle flame but, unlike Kimura, included buoyancy in the calculation. Their calculation resulted in a flicker frequency that was in good agreement with experiments. An unsatisfactory aspect of their inviscid analysis, however, was that their theory resulted in a flicker frequency that was dependent on streamwise distance to the one-fourth power. Even though this was a weak dependence, it caused a problem in choosing a distance for estimating the flicker frequency that was consistent with the inviscid and large-Reynolds-number assumptions used in their analysis and yet was sufficiently close to the nozzle where the instability was thought to originate. They chose a distance of 3 cm, the approximate location where the outer structures begin to form. Mahalingam et al.¹³ questioned the dependence of frequency on streamwise distance. They argued that the instability is present even at the exit of the nozzle where, according to the inviscid analysis, the frequency should be zero. Experimental evidence also indicates that the frequency of the outer instability does not change with streamwise distance within the first 10 nozzle diameters.¹⁴ Buckmaster and Peters recognized the uncertainties associated with the inviscid and parallel-flow assumptions used in their analysis and suggested the formidable task of conducting a detailed viscous analysis of the complete flowfield to examine the points made in their paper.

Recently, direct numerical simulations of buoyant jet flames have provided support and given additional insight into the findings of Buckmaster and Peters and others. By adopting a flame-sheet model, Davis et al.¹⁵ successfully simulated the dynamic structure of a 12-cm/s buoyant propane jet diffusion flame established with a 2.2-cm-diam tube. They showed that the flame is stationary and has no outside vortices when $g = 0$. In the presence of buoyancy, the outer vortex structures develop, and their upward convective motion is shown to be responsible for the 13-Hz flicker frequency associated with the flame bulge. Thus, they confirmed the basic premise of Buckmaster and Peters¹² that buoyancy is the source of flame flicker. Ellzey et al.¹⁶ successfully simulated a transitional hydrogen-nitrogen jet diffusion flame established by a 5-mm contoured nozzle having an exit velocity of 10 m/s. They also showed that the convective motion of the outside vortex structures is responsible for flame flicker and that buoyancy is required to produce these structures. The flicker frequencies computed by Davis et al.¹⁵ and Ellzey et al.¹⁶ were in the range of 11–15 Hz, in agreement with the experimental results. These combined results show that the outer vortex motion and, thus, the flicker frequency, are relatively insensitive to fuel type, Reynolds number, and jet diameter, as demonstrated by experiments.^{9–11} This also supports the argument made by Buckmaster and Peters that the buoyancy-induced instability is decoupled from the jet characteristics. However, this point must be examined in flames having inner structures.

The velocity of the flame studied by Ellzey et al. was sufficiently high that one might expect organized inner vortex structures. Although such inner structures did initially form in their calculation, they dissipated rather rapidly due supposedly to volumetric expansion and increased viscosity. Yamashita et al.¹⁷ conducted a numerical study of the laminar-to-turbulent transition in a two-dimensional planar jet diffusion flame in a coflowing air-

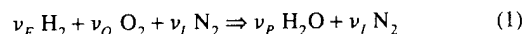
stream. Their results clearly show that the inner structures can interact with the flame and can even produce a low-frequency instability outside the flame surface. However, the impact of this interaction on the outside vortex structures was not studied since buoyancy was not included in their calculations. Recently, Katta and Roquemore performed a numerical study of a transitional propane jet diffusion flame in which the dynamic characteristics of both the inner and the outer vortex structures were captured.¹⁸ Their results suggest that buoyancy—and not viscosity (as suggested by several authors^{1,2,5})—is mainly responsible for the long coherence lengths of the inner structures in transitional jet flames. They also showed that small-scale wrinkles occur on the flame surface as a result of the convective motion of the inner vortices but that their overall effect on combustion is small.

In the present paper, the interactions of the outer and inner vortices in a transitional H_2/N_2 jet diffusion flame similar to that shown in Fig. 1 are examined. A numerical method for accurately simulating the time and spatial characteristics of the inner and outer vortex structures is described in detail. This method incorporates buoyancy, a simple one-step chemistry model, and transport coefficients that depend on temperature and species concentration. Predictions of the structural features, the mean and fluctuating velocity profiles, and the time-evolving temperature at a fixed axial location compare favorably with experimental results for an H_2/N_2 flame having a laminar potential core. The predicted structural features of a transitional H_2/N_2 flame having coherent inner structures in the potential core also compare favorably with experimental results. Numerical experiments are used to investigate the source of the inner structures, their growth process, their spectral characteristics, and the influence of the outer structures on these properties.

Theory

Mathematical Model

A simple chemistry model is used in which fuel (H_2), oxidizer (O_2), products (H_2O), and inert gas (N_2) are assumed to undergo a single global reaction step given as



The subscripts F , O , I , and P represent fuel, oxidizer, inert gas, and products, respectively, and ν is the corresponding stoichiometric coefficient. The problem is further simplified by adopting a Shvab-Zel'dovich formulation for the species and energy equations that are written in terms of two scalar variables β_1 and β_2 , defined as

$$\beta_1 = \frac{\alpha Y_O + Y_F^i - Y_F}{\alpha Y_O^i + Y_F^i} \quad (2)$$

and

$$\beta_2 = \frac{h - h_O^i + (Y_F/\alpha) Q}{(Y_F^i/\alpha) Q + h_F^i - h_O^i} \quad (3)$$

where α is the fuel-oxidizer ratio ($\nu_F M_F/\nu_O M_O$); Y_m and h_m are the mass fraction and enthalpy of the m th species, respectively; h is the mixture enthalpy; Q is the heat release per unit mass of oxygen consumed; M is the molecular weight; and the superscript i represents the initial values. It is assumed that 1) the reaction represented by Eq. (1) occurs at an infinitely fast rate, resulting in an infinitely thin reaction zone or flame sheet, 2) the Lewis number (Le = rate of energy transport/rate of mass transport) is equal to unity, and 3) the Soret and Dufour effects can be neglected. Use of $Le = 1$ with respect to hydrogen flames may not represent the details of the flame structure accurately; however, it is believed that the dynamics of the flames considered in this study are not affected significantly by this assumption. A more recent analysis has also shown that relaxation of this constraint has only negligible

impact on the flame dynamics but significantly increases the computational time.¹⁹

The time-dependent governing equations written in the cylindrical (z, r) coordinate system for an axisymmetric reacting flow are

$$\frac{\partial p}{\partial t} + \frac{\partial \rho u}{\partial z} + \frac{1}{r} \frac{\partial (r p v)}{\partial r} = 0 \quad (4)$$

and

$$\begin{aligned} \frac{\partial (\rho \Phi)}{\partial t} + \frac{\partial (\rho u \Phi)}{\partial z} + \frac{\partial (\rho v \Phi)}{\partial r} &= \frac{\partial}{\partial z} \left(\Gamma^\Phi \frac{\partial \Phi}{\partial z} \right) \\ &+ \frac{\partial}{\partial r} \left(\Gamma^\Phi \frac{\partial \Phi}{\partial r} \right) - \frac{\rho v \Phi}{r} + \frac{\Gamma^\Phi}{r} \frac{\partial \Phi}{\partial r} + S^\Phi \end{aligned} \quad (5)$$

where ρ represents density; u and v are the axial and radial components of the velocity vector, respectively; and p is the pressure. The general form of Eq. (5) represents the momentum, species, or energy-conservation equation, depending on the variable used in place of Φ . Table 1 gives the transport coefficients Γ^Φ and the source terms S^Φ that appear in the governing equations. Here μ is the viscosity of the mixture; D is the local binary diffusion coefficient between any two species; ρ_0 is the density of air; and g is the gravitational acceleration. The set of equations given by Eqs. (4) and (5) can be completed using the state equation

$$p = \rho T R_0 \left(\frac{Y_F}{M_F} + \frac{Y_O}{M_O} + \frac{Y_P}{M_P} + \frac{Y_I}{M_I} \right) \quad (6)$$

where R_0 is the universal gas constant; and T is the temperature.

Thermodynamic and Transport Properties

The enthalpy of each species is calculated using the polynomial curve fits compiled by Burcat.²⁰ The mixture enthalpy h is estimated as

$$h = (Y_F h_F + Y_O h_O + Y_P h_P + Y_I h_I) \quad (7)$$

The temperature- and species-dependent transport properties are used in this analysis. First, the viscosity of the individual species is estimated based on the Chapman-Enskog collision theory and then that of the mixture is determined using the Wilke formula.²¹ Although four species are involved in the problem, the assumption of infinitely fast chemical reaction will not allow the fuel and oxidizer to be present simultaneously. This means that either Y_F or Y_O should be zero at any time and location and that, at the flame sheet, both vanish. The flame surface can be identified when

$$\beta_1 \equiv \beta_1^* = \frac{Y_F^i}{\alpha Y_O^i + Y_F^i} \quad (8)$$

Table 1 Coefficients and source terms appearing in governing equations

Φ	Γ^Φ	S^Φ
u	μ	$-\frac{\partial p}{\partial z} + (\rho_0 - \rho)g + \frac{\partial}{\partial z} \left(\mu \frac{\partial u}{\partial z} \right) + \frac{\partial}{\partial r} \left(\mu \frac{\partial v}{\partial z} \right) + \frac{\mu}{r} \frac{\partial v}{\partial z}$ $-\frac{2}{3} \left[\frac{\partial}{\partial z} \left(\mu \frac{\partial u}{\partial z} \right) + \frac{\partial}{\partial z} \left(\mu \frac{\partial v}{\partial r} \right) + \frac{\partial}{\partial r} \left(\mu \frac{\partial v}{\partial z} \right) \right]$
v	μ	$-\frac{\partial p}{\partial r} + \frac{\partial}{\partial z} \left(\mu \frac{\partial u}{\partial r} \right) + \frac{\partial}{\partial r} \left(\mu \frac{\partial v}{\partial r} \right) + \frac{\mu}{r} \frac{\partial v}{\partial r} - 2\mu \frac{v}{r^2}$ $-\frac{2}{3} \left[\frac{\partial}{\partial r} \left(\mu \frac{\partial u}{\partial z} \right) + \frac{\partial}{\partial r} \left(\mu \frac{\partial v}{\partial r} \right) + \frac{\partial}{\partial r} \left(\mu \frac{\partial v}{\partial z} \right) \right]$
β_1	ρD	0
β_2	ρD	0

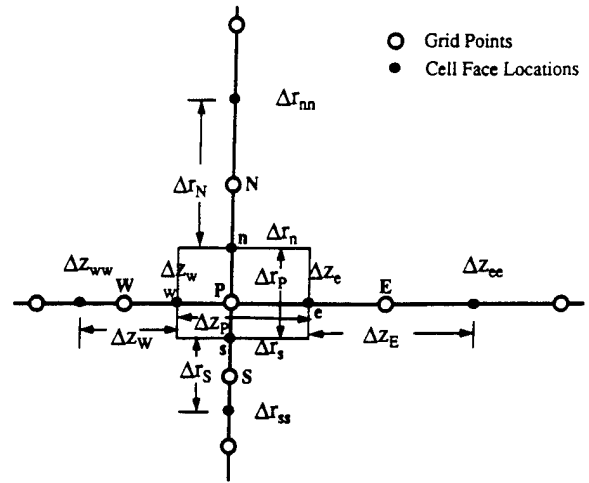


Fig. 2 Grid spacings and notations used in constructing finite difference scheme.

The binary diffusion coefficient between any two species is assumed to be identically equal to that of the fuel and nitrogen on the fuel side of the flame and is set identical to that of the oxidizer and nitrogen on the oxidizer side of the flame. The Chapman-Enskog theory and the Lennard-Jones potentials²² have been used to estimate the previous two binary diffusion coefficients. This approach allows the fuel (H_2) and the oxidizer (O_2) to diffuse at different rates.

Numerical Scheme

While studying the cold jet shear layers using the explicit quadratic upstream interpolation for convective kinematics with estimated streaming terms (QUICKEST) scheme,²³ Davis and Moore²⁴ found that the low numerical diffusion associated with a finite difference scheme is very important in capturing the small-scale structures. Using the same scheme, Davis et al.¹⁵ were also successful in simulating the large-scale buoyancy-driven structures in a jet diffusion flame. The flame investigated in the present study exhibits not only the large-scale buoyancy-driven structures outside the flame but also the shear buoyancy structures inside the flame that are about the same size as the momentum thickness of the jet. An implicit approach for the QUICKEST scheme has been developed and used successfully to provide a more efficient treatment of the different time scales of the large- and small-scale structures and the source terms that arise from chemical reactions.

A control volume within a staggered grid system and the various distances associated with it are shown in Fig. 2. By adopting the QUICKEST approach for this control volume and calculating the fluxes at the cell faces based on the unknown variable Φ at the $N+1$ th time step, the finite difference form of the scalar equation [Eq. (5)] can be written as follows:

$$\begin{aligned} A_P \Phi_P^{N+1} + A_{EE} \Phi_{EE}^{N+1} + A_E \Phi_E^{N+1} + A_W \Phi_W^{N+1} + A_{WW} \Phi_{WW}^{N+1} \\ + A_{NN} \Phi_{NN}^{N+1} + A_N \Phi_N^{N+1} + A_S \Phi_S^{N+1} + A_{SS} \Phi_{SS}^{N+1} \\ = \Delta t S_P^\Phi + \rho_P \Phi_P^N \end{aligned} \quad (9)$$

where the superscripts N and $N+1$ represent the known variables at the N th time step and the unknown variables at the $N+1$ th time step, respectively. The subscripts indicate the location of the variables in Fig. 2. The coefficients in the previous equation are

$$A_{NN} = \frac{\Delta t}{\Delta r_p} [-(\rho_n v_n) \Delta r_n^2 (1/6 - \gamma_n - 1/6 C_n^2) c_1]$$

$$A_N = \frac{\Delta t}{\Delta r_p} \left\{ (\rho_n v_n) \left[\frac{1}{2} - \frac{C_n}{2} - \Delta r_n^2 (1/6 - \gamma_n - 1/6 C_n^2) c_2 \right] \right\}$$

$$\begin{aligned}
& + (\rho_s v_s) \Delta r_s^2 \left(\frac{1}{6} - \gamma_s - \frac{1}{6} C_s^2 \right) d_1 - \frac{\Gamma_n}{r_n} \left\} - \frac{\Delta t}{r_p} \frac{\Gamma_p}{2 \Delta r_n} \right. \\
A_s = & \frac{\Delta t}{\Delta r_p} \left\{ -(\rho_n v_n) \Delta r_n^2 \left(\frac{1}{6} - \gamma_n - \frac{1}{6} C_n^2 \right) c_4 \right. \\
& - (\rho_s v_s) \left[\frac{1}{2} + \frac{C_s}{2} - \Delta r_s^2 \left(\frac{1}{6} - \gamma_s - \frac{1}{6} C_s^2 \right) d_3 \right] - \frac{\Gamma_s}{\Delta r_s} \left\} \right. \\
& + \frac{\Delta t}{r_p} \frac{\Gamma_p}{2 \Delta r_s} \\
A_{ss} = & \frac{\Delta t}{\Delta r_p} [(\rho_s v_s) \Delta r_s^2 \left(\frac{1}{6} - \gamma_s - \frac{1}{6} C_s^2 \right) d_4]
\end{aligned}$$

and

$$A_p = \rho_p^N - \{A_{NN} + A_N + A_s + A_{ss} + A_{EE} + A_E + A_w + A_{ww}\}$$

The expressions for A_{EE} , A_E , A_{ww} and A_{ww} can be written similarly. The local Courant numbers (C_n , C_s , etc.) and the physical diffusion parameters (γ_n , γ_s , etc.) appearing in these coefficients are given by

$$\begin{aligned}
C_n = v_n \frac{\Delta t}{\Delta r_n}, \quad \gamma_n = \Gamma_n \frac{\Delta t}{\Delta r_n^2}, \quad C_s = v_s \frac{\Delta t}{\Delta r_s}, \\
\gamma_s = \Gamma_s \frac{\Delta t}{\Delta r_s^2}, \quad \text{etc.}
\end{aligned}$$

The previous coefficients become functions of the velocity direction as a result of the upwind quadratic differencing that is inherent in the constants a , b , c , and d as follows:

$$\begin{aligned}
v_n \geq 0 \quad & \begin{cases} c_1 = 0 \\ c_2 = \left(\frac{1}{\Delta r_p} \frac{1}{\Delta r_n} \right) \\ c_3 = -\left(\frac{1}{\Delta r_p} \frac{1}{\Delta r_n} + \frac{1}{\Delta r_p} \frac{1}{\Delta r_s} \right) \\ c_4 = \left(\frac{1}{\Delta r_p} \frac{1}{\Delta r_s} \right) \end{cases} \\
v_n < 0 \quad & \begin{cases} c_1 = \left(\frac{1}{\Delta r_n} \frac{1}{\Delta r_n} \right) \\ c_2 = -\left(\frac{1}{\Delta r_n} \frac{1}{\Delta r_n} + \frac{1}{\Delta r_n} \frac{1}{\Delta r_s} \right) \\ c_3 = \left(\frac{1}{\Delta r_n} \frac{1}{\Delta r_s} \right) \\ c_4 = 0 \end{cases}
\end{aligned}$$

$$\begin{aligned}
v_s \geq 0 \quad & \begin{cases} d_1 = 0 \\ d_2 = \left(\frac{1}{\Delta r_s} \frac{1}{\Delta r_s} \right) \\ d_3 = -\left(\frac{1}{\Delta r_s} \frac{1}{\Delta r_s} + \frac{1}{\Delta r_s} \frac{1}{\Delta r_{ss}} \right) \\ d_4 = \left(\frac{1}{\Delta r_s} \frac{1}{\Delta r_{ss}} \right) \end{cases}
\end{aligned}$$

$$\begin{aligned}
v_s < 0 \quad & \begin{cases} d_1 = \left(\frac{1}{\Delta r_p} \frac{1}{\Delta r_n} \right) \\ d_2 = -\left(\frac{1}{\Delta r_p} \frac{1}{\Delta r_n} + \frac{1}{\Delta r_p} \frac{1}{\Delta r_s} \right) \\ d_3 = \left(\frac{1}{\Delta r_p} \frac{1}{\Delta r_s} \right) \\ d_4 = 0 \end{cases}
\end{aligned}$$

Expressions can be written in a similar fashion for the other constants.

The previous finite difference scheme [Eq. (9)] is third order accurate both spatially and temporally. Although Eq. (9) is written in the general form of the scalar equation [Eq. (5)], care must be exercised when generating the finite-difference schemes for the u and v momentum equations because of the staggered grid adopted. The four equations represented by Eq. (9) are solved individually using an iterative alternative direction implicit (ADI) technique that involves obtaining solutions for pentadiagonal matrices in the z and r directions iteratively until the residual drops below a specified value. Although these equations are solved independently, a consistent sequence should be followed for simulating time-dependent combustions flows. In the present simulation the equations for β_1 and β_2 are solved first, and then the temperature and density at the $N + 1$ th time step are obtained. Based on the previous density, the u and v momentum equations are solved next.

Pressure Solver

Solution at the $N + 1$ th time step is completed by solving the mass continuity equation [Eq. (4)] for pressure. The slowly moving buoyant structures are extremely sensitive to the accuracy of the pressure field. The SIMPLE method²⁵ for solving the pressure field was used in earlier attempts to simulate the buoyancy-driven structures for an H_2/N_2 diffusion flame; these attempts failed, although success was achieved in the case of a propane flame. This iterative pressure solver could not determine the pressure field around the large-scale buoyant structures with sufficient accuracy because of the additional pressure drop that occurred due to the natural buoyant acceleration of the hydrogen. The result was an oscillating flame that did not have the well-defined structures observed in the experiments. The projection method suggested by Chorin²⁶ was used to circumvent this difficulty. Earlier Peyret and Taylor²⁷ used this method in simulating the unsteady jet flowing into a stratified fluid, and Davis et al.¹⁵ employed it in simulating buoyant propane flames.

The projection method along with the direct solver used in the present study are described later. At every time step, the u and v momentum equations are solved for u^* and v^* , with the assumption that the pressure is uniform everywhere in the flowfield. The actual velocities u^{N+1} and v^{N+1} at this time step can be written as

$$u^{N+1} = u^* + u' \quad (10)$$

$$v^{N+1} = v^* + v' \quad (11)$$

where u' and v' are the errors in the velocity field due to the constant pressure assumption. By substituting Eqs. (10) and (11) into the momentum equations [Eq. (9)], the following relations between the error velocities and the pressure gradients can be obtained:

$$\rho_e^{N+1} u_e' = -\Delta t \left(\frac{p_E^{N+1} - p_P^{N+1}}{\Delta z_p^u} \right) \quad (12)$$

$$\rho_n^{N+1} v_n' = -\Delta t \left(\frac{p_N^{N+1} - p_P^{N+1}}{\Delta r_p^v} \right) \quad (13)$$

where the superscripts u and v to the geometrical parameters indicate the grid sizes used in solving the u and v momentum equations, respectively. Now the pressure Poisson equation is obtained by substituting Eqs. (10–13) into the finite difference form of the continuity equation [Eq. (4)]:

$$\begin{aligned} & \frac{\rho_e^{N+1} u_e' - \rho_w^{N+1} u_w'}{\Delta z_p} + \frac{r_n \rho_n^{N+1} v_n' - r_s \rho_s^{N+1} v_s'}{r_p \Delta r_p} \\ &= - \left(\frac{\rho_e^{N+1} u_e^* - \rho_w^{N+1} u_w^*}{\Delta z_p} + \frac{r_n \rho_n^{N+1} v_n^* - r_s \rho_s^{N+1} v_s^*}{r_p \Delta r_p} \right) \\ &= -\dot{m} \end{aligned} \quad (14)$$

If Eq. (14) is multiplied by $r_p \Delta r_p \Delta z_p$, the following symmetric-pressure Poisson equation for an orthogonal grid system is obtained:

$$\begin{aligned} & r_p \Delta r_p \left[\left(\frac{p_E^{N+1} - p_P^{N+1}}{\Delta z_e^u} \right) - \left(\frac{p_P^{N+1} - p_W^{N+1}}{\Delta z_w^u} \right) \right] \\ &+ \Delta z_p \left[r_n \left(\frac{p_N^{N+1} - p_P^{N+1}}{\Delta r_n^v} \right) - r_s \left(\frac{p_P^{N+1} - p_S^{N+1}}{\Delta r_s^v} \right) \right] \\ &= \frac{r_p \Delta z_p \Delta r_p}{\Delta t} \dot{m} \end{aligned} \quad (15)$$

The previous equation represents a system of algebraic expressions, with one equation at each grid point. Equation (15) is solved directly using the matrix inversion method in conjunction with the lower and upper (LU) decomposition technique. Finally, the velocities are corrected based on Eqs. (10) and (11), and then the temperature and density are updated.

Grid System and Boundary Conditions

Since the flowfield associated with a transitional jet diffusion flame can be complicated by the presence of the localized small-scale flow structures within a large domain, careful grid management is required. An orthogonal grid system having rapidly expanding cell sizes in both the z and r directions was used in the

present analysis. A typical grid system is shown in Fig. 3. Grid lines are clustered within the shear layer to resolve the small-scale structures, and the boundaries are shifted sufficiently to minimize the propagation of disturbances (which arise due to the inaccuracies in the boundary conditions) in the region of interest. As shown in the figure, most of the grid points in the radial direction are concentrated within the flame zone. The grid spacing in the axial direction is gradually increased to take advantage of the fact that the small-scale structures grow as they are convected downstream. The large outside structures can be accurately captured, even with a coarse grid; hence, no special consideration was given to these structures during construction of the grid system.

The outflow boundary is the most difficult one to treat in these flows because the flow leaving this boundary continuously evolves in time as the large outside and small inside vortices are convected through the boundary. In incompressible and subsonic flows, the flowfield at the outflow boundary cannot be determined solely from the upstream flow conditions. Several procedures²⁴ are cited in the literature for dealing with outflow boundaries; however, none proved to be adequate for the present calculation because of the passage of structures having different length scales. Thus, a simple extrapolation procedure with weighted zero and first-order terms was used. The main criterion used in selecting the weighting functions was that the vortices crossing this outflow boundary should exit without being distorted. Although this procedure is simple and accurate, some judgment is required on a case-by-case basis.

Calculations are usually initiated with uniform flow conditions everywhere; however, during the first few (<100) time steps, the simulations are forced for a steady-state solution. This can easily be accomplished by updating the temperature and density immedi-

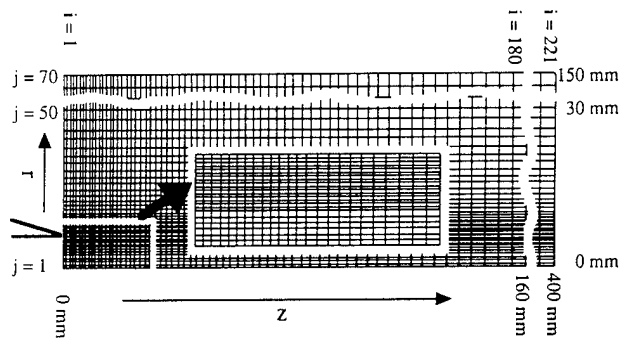


Fig. 3 Typical grid system used for simulations.

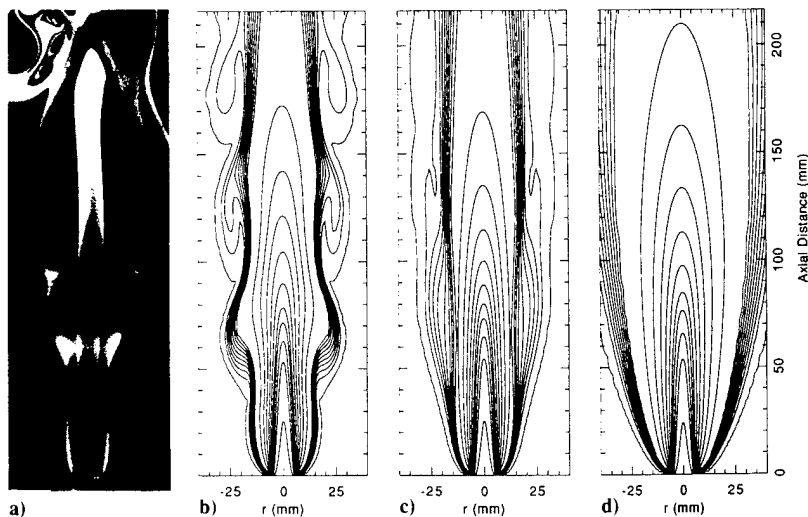


Fig. 4 Comparison of experimental and computed flames for fuel-jet velocity of 3.26 m/s: a) reactive-Mie-scattering image of experimental flame, b) instantaneous temperature contours of oscillating flame, c) isotherm contours obtained from averaged flame, and d) isotherm contours of predicted flame when gravitational force is neglected.

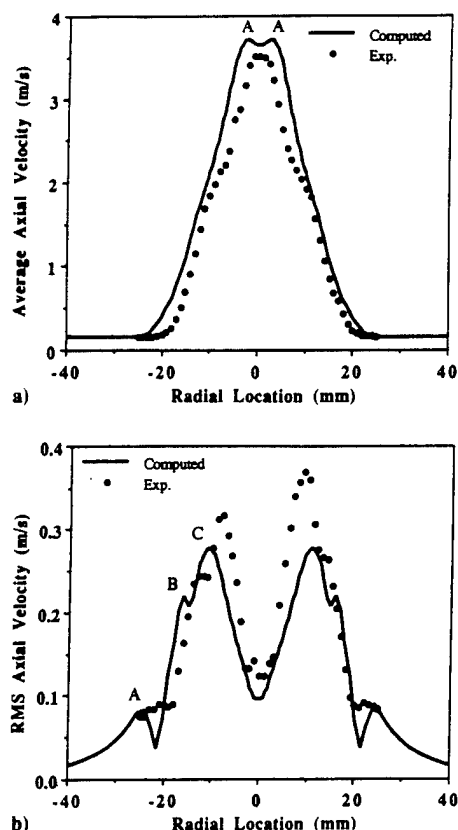


Fig. 5 Computed and measured axial-velocity distributions in radial direction at height of 40 mm above nozzle: a) average velocities and b) rms velocities.

ately after solving the β_1 and β_2 equations. For a typical calculation, a 221×70 grid system is used, and the stable solution is usually obtained in about 5000 time steps, which requires ~ 50 min of CPU time on a Cray XMP.

Results And Discussion

Two types of structures can develop in transitional jet diffusion flames: the large-scale vortices outside the flame sheet and the small-scale vortex structures enclosed by the flame sheet. The ability of the numerical model to simulate these outer and inner structures was evaluated for two flames in the present study. The first flame is characterized by the large outside structures and a laminar potential core. The advantage of studying this flame is that the effects of the dynamic motion of the outside structures on the velocity profiles and the time-dependent temperature field can be addressed without concern for the impact of the inner structures. The second flame has both inner and outer structures. The stability characteristics of the inner structures, their interaction with the larger outside structures, and their frequency characteristics were examined.

Buoyant H_2/N_2 Jet Diffusion Flame Having Laminar Potential Core

Extensive experimental studies have been conducted on the buoyant, laminar jet flame chosen for the model-evaluation study.²⁸⁻³⁰ The fuel was a mixture of hydrogen and nitrogen in a volumetric ratio of 3.5 to 1. The flame was stabilized on a contoured nozzle having an exit diameter of 10 mm. The fuel jet was mounted vertically and had a mass-averaged exit velocity of 3.26 m/s. The flame was surrounded by a 150-mm-diam coannular air jet having a velocity of 15 cm/s, which helped to shield the central jet flame from room air disturbances. Flow visualizations, mean and rms velocities, and time-dependent temperature data have been collected for this flame. The measured peak flame temperature was ~ 1900 K. Preliminary calculations under these conditions resulted in an oscillating flame having a flame temperature of ~ 2600 K.

~ 2600 K. The difference in the calculated and measured temperatures is believed to be due to the lack of radiation and finite rate chemistry models and the use of the unity-Lewis-number assumption in the numerical simulation. More realistic calculated temperatures were obtained by reducing the heat-release parameter $[Q$ in Eq. (3)] by 20%. This lowered the calculated flame temperature to ~ 2100 K. An instantaneous image of the experimental flame visualized by the reactive-Mie-scattering technique is shown in Fig. 4a.²⁸ At this low jet velocity, the shear layer is laminar in nature, and shear-layer instabilities have not developed. Two outside large-scale structures are clearly visible, and a portion of a third one at the top is somewhat smeared by the room air.

An instantaneous isotherm contour plot of the computed flame is shown in Fig. 4b at a phase very near that of the experimental image in Fig. 4a. It should be pointed out that no artificial perturbations were introduced to generate these buoyancy-driven structures. It is not clear how the first vortex is generated; once developed, however, it rolls along the flame surface as it is convected downstream. During this process, the vortex interacts strongly with the flame, making the flame surface bulge and squeeze. This motion is simulated by the time-dependent calculations, as observed in animations of the dynamic characteristics of the flame. Freezing of the flame motion, as in Figs. 4a and 4b, shows that the bulging and squeezing of the experimental and computed flame surfaces occur at about the same heights. It should also be noted that the computed flame has three outer vortices, whereas the experimental image shows only two and one-half vortices. The reduced amount of heat release used in the calculations to compensate for the radiation heat losses accounts for this difference. This reduction lowered not only the peak temperature but also the temperature outside the flame surface. The weaker buoyancy forces associated with the reduced temperature (or higher density) around the computed flame surface reduce the size of the vortical structures, as confirmed by calculations made without modifying the heat-release value. Excellent agreement was obtained between the calculated and measured flame-flicker frequency. At 80 mm above the nozzle, a 12.8-Hz frequency was

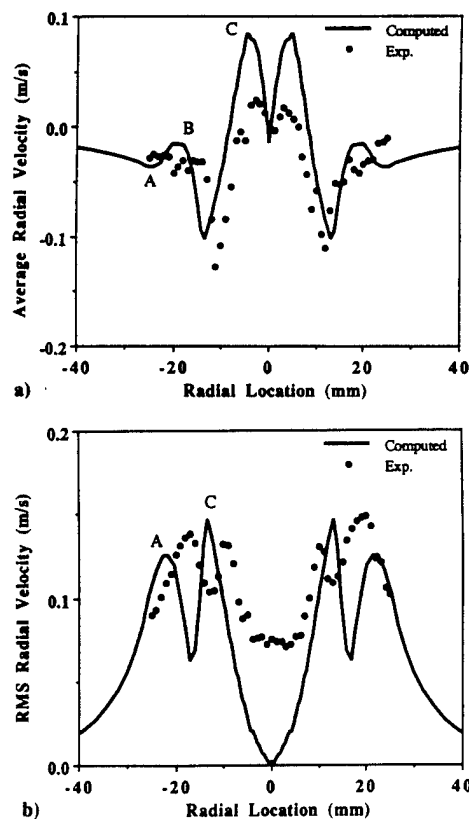


Fig. 6 Computed and measured radial-velocity distributions in radial direction at height of 40 mm above nozzle: a) average velocities and b) rms velocities.

obtained from the computed temperature fluctuations, whereas the frequency was observed to be ~ 13 Hz in the experiments.

The average of several instantaneous temperature contours is plotted in Fig. 4c. In the averaged view, the second and third buoyant structures have disappeared, but the first structure is still evident as a locally diffused flame. Since the mean temperature reflects the time the flame spends in a given location, the presence of the first bulge indicates that the flame spends considerable time in the bulged position at an axial location between 50 and 100 mm. The isotherms in the interior of the jet ($r < 10$ mm) are only moderately affected by the dynamic motion of the outer structures, as evidenced by the similarity of the instantaneous (Fig. 4b) and averaged (Fig. 4c) isotherms.

To illustrate that gravity is an essential factor in generating the outside structures, calculations were also performed with a zero gravitational field. Solution for this case converged to a steady-state flame having a perfectly smooth flame surface. Isotherm contours in the flow are shown in Fig. 4d. In the middle of the calculation, the flame surface was artificially disturbed to determine whether it would become unsteady. The disturbance was damped, and the flowfield converged to a steady-state solution. Without buoyancy, the flame has no outside structures and is very fat compared with the laboratory flame. The flame diameter at 200 mm above the nozzle in this case is ~ 70 mm, whereas it is only 20 mm in the experimental flame and 21 mm in the calculated dynamic flame. When the buoyancy terms are activated in Eq. (9),

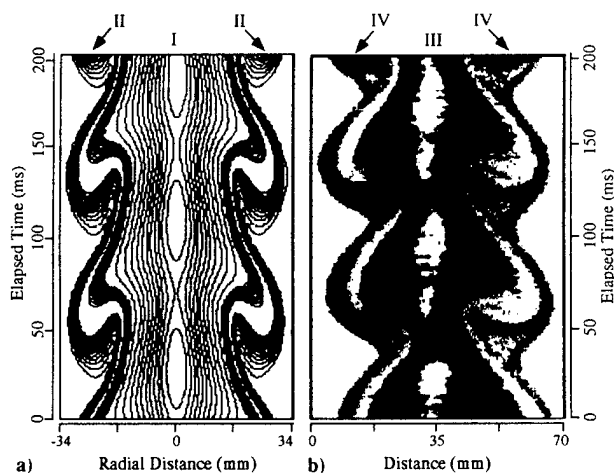


Fig. 7 Comparison of dynamic behavior of flame at height of 80 mm above nozzle: a) isotherm contours from calculated data, b) temperature history of experimental flame recorded by thin-filament pyrometry technique.

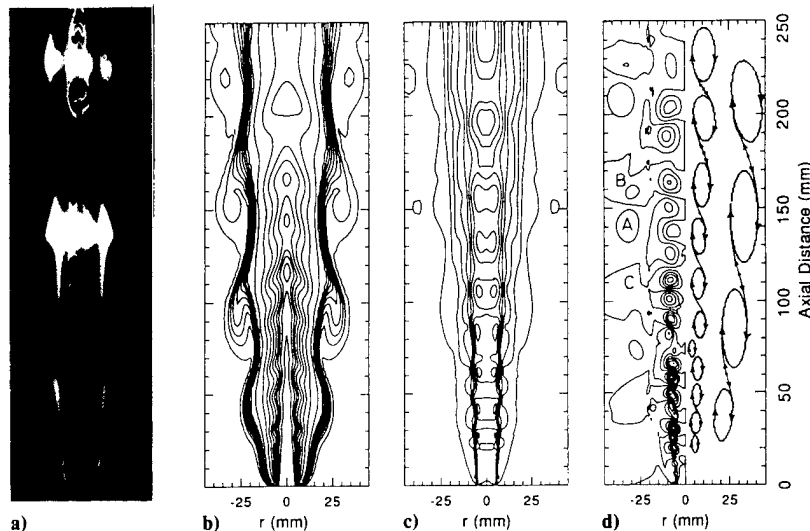


Fig. 8 Visualization of large-scale outer and small-scale inner vortices of 7.64 m/s flame: a) experimental flame obtained with reactive-Mie-scattering technique, b) instantaneous isotherm contours of computed flame, c) instantaneous isoaxial velocity map, and d) instantaneous isoradial velocity contours (left side) and speculated vortex structure (right side).

the flame quickly settles into periodic oscillation, with an instantaneous structure similar to that in Fig. 4b. These observations are similar to those of Davis et al.¹⁵ and Ellzey et al.¹⁶ for propane and hydrogen flames, respectively.

Radial profiles of mean and rms values of axial and radial velocities at a height of 40 mm above the nozzle are shown in Figs. 5 and 6. The measured^{28,29} values are represented by solid circles and the computed results by lines. It is evident that the simulation correctly predicts the unusual shape of the mean and rms profiles presented. The simulation predicts the change in slope of the profile at 15 and 12 mm in Fig. 5a. Also, it correctly predicts the peaks and valleys in Figs. 5b and Fig. 6. To a great extent, the shape of the profiles is the result of the flame oscillations induced by the convective and rotational motion of the outer vortices. For example, the two peaks in the rms axial velocity denoted by A and B in Fig. 5b appear as a result of the periodic passage of vortices across this section. Since these vortices are convected axially, only one peak appears in the rms radial-velocity profile (A in Fig. 6b). Had the outer vortices been perfectly symmetric about the vortex center, then averaging would have eliminated this peak. The presence of a valley (A) and a peak (B) in Fig. 6a indicates that the structure of the vortex is very complex. The other peaks (C in Figs. 5b and 6b) arise from the radial oscillation of the flame surface. The reasonable predictions of the shape of the profiles indicate that the simulation is capturing the essential dynamic features of the outside vortices and the induced flame oscillations.

The simulation typically overestimates the radial locations of the peaks, inflection points, and other distinguishing features of the mean and rms profiles in Figs. 5 and 6. Also, the magnitude of the peaks is not always correctly predicted. These problems are believed to be due, in part, to the lack of a radiation model and insufficient modeling of the attachment of the flame at the nozzle tip. It is known, and also clear from Fig. 4a, that the hydrogen diffusion flame is anchored a few millimeters upstream of the nozzle exit. This means that the flame surface is outside the shear layer of the jet, even at the nozzle lip. Since the nozzle lip is not considered in the calculations, the calculated flame develops in the shear layer at the nozzle exit; however, it rapidly moves out of the shear layer as the flow progresses downstream. The proximity of the flame to the shear layer at the first few grid points heats up the cold fuel jet and creates an overshoot in the axial velocity at the shear layer due to the gravitational acceleration. This overshoot, which remains up to about 80 mm above the nozzle exit can be seen at the edge of the shear layer in the computed velocity profile at point A in Fig. 5a.

The dynamic temperature characteristics of both the computed and the laboratory flames are compared in Fig. 7. The computed time-evolving isotherm contours are shown in Fig. 7a as the large outer structures are convected past a fixed radial line 80 mm above the nozzle tip. The data shown at $t = 200$ ms represent the

temperature recorded 200 ms before that shown at 0 ms. Two different contour levels were chosen to highlight the motion of the outer structures and the flame oscillation. In the high-temperature region (I in Fig. 7a), 20 equally spaced contours are plotted between 1500 and 2400 K. The convective motion of the outer vortex is marked (II in Fig. 7a) by the 12 equally spaced contours between 400 and 800 K. Bulging and squeezing of the flame due to the convective motion of the outer vortices cause the periodic oscillation in the flame surface and create the elliptical-shaped islands of relatively cold fuel (<1500 K) near the centerline of the jet. The temperature evolution of the experimental flame at the same height ($z = 80$ mm) was obtained by the thin-filament-pyrometry³⁰ technique and is plotted in Fig. 7b; the spatial and temporal scales are those used for plotting the computed results. The data shown in region III of Fig. 7b represent the temperature recorded by the filament that is sensitive to temperatures above 1100 K. The reactive-Mie-scattering data³⁰ shown in Region IV and the temperature data were obtained simultaneously and are superimposed in Fig. 7b. A comparison of Figs. 7a and 7b shows that the calculations have accurately captured the time-evolving temperature field. However, the computed outer vortex is smaller in Fig. 7a. This is believed to be due to the reduced value of Q in the calculation and the differences in the visualization techniques used in the experiment and calculations. The computed outer vortex is identified from the temperature contours; in the experiment it is identified by illuminating the TiO_2 particles trapped inside the vortex. The period of oscillation measured from this plot (~78.8 ms) matches that obtained from the frequency data.

The analysis presented here shows that the numerical simulation predicts the flame structure, mean and rms velocity profiles, and the time-evolving temperature profile reasonably well for the 3.26-m/s jet flame having a laminar potential core. The next test of the model is to determine whether it can be used to simulate a transitional jet flame having both inner and outer structures.

Buoyant Transitional H_2/N_2 Jet Diffusion Flame Having Outer and Inner Structures

Coherent small-scale structures were experimentally observed when the fuel velocity was increased to 7.64 m/s. The volumetric ratio between the hydrogen and nitrogen in this case was 3.44 to 1. A reactive-Mie-scattering image of an instantaneous flame is shown in Fig. 8a. This flame is highly symmetric, even up to a height of 250 mm (25 diameters) and has well-organized structures both outside and inside the flame surface. As the inner vortices move downstream, they are squeezed radially and elongated axially but still retain their symmetry.

Numerical simulations of this flame were conducted using a flat velocity profile at the nozzle exit. The outside structures appeared shortly after the calculation was initiated and settled into a repetitive pattern. However, the inner shear layer became very laminar in nature, having no structures. Although the outside vortices cause the jet shear layer to oscillate, even at the fuel nozzle exit, this low-frequency disturbance was not amplified in the jet shear layer and, thus, did not stimulate the growth of the small-scale structures. Extensive efforts were made to determine whether changes in grid spacing, time step, and physical properties of the species would cause the inner vortices to appear. These attempts were unsuccessful. In the experiments, both the outer and inner vortices were always present, with no apparent driving of the flow. A review of the literature suggested that the noise that is inevitably present in experiments initiates the instability. This noise was not being taken into account in the simulation.

Gutmark and Ho,³¹ in an extensive review of spreading rates and preferred modes in cold jets, pointed out that both the data scatter in reported values of the preferred frequency mode and the spreading rate are larger than expected, based on experimental error. After studying jets in different facilities, they came to the conclusion that the dynamics of a laminar shear layer are controlled by an instability and that the small background perturbations always present in a test facility initiate the instability. They suggested that the development of a shear layer is strongly dependent on the nature of the background perturbations at the nozzle exit. The

background noise in the numerical model used to calculate the H_2/N_2 flame structure is considerably smaller than that in the experiments. A contoured nozzle was used in the jet flame experiments to generate a flat velocity profile at the nozzle exit having an estimated rms value of ~2.5% of the mean velocity. The spectral characteristics of this fluctuation were not measured. The possibility cannot be ruled out that the fluctuations at the nozzle exit provided the background perturbations needed to stimulate the inner structures in the experiments. Indeed, the work of Gutmark and Ho suggests that this is the case.

In the next attempt to generate the shear-layer instabilities in the calculations, different types of disturbances were introduced at the fuel-jet exit. All led to the development of small-scale structures. To avoid driving the shear layer with perturbations having a frequency or magnitude bias, we used the following procedure for introducing disturbances in subsequent calculations. A few millimeters above the nozzle, but within the shear layer, a circular zone having a radius of three grid spacings was chosen. At all of the grid points within this zone, disturbances were introduced in the axial-velocity component. At every point a random number between -0.5 and +0.5 was generated. The axial velocity at that grid point was then modified as follows:

$$u = u^* (1.0 + 0.01 * \text{random number}) \quad (16)$$

This introduced a maximum of 1% unbiased fluctuation in the axial velocity. Velocity fluctuations at every grid point within the selected zone of disturbance were introduced after every time step. Perturbations triggered the instabilities in the calculations; however, sustaining them required sufficient grid spacings and time steps. The former was easily determined by allowing at least seven grids in each direction to lie within the expected vortex. A decision on the time step was made based on trial-and-error calculations. A time step corresponding to a Courant-Friedrichs-Levy (CFL) number of 1.0 was used in the final calculations. The CFL number is defined as $\Delta t * U_{\text{jet}} / \min(\Delta z_{\text{min}}, \Delta r_{\text{min}})$.

A computed solution of the flame with 1% random noise at the nozzle exit is shown in Fig. 8, along with the experimental image. The phase of the computed and experimental flames has been matched reasonably well. Computed isotherms and axial- and radial-velocity contours are shown in Figs. 8b-d, respectively. In each of the figures, it is evident that the inner vortices are present; however, their features are dependent on the visualization technique employed. In the isotherms, the vortices appear as wavy lines; in the isoaxial velocity contours, they are shown as packets of fluid that appear to be coupled in some way. The inner vortices are more evident in the isoradial-velocity contours of Fig. 8d. Constant radial-velocity contours are plotted in the left half of Fig. 8d; interpretation of these contours in terms of vortex structures is difficult because each vortex is composed of both positive (outward) and negative (inward) radial velocities. For example, point A in Fig. 8d represents a radially inward velocity contour that would be present at the trailing edge of a vortex. Points B and C represent outward velocities that would be at the leading edge of a vortex. Pair B and A would represent one vortex. It is much easier to use color contours to match a pair of isoradial-velocity contours with a vortex. The elliptical-shaped inner and outer structures identified from color contours (not shown in the figure) are displayed in the right half of Fig. 8d.

Streakline plots were also used to highlight the inner and outer vortex structures. These plots can be interpreted more easily than the radial-velocity contours, as shown in Fig. 9 where the streaklines are generated by injecting massless particles at a fixed rate from the fixed spatial locations indicated by open circles. The particles were then visualized in the flowfield at one instant in time. The solid circles in Fig. 9 show the location of the flame surface that was identified from the computed peak temperatures. For entraining particles into the outer vortices, particles were injected along a line near the outer vortex. As expected, the particles injected within the shear layer at the nozzle exit entered the inner vortices and remained there. However, this was not the case with the outer vortices. Each outer vortex continuously entrained new

particles from the annulus airflow as it lost some to the flame zone. The loss of fluid from the outer vortices reduces their growth rate.

A comparison of the calculated flame in Figs. 8 and 9 with the experimental flame in Fig. 8a shows that the simulation provides a good prediction of the structural features of the inner vortices. The numerical model is able to predict the flame surface location with reasonable accuracy up to a location of ~ 200 mm above the nozzle. For example, the computed flame diameters at the first three flame bulges from the nozzle are 37, 41, and 42 mm, respectively, as compared with 32, 41, and 41 mm measured from the experimental image. Also, the frequency of the computed inner vortices, as noted by the number of vortices per unit length, is about the same as that in the experiments. The simulation also correctly predicts the unusual spatial development of the vortices as they are convected downstream. Note that in the experiment, Fig. 8a, the vortices in the shear layer of the jet do not grow radially as they do in cold jets. Instead, the vortices grow axially and become elongated as they are convected downstream. The computed inner vortices in Figs. 8d and 9 exhibit these same characteristics.

These calculations showed that the development and growth of the inner structures have little impact on the outer structures. However, some secondary effects are present. The inner vortices perturb the temperature field slightly, as evidenced by the small wiggles superimposed on the long-wavelength spatial oscillation in the isotherm contours near the shear layer in Fig. 8b. No other effects of small-scale structures on large-scale ones were observed. However, the large-scale structures have a major impact on the small-scale ones.

The large-scale structures contribute to a very different type of growth and merging process in the small-scale structures. In Fig. 9 the flame location is marked by the large dots. Note that the inner vortices located where the flame is squeezed are longer than their neighbors. This can be understood in terms of the dynamics of the radial flame oscillations induced by the outer vortices. As the

flame is squeezed toward the centerline, the fluid inside it accelerates in much the same way as it would if it were flowing in a flexible tube in which the walls were flexing in and out. The dynamics of the flame oscillation are such that all of the inner vortices that pass locations where the flame is moving inward undergo a local axial stretching or elongation due to the acceleration of the inner fluid. Elongation of the inner fluid also takes place in the absence of inner vortices. The dynamics of this process can be seen in Fig. 7. The elongation process can also result in a head-to-tail type of merging of the inner vortices, as can be observed at a height of ~ 80 cm in Fig. 9. This merging is very different from that observed in conventional shear layers where the vortices roll around each other and grow radially. The elongation process and the axial merging are also evident from a careful inspection of the visualized flame in Fig. 8a. Similar growth and merging processes are also evident in the propane and methane transitional jet flame visualizations published in Ref. 5. The elongation and axial-merging process has a significant impact on the spectrum of the transitional flame.

Calculated Spectrum of Transitional H_2/N_2 Flame

Figure 10 shows frequency spectra obtained from temperature data collected at a radial location of 5 mm within the shear-layer at different axial distances from the nozzle exit. The data stored from 10,000 time steps covered a real time of 0.75 s. The calculated spectra compare favorably with those recently measured by Lee in a 10-mm-diameter jet diffusion flame fueled by hydrogen and nitrogen in a mixture ratio of 3.5 to 1 at an exit velocity of 7.8 m/s.³² Lee used Fourier transforms to obtain the spectrum from time and spatially resolved temperature measurements made using thin filament pyrometry at several heights in the flame. The spectral peaks at a height of 51 mm were compared with those shown in Fig. 10 at a height of 50 mm. The measured peak frequency was ~ 340 Hz, with smaller peaks at $\sim 380, 480, 300, 240$, and 15.6 Hz. This compares favorably with the calculated peak frequency of 350 Hz and smaller peaks at $\sim 380, 420, 300, 260$, and 14 Hz. Spectra measured at downstream locations showed the same trends as those in Fig. 10. That is, the peak frequencies decreased with height. A similar shift from high to low frequency with height in the flame was also observed by Yule et al.¹ for a 6-m/s methane flame having well-organized inner vortices. From this limited analysis, the simulation appears to calculate the spectrum reasonably well, which suggests that it has captured the essential physics of the problem.

The high-frequency bands in the spectra in Fig. 10 show the frequency distribution at which the inner vortices are convected past the measurement point in the flame. The distribution of the frequencies is the result of the unusual axial growth and merging process of the inner structures induced by the outer structures. As previously discussed, the inner vortices undergo axial elongation and merging due to oscillations of the flame surface. It should also be noted in Figs. 8a and 9 that the elongation process is not the same for all inner vortices or even neighboring vortices since the inner vortices have different spatial and time histories as they are convected downstream. For example, during one period of the 14-Hz flame oscillation, the number of 1-cm-long inner structures that will pass the measurement point at a fixed height is ~ 55 . Also, in an axial direction, the inner vortices are moving much faster than the outer ones, but not so fast that they would be affected by some radial displacement of the flame during the time it takes them to pass along the length of the flame. The flame is in a slightly different position at the time of formation of each inner vortex. As each vortex is convected downstream, it experiences a slightly different acceleration and deceleration than its neighbor due to the influence of flame oscillation. The result of this process is that vortices have different axial growth rates or lengths. The different frequencies at one axial location in Fig. 10 result from the different lengths and axial velocities of the vortices. The frequencies are bunched relatively close together because the time and spatial history differs only slightly from vortex to vortex. The decrease in frequency with axial distance is a result of the general axial growth of the vortices as they move downstream. The axial growth with downstream dis-

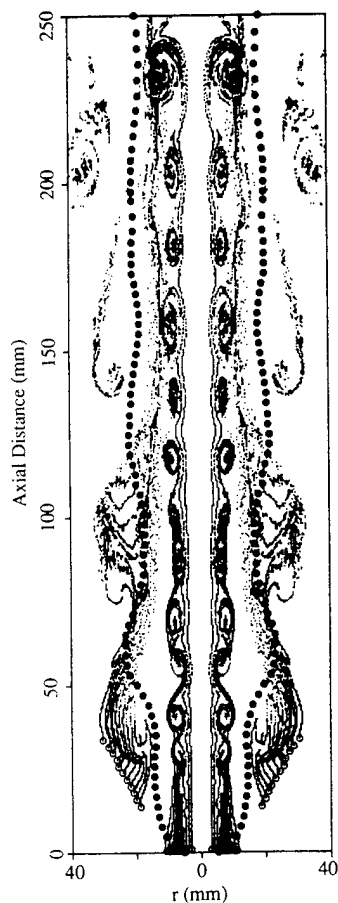


Fig. 9 Streaklines obtained from particles released at nozzle exit and at locations marked with open circles in annular flow.

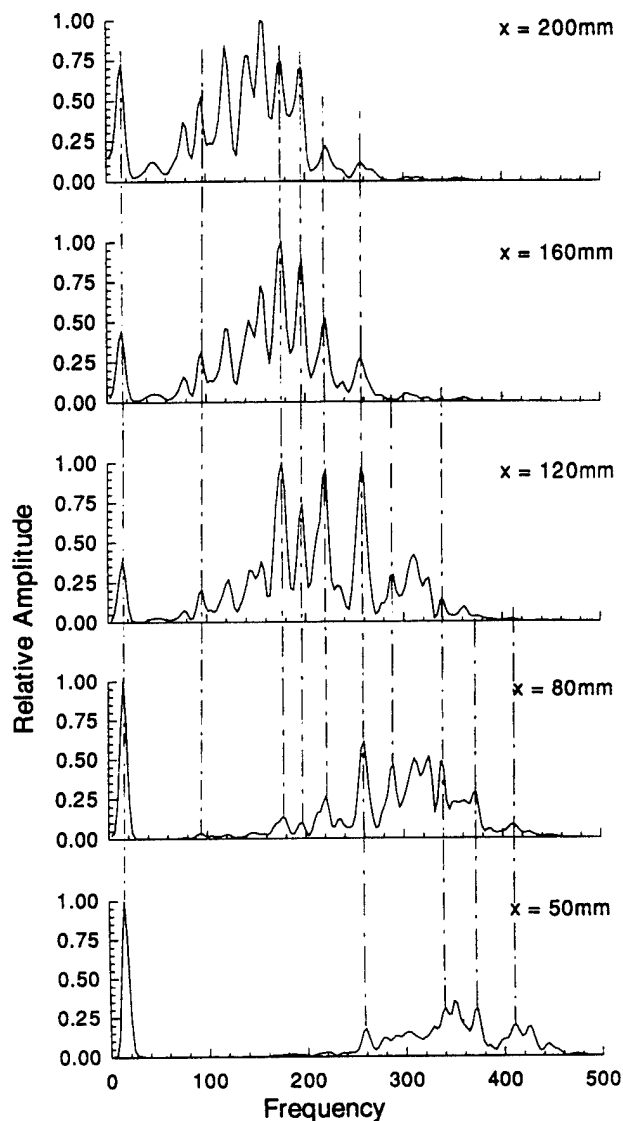


Fig. 10 Frequency spectra obtained from temperature data recorded within the shear layer at different axial locations.

tance is due to the repeated elongations and possibly to mergings that occur as the inner vortices pass along the length of the flame. The mergings, however, do not necessarily produce a subharmonic frequency, as noted by inspection of Fig. 10. This is probably due to the complex acceleration experienced by different axial segments of a vortex or merged vortex pair.

The low-frequency component in the spectra in Fig. 10 is the result of the convective motion of the large outside vortex. The computed 14-Hz oscillation of the flame is in reasonable agreement with the 15.6-Hz measured value of Lee in a slightly higher velocity (7.8 m/s as compared with 7.6 m/s) H_2/N_2 flame.³² Note that the lower frequency component remains unaltered at 14 Hz up to a height of 200 mm or 20 jet diameters. That the vortex frequency is independent of axial distance is inconsistent with the results of the linear, inviscid stability analysis of the infinite candle flame performed by Buckmaster and Peters.¹² Their analysis resulted in a frequency dependence of $x^{1/4}$. They also estimated that the frequency of the instability would vary with gravitational constant to the three-fourths power. A recent study³³ by the authors using the simulation described in this paper yielded a frequency dependence of $g^{1/2}$. Furthermore, viscosity was shown to have no effect on the frequency of the outer structures.³³ These discrepancies have raised some concern about the ability of a linear instability analysis to capture the physics of the buoyancy-related instabil-

ity problem. However, the results of the present paper should resolve any problems concerning the basic assumption made in the analysis by Buckmaster and Peters¹²; this assumption—that the instability associated with the outer structures is essentially decoupled from the forced flow—is correct, even for transitional flames with inner vortex structures. The reason for the decoupling is evident in Fig. 9. The flame surface, established at the location where the fuel and oxygen meet in stoichiometric proportions, lies several millimeters outside the jet shear layer. As the jet velocity increases, the separation between the flame and the jet shear layer decreases and the outer vortex structures weaken as they become an increasing part of the forced flow.

Summary and Conclusions

A direct numerical method for accurate simulation of the time and spatial characteristics of the inner and outer vortex structures in two transitional H_2/N_2 jet diffusion flames has been presented. The numerical method incorporating an implicit, third-order-accurate, upwind scheme with very low numerical diffusion has been described in detail. This method provides direct numerical solutions to the time-dependent conservation equations and incorporates buoyancy, a simple one-step chemistry model, and transport coefficients that depend on temperature and species concentration.

The ability of the numerical model to predict accurately the time-averaged and dynamic characteristics of a low-speed buoyant H_2/N_2 jet diffusion flame having a laminar potential core is evaluated. The flame chosen for this evaluation had been extensively studied experimentally. The model correctly predicted the structural features of this flame, including the large vortices outside of the flame surface. The vortices had a measured frequency of 13 Hz, which compared favorably with a calculated frequency of 12.8 Hz. Mean and rms velocity profiles were obtained by averaging instantaneous velocity flowfield calculations over several cycles of the outer structures. Model predictions of the axial and radial velocities and their rms values compared favorably with the experimental results, even revealing the irregular features in the profiles due to the convective motion of the outer vortices. Time-evolving temperature along a radial line eight nozzle diameters downstream also compared favorably with measured data. However, the predicted flame temperature was ~ 700 K higher than that measured; this is believed to be due to a lack of radiation and finite rate chemistry models in the simulation. To compensate for this temperature difference, the fuel heating value in the calculations was reduced by 20%, which not only lowered the predicted temperature but also reduced the size of the outer structures. When g was set equal to zero in the calculation, the outside structures disappeared and the flame became perfectly laminar, which confirms the findings of others, i.e., that buoyancy is required to form the outside structures.

Constant external forcing in the form of background noise at the exit of the jet was required to initiate and sustain the instabilities that give rise to the inner vortices. This finding is not surprising to the community that studies instabilities, but its importance in both experimental and computational studies is often overlooked. In the presence of buoyancy, the outer structures formed without any intentional application of perturbation to the flow. The instability responsible for the initiation of the outer vortices is felt to be absolutely unstable; thus, only one-time perturbation is required to initiate the oscillation. Such a perturbation can arise from a slight mismatch in the initial, assumed starting solution and the first iterated solution. Once the oscillation begins, it is self-sustaining. This view is currently being examined in some detail.

Predictions of a flame having inner and outer vortices compared favorably with experiments. An examination of the computed and experimental results shows that the growth and merging of the inner vortices are dominated by the motion of the outside structures. The outer vortices cause the flame surface to oscillate. As the inner vortices pass through the contracted and expanded regions of the flame, they become stretched axially (elongated) by the acceleration of the flow, and axial merging can take place. As a result the shear layer experiences very little radial growth. This radial growth and merging process is very different from that in

cold jets and in higher speed jet diffusion flames. The predicted frequency spectra, which compared favorably with the limited experimental results, could be physically interpreted in terms of the axial-growth process of the inner vortices.

Acknowledgments

This work was supported, in part, by Air Force Contract F33615-90-C-2033. The first author also acknowledges the National Research Council and Air Force Systems Command for sponsoring him on the Postdoctoral Fellowship Program during 1989-91. This research was also supported, in part, by the Aerospace Sciences Directorate of the Air Force Office of Scientific Research. The authors would like to thank Marian Whitaker for her help in preparing the manuscript.

References

- ¹Yule, A. J., Chigier, N. A., Ralph, S., Boulderstone, R., and Ventura, J., "Combustion-Transition Interaction in a Jet Flame," *AIAA Journal*, Vol. 19, No. 6, 1981, pp. 752-760.
- ²Eickhoff, H., and Winandy, A., "Visualization of Vortex Formation in Jet Diffusion Flames," *Combustion and Flame*, Vol. 60, No. 1, 1985, pp. 99-101.
- ³Savas, O., and Gollahalli, S. R., "Flow Structure in Near-Nozzle Region of Gas Jet Flames," *AIAA Journal*, Vol. 2, No. 7, 1986, pp. 1137-1140.
- ⁴Coats, C. M., and Zhao, H., "Transition and Stability of Turbulent Jet Diffusion Flames," *Twenty-Second Symposium (International) on Combustion*, The Combustion Inst., Pittsburgh, PA, 1988, pp. 685-692.
- ⁵Roquemore, W. M., Chen, L.-D., Goss, L. P., and Lynn, W. F., "Structure of Jet Diffusion Flames," *Turbulent Reactive Flows*, edited by R. Borghi and S. N. B. Murthy, Vol. 40, Lecture Notes in Engineering, Springer-Verlag, Berlin, Germany, 1989, pp. 49-63.
- ⁶Cabelli, A., Pearson, I. C., Shepherd, I. C., and Hamilton, N. B., "Fluid Dynamic Structures in Jet Diffusion Flames: Acoustic Effects," *Experimental Heat Transfer, Fluid Mechanics, and Thermodynamics*, First World Conference on Experimental Heat Transfer, Fluid Mechanics, and Thermodynamics (Dubrovnik, Yugoslavia), Elsevier, New York, Sept. 1988, pp. 627-631.
- ⁷Takahashi, F., Mizomoto, M., and Ikai, S., "Transition from Laminar to Turbulent Free Jet Diffusion Flames," *Combustion and Flame*, Vol. 48, No. 1, 1982, pp. 85-95.
- ⁸Chamberlin, D. S., and Rose, A., "The Flicker of Luminous Flames," *Industrial and Engineering Chemistry*, Vol. 20, No. 10, 1928, pp. 1013-1016.
- ⁹Kimura, I., "Stability of Laminar-Jet Flames," *Tenth Symposium (International) on Combustion*, The Combustion Inst., Pittsburgh, PA, 1965, pp. 1295-1300.
- ¹⁰Durao, D. F., and Whitelaw, J. H., "Instantaneous Velocity and Temperature Measurements in Oscillating Diffusion Flames," *Proceedings of Royal Society of London, Series A: Mathematical and Physical Sciences*, Vol. 338, No. 1615, 1974, pp. 479-501.
- ¹¹Grant, A. J., and Jones, J. M., "Low Frequency Diffusion Flame Oscillations," *Combustion and Flame*, Vol. 25, No. 2, 1975, pp. 153-160.
- ¹²Buckmaster, J., and Peters, N., *Twenty-First Symposium (International) on Combustion*, The Combustion Inst., Pittsburgh, PA, 1986, pp. 1829-1836.
- ¹³Mahalingam, S., Cantwell, B. J., and Ferziger, J. H., "Stability of Low-Speed Reacting Flows," *Physics of Fluids A*, Vol. 3, No. 6, 1991, pp. 1533-1543.
- ¹⁴Chen, L.-D., Seaba, J. P., Roquemore, W. M., and Goss, L. P., "Buoyant Diffusion Flames," *Twenty-Second Symposium (International) on Combustion*, The Combustion Inst., Pittsburgh, PA, 1988, pp. 677-684.
- ¹⁵Davis, R. W., Moore, E. F., Roquemore, W. M., Chen, L.-D., Vilimpoc, V., and Goss, L. P., "Preliminary Results of a Numerical-Experimental Study of the Dynamic Structure of a Buoyant Jet Diffusion Flame," *Combustion and Flame*, Vol. 83, Nos. 3 & 4, 1991, pp. 263-270.
- ¹⁶Ellzey, J. L., Laskey, K. J., and Oran, E. S., "Effects of Heat Release and Gravity on an Unsteady Diffusion Flame," *Twenty-Third Symposium (International) on Combustion*, The Combustion Inst., Pittsburgh, PA, 1990, pp. 1635-1640.
- ¹⁷Yamashita, H., Kushida, G., and Takeno, T., "A Numerical Study of the Transition of Jet Diffusion Flames," *Proceedings of Royal Society of London, Series A: Mathematical and Physical Sciences*, Vol. 431, No. 1882, 1990, pp. 301-314.
- ¹⁸Katta, V. R., and Roquemore, W. M., "Role of Inner and Outer Structures in a Transitional Diffusion Flame," *Combustion and Flame*, Vol. 92, No. 2, 1993, pp. 274-282.
- ¹⁹Katta, V. R., Goss, L. P., and Roquemore, W. M., "Effect of Nonunity Lewis Number on the Dynamics of a Hydrogen-Air Jet Diffusion Flame," *AIAA Paper 93-0454*, Jan. 1993.
- ²⁰Burcat, A., "Thermochemical Data for Combustion Calculations," *Combustion Chemistry*, Springer-Verlag, New York, 1984, pp. 455-473.
- ²¹Wilke, C. R., "Viscosity Equation for Gas Mixtures," *Journal of Chemical Physics*, Vol. 18, No. 4, 1950, pp. 517-519.
- ²²Reid, R. C., Prausnitz, J. M., and Poling, B. E., *The Properties of Gases and Liquids*, McGraw-Hill, New York, 1987, pp. 733, 734.
- ²³Leonard, B. P., "A Stable and Accurate Convective Modeling Procedure Based on Quadratic Upstream Interpolation," *Computer Methods in Applied Mechanics and Engineering*, Vol. 19, No. 1, 1979, pp. 59-98.
- ²⁴Davis, R. W., and Moore, E. F., "A Numerical Study of Vortex Shedding from Rectangles," *Journal of Fluid Mechanics*, Vol. 116, March, 1982, pp. 475-506.
- ²⁵Patankar, S. V., *Numerical Heat Transfer and Fluid Flow*, McGraw-Hill, New York, 1980.
- ²⁶Chorin, A. J., "A Numerical Method for Solving Incompressible Viscous Flow Problems," *Journal of Computational Physics*, Vol. 2, No. 1, 1967, pp. 12-26.
- ²⁷Peyret, R., and Taylor, T. D., *Computational Methods for Fluid Flow*, Vol. X, Springer Series in Computational Physics, Springer-Verlag, New York, 1983, pp. 143-215.
- ²⁸Vilimpoc, V., Systems Research Lab., Inc., unpublished data, Dayton, OH, 1988.
- ²⁹Lynn, W. F., Goss, L. P., Chen, T. H., and Trump, D. D., "Two Component Velocity Measurements on an Axially Symmetric H₂-N₂ Jet Diffusion Flame," *Proceedings of Central States Section Meeting of the Combustion Inst.* (Indianapolis, IN), May 1988 (Paper No. 23).
- ³⁰Vilimpoc, V., and Goss, L. P., "SiC-Based Thin-Filament Pyrometry: Theory and Thermal Properties," *Twenty-Second Symposium (International) on Combustion*, The Combustion Inst., Pittsburgh, PA, 1988, pp. 1907-1914.
- ³¹Gutmark, E., and Ho, C.-M., "Preferred Modes and the Spreading Rates of Jets," *Physics of Fluids*, Vol. 26, No. 10, 1983, pp. 2932-2938.
- ³²Lee, S., "Flow-Flame Interactions of Transitional Nitrogen Diluted Hydrogen Jet Diffusion Flames," Ph.D. Thesis, Univ. of Iowa, Iowa City, IA, Dec. 1992.
- ³³Katta, V. R., Goss, L. P., and Roquemore, W. M., "Numerical Investigations on the Dynamic Behavior of a H₂-N₂ Diffusion Flame Under the Influence of Gravitational Force," *AIAA Paper 92-0335*, Jan. 1992.

Role of Inner and Outer Structures in Transitional Jet Diffusion Flame

V. R. KATTA

*Systems Research Laboratories, Inc., A Division of Arvin / Calspan, 2800 Indian Ripple Road,
Dayton, OH 45440-3696*

and

W. M. ROQUEMORE

Wright Laboratory, Aero Propulsion and Power Directorate, Wright-Patterson Air Force Base, OH 45433-6563

A jet diffusion flame was studied using a time-dependent, axisymmetric, third-order-accurate computational-fluid-dynamics-based model. In a previous investigation, this vertical, unconfined propane jet flame at transitional fuel-jet velocity was studied experimentally and found to have a double-vortex structure with large-scale buoyancy-driven vortices outside the flame surface and smaller Kelvin-Helmholtz-type vortices in the shear layer of the fuel jet inside the flame surface. In the calculations the outer-vortex structures were developed as part of the solution, while a weak shear-layer perturbation was required to generate the inner structures. The computed shapes and the time and spatial evolution of these complex structures closely match those observed in the real flame. The model also correctly predicted the change in the direction of rotation of the inner vortices, which was observed 15 nozzle diameters downstream of the fuel-jet exit in the experiments. The computed results are used to explain this phenomenon. The detailed shapes of the time-averaged and root-mean-square temperature profiles at different heights in the flame are well predicted by the model and are shown to be due to the dynamic motion of the outer-vortex structures. Computational experiments have been performed to examine the long-standing question regarding why the vortices inside a transitional jet flame have a very long coherence length as compared with that of cold jets. Buoyancy was found to be a major factor. The buoyant acceleration of the hot gases of the flame entrains fluid that would normally be entrained by the inner vortices of the jet shear layer and causes their rapid dissipation. The buoyant acceleration also reduces the velocity gradient in the jet shear layer which, in turn, weakens the process that drives the growth of the vortices.

INTRODUCTION

A jet diffusion flame at transitional fuel-jet velocities exhibits two distinct vortex structures—one inside and the other outside the flame surface. This double-vortex structure of a transitional jet diffusion flame was first observed by Yule et al. [1] and subsequently by Eickhoff [2], Eickhoff and Winandy [3], and Roquemore et al. [4]. While the slowly moving outer vortices are associated with the low-frequency flame-flickering phenomenon, the small-scale inner vortices lead to the development of turbulence in diffusion flames. The first comprehensive investigation of the low-frequency oscillations (flame flicker) in near-laminar and transitional-jet diffusion flames was conducted

by Chamberlin and Rose [5] in 1928. Nearly 60 years later Buckmaster and Peters [6], following the work of Kimura [7] and Toong et al. [8], clearly identified the origin of these oscillations as a modified Kelvin-Helmholtz-type buoyancy-driven instability. They speculated that the vortex structures outside the flame sheet observed by Roquemore et al. [4] result from the nonlinear growth of the low-frequency instability. With the help of high-speed Reactive-Mie-Scattering visualization movies, Chen et al. [9] demonstrated that the low-frequency flame oscillation is the result of the convective motion of the large outer toroidal vortex. This was shown conclusively in recent numerical studies by Davis et al. [10] and Ellzey and Oran [11] in which jet diffusion flames did not oscil-

late when gravity was not taken into account; where gravity was included, however, low-frequency oscillations were induced by the motion of outer vortices which caused the flames to flicker in the way described by Chen et al. [9].

The smaller vortex structures inside the flame surface are believed to be a Kelvin-Helmholtz-type instability of the jet shear layer. However, these inner vortices differ significantly from those generated in cold jets in that they have a longer potential core and maintain their coherence for longer distances downstream. This long coherence length of the inner vortices has been attributed to the decrease in effective Reynolds number which results from combustion [1]. However, the inviscid numerical simulations of Ellzey et al. [12] and the analytical results of Mahalingam et al. [13] suggest that heat release may cause the inner vortices to dissipate rapidly. The change in direction of rotation of the small inner vortices caused by the rotation of the large vortex structures outside the flame surface, as observed by Eickhoff and Winandy [3] and Roquemore et al. [4], suggests that buoyancy may contribute to the long coherence length of the inner structures.

In the present article the first numerical results to capture the temporal and spatial development of both the outer and the inner vortex structures of a transitional jet diffusion flame are presented. The validity of the predictions was examined by comparison with experimental results. Computational experiments were performed to investigate the effects of transport coefficients, volumetric expansion, and buoyancy on the coherence of the inner structures.

MODEL FORMULATION

The diffusion flame in this study was formed between a propane jet and a very low speed co-annular air flow. Axisymmetric simulations for this flame were made using a simple global-chemistry model in which fuel (C_3H_8) and oxidizer (O_2) undergo a single irreversible reaction to give products (CO_2 and H_2O). The problem is further simplified by adopting the Shvab-Zel'dovich formulation and introducing

two scalar variables, β_1 and β_2 , which are defined as

$$\beta_1 = \frac{\alpha Y_O + Y_F^i - Y_F}{\alpha Y_O^i + Y_F^i} \quad \text{and}$$

$$\beta_2 = \frac{h - h_O^i + (Y_F/\alpha)Q}{(Y_F^i/\alpha)Q + h_F^i - h_O^i},$$

for the species and energy-conservation equations, respectively. Here α is the Fuel-Oxidizer Ratio ($\nu_F M_F / \nu_O M_O$); Y_m and h_m are the mass fraction and enthalpy of the m th species, respectively; h is the mixture enthalpy; Q is the heat release per unit mass of oxygen consumed; M is the molecular weight; and the superscript i represents the initial values. It is also assumed that (1) all species locally have the same diffusion coefficient, (2) the reaction among the species occurs at an infinitely fast rate, resulting in an infinitely thin reaction zone or "flame sheet," and (3) the Lewis number is equal to unity.

The time-dependent governing equations, expressed in cylindrical (z, r) coordinates, are

$$\frac{\partial \rho}{\partial t} + \frac{\partial \rho u}{\partial z} + \frac{1}{r} \frac{\partial (r \rho v)}{\partial r} = 0, \quad (1)$$

and

$$\begin{aligned} & \frac{\partial (\rho \Phi)}{\partial t} + \frac{\partial (\rho u \Phi)}{\partial z} + \frac{\partial (\rho v \Phi)}{\partial r} \\ &= \frac{\partial}{\partial z} \left(\Gamma^\Phi \frac{\partial \Phi}{\partial z} \right) + \frac{\partial}{\partial r} \left(\Gamma^\Phi \frac{\partial \Phi}{\partial r} \right) \\ & \quad - \frac{\rho v \Phi}{r} + \frac{\Gamma^\Phi}{r} \frac{\partial \Phi}{\partial r} + S^\Phi, \end{aligned} \quad (2)$$

where ρ represents density; u and v are the axial and radial components of the velocity vector, respectively; and p is the pressure. The general form of Eq. 2 represents the axial momentum, radial momentum, species, or energy-conservation equation depending on the variable used in place of Φ . The transport coefficients Γ^Φ and the source terms S^Φ that appear in the governing equations are given in Table 1.

TABLE 1
Transport Coefficients and Source Terms Appearing in Governing Equations

Φ	Γ^Φ	S^Φ
u	μ	$-\frac{\partial p}{\partial z} + (\rho_0 - \rho)g + \frac{\partial}{\partial z} \left(\mu \frac{\partial u}{\partial z} \right) + \frac{\partial}{\partial r} \left(\mu \frac{\partial v}{\partial z} \right) + \frac{\mu}{r} \frac{\partial v}{\partial z}$ $-\frac{2}{3} \left\{ \frac{\partial}{\partial z} \left(\mu \frac{\partial u}{\partial z} \right) + \frac{\partial}{\partial z} \left(\mu \frac{\partial v}{\partial r} \right) + \frac{\partial}{\partial z} \left(\mu \frac{v}{r} \right) \right\}$
v	μ	$-\frac{\partial p}{\partial r} + \frac{\partial}{\partial z} \left(\mu \frac{\partial u}{\partial r} \right) + \frac{\partial}{\partial r} \left(\mu \frac{\partial v}{\partial r} \right) + \frac{\mu}{r} \frac{\partial v}{\partial r}$ $-2\mu \frac{v}{r^2} - \frac{2}{3} \left\{ \frac{\partial}{\partial r} \left(\mu \frac{\partial u}{\partial z} \right) + \frac{\partial}{\partial r} \left(\mu \frac{\partial v}{\partial r} \right) + \frac{\partial}{\partial r} \left(\mu \frac{v}{r} \right) \right\}$
β_1	ρD	0
β_2	ρD	0

The body-force term due to the gravitational field is included in the axial-momentum equation. Here μ is the viscosity of the mixture; D is the local binary diffusion coefficient between any two species; ρ_0 is the density of air; and g is the gravitational acceleration. The system of governing equations is completed using the state equation

$$p = \rho TR_0 \left\{ \frac{Y_F}{M_F} + \frac{Y_O}{M_O} + \frac{Y_P}{M_P} + \frac{Y_I}{M_I} \right\}, \quad (3)$$

where R_0 is the universal gas constant and T is the temperature. The subscript I in the above equation represents nitrogen, which is assumed to be an inert gas in the present simulation.

The enthalpy of each species is calculated from the polynomial curve fits, while the viscosity of the individual species is estimated from Chapman-Enskog collision theory. The binary-diffusion coefficient between any two species on the fuel side of the flame is assumed to be identically equal to that of the fuel and nitrogen. Similarly, on the oxidizer side of the flame, this coefficient is set equal to that of the oxidizer and nitrogen. Chapman-Enskog theory and the Lennard-Jones potentials have been used to estimate the above two binary-diffusion coefficients.

The finite-difference form of the governing equations is constructed on a staggered grid system based on an implicit QUICKEST [14, 15] numerical scheme that is third-order accurate in both space and time and has a very low numerical diffusion error. At every time-step,

the pressure field is accurately calculated by solving the system of algebraic pressure Poisson equations at all grid points using the LU decomposition technique. An orthogonal grid system with rapidly expanding cell sizes in both the z and r directions is utilized. The outer boundaries of the computational domain are shifted sufficiently far to minimize the propagation of disturbances into the region of interest. The outflow boundary in the unsteady flows is the most difficult one to treat because the flow crossing this boundary continuously evolves in time as the large outer and small inner vortices are convected through it. A simple extrapolation procedure with weighted zero- and first-order terms was used to estimate the flow variables on the boundary in the present calculations. The main criterion used in selecting the weighting functions is that the vortices should cross the outflow boundary smoothly without being distorted. Recent work on hydrogen diffusion flames in this laboratory [15] indicates that this procedure for treating the outflow boundary in conjunction with the above-discussed numerical algorithm is accurate in predicting the dynamic behavior of the flames.

Initial calculations are generally made with very large time-steps to establish the slowly moving outer structures of the flame; then a smaller time-step is employed to allow the growth of the small-scale structures. A typical calculation on a mesh system having 241 and 70 grid points in z and r directions, respectively, requires ~ 0.75 s per time-step on a Cray-XMP.

RESULTS

The inflow conditions in the present calculations are the same as those used for a laboratory flame studied experimentally by Roquemore et al. [4]. A vertically mounted jet diffusion flame was established by burning pure propane emerging from a 10-mm-diameter contoured nozzle. Flat initial velocity profiles with measured average velocities of 2.22 and 0.15 m/s were used in the calculations at the exits of the fuel nozzle and annulus duct, respectively.

An instantaneous image of the flame obtained by the Reactive-Mie-Scattering visualization technique [4] is shown in Fig. 1a. With this technique, the micron-sized TiO_2 particles that are formed from the spontaneous reaction between the seeded TiCl_4 vapor and the water vapor produced during combustion are visualized by the Mie scattered light from a laser sheet. In Fig. 1a the luminous (soot) flame surface is the yellow boundary that begins just outside the nozzle lip and has outward bulges at $z = 100, 160$, and 230 mm. The large toroidal vortices outside the flame surface and the smaller coherent vortices inside the flame surface are identified by the green scattered light from the laser.

The time-averaged (right of centerline) and root-mean-square (RMS) (left of centerline) temperatures measured [4] with a Coherent Anti-Stoke Raman Spectroscopy (CARS) system are superimposed on the flame in Fig. 1a. These measured temperatures are also shown in Fig. 1b along with the time-averaged and RMS temperatures calculated with the model. The heat-release rate used in the definition of the scalar variable β_1 has been reduced by a factor of 0.15 as a first-order estimate of the heat lost due to radiation from soot.

Instantaneous iso-temperature contours of the calculated flame are shown in Fig. 1c. The calculated flame has the same spatial scale and roughly the same phase as the experimentally observed flame. The flame surface (solid circles in the figure) was identified from the peak temperature locations. The vortices outside the flame surface develop as part of the solution, and the responsible parameter is identified as the buoyancy term in the momentum equation

[10, 15]. No artificial disturbances were needed for generation of these large outer vortices. A small perturbation, however, was required to generate the inner vortices. Earlier attempts without introducing the perturbations in this flame generated only a laminar-like shear layer, which indicates that the low-frequency oscillations in the flowfield induced by the convective motion of the outer vortices are ineffective in triggering shear-layer instabilities. Therefore, sinusoidal velocity perturbations of $\sim 0.3\%$ were introduced at the shear layer near the nozzle exit to initiate the development of the inner structure. Inviscid stability analysis [16] suggests that the most amplified frequency for the co-annular jet shear layer under consideration would be ~ 400 Hz. In actual calculations the perturbations introduced at this frequency did not travel beyond 80 cm which could be attributed to the viscosity of the fluid and the assumptions used in the model which become increasingly significant at downstream locations. In order to account for these differences, the most amplified frequency is determined by virtually repeating several calculations and varying the perturbation frequency. At 190 Hz, the disturbances traveled farther downstream. Blowups of the iso-temperature contours of the internal structures at three axial locations are shown in the boxes to the right of Fig. 1c.

The rotational characteristics of the outer and inner structures are shown in Fig. 2 with the aid of velocity vectors and color contours of density. Red represents the low-density gases or high-temperature region of the flame. The flame surface is denoted by solid circles. The highest-density fluid is the cold propane fuel, represented by purple; the air density is blue. The flame is normally calculated as observed from the laboratory reference frame. However, this is not the best reference frame for viewing the rotational characteristics of the vortices. The velocity-vector field in Fig. 2 represents what an observer would view if moving at the spatially averaged axial velocity at the time of image capture. The advantage of this reference frame is that the internal fluid motion of the large outer vortices can be recognized easily. This view is calculated by subtracting the spatially averaged axial velocities at all grid points shown in the figure from the local axial veloci-

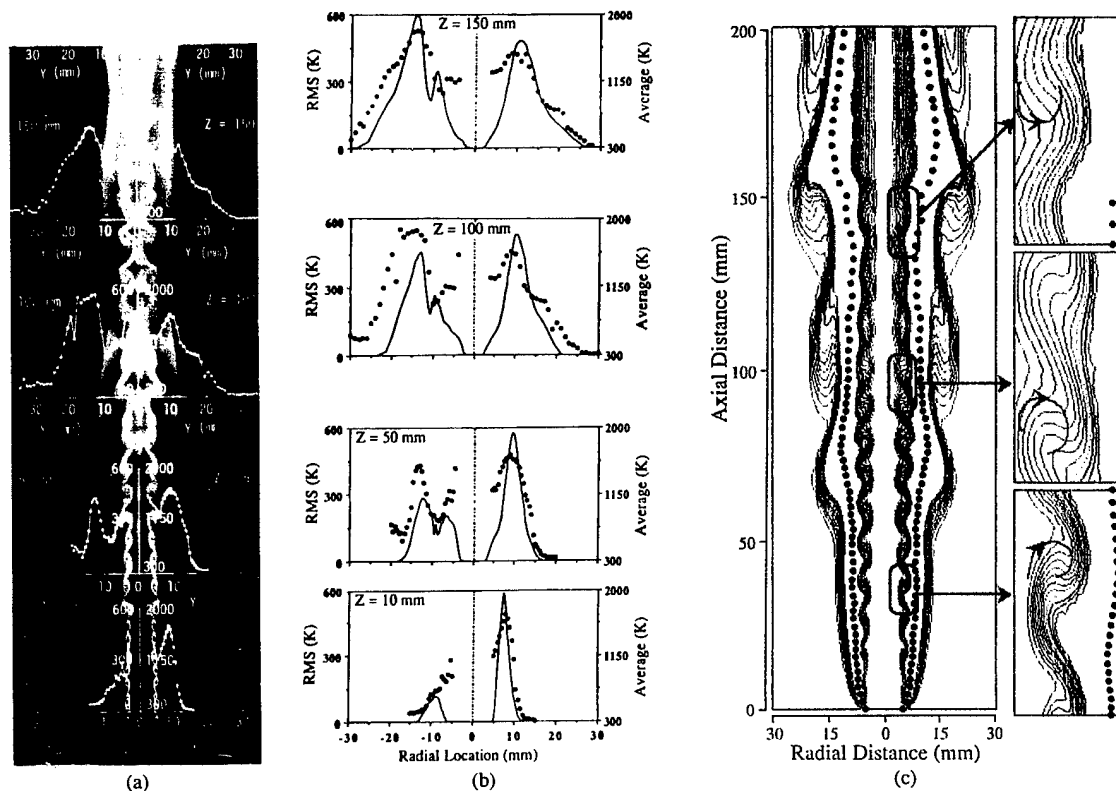
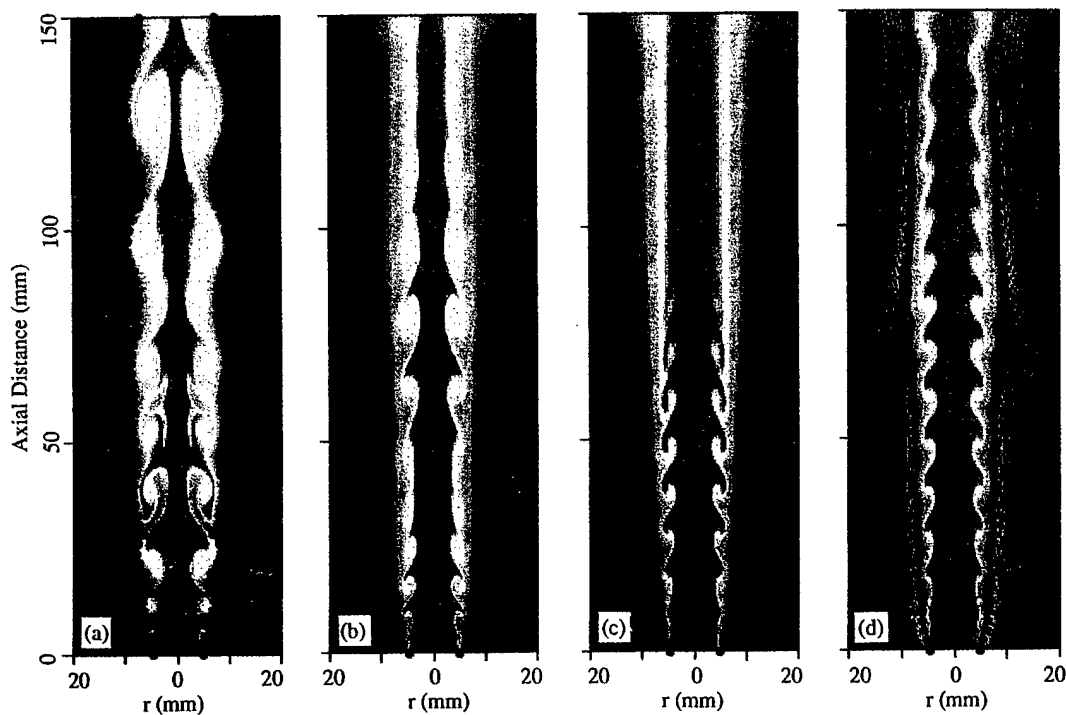


Fig. 1. Visualizations of experimental and computed transitional propane diffusion flame: (a) Reactive-Mie-Scattering image of flame, with bright region between inner and outer vortices indicating flame (soot) surface; (b) RMS and average temperature at different axial locations, with lines and solid circles indicating computed and measured values, respectively; (c) Instantaneous iso-temperature contours obtained from computed flowfield, with solid circles indicating flame surface identified from peak temperatures.

Fig. 3. Mixture-fraction distribution for different cases showing effect of viscosity, heat-release, and buoyancy on internal structures. Solid circles indicate stoichiometric surface. (a) Noncombusting flow; (b) Fictitious flame in absence of volumetric expansion; (c) Fictitious flame in absence of gravity; (d) Present model.



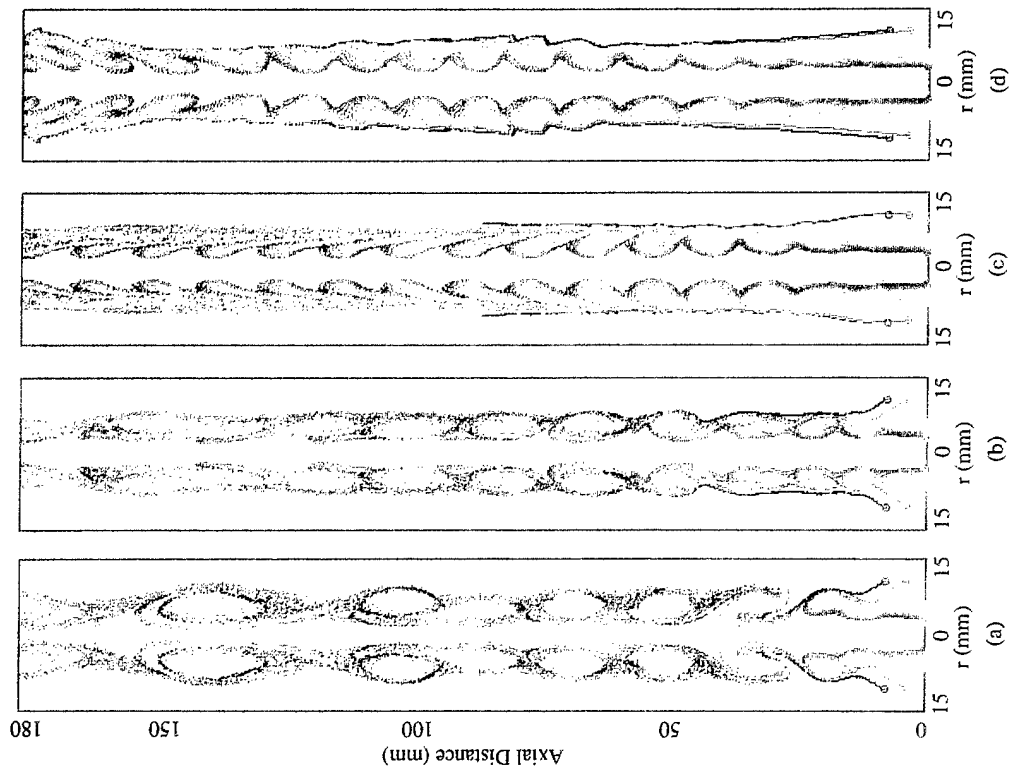


Fig. 4. Streaklines obtained from particles released from locations at nozzle exit for four cases shown in Fig. 3.

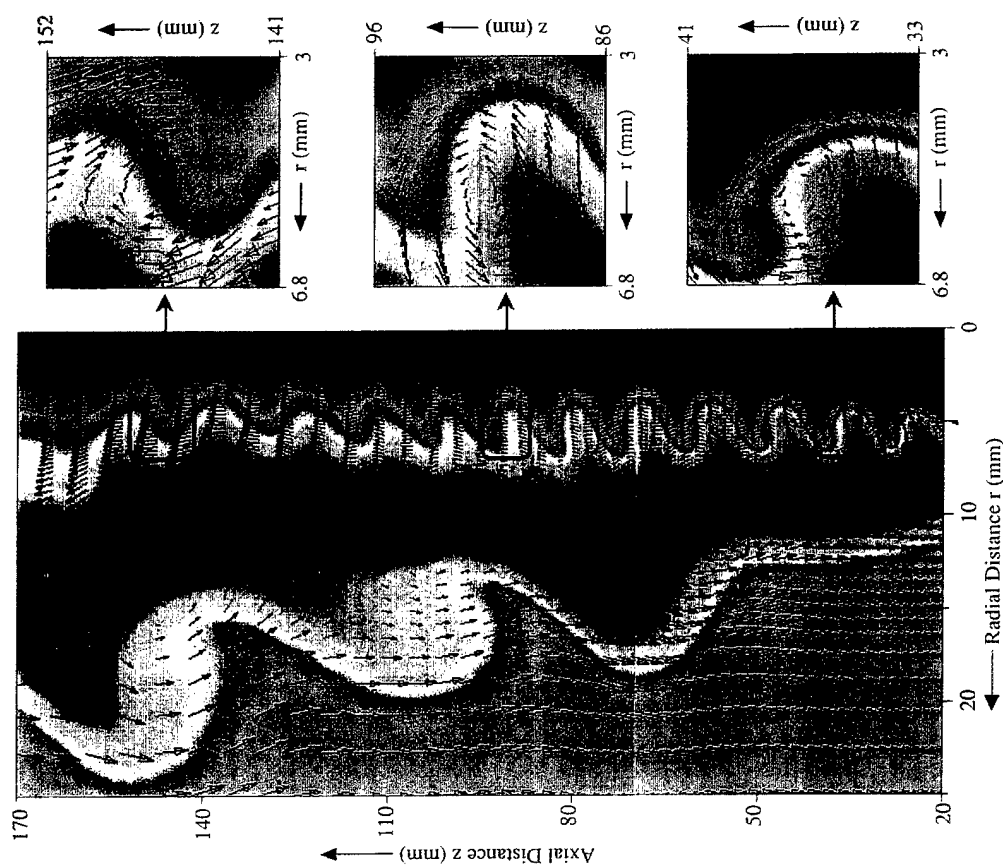


Fig. 2. Flowfield between $z = 20$ and 140 mm showing structural details of flame. Density is color coded between red and purple to represent lowest and highest values, respectively. Velocity vectors represent velocity field seen by observer moving at averaged velocity of respective frame. Blow-ups for three vortices are shown in insets.

ties. The spatially averaged axial velocity was 1.63 m/s; therefore, fluid moving with a lower axial velocity will appear to be traveling upstream, as is evident for the outer air flow which has a velocity of 0.15 m/s at the annular-jet exit. The inner vortices cannot be recognized easily in this reference frame because the large spatially averaged velocity is lower than the convective velocity of these vortices. The velocity-vector fields in the three inserts in Fig. 2 depict what an observer would view if moving at the spatially averaged axial velocity of the inner vortex at the instant of flame visualization. The inserts in Fig. 2 correspond to the same spatial locations as those in the boxes in Fig. 1c. The rotation of the inner structures can be clearly visualized from this reference frame.

Figure 3 contains mixture-fraction contours of four jet flows, calculated for the same configuration and inlet conditions as those in Fig. 1c. These flames have different values of heat release, volumetric expansion, and gravitational constant g . In a flame, temperature affects the fluid dynamics of the flow by changing the density (or volumetric expansion) and the transport properties. The effects of these two changes on the vortex dynamics are studied in the first two simulations. Figure 3a is an instantaneous mixture-fraction color contour plot for a jet with zero heat release (cold jet). Since heat release was not taken into account in this calculation, changes in density and transport properties due to combustion are not present. However, property changes due to the mixing of fuel and air were considered. The solid circles represent the stoichiometric-mixture-fraction surface. Figure 3b shows instantaneous-mixture-fraction contours of a flame with $g = 0$ and zero volumetric expansion. The latter was achieved by maintaining the density of the fluid constant (incompressible) while allowing the viscosity, diffusion, and other transport properties of the flow to change with the calculated temperature. Pressure in this incompressible calculation becomes a function of velocity only. Finally, Fig. 3c contains an instantaneous-mixture-fraction contour for a flame with $g = 0$ and all other properties being the same as those in Fig. 1c. The flame in Fig. 3d is the mixture-fraction contour visualization for the flame in Fig. 1c.

Figures 4a–4d show streaklines marking the roll up of fluid into the inner vortices for the cases considered in Figs. 3a–3d, respectively. In these calculations massless particles were released at a constant rate from the fixed spatial locations (shown by open circles) clustered near the exit of the nozzle. All particles released from a given location are shown by the same color.

DISCUSSION

Evaluation of the Model

The model simulated the detailed shapes of the mean temperature profiles shown in Figs. 1a and 1b. The shapes of the profiles are primarily determined by the oscillation of the flame surface that results from the rotational and convective motions of the outer vortices. The rotation of the vortices forces the flame outward at some axial locations and inward at others (see $z = 155$ and 140 mm locations in Fig. 2). The result is a flame surface that oscillates radially as the large outer vortices are convected past a fixed axial location. The measured frequency of this oscillation was 15 Hz, which compares well with the calculated value of 15.8 Hz. This oscillation is responsible for the inflection of the mean temperature profile at a radial location of 20 mm at $z = 100$ and 150 mm in Fig. 1b. The inflection is predicted by the model and corresponds to the maximum radial location of the flame oscillation. This inflection occurs because the flame spends a large fraction of the oscillation cycle in the region of the inflection as it slows down and then stops before being pushed back toward the centerline. Also note in Fig. 1b that with adjustment for radiation loss, the model yields reasonably good estimates of the magnitude of the mean-temperature profiles, except near the centerline of the fuel jet. Measurements show higher average and RMS temperatures inside the flame. The additional transport mechanism that governs this enhanced combustion inside the flame is not well understood. One speculation is that radiation from soot and nitric oxide at the flame surface heats the potential core significantly. However, some degree of uncertainty is associated with temperature measurements inside the flame because of

the scarcity of the nitrogen molecules there (pure propane was used as the fuel). CARS actually measures the temperature of N_2 , which, inside the flame surface, would be hot because these N_2 molecules gain heat as they diffuse through the flame. The cooler fuel temperatures inside the flame, however, would not be recorded by the CARS measurements; thus, the measured mean temperatures could be biased high, well inside the flame surface.

The model predicts and experiments confirm that two peaks are present in the RMS profiles (see Fig. 1b). The oscillation of the flame surface due to the outer vortices is responsible for the peak RMS temperatures noted at $r \approx 15$ mm in Fig. 1b. At $z = 100$ and 150 mm, an inflection is also present in the predicted and measured RMS temperatures (at $r \approx 20$ mm) because, as described above, the flame ceases to move as it approaches its maximum radial location. The second peak in the RMS profiles, between $r = 5$ and 10 mm, is the result of an oscillation in the temperature field induced by the rotational and convective motions of the inner vortices. This interaction process is indicated by the temperature contours in Fig. 1c and clearly shown by the density oscillations and velocity vectors in the inserts in Fig. 2. The calculations in Fig. 2 also show that small wrinkles occur in the flame surface (solid circles) at the location where the flame approaches the inner vortices (see $z = 100$ and 130 mm in Fig. 2). These small wrinkles in the flame surface, which are weak and not a major contributor to the RMS profiles in Fig. 1b, have also been observed recently by Chen et al. [17] in studies of this flame.

It is well known that the vortices inside transitional jet diffusion flames maintain their coherence for long distances downstream [1]. Comparison of Fig. 1a with Figs. 1c and 2 shows that the model has captured this important feature. Even the coherence lengths in the calculated and measured flames are about the same. The inner structures of the experimental flame are weakened at $z = 165$ mm and completely dissipated at a height of ~ 210 mm. This weakening of the inner vortices appears to be associated with the third flame bulge and the change in direction of rotation of the vortices as seen in Fig. 1a. For the calculated flame in Fig. 2, the inner vortices begin to

change their direction of rotation at the location where the flame begins to bulge outwardly (second flame bulge). The reversal in the direction of rotation of the inner vortices is complete at a height of 147 mm, leading to their dissipation at about $z = 165$ mm. From Figs. 1c and 2, it is clear that the model reproduces this complicated rotational reversal process. However, some disagreement exists concerning the frequencies of the inner vortices. Although the measured frequency of the inner structures was 320 Hz, a lower-amplitude peak at 180 Hz was also measured. Amplification in the calculations is maximum for the driving frequency of 190 Hz. The calculations appear to be amplifying this lower-frequency component more than the higher-frequency one. The reason for this is presently under investigation.

The overall assessment of the model is that it has correctly predicted most of the detailed structural features of this rather complex transitional propane jet diffusion flame. Thus, it can be used to gain insight into the physics associated with some of the observed characteristics of this flame. In the next two sections, model results will be examined to determine the cause of the rotational reversal of the inner vortices and to provide insight into the reason for the inner vortices maintaining their coherence for long distances.

Reversal in Direction of Rotation of Vortices Inside the Flame

The reversal of the inner structures was first observed by Eickhoff and Winandy [3]. They postulated that this phenomenon was induced by the motion of the outer vortices. Roquemore et al. [4] also observed this phenomenon and speculated that buoyancy accelerates the hot gases of the flame in such a way that at some distance downstream, they have a higher velocity than the potential flow for the fuel jet. This reversal in the slope of the velocity gradient causes the vortices to change their direction of rotation. The computational data obtained for this flame will be used to examine these points.

Figure 2 shows the origin of the reversal in the rotation of the inner structures. At a height of 147 mm, the inner vortices change their direction of rotation (see small inserts in Fig.

2). At this location the velocity vectors in the high-temperature region of the flame (red contour) are higher than those of the potential core, which is not the case low in the flame. This occurs because the rotational motion of the buoyancy-generated outside vortex, centered at $z \approx 147$ mm, induces an acceleration of the fluid between the flame and the potential core as the flame is pulled in an outward direction. When this motion is combined with the acceleration due to the buoyancy force, the velocity of the fluid surrounding the inner vortices becomes locally higher than the convective velocity of the potential core. This creates a recirculation, which rotates in the direction opposite to that of the inner vortices, within the enclosed central-jet (potential-core) fluid. If an inner vortex is present as the recirculation zone is formed and if the recirculation zone has sufficient strength, then the direction of rotation of the inner vortex will change to that of the recirculation zone. This has a dissipating effect on the inner vortices. The formation of a recirculation zone as the outer vortices pull the flame in an outward direction has been observed in lower speed jet diffusion flames and occurs irrespective of the presence of the inner vortices [3, 4, 18].

Eickhoff and Winandy [3] noted that the range of jet velocities over which the inner vortices are observed to reverse their direction of rotation is relatively small, the reason being that the following two effects must exist simultaneously for this to happen. The outer vortices must have sufficient strength and time to induce an outward motion of the flame, and the fuel jet velocity must be sufficiently high to generate the velocity gradients which lead to the formation and growth of the inner vortices. These two requirements are only satisfied over a small range of velocities. For example, the inner vortices form at a velocity of about 1 m/s for both methane [4] and propane [18] flames. At jet velocities above ~ 3 m/s, the convective velocity of the flame becomes sufficiently high and the strength of the outer vortices is sufficiently weak that very little outward deflection of the flame is induced and, hence, a very weak recirculating flow is created. Thus, the reversal phenomenon might be expected for hydrocarbon jet flames at velocities between about 1 and 3 m/s. Although this

velocity range is only approximate and varies significantly with annulus-air velocity and nozzle design, it is only slightly different from the values quoted by Eickhoff and Winandy [3].

Coherent Nature of Internal Structures

The realization that buoyancy can affect the inner vortices raises the possibility that it also contributes to the long coherence length of the inner vortices. The results in Fig. 2 indicate that this may be the case. The inner vortices are located in the green region of Fig. 2, at a radial position between 4 and 7 mm. Two points can be made from inspection of the velocity vectors in this region and the adjacent region of hot (red) fluid. First, as the flow progresses downstream, the directions of the velocity vectors indicate that very little fluid is being transported into the small vortices. It appears that most of the fluid is being accelerated upward by buoyancy or entrained into the hot region near the flame. Second, the axial-velocity gradient is initially positive (see $z \approx 30$ mm location), progresses to zero at $z \approx 100$ mm, and becomes negative at higher axial locations, as is evident from the change in magnitude of the velocity vectors with radial location. The axial-velocity gradient is thought to be responsible for the formation of the inner vortices and, in the case of cold jets, also to be responsible for their destruction because it leads to the entrainment of the lower speed fluid into the vortices. This entrainment results in the dissipation of the vortices and a reduction in the axial-velocity gradient. Thus, the jet flame and the cold jet differ in several important ways. In the flame case, fluid is entrained into the hot buoyant accelerated flame rather than into the inner vortices. The buoyant acceleration reduces the axial-velocity gradient of the jet shear layer, which, in turn, reduces the tendency of fluid to be entrained into the inner vortices. In a cold jet significant entrainment of the low-speed fluid into the vortices leads to the loss of coherence of the vortices.

Factors other than buoyancy may be involved in maintaining the long coherence length of the inner vortices (or, in other words, in delaying their transition to turbulence). Yule et al. [1] have suggested that a decrease in the effective Reynolds number due to the higher

viscosity of the hot products contributes to the coherence of the inner vortices [1]. Recently, Chen et al. [18] suggested that vorticity destruction inside the flame due to the baroclinicity and volumetric expansion contributes to the long coherence length. They showed the impact of volumetric expansion due to heat release on the vortices by presenting near-field visualizations of the flame in Fig. 1a and the unreacted cold jet for the same flow conditions. For the cold jet, coherent vortices that were formed in the shear layer began to coalesce and lose their coherence at ~ 2 nozzle diameters downstream. The first vortex-merging in the experiments led to a fine-scale turbulent structure, and the flow became three dimensional. Figure 3a is a mixture-fraction visualization of the computed cold jet with $g = 0$ and is similar to the flow which was observed experimentally [18]. Figure 3a and particle traces in Fig. 4a show that the vortices in the computed cold jets are growing rapidly and losing coherence. In fact, the vortices are merging at two different locations—first at ~ 2 nozzle diameters and later at 10 nozzle diameters downstream. After merging, the vortices develop into a larger vortex. The axisymmetric nature of the present calculations prevents the growth of the azimuthal instabilities and thereby, the breakup of vortices into smaller ones.

As described earlier, Fig. 3b examines the effects of the temperature dependence of the viscosity and other diffusion coefficients, neglecting volumetric expansion. The stoichiometric surface moves away from the shear layer due to increased diffusion, and the viscous layer along the stoichiometric surface appears to dampen the growth of the inner vortices (compare Figs. 3a and 3b). The first vortex-merging in this case takes place at a location between 3 and 4 nozzle diameters downstream (Fig. 4b), and the particles that were released at the black open circles are entering the vortex train only at a height of 50 mm above the nozzle. Since the viscous layer surrounding the shear layer acts as a shield to the shear-layer vortices, these vortices are stretched axially more than radially.

When heat release was also added to the calculations (Fig. 3c), the inner vortices did not grow significantly and were completely dissi-

pated at ~ 100 mm above the nozzle. The reason for this is that the volumetric expansion moves the stoichiometric surface closer to the shear layer, and viscous fluid near the flame surface is entrained into the vortices, leading to their dissipation. A completely dissipated shear layer can be clearly identified from the thick layer of particles outside the fuel jet which is a blend of all colors (Fig. 4c). The oscillations generated inside the potential core (fuel jet) due to the motion of the vortices at the upstream locations are present throughout the length considered in Fig. 4c, and very weak roll-ups within these oscillations may be seen from the blue-color particle traces. When buoyancy is added to the computation (Fig. 3d), the flame surface moves even closer to the shear layer and one might expect the inner structures to decay more quickly than for the condition in Fig. 3c because more viscous fluid is expected to be entrained into the vortices. Instead, the inner vortices in Fig. 3d travel farther downstream without growing significantly, which indicates that buoyancy reduces the amount of hot viscous fluid entrained into the vortices and, as described earlier, also reduces the potential of the vortices to entrain fluid by reducing the velocity gradient. This analysis suggests that buoyancy is a major factor in maintaining the long coherence length of the inner vortices since it must overcome the dissipative effects of viscosity and volumetric expansion due to heat release. The particle traces in the shear layer (Fig. 4d) closely resemble those in the experimental flame image (Fig. 1a). The motion of the outer vortices causes the potential core to bulge and squeeze as seen in Fig. 4d at axial locations of ~ 80 and 140 mm, respectively. A comparison of streakline plots for the four cases indicates that the change in the size of the inner vortices observed in the transitional diffusion flame (Fig. 4d) is caused by the motion of the buoyancy-driven outer structures.

CONCLUSIONS

Past experiments have demonstrated the double-vortex structure in transitional jet diffusion flames. In the present work a CFD-based model, with an implicit numerical method that is third-order accurate in space and time and a

simple flame-sheet chemistry submodel, successfully simulated the slowly moving large vortices outside the flame and the small-scale inner vortices. The salient features of this flame such as the existence of coherent inner vortices and the change in their direction of rotation are well captured by the model. Buoyancy was found to play a significant role in maintaining the coherence of the inner structures over long distances and, thus, retarding the transition to turbulence. The inner vortices in the computed flame cause small-scale wrinkles to occur in the flame surface, but their overall impact on the combustion process is negligible. However, at higher jet-flow velocities, these vortices interact more strongly with the flame surface, which will be investigated in the future.

This work was supported, in part, by U. S. Air Force Contract F33615-90-C-2033. The first author acknowledges NRC and AFSC for sponsoring him on the Postdoctoral Fellowship Program during 1989-91. The authors would like to thank Professor L.-D. Chen, Dr. D. R. Ballal, and Mr. R. Bradley for their helpful discussions and Mrs. M. Whitaker for help in preparation of the manuscript.

REFERENCES

1. Yule, A. J., Chigier, N. A., Ralph, S., Boulderstone, R., and Ventura, J., *AIAA J.* 19:752 (1981).
2. Eickhoff, H., *Instability and Coherent Structures in Jet Flames. Recent Contributions to Fluid Mechanics*, Springer-Verlag, Berlin, 1982, pp. 50-57.
3. Eickhoff, H., and Winandy, A., *Combust. Flame* 60:99 (1985).
4. Roquemore, W. M., Chen, L.-D., Goss, L. P., and Lynn, W. F., in *Turbulent Reactive Flows, Lecture Notes in Engineering* (R. Borghi and S. N. B. Murthy, Eds.), Springer-Verlag, Berlin, 1989, Vol. 40, p. 49.
5. Chamberlin, D. S., and A. Rose., *Ind. Eng. Chem.* 20:1013 (1928).
6. Buckmaster, J., and N. Peters., *Twenty-First Symposium (International) on Combustion*, The Combustion Institute, Pittsburgh, 1986, p. 1829.
7. Kimura, I., *Tenth Symposium (International) on Combustion*, The Combustion Institution, Pittsburgh, 1965, p. 1295.
8. Toong, T.-Y., Salant, R. F., Stopford, J. M., and Anderson, G. Y., *Tenth Symposium (International) on Combustion*, The Combustion Institute, Pittsburgh, 1965, p. 1301.
9. Chen, L.-D., Seaba, J. P., Roquemore, W. M., and Goss, L. P., *Twenty-Second Symposium (International) on Combustion*, The Combustion Institute, Pittsburgh, 1988, p. 677.
10. Davis, R. W., Moore, E. G., Roquemore, W. M., Chen, L.-D., Vilimpoc, V., and Goss, L. P., *Combust. Flame* 83:263 (1991).
11. Ellzey, J. L., and Oran, E. S., *Twenty-Third Symposium (International) on Combustion*, The Combustion Institute, Pittsburgh, 1990, p. 1635.
12. Ellzey, J. L., Laskey, K. J., and Oran, E. S., *Prog. Astronaut. Aeronaut.* 131:179 (1989).
13. Mahalingam, S., Cantwell, B., and Ferziger, J., *AIAA Paper 89-0661*, 27th Aerospace Sciences Meeting, Reno, 1989.
14. Leonard, B. P., *Comp. Meths. Appl. Mech. Eng.* 19:59 (1979).
15. Katta, V. R., Goss, L. P., and Roquemore, W. M., *AIAA Paper 92-0335*, 30th Aerospace Sciences Meeting, Reno, 1992 (submitted for publication).
16. Michale, A., and Hermann, G., *J. Fluid Mech.* 114:343 (1982).
17. Chen, L.-D., Private communication.
18. Chen, L.-D., Roquemore, W. M., Goss, L. P., and Vilimpoc, V., *Combust. Sci. Technol.* 77:41 (1991).

Received 14 April 1992; revised 22 September 1992

SIMULATION OF VORTICAL STRUCTURES IN A JET DIFFUSION FLAME

V. R. KATTA, L. P. GOSS

*Systems Research Laboratories, Inc., A Division of Arvin/Calspan, 2800 Indian Ripple Road,
Dayton, OH 45440-3696, USA*

AND

W. M. ROQUEMORE

Wright Laboratory, Aero Propulsion and Power Directorate, Wright-Patterson Air Force Base, OH 45433-7103, USA

ABSTRACT

The dynamics of a transitional propane jet diffusion flame with a fuel-jet velocity of 2.2 m/s has been studied using an implicit, third-order-accurate, upwind numerical scheme. The large-scale vortices outside the flame surface and the small-scale ones inside were simulated simultaneously, and their interactions with the flame surface were investigated. Numerical experiments were conducted to gain insight into the influence of buoyancy and shear-layer forcing on the development of the outer and inner vortices. In the presence of buoyancy forces, the outer vortices developed as part of the solution, and the vortex-crossing frequency was approximately 15 Hz. The inner structures were manifested from a weak perturbation in the vorticity that was introduced at the nozzle exit, and, at 185 Hz, these vortices were found to travel farther downstream. It was also found that the inner vortices do not play a role in the formation of the outer vortices, and vice versa. However, the growth of the inner vortices in the downstream locations is strongly influenced by the slowly moving outer vortices.

KEY WORDS Jets Diffusion flame Vortices Upwind

INTRODUCTION

The existence of vortex structures inside and outside the flame surface that become a characteristic of transitional jet diffusion flames was first observed by Yule *et al.*¹ and subsequently by Eickhoff² and Roquemore *et al.*³. The inner small-scale structures in flames that develop due to the instability of the jet shear layer are different from those in cold jets⁴. The vortices in a reacting flow grow very slowly and maintain their identities over a long distance, as compared to the rapid formation and growth of these structures in cold flows. However, in both reacting and cold flows, the frequency of the inner vortices depends on the velocity gradient across the shear layer and the viscosity. The large vortices in flames, on the other hand, are generated outside the flame surface and are analogous to the structures observed along heated vertical walls⁵. These slowly moving outer vortices are, in general, not sensitive to the fuel-jet velocity, fuel composition, or geometrical dimensions. Buckmaster and Peters⁶ have provided a theoretical background for this phenomenon by isolating the natural convective flow from the forced one.

Both the outer and inner vortices interact with the flame surface and create wrinkles on it. With the help of high-speed movies, Chen *et al.*⁷ confirmed that low-frequency flame oscillation (flame-flicker) is the result of the convective motions of the wrinkled flame and the large outer vortices. These visualizations also indicated that the shape and rotational characteristics of the inner vortices seem to change at certain locations inside the flame, which suggests that the development and growth of the inner vortices are influenced by the motion of the outer vortices.

Numerical studies by Davis *et al.*⁸ and Ellzey *et al.*⁹ have demonstrated that the large vortices outside the flame result from the buoyant acceleration of the hot gases along the flame surface. In the present paper, direct numerical simulations are presented which capture the temporal and spatial development of both the outer and the inner vortex structures of a transitional propane jet diffusion flame. Computational experiments were performed to investigate the importance of buoyancy and shear-layer forcing on the development of the outer and inner vortices. Changes in the growth of the inner vortices due to the presence of the outer vortices are also discussed.

MATHEMATICAL MODEL

The diffusion flame studied in this work is formed between a central propane jet and a very low speed co-annular air flow. The time-dependent governing equations, expressed in cylindrical coordinates (z, r), are:

$$\frac{\partial \rho}{\partial t} + \frac{\partial \rho u}{\partial z} + \frac{1}{r} \frac{\partial (r \rho v)}{\partial r} = 0 \quad (1)$$

$$\frac{\partial (\rho \Phi)}{\partial t} + \frac{\partial (\rho u \Phi)}{\partial z} + \frac{\partial \rho v \Phi}{\partial r} = \frac{\partial}{\partial z} \left(\Gamma^\Phi \frac{\partial \Phi}{\partial z} \right) + \frac{\partial}{\partial r} \left(\Gamma^\Phi \frac{\partial \Phi}{\partial r} \right) - \frac{\rho v \Phi}{r} + \frac{\Gamma^\Phi}{r} \frac{\partial \Phi}{\partial r} + S^\Phi \quad (2)$$

where ρ represents density; u and v are the axial and radial components of the velocity vector, respectively; and p is the pressure. The general form of (2) represents the axial momentum, radial momentum, species, or energy-conservation equation, depending on the variable used in place of Φ . The conserved scalar variables β_1 and β_2 defined as

$$\beta_1 = \frac{\alpha Y_O + Y_F^i - Y_F}{\alpha Y_O^i + Y_F^i}, \quad \text{and} \quad \beta_2 = \frac{h - h_O^i + (Y_F/\alpha)Q}{(Y_F^i/\alpha)Q + h_F^i - h_O^i},$$

are used to represent the species mixture fraction and enthalpy, respectively. Here α is the fuel-oxidizer ratio ($v_F M_F / v_O M_O$); Y_m and h_m are the mass fraction and enthalpy of the m th species, respectively; h is the mixture enthalpy; Q is the heat release per unit mass of oxygen consumed; M is the molecular weight; and the superscript i represents the fuel-jet and air-flow values. The chemical reaction between the fuel and the oxygen is assumed to occur at an infinitely fast rate, yielding an infinitely thin sheet of flame at:

$$\beta_1 = \beta_1^* = \frac{Y_F^i}{\alpha Y_O^i + Y_F^i}.$$

The transport coefficients Γ^Φ and the source terms S^Φ that appear in (2) are given in Table 1. The body force term due to the gravitational field is included in the axial-momentum equation. Here μ is the viscosity of the mixture; D is the local binary diffusion coefficient between any two species; ρ_0 is the density of air; and g is the gravitational acceleration. The system of governing equations is completed using the state equation:

$$p = \rho T R_0 \left\{ \frac{Y_F}{M_F} + \frac{Y_O}{M_O} + \frac{Y_P}{M_P} + \frac{Y_I}{M_I} \right\} \quad (3)$$

Table 1 Transport coefficients and source terms appearing in governing equations

Φ	Γ^Φ	S^Φ
u	μ	$-\frac{\partial p}{\partial z} + (\rho_0 - \rho)g + \frac{\partial}{\partial z}\left(\mu \frac{\partial u}{\partial z}\right) + \frac{\partial}{\partial r}\left(\mu \frac{\partial v}{\partial z}\right) + \frac{\mu}{r} \frac{\partial v}{\partial z} - \frac{2}{3} \left\{ \frac{\partial}{\partial z}\left(\mu \frac{\partial u}{\partial z}\right) + \frac{\partial}{\partial z}\left(\mu \frac{\partial v}{\partial r}\right) + \frac{\partial}{\partial z}\left(\mu \frac{v}{r}\right) \right\}$
v	μ	$-\frac{\partial p}{\partial r} + \frac{\partial}{\partial z}\left(\mu \frac{\partial u}{\partial r}\right) + \frac{\partial}{\partial r}\left(\mu \frac{\partial v}{\partial r}\right) + \frac{\mu}{r} \frac{\partial v}{\partial r} - 2\mu \frac{v}{r^2} - \frac{2}{3} \left\{ \frac{\partial}{\partial r}\left(\mu \frac{\partial u}{\partial z}\right) + \frac{\partial}{\partial r}\left(\mu \frac{\partial v}{\partial r}\right) + \frac{\partial}{\partial r}\left(\mu \frac{v}{r}\right) \right\}$
β_1	ρD	0
β_2	ρD	0

where R_0 is the universal gas constant; and T is the temperature. The subscript I in the above equation represents nitrogen which is assumed to be an inert gas in the present simulation.

Temperature- and species-dependent thermodynamic and transport properties are used in this formulation. The enthalpy of each species is calculated from polynomial curve-fits, while the viscosity of the individual species is estimated from the Chapman-Enskog collision theory¹⁰. The binary diffusion coefficient between any two species on the fuel side of the flame is assumed to be identically equal to that of the fuel and nitrogen. Similarly, on the oxidizer side of the flame, it is assumed identical to that of the oxidizer and nitrogen. The Chapman-Enskog theory and the Lennard-Jones potentials have been used to estimate the above two binary diffusion coefficients.

Numerical scheme

An orthogonal, staggered grid system with rapidly expanding cell sizes in both the z and r directions is utilized. The governing equations are integrated using an implicit QUICKEST (Quadratic Upstream Interpolation for Convective Kinematics with Estimated Streaming Terms) numerical scheme^{11,12} which is third-order accurate in both space and time and has a very low numerical diffusion error. After rearrangement of terms, the finite-difference form of (2) for the variable Φ at a grid point P can be written as an algebraic equation as follows:

$$A_P \Phi_P^{N+1} + A_{z^+} \Phi_{z^+}^{N+1} + A_{z^-} \Phi_{z^-}^{N+1} + A_{z^{++}} \Phi_{z^{++}}^{N+1} + A_{z^{--}} \Phi_{z^{--}}^{N+1} + A_{r^+} \Phi_{r^+}^{N+1} + A_{r^-} \Phi_{r^-}^{N+1} + A_{r^{++}} \Phi_{r^{++}}^{N+1} + A_{r^{--}} \Phi_{r^{--}}^{N+1} = S_P^\Phi + \Delta t \cdot \rho_P \Phi_P^N \quad (4)$$

The time increment, Δt , is determined from the stability constraint and maintained as a constant during the entire calculation. The superscripts N and $N+1$ represent the known variables at the N th time step and the unknown variables at the $(N+1)$ th time step, respectively; the subscripts z^+ and z^- indicate the values at the grid points immediately adjacent to point P in the positive and negative z -directions, respectively. Similarly, the subscripts z^{++} and z^{--} represent the values at two grid points away from P in the respective directions. The coefficients A and the terms on the right hand side of (4) are calculated from the known flow variables at the N th time step. Although, the above equation is written in general form, care must be exercised while generating the finite-difference schemes for the u and v momentum equations because of the staggered grid adopted. The four equations represented by (4) are solved individually using an iterative ADI (Alternative Direction Implicit) technique. This involves obtaining solutions for pentadiagonal matrices in the z and r directions iteratively, until the total residual drops below a specified value. Although the momentum and scalar equations represented by (4) are solved independently, a consistent sequence should be followed for simulating time-dependent reacting flows. In the present simulation the equations for β_1 and β_2 are solved first, and then the temperature and density at the $(N+1)$ th time step are obtained. Based on the previous

density, the u and v momentum equations are solved next. The pressure field at every time step is accurately calculated by simultaneously solving the system of algebraic pressure Poisson equations at all grid points using the LU (Lower-Upper) decomposition technique.

Initial and boundary conditions

The flowfield considered in the present study has vortical structures of two different scales. While the smaller-scale vortices develop inside the flame surface along the shear layer of the fuel jet, the larger-scale outer vortices form outside the flame surface. The computational domain and the boundary conditions employed to capture these vortical structures are shown in *Figure 1*. The outer boundaries II and IV (cf. *Figure 1*) of the computational domain are located sufficiently far from the nozzle exit (40 nozzle diameters) and symmetry axis (15 nozzle diameters), respectively to minimize the propagation of disturbances into the region of interest. Flat velocity profiles are used at the fuel and air inflow boundaries. The outflow boundary in these flows is the most difficult one to treat because the flow leaving this boundary continuously evolves in time as the large outside and small inside vortices cross this boundary. A simple extrapolation procedure with weighted zero- and first-order terms was used to estimate the flow variables on the boundary in the present calculations. The weighting functions, w_1 and w_2 (cf. *Figure 1*), are selected by the trial-and-error approach, and the main criterion used is that the vortices crossing the outflow boundary should leave smoothly without being distorted.

RESULTS AND DISCUSSION

The inflow conditions used in the present calculations are for a laboratory flame studied experimentally by Roquemore *et al.*³. A vertically mounted jet diffusion flame was established by burning pure propane emerging from a 10-mm-diameter contoured nozzle. Flat initial velocity profiles with measured average velocities of 2.22 m/s and 0.15 m/s were used in the calculations at the exit of the fuel nozzle and the annular duct, respectively.

Development of vortices

Laboratory experiments on this flame indicate that vortices having two different scales (referred to as large- and small-scale) can develop when the fuel jet velocity is greater than 1 m/s. According to Buckmaster and Peters⁶, the large-scale vortices that are located outside the flame surface are small perturbations amplified by a modified Kelvin-Helmholtz-type instability. In their analysis they separated the natural convection of the hot gases due to buoyancy from the forced convective flow and obtained this modified instability. The small-scale vortices are usually enclosed within the flame; hence, they are often referred to as inner vortices. It is speculated that these inner vortices are generated by the flow perturbations at the nozzle exit and amplified by the Kelvin-Helmholtz-type flow instability of the fuel-jet shear layer. The issues concerning the inner and outer vortices are difficult to address experimentally because of the inherent noise in the flow systems. On the other hand, numerical experiments can offer dissection of the complex flowfield resulting from different external forces.

Simulations of Davis *et al.*⁸ and Ellzey *et al.*⁹ indicate that the outer vortices on the flame form when the gravity force is included in the calculations. Similarly, Katta *et al.*¹¹ showed that the inner vortices do not become established without introducing noise into the fuel-jet shear layer. Therefore, four different calculations (identified as *Flames 1-4*) were performed in the present study to gain insight into the factors that might influence the development and growth of the vortices in the flame under study. The gravity term in the axial-momentum equation was neglected in the first two cases, and shear-layer perturbations were not introduced in the first and third calculations. Results in the form of iso-temperature contours are plotted in *Figures*

2(a)–2(d). When both gravity and shear-layer perturbations were absent in the *Flame-1* calculation, the solution converged to a steady flame, as seen in *Figure 2(a)*. The possibility that the inner structures generate the outer structures may be ruled out as a result of the second calculation (*Flame 2*). Velocity perturbations of $\sim 0.3\%$ in magnitude and at a frequency of 185 Hz were introduced at the shear layer near the nozzle exit in this calculation. Inviscid stability analysis¹³ suggests that the most amplified frequency for the co-annular jet shear layer considered is ~ 400 Hz. In actual calculations, the perturbations introduced at this frequency did not travel beyond a few nozzle diameters downstream. This could be due to the viscosity of the combustion products. However, the most amplified frequency in these viscous calculations is determined by repeating several calculations and varying the perturbation frequency. At 185 Hz the disturbances travelled farther downstream and developed into a train of inner vortices. The highly viscous fluid resulting from the combustion along the flame surface is entering into the inner vortices and causing them to dissipate at $z = 100$ mm. When the buoyancy force was neglected in this simulation, even the inner vortices did not cause the outer vortices to form (*Figure 2(b)*). However, the flame surface in the downstream locations exhibits weak oscillations, with scales on the order of those of the outer vortices. These oscillations may be due to another type of flow instability which is developing in the low-density flame zone.

When the buoyancy term was activated in the axial-momentum equation, the flame began to oscillate immediately and quickly settled into periodic oscillations, as seen in *Figure 2(c)*. It is important to note that no artificial perturbation was used in this calculation (*Flame 3*). In the presence of a gravity force, the acceleration of hot gases along the flame surface generated the outer structures as part of the solution. The frequency corresponding to the passage of the outer vortices is ~ 15 Hz. Although the entire flow including the fuel-jet shear layer is oscillating at this low-frequency, it did not initiate the small-scale inner structure; therefore, the potential core remained laminar. In the last calculation (*Flame 4*), the shear-layer perturbations introduced at

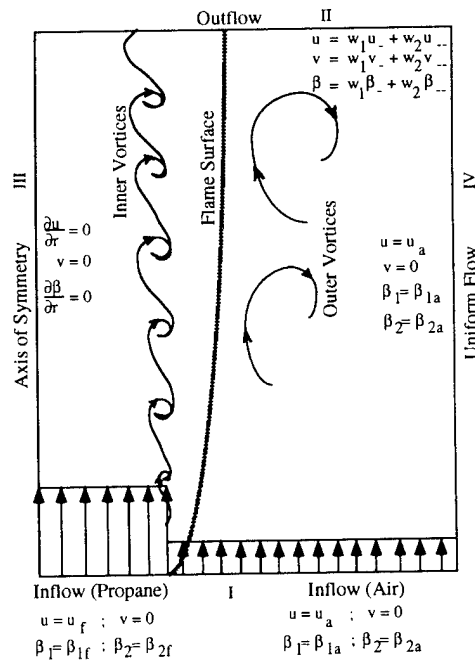


Figure 1 Computational domain and boundary conditions used in calculations

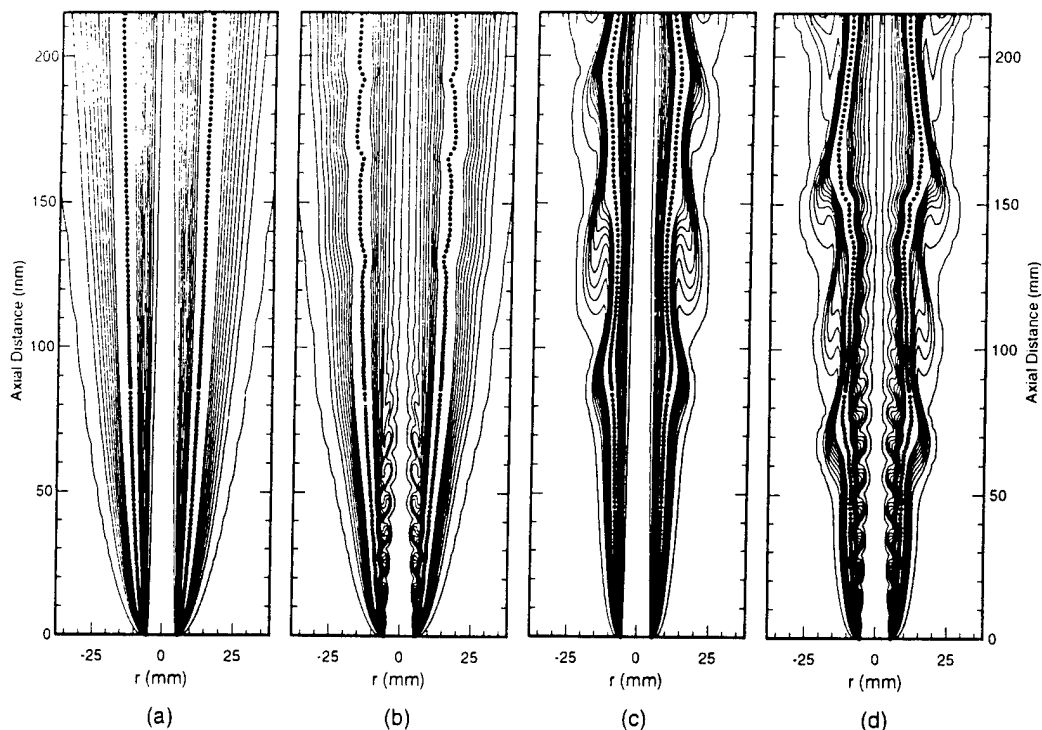


Figure 2 Iso-temperature contours of propane jet diffusion flame obtained from different calculations. Solid circles indicate stoichiometric flame surface. Flame in absence of buoyancy forces (a) without and (b) with shear-layer perturbations. Flame under influence of buoyancy (c) without and (d) with shear-layer perturbations

185 Hz developed into long coherent inner structures. This flame appears to be very similar to the laboratory flame³ and captures its salient features such as the existence of outer and inner structures, longer coherence length for the inner vortices, and relaminarization (losing flow instabilities) of the potential core downstream of $z = 160$ mm. The outer vortices in this flame seem to form earlier than those in the flame without the inner vortices (*Flame 3*).

Influence of double-vortex structure on flame

The radial distributions of temperature and axial velocity at an axial location of 100 mm are compared for different cases in Figures 3 and 4, respectively. Since *Flame 1* is a steady flame without inner or outer vortices, the RMS (Root Mean Square) values for this case are zero. The flame surface in this case (Figure 3(a)) is located farther away from the center than that in the experiment, and both the temperature and velocity are poorly predicted; these results indicate the importance of buoyancy in this transitional jet flame. The predictions of the current model (*Flame 4*) are in good agreement with the experimental data. The inflection points in the temperature profiles (at $r = 13$ mm in Figures 3(a) and 3(b)) that arise from the motion of the outer vortices are correctly predicted. However, inside the flame the temperature measurements show higher average and RMS values. It is not clear what additional transport mechanism is leading to the enhanced combustion inside the flame. One speculation is that the fine-scale turbulence originating from the nozzle walls is increasing the mixing between the fuel and the oxidizer. However, some degree of uncertainty is associated with temperature measurements (based on the temperature of the nitrogen molecules) inside the flame because of the scarcity of

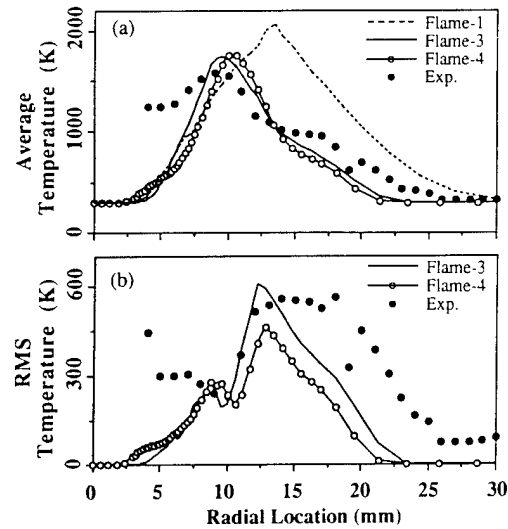


Figure 3 Radial distributions of computed and measured temperature at $z = 100$ mm. (a) Average; (b) RMS

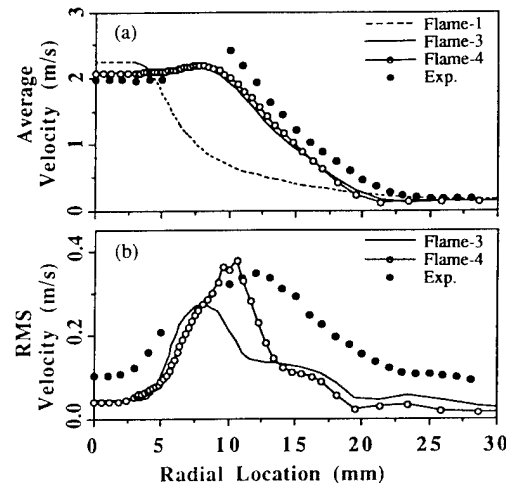


Figure 4 Radial distributions of computed and measured axial velocity at $z = 100$ mm. (a) Average; (b) RMS

the nitrogen molecules there. Closer agreement for the predicted velocities can be seen in *Figures 4(a) and 4(b)*. The potential core emanating from the 5-mm-radius nozzle is decaying quickly in the nonbuoyant flame calculation (*Flame 1*). The acceleration of hot gases due to buoyancy in *Flames 3 and 4* reduced the velocity gradient to almost zero at the edge of the potential core. This led to a much slower growth rate for the inner vortices in the case of *Flame 4*, as compared to that of the nonbuoyant case, *Flame 2* (cf. *Figure 2*). Although the presence of the inner vortices in *Flame 4* improved the predictions of the average temperature and velocity, their impact on the overall flame seems to be very small up to $z = 100$ mm. This is to be expected since in diffusion flames, the high-temperature surface separates the fuel and the oxidizer. The internal

structures formed along the edge of the potential core which is well inside the flame surface do not enhance mixing between the fuel and the oxidizer; instead, they improve mixing of burnt products with the fuel. This results in only small changes in the temperature and velocity distributions inside the flame.

Temperature evolutions and the corresponding pdf's (probability density functions) at two axial locations ($z = 50$ and 150 mm) for the *Flame-4* case are plotted in *Figures 5* and *6*, respectively. At the former axial location, the inner vortices are stronger and the outer vortices weaker than the respective ones at the latter axial location. The computed temperature data along the radial direction at these axial locations are first recorded over several flame-flicker cycles. The time evolution of the temperature is then obtained by plotting constant-temperature contours. Data for about one flickering cycle (~ 80 ms) are shown in *Figures 5(a)* and *6(a)*. The pdf plots (*Figures 5(b)* and *6(b)*) are obtained by calculating the probability density of the temperature at each radial location from the recorded data and then drawing constant-probability contour lines. The convergence of contour lines at $r = 16$ mm in *Figure 6(b)* indicates that the vortex at this axial location is well separated from the flame. The bi-modal probability distribution of temperature at a given radial location is due to the flame oscillation or flicker which, in turn, results from the convective motion of the vortices. The radial movements of the flame surface (width of the pdf plots in *Figure 5(b)* and *6(b)* at peak temperature) at $z = 50$ and 150 mm are about 1.2 and 2.8 mm, respectively.

Rotation of the fluid in the outer vortex is such that it pulls the hot gases from the flame surface on the leading side of the vortex and brings the outside air into the flame zone on the trailing side. On the other hand, the inner vortices add fuel to the flame zone on the leading side and take away combustion products on the trailing side. In both situations, wrinkles (cf. *Figures 2(d)*, *5(a)*, and *6(a)*) having scales corresponding to the interacting vortices form on the

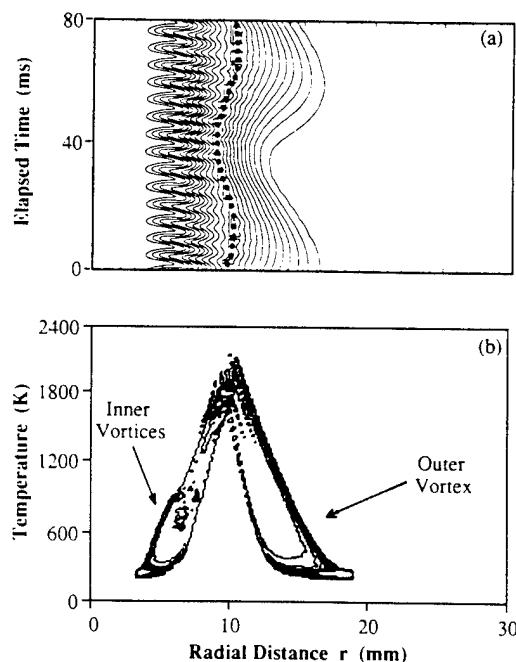


Figure 5 (a) Temperature history of computed flame at $z = 50$ mm. (b) Iso-probability-density contours obtained from temperature data

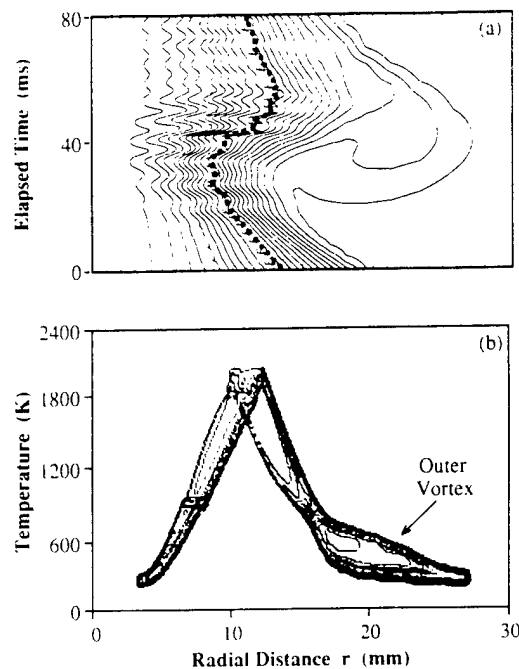


Figure 6 (a) Temperature history of computed flame at $z = 150$ mm. (b) Iso-probability-density contours obtained from temperature data

flame surface. The small-scale wrinkles on the flame surface in the calculations occur at the instant when the flame is pushed closer to the potential core by the outer vortex. Although these small-scale wrinkles are weak and not a major contributor to the RMS profiles in *Figure 3(b)*, they have been recently observed by Chen *et al.*¹⁴ in the studies of this flame using the thin-filament-pyrometry technique. However, at higher jet flow velocities, the inner vortices grow much more rapidly and may interact with the flame surface strongly.

Evolution of vortices

Frequency spectra at different axial locations for the flame under consideration were obtained from the temperature data collected at a radial location within the shear layer ($r = 5$ mm) and are shown in *Figure 7*. Two different modes of shear-layer oscillations are evident from these spectra. The lower-frequency component results from the convective motion of the outer vortices and the higher-frequency one from the inner vortices. At $z = 50$ and 100 mm, the outer vortices create weaker fluctuations within the shear layer than the inner ones. This process is reversed at $z = 200$ mm, indicating relaminarization of the shear layer. Absence of frequencies other than the natural 15 Hz and the forced 185 Hz suggests that no vortex merging is taking place in this flame. However, the peaks—especially at 185 Hz—become broad at the downstream locations. This could be due to the influence of the outer vortices on the inner ones. The squeezing action of the outer vortex not only increases the local axial velocity but also brings the viscous fluid of the flame zone closer to the inner vortices, which could affect the growth of the nearby inner vortex. Therefore, the instantaneous inner-vortex structure shown in *Figure 2(d)* might change when the outer vortices are located at a different position at another instant of time.

The evolution of the inner and outer vortices is visualized in *Figure 8* using a particle-tracking technique. During the calculations for *Flame 4*, massless particles were released in the shear

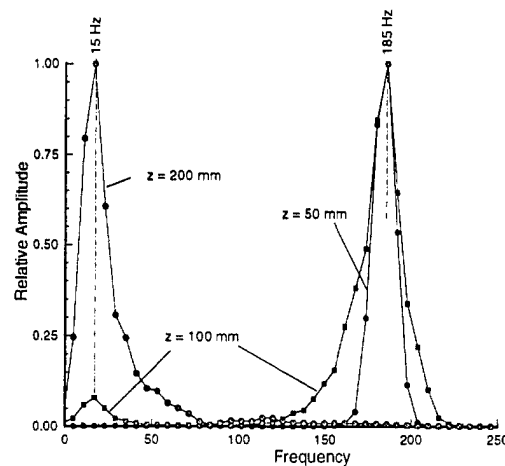


Figure 7 Frequency spectra at different axial locations obtained from temperature data

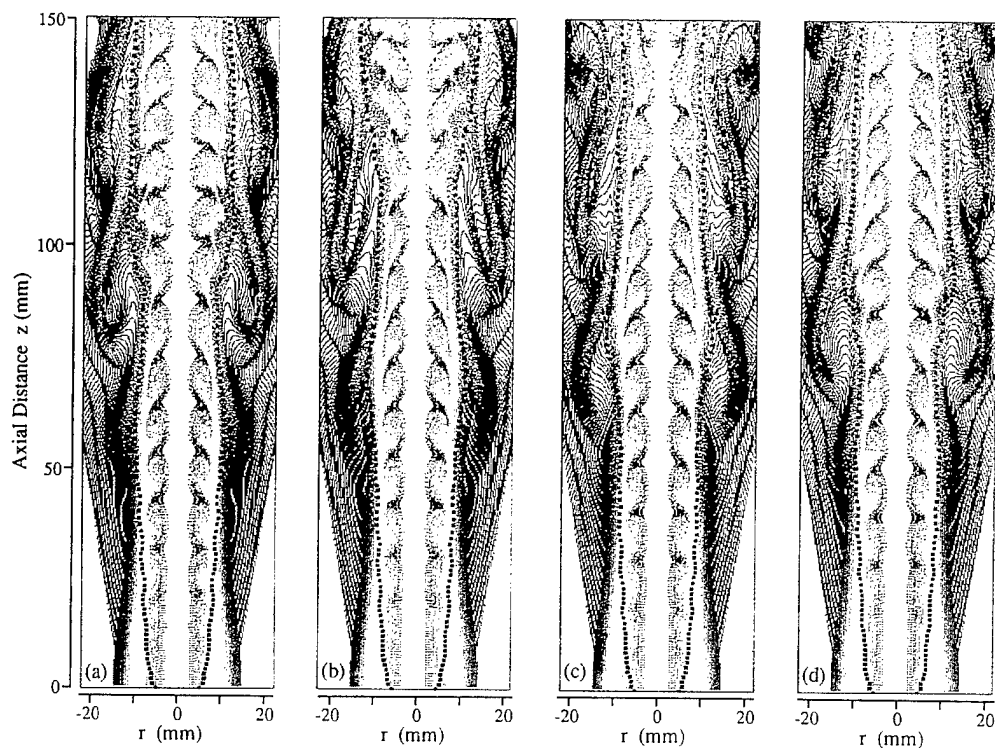


Figure 8 Evolution of inner and outer vortices visualized by particle traces. Massless particles are continuously released at the nozzle exit and along inclined line in annular air flow. Instantaneous locations of all particles released from the same location are plotted with same color. Black solid squares indicate stoichiometric flame surface. (a) $t = 0$; (b) $t = 17.7$ ms; (c) $t = 35.5$ ms; (d) $t = 53.2$ ms

layer at the nozzle exit and along the inclined line in the outer-annulus air flow. At a given instant of time, the locations of all particles released from a common point were plotted with the same color. Therefore, the particles represented with the color green in *Figures 8(a)–8(d)* were released inside the flame and at the nozzle exit. Similarly, the particles represented with the color blue were released at a location farther outside the flame and in the annular air flow. Four instantaneous images with a phase difference of 17.75 ms, which is about one-fourth of the flame-flicker cycle, are shown in *Figures 8(a)–8(d)*. The vortex structures are more easily identified in these plots than in the contour plot of *Figure 2(d)*. The solid squares indicate the instantaneous location of the stoichiometric flame surface. The particles that were released in the annular-air flow cross the flame surface, which shows an important characteristic of a diffusion flame—that the external fluid is continuously entrained into the flame zone¹⁵.

The shape of the inner vortices up to $z = 50$ mm is very similar in all four phases. In these figures no effort was made to match the phases of the inner vortices. At this location, the outer vortex begins to affect the flame. It is clear that the inner vortices are stretched axially, while the flame is squeezed by the outer vortex (at $z = 80$ mm in *Figure 8(a)*, at $z = 110$ mm in *Figure 8(b)*, and at $z = 150$ mm in *Figure 8(c)*). Similarly, when the flame bulges out, the inner vortices are pulled radially or, in other words, compressed axially. These structural changes are reflected in the broadening of the frequency spectra in *Figure 7*. The inner vortices of this flame exhibit an interesting characteristic. At $z = 145$ mm and $t = 17.75$ ms, the inner vortices change their direction of rotation¹⁶. This phenomenon occurs due to a combination of the two fluid accelerations which result from (1) the rotational motion of the buoyancy-generated outside vortex and (2) the buoyancy force on the hot gases. The change in rotation of the inner vortices was also observed in the experiments³ at about the same height from the nozzle exit.

CONCLUSION

A third-order accurate, upwind numerical scheme is used to capture the complex dynamics of a transitional jet diffusion flame. The two distinct vortex structures—one inside and the other outside the flame surface—were simulated simultaneously, and the flame surface was found to be located between these vortex structures. Buoyancy is responsible not only for generating the outside structures but also for maintaining the coherence (or identity) of the inner structures over a long distance downstream. The low-frequency perturbations (~ 15 Hz) generated by the motion of the outer vortices do not initiate the development of the inner vortices. When the fuel-jet shear layer was forced with higher-frequency perturbations, the response was observed to be maximum at 185 Hz. Although the inner vortices create small wrinkles on the flame surface, their overall impact on the flame is insignificant. The presence of the outer vortices, however, has a significant effect on the development of the inner vortices. When the flame is pulled out by the outer vortex, the nearby inner vortices become compressed axially. In a near-turbulent flame, such compression of vortices results in merging vortices.

ACKNOWLEDGEMENT

This work was supported, in part, by US Air Force Contract F33615-90-C-2033. The authors would like to thank Mrs. M. Whitaker for help in the preparation of the manuscript.

REFERENCES

- 1 Yule, A. J., Chigier, N. A., Ralph, S., Boulderstone, R. and Ventura, J. Combustion-transition interaction in a jet flame. *AIAA J.*, 19 (6), 752–760 (1981)

- 2 Eickhoff, H. Instability and coherent structures in jet flames, *Recent Contributions to Fluid Mechanics*, Springer-Verlag, Berlin and Heidelberg, 50–57 (1982)
- 3 Roquemore, W. M., Chen, L.-D., Goss, L. P. and Lynn, W. F. The structure of jet diffusion flames, *Turbulent Reactive Flows, Lecture Notes in Engineering*, 40 (R. Borghi and S. N. B. Murthy, Eds.), Springer-Verlag, Berlin, 49–63 (1989)
- 4 Savas, O. and Gollahalli, S. R. Flow structure in near-nozzle region of gas jet flames, *AIAA J.*, 2 (7), 1137–1140 (1986)
- 5 Holman, J. P., Gartrell, H. E. and Soehngen, E. E. An interferometric method of studying boundary layer oscillations, *J. Heat Trans.*, 82, 263–264 (1960)
- 6 Buckmaster, J. and Peters, N. The infinite candle and its stability—A paradigm for flickering diffusion flames, *Twenty-First Int. Symp. on Combustion*, The Combustion Institute, Pittsburgh, PA, 1829–1836 (1986)
- 7 Chen, L.-D., Seaba, J. P., Roquemore, W. M. and Goss, L. P. Buoyant diffusion flames, *Twenty-Second Int. Symp. on Combustion*, The Combustion Institute, Pittsburgh, PA, 677–684 (1988)
- 8 Davis, R. W., Moore, E. F., Roquemore, W. M., Chen, L.-D., Vilimpoc, V. and Goss, L. P. Preliminary results of a numerical-experimental study of the dynamic structure of a buoyant jet diffusion flame, *Combust. Flame*, 83, 263–270 (1991)
- 9 Ellzey, J. L., Laskey, K. J. and Oran, E. S. Effects of heat release and gravity on an unsteady diffusion flame, *Twenty-Third Int. Symposium on Combustion*, The Combustion Institute, Pittsburgh, PA, 1635–1640 (1990)
- 10 Reid, R. C., Prausnitz, J. M. and Poling, B. E. *The Properties of Gases and Liquids*, McGraw-Hill Book Company, New York (1987)
- 11 Katta, V. R., Goss, L. P. and Roquemore, W. M. Numerical investigations on the dynamic behaviour of a H_2 - N_2 diffusion flame under the influence of gravitational force, *AIAA Paper 92-0335*, Reno, NV (1992)
- 12 Leonard, B. P. A stable and accurate convective modelling procedure based on quadratic upstream interpolation, *Comp. Meth. Appl. Mech. Eng.*, 19, 59–98 (1979)
- 13 Michalke, A. and Jermann, G. On the inviscid instability of a circular jet with external flow, *J. Fluid Mech.*, 114, 343–350 (1982)
- 14 Chen, L.-D. Private communication (University of Iowa, Iowa City, Iowa) (1991)
- 15 Takahashi, F., Mizomoto, M. and Ikai, S. Structure of the stabilizing region of a laminar jet diffusion flame, *J. Heat Trans.*, 110 (2), 192–189 (1988)
- 16 Katta, V. R. and Roquemore, W. M. Role of inner and outer structures in a transitional diffusion flame, *Comb. Flame*, 92, 274–282 (1993)



AIAA 93-0454

**Effect of Nonunity Lewis Number and Finite-Rate
Chemistry on the Dynamics of a Hydrogen-Air
Jet Diffusion Flame**

V. R. Katta and L. P. Goss
Systems Research Laboratories, Inc.
Dayton, OH

W. M. Roquemore
Wright Laboratory
Wright-Patterson Air Force Base, OH

**31st Aerospace Sciences
Meeting & Exhibit**
January 11-14, 1993 / Reno, NV

Effect of Nonunity Lewis Number and Finite-Rate Chemistry on the Dynamics of a Hydrogen-Air Jet Diffusion Flame

V. R. Katta* and L. P. Goss*
Systems Research Laboratories, Inc.
A Division of Arvin/Calspan
2800 Indian Ripple Road
Dayton, OH 45440-3696

and

W. M. Roquemore†
Wright Laboratory
Aero Propulsion and Power Directorate
Wright-Patterson Air Force Base, OH 45433-6563

ABSTRACT

In jet diffusion flames buoyancy-influenced toroidal vortices roll outside the flame surface when the annulus air flow is low. The temporal and spatial evolution of these vortices change the stretch along the flame surface, which results in a wrinkled laminar flame. A time-dependent, axisymmetric mathematical model with a detailed chemical kinetics mechanism is used to simulate such a wrinkled flame of a low-speed H₂-Air jet diffusion flame. The effects of Lewis number and finite-rate chemistry on the steady-state and the dynamic flame structures are examined. Results obtained with different models indicate that the size and shape of the outer structures are unaffected by the unity-Lewis-number and fast-chemistry assumptions. Experiments showed that the flame temperature tends to increase when the flame is bulging out and decrease when it is squeezing in. The lower Lewis number inside the flame—not the increased Damkohler number—was found to be responsible for the observed fluctuations in the flame temperature. Preferential mass diffusion of different species causes an increase in water in the bulge regions of the flame and radicals in the squeezing regions.

INTRODUCTION

The most commonly used flames in a practical combustor device are the nonpremixed (or diffusion) type. In these flames the reactants remain separated until the end of the activation process. Since the inception of the Burke-Schumann flame-sheet model,¹ considerable progress has been made over the past 60 years in understanding a jet diffusion flame. However, several important questions about the turbulent combustion process such as the existence of strained/stretched laminar flamelets² and distributed reaction zones³ must be answered if an accurate design model is to be developed for the practical combustors.

According to Hottel and Hawthorne,⁴ a flame is considered to be fully turbulent when its entire surface area becomes a flame brush. Under this condition the flame appears highly wrinkled, bumpy, and rough. Improved visualization techniques have provided additional insight into the structure of the turbulent flame and the activity within the flame. The wrinkles and bumps in the flame are believed to be localized protrusions of the flame surface that result when three-dimensional fluid elements (often associated with vortices) of different size, shape, velocity and rotational strength interact with reaction zones of different thickness. An ensemble of these events result into a turbulent flame structure. An accurate representation of this statistical process, requires an understanding of the individual flame-vortex interactions.

A simple vertically mounted jet diffusion flame, formed between coannulus fuel and air jets, provides a fundamental flame-vortex interaction. When the annulus air flow is low, buoyancy-influenced toroidal vortices form outside the flame surface. As these vortices convect downstream, they interact with the flame and create small wrinkles on the flame surface. Three important observations are made from Reactive-Mie-Scattering images⁵ of a hydrogen jet flame: (1) large toroidal vortices develop outside the flame surface and the flame flicker resulting from their convective motion is ~ 13 Hz, (2) the potential core is laminar; and (3) the soot intensity, in general, decreases with axial distance; however, locally it increases near the braid regions of the outer vortices. Since in the low-speed diffusion flame the soot intensity seems to be coupled with the temperature, similar variations in the flame temperature might be expected. In fact, the Thin-Filament-Pyrometry technique⁶ confirmed that the temperature actually increases when the flame is bulging out. Recently, theoretical investigations on this flame were carried out by Katta et al.⁷ using a flame-sheet model. The toroidal vortices that developed from the buoyancy-induced instability were accurately captured in that study. However, the limitation of that model arising from the fast-chemistry and unity-Lewis-number assumptions is apparent from the near-constant flame temperature that was predicted all along the

* Research Applications Division

† Fuels and Lubrication Division

This paper is declared a work of the U.S. Government and is not subject to copyright protection in the United States

Table 1

Φ	Γ^Φ	S^Φ
u	μ	$-\frac{\partial p}{\partial z} + (\rho_0 - \rho)g + \frac{\partial}{\partial z}\left(\mu \frac{\partial u}{\partial z}\right) + \frac{\partial}{\partial r}\left(\mu \frac{\partial v}{\partial z}\right) + \frac{\mu}{r} \frac{\partial v}{\partial z} - \frac{2}{3} \left\{ \frac{\partial}{\partial z}\left(\mu \frac{\partial u}{\partial z}\right) + \frac{\partial}{\partial z}\left(\mu \frac{\partial v}{\partial r}\right) + \frac{\partial}{\partial z}\left(\mu \frac{v}{r}\right) \right\}$
v	μ	$-\frac{\partial p}{\partial r} + \frac{\partial}{\partial z}\left(\mu \frac{\partial u}{\partial r}\right) + \frac{\partial}{\partial r}\left(\mu \frac{\partial v}{\partial r}\right) + \frac{\mu}{r} \frac{\partial v}{\partial r} - 2\mu \frac{v}{r^2} - \frac{2}{3} \left\{ \frac{\partial}{\partial r}\left(\mu \frac{\partial u}{\partial z}\right) + \frac{\partial}{\partial r}\left(\mu \frac{\partial v}{\partial r}\right) + \frac{\partial}{\partial r}\left(\mu \frac{v}{r}\right) \right\}$
Y_i ($i = 1 \sim N_s - 1$)	ρD_i	$\dot{\omega}_i$
H	$\frac{\lambda}{c_p}$	$\nabla \left[\frac{\lambda}{c_p} \sum_1^{N_s} \left\{ (Le_i^{-1} - 1) H_i \nabla Y_i \right\} \right] - \sum_1^{N_s} (h_{f,i}^0 \dot{\omega}_i)$

wrinkled flame surface.

The laminar flamelet theory² suggests that when a diffusion flame is stretched, the flame temperature drops due to the increased reactant fluxes and the Damkohler number. Studies of Mizomoto et al.⁸ on premixed flames indicate that the preferential diffusion resulting from non-unity Lewis number has strong influence on the flame temperature, especially when the flame is unsteady and subjected to non-uniform flow. Therefore, the variation in the flame temperature of the dynamic hydrogen flame of Vilimovic and Goss⁶ could be due to the chemistry-related stretch effect and/or the preferential diffusion. In the present study, these issues were examined using a time-dependent, axisymmetric computational-fluid-dynamics model with a detailed H₂-O₂ chemical-kinetics mechanism. Numerical experiments were performed by introducing different chemistry and Lewis-number assumptions and the results are compared to explore their effects on the development of the vortices and the flame-vortex interaction process.

FORMULATION

Governing Equations

The time-dependent governing equations for an axisymmetric reacting flow that consists of a number of species N_s can be written in the cylindrical (z, r) coordinate system as

$$\frac{\partial \rho}{\partial t} + \frac{\partial \rho u}{\partial z} + \frac{1}{r} \frac{\partial (r p v)}{\partial r} = 0, \quad (1)$$

and

$$\begin{aligned} \frac{\partial (\rho \Phi)}{\partial t} + \frac{\partial (\rho u \Phi)}{\partial z} + \frac{\partial (\rho v \Phi)}{\partial r} = & \frac{\partial}{\partial z} \left(\Gamma^\Phi \frac{\partial \Phi}{\partial z} \right) + \frac{\partial}{\partial r} \left(\Gamma^\Phi \frac{\partial \Phi}{\partial r} \right) \\ & - \frac{\rho v \Phi}{r} + \frac{\Gamma^\Phi}{r} \frac{\partial \Phi}{\partial r} + S^\Phi, \end{aligned} \quad (2)$$

where ρ represents density; u and v are the axial and radial components of the velocity vector, respectively; and p is pressure. The general form of Eq. (2) represents the momentum, the species, or the energy conservation equation, depending on the variable used in place of Φ . In the solution for weakly compressible flows, the choice of an appropriate form for the energy equation eliminates numerical-instability problems. Details of the energy equation used in the present study are given in the Appendix. In Table 1 the transport coefficients Γ^Φ and the source terms S^Φ that appear in the governing equations are given. Here μ , λ , and c_p are the viscosity, thermal conductivity, and specific heat of the mixture, respectively; Y_i is the mass fraction; D_i is the self-binary diffusion coefficient; and $\dot{\omega}_i$ is the mass-production rate of the i -th species; ρ_0 is the density of air; and g is the gravitational acceleration. The subscript i indicates the i -th species. Enthalpy H is defined as

$$H \equiv \int_{T_0}^T c_p dT \equiv \sum_1^{N_s} H_i \equiv \sum_1^{N_s} Y_i (h_i - h_{f,i}^0),$$

where h and h_f^0 represent the total enthalpy and the heat of formation at standard state (temperature T_0), respectively. Finally, Le_i is the Lewis number of the i -th species, which is defined as

$$Le_i \equiv \frac{\lambda}{\rho D_i c_p}.$$

The set of equations given by (1) and (2) can be completed using the global-species-conservation equation

$$Y_{N_s} = 1.0 - \sum_1^{N_s-1} Y_i \quad (3)$$

Table 2

No.	Reaction	α_f	A_f (mole, cm, s)	E_{af} (cal/mole)	α_b	A_b (mole, cm, s)	E_{ab} (cal/mole)
R1	$H_2 + O_2 \rightleftharpoons 2 OH$	0	1.7E+13	47,780	0	1.7E+13	40,000
R2	$H_2 + OH \rightleftharpoons H_2O + H$	0	2.2E+13	5,146	0	9.5E+13	20,300
R3	$H + O_2 \rightleftharpoons OH + O$	-0.82	5.13E+16	16,510	0	1.305E+13	677
R4	$O + H_2 \rightleftharpoons OH + H$	1.0	1.8E+10	8,900	1.0	8.3E+09	6,950
R5	$H + O_2 + M \rightleftharpoons HO_2 + M$	0	1.65E+15	-1,000	0	2.31E+15	45,900
R6	$OH + HO_2 \rightleftharpoons H_2O + O_2$	0	5.0E+13	1,000	0	6.33E+14	73,860
R7	$H + HO_2 \rightleftharpoons 2 OH$	0	2.5E+14	1,900	0	1.2E+13	40,100
R8	$O + HO_2 \rightleftharpoons O_2 + OH$	0	5.0E+13	1,000	0	6.42E+13	56,610
R9	$OH + OH \rightleftharpoons O + H_2O$	0	6.3E+12	1,100	0	6.8E+13	18,350
R10	$H_2 + M \rightleftharpoons H + H + M$	0	2.2E+14	96,000	0	3.0E+15	0
R11	$O_2 + M \rightleftharpoons O + O + M$	0	5.1E+15	115,000	-0.28	4.7E+15	0
R12	$H + OH + M \rightleftharpoons H_2O + M$	-2.0	1.4E+23	0	-2.0	3.8E+16	119,282
R13	$H + HO_2 \rightleftharpoons H_2 + O_2$	0	2.5E+13	700	0	5.5E+13	57,800

and the state equation

$$p = \rho T R_0 \sum_i \left(\frac{Y_i}{M_i} \right), \quad (4)$$

where R_0 is the universal gas constant; T is the temperature; and M_i is the molecular weight of the i -th species.

Thermodynamic and Transport Properties

Solution of the governing equations [(1)-(4)] requires information on the thermodynamic and transport properties that appear in Table 1. Temperature- and species- dependent properties are incorporated in this study. The enthalpy h and specific heat c_p of each species are calculated using the polynomial curve fits compiled by Burcat.⁹ First the viscosity and thermal conductivity of the individual species are estimated based on Chapman-Enskog collision theory; then those of the mixture are determined using Wilke's semi-empirical formulae. Chapman-Enskog theory and the Lenord-Jones potentials have been used to estimate the self-diffusion coefficient of each species.

Chemical Kinetics

The fluid model used in the present analysis consists of eight species ($N_s = 8$); namely, H_2 , O_2 , H , O , OH , H_2O , HO_2 and N_2 . The reaction mechanism used among these

constituent species to represent hydrogen combustion¹⁰ is given in Table 2. Here, M is any third molecule serving to absorb excess energy released during the collision process. Nitrogen in the present calculations is assumed to be an inert gas and is not participating in the reactions.

The net rate of production of the i -th species due to the number of reactions N_r is obtained by summing the individual contributions from each reaction (δ_j) and is given by the following expression:

$$\dot{\omega}_i = M_i \sum_j \{ (v_{ji}'' - v_{ji}') \delta_j \}, \quad (5)$$

$$= M_i \sum_j \left\{ (v_{ji}'' - v_{ji}') \left[k_{fj} \prod_i C_i^{v_{ji}'} - k_{bj} \prod_i C_i^{v_{ji}''} \right] \right\}. \quad (6)$$

Here, v_{ji}' and v_{ji}'' are the stoichiometric coefficients of the i -th species in the j -th reaction in forward and backward directions, respectively. C_i represents the molar concentration of the i -th species; k_{fj} and k_{bj} are the forward and backward specific reaction-rate constants of the j -th reaction and are represented by the modified Arrhenius law

$$k_{fj} = A_{fj} T^{\alpha_{fj}} \exp \left(\frac{-E_{afj}}{R_0 T} \right) \text{ and } k_{bj} = A_{bj} T^{\alpha_{bj}} \exp \left(\frac{-E_{abj}}{R_0 T} \right). \quad (7)$$

The constants appearing in Eq. 6, obtained from Ref. 11, are also listed in Table 2.

NUMERICAL SCHEME

The governing equations [(1)-(4)] are integrated on a nonuniform staggered-grid system. The finite-difference forms of the momentum equations are obtained using an implicit QUICKEST scheme¹² while those of the species and energy equations are obtained using the hybrid scheme of Spalding.¹³ The resulting (N_s+3) sets of algebraic equations are then solved using an iterative Alternative Direction Implicit technique. A stable numerical-integration procedure is achieved by coupling the species and energy equations through the source terms (cf Table 1). At every time step, the pressure field is calculated by solving the pressure Poisson equations simultaneously and utilizing the LU (Lower and Upper diagonal) matrix-decomposition technique.

Grid lines are clustered near the flame surface to resolve the steep gradients of the dependent variables. Boundaries of the computational domain are shifted sufficiently to minimize the propagation of disturbances (due to inaccuracies in boundary conditions) into the region of interest. The flow variables at the outflow boundary are obtained using an extrapolation procedure with weighted zero and first-order terms.⁷

RESULTS AND DISCUSSION

The inflow conditions used in the present calculations are those of the laboratory flame investigated experimentally by Lynn et al.¹⁴ and Vilimpoc and Goss.⁶ A vertically mounted jet diffusion flame was established by burning a mixture of hydrogen and nitrogen emerging from a 10-mm-diameter contoured nozzle. The volumetric ratio between the fuel and nitrogen was 3.5. Flat initial velocity profiles with measured average velocities of 3.26 and 0.15 m/s were used at the exits of the fuel nozzle and annulus duct, respectively. The influence of nonequilibrium chemistry and heat transfer on the structure of the flame was studied by simulating the flame using the following four models:

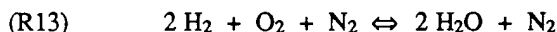
M1: Fast global chemistry and $Le_i = 1$

M2: Fast global chemistry and $Le_i \neq 1$

M3: Finite-rate chemistry and $Le_i = 1$

M4: Finite-rate chemistry and $Le_i \neq 1$

The Shvab-Zel'dovich formulation of Model M1, described in detail in Ref. 7, is based on two conserved scalar variables (one for the species and the other for the enthalpy). A global-chemical-kinetics model



is used in place of Reactions (R1)-(R12) to obtain Model M2. A very high value for the pre-exponential in the rate equation of Reaction (R13) is chosen to simulate fast global chemistry. While Model M4 represents the formulation described in this paper, Model M3 is deduced from this by simplifying the source term of the energy equation (cf Table 1) with an assumption $Le_i = 1$.

Steady-State Flame Structure

In the presence of gravitational force, the low-speed hydrogen diffusion flame studied here tends to oscillate at a frequency corresponding to the convective motion of the outer vortices. To understand the differences in the flame structure due to the unity-Lewis-number assumption, calculations for the steady-state flames were made by neglecting the time-dependent terms in the governing equations [Eqs. (1) and (2)]. Results obtained with Models M4 and M3 are shown in Figs. 1(a) and 1(b), respectively. Here, iso-temperature contours are plotted with a contour-level difference of 400 K. Flame tips were marked by plotting a contour of the maximum centerline temperature [2190 K in Fig. 1(a) and 2450 K in Fig. 1(b)]. It is evident from comparing these Figures that the temperature distribution inside the flame is different without and with the unity-Lewis-number assumption; however, the difference is not significant outside the flame. This has an interesting effect on the dynamics of the flame, as will be discussed in the next section.

The unity-Lewis-number assumption in this hydrogen diffusion flame resulted in a shorter flame and a different flame structure than that predicted by Model M4. The closed contours along the flame surface in Fig. 1(a) show that the flame temperature decreases with axial distance, whereas it is constant from the flame shoulder to the tip in Fig. 1(b). The flame temperature (T_f) and the total-heat-release rate (ΔH) at the flame surface that results from

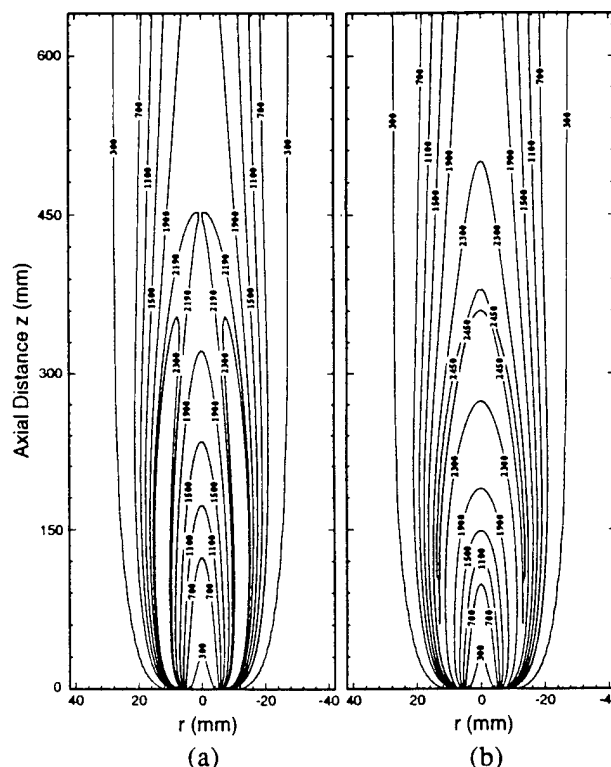


Fig. 1. Steady-state flame calculated a) without $Le_i = 1$ and b) with $Le_i = 1$ assumption.

chemical reactions are plotted as functions of axial distance from nozzle exit in Figs. 2(a) and 2(b), respectively. Here ΔH is defined as

$$\Delta H = \sum_1^{N_r} \Delta H_j = \sum_1^{N_r} \sum_1^{N_s} \left\{ (v_{ji} - v_{ji}) \frac{\delta_j}{\rho} h_i \right\}. \quad (8)$$

Note from Fig. 1 that with and without the unity-Lewis-number assumptions the flame has converged to the centerline. Therefore, beyond the flame tip, the flame temperature indicates the temperature at the centerline. As expected, the flame temperature of 2460 K for the $Le_i = 1$ case is very near the adiabatic flame temperature ($T_{ad} = 2450$ K) for the hydrogen-air mixture considered. The major heat-releasing chemical reactions are complete at the flame tip ($z \sim 390$ mm), and the temperature drop beyond this location is mainly due to convective and conductive heat diffusion. It is known that lighter species such as H_2 have higher Lewis numbers (~ 2); therefore, one might expect a flame temperature that is lower than T_{ad} in hydrogen diffusion flames. However, when no assumption for species Lewis number is made, the Model M4 yields a flame temperature of 2750 K (300 K above the adiabatic value) near the flame base (or shoulder) that gradually decreased to 2200 K (250 K below the adiabatic value) at

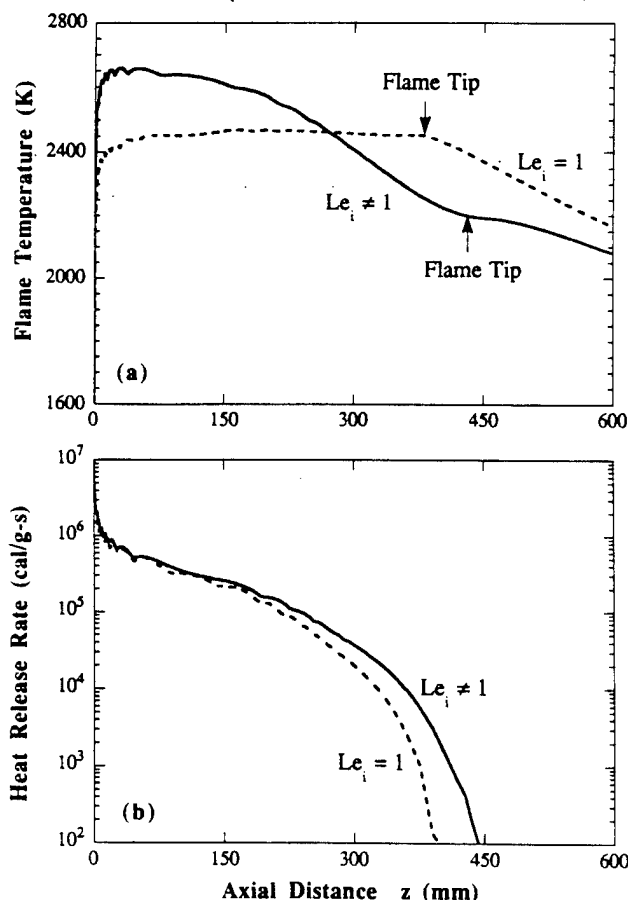


Fig. 2. Variation of a) flame temperature and b) chemical heat release rate at flame surface with axial distance for steady-state flames shown in Fig. 1.

the tip. Since the initial heat-release rate is the same in both cases [up to $z = 150$ mm in Fig. 2(b)], the higher flame temperature in the $Le_i \neq 1$ case is due to lower heat transfer in the flame zone which is contrary to the general concept of the H_2 -air flame (Lewis number greater than unity represents higher heat-transfer rate). To explain this, distributions of species mole fractions, temperature, and different transport coefficients within the flame zone at a height of 150 mm are plotted in Figs. 3-5.

The major species in the flame zone are hydrogen, oxygen, nitrogen, and water. The peak OH concentration in this flame seems to occur outside the high-temperature region and on the oxidizer side. The reaction zone, in which both fuel and oxygen exist (Fig. 3), is ~ 2 mm thick; the maximum temperature occurs within this zone. The local Lewis number of a species is the ratio of the mixture conductive heat transport and the mass transport of the species. The thermal conductivity and viscosity of the

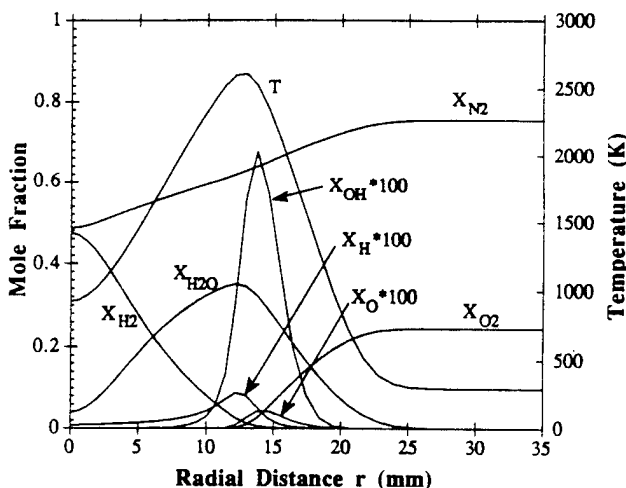


Fig. 3. Radial distribution of temperature and mole fractions of different species at $z = 150$ mm in $Le_i \neq 1$ simulation.

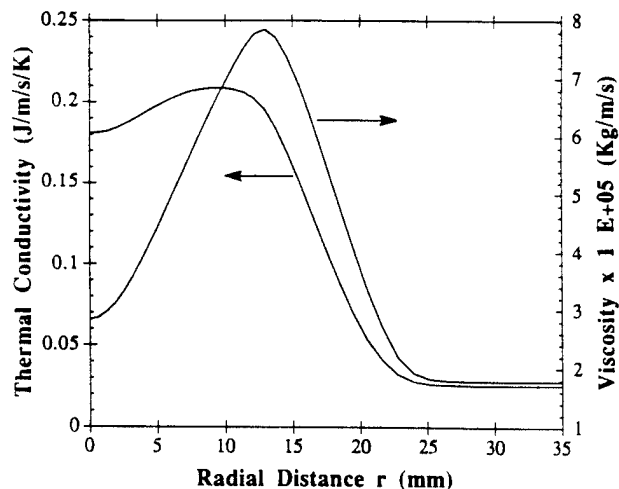


Fig. 4. Thermal conductivity and viscosity across flame at $z = 150$ mm.

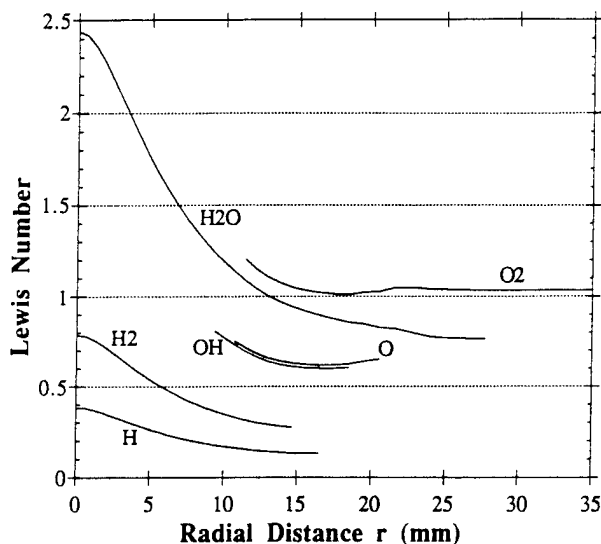


Fig. 5. Lewis number of different species in mixture across flame at $z = 150$ mm.

mixture across the flame at $z = 150$ mm are shown in Fig. 4. The higher thermal conductivity of the hydrogen molecules caused the thermal conductivity of the mixture in the potential core to be as high as that of the products in the high-temperature flame zone. On the other hand, as with any flame, the viscosity of the mixture becomes very high in the flame zone.

The thermal conductivity and Lewis number of a species become effective in the energy equation (cf Table 2) only if that species is present locally in sufficient concentration. Therefore, if mole fraction of a species is small ($<10^{-4}$), then the corresponding Lewis number is not shown in Fig. 5. In a mixture resulting from H_2 - O_2 combustion, only O_2 has a Lewis number near unity. H_2O has a Lewis number greater than one on the fuel side of the flame and less than one on the oxygen side. All other species including H_2 have Lewis numbers smaller than unity. Therefore, on the fuel side of the flame zone, the overall heat-transfer rate is lower than the diffusive mass-transfer rate. This affects the structure of the flame in two ways. Near the shoulder region, where the general flow direction is parallel to the flame surface, the lower heat-conduction rate, as compared to the mass-diffusion rate ($Le < 1$), increases the flame temperature above T_{ad} . In the downstream locations, i.e., $100 \text{ mm} < z < 440 \text{ mm}$, the flame surface is concave with respect to the incoming fuel. Because of this curvature conduction of heat away from the flame focuses heat inside the flame and, hence, tends to raise the flame temperature. On the other hand, the same curvature has a defocussing effect on the fuel diffusing toward the flame surface and tends to lower the flame temperature. When the Lewis number is unity, these opposite effects on T_f due to the concave flame surface cancel each other, yielding $T_f = T_{ad}$. However, in the hydrogen flame under consideration here ($Le_{H_2} < 1$), the influence of the curvature on mass diffusion (cooling effect) is dominant. As a result the flame temperature

monotonically decreases from $z = 100$ mm to the tip of the flame.

In Model M4 the heat concentration in the flame zone near the shoulder region and the cooling of the flame in the remaining section resulted in a lower temperature inside the flame (i.e., on the fuel side), which increased the overall flame height (440 mm in the $Le_j \neq 1$ case and 390 mm in the $Le_j = 1$ case). Since the Lewis number of oxygen is near unity, the temperature distribution outside the flames predicted by Models M3 and M4 is similar [cf Figs. 1(a) and 1(b)].

Dynamic Flame-Structure

Buoyant acceleration of hot gasses outside the flame surface is responsible for the flame-flickering phenomenon which is commonly observed in low-speed annulus-air diffusion flames. Several experimental studies have shown that the flame-flickering frequency is insensitive to fuel type, nozzle size, and fuel velocity and is weakly dependent on the annulus-air velocity. Buckmaster and Peters¹⁵ have provided theoretical support to this by isolating the convective flow from the forced one. They argued that the Kelvin-Helmholtz instability associated with this convective flow is primarily responsible for the roll-up of the large toroidal vortices outside the flame. Chen et al.¹⁶ have shown that the convective motion of these vortices squeezes the flame at certain locations and bulges it at others and, thereby, is responsible for the flame flickering. Numerical studies of these dynamic flames also confirmed the role of buoyancy forces in the roll-up of the outer vortices. Recent simulations of Katta et al.⁷ showed that the flickering frequency of a flame increases in proportional to the square-root of the gravitational acceleration and is also insensitive to the viscosity of the fluid. In the numerical simulations^{7,17,18,19} made to date for these buoyancy-influenced dynamic flames, a one-step global-chemistry model was used. The simulations of Ellzey et al.¹⁷ without and those of Davis et al.¹⁸ with the unity-Lewis-number assumption, predicted flickering frequencies very accurately. However, these studies did not address the effect of Lewis number on the dynamics of the flame. According to Law,²¹ the preferential diffusion due to nonunity-Lewis number has significant effect on a stretched flame. Also, the nonequilibrium nature of the flame chemistry will be affected by stretching as the Damkohler number (ratio between reaction time and residence time) changes. The experiments of Vilimpoc and Goss on hydrogen flames indeed show variations in the flame temperature that result from the dynamics of the flow. Therefore, in order to understand the effects of Lewis number and finite-rate chemistry on the flame dynamics, simulations were made for the buoyancy-influenced dynamic flames using Models M1, M2, and M4.

Because of the gravity term in the axial-momentum equation (1), the solution of governing equations (1)-(5) for the low-speed annulus flow always results in a dynamic flame. The instantaneous temperature fields obtained from different models for the flame described in the previous section are shown in Fig. 6. In each flame, eight contour

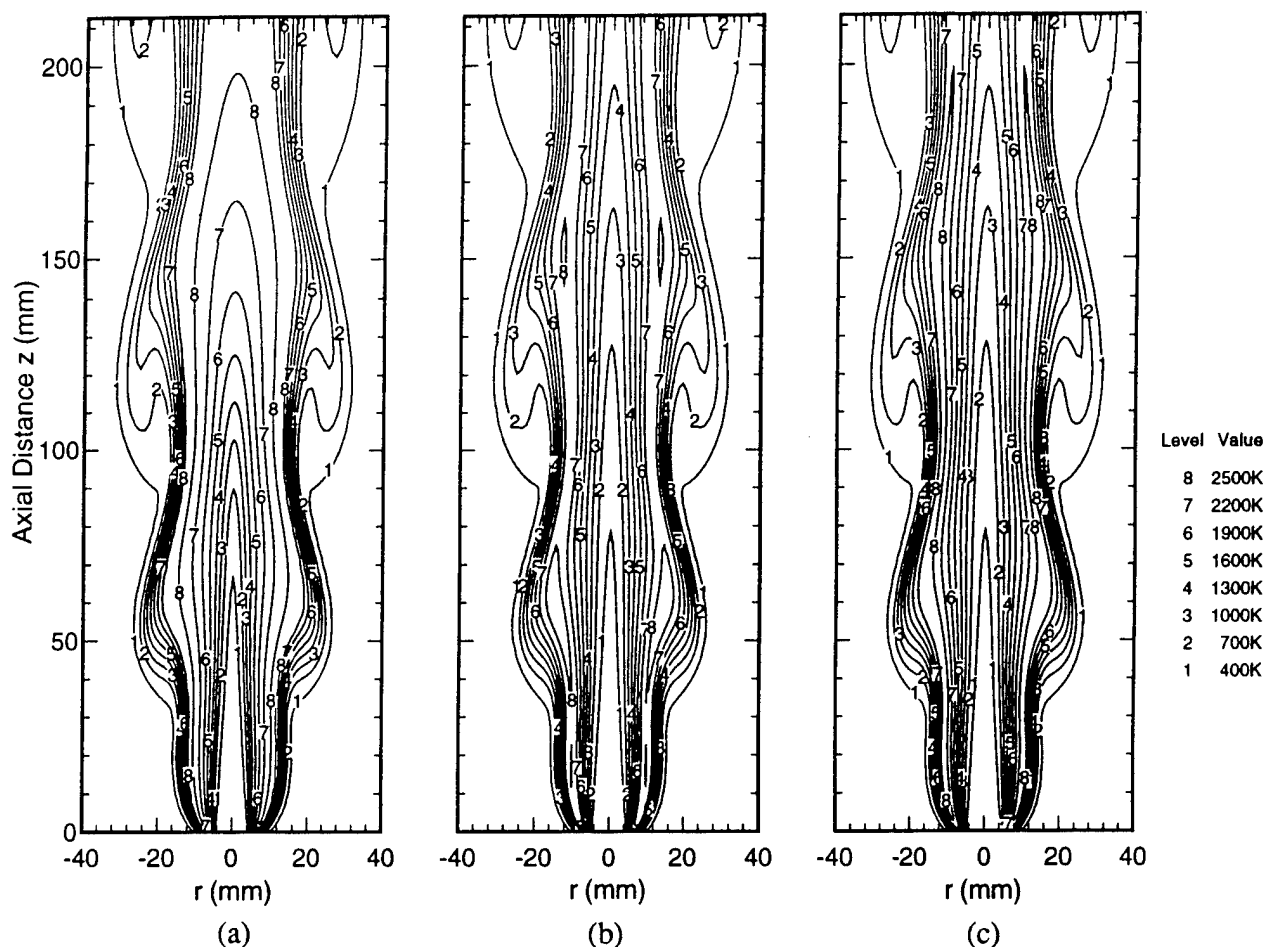


Fig. 6. Instantaneous iso-temperature contours of dynamic flame obtained with different models. a) Fast chemistry and $Le_1 = 1$. b) Fast chemistry and $Le_1 \neq 1$. c) Finite-rate chemistry and $Le_1 \neq 1$. Eight equally spaced contours are plotted in each figure; temperatures corresponding to contour numbers are shown in insert.

levels (1-8) are plotted, and the temperatures corresponding to these contour levels are shown in the insert. It is useful to recall that Fig. 6(a) was obtained using a model which has fast-chemistry and $Le_1 = 1$ assumptions; in Fig. 6(b) only the former assumption was used; and the simulation with neither of these assumptions yields the flame in Fig. 6(c). The grid system and time step were identical in all the three simulations. For comparison purposes the same phases were chosen for all three flames.

The flames shown in Fig. 6 have two and one-half vortex structures formed outside the flame surface. The crossing frequency of these vortices is ~ 13 Hz. It is interesting to note from Fig. 6 that the size and shape of the outer vortices in the three flames are very similar. In fact, even the contours downstream of $z = 200$ mm are identical (for example, the U-shaped 700-K contours). It should be pointed out that the temperatures within the flame zone and inside the flame are significantly different in Figs. 6(a) and 6(b) [or 6(c)], mainly due to the fact that the Lewis number is much less than unity for the hydrogen molecules inside the flame (cf Fig. 5). The temperature distributions of Figs. 6(b) and 6(c) are similar everywhere except in the thin flame zone, indicating that the effects of

finite-rate-chemistry on the temperature distribution are negligible in these flames.

The similarity in the outer structures obtained under different assumptions may be explained by referring to the earlier discussions on the steady-state flames (Fig. 1). The vortices outside the flame form as a consequence of the buoyant acceleration of the hot gases that results from the temperature distribution outside the flame surface. Because of the unity Lewis number of the oxygen molecules outside the flame, the temperature distribution outside the steady-state flame was not affected by the $Le_1 = 1$ assumption over the entire flow. Since the finite-rate-chemistry effects are confined to a narrow flame zone, the temperature outside the flame zone and, hence, the outer structures are almost independent of the assumptions used in Models M1-M3. For the above-mentioned reasons and due to the lack of preferential diffusion for oxygen molecules (arising from $Le_{O_2} = 1$), it is possible to predict the temperature distribution outside the flame surface for any diffusion flame using an accurate diffusion model. This is evident from the accurate predictions for the outer structures of propane,^{18,19} methane,²⁰ and hydrogen flames⁷ made with simple models such as Model M1.

Preferential Diffusion Effect on the Flame Dynamics

The motion of the large torroidal vortices outside the flame induces stretch on the flame at different locations. A close look at the flame zones in Figs. 6(b) and 6(c) indicates that the temperature peaks when the flame is bulging out and drops to a minimum when it is squeezing in. This is more evident from the temperature-evolution plots shown in Fig. 7; these plots were obtained from the flame simulated using Model M4 [Fig. 6(c)]. Computed temperature data at two axial locations, $z = 40$ and 80 mm, were recorded over a time period of ~ 290 ms, and the fluctuations are plotted in Figs. 7(a) and 7(b), respectively, in the form of iso-temperature contours. These two locations were chosen because experimental data⁶ and numerical results obtained with a simplified model⁷ were available in the literature. The data shown at any time t , at the given axial location, should be interpreted as the radial-temperature distribution that was seen at this location t ms prior to 0 ms. Two observations can be made from these plots: (1) The oscillations are highly periodic and does not change with axial distance; the frequency of oscillation is 12.7 Hz. (2) At a given location the flame temperature oscillates between a minimum and a maximum as the outer vortex passes by (refer to the closed contours in the flame zone). The later observation was also made by Vilimpoc and Goss while studying this flame experimentally.⁶ The flame predicted using the flame-sheet Model M1 [Fig. 6(a) and time-evolution plot in Ref. 7] did not exhibit this characteristic, which indicates that the chemical nonequilibrium and preferential diffusion arising from $Le_i \neq 1$ in the flame zone may be responsible for the observed fluctuations in the flame temperature. The results obtained with Models M1–M4 were used in an attempt to understand this phenomenon.

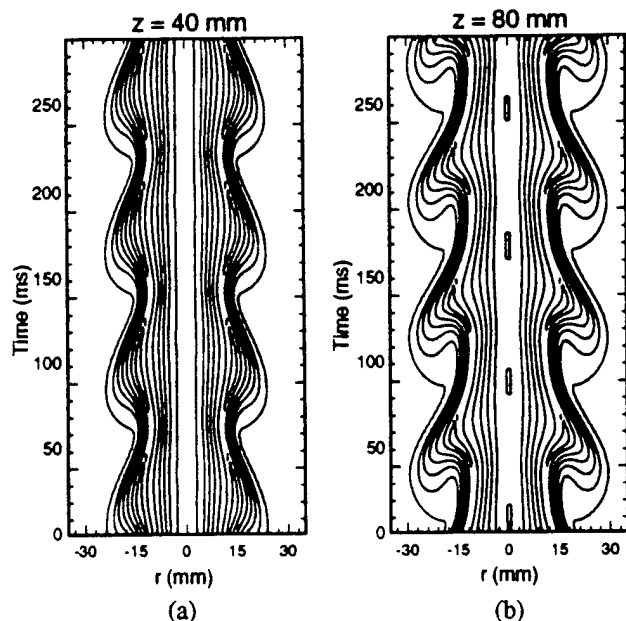


Fig. 7. Evolution of temperature at different heights in flame. Flame surface is located at $\sim r = 15$ mm.

The simulations with fast-global and finite-rate chemistry ($Le_i \neq 1$ in both cases) showed that the temperature peaks in the flame-bulge region [Figs. 6(b) and (c)]. The predictions of model M1 [Fig. 6(a)] resulted in a flame with a constant flame temperature near T_{ad} . Finally, the flame obtained with Model M3 (not shown) is very similar to that in Fig. 6(a). Combining the results from the four models suggests that $Le \neq 1$ is essential in predicting flame-temperature oscillations in a dynamic hydrogen diffusion flame.

Referring to Fig. 6(c) it can be noticed that the flame at this phase is squeezed in at $z = 100$ mm and bulged out at $z = 63$ mm. From several animations made on this flame, it is evident that the first torroidal vortex from the nozzle exit with a vorticity vector running counterclockwise in the top view is pulling the hot gases out of the flame and creating a bulge at $z = 63$ mm. Similarly, the second vortex from the nozzle exit is squeezing the flame by bringing more air into the flame zone at $z = 100$ mm and bulging it by pulling the hot gasses out at $z = 140$ mm. Molar concentrations of different species in the flame of Fig. 6(c) are shown in Fig. 8. In the bulge region ($z = 63$ mm), both H_2 and O_2 spread out, indicating slower diffusion rate. On the other hand, the diffusion fluxes are high for both H_2 and O_2 at $z = 100$ mm. The temperature and heat-release-rate [ΔH in Eq. (8)] variations across the flame at heights of $z = 100$ and 63 mm are plotted in Figs. 9 and 10, respectively. The variations of the corresponding steady-state flame (obtained with Model M4) are also shown in these figures.

At $z = 100$ mm, the flame is pushed toward the centerline (cf Fig. 9) and the flame zone becomes thin compared to that of the steady-state solution. Because of the increased fuel and oxidizer fluxes at this location (cf Fig. 8) in the dynamic flame, the chemical-heat-release rate has increased significantly. However, the flame temperature has been reduced by 65 K. The decrease in flame temperature with increase in mass fluxes was also observed in a counterflow hydrogen diffusion flame.²² In that study it was concluded that insufficient consumption of reactants by chemical reactions reduced the flame temperature; this is in agreement with the theory of Peters² and numerical simulations of Givi.²³ However, this is not the case with the flame shown in Fig. 6(c) because (i) simulations with the finite-rate-chemistry and $Le_i = 1$ assumption did not show the decrease in temperature (ii) simulation with fast-chemistry assumption but without the $Le_i = 1$ restriction showed the decrease in temperature when the flame was squeezed in. It is important to note that the flame in Fig. 6(c) is a low-speed diffusion flame ($V_{fuel} = 3.26$ m/s) in which one might expect that the residence time is ample for consuming the slightly increased reactant fluxes. The flame structure at $z = 63$ mm (flame bulging in Fig. 10) is different from that at $z = 100$ mm. Here, the flame zone becomes thicker, the heat-release-rate drops, and the flame temperature increases by 30 K as compared to that of the steady-state flame (shown with solid circles in Fig. 10).

The changes in flame temperature due to preferential diffusion may be explained using the cartoon shown

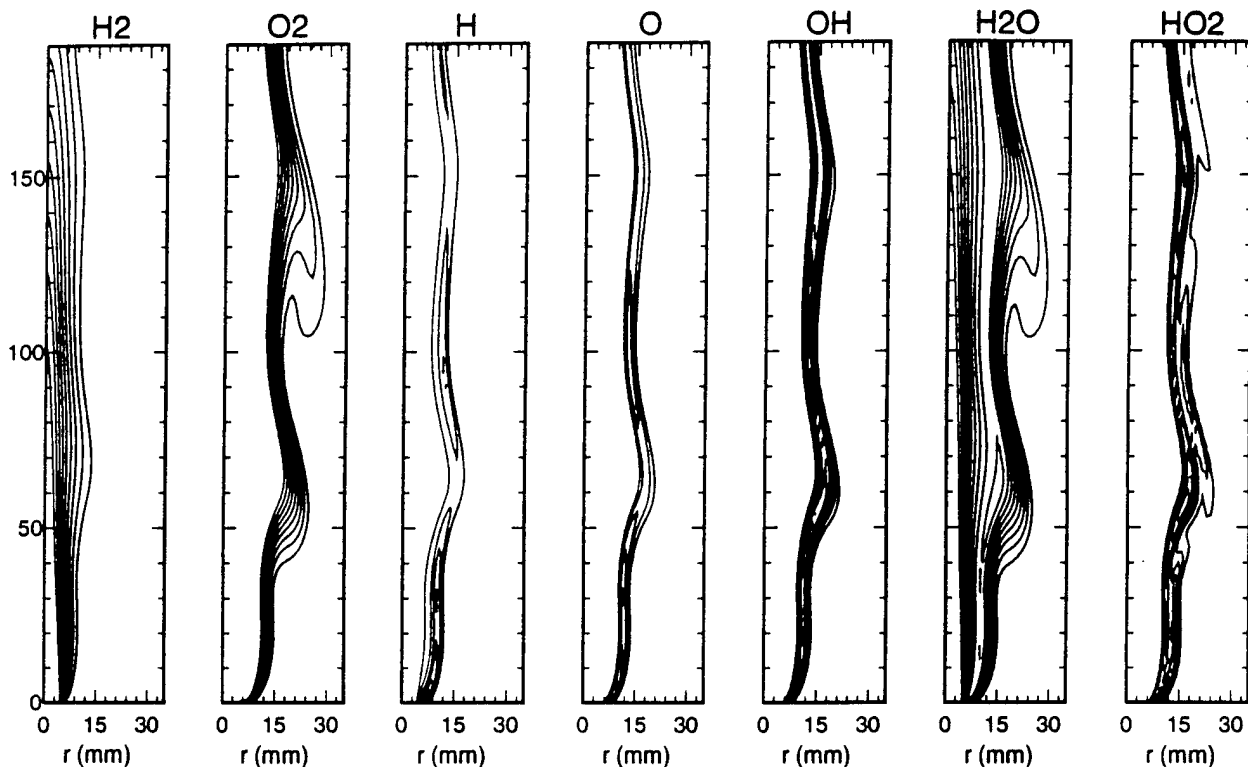


Fig. 8. Molar distributions of different species in dynamic H₂-Air diffusion flame. Nine iso-molar contours are plotted between minimum and maximum in each plot.

in Fig. 11. Here, the buoyancy-influenced vortex is formed outside the flame surface (on the air side) and induces a velocity field in indicated. The vortex strength decreases with decreasing radial distance ($du/dr > 0$) on the fuel side. The increased air flow develops a positive stretch in the flame zone and, hence, the oxygen-concentration gradient becomes steep. Since $Le_i \sim 1$ on the oxygen side of the flame, the temperature gradient also increases (cf Fig. 9). On the other hand, the nonuniform flow on the fuel side tends to increase the flame temperature by increasing the incoming fuel mass flux and, at the same time, to decrease the flame temperature (cooling effect) by removing the heat in the flame zone. If the Lewis number of the fuel were unity, then these two effects would cancel each other resulting in a flame temperature equal to T_{ad} . However, when $Le_i < 1$ (as in the hydrogen flame considered here), more heat will be concentrated in the flame zone and, hence, the cooling effect will be dominant. This results in a decrease in the flame temperature (not lower than T_{ad} but lower than that of steady-state flame). In the bulge region, the vortex pulls the flame in such a way that its surface is convex to the incoming fuel. As discussed by Law,²¹ this curvature has a focussing effect on the incoming fuel and a defocussing effect on the heat ahead of the flame. The preferential diffusion in this case results in a higher flame temperature for the $Le_i < 1$ flows.

Preferential diffusion affects not only the temperature in the bulging and squeezing regions of a dynamic flame but also the species concentrations there. From Fig. 8 it

should be noted that the intermediate-radical concentrations are minimum in the bulge region and maximum in the squeeze region. While H₂O species show exactly the opposite trend (they peak in the bulge region), the variation in peak-OH concentration is not significant. HO₂ is very weak in this flame and is confined to a thin region in the flame zone. At 2500 K the self-diffusion coefficients of different species with respect to that of H₂ are as follows;

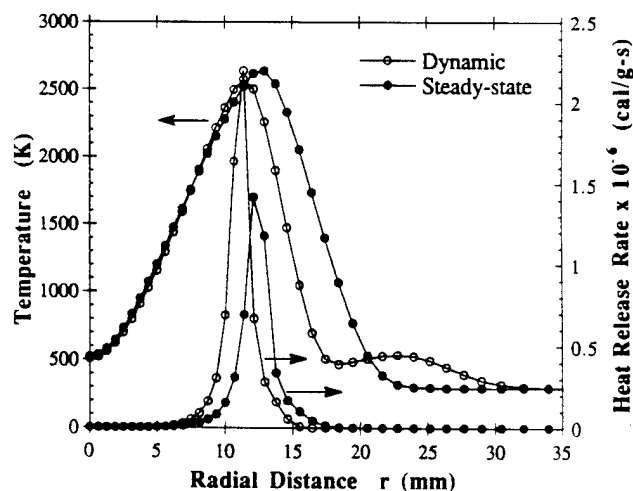


Fig. 9. Temperature and heat-release rate of dynamic and steady-state flames at $z = 100$ mm.

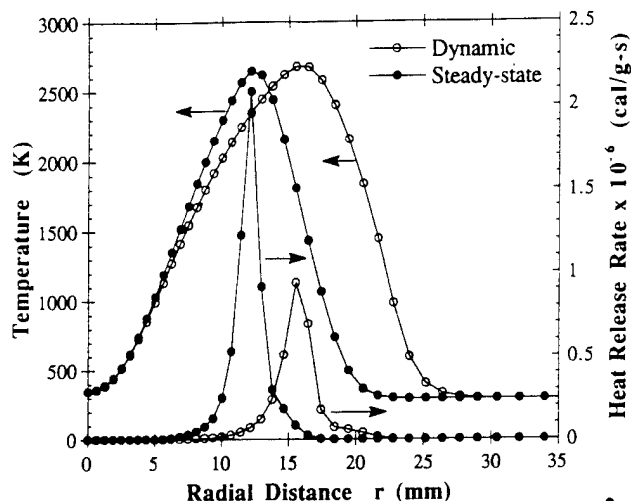


Fig. 10. Temperature and heat-release rate of dynamic and steady-state flames at $z = 63$ mm.

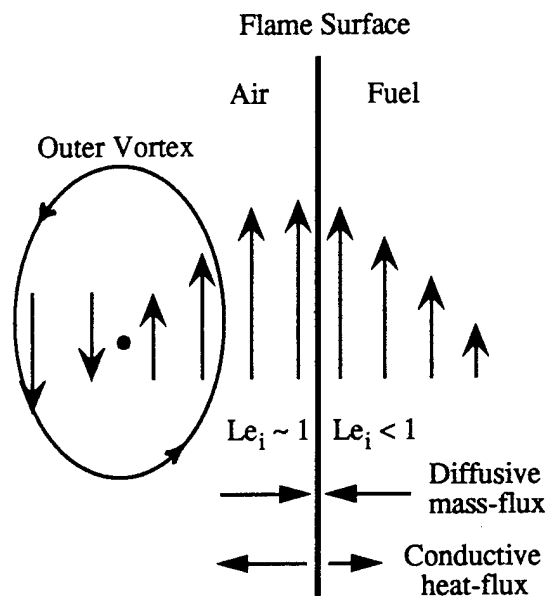


Fig. 11. Nonuniform flow resulting from buoyancy-influenced outer vortex and effect of preferential diffusion on flame temperature.

$$\frac{D_H}{D_{H_2}} = 2.0, \quad \frac{D_O}{D_{H_2}} = 0.8, \quad \frac{D_{OH}}{D_{H_2}} = 0.7, \quad \frac{D_{H_2O}}{D_{H_2}} = 0.3.$$

The intermediate species result from the combustion process within the flame zone as does the heat energy (or temperature); the arguments made with respect to Lewis number are valid for the structure of the species in the flame zone. The relative diffusion coefficient of H_2O is less than one; hence, it peaks in the bulge region. On the other hand, the H radical peaks in the squeeze region because its relative diffusion coefficient is greater than one. The diffusion coefficients of O and OH are near that of H_2 ,

and their concentrations do not exhibit much variation due to the bulging and squeezing of the flame. In a complex mixture of several species, the value at which the change in structural behavior due to preferential molecular diffusion occurs may shift from unity to a critical number. In this flame this critical relative diffusion coefficient may be between 0.8 and 0.7 since OH tends to peak in the bulge region while O tends to peak in the squeeze region.

CONCLUSIONS

A time-dependent, axisymmetric computational-fluid-dynamics model with detailed H_2 - O_2 chemistry is developed and used to simulate a low-speed hydrogen-air diffusion flame that had been experimentally studied previously. Different assumptions on Lewis number and chemistry are made to examine the flame dynamics. Buoyancy-influenced vortices developed in all these simulations in the same way. It was found that neither the Lewis number nor the nonequilibrium chemistry influences the size, shape and frequency of these vortices. The large outer vortices develop as a result of temperature distribution on the air side of a diffusion flame. Since the Lewis number on the air side of a hydrogen flame (and other flames) is near unity the vortex (outer) development, in turn, depends on the mass diffusion. Therefore, the outer vortices predicted by a simple model based on the Shvab-Zeldovich formulation are identical to those predicted by a complex model with detailed chemistry and no assumption for Lewis number (cf Fig. 6).

The Lewis number of hydrogen molecules in a pure mixture is ~ 2 ; however, in a diffusion flame it becomes less than unity. Therefore, the shoulder region of the hydrogen flame burns more intensely than the tip. The convective motion of the outer vortices induce stretch along the flame surface by squeezing the flame at some locations and bulging it at others. The model was able to predict the experimentally observed fluctuations in the flame temperature that arise due to changes in flame stretch. It was found that the lower Lewis number of the hydrogen species on the fuel side of the flame is responsible for increasing the temperature of the stretched flamelet. In the low-speed diffusion flame studied here, the nonequilibrium chemistry is not a factor in determining the stretched-flamelet temperature. The temperature drop of a stretched flamelet due to the supply of reactants in excess of the consumption rate may occur only at higher fuel jet velocities. However, the Lewis number effects discussed here may be present in those flames also. The preferential-mass-diffusion effects seem to complicate the flame-stretching phenomenon.

ACKNOWLEDGEMENT

This work was supported in part by Air Force Contract F-33615-90-C-2033 and the Air Force Office of Scientific Research. The authors would like to thank Dr. Fumiaki Takahashi for helpful discussions and Mrs. Marian Whitaker for the help in preparing the paper.

APPENDIX

The time-dependent energy equation can be written after neglecting body forces, Soret and Dufour effects, pressure-gradient diffusion, and the dissipation by viscous stresses as

$$\rho \frac{\partial h}{\partial t} + \rho \vec{V} \cdot \nabla h = \nabla \cdot (\lambda \nabla T) - \nabla \cdot \left(\rho \sum_1^{N_s} h_i Y_i \vec{V}_i \right)$$

Here, \vec{V}_i is the diffusion velocity of the i -th species. By use of mass continuity (Eq. 1) and Fick's Law for binary diffusion, the above energy equation can be rewritten as follows:

$$\frac{\partial \rho h}{\partial t} + \nabla \cdot \left[\rho \sum_1^{N_s} h_i Y_i \vec{V} - \rho \sum_1^{N_s} D_i h_i \nabla Y_i - \lambda \nabla T \right] = 0.$$

Through the fact that

$$h = \sum_1^{N_s} h_i Y_i = \sum_1^{N_s} \int_{T_0}^T Y_i c_{pi} dT + \sum_1^{N_s} Y_i h_{fi}^0$$

one can obtain

$$\begin{aligned} \frac{\partial \rho h}{\partial t} + \nabla \cdot \left[\rho \vec{V} \sum_1^{N_s} \int_{T_0}^T Y_i c_{pi} dT + \rho \vec{V} \sum_1^{N_s} Y_i h_{fi}^0 \right. \\ \left. - \rho \sum_1^{N_s} D_i \left(\int_{T_0}^T c_{pi} dT + h_{fi}^0 \right) \nabla Y_i \right] - \lambda \nabla T = 0. \end{aligned}$$

Here, T_0 is the reference temperature. By rearrangement of the terms, the above equation becomes

$$\begin{aligned} \frac{\partial \rho h}{\partial t} + \nabla \cdot \left[\rho \vec{V} \int_{T_0}^T \left(\sum_1^{N_s} Y_i c_{pi} dT \right) - \sum_1^{N_s} D_i \left(\int_{T_0}^T c_{pi} dT + h_{fi}^0 \right) \nabla Y_i \right] \\ - \nabla \cdot (\lambda \nabla T) + \nabla \cdot \left[\rho \vec{V} \sum_1^{N_s} Y_i h_{fi}^0 - \sum_1^{N_s} D_i (\nabla Y_i) h_{fi}^0 \right] = 0 \end{aligned}$$

and then

$$\begin{aligned} \frac{\partial \rho h}{\partial t} + \nabla \cdot \left[\rho \vec{V} \int_{T_0}^T \left(\sum_1^{N_s} Y_i c_{pi} dT \right) - \sum_1^{N_s} D_i \left(\int_{T_0}^T c_{pi} dT + h_{fi}^0 \right) \nabla Y_i \right] \\ - \nabla \cdot (\lambda \nabla T) + \sum_1^{N_s} h_{fi}^0 \dot{\omega}_i - \sum_1^{N_s} \left(h_{fi}^0 \frac{\partial \rho Y_i}{\partial t} \right) = 0 \end{aligned}$$

Note that

$$\begin{aligned} \nabla \int_{T_0}^T c_p dT &= \nabla \left(\sum_1^{N_s} Y_i \int_{T_0}^T c_{pi} dT \right) \\ &= \sum_1^{N_s} (\nabla Y_i) \int_{T_0}^T c_{pi} dT + \left(\sum_1^{N_s} Y_i c_{pi} \right) (\nabla T), \\ &= \sum_1^{N_s} (\nabla Y_i) \int_{T_0}^T c_{pi} dT + c_p \nabla T. \end{aligned}$$

$$\Leftrightarrow \lambda \nabla T = \frac{\lambda}{c_p} \left[\nabla \int_{T_0}^T c_p dT - \sum_1^{N_s} (\nabla Y_i) \int_{T_0}^T c_{pi} dT \right]$$

Substitution of this into the energy equation results in

$$\begin{aligned} \frac{\partial \rho h}{\partial t} + \nabla \cdot \left[\rho \vec{V} \int_{T_0}^T \left(\sum_1^{N_s} Y_i c_{pi} dT \right) - \frac{\lambda}{c_p} \nabla \int_{T_0}^T c_p dT \right] \\ = \nabla \cdot \left[\sum_1^{N_s} \left(\rho D_i - \frac{\lambda}{c_p} \right) \left(\int_{T_0}^T c_{pi} dT \right) \nabla Y_i \right] \\ - \sum_1^{N_s} h_{fi}^0 \dot{\omega}_i + \sum_1^{N_s} \left(h_{fi}^0 \frac{\partial \rho Y_i}{\partial t} \right) \end{aligned}$$

By combining the time-dependent terms, one obtain

$$\begin{aligned} \frac{\partial}{\partial t} \left(\rho \int_{T_0}^T c_p dT \right) + \nabla \cdot \left[\rho \vec{V} \int_{T_0}^T \left(\sum_1^{N_s} Y_i c_{pi} dT \right) - \frac{\lambda}{c_p} \nabla \int_{T_0}^T c_p dT \right] \\ = \nabla \cdot \left[\sum_1^{N_s} \left(\rho D_i - \frac{\lambda}{c_p} \right) \left(\int_{T_0}^T c_{pi} dT \right) \nabla Y_i \right] - \sum_1^{N_s} h_{fi}^0 \dot{\omega}_i. \end{aligned}$$

By definition of

$$H \equiv \int_{T_0}^T c_p dT \equiv \sum_1^{N_s} \int_{T_0}^T (Y_i c_{pi} dT) \equiv \sum_1^{N_s} Y_i (h_i - h_{fi}^0) \equiv \sum_1^{N_s} H_i$$

and

$$Le_i \equiv \frac{\lambda}{\rho D_i c_p}$$

the final energy equation can be obtained

$$\frac{\partial \rho H}{\partial t} + \nabla \cdot \left(\rho \vec{V} H - \frac{\lambda}{c_p} \nabla H \right) \\ = \nabla \cdot \left(\sum_1^{N_t} (Le_i^{-1} - 1) H_i \nabla Y_i \right) - \sum_1^{N_t} h_{f,i}^0 \dot{\omega}_i.$$

REFERENCES

- Burke, S. P., and Schumann, T. E. W., Diffusion Flames, *Industrial Engineering Chemistry*, Vol. 20, No. 10, pp. 998-1004, 1928.
- Peters, N., and Williams, F. A., Liftoff Characteristics of Turbulent Jet Diffusion Flames, *AIAA Journal*, Vol. 21, No. 3, pp. 423-429, March 1983.
- Bilger, R. W., "The Structure of Turbulent Nonpremixed Flames," Twenty-Second (International) Symposium on Combustion, The Combustion Institute, Pittsburgh, PA, pp. 475-488, 1989.
- Hottel, H. C. and W. R. Hawthorne, "Diffusion in Laminar Flame Jets," Third Symposium (International) on Combustion, Flame and Explosive Phenomena, PP 254-266, 1949.
- Roquemore, W. M., L.-D. Chen, L. P. Goss and W. F. Lynn, "Structure of Jet Diffusion Flames", *Turbulent Reactive Flows*, Lecture Notes in Engineering. Vol. 40, pp. 49-63, 1988.
- Vilimpoc, V., and Goss, L. P., SiC-Based Thin-Filament Pyrometry: Theory and Thermal Properties, Twenty-second Symposium (International) on Combustion, The Combustion Institute, Pittsburgh, PA, pp. 1907-1914, 1988.
- Katta, V. R., Goss, L. P., and Roquemore, W. M., Numerical Investigations on the Dynamic Behavior of a H₂-N₂ Diffusion Flame under the Influence of Gravitational Force, *AIAA Paper 92-0335*, 30th Aerospace Sciences Meeting, Reno, 1992.
- Mizomoto, M., Asaka, Y., Ikai, S., and Law, C. K., Effects of Preferential Diffusion on the Burning Intensity of Curved Flames, Twentieth Symposium (International) on Combustion, The Combustion Institute, Pittsburgh, PA, pp. 1933-1939, 1984.
- Burcat, A., Thermochemical Data for Combustion Calculations, in *Combustion Chemistry*, Springer-Verlag, New York, NY, pp. 455-473, 1984.
- Miller, J. A., and Kee, R. J., Chemical Non-Equilibrium Effects in Hydrogen-Air Laminar Jet Diffusion Flames, Central States Section Spring Meeting, Combustion Institute, March 28-30, 1977.
- Cowart, J. S., Keck J. C., Heywood J. B., Westbrook C. K., and Pitz, W. J.; Comparison of Engine Knock Predictions using a Fully-Detailed and a Reduced Chemical Kinetics Mechanism, Western States Section Meeting of the Combustion Institute, October 23-24, 1989.
- Leonard, B. P., A Stable and Accurate Convective Modelling Procedure Based on Quadratic Upstream Interpolation, *Computer methods in Applied Mechanics and Engineering*, Vol. 19, pp. 59-98, 1979.
- Spalding, D. B., A Novel Finite Difference Formulation for Difference Expressions involving both First and Second Derivatives, *International Journal for Numerical Methods in Engineering*, Vol. 4, 1972, pp. 551-559.
- Lynn, W. F., Goss, L. P., Chen, T. H., and Trump, D. D., Two-Dimensional Velocity Measurements on an Axially Symmetric H₂-N₂ Jet Diffusion Flame, Presented at the Central States section of the Combustion Institute Meeting, Indianapolis, IN, May 2-3, 1988.
- Buckmaster, J., and Peters, N., Twenty-First Symposium (International) on Combustion, The Combustion Institute, Pittsburgh, PA, pp. 1829-1836, 1986.
- Chen, L.-D., Seaba, J. P., Roquemore, W. M., and Goss, L. P., Buoyant Diffusion Flames, Twenty-Second Symposium (International) on Combustion, The Combustion Institute, Pittsburgh, PA, pp. 677-684, 1988.
- Ellzey, J. L., Laskey, K. J., and Oran, E. S., Effects of Heat Release and Gravity on an Unsteady Diffusion Flame, Twenty-Third Symposium (International) on Combustion, The Combustion Institute, Pittsburgh, PA, pp. 1635-1640, 1990.
- Davis, R. W., Moore, E. F., Roquemore, W. M., Chen, L.-D., Vilimpoc, V., and Goss, L. P., Preliminary Results of a Numerical-Experimental Study of the Dynamic Structure of a Buoyant Jet Diffusion Flame, *Combustion and Flame*, Vol. 83, pp. 263-270, 1991.
- Katta, V. R., and Roquemore, W. M., Role of Inner and Outer Structures in a Transitional Diffusion Flame, to appear in *Combustion and Flame*, Feb. 1993.
- Hsu, K. Y., Chen, L.-D., Katta, V. R., Goss, L. P., and Roquemore, W. M., Experimental and Numerical Investigations on the Flame-Vortex Interactions in a Driven Jet Diffusion Flame, *AIAA Paper 93-0455*, 31th Aerospace Sciences Meeting, Reno, 1992.
- Law, C. K., *Heat and Mass Transfer in Combustion: Fundamental Concepts and Analytical Techniques*, *Progress in Energy and Combustion Science*, Vol 10, pp. 295-318, 1984.
- Dixon-Lewis, G., Structure of Laminar Flames, Twenty-third Symposium (International) on Combustion, The Combustion Institute, Pittsburgh, PA, pp. 305-324, 1990.
- Givi, P., Jou, W. -H., and Metcalfe, R. W., Flame Extinction in a Temporally Developing Mixing Layer, Twenty-first Symposium (International) on Combustion, The Combustion Institute, Pittsburgh, PA, pp. 1251-1261, 1986.

On the Structure of a Stretched/Compressed Laminar Flamelet—Influence of Preferential Diffusion

V. R. KATTA*

Systems Research Laboratories, Inc. A Division of Calspan Corporation, 2800 Indian Ripple Road, Dayton, OH 45440-3696

W. M. ROQUEMORE

Wright Laboratory, Aero Propulsion and Power Directorate, Wright-Patterson Air Force Base, OH 45433-7103

The local Lewis number on the fuel side of a H_2 /air diffusion flame is known to be lower than unity. When a high-Damkohler-number hydrogen flame is stretched, the flame temperature changes—not because of incomplete chemical reactions, but due to the preferential diffusion resulting from the nonunity Lewis number. These changes are examined using a Computational Fluid Dynamics with Chemical reactions (CFDC) code that is third-order accurate. Detailed chemical kinetics including NO reactions is used to investigate the effects of stretch on the flame structure. A low-speed H_2 /air diffusion flame having a fuel-jet velocity of 3.26 m/s is subjected to stretch using two vortices—one located on the fuel side of the flame and the other on the air side. Both vortices create positive (stretch) and negative (compression) flame-stretch factors when interacting with the flame. The temperature of the positively stretched flamelet was found to decrease when the vortex is located on the air side and to increase when it is on the fuel side. Similarly, compression of the flamelet resulting from the air-side vortex increases the flame temperature, whereas fuel-side vortex decreases the flame temperature. Among the eleven species considered in this model, production of NO in the flame zone appears to be the most sensitive to flame stretching or compression. Concentration of NO is found to be maximum in the compressed flamelet formed during the outside vortex-flame interaction. Finally, a comparison of the mean-NO-concentration profiles obtained by averaging over several cycles of outside vortex-flame interactions and the time-averaged measurements yielded favorable agreement.

INTRODUCTION

Two classes of vortex-flame interactions have been observed in jet diffusion flames. In one class, the vortex is formed outside the flame surface and in the other, the vortex is formed inside the flame surface. A conventional vertically mounted jet diffusion flame (central fuel jet surrounded by a coannular air flow) may contain either or both of these vortices, depending on the fuel and air-jet velocities. When the annular-air velocity is low, buoyancy-induced vortices form outside (i.e., on the air side) the flame surface. Similarly, shear-layer vortices develop inside (i.e., on the fuel side) the flame surface at a sufficiently high fuel jet velocity. In transitional jet diffusion flames [1]

both outer and inner vortices are observed, whereas in turbulent flames only inner vortices are observed. As the outer and inner vortices are convected downstream, they interact with the flame surface and create locally stretched and compressed flamelets.

The structural changes in a stretched or compressed flamelet are dependent on the local Damkohler number of the flow [2] and the specific manner in which the flame is stretched [3]. The latter dependence results from the difference in heat- and mass-transport rates (nonunity Lewis number) that prevail locally in a flame zone. The structure of a stretched flamelet for different Damkohler numbers has been studied extensively in stagnation-point [4] and counterflow [5, 6] flames. These configurations eliminate the effects of nonuniform flow and flame curvature, thereby reducing the nonunity-Lewis-number effects. As a result such studies were focused mainly on Damkohler-number effects. Most of the studies on flame

* Corresponding author.

Presented at the Twenty-Fifth Symposium (International) on Combustion, Irvine, California, 31 July–5 August 1994.

COMBUSTION AND FLAME 100: 61–70 (1995)

Copyright © 1995 by The Combustion Institute

Published by Elsevier Science Inc.

0010-2180/95/\$9.50
SSDI 0010-2180(94)00077-6

stretch in vortex-flame interactions were conducted on premixed systems [7–9]; however, a few were conducted in diffusion flames on outside vortex-flame type interactions [10, 11]. To the authors' knowledge, only two vortex-flame-interaction studies have been performed in which vortices have formed inside the flame [12, 13].

Although the reduction in flame temperature due to stretch has been of primary concern in the vortex-flame interaction studies, the impact of local nonunity Lewis number has not been examined. What has not been fully appreciated is that a local nonunity Lewis number can have a significant impact on vortex-flame interaction, causing temperature increases and decreases in different regions of the flame. The locations where the temperature increases and decreases depend on whether the interacting vortex is inside or outside the flame surface and whether the flame-stretch factor is positive (stretch) or negative (compression).

In the present study, the effects of nonunity Lewis number on vortex-flame interactions were computationally investigated in two high-Damkohler-number (or low-speed) H_2 /air jet diffusion flames. In the first case (Flame A) interaction with an inside vortex and in the other case (Flame B) interaction with an outside vortex were considered. The flow conditions for the second were chosen to coincide with those employed for a laboratory flame that has been extensively investigated [14].

MATHEMATICAL MODEL

In the present analysis, time-dependent, axisymmetric Navier-Stokes equations written in the cylindrical-coordinate system are solved along with species- and energy-conservation equations [15]. The body-force term due to the gravitational field is included in the axial-momentum equation. A detailed chemical-kinetics model is used to describe the hydrogen-air combustion. This model consists of eleven species (H_2 , O_2 , H , O , OH , H_2O , HO_2 , H_2O_2 , N , NO , and N_2) and 40 elementary reactions [16]. Temperature- and species-dependent properties are incorporated. The enthalpy of each species is calculated from polynomial

curve-fits, while the viscosity and thermal conductivity are estimated from Chapman-Enskog collision theory. The effective binary-diffusion coefficient [17] of individual species in the local mixture is calculated using molecular dynamics and Lennard-Jones potentials.

The governing equations are integrated on a nonuniform staggered-grid system. An orthogonal grid having rapidly expanding cell sizes in both the axial and the radial direction is employed. The finite-difference forms of the momentum equations are obtained by an implicit QUICKEST scheme [18] and those of the species and energy equations by a hybrid scheme of upwind and central differencing. At every time-step, the pressure field is calculated by solving all the pressure Poisson equations simultaneously and utilizing the LU (Lower and Upper diagonal) matrix-decomposition technique.

The computational domain is bounded by the axis of symmetry and an outflow boundary in the radial direction and by the inflow and another outflow boundary in the axial direction. The outer boundaries in the z and r directions are located sufficiently far from the nozzle exit (40 nozzle diameters) and the axis of symmetry (15 nozzle diameters), respectively, to minimize the propagations of boundary-induced disturbances into the region of interest. Flat velocity profiles are used at the fuel and air inflow boundaries. An extrapolation procedure with weighted zero- and first-order terms is used to estimate the flow variables at the outflow boundary. The weighting functions are selected using the trial-and-error approach, and the main criterion used is that the vortices crossing the outflow boundary leave smoothly without being distorted.

RESULTS

Two laminar jet diffusion flames (A and B) were simulated for a mixture of hydrogen and nitrogen emerging from a 10-mm-diameter nozzle. The volumetric ratio between the fuel and nitrogen was 3.5. A fuel-jet velocity of 3.26 m/s was used for both flames. These flow conditions are the same as those of the laboratory flame that was studied by Vilimpoc et. al. [14]. The annulus-air velocity was 0.6 and 0.15

m/s for Flames A and B, respectively. The flames were calculated in a physical domain of 400×150 mm using a 201×71 grid.

The steady-state solutions for Flames A and B were first obtained by performing the calculations while neglecting the unsteady terms in the governing equations. These solutions were used as the initial conditions for the present studies on dynamic vortex-flame interactions.

Formation of Fuel-Side Vortex

Unsteady simulations made on Flame A did not result in any vortices either inside or outside the flame surface. The relatively high annulus-air flow delayed the formation of buoyancy-induced vortices [19] outside the flame surface, and the flame was oscillation free up

to $z = 150$ mm. Although at locations farther downstream, the flame was observed to be oscillating at a low frequency with the onset of buoyancy-induced vortices, it does not have any influence on the present results which are focused in the region $z < 100$ mm. Fuel-side vortices in this flame were introduced periodically (30 Hz) by perturbing the fuel-jet velocity at the exit of the nozzle [14].

Particles were introduced at the nozzle exit to trace the introduced vortex. Instantaneous locations of the particles are shown in Fig. 1a. Flame surface that was identified by locating the peak temperatures in the radial directions is shown by solid circles. The flame location and the temperature contours obtained from the steady-state solution are plotted in Fig. 1b and those obtained from the flame having a fuel-side vortex are plotted in Fig. 1c. The

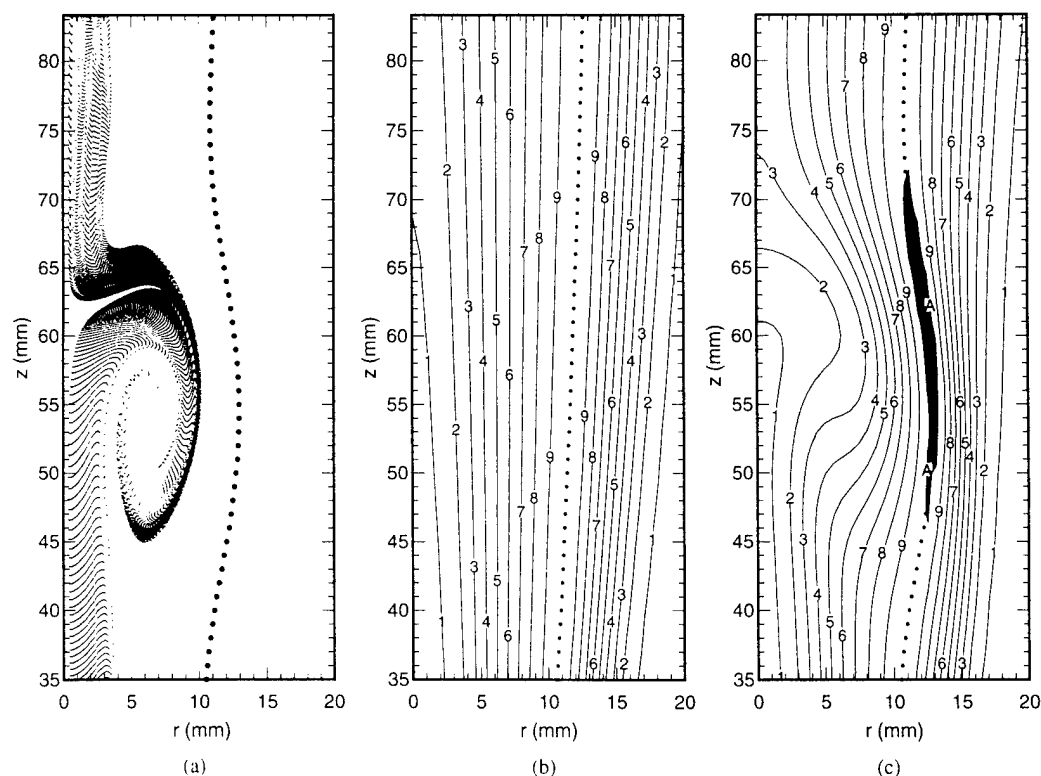


Fig. 1. Interaction of fuel-side vortex with laminar diffusion flamelet. (a) Instantaneous locations of particles that were injected continuously at nozzle exit. Large solid circles indicate flame surface which was obtained by tracing peak temperature at every axial position. (b) Instantaneous iso-temperature contours of steady-state flame. (c) Modified temperature field as result of interaction. Nine equally spaced contours (1–9) were plotted between 400 and 2400 K. Shaded contour A indicates region with temperature higher than 2580 K, which is peak value in steady-state flame.

contours in Figs. 1b and 1c are labeled in such a way that the numbers 1–9 correspond to equally spaced temperatures between 400 and 2400 K. As expected, the temperature in the steady-state flame is maximum along the flame surface and equal to 2580 K. The interaction of the vortex and the flame surface created locally stretched and compressed flamelets. As a result, the temperature along the flame surface was no longer constant in Fig. 1c. Contour A represents a temperature of 2580 K, and the region where the temperature is above this value is shaded. It should be noted from Figs. 1a and 1b that the fuel-side vortex centered at $z \sim 55$ mm has pushed the flame radially outward by ~ 1.3 mm. The stretch induced on the flame surface and its effects on the flame structure will be discussed later.

Formation of Air-Side Vortex

Unsteady simulations on Flame B were made using the steady-state solution as the initial condition. The low annulus-air flow in this case

yielded a train of large toroidal vortices outside the flame surface, i.e., on the air side. It is important to note that no external perturbation was used in this simulation and that the buoyant acceleration of hot gases along the flame surface is responsible for the formation of these vortices [19]. No vortices on the fuel side were formed and the jet shear layer remained laminar. Instantaneous particle locations in the neighborhood of an air-side vortex are shown in Fig. 2a. The center of the vortex is located at $z = 55$ mm. Iso-temperature contours of the steady-state and dynamic flame are shown in Figs. 2b and 2c, respectively. Labeling of the contours is identical to that used in Figs. 1b and 1c. The air-side vortex has pushed (squeezed) the flame toward the axis by 2 mm at $z = 55$ mm and pulled (bulged) it radially outward by 3.4 mm at $z = 80$ mm. The closed iso-temperature contour (A) in the flame-bulging region ($z = 80$ mm) of Fig. 2c indicates that the temperature along the flame surface is not constant and is higher than 2580 K in the shaded region.

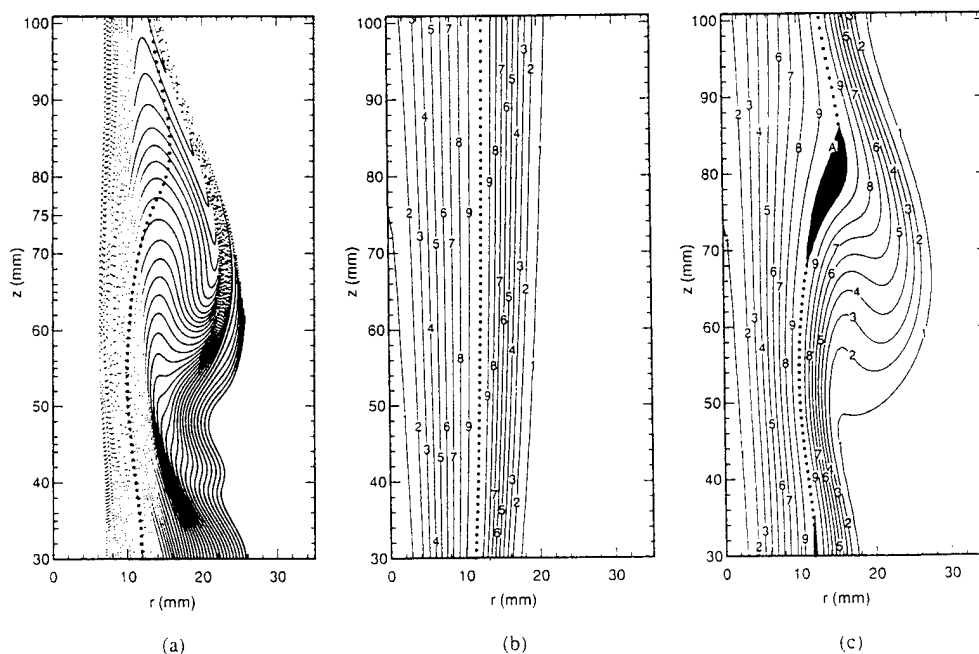


Fig. 2. Interaction of air-side vortex with laminar-diffusion flamelet. (a) Instantaneous locations of particles that were injected continuously at nozzle exit. Large solid circles indicate flame surface which was obtained by tracing peak temperature at every axial position. (b) Instantaneous iso-temperature contours of steady-state flame. (c) Modified temperature field as result of interaction. Contour labeling is identical to that of Fig. 1.

DISCUSSION

The local flame structure is altered when a vortex interacts with the flame. A comparison of the iso-temperature contours of Flames A and B (Figs. 1c and 2c, respectively) with those of the steady-state flames (Figs. 1b and 2b, respectively) reveals that the local flamelets near the centers of the vortices are stretched (squeezed contours) and compressed in the leading and trailing edges (spread-out contours). It is known that the fuel and oxidizer fluxes into the flame zone increase with flame stretching [17]. Laminar flamelet theory [2] suggests that as the flame is stretched, the chemical-reaction rates cannot keep pace with the increase in the reactant fluxes in consuming them; hence, the temperature of the flame decreases. However, the shaded regions ($T > 2580$ K) of Figs. 1c and 2c show that the flame temperature increases when the flame is pushed radially outward, even though this bulge is associated with flame stretching in the former case and with flame compression in the latter.

Intuitively, it may be argued that in a high-Damkohler-number flow (i.e., residence time \gg reaction time), small variations in the reactant fluxes due to flame stretch would not overwhelm the chemistry. In fact, our previous study on the effects of finite-rate chemistry and nonunity Lewis number on this flame [20] stressed that the fluctuations in flame temperature observed when the flame was periodically stretched and compressed are due not to finite-rate chemistry but to preferential diffusion. In order to correlate the flame stretch and the changes in temperature in Flames A and B, the stretch factor k is calculated using the expression [21],

$$k = \frac{1}{A} \frac{\partial A}{\partial t} = \vec{\nabla}_s \cdot \left\{ \hat{n} \times (\vec{V}_f \times \hat{n}) \right\} + (\vec{v} \cdot \hat{n}) (\vec{\nabla}_s \cdot \hat{n}).$$

Here, \vec{V}_f represents the fluid velocity at the flame surface and \vec{v} is the flame velocity. In order to calculate k using this expression, at least two solutions at times t_0 and $t_0 + \Delta t$ are required.

The flame-surface locations of Flames A and B are plotted with broken lines at time $t_0 + \Delta t$ in Figs. 3a and 4a, respectively, and with solid lines at time t_0 . The normal flame velocity ($\vec{V}_n \equiv \vec{v} \cdot \hat{n}$) calculated from these two instantaneous flame surfaces is also shown in these plots. In both flames, the flame surface is moving downstream with the convective motion of the vortex, without being pushed further in or out radially. Therefore, the normal flame velocity at the vortex center (at $z = 55$ mm in both flames) is zero which suggests that the local flow is parallel to the flame surface.

The flame-stretch factor (k) and temperature along the flame surface at different axial locations are plotted for Flames A and B in Figs. 3b and 4b, respectively. Due to the fuel-side vortex (Fig. 3b), the flame is stretched (k is $+ve$) in the regions where it is pushed radially outward. When the flame is pulled

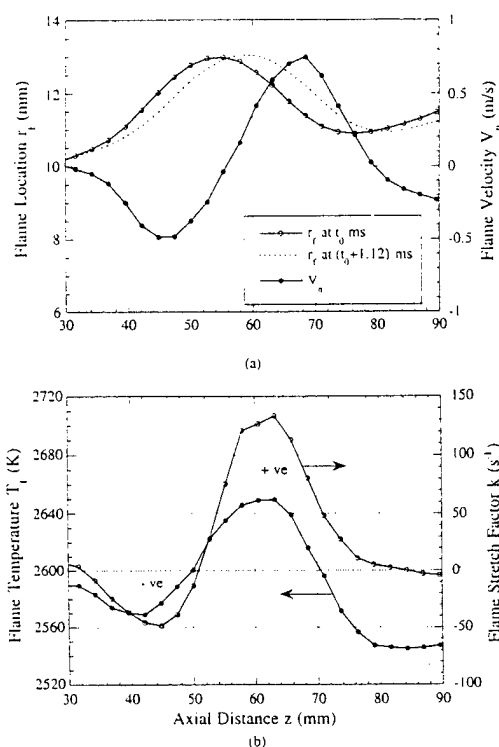


Fig. 3. Flame-surface response to moving fuel-side vortex plotted at different axial locations. (a) Location of flame surface at two instants in time. Normal flame velocity with reference to laboratory frame is also shown. (b) Temperature and stretch factor along flame surface.

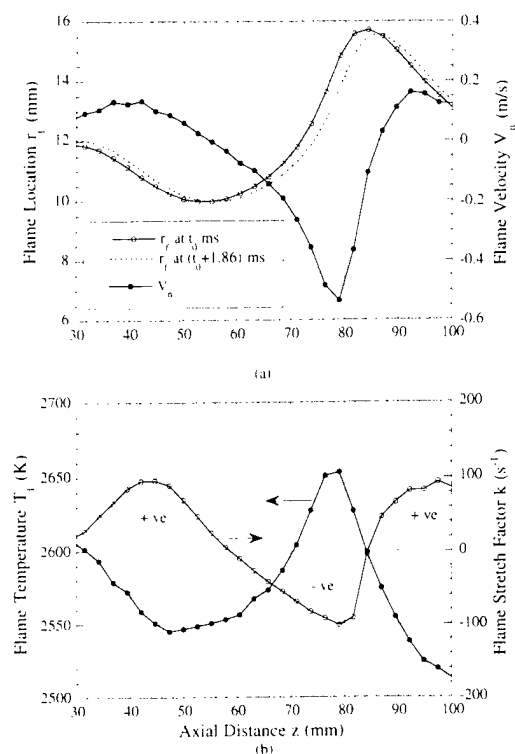


Fig. 4. Flame-surface response to moving air-side vortex plotted at different axial locations. (a) Location of flame surface at two instants in time. Normal flame velocity with reference to laboratory frame is also shown. (b) Temperature and stretch factor along flame surface.

back in the trailing edge of the vortex, the flame-stretch factor becomes $-ve$, indicating that the local flamelet is compressed. Note that the flame stretch is maximum at a location slightly downstream of the vortex center ($z = 55$ mm).

Flame temperature, which was nearly constant in the steady-state flame, is changing with the axial distance in Flame A (Fig. 3b). When the flame is stretched (i.e., for $k + ve$), the temperature also increases. Similarly, when it is compressed (i.e., for $k - ve$), the flame temperature decreases. This correlation between the flame-stretch and temperature behavior is in contrast to what might be expected from the laminar-flamelet theory [2]. Due to the large Damkohler number associated with these flows, chemical reactions are not responsible for the changes in flame temperature; therefore, the laminar-flamelet theory [2] is not applicable in this context.

It is known that the H_2 /air diffusion flame has a Lewis number that is less than unity on the fuel side of the high-temperature surface. Preferential diffusion resulting from this nonunity Lewis number alters the flame temperature when a vortex interacts with the flame. Clockwise rotation of the fluid due to the fuel-side vortex in Fig. 1a induces a velocity field in the stretched-flame region in a way that the superimposed axial velocity u' decreases with radial distance from the vortex core. Since the Lewis number is less than unity in the flame zone, the negative velocity gradient with respect to the radial distance (i.e., $du'/dr < 0$) has less effect on the heat transported away from the flame zone than on the mass transported into the flame zone. Accumulation of heat in the stretched-flame zone results in an increase in temperature. The interaction of the vortex and the flame makes the flame surface concave with respect to the vortex and, hence, to the incoming fuel (vortex located on fuel side). This curvature in conjunction with the preferential diffusion that arises from the Lewis number being less than unity resulted in the flame temperature decreasing in the compressed region [3, 20].

When the air-side vortex interacts with the flame (B), the maximum stretch (Fig. 4b) is occurring at a location 10 mm upstream of the vortex center ($z = 55$ mm). The buoyancy-induced vortex in this flame has developed locally stretched flamelets having a stretch factor of up to 100 s^{-1} and compressed flamelets having k as low as -100 s^{-1} . In contrast to the results obtained with the fuel-side vortex-flame interaction, flame temperature in the air-side case decreases when the flamelet is stretched and increases when it is compressed. The air-side vortex in this flame is associated with the fluid that rotates in the clockwise direction (Fig. 2a), and induces an axial velocity u' in the flame zone that decreases with decreasing radial distance. The positive velocity gradient (i.e., $du'/dr > 0$) has more effect on the heat transport than on the mass transport in the H_2 /air diffusion flame which has a Lewis number less than unity on the fuel side. The faster removal of heat from the flame zone due to this velocity gradient in the stretched flamelet ($z \sim 47$ mm) decreased the

flame temperature (Fig. 4b) by about 40 K. Since the vortex is on the air side, the flame has a convex curvature with respect to the incoming fuel which increases the flame temperature in the compressed flamelet due to preferential diffusion.

The temperature response to the flame stretch in Flame B is similar to what one might expect from finite-rate chemistry if the reaction and residence times are of the same order. Therefore, in a low-Damkohler-number H_2 /air flame, preferential diffusion and finite-rate chemistry work together to decrease the temperature when the flamelet is stretched and to increase it when the flamelet is compressed. However, if the vortex is on the air side, finite-rate chemistry effects must overcome those resulting from preferential diffusion in order to see the phenomenon that a laminar flamelet theory suggests.

Structures of the stretched and compressed flamelets of Flame B are shown in Figs. 5a and 5b, respectively. As described earlier, the air-side vortex is interacting with the flame in this case. Temperature and mole fractions of H_2 , O_2 , OH, and NO are plotted as functions of radial distance. Figures 5a and 5b correspond to axial locations of 55 and 80 mm from the nozzle exit (cf. Fig. 2). Flame thicknesses (width of the temperature profile at $0.5T_f$) measured from the steady-state solution (Fig. 2b) at these two locations are 9.7 and 10.8 mm, respectively. The direct effect of stretch on a flamelet is to increase the reactant fluxes into the flame zone and that of compression is to decrease them. This is evident from the changes in flame-zone thickness in Figs. 5a and 5b. The thickness of the flame zone in the case of the stretched flamelet has decrease to 6.9 mm, while it has increased to ~ 17.3 mm in the compressed flamelet. Referring Fig. 4b it should be noted that the difference in the stretch factor between these two flamelets is nearly 200 s^{-1} .

The peak OH concentration in the compressed flamelet (Fig. 5b) is 26% lower than that in the stretched flamelet (Fig. 5a). Among the 11 species considered in this study, NO seems to be the most sensitive to flame stretching. The peak NO concentration in the compressed flamelet is 54% higher than that in the

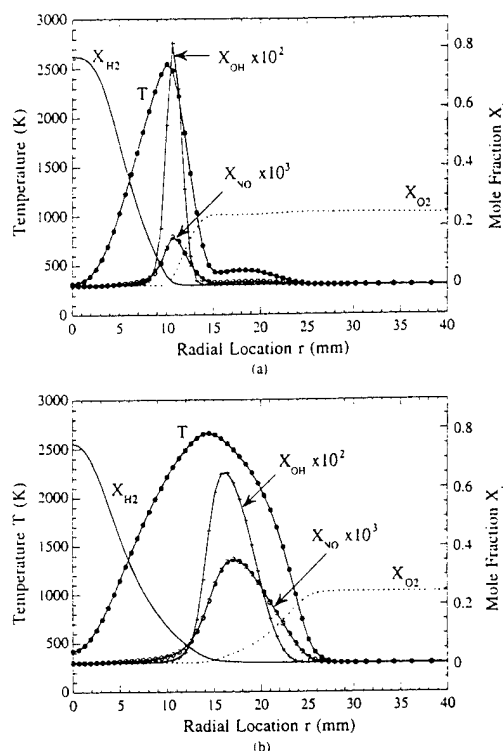


Fig. 5. Flame structure in (a) stretched and (b) compressed regions of the laminar flamelet. Interacting vortex is on air side. Radial distributions of instantaneous temperature and mole fractions of four species are plotted.

stretched flamelet. While the preferential diffusion arising from the nonunity Lewis number affects the temperature of a stretched flamelet, the nonunity relative Schmidt number of the species with respect to the fuel (D_{H_2}/D_i) affects the species distribution in the flame zone [20]. During the vortex-flame interactions in diffusion flames, the combined effect of Lewis and Schmidt numbers complicates the flame-zone structure.

Variations in temperature and molar concentration of OH and NO across the flame with time at an axial distance of 80 mm are plotted in Fig. 6. Data at elapsed time τ represent the flame one might have observed at τ ms prior to zero. Closed contours in the bulge regions of Fig. 6a reflect the increase in temperature which was also observed by Vilimpoc [14] while measuring temperature using the Thin-Filament-Pyrometry technique. The species OH is confined in a narrow zone of the flame and is mostly on the air side. Its concen-

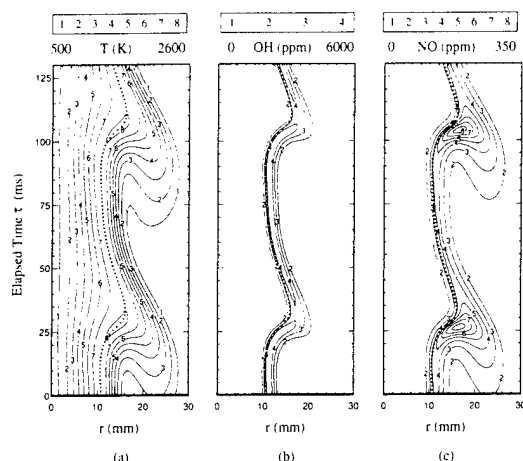


Fig. 6. Evolution of (a) temperature, (b) OH concentration, and (c) NO concentration of dynamic flame at axial location of 80 mm from nozzle exit. Data at any given elapsed time, τ , represents that the observer might have seen τ ms prior to 0. Contour table for each plot is given at the top. High-temperature surface is marked with solid circles.

tration decreases as the flame is pulled radially outward. Hsu [22] recently visualized this behavior of OH using the Laser-Induced-Fluorescence technique.

Figure 6c indicates that all or most of the generated NO is on the air side of the high-temperature surface. Entrainment of NO into the air-side vortex indicates the longevity of the NO molecules. In contrast to the behavior of OH, NO production becomes maximum when the flame is bulging outward. Time-averaged NO profiles obtained at two axial locations are compared with the recently measured ones in Fig. 7. The overall agreement seems to be reasonable considering the uncertainties associated with the experimental procedure and the NO-mechanism adopted in this study. However, based on the comparisons made for temperature and OH and NO concentration, it is clear that the mathematical model has correctly captured the effects of preferential diffusion on temperature and species in a dynamic flame.

CONCLUSION

A vortex (either fuel side or air side) develops a positive stretch on the flame near the center of the vortex and a negative stretch (compres-

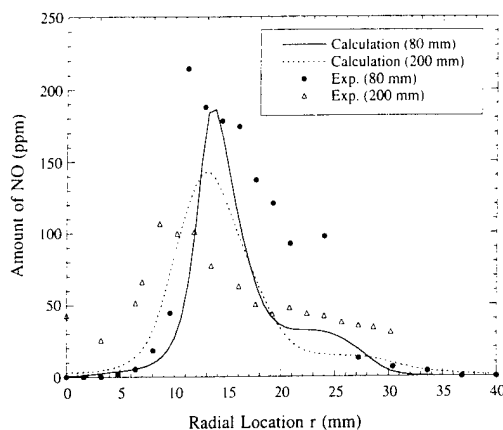


Fig. 7. Comparison of measured and computed NO-profiles of averaged flame at two different axial locations.

sion) in the trailing and leading edges. In large-Damkohler-number flames, the chemistry is not affected by this stretch. However, because of the preferential diffusion in hydrogen flames (arising from the nonunity Lewis number), the temperature of the local flamelet changes during the vortex-flame interaction and its response to stretching or compression is dependent on the location of the interacting vortex with respect to the flame surface. It was found that the flame temperature increases in the leading and trailing edges of an air-side vortex (compressed flamelets) and near the center of a fuel-side vortex (stretched flamelet). Similarly, the temperature decreases when the flamelet is stretched by the air-side vortex or compressed by the fuel-side vortex. At lower Damkohler numbers, the flame temperature changes as a result of both the incompleteness of the chemistry and preferential diffusion. Therefore, in a low-Damkohler-number hydrogen diffusion flame, preferential diffusion enhance the chemistry effects if the vortex is on the air side and diminishes them if the vortex is on the fuel side.

It was also found that when the flamelet is stretched by an air-side vortex, production of OH increases and that of NO decreases. This is due, in part, to the nonunity relative Schmidt numbers of the different species with respect to the fuel and, in part, to the decrease in temperature. Since NO generation is very sensitive to flame temperature, its concentration in the stretched flamelet is 54% lower than

that in the compressed flamelet, even though the temperature difference is only 110 K in these two flamelets.

This work was supported, in part, by US Air Force Contract F 33615-90-C-2033 and the Air Force Office of Scientific Research. The authors would like to thank Dr. K. Y. Hsu for providing us with the prepublished OH data, Messrs. C. Frayne, and R. Britton, and J. Zelina for allowing us to use the NO data, and Mrs. M. Whitaker for the help in preparing the manuscript.

REFERENCES

1. Yule, A. J., Chigier, N. A., Ralph, S., Boulderstone, R., and Ventura, J., *ALAA J.* 19:752 (1981).
2. Peters N., and Williams, F. A., *ALAA J.* 21:423 (1983).
3. Law, C. K., in *Prog. Ener. Combust. Sci.*, 10:295 (1984).
4. Tsuji, H., and Yamaoka, I., *Thirteenth Symposium (International) on Combustion*, The Combustion Institute, Pittsburgh, 1971, p. 723.
5. Dixon-Lewis, G., *Twenty-Third Symposium (International) on Combustion*, The Combustion Institute, Pittsburgh, 1990, p. 305.
6. Chelliah, H. K., Law, C. K., Ueda, T., Smooke, M. D., and Williams, F. A., *Twenty-Third Symposium (International) on Combustion*, The Combustion Institute, Pittsburgh, 1991, p. 503.
7. Roberts, W. L., Driscoll, J. F., Drake, M. C., Ratcliffe, J. W., *Twenty-Fourth Symposium (International) on Combustion*, The Combustion Institute, Pittsburgh, 1992.
8. Rutland, C., and Ferziger, J., *AIAA Paper 89-0127*, 27th Aerospace Sciences Meeting and Exhibit, Reno, 1989.
9. Poinso, T., Veynante, D., and Candel, S., *J. Fluid Mech.* 22:561 (1991).
10. Karagozian, A. R., Marble, R. E., *Combust. Sci. Technol.* 45:65 (1986).
11. Laverdant, A., and Candel, S., *ALAA J. Propul. Power* 5:134 (1989).
12. Lewis, G. S., in *Twenty-Second Symposium (International) on Combustion*, The Combustion Institute, Pittsburgh, 1988, p. 515.
13. Hsu, K. Y., Chen, L.-D., Katta, V. R., Goss, L. P., and Roquemore, W. M., *AIAA Paper 93-0455*, 31st Aerospace Sciences Meeting and Exhibit, Reno, Jan., 1993.
14. Vilmpoc, V., and Goss, L. P., *Twenty-Second Symposium (International) on Combustion*, The Combustion Institute, Pittsburgh, 1988, p. 1907.
15. Katta, V. R., Goss, L. P., and Roquemore, W. M., *ALAA J.* 32:84 (1994).
16. Katta, V. R., and Roquemore, W. M., *AIAA Paper 94-0454*, 32nd Aerospace Sciences Meeting and Exhibit, Reno, Jan., 1994.
17. Williams, F. A., *Combustion Theory—The Fundamentals of Chemically Reacting Flow Systems*, Addison-Wesley, Reading, Mass., 1985.
18. Leonard, B. P., *Comp. Meth. Appl. Mech. Eng.* 19:59 (1979).
19. Chen, L.-D., Seaba, J. P., Roquemore, W. M., and Goss, L. P., *Twenty-Second Symposium (International) on Combustion*, The Combustion Institute, Pittsburgh, 1988, p. 677.
20. Katta, V. R., Goss, L. P., and Roquemore, W. M., *Combust. Flame* 96:60 (1994).
21. Chung, S. H., and Law, C. K., *Combust. Flame* 55:123 (1984).
22. Hsu, K. Y., Private communication, SRL, Dayton, Nov. 1993.

Received 1 December 1993; revised 20 April 1994

Comments

R. V. Serauskas, Gas Research Institute, USA. 1. By how much is the adiabatic flame temperature exceeded in the compressed vortex regions (induced by non-unity Lewis numbers)?

2. Since present precision of in-flame measurements of temperature fields are on the order of ± 60 K at best, how good are prospects that such excursions (and implications for NO_x) can be validated?

Authors' Reply. Calculations made for a diffusion flame using unity-Lewis-number and infinitely fast-chemical kinetics assumptions yield a constant flame temperature that is equal to the adiabatic value (T_{ad}). However, as dis-

cussed in Ref. 1, relaxation of these assumptions for a H_2 air jet diffusion flame results in a flame temperature that decreases with flame height. Near the flame base flame temperature is higher than T_{ad} ; near the flame tip it is lower. When such a flame is stretched or compressed by a vortex, the local flame temperature may change. In the present calculations near the compressed region of the air-side vortex, the flame temperature exceeded the steady-state value by 70 K and the adiabatic value by 200 K.

Although the precision for the instantaneous-temperature measurements in flames is only about ± 60 K, the current instruments (for example, CARS) can measure quite accu-

rately the average temperatures (up to 20 K). The flame-vortex phenomenon represents an unsteady process. However, by periodically introducing vortices into the flame and by phase-locking the measurements to the vortices, one can obtain several instantaneous shots of the same event and, thus, cancel out the random errors of the instrument. Experiments are currently underway for making simultaneous temperature and NO_x measurements with respect to the air-side vortex-flame interactions.

K. Yamamoto, University of Tokyo, Japan. In general, when the Lewis number is not equal to unity, the temperature and concentration fields are very different. In your study, the flame surface was identified only by locating the peak temperature in the radial directions to calculate the flame stretch. In a diffusion flame, the flame position is also affected by the flux of fuel and oxidant. Will you calculate the flame surface by means of the velocity vector and H_2 , O_2 etc. mole fraction, if possible?

Authors' Reply. Because of the non-unity Lewis number and finite-rate chemistry used in the calculations, one can determine the flame-surface location from the temperature field, reactant molar fluxes, heat-release rate, etc. However, in a diffusion flame, all of these surfaces lie within the reaction zone which has a thickness on the order of 2 mm. Since changes in the velocity field are negligible within the reaction zone, the flame-stretch factors calculated using different methods for identifying flame surface locations should be the same for all practical purposes.

Y. C. Chao, National Cheng Kung University, Republic of China. What is the effect of the grid size on the determination of the flame surface, the stretch factor, and the diffusion process in your cases?

Authors' Reply. Since the discussed fluctuations in flame temperature and NO concentration result from physical processes that occur in a narrow region of the flame zone, finite-difference calculations should resolve the flame zone accurately. Our mathematical formula-

tion is based on a non-uniform mesh system and the grid spacing in the flame region is 0.4 mm. Based on the calculations performed with different grids that were coarser than the one used in the present paper we found that further refinement in grid does not change the results presented here.

R. W. Dibble, University of California-Berkeley, USA. Can you compare total NO_x production for two cases? Case 1: Lewis number is one; Case 2: Lewis number is not one.

Authors' Reply. We have not made calculations using the unity-Lewis-number assumption in conjunction with the present chemistry model that takes NO reactions into account. However, our earlier calculations using a chemistry model that did not consider NO reactions suggested that the unity-Lewis-number assumption eliminates the fluctuations in flame-surface temperature and species concentrations during flame-vortex interactions. Since the total NO (thermal) increases with fluctuations in temperature, one might expect much lower total NO for the case of unity Lewis number as compared to the case of non-unity Lewis number.

B. Categer. When the vortex resides on the fuel side, the temperature increases above its stoichiometric adiabatic value, yet the NO formation decreases. Is this a result of the change in the composition field and if so, how does this effect come about?

Authors' Reply. In high-Damkohler-number flames, the flame-vortex interactions leads to fluctuations in flame temperature if the local Lewis number is not equal to unity. On the other hand, the species distributions are affected, in part, by the differences in the mass diffusion rates and in part, by the changes in the reaction rates. The decrease in NO concentration in the stretched region when a fuel-side vortex interacts with the flame is believed to be the result of a decrease in the concentration of O-radicals. In order to clarify this, one needs to perform some numerical experiments by changing the mass-diffusion rates of different species.

Numerical Studies on the Structure of Two-Dimensional H_2 /Air Premixed Jet Flame

V. R. KATTA*

Systems Research Laboratories, Inc., A Division of Calspan Corporation, 2800 Indian Ripple Road, Dayton, OH 45440-3696

W. M. ROQUEMORE

Wright Laboratory, Aero Propulsion and Power Directorate, Wright-Patterson Air Force Base, OH 45433-7103

The burning characteristics of a premixed, H_2 /air Bunsen-type flame are investigated using a time-dependent, axisymmetric numerical model with variable transport properties and a detailed-chemical-kinetics mechanism. The temperature, species concentration, and velocity fields are investigated under fuel-lean, stoichiometric, and fuel-rich conditions. The calculations show that under fuel-lean conditions the flame exhibits the "tip-opening" phenomenon, while under fuel-rich condition the tip of the flame burns intensely. These results are in agreement with the experimental findings of Mizomoto et al. who have suggested that the tip-opening phenomenon results from the nonunity Lewis number. To further investigate the impact of local Lewis number on the premixed-flame structure, numerical experiments are performed by modifying the local Lewis numbers of the individual species. Results for the fuel-lean condition confirm that the local Lewis number is responsible for the tip-opening phenomenon. Indeed, when the local Lewis number is set equal to 2, the burning pattern of the fuel-lean premixed flame resembles that of a fuel-rich flame with a closed tip. The spatial distributions of NO in the fuel-lean, stoichiometric, and fuel-rich flames are also examined. Under the fuel-lean and stoichiometric conditions, the NO is formed along the high-temperature cone of the flame, as expected. In the fuel-rich case, a dual flame structure is observed. The NO production occurs primarily in the secondary "diffusion" flame which is established at the interface of the excess fuel and ambient oxygen. Buoyancy-induced toroidal vortices are found to form in the vertically mounted premixed flames. However, the dynamic characteristics of a premixed flame, in contrast to those of a jet diffusion flame, are observed to be dependent on the inlet velocity profile of the fuel jet.

INTRODUCTION

Premixed flames in which the fuel and oxidizer are mixed prior to burning have considerable industrial importance since they produce clear flames with intense combustion and less soot. These premixed combustion systems are commonly used in applications such as domestic heating and gas fires. Most large-scale practical combustors also contain flame zones, especially near the flame base, that are of the premixed type. In this context knowledge of the structure of the premixed flame plays a key role in the development of flame-stabilization techniques.

Premixed flames have been the subject of scientific investigation over the past several years not only because of their practical importance but also because of their ability to provide information on a number of fundamental

properties of the gas mixture such as adiabatic flame temperature and burning velocity; such information is useful in understanding the chemical and physical process of combustion and in validating mathematical models. Since the invention of the first laboratory premixed-flame burner by Bunsen in 1855, several investigators have adopted this burner for studies on premixed flames; a summary of conclusions from many such studies is given by Lewis and von Elbe [1]. An interesting feature of the Bunsen-type flame is that the flame structure changes with the fuel/air (or equivalence) ratio. For example, fuel-lean and near-stoichiometric flames of natural gas have fork-like temperature distributions, with maximum temperature occurring at the flame tip. On the other hand, in a fuel-rich flame the high temperature is concentrated along the sides—often referred to as the tip-opening phenomenon [1].

Extensive experimental efforts [2, 3] have been made to explore the physics associated with the variation in burning intensity of Bun-

* Corresponding author.

sen-type flames. After considering the data obtained with several fuels and equivalence ratios, Mizomoto et al. [2] and Law et al. [3] proposed that preferential diffusion (resulting from nonunity Lewis number) in conjunction with the flame curvature is responsible for the tip-opening phenomenon. The importance of Lewis number in characterizing the structure of a flame (or reaction) zone was recognized in 1934 by Lewis and von Elbe in their work on minimum ignition energies [4]. The small differences in the mass and heat diffusion rates of various species (nonunity Lewis number) result in flame temperatures that differ from the adiabatic temperatures. When a flame is subjected to aerodynamic stretching and/or is curved, preferential-diffusion effects arising from nonunity Lewis number can be pronounced. However, since it is very difficult to vary the Lewis number in an experiment without perturbing the other flow characteristics, data from previous experimental studies [2, 3] on Bunsen-type flames lead to some uncertainty in providing a conclusive evidence regarding the proposed preferential diffusion effects [5] on flame structure.

An alternative approach to investigating the burning characteristics of a Bunsen-type flame involves direct numerical simulation. This approach was successfully used with respect to jet diffusion flames by Yamashita et al. [6] and Ellzey et al. [7] while investigating the role of viscosity on the flame dynamics and recently, by Takagi and Xu [8] and Katta et al. [9] for predicting the preferential diffusion effects. Even though, several mathematical models for simulating premixed flames have been developed [10–12], the incorporated assumptions concerning one-dimensional-flow, unity-Lewis-number, or global chemistry render those models not suitable for exploring the preferential diffusion effects in a Bunsen flame which is of multidimensional in nature.

In the present investigation the burning characteristics of axisymmetric premixed jet flames of the Bunsen type were studied using a Computational Fluid Dynamics with Chemistry (CFDC) code [13] that has been extensively tested for its ability to predict the dynamic characteristics of a diffusion flame [9, 13, 14]. Numerical experiments were also conducted in

an attempt to understand the influence of Lewis number, equivalence ratio, and velocity-profile shape on the structure of a two-dimensional H_2 /air premixed flame.

MODELING

Time-dependent, axisymmetric Navier-Stokes equations written in the cylindrical-coordinate system are solved along with the species- and energy-conservation equations [9]. The body-force term due to the gravitational field is included in the axial-momentum equation. A detailed-chemical-kinetics model has been used to describe the H_2 -air combustion. This model consists of eleven species; namely, H_2 , O_2 , H , O , OH , H_2O , HO_2 , H_2O_2 , N , NO , and N_2 . The H_2 - O_2 - N_2 reactions used among the constituent species are given in Table 1. Here, M is any third molecule serving to absorb excess energy released during the collision process. The rate constants for the H_2 - O_2 reaction system are taken from Cowart et al. [15] and those for the N_2 reactions are taken from Miller and Bowman [16] and Hanson and Salimian [17].

Temperature- and species-dependent property calculations are incorporated in the model. The enthalpy of each species is calculated from polynomial curve fits [18]. While the viscosity and the thermal conductivity of individual species are estimated from the Chapman-Enskog collision theory [19, 20], the mixture properties are obtained by employing Wilke's semiempirical formulae. The effective binary-diffusion coefficient [21] of individual species in the local mixture is calculated using the kinetic theory [19]. The collision diameter and the Lennard-Jones potential for each species needed for calculating thermodynamic properties are obtained from Ref. 20.

The governing equations are integrated on a nonuniform staggered-grid system. An orthogonal grid having rapidly expanding cell sizes in both the axial and the radial direction is employed. The finite-difference forms of the momentum equations are obtained using QUICK-EST scheme [22], and those of the species and energy equations are obtained using a hybrid scheme of upwind and central differencing [23]. At every time-step, the pressure field is calcu-

TABLE I
Chemical Kinetics Used for the Simulation of H₂-O₂-N₂ Combustion

No.	Reaction	α_f	A_f (mol, cm, s)	E_{a_f} (cal/mol)	α_b	A_b (mol, cm, s)	E_{a_b} (cal/mol)
R1-2	H ₂ + O ₂ \rightleftharpoons 2OH	0	1.70E + 13	47,780	0	1.70E + 13	40,000
R3-4	H ₂ + OH \rightleftharpoons H ₂ O + H	0	2.20E + 13	5,146	0	9.50E + 13	20,300
R5-6	O ₂ + H ₂ \rightleftharpoons OH + O	-0.82	5.13E + 16	16,510	0	1.31E + 13	677
R7-8	O + H ₂ \rightleftharpoons OH + H	1.0	1.80E + 10	8,900	1.0	8.30E + 09	6,950
R9-10	H + O ₂ + M \rightleftharpoons HO ₂ + M	0	1.65E + 15	-1,000	0	2.31E + 15	45,900
R10-12	OH + HO ₂ \rightleftharpoons H ₂ O + O ₂	0	5.00E + 13	1,000	0	6.33E + 14	73,860
R13-14	H + HO ₂ \rightleftharpoons 2OH	0	2.50E + 14	1,900	0	1.20E + 13	40,100
R15-16	O + HO ₂ \rightleftharpoons O ₂ + OH	0	5.00E + 13	1,000	0	6.42E + 13	56,610
R17-18	OH + OH \rightleftharpoons O + H ₂ O	0	6.30E + 12	1,100	0	6.80E + 13	18,350
R19-20	H ₂ + M \rightleftharpoons H + H + M	0	2.20E + 14	96,000	0	3.00E + 15	0
R21-22	O ₂ + M \rightleftharpoons O + O + M	0	5.10E + 15	115,000	-0.28	4.70E + 15	0
R23-24	H + OH + M \rightleftharpoons H ₂ O + M	-2.0	1.40E + 23	0	-2.0	3.80E + 16	119,282
R25-26	H + HO ₂ \rightleftharpoons H ₂ + O ₂	0	2.50E + 13	700	0	5.50E + 13	57,800
R27-28	HO ₂ + HO ₂ \rightleftharpoons H ₂ O ₂ + O ₂	0	3.02E + 12	1,390	0	2.96E + 12	38,150
R29-30	H ₂ O ₂ + M \rightleftharpoons OH + OH + M	0	1.20E + 17	45,500	0	9.10E + 14	-5,070
R31-32	H ₂ O ₂ + H \rightleftharpoons HO ₂ + H ₂	0	1.70E + 12	3,750	0	7.30E + 11	18,700
R33-34	H ₂ O ₂ + OH \rightleftharpoons H ₂ O + HO ₂	0	1.00E + 13	1,800	0	2.80E + 13	32,790
R35-36	N ₂ + O \rightleftharpoons NO + N	0.0	1.82E + 14	76,241	0.3	3.31E + 12	0
R37-38	N + O ₂ \rightleftharpoons NO + O	1.0	6.46E + 09	6,280	1.0	3.80E + 09	41,370
R39-40	N + OH \rightleftharpoons NO + H	0	3.80E + 13	0	0	2.63E + 14	50,410

lated by solving all the pressure Poisson equations simultaneously and utilizing the LU (Lower and Upper diagonal) matrix-decomposition technique.

Burner Geometry and Flow Conditions

Mizomoto et al. [2] have conducted several experiments on H₂/air premixed flames to study the tip-opening phenomenon. Their comprehensive plot presented in Ref. 2 covers a fuel-jet velocity ranging from 7–17 m/s and suggests that the tip of the H₂/air flame, independent of velocity, opens when the fuel/air ratio is less than 1.1. Through use of the guidelines from that study, the flow conditions were determined for the present numerical investigations on a vertically mounted H₂/air Bunsen flame.

The burner assembly consists of a 7.1-mm-diameter central fuel nozzle and a large coannular air duct. A mixture of H₂ and air was used as the fuel. The flow rate chosen for the present investigations was such that the average fuel velocity at the central-tube exit is 8 m/s. A low uniform shroud flow of air at 0.15 m/s was used in the annular duct.

Initial and Boundary Conditions

Axisymmetric calculations were made on a physical domain of 200 × 150 mm utilizing a 251 × 91 nonuniform grid system (Fig. 1). Since most of the chemical reactions occur within a narrow zone surrounding the Bunsen cone of the premixed flame, grid points are clustered near the fuel tube such that the spacings in the radial and axial directions do not exceed 0.1 and 0.25 mm, respectively. The computational domain is bounded by the axis of symmetry and an outflow boundary in the radial direction and by the inflow and another outflow boundary in the axial direction. Parabolic and flat velocity profiles are imposed at the fuel and air inflow boundaries, respectively. The outer boundaries in the z and r directions are located sufficiently far from the nozzle exit (~ 30 nozzle diameters) and the symmetry axis (~ 20 nozzle diameters), respectively, that the propagation of boundary-induced disturbances into the region of interest is minimized. An extrapolation procedure with weighted zero- and first-order terms is used to estimate the flow variables at the outflow boundary [13].

For the given flow conditions, a steady-state solution was first obtained by neglecting the

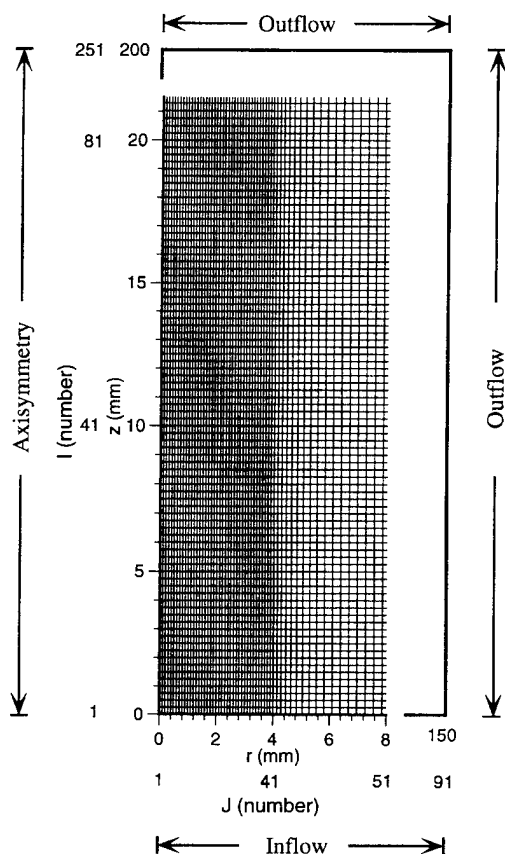


Fig. 1. Grid system and physical domain considered for the simulation of premixed jet flames.

unsteady terms in the governing equations. Flame in these calculations was ignited by temporarily increasing the temperature (to ~ 1000 K) at a few grid points near the fuel-tube exit during the first 10 time-steps. Finally, the dynamic-flame simulations were performed using the previously obtained steady-state solution as the initial flow condition. It should be noted that due to the buoyancy force in the lengthwise direction, these jet flames tend to flicker naturally in the absence of any finite flow disturbances.

RESULTS

Calculations for H_2 /air premixed flames were made using the procedure described in the previous section for different equivalence ratios (ratio between the mole fraction of H_2 with respect to O_2 and that of the stoichiomet-

ric H_2 /air mixture), Lewis numbers (ratio between the diffusive heat transport and the diffusive mass transport), and the inlet velocity profiles of the H_2 /air mixture. Results are used for evaluating the mathematical model and to investigate the premixed-flame structure.

Validation of the Model

An important parameter in premixed-flame theory is the burning velocity (or flame speed) which is defined as the velocity of the unburned gases normal to the inner cone as they move into the combustion zone. This quantity is often used to validate physical and chemical models for laminar premixed flames.

To determine the burning velocity in a jet flame geometrical information about the inner cone and the local unburned-fuel velocity are required. In experiments the inner cone is usually identified from the shadowgraphs of the flame which highlight the regions having a steep density gradient. Similarly, the location of the inner cone can be determined from the computed density or temperature field; however, a theoretically more sound procedure involves the heat-release rate which precisely identifies the onset of chemical reactions. The heat-release rate (ΔH) is defined as

$$\Delta H \equiv \sum_1^{N_r} \Delta H_j = \sum_1^{N_r} \sum_1^{N_s} \left\{ (v_{ji}'' - v_{ji}') \frac{\delta_j}{\rho} h_i \right\}. \quad (1)$$

Here, N_j and N_s are the numbers of reactions and species, respectively, considered in the model; v_{ij}' and v_{ij}'' are the stoichiometric coefficients of the i th species on the reactants and products sides of the j th reaction, respectively; ρ is the density; h_i is the enthalpy of the i th species; and δ_j is the specific rate of production of the j th reaction. The heat-release rate is calculated first from the computed flame solution; then the location of the inner cone is obtained by tracking a very-low-value ΔH . Finally, the local unburned-gas velocity which is also needed for the calculation of burning velocity is obtained at the inner cone. Note that along the inner cone the radial-velocity component of the unburned gases

is negligible and the local density differs from that of the unburned gases by only 0.001%.

As the inner-cone angle with respect to the flow direction and the local unburned gases velocity of a jet flame change with the flame height, the global burning velocity (\bar{S}_L) is obtained using the integral equation

$$\bar{S}_L = \frac{1}{A_c} \int_{z=0}^{z=z_{tip}} S_L \cdot dA. \quad (2)$$

Here, S_L represents the local burning velocity and A_c is the surface area of the inner cone. The upper limit for integration z_{tip} represents the inner-cone height.

Calculations for H₂/air premixed flames having different equivalence ratios were made using the numerical procedure described in the Modeling section. The predicted burning velocities (\bar{S}_L) for different flames are plotted in Fig. 2. Also shown are the experimental data obtained by Takahashi et al. [24] who used shadowgraphs and laser doppler velocimetry (LDV) for locating the inner cone and measuring the local unburned-gas velocity, respectively. These authors also presented a comprehensive plot of measured burning velocities of the H₂/air system using different experimental techniques [24], which showed that their data pass through the widely scattered data points obtained by several other investigators. The upper and lower limits for the measured burning velocities reported in Ref. 24 are

shown in Fig. 2 with + and - symbols, respectively.

As expected, the burning velocity increased initially with equivalence ratio (Φ) and then decreased. The predicted maximum burning velocity and the corresponding Φ are 3.16 m/s and 1.8, respectively, which agree well with the data of Takahashi et al. [24]. Overall, the agreement between the computed and measured burning velocities is excellent for the fuel-lean and slightly fuel-rich cases. Even though there is a considerable data scatter in the measured burning velocities, the calculations seem to underpredict \bar{S}_L for $\Phi > 2$ when compared to the data of Takahashi et al. A possible explanation for this underprediction of \bar{S}_L is that the finite-rate-chemistry model considered may not be sufficiently accurate to describe the fuel-rich situations. Nevertheless, the present work on burning patterns of H₂/air jet flames is focused in the range $0.6 < \Phi < 1.4$ where the model predictions are very good.

Influence of Equivalence Ratio on Flame Structure

Burning intensity along the inner cone of a H₂/air premixed flame changes with the flame height. The pattern in which the burning intensity changes depends on the equivalence ratio of the fuel/air mixture. Mizomoto et al. [2] have conducted several experiments by varying Φ and observed that the flame intensity: (1)

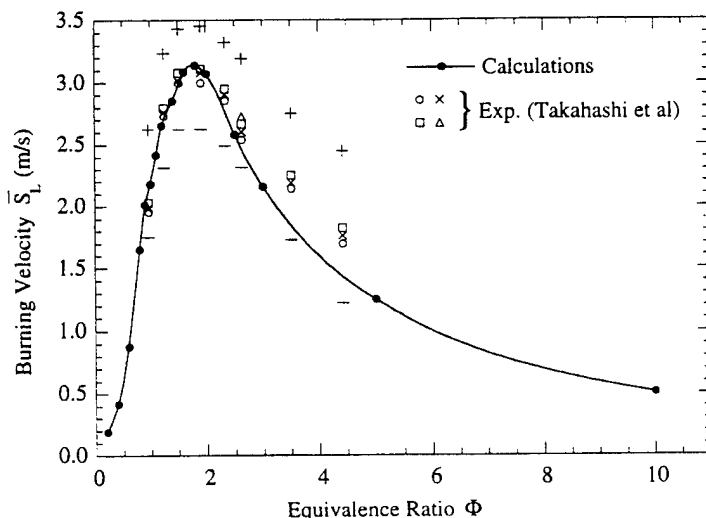


Fig. 2. Comparison of predicted and measured burning velocities at different equivalence ratios for the H₂/air system.

decreases with the flame height leading to the "tip-opening" phenomenon under fuel-lean conditions, (2) increases with the flame height under fuel-rich conditions representing a "tip-burning" situations and (3) is uniform all along the inner cone for near-stoichiometric conditions.

In order to test how well the present mathematical model captures the dependence of burning pattern on equivalence ratio, calculations were made for fuel lean ($\Phi = 0.6$), stoichiometric ($\Phi = 1.0$), and fuel-rich ($\Phi = 1.4$) flame conditions. The fully developed parabolic velocity profiles used in these simulations are identical for all the three cases. Results in the form of temperature, heat-release-rate, OH-, and NO-mole-fraction distributions are plotted in Figs. 3-5 for the fuel-lean, stoichiometric and fuel-rich cases, respectively.

Computed premixed flame structure for the fuel-lean case is shown in Fig. 3. The equivalence ratio of 0.6 used in this case corresponds to a mole fraction of 0.209 for hydrogen (X_{H_2})

in the fuel/air mixture. Although the calculations were made for one side only, the entire flame is shown in this and the other contour plots through the use of mirror-image data. The flame for this fuel-lean condition is steady without flow instabilities or flame flicker. The computed temperature field in the form of equally spaced iso-contours ($\Delta T = 200$ K) is shown in Fig. 3a. Fuel that is issued from the central tube at room temperature is burning along the conically shaped flame surface, which may be identified from the clustered contours. The predicted maximum flame temperature for this case is 1920 K, which, matches reasonably well with the theoretical adiabatic flame temperature ($T_{ad} = 1884$ K).

Temperature distribution around the inner cone indicates that a high-temperature region (contour 8) is located along the sides of the flame. At the cone tip, temperature is spread-out and the flame appears to be an open-tipped one. However, this cannot be stated conclusively from temperature data as the combus-

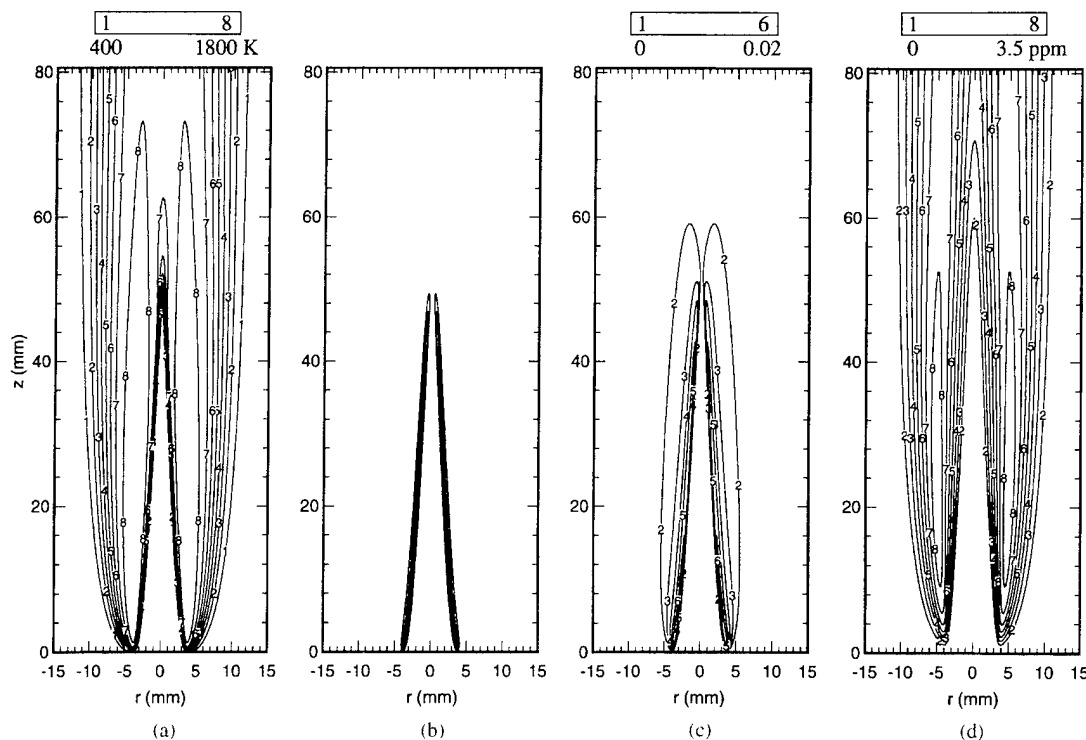


Fig. 3. Fuel-lean premixed H_2 /air laminar jet flame. $\Phi = 0.6$ and $V_u = 8$ m/s. Distributions of (a) temperature, (b) heat-release rate, (c) OH mole fraction, and (d) NO mole fraction. Tables of equally spaced contour values are given at the top of each plot.

tion products generated along the sides of the flame eventually approach the axis and raise the local temperature. Experimentally, Mizomoto et al. [2] found that the tip of a H_2 /air flame opens at $\Phi = 0.6$. Their finding is based on visual observation along the luminous cone which, may be identified more clearly from the heat-release data shown in Fig. 3b. The rate of heat release is decreasing with flame height; and at the inner (or burning) cone tip, it became zero. This clearly shows that no combustion is taking place at the end of the inner cone and that the tip of the luminous cone is open. The "tip-opening" phenomenon is discussed further in a latter section.

Chemical activity along the inner cone is shown in Fig. 3c by plotting the OH-concentration distribution. The mole fraction of OH is maximum at the base of the flame and decreases with the flame height. Absence of OH in the tip region indicates that the reactions are locally quenched. The distribution of NO in the fuel-lean flame is shown in Fig. 3d.

Except at very near the base region, the production of NO followed the temperature distribution. The peak concentration of predicted NO in this flame is only 3.8 ppm. A discussion on the formation of NO in premixed flames is given in a latter section.

The temperature variation of the stoichiometric flame (Fig. 4a) resembles that of the fuel-lean flame (Fig. 3a), with high temperatures being concentrated along the sides of the flame. Heat-release rate along the burning cone in Fig. 4b at different heights between the tube exit and the tip of the cone is distributed similarly, except at the location very near to the cone tip. The low heat-release rate at the cone tip indicates that the flame under stoichiometric conditions is still of the open-tip type. A similar observation was made by Mizomoto et al. [2] while conducting experiments for different equivalence ratios. They found that the tip of the flame closes completely only when Φ is above 1.15. Indeed, the present simulations made for the fuel-rich case yielded

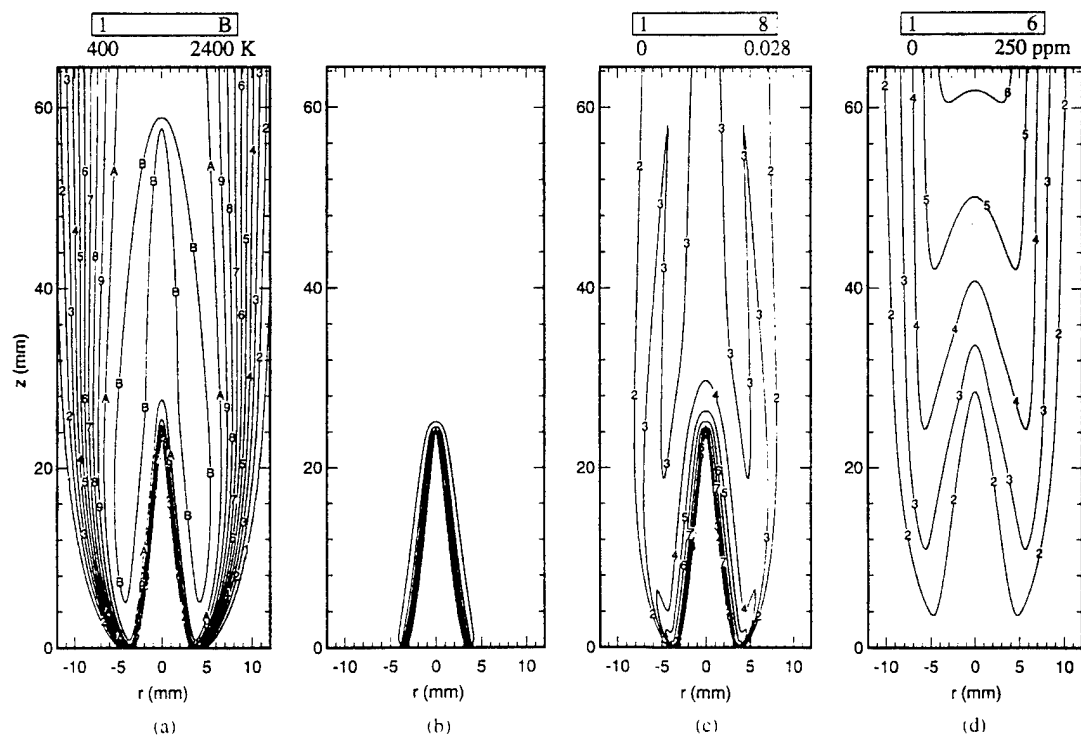


Fig. 4. Stoichiometric premixed H_2 /air laminar jet flame. $\Phi = 1.0$ and $V_u = 8$ m/s. Distributions of (a) temperature, (b) heat-release rate, (c) OH mole fraction, and (d) NO mole fraction. Tables of equally spaced contour values are given at the top of each plot.

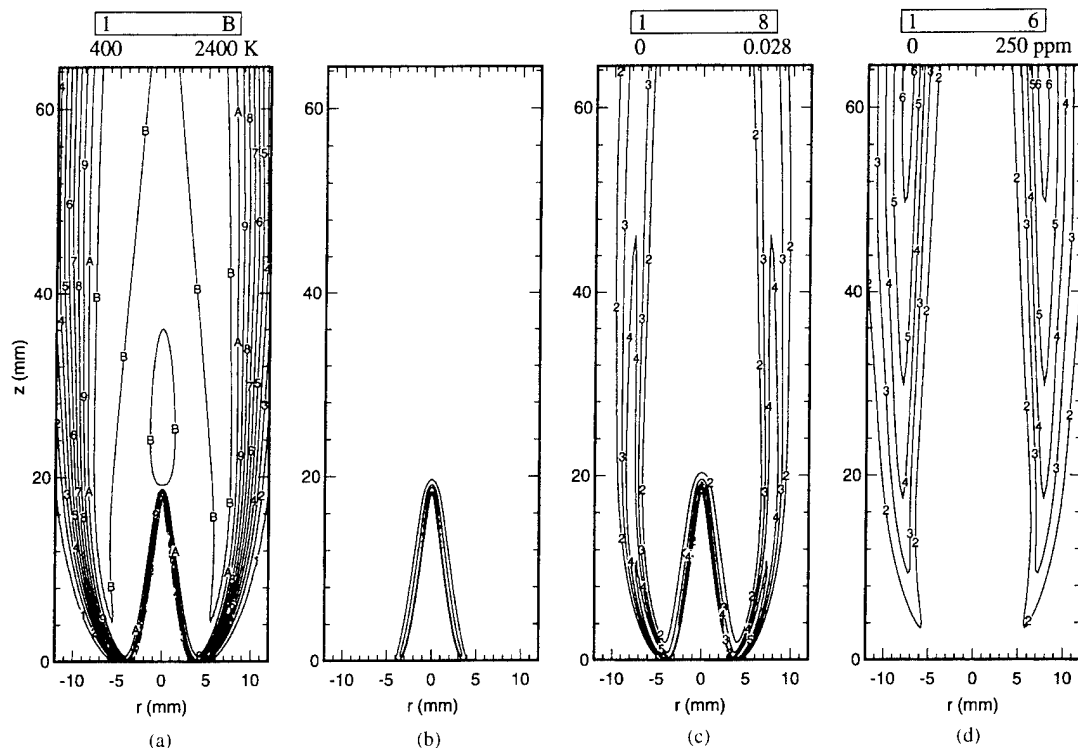


Fig. 5. Fuel-rich premixed H_2 /air laminar jet flame. $\Phi = 1.4$ and $V_a = 8$ m/s. Distributions of (a) temperature, (b) heat-release rate, (c) OH mole fraction, and (d) NO mole fraction. Tables of equally spaced contour values are given at the top of each plot.

a closed-tip flame. The heat-release rate in this case (Fig. 5b) increased with flame height with a maximum occurring at the tip of the inner cone.

Temperature of the fuel-rich flame (Fig. 5a) is higher at the tip which represents an intensely burning flame tip. Note, there is another temperature peak located in the mixing region of the combustion products and surrounding air. This indicates the presence of a secondary flame. Due to the insufficient amount of oxygen in the H_2 /air mixture, hydrogen is not completely burned in the fuel-rich flame. The excess hydrogen then diffuses farther into the combustion products and reacts with the additional oxygen that is diffusing from the annulus flow into the flame zone and establishes a diffusion flame. This is evident from the OH-concentration plot of Fig. 5c.

Blown-up views of the flame tips for the fuel-lean, stoichiometric, and fuel-rich conditions are shown in Fig. 6. Heat-release rates, OH mole fractions, and fuel mole fractions

plotted in this figure are color coded between the red (representing the maximum of the corresponding variable) and the purple (representing zero). From the heat-release-rate and OH-mole-fraction plots it is evident that for both the fuel-lean and stoichiometric flames the tips are opened and for the fuel-rich flame it is closed and burning intensely. Even though, the flame is open at the tip for the fuel-lean case, it should be noted from the X_{H_2} plot that no fuel is leaking through the flame. This is in contrast to some theories on tip-opening phenomenon that when the tip of a flame is opened then some unburned fuel escapes through the flame [1]. Present calculations indicate that all the fuel at the flame tip diffuses in a radially outward direction and burns slowly along the inner cone, yielding a longer cone.

Flow patterns obtained by plotting streamlines associated with the fuel-lean, stoichiometric, and fuel-rich premixed flames are shown in Figs. 7a-c, respectively. Both the inner and outer cones of the different pre-

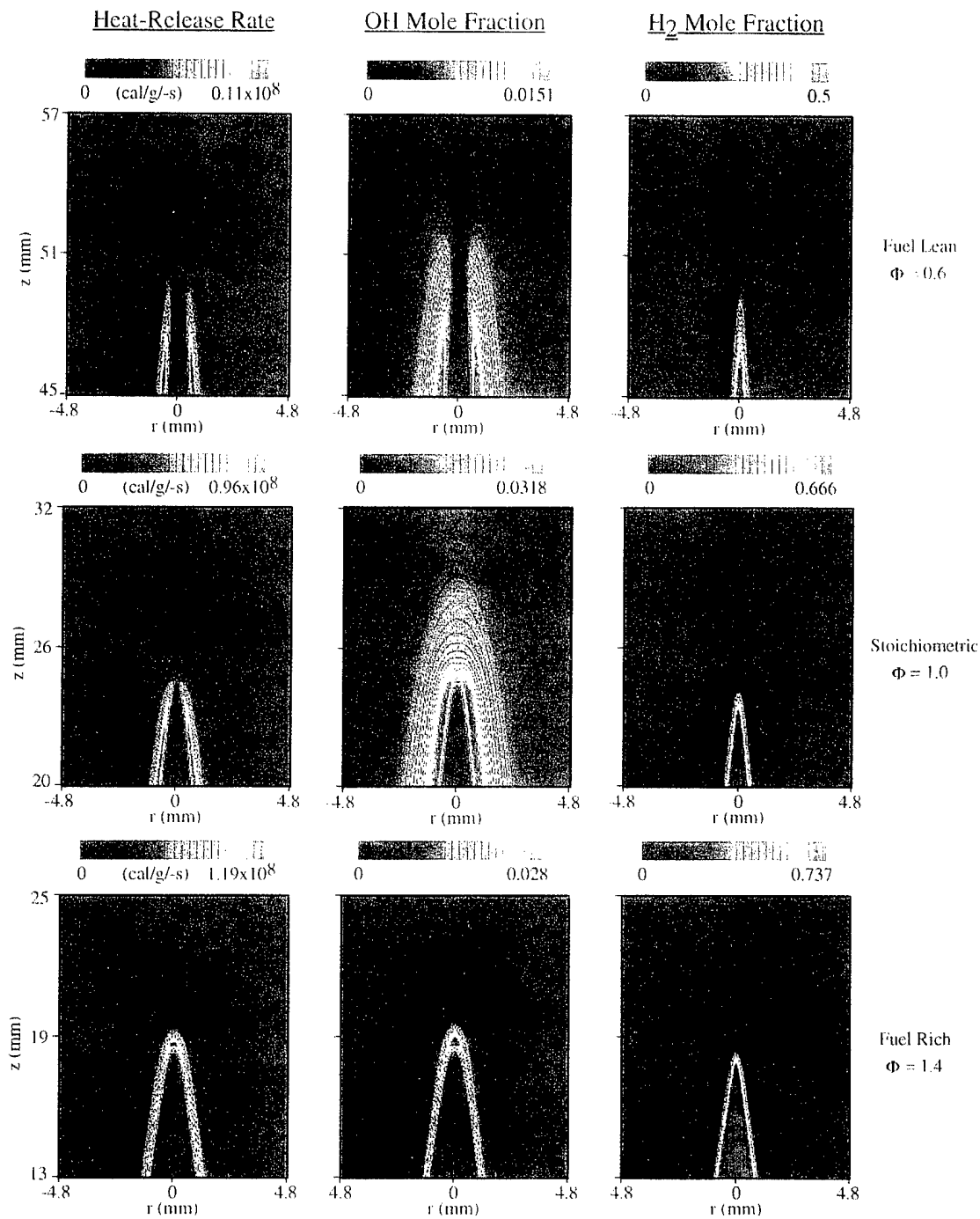


Fig. 6. Flame tips of premixed H_2 /air laminar jet flames under fuel-lean, stoichiometric, and fuel-rich conditions.

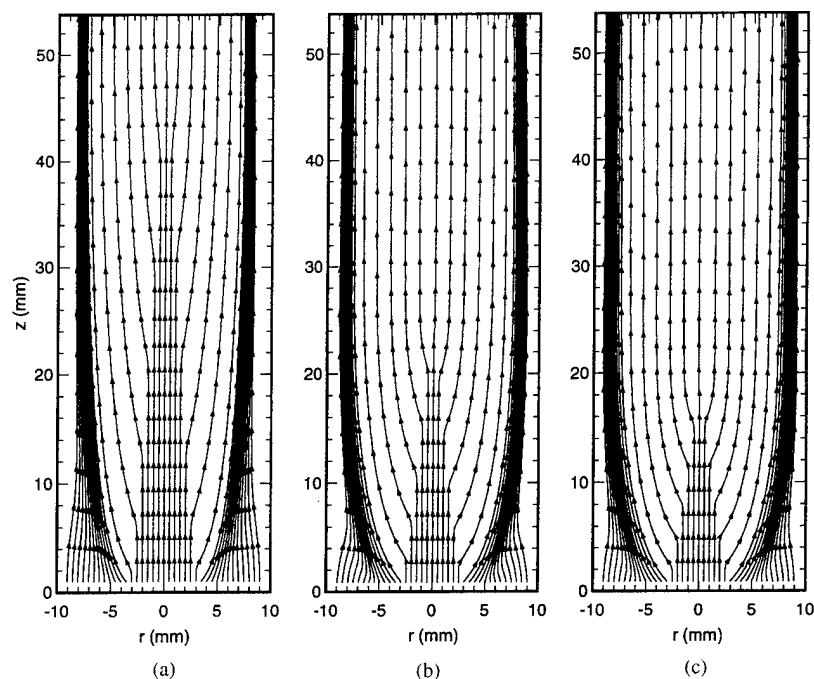


Fig. 7. Flow patterns of (a) fuel-lean, (b) stoichiometric, and (c) fuel-rich premixed flames.

mixed flames can be identified from these plots. Burning of incoming fuel/air mixture deflects the streamlines along the inner cone and the entrainment of annulus air by the higher velocity combustion products converges the streamlines to the outer cone. Surprisingly, no significant change in the streamline patterns in the neighborhood of the outer cone is noted between the fuel-lean (Fig. 7a) and fuel-rich (Fig. 7c) cases; even though, the latter one has a diffusion flame along the outer cone in addition to the premixed flame. This elucidates the fact that the diffusion flame does not represent a combustion wave and does not have a burning velocity associated with it. In general, flow patterns for the three cases are similar and represent that of a typical premixed flame.

Plotted in Fig. 8 are the variations of major species and temperature at a height of 10 mm above the burner exit across the three flames shown in Figs. 3–5. Temperatures resulting from the premixed combustion in lean, stoichiometric, and rich flames at this axial location are 1902, 2490, and 2355 K, respectively, and compare well with corresponding theoretical adiabatic flame temperatures (1884, 2580, and 2275 K for $\Phi = 0.6$, 1.0, and 1.4, respec-

tively). The flame thickness (high-temperature region), in general, is increasing with equivalence ratio and a secondary flame may be observed at $r = 6.6$ mm for $\Phi = 1.4$ (Fig. 8c). In contrast to that observed for diffusion flames [9], the concentration of H atoms in the premixed H_2 /air flames is significant and is comparable to the concentration of OH. As expected, oxygen is available everywhere in the fuel-lean flame. However, in the stoichiometric flame (Fig. 8b) the consumption of fuel and oxygen has slowed-down significantly when the reactant concentrations become low. As a result oxygen molecules are present everywhere in this flame also. On the other hand, in the fuel-rich flame, oxygen is absent everywhere in the region between the inner cone and the outer diffusion flame. Distribution of oxygen in H_2 /air flames has important bearing on the production of NO, which will be discussed in a latter section.

Role of Lewis Number on Burning Pattern

The contour plot in Fig. 3a indicates that the temperature is higher along the sides of the flame and decreases with flame height. This

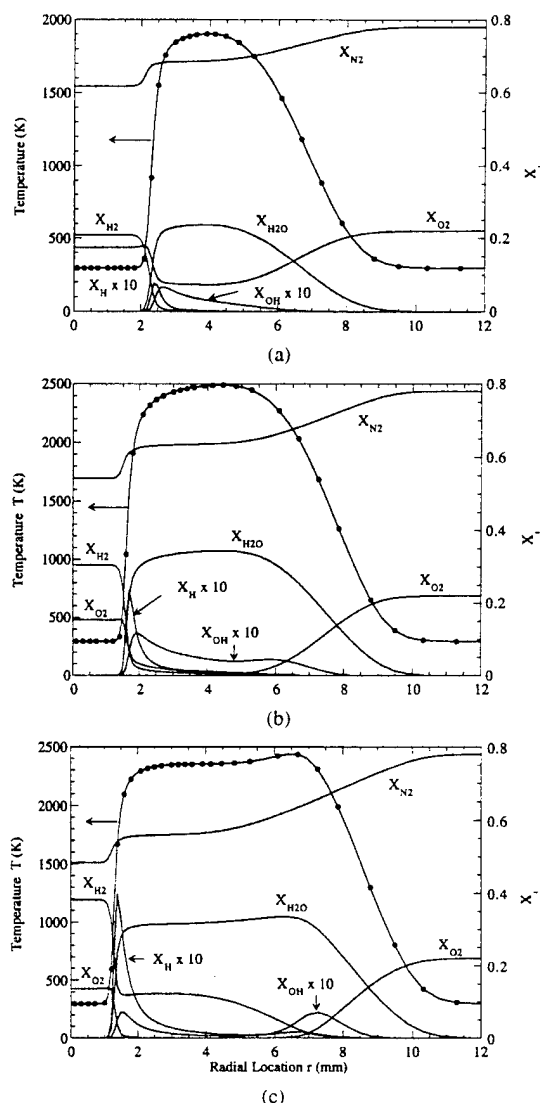


Fig. 8. Temperature and major-species distributions across the flame at a location 10 mm above the burner. (a) Fuel-lean premixed flame with $\Phi = 0.6$, (b) stoichiometric flame, and (c) fuel-rich flame with $\Phi = 1.4$.

type of temperature distribution in a premixed flame was experimentally observed [1]. Law [5] has explained that the preferential diffusion resulting from the nonunity Lewis number can give rise to increasing or decreasing temperature along the length of the flame, depending on whether the Lewis number of the fuel is greater or less than unity, respectively. The Lewis number of a species in a mixture (Le_i) is defined as the ratio of the thermal-diffusion

rate to the mass-diffusion rate and is written as

$$Le_i \equiv \frac{\lambda}{\rho D_{im} c_p}, \quad (3)$$

where λ and c_p are the thermal conductivity and specific heat of the mixture, respectively, and D_{im} is the effective binary-diffusion coefficient of the i th species. It is known that the Lewis number of hydrogen is less than unity in a fuel-lean mixture of H_2 /air and increases as the fuel becomes hydrogen-rich. Therefore, the predicted temperature pattern in the fuel-lean flame supports the explanation given by Law [5] for a flame with $Le_i < 1$.

In an attempt to provide additional evidence for the noted temperature-distribution behavior with respect to the nonunity Lewis number, three calculations were made for the fuel-lean premixed flame of Fig. 3a. In these calculations, the local Lewis number of the individual species was assumed to be constant and equal to (a) one half, (b) one, and (c) two. These assumptions were implemented in the simulation by setting $D_{im} = D_{O_2-N_2}$ and then calculating λ from Eq. 3 rather than using kinetic theory, as discussed in the Modeling Section. Since the calculations made by assuming $D_{im} = D_{H_2-N_2}$ instead of $D_{im} = D_{O_2-N_2}$ gave similar conclusions, only the results obtained with the latter assumption are discussed in the present study. Note that neither the chemistry nor the flow conditions were altered in these simulations. The computed results in the form of isotherms for $Le_i = 0.5$, $Le_i = 1$, and $Le_i = 2$ cases are plotted in Figs. 9a, 9b, and 9c, respectively. Eight equally spaced contours between 400 and 1800 K and a flooded contour (labeled 9) representing the region of high temperature ($T > 1850$ K) are drawn in these figures.

Similar to that of the fuel-lean-flame simulation without imposing any assumption on Lewis number (Fig. 3a) the high temperature in Fig. 9a is concentrated at the sides of the flame. However, since the flame with $Le_i = 0.5$ has lower diffusion coefficient and thermal conductivity, it differs from the flame of Fig. 3a in several ways—the inner-cone height (z_f) increased from 48 to 84 mm; the burning velocity (\bar{S}_L) decreased from 0.8781 to 0.492 m/s; and finally, the flame became dynamic in nature,

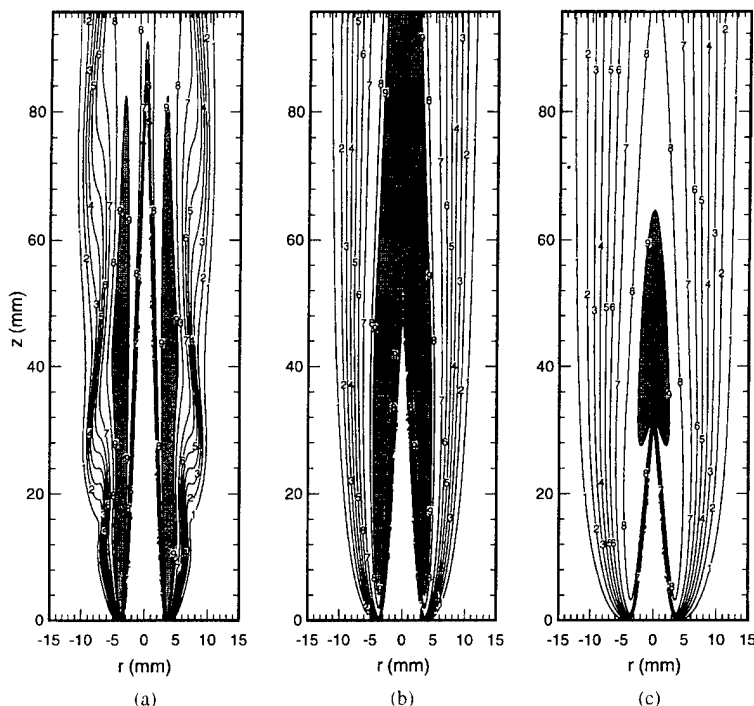


Fig. 9. Temperature distributions in a lean premixed ($\Phi = 0.6$) flame calculated using the assumptions (a) $Le_i = 0.5$, (b) $Le_i = 1$, (c) $Le_i = 2.0$. Contours 1 through 8 represent equally spaced temperatures between 400 and 1800 K. Flooded contour (no. 9) in each plot represents region of high temperature.

with large buoyancy-induced vortices [25] developing outside the flame surface.

When the local Lewis number of each species was increased to unity, it is observed (Fig. 9b) that the inner-cone height decreased to 50 mm, the burning velocity increased to 0.815 m/s, and the high-temperature region (shaded) spread around the conical portion of the unburned fuel. The last observation indicates that burning is uniform along the inner (or burning) cone. On the other hand, for the $Le_i = 2$ case (Fig. 9c) the high-temperature region moved to the tip of the inner cone resulting in the intensive tip-burning pattern. The burning velocity of 1.262 m/s in this case is higher than that of the flame in Fig. 3a in which no assumption on Lewis number was made. The significant variation in the heights of the inner cones and the burning velocities in Fig. 9 demonstrate the need for accurate transport-property calculations in simulating a premixed jet flame.

Flame locations at different axial distances identified by radially scanning for the peak

temperature are plotted in Fig. 10a for the three flames obtained with different assumptions on Lewis number. The variations in temperature along these flame surfaces are shown in Fig. 10b. Temperature downstream of the flame tip for $Le_i = 1.0$ and $Le_i = 2.0$ cases represent that at the axis of symmetry. When the Lewis number is less than unity then the flame temperature in the base region increased above the adiabatic flame temperature ($T_{ad} = 1884$ K) and then decreased with flame height. On the other hand, the flame temperature is quite uniform all along the flame surface of the unity-Lewis-number case and is very close to T_{ad} . Interestingly, for the $Le_i = 2$ case, the flame temperature increased slowly up to the tip of the flame ($z = 32$ mm) and then it jumped to 1955 K (i.e., 81 K above the adiabatic value). Downstream of the flame tip the temperature at the axis gradually decreased due to heat conduction and product diffusion.

Premixed jet flames are curved concave with respect to the incoming fuel/air mixture. The

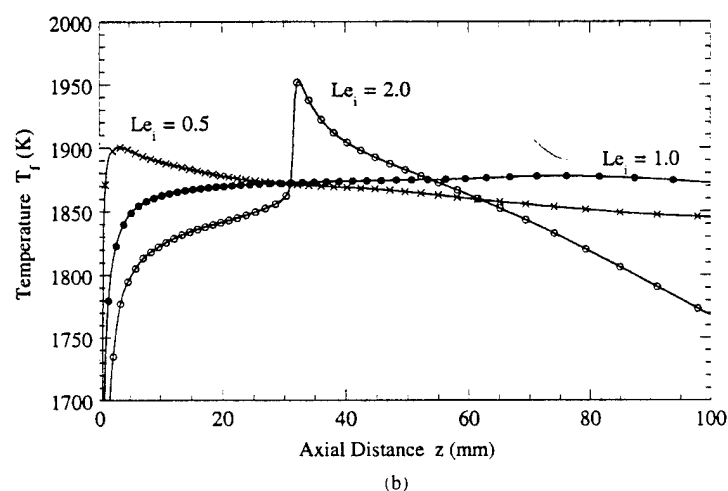
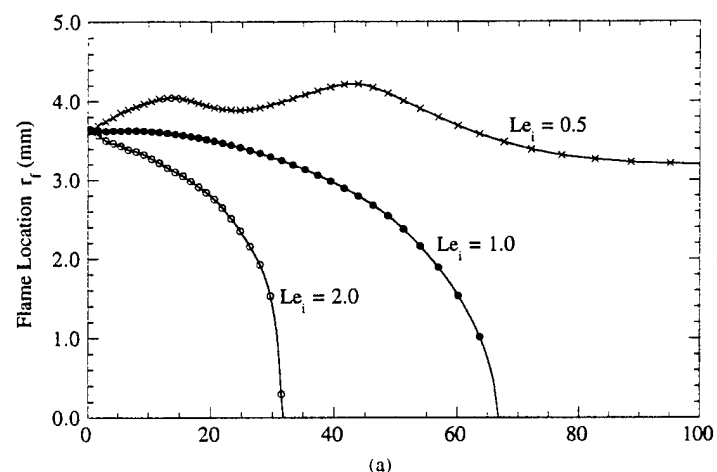


Fig. 10. Characteristics of the fuel-lean flame under different assumptions concerning Lewis number. (a) Locations of the flame surface at different axial distances obtained by scanning radially for the peak temperature. (b) Temperature along the flame surface.

nonunity Lewis numbers associated with the H_2 /air flames in conjunction with this flame curvature is responsible for the observed variations in the burning patterns. The transport zones near the premixed flame tips under different assumptions on Lewis number are shown in Fig. 11. A discussion on the role of nonunity Lewis number and flame curvature on the "tip-opening" and "tip-burning" phenomena is given in a latter section.

Influence of Inlet Velocity Profile

Studies on vertically mounted jet diffusion flames indicated that buoyancy-induced toroidal vortices develop outside the flame surface and that their convective motion induces the flame flicker. These dynamic flames were

successfully simulated by Davis et al. [26], Katta et al. [14], and Ellzey et al. [27] using different fuels. These numerical investigations on jet diffusion flames led to the same conclusion—that in the presence of gravitational force, the flame tends to flicker in a natural way without requiring any external disturbances. As mentioned previously, the present simulations considered gravitational force acting in the axial direction. However, the three flames shown in Figs. 3–5 are steady in nature and flame flickering is not observed in any of them. One exception is the fuel-lean flame calculated assuming $Le_i = 0.5$ (Fig. 9a), which has the buoyancy-induced fluctuations.

To determine the flow conditions for which the buoyancy-induced vortices develop on a premixed flame, several calculations were made

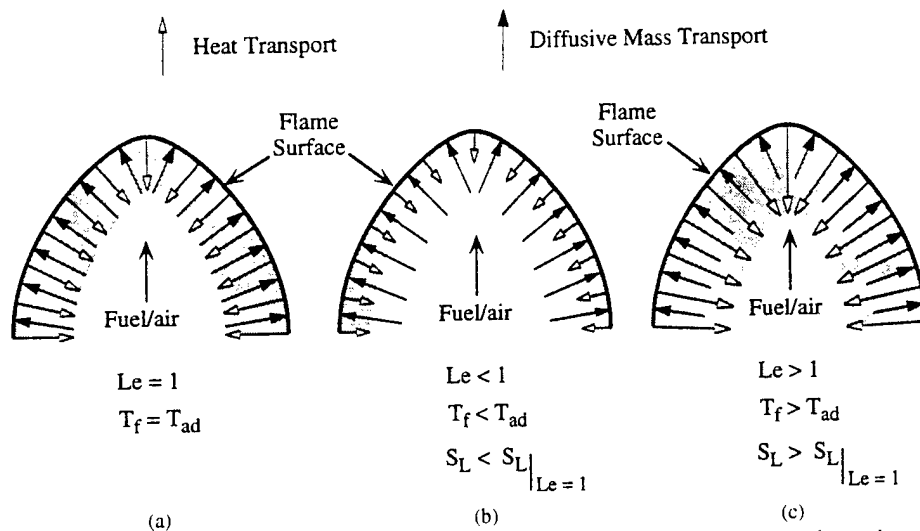


Fig. 11. Diffusive-heat and diffusive-mass transport near the flame tip for different Lewis numbers.

by varying the equivalence ratio and velocity profile at the exit of the fuel tube. The mean exit velocity of the fuel was kept constant. The simulations of Figs. 2–10 were made by assuming a parabolic velocity profile at the fuel-tube exit which represents a fully developed flow associated with straight tubes. A partially developed velocity profile at the exit of a contoured nozzle may be represented using a flat-topped parabolic type. The ratio between the flat portion (r_{flat}) of the velocity profile and the burner radius (r_b) is used in this study to represent varying degrees of partially developed flows. In order to obtain the same mean velocity for different velocity profiles the peak value was adjusted (changes from 8 m/s for a flat profile to 16 m/s for a fully developed parabolic one). Interestingly, the simulations made under near-stoichiometric conditions and with some flatness in the inlet velocity profile resulted in dynamic flames with large toroidal vortices convecting downstream along the flame surface.

Results in the form of iso-temperature distributions obtained from the simulations made with $\Phi = 0.9$ and for different r_{flat}/r_b values are shown in Fig. 12. For comparison purpose calculations were also made for a highly fuel-rich ($\Phi = 10$) case, which is dominated by the outer diffusion flame. Temperature distributions for the latter case for different velocity profiles are plotted in Fig. 13. The inlet veloc-

ity profile used in each of the calculations of Figs. 12 and 13 is also shown. Figures 12a and 13a represent the flames calculated using a parabolic profile ($r_{flat}/r_b = 0.0$), and Fig. 12d and 13d show the flames obtained using a nearly flat ($r_{flat}/r_b = 0.8$) velocity profile. Note, in all these simulations (Figs. 12a–12d and 13a–13d) the mean velocity used for the fuel was 8 m/s and the Reynolds number based on the fuel-tube diameter is 3300. Ten equally spaced contours between 350 and 2600 K are plotted in each of these figures.

The near-stoichiometric flame in Fig. 12a is steady and has a burning pattern similar to that of the fuel-lean flame (Fig. 3). The tip of this flame is open. As the velocity profile deviates from a parabolic shape, the inner-cone height decreases. The flame with $r_{flat}/r_b = 0.2$ is weakly oscillating, and the unsteadiness of the flow is noticeable only at $z > 150$ mm. A dynamic premixed flame (Fig. 12c) is obtained when r_{flat}/r_b was set equal to 0.5. The flow oscillations are observed at a location near the tip of the cone and grow as they are convected downstream. The frequency of oscillation is found to be 120 Hz and is the same at axial locations up to 150 mm. The flow oscillations grew to large toroidal vortices in the near-stoichiometric premixed flame (Fig. 12d) when the velocity at the fuel-tube exit was near uniform ($r_{flat}/r_b = 0.8$). Under these conditions the burning cone became flat at the edges.

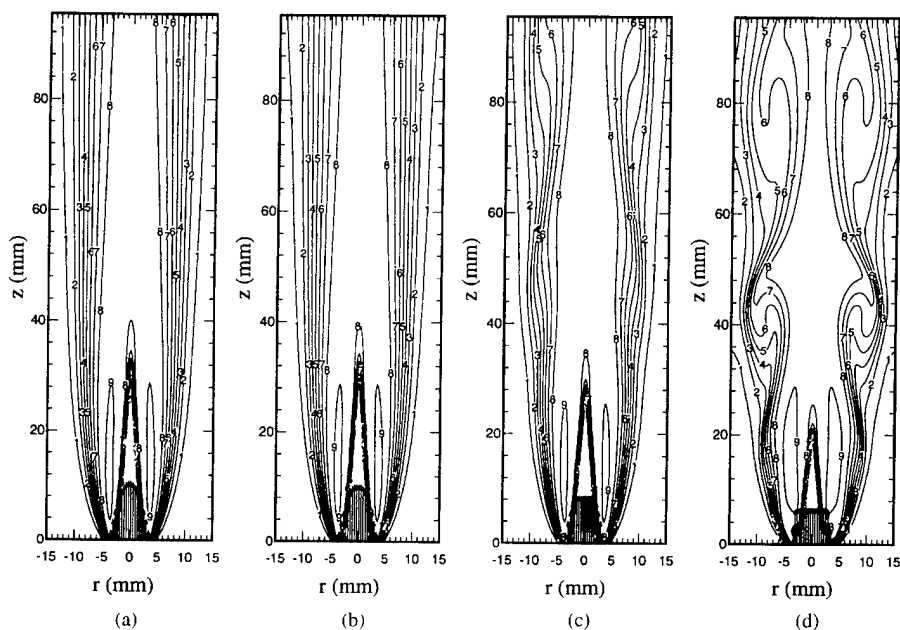


Fig. 12. Influence of the inlet-velocity profile on the structure of a near-stoichiometric premixed flame ($\Phi = 0.9$). Calculations were made using (a) fully, (b) 80 percent, (c) 50 percent, and (d) 20 percent developed parabolic profiles. Temperature distributions are shown with ten equally spaced contours between 350 and 2600 K. Corresponding fuel-jet velocities at the burner exit are also shown.

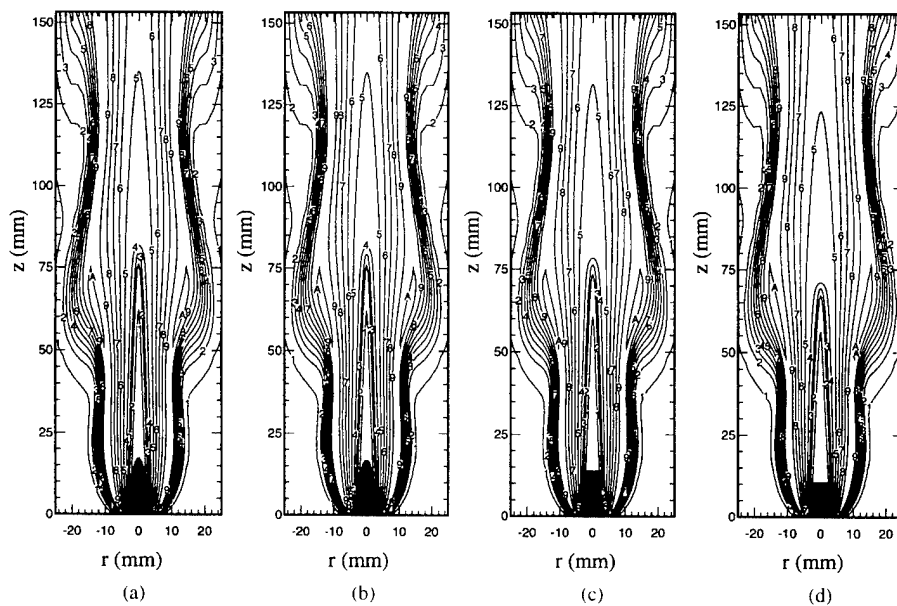


Fig. 13. Influence of the inlet-velocity profile on the structure of a highly fuel-rich premixed flame ($\Phi = 10.0$). Calculations were made using (a) fully, (b) 80 percent, (c) 50 percent, and (d) 20 percent developed parabolic profiles. Contour numbering follows that used for Fig. 12.

In fact, under some fuel-lean flow conditions, such flat-edged burning cones are observed experimentally [2]. From the studies reported in the present paper it is not clear which mechanism is responsible for such burning patterns of uniform velocity profiles.

As shown in Fig. 13 the velocity profile does not have much impact on the flame structure of a highly fuel-rich case. Both the premixed and diffusion type combustion is taking place in this flame. It is known that the H_2 /air premixed flame with an average flow velocity of 8 m/s is not self-supported for an equivalence ratio of 10. However, the diffusion flame established between the excess fuel and the annulus air is supporting the premixed combustion at the flame base and as a result, stable inner cones are seen for all the velocity profiles shown in Fig. 13. The flame is dominated by the outer diffusion flame and hence, buoyancy induced instabilities [25] have developed outside the diffusion-flame surface in much the same way as seen in a typical diffusion flame. The vortex-crossing frequency for the four flames shown in Fig. 13 is the same and equal to 14 Hz. The temperature and velocity distributions across the flames of Figs. 12d and 13d at an axial location of 2 mm above the burner exit (note, it is known that buoy-

ancy-induced instabilities manifest at a location very close to the flame base) are plotted in Fig. 14. A further discussion on the buoyancy-induced instabilities in a premixed flame based on the current understanding on their manifestation in jet diffusion flames is given in the next section.

DISCUSSION

Burning Pattern

Flame height, stability, and extinction characteristics of a premixed flame are influenced by the burning pattern. Based on the experimental observations and asymptotic mathematical analysis, Buckmaster and Crowley [28] and Law [5] have provided insights for the variations of burning patterns of Bunsen-type premixed flames. However, as the proposed theories involve local Lewis number of the gas and the flame curvature, a direct validation for those theories may not be provided using the asymptotic and one-dimensional analyses. The multi-dimensional analysis described in the present work has the elements required for a study of Lewis-number effects in a curved flame and the results obtained using this model compare favorably with the experiments of Takahashi

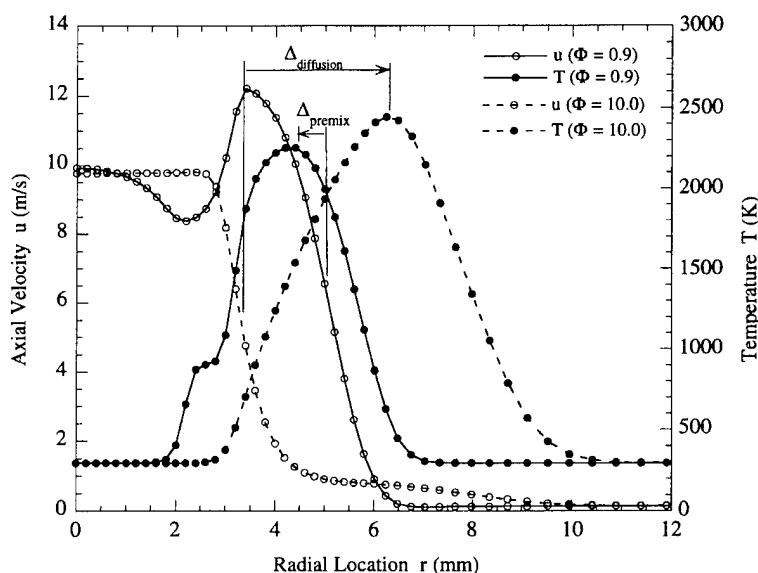


Fig. 14. Velocity and temperature profiles across the near-stoichiometric and highly fuel-rich flames of 9 mm above the burner exit.

et al. [24] and Mizomoto et al. [2]. Hence, these results are used further, within the theoretical framework of Buckmaster and Law, to investigate the burning patterns of Bunsen-type flames.

The burning pattern of a premixed flame depends largely on the Lewis numbers of the incoming fuel and oxidizer, even though in a multi-component reacting flow (e.g., the one shown in Fig. 3a) the value of the Lewis number depends on the local physical properties and the species under consideration. Typical Lewis numbers for hydrogen and oxygen in a mixture of H_2 /air obtained from the transport-property models used in the present analysis are given in Table 2. It should be noted that the Lewis number for oxygen is greater than unity for all equivalence ratios, whereas that for hydrogen increases with Φ from a value less than unity to a value greater than unity. Therefore, the effective Lewis number of a H_2 /air mixture changes from less than unity for fuel-lean mixtures to greater than unity for fuel-rich mixtures.

As expected, the burning pattern of the fuel-lean flame (Fig. 3a) is qualitatively similar to that of the flame simulated using the assumption of $Le_i = 0.5$ (Fig. 9a). In both the cases the high temperature is concentrated along the sides of the inner cones and the flames are open at the tips. Similarly, the tip-burning pattern of the fuel-rich flame (Fig. 5a) resembles that of Fig. 9c, which was a fuel-lean flame simulated assuming $Le_i = 2.0$. Additional calculations made for the fuel-rich flame ($\Phi = 1.4$) by imposing $Le_i = 0.5$ gave an open-tipped temperature distribution (similar to that of Fig. 3a) with high-temperature regions being on the sides of the inner cone. All these results suggest that in a given flame if

$Le_i > 1$, the sides of the flame burn intensely; if $Le_i < 1$, the tip of the flame burns intensely. From the equivalence ratio view point, the burning pattern of a H_2 /air premixed flame changes to intensely burning tip from an open-tip condition as the flame becomes fuel-rich from fuel-lean situation. Interestingly, calculations performed for the stoichiometric H_2 /air mixture (Figs. 4 and 6) yielded a flame with the burning intensity being nearly uniform along the inner cone. However, the tip of the flame seems to be open by a very small amount. This means that the effective Lewis number of the H_2 /air mixture under stoichiometric conditions is slightly less than unity.

It is known that the Lewis number does not influence the temperature distribution of a flame solely by itself but does in conjunction with the nonuniform flow or flame curvature [5, 29]. Hence, the explanation for the previously mentioned burning-pattern behavior of a premixed flame with respect to Lewis number (or equivalence ratio) may then be given using the cartoons sketched in Fig. 11.

Premixed jet flames are curved concave at the tip with respect to the incoming fuel/air mixture as shown in Fig. 11. Note from the directions of transport fluxes that the concavity of the flame surface focuses heat on the incoming fuel/air mixture and defocuses fuel and air masses from the incoming fuel/air mixture. The former effect enhances the preheating and raises the temperature of the incoming reactants and thereby, increases the flame temperature. In contrast to this, the defocusing effect reduces the reactant concentration in the reaction zone and thereby, the flame temperature.

In the case of unity-Lewis-number situation (Fig. 11a), as the heat and mass transports are equally distributed in the transport zone, the focusing effect on heat flux cancels with the defocusing effect on mass flux: which, yields the flame temperature that is equal to the adiabatic value. Since the concavity of the flame is not effective in this case, the temperature will be constant and independent of curvature all along the flame surface. However, if the Lewis number is less than unity (Fig. 11b) then the region of preheating in the transport zone will be smaller in comparison to that of the

TABLE 2

Lewis Numbers of Hydrogen and Oxygen in Different Mixtures

Φ	Le_{H_2}	Le_{O_2}
0.4	0.442	1.415
0.6	0.510	1.534
1.0	0.629	1.708
1.4	0.732	1.826
5.0	1.263	2.123

mass diffusion. Therefore, in the case of $Le < 1$, reduction in temperature due to the defocusing effect of reactant diffusion dominates the temperature increase resulting from the focusing effect of heat. This yields a flame temperature that is less than the adiabatic value—the difference obviously, depends on the curvature of the flame. Because of the decrease in preheating efficiency of a curved flame, the burning velocity also decreases with Lewis number (0.815 and 0.492 m/s for the flames in Fig. 9b and 9a, respectively).

When the Lewis number is greater than unity, the preheating zone is larger than the reactant diffusion zone; and thus in a flame that is curved concave, it makes the focusing effects of heat transport stronger than the defocusing effects of reactant diffusion. As a result, the flame temperature, in general, will be above the adiabatic value and locally along the flame surface it increases with the curvature. This is evident in Figs. 9c and 10b. In a jet flame the curvature of the inner cone (and hence, that of the flame surface) changes rapidly in a short region around the tip and increases to a maximum value at the tip. This leads to a tip-opening situation in a flame when the Lewis number is less than unity and to a tip-burning situation when $Le_i > 1$. The jump in temperature at the flame tip in Fig. 10b is also due to the rapid change in curvature of the inner cone at the tip.

Thermal-NO Formation

The three important pathways for the formation of Nitric Oxide (NO) in the flames, as summarized by Miller and Bowman [16], are the thermal-NO mechanism (dissociation of N_2 molecules at high temperature), mechanism involving intermediate N_2O , and the prompt mechanism (attack by hydrocarbons). However, because of the absence of hydrocarbon molecules the prompt mechanism does not involve in the production of NO in the H_2 /air flames. Since the formation of NO through N_2O molecules is important only in the fuel-lean flames in which the temperature is low, the second pathway was not considered. Thus, only the formation of "thermal NO" in the premixed flames is investigated in the present

work. A well-known Zeldovich mechanism 1161 for thermal NO is incorporated in the chemical-kinetics model (cf. Table 1).

The distribution of NO in the fuel-lean flame is shown in Fig. 3d. Except at very near the base region, the production of NO follows the temperature distribution. The peak concentration of thermal NO predicted in this flame is only 3.8 ppm. The delay in the generation of NO near the base results from the smaller Damkohler number (ratio between the residence and reaction times) associated with the thermal-NO reactions.

An interesting pattern appears for the generation of thermal NO in the stoichiometric and fuel-rich flames (Figs. 4d and 5d, respectively). In the former case, thermal NO is observed along with the other combustion products in the regions where the temperature is higher than that of the incoming fuel. However, due to their longevity, NO molecules accumulate and, hence, their concentration increases with flame height. A similar pattern was also observed in the fuel-lean flame. On the other hand, under fuel-rich conditions (Fig. 5d), most of the thermal NO is found near the secondary (diffusion) flame. Reactions R35–R38 (cf. Table 1) of the Zeldovich (NO) mechanism require oxygen molecules in order to break down N_2 . In the fuel-rich flame, the available oxygen in the H_2 /air mixture is depleted along the reaction cone of the premixed flame; when the temperature of the gas becomes sufficiently high, nitrogen is not dissociated because of the absence of O_2 molecules. As a result, NO is not produced in the premixed-flame region. Ambient oxygen from the annulus flow diffuses into the combustion products and produces NO near the secondary flame. Since the oxygen molecules do not penetrate through the secondary flame, which is of the diffusion type, the NO is not generated between the secondary flame and the axis of symmetry. In the stoichiometric and fuel-lean flames (Figs. 4d and 3d), on the other hand, ambient oxygen is able to penetrate well into the combustion products (since there is no secondary flame) and produced thermal NO over wide regions.

Studies of the NO distributions suggest that the production of thermal NO increases with

temperature and the local oxygen concentration. In jet flames with low or no annulus air flow the buoyancy-induced instabilities may manifest into large toroidal vortices, which, in turn, entrain ambient air into the combustion products and thereby increase the production of thermal NO. The conditions under which a premixed jet flame becomes dynamic with convecting vortices outside the flame is addressed in the following sub-section.

Instabilities

It is known that the natural convection of hot combustion products in jet flames leads to buoyancy-induced instabilities and thereby to a periodically oscillating flame [25]. Some recent studies further indicate that these buoyancy-induced instabilities manifest into large vortices through a limit-cycle process, which is a characteristic of an absolutely unstable instability [30]. Therefore, in order to simulate such dynamic flames experimentally or numerically it is not necessary to continuously provide the jet with artificial perturbations. Several numerical models, including the one used in the present work, have successfully simulated periodically oscillating jet diffusion flames without the use of artificial perturbations. The models have also correctly predicted the insensitivity of the oscillation frequency to fuel type, Reynolds number, and jet diameter [13, 14, 26, 27]. Therefore, it may be expected that these models might also capture the dynamic behavior of a premixed jet flame. Indeed, as demonstrated in Fig. 13, the present mathematical model is able to simulate the buoyancy-induced vortices outside flame surface for the highly fuel-rich case. Since no artificial disturbances are introduced in the calculations, it should be noted that the well-known Kelvin-Helmholtz instabilities of shear layer [31] are not simulated in the present study.

The premixed flames for the fuel-lean (Fig. 3), stoichiometric (Fig. 4), and fuel-rich (Fig. 5) cases are steady in nature. When the Lewis number of a fuel-lean flame is fixed at 0.5 then the flame becomes oscillatory (Fig. 9a) in much the same way as that of a diffusion flame. However, the calculations made for the hydro-

gen jet diffusion flame using fixed and varying Lewis numbers yielded identical oscillating flames. Also, the simulations made using different velocity profiles for the near-stoichiometric premixed flame resulted in varying degrees of oscillatory flames (Fig. 12). Further investigations on premixed flames by neglecting the gravitational force in the governing equations resulted in steady flames for all the conditions. This suggests that the large vortices seen in the premixed flames are similar to those observed in jet diffusion flames in a sense that in both cases these vortices are induced by the buoyant acceleration of hot combustion products. However, unlike a diffusion flame, the dynamic behavior of a premixed jet flame depends on the fuel type and flow conditions.

Another important difference between the dynamically oscillating jet diffusion flame and premixed flame is that the frequency of oscillations. In diffusion flame studies [13] it is found that the vortex-crossing (or flame-flicker) frequency, under the fuel-jet and annulus-air velocity conditions similar to those used in the present study, is ~ 15 Hz. On the other hand, the near-stoichiometric premixed flame tends to oscillate at ~ 120 Hz and the highly fuel-rich flame at ~ 14 Hz. This difference in vortex-crossing frequency may be explained by considering the separation between the fuel-jet shear layer and the flame surface (Δs in Fig. 14). The flame surface of a diffusion-dominated flame is well separated from the fuel-jet shear layer ($\Delta_{\text{diffusion}} \approx 2.5$ mm), hence the buoyancy-induced vortices formed outside the flame surface are well into the annulus air flow. As a result, the vortex-crossing frequency becomes independent of fuel-jet velocity and becomes a function of annulus air flow. Whereas in the premixed flames the flame (high-temperature) surface and hence, the buoyancy-induced vortices are located well inside the high-velocity region ($\Delta_{\text{premix}} \approx -0.6$ mm). As a result, the vortex-crossing frequency of a premixed flame is high compared to that of a diffusion flame and becomes a function of fuel jet velocity.

In jet diffusion flames it is also noted that an increase in annulus velocity brings the flame closer to the shear layer and decreases the

flickering amplitude, which led to a proposal that the separation between the flame surface and the fuel-jet shear layer could be used as a parameter for characterizing the flame flicker. However, the present study on premixed flames does not support that concept. The fuel/product shear layer in a near-stoichiometric flame (Fig. 14) is outside the high-temperature surface (i.e., the separation between the flame surface and the shear layer is negative) and yet the flame flicker is strong. In fact, the buoyancy-induced vortices in Fig. 12d may no longer be identified as outer vortices.

Observations from experiments and calculations indicate that the buoyancy-induced instabilities in jet flames (diffusion and premixed) fall under absolutely-unstable category of the hydrodynamic instability. Attempts are being made to treat the diffusion-flame instabilities mathematically adopting the analysis given by Ragu and Monkewitz [32] for the absolute instability of heated jets. However, due to the very low frequency associated with diffusion flames (~ 15 Hz) a conclusive formulation could not be made. It is expected that the relatively high vortex-crossing frequencies of the premixed flames (~ 120 Hz) might help in successfully extending the analysis of Ragu and Monkewitz [32] to jet flames which will be investigated in the future.

CONCLUSIONS

A time-dependent, axisymmetric computational-fluid-dynamics model with finite-rate chemistry has been used to simulate vertically mounted H_2 /air premixed jet flames. A detailed H_2 - O_2 - N_2 chemistry model was incorporated to provide an accurate description of the combustion process and thermal-NO production in these flames. A fine-mesh system with a grid spacing of 0.1 mm was employed to resolve the reaction cone of the premixed flame. Very good agreement between measured and predicted burning velocities is found over a wide range of equivalence ratios. The model is successful in predicting the dual-flame structure (both premixed and diffusion) for fuel-rich cases. Numerical experiments were conducted by varying the fuel/air ratio, trans-

port properties, and fuel-jet-velocity profile at the burner exit. Important conclusions drawn from this study are as follows:

1. The heat-release rate is maximum and the temperature rises above the adiabatic value at the tip of a fuel-rich premixed flame which results in an intensely burning tip.
2. In the lean and stoichiometric H_2 /air flames, the heat-release rate decreases with flame height, and combustion does not extend to the tip of the flame (tip-opening phenomenon).
3. When the local Lewis numbers of the species were set equal to 2, the lean flame exhibited the combustion characteristics of a rich flame, which confirms the speculations of Law and Mizomoto et al. that the nonunity Lewis number is responsible for the non-uniform burning pattern of a premixed flame.
4. As expected, distribution of thermal NO in fuel-lean and stoichiometric flames was found to follow that of the temperature. However, in the fuel-rich flames thermal NO is formed only along the outer diffusion flame.
5. Flame flickering resulting from the convective motion of buoyancy-induced vortices that is often observed in jet diffusion flames was also observed in premixed flames. However, flame flickering in premixed flames is strongly dependent on the fuel-air ratio and the velocity profile at the burner exit.

This work was supported, in part, by Air Force Contract F33615-90-C-2033 and the Air Force Office of Scientific Research. The authors would like to thank Dr. Fumiaki Takahashi for helpful discussions and Mrs. Marian Whitaker for editorial comments on the manuscript.

REFERENCES

1. Lewis, B., and von Elbe, G., *Combustion, Flames, and Explosions of Gases*, Academic Press, New York, 1961.
2. Mizomoto, M., Asaka, Y., Ikai, S., and Law, C. K. *Twentieth Symposium (International) on Combustion*, The Combustion Institute, Pittsburgh, 1984, p. 1933.
3. Law, C. K., Cho, P., Mizomoto, M., and Yoshida, H., *Twenty-first Symposium (International) on Combustion*, The Combustion Institute, Pittsburgh, 1985, p. 1933.

- tion, The Combustion Institute, Pittsburgh, 1986, p. 1803.
4. von Elbe, G., and Lewis, B., *Seventh Symposium on Combustion*, Butterworths, London, 1959, p. 342.
5. Law, C. K., *Prog. Ener. Combust. Sci.* 10:295 (1984).
6. Yamashita, H., Kushida, G., and Takeno, T., *Proc. of R. Soc. of Lond. A* 431:301-314 (1990).
7. Ellzey, J. L., Laskey, K. J., and Oran, E. S., *Progr. Astronaut. Aeronaut.* 131:179 (1989).
8. Takagi T., and Xu, Z., *Combust. Flame* 96:50-59 (1994).
9. Katta, V. R., and Roquemore, W. M. *Combust. Flame* 92:274-282 (1993).
10. Smith, H. W., Schmitz, R. A., and Ladd, R. G., *Combust. Sci. Technol.* 4:131 (1971).
11. Smooke, M. D., Crump, J., Seshadri, K., and Giovangigli, V., *Twenty-Third Symposium (International) on Combustion*, The Combustion Institute, Pittsburgh, 1990, p. 463.
12. Dixon-Lewis, G., *Twenty-Third Symposium (International) on Combustion*, The Combustion Institute, Pittsburgh, 1990, p. 305.
13. Katta, V. R., Goss, L. P., and Roquemore, W. M., *AIAA J.* 32:84-94 (1994).
14. Katta V. R., Goss, L. P., and Roquemore, W. M., *Combust. Flame* 96:60-74 (1994).
15. Cowart, J. S., Keck J. C., Heywood J. B., Westbrook C. K., and Pitz, W. J., Western States Section Meeting of the Combustion Institute, October 23-24, 1989.
16. Miller, J. D., and Bowman, C. T., *Prog. Energy Combust. Sci.* 15:287-338 (1989).
17. Hanson, R. K., and Salimian, S., in *Combustion Chemistry*, Springer-Verlag, New York, 1984, pp. 410.
18. Burcat, A., in *Combustion Chemistry*, Springer-Verlag, New York, 1984, pp. 455-473.
19. Hirschfelder, J. O., Curtiss, C. F., and Byron, R., *Molecular Theory of Gases and Liquids*, Wiley, New York, 1954.
20. Svehla, R. A., NASA Technical Report R-132, Washington, D.C., 1962.
21. Williams, F. A., *Combustion Theory—The Fundamentals of Chemically Reacting Flow Systems*, Addison-Wesley, Reading, MA, 1985.
22. Leonard, B. P., *Comp. Meth. Appl. Mech. Eng.* 19:59-98 (1979).
23. Spalding, D. B., *Int. J. Numerical Meth. Eng.*, 4:551-559 (1972).
24. Takahashi, F., Mizomoto, M., and Ikai, S., *Alternative Energy Sources III* (T. Nejat Veziroglu, Ed.), Vol. 5 Nuclear Energy/Synthetic Fuels, p. 447, 1983.
25. Chen, L.-D., Seaba, J. P., Roquemore, W. M., and Goss, L. P., *Twenty-second Symposium (International) on Combustion*, The Combustion Institute, Pittsburgh, 1988, p. 677.
26. Davis, R. W., Moore, E. F., Roquemore, W. M., Chen, L.-D., Vilimpoc, V., and Goss, L. P., *Combust. Flame* 83:263-270 (1991).
27. Ellzey, J. L., Laskey, K. J., and Oran, E. S., *Twenty-Third Symposium (International) on Combustion*, The Combustion Institute, Pittsburgh, 1990, p. 1635.
28. Buckmaster, J. D., and Crowley, A. B., *J. Fluid Mech.* 131:341 (1983).
29. Asato, K., Kawamura, T., and Ban, T., *Twenty-Second Symposium (International) on Combustion*, The Combustion Institute, Pittsburgh, 1988, p. 1509.
30. Monkewitz, P. A., and Sohn K. D., *AIAA J.* 26:911-916 (1988).
31. Brown, G. L., and Roshko, J., *J. Fluid Mech.* 64:775-816 (1974).
32. Ragu, S., and Monkewitz, P. A., *Phys. Fluids A* 3:501-503 (1991).

Received 23 September 1993; 16 September 1994

Numerical Experiments on the Vortex-Flame Interactions in a Jet Diffusion Flame

Fumiaki Takahashi*

University of Dayton, Dayton, Ohio 45469

and

Viswanath R. Katta†

Systems Research Laboratories, Inc., Dayton, Ohio 45440

Dynamic behavior of a laminar jet diffusion flame in response to an artificial vortex that issues radially from the fuel-jet core toward the flame zone has been studied numerically to illustrate essential physics of a naturally-forming shear layer vortex that has some radial velocity. A time-dependent, axisymmetric, implicit, third-order accurate numerical model is used with the infinitely-fast chemistry and unity Lewis number assumptions. A packet of fuel (methane) is ejected as a single-pulsed "side jet" at given initial and boundary conditions (the ejection velocity and period), which cover an order of magnitude in the time scale of the vortex-flame interaction. A vortex system with a pair of counter-rotating toroidal vortex rings is generated and penetrated into the high-temperature (highly viscous) layer with "solid-body" rotation. If the Peclet number Pe defined as the ratio of the characteristic diffusion to convection times, is small (the order of 10 or less), the vortex system pushes out the flame surface. If Pe is large (the order of 100), the vortex system nearly cuts through the high-temperature layer with a minimal flame movement, thus creating a significantly thin diffusive-thermal layer. In both cases, as the vortex approaches the flame surface, the net radial velocity of the incoming oxidizer stream crossing the flame and the reactants' diffusive fluxes into the flame increase. As a result, the flame structure similar to that of a strained counterflow diffusion flame is formed. A periodically-pulsed side jet has also been studied; the fuel packets ejected (at 500 Hz) induces the development of a large-scale vortex train in the shear layer of the primary jet, interacting with the flame zone.

Introduction

IN most combustion systems of practical interest such as gas turbine combustors and industrial furnaces, turbulence plays an important role in determining various aspects of performance and efficiency, because it provides the most effective means of stirring fluids and enhancing molecular mixing and reactions. However, flow visualization in combustion systems shows inhomogeneous stirring of fluids, composed of packets and parcels of fuel, oxidizer, and products, because of large-scale turbulent structures generated in the shear layer. Therefore, the interactions between the large vortices and the flame zone are of essential importance as they relate to various aspects of combustion phenomena such as the transition to turbulent flames, flame stability, and local extinction.^{1–21}

In a jet diffusion flame for which the flame base is securely stabilized, the local flame extinction occurs near the laminar-to-turbulent flame transition point (breakpoint) as the fuel jet velocity is increased.¹⁷ Takeno and Kotani¹ postulated for hydrogen flames that the local extinction is a result of the excess transport rate as compared to the reaction rate at the breakpoint. The event when the vortex was ejected radially and interfered with the flame zone was captured in methane flames by using flow visualization techniques.^{5,8,9} Eickoff et al.⁵ speculated that the diffusion flame was quenched because too much heat was diffused by the small-scale turbulence superimposed in these vortices. However, in the near-

jet field of hydrocarbon-air flames, the flame zone is generally formed in the external fluid, not in the jet fluid, because of low stoichiometric fuel concentration and a high Damköhler number. It is, therefore, less likely that the flame zone interacts directly with the small-scale, high-intensity turbulence confined in the jet fluid.

A series of recent experiments^{15,17,19–21} using a variety of diagnostic techniques revealed the essential features of the vortex-flame interactions that lead to the local extinction of methane jet diffusion flames. Figure 1 shows a schematic of

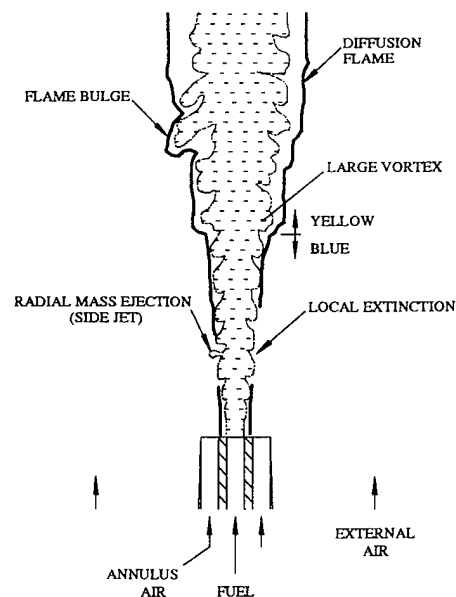


Fig. 1 Vortex-flame interactions observed in methane-air turbulent jet diffusion flames.

Presented as AIAA Paper 93-0456 at the AIAA 31st Aerospace Sciences Meeting and Exhibit, Reno, NV, Jan. 11–14, 1993; received Feb. 24, 1993; revision received March 21, 1994; accepted for publication April 14, 1994. Copyright © 1994 by the American Institute of Aeronautics and Astronautics, Inc. All rights reserved.

*Research Engineer, Research Institute, 300 College Park. Senior Member AIAA.

†Senior Engineer, Research Applications Division, 2800 Indian Ripple Road. Member AIAA.

some features of a locally extinguished turbulent flame based on the flow visualization.^{17,19,20} In the near-exit region (less than several jet diameters), the flame zone is close to the jet-fluid core and is blue in color. The flame zone shifts away from the core downstream and becomes yellow because of the soot formation. The local extinction occurs in the blue flame region near the jet exit when fuel packets, conveyed by the large-scale vortices or more rapid radial mass ejection (side jet), reach the flame zone location. The flame bulge is observed generally downstream (typically more than 10 jet diameters) in the yellow flame region. The time required for the fuel packet to reach the flame zone location in turbulent flames (typically less than 1 ms) is, at least, an order of magnitude shorter than the characteristic diffusion time required to re-establish the reactant concentration field (typically >10 ms).^{19,20} In an axially-pulsed laminar flame,²¹ the interaction between the flame zone and a large-scale vortex with a radial transit velocity of ~ 2 m/s occurred over a longer time (~ 10 ms), and the local quenching was observed near the leading edge of the vortex.

Recent developments of numerical models to simulate various aspects of the transient behavior of diffusion flames²¹⁻²⁶ enable more challenging numerical experiments on the dynamic vortex-flame interactions with sufficient accuracy. The computer code^{21,24-26} used in this paper employs a time-dependent, axisymmetric, implicit, third-order accurate, upwind numerical scheme with assumptions of infinitely fast, one-step chemical kinetics and unity Lewis number. In laminar diffusion flames, the second Damköhler number, defined as the ratio of the mass source from chemistry to diffusive transport²⁷ (or the characteristic diffusion to chemical reaction times), is generally large, and therefore, the diffusion process is the rate-determining factor. As a vortex approaches the flame zone and the diffusion layer becomes thin (reducing the Damköhler number), finite-rate chemistry must become important in the process, eventually leading to local extinction. Because of the axisymmetry and infinitely fast chemistry assumptions, the current model cannot simulate the three-dimensional nature of a vortex, nor can the flame extinction condition. However, it must provide global information on the physical nature (fluid-dynamic and transport aspect) of the vortex-flame interaction before local extinction. This study attempts to simulate numerically the transient response of a laminar jet diffusion flame to an artificial vortex that issues from a side jet. The primary objective of this study is to gain a better understanding of essential physical features of the interactions between the flame zone and a naturally-forming shear-layer vortex that has some radial velocity.

Numerical Experiment

Numerical Scheme

The laminar diffusion flame considered in this article is formed between a central methane jet and a concentric annulus airflow. Time-dependent governing equations, expressed in cylindrical coordinates, consist of mass continuity, axial and radial momentum conservation, and two scalar conservation equations.^{24,25} Shvab-Zel'dovich formulation,²⁸ in conjunction with the flame-sheet assumption, is utilized. Body-force term caused by the gravitational field is included in the axial momentum equation. The system of governing equations is completed by using the equation of state. Transport properties are considered to vary with temperature and species concentrations. Enthalpy of each species is calculated from polynomial curve-fits, whereas the viscosity of the individual species is estimated from Chapman-Enskog collision theory.²⁹ The binary diffusion coefficient between any two species on the fuel side of the flame is assumed to be identically equal to that of the fuel and nitrogen. Similarly, on the oxidizer side of the flame, it is made identical to that of the oxygen and nitrogen. The Chapman-Enskog theory and the Lennard-Jones potentials²⁹ have been used to estimate these two binary diffusion coefficients.

The finite difference form of the governing equations is constructed on a staggered grid system based on an implicit QUICKEST numerical scheme. It is third-order accurate in both space and time and has a very low numerical diffusion error. At every time-step, the pressure field is accurately calculated by solving the system of algebraic pressure Poisson equations simultaneously. An orthogonal grid system (Fig. 2) with rapidly expanding cell sizes in both z and r directions is utilized. The computational domain of 150×60 mm in axial z and radial r directions, respectively, is represented by a mesh system of 241×71 . The i.d. of the fuel tube ($d = 9.6$ mm) is almost the same as that used in the experiments.^{15,17,19,20} Grid lines are clustered near the burner lip and side jet locations. The outer boundaries of the computational domain are shifted sufficiently far enough to minimize the propagation of disturbances into the region of interest.

The initial and boundary conditions for the axial U and radial V velocities, and the scalar variables for species β_1 and energy β_2 ,^{24,25} at different flow boundaries are shown in Fig. 3. The fully developed pipe flow and flat-velocity profiles are used at the exits of the fuel tube and the annulus air channel, respectively. Along the burner-lip walls, no-slip boundary conditions are enforced. An extrapolation procedure with weighted zero- and first-order terms is used to estimate the flow variables on the outflow boundary. During the calculations, radial side jets are introduced from different locations in the flowfield.

Test Conditions

The primary test cases reported in this article are listed in Table 1. Case 1 represents a laminar jet diffusion flame with low velocities of the primary jet U_p , annulus air U_a , and side jet V_s , and a long pulse width t_p . At the grid points within the side jet, the radial component of the local velocity and the scalar variables are replaced by V_s , $\beta_{1,s}$ ($=\beta_{1,r}$), and $\beta_{2,s}$ ($=\beta_{2,r}$), respectively, for a time-period of t_p . The primary jet has a

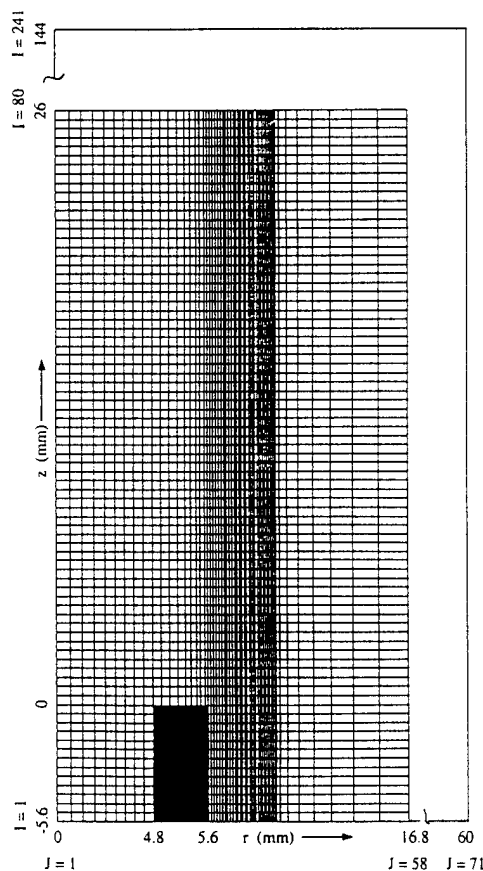


Fig. 2 Grid system.

Table 1 Test conditions

Case no.	Primary jet		Annulus air		Side jet			Pulse mode
	U_j , m/s	Velocity profile	U_a , m/s	r_a , mm	z_s , mm	V_s , m/s	t_s , μ s	
1	1.5	Parabolic	1.5	4.8	14.2–16.5	2.0	300	Single-shot
2a	15	$\frac{1}{n}$ th power	3	4.8	14.2–16.5	8.6	30	Single-shot
2b	15	$\frac{1}{n}$ th power	3	4.8	14.2–16.5	8.6	60	Single-shot
2c	15	$\frac{1}{n}$ th power	3	4.8	14.2–16.5	4.3	30	Single-shot
3	15	$\frac{1}{n}$ th power	3	4.8	4.2–9.5	2.0	30	Periodic, 500 Hz

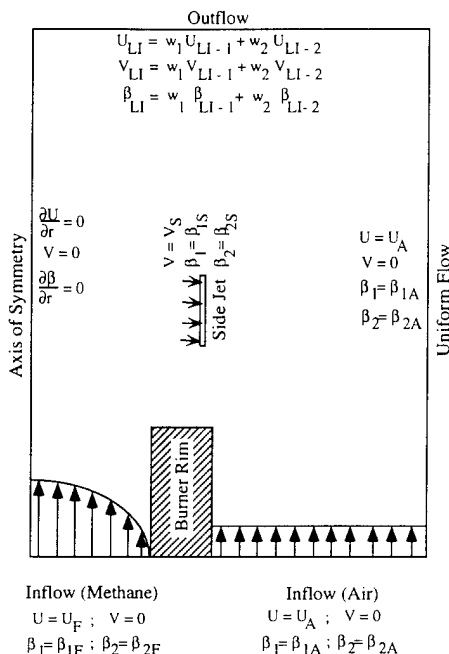


Fig. 3 Boundary conditions.

parabolic velocity distribution, representing the fully developed laminar pipe flow. The side-jet velocity in case 1 is the same magnitude as the radial velocity component of a large-scale vortex observed experimentally in the axially-pulsed laminar methane flame.²¹ The radial location of the side jet ($r_s = d/2$) is nearly coincident with a dividing streamline between the jet and external fluids. The height of the side jet is chosen near the jet exit such that the flame zone interacts with the vortex intensely because of the flame proximity to the jet-fluid core. Case 2a represents a flame with higher velocities of the primary jet, annulus air, and side jet, and a shorter pulse width in consideration of a naturally-forming radial mass ejection observed in turbulent flames.^{17,19,20} In the turbulent methane jet diffusion flame stabilized on a thick burner lip, the local flame extinction occurred at the mean primary jet velocity of ~ 15 m/s,^{15,17} and the maximum radial velocity component (the mean plus three times the rms fluctuation) observed was ~ 7 m/s.¹⁹ The velocity distribution of the primary jet is given by using the empirical equation of the $1/n$ th-power law³⁰ for the fully developed turbulent pipe flow with the exponent $n = 6$ for a moderate Reynolds number (although the simulation considers laminar flows only). In case 2b, the pulse width of the side jet is doubled from case 2a to see the effect of the total mass ejected. In case 2c, the side jet velocity is halved from case 2a to test the effect of momentum at a same total mass ejection. Case 3 is an attempt to simulate a naturally-forming train of large-scale vortices in the shear layer, observed experimentally,^{3,8,9,12,25} and their interaction with the flame zone. A moderate-speed periodically-pulsed (50% duty cycle) side jet is ejected into the flame under the condition of the same primary jet velocity as that in case 2a.

Results and Discussion

Single Vortex vs Flame Interactions

A steady-state solution for the diffusion flame structure without a side jet was obtained first for each case by numerous (typically several tens thousand times) iterative calculations using a long time step ($\sim 183 \mu$ s in case 1; $\sim 37 \mu$ s in case 2). By using the steady-state solution as the initial condition, the temporal changes in the flame structure in response to the side-jet ejection were calculated using a short time step ($\sim 12.2 \mu$ s in case 1; $\sim 2.4 \mu$ s in cases 2a–2c and 3). Figures 4 and 5 show the flame structure near the side jet for cases 1 and 2a, respectively: a color-coded mapping of the gas temperature T and a superimposed tracer particles image (Figs. 4a and 5a) and a color-coded mapping of the mole fractions of methane and oxygen X_{CH_4} , X_{O_2} with superimposed velocity vectors (Figs. 4b and 5b). The tracer particles in Figs. 4a and 5a were injected in front of the side jet (at $r = 4.9$ mm) over the axial distance of 4 mm at every time step. Notice that the elapse time after ejection t is an order of magnitude longer for case 1 ($t = 3.91$ ms) than case 2a ($t = 0.391$ ms). Despite the difference in the magnitude of side-jet velocity and, in turn, the time scale of the process, the two cases show the following common features in the flame structures, because the vortex system formed dominates the global flow structure.

As a fuel packet issues from the side jet in the jet-fluid core toward the flame surface, a sudden change in the radial-velocity distribution near the edges of the side jet induces the roll-up of fluid and the subsequent formation of a vortex system composed of a pair of counter-rotating vortex rings. The vortex system grows as it engulfs surrounding gases and penetrates into a high-temperature (highly viscous) layer toward the flame surface. The vortex structure rotates as a whole naturally because of the uneven axial-velocity distribution in the shear layer. This tendency is more evident in case 2a because of its higher velocity gradient, and consequently, the upper portion of the double-vortex structure shrinks (Fig. 5a). The formation of the vortex structure with counter-rotating vortex rings and the subsequent solid-body rotation have been observed experimentally.²¹ The vortex evolution processes described are depicted well by the injected particle images (such as Figs. 4a and 5a), and the consecutive time-series animation of the particle images and the color-coded temperature mappings on a computer display. The velocity vectors (Figs. 4b and 5b) show a zigzag motion (with respect to the stationary coordinate) typical of large-scale vortices. The rotating motion is more clearly seen in case 2a. The velocity vectors also show that the bulk flow comes into the upstream portion of the vortex system from the oxidizer side, crossing the flame surface, and goes out from the downstream portion, crossing the flame again. However, because the contribution of convection to the reactant fluxes vanishes at the flame surface (as will be described later), the reactant species enter the flame surface solely by diffusion from opposite directions, typical of diffusion flames.

Major differences in the response of the flame to the vortex movement between the two cases stem from the an-order-of-magnitude difference in the time scale of the process. In case 1, the vortex system pushes out the flame zone along with

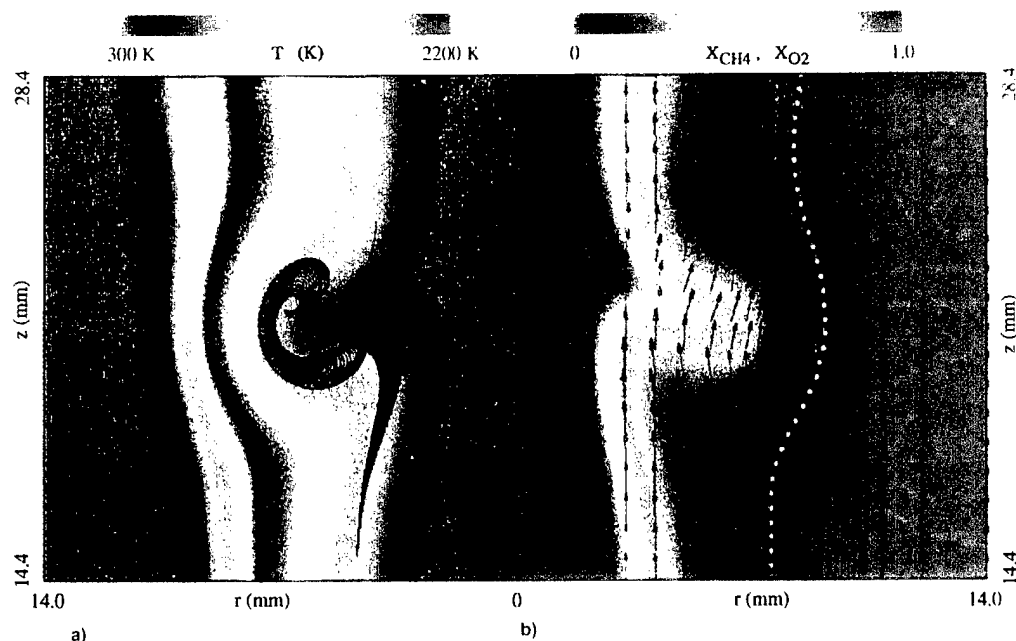


Fig. 4 Structure of a methane jet diffusion flame with a single side jet (case 1), $t = 3.91$ ms: a) temperature field and injected particles and b) mole fraction field of CH_4 and O_2 and velocity vectors.

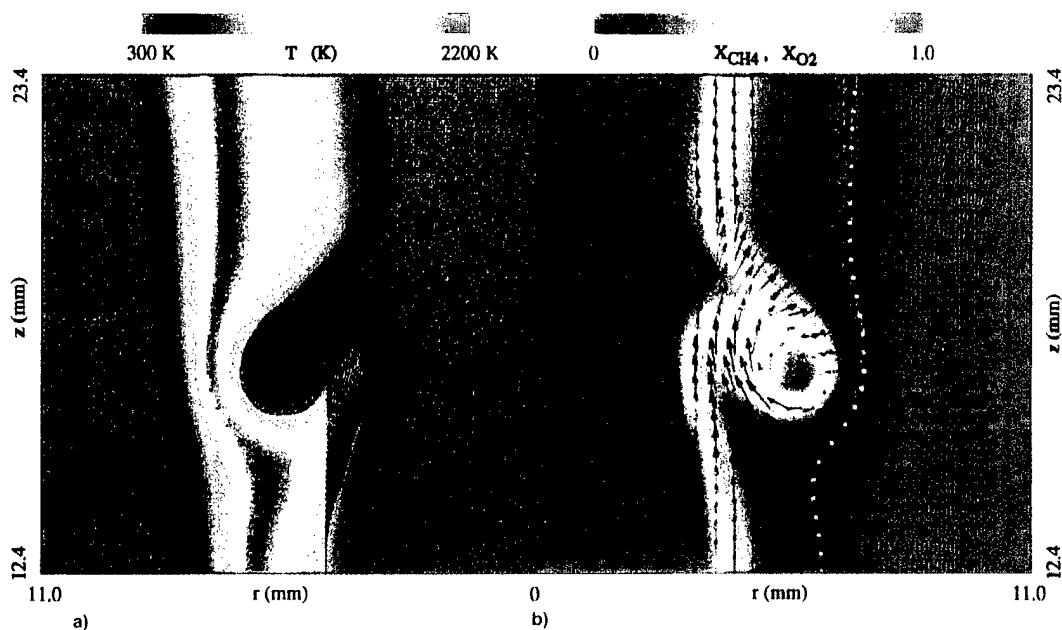


Fig. 5 Structure of a methane jet diffusion flame with a single side jet (case 2a), $t = 0.391$ ms: a) temperature field and injected particles and b) mole fraction field of CH_4 and O_2 and velocity vectors.

the isothermal layers well before the vortex leading edge reaches the initial flame surface location (Fig. 4a). By contrast, in case 2a, the vortex almost cuts across the high-temperature zone while the flame zone shifts slightly at a very last stage of the process (Fig. 5a). Consequently, the thermal layer ahead of the vortex becomes significantly thin as the leading edge of the vortex reaches the initial flame surface location. Furthermore, although the total mass ejected is more than twice of that in case 1, the methane mole fraction in the vortex system becomes lower than case 2a because of the excess diffusion of the fuel molecules to the surroundings over a longer elapse time (Figs. 4b and 5b).

Figures 6 and 7 show the radial distributions of the mean axial and radial flow components (Figs. 6a and 7a); the gas temperature, the mole fractions of methane and oxygen (Figs. 6b and 7b); and the instantaneous total (axial and radial) mole fluxes of methane and oxygen by convection ($\dot{M}_{\text{CH}_4, \text{conv}}$, $\dot{M}_{\text{O}_2, \text{conv}}$) and diffusion ($\dot{M}_{\text{CH}_4, \text{diff}}$, $\dot{M}_{\text{O}_2, \text{diff}}$) at a height near the center of the vortex system for cases 1 and 2a, respectively (Figs. 6c and 7c). The results at $t = 0$ rep-

resent the steady-state solution. The radial location of the flame surface r_f at the height of the center of the side jet at $t = 0$ is ~ 7.3 mm in case 1, and ~ 6.5 mm in case 2a. For the lower velocity condition (case 1) at $t = 0$, the axial velocity component shows a velocity overshoot near the flame because of the buoyancy effect. That is not seen in case 2a, in which the external air velocity is ~ 3 m/s.

Because of the unity Lewis number assumption, heat transfer and mass diffusion processes must be similar. Therefore, the thickness of the layer in which the temperature varies is coincident with that for the (fuel and oxygen) mole fractions. The thickness of this layer (the diffusive-thermal layer) can be characterized using the full width at half-maximum (FWHM) of the temperature distribution w_T ; $w_T = 3.6$ mm in case 1 and $w_T = 2.4$ mm in case 2a at $t = 0$. The higher primary jet and air velocity in case 2a result in a higher bulk flow velocity coming into the flame zone from the air side, pushing the contour of a stoichiometric mole-flux balance (where the flame surface is located) inward to the region where gradients of variables (velocity, temperature, and methane mole frac-

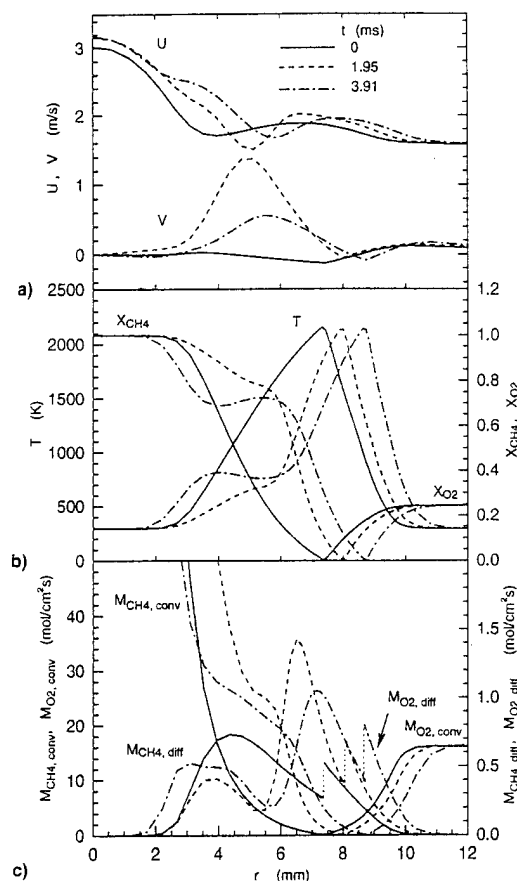


Fig. 6 Radial profiles of a) the axial and radial velocities; b) temperature, mole fractions of CH_4 and O_2 ; and c) mole fluxes of CH_4 and O_2 (case 1).

tion) are larger. Thus, the diffusive-thermal layer becomes thinner and the flame zone is more strained.

The magnitude of the instantaneous mole fluxes of the reactants by convection are large in the region away from the flame and decrease to zero at the flame surface, because the convection terms ($\rho_i Y_i v / W_i$, where ρ is density, Y is mass fraction, v is velocity vector, W is molecular weight, subscript i : species i for CH_4 and O_2) vanish as $Y_i \rightarrow 0$ at $r \rightarrow r_f$. On the other hand, the diffusion terms ($\rho_i D \nabla Y_i / W_i$) have finite values at $r = r_f$. The mole flux of methane by diffusion on the flame surface at $t = 0$ is $M_{\text{CH}_4, \text{diff}} = 0.27 \text{ mole/m}^2\text{s}$ ($M_{\text{O}_2, \text{diff}} = 0.54 \text{ mole/m}^2\text{s}$) in case 1 and $M_{\text{CH}_4, \text{diff}} = 0.40 \text{ mole/m}^2\text{s}$ ($M_{\text{O}_2, \text{diff}} = 0.80 \text{ mole/m}^2\text{s}$) in case 2a. Because of the null contribution of convection to the methane and oxygen mole fluxes at the flame surface, the diffusion contribution is always at a stoichiometric ratio (1:2). Incidentally, the oxygen mole flux determined experimentally³¹ in the luminous zone near the base of a laminar diffusion flame of methane is $\sim 1 \text{ mole/cm}^2\text{s}$.

At $t > 0$ in both cases, the peak temperature remains nearly constant (2100–2150 K), and a secondary temperature peak appears on the fuel side of the flame as a result of the roll-up of hot surrounding gases into the vortex structure. The diffusive-thermal layer becomes thinner ($w_T = 2.4 \text{ mm}$ at $t = 3.91 \text{ ms}$ in case 1, and $w_T = 1.0 \text{ mm}$ at $t = 0.391 \text{ ms}$ in case 2a), and the methane mole flux by diffusion increases with time ($M_{\text{CH}_4, \text{diff}} = 0.40 \text{ mole/m}^2\text{s}$ at $t = 3.91 \text{ ms}$ in case 1, and $M_{\text{CH}_4, \text{diff}} = 0.75 \text{ mole/m}^2\text{s}$ at $t = 0.391 \text{ ms}$ in case 2a). The reactant mole fluxes on the flame surface are thus almost proportional to w_T . In case 2a, in particular, the radial gradient of the methane mole fraction becomes significantly steep, thus resulting in the high methane flux diffusing into the flame zone (Fig. 7a).

Figure 8 shows the comparisons between the flame structures for cases 2a, 2b, and 2c at a fixed elapse time ($t = 0.293$

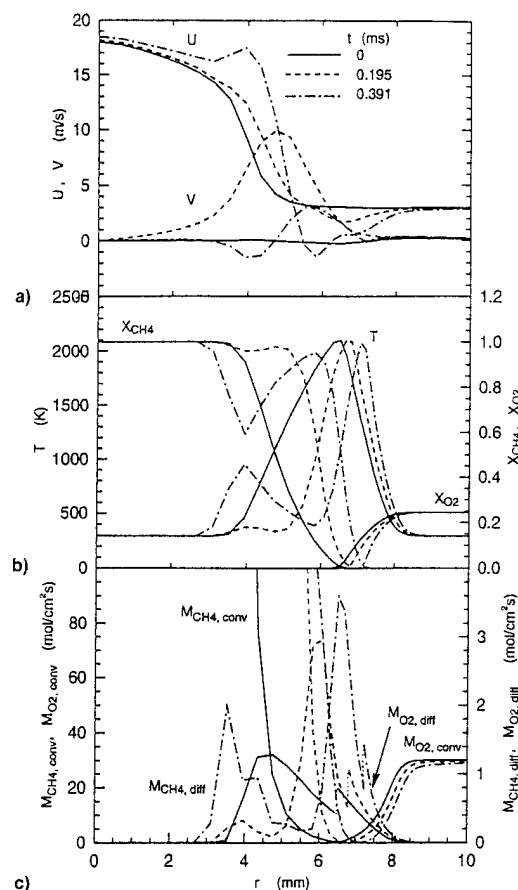


Fig. 7 Radial profiles of a) the axial and radial velocities; b) temperature, mole fractions of CH_4 and O_2 ; and c) mole fluxes of CH_4 and O_2 (case 2a).

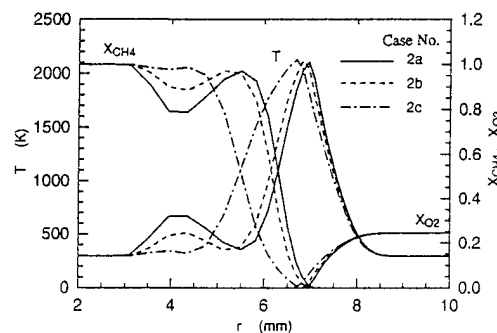


Fig. 8 Radial profiles of the temperature and mole fractions of CH_4 and O_2 .

ms). In case 2b, the ejection period and, in turn, the total mass of the side jet is doubled from case 2a. Although the size of the vortex system becomes larger in the temperature field mapping (not shown) in case 2b, the structure remained similar because the vortex system penetrated into the hot zone at almost the same degree. In case 2c, the velocity of the side jet is halved under a fixed total mass. Because of the lower momentum of the vortex system in case 2c, it could not penetrate into the hot zone to reach the flame zone location and, thus, drifted away downstream.

If the movement of the vortex system toward the flame surface was extremely slow, changes in the fuel concentration by the movement would propagate around the vortex by diffusion simultaneously. As a result, a quasi-steady-state concentration field would be re-established in time, and thus, the flame surface would be shifted to a renewed equilibrated position. On the other hand, if the vortex speed was extremely fast compared to the rate required for the diffusion process, the surrounding concentration field would not be able to re-

spond to the changes except for a narrow region in the immediate vicinity of the vortex. Therefore, the Peclet number Pe for mass transfer, defined as the ratio of the convective to conductive (diffusive) mass transfer²⁷ (or the characteristic diffusion to convection times), must be an important dimensionless parameter in determining the degree of the vortex-flame interaction. Because of the unity Lewis number assumption, the Peclet number for mass transfer is identical to its counterpart for heat transfer.²⁷ In the previous paper,^{19,20} the characteristic diffusion time τ_d , and the convection time caused by radial mass ejection τ_m were determined as $\tau_d = (\delta_d)^2/D$ (δ_d is diffusive transport layer thickness, D is diffusion coefficient), and $\tau_m = \delta_d/V_m$ (V_m is radial mass ejection velocity), respectively. Therefore, the Peclet number relevant to the side-jet ejection under current consideration becomes

$$Pe = (\tau_d/\tau_m) = (\delta_d V_m/D) \quad (1)$$

It was estimated^{19,20} that $\tau_d \sim 30$ ms and $\tau_m \sim 0.2$ ms using $\delta_d \sim 1.5$ mm, $D \sim 0.7$ cm²/s (methane at 1500 K), and $V_m = 6.6$ m/s, resulting in $Pe \sim 150$. By substituting $(r_f - r_s)$ at $t = 0$ for δ_d and V_s for V_m , for the flames under investigation in this article, $Pe \sim 71$ ($\tau_d \sim 89$ ms, $\tau_m \sim 1.25$ ms) was obtained for case 1, and $Pe \sim 209$ ($\tau_d \sim 41$ ms, $\tau_m \sim 0.2$ ms) for case 2a. Thus, the characteristic convection time is one to two orders of magnitude shorter than the characteristic diffusion (or heat transfer) time.

Figure 9 shows the temporal variations in the radial locations and transit velocities of the leading edge of the vortex system (r_l , V_l), the flame surface (r_f , V_f), and the width at half-maximum of the temperature distribution for cases 1 and 2a. As the vortex approaches the flame zone at $t < 2$ ms in case 1 (Fig. 9a), the vortex loses its speed while the flame surface gains its moving velocity. As the vortex pushes the flame, $(r_f - r_l)$ and w_T decrease and become nearly constant, and $V_l \approx V_f$ at $t > 2$ ms. Because of unity Lewis number, w_T is almost proportional to $(r_f - r_l)$. In case 2a (Fig. 9b), $(r_f - r_l)$, w_T , and V_l continue to decrease and V_f increases until the leading edge of the vortex reaches the initial flame zone location at $t \sim 0.4$ ms. The V_f curve changes its slope as the vortex starts the "solid-body" rotation described before.

Since the flame surface moves outward as the vortex system approaches, it is necessary to consider the net radial velocity

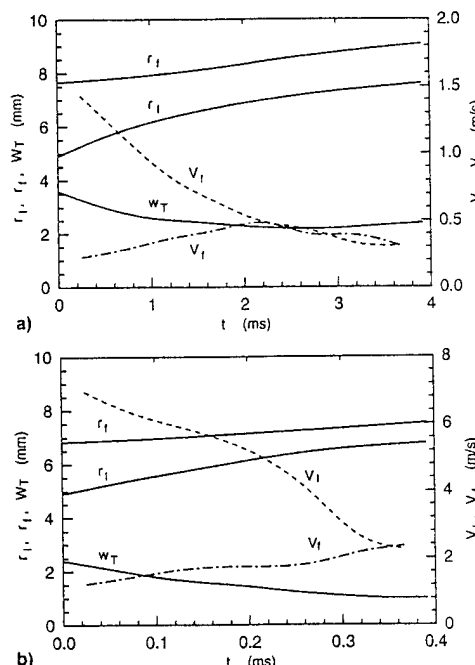


Fig. 9 Temporal variations in the radial locations and velocities of the vortex leading edge and flame surface and the FWHM of the temperature distribution: a) case 1 and b) case 2a.

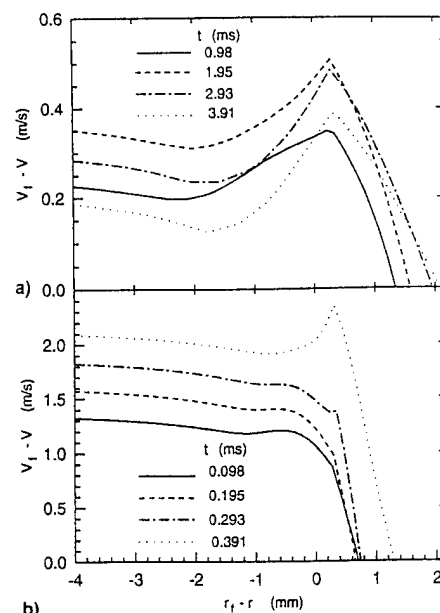


Fig. 10 Radial profiles of the net radial velocity relative to the flame surface.

component relative to the flame surface in order to examine the instantaneous structure near the flame. Figure 10 shows the relative radial velocity component ($V_l - V$), which is positive for the incoming flow direction crossing the flame surface, as a function of the relative location ($r_f - r$) in the near-flame region for cases 1 and 2a. In case 1 (Fig. 10a), as the vortex system approaches the flame surface, the profile of ($V_l - V$) becomes similar to the one observed in strained counterflow diffusion flames^{32,33} (with a peak at slightly downstream of the flame surface) at a relatively early stage of the vortex-flame interaction process. In case 2a (Fig. 10b), the temperature peak does not appear until a later stage of the process when the vortex leading edge approaches the close proximity of the flame surface and $(r_f - r_l)$ becomes constant. Because the velocity peak is caused by the longitudinal acceleration by gas expansion at high temperatures, the peak would not appear (or would be small, if any) if the gases (stream tubes) were able to expand laterally under a given flow configuration. Furthermore, unlike the counterflow diffusion flames, the velocity gradient (deceleration) of the approach flow just before entering the flame (which is normally used to assess the strain rate in the counterflow diffusion flames), is small because the net radial velocity component is nearly constant ($\sim V_f$) away from the flame surface as the actual velocity with respect to the laboratory coordinate is nearly zero. In jet diffusion flames, in general, the streamlines are nearly parallel to the flame surface (and thus, the velocity component perpendicular to the flame is small), while in counterflow diffusion flames, the streamlines are perpendicular for the stagnation-point flow. The radial side jet ejection has altered the normal jet diffusion flame structure. Therefore, the differences in the geometric configuration and velocity of the incoming flow play an important role in determining the flame structure, and a proper consideration needs to be made when applying a property (such as the critical strain rate for extinction) of one type of flames to another type.

Periodic-Vortices vs Flame Interactions

In case 3, the periodically-pulsed side jet induced the development of a train of large-scale vortices in the shear layer, similar to the structure observed experimentally.^{8,9,12} A preliminary test showed that the evolution frequency of the large structure was ~ 500 Hz and nearly independent of the side jet frequency in the range of 500–1000 Hz. Figure 11 shows the structure of the flame with a periodic (500-Hz) side-jet ejection: a color-coded mapping of the temperature field (Fig.

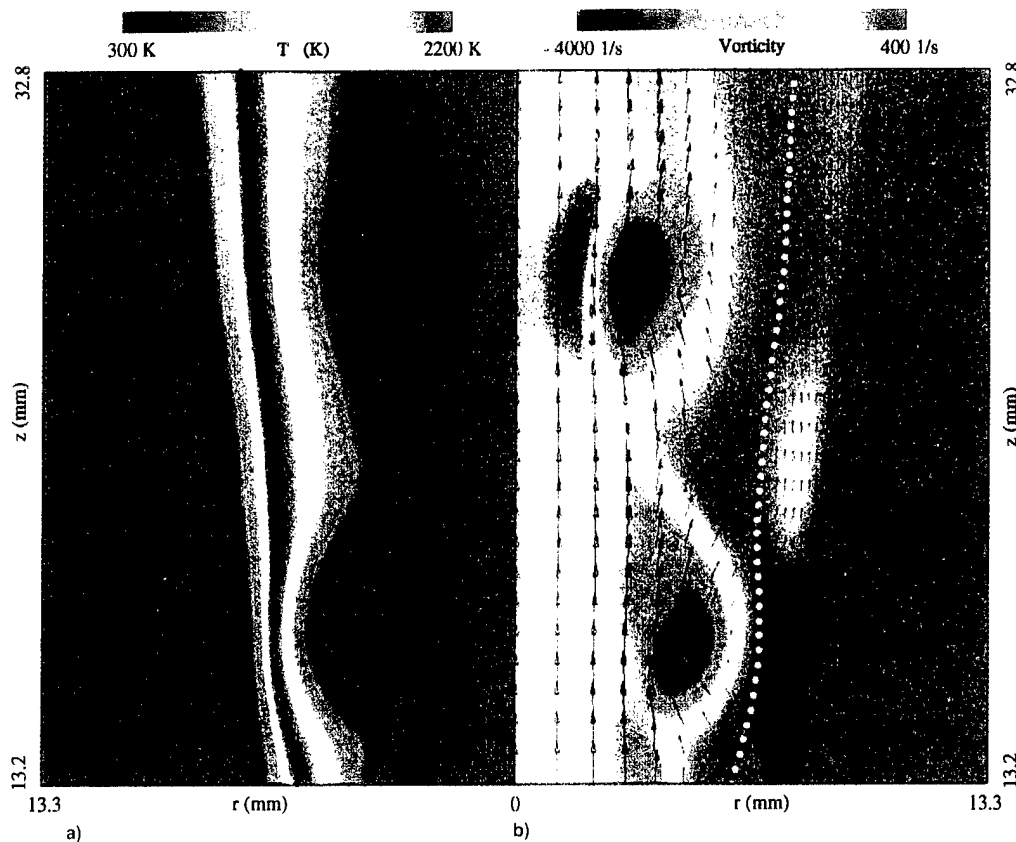


Fig. 11 Structure of a methane jet diffusion flame with a periodically-pulsed (500-Hz) side jet (case 3): a) temperature field and b) vorticity field and velocity vectors.

11a) and the vorticity field with superimposed velocity vectors (Fig. 11b). The temperature field image (Fig. 11a) shows the engulfment of the hot combustion products into the upstream side of the vortex and the thinned diffusive-thermal layer near the vortex upstream. Although the vortex interacts with the flame in a similar manner with the single-pulsed cases in the upstream region, the interaction becomes weaker downstream as the vortex loses its radial momentum and the distance between the vortex and the flame (or the diffusive-thermal layer thickness) increases. Unlike the single-shot side jet described before, the large vortex has the only one rotation direction as is normally seen in the shear layer. Thus, the vorticity (Fig. 11b) shows a negative peak. The velocity vectors again show a zigzag motion because of the large vortices.

Conclusions

A unique numerical experiment, in which a packet of fuel issues from a side jet toward a flame zone, has illustrated essential physics of the interactions between a large-scale vortex and a laminar diffusion flame. The following are among major conclusions.

The formation of a large-scale vortex structure composed of a pair of counter-rotating vortex rings and subsequent solid-body rotation of the vortex structure caused by the uneven axial-velocity distribution in the shear layer, observed experimentally, are simulated numerically. If the side-jet velocity (or momentum) is large, the vortex system penetrates into the high-temperature (highly viscous) layer; otherwise, it drifts away downstream before reaching the initial flame surface location. The level of penetration is nearly independent of the total mass ejected. The solid-body rotation of the vortex system is more evident in the higher primary jet velocity case because of the higher velocity gradient.

A Peclet number, defined as a ratio of the characteristic diffusion (or thermal conduction) to convection times for the side jet, is an important parameter in determining the level of the vortex-flame interactions. If Pe is small (the order of 10 or less), the vortex system pushes out the flame surface

over the majority of the interaction period. If Pe is large (the order of 100), the vortex system nearly cuts through the high-temperature layer with a slight flame movement, thus resulting in an extremely thin diffusive-thermal layer with large gradients of the temperature and reactant concentrations. In both cases, as the vortex system approaches the flame surface, both the bulk flow velocity and the diffusive fluxes of reactants into the flame surface increase, and a flame structure becomes similar to that of a strained laminar counterflow diffusion flame. Therefore, the geometric flow configuration and incoming flow velocity, created by the large-scale vortex, are important factors in determining the flame structure.

The development of a train of large-scale vortices in the shear layer, observed experimentally, is simulated numerically by ejecting consecutive packets of fuel from the side jet periodically. Although the vortex-flame interactions similar to the single-pulsed cases take place in the upstream region, the level of the interactions decreases rapidly downstream, as the vortex loses its radial momentum.

Acknowledgments

This work was supported by the U.S. Air Force, Wright Laboratory, Aero Propulsion and Power Directorate, Fuels and Lubrication Division, Wright-Patterson Air Force Base, Ohio, under Contract F33615-92-C-2207 (Technical Monitor: C. W. Frayne). The authors would like to thank W. M. Roquemore for helpful discussions.

References

1. Takeno, T., and Kotani, Y., "An Experimental Study on the Stability of Jet Diffusion Flames," *Acta Astronautica*, Vol. 2, 1975, pp. 999-1008.
2. Yule, A. J., Chigier, N. A., Ralph, S., Boulderstone, R., and Ventura, J., "Combustion Transition Interaction in a Jet Flame," *AIAA Journal*, Vol. 19, No. 6, 1981, pp. 752-760.
3. Eickhoff, H., "Instability and Coherent Structures in Jet Flames," *Recent Contributions to Fluid Mechanics*, edited by W. Haase, Springer-Verlag, 1981, pp. 1-10.

ger-Verlag, New York, 1982, pp. 50-57.

⁴Takahashi, F., Mizomoto, M., and Ikai, S., "Transition from Laminar to Turbulent Free Jet Diffusion Flames," *Combustion and Flame*, Vol. 48, No. 1, 1982, pp. 85-95.

⁵Eickoff, H., Lenze, B., and Leuckel, W., "Experimental Investigation on the Stabilization Mechanism of Jet Diffusion Flames," *Twentieth Symposium (International) on Combustion*, The Combustion Inst., Pittsburgh, PA, 1984, pp. 311-318.

⁶Gollahalli, S. R., Savas, Ö., Huang, R. F., and Rodriguez Azara, J. L., "Structure of Attached and Lifted Gas Jet Flames in Hysteresis Region," *Twenty-First Symposium (International) on Combustion*, The Combustion Inst., Pittsburgh, PA, 1988, pp. 1463-1471.

⁷Shekarchi, S., Savas, Ö., and Gollahalli, S. R., "Structure of a Split Gas Flame," *Combustion and Flame*, Vol. 73, 1988, pp. 221-232.

⁸Eickoff, H., Lehmann, B., Barsikow, B., and Winandy, A., "Instability of Ring Vortices and the Formation of Side Jets in Diffusion Flames and Hot Jets," 5th International Symposium on Flow Visualization, Prague, Czechoslovakia, Aug. 1989.

⁹Roquemore, W. M., Chen, L.-D., Goss, L. P., and Lynn, W. F., "The Structure of Jet Diffusion Flames," *Turbulent Reactive Flows*, edited by R. Borghi and S. N. B. Murthy, Springer-Verlag, Berlin, Vol. 40, 1989, pp. 49-63.

¹⁰Lewis, G. S., Cantwell, B. J., Vandsburger, U., and Bowman, C. T., "An Investigation of the Structure of a Laminar Non-Premixed Flame in an Unsteady Vortical Flow," *Twenty-Second Symposium (International) on Combustion*, The Combustion Inst., Pittsburgh, PA, 1989, p. 515.

¹¹Gutmark, E., Parr, T. P., Parr, D. M., and Schadow, K. C., "Evolution of Vortical Structure in Flames," *Twenty-Second Symposium (International) on Combustion*, The Combustion Inst., Pittsburgh, PA, 1989, pp. 523-529.

¹²Chen, L.-D., Seaba, J. P., Roquemore, W. M., and Goss, L. P., "Buoyant Diffusion Flames," *Twenty-Second Symposium (International) on Combustion*, The Combustion Inst., Pittsburgh, PA, 1989, pp. 677-684.

¹³Coats, C. M., and Zhao, H., "Transition and Stability of Turbulent Jet Diffusion Flames," *Twenty-Second Symposium (International) on Combustion*, The Combustion Inst., Pittsburgh, PA, 1989, pp. 685-692.

¹⁴Takahashi, F., Mizomoto, M., Ikai, S., and Tsuruyama, K., "Stability Limits of Hydrogen/Air Coflow Jet Diffusion flames," AIAA Paper 90-0034, Jan. 1990.

¹⁵Takahashi, F., Schmoll, W. J., and Vangsness, M. D., "Effects of Swirl on the Stability and Turbulent Structure of Jet Diffusion Flames," AIAA Paper 90-0036, Jan. 1990.

¹⁶Pitts, W. M., "Large-Scale Turbulent Structures and the Stabilization of Lifted Turbulent Jet Diffusion Flames," *Twenty-Third Symposium (International) on Combustion*, The Combustion Inst., Pittsburgh, PA, 1991, pp. 661-668.

¹⁷Takahashi, F., and Schmoll, W. J., "Lifting Criteria of Jet Diffusion Flames," *Twenty-Third Symposium (International) on Combustion*, The Combustion Inst., Pittsburgh, PA, 1991, pp. 677-683.

¹⁸Chen, T. H., and Goss, L. P., "Statistical OH-Zone Structure of Turbulent Jet Flames from Liftoff to Near-Blowout," *Combustion*

Science Technology, Vol. 79, 1991, pp. 311-324.

¹⁹Takahashi, F., and Goss, L. P., "Near-Field Turbulent Structures and the Local Extinction of Jet Diffusion Flames," *Twenty-Fourth Symposium (International) on Combustion*, The Combustion Inst., Pittsburgh, PA, 1992, pp. 351-359.

²⁰Takahashi, F., and Vangsness, M. D., "Near-Field CARS Measurements and the Local Extinction of Turbulent Jet Diffusion Flames," *Dynamics of Heterogeneous Combustion and Reacting Systems*, edited by A. L. Kuhl, J.-C. Leyer, A. A. Borisov, and W. A. Sirignano, Vol. 152, Progress in Astronautics and Aeronautics, AIAA, Washington, DC, 1993, pp. 37-55.

²¹Hsu, K. Y., Chen, L. D., Katta, V. R., Goss, L. P., and Roquemore, W. M., "Experimental and Numerical Investigations of the Vortex-Flame Interactions in a Driven Jet Diffusion Flames," AIAA Paper 93-0455, Jan. 1993.

²²Davis, R. W., Moore, E. F., Roquemore, W. M., Chen, L.-D., Vilimpoc, V., and Goss, L. P., "Preliminary Results of a Numerical-Experimental Study of the Dynamic Structure of a Buoyant Jet Diffusion Flames," *Combustion and Flame*, Vol. 83, Nos. 3/4, 1991, pp. 263-270.

²³Ellzey, J. L., Laskey, K. J., and Oran, E. S., "Effects of Heat Release and Gravity on an Unsteady Diffusion Flame," *Twenty-Third Symposium (International) on Combustion*, The Combustion Inst., Pittsburgh, PA, 1991, pp. 1635-1640.

²⁴Katta, V. R., Goss, L. P., and Roquemore, W. M., "Numerical Investigations of Transitional H₂/N₂ Jet Diffusion Flames," *AIAA Journal*, Vol. 32, No. 1, 1994, pp. 84-94.

²⁵Katta, V. R., and Roquemore, W. M., "Role of Inner and Outer Structures in Transitional Jet Diffusion Flame," *Combustion and Flame*, Vol. 92, No. 2, 1993, pp. 274-282.

²⁶Katta, V. R., Goss, L. P., and Roquemore, W. M., "Effect of Nonunity Lewis Number and Finite-Rate Chemistry on the Dynamics of a Hydrogen-Air Jet Diffusion Flames," *Combustion and Flame*, Vol. 96, Nos. 1/2, 1994, pp. 60-74.

²⁷Strehlow, R. A., *Combustion Fundamentals*, McGraw-Hill, New York, 1984, p. 120.

²⁸Williams, F. A., *Combustion Theory*, 2nd ed., The Benjamin/Cummings, Menlo Park, CA, 1985, p. 10.

²⁹Hirschfelder, J. O., Curtis, C. F., and Bird, R. B., *The Molecular Theory of Gases and Liquids*, Wiley, New York, 1954.

³⁰Schlichting, H., *Boundary-Layer Theory*, 7th ed., translated by J. Kestin, McGraw-Hill, New York, 1979, p. 599.

³¹Robson, K., and Wilson, M. J. G., "The Stability of Laminar Diffusion Flames of Methane," *Combustion and Flame*, Vol. 13, 1969, pp. 626-634.

³²Tsuji, H., and Yamaoka, I., "Structure Analysis of Counterflow Diffusion Flames in the Forward Stagnation Region of a Porous Cylinder," *Thirteenth Symposium (International) on Combustion*, The Combustion Inst., Pittsburgh, PA, 1971, pp. 723-731.

³³Chelliar, H. K., Law, C. K., Ueda, T., Smooke, M. D., and Williams, F. A., "An Experimental and Theoretical Investigation of the Dilution, Pressure and Flow-Field Effects on the Extinction Condition of Methane-Air-Nitrogen Diffusion Flames," *Twenty-Third Symposium (International) on Combustion*, The Combustion Inst., Pittsburgh, PA, 1991, pp. 503-511.

VORTEX DYNAMICS IN A DRIVEN JET DIFFUSION FLAME

V. R. Katta*, K. Y. Hsu*, L. P. Goss* and W. M. Roquemore†

*Systems Research Laboratories, Inc., A Division of Arvin/Calspan, 2800 Indian Ripple Road, Dayton, OH 45440-3696, U.S.A.

†Wright Laboratory, Aero Propulsion and Power Directorate, Wright-Patterson Air Force Base, OH 45433-7103, U.S.A.

The evolution of forced vortices in a laminar jet diffusion flame was studied using a time-dependent mathematical model. The governing equations in axisymmetric form were integrated on a staggered-mesh system using a finite-difference scheme that is third-order accurate in space and time. The chemistry was simplified by assuming an infinitely fast reaction and adopting the Shvab-Zel'dovich formulation. Large vortices were generated inside the flame by ejecting additional fuel from the central nozzle periodically. Particle traces have shown that these vortices are of mushroom type having a pair of counter-rotating ring vortices. Aerodynamic stretch induced by the vortex on the flame surface is discussed in terms of instantaneous velocity and temperature fields and flame-surface movement. The calculations predicted the high fuel and oxidizer fluxes near the flame surface where local quenching was observed in the experiment.

1. INTRODUCTION

Lean blowout, high-altitude relight, emissions, and combustion efficiency are of practical importance in the design of gas turbine combustors. If accurate combustor design models are to be developed, a better understanding of the turbulent-chemistry interactions that involved in these characteristics is required. Turbulent jet diffusion flames are often studied to gain the insight needed to develop such interaction models. The classical definition of an unconfined turbulent jet diffusion flame is provided by Hottel and Hawthorne [1], i.e., a vertically-mounted jet diffusion flame is considered to be fully turbulent when its entire surface area becomes a flame brush, which means that the flame has a highly wrinkled, bumpy, or rough appearance.

Improved visualization techniques have provided additional insight into the structure of turbulent flames and the events occurring as the flame becomes turbulent [2]. The wrinkles or bumps in the flame are observed to be localized protrusions of the flame surface that result when three-dimensional fluid elements (often associated with vortices) of different size, shape, velocity, and rotational strength interact with reaction zones of different thicknesses. This interaction processes is commonly referred to as vortex-flame interaction.

An understanding of individual vortex-flame interactions is important since they form building blocks for statistical theories of turbulent flames. It is conceivable that an ensemble of only a relatively few basic types of vortex-flame interactions need to be considered to represent accurately the statistical result of what might appear, at first glance, to be an endless number of interactions.

This paper describes a numerical study on a particular type of flame-vortex interaction that was obtained in a laboratory jet diffusion flame [3]. Details on the formation of a mushroom vortex and its evolution in the flame are presented. Aerodynamic stretch that led to local quenching of the flame is discussed.

2. DRIVEN-FLAME EXPERIMENT

The experimental set-up used to generate vortices inside a laminar diffusion flame is described in detail in Ref. 3. This simple, axisymmetric, unconfined burner consists of a central fuel nozzle and a coannular air duct with exit diameters of 10 and 152 mm, respectively. The fuel nozzle is connected to the speaker chamber by means of a long tapered tube. Fuel is pumped through the side ports of the speaker chamber. An audio speaker is mounted in this chamber in such a way that the hollow cone of the

diaphragm is toward the nozzle exit. While a steady flow of fuel is maintained throughout the experiment, puffs of fuel are periodically ejected out of the nozzle by driving the speaker with a pulse generator. The flame is shielded from room-air disturbances using a low-speed air flow in the coannular duct; the duct consists of a diffuser, a contraction section and several layers of screens and honeycomb flow straighteners. This system permits a precise control of the frequency, strength, and shape of the vortex that emerges from the fuel nozzle.

Several visualization and measurement techniques are used to capture the vortex-flame interaction process. An instantaneous (phase) image obtained with the Reactive-Mie-scattering (RMS) technique [2,3] is shown in Fig. 1. With this method micron-sized TiO_2 particles, formed from the spontaneous reaction between the seeded- TiCl_4 vapor and the water vapor produced during combustion, are visualized using the Mie-scattered light from a laser sheet. TiCl_4 is seeded into the fuel flow, and the laser firing is synchronized with the speaker driving signal. Images at different phases are obtained by changing the delay between the laser firing and speaker driving signals. The luminous flame surface is also captured in Fig. 1; however, it represents the flame that is integrated over the period during which the camera shutter is open.

Figure 1 illustrates that the vortices generated are quite symmetric. The vortices are introduced into the flame at a rate of 30 per second which corresponds to the driving frequency set for the speaker pulse generator. The thin lines surrounding the vortices and the bright region near the axis of symmetry result from the green light scattered by the TiO_2 particles. The motion of the vortices has pushed the flame surface radially outward to the point where it is locally and temporally quenched.

3. MATHEMATICAL MODEL

The diffusion flame described in the previous section is formed between a central methane jet and a low-speed coannular air flow. The time-dependent governing equations which consist of mass continuity, axial and radial momentum conservation, and two scalar conservation equations [4] are solved in a cylindrical coordinate system. The body-force term due to the gravitational field is included in the axial-momentum equation. The Shvab-Zel'dovich formulation in

conjunction with the flame-sheet-reaction model is utilized to simplify the chemical-kinetics calculations. Because of this fast chemistry assumption, the present mathematical formulation cannot predict flame extinction; however, it is used primarily to explore the vortex dynamics and the aerodynamic stretch that leads to local extinction of the flame in the experiment.

The transport properties are considered to vary with temperature and species concentration. The enthalpy of each species is calculated from polynomial curve fits, while the viscosity of the individual species is estimated from Chapman-Enskog collision theory. The binary-diffusion coefficient between any two species on the fuel side of the flame is assumed to be identically equal to that between fuel and nitrogen; similarly on the oxidizer side of the flame, it is set identical to that between oxygen and nitrogen. Chapman-Enskog theory and Lennard-Jones potentials have been used to estimate these two binary-diffusion coefficients.

The finite-difference form of the governing equations is constructed on a staggered-grid system based on an implicit QUICKEST numerical scheme [4] which is third-order accurate in both space and time and has a very low numerical diffusion error. At every time-step, the pressure field is accurately calculated by solving the system of algebraic pressure Poisson equations at all grid points simultaneously using the Lower and Upper Diagonal decomposition technique. An orthogonal grid system with rapidly expanding cell sizes in both the z and r directions is utilized. The outer boundaries of the computational domain are shifted sufficiently to minimize the propagation of disturbances into the region of interest.

3. RESULTS AND DISCUSSION

Flat initial velocity profiles with measured mass-averaged values of 1.5 and 0.4 m/s are used at the exit planes of the fuel nozzle and the annulus air duct, respectively. Using a mesh size of 151×61 , calculations were first made for the unsteady flow in a 250 mm \times 150 mm computational domain. The buoyancy-influenced instability resulted in a weak, low-frequency flame oscillation (~ 20 Hz), but no vortex roll up [4] developed outside the flame surface. This is a result of the relatively high air-flow rate (0.4 m/s) used in the annulus duct.

The computational flame was driven periodically by perturbing the fuel mass-flow rate at the exit of

the fuel nozzle at a frequency of 30 Hz. The imposed velocity for a period of three perturbation cycles shown in Fig. 2 represents a weak-suction pulse for about 15 ms, followed by a sharp mass ejection for a period of 6 ms. This velocity profile was obtained using the experimentally measured maximum and minimum velocities at the center of the nozzle exit. The duration of the suction and mass-ejection pulses were then adjusted to achieve a vortex growth similar to that observed in the experiment.

3.1 Flame and vortex structures

The computed instantaneous-temperature and -velocity fields at a phase near that of the image in Fig. 1 are plotted on the left- and right-hand sides of Fig. 3, respectively. The flame surface, as identified by the mixture fraction, is also shown in Fig. 3 by solid circles. Calculations were performed for several perturbation cycles prior to the solution shown in Fig. 3 which represents the flame at (t_0+24) ms. The mass ejection at (t_0+20) ms (cf Fig. 2) has created a large vortex between the jet shear layer and the flame surface. The growth and dynamics of this vortex will be discussed in the next section.

Referring to the velocity field of Fig. 3 it should be noted that the flow at the flame surface near the vortex center (Region C in Fig. 3) is parallel to the flame surface. On the other hand, an outward flow and an inward flow are observed at the flame surfaces downstream of the vortex center (Region A) and upstream of the vortex center (Region B), respectively. The velocity normal to the flame surface in Regions A and B resembles the flow pattern of a counter-flow diffusion flame [5]. The aerodynamic stretch calculated using the instantaneous velocity field and the flame surface yielded high values in these regions. As a result one might expect local quenching in Regions A and/or B. However, in the experiment local quenching was observed near the vortex center (cf Fig. 1). The temperature field of Fig. 3 indicates that the contours are clustered in Region C and dispersed in Regions A and B. Because of the unity-Lewis-number assumption used in this calculation, the distributions of fuel and oxidizer follow that of temperature. Therefore, the higher fuel and oxidizer fluxes in Region C are indicative of greater local flame stretch compared to that in Region A or B. A simulation with finite-rate chemistry might also predict local quenching in Region C because of the higher mass fluxes.

The confusion with flame stretch calculated using instantaneous velocity data may be resolved by considering the dynamics of the flame. In a diffusion flame the stoichiometric (or flame) surface becomes established at a location where the fuel- and oxidizer-mass fluxes are balanced. The outward flow along the flame surface in Region A increases the fuel flux and decreases the oxidizer flux. As a result, the flame at this location moves toward the air side. Similarly, the flame surface upstream of the vortex center (Region B) penetrates into the region between the vortex and the fuel jet. The motion of the flame surface in these two regions (A and B) is such that it reduces the aerodynamic stretch on the flame. On the other hand, the flame surface in Region C has been radially pushed to $r = 15$ mm from the unperturbed-flame location of $r = 8.5$ mm, and this displacement is the maximum compared to that at any other location on the flame surface. This rapid motion creates a strong stretch on the flame in Region C, even though the instantaneous velocity field is generating a negligible stretch there.

3.2 Vortex and flame evolution

The Reactive-Mie-Scattering image of Fig. 1 shows a double-vortex (or mushroom-vortex) structure, whereas the calculations in Fig. 3 indicate only a single-vortex structure. This is resulting from the differences in the visualization techniques used in the experiment and the calculation. As discussed earlier, the image in Fig. 1 represents the location of TiCl_4 particles at the instant of laser firing. Thus, particle traces and streaklines might provide an image that is similar to the one obtained using the experimental visualization technique.

The vortex structure and flame surface at different times between t_0+24 and t_0+30 ms are shown in Fig. 4. Sets of massless particles along a line at the fuel nozzle exit were released at a rate of 20 sets per ms. Instantaneous locations of all the particles are plotted at four different times in Fig. 4. The location of the stoichiometric (or flame) surface is shown by solid circles. Note that Figs. 4(b) and 3 represent solutions at the same instant of time. Particle-trace plots clearly identify the mushroom-vortex structure associated with mass ejection. The scenario for the formation of the mushroom-vortex and its evolution in a diffusion flame is as follows.

When the fluctuating velocity (Fig. 2) was superimposed on the steady-fuel flow of 1.5 m/s, the

resulting velocity at the nozzle exit temporarily became zero between t_0+12 and t_0+20 ms. This stagnant flow condition at the nozzle exit caused the flame surface and, thereby, the viscous fluid to approach the axis. The additional fuel ejected suddenly with a velocity of 6 m/s (modified velocity of 7.5 m/s) collided with the column of viscous combustion products and then traveled radially outward. As the density of this column decreased with radial distance (minimum at the flame surface), the ejected fuel moved downstream more easily near the flame surface than at the center, as is evident from the convex-shaped (with respect to the fuel flow) particle line, P, in Fig. 4(a). This process resulted in a mushroom vortex that traveled radially toward the flame surface [cf Figs. 4(a) and (b)]. The higher viscosity of the combustion products in the secondary vortex is partly responsible for its smaller size as compared to that of the primary vortex.

The mass-ejection pulse is complete at about t_0+25 ms (cf Fig. 2), and maximum growth for the mushroom vortex is reached at a phase shown in Fig. 4(b). The particle line, P, is nearly horizontal and compares favorably with that observed in the experiment (Fig. 1). In 2 ms [Figs. 4(a) and (b)], the flame surface near the vortex center has moved radially from 10 to 15 mm, yielding an average velocity of ~ 2 m/s. The mushroom vortex at times greater than t_0+26 ms is simply rotating counterclockwise [Figs. 4(c) and (d)] without having a further radial movement. The higher fuel jet velocity (1.5 m/s) is responsible for this rotation. When the secondary vortex [upper one in Fig. 4(b)] moved to the left of the primary vortex in Fig. 4(c), it also approached the flame surface. Entrainment of viscous combustion products into the secondary vortex further dissipated it. The general entrainment of fluid by the fuel jet in Fig. 4(d) pulled the mushroom vortex near the axis. Acceleration of the primary vortex by the fuel jet began to cause its separation from the secondary one. Meanwhile, the flame structure upstream of $z = 25$ mm returned to its unperturbed position, and another driving cycle followed.

4. CONCLUSIONS

The dynamic characteristics of a vortex-flame interaction that had been studied experimentally were examined using numerical simulations. Large mush-

room vortices inside a laminar, methane jet diffusion flame were generated by periodical perturbation of the fuel jet velocity. The simulated vortex structure and its evolution closely resembled that observed in the experiment. It was found that instantaneous flowfield data are insufficient to present a correct description of the aerodynamic stretch along the flame surface. Rapid movement of the flame surface (~ 2 m/s) is believed to be responsible for developing localized high-stretch regions in the diffusion flame considered here. The model was able to predict the high concentrations of species near the flame surface where quenching was experimentally observed. However, because of the fast-chemistry assumption the model could not predict the local and temporal quenching of flame.

5. ACKNOWLEDGEMENT

This work was supported in part by Air Force Contract F33615-90-C-2033 and the Air Force Office of Scientific Research. The authors would like to thank Mrs. Marian Whitaker for help in preparing the paper.

REFERENCES

1. Hottel, H. C. and Hawthorne, W. R., in 3rd Symp. (Int.) on Combustion, Flame and Explosive Phenomena, The Combustion Institute, 1949, 254-266.
2. Roquemore, W. M., Chen, L.-D., Goss, L. P., and Lynn, W. F., in Turbulent Reactive Flows, Lecture Notes in Engineering, Vol. 40, Springer Verlag, 1989, 49-63.
3. Hsu, K.Y., Chen, L.-D., Katta, V. R., Goss, L. P., and Roquemore W. M., AIAA Paper 93-0455, 31st Aerospace Sciences Meeting, Reno, 1992.
4. Katta, V. R., Goss, L. P., and Roquemore, W. M., AIAA Paper 92-0335, 30th Aerospace Sciences Meeting and Exhibit, Reno, 1992.
5. Dixon-Lewis, G., in 23rd Symp. (Int.) on Combustion, The Combustion Institute, 1990, 305-324.



Fig. 1 Driven methane jet diffusion flame. Instantaneous Reactive-Mie-Scattering Image.

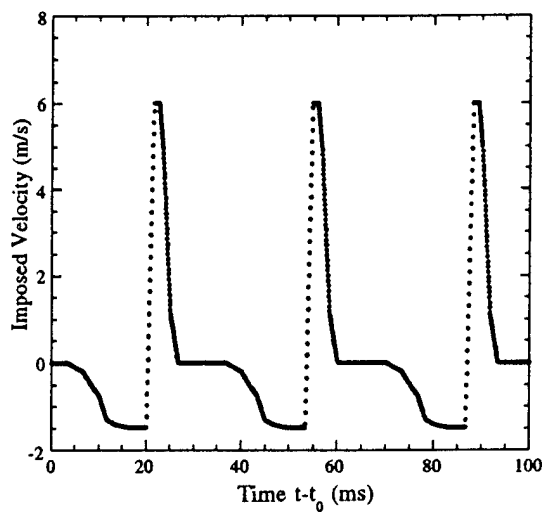


Fig. 2. Velocity fluctuations used in numerical simulation. Unperturbed fuel jet velocity is 1.5 m/s.

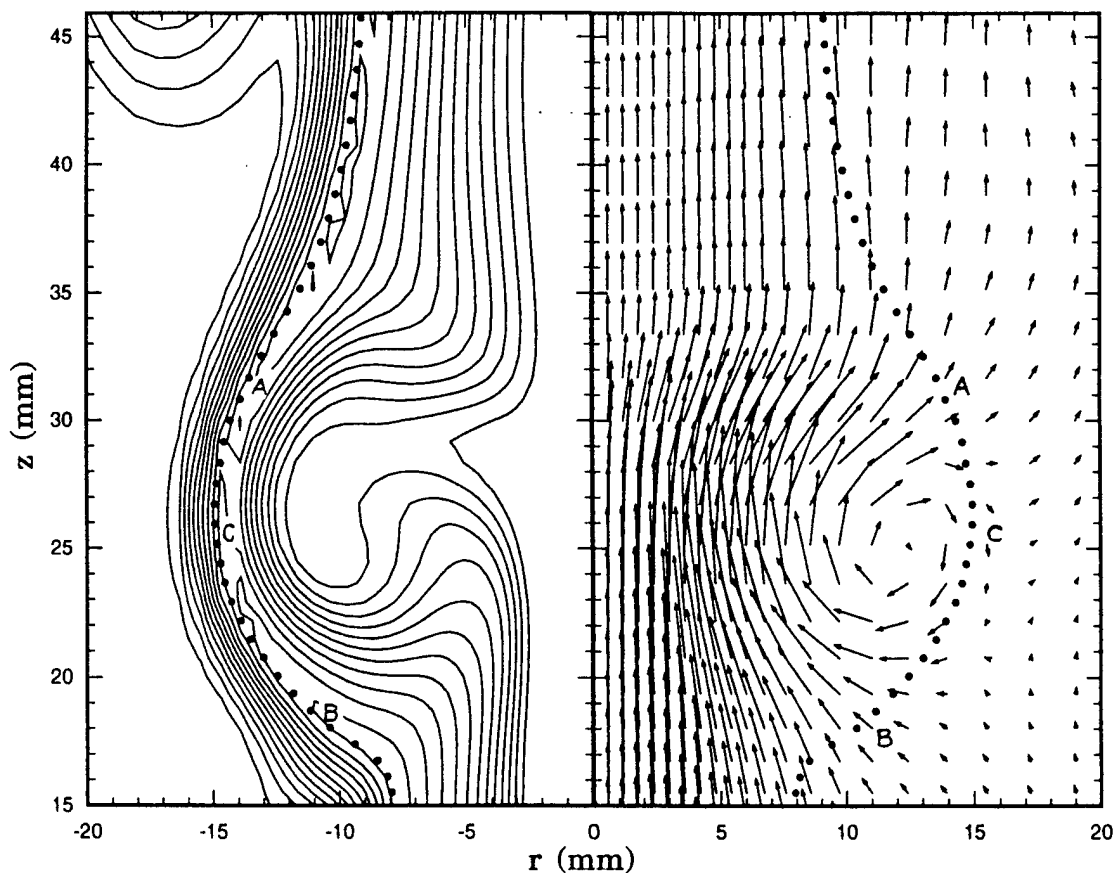


Fig. 3 Computed iso-temperature contours and velocity field at $t_0 + 26$ ms.

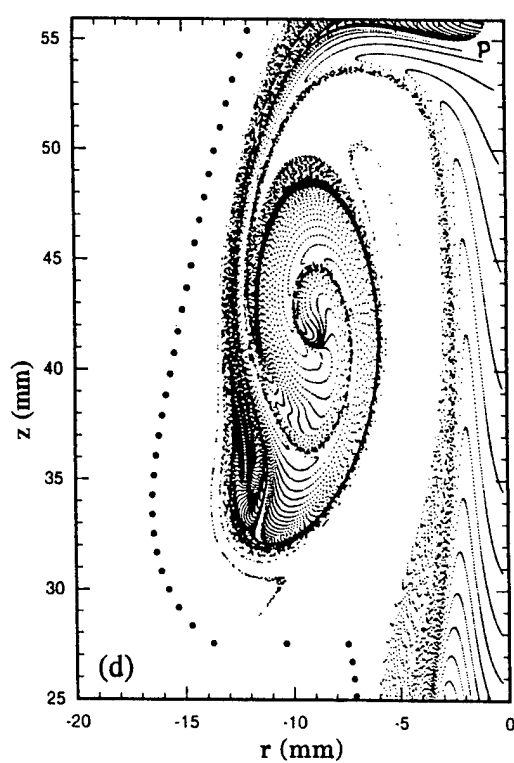
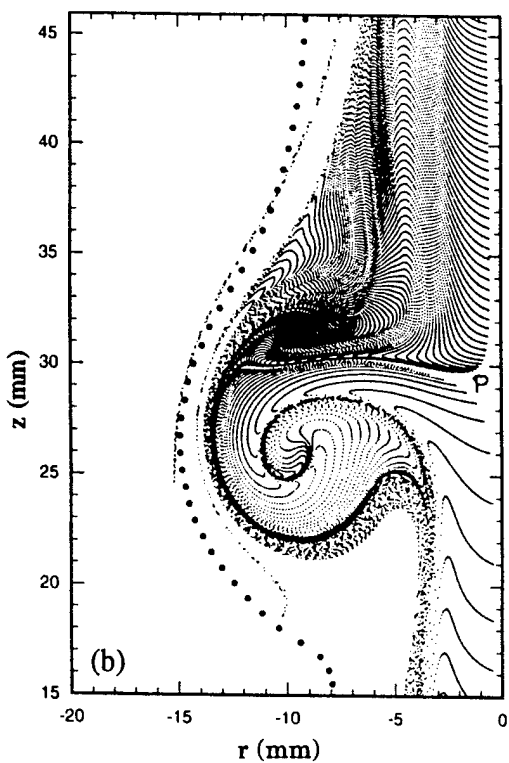
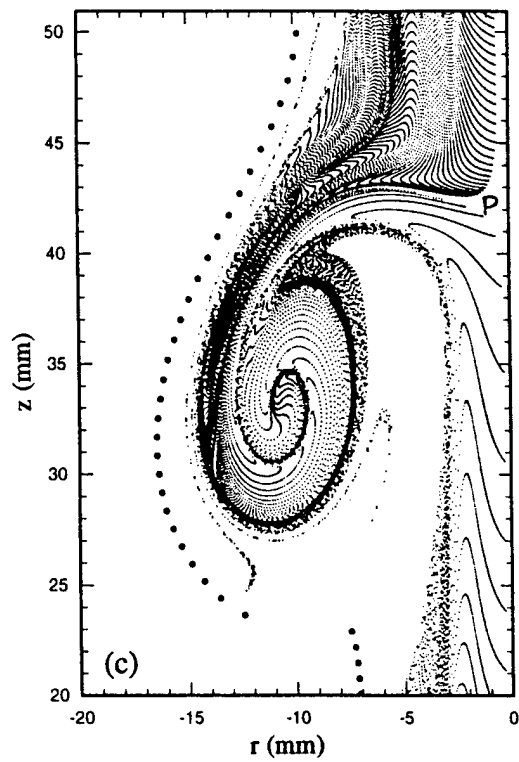
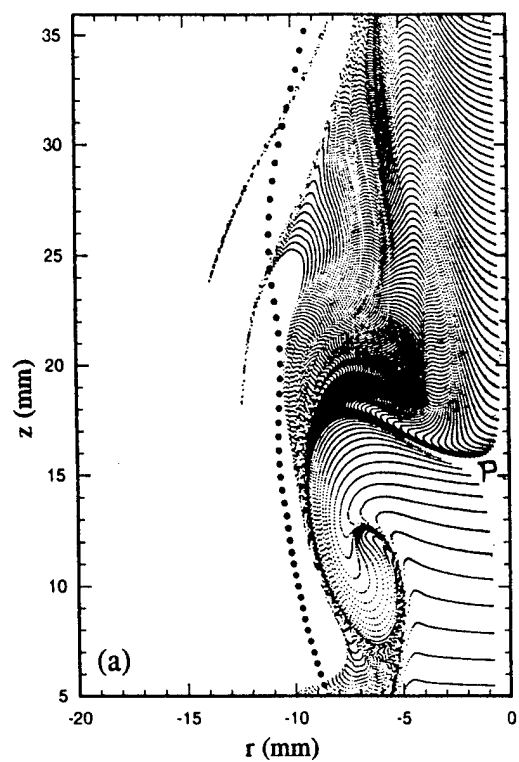


Fig. 4 Vortex evolution. a) $t_0 + 24$ ms, b) $t_0 + 26$ ms, c) $t_0 + 28$ ms, and c) $t_0 + 30$ ms.

Study of Flame Stability in a Step Swirl Combustor

M. D. Durbin

M. D. Vangsness

D. R. Ballal

Fellow ASME

University of Dayton,
Dayton, OH 45469

V. R. Katta

Innovative Scientific Solutions, Inc.,
Dayton, OH 45430

A prime requirement in the design of a modern gas turbine combustor is good combustion stability, especially near lean blowout (LBO), to ensure an adequate stability margin. For an aeroengine, combustor blow-off limits are encountered during low engine speeds at high altitudes over a range of flight Mach numbers. For an industrial combustor, requirements of ultralow NO_x emissions coupled with high combustion efficiency demand operation at or close to LBO. In this investigation, a step swirl combustor (SSC) was designed to reproduce the swirling flow pattern present in the vicinity of the fuel injector located in the primary zone of a gas turbine combustor. Different flame shapes, structure, and location were observed and detailed experimental measurements and numerical computations were performed. It was found that certain combinations of outer and inner swirling air flows produce multiple attached flames, a flame with a single attached structure just above the fuel injection tube, and finally for higher inner swirl velocity, the flame lifts from the fuel tube and is stabilized by the inner recirculation zone. The observed difference in LBO between co- and counterswirl configurations is primarily a function of how the flame stabilizes, i.e., attached versus lifted. A turbulent combustion model correctly predicts the attached flame location(s), development of inner recirculation zone, a dimple-shaped flame structure, the flame lift-off height, and radial profiles of mean temperature, axial velocity, and tangential velocity at different axial locations. Finally, the significance and applications of anchored and lifted flames to combustor stability and LBO in practical gas turbine combustors are discussed.

Introduction

A prime requirement in the design of a modern gas turbine combustor is good combustion stability, especially near lean blowout (LBO), to ensure an adequate stability margin. For an aircraft engine, combustor blow-off limits are encountered during low engine speeds at high altitudes over a range of flight Mach numbers and a good design ensures that the combustor steady-state burning remains within the operating envelope. This envelope should be extensive enough to encompass the under- and overshoots associated with the different response rates to the throttle movements of the fuel system and the rotating machinery. For an industrial combustor, requirements of ultralow NO_x emissions coupled with high combustion efficiency demand operation at or close to LBO, thereby eroding the safety margins. Therefore, a fundamental study of flame stability in a model step swirl combustor (SSC) has important practical applications, and this provided a strong motivation to undertake the present investigation.

The physical mechanisms responsible for the stabilization of a flame on the fuel injector lip (in the near-field region) are not fully understood. In the past, the stabilization mechanism of free jet diffusion flames has been investigated by Vanquickenborne and van Tiggelen (1966), Gollahalli et al. (1985), Pitts (1988, 1990), Bradley et al. (1990), Takahashi et al. (1984, 1990), and Takahashi and Goss (1992). A prime goal of these investigations was to predict flame blowout accurately. For example, Vanquickenborne and van Tiggelen (1966) developed the stabilization criterion that the total approach velocity should be balanced by the turbulent burning velocity of the mixture. Takahashi et al. (1984) found that the local velocities in the vicinity of an attached flame are laminar, and the flame stability mechanism is the balance of the total approach velocity

in the attached flame zone with the laminar burning velocity of the mixture. However, in a modern annular gas turbine combustor, the flame is stabilized by producing a swirl-induced recirculation zone in the flow field. This zone is generated by a combination of three mechanisms: an axial swirling air jet associated with each fuel introduction, sudden expansion of the axial swirling jets as they enter the primary zone, and back pressure provided by an array of radial air jets at the end of the primary zone. An SSC was designed to reproduce this type of complicated recirculation flow pattern. This paper discusses the different shapes, structure, and location of the stabilized flame in the SSC and how these various factors affect LBO.

Test Facility

The SSC. Figure 1 shows a schematic diagram of the SSC, which has a 150 × 150-mm cross section with rounded corners, length of 754 mm, and a step height of 55 mm. The SSC provides a geometrically simple, optically accessible research combustor capable of reproducing the fuel-air mixing pattern downstream of the airblast atomizer located in the dome region of a modern annular gas turbine combustor. The SSC also offers independent control over inner and outer airstreams. The SSC was mounted on a vertical combustion tunnel with a three-axis traversing mechanism.

Fuel was supplied to the combustor by the annular fuel tube (20 mm i.d. and 29 mm o.d.), which is coaxially sandwiched between swirling airstreams: the inner air jet (20-mm-dia) and the outer annular air jet (29 mm i.d. and 40 mm o.d.). The combustor exit has a 45 percent blockage orifice plate on top, which simulates the back pressure exerted by the dilution jets in a practical gas turbine combustor (see Sturgess et al., 1990). The SSC has quartz windows on all four sides to permit visual observations and laser diagnostics measurements. The stationary helical vane swirlers were located 25 mm upstream from the burner tube exit in each of the air passages. The inner swirler has six vanes with a central 1.4-mm-dia hole to prevent the flame from anchoring to the swirler. The outer swirler has

Contributed by the International Gas Turbine Institute and presented at the 40th International Gas Turbine and Aeroengine Congress and Exhibition, Houston, Texas, June 5-8, 1995. Manuscript received by the International Gas Turbine Institute February 10, 1995. Paper No. 95-GT-111. Associate Technical Editor: C. J. Russo.

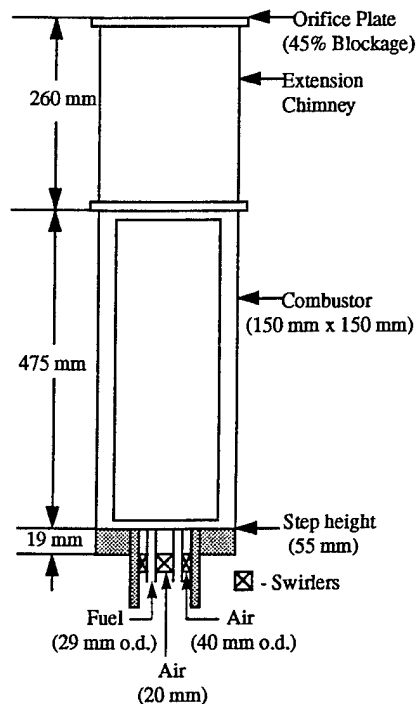


Fig. 1 Schematic diagram of a step swirl combustor

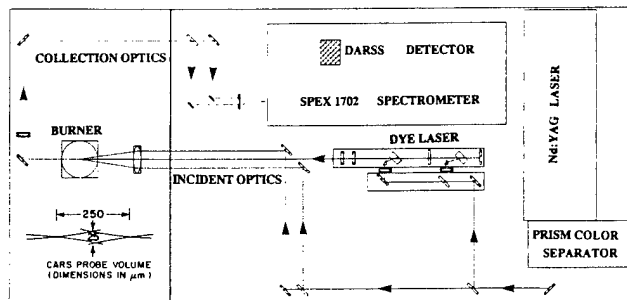


Fig. 2 Schematic of the CARS system optics

twelve vanes. Inner swirler lengths are 25 and 19 mm, respectively, for 30 and 45 deg swirlers; outer swirler length was 32 mm for the 30 deg swirler. Swirler lengths and number of vanes were adequate to ensure that the air closely follows the swirl vane angle. The swirlers were precision-fabricated in a rapid prototype manufacturing process known as stereolithography. These swirlers performed satisfactorily at the level of high temperatures present in the SSC.

Instrumentation

CARS System. Figure 2 shows a schematic of a Coherent Anti-Stokes Raman Spectroscopy (CARS) optics system, which was used for nonintrusive flame temperature measurements. Pan et al. (1991) have provided detailed information on

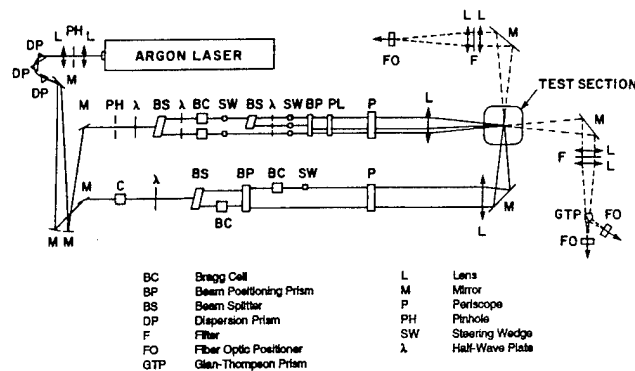


Fig. 3 Schematic of the LDA system optics

CARS measurements. Briefly, the CARS signal was generated by combining two 30 mJ doubled Nd:Yag beams at 532 nm and one 25 mJ broad band dye laser beam centered at 607 nm and pumped by the same Nd:Yag laser. The pulse laser and detector camera run at 10 Hz. A Boxcars configuration with an ellipsoidal probe volume approximately $25 \mu\text{m}$ (dia) \times $250 \mu\text{m}$ (length) was used for collecting the signal. The detector is a Princeton Instruments intensified 576×384 charge coupled device (CCD). The intensifier is triggered by a Princeton PG-10 pulser. A Princeton ST-130 controller operates the camera and the detector chiller. The collection process is controlled by Princeton's ST-130 CSMA software package running on a personal computer. Spectra are fit to a library of spectra by a nonlinear fitting routine running on a personal computer. A total of 250 samples were taken for each CARS temperature measurement.

LDA System. Figure 3 illustrated the optical setup of the LDA system. Nonintrusive velocity measurements were made using a Dantec Fiber-Flow LDA system. Essentially, this LDA system is an upgraded version of the system used by Durbin and Ballal (1996). The two-dimensional LDA system uses the 514 nm and 488 nm lines from an argon-ion laser. The laser output is directed into a Dantec Fiber flow transmitter where the colors are separated and directed to optical fiber couplers by a Bragg cell operating at 40 MHz. The four beams are guided to the probe via polarization preserving fibers. The recollimated and focused laser beams cross to produce an ellipsoidal probe volume approximately $100 \mu\text{m}$ (dia) \times $1000 \mu\text{m}$ (length). A fluidized-bed seeder was used to inject submicron-sized (97 percent $< 1 \mu\text{m}$) ZrO_2 particles into each burner tube passage. Velocity biasing was resolved by seeding one passage at a time in a manner similar to Takahashi et al. (1992). The forward scattered signal is collected and separated by dichroic mirrors before it is detected by photomultiplier tubes and processed by individual TSI burst counters. Typical coincident sampling rates exceeded 1 kHz in flames. A total of 2048 coincident samples were collected for each velocity measurement. Custom-designed software was used to reduce the data on a personal computer. Three-component noncoincident velocity measurements were made with the two-dimensional LDA system by scanning in the transverse and radial directions to get axial and

Nomenclature

k = turbulent kinetic energy
 Re = Reynolds number
 T = mean temperature
 U, W = mean axial and tangential velocities, respectively

X, Y, Z = transverse, radial, and axial directions, respectively
 ϵ = turbulent-energy dissipation rate
 θ = swirl vane angle
 ϕ = overall equivalence ratio

Subscripts

f = fuel
 i = inner
 o = outer

Table 1 Test matrix for the step swirl combustor experiments (all tests at room temperature and atmospheric pressure)

Variable	Range
Inner vane angle, θ_i , degrees	0, 30 and 45
Outer vane angle, θ_o , degrees	30
Vane configuration	co and counter-swirl
Inner air velocity, U_i , m/s	14.4
Re	18.0×10^3
Outer air velocity, U_o , m/s	8.6
Re	14.8×10^3
Fuel velocity, U_f , m/s	2.5
Re	3.2×10^3
Equivalence ratio, ϕ	0.9
Fuel	methane

tangential velocities, and axial and radial velocities, respectively.

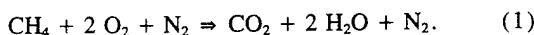
Test Conditions. Table 1 lists all the test conditions. Durbin and Ballal (1996) have shown that increasing the inner vane angle increases turbulent mixing and strengthens the inner recirculation zone; these changes dramatically affect the flame structure and the stability characteristics. Therefore, experiments were performed to reveal the differences in flame structure by changing the inner vane angle. Test conditions were also chosen to compare: (i) attached versus lifted flames and (ii) co-versus counterswirl configurations.

Experimental measurements included flame photography, three-component mean and rms velocities, mean and rms temperatures, and LBO. The LBO data were collected by maintaining a constant airflow rate, heating the combustor to a near steady-state temperature at stoichiometric fuel-air ratio, and then gradually decreasing the fuel flow rate until blowout occurred. This is a standard procedure that has been adopted in our laboratory since the work of Sturgess et al. (1991).

Turbulent Combustion Model

A time-dependent axisymmetric model, which solves axial and radial-momentum equations, continuity, swirl, turbulent energy (k), turbulent-energy dissipation (ϵ), and enthalpy and species conservation equations was used to simulate the flow-field in the SSC. The standard isotropic κ - ϵ turbulence model was incorporated into this code. Details are described by Katta and Roquemore (1993) and Katta et al. (1994). Briefly, in this turbulence model, density (ρ) was obtained by solving the state equation while pressure field at every time step is determined from pressure Poisson equations. Even though all the governing equations were solved in an uncoupled manner, the turbulence and species conservation equations are coupled through the source terms during the solution process to improve the stability of the algorithm.

In the present analysis of reacting flows, a simple global-chemical-kinetics model involving methane, oxygen, water, carbon dioxide, and nitrogen was used as follows:



The specific reaction rate for Eq. (1) was written in Arrhenius form with an activation energy of 20 kcal/mole and pre-exponential of $2.0 \times 10^{19} \text{ m}^6/\text{mole}^2/\text{s}$. These rate constants were determined by predicting the lift-off of a 8 m/s laminar methane jet flame (Katta, 1995).

An orthogonal, staggered grid system with varying cell sizes in both the z and y directions was utilized. The momentum and swirl equations were integrated using an implicit Quadratic Upstream Interpolation for Convective Kinematics with Estimated Streaming Terms (QUICKEST) numerical scheme

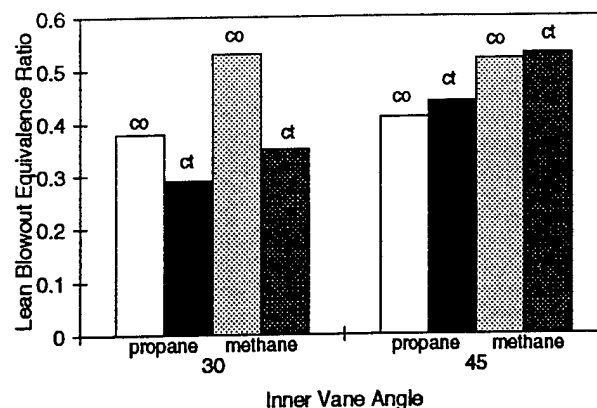


Fig. 4 Lean blowout data comparing inner vane angle, co-swirl (co) and counter-swirl (ct), and methane with propane. Test conditions were $\theta_o = 30^\circ$, $\phi = 0.9$, $U_i = 14.4 \text{ m/s}$, $U_o = 8.6 \text{ m/s}$, $U_f = 2.5 \text{ m/s}$.

(Katta et al., 1994; Leonard 1979), which is third-order accurate in both space and time and has a very low numerical diffusion error. On the other hand, the species, enthalpy, and turbulence-energy conservation equations, which have relatively large source terms, were integrated using the hybrid scheme of Spalding (1972). By rearranging the terms, the finite-difference form of each governing equation at all grid points was written as a system of algebraic equations, which was then solved by using Alternative Direction Implicit (ADI) technique. The time increment, Δt , was determined from the stability constraint and maintained as a constant during the entire calculation. The pressure field at every time step was accurately calculated by simultaneously solving the system of algebraic pressure Poisson equations at all grid points using the LU (Lower-Upper) decomposition technique.

Temperature- and species-dependent thermodynamic and transport properties were used in this formulation. The enthalpy of each species was calculated from polynomial curve-fits, while the viscosity, thermal conductivity, and diffusion coefficients of the species were estimated from the Leonard-Jones potentials. Measured velocity profiles were used at the fuel and air inflow boundaries. All other flow variables (k , ϵ , mass fractions, and T) along these boundaries were assumed to be distributed uniformly. A simple extrapolation procedure (Katta et al., 1994) with weighted zero- and first-order terms was used to estimate the flow variables on the outflow boundary. The usual no-slip, adiabatic, and chemically inert boundary conditions were applied at the walls. Wall functions were used for determining the gradients of the flow variables near the walls.

Results and Discussion

Experimental Observations

Flame Stability. LBO data were collected for all test conditions. In addition, some propane LBO data were collected to examine fuel effects on flame stability. Figure 4 shows LBO data comparing co- and counterswirl and propane with methane. These differences will be discussed after examining flame characteristics utilizing long exposure flame photographs taken with a 35-mm camera. Figure 5(a-e) reveal dramatic flame structure differences in the five test configurations. The only two variables in test conditions for the five cases were inner vane angle and co- or counterswirl configuration. Test conditions were $\theta_o = 30^\circ$, $\phi = 0.9$, $U_i = 14.4 \text{ m/s}$, $U_o = 8.6 \text{ m/s}$, $U_f = 2.5 \text{ m/s}$, using methane fuel.

Figure 5(a) shows that no swirl in the inner air stream produces a long tubelike central flame structure. The 30 deg outer swirl produces an outer flame structure, which approximates the 30 deg pattern. The attached flame appears to be stabilized

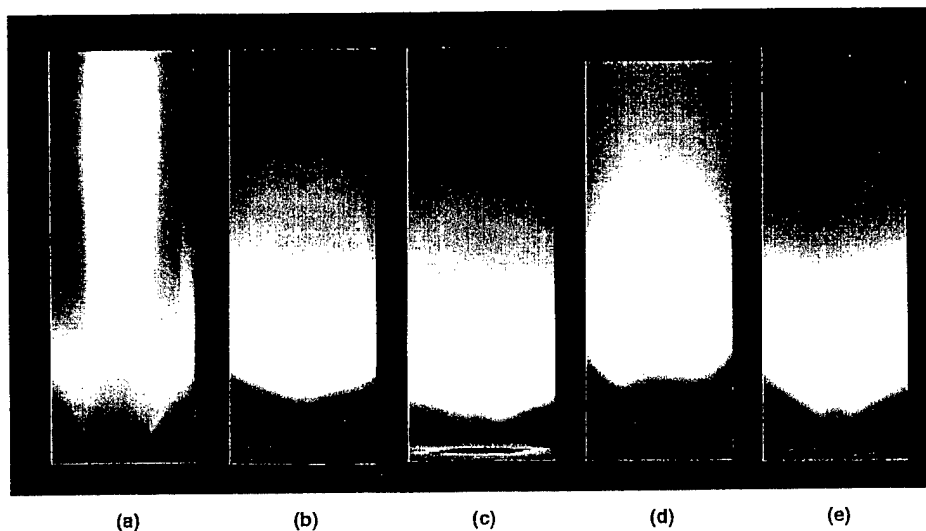


Fig. 5 Photographs illustrating the flame structure for (a) $\theta_i = 0$ deg, (b) $\theta_i = 30$ deg coswirl, (c) $\theta_i = 45$ deg coswirl, (d) $\theta_i = 30$ deg counterswirl, and (e) $\theta_i = 45$ deg counterswirl. Test conditions were $\theta_o = 30$ deg, $\phi = 0.9$, $U_i = 14.4$ m/s, $U_o = 8.6$ m/s, $U_r = 2.5$ m/s, methane.

at the inner air side of the fuel tube and also at the outer air side of the fuel tube. Small traces of flame structure outside the outer air stream are also visible and this can only occur if the fuel penetrates the fast-moving outer air stream or if the fuel recirculates in the outer recirculation zone before burning. It is suspected that the dynamic characteristics of the turbulent flow bring packets of fuel into the recirculation zone and these packets, in turn, burn in the mixing layer of the outer air and the recirculation zone. Sturgess et al. (1991) have observed similar results for a flame stabilized in the outer recirculation zone. This dynamic turbulent exchange phenomenon is more dramatic for an outer vane angle of 60 deg, which produces a stronger outer recirculation zone.

Figure 5(b) shows a flame photograph with coswirl configuration and 30 deg inner vane angle. The flame is lifted, there is premixing at its base, and it stabilizes with a dimple shape within the inner recirculation zone. The flame lifts because the

inner air stream penetrates the fuel stream with a velocity too high for an attached flame to stabilize and the flame is blown downstream. Also, the inner recirculation is caused by the inner air stream pushing out toward the wall, leaving a low-pressure region in the central portion of the combustor. Chen and Driscoll (1988) have made similar observations on the formation and structure of an inner recirculating vortex. Figure 5(c) shows that increasing the inner vane angle from 30 deg coswirl to 45 deg coswirl widens the flame shape and decreases the lift height. This occurs because an increase in vane angle increases the size and strength of the inner recirculation zone but it does not change the stability mechanism; i.e., flame is still stabilized within the inner recirculation zone.

Figure 5(d) shows the flame structure for 30 deg inner vane angle counterswirl. The flame has a bulbish shape above the fuel tube. Decreasing the fuel flow velocity causes the flame attachment just above the fuel tube. Figure 5(e) shows that

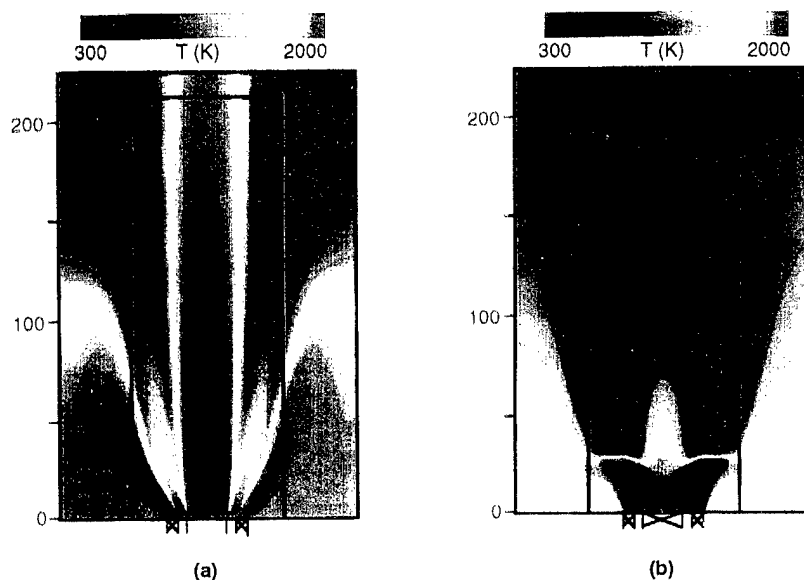
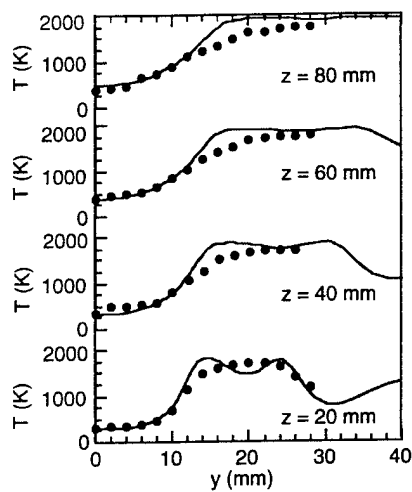
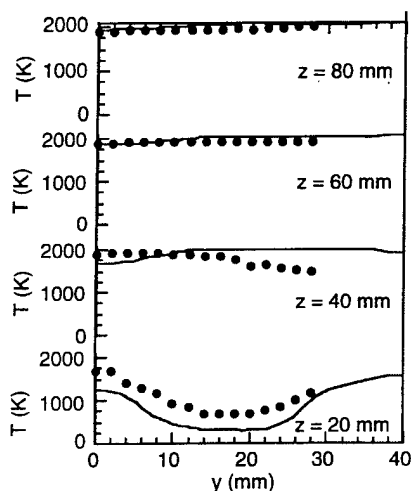


Fig. 6 Computed temperature distribution in SSC for (a) $\theta_i = 0$ deg and (b) $\theta_i = 30$ deg coswirl. Test conditions are identical to Figs. 5(a) and 5(b), respectively.



(a)



(b)

Fig. 7 Radial temperature profiles at different axial locations for (a) $\theta_i = 0$ deg, and (b) $\theta_i = 30$ deg. Test conditions correspond with Figs. 5(a) and 5(b), respectively. ● Experimental, — computational.

increasing the inner vane angle from 30 deg counterswirl to 45 deg counterswirl causes too much penetration of the inner air into the fuel zone and this causes the flame to lift and stabilize within the inner recirculation zone.

Lean Blowout. Figure 4 shows LBO data comparing co- and counterswirl for two values of the inner vane angle, namely 30 and 45 deg, for both methane and propane gaseous fuels. The propane data were taken at identical test conditions for comparison purposes. Three observations can be made:

1 LBO values were found to be lower with propane fuel than with methane fuel for all the conditions of the tests. A plausible explanation is that the air/methane mass velocity ratio $(\rho U)_a/(\rho U)_m$ is higher than the corresponding air/propane ratio; this produces enhanced methane-air mixing (as compared to propane-air mixing) and hence a higher value of LBO. Figures 5(b), 5(c), and 5(e) for methane flames clearly show an evidence of premixing at the flame base followed by a lifted flame structure stabilized in the inner recirculation zone.

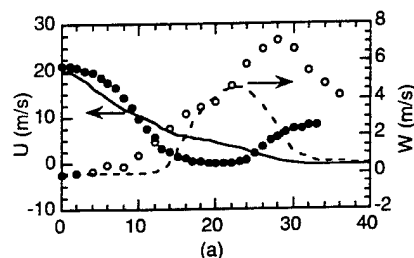
2 For a 30 deg inner vane angle, LBO values were lower for counterswirl as opposed to coswirl flow direction. This result

arises because for the counterswirl flow, shearing braids cause lower air velocities just above the fuel tube leading to an attached flame (which has a lower value of LBO); in contrast the coswirl flow gives higher axial mean velocity directly above the fuel tube, causing the flame to lift from the fuel tube thereby compromising flame stability; i.e., higher values of LBO are obtained.

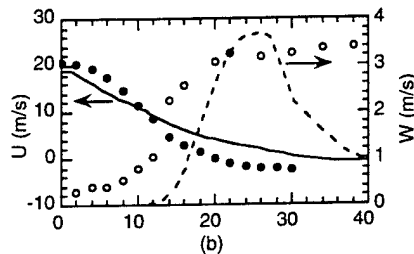
3 As the inner vane angle is increased from 30 to 45 deg, LBO values increase correspondingly and also LBO becomes less sensitive to swirl flow direction. This happens because the higher (45 deg) inner swirl angle directs more inner airflow toward the fuel tube, causing the flame to lift. This lifted flame produces higher values of LBO.

Analysis

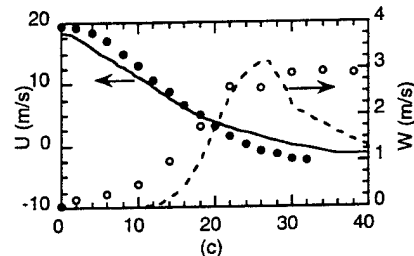
Flame Stability—Computed Results. Predictions were made for different flow conditions using the turbulent combustion model described earlier. Results in the form of temperature distributions for zero- and 30 deg inner coswirl cases (corresponding to Figs. 5(a) and 5(b) are shown in Figs. 6(a) and 6(b), respectively. Measured axial, radial, and tangential velocity profiles at the exits of the inner-air and fuel tubes and turbulent mass-averaged outer air velocity obtained from the volu-



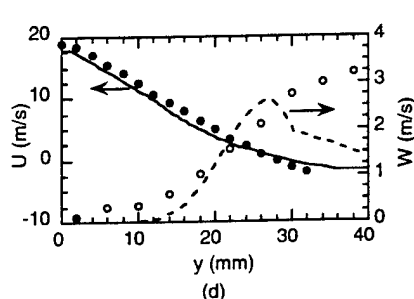
(a)



(b)



(c)



(d)

Fig. 8 Calculated and measured velocities for $\theta_i = 0$ deg case at axial locations (a) 20 mm, (b) 40 mm, (c) 60 mm, and (d) 80 mm. Circles and lines represent measured and computed velocities, respectively.

metric flow rate provided the inlet boundary conditions for these predictions. Figures 6(a) and 6(b) show the predicted flame images, i.e., temperature distributions corresponding to flame photographs shown in Figs. 5(a) and 5(b). Note, the inner box marked on the computed-flame images corresponds with the dimensions of the flame photographs. The following observations were made from the calculated temperature fields: (i) In Fig. 6(a) (zero inner swirl), the computations correctly predicted the locations of flames on either side of the fuel jet. (ii) In Fig. 6(b) (30 deg coswirl), a recirculation bubble develops inside the inner air jet and it produces the dimple-shaped flame, and (iii) the lift-off height for case (ii) predicted by the model matches well with the experimental data. These computations support the qualitative observations on flame photographs described above.

The calculated radial temperature profiles at different axial locations are compared with the measured data in Figs. 7(a) and 7(b) for zero swirl and 30 deg swirl cases, respectively. In Fig. 7(a), in the absence of swirl, the inner air jet spreads gradually, leading to a long tubelike inner flame. Both the calculations and measurements show that the temperature at the center of the SSC over the measurement range ($z = 0$ to 80 mm) is nearly the same as that of the room temperature air.

Figures 8 and 9 illustrate a comparison between predicted and measured velocities for the zero and 30 deg swirl cases, respectively. Axial (U) and swirl (W) velocity components were compared at different axial locations. For the no-swirl case, calculated velocity profiles agreed well with the experimental data. With 30 deg inner swirl, the measured swirl velocity was generally higher than the predictions, especially in the regions $Y > 22$ mm. Since the outer air was not seeded and the outer velocity profile was approximated, there are discrepancies at locations radially away from the outer jet.

In summary, our simple turbulence model with a single-step global-chemical-kinetics provides a reasonable prediction of flame shape and location, flame temperatures, and axial and swirl velocities. Wherever differences exist between predictions and measurements, an explanation is offered and further investigations along those lines are proceeding.

Flame Shape, Structure, and Location. From the examination of numerous flame photographs and the detailed numerical computations, flame stability in the SSC at the tested flow conditions primarily depends upon the attached flame and the lifted flame processes as sketched in Fig. 10 and described below. Sturgess et al. (1991) and Sturgess and Shouse (1993) have found that studies of such fundamental flame stability processes have great relevance to flame stability in modern annular gas turbine combustors.

1 Multi-attached flame. This type of attached flame is sketched in Figs. 10(a, b). As shown in Fig. 10(a), for the combination of strong outer swirl (60 deg) and zero inner swirl, the flame is simultaneously attached at three locations: (i) inner air side of the fuel stream, (ii) outer air side of the fuel stream, and (iii) outside of the outer air stream. It may be postulated that the dynamic characteristics of the flow bring packets of fuel into the outer recirculation zone, then burn in the mixing layer of the outer air and the recirculation zone. As the strength of the outer air swirl is decreased (30 deg) the attached flame structure shifts to that sketched in Fig. 10(b) where the flame no longer has an attachment on the outer air side of the fuel stream.

2 Single-attached flame. Figure 10(c) illustrates this single attached flame structure. This type of attached flame is observed for low inner (30 deg) and outer (30 deg) counterswirling air flows. Such flow conditions cause the collapse of the twin attached flame structure sketched in Fig. 10(b) to a

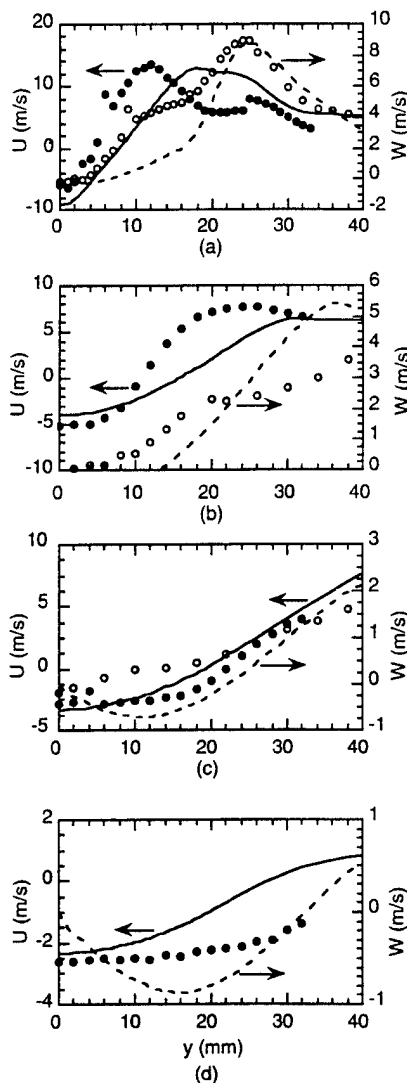


Fig. 9 Calculated and measured velocities for $\theta_i = 30$ deg case at axial locations (a) 20 mm, (b) 40 mm, (c) 60 mm, and (d) 80 mm. Circles and lines represent measured and computed velocities, respectively.

single attachment just above the fuel tube. This type of attached flame was also observed for the coswirl configuration but at a lower combustor loading.

3 Lifted flame. Figure 10(d) illustrates this type of flame; also it is observed in the photographs of Figs. 5(b), 5(c), and 5(e). The flame lifts from the fuel tube lip because of the high mean axial velocity in the near-field region above the fuel tube. The lifted flame is stabilized by the inner recirculation zone. However, increasing the swirl intensity and/or combustor loading only slightly changes flame stability, i.e., LBO values remain fairly constant for lifted flames. This is because the lifting of a flame is usually accompanied by a premixing of fuel and air at the base of the flame. This premixing compromises the stability of the lifted flame over that of an attached flame, i.e., LBO values are higher for a lifted flame than for an attached flame.

Now, it is also clear that the observed difference in LBO between co- and counterswirl configurations, as shown in Fig. 4, is primarily a function of how the flame stabilizes. Counterswirl conditions readily produce an attached flame for moderate inner swirl intensity (30 deg); however, both configurations produce lifted flames for higher swirl intensity (45 deg) and for this

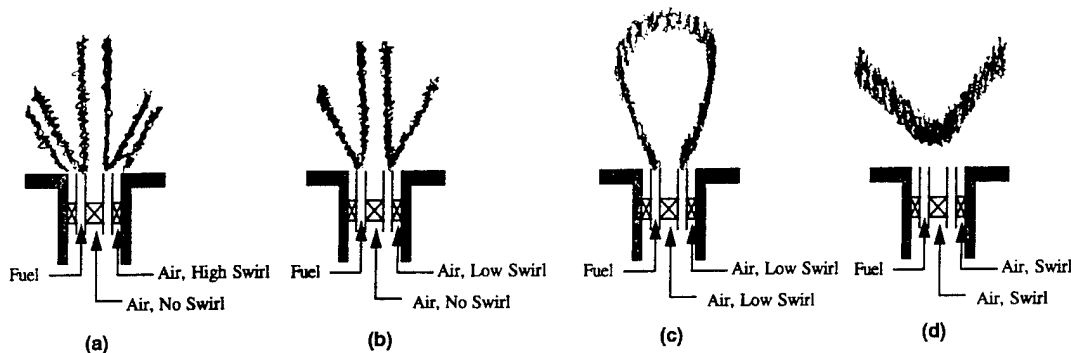


Fig. 10 Sketches illustrating the flame shape, structure, and location in the SSC

latter condition the LBO values are very similar. Finally, Sturgess et al. (1991) and Sturgess and Shouse (1993) have elucidated the significance and applications of anchored and lifted flames to practical gas turbine combustor stability and LBO. They observe three basic flame conditions: a thin sheathlike pilot anchored flame, a shear layer flame associated with the inner and outer recirculation zones, and a lifted main flame, which allows considerable premixing of reactants to take place prior to combustion. These observations further confirm the relevance and importance of the present work to practical gas turbine combustors.

Conclusions

An SSC was designed to reproduce the swirling flow pattern present in the vicinity of the fuel injector located in the primary zone of a gas turbine combustor. Different flame shapes, structure, and location were observed and detailed experimental measurements and numerical computations were performed.

1 For the combination of strong outer swirl and zero inner swirl, a multiple attached flame exists simultaneously over the fuel and air injection tubes. As the strength of the outer air swirl is decreased and that of the inner swirl increased, the flame structure gradually shifts to a single attachment above the fuel injection tube.

2 For higher inner swirl velocity, the flame lifts from the fuel tube and is stabilized by the inner recirculation zone. Premixing of fuel and air at the base of the flame compromises the stability of the lifted flame over that of an attached flame, i.e., LBO values are higher for a lifted flame than for an attached flame.

3 The observed difference in LBO between co- and counterswirl configurations is primarily a function of how the flame stabilizes. Counterswirl conditions readily produce an attached flame for moderate inner swirl intensity; however, both configurations produce lifted flames for higher inner swirl intensity and for this latter condition the LBO values are very similar.

4 Computations based upon a turbulent combustion model correctly predict the attached flame locations, the development of an inner recirculation zone, which produces a dimple-shaped flame structure, and finally the flame lift-off height. The calculated radial mean temperature profiles at different axial locations agreed well with the measured CARS temperature. Also, the calculated velocity profiles agree reasonably well with the LDA measurements of mean axial and mean tangential velocities. These computations show the presence of a strong inner recirculation zone in the SSC, provide the location of the reattachment point of this recirculation bubble, and confirm the transport of combustion products upstream.

Finally, Sturgess et al. (1991) and Sturgess and Shouse (1993) have elucidated the significance and applications of an-

chored and lifted flames to practical gas turbine combustor stability and LBO. This confirms the importance and relevance of the present work to gas turbine combustors.

Acknowledgments

This work was supported by the U.S. Air Force, Wright Laboratory, Fuels and Lubrications Division, Aero-Propulsion and Power Directorate, Wright Patterson Air Force Base, Dayton, OH, under contract No. F33615-92-C-2207, with Mr. Charles W. Frayne serving as the Air Force Technical Monitor. The authors wish to thank Mr. W. John Schmoll for the custom LDA processing software.

References

- Bradley, D., Gaskell, P. H., and Lau, A. K. C., 1990, "A Mixedness-Reactedness Flamelet Model for Turbulent Diffusion Flames," *Twenty-Third Symposium (International) on Combustion*, The Combustion Institute, p. 685.
- Chen, R. H., and Driscoll, J. F., 1988, "The Role of the Recirculation Vortex in Improving Fuel-Air Mixing Within Swirling Flames," *Twenty-Second Symposium (International) on Combustion*, The Combustion Institute, p. 281.
- Durbin, M. D., and Ballal, D. R., 1996, "Studies of Lean Blowout in a Step Swirl Combustor," *ASME JOURNAL OF ENGINEERING FOR GAS TURBINES AND POWER*, Vol. 118, pp. 72-78.
- Gollahalli, S. R., Savas, O., Huang, R. F., and Rodriguez Azara, J. L., 1985, "Structure of Attached and Lifted Gas Jet Flames in Hysteresis Region," *Twenty-First Symposium (International) on Combustion*, The Combustion Institute, p. 295.
- Katta, V. R., and Roquemore, W. M., 1993, "Numerical Method for Simulating Fluid-Dynamic and Heat-Transfer Changes in Jet Engine Injector Feed-Arm Due to Fouling," *Journal of Thermophysics and Heat Transfer*, p. 651.
- Katta, V. R., Goss, L. P., and Roquemore, W. M., 1994, "Numerical Investigations of Transitional H₂/N₂ Jet Diffusion Flames," *AIAA Journal*, Vol. 32, p. 84.
- Katta, V. R., 1995, internal report in preparation.
- Leonard, B. P., 1979, "A Stable and Accurate Convective Modeling Procedure Based on Quadratic Upstream Interpolation," *Computational Methods in Applied Mechanics and Engineering*, Vol. 19, p. 51.
- Pan, J. C., Vangsness, M. D., Heneghan, S., and Ballal, D. R., 1991, "Scalar Measurements of Bluff Body Stabilized Flames Using CARS Diagnostics," *ASME Paper No. 91-GT-302*.
- Pitts, W. P., 1988, "Assessment of Theories for the Behavior and Blowout of Lifted Turbulent Jet Diffusion Flames," *Twenty-Second Symposium (International) on Combustion*, The Combustion Institute, p. 809.
- Pitts, W. P., 1990, "Large-Scale Turbulent Structures and the Stabilization of Lifted Turbulent Jet Diffusion Flames," *Twenty-Third Symposium (International) on Combustion*, The Combustion Institute, p. 661.
- Spalding, D. B., 1972, "A Novel Finite Difference Formulation for Difference Expressions Involving Both First and Second Derivatives," *International Journal for Numerical Methods in Engineering*, Vol. 4, p. 551.
- Sturgess, G. J., Lesmerises, A. L., Heneghan, S. P., and Ballal, D. R., 1990, "Design and Development of a Research Combustor for Lean Blowout Research," *ASME JOURNAL OF ENGINEERING FOR GAS TURBINES AND POWER*, Vol. 114, p. 13.
- Sturgess, G. J., Sloan, D. G., Roquemore, W. M., Shouse, D., Lesmerises, A. L., Ballal, D. R., Heneghan, S. P., Vangsness, M. D., and Hedman, P. O., 1991, "Flame Stability and Lean Blowout—A Research Program Progress Report," Paper No. 91-7037, *Proceedings of Tenth ISABE*, Nottingham, United Kingdom.
- Sturgess, G. J., and Shouse, D., 1993, "Lean Blowout Research in a Generic Gas Turbine Combustor With High Optical Access," Paper No. 93-GT-332, to appear in the *Transactions of the ASME*.

Takahashi, F., Mizomoto, M., Ikai, S., and Fukati, N., 1984, "Lifting Mechanism of Free Jet Diffusion Flames," *Twentieth Symposium (International) on Combustion*, The Combustion Institute, p. 295.

Takahashi, F., Schmoll, W. J., and Vangsness, M. D., 1990, "Effects of Swirl on the Stability and Turbulent Structure of Jet Diffusion Flames," Paper No. AIAA-90-0036.

Takahashi, F., and Goss, L. P., 1992, "Near-Field Turbulent Structures and

the Local Extinction of Jet Diffusion Flames," *Twenty-Fourth Symposium (International) on Combustion*, The Combustion Institute, p. 351.

Takahashi, F., Vangsness, M. D., and Belovich, V. M., 1992, "Conditional LDV Measurements in Swirling and Non-swirling Coaxial Turbulent Air Jets for Model Validation," Paper No. AIAA-92-0580.

Vanquickenborne, L., and van Tiggelen, 1966, "The Stabilization Mechanism of Lifted Diffusion Flames," *Combustion and Flame*, Vol. 10, p. 59.

4.1.3 Numerical Simulations of Droplet Combustion.

Maximum-Entropy Formulation of Droplet Distribution in Spray. One aspect in the modeling of sprays is to describe their characteristics systematically. A theoretical formulation based on the maximum-entropy principle was developed to predict the droplet size, velocity, and temperature distribution of sprays. A joint droplet distribution function was derived by maximizing Shannon's entropy, subject to a set of physical constraints that conserve the mass, momentum, and various modes of energy (surface, kinetic, and thermal) of the liquid phase of sprays. Different types of droplet distributions that have been identified and observed in various spray systems can be successfully predicted using this model without detailed information on the atomization processes. Three different types of droplet size distribution--positively skewed mono-modal, uniform (in the limit approaching a delta function), and bi-modal--were predicted and compared with data obtained from experiments ["Comparison Between Experiments and Predictions Based on Maximum Entropy for Sprays from a Pressure Atomizer" (pp. 716 - 732), "Comparisons Between Experiments and Predictions Based on Maximum Entropy for the Breakup of a Cylindrical Liquid Jet" (pp. 733 - 750), and "Bi-Modal Size Distributions Predicted by Maximum Entropy are Compared with Experiments in Sprays" (pp. 751 - 768)]. A simplified model that reduces the number of constraints by three was also derived to improve the calculation efficiency for less complicated spray systems. The derived model shows that the velocity distribution is Gaussian and the temperature distribution is exponential.

Droplet/Vapor/Vortex Interaction. The interaction between droplet and vortex is important in the determination of the combustion characteristics of sprays. Only limited information is available at the present time on vapor after it leaves the surface of evaporating droplets. A numerical model based on the Marker and Cell (MAC) method was developed to simulate the vaporline of droplets in a two-dimensional shear layer ["Characterization of Droplet/Vapor/Vortex Interactions in a Two-Dimensional Shear Layer" (pp. 769 - 772)]. For visualizing the flow patterns (e.g., streaklines and vaporlines of droplets), massless markers convected by the velocity field were introduced. The trajectories of droplets in the flow field can be calculated using drag correlation for the droplets. This model is useful in characterizing the convective transport of vapor from evaporating droplets.

The droplet-vortex interactions that determine the structural and dynamic characteristics of a spray-jet flow were investigated using a time-dependent axisymmetric numerical simulation of an n-heptane evaporating spray ["Gravity Effects on the Dynamics of Evaporating Droplets in a Heated Jet" (pp. 773 - 782) and "A Numerical Study of Droplet-Vortex Interactions in an Evaporating Spray" (pp. 783 - 797)]. The spray was formed between a droplet-laden heated-nitrogen jet and a coflowing air stream.

A detailed, multidimensional two-phase algorithm was developed for the simulation. Monodisperse spray was introduced into the large vortex structures generated by the buoyancy-induced hydrodynamic instability of the heated jet. Results [reported in "A Numerical Study of Droplet-Vortex Interactions in an Evaporating Spray" (pp. 783 - 797)] focused on the two-way interactions between vortical structures and droplets and the dynamics of both nonevaporating and evaporating sprays. The vortex structures cause droplets to disperse radially outward which, in turn, determines the fuel vapor distribution and also modifies the vortex dynamics. Thus, the dynamics and structural characteristics of evaporating sprays are strongly influenced by the two-way transient interactions. The effects of initial droplet size, injection location, and liquid-to-gas mass loading ratio on these interactions are reported in the paper entitled, "A Numerical Study of Droplet-Vortex Interactions in an Evaporating Spray" (pp. 783 - 797).

Droplet-Vortex-Flame Interactions. The effects of gravity on the structure of a spray flame were investigated by simulating an unsteady n-heptane spray flame ["Effect of Gravity on the Structure of an Unsteady Spray Diffusion Flame" (pp. 798 - 805)]. The flame was formed between a droplet-laden nitrogen jet and a coflowing air stream. A detailed, multidimensional two-phase algorithm was developed for the simulation. The gas-phase model included a one-step global-chemistry model, multicomponent diffusion, and variable transport properties. A comprehensive vaporization model was employed for calculating the instantaneous droplet size and surface temperature along the trajectory of each droplet group. The model includes the effects of variable thermophysical properties, nonunity Lewis number in the gas film, the effect of Stefan flow on the heat and mass transfer between the droplet and the gas, and the effect of transient liquid heating. Results indicated that the laminar spray flame structure is strongly influenced by gravity. Large-scale buoyancy-driven structures were observed outside the flame surface, similar to those in a gaseous jet diffusion flame. These outer structures developed naturally and sustained themselves without any external excitation. Results also indicated the occurrence of strong two-way interactions between droplets and large structures. The large vortex structures cause droplets to disperse radially outward which, in turn, modifies the vortex dynamics. The dynamics of spray flames and their structural characteristics are strongly influenced by these interactions.

Comparison Between Experiments and Predictions Based on Maximum Entropy for Sprays from a Pressure Atomizer

X. LI*, L. P. CHIN, and R. S. TANKIN,
Northwestern University, Evanston, IL

T. JACKSON and J. STUTRUD,
Wright-Patterson AFB, Dayton, OH

G. SWITZER
Systems Research Laboratories, Inc., Dayton, OH

Measurements were made of the droplet size and velocity distributions in a hollow cone spray from a pressure atomizer using a phase/Doppler particle analyzer. The maximum entropy principle is used to predict these distributions. The constraints imposed in this model involve conservation of mass, momentum, and energy. Estimates of the source terms associated with these constraints are made based on physical reasoning. Agreement between the measurements and the predictions is very good.

INTRODUCTION

Sprays play an important role in many engineering applications, for example, in combustion of liquid fuels, agricultural applications, painting, direct injection condensers, cooling, etc. In all these applications, droplet size and velocity distributions are important parameters in addition to the spray cone angle and droplet penetration. Until recently the main interest of researchers has been on the droplet size distribution. This was primarily due to the fact that it was nearly impossible to measure droplet velocity distributions. It was often assumed that the droplets leave the spray with a uniform velocity, equal to the sheet velocity at breakup (for pressure atomizers). However, with the advent of the phase/Doppler particle analyzer (PDPA), it is possible to measure both the local droplet size and velocity distributions. The PDPA is a single point, scattering technique, making a measurement of each droplet as it passes through a small probe volume. Results are reported at an isolated point (or several points) in the spray. For example, Bhatia and Durst [1] made measurements along the center-

line of a spray at various axial locations, and compared their results with various models. In this article, we report measurements across a selected plane in the spray and compare these results with predictions obtained using the maximum entropy principle.

The concept of information entropy was developed by Shannon [2], and Jaynes [3], who later extended this concept into the now well-known method of maximum entropy formalism. This formalism can be applied to problems that involve probability, i.e., where insufficient information is available to obtain exact solutions. Tribus [4] used the principle of this formalism in thermodynamics and showed that the concepts of heat and temperature in thermodynamics could be defined through the formalism of maximum entropy. We were originally influenced by Haken's book on synergetics [5], which establishes links between dynamical systems theory and statistical theory with information theory as its basis. This maximum entropy formalism allows one to determine the probability distribution functions for complex systems in physics, chemistry, and biology, as well as in many other disciplines by measuring relatively few average (macroscopic) quantities. In the present article, we will confine our attention to its application to liquid sprays in order to predict the droplet size and velocity

*Present address: Mechanical Engineering Department, University of Waterloo.

distributions in sprays. Since the application to this kind of problems has been adequately discussed by several researchers—Kelly [6], Sellens and Brzustowski [7, 8], Sellens [9, 10], and Li and Tankin [11, 12–13] it will not be necessary to develop the background materials once again.

The primary purpose of this article is to compare the theoretical predictions based on maximum entropy principle of Li and Tankin [11–13] concerning droplet size and velocity distributions with experimental results. In the process of making these comparisons, estimates will be made of the source terms that appear in the equations. To accurately compare theory and experiment it is necessary to account for drag effects on the droplet velocity distributions.

EXPERIMENT

The test article in these experiments was a hollow cone spray nozzle manufactured by Delavan (WDA-2 with a 60° spray angle). The spray of distilled water issues into a quiescent, saturated air environment at 295 K. The flow rate is $2.39 \times 10^{-6} \text{ m}^3/\text{s}$ (2.2 g/h) at a pressure drop across the nozzle of 1.3 MPa (190 psig). The water exiting the nozzle forms a liquid sheet, hollow cone in shape, which breaks up into ligaments that form droplets. It is desirable to measure the spray as close as possible to the sheet breakup region. Measurements beyond this will be influenced by local gas aerodynamics and complicate the comparison with prediction. Photographs of the spray (Fig. 1) indicate that sheet breakup occurs at approximately 7.5 mm from the nozzle face. At 10 mm the droplets have formed. Based on the photographs, the measurement plane was set at 10 mm from the nozzle discharge plane, 2.5 mm past the sheet breakup.

Droplets are sized with an Aerometrics, Inc., two-color, four-beam PDPA. This instrument measures the radius of curvature of droplets passing through the probe volume. A complete discussion of the theory of operation can be found in Bachalo and Houser [14]; a discussion of the operational constraints in practical environments can be found in Jackson [15]. The instrument is configured like a standard laser Doppler anemometer with each beam pair measuring one component of the droplet velocity. At each measurement station 10,000 droplets are measured.

Collection times for this many samples are of the order of seconds. Sample sizes as large as 20,000 were acquired before determining that 10,000 samples are sufficient to yield stable mean and RMS velocity statistics. The nominal probe volume size is 0.002 mm^3 .

Comparison between experiment and prediction demands that the measured values of droplet size and velocity near sheet breakup be representative of the behaviour of the entire spray. Several constraints inherent in the PDPA must be addressed. First, measured droplets must be spherical. This requires that the measurement station be sufficiently far from the sheet breakup region that droplets are not oscillating. Second, the PDPA has a dead time of 16 μs associated with each measured droplet. Another droplet entering the probe volume during this period will not be measured and may prevent the measurement of the first droplet. Thus, in dense spray regions, typical of the sheet breakup area, not all droplets may be counted. If the rejection is completely random (not based on a particular droplet size or velocity class), the measurements are still suitable for this purpose. Third, the cross-sectional area of the optical probe volume is small compared with the cross-sectional area around the sheet breakup. Data collected by the PDPA must be extrapolated to the entire spray area at the measurement plane located 10 mm from the nozzle.

The first two considerations influence the percentage of valid signals versus the total attempts. That is, the PDPA attempts to process all Doppler signals. It performs checks on the quality of each signal and rejects those that exceed certain limits. In these experiments valid signals range from 25% to 70% of the signals collected. Thus, to collect 10,000 valid signals at a challenging location in the spray it was necessary to make as many as 40,000 attempts. The third consideration is one of spray symmetry and of specifying the probe volume cross section. For the symmetry evaluation, two orthogonal, full-diameter traverses were made. The axis of the spray was horizontal for all measurements. A horizontal traverse through the spray yielded measurements of droplet size and its axial and azimuthal velocities; a vertical traverse yielded measurements of droplet size and its axial and radial velocities. Measurements were made at 0.5-mm intervals.

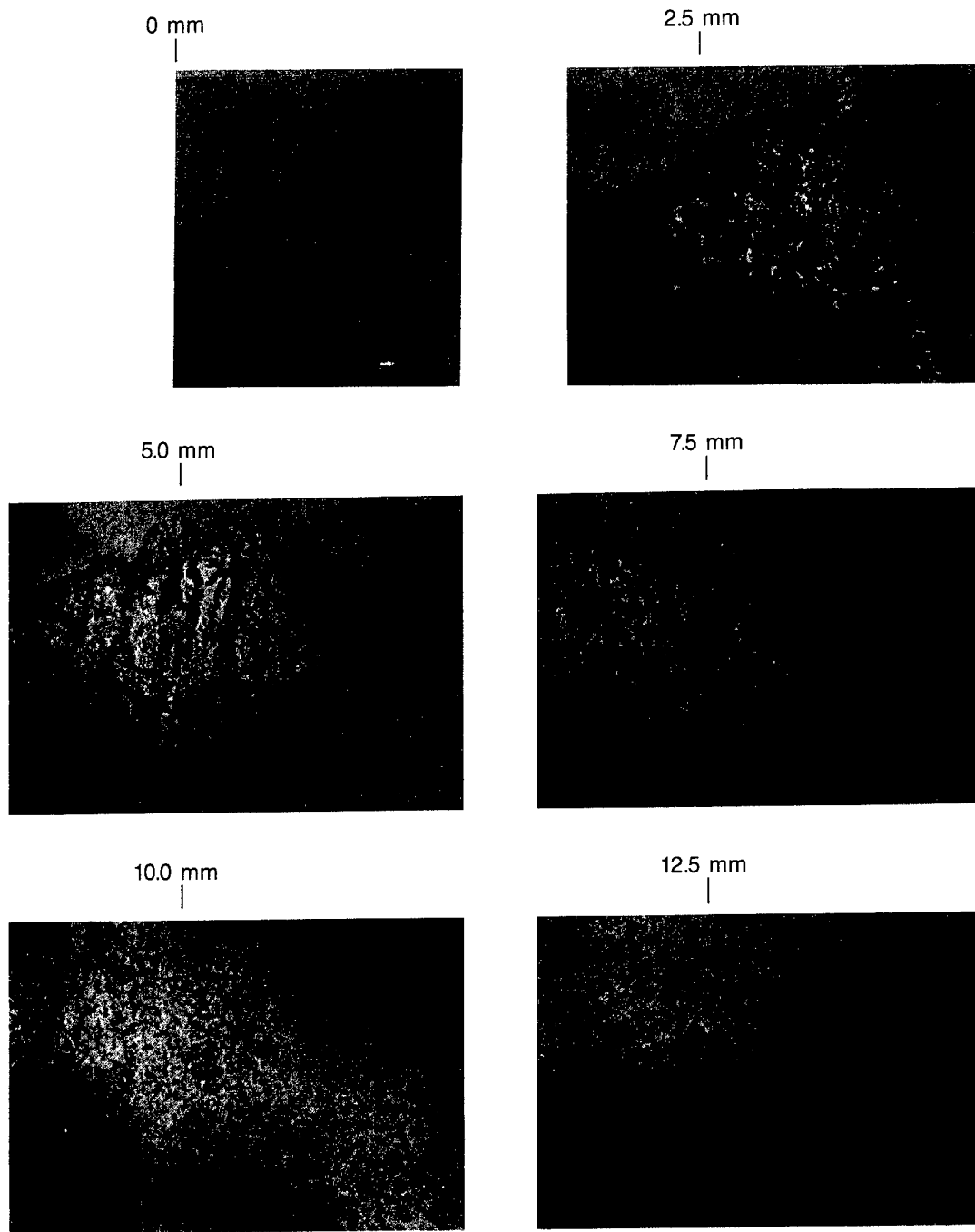
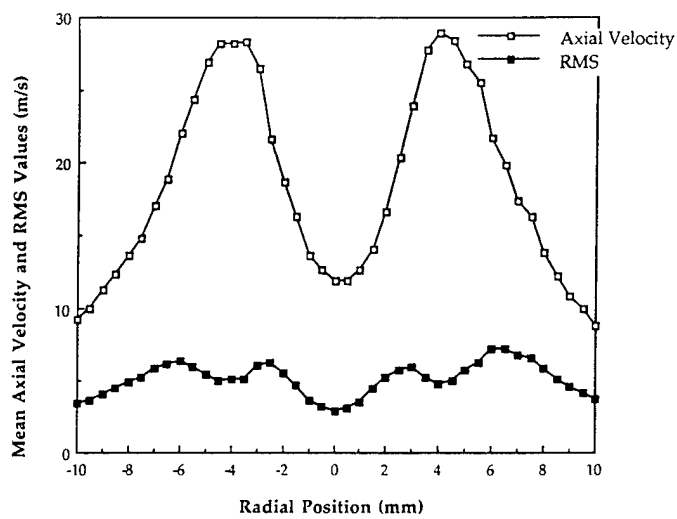


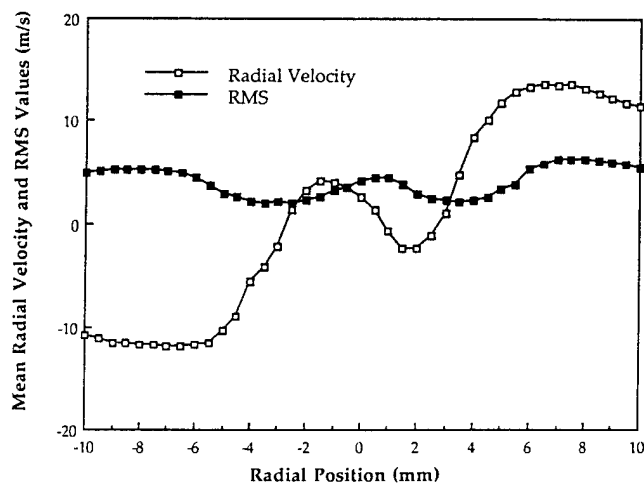
Fig. 1. Photographs of the spray taken at designated axial distances from the nozzle exit.

Figure 2 depicts the axial and radial velocity along with their root mean square (rms) values, and the Sauter mean diameter (SMD) measurements from the vertical traverse. The axial and azimuthal velocity along with their rms and SMD

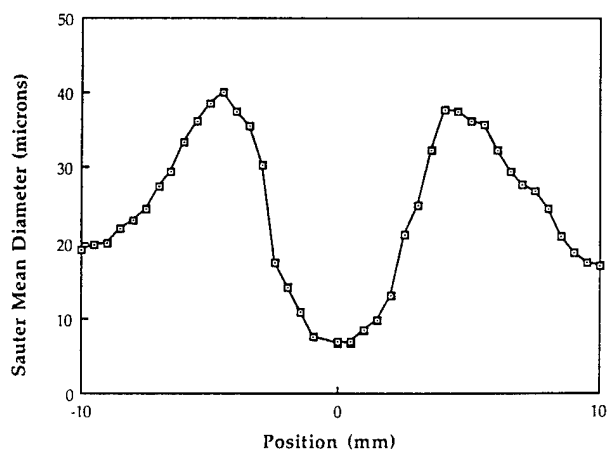
profiles from the horizontal traverse are illustrated in Fig. 3. The two axial velocity profiles and the two SMD profiles are replotted in Fig. 4 for comparison. The velocity and droplet size profiles along two orthogonal traverses through



(a)

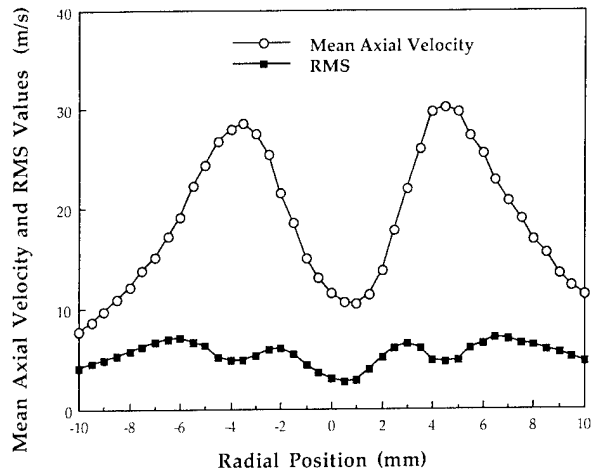


(b)

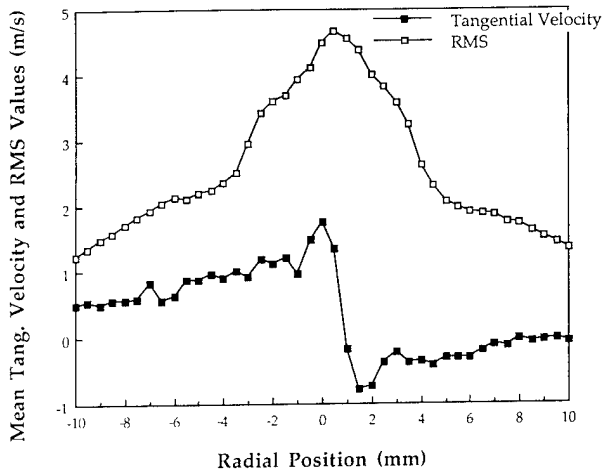


(c)

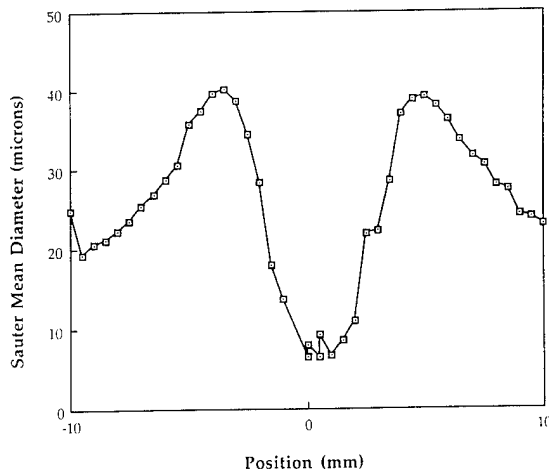
Fig. 2. (a) Plot of the axial mean velocity and RMS values as a function of radial position obtained from a vertical traverse. (b) Plot of the mean radial velocity and RMS values as a function of radial position obtained from a vertical traverse. (c) Plot of the Sauter mean diameter as a function of radial position obtained from a vertical traverse.



(a)



(b)



(c)

Fig. 3. (a) Plot the axial mean velocity and RMS values as a function of radial position obtained from a horizontal traverse. (b) Plot of the mean tangential velocity and RMS values as a function of radial position obtained from a horizontal traverse. (c) Plot of the Sauter mean diameter as a function of radial position obtained from a horizontal traverse.

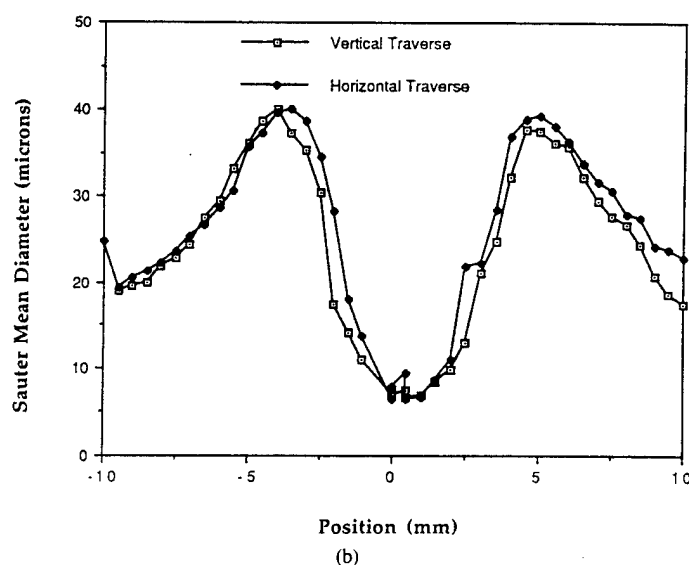
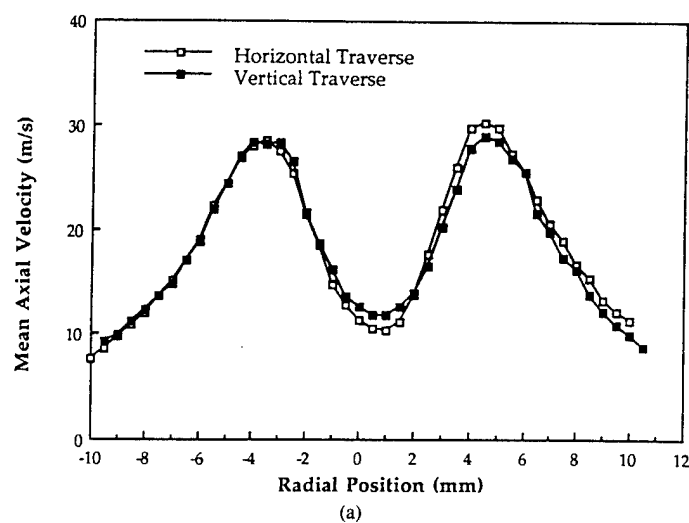


Fig. 4. (a) Plot comparing the axial velocity components obtained from horizontal and vertical traverses. (b) Plot comparing the Sauter mean diameters obtained by vertical and horizontal traverses.

the spray are nearly identical, indicating the spray has good symmetry about its axis. Thus, size and velocity distributions, obtained from the point measurements, can be integrated over the ring area associated with each measurement point to yield a total spray measurement.

After initial spray symmetry checks, data were collected to evaluate the predictions. One detailed radial profile was taken at the 10-mm location where measurements were made at 22 radial points from the spray center to its edge. Ten thousand valid samples were taken at each location. A joint size-axial velocity distribution function is constructed from the individual point mea-

surements, weighing each measurement by their time of collection and the ratio of their optical probe area to the ring area represented at that location. This experimentally determined joint distribution function can be compared to that predicted by the maximum entropy analysis. Droplet size is normalized by the mass mean diameter, D_{30} , determined from measurements to be $25.3 \mu\text{m}$. Droplet velocity is normalized by the computed axial velocity of the sheet at the nozzle exit, U_0 . This value is determined from the measured flow rate of the nozzle and the size of the air core at the nozzle exit plane. This latter value is determined from the spray cone angle,

photographically determined to be 58° , and the discharge coefficient of the atomizer [16]. The computed axial velocity of the sheet is 30 m/s; its tangential velocity is 23.5 m/s. As an aside, using this tangential velocity at the nozzle exit and assuming a free vortex flow one can compute the tangential velocity as a function of radius. Comparison between this result and measurements is shown in Fig. 5. It is noted that the measured values have been shifted 0.5 mm horizontally due to error in exactly locating the nozzle center.

THEORY

Since all the detailed formulation and derivation have been published [12], we do not reiterate them but just give the final pertinent equations. The constraints imposed on liquid atomization processes are conservation of mass, momentum, and total energy—the sum of kinetic energy and surface energy. In addition there is the requirement that the sum of the joint probabilities be unity. Thus,

$$\text{Mass: } \iint f \bar{D}^3 d\bar{U} d\bar{D} = 1 + \bar{S}_m. \quad (1)$$

$$\text{Momentum: } \iint f \bar{D}^3 \bar{U} d\bar{U} d\bar{D} = 1 + \bar{S}_{mv}. \quad (2)$$

$$\begin{aligned} \text{Energy: } \iint f(\bar{D}^3 \bar{U}^2 + B \bar{D}^2) d\bar{U} d\bar{D} \\ = 1 + \bar{S}_e. \end{aligned} \quad (3)$$

$$\text{Normalization: } \iint f d\bar{U} d\bar{D} = 1. \quad (4)$$

Here \bar{S}_m , \bar{S}_{mv} , and \bar{S}_e are the nondimensional mass, momentum, and energy source terms, respectively, and f is the joint droplet size and velocity distribution function, which maximizes the Shannon's entropy subject to the constraints of Eqs. 1-4. Thus, f can be shown to have the following form:

$$\begin{aligned} f = 3 \bar{D}^2 \exp \{ -a_0 - a_1 \bar{D}^3 - a_2 \bar{D}_3 \bar{U} \\ - a_3 (\bar{D}^3 \bar{U}^2 + B \bar{D}^2) \}, \end{aligned} \quad (5)$$

where

$$\bar{D} = \frac{D}{D_{30}}$$

is the dimensionless droplet diameter,

$$\bar{U} = \frac{U}{U_0}$$

is the dimensionless droplet velocity,

$$B = \frac{12}{We}$$

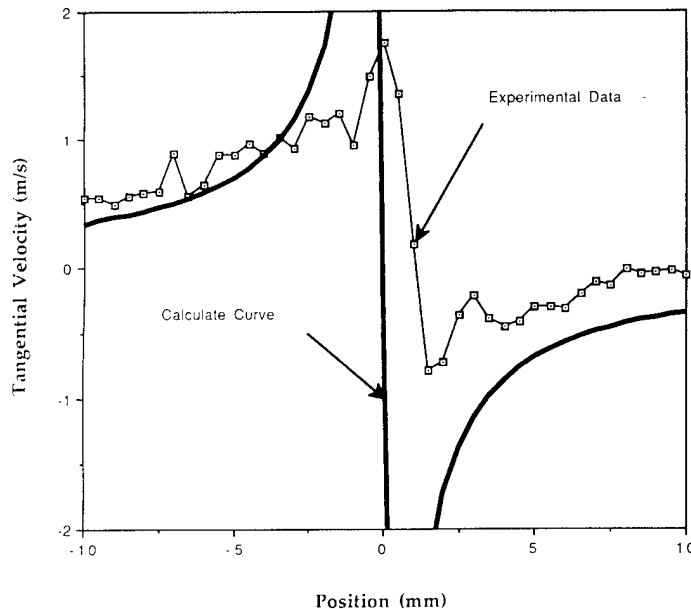


Fig. 5. Plot comparing the measured and computed (free vortex) tangential velocities.

and

$$a_0, a_1, a_2, a_3$$

are Lagrangian multipliers, and

$$W_e = \frac{\rho_l U_0^2 D_{30}}{\sigma} \quad (5a)$$

is the Weber number, representing, within a constant factor, the ratio of the total droplet energy available (i.e., the liquid kinetic energy at nozzle exit to the droplet surface energy) where ρ_l is the liquid density and σ is the surface tension. Equation 5 shows that for any particular droplet size, the velocity distribution appears Gaussian. However, the droplet velocity in a spray (at the breakup region) cannot be negative; thus, the resulting velocity distribution is a truncated Gaussian distribution. The mean and variance of the droplet velocity distribution depend on the droplet size. Equation 5 can be integrated over velocity space from minimum to maximum velocity to yield the number-based droplet size distribution

$$dN/d\bar{D} = \frac{3}{2} \left(\frac{\pi \bar{D}}{a_3} \right)^{1/2} \left\{ \text{erf}(x_{\max}) - \text{erf}(x_{\min}) \right\} \exp \left\{ -a_0 - a_3 B \bar{D}^2 - \left(a_1 - \frac{a_2}{4a_3} \right) \bar{D}^3 \right\}, \quad (6)$$

where

$$x_{\max} = \left(\bar{U}_{\max} + \frac{a_2}{2a_3} \right) (a_3 \bar{D}^3)^{1/2},$$

$$x_{\min} = \left(\bar{U}_{\min} + \frac{a_2}{2a_3} \right) (a_3 \bar{D}^3)^{1/2},$$

$\text{erf}(x)$ represents the error function, and N is the normalized droplet numbers. Equation 6 shows that the number distribution vanishes as the droplet diameter \bar{D} equals zero—just as experimental evidence and physical reasoning require.

It is necessary to estimate the following quantities: \bar{S}_m , \bar{S}_{mv} , \bar{S}_e . Values of U_0 and D_{30} are determined from the experiment. It is important to restate that the control volume (shown schematically in Fig. 6) extends from the nozzle

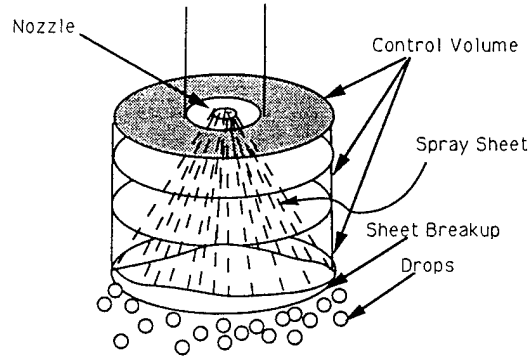


Fig. 6. Schematic drawing showing the control volume used in the maximum entropy model.

exit to the breakup region. This is an important point because this control volume differs from that of Sellens and Brzustowski's [7, 8], which extends from the tip of the sheet breakup region to the droplet region.

The spray is isothermal and issues into a saturated air environment. Therefore, the mass source term, \bar{S}_m is assumed to be zero. The momentum source term, \bar{S}_{mv} , is estimated as follows. The spray discharges into a quiescent air environment, creating a drag on the spray sheet. To estimate this drag, the hollow cone liquid sheet is unfolded into a triangular shape (Fig. 7) having an altitude of 7.5 mm and a base equal to 26 mm (which is $2\pi r$). Using laminar boundary layer flow (Reynolds number based on 7.5 mm is well below the critical Reynolds number of 5×10^5) past a flat plate yields $C_f = 0.02$ on one surface (outside) of the triangular sheet. Since the air flow inside the hollow cone consists of vortical structures (see Ref. 17, Fig. 3), the drag of this air flow on the liquid sheet is neglected. Using the computed value for C_f , yields a value for \bar{S}_{mv} of -0.017 . The energy source term, \bar{S}_e ,

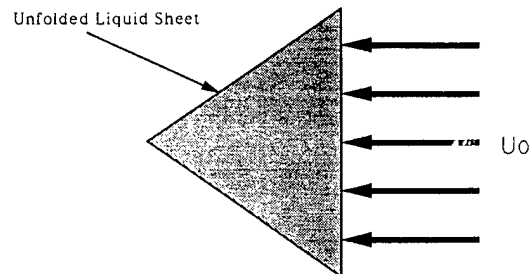


Fig. 7. Drawing showing the model used to estimate the momentum source, \bar{S}_{mv} .

consists of kinetic and surface energy components. The surface energy is a function of the surface area, which increases between the nozzle exit and the drop formation zone located just beyond the tip of the sheet breakup. On the other hand, the kinetic energy component of \bar{S}_e decreases between nozzle exit and breakup. Thus, \bar{S}_e is estimated to be zero. Admittedly, the estimates for \bar{S}_{mv} and \bar{S}_e are very crude but their accuracy is not a critical aspect of this paper; they serve as a reasonable first estimate. Knowing D_{30} and U_0 from the experiments, the Weber number (Eq. 5a) is determined to be 311. It should be noted that the Weber number is not the usual one associated with sprays. It is based on the fluid (water) density and not the gas (air) density. When comparisons are made between experiments and theory, it may be necessary to adjust the values of \bar{S}_{mv} and \bar{S}_e , the only two adjustable constants in the theory.

COMPARISONS BETWEEN THEORY AND EXPERIMENTS

The predicted and measured joint size-velocity probability distributions are illustrated in the three-dimensional plots of Fig. 8. The predicted results are shown in Fig. 8a and the experimental results in Fig. 8b. The corresponding iso-probability contours are presented in Figs 9a. and 9b. Clearly the predicted joint probability distribution is symmetric about $U/U_0 = 1$, in contrast to the experimentally determined distribution. By summing the values of the probability function, f , over all velocities for each drop size, the size distribution function of the spray is generated. Figure 10 shows the predicted and measured values. Agreement between prediction and experiment is very good. The predicted and measured droplet size-velocity correlations for the spray, Fig. 11, are not in agreement, however. The discrepancy lies in the separation between the sheet breakup location (7.5 mm) where the predictions are valid and the measurement location (10 mm). Over this 2.5-mm separation it is necessary to account for the drag of the quiescent ambient air on the droplets. The drag correlations are tabulated in Table 1, which was taken from Clift, et al. [18]. Since the maximum Reynolds number is less than 260, only the following correlations were used:

Range	Correlation
$Re < 0.01$	$C_d = 3/16 + 24/Re$
$0.01 < Re < 20$	$C_d = 24/Re[1 + 0.1315 Re^{(0.82 - 0.05 \log Re)}]$
$20 < Re < 260$	$C_d = 24/Re[1 + 0.1935 Re^{0.6305}]$

The 2.5-mm region between the sheet breakup region and the measuring plane is divided into 100 equal intervals of 0.025 mm. The drag correlations are used to compute the new velocity distributions using particle mechanics. It is assumed the droplets leave the sheet region with the joint pdf predicted in Fig. 8a and move into quiescent air. After accounting for the drag on the droplets, the resultant three-dimensional joint probability plot and its associated iso-probability contours seen in Fig. 12 are similar to the measured values of Figs. 8b and 9b. The predicted size distribution function shown in Fig. 10 does not change due to drag effects. However, the mean velocity changes significantly as a function of droplet diameter. This is seen in Fig. 13, where predicted values are compared with measured values. This agreement is reasonably good. Also shown is the effect that the distance between the breakup plane and the measuring plane has on the mean velocity values. A difference in only 1 mm has a meaningful effect. Referring to Fig. 1, it is difficult to be more precise than about 1 mm in determining the position of the breakup region. At different diameters, one can plot the probability distribution function for velocity and compare the results between theory and experiment. This was done in Fig. 14 for $D/D_{30} = 0.5, 1.0, 1.5$, and 2.0. Again the agreement is reasonable.

DISCUSSION

The computed joint probability distribution function is dependent on the following: We , \bar{S}_m , \bar{S}_{mv} , and \bar{S}_e . There is little doubt that one can better match the theory with the experiments if one selects values for these nondimensional quantities without physically justifying their magnitude. Figure 15 indicates the sensitivity of $dN/d\bar{D}$ on Weber number. With a decrease in Weber number, the peak of this curve increases and moves to smaller D/D_{30} values—thus agreement with experimental data improves if one assumes $We = 250$. On the other hand, one can decrease the

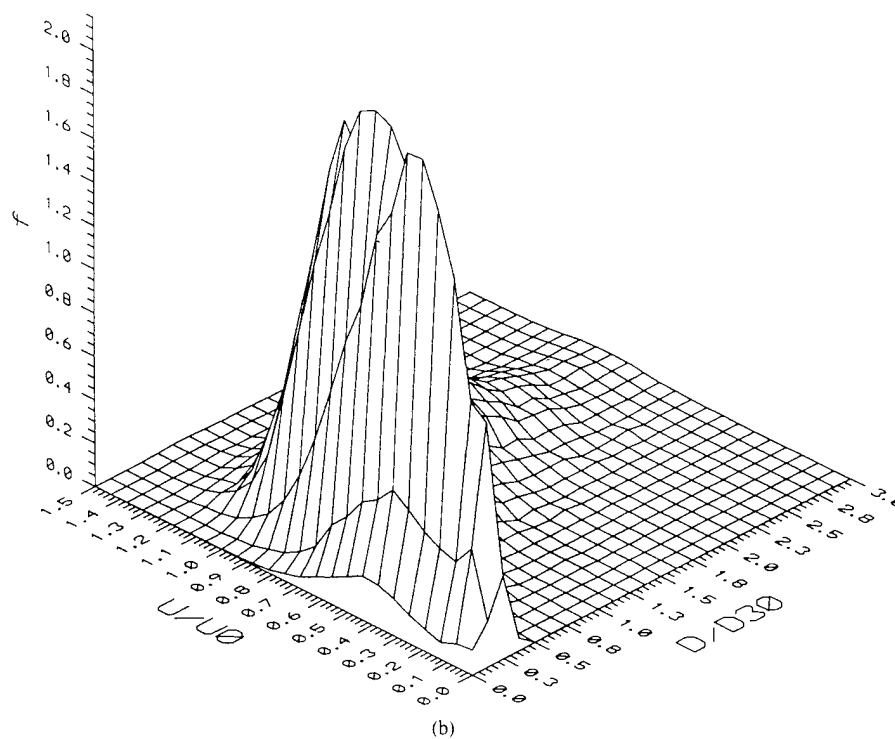
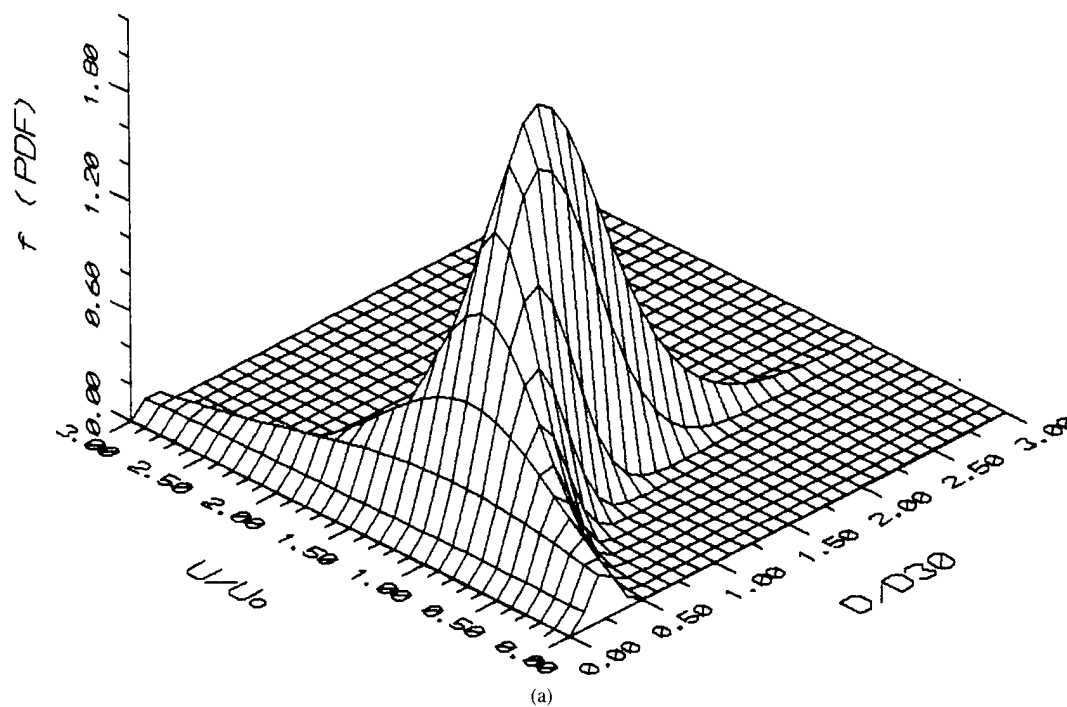


Fig. 8. (a) Three-dimensional plot of the predicted joint probability distribution function. (b) Three-dimensional plot of the experimentally determined joint probability distribution function.

peak of the computed $dN/d\bar{D}$ by increasing the energy source term (\bar{S}_e) or decreasing the momentum source term (\bar{S}_{mv}); these are shown in Figs. 16 and 17, respectively. It would be desirable if the trends of the curves in Figs. 15–17 could be verified using data of other researchers,

for example, the affect of the Weber number on $dN/d\bar{D}$ as seen in Fig. 15, that is, $dN/d\bar{D}$ shifts to smaller values of D/D_{30} with decrease in Weber number ($(\rho_l U_0^2 D_{30} / \sigma)$). Jones [19] used high-speed photographic techniques to investigate the mean droplet size, and obtained the following

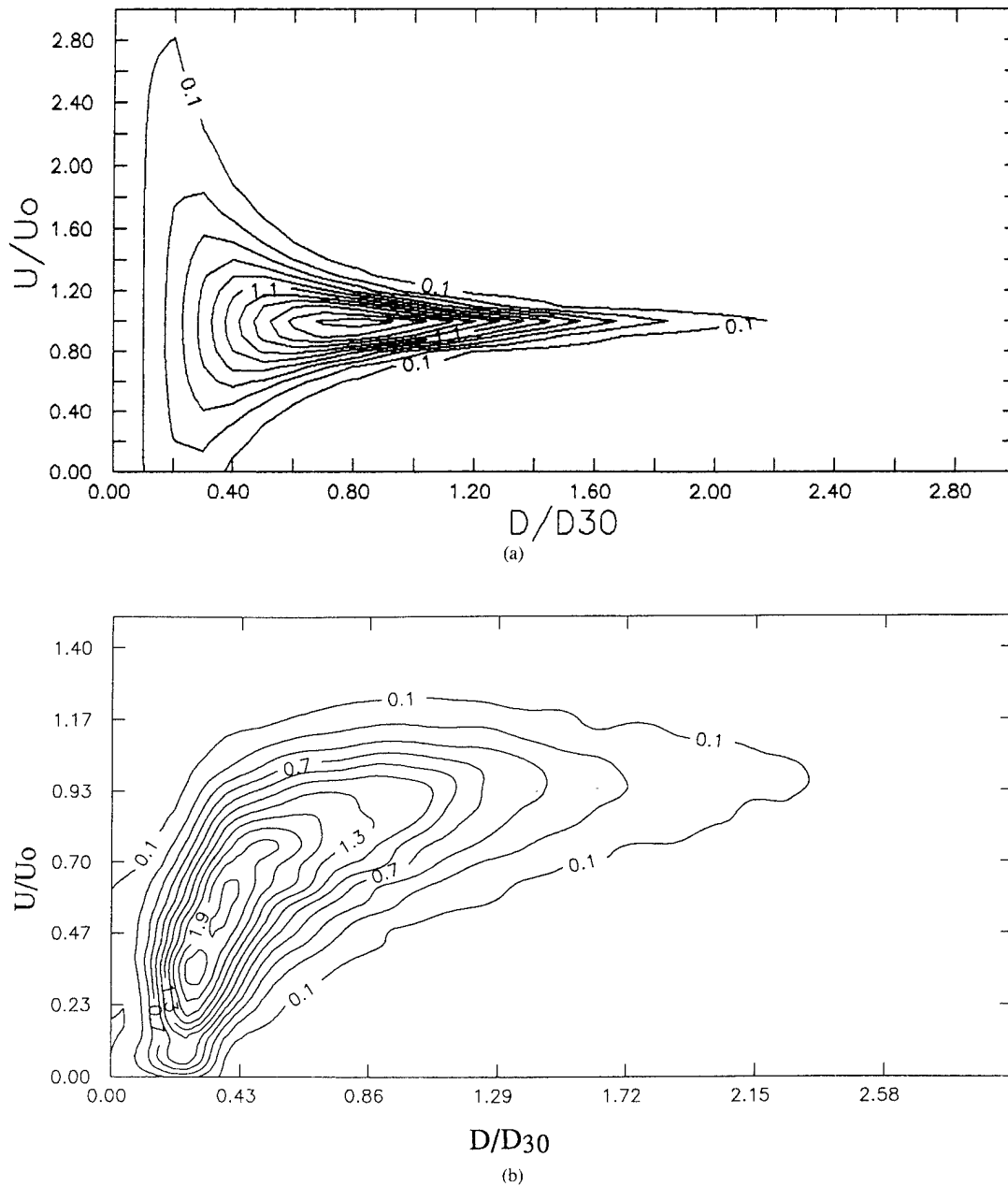


Fig. 9. (a) Iso-contour plot of the predicted joint probability distribution function. (b) Iso-contour plot of the experimentally determined joint probability distribution function.

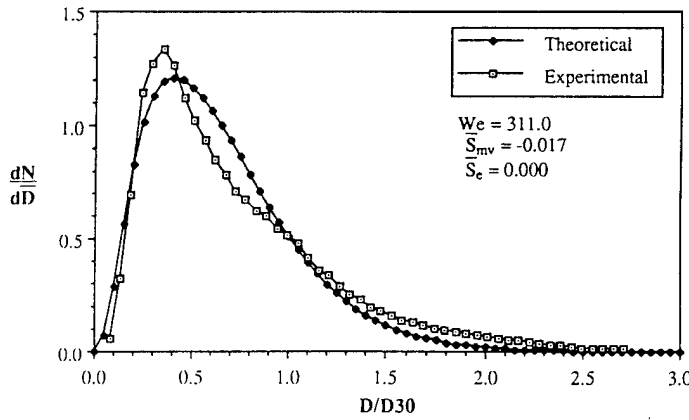


Fig. 10. Plot of experimental and predicted droplet size distribution.

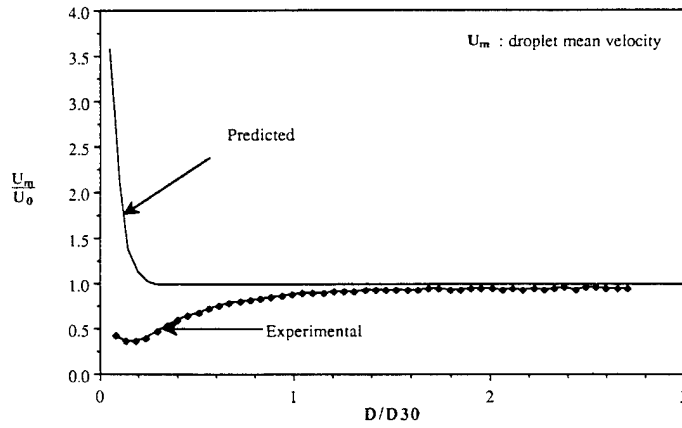


Fig. 11. Plot of experimental and predicted mean velocity as a function of droplet diameter.

TABLE 1

Recommended Drag Correlations, Where $w = \log_{10} \text{Re}$, Taken from Clift. et al. [18]

Range	Correlation
(A) $\text{Re} < 0.01$	$C_D = 3/16 + 24/\text{Re}$
(B) $0.01 < \text{Re} \leq 20$	$\log_{10} \left[\frac{C_D \text{Re}}{24} - 1 \right] = -0.881 + 0.82w - 0.05w^2$ i.e., $C_D = \frac{24}{\text{Re}} [1 + 0.1315 \text{Re}^{(0.82 - 0.05w)}]$
(C) $20 \geq \text{Re} \leq 260$	$\log_{10} \left[\frac{C_D \text{Re}}{24} - 1 \right] = -0.7133 + 0.6305w$ i.e., $C_D = \frac{24}{\text{Re}} [1 + 0.1935 \text{Re}^{0.6305}]$
(D) $260 \leq \text{Re} \leq 1500$	$\log_{10} C_D = 1.6435 - 1.1242w + 0.1558w^2$
(E) $1.5 \times 10^3 \leq \text{Re} \leq 1.2 \times 10^4$	$\log_{10} C_D = -2.4571 + 2.5558w - 0.9295w^2 + 0.1049w^3$
(F) $1.2 \times 10^4 < \text{Re} < 4.4 \times 10^4$	$\log_{10} C_D = -1.9181 + 0.6370w - 0.0636w^2$
(G) $4.4 \times 10^4 < \text{Re} \leq 3.38 \times 10^5$	$\log_{10} C_D = -4.3390 + 1.5809w - 0.1546w^2$
(H) $3.38 \times 10^5 < \text{Re} \leq 4 \times 10^5$	$C_D = 29.78 - 5.3w$
(I) $4 \times 10^5 < \text{Re} \leq 10^6$	$C_D = 0.1w - 0.49$
(J) $10^6 < \text{Re}$	$C_D = 0.19 - 8 \times 10^4/\text{Re}$

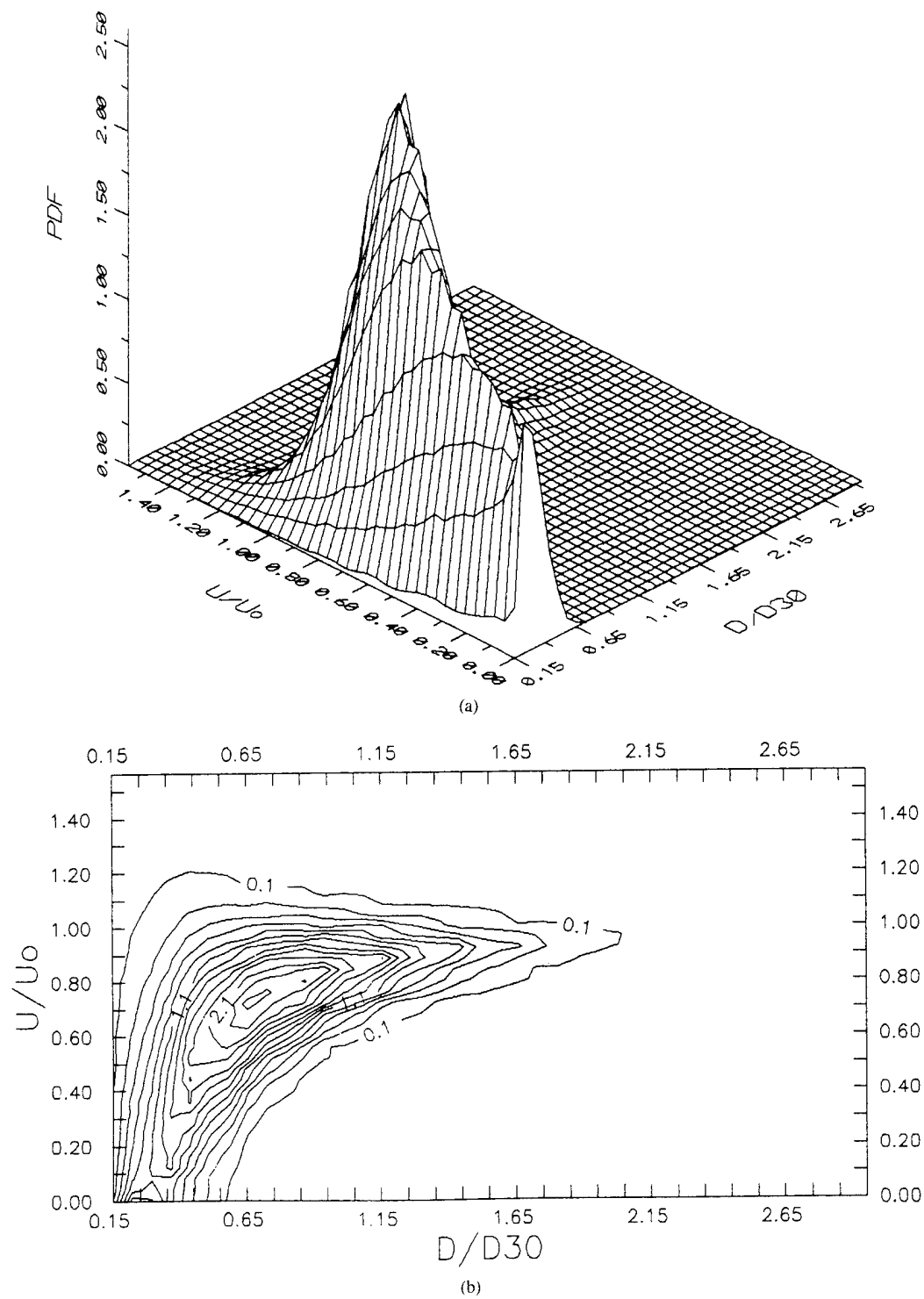


Fig. 12. (a) Three-dimensional plot of the predicted joint probability distribution function accounting for drag on the droplets. (b) Iso-contour plot of the predicted joint probability distribution function accounting for drag on the droplets.

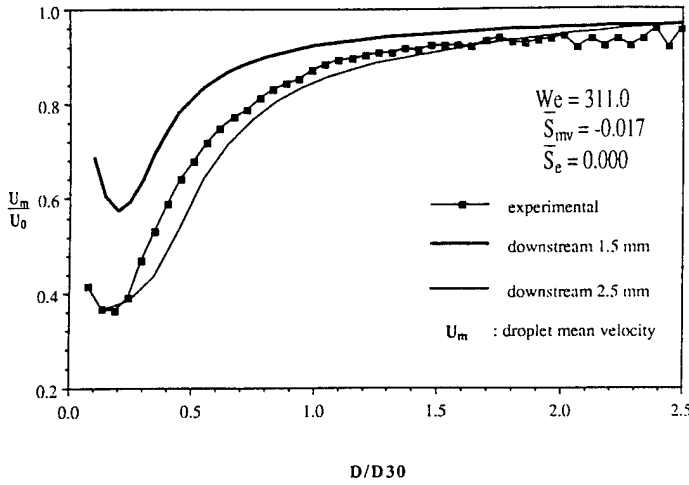


Fig. 13. Plot of the experimental and predicted mean velocity as a function of droplet diameter. The predicted values are shown where the distance between the breakup region and the measuring plane is 1.5 and 2.5 mm.

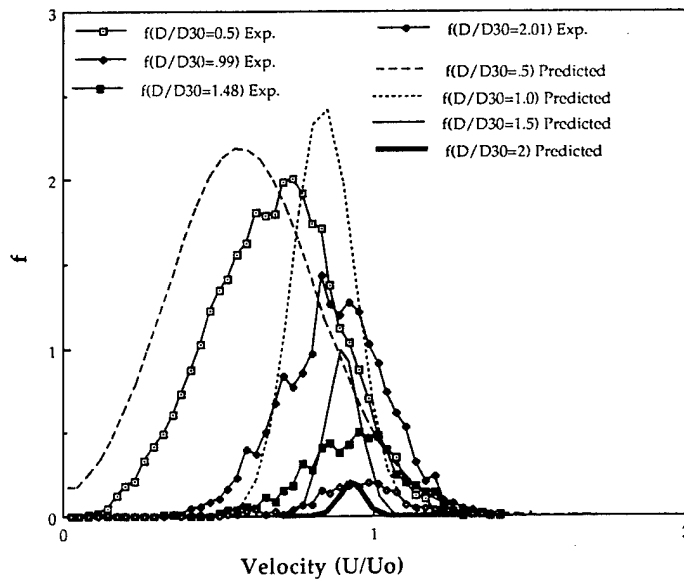


Fig. 14. Plots comparing the experimental and predicted velocity distributions at selected droplet diameters.

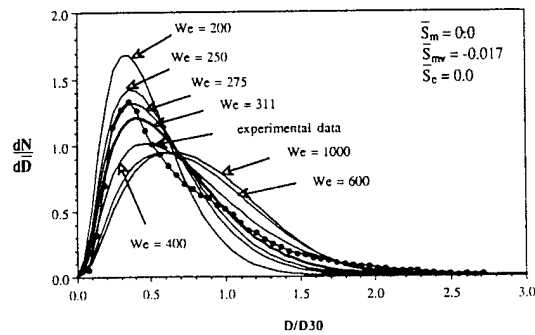


Fig. 15. Plots indicating the sensitivity of the Weber number on dN/dD , where $\bar{S}_m = 0$, $\bar{S}_{mv} = -0.017$, and $\bar{S}_e = 0$.

expression for D_{30} :

$$D_{30} = 2.47\sigma^{0.25}\mu_l^{0.16}m_l^{0.315}\Delta P_l^{-0.47}m_a^{-0.04}\rho_l^{0.22} \quad (7)$$

(geometric parameters for swirl atomizers).

According to Eq. 7, D_{30} increases with an increase in σ . One way to decrease the Weber number is to increase σ -holding ρ_l and U_0 constant. This may be an explanation of why the size distribution curves in Fig. 15 shift to smaller D/D_{30} values with decrease in Weber number by increasing σ . However, this explanation is

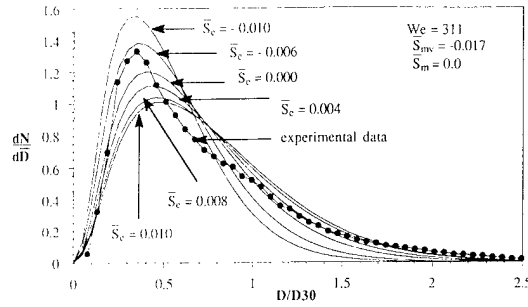


Fig. 16. Plots indicating the sensitivity of \bar{S}_c on $dN/d\bar{D}$, where $\bar{S}_m = 0$, $We = 311$, and $\bar{S}_{mv} = -0.017$.

pure conjecture because the effect of σ on D is not known.

Our goal was to estimate, however crudely, the magnitude of these source terms (and We) based on the physical aspects of the problem under consideration. Then to compare the theoretical results with the experiments and make adjustments, if necessary, in the source terms. The predicted results agree reasonably well with the experiments using the estimated source terms.

One inconsistency in this study should be noted. The metered mass flow of water through the nozzle is an order of magnitude greater than the mass flow computed from the optical measurements (PDPA) using the following:

$$\rho_l \frac{\pi}{6} \sum_i \left(\frac{\text{validations}}{\text{time}} \right)_i \left(\frac{\text{ring area}}{\text{probe area}} \right)_i (D_{30})_i^3 \quad (i = 1, 20). \quad (8)$$

There are two possible sources of error responsible for this discrepancy: (1) defining the optical probe measurement cross section, and (2) high rates of data rejection.

The effective cross sectional area of the optical

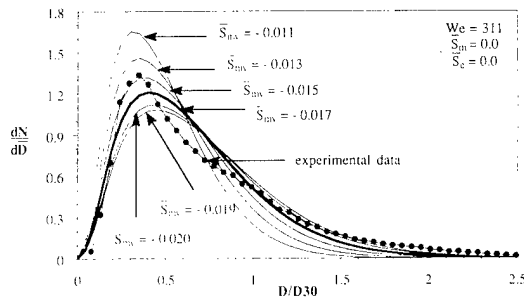


Fig. 17. Plots indicating the sensitivity of \bar{S}_{mv} on $dN/d\bar{D}$, where $\bar{S}_m = 0$, $We = 311$, and $\bar{S}_c = 0$.

measurements must be carefully defined. Measurements are taken at discrete points in the spray field and the optical probe areas are of the order of 10^{-2} mm^2 . The entire spray, however, covers an area of order 10^2 mm^2 at the axial measurement position of this experiment. Extrapolation of the measured flux at the discrete measurement stations to the total nozzle mass flux is a major step, relying heavily upon the probe area definition. The nature of the probe area is such that it changes with particle size, photodetector voltage, and the optical thickness of the spray.

Data are rejected from the PDPA measurement for a multitude of reasons. In a complex spray several of the rejected criteria are most prevalent: (1) Drops to be measured may be beyond the range of the instrument settings—out of the 35:1 sizing range or outside the frequency filter band. (2) The droplet trajectory may take it through one beam pair, but not the other; resulting in a violation of the two-color system's minimum requirement for a simultaneous measurement on two channels. (3) More than one droplet may be in the probe volume at a given time. At locations where the rejection rates were high, there are indications that the errors were predominately in the first two categories above. As indicated in Fig. 18, the central region of the spray produced the lowest ratio of validations to attempts (acceptance ratio). This is not surprising since in this hollow cone spray, the central region is dominated by an intense recirculation zone. In such an environment the droplet trajectories are not well behaved and droplet velocities vary widely. Such behavior leads to the types of errors noted. Plotted in Fig. 18 is Eq. 8 normalized ("Normalized Cumulative Flow Rate"). While these large rejection levels can be a problem, Fig. 18 reveals that they are confined to the central region of the spray where little of the spray mass is concentrated ($< 10\%$).

The mismatch in metered and optically measured mass flux is disturbing but not unusual and not indicative of any serious problem with the measurements. Extrapolation of the local flux data via the ratio of optical probe area to spray area represents a significant source of potential error. Also, the high rates of data rejection at certain areas in the spray may contribute to the flux mismatch. This latter issue would be a problem in the analysis presented in this article if the

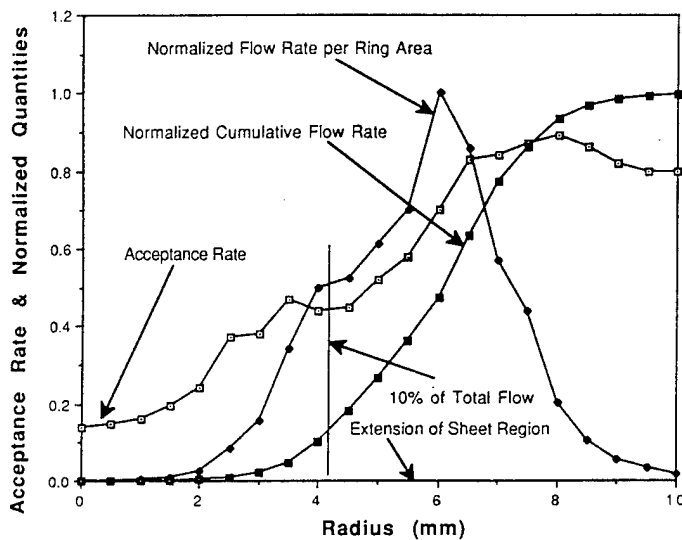


Fig. 18. Plots of acceptance rates, normalized flow rate per ring area, and normalized cumulative flow rate as a function of radial position.

rejections were not randomly distributed across all size classes. However, this is not likely to be the case because a large amount of the errors are associated with coincidence errors—typically a function of local droplet trajectories. Furthermore, the high rejection rates are confined to the central spray region (radial position between 0 and 2 mm) which contains the least amount of mass.

Three other runs (two from the horizontal traverse and another from a vertical traverse) resulted in similar data as those presented in this paper. Sensor [20] also had large discrepancy between similarly measured flow rates—particularly near the breakup region—in the dense portion of the spray. Also shown in Fig. 18 is a normalized plot of

$$\rho_l \frac{\pi}{6} \left(\frac{\text{volidations}}{\text{time}} \right)_i \left(\frac{\text{ring area}}{\text{probe area}} \right)_i (D_{30})_i^3$$

which is labeled “Normalized Flow Rate per Ring Area.” The maximum of this curve occurs near the extension of the sheet region (which is at a radius of 5.6 mm), as expected.

In the formulation presented in this article, one starts at one local equilibrium state (the nozzle exit) and ends at another local equilibrium state (where the droplets are formed) using the maximum entropy principle. From a statistical point of view, we are interested in determining the second

local equilibrium states (pdf) for a given initial state. The details of how one goes from one local equilibrium state to another is not important, except in a gross manner—through physically motivated source terms (mass, momentum, and energy). One need not be involved in the details of the sheet instability, the breakup process, the formation of ligaments, and their final breakup into droplets. In fact, these are just a way or means of converting part of kinetic energy (at the nozzle exit) into surface energy (when droplets are formed). The detailed physical processes of the transition plays no role in the maximum entropy approach. How one proceeds from one local equilibrium state to another is linked through the physical conservation laws—conservation of mass, momentum, and energy.

CONCLUSIONS

Experiments were performed on a pressure-atomizing nozzle that operated at its normal operating conditions. The drop sizes and velocities were measured. Predicted values for velocity and size distributions were obtained using the maximum entropy principle. The size distribution agrees reasonably well with the measured values, but the velocity predictions did not. By accounting for the drag on the droplets between the breakup region (where predictions were made) and the measuring plane, the results obtained agree with experiments. It should be noted that the droplet

size for the measured and predicted distribution deviates significantly from a Gaussian distribution. Physically justified source terms were used in the predictions. Using the maximum entropy principle to obtain the joint pdf as formulated in this article can serve as the initial input to a computer program that computes the droplet trajectories in a complicated air flow situation.

REFERENCES

1. Bhatia, J. C., and Durst, F., *Part. Part. Syst. Charact.* 6:151-162 (1989).
2. Shannon, C. E., *Bell Syst. Tech. J.* 27:379-423 (1948).
3. Jaynes, E. T., *Phys. Rev.* 106:620-630, 108:171-190 (1957).
4. Tribus, M., *Thermostatistics and Thermodynamics*, Van Nostrand, Princeton, NJ, 1961.
5. Haken, H., *An Introduction to Synergetics*, Springer-Verlag, Berlin, 1978.
6. Kelly, A. J., *J. Appl. Phys.*, 47:5264-5271 (1976).
7. Sellens, R. W., and Brzustowski, T. A., *Atomizat. Spray Technol.* 1:89-102 (1985).
8. Sellens, R. W., and Brzustowski, T. A., *Combust. Flame* 65:273-279 (1986).
9. Sellens, R. W., *Second Symposium on Liquid Particle Size Measurement Techniques*, ASTM, Atlanta, GA, 1988.
10. Sellens, R. W., *Part. Part. Syst. Charact.* 6:17-27 (1989).
11. Li, X., and Tankin, R. S., *Combust. Sci. Technol.* 56:65-76 (1987).
12. Li, X., and Tankin, R. S., *Combust. Sci. Technol.* 60:345-357 (1988).
13. Li, X., Ph.D thesis, Northwestern University, 1989.
14. Bachalo, W. D., and Houser, M. J., *Opt. Engi.* 23:583-590 (1984).
15. Jackson, T. A., in *Liquid Particle Size Measurement Techniques*, ASTM STP 1083 (E. D. Hirtleman, W. D. Bachalo, and P. G. Felton, Eds.), ASTM, Philadelphia, 1990, vol. 2, p. 151.
16. Giffen, E., and Muraszew, A., *The Atomization of Liquid Fuels*, Chapman and Hall, London, 1953.
17. Lee, S. Y., and Tankin, R. S., *Int. J. Heat Mass Transf.* 27:351-361 (1984).
18. Clift, R., Grace, J. R., and Weber, M. E., *Bubbles, Drops, and Particles*, Academic, New York, 1978.
19. Jones, A. R., *Proceedings of the International Conference on Liquid Atomization and Spray Systems*, Madison, WI, 1982.
20. Sensor, D., Private communication, 1990.

Received 29 June 1990; revised 28 February 1991

COMPARISONS BETWEEN EXPERIMENTS AND PREDICTIONS BASED ON MAXIMUM ENTROPY FOR THE BREAKUP OF A CYLINDRICAL LIQUID JET

L. P. Chin

Systems Research Laboratories, Inc.

P. C. Hsing and R. S. Tankin

Northwestern University, Evanston, Illinois, USA

T. Jackson

Wright Patterson Air Force Base, Ohio, USA

A motion analyzer was used to measure the size and velocity distributions of droplets generated by the disintegration of a cylindrical liquid jet. The breakup of the liquid jet under consideration contains satellite droplets interspersed among the primary droplets, thus resulting in a bimodal distribution in size. The integrated velocity distribution of droplets is not Gaussian. The maximum entropy principle is used to model this phenomenon. Agreement between the model and the measurements is reasonably good.

INTRODUCTION

The process of producing droplets by the breakup of a cylindrical liquid jet is commonly called Rayleigh breakup [1, 2]. The use of a stimulated mechanism (forcing function) has been widely employed to obtain uniform droplets; this can be represented by $\delta(D - D_0) \delta(U - U_0)$, a coupled delta function where D_0 denotes uniform droplet size and U_0 denotes uniform droplet velocity. Such droplets are essential in calibrating spray sizing instruments and in studying the fundamental aspects of spray evaporation and combustion. In general, a stream of droplets having uniform size is difficult to achieve without external stimulation, even when experiments are carefully conducted in a vibration-isolated environment. Such a jet, as a result of nonlinear instability, frequently has a propensity to produce relatively small "satellite" droplets interspersed among the main large droplets [3]. The existence and behavior of these satellite droplets depends on the initial flow conditions and the physical properties of the liquid jet.

The maximum entropy principle has been used successfully to study the droplet size and velocity distributions for nonstimulated cylindrical water jets without satellite droplets [4]. Unforced disturbances and complicated nonlinear breakup mechanisms produce a stream of droplets that deviates from the ideal (deterministic) uniform distributions in size

This work was supported in part by the Air Force Office of Scientific Research under contract F49620-92-J-0389. The authors would like to thank Prof. Xiang Li of the University of Victoria in Canada for his valuable comments.

NOMENCLATURE

A_e	area of prolate spheroid	k	nondimensional wave number
A_s	area of sphere	N	normalized droplet number
B	$12/We$	P_{ij}	joint probability
\overline{C}_{+1}	constant associated with constraint of primary (prolate spheroid) drops	S	information entropy
\overline{C}_{-1}	constant associated with constraint of satellite (spherical) drops	S_m	mass source term
D	diameter of droplet	S_{mv}	momentum source term
\overline{D}	nondimensional droplet diameter (D/D_{30})	S_{ke}	kinetic energy source term
D_c	diameter of liquid column near breakup	S_{se}	surface energy source term
D_{jet}	diameter of nozzle exit	\overline{U}	nondimensional velocity (U/U_{jet})
D_1	mean diameter of satellite droplets	U_{jet}	velocity of liquid column at nozzle exit
D_2	mean diameter of primary droplets	We	Weber number ($\rho U_{jet}^2 D_{30} / \sigma$)
D_{30}	mass mean diameter of droplets	$\alpha_0, \alpha_1, \dots, \alpha_6$	Lagrangian multipliers
D_{32}	sauter mean diameter	λ	Wavelength of instabilities in liquid column

and velocity. The present study extends the use of the maximum entropy principle to a stream of primary and satellite droplets whose size and velocity distributions are not deterministic and thus are described by probability distribution functions.

The concept of information entropy was developed by Shannon [5], and Jaynes [6] later extended this concept to the well-known method of maximum entropy formalism. This formalism can be applied to problems that involve probability, i.e., where insufficient information is available to obtain exact solutions. Tribus [7] showed that the concepts of heat and temperature in thermodynamics could be defined through the formalism of maximum entropy. The maximum entropy formalism asserts that the least prejudiced (biased) or most appropriate probability distribution is the one that maximizes Shannon's entropy—subject to the given constraints imposed on a physical probabilistic system (or process). The maximum entropy formalism can be applied to a system (or process) about which the available knowledge or information is limited and insufficient to permit predictions that are certain to be correct by a conventional deterministic approach.

Although there is no way, at present, of proving the maximum entropy principle, its physical meaning can be understood (or interpreted) from the thermodynamic point of view by the fact that both entropies, one defined by Shannon and the other defined in classic thermodynamics, are equivalent. The second law of thermodynamics dictates that the entropy of an isolated system always increases for any natural processes. When the entropy of the system reaches its maximum value, the system is in thermodynamic equilibrium. Therefore, the probability distribution derived from the maximum entropy principle can be interpreted as the probability distribution for the system that reaches local equilibrium under given conditions (constraints). Since the equilibrium state is unique for a given set of conditions, the probability distribution corresponding to an equilibrium state is also unique.

In addition to applying the maximum entropy principle to the breakup of a cylindrical jet, the maximum entropy principle also has been used to model the spray from a pressure atomizer, and a skewed monomodal size distribution was derived [8–12]. The predicted

size distributions as well as the velocity distributions agreed with the experimental measurements [4, 8, 11, 12]. The experimental results reported in these earlier articles were obtained using a phase Doppler particle analyzer (PDPA). In a recent article by van der Geld and Vermeer [13], a size distribution function of a spray having satellite drops was derived using maximum entropy formalism. In their derivation, however, the size distribution for the primary droplets is assumed to be Gaussian. Maximum entropy theory was used to obtain the size distribution for the satellite drops; the final distribution is a composite distribution. In the study presented here, no assumption was made a priori with regard to either the primary or satellite droplet distributions. A single probability distribution function, not a composite type, was obtained that incorporates both primary and satellite drops.

The goal of this article is to examine a flow system having a strong bimodal size distribution. Rayleigh breakup of a cylindrical liquid jet with satellite droplets is an ideal candidate. This is essentially a simple spray, which, however, has complex size and velocity distributions. Stimulating the flow (piezoelectrically, acoustically, etc.) can produce very reproducible flows having a bimodal size distribution that incorporates essentially two delta functions—one for the primary drops and another for the satellite drops. These flows have been studied by conventional deterministic approaches—linear or nonlinear stability analyses [14–18]. However, a Rayleigh liquid jet that is not externally stimulated produces droplets that vary in size and velocity and thus are described by probability distribution functions that are amenable to the maximum entropy approach used in this study.

EXPERIMENT

Background

The experimental setup used in this study is similar to that described by Chin et al. [4]. In that setup, the nozzle assembly had an orifice that was 50 μm in diameter. The 50 μm orifice was formed in a bimetal nozzle plate by the fabrication technique called electroforming [19]. By adjusting the flow rate (air pressure) and observing the breakup with a microscope, one can locate a range of flow rates where satellite drops have occurred. However, when attempting to use the PDPA, three problems became apparent.

1. The satellite drop is usually captured by either the succeeding or preceding primary (large) drop within several wavelengths downstream of the breakup plane. Which primary drop captures the satellite drop depends on where the ligament separation occurs first—on the fore side or the aft side of the primary drop [3]. In the meantime, the effect of aerodynamic drag on a satellite drop is greater than that on a primary drop, which results in coalescence of the satellite drop and the primary drop—even if the ligament separation from the fore and aft primary drops occurs simultaneously. Because of the wide probe area of the PDPA ($\sim 10^{-2} \text{ cm}^2$), the measurement must be made within the first few wavelengths after the breakup plane of the liquid jet; otherwise the close proximity of the primary droplet interferes with the measurement of the satellite droplet.
2. Because the breakup plane fluctuates more than several wavelengths, the PDPA normally “sees” the cylindrical column of liquid (upstream of breakup) or the

large droplets without the satellites (too far downstream of breakup, where coalescence has occurred or is about to occur). This became obvious when we examined printouts obtained from an ICCD camera focused through a microscope on the breakup region.

3. The PDPA size measurements are based on the assumption that the droplets are spherical, which is not the case—particularly with regard to the primary (large) droplets. They oscillate between different modes ("ellipsoidal"-like shapes).

In the present study, the experimental setup has been modified to overcome the difficulties described above. Microscopic photography was used instead of PDPA to measure the droplet size and droplet velocity.

Nozzle Assembly

A schematic diagram of the apparatus used to study the evolution of droplets is illustrated in Fig. 1. A compressed-air supply forces the water from a reservoir through a filter to the nozzle assembly. The nozzle assembly, which is positioned vertically with the fluid exiting downward, has an inner diameter of about 2.54 cm. Inside the nozzle assembly are three fine stainless steel screens; above these screens are several layers of glass beads that are 0.47 cm in diameter. Thus nonuniformity and rotation of the liquid flow are removed. The orifice in the nozzle assembly consists of a sapphire orifice with a 0.08-cm hole. The flow is accurately controlled by a needle valve placed between the pressure source and the pressurized water tank, and a ball valve placed upstream of the water filter. The operating pressure drop across the nozzle assembly for this test was 7.6 kPa, yielding a volumetric flow rate of 2 ml/s. The volumetric flow rate was measured by weighing the total mass of water collected over a selected interval of time.

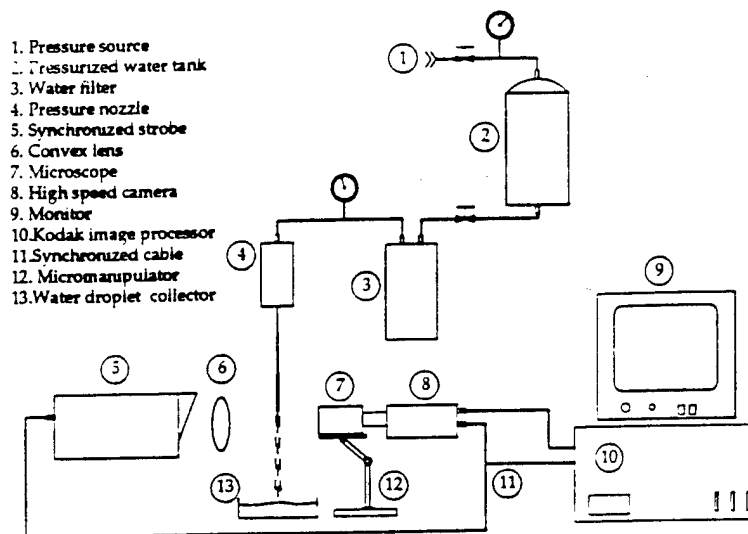


Fig. 1 Schematic drawing of the droplet generator setup.

Image Analysis System

A Kodak image analyzer was used to take pictures of the water droplets. The water issues from the nozzle assembly as a liquid column. This liquid column breaks up into droplets about 10 cm downstream from the orifice. The motion analyzer was set up about 10 cm downstream of the orifice to record the droplet formation in the vicinity of the breakup region. A strobe light having a very short pulse duration (less than a microsecond) was used to provide illumination of the droplets. The strobe flash is of sufficiently short exposure time to provide images of the droplets with little distortion due to droplet motion—which is particularly important for measuring the size of the satellite droplets. To increase the intensity of the strobe light at the test section, a convex lens was used to focus the strobe light to a circle about 2.54 cm in diameter at the plane of the droplets. The illuminating strobe light and the image camera were both triggered by a synchronized signal from the image processor. The images "seen" by the camera were enlarged 10-fold by a microscope. The strobe light, which back-lighted the droplets, was slightly offset from the line of sight.

As stated earlier, measurements must be made on droplets near the breakup region, otherwise many of the satellite drops may have coalesced with primary (large) drops. Due to the influence of inherent instabilities from various sources, the breakup plane is not fixed in space and was found to fluctuate about ± 1.5 cm. This fluctuation was more than the view area seen through the microscope. Thus, some of the images had only a cylindrical column of water with no droplets (the image is upstream of the breakup plane), whereas some of the other images have satellite droplets on the verge of coalescing with the primary drop. Possibly some satellite drops may have already coalesced with primary drops and we missed counting them. In the experiment, a total of 1017 primary droplets and 877 satellite droplets were counted and analyzed. Thus, the measured number ratio of primary droplets to satellite droplets at breakup is 1.16.

Results and Analysis

Figure 2 shows the images taken at a framing rate of 1500 pictures per second. In these images the droplets are traveling from left to right. Both primary and satellite droplets appear. In Fig. 2a, no satellite drop is seen between droplets labeled "b" and "c" in the first frame nor between "e" and "d" of the third frame. In Fig. 2b, the satellite drop between droplets "b" and "c" in the first frame is about to coalesce with droplet "b" in the second frame. There are some instances where there are two satellite drops between the two primary drops.

The satellite drops are nearly spherical in shape; on the other hand, the primary drops are relatively large in size, but are far from spherical. It was necessary to characterize the drop sizes by an effective diameter. It was assumed that all the droplets are ellipsoidal in shape (either prolate or oblate spheroids), with their axes of symmetry along the flow direction (vertical in experiments and horizontal in images shown in Fig. 2). By measuring the major and minor axes of the droplet, the volume of the droplet was calculated. The diameter of a sphere with an equivalent volume was obtained and its diameter was defined as the effective diameter for the droplet. The accuracy of the measurements of the major and minor axes for an individual drop is ± 22.5 μm . The standard deviation of the mean was computed from 50 such measurements on a typical satellite drop and primary drop—the values were 2.2 μm

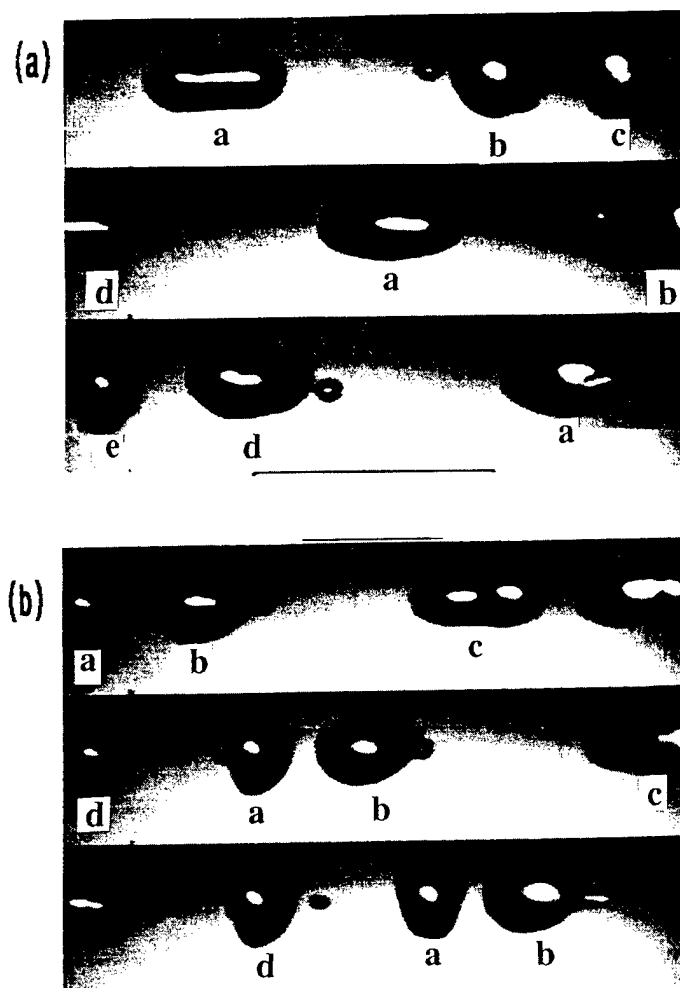


Fig. 2 Typical images taken with the Ektapro motion analyzer 10 cm from the nozzle.

(mean diameter is 0.32 mm) for the satellite drop and 3.5 μm (mean diameter is 1.35 mm) for the primary drop. Thus the measured effective diameters of the droplets are a good representation of the droplet sizes. There may be some question concerning their accuracy, but they do not have to be any more accurate because the effective diameters are nondimensionalized with the mass mean diameter (D_{30}), and D_{30} is computed based on the measured effective diameters. As a further verification of the measured diameters of the nonspherical primary drops, measurements were made far downstream (approximately 50 cm from the nozzle). At this location (see Fig. 3), the primary drops are round and their diameters (equal to effective diameters) can be measured directly (the increase in volume due to coalescence with a satellite drop is negligible). Although there may be coalescence between some primary drops at 50 cm from the nozzle, the diameters at the peak of the distribution curves in both cases (at 10 and 50 cm from the nozzle) agree at 1.37 mm.

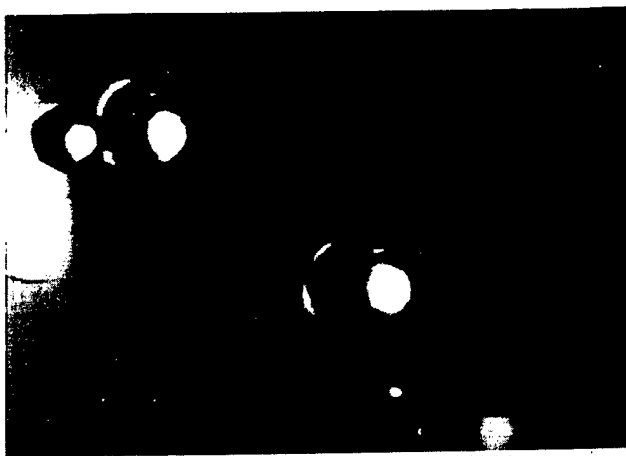


Fig. 3 Typical image taken with the Ektapro motion analyzer 50 cm from the nozzle.

The measured droplet size distribution is shown in Fig. 4. There are two peaks, one for the satellite droplets and the other for the primary droplets. The amplitude of the peak for the primary droplets is slightly larger than that for the satellite droplets. As mentioned earlier, a few satellite drops may not have been counted because of coalescence prior to the time of the images under consideration. Using the measured effective diameters, D_{30} was

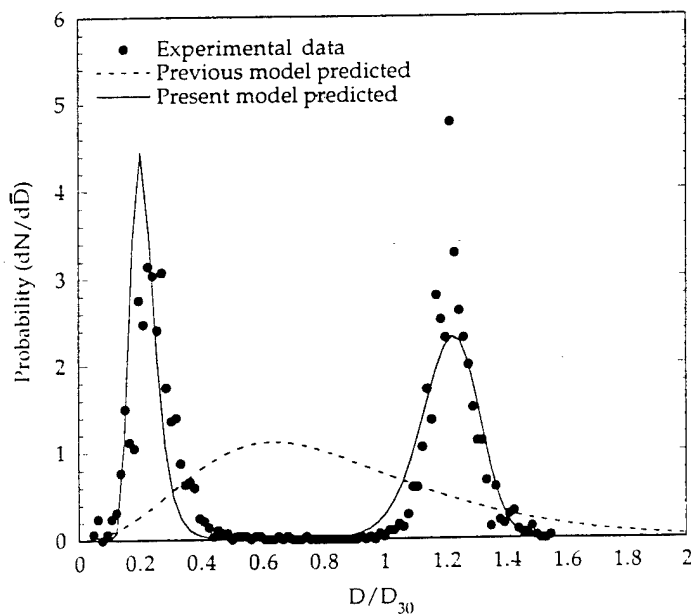


Fig. 4 Comparison between experimental and predicted droplet size distributions.

calculated to be 1.1 mm. From recorded images similar to those shown in Fig. 2, the velocities of the droplets at the breakup plane were measured. The mean velocity of the droplets at the breakup region was found to be 4.15 m/s. An experimentally measured velocity distribution will be presented later and compared with the predicted velocity distribution function.

In order to compare the drop size measurements with data in the literature, it is necessary to determine the nondimensional wave number, $k = \pi D_c / \lambda$. λ , the wavelength, was measured from data such as that shown in Fig. 5. λ equals 3.5 mm and D_c (the diameter of the liquid column near breakup) equals 0.79 mm; thus, k equals 0.71. This agrees well with the wave number at maximum growth rate ($k = 0.698$) under unforced Rayleigh breakup condition. Figure 6 is a plot showing data presented by Lefrance [18] and by Rutland and Jameson [17]. On this plot the theoretically predicted drops sizes (primary and satellite) from [18] are also presented, and these are seen as solid and dashed curves. Two data points obtained from our measurements are marked by triangles in Fig. 6, and they are found to agree with the data in [18] and [17]. This agreement further enhances confidence in our experimental data.

THEORETICAL MODEL

The maximum entropy principle is applied from one local equilibrium state (at the nozzle exit) to another local equilibrium state (where the droplets are formed) and does not become involved with the details of the liquid column instability characteristics such as the random onset and selective growth of undulations, the breakup mechanisms, the ligament formation between two primary drops, their final breakup into satellite droplets, etc. These processes are just the physical mechanisms required for the natural occurrence of the transition from one equilibrium state (at the nozzle exit) to another (where the droplets are formed). (The droplets that are formed are oscillating and thus not strictly in equilibrium. However, the energy due to the oscillations is small compared to the translational kinetic

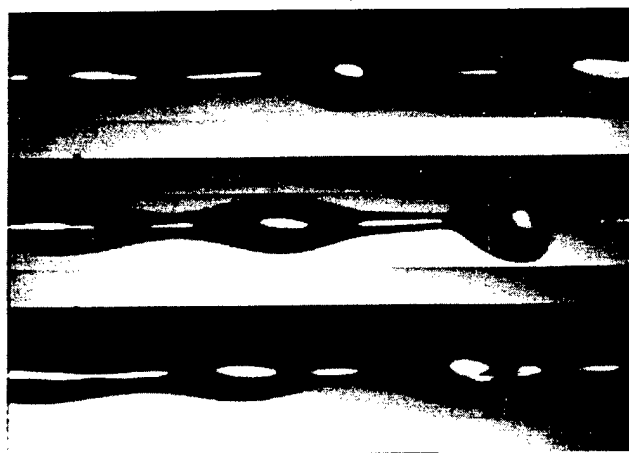


Fig. 5 Typical image of the surface of the cylindrical jet prior to breakup.

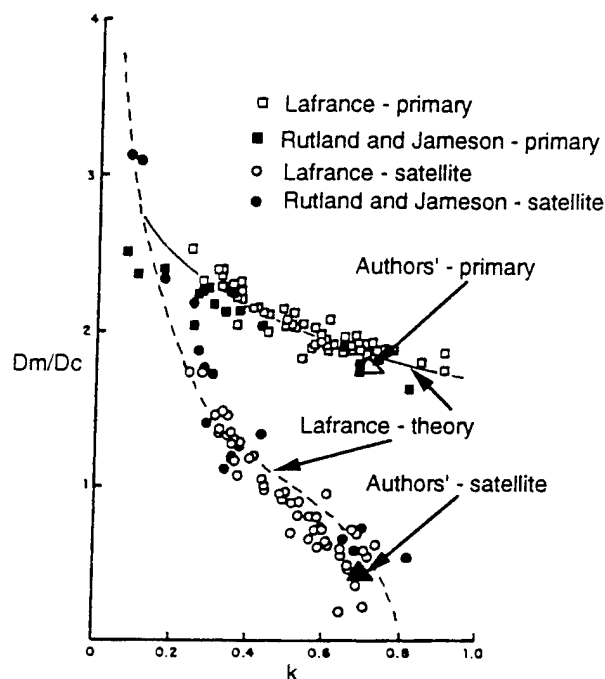


Fig. 6 Comparison of wave-number and results obtained in present experiments and those of Lafrance [18] and Rutland and Jameson [17].

energy. Therefore we modeled this problem as a quasi-equilibrium process—that is, the oscillating drops are infinitesimally near equilibrium.) The detailed physical processes of the transition plays no role in the maximum entropy approach, which only takes into account, from a statistical point of view, the macroscopic average quantities constraining an indeterminate process. In maximum entropy formalism, the transition from one local equilibrium state to another is linked through physical laws such as conservation of mass, momentum, and energy. We do not imply that the maximum entropy approach will replace the conventional deterministic approach; whenever possible, the deterministic approach should be used. However, for a stochastic process such as the one under consideration, the experimental results are represented by a probability distribution function, for which a deterministic approach is not appropriate. For this problem, the maximum entropy approach may prove useful.

Detailed formulation and derivation of the maximum entropy principle, as presented here, have been published [4, 8, 20]. However, there is one significant modification for the model presented here. The previously presented model is derived based on the assumption that the droplets are spherical. In the present study, the satellite drops in most instances are nearly spherical; however, the primary (large) drops are far from spherical. Their actual shapes, which vary from frame to frame, are complicated and difficult, if not impossible, to describe mathematically. To account for these nonspherical shapes, two new constraints are introduced—one related to the surface/volume ratio of small droplets and the other related to the nonsphericity of large droplets.

1. Since the small drops (satellite) are nearly spherical, the area/volume ratio of a satellite drop is equal to $6/D$ (where D is the diameter of the droplet). Therefore, it was assumed in this model that the mean area/volume ratio for the group of small satellite droplets varies inversely with \bar{D} (D/D_{30}). This constraint is dominated by small droplets ($\bar{D} \ll 1$).
2. It is known that the surface-to-volume ratio for a sphere is smaller than that of any other shape having the same volume. From the examination of experimental data, it is observed that the larger the drops, the greater is the deviation from spherical shape. A mathematical model for large droplets based on experimental observations can be established by describing the large droplet as a prolate spheroid having a major axis a and a minor axis b . The surface area for a prolate spheroid (A_p) is greater than the surface area of a sphere (A_s) having the same volume. The greater the ratio of the major axis to the minor axis, the greater is the ratio A_p/A_s . If we assume that the ratio between the major axis and the minor axis follows this relationship, $a/b = \delta D_{eq}^\beta$, as the droplet size increases, then it is found that the ratio A_p/A_s is proportional to D_{eq} as shown in Fig. 7. D_{eq} is defined as the diameter of a sphere having the same volume as the prolate spheroid. The proportionality between A_p/A_s and D_{eq} depends on the values of δ and β , which indicate the degree of deviation for the shape of droplet from a sphere. It is clearly seen in Fig. 7 that the curves are approximately linear with D_{eq} . Therefore, as a second constraint, we assumed that A_p/A_s varies linearly with \bar{D} ($\bar{D} = D_{eq}/D_{30}$). This constraint is dominated by large (primary) droplets.

A schematic drawing for the breakup of a liquid jet and its control volume is shown in Fig. 8. The control volume begins at the orifice and extends several (wavelengths

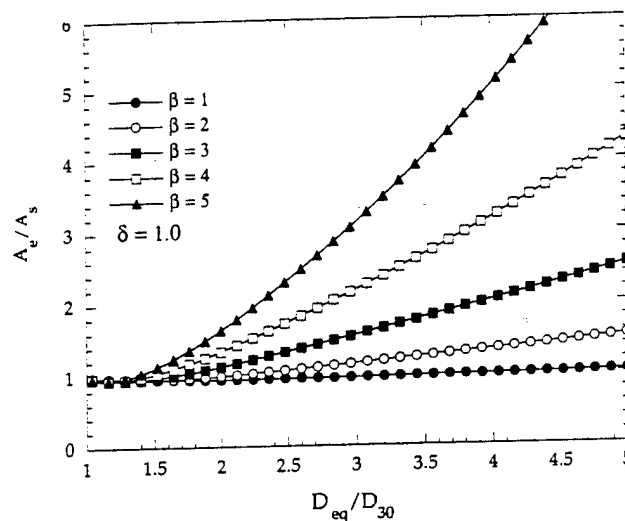


Fig. 7 A plot of A_p/A_s versus D_{eq} , where A_p is the area of a prolate spheroid, A_s is the area of a sphere having the same volume, a and b are the major and minor axes of the spheroid, and $a/b = \delta D_{eq}^\beta$.

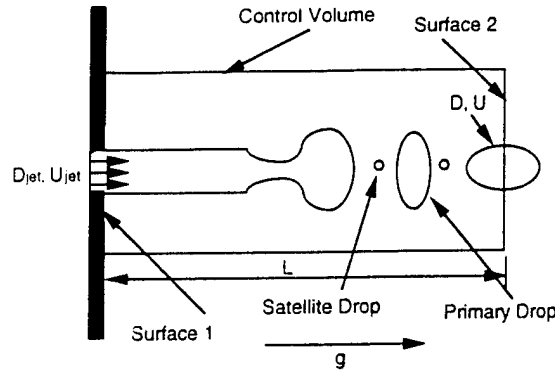


Fig. 8 Schematic drawing of the control volume chosen in this study to model the breakup of a liquid jet into droplets.

downstream of breakup. The liquid jet that enters the control volume through surface 1 has a diameter D_{jet} , and velocity U_{jet} . The droplets that emerge from the control volume through surface 2 have diameter D and velocity U . Because of the existence of individual droplets crossing surface 2, the mass, momentum, and energy leaving the control volume are not constant in time. Not only are there variations in diameter and velocity within the primary and satellite droplets, but at some instances the primary drop crosses surface 2 (as in Fig. 8) and at other instances the satellite drop crosses surface 2. Thus there are changes of these quantities (mass, momentum, kinetic energy flux, and surface energy flux) within the control volume in time. To maintain steady-state formulation, the conservation equations employed here will be derived using a time-averaged base.

Constraints Selected in Maximum Entropy Formulation

The entropy defined by Shannon [5] is expressed in the form

$$S = -K \sum_i \sum_j P_{ij} \ln(P_{ij}) \quad (1)$$

where S is called the information entropy, K is a constant, and P_{ij} is the relative frequency or joint probability of the occurrence of certain realizations (or results). The goal is to find the joint probability distribution, P_{ij} , that is realized with the greatest probability. Hence it is required that S is an extreme under whatever constraints are imposed in the physical system considered. Similar to the constraints used in the previous study for a liquid cylindrical jet [4] without satellite droplets, the balance of mass flux, momentum flux, and energy fluxes between the nozzle exit and the liquid breakup plane (in Fig. 8) can be expressed as follows:

$$\text{Mass flux:} \quad \frac{\pi}{6} \rho \dot{n} \sum_i \sum_j P_{ij} D_i^3 = \dot{m} + S_m = \frac{\pi}{4} \rho D_{jet}^2 U_{jet} + S_m \quad (2)$$

$$\text{Momentum flux:} \quad \frac{\pi}{6} \rho \dot{n} \sum_i \sum_j P_{ij} D_i^3 U_j = \dot{m} U_{jet} + S_{mv} = \frac{\pi}{4} \rho D_{jet}^2 U_{jet}^2 + S_{mv} \quad (3)$$

$$\text{Kinetic energy flux: } \frac{\pi}{12} \rho \dot{n} \sum \sum P_{ij} D_i^3 U_j^2 = \frac{1}{2} \dot{m} U_{\text{jet}}^2 + S_{ke} = \frac{\pi}{8} \rho D_{\text{jet}}^2 U_{\text{jet}}^3 + S_{ke} \quad (4)$$

$$\text{Surface energy flux: } \pi \sigma \dot{n} \sum \sum P_{ij} D_i^2 = \pi \rho D_{\text{jet}} U_{\text{jet}} + S_{se} \quad (5)$$

In these constraints, P_{ij} represents the joint probability of finding a droplet having diameter D_i and velocity U_j ; D_{jet} and U_{jet} are the diameter of the nozzle exit and the mean liquid velocity leaving the nozzle exit; ρ and σ are the density and the surface tension of the liquid at room temperature; \dot{n} is the number of droplets produced per unit time. The source terms, S_m , S_{mv} , S_{ke} , and S_{se} , account for the transport effects of mass, momentum, and energy between the two phases (liquid and gas) in the region of continuous liquid jet column. In addition, the sum of probability equals 1; that is, $\sum \sum P_{ij} = 1$.

The two new constraints mentioned above can be expressed as follows:

$$\text{Spherical droplets: } \dot{n} \sum \sum P_{ij} \left(\frac{A}{V} \right)_i \propto \dot{n} \sum \sum P_{ij} D_i^{-1} = \dot{n} C_{-1} D_{30}^{-1} \quad (6)$$

$$\text{Nonspherical droplets: } \dot{n} \sum \sum P_{ij} \left(\frac{A_e}{V_s} \right)_i \propto \dot{n} \sum \sum P_{ij} D_i^{+1} = \dot{n} C_{+1} D_{30}^{+1} \quad (7)$$

D_{30} (mass mean diameter) and U_{jet} (initial mean liquid velocity) are chosen to nondimensionalize the size ($\bar{D} = D/D_{30}$) and velocity ($\bar{U} = U/U_{\text{jet}}$) of the droplets, respectively. Thus, the constraint of normalization can be expressed in integral form as

$$\iint f \bar{D} d\bar{D} d\bar{U} = 1.$$

Since the droplets are assumed to be produced in a saturated air environment, there is no mass flux loss or gain during the breakup process, and, the mass flow rate at surface 1 and surface 2 are equal on a time-averaged basis ($S_m = 0$). The constraints defined in Eqs. (2)–(7) have the following integral form:

$$\iint f \bar{D}^3 d\bar{D} d\bar{U} = 1 \quad (8)$$

$$\iint f \bar{D}^3 \bar{U} d\bar{D} d\bar{U} = 1 + \bar{S}_{mv} \quad (9)$$

$$\iint f \bar{D}^3 \bar{U}^2 d\bar{D} d\bar{U} = 1 + \bar{S}_{ke} \quad (10)$$

$$B \iint f \bar{D}^2 d\bar{D} d\bar{U} = 2B/3\bar{D}_{\text{jet}} + \bar{S}_{se} \quad (11)$$

$$\iint (f/\bar{D}) d\bar{D} d\bar{U} = C_{-1} \quad (12)$$

$$\iint f \bar{D} d\bar{D} d\bar{U} = C_{+1} \quad (13)$$

Here, $B = 12/We$ and $We = \rho U_{jet}^2 D_{30} / \sigma$ in Eq. (11). f is the continuous joint probability density function (PDF) of P_{ij} . By maximizing Shannon's entropy (S) subject to the above constraints [Eqs. (8)–(13)], f will have the following form:

$$f = 3\bar{D}^2 \exp\left(-\alpha_0 - \alpha_1 \bar{D}^3 - \alpha_2 \bar{D}^3 \bar{U} - \alpha_3 \bar{D}^3 \bar{U}^2 - \alpha_4 B \bar{D}^2 - \alpha_5 \bar{D}^{+1} - \alpha_6 \bar{D}^{-1}\right) \quad (14)$$

Further discussion of the constraint given in Eq. (12) is necessary because this constraint is similar to one used by Sellens [11]. However, the physical motivation is entirely different. In Sellen's formulation this constraint is introduced to reduce his PDF at small droplet sizes—otherwise the PDF does not go to zero as droplet sizes go to zero. In our formulation, the PDF goes to zero as droplet sizes go to zero without this constraint [Eq. (12)]. The two new constraints introduced in this model account for the sphericity of the small satellite drops [Eq. (12)] and the nonsphericity of the large primary drops [Eq. (13)].

Estimates of Source Terms and Constants: \bar{S}_{mv} , \bar{S}_{ke} , \bar{S}_{se} , C_{-1} , and C_{+1}

In order to predict the droplet size distribution from a liquid cylindrical jet, the quantities on the right-hand side of the constraints [Eqs. (8)–(13)] are required to be known. Similar to the procedure used in the previous studies [4, 8], the source terms and the two constants C_{-1} and C_{+1} are estimated based on some measured mean droplet data, such as mass mean diameter (D_{30}), Sauter mean diameter (D_{32}), mean velocity (U_m), etc. The following source terms were obtained (explanation will follow): $\bar{S}_{mv} = 0.037$, $\bar{S}_{ke} = 0.08$, $\bar{S}_{se} = 0.041$, $C_{-1} = 2.23$ and $C_{+1} = 0.76$.

The values of \bar{S}_{mv} and \bar{S}_{ke} were obtained from the measurements of U_{jet} and U_m . Using the control volume shown in Fig. 8, and knowing \dot{m} and the velocities into and out of the control volume ($U_{jet} = 4.0$ m/s and $U_m = 4.15$ m/s), \bar{S}_{mv} and \bar{S}_{ke} were computed. They were found to be 0.037 and 0.08, respectively. Since total energy must be conserved for the sum of kinetic energy, surface energy, and potential energy ($2gh/U_{jet}^2 = 0.12$), \bar{S}_{se} is determined to be about 0.04.

There are two ways of evaluating C_{-1} and C_{+1} .

1. C_{-1} and C_{+1} can be estimated from measured values of D_{30} and D_{32} . In this case, D_{30} and D_{32} were found to be 1.10 and 1.33 mm, respectively. If one assumes that the number of satellite drops equals the number of primary drops, then

$$D_{30} \approx \left(\frac{D_1^3 + D_2^3}{2} \right)^{1/3} \quad (15)$$

$$D_{32} \approx \frac{D_1^3 + D_2^3}{D_1^2 + D_2^2} \quad (16)$$

where D_1 is the mean diameter of the satellite drops, and D_2 is the mean diameter of the primary drops. Solving Eqs. (15) and (16) for D_1 and D_2 yields $D_1 = 0.30$ mm and $D_2 = 1.37$ mm. Because

$$C_{-1} = \left(\frac{1}{D_1} + \frac{1}{D_2} \right) \times \frac{D_{30}}{2} \quad (17)$$

$$C_{+1} = \frac{D_1 + D_2}{D_{30}/2} \quad (18)$$

Eq. (17) yields $C_{-1} = 2.23$ and Eq. (18) yields $C_{+1} = 0.76$. In summary, to evaluate the constraints using this method, the following measurements are required: D_{32} , D_{30} , U_{jet} , U_m , and breakup length, h (where the measurements were made).

- Equations (12) and (13) are used to calculate C_{-1} and C_{+1} directly from experimental measurements on individual droplets. This yields $C_{-1} = 2.49$ and $C_{+1} = 0.77$. The resulting distribution is essentially the same as that shown in Fig. 4.

It is very important to emphasize that the procedure described above is not merely a curve-fitting technique. Although the continuous joint probability distribution function [Eq. (14)] has seven constants (Lagrange multipliers $\alpha_0 - \alpha_6$), it was derived from a well-established statistical method in terms of a set of physical constraints. These constants cannot be chosen freely, but are solved according to the seven constraints imposed. If a pure curve-fitting method (e.g. least-squares method) is used to calculate the seven constants based on direct experimental measurements, the resulting distribution function will not be guaranteed to satisfy all the constraints [normalization and Eqs. (8)–(13)] required physically.

Domain of Integration

In this section we will respond to a point raised by van der Geld and Vermeer [13] regarding the sensitivity of the predicted size distribution function to the domain of integration. The limits of integration chosen to predict the droplet distributions are important only when the resulting probabilities do not approach zero near the integration limits. For the domain of droplet size, the upper limit should be chosen such that the PDF approaches zero at the limit of integration. The results presented in Figs. 7 and 8 of [13] clearly show several distributions that increase exponentially near the upper limit of integration. This, of course, is not physically reasonable. If we obtained such a result, which we did not, it would not be accepted as a correctly predicted distribution. The reasons for predicting such unrealistic distributions are twofold: (1) The spray quantities [right-hand sides of Eqs. (9)–(13)] in the set of constraints are not prescribed appropriately, that is, unreasonable estimates are made of the spray quantities; (2) an incomplete set of constraints are imposed, thus resulting in a distribution of improper functional form. In our opinion, it is not appropriate to justify the sensitivity of integration domains based on results (as presented in [13]) that were obtained using either unreasonable estimates of the spray quantities or an incomplete set of constraints. For the present model, if the predicted

droplet size distribution is physically reasonable (as in the case presented in this article as well as those in [4] and [8]), then the integration limits will not have an effect on the results.

In the integration domain for droplet velocity, the effect of integration limits appears only for small droplets ($\bar{D} \ll 1$), because the amplitude of velocity PDF for small droplet sizes approaches zero at both velocity limits very slowly. As a result, the velocity distribution for small droplets is much wider than that for large droplets (see Fig. 8a in [8]). To minimize the influence of the velocity domain, one can expand the velocity domain further such that the PDF becomes sufficiently small near the limits (an infinite velocity domain is ideal, but computationally impossible). It is important to emphasize, however, that the velocity domain has very little influence on the droplet size distribution as long as the domain is sufficiently large. The sensitivity of the predicted PDF on the integration domain as presented by van der Weld and Vermeer has not been observed by us.

RESULTS AND DISCUSSION

Once the source terms and constants in the constraints are determined, the droplet size distribution is obtained by integrating Eq. (14) over \bar{U} . This yields

$$\frac{dN}{d\bar{D}} = \frac{3}{2} \sqrt{\frac{\pi \bar{D}}{\alpha_3}} \theta(\bar{D}, \bar{U}) \exp \left[-\alpha_0 - \left(\alpha_1 - \frac{\alpha_2^2}{4\alpha_3} \right) \bar{D}^3 - \alpha_4 B \bar{D}^2 - \alpha_5 \bar{D}^{+1} - \alpha_6 \bar{D}^{-1} \right] \quad (19)$$

where $\theta(\bar{D}, \bar{U}) = \text{erf}(X_{\max}) - \text{erf}(X_{\min})$ and $\text{erf}(X)$ is the error function of X :

$$X_{\max} = \left(\bar{U}_{\max} + \frac{\alpha_2}{2\alpha_3} \right) \sqrt{\alpha_3 \bar{D}^3} \quad X_{\min} = \left(\bar{U}_{\min} + \frac{\alpha_2}{2\alpha_3} \right) \sqrt{\alpha_3 \bar{D}^3} \quad (20)$$

Here, N is the normalized droplet number, and \bar{U}_{\max} and \bar{U}_{\min} are the integration limits.

The solid line in Fig. 4 shows the predicted size distribution from Eq. (19), where the values of the source terms, C_{-1} , and C_{+1} listed above, are used. One can see that there is reasonably good agreement between the experimental size distribution and the computed size distribution. A predicted size distribution having the same source terms without constraints C_{-1} , and C_{+1} is also shown in Fig. 4. This plot is not bimodal and does not agree with the experimental data. Thus, to obtain a bimodal size distribution for Rayleigh breakup of a cylindrical jet using the maximum entropy principle, one must introduce additional constraints such as C_{-1} , and C_{+1} in our model.

In Fig. 9 are plots of the experimental and computed velocity distributions obtained from the probability density function [Eq. (14)]. Again, it is seen that there is reasonably good agreement between experimental and computed velocity distributions. It should be noted that the velocity distribution for both the experimental and computed curves are broad at the base and merge rather abruptly into a rather narrow distribution that is not a Gaussian shape. To further explain this non-Gaussian shape, the joint probability distribution function, $f(\bar{D}, \bar{U})$, is plotted in Fig. 10. The velocity distributions for the satellite drops and the primary drops are Gaussian individually, but the integrated velocity distribution is a non-Gaussian distribution. Figure 10 shows that the satellite drops have a much

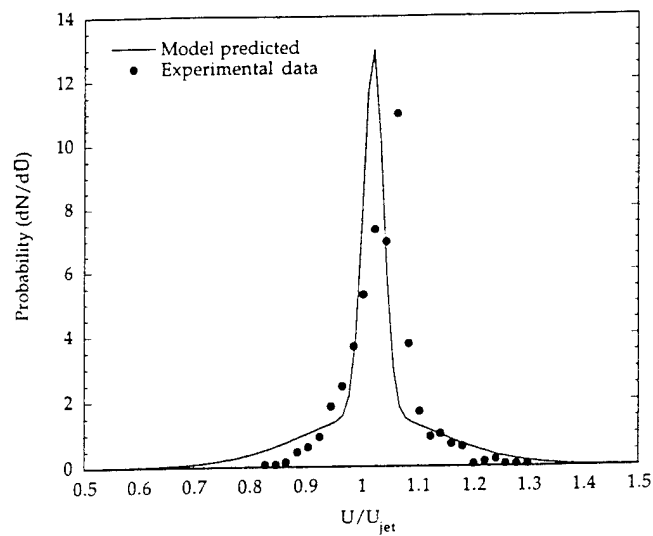


Fig. 9 Comparison between experimental data and predicted droplet velocity distribution.

broader velocity distribution than the primary drops. Physically, one would expect a broader velocity distribution for the satellite drops because their velocity variance depends to a large extent on where the ligament separation first occurs—on the fore side of the primary drop (giving the satellite a higher velocity) or on the aft side of the primary drop

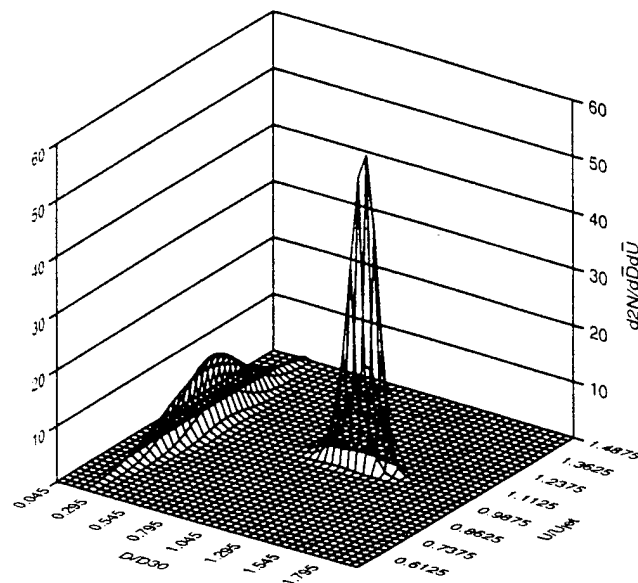


Fig. 10 Three-dimensional plot of predicted joint probability distribution function.

(giving the satellite a lower velocity). Thus, the maximum entropy solution predicts a velocity distribution that accounts for the effect of ligament separation without specifically considering this in the formulation of the problem. This illustrates the point that the detailed physical processes involving the transition from one equilibrium state to another equilibrium state play no role in the maximum entropy approach.

A question arises: What would happen if the constraints involving nonsphericity (C_{-1} and C_{+1}) were introduced to formulate a pressure atomizer experiment [8] where the measured size distribution is not bimodal? Figure 11 shows the predicted droplet size distribution (labeled Model A) presented in [8] without the constraints C_{-1} and C_{+1} . The curve labeled Model B is a plot where $C_{-1} = 2.10$ and $C_{+1} = 0.73$ (the other constraints in both models are kept the same). The values of C_{-1} and C_{+1} were obtained by evaluating Eqs. (12) and (13) from the measurement data for the pressure atomizer. Even though C_{-1} and C_{+1} were introduced, there is no bimodal size distribution (Model B)—it remains skewed monomodal. Thus the introduction of the constraints C_{-1} and C_{+1} does not necessarily result in a bimodal size distribution. A bimodal size distribution depends on the other constraints (involving conservation of mass, momentum, surface energy, and kinetic energy) as well.

Rayleigh breakup of a cylindrical liquid jet without satellites was also examined [4]. This system results in a distribution that is uniform in size and velocity. The values of C_{-1} and C_{+1} obtained from experimental data are 1^+ and 1^- , respectively. Using $C_{-1} = 1.04$ and $C_{+1} = 0.98$, the resulting droplet size (and velocity) is uniform—not exhibiting any bimodal shape.

In summary, the occurrence of a bimodal size distribution depends on the entire set of constraints imposed, not just the introduction of C_{-1} and C_{+1} .

CONCLUSIONS

A model based on the maximum entropy formulation has been derived for a system experiencing Rayleigh jet breakup with satellite droplets. The agreement between theory

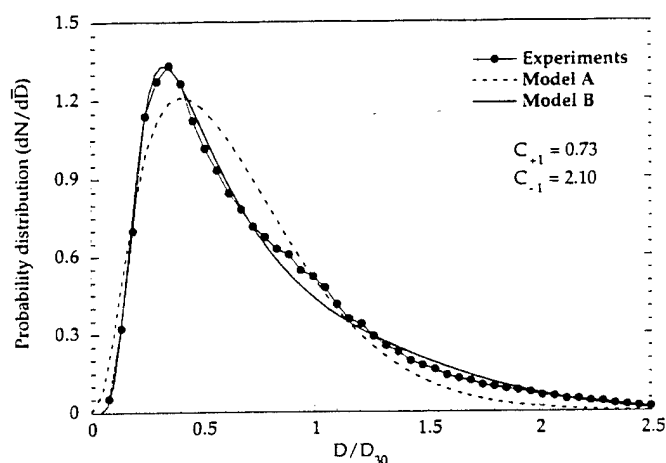


Fig. 11 Plot of computed and measured droplet size distribution from a pressurized atomizer.

and experiment is reasonably good. Both the computed velocity and the size distributions agree with the measured distributions. In order to obtain a bimodal size distribution function, it was necessary to modify the previous model [4] to account for the nonsphericity of the large droplets. Two new constraints as expressed in Eqs. (12) and (13) were introduced. The integrated velocity distributions from both the experiments and the model were not Gaussian. In conclusion, the maximum entropy model is very robust for predicting complicated droplet size and velocity distributions of sprays under a variety of flow conditions.

REFERENCES

1. L. Rayleigh, On the Instability of Jets, *Proc. London Math. Soc.*, vol. 10, 1879.
2. L. Rayleigh, Further Observations upon Liquid Jets, *Proc. R. Soc. London*, vol. 34, 1882.
3. D. B. Boggy, Drop Formation in a Circular Liquid Jet, *Annu. Rev. Fluid Mech.*, vol. 11, 1979.
4. L. P. Chin, P. G. LaRose, R. S. Tankin, T. Jackson, J. Stutrud, and G. Switzer, Droplet Distributions from the Breakup of a Cylindrical Liquid Jet, *Phys. Fluids A*, vol. 3, no. 8, 1991.
5. C. E. Shannon, A Mathematical Theory of Communication, *Bell System Tech. J.*, vol. 27, 1948; Also in D. Slepian (ed.), *Key Papers in the Development of Information Theory*, IEEE Press, New York, NY, 1974.
6. E. T. Jaynes, Information Theory and Statistical Mechanics, *Phys. Rev.*, vol. 106, vol. 108, 1957.
7. M. Tribus, *Thermostatistics and Thermodynamics*, Van Nostrand, New York, NY, 1961.
8. X. Li, L. P. Chin, R. S. Tankin, T. Jackson, J. Stutrud, and G. Switzer, Comparison between Experiments and Predictions Based on Maximum Entropy for Sprays from a Pressure Atomizer, *Combustion and Flame*, vol. 86, 1990.
9. R. W. Sellens and T. A. Brzustowski, A Prediction of Drop Size Distribution in a Spray from First Principles, *Atomization and Spray Technol.*, vol. 1, pp. 89–102, 1985.
10. R. W. Sellens and T. A. Brzustowski, A Simplified Prediction of Droplet Velocity Distributions in a Spray, *Combustion and Flame*, vol. 65, pp. 273–279, 1986.
11. R. W. Sellens, Prediction of the Droplet Size and Velocity Distribution in a Spray Based on the Maximum Entropy Formalism, *Particle Particle Syst. Charact.*, vol. 6, pp. 17–27, 1989.
12. R. W. Sellens, *Atomization and Sprays*, vol. 3, pp. 2910–310, 1993.
13. C. W. M. van der Geld and H. Vermeer, Prediction of Droplet Size Distributions in Sprays Using the Maximum Entropy Formalism: The Effect of Satellite Formation, *Int. J. Multiphase Flow*, vol. 20, pp. 363–381, 1994.
14. M. C. Yuen, Nonlinear Capillary Instability of a Liquid Jet, *J. Fluid Mech.*, vol. 33, p. 151, 1968.
15. E. F. Goedde and M. C. Yuen, Experiments on Liquid Jet Instability, *J. Fluid Mech.*, vol. 40, p. 495, 1970.
16. A. H. Nayfeh, Nonlinear Stability of a Liquid Jet, *Phys. Fluids*, vol. 13, p. 841, 1970.
17. D. F. Rutland and G. J. Jameson, Theoretical Prediction of the Size of Drops Formed in the Breakup of Capillary Jets, *Chem. Eng. Sci.*, vol. 25, p. 1689, 1970.
18. P. Lafrance, Nonlinear Breakup of a Laminar Jet, *Phys. Fluids*, vol. 17, p. 1913, 1974.
19. J. L. Dressler, Two-Dimensional, High Flow, Precisely Controlled Monodispersed Drop Source, Final Report, Wright Laboratory, WL-TR-2049, 1993.
20. X. Li and R. S. Tankin, Droplet Size Distribution: A Derivation of a Nukiyama-Tanasawa Type Distribution Function, *Combustion Sci. and Technol.*, vol. 57, p. 65, 1987.

BI-Modal Size Distributions Predicted by Maximum Entropy are Compared with Experiments in Sprays

L. P. CHIN and G. SWITZER *Systems Research Laboratories, Inc. Dayton, Ohio 45433*

R. S. TANKIN *Northwestern University Evanston, Illinois 60208*

T. JACKSON and J. STUTRUD *Wright-Patterson Air Force Base, Dayton, Ohio 45433*

(Received July 6, 1994; in revised form July 5, 1995)

ABSTRACT—A theoretical formulation based on maximum entropy principles is presented to predict the droplet size and velocity distributions of sprays in an isothermal environment. The joint droplet distribution function is derived subject to the constraints of mass flow rate, momentum flux, and two modes of energy fluxes (kinetic and surface). A simpler model, which reduces the number of constraints by three, is derived by choosing an adequate velocity integration range. This maximum entropy principle spray model is tested by comparing the calculated distributions with experimental measurements presented by the authors for a hollow cone, non-swirl spray nozzle and the experimental results obtained by other researchers for hollow cone, swirl spray nozzles. For a specific droplet size, the droplet velocity distribution is Gaussian. The droplet size distribution is much more complicated; three types of distributions may occur—positively skewed mono-modal, uniform size (in the limit approaching a delta function), and bi-modal. This study is concerned mainly with the bi-modal size distribution.

Key Words: Sprays, maximum entropy, bi-modal distributions

INTRODUCTION

Sprays play an important role in the operation of combustion systems and can improve performance and reduce pollutant emission. The spray characteristics due to the atomization of liquid fuel, such as occurs in gas turbine engines, internal combustion engines, industrial furnaces, etc., have been the focus of research for many years. One aspect in the modeling of sprays is to understand the detailed information about the droplet distributions in size and velocity. Several famous droplet size distribution functions (Mugele and Evans, 1951 and Tishkoff and Law, 1977) are widely used by many researchers and engineers. However, due to the complicated nature of sprays in various combustion systems, none of these functions can adequately describe all sprays.

In statistical mechanics, Jaynes', 1957 maximum entropy principle is a method of statistical inference to solve a probability problem when the information available is limited to some average quantities (constraints); such as, the mean, variance, etc. From this limited information, the most probable probability distribution will be the one that maximizes the Shannon entropy. Maximum entropy principle has been successfully applied in many problems arising out of several disciplines, e.g., thermodynamics,

economics, business and finance, transportation, geography, fluid dynamics, image processing, etc. The basic concept and derivation of the maximum entropy principle can be found in several books (Levine and Tribus, 1979; Kapur and Kesavan, 1992).

Recently, the maximum entropy principle has become a useful tool in the area of spray combustion to obtain droplet distributions. The diversity in the results is due to different choice of constraints imposed on sprays. A model with fewer constraints may simplify the problem as far as computations concerned, but may not be valid for the sprays in a complicated system. There are several examples of maximum entropy spray models developed since the mid-1980's: a Nukiyama-Tanasawa type model (Li and Tankin, 1987); a one-velocity/combined energy model (Li and Tankin, 1988; Li, Chin *et al.*, 1991); a one-velocity/separate energy model (Sellens and Brzustowski, 1985; Chin *et al.*, 1991); and a two-velocity model (Sellens, 1987; Sellens, 1989). These models differ primarily by the number of droplet velocity components modeled and the energy flux (surface energy flux and kinetic energy flux) constraints imposed. All these models have been tested by comparing the calculated results with experimental data and agreement is reasonably good.

Our previous models (Li *et al.*, 1991 and Chin *et al.*, 1991) will be modified and extended in this paper. In an earlier paper by Chin and Tankin 1991, bi-modal size distributions were predicted using the maximum entropy model, but no experimental observations were known by the authors, at the time, to corroborate this prediction. Thus, one of the main purposes of this paper is to compare the maximum entropy model with an experimentally determined bi-modal size distributions. In a recent paper by van der Geld and Vermeer [1994], a bi-modal size distribution was discussed using maximum entropy formalism. However in their derivation, the size distribution for the primary (large) drops was assumed to be Gaussian. The maximum entropy theory was used to obtain the size distribution of the satellite (smaller) drops; the final distribution is a composite distribution. In the study presented here, no assumption was made *a priori* with regard to the size distribution. A single probability distribution, not a composite type, was obtained that yielded a bi-modal size distribution. All three droplet velocity components for any coordinate system will be included in the momentum flux and kinetic energy flux constraints. As a result, the previous models with fewer velocity components are special cases of this more general model.

THEORETICAL FORMULATION

1. Jaynes' Maximum Entropy Principle

Entropy, defined by C. E. Shannon [1948], has been used to measure the uncertainty of a probability distribution in a statistical system. The probability distribution function that maximizes the Shannon entropy will be chosen out of all the probability distributions satisfying a given set of constraints (given information). Let $\mathbf{p} = (p_1, p_2, \dots, p_n)$ be a probability distribution, such that $p_i \geq 0$ for all i , and

$$\sum_{i=1}^n p_i = 1 \quad (1)$$

Shannon's measure of entropy for this distribution is given by

$$S(p) = -k \sum_{i=1}^n p_i \ln p_i; k \text{ is an arbitrary positive constant.} \quad (2)$$

For a random variable X having the discrete values x_1, x_2, \dots, x_n with the corresponding probabilities p_1, p_2, \dots, p_n , the expected values of the functions $g_1(X), g_2(X), \dots, g_m(X)$ are determined from the following relation for a positive r :

$$\sum_{i=1}^n p_i g_r(x_i) = \sum_{i=1}^n p_i g_{ri} = a_r, \quad r = 1, 2, 3, \dots, m \quad (3)$$

If $m+1 < n$, Eqs. (1) and (3) will not be sufficient to determine a unique set of p_1, p_2, \dots, p_n . To find the probability distribution with maximum Shannon's entropy, Eqs. (1) and (3) can be solved by using the method of Lagrange multipliers. Thus, we have

$$p_i = \exp(-\lambda_0 - \lambda_1 g_{1i} - \lambda_2 g_{2i} - \dots - \lambda_m g_{mi}) \quad (4)$$

where

$$\exp(\lambda_0) = \sum_{i=1}^n \exp\left(-\sum_{j=1}^m \lambda_j g_{ji}\right) \quad (5)$$

$$a_r = \sum_{i=1}^n g_{ri} \exp\left(-\sum_{j=1}^m \lambda_j g_{ji}\right) / \sum_{i=1}^n \exp\left(-\sum_{j=1}^m \lambda_j g_{ji}\right) \quad (6)$$

The Lagrange multipliers $\lambda_0, \lambda_1, \dots, \lambda_m$ are determined from Eqs. (5) and (6).

2. Maximum Entropy Spray Model

To apply the maximum entropy principle to a spray system, a joint probability distribution $p_{ijkl} = p(V_i, U_{1,j}, U_{2,k}, U_{3,l})$ is defined as the number probability of finding a droplet in a spray with volume $V_i (V_i = \pi D_i^3/6)$; and velocity $U = (U_{1,j}, U_{2,k}, U_{3,l})$. The three components of U represent the three orthogonal velocity components in any coordinate system (Cartesian, cylindrical, or spherical) depending on the geometrical configuration of spray system. The first constraint imposed on this probability distribution is the normalization constraint expressed as follows:

$$\sum_i \sum_j \sum_k \sum_l p(V_i, U_{1,j}, U_{2,k}, U_{3,l}) = 1 \quad (7)$$

If there are no further constraints for the spray system, then the probability distribution of droplets having a maximum Shannon's entropy is a uniform distribution. This is not a realistic case for a usual spray system. The other probable constraints for a spray system can be obtained by choosing a set of given functions $g_1(X), g_2(X), \dots, g_m(X)$ such that their mean values can be determined either experimentally or theoretically. Here, X denotes the droplet variables V and U . The chosen functions, $g_1(X), g_2(X), \dots, g_m(X)$, are related to some physical quantities of the spray. In this study, the following functions are chosen to construct the constraint equations for the spray. Note

that each droplet is assumed to be spherical in shape.

$$g_1(V, \mathbf{U}) = \rho_d V \quad \text{mass of droplet}$$

$$g_2(V, \mathbf{U}) = \sigma(6\sqrt{\pi}V)^{2/3} \quad \text{surface energy of droplet}$$

$$g_{p+2}(V, \mathbf{U}) = \rho_d U_p V \quad \text{momentum of droplet in } q \text{ component } (q = 1, 2, 3)$$

$$g_6(V, \mathbf{U}) = (\rho_d V \Sigma U_q^2)/2 \quad \text{kinetic energy of droplet}$$

where ρ_d is the density of the droplet; σ is the surface tension of the droplet;

Based on the functions defined above, the constraint equations for the spray can be obtained from Eq. (3). If we multiply both sides of the constraint equations by \dot{n} , which denotes the number of droplets formed per unit time under steady-state condition, then the constraint equations become

$$\dot{n} \sum_i \sum_j \sum_k \sum_l \rho_d p_{ijkl} V_i = \dot{m} \quad \text{mass flow rate of spray} \quad (8)$$

$$\dot{n} \sum_i \sum_j \sum_k \sum_l \sigma p_{ijkl} (6\sqrt{\pi} V_i)^{2/3} = \dot{E}_s \quad \text{surface energy flux of spray} \quad (9)$$

$$\dot{n} \sum_i \sum_j \sum_k \sum_l \rho_d p_{ijkl} U_{p,q} V_i = \dot{M}_p \quad \text{momentum flux of spray in } p$$

$$(p = 1, 2, 3; q = j, k, l) \quad (10)$$

$$\dot{n} \sum_i \sum_j \sum_k \sum_l \rho_d p_{ijkl} (\Sigma U_{p,q}^2) V_i / 2 = \dot{E}_k \quad \text{kinetic energy flux of spray} \quad (11)$$

When the number of droplets, \dot{n} , is large; it is reasonable to transform the probability distribution and the droplet variables (V and \mathbf{U}) from the discrete domain to the continuous domain by replacing the sums in Eqs. (8)–(11) by integrals. This maximum entropy spray model is further modified by expressing the constraints in terms of droplet diameter (D) instead of droplet volume ($V = \pi D^3/6$). To non-dimensionalize the constraint equations, the mass mean diameter of the droplets, D_{30} (where $D_{30} = [6\dot{m}/\dot{n}\pi\rho_d]^{1/3}$), is chosen as the characteristic length ($\bar{D} = D/D_{30}$); and the initial mean velocity of the liquid before atomization, U_0 , is chosen as the characteristic velocity ($\bar{\mathbf{U}} = \mathbf{U}/U_0$). In summary, the complete maximum entropy spray model derived in this study results in a continuous joint droplet distribution function of spray, $f(\bar{D}, \bar{\mathbf{U}})$, subject to the following constraints (from (8)–(11)):

$$\iint f(\bar{D}, \bar{\mathbf{U}}) d\bar{D} d\bar{\mathbf{U}} = 1 \quad (12)$$

$$\iint f(\bar{D}, \bar{\mathbf{U}}) \bar{D}^3 d\bar{D} d\bar{\mathbf{U}} = \bar{m} \quad (13)$$

$$\iint B f(\bar{D}, \bar{\mathbf{U}}) \bar{D}^2 d\bar{D} d\bar{\mathbf{U}} = \bar{E}_s \quad (14)$$

$$\iint f(\bar{D}, \bar{U}) \bar{D}^3 \bar{U}_p d\bar{D} d\bar{U} = \bar{M}_p \quad (p = 1, 2, 3) \quad (15)$$

$$\iint f(\bar{D}, \bar{U}) \bar{D}^3 (\sum \bar{U}_p^2) d\bar{D} d\bar{U} = \bar{E}_k \quad (16)$$

the function, $f(\bar{D}, \bar{U})$, that maximizes the Shannon entropy is

$$f(\bar{D}, \bar{U}) = 3 \bar{D}^2 \exp \{ -\lambda_0 - \lambda_1 \bar{D}^3 - \lambda_2 B \bar{D}^2 - (\sum \lambda_{p+2} \bar{U}_p) \bar{D}^3 - \lambda_6 (\sum \bar{U}_p^2) \bar{D}^3 \} \quad (17)$$

The dimensionless parameters appearing in Eqs. (14) and (17) are defined as

$$B = 12/We; \quad \text{where } We = \rho_a D_{30} U_0^2 / \sigma.$$

The Weber number for a droplet, We , is the ratio of the initial kinetic energy of the liquid to the surface energy of droplet (note: the Weber number used in sprays is frequently defined as $We = \rho_a D_{30} U_0^2 / \sigma$, where ρ_a is the density of air).

When a spray nozzle is modeled, the control volume in cylindrical coordinates is shown in Figure 1. The liquid fuel that enters the control volume through surface 1(s1) has density ρ_a , surface tension σ , specific heat at constant pressure c_p , and mass flow rate \dot{m} . The mean velocity averaged over the area of the nozzle exit will be used to characterize the initial velocity condition of the liquid. The three components of initial mean liquid velocity in cylindrical coordinates at surface S1 are defined as follows:

$$U_{1,0} = U_{r,0} = \{ \rho_a \int V_r(A) V_z(A) dA_{(s1)} \} / \dot{m}$$

$$U_{2,0} = U_{\theta,0} = \{ \rho_a \int V_{\theta}(A) V_z(A) dA_{(s1)} \} / \dot{m}$$

$$U_{3,0} = U_{z,0} = \{ \rho_a \int V_z(A) V_z(A) dA_{(s1)} \} / \dot{m}$$

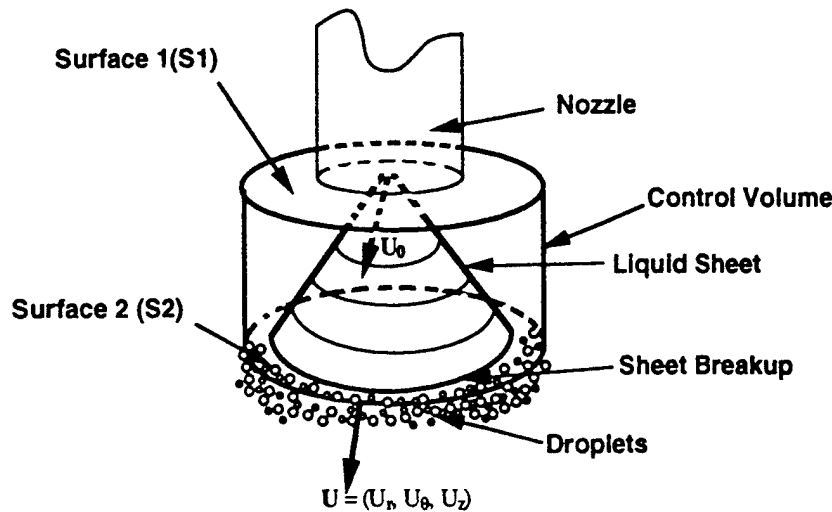


FIGURE 1 Schematic drawing of the control volume for a spray nozzle.

At surface 2(S2), the droplets that emerge from the control volume have diameter D , and velocity vector $\mathbf{U} = \{U_r, U_\theta, U_z\}$. The physical properties of liquid droplets (ρ_d, σ, c_p) at surface 2 have been defined. The basic idea of this approach is to relate the spray quantities, $(\bar{m}, \bar{E}, \bar{M}_p, \bar{E}_k)$, in the constraint equations (Eqs. 13–16) to the same quantities at the initial stage of the continuous liquid phase (e.g., the nozzle exit in Fig. 1).

3. Comments on the Number of Velocity Components Modeled:

In the previous models, either one or two components of droplet velocity are considered (to simplify computations). For example, the one velocity component model was applied to a cylindrical liquid jet by Chin *et al.* [1991]; in this case there is only one dominant velocity component and this assumption is reasonable. In the swirl jet nozzle Li *et al.* [1991], the one velocity component model was applied with success; although all three components of velocity are present and of same order of magnitude. Thus, it isn't just the magnitude of the velocity components that determine the suitability of the one component model, the two component model and the three component model. The spray quantities $(\bar{m}, \bar{M}_p, \bar{E}_p, \bar{E}_k)$ and the Weber number determine whether the one or two component model will describe the spray with reasonable accuracy.

The general maximum entropy model, derived in this study, consisting of all three velocity components can be applied to various spray systems. If any of the velocity components are small enough to be neglected, this general maximum entropy model can easily be modified by dropping the corresponding momentum flux constraints and the corresponding kinetic energy terms (Eqs. 15 and 16). Also, the terms involving these small components in the joint droplet distribution function are omitted. However, if one is not sure about the influence of small velocity components on the droplet distribution, the general model is recommended.

4. Model Simplification

If the joint droplet distribution function f is differentiated with respect to \bar{U}_p ($p = 1, 2, 3$) respectively and set equal to zero, the following relation is obtained:

$$\frac{\partial f}{\partial \bar{U}_p} = -(\lambda_{p+2} + 2\lambda_6 \bar{U}_p) \bar{D}^3 f = 0 \Rightarrow \bar{U}_{\text{peak},p} = -\frac{\lambda_{p+2}}{2\lambda_6} \quad (18)$$

where $\bar{U}_{\text{peak},p}$ is the droplet velocity at which the probability is maximum. $\bar{U}_{\text{peak},p}$ is not a function of droplet size. Because $\bar{U}_{\text{peak},p}$ is independent of droplet size, the droplet velocity distribution ($d\bar{N}/d\bar{U}_p$, \bar{N} is the normalized number of droplets with velocity \bar{U}_p) has its maximum probability at the same $\bar{U}_{\text{peak},p}$. This result will be used in simplifying the maximum entropy spray model. The constraint equation for the spray momentum flux (Eq. 15) can be integrated over the velocity range as follows:

$$-\int \left\{ \frac{\pi}{8\lambda_6^2 \bar{D}^3} \Omega(\bar{D}) \left[\prod_{q=1}^3 \exp(\gamma_q^2 \bar{D}^3) \right] Q_p'' \prod_{q \neq p} Q_q' \right\} d\bar{D} = \bar{M}_p + \gamma_p \quad (p = 1, 2, 3) \quad (19)$$

where

$$\Omega(\bar{D}) = 3\bar{D}^2 \exp(-\lambda_0 - \lambda_1 \bar{D}^3 - \lambda_2 B \bar{D}^2)$$

is the size distribution function for droplets having zero velocity ($\bar{U}_p = 0$) $\gamma_p = \lambda_{p+2}/2\lambda_6 = -\bar{U}_{\text{peak},p}$ is the coefficient related to the peak velocity.

$$Q_p'' = \exp(-\chi_{\text{max},p}^2) - \exp(-\chi_{\text{min},p}^2)$$

$$Q_p' = \text{erf}(-\chi_{\text{max},p}) - \text{erf}(-\chi_{\text{min},p})$$

$$\chi_{\text{max},p} = (\bar{U}_{\text{max},p} + \gamma_p) \sqrt{\lambda_3 \bar{D}^3}; \bar{U}_{\text{max},p} \text{ is the upper velocity integration limit.}$$

$$\chi_{\text{min},p} = (\bar{U}_{\text{min},p} + \gamma_p) \sqrt{\lambda_3 \bar{D}^3}; \bar{U}_{\text{min},p} \text{ is the lower velocity integration limit.}$$

If the upper and lower integration limits for the velocity are chosen as

$$\bar{U}_{\text{min},p} = \bar{U}_{\text{peak},p} - \Delta \bar{U}_p = -\Delta \bar{U}_p - \gamma_p; \bar{U}_{\text{max},p} = \bar{U}_{\text{peak},p} + \Delta \bar{U}_p = \Delta \bar{U}_p - \gamma_p,$$

then $Q_p'' = \exp(-\Delta \bar{U}_p^2) - \exp(-\Delta \bar{U}_p^2) \equiv 0$; and $\bar{M}_p = -\gamma_p$ from Eq. (19).

This relationship, $\bar{M}_p = -\gamma_p$, can be applied to modify the general maximum entropy spray model to a simpler model with fewer unknown coefficients and fewer constraints by using $\lambda_{p+2} = -2\lambda_6 \bar{M}_p$. The constraints for the simplified model become:

$$\iint f(\bar{D}, \bar{U}) d\bar{D} d\bar{U} = 1 \quad (20)$$

$$\iint f(\bar{D}, \bar{U}) \bar{D}^3 d\bar{D} d\bar{U} = \bar{m} \quad (21)$$

$$\iint B f(\bar{D}, \bar{U}) \bar{D}^2 d\bar{D} d\bar{U} = \bar{E}_s \quad (22)$$

$$\iint f(\bar{D}, \bar{U}) \bar{D}^3 (\sum_p \bar{U}_p^2) d\bar{D} d\bar{U} = \bar{E}_k \quad (23)$$

and the joint droplet distribution function, f , becomes

$$f(\bar{D}, \bar{U}) = 3\bar{D}^2 \exp \left\{ -\lambda_0 - \lambda_1 \bar{D}^3 - \lambda_2 B \bar{D}^2 - \lambda_6 \sum_{p=1}^3 (-2\bar{M}_p \bar{U}_p + \bar{U}_p^2) \bar{D}^3 \right\} \quad (24)$$

Note that the momentum constraints are no longer required. One still needs to know \bar{M}_p to evaluate Eq. (24), but it not a constraint and therefore the Lagrange multipliers λ_3, λ_4 , and λ_5 in Eq. (15) do not appear. This is a mathematical simplification of the problem; the number of λ 's to evaluate has been reduced from six in Eq. (17) to four in Eq. (24). Thus, the numerical computations become simpler.

5. Determination of Spray Quantities in the Constraints

As mentioned earlier, the spray quantities ($\bar{m}, \bar{M}_p, \bar{E}_s, \bar{E}_k$) on the right hand side of the constraint equations (Eqs. 13-16) must be given (computed or assumed) before any

probability distribution of spray can be determined. These spray quantities are physical quantities and represent the mean values of the chosen functions $g_i(X)$.

Several averaged experimental data such as mean diameter, mean velocity, etc., are used in the following manner as a first estimate of the spray quantities (\bar{m} , \bar{M}_p , \bar{E}_s , \bar{E}_k):

$$\bar{m} = \frac{6\dot{m}}{\pi\rho_d\bar{D}_{30}^3} = \iint f \bar{D}^3 d\bar{D}d\mathbf{U} = \bar{D}_{30}^3 = 1 \quad (25)$$

$$\bar{E}_s = \frac{2\dot{E}_s}{\dot{m}U_0^2} = \iint B f \bar{D}^2 d\bar{D}d\mathbf{U} = B\bar{D}_{20}^2/\bar{D}_{30}^3 = B/\bar{D}_{32} \quad (26)$$

$$\bar{M}_p = \frac{\dot{M}_p}{\dot{m}U_0} = \iint f \bar{D}^3 U_p d\bar{D}d\mathbf{U} = \bar{D}_{30}^3 \bar{U}_{m,p} = \bar{U}_{m,p} \quad (27)$$

$$\begin{aligned} \bar{E}_k &= \frac{2\dot{E}_k}{\dot{m}U_0^2} = \iint f \bar{D}^3 (\sum U_p^2) d\bar{D}d\mathbf{U} = \bar{D}_{30}^3 \iint f (\sum U_p^2) d\bar{D}d\mathbf{U} \\ &= \iint f (\sum (U_p - \bar{U}_{m,p})^2) d\bar{D}d\mathbf{U} + 2 \sum \left\{ \bar{U}_{m,p} \iint f U_p d\bar{D}d\mathbf{U} \right\} - \sum \bar{U}_{m,p}^2 \\ &= \sum (\bar{U}_{m,p}^2 + \bar{U}_{var,p}^2) \end{aligned} \quad (28)$$

where \bar{D}_{32} denotes the Sauter mean diameter of spray
 $\bar{U}_{m,p}$ denotes the mean velocity of spray in component p
 $\bar{U}_{var,p}$ denotes the velocity variance of spray in component p
 B is assumed independent of temperature

These approximations are based on the assumption that all the droplets have the same diameter ($\bar{D} = \bar{D}_{30}$). Obviously, this assumption is unrealistic for a general spray system under normal operating conditions. However, the estimates based on this assumption, as stated, provide a first approximation of the spray quantities yielding a droplet distribution that may be reasonably close to the experimentally measured results. The error induced by this approximation (the assumption for the droplet size ($\bar{D} = \bar{D}_{30}$)) is reduced by adjusting the estimated spray quantities \bar{E}_k and \bar{E}_s . Generally, \bar{E}_s is responsible only for the droplet size distribution; and \bar{E}_k is responsible for both droplet size and droplet velocity distributions. An example using this approach was the study of droplet distributions from a cylindrical liquid jet Chin *et al.* [1991]. In that case, the computed distributions agree well with the data using the first approximations for the spray quantities. The reason that the agreement was so good in that particular case is because the assumption that all droplets have the same diameter is a very good assumption (see Fig. 6 in Chin *et al.*, 1991). That study also indicates the sensitivity of the distributions on the spray quantities when the distribution functions approach a delta function.

MODEL TEST

This section will demonstrate how to apply the maximum entropy spray model to a spray system and compare the calculated droplet size distributions with experimental

measurements. Our interest is focused on bi-modal size distributions, since we have already demonstrated successfully the application of maximum entropy to sprays having uniform (Chin *et al.*, 1991) and skewed mono-modal (Li *et al.*, 1991) size distributions. The experiments were carried out at Wright Laboratories using PDPA to measure the droplet size/velocity distributions from a pressurized spray nozzle.

1. Experiment

The nozzle used in these experiments was an Allison hollow cone, non-swirl spray nozzle having a 90° spray angle. A spray of water issues into a quiescent, saturated air environment at 295 °K. The flow rate is $2.75 \times 10^{-6} \text{ m}^3/\text{s}$ (2.6 gallons/hr) at a pressure drop across the nozzle of 0.27 MPa (40 psig). The water exiting the nozzle forms a liquid, hollow cone sheet, which breaks up into ligaments and droplets. The ligaments breakup into droplets further downstream. It is desirable to measure the spray as close as possible to the sheet break-up region—but downstream of the ligament region. Measurements beyond this point may be significantly influenced by local gas aerodynamics and complicate the comparison with calculations. In addition, if measurements are made far downstream, a large diameter measuring plane will require measurements at many radial positions to account for all the droplets from the spray. Photograph of the spray (Fig. 2) indicates that sheet breakup occurs at approximately 7.5 mm from the nozzle face. The laser beams that appear in Figure 2 are located 10 mm from the nozzle exit. At 10 mm, droplets have formed. It should be mentioned that several such photographs were taken and the location of the sheet breakup plane oscillates. This was seen more clearly from video tapes taken of the spray. Based on the photographs

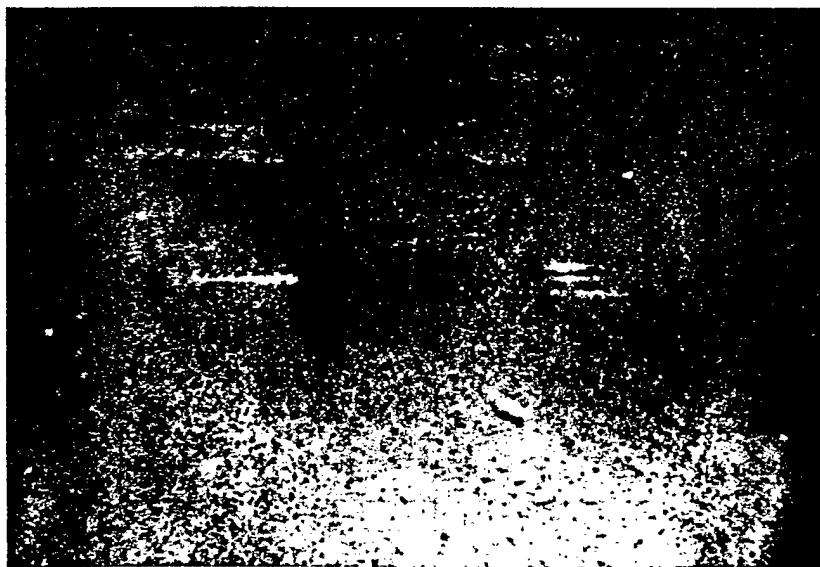


FIGURE 2 Photograph showing the spray from a pressurized nozzle. See Color Plate I.

and video tapes, the measurements plane was set at 10 mm from the nozzle discharge plane, which is about 2.5 mm beyond the mean position of the sheet break up.

Droplets are sized with an Aerometrics, Inc. two-color, four-beam PDPA. A complete discussion of the theory of operation can be found in Bachalo and Houser [1984]; a discussion of the operational constraints in practical environments can be found in Jackson [1990]. At each measurement station 5,000 droplets are measured. Collection times for these many samples are of the order of seconds.

Comparison between experiment and calculation demands that the measured values of droplet size and velocity near the sheet break-up region be representative of the behavior of the entire spray. Several constraints inherent in the PDPA that must be addressed are listed by Li *et al.* [1991]. In the experiments in this study, valid signals range from about 50–75% of the signals collected. Thus, to collect 5,000 valid signals at a challenging location in the spray it was necessary to make as many as 10,000 attempts. The method of analysis of the data described by Li *et al.* [1991], requires the spray to be axially symmetric. For the symmetry evaluation two orthogonal, full diameter traverses were made. The axis of the spray was vertical for all measurements. An *x* traverse through the spray yielded measurements of droplet size and axial and radial droplet velocities; a *y* traverse yielded measurements of droplet size and axial and tangential droplet velocities. Measurements were made at radial intervals of 0.5 mm. Figure 3 shows the axial velocity measurements from the *x* and *y* traverses. Figure 4 shows the Sauter mean diameter profiles associated with the *x* and *y* traverses. The velocity and droplet size profiles along two orthogonal traverses through the spray are in reasonable agreement, indicating the spray has good symmetry about its axis. Thus, the droplet size and velocity distributions obtained from point measurements can be integrated over the ring areas associated with each measurement point to yield a total spray measurement.

After initial spray symmetry checks, data were collected to evaluate the calculations. A detailed radial profile was taken at the 10 mm location where measurements were

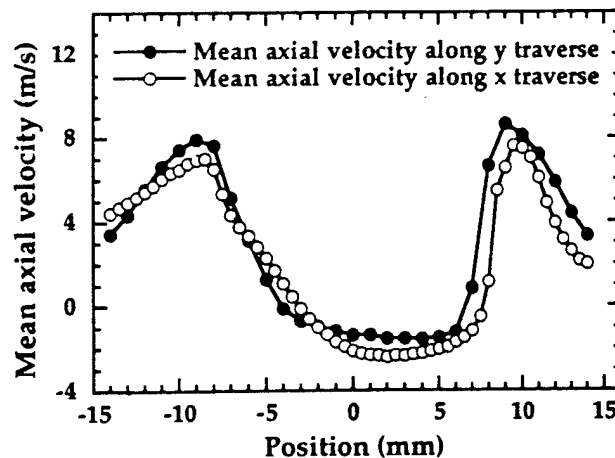


FIGURE 3 Experimentally measured axial velocities obtained from *x* and *y* traverses.

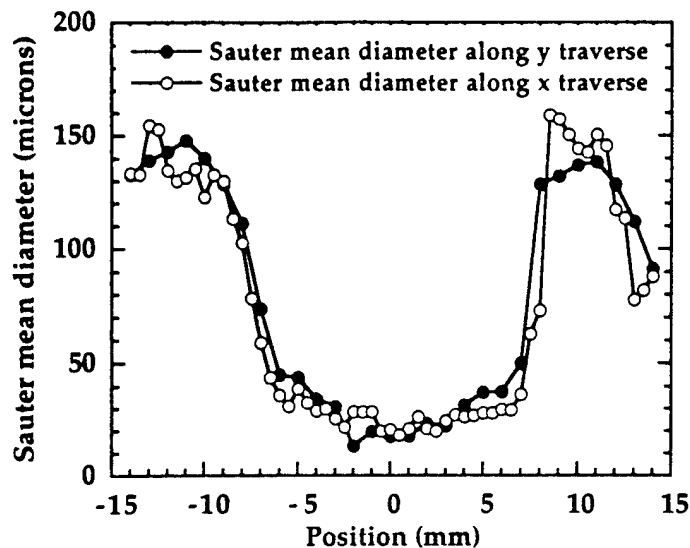


FIGURE 4 Experimentally measured Sauter mean diameters obtained from x and y traverses.

made at 21 radial points from the spray center to its edge. In looking at the data in Figure 3, a plot of mean axial velocity profiles, it was observed that there is a rather strong negative (upward) axial velocity in the central portion of the spray (see, for example, Fig. 5 that shows data taken at 3.0 mm from the spray centerline). These

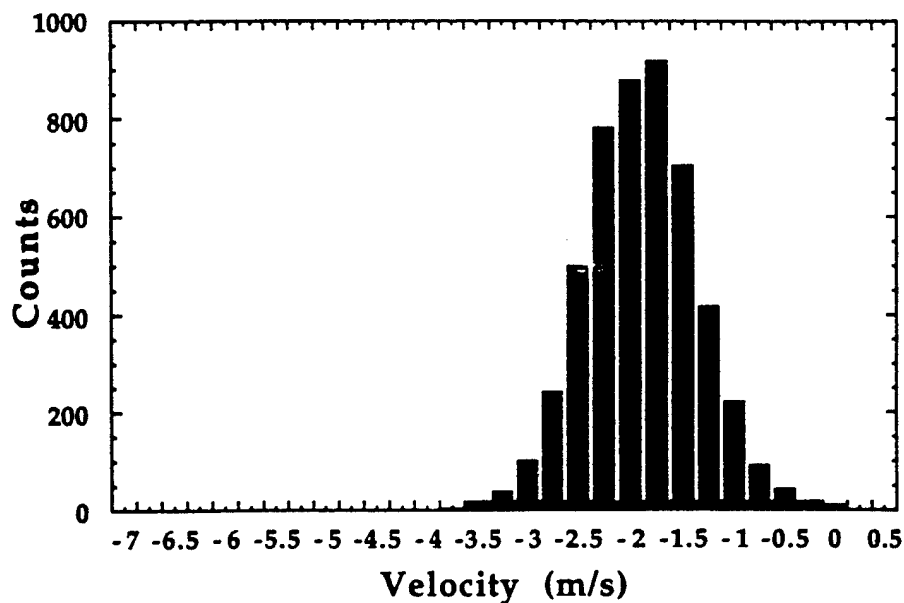


FIGURE 5 Mean axial velocity distribution of droplets located 3 mm from centerline.

negative mean axial velocities extend from the spray centerline to a radial position of about 8 mm. Since the droplets in the central region of the spray are relatively small (see Fig. 4, containing a plot the Sauter mean diameter profiles), they more or less follow the air flow. The axial velocity of the air in a hollow cone spray close to the sheet region is positive (downward) because of the drag of the liquid sheet on the surrounding air. To balance this mass flux of air leaving the interior of the hollow cone, there must be a flow of air upward (negative axial velocity) in the central portion of the hollow cone spray. At 9 mm from the centerline of the spray, the axial velocity data exhibit a bi-modal distribution. This is shown in Figure 6. We believe this is due to fluctuations of the sheet region—both spatially and temporally. All the other velocity profiles (at radii $\neq 9$ mm) have one peak (mono-modal). The data taken at radii less than 9 mm have peaks with negative velocities; those at greater radii have peaks with positive velocities.

The air flow (caused by the liquid sheet) carries many of the small droplets (that originate at the breakup of the liquid sheet) some distance downstream, then inward toward the axis of the spray, upward by the vortical structures formed in the air that is interior of the hollow spray cone, and finally downward again in a region close to the interior surface of the liquid sheet. It is the boundary layer due to the liquid sheet that drives the air recirculating zone. This flow pattern was deduced in an earlier paper (Fig. 3, Lee and Tankin [1984]) where negative droplet velocities were observed along the centerline of a hollow cone spray. Therefore, if one were to count the droplets from the centerline of the spray outward to the outer edge of the spray, the small droplets in the interior (radius ≤ 9 mm) would be counted three times. Figure 7 shows the normalized axial velocity and Sauter mean diameter profiles. There is a strong spatial correlation

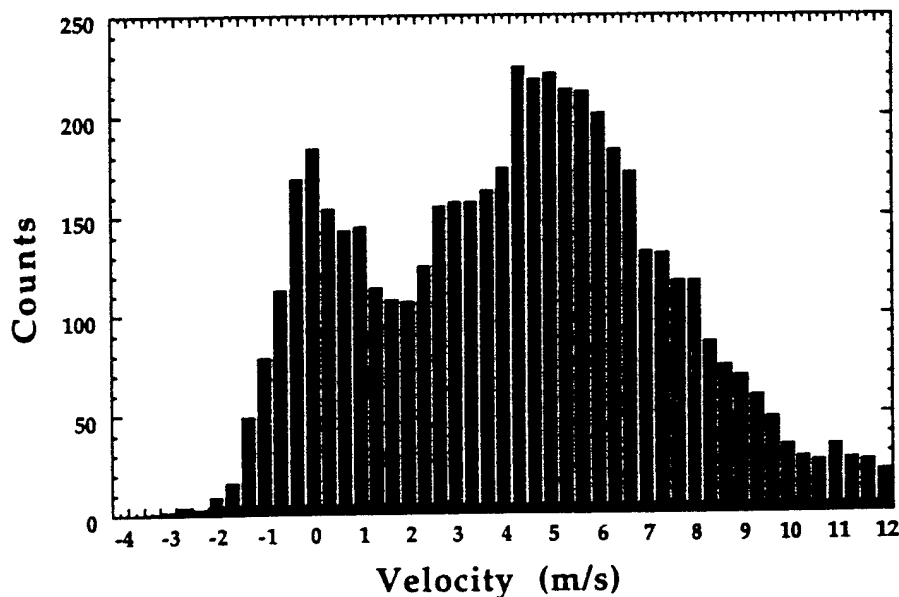


FIGURE 6 Mean axial velocity distribution of droplets located 9 mm from centerline.

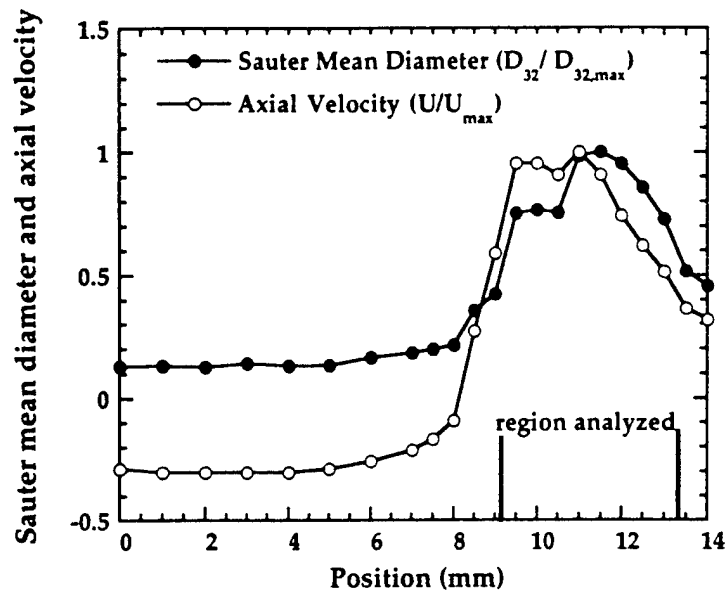


FIGURE 7 Experimentally measured profiles of mean axial velocity and Sauter mean diameter.

between the small droplets and the negative velocities. To avoid this problem of multiple counting of the small droplets, the region analyzed was restricted to radii that are ≥ 9.5 mm. For these measurements the acceptance ratio (validations/attempts) is around 60%- varying from 55% at a radius of 9.5 mm increasing to about 75% at a radius of 11.5 mm and then tapering off to about 70% at larger radial positions. The PDPA determines droplet diameter by measuring the phase shift of light refracted through the droplet. Making this measurement requires two spatially separated detectors. The PDPA uses three detectors, computing multiple phase differences. These two measurements are compared and must match within a prescribed tolerance; otherwise the measurement is rejected. Multiple droplets in the probe volume is a leading cause of such rejections. Most of the rejected measurements were of this type (failure to match the multiple phase shift measurements). The highest density of droplets occurs at a radial position of about 10 mm (this nozzle has a 90 degree cone angle and the measuring volume is 10 mm from the nozzle). We believe the main cause for the rejections is due to multiple droplets within the measuring volume.

A droplet size distribution is constructed from the individual point measurements, weighting each measurement by their time of collection and the ratio of their optical probe area to the ring area represented at that location. This experimentally determined droplet size distribution will be compared to that calculated by the maximum entropy spray model. Droplet size is normalized by the mass mean diameter, D_{30} , which was determined from measurements to be 81.43 microns. The resulting experimentally determined probability size distribution is shown in Figure 8(a). It should be noted that this is evidence of a bi-modal size distribution-although not a strong

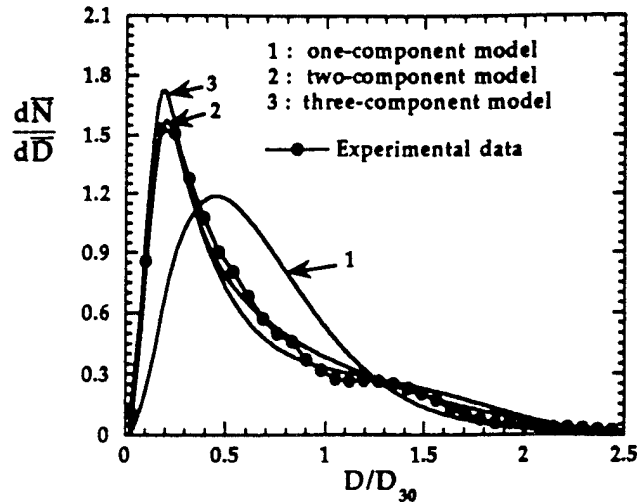


FIGURE 8a Comparisons between experimentally measured droplet size distribution and calculated values. In the three-component model, the kinetic energy due to the tangential velocity (third component) is 4% of the total kinetic energy.

bi-modal distribution. One peak occurs at $\bar{D} = 0.2$ and the second peak at $\bar{D} = 1.3$. A physical explanation for the origin of these peaks is as follows: There are two main sources for the droplets in this spray – the droplets that form from the ligaments and those that form from the thin sheet of liquid that lies between the ligaments at breakup. From Figure 2 it appears that the ligaments are related to the instabilities seen on the liquid sheet prior to breakup. Then, the ligaments breakup via Rayleigh's capillary instability and form the larger droplets associated with those centered around $\bar{D} = 1.3$ (in Fig. 8a). The droplets that originate from the thin sheet are associated with those centered around $\bar{D} = 0.2$.

As already mentioned, in an earlier paper by Chin and Tankin [1991], bi-modal size distributions were predicted using the maximum entropy model, but no experimental observations were presented to corroborate this prediction. Only when the nozzle in this study was operated at very low flow rates – $2.75 \times 10^{-6} \text{ m}^3/\text{s}$ (40 psig) – does a weak bi-modal size distribution appear. If the nozzle is operated at higher flow rates (but still below its designed operating range), no bi-modal size distributions were obtained. That was the motivation for operating this nozzle at such low flow rates.

2. Calculation

To compare the experimental droplet size distribution shown in Figure 8(a) with our maximum entropy spray model, the Lagrange multipliers, λ 's, in Eq. (24) are solved by using the modified Newton-Raphson method, the same scheme that was used in all the previous studies. To estimate the spray quantities required in the constraints (Eqs. 13–16), the averaged data from the experiments and the estimated spray quantities are

listed below:

$$\begin{aligned}
 D_{30} &= 81.4 \mu\text{m}; \quad U_{z,0} = 8.0 \text{ m/sec} \Rightarrow We = 71; \quad B = 0.17 \\
 D_{32} &= 120.8 \mu\text{m}; \quad \Rightarrow \dot{E}_s = 0.11 \\
 U_{m,r} &= 5.4/\text{sec}; \quad U_{var,r} = 10.8 \text{ m}^2/\text{sec}^2 \\
 U_{m,z} &= 4.9 \text{ m/sec}; \quad U_{var,z} = 8.8 \text{ m}^2/\text{sec}^2 \\
 U_{m,\theta} &= 0.34 \text{ m/sec} \Rightarrow \dot{M}_r = 0.68; \quad \dot{M}_z = 0.61; \quad \dot{M}_\theta = 0.04; \quad \dot{E}_k = 1.1 \quad (29)
 \end{aligned}$$

The solved λ 's for the conditions described above are: $\lambda_0 = -0.696$; $\lambda_1 = 36.150$; $\lambda_2 = -7.108$; and $\lambda_6 = 0.124$

Axial and radial droplet velocity components have been measured simultaneously in the experiments. The third droplet velocity component (tangential) is small (but still present) compared to the other two components since this hollow cone spray is formed without swirl. The contribution of the variance of the tangential velocity component on the estimate of \dot{E}_k has been neglected. After adjustments (due primarily to the assumption that all droplets have the same diameter) were made on the values of $\dot{E}_k (= 0.87)$ and $\dot{E}_s (= 0.12)$, the computed curve agrees reasonably well with the experiments. (See Fig. 8(a)). It should be mentioned that \dot{E}_k and \dot{E}_s are not independent of each other. Conservation of energy requires that the sum of potential energy, surface energy (\dot{E}_s), and kinetic energy (\dot{E}_k) of the droplets should equal to the sum of the kinetic energy and potential energy of the liquid at the nozzle. Thus the sum $[\dot{E}_s + \dot{E}_k]$ for this flow should be equal to approximately 1. The sum of these two terms equals 0.99.

To compare this general model with other models having fewer velocity components, the droplet size distributions obtained from a two-component model (without tangential velocity) and a one-component model (vector sum of velocities as a single velocity) are also shown in Figure 8(a) – curves “1” and “2” respectively. It is noted that the results obtained from the one-component model do not agree with the experiments. The dominant droplet size for the one-component model is too large ($\bar{D} \approx 0.5$) compared with the experimental measurements ($\bar{D} \approx 0.2$). The calculated droplet size distributions for both two-component and three-component models agree with the \bar{D}_{peak} of the experimental data. However by adding the third component (three-component model) one begins to see evidence of a bi-modal droplet size distribution. The experimental result shown in Figure 8(a) has a second peak around $\bar{D} \approx 1.3$ – the same location as the three component model. Although the amplitude of this second peak is small compared to the first peak ($\bar{D} \approx 0.2$), it is easily identified.

The influence of the small velocity component (tangential component in this case) on the droplet size distribution will be examined. Figure 8(b) shows a set of droplet size distributions obtained by assigning different values of \dot{M}_θ (the tangential momentum flux) while the other constraints (\dot{m} , \dot{E}_k , \dot{E}_s) are not changed. Each droplet size distribution in Figure 8(b) is characterized by the ratio of the kinetic energy flux of the tangential component in the total kinetic energy flux. It is noted that the bi-modal distribution can be enhanced by increasing the magnitude of the third velocity (tangential) component. Curve “2” (4%) in Figure 8(b) corresponds to curve “3” (three-component model) in Figure 8(a). 4% of the total kinetic energy amounts to

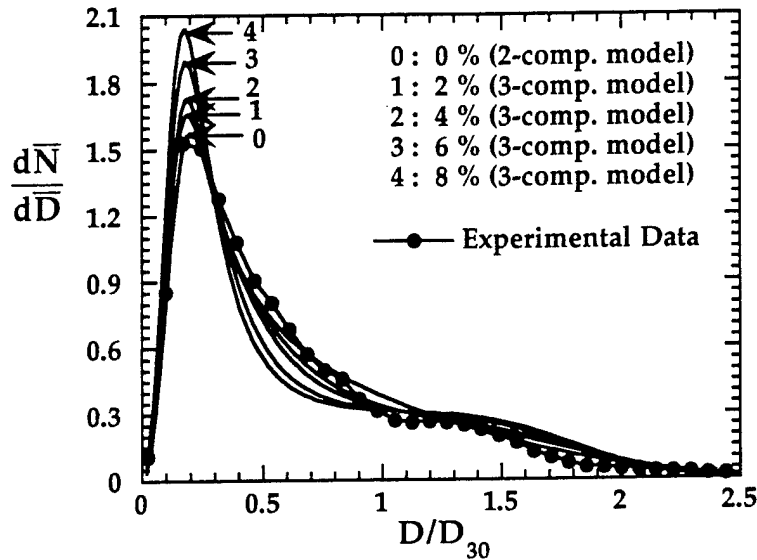


FIGURE 8b Droplet size distributions for various percentages of tangential kinetic energy to total kinetic energy. Curve "2" is the same as curve "3" in Figure 8a.

a tangential velocity of only 0.35 m/sec. This is reasonable from values of the tangential velocity that were determined experimentally.

Presser *et al.* [1990] and Gulder [1990] obtained significantly strong bi-modal size distributions in their experiments. Presser *et al.* represented their bi-modal size dis-

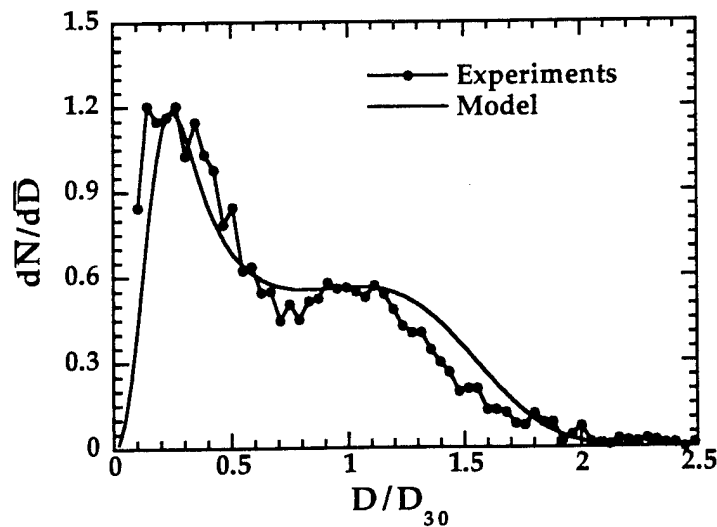


FIGURE 9 Comparison of droplet size distribution between model and experiments of Gupta *et al.* [1986].

tribution function by the sum of two mono-modal log-normal distribution functions with a weighing factor. To properly fit the data, they had to determine five fitting parameters. Cary Presser has been kind enough to provide us with his experimental data that he published with Gupta, Santoro, and Semerjian [1986]. This experimental data is for a swirl nozzle and exhibits a strong bi-modal size distribution. The computed size distribution curve using the procedures presented in this paper agrees reasonably well with their experiments as seen in Figure 9. Note that the velocity in this experiment is relatively small for a pressure atomizing nozzle, and that the spray has swirl. In our experiments, we only observed a bi-modal distribution at low flow rates (low U_0) and the computations predict that increasing the tangential velocity component (swirl) strengthens the bi-modal distribution (see Fig. 8b). It has been shown that the maximum entropy principle will yield directly a bi-modal size distribution for a particular set of spray quantities (\bar{m} , \bar{M}_p , \bar{E}_k , \bar{E}_s). Prior to this paper, the maximum entropy principle has successfully yielded skewed mono-modal and uniform (approximating a delta function) distributions (see Li *et al.*, 1991 and Chin *et al.*, 1991 respectively).

CONCLUSIONS

A theoretical spray model based on Jaynes' maximum entropy principle has been derived. From this model, the joint distribution function of droplet size and velocity can be obtained without knowing detailed information of the atomization process. Two examples have been presented to compare this model with experiments that have a bi-modal size distributions. There is reasonably good agreement between the experiments and the computed results. This model is the only model known to the authors which has been used successfully to yield skewed mono-modal size distributions, uniform size distributions, and now bi-modal size distributions.

The maximum entropy spray model has been further simplified by choosing the velocity integration limits to be mirror images about the peak droplet velocity. This simplifies the computations required in the maximum entropy spray model, since the constraints involving the momentum flux of droplets can be omitted.

ACKNOWLEDGEMENTS

This work was supported in part by the Air Force Office of Scientific Research under contract No. F49620-92-J-0389.

REFERENCES

- Bachalo, W. D. and Houser, M. J. (1984). Phase/Doppler spray analyzer for simultaneous measurement of drop size and velocity distributions. *Optical Engineering*, 23, 583-590.
- Chin, L. P., LaRose, P. G., Tankin, R. S., Jackson, T., Stutrud, J. and Switzer, G. (1991). Droplet Distributions From the Breakup of a Cylindrical Liquid Jet. *Physics of Fluids* 3, (8), 1897-1906.
- Chin, L. P. and Tankin, R. S. (1991). Theoretical Prediction of Droplet Distributions in Sprays Based on Maximum Entropy Theory. HTD, *Winter Annual Meeting ASME*, pp. 1-10.
- Dressler, J. L. and Kraemer, G. O. (1990). A Multiple Drop-Size Drop Generator for Calibration of A Phase-Doppler Particle Analyzer. *Liquid Particle Size Measurement Technique-ASTM*, II, pp. 30-44.

- Gulder, O. L. (1990). Multiple Scattering Effects in Dense Spray Sizing by Laser Diffraction. *Aerosol Science and Technology*, **12**, 570–577.
- Jackson, T. A. (1990). Liquid Particle Size Measurement Techniques. "Liquid Particle Size Measurement Technique," ASTM, II, p. 151.
- Jaynes, E. T. (1957). Information Theory and Statistical Mechanics, I and II. *Physical Review*, **106**, 620–630, and **108**, 171–190.
- Kapur, J. N. and Kesavan, H. K. (1992). *Entropy Optimization Principles with Applications*, Academic Press, Inc., San Diego, California.
- Lee, S. Y. and Tankin, R. S. (1984). A Study of Liquid Spray (Ware) in a Non-Condensable Environment. *Int. J. Heat and Mass Transfer*, **27**, 351–361.
- Levine, R. D. and Tribus, M. (1979). *The Maximum Entropy Formation*, MIT Press, Cambridge, Mass.
- Li, X. and Tankin, R. S. (1987). Droplet Size Distribution: A Derivation of a Nukiyama-Tanasawa Type Distribution Function. *Combustion Science and Technology*, **56**, 65–76.
- Li, X. and Tankin, R. S. (1988). Derivation of Droplet Size Distribution of Sprays Using Information Theory. *Combustion Science and Technology*, **60**, 345–357.
- Li, X., Chin, L. P., Tankin, R. S., Jackson, T., Stutrud, J. and Switzer, G. (1991). Comparison Between Experiments and Predictions Based on Maximum Entropy for Sprays from a Pressure Atomizer. *Combustion and Flame*, **86**, 73–89.
- Mugele, R. and Evans, H. D. (1951). Droplet Distribution in Sprays. *Industrial Engineering Chemistry*, **43**, 1317–1324.
- Presser, C., Gupta, A. K., Dobbins, A. and Semerjian, H. G. (1990). Influence of Size Distribution on Droplet Mean Diameter Obtained by Ensemble Light Scattering. *Liquid Particle Size Measurement Technique—ASTM II*, pp. 93–111.
- Presser, C., Gupta, A. K., Santoro, R. J. and Semerjian, H. G. (1986). Laser Diagnostics for Characterization of Fuel Sprays. *Proceedings ICALEO*, **58**.
- Sellens, R. W. and Brzustowski, T. A. (1985). A Prediction of the Drop Size Distribution in a Spray from First Principle. *Atomization and Spray Technology*, **1**, 89–102.
- Sellens, R. W. (1987). Ph. D. thesis, University of Waterloo.
- Sellens, R. W. (1989). Prediction of The Drop Size and Velocity Distributions A Spray, Based on the Maximum Entropy Principle. *Part. Part. Syst. Charact.*, **6**, 17–27.
- Shannon, C. E. (1948). A Mathematical Theory of Communication. *Bell System Tech. J.*, **27**, 379–423, 623–659.
- Tishkoff, J. M. and Law, C. K. (1977). Application of a Class of Distribution Functions to Drop-Size Data by Logarithmic Least Squares Technique. *Journal of Engineering for Power*, **99**, 684–688.
- van Der Geld, C. W. M. and Vermeer, H. (1994). Prediction of Droplet Size Distributions in Sprays Using the Maximum Entropy Formalism: The Effect of Satellite Formation, *Int. J. Multiphase Flow*, **20**, 363–381.

Characterization of Droplet/Vapor/ Vortex Interactions in a Two-Dimensional Shear Layer

R. D. Hancock*

U.S. Air Force Wright Laboratory,
Wright-Patterson Air Force Base, Ohio 45433
and

L. P. Chint†

Systems Research Laboratories, Inc., Dayton, Ohio 45440

Introduction

TWO-PHASE flows are often difficult to characterize because of the complex interaction of the solid particles or liquid droplets and the gas. These flows become even more complicated when the fundamental characteristics of the particles or droplets change due to such processes as evaporation and combustion. These complex flows are commonplace in such devices as industrial burners, internal-combustion engines, and gas turbine combustors. In many cases, the droplet or particle sizes and velocities can be measured, and the gas velocity can also be determined using a variety of velocimetry techniques. However, little information is available on the vapor after it leaves the surface of the evaporating droplet.¹⁻⁴ This information is particularly important in combusting sprays because combustion typically takes place away from the surface of the droplet where the fuel-to-air ratio is appropriate.

The visualization technique presented in this Note is a new method for accurate visualization and prediction of the convective transport of vapor in two-phase flows. Water droplets are injected into a TiCl_4 -laden gaseous flow where they evaporate. The water vapor reacts spontaneously with the TiCl_4 vapor to form micrometer-sized TiO_2 particles. The particles are sufficiently small to accelerate rapidly to the velocity of the carrier gas but are too large to diffuse readily. Thus, they are convected along the path that the water vapor follows as it leaves the droplets. The instantaneous locus of the TiO_2 particles is defined as a "vaporline" and can be visualized using Mie scattering. Although the technique for visualizing vaporlines is relatively simple, the physics required to interpret the vaporlines in terms of the droplet, vapor, and fluid interactions can be complicated. The goal of this study was to provide insight into the physics needed to understand and interpret vaporlines. Additionally, predictions from a computer model are presented that support the qualitative interpretation of the vaporline data.

Experimental

The experimental data presented in this Note were obtained in the two-dimensional shear-layer facility described in more detail elsewhere.⁵ The splitter plate divides a 12.7-cm-square duct equally. Dry air was used in both airstreams. The gas velocities were set at 0.70 m/s and 0.35 m/s for the high- and low-speed sides of the flow giving localized Reynolds numbers of less than 1000. The higher-speed air was passed over a liquid TiCl_4 bath for collection of TiCl_4 vapor, as is done in reactive Mie scattering (rms).⁶ For rms, two gaseous flows—one seeded with water vapor, the other with TiCl_4 vapor—must come in molecular contact. When the TiCl_4 reacts with the water vapor, TiO_2 particles are formed that act as light scatterers to mark the interaction of the two streams. The products of the TiCl_4 and H_2O reaction are HCl and TiO_2 . The TiO_2 is a fine white powder that is quite inert, but the HCl can create problems because of its corrosive nature. The quantity of HCl produced is quite low, but a hood should always be used when trying to visualize a flow with TiCl_4 .

Droplets were injected through a slot in the Plexiglas duct on the low-speed side of the flow. The droplets were $\sim 60\text{ }\mu\text{m}$ in diameter and had sufficient momentum to cross the shear layer to the high-speed, TiCl_4 -laden side of the flow. Micrometer-sized TiO_2 particles were formed as the water vapor mixed with the TiCl_4 . The flowfield was illuminated by the 532-nm light output of a frequency-doubled Nd:YAG laser. Water droplets and the TiO_2 particles were the only scatters in the flowfield, and they could be easily distinguished by their 50:1, or greater, diameter ratio. Water-droplet injection was controlled using a droplet-on-demand generator that was driven by a piezoelectric crystal transducer.⁷

Vortices form at roughly 20 Hz for the undriven shear layer, but they are not as stable as desired for the collection of phase-locked measurements and photographs. Therefore, vortex formation was controlled by acoustically driving the low-speed airstream at 20 Hz. A 1% velocity fluctuation was introduced into the low-speed side of the flow due to the acoustic driving. The natural shear layer and driven shear layer are very similar in appearance, but the vortices in the driven shear layer are more controlled and equally spaced. The location of the water droplets and the entrainment of the water vapor into the individual vortices of the shear layer, as marked by TiO_2 particles, were recorded with a digitizing camera. The curve identified by the location of the TiO_2 particles at the instant of visualization is referred to as a vaporline.

Results and Discussion

A vaporline image of a two-dimensional shear layer in which a vortex is forming is shown in Fig. 1. The high-speed side of the flow is on the left and the low-speed side of the flow is on the right with flow from bottom to top. The left side of the flow is seeded with TiCl_4 vapor that reacts quickly and spontaneously with the water vapor from the droplets to form TiO_2 particles. Seven water droplets are visible in this particular image. The air on the left of the shear layer is moving faster than the droplets, and this causes the vapor to precede the droplets as they move downstream. Each droplet has a vaporline associated with it. More detailed analysis of images such as that shown in Fig. 1 led to the development of the schematic shown in Fig. 2 for describing the time and spatial development of the vaporlines.⁵

The vaporline schematic illustrates a specific case in which each droplet is introduced into a driven laminar flow at the same fre-

Presented as Paper 93-0416 at the AIAA 31st Aerospace Sciences Meeting, Reno, NV, Jan. 11-14, 1993; received Feb. 10, 1993; revision received July 20, 1993; accepted for publication July 26, 1993.

*Captain, Wright Laboratory, WL/POSF Bldg. 490, 1790 Loop Road N. Member AIAA.

†Senior Research Engineer, 2800 Indian Ripple Road. Member AIAA.

quency and phase angle (relative to the vortex generation) as the previous droplet. Therefore, this schematic provides an instantaneous picture of the flow that allows one to follow the development of vaporlines at a given flow phase angle, separated by 360-deg phase increments. The thick solid line represents a streakline that would form if dye or seed particles were emitted from the tip of the splitter plate. This streakline is shown to illustrate what the shear layer would look like using traditional methods. It is not created in the experimental shear layer unless a small droplet of water is placed on the tip of the splitter plate where it can react with TiCl_4 in the airflow to form TiO_2 particles. These particles would then be swept downstream from their origination site at the tip of the splitter plate. The dashed lines represent the particle trajectories that specific water droplets and TiO_2 particles would follow. The thin solid lines represent the vaporlines from each droplet. The open circles indicate the locations of the first TiO_2 seed particles formed when each water droplet first passed through the shear layer and to the TiCl_4 -laden side of the flow. The same number is assigned to the head (water droplet) and the tail (first TiO_2 particle formed) of each vaporline. A continuous line of seed particles exists between each identically numbered droplet and seed particle. This line of seed (or vaporline) grows and stretches as it moves downstream, due to gaseous velocity gradients. It should be noted that the convective vaporline remains fairly thin and well defined over a long distance for the two-dimensional gaseous flows investigated, because these flows are laminar and well behaved. If the flow were turbulent, the vaporline would be a more disperse three-dimensional curve, and only a broken line might appear in a two-dimensional visualization.

Notice that the open-circle particles all lie on the streakline that originates at the tip of the splitter plate. It should not be assumed that as these individual seed particles move downstream, they remain on a path identical to the streakline shown. This would be the case only if the flow did not vary with time. However, since this flow is time-dependent, successive snapshots collected at other times (phase angles) would show the streaklines at different stages of their development. Furthermore, if the droplets are introduced at different times relative to the vortex generation, then the vaporlines will have slightly different shapes. This is because the droplets will see different surrounding airflows depending on where they are relative to the vortices. It would be easy to conclude that

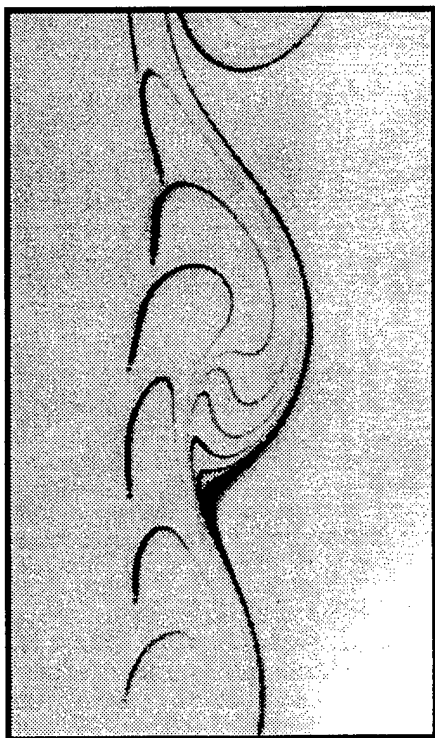


Fig. 1 Vaporlines in a two-dimensional shear layer.

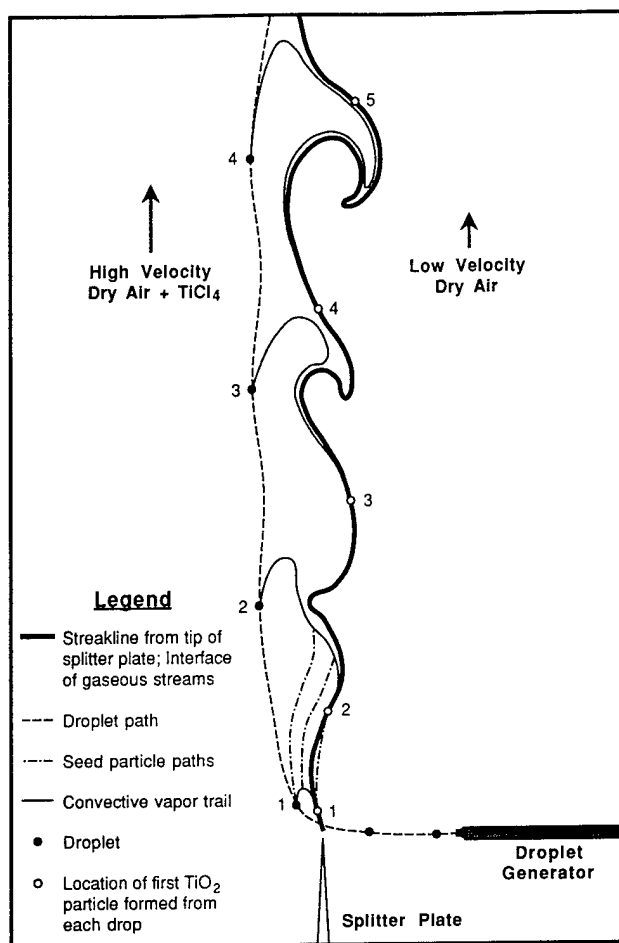


Fig. 2 Vaporline schematic.

the vapor from the droplets follows the path marked out by the vaporlines; this is not the case. The vaporlines are not streamlines or particle trajectories, but evolutionary histories of the convective vapor transport from a droplet relative to a specific flow. In this experiment no droplets, seed particles, or fluid elements move upstream, as observed from the laboratory reference frame. The fluid elements are moving downstream, but certain parts of the flow are moving faster than others, as reflected by the shape of the vaporline. The relative velocity of the droplet to the flow also plays a major role in defining the shape of the convective vaporline. In the extreme case, where the droplet is moving at the same velocity as the gas, no vaporline would exist—only a small spherical cloud of particles around the droplet where the evaporating water is reacting with the TiCl_4 would appear.

The vaporline visualization technique is fairly easy to use in low-velocity flows that are two-dimensional. However, if the flow is three-dimensional, this technique would be difficult using standard sheet-lighting techniques. Obviously, the TiO_2 vaporlines will form independent of the dimensionality of the flow or the method of flow illumination. However, in more turbulent flows the TiO_2 seed vaporlines will become more disperse, requiring a higher intensity light source to maintain sufficient light scattering for observation or recording. Furthermore, a nucleation time is associated with the growth of TiO_2 particles that are large enough to scatter sufficient light for observation. In the images shown in this Note, the time required for the TiO_2 particle to reach sufficient size for observation was $\sim 2\text{--}3$ ms. This could present a problem in high-velocity flows where the interesting fluid dynamics occurs over a time period much less than a few milliseconds.

With confidence that the basic fluid dynamics associated with these vaporlines was understood, attention was turned to the development of a numerical model to calculate vaporlines for comparison with experimental data. It was felt that if the vaporlines could

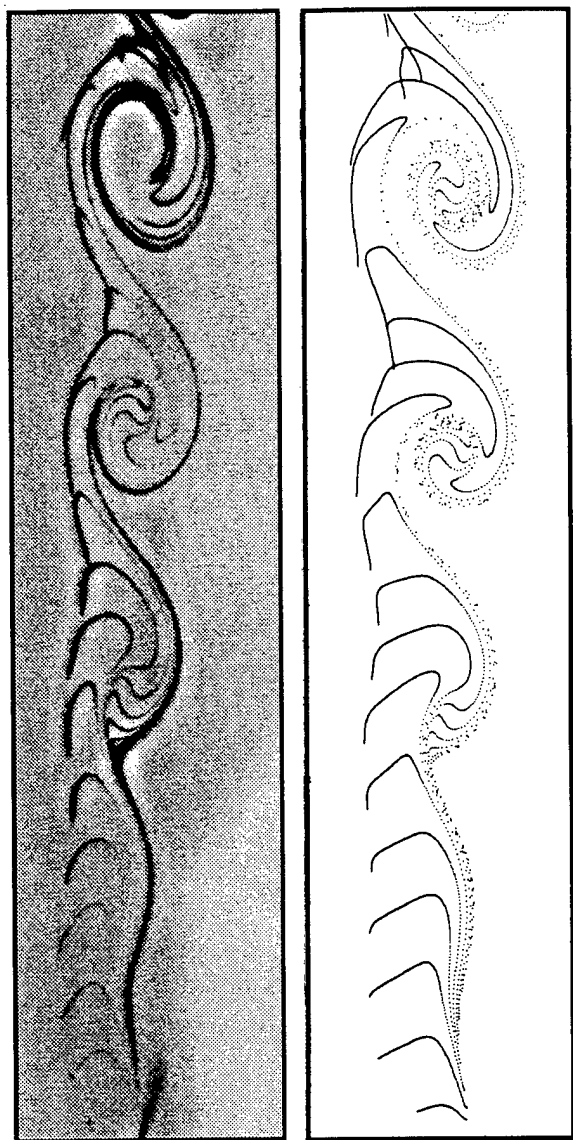


Fig. 3 Vaporlines from tip of splitter plate for a two-dimensional shear layer (left: 0.70 m/s; right: 0.35 m/s; drive: 20 Hz; droplets: 100 Hz; and image: 3 × 12 cm).

be modeled for a relatively simple two-dimensional flow, then it might be possible to extend this visualization technique to more complex flows such as boundary layers, jets in a crossflow, or other higher velocity flows.

The marker and cell (MAC) method was used to simulate the vaporlines of droplets in a two-dimensional shear layer. This numerical method was originally developed by Welch et al.⁸ to solve flow systems with free surfaces. Later, it was modified by Hirt and Cook⁹ to allow the pressure field to be solved more readily. The MAC method is characterized by the use of a staggered grid and the solution of the Poisson equation for pressure at every time step. Also, the pressure solution has the auxiliary task of satisfying the continuity condition. For visualization of the flow patterns (e.g., streaklines, vaporlines of droplets), massless markers (particles) convected by the velocity field were introduced. These markers play no role in determining the velocity and pressure fields.

Uniformly spaced MAC cells (0.1 × 0.05 cm) are distributed throughout the computational domain which is 30 cm long and 12.8 cm wide. The total number of cells is 300 × 256. To handle the outflow boundary condition, the "guard cells"¹⁰ were used to extrapolate the velocity and pressure according to the following equations:

$$\left(\frac{\partial u}{\partial x}\right)_g = \left(\frac{\partial u}{\partial x}\right)_n \quad (1a)$$

$$P_g = P_n + (P_o - P_n) \left(\frac{X_g - X_n}{X_o - X_g} \right) \quad (1b)$$

where the subscript g denotes the guard cell, and n denotes the boundary cell. X_g is the position of the guard cell relative to the origin. X_n is the position of the boundary cell relative to the origin, and X_o is the specified position of the ambient relative to the origin. In this program, artificial disturbances (1% and 20 Hz) were introduced along inflow boundaries to trigger the vortical-shedding process. The vaporlines of droplets observed in the experiments can be produced numerically by tracing a number of massless particles being emitted from the droplets while the droplets are traveling through the simulated flowfield. To obtain the particle velocities in the discretized flowfield numerically, an accurate second-order interpolation scheme from Chan et al.¹¹ was used.

The trajectories of droplets in the flowfield were calculated by employing the following drag correlation of droplets:¹²

$$C_D = \frac{3}{16} + \frac{24}{Re_d}, \quad \text{for } Re_d \leq 0.01 \quad (2a)$$

$$C_D = \frac{24}{Re_d} \{ 1 + 0.1315 Re_d^{[0.82 - 0.05 \log_{10}(Re_d)]} \} \quad (2b)$$

for $0.01 < Re_d \leq 20$

$$C_D = \frac{24}{Re_d} \{ 1 + 0.1935 Re_d^{0.6305} \}, \quad \text{for } 20 < Re_d \leq 260 \quad (2c)$$

The code was first used to predict the shape of the two-dimensional shear layer as marked by a streakline originating from the tip of the splitter plate. The experimental streakline was obtained by placing a small drop of water on the tip of the splitter plate and seeding the high-speed side of the flow with TiCl_4 . The correlation between the experimental data and the model predictions is quite good. When droplets were introduced into the experimental shear layer, the image on the left in Fig. 3 was obtained. The resulting numerical simulation of this flowfield is shown on the right in the figure. The experimental data and the numerical results matched quite closely, despite limited information on the inlet velocity profile. Furthermore, the model does not account for a reduction in droplet diameter and weight due to evaporation. These droplets emit massless particles as they move in the flow to simulate the TiO_2 seed particle vaporlines formed when the water vapor comes in contact with the TiCl_4 in the flow.

Conclusions

This Note describes a vaporline visualization technique and associated numerical model that are useful in characterizing the convective transport of vapor from evaporating droplets. The physical process has been modeled successfully, and the correlation between experimental data and model predictions is excellent. This visualization technique is easy to apply to low-velocity, two-dimensional flows, but its application becomes increasingly difficult in three-dimensional and high-velocity flows. However, it is anticipated that this visualization technique will be applied with some success to flows that are more complex than a two-dimensional shear layer.

Acknowledgments

The authors acknowledge M. E. Post, V. R. Katta, D. Tankin, W. M. Roquemore, L. P. Goss, L. Brainard, D. D. Trump, and M. Whitaker for valuable insight and technical assistance. This work is supported by the Air Force Office of Scientific Research.

References

- 1 Melton, L. A., "Spectrally Separated Emissions for Diesel Fuel Droplets and Vapor," *Applied Optics*, Vol. 22, No. 14, 1983, pp. 2224-2226.
- 2 Melton, L. A., and Verdieck, J. F., "Vapor/Liquid Visualization in Fuel

Sprays," *Twentieth Symposium (International) on Combustion*, Combustion Inst., Pittsburgh, PA, 1984, pp. 1283–1290.

³Ball, G. J., and Pratt, N. H., "Laser Induced Fluorescence Imaging of Interphase Mass Transfer in Steam/Water Flows," *Proceedings of the VI International Conference Photon Correlation and Other Techniques in Fluid Mechanics*, Inst. of Physics Conf. (Cambridge, England, UK), Serial 77, Session 3, 1985, pp. 111–116.

⁴Allen, M. G., and Hanson, R. K., "Digital Imaging of Species Concentration Fields in Spray Flames," *Twenty-First Symposium (International) on Combustion*, Combustion Inst., Pittsburgh, PA, 1986, pp. 1755–1761.

⁵Hancock, R. D., Jackson, T. A., and Nejad, A. S., "Technique for Visualizing Vaporlines Emanating from Water Droplets," *Applied Optics*, Vol. 31, No. 9, 1992, pp. 1163–1166.

⁶Chen, L.-D., and Roquemore, W. M., "Visualization of Jet Flames," *Combustion and Flame*, Vol. 66, No. 1, 1986, pp. 81–86.

⁷Switzer, G. L., "A Versatile System for Stable Generation of Uniform Droplets," *Review of Scientific Instruments*, Vol. 62, No. 11, 1991, pp. 2765–2771.

⁸Welch, J. E., Harlow, F. H., Shannon, J. P., and Daly, B. J., "The MAC Method, a Computing Technique for Solving Viscous, Incompressible Transient Fluid Involving Free Surface," Los Alamos Scientific Lab., Rept. LA-3425, Los Alamos, NM, 1966.

⁹Hirt, C. W., and Cook, J. L., "Calculating Three-Dimensional Flows Around Structures and Over Rough Terrain," *Journal of Computational Physics*, Vol. 10, No. 2, 1972, p. 324–340.

¹⁰Boris, J. P., Oran, E. S., Fritts, M. J., and Oswald, C. E., "Time Compressible Similarities of Shear Flows," Naval Research Lab., NRL Memo Rept. 5249, Washington, DC, 1983.

¹¹Chan, R. K. C., Street, R. L., and Strelkoff, T., "Computer Studies of Finite Amplitude Water Waves," Stanford Univ., Dept. of Civil Engineering, TR 104, Stanford, CA, 1969.

¹²Clift, R., Grace, J. R., and Weber, M. E., *Bubbles, Drops, and Particles*, Academic Press, San Diego, CA, 1978, Chap. 5.

Gravity Effects on the Dynamics of Evaporating Droplets in a Heated Jet

T. W. Park* and S. K. Aggarwal†

University of Illinois at Chicago, Chicago, Illinois 60607
and

V. R. Katta‡

System Research Laboratory, Inc., Dayton, Ohio 45440

Dispersion and vaporization behavior of liquid fuel droplets in a heated axisymmetric jet is studied using detailed flow visualization based on numerical simulations. Results show that the gravity has a strong effect on the dynamics of jet shear layer and droplets. The presence of gravity introduces the buoyancy-induced hydrodynamic instability, causing the large vortical structures to appear without any external perturbation. The droplet dispersion and vaporization behavior is influenced by both the vortex structures and the gravity. Three regimes, distinguished by the Stokes number St and the ratio of droplet terminal velocity to characteristic gas velocity V_r , are identified to characterize the effects of vortex structures and gravity on droplet dispersion. At low St and V_r , the droplets behave like gas particles. In the second regime, $0.1 < St < 0.64$ and $0.04 < V_r < 0.3$, due to the centrifugal action of the vortex structures the droplets are dispersed more than the gas particles. At the lower end of the third regime, the droplet motion is affected by both the vortex structures and the gravity, whereas at the higher end it is affected more by gravity. The effect of vaporization is to shift the Stokes number range for the three regimes.

Nomenclature

B = Spalding transfer number
 C_D = droplet drag coefficient
 C_p = specific heat
 D = vapor/air binary diffusion coefficient
 d_k = droplet diameter
 g = acceleration of gravity
 H = heat transferred from gas phase to droplet per unit mass of fuel vaporized
 \bar{H} = H/L
 h = heat transfer coefficient
 L = latent heat of vaporization
 Le = Lewis number, $\lambda/(\rho DC_p)$
 M = molecular weight
 \dot{m}_k = droplet vaporization rate
 \dot{m}_k'' = droplet vaporization flux rate, $\dot{m}_k/(\pi d_k^2)$
 \bar{m}_k = normalized droplet vaporization rate, $\dot{m}_k/(2\pi\rho D d_k)$
 Nu = Nusselt number
 P = pressure
 Pe = Peclet number, $RePr$
 Pr = Prandtl number
 R = universal gas constant
 Re = Reynolds number
 r = radial distance for gas-phase
 Sc = Schmidt number
 Sh = Sherwood number
 St = Stokes number, t_k/t_f
 T = temperature
 T_b = boiling temperature
 T_0 = initial droplet temperature

t = time
 t_f = characteristic flow time
 t_k = droplet aerodynamic response time, $\rho_k d_k^2/(18\mu_g)$
 u = axial velocity
 V_r = droplet terminal velocity, $\rho_k d_k^2 g/(18\mu_g)$
 v = radial velocity
 x = axial location of droplet
 Y = mass fraction
 y = radial location of droplet
 z = axial distance
 α = thermal diffusivity
 λ = thermal conductivity
 μ = dynamic viscosity
 ρ = density

Subscripts

F = fuel vapor
 g = gas-phase
 i = i th species
 k = droplet characteristic or group
 l = liquid-phase
 s = surface
 ∞ = ambient condition

Introduction

GRAVITY influences combustion phenomena in many significant ways. Combustion systems where gravity plays a key role include burning droplets, jet diffusion flames, freely propagating premixed flames, candle flames, flames over solid and liquid pools, and other heterogeneous flames.¹ Since the pioneering work of Burke and Schumann² and Hottel and Hawthorne,³ the gaseous diffusion flames, because of their practical and scientific importance, have been extensively studied over many decades. More recently, opportunities provided by the microgravity (μg) environment at ground-based and space facilities have motivated additional research in this area, focusing on the effects of gravity on the diffusion flames.^{4–9} It has been found^{4–9} that the reduction of gravity introduces drastic changes in both the steady-state and the dynamic characteristics of these flames. Under μg conditions,

Received May 27, 1994; revision received Sept. 2, 1994; accepted for publication Sept. 16, 1994. Copyright © 1994 by the authors. Published by the American Institute of Aeronautics and Astronautics, Inc., with permission.

*Graduate Student, Department of Mechanical Engineering, Student Member AIAA.

†Associate Professor, Department of Mechanical Engineering, Associate Fellow AIAA.

‡Senior Engineer, Member AIAA.

the diffusion becomes a more dominant transport mechanism and the residence time is increased. Consequently, the μg diffusion flames are much taller, wider, sootier, and more radiating compared to the corresponding normal gravity (1g) flames. The μg and 1g flames also differ in structural details and their dependence on pressure, oxygen concentration, and Reynolds number. In addition, the 1g flames are subjected to the buoyancy-induced hydrodynamic instability, which is responsible for the presence of large vortical structures outside of the flame.⁷⁻⁹ These low-frequency, slowly moving outer structures interact strongly with the flame surface, creating a wrinkled flame, and are responsible for the flame flicker. In μg conditions, these structures are not present.

The transitional behavior of diffusion flames also exhibit fundamental differences in 1g and μg conditions.^{5,6} At 1g, transition is first observed at the flame tip, and with increasing Reynolds number, instability moves closer to the flame base. At μg , transition is associated with the appearance of intermittent disturbances that form at the base and move downstream. In addition, the buoyancy-generated turbulence aids in transition to turbulent flame at 1g, whereas the transition occurs over a much longer range of Reynolds number at μg . The blowoff limits are also significantly extended for μg diffusion flames.

While the gaseous diffusion flames under 1g and μg conditions have been extensively investigated, the research focusing on the effects of gravity on liquid-fuel spray diffusion flames is rather limited. Additional complications arising from gravity in a spray flame are due to the effect of gravity on droplet motion, causing droplet settling and stratification in droplet concentration, and the dynamic interactions of droplets with outer buoyancy-driven structures. These interactions, which involve the influence of outer structures on the dispersion and vaporization behavior of droplets, and the effect of dispersed phase on the development of buoyancy-driven instability, are expected to play an intrinsic role in the dynamics of spray flames.

In this article, the dynamics and dispersion behavior of *n*-heptane droplets in a heated axisymmetric jet is studied via numerical simulations. The gravity is considered a parameter. The overall objective is to study the fundamental processes of spray diffusion flames in laminar and transitional regimes under the influence of gravity. In this first study, the physical model is simplified by considering a heated jet issuing into a slower cold coflow, so that the complexities due to chemical reactions and the effects of dispersed phase on gas-phase processes can be avoided. The dispersion behavior of nonevaporating and evaporating droplets injected into the jet shear layer, where the fluid dynamics and heat transport processes are dominated by buoyancy-induced vortical structures, is investigated. Results presented focus on the effect of evaporation on the droplet dispersion behavior in the presence of large vortex structures, and the role of gravity in the dispersion process. Several experimental and computational studies¹⁰⁻¹⁸ have been reported in recent years, examining the dispersion behavior of particles or nonevaporating droplets in the presence of shear-induced vortex structures. These studies indicate that the dynamics of particles in the near shear-layer region is controlled by the large structures, which enhance the dispersion of intermediate size particles. The effect of vortex structures on particle dispersion is characterized by *St*, defined as the ratio of the particle response time to the characteristic flow time. The cited studies, however, do not consider the effect of evaporation on the dispersion behavior.

Physical Model

Figure 1 shows the physical system simulated in the present study. The heated air jet at a velocity of 1.0 m/s and temperature of 1200 K issuing into a coflow at velocity of 0.2 m/s and temperature of 294 K is considered. The jet diameter is 2.54 cm, and the computational domain in the radial di-

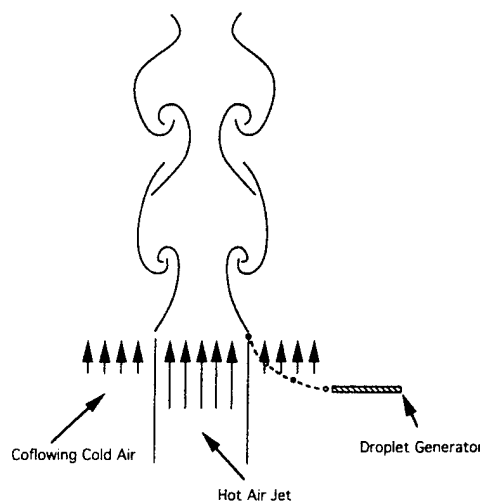


Fig. 1 Schematic of a buoyant hot air jet in a coflowing cold airstream at 1g.

rection is 15 cm. For the heated jet at 1g, the buoyancy-induced vortex structures are observed in the jet shear layer. The dynamics of these structures is simulated by solving the time-dependent, axisymmetric gas-phase equations. The *n*-heptane droplets of different diameters are then injected into the jet shear layer from the specified radial locations, and their dispersion and vaporization behavior is investigated by solving the appropriate droplet equations.

Gas-Phase Equations

The time-dependent governing equations written in cylindrical (*z*, *r*) coordinate system for an axisymmetric heated jet are

$$\begin{aligned} \frac{\partial(\rho\Phi)}{\partial t} + \frac{\partial(\rho u\Phi)}{\partial z} + \frac{\partial(\rho v\Phi)}{\partial r} = \frac{\partial}{\partial z} \left(\Gamma^\Phi \frac{\partial\Phi}{\partial r} \right) \\ + \frac{\partial}{\partial r} \left(\Gamma^\Phi \frac{\partial\Phi}{\partial z} \right) - \frac{\rho v\Phi}{r} + \frac{\Gamma^\Phi}{r} \frac{\partial\Phi}{\partial r} + S_s^\Phi \end{aligned} \quad (1)$$

The general form of Eq. (1) represents the continuity, momentum, or energy equation, depending on the variable used for Φ . Table 1 gives the transport coefficients Γ^Φ and the source terms S_s^Φ that appear in the governing equations. In this table, μ , λ , and C_p are, respectively, the viscosity, thermal conductivity, and specific heat of air. They are considered functions of temperature.

Liquid-Phase Equations

The Lagrangian approach is employed to compute the properties of each droplet as it travels in a heated jet shear flow. The equations governing the variation of position, velocity, and size for a given droplet *k* along its trajectory are

$$\frac{dx_k}{dt} = u_k \quad (2)$$

$$\frac{dy_k}{dt} = v_k \quad (3)$$

$$\frac{du_k}{dt} = \frac{3C_D\rho_g}{4d_k\rho_k} |u_g - u_k| (u_g - u_k) + \left(\frac{\rho_g}{\rho_k} - 1 \right) g \quad (4)$$

$$\frac{dv_k}{dt} = \frac{3C_D\rho_g}{4d_k\rho_k} |v_g - v_k| (v_g - v_k) \quad (5)$$

$$\frac{dd_k}{dt} = -\frac{2\dot{m}_k''}{\rho_k} \quad (6)$$

Table 1 Transport coefficients and source terms appearing in governing equations

Equations	Φ	Γ^Φ	S_κ^Φ
Continuity	1	0	0
Axial momentum	u	μ	$-\frac{\partial p}{\partial z} + (\rho_0 - \rho)g + \frac{\partial}{\partial z} \left(\mu \frac{\partial u}{\partial z} \right) + \frac{\partial}{\partial r} \left(\mu \frac{\partial v}{\partial z} \right) + \frac{\mu}{r} \frac{\partial v}{\partial z} - \frac{2}{3} \left[\frac{\partial}{\partial z} \left(\mu \frac{\partial u}{\partial z} \right) + \frac{\partial}{\partial z} \left(\mu \frac{\partial v}{\partial r} \right) + \frac{\partial}{\partial z} \left(\mu \frac{v}{r} \right) \right]$
Radial momentum	v	μ	$-\frac{\partial p}{\partial r} + \frac{\partial}{\partial z} \left(\mu \frac{\partial u}{\partial r} \right) + \frac{\partial}{\partial r} \left(\mu \frac{\partial v}{\partial r} \right) + \frac{\mu}{r} \frac{\partial v}{\partial r} - 2\mu \frac{v}{r^2} - \frac{2}{3} \left[\frac{\partial}{\partial r} \left(\mu \frac{\partial u}{\partial z} \right) + \frac{\partial}{\partial r} \left(\mu \frac{\partial v}{\partial r} \right) + \frac{\partial}{\partial r} \left(\mu \frac{v}{r} \right) \right]$
Energy	T	λ/C_p	0

where

$$C_D = \frac{24}{Re_k} \left(1 + \frac{Re_k^{2/3}}{6} \right) \quad (7)$$

$$Re_k = \frac{\rho_s [(u_g - u_k)^2 + (v_g - v_k)^2]^{1/2} d_k}{\mu_k} \quad (8)$$

The following expressions¹⁹ are used for heat and mass transfer rates to the drop:

$$\frac{hd_k}{\lambda} = \frac{2(N_p/Le)^{1/4}(1+B)}{(1+B)^{1/4} - 1} \quad (9)$$

$$\frac{\dot{m}_k d_k}{\rho D} = 2N_s^{1/4}(1+B) \quad (10)$$

and B is given by

$$B = (Y_{F_s} - Y_{F_\infty})/(1 - Y_{F_s}) \quad (11)$$

N_p and N_s are the corrective factors to consider the convective effect on heat and mass transfer, and are calculated using semi-empirical relations¹⁹:

$$N_p \text{ or } N_s = 1 + \frac{0.278 Re_k^{1/2} (Pr \text{ or } Sc)^{1/3}}{[1 + 1.232/(Re_k (Pr \text{ or } Sc)^{4/3})]^{1/2}} \quad (12)$$

In order to complete the solution, the drop surface temperature and the fuel mass fraction at the drop surface must be known. The two equations required to solve for these quantities are provided by the fuel vapor pressure relationship and the energy equation in the liquid. The vapor pressure relationship has the form

$$Y_{F_s} = f(T, P, Y_\infty) \quad (13)$$

The transient heat transport within the droplet is represented by the unsteady heat diffusion equation in a spherically symmetric geometry. The solution of this equation involves a moving boundary-value problem as the droplet is evaporating. This problem can be reformulated by using a transformation to make the boundary stationary. The transformed governing equation²⁰ is

$$\frac{\partial \tilde{T}_l}{\partial \tilde{t}} = \frac{1}{\tilde{r}^2} \frac{\partial}{\partial \tilde{r}} \left(\tilde{r}^2 \frac{\partial \tilde{T}_l}{\partial \tilde{r}} \right) - \frac{\tilde{r} \tilde{m}_k \lambda}{Le C_p \rho \alpha_l} \left(\frac{\partial \tilde{T}_l}{\partial \tilde{r}} \right) \quad (14)$$

with the initial and boundary conditions as

$$\tilde{T}_l = 0 \quad \text{at} \quad \tilde{t} = 0 \quad (15)$$

$$\frac{\partial \tilde{T}_l}{\partial \tilde{r}} = 0 \quad \text{at} \quad \tilde{r} = 0 \quad (16)$$

$$\frac{\partial \tilde{T}_l}{\partial \tilde{r}} = \frac{\tilde{m}_k (\tilde{H} - 1) L \lambda}{Le C_p \lambda_l (T_B - T_0)} \quad \text{at} \quad \tilde{r} = 1 \quad (17)$$

where $\tilde{T}_l(\tilde{r}, \tilde{t})$ and \tilde{r} are, respectively, the normalized liquid temperature and radial location inside the droplet, and \tilde{t} is the normalized time variable. These are given by

$$\tilde{T}_l = (T_l - T_0)/(T_B - T_0) \quad (18)$$

$$\tilde{r} = 2r/d_k \quad (19)$$

$$\tilde{t} = \alpha_l \int_0^t \frac{4}{d_k^2} dt \quad (20)$$

The vapor pressure relationship and other properties used for the liquid and gas phases are summarized in the Appendix. The droplet model includes the effects of variable thermophysical properties and nonunity Lewis number in the gas film outside the droplet. The thermophysical properties are calculated at an average reference state defined as

$$\Phi_{\text{avg}} = \alpha \Phi_{gs} + (1 - \alpha) \Phi_g \quad (21)$$

where Φ is a generic quantity representing either mass fraction or temperature, and α is selected to be 0.7. The subscripts gs and g represent the gas-phase property at the droplet surface and outside the gas film, respectively.

It should be noted that in the present vaporization model, the effect of transient heating is incorporated by using the conduction-limit model.²⁰ This model is deemed satisfactory in the present study, since the maximum droplet Reynolds number during droplet lifetime is less than 10, and, therefore, the effect of internal circulation is expected to be negligible. For the same reason, the effect of gas-phase convection on the heat and mass transport is represented by semi-empirical correlations, Eq. (12).

Numerical Model

An implicit algorithm is employed to solve the unsteady gas-phase equations. The finite difference forms of the momentum equations are obtained using an implicit QUICKEST scheme.²¹ The governing equations are integrated on a non-uniform staggered-grid system. An iterative alternative direction implicit (ADI) technique is used for solving the resulting sets of algebraic equations. At every time step, the pressure field is calculated by solving the pressure Poisson equations simultaneously and utilizing the lower and upper diagonal (LU) matrix decomposition technique.

Figure 2 shows the grid system and the computational domain used in the present study. Grid lines are clustered near the shear layer to resolve the steep gradients of the dependent variables. Boundaries of the computational domain are shifted sufficiently to minimize the propagation of disturbances into region of interest. The flow variables at the outflow boundary are obtained using an extrapolation procedure with weighted zero and first-order terms. The main criterion used in selecting the weighting functions is that the vortices crossing this outflow boundary should leave smoothly without being distorted.

The liquid-phase equations are advanced in time by a second-order accurate Runge-Kutta method. Since the gas-phase

solution employs an implicit procedure, the temporal step size used for integrating the liquid-phase equations is usually smaller than that for gas-phase equations. An automatic procedure is implemented in order to select an optimum liquid-phase time step. The procedure involves calculating the characteristic thermal response time, velocity response time, and vaporization time for each droplet group, and then selecting the temporal step size as a fraction (two-hundredth) of the smallest of these time scales. A detailed examination of the various time scales, based on numerical experiments, revealed that the temporal step size is determined by either the thermal response time or the velocity response time of a given droplet group. The number of subcycles for advancing the liquid-phase solution for each gas-phase cycle typically varies from 1 to 30, depending upon the droplet size.

The procedure to advance the two-phase solution over one gas-phase time step Δt_k is as follows. Using the known gas-phase properties, the liquid-phase equations are solved over the specified number of liquid-phase subcycles. A third-order accurate Lagrangian polynomial method is used for interpolating the gas-phase properties from the nonuniform fixed grid to the droplet characteristic location. Figure 3 shows the gas-phase cells surrounding a droplet characteristic. The variable $\Phi_{g,k}$ represents the interpolated value of the gas-phase variable at the k -characteristic location. It should be noted that the interpolation scheme for the gas-phase velocities u and v

is based on their respective grid cells because of the use of a staggered grid in gas-phase calculation. It is also important to find the best-fit nine grid points at each characteristic location for better interpolation. The nine grid points shown in Fig. 3 correspond to the characteristic location in the shaded region. The droplet properties are updated after every liquid-phase subcycle. The gas-phase properties are then updated by solving Eq. (1), as described earlier.

Results and Discussion

For the base case, a jet at a velocity of 1.0 m/s and temperature of 1200 K issuing into a coflow at a velocity of 0.2 m/s and temperature of 294 K is considered. The computational domain is 15 cm in the radial direction and 40 cm in the axial direction. The jet diameter is 2.54 cm. A nonuniform grid system with 151×61 grid points, with a large number of grid points clustered in the shear layer, is utilized. The minimum grid spacing is about 0.079 cm, and the Courant, Friedrichs, and Lewy (CFL) number is 0.2. Several diagnostic runs were made to assure that the gas-phase simulations are reasonably independent of the grid size and CFL number. Results from one of these runs, indicating the grid-independence of the gas-phase solution, are given in Fig. 4, which shows the instantaneous iso-temperature contours for two grid densities for the heated jet at 1g. The effect of CFL number on the gas-phase solution was also evaluated, and the CFL number of 0.2 was found to be in the range where the solution is insensitive to the temporal step size Δt_k . The temporal step size for droplet calculation Δt_p was also taken in the range where the droplet results are independent of Δt_p , as described earlier.

Dynamics of Cold and Heated Jets

The stability characteristics of cold and heated jets under 0 and 1g conditions are examined first without injecting droplets into the jet shear layer. Based on the jet velocity of 1.0 m/s and the diameter of 2.54 cm, the cold and heated jets represent flows with Reynolds number of 1.546×10^3 and 1.50×10^2 , respectively. The latter is calculated using the density and viscosity of air at 1200 K. Due to the velocity gradient, the jet shear layer exhibits Kelvin-Helmholtz-type instability, which is characterized by the formation of large toroidal vortices. However, to simulate these vortices a low-amplitude perturbation, either external or inherent in the calculations, is required. Numerical experiments were per-

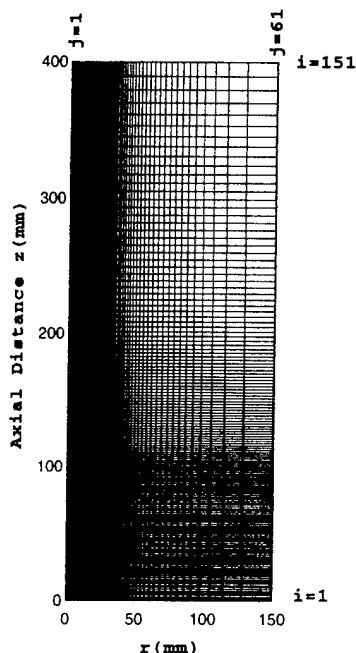


Fig. 2 Typical grid system used for simulations.

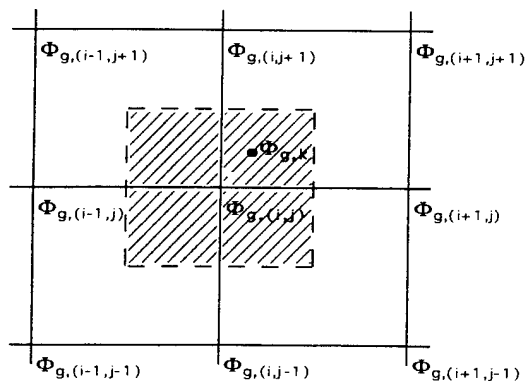


Fig. 3 Best-fit grid cells for the interpolation.

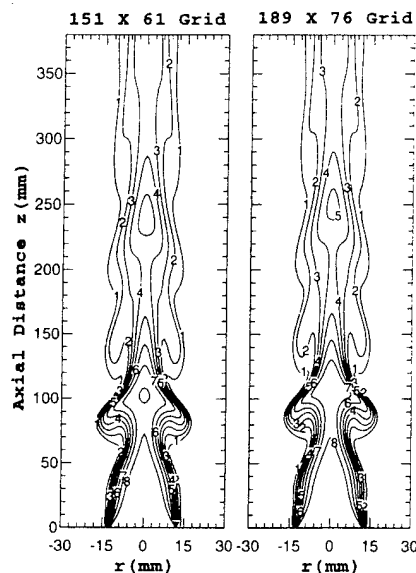


Fig. 4 Comparison of temperature contours for the heated jet with two grid densities.

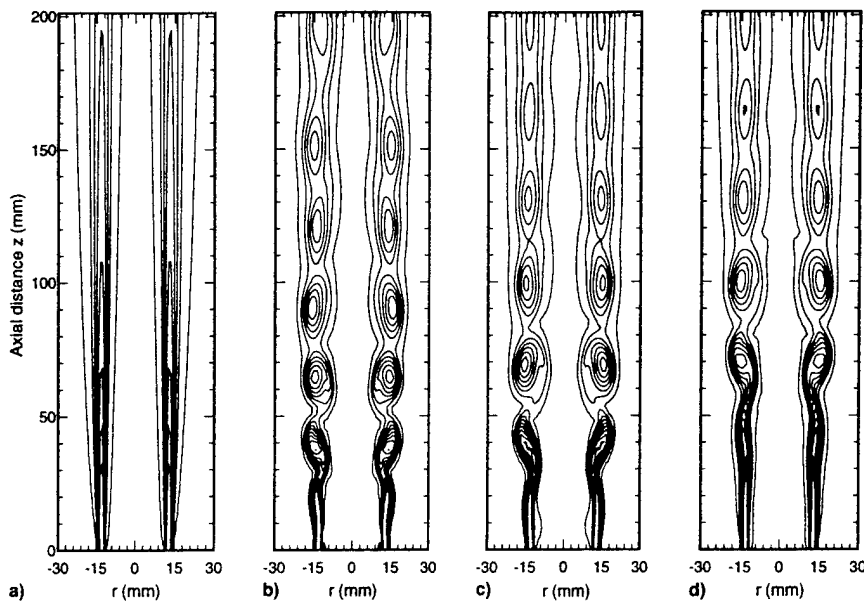


Fig. 5 Iso-vorticity contours for the cold jet for four different cases: a) without external forcing, b) white-noise forcing, c) forcing the central high-speed jet at a frequency of 20 Hz, and d) forcing the low-speed annulus flow at a frequency of 20 Hz. Jet Reynolds number is 1.546×10^3 .

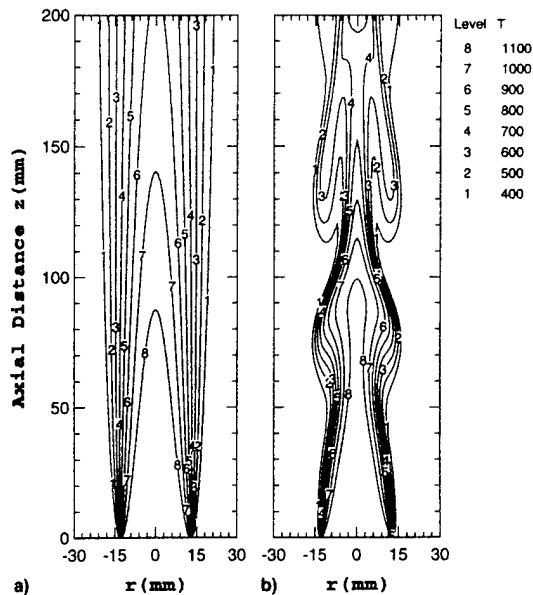


Fig. 6 Iso-temperature contours for the hot jet at a) 0 and b) 1g.

formed on these jets for triggering the shear-layer instability and the results are summarized in Figs. 5 and 6.

To determine whether the noise inherent in the calculations is sufficient or not for the development of the shear-layer instabilities, both the cold and heated jets are simulated without introducing any external perturbation. Cold-jet calculations performed with different grid systems and time steps have converged to a steady-state solution that is given in Fig. 5a. The iso-vorticity contours of this figure show that the shear layer is laminar without having flow instabilities. These calculations suggest that the noise in the present simulations is not sufficient for the manifestation and growth of the shear-layer instabilities. Therefore, as an alternative, attempts were made to make the calculated jet shear layer unsteady by providing it with external perturbations.

The following types of external perturbations are considered in the present study: 1) computer-generated white noise superimposed on the convective flow at all the grid points within a circular region of two-grid radius and centered in the jet shear layer at $z = 8$ mm, 2) forcing the entire central high-

speed jet to oscillate at a frequency of 20 Hz, and 3) forcing the low-speed annulus flow to oscillate at 20 Hz. Instantaneous vorticity fields resulting from the calculations using the above three types of perturbations are depicted in Figs. 5b–5d, respectively. The magnitude of forcing (velocity fluctuation) for different perturbation modes was fixed at 3% of the local axial velocity. Forcing frequency (20 Hz) used for the latter two modes was equal to the peak-amplification frequency noted from the calculations made with white-noise perturbations (obtained from the fast Fourier transformation of the time data). The iso-vorticity contours of Figs. 5b–5d indicate that all the three types of external perturbation are magnified similarly and resulted in toroidal vortices of same size. Due to the lower-magnitude velocity fluctuations used in the last case (3% of the annulus air velocity of 0.2 m/s) the instability is somewhat weaker (Fig. 5b) in the region $z < 80$ mm compared to that seen for the other two cases (Fig. 5c and 5d).

It is clearly evident from Fig. 5 that the shear layer of the cold jet ($Re = 1.546 \times 10^3$) becomes unsteady only in the presence of external perturbations, and the flow structure seems to be insensitive to the type of perturbation used. For the corresponding heated jet case (jet velocities the same as those of the cold-flow case) the shear layer might be expected to be stable as the effective Reynolds number based on air density and viscosity at 1200 K is reduced by a factor of about 10. Because of the presence of density variation in the heated-jet case, simulations are made by 1) neglecting the gravitational force and 2) assuming that gravity acts in a direction opposite to that of the jet flow, which represents the vertically mounted jets. Computed jets for both the cases are shown in Fig. 6 using iso-temperature contours.

Calculations made by neglecting gravitational force yielded a solution that has no vortical structures in the shear layer (Fig. 6a). Kelvin-Helmholtz instabilities did not develop even when the shear layer was excited using the previously described perturbation methods. However, when the gravity term was introduced in the axial momentum equation, large-scale vortex structures appeared due to the buoyancy-induced instability of the heated-jet shear layer (Fig. 6b). It is important to note that these structures are produced without using any external forcing, and their dynamics are found to be unaltered by the superimposition of the three different external perturbations discussed earlier. This is in contrast to the dynamics of shear-induced vortex structures. The buoyant

acceleration of hot gases at 1g helps the formation of large vortex structures, while at 0g, due to the low Reynolds number, the jet shear layer exhibits a behavior typical of a laminar flow. The temporal evolution of buoyancy-induced vortices for the 1g case is shown in Fig. 7. Computed temperature data along the radial direction at two axial locations are recorded over a period of 250 ms, and the evolution is shown in the form of iso-temperature contours. It can be seen that the vortex structures are highly coherent and periodic. The frequency of oscillation is 15.8 Hz. Even though the frequencies of the Kelvin-Helmholtz instability of the cold jet and the buoyancy-induced instability of the heated jet are not much different (20 and 15.8 Hz, respectively), the sizes of the vortical structures in these two cases (Figs. 5b and 6b) are significantly different. The number of vortical structures present within an axial distance of 200 mm in the cold and heated jets are about 6 and 2, respectively. Based on the average vortex size and the crossing frequency, the average convective velocities for the cold and heated jets must be approximately 0.6 and 1.5 m/s, respectively. The higher convective velocity in the case of heated jet is the result of buoyancy.

Effect of Gravity on Droplet Motion

The motion and dispersion characteristics of droplets in the dynamically evolving flow of heated jet (Fig. 6b) are studied by injecting droplets of varying size into the shear layer. Figure 8 shows the effect of gravity on the trajectories of evaporating droplets that are injected at the nozzle rim and traverse the unsteady flowfield dominated by large-scale vortical structures. For this case, the gas-phase simulation is started at $t = 0$ and the droplets are injected at $t = 0.954$ s. During the period of $0 < t < 0.954$ s, the initial flow transient is convected out of the computational domain. The trajectories shown in Fig. 8 are computed from $t = 0.954$ –2.226 s by solving the gas-phase and the droplet equations simultaneously. For all the cases considered, the initial droplet velocity is assumed to be equal to the jet velocity. For the 0g case (Fig. 8b), due to the absence of buoyant vortex structures, the jet flow has little influence on the droplet trajectory. In particular, there is virtually no radial dispersion of droplets, and the initial droplet size does not have much effect on the trajectory. For the corresponding 1g case, however, the droplet motion is strongly influenced by the buoyancy-induced vortex structures. In addition, it may also be affected by grav-

ity directly, depending upon the initial droplet size. In fact, we can identify three different droplet-size regimes given in Table 2, that are distinguished by the Stokes number and the ratio of droplet terminal velocity [$V_t = \rho_k d_k^2 g / (18 \mu g)$] to characteristic gas velocity. Here, the Stokes number is defined by the ratio of t_k to t_f , the latter defined by the time scale of large structures. At low Stokes number (initial diameter $d_0 < 50 \mu\text{m}$), the droplets behave like gas particles, and gravity has no direct influence on their motion as their terminal velocity is small compared to the characteristic gas velocity ($V_{\text{gas}} = 1.5$ m/s), the latter being taken as the average convective velocity of the buoyancy-induced structures. In the second regime, the Stokes number is in the range $0.1 < St < 0.64$, the droplet terminal velocity is still small relative to V_{gas} . In this regime, due to the centrifugal action of the vortex structures,^{10,16,17} the droplets are dispersed more than the gas particles. This will be discussed quantitatively in the next section. The third regime is characterized by intermediate to large values of the Stokes number. At the lower end of this regime, the droplet motion is affected by both the vortex structures and the gravity, whereas at the higher end, it is affected more strongly by gravity. For example, as shown in Fig. 8, the 500- μm evaporating droplets fall back to the inner jet region due to the strong effect of gravity.

Table 2 Stokes numbers and droplet terminal velocities for various droplet diameters

$d_k, \mu\text{m}$	St	$V_t, \text{m/s}$
25	0.01	0.006
50	0.04	0.025
100	0.16	0.10
150	0.36	0.23
200	0.64	0.40
250	1.00	0.63
300	1.44	0.90
500	4.00	2.52

Characteristic flow time used in the calculation of Stokes numbers is 0.063 s based on a vortex frequency of 15.8 Hz.

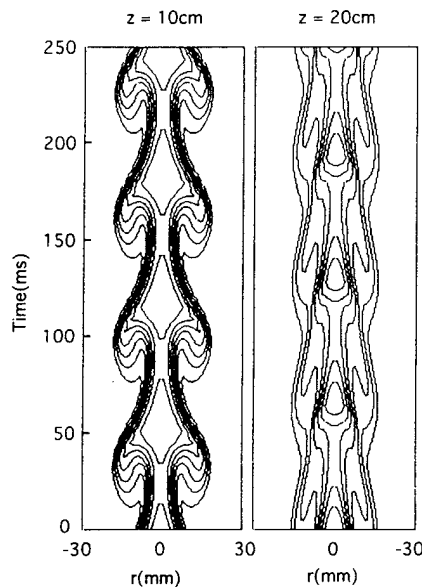


Fig. 7 Temporal evolution of buoyancy-generated vortex structures in terms of iso-temperature contours at two axial locations for the 1g case of Fig. 6.

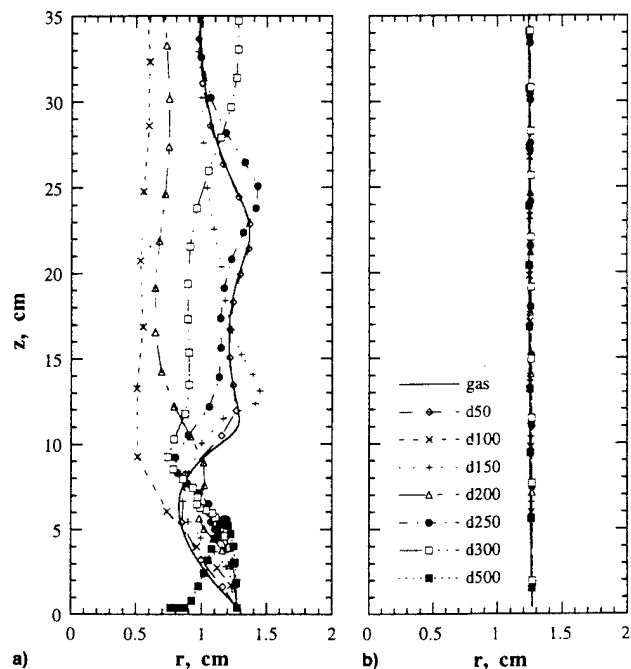


Fig. 8 Trajectories of evaporating droplets injected into the hot jet shear layer under a) 1 and b) 0g conditions. Results are shown for a gas particle and droplets of different initial diameters, with d50 representing diameter of 50 μm , etc.

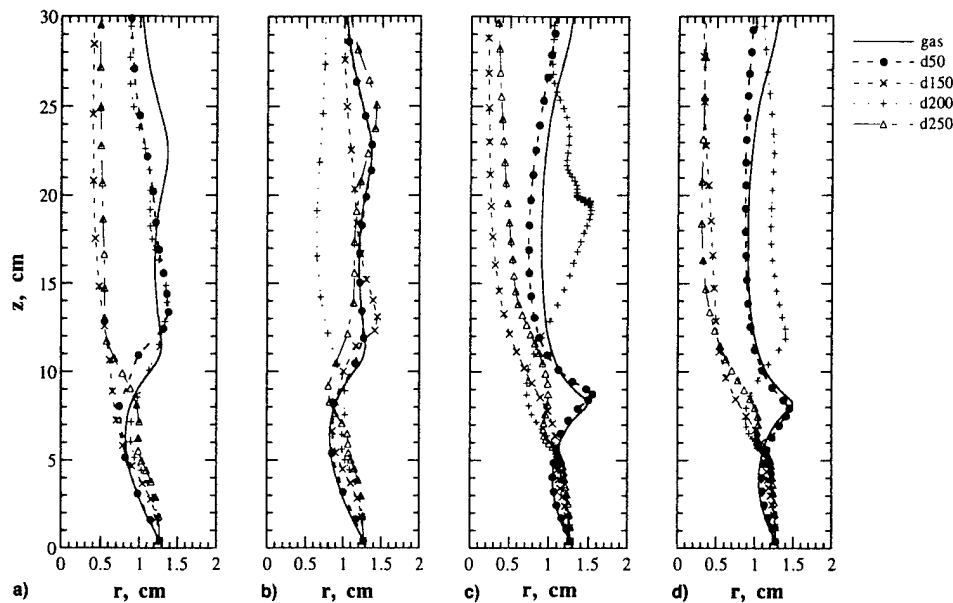


Fig. 9 Trajectories of nonevaporating (a and c) and evaporating (b and d) droplets injected at two different injection times for the 1g case. Droplets in a) and b) are injected at $t = 0.954$ s and those in c) and d) at $t = 0.986$ s.

The effect of evaporation on droplet trajectories for the 1g case is portrayed in Fig. 9, which shows the trajectories of nonevaporating and evaporating droplets injected at two different times. The difference in the two injection times (t_{diff}) is one-half the time period of the dominant instability frequency, i.e., the droplets in Figs. 9a and 9b are injected at time $t = t_{\text{inj}}$, while those in Figs. 9c and 9d are injected at $t = t_{\text{inj}} + t_{\text{diff}}$. Important observations from this figure are as follows:

1) In the low Stokes number range, the trajectories of evaporating droplets are qualitatively similar to those of nonevaporating droplets, except that the Stokes number decreases along the trajectory for the evaporating case. As a consequence, the evaporating droplets follow the gas motion more closely than the corresponding nonevaporating droplets (see Figs. 9a and 9b).

2) In the intermediate Stokes number range ($0.36 < St < 1.4$), due to the combined effect of vaporization and large structures in a dynamically evolving flowfield, the trajectories of evaporating and nonevaporating droplets are significantly different. For example, compare the trajectories of 200- μm nonevaporating and evaporating droplets in Figs. 9a and 9b, respectively.

3) The droplet trajectory exhibits strong sensitivity to the time (during the dominant instability period) as to when the droplet is introduced into the shear layer. This can be seen by comparing the trajectories of same-size droplets in Figs. 9a and 9c. This sensitivity is important, however, only over the time scale of the dominant frequency. For example, in the dispersion analysis that involves a time scale much longer than the instability time scale, this sensitivity would not be important.

4) The trajectory of a 200- μm droplet is distinctly different from those of 150- and 250- μm droplets. This has some important implication in the size-dependence of the dispersion function discussed in the next section.

Dispersion Behavior

In order to quantify the effects of vortex structures and gravity on droplet dispersion, the dispersion function is defined as

$$D(t, N) = \left(\left\{ \sum_{i=1}^N [r_i(t) - r_m]^2 \right\} / N \right)^{1/2} \quad (22)$$

where N is the total number of droplets in the flowfield at time t , r_i the radial location of droplet i at time t , and r_m the radial injection location of the same droplet at nozzle exit. It can be expected that the dispersion function is a strong function of t and droplet diameter d_p . In addition, it may be a function of r_m , N , and starting time of injection t_0 . In the results presented here, the dispersion function was made statistically independent of N by using a sufficiently large number of droplets in the dispersion calculation, and of t_0 by performing calculations over a sufficiently large time t . It is also worth noting that the above dispersion function does not distinguish between the droplets that move away from the jet axis and those that move toward it.

Dispersion behavior of droplets in the heated-jet flow is investigated by continuously injecting single-sized droplets from a given location. Results of the calculations made with a large number of droplet injections are shown in Fig. 10 in the form of simultaneous snapshots (or instantaneous images) of the flow and droplets. Iso-temperature contours are plotted using broken lines and the droplet locations are marked with solid circles. Snapshots for different size droplets are depicted in this figure, whereas in each individual snapshot locations of the evaporating and nonevaporating droplets are plotted on the left and right sides of the symmetric jet, respectively. Color (represents the size) of the droplet changes from red to blue as it evaporates from the initial size (at the instant of injection) to the size of a gas particle, which is taken as 10 μm or one-tenth of the initial size, whichever is smaller. Since the droplets on the right side of the jet represent nonevaporating ones, the color of the droplets remains red. As expected, the snapshot of 50- μm -evaporating droplets shows that these droplets behave like tracer particles and follow the iso-temperature contours. In general, due to the higher momentum, the nonevaporating droplets deviate more from the iso-temperature contours compared to the evaporating ones.

Dispersion of evaporating and nonevaporating droplets in a dynamically evolving flow are quite different. The instantaneous flowfield shown in Fig. 10 has two large-scale vortices that are located approximately at $z = 70$ and 140 mm. The first vortex ($z = 70$ mm) is pulling the smaller size droplets (both the evaporating and nonevaporating ones) radially outward and has little impact on the droplets that are larger than 150 μm . On the other hand, the medium-sized (~ 150 μm) nonevaporating and smaller evaporating droplets are impacted more by the second vortex ($z = 140$ mm). It may also

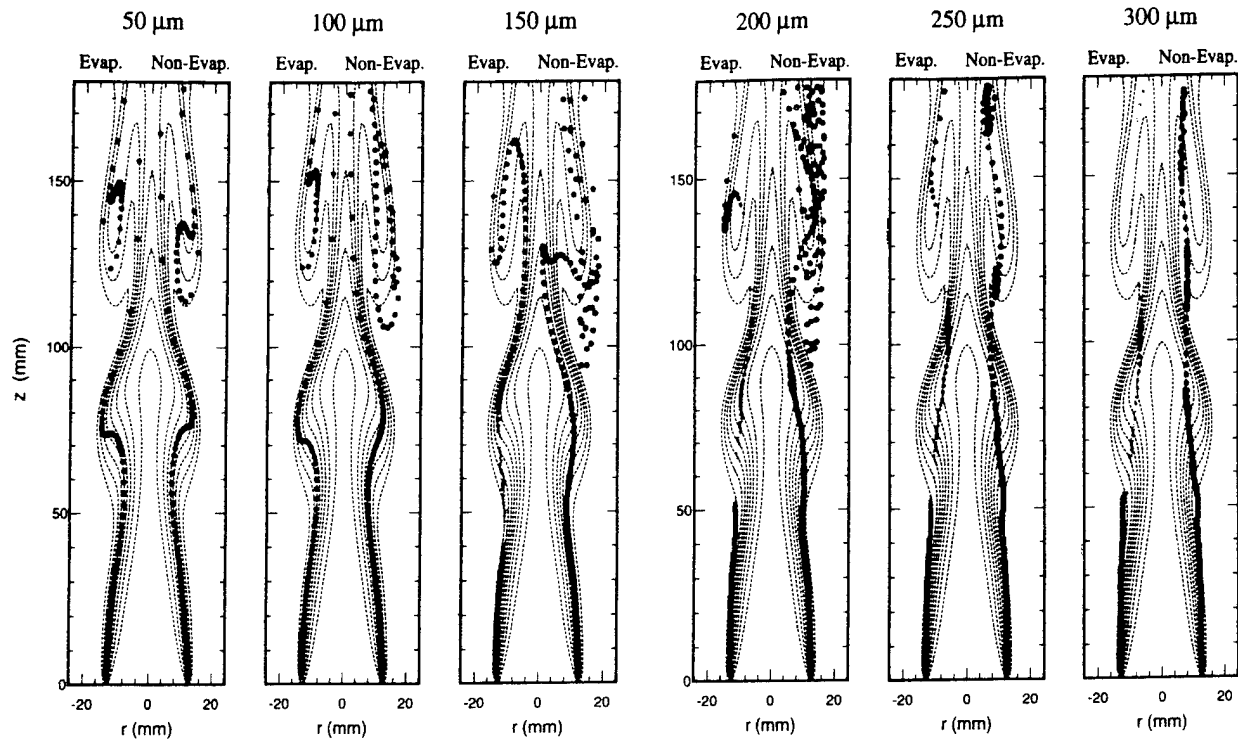


Fig. 10 Simultaneous snapshots of the flow (iso-temperature contours) and droplets (solid circles) of different initial sizes; in each individual snapshot locations of the evaporating and nonevaporating droplets are plotted on the left and right sides of the symmetric jet, respectively.

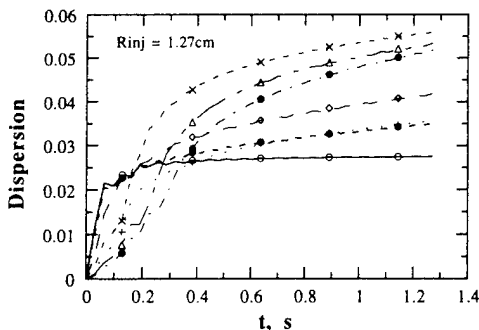


Fig. 11 Variation of dispersion function with time for evaporating droplets at 1g.

be noted from Fig. 10 that in the neighborhood of the second vortex the evaporating droplets are not dispersed as much as the nonevaporating ones. The reason for this difference may be explained as follows:

The flowfield and the droplet locations near the second vortex are, in fact, the evolution of the respective ones associated with the first vortex. It is known that the entrainment of droplets into the first vortex decreases with the size of the droplet with a maximum occurring for the gas-like particles. On the other hand, as the vortex evolves in space and time, the entrained droplets are centrifuged out of the vortex due to their inertia, which increases with the droplet size. As a result, dispersion of nonevaporating droplets in the neighborhood of the second vortex is more for the medium-sized droplets ($\sim 150 \mu\text{m}$). However, evaporating droplets exhibit a different behavior. Due to the evaporation process that occurs during the evolution of the flowfield in time and space, the smaller- and medium-sized droplets are not centrifuged out of the second vortex. On the other hand, the larger-sized droplets are not entrained by the first vortex, and hence, are not dispersed in the neighborhood of the second vortex.

Figure 11 shows the variation of dispersion function with time for the gas particle and evaporating droplets for different

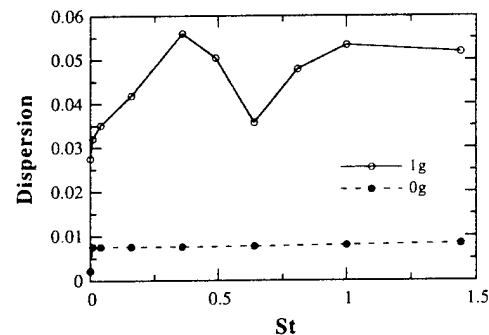


Fig. 12 Variation of dispersion function with Stokes number for the evaporating case at 1 and 0g.

initial diameter for the 1g case. The dispersion function generally increases with time as the droplets, that are continuously being injected into the shear layer, are either pulled radially inward by the heated jet or dispersed radially outward by the large structures. After $t = 0.8 \text{ s}$, the dispersion function starts leveling out, since some of the injected droplets are being convected out of the computational domain. In order to examine the effect of initial droplet size, it is convenient to plot dispersion function vs size at a fixed t . Figure 12 shows this plot for the 1 and 0g cases, where the dispersion function at $t = 1.27 \text{ ms}$ is plotted vs the Stokes number. Three observations can be made from this figure. First, as expected and consistent with the results in Fig. 8, the droplet dispersion for the 0g case is negligible compared to that for the 1g case. Second, the effect of large vortex structures is to enhance the dispersion of intermediate size droplets. Third, there is a range of Stokes number near $St \sim \mathcal{O}(1)$, where the droplet dispersion behavior is modified by the direct effect of gravity. For example, the maximization of dispersion function for the intermediate Stokes numbers, which is typically observed in the shear-induced vortical structures,^{16,17} is modified by gravity. As indicated in Fig. 12, there is a drop in the dispersion

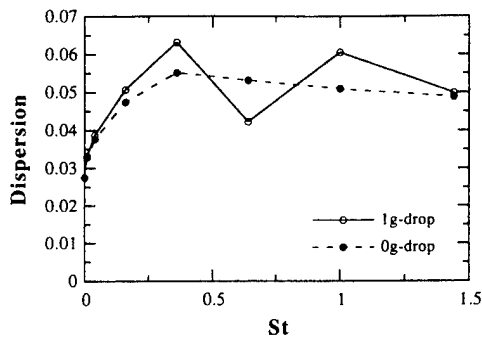


Fig. 13 Variation of dispersion function with Stokes number for nonevaporating droplets with and without the effect of gravity on droplet motion.

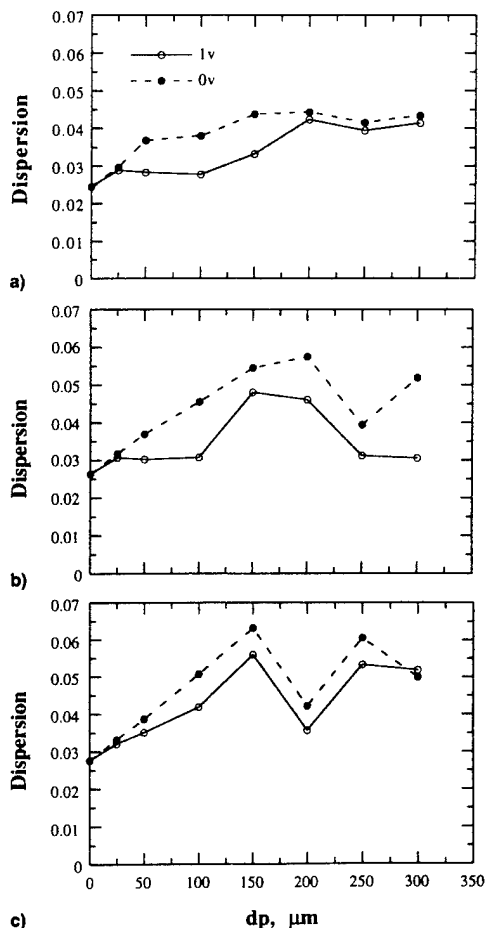


Fig. 14 Variation of dispersion function with initial droplet size for three different injection locations: r_{inj} = a) 1.10, b) 1.20, and c) 1.27 cm. 1v and 0v represent evaporating and nonevaporating cases, respectively.

function near $St = 0.64$ ($d_p = 200 \mu m$), which is believed to be due to the fact that the effect of gravity on droplet motion becomes comparable to that of large-scale structures. This is confirmed by performing a dispersion calculation without the effect of gravity on droplet motion. The result given in Fig. 13 for the nonevaporating case indicates that the dispersion function does not experience a drop near $St = 0.64$ ($d_p = 200 \mu m$), when the gravity term is excluded from the droplet equations. Rather, an optimum droplet size is seen to exist, where the dispersion is maximized. This is consistent with the results of previous experimental^{15,16} and computational results.^{10,17}

Figure 14 shows the effect of injection location on droplet dispersion for evaporating and nonevaporating droplets at 1g. The dispersion function is plotted vs initial droplet size for three injection locations. The important observation is that the maximum droplet dispersion is achieved by injecting droplets in the jet shear layer ($r_{inj} = 1.27$ cm), and that the evaporating droplets are dispersed less compared to the nonevaporating droplets. It is also important to note that as the injection location is moved to the jet core, the dispersion function does not show a sudden drop near $d_p = 200 \mu m$. This is related to the fact that the direct effect of gravity is not as strong in the jet core region as it is in the shear layer region.

Conclusions

Dynamics and dispersions of *n*-heptane liquid fuel droplets in a heated jet are studied via numerical simulations and flow visualization. The objective of this study is to investigate the droplet dynamics and vaporization behavior in a heated shear layer under normal-gravity and zero-gravity environments. An implicit, third-order accurate upwind numerical scheme is used to solve the unsteady gas-phase equations. The Lagrangian approach is employed to study the droplet dynamics and dispersion in a heated shear layer.

Results show that the gravity has a strong effect on the dynamics of the heated jet shear layer, as well as on the dispersion and vaporization behavior of droplets. The presence of gravity introduces the buoyancy-induced hydrodynamic instability, causing the large vortical structures to appear without any external perturbation. The dynamics of the buoyancy-induced instability in a hot jet is compared to that of the Kelvin-Helmholtz instability in a cold jet. While the large-scale structures in both these cases are highly coherent and periodic with the respective frequencies of 15.8 and 20 Hz, their sizes and convective velocities are significantly different.

The droplets trajectory plots and the simultaneous snapshots of the flow and droplets are employed to analyze the dynamics of nonevaporating and evaporating droplets under the influence of buoyancy-induced vortex structures and gravity. Three different droplet-size regimes are identified to characterize the effects of large structures and gravity. These regimes are distinguished by the values of St and Vr . In the first regime, characterized by small values of St and Vr , the droplet behavior is akin to that of gas particles. In the second regime, the droplet dispersion and vaporization behavior is strongly influenced by large vortical structures and gravity, whereas in the third regime, the droplet motion is more strongly affected by the direct effect of gravity.

In order to quantify the effect of gravity and large vortex structures on droplet dynamics, the dispersion function is calculated as a function of initial droplet size for evaporating and nonevaporating droplets for 1 and 0g conditions. The important observations are as follows:

- 1) At zero gravity, in the absence of buoyancy-induced vortex structures, the droplet dispersion is negligibly small compared to that at normal gravity.
- 2) The effect of large buoyant structures is to enhance the dispersion of intermediate size droplets, and can be represented in terms of the Stokes number.
- 3) There is a range of Stokes number near unity, where the correlation between dispersion function and Stokes number, reported previously for particle-laden shear flows,^{16,17} is modified by the direct effect of gravity.
- 4) The dispersion behavior of nonevaporating droplets is quite different from that of evaporating droplets. Due to the centrifugal action of the vortical structures, the intermediate-sized nonevaporating droplets disperse more than the gas particles. However, due to the evaporation process, the intermediate-sized evaporating droplets are not centrifuged out of the vortical structures and consequently disperse less than the nonevaporating droplets.

Appendix: Mixture and Fuel Properties

The viscosity and thermal conductivity of the gas mixture are calculated by using the semiempirical formula of Wilke:

$$\mu_m \text{ or } \lambda_m = \sum_{i=1}^N \left[X_i (\mu_i \text{ or } \lambda_i) / \left(\sum_{i=1}^N X_i \varphi_i \right) \right]$$

where

$$\varphi_i = \{1 + [(\mu_i \text{ or } \lambda_i)/(\mu_j \text{ or } \lambda_j)]^{1/2} (M_j/M_i)^{1/4}\}^2 / (8 + 8M_j/M_i)^{1/2}$$

The mixture specific heat was calculated as a mole fraction weighted average of the specific heats of each contributing species:

$$C_{pm} = \left(\sum_{i=1}^N X_i C_{pi} \right) / M$$

Fuel properties for *n*-heptane were approximated as a function of the temperature from the various sources.^{22,23} In this study, the following correlations were used:

latent heat of vaporization

$$L = 316.3(3.204 - T/168.6)^{0.38}, \text{ kJ kg}^{-1}$$

vapor mass fraction at the droplet surface

$$Y_{F_s} = \left(1 + \frac{M_g}{M_F} \left\{ \exp \left[\frac{LM_F}{R} \left(\frac{1}{T} - \frac{1}{T_B} \right) \right] - 1 \right\} \right)^{-1}$$

binary diffusion coefficient

$$D = 5.94 \times 10^{-6} (T/273)^{1.60} P^{-1}, \text{ m}^2 \text{ s}^{-1}, \text{ with } P \text{ in atm}$$

vapor specific heat

$$C_{pF} = -51.56 + 6.776T - 3.658 \times 10^{-3} T^2 - 7.673 \times 10^{-7} T^3, \text{ J kg}^{-1} \text{ K}^{-1}$$

vapor thermal conductivity

$$\lambda_F = -4.401 \times 10^{-2} + 2.514 \times 10^{-4} T - 3.173 \times 10^{-7} T^2 + 2.487 \times 10^{-10} T^3, \text{ J m}^{-1} \text{ s}^{-1} \text{ K}^{-1}$$

vapor dynamic viscosity

$$\mu_F = 3.83 \times 10^{-6} - 3.613 \times 10^{-9} T + 4.911 \times 10^{-11} T^2 - 3.577 \times 10^{-14} T^3, \text{ kg m}^{-1} \text{ s}^{-1}$$

Liquid fuel properties were assumed to be constant and evaluated at some average temperature $T_l = (T_o + T_B)/2 = 332.8 \text{ K}$. They are as follows:

$$\begin{aligned} C_{pl} &= 2383.89, \text{ J kg}^{-1} \text{ K}^{-1} \\ \lambda_l &= 1.1768 \times 10^{-1}, \text{ J m}^{-1} \text{ s}^{-1} \text{ K}^{-1} \\ \rho_l &= 649.38, \text{ kg m}^{-3} \end{aligned}$$

Acknowledgments

This work is supported by AFOSR Grant F49620-92-J-0231, with Julian M. Tishkoff as the Program Manager. Many fruit-

ful discussions with W. M. Roquemore at Wright-Patterson Air Force Base, Dayton, Ohio, are greatly appreciated.

References

- Ross, H. D., "Overview of NASA's Microgravity Combustion Science and Fire Safety Program," Second International Microgravity Combustion Workshop, Cleveland, OH, 1992.
- Burke, S. P., and Schumann, T. E. W., *Industrial and Engineering Chemistry*, Vol. 20, 1928, p. 998.
- Hottel, H. C., and Hawthorne, W. R., *Third Symposium on Combustion*, Williams and Wilkins, Baltimore, MD, 1949, p. 254.
- Bahadori, M. Y., Edelman, R. B., Stocker, D. P., and Olson, S. L., "Ignition and Behavior of Laminar Gas-Jet Diffusion Flames in Microgravity," *AIAA Journal*, Vol. 28, No. 2, 1990, pp. 236-244.
- Bahadori, M. Y., Stocker, D. P., Vaughan, D. F., Zhou, L., and Edelman, R. B., "Effects of Buoyancy on Laminar, Transitional, and Turbulent Gas Jet Diffusion Flames," Second International Microgravity Combustion Workshop, NASA CP 10113, Cleveland, OH, 1992.
- Bahadori, M. Y., Hegde, U., Zhou, L., and Stocker, D. P., "Effect of Gravity on the Transition to Turbulence of Gas-Jet Diffusion Flames," AIAA Paper 93-0710, Jan. 1993.
- Davis, R. W., Moore, E. F., Roquemore, W. M., Chen, L. D., Vilmpoc, V., and Goss, L. P., *Combustion and Flame*, Vol. 83, 1991, pp. 263-270.
- Katta, V. R., and Roquemore, W. M., "Role of Inner and Outer Structures in Transitional Jet Diffusion Flame," *Combustion and Flame*, Vol. 92, 1993, pp. 274-282.
- Katta, V. R., Goss, L. P., and Roquemore, W. M., "Effect of Nonunity Lewis Number and Finite-Rate Chemistry on the Dynamics of a Hydrogen-Air Jet Diffusion Flame," *Combustion and Flame*, Vol. 96, 1994, pp. 60-74.
- Chung, J. N., and Troutt, T. R., "Simulation of Particle Dispersion in an Axisymmetric Jet," *Journal of Fluid Mechanics*, Vol. 186, 1988, pp. 199-222.
- Hansell, D., Kennedy, I. M., and Kollmann, W., "A Simulation of Particle Dispersion in a Turbulent Jet," *International Journal of Multiphase Flow*, Vol. 18, No. 4, 1992, pp. 559-576.
- Lazaro, B. J., and Lasheras, J. C., "Particle Dispersion in the Developing Free Shear Layer, Part 1-Unforced Flow," *Journal of Fluid Mechanics*, Vol. 235, 1992, pp. 143-178.
- Lazaro, B. J., and Lasheras, J. C., "Particle Dispersion in the Developing Free Shear Layer, Part 2-Forced Flow," *Journal of Fluid Mechanics*, Vol. 235, 1992, pp. 179-221.
- Samimy, M., and Lele, S. K., "Motion of Particles with Inertia in a Compressible Free Layer," *Physics of Fluids*, Vol. A3, 1991, pp. 1915-1923.
- Hishida, K., Ando, A., and Maeda, M., "Experiments on Particle Dispersion in a Turbulent Mixing Layer," *International Journal of Multiphase Flow*, Vol. 18, No. 2, 1992, pp. 181-194.
- Longer, E. K., and Eaton, J. K., "Structure of a Particle-Laden Round Jet," *Journal of Fluid Mechanics*, Vol. 236, 1992, pp. 217-257.
- Uthuppan, J., Aggarwal, S. K., Grinstein, F. F., and Kailasanath, K., "Particle Dispersion in a Transitional Axisymmetric Jet: A Numerical Simulation," AIAA Paper 93-0105, Jan. 1993.
- Aggarwal, S. K., "Relationship Between Stokes Number and Intrinsic Frequencies in Particle Laden Flows," *AIAA Journal*, Vol. 32, No. 6, 1994, pp. 1322-1325.
- Faeth, G. M., "Evaporation and Combustion of Sprays," *Progress in Energy and Combustion Science*, Vol. 9, No. 2, 1983, pp. 1-76.
- Aggarwal, S. K., Tong, A., and Sirignano, W. A., "A Comparison of Vaporization Models for Spray Calculation," *AIAA Journal*, Vol. 22, No. 10, 1984, pp. 1448-1457.
- Leonard, B. P., "A Stable and Accurate Convective Modelling Procedure Based on Quadratic Upstream Interpolation," *Computational Methods in Applied Mechanics and Engineering*, Vol. 19, 1979, pp. 59-98.
- Vargaftik, N. B., *Handbook of Physical Properties of Liquids and Gases*, 2nd ed., Hemisphere, New York, 1983, pp. 632-643.
- Ho, C. Y., Liley, P. E., Makita, T., and Tanaka, Y., *Properties of Inorganic and Organic Fluids*, Hemisphere, New York, 1988, pp. 137-150.



0017-9310(95)00324-X

A numerical study of droplet–vortex interactions in an evaporating spray

T. W. PARK† and S. K. AGGARWAL‡

Department of Mechanical Engineering, University of Illinois at Chicago, Chicago, IL 60607, U.S.A.

and

V. R. KATTA§

System Research Laboratory, Inc., Dayton, OH 45440, U.S.A.

(Received 23 March 1995 and in final form 28 August 1995)

Abstract—In this paper, we present the time-dependent axisymmetric numerical simulation of a *n*-heptane evaporating spray, and investigate the droplet–vortex interactions which determine the structural and dynamic characteristics of a spray jet flow. The spray is formed between a droplet-laden heated nitrogen jet and a coflowing air stream. A detailed, multidimensional, two-phase algorithm is developed for the simulation. Monodisperse spray is introduced into the large vortex structures that are generated by the buoyancy-induced hydrodynamic instability of the heated jet. Results focus on the two-way interactions between vortical structures and droplets, and the dynamics of both non-evaporating and evaporating sprays. The vortex structures cause droplets to disperse radially outward, and this in turn determines the fuel vapor distribution and also modifies the vortex dynamics. Thus, the dynamics and structural characteristics of evaporating sprays are strongly influenced by the two-way transient interactions. The effects of initial droplet size, injection location, and liquid-to-gas mass loading ratio on these interactions are investigated. These studies indicate that the effect of dispersed phase on gas phase is negligible for mass loading ratio less than 0.5. At higher mass loading ratios, the dispersed phase modifies the dynamics of vortex structures but not the time-average behavior for non-evaporating spray, while for evaporating spray it influences both the dynamics and the time-averaged behavior. It is also found that the spray injection characteristics have strong influence on the processes of droplet–vortex interactions. Copyright © 1996 Elsevier Science Ltd.

INTRODUCTION

Large-scale, coherent vortical structures have been found to exist in a variety of shear flows including those involving combustion and multiple phases [1–4]. In two-phase shear flows involving solid particles or liquid droplets, the transient interactions between dispersed phase and large vortical structures are expected to play a central role in determining the dynamics and structural characteristics of these flows. The transient interactions pertain to the effect of large vortical structures on the behavior of droplets/particles, and the influence of droplets on the dynamics of large vortical structures. These two effects coupled in a nonlinear manner; the vortex structures determine the droplet dispersion and gasification behavior, which in turn affects the local environment surrounding each droplet and thereby the dynamics

of the two-phase system under consideration. Several numerical [5, 6] and experimental [7–10] studies in recent years have focused on the one-way coupling, examining the influence of large eddies on the dynamics of droplets/particles injected into a shear flow. These studies show that the effect of large structures on particle motion is characterized by the ratio of particle response time to characteristic time of structures. This ratio is defined as the Stokes number (St). When the particle response time is of the same order of magnitude as the vortex time scale, $St \sim O(1)$, particles can disperse significantly more than the fluid particles, the enhanced dispersion being attributed to the centrifugal action of vortices. For small Stokes number, $St \ll 1.0$, particles behave similar to the fluid particles, while for large Stokes number, particles remain largely unaffected by the vortices. More recent works [11, 12] on particle-laden flows have examined the effect of external forcing on the particle dispersion behavior. A general observation from these studies [11, 12] is that the dynamics of vortex structures, and thereby the dispersion behavior of particles in a shear layer can be manipulated by a subharmonic forcing of the shear layer.

Particle-laden shear flows in practical applications

† Currently at Wright Laboratory, Aero Propulsion and Power Directorate, Wright-Patterson Air Force Base, OH 45433, U.S.A., as a National Research Council Research Associate.

‡ Author to whom correspondence should be addressed.

§ Present address: Innovative Scientific Solutions, Inc., Dayton, OH 45430, U.S.A.

NOMENCLATURE

C_p	specific heat	u	axial velocity
d_o	initial droplet diameter	v	radial velocity
D	vapor/air binary diffusion coefficient	Y	mass fraction
g	acceleration of gravity	z	axial distance.
h_{fs}	enthalpy of fuel vapor at droplet surface		
$l_{k,eff}$	effective latent heat, or the heat transferred from gas phase to droplet	Greek symbols	
\dot{m}_k	droplet vaporization rate	μ	dynamic viscosity
M	ratio of the liquid fuel mass flow rate to the nitrogen mass flow rate	λ	thermal conductivity
M_k	mass of each group of droplets	ρ	density.
n_k	number of droplets in each group	Subscripts	
p	pressure	f	fuel vapor
r	radial distance	g	gas-phase
t	time	k	droplet characteristic
T	temperature	l	liquid-phase
		o	oxygen
		s	surface.

involve two-way, nonlinear interactions between the continuous and dispersed phases. Previous studies cited above focus mainly on the one-way interactions, i.e. on characterizing the effect of vortex structures on droplet motion and dispersion behavior. The effects of dispersed phase on vortex dynamics, and subsequently on fuel vapor distribution and flame behavior remain largely unexplored. In this paper, we report a numerical study of two-way droplet-vortex interactions in an unsteady evaporating spray. The spray is formed between a droplet-laden heated nitrogen jet and a coflowing air stream. The jet velocity and temperature are considered in a range where the large vortical structures are generated due to the buoyancy-induced hydrodynamic instability rather than the shear-induced Kelvin-Helmholtz instability. The vaporization characteristics of n-heptane fuel spray under the influence of two-way droplet-vortex interactions are investigated. The additional complexities due to chemical reactions and heat release are avoided so as to focus on the dynamics of two-way interactions. A non-evaporating spray is also analyzed in order to distinguish the interactions involving only momentum transfer between the phases from those involving mass, momentum, and energy transfer. Results are presented that highlight the dynamics as well as the time-averaged structure of these sprays.

PHYSICAL MODEL

The evaporating spray investigated in the present study is shown schematically in Fig. 1. It consists of a central fuel jet which is a two-phase mixture of gaseous nitrogen and liquid fuel droplets and a low-speed coannulus air flow. The central jet is heated primarily to enhance the fuel evaporation; however, in the pre-

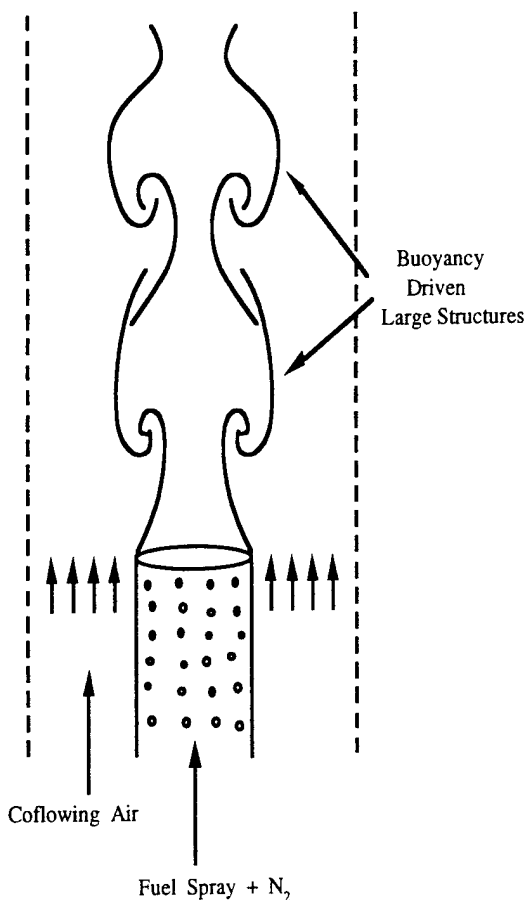


Fig. 1. A schematic of evaporating spray jet at 1 g.

sent studies, it also plays a key role for the formation of buoyancy induced vortical structures. Numerical studies on the two-way interactions between the vor-

Table 1. Transport coefficients and source terms appearing in governing equations

Equations	Φ	Γ^Φ	S_g^Φ	S_l^Φ
Continuity	1	0	0	$\sum_k n_k \dot{m}_k$
Axial momentum	u	μ	$-\frac{\partial p}{\partial z} + (\rho_o - \rho)g + \frac{\partial}{\partial z}\left(\mu \frac{\partial u}{\partial z}\right) + \frac{\partial}{\partial r}\left(\mu \frac{\partial v}{\partial z}\right) + \frac{\mu}{r} \frac{\partial v}{\partial z}$ $-\frac{2}{3}\left\{\frac{\partial}{\partial z}\left(\mu \frac{\partial u}{\partial z}\right) + \frac{\partial}{\partial z}\left(\mu \frac{\partial v}{\partial r}\right) + \frac{\partial}{\partial z}\left(\mu \frac{v}{r}\right)\right\}$	$\sum_k \left(n_k \dot{m}_k u_k - n_k M_k \frac{du_k}{dt}\right)$
Radial momentum	v	μ	$-\frac{\partial p}{\partial r} + \frac{\partial}{\partial z}\left(\mu \frac{\partial u}{\partial r}\right) + \frac{\partial}{\partial r}\left(\mu \frac{\partial v}{\partial r}\right) + \frac{\mu}{r} \frac{\partial v}{\partial r} - 2\mu \frac{v}{r^2}$ $-\frac{2}{3}\left\{\frac{\partial}{\partial r}\left(\mu \frac{\partial u}{\partial z}\right) + \frac{\partial}{\partial r}\left(\mu \frac{\partial v}{\partial r}\right) + \frac{\partial}{\partial r}\left(\mu \frac{v}{r}\right)\right\}$	$\sum_k \left(n_k \dot{m}_k v_k - n_k M_k \frac{dv_k}{dt}\right)$
Mass fraction of fuel	Y_f	ρD_f	0	$\sum_k n_k \dot{m}_k$
Mass fraction of oxygen	Y_o	ρD_o	0	0
Energy	T	λ/C_p	0	$\sum_k n_k \dot{m}_k (h_{fs} - I_{k,eff})$

tex structures and the evaporating droplets are conducted by solving the unsteady, axisymmetric gas-phase equations that include the droplet source terms, and the appropriate droplet equations.

The unsteady, axisymmetric governing equations in cylindrical (z, r) coordinate system for a droplet-laden heated jet are

$$\begin{aligned} \frac{\partial(\rho\Phi)}{\partial t} + \frac{\partial(\rho u\Phi)}{\partial z} + \frac{\partial(\rho v\Phi)}{\partial r} \\ = \frac{\partial}{\partial z}\left(\Gamma^\Phi \frac{\partial\Phi}{\partial z}\right) + \frac{\partial}{\partial r}\left(\Gamma^\Phi \frac{\partial\Phi}{\partial r}\right) \\ - \frac{\rho v\Phi}{r} + \frac{\Gamma^\Phi}{r} \frac{\partial\Phi}{\partial r} + S_g^\Phi + S_l^\Phi. \quad (1) \end{aligned}$$

The general form of equation (1) represents the continuity, momentum, species, or energy conservation equation depending on the variable used for Φ . Table 1 gives the transport coefficients Γ^Φ and the source terms S_g^Φ and S_l^Φ that appear in the governing equations. In this table, μ , λ and C_p represent the viscosity, the thermal conductivity and the specific heat, respectively. They are considered functions of temperature and species concentration.

The effect of dispersed phase on gas-phase properties is incorporated through the source/sink terms (S_l^Φ), representing the exchange of mass, momentum, and energy between the gas and liquid phases. In order to evaluate these terms, it is necessary to establish droplet trajectories, size and temperature histories. The Lagrangian approach is employed to solve the liquid-phase governing equations for the dynamics and vaporization history of each droplet group. The spray is characterized by a discrete number of droplet groups, distinguished by their injection location, initial size and time of injection. A droplet group in a Lagrangian treatment represents a characteristic containing a finite number of droplets. Since an axi-

symmetric configuration is analyzed, the liquid properties are implicitly averaged in the azimuthal direction and the number of droplets associated with each characteristic represents droplets uniformly distributed in an annual ring. The equations governing the variation of position, velocity, and size for each droplet group and other expressions are available in ref. [13]. A comprehensive vaporization model is employed to calculate the instantaneous droplet size and surface temperature along the trajectory of each group. The model includes the effects of variable thermophysical properties, non-unity Lewis number in the gas film outside the droplet, the effect of Stefan flow on the heat and mass transfer between the droplet and the gas, and the effect of transient liquid heating. The variable thermophysical properties are calculated at reference film temperature and concentrations, obtained by using the 1/3 rule, except for the gas density which is calculated at the free stream value [14]. The Wilke rule [15] is used to calculate the dynamic viscosity and thermal conductivity of the gas film. The liquid fuel ($n\text{-C}_7\text{H}_{16}$) properties are collected from the various sources and approximated as a function of the temperature [13]. The effect of transient liquid heating is incorporated by using the finite-conductivity model [16]. This model is deemed satisfactory in the present study, since the maximum droplet Reynolds number during droplet lifetime is less than ten and thus the effect of internal circulation is expected to be negligible. For the same reason, the effects of gas-phase convection on the heat and mass transport are represented by the Ranz-Marshall correlation [16].

SOLUTION PROCEDURE

The numerical solution of the unsteady two-phase equations employs an implicit algorithm for solving the gas-phase equations, and an explicit Runge-Kutta procedure for the liquid-phase equations. The finite-

difference forms of the momentum equations are obtained using an implicit QUICKEST scheme [17], while those of the species and energy equations are obtained using a hybrid scheme of Spalding [18]. A "finite control volume" approach with a staggered, non-uniform grid system is utilized. Body force term due to gravitational field is included in the axial momentum equation for gas-phase and the droplet motion equation for liquid-phase. An iterative ADI (Alternative Direction Implicit) technique is used for solving the resulting sets of algebraic equations. A stable numerical integration procedure is achieved by coupling the species and energy equations through the source terms (cf. Table 1). At every time step, the pressure field is calculated by solving the pressure Poisson equations simultaneously and utilizing the LU (Lower and Upper diagonal) matrix decomposition technique. It should be noted that the pressure Poisson equations consider the effect of mass transfer from the liquid phase to the gas phase, represented by a source term in the gas-phase mass continuity equation.

The liquid-phase equations are advanced in time by a second-order accurate Runge-Kutta method. Since the gas-phase solution employs an implicit procedure, the temporal step size used for integrating the liquid-phase equations is smaller than that for gas-phase equations. An automatic procedure is implemented in order to select an optimum liquid-phase time step. The procedure involves calculating the characteristic thermal response time, velocity response time and vaporization time for each droplet group, and then selecting the temporal step size as a fraction (one-hundredth) of the smallest of these time scales. A detailed examination of the various time scales, based on numerical experiments, revealed that the temporal step size is determined by either the thermal response time or the velocity response time of a given droplet group. The number of subcycles for advancing the liquid-phase solution for each gas-phase cycle typically varies from two to ten, depending upon the droplet size.

The procedure to advance the two-phase solution over one gas-phase time step is as follows. Using the known gas-phase properties, the liquid-phase equations are solved over a specified number of liquid-phase subcycles. A third-order accurate Lagrangian polynomial method is used for interpolating the gas-phase properties from the non-uniform fixed grid to the droplet characteristic location. It should be noted that the interpolation scheme for the gas-phase velocities u and v is based on their respective grid cells because of the use of a staggered grid in gas-phase calculation. The droplet properties are updated after every liquid-phase subcycle. Also, during each subcycle, the liquid-phase source terms appearing in the gas-phase equations are calculated at the characteristic location, and then distributed to the surrounding gas-phase grid points. These source terms are added at each gas-phase grid points during one gas-phase time step and then used in the implicit solution of the gas-phase equations.

RESULTS

The jet diameter of the vertically mounted evaporating spray considered in the present study is 2.54 cm. The jet velocities for the central fuel and coannular air streams are 1.0 and 0.2 m s⁻¹, respectively. Flat velocity profiles are used as the inflow conditions. Temperature chosen for the fuel jet is 1200 K while that of the surrounding annulus air is 294 K. Calculations are made for a physical domain having dimensions of 15 and 40 cm in the radial and axial direction, respectively. It should be noted that the physical domain used in the calculations is much larger than the domain of interest (3 × 20 cm) and hence, the results are not influenced by the computational boundaries. Results reported in the present paper are obtained using a grid system having 151 and 61 points in the axial and radial directions, respectively. Grid lines are clustered near the shear layer to resolve the steep gradients of the dependent variables. Calculations are advanced in time utilizing a low CFL number of 0.2. In an earlier study [13], it was found that the results obtained on a 151 × 61 mesh system (with grid spacings similar to the ones used in the present investigation) and using a CFL number less than 0.5 are grid independent and time accurate.

Numerical experiments are conducted by injecting different groups of droplets into the fuel stream to examine the changes in the flow structure due to the two-way nonlinear, two-phase interactions. The injection process consists of introducing a group of monodisperse droplets at a given instant of time. The number of droplets in each group depends on the mass loading (ratio of the liquid fuel mass flow rate to the nitrogen mass flow rate), initial droplet size, and injection time interval. As a base case for the spray calculations reported in this work, a monodisperse *n*-heptane spray with an initial diameter of 200 μm and mass loading of unity is considered. At a mass loading of unity, the volume occupied by liquid phase is about three orders of magnitude smaller than that of the gas-phase volume due to the high density of the liquid fuel and hence, the dilute-spray assumption is still valid. At higher mass loading, however, the assumption would become increasingly more questionable. For this reason, the mass loading of unity is the highest loading considered in the present study. The droplets are injected continuously into the jet shear layer from a radial location of 1.25 cm. A time difference of 1.428 ms ($= 9 \Delta t_{\text{gas}}$) is used between two consecutive injections for all the spray calculations reported in this work. This time interval was determined based on the constraint that the spatial separation between two successive droplet groups is large enough for neglecting the interaction between the droplets. This yields the number of droplets in each group to be 76. Three different droplet injection intervals are chosen to examine their effect on the time-averaged temperature and axial velocity profiles in the flow field. Figure 2 shows the time-averaged axial profiles of

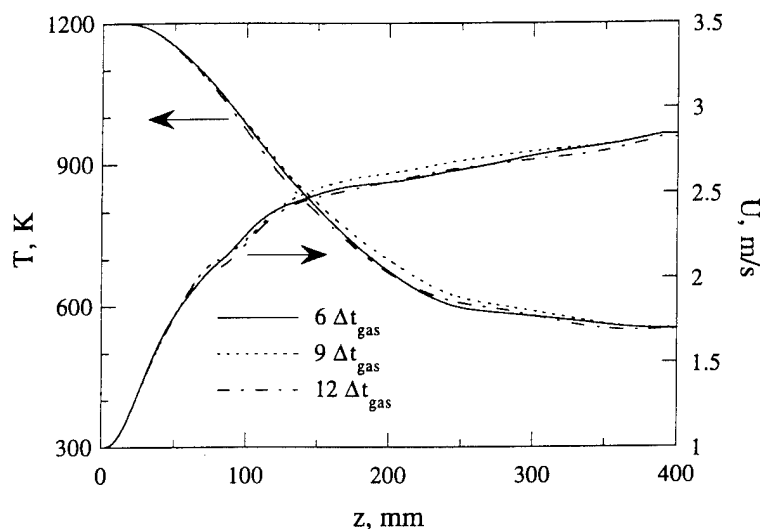


Fig. 2. Effect of droplet interval on the time-averaged temperature and axial velocity profiles of 200- μ m evaporating spray with mass loading value of $M = 1.0$.

temperature and axial velocity for the three cases. As expected, the average temperature decreases along the jet axis due to gas-phase heat transport processes and cooling caused by the dispersed phase. The average axial velocity, however, increases in the axial direction due to buoyant acceleration. The important observation is that the gas-phase calculations are not sensitive to the droplet injection interval used for the base case.

The effect of dispersed phase on the dynamics of vortex structures and heated jet is portrayed in Figs. 3 and 4. Calculations are initially made without inject-

ing droplets into the fuel stream. The shear layer between the 1200-K nitrogen jet and the cold annulus air flow became unsteady with the development of large-scale vortices. Iso-temperature contours of this heated jet are shown in Fig. 3(a). It is important to note that these vortical structures are generated without using any external forcing, and their dynamics is found to be highly periodic. The role of gravity on the

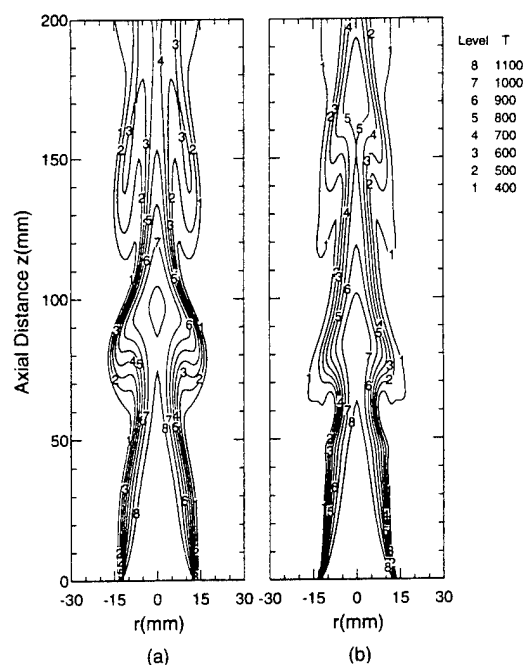


Fig. 3. Instantaneous iso-temperature contours for the heated jet: (a) without fuel spray; (b) with fuel spray.

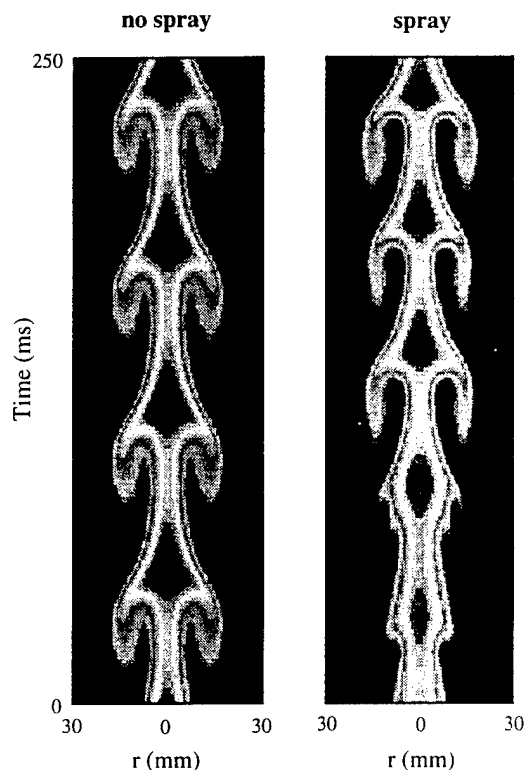


Fig. 4. Time evolution of temperature contours at axial location of 10 cm above the inlet for the cases of Fig. 3.

dynamics of the heated jet was confirmed by performing numerical experiments. When the gravitational term in the axial momentum was set equal to zero, the simulation yielded a steady laminar jet flow. This observation is in contrast with that made for heated jet flows at higher Reynolds number, in which Kelvin–Helmholtz instabilities develop independent of the assumption made for gravitational force. Most of the experimental studies on heated jets [19, 20] were focused on the higher Reynolds-number flow and did not provide insight on buoyancy-induced instabilities. However, the latter ones were extensively investigated experimentally in jet diffusion flames [21, 22] and helium jets [23]. The numerical studies [24, 25] performed on these flames and helium jet flows using the code discussed in the present study predicted the growth of buoyancy-induced instabilities very accurately.

Instantaneous iso-temperature contours for the case with fuel spray [plotted in Fig. 3(b)] are compared with the ones obtained without introducing fuel spray in Fig. 3(a). All the droplet source terms (Table 1) are incorporated in the gas-phase equations for the simulation with fuel spray. For both the cases, the buoyancy-induced vortex structures shown in Fig. 3 appear naturally without any external forcing. It is apparent from the figure that the injection of 200- μm droplets into the shear layer weakened the vortical structures and decreased the spreading of the heated jet. The weakening of vortical structures is probably caused by the cooling effect of the dispersed plane, while the decrease in the spreading rate may be expected due to fact that the addition of fuel spray to the nitrogen gas increases the jet momentum. Figure 3 further indicates that the jet oscillations are highly coherent for the gaseous (no spray) case and somewhat less coherent for the spray case. Since the presence of liquid phase modifies the spectral characteristics or the dominant instability frequency, an attempt was made to phase-lock the instantaneous images for the two cases. Consequently, the temperature contour plots in Fig. 3 for the gaseous and spray cases represent the results that are obtained at slightly different times from the start of the respective calculation.

The dynamics of vortex structures is examined by plotting the time evolution of temperature contours in Fig. 4. Temperature data along the radial location at an axial location of 10 cm above the jet exit for the gaseous and spray cases are recorded over a time period of 250 ms and shown in this figure. Again, an attempt was made to phase-lock the images for the gaseous and spray case. It can be seen from Fig. 4(a) that the vortex structures in the case of gaseous jet are highly coherent and periodic. With the addition of fuel spray the dynamics of jet has become aperiodic and the vortex crossing frequency (obtained by counting the number of vortices in a fixed time interval) has increased by about 30%. This can be confirmed by performing the spectral analysis at different axial

locations in the shear layer. Temperature data were recorded at different locations during more than 10 vortex crossing times ($4096 \Delta t_{\text{gas}}$). Figure 5 clearly shows that the dominant frequency for the spray case is increased to 20.5 Hz which is about 30% higher compared to the frequency observed for the gaseous jet case. In addition, the deterioration in coherency can be seen for the spray case. The increase in frequency for the spray case is resulting from the momentum transfer between the liquid drops and the gaseous flow. The fuel drops are injected into the gaseous jet shear layer at the same velocity as that of the local gas velocity which yields higher momentum to the fuel drops. As the gaseous flow and drops convect downstream, the higher momentum of the latter transfer to the former which, in turn, increases the local gas velocity. As a result, the crossing frequency of the vortices in the shear layer, which is proportional to the local gas velocity, also increases. The increase in frequency is observed for both non-evaporating and evaporating sprays, implying again that this is primarily a momentum-transfer effect. It is also interesting to note that no vortex merging is observed for these two cases.

Effect of liquid mass loading

The structural changes noted in a buoyancy driven heated jet with the addition of fuel spray are resulting from (1) liquid mass loading, (2) droplet evaporation and (3) the two-way interaction between vortices and droplets. To further understand the impact of the above individual parameters, numerical experiments are performed by changing the liquid mass loading, evaporation characteristics, spray injection location and droplet size.

The instantaneous iso-temperature contours for five different mass loading values ($M = 0, 0.125, 0.25, 0.5$ and 1.0) for a non-evaporating spray are shown in Fig. 6. Again, the images shown in Fig. 6 are phase locked. Liquid mass flow rate is controlled by changing the number of droplets in each injected group. As the droplets are assumed to be non-evaporating in this case, only the source terms in the momentum equation (cf. Table 1) are considered in the gas-phase equations. In other words, only the momenta are exchanged in this two-phase flow calculation. The single-phase gaseous flow shown in Fig. 3(a) may be approximated as a non-evaporating spray in the limiting case of $M = 0$ [Fig. 6(a)]. It seems that the structural characteristics of low mass loading cases like $M = 0.125$ and 0.25 are similar to that of single-phase flow even though the vortex-crossing frequencies in these flows are somewhat different. The time history plots of the dynamic heated jets for different mass loading values are shown in Fig. 7. This plot clearly shows the changes in the sizes of the vortex structures and their crossing frequency for different cases. It may be observed from Fig. 7 that as the mass loading ratio is increased, the crossing frequency of vortex structures is also increasing. At higher mass loading

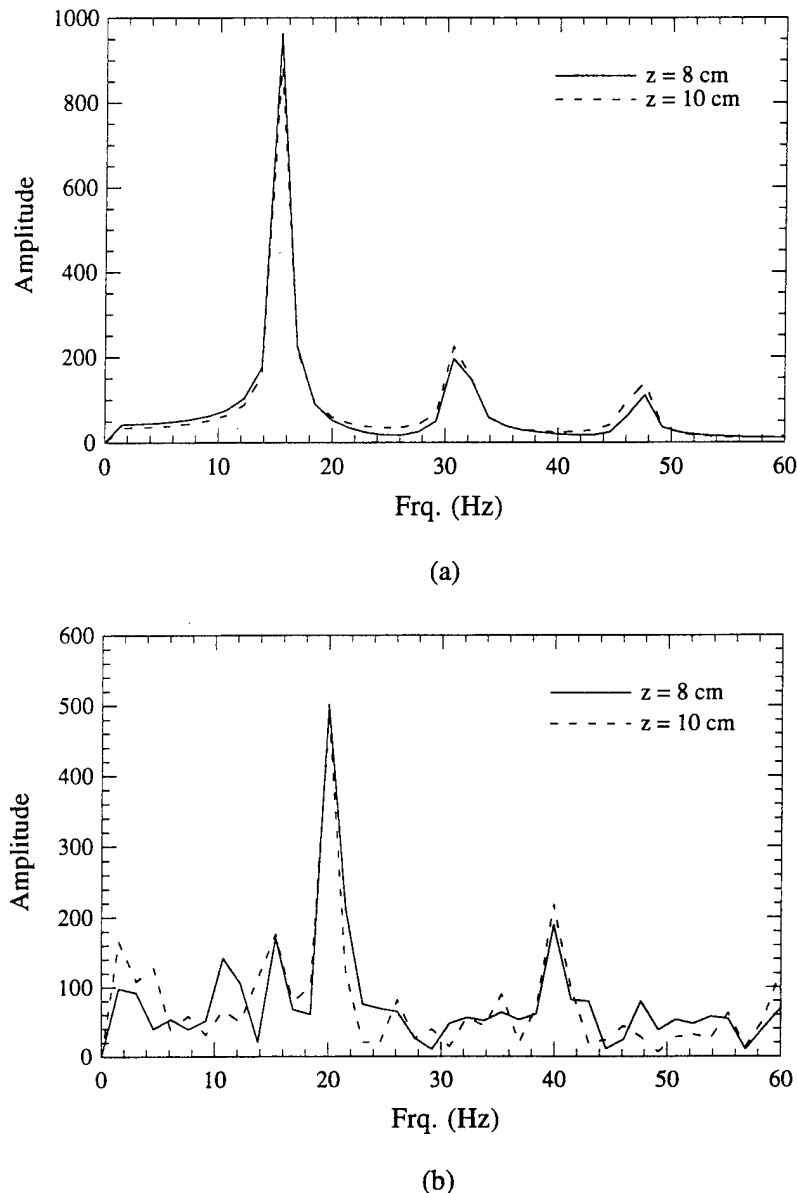


Fig. 5. Frequency spectra obtained from temperature data recorded within the shear layer at two different axial locations.

values ($M = 0.5$ and 1.0), the structural characteristics seem to change more significantly.

The effect of mass loading in an evaporating spray is depicted in Fig. 8 by plotting the phase-locked instantaneous temperature contours for the three different mass loading values ($M = 0.25, 0.5$ and 1.0). The gas-phase governing equations for this case include all the source/sink terms due to the exchange of mass, momentum and energy due to droplet dynamics and vaporization. Structure of the heated jet seems to change more significantly with the addition of evaporating spray compared to that of a non-evaporating one. Figure 9 shows the time evolution of temperature contours at $z = 7.5$ cm for the three cases shown in Fig. 8. It is interesting to compare

the structures of high mass loading values ($M = 0.5$ and 1.0) for the evaporating (Fig. 9) and non-evaporating (Fig. 7) cases. The development of vortical structures for evaporating spray is more periodic than that observed in the corresponding non-evaporating cases. This is probably due to the fact that for the evaporating case the effect of momentum coupling between the phases is reduced due to droplet vaporization.

The effect of dispersed phase on the time-averaged gas-phase properties for both non-evaporating and evaporating sprays with different mass loading values is portrayed in Fig. 10. The time period used in obtaining the average values was at least 10 vortex periods. In addition, it was verified that the average values

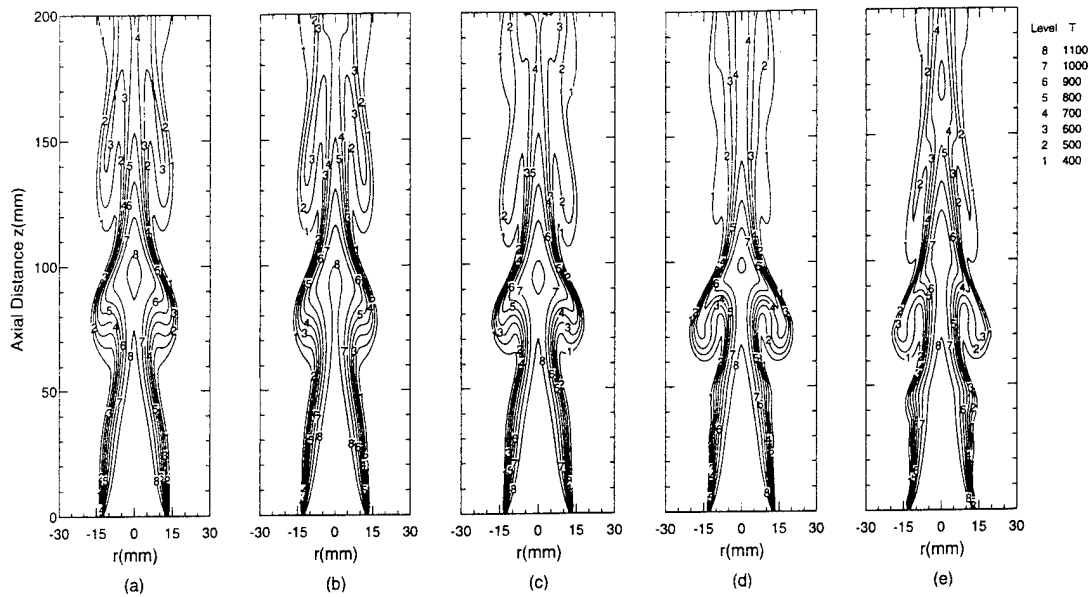


Fig. 6. Instantaneous iso-temperature contours for a 200- μ m non-evaporating spray jet with five different mass loading values: (a) $M = 0$, (b) $M = 0.125$, (c) $M = 0.25$, (d) $M = 0.5$ and (e) $M = 1.0$.

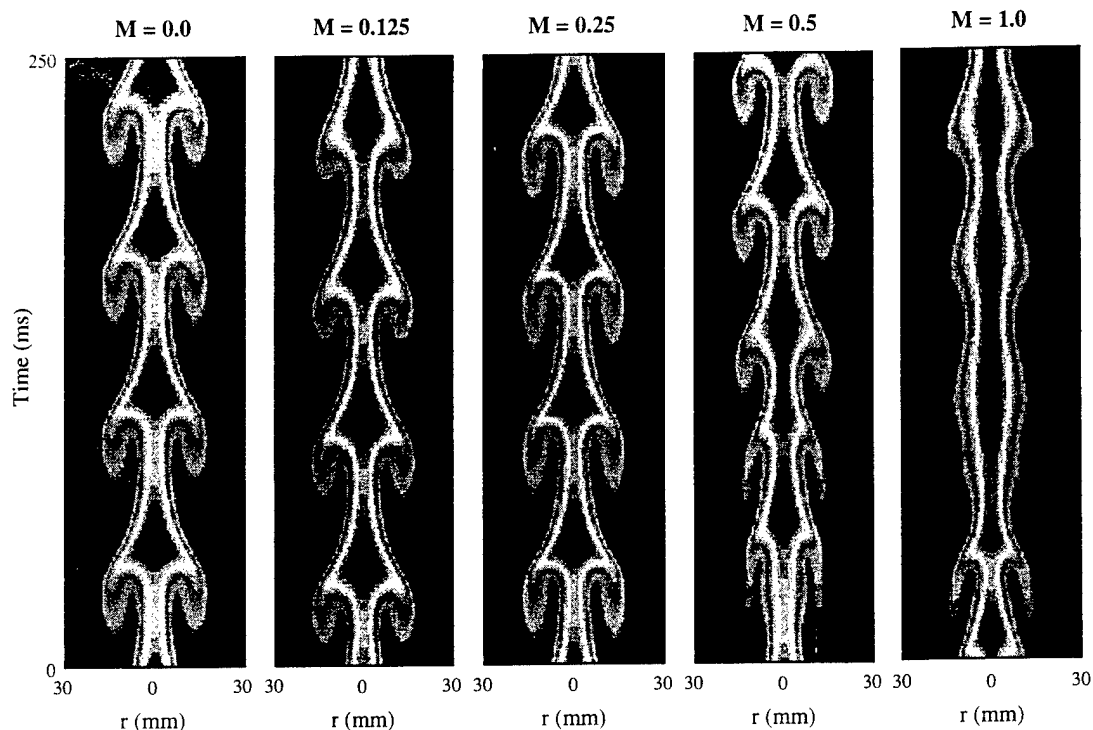


Fig. 7. Time evolution of temperature contours at axial location of 10 cm above inlet for the cases of Fig. 6.

shown in Fig. 10 were independent of this time period. An important observation is that the dispersed phase does not have any discernible influence on the time-averaged properties of non-evaporating spray jet. This is especially interesting in view of the fact that the vortex dynamics for the non-evaporation spray case is modified by the presence of the dispersed phase. As

expected, the average gas-phase properties of evaporating spray are significantly affected by the dispersed phase. The average gas temperature decreases along the jet axis due to the cooling caused by droplet vaporization. The decrease in gas temperature reduces the magnitude of buoyant acceleration, resulting in a lowering of average gas velocity compared to that for

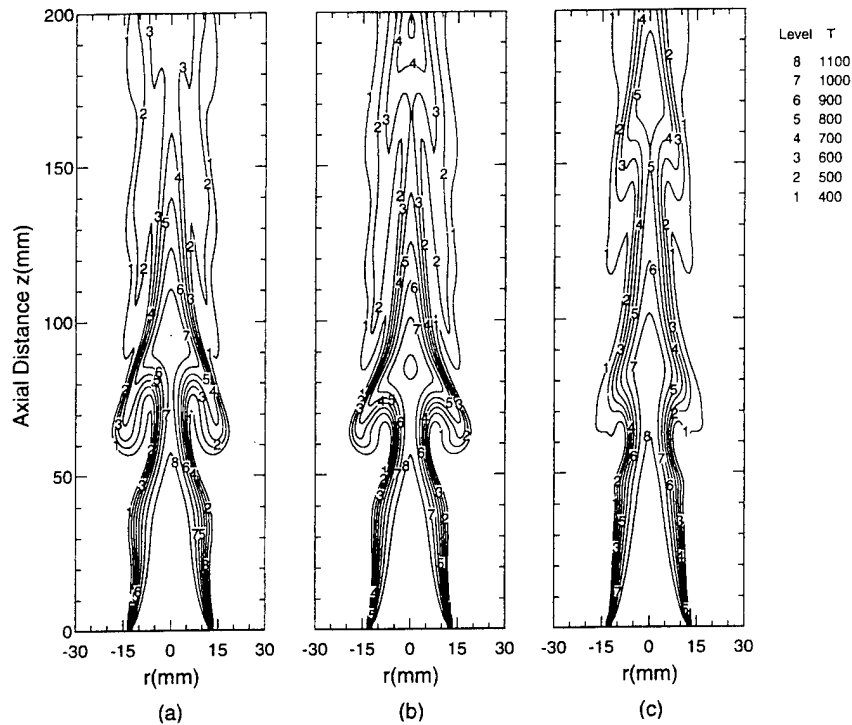


Fig. 8. Instantaneous iso-temperature contours for a 200- μm evaporating spray jet with three different mass loading values; (a) $M = 0.25$, (b) $M = 0.5$ and (c) $M = 1.0$.

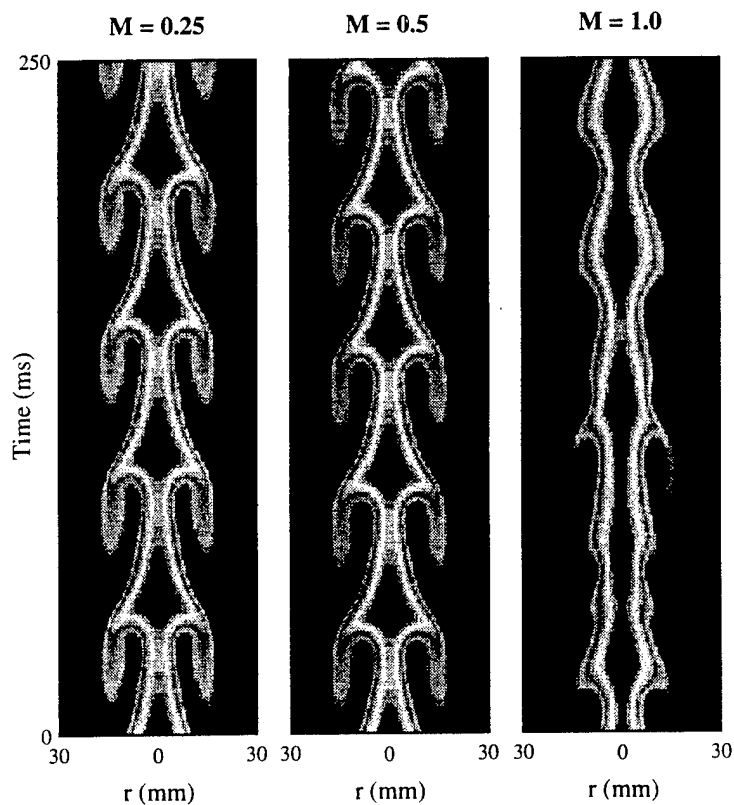
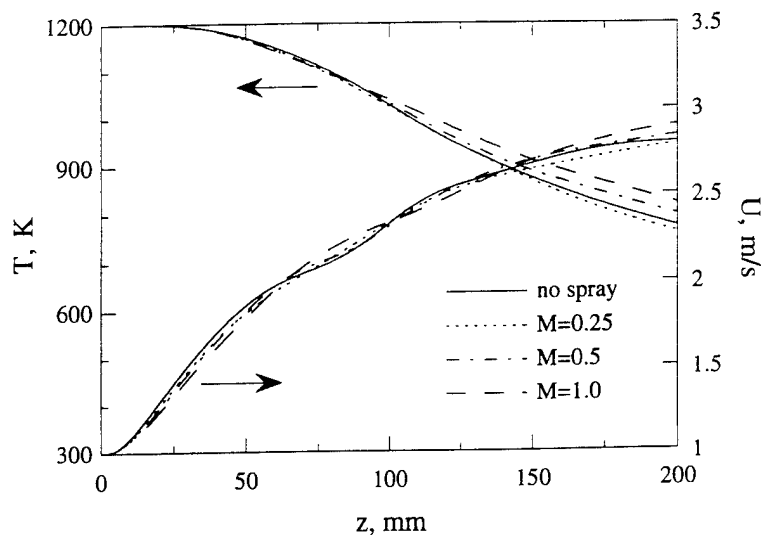
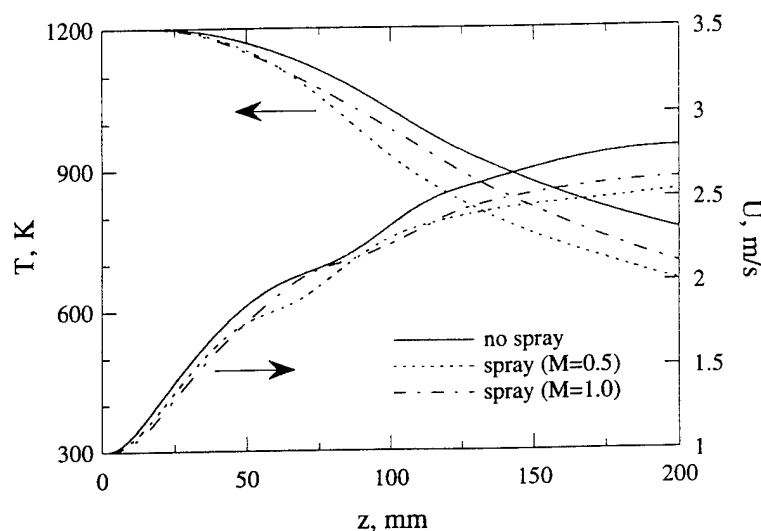


Fig. 9. Time evolution of temperature contours at a location of 7.5 cm above the inlet for the cases of Fig. 8.



(a)



(b)

Fig. 10. Time-averaged axial profiles of gas temperature and axial velocity for (a) non-evaporating and (b) evaporating sprays with different liquid-to-gas loading ratios.

the gaseous case. Note that a reduction in the buoyant acceleration makes the vortex structures weaker as mentioned earlier.

Effect of injection characteristics

The effect of initial droplet distribution on the structural characteristics and dynamics of evaporating spray jet is studied by changing the injection characteristics. The mass loading ratio and droplet diameter are fixed at 1.0 and 200 μm , respectively. The instantaneous temperature contours for three cases having different droplet injection locations are shown in Fig. 11. The three distributions of injection locations used are as follows: (1) $r_k = 1.25$ cm, one injection

location, (2) $r_k = 0.625$ and 1.25 cm, two injection locations and (3) $r_k = 0.25, 0.50, 0.75, 1.00$ and 1.25 cm, five injection locations. The mass loading ratio is kept constant by using a different number of droplets in each group for different cases. It is seen that the characteristics of the core region near the nozzle exit are quite different for the three cases due to different droplet injection processes. The use of more injection locations apparently leads to a dynamic heated spray jet with well-organized vortical structures [Fig. 11(c)]. It is known that the vaporization of a liquid droplet absorbs thermal energy and hence reduces the local temperature. This is evident in Figs. 11(b) and (c). In the former figure a valley in the temperature contours

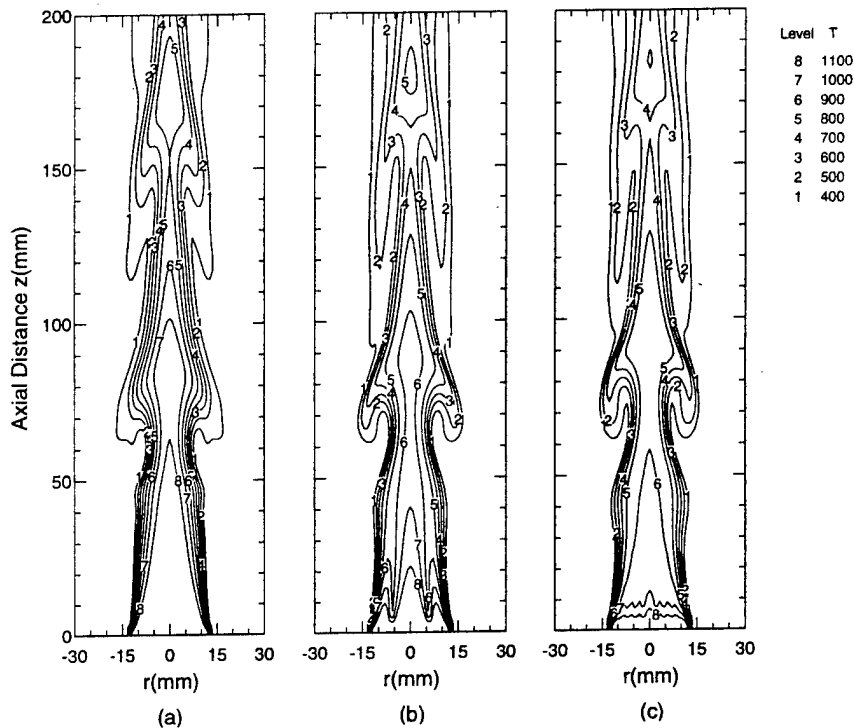


Fig. 11. Instantaneous iso-temperature contours for an evaporating spray jet with three different injection distributions: (a) $r_k = 1.25$ cm, one injection location, (b) $r_k = 0.625$ and 1.25 cm, two injection locations, (c) $r_k = 0.25, 0.5, 0.75, 1.0$ and 1.25 cm, five injection locations.

developed in the downstream region of the inner injection location (i.e. $r_k = 0.625$ cm) as the injected droplet vaporized. However, in the latter figure, the choice of more injection locations reduced the entire jet temperature uniformly leading to near flat contours for 1000 and 1100 K [contours 7 and 8 in Fig. 11(c)]. The time evolution of temperature contours at an axial location of 7.5 cm for the above three cases is plotted in Fig. 12. It clearly shows that the vortex structures are well organized and highly periodic similar to that of a single-phase flow (Fig. 3a) when the number of injection locations is increased. However, the vortex passage frequency for the spray case is different from that for the single-phase jet.

Effect of droplet size

In order to examine the effect of initial droplet size on the processes of droplet-vortex interactions, three different spray cases with initial droplet diameters of 200, 100 and $50 \mu\text{m}$ are considered. A constant mass loading ratio of $M = 1.0$ is maintained by increasing the number of droplets in each group as its initial size is decreased, and the droplets are injected in the shear layer ($r_k = 1.25$ cm). Results are portrayed in Fig. 13 in the form of snap shots of the flow field. For each case, instantaneous iso-temperature contours and velocity vectors are plotted on the left-hand and right-hand sides of the symmetric jet, respectively. It is quite evident from Fig. 13 that the initial droplet size has a strong influence on the dynamic and structural characteristics of the evaporating spray. For all three cases

shown in the figure, there is a reduction in gas temperature due to the vaporization of liquid fuel. However, as the initial droplet size decreases, there is increasingly pronounced cooling in the initial part of the jet caused by droplet vaporization, which affects both the shape and the dynamics of vortex structures. This can be seen more clearly in Fig. 14 which shows the time evolution of vortical structures for the three cases. In fact, when the initial droplet size is sufficiently small ($d_0 = 50 \mu\text{m}$), the jet temperature downstream of $z = 6$ cm is reduced to less than 500 K, and vortex structures seem to be destroyed. This drastic reduction in gas temperature is caused by the increased total liquid-phase surface area and entrainment of colder fluid into the jet interior. The latter is due to the vortex merging process and subsequent enlargement of vortex structures for the $50\text{-}\mu\text{m}$ spray case. Note that the vortex merging which occurs at an axial location between $z = 2.5$ and 5 cm is not shown in the figures (although there is some evidence of it in Fig. 13). However, the enlargement of vortex structures for the $50\text{-}\mu\text{m}$ spray can be clearly seen in Fig. 14. The vortex-merging process enhances the entrainment of colder fluid, which further reduces the gas temperature and weakens the vortex structures drastically. Figure 15 shows the effect of initial droplet size on the time-averaged axial profiles of temperature and axial velocity. The drastic reduction in gas temperature caused by droplet vaporization and entrainment of colder fluid, and the subsequent destruction of vortex structures can be clearly seen in this figure. Thus the

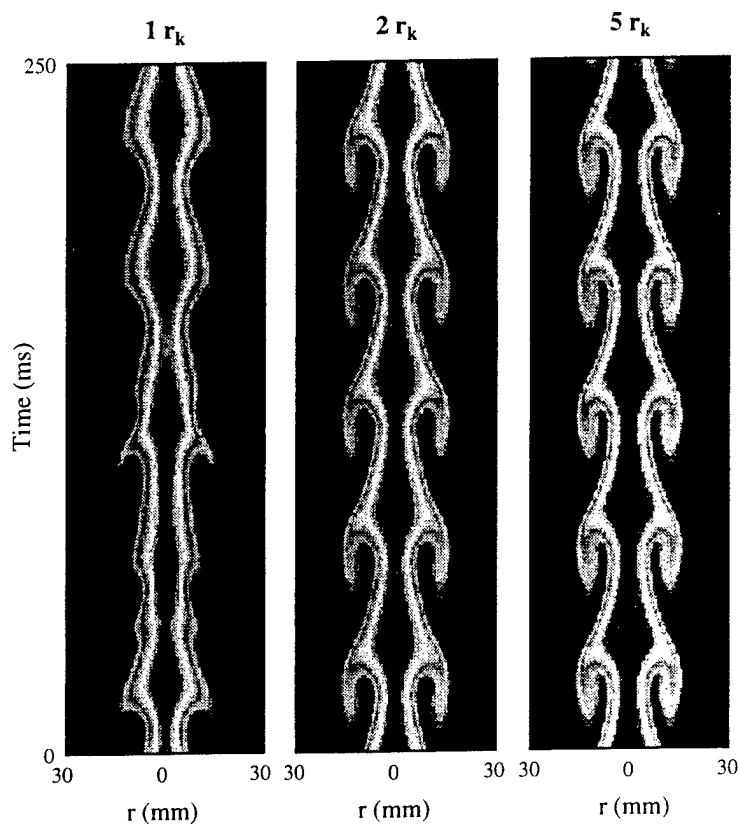


Fig. 12. Time evolution of temperature contours at axial location of 7.5 cm above inlet for the cases of Fig. 10.

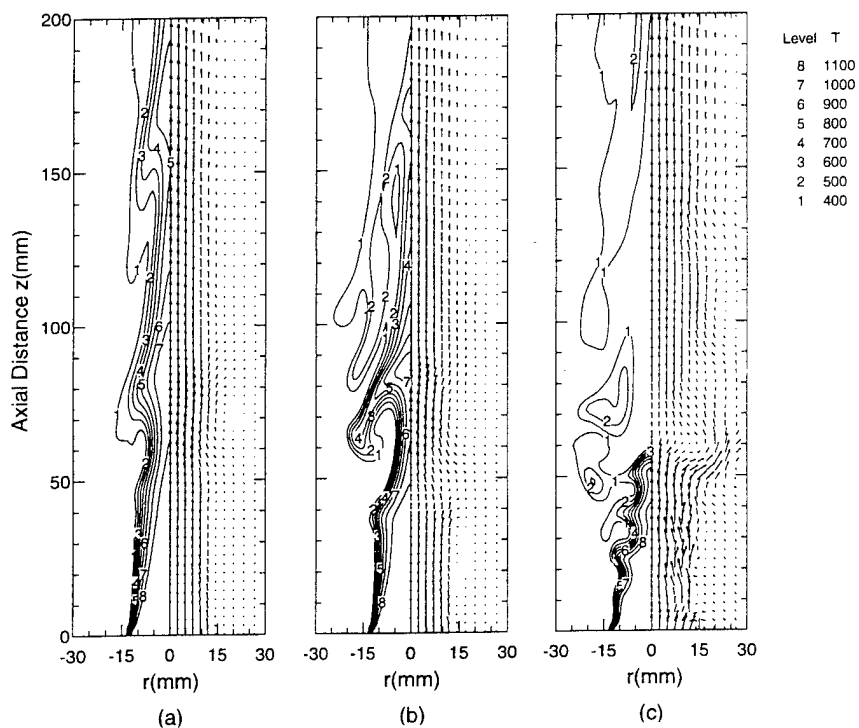


Fig. 13. Simultaneous snapshots of iso-temperature contours and velocity vectors for an evaporating spray for three different initial droplet diameters: (a) $d_o = 200 \mu\text{m}$, (b) $d_o = 100 \mu\text{m}$ and (c) $d_o = 50 \mu\text{m}$.

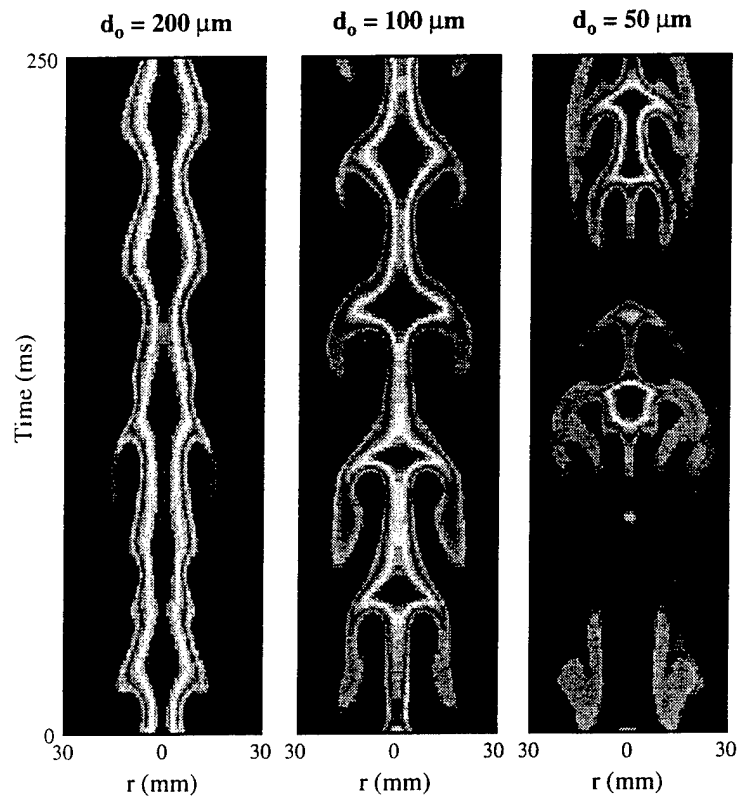


Fig. 14. Time evolution of temperature contours at a location of 7.5 cm above the inlet for the cases of Fig. 12.

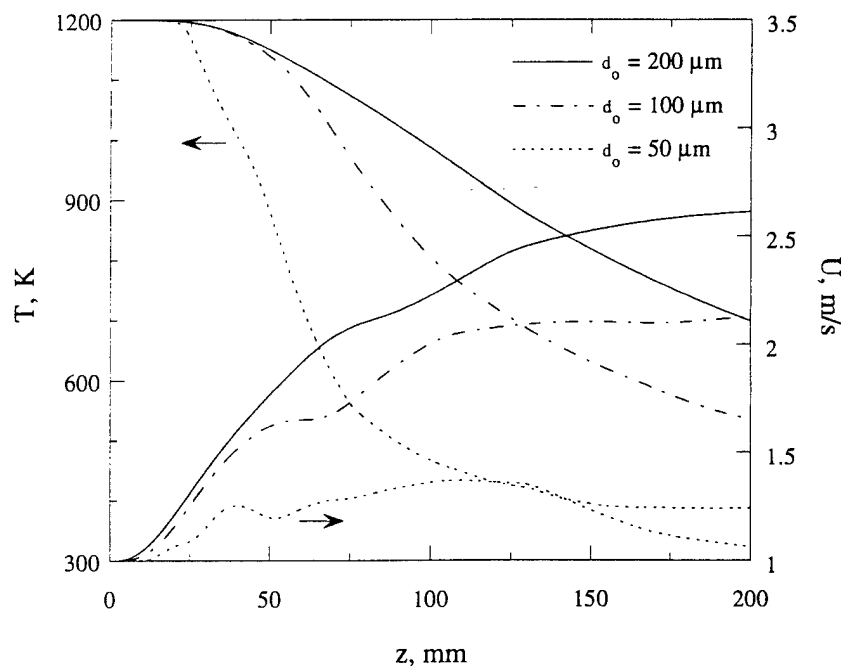


Fig. 15. Time-averaged axial profiles of gas temperature and axial velocity for an evaporating spray with three different initial droplet diameters and $M = 1.0$.

two-way nonlinear interactions seem to become stronger due to fast vaporization of 50- μm spray.

CONCLUSIONS

In this paper, we have investigated the dynamics of two-way droplet-vortex interactions and their influence on the structure of an evaporating spray. A low-speed spray formed (jet Reynolds number based on a jet temperature of 1200 K and velocity of 1.0 m s^{-1} is 154) between a droplet-laden heated nitrogen jet and a coflowing air stream has been simulated. Gravity has been used to generate large-scale vortical structures in the jet shear layer. The density difference between the heated fluid and the cold coflowing fluid gives rise to buoyant acceleration causing vortical structures to appear without any external perturbation. Liquid fuel (n-heptane) droplets are introduced into the vortex structures, and processes of droplet-vortex interactions are studied numerically by developing a time-accurate, multidimensional, two-phase algorithm. The effect of dispersed phase is incorporated through the source/sink terms in the gas-phase governing equations, representing the exchange of mass, momentum, and energy between the gas and liquid phases.

Snapshots and time evolution plots of vortex structures have been employed to analyze the effect of dispersed phase on their dynamics and time-averaged behavior under different mass loadings for both non-evaporating and evaporating sprays. The vortex structures cause droplets to disperse radially outward, and this in turn determines the fuel vapor distribution and also modifies the vortex dynamics. Thus, the dynamics and structural characteristics of the evaporating spray are strongly influenced by these interactions. The effects of initial droplet size, injection location, and liquid-to-gas mass loading ratio on the droplet-vortex interaction have been investigated by performing numerical experiments.

For both non-evaporating and evaporating sprays, the effect of dispersed phase on vortex dynamics is found to be negligible for mass loading ratio (M) less than 0.5. However, at higher loading ratios, depending upon the droplet injection characteristics, the vortex dynamics as well as the spray jet behavior may be strongly influenced by the dispersed phase. For a non-evaporating spray, the dispersed phase modifies the dynamics of vortex structures but not the time-average behavior, while it modifies both the dynamics and time-averaged behavior for an evaporating spray. For example, for 200- μm spray at $M = 1.0$ and with droplets injected into the shear layer, the vortex passage frequency is increased by about 30% and the vortex structures become weaker and less coherent compared to the gaseous jet case. This has important implications in spray applications such as gas turbine and ramjet combustors, especially when the system performance is strongly linked to some underlying unsteady phenomenon. Results also indicate that the initial droplet size has a strong influence on the two-

way interactions. Due to spray vaporization, gas temperature in the jet interior decreases, which modifies the vortex dynamics and consequently the droplet dynamics and vaporization. In fact, for 50- μm spray at $M = 1.0$, the vortex dynamics is drastically modified and a vortex pairing phenomenon is observed. The latter results in a much larger entrainment of colder fluid causing a subsequent destruction of vortex structures. Thus the spray injection characteristics have strong influence on the processes of droplet-vortex interactions.

Acknowledgements—This work was funded by the AFOSR under Grant F49620-93-1-0400 monitored by Dr Julian M. Tishkoff. Many fruitful discussions with Dr W. M. Roquemore at Wright-Patterson Air Force Base are greatly appreciated. Computations were performed on Cray C-90 at the Pittsburgh Supercomputing Center.

REFERENCES

1. G. L. Brown and A. Roshko. Density effects and large scales in the developing mixing layer. *J. Fluid Mech.* **64**, 775–816 (1974).
2. A. J. Yule. Large scale structure in the mixing layer of a round jet. *J. Fluid Mech.* **89**, 413–432 (1978).
3. V. R. Katta, L. P. Goss and W. M. Roquemore. Effect of nonunity Lewis number and finite-rate chemistry on the dynamics of a hydrogen–air jet diffusion flame. *Combust. Flame* **96**, 60–74 (1994).
4. E. K. Longmire and J. K. Eaton. Structure of a particle-laden round jet. *J. Fluid Mech.* **236**, 217–257 (1992).
5. J. N. Chung and T. R. Troutt. Simulation of particle dispersion in an axisymmetric jet. *J. Fluid Mech.* **186**, 199–222 (1988).
6. D. Hansell, I. M. Kennedy and W. Kollmann. A simulation of particle dispersion in a turbulent jet. *Int. J. Multiphase Flow* **18**, 559–576 (1992).
7. B. J. Lazaro and J. C. Lasheras. Particle dispersion in the developing free shear layer—I. Unforced flow. *J. Fluid Mech.* **235**, 143–178 (1992).
8. B. J. Lazaro and J. C. Lasheras. Particle dispersion in the developing free shear layer—II. Forced flow. *J. Fluid Mech.* **235**, 179–221 (1992).
9. M. Samimy and S. K. Lele. Motion of particles with inertia in a compressible free layer. *Phys. Fluids* **A3**, 1915–1923 (1991).
10. K. Hishida, A. Ando and M. Maeda. Experiments on particle dispersion in a turbulent mixing layer. *Int. J. Multiphase Flow* **18**, 181–194 (1992).
11. J. Uthuppan, S. K. Aggarwal, F. F. Grinstein and K. Kailasanath. Particle dispersion in a transitional axisymmetric jet: a numerical simulation. *AIAA J.* **32**, 2004–2014 (1994).
12. S. K. Aggarwal. Relationship between stokes number and intrinsic frequencies in particle laden flows. *AIAA J.* **32**, 1322–1325 (1994).
13. T. W. Park, S. K. Aggarwal and V. R. Katta. Gravity effects on the dynamics of evaporating droplets in a heated jet. *AIAA J. Propulsion Power* **11**, 519–528 (1995).
14. B. Abramzon and W. A. Sirignano. Droplet vaporization model for spray combustion calculations. *Int. J. Heat Mass Transfer* **32**, 1605–1618 (1989).
15. D. K. Edwards, V. E. Denny and A. F. Mills. *Transfer Processes: An Introduction to Diffusion, Convection and Radiation* (2nd Edn). McGraw-Hill, New York (1979).
16. S. K. Aggarwal, A. Tong and W. A. Sirignano. A comparison of vaporization models for spray calculation. *AIAA J.* **22**, 1448–1457 (1984).
17. B. P. Leonard. A stable and accurate convective mod-

- elling procedure based on quadratic upstream interpolation. *Comput. Meth. Appl. Mech. Engng* **19**, 59–98 (1979).
18. D. B. Spalding, A novel finite difference formulation for difference expressions involving both first and second derivatives. *Int. J. Numer. Meth. Engng* **4**, 551–559 (1972).
 19. P. A. Monkewitz and K. D. Sohn, Absolute instability in hot jets, *AIAA J.* **26**, (8), 911–916 (1988).
 20. S. Ragu and P. A. Monkewitz, The bifurcation of a hot round jet to limit-cycle oscillations, *Phys. Fluids A* **3**, 501–503 (1991).
 21. L.-D. Chen, J. P. Seaba, W. M. Roquemore and L. P. Gross, Buoyant diffusion flames, *Proceedings Twenty-Second International Symposium on Combustion*, pp. 677–684. The Combustion Institute, Pittsburgh, PA (1988).
 22. H. Eickhoff and A. Winandy, Visualization of vortex formation in jet diffusion flames, *Combust. Flame* **60** (1), 99–101 (1985).
 23. T. Yuan, D. Durox and E. Villermaux, An analog study for flame flickering, *Expts Fluids* **17** (5), 337–349 (1994).
 24. R. W. Davis, E. F. Moore, W. M. Roquemore, L.-D. Chen, V. Vilimpoc and L. P. Goss, Preliminary results of a numerical-experimental study of the dynamic structure of a buoyant jet diffusion flame, *Combust. Flame* **83** (3/4), 263–270 (1991).
 25. V. R. Katta, L. P. Goss and W. M. Roquemore, Numerical investigations of transitional H_2/N_2 jet diffusion flames, *AIAA J.* **32**, 84–94 (1994).

Effect of Gravity on the Structure of an Unsteady Spray Diffusion Flame

T. W. PARK and S. K. AGGARWAL*

Department of Mechanical Engineering, University of Illinois at Chicago, Chicago, IL 60607

and

V. R. KATTA

Systems Research Laboratories, Inc., A Division of Arvin/Calspan, 2800 Indian Ripple Road, Dayton, OH 45440-3696

In this paper, we present time-dependent axisymmetric numerical simulation of an unsteady *n*-heptane spray flame, and examine the effects of gravity on the flame structure. The flame is formed between a droplet-laden nitrogen jet and a coflowing air stream. A detailed, multidimensional two-phase algorithm is developed for the simulation. The gas-phase model includes a one step global chemistry model, multicomponent diffusion, and variable transport properties. A comprehensive vaporization model is employed to calculate the instantaneous droplet size and surface temperature along the trajectory of each droplet group. The model includes the effects of variable thermophysical properties and nonunity Lewis number in the gas film, the effect of Stefan flow on the heat and mass transfer between the droplet and the gas, and the transient liquid heating. Results indicate that the laminar spray flame structure is strongly influenced by gravity. Large-scale buoyancy-driven structures are observed outside the flame surface, similar to those in a gaseous jet diffusion flame. These outer structures develop naturally and sustain themselves without any external excitation. Results also indicate the occurrence of strong two-way interactions between droplets and large structures. The large vortex structures cause droplets to disperse radially outward, and this in turn modifies the vortex dynamics. The dynamics of spray flames and their structural characteristics are strongly influenced by these interactions.

INTRODUCTION

Gravity plays an intrinsic role in determining the structure of gaseous jet diffusion flames [1-8]. At normal gravity, the diffusion flame at laminar and transitional speeds is subjected to the buoyancy-induced hydrodynamic instability, which is responsible for the presence of large vortical structures outside the flame surface. These low-frequency, slowly moving structures are known [5-8] to interact strongly with the flame surface, creating a wrinkled flickering flame. In addition, the shear-induced smaller structures from a Kelvin-Helmholtz instability develop inside the flame surface. The dynamics of these smaller structures may also be significantly influenced by the presence of buoyancy-induced outer structures. The

structural and transitional characteristics of normal-gravity ($1\ g$) and microgravity (μg) diffusion flames also differ in other important aspects [4-7]. These include their global behavior, sooting characteristics, dependence on pressure and oxygen concentration, and transition to turbulence.

While the gaseous jet diffusion flames under $1\text{-}g$ and $\mu\text{-}g$ conditions have been investigated extensively, the corresponding research on spray diffusion flame has been rather limited [9-12]. Levy and Bulzan [9] report an experimental study of a laminar spray flame in a coaxial flow system with the inner nitrogen stream carrying liquid fuel droplets and fuel vapor in a coflowing air stream. The spray flame exhibits large-amplitude self-induced oscillations that are unique to the spray case (not observed for the gaseous fuel case) and believed to be due to a nonlinear coupling of two-phase flow dynamics and gravity effects. Li et al. [10] and Lucas et al. [11] employ a

* Corresponding author.

Presented at the Twenty-Fifth Symposium (International) on Combustion, Irvine, California, 31 July-5 August 1994.

counterflow spray burner to investigate experimentally and theoretically the structure of a laminar spray flame. Chen and Gomez [12] use an electrostatic spray generator in a counterflow spray burner and report an experimental study of a laminar spray flame. All of these investigations are performed under 1-g conditions. It may be argued that compared with a gaseous diffusion flame, the role of gravity in a spray flame is even more complex and scientifically more interesting to study. The additional complications arising from gravity are due to the effect of gravity on droplet motion, causing droplet settling and stratification in droplet concentration at low flow speeds, and the dynamic interactions of droplets with the outer buoyancy-driven structures. The influence of outer structures in dispersing the droplets and the effect of dispersed phase on the development of buoyancy-driven instability need to be understood in order to quantify the gravity-induced interactions between the phases and the effects of these interactions on the dynamics of spray flame. The understanding of these interactions is also relevant to the dynamics of fires in earth as well as space environments.

In this paper, we present time-dependent axisymmetric numerical simulation of an unsteady spray flame. The flame is formed between a droplet-laden nitrogen jet and a coflowing air stream. The major objective is to investigate the effect of gravity on the dynamics and structural characteristics of spray flames at laminar speeds. A time-dependent, multidimensional, two-phase algorithm is developed for the simulation. Following a brief description of the physical and numerical models, the computational results are reported for a *n*-heptane spray flame at 1 *g* and 0 *g*. The results although qualitative highlight the presence of large-scale buoyancy-generated structures outside the flame surface, the strong two-way interactions between droplets and large structures, and the influence these interactions have on the dynamics of spray flames at 1 *g*.

THE PHYSICAL MODEL

The spray flame simulated in the present study is shown schematically in Fig. 1. The flame is supported by a droplet-laden nitrogen jet issu-

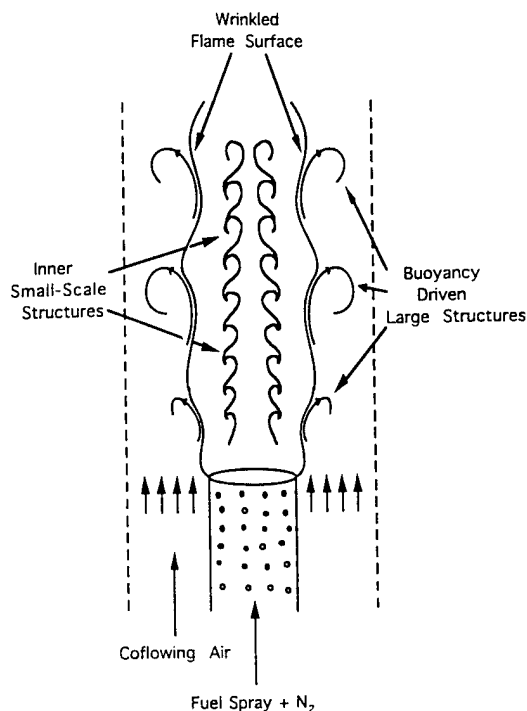


Fig. 1. A schematic of a spray diffusion flame at normal-gravity.

ing into a coflowing oxidizer medium. At normal gravity, the structural characteristics of this spray flame are strongly influenced by gravity. First of all, the buoyancy-driven large-scale structures outside the flame surface interact with the flame surface, creating a wrinkled, flickering flame. The outer structures also modify the dispersion and vaporization behavior of droplets, which in turn modify the development of outer structures and their subsequent dynamic behavior. In addition, if the jet Reynolds number is in the transitional range, the small structures due to the Kelvin-Helmholtz instability develop inside the flame. In the present study, however, the jet Reynolds number is in the laminar range and the inner structures are not observed.

The spray flame dynamics is simulated by developing a detailed reacting two-phase flow algorithm. The solution of gas-phase properties is based on the time-dependent equations [8] for the species densities, axial and radial velocities, and enthalpy, written for an axisymmetric flow. The gas-phase model used includes multicomponent diffusion, variable

transport properties, and finite-rate chemistry. The gas-phase fluid consists of five species (nC_7H_{16} , O_2 , CO_2 , H_2O , and N_2). Nitrogen in the present model is assumed to be an inert species and is obtained from the global mass continuity. A single-step, global reaction mechanism is used to describe the combustion process. However, the activation energy is assumed to be small in order to simulate a "flame sheet" approximation. The effect of dispersed phase is incorporated through the source/sink terms, representing the exchange of mass, momentum, and energy between the gas and liquid phases. The liquid-phase equations are based on the Lagrangian formulation. Using the dilute-spray assumption, the spray is characterized by a discrete number of droplet groups, distinguished by their injection location, initial size, and time of injection. The governing equations are written for the dynamics and vaporization history of each droplet group. These include equations for the position and velocity vectors, and the instantaneous size of each group. A comprehensive vaporization model is employed to calculate the instantaneous droplet size and surface temperature along the trajectory of each group. The model includes the effects of variable thermophysical properties and nonunity Lewis number in the gas film outside the droplet, the effect of Stefan flow on the heat and mass transfer between the droplet and the gas, and the transient liquid heating. The variable thermophysical properties are calculated at reference film temperature and concentrations, obtained by using the 1/3 rule, except for the gas density which is calculated at the free stream value [13]. The Wilke rule [14] is used to calculate the dynamic viscosity and thermal conductivity of the gas film. The fuel (nC_7H_{16}) properties are collected from the various sources and approximated as a function of the temperature. The effect of transient liquid heating is incorporated by using the conduction-limit model [15]. This model is deemed satisfactory in the present study, since the maximum droplet Reynolds number during droplet lifetime is less than ten and thus the effect of internal circulation is expected to be negligible. For the same reason, the effects of gas-phase convection on the heat and mass trans-

port are represented by the Ranz-Marshall correlation [15]. It should be noted, however, that the two-phase algorithm developed is quite general and more refined models [13] such as the "effective conductivity" model for transient liquid heating and the "film theory" model for gas-phase convection can be easily implemented in the algorithm.

THE NUMERICAL MODEL

The numerical solution of the unsteady two-phase equations employs an implicit algorithm for solving the gas-phase equations, and an explicit Runge-Kutta procedure for the liquid-phase equations. The finite-difference forms of momentum equations are obtained using an implicit QUICKEST scheme [16] which is fourth-order in space and third-order accurate temporally, while those of species and energy equations are obtained using an hybrid scheme of Spalding [17]. A "finite control volume" approach with a staggered, non-uniform grid system is utilized. An iterative ADI (Alternating Direction Implicit) technique is used for solving the resulting sets of algebraic equations. A stable numerical integration procedure is achieved by coupling the species and energy equations through the source terms. At every time step, the pressure field is calculated by solving the pressure Poisson equations using the LU matrix decomposition technique. It should be noted that the pressure Poisson equations consider the effect of mass transfer from the liquid phase to the gas phase, represented by including a source term in the gas-phase mass continuity equation.

The liquid-phase equations are advanced in time by a second-order accurate Runge-Kutta method. Since the gas-phase solution employs an implicit procedure, the temporal step size used for integrating the liquid-phase equations is smaller than that for gas-phase equations. An automatic procedure is implemented in order to select an optimum liquid-phase time step. The procedure involves calculating the characteristic thermal response time, velocity response time, and vaporization time for each droplet group, and then selecting the temporal step size as a fraction (at least one-hundredth) of the smallest of these time scales. A detailed

examination of various time scales based on numerical experiments revealed that the temporal step size is determined by either the thermal response time or the velocity response time of a given droplet group. The number of subcycles for advancing the liquid-phase solution for each gas-phase cycle varies typically from two to ten, depending upon the droplet size.

The procedure to advance the two-phase solution over one gas-phase time step is as follows. Using the known gas-phase properties, the liquid-phase equations are solved over a specified number of liquid-phase subcycles. A third-order accurate Lagrangian polynomial method is used for interpolating the gas-phase properties from the nonuniform fixed grid to the instantaneous droplet location. The droplet location and other properties are updated after every liquid-phase subcycle. Also, during each subcycle, the liquid-phase source terms appearing in the gas-phase equations are calculated at the characteristic location, and then distributed to the surrounding gas-phase grid points. These source terms are then used in the implicit solution of the gas-phase equations. At each time-step, the four species conservation equations and the energy equation are first solved simultaneously to obtain the new density and temperature of the mixture. The momentum and mass continuity equations are then solved to complete the gas-phase calculations.

Flat initial profiles are used at the exit of the central fuel (or nitrogen) nozzle and the coannular air duct. The outflow boundaries are shifted sufficiently to minimize the propagation of any disturbance from the boundaries into the region of interest. The flow variables at the outflow boundary are obtained by using an interpolation procedure with weighted zero- and first-order terms. The weighting functions are selected by the trial-and-error approach, and the main criterion used is that the vortices crossing the outflow boundary should leave smoothly without being distorted.

RESULTS

The spray flame is established between a droplet-laden nitrogen jet and a coannular air flow.

The liquid fuel is *n*-heptane. Since the objective of this study is to investigate the behavior of laminar spray flame under the influence of gravity, a low-speed nitrogen jet at room temperature and at a velocity of 20 cm/s is considered for the base case. The jet Reynolds number based on the jet velocity and diameter is about 350. The computational domain is 15×80 cm and has 151×51 grid points. A nonuniform grid system, with a large number of grid lines clustered near the flame surface to resolve the steep gradients, is utilized. The minimum grid spacing is approximately 0.1 cm. The CFL number of 0.1 is used in all the spray flame simulations discussed in this paper. It should be noted that several diagnostic runs were first made to assess the grid-independence of gas-phase calculations, and the effects of temporal step size and droplet injection frequency. The details of these results, and of physical-numerical model are given in Ref. [18].

Figure 2 shows the instantaneous iso-temperature contours for the spray flames at 1 g and 0 g. The spray injection process is simulated by injecting monodisperse droplets into the jet shear layer. The number of droplets

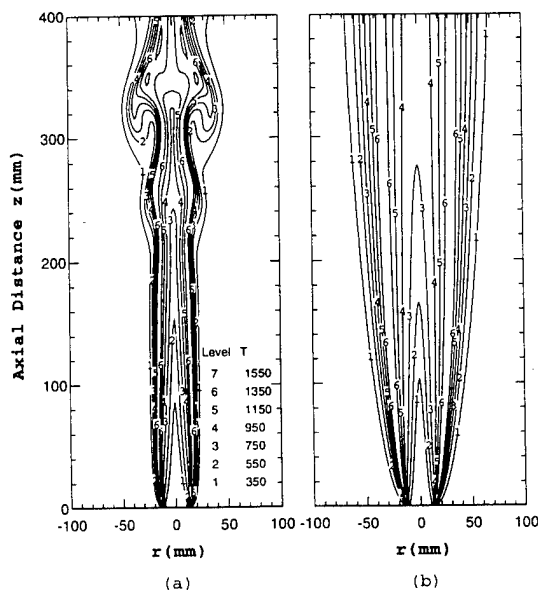


Fig. 2. Temperature contours for (a) normal-gravity and (b) zero-gravity spray flames. The droplet diameter is 200 μ m.

injected per unit time is determined from the overall liquid flow rate and the droplet diameter. For the results shown in Fig. 2, the droplet diameter is $200\text{ }\mu\text{m}$ and one droplet group with 50 droplets is injected every five gas-phase time steps. The outer toroidal vortices shown for the 1-g case appear as a part of the solution resulting from the buoyancy-driven instability; no artificial (external) excitation is needed to generate the outer structures. If the gravity is removed from the simulation, a steady laminar spray flame is obtained, as shown in Fig. 2b. It should also be noted that the smaller Kelvin-Helmholtz type vortices inside the flame, as discussed by Chen et al. [6], are not observed in the present simulations, since the jet Reynolds number is in the laminar range and no external perturbation is used to drive the jet instability. In this context, it is also important to note the differences between the shear-layer and buoyancy-induced instabilities. While the shear-layer instability is described as a convective instability, the buoyancy-induced instability is an absolute one [19].

The contours of fuel vapor mass fraction for the above two cases are portrayed in Fig. 3. The maximum fuel mass fraction occurs in the jet shear region, where the droplets are in-

jected. The flame is located outside the shear layer as fuel vapor diffuses radially outward, and mixes with the inwardly diffusing oxygen. As the mixing occurs, the chemical reaction occurs immediately due to the low activation energy used. The buoyant convection resulting from the heat release is believed to be responsible for the generation of large-scale outer structures.

The temporal evolution of toroidal vortices for $200\text{-}\mu\text{m}$ spray flame is shown in Fig. 4. Computed temperature data along the radial direction at two axial locations are recorded over a period of 600 ms, and the evolution is shown in the form of iso-temperature contours. The plots indicate a vortex-pairing interaction, which we believe is unique to the spray flame and has not been observed previously in gaseous diffusion flames at 1 g. The plot at $z = 30\text{ cm}$ shows a sequence of vortex pairs, with a smaller vortex following a larger one. By the time these vortices reach a height of 40 cm from the nozzle exit, the fast-moving smaller vortices are penetrating into the slowly moving larger ones causing a merging. The vortex frequency is found to be 14 Hz with a subharmonic of 7 Hz. When the droplet size was reduced to $100\text{ }\mu\text{m}$, outer vortices established (Fig. 6) at a location very close to the nozzle exit (closer than that of the gaseous flame) and vortex merging (not shown) took place at an height less than 20 cm.

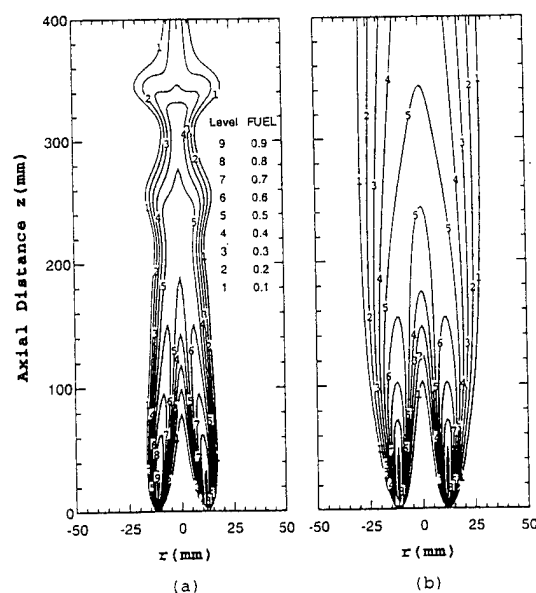


Fig. 3. Contours of fuel vapor mass fractions for (a) normal-gravity and (b) zero-gravity spray flames. The droplet diameter is $200\text{ }\mu\text{m}$.

Droplet-Vortex Interactions: Effects of Gravity and Droplet Size

In addition to the direct effect of gravity, the droplet trajectory and vaporization history may also be affected by the buoyancy-generated large structures. In order to examine these effects, the histories of droplet diameter, surface temperature, and droplet Reynolds number are plotted in Fig. 5 for 1-g and 0-g cases. One striking observation is that due to the buoyancy-generated convection, the droplet Reynolds number is much larger (maximum value ~ 9.0) for 1-g case compared with that (maximum value ~ 1.0) for 0-g case. In addition, Fig. 5 indicates that the droplet lifetime is shorter, although the surface temperature is mostly lower for 1-g case compared with that

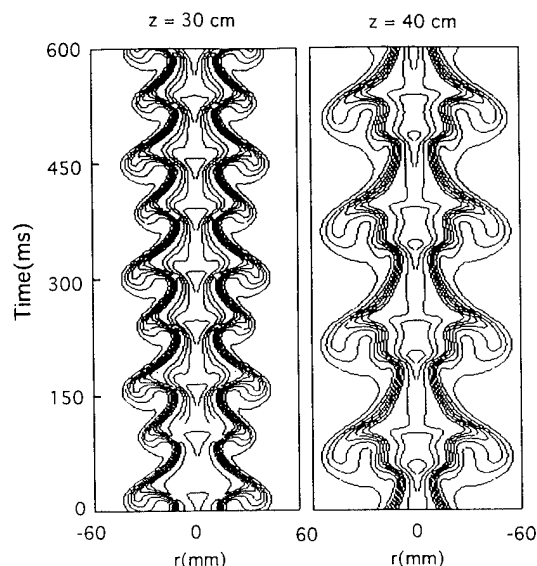


Fig. 4. Temporal evolution of buoyancy-generated outer structures at three axial locations for the spray flame (of Fig. 2) at 1 g.

for 0-g case. This is probably due to the relatively large droplet Reynolds number for 1-g case. The important conclusion seems to be that the droplet behavior in a 1-g laminar spray flame is strongly influenced by the large vortex structures. This effect is further highlighted in Fig. 5c, which shows the plot of droplet Reynolds number history for a 1-g spray flame with initial droplet diameter of 100 μm . The comparison of Reynolds number histories for the 100- and 200- μm cases shows that the vortex structures affect the motion of the 100- μm droplet more strongly than that of the 200- μm droplet. This has important implications for the two-way droplet-vortex interactions discussed next.

Effect of Droplet Size

Figure 6 shows the iso-temperature contours for three computed flames at 1 g, namely a *n*-heptane gaseous diffusion flame (Fig. 6a) and two spray diffusion flames (Figs. 6b and 6c) with initial droplet diameters of 100 and 200 μm , respectively. The corresponding flames computed at 0 g are shown in Fig. 7. The gaseous flame is calculated by assuming that the jet carries a mixture of N_2 and *n*-heptane

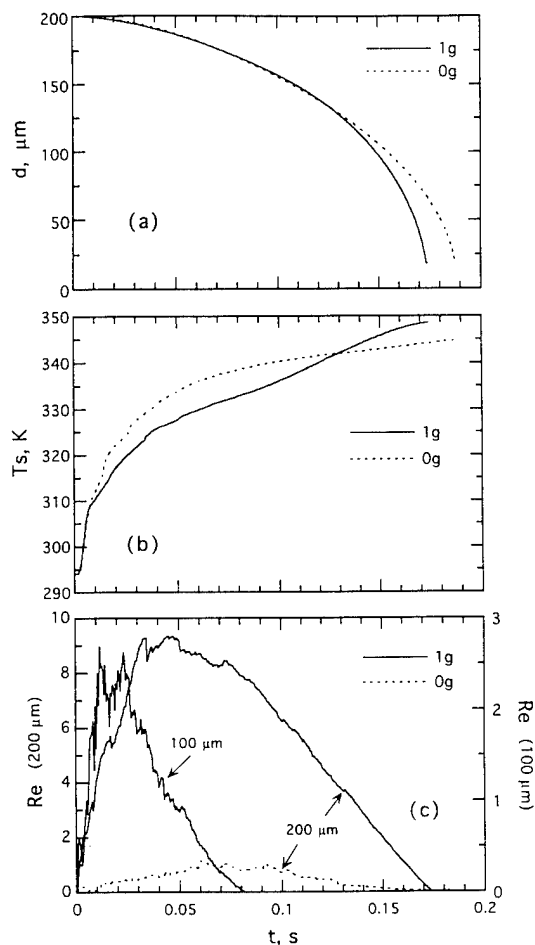


Fig. 5. Histories of (a) droplet diameter, (b) surface temperature, and (c) droplet Reynolds number for 200- and 100- μm spray flames at 1 g and 0 g.

in gaseous form, and may be approximated as a spray flame in the limit of initial droplet diameter going to zero. The important observation from these figures is that the initial droplet size has a strong influence on the structural characteristics of 1-g spray flames, but negligible effect on 0-g spray flames. For the latter, three flames (Fig. 7) appear to be qualitatively similar, although there are quantitative differences; the spray flame is generally thicker due to the distribution of droplets, but develops faster compared to the gaseous flame. Figure 6 clearly highlights the strong interaction between droplets and buoyancy-driven vortex structures, and the significant effect these interactions have on the dynamics of 1-g spray flames. Moreover, the droplet-vortex in-

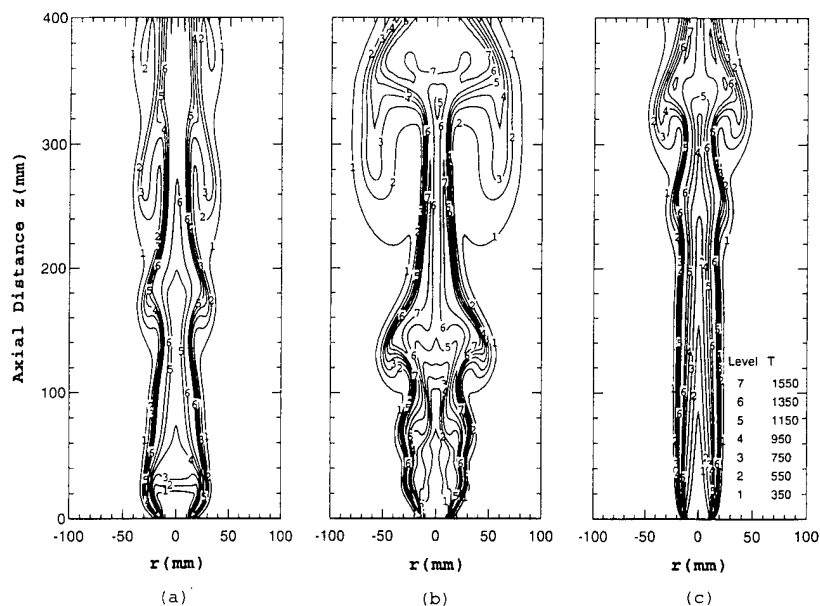


Fig. 6. Iso-temperature contours for three different flames at 1 g. (a) *n*-heptane gaseous diffusion flame (b) and (c) *n*-heptane spray diffusion flame with initial droplet diameter of 100 and 200 μm , respectively.

teraction is clearly a two-way interaction. The initial development of buoyancy-driven instability seems to depend upon the droplet size, which can be seen by comparing the initial appearance of vortex structures for the 100- and 200- μm cases in Fig. 6. The vortex struc-

tures, once they develop, influence the droplet dispersion and vaporization behavior, which in turn modifies the heat release process and thus the dynamics of vortex structures. Another important observation is that the effect of droplet size is not monotonic, i.e., there appears to be

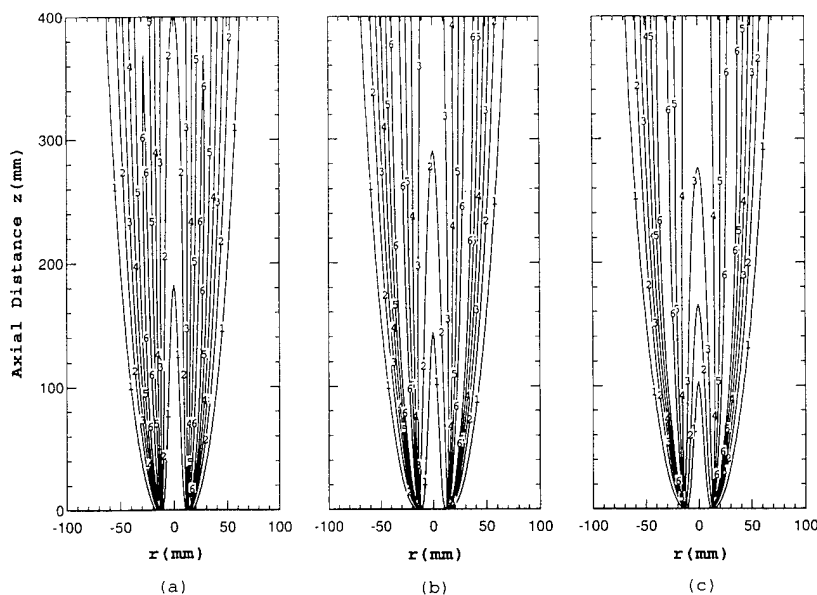


Fig. 7. Iso-temperature contours for three different flames at 0 g. For details see caption of Fig. 6.

an intermediate droplet size where the droplet-vortex interactions are the strongest. Whether this can be explained in terms of an intermediate Stokes number (ratio of droplet response time to time scale of large structures) remains to be investigated. For nonevaporating droplets in shear layers, it is found [20, 21] that the droplet dispersion in the presence of large vortical structures maximizes near Stokes number of unity. More detailed numerical experiments are needed to examine if a similar behavior exists in the presence of two-way droplet-vortex interactions.

CONCLUSIONS

A detailed multidimensional two-phase algorithm is developed to study the dynamics of laminar spray flames under the influence of gravity. The flame is formed between a droplet-laden nitrogen jet and a coflowing air stream. Results indicate that the dynamics of laminar spray flames is strongly influenced by gravity. While the computed spray flame at 0 g exhibits a steady laminar behavior, the simulations at 1 g show an oscillating flame, which is due to the presence of large-scale buoyancy-driven structures outside the flame surface. These large outer structures develop naturally as a part of the solution, without any external excitation. Results further indicate the occurrence of strong two-way interactions between large vortex structures and droplets. The relative intensity of two-way interactions appears to depend upon the initial droplet size. The dynamics and structural characteristics of laminar spray flames at 1 g are determined by these droplet-vortex interactions. Another effect of these interactions is the pairing of vortex structures, which we believe is unique to spray flames, and not observed previously for gaseous diffusion flames. It should be noted, however, that the results at this time can only be considered qualitative rather than quantitative.

This work was supported by AFOSR Grant F49620-92-J-0231, with Dr. Julian M. Tishkoff as the Program Manager. Many fruitful discussions with Dr. W. M. Roquemore at Wright-Patterson Air Force Base are greatly appreciated.

REFERENCES

1. Law, C. K., AIAA-90-0120, Twenty-Eighth Aerospace Sciences Meeting, Reno, January, 1990.
2. Bahadori, M. Y., Edleman, R. B., Stocker, D. P., and Olson, S. L., *AIAA J.* 28:236-244 (1990).
3. Ellzey, J. L., and Oran, E. S., *Twenty-Third Symposium (International) on Combustion*, The Combustion Institute, Pittsburgh, 1991, pp. 1635-1640.
4. Bahadori, M. Y., Hegde, U., Zou, L., and Stocker, D. P., Paper 93-0710, Thirty-First Aerospace Sciences Meeting and Exhibit, Reno, Nevada, January 11-14, 1993.
5. Davis, R. W., Moore, E. F., Roquemore, W. M., Chen, L. D., Vilimpoc, V., and Goss, L. P., *Combust. Flame* 83:263-270 (1991).
6. Chen, L.-D., Roquemore, W. M., Goss, L. P., and Vilimpoc, V., *Combust. Sci. Technol.* 77:41 (1991).
7. Katta, V. R., Goss, L. P., and Roquemore, W. M., AIAA Paper 93-0454, Thirty-First Aerospace Sciences Meeting and Exhibit, Reno, Nevada, January 11-14, 1993.
8. Katta, V. R., Goss, L. P., and Roquemore, W. M., *Combust. Flame* 96:60-74 (1994).
9. Levy, Y., and Bulzan, D. L., *Proceedings of the Fifth International Conference on Liquid Atomization and Spray Systems, ILASS-91*, Gaithersburg, MD, 1991.
10. Li, S. C., Libby, P. A., and Williams, F. A., *Twenty-Fourth Symposium (International) on Combustion*, The Combustion Institute, Pittsburgh, 1992, pp. 1503-1512.
11. Lacas, F., Darabiha, P., Versaev, P., Rolon, J. C., and Candel, S., *Twenty-Fourth Symposium (International) on Combustion*, The Combustion Institute, Pittsburgh, 1992, pp. 1523-1529.
12. Chen, G., and Gomez, A., *Twenty-Fourth Symposium (International) on Combustion*, The Combustion Institute, Pittsburgh, 1993, pp. 1531-1539.
13. Abramzon, B., and Sirignano, W. A., *Int. J. Heat Mass Trans.*, 32:1605-1618 (1989).
14. Edwards, D. K., Denny, V. E. and Mills, A. F., *Transfer Processes: An Introduction to Diffusion, Convection and Radiation*, 2nd ed., McGraw-Hill, New York, 1979.
15. Aggarwal, S. K., Tong, A. Y., and Sirignano, W. A., *AIAA J.* 22:1448-1457 (1984).
16. Leonard, B. P., *Comput. Methods Appl. Mech. Eng.* 19:59 (1979).
17. Spalding, D. B., *Int. J. Num. Meth. Eng.* 4:551-559 (1972).
18. Park, T. W., Aggarwal, S. K., and Katta, V. R., AIAA Paper 94-0684, Thirty-Second Aerospace Sciences Meeting and Exhibit, Reno, 1994.
19. Katta, V. R., Goss, L. P., and Roquemore, W. M., *AIAA J.* 32:84-94 (1994).
20. Crowe, C. T., Chung, J. N., and Trout, T. R., *Prog. Ener. Combust. Sci.* 14:171-194 (1988).
21. Aggarwal, S. K., *AIAA J.* 32:1322-1325 (1994).

Received 1 December 1993; revised 19 April 1994

4.2 Thermally Stressed Jet-Fuel Studies

4.2.1 General Overview. The thermal stability of jet fuels has been studied for many years, and a considerable amount of data has been collected under various experimental conditions using different types of experimental arrangements. However, the overall complexity and a lack of fundamental understanding of the processes leading to fouling have hindered the development of a general theoretical framework which can be used to interpret or predict different types of experimental results. The primary goal of this portion of the program was to develop numerical models for the accurate prediction of fuel fouling in a variety of environments. The methods used to accomplish this difficult task are discussed below.

4.2.2 Numerical Simulations of Jet-Fuel Thermal Stability. High fuel and surface temperatures make the heated tubes susceptible to fouling because of decomposition of the fuel. As a deposit begins to grow on the tube wall, it offers resistance to the heat flow and blocks the fuel flow. A mathematical approach was developed to provide a direct coupling between the CFDC simulations of turbulent fuel flow and the variable boundary conditions that arise from the buildup of deposits on the walls of heated tubes. Details of the model are given in the paper entitled, "Numerical Method for Simulating Fluid-Dynamic and Heat-transfer Changes in Jet-Engine Injector Feed-Arm Due to Fouling" (pp. 808 - 817).

The nonuniform temperature distribution in thermal-stability rigs such as the Phoenix Rig triggers buoyancy-induced turbulence before the convective flow induces turbulence that may influence the relationship between deposit formation and wall temperature. A unique methodology was developed to investigate the effects of gravity on fuel flowing through small-bore heated tubes. The copper block that houses the fuel tube (or test section) is located on a swivel, and experiments are conducted for different tube orientations, namely, horizontal, vertical with flow from bottom to top, and vertical with flow from top to bottom. Calculations for each of these configurations were made using the "foul2d" time-dependent code and compared with the experimental data. Results obtained for different fuel-flow rates and block temperatures are discussed in a paper entitled, "Role of Buoyancy in Fuel-Thermal-Stability Studies" (pp. 818 - 827). Natural flow resulting from buoyancy was found to have a significant effect on heat transfer and oxygen consumption for fuel-flow rates up to 100 cc/min (Reynolds numbers up to 2300). Flow instabilities were observed when the fuel was flowing downward in a vertically mounted test section.

The "foul2d" code was extended to simulate deposition in the Air Force Phoenix Rig and Isothermal Rig for different fuels. The autoxidation process of a Jet-A fuel, designated POSF-2827, was remodeled, assuming a zeroth-order dependence with respect to the dissolved oxygen. It was found that the two-step global-chemistry model is not sufficient to describe the autoxidation and deposition processes simultaneously in certain fuels. A new global-chemistry model ["Development of a Global-Chemistry Model for Jet-Fuel Thermal Stability Based on Observations

from Static and Flowing Experiments" (pp. 828 - 838)] was developed for simulating the deposition process for a wide range of flow and thermal conditions. A second-generation "foul2d" code was developed for simulating multiple passages of fuel in an aircraft fuel nozzle ["Numerical Modeling of Deposition in Fuel-Injection Nozzles" (pp. 839 - 848)]. The new global-chemistry model was incorporated into this second-generation "foul2d" code, and its abilities in predicting flow patterns, heat-transfer distribution, and deposit formation were demonstrated by simulating a modified aircraft fuel nozzle; the results were reported in a paper entitled, "Numerical Modeling of Deposition in Fuel-Injection Nozzles" (pp. 849 - 855).

The autoxidation mechanism is strongly coupled with the formation of deposits in jet fuel. Since the chemical kinetics involved in the process are complex, the usual one-step global oxidation concept may not be applicable over a wide range of operating conditions. A new oxidation model proposed by Heneghan¹⁷ that treats the specific reaction rate for global oxidation as a function of the reaction progress variable was incorporated into the "foul2d" CFDC code; the feasibility of such oxidation models as they applying to flowing systems was investigated, and the results are presented in a paper entitled, "Numerical Modeling of Jet-Fuel Autoxidation in Flowing Systems" (pp. 856 - 862).

Numerical Method for Simulating Fluid-Dynamic and Heat-Transfer Changes in Jet-Engine Injector Feed-Arm Due to Fouling

V. R. Katta*

Systems Research Laboratories, Inc., Dayton, Ohio 45440
and

W. M. Roquemore†

Wright Laboratory, Wright-Patterson Air Force Base, Ohio 45433

A computational method for integrating fluid-dynamic simulations and heat-transfer calculations in different segments of solid boundaries has been developed to predict deposition inside tubes. The fuel thermal-degradation mechanism is treated mathematically using a four-step global-chemistry model. Deposits are allowed to grow on the wall surface, and the resulting fluid-dynamic and heat-transfer changes are implicitly computed using a time-dependent formulation. Turbulent-flow simulations for the fuel flow bounded by the fuel-deposit interface are made on a body-oriented coordinate system. The induction period, which is associated with the slower deposition during the initial hours of exposure, is modeled by introducing a wall-reaction-type mechanism for the surface sticking phenomenon. Calculations are made for full-scale and half-scale gas-turbine injector feed-arm rigs. The temperature at the deposit-tube interface is found to increase with deposition. Computed accumulated deposit weight and changes in the tube-inner-wall temperature with time are compared with the experimental data. The effects of fouling on heat transfer and blockage to the fuel flow are discussed.

Introduction

IN a gas-turbine engine, fuel is fed to the atomizers through the injector feed-arms. Attempts by designers to increase engine performance result in increasing compressor-exit and, thereby, feed-arm temperatures. Bulk-fuel temperatures are also expected to increase in high-performance aircraft due to the higher heat loads which the fuel will experience as it is used to cool the engine lube oil, avionics, environmental systems, and fuel controls.¹ The combination of high fuel-inlet and tube-wall surface temperatures makes the injector feed-arm very susceptible to fouling due to decomposition of the fuel. When fuel degrades and forms insoluble gums and hard carbonaceous deposits, the small apertures in the fuel nozzles and atomizers can become clogged, or fouled, leading to spray-pattern distortions, unscheduled overhauls, and, potentially, engine malfunction.² This will constitute a serious problem in future high-speed aircraft.

The thermal stability of jet fuels has been studied for many years, and a considerable quantity of data has been collected under various experimental conditions and for different types of experimental arrangements. However, the overall complexity and a lack of fundamental understanding of the processes leading to fouling have hindered the development of a general theoretical framework which can be used to interpret or predict different types of experimental results. Empirically based fouling models^{3,4} are potentially applicable to many engineering problems; however, they cannot be generally applied to different experimental configurations and they do not provide fundamental insight into the deposition processes.

Time-averaged computational-fluid-dynamic and chemistry (CFDC) models⁵ based on numerical solutions of conservation of mass, momentum, and energy are much more general than empirical models, and can be applied to different test-section geometries over a wide range of test conditions. Thus, the time-averaged CFDC models represent a significant advancement; however, they are most applicable to a thin deposition layer which does not appreciably affect the heat-transfer and fuel-flow characteristics—a limitation which results from these models providing the deposition rate rather than the actual time evolution of deposits in the system.

The real-time evolution of deposits is important in fuel-system components such as the nozzle feed-arm because it can be used to determine the change in performance of a fuel-system component as a function of time. As deposits begin to grow on the tube walls, they offer resistance to the heat flow and block the fuel flow.

A cross section of a typically fouled tube is depicted in Fig. 1. Usually, peak deposition occurs somewhere along the tube, depending on the thermo-fluid-dynamic stressing of the fuel. Wall deposition inside the tube alters the fluid dynamics and heat transfer which, in turn, modify the fuel degradation. The fluid-dynamic changes due to deposition are apparent; however, changes in heat transfer depend on the heating environment. In laboratory experiments which study fouling problems, tubes are often heated by passing electric current through the tube walls. In this case, because of the constant heat flux across the tube wall, the temperature at the outer wall increases with deposition, while that at the fuel-deposit interface (and, hence, that of the fuel) remains more or less undisturbed. Therefore, the chemical kinetics of fuel degradation may not be affected by the accumulation of deposits on the tube wall, which somewhat simplifies the problem. However, the higher temperatures within the deposits chemically alter their morphology, resulting in layers of deposits having different densities⁶ which is misrepresented as a change in the rate of deposition. Normally, heating in a fuel-nozzle feed-arm does not take place in this way. These tubes are usually heated with a constant-temperature heat source, and the temperature at the fuel-deposit interface decreases with deposi-

Presented as Paper 92-0768 at the AIAA 30th Aerospace Sciences Meeting and Exhibit, Reno, NV, Jan. 6-9, 1992; received Jan. 31, 1992; revision received Sept. 9, 1992; accepted for publication Sept. 9, 1992. This paper is declared a work of the U.S. Government and is not subject to copyright protection in the United States.

*Senior Engineer, Research Applications Division, Arvin/Calspan, 2800 Indian Ripple Road. Member AIAA.

†Senior Scientist, Fuels and Lubrication Division, Aero Propulsion and Power Directorate. Member AIAA.

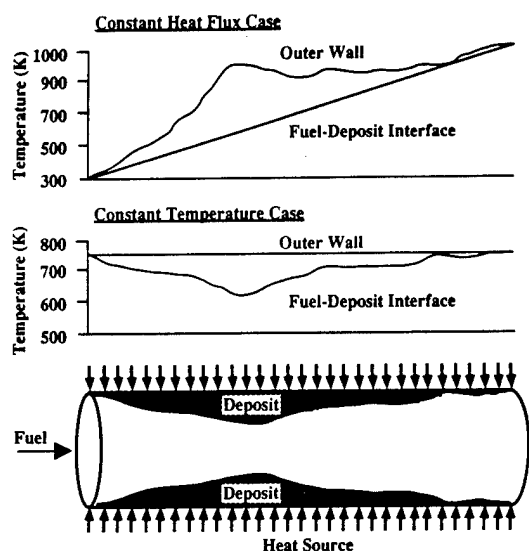


Fig. 1 Effect of deposition on heat transfer in tubes under different heating conditions.

tion. The lower fuel temperature alters the decomposition process inside the tube. A computational technique capable of simulating the time evolution of deposition would be useful in addressing this problem. A time-dependent model⁷ was recently developed in this laboratory to predict deposit formation in electrically heated tubes over long periods of time. By varying the deposit density as a function of exposure time, reasonable comparisons between predicted and measured values have been obtained. Since these experiments were conducted under fixed electrical power conditions, the temperature distribution of the fuel did not change with deposition (cf. Fig. 1), simplifying the boundary conditions.

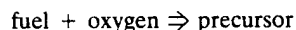
In the present study, a mathematical approach was developed to provide a direct coupling between the CFDC simulations of the turbulent fuel flow and the variable boundary conditions which arise from the buildup of deposits on the walls of fuel-injector feed-arms.

Formulation

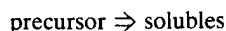
Fluid flow, heat transfer, and deposit formation are treated by means of an integrated approach to simulate the time evolution of deposition inside heated tubes.

Chemical Kinetics

A simple global-chemistry kinetics model has been used to describe fuel degradation. The deposit-forming precursors in the fuel were assumed to be a separate species, along with the dissolved oxygen in this model. The crucial autoxidation reaction is modeled using a single irreversible reaction⁴ as (reaction 1)

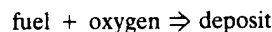


In order to limit the concentration of precursors at higher temperatures (>500 K), another global reaction⁵ (reaction 2)



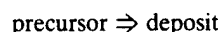
has been added.

The high viscosity of the fuel causes a sublayer of very slowly moving fluid to form adjacent to the walls. The longer residence time associated with this fluid and other factors cause the autoxidation reaction (reaction 1) to underpredict the chemical reaction rate within this laminar sublayer. Therefore, another autoxidation reaction is included in the model as a wall reaction (reaction 3)



The rates for reactions 1–3 are assumed to be governed by Arrhenius expressions.

The precursors formed within the fuel are transported to the wall surface as a result of convective fluid motion and molecular and turbulent diffusion processes. These precursors may stick to the wall surface and form deposits. Their sticking probability depends on several factors such as temperature, surface and precursor characteristics, and flow velocity. The lack of a fundamental understanding of the processes involved in sticking makes it difficult to obtain, from first principles, a functional form for the sticking phenomenon. Hence, in the present study, a simple model which considers only the homogeneity of the tube wall is proposed. This process is mathematically represented as a wall reaction (reaction 4)



The rate for this reaction is expressed as a function of deposit thickness as

$$\text{reaction rate} = A_4 \exp(-E_4/\Delta\text{Dep}) \quad (1)$$

where A_4 and E_4 are the pre-exponential and activation thickness, respectively. The deposit thickness ΔDep is the net result of deposition due to reactions 3 and 4.

Experiments conducted by Giovanetti⁴ and Marteney⁶ over long periods of time indicate that the deposition rate increases with exposure time. Since the clean fuel was driven throughout the testing period, these changes in deposition rate with exposure time may be attributed to changes in surface characteristics, deposit morphology, chemical reactions occurring near the wall, and the fluid dynamics within the test section (heat-transfer changes due to deposit buildup are negligible in this electrically resistance-heated experiment). Microscopic analysis revealed that the deposit surface is highly irregular and granular, and that the surface irregularity and structure of the cavities depend mainly on the fluid velocity and the deposit thickness. This rough surface, in turn, affects the deposit growth rate—less significantly by altering the surface sticking properties, but more significantly by trapping fuel and sucking it into the cavities. Since the fuel in the feed-arms flows at appreciable rates (velocities > 1 m/s), the deposits inside the tubes may be dense, as suggested by Marteney.⁶ Also, the exposure times considered in the present study are not sufficiently long to result in thick deposits; therefore, reactions 1–4 in this analysis are assumed to be independent of morphological history of the deposit.

Governing Equations

Fluid motion inside the tube is assumed to be axisymmetric and is bounded by the fuel-deposit interface. Time-dependent Navier-Stokes equations along with turbulent-energy, species-conservation, and enthalpy equations are written in the z - r cylindrical coordinate system as follows:

$$\frac{\partial \rho}{\partial t} + \frac{\partial \rho u}{\partial z} + \frac{\partial (\rho v)}{\partial r} + \frac{(\rho v)}{r} = 0 \quad (2)$$

$$\begin{aligned} \frac{\partial (\rho \Phi)}{\partial t} + \frac{\partial (\rho u \Phi)}{\partial z} + \frac{\partial \rho v \Phi}{\partial r} &= \frac{\partial}{\partial z} \left(\Gamma^* \frac{\partial \Phi}{\partial z} \right) \\ &+ \frac{\partial}{\partial r} \left(\Gamma^* \frac{\partial \Phi}{\partial r} \right) - \frac{\rho v \Phi}{r} + \frac{\Gamma^*}{r} \frac{\partial \Phi}{\partial r} + S^* \end{aligned} \quad (3)$$

Here ρ , u , and v are the density and the axial and radial velocity components, respectively. Equation (3) represents different conservation equations, depending on the variable assigned to Φ . The source terms S^* and the transport coefficients Γ^* associated with each of these equations are given in Table 1.

In the table, μ , κ , and c_p are the viscosity, thermal conductivity, and specific heat of the fuel, respectively, and μ_t is the turbulent viscosity incorporated through use of the k - ϵ turbulence model. The variables p , h , k , and ϵ are the pres-

Table 1 Source terms and transport coefficients appearing in governing equations

Φ	Γ^Φ	S^Φ
u	$\mu + \mu_t$	$-\frac{\partial p}{\partial z} + \frac{\partial}{\partial z} \left(\Gamma^u \frac{\partial u}{\partial z} \right) + \frac{\partial}{\partial r} \left(\Gamma^u \frac{\partial v}{\partial z} \right) + \frac{\Gamma^u}{r} \frac{\partial v}{\partial z}$
v	$\mu + \mu_t$	$-\frac{\partial p}{\partial r} + \frac{\partial}{\partial z} \left(\Gamma^v \frac{\partial u}{\partial r} \right) + \frac{\partial}{\partial r} \left(\Gamma^v \frac{\partial v}{\partial r} \right) + \frac{\Gamma^v}{r} \frac{\partial v}{\partial r} - 2\Gamma^v \frac{v}{r^2}$
k	$\mu + \frac{\mu_t}{\sigma_k}$	$G - \rho \epsilon$
ϵ	$\mu + \frac{\mu_t}{\sigma_\epsilon}$	$C_1 G \frac{\epsilon}{k} - C_2 \rho \frac{\epsilon^2}{k}$
h	$\frac{\kappa}{c_p} + \frac{\mu_t}{\sigma_h}$	0
Y_i	$\rho D_i + \frac{\mu_t}{\sigma_{Y_i}}$	$\dot{\omega}_i$

sure, enthalpy, and turbulence kinetic energy and its dissipation, respectively, and σ is the turbulent Prandtl number (or Schmidt number) associated with a specific transport equation. Y_i , $\dot{\omega}_i$, and D_i are the mass fraction, rate of production, and diffusion coefficient of the i th species, respectively. The other variables and constants appearing in the table are defined below:

$$G = \mu_t \left\{ 2 \left[\left(\frac{\partial u}{\partial z} \right)^2 + \left(\frac{\partial v}{\partial r} \right)^2 + \left(\frac{v}{r} \right)^2 \right] + \left(\frac{\partial v}{\partial z} + \frac{\partial u}{\partial r} \right)^2 \right\}$$

$$\mu_t = C_\mu \rho k^2 / \epsilon$$

$$C_1 = 1.47, \quad C_2 = 1.92, \quad \text{and} \quad C_\mu = 0.09$$

$$\sigma_k = 1.0, \quad \sigma_\epsilon = 1.3, \quad \sigma_h = 1.0, \quad \text{and} \quad \sigma_{Y_i} = 1.0$$

Since a wide range of temperatures exists within the test section, the transport properties of the fluid vary significantly. A "typical" Jet-A fuel is used as the fluid in the present calculations, and the transport properties along with the enthalpy and density at the given temperature are obtained from the curve fits developed for Jet-A fuel.

For an accurate treatment of the boundary conditions, a body-oriented curvilinear coordinate system (Fig. 2) was used. The contravariant velocities and the inverse of the Jacobian associated with this ξ - η coordinate system are related to those of the z - r orthogonal system as follows:

$$U = \xi_z u + \xi_r v \quad (4)$$

$$V = \eta_z u + \eta_r v \quad (5)$$

$$J^{-1} = (z_\xi r_\eta - z_\eta r_\xi) \quad (6)$$

and the governing equations [Eqs. (2) and (3)] are rewritten as

$$\frac{\partial \rho}{\partial t} + \frac{\partial (J^{-1} \rho U)}{\partial \xi} + \frac{\partial (J^{-1} \rho V)}{\partial \eta} + \frac{J^{-1}}{r} (\rho v) = 0 \quad (7)$$

$$\begin{aligned} \frac{\partial (J^{-1} \rho \Phi)}{\partial t} + \frac{\partial (J^{-1} \rho U \Phi)}{\partial \xi} + \frac{\partial (J^{-1} \rho V \Phi)}{\partial \eta} &= \frac{\partial}{\partial \xi} \left[J^{-1} (\xi_z^2 \right. \\ &+ \xi_r^2) \Gamma^\Phi \frac{\partial \Phi}{\partial \xi} \left. \right] + \frac{\partial}{\partial \eta} \left[J^{-1} (\eta_z^2 + \eta_r^2) \Gamma^\Phi \frac{\partial \Phi}{\partial \eta} \right] \\ &- J^{-1} \frac{\rho v \Phi}{r} + J^{-1} \frac{\Gamma^\Phi}{r} \left(\xi_r \frac{\partial \Phi}{\partial \xi} + \eta_r \frac{\partial \Phi}{\partial \eta} \right) + S^\Phi \end{aligned} \quad (8)$$

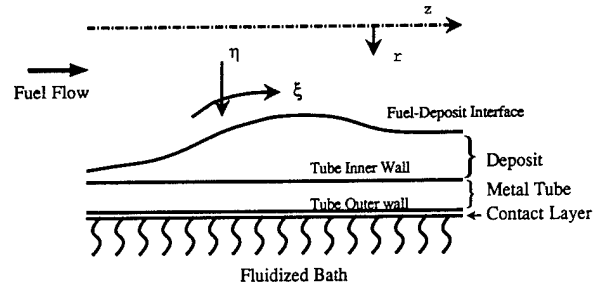


Fig. 2 Boundary segments and coordinate system used in calculations.

where

$$\begin{aligned} S^\Phi &= \frac{\partial}{\partial \xi} \left[J^{-1} (\xi_z \eta_z + \xi_r \eta_r) \Gamma^\Phi \frac{\partial \Phi}{\partial \eta} \right] \\ &+ \frac{\partial}{\partial \eta} \left[J^{-1} (\xi_z \eta_z + \xi_r \eta_r) \Gamma^\Phi \frac{\partial \Phi}{\partial \xi} \right] + S^\Phi \end{aligned}$$

Here the subscripts z and r indicate partial derivatives.

The governing equations [Eqs. (7) and (8)] are discretized utilizing a hybrid scheme⁸ which is a second-order central-differencing scheme everywhere, but changes to a first-order upwind scheme when the local Peclet number $[(J^{-1})^2 U \Delta \xi / \Gamma^\Phi]$ becomes greater than two. An implicit approach is employed to advance the calculations using a large time-step (enabling the computation of several hours of real time to be made in a few minutes of computational time). After rearrangement of the terms, the finite-difference form of Eq. (8) for the variable Φ at a grid point P can be written into an algebraic equation as follows:

$$\begin{aligned} A_P^\Phi \Phi_P^{n+1} + A_{\xi^+}^\Phi \Phi_{\xi^+}^{n+1} + A_{\xi^-}^\Phi \Phi_{\xi^-}^{n+1} + A_{\eta^+}^\Phi \Phi_{\eta^+}^{n+1} \\ + A_{\eta^-}^\Phi \Phi_{\eta^-}^{n+1} = \text{RHS} \end{aligned} \quad (9)$$

Here, the subscripts ξ^+ and ξ^- indicate the values at the grid points immediately adjacent to point P in the positive and negative ξ directions, respectively. The coefficients A and the terms on RHS (right-hand side) are calculated from the known flow variables at the n th time step. The u and v momentum, k and ϵ turbulence, enthalpy, and the three species equations represented by Eq. (9) are solved individually using the alternate direction implicit (ADI) method. Finally, the pressure field is obtained through the use of the SIMPLE technique.⁹

The present formulation allows the deposit to grow on the wall surface. In other words, after each time-step the geometry of the fuel-deposit interface is allowed to change as part of the solution procedure. If Ω is the deposition rate in micrograms per square centimeter per hour, ρ_D is the deposit density in kilograms per cubic meter, and Δt is the time-step in hours, then the new fuel-deposit interface shape (r_{int}) is calculated from

$$r_{\text{int}}^{\text{new}} = r_{\text{int}}^{\text{old}} \sqrt{1 - (2\Omega \Delta t / 10^3 \rho_D r_{\text{int}}^{\text{old}})} \quad (10)$$

The computational domain is bounded by the axis of symmetry and the fuel-deposit interface, and the grid system is reconstructed after each time step to take into account the changes in the boundary shape.

Boundary Conditions

The usual no-slip conditions are imposed at the fuel-deposit interface for the velocities. The normal derivative of a variable f at the boundary is written as

$$\frac{\partial f}{\partial n} = \frac{\xi_z \eta_z + \xi_r \eta_r}{\sqrt{\eta_z^2 + \eta_r^2}} f_\xi + \sqrt{\eta_z^2 + \eta_r^2} f_\eta \quad (11)$$

and is set equal to zero or a specified value, depending on the variable. With the use of central differencing in the ξ direction and first-order backward differencing in the η direction, Eq. (11) can be solved for the variable at the interface. The normal derivatives specified for different variables under laminar flow conditions are as follows:

Pressure

$$\frac{\partial p}{\partial n} = 0$$

Enthalpy

$$\frac{\partial h}{\partial n} = 0 \quad \text{for adiabatic wall}$$

$$= \left(\frac{c_p}{\kappa} \right) \dot{q}_{\text{int}} \quad \text{for constant heat flux}$$

$$T = T_{\text{int}} \quad \text{for constant wall temperature}$$

Species

$$\frac{\partial Y}{\partial n} = \left(\frac{1}{\rho D_{O_2}} \right) \dot{\omega}_{O_2}|_{\text{int}} \quad \text{for oxygen}$$

$$= \left(\frac{1}{\rho D_P} \right) \dot{\omega}_P|_{\text{int}} \quad \text{for precursor}$$

Here, the subscript int represents the values at the fuel-deposit interface. The species production rates $\dot{\omega}_{O_2}$ and $\dot{\omega}_P$ are calculated from the wall reactions 3 and 4, respectively, and the heat flux \dot{q}_{int} must be obtained by solving the heat-transfer equations for the deposit and the tube wall.

For the turbulent-flow conditions, wall functions¹⁰ have been used to determine the variations of the flow variables near the fuel-deposit interface. Usually, wall functions relate the normal stresses (or the derivatives of the flow variables) in the Cartesian coordinate system at the wall to the k, ϵ values at a grid point inside the flowfield. Therefore, for the body-oriented curvilinear coordinate system, the wall functions proposed in Ref. 9 can be appropriately modified using Eq. (11).

Heat Transfer

The direct impact of deposits on heat exchangers is evident in the deteriorating heat-transfer characteristics. As deposits form on the wall surface, they offer resistance to the heat flow from the fuel in the tubes to the wall surface or vice versa. Therefore, complete definition of the problem necessitates solving for the heat distribution in the deposits and tube walls simultaneously with that of the flowing fuel. An analysis in the z - r coordinate system is presented for simplicity, although a similar approach in the ξ - η system was used in the actual calculations.

Since the deposit and tube-wall thicknesses are very small compared to the tube length, the heat equation for the heat flux can be written, after neglecting the heat conduction in the axial direction, as

$$\frac{\partial \dot{q}}{\partial r} + \frac{\dot{q}}{r} = 0 \quad (12)$$

The following analytical expressions for the heat-flux distributions in the deposit and the tube walls can be obtained by integration of the above equation:

$$\dot{q} = \dot{q}_o \frac{r_o}{r} = \dot{q}_{\text{wall}} \frac{r_{\text{wall}}}{r} = \dot{q}_{\text{int}} \frac{r_{\text{int}}}{r} \quad (13)$$

Here, the subscripts o and wall represent the outer and inner tube walls, respectively. If the thermal conductivities of the deposit and tube metal are denoted by κ_d and κ_r , respectively, their corresponding temperature distributions can be obtained by integrating

$$\dot{q} = \kappa \frac{dT}{dr} \quad (14)$$

as

$$T = T_{\text{int}} + \int_{r_{\text{int}}}^r \left(\frac{\dot{q}_{\text{int}} r_{\text{int}}}{\kappa_d} \right) \frac{1}{r} dr \quad (15)$$

$$T = T_{\text{wall}} + \int_{r_{\text{wall}}}^r \left(\frac{\dot{q}_{\text{wall}} r_{\text{wall}}}{\kappa_r} \right) \frac{1}{r} dr \quad (16)$$

If κ_r is independent of temperature, and the tube wall is assumed to have homogeneous properties, then an expression for the tube-outer-wall temperature can be obtained by solving Eq. (16) as

$$T_o = T_{\text{wall}} + \frac{\dot{q}_{\text{wall}} r_{\text{wall}}}{\kappa_r} \ln \left(\frac{r_o}{r_{\text{wall}}} \right) \quad (17)$$

For the constant heat-flux boundary condition (i.e., for the given \dot{q}_o), at each time step, first Eq. (13) is solved for the value of \dot{q}_{int} , and then the fuel-flow calculations are performed using this value in the boundary condition described by Eq. (11). The given constant outer-wall-temperature condition can be implemented using the iterative procedure given below:

1) At a given axial location and time $t + \Delta t$, assume that the temperature at the fuel-deposit interface is equal to that at time t and calculate the heat flux \dot{q}_{int} from the turbulent fuel-flow solution.

2) Obtain \dot{q}_{wall} by solving Eq. (13).

3) Determine the tube-outer-wall temperature T_o from Eq. (17); T_o will be greater than the actual wall temperature because of the additional amount of deposition during Δt .

4) Now, relax the assumption made in step 1 to obtain a better value for the interface temperature and repeat steps 2 and 3; the entire procedure must be repeated until the calculated outer-wall temperature matches the specified value.

Results and Discussion

Evaluation of the Model

The mathematical model described above involves global-chemistry parameters which must be obtained, or calibrated, from well-controlled experiments for a given fuel. The global-reaction scheme (reactions 1–3) has been calibrated by Krazinski et al.⁵ for a CFDC steady-state computational code using data from an electrically heated tube.¹¹ The pre-exponentials and the activation energies corresponding to each of these reactions are given in Table 2 under model A. The assumption of Krazinski et al.⁵—that the precursors transported near the wall stick to the wall instantaneously—may be treated in this model using a large value for the pre-exponential and zero for the activation thickness of the deposit-formation reaction (reaction 4).

For validation of the present code, which was developed based on the unsteady formulation, a short-duration experiment conducted by Marteney¹¹ was numerically simulated. Marteney¹¹ obtained deposition rates for a JP-5 fuel flowing through an electrically heated 2.25-mm-i.d. steel tube after a test time of <6 h. A fuel velocity of 2.12 m/s at the tube entrance triggered flow turbulence inside the tube. Calculations for this situation have been made using the reaction kinetics given by model A in Table 2. Perhaps the most sensitive parameter in deposit formation in the heated-tube ex-

Table 2 Rate constants and units used in global chemistry model

	Reaction 1		Reaction 2		Reaction 3		Reaction 4	
	$\frac{\text{m}^3}{\text{mole s}}$	$\frac{\text{cal}}{\text{mole K}}$	$\frac{1}{\text{s}}$	$\frac{\text{cal}}{\text{mole K}}$	$\frac{\text{m}^4}{\text{mole s}}$	$\frac{\text{cal}}{\text{mole K}}$	$\frac{\text{m}}{\text{s}}$	mm
Model A	1.0E + 08	30,000	3.0E + 15	35,000	6.34E - 08	8,000	1.0E + 20	0
Model B	3.0E + 08	27,000	1.0E + 18	40,000	6.34E - 08	8,000	1.0E + 20	0.1

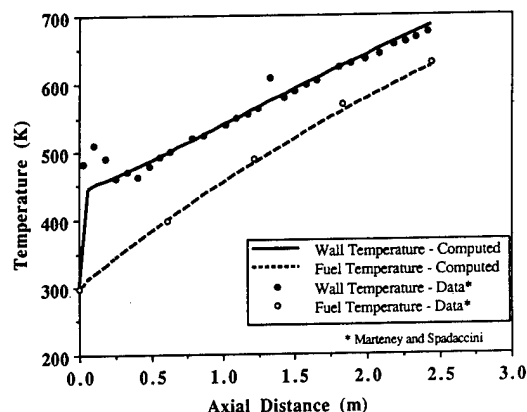


Fig. 3 Comparison of calculated and measured temperatures for constant heat-flux case.

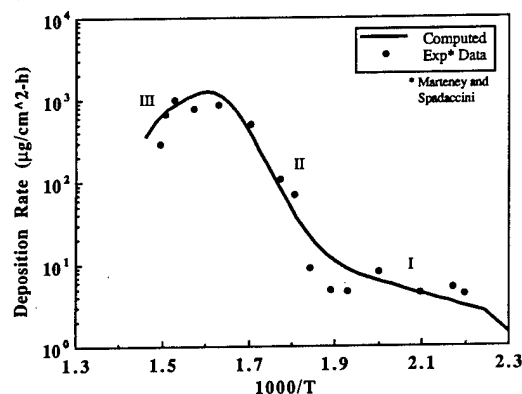


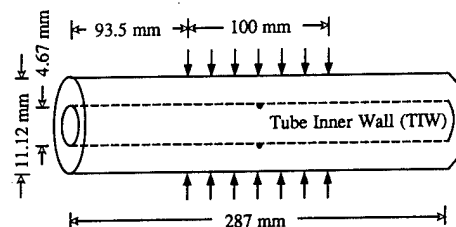
Fig. 4 Deposition rate computed with three-step global-chemistry reaction model.

periments is the wall temperature. Therefore, the numerical model to be used for thermal-degradation investigations should be first validated for its ability to predict wall temperature.

The wall and bulk-fuel temperatures along the tube length are shown in Fig. 3. The turbulence model and the wall functions used in the code accurately predicted these temperatures. The overshoot in the wall temperature near the tube entrance observed in the experimental data is due to the transition from laminar to turbulent flow. Since the code has no submodel for predicting the flow transition, calculations were made assuming a fully developed turbulent flow inside the tube. The deposition rate obtained by the code is plotted as a function of the inverse of temperature in Fig. 4 along with the experimental data. The global-chemistry model was partially calibrated⁵ for this experiment. The computed deposition-rate curve closely follows the experimental data. The portion of the curve in the lower temperature range marked "I" in Fig. 4 is caused by the wall autoxidation reaction 3. In the moderate temperature regime (segment II), the bulk-fuel autoxidation reaction 1 is dominant. The impact of the precursor-controlling reaction 2 can be seen in Fig. 4 along the descending portion (segment III) of the deposition-rate curve.

Simulations for the Injector Feed-Arm

The next goal of the present study was to determine how well the numerical model described above would predict

Fig. 5 Schematic diagram of model feed-arm used by Kendall et al.¹²

deposition in a more practical system. Kendall et al.¹² studied experimentally the fouling characteristics of a model gas-turbine injector feed-arm. Recently, Clark and Stevenson¹³ conducted experiments on a half-scale model of the feed-arm under very similar thermal-stressing conditions in order to understand the effects of scaling on fouling. Both studies indicate three distinct phases of the deposition process. Insignificant deposition occurs during the initial "induction period," followed by a near-constant rate of deposition over a long period; in some cases, a decrease in deposition rate was observed near the end of the test. The initial low deposition rate during the induction period is generally thought to be a result of the initial clean tube surface. The activation thickness [Eq. (1)] in the present model may be related to the experimentally observed induction period. It should be noted that the fuels used by Kendall et al.¹² and Clark and Stevenson¹³ are not the same fuels used in the experiments of Marteny,¹¹ for which the global-chemistry model was calibrated. Thus, it might be expected that the difference in fuels would make some changes in the pre-exponential and activation energies in the global-chemistry model.

Full-Scale Tests

The feed-arms were designed¹² to simulate the burner tubes leading to the nozzles of a large gas turbine. These are straight, thick-walled tubes (Fig. 5) of 4.76-mm bore. The central 100-mm section of the feed-arm was immersed in a fluidized bath. The aviation fuel (Jet A), preheated to a bulk temperature of 438 K, was pumped through the feed-arm at flow rates of 72 and 36 kg/h. The temperature of the fluidized bath was 813 K which resulted in a temperature of 573 K at the inner wall of the tube (TIW). Tests were conducted for time periods of up to 80 h, and changes in the tube inner-wall temperature (Δ TIW) were monitored as a function of time.

Numerical simulations were first made for the higher-flow-rate case (identified as case 1), i.e., 72 kg/h, which corresponds to a 1.5-m/s flat velocity ($Re = 25,034$) at the tube entrance. The fluidized-bath temperature was set at 813 K to match the temperature used in the experiments. Since the fluidized bath around the tube does not make perfect contact with the tube outer wall, a temperature drop occurs across a thin layer between the fluidized bath and the tube. This is treated as a contact layer (cf. Fig. 2) in the simulations. Turbulent-flow and heat-transfer calculations were carried out initially without activating the chemical reactions within the bulk fuel or on the wall surface. The resistance of the contact layer was adjusted in such a way that the temperature at TIW (Fig. 5) would be 438 K. Once the initial fuel flow was established, the unsteady calculations were performed using the reaction-rate constants of model A (see Table 2) which was calibrated for a constant-heat-flux experiment. After each 1-min time step, the amount of deposit on the tube wall was

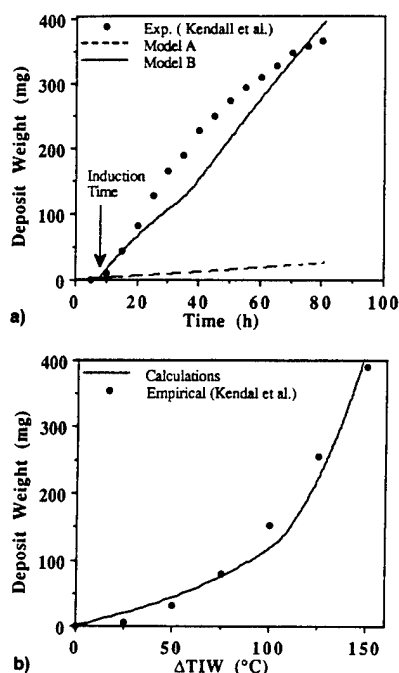


Fig. 6 Results for case 1: a) calculated and measured deposition at different times during 80-h test (used for calibration), and b) relationship between amount of deposition on tube walls and associated rise in Δ TIW.

calculated by integrating the deposition over the entire tube length. A deposit density of 1 gm/cm^3 was used. This value was determined experimentally by Marteney⁶ under similar velocity conditions. The value of $0.1 \text{ W/m}^2\text{C}$ used for the thermal conductivity of the deposit is close to that of $\sim 0.16 \text{ W/m}^2\text{C}$ found by Goodman and Bradley.¹⁴

The total weight of the deposit collected on the tube inner wall at different exposure or run times up to 80 h is plotted in Fig. 6a (broken line); measured values obtained by Kendall¹² are also plotted in this figure (solid circles). The very small amount of deposition predicted by the model indicates that the global-reaction scheme calibrated for the JP-5 fuel used by Marteney¹¹ was not applicable for the present feed-arm experiment. Therefore, the global-chemistry model was recalibrated for the Jet-A fuel by repeating the calculations, choosing different values for the pre-exponentials and activation energies for reactions 1–4. The calculated deposition weights which best fit the experimental data are shown in Fig. 6a, and the constants associated with reactions 1–4 are given in Table 2 under model B. The value of 0.1 mm used for the activation thickness appears to be sufficient for reproducing the observed induction period. The differences in the shapes of the measured and calculated deposition curves indicate the limitations of the global-chemistry model.

Kendall et al.¹² obtained the weight of the deposit by an indirect method. For each flow condition, a few specific experiments were conducted using different run times. The information on the change in the Δ TIW and the weight of the deposit measured at the end of each run was recorded and later used to obtain an empirical relation between the deposit weight and Δ TIW. In the actual deposition experiments, only Δ TIW was measured and the deposit weight was obtained using the predetermined empirical relation. Figure 6b shows the computed Δ TIW due to deposition for case 1. The empirical relation for this flow rate determined by Kendall et al.¹² is $W_D = 0.00367(\Delta\text{TIW})^{2.31}$, and the data obtained from this relation are plotted in Fig. 6b (solid circles). After 80 h of exposure, the tubes accumulated $\sim 400 \text{ mg}$ of deposit; as a result, the inner-wall temperature at the center of the tube changed by $\sim 150^\circ\text{C}$. This clearly indicates the severe effect of fouling on heat transfer in a tube surrounded by a fluidized

bath. The good agreement between calculated and experimental results demonstrates the ability of the present model to predict the changes in heat transfer due to deposition.

Effect of Velocity

The deposit weight as a function of time measured by Kendall et al.¹² at a fuel flow rate of 36 kg/h and a fuel velocity of 0.75 m/s (identified as case 2) is plotted in Fig. 7a (solid circles). One might expect that because the fuel velocity in case 2 is lower than that in case 1, the deposition rate would be higher for case 2 since the fuel residence time in the tube is longer. Direct comparison of the experimental data in Figs. 6a and 7a indicates that this is not the case. The measured deposition rate actually decreased with fuel velocity.

The calibrated model was used to predict deposit weight as a function of test time under case 2 conditions. The calculated results are plotted in Fig. 7a. The induction time did not change appreciably with velocity, and good agreement is observed between predicted and measured values. In fact, the calculations also show a reduction in deposition rate compared to that of the higher velocity case. The value of a CFDC-based model is that it can be used to examine why the deposition rate decreases with fuel velocity. For both flow rate cases, the inlet-fuel temperature and the initial TIW were maintained identical. An examination of the model data showed that the bulk-fuel temperatures were higher under case 2 than under case 1 conditions. This is true, because at lower velocity the fuel in case 2 spends more time in the tube and thereby receives more heat from the wall surface which was maintained at a temperature of 573 K in both cases. The higher fuel temperatures in case 2 decreased the precursor concentration due to reaction 2, which converts precursors to soluble products. This results in a lower deposition rate, as compared to that in case 1. This simple explanation is only as good as the global-chemistry model used in the CFDC calculations. However, it illustrates the potential of the model for exploring the physical and chemical processes which might explain otherwise confusing results.

The model has provided an explanation that can be examined directly in future experiments. Reaction 2 was introduced into the global-chemistry model for deposition⁵ to take into account two experimental observations:¹¹ 1) the deposition rate decreases at higher temperatures, and 2) an appreciable amount of oxygen is still present at those temperatures. These observations were made on a particular JP-5 fuel. How-

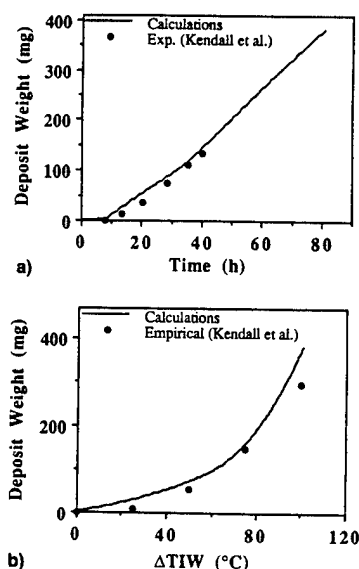


Fig. 7 Results for case 2: a) comparison of predicted and measured relationships, and b) comparison of calculated and experimental relationships between amount of deposition on tube walls and associated rise in tube-inner-wall temperature.

ever, recent experiments on heated tubes by Heneghan¹⁵ and Jones¹⁶ with different fuels indicate that the oxygen inside the tubes has been consumed by the time the fuel has attained a temperature of 460 K; they attribute the decrease in deposition at higher temperature to the depletion of oxygen in the fuel. In such fuels, reaction 2 may be overwhelmed by reaction 1, and the present model cannot predict higher deposition rates with an increase in fuel velocity. The calibrated global-chemistry model for Jet-A fuel used in the feed-arm experiment predicts that the dissolved oxygen will not be totally consumed and that a considerable amount of oxygen will remain in the outgoing fuel. In order to validate the model, additional measurements for species such as dissolved oxygen should be made in future experiments. Despite the outcome of such an examination, the model predictions clearly indicate that the heat-transfer effects overcome the chemical effects expected from a longer residence time and, in turn, cause a decrease in the deposition rate.

For the lower flow rate (case 2), the deposit weight and ΔTIW were found¹² to be related by the empirically derived expression $W_D = 0.00407(\Delta TIW)^{2.43}$. Values obtained from this relation are shown in Fig. 7b along with those predicted by the model. A comparison with the results in Fig. 6b show that for the same deposit weight (or deposit thickness), the temperature change at the inner wall (ΔTIW) is larger for the higher flow rate case, which means that the effects of deposition on heat-transfer characteristics will increase with increasing fuel flow rate or, conversely, decrease with decreasing fuel flow rate.

Half-Scale Tests

A half-scale apparatus having a feed-arm tube similar in length to the full-scale tube sketched in Fig. 5 and operating at identical temperatures was designed by Clark and Stevenson¹³ to reduce the amount of fuel required for their experiment. The wall thickness of the half-scale tube is 2.032 mm, and the bore is 2.286 mm. Jet-A aviation fuel, preheated to 438 K, passed through the tube at a rate of 300 ml/min, which corresponds to a mass-averaged velocity of 1.218 m/s ($Re = 9950$). The fluidized-bath temperature in the calculations (identified as case 3) was set equal to 700 K, a value chosen in the range 683–723 K used in the experiments. The contact resistance was then adjusted to obtain the specified clean-tube inner-wall temperature (TIW) of 573 K at the midsection.

The computed and measured deposit weights at different exposure times are plotted in Fig. 8a. The deposit weight

increased very slowly (0.0132 mg/cm²/h) up to 6–7 h and, thereafter, rapidly at a rate of 0.275 mg/cm²/h. Induction time in the calculations was modeled using an activation thickness of 0.1 mm in Eq. (1). When the tube is clean, deposition on the wall surface occurs as a result of the wall reaction only. On the fouled surface, the deposition rate approaches that given by the bulk reactions in an exponential manner. This is analogous to the argument¹³ that the reciprocal induction period is a measure of fuel-deposition rate on a clean metal surface, whereas the postinduction rate is a measure of the deposition rate on a fouled surface. The good agreement obtained for the calculated and measured induction times (Fig. 8a) supports this idea.

Changes in the TIW with deposition weight are plotted in Fig. 8b. The computations show a nonlinear relationship between ΔTIW and the amount of deposit. Clark and Stevenson¹³ observed that a linear relationship fit the data (not shown in their paper), and speculated that the difference in the fluidized-bath temperatures for the full-scale and half-scale rigs could result in changes in heat-transfer characteristics between the fluidized bath and the feed-arm and, hence, in relationships between ΔTIW and deposit weight. This is not the case, because the temperature drop across the solid deposit is always a logarithmic function of deposit thickness. However, in case 3, the temperature drop per unit thickness of deposit could be sufficiently small that a linear approximation of the logarithmic behavior might be reasonable. This idea is supported by the following two observations:

- 1) The temperature drop across the deposit in case 3 is only 47.5°C as compared to those of 124 and 82°C for cases 2 and 3, respectively.
- 2) Although the rate of deposition is low in case 3 as compared to that observed in either case 1 or case 2, the deposit thickness at 50 h of test time is approximately the same for all three cases because of the difference in innertube radii. This implies that the relatively slow temperature drop with deposition in case 3 results in a linearizing effect on the empirical curve fits.

Details Along the Tube Length

In the previous sections, computed results were presented in the form of total deposits accumulated inside the tube and the temperature changes at the inner wall of the midsection; these results compared favorably with the experimental data. In this section details along the tube length are discussed.

Since the temperature inside the tube is not uniform, the growth of deposits on the tube wall surface will be uneven. The location of the fuel-deposit interface along the length of the tube is shown in Fig. 9a. At time $t = 0$ this interface coincides with the tube-inner-wall surface. Although only the 0.1-m central section was heated by the fluidized bath, the flow of hot fuel before and after the heated section caused fouling on these sections as well. Deposit growth at the center of the tube ($z = 0.1435$ m) is less during the 40–80 h period than during the 0–40 h period. This reduction in deposition for longer times was also observed by Clark and Stevenson¹³ and is due to the insulating effect of the cumulative deposit, as can be seen in Fig. 9b where the instantaneous deposition rates at three different times are plotted. The rate of deposition at the center at 80 h is lower than that at 40 h. At time $t = 0$, the deposition rate is very low along the entire length of the tube, corresponding to the wall autooxidation reaction 3 only. The induction submodel in the present study prevents precursors formed within the bulk fuel from sticking on the wall surface at this time. The lower wall temperature of the preheater section (438 K) yields a clean-tube deposition rate which is lower than that at the midsection. As a result, the induction period in this section extends beyond 40 h. This effect of temperature on induction period may be viewed as the tendency of fuels having lower thermal stability to exhibit shorter induction periods.

Heat and fuel flow are visualized in Fig. 10 in the form of isotherm and isoturbulent energy contours beyond 80

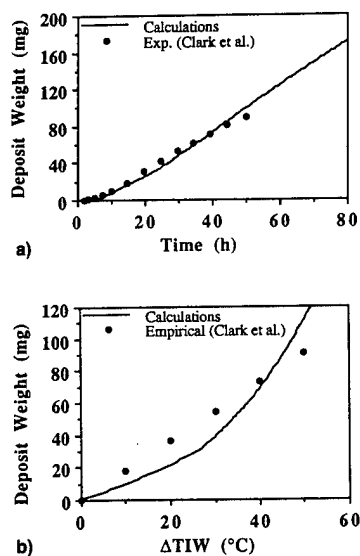


Fig. 8 Results for half-scale feed-arm rig (case 3): a) calculated and measured deposits, and b) calculated and experimentally observed relationships between amount of deposit and associated ΔTIW .

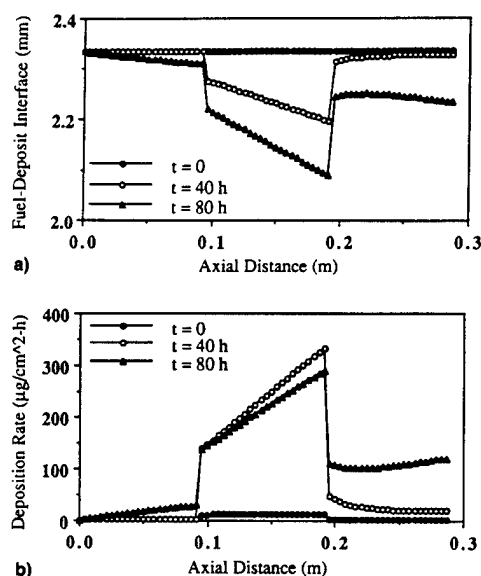


Fig. 9 Changes in a) deposit-fuel interface geometry and b) deposition rate at different axial locations after 40 and 80 h.

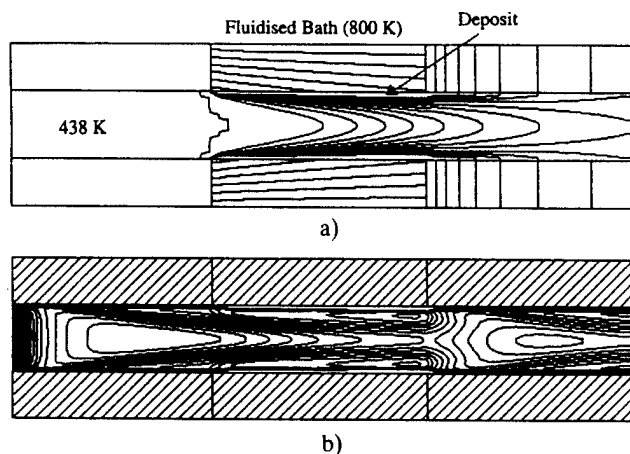


Fig. 10 Flow and heat distributions at the end of 80-h test on full-scale rig: a) temperature within tube wall and fuel and b) turbulent kinetic energy.

h. Deposits on the tube wall are also shown in these figures between the inner-wall surface and the contour lines in the fuel. Because of the adiabatic wall conditions imposed on the preheater section, both the fuel and tube wall are at the same temperature which, in this case, is identical to that of the inlet fuel (438 K). As fuel passes through the heater section, its temperature increases, as evidenced by the parabolic contours in the temperature field. The temperature distribution within the tube wall is dependent on the heat flux entering into the fuel at any cross section. The heat flux will be at a maximum at the entrance section of the heated zone and at a minimum at the exit section. In the postheater portion of the tube, equilibration of the fuel temperature results in a decrease in temperature at the tube-inner-wall surface. Again, because of the adiabatic wall conditions used in this section, a uniform temperature is obtained within the wall at an axial location.

Deposit growth not only affects the heat transfer, but also blocks the fuel flow. Uneven deposition along the tube wall is evident in Fig. 9a. The blockage (percentage ratio of blocked to clean-tube area) gradually increases in the heater section, reaching a maximum of $\sim 20\%$ near the tube end. This contraction causes fuel inside the tube to accelerate, resulting in a higher turbulent energy, as indicated by the closed isoenergy contours (Fig. 10b) near the deposition. The sudden expansion resulting from a decrease in blockage from 20 to 7.7%

immediately after the heater section relaxes the turbulent energy, as shown by the diverging contours. The actual velocity distribution along the centerline is plotted in Fig. 11a. Calculations were initiated with a flat velocity profile at the entrance of the tube. As the fuel flows through the preheater section, a fully developed turbulent velocity profile is established, and the centerline velocity levels off at a value of 1.94 m/s just before the heater section. Within the heater section, wall heating causes the fuel nearer the wall to become hotter than that at the center. The lower density and viscosity of the higher temperature fuel accelerates the flow near the wall which, in turn, reduces the fuel velocity at the center (seen as a valley in the velocity distribution) (Fig. 11a) at $t = 0$. At all other times $t > 0$, the centerline velocity increases with the blockage. Interestingly, just after the heater section, the velocity of the fuel at the centerline actually decreases. Expansion around the backward-facing step-type deposit geometry creates vorticity in that region.

The temperature distribution at different boundaries along the tube length is shown in Fig. 11b for three instants of time. When the tube is clean (i.e., at $t = 0$), the fuel-deposit interface becomes the fuel-inner wall interface. As the exposure time increases, the deposits accumulate on the inner wall, and a temperature drop develops across the deposit; this drop is actually shared by the fuel and the tube wall. The temperature at the inner wall increases, approaching the fluidized bath temperature; at the fuel-deposit interface, it decreases, approaching the inlet-fuel temperature. After 80 h the temperature of the inner wall at the midsection ($z = 0.1435$ m) is 722 K—a rise of 149°C from the initial temperature. This compares favorably with the measured ΔTIW of 150°C . On the other hand, the temperature at the fuel-deposit interface has decreased by 84°C . The insulation effect of the deposit is evident in the bulk-fuel temperature plot (Fig. 11c). Because of the high flow rate (72 kg/h) and short heater section, the fuel temperature increased by only 11°C when the tube was clean and by only 4°C near the end of the experiment.

Deposition occurs in heated tubes primarily as a result of temperature. The presence of deposits changes the heat-transfer characteristics and blocks the tube. Heat usually comes into the fuel from the outside environment after passing through several layers of resisting materials. Any computational method designed to predict deposition should be accurate in treating this complex transfer of heat. The present formulation with a body-oriented coordinate system and an iterative method used to link the fluid flow and boundary calculations is very effective in solving this problem. The accuracy of the calculations may be validated by comparing the amount of heat energy supplied to the system with that actually present in the fuel.

The heat energy available in the fuel in a given cross section ($z = L$) may be obtained by mass averaging the local enthalpy as

$$h_{\text{fuel}} = h_{\text{in}} + \frac{1}{\dot{m}} \int_0^{r_{\text{int}}} (2\pi r) \rho u h \, dr \quad (18)$$

Similarly, the heat energy supplied to the section at $z = L$ is calculated by integrating the heat flux at the outer wall and is given by

$$h_{\text{supplied}} = h_{\text{in}} + \frac{(2\pi r_o)}{\dot{m}} \int_0^L (\dot{q}_o) \, dz \quad (19)$$

The supplied and available energy distributions along the axial distance are compared in Fig. 11d at time $t = 0$ and at the conclusion of the test. The heat energy increased linearly in the clean heater section; since no losses are incorporated into the model, this energy remained constant in the other sections. The small discrepancy between the supplied and available energy is mainly due to the error involved in the numerical integration of Eq. (18). The heating efficiency (per-

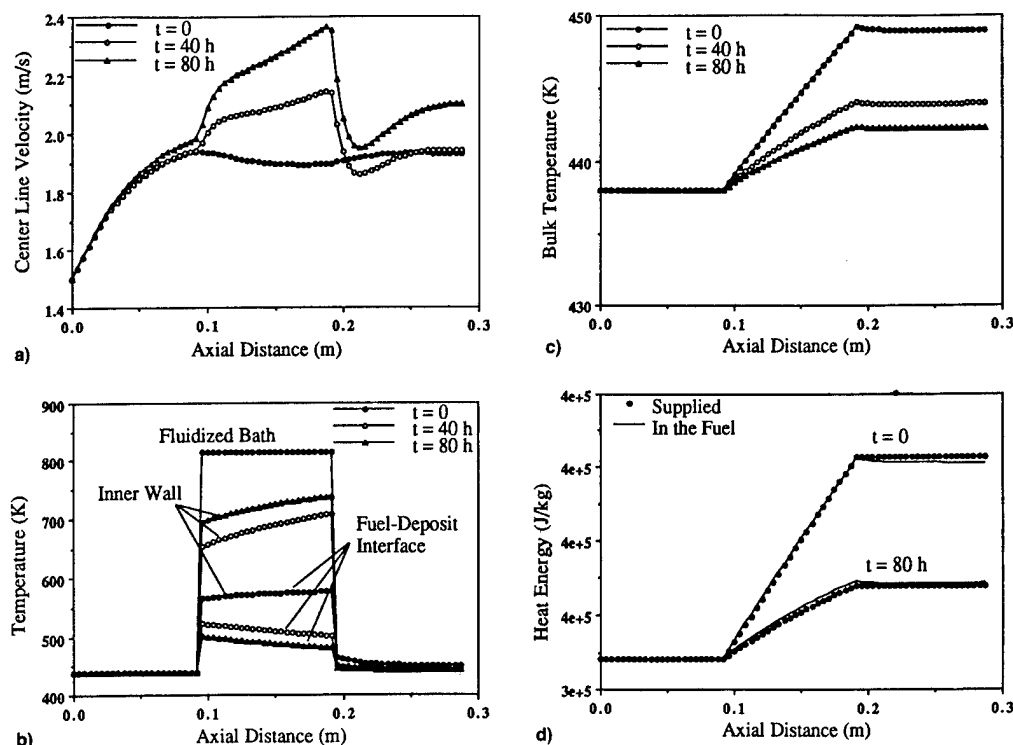


Fig. 11 Effect of deposition on a) fuel velocity, b) temperature at different interfaces, c) bulk-fuel temperature, and d) added and available heat energies.

centage ratio of heat energy received at a particular time to that received when the tube was clean) of the rig has been reduced to 36.6% by the end of the 80th hour. As mentioned earlier, the blockage to the fuel flow at this instant was 20%. On the other hand, in the half-scale rig (case 3) the blockage was 30%, but the heating efficiency remained at 46.6%.

Conclusions

A numerical method for simulating deposit growth inside a fuel-injector feed-arm has been presented. The global-chemistry model calibrated for a series of electrically resistance-heated tubes failed to generate deposits in the feed-arms. This is thought to be due to the difference in the fuel used in the electrically heated tube and that used in the feed-arm experiments. Bulk reaction rates were recalibrated to correlate the predicted deposition with the measured data for an experiment conducted on the full-scale feed-arm rig. The induction period observed in the deposition growth was mathematically treated by introducing a wall-reaction-type mechanism for sticking. An activation thickness of 0.1 mm was sufficient to reproduce the measured induction time. Through use of the same chemistry, simulations were made for a half flow rate case on a full-scale rig and a quarter flow rate case on a half-scale rig. Good agreement was obtained for both deposit growth and temperature changes. The flow rate appeared to have no direct effect on deposition; however, the heat-transfer changes resulting from the flow rate perturb deposit growth. It was observed in the present study that in identical thermal environments 1) the impact of fouling on heat-transfer is less at lower fuel flow rates, and 2) blockage to the fuel flow is less for larger tube bores. Present calculations in fairly uniform temperature environments and earlier calculations in a tube where the temperature was rapidly increasing, suggest that deposition depends strongly on wall temperature and weakly on bulk-fuel temperature. Recent experimental studies on the "Phoenix Rig"¹⁵ lend support to this concept. The four-step global-reaction model used in the current study lacks this important element. Development efforts on the next-generation global-reaction model for deposition will be based on the vast amount of data being gathered from the Phoenix Rig.

Thermal decomposition of fuel is the result of highly complex chemical kinetics which depend not only on the type of fuel, but also on the batch. Development of a mathematical model for predicting the deposition process inside heated tubes based on elementary reactions is, therefore, not feasible in the near term. The fouling problem is further complicated by the lack of fundamental understanding of the surface sticking phenomenon. The global-chemistry models proposed in Ref. 5 and in this article seem promising for predicting performance deterioration due to fouling; however, such models must be calibrated a priori for the given fuel. Until recently, such calibration was made using the data obtained in flowing experiments. A more scientific approach to the problem would be to calibrate the global-chemistry model using data collected from quick static experiments. Future work should be focused on designing simple experiments which can be utilized to improve the chemistry and sticking models.

Acknowledgments

This work was supported, in part, by U.S. Air Force Contract F33615-90-C-2033. V. R. Katta acknowledges NRC and AFSC for sponsoring him under the Postdoctoral Fellowship Program during 1989-91. The authors would like to thank Marian Whitaker, Royce Bradley, Donn Storch, and Tim Edwards for their helpful comments.

References

- Koff, B. L., "The Next 50 Years of Jet Propulsion, the Global Anniversary of Jet Powered Flight: 1939-1989," Dayton and Cincinnati AIAA Meeting, Dayton, OH, Aug. 1989.
- "CRC Literature Survey on the Thermal Oxidation Stability of Jet Fuel," Coordinating Research Council Rept. 509, Atlanta, GA, April 1979.
- Deshpande, G. V., Serio, M. A., Solomon, P. R., and Molhotra, R., "Modeling of the Thermal Stability of Aviation Fuels," *Preprints from the Symposium on the Chemical Aspects of Hypersonic Propulsion*, American Chemical Society, Div. of Petroleum Chemistry, Miami, FL, Vol. 34, No. 3, 1989, p. 955.
- Giovanetti, A. J., and Szetela, E. J., "Long Term Deposit Formation in Aviation Turbine Fuel at Elevated Temperature," AIAA 24th Aerospace Sciences Meeting, AIAA Paper 86-0525, Reno, NV, Jan. 6-9, 1986.

- ⁵Krazinski, J. L., Vanka, S. P., Pearce, J. A., and Roquemore, W. M., "A Computational Fluid Dynamics and Chemistry Model for Jet Fuel Thermal Stability," *Journal of Engineering for Gas Turbines and Power*, Vol. 114, Jan. 1992, pp. 104-110.
- ⁶Marteney, P. J., "Thermal Decomposition of JP-5 in Long Duration Tests," Naval Propulsion Center, TR NAPC-PE-201C, Trenton, NJ, 1988.
- ⁷Reddy, K. V., and Roquemore, W. M., "A Time-Dependent Model with Global Chemistry for Decomposition and Deposition of Aircraft Fuels," *Preprints from the Symposium on the Stability and Oxidation Chemistry of Middle Distillate Fuels*, American Chemical Society, Washington, DC, Aug. 1990.
- ⁸Spalding, D. B., "A Novel Finite Difference Formulation for Difference Expressions Involving Both First and Second Derivatives," *International Journal for Numerical Methods in Engineering*, Vol. 4, No. 4, 1972, pp. 551-559.
- ⁹Patankar, S. V., and Spalding, D. B., "A Calculation Procedure for Three-Dimensional Parabolic Flows," *International Journal of Heat and Mass Transfer*, Vol. 15, Oct. 1972, pp. 1787-1805.
- ¹⁰Launder, B. E., and Spalding, D. B., "The Numerical Computation of Turbulent Flows," *Computer Methods in Applied Mechanics and Engineering*, Vol. 3, No. 2, 1974, pp. 269-289.
- ¹¹Marteney, P. J., and Spadaccini, L. J., "Thermal Decomposition of Aircraft Fuels," *Journal of Engineering for Gas Turbines and Power*, Vol. 108, Oct. 1986, pp. 648-653.
- ¹²Kendall, D. R., Houlbrook, G., Clark, R. H., Bullock, S. P., and Lewis, C., "The Thermal Degradation of Aviation Fuels in Jet Engine Injector Feed-Arms: Part 1—Results from a Full-Scale Rig," 30th International Gas Turbine Congress, Tokyo, Oct. 1987.
- ¹³Clark, R. H., and Stevenson, P. A., "The Thermal Degradation of Aviation Fuels in Jet Engine Injector Feed-Arms: Results from a Half-Scale Rig," *Preprints from the Symposium on the Stability and Oxidation Chemistry of Middle Distillate Fuels*, American Chemical Society, Washington, DC, Aug. 1990.
- ¹⁴Goodman, H., and Bradley, R., "High Temperature Hydrocarbon Fuels Research in an Advanced Aircraft Fuel System Simulator," Air Force Aero Propulsion Lab. TR-70-13, Wright-Patterson AFB, OH, March 1970.
- ¹⁵Heneghan, S. P., Martel, C. R., Williams, T. F., and Ballal, D. R., "Studies of Jet Fuel Thermal Stability in a Flowing System," International Gas Turbine and Aeroengine Congress and Exposition, American Society of Mechanical Engineers Paper 92-GT-106, Cologne, Germany, June 1-4, 1992.
- ¹⁶Jones, E. G., and Balster, W. J., "Application of a Sulphur-Doped System to the Study of Thermal Oxidation of Jet Fuels," International Gas Turbine and Aeroengine Congress and Exposition, American Society of Mechanical Engineers Paper 92-GT-122, Cologne, Germany, June 1-4, 1992.

Role of Buoyancy in Fuel-Thermal-Stability Studies

V. R. Katta*

Systems Research Laboratories, Inc., Dayton, Ohio 45440
and

J. Blust,† T. F. Williams,‡ and C. R. Martel‡

University of Dayton Research Institute, Dayton, Ohio 45469

A unique methodology is used to investigate the effects of gravity on fuel flowing through the small-bore heated tubes that are often used in the study of fuel-thermal-stability characteristics. The copper block that houses the fuel tube (or test section) is located on a swivel, and experiments are conducted for different tube orientations, namely; horizontal, vertical with flow from bottom to top and vice versa. Results obtained for different fuel-flow rates and block temperatures are discussed. An axisymmetric, time-dependent numerical model is used to simulate the flow patterns in the test section. This model solves momentum, energy, species, and $k-\epsilon$ turbulence equations. The buoyancy term is included in the axial-momentum equation. Natural flow resulting from buoyancy was found to have a significant effect on heat transfer and oxygen consumption for fuel-flow rates up to 100 cc/min (Reynolds numbers up to 2.3×10^3). Flow instabilities were observed when the fuel was flowing downward in a vertically mounted test section. The effect of block temperature and flow rate on these instabilities was also studied.

Introduction

IN aircraft, before fuel is burned in the combustion chamber, it is used to cool several engine and airframe components as well as electronic equipment.¹ The bulk-fuel temperature and the high wall temperature of these components lead to degradation of the fuel (i.e., chemical decomposition of fuel to form gums and solids that cause fouling of fuel nozzles and heat exchangers). Several laboratory experiments of the flowing^{2,3} and static⁴ type have been designed to study the thermal stability of jet fuel. Temperature is usually treated as an effective parameter⁵ for correlating experimentally obtained data and fuel behavior in aircraft. Recent studies^{6,7} have indicated strong involvement of certain species such as dissolved oxygen and hydroperoxides in the fouling process. In order to extend the findings derived from these laboratory experiments to real aircraft fuel systems, a thorough understanding of the experimental data is needed. Knowledge of the temperature and species distributions within the test section of an experiment is essential for analyzing the complex data on deposition.

In commonly used flowing experiments^{2,3,5,6} in fuel-thermal-stability studies, fuel is passed continuously through a long, small-bore heated tube (test section). The tube is heated by either passing electric current through the tube wall² (constant heat flux) or using an external, constant-temperature heat source.^{3,5,6} The test sections are mounted either horizontally^{3,5} or vertically,² with fuel flowing from top to bottom or vice versa. In each of these situations, the forced laminar or turbulent convection is altered in a different way by the free (or natural) convective flow.

During heating, the fluid near the wall is warmer and, therefore, lighter than the bulk fluid in the core. As a consequence, in a horizontally mounted tube, two upward currents flow along the side walls and, by continuity, the heavier fluid near the center of the tube flows downward. This establishes two spiral vortices that are symmetrical about a vertical meridional

plane.⁸ This combined forced and natural convective flow causes the heat-transfer coefficient to be higher than that predicted using laminar-flow assumptions. The secondary motion with the uniform-temperature boundary condition develops to a maximum intensity and then diminishes to zero as the temperature gradients in the fuel decrease. If the tube is placed vertically, then the fuel near the side wall is accelerated along the tube length for the bottom-to-top forced flow and decelerated for the top-to-bottom forced flow. The greater shear between the core and the near-wall fluid in the former case could establish ring vortices that are symmetric about the axis of the tube as a result of the Kelvin-Helmholtz-type instability.⁹ Similar vortices could develop in the latter case (top-to-bottom forced flow) also, resulting from the Taylor instability.¹⁰ As these vortices enhance mixing, the heat-transfer coefficient increases above its expected laminar value, but remains less than its turbulent value. Although the effects of natural flow on convective flow have been addressed in the past,¹¹ those studies were limited to relatively large cross sections (>1 cm) and, hence, are not relevant for the small-bore tubes used in fuel-thermal-stability studies.

In the present study, the effects of free convection on forced flow in a long, small-bore tube for different test-section orientations were investigated experimentally and theoretically using a time-dependent mathematical model. The tube was heated with a constant-temperature copper block. An aviation fuel, Jet A, was used as the flow media. The results are characterized by the Reynolds and Grashof numbers.

Experimental Arrangement

Several fuel-thermal-stability experiments were conducted on a single-pass, flowing fuel system known as the Phoenix rig.³ Figure 1 is a schematic diagram of the rig that consists of two test sections, two copper blocks (one for heating and the other for cooling), a fuel-supply system, filters, and several measuring instruments. Small-bore stainless steel tubes, 0.3175 cm o.d., 0.216 cm i.d., and 55.9 cm in length, are used as the test sections. The internal surface of the tube is not electropolished, having a roughness of 0.2–0.38 μm . The heating block consists of a copper cylinder measuring 45.7 cm in length and 7.6 cm in diam. The copper cylinder is split lengthwise in two halves, with each section containing a full-length cartridge heater. A lengthwise groove on the flat face of each

Received March 7, 1994; revision received June 29, 1994; accepted for publication June 30, 1994. Copyright © 1994 by the American Institute of Aeronautics and Astronautics, Inc. All rights reserved.

*Senior Engineer, Research Applications Division, Member AIAA.

†Graduate Student, Research Institute, Student Member AIAA.

‡Research Engineer, Research Institute.

Table 1 Source terms and transport coefficients appearing in governing equations

Φ	Γ^Φ	S^Φ
u	$\mu + \mu_t$	$-\frac{\partial p}{\partial z} + \frac{\partial}{\partial z} \left(\Gamma^u \frac{\partial u}{\partial z} \right) + \frac{\partial}{\partial r} \left(\Gamma^u \frac{\partial v}{\partial r} \right) + \frac{\Gamma^u}{r} \frac{\partial v}{\partial z} + \rho g$
v	$\mu + \mu_t$	$-\frac{\partial p}{\partial r} + \frac{\partial}{\partial z} \left(\Gamma^v \frac{\partial u}{\partial r} \right) + \frac{\partial}{\partial r} \left(\Gamma^v \frac{\partial v}{\partial r} \right) + \frac{\Gamma^v}{r} \frac{\partial v}{\partial r} - 2\Gamma^v \frac{v}{r^2}$
k	$\mu + \frac{\mu_t}{\sigma_k}$	$G - \rho \epsilon$
ϵ	$\mu + \frac{\mu_t}{\sigma_\epsilon}$	$C_1 G \frac{\epsilon}{k} - C_2 \rho \frac{\epsilon^2}{k}$
h	$\frac{k}{c_p} + \frac{\mu_t}{\sigma_h}$	0
Y_i	$\rho D_i + \frac{\mu_t}{\sigma_{Y_i}}$	\dot{w}_i

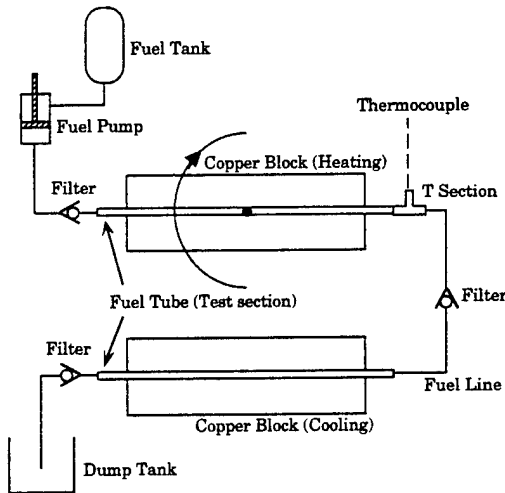


Fig. 1 Schematic diagram of single-pass, flowing system (Phoenix Rig) used for studies of fuel-thermal-stability characteristics.

cylinder section was provided in order that a 0.3175-cm-diam hole would form to house the test section when the copper-block sections were clamped together. The cooling block is designed similarly, except that it is not provided with cartridge heaters.

Only the central 45.7-cm section of each stainless steel tube was clamped inside the heated copper block, leaving the 5.1-cm-long tube sections on both ends unheated. However, both the end sections of the tube were insulated by wrapping them using fiberglass. The end of the fuel tube was connected to a T section for measuring the bulk fuel temperature T_{BE} . Several thermocouples were also connected to the fuel tube in order to profile the tube-outer-wall temperature T_w . The temperature of the copper block T_{CB} was maintained at the desired value using a on-line-monitoring computer. In order to avoid vaporization of fuel the system was pressurized to 350 psi.

The heated copper block was mounted on a swivel system to permit its rotation up to 270 deg from the horizontal position. This would allow horizontal (0 deg), vertical with flow-up (90 deg), and vertical with flow-down (270 deg) configurations. The second copper block is generally used to study the fuel-thermal-stability characteristics during the cooldown process; however, in the present investigation of the flow characteristics, it was used as a means to cool fuel prior to its return to the dump tank.

Mathematical Model

Fluid motion inside the tubular test section is assumed to be axisymmetric. The time-dependent Navier-Stokes equations along with the turbulent-energy, species-conservation,

and enthalpy equations that are solved in the z - r cylindrical coordinate system are as follows¹²:

$$\frac{\partial \rho}{\partial t} + \frac{\partial \rho u}{\partial z} + \frac{\partial \rho v}{\partial r} + \frac{\rho v}{r} = 0 \quad (1)$$

$$\frac{\partial \rho \Phi}{\partial t} + \frac{\partial \rho u \Phi}{\partial z} + \frac{\partial \rho v \Phi}{\partial r} = \frac{\partial}{\partial z} \left(\Gamma^\Phi \frac{\partial \Phi}{\partial z} \right) + \frac{\partial}{\partial r} \left(\Gamma^\Phi \frac{\partial \Phi}{\partial r} \right) - \frac{\rho v \Phi}{r} + \frac{\Gamma^\Phi}{r} \frac{\partial \Phi}{\partial r} + S^\Phi \quad (2)$$

Here, ρ , u , and v are the density and the axial and radial velocity components, respectively. Equation (2) represents different conservation equations, depending on the variable assigned to Φ . The source terms S^Φ and the transport coefficients Γ^Φ associated with each of these equations are given in Table 1. The gravity term is added to the axial-momentum equation to simulate the flow-up or flow-down in a vertically mounted tube.

In Table 1, μ , k , and c_p are the viscosity, thermal conductivity, and specific heat of the fuel, respectively, and μ_t is the turbulent viscosity incorporated through use of the k - ϵ turbulence model. The variables p , h , k , and ϵ are the pressure, enthalpy, and turbulence energy and its dissipation, respectively, and σ is the turbulent Prandtl number (or Schmidt number) associated with a specific transport equation. Y_i , w_i , and D_i are the mass fraction, rate of production, and diffusion coefficient of the i th species, respectively. The other variables and constants appearing in the table are defined below:

$$G = \mu_t \left\{ 2 \left[\left(\frac{\partial u}{\partial z} \right)^2 + \left(\frac{\partial v}{\partial r} \right)^2 + \left(\frac{v}{r} \right)^2 \right] + \left(\frac{\partial v}{\partial z} + \frac{\partial u}{\partial r} \right)^2 \right\}$$

$$\mu_t = C_\mu \rho k^2 / \epsilon$$

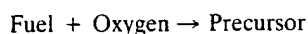
$$C_1 = 1.47, \quad C_2 = 1.92, \quad \text{and} \quad C_\mu = 0.09$$

$$\sigma_k = 1.0, \quad \sigma_\epsilon = 1.3, \quad \sigma_h = 1.0, \quad \text{and} \quad \sigma_{Y_i} = 1.0$$

The transport properties, enthalpy, and density at a given temperature are obtained from the curve fits developed for the available Jet-A fuel data.¹³ The governing equations are discretized utilizing a hybrid scheme,¹⁴ which is a second-order central differencing scheme everywhere, but changes to a first-order upwind scheme when the local cell-Reynolds number becomes greater than 2. The finite difference form of the governing equations are solved sequentially adopting an implicit approach¹² and a uniform grid system having 31 points in the radial direction and 101 points in the axial direction. This grid density was found to be yielding results that are only weakly sensitive to the further grid refinement. While

flat velocity profiles were used at the tube entrance as initial conditions, values of the flow variables at the tube exit plane were obtained by extrapolating the data at the interior grid points. For the turbulent-flow calculations, wall functions¹⁵ have been used to determine the gradients of the flow variables near the wall boundary. Due to the destructive procedure adopted in the experiments to measure carbon deposition, low-cost fuel tubes with medium surface finish were used. The surface roughness could influence the growth of the boundary layer in the fuel tube; however, to simplify the mathematical modeling, it is not taken into account.

The chemical-kinetics models described by Krazinski et al.¹⁶ and Katta et al.¹⁷ are capable of predicting carbon deposition on the tube wall. However, since the present study was limited to the effects of buoyancy on heat transfer and oxygen depletion, the deposit-formation chemistry was not considered. The oxygen consumption is governed by the single irreversible reaction



The reaction rate for the above equation is assumed to be governed by an Arrhenius expression and of zeroth order with respect to the reactants. The pre-exponential (2.53×10^{13} mole/m³/s) and activation energy (32 kcal/mole) were determined for the Jet A fuel used by Katta et al.¹⁷ The same values were selected for the present simulations since the Jet A fuel used in these studies is only slightly different from that of Katta et al.¹⁷

Results and Discussion

The bulk temperature measured at the exit of the horizontal fuel tube for different flow rates is shown in Fig. 2. The copper-block temperature T_{CB} was 573 K. The temperature of the fuel before entering the tube was 292 K. The Reynolds

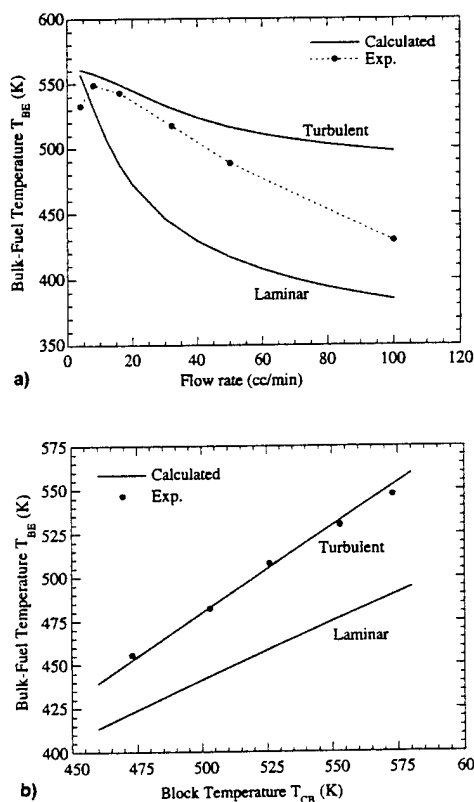


Fig. 2 Comparison of predicted and measured bulk fuel temperature in horizontal position at exit of fuel tube: a) for different flow rates, block temperature is 573 K and b) for different block temperatures, flow rate is 16 cc/min.

number (based on the diameter of the fuel tube and the fuel properties at the end of the tube) obtained for the highest flow rate of 100 cc/min was $\sim 2.3 \times 10^3$, which suggests that the flow inside the test section should be laminar for all flow rates used in this experiment. Note that the Reynolds numbers calculated based on the fuel properties at the inlet are an order of magnitude lower than those obtained at the end of the tube. As expected, the measured bulk-fuel temperature decreased with the flow rate. However, at a very low flow rate of 4 cc/min, the bulk-fuel temperature is lower than that measured at 8 cc/min. This is believed to be resulting from the insufficient insulation provided between the end of the heated section and the thermocouple location.

Calculations were initially made by neglecting gravity term in the axial-momentum equation (Table 1) and by assuming a laminar-type flow inside the test section, and the results are shown in Fig. 2a. The bulk-fuel temperature predicted for different flow rates is significantly lower than the measured value. Based on the facts that 1) the present calculations employed widely accepted temperature-dependent density and transport coefficients¹³ for a Jet-A fuel, 2) the code used for these simulations was well tested in the past for its accuracy in predicting the wall and fuel temperatures in similar heating systems but operating at higher flow rates, and 3) the pressure (350 psi) and the copper-block temperature (< 573 K) adopted in the present experiments guarantee a single-phase flow in the fuel tube; one might question, in light of the differences noted between the theory and experiment, the use of laminar-flow assumption. The higher temperatures (compared to the laminar predictions) in the experiment then could be due to some kind of flow turbulence. To investigate the possibility of flow being turbulent inside the tube, calculations were made assuming a turbulent flow in the test section. However, a very low level of fluctuating velocity ($\sim 1\%$ of the mean) was used at the tube entrance.

The exit bulk temperatures obtained under the assumption of turbulent flow are also compared with the experimental data in Fig. 2a. It should be noted from this figure that when the flow rate is low (< 40 cc/min), the turbulent simulation predicts the T_{BE} more accurately than the laminar simulation. A similar observation was made from calculations obtained under an experiment in which the flow rate was fixed (16 cc/min) and the block temperature was varied. Both the computed and the measured data are plotted in Fig. 2b. Close agreement between the measured values and those predicted by the turbulent-flow simulation is evident. It should also be noted from Fig. 2a that as the flow rate increases, the measured values approach the calculated laminar data. This raises two questions: 1) is the flow at lower flow rates (or Reynolds numbers) turbulent and, if so, 2) why does it become laminar at higher flow rates. These issues will be addressed both theoretically and experimentally in the following sections.

Influence of Buoyancy

The density of the fuel changes significantly with temperature (840 kg/m³ at room temperature and 650 kg/m³ at 500 K), which gives rise to considerable buoyancy force on the fuel near the tube wall. As the test section is mounted horizontally, the buoyancy force acts in the direction normal to the fuel flow. It is known that such a buoyancy force on the fluid passing between two horizontally mounted parallel plates gives rise to Taylor instabilities,¹⁰ which, in turn, develop into large vortices. However, in the case of circular tubes, the Taylor instabilities result in a three-dimensional flow. In both situations, the induced flow normal to the heated walls increases the heat transfer coefficient.

Since the inside diameters of tubes used in fuel-thermal-stability experiments are usually smaller than 0.5 cm, one might intuitively expect that the large three-dimensional vortices break down into smaller ones, yielding a flow pattern that resembles a turbulent flow. The induced free flow (or

natural flow) is significant when the convective flow (or flow rate) is low and becomes less significant as the flow rate increases. This results in laminarization of the flow in the tube. Therefore, the fluid flow in a horizontally mounted, heated tube can be characterized as a turbulent flow when the flow rate is small, approaching a laminar flow as the flow rate increases. At much higher flow rates (Reynolds numbers above 2.3×10^5), the convective flow itself becomes turbulent and the buoyancy forces become negligible. The data shown in Fig. 2a support these concepts on free flow in horizontally mounted, small-bore circular tubes. The bulk exit temperature follows turbulent-flow predictions initially and, as the flow rate is increased, it shifts toward laminar-flow predictions. Neither the exit bulk temperature nor the wall temperature in the experiment exhibited fluctuations that would indicate that large-scale vortices similar to those observed in large-bore tubes¹¹ are not present in the present experiment.

Although temperature predictions for a horizontally mounted heated tube suggest that the flow within the test section is turbulent (induced by buoyancy), evidence could not be obtained in this enclosed system using the recently developed visualization techniques¹⁶ because the tube bore is too small and tube itself is embedded in a copper block. Also, the dynamics of the flow were not captured by the numerical simulation since the mathematical formulation was based on the assumption that the flow is axisymmetric. In order to gain a better understanding of the importance of buoyancy in these flows, different experiments were designed. The problem associated with three dimensionality of the flow was eliminated by mounting the test section vertically. In this configuration the buoyancy forces are parallel to the flow direction; hence, buoyancy does not induce three dimensionality in the flow. The flow rates and block temperatures used were identical to those in Fig. 2; however, the fuel temperature was different at the entrance of the fuel tube. Usually, the fuel was driven from bottom to top. The heater block in the experiment is fabricated in such a way that it can be rotated counterclockwise 90 deg, and clockwise by 180 deg for studying the horizontal and flow-down conditions, respectively.

Experiments and numerical simulations for different test-section orientations were made to investigate the changes in heat-transfer characteristics. The predicted and measured bulk fuel temperatures at the exit of the fuel tube for different flow rates are shown in Fig. 3. The block temperature was fixed at a value of 573 K. For each flow rate, four different calculations were performed, using the following assumptions concerning the flowfield: 1) flow is turbulent and buoyancy forces in the axial direction are negligible—to simulate the flow inside the horizontally mounted tube; 2) laminar flow without buoyancy terms—to provide an estimate for the effects of natural flow in this system; 3) laminar flow and buoyancy forces act along the convective flow—to simulate the vertically upward flow and; 4) laminar flow on which buoyancy acts in the direction opposite that of the convective-flow direction—to represent the vertically downward flow.

For all flow rates considered in this study (2–100 cc/min), the first three assumptions yielded steady-state flows. However, the vertically downward flow calculations resulted in large fluctuations in the bulk temperature at the exit of the fuel tube. This was found to result from the convective motion of the large-scale vortices that developed inside the heated section of the tube. The formation of these vortices and their characteristics will be discussed later. Results obtained with the above four models are presented in Fig. 3 along with the respective experimental data.

As expected, for all flow rates the horizontal configuration yielded the highest bulk temperatures at the end of the test section. Calculations made under the assumption of turbulent flow yielded accurate predictions for these flows up to a flow rate of 50 cc/min. For higher flow rates the measurements are shifted toward the laminar predictions. As seen from Fig. 3,

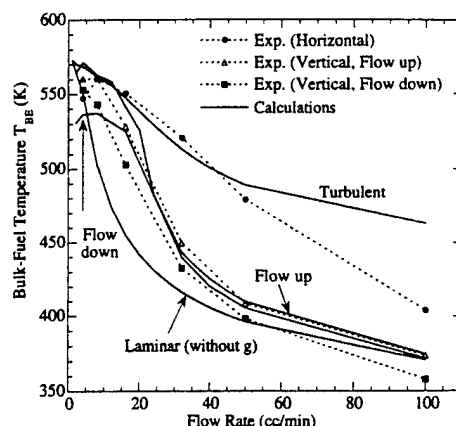


Fig. 3 Computed and measured bulk fuel temperature at exit of fuel tube for different test-section orientations ($T_{CB} = 573$ K).

the agreement between the measured and calculated bulk temperatures for the vertically upward flow is very good for all flow rates considered. This suggests that the highest fuel flow rate (or Reynolds number) used in these heated-tube experiments, i.e., 100 cc/min, does not produce turbulent flow. Therefore, the turbulent-type flows observed for the lower flow rates in the horizontally mounted tubes result from free convection in the radial direction rather than due to the forced convection in the axial direction.

A comparison of the bulk temperatures predicted for laminar flows (Fig. 3) with and without the gravity term in the governing equations indicates that the influence of free convection on forced convection decreases with flow rate and is almost negligible at a flow rate of 100 cc/min. This in conjunction with the earlier discussion on the flow-up case in the vertically mounted configuration indicates that, as the flow rate increases, the flow inside a horizontally mounted, heated tube approaches laminar conditions. This phenomenon was also observed in buoyancy-dominated combustor flows and is often referred to as "relaminarization."¹⁸

For a given flow rate, the vertically mounted configuration with fuel flowing downward yielded the lowest bulk temperatures at the tube exit (cf. Fig. 3). This means that heat transfer occurs in a very inefficient way when free (or natural) convection opposes forced convection. Since the simulations for this case were unsteady in nature, the T_{BE} profile shown in Fig. 3 was obtained by time-averaging the data. For flow rates greater than or equal to 32 cc/min, the calculated T_{BE} for flow-down case closely followed that of the flow-up case.

Temperature Distribution Obtained with Different Models

Experiments conducted at different block temperatures and fuel-flow rates have indicated similar behavior, as discussed in the previous section. However, when the heated tube was placed in a vertical position and with fuel flowing downward, the exit bulk temperatures showed strong fluctuations for certain flow and block-temperature conditions. The periodic nature of these oscillations gave the first indication about the Taylor instabilities developing inside the small-bore heated tubes that are generally used for fuel thermal studies. To understand the growth and nature of these instabilities, flow simulations were made using the four models described previously with different block temperatures and flow rates.

Temperature distributions for a flow rate of 32 cc/min and a block temperature of 573 K predicted by the previously discussed models are shown in Fig. 4. Eleven equally spaced isotherm contours between 290–590 K are plotted in each case. Velocity fields associated with the four cases of Fig. 4 are shown in Figs. 5a–5d, respectively. A low turbulent kinetic energy was used at the inlet for the turbulent flow simulation. However, as the fuel temperature increased (and

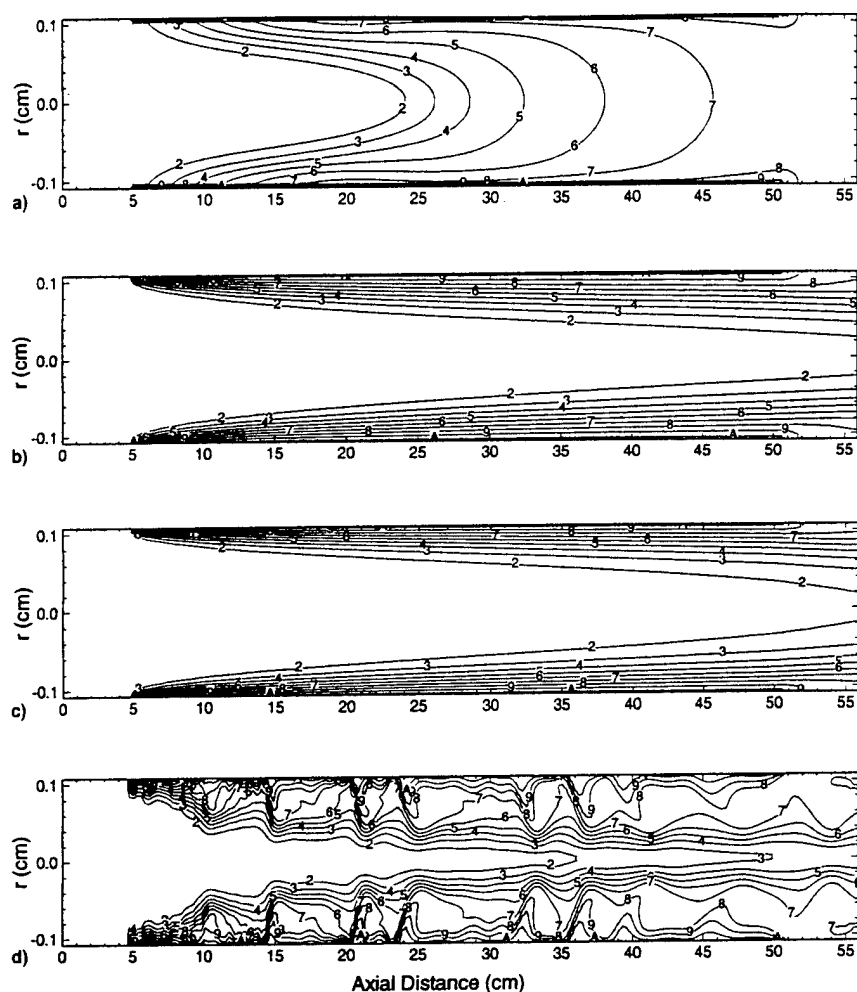


Fig. 4 Temperature distributions predicted for fuel flow rate of 32 cc/min using assumptions of a) turbulent flow, b) laminar flow with no gravity, c) laminar flow with buoyancy force acting in same direction of forced flow and, d) laminar flow with buoyancy force acting in opposite direction of forced flow. Eleven equally spaced contours are plotted between 290–590 K.

density decreased) with axial distance, the velocity and, hence, the turbulent kinetic energy increased. This introduced higher heat flux into the fuel from the tube wall, as indicated by the higher fuel temperature in Fig. 4a. As discussed earlier, this turbulent simulation globally represents the flow inside a horizontally mounted heated tube.

The gravitational force was neglected in the simulation of Figs. 4b and 5b. Under the laminar-flow assumption, the thermal layer (region between contours A and 2) became thinner (cf. Fig. 4b), and most of the fuel at the tube center was cold, having a temperature very near that of the incoming fuel. The fuel velocity within the thermal layer increased (cf. Fig. 5c) due to the natural flow in the flow-up case. As a result, the higher temperature contours were pushed towards the wall (cf. Figs. 4b and 4c). However, as seen from Fig. 3, the bulk fuel temperature in this case is greater than that of the laminar flow. The buoyant acceleration of the hot fuel along the heated wall entrained more cold fuel into the thermal layer, leading to an increase in the heated-fuel flow along the wall and, hence, to a higher bulk fuel temperature. This acceleration did not initiate any flow instabilities (Kelvin-Helmholtz type), and the entire flow remained steady state (Fig. 5c).

When the buoyancy force was opposite to the forced-flow direction (flow-down configuration), several vortices developed along the heated wall (Figs. 4d and 5d) and the flow became unsteady. Unlike the vortices in other buoyancy-dominated flows such as diffusion flames^{18,19} and flow over a heated plate,²⁰ the vortices in these heated tubes are noncoherent and irregular in size and shape. This is due, in part, to the very large aspect ratio (length-to-diameter of ~200) associ-

ated with the small-bore tubes used in this study. Note that the scales in the axial and radial directions in Figs. 4 and 5 are not the same. Nevertheless, the thermal layer resulting from the presence of vortices is significantly increased. The convective motion of these vortices led to fluctuations in bulk temperature at the exit of the fuel tube. Interestingly, the fuel velocity in the thermal layer is reduced in this case (Fig. 5d) when compared to that in the other three cases (Figs. 5a–5c). Due to continuity of mass, fuel velocity near the center of the tube in the flow-down case has increased appreciably. The higher cold-fuel flow at the tube center resulted in a bulk-fuel-exit temperature that is less than that obtained in flow-up case (Fig. 3).

Predicted and measured bulk-fuel temperatures as functions of time are plotted in Fig. 6. The Fourier analysis of the data shows that the computed flow is fluctuating with frequencies near 0.5 and 3.0 Hz. On the other hand, the dominating frequency of the measured fluctuations is ~0.4 Hz. In the numerical simulations the bulk exit temperature was calculated by integrating the mass-weighted temperature at the exit of the tube at a given instant of time. The bulk-fuel temperature in the experiment was obtained by passing the fuel through a "T section," which was assumed to provide an equilibrium temperature through mixing. However, this procedure could easily destroy small vortices and fail to reproduce the higher frequencies associated with small-scale vortices. Considering the differences in the data-acquisition techniques and the assumption made concerning tube surface roughness, the calculations seem to predict the magnitude and lower frequency of the temperature fluctuations reasonably well.

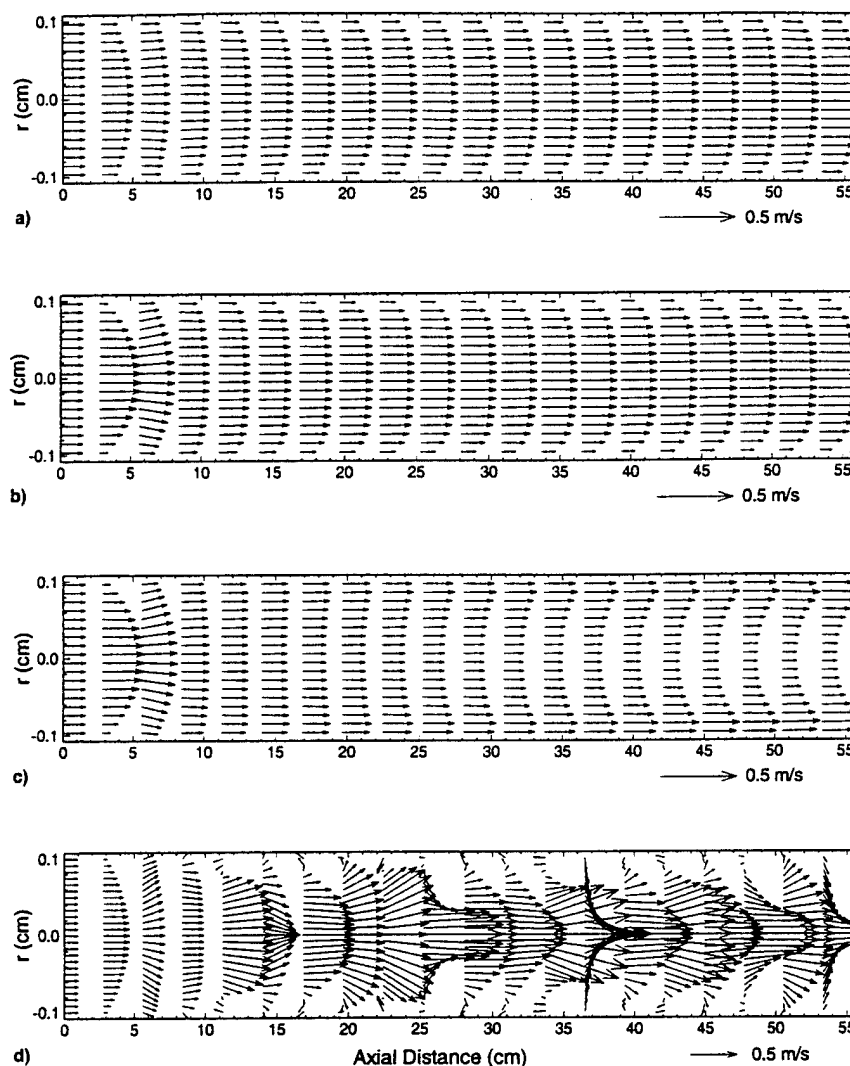


Fig. 5 Velocity fields corresponding to the four calculations of Fig. 4.

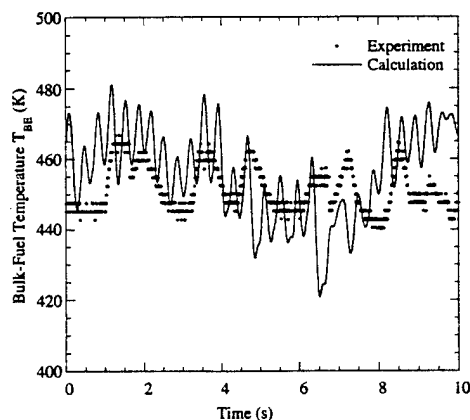


Fig. 6 Computed and measured temperature fluctuations obtained for fuel flow rate of 32 cc/min and block temperature of 573 K in vertically mounted heated tube with fuel flowing from top to bottom.

Effect of Block Temperature on Instabilities

Both the simulations and the experiments demonstrated that instabilities can develop in a vertically mounted heated tube when the fuel is flowing from top to bottom. The effect of block temperature on these instabilities was studied by maintaining the flow rate constant at 32 cc/min. The computed temperature distributions inside the fuel tube obtained with

the flow-down model are plotted in Fig. 7. Results for block temperatures of 473, 513, and 553 K are shown here. For the three block temperatures, the initial thermal layer became unstable. However, at $T_{CB} = 473$ K (Fig. 7a), the instabilities seem to be organized and dampened within 5.0 cm of the tube, and the remainder of the flow became laminar. No fluctuations were observed in the exit bulk temperature, which was steady at a value of 357 K. As the block temperature was increased, the hot fuel along the wall penetrated farther upstream into the preheater section. The stronger buoyancy force in the cases of $T_{CB} = 513$ and 553 K led to destruction of the orderliness of the vortices. Large-scale vortices formed through vortex merging, and the entire thermal layer became unsteady. For a block temperature of 513 K, only the large-scale vortices survived at the tube exit, and the bulk-fuel temperature there fluctuates at ~ 0.9 Hz only. On the other hand, at $T_{CB} = 553$ K both the small- and large-scale vortices are passing through the tube. The exit bulk temperature displays fluctuations similar to those observed for $T_{CB} = 573$ K (Figs. 4d and 6). It may be speculated that for higher block temperatures, the thermal layer becomes turbulent.

Weakening of flow instabilities at lower block temperatures is in qualitative agreement with the observations made in the experiments. The bulk-fuel temperatures measured at the tube exit were found to fluctuate when the block temperature was higher than 560 K. This cutoff temperature compares favorably with that of 513 K obtained from the simulations.

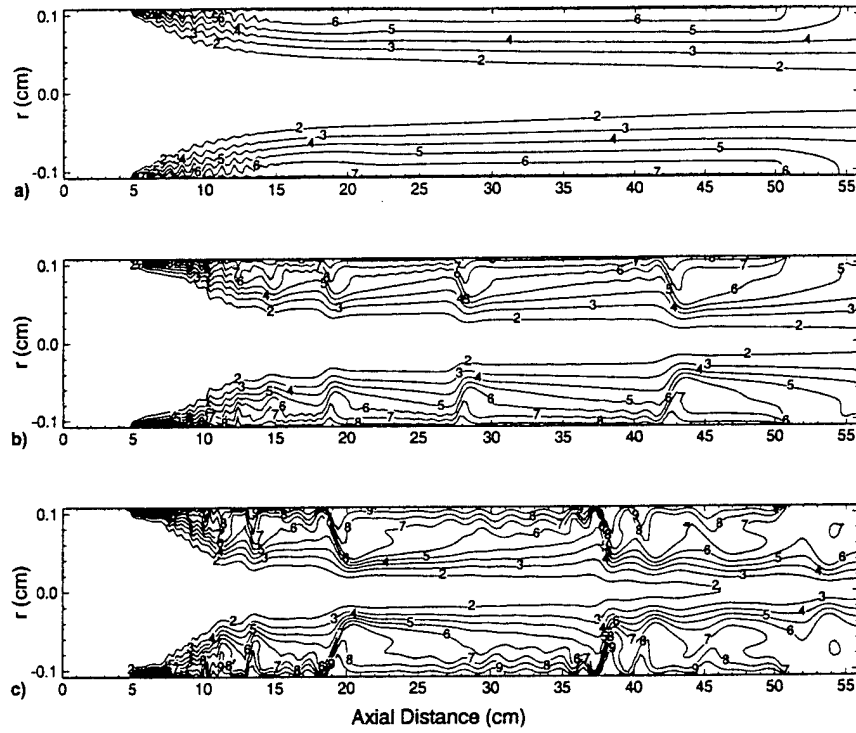


Fig. 7 Temperature distributions obtained for block temperatures of a) 473, b) 513, and c) 553 K in vertically mounted heated tube with fuel flowing from top to bottom. Fuel-flow rate is 32 cc/min.

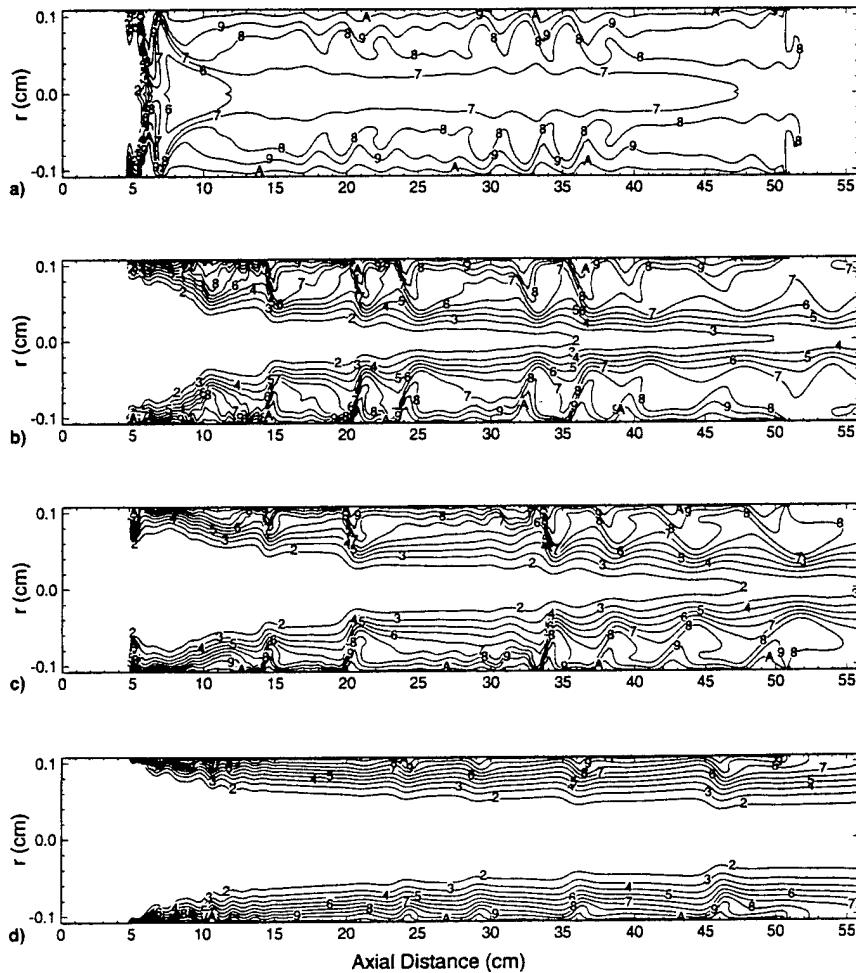


Fig. 8 Temperature distributions obtained for fuel-flow rates of a) 8, b) 32, c) 50, and d) 100 cc/min in vertically mounted heated tube with fuel flowing from top to bottom. Block temperature is 573 K.

Effect of Flow Rate on Instabilities

From Figs. 2 and 3 it can be observed that the influence of gravity on the convective flow in a heated tube decreases with flow rate. In order to understand how the flow rate modifies the instabilities in the flow-down configuration, simulations were made for different fuel flow rates. Instantaneous temperature fields obtained for flow rates of 8, 32, 50, and 100 cc/min are shown in Figs. 8a–8d, respectively. Copper-block temperature in all these cases was 573 K. Two interesting observations may be made from these figures. First, the thermal-layer thickness decreases, and secondly, the instabilities become weaker with increased flow rate. The instabilities in the case of the 8-cc/min flow rate grew rapidly to the scale of the tube radius. Figure 8a indicates that the fuel toward the end of the tube is approaching an equilibrium value. The well mixedness of the fuel inside the tube gave rise to weak temperature fluctuations, although large-scale vortices are continuously passing at the tube exit. Stronger fluctuations in the bulk fuel temperature are observed at the tube exit for flow rates of 32 and 50 cc/min (Figs. 8b and 8d). The weaker instabilities in the 100-cc/min flow-rate case gave rise to weak oscillations in the bulk-fuel temperature, confirming the relaminarization of the flow.

Similar behavior between the bulk-fuel temperature at the exit and the flow rate was observed while conducting flow-down experiments in the vertically mounted heated tube. These results are plotted in Fig. 9 in the form of standard deviations for the measured bulk-temperature fluctuations for different flow rates. The Reynolds and Richardson numbers obtained based on the tube i.d. and length, respectively, and the fuel properties at the inlet are given along with the flow rates. The block temperature in these calculations was maintained at 573 K. The average bulk-fuel temperature at the tube exit and the Grashof number are also plotted in Fig. 9. The Grashof number at a given flow rate was calculated based on tube length and the fuel properties corresponding to the bulk-fuel temperature at the exit of the fuel tube. It is clear from this plot that fluctuations in the bulk-fuel temperature were strong when the flow rate was between 16–47 cc/min. At flow rates higher than 47 cc/min, the forced flow dominated the buoyancy-induced natural flow that resulted in reduced fluctuations in temperature.

It is common to characterize the flow in terms of whether it is dominated by buoyancy based on Grashof number. Figure 9 indicates that in the flow-down cases, the flow becomes buoyancy dominated when the Grashof number is $>6.0 \times 10^{11}$. However, the Grashof number does not correctly char-

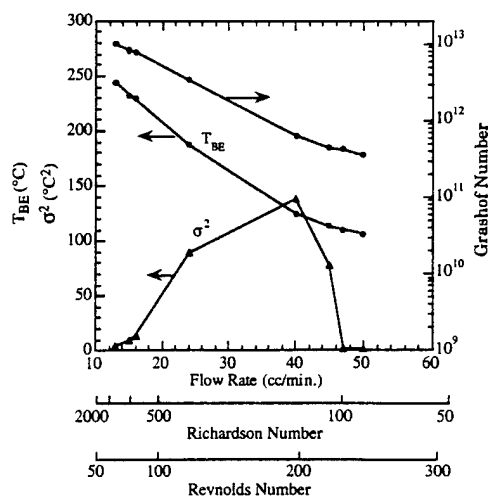


Fig. 9 Measured average and standard deviation of fuel bulk temperature and associated Grashof numbers for different flow rates in vertically mounted heated tube with fuel flowing from top to bottom. Block temperature is 573 K.

acterize the flow oscillations that result from the natural flow. Fluctuations in temperature are observed only when the Grashof number is $<9.0 \times 10^{12}$ and $>6.0 \times 10^{11}$.

Effect of Buoyancy on Oxygen Consumption

Fouling in heated tubes is strongly coupled to the consumption of dissolved oxygen, which, in turn, is dependent on the temperature distribution. The global-chemistry model developed for predicting deposition in heated tubes was successfully used in the Phoenix-rig experiments.³ The same model was used in the present study to understand the influence of buoyancy on oxygen consumption.

Concentration of dissolved oxygen in the fuel before it enters the heated tube was assumed to be 50 ppm, which represents the level in the air-saturated fuel. Calculations were made using the four mathematical models discussed previously under the same conditions used with reference to Fig. 4. The remaining oxygen and the temperature of the bulk fuel (obtained by mass-weighted integration) at different axial locations are plotted in Fig. 10. The turbulent-flow simulation that represents the horizontal configuration of the tube predicts a significant amount of oxygen present throughout the tube. Interestingly, from Fig. 10, it may be noted that the fuel was heated to the highest temperature in this simulation. This is in contrast to the general belief on fuel oxidation that higher bulk fuel temperature leads to a greater consumption of dissolved oxygen. The inconsistency of the lower oxygen consumption for higher bulk-fuel temperature results from 1) turbulent conditions transport heat readily in the radial direction and, thus, do not generate a high-temperature thermal boundary layer along the heated wall and 2) the higher velocity near the wall that reduces the residence time necessary for chemical reaction to occur.

The reduced velocity in the thermal layer in the laminar simulation (Fig. 5b) yielded high consumption of oxygen along the tube wall. The buoyant flow along the wall in the vertical, flow-up configuration increased the entrainment of fuel into the thermal layer. The oxygen consumption was initially decreased compared to that of the laminar flow (Fig. 10) up to $z \approx 35$ cm because of the increased velocity (or reduced residence time), and then increased due to entrainment. A significant amount of oxygen is consumed in the vertically mounted heated tube when the fuel is flowing from top to

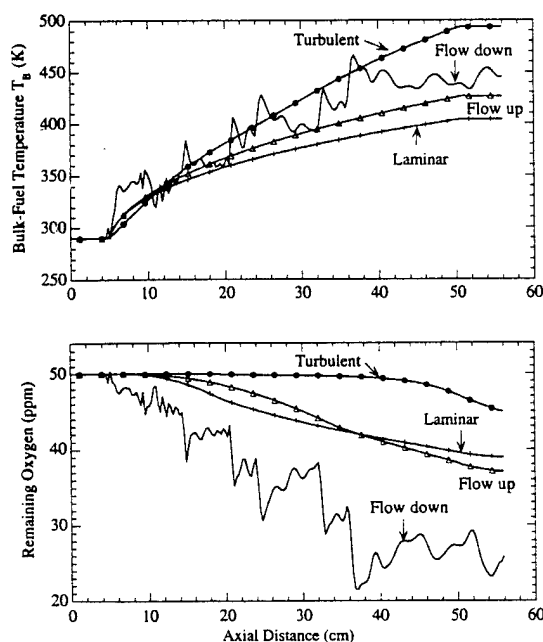


Fig. 10 Remaining oxygen and bulk fuel temperature at different axial locations predicted by different models. Fuel-flow rate and block temperature are 32 cc/min and 573 K, respectively.

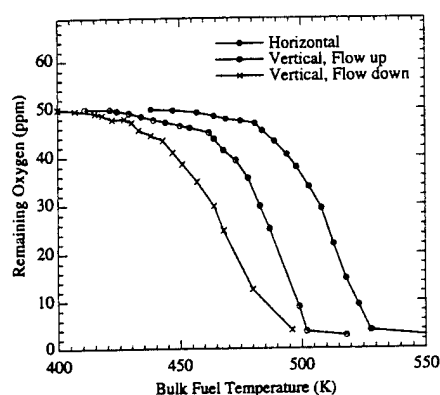


Fig. 11 Remaining oxygen vs bulk fuel temperature measured with different orientations of heated tube. Flow rate is 16 cc/min.

bottom as a result of the increased residence time in the thermal layer. In fact, consumption of oxygen is maximum in this case compared to the other three simulations.

The oxygen consumption in the Jet A fuel was measured using on-line instrumentation of Phoenix rig³ for the three tube orientations. Data in the form of remaining oxygen vs bulk fuel temperature at the exit of the heated tube is plotted in Fig. 11. All these measurements were made for a flow rate of 16 cc/min and by varying the copper-block temperature. Figure 11 shows that for a given value of T_{BE} , consumption of dissolved oxygen is the highest in a vertically mounted tube with fuel flowing from top to bottom and the lowest when the tube was placed horizontally. This qualitatively supports the predictions discussed previously. Note, Fig. 3 indicates that for the given fuel-flow rate and block-temperature, the vertically mounted tube with fuel flowing down yields the lowest bulk fuel temperature at the tube exit.

It is known that deposition on the wall increases with consumption of oxygen.^{3,6,16,17} Therefore, it may be expected that maximum deposition occurs on the tube walls in a vertically mounted, heated tube when the fuel is flowing top to bottom and minimum deposition occurs in a horizontally oriented fuel tube. Due to the nonmonotonic behavior of deposition with temperature (i.e., deposition initially increases and then decreases with fuel temperature^{2,3}), the vertically mounted, heated tube with flow-down configuration may not represent the worst scenario for all block temperatures. Global-reaction models proposed such as those in Refs. 16 and 17 are capable of predicting the deposition by taking into account the fluid-dynamics and heat-transfer effects on the fuel flow. Future studies with theoretically and experimentally obtained deposition data for different fuel-tube orientations may be useful in validating such global-chemistry models.

Conclusions

The flow structure in a small-bore heated tube was studied experimentally and theoretically. It was found that buoyancy has a significant impact on the temperature field. Because of the difficulties associated with extending currently available flow-visualization techniques to small-bore tubes, the influence of natural flow on forced flow was investigated by conducting unique experiments and performing time-dependent numerical simulations for different heated-tube orientations. Experiments yielded the highest bulk-fuel exit temperature when the test-section was mounted horizontally and the lowest in a vertically mounted test-section with fuel flowing from top to bottom. Numerical simulations have reproduced most of the observed features.

The following conclusions are drawn from the comparative experimental and numerical studies made in this article.

1) When the fuel is flowing in a horizontally mounted, small-bore tube, the flow pattern is more turbulent in nature

at very low Reynolds numbers and becomes laminar in nature as the Reynolds number increases to 2300.

2) It is hypothesized that the buoyancy forces normal to the force-flow direction increase mass and heat transport, develop three dimensionality, and, thereby, render the flow turbulent.

3) An axisymmetric code with the $k-\epsilon$ turbulent model is found to yield reasonable predictions for horizontal flow. However, a more realistic simulation of buoyancy dominated fuel flow in a horizontally mounted, heated tube should be performed using a three-dimensional code.

4) Vertically mounted, heated tube with fuel flowing from bottom to top is observed to yield axisymmetric, laminar flows up to a flow rate of 100 cc/min in the 0.3175-cm-diam tubes considered in this study.

5) Fuel flowing from top to bottom in a vertically mounted, heated tube develops flow instabilities when the flow rate is moderate.

6) Oxygen consumption is found to be minimum in the horizontal case and maximum when the fuel is flowing from top to bottom in a vertically mounted tube.

Acknowledgments

This work was supported by the U.S. Air Force under Contracts F33615-90-C-2033 and F33615-92-C-2207. The authors would like to thank the principal investigators, Larry Goss and Dilip Ballal, and the Air Force Technical monitor, Mel Roquemore, for supporting this work and participating in the stimulating discussions.

References

- Koff, B. L., "The Next 50 Years of Jet Propulsion, the Global Anniversary of Jet Powered Flight: 1939-1989," Dayton and Cincinnati AIAA Meeting, Dayton, OH, Aug. 1989.
- Marteney, P. J., and Spadaccini, L. J., "Thermal Decomposition of Aircraft Fuels," *Journal of Engineering for Gas Turbines and Power*, Vol. 108, Oct. 1986, pp. 648-653.
- Ballal, D. R., Byrd, R. J., Heneghan, S. P., Martel, C. R., Williams, T. F., and Zabarnick, S., "Combustion and Heat Transfer Studies Utilizing Advanced Diagnostics: Fuel Research," Wright Lab. TR WR-TR-92-2112, Wright-Patterson AFB, OH, Nov. 1992.
- Jones, E. G., and Balster, W. J., "Application of a Sulphur-Doped System to the Study of Thermal Oxidation of Jet Fuels," International Gas Turbine and Aeroengine Congress and Exposition, American Society of Mechanical Engineers, Paper 92-GT-122, Cologne, Germany, June 1992.
- Chin, J. S., and Lefebvre, A. H., "Influence of Flow Conditions on Deposits from Heated Hydrocarbon Fuels," International Gas Turbine and Aeroengine Congress and Exposition, American Society of Mechanical Engineers, Paper 92-GT-114, Cologne, Germany, June 1992.
- Jones, G., Balster, W. J., and Post, M. E., "Degradation of a Jet-A Fuel in a Single-Pass Heat Exchanger," International Gas Turbine and Aeroengine Congress and Exposition, American Society of Mechanical Engineers, Paper 93-GT-334, Cincinnati, OH, May 1993.
- Heneghan, S. P., and Zabarnick, S., "Oxidation of Jet Fuels and the Formation of Deposits," *Fuel*, Vol. 73, No. 1, 1994, p. 35.
- Mori, Y., Futagami, K., Tokuda, S., and Nakamura, M., "Forced Convective Heat Transfer in Uniformly Heated Horizontal Tubes," *International Journal of Heat and Mass Transfer*, Vol. 9, No. 5, 1966, pp. 453-463.
- Brown, G. L., and Roshko, A., "On Density Effects and Large Structure in Turbulent Mixing Layers," *Journal of Fluid Mechanics*, Vol. 64, No. 4, 1974, pp. 775-816.
- Busse, F. H., "Transition to Turbulence in Rayleigh-Benard Convection," *Hydrodynamic Instabilities and the Transition to Turbulence*, edited by H. L. Swinney and J. P. Gollub, Springer-Verlag, Berlin, 1981.
- Mori, Y., and Futagami, K., "Forced Convective Heat Transfer in Uniformly Heated Horizontal Tubes," *International Journal of Heat and Mass Transfer*, Vol. 10, No. 12, 1967, pp. 1801-1813.
- Katta, V. R., and Roquemore, W. M., "Numerical Method for Simulating Fluid-Dynamic and Heat-Transfer Changes in Jet-Engine

Injector Feed-Arm Due to Fouling," *Journal of Thermophysics and Heat Transfer*, Vol. 7, No. 4, 1993, pp. 651-660.

¹³Nixon, A. C., Ackerman, G. H., Faith, L. E., Henderson, H. T., Ritchie, A. W., Ryland, L. B., and Shryne, T. M., "Vaporizing and Endothermic Fuels for Advanced Engine Application: Part III, Studies of Thermal and Catalytic Reactions, Thermal Stabilities, and Combustion Properties of Hydrocarbon Fuels," Air Force Aero Propulsion Lab., AFAPL-TR-67-114, Pt. III, Vol. II, Wright-Patterson AFB, OH, 1967.

¹⁴Spalding, D. B., "A Novel Finite Difference Formulation for Difference Expressions Involving Both First and Second Derivatives," *International Journal for Numerical Methods in Engineering*, Vol. 4, No. 4, 1972, pp. 551-559.

¹⁵Launder, B. E., and Spalding, D. B., "The Numerical Computation of Turbulent Flows," *Computer Methods in Applied Mechanics and Engineering*, Vol. 3, No. 2, 1974, pp. 269-289.

¹⁶Krazinski, J. L., Vanka, S. P., Pearce, J. A., and Roquemore, W. M., "A Computational Fluid Dynamics and Chemistry Model for

Jet Fuel Thermal Stability," *Journal of Engineering for Gas Turbines and Power*, Vol. 114, Jan. 1992, pp. 104-110.

¹⁷Katta, V. R., Jones, E. G., and Roquemore, W. M., "Development of Global-Chemistry Model for Jet-Fuel Thermal Stability Based on Observations from Static and Flowing Experiments," *Fuels and Combustion Technology for Advanced Aircraft Engines*, Paper 19, AGARD, Loughton, Essex, England, UK, Sept. 1993, pp. 19-1-19-11 (AGARD CP-536).

¹⁸Roquemore, W. M., Chen, L.-D., Goss, L. P., and Lynn, W. F., "Structure of Jet Diffusion Flames," *Turbulent Reactive Flows, Lecture Notes in Engineering*, edited by R. Borghi and S. N. B. Murthy, Vol. 40, Springer-Verlag, Berlin, 1989, pp. 49-63.

¹⁹Chen, L.-D., Roquemore, W. M., Goss, L. P., and Vilimpoc, V., "Vorticity Generation in Jet Diffusion Flames," *Combustion Science and Technology*, Vol. 77, Nos. 1-3, 1991, pp. 41-57.

²⁰Holman, J. P., Gartrell, H. E., and Soehngen, E. E., "An Interferometric Method of Studying Boundary Layer Oscillations," *Journal of Heat Transfer*, Vol. 82, Aug. 1960, pp. 263, 264.

DEVELOPMENT OF GLOBAL-CHEMISTRY MODEL FOR JET-FUEL THERMAL STABILITY BASED ON OBSERVATIONS FROM STATIC AND FLOWING EXPERIMENTS

V. R. Katta and E. G. Jones
Systems Research Laboratories, Inc.
A Division of Arvin/Calspan
2800 Indian Ripple Road
Dayton, OH 45440-3696
USA

and

W. M. Roquemore
Wright Laboratory, Aero Propulsion and Power Directorate
Wright-Patterson Air Force Base, OH 45433-7103
USA

ABSTRACT

Two global-chemistry models for oxidative deposition of jet fuels are evaluated by integrating them into a Computational Fluid Dynamics with Chemistry (CFDC) code. A previously developed two-step global-chemistry model was found to be insufficient to describe the thermal-oxidation and -deposition rates associated with a Jet-A fuel. A new global-chemistry model has been developed systematically based on observations from flowing and static experiments. The global-oxidation reaction is modified such that the reaction rate becomes zeroth-order with respect to the dissolved oxygen concentration. The generation of deposit-forming precursor is coupled with the oxidation reaction by introducing a radical species ROO^* . A formulation for the sticking probability has also been developed. Deposition profiles are well represented by this new model under a variety of temperature and flow conditions. The model correctly predicts the changes in magnitude and spatial location of the deposition peak due to changes in flow. The CFDC model, which is designed for flowing systems, has been extended to static experiments. The model incorporates a non-depleting species F_s representing all non-oxygen compounds responsible for deposition. Static experiments were found to provide a useful and inexpensive method for estimating the concentration of F_s in the fuel.

1 INTRODUCTION

An increase in the operating temperatures of fuel-system components in future high-performance aircraft requires improvement of the thermal-stability of jet fuels.¹ Several laboratory methods^{2,3} have been developed for evaluating the thermal stability of current and future fuels. High temperatures are normally used to accelerate these experiments. Often there is neither clear correlation between the results of the different laboratory experiments nor knowledge of how the results are related to the thermal decomposition of the fuel in aircraft fuel-system components. Recently a general theoretical framework has been established by integrating the Computational Fluid Dynamics

conservation equations with global-chemistry models for thermal-decomposition processes.⁴ The resulting CFDC-type models offer potential for predicting fuel behavior in an engine component based on knowledge gained from laboratory experiments. The success of this approach depends on the development of a universal global-chemistry model that can be calibrated for each fuel by laboratory experiments and the ability of the model to predict deposition over a wide range of flow and temperature conditions for any fuel-system component.

Although CFD part of the model is well developed, the global chemistry for thermal oxidation and deposition part is not. Significant progress has been made in using CFD models to predict fluid and thermal characteristics in the complex geometries of practical systems. On the other hand, development in the chemistry modeling of thermal deposition has been hindered by the lack of fundamental understanding of the complex fuel-degradation processes. Krazinski et al.⁴ and Katta and Roquemore⁵ have achieved some success in the use of the CFDC approach with simple global-chemistry models to predict fuel fouling under different conditions in heated-tube experiments. These successes offer hope that CFDC models will become useful tools for research as well as fuel-system component design.

This paper demonstrates that the previously developed global-chemistry models^{5,6} were insufficient for predicting both oxidation and deposition rates in recent experiments. A new global-chemistry model is presented which uses knowledge gained from a variety of flowing and static experiments conducted with the same fuel. The ability of the new model to predict both oxidation and deposition rates in the test sections of the heated tube and near-isothermal rigs is evaluated. Finally, a calibration procedure is discussed for extending this model to a different fuel.

2 FLUID-DYNAMIC AND HEAT-TRANSFER MODELING

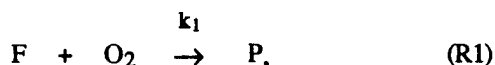
Fluid motion inside the tubular test section is assumed to be axisymmetric and bounded by the fuel-deposit interface. The time-dependent Navier-Stokes

equations along with the turbulent-energy, species-conservation, and enthalpy equations are solved in the z - r cylindrical coordinate system. The transport properties along with the enthalpy and density at a given temperature are obtained from the curve fits developed for Jet-A fuel. The governing equations are discretized utilizing a hybrid scheme⁶ which is a second-order central-differencing scheme everywhere but changes to a first-order upwind scheme when the local Peclet number becomes greater than two. An implicit approach is employed to advance the calculations using a large time-step. This allows the calculations to be performed for real times ranging from minutes to thousands of hours. For the turbulent-flow calculations, wall functions have been used to determine the variations of the flow variables near the fuel-deposit interface.

The mathematical formulation of the problem⁵ takes into account the changes in fluid and thermal characteristics of the system as the deposit builds up on wall surfaces. After each time-step the geometry of the fuel-deposit interface is allowed to change as part of the solution procedure. The computational domain is bounded by the axis of symmetry and the fuel-deposit interface, and the grid system is reconstructed after each time-step to take into account the changes in the boundary shape. Fluid flow, heat transfer, and deposit formation are treated using an integrated approach to simulate the time evolution of deposition inside heated tubes. Conjugate heat-transfer calculations are performed to obtain the heat distribution in the deposits, tube walls, and bulk fuel simultaneously.

3. AUTOXIDATION MODELING

Jet fuels are composed of hundreds of compounds. Dissolved oxygen is one of the most important species in the fuel contributing to deposition on metal walls. Several experiments^{7,8} have shown strong coupling between oxygen depletion rate and deposit growth. Several reaction mechanisms^{8,9} have been proposed to describe autoxidation in fuels. Variations in the reaction kinetics itself indicate that the autoxidation process is also dependent on the fuel under study. The previous and new CFDC models attempt to represent this complex autoxidation process by the following single-step global-reaction equation



which requires calibration for the reaction rate for a given fuel. Here, F and P represent the fuel and precursor to deposit, respectively. As the mass fraction of the base fuel is far greater than those of the species that involve in thermal-decomposition process, the value of the fuel concentration in the rate expression is treated as a part of the pre-exponential. To date calibration for different fuels has been limited to determining the pre-exponential factor and the

activation energy of the global-autoxidation reaction. Recent experiments where an abundance of oxygen-depletion-rate data has been collected using gas chromatography (GC)^{7,10} suggest that the rate of oxygen depletion in some fuels is not a function of dissolved-oxygen concentration. This means that calibration of global-chemistry model for such fuels should also include estimates of the order of the reaction with respect to the oxygen.

Dissolved oxygen measured in a Jet-A fuel identified as 2827 by the U. S. Air Force at different temperatures is shown in Fig. 1. These experiments were conducted in a constant-temperature heated-tube test apparatus referred to as the Phoenix rig.⁷ The heated tube consists of a 0.3175-cm-o.d. and 50.8-cm-long stainless-steel fuel tube and a 40.64-cm-long heated copper block. The fuel tube was clamped inside the copper block in such a way that only the central 40.64-cm section was heated. Temperature of the copper block was maintained at 573 K. Fuel was passed through the fuel tube at a steady flow rate, and measurements for bulk-fuel temperature and oxygen were made at the exit of the tube. Oxygen content in the fuel at different temperatures was obtained by changing the fuel-flow rate (i.e., indirectly, the heat flux). Oxygen depletion with temperature for different initial levels of dissolved oxygen was then obtained by repeating the experiments. Calculations for the same experimental conditions (initial dissolved oxygen of 65 ppm) were made using the global-chemistry model that was calibrated for a JP-5 fuel used in experiments at United Technologies Research Center (UTRC).⁴ The results are shown in Fig. 1 (short-dashed line). Model predictions indicate that the consumption of oxygen in

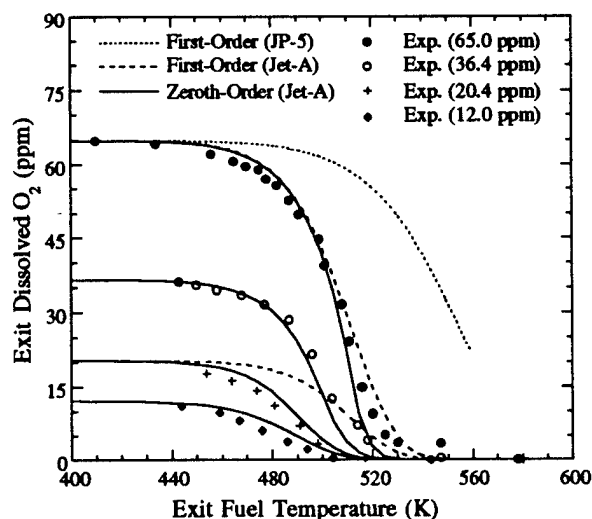


Fig. 1. Oxygen depletion as function of fuel temperature in Jet-A fuel for different levels of initial dissolved oxygen. Data were obtained at end of 50.4-cm-long tube heated with a 573-K copper block and by varying the flow rate. Calculations were made using different global-oxygen-consumption models.

the Jet-A (USAF-2827) fuel is much more rapid than in the JP-5 fuel used by UTRC.¹¹ Interestingly, the latter fuel yielded peak deposit of $\sim 1000 \mu\text{g}/\text{cm}^2/\text{h}$ —an order of magnitude greater than that of the Jet-A fuel. The very large deposition rate with JP-5 could be partly due to the high flow rates used in the UTRC experiments. However, Heneghan and Zabarnick⁹ have also observed this inverse behavior—fuels that oxidize easily tend to produce less solids—and attributed it to the natural antioxidant molecules inherently present in nonhydrotreated fuels.

The global-autoxidation rate

$$k_1 = [\text{O}_2]^\alpha A_1 e^{(-E_a/RT)}, \quad (1)$$

was recalibrated for the Jet-A (USAF-2827) fuel, and the best fit to the oxygen-depletion data with initial oxygen concentration of 65 ppm is shown by the long-dashed line in Fig. 1. In the above equation, α represents the order of the reaction with respect to the oxygen concentration. In this model, α was assumed to be equal to one, which is consistent with the model developed by Krazinski et al.⁴ The new Arrhenius parameters ($A = 1.65 \times 10^{14} \text{ s}^{-1}$, $E_a = 35.5 \text{ kcal/mole}$) resulted a good fit to the experimental data with an initial oxygen concentration of 65 ppm. However, the predictions of oxygen depletion for the 19.5-ppm oxygen level are not so good as noted in Fig. 1. Since the global autoxidation reaction is first-order with respect to oxygen concentration, the depletion rate is much lower than that observed when the initial oxygen concentration was 65 ppm. However, the experimental data show a higher depletion rate, even when the initial dissolved oxygen was 19.5 ppm, suggesting that the autoxidation reaction depends only weakly on oxygen concentration. The global-autoxidation reaction was recalibrated for the Jet-A fuel using different values for α in the rate expression (1). The best representation of the experimental data was achieved when α was set equal to zero. Also the autoxidation reaction with respect to oxygen was assumed to change from zeroth order to first order when the amount of dissolved oxygen fell below the 10-ppm level. The lower depletion rates observed in the experiments at lower oxygen levels support this assumption. The recalibrated oxygen depletion from the 65-ppm level and the predicted depletion curves from different lower initial oxygen concentrations are plotted in Fig. 1 with solid lines. The Arrhenius parameters for this model are $A = 2.53 \times 10^{13} \text{ mole}/\text{m}^3/\text{s}$ and $E_a = 32 \text{ kcal/mole}$. Agreement between the zeroth-order model predictions and the experiments is favorable for all initial oxygen concentrations. Choice of $\alpha = 0$ in Eq. (1) is also in agreement with the recent findings of Jones et al.⁸

4 DEPOSITION MODELING

Hydroperoxides are felt to have direct bearing on wall deposition. Although, the formation of hydroperoxides in the fuel through the peroxy radicals

is reasonably well understood, the transformation mechanism of hydroperoxides into deposits is not. However, hydroperoxides are assumed to produce a precursor to deposits which can be transported by convective and diffusive motions to the wall surface and adhere to it. The precursor is then transformed to deposit. It should be noted that this assumed wall-deposition process is dependent on a sticking phenomenon which must also be modeled.

Carbon-deposition experiments were conducted using the Phoenix rig⁷ for the oxygen concentrations shown in Fig. 1. Jet-A (USAF-2827) fuel was continuously passed through the test section at a constant flow rate and copper-block temperature. The fuel was sparged with ambient air to yield a 65-ppm initial concentration of dissolved oxygen before being passed through the test section. After 6 h, the tube was removed from the copper block and cut into 2.54- or 5.08-cm-long sections. The total deposit inside each of these small sections was measured using the carbon-burn-off technique. The deposition rate along the length of the tube in units of $\mu\text{g}/\text{cm}^2/\text{h}$ is shown in Fig. 2 for two different block temperatures and a flow rate of 16 cc/min. In the present paper, these data are used to calibrate the deposition part of the Krazinski et al.⁴ model and the new model. The calibrated models are then used to predict the deposition for the 4-cc/min flow-rate data shown in Fig. 3.

Two-Step Chemistry Model

In the two-step global-chemistry model proposed by Krazinski et al.,⁴ a precursor to the wall deposits was assumed to be formed directly from the autoxidation reaction. A unity sticking probability for the precursor was also assumed. A precursor removal reaction was

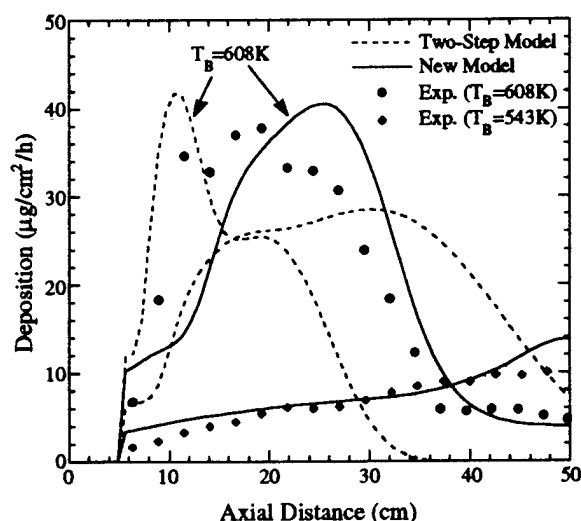


Fig. 2. Deposition as function of tube length or axial distance. Measurements made using carbon burn-off technique. Fuel flow rate was 16 cc/min. Global-chemistry models were calibrated for these data.

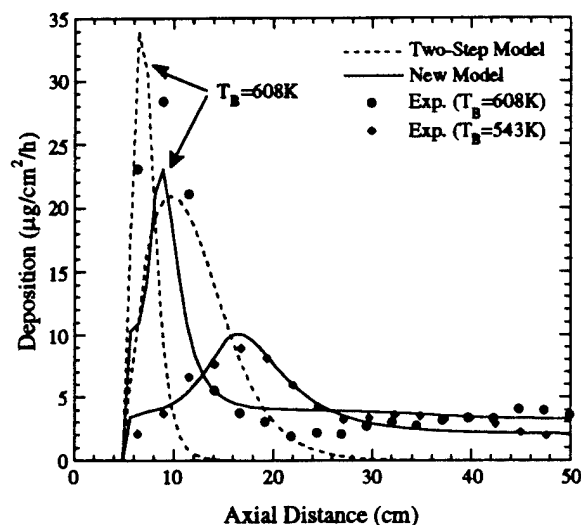


Fig. 3. Predicted and measured deposition in heated tube for different wall temperatures at fuel-flow rate of 4 cc/min.

introduced to limit the deposition at higher temperatures (> 500 K). The deposition model is as follows:



The strategy for calibrating this model for a given fuel is to determine the Arrhenius parameters for the autoxidation reaction using the oxygen-depletion data and then for the precursor-removal reaction using wall-deposition data. As discussed in the previous section, the autoxidation reaction for the Jet-A fuel was calibrated using the 65-ppm initial dissolved-oxygen-concentration data (short-dashed line in Fig. 1). Calculations for the 16-cc/min flow rate and $T_B = 608$ K were repeated by adjusting the Arrhenius parameters of the precursor-controlling reaction (R2) to obtain a wall-deposition profile close to that of the experiment. The best-fit profile was obtained with $A = 2.1 \times 10^{14} \text{ s}^{-1}$, $E_a = 30 \text{ kcal/mole}$ and is shown by the broken line in Fig. 2. Also shown are predictions in Fig. 2 for a lower block temperature of 543 K using this model. Since the initial 5-cm section of the tube was not heated, deposition did not occur there.

A comparison of calculations and experimental data (cf Fig. 2) elucidate the limitations of the two-step chemistry model. The first important difference is that calculations at $T_B = 608\text{K}$ yielded a deposition peak which is narrower than that observed in the experiments. This is due to the direct transformation of oxygen to the precursor [cf reaction (R1)] in the model. The high rate of oxygen depletion gives rise to a rapid increase in the deposition rate (from 10 to $40 \mu\text{g/cm}^2/\text{h}$) when the fuel enters the heated section. A high precursor-removal reaction rate is used to limit the peak

deposition at $\sim 40 \mu\text{g/cm}^2/\text{h}$ which, in turn, yielded a narrow peak. A change in the calculated deposition rate seen at $x = 16 \text{ cm}$ is due to the flow transition to turbulence. The increased mixing due to turbulence transported more precursors to the wall; hence, more deposition occurred. The dip in the experimental data at $x = 14 \text{ cm}$ is believed to be due to the same flow transition. The second important difference is that at downstream locations ($x > 35 \text{ cm}$), the model tends to decrease the deposition rate to zero, whereas the experiments show a deposition of the order of $5 \mu\text{g/cm}^2/\text{h}$. Once the oxygen in the fuel is completely depleted, the precursor concentration decreases exponentially due to the precursor removal reaction. After a certain residence time, the precursors have either been transported to the walls or become solubles leaving fuel downstream precursor-free. This poses a serious problem in the prediction of fouling associated with pre-heated fuel systems. For example, in the experiments of Chin et al.,¹² fuel pre-heated to about 550 K was used. They observed significant deposition in the test section under a variety of flow and block-temperature conditions. Two-step chemistry-model calculations of this experiment predict no deposition in the test section because the chemistry described by the two-step model is completed within the pre-heater, leaving the fuel throughout the test-section precursor-free. The third important difference is that when the block temperature is reduced from 608 to 543 K, the peak measured deposition rate decreases from 40 to $10 \mu\text{g/cm}^2/\text{h}$, while the location of the peak shifts axially from 20 cm to the end of the tube. These changes in the deposition rate are poorly predicted by the two-step chemistry model, as noted in Fig. 2. At $T_B = 543 \text{ K}$ the calculations show a significant amount of deposition along the length of the tube, with a peak at $\sim 18 \text{ cm}$. In fact, the total amount of deposit predicted inside the tube at $T_B = 543 \text{ K}$ is more than that obtained at 608 K. This result is not in agreement with the experimental results. The inability to predict the correct wall temperature dependence of the deposition rate is felt to be due in part to the unity-precursor-sticking-probability assumption.

Predictions made with the two-step global-chemistry model for a fuel-flow rate of 4 cc/min (broken lines) are compared with the experimental data in Fig. 3. The peaks in the deposition have moved closer to the tube entrance; however, again their location and magnitude are not in agreement with the experiments. Because of the longer residence time ($\sim 30 \text{ s}$), no deposition is predicted beyond $x = 30 \text{ cm}$.

The above comparisons of model predictions and experimental data indicate that the simple two-step global-chemistry model can not adequately describe the deposition process for a fuel such as the Jet-A (USAF-2827). In general, the model provides reasonable predictions when the flow and heating conditions are only slightly different from those used for calibration, as noted in Fig. 2. However, a more robust global-chemistry model must be developed if CFD codes are expected to predict fouling in experiments where flow conditions differ greatly.

New Chemistry Model

Experiments of Kauffman et al.¹³ suggest that deposit-forming precursors are generated through chemical reactions involving hydroperoxides but not directly formed from the autoxidation process. Therefore, with this in mind, the peroxy-radical was introduced in the new model as a separate species. Jones et al.¹⁴ conducted non-flowing, static experiments by heating a flask containing fuel and metal coupons. Deposition on the metal-coupon surfaces and growth of insoluble particles in the bulk fuel were studied as functions of time for a fixed temperature. They observed that the deposition rate on the metal coupons remained constant, even though the concentration of the

bulk-insoluble materials increased linearly with time which implies that the deposition rate is independent of bulk-insoluble concentration in the bulk fuel. This led to the interesting conclusion that the bulk-insoluble materials and the deposit-forming precursors are generated through separate pathways but probably involve the same hydroperoxides. In time, the bulk insolubles probably agglomerate; and, in a flowing system, the large bulk-insoluble particles may stick to the walls upon collision and become deposits. The new global-chemistry model developed using these ideas, consists of four species; namely, O_2 , ROO° , P , and D_{Bulk} . The global-chemical kinetics involving the above species is given in Tables 1 and 2.

Table 1: Bulk-fuel reactions used in new global-chemistry model

Reaction				Activation Energy (kcal/mole/K)	Pre-Exponential	Reaction No
F	+	O_2	$\xrightarrow{k_4} ROO^\circ$	32.0	$2.5 \times 10^{13} \left(\frac{\text{mole}}{\text{m}^3 \text{s}}\right)$	(R4)
ROO°	+	F	$\xrightarrow{k_5} \text{Solubles}$	10.0	$1.0 \times 10^4 \text{ (s}^{-1}\text{)}$	(R5)
ROO°	+	F_s	$\xrightarrow{k_6} P$	15.0	$8.0 \times 10^9 \text{ (s}^{-1}\text{)}$	(R6)
ROO°	+	F	$\xrightarrow{k_7} D_{Bulk}$	10.0	$2.0 \times 10^2 \text{ (s}^{-1}\text{)}$	(R7)
P	+	F	$\xrightarrow{k_8} \text{Solubles}$	30.0	$3.2 \times 10^{12} \text{ (s}^{-1}\text{)}$	(R8)
D_{Bulk}	+	F	$\xrightarrow{k_9} 2 D_{Bulk}$	0	$1.0 \times 10^{-3} \text{ (s}^{-1}\text{)}$	(R9)

Table 2: Wall reactions used in new global-chemistry model

Reaction				Activation Energy (kcal/mole/K)	Pre-Exponential	Reaction No.
O_2	+	F	$\xrightarrow{k_{10}} P$	12.0	$5.2 \times 10^{-3} \text{ (m/s)}$	(R10)
		P	$\xrightarrow{k_{12}} D_{Wall}$	17.0	260 (m/s)	(R11)
		D_{Bulk}	$\xrightarrow{k_{12}} D_{Wall}$	10.0	0.80 (m/s)	(R12)

Reactions (R4) - (R9) occur in the fuel, whereas (R10) - (R12) are the termination reactions that occur on the walls. With this chemical mechanism, the peroxy radicals that are generated through the autoxidation reaction (R4) are assumed to have zeroth-order with respect to dissolved-oxygen concentration. However, as the oxygen concentration falls below the 10-ppm level, the mechanism switches to first-order reaction with oxygen. Some of the peroxy radicals are assumed to decompose to solubles through the reaction (R5). The remaining peroxide radicals are assumed to be involved in the generation of deposit-forming precursors (P) and bulk insolubles (D_{Bulk}) through separate pathways (R6) and (R7). Here, F_s is the component of the fuel that is assumed to be responsible for characterizing the thermal stability of the overall fuel. It could represent species such as copper, sulfur, and nitrogen. Note that F_s is a non-depleting species in the model and therefore, can also be viewed as a part of the pre-exponential of the Arrhenius rate expression for (R6). The precursor-removal reaction is retained in this model as (R8). Finally, the agglomeration of the bulk insolubles is chemically expressed as (R9). A zero activation energy for this reaction allows the growth of large-size particles in time. Note that the units for pre-exponentials in Tables 1 and 2 do not correspond to the bimolecular reactions as the concentrations of species F and F_s are assumed to be constant and are treated as portions of the respective pre-exponentials.

The above reaction mechanism yields precursors and bulk insolubles in the fuel which are then transported to the walls by diffusion and convection. All species except D_{Bulk} are assumed to have the same diffusion coefficient as oxygen. A measured value of $8.0 \times 10^{-8} \text{ cm}^2/\text{s}$ is used for the diffusion coefficient for the large D_{Bulk} particles;¹⁵ this is $\sim 10,000$ times smaller than the diffusion coefficient of the oxygen molecules and corresponds to a particle having a diameter of $0.3 \mu\text{m}$. The number of P and D_{Bulk} particles that attach to the wall and transform into wall deposit, D_{wall} , is dependent on the sticking probability and the concentration gradient of the respective species. The sticking probability is defined as the probability that a particle reaching the wall will remain at the wall and is usually characterized by an Arrhenius-type dependence on surface temperature.¹⁶ It is also known that the sticking probability decreases with increasing fuel velocity or flow rate due to shear force. Watkinson and Epstein¹⁷ argued that the sticking probability might display a stronger-than-linear dependence on the reciprocal of friction velocity (or square root of shear stress). Table 2 shows the wall reaction mechanism that is developed by considering the effect of temperature and velocity on the sticking probability.

The high viscosity of the fuel causes a laminar sub-layer of very slowly moving fluid to form adjacent to the walls. The longer residence time associated with this fluid and other unknown factors appear to cause the autoxidation reaction (R4) to under predict the chemical-reaction rate within this layer. Therefore, another autoxidation reaction which yields precursors directly is

included as a wall reaction (R10) in the model. The reactions (R11) and (R12) represent the attachment of particles P and D_{Bulk} to the wall. Finally, the rate of deposition on the wall is expressed as

$$\frac{d[D_{\text{wall}}]}{dt} = \frac{c}{(\tau_{\text{wall}})^{0.7}} \left\{ [P]_{\text{wall}} A_{11} e^{\left(-\frac{E_{11}}{RT}\right)} + [D_{\text{Bulk}}]_{\text{wall}} A_{12} e^{\left(-\frac{E_{12}}{RT}\right)} \right\} \quad (2)$$

where τ_{wall} is the shear stress at the wall and c is a constant that takes the units of $\tau^{0.7}$.

The new global-chemistry model described above is calibrated for Jet-A (USAF-2827) fuel using the experimental data in Figs. 1 and 2. It is assumed that the concentration of sulfur and other deposit-generating species (F_s) in this fuel is ~ 100 ppm. Values obtained for the pre-exponential and activation energy of each of the reactions (R4) - (R12) are given in Tables 1 and 2.

The calibrated deposition profiles at $T_B = 608$ and 543 K are shown in Fig. 2 with solid lines. The new model is able to correctly represent the changes in the magnitude and location of the deposition peaks for the two block temperatures. The broad-peak characteristic at higher block temperatures is well reproduced. At downstream locations ($x > 40 \text{ cm}$), the attachment of bulk-insoluble particles to the walls yields a fairly constant deposition which matches the experimental data. Overall, the new model yields a fairly accurate calibration for the experimental data.

With all values in Tables 1 and 2 being maintained constant, predictions are made for the 4-cc/min flow-rate case. Results in the form of deposition rate are shown with solid lines for the two block temperatures in Fig. 3. The deposition peak at this flow rate has moved from 9 to 16 cm when the block temperature was decreased from 608 to 543 K. This agrees favorably with the experimental results. The predicted shift in peak-deposition location with block temperature is due in part to the low activation energy (15 kcal/mole) used for the precursor-generation reaction (R6) and in part to the change in heat transfer. On the other hand, the shift in the peaks obtained by the simple two-step global-chemistry model (cf dashed lines in Fig. 3) was mainly due to the change in heat transfer as a result of the high activation energy (32.5 kcal/mole) of the autoxidation/precursor formation reaction. Choice of such a low activation energy for reactions similar to (R6) can also be found in the literature. In a study of autoxidation chemistry, Zabarnick¹⁸ proposed an activation energy of 10 kcal/mole for hydroperoxides formation based on H-atom abstraction reactions.¹⁹

The new model predictions for deposition profiles, including the tail regions at both block temperatures (solid lines in Fig. 3), are in good agreement with the experimental data. It is apparent from the shapes of the deposition profiles at $T_B = 608 \text{ K}$ in Figs. 2 and 3 that 1) the chemistry shown in Tables 1 and 2, except for reactions (R9) and (R12), is completed within the test-section and 2) the total deposition (i.e., area under the

curve) of $620 \mu\text{g/h}$ at 16 cc/min is nearly four times that of $182 \mu\text{g/h}$ at 4 cc/min . Reaction (R9) progresses very slowly and yields only small amounts of deposit at these flow rates. Since oxygen is the only consumable reactant in the model, the observation that the chemistry is completed in the test section suggests that the incoming oxygen is being totally consumed within the test section at both the 4- and 16 cc/min flow rates. Also, the total deposition for 16 cc/min is about 4 times that at 4 cc/min which, suggests that the total deposition is nearly proportional to the total amount of oxygen flowing through the tube.

The strong dependence of deposition on oxygen was studied experimentally by changing the amount of initial dissolved oxygen in the Jet-A fuel. The block temperature and fuel-flow rate were fixed at 573 K and 16 cc/min , respectively. The desired concentration of dissolved oxygen was achieved by initially sparging the fuel with nitrogen and then with a mixture of oxygen and nitrogen with a specified volumetric ratio. A GC system was used to measure the relative dissolved-oxygen concentration.¹⁰ This system was calibrated by assuming that the oxygen level obtained when the fuel was sparged with pure oxygen was the saturation value of 298 ppm . The total deposit inside the test section after 6 h of stressing was measured and the data are plotted in Fig. 4 for different initial dissolved-oxygen concentrations. The data show that the total deposition increases linearly with the amount of dissolved oxygen. Extrapolation of these data to very low oxygen concentrations indicates a threshold concentration below which no deposition occurs. This could be due to the well-known induction phenomenon²⁰ associated with fouling.

Calculations have been made for the same conditions using the two chemistry models discussed earlier. The results are shown in Fig. 4 along with the experimental data. It is important to note that the two-

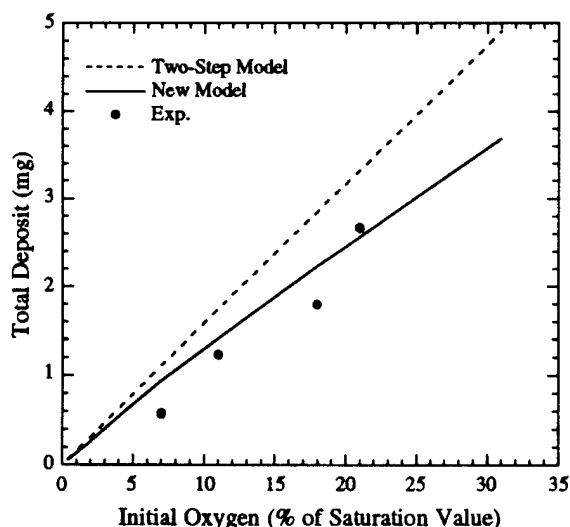


Fig. 4. Total deposit in tube for different levels of initial dissolved oxygen. Fuel flow rate 16 cc/min and $T_B = 573 \text{ K}$.

step and new global-chemistry models have been calibrated for the experimental data obtained with $T_B = 608 \text{ K}$. Both the two-step (dashed line) and new (solid line) models predict zero deposition only when no dissolved oxygen is present initially. This is expected since neither model takes into account induction behavior. In general, the two-step model over predicts deposition; however, it predicts the linear dependence between deposition and initial oxygen concentration. Predictions of the new model are in good agreement with the experimental results. The change in slope for the new-model calculations at about 7% initial oxygen concentration is due to the constraint that autoxidation switches from zeroth to first-order when the local oxygen level falls below the 10-ppm level used in the model.

Near-Isothermal Experiment

The ability of the models was further tested through prediction of deposition under different flow and temperature conditions. Using very low flow rates and longer test sections, Jones et al.⁸ were able to develop a near-isothermal heated-tube test section. They used the same Jet-A (USAF-2827) fuel as that employed in the Phoenix rig. The outside diameter and the length of the standard fuel tube were 0.3175 and 91.44 cm , respectively. Experiments were also conducted with tubes having a bore size about twice that of the standard ones. The central 81.28-mm section of the fuel tube was heated with a copper block which was maintained at a constant temperature. In some experiments a second heated test section was connected in series with the first one to capture the entire deposition profile. The experiments reported here were made at a copper block temperature of 458 K . Because of the low flow rates (usually less than 1 cc/min), fuel attains the block temperature within the initial 10 cm of the test section and remains isothermal in the remainder of the test section.

For a flow rate of 0.5 cc/min , the predicted and measured deposition inside the standard-size and larger-bore tubes is plotted in Fig. 5. In both tubes the deposition peaks predicted by the simple two-step model (dashed lines) are very close to the entrance to the heated section (note that the initial 5.08 cm of the tube was not heated). Whereas, in experiments, deposition peaks in the standard-size and larger-bore tubes occurred at about $x=70$ and 35 cm , respectively.

Results obtained with the new model are shown in Fig. 5 with the solid lines. The new model estimated the maximum deposition fairly well, but the locations of the predicted peaks do not match with those obtained in the experiments. However, the model predicted a shift in the locations of the peak deposition from $x = 27$ to 11 cm when the tube size was changed from standard to larger bore, which qualitatively agrees with experiments. The shift in deposition profiles in the calculations is occurring due to the difference in fuel residence times (fuel velocities) in the two tubes. Since the fuel in the two tubes is at a nearly constant temperature, the chemical reactions should progress

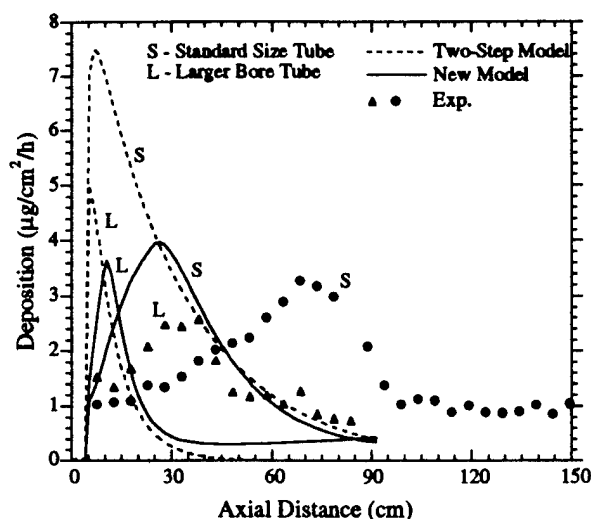


Fig. 5. Predicted and measured deposition in near-isothermal (458 K) heated-tube experiment using two different bore sizes.

identically with respect to residence time. As the same flow rate is employed, fuel in the larger-bore tube flows at a velocity equal to one-fourth that in the standard-size tube. If the initial 5.08 cm of tube section which is not heated is neglected, the two predicted spatial locations of the deposition peaks correspond to the same point on the residence time scale. However, the experimental data do not support this prediction. Peak deposition in the larger-bore tube occurs much later in time than that in the smaller, standard-size tube. In order to understand this difference between the calculations and the experimental data, oxygen consumption in the near-isothermal system is examined.

The expected amount of dissolved oxygen remaining in the fuel along the length of the standard-size tube is plotted in Fig. 6. Note that axial distance is replaced by residence time in this plot. Both the experimental and computed data were obtained by measuring oxygen content in the fuel at the exit of the tube at different flow rates (or residence times). It is evident that oxygen is depleting in the model much earlier than in the experiment (Fig. 6). This is felt to be the reason for the difference in the predicted and experimental deposition profiles in Fig. 5. The zeroth-order autoxidation reaction in the new model was actually calibrated using the data obtained at higher temperatures on a different rig. The data of Fig. 6 suggest that a single set of Arrhenius parameters is not sufficient to describe the autoxidation process in Jet-A fuel over a wide range of temperatures. These experimental data also indicate that initially oxygen consumption progresses very slowly and then at a rapid rate—a feature not observed at elevated temperatures. Jones et al.⁸ felt that some sort of autocatalysis mechanism triggers the higher oxygen consumption rate, while Heneghan and Zabarnick⁹ argued that radical chain reactions are responsible for this behavior. In either case, a single-step autoxidation

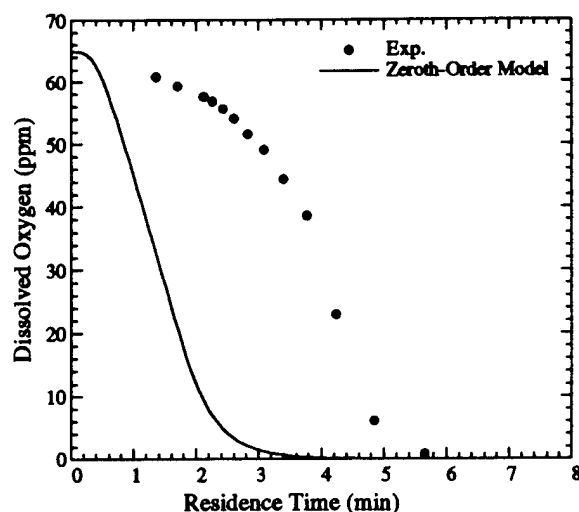


Fig. 6. Measured and computed dissolved oxygen for different residence times in near-isothermal (458 K) heated-tube experiment.

reaction cannot explain the change in oxygen consumption rate. Future efforts should be focused on improving the autoxidation reaction for a global-chemistry model which will be valid over a wide range of temperatures.

Overall, the new model has provided significant improvement in the prediction of fouling in heated tubes (cf Figs. 2 - 5). Although the chemistry model (cf Tables 1 and 2) contains several constants, most of them are felt to be fuel independent. To extend this model to a different fuel, one must calibrate the autoxidation reaction (R4) and determine the concentration of F_s in the fuel. Since F_s represents unknown species in the fuel, it will not be possible to measure its concentration in the near future. However, it may be possible to estimate F_s by conducting some simple static experiments.

Calibration of New Model with Static Experiments

Jones et al.¹⁵ have conducted static experiments in which a small amount of Jet-A fuel (330 cc) was placed in a flask and heated it to 485 K. Oxygen was continuously bubbled into the fuel at ~ 0.2 cc/min/cc of fuel. This agitation helped maintain equilibrium conditions for the fuel in the flask and replenished the fuel with oxygen as it was consumed. Off-line GC measurements showed a constant 49.5-ppm concentration of dissolved oxygen in the fuel. Small metal coupons, suspended in the flask, were submerged completely in the fuel. Typically, the experiments were conducted over a period of 6 h. Periodically, some of the metal coupons and small quantities of the fuel were extracted from the flask to determine the amount of insoluble solids present. The static flask experiments

are examined below to determine their usefulness in estimating values of F_8 in the new model.

The static experiment may be treated mathematically as a flowing system under the following conditions. First, the fuel is made to flow at a sufficiently low velocity through a tube such that it is basically static in the tube for the duration of the experiment. The tube is assumed to be heated with a copper block. The tube surface represents the metal coupons in the flask, and the bulk fuel in the tube represents the bulk fuel in the flask. Second, the isothermal conditions in the flask are simulated by instantaneously preheating the fuel to 485 K, the flask temperature, at time $t = 0$. This temperature is maintained for the duration of the experiment. Third, the dissolved oxygen in the fuel is replenished continuously as it is consumed (i.e., mathematically, the net rate of consumption of oxygen = 0). Because of the very low flow rate, fuel inside the tube attains chemical equilibrium very quickly which results in a uniform deposition rate along the tube. Assuming that all the constants in Tables 1 and 2 are fixed for the given fuel (for example Jet-A) then this deposition rate becomes a function of the concentration of F_8 only.

Predicted depositions on the tube wall for different concentrations of F_8 are shown in Fig. 7 as functions of stress duration (not residence time, since the fuel velocity is extremely low and only a small amount of fuel exits the tube). The computed deposition rates for F_8 concentrations of 150, 100 and 50 ppm are 6.25, 4.84, and 3.04 $\mu\text{g}/\text{cm}^2/\text{h}$, respectively. Experimental data obtained from the metal coupons are also plotted in Fig. 7. The slope of the bestfit line representing the experimental data is 3.58 $\mu\text{g}/\text{cm}^2/\text{h}$. This rate could be slightly higher since the deposit on the metal coupons in a static experiment is loosely bonded, and a fraction of

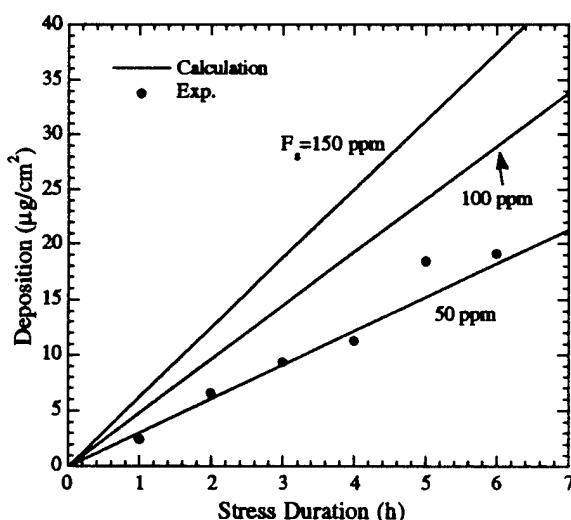


Fig. 7. Calculated and measured deposition on discs in static experiment. Small metal coupons (discs) were immersed in fuel at 485 K contained in a flask. Calculations were used to estimate concentration of F_8 in Jet-A fuel.

the total deposit might be lost during the washing and rinsing processes. With this in mind, a comparison between the calculated and experimental data yields a concentration between 50 and 100 ppm for F_8 in Jet-A. As seen from Figs. 2 - 5, a value of 100 ppm for F_8 yielded reasonable predictions for deposition for different temperatures and flow rates. A possible strategy for calibrating the new global-chemistry model given in Tables 1 and 2 for a new fuel is as follows: 1) determine the Arrhenius parameters for the autoxidation reaction (R4) by conducting relatively simple oxidation experiments using flowing systems such as the Phoenix rig, and 2) with all other constants unaltered, estimate the amount of F_8 present in the fuel by performing the inexpensive static experiments discussed above.

5 SUMMARY AND CONCLUSIONS

The simplified two-step global-chemistry models developed previously are not sufficient for simultaneous prediction of the deposition and oxidation rates associated with different fuels and operating conditions. Recent experiments with a Jet-A fuel have suggested that: 1) the rate of oxygen consumption is independent of the amount of dissolved oxygen, 2) wall deposition is not closely following the oxygen depletion even though the former strongly depends on the latter, and 3) wall temperature has a pronounced effect on deposition. Static experiments with this fuel also indicate that bulk insolubles and wall deposits are generated through separate chemical pathways. Based on these observations a new global-chemistry model was developed for fouling in heated tubes. A zeroth-order autoxidation reaction is incorporated into the model and is found to predict correctly oxygen depletion starting from different initial concentrations. More realistic wall-deposition profiles are obtained by introducing an intermediate species ROO^* , which is felt to be a product of fuel autoxidation, for the generation of deposit-forming precursors. Bulk insolubles are generated through the reaction (R7) and are allowed to agglomerate. The sticking probability which is a function of both wall temperature and friction velocity is incorporated into the new model for the attachment of precursors and bulk particles to the wall. The model has been successfully used to predict the changes in magnitude and location of the deposition peaks for the high temperatures and flow velocities of the Phoenix-rig experiments.

For near-isothermal, lower temperature, long-residence-time experiments, the new model did not correctly predict the location of peak deposition for two different tube diameters. The model predicted consumption of oxygen much earlier in these tubes than what was observed in the experiments. The disagreement between experimental results and predictions of the new model is possibly due to the lack of an autocatalysis-type mechanism in the global-chemistry model. Since the predicted deposition profiles for low-temperature conditions seem to be shifted only spatially from the experimental profiles (cf

Fig. 5), introduction of autocatalysis into the model might alleviate this problem.

The bulk insolubles D_{Bulk} in this study were used only to provide small amounts of deposit toward the end of the test section. In flowing experiments which employ pre-heated fuel, part or all of the precursor related-reactions could be completed within the pre-heater. Therefore, D_{Bulk} is expected to be the major contributor to wall deposition in preheated experiments. The new model has the potential for predicting deposition in such pre-heated-type flow systems. In order to explore this capability, the reactions (R7) and (R8) must be calibrated more accurately. Bulk insolubles that remain in the fuel also represent the filterable bulk deposits. Since the deposits that are collected by filters in the experiments represent only a fraction of the total bulk deposits (due to the practical size of the filter), no attempt is made to calibrate the model for bulk insolubles. However, future experiments with filters of different sizes might facilitate the determination of Arrhenius parameters for the reactions (R7) and (R8).

The CFDC model designed for flowing experiments has been successfully extended to simulation of static flask experiments in which metal coupons are used. Results suggest that the concentration of F_2 in a given fuel can be estimated using the quick and inexpensive static experiments. The flask experiments of Jones et al.¹⁵ also provide information on the growth of insolubles in the bulk fuel, in addition to the deposits on the metal coupons. If the reactions (R7) and (R8) could be calibrated using this information, then the static experiments would become an important tool in model calibration and development. However, this procedure must be examined in the future.

6 ACKNOWLEDGMENT

This work is supported, in part, by U. S. Air Force Contract F33615-90-C-2033 and, in part, by the Aerospace Sciences Directorate of the Air Force Office of Scientific Research under Work Unit 2308P700. The authors would like to thank Messrs. Chuck Martel and Ted Williams for providing with Phoenix-rig data and Steve Zabarnick and Shawn Heneghan for their helpful comments. Special thanks is given to Mrs. Marian Whitaker for editing this paper.

7 REFERENCES

1. Edwards, T., Anderson S. D., Pearce, J. A., and Harrison, W. E., "High Temperature Thermally Stable JP Fuels--An Overview," AIAA 92-0683, Presented at 30th Aerospace Sciences Meeting and Exhibit, Jan. 6-9, 1992, Reno, NV.
2. Marteney, P. J., and Spadaccini, L. J., "Thermal Decomposition of Aircraft Fuels," ASME Journal of Engineering for Gas Turbines and Power, Vol. 108, October 1986, pp. 648-653.

3. Edwards, T., Roquemore, W. M., Harrison, W. E., and Anderson S. D., "Research and Development of High Thermal Stability Fuels," Paper to be presented at AGARD Meeting on Fuels and Combustion Technology for Advance Aircraft Engines, Paper No. PEP-18, May 10-14, 1993, Colliferro, Italy.
4. Krazinski, J. L., Vanka, S. P., Pearce, J. A., and Roquemore W. M., "A Computational Fluid Dynamics and Chemistry Model for Jet Fuel Thermal Stability," Journal of Engineering for Gas Turbines and Power, Vol. 114, January 1992, pp. 104-110.
5. Katta, V. R., and Roquemore, W. M., "Numerical Method for Simulating Fluid-Dynamic and Heat-Transfer Changes in Jet-Engine Injector Feed-Arm due to Fouling," Journal of Thermophysics and Heat Transfer, Vol. 7, No. 3, July-Sept. 1993.
6. Patankar, S. V., and Spalding, D. B., "A Calculation Procedure for Three-Dimensional Parabolic Flows," International Journal of Heat and Mass Transfer, Vol. 15, October 1972, pp. 1787-1805.
7. Ballal, D. R., Byrd, R. J., Heneghan, S. P., Martel, C. R., Williams, T. F., and Zabarnick, S., "Combustion and Heat Transfer Studies Utilizing Advanced Diagnostics: Fuels Research," Wright Laboratory Technical Report WL-TR-92-2112, Nov. 1992, Wright-Patterson AFB, OH.
8. Jones, G., Balster, W. J., and Post, M. E., "Degradation of a Jet-A Fuel in a Single-Pass Heat Exchanger," to be presented at the International Gas Turbine and Aeroengine Congress and Exposition, May 24-27, 1993, Cincinnati, Ohio.
9. Heneghan, S. P., and Zabarnick, S., "Oxidation of Jet Fuels and the Formation of Deposits," To appear in Fuels, 1993.
10. Rubey, W. A., Tissandier, M. D., Striebach, R. C., and Tirey, D. A., "In Line Gas Chromatographic Measure of Trace Oxygen and other Dissolved Gases in Flowing, High Pressure, Thermally Stressed Fuel," Preprints Symposia - Structure of Jet Fuels III, Division of Petroleum Chemistry, American Chemical Society, Washington, D. C., Vol. 37, No. 2, pp. 371-376.
11. Marteney, P. J., "Thermal Decomposition of JP-5 in Long Duration Tests," Technical Report NAPC-PE-201C (Naval Propulsion Center, Trenton, NJ, 1988).
12. Chin, J. S., and Lefebvre, A. H., "Influence of Flow Conditions on Deposits from Heated Hydrocarbon Fuels," ASME Paper 92-GT-114.
13. Kauffman, R. E., University of Dayton Research Institute, Ohio, Private communications, 1993.
14. Jones, E. G., Balster, W. J., and Anderson, S. D., "Formation of Insolubles in Jet Fuels: Effects of Oxygen," Preprints Symposia-Structure of Jet Fuels III,

Division of Petroleum Chemistry, American Chemical Society, Washington, D. C., Vol. 37, No. 2, pp. 393-402

15. O'Hern, T., Sandia National Laboratories, Albuquerque, New Mexico, Private communication, Feb, 1993.

16. Epstein, N., "Fouling of Heat Exchangers," in Heat Exchangers Sourcebook, Ed., Pale, J. W., Hemisphere Publishing Co., Washington, D.C.

17. Watkinson, A. P., and Epstein, N., "Particulate Fouling of Sensible Heat Exchangers," in Proceedings of the 4th International Heat Transfer Conference, Vol. 1, Paper HE 1.6, pp. 12.

18. Zabarnick, S., "Chemical Kinetics Modeling of Jet Fuel Autoxidation and Antioxidant Chemistry," To be published in Fuels, 1993.

19. Benson, S. W., Thermochemical Kinetics, Wiley, New York, 1976.

20. Kendall, D. R., Houlbrook, G., Clark, R. H., Bullock, S. P., and Lewis, C., "The Thermal Degradation of Aviation Fuels in Jet Engine Injector Feed-Arms: Part 1 - Results from a Full-Scale Rig," Presented at the 30th International Gas Turbine Congress, Tokyo, October 1987.

Discussion

Question 1. M.F. Bardon

Are the various high temperature targets technically possible but too expensive at present, or are the higher ones, such as 900 degrees F, impossible at any price right now?

Author's Reply

The aircraft fuel with the highest thermal stability is JP-7. If one removes the dissolved oxygen from this fuel, it will come close to being JP-900 fuel. Our research is not far enough along to know if a JP-900 fuel can be developed when dissolved oxygen remains in the fuel.

Question 2. Dr L. Janovski

Your new global chemical model is approximate. How have you determined the values of the kinetic parameters? Metal is deactivated by coke deposits. What methods are used to take this into account in your model?

Author's Reply

The values of the parameters given in Tables 1 and 2 were determined by experience and the trial and error fitting with experimental data. A more systematic approach is needed but we have not yet looked into how to do this.

The model has a surface activation term that is important at low temperatures. In Reference 5, we used an empirically determined surface thickness term to change the rate of surface reaction. This term has not been put into the present model because there is concern about it being physically correct.



AIAA 95-0497

**Numerical Modeling of Deposition in
Fuel-Injection Nozzles**

L. P. Chin and V. R. Katta
System Research Laboratories, Inc.
A Division of Space Industries International, Inc.
Dayton, OH

**33rd Aerospace Sciences
Meeting and Exhibit
January 9-12, 1995 / Reno, NV**

NUMERICAL MODELING OF DEPOSITION IN FUEL-INJECTION NOZZLES

Long P. Chin* and Viswanath R. Katta†

Systems Research Laboratories, Inc.

A Division of Space Industries International, Inc.

Dayton, Ohio

ABSTRACT

A computational model based on the finite-difference method has been developed to simulate coke-deposition phenomena inside a fuel-injection nozzle. The conjugated heat transfer among gaseous-air, liquid-fuel, and solid metallic sections of the nozzle is treated by balancing the heat fluxes and temperatures at the interfaces. To account for the geometrical change of interface resulting from the buildup of deposits on the metal surface, the model is constructed using a separate boundary-oriented coordinate system in each section of the nozzle. The chemical kinetics of the deposition mechanism is treated mathematically using a global-chemistry model that was developed based on observations from some simple experiments. The primary focus of this paper is the prediction of the complex flow pattern, heat distribution, chemical activity, and, hence, deposition in a fuel-injection nozzle of an aircraft engine. An example is presented to demonstrate the capability of this model for a fuel nozzle with simplified geometry (axisymmetric). Results of flow visualization and calculated deposition rate along the fuel/wall interfaces are presented. As deposits begin to form on the inner surfaces of the nozzle, transient simulations show that the temperature on the outside metal wall of the nozzle is increasing and the temperature of the bulk fuel at the exit is decreasing slightly with time.

NOMENCLATURE

D diffusion coefficient
P control parameter used in stretching function
Q control parameter used in stretching function
T temperature
Y species mass concentration
c specific heat of fuel
h enthalpy

k turbulent kinetic energy
p pressure
s variable used in stretching function
r radial direction in cylindrical-coordinate system
z axial direction in cylindrical-coordinate system
u axial flow velocity
v radial flow velocity
t time

Greek symbols

Ω deposition rate in $\mu\text{g}/\text{cm}^2/\text{h}$
 Γ transport coefficient
 α geometrical parameter from coordinate transformation
 ξ generalized coordinate
 η generalized coordinate
 ρ density of fuel
 ε turbulent dissipation
 σ turbulent Prandtl number (or Schmidt number)
 μ viscosity of fuel
 κ thermal conductivity
 θ geometrical parameter of nozzle
 δ thickness of deposit
 τ shear stress
 $\dot{\omega}$ rate of reaction

Subscripts

d deposit
f interface between fuel and deposit
w interface between wall and deposit
n direction normal to an interface
i chemical species
t turbulence

INTRODUCTION

Studies on fuel-thermal-stability characteristics are important in the design of advanced aircraft engines. When a jet fuel is exposed to a wide range of thermal stresses for a

*Research Engineer, Research and Systems Engineering, 2800 Indian Ripple Road.

†Senior Engineer, Research and Systems Engineering, 2800 Indian Ripple Road. Member AIAA.

prolonged period of time in different components of the aircraft fuel system such as fuel-control valves, fuel nozzles, and injector feed-arms, it experiences thermal breakdown and forms insoluble gums and hard carbonaceous deposits which eventually lead to severe engine-fouling problems. In an aircraft engine the fuel-injection nozzle typically operates under high fuel- and wall-temperature conditions. As the fuel decomposes, the small passages and atomizers of the nozzle may become clogged which, in turn, will affect the characteristics of the spray pattern. For evaluation of the thermal stability of jet fuel in injection nozzles, several full-scale laboratory tests¹⁻³ have been conducted; from these the parameters of fuel thermal stability have been determined for different fuels in a variety of injection nozzles. Since each nozzle exhibits a different pattern of fuel thermal stability, test results from one type of fuel nozzle cannot be used for interpreting the deposition occurring in another type. This makes it difficult to design a fuel-injection nozzle based on the data acquired for the design of a previous one.

As an alternative approach, deposition problems in fuel-injection nozzles can be explored using numerical techniques such as the one described in this paper. In recent years, through integration of the Computational Fluid Dynamics with Chemistry (CFDC) models, several numerical codes⁴⁻⁶ have been developed for studying the fundamental mechanism governing fuel degradation. Because of past success in predicting deposition rates in some simple flowing systems, this type of CFDC model has become a useful research tool in the design of fuel-injection nozzles.

The numerical model used in this study is an extension of previous CFDC codes^{5,6} that were designed to study the deposition phenomena inside a heated straight tube. Because of the complicated structures of actual nozzles that are composed of more than one fuel passage, the conjugated heat transfer between the fuel passages has been taken into account in the present model.

In the present paper, results obtained for a typical fuel-injection nozzle with simplified geometry (axisymmetric) are presented. The configuration of the modeled nozzle is modified in such a way that it retains the important features of an actual pressurized fuel-injection nozzle. Since direct-deposition measurement results for the fuel nozzle are not available from thermal-stability tests, comparison with experiments is not made in this study. However, the results presented are explained based on the knowledge gained from previous applications of this model to simple flowing systems.⁵

MATHEMATICAL MODEL

Fuel-nozzle configuration and grid generation

The configuration and the geometrical parameters of the modeled fuel-injection nozzle used in the present study are shown in Fig. 1. The configuration shown was achieved by simplifying an actual pressurized fuel-injection nozzle for modeling with the present code and, at the same time, retaining important features such as flow passages and air

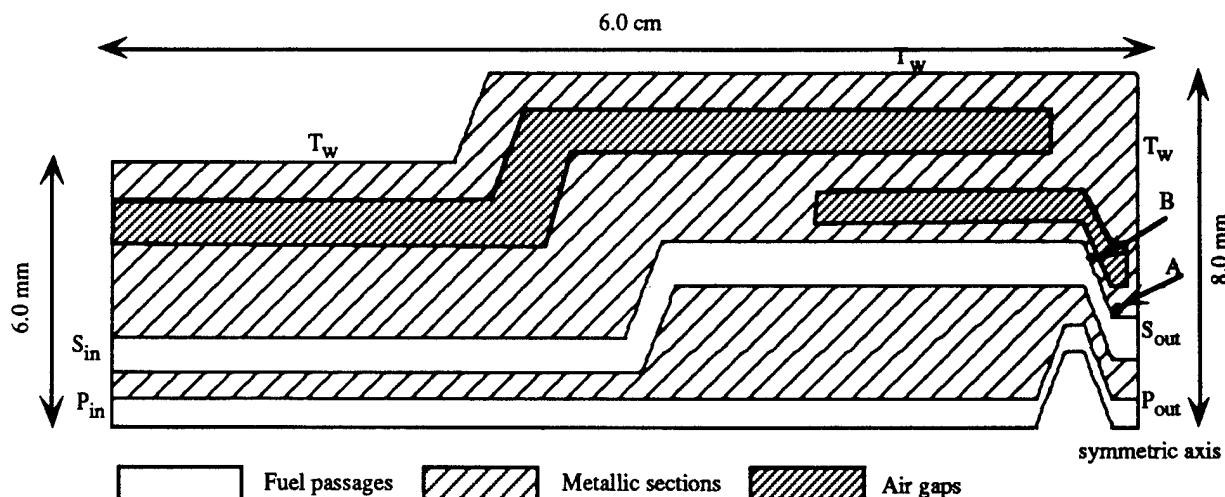


Figure 1. Configuration of modeled fuel-injection nozzle:

- P_{in} is the inlet of primary fuel passage (0.6 mm in radius); P_{out} is the exit of primary fuel passage;
- S_{in} is the inlet of secondary fuel passage (0.8 mm in width); S_{out} is the exit of secondary fuel passage;
- T_w is the outer-wall temperature specified as the thermal boundary condition for the nozzle;
- A and B are two selected locations where the data are shown in Fig. 7.

and metal gaps. The modeled nozzle is assumed to be of axisymmetric geometry and consists of two fuel passages--one for the primary fuel and the other for the secondary fuel. The primary fuel passes through the center of the nozzle and then splits into an annular passage that forms a "bridge"-shaped channel near the nozzle exit. The air gaps inserted annularly between the outside metal wall and the secondary fuel passage serve as thermal-insulation layers to prevent overheating of the fuel.

The grid system is generated for each section (air gap, liquid fuel, and metal wall) of the modeled nozzle using a two-boundary technique. Distribution of grids in each section is determined by the stretching functions imposed on the inner and outer boundaries. The stretching function

$$s = P\bar{z} + (1-P) \times \left(1 - \frac{\tanh[Q(1-\bar{z})]}{\tanh Q} \right); \quad 0 \leq \bar{z} \leq 1 \quad (1)$$

given by Eiseman⁷ was applied for all domains. Here P and Q are the parameters used to control the spacing between the grid points. For accurate resolution of the flow turning within the bends, finer grids in the bent regions of the fuel passages are incorporated.

Governing equations

Flow and thermal structures in the two fuel passages are simulated by solving the time-dependent Navier-Stokes equations along with the turbulent-energy, species-conservation, and enthalpy equations. Written in the z - r cylindrical coordinate system, these equations are expressed as follows:

$$\frac{\partial \rho}{\partial t} + \frac{\partial(\rho u)}{\partial z} + \frac{\partial(\rho v)}{\partial r} + \frac{\rho v}{r} = 0 \quad (2)$$

$$\begin{aligned} \frac{\partial(\rho \Phi)}{\partial t} + \frac{\partial(\rho u \Phi)}{\partial z} + \frac{\partial(\rho v \Phi)}{\partial r} &= \frac{\partial}{\partial z} \left(\Gamma_{\Phi} \frac{\partial \Phi}{\partial z} \right) \\ &+ \frac{\partial}{\partial r} \left(\Gamma_{\Phi} \frac{\partial \Phi}{\partial r} \right) - \frac{\rho v \Phi}{r} + \frac{\Gamma_{\Phi}}{r} \frac{\partial \Phi}{\partial r} + S_{\Phi} \end{aligned} \quad (3)$$

Here ρ , u , and v are the density and the axial and radial velocity components, respectively. Φ in Eq. (3) represents different variables conserved in the system. The source term S_{Φ} and the transport coefficients Γ_{Φ} associated with each of these equations are given in Table I. In the table, μ , κ , and c_p are the molecular viscosity, thermal conductivity, and specific heat of the fuel, respectively, and $\mu_t(C_{\mu}\rho k^2/\epsilon)$ is the turbulent viscosity incorporated through use of the $k-\epsilon$ turbulence model. G is the generation of turbulent energy by turbulent stress. The variables p , h , k , and ϵ are the pressure, enthalpy, and turbulent kinetic

Table I. Source terms and transport coefficients in governing equations.

Φ	Γ_{Φ}	S_{Φ}
u	$\mu + \mu_t$	$\frac{\partial}{\partial z}(\Gamma_u \frac{\partial u}{\partial z}) + \frac{\partial}{\partial r}(\Gamma_u \frac{\partial v}{\partial z}) - \frac{\partial p}{\partial z} + \frac{\Gamma_u}{r} \frac{\partial v}{\partial z}$
v	$\mu + \mu_t$	$\frac{\partial}{\partial z}(\Gamma_u \frac{\partial u}{\partial r}) + \frac{\partial}{\partial r}(\Gamma_u \frac{\partial v}{\partial r}) - \frac{\partial p}{\partial r} + \frac{\Gamma_v}{r} \frac{\partial v}{\partial r}$ $- 2\Gamma_v \frac{v}{r^2}$
k	$\mu + \frac{\mu_t}{\sigma_k}$	$G - \rho \epsilon$
ϵ	$\mu + \frac{\mu_t}{\sigma_{\epsilon}}$	$C_1 G \frac{\epsilon}{k} - C_2 \rho \frac{\epsilon^2}{k}$
h	$\frac{\kappa}{c_p} + \frac{\mu_t}{\sigma_h}$	0
Y_i	$\rho D_i + \frac{\mu_t}{\sigma_i}$	$\dot{\omega}_i$

energy and its dissipation, respectively, and σ is the turbulent Prandtl number (or Schmidt number) associated with a specific transport equation. Y_i , $\dot{\omega}_i$, and D_i are the mass fraction, rate of production, and diffusion coefficients of the i th species, respectively. The values of the constants used in the $k-\epsilon$ turbulence model are as follows: $C_{\mu} = 0.09$, $C_1 = 1.47$, $C_2 = 1.92$, $\sigma_k = 1.0$, $\sigma_{\epsilon} = 1.3$, $\sigma_h = 1.0$, and $\sigma_i = 1.0$. Since a wide temperature range exists within a fuel nozzle, the thermo-physical properties of the fluids vary significantly. In the present study, the transport properties along with the enthalpy and density of the fluid at a given temperature were obtained from the curve fits developed for Jet-A fuel and air. For the metal sections of the nozzle, the heat-conduction equation was solved using a constant value for the thermal conductivity.

To treat the boundary conditions accurately, a boundary-oriented curvilinear coordinate system in the ξ and η directions is used (see Fig. 2). The governing equations are discretized utilizing a hybrid scheme⁸ which is a second-order upwind scheme when the local Peclet number is greater than two. An implicit approach is employed to advance the calculations in time. The algebraic equations resulting from the discretized governing equations were solved using an Alternate Direction Implicit (ADI) algorithm.

The finite-difference form of the pressure Poisson equation is obtained by applying the "SIMPLE" technique⁸ developed for weakly compressible flows. In a generalized coordinate system, this SIMPLE method represents a nine-point pressure-correction scheme. Since the length of the fuel passage in a fuel-injection nozzle is usually much greater than the width, the ADI scheme will not yield an

accurate solution for the pressure at all grid points. Therefore, an iterative Modified Strongly Implicit Procedure (MSIP)⁹ which solves the system of equations to machine accuracy was employed for obtaining the pressure fields in different passages of the fuel-injection nozzle.

Interface formulations

The present model takes into account the changes in fluid-motion and heat-transfer characteristics in the fuel-injection nozzle as deposits build up on the metal surfaces. After each time step the geometries of the fuel/deposit interfaces in the fuel passages are allowed to change as part of the solution procedure. If Ω is the deposition rate in micrograms per square centimeter per hour, ρ_d is the deposit density in kilograms per cubic meter, and Δt is the time-step in hours, then the change in deposit thickness ($\Delta\delta_d = \delta_d^{n+1} - \delta_d^n$) after each time-step is calculated from (refer to Fig. 2)

$$\Delta\delta_d = r_d \left\{ 1 - \sqrt{(2\Omega\Delta t \cos \theta) / (10^3 \rho_d r_d)} \right\} \times \sqrt{1/\cos^2 \theta} \quad (4)$$

Once deposits form, they offer resistance to heat flow from the fuel to the metal surface and *vice versa*. Therefore, in balancing heat transfer along the fuel-deposit interfaces, the conduction of heat through the deposit must be taken into account. If the heat conduction in the ξ direction within the deposit is neglected, then the heat fluxes and the temperatures of the two interfaces (fuel-deposit and metal-deposit interfaces shown in Fig. 2) satisfy the following relationships:

$$T_f - T_w = \left(\frac{\eta_r}{\kappa_d} \right) \int_{r_w}^{r_f} \{ q_{n,w} \left(\frac{r_w}{r_f} \right)^\alpha \} dr \quad (5a)$$

$$\frac{q_{n,w}}{q_{n,f}} = \left(\frac{r_f}{r_w} \right)^\alpha; \quad \alpha = \left(\frac{\eta_r^2}{\eta_z^2 + \eta_r^2} \right)_d \quad (5b)$$

where subscript "n" denotes the direction normal to the interface, "w" represents the interface between the deposit and the metal wall, and "f" denotes the interface between the deposit and the fuel. κ_d is the thermal conductivity of the deposit, and α is a geometrical parameter evaluated based on the shape of the deposit. If overall heat balance in the entire fuel nozzle is to be achieved, Eqs. (5a) and (5b) must be satisfied at each time-step.

Deposition model

The global-chemistry-kinetics model developed by Katta et al.⁵ was incorporated in the present model to simulate the kinetic mechanism governing fuel deposition. This deposition model was successful in predicting deposition rates under a variety of thermal and flow conditions in several

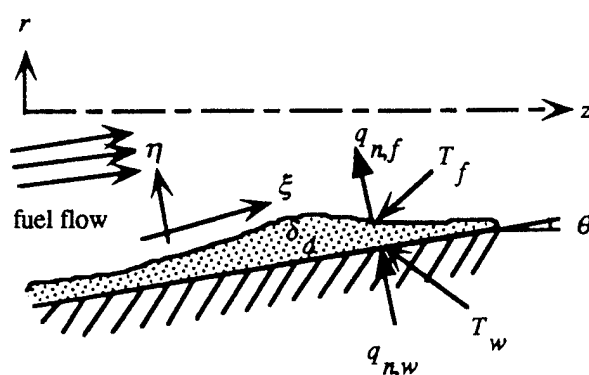
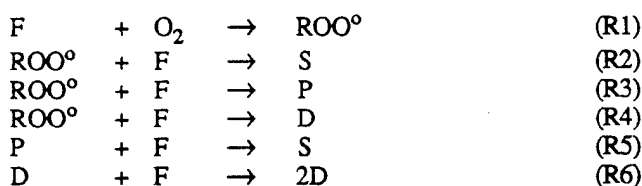
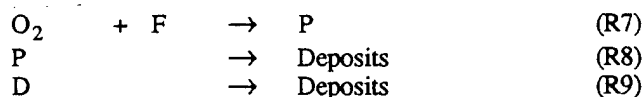


Figure 2. Interface models for deposition and heat transfer.

simple flowing thermal-stability rigs.^{10,11} Two types of reaction mechanisms are included in this model. The first--reactions that occur in bulk fuel--is represented by a type of mechanism which has the following six steps:



The peroxy radical [ROO°] generated through the autoxidation reaction (R1) is an intermediate species that reacts with the bulk fuel to produce solubles (S) through R2, deposit-forming precursors (P) through R3, and bulk insolubles (D) through R4. Decomposition of the precursor (R5) that is known to occur at high temperatures is also considered in this model. Finally, the agglomeration process of bulk insolubles is represented by R6. The second type of reaction mechanism proposed in this model--wall reactions--involves the following three steps:



As a result of convection and diffusion, the precursors (P) and bulk insolubles (D) generated in the bulk fuel (through R1-R6) stick to the metallic wall surface and form deposits through R8 and R9. The sticking probability for P and D particles that transform into wall deposits is assumed to have an Arrhenius-type dependence on surface temperature. The rate of deposition on the wall surface is expressed as⁵

$$\Omega = \frac{c}{(\tau_w)^{0.7}} \{ [P]_w \dot{\omega}_8 + [D]_w \dot{\omega}_9 \} \quad (6)$$

where $[D]_w$ and $[P]_w$ are the concentrations of precursors and bulk insolubles on the wall, respectively, $\dot{\omega}_8$ and $\dot{\omega}_9$ are the reaction rates of R8 and R9, respectively, and τ_w is the shear stress at the wall.

The global-chemistry model described above has been calibrated for a Jet-A fuel (referred to as POSF-2827 by the U. S. Air Force, Wright Laboratory) using the data obtained from two flowing experiments.^{10,11} Values obtained for the pre-exponential and the activation energy of each of the reactions (R1-R9) have been reported by Katta et al.⁵ The simulated results for the fuel-injection nozzle presented in the following sections were obtained based on this fuel.

RESULTS AND DISCUSSION

The simulations for a thermal and fluid condition which result in typical characteristics of deposition in a fuel-injection nozzle are presented and discussed. The mass flow rates of the fuel at two inlets and the boundary temperatures selected for this test are as follows:

- Inlet mass flow rate of the primary fuel: 6.4 kg/h
- Inlet mass flow rate of the secondary fuel: 6.4 kg/h
- Inlet temperature of the primary fuel: 177°C
- Inlet temperature of the secondary fuel: 177°C
- Outer wall temperature of the nozzle: 827°C

Based on the inlet flow rates selected for this test, the mean velocities at the entrances of the primary and secondary fuel passages are 2.0 and 0.4 m/s, respectively. Because of these high velocities, turbulent-flow calculations were performed. The outer-wall temperature of the nozzle (T_w) is used in the simulations as a constant-wall-temperature boundary condition at the outer and the right-side wall boundaries, as indicated in Fig. 1.

It is well known that temperature plays an important role in the phenomenon of decomposition of jet fuel. Generally speaking, when the fuel is near or above a certain temperature [e.g., JFTOT (Jet Fuel Thermal Oxidation Tester) breakpoint], decomposition begins and becomes progressively worse as the temperature increases. However, at very

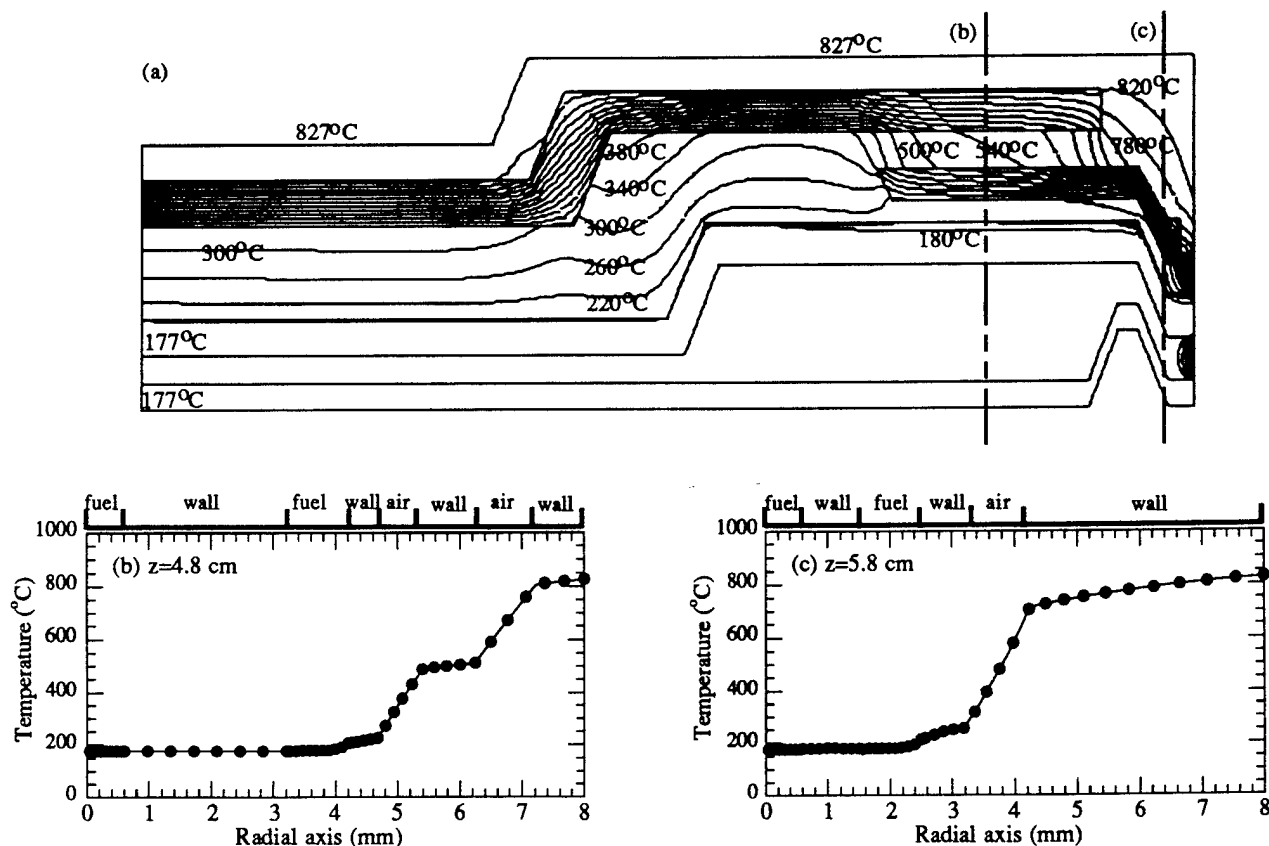


Figure 3. Calculated temperature distributions of the fuel nozzle. (a) iso-contours of the whole nozzle; (b) radial distribution at $z = 4.8$ cm; (c) radial distribution at $z = 5.8$ cm.

high temperatures the deposition on the walls and the concentration of peroxide radicals in the bulk fuel are known to decrease. The drop-off in deposition rate at higher temperatures has been taken into account in the global-chemistry model, as represented by R5. In Fig. 3, the iso-contours of calculated temperature for the entire fuel nozzle are shown along with the radial distributions at two selected axial locations ($z = 4.8$ and 5.8 cm from the inlet of the nozzle). It can be clearly seen that the temperature decreases significantly from the outer walls of the nozzle toward the inner fuel passages as a result of cooling conducted by the fast-flowing fuels having low inlet temperatures. Since the thermal conductivity of air is much lower than that of the metallic part of the nozzle, the temperature profiles within the air gaps have much steeper slopes than those in the metallic parts of the nozzle [refer to Figs. 3(b) and (c)]. It should be mentioned that the radiative and convective (particularly, natural convection) heat-transfer mechanisms are not included in the present model. However, these two factors will be incorporated into the thermal model when it is extended to 3-D applications.

Figures 4(a) and 4(b) show the calculated bulk-fuel and wall-temperature profiles along the streamwise direction of the two fuel passages. Note that data for only a 0.3-cm segment of the primary fuel passage [Fig. 4(a)] and a 4-cm segment of the secondary fuel passage [Fig. 4(b)] near the exits of the nozzle are shown. The bulk-fuel temperature was obtained by mass averaging the radial-temperature profile across the cross section of the fuel passage at a given axial location. Because of the high flow rates employed in the test, the increase of bulk-fuel temperature is very small throughout the nozzle ($< 1^\circ\text{C}$ for the fuel in the primary passage and 5°C for the fuel in the secondary passage). Temperatures on the wall surfaces (interfaces between deposit and wall) in both fuel passages increase rapidly near the exits where the nozzle is exposed to a high-temperature environment. The temperature distribution along the outer wall surface of the secondary fuel passage is more complicated as seen in Fig. 4(b). Two sharp temperature peaks appearing at $z = 3.3$ and 5.7 cm correspond to regions in the secondary passage where the fuel turns upward and downward in the bent segments, respectively. The drop-off in temperature at about $z = 4.2$ cm between the two peaks mentioned above results from insertion of the second (shorter) air gap that becomes effective at this location.

Since the bulk-fuel temperature under this test condition is below the breakpoint temperature (225°C) of this fuel (POSF-2827) and the residence time of fuel in the nozzle is very short (< 0.03 s in the primary fuel passage and < 0.1 s in the secondary passage), it is expected that the deposition on the wall surface is primarily determined by the temperature on the wall rather than the temperature of the bulk fuel. In other words, the wall reactions (R7-R9) presented in the global-chemistry model are the dominant mechanisms for the deposition process. The calculated deposition rates on the wall surfaces in the secondary fuel passage are shown in Fig. 5. The calculated deposition rates

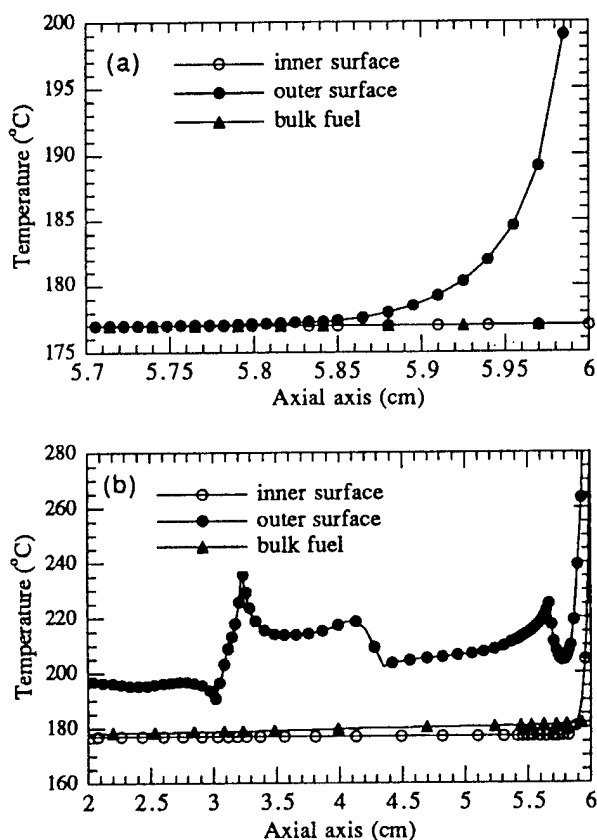


Figure 4. Calculated axial-temperature distributions in (a) primary fuel passage and (b) secondary fuel passage.

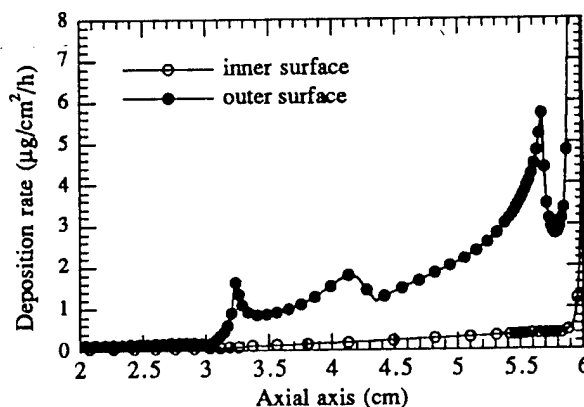


Figure 5. Predicted deposition rates on the two surfaces of the secondary fuel passage.

for the primary fuel passage are not shown in this paper because the amount of deposits predicted is too small to be meaningful compared with the noise level usually measured in actual thermal-stability tests. Figure 5 shows that the profiles of deposition rate on both the inner and the outer walls have a strong dependence on wall temperature. This phenomenon has also been observed in experiments on the EDTST¹² (Extended Duration Thermal Stability Test) system conducted at Wright Laboratory. The EDTST system was designed to evaluate fuel thermal stability in straight tubes under flow and temperature conditions similar to those experienced by an actual aircraft engine. The EDTST system results show that deposits increase exponentially as a function of wetted-wall temperature (peak temperature on the wall in the EDTST system). Because of the similarity between the EDTST system and the fuel-injection nozzle, the experimental data obtained from the EDTST tests are valuable for calibrating the wall-reaction parameters of the global-chemistry model.

The two sharp temperature peaks on the outer surface of secondary fuel passage result in two corresponding peaks in the distribution of deposition rate, as shown in Fig. 5. It is interesting to note that the sharp peak in deposition rate downstream (at $z = 5.7$ cm) is four times larger in amplitude than for the sharp peak upstream (at $z = 3.3$ cm), despite the fact that the wall temperature at $z = 5.7$ cm is slightly lower than that at $z = 3.3$ cm. In order to understand this inverse dependence of deposition rate on wall temperature, another variable--the concentration of main reacting species--that affects the deposition process must be examined. As expressed in Eq. (6), the deposition rate is influenced by the following four variables: (1) shear stress at the wall (τ_w), (2) temperature on the wall surface (T_w), (3) precursor concentration ($[P]$) near the wall, and (4) bulk-insoluble concentration ($[D]$) near the wall. For the given flow conditions, if the reaction rate of R9 (i.e., $\dot{\omega}_9$) is much smaller than the reaction rate of R8 ($\dot{\omega}_8$) because of the lower concentration of $[D]$, then the amount of deposits transformed from bulk insolubles (D) will be negligibly small in comparison to that transformed from the precursors.

The iso-contours of concentration for two main species (dissolved oxygen and precursor) in the straight segment (from $z = 3.3$ to $z = 5.7$ cm) between two bent regions of the secondary passage are shown in Figs. 6(a) and 6(b). Since the rates for all the reactions (R1 - R9) in the present deposition model are assumed to have an Arrhenius form with positive activation energies, the consumption of dissolved oxygen will be faster in the high-temperature regime [upper-right-side region in Figs. 6(a) and 6(b)] than in the low-temperature regime [lower-left-side region in Figs. 6(a) and 6(b)]. As Fig. 6(a) shows, the iso-contours for oxygen concentration closely reflect the distribution of fuel temperature. An initial level of 50 ppm (parts per million by weight) for dissolved oxygen was used for this fuel.

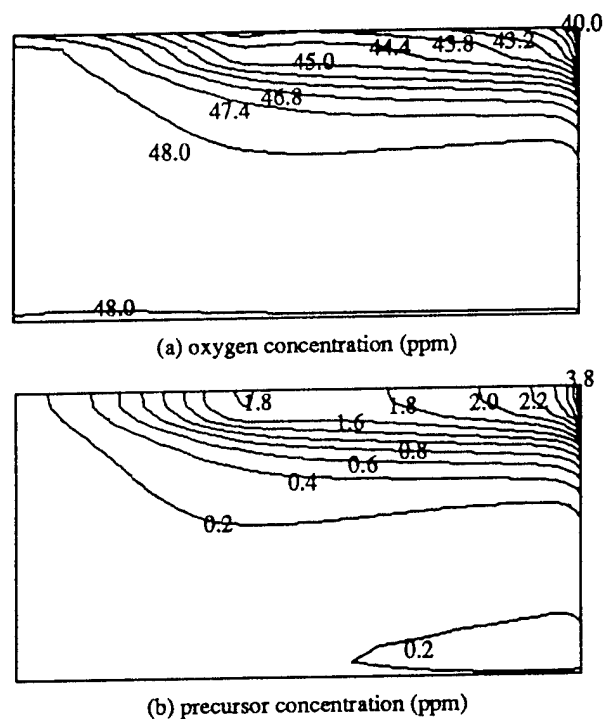


Figure 6. Iso-contours of concentration of dissolved oxygen and deposit-forming precursor in the secondary fuel passage. Plots are shown only in the straight segment from $z = 3.3$ to 5.7 cm.

Similarly, the precursors generated through reaction R3 should have a higher concentration in the high-temperature regime. The distribution of precursor concentration may become complicated as the decomposition of precursor through R5 consumes part of the precursors generated in the high-fuel-temperature regime. However, the resulting distribution of precursor concentration as shown in Fig. 6(b) does not reveal significant influence from the mechanism of precursor decomposition in this straight region. As a result of the combined effects of the wall temperature and the precursor concentration, the deposition in a low-temperature region will become worse if the deposit-forming precursor is sufficiently high in concentration. This suggests that the worst deposition will not always occur where the temperature is highest in the nozzle.

Finally, the results of the transient simulation, which was performed to explore the influence of deposits accumulated inside the fuel nozzle on the metal-wall and fuel temperature, are presented and discussed. A deposit density of 1 gm/cm^3 determined experimentally by Marteney¹³ was used in the model. The value of $0.1 \text{ W/m}^2\text{C}$ used for the thermal conductivity of the deposit is near that of $\sim 0.16 \text{ W/m}^2\text{C}$ found by Goodman and Bradley.¹⁴ The total weight of the deposits collected on the walls of the secondary fuel passage for a 30-hr period is plotted in Fig. 7. Also in this

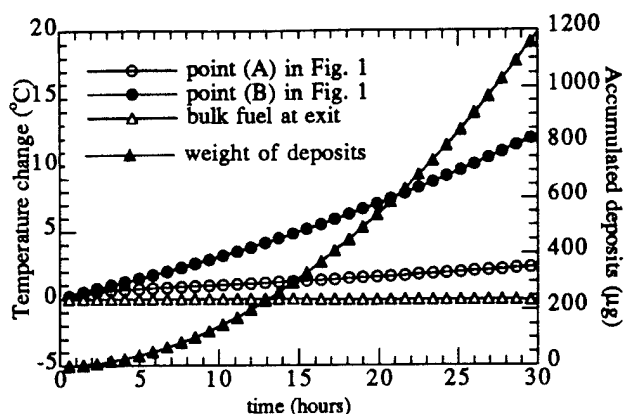


Figure 7. Temperature changes in the nozzle resulting from the increase in deposits accumulated on the wall surfaces in the secondary passage.

plot are the calculated temperature history of the wall at the two locations marked in Fig. 1 and the calculated temperature history of the bulk fuel at the nozzle exit. As mentioned earlier, the deposits offer resistance to heat flow from the fuel to the metal surface and *vice versa*. The growth of deposits on the wall surface reduces the heat transport from the high-temperature side (i.e., outer metallic part) to the low-temperature side (i.e., fuel passages) of the nozzle. As a result, the temperature in the outer metal part of the nozzle increases, whereas the temperature of bulk fuel decreases with time. As can be seen in Fig. 7, the temperatures at locations (A) and (B) increase around 12 and 30°C, respectively, during the 30-hr period. However, the temperature of the bulk fuel at the nozzle exit changes only slightly, and a total decrease of 0.5°C is recorded in 30 hr. The high flow rates employed in this test and the large percentage of deposits formed near the nozzle exit contribute to this small decrease in bulk-fuel temperature.

CONCLUSIONS

A numerical model for studying the formation of deposits in a fuel-injection nozzle has been presented. A global-deposition model which has been successfully used in predicting deposition rates for thermally stressed fuel in straight tubes was employed to simulate the chemical kinetics of the fuel-degradation process in fuel-injection nozzles. The characteristics and pattern of the deposition rate under practical flow conditions were obtained and discussed. The deposition rates predicted result primarily from wall reactions that are strongly dependent on the wetted-wall temperature and precursor concentration. For the transient study, the buildup of deposits on the wall surfaces is accompanied by an increase in outer-wall temperature and a decrease of bulk fuel near the nozzle exit. The present work primarily illustrates the usefulness of the Computational Fluid Dynamics with

Chemistry (CFDC) model in understanding the deposition process in a fuel-injection nozzle. In the future, predictions will be compared with the results of direct measurements of deposits when they become available.

ACKNOWLEDGMENTS

This work was supported by the U. S. Air Force under Contract F33615-90-C-2033. The authors would like to thank Dr. Mel Roquemore and Dr. Andy Brankovic for their valuable comments on this work. Special thanks to Ms. Marian Whitaker for editorial comments and preparation of the manuscript.

REFERENCES

1. Gleason, C. C., Oller, T. L., Shayeson, M. W., and Bahr, D. W., 1979, "Evaluation of Fuel Character Effects on the F101 Engine Combustion System," Technical Report AFAPL-TR-79-2018, Air Force Aero Propulsion Laboratory, Wright-Patterson Air Force Base, OH.
2. Morton, H. L., 1986, "Effects of Fuel Composition on T700 and F404 Engine Hot Section Components - Lot II," Report No. NAPC-PE-117C, Final Report, Vol. I, Naval Aero Propulsion Center, Trenton, NJ.
3. Tyler, J. C., Cuellar, J. P., Jr., and Moses, C. A., 1987, "Alternate Test Procedure to Qualify Fuels for Navy Aircraft, Phase II Continuation," Final Report, Vol. I, "Hot Fuel Nozzle Fouling," Report No. NAPC-PE-176C, Naval Aero Propulsion Center, Trenton, NJ.
4. Krazinski, J. L., Vanka, S. P., Pearce, J. A., and Roquemore, W. M., 1992, "A Computational Fluid Dynamics and Chemistry Model for Jet Fuel Thermal Stability," Journal of Engineering for Gas Turbines and Power, Vol. 114, pp. 104-110.
5. Katta, V. R., Jones, E. G., and Roquemore, W. M., 1993, "Development of Global-Chemistry Model for Jet-Fuel Thermal Stability Based on Observations from Static and Flowing Experiments," Report No. AGARD-CP-536, Paper No. 19, Advanced Group on Aerospace Research and Development, Neuilly sur Seine, France.
6. Katta, V. R., and Roquemore, W. M., 1993, "Numerical Method for Simulating Fluid-Dynamic and Heat-Transfer Changes in Jet-Engine Injector Feed-Arm Due to Fouling," Journal of Thermophysics and Heat Transfer, Vol. 7, No. 4, pp. 651-660.
7. Eiseman, P. R., 1978, "A Coordinate System for a Viscous Transonic Cascade Analysis," Journal of Computational Physics, Vol. 26, pp. 307-338.

8. Patankar, S. V., 1980, "Numerical Heat Transfer and Fluid Flow," Hemisphere Publishing Corp., Washington, D. C.
9. Schneider, G. E., and Zedan, M., 1981, "A Modified Strongly Implicit Procedure for the Numerical Solution of Field Problems," *Journal of Computational Physics*, Vol. 4, pp. 1-19.
10. Ballal, D. R., Byrd, R. J., Heneghan, S. P., Martel, C. R., Williams, T. F., and Zabarnick, S., 1992, "Combustion and Heat Transfer Studies Utilizing Advanced Diagnostics: Fuels Research," Technical Report WL-TR-92-2112, Wright Laboratory, Wright-Patterson Air Force Base, OH.
11. Jones, G., Balster, W. J., and Post, M. E., 1993, "Degradation of a Jet-A Fuel in a Single-Pass Heat Exchanger," ASME Paper No. 93-GT-334, Presented at the International Gas Turbine and Aeroengine Congress and Exposition, Cincinnati, OH.
12. Dieterle, G. L., and Binns, K. E., 1994, "Evaluation of High Thermal Stability Fuels for Future Aircraft," AIAA Paper No. 94-3171, Presented at the 30th AIAA/ASME/SAE/ASEE Joint Propulsion Conference, Indianapolis, IN.
13. Marteney, P. J., 1988, "Thermal Decomposition of JP-5 in Long Duration Tests," Technical Report TR NAPC-PE-201C, Naval Propulsion Center, Trenton, NJ.
14. Goodman, H., and Bradley, R., 1970, "High Temperature Hydrocarbon Fuels Research in an Advanced Aircraft Fuel System Simulator," Technical Report TR-70-13, Air Force Aero Propulsion Laboratory, Wright-Patterson AFB, OH.

In *Emerging Energy Technology* (Proc. ASME Emerging Energy Symposium, 29 January - 6 February 1995, Houston, TX) (G. A. Karim, Ed.) (American Society of Mechanical Engineers, New York, 1995), PD-Vol. 6, pp. 67-74.

NUMERICAL MODELING OF DEPOSITION IN FUEL-INJECTION NOZZLES

Long P. Chin and Viswanath R. Katta
Systems Research Laboratories, Inc.
A Division of Space Industries International, Inc.
Dayton, Ohio

ABSTRACT

A computational model based on the finite-difference method has been developed to simulate coke-deposition phenomena inside a fuel-injection nozzle. The conjugated heat transfer among gaseous air, liquid fuel, and solid metallic sections of the nozzle is treated by balancing the heat fluxes and temperatures at the interfaces. To account for the geometrical change of interface resulting from the buildup of deposits on the metal surface, the model is constructed using a separate boundary-oriented coordinate system in each section of the nozzle. The chemical kinetics of the deposition mechanism is treated mathematically using a global-chemistry model that was developed based on observations from some simple experiments. This paper is primarily focused on the prediction of the complex flow pattern, heat distribution, chemical activity, and, hence, deposition in a simplified fuel nozzle of an aircraft engine. Calculations are made for two cases by choosing different flow and temperature conditions. Results in terms of flow visualization and deposition rate along the fuel/wall interfaces are presented.

NOMENCLATURE

P control parameter used in stretching function
Q control parameter used in stretching function
T temperature
c constant in Eq. (3)
s variable used in stretching function
r radial direction in cylindrical-coordinate system.
z axial direction in cylindrical-coordinate system
t time

Greek symbols

Ω deposition rate in $\mu\text{g}/\text{cm}^2/\text{h}$
 α geometrical parameter from coordinate transformation
 ξ generalized coordinate
 η generalized coordinate
 θ geometrical parameter of nozzle
 δ thickness of deposit

τ shear stress
 $\dot{\omega}$ rate of reaction

Subscripts

d deposit
f interface between fuel and deposit
w interface between wall and deposit
n direction normal to interface

INTRODUCTION

Studies on fuel-thermal-stability characteristics are important in the design of advanced aircraft engines. When a jet fuel is exposed to a wide range of thermal stress for a prolonged period of time in components of the aircraft fuel system, it experiences thermal breakdown, forming insoluble gums and hard carbonaceous deposits which eventually lead to severe engine-fouling problems. In an aircraft engine the fuel-injection nozzle typically operates under high fuel and wall-temperature conditions. As the fuel decomposes, the small passages and atomizers of the nozzle may become clogged which, in turn, will affect the characteristics of the spray pattern. For evaluation of the thermal stability of jet fuel in injection nozzles, several full-scale laboratory tests (Gleason et al., 1979; Morton, 1986) have been conducted from which the parameters of fuel thermal stability have been determined for different fuels in a variety of injection nozzles. Since each nozzle exhibits a different pattern of fuel thermal stability, test results from one type of fuel nozzle cannot be used for interpreting the deposition occurring in another type.

As an alternative approach, deposition problems in fuel-injection nozzles can be explored using numerical techniques such as the one described in this paper. In recent years, by integration of the Computational Fluid Dynamics with Chemistry (CFDC) models, several numerical codes (Krazinski et al., 1992; Katta et al., 1993a; Katta and Roquemore, 1993b) have been developed for studying the fundamental mechanism governing fuel degradation. Past success in predicting deposition rates in some simple

flowing systems has made this type of CFDC model a useful research tool in the design of fuel-injection nozzles.

The numerical model used in this study is an extension of the previous CFDC codes (Katta et al., 1993a; Katta and Roquemore, 1993b) that were designed to study the deposition phenomena inside a heated straight tube. In order to consider the complicated structures of actual nozzles that are composed of more than one fuel passage, the conjugated heat transfer between the fuel passages has been taken into account in this model.

From the present study, results obtained for a typical fuel-injection nozzle with simplified geometry (axisymmetric) are presented. Since the direct deposition measurement results for the fuel nozzle are not available from the thermal-stability tests, comparison with experiments is not made in this study. However, the results presented are explained based on the knowledge gained from previous applications of this model to simple flowing systems (Katta et al., 1993a).

MATHEMATICAL MODEL

Fuel-nozzle configuration and grid generation

The configuration and the geometrical parameters of the modeled fuel-injection nozzle used in the present study are shown in Fig. 1. The configuration shown was obtained by simplifying an actual pressurized fuel-injection nozzle for modeling with the present code and, at the same time, retaining the important features such as flow passages and air and metal gaps. The modeled nozzle is assumed to be axisymmetric in geometry and consists of two fuel passages—one for the primary fuel and the other for the secondary fuel. The primary fuel passes through the center of the nozzle and then splits into an annular passage, forming a "bridge"-shaped channel near the nozzle exit. The air gap inserted annularly between the outside metal wall and the secondary fuel passage serves as a thermal-insulation layer to prevent the fuel from becoming overheated.

The grid system is generated for each section (air gap, liquid fuel, and metal wall) of the modeled nozzle using a two-boundary technique. The stretching function

$$s = Pz^* + (1 - P)\left(1 - \frac{\tanh[Q(1 - z^*)]}{\tanh Q}\right); \quad 0 \leq z^* \leq 1 \quad (1)$$

given by Eiseman (1978) was applied for all domains. Here P and Q are the parameters used to control the spacing between the grid points.

Governing equations

Flowfields in the two fuel passages and in the air gap are simulated by solving the time-dependent Navier-Stokes equations along with the turbulent-energy, species-conservation, and enthalpy equations in the z - r cylindrical coordinate system. Since a wide range of temperature exists within a fuel nozzle, the thermo-physical properties of the fluids vary significantly. In the present study, the transport properties along with the enthalpy and density of the fuel at a given temperature were obtained from the curve fits developed for Jet-A fuel and air. For the metal sections of the nozzle, the heat-conduction equation was solved using a constant value for the thermal conductivity. The algebraic equations resulting from the discretized governing equations were solved using an Alternate Direction Implicit (ADI) algorithm.

The finite-difference form of the pressure Poisson equation is obtained by applying the "SIMPLE" technique (Patankar, 1980). In a generalized coordinate system, this "SIMPLE" method represents a nine-point pressure-correction scheme. Since the width of the flow passage in a fuel-injection nozzle is usually much smaller than the passage length, the ADI scheme will not yield an accurate solution for the pressure at all grid points. Therefore, an iterative Modified Strongly Implicit Procedure (MSIP) (Schneider and Zedan, 1981) which solves the system of equations to machine

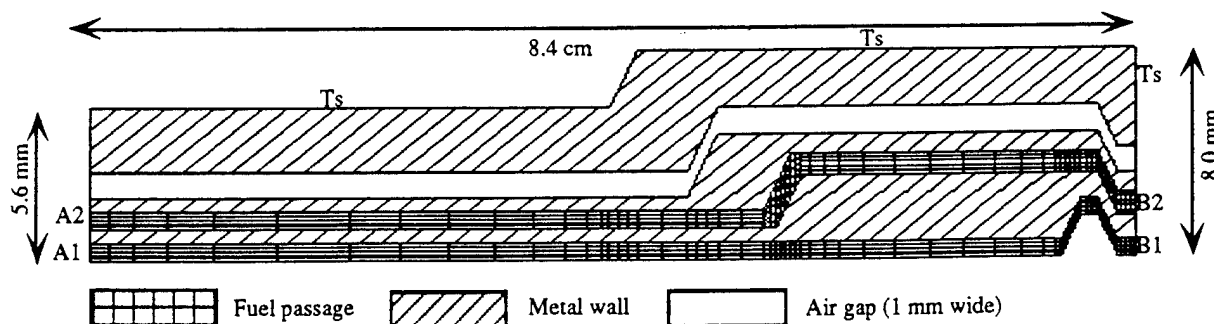


Figure 1. Configuration of modeled fuel-nozzle :

A1 is the inlet of primary fuel passage (0.64 mm in radius); B1 is the exit of primary fuel passage;
A2 is the inlet of secondary fuel passage (0.68 mm in width); B2 is the exit of secondary fuel passage;
Ts is the outer wall temperature specified as the thermal boundary condition for the nozzle.

accuracy was employed for obtaining the pressure fields in different passages of the fuel-injection nozzle.

Interface formulations

The present model takes into account the changes in fluid motion and heat-transfer characteristics in the injection nozzle as deposits build up on the metal surfaces. Once the deposits form, they offer resistance to the heat flow from the fuel to the metal surface and *vice versa*. Therefore, in balancing heat transfer along the fuel-deposit interfaces, the conduction of heat through the deposit must be considered. If the heat conduction in the ξ direction is neglected within the deposit, then the heat fluxes and the temperatures of the two interfaces (fuel-deposit and metal-deposit interfaces shown in Fig. 2) satisfy the following relationships:

$$T_f - T_w = \left(\frac{\eta_f}{\kappa_d} \right) \int_{r_w}^{r_f} \left(q_{n,w} \left(\frac{r_w}{r_f} \right)^\alpha \right) dr \quad (2a)$$

$$\frac{q_{n,w}}{q_{n,f}} = \left(\frac{r_f}{r_w} \right)^\alpha; \quad \alpha = \left(\frac{\eta_f^2}{\eta_z^2 + \eta_r^2} \right)_d \quad (2b)$$

where subscript "n" denotes the direction normal to the interface, "w" represents the interface between the deposit and the metal wall, and "f" denotes the interface between the deposit and the fuel. κ_d is the thermal conductivity of the deposit, and α is a geometrical parameter evaluated based on the shape of the deposit. If overall heat balance in the entire fuel nozzle is to be achieved, Eqs. (2a) and (2b) must be satisfied at each time-step.

Deposition model

The global-chemistry-kinetics model developed by Katta et al. (1993a) was incorporated in the present model to simulate the kinetic mechanism governing fuel deposition. This deposition model was successful in predicting the deposition rates in several simple flowing thermal-stability rigs (Ballal et al., 1992; Jones et al., 1993) under a variety of thermal and flow conditions. Two types of reaction mechanisms are included in this model. The first-reactions that occur in bulk fuel--is represented by a type of mechanism which has the following six steps:

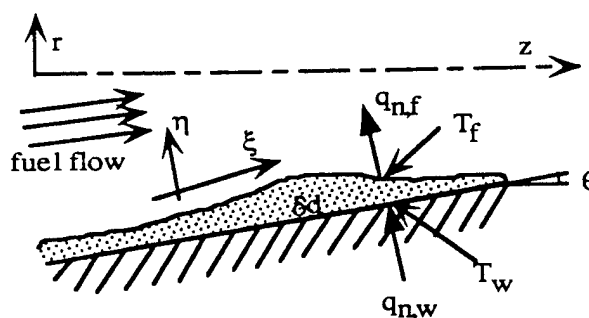
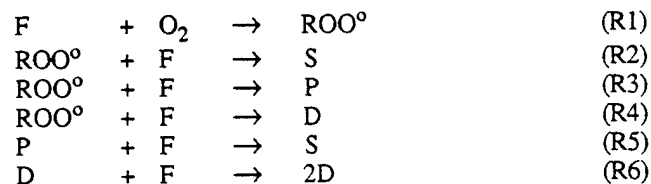
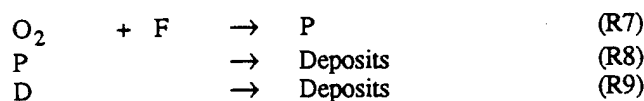


Figure 2. Interface models for deposition and heat transfer.

The peroxy radicals (ROO°) generated through the auto-oxidation reaction (R1) react with the bulk fuel to produce solubles (S) through R2, deposit-forming precursors (P) through R3, and bulk insolubles (D) through R4. The decomposition of the precursor (R5) that is known to occur at high temperatures is also considered in this model. Finally, the agglomeration process of bulk insolubles is represented by R6. The second type of reaction mechanism proposed in this model--wall reactions--involves the following three steps:



As a result of convection and diffusion, the precursors (P) and bulk insolubles (D) generated in the bulk fuel (through R1-R6) stick to the metallic wall surface and form deposits through R8 and R9. The sticking probability for P and D particles that transform into wall deposits is assumed to have an Arrhenius-type dependence on surface temperature. The rate of deposition on the wall surface is expressed as (Katta et al., 1993a)

$$\Omega = \frac{c}{(\tau_w)^{0.7}} ([P]_w \dot{\omega}_8 + [D]_w \dot{\omega}_9) \quad (3)$$

where $[D]_w$ and $[P]_w$ are the concentrations of precursors and bulk insolubles on the wall, respectively, $\dot{\omega}_8$ and $\dot{\omega}_9$ are the reaction rates of R8 and R9, and τ_w is the shear stress at the wall.

The global-chemistry model described above has been calibrated for a Jet-A fuel (referred to as POSF-2827 by the U. S. Air Force, Wright Laboratory) using the measured data obtained from two flowing experiments (Ballal et al., 1992; Jones et al., 1993). The simulated results for the fuel-injection nozzle presented in the following sections were obtained based on this fuel.

RESULTS AND DISCUSSION

Simulations for two thermal and fluid conditions which result in different characteristics of deposition are presented and discussed. The conditions for temperature and fuel-flow rate used in these two cases are given in Table 1. In each case, the inlet fuel-flow rates were chosen to provide essentially the same mean velocity in the entrances of the two fuel passages. Based on these inlet mean velocities, turbulent-flow calculations were performed in Case I, while laminar-flow calculations were made for Case II.

		Flow rate (Jet-A fuel)	Inlet temp.	Wall temp.
Case I	primary	18.5 kg/hour (5 m/sec)	180°C	530°C
	secondary	93.8 kg/hour (5 m/sec)	180°C	
Case II	primary	0.20 kg/hour (0.05 m/sec)	180°C	330°C
	secondary	0.90 kg/hour (0.05 m/sec)	180°C	

Table 1. Flow and thermal conditions for two tests.

It is well known that temperature plays an important role in the phenomena of decomposition of jet fuel. Generally speaking, when the fuel is near or above a certain temperature [e.g. JFTOT (Jet Fuel Thermal Oxidation Tester) breakpoint], decomposition begins and becomes progressively worse as the temperature increases. At very high temperatures the deposition on the walls and the concentration of peroxide radicals in the bulk fuel are known to decrease. The drop-off in deposition rate at higher temperatures has been taken into account in the global-chemistry model as represented by R5.

Figure 3(a) shows the calculated bulk-fuel and wall-temperature profiles along the streamwise direction of the primary fuel passage in Case I. Note that data for only a 9-mm segment of the nozzle near the exit are shown. Because of the high flow rate employed in this case, the increase of bulk-fuel temperature is very small throughout the nozzle (25°C in the primary passage). Temperatures on both wall boundaries increase rapidly near the exit of the nozzle. Since the bulk-fuel temperature for this condition (Case I) is below the breakpoint temperature (225°C) of this fuel (POSF-2827) and the residence time of fuel in the nozzle is very short (< 0.03 s), it is expected that the deposition on the wall surface is primarily determined by the temperature on the wall instead of the temperature of the bulk fuel. The calculated deposition rates on two wall boundaries in the primary fuel passage are shown in Fig. 3(b). It should be noted that the profiles of deposition rate show a strong dependence on wall temperature. This phenomenon has also been observed in the experiments on the EDTST (Extended Duration Thermal Stability Test) system conducted at Wright Laboratory (Dieterle and Binns, 1994). The EDTST system was designed to evaluate fuel thermal stability in straight tubes for flow and temperature conditions similar to those experienced by an actual aircraft

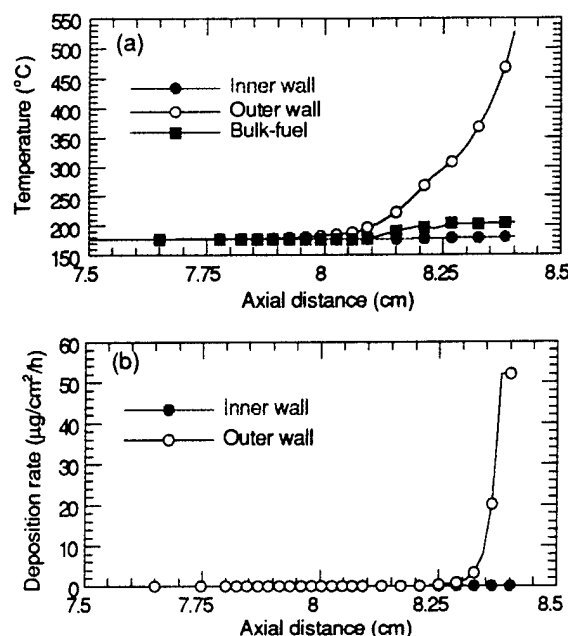


Figure 3. Temperature distributions (a) and deposition rates (b) on walls of primary fuel passage for Case I.

engine. The results on the EDTST system show that deposits increase exponentially as a function of wetted-wall temperature (peak temperature on the wall in the EDTST system). Because of the similarity between the EDTST system and the fuel-injection nozzle, the experimental data obtained from the EDTST tests are valuable for calibrating the wall-reaction parameters of the global-chemistry model.

A different pattern of deposition is likely to occur if the flow rate of the fuel is reduced to allow the fuel to be heated to a temperature above that of the breakpoint. This condition normally occurs when an aircraft is operating in the descent (or idle) mode. To simulate this situation, the flow rates of fuel in both passages are reduced to < 1.0 kg/h (Case II). The residence time of the fuel in the nozzle is ~ 1 s.

The temperature distributions in both fuel passages are shown in Fig. 4. The bulk fuel is heated to the breakpoint temperature at axial locations ~ 6 and 4 cm from the inlet in the primary and secondary passages, respectively. Once the temperature of the bulk fuel exceeds the breakpoint temperature of the fuel, it is expected that deposition rates in the primary and secondary passages will increase significantly. Since the nozzle is heated from the outer and right-side wall boundaries, the temperature on the inner-wall boundary of the fuel passage is lower than that on the outer-wall boundary at a given axial location (see Fig. 4). The temperature gradient across the fuel passage results in a complex distribution for the reacting species and changes the deposition characteristics on the inner and outer walls. The predicted distributions of deposition rates in the two fuel passages for Case II are shown in Fig. 5. It is evident that the peaks in

deposition rates on both walls occur within the nozzle rather than at the tip of the nozzle. In fact, two peaks (a broad peak followed by a sharp one) are noted on the outer wall of both passages. The peak on the inner wall is located farther downstream than those on the outer wall.

Referring to the configuration shown in Fig. 1, it was found that the sharp peak on the outer wall occurs at a location where the fuel turns upward in the bent regions of the fuel passages ($z = 7.8$ cm in the primary passage and $z = 5.7$ cm in secondary passage). On the other hand, no corresponding sharp peak is observed in the bent region where the fuel turns downward. In order to understand the mechanism responsible for this sharp peak in deposition rate on the outer wall, the flow structures, temperature field, and concentration distributions of the two species (dissolved oxygen and deposit-forming precursor) in the bent region of the fuel passage were examined. As expressed in Eq. (3), it is clear that deposition rate is influenced by the following four variables: (a) shear stress at the wall (τ_w), (b) temperature on the wall (T_w), (c) precursor concentration ($[P]$) near the wall, and (d) bulk-insoluble concentration ($[D]$) near the wall. If the reaction rate of R9 (i.e., $\dot{\omega}_9$) is much smaller because of the lower concentration of $[D]$ than the reaction rate of R8 ($\dot{\omega}_8$) for the given flow conditions, then the amount of deposits transformed from bulk insolubles (D) will be negligibly small in comparison to that transformed from the precursors.

The detailed structures of fuel flow, temperature field, and species concentration in the "bridge" region of the primary passage are shown in Fig. 6. Since the rates for all the reactions (R1-R9) in the present deposition model are assumed to have an Arrhenius form with positive activation energies, the consumption of dissolved oxygen will be faster in the high-temperature regime [upper-right-side region in Fig. 6(b)] than in the low-temperature regime [lower-left-side region in Fig. 6(b)]. As Figs. 6(b) and (c) show, the iso-contours for oxygen concentration closely reflect the distribution of fuel temperature. An initial level of 65 ppm (parts per million by weight) for dissolved oxygen was used for this fuel. Similarly, the precursor generated through the reaction of R3 should have a higher concentration in the high-temperature regime. However, the distribution of precursor concentration becomes complicated since the decomposition of precursor through R5 consumes most of the precursors generated in the high-fuel-temperature regime. The resulting distribution of precursor concentration is shown in Fig. 6(d). Two local maxima for precursor concentration exist; one is located at $z = 8.1$ cm near the inner wall and the other at $z = 7.9$ cm near the outer wall. The precursor concentrations along both wall boundaries are plotted in Fig. 7 along with the deposition rates calculated in this region.

The shear stress at the wall is an important physical parameter that influences the probability of deposit particles sticking to the wall, particularly under low-flow-rate

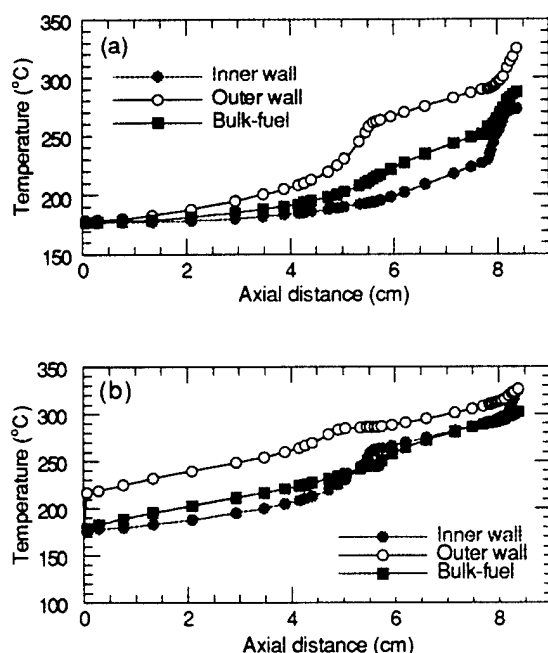


Figure 4. Temperature distributions in fuel passages for Case II. (a) Primary fuel (b) Secondary fuel.

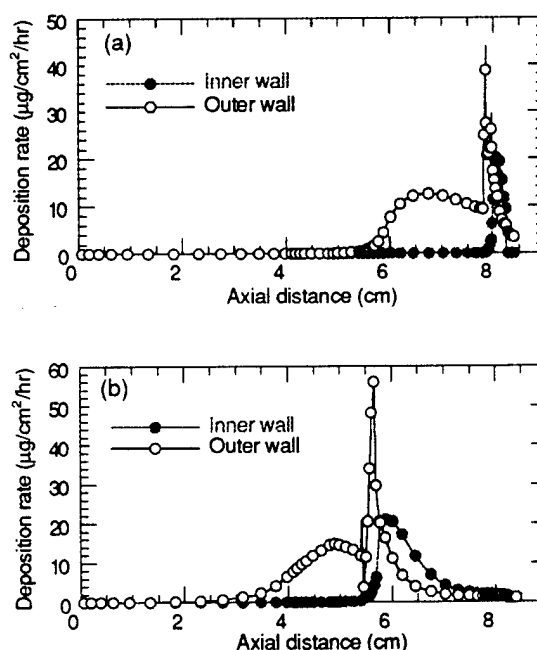


Figure 5. Deposition rates on walls of fuel passages for Case II. (a) Primary fuel (b) Secondary fuel.

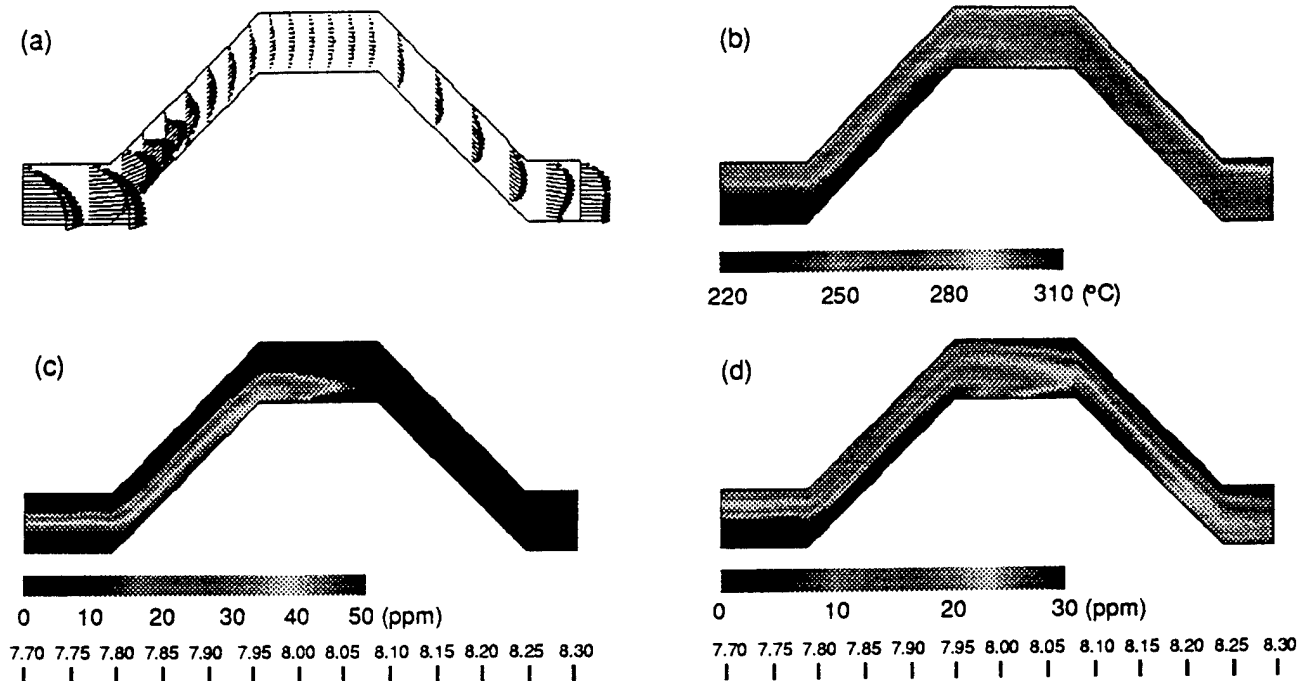


Figure 6. Flow structures, temperature fields, and species concentrations in "bridge"-shaped region of primary fuel passage. (a) Velocity vectors of fuel flow. (b) Iso-contours of fuel temperature. (c) Iso-contours of oxygen concentration, and (d) Iso-contours of precursor concentration.

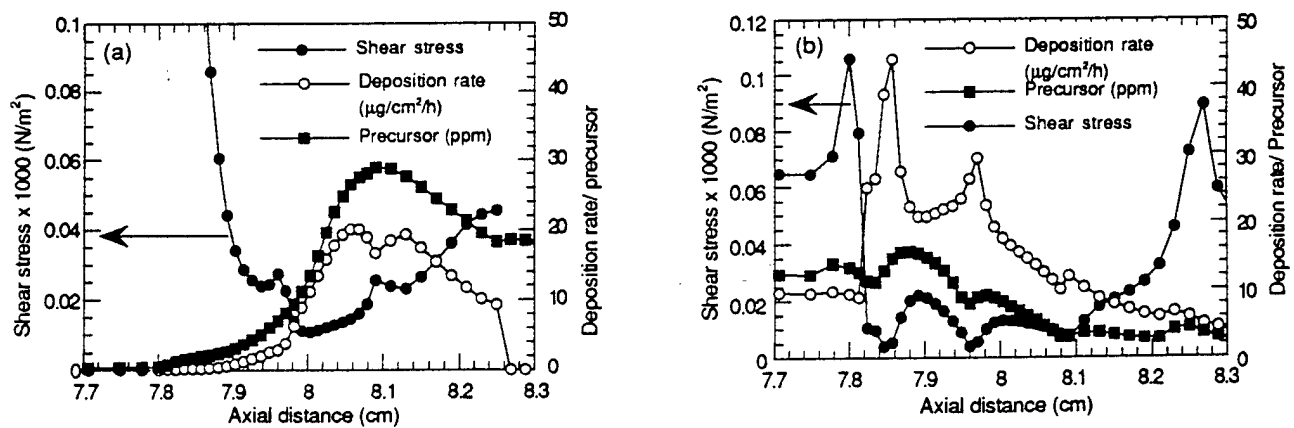


Figure 7. Deposition rate, precursor concentration, and shear stress on walls of primary fuel passage. Data are shown in "bridge"-shaped region only. (a) Inner wall and (b) Outer wall.

conditions. The higher shear stress near the wall makes the deposit particles less likely to stick to the wall. The plot of velocity vectors [Fig. 6(a)] clearly shows that the velocity is significantly reduced in the middle of the "bridge" where the

annular area of cross section is largest. The decreasing velocity in the front part of the "bridge" section induces a nearly stagnant flow region near the outer wall around $z = 7.85$ cm. The shear stress at the wall in this region is

expected to be very small. The shear stresses at the two walls are also plotted in Fig. 7. The reciprocal relationship between shear stress and deposition rate is evident from these figures. A second peak in deposition on the outer wall is shown in Fig. 7(b) at the location $z = 7.95$ cm where the fuel has just reached the middle of the "bridge."

Generally speaking, the formation of deposits under this condition (Case II) is not reflected by the wall temperature. Instead, detailed information on the flow structure, temperature field, and species concentration is required for understanding the mechanism of deposition in a complex fuel system.

CONCLUSIONS

A numerical model for studying the formation of deposits in a fuel-injection nozzle has been presented. A global-deposition model which was successfully used in predicting the deposition rates for thermally stressed fuel in straight tubes was employed to simulate the chemical kinetics of the fuel-degradation process in fuel-injection nozzles. Two patterns of deposition were obtained from this model under two different fuel-flow and temperature conditions. The deposition calculated in Case I (high flow rate of fuel) primarily results from the wall reactions that strongly depend on the wetted-wall temperature. On the other hand, the deposition calculated in Case II (low flow rate of fuel) shows a pattern that results from the integrated effects of fluid dynamics, heat transfer, and chemical reactions. The present work primarily illustrates the usefulness of the Computational Fluid Dynamics with Chemistry (CFDC) model in understanding the deposition process in a fuel-injection nozzle. In the future, predictions will be compared with the results of direct measurements of deposits when they become available.

ACKNOWLEDGMENTS

This work was supported by the U. S. Air Force under Contract F33615-90-C-2033. The authors would like to thank Dr. Mel Roquemore and Dr. Andy Brankovic for their valuable comments on this work. Special thanks to Ms. Marian Whitaker for editorial comments and preparation of the manuscript.

REFERENCES

- Ballal, D. R., Byrd, R. J., Heneghan, S. P., Martel, C. R., Williams, T. F., and Zabarnick, S., 1992, "Combustion and Heat Transfer Studies Utilizing Advanced Diagnostics: Fuels Research," Technical Report WL-TR-92-2112, Wright-Patterson Air Force Base, OH.
- Dieterle, G. L., and Binns, K. E., 1994, "Evaluation of High Thermal Stability Fuels for Future Aircraft," AIAA Paper No. 94-3171, Presented at the 30th AIAA/ASME/SAE/ASEE Joint Propulsion Conference, Indianapolis, IN.
- Eiseman, P. R., 1978, "A Coordinate System for a Viscous Transonic Cascade Analysis," *Journal of Computational Physics*, Vol. 26, pp. 307-338.
- Gleason, C. C., Oller, T. L., Shayeson, M. W., and Bahr, D. W., 1979, "Evaluation of Fuel Character Effects on the F101 Engine Combustion System," Technical Report AFAPL-TR-79-2018, Air Force Aero Propulsion Laboratory, Wright-Patterson Air Force Base, OH.
- Jones, G., Balster, W. J., and Post, M. E., 1993, "Degradation of a Jet-A Fuel in a Single-Pass Heat Exchanger," ASME Paper No. 93-GT-334, Presented at the International Gas Turbine and Aeroengine Congress and Exposition, Cincinnati, OH.
- Katta, V. R., Jones, E. G., and Roquemore, W. M., 1993a, "Development of Global-Chemistry Model for Jet-Fuel Thermal Stability Based on Observations from Static and Flowing Experiments," Report No. AGARD-CP-536, Paper No. 19, Advanced Group on Aerospace Research and Development, Neuilly sur Seine, France.
- Katta, V. R., and Roquemore, W. M., 1993b, "Numerical Method for Simulating Fluid-Dynamic and Heat-Transfer Changes in Jet-Engine Injector Feed-Arm Due to Fouling," *Journal of Thermophysics and Heat Transfer*, Vol. 7, No. 4, pp. 651-660.
- Krazinski, J. L., Vanka, S. P., Pearce, J. A., and Roquemore, W. M., 1992, "A Computational Fluid Dynamics and Chemistry Model for Jet Fuel Thermal Stability," *Journal of Engineering for Gas Turbines and Power*, Vol. 114, pp. 104-110.
- Morton, H. L., 1986, "Effects of Fuel Composition on T700 and F404 Engine Hot Section Components - Lot II," Report No. NAPC-PE-117C, Final Report, Vol. I, Naval Aero Propulsion Center, Trenton, NJ.
- Patankar, S. V., 1980, "Numerical Heat Transfer and Fluid Flow," Hemisphere Publishing Corp., Washington, D. C.
- Schneider, G. E., and Zedan, M., 1981, "A Modified Strongly Implicit Procedure for the Numerical Solution of Field Problems," *Journal of Computational Physics*, Vol. 4, pp. 1-19.

Symposium on Distillate Fuel Auto-Oxidation Chemistry
Presented before the Division of Petroleum Chemistry, Inc.
207th National Meeting, American Chemical Society
San Diego, CA, March 13-18, 1994

Numerical Modeling of Jet-Fuel Autoxidation in Flowing Systems

Long P. Chin and Viswanath R. Katta
Systems Research Laboratories, Inc.
A Division of Calspan Corporation
2800 Indian Ripple Road
Dayton, OH 45440-3696

Shawn P. Heneghan
University of Dayton
300 College Park Avenue
Dayton, OH 45469-0140

INTRODUCTION

As the operating temperature in aircraft fuel systems is increased, the thermal stability of the jet fuel must be improved to minimize the fouling problem in fuel components. For many years studies in this field have been focused on the development of experimental techniques (1, 2) to evaluate the thermal stability of various fuels. Recently the development of the Computational Fluid Dynamics with Chemistry (CFDC) code (3, 4) has provided a useful tool to aid the understanding of the fundamental phenomena of jet-fuel degradation; the information obtained from CFDC modeling is valuable in explaining experimental results. Successful application of the CFDC approach requires establishment of a global-chemistry model that takes into account the complicated thermal-decomposition processes. The calibrated parameters of the global-chemistry model for each fuel should be valid over a wide range of flow and temperature conditions.

It is well known that the consumption of dissolved oxygen is strongly coupled to the formation of deposits in jet fuels (5). Since the chemical kinetics involved in the autoxidation process in jet fuel are complex, the global-oxidation concept has normally been used in the modeling to represent a series of elementary reactions (6). Typically the reaction-rate parameters of the global-kinetic model are assumed to be in Arrhenius form (in terms of activation energy and pre-exponential) and independent of temperature and

time. However, the Arrhenius-type global-kinetic model may not be adequate for the autoxidation process that occurs in jet fuel because the decomposition of the oxidation products has a tendency to increase the rate of reaction (7, 8). The non-Ar-

renius behavior of the reaction rate has been studied by Semenov (9) using a probability approach to illustrate that the activation energy increases with temperature without bound. Katta et al. (4) also observed this effect when predicting the deposition profiles in an isothermal flowing experiment and attributed it to the overestimation of the oxidation rate at low temperature. Recently, Heneghan (10) studied the global rate constants for a chain autoxidation mechanism having an autocatalysis reaction. In that study he derived the reaction-rate equation and showed that the global rate constants are neither constant in time nor Arrhenius in form at a given time.

In the present study the autoxidation process of jet fuel in flowing systems was simulated numerically using the CFDC code of Katta et al. (4). This code was modified to implement the new global-oxidation model of Heneghan (10). The new model for a given jet fuel was evaluated based on two sets of flowing experiments under different flow and temperature conditions. The role of fluid dynamics in the autoxidation of fuel in flowing systems was also examined.

GLOBAL-OXIDATION MODEL

The following autoxidation mechanism was used by Heneghan (10) to derive the new global-oxidation model:

Initiation	Initiation of $R\cdot$ (R_i)	R1)
Propagation	$R\cdot + O_2 \rightarrow RO_2\cdot$	R2)
	$RO_2\cdot + RH \rightarrow RO_2H + R\cdot$	R3)
Termination	$RO_2\cdot + RO_2\cdot \rightarrow \text{products}$	Rt)
Chain-Transfer Reactions	$RO_2\cdot + AH \rightarrow RO_2H + A\cdot$	R3')
Autocatalysis	$RO_2H \rightarrow RO_2\cdot + OH\cdot$	Ru)

The global-oxidation rate constant k_o of this new model can be expressed as (10):

$$k_o = \frac{-d[O_2]}{dt} = k' (k_u \int k_o dt + B_i) \quad (1)$$

where

- k' is the chain length of oxidation [unitless],
- k_u is the rate of unimolecular decomposition of oxidation products [1/s],
- B_i is the baseline initiation rate at time zero [moles/m³/s], and
- t is time [s].

Since k' , k_u , and B_i have an Arrhenius form, this model has six rate parameters--three pre-exponentials (A' , A_u , and A_i) and three activation energies (E' , E_u , and E_i). However, Equation 1 can be arranged into an expression [Equation 2] having only four rate parameters by defining $k_u = k'k_u$ and $k_i = k'B_i$:

$$k_o = \bar{k}_u \int k_o dt + \bar{k}_i \quad (2)$$

The solution of Equation 2 for k_o is:

$$k_o = \bar{k}_i + \bar{k}_u \Psi \int (\bar{k}_i / \Psi) dt; \quad \Psi = \exp(\int \bar{k}_u dt) \quad (3)$$

If \bar{k}_u and \bar{k}_i are constant in time (fuel is near isothermal), k_o can be simplified to Equation 4 using the initial condition $k_o = \bar{k}_i$:

$$k_o = \bar{k}_i \exp(\bar{k}_u t) \quad (4)$$

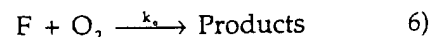
Since \bar{k}_u is a first-order rate constant and \bar{k}_i is a zero-order rate constant, the oxidation rate constant k_o will have zero-order dependence upon oxygen concentration (7). The order of oxygen dependence increases as oxygen concentration diminishes in the system (11). The change of oxidation order was incorporated in the CFDC code.

The time t in this model is the residence time of the oxygen molecule in the system under study. In flowing systems, the residence time of the oxygen molecule at a given location is very difficult to determine because it depends on the pathway of the oxygen molecule upstream. This pathway is affected by the convective and diffusive motions in the flow field. To apply the model more simply in the present study, t was estimated by integrating the convective time of the oxygen molecule along the streamwise flow direction:

$$t = \int_{x=0}^{x=L} d\tau = \int_{x=0}^{x=L} dx / v(x) \quad (5)$$

EVALUATION OF OXIDATION MODEL

The k_o from Equation 3 is used to represent the global-oxidation rate constant for the following single-step global-oxidation equation:



To calibrate k_o for a given jet fuel, the rate parameters ($A'A_u$, $A'A_i$, $E' + E_u$, and $E' + E_i$) can be determined from the results of oxygen measurements in flowing experiments. In the present study, a Jet-A fuel identified as POSF-2827 by the U. S. Air Force was used, and the results presented in the following sections are for this fuel.

The results of dissolved-oxygen measurements from two flowing test rigs were chosen for calibration of this oxidation model. One, the Phoenix rig (12), consists of a 0.3175-cm-o.d. and 45.8-cm-long heated tube with the fuel passing through at a steady flow rate. The second, the near-isothermal flowing experiment (7), has a 0.3175-cm-o.d. and 81.3-cm-long heated tube. Normally the tests conducted in the Phoenix rig are under high-temperature, high-flow-rate conditions, whereas the near-isothermal experiments are performed at

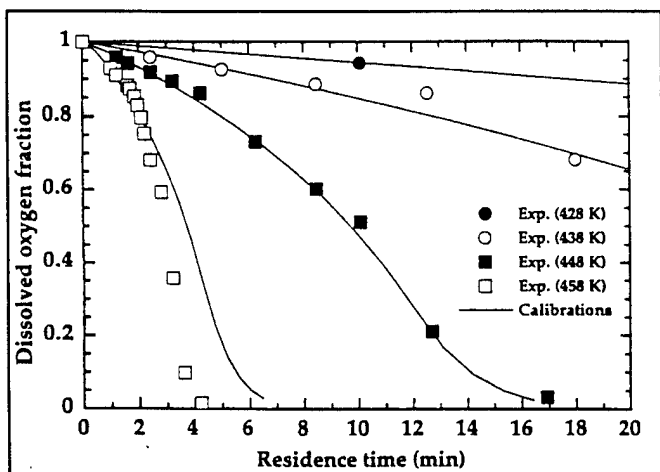


Figure 1. Measured and calibrated oxygen-consumption curves in near-isothermal experiments for four temperatures.

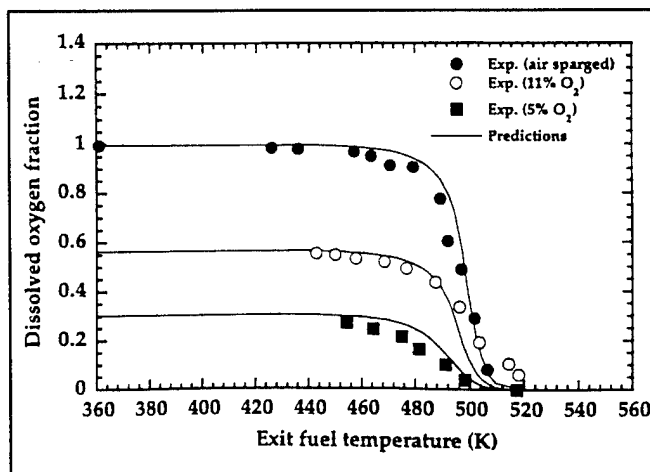


Figure 2. Measured and predicted oxygen-consumption curves in Phoenix-rig experiments for three initial levels of oxygen.

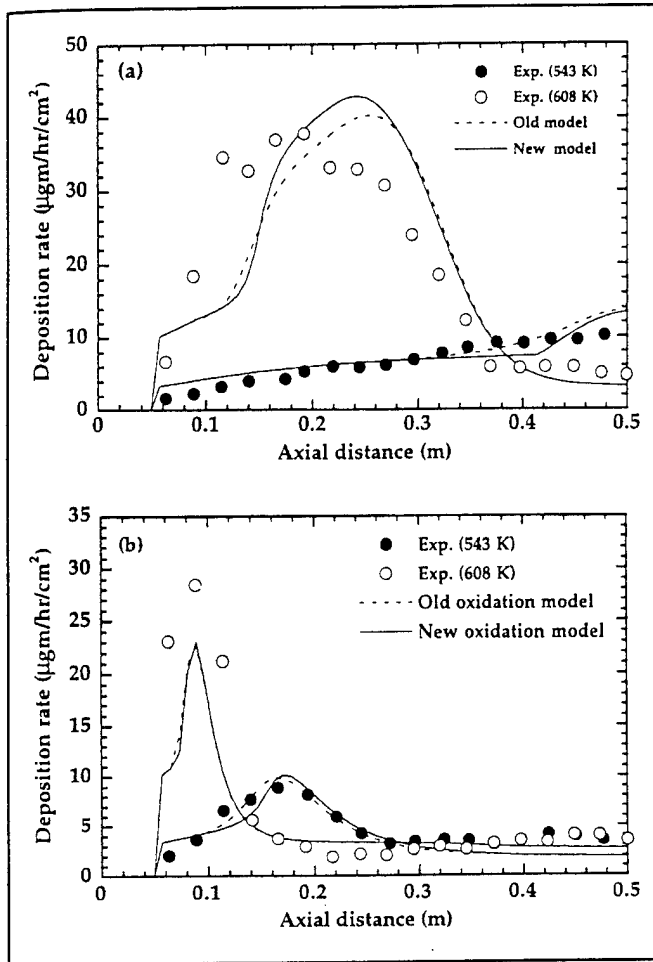


Figure 3. Measured and predicted deposition profiles in Phoenix-rig experiments for two temperatures. Predictions made for two oxidation models. Flow rate is 16 cc/min in (a) and 4 cc/min in (b).

lower temperatures and flow rates to achieve isothermal conditions in a minimum length of tube.

Results of measurements of dissolved-oxygen content for the Jet-A (POSF-2827) fuel at the exit of the tube in the near-isothermal experiments (7) are plotted in Figure 1. These data represent four block temperatures—428, 438, 448, and 458°K at different flow rates (or residence times of fuel). The sequence of events that led to determination of the rate parameters of the new oxidation model is as follows: (a) By fitting the initial slopes of each experimental curve in Figure 1 to an Arrhenius plot, Jones (7) obtained $A'A_i = 2 \times 10^{14}$ moles/m³/s and $E' + E_i = 35.8$ kcal/mole/K—the two rate parameters of k_i . (b) The two rate parameters of k' — $A' = 2 \times 10^4$ and $E' = 5$ kcal/mole/K—have been

10^{15} s⁻¹ and $E_u = 42$ kcal/mole/K. For an initial oxygen content of 65 ppm in the fuel, the best fit to the data shown in Figure 1 is $A_u = 0.7 \times 10^{15}$ s⁻¹, $E_u = 40$ kcal/mole/K. (4) $A'A_u = 0.7 \times 10^{20}$ s⁻¹ and $E' + E_u = 45$ kcal/mole/K are determined from (b) and (c).

For evaluation of this new oxidation model, the rate parameters calibrated above were used to predict the behavior of oxygen depletion in the Phoenix-rig experiments at higher flow rates and higher temperatures. A comparison of experimental and predicted results for three different initial levels of dissolved oxygen is shown in Figure 2. In the experiments fuel was passed through the heated tube at a constant flow rate of 16 cc/min, and measurements for bulk-fuel temperature and oxygen content were made at the exit of the tube. The

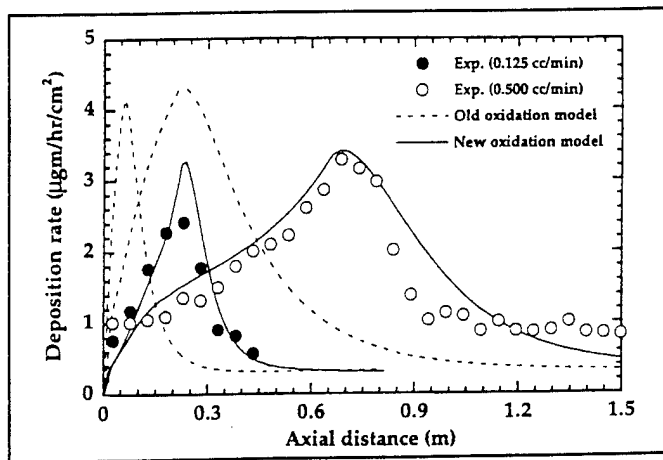


Figure 4. Measured and predicted deposition profiles in near-isothermal experiments for two flow rates. Block temperature is 458°K. Predictions made for two oxidation models.

given by Zabar-nick (8) for a strongly terminated oxidation system. Therefore, the rate parameters of B_i are $A_i = 1 \times 10^{10}$ moles/m³/s and $E_i = 30.8$ kcal/mole/K from (a).

(c) According to Benson (13) the rate parameters of k_u are expected to be near $A_u \approx 1 \times$

oxygen content in the fuel at different outlet temperatures was determined by changing the temperature of the heated block. The reasonably good agreement shown in Figure 2 confirms that the new oxidation model provides an adequate description of the autooxidation process in fuel over a wide range of flow and temperature conditions.

This new oxidation model was further evaluated through prediction of the deposition profiles observed from the two flowing profiles experiments mentioned above. The deposition model proposed by Katta et al. (4) includes five steps for bulk-fuel reactions and three steps for wall reactions. This deposition model was calibrated based on the Phoenix-rig experiments at a flow rate of 16 cc/min and two block temperatures of 608 and 543°K. Using this deposition model in conjunction with the new global oxidation model, the deposition profiles for two flow rates (16 and 4 cc/min) and two block temperatures (608 and 543°K) in the Phoenix-rig experiments were predicted. The calculated results along with experimental data are shown in Figure 3. Also shown are the deposition profiles predicted by the global-oxidation model used in the previous study (4). This model was assumed to have an Arrhenius-type reaction-rate constant k_o ($A_o = 2.53 \times 10^{13}$ moles/m³/s and $E_o = 32$ kcal/

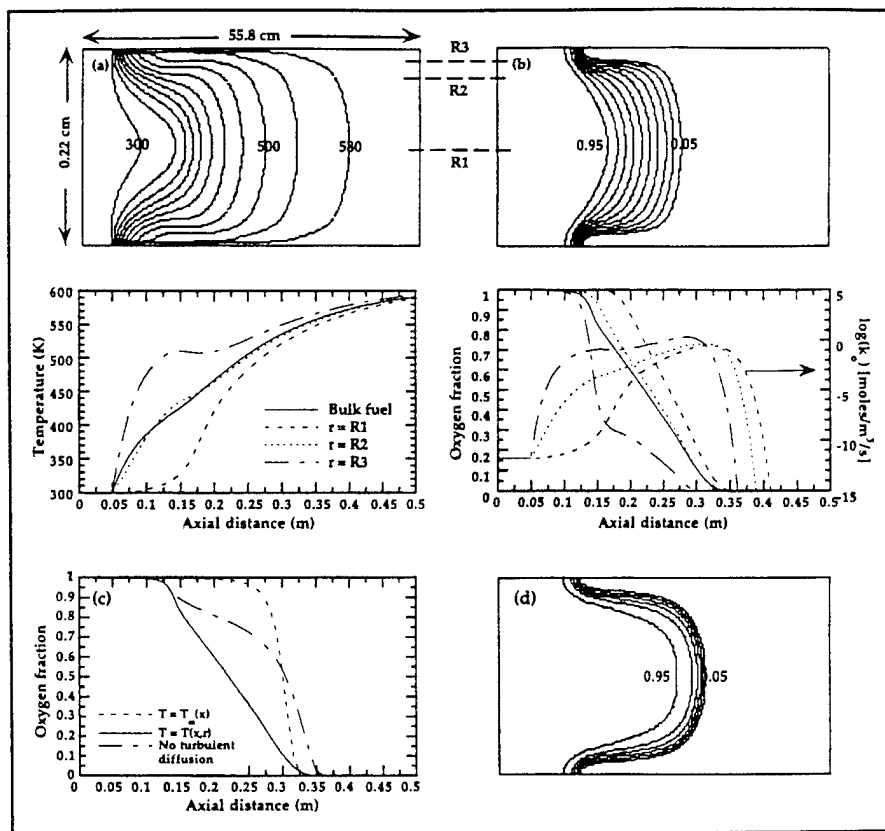


Figure 5. Simulations of oxygen depletion in Phoenix-rig experiments. Flow rate is 16 cc/min, and block temperature is 608°K. (a) Fuel temperature. top - contours, bottom-axial profiles. (b) Oxygen concentration. top - contours, bottom - axial profiles. (c) Bulk oxygen profiles. (d) Contours of oxygen concentration without turbulent diffusion.

mole/K) and was calibrated based on the oxygen data shown in Figure 2. Agreement between experimental results and predictions is reasonably good. The discrepancy in the deposition profiles predicted using the two global-oxidation models is expected to be small because both models were able to predict oxygen depletion at such high temperatures and flow rates (Figure 2 in this study and Figure 1 in Reference 4).

It has been noted by Katta et al. (4) that a single set of Arrhenius parameters (A_0 and E_0) is not sufficient to describe the autoxidation process in jet fuel over a wide range of temperatures. The two global-oxidation models were further compared by predicting the deposition profiles at low temperature (458 K) for two flow rates (0.125 and 0.5 cc/min) in near-isothermal experiments (7); the results are shown in Figure 4. It is apparent that the oxidation model

described in Reference 4 (dashed curves in Figure 4) failed to predict the correct locations of the deposition peaks for both flow rates, whereas the predictions of the new oxidation model (solid curves in Figure 4) match the measurement results extremely well. The reason for this difference is that the oxidation model of Reference 4 (calibrated based on high-temperature data) over-predicts the oxygen-consumption rate at low temperature.

DISCUSSION

In a flowing fuel system, the roles of fluid dynamics and chemical kinetics are equally important in determining the behavior of dissolved oxygen in the fuel. The overall consumption rate of oxygen is controlled not only by the kinetics of oxidation (chemistry) but also by the mechanism of species transport (physics). The degree of the interaction between these two

phenomena is dependent on the characteristics of the temperature and flow fields established in the system. Generally speaking, the fuel flowing near the wall is heated at a faster rate and has a longer residence time (due to the boundary layer) than the fuel passing through the center of the tube. The spatial non-uniformity of either the temperature or the residence time of the fuel has a pronounced effect on the rate of oxygen consumption. This phenomenon can be examined in detail through the two following examples of simulations based on the new oxidation model.

Phoenix-Rig Experiment at 16 cc/min and 608°K

The calculated distributions of temperature and oxygen concentration under these conditions are plotted in Figures 5(a) and 5(b). Iso-contour plots of temperature and oxygen concentration in the tube are shown at the top; at the bottom their distribution profiles are shown along the tube length at three radial locations (R1, R2, and R3). Also shown in Figure 5(b) are the corresponding oxidation rates for the three concentration profiles in this plot. The rapid decrease of the calculated reaction rate is a result of a change in the reaction order from zero to one as the oxygen concentration decreases below 20% of the initial level. Because the temperature near the wall is higher than that in the center [Figure 5(a)], the oxygen near the wall is consumed faster than that in the center [Figure 5(b)]. As shown in Figure 5(b), oxygen is completely consumed at $x = 35$ cm for $r = R1$ and $x = 30$ cm for $r = R3$. Near the wall, oxygen is completely consumed at $x = 15$ cm.

A comparison of Figures 5(a) and 5(b) shows that the system exhibits noticeable oxygen depletion [e.g., beginning from the contour of 0.95 in Figure 5(b)] at the locations corresponding to the temperature level between 350 and 400°K [Figure 5(a)]. At this low temperature level, this par-

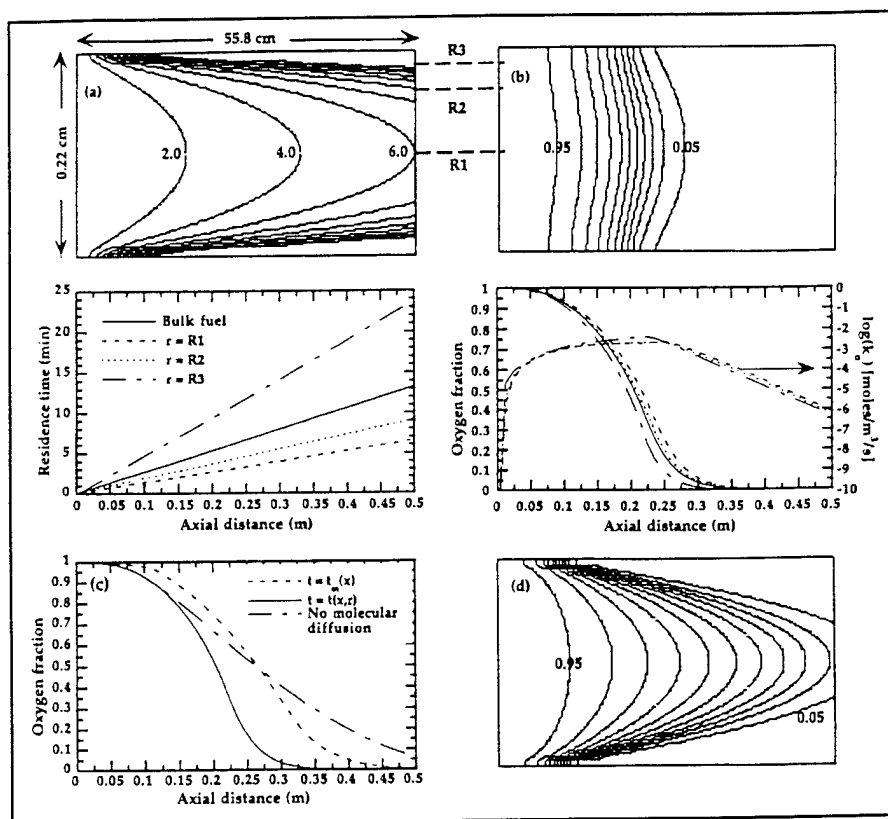


Figure 6. Simulations of oxygen depletion in near-isothermal experiments. Flow rate is 0.125 cc/min, and block temperature is 458°K. (a) Residence time of fuel. top - contours, bottom-axial profiles. (b) Oxygen concentration. top - contours, bottom - axial profiles. (c) Bulk oxygen profiles. (d) Contours of oxygen concentration without molecular diffusion.

ticular fuel (Jet-A: POSF-2827) cannot oxidize at such a high rate. The oxidation rate for this temperature level is below 10^{-8} moles/m³/s where over 1,000 hr is required for consumption of 5% of the oxygen at an initial level of 65 ppm. It is thought that the more rapid oxygen depletion in the center results from the effect of a non-uniform temperature field in the radial direction. This factor was examined by calculating the concentration profiles of bulk oxygen along the tube length for two different conditions; these profiles are presented in Figure 5(c). The solid curve in this figure was obtained based on the temperature field shown in Figure 5(a), and the dashed curve was obtained based on a radially uniform temperature field [i.e., $T(x, r) = T_m(x)$]. The radially uniform temperature field chosen was one which would result in the same total amount of oxygen being consumed as that for the temperature field shown in Figure 5(a) without the effect of fluid dynamics. The total

amount of oxygen consumed increased by about 30% as a result of the radially non-uniform temperature field under this flow condition.

Since the fuel tube is small (0.22-cm o.d.), a steep gradient of oxygen concentration in the radial direction is expected because of the radial gradient of the temperature field when fluid dynamics is not taken into account. The steep gradient of oxygen concentration provides a strong driving mechanism to force the oxygen from the high-concentration region to the low-concentration region (radially outward) as a result of turbulent diffusion (molecular diffusion is small compared to turbulent diffusion for this flow condition). The fresh oxygen driven to the high-temperature region near the wall will be consumed immediately under the rapid oxidation rate. Once the oxygen near the wall is consumed, fresh oxygen is continuously supplied from the central region. The contours of

oxygen concentration shown in Figure 5(b) represent an equilibrium state where the oxygen consumed as a result of the oxidation reaction is balanced locally by the oxygen supplied from turbulent diffusion and convection.

The explanation above for more rapid oxygen depletion in the center of the tube can be verified by calculating the distribution of oxygen concentration without the effect of turbulent diffusion on oxygen transport. The contours of oxygen concentration shown in Figure 5(d) reveal shapes similar to those of the temperature field in Figure 5(a). Oxygen depletion without turbulent diffusion [Figure 5(d)] has been delayed to locations where the fuel temperature is about 500°K [Figure 5(a)] which yields an oxidation rate of around 10^{-1} moles/m³/s [Figure 5(b)]. The concentration profile of bulk oxygen without turbulent diffusion [solid-dashed curve in Figure 5(c)] shows that the total amount of oxygen consumed is very near that in a radially uniform temperature field [dashed curve in Figure 5(c)]. Therefore, it is evident that enhancement of oxygen depletion resulting from a non-uniform temperature field is driven by turbulent diffusion under this flow and temperature condition.

Near-Isothermal Experiment at 0.125 cc/min and of 458°K

Since the temperature of fuel under this flow condition is nearly constant throughout the tube, the more rapid oxygen depletion observed in the first example does not occur. However, because of the low fuel velocity (< 0.06 cm/s), the wide range of residence times (up to 30 min) results in different characteristics of oxygen depletion than those expected from an oxidation-kinetics viewpoint. The distributions of residence time and oxygen concentration are shown in Figures 6(a) and 6(b). The oxygen depletion across the fuel tube is fairly uniform compared to that observed in the Phoenix-rig experiments. Oxy-

gen is completely consumed at $x = 37$ cm in the center and at $x = 32$ cm near the wall. If oxidation kinetics only is considered, it is expected that the location for complete oxygen consumption will be nearly inversely proportional to the residence time of the fuel. The more uniform oxygen depletion in the radial direction is thought to result from molecular diffusion that transports oxygen from the center to the wall. The radially diffused oxygen moves the location of consumption upstream in the center and downstream near the wall. The concentration profiles of bulk oxygen along the tube length [Figure 6(c)] were calculated to permit comparison of the total amount of oxygen consumed in the two cases. The amount of oxygen consumed increased by about 18% as a result of the radial non-uniformity of the residence time (or reaction time). To verify the effect of molecular diffusion on oxygen depletion, the oxygen concentration without molecular diffusion was calculated and is presented in Figure 6(d). The resulting contours are similar to those of the residence time in Figure 6(a).

CONCLUSIONS

A new global-oxidation model that describes the autoxidation process in jet fuel has been evaluated numerically. The model takes into account rate acceleration resulting from autocatalysis. The new oxidation model was calibrated for a given jet fuel based on the results of oxygen measurements in near-isothermal flowing experiments under low-temperature, low-flow-rate conditions, and the calibration procedure has been described. The six calibrated rate parameters of the model are consistent with the estimates from theoretical considerations. The new model has been used successfully to predict the characteristics of oxygen depletion over a wide range of flow and temperature conditions. This type of prediction was not possible with the oxidation model in which the oxidation rate is assumed to be in

a simple Arrhenius form. Improvement of the autoxidation model has made the CFDC model (4) more powerful and accurate in predicting deposition profiles under a variety of experimental conditions.

Numerical modeling has the advantage that a mechanism can be isolated in order to study a specific phenomenon. Through this procedure, diffusive transport was found to have a significant effect on oxygen depletion in flowing systems. Under high-temperature, high-flow-rate conditions, turbulent diffusion is responsible for the increase in oxygen consumption which results from a radially non-uniform temperature field. On the other hand, the enhancement of oxygen consumption resulting from the wide range of residence times under low-temperature, low-flow-rate conditions is driven by molecular diffusion.

ACKNOWLEDGMENTS

This research was sponsored by Wright Laboratory, Aero Propulsion and Power Directorate, Wright-Patterson Air Force Base, Ohio, under USAF Contracts F33615-90-C-2033 and F33615-92-C-2207. The authors would like to thank Mrs. Marian Whittaker for editorial comments on the paper.

LITERATURE CITED

- (1) Marteney, P. J. and Spadaccini, L. J., *ASME J. Eng. Gas Turb. Power*, **108**, 648 (1986).
- (2) Edwards, T., Roquemore, W. M., Harrison, W. E. and Anderson S. D., Research and Development of High Thermal Stability Fuels, Paper No. PEP-18 presented at the 81st AGARD Symposium on Fuels and Combustion Technology for Advanced Aircraft Engines, May 10-14, 1993, Colliferro, Italy.
- (3) Krazinski, J. L., Vanka, S. P., Pearce, J. A. and Roquemore W. M., *J. Eng. Gas Turb. Power*, **114**, 104 (1992).
- (4) Katta, V. R., Jones, E. G. and Roquemore, W. M., Development of Global-Chemistry Model for Jet-Fuel Thermal Stability Based on Observations from Static and Flowing Experiments, Paper No. PEP-19 presented at the 81st AGARD Symposium on Fuels and Combustion Technology for Advanced Aircraft Engines, May 10-14, 1993, Colliferro, Italy.
- (5) Hazlett, R. N., Thermal Oxidation Stability of Aviation Turbine Fuels, ASTM, Philadelphia, PA (1991).
- (6) Hautman, J., Dryer, F. L., Schug, K. P. and Glassman, I., *Comb. Sci. Tech.*, **25**, 219 (1981).
- (7) Jones, E. G., Balster, W. J. and Post, M. E., Thermal Degradation of Jet-A Fuel in a Single-Pass Heat Exchanger, ASME Paper 93-GT-334 presented at the International Gas Turbine and Aeroengine Congress and Exposition, May 24-27, 1993, Cincinnati, OH.
- (8) Zabarnick, S., Chemical Kinetic Modeling of Jet Fuel Autoxidation and Antioxidant Chemistry, *Ind. Eng. Chem. Rev.*, In press (1993).
- (9) Semonov, N., Chemical Kinetics and Chain Reactions, Clarendon Press, Oxford (1935).
- (10) Heneghan, S. P., Understanding Global Oxidation Rates: Their Origin, Time and Temperature Behavior, To be presented at the 207th National Meeting of the American Chemical Society, Division of Petroleum Chemistry,

March 13-18, 1994, San Diego, CA.

- (11) Heneghan, S. P. and Zabarnick, S., Oxidation and the Formation of Deposits in Jet Fuels, Fuels, In press (1993).
- (12) Heneghan, S. P., Williams, T. F., Martel, C. R. and Ballal, D. R., Studies of Jet Fuel Thermal Stability in a Flowing System, ASME Paper 92-GT-106 presented at the 37th ASME International Gas Turbine and Aeroengine Congress and Ex-
- position, June 1-4, 1992, Cologne, Germany.
- (13) Benson, S. W., J. Chem. Phys., 40, 1007 (1964).

5. REFERENCES

1. G. Langer, "JP-4 Fuel System Icing," WADD Technical Report 60-826 (Wright Air Development Division, Wright Patterson Air Force Base, OH, 1960)
2. D. A. Netzel, R. L. Elliot, and G. F. Bechtle, "A Study of JP-4 Additives: Their Chemical Correlation and Physical Parameters as Effective Anti-Icing Agents," WADD Technical Report 60-226, Part II (Wright Air Development Division, Wright Patterson Air Force Base, OH, 1960)
3. C. R. Martel, "Military Jet Fuels, 1944-1987," AFWAL Technical Report AFWAL-TR-87-2062 (Air Force Wright Aeronautical Laboratories, Air Force Systems Command, Wright Patterson Air Force Base, Ohio, November 1987)
4. G. W. Mushrush, W. M. Stalick, E. J. Beal, S. C. Basu, and J. E. Slone, "The Synthesis of Acetals and Ketals of the Reduced Sugar Manose as Fuel System Icing Inhibitors," Presented at the ACS National Meeting, New Orleans, 24-28 March 1996.
5. J. Cummings, Naval Air Warfare Center Aircraft Division, Trenton, NJ, Private Communication.
6. G. W. Mushrush, George Mason University, Chemistry Department, Fairfax, VA, Private Communication.
7. J. Krautkramer and H. Krautkramer, Ultrasonic Testing of Materials, 4th Ed. (Springer-Verlag, New York, 1990).
8. "Handbook of Aviation Fuel Properties," CRC Report No. 503 (Coordinating Research Council, Inc., Atlanta, GA, 1983).
9. See, for example, S. J. Martin, V. E. Granstaff, and G. C. Frye, "Characterization of a Quartz Crystal Microbalance with Simultaneous Mass and Liquid Loading," *Anal. Chem.* **63**, 2272-2281 (1991).
10. See, for example, P. S. Russo, M. J. Saunders, L. M. DeLong, S. Kuehl, K. H. Langley, and R. W. Detenbeck, "Zero-Angle Depolarized Light Scattering of a Colloidal Polymer," *Anal. Chem. Acta* **189**, 69-87 (1986).
11. See, for example, B. Chu, Laser Light Scattering: Basic Principles and Practice, 2nd Ed. (Academic Press, Boston, 1991).
12. L. Gabriel, "Development of JP-5 Icing Inhibitor and Biocide Additive Package," NAPC Interim Report No. NAPC-LR-76-3 (Naval Air Propulsion Center, Trenton, NJ, February 1976).
13. A Guide to Glycols (Dow Chemical USA, Midland, MI, 1989).
14. Dow Chemical USA, The Glycol Ethers Handbook (Dow Chemical USA, Chemicals and Performance Products, Midland, MI, 1989).

15. Kinetica, Inc., Mound Advanced Technology Center, 1 Mound Road, Miamisburg, Ohio.
16. ASTM D-1177-94, "Standard Test Method for Freezing Point of Aqueous Engine Coolants" (American Society for Testing and Materials, Philadelphia, Pennsylvania, 1994).
17. S. P. Heneghan, "Global Oxidation of Jet Fuels: Determining and Understanding the Parameters," Polymer Prepr. 39(1), 14-18 (February 1994) (Presented at the 207th National Meeting of the American Chemical Society, Division of Petroleum Chemistry, San Diego, CA, March 13-18, 1994).

APPENDIX

Presentations, Publications, and Patents

"Two-Dimensional Temperature and Velocity-Measurement Techniques in a Sooty Jet Diffusion Flame," V. Vilimpoc, L. P. Goss, M. E. Post, B. Sarka, and D. D. Trump, Presented at the 1990 ASME Fluids Engineering Division Meeting, 4-7 June 1990, Toronto, Canada.

"Planar Visualization of Propane Jets and Propane Jet Diffusion Flames," L.-D. Chen, W. M. Roquemore, L. P. Goss, and V. Vilimpoc, Presented at the ASME Fluids Engineering Division Meeting, Fluid Measurements and Instrumentation Forum, 4-7 June 1990, Toronto, Canada.

"Conditional Velocity Measurements at the Base of Turbulent, Lifted Diffusion Flames," T. H. Chen, D. D. Trump, and L. P. Goss, Presented at the 26th AIAA/ASME/SAE/ASEE Joint Propulsion Conference and Exhibit, 16-18 July 1990, Orlando, FL.

"Effect of Droplet-Induced Breakdown on CARS Temperature Measurements," D. Dunn-Rankin, G. L. Switzer, C. A. Obringer, and T. A. Jackson, Appl. Opt. 29(21), 3150 (July 20, 1990).

"A Numerical/Experimental Study of Buoyant Jet Diffusion Flame," L.-D. Chen, J.-G. Lee, S.-H. Wu, R. W. Davis, E. F. Moore, W. M. Roquemore, L. P. Goss, and V. Vilimpoc, 1990 Fall Technical Meeting of the Eastern Section of the Combustion Institute (The Combustion Institute, Pittsburgh, PA, 1990), pp. 123-1 - 123-4.

"Model Compound Studies," E. G. Jones, Presented at the Advanced Thermally Stable Jet Fuels Progress Review, 2-3 October 1990, Wright-Patterson Air Force Base, OH.

"Dynamic Structure of a Buoyant Jet Diffusion Flame," W. M. Roquemore, L.-D. Chen, J.-G. Lee, S.-H. Wu, V. Vilimpoc, L. P. Goss, R. W. Davis, and E. F. Moore, Presented at the 43rd Annual Meeting of the American Physical Society, Division of Fluid Dynamics, 1990.

"Velocity Measurements in an Axisymmetric Swirl Combustor Using a Two-Component LDV System," R. Govind, M. E. Post, and S. Jeng, Presented at the Second Annual Health Monitoring Conference for Space Propulsion Systems, 14-15 November 1990, Cincinnati, OH.

"A Numerical Investigation of the Dynamic Structure of a Buoyant Jet Diffusion Flame," R. W. Davis, E. F. Moore, L.-D. Chen, W. M. Roquemore, and L. P. Goss, 1991 SIAM Numerical Combustion.

"Advanced Optical Diagnostics at Wright-Patterson Air Force Base by SRL," L. P. Goss, Invited Presentation to the AIAA Technical Committee on Aerodynamic Measurement Technology in conjunction with the AIAA 29th Aerospace Sciences Meeting, 7-10 January 1991, Reno, NV.

"Two-Color Particle-Imaging Velocimetry in a Turbine Cascade," M. E. Post, L. P. Goss, and L. F. Brainard, AIAA Paper 91-0274, Presented at the AIAA 29th Aerospace Sciences Meeting, 7-10 January 1991, Reno, NV.

"Experimental and Theoretical Studies in a Gas-Fueled Research Combustor," W. M. Roquemore, V. K. Reddy, P. O. Hedman, M. E. Post, T. H. Chen, L. P. Goss, D. D. Trump, V. Vilimpoc, and G. J. Sturgess, AIAA Paper 91-0639, Presented at the AIAA 29th Aerospace Sciences Meeting, 7-10 January 1991, Reno, NV.

"OH-Flow-Tagging Velocimetry," T. H. Chen, Invited Presentation at the University of Dayton Electro-Optics Seminar, 11 February 1991, Dayton, OH.

"Preliminary Results of a Numerical-Experimental Study of the Dynamic Structure of a Buoyant Jet Diffusion Flame," R. W. Davis, E. F. Moore, W. M. Roquemore, L.-D. Chen, V. Vilimpoc, and L. P. Goss, Comb. Flame 83, 263 (1991).

"Comparison Between Experiments and Predictions Based on Maximum Entropy for Sprays from a Pressure Atomizer," X. Li, L. P. Chin, R. S. Tankin, T. Jackson, J. Stutrud, and G. Switzer, *Comb. Flame* 86, 73 (1991).

"Uniform Droplet Generator: A Versatile System for Stable Generation of Uniform-Size Droplets," G. L. Switzer and B. Sarka, Invention Disclosure submitted 15 April 1991.

"Experimental Studies in a Gas-Fueled Research Combustor," M. E. Post, L. P. Goss, T. H. Chen, D. D. Trump, B. Sarka, and W. M. Roquemore, Presented at the 1991 Spring Technical Meeting of the Central States Section of the Combustion Institute, 22-24 April 1991, Nashville, TN; published in *Combustion Fundamentals and Applications* (The Combustion Institute, Pittsburgh, PA, 1991), pp. 397-402.

"Two-Color Particle-Imaging Velocimetry in a Diffusion Flame," M. E. Post, L. P. Goss, and L. F. Brainard, Presented at the 1991 Spring Technical Meeting of the Central States Section of the Combustion Institute, 22-24 April 1991, Nashville, TN; published in *Combustion Fundamentals and Applications* (The Combustion Institute, Pittsburgh, PA, 1991), pp. 215-220.

"Low-Frequency Flame Oscillation of a Nitrogen-Diluted Hydrogen Jet Diffusion Flame," S. Lee, L.-D. Chen, W. M. Roquemore, and L. P. Goss, Presented at the 1991 Spring Technical Meeting of the Central States Section of the Combustion Institute, 22-24 April 1991, Nashville, TN; published in *APS Bull.* 36(10), 2640 (1991) and in *Combustion Fundamentals and Applications* (The Combustion Institute, Pittsburgh, PA, 1991), pp. 119-124.

"Multiple-Line Thermometry in Sooting Flames Using Thin-Filament Pyrometry," L. P. Goss, V. Vilimpoc, and M. E. Post, Presented at the 1991 Spring Technical Meeting of the Central States Section of the Combustion Institute, 22-24 April 1991, Nashville, TN; published in *Combustion Fundamentals and Applications* (The Combustion Institute, Pittsburgh, PA, 1991), pp. 169-174.

"Model Compound Development," E. G. Jones, Presented at the Coordinating Research Council - Aviation Group Meeting, 22-25 April 1991, Alexandria, VA.

"Recent Developments in Optical Diagnostics," L. P. Goss, Invited Presentation at the Society of Automotive Engineers Aerospace Atlantic Conference, 22-26 April 1991, Dayton, OH.

"Velocity Measurements of Non-Reacting and Reacting Flows in a Research Combustor," T. H. Chen, M. E. Post, L. P. Goss, V. Vilimpoc, D. D. Trump, and B. Sarka, Presented at the International Union of Theoretical and Applied Mechanics (IUTAM) Symposium on Aerothermodynamics in Combustors, 3-5 June 1991, Taiwan, Republic of China.

"Development and Application of Laser Diagnostics for Reacting and Non-Reacting Flow Measurements," T. H. Chen, Invited Seminar at the Institute of Applied Mechanics, National Taiwan University, 11 June 1991, Taiwan, Republic of China.

"Development and Application of Laser Diagnostics for Studying Reacting and Non-Reacting Flow Measurements," T. H. Chen, Invited Seminar at the Industrial Technology Research Institute, 12 June 1991, Taiwan, Republic of China.

"Development of an Additive Package for Improving the Thermal Stability of Aviation Turbine Fuel," S. D. Anderson, J. T. Edwards, E. M. Steward, S. P. Heneghan, R. J. Byrd, T. B. Biddle, W. H. Edwards, and E. G. Jones, Presented at the ASTM Symposium on Aviation Fuel Thermal Stability Requirements, 23-27 June 1991, Toronto Ontario, Canada.

"Vorticity Generation in Jet Diffusion Flames," L-D. Chen, W. M. Roquemore, L. P. Goss, and V. Vilimpoc, Comb. Sci. Technol. 77, 41 (1991).

"Two-Color Particle-Imaging Velocimetry in a Two-Dimensional Vortex," M. E. Post, L. P. Goss, D. D. Trump, L. F. Brainard, and R. D. Hancock," Poster presented at the 1991 Gordon Research Conference on the Physics and Chemistry of Laser Diagnostics in Combustion, 15-19 July 1991, Plymouth, NH.

"Droplet Distributions from the Breakup of a Cylindrical Liquid Jet," L. P. Chin, P. G. LaRose, R. S. Tankin, T. Jackson, J. Stutrud, and G. L. Switzer, Phys. Fluids A. 3(8), 1897 (August 1991).

"Statistical OH-Zone Structures of Turbulent Jet Flames from Liftoff to Near-Blowout," T. H. Chen and L. P. Goss, Comb. Sci. Technol. 79, 311 (October 1991).

"Vaporization Behavior of Fuel Droplets in a Hot Air Stream," S. K. Aggarwal, C. Chen, T. A. Jackson, and G. L. Switzer, Int. J. Heat Mass Trans. 43(10), 2669 (October 1991).

"A Versatile System for Stable Generation of Uniform Droplets," G. L. Switzer, Rev. Sci. Instrum. 62(11), 2765 (November 1991).

"New Insights into the Recirculation Process of Research Combustors Gained Through the Use of Optical Diagnostics," T. H. Chen, L. P. Goss, and W. M. Roquemore, Invited Presentation at the 28th Annual Technical Meeting of the Society of Engineering Science, 6-8 November 1991, Gainesville, FL.

"Some Combustion Experiments at Wright Laboratory," T. H. Chen, Invited Presentation to the Junior and Senior Chemical Engineering Students, Chemical Engineering Department, University of Dayton, 22 November 1991, Dayton, OH.

"Interaction of 2D Wake and Plume," W. M. Roquemore, R. L. Britton, R. S. Tankin, C. A. Boedicker, M. M. Whitaker, and D. D. Trump, Photograph chosen for the cover of Bull. Am. Phys. Soc. 36(1) (November 1991).

"Evolution of a Buoyant Jet Diffusion Flame," L-D. Chen, J-G. Lee, S. H. Wu, R. W. Davis, E. F. Moore, V. Vilimpoc, L. P. Goss, and W. M. Roquemore, Poster presented at the 44th Annual Meeting of the American Physical Society, Fluid Dynamics Division, Gallery of Fluid Motion, 24-26 November 1991, Scottsdale, AZ.

"Manipulation of a Square Jet by Piezoelectric Actuators," R. D. Hancock, W. M. Roquemore, A. Glezer, and D. D. Trump, Poster presented at the 44th Annual Meeting of the American Physical Society, Fluid Dynamics Division, Gallery of Fluid Motion, 24-26 November 1991, Scottsdale, AZ. Of the fifty posters presented at this meeting (international), this poster was one of eight selected to receive an award.

"Velocity Effects on the Dynamic Behavior of H₂-N₂ Diffusion Flame," V. R. Katta and W. M. Roquemore, Presented at the 4th International Conference on Numerical Combustion, 2-4 December 1991, St. Petersburg Beach, FL.

"Two-Color Particle Velocimetry," L. P. Goss, M. E. Post, B. Sarka, and D. D. Trump, J. Laser Appl. 3(1), 36 (Winter 1991).

"Two-Dimensional Shear-Layer Entrainment and Interface-Length Measurements," T. H. Chen and R. D. Hancock, AIAA Paper 92-0382, Presented at the AIAA 30th Aerospace Sciences Meeting, 6-9 January 1992, Reno, NV.

"A Numerical Method for Simulating the Fluid-Dynamic and Heat Transfer Changes in a Jet Engine Injector Feed-Arm Due to Fouling," V. R. Katta and W. M. Roquemore, AIAA Paper 92-0768, Presented at the AIAA 30th Aerospace Sciences Meeting, 6-9 January 1992, Reno, NV.

"Numerical Investigations on the Dynamic Behavior of a H_2 - N_2 Diffusion Flame under the Influence of Gravitational Force," V. R. Katta, L. P. Goss, and W. M. Roquemore, AIAA Paper 92-0335, Presented at the AIAA 30th Aerospace Sciences Meeting, 6-9 January 1992, Reno, NV.

"Propagation and Fractals of Turbulent Jet Diffusion Flames," T. H. Chen and L. P. Goss, J. Propul. Power 8(1), 16 (January-February 1992).

"Autoxidation of Jet Fuels: Formation of Bulk and Surface Solubles," E. G. Jones and W. J. Balster, Presented at the American Chemical Society Meeting, Dayton Section, Membership Poster Session, 13 February 1992, Dayton, OH.

"Formation of Insolubles in Jet Fuels: Effects of Oxygen," E. G. Jones, W. J. Balster, and S. D. Anderson, Presented at the ACS National Meeting, 5-10 April 1992, San Francisco, CA; published in Molecular Modeling of Petroleum Processes and Catalysis, Prepr. Symp.-Structure of Jet Fuels III, Div. Pet. Chem., ACS 37(2), 393 (March 1992).

"Correlation Between Flask and Flowing Tests for Determining Thermal Oxidative Stability," E. G. Jones and W. J. Balster, Presented to the Coordinating Research Council - Aviation Oxidation Stability of Gas Turbine Fuels Group, 21 April 1992, Alexandria, VA.

"Computational Fluid Dynamics and Chemistry Modeling of Fouling," V. R. Katta and W. M. Roquemore, Presented to the Coordinating Research Council - Aviation Oxidation Stability of Gas Turbine Fuels Group, 21 April 1992, Alexandria, VA.

"Thin-Filament Velocimetry," M. E. Post, J. R. Gord, L. P. Goss, D. D. Trump, B. Sarka, L. F. Brainard, and R. Govind, Presented at the 1992 Technical Meeting of the Central States Section of the Combustion Institute, 27-28 April 1992, Columbus, OH.

"Two-Color Particle-Imaging Velocimetry in a Two-Dimensional Vortex," M. E. Post, L. P. Goss, D. D. Trump, L. F. Brainard, and R. D. Hancock, Presented at the 1992 Technical Meeting of the Central States Section of the Combustion Institute, 26-28 April 1992, Columbus, OH.

"Dynamic Vortex-Flame Interactions in Turbulent Jet Diffusion Flames Near Local Extinction," F. Takahashi, M. D. Vangsness, and L. P. Goss, Presented at the 1992 Technical Meeting of the Central States Section of the Combustion Institute, 26-28 April 1992, Columbus, OH.

"Studies of the Double-Vortex Structure of a Propane Jet Diffusion Flame Near Transitional Speed," V. R. Katta, L. P. Goss, and W. M. Roquemore, Presented at the 1992 Technical Meeting of the Central States Section of the Combustion Institute, 26-28 April 1992, Columbus, OH.

"A Numerical and Experimental Study of Vortical Structures of a Jet Diffusion Flame," S. Lee, L. D. Chen, W. M. Roquemore, and L. P. Goss, Presented at the 1992 Technical Meeting of the Central States Section of the Combustion Institute, 26-28 April 1992, Columbus, OH.

"Computational Fluid Dynamics and Chemistry Modeling of Fouling," V. R. Katta and W. M. Roquemore, Presented at Parker Hannifin Corporation, 14 May 1992, Cleveland, OH.

"Dynamic Stabilization Zone Structure of Jet Diffusion Flames from Liftoff to Blow-out," T. H. Chen, L. P. Goss, D. Talley, and D. Mikolaitis, *J. Propul. Power* 8(3), 548 (May- June 1992).

"Application of a Sulphur-Doped Alkane System to the Study of Thermal Oxidation of Jet Fuels," E. G. Jones and W. J. Balster, ASME Paper 92-GT-122, Presented at the 37th ASME International Gas Turbine and Aeroengine Congress and Exposition (1992 ASME Turbo Expo - Land, Sea, and Air), 1-4 June 1992, Cologne, Germany.

"Overview of Combustion Diagnostics at Wright-Patterson Air Force Base," L. P. Goss, Presented at the 28th AIAA/SAE/ASME/ASEE Joint Propulsion Conference and Exhibit, 6-8 July 1992, Nashville, TN.

"Time Evolution of a Buoyant Jet Diffusion Flame," L-D. Chen, V. Vilimpoc, L. P. Goss, R. W. Davis, E. F. Moore, and W. M. Roquemore, Presented at the Twenty-Fourth International Symposium on Combustion, 5-10 July 1992, Sydney, Australia; published in Twenty-Fourth Symposium (International) on Combustion (The Combustion Institute, Pittsburgh, PA, 1992), pp. 303-310.

"Near-Field Turbulent Structures and the Local Extinction of Jet Diffusion Flames," F. Takahashi and L. P. Goss, Presented at the Twenty-Fourth International Symposium on Combustion, 5-10 July 1992, Sydney, Australia; published in Twenty-Fourth Symposium (International) on Combustion (The Combustion Institute, Pittsburgh, PA, 1992), pp. 351-359.

"Computational Method for Predicting Deposition in Fuel System Components," V. R. Katta and W. M. Roquemore, Invited Presentation to Fuel Systems, Textron, 7 July 1992, Zeeland, MI.

"Simulation of Vortical Structures in a Jet Diffusion Flame," V. R. Katta, L. P. Goss, and W. M. Roquemore, Presented at the Sixth International Conference on Boundary and Interior Layers - Computational and Asymptotic Methods, 17-20 August 1992, Copper Mountain, CO.

"Direct Numerical Simulation of Transitional Jet Diffusion Flames," V. R. Katta and W. M. Roquemore, Invited Presentation at the World Congress of Nonlinear Analysts, 19-26 August 1992, Tampa, FL.

"Comparison of Jet Fuels. Jet A-1 POSF-2747: Jet A (SUN) and Jet A POSF-2827: Jet A (SHELL)," E. G. Jones and W. J. Balster, Presented at the Air Force-Navy Fuel Thermal Stability Meeting, 25-26 August 1992, Wright-Patterson Air Force Base, OH.

"Modeling of Deposition Process for Predicting Fouling in Heated Tubes," V. R. Katta and W. M. Roquemore, Presented at the Air Force-Navy Fuel Thermal Stability Meeting, 25-26 August 1992, Wright-Patterson Air Force Base, OH.

"Manipulation of a Square Jet by Piezoelectric Actuators," R. D. Hancock, A. Glezer, D. D. Trump, and W. M. Roquemore, *Phys. Fluids A* 4(9), 1877 (September 1992). One of the photographs from this paper was selected for the cover of this issue.

"Numerical Simulation of a Near-Turbulent Jet Diffusion Flame," V. R. Katta, L. P. Goss, and W. M. Roquemore, Presented at the 45th Annual Meeting of the Division of Fluid Dynamics of the American Physical Society, 22-24 November 1992, Tallahassee, FL.

"Visualization of the Liquid Motion During Formation of Rayleigh-Regime Drops," L-D. Chen, P. C. Sui, G. Switzer, J. Gord, C. Obringer, and W. M. Roquemore, Presented at the 45th Annual Meeting of the Division of Fluid Dynamics of the American Physical Society, 22-24 November 1992, Tallahassee, FL. Published in APS Bull. 37(10), 1992.

"Flame-Vortex Interactions in a Driven Jet Diffusion Flame," W. M. Roquemore, K. Y Hsu, L-D. Chen, V. R. Katta, and L. P. Goss, Presented at the 45th Annual Meeting of the Division of Fluid Dynamics of the American Physical Society, 22-24 November 1992, Tallahassee, FL.

"Flame-Vortex Interactions in a Driven Diffusion Flame," K. Y. Hsu, W. M. Roquemore, V. Katta, L. P. Goss, and D. D. Trump, Poster presented at the 10th Annual Gallery of Fluid Motion in conjunction with the 45th Annual Meeting of the Division of Fluid Dynamics of the American Physical Society, 22-24 November 1992, Tallahassee, FL. Of the fifty posters and videos presented at this meeting (international), this poster was one of fifteen selected to receive an award.

"Vortex Dynamics in a Flame--Influence of Combustion and Gravity," V. R. Katta and W. M. Roquemore. Video presented at the 10th Annual Gallery of Fluid Motion in conjunction with the 45th Annual Meeting of the Division of Fluid Dynamics of the American Physical Society, 22-24 November 1992, Tallahassee, FL.

"CARS Instrumentation for Combustion Applications," L. P. Goss, Invited Book Chapter in Instrumentation for Flows with Combustion (A. Taylor, Ed.) (Academic Press Ltd., United Kingdom, 1993), Chapter 4, pp. 251-322.

"Role of Inner and Outer Structures in Transitional Jet Diffusion Flame," V. R. Katta and W. M. Roquemore, Comb. Flame 92, 274 (1993).

"Images of the Quenching of a Flame by a Vortex - To Quantify Regimes of Turbulent Combustion," W. L. Roberts, J. F. Driscoll, M. C. Drake, and L. P. Goss, Comb. Flame 94, 58 (1993).

"Two-Color Particle-Imaging Velocimetry in Vortex Structures," M. E. Post and L. P. Goss, AIAA Paper 93-0412, Presented at the AIAA 31st Aerospace Sciences Meeting and Exhibit, 11- 14 January 1993, Reno, NV. Also published in Selected Technical Papers from the Aerodynamic Measurement Technology Committee, 31st AIAA Aerospace Sciences Meeting and Exhibit, January 11-14, 1993, Reno, NV (AIAA, Washington, D. C., 1993).

"Thin-Filament Velocimetry," L. P. Goss, J. R. Gord, D. D. Trump, and M. E. Post, AIAA Paper 93-0518, Presented at the AIAA 31st Aerospace Sciences Meeting and Exhibit, 11-14 January 1993, Reno, NV. Also published in Selected Technical Papers from the Aerodynamic Measurement Technology Committee, AIAA 31st Aerospace Sciences Meeting and Exhibit, January 11-14, 1993, Reno, NV (AIAA, Washington, D. C., 1993).

"Effect of Nonunity Lewis Number and Finite-Rate Chemistry on the Dynamics of a Hydrogen-Air Jet Diffusion Flame," V. R. Katta, L. P. Goss, and W. M. Roquemore, AIAA Paper 93-0454, Presented at the AIAA 31st Aerospace Sciences Meeting and Exhibit, 11-14 January 1993, Reno, NV.

"Experimental and Numerical Investigations of the Vortex-Flame Interactions in a Driven Jet Diffusion Flame," K. Y. Hsu, L-D. Chen, V. R. Katta, L. P. Goss, and W. M. Roquemore, AIAA Paper 93-0455, Presented at the AIAA 31st Aerospace Sciences Meeting and Exhibit, 11-14 January 1993, Reno, NV.

"Numerical Experiments on the Vortex-Flame Interactions in a Jet Diffusion Flame," F. Takahashi and V. R. Katta, AIAA Paper 93-0456, Presented at the AIAA 31st Aero-space Sciences Meeting and Exhibit, 11-14 January 1993, Reno, NV.

"The Strain Exerted by a Vortex on a Flame - Determined from Velocity Field Images," J. F. Driscoll, D. J. Sutkus, W. L. Roberts, M. E. Post, and L. P. Goss, AIAA Paper 93-0362, Presented at the AIAA 31st Aerospace Sciences Meeting and Exhibit, 11-14 January 1993, Reno, NV. Selected by the AIAA Technical Committee on Propellants and Combustion as the outstanding technical paper in this area. Award presented at the 30th AIAA/ASME/SAE/ASEE Joint Propulsion Conference, 27-29 June 1994, Indianapolis, IN.

"Formation of Insolubles in Aviation Fuels," E. G. Jones and W. J. Balster, Poster presented at the American Chemical Society Meeting, Dayton Section, Membership Poster Session, 4 February 1993, Dayton, OH.

"Numerical Study of the Vortex-Flame Interactions in a Jet Diffusion Flame," F. Takahashi and V. R. Katta, Presented at the 19th Mini-Symposium on Aerospace Science and Technology, 25 March 1993, Dayton, OH.

"Isothermal Fuel Degradation in a Single-Pass Heat Exchanger," E. G. Jones and W. J. Balster, Presented at the Coordinating Research Council Meeting, 21 April 1993, Washington, D. C.

"Degradation of a Jet-A Fuel in a Single-Pass Heat Exchanger," E. G. Jones, W. J. Balster, and M. E. Post, ASME Paper 93-GT-334, Presented at the 38th ASME International Gas Turbine and Aeroengine Congress and Exposition, 24-27 May 1993, Cincinnati, OH.

"Development of a Global-Chemistry Model for Jet-Fuel Thermal Stability Based on Observations from Static and Flowing Experiments," V. R. Katta, E. G. Jones, and W. M. Roquemore, Paper PEP-19, Presented at the AGARD-Propulsion and Energetics Panel 81st Symposium on Fuels and Combustion Technology for Advanced Aircraft Engines, 10-14 May 1993, Colliferno, Italy; published in AGARD-CP-536, Fuels and Combustion Technology for Advanced Aircraft Engines (AGARD, Neuilly sur Seine, France, September 1993), pp. 19-1 - 19-10.

"Periodic Vortex-Flame Interactions in a Diffusion Flame," K. Y. Hsu and L. P. Goss, Poster presented at the Gordon Research Conference on the Physics and Chemistry of Laser Diagnostics in Combustion, 11-16 July 1993, Plymouth, NH.

"Trace Analysis by Two-Photon Excited Fluorescence," F. E. Lytle, K. Grinstead, J. Gord, W. Weaver, W. Fisher, and D. Dinkel, Invited Presentation at the 206th ACS National Meeting, Spectrochemical Awards Symposium to Honor Richard Keller, 23 August 1993, Chicago, IL.

"Transient Behavior of Chemical Species in a Dynamic Hydrogen Jet Diffusion Flame," V. R. Katta and W. M. Roquemore, Presented at the 5th International Symposium on Computational Fluid Dynamics, 31 August - 3 September 1993, Sendai, Japan; published in Proceedings, Vol II (H. Daiguji, Ed.) (Japan Society of Computational Fluid Dynamics, Koganei, Japan, 1993), pp. 7-12.

"Vortex Dynamics in a Driven Jet Diffusion Flame," V. R. Katta, K. Y. Hsu, L. P. Goss, and W. M. Roquemore, Poster presented at the 5th International Symposium on Computational Fluid Dynamics, 31 August - 3 September 1993, Sendai, Japan; published in Proceedings, Vol II (H. Daiguji, Ed.) (Japan Society of Computational Fluid Dynamics, Koganei, Japan, 1993), pp. 13-18.

"Flame-Vortex Interactions in a Driven Diffusion Flame," K. Y. Hsu, L-D. Chen, V. R. Katta, L. P. Goss, D. D. Trump, and W. M. Roquemore, *Phys. Fluids A* 5, S4 (September 1993).

"Numerical Method for Simulating Fluid-Dynamic and Heat-Transfer Changes in Jet-Engine Injector Feed-Arm Due to Fouling," V. R. Katta and W. M. Roquemore, *AIAA J. Thermophys. Heat Trans.* 7(4), 651 (October-December 1993).

"Effects of Preferential Diffusion on Temperature During Flame-Vortex Interactions," V. R. Katta and W. M. Roquemore, Presented at the Fall Technical Meeting of the Eastern States Section of the Combustion Institute, 25-27 October 1993, Princeton, NJ.

"Trace Analysis by Two-Photon Excited Fluorescence," F. E. Lytle, K. Grinstead, J. Gord, W. Weaver, W. Fisher, and D. Dinkel, Invited Presentation at the 28th ACS Midwest Regional Meeting, 11 November 1993, Columbia, MO.

"Flame-Vortex Interactions in Nonpremixed Flames," V. R. Katta and W. M. Roquemore, Presented at the 1993 Meeting of the American Physical Society, Division of Fluid Dynamics, 21-23 November 1993, Albuquerque, NM.

"Stable Vortex Combustor (SVC)," W. M. Roquemore, K. Y. Hsu, L. P. Goss, and S. Raghu, Presented at the 1993 Meeting of the American Physical Society, Division of Fluid Dynamics, 21-23 November 1993, Albuquerque, NM.

"Simulation of Flame-Vortex Interaction in a Jet Diffusion Flame," V. R. Katta, K. Y. Hsu, M. Whitaker, and W. M. Roquemore, Poster presented at the 11th Annual Picture Gallery of Fluid Motion in conjunction with the 46th Annual Meeting of the Division of Fluid Dynamics of the American Physical Society, 21-23 November 1993, Albuquerque, NM. Of the 30 posters presented at this meeting (international), this poster was one of six selected to receive an award.

"Phenomenological Study of the Formation of Insolubles in a Jet-A Fuel," E. G. Jones and W. J. Balster, *Energy Fuels* 7, 968 (1993).

"A Numerical/Experimental Study of the Dynamic Structure of a Buoyant Jet Diffusion Flame," R. W. Davis, E. F. Moore, L-D. Chen, W. M. Roquemore, V. Vilimpoc, and L. P. Goss, Invited Paper, *Theoret. Comput. Fluid Dynamics* 6, 113 (1994).

"Effect of Nonunity Lewis Number and Finite-Rate Chemistry on the Dynamics of a Hydrogen-Air Jet Diffusion Flame," V. R. Katta, L. P. Goss, and W. M. Roquemore, *Comb. Flame* 96, 60 (1994).

"Numerical Investigations of Transitional H₂/N₂ Jet Diffusion Flames," V. R. Katta, L. P. Goss, and W. M. Roquemore, *AIAA J.* 32, 84 (January 1994).

"Simultaneous Thin-Filament Velocimetry and Pyrometry," L. P. Goss, W. L. Weaver, D. D. Trump, and J. R. Gord, AIAA Paper No. 94-0495, Presented at the AIAA 32nd Aero-space Sciences Meeting and Exhibit, 10-13 January 1994, Reno, NV.

"Gravity Effects on the Dynamics of Evaporating Droplets in a Heated Jet," S. Aggarwal, T. Park, and V. R. Katta, AIAA Paper No. 94-0684, Presented at the AIAA 32nd Aerospace Sciences Meeting and Exhibit, 10-13 January 1994, Reno, NV.

"Numerical Studies on Multidimensional H₂/O₂/N₂ Premixed Jet Flame," V. R. Katta and W. M. Roquemore, AIAA Paper No. 94-0549, Presented at the AIAA 32nd Aero-space Sciences Meeting and Exhibit, 10-13 January 1994, Reno, NV.

"Two-Color Particle-Imaging Velocimetry Using a Single Argon-Ion Laser," M. E. Post, D. D. Trump, L. P. Goss, and R. D. Hancock, *Exp. Fluids* 16, 263 (February 1994).

"Improvements and Expectations of a Two-Photon Second-Harmonic Detection Fluorometer," K. D. Grinstead, Jr., F. E. Lytle, J. R. Gord, W. L. Weaver, and W. G. Fisher, Presented at the Pittsburgh Conference, 27 February 1994, Chicago, IL.

"Temperature Effects in Fuel Fouling," E. G. Jones and W. J. Balster, Poster presented at the ACS Dayton Section Membership Poster Session, 8 March 1994, Dayton, OH.

"Numerical Modeling of Jet-Fuel Autoxidation in Flowing Systems," L. P. Chin, V. R. Katta, and S. P. Heneghan, Presented at the 207th National Meeting of the American Chemical Society, Division of Petroleum Chemistry, 13-18 March 1994, San Diego, CA; *Polymer Prepr.* 39(1), 19 (February 1994).

"Kinetics and Modeling for Jet-Fuel Autoxidation," E. G. Jones, W. J. Balster, M. R. Vonada, and J. M. Pickard, Presented at the 207th National Meeting of the American Chemical Society, Division of Petroleum Chemistry, 13-18 March 1994, San Diego, CA; *Polymer Prepr.* 39(1), 10 (February 1994).

"Formation of Insolubles in a Jet-A Fuel: Temperature Effects," E. G. Jones and W. J. Balster, Presented at the 207th National Meeting of the American Chemical Society, Division of Petroleum Chemistry, 13-18 March 1994, San Diego, CA; *Polymer Prepr.* 39(1), 78 (February 1994).

"Simulation of a Multidimensional Premixed Flame," V. R. Katta and W. M. Roquemore, Presented at the AIAA Dayton-Cincinnati Section 20th Annual Minisymposium of Aerospace Science and Technology, 31 March 1994, Dayton, OH.

"Structure of a Spray Flame Stabilized on a Production Engine Combustor Swirl Cup," F. Takahashi, W. J. Schmoll, G. L. Switzer, and D. T. Shouse, Presented at the AIAA Dayton-Cincinnati Section 20th Annual Minisymposium of Aerospace Science and Technology, 31 March 1994, Dayton, OH.

"Characterization of Droplet/Vapor/Vortex Interactions in a Two-Dimensional Shear Layer," R. D. Hancock and L. P. Chin, *AIAA J.* 32, 881 (April 1994).

"Surface Deposition - Sulphur Aspects," E. G. Jones and W. J. Balster, Presented at the Seminar on Sulphur Chemistry of Jet Fuels, Sponsored by Wright Laboratory, Aero Propulsion and Power Directorate, Fuels and Lubrication Division, Fuel Development Section, 6 April 1994, Wright-Patterson Air Force Base, OH.

"Fouling of Jet Fuel: Near-Isothermal Studies," E. G. Jones and W. J. Balster, Presented at the Coordinating Research Council - Aviation Group on Low Temperature Flow Performance of Aviation Turbine Fuels, 25-28 April 1994, Alexandria, VA.

"Composition of Aviation-Fuel Gums," E. G. Jones, J. M. Lavoie, and S. H. Hoke, Poster presented at the 42nd American Society for Mass Spectrometry Conference on Mass Spectrometry and Allied Topics, 29 May - 3 June 1994, Chicago, IL; published in *Proceedings (American Society for Mass Spectrometry, Santa Fe, NM, 1994)*, p. 537.

"Thin-Filament Velocimetry and Pyrometry," L. P. Goss, W. L. Weaver, D. D. Trump, and J. R. Gord, Presented at the 1994 Technical Meeting of the Central States Section of the Combustion Institute, 5-7 June 1994, Madison, WI; published in Combustion Fundamentals and Applications (The Combustion Institute, Pittsburgh, PA, 1994), pp. 243-248.

"Characteristics of a Trapped-Vortex (TV) Combustor," K. Y. Hsu, L. P. Goss, D. D. Trump, and W. M. Roquemore, Presented at the 1994 Technical Meeting of the Central States Section of the Combustion Institute, 5-7 June 1994, Madison, WI; published in Combustion Fundamentals and Applications (The Combustion Institute, Pittsburgh, PA, 1994), pp. 424-429.

"Fuel-Thermal-Stability Studies with Two-Photon Fluorescence Spectroscopy," J. R. Gord, W. L. Weaver, K. D. Grinstead, and F. Lytle, Presented at the 1994 Technical Meeting of the Central States Section of the Combustion Institute, 5-7 June 1994, Madison, WI; published in Combustion Fundamentals and Applications (The Combustion Institute, Pittsburgh, PA, 1994), pp. 249-254.

"The Effect of a DC Electric Field on the Velocity and Temperature of a Premixed Propane-Air Flame," D. F. Grosjean, Presented at the 1994 Technical Meeting of the Central States Section of the Combustion Institute, 5-7 June 1994, Madison, WI; published in Combustion Fundamentals and Applications (The Combustion Institute, Pittsburgh, PA, 1994), pp. 207-212.

"Two-Color Particle-Imaging Velocimetry Employing a Single CCD Camera," L. P. Goss, D. D. Trump, B. Sarka, and J. H. Frank, Presented at the 1994 Technical Meeting of the Central States Section of the Combustion Institute, 5-7 June 1994, Madison, WI; published in Combustion Fundamentals and Applications (The Combustion Institute, Pittsburgh, PA, 1994), pp. 237-242.

"Transition of a Laminar Jet Flame from Premixed to Diffusion Type," V. R. Katta and W. M. Roquemore, Presented at the 1994 Technical Meeting of the Central States Section of the Combustion Institute, 5-7 June 1994, Madison, WI; published in Combustion Fundamentals and Applications (The Combustion Institute, Pittsburgh, PA, 1994), pp. 195-200.

"Numerical Studies on the Structure of an Unsteady Spray Diffusion Flame under the Influence of Gravity," T. W. Park, S. K. Aggarwal, and V. R. Katta, Presented at the 1994 Technical Meeting of the Central States Section of the Combustion Institute, 5-7 June 1994, Madison, WI; published in Combustion Fundamentals and Applications (The Combustion Institute, Pittsburgh, PA, 1994), pp. 159-164.

"Effects of Buoyancy on Heat Transfer and Oxygen Consumption in Fuel-Thermal-Stability Studies," V. R. Katta, T. F. Williams, J. Blust, and C. R. Martel, Presented at the 39th International Gas Turbine and Aeroengine Congress and Exposition, 13-16 June 1994, The Hague, Netherlands.

"Observations of Flame Behavior from a Practical Fuel Injector Using Gaseous Fuel in a Technology Combustor," P. O. Hedman, G. J. Sturgess, D. L. Warren, L. P. Goss, and D. T. Shouse, ASME Paper 94-GT-389, Presented at the 39th International Gas Turbine and Aeroengine Congress and Exposition, 13-16 June 1994, The Hague, Netherlands.

"Relation of CARS Temperature Fields to Lean Blowout Performance in an Aircraft Gas Turbine Generic Combustor," G. L. Switzer, G. F. Sturgess, D. G. Sloan, and D. Shouse, AIAA Paper No. 94-3271, Presented at the 30th AIAA/ASME/SAE/ASEE Joint Propulsion Conference, 27-29 June 1994, Indianapolis, IN.

"A Numerical Study of Droplet-Vortex Interactions in an Evaporating Spray," T. W. Park, S. K. Aggarwal, and V. R. Katta, AIAA Paper No. 94-3276, Presented at the 30th AIAA/ASME/SAE/ASEE Joint Propulsion Conference, 27-29 June 1994, Indianapolis, IN.

"On the Structure of Stretched/Compressed Laminar Flamelet--Influence of Preferential Diffusion," V. R. Katta and W. M. Roquemore, Presented at the Twenty-Fifth International Symposium on Combustion, 31 July - 5 August 1994, Irvine, CA.

"Effect of Gravity on the Structure of an Unsteady Spray Diffusion Flame," T. W. Park, S. K. Aggarwal, and V. R. Katta, Presented at the Twenty-Fifth International Symposium on Combustion, 31 July - 5 August 1994, Irvine, CA.

"Structure of a Spray Flame Stabilized on a Production Engine Combustor Swirl Cup," F. Takahashi, W. J. Schmoll, G. L. Switzer, and D. T. Shouse, Presented at the Twenty-Fifth International Symposium on Combustion, 31 July - 5 August 1994, Irvine, CA. A photograph from this paper was selected for the cover of the August 1994 issue of Aerospace America.

"Surface Fouling: Short- vs. Long-Term Tests," E. G. Jones and W. J. Balster, Presented at the ACS National Meeting, 21-26 August 1994, Washington, D. C.; published in Prepr.-ACS, Div. Fuel Chem. 39(3), 952 (1994).

"Simulation of Flame-Vortex Interaction in a Jet Diffusion Flame," V. R. Katta, K. Y. Hsu, M. Whitaker, and W. M. Roquemore, Phys. Fluids 6(9), S3 (September 1994).

"Characteristics of a Trapped Vortex (TV) Combustor," K. Y. Hsu, L. P. Goss, D. D. Trump, and W. M. Roquemore, Presented at the Sixth Annual Propulsion Symposium, 13-14 September 1994, Cleveland, OH.

"Simulation of Vortical Structures in a Jet Diffusion Flame," V. R. Katta, L. P. Goss, and W. M. Roquemore, Inter. J. Numer. Meth. Heat Fluid Flow 4(5), 413 (October 1994).

"Detailed Numerical Simulations for Premixed Flame Structure," V. R. Katta and W. M. Roquemore, Poster presented at the 1994 Ohio Supercomputer Conference on Combustion, Environment, and Heating Technology - The Role of High Performance Simulation, 6-7 October 1994, Columbus, OH.

"The Effect of Additives on the Formation of Insolubles in a Jet A Fuel," S. D. Anderson, E. G. Jones, L. P. Goss, and W. J. Balster, Presented at the 5th International Conference on Stability and Handling of Liquid Fuels, 3-7 October 1994, Rotterdam, The Netherlands; published in Proceedings, Vol. 1 (H. N. Giles, Ed.) (U. S. Department of Energy, Washington, D. C., 1994), pp. 291-301.

"Burning Characteristics of Fuel-Lean and Fuel-Rich Premixed Flames," V. R. Katta and W. M. Roquemore, Presented at the 47th Annual Meeting of the Division of Fluid Dynamics of the American Physical Society, 20-22 November 1994, Atlanta, GA.

"Dynamics of Jet in Cross Flow," S. P. Gogineni, W. M. Roquemore, M. M. Whitaker, and L. P. Goss, Poster presented at the 12th Annual Picture Gallery of Fluid Motion in conjunction with the 47th Annual Meeting of the Division of Fluid Dynamics of the American Physical Society, 20-22 November 1994, Atlanta, GA. Of the 51 posters presented at this international meeting, this poster was one of seven selected to receive an award (selected as best poster by all 15 judges).

"Effect of Droplet Size on Vortex-Droplet Interaction," V. R. Katta, M. M. Whitaker, S. K. Aggarwal, T. W. Park, and W. M. Roquemore, Poster presented at the 12th Annual Picture Gallery of Fluid Motion in conjunction with the 47th Annual Meeting of the Division of Fluid Dynamics of the American Physical Society, 20-22 November 1994, Atlanta, GA.

"Effect of Gravity on the Structure of an Unsteady Spray Diffusion Flame," T. W. Park, S. K. Aggarwal, and V. R. Katta, Comb. Flame 99(10), 767 (1994).

"On the Structure of Stretched/Compressed Laminar Flamelet--Influence of Preferential Diffusion," V. R. Katta and W. M. Roquemore, Comb. Flame 100(1), 61 (1995).

"Role of Buoyancy in Fuel-Thermal-Stability Studies," V. R. Katta, J. Blust, T. F. Williams, and C. R. Martel, J. Thermophys. Heat Transfer 9(1), 159 (January-March 1995).

"Degradation of a Jet-A Fuel in a Single-Pass Heat Exchanger," E. G. Jones, W. J. Balster, and M. E. Post, J. Eng. Gas Turb. Power 117, 125 (January 1995).

"Numerical Experiments on the Vortex-Flame Interactions in a Jet Diffusion Flame," F. Takahashi and V. R. Katta, J. Propul. Power 11(1), 170 (January-February 1995).

"Numerical Modeling of Deposition in Fuel-Injection Nozzles," L. P. Chin and V. R. Katta, AIAA Paper No. 95-0497, Presented at the AIAA 33rd Aerospace Sciences Meeting and Exhibit, 9-12 January 1995, Reno, NV.

"Vortex-Flame Interaction in Premixed Jet Flames," V. R. Katta and W. M. Roquemore, AIAA Paper No. 95-0871, Presented at the AIAA 33rd Aerospace Sciences Meeting and Exhibit, 9-12 January 1995, Reno, NV.

"Investigation of a Jet in a Crossflow Using PIV," S. P. Gogineni, D. Sutkus, L. Goss, and A. Glezer, AIAA Paper No. 95-0790, Presented at the AIAA 33rd Aerospace Sciences Meeting and Exhibit, 9-12 January 1995, Reno, NV.

"Performance of a Trapped-Vortex (TV) Combustor," K.-Y. Hsu, L. P. Goss, D. D. Trump, and W. M. Roquemore, AIAA Paper No. 95-0810, Presented at the AIAA 33rd Aerospace Sciences Meeting and Exhibit, 9-12 January 1995, Reno, NV.

"Vortex-Flame Interactions and the Local Extinction of Turbulent Jet Diffusion Flames," F. Takahashi, W. J. Schmoll, D. D. Trump, and L. P. Goss, AIAA Paper No. 95-0139, Presented at the AIAA 33rd Aerospace Sciences Meeting and Exhibit, 9-12 January 1995, Reno, NV.

"Laser Diagnostic Development for the Characterization of the Chemistry and Kinetics in Combustion and Decomposition of Hydrocarbon Jet Fuels," W. L. Weaver, Invited presentation at the Meeting of the Ohio Valley Section of the Society for Applied Spectroscopy, 25 January 1995, Dayton, OH.

"Numerical Modeling of Deposition in Fuel-Injection Nozzles," L. P. Chin and V. R. Katta, Presented at the ASME Emerging Energy Technology Symposium, 29 January - 6 February 1995, Houston, TX; published in Emerging Energy Technology (G. A. Karim, Ed.) (American Society of Mechanical Engineers, New York, 1995), PD-Vol. 66, pp. 67-74.

"Using Lasers to Improve Aviation Fuel," J. R. Gord and W. L. Weaver, Presented at the Dayton Museum of Natural History, Affiliate Societies Council Career Exploration Day, 4 February 1995, Dayton, OH.

"Autoxidation in Aviation Fuels: Reaction of Oxygen and Formation of Hydroperoxides Leading to Surface Fouling," L. M. Balster, W. J. Balster, and E. G. Jones, Poster presented at the ACS Dayton Section Membership Poster Session, 14 February 1995, Dayton, OH.

"Simulation of Preferential Diffusion Effects in Jet Flames," V. R. Katta and W. M. Roquemore, Invited presentation at the European Science Foundation/FBP Workshop on Free Boundary Problems in Combustion, 22-24 March 1995, Arcachon, France.

"Diagnostics for Aviation-Fuel Thermal Decomposition Studies," W. L. Weaver, V. Vilimpoc, S. W. Buckner, and J. R. Gord, Presented at the 21st Annual Mini-Symposium on Aerospace Science and Technology, Dayton-Cincinnati Section of AIAA, 30 March 1995, Dayton, OH.

"Quantitation of Key Combustion Species Through Picosecond Laser Techniques," J. R. Gord, M. A. Linne, G. J. Fiechtner, and W. L. Weaver, Presented at the 21st Annual Mini-Symposium on Aerospace Science and Technology, Dayton-Cincinnati Section of AIAA, 30 March 1995, Dayton, OH.

"Vortex-Flame Interactions in a Hydrogen Jet Diffusion Flame," V. R. Katta, F. Grisch, B. Attal-Tretout, P. Bouchardy, and W. M. Roquemore, Paper No. 95S-033, Presented at the Spring Meeting of the Central States/Western States/Mexican National Sections of the Combustion Institute and American Flame Research Committee, 23-26 April 1995, San Antonio, TX; published in Combustion Fundamentals and Applications (The Combustion Institute, Pittsburgh, PA, 1995), pp. 173-178.

"The Structure of a Dynamic Non-premixed H₂-Air Flame," C. D. Carter, L. P. Goss, K. Y. Hsu, V. R. Katta, and D. D. Trump, Paper No. 95S-080, Presented at the Spring Meeting of the Central States/Western States/Mexican National Sections of the Combustion Institute and American Flame Research Committee, 23-26 April 1995, San Antonio, TX; published in Combustion Fundamentals and Applications (The Combustion Institute, Pittsburgh, PA, 1995), pp. 429-434.

"Finite-Rate Chemistry Effects During Vortex-Flame Interactions in a Driven-Jet Diffusion Flame," R. D. Hancock, R. P. Lucht, V. R. Katta, and K. Y. Hsu, Paper No. 95S-034, Presented at the Spring Meeting of the Central States/Western States/Mexican National Sections of the Combustion Institute and American Flame Research Committee, 23-26 April 1995, San Antonio, TX; published in Combustion Fundamentals and Applications (The Combustion Institute, Pittsburgh, PA, 1995), pp. 179-184.

"Unsteady Spray Behavior in a Heated Jet Shear Layer," S. K. Aggarwal, T. W. Park, and V. R. Katta, Paper No. 95S-142, Presented at the Spring Meeting of the Central States/Western States/Mexican National Sections of the Combustion Institute and American Flame Research Committee, 23-26 April 1995, San Antonio, TX; published in Combustion Fundamentals and Applications (The Combustion Institute, Pittsburgh, PA, 1995), pp. 754 - 759.

"Relationships Among Nitric Oxide, Temperature, and Mixture Fraction in Hydrogen Jet Flames," R. S. Barlow and C. D. Carter, Paper No. 95S-054, Presented at the Spring Meeting of the Central States/Western States/Mexican National Sections of the Combustion Institute and American Flame Research Committee, 23-26 April 1995, San Antonio, TX; published in Combustion Fundamentals and Applications (The Combustion Institute, Pittsburgh, PA, 1995), pp. 275 - 280.

"Effect of Additives on the Formation of Insolubles in Two Jet Fuels," E. G. Jones, L. M. Balster, and W. J. Balster, Presented at the Coordinating Research Council Meeting, Aviation Oxidation Stability Gas Turbine Fuels Group, 25 April 1995, Alexandria, VA.

"Two-Dimensional Shear-Layer Entrainment and Interface-Length Measurements," T. H. Chen and R. D. Hancock, AIAA J. 33(5), 949 (May 1995).

"Gravity Effects on the Dynamics of Evaporating Droplets in a Heated Jet," T. K. Park, S. K. Aggarwal, and V. R. Katta, *J. Propul. Power* 11(3), 519 (May-June 1995).

"Combustor Flame Stabilizing Structure," W. M. Roquemore, D. T. Shouse, and K-Y. Hsu, Air Force Invention No. 21286 assigned 14 June 1995.

"A Numerical Study of Droplet-Vortex Interactions in an Evaporating Spray," T. W. Park, S. K. Aggarwal, and V. R. Katta, Accepted in June 1995 for publication in the *International Journal of Heat and Mass Transfer*.

"Surface Fouling in Aviation Fuels: An Isothermal Chemical Study," E. G. Jones, W. J. Balster, and J. M. Pickard, ASME Paper No. 95-GT-45, Presented at the 40th ASME Gas Turbine and Aeroengine Congress, 5-8 June 1995, Houston, TX.

"Studies on Lean-Blowout Characteristics of a Premixed Jet Flame," V. R. Katta and W. M. Roquemore, ASME Paper No. 95-GT-115, Presented at the 40th ASME Gas Turbine and Aeroengine Congress, 5-8 June 1995, Houston, TX.

"Study of Flame Stability in a Step Swirl Combustor," M. D. Durbin, D. Vangsness, D. R. Ballal, and V. R. Katta, ASME Paper No. 95-GT-111, Presented at the 40th ASME Gas Turbine and Aeroengine Congress, 5-8 June 1995, Houston, TX; accepted for publication in *Transactions of the ASME*.

"Observations of Flame Behavior from a Practical Fuel Injector Using Gaseous Fuel in a Technical Combustor," P. O. Hedman, G. J. Sturgess, D. L. Warren, L. P. Goss, and D. T. Shouse, *J. Eng. Gas Turb. Power* 117(3), 441 (July 1995).

"Numerical Studies on the Structure of Two-Dimensional H₂/Air Premixed Jet Flame," V. R. Katta and W. M. Roquemore, *Combust. Flame* 102(1/2), 21 (July 1995).

"Dynamics of Propane Jet Diffusion Flames," V. R. Katta, L. P. Goss, W. M. Roquemore, and L. D. Chen, Invited paper submitted in July 1995 to *Atlas of Flow Visualization*, Vol. 3 (Visualization Society of Japan, 1995).

"Surface Fouling in Aviation Fuel: Short- vs Long-Term Isothermal Tests," E. G. Jones and W. J. Balster, *Energy Fuels* 9, 610 (July/August 1995).

"Effects of Dilution on Burning Characteristics and Dynamics of H₂/O₂ Premixed Flame," V. R. Katta and W. M. Roquemore, Presented at the 8th International Symposium on Transport Phenomena in Combustion, 16-20 July 1995, San Francisco, CA.

"Dissolved Oxygen Quantitation in Fuel Through Measurements of Dynamically Quenched Fluorescence Lifetimes," J. R. Gord, S. W. Buckner, and W. L. Weaver, Presented at the 16th International Congress on Instrumentation in Aerospace Simulation Facilities, 18-21 July 1995, Wright-Patterson Air Force Base, OH.

"Diagnostics for Simultaneous Quantitation of Dissolved Oxygen Concentration, Particle Size, and Surface Mass Deposition Rate in Thermally Stressed Aviation Fuel," J. R. Gord, W. L. Weaver, V. Vilimpoc, and S. W. Buckner, Presented at the 37th Rocky Mountain Conference on Analytical Chemistry, 23-28 July 1995, Denver, CO.

"Unsteady Spray Behavior in a Heated Jet Shear Layer: Droplet-Vortex Interactions," S. K. Aggarwal, T. W. Park, and V. R. Katta, Presented at the 15th International Colloquium on Dynamic Reacting Flows, 31 July - 4 August 1995, Boulder, CO; accepted for publication in *Combustion Science and Technology*.

"Numerical Experiments on the Vortex-Flame Interactions in a Jet Diffusion Flame," F. Takahashi and V. R. Katta, Presented at the 15th International Colloquium on Dynamic Reacting Flows, 31 July - 4 August 1995, Boulder, CO.

"PIV Measurements of a Jet in a Cross Flow," S. P. Gogineni, D. D. Trump, and L. P. Goss, Presented at the Joint ASME/JSME Fluids Engineering Conference, Fourth Symposium on Experimental and Numerical Flow Visualization, 13-18 August 1995, Hilton Head, SC; published in *Experimental and Numerical Flow Visualization - 1995*, FED-Vol. 218 (B. Khalighi, T. Kobayashi, D. H. Fruman, M. J. Braun, C. J. Freitas, and F. Balban, Eds.) (American Society of Mechanical Engineers, New York, 1995), pp. 71-75.

"Simultaneous Application of Photon Correlation Spectroscopy and Quartz Crystal Microbalance to the Study of Thermally Stressed Jet Fuel," V. Vilimpoc and B. Sarka, Presented at the Fall 1995 ACS 210th National Meeting, Symposium on Coke Formation and Mitigation, 20-24 August 1995, Chicago, IL; published in *Prepr. Symp.-ACS, Div. Pet. Chem.* 40(4), 666 (August 1995).

"Fouling of Stainless Steel and Silcosteel Surfaces during Aviation Fuel Autoxidation," E. G. Jones, W. J. Balster, and W. A. Rubey, Presented at the Fall 1995 ACS 210th National Meeting, Symposium on Coke Formation and Mitigation, 20-24 August 1995, Chicago, IL; published in *Prepr. Symp.-ACS, Div. Pet. Chem.* 40(4), 655 (August 1995).

"Dynamics of Jet in Cross Flow," S. P. Gogineni, M. M. Whitaker, L. P. Goss, and W. M. Roquemore, *Phys. Fluids* 7(9), A5 (September 1995).

"Application of Isothermal Calorimetry to Jet Fuel Autoxidation Kinetics," J. M. Pickard, E. G. Jones, and W. J. Balster, Presented at the 24th North American Thermal Analysis Society Conference, 10-13 September 1995, San Francisco, CA; published in *Proceedings* (S. A. Mikhail, Ed.) (CANMET, Ottawa, Ontario, Canada, 1995), pp. 216-221.

"Influence of Combustion Air Jets on Primary Zone Characteristics for Gas Turbine Combustors," S. Gogineni, D. Shouse, C. Frayne, J. Stutrud, and G. Sturgess, Paper No. ISABE 95-704, Presented at the 12th International Symposium on Air Breathing Engines, XII ISABE, 10-15 September 1995, Melbourne, Australia; published in *Proceedings* (F. S. Billig, Ed.) (American Institute of Aeronautics and Astronautics, Washington, D. C., 1995), Vol. 1, pp. 475-487.

"Two-Color Particle-Image Velocimetry Employing a Color CCD Camera," D. D. Trump, S. P. Gogineni, and L. P. Goss, Presented at the 7th International Symposium on Flow Visualization, 11-14 September 1995, Seattle, WA; published in *Flow Visualization VII* (J. P. Crowder, Ed.) (Bagell House, Inc., New York, 1995), pp. 622-627.

"Quantitative Evaluation of Jet-Fuel Fouling and the Effect of Additives," E. G. Jones, L. M. Balster, and W. J. Balster, *Energy Fuels* 9, 906 (September/October 1995).

"Particle Image Velocimetry (PIV) for Research in Fluid Processes and Flow Measurement at NIST," S. P. Gogineni, Invited presentation to the National Institute of Standards and Technology, 18 October 1995, Gaithersburg, MD.

"Titanium:Sapphire-Based Laser Sources for Two-Photon Fluorescence Spectroscopy," K. D. Grinstead, F. E. Lytle, W. L. Weaver, and J. R. Gord, Presented at the 22nd Annual Conference of the Federation of Analytical Chemistry and Spectroscopy Societies, 15-20 October 1995, Cincinnati, OH.

"Ultrafast Pump-Probe Studies of Rotational Diffusion in Supercritical Fluids," J. R. Gord, W. L. Weaver, E. Niemeyer, and F. V. Bright, Presented at the 22nd Annual Conference of the Federation of Analytical Chemistry and Spectroscopy Societies, 15-20 October 1995, Cincinnati, OH.

"Quantitation of Dissolved Oxygen Concentration, Particle Size, and Surface Mass Deposition Rate in Thermally Stressed Aviation Fuel," W. L. Weaver, V. Vilimpoc, S. W. Buckner, and J. R. Gord, Presented at the 22nd Annual Conference of the Federation of Analytical Chemistry and Spectroscopy Societies, 15-20 October 1995, Cincinnati, OH.

"Time-Correlated Single-Photon Counting Investigations of the Effects of Temperature, Solvent, and Excitation Energy on the Fluorescence Lifetime of Adamantyl Diazirine," J. S. Buterbaugh, J. P. Toscano, W. L. Weaver, J. R. Gord, T. L. Gustafson, and M. S. Platz, Presented at the 22nd Annual Conference of the Federation of Analytical Chemistry and Spectroscopy Societies, 15-20 October 1995, Cincinnati, OH.

"The Structure of a Dynamic Nonpremixed H₂-Air Flame," C. D. Carter, R. D. Gould, L. P. Goss, V. R. Katta, and K. Y. Hsu, Presented at the Fall Meeting of the Western States Section of the Combustion Institute, 30-31 October 1995, Stanford, CA, and published as Paper No. WSS/CI 95F-222.

"Comparisons Between Experiments and Predictions Based on Maximum Entropy for the Breakup of a Cylindrical Liquid Jet," L. P. Chin, R. S. Tankin, and T. Jackson, *Atomization and Sprays* 5, 603 (November/December 1995).

"An Experimental Investigation of the Unsteady Structure of a Transitional Plane Wall Jet," S. P. Gogineni and C. Shih, Submitted in November 1995 to *Experiments in Fluids*.

"Simultaneous Measurement of Particle Size, Mass Rate of Deposition, and Oxygen Concentration in Thermally Stressed Jet Fuel," V. Vilimpoc, B. Sarka, W. L. Weaver, and J. R. Gord, Presented at the 1995 International Mechanical Engineering Congress and Exposition, 12-17 November 1995, San Francisco, CA, and published in *Proceedings*.

"Fluorescence Imaging of Droplet Internal Fluid Motion," J. M. Hartings, G. L. Switzer, K.-Y. Hsu, and J. R. Gord, Poster presented at the 13th Annual Picture Gallery of Fluid Motion in conjunction with the 48th Annual Meeting of the Division of Fluid Dynamics of the American Physical Society, 19-21 November 1995, Irvine, CA.

"High Free Stream Turbulence Influence on Turbine Film Cooling Flows," S. P. Gogineni, R. B. Rivir, D. J. Pestian, and L. P. Goss, Poster presented at the 13th Annual Picture Gallery of Fluid Motion in conjunction with the 48th Annual Meeting of the Division of Fluid Dynamics of the American Physical Society, 19-21 November 1995, Irvine, CA. Of the 50 posters presented, this was one of six selected to receive an award. To be published in the September 1996 issue of *Physics of Fluids*.

"Two-Color PIV Employing a Color CCD Camera," S. Gogineni, D. Trump, and L. Goss, Presented at the 48th Annual Meeting of the Division of Fluid Dynamics of the American Physical Society, 19-21 November 1995, Irvine, CA, and abstract published in Bull. APS 40(12), 1950 (1995).

"Influence of Combustion Air Jets in the Formation of Gas Turbine Emissions," M. Roquemoire, D. Shouse, S. Gogineni, and G. Sturgess, Presented at the 48th Annual Meeting of the Division of Fluid Dynamics of the American Physical Society, 19-21 November 1995, Irvine, CA, and abstract published in Bull. APS 40(12), 1979 (1995).

"Effect of High Free Stream Turbulence on Flat Plate Film Cooling Flows," D. Pestian, S. Gogineni, D. Trump, and R. Rivir, Presented at the 48th Annual Meeting of the Division of Fluid Dynamics of the American Physical Society, 19-21 November 1995, Irvine, CA, and abstract published in Bull. APS 40(12), 2035 (1995).

"Application of Photon-Correlation Spectroscopy and Quartz-Crystal Microbalance to the Study of Thermally Stressed Jet Fuel," V. Vilimpoc and B. Sarka, Submitted in December 1995 to Industrial and Engineering Chemistry Research.

"Bi-Modal Size Distributions Predicted by Maximum Entropy are Compared with Experiments in Sprays," L. P. Chin, G. Switzer, R. S. Tankin, T. Jackson, and J. Stutrud, Combust. Sci. Technol. 109(1-6), 35 (1995).

"The Role of Transverse Air Jets in the Formation of Gas Turbine Emissions," D. Shouse, C. Frayne, J. Stutrud, S. Gogineni, and G. J. Sturgess, AIAA Paper No. 96-0705, Presented at the AIAA 34th Aerospace Sciences Meeting and Exhibit, 15-18 January 1996, Reno, NV.

"PIV Measurements of Flat Plate Film Cooling Flows with High Free Stream Turbulence," S. P. Gogineni, R. B. Rivir, D. J. Pestian, and L. P. Goss, AIAA Paper No. 96-0617, Presented at the AIAA 34th Aerospace Sciences Meeting and Exhibit, 15-18 January 1996, Reno, NV.

"Thermal Stability of Jet-A Fuel Blends," E. G. Jones, L. M. Balster, and W. J. Balster, Energy and Fuels 10(2), 509 (March/April 1996).

"Vortex Interactions in Jet in a Cross Flow," S. P. Gogineni, Presented at the Windows-on-Science Vortex-Flame Interactions Colloquium, 11-14 March 1996, Wright-Patterson AFB, OH.

"Application of JFA-5 as an Anti-Fouling Additive in a Jet-A Fuel," E. G. Jones, W. J. Balster, and L. P. Goss, Ind. Eng. Chem. Res. 35(3), 837 (March 1996).

"Use of MDA, BHT, and Dispersant Singly and in Combination as Jet-Fuel Additives," W. J. Balster, L. M. Balster, and E. G. Jones, Presented at the American Chemical Society National Meeting, 24-28 March 1996, New Orleans, LA; published in Prepr., Div. Pet. Chem., ACS 41(2), 446 (March 1996).

"Quantification of Thermal Stability of Blended Fuels," L. M. Balster, W. J. Balster, and E. G. Jones, Presented at the American Chemical Society National Meeting, 24-28 March 1996, New Orleans, LA; published in Prepr., Div. Pet. Chem., ACS 41(2), 464 (March 1996).

"Vortex/Boundary-Layer Interactions in a Wall Jet," S. P. Gogineni, Presented at the 22nd Annual Mini-Symposium on Aerospace Science and Technology, 28 March 1996, Dayton, OH.

"Autoxidation of Aviation Fuels in Heated Tubes: Surface Effects," E. G. Jones, L. M. Balster, and W. J. Balster, Energy and Fuels 10, 831 (1996).

"Surface Fouling in Aviation Fuels: An Isothermal Chemical Study," E. G. Jones, W. T. Balster, and J. M. Pickard, Tr. ASME: J. Eng. Gas Turb. Power 118, 287 (1996).